Lecture Notes in Electrical Engineering 326

C. Kamalakannan
L. Padma Suresh
Subhransu Sekhar Dash
Bijaya Ketan Panigrahi
Editors

Power Electronics and Renewable Energy Systems

Proceedings of ICPERES 2014

Springer

Lecture Notes in Electrical Engineering

Volume 326

About this Series

"Lecture Notes in Electrical Engineering (LNEE)" is a book series which reports the latest research and developments in Electrical Engineering, namely:

- Communication, Networks, and Information Theory
- Computer Engineering
- Signal, Image, Speech and Information Processing
- Circuits and Systems
- Bioengineering

LNEE publishes authored monographs and contributed volumes which present cutting edge research information as well as new perspectives on classical fields, while maintaining Springer's high standards of academic excellence. Also considered for publication are lecture materials, proceedings, and other related materials of exceptionally high quality and interest. The subject matter should be original and timely, reporting the latest research and developments in all areas of electrical engineering.

The audience for the books in LNEE consists of advanced level students, researchers, and industry professionals working at the forefront of their fields. Much like Springer's other Lecture Notes series, LNEE will be distributed through Springer's print and electronic publishing channels.

More information about this series at http://www.springer.com/series/7818

C. Kamalakannan · L. Padma Suresh
Subhransu Sekhar Dash
Bijaya Ketan Panigrahi
Editors

Power Electronics and Renewable Energy Systems

Proceedings of ICPERES 2014

Springer

Editors
C. Kamalakannan
Department of Electrical and Electronics Engineering
Rajalakshmi Engineering College
Chennai
Tamil Nadu
India

L. Padma Suresh
Department of Electrical and Electronics Engineering
Noorul Islam College of Engineering
Kumaracoil
Tamil Nadu
India

Subhransu Sekhar Dash
Department of Electrical and Electronics Engineering
SRM Engineering College
SRM University
Chennai
Tamil Nadu
India

Bijaya Ketan Panigrahi
Department of Electrical Engineering
Indian Institute of Technology
New Delhi
India

ISSN 1876-1100 ISSN 1876-1119 (electronic)
ISBN 978-81-322-2118-0 ISBN 978-81-322-2119-7 (eBook)
DOI 10.1007/978-81-322-2119-7

Library of Congress Control Number: 2014950395

Springer New Delhi Heidelberg New York Dordrecht London

Printed on acid-free paper

Springer is part of Springer Science+Business Media (www.springer.com)

Preface

This LNEE volume contains the papers presented at the International Conference on Power Electronics and Renewable Energy Systems (ICPERES 2014) held during April 25 and 26, 2014 at Rajalakshmi Engineering College, Chennai, India. ICPERES 2014 received 250 paper submissions from various countries across the globe. After a rigorous peer-review process, 110 full-length articles were accepted for oral presentation at the conference. This corresponds to an acceptance rate of 44 % and is intended for maintaining the high standards of the conference proceedings. The papers included in this LNEE volume cover a wide range of topics in Wind Energy Electric Conversion Systems, Solar Energy, Fuel Cells, Hybrid Energy Systems, Energy Conservation and Auditing, FACTS, Smart Grid Systems, Power Quality, Power Electronic Converters, Power System Operation and Control, Power Factor and Efficiency improvement, Induction Machines, Special Machines, Optimization Techniques, and their applications for solving problems in these areas.

The conference also featured four distinguished keynote speakers. The lecture by B.K. Panigrahi of IIT Delhi, India on "Applied Swarm Intelligence: A power system perspective" included the application of swarm algorithms to power systems, power electronics and drives. The lecture made an excellent start to the two-day conference. P. Valsalal from Anna University, Chennai, India gave a talk on "Sustainable energy for modern energy requirements." P. Dananjayan from Pondicherry Engineering College, in his lecture on "Quasi-Resonant converter-fed DC Drives" described in detail various considerations in the design of these drives. G. Uma from Anna University, Chennai in her lecture on "Micro grid and its control algorithms" gave an elaborate explanation of the analysis, modeling, and working of the different components which form the Micro grid. All these lectures generated great interest among the participants of ICPERES 2014 in paying more attention to these important topics in their research work.

We take this opportunity to thank the authors of all the submitted papers for their hard work, adherence to the deadlines and suitably incorporating the changes suggested by the reviewers. The quality of a refereed volume depends mainly on the expertise and dedication of the reviewers. We are indebted to the Program Committee members for their guidance and coordination in organizing the review process.

We would also like to thank our sponsors for providing all the support and financial assistance. We are indebted to the Chairman, Chairperson, CEO, Advisor, Principal, Vice-principal, faculty members, and administrative personnel of Rajalakshmi Engineering College for supporting our cause and encouraging us to organize the conference in a grand scale. We would like to express our heartfelt thanks to B.K. Panigrahi and S.S. Dash for providing valuable guidelines and suggestions in the conduct of the various parallel sessions in the conference. We would also like to thank all the participants for their interest and enthusiastic involvement. Finally, we would like to thank all the volunteers, whose tireless efforts in meeting the deadlines and arranging every detail meticulously, made sure that the conference could run smoothly. We hope the readers of these proceedings find the papers useful, inspiring, and enjoyable.

April 2014

C. Kamalakannan
L. Padma Suresh
Subhransu Sekhar Dash
Bijaya Ketan Panigrahi

Organizing Committee

Chief Patrons
Mr. S. Meganathan, Chairman
Dr. (Mrs.) Thangam Meganathan, Chairperson

Patrons
K. Jayaram Krishnan, CEO, RI
C.R. Muthukrishnan, Advisor, RI
G. Thanigaiyarasu, Principal, REC
V. Prithiviraj, Principal, RIT

Programme Advisor
M. Subbiah, REC, Chennai
S. Renganarayanan, REC, Chennai

General Chairs
B.K. Panigrahi, IIT Delhi
S.S. Dash, SRM University, Chennai

Programme Chairs
C. Kamalakannan, REC, Chennai
L. Padma Suresh, NICHE, India
Florian Misoc, USA
Ramazan Bayindir, Turkey

Programme Co-Chairs
I. Philip Praveen
R. Essaki Raj

Special Session Chairs
Adel Nasiri, USA
P.N. Suganthan, Singapore
Kishore Chatterjee, India

Publicity Chairs
B. Venkatachalapathi
Natteri M. Sudharsan
T.M. Sridhar

International Advisory Committee

Ahmed Faheem Zobaa, UK
Akhtar Kalam, Australia
Alfredo Vaccaro, Italy
David YU, US
Dmitri Vinnikov, Estonia
Gorazd Štumberger, Slovenia
Hussain Shareef, Malaysia
Joseph Olorunfemi Ojo, USA
Junita Mohamad-Saleh, Malaysia
Mohamed A. Zohdy, MI
Murad Al-Shibli, Abu Dhabi
Nesimi Ertugrul, Australia
Omar Abdel-Baqi, USA
Richard Blanchard, UK
Shashi Paul, UK
Zhao Xu, Hong Kong

National Advisory Committee

Ammasai Gounden
Ashok Kumar Pradhan
S. Baskar
Bhim Singh
P. Dananjayan
Ganapati Panda
K. Jayaraman
P. Jeevanandhan
V. Kamaraj
D.P. Kothari

V. Kumaresan
Ling Siddhaiah
M.R. Mohan
S.P. Natarajan
N.P. Padhy
Pashupathy gopalan
S. Paramasivam
S.R. Paranjothi
S.K. Patnaik
S. Rama Reddy
P. Rangarajan
M. Ravi
P. Somasundaram
S. Usa
S. Velusami

About the Editors

Dr. Subhransu Sekhar Dash is presently working as a Professor in the Department of Electrical and Electronics Engineering, SRM Engineering College, SRM University, Chennai, India. He received his Ph.D. from College of Engineering, Guindy, Anna University. He has more than 17 years of research and teaching experience. His research areas are Power Electronics and Drives, Modeling of FACTS Controller, Power Quality, Power System Stability and Smart Grid. He is a Visiting Professor at Francois Rabelais University, POLYTECH, France. He is the Chief Editor of *International Journal of Advanced Electrical and Computer Engineering*.

Dr. C. Kamalakannan is presently working as a Professor and Head in the Department of Electrical and Electronics Engineering, Rajalakshmi Engineering College, Chennai, India. He has completed his graduation degree in Electrical Engineering from Institution of Engineers (India), Kolkata, Master's and Doctorate from Anna University, Chennai, India. He has more than 13 years of research and teaching experience. He has published more than 15 papers in refereed international journals and conferences. His research areas are Power Electronics and Drives, Electrical Machines. He is a life member of Indian Society for Technical Education, Institution of Engineers (India).

Dr. Bijaya Ketan Panigrahi is an Associate Professor of Electrical and Electronics Engineering Department in Indian Institute of Technology Delhi, India. He received his Ph.D. from Sambalpur University. He is serving as a Chief Editor to the *International Journal of Power and Energy Conversion*. His interests focus on Power Quality, FACTS Devices, Power System Protection, and AI Application to Power System.

Dr. L. Padma Suresh obtained his doctorate from MS University and Dr. M.G.R University, respectively. He is presently working as a Professor and Head in Department of Electrical and Electronics Engineering, Noorul Islam University, Kumaracoil, India. Dr. Suresh is well known for his contributions to the field in both research and education contributing over 50 research articles in journal and conferences. He is an editorial member of *International Journal of Advanced Electrical and Computer Engineering* and also served as reviewer for various reputed journals. He has been a life member of the Indian Society for Technical Education. He also served in many committees as Convener, Chair, and Advisory member for various external agencies. His research is currently focused on Artificial Intelligence, Power Electronics, Evolutionary Algorithms, Image Processing, and Control Systems.

Contents

1 **Analytical and Simulation Analysis of Stator Tooth on Cogging Torque of Brushless DC Motor Using Finite Element Analysis** 1
M. Arun Noyal Doss, V. Ganapathy, R. Sridhar, S.S. Dash and D. Mahesh

2 **Application of Sinusoidal Pulse Width Modulation Based Matrix Converter as Revolutionized Power Electronic Converter** 9
K. Vijayakumar, R. Sundar Raj and S. Kannan

3 **Performance Analysis of Biofuels and Gasoline in SI Engines** . . . 19
S.P. Karthick, R.L. Helen Catherine and N. Premaanand

4 **Simulation of Open Loop and Feed-Back Controlled Bridgeless PFC Boost Converter** 29
K. Mohanraj, C. Danya Bersis and Subhransu Sekhar Dash

5 **Modeling and Simulation of Three-Phase DCMLI Using SVPWM for Photovoltaic System** 39
M. Valan Rajkumar and P.S. Manoharan

6 **Quantification of Voltage Unbalance Conditions** 47
Abhishek Chauhan, Padhmanabh Thakur and D. Raveendhra

7 **Short-Term Hydrothermal Scheduling of an Indian Utility System Using an Enhanced Bacterial Foraging Algorithm** 57
S. Padmini, R. Jegatheesan, Subhransu Sekhar Dash and S. Hemanth

8 **Efficiency Modeling of High Gain DC-DC Converter for Renewable Energy Application** 67
J. DivyaNavamani, A. Lavanya, K. Vijayakumar and A. Navauga

9 **Reactive Power Optimization Using Firefly Algorithm** 83
G. Kannan, D. Padma Subramanian and R.T. Udaya Shankar

10 **A New Real Time Approach for Reactive Power Control by STATCOM in Autonomous Wind-Diesel Hybrid Power System** 91
M. Mynavathi, V. Kumar Chinnaiyan, P. Venkatesh and S. Balamurugan

11 **Improving the Reliability of Wind Generators Using Dynamic Voltage Restorer** 101
G. Sivasankar and V. Suresh Kumar

12 **Rule Weight Tuned Fuzzy Controller for Robot Manipulator Using Quantum Inspired Firefly Algorithm** 111
A. Manju and A. Monasubramaniam

13 **Design and Investigation of Solar Powered Soft Switched Z-Source Inverter** 121
R. Uthirasamy, U.S. Ragupathy and R. Mithra

14 **An Integrated Passive Islanding Detection Method for Grid Connected PV Distributed Generators** 131
Almoataz Y. Abdelaziz, Mohmmed Ezzat, Walid Sameh, R.K. Saket and K.S. Anand Kumar

15 **Acoustic Echo Cancellation Using Variable Step Size Based Adaptive Filtering with Performance Measure** 145
Srilakshmi Gubbala, K. Srinivas and Rangarao Orugu

16 **Simulation and Experimental Verification of MPPT Algorithms for Partially Shaded Stand Alone Photovoltaic Systems** 153
M. Muthuramalingam and P.S. Manoharan

17 **Performance Comparison of D-STATCOM and SVC for Mitigation of Voltage Flicker in Electric Arc Furnace Using PSCAD/EMTDC** 163
A. Pandiyarajan and S. Latha

18 **The Influence of Floor Tile Colour on Lighting and Energy Saving** 177
P. Ganesan, S. Rajakarunakaran, M. Thirugnanasambandam and D. Devaraj

19 **Voltage Control of Fixed Speed Wind Farm Under Unbalanced Grid Faults Using DVR** 183
B. Ashok Kumar, N. Kamaraj and C.K. Subasri

20 **Smart Indian Railways: An Environment Friendly Model**. 193
Nitish Kumar Singh, Yashwant Singh Patel, Subnum Begum and Ananya Chatterjee

21 **Grid Connected Multilevel Inverter and MPPT for Photovoltaic System**. 201
R. Santhiya, A. Senthilnathan, V. Kumar Chinnaiyan and R. Nithya Priya

22 **Implementation of Anti-islanding Scheme for a Grid Connected Inverter**. 213
Arup Kumar Saikia and P.N. Kapil

23 **THD Analysis of One-Cycle and PWM Controlled Active Power Filters** 225
Sravani Jennela and V. Raj Kumar

24 **Simulation of PWM Controlled Double Half Bridge Inverter for Partly Coupled Induction Cooking System** 237
Nagarajan Booma, Sathi Rama Reddy and Vishnuram Pradeep

25 **Maximum Power Point Tracking of Photovoltaic System Using Two Input and Two Output Fuzzy System** 245
Luckey Chouksey, P. Akash Pattanaik and R.K. Saket

26 **Performance of High Voltage Bushings Under Polluted Conditions**. 255
Avik Ganguly and R.S. Gorayan

27 **Simulation of Static Var Compensator in IEEE 14 Bus System for Enhancing Voltage Stability and Compensation**. 265
M. Priyadhershni, C. Udhayashankar and V. Kumar Chinnaiyan

28 Study on Reflector Material Optimization of a Parabolic Solar Concentrator 275
A.B. Auti, D.R. Pangavane, T.P. Singh, M. Sapre and A.S. Warke

29 A New Approach for Torque Ripple Minimization of PMBLDC Motor Drive 285
J. Gayathri Monicka, V. Jamuna and K. Hemalatha

30 Grid Integration of Hybrid Generation Scheme for Optimal Switching Pattern Based Asymmetrical Multilevel Inverter 295
G. Satyanarayana and K. Lakshmi Ganesh

31 Reactive Power Pricing Using Group Search Optimization in Deregulated Electricity Market 305
G. Kannan, D. Padma Subramanian and S. Siva Subramanian

32 Enhanced Controllers of DFIG with Unbalanced and Distorted Grid Voltage Conditions 313
A. Ramkumar, S. Durairaj and K. Dhivya

33 FPGA Controlled Power Conditioning System for Solar PV Fed PMDC Motor 321
Dogga Raveendhra, Padmanabh Thakur and Abhisekh Chauhan

34 Genetic Algorithm Based Wind-Thermal Coordination Dispatch Including Transmission Losses 329
K. Dhayalini, S. Sathiyamoorthy and C. Christober Asir Rajan

35 A Novel MLI Topology with Reduced Power Switches 341
N. Vinothkumar, V. Arunachalam and V. Kumar Chinnaiyan

36 Optimal Placement and Sizing of Solar and Wind Based DGs in Distribution Systems for Power Loss Minimization and Economic Operation 351
Bibhudatta Patnaik, D. Sattianadan, M. Sudhakaran and S.S. Dash

37 Control of Three Phase to Three Phase Matrix Converter—A Direct Transfer Function Approach 361
A. Jamna, V. Jamuna and S. Rama Reddy

38 **Comparison of PI and PIR Regulators for DFIG During Unbalanced Grid Voltage Conditions** . . . 373
A. Ramkumar, S. Durairaj and N. Arun

39 **Implementation of Direct Torque Control for Matrix Converter Fed Induction Motor Drive Using Fuzzy Logic Controller** . . . 383
J. Karpagam, A. Nirmal Kumar, V. Kumar Chinnaiyan and M. Surya

40 **Improvement of Power Quality in Distribution System Using D-STATCOM** . . . 395
Pravati Nayak, Amruta Pattnaik, Mihir N. Mohanty and Ranjan Kumar Mallick

41 **Simulation and Optimization of Biomass Based Hybrid Generation System for Rural Electrification** . . . 407
M. Mahalakshmi and S. Latha

42 **Application of H-Bridge Converter Based Dynamic Voltage Restorer to Protect a Sensitive Load on Polluted Distribution Network** . . . 417
M.R.V. Murali and S. Latha

43 **Power Control of Wind Turbine Driven Permanent Magnet Synchronous Generator Using Maximum Power Point Tracking Algorithm** . . . 425
K. Devi Anusha and K.C. Jayasankar

44 **Performance Evaluation of Differential Evolution and Particle Swarm Optimization Algorithms for Optimizing Power Loss in a Worm Gear Mechanism** . . . 433
P. Sabarinath, M.R. Thansekhar and R. Saravanan

45 **An Improved Buck Boost Converter Using Auxiliary Resonance for Photo Voltaic Based Dynamic Voltage Restorer** . . . 443
G. Ezhilarasan, Subhransu Sekar Dash and Chinmaya Samanta

46 **A Fuzzy Logic Controller Based Multi Converter UPQC to Enhance the Power Quality Problems** . . . 453
Paduchuri Chandra Babu, Subhransu Sekhar Dash, C. Subramani, Navya Tejaswini and Y. Sravan Kumar Reddy

47 Artificial Neural Network and Fuzzy Logic Controlled Single Phase Active Power Line Conditioner Under Non Sinusoidal Supply Condition: A Comparison 465
D. Kavitha, P. Renuga and V. Suresh Kumar

48 Design and Implementation of SMR Based Bidirectional Laptop Adapter 475
M. Gowrinathan, V. Devi Maheswaran and V.T. Sreedevi

49 Analysis of Different Current Commutation Technique in Matrix Converter 485
S.K. Das and P. Syam

50 Performance Comparison of DC to DC Boost Converters for Solar Power Installation System 497
A. Kalirasu, Subhransu Sekhar Dash and M.V. Muthukumar

51 DC-DC Converter Based on Cockcroft-Walton for High Voltage Gain 509
D. Parameswara Reddy, V. Suvitha and K. Somasekhar

52 New Direct Torque Control Algorithm for High Performance Induction Motor 523
S. Srinivasan and A. Sabari Raja

53 Performance Analysis of Induction Generator Using Computational Technique 535
R. Gopikaramanan, R. Sridevi and C. Kumar

54 Performance Analysis of Efficiency Enrichment Technique for SPVPGS: An Experimental Assessment 545
K.R. Chairma Lakshmi

55 Cable Laying Precautions in Offshore Wind Farms with Reactive Power Compensation 553
Ahmed M. Atallah, Almoataz Y. Abdelaziz, Mohamed Ali, R.K. Saket and K.S. Anand Kumar

56 Single Phase Soft Switching Techniques Power Factor Correction Converter 563
P. Anjappa, K. Naresh, V. Ramesh, P. Lakshmipathi and K. Reddy Swathi

57 **Cuckoo Search Algorithm for Short Term Hydrothermal Scheduling** 573
Hari Mohan Dubey, Manjaree Pandit and B.K. Panigrahi

58 **Performance of Phase-Shift Control Using High-Efficiency Switched-Capacitor-Based Resonant Converter** 591
K. Naresh, K. Kareemulla Khan, V. Ramesh, Mohan Bukya and K. Chaitanya Kumar

59 **Single Stage High Voltage Gain Boost Converter for Battery Charging Using PV Panels** 601
P.M. Midhun

60 **Performance Assessment of Photovoltaic Predicated Dynamic Voltage Restorer Using PI and Fuzzy Logic Controller** 611
Greeshma Govind, R. Suresh Kumar and M. Maheswari

61 **Multiple Winding Linear Transformer for Interleaved Step-up ZVT Converter** 621
Nidhin Antony and K. Karthikeyan

62 **Embedded Based PFC Converter for an Air Conditioner with BLDC Motor** 631
Tinu Francis and P. Gokulakrishnan

63 **Photovoltaic Power System Application Using Energy Stored Quasi Z Source Inverter** 643
S. Aysha and P. Selvakumar

64 **Power Management of a Grid Connected PV/Battery** 653
Chinmaya Samanta, Subhransu Sekhar Dash, G. Ezhilarasan and N.K. Rayaguru

65 **Design and Comparative Analysis of Diode Clamped Multilevel Inverter for Eliminating Total Harmonics Using High Switching Frequency Techniques** 665
P.K. Dhal and C. Christober Asir Rajan

66 **PID Control of SAPF for Elimination of Harmonics in Power System Based on DQ Reference Frame Theory** 679
Pradeep Katta, Arun, D. Atul Kumar Mishra and H. Vignesh

67 **Power Quality Improvement in Distribution System Using Unified Power Quality Conditioner** 689
D. Rajasekaran, Subhransu Sekhar Dash, C. Subramani, Arun Bhaskar Mayilvaganan and Yarralinganagari Venkatesh

68 **Hybrid Power System Based Load Sharing and Maintaining the DC Voltage in UPS System** 699
R. Jaiganesh and S. Sharmila

69 **Analysis of Full Bridge LCC Resonant Converter for Wide Load Variations** 709
M. Santhosh Rani, Subhransu Sekhar Dash and Julie Samantaray

70 **Power Quality Improvement Using Multilevel Inverter Based Dynamic Voltage Restorer with PI Controller** 721
M. Maheswari, S. Thangavel, R. Suresh Kumar and C. Vivekanandan

71 **Design and Implementation of Fractional Order Proportional Integral Controller for the Control of Aircraft Pitch Dynamics** 731
Abdul Wahid Nasir and U. Sabura Banu

72 **Retracted: An Independent Reconstruction Error Using Randomized Quantization** 743
S. Arunadevi and S. Sathya

73 **Mitigation of Power Quality Issues in Three-Phase Four-Wire Distribution System Employing Four-Leg DSTATCOM** 753
C.K. Sundarabalan, K. Selvi and P. Shirley Vaz

74 **Performance Investigation of Fuzzy Logic Controlled MPPT for Energy Efficient Solar PV Systems** 761
C.K. Sundarabalan, K. Selvi and K. Sakeenathul Kubra

75 **Identification of the Fractional Order First Order Plus Dead Time Parameters of Two Interacting Conical Tank Process Using Bee Colony Optimization Technique Minimizing Root Mean Square Error** 771
S.K. Lakshmanaprabu, U. Sabura Banu and N. Sivaramakrishnan

76 **Real Time Simulation of Single Machine Infinite Bus System Using dSPACE Controller Board** 783
R. Ramya and K. Selvi

77 **RGA Based Fractional Order PI Controller Design for Speed Control of IPMSM** 793
A. Shakila Banu and R.S.D. Wahidabanu

78 **Optimization of Photovoltaic Power Using PID MPPT Controller Based on Incremental Conductance Algorithm** 803
B. Ashok Kumar, M. Srinivasa Venkatesh and G. Mohan Muralikrishna

79 **Development of a Universal Controller for Converter Based Switched Reluctance Motors** 811
P. Avirajamanjula and P. Palanivel

80 **PSO Based Social Welfare Maximization of Wind Thermal Coordinated System in a Deregulated Power Market** 819
R. Manimegalai, S. Visalakshi and Lucina Joseph

81 **Microcontroller Based BLDC Motor Drive for Commercial Applications** 829
Shanmugam Sathishkumar, R. Meenakumari, Eswaramoorthi Jobanarubi, Pattu John Samuel Anitta and Premkumar Ravikumar

82 **Forecasting India's Electricity Consumption Using Particle Swarm Optimization** 843
S. Saravanan, R. Nithya, S. Kannan and C. Thangaraj

83 **Frequency Regulation of Isolated Hybrid Wind/Diesel, Power Generation with Fuel Cell System** 853
Shailendra Singh, Munendra Singh, S. Chanana and S. Semwal

84 **Residential Load Signature Analysis for Their Segregation Using Wavelet—SVM** 863
Munendra Singh, Sanjeev Kumar, Sunil Semwal and R.S. Prasad

85 **Fuzzy-Based Torque Ripple Optimization and Digitalized Sector Selection in DTC Scheme** 873
D. Deenadayalan and I. Alexandar Beski

86 A Mobile Based Novice Detection of Driver's Fatigue Level and Accident Reporting Solution 883
Jay Lavanya and R. Essaki Raj

87 Analysis and Position Control of Switched Reluctance Motor Drives by Using Fuzzy Logic 893
K.S. Srikanth, L.V. Narasimha Rao, D. Ravikrishore, K. Naresh and V. Ramesh

88 Assessment of Six Phase Synchronous Generator Using Fuzzy Controller 903
N. Rathika, A. Senthil Kumar and S. Rahul

89 Power Loss Minimization in Presence of Distributed Generation by DSM 913
S. Sambath and P. Palanivel

90 Comparative Study of Prototype and Simulation of SVC for Transmission Congestion Management 923
Khatavkar Vrushali, Redekar Abhijeet and Dharme Anjali

91 Design Aspects of Blade Shape and Position for the MAGLEV Vertical Axis Wind Turbine 933
G.P. Ramesh and C.V. Aravind

92 Placement and Sizing of D-STATCOM Using Particle Swarm Optimization 941
S. Devi and M. Geethanjali

93 Fault Tolerant Soft Starter Control for Induction Motors 953
V. Jaikrishna, Linss T. Alex, Subhranhsu Sekhar Dash and Susanta Kumar Gachhayat

94 A Novel Soft Switched Positive Output Super Lift Luo Converter for Li-Ion Battery Charging 963
Winnie Raghu and T.S. Saravanan

95 Reduction in Ripples Using Interleaved Soft Switching Boost Converter for Hybrid Power Generation System 973
A. Alice Hepzibah, A. Senthil Kumar and R. Joylin Rini

96 Implementation of Reactor and Capacitor in Adjustable Speed Drive for Power Quality Problem 985
R. Suganthi, V. Kumar Chinnaiyan and M. Gopinath

97 **Yaw Control of Wind Turbine Using Fuzzy Logic Controller** . . . 997
R. Bharani and K.C. Jayasankar

98 **Overload Protection and Speed Monitoring of Induction Motor Using ZigBee Wireless Sensor Networks and GSM Technology** . . . 1007
P.E. Elavenil and R. Kalaivani

99 **Thermal Analysis of Switched Reluctance Machine Under Steady State and Transient Conditions Using Finite Element Method** . . . 1017
E. Annie Elisabeth Jebaseeli and S. Paramasivam

100 **Design and Analysis of Three Phase Four Wire Shunt Active Filter with Neural Network Controller for Different Loading Conditions** . . . 1027
V.V. Karthikeyan, S. Thangavel, Sreedendu and R. Sasikala

101 **MPPT Measurement of Photovoltaic System Under Partial Shading Condition Using DPSO Algorithm** . . . 1037
D. Gokilapriya and S. Barvin Banu

102 **Cascaded Dual Buck Inverter with Sensorless Current Control Method for Grid Connected Photovoltaic Systems** . . . 1047
Sumith Surendran and R.B. Selvakumar

103 **Steady State Analysis and Open Loop Modeling of Permanent Magnet Stepper Motor** . . . 1057
S. Vijaya, A. Senthil Kumar and R. Suganya

104 **Reliability Evaluation of Tamil Nadu Power Grid for the Year 2012** . . . 1067
K. Karunanithi, S. Kannan and C. Thangaraj

105 **Implementation of Low Cost Single Switch Based Switched Reluctance Motor Drive** . . . 1077
S. Rajagopal and S.S. Dash

106 **A Novel Block-Based Selective Embedding Type Video Data Hiding Using Encryption Algorithms** . . . 1087
P. Saravanan and K.K. Thyagarajan

107 **General Regression Neural Network for Software Effort Estimation of Small Programs Using a Single Variable** . . . 1099
S.K. Pillai and M.K. Jeyakumar

108 EBRP: Evolutionary Backup Routing Protocol for Mobile Ad Hoc Networks 1109
A. Samuel Chellathurai and E. George Dharma Prakash Raj

109 A QCP Approach for Bandwidth Reallocation in Integrated Cellular Network 1117
C.P. Maheswaran and C. Helen Sulochana

110 A Grade Prediction Methodology for Astrocytoma Using Modified K-Clustering Network 1127
M. Monica Subashini, Sarat Kumar Sahoo, S. Prabhakar Karthikeyan and I. Jacob Raglend

111 Simulation and Application on Power System Reliability for Bulk Electrical System 1139
N. Mahiban Lindsay and A.K. Parvathy

112 Intelligent Load Shedding Using Ant Colony Algorithm in Smart Grid Environment 1149
V. Margaret, K. Uma Rao and G.G. Ganeshprasad

113 Design of ANFIS Controller for Power System Stability Enhancement Using FACTS Device 1163
G.Y. Sree Varshini, S. Charles Raja and P. Venkatesh

114 Application of Bacterial Foraging Optimization for Elimination of Lower Order Harmonics in Seven Level Inverter 1173
W. Razia Sultana, Sarat Kumar Sahoo, S. Prabhakar Karthikeyan, I. Jacob Raglend, A. Chandrashekar and A. Syam Pradeep

115 Affine Invariant Shape Descriptor Using Object Area Normalization 1183
P. Arjun, T.T. Mirnalinee, S. Sindhuja and G. Bharathi Raja

116 Automatic Classification of CC View and MLO View in Digital Mammograms 1193
K. Vaidehi and T.S. Subashini

117 Power Quality Improvement in a Wind Farm Connected to Grid Using FACTS Device 1203
C.K. Subasri, S. Charles Raja and P. Venkatesh

118 Development of Power Backup Device Using Solar Energy Harvesting for Real Time Industrial Applications 1213
K. Janakiraman, D. Manivannan and R. Winnie Beulah

119 An Image Watermarking Scheme Resilient to Geometric Distortions 1225
D. Vaishnavi and T.S. Subashini

120 Intensification of Available Transfer Capability Via Real Coded Biogeography Based Optimization 1235
A. Ramesh Kumar and L. Premalatha

121 Application of SRF Algorithm and SVPDM Concept in Power Electronic Transformer 1245
T. Ruban Deva Prakash and R. Shiju Kumar

122 Investigations on the Dynamics of Seven Level Inverter Fed Induction Motor Drive with Neural Based Rotor Resistance Estimator 1261
A. Chitra and S. Himavathi

123 Comparison of Single Layer and Multilayer Feed-Forward Architecture for On-line Economic Load Dispatch Problem 1273
C.S. Boopathi, Subhransu Sekhar Dash, A. Venkadesan, C. Subramani and G.V. Anilkumar

124 Prediction of India's Industrial Sector Electricity Consumption Using ANFIS 1281
S. Saravanan, S. Kannan and C. Thangaraj

125 Enhancing the Security of AES Algorithm in Wireless Network 1289
R. Velayutham, E. Siva Ganesh and D. Manimegalai

126 Effect of Grid Impedance Variation on the Control of Grid Connected Converters with Synchronous Reference Frame Controllers in Micro-Grids 1297
A. Vijayakumari, A.T. Devarajan and N. Devarajan

127 Application of SVM as Classifier in Estimating Market Power Under Deregulated Electricity Market 1309
S. Prabhakar Karthikeyan, I. Jacob Raglend, K. Sathish Kumar, Sarat Kumar Sahoo and B. Priya Esther

128 **Optimal Capacitor Placement in Radial Distribution System to Minimize the Loss Using Fuzzy Logic Control and Hybrid Particle Swarm Optimization** 1319
S. Joyal Isac and K. Suresh Kumar

129 **Vector Control Based Dynamic Voltage Restorer for Fault Ride Through of Doubly Fed Induction Generator** 1331
G. Sivasankar and V. Suresh Kumar

130 **Design of PSO-Fuzzy MPPT Controller for Photovoltaic Application** 1339
J. Prakash, Sarat Kumar Sahoo, S. Prabhakar Karthikeyan and I. Jacob Raglend

131 **Voltage Control of a STATCOM at a Fixed Speed Wind Farm Under Unbalanced Grid Faults Using Fuzzy Logic Technique** 1349
B. Ashok Kumar, N. Kamaraj and C.K. Subasri

132 **Evaluation and Prediction of Contamination Level in Insulators Based on the Leakage Current Characteristics Using Neural Network**. 1359
A. Sheik Sidthik, A. Raymon and L. Seenivasagam

133 **A Hybrid PSO-SFS-SBS Algorithm in Feature Selection for Liver Cancer Data**. 1369
S. Gunasundari and S. Janakiraman

134 **Heart Disease Prediction System Using Intelligent Network**. 1377
R. Chitra and V. Seenivasagam

135 **Performance Comparison of AI Controllers for DC Link Voltage of SAPF System for Power Quality Enhancements** 1385
P.M. Balasubramaniam and S.U. Prabha

136 **Online Fuzzy Supervised Learning of Radial Basis Function Neural Network Based Speed Controller for Brushless DC Motor** 1397
K. Premkumar and B.V. Manikandan

137 **Modeling of Wind Turbine Power Curves Using Firefly Algorithm** 1407
N. Karthik, R. Arul and M.J. Hari Prasad

138 An Innovative Classification Model for CAD Dataset Using SVM Based Iterative Linear Discriminant Analysis 1415
G. Nalini Priya and A. Kannan

139 Phenotypic Evolutionary Programming for Economic Operation of Thermal—Wind Coordination 1425
W.A. Augusteen, R. Rengaraj and N.B. Muthu Selvan

140 Mathematical Modeling of BLDC Motor Using Two Controllers for Electric Power Assisted Steering Application 1437
G.R. Puttalakshmi and S. Paramasivam

141 Comparison and Simulation of Various PFC Boost Converters 1445
K. Mohanraj, C. Danya Bersis and Subhransu Sekhar Dash

142 Modified LBP Based Region Growing Segmentation of MR Brain Images 1453
K.S. Angel Viji and J. Jayakumari

143 A Novel Reference Current Generation Algorithm for Three Phase Shunt Active Power Filter 1467
Deepthi Joseph, N. Kalaiarasi and K. Rajan

144 Mathematical Model of Brushless Doubly Fed Induction Generator Based Wind Electric Generator 1477
Anjana Suresh, R. Resmi and V. Vanitha

145 Design of Wideband Widescan Linear Tapered Slot Antenna for an Active Electronically Scanned Array Antenna 1489
Babu Saraswathi K. Lekshmi and Jacob I. Raglend

146 Energy Efficient Decoder Design for Non-binary LDPC Codes 1497
T. Yasodha, I. Jocobraglend and K. Meena Alias Jeyanthi

147 Automated Segmentation of MR Images by Implementing Multi SVM Technique 1509
G. Paul, Tinu Varghese, K.V. Purushothaman and Albert Singh

148 Implementation of ARM Processor Based Online Learning Neural Network Controller for Buck-Boost Converter 1517
M.V. Mini and L. Padma Suresh

149 **A Control Strategy for Harmonic Reduction in a Single Phase High Step up AC–DC Converter Based on Matrix Converter and Cockcroft-Walton Voltage Multiplier with PFC for Low Power Applications** . . . 1525
S. Anuraj, M.R. Rashmi and A. Suresh

150 **Classification of ECG Signal Using Hybrid Feature Extraction and Neural Network Classifier** . . . 1537
K. Muthuvel, L. Padma Suresh, T. Jerry Alexander and S.H. Krishna Veni

151 **Power Flow Constrained Unit Commitment Problem Using Improved Shuffled Frog Leaping Algorithm** . . . 1545
J. Mary Anita and I. Jacob Raglend

152 **Investigation and Control of Principal Axes of Aircraft Using Robust Method** . . . 1557
V. Rajeswari and L. Padma Suresh

153 **Secret Key Sharing in Networks Using Classical Cryptography Based Quantum Stratagem Approach** . . . 1565
R. Sarath, A. Shajin Nargunam and R.P. Sumithra

154 **Cuckoo Search Based Color Image Segmentation Using Seeded Region Growing** . . . 1573
M. Mary Synthuja Jain Preetha, L. Padma Suresh and M. John Bosco

155 **Comparative Study of PI and PID Controller for Non Linear MIMO System** . . . 1585
S. Anitha Janet Mary, L. Padma Suresh, Rini Valsa Mathew and N. AlbertSingh

156 **A Simple Cascade NN Based Flux Estimator to Overcome Low Speed Problems in Sensor-Less Direct Vector Controlled IM Drives** . . . 1593
A. Venkadesan, S. Himavathi and A. Muthuramalingam

Retraction Note to: An Independent Reconstruction Error Using Randomized Quantization . . . E1

Author Index . . . 1603

Chapter 1
Analytical and Simulation Analysis of Stator Tooth on Cogging Torque of Brushless DC Motor Using Finite Element Analysis

M. Arun Noyal Doss, V. Ganapathy, R. Sridhar, S.S. Dash and D. Mahesh

Abstract This paper discusses the analytical and simulation analysis of cogging torque in stator tooth of Brushless DC motor (BLDC). Cogging torque causes direct impact on the performance of motor. The various techniques applies in stator tooth, such as Dual bifurcated, Dummy slot and Reduced stator tooth width were analysed and simulated in 2-D Finite Element Analysis (FEA). The analysis of variations in cogging torque, flux density, output power and efficiency for different stator tooth shapes are evaluated and compared.

Keywords Cogging torque · Finite element analysis (FEA) · BLDC motor

1.1 Introduction

BLDC motor has been widely accepted in industrial drives for high performance applications due to its various attractive features such as high torque density and low acoustic noise. Although PM machines are high performance devices, the cogging torque components that affect their output produced from the harmonic content of the current and voltage waveforms in the machine. The cogging torque is due to the physical structure of the machine. The cogging torque is produced by the magnetic attraction between the rotor mounted permanent magnets and the stator teeth [1–3]. Cogging torque is also detrimental to the performance of position control systems such as robots and to the performance of speed control systems particularly at low speed [4–7].

M. Arun Noyal Doss (✉) · V. Ganapathy · R. Sridhar · S.S. Dash · D. Mahesh
Department of Electrical and Electronics, SRM University, Chennai, India
e-mail: arunnoyal@gmail.com

C. Kamalakannan et al. (eds.), *Power Electronics and Renewable Energy Systems*,
Lecture Notes in Electrical Engineering 326, DOI 10.1007/978-81-322-2119-7_1

Table 1.1 Specifications of the motor

Parameters	Value
Connection	Star
Speed	3,000 rpm
Number of phases	3
Air gap	1 mm
Magnet depth	30 mm
Motor diameter	80 mm
Outer radius of stator	40 mm
Winding pitch	6/9
Tooth width	5.3 mm
Tooth depth	17.2 mm
Number of slots	60, 72
Number of poles	8

Reduction of cogging torque in permanent magnet motors is gaining increasing importance along with the demand for high-performance brushless motors. The torque ripple can be minimized both by the proper motor design and motor control [8]. There are various methods available in design perspective to reduce cogging torque in brushless machines. They are slot-less windings, skewing of stator slots and Permanent Magnets (PM), shaping of stator slots and PMs, adjusting slot opening, shifting PM segments, selection of PMs width, and creating Magnetic circuit asymmetry [9].

The electromagnetic torque can be calculated analytically or numerically in a variety of ways such as by the Maxwell stress and co-energy methods. They need very accurate global and local field solutions particularly for the determination of cogging torque. The analytical model used for predicting the cogging torque is also capable of quantifying the effects of the various design parameters [10, 11]. Cogging torque can be determined analytically as well as by finite element methods. The FEM is a powerful and economical approach to characterize the torque ripple of a given design without hardware proto type. The main objective of the present chapter is to demonstrate that cogging torque can be reduced to generally acceptable levels by appropriate selection of motor design. For certain standard stator slot (teeth) shapes the cogging torque can be determined. The specification of the motor is shown in the Table 1.1.

1.2 Determination of Cogging Torque

Cogging torque is also called detent torque, and it is one of the inherent characteristics of PMEM. Theoretically, cogging torque is caused by the reluctance change between the stator teeth and magnet poles on the rotor, and it is mainly the magnet poles corners, not the whole magnet poles, which create the cogging torque.

Cogging torque is influenced by a variety of design factors of BLDC Motor. Among the factors, air gap length, slot opening, and magnet pole pitch play important roles [12, 13].

Cogging torque sometimes may cause excessive acoustic noise and harmful vibration to the machine itself as well as to its load (or driver), and in many serious cases, a mechanical resonant may occur so that serious destruction is caused. To significantly reduce harmful cogging torque of BLDC has become one of the most interesting research topics in the machine design and application fields [14–16]. The cogging torque calculating methods and reduction measures will be discussed in the following sections.

$$T_{cog} = \sum_{k=1}^{\alpha} T_{ck} \cos kq\,\theta \tag{1.1}$$

T_{ck} is the amplitude of the kth harmonic component of the cogging torque, Q is the no. of slots, k is the order of cogging harmonics.

The theoretical analysis of cogging torque has following assumption:

(1) End effect of the motor and flux leakage is negligible. (2) Permeability of the iron is infinite. (3) Permeability of permanent magnet is equal to that of the vacuum.

The various design of BLDC motor's magnetic field distribution in air gap is schematically shown in Fig. 1.1.

According to the consideration of Assumption the coenergy in the air gap can be expressed as

$$w'_{fld} = w'\mathrm{d}v = \int \frac{B^2}{2\mu_0}\mathrm{d}v \tag{1.2}$$

$$w'(\theta) = \frac{1}{2\mu_0}\int Br^2(\theta,\alpha)G^2(\theta)\mathrm{d}v \tag{1.3}$$

When energy method is used to analyse the cogging torque can be expressed as:

$$T_{cog(\theta)} = \frac{-\partial w'(\theta)}{\partial\theta} \tag{1.4}$$

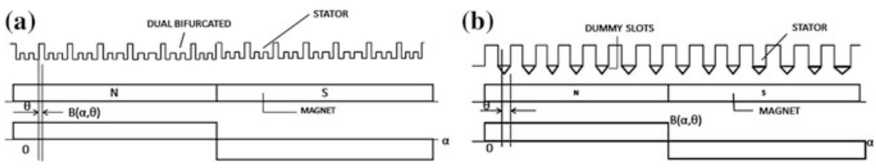

Fig. 1.1 Distribution of air gap magnetic field in **a** dual bifurcated **b** dummy slot

$$= \frac{\partial}{\partial\theta}[\frac{1}{4\mu_0}L(R_m^2 - R_s^2)\int_0^{2\pi} G^2(\theta)B^2(\theta,\alpha)\mathrm{d}\alpha \tag{1.5}$$

$$= \frac{\pi L}{4\mu_0}(R_m^2 - R_s^2)\sum_{n=0}^{\alpha} nN_{nL}G_{nL}B_{nL}\sin(nN_L\theta) \tag{1.6}$$

where B_r is the magnet renaissance, R_{in}, R_s, R_r respectively the radii at the stator surface, magnet surface and rotor core surface. α_p is the number of pole pairs, P is the magnet pole-arc factor, $w'(\theta)$ is the co-energy in the air gap, $G(\theta)$ and $B(\theta,\alpha)$ are respectively the relative permeance and the flux density in the air gap; they can be expressed with Fourier series G_{nL} and B_{nL} are respectively the Fourier series coefficients of $G^2(\theta)$, $B^2(\theta,\alpha)$, N_L is the least common multiple (LCM) of stator slot number S and p. Through suitable design $G(\theta)$ and $B(\theta,\alpha)$ can be decreased thus cogging torque can be reduced.

1.3 Implementation of Adopted Technique

The implementation of adopted techniques involved in simulations of cogging torque in stator tooth of BLDC motor was follows.

1. Dual bifurcated
2. Dummy slots.

1.3.1 Dual Bifurcated

The cogging torque can be considerably reduced by using the dual bifurcated surface in the stator which is more efficient compare with bifurcated, the shape of dual bifurcated 8-pole 60 slot machine is shown in Fig. 1.2a. Dual bifurcation is made in stator slots, which helps to reduce the cogging torque. The bifurcation is in the shape of semicircle (or) square shape in the stator slots. This technique which is varies the rate of change of reluctance in between the slots and PMs. The modification and optimising analysis in the stator slots and the removal of particular area in the slots held in this model.

1.3.2 Dummy Slot

Cogging torque can be reduced by using the dummy slots in the stator teeth. They are equally spaced as wide as the opening of stator slots. The no of dummy slots selected must be represented in order to achieve effective reduction in cogging

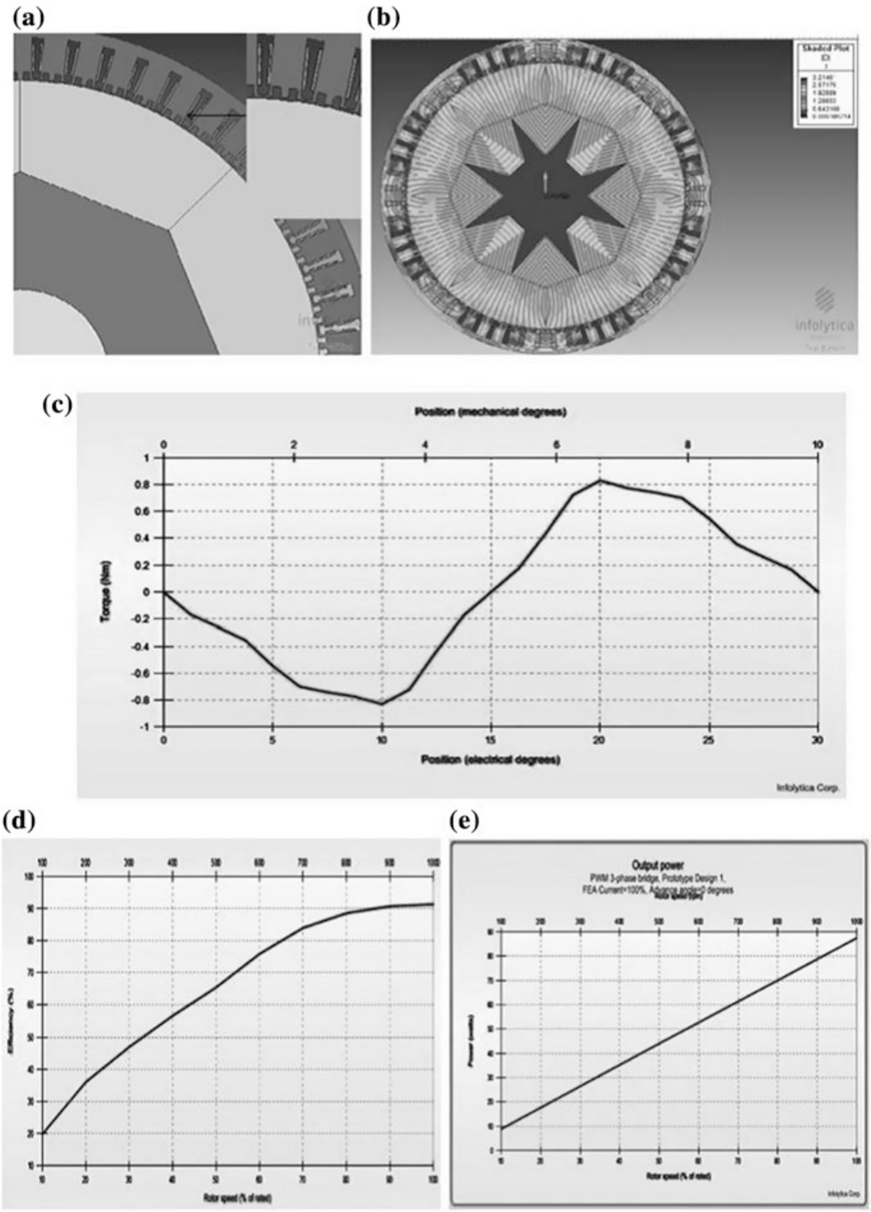

Fig. 1.2 **a** Dual bifurcated model, **b** flux density, **c** cogging torque, **d** efficiency and **e** output power

torque of BLDC motor. Different shapes of dummy slots can be available but in these model triangular dummy slots is introduced in 8-pole 60 slot model and shown in Fig. 1.3a. Hence, dummy slot shape has significant influence on reducing

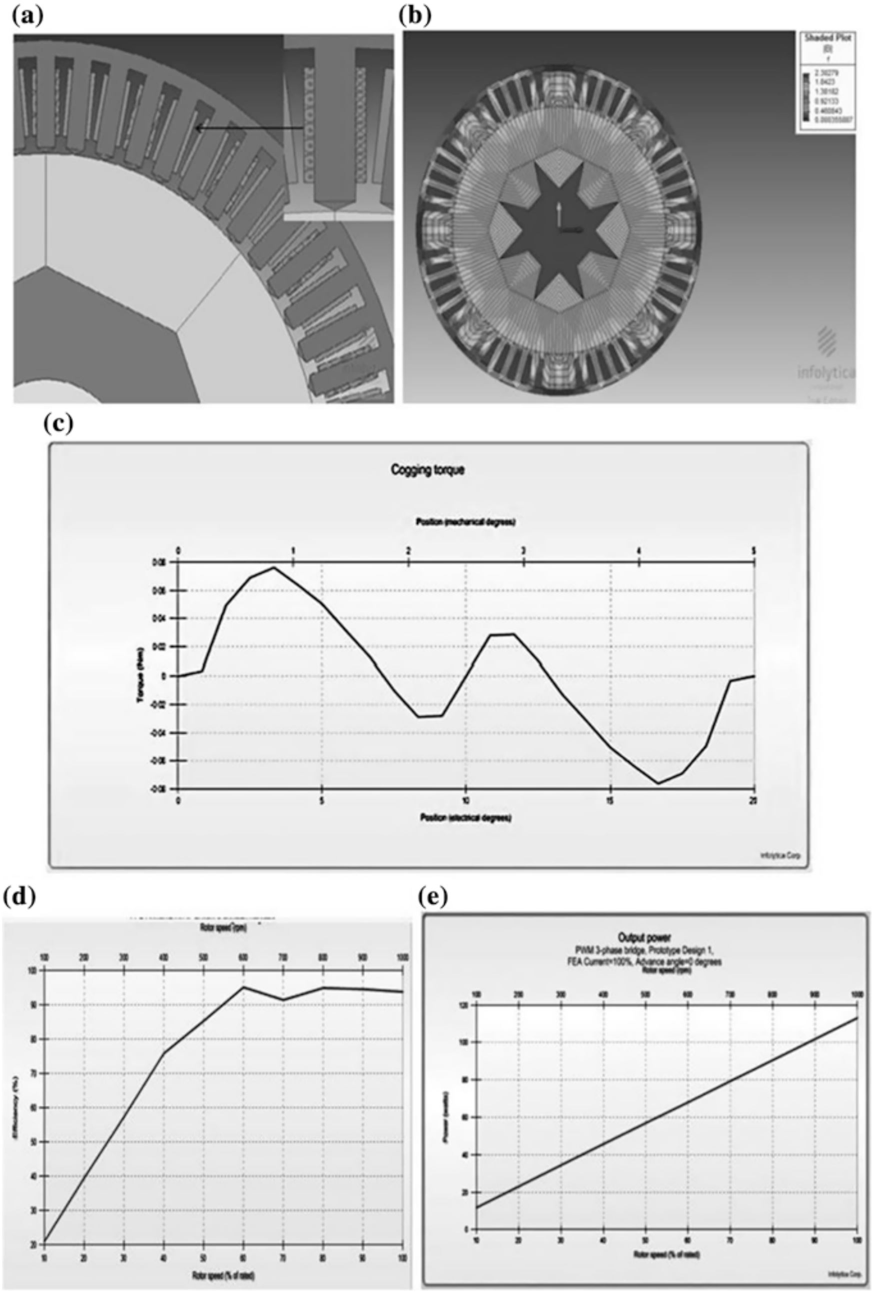

Fig. 1.3 **a** Dummy slots, **b** flux density, **c** cogging torque, **d** efficiency and **e** output power

Table 1.2 Performance of different motor models

Performance	Dual bifurcation	Dummy slots
Cogging torque (N-m)	0.8	0.078
Efficiency	91 %	93 %
Output power (W)	88	120
Flux density (Wb/m^2)	3.21	2.30
Power factor	0.62	0.69

cogging amplitude in this case. This could be useful, especially for a trapezoidal type of machine if used in conjunction with some other methods for reducing cogging torque. Since with one dummy slot, the CPMR is doubled, only half-slot pitch skewing is enough compared to the full-slot pitch skewing with no dummy slots. Saturation of the stator teeth must be considered before selecting the shape of the dummy slots, which may increase the harmonic contents in the back EMF, resulting in higher torque ripple in sinusoidal back-EMF machines and may decrease the torque-per-ampere ratio for such machines.

1.4 Analysis of Results

The cogging torque suppression techniques are investigated in various designs bifurcated, increasing no of slots, dummy slots. In this for bifurcated 8 pole 60 slots cogging torque are 0.8 N-m and efficiency 91 % with low power factor and high flux density as shown in Fig. 1.2. Figure 1.3 represent the 8 poles 60 slots with dummy slots, which the cogging torque is 0.078 N-m and efficiency 93 % with high output power and low flux density. Comparing these two designs is clearly clarified in performance Table 1.2. In this cogging torque is low in dummy slots and high power factor, high efficiency, less flux density, and high output power. For the two motor designs torque developed by the motor, peak to peak values of the cogging torque output power the efficiency are recorded.

1.5 Conclusion

The paper has discussed the comparison of results with various techniques like dual bifurcated and dummy slot for reducing cogging torque in BLDC motor. Also the characteristics curve for the flux density, efficiency and output power is discussed. From this results reduced stator tooth width method is more efficient when compared with other two prototypes. The cogging torque may not be eliminated completely due to variation and tolerance but can be minimized to satisfactory level. The performance of the BLDC motor has been verified by geometrically and analytically. The effectiveness of analysis and simulations results is evaluated and compared by 2-D FEA.

References

1. Studer C, Keyhani A, Sebastian T, Murthy SK (1997) Study of cogging torque in permanent magnet machines. In: IEEE IAS annual meeting, USA, pp 42–49
2. Li T, Slemon G (1998) Reduction of cogging torque in permanent magnet motors. IEEE Trans Magn 6:2901–2903
3. Steinbrink J (2007) Analytical determination of the cogging torque in brushless motors excited by permanent magnets.In: Proceedings of IEEE international conference on electric machines and drives (IEMDC'07), vol 1, pp 172–177, May 2007
4. Gieras JF, Wing M (2002) Permanent magnet motor technology, design and applications, 2nd edn. Marcel Dekker Inc., New York
5. Ackermann B, Janssen JHH, Sotteck R, van Steen RI (1992) New technique for reducing cogging torque in a class of brushless DC motors. IEE Proc B-Electr Power Appl 139 (4):315–320
6. Zhu ZQ, Howe D (2000) Influence of design parameters on cogging torque in permanent magnet machines. IEEE Trans Energy Convers 15(4):407–412
7. Zarko D, Ban D, Lipo TA (2008) Analytical solution for cogging torque in surface permanent-magnet motors using conformal mapping. IEEE Trans Magn 44(1):52–65
8. Ishikawa T, Slemon GR (1993) A method of reducing ripple torque in permanent magnet motors without skewing. IEEE Trans Magn 29(2):2028–2031
9. Yang Y, Wang X, Zhang R, Zhu C, Ding T (2005) Research of cogging torque reduction by different slot width pairing permanent magnet motors. In: Proceedings of 8th international conference on electrical machines and systems (ICEMS'05), vol 1, pp 367–370, Sept 2005
10. Islam MS, Mir S, Sebastian T (2004) Issues in reducing the cogging torque of mass-produced permanent-magnet brushless DC motor. Ind App IEEE Trans Magn 40(3):813
11. Lateb R, Takorabet N, Meibody-Tabar F (2006) Effect of magnet segmentation on the cogging torque in surface-mounted permanent magnet motors. IEEE Trans Magn 42(3):442
12. Koh CS, Seol J-S (2003) New cogging torque reduction method for brushless permanent-magnet motors. IEEE Trans Magn 39(6):3503–3506
13. Dosiek L, Pillay P (2007) Cogging torque reduction in permanent magnet machines. IEEE Trans Ind Appl 43(6):1565–1571
14. Jahns TM, Soong WL (1996) Pulsating torque minimisation techniques for permanent magnet AC motor drives: a review. IEEE Trans Industrial Electronics 43(2):321–330
15. Breton C, Bartolome J, Benito JA, Tassinario G, Flotats I, Lu CW, Chalmers BJ (2000) Influence of machine symmetry on reduction of cogging torque in permanent-magnet brushless motors. Magn IEEE Trans Magn 36(5):3819
16. Zhu ZQ, Ruangsinchaiwanich S, Schofield N, Howe D (2003) Reduction of cogging torque in interior-magnet brushless machines. IEEE Trans Magn 39(5):3238–3240

Chapter 2
Application of Sinusoidal Pulse Width Modulation Based Matrix Converter as Revolutionized Power Electronic Converter

K. Vijayakumar, R. Sundar Raj and S. Kannan

Abstract This Paper presents the application of Single Phase Matrix converter as a Cycloconverter and Cycloinverter. Sinusoidal Pulse Width Modulation (SPWM) technique is used to generate control pulses for the Matrix Converter switches to produce output. The switching sequences for the Matrix Converter to operate as Cycloconverter and Cycloinverter are presented and evaluated using MATLAB/Simulink. The simulation results prove Single Phase Matrix Converter functionality as several power electronics converters by switching sequence via SPWM technique.

Keywords SPWM · Matrix converter · Cycloconverter

2.1 Introduction

Nowadays power electronics converters are used in many applications such as Industrial, Medical and Railways etc. Optimization of power electronic system design and operation is important to hold the growing need for energy efficiency in portable electric devices and respond to their increasing functional features. These features stipulate extra electric power while the devices must be reduced in size and weight. Power electronics converters like Rectifier and Inverters are used in various commercial and industrial applications. Inverters are used widely in many applications in which the required voltage is AC in nature. But still in most of the electrical drive system DC voltage is required due to ease of speed control in all the four quadrants. So rectifier find its part in which the voltage generated is DC. Power electronics converter also plays a major applicable role in DC motor drive con-

---

K. Vijayakumar (✉) · R.S. Raj · S. Kannan
Department of EEE, Kalasalingam University, Krishnankoil 626126, India
e-mail: kumark86@gmail.com

C. Kamalakannan et al. (eds.), *Power Electronics and Renewable Energy Systems*,
Lecture Notes in Electrical Engineering 326, DOI 10.1007/978-81-322-2119-7_2

trolling the speed in both forward and reverse direction by controlling the current in both the directions as well [1]. The Matrix Converter is a smart topology of power converter for direct power supply application with absence of electrolytic capacitors, potentiality of increasing power density, reduced size, weight and good input power quality [2]. An improved control structure for single phase Matrix Converter such that it can be used for different applications, is proposed in this paper. Development of control signals through Sinusoidal Pulse Width Modulation is presented and the Matrix Converter is evaluated for its operation based on switching sequence.

2.2 Single Phase Matrix Converter Topology

The circuit topology consists of four bi-directional IGBT switches which are configured in anti-parallel Common Emitter (CE) configuration. Matrix Converter in the three-phase variant is extensively researched at the same time as the single phase Matrix Converter had very little attention while offering the possibility of a very wide application. Single phase matrix converter was first released by Zuckerberger in 1997 as the direct single phase AC-AC converter [3]. The Single phase Matrix Converter can perform all the function of a generalized single phase power electronics converter only by varying the input parameters though having possibilities of single phase to three phase conversion in Matrix Converters [4]. The Matrix converter in single phase configuration is shown in Fig. 2.1. It consists of matrix of switches with two IGBTs connected back to back in CE configuration. The input to the Matrix Converter may be AC or DC depending on which the converter operation is made. The load is connected to supply directly through Matrix converter topology without any DC link (reactive energy storage elements). The output from the Matrix Converter is obtained by toggling of switches with control signals developed via SPWM. It is to ensure that the switches do not short-circuit voltage sources and open-circuit current sources [5].

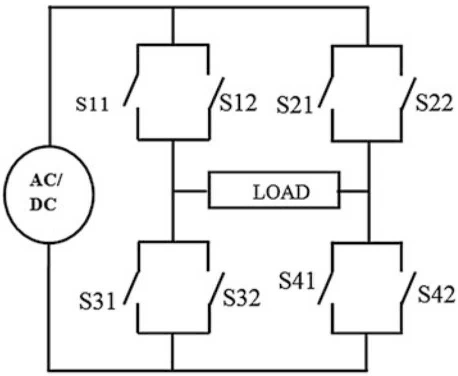

Fig. 2.1 Single phase matrix converter topology

2.3 Proposed Functionality of Matrix Converter

Figure 2.2 represents the functional block diagram in which the following operations possibilities could be elucidated as follows.

2.3.1 Matrix Converter Applicable as a Cycloconverter

The input supply to the Matrix Converter is chosen as AC for its operation as a Cycloconverter. In this condition if the related switches of the Matrix converter are toggled with control signals, then the Matrix converter will generate AC, which is called as Cycloconverter (AC-AC). For Cycloconverter mode of operation, the output frequency obtained is given by, $f_o = f_{in}/N_{r,}$ Where, f_o = Output frequency, f_{in} = Input frequency and N_r = Real number. Here the desired output from the Matrix Converter could be used for variable frequency applications of AC drives and AC load purpose. The control signals when given to the switches S11, S41 & S22, S32 of the pair, positive load voltage is obtained across the load for the positive and negative cycles of the input AC voltage. Similarly when the switches S21, S31 & S12, S42 of the pair are toggled, negative load voltage is obtained across the load for the positive and negative cycles of the input voltage thus giving off the Cycloconverter function.

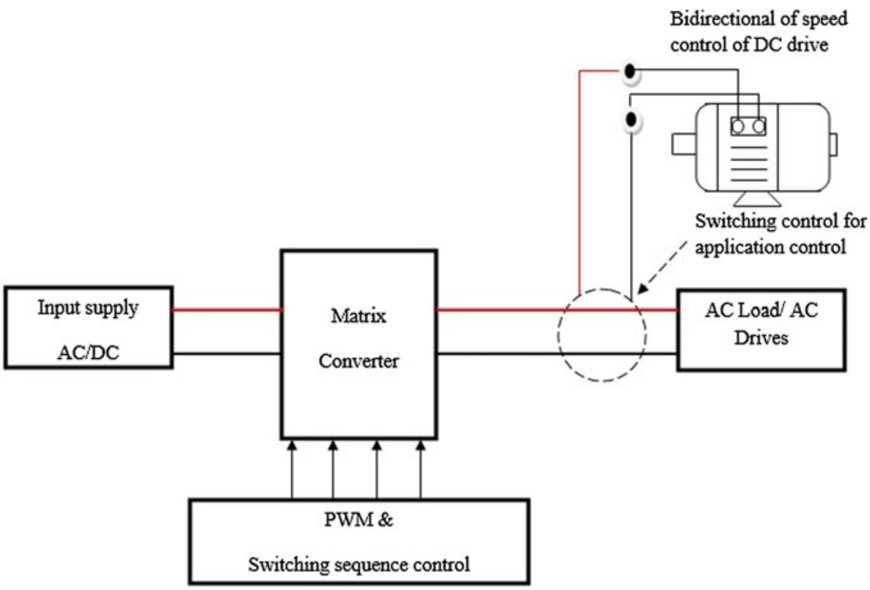

Fig. 2.2 Functional block diagram of matrix converter

2.3.2 Matrix Converter Applicable as a Cycloinverter

Similarly, if the Matrix converter is chosen with input supply AC, it operates as Cycloinverter in which the output frequency f_o will be $f_o = f_{in} \times N_r$, Where, f_o = Output frequency, f_{in} = Input frequency and N_r = Real number. In this condition if the related switches of the Matrix converter are toggled, it will generate AC, which is called as AC-AC Cycloinverter.

2.3.3 Matrix Converter Applicable as a Dual Converter, Rectifier and Inverter

With appropriate switch control for selecting application, the Matrix converter could be reliably used for bi-directional speed control of DC drive as in dual converter. The DC motor could be run in the positive direction by the toggling of switches S11 & S41 for the positive half cycle of the input AC voltage and S22 & S32 for the negative cycle of the input. For the DC motor to run in the reverse direction, the switches S21 & S31 and S12 & S42 are toggled with control signals for the positive and negative cycles of the AC input respectively. Similarly, the Matrix Converter could also be made applicable as Rectifier and Inverter [6].

2.4 Sinusoidal Pulse Width Modulation Technique

Sinusoidal Pulse Width Modulation (SPWM) technique is one of the simplest carrier-based modulation methods for the control of Matrix Converters. The SPWM is a familiar shaping technique in the field of Power Electronics where a high-frequency triangular carrier signal is compared with a sinusoidal reference signal. The main advantage of carrier based SPWM is that the complexity is very low and the dynamic response is also good for Matrix Converters [7]. The number of pulses per cycle is being decided by ratio of the triangular carrier frequency to that of modulating sinusoidal frequency. Modulation ratio (M_R) is given by the relation,

$$M_R = \frac{\text{Frequency of Carrier Waveform}}{\text{Frequency of the Modulating Waveform}} \tag{2.1}$$

M_R is related to the harmonic frequency and the harmonics are normally located at:

$$f = kM_R(f_m) \tag{2.2}$$

where f_m is the frequency of the modulating signal and k is an integer (1, 2, 3…)

Modulation index (M_I) is given by the ratio of Amplitude of modulating reference waveform to that of the Amplitude of carrier waveform and is denoted by,

$$M_I = A_r/A_c \tag{2.3}$$

where A_r is the reference amplitude and A_c the carrier amplitude

M_I is related to the fundamental (sine wave) output voltage magnitude. If M_I is high, then the sine wave output is high and vice versa.

When $0 < M_I < 1$, the linear relationship holds: $V_1 = M_I\ V_{in}$, where V_1, V_{in} are fundamental of the output voltage and input voltage, respectively.

2.5 Simulation Model

The simulation is carried out using MATLAB/Simulink and the implementation of SPWM is presented in Fig. 2.3. Here the triangular carrier signal of the switching frequency is compared with the sinusoidal reference signal and the control signals (pulses) are obtained for the positive and negative cycles of the sequence. The simulation output of SPWM is shown in Fig. 2.4.

The Cycloconverter operation is implemented using MATLAB/Simulink and is shown in Fig. 2.5. The operation of the Matrix Converter as Cycloconverter for positive output load voltage is obtained by the conduction of the switches S11, S41 for the positive half cycle of the AC input, and S22 & S32 for the negative half cycle of the input and similarly S21, S31, & S12, S42 for the negative output load

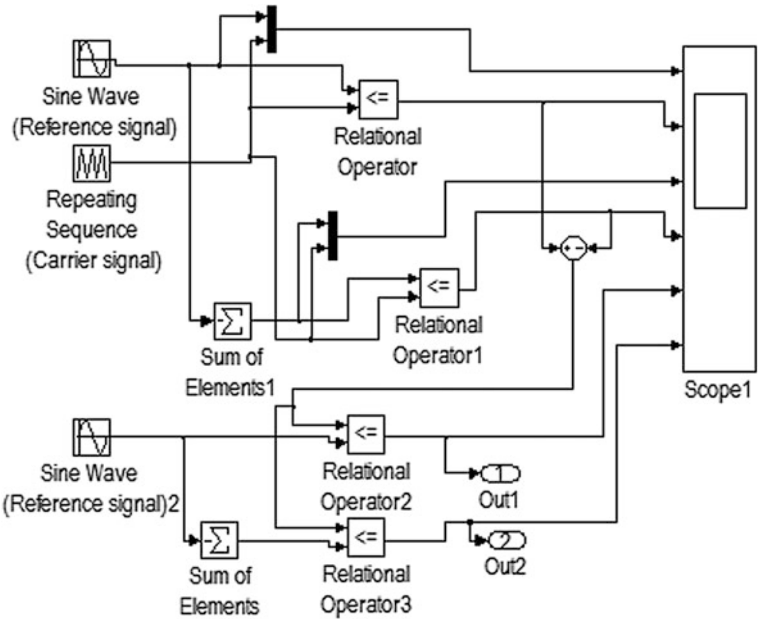

Fig. 2.3 SPWM implementation in MATLAB/Simulink

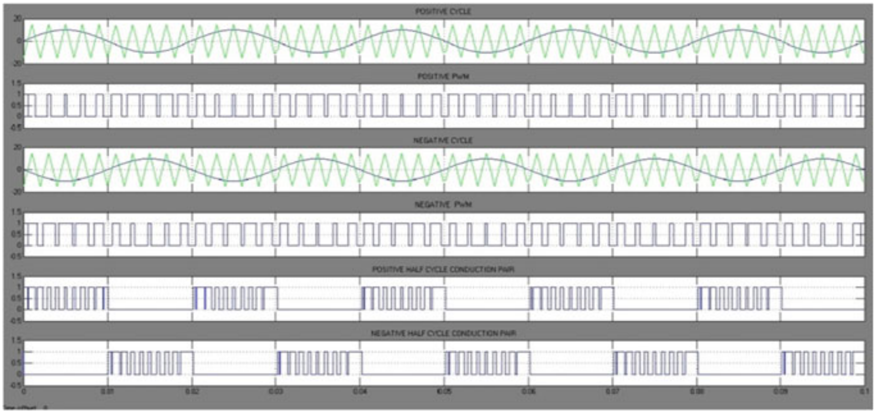

Fig. 2.4 SPWM output in MATLAB/Simulink

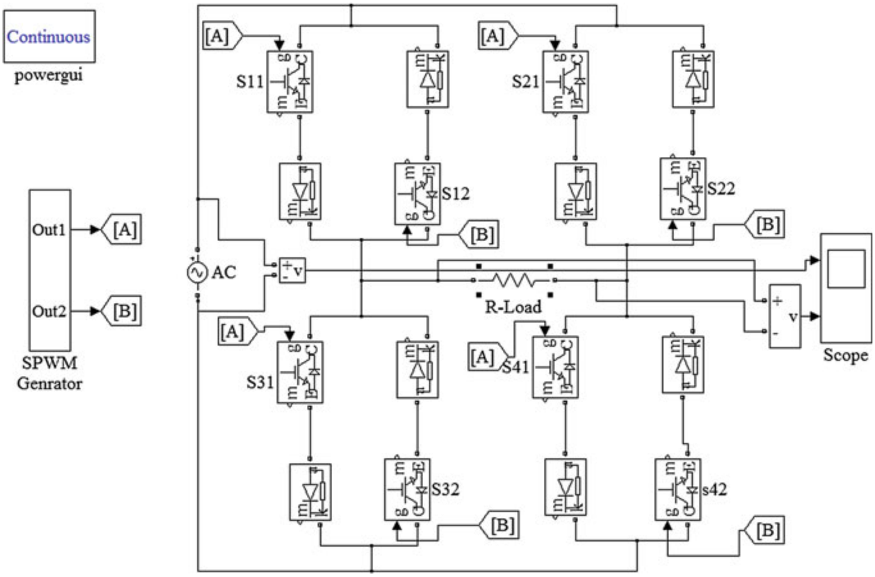

Fig. 2.5 Cycloconverter implementation in MATLAB/Simulink

voltage. For Cycloconverter mode of operation, the output frequency obtained is given by, $f_o = f_{in}/N_r$, Where, f_o = Output frequency, f_{in} = Input frequency and N_r = Real number. The operation of Matrix Converter as Cycloconverter could be easily understandable from the following simulation circuit and output.

An AC output voltage of 325 V peak and 50 Hz is obtained for the input voltage and switching frequency of 325 V DC and 5 kHz respectively for a resistive load of

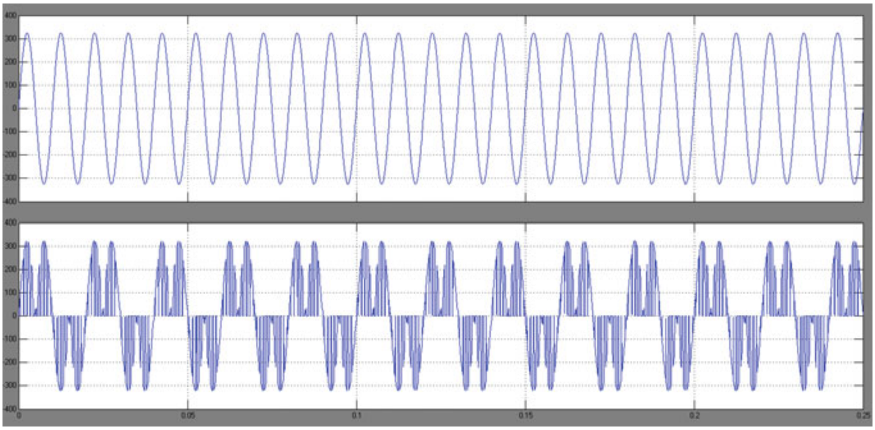

Fig. 2.6 Simulation output of Cycloconverter (100 Hz input voltage vs. 50 Hz output voltage)

50 Ω. The control signals are given by the SPWM technique as mentioned in Chap. 4. The simulation output is shown in Fig. 2.6.

Similarly, the Cycloinverter is implemented using MATLAB/Simulink. The operation as Cycloinverter is obtained by the conduction of switches S11, S41, S21, & S31 for the positive half cycle of the input and S22, S32, S12 and S42 for the negative half cycle of the input in which the output frequency f_o will be $f_o = f_{in} \times N_r$, Where, f_o = Output frequency, f_{in} = Input frequency and N_r = Real number. The output frequency of the Matrix Converter when working as Cycloinverter will be of the necessary value depending on the developed SPWM cycle frequency in which the output frequency is 100 Hz for an input of 50 Hz AC supply as shown in Fig. 2.7.

The Matrix Converter is implemented as dual-converter in MATLAB/Simulink with AC as supply input to the converter. When the control signals are given to the

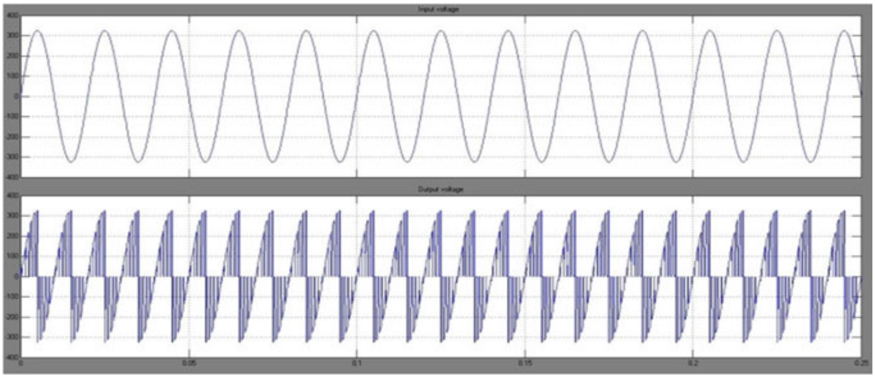

Fig. 2.7 Simulation output of Cycloinverter (50 Hz input voltage vs. 100 Hz output voltage)

Table 2.1 Matrix converter switching sequence and modes of operation

Supply sequence	Switching sequence	Mode of operation	Utility
Positive	S11 S41 & S22 S32	Cycloconverter operation	AC load/AC drive
Negative	S21 S31 & S12 S42		
Positive	S11 S41 & S21 S31	Cycloinverter operation	AC load/AC drive
Negative	S12 S42 & S22 S32		

switches S11 & S41 for the positive half cycle of the input AC voltage and S22 & S32 for the negative cycle of the input, the DC output is obtained in the positive potential. This positive load voltage serves running the DC motor in forward direction. The speed control is achieved by a change in the Modulation index M_I as given in Eq. 2.3 Similarly for the DC motor to run in the reverse direction the switches S21 & S31 and S12 & S42 are toggled with control pulses through SPWM for the positive and negative cycles of the AC input respectively. With a change in the Modulation index M_I, the speed is also controlled in the reverse direction of the DC motor. The operation of Matrix Converter as rectifier (switching states) is similar to the operation of dual-converter in obtaining positive load voltage. The switching states are presented in Table 2.1.

2.6 Conclusion

Generally the operation of converters and maintenance needs expertise and skilled manpower. But as proposed in this paper generalized functionality of Matrix Converter reduces the need for new converter hardware. The use of a Matrix Converter in the future reduces the need for learning many varying converter topologies. The Single phase Matrix Converter can perform all the functions of a generalized single phase power electronics converter only by changing the input parameters though having possibilities of single phase to three phase conversion in Matrix Converters.

Acknowledgments The authors are grateful to the management and the head of the Institution of Kalasalingam University for giving all necessary support and providing facilities for making this research paper a successful one.

References

1. Mohammad Noor SZ, Abdul Rahman NF, Hamzah MK (2011) Single phase matrix converter operating as a four quadrant dc chopper controlled using xilinx FPGA. Int J Electr Electron Syst Res, vol 4
2. Babaei E, Hosseini SH, Gharehpetian GB (2010) Reduction of THD and low order harmonics with symmetrical output current for single-phase ac/ac matrix converters. J Electr Power Energy Syst 32:225–235

3. Friedli T, Kolar JW (2012) Milestones in matrix converter research. IEE J Ind Appl 1(1):2–14
4. Baskaran B, Natarajan SP, Sivagamasundari S, Thamilarasi D (2009) A novel matrix converter based single phase to three phase converter. Int J Sci Techniques Autom Control Comput Eng IJ-STA 3(2):1092–1107
5. Gola AK, Agarwal V (2009) Implementation of an efficient algorithm for a single phase matrix converter. J Power Electron 9(2):198–206
6. Vijayakumar K, Raj RS (2013) Realization of matrix converter as revolutionized power electronic converter employing sinusoidal pulse width modulation. IEEE international conference on computational intelligence and computing research (ICCIC), 26–28 Dec 2013, pp 1–5
7. Rodriguez J, Rivera M, Kolar JW, Wheeler PW (2012) A review of control and modulation methods for matrix converters. IEEE Trans Ind Electron 59(1):58–70

Chapter 3
Performance Analysis of Biofuels and Gasoline in SI Engines

S.P. Karthick, R.L. Helen Catherine and N. Premaanand

Abstract Considering energy crises and pollution problems today, investigations have been concentrated on decreasing fuel consumption by using alternative fuels and on lowering the concentration of toxic components in combustion products. In the present work, the variable compression ratio spark ignition engine designed to run on gasoline has been tested with pure gasoline, and bio-alcohols namely ethanol, butanol and acetone mixed with different proportions by volume without any engine modifications has been tested and presented the result. Brake thermal and volumetric efficiency variation with brake power is compared and presented. CO_2, CO, O_2, HC and NOx emissions have been also compared for all tested fuels.

Keywords SI engines · Specific fuel consumption (sfc) · Biofuel · Gasoline

3.1 Introduction

The world is presently confronted with the twin crises of fossil fuel depletion and environmental degradation. Indiscriminate extraction and lavish consumption of fossil fuels have led to reduction in underground-based carbon resources. Alcohol fuels particularly ethanol can be produced by fermentation of bio mass crops, mainly sugar cane, wheat and wood. Usage of alcohols as a fuel for spark ignition

S.P. Karthick (✉)
Department of Electrical and Electronics Engineering, PSNA College of Engineering and Technology, Dindigul, Tamil Nadu, India
e-mail: karrthicksp@gmail.com

R.L.H. Catherine
Sri Krishna College of Engineering and Technology, Coimbatore, Tamil Nadu, India
e-mail: rl.helencatherine@gmail.com

N. Premaanand
Aiswarya College of Engineering and Technology, Erode, Tamil Nadu, India
e-mail: premaanandkct32@gmail.com

C. Kamalakannan et al. (eds.), *Power Electronics and Renewable Energy Systems*, Lecture Notes in Electrical Engineering 326, DOI 10.1007/978-81-322-2119-7_3

engines has some advantage to compare the gasoline. The engine thermal efficiency can be improved with increasing of compression ratio. Alcohols burns with lower flame temperatures and luminosity owing to decreasing the peak temperature inside the cylinder and hence the heat losses and NOx emissions are lower. The gasoline engine became the preferred engine for the automobile because gasoline was cheaper than alcohol, not because it was a better fuel. And, because alcohol was not available at any price from 1920 to 1933, a period during which the sale, manufacture, and transportation of alcohol was banned nationally as mandated in the Eighteenth Amendment to the United States Constitution. The amendment was repealed by the Twenty-First Amendment on December 5, 1933.

3.2 Literature Review

By using ethanol with gasoline they blend in the availability of a spark ignition engine was experimentally investigated [1]. Sixty percent ethanol and 40 % gasoline blend was exploited to test the performance, the fuel consumption and the exhaust emissions. Methanol and ethanol have some advantages, but also have some disadvantages at the same time which make their usages limited shown [2, 3]. Butanol has the physical and chemical properties more close to gasoline fuel than ethanol. The studies of [4] show that butanol is a good alternative fuel for gasoline engine. At medium loads, the efficiency variation is small shown [1]. It is recommended that the petrol should not mix with the commercially available kerosene as it gives high carbon monoxide emission. According to [5], using ethanol-gasoline blend fuel in SI engines lead to higher engine torque in comparison with gasoline fuel. Using E40 and E60 blends led to a significant reduction of CO and HC emissions. It was also reported by [6] that blends with ethanol allowed the compression ratio to increase by 50 % without knock. The most suitable ethanol-gasoline fuel blend in terms of performance and emissions was E50 in a small gasoline engine with low efficiency shown [7]. Engine power increased by about 29 % running with E50 fuel at high compression ratio compared to running with E0 fuel. The specific fuel consumption, CO, CO_2, HC emissions were reduced by approximately 3, 53, 10 and 12 % respectively.

3.3 Experimental Setup

The internal combustion engine performance is generally indicated by the term efficiency (η). The break thermal efficiency (ηbth) and mechanical efficiency of the engine (ηm). These two important parameters apart from exhaust gas analysis have been aimed at in this study.

Performance and exhaust gas analysis of variable compression ratio spark ignition engine, which has been designed for gasoline, is tested with ethanol, butanol and acetone at different proportions by volume without modifications of the engine has set and performance of the engine has made. The engine used here is Four stroke single cylinder engine with variable compression ratio. Experimental apparatus included three major systems, i.e. the engine system, the power measurement system, and the exhaust measurement system.

This engine is a four stroke single cylinder, air cooled, spark ignition type petrol engine. It is coupled to a loading system which is in this case is an Eddy current dynamometer, the output shaft of the dynamometer is arrested with an arm which rests on the load cell provided. In the experimental study, a single cylinder variable compression ratio spark ignition engine was used. Typical views of test engine have shown in Figs. 3.1 and 3.2. The specifications of test engine are shown in Table 3.1. The tests were performed by keeping the torque varied. The test fuels used are gasoline(mono), and bio-alcohols(ethanol, butanol and acetone) at different proportions by volume (EBA 45 50 5, 55 35 10, 68 22 10, 70 25 5 and 65 25 10). The performance test generally includes brake power, specific fuel consumption, total fuel consumption, swept volume, actual volume, volumetric efficiency and overall efficiency. Before conducting the experiment, the property test is conducted . The property test includes calorific value using bomb calorimeter, viscosity by using poiseuille's method, density and specific weight using electronic weight balance. After getting the property of the fuels i.e. all ten different proportions of ethanol, butanol and acetone. All the ten different proportions are tested in the engine and exhaust analysis has been done by using exhaust gas analyzer. Among the ten different proportions, best five proportions has been selected and performance exhaust analysis has been made.

The experiment was performed at four different compression ratios (3.5:1, 4.6:1, 6:1, and 8:1) for each fuel and the effect of engine performance was investigated. The engine to be tested was started and allowed to run at no load for about 10 min to reach the steady state for each fuel to be tested. Air consumption was measured with orifice meter and the liquid fuel consumption was measured with burette. Fuel

Fig. 3.1 Photograph of *front* and *side* view of SI engine experiment test rig

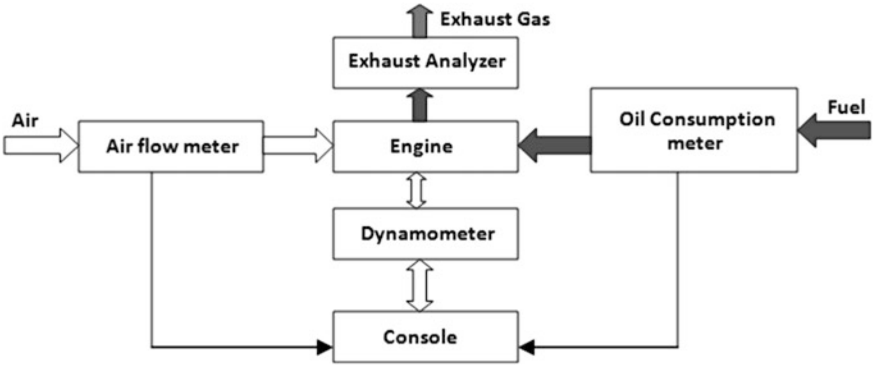

Fig. 3.2 Sketch of experiment system

Table 3.1 Properties of tested biofuels

Biofuels proportions (ml)			Density (kg/m^3)	Specific weight (N/m^3)	Calorific value (kJ/kg)	Dynamic viscosity (N s m^{-2})	Kinematic viscosity (N s m/kg) × 10^{-5}
E	B	A					
65	25	10	771.368	7,559.41	69,775.99	0.02537	3.28896
60	35	5	777.708	7,621.541	54,658.56	0.04019	5.16774
70	30	0	765.51	7,502	75,168.12	0.0212517	2.7759
40	60	0	770.408	7,550	56,888.41	0.02476	3.21388
45	50	5	772.708	7,572.541	59,607.54	0.024017	3.10815
50	40	10	777.239	7,616.934	48,120.55	0.036887	4.7449
40	55	5	778.465	7,628.965	55,256.727	0.02618	3.36302
70	25	5	773.279	7,578.134	61,469.5	0.02677	3.4618
60	40	0	770.872	7,554.548	47,256.55	0.048623	6.3075
60	30	10	774.19	7,587.062	59,392.72	0.01872	2.41801

where *E* Ethanol, *B* Butanol, *A* Acetone

consumption, temperature at corresponding positions, rpm, and exhaust gas temperature were noted for no load condition. After this the engine was loaded in steps and corresponding data for each load was noted. Exhaust gas analysis has been done with the help of exhaust gas analyzer (Model:ECOGAS-4) of CO range from 0 to 9.99 %, CO_2 range from 0 to 19.9 %, HC range from 0 to 15,000 ppm, O_2 range from 0 to 25 % and NOx range from 0 to 5,000 ppm. Measured NOx and carbon dioxide emissions when the above said different fuels used and comparative statement has been made.

3.4 Results and Discussion

Gasoline has density of 800 kg/m^3 and calorific value of 46,500 kJ/kg, so that the above bio-alcohol combinations has relatively equivalent to that of gasoline and it can be seen practically by below results in Figs. 3.3, 3.4, 3.5, 3.6, 3.7, 3.8, 3.9 and 3.10. From the test conducted below, it can be evident that the property of bio-alcohols tested below will be equivalent to that of gasoline. The theoretical AFR of gasoline is 1.6 times that of ethanol; therefore the specific fuel consumption (sfc) should be increased with the increase of ethanol content. The engine performance and the pollutant emission of a commercial SI engine were investigated by using an bio-alcohols combination without blending of gasoline. Gasoline performance and exhaust will be taken as reference for the below comparison.

The above graph (Figs. 3.3, 3.4, 3.5 and 3.6) shows that the volumetric efficiency of the bio-alcohols mentioned in the graph has been high compared to gasoline and overall efficiency is been quite low because of the air-fuel ratio and increase in fuel consumption. So that if the engine is modified with increase in the

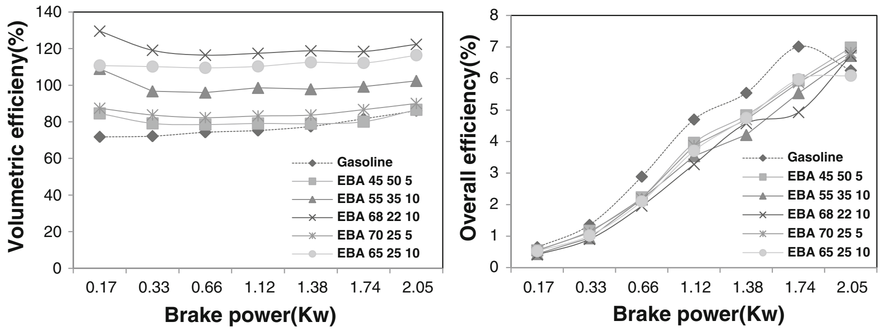

Fig. 3.3 Comparative and performance of bio-alcohols and gasoline in compression ratio 3.5

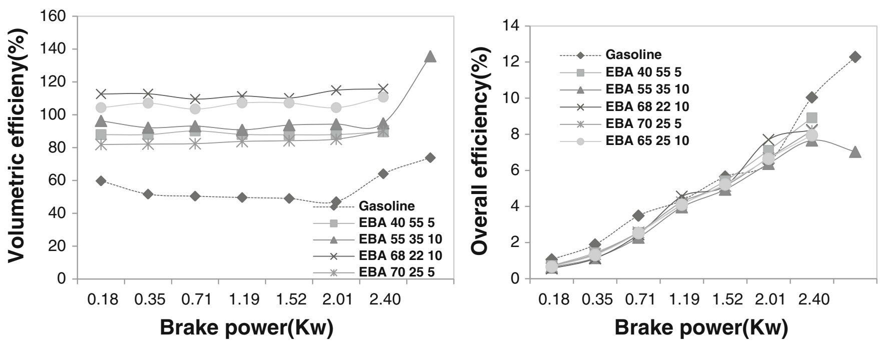

Fig. 3.4 Comparative and performance of bio-alcohols and gasoline in compression ratio 4.67

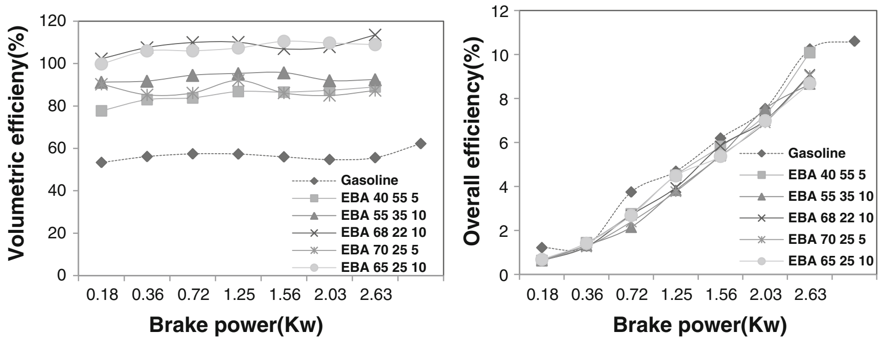

Fig. 3.5 Comparative and performance of bio-alcohols and gasoline in compression ratio 6

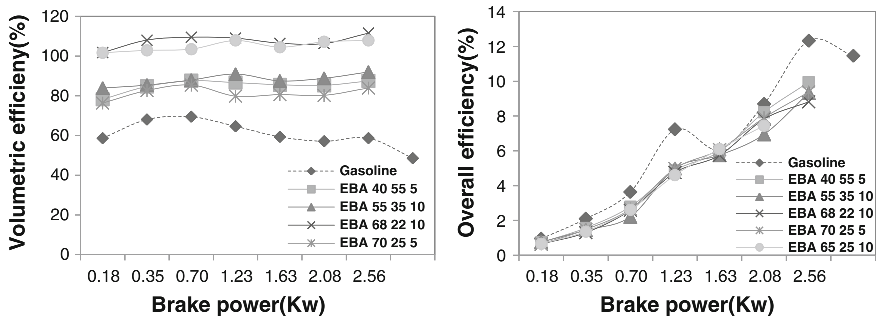

Fig. 3.6 Comparative and performance of bio-alcohols and gasoline in compression ratio 8

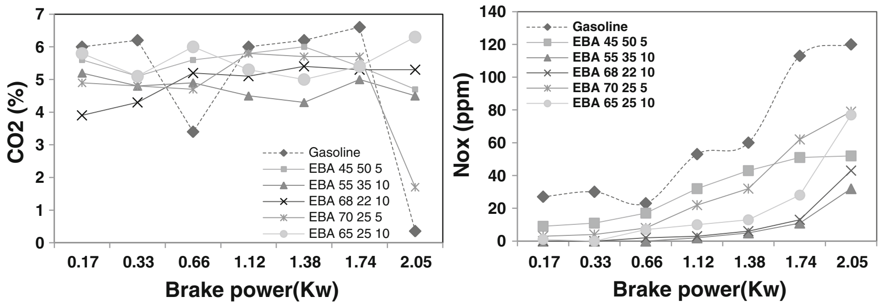

Fig. 3.7 Comparative exhaust analysis of bio-alcohols and gasoline in compression ratio 3.5

spark produced by spark plug and increase the diameter of the incoming valve to the carburetor (to increase the quantity of bio-alcohols burned), we can get high efficiency rather than the above results without any modification.

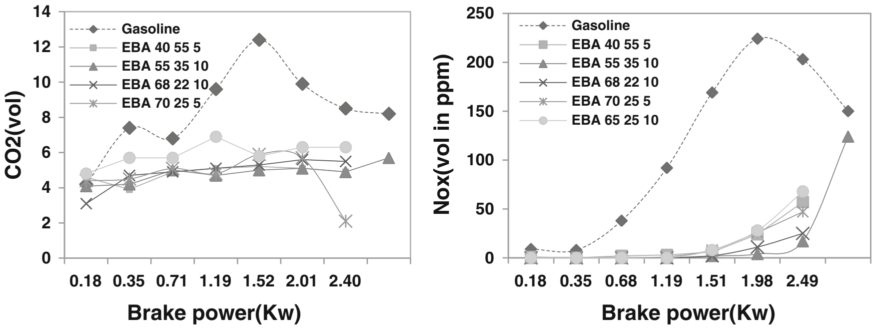

Fig. 3.8 Comparative exhaust analysis of bio-alcohols and gasoline in compression ratio 4.67

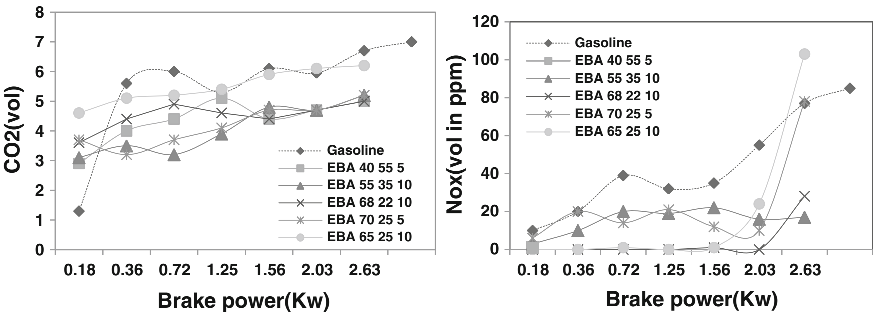

Fig. 3.9 Comparative exhaust analysis of bio-alcohols and gasoline in compression ratio 6

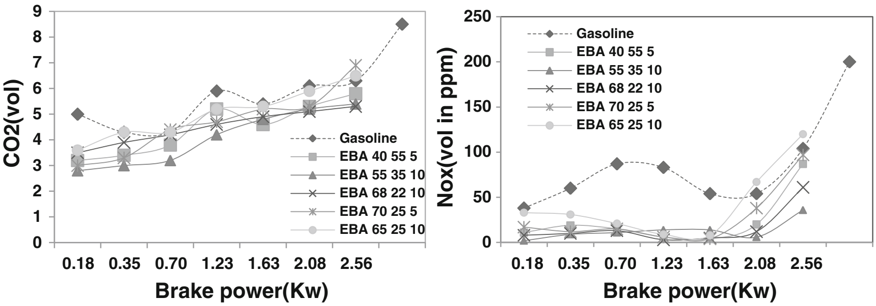

Fig. 3.10 Comparative exhaust analysis of bio-alcohols and gasoline in compression ratio 8

The exhaust chart Figs. 3.7, 3.8, 3.9 and 3.10 shows that both CO_2 and NOx is reduced in the bio-alcohol fuels rather than gasoline because of low hydrocarbon content when compared to gasoline. The emission of these both pollutants has been drastically reduced by using these combination of bio-alcohols without compensating the performance of the engine. EBA 68 22 10 will emit low CO_2 in low torque and during high torque it emit CO_2 in moderate concentration. Remaining four samples has low CO_2 emission when compared to gasoline and high when compared to EBA 68 22 10. The concentration of NOx emission is rapidly decreased in the four bio-alcohol combination when compared to the gasoline which has been shown clearly in Figs. 3.7, 3.8, 3.9 and 3.10. Among that once again EBA 68 22 10 will be the best because of their low Nox emission.

3.5 Conclusion

The effect of alcohol and gasoline on engine performance was investigated. Similarly, the flue gas analysis has been done for all the fuels and compared the results. Brake thermal efficiency and volumetric efficiency of the spark ignition engine at different compression ratio is analyzed. Variation of engine brake thermal efficiency with gasoline and different proportions of bio-alcohol fuels has been compared at different load conditions as shown in Figs. 3.3, 3.4, 3.5 and 3.6. Relatively the brake thermal efficiency is less for all the fuels due to their practical limitations on the research engine. The variation is similar for all the engines, and highest efficiency is seen with pure petrol. The lowest brake thermal efficiency is with EBA 55 35 10. This may be due to pre-ignition combustion. The same type of tendency is observed at all tested compression ratios are in Figs. 3.3, 3.4, 3.5 and 3.6. Among the combination EBA 68 22 10 has been high in the volumetric efficiency in the CR 3.5, 4.67, 6 and 8. In order to enhance engine efficiency and decrease pollution emission, the relative experiments with mixed fuels were involved in this project. So that the fuels chosen for the mixing was butanol, acetone and ethanol because of their relative equivalent characteristics of gasoline without any blending. So that to enhance the performance and efficiency, engine is modified with increase in the spark produced by spark plug and increase the diameter of the incoming valve to the carburetor (to increase the quantity of bio-alcohols burned), we can get high efficiency rather than the above results without any modification. Using ethanol as a fuel additive to unleaded gasoline causes an improvement in engine performance and exhaust emissions.

References

1. Yuksel F, Yuksel B (2004) The use of ethanol-gasoline blend as a fuel in SI engine. Renewable Energy 29:1181–1191
2. Al-Hasan M (2003) Effect of ethanol-unleaded gasoline blends on engine performance and exhaust emissions. Energy Convers Manage 44:1547–1561
3. El-Kassaby MM (1993) Effect of using differential ethanol–gasoline blends at different compression ratio on SI engine. Alexandria Eng J 32(3):A135–A142
4. Celik MB (2008) Experimental determination of suitable ethanol–gasoline blend rate at high compression ratio for gasoline engine. Appl Therm Eng 28(396):404

5. Leu J-H, Huang M-Y (2009) Alternative fuel test study of an diesel engine fed by synthetic fuel derived from waste bilge oil. J Mar Sci Technol 17(1):7–12
6. Hamdan MA, Jubran BA (1986) The effect of ethanol addition on the performance of diesel and gasoline engines. Dirasat XIII(10):229–44
7. Jaichandar S, Annamalai K (2011) The status of biodiesel as an alternative fuel for diesel engine—an overview. J Sustain Energy Environ 2:71–75

Chapter 4
Simulation of Open Loop and Feed-Back Controlled Bridgeless PFC Boost Converter

K. Mohanraj, C. Danya Bersis and Subhransu Sekhar Dash

Abstract Conventional Bridge PFC Boost converter has higher conduction losses and less efficiency. To avoid this Bridgeless PFC Boost converter is used. This paper proposes a new closed-loop controlled Bridgeless PFC Boost Converter. Unity Power Factor can be obtained by using feed forward and feed-back control unit and the output voltage of the converter has greatly increased. Performance of the circuit and efficiency also get increased. Since input voltage drop get reduced. This paper also compares conventional Bridgeless PFC Boost converter with feed forward and feedback controlled Bridgeless PFC Boost converter. MATLAB simulation result shows that the Power Factor is Unity.

Keywords Power factor correction (PFC) · Feed forward and feedback control · Boost converter

4.1 Introduction

Power Factor Correction (PFC) is one of the most important topics in power electronics and drives. Power Factor is the angle by which the load current lags or leads the supply voltage. When they are in phase power factor is unity. When they are in out of phase power factor is zero. If it is poor power factor, supply voltage drop and efficiency get reduced. So power factor should be maintained to unity or nearer to unity. Power Factor Correction (PFC) is used to shape the input current. Various Power Factor Correction techniques are used to control quality problems. PFC Boost converters are used to decrease conduction losses by reducing switches and increase efficiency [1–4]. Active Power Filter (APF) is used to increase the power factor at the input ac line which is mentioned in [5]. Passive Power Factor Correction techniques are used in low power cost sensitive application and Active

K. Mohanraj · C.D. Bersis (✉) · S.S. Dash
Department of EEE, SRM University, Chennai 603203, India
e-mail: danyabersis@gmail.com

C. Kamalakannan et al. (eds.), *Power Electronics and Renewable Energy Systems*,
Lecture Notes in Electrical Engineering 326, DOI 10.1007/978-81-322-2119-7_4

Power Factor Correction techniques are used in many applications. Buck, Boost and Buck Boost converters are used in Active Power Factor Correction techniques. Bridge PFC Boost converter uses diode-bridge which is used to improve the Power Factor. It has high conduction losses and efficiency is less. In recently used power factor improvement technique is Bridgeless PFC boost converters. Here, Diode Bridge is not required. Two inductors, two switches and four diodes are used. But the Power Factor is not unity. Totem pole Bridgeless PFC Boost converter and Pseudo-Totem pole PFC Boost converters are used to require complex control methods.High performance single phase rectifier is used to converter is used to improve power factor [6]. Dual PFC Boost converters mentioned in [7] produces less THD and more power factor.Continuous Conduction Mode (CCM) Boost converters presented in [8] are used as power factor correction converters which are used in high power applications. In general, dc power supplies are used in computers, televisions, audio sets and etc. The high power non linear loads like adjustable speed drives and low power loads like computers are used to produce harmonics which leads to poor power factor operation. Power factor can increase the input line current as well as performing voltage regulation i.e. regulate over and under voltage [9]. Interleaved PFC Boost converters mentioned in [10] high efficient and high input power factor converters. Zero Voltage Switching and Zero Voltage Transition PFC Boost converters are used to produce less conduction loss [11–13]. ZVS interleaved Boost converter is used to improve the power factor which is used to turn on under zero voltage condition. This type of converters is used in Plug-In Electric Vehicles [14]. The proposed methodology of this paper is to increase the power factor to unity. In this Bridgeless PFC boost converter with only one inductor and two diodes are used. This converter is controlled by feedback and feed forward control system. It consists of Proportional Integral (PI) controller, reference current generator, unit vector generator and Hysteresis controller. In this, efficiency and the performance of the converters are greatly increased.

4.2 Open Loop PFC Boost Converters

Figure 4.1 shows Conventional Bridge PFC Boost converter. During the positive half cycle D1, D2 and switch S1 will conduct and the negative half cycle D3 and D4 will conduct. Diode D4 and D2 are slow recovery diodes.

Figure 4.2 shows Conventional Bridgeless PFC Boost converter. In this, two switches are used S_A and S_B. D_1 and D_2 diodes are slow recovery diodes. Inductors are used to increase the output voltage of the dc-dc boost converters. During the positive half cycle first dc-dc converter (L_1-S_A-D_A) will conduct through diode D_2. During the negative half cycle second dc-dc converter (L_2-S_B-D_B) will conduct through diode D_1. In this, number of diodes used is more.

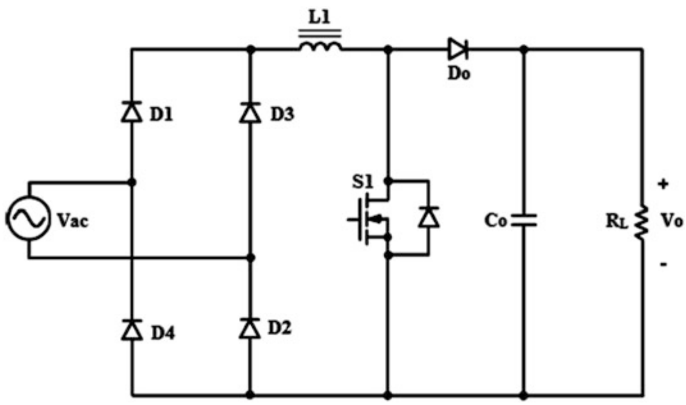

Fig. 4.1 Conventional bridge PFC boost converter

Fig. 4.2 Conventional bridgeless PFC boost converter

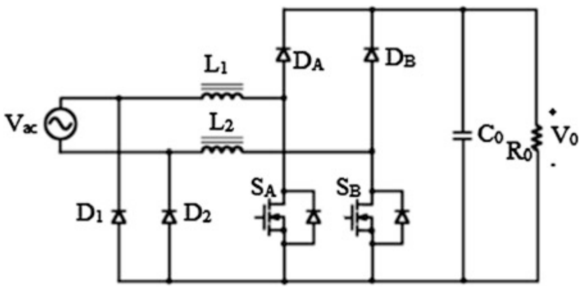

4.3 Closed Loop Controlled Bridgeless PFC Boost Converter

Figure 4.3 shows Feedback and Feed-forward controlled Bridgeless Boost converter. In this, two diodes, two IGBT switches and only one inductor are used. So switching losses of this circuit is greatly reduced. There are four modes of operations are performed. In first mode D3 and S2 will conduct. Current flows from source—Lin—D3-Capacitor—S2. In case of mode 2, current flows through switch S1 and S2. At this time capacitor discharges. In mode 3, diode D2 and S1 will conduct. Mode 4, S2 and S1 will conduct. Current flows through S1–S1 and inductor. At this time capacitor discharges and supplies current to the load.

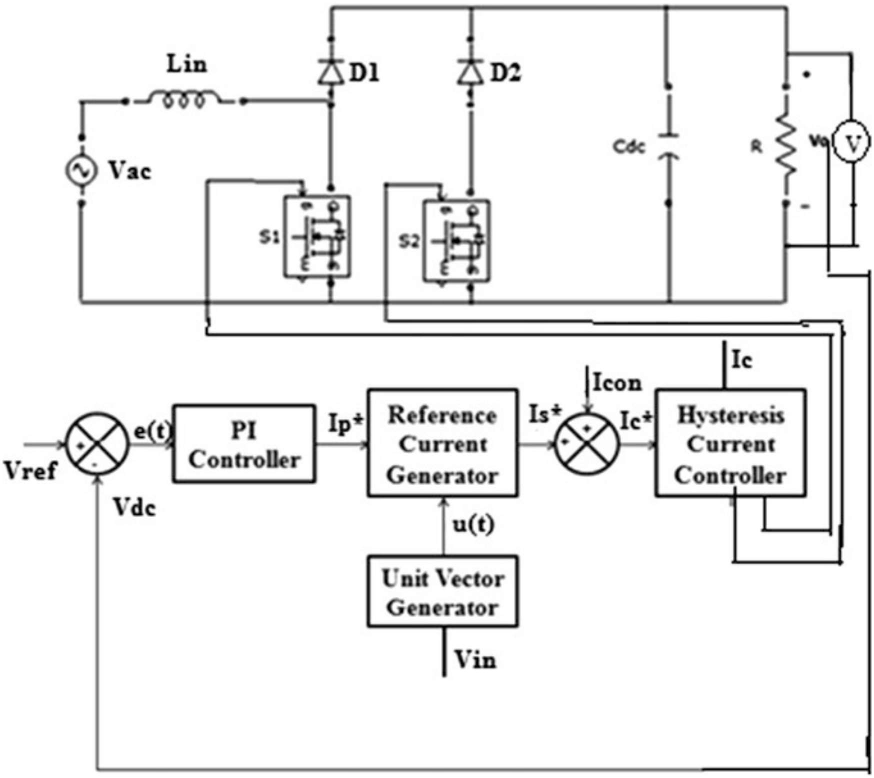

Fig. 4.3 Feedback and feed-forward controlled bridgeless boost converter

4.4 Control Unit

Figure 4.4 shows feedback and feed-forward control scheme of Bridgeless Boost converter. In this, feed-forward and feedback loop is connected to the Bridgeless PFC Boost converter.

Closed-loop consists of PI controller, reference current generator, unit vector generator and hysteresis current controller. Output voltage of the converter (Vdc) is compared with reference voltage (Vref) by using comparator which produces error signal e(t). PI (Proportional Integral) is used to minimize the error signal and it produces peak value of reference current (Ip*). Unit vector of supply voltage is fed to reference current generator which will produce reference sinusoidal unit vector current (Is*). It is compared with converter current by using comparator which produces reference converter current. It is processed in hysteresis current controller which produces switching signals to the MOSFETs. This corrective action will takes place in each and every half cycle of the ac supply and produces fast dynamic response of Bridgeless PFC Boost converter. The output voltage of the PFC Boost converter is regulated by controlling the duty cycle ratio or by varying the switching frequency.

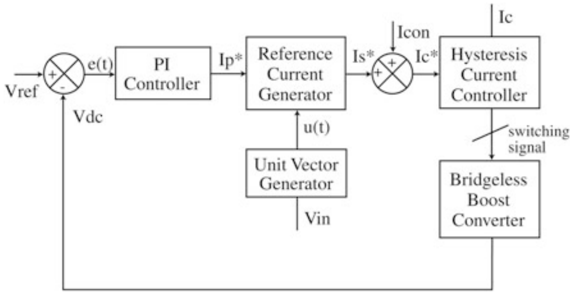

Fig. 4.4 Feed forward and feed-back control system

4.5 Equations of Feed Forward Control System

Error signal $e(t)$ is given by,

$$e(t) = V_{ref} - V_{dc} \tag{4.1}$$

$$I_p^* = e(t) \cdot K_p + K_i T_i \int e(t)\mathrm{dt} \tag{4.2}$$

where, K_i and K_p are integral and proportionality gain constant of PI controller.

I_p^*—Peak value of reference supply current.

$$I_s^* = u(t) \cdot I_p^* \tag{4.3}$$

where,

$I_p{}^*$—Reference sinusoidal unit vector current
$u(t)$—Unit vector for the input supply voltage
I_{con}—Converter current
$I_s{}^*$—Reference supply current

$$I_c{}^* = I_s{}^* + I_{con} \tag{4.4}$$

If $(i_c > i_c{}^* + h_b)$ Switch S1 ON
If $(i_c < i_c{}^* - h_b)$ Switch S2 ON

where, h_b—Hysteresis bandwidth in ampere

4.6 Simulation Results for Open Loop PFC Boost Converters

Conventional Bridge PFC Boost converter gives 0.637 power factor. Input line voltage of the converter is 250 V and the output voltage is 302 V (Figs. 4.5, 4.6).

Figures 4.7 and 4.8 show simulation circuit and output voltage waveform of Conventional Bridgeless PFC Boost Converter. Output voltage obtained is 345 V and the power factor at the supply side is 0.9923.

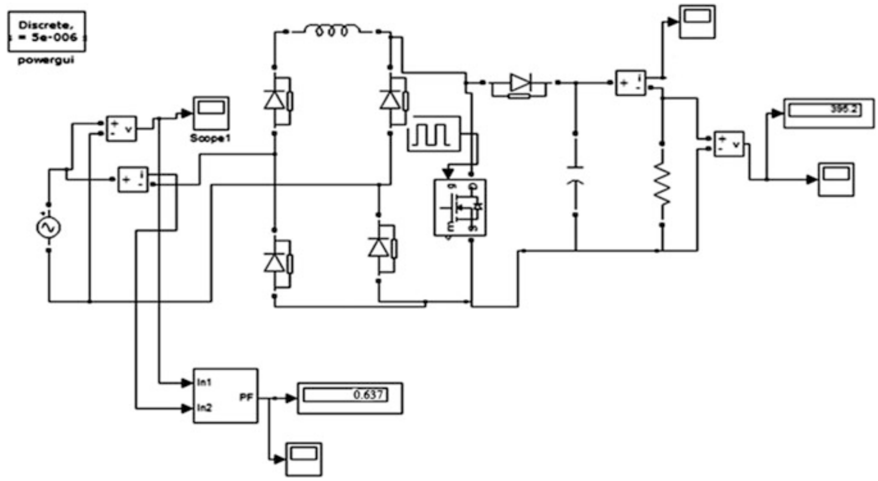

Fig. 4.5 Simulation circuit of conventional bridge PFC boost converter

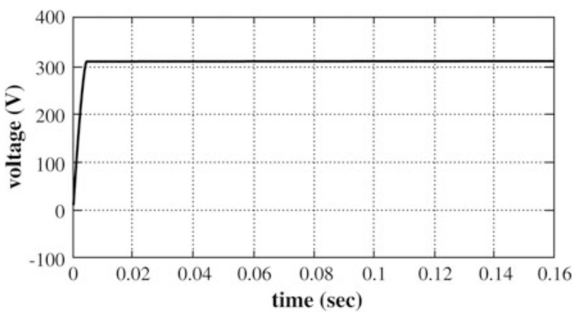

Fig. 4.6 Output voltage waveform of conventional bridge PFC boost converter

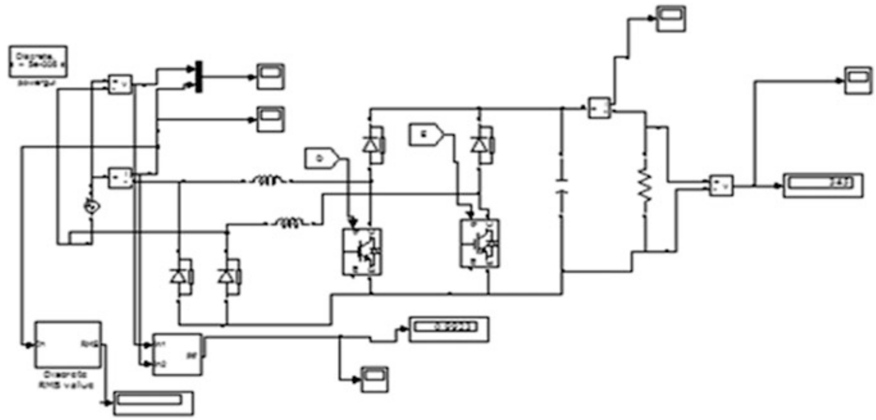

Fig. 4.7 Simulation circuit of conventional bridgeless PFC boost converter

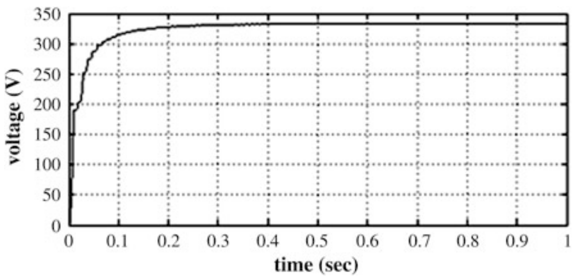

Fig. 4.8 Output voltage waveform of conventional bridgeless PFC boost converter

4.7 Simulation Results of Feed-Forward Bridgeless Boost Converter

Circuit diagram of proposed converter by using MATLAB/SIMULINK is shown in Fig. 4.9. Conventional PFC Boost converter gives less power factor but the proposed converter gives unity power factor. Switching pulses produced by feed forward and feed-back loop is shown in Fig. 4.10.

Figure 4.11 shows input voltage and current waveform of proposed Bridgeless PFC Boost converter. In this, line voltage is 250 V. This waveform shows that input supply voltage and current are in phase. So the power factor at the supply side is unity. Output voltage of the converter obtained is 645 V which is shown in Fig. 4.12.

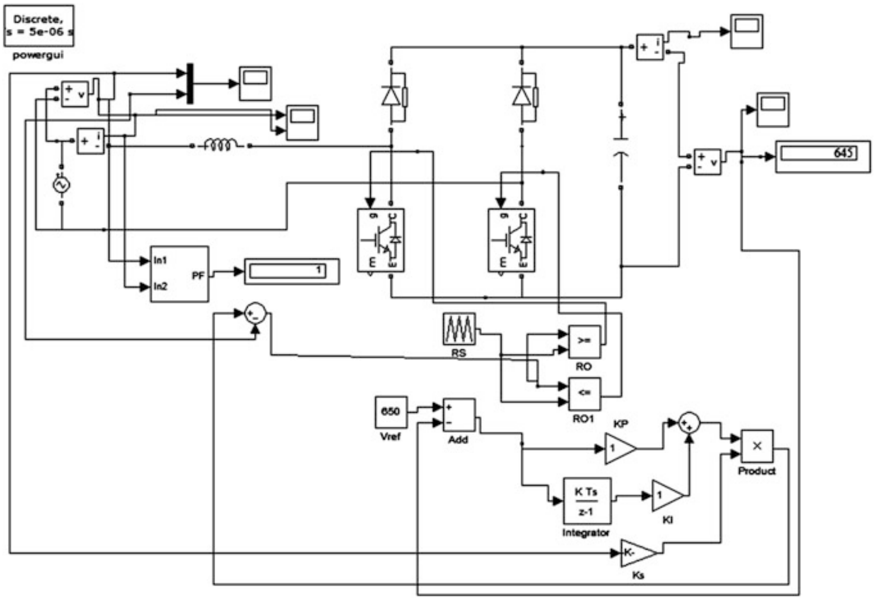

Fig. 4.9 Simulation circuit of proposed bridgeless PFC boost converter

Fig. 4.10 Switching pulses of MOSFETs

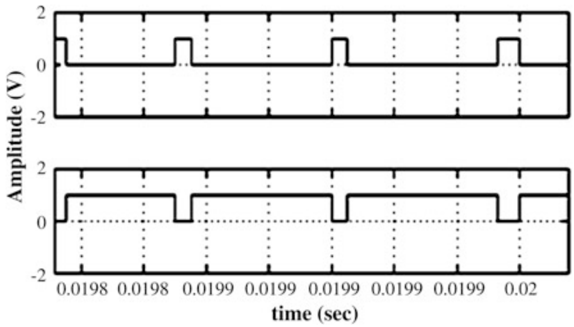

Fig. 4.11 Unity power factor at the supply

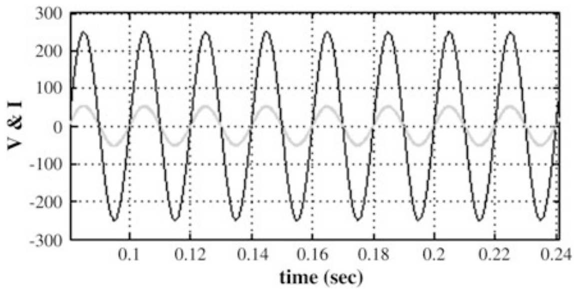

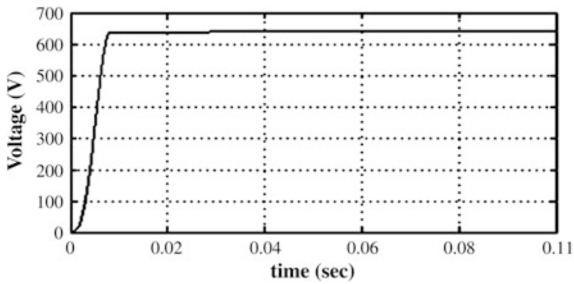

Fig. 4.12 DC output voltage waveform

4.8 Conclusions

A feed-forward and feedback controlled Bridgeless PFC Boost converter is presented and simulated by using MATLAB/SIMULINK. Compared to the Conventional Bridge and Bridgeless PFC Boost converters, proposed feed forward and feed-back controlled Bridgeless PFC Boost converter gives high dc output voltage and also it gives unity power factor at the supply side. So the efficiency and performance of the proposed closed loop controlled Bridgeless PFC Boost converter has greatly increased.

References

1. Martinez R, Enjeti PN (1996) A high performance single phase AC to DC rectifier with input power factor correction. IEEE Trans Power Electron 11(2):311–317
2. Lim J-W, Kwon B-H (1999) A power-factor controller for single-phase PWM rectifiers. IEEE Trans Ind Electron 46(5):1035–1037
3. Maswood AI, Liu F (2011) A unity power factor front and rectifier with hysteresis current control. IEEE Trans Energy Convers 21(1):153–160
4. Martinez R, Enjeti PN (1996) A high-performance single-phase rectifier with input power factor correction. IEEE Trans Power Electron 11(2):311–317
5. Anita U, Boini SK (2012) AC to DC conversion using active PFC. Proc Int J Mod Eng Res 2 (6):4220–4223
6. Huber L, Jang Y, Jovanovic MM (2008) Performance evaluation of bridgeless PFC boost rectifiers. IEEE Trans Power Electron 23(3):1381–1390
7. Prasuna PV, Rama Rao JVG, Lakshmi ChM (2013) Improvement in power factor and THD using dual boost converter. Int J Eng Res Appl 2:2368–2376
8. Park S, Choi S (2010) Soft- switched CCM boost converters with high power application. IEEE Trans Power Electron 25(5):1296–1309
9. Gopinath M (2011) Bridgeless PFC converter for power factor correction. Int J Adv Eng Sci Technol 9:1049–1054
10. Jaya Kumar MS, Ajeesh G (2012) A high efficient high input power factor interleaved boost converter. Proc Int J Electr Comput Eng 2(3):339–344
11. Souza AF, Barbi I (1999) A new ZVS semi-resonant high power factor rectifier with reduced conduction losses. IEEE Trans Ind Electron 46(1):82–90

12. Souza AF, Barbi I (1995) A new ZVS-PWM unity power factor rectifier with reduced conduction losses. IEEE Trans Power Electron 10(6):746–752
13. Kin I-D, Choi S-H, Nho E-C, Ahn J-W (2007) A simple ZVT PWM single-phase rectifier with reduced conduction loss and unity power factor. Proc J Power Electron 7(1)
14. Pahlevaninezhad M, Das P, Drobnik J, Jain PK, Bakhshai A (2012) A ZVS interleaved boost AC/DC converter used in plug-in electric vehicles. IEEE Trans Power Electron 27 (8):3513–3529

Chapter 5
Modeling and Simulation of Three-Phase DCMLI Using SVPWM for Photovoltaic System

M. Valan Rajkumar and P.S. Manoharan

Abstract A control of an eleven-level diode-clamped multilevel inverter (DCMLI) for photovoltaic (PV) systems is proposed in this paper. The fuzzy logic MPPT is used to track the maximum power. Space vector pulse width modulation (SVPWM) algorithm is used to control the DCMLI. In addition, this algorithm is used to determine to achieve low total harmonic distortion (THD). The proposed theory is validated by the simulation results. The operation and performance of the proposed multilevel inverter are evaluated using MATLAB/Simulink and compared with seven-level and nine-level DCMLI.

Keywords Space vector pulse width modulation (SVPWM) · Diode-clamped multilevel inverter (DCMLI) · Total harmonic distortion (THD)

5.1 Introduction

Applications of the photovoltaic as renewable distributed generations provide evidence the importance to study the photovoltaic systems, which consist of solar cells and inverter [1]. Different types of multilevel inverter topologies and PWM algorithms are presented [2, 3]. A novel simplified multilevel space vector modulation scheme based on two-level inverter [4] and produces three dodecagonal voltage space vectors is presented [5].

In a PV system, different controller scheme is used to maintain the sinusoidal output with various climate conditions [6]. Simulation and experimental investigation of SVPWM technique on a multilevel voltage source inverter for PV system

M. Valan Rajkumar (✉)
SSM Institute of Engineering and Technology, Dindigul, India
e-mail: valanrajkumar@gmail.com

P.S. Manoharan
Thiagarajar College of Engineering, Madurai 625015, India
e-mail: psmeee@tce.edu

C. Kamalakannan et al. (eds.), *Power Electronics and Renewable Energy Systems*,
Lecture Notes in Electrical Engineering 326, DOI 10.1007/978-81-322-2119-7_5

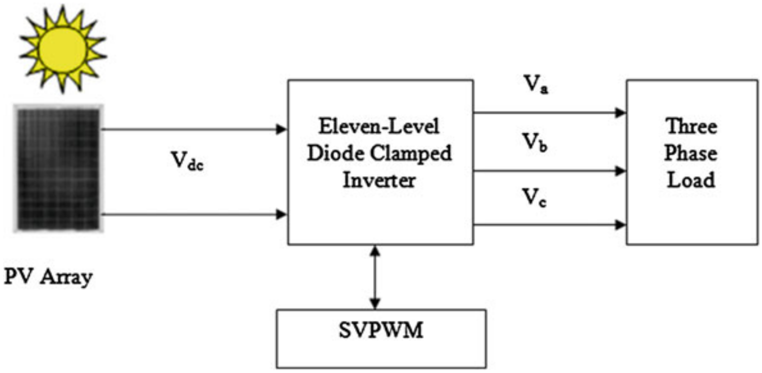

Fig. 5.1 General diagram of proposed system

is discussed in [7]. The modeling and simulation of three-phase five-level DCMLI using SPWM for grid connected photovoltaic system with fuzzy MPPT in [8, 9]. The THD minimization of the output voltage of multilevel inverters is discussed [10, 11].

This paper focuses the control structure of the proposed system is composed of MPPT control and inverter control. These structures are used to control DC bus voltage, to convert DC input to AC output waveforms (Fig. 5.1).

5.2 Solar Array Mathematical Formulation

The equivalent circuit of PV array (KC200GT) is shown in Fig. 5.2. The PV array mathematical model is given as [12],

$$I = IPhoto - IRSat\{\exp\,[\frac{q}{AD\,KB\,T}(V + IRSe)] - 1\} - \frac{V + RSe\,I}{RP} \tag{5.1}$$

$$\text{where,}\quad IPhoto\,(Gira) = ISC(\frac{Gira}{Giras}) \tag{5.2}$$

$$ISC(T) = ISCSat[1 + \Delta ISC(T - TSt)] \tag{5.3}$$

The solar cell temperature and irradiation can be expressed as

$$IPhoto\,(Gira,\,T) = ISCSat(\frac{Gira}{Giras})[1 + \Delta ISC\,(T - TSt)\,] \tag{5.4}$$

$$IRSat\,(Gira,\,T) = \frac{IPhoto\,(Gira,\,T)}{e^{(\frac{VOC}{Vt})} - 1} \tag{5.5}$$

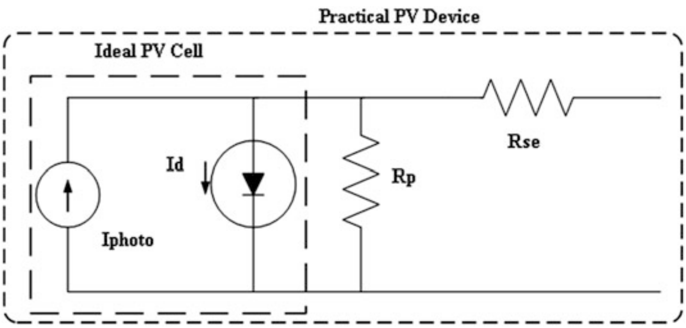

Fig. 5.2 Equivalent circuit of a PV cell physical model

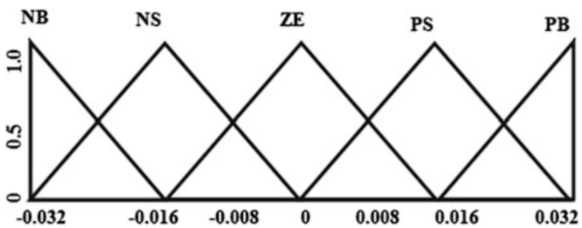

Fig. 5.3 Fuzzy input and output membership function

5.3 Methodology

Fuzzy MPPT control is used to control a switch of the DCMLI [7]. FLC depends on the membership function and rule base [7]. The value of input error and change in error are normalized by an input scaling factor is shown in Fig. 5.3.

5.4 MATLAB/Simulink Results

In the proposed system, SVPWM algorithm is used to control the inverter based on [7]. The SVPWM output is generated from this simulink module. The simulation was carried out for 0.2 s and sampling frequency f_s = 10 kHz. FLC controlled MPPT tracks the maximum operating point quickly and accurately with and without change irradiance level. In the proposed system, the output line-to-line voltage of the three-phase seven-level, nine-level and an eleven-level DCMLI is shown in Fig. 5.4. This shows that the generated line-to-line voltage is much improved with the level of inverter. The performance of the FLC with the three-phase an eleven-level DCMLI also shows the output of PV follows its reference and there are no effects for the load variation. This proves that the proposed scheme can reduce the THD which is an indispensable condition for PV system.

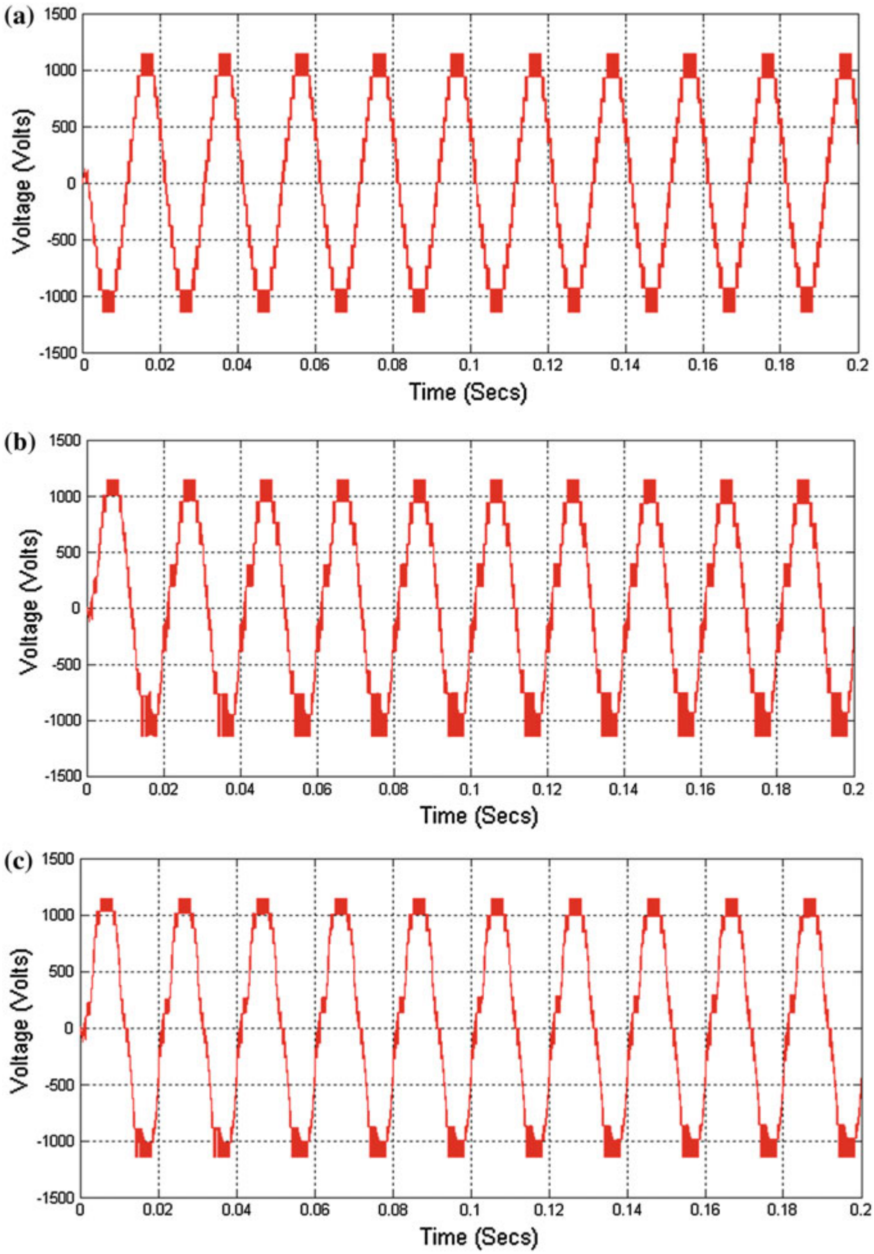

Fig. 5.4 Simulation result of a three-phase line-to-line (V_{ab}) voltage of DCMLI **a** seven-level, **b** nine-level and **c** eleven-level

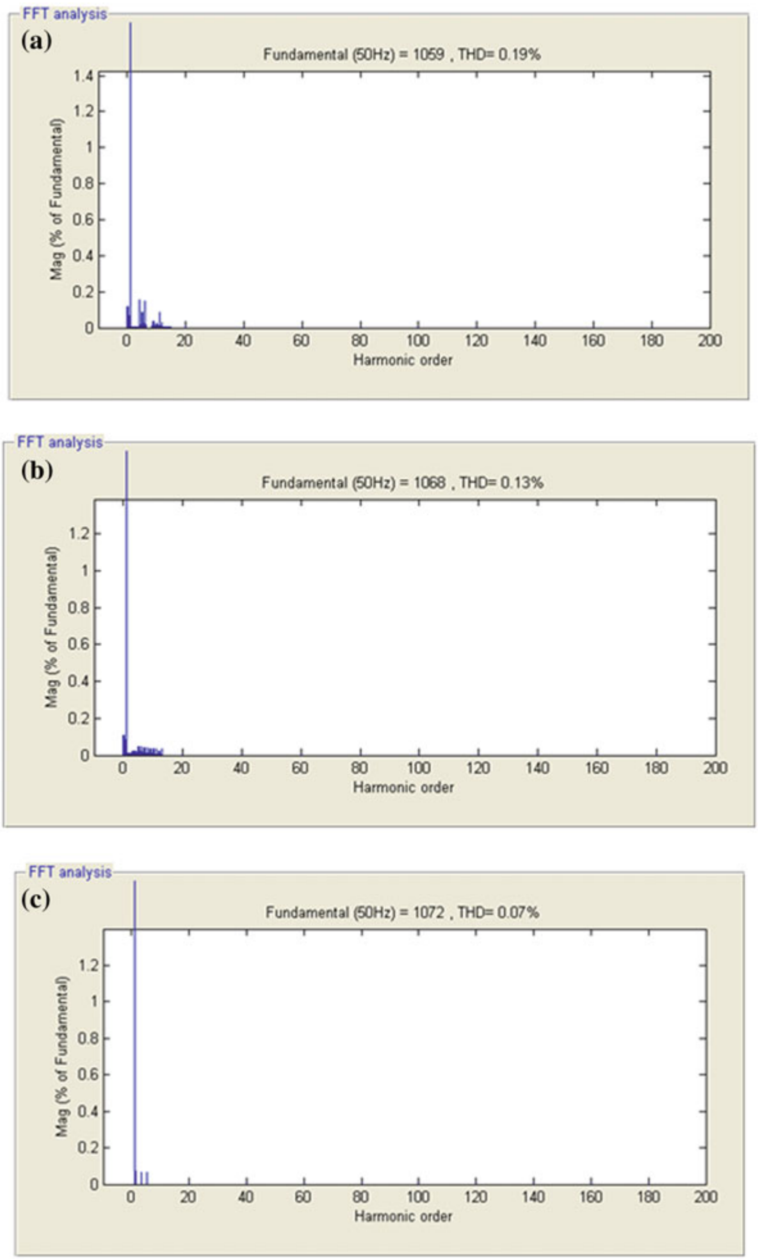

Fig. 5.5 THD measurement for DCMLI **a** seven-level, **b** nine-level and **c** eleven-level

Table 5.1 Comparison between THD for proposed system with SVPWM

No. of levels	Proposed SVPWM (%)
7	0.19
9	0.13
11	0.07

According to the standard Std IEEE-929-2000, the THD of inverters output voltage waveforms must be less than 5 %. The THD of seven-level, nine-level and an eleven-level DCMLI is shown in Fig. 5.5. The THD measurement of SVPWM seven-level and nine-level are 0.19 and 0.13 %. From the results it is observed that the generated voltage spectrum is very much increased with the level of inverter. The THD measurement of the proposed SVPWM an eleven-level inverter is 0.07 %. The THD levels of proposed SVPWM three-phase seven-level, nine-level and eleven-level inverters are compared in Table 5.1. This proves that the proposed scheme can reduce the THD.

5.5 Conclusion

This paper presents multilevel operation of DCMLI using SVPWM for PV systems. This paper investigates the use of SVPWM of a three-phase DCMLI for photovoltaic systems and improves the quality of output voltage. FLC can provide more efficient than the conventional controller for nonlinear systems. It is seen from the results revels that to minimize the overall THD of the output voltage of a multilevel inverter. Reduction of THD of the proposed topology in comparison other topology is another advantage of the proposed inverter for PV systems.

References

1. Villalva MG, Gazoli JR, Filho ER (2009) Comprehensive approach to modelling and simulation of photovoltaic arrays. IEEE Trans Power Electron 24:1198–1208
2. Rodriguez J, Lai J-S, Peng FZ (2002) Multilevel inverters: a survey of topologies, controls, and applications. IEEE Trans Ind lectron 49:724–738
3. Colak I, Kabalci E, Bayindir R (2011) Review of multilevel voltage source inverter topologies and control schemes. Energy Convers Manage 52:1114–1128
4. Wu FJ, Zhao K, Sun L (2012) Simplified multilevel space vector pulse-width modulation scheme based on two-level space vector pulse-width modulation. IET Power Electron 5:609–616
5. Mathew K, Mathew J, Azeez NA, Dey A, Umanand L, Gopakumar K (2012) Multilevel dodecagonal space-vector generation for induction motor drives by cascading three-level and two-level inverters. IET Power Electron 5:1324–1332

6. Selvaraj J, Rahim NA (2009) Multilevel inverter for grid-connected PV system employing digital PI controller. IEEE Trans Ind Electron 56:149–158
7. Valan Rajkumar M, Manoharan PS, Ravi A (2013) Simulation and an experimental investigation of SVPWM technique on a multilevel voltage source inverter for photovoltaic system. Electr Power Energy Syst 52:116–131
8. Ravi A, Manoharan PS, Vijay Anand J (2011) Modeling and simulation of three phase multilevel inverter for grid connected photovoltaic systems. Sol Energy 85:2811–2818
9. Valan Rajkumar M, Manoharan PS (2013) Modeling and simulation of five-level five-phase voltage source inverter for photovoltaic system. Przeglad Elektrotechniczny 2013 (10):237–241
10. Yousefpoor N, Fathi SH, Farokhnia N, Abvaneh HA (2012) THD minimization applied directly on the line-to-line voltage of multilevel inverters. IEEE Trans Ind Electron 59:373–380
11. Valan Rajkumar M, Manoharan PS (2013) Harmonic reduction of fuzzy PI controller based three-phase seven-level DCMLI with SVPWM for grid connected photovoltaic system. Int Rev Model Simul 6:684–692
12. Valan Rajkumar M, Manoharan PS (2013) FPGA based multilevel inverters with SVPWM algorithm for photovoltaic system. Sol Energy 87:229–245

Chapter 6
Quantification of Voltage Unbalance Conditions

Abhishek Chauhan, Padhmanabh Thakur and D. Raveendhra

Abstract This paper confers the various effects of voltage unbalance on the performance of three-phase induction motor (3-Φ IM). The need of quantification of the voltage unbalance conditions is asserted to make precise and unique assessment of the performance 3-Φ IM. Further, the slip of 3-Φ IM is evaluated under different conditions and values of degree of voltage unbalance. It is revealed that the slip is not affected with the change in degree while change of the conditions of voltage unbalance greatly affects its value. Hence, slip can be considered as suitable index for the quantification of the various conditions of supply voltage unbalance. Additionally, the variations of performance parameters of 3-Φ IM, viz., efficiency, input power, power factor, copper loss, etc., with respect to slip are investigated. It is found that, these performance parameters are not only dependent on the degree of voltage unbalance but the information of slip is also required for accurate and inimitable assessment of these performance parameters.

Keywords Induction motor · Power quality · Voltage unbalance · P.F.

6.1 Introduction

The worsening of power quality (PQ) is the foremost concern when stress is on the power system restructuring. The voltage unbalance (VU) in supply is one of the prominent causes of worsening of PQ that result in the variations of the machine parameters associated with the power system networks. Although, three-phase (3-Φ) power systems are usually designed for the balance magnitude and phase, but

A. Chauhan (✉) · P. Thakur · D. Raveendhra
Graphic Era University, Dehradun, India
e-mail: mtechabhi1990@gmail.com

C. Kamalakannan et al. (eds.), *Power Electronics and Renewable Energy Systems*,
Lecture Notes in Electrical Engineering 326, DOI 10.1007/978-81-322-2119-7_6

uneven distribution of single phase loads, incomplete transposition of transmission lines, single-phase tractions, blown fuses on 3-Φ capacitor banks, and open delta transformer connections in the distribution system results unbalance in supply voltage [1].

The 3-Φ IMs are considered as the most preferred machine for the industrial applications, due to its ruggedness and relatively low operating cost, but it is found as very sensitive to voltage unbalance (VU), simultaneously. The adverse effects of VU on the performance of 3-Φ IM were discussed in numerous studies [2–7]. The strange consequence of VU as reduction of efficiency [2], increase of winding temperature and shortening of machine operational life [3–5], de-rating in the machine [6] increase in loss and faster aging of the insulation system [7], have been discussed in these studies. However, the degree and conditions of VU and resulting motor characteristics have been ignored, and qualitative results of the effects of VU were discussed in these studies [8]. Further, the various conditions and degree of VU have been incorporated in [9], to reveal the negative consequence of VU on the performance of 3-Φ IM. Considering IEC defined VU index [10], namely, voltage unbalance factor (*VUF*), it has been shown that the degree of VU, i.e., voltage unbalance factor (*VUF*), is not sufficient to evaluate the performance parameters of 3-Φ IM but conditions of VU are required, also. In this paper, positive sequence voltage has been considered to define the condition of VU. But this study suffers from two major drawbacks. First, the angle of *VUF*, necessary for the accurate prediction of peak copper and stator loss, has not been considered. Second, the most basic characteristic, namely, slip (‘s’), responsible for the change in the performance parameters of 3-Φ IM under VU condition, has been ignored. Additional efforts toward the precise and complete assessment of the performance of 3-Φ IM under unbalance condition have been made in [11–13]. These studies assert the need to include the condition or nature of VU along with its degree. But the basic cause of inclusion of condition along with degree of VU has not been discussed.

For the better understanding of the event and to apply proper mitigation scheme, protection scheme, and in reducing the cost of downtime associated with it, the knowledge of the basic cause of inclusion of condition or nature of unbalance, is an essential requirement. Further, to extract the precise and relevant information about the condition of VU its quantification is also required. However, the index for the quantification of degree of VU, namely, *VUF*, *PVUR*, *LVUR*, etc., has been defined in various standards [10, 14, 15], but these standards do not provide definition for the quantification of VU.

In this paper, it is shown that the ‘s’ of 3-Φ IM is suitable parameter to quantify the condition of VU. It is revealed that the value of ‘s’ changes with change in condition of VU while it is unaffected due to change of degree of VU. Additionally, it is shown that the knowledge of degree of VU, namely, *VUF*, along with knowledge of VU condition, namely, ‘s’, makes the assessment of the performance parameters accurate and unique.

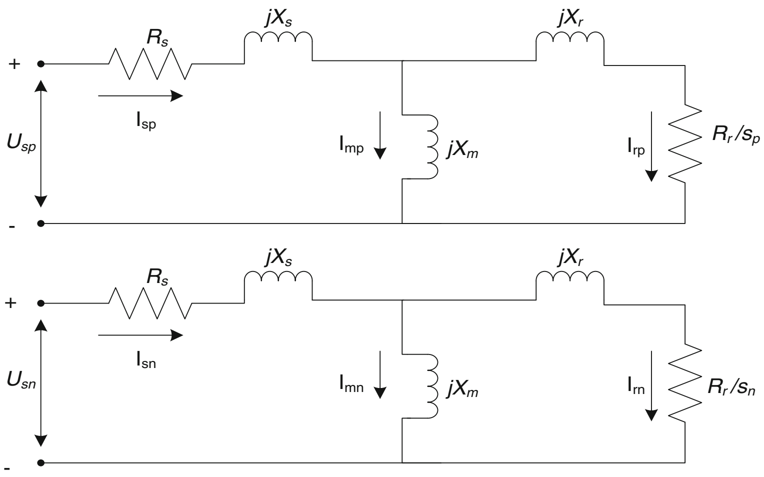

Fig. 6.1 Sequence equivalent circuit of three-phase induction motor

6.2 Symmetrical Component Theory

Three unsymmetrical and unbalanced phasors of three-phase systems can be resolved into positive, negative and zero sequence component set of balanced phasors. The effects of the zero sequence components are neglected in this study, as the 3-Φ IM is either ungrounded wye (Y) or delta (Δ) connected. Positive and negative sequence equivalent circuits of 3-Φ IM are shown in Fig. 6.1. Equivalent circuit has R_s and R_r as the stator and rotor resistance, X_m, X_s and X_r are the magnetizing reactance, stator and rotor reactance respectively, I_{sp} and I_{sn} represent stator positive and negative sequence current, I_{rp} and I_{rn} represent the rotor positive and negative-sequence currents and U_{sp} and U_{sn} are the positive and negative sequence component of voltage for stator.

It is assumed that all the circuit elements are constant, mechanical and stray losses are neglected, and the motor is Δ-connected. In this condition, U_{sp} and U_{sn} run the 3-Φ IM with forward (s_p) and backward (s_n) slip, respectively as there is no zero sequence network. The expressions for torque, power factor (p.f.), output power, efficiency, stator/rotor copper loss, sequence current, etc., in unbalance condition were discussed and derived in numerous studies [11, 12]. In this paper, these expressions are directly adopted to analyze the behavior of 3-Φ IM under the various conditions and degree of VU.

6.3 Quantification of Condition of Voltage Unbalance

In this section the performance parameter, specially, ‘s’ of 3-Φ IM, is determined under various condition and degree of VU. It is reveal that the ‘s’ of 3-Φ IM changes due to change of unbalance condition, only. The change of degree of VU, i.e., *VUF*, does not affect the value of ‘s’, if the condition of unbalance is fixed. Here, $U_{sp} < 1$, and $U_{sp} > 1$, considered as under- and over-voltage condition [9], respectively. Two types of 3-Φ IMs and various conditions and degree of VU are considered to reveal the dependence of ‘s’ of 3-Φ IM on the condition of VU. The ratings of 3-Φ IMs are considered as follows:

- Motor-I ratings [12, 13]: 240 V (line-to-line), 7.5 kW, 60 Hz, six poles, Δ-connected. The resistance and reactance of its equivalent circuit in ohms per phase referred to the stator are: $R_s = 0.294\ \Omega$, $X_s = 0.503\ \Omega$, $R_r = 0.144\ \Omega$, $X_r = 0.209\ \Omega$, $X_m = 13.25\ \Omega$.
- Motor-II ratings [16]: 460 V (line-to-line), 18.64 kW, 60 Hz, six poles, Δ-connected. The resistance and reactance of its equivalent circuit in ohms per phase referred to the stator are: $R_s = 0.641\ \Omega$, $X_s = 1.106\ \Omega$, $R_r = 0.332\ \Omega$, $X_r = 0.464\ \Omega$, $X_m = 26.3\ \Omega$.

Considering basic circuit of sequence networks of 3-Φ IM, as shown in Fig. 6.1, the values of ‘s’ are evaluated under various conditions and degree of voltage unbalance and are shown in Fig. 6.2. Here, two values of *VUF* (K_v), 3 and 5 % are considered.

The following observations are extracted from Fig. 6.2:

- The value of ‘s’, for both of 3-Φ IMs, changes only due to change in conditions of unbalance, i.e., U_{sp}. It is not affected due to the change of K_v. An upper curve represents the values of ‘s’, under different conditions of VU, for VUF equals to 3 and 5 %, for Motor-I, while lower curve is same for Motor-II.
- In under-voltage condition, i.e., $U_{sp} < 1$, ‘s’ is more than the values of ‘s’ in over-voltage conditions, i.e., $U_{sp} > 1$. The ranges of ‘s’ in over- and under-voltage

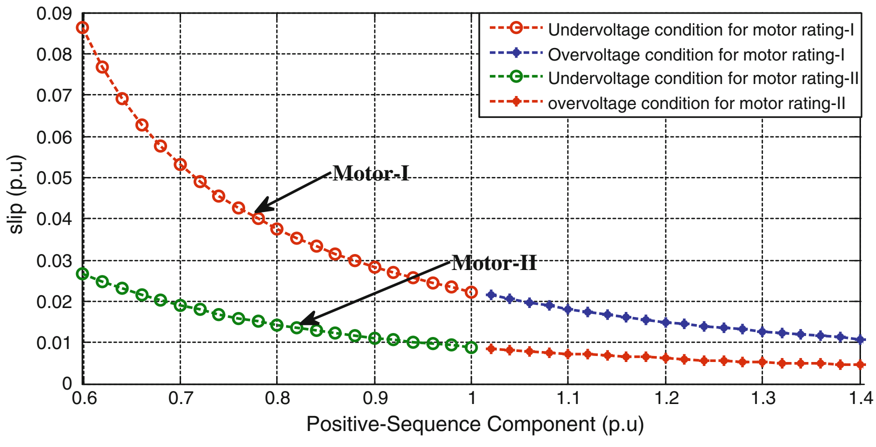

Fig. 6.2 Change in slip (‘s’) with positive- sequence component of voltage for a *VUF* (K_v) of 3 and 5 %

conditions depend on the rating of the 3-Φ IM. For example, ranges of 's' in under-voltage conditions, for Motor-I, are 0.02–0.09, whereas same, for Motor II, are 0.01–0.03, respectively.

From these observations, it can be concluded that the value 's' of 3-Φ IM gives the reflection of the conditions of VU. Hence, it can be considered as a suitable index to quantify the conditions of VU. In the following sections, it is shown that the simultaneous knowledge of 's' and *VUF*, only, makes the assessment of performance parameters accurate and unique. Therefore, to make assessment precise, the need of inclusion of 's' along with *VUF* is suggested in this study.

6.4 Assessment of Performance Parameters

6.4.1 Efficiency and Input Power

The downgrading in efficiency is reported in various literatures, when operation of 3-Φ IM is under unbalanced supply, hence, inclusion of preciseness in the assessment of efficiency gain tremendous popularity. From the basic of sequence network, as shown in Fig. 6.1, the values of efficiency (η) and input power (P_{in}) are evaluated under various conditions and degree of VU, for Motor-I, and are shown in Figs. 6.3 and 6.4. The following results are extracted after analysis of Figs. 6.3 and 6.4:

- The accurate values of η depend on degree as well as the conditions of VU. The knowledge of either VUF or 's', only, is not sufficient to estimate its value accurately. For example, for VUF equals to 3 %, the values of efficiency lies in range between 76 and 94 %. It is obvious that the value of η can be determined

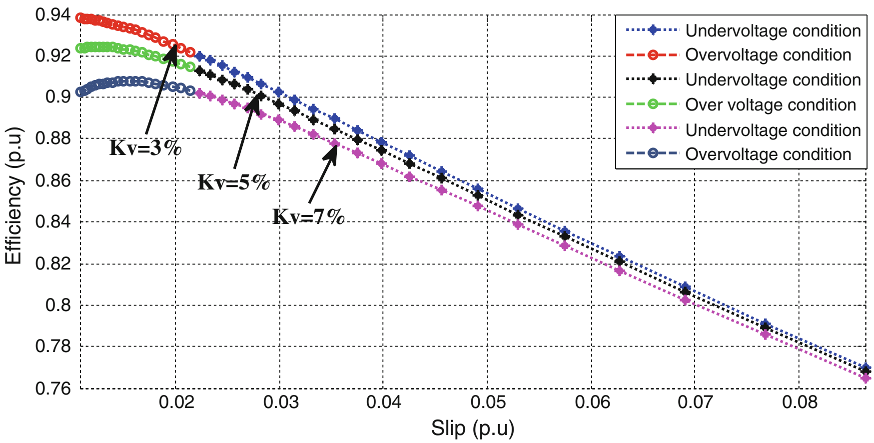

Fig. 6.3 Variation of efficiency with change in 's'

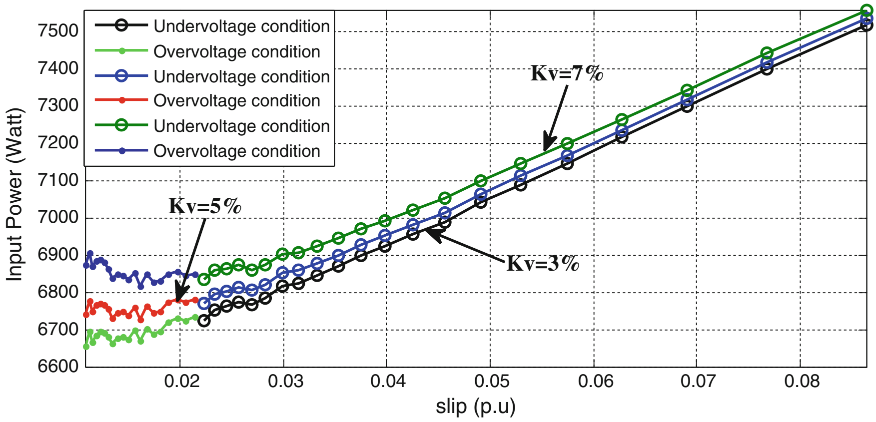

Fig. 6.4 Variation of input power with change in 's'

accurately and unique only when the information of, 's' and K_v, are available simultaneously. The similar observation can be made for P_{in} from Fig. 6.4.

- The motor efficiency is higher in over-voltage than under-voltage condition for fixed value of K_v. This observation is in tune with [9]. The similar observation can be made for speed, i.e., higher speed in over-voltage than under-voltage condition.
- The input power is lower in over-voltage than under-voltage conditions. Further, it can be seen that for fixed value of K_v, the exact value of P_{in} depends on 's'. Hence, unique and accurate value of P_{in} can be estimated only when information of both K_v and 's' are available.

6.4.2 Power Factor (p.f.)

The values of p.f. are estimated under different conditions and degree of VU and are shown in Fig. 6.5. From Fig. 6.5, the following observation can be highlighted:

- The value p.f. is slightly affected with change of degree of unbalance (K_v) but change of conditions ('s') greatly affects its value. Hence, the 's', alone, is sufficient to estimate its value, accurately. However, more precise estimation is possible only when information of K_v and 's' are available, simultaneously.
- The value of p.f. is lower in over-voltage than under-voltage conditions. As the intensity of under-voltage conditions increases, the value p.f. increased, further.

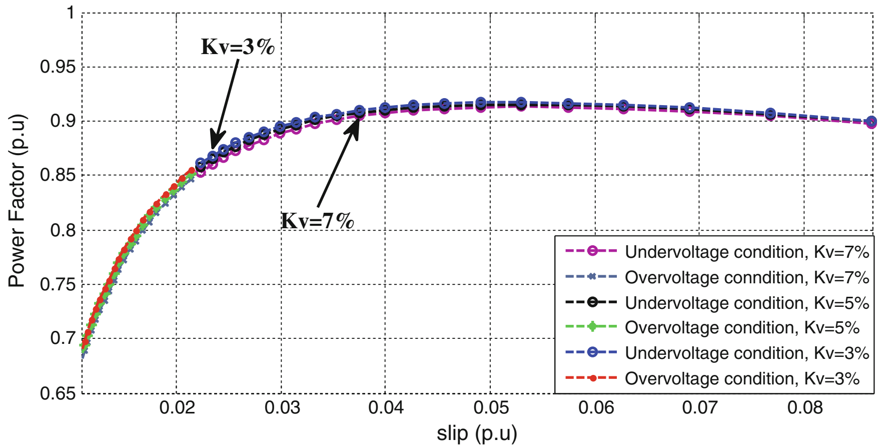

Fig. 6.5 Variation of power factor with change in ‘s’

6.4.3 Stator and Rotor Copper Losses

The values of stator and rotor copper losses are estimated under various conditions and degree of voltage unbalance and are shown in Figs. 6.6 and 6.7.

From Figs. 6.6 and 6.7, the following observations are highlighted:

- The value of stator and rotor copper loss depends on the ‘s’ as well as K_v. For fixed value of K_v (e.g., 7 %), the value of stator copper loss lies between 500 and 1,200 W, whereas rotor copper loss lies between 190 and 570 W. Hence, accurate and unique value of these losses can be estimated only when, the

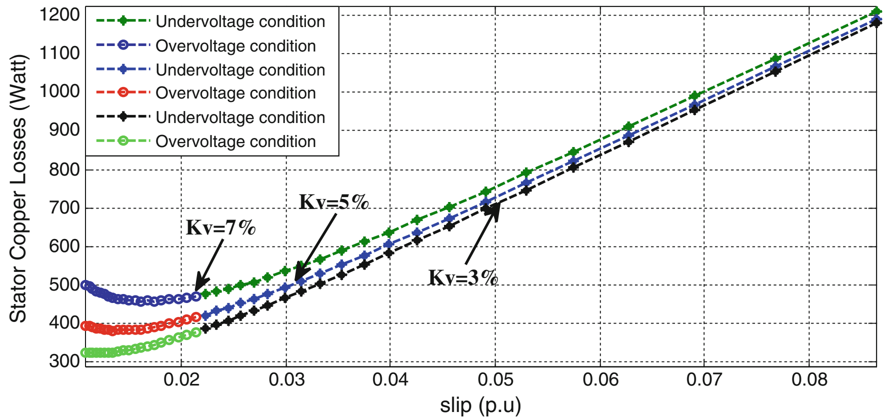

Fig. 6.6 Variation of stator copper loss with change in ‘s’

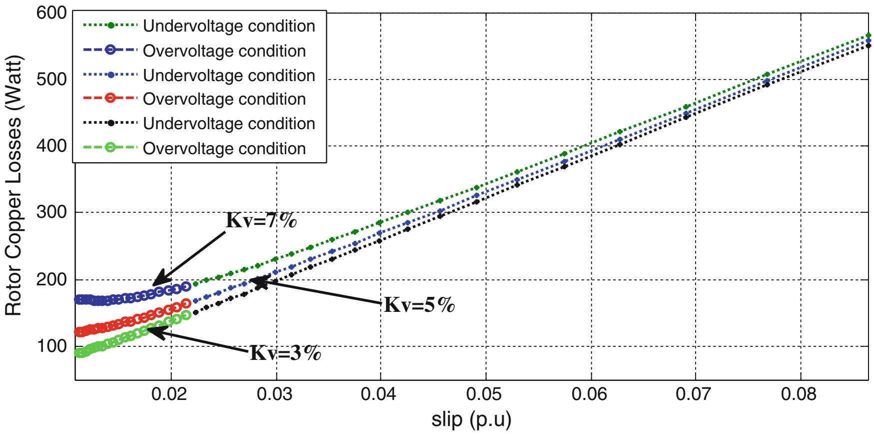

Fig. 6.7 Variation of rotor copper loss with change in ‘s’

information of degree (K_v) and condition (‘s’) of VU are available, simultaneously.

- The values of these losses are lower in over-voltage than under-voltage condition if degree of VU is fixed.
- For fixed condition of voltage unbalance, these losses increase with increase of degree of voltage unbalance.

6.5 Conclusion

This paper highlights the impact of unbalance supply on the performance of 3-Φ IM. The need of quantification of voltage unbalance condition has been asserted. It is shown that the information of degree (K_v) and condition of unbalance, are essential to make complete and accurate assessment. Further, it has been shown that the “s’ of 3-Φ IM’ is the important parameter which can be used as index for quantification of the conditions of voltage unbalance. Additionally performance parameters of 3-Φ IM are evaluated for various condition (‘s’) and degree of voltage unbalance (K_v). The major highlights of the assessment are as follows:

- The efficiency is higher in over-voltage than under-voltage condition for the fixed degree of voltage unbalance. Further, it is shown that, for fixed condition of voltage unbalance, efficiency decreases with increasing of degree of voltage unbalance.
- Stator and rotor copper losses are smaller in over-voltage than under-voltage condition, if degree of voltage unbalance is kept constant. For fixed condition of voltage unbalance, these losses increase with increase of degree of voltage unbalanced.

- The effect of the degree of voltage unbalance is negligible small on the p.f. of 3-Φ IM while it is greatly affected from the condition of voltage unbalance. The p. f. is found as lower in over-voltage than under-voltage condition for any degree of voltage unbalance.

References

1. Jouanne AV, Banerjee B (2001) Assessment of voltage unbalance. IEEE Trans Power Deliv 16(4):782–790
2. Williams JW (1954) Operation of 3 phase induction motors on unbalanced voltages. AIEE Trans Power Appl Syst PAS-73:125–133
3. Gafford BN, Duesterhoeft WC, Mosher CC (1959) Heating of induction motors on unbalanced voltages. AIEE Trans Power Apparatus Syst PAS-78(III-A):282–297
4. Oraee H (2000) A quantative approach to estimate the life expectancy of motor insulation systems. IEEE Trans Dielectr Electr Insul 7(6):790–796
5. Cummins PB, Dunki-Jacobs JR, Kerr RH (1985) Protection of induction motors against unbalanced voltage operation. IEEE Trans Ind Appl IA-21(4):778–792
6. Schmitz NL, Berndt MM (1963) Derating poly-phase induction motors operated with unbalanced line voltages. IEEE Trans Power Appl Syst 680–686
7. Woll RF (1975) Effect of unbalanced voltage on the operation of poly-phase induction motors. IEEE Trans Ind Appl IA-11:38–42
8. Faiz J, Ebrahimpour H, Pillay P (2004) Influence of unbalanced voltage on the steady-state performance of a three-phase squirrel-cage induction motor. IEEE Trans Energy Convers 19 (4):657–662
9. Lee CY (1999) Effects of unbalanced voltage on the operation performance of a three-phase induction motor. IEEE Trans Energy Convers 14(2):202–208
10. Testing and measurement techniques—unbalance, immunity test, IEC Standard 61000-4-27, Aug 2000
11. Singh SB, Singh AK, Thakur P (2012) Assessment of induction motor performance under voltage unbalance condition. In: Proceedings of harmonics and quality of power conference, Hong Kong, 17–20 Jun 2012, pp 256–261
12. Anwari M, Hiendro A (2010) New unbalance factor for estimating performance of a three-phase induction motor with under and overvoltage unbalance. IEEE Trans Energy Convers 25 (3):619–625
13. Wang YJ (2001) Analysis of effects of three-phase voltage unbalance on induction motors with emphasis on the angle of the complex voltage unbalance factor. IEEE Trans Energy Convers 16(3):270–275
14. Motors and generators, ANSI/NEMA Standard MG1-1993
15. IEEE standard test procedure for polyphase induction motors and generators, IEEE Standard 112, 1991
16. (2005) Energy matters industrial technology program: the effects of unbalanced voltage on the life and efficiency of three-phase electric motors. U.S Department of Energy and Renewable Energy, Mar 2005

Chapter 7
Short-Term Hydrothermal Scheduling of an Indian Utility System Using an Enhanced Bacterial Foraging Algorithm

S. Padmini, R. Jegatheesan, Subhransu Sekhar Dash and S. Hemanth

Abstract The Short-Term Hydrothermal Scheduling (STHTS) problem is treated as a dynamic large scale optimization problem. The Bacteria Foraging Algorithm (BFA) is a recently developed evolutionary optimization technique which is based on the foraging behavior of the *E. coli* bacteria. The BFA has been successfully implemented to solve various optimization problems. To solve STHTS problem, considering its high dimension search space, some critical improvements are introduced into the basic BFA to improve convergence. Here the chemotactic step is modified, so that better exploration of the search space can be obtained. An Enhanced Bacteria Foraging Algorithm (EBHA) is presented to solve the short term hydrothermal coordination problem. The developed algorithm is illustrated for a test system consisting of four hydro and seven thermal plants of an Indian Utility system. It is found that convergence characteristic is excellent and the result obtained by the proposed method is better in terms of fuel cost.

Keywords Short-term hydrothermal scheduling · Bacteria foraging algorithm

7.1 Introduction

The optimal scheduling of an electric power system is the determination of the generation for every plant such that the total generation cost is minimum while satisfying the system constraints. However, due to insignificant operating of hydro

S. Padmini (✉) · R. Jegatheesan · S. Hemanth
SRM University, Chennai 603203, India
e-mail: padmini.s@ktr.srmuniv.ac.in

S.S. Dash
Department of Electrical and Electronics Engineering,
SRM University, Chennai 603203, India
e-mail: munu_dash_2k@yahoo.com

C. Kamalakannan et al. (eds.), *Power Electronics and Renewable Energy Systems*,
Lecture Notes in Electrical Engineering 326, DOI 10.1007/978-81-322-2119-7_7

plants the scheduling problem essentially reduces the fuel cost of the thermal plants. The generation of hydro plants reduces the power demand, which must be fulfilled by the thermal power plants. The electrical output depends on the water discharge, the head and efficiency of the hydro plants. The efficiency itself is a function of the water discharge and head.

STHTS problem is to determine the optimal generation level for each thermal and hydro plant to meet the total load demand over a scheduling period. This is to determine, optimally, which of the committed thermal generating units should run and how much power is generated by the hydro and thermal plants, so as the total operating cost is minimized. Hydraulic and thermal constraints may include load balance, generation limits, water discharge, starting and ending storage volume of water and spillage discharge rate [1]. The STHTS problem has been solved by various methods. The method reported in the literature includes classical methods such as Gradient descent method [1] and Lagrange Relaxation method [2]. The STHTS is a large-scale nonlinear and complicated constrained power system optimization problem which has been solved using calculus-based programming algorithms such as augmented lagrangian relaxation method [3], linear and non-linear programming [4, dynamic programming [4], interior point methods [5], bundle trust method [6] and mixed integer programming [7]. Various stochastic search algorithms such as Simulated annealing (SA) [8, 9], Genetic algorithm (GA) [10], Evolutionary Programming (EP) [11–13] and Particle Swarm Optimization (PSO) [14–17] have been implemented for the solution of hydrothermal scheduling problem.

Bacterial foraging algorithm is a recently introduced optimization technique inspired by the foraging behavior of the *E. coli* bacteria [18–21]. These techniques can generate solution within shorter calculation time and has more stable convergence characteristics. Many researches are still proving its potential in solving complex power system problems.

7.2 Problem Formulation

7.2.1 Objective Function

The STHTS problem is designed to determine the optimum loading of all thermal and hydro generation units to minimize the cost function.

$$\min(f) = \sum_{j=1}^{N} n_j f_j\left(PT_j\right) \tag{7.1}$$

subjected to power balance, discharge, steam and hydro demand constraints, volume storage constraints and reservoir limit constraints.

$$\left(P_{dj} + P_{Loss_j}\right) - \left(PH_j + PT_j\right) = 0 \tag{7.2}$$

$$PH_j = g\left(q_j\right) \tag{7.3}$$

$$q_{j\min} \le q_j \le q_{j\max} \tag{7.4}$$

$$PT_{j\min} \le PT_j \le PT_{j\max} \tag{7.5}$$

$$PH_{j\min} \le PH_j \le PH_{j\max} \tag{7.6}$$

$$Volume_{j+1} = Volume_j + n_j\left(r_j - q_j - s_j\right) \tag{7.7}$$

$$Volume_{j\min} \le Volume_j \le Volume_{j\max} \tag{7.8}$$

7.3 The Proposed BFA Algorithm

7.3.1 Bacteria Foraging Algorithm

The biological aspects of the bacterial foraging strategies and their motile behavior as well as their decision making mechanisms can be found in [18]. As a heuristic method, BFA is designed to tackle non-gradient optimization problems and to handle complex and non-differentiable objective functions. The BFA algorithm can be performed through three main operations, namely; chemotaxis, reproduction and elimination dispersal activities [18]. The chemotaxis process is performed through swimming and tumbling. The bacterium spends its lifetime alternating between these two modes of motion. In the BFA, a tumble is represented by a unit length in a random direction, $\phi(j)$, which specifies the direction of movement after a tumble. The size of the step taken in the random direction is represented by the constant run-length unit, $C(i, j)$. For a population of bacteria, the location of the bacterium at the jth chemotactic step, kth reproduction step and lth elimination/dispersal event is represented by $\theta^i(i,j,l) \in R^p$. At this location the cost function is denoted by $J(i,j,k,l)$, which is also known as the nutrient function. After a tumble, the location of the ith bacterium is represented by

$$\theta^i(j+1,k,l) = \theta^i(j,k,l) + C(i,j)\phi(j) \tag{7.9}$$

When at $\theta^i(j+1,k,l)$, the cost function $J(i,j+1,k,l)$ is better (lower) than $J(i,j,k,l)$, another step of size $C(i, j)$ in the same direction is taken. This swimming operation is repeated as long as a lower cost is obtained until a maximum preset number of steps, Ns, is reached.

This swarming is expressed as follows:

$$\begin{aligned} J_{cc}(\theta, P(j,k,l)) &= \sum_{i=1}^{s} J_{cc}(\theta, \theta^{i}(j,k,l)) \\ &= \sum_{i=1}^{s}\left[-d_{attract}\exp\left(-\omega_{attract}\sum_{m=1}^{p}(\theta_m-\theta_m^i)^2\right)\right] \\ &\quad+\sum_{i=1}^{s}\left[h_{repellant}\exp\left(-\omega_{repellant}\sum_{m=1}^{p}\left(\theta_m-\theta_m^i\right)^2\right)\right] \end{aligned} \tag{7.10}$$

where $d_{attract}$, $\omega_{attract}$, $h_{repellant}$ and $\omega_{repellant}$ are coefficients representing the characteristics of the attractant and repellant signals released by the cell and θ_m^i is the m^{tk} component of ith bacterium position.

The function (14) which represents the cell-to-cell signaling effect is added to the cost function.

$$J(i,j,k,l) + J_{cc}(\theta, P) \tag{7.11}$$

A reproduction process is performed after taking a maximum number of chemotactic steps, Nc. The population is halved so that the least healthy half bacteria dies and each bacterium in the other healthiest one splits into two bacteria that take the same position. After Nre reproduction steps an elimination/dispersal event takes place for Ned number of executions. In this operation each bacterium could be moved to explore other parts of the search space. The probability for each bacterium to experience the elimination/dispersal event is determined by a predefined fraction P_{ed}.

7.3.2 Enhanced Bacterial Foraging Algorithm

The unit step length of the basic BFA is a constant parameter which may guarantee good searching results for small optimization problems. However, when applied to complex large scale problems with high dimensionality it shows poor performance. The run-length parameter is the key factor for controlling the local and global search ability of the BFA. From this perspective, balancing the exploration and exploitation of the search could be achieved by adjusting the run-length unit. In this paper we propose a decreasing dynamic function to perform the swim walk instead of the constant step. This function is expressed as:

$$C(i,j) = C(N_c) + (C(1) - C(N_c))\frac{(N_c - j)}{(N_c)} \tag{7.12}$$

The algorithm of the proposed technique is as follows:

Step 1: Initialization of the following parameters:

P:	Dimension of the search space
S:	The number of bacteria in the population
Nc:	Number of chemotactic steps
Ns:	The length of a swim when it is on a gradient
Nre:	The number of reproduction steps
Ned:	The number of elimination-dispersal events
ped:	The probability that each bacterium will be eliminated/dispersed
C(i, j)|j = 1:	Initial run-length unit
C(Nc):	The run-length unit at the end of the chemotactic steps (j = Nc)

Step 2: Elimination/dispersal loop, $l = l + 1$

Step 3: Reproduction loop, k = k + 1

Step 4: Chemotaxis loop, j = j + 1

- For i = 1, 2, …, S, execute the chemotactic step for each bacterium as follows:
  - Evaluate the cost function J(i, j, k, l)
  - Let $J_{last} = J(i, j, k, l)$ so that a lower cost could be found.
  - Tumble: generate a random vector $\Delta(i) \in R^p$ and $\Delta_m(i)$ m = 1, 2, …, p is a random number in the range [−1,1].
    Compute $\phi(i)$:
    Move using (13)
  - Compute J(i, j + 1, k, l) and also compute $J_{cc}(\theta, P(j+1, k, l))$ then find new J(i, j + 1, k, l).
  - Swim: let $m = 0$ (counter for swim length)
    While $m < Ns$ (no climbing down long)
    Let $m = m + 1$
    If $J(i, j + 1, k, l) < J_{last}$ let $J_{last} = J(i, j + 1, k, l)$
    then take another step in the same direction and compute the new $J(i, j + 1, k, l)$.
  - Go to the next bacterium ($i = i + 1$ *if* $i \neq S$).
  - Update the run length unit

Step 5: If $j < Nc$ go to step 4 ($j = j + 1$)

Step 6: Reproduction:

- For the given k and l, evaluate the health of each bacterium i as follows:

Table 7.1 Hydrothermal generation (MW) using Lagrangian method

Hour	PS1	PS2	PS3	PS4	PS5	PS6	PS7	PH1	PH2	PH3	PH4
h	MW	MW	MW	MW	MW	MW	MW	MW	MW	MW	MW
1	28.45	20	30	120	95.75	96.48	75	319.5	294.95	319.8	500
2	15	25.3	64.1	120	95.94	65.57	75	350.1	301.03	319.5	500
3	33.44	23.53	45.88	25	70.6	50	75	324	298.88	346.5	50
4	15	57.01	30	120	50	76.55	99.4	262.5	268.49	345.7	475.1
5	31.92	45.28	30	120	65.5	50	75	264.5	272.35	263.6	446.5
6	15	45.07	30	120	69.9	89.09	119.9	268.3	309.12	266.9	418.9
7	37.83	20	56.99	25	92.92	50	75	281.6	269.18	245.9	392.4
8	37.38	35.11	38.48	120	50	75.72	94.21	281.2	271.12	235.2	366.8
9	23.88	46.75	65.38	25	56.88	50	75	291.2	275.01	223.5	342.2
10	23.78	20	42.13	25	65.4	68.92	93.51	303.6	280.91	258.4	318.7
11	15	49.54	37.68	120	50	50	75	318.4	286.88	193.7	296.2
12	39.09	20	30	25	80	50	113.8	411.8	290.91	222.8	274.7
13	39.11	34.78	38.49	25	85.3	62.2	75	332.2	294.97	170.7	254.2
14	15	20	30	120	50	90.27	118.1	350	301.12	162.7	234.7
15	16.61	20	54.61	120	50	50	75	361.2	307.35	154.9	216.2
16	15	20	30	120	50	50	75	372.8	344.44	208.7	198.7
17	24.61	20	52.12	25	68.67	50	75	407.9	315.88	146	182.3
18	34.9	29.2	30.51	120	50	50.85	75	407.4	320.34	121.2	166.9
19	36.52	31.96	30	120	87.59	55.01	77.8	444.4	322.02	126.1	152.5
20	15	50.65	30	25	50	50	75	397.2	308.94	97.29	139.1
21	40.71	58.78	30.72	25	50	50	75	385.2	345.84	99.94	126.7
22	15	20	30	120	50.78	50	75	392.4	316.72	97.6	115.3
23	21.98	34.71	30	120	96.3	54.68	75	456.1	320.99	95.85	104.9
24	17.79	22.04	69.15	25	88.51	91.32	99.52	407	325.29	62.78	95.59

Table 7.2 Hydrothermal generation (MW) using EBFA method

Hour	PS1	PS2	PS3	PS4	PS5	PS6	PS7	PH1	PH2	PH3	PH4
h	MW	MW	MW	MW	MW	MW	MW	MW	MW	MW	MW
1	23.64	31.82	60.27	120	50	67.14	92.65	267.05	140.27	352.25	500
2	15	20	52.84	25	50	68.77	75	277.97	142.78	302.24	500
3	19.9	20	30	120	50	50	102.7	319.37	146.61	330.76	500
4	17.85	48.51	52.85	120	50	79.04	118.7	279.66	175.41	285.12	475.14
5	34.59	20	60.33	120	51.44	88.42	75	281.65	151.02	267.11	446.53
6	37.15	47.39	30	120	50	50	75	285.65	151.79	258.67	418.93
7	15	20	59.54	120	92.96	69.66	75	321.01	151.79	249.15	392.35
8	38.94	36.75	69.29	120	50	80.13	75	349.8	177.01	329.25	366.78
9	33.23	35.15	30	120	50	62.59	82.61	300.06	179.71	235.18	342.22
10	26.16	55.69	40.6	25	50	86.27	75	351.26	179.72	280.92	318.68
11	15	36.88	30	25	50	50	75	382.59	155.75	186.08	296.16
12	28.58	20	37.7	120	50	53.58	75	326.07	158.46	168.26	274.65
13	15	20	39.54	120	50	50	118.5	339.26	161.2	205.64	254.15
14	27.94	34.42	30	120	72.86	73.78	75	355.03	165.38	146.01	234.66
15	35.35	30.8	30	120	50	50	117.4	433.29	200.3	201.1	216.19
16	29.16	20	58.95	120	85.41	50	75	372.14	169.05	120.4	198.74
17	40.43	20	69.18	120	70.69	99.94	75	381.59	170.48	127.77	182.29
18	15	20	30	25	52.18	50	75	388.76	170.48	123.9	166.87
19	41.04	20	52.18	120	56.18	50	75	393.59	199.1	110.94	152.45
20	15	20	30	120	50	89.71	75	396.01	171.71	77.84	139.05
21	44.79	20	30	25	50	50	75	400.89	176.08	71.14	126.66
22	34.97	54.3	37.36	25	82.58	50	75	454.88	180.52	64.64	115.29
23	27.15	31.56	51.07	120	78.13	50	86.56	455.55	183.53	57.58	104.93
24	15.19	36.47	51.88	25	50	54.95	75	427.71	186.57	50.03	95.59

Table 7.3 Comparison of costs between two methods

Parameter	Lagrangian method ($)	Enhanced bacterial foraging algorithm ($)	Difference ($)
Total operating cost	113,470.00	111,740.00	1,730.00

Sort bacteria according to their health J^i_{health} in ascending order.

- The bacteria with the highest J^i_{health} values, computed by (7.12) die while the other S_r with the lowest values split and take the same location of their parents.

Step 7: If $k < Nre$, go to step 3 ($k = k + 1$)
Step 8: Elimination/dispersal

- With probability *ped,* randomly eliminate and Dispersal each bacterium i, keeping the size of the population constant.

Step 9: If $l < N$, go to step 2 ($l = l + 1$), otherwise end

7.4 Simulation Results

In this study, a test case have been considered from [10] which consists of four hydro multi-chain cascaded reservoir and seven thermal plants over a period of 24 h. Table 7.1 presents the optimal hydrothermal scheduling using Conventional method i.e. lagrangian method and Table 7.2 using EBFA algorithm respectively. Table 7.3 gives the improved effectiveness of the proposed method compared with the conventional method.

7.5 Conclusion

In this paper, an enhanced bacterial foraging algorithm is introduced for solving the short-term hydrothermal scheduling problem. The proposed algorithm employs the modified chemotactic steps into the basic Bacteria Foraging Algorithm, so that better exploration of the search space is obtained resulting in improved convergence characteristics. Simulated results for the four hydro and seven thermal plants of an Indian Utility system shows the effectiveness of the proposed algorithm. The results yields better optimal solution when compared with the conventional technique.

References

1. Wood AJ, Wollenberg BF (1984) Power generation, operation and control. Wiley, New York
2. Ngundam JM, Kenfack F, Tatietse TT (2002) Optimal scheduling of large scale hydro thermal power system using the lagrangian relaxation technique. Int J Electr Power Energy Syst 22:237–245
3. Tan H, Luh PB, Zhang L (1994) Scheduling of hydrothermal power system using the augmented lagrangian decomposition and coordination technique. Am Control Conf 2:1558–1562
4. Momoh JA, Adapa R, El-Hawary ME (1996) A review on selected optimal power flow literature to non- linear and quadriatic programming approaches. IEEE Trans Power Syst 14 (1):96–104
5. Ferrero RW, Rivera JF, Shahidehpour SM (1998) A dynamic programming two-stage algorithm for long-term hydrothermal scheduling of multi reservoir systems. IEEE Trans Power Syst 13(4):1534–1540
6. Borghetti A, Frangioni A, Lacalandra F, Nucci CA (2002) Lagrangian heuristics based on disaggregated bundle methods for hydro thermal unit commitment. IEEE Trans Power Syst 14 (1):313–323
7. Luh PB, Zhang L, Tomastik RN (1998) An algorithm for solving the dual problem of hydrothermal scheduling. IEEE Trans Power Syst 13:593–600
8. Wong KP, Wong YW (1994) Short-term hydrothermal scheduling, part-I: simulated. annealing approach. IEEE Proc. Part-C 141(5):497–501
9. Malekshah ARS, Mahvy M, Jahani R, Shayanfar HA (2010) Optimal bidding strategy in electricity markets by considering emission constraints using simulated annealing algorithm and comparison with other heuristic methods. Int Rev Electr Eng 3(6):1183–1188
10. Padmini S, Christober Asir R, Chaudhuri S, Chakraborty A (2012) Optimal scheduling of short term hydrothermal coordination for an indian utility system using genetic algorithm. Adv Intell Syst Comput 453–459
11. Sinha N, Chakrabarti R (2003) Fast evolutionary programming techniques for short-term hydrothermal scheduling. IEEE Trans PWRS 18(1):214–219
12. Suman DS, Nallasivan Joseph Henry C, Ravichandran S (2006) A novel approach for short-term hydrothermal scheduling using hybrid technique. In: IEEE Power India Conference, Apr 2006
13. Padmini S, Jegatheesan R, Dash SS, Rajan A, Christober C (2013) Evolutionary programming based hydrothermal commitment scheduling for maximizing the profit of GENCO considering the effect of reserve in a deregulated energy market. Int Rev Electr Eng 8(4):1279–1286
14. Samudi C, Das GP, Ojha PC, Sreeni TS, Cherian S (2008) Hydrothermal scheduling using particle swarm optimization. IEEE
15. Hotaa PK, Barisala AK, Chakrabarti R (2009) An improved PSO technique for short-term optimal hydrothermal scheduling. Electr Power Syst Res 79(7):1047–1053
16. Padmini S, Rajan CA, Murthy P (2011) Application of improved PSO technique for short term hydrothermal generation scheduling of power system. Lect Notes Comput Sci 2:1176–1182
17. Liang JJ, Qin AK, Suganthan PN, Baskar S (2006) Comprehensive learning particle swarm optimizer for global optimization of multimodal functions. IEEE T Evol Comput 10 (3):281–295
18. Tang WJ, Wu QH, Saunders JR (2006) Bacteria foraging algorithm for dynamic environments. IEEE Congr Evol Comput 1324–1330
19. Chen H, Zhu Y, Hu K (2008) Self-adaptation in bacterial foraging optimization algorithm. In: .3rd international conference on intelligent systems and knowledge engineering, vol 1, pp 1026–1031
20. Chu Y, Mi H, Liao H, Ji Z, Wu QH (2008) A fast bacteria swarming algorithm for high dimensional function optimization. IEEE World Congr Evol Comput 3135–3140
21. Passino KM (2002) Biomimicry of bacterial foraging distributed optimization and control. Control Syst Mag IEEE 22:52–67

Chapter 8
Efficiency Modeling of High Gain DC-DC Converter for Renewable Energy Application

J. DivyaNavamani, A. Lavanya, K. Vijayakumar and A. Navauga

Abstract This paper presents a high efficiency step-up DC-DC converter for Low-DC renewable energy sources. Conventional DC converters can offer limited gain and their efficiency drops as the gain requirement increases. Efficiency modeling of each dc-dc converter accurately predicts the behavior of DC-DC converter. A comparison is made in this paper between a number of high gain DC-DC converter topologies, and it is shown that the proposed converter outperforms other topologies in terms of efficiency and component utilization. Thus, the achieved low cost and high efficiency of the proposed converter make it suitable for low-PV application.

Keywords DC-DC converter · Renewable energy source · PV application

8.1 Introduction

Utilization of renewable energy, efficient conversions of fossil fuel are not only environmentally and climatically beneficial, they also preserve the finite energy sources. The search for alternative energy sources is strongly rooted in the realization that the conventional energy sources are polluting and they are not renewable and thus limited. India has made rapid strides towards economic self reliance over the last few years. On the energy demand and supply side, India is facing severe shortages. To overcome energy crisis, government has developed many projects related to alternative energy sources [1, 2]. The new agricultural technologies have also been developed based on non-conventional energy sources. Power plays a

J. DivyaNavamani (✉) · A. Lavanya · K. Vijayakumar · A. Navauga
SRM University, Kattankulatur, India
e-mail: divyateddy1@gmail.com

C. Kamalakannan et al. (eds.), *Power Electronics and Renewable Energy Systems*,
Lecture Notes in Electrical Engineering 326, DOI 10.1007/978-81-322-2119-7_8

great role wherever man lives and works. The living standard and prosperity of a nation vary directly with the increase in the use of power. The electricity requirement of the world is increasing at an alarming rate due to industrial growth, increased and extensive use of electrical gadgets. Thus, various ways possible to increase the power that is required is being done. Adaptation to renewable energy sources is being increased nowadays. Still there are so many disadvantages in that field which, are being improvised day by day. One amongst those is the efficiency improvement. In a renewable energy system, the output obtained is very less compared to the non renewable system. Thus obtaining maximum of the output is very important. In this paper, efficiency modeling of three converters namely, double dual interleaved boost converter (DDIBC), interleaved voltage multiplier boost converter (IVMBC), multi-device interleaved boost converter (MDIBC) are done [3, 4]. A systematical losses evaluation gives us a global view on the interesting features of the Interleaved boost, the interests and limits of the interleaving technique, the components choice strategy and the optimal system architecture. Their theoretical and simulated efficiencies are compared to find the best converter for renewable energy application [5–12].

8.2 Efficiency Modeling of Converters

8.2.1 Double Dual Interleaved Boost Converter

The interleaved double dual boost (IDDB) is a non-isolated step-up dc-dc converter capable of high voltage gain and suitable to high-power applications (Fig. 8.1). The interleaving technique is introduced to solve the problem of high current—low voltage and low current ripple imposed by FC, to reduce the average current, to minimize components losses and to facilitate inductors manufacture. The configuration is composed of two conventional boosts with input coupled inversely. Switches commands of each boost are delayed of a half switching period each. The advantage of DDIBC converter compared with a classical boost in the case of the same power, same input and output voltage is that the. In addition, the dimensioning voltage is not output voltage but capacitor voltage, which is lower than output voltage. The applications of this converter include electrical vehicles and renewable energy conversion.

There are two modes of operation in this converter.

In the first mode, the switch S_1 is ON. Therefore both the inductors conduct and the capacitors also conduct. Only one diode, D_2 conducts. Figure 8.2 explains the mode 1 operation. Figure 8.3, explains Mode 2 operation. In this mode, the other switch is ON. Thus diode D1 conducts and D2 is in OFF state.

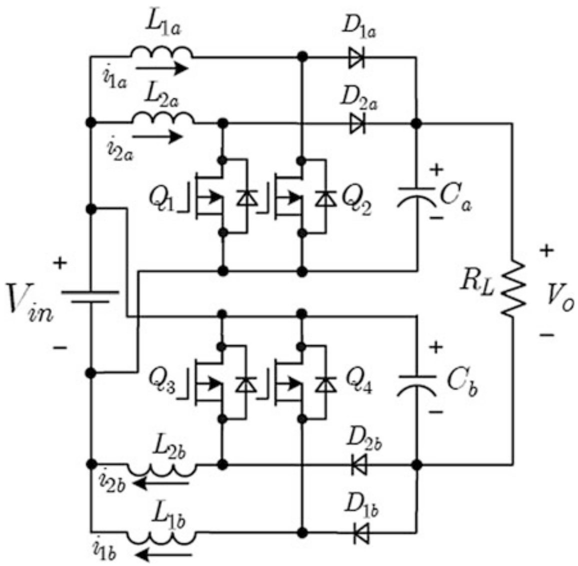

Fig. 8.1 Circuit diagram of double dual interleaved boost converter

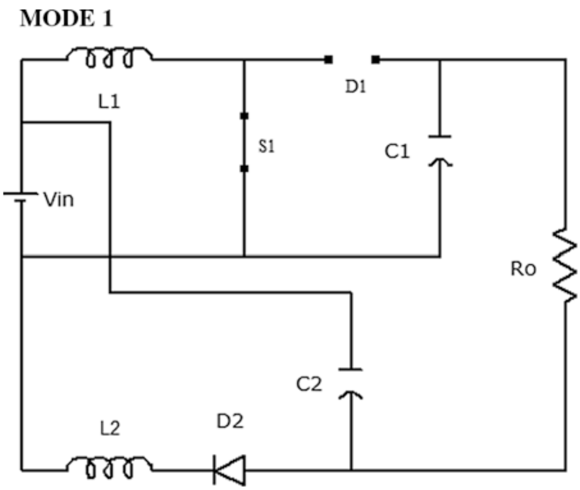

Fig. 8.2 Circuit diagram of mode 1 of DDIBC

The mathematical expression for this is given as,

$$P_{L1} = P_{L2} = T_{L1}(I_{L1})^2 \times R_L \tag{8.1}$$

$$P_{S1} = P_{S2} = T_{S1}\left(\frac{I_{IN}}{2}\right)^2 \times R_S \tag{8.2}$$

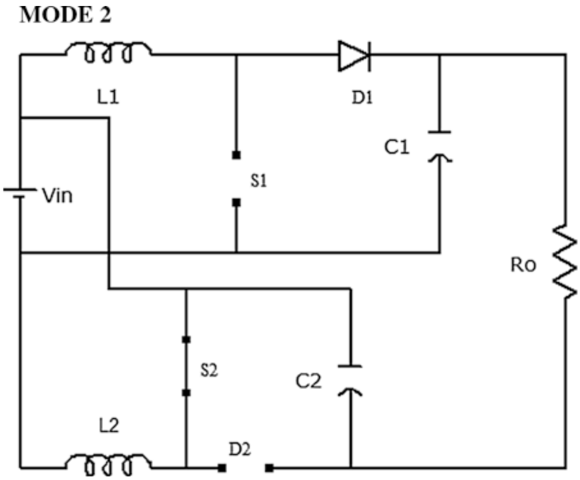

Fig. 8.3 Circuit diagram of mode 2 of DDIBC

$$P_{DS1} = P_{DS2} = T_{DS2}(I_{DS2})^2 \times R_D + V_D I_{DS2} \tag{8.3}$$

$$P_{C2} = P_{C1} = T_C\left(\left((I_0)^2 \times R_C\right) + \left((I_{L1} - I_0)^2 R_{CM1}\right)\right) + \left((I_0)^2 R_C\right) \tag{8.4}$$

T represents the total time period of conduction. Here the values are calculated for the maximum duty cycle of 40 %. The values of the internal resistance are assumed depending upon the value of various components. Similarly the value of mode 2 is also calculated. Then the total power loss found. Finally the efficiency is calculated, EFFICIENCY $= (TP_0 + P_{LOSS})/TP_0$ the efficiency is found to be 75 %.

8.2.2 Interleaved Voltage Multiplier Boost Converter

This converter is based on the interleaved boost converter, integrated with multiplier capacitors connected in series as shown in Fig. 8.4. These capacitors present comportment similar to the series capacitor of the Sepic converter, however these capacitors allow to obtain high static gain. The number of parallel stages is represented by the parameter "**P**" and the number of multiplier stages is represented by the parameter "M", that are defined by the number of the multiplier capacitors in series with each switch.

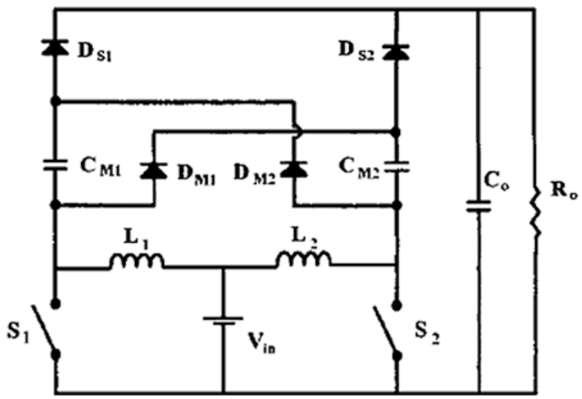

Fig. 8.4 Interleaved voltage multiplier boost converter

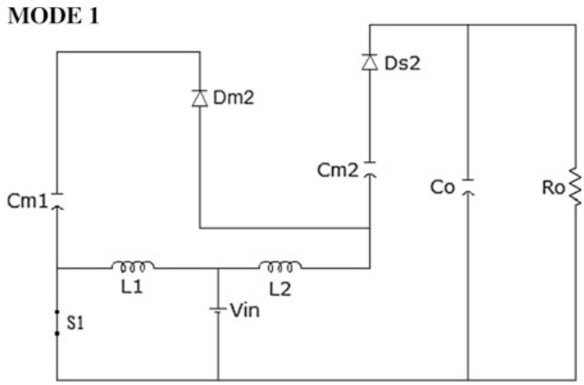

Fig. 8.5 Circuit diagram of mode 1 of IVMBC

There are two modes of operation,

Switch one, S_1 ON when diodes, D_{M2}, D_{S2} conducts. Also C_{M1}, C_{M2}, L_1, L_2 conducts as shown in Fig. 8.5.

Switch two, S_2 ON—D_{M1}, D_{S1} conducts. Also C_{M1}, C_{M2}, L_1, L_2 conducts as shown in Fig. 8.6.

The mathematical expression for this are given as,

$$\mathrm{ID_{M2}} = \frac{\mathrm{I_{IN}}}{4} \tag{8.5}$$

$$\mathrm{I_{S1}} = \mathrm{I_{L1}} + \mathrm{I_{DM2}} \tag{8.6}$$

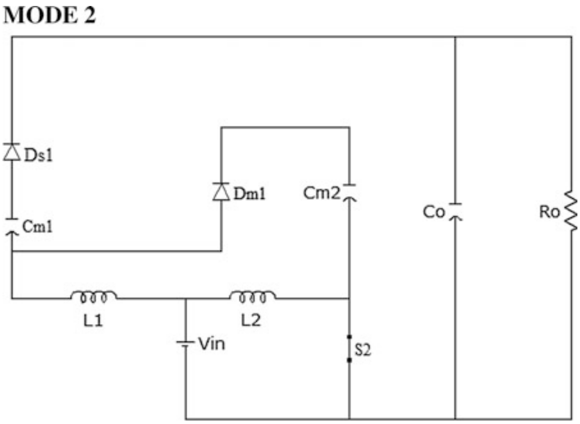

Fig. 8.6 Circuit diagram of mode 2 of IVMBC

$$\mathrm{I}_{L1} = \mathrm{I}_{L2} = \frac{\mathrm{I_{IN}}}{2} \tag{8.7}$$

$$\mathrm{P}_{L1} = T_{L1}\left(\frac{I_{\mathrm{IN}}}{2}\right)^2 \times R_L \tag{8.8}$$

$$\mathrm{P}_{L2} = T_{L2}\left(\frac{I_{IN}}{2}\right)^2 \times R_L \tag{8.9}$$

$$\mathrm{P}_{S1} = T_{S1}\left(\frac{I_{\mathrm{IN}}}{2}\right)^2 \times R_S \tag{8.10}$$

$$\mathrm{P}_{S2} = T_{S2}\left(\frac{I_{\mathrm{IN}}}{2}\right)^2 \times R_S \tag{8.11}$$

$$\mathrm{P}_{CM1} = T_{CM1}\left(\left((I_{DM2})^2 \times R_{M1}\right) + \left(\left(\frac{I_{IN}}{2}\right) - (I_{DM1})^2 R_{CM1}\right)\right) \tag{8.12}$$

$$\mathrm{P}_{CM2} = T_{CM2}\left(\left(\left(\frac{I_{IN}}{2} - I_{DM2}\right)^2 \times R_{M1}\right) + \left(\left(\left(\frac{I_{IN}}{2}\right) - (I_{S1})\right)^2 R_{CM2}\right)\right) \tag{8.13}$$

$$P_{DM1} = T_{DM1}\left((I_{DM1})^2 \times R_D + V_D I_{DM1}\right) \tag{8.14}$$

$$P_{DM2} = T_{DM2}\left((I_{DM2})^2 \times R_D + V_D I_{DM2}\right) \tag{8.15}$$

$$P_{DS1} = T_{DS1}\left((I_{DS1})^2 \times R_D + V_D I_{DS1}\right) \tag{8.16}$$

$$P_{DS2} = T_{DS2}\left((I_{DS2})^2 \times R_D + V_D I_{DS2}\right) \tag{8.17}$$

$$P_{C0} = T_{C0}(I_O)^2 R_{C0} \tag{8.18}$$

$$\begin{aligned} P_{M1} = {} & P_{L1} + P_{L2} + P_{S1} + P_{S2} + P_C + P_{CM1} \\ & + P_{CM2} + P_{DM1} + P_{DM2} + P_{DS1} + P_{DS2} + P_{C0} \end{aligned} \tag{8.19}$$

Here the values are calculated for the maximum duty cycle of 70 %. The values of the internal resistance are assumed depending upon the value of various components. Similarly the value of mode 2 is also calculated. Then the total power loss found. Finally the efficiency is calculated and found to be 83 %.

8.2.3 Multi Device Interleaved Boost Converter

This converter consists of two-phase interleaved with two switches and two diodes connected in parallel per phase as shown in Fig. 8.7. The easy way to reduce the size of the inductor, capacitor, and input/output EMI filter is by increasing the frequency of the inductor current ripple and the output voltage ripple. The phase-shift interleaved control is proposed to achieve the control strategy. This control strategy will provide a doubled ripple frequency in inductor current at the same switching frequency, which can contribute to a higher system bandwidth. This bandwidth achieves a fast dynamic response for the converter and reduces the size of the passive components.

- There are 8 modes of operation
- They are,

    S1, S4-ON
    S1, S3-ON
    S2, S3-ON
    S2, S4-ON
    S1-ON
    S3-ON
    S2-ON
    S4-ON

where, S1, S2, S3, S4 are the switches.

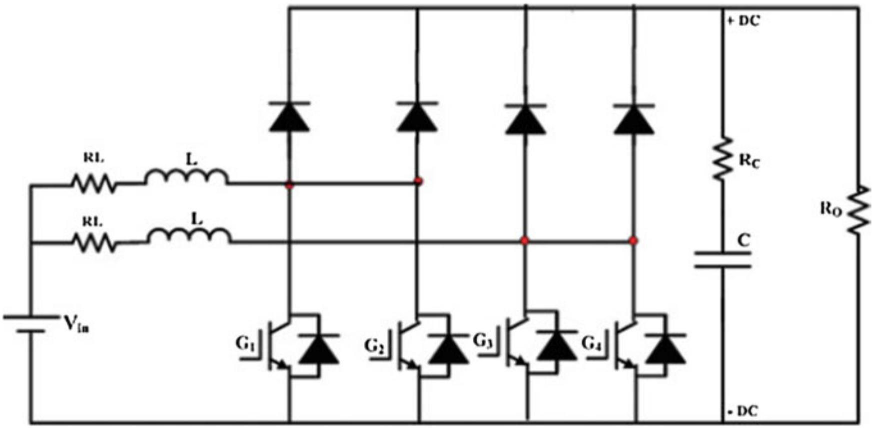

Fig. 8.7 Circuit diagram of multidevice interleaved boost converter

Fig. 8.8 Circuit diagram of mode 1 of MDIBC

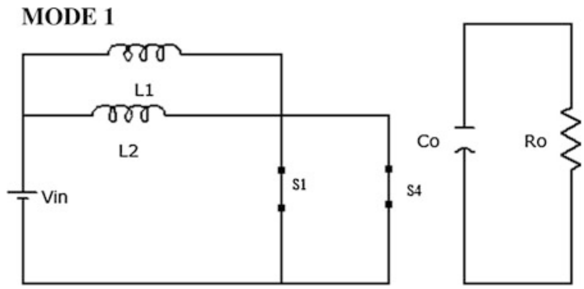

Mode operation when two switches are ON. Figures: 8.8, 8.9, 8.10 and 8.11, represents the mode of operation of MDIBC.

The mathematical expression for this is given as,

$$P_{L1} = T_L \left(\frac{T_{IN}}{2} \right)^2 \times R_L \tag{8.20}$$

$$P_{L2} = T_L \left(\frac{T_{IN}}{2} \right)^2 \times R_L \tag{8.21}$$

$$P_{S1} = T_{S1} \left(\frac{I_{IN}}{2} \right)^2 \times R_S \tag{8.22}$$

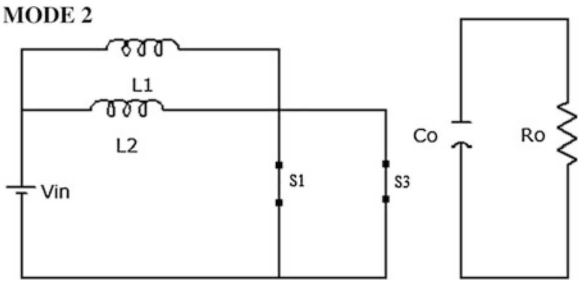

Fig. 8.9 Circuit diagram of mode 2 of MDIBC

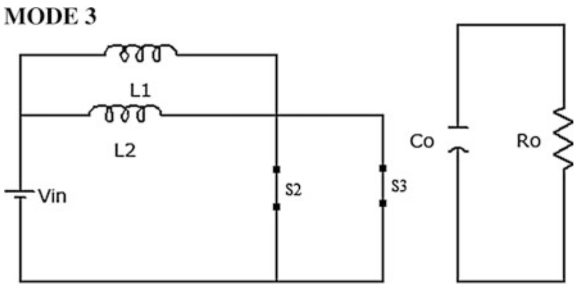

Fig. 8.10 Circuit diagram of mode 3 of MDIBC

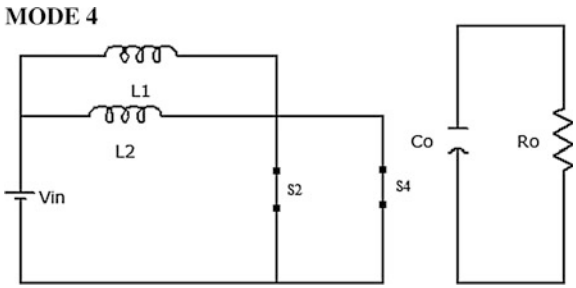

Fig. 8.11 Circuit diagram of mode 4 of MDIBC

$$P_{S2} = T_{S2}\left(\frac{I_{IN}}{2}\right)^2 \times R_S \tag{8.23}$$

$$P_C = T_C\left(\frac{I_{IN}}{2}\right)^2 \times R_C \tag{8.24}$$

$$P_{M1} = P_{L1} + P_{L2} + P_{S1} + P_{S2} + P_C \tag{8.25}$$

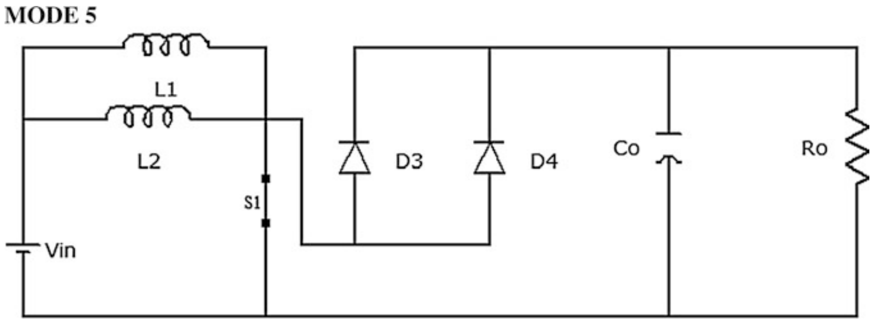

Fig. 8.12 Circuit diagram of mode 5 of MDIBC

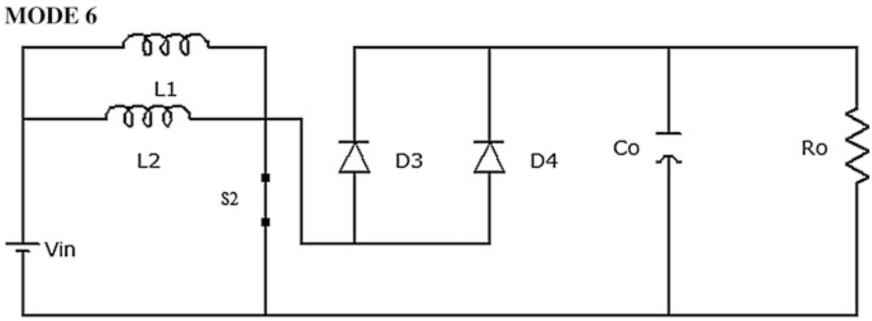

Fig. 8.13 Circuit diagram of mode 6 of MDIBC

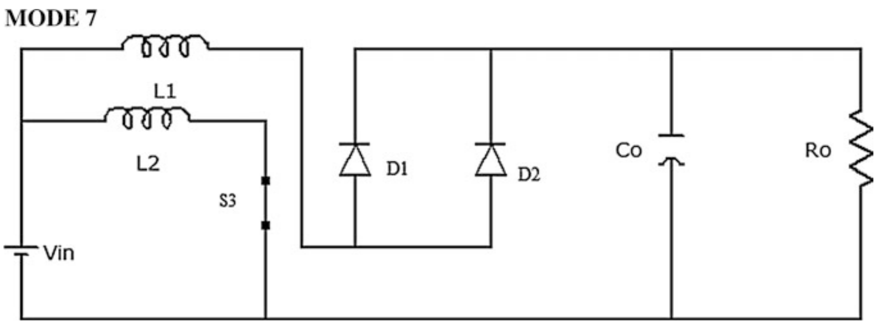

Fig. 8.14 Circuit diagram of mode 7 of MDIBC

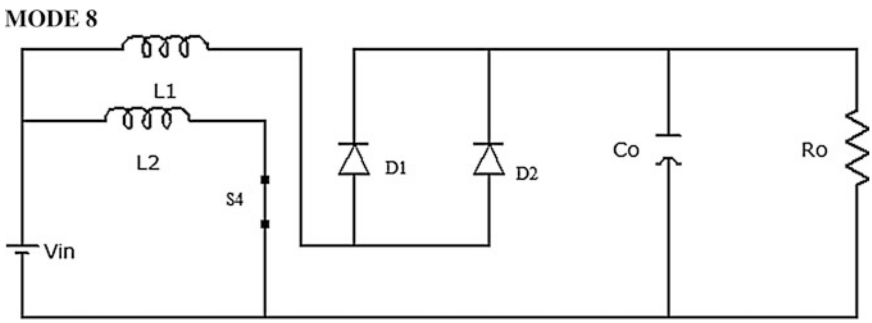

Fig. 8.15 Circuit diagram of mode 8 of MDIBC

Mode operation when one switch is ON. Figures: 8.12, 8.13, 8.14 and 8.15, represents this mode of operation. The mathematical expression for this is given as,

$$P_{L1} = T_L \left(\frac{T_{IN}}{2} \right)^2 \times R_L \tag{8.26}$$

$$P_{L2} = T_L \left(\frac{T_{IN}}{2} \right)^2 \times R_L \tag{8.27}$$

$$P_{S1} = T_{S1} \left(\frac{I_{IN}}{2} \right)^2 \times R_S \tag{8.28}$$

$$P_{D3} = T_{D3} \left(\frac{I_{IN}}{4} \right)^2 \times R_D + V_D \left(\frac{I_{IN}}{4} \right) \tag{8.29}$$

$$P_{D4} = T_{D4} \left(\frac{I_{IN}}{4} \right)^2 \times R_D + V_D \left(\frac{I_{IN}}{4} \right) \tag{8.30}$$

$$P_C = T_C \left(\frac{I_{IN}}{2} - I_0 \right)^2 \times R_S \tag{8.31}$$

$$P_{M1} = P_{L1} + P_{L2} + P_{D3} + P_{D4} + P_C \tag{8.32}$$

Here the values are calculated for the maximum duty cycle of 40 %. Because, when the duty cycle is increased more than 0.5 the converter will give negative output voltage. The values of the internal resistance are assumed depending upon the value of various components. Similarly the value for the other 8 modes is also calculated. Then the total power loss is found. Finally the efficiency is calculated and is found to be 96 %.

8.3 Simulation Result and Comparison

8.3.1 Efficiency Modeling of Double Dual Interleaved Boost Converter

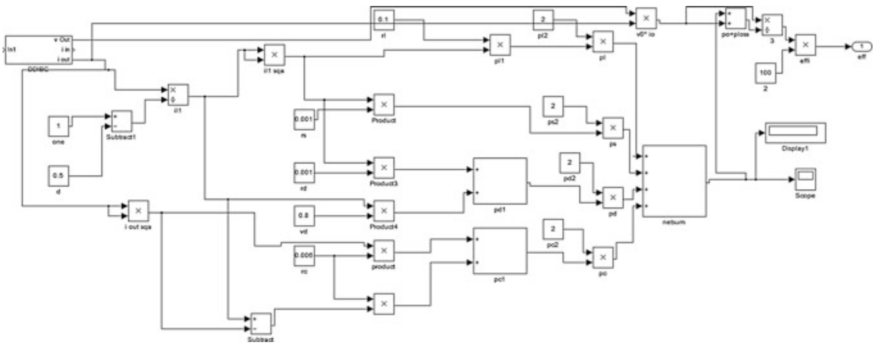

Fig. 8.16 Simulation circuit of efficiency modeling of DDIBC

8.3.2 Efficiency Modeling of Interleaved Voltage Multiplier Boost Converter

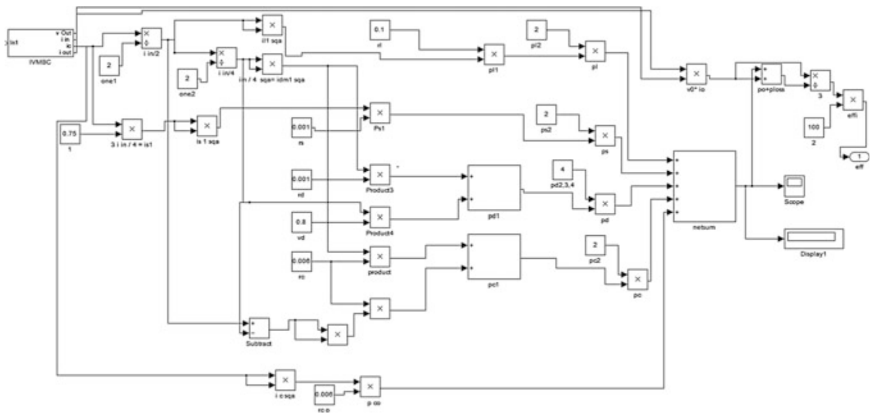

Fig. 8.17 Simulation circuit of efficiency modeling of IVMBC

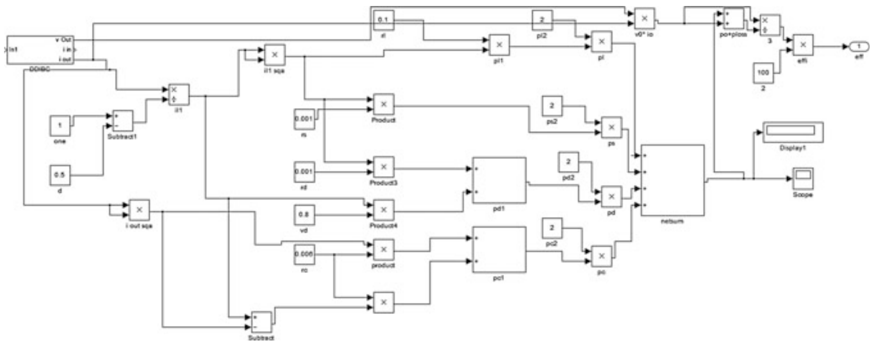

Fig. 8.18 Simulation circuit of efficiency modeling of MDIBC

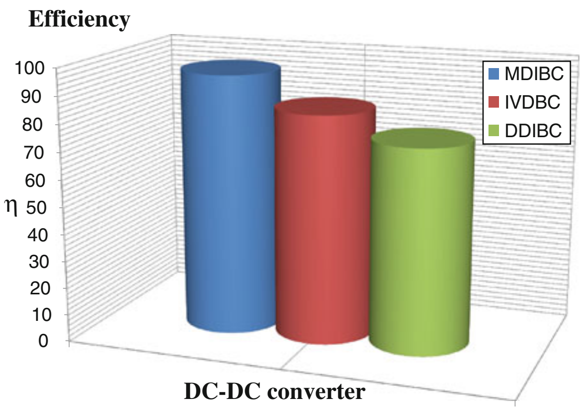

Fig. 8.19 Comparison of efficiency for all the three converters

8.3.3 Efficiency Modelling of Multi Device Interleaved Boost Converter

The simulated modeling circuit for efficiency calculation which is done MATLAB/SIMULINK in shown in Figs. 8.16, 8.17 and 8.18 for various converter. This is a comparison graph between the various converters. Thus the efficiency of MDIBC is found to be higher than the other converters through this analysis as shown in Fig. 8.19.

Table 8.1 Efficiency comparison

Sl. no.	Converter	Theoretical	Simulated
1	DDIBC	75	77
2	IVMBC	84	82.1
3	MDIBC	96	95.66

Table 8.1 shows the efficiency comparison of different high step up DC-DC converter. The theoretical efficiency and simulated result efficiency are compared. The values are approximately equal. Again, MDIBC is found to the highest efficiency.

8.4 Conclusion

The efficiency of the MDIBC is found to be greater than 95 %. Two important conclusions are reached: first, DC-DC power converters have sufficiently high efficiency for PV applications; and secondly losses in the power converters can be calculated with reasonable accuracy if the device parameters are known.

References

1. Hegazy O (2012) Analysis, modeling, and implementation of a multidevice interleaved DC/DC converter for fuel cell hybrid electric vehicles. IEEE Trans Power Electron 27 (11):4445–4458
2. Plesko H, Biela J, Luomi J, Kolar JW (2008) Novel concepts for integrating the electric drive and auxiliary DC/DC converter for hybrid vehicles. IEEE Trans Power Electron 23(6)
3. Lujara NK, Van Wyk JD, Materu PN (1998) Power electronic loss models of DC-DC converters in photovoltaic applications. In: Proceedings. ISIE '98, IEEE international symposium on industrial electronics, Jul 1998, vol 1, pp 35–39
4. Torrico-Bascope RP, Oliveira DS, Antunes FLM (2006) A generalised high voltage gain boost converter based on three state switching cell. In: IECON 2006—32nd annual conference on IEEE industrial electronics, Nov 2006
5. Krykunov O (2007) Comparison of the DC/DC-converters for fuel cell applications. Int J Electr Electr Eng, Int Sci Index 1(3)
6. Li W, Lv X, Deng Y, Liu J, He X (2009) A review of non-isolated high step-up DC/DC converters in renewable energy applications. In: IEEE 24th applied power electronics conference and exposition
7. Tomaszuk A, Krupa A (2011) High efficiency high step-up DC/DC converters—a review. Bull Polish Acad Sci Tech Sci 59(4):475–483
8. Chunliu C, Chenghua W, Feng H (2009) Research of an interleaved boost converter with four interleaved boost converter cells. In: Asia Pacific conference on postgraduate research in microelectronics and electronics (PrimeAsia) IEEE vol 1, pp 396–399

9. Yu W, Hutchens C, Lai J-S, Zhang J, Lisi G, Djabbari A, Smith G, Hegarty T (2009) High efficiency converter with charge pump and coupled inductor for wide input photovoltaic AC module applications. Energy Conv Congr Exposition (ECCE) IEEE 1:3895–3900
10. Changchien SK, Liang TJ (2010) Novel high step-up DC–DC converter for fuel cell energy conversion system. IEEE Trans Ind Electr 57(6):2007–2017
11. Garcia FS, AntenorPomilio J (2013) Modeling and control design of the interleaved double dual boost converter. IEEE Trans Ind Electr 60(8):3283–3290
12. Gules R, Pfitscher LL, Franco LC (2003) An interleaved boost DC-DC converter with large conversion ratio. In: IEEE international symposium on industrial electronics (ISIE '03)

Chapter 9
Reactive Power Optimization Using Firefly Algorithm

G. Kannan, D. Padma Subramanian and R.T. Udaya Shankar

Abstract This paper presents a Firefly algorithm to minimize the real power losses and to improve the voltage profile. This problem is a nonlinear combinatorial optimization with constraints. Newton-Raphson method of power flow is used in conjunction with Firefly algorithm to obtain the optimal values of the control variables. The control variables for this problem are the Generator bus voltages, Transformer Tap positions and the MVAR at the capacitor Banks. The performance of the proposed algorithm has been demonstrated with the IEEE 30-bus system. The algorithm used in this problem is compared to another nature-inspired metaheuristic algorithm (PSO). The simulated result shows improved results both in terms of convergence time and reduction of real power loss.

Keywords Reactive power optimization · Fire fly algorithm · IEEE 30-bus system · GA · PSO

9.1 Introduction

Reactive power optimization is needed in a system to minimize the real power losses and also to improve the voltage profile. It involves the identification of the optimal values of transformer tap-settings, generator bus voltage magnitudes, the reactive power output of capacitor and the generator bus reactive power. This problem thus includes various equality and inequality constraints and it is a non-linear combinatorial problem.

Conventional methods used in reactive power optimization are based on linear programming [1] and non-linear programming. Fast Quadratic Programming [2]

G. Kannan (✉) · R.T. Udaya Shankar
SMIT, Chennai, India
e-mail: ganapathykannan@yahoo.com

D. Padma Subramanian
Faculty of Electrical and Electronics Engineering, Director-Centre for Renewable Energy and Robotic Automation, AMET University, Chennai, India
e-mail: jceprincipal2013@gmail.com

C. Kamalakannan et al. (eds.), *Power Electronics and Renewable Energy Systems*,
Lecture Notes in Electrical Engineering 326, DOI 10.1007/978-81-322-2119-7_9

has also been used for large scale VAR optimization. The major drawback of these methods includes the time consumption and the local minima criterion. It is difficult to handle discrete variables.

In order to overcome these drawbacks, evolutionary techniques such as Genetic Algorithm [3] Hybrid Stochastic search Algorithm [4] Ant colony search Algorithm [5] PSO Algorithm and its several modification such as HPSO and HMAPSO [6, 7] were proposed. Differential Evolution [8] approach which uses differential operators has also found its use in reactive power optimization. Recent works on reactive power optimization includes various algorithms like Biogeography-Based optimization (BBO) [9], Harmony search Algorithm (HSA) [10] and teaching learning based optimization (TLBO) [11] for real power loss minimization.

In 2007 Firefly Algorithm was developed by Dr. Xin-She Yang [12] at Cambridge University based on the flashing behavior of fireflies. The objective function of the problem is related to that of the brightness of firefly and based on the movement of the fireflies to the brighter one in the given population thus solving the problem.

The rest of this paper is organized as follows. The mathematical formulation of the optimal reactive power dispatch is presented in Sect. 2. In Sect. 3, firefly algorithm and its implementation in reactive power optimization is described in detail. The numerical results on IEEE 30 bus system and the comparison with the results provided by other methods such as genetic algorithm (GA) and particle swarm optimization (PSO) techniques is shown in Sect. 4. In Sect. 5 final conclusions are given.

9.2 Mathematical Problem Formulations

The main objective of reactive power optimization is to minimize the active power loss in the transmission network, which is defined as follows:

$$f_1 = \min \sum_{n=1}^{nl} P_{loss} \tag{9.1}$$

Another objective of this problem is to improve the voltage profile which is formulated mathematically as follows,

$$f_2 = \alpha(1.1 - \mathrm{abs}(\max(V_{mag}))) + \beta(0.95 - \mathrm{abs}(\min(V_{mag}))) \tag{9.2}$$

The overall objective function of the problem is thus formulated as follows,

$$f = \min \sum_{n=1}^{nl} P_{loss} + \alpha(1.1 - \mathrm{abs}(\max(V_{mag}))) + \beta(0.95 - \mathrm{abs}(\min(V_{mag}))) \tag{9.3}$$

where, P_{loss} = active power loss in the transmission network, α, β are the penalty factors.

9.2.1 Constraints

Equality Constraints. The equality constraints include the real and reactive power constraints which is given as follows,

Real Power Constraint

$$P_i(V,\theta) = \sum_{j=1}^{n} V_i V_j (G_{ij} \cos\theta_{ij} + B_{ij} \sin\theta_{ij}) \tag{9.4}$$

where,

n number of buses, except swing bus

G_{ij} mutual conductance between bus i and j

B_{ij} mutual susceptance between bus i and j

P_i Real power injected into network at bus i

Reactive Power Constraint

$$Q_i(V,\theta) = \sum_{j=1}^{n} V_i V_j (G_{ij} \sin\theta_{ij} + B_{ij} \cos\theta_{ij}) \tag{9.5}$$

where,

n number of buses, except swing bus

Q_i Reactive power injected into network at bus i

Inequality Constraints. The inequality constraints include the following,

Bus Voltage Magnitude Constraint

$$V_{i,min} \leq V_i \leq V_{i,max};\ i \in N_B \tag{9.6}$$

where,

V_i Voltage magnitude at bus i

N_B Total number of buses

Generator Bus Reactive Power Constraint

$$Q_{Gi,min} \leq Q_{Gi} \leq Q_{Gi,max};\ i \in N_g \tag{9.7}$$

where,

Q_{Gi} Reactive power generation at bus i

N_g Number of generator buses

Reactive Power Source Capacity Constraints

$$Q_{Ci,min} \leq Q_{Ci} \leq Q_{Ci,max};\ i \in N_c \tag{9.8}$$

where,
Q_{Ci} Reactive power generated by ith capacitor bank
N_C No. of capacitor banks

Transformer Tap Position Constraints

$$T_{k,min} \leq T_k \leq T_{k,max};\ i \in N_T \tag{9.9}$$

where,
T_k Tap setting of transformer at branch k
N_T No. of tap-setting transformer branches.

9.3 Firefly Algorithm

9.3.1 Introduction

The firefly algorithm is based on randomization of movements of fireflies in space. It involves updating the position of flies with respect to attractiveness and distance. Three idealized rules being followed during optimization using firefly algorithm is as follows,

1. All fireflies are unisexual so that one firefly will be attracted to other fireflies regardless of sex.
2. Attractiveness is proportional to brightness, thus for any two flashing fireflies the less bright one will move towards the brighter one. The attractiveness is proportional to the brightness and they both decrease as their distance increases. If there is no brighter one than a particular firefly it will move randomly.
3. The brightness of the firefly is affected or determined by the landscape of the objective function.

9.3.2 Algorithm and Flowchart

The flowchart for firefly algorithm in reactive power optimization is given in Fig. 9.1 and the steps included is given as follows,

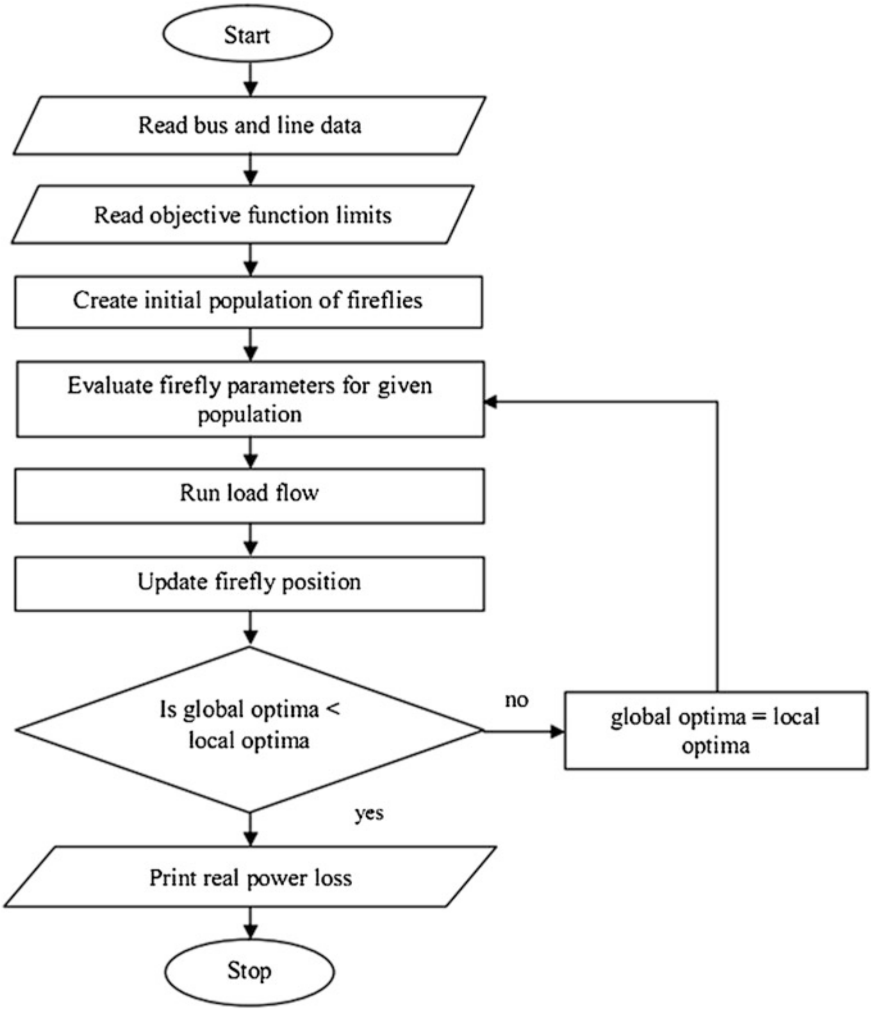

Fig. 9.1 Flowchart of firefly algorithm for reactive power optimization

1. Read the objective function limits which include the generator limits (bus voltages), MVAR limits and transformer tap setting positions.
2. Create initial set of fireflies.
3. Evaluate firefly parameters for initial population

   (a) Attractiveness

$$\beta(r) = \beta_0 * \exp(-\gamma r^m) \tag{9.10}$$

where,

β_0 initial attractiveness at r = 0

γ absorption co-efficient

r distance between two flies.

(b) Distance

The distance can be found by Euclidean distance formula,

$$r_{ij} = \|x_i - x_j\| \tag{9.11}$$

where, r_{ij} = distance between two flies at positions i and j respectively.

(c) Movement

$$x_i = x_{i(old)} + \beta_0 * \exp(-\gamma r_{ij}^2) * (x_i - x_j) + a * (rand - \frac{1}{2}) \tag{9.12}$$

where, rand = random number generator.

4. Run load flow.
5. Update the flies' position and check if global optima is less than local optima, if yes then got to step 6, else update global optima = local optima and go to step 3.
6. Print the values of the control variables and loss.
7. Stop.

9.4 Numerical Example and Results

The Firefly Algorithm [13] has been implemented to IEEE 30-bus system using MATLAB and the results are compared with PSO.

The IEEE 30-bus network consists of 6 generators, 4 transformers, and 41 branches. The voltage and tap settings limits for the IEEE 30-bus is shown in Table 9.2. The reactive power generation limits for the IEEE 30-bus system are listed in Table 9.1. The base case real power loss is obtained as 0.17557 p.u. The analysis of the voltage levels shows the 30th bus is a weak bus.

Table 9.1 Limit for reactive power generation

Bus no.	1	2	5	8	11	13
$Q_{g\,min}$(Mvar)	0	−40	−40	−10	−6	−6
$Q_{g\,max}$(Mvar)	10	50	40	40	24	24

Table 9.2 Limits for voltage and tap-setting (in p.u.)

$V_{G,max}$	$V_{G,min}$	$V_{load,max}$	$V_{load,min}$	$T_{k,max}$	$T_{k,min}$
1.1	0.9	1.05	0.95	1.05	0.95

Table 9.3 Comparison of simulated results for IEEE 30-bus system (real power loss minimization)

	Base case	GA	PSO	FIREFLY
P_{loss} (p.u.)	0.17557	0.17180	0.15813	0.155084

Table 9.4 Optimal values of the control variables in p.u. obtained using firefly algorithm

V_1	1.1	Q_{C10}	0.29094	Q_1	0.012295
V_2	1.0851	Q_{C24}	0.21169	Q_2	0.029082
V_5	1.0538	T_1	1.0191	Q_5	0.218592
V_8	1.1	T_2	0.9	Q_8	0.034493
V_{11}	1.1	T_3	0.9415	Q_{11}	0.086045
V_{13}	1.1	T_4	0.9254	Q_{13}	0.095031

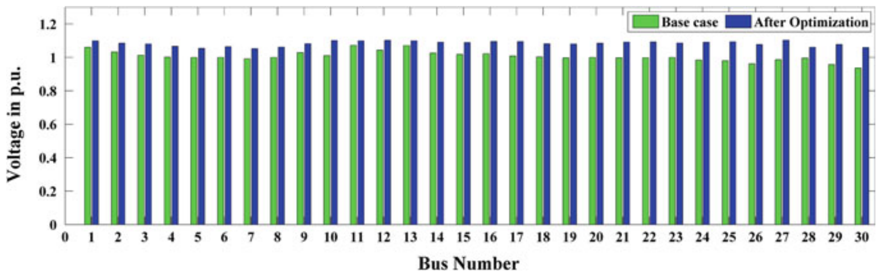

Fig. 9.2 Comparison of voltage levels before and after optimization

The real power loss obtained after optimization using firefly algorithm is obtained as 15.5084 (MW). The result obtained from firefly algorithm is compared with that of the GA and PSO in Table 9.3. The optimal value of the control variables is provided in Table 9.4. It is noted that all the control variables are within their specified limits. The comparison of voltage levels before and after optimization is shown in Fig. 9.2 and it is seen that the voltage profile of the system has improved after reactive power optimization using Firefly Algorithm.

9.5 Conclusion

Reactive power optimization for IEEE 30-bus system is reported. Firefly algorithm has been successfully implemented using MATLAB to minimize the active power losses in the system satisfying all the power system constraints. The proposed method has been found to be better both in terms of convergence time and reduction in losses when compared to that of GA and PSO.

References

1. Venkatesh B, Sadasivam G, Abdullah M (1999) Khan fuzzy logic based successive L.P. method for reactive power optimization. Electr Mach Power Syst 27:1141–1160
2. Sayed MAH El, Abdel-Rahman TM, Mansour MO Fast quadratic programming approach for large scale reactive power optimization
3. Iha K (1994) Reactive power optimization by genetic algorithm. IEEE Trans Power Syst 9(2), Mitsubishi Electric Corp., Kobe, Japan
4. Bhagwan Das D, Patvardhan C (2002) Reactive power dispatch with a hybrid stochastic search technique. Electrl Power Energy Syst 24:731–736
5. Lenin K, Mohan MR (2006) Ant colony search algorithm for optimal reactive power optimization Serbian. J Electr Eng 3(1):77–88
6. Shunmugalatha A, Raja Slochanal SMR (2008) Application of hybrid multiagent-based particle Swarm optimization to optimal reactive power dispatch. Electr Power Compon Syst 36:788–800
7. Bhattacharya B, Goswami SK (2007) Reactive power optimization through evolutionary techniques: a comparative study of the GA, DE and PSO algorithms. Intell Autom Soft Comput 13(4):453–461
8. Varadarajan M, Swarup KS (2008) Differential evolution approach for optimal reactive power dispatch. Appl Soft Comput 8:1549–1561
9. Bhattacharya A, Chattopadhyay PK (2010) Solution of optimal reactive power flow using biogeography-based optimization. Int J Electr Electron Eng 4:8
10. Khazali AH, Kalantar M (2011) Optimal reactive power dispatch based on harmony search algorithm. Electr Power Energy Syst 33:684–692
11. Mandal B, Roy PK (2013) Optimal reactive power dispatch using quasi-oppositional teaching learning based optimization. Electr Power Energy Syst 53:123–134
12. Yang X-S Firefly algorithms for multimodal optimization
13. Yang X-S Nature inspired meta-heuristic algorithms. Luniver press

Chapter 10
A New Real Time Approach for Reactive Power Control by STATCOM in Autonomous Wind-Diesel Hybrid Power System

M. Mynavathi, V. Kumar Chinnaiyan, P. Venkatesh and S. Balamurugan

Abstract This paper presents the reactive power control of Autonomous Wind-Diesel Hybrid Power Systems (AWDHPS) under dSPACE real time environment. The reactive power absorption and supply is done by a Static Compensator (STATCOM) controlled by proportional plus integral controller and tuned by dSPACE DS 1104. The disturbance parameters in the models were the change in reactive power of the load (ΔQ_L), the change in mechanical power input of the induction generator (ΔP_{IW}) respectively. The parameters were dynamically varied in control desk of dSPACE Software.

Keywords Autonomous wind-diesel hybrid power system · dSPACE · Induction generator · Synchronous generator · Static compensator

M. Mynavathi (✉) · V. Kumar Chinnaiyan
Department of Electrical and Electronics Engineering, Dr. N.G.P. Institute of Technology, Coimbatore, India
e-mail: mynavathimani@gmail.com

V. Kumar Chinnaiyan
e-mail: kumarchin@hotmail.com

P. Venkatesh
Department of Electrical and Electronics Engineering, Thiagarajar College of Engineering, Madurai, India

S. Balamurugan
Department of Electronics and Instrumentation Engineering, K.L.N. College of Engineering, Madurai, India

C. Kamalakannan et al. (eds.), *Power Electronics and Renewable Energy Systems*, Lecture Notes in Electrical Engineering 326, DOI 10.1007/978-81-322-2119-7_10

10.1 Introduction

Wind energy has gained a large momentum during the past two decades. The total installed wind capacity of the world reached nearly 283 GW in 2013. India ranks fifth in the world with an installed capacity of around 20 GW. In the Sagar Island, West Bengal of India a wind-diesel system comprising of 200 kW wind power and 280 kW diesel generator set is providing electricity to the villages in that island. Autonomous power systems produce electricity near the location of use and restrict grid expansion. The integration of wind energy system into the existing autonomous power system leads to a wind energy based autonomous hybrid power system [1]. The AWDHPS is becoming a viable and cost effective approach for remotely located communities. In AWDHPS the wind energy system is the main constituent and diesel system forms the back up. This type of hybrid power system saves fuel cost, improves power capacity to meet the increasing demand and maintains the continuity of supply in the system [1, 2].

The reactive power control of AWDHPS is based on the mathematical modelling of the system using power equations [3, 4]. The Components of AWDHPS such as induction generator, synchronous generator, IEEE type—I excitation system and STATCOM are modelled individually to achieve their transfer functions [5]. Then these transfer function blocks are combined together to build the MATLAB/Simulink model of the AWDHPS. The STATCOMs are used to control the reactive power. The MATLAB/Simulink models of the AWDHPS were developed to perform the reactive power control under variable slip condition [5].

This paper presents the reactive power control of Autonomous Wind-Diesel Hybrid Power Systems (AWDHPS) using dSPACE DS 1104. The reactive power absorption and supply is done by a Static Compensator (STATCOM) controlled by proportional plus integral controller and tuned by dSPACE DS 1104. The MATLAB/simulink block diagrams of AWDHPS were built in dSPACE real time environment. The reactive power control simulation was performed for three models of AWDHPS. The disturbance parameters in the models were the change in reactive power of the load (ΔQ_L) and the change in mechanical power input of the induction generator (ΔP_{IW}). The parameters were dynamically varied in control desk of dSPACE Software with DS1104 Research and Development (R&D) controller board mounted in personal computer under real time environment. The static and dynamic response curves were depicted and the time domain response specifications were tabulated.

10.2 Mathematical Model of the System

The wind-diesel power system in general comprises induction generator, synchronous Generator, electrical loads and reactive power compensator (SVC or STATCOM) and a control mechanism [6]. A diagram of the system is shown in Fig. 10.1.

The active power demand of the load is fulfilled by the synchronous generator and the induction generator.

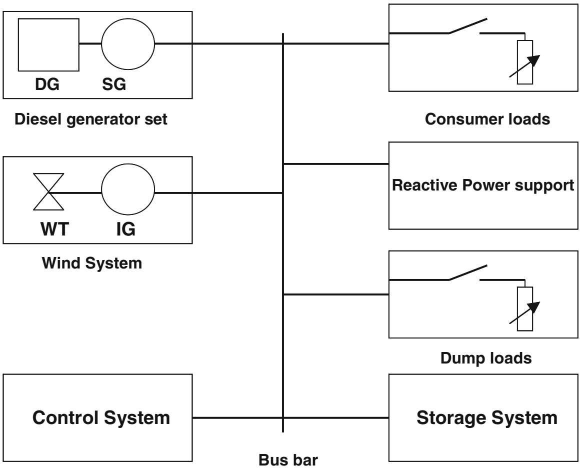

Fig. 10.1 Block diagram of autonomous wind-diesel hybrid power system

$$\mathrm{P_{IG} + P_{SG} = P_L} \tag{10.1}$$

The reactive power is supplied by means of STATCOM or SVC and partially by means of Synchronous generator.

For STATCOM

$$Q_{SG} + Q_{STATCOM} = Q_L + Q_{IG} \tag{10.2}$$

Due to disturbance in load reactive power ΔQ_L, the system voltage may change which results incremental change in reactive power of other components. The net reactive power surplus is

$$\Delta Q_{SG} + \Delta Q_{STATCOM} - \Delta Q_L - \Delta Q_{IG} \tag{10.3}$$

Further calculating,

$$\Delta Q_{SG} + \Delta Q_{SVC} - \Delta Q_L - \Delta Q_{IG} = \frac{d}{dt}\Delta E_M + D_V \Delta V \tag{10.4}$$

Further simplifying we get,

$$\begin{aligned} \Delta V(s) = \frac{K_V}{1 + T_V}&(\Delta Q_{SG}(s) + \Delta Q_{SVC}\,(s) \\ &- \Delta Q_L(s) - \Delta Q_{IG}\,(s)) \end{aligned} \tag{10.5}$$

$$\text{where } \mathrm{T_v = \frac{2H_r}{D_V V^0}} \tag{10.6}$$

$$\text{and } \mathrm{K_v = \frac{1}{D_V}} \tag{10.7}$$

10.2.1 Synchronous Generator Equation

The mathematical model of synchronous generator is given by

$$\Delta Q_{SG} = K_1 \Delta E'_q + K_2 \Delta V \tag{10.8}$$

$$\text{where } K_1 = \frac{V\cos\delta}{x'_d} \tag{10.9}$$

$$K_2 = \frac{E'_q\cos\delta - 2V}{x'_d} \tag{10.10}$$

10.2.2 Static Compensator Equations

The commonly used lead-lag structure is chosen in this study as STATCOM based controller [7]. The structure consists of gain block, signal washout block and two stage phase compensation block. The phase compensation block provides the appropriate phase lead characteristics to compensate for the phase lag between input and output signals [8, 9]. The signal washout block serves as a high-pass filter which allows signals associated with oscillations in input signal to pass unchanged. Without it steady changes in input would modify the output. Washout function value of time constant is not critical T_{ws} in range of 1–20 s. In this structure T_{ws} is washout constant and T_{2s}, T_{3s} are time constants. T_{ws} = 10 s; T_{2s} = T_{4s} = 0.3 s.

$$Washout\ block = \frac{sT_{ws}}{1 + sT_{ws}} \tag{10.11}$$

$$Two\ stage\ leadlag = \frac{(1 + sT_{1s})(1 + sT_{3s})}{(1 + sT_{2s})(1 + T_{4s})} \tag{10.12}$$

10.2.3 The Flux Linkage Equation

The flux linkage equations of the round rotor synchronous machine are as follows

$$(1 + sT_G)\Delta E'_q(s) = K_1 \Delta E_{fd}(s) + K_2 \Delta V(s) \tag{10.13}$$

10.2.4 Induction Generator Equation

The reactive power requirement of induction generator keeps on changing with the change of wind input power. For this purpose variable slip/speed model of induction generators has-been considered .The real power input, P_{IW} and reactive power, Q_{IG} absorbed by the induction generator can be written in terms of generator terminal voltage, slip and generator parameters. These equations can be written for small perturbation, by eliminating deviation in slip, Δs as

$$\Delta Q_{IG}(s) = K_7 \Delta P_m(s) + K_8 \Delta V(s) \tag{10.14}$$

10.3 dSPACE Simulation of AWDHPS

The dSPACE system consists of three components: the DS1104 controller board mounted within a personal computer, a breakout panel for connecting signal lines to the DS 1104 controller board and software tools for operating the DS1104 controller board through the Simulink environment [10]. The Real Time Interface data of AWDHPS Model - III is shown in Fig. 10.2. The step by step procedure of dSPACE simulation of AWDHPS [11, 12, 13] is given below:

1. Start Matlab and Simulink.
2. Prepare the AWDHPS model in Simulink as shown in Fig. 10.2.
3. Start Control Desk Software.
4. Build the Simulink model. During the build process Matlab converts Simulink model into system description file (sdf) and stores on the DS 1104 Processor.

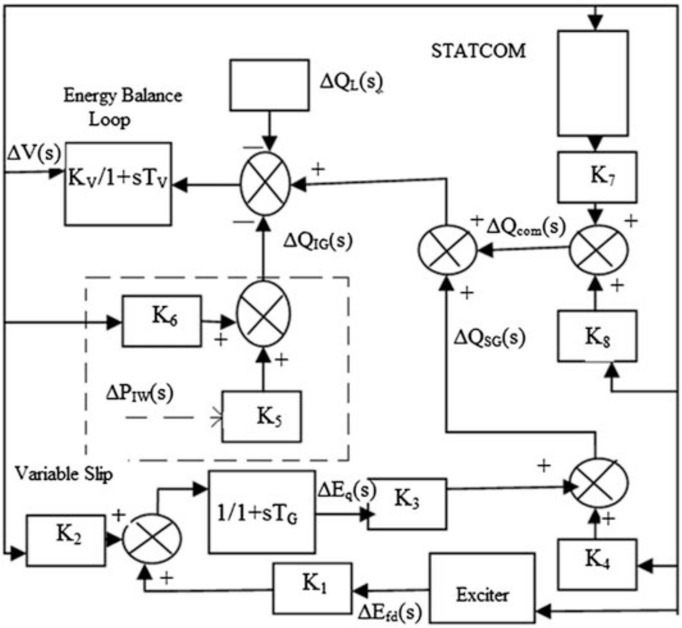

Fig. 10.2 Simulink model of AWDHPS model

5. After the building process sdf file is transferred to control desk environment automatically. This file contains information of variables used in simulink model. These variables can be directly plotted using control desk software environment.
6. Start new layout file in control desk and select capture setting block from instrument panel and draw on the layout screen. Similarly select a plotter array and draw it on layout. Select an appropriate variable from down menu and drop into the plotter block.
7. Start animation mode and observe the variation of variables on the plotter array.
8. To save the information use save button on capture setting window and give the name of mat file.

10.4 Results and Discussion

The simulink models used in the study are referred from [5]. The parameters used are given in Appendix. The real time simulation study is carried out using the computer with dSPACE DS1104 R&D controller board. AWDHPS Model is implemented as per the steps given in Sect. 10.3. The reactive power load change is a disturbance parameter in the model (It is assumed as a step block). The reactive power load change is compensated by the components such as STATCOM and SG in the model as given in Eq. (10.5). In the AWDHPS the reactive power demanded by the induction generator and load are supplied by STATCOM and Synchronous Generator. The AWDHPS is modelled as shown in Fig. 10.3 by assigning suitable parameters. In this paper performance curves obtained for various slip conditions under real time environment were presented. From the curve it is clear that the system satisfies Eq. (10.2).

10.4.1 Real Time Control of AWDHPS

It is seen from Fig. 10.4 that the real time control satisfies the reactive power compensation as mentioned by Eq. (10.2). Thus using dSPACE real time control can be done effectively.

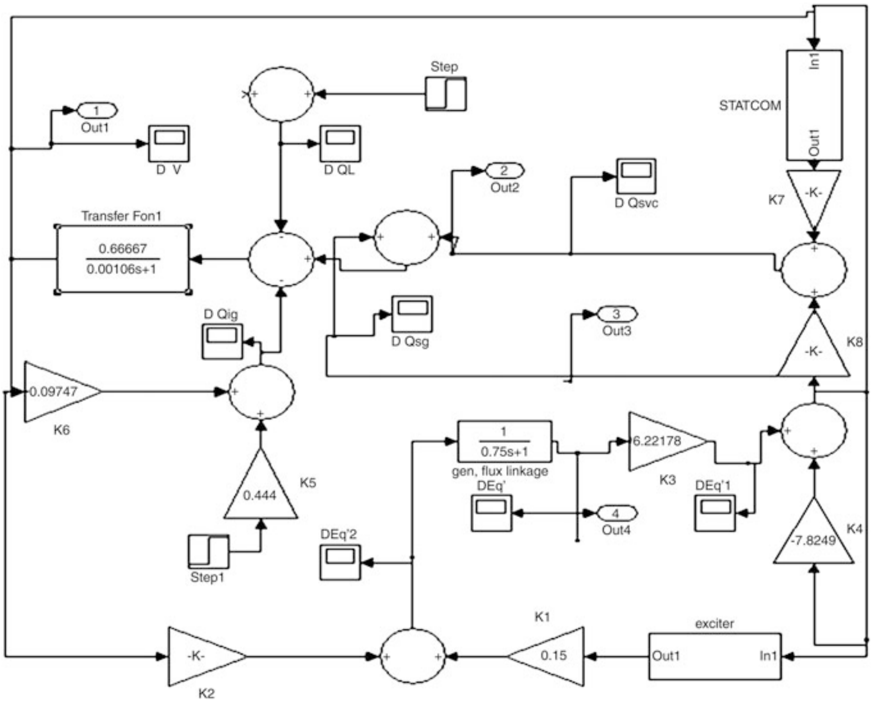

Fig. 10.3 Transfer function block diagram for the system data 1

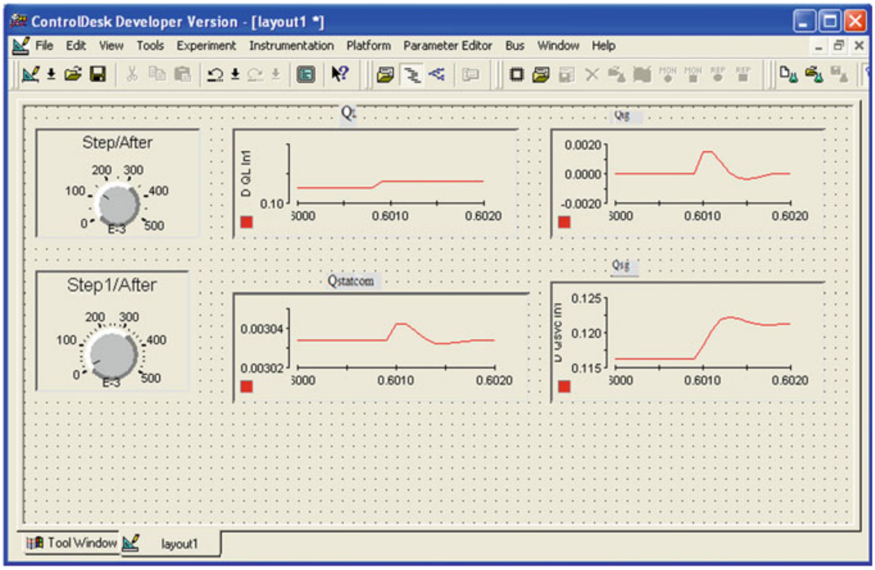

Fig. 10.4 Real time control of AWDHPS (system data 3)

10.5 Conclusion

The reactive power control of the autonomous wind-diesel hybrid power system has been presented in this paper. An IG has been considered for electric power generation from wind turbine and STATCOM is used for providing variable reactive power required by the system [14]. To study the effect of the size of the wind-turbine unit of the system on the dynamic performance, three examples of the wind-diesel hybrid system are considered with different wind-power generation capacities [15]. A complete dynamic model of the system has been derived to study the effect of load disturbances and input wind power disturbances. Some of the dynamic responses of the hybrid system have also been presented. It has been observed that during dynamic condition, the STATCOM eliminate the oscillations effectively within 0.01 s. caused by disturbances, for variable slip condition. As steady state condition reaches, the STATCOM provides the additional reactive power required by the load. The MATLAB/simulink block diagrams of three models of AWDHPS are built in dSPACE real time environment. The reactive power control simulation was performed for three models of AWDHPS. The disturbance parameters in the models are the change in reactive power of the load (ΔQ_L) and the change in mechanical power input of the induction generator (ΔP_{IW}) respectively. The parameters are dynamically varied using knobs in dSPACE DS1104 R&D controller board. The real time performance curves of the hybrid power system were presented. The desired dynamic response behavior of the three models is observed from the performance curves of the components present in them.

Appendix

System parameters	System data 1	System data 2	System data 3
System load capacity (wind)	150	100	50
Diesel capacity (kW)	150	150	150
Load capacity (kW)	250	200	150
Base power (kVA)	250	200	150
P_{SG} (p.u. kW)	0.4	0.5	0.6666
Q_{SG} (p.u. kVAR)	0.2	0.242	0.3333
Eq (p.u.)	1.1136	1.1108	1.094
E′q (p.u.)	0.9603	0.9256	0.838
QIG (p.u. kVAR)	0.6	0.5	0.333
S (%)	−4	−4	−2

References

1. Bansal RC (2007) Modelling and automatic reactive power control of isolated wind-diesel hybrid power systems using ANN. Sci Direct Energy Convers Manage 49:357–364
2. Panda S, Padhy NP (2007) Optimal location and controller design of STATCOM for power system stability improvement using PSO. Sci Direct J Franklin
3. Bansal RC, Zobaa AF, Saket RK (2005) Some issues related to power generation using wind energy conversion systems: an overview. Int J Emerg Electr Power Syst 3(2):1–17
4. Bansal RC, Bhatti TS, Kumar V (2007) Reactive power control of autonomous wind-diesel hybrid power systems using ANN. In: The 8th international power engineering conference (IPEC 2007)
5. Sivachandran P, Venkatesh P, Kamaraj N (2007) A review of wind energy based decentralized power generation systems with new developments in India. Int J Energy Environ 6:102–107. ISSN:1563-1362
6. Bansal RC, Bhatti TS (2008) Small signal analysis of isolated hybrid power systems. Narosa Publishing House, New Delhi
7. Sharma P, Saxena NK, Bhatti TS (2009) Study of autonomous hybrid power system using SVC and STATCOM. In: 3rd international conference on power systems, Kharagpur, India 27–29 Dec 2009
8. Kouadri B, Tahir Y (2008) Power flow and transient stability modelling of a 12-pulse Statcom. J Cybern Inf 7:9–25
9. Dizdarevic N, Majstrovic M, Andersson G (2003) FACTS-based reactive power compensation of wind energy conversion system. IEEE Bologna Power Tech Conference, Bologna, Italy
10. Sharma P, Bhatti TS, Ramakrishna KSS (2010) Control of reactive power of autonomous wind-diesel hybrid power systems. In: 2010 joint international conference, power electronics, drives and energy system and 2010 power India
11. Quijano N, Passino K (2002) A tutorial introduction to control systems development and implementation with dSPACE. Department of Electrical Engineering, The Ohio State University
12. dSPACE DS 1104 Technical data manual, dSPACE Inc., Gmbh
13. www.dspaceinc.com
14. Sharma1 P, Bhatti TS, Ramakrishna KSS (2010) Performance of a wind-diesel hybrid power system with STATCOM as a reactive power compensator. Smart Grid Renew Energy 1:153
15. Sharma P (2010) Transient stability investigation of the wind-diesel hybrid power system. Int J Energy Inf Commun 1(1):49–63

Chapter 11
Improving the Reliability of Wind Generators Using Dynamic Voltage Restorer

G. Sivasankar and V. Suresh Kumar

Abstract The increasing wind power integration with power grid has forced the situation to improve the reliability of wind generators for stable operation. One important problem with induction generator based wind farm is its low ride through capability to the grid voltage disturbance. Any disturbance such as voltage dip may cause wind farm outages. Since wind power contribution is in predominant percentage, such outages may lead to stability problem. The proposed strategy is to use dynamic voltage controller (DVR) to compensate the voltage disturbance. The DVR provides the wind generator the ability to remain connected in grid and improve the reliability. Extensive simulation results are included to illustrate the control and operation of DVR.

Keywords Wind generator · Power grid · Induction generator · Voltage controller

11.1 Introduction

The Wind power integration with power grid has increased significantly. An important problem with induction generator based wind farm is the inability to stay connected to the grid during a fault due to its low voltage ride through capability [1]. The fault such as dip may lead to wind generators outages and severe damage. Hence wind generators are usually disconnected from the grid for safety. In the past the wind power penetration was low in percentage, hence any outage may not affect the system stability. But in recent years wind generation is in rapid expansion and its contribution to grid is as do conventional generation plant [2–4]. Hence mitigation of fault can only

G. Sivasankar (✉) · V. Suresh Kumar
Department of Electrical and Electronics Engineering, Thiagarajar College of Engineering, Madurai 625015, Tamil Nadu, India
e-mail: g.sivasankar@live.in

C. Kamalakannan et al. (eds.), *Power Electronics and Renewable Energy Systems*,
Lecture Notes in Electrical Engineering 326, DOI 10.1007/978-81-322-2119-7_11

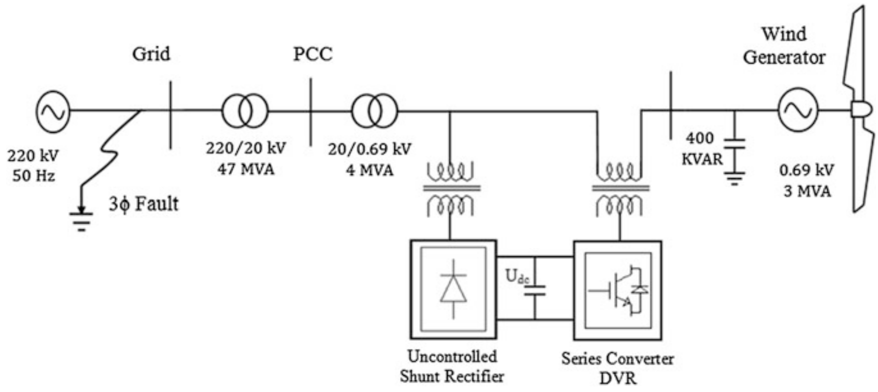

Fig. 11.1 Wind generator connected to grid with DVR protection

be a complete solution for the aforementioned problems [5]. There are several methods and techniques that use STATCOM, SVC for dip mitigation [6]. However use of DVR is an appropriate solution for dip and its related issues [7]. In this paper the effect of symmetrical and unsymmetrical voltage dip on fixed speed wind generators and the associated problems caused in the grids are discussed. The proposed strategy is to use dynamic voltage restorer (DVR) for voltage dip compensation by series voltage injection (shown in Fig. 11.1). Vector control scheme is employed to compensate for both voltage magnitude and phase jump [8]. The proposed DVR can also exchange real and reactive power demand of wind generator [9]. Matlab simulink is used for wind farm modeling and to realize DVR control strategies.

11.2 Control of the DVR

The considerations for control of the DVR include: reference voltage generation, control of injection voltage, real and reactive power exchange and protection of DVR. A high performance control is required for a grid integration system [10]. Hence vector control scheme is employed for control of the DVR (shown in Fig. 11.2). A vector-controller generates continuous control signals for instantaneous current and voltage values to be controlled in a system. The controller has to generate a accurate reference voltage for successful compensation. Software phase locked loop (SPLL) circuit is used for synchronization of the system [11]. Frequency adaptive performance, low computational burden and relatively high filtering capability are the advantages of this method, which make it a successful solution for voltage distorted and frequency-varying conditions.

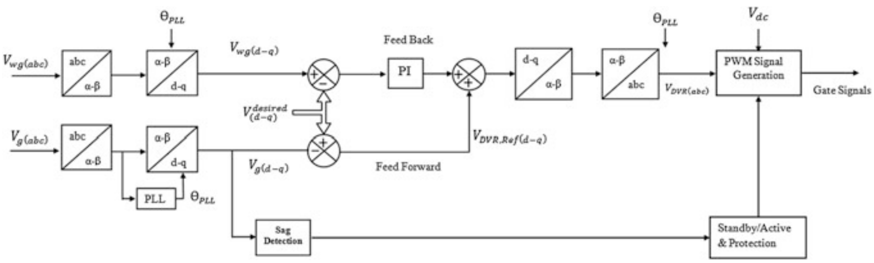

Fig. 11.2 Vector control in the rotating dq reference frame

11.3 Series Voltage Control Scheme

The control scheme uses Park (dq0) transformation to obtain d–q component, which is a widely used transformation. It is applied for time-dependent arbitrary three-phase system which is used to decouple variables and refer to common reference frame. The grid voltage may contain negative and zero-sequence components due to unbalanced voltage. For categorizing the sequence components the system voltage is transformed into the synchronous *dq0* reference frame. For an unbalanced voltage, the Park transformation results in

$$U^{ref}_{DVR(d-q)} = U^{ref}_{(d-q)} - U_{g(d-q)} \tag{11.1}$$

The voltage dip detection is carried out by comparing the grid voltage with the reference voltage to obtain the value of the setting voltage $U^{ref}_{DVR(d-q)}$ to be generated in the DVR, so that the restored wind generator voltage reaches its nominal value. The $U^{ref}_{DVR(d-q)}$ reference voltage of Eq. 11.1 is then inversely transformed into the abc reference frame. Finally, a sinusoidal pulse width modulation (SPWM) is used for the inverter switching and voltage dip is compensated.

The fault ride through capability of wind generator is not only affected by voltage disturbance but also due to power dearth. The proposed DVR is capable of providing real and reactive power support. The uncontrolled shunt rectifiers are used to maintain a strong dc link which acts as a source to meet the real power demand. The reactive power compensation is done by switching the series converter in appropriate phase angle. The series connected DVR inverter may face severe problem due to transients or fault current in the grid. And there is a chance of high in-rush of current reflects into DVR, if the dip is not completely compensated. A proper protection of DVR inverter is one of the important aspects of the design which can be done using the design scheme presented in [12].

11.4 Results and Discussion

In this section, two different fault cases are considered for compensation. In case I, voltage dip due to symmetrical three-phase to ground fault is investigated and it is assumed that there is no phase jump. The dip mitigation is done by in phase voltage insertion. In case II unbalanced dip due to unsymmetrical phase-to-phase grounded fault is investigated.

11.4.1 Three-Phase-to-Ground Fault and Mitigation

A three-phase-to-ground fault is evolved near the grid which starts at 500 ms and lasts for about 100 ms with a voltage dip of 40 % at grid is shown in Fig. 11.3a. The effect of fault on wind generator was synthesized by d–q component. Since it is a balanced fault, only positive sequences are represented, as depicted in Fig. 11.3b. The real power contributed by the wind farm to the grid is limited by the fault and the reactive power supplied to the wind farm is also restricted as shown in Fig. 11.3c.

Using the vector control strategy, voltage dip magnitude was calculated and DVR compensation voltage is generated as shown in Fig. 11.4a. The dip is compensated by an in-phase insertion of voltage in series with the line. The Fig. 11.4b shows the compensated voltage of the wind generator. The real and reactive power at wind generator bus after compensation of three-phase-to-ground fault is depicted in Fig. 11.4c.

11.4.2 Phase-to-Phase Grounded Fault and Mitigation

Unbalanced dip is realized using phase-to-phase grounded fault near grid. The voltage variation at wind generator is as shown in Fig. 11.5a. The d–q components of positive and negative sequences of wind generator bus during fault condition are obtained as shown in Fig. 11.5b, c. The Fig. 11.5d shows the real and reactive power at wind generator bus during the fault. The DVR control reference signal is depicted in Fig. 11.6a. Figure 11.6b shows the voltage level after the compensation. Real and reactive power at wind generator bus after compensation of phase-to-phase ground fault is show in Fig. 11.6c.

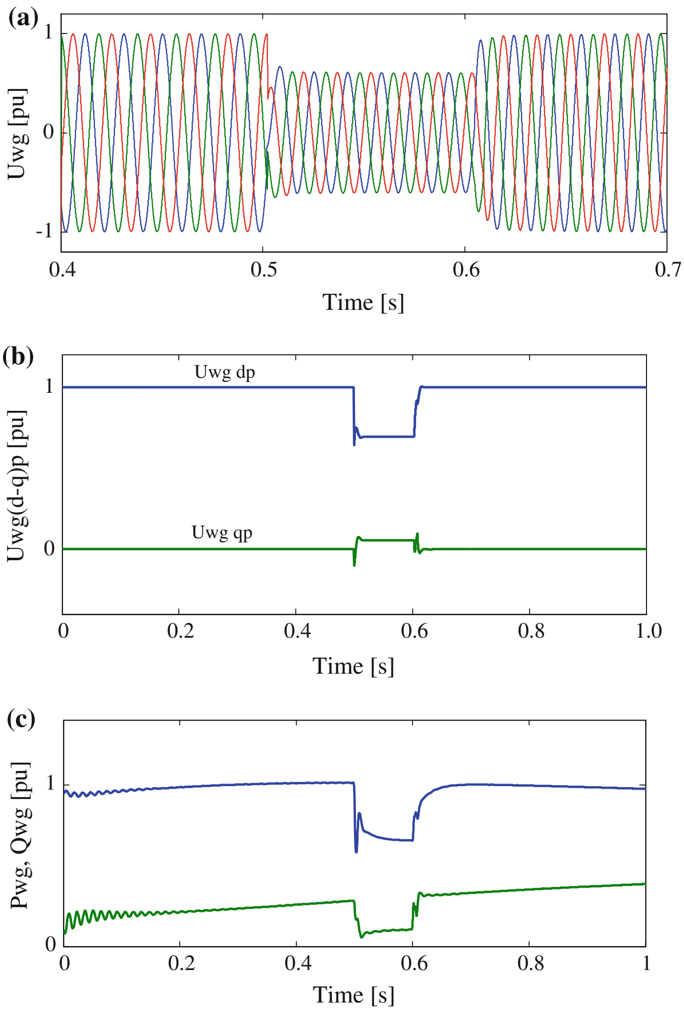

Fig. 11.3 The grid connected wind generator during three- phase-to-ground fault. **a** Voltage dip. **b** Positive sequence components. **c** Active and reactive power at wind generator

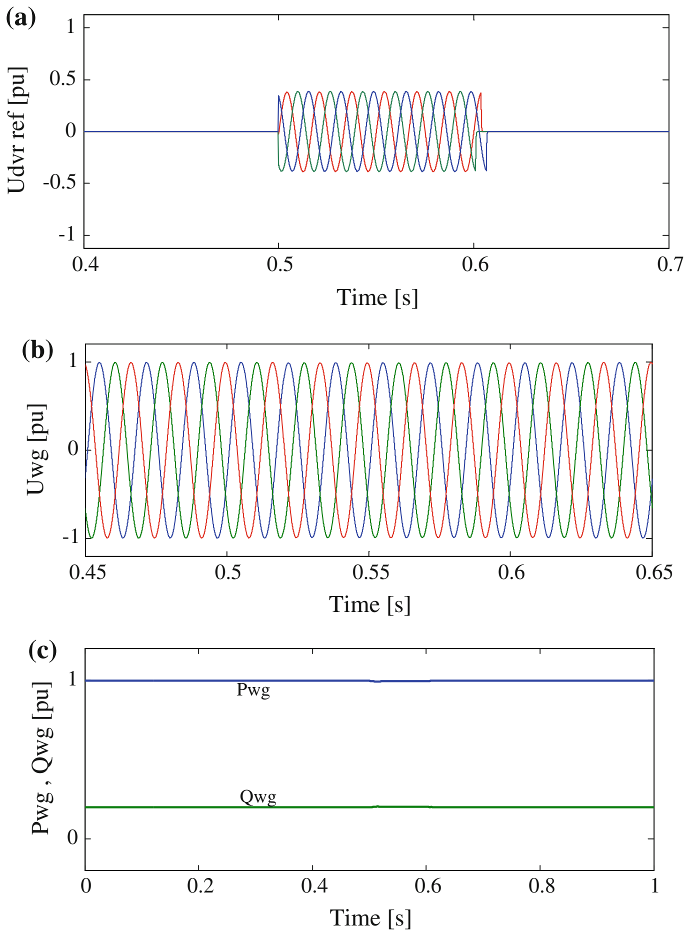

Fig. 11.4 The grid connected wind generator after three- phase-to-ground fault compensation. **a** DVR reference signal. **b** Compensated voltage. **c** Active and reactive power at wind generator

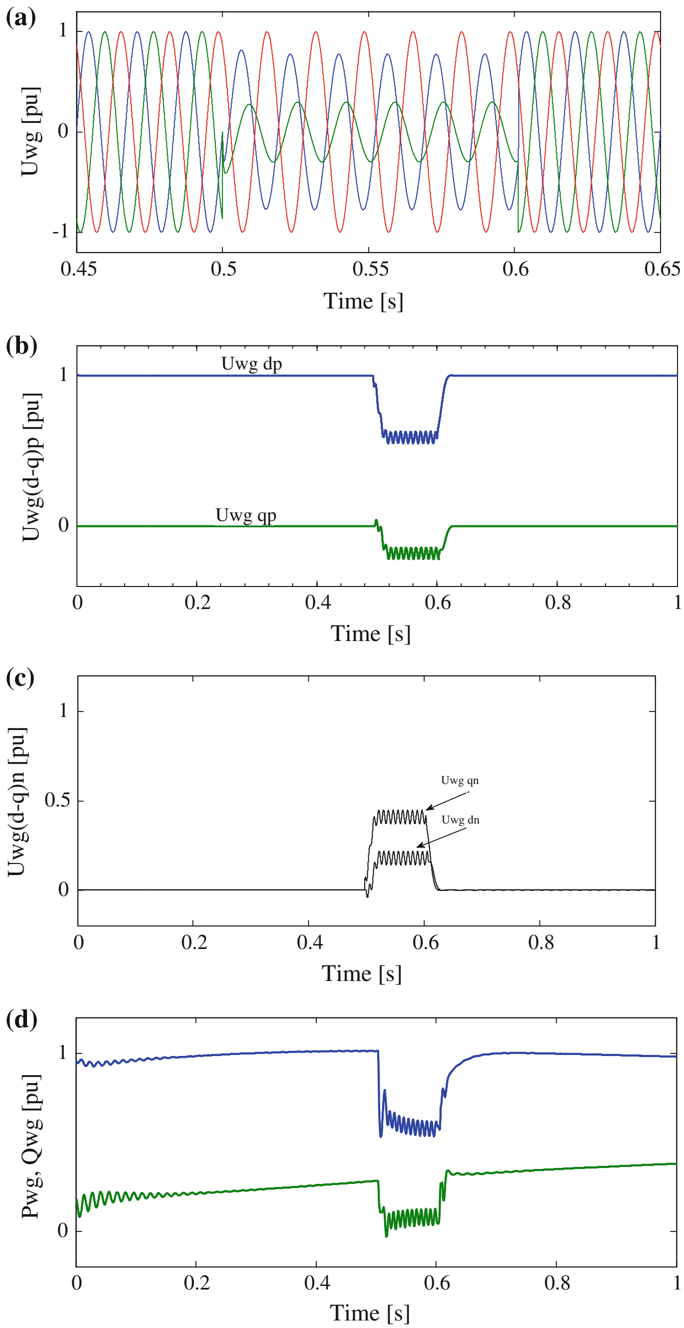

Fig. 11.5 The grid connected wind generator during phase-to-phase fault. **a** Voltage dip. **b** Positive sequence components. **c** Negative sequence component. **d** Active and reactive power at wind generator

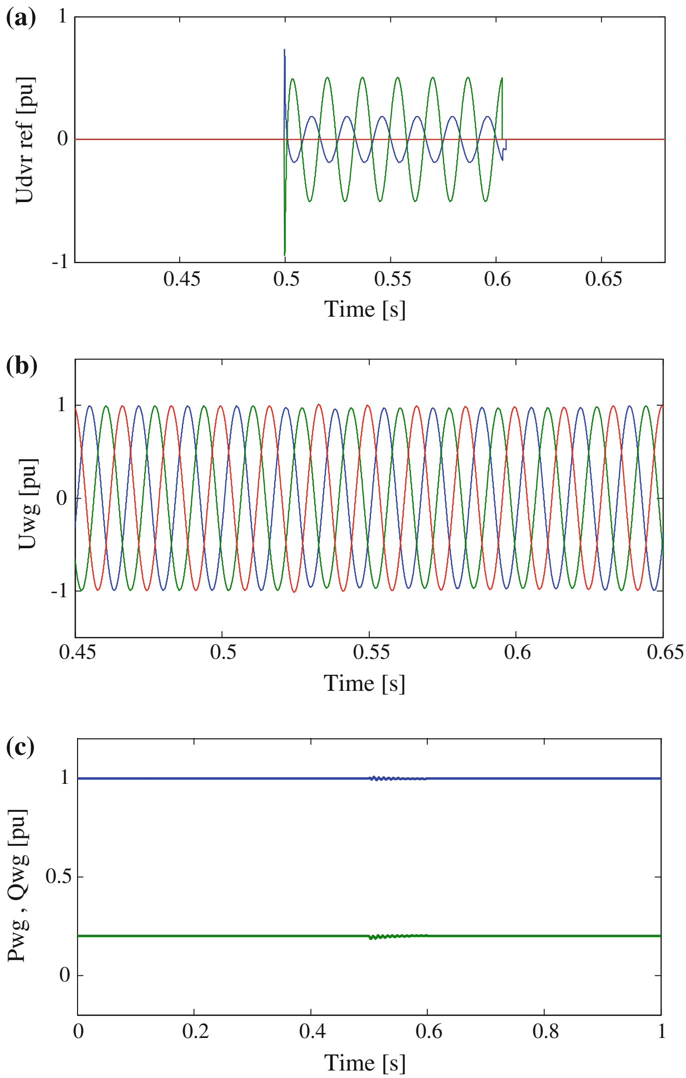

Fig. 11.6 The grid connected wind generator after phase-to-phase fault compensation. **a** DVR reference signal. **b** Compensated voltage. **c** Active and reactive power at wind generator

11.5 Conclusion

The proposed DVR can recover voltage dip and provide real and reactive power support. Hence fault ride through capability of the Induction generator based wind farm is improved with the aid of a DVR. The wind generator is able to remain connected to the grid without loss of stability. The proposed control scheme can also protect the wind generator from destruction. Wind farm modeling and DVR control strategies are simulated using matlab simulation, which demonstrates the viability of the proposed scheme. The results show that the control technique is very effective and yield excellent compensation for voltage dip and associated problems.

References

1. Freitas W, Vieira JCM, Morelato A, da Silva LCP, da Costa VF, Lemos Flavio AB (2006) Synchronous and induction machines for distributed generation applications. IEEE Trans Power Syst 21(1):301–311
2. Bollen, MHJ, Hager, M (2005) Impact of increasing penetration of distributed generation of the number of voltage dips experienced by end-customers. Presented at the 18th International Conference Electricity Distribution, Turin, Italy, 6–9 June 2005
3. Singh Mukhtiar, Khadkikar Vinod, Chandra Ambrish, Varma RK (2011) Grid interconnection of renewable energy sources at the distribution level with power-quality improvement features. IEEE Trans Power Syst 26(1):307–315
4. Begovic PM, Rohatgi A (2006) Recloser allocation for improved reliability of DG enhanced distribution networks. IEEE Trans Power Syst 21(3):1442–1449
5. Bollen MHJ (1999) Understanding power quality problems: voltage sags and interruptions. IEEE Press, New York
6. Molinas M, Suul JA, Undeland T (2008) Low voltage ride through of wind farms with cage generators: STATCOM versus SVC. IEEE Trans Power Electron 23(3):1104–1117
7. Nielsen JG, Newman M, Nielsen H, Blaabjerg F (2004) Control and testing of a dynamic voltage restorer (DVR) at medium voltage level. IEEE Trans Power Electron 19(3):806–813
8. Awad H, Svensson J, Bollen MHJ (2004) Mitigation of unbalanced voltage dips using static series compensator. IEEE Trans. Power Electron. 19(3):837–846
9. Ottersten R, Svensson J (2002) Vector current controlled voltage source converter—deadbeat control and saturation strategies. IEEE Trans Power Electron 279–285
10. Muyeen SM, Takahashi R, Murata T, Tamura J (2010) A variable speed wind turbine control strategy to meet wind farm grid code requirements. IEEE Trans Power Syst 25(1):331–340
11. Awad H, Svensson J, Bollen MJ (2005) Tunning phase locked loop for series connected converters. IEEE Trans Power Deliv 20(1):300–308
12. Newman MJ, An Holes DG (2002) integrated approach for the protection of series injection inverters. IEEE Trans Ind Appl 38(3):679–687

Chapter 12
Rule Weight Tuned Fuzzy Controller for Robot Manipulator Using Quantum Inspired Firefly Algorithm

A. Manju and A. Monasubramaniam

Abstract One of the most important factors in designing controller is the tuning of controller parameters which is basically an optimization problem. In this paper, weights of the consequent part of fuzzy PD+I type-I controller employed for Trajectory control of Puma560 Robot manipulator is tuned using Quantum inspired Firefly Algorithm. A comparative study on above tuning strategy using other metaheuristic algorithms like GA, PSO, QPSO, and FA are also performed to exhibit the potential of Quantum inspired algorithm.

Keywords Optimization · Firefly algorithm · GA · PSO

12.1 Introduction

Robots will be eventual in future due to the increasing demand in productivity and quality of the products in manufacturing process. The then problem is to control such Industrial Robot manipulators, mainly to make the manipulator follow a desired trajectory. Owing to the strong non-linear characteristics and parameter variations in real environments, tracking control of a robot arm system becomes quite difficult. PUMA 560 is an important class of Robots, which are widely used for material handling, welding, assembling, painting, grinding and other industrial applications [1]. Fuzzy PD+I controllers are the most generally used fuzzy controller as it has the following advantages of being Simple, having Less overshoot, Removes steady state error, and smoothens control signal [2].

A. Manju (✉)
SKP Engineering College, Tiruvannamalai 606611, Tamil Nadu, India
e-mail: manju.senthil@gmail.com

A. Monasubramaniam
Galgotias College of Engineering and Technology,
Greater Noida 201306, Uttar Pradesh, India

C. Kamalakannan et al. (eds.), *Power Electronics and Renewable Energy Systems*,
Lecture Notes in Electrical Engineering 326, DOI 10.1007/978-81-322-2119-7_12

Fuzzy controllers can be tuned by various methods of which the changing the Rule-weights enhances the robustness, flexibility and system modeling capability [3]. Moreover complexity is increased in parallel to accuracy providing a tradeoff relation between the accuracy and complexity [4]. If a rule weight is applied to the consequent part of the rule, it modifies the size of the rule's output value [5].

Nature inspired optimization algorithms have been gaining its importance over past several decades, of which the recent member is Firefly algorithm (FA). FA, inspired by social behavior of fireflies was found to handle multimodal problems of combinational and numerical optimization more naturally and efficiently. Fireflies are assumed to be present in atmosphere of uniform density [6]. The authors formulated a quantum Delta potential well model for Firefly Algorithm by placing the fireflies in an exponent atmosphere with global updating operator and weighting function [7]. Employing above Quantum inspired FA (QFA) on well known Benchmark problems exhibits stronger local and global searching capability of the algorithm as many other quantum inspired versions outperforming their counterparts [8].

In this paper above QFA is employed to tune the Fuzzy PD+I controller to control PUMA 560 robot. The reference fuzzy controller is obtained by tuning the scaling parameters, which is then followed by the tuning of the rule-weights. To exhibit the superiority, the controller is also tuned with algorithms like Genetic algorithm (GA), particle swarm optimization (PSO), FA and quantum inspired particle swarm optimization (QPSO).

Rest of the paper is organized as follows: Sect. 12.2 gives a brief introduction to PUMA560 robot arm and its dynamics and Sect. 12.3 describes the employed fuzzy controller. In Sect. 12.4 the basic QFA is outlined, and Sect. 12.5 gives the results and discussion.

12.2 Dynamics of Puma560

Dynamics of a serial n-link rigid robot can be written as:

$$M(q)\ddot{q} + c(q,\dot{q}) + g(q) = \tau \tag{12.1}$$

where q is the $n \times 1$ vector of joint displacements, $\dot{q}$ is the $n \times 1$ vector of joint velocities, τ is the $n \times 1$ vector of actuators applied torques, $M(q)$ is the $n \times n$ symmetric positive definite manipulator inertia matrix, $c(q,\dot{q})$ is the $n \times 1$ vector of centripetal and Coriolis torques and $g(q)$ is the $n \times 1$ vector of gravitational torques due to gravity. We assume that the robot joints are joined together with revolute joints.

Let the desired joint position q_d be a twice differentiable vector function. We define a control problem to determine the actuator torques in such a way that the following control aim be achieved.

$$\lim_{t \to \inf} q(t) = q_d(t) \tag{12.2}$$

A six DOF PUMA-560 robot is considered for the simulation, the Kinematical and dynamical parameters of the arm and the torque limitations are adopted from the work of Srinivasan and Nigam [9] and references therein.

12.3 Fuzzy PD+I Controller

The fuzzy PD+I controller given in Fig. 12.1 uses linear fuzzy inference method. In this structure, the fuzzy system is applied only to the proportional and derivative signal of the linear PID controller [10]. The integral signal uses conventional linear method. The major roll of the integral signal is to eliminate the steady state error. The transient response is affected mostly by the proportional signal and the derivative signal. For the enhancement of the transient response, the varying gains are implemented on the proportional and derivative parts using two-input fuzzy system. The nonlinearities that make the varying gains possible are added by the fuzzy control rules and the membership functions.

Initially above gains are coarsely tuned in order to produce base or reference system. Gaussian membership function with negative, zero and positive fuzzy sets are used to represent the inputs and outputs of the controller as shown in Fig. 12.2. The rule base is shown in Table 12.1.

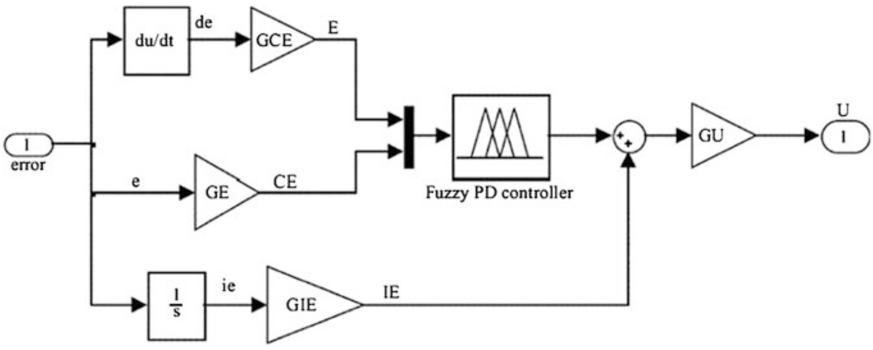

Fig. 12.1 Fuzzy PD+I controller

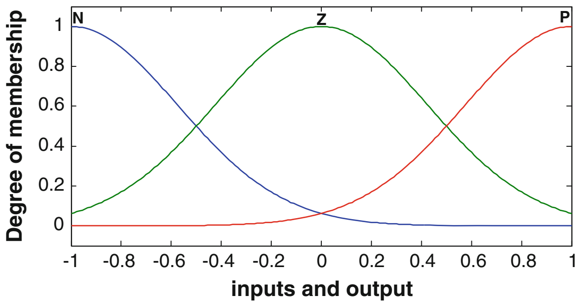

Fig. 12.2 Membership functions for fuzzy PD input and output variables

Table 12.1 Fuzzy PD control rules

		Change of error ($\dot{e}$)		
		N	Z	P
Error (e)	N	N	N	Z
	Z	N	Z	Z
	P	Z	P	P

12.4 Quantum Inspired Firefly Algorithm

FA proposed by Yang [6] and other researchers employed either constant or varying attenuation coefficient based on characteristic length of the search space. In all the above cases, Fireflies are assumed to be present in atmosphere of uniform density. But typically, the density of the atmosphere decays exponentially with height as in exponential atmosphere model [11].

Using the above concept the attenuation coefficient is assumed to be exponentially varying with distance [12]. Inspired by Quantum mechanics and trajectory analysis of PSO by Clerc and Kennedy [13] Delta potential well model of PSO was introduced by Sun et al. [14]. Unlike PSO, QPSO needs no velocity vectors for particles, and has fewer parameters to adjust, making it easier to implement. The iterative equation of QPSO is very different from that of PSO as given below

$$X_i(t+1) = p_i(t) \pm \beta \cdot |mbest(t) - X_i(t)| \cdot \ln(1/u) \tag{12.3}$$

where *mbest* is the mean value of the pbest positions of all particles [14] and β is the only parameter of adjustment of speed of convergence, named as contraction–expansion coefficient.

Adding a global updation term and inertia weight factor to the FA updation formula (as given in Eq. 12.4) of fireflies in exponential atmosphere, a quantum Delta potential well model for FA (QFA) has been arrived [7].

$$x_i = x_i + \beta_0 e^{-\gamma r_{i,j}^2}(x_j - x_i) + u_i \tag{12.4}$$

$$\beta = \beta_0 e^{-\gamma r_j} \tag{12.5}$$

where x_i represents a solution for firefly i in whereas β denotes its attractiveness. Attractiveness is represented by the monotonic decreasing function as given in Eq. 12.5. $\beta_0 \in (0, 1)$ and $\gamma \in (0, 1)$ are predetermined algorithm parameters: maximum attractiveness value and absorption coefficient, respectively.

In the process of formulation of QPSO in [14] the potential energy of the particle, $V(x)$ is equated to a dirac delta function. In Basic FA with fireflies in atmosphere with constant attenuation coefficient, the velocity function does not constitute a dirac delta function. But when the fireflies are placed in exponentially varying attenuation coefficient, the potential energy of the particle can be equated to the function $V(x)$ in [14]. Searching procedure of proposed QFA is similar to that of QPSO except for the updation part which happens only when it finds the brighter ones.

12.5 Results and Discussion

GA, PSO, QPSO, FA and QFA are employed to coarsely tune the gains of the fuzzy controller employed to PUMA 560 robot with input Sine wave trajectory [15]. The coarsely tuned base system is later subjected to rule weight tuning. In case of GA the chromosomes are encoded with the values of weights of consequent part of the if-then rule of the fuzzy rule base. Whereas in case of other swarm based algorithms like PSO and QPSO the rule weights are encoded as swarm positions and as locations of fireflies in FA and QFA. For GA the default settings are employed except for the population size which is set to be slightly higher than the number of variables to be tuned. In case of other algorithms like PSO, QPSO, FA and QFA the

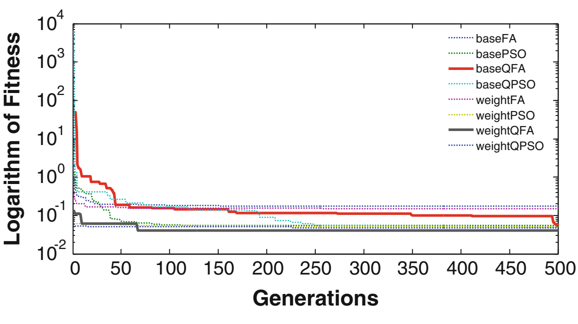

Fig. 12.3 Convergence of fuzzy PD+I type 1 controller using various algorithms

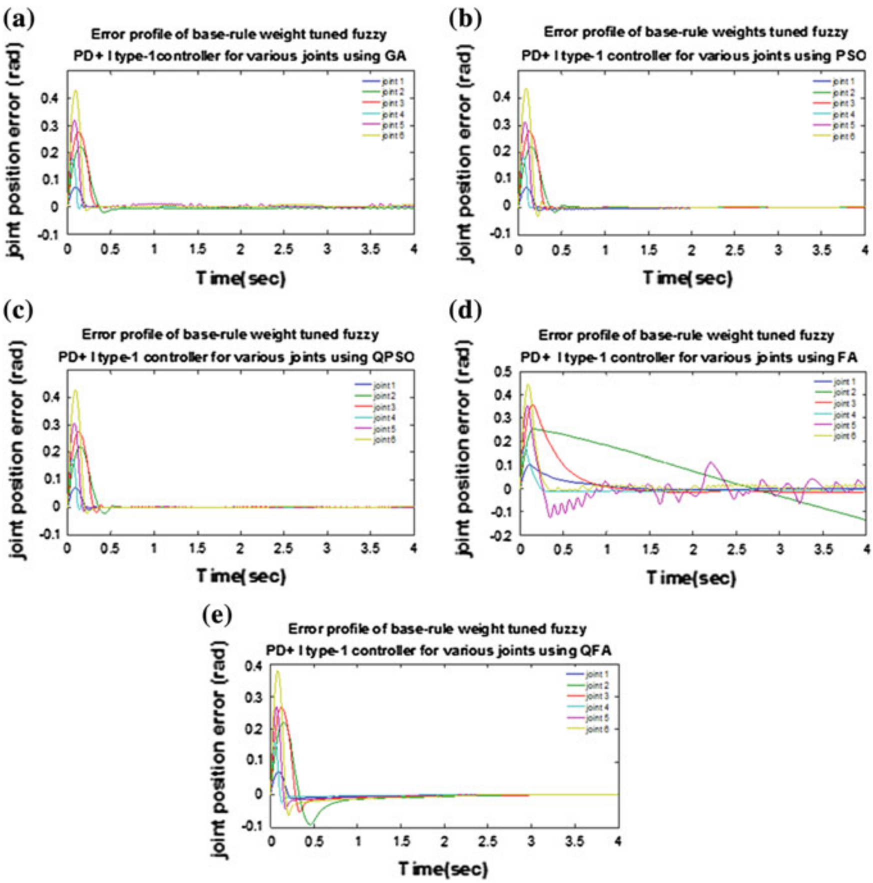

Fig. 12.4 Joint position error profiles using **a** GA, **b** PSO, **c** QPSO, **d** FA, **e** QFA

Table 12.2 Results of scalar tuning and rule-weight tuning using various algorithms

Algorithm	Type	ISE	IAE	ITAE	ITSE
GA	Scalar tuning	0.05	0.2587	0.1023	0.0057823
	Base-rule weight tuning	0.0488	0.2576	0.116	0.0057782
PSO	Scalar tuning	0.0537	0.3886	0.3225	0.009046
	Base-rule weight tuning	0.0499	0.2384	0.0594	0.0055786
QPSO	Scalar tuning	0.0496	0.2293	0.0495	0.0054983
	Base-rule weight tuning	0.048	0.2356	0.0697	0.0053466
FA	Scalar tuning	0.1735	1.1689	1.6082	0.17559
	Base-rule weight tuning	0.15	0.9977	1.2067	0.10229
QFA	Scalar tuning	0.0544	0.3434	0.1484	0.007537
	Base-rule weight tuning	0.0413	0.2978	0.1237	0.0056089

Table 12.3 Results of scalar tuning and rule-weight tuning for individual joints using various algorithms

Algorithm	Joint 1		Joint 2		Joint 3		Joint 4		Joint 5		Join
	RMS	MAX	RMS	MAX	RMS	MAX	RMS	MAX	RMS	MAX	RMS
GA	0.011972	0.073366	0.045352	0.2218	0.054714	0.27838	0.023199	0.18445	0.045482	0.31364	0.068449
	0.011575	0.071502	0.045214	0.22035	0.054131	0.27587	0.021929	0.17723	0.046374	0.31749	0.066753
PSO	0.012722	0.073288	0.048985	0.22478	0.055819	0.27736	0.025517	0.1827	0.048296	0.3276	0.069023
	0.012145	0.072149	0.045364	0.22179	0.05497	0.27956	0.022778	0.1827	0.04547	0.31364	0.068266
QPSO	0.011652	0.071916	0.045429	0.22211	0.054409	0.27728	0.022766	0.1827	0.045407	0.31364	0.068246
	0.011588	0.0714	0.045148	0.22094	0.0542	0.27631	0.021922	0.17723	0.044175	0.3067	0.066691
FA	0.021473	0.081433	0.14607	0.25224	0.099332	0.35399	0.043409	0.21642	0.062722	0.35527	0.076763
	0.0249	0.10115	0.13555	0.25225	0.087376	0.35484	0.026816	0.17724	0.06938	0.35274	0.073088
QFA	0.012766	0.074237	0.049424	0.22298	0.05725	0.28104	0.024252	0.19008	0.046937	0.31552	0.070112
	0.011816	0.07039	0.049038	0.22177	0.052442	0.26705	0.019263	0.16178	0.037159	0.26822	0.057201

swarm size is set to be twice the number of variables to be tuned. Computational steps of PSO and QPSO is given in [Xi 200]. Inertia weight is taken to be linearly decreasing from 0.9 to 0.4 [16] and the acceleration constants c_1 and c_2 are taken as 2.0. Maximum number of generations is equal to 500 which is the stopping criterion. For QPSO algorithm, the parameter β is linearly decreased from 1.0 to 0.5. Computational steps and settings of FA and QFA is as in [7]. Objective function being the overall ISE given by

$$ISE = \sum_{i=1}^{6} \int e_i^2(t)dt \tag{12.6}$$

where $e_i(t)$ is the error signal for the ith joint. Here i can take values from 1 to 6 corresponding to 6 joints.

Numerical simulations of proposed controllers are performed in MATLAB. Figure 12.3 shows the Convergence graph of fuzzy PD+I type 1 controller using various algorithms. Faster convergence is observed in case of QFA for both scalar tuning and rule weight tuning process. But the speed of convergence is higher in case of rule weight tuning process. Figure 12.4a–e shows the joint position error profile for various tuning strategies. Performance indices of Root Mean Square error (RMS) and Maximum error (Max) are used for comparison. The values of performance indices for various control strategies and various joints are tabulated in Tables 12.2 and 12.3. Above tabulation emphasize that a satisfactory tracking precision could be achieved using rule tuned fuzzy PD+I controller and Quantum inspired algorithms. Moreover it is observed that QFA outperforms other algorithms.

References

1. Mazhari SA, Kumar S (2008) PUMA 560 optimal trajectory control using genetic algorithm, simulated annealing and generalized pattern search techniques. Int J Electr, Comput Syst Eng 2(1):71–80
2. Jantzen J (2007) Foundations of fuzzy control. Wiley, Hoboken. ISBN 978-0-470-02963-3
3. Alcala R, Cordon O, Herrera F (2003) Combining rule weight learning and rule selection to obtain simpler and more accurate linguistic fuzzy models. Modelling with words, LNAI 2873, Springer, Berlin, pp 44–64
4. Ishibuchi H, Kaisho Y, Nojima Y (2003) Complexity, interpretability and explanation capability of fuzzy rule-based classifiers. FUZZ-IEEE 2009, Korea. ISBN: 978-1-4244-3597-5, 20–24 Aug 2009
5. Nauck D (2000) Adaptive rule weights in neuro-fuzzy systems. Neural Comput Appl 9:60–70
6. Yang XS (2008) Nature-inspired metaheuristic algorithms. Luniver Press, UK
7. Manju A, Nigam MJ (2012) Firefly algorithm with fireflies having quantum behavior. In: Proceedings of the 2012 international conference on radar, communication and computing (ICRCC), pp 117–119. doi:10.1109/ICRCC.2012.6450559
8. Manju A, Nigam MJ (2012) Applications of quantum inspired computational intelligence: a survey. Artif Intell Rev. doi:10.1007/s10462-012-9330-6

9. Srinivasan A, Nigam MJ (2008) Fuzzy PD+I control of a six DOF robot manipulator. Ind Rob: Int J 35(2):125–132
10. Kim BJ, Chung CC (2002) Design of Fuzzy PD+I controller for tracking control. In: Proceedings of the American control conference anchorage, AK, May 8–1, AACC, pp 2124–2129
11. Tewari A (2007) Atmospheric and space flight dynamics modeling and simulation with MATLAB and Simulink. Birkhäuser, Basel, Berlin, Boston
12. Manju A, Nigam MJ (2012) Application of exponential atmosphere concept in improving Firefly Algorithm. In: 3rd international conference on computing communication and networking technologies (ICCCNT), pp 1–6. doi:10.1109/ICCCNT.2012.6395946
13. Clerc M, Kennedy J (2002) The particle swarm: explosion, stability, and convergence in a multidimensional complex space. IEEE Trans Evol Comput 6:58–73
14. Sun J, Feng B, Xu WB (2004) Particle swarm optimization with particles having quantum behavior. In: IEEE proceedings of congress on evolutionary computation, pp 325–331
15. Srinivasan A, Nigam MJ (2009) New hybrid adaptive neuro-fuzzy algorithms for manipulator control with uncertainties-comparative study. ISA Trans 48:497–502
16. Xi M, Sun J, Xu W (2008) An improved quantum-behaved particle swarm optimization algorithm with weighted mean best position. Appl Math Comput 205:751–759

Chapter 13
Design and Investigation of Solar Powered Soft Switched Z-Source Inverter

R. Uthirasamy, U.S. Ragupathy and R. Mithra

Abstract This paper introduces the design and analysis of Zero Voltage Switching (ZVS) scheme of solar powered Z-Source Inverter (ZSI) topology for the UPS applications. The ZSI topology employs a unique impedance network which couples the solar power and the utility. A resonant circuit is designed to obtain ZVS of ZSI, thereby voltage stress across the inverter switches are minimized. The proposed configuration reduces the switching loss and improves the utilization of solar power. Moreover, it highly enhances the reliability of the inverter because the shoot through no longer destroys the inverter. The entire system is developed and simulated using SIMULINK tools. The performance of the proposed system is analyzed and necessary simulation results are obtained. A prototype model of single phase soft switched ZSI is developed and its results are validated.

Keywords Solar PV · Irradiance · Soft switching · Z-Source inverter · H-Bridge · Total harmonic distortion

13.1 Introduction

Soft switching techniques have been analyzed and enhanced in recent years for power converters to reduce voltage stress across the switches. Traditional inverters are Voltage Source Inverter (VSI) and Current Source Inverter (CSI), which can

R. Uthirasamy (✉) · R. Mithra
Department of Electrical and Electronics Engineering, Jansons Institute of Technology, Karumathampatti, Coimbatore, India
e-mail: rusamy83@gmail.com

R. Mithra
e-mail: mithraece31@gmail.com

U.S. Ragupathy
Department of Electronics and Instrumentation Engineering, Kongu Engineering College, Perundurai, Erode, India
e-mail: ragupthy.us@gmail.com

C. Kamalakannan et al. (eds.), *Power Electronics and Renewable Energy Systems*, Lecture Notes in Electrical Engineering 326, DOI 10.1007/978-81-322-2119-7_13

operate in either as a boost or buck inverter and cannot be a buck-boost inverter. To achieve buck and boost operation, separate chopper circuit is required. These limitations can be rectified through ZSI [1]. Normally, in AC–DC–AC converter system the rectified output voltage acts as an input voltage to ZSI and in solar powered AC system, solar panel output acts as an input to ZSI. The peak output DC voltage of both the systems is still high which acts as a voltage stress across the ZSI switches. To obtain ZVS of power converters, a resonant circuit module is required. The developed ZVS scheme averts any voltage or current spikes happening during switching operation. Soft switching techniques are not only adopted for inverter circuits but also for DC-DC converter circuits [2, 3]. A modular soft switched Pulse Width Modulation (PWM) technique is introduced to reduce high voltage and current stress in DC-DC converters, Flying capacitor and Diode Clamped Multilevel Inverter (DCMLI) [4, 5]. In the proposed paper ZVS technique is achieved through the development of resonant soft switching circuits in order to reduce voltage stress across solar powered ZSI switches. This paper is organized as follows; Sect. 13.1 shows the introduction of soft switched solar powered ZSI system. Solar PV panels are designed and analyzed in Sect. 13.2. Soft switching technique is analyzed in Sect. 13.3. Simulation of solar PV and soft switched solar powered ZSI is addressed in Sect. 13.4. Results and discussions are presented in Sect. 13.5. In Sect. 13.6 hardware model and its results are validated. Section 13.7 concludes the development of soft switched ZSI. The general structure of solar powered ZSI is shown in Fig. 13.1a. The voltage stress between the impedance source (Z-Source) and inverter switches are high. To minimize the voltage stress across the inverter switches, a resonant circuit is developed with solar powered ZSI is shown in Fig. 13.1b.

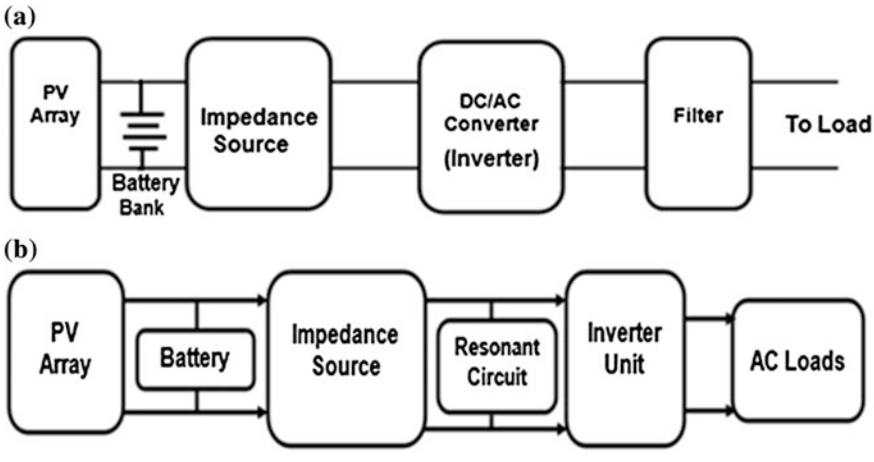

Fig. 13.1 **a** Block diagram of solar powered ZSI. **b** Block diagram of soft switched solar powered ZSI

13.2 Modeling of Solar PV

The basic equation from the theory of semiconductors that mathematically describes the I-V characteristics of the ideal photovoltaic cell:

$$I = I_{pv,cell} - I_{0,cell}\left[\exp\left(\frac{qV}{akT}\right) - 1\right]. \tag{13.1}$$

where, $I_{pv,cell}$ is incident current generated, $I_{0,cell}$ is reverse saturation current of diode, T is the temperature of p-n junction and 'a' is diode ideality constant. A single cell has a rated voltage of 0.5 V and rated power of 0.3 W. Practical arrays are composed of several connected photovoltaic cells [6–9].

13.3 Analysis of Soft Switched Z-Source Inverter

Design and analysis of ZSI is investigated [10–13], but in the analysis, voltage stress is not taken into account. The proposed system is used to reduce voltage stress across ZSI. The equivalent circuit of soft switched ZSI is shown in the Fig. 13.2. Solar panel voltage is stored in the battery bank and then it is get boosted through the Z-source network (L&C). The boosted voltage is transferred to the load by the proper switching of H-bridge inverter.

Resonant circuit is interfaced between the Z-source network and the H-bridge inverter to reduce the voltage stress in inverter switches.

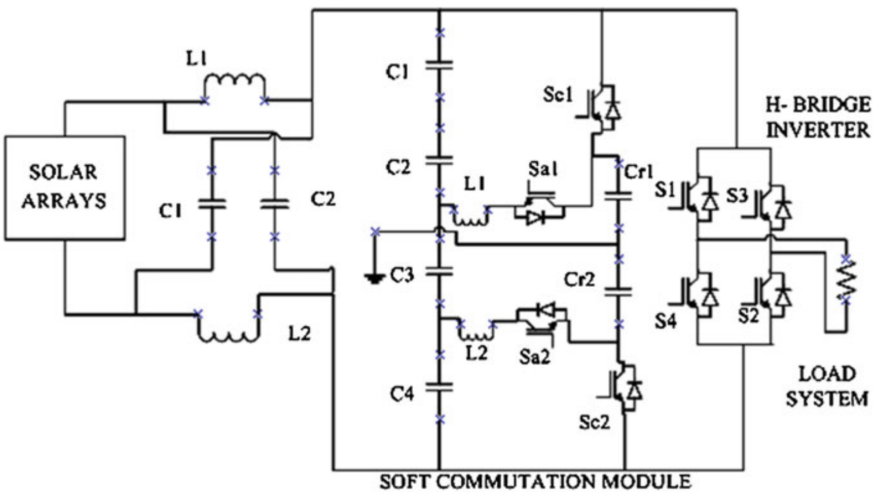

Fig. 13.2 Equivalent circuit of soft switched ZSI

Voltage across the inductor during energizing;

$$V_L = L\left(\frac{dI_l}{dt}\right). \tag{13.3}$$

Current flowing through the capacitors;

$$Ic = C\left(\frac{dVc}{dt}\right). \tag{13.4}$$

Source voltage is the summation of V_L and V_P

$$V_s = V_P + V_L. \tag{13.5}$$

where, V_L—Voltage across the inductor, V_p—Panel voltage, V_s—Source voltage (Boost voltage). By applying the Law of KVL and KCL, following are the expressions of Z-source network. The operation of soft switched ZSI has two modes of operation as those of ZSI are Non shoot through state and Shoot through state. Non shoot through state is considered as the normal switching state of ZSI as similar to that of VSI. It can be analyzed as follows; in Non Shoot-Through State 1, diode D and inverter switches S_1 and S_2 are in ON state and in Non Shoot-Through State 2, diode D and inverter switches S_3 and S_4 are in ON state. In Shoot-through state the inverter switches of the same-phase leg are gated ON at the same time. In shoot through state 1, diode D is in OFF state and the same leg switches S_1 and S_4 are get triggered and in shoot through state 2, diode D is in OFF state and the same leg switches S_3 and S_2 are get triggered. Resonant circuit is used to achieve zero voltage switching of inverter with Z-source network [14–16]. The resonant circuit can be operated into the following modes of operation;

(a) **Upper Bank Circuit Operation**

Mode 1 The resonant capacitor, C_{r1}, has been charged up to one-half of the normal bus voltage. The clamping switch, $S_{C1,}$ is in the ON-state, and the positive bus voltage is clamped to the capacitor's level, which is equal to $V_s/2$.

Mode 2 The clamping switch, S_{C1} gets turn OFF so that the positive bus terminal is released from the capacitor bank. By turn ON the auxiliary switch, S_{a1}, a resonant path is formed with L_{r1} and C_{r1}. The energy stored in C_{r1} is transferred to the large capacitor bank through the inductor and the voltage crossing C_{r1} is decreasing.

Mode 3 At the end of one-half resonant cycle, the voltage across C_{r1} has been discharged to zero. Any excess current in the inductor will flow through the anti parallel diodes of the inverter switches, as the voltage remains at zero. During this time, the positive bus, across the inverter is in the same potential as the neutral line. If the negative bus has also swung to the neutral line at that time, all the inverter switches will experience zero crossing-voltage and they are ready to safely turn ON and OFF according to the new PWM gating patterns.

Mode 4 As the inductor current reverses, the anti parallel diode of the auxiliary switch will conduct and provide a path to charge C_{r1}. As a result, another resonance occurs between L_{r1} and C_{r1} with an opposite direction of current. The resonant energy is being transferred back to C_{r1}.

Mode 5 When the voltage across C_{r1} reaches its peak value, the clamping switch, S_{C1}, is turn ON at zero voltage, and the positive bus is clamped to the capacitor bank again. Thus, the entire soft commutation is completed.

(b) **Lower Bank Circuit Operation**

Similarly lower bank modes of operation are achieved to obtain the negative side peak voltage to zero.

13.4 Simulation of Solar Panels and Soft Switched ZSI

The SIMULINK model of the solar PV is shown in Fig. 13.3. Developed solar panel generates the output voltage of 96 V and the output current of 16 A at the irradiance of 1,000 W/m^2 and at the panel temperature of 25 °C. The solar panel output is fed to the Z-source network. Through the proper switching of resonant circuit and inverter switches solar panel voltage is utilized by the load system. The simulated model of soft switched ZSI system is shown in Fig. 13.4. Solar panel output voltage is boosted using ZSI circuit and soft switched by resonant circuit.

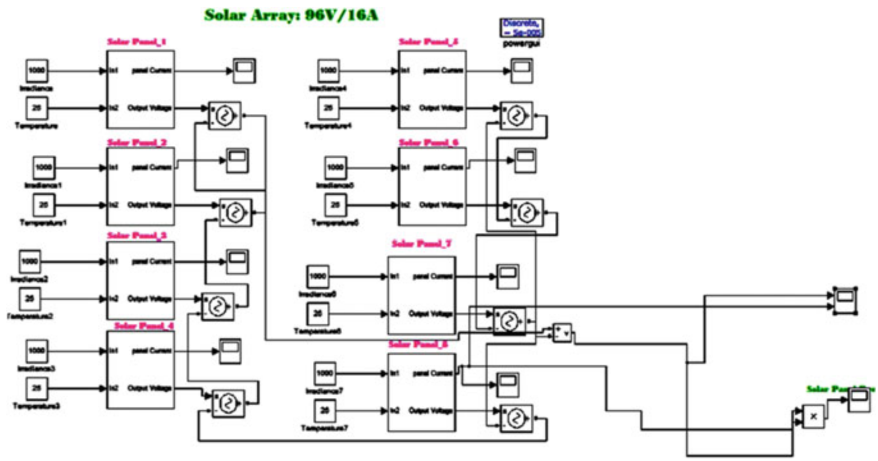

Fig. 13.3 Simulation model of solar PV panels

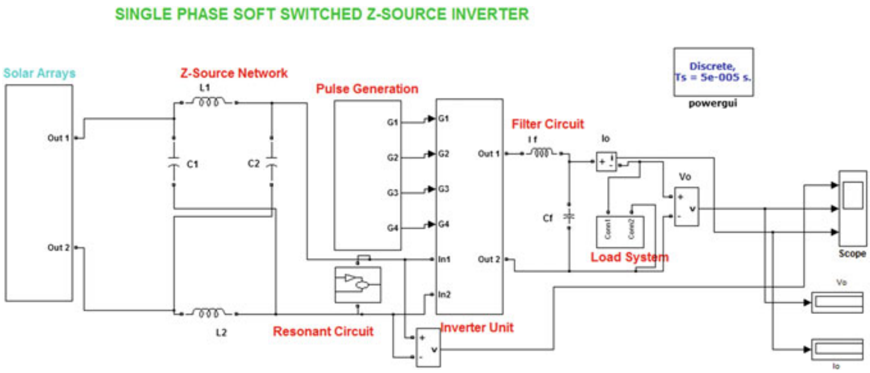

Fig. 13.4 Simulation model of soft switched ZSI system

13.5 Results and Discussion of the Proposed System

For the maximum irradiance, the solar panels are developed to obtain 96 V and 16 A. The obtained solar panel output voltage of 96 V is stored in battery bank. Battery bank voltage is boosted through Z-Source network and H-Bridge inverter switches. The output voltage of resonant soft switching circuit is shown in Fig. 13.5. The main aim of the proposed system is to develop the zero voltage state of battery output voltage for soft switching of inverter switches. The obtained output voltage is fed to the H-bridge inverter switches.

Figure 13.6a, b represents switching pattern for resonant circuits and inverter switches S_1, S_2, S_3 and S_4 respectively. The starting time of resonant switch pulse and non shoot through time period of inverter switches coincides with each other. Figure 13.6c shows the soft switched ZSI AC output voltage of 283.7 V (V_{max}),

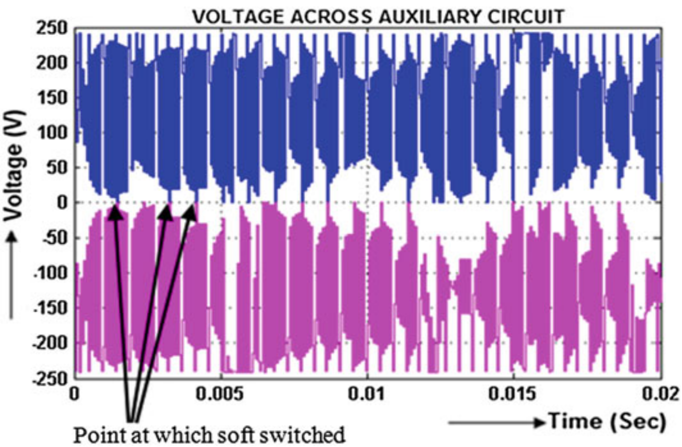

Fig. 13.5 Soft switched output voltage

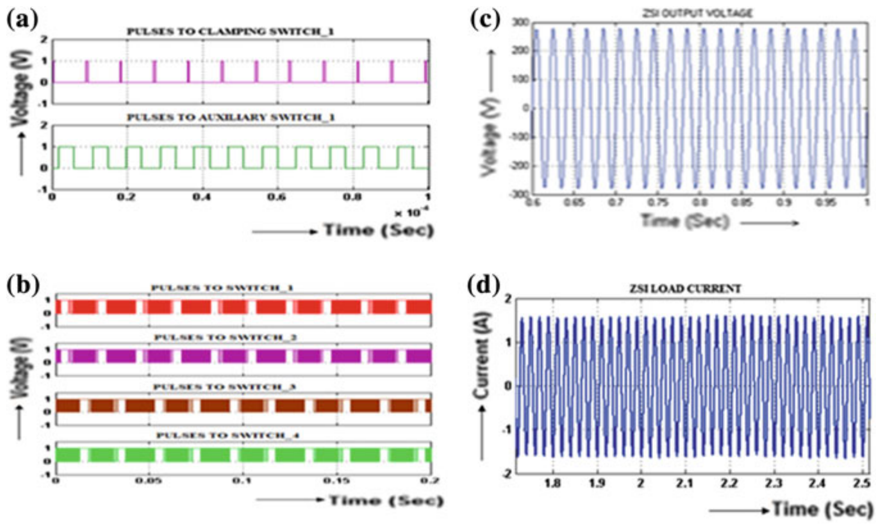

Fig. 13.6 Firing pulses to **a** resonant circuit switches **b** inverter switches **c** output voltage waveform **d** output load current waveform

50 Hz and Fig. 13.6d shows the load current of 1.5 A, 50 Hz for the following load parameters. Proposed system has following load arrangements; Compact Florescent Lamp (2 Nos.) = (20 * 2) W = 40 W; Fan (1 No.) = 60 W; Mixer = 75 W; Personal computer = 100 W; Total power consumption = 275 W.

The output voltage harmonic analysis for the proposed system with Total Harmonic Distortion (THD) value of 2.83 %. As per IEEE standard 519: 1992 the acceptable THD is less than 5 %.

13.6 Experimental Results and Analysis

Figure 13.7a shows output voltage of resonant circuit (soft switched voltage). At time of every zero crossing state of DC voltage, H-bridge inverter switches get triggered.

Figure 13.7b shows the output voltage of soft switched Z-source inverter. Inverter gets the input from the solar panel through the Z-source network and resonant circuit.

Figure 13.7c shows the prototype setup of the proposed system. The entire system is assembled in a single board.

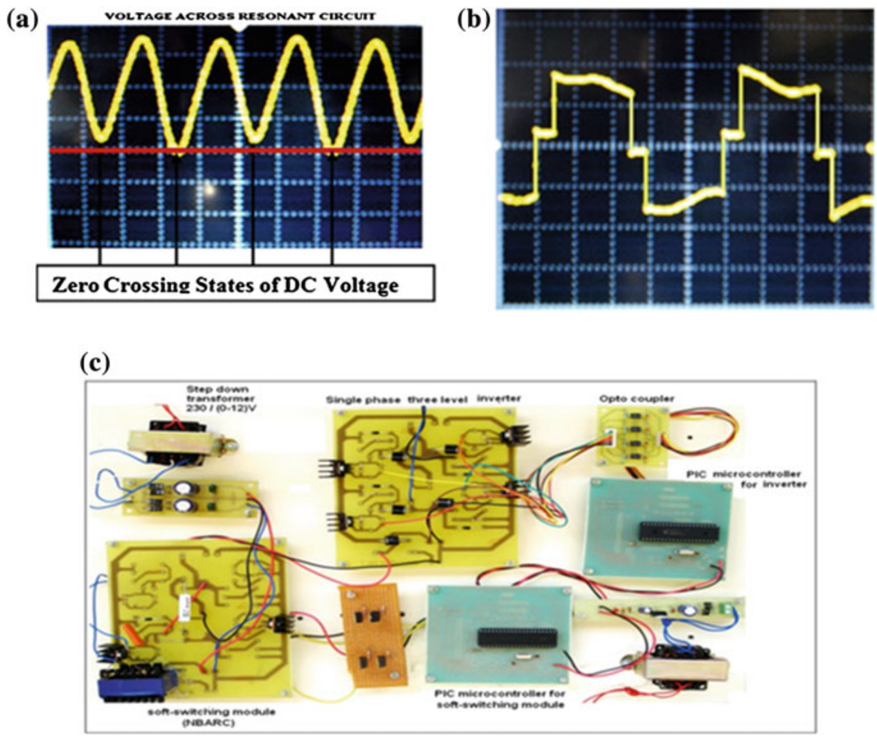

Fig. 13.7 **a** Output voltage of resonant circuit **b** output voltage of soft switched ZSI **c** prototype model of soft switched ZSI

13.7 Conclusion

In this paper a solar powered soft switched ZSI system is obtained using LC resonant circuit. The proposed system has maximum boost capability with high efficiency. The voltage stress across the inverter switches can be minimized through the proposed system. The proposed system enhances the maximum utilization of solar power.

References

1. Peng FZ (2003) Z-source inverter. IEEE Trans Ind Appl 39(2):504–510
2. Jay J, Hu J (2006) Modular: design of soft-switching circuits for two level and three-level inverters. IEEE Trans Power Electron 21(1):131–139
3. Yuan X, Barbi I (2000) Soft-switched three-level capacitor clamping inverter with clamping voltage stabilization. IEEE Trans Ind Appl 36(4)

4. Amini MR, Farzanehfard H (2009) Novel family of PWM soft-single-switched DC–DC converters with coupled inductors. IEEE Trans Ind Electron 56(6)
5. Divan DM, Skibinski G (1989) Zero-switching-loss inverters for high-power application. IEEE Trans Ind Appl 25(4):634–643
6. Xiao W, Dunford WG, Capel A (2004) A novel modeling method for photovoltaic cells. In: Proceedings of IEEE 35th annual power electronics spectrum conference (PESC), vol 3, pp 1950–1956
7. Jensen M, Louie R, Etezadi-Amoli M, Fadali MS (2010) Model and simulation of a 75 KW PV solar array. IEEE conference on power electron, Oct 2010
8. Sera D, Teodorescu R, Rodriguez P (2007) PV panel model based on datasheet values. IEEE international symposium on industrial electronics, pp 2392–2396, Jun 2007
9. Kuo YC, Liang TJ (2001) Novel maximum power point tracking controller for photovoltaic energy conversion system. IEEE Trans Ind Electron 48(3):594–601
10. Zhou ZJ, Zhang X, Xu P, Shen WX (2008) Single phase uninterruptible power supply based on Z-source inverter. IEEE Trans Ind Electron 55(8)
11. Peng FZ, Shen M, Qian Z (2004) Maximum boost control of the Z-source inverter. In: Proceedings of 39th IEEE industry applications conference, vol 1
12. Loh PC, Vilathgamuwa DM, Lai YS, Tin CG, Li Y (2005) Pulse width modulation of Z-source inverters. IEEE Trans Power Electron 20(6):1346–1355
13. Peng FZ, Shen M, Qian Z (2005) Maximum boost control of the Z-source inverter. IEEE Trans Power Electron 20(4):833–838
14. Divan DM (1989) The resonant dc link converter-a new concept in static power conversion. IEEE Trans Ind Appl 25(2):629–637
15. De Doncker RD, Lyons JP (1990) The auxiliary resonant commutated pole converter. In: The proceedings of IEEE IAS Conference, pp 1228–1235
16. Uthirasamy R, Ragupathy US (2013) Design and realization of maximum boost Z-source inverter for solar power applications, IEEE International Conference on Electronics, Computing, Communication Technologies (IEEE CONECCT2013), IEEE Bangalore Section

Chapter 14
An Integrated Passive Islanding Detection Method for Grid Connected PV Distributed Generators

Almoataz Y. Abdelaziz, Mohmmed Ezzat, Walid Sameh, R.K. Saket and K.S. Anand Kumar

Abstract This study proposes an islanding detection method for use with grid-interconnected distributed generators (DGs). The method is based on two indices; the rate of change of frequency (ROCOF) and the rate of change of voltage (ROCOV). When a DG is connected to grid, the ROCOF and ROCOV are lower than the threshold value. In contrast, as an islanding occurs, the ROCOF or ROCOV become much higher than the threshold values. Detection systems monitor terminal voltage at the grid-interconnected point to calculate ROCOF and ROCOV, and issue an operating signal when the value and exceed a given threshold. In this study, simulations are performed to illustrate the principles of the proposed technique for grid connected photo-voltaic (PV) generator. The test results show that the proposed method is reliable, economical, and easy to implement for islanding detection of distributed generators. Islanding detection methods are investigated, simulated and evaluated using MATLAB /SIMULINK package.

Keywords Islanding detection · Distributed generators · ROCOF · ROCOV and photovoltaic

A.Y. Abdelaziz (✉) · M. Ezzat · W. Sameh
Ain Shams University, Cairo, Egypt
e-mail: almoatazabdelaziz@hotmail.com

M. Ezzat
e-mail: moh_ezzat@yahoo.com

W. Sameh
e-mail: walidsameh@ymail.com

R.K. Saket
Department of Electrical Engineering, Indian Institute of Technology, Banaras Hindu University, Varanasi, Uttar Pradesh, India
e-mail: rksaket.eee@iitbhu.ac.in

K.S. Anand Kumar
National Aerospace Laboratory, Bangalore, Karnataka, India
e-mail: anand_kumarks@nal.res.in

C. Kamalakannan et al. (eds.), *Power Electronics and Renewable Energy Systems*, Lecture Notes in Electrical Engineering 326, DOI 10.1007/978-81-322-2119-7_14

14.1 Introduction

Since the society becomes increasingly concerned to save energy and preserve the environment, the interest toward the distributed generation systems, such as photovoltaic arrays and wind turbines, increases year after year. But as photovoltaic arrays and generally DGs will have affects in the network that one of these influences is an islanding phenomenon [1]. Islanding is the situation in which a distribution system becomes electrically isolated from the remainder of the power system, yet the system continues to be energized by DG connected to it. Islanding situations can damage the grid itself or equipments connected to the grid and can even compromise the security of the maintenance personnel that service the grid. Therefore, according to IEEE standard, islanding state should be identified and disconnected in 2 s [2]. There are quite a few different methods used to detect islanding. All methods have benefits and drawbacks. Islanding detection techniques can broadly be divided into remote and local techniques.

Remote islanding detection techniques are based on the communication between utilities and DGs. Supervisory Control and Data Acquisition (SCADA) [3] or power line signaling scheme [4, 5] can be used to determine when the distribution system is islanded. These techniques have better reliability but they are expensive to implement especially for small systems.

Therefore, local techniques are widely used to detect islanding and they can further be divided into passive and active techniques.

Passive methods continuously monitor the system parameters such as voltage, frequency, harmonic distortion, etc. Based on the system characteristics, one or more of these parameters may vary greatly when the system is islanded. Setting a proper threshold can help to differentiate between an islanding and a grid connected condition. Rate of change of output power of DG [3, 6], rate of change of frequency [7], rate of change of frequency over power [8], change of source impedance [9, 10], and harmonic distortion [11–13], are a few examples of passive islanding detection techniques. A detection technique that looks into a database created by extensive offline calculations is presented in [14] to overcome some of the limitations of existing passive techniques. The main problem with the passive techniques is that, it is difficult to detect islanding when the load and generation in the islanded system closely match. Furthermore, special care has to be taken while setting the thresholds for these parameters.

Active methods directly interact with the power system operation by introducing perturbations. These small perturbations will result in a significant change in system parameters when the DG is islanded, whereas the change will be negligible when the DG is connected to the grid. Reactive power export error detection method [7], impedance measurement method [9], slip mode frequency shift algorithm (SMS) [3], active frequency drift (AFD) [15], automatic phase-shift (APS) [16], and adaptive logic phase shift (ALPS) are a few examples of active islanding detection techniques. The problems with these techniques are that they introduce perturbations in

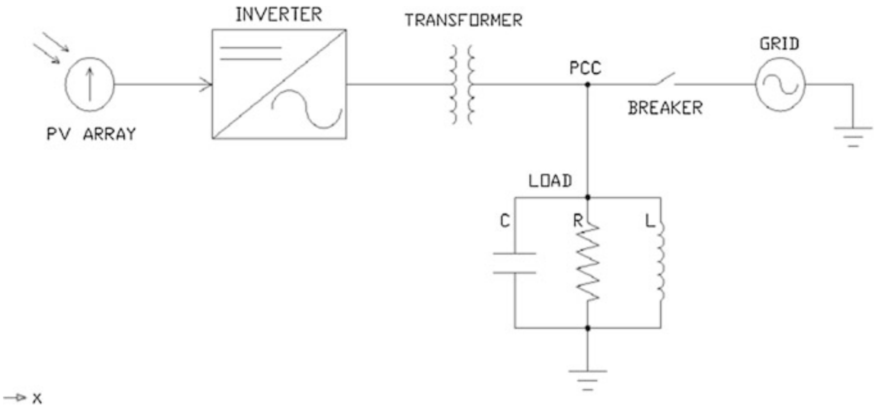

Fig. 14.1 Configuration of the grid connected PV system with local load

the system and detection time is slow as a result of extra time needed to analyze the system response of the perturbations.

Applications of active techniques are limited to the DG type and/or load, i.e. reactive power export error detection method cannot be used when the DG has to operate at the unity power factor and methods based on phase shift are mostly useful for inverter based DGs. Also, AFD is very effective for purely resistive loads but it may fail for other loads [3].

In this study, we assume that a grid connected PV system consists of local load RLC, a transformer, a switch and the utility voltage source as an example of dg system shown in Fig. 14.1.

14.2 The Proposed Techniques Basic Principle

The ROCOF detection method is based on the feature that the real power imbalance causes transients in an islanded systems and the system frequency starts to vary dynamically during the islanding operation. Such system behavior can be used to detect an islanding condition. Therefore, measuring the ROCOF would show whether the DG is operating in parallel with the grid or functioning independently of the grid. The equivalent circuit of a DG interconnected to the grid in normal operation is shown in Fig. 14.2, where PL is the local load demand; P_g is the active power generation of the DG; P_u is the active power supplied by the power grid. The active power balance equation when the DG is interconnected to the grid is expressed as:

$$P_u + P_g = P_L \tag{14.1}$$

The equivalent circuit of a DG subject to islanding operation is shown in Fig. 14.2. After opening of the tie switch S1, the DG starts running in an islanded

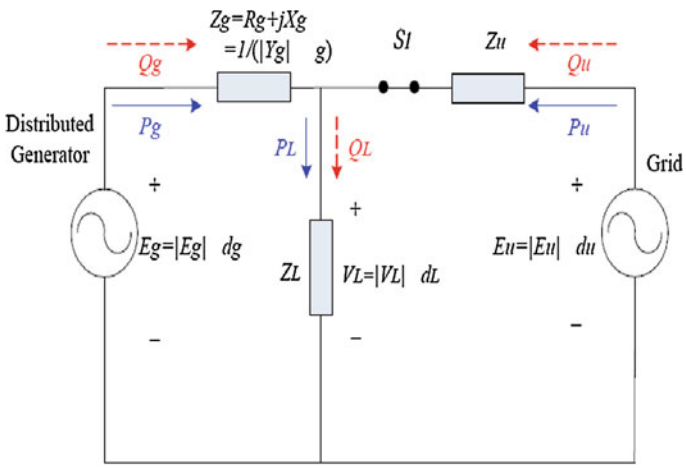

Fig. 14.2 Equivalent circuits of a DG parallel with the grid

mode and a power imbalance exists due to the lost grid power P_u. Such active power imbalance ΔP is described as follows:

$$\Delta P = P_g - P_L = - P_u \tag{14.2}$$

The swing equation of the DG during islanding operation is given by:

$$\frac{2H}{\omega_0} \times \frac{d\omega}{dt} = \Delta P = P_g - P_L \tag{14.3}$$

where, H is the inertia constant of the DG, ω is the rotor speed of the DG, ω_0 is the synchronous speed in normal operation. The derivative of ω can be solved from (14.3) as:

$$\frac{d\omega}{dt} = \frac{\omega_0 \times \Delta P}{2H} \tag{14.4}$$

Since ω and ω_0 can be described as $\omega = 2\pi f$ and $\omega_0 = 2\pi f_0$, where f is the system frequency in an islanding operation, f_0 is the system synchronous frequency in normal operation. The ROCOF ($\Delta f/\Delta t$) can be solved from (14.4) as:

$$\frac{\Delta f}{\Delta t} = \frac{df}{dt} = \frac{f_0 \times \Delta P}{2H} \tag{14.5}$$

As shown in (14.5), when the real power imbalance ΔP causes transients in the islanded system, the frequency of the system drifts up or down, making the frequency of the system deviate from its nominal value until frequency relay is triggered. However, if the power imbalance ΔP in the islanded system is small, then the frequency will change slowly. Thus, ROCOF can be used as a detection index under this islanding situation. The ROCOV detection method is based on the feature that the reactive power imbalance causes transients in an islanded system and the terminal voltage starts to vary dynamically during the islanding operation. As in the principle of the ROCOF mentioned above, such system behavior can also be used to detect an islanding condition. Therefore, measuring the ROCOV would show whether the DG is operating in parallel with the grid or functioning independently of the grid. As shown in Fig. 14.1, we have the equivalent circuit of a DG parallel with the grid in normal operation, where $E_u = |E_u| < \delta_u$ and $E_g = |E_g| < \delta_g$ are the open circuit voltages of the utility and the DG; $V_L = |V_L| < \delta_L$ is the terminal voltage of the local load; Zu is the source impedance of the utility grid; $Z_g = R_g + jX_g = 1/(|Y_g| < \Theta_g)$ is the source impedance of the DG; ZL is the local load impedance; Q_L is the local reactive load demand; Q_g is the reactive power generation of the DG; Q_u is the reactive power provided by the power grid. The reactive power balance equation when the DG is interconnected to the grid is expressed as:

$$Q_u + Q_g = Q_L \tag{14.6}$$

As shown in Fig. 14.3, after opening the tie switch *S*1, the DG starts running in an islanded mode and a reactive power imbalance exists due to the lost grid reactive power *Qu*. Such reactive power imbalance ΔQ is described as follows:

$$\Delta Q = Q_g - Q_L = -Q_u \tag{14.7}$$

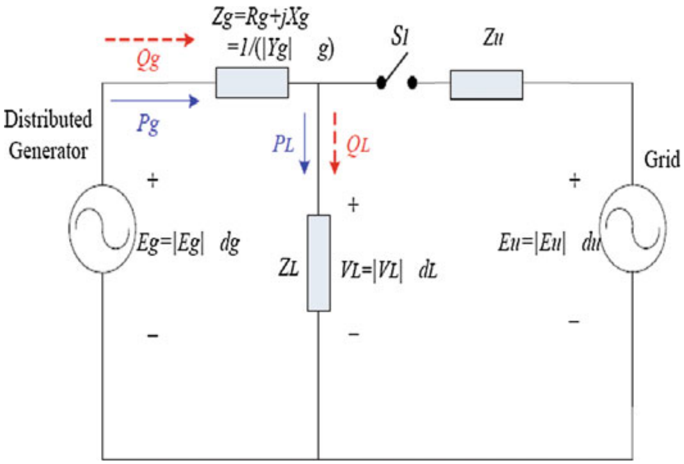

Fig. 14.3 Equivalent circuits of a DG Parallel with the grid

The reactive power generation of DG is given by

$$Q_g = -|E_g||V_L||Y_g|\sin(\Theta_g - \delta_g + \delta_L) \tag{14.8}$$

The partial derivative of Q_g can be solved from Eq. (14.8) as:

$$\frac{\partial \mathrm{Q_g}}{\partial \mathrm{V_L}} = -|E_g||Y_g|\sin(\Theta_g - \delta_g + \delta_L) \tag{14.9}$$

$\Theta_g - \delta_g + \delta_L = \delta_g$ can be approximately expressed as:

$$\frac{\partial \mathrm{Q_g}}{\partial \mathrm{V_L}} = -|\ \mathrm{E_g}||\ \mathrm{Y_g}|\sin(\delta_g) = -\ |\mathrm{E_g}|\ \mathrm{B_g} \tag{14.10}$$

where B_g is the imaginary part of Y_g. Equation (14.10) can be solved as:

$$\frac{\Delta \mathrm{Q_g}}{|\mathrm{E_g}|} = -\mathrm{B_g}|\Delta|\mathrm{V_L}| \tag{14.11}$$

Because $\Delta Q_g = -\Delta Q$, Eq. (14.11) can be written as:

$$\Delta|\mathrm{V_L}| = \frac{1}{\mathrm{B_g}} \times \frac{\Delta Q}{|\mathrm{E_g}|} \tag{14.12}$$

If the resister of the DG (R_g) is ignored, B_g can be approximately expressed as $1/X_g$, where X_g is the source reactance of the DG. Then, ROCOV ($\Delta|V_L|/\Delta t$) can be solved as:

$$\frac{\Delta \mathrm{V_L}}{\Delta \mathrm{t}} = \frac{\mathrm{X_g}}{\mathrm{E_g}} \times \frac{\Delta \mathrm{Q}}{\Delta \mathrm{t}} \tag{14.13}$$

As shown in Eq. (14.13), when the reactive power imbalance ΔQ causes transients in the islanded system, the terminal voltage drifts up or down, making the terminal voltage deviate from its nominal value until voltage relay is triggered. However, if the reactive power imbalance ΔQ in the islanded system is small, then the terminal voltage will change slowly, due to small value of ROCOV. Thus, ROCOV can be used as an alternative detection index in this kind of islanding situation.

14.3 Simulation Model and Results

The simulation mainly uses MATLAB/Simulink software to build a three phase grid connected PV generation system which shown in Fig. 14.4. In the example, the voltage of the PV is set to be 400 V. The system is mainly composed of PV array

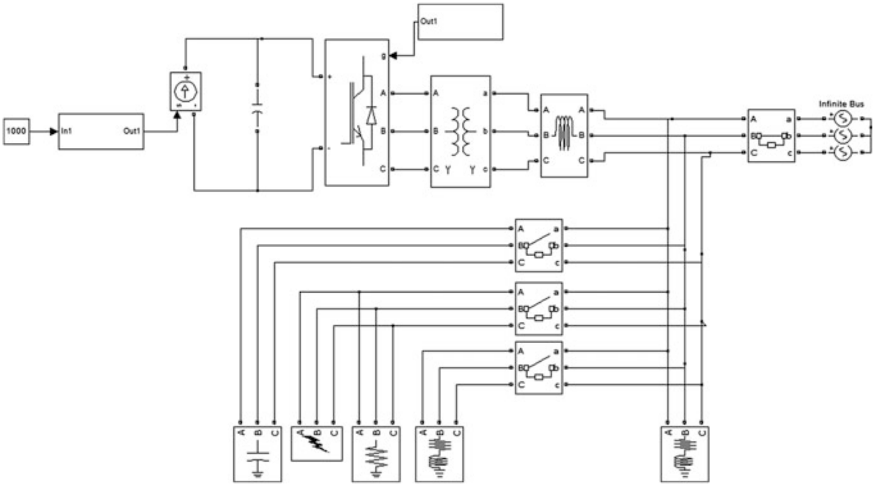

Fig. 14.4 Three phase grid connected PV generation system

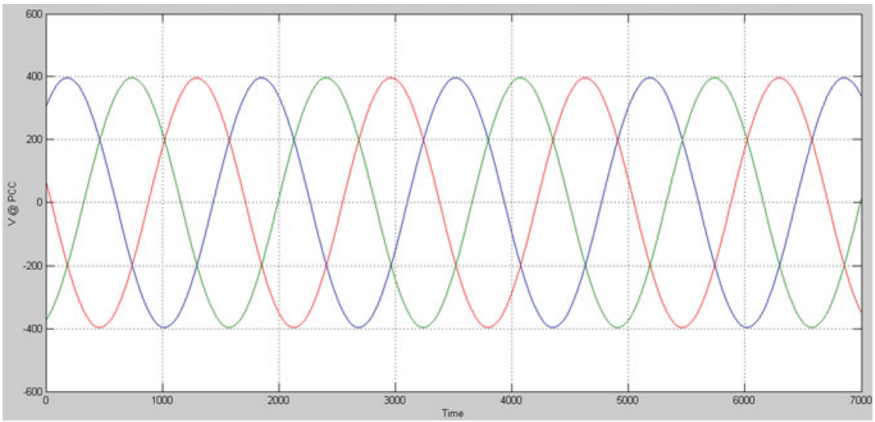

Fig. 14.5 Three phase PCC voltage

module, IGBT inverter module and its control, transformer, LC filter, load which is formed from parallel RLC and the grid. Various events (islanding, load change, capacitor switching, and short circuit) have been simulated to show the effectiveness of the proposed technique. The output voltage wave form from and the point of common coupling (PCC) is shown in Fig. 14.5, the various events are tabled in Table 14.1 as shown and its results are shown in figures from Figs. 14.6, 14.7, 14.8, 14.9, 14.10, 14.11, 14.12, 14.13, 14.14, 14.15, 14.16, 14.17, 14.18 and 14.19.

Table 14.1 Studied cases

Case #	Time	Active power	Reactive power L	Reactive power C
Case 1	0	5 kW	1 kvar	0.7 kvar
	0.3	+1 kW	+0.1 kvar	+0.1 kvar
	0.6	−1 kW	−0.1 kvar	−0.1 kvar
	0.8	Islanding occurred		
Case 2	0	5 kW	1 kvar	0.7 kvar
	0.3	–	–	+0.3 kvar
	0.6	Islanding occurred		
Case 3	0	5 kW	1 kvar	0.7 kvar
	0.3	+3 kW	–	–
	0.6	3ph Short circuit @3 kW load		
	1.2	Islanding occurred		
Case 4	0	5.5 kW	1 kvar	0.7 kvar
	0.3	1ph(A) to ground fault @0.5 kW load		
	0.6	Islanding occurred		
Case 5	0	5.5 kW	0	5.5 kW
	0.3	2ph(A,B) to ground fault @0.5 kW load		
	0.6	Islanding occurred		
Case 6	0	2 kW	1 kvar	0.7 kvar
	0.6	Islanding occurred		
Case 7	0	7.5 kW	1 kvar	0.7 kvar
	0.6	Islanding occurred		

Fig. 14.6 Frequency at PCC

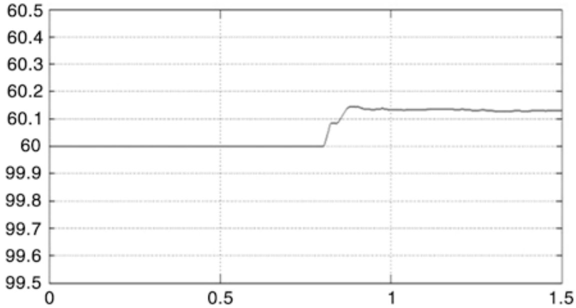

Figure 14.6 shows the frequency of the PV at normal operation and at load increasing and decreasing and at islanding condition. Figure 14.7 shows the per unit voltage of the PV at the same conditions. Figure 14.8 shows the frequency of the PV at normal operation and at switching a capacitor bank (0.3) kvar and then Islanding took place. Figure 14.9 shows the per unit voltage of the PV at the same conditions.

Fig. 14.7 Voltage at PCC

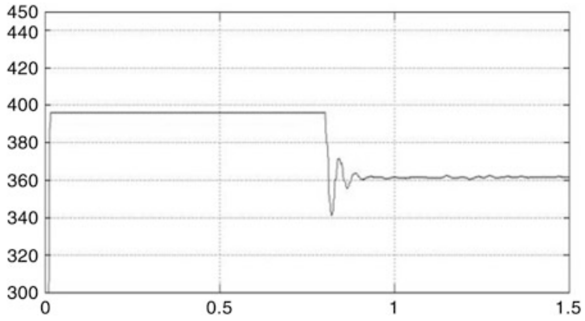

Fig. 14.8 Frequency at PCC

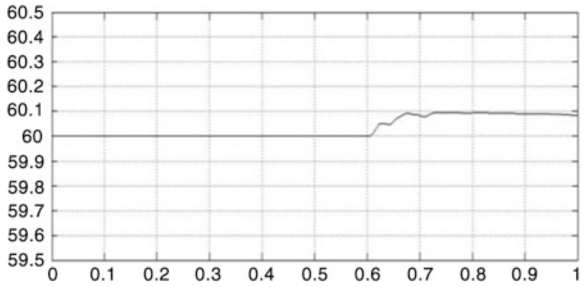

Fig. 14.9 Voltage at PCC

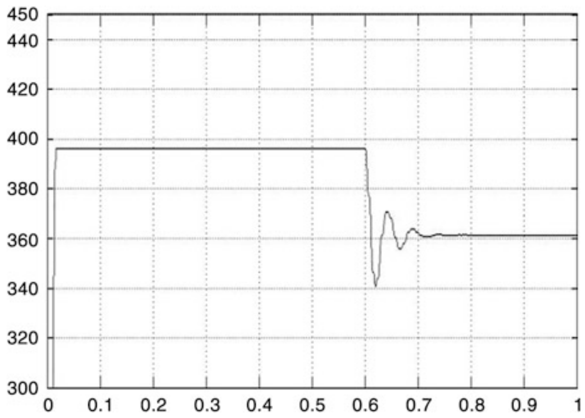

Figure 14.10 shows the frequency of the PV at normal operation. Then, a 3 kW local load was added. Then, a three phase short circuit at the 3 kW load took place and cleared. Then, islanding took place. Figure 14.11 shows the per unit voltage of the PV at the same conditions. Figure 14.12 shows the frequency of the PV at normal operation. Then a 0.5 kW local load was added. Then, a single phase short circuit at the 0.5 kW load took place ant cleared. Then, islanding took place. Figure 14.13 shows the per unit voltage of the PV at the same conditions.

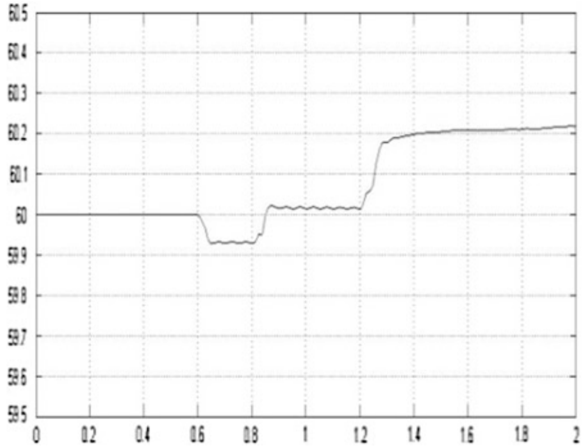

Fig. 14.10 Frequency at PCC

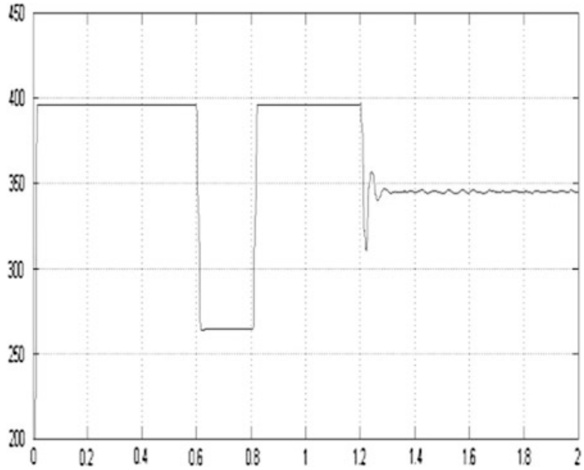

Fig. 14.11 Voltage at PCC

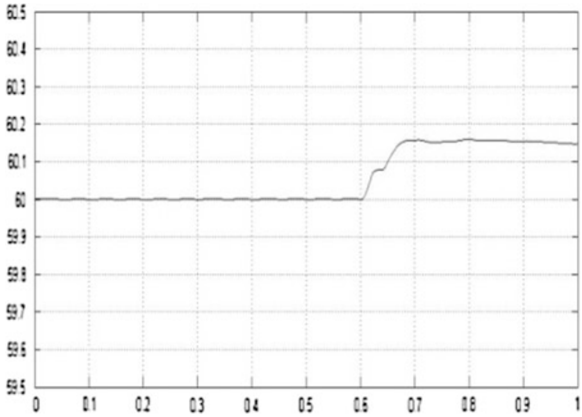

Fig. 14.12 Frequency at PCC

Fig. 14.13 Voltage at PCC

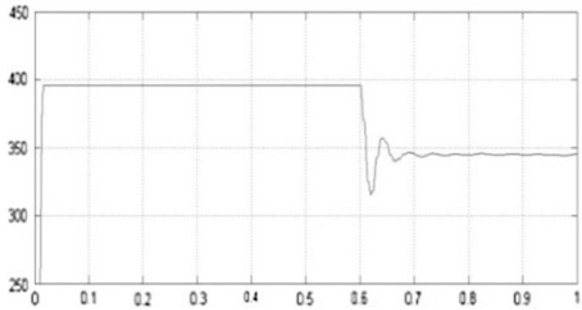

Fig. 14.14 Frequency at PCC

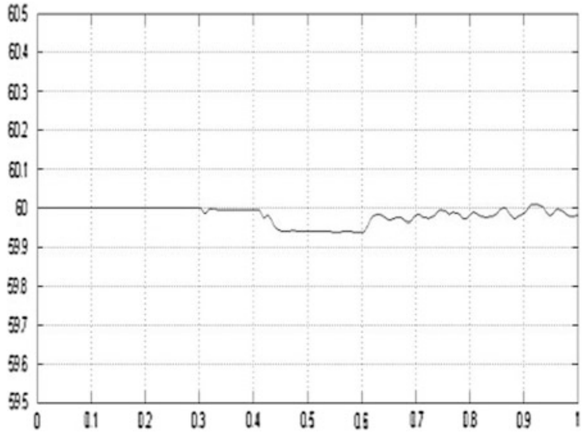

Fig. 14.15 Voltage at PCC

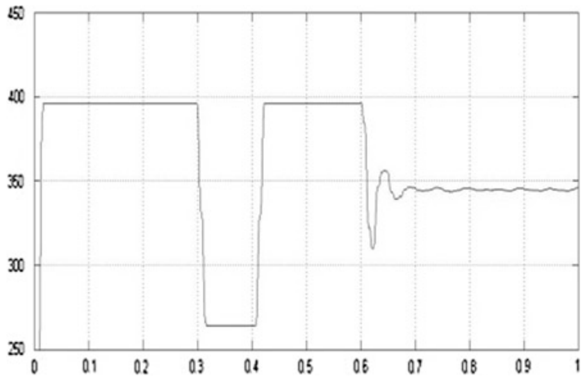

Figure 14.14 shows the frequency of the PV at normal operation. Then, a 0.5 kw local load was added. Then, we apply a two phase short circuit at the 0.5 kW load and cleared. Then, islanding took place. Figure 14.15 shows the per unit voltage of the PV at the same conditions. Figure 14.16 shows the frequency of the PV at

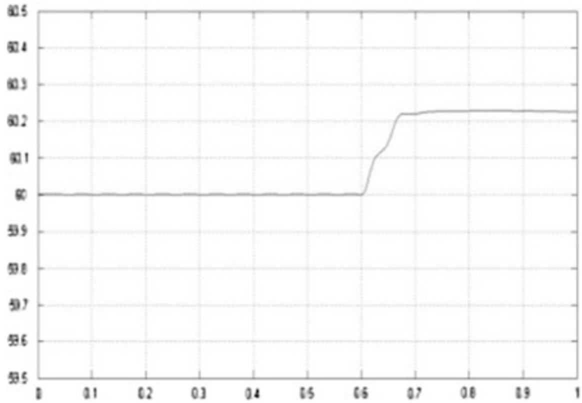

Fig. 14.16 Frequency at PCC

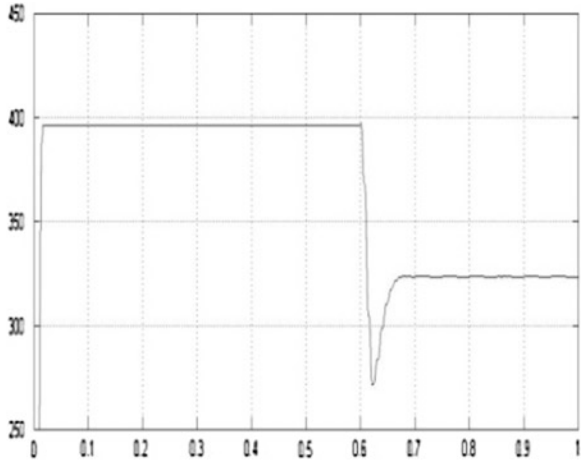

Fig. 14.17 Voltage at PCC

normal operation but the local load is 2 kW and 0.3 kvar. Then, islanding took place. Figure 14.17 shows the per unit voltage of the PV at the same conditions. Figure 14.18 shows the frequency of the PV at normal operation but the local load is 7.5 kW and 0.3 kvar. Then, islanding took place. Figure 14.19 shows the per unit voltage of the PV at the same conditions.

Fig. 14.18 Frequency at PCC

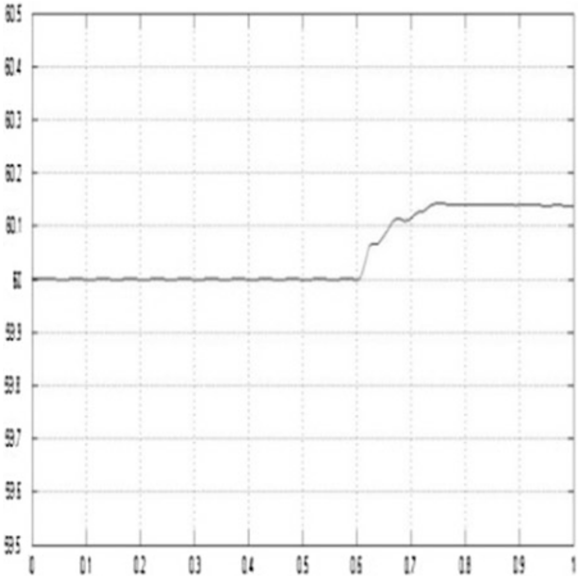

Fig. 14.19 Voltage at PCC

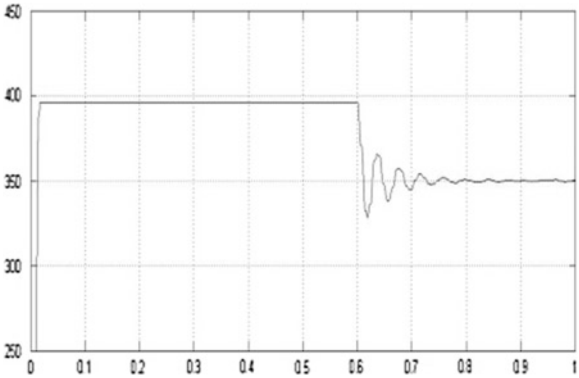

14.4 Conclusion

This paper has given a short overview of the ROCOF and ROCOV techniques to detect islanding operation for PV grid connected generators. To verify the effectiveness of the proposed techniques, experiments using different kinds of typical loads were used in this study. The experiment results show that the proposed indices of the islanding detection of ROCOF and ROCOV can detect the islanding operations satisfactorily for the different kinds of loads. The detection performance is verified to be less dependent on the load quality factor and power level.

References

1. Karrari M, Rosehart W, Malik OP (2003) Nonlinear modeling and simulation of a wind generation unit for transient and stability analysis. Technical Report, University of Calgary, Calgary
2. Nikkhajoei H, Iravani R (2007) Steady-State Model and Power Flow Analysis of Electronically-Coupled Distributed Resource Units. IEEE Trans Power Deliv 22(5):335–341
3. Smith GA, Onions PA, Infield DG (2000) Predicting islanding operation of grid connected PV inverters. Proc IEE Electric Power Appl 147:1–6
4. Wang G, Kliber J, Zhang G, Xu W, Howell B, Palladino T (2007) A power line signaling based technique for anti-islanding protection of distributed generators—part II: field test results. IEEE Trans Power Deliv 22(3):1767–1772
5. Ropp M, Aaker K, Haigh J, Sabhah N (2000) Using power line carrier communications to prevent islanding. In: Proceedings of 28th IEEE photovoltaic specialist conference 2000, pp 1675–1678
6. Redfern MA, Barren JI, Usta O (1995) A new microprocessor based islanding protection algorithm for dispersed storage and generation units. IEEE Trans Power Deliv 10 (3):1249–1254
7. Warin J, Allen WH (1990) Loss of mains protection. In: Proceedings of 1990 ERA conference circuit protection for industrial and commercial installation, London, UK, pp 4.3.1–4.3.12
8. Pai F, Huang S (2001) A detection algorithm for islanding-prevention of dispersed consumer-owned storage and generating units. IEEE Trans Energy Convers 16(4):346–351
9. O'Kane P, Fox B (1997) Loss of mains detection for embedded generation by system impedance monitoring. In: Proceedings of 6th International conference developments in power system protection, March 1997, pp 95–98
10. Hopewell PD, Jenkins N, Cross AD (1996) Loss of mains detection for small generators. Proc IEE Electric Power Appl 143(3):225–230
11. Kabayashi H, Takigawa K, Hashimato E (1991) Method for preventing islanding phenomenon on utility grid with a number of small scale PV systems. In: Proceedings of 2nd IEEE photovoltaic specialists Conference, 1991, vol 1, pp 695–700
12. Jang SI, Kim KH (2004) A new islanding detection algorithm for distributed generations interconnected with utility networks. In: Proceedings of IEE International conference developments in power system protection, April 2004, vol 2, pp 571–574
13. Jang SI, Kim KH (2004) An islanding detection method for distributed generations using voltage unbalance and total harmonic distortion of current. IEEE Trans Power Deliv 192 (2):745–752
14. El-Arroudi K, Joos G, Kamwa I, McGillis DT (2007) Intelligentbased approach to islanding detection in distributed generation. IEEE Trans Power Deliv 22(2):828–835
15. Ropp ME, Begovic M, Rohatgi A (1999) Analysis and performance assessment of the active frequency drift method of islanding prevention. IEEE Trans Energy Convers 14(3):810–816
16. Hung G, Chang C, Chen C (2003) Automatic phase shift method for islanding detection of grid connected photovoltaic inverter. IEEE Trans Energy Convers 18(1):169–173

Chapter 15
Acoustic Echo Cancellation Using Variable Step Size Based Adaptive Filtering with Performance Measure

Srilakshmi Gubbala, K. Srinivas and Rangarao Orugu

Abstract Acoustic echo is a most frequent occurrence in modern telecommunication systems. This paper describes the different adaptive filtering algorithms to minimize an unwanted echo and improves quality of speech signals. Adaptive filtering has been an active area of research. Here we are using NLMS, MMAX-NLMS and MMAX-NLMSvss algorithms to analyze speech signal. In both NLMS and MMAX-NLMS algorithms the step size parameter is fixed. That forces a performance compromise between fast convergence and small steady state misadjustment. So, Partial update adaptive algorithms have been proposed by deriving a variable step-size for the MMAX-NLMS algorithm using its mean square deviation. The proposed MMAX-NLMSvss algorithm is tested with speech input signal and the result shows that it has fast convergence time, lower intricacy compared to the NLMS, MMAX-NLMS algorithm.

Keywords Adaptive filtering · NLMS and MMAX-NLMS algorithm

15.1 Introduction

One of the important applications of adaptive filter is AEC. The key to eliminating the undesirable echoes is that a replica of the echo signal is generated by using an adaptive filter and subtracts it from the actual microphone signal from Loudspeaker-Room-Microphone (LRM) system as shown in Fig. 15.1. Here the NLMS algorithm requires $O(2L)$ multiply accumulate (MAC) operations per sampling period. It is

S. Gubbala (✉) · K. Srinivas · R. Orugu
Vishnu Institute of Technology, Bhimavaram, Andhra Pradesh, India
e-mail: y.lakshminivas@gmail.com

K. Srinivas
e-mail: srkanuri@yahoo.com

R. Orugu
e-mail: ranga.mouni@gmail.com

C. Kamalakannan et al. (eds.), *Power Electronics and Renewable Energy Systems*,
Lecture Notes in Electrical Engineering 326, DOI 10.1007/978-81-322-2119-7_15

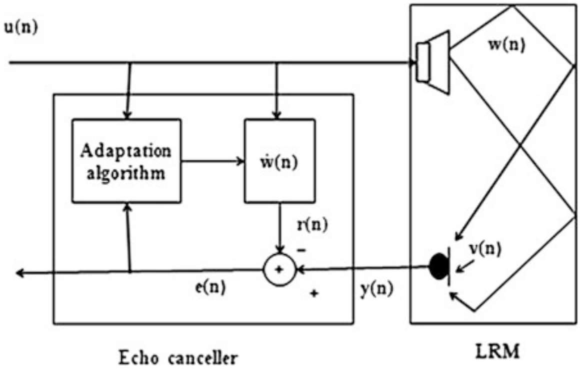

Fig. 15.1 Acoustic echo canceller

required to minimize the computational complexity of the filter, so that MMAX-NLMS [1] have also been proposed. In a MMAX tap selection the filter coefficients updated per iteration is lower, the complexity is also lowered but there is some loss in performance. The first step here is evaluating the mean-square deviation of MMAX-NLMS and deriving a variable step-size in order to improve convergence.

15.2 Normalized Least Mean Square (NLMS) Algorithm

The step size parameter of the NLMS algorithm is selected based on the present input values. The following steps are required by the NLMS algorithm for each iteration.

An adaptive filter output is

$$r(n) = \sum_{i=0}^{N-1} \widehat{w}(n)u(n-i) = \widehat{w}^T(n)u(n)$$

An error signal is

$$\mathrm{e(n) = y(n) - r(n)}$$

The input vector step size value is

$$\mu(\mathrm{n}) = \frac{1}{\boldsymbol{u^T(n)u(n)}}$$

An updated filter taps weights for the next iteration.

$$\widehat{w}(n+1) = \widehat{w}(n) + \mu(\mathrm{n})e(n)u(n)$$

15.3 The MMAX-NLMS Algorithm

As shown in Fig. 15.1, an echo canceller in which, at the nth iteration, the tap-input vector is $y(n) = U^T(n)h(n)$ $U(n) = [u(n), \ldots, u(n-L+1)]^T$ than the unknown LRM system $w(n) = [w_0(n), \ldots, w_{L-1}(n)]^T$ is of length L. An adaptive filter $\hat{w}(n) = [\hat{w}_0(n), \ldots, \hat{w}_{L-1}(n)]^T$, and that we assume [2] $w(n)$ is an unknown system having equal length, it is used to estimate $w(n)$ by adaptively reducing the a priori error signal $e(n)$ using $r(n)$ defined by

$$e(n) = u^T(n)\ w\ (n)\ \ - r\ (n) + v(n), \tag{15.1}$$

$$r(n) = U^T(n)\ \hat{w}\ (n-1), \tag{15.2}$$

and the measurement noise is $v(n)$. In the MMAX-NLMS algorithm [3], only those taps corresponding to the M largest magnitude tap-inputs are chosen for updating at each iteration with $1 \leq M \leq L$. Determining the sub selected tap-input vector.

$$\tilde{u}\ (n) = Q\ (n) u\ (n), \tag{15.3}$$

where $Q(n)$ diagonal {q(n)} is a L × L tap selection matrix and $q(n) = [qo(n), \ldots, qL-1(n)]^T$, element $q_i(n)$ for $i = 0, 1, \ldots,\ L-1$ is given by,

$$q_i(n) = \begin{cases} 1\ |u(n-i)| \in \{M \max ima\ of\ |U(n)|\} \\ 0\ otherwise \end{cases}, \tag{15.4}$$

where the input $|U(n)| = [|u(n)|, \ldots, |u(n-L+1)|]^T$. Defining $|| \cdot ||^2$ as the squared l_2-norm, the MMax-NLMS tap-update equation is

$$\hat{\mathrm{w}}(n) = \hat{w}(n-1) + \frac{\mu Q(n)U(n)e(n)}{||U(n)||^2 + \delta}, \tag{15.5}$$

where δ is the regularization parameter. Defining $I_{L\times L}$ as the $L \times L$ identity matrix, we note that if $Q(n) = I_{L\times L}$, i.e., with M = L, the update equation in (15.5) is equivalent to the NLMS algorithm. That is, the step-size μ in (15.5) controls the ability of MMAX-NLMS to track the unknown system which is reflected by its rate of convergence. To select the M maxima of input $|U(n)|$ in (15.4), The computational intricacy in terms of multiplications for MMAX-NLMS is Ó (L + M) compared to NLMS of $O(2L)$. As seen in Sect. 15.1, the performance of MMAX-NLMS generally minimizes with the number of filter coefficients updated per iteration. Then this trade-off between convergence and complexity can be shown by first specifying

$$\eta(n) = \|w(n) - \hat{w}(n)\|^2 / \|w(n)\|^2, \tag{15.6}$$

15.4 Mean Square Deviation of MMAX-NLMS

In this section, the convergence performance of MMAX-NLMS is dependent on the step-size μ when recognizing a LRM system as proved in [4]. But our goal is to reduce the degradation of convergence rate due to partial updating of the filter coefficients, The MSD of MMAX-NLMS can be obtained by defining the system deviation as

$$\in (n) = w(n) - \hat{w}(n), \tag{15.7}$$

$$\in (n-1) = w(n) - \hat{w}(n-1), \tag{15.8}$$

Subtracting (15.8) from (15.7) and using (15.5), we obtain

$$\in (n) = \in (n-1) - \frac{\mu Q(n) U(n) e(n)}{U^T(n) U(n) + \delta}, \tag{15.9}$$

Defining $\varepsilon\{\cdot\}$ as the expectation operator, the mean square of (15.9) gives the MSD of MMAX-NLMS can be determined iteratively as

$$\varepsilon\left\{||\in (n)||^2\right\} = \varepsilon\left\{\in^T (n) \in (n)\right\} = \varepsilon\left\{||\in (n-1)||^2\right\} - \varepsilon\{\varphi(\mu)\}, \tag{15.10}$$

where,

$$\varepsilon\{\varphi(\mu)\} = \varepsilon\left\{\frac{2\mu U^T(n)\varepsilon(n-1)e(n)}{|U|^2} - \frac{\mu^2 ||U(n)||^2 e^2(n)}{\left[||U(n)||^2\right]^2}\right\}, \tag{15.11}$$

And similar to (15.13), here we assume that the MSD is small due to effect of the regularization term δ. The sub selected tap-input vector $\widetilde{U}(n)$ is defined by (15.3). from Eq. (15.10), in order to increase the convergence rate for the MMAX-NLMS algorithm, we select step-size μ such that $\varepsilon\{\varphi(\mu)\}$ is maximized.

15.5 The Proposed MMAX-NLMS VSS Algorithm

In this part, from the approach of [5] The MMAX-NLMSvss algorithm was proposed, differentiate (15.11) with respect to μ. Setting the result to zero, we obtain

$$\varepsilon\left\{\frac{\mu(n)e(n)||\tilde{U}(n)||^2 e(n)}{\left[||U(n)||^2\right]^2}\right\} = \varepsilon\left\{\in^T (n-1)\tilde{U}(n)\left[||U(n)||^2\right]^{-1} e(n)\right\}$$

Giving the variable step-size $\mu(n) = \mu \max U$

$$\frac{\in^T (n-1)\tilde{U}(n)\left[||U(n)||^2\right]^{-1} U^T(n) \in (n-1)||U(n)||^2}{||\tilde{U}(n)||^2 \varepsilon^T(n-1)U(n)\left[||U(n)||^2\right]^{-1} U^T(n)\varepsilon(n-1) + \sigma_w^2 M(n)}$$

where $0 < \mu$ max ≤ 1 limits the maximum of μ(n) and we have defined (15.9)

$$M(n) = \frac{||\tilde{U}(n)||^2}{||U(n)||^2}, \tag{15.12}$$

In this as the ratio between energies of the sub selected tap-input vector $\tilde{U}(n)$ and the completed tap-input vector $U(n)$, than $\sigma_w^2 = \varepsilon\{w^2(n)\}$. To simplify the numerator of $\mu(n)$, further, we employ the relationship $\tilde{U}(n)U^T(n) = \tilde{U}(n)\tilde{U}^T(n)$ giving $\mu(n) = \mu \max U$

$$\frac{\varepsilon^T(n-1)\tilde{U}(n)\left[||U(n)||^2\right]^{-1} \tilde{U}^T(n)\varepsilon(n-1)||U(n)||^2}{||\tilde{U}(n)||^2 \varepsilon^T(n-1)U(n)\left[||U(n)||^2\right]^{-1} U^T(n)\varepsilon(n-1) + \sigma_w^2 M(n)}$$

We can now simplify $\mu(n)$ further by letting

$$\tilde{P}(n) \tilde{=} U(n)\left[U^T(n)U(n)\right]^{-1} \tilde{U}^T(n)\varepsilon(n-1), \tag{15.13}$$

$$P(n) = U(n)\left[U^T(n)U(n)\right]^{-1} U^T(n)\varepsilon(n-1), \tag{15.14}$$

From which we can then show that

$$||\tilde{P}(n)||^2 = M(n)\varepsilon^T(n-1)\tilde{U}(n)\left[||U(n)||^2\right]^{-1} \tilde{U}^T(n)\varepsilon(n-1)$$
$$||P(n)||^2 = \varepsilon^T(n-1)U(n)\left[|U|^2\right]^{-1} U^T(n)\varepsilon(n-1)$$

Following the approach in (15.13), and defining $0 \ll \alpha < 1$ as the smoothing parameter, we can estimate $\tilde{P}(n)$ and $P(n)$ iteratively by

$$p(n) = \alpha\tilde{p}(n-1) + (1-\alpha)\tilde{U}(n)\left[U^T(n)U(n)\right]^{-1} e_a(n), \tag{15.15}$$

$$P(n) = \alpha P(n-1) + (1-\alpha)U(n)\left[U^T(n)U(n)\right]^{-1} e(n), \tag{15.16}$$

where we have used $e(n) = U^T(n)(n-1)$ in (15.16) while the error $e_a(n)$ due to active filter coefficients $\tilde{U}(n)$ in (15.15) is given as

$$e_a(n) = \tilde{U}^T(n)\varepsilon(n-1) = \tilde{U}^T(n)[w(n) - \hat{w}(n-1)] \tag{15.17}$$

It is important to note that since $\tilde{U}^T(n)h(n)$ is unknown, it is required to approximate $e_a(n)$. Defining $\overline{Q}(n) = L_{LXL} - Q(n)$ as the tap-selection matrix it selects the inactive taps, we can express

$$e_i(n) = \left[\overline{Q}(n)U(n)\right]^T \varepsilon(n-1)$$

Here the error contribution due to the inactive filter coefficients that the total error $e(n) = e_a(n) + e_i(n)$. As explained in (15.9), for $0.5L \le M < L$, the degradation in $M(n)$ caused by tap-selection is negligible. Since for M large enough, elements in $\overline{Q}(n)U(n)$ are small and hence the errors $e_i(n)$ are small, the general motivation for MMAX tap-selection (15.7). We can make approximate $e_a(n) \approx e(n)$ in (15.15) giving

$$\tilde{P}(n) \approx \alpha\tilde{P}(n-1) + (1-\alpha)\tilde{U}(n)\left[U^T(n)U(n)\right]^{-1}e(n), \tag{15.18}$$

By using Eqs. (15.16) and (15.18), the variable step-size is given by

$$\mu(n) = \mu \max \frac{\left|\left|\tilde{P}(n)\right|\right|^2}{M^2(n)||P(n)||^2 + C}, \tag{15.19}$$

where, $C = M^2(n)\alpha_w^2$. Since α_w^2 is unknown, here we can approximate C by a small constant, typically 0.01 (15.13). The computation of (15.16) and (15.18) each requires M additions. To reduce computation further then for M large enough the elements in $\overline{Q}(n)U(n)$ are small, we can approximate $||P(n)||^2 \approx \left|\left|\tilde{P}(n)\right|\right|^2$ giving,

$$\mu(n) \approx \mu \max \frac{\left|\left|\tilde{P}(n)\right|\right|^2}{M^2(n)\left|\left|\tilde{P}(n)\right|\right|^2 + C}, \tag{15.20}$$

When $Q(n) = I_{LXL}$, that is, M = L, MMAX-NLMS is equivalent to the NLMS algorithm and from (15.12), $M(n) = 1$ *and* $\left|\left|\tilde{P}(n)\right|\right| = ||P(n)||^2$. As the variable step-size $\mu(n)$ in (15.20) is stable with that presented in (15.13) for M = L.

15.6 Simulation Result

In this section, our analysis of the performance of NLMS, MMAX-NLMS and MMAX-NLMSvss algorithms is validated in terms of the normalized misalignment using WGN and speech inputs. Impulse response is h(n) of length of L. The adaptive

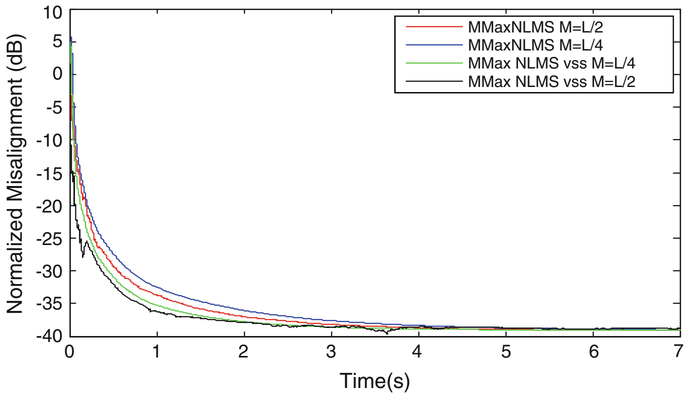

Fig. 15.2 Comparison between convergence rate of MMax-NLMSvss and MMax-NLMS for L = 50 and SNR = 20 dB

filter length also is L. From Fig. 15.2 an improvement in convergence rate of MMAX-NLMSvss over MMAX-NLMS for the cases of M = L/2 and L/4.

Figure 15.3 shows that the performance of MMAX-NLMSvss for speech input. In this simulation, In order to verify the benefits of the proposed algorithm, M = 512 taken for both MMAX-NLMS and MMAX-NLMSvss. This gives a 25 % savings in multiplications per iteration for MMAX-NLMSvss over NLMS. We can conclude that, even with this computational savings, the proposed MMAX-NLMSvss algorithm achieves an improvement of 3.5 dB in terms of normalized misalignment over NLMS.

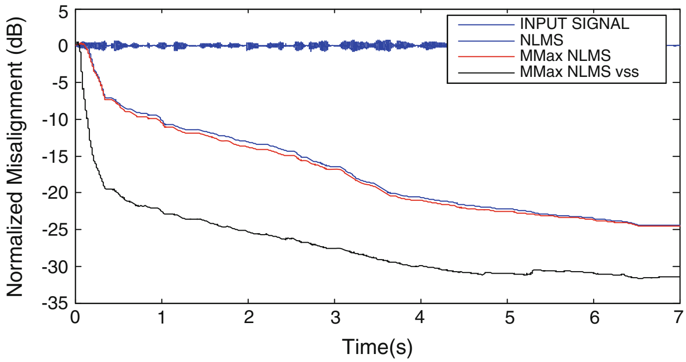

Fig. 15.3 Speech input: comparison between convergence rate of MMax-NLMSvss with NLMS for L = 2,048, M = 512 and SNR = 20 dB. Computational time: MATLAB 7.8 (R2009a) with processor P IV CPU, 3.0 GHz, The time elapsed for NLMS is 352.613455 s

15.7 Conclusion

This paper gives the frame work for comparing three adaptive algorithms for Acoustic Echo Cancellation. We proposed improved convergence characteristics and reduced complexity MMAX-NLMS algorithm by introducing a variable step-size. We proposed MMAX-NLMSvss algorithm by deriving a variable step size for the MMAX-NLMS algorithm using its mean square deviation. In terms of convergence performance, the proposed MMAX-NLMSvss algorithm achieves approximately 7 and 3.5 dB improvement in normalized misalignment over NLMS for WGN and speech input respectively. We can conclude that the proposed algorithm can attain good convergence rate with reduced computational complexity compared to NLMS.

Acknowledgments We are very grateful for the support by the Vishnu Institute of Technology for providing an opportunity to utilize laboratories. We would like to express sincere thanks to Prof. K. Srinivas for providing his guidance and support.

References

1. Dogancay K, Tanrikulu O (2001) Adaptive filtering algorithms with selective partial updates. IEEE Trans Circuits Syst II 48(8):762–769
2. Hänsler E (2000) Hands-free telephones—joint control of echo cancellation and postfiltering. Sig Process 80(11):2295–2305
3. Aboulnasr T, Mayyas K (1997) Selective coefficient update of gradient based adaptive algorithms. In: Proceedings of IEEE international conference on acoustics speech signal processing, vol 3, pp 1929–1932
4. Khong AWH, Naylor PA (2007) Selective-tap adaptive filtering with performance analysis for identification of time-varying systems. IEEE Trans Audio Speech Lang Process 15(5):1681–1695
5. Shin H-C, Sayed A, Song W-J (2004) Variable step-size NLMS and affine projection algorithms. IEEE Signal Process Lett. 11(2):132–135

Chapter 16
Simulation and Experimental Verification of MPPT Algorithms for Partially Shaded Stand Alone Photovoltaic Systems

M. Muthuramalingam and P.S. Manoharan

Abstract The characteristics of a photovoltaic (PV) array are affected by temperature, solar insolation, and shading. In this paper each cascaded H-bridge inverter (CHBMLI) unit is connected to an individual PV module through an interleaved soft switching boost inverter (ISSBC) and controlled with incremental conductance (INC) and adaptive neuro-fuzzy inference system (ANFIS) maximum power point techniques, is studied and simulation and experimental implementation Matlab/Simpowersystem software. The generated PV voltages of each PV module are unequal. In this topology the selective harmonic elimination (SHE) PWM, with a trained ANN sub system for a single phase CHBMLI to generate balanced output voltage even under partially shadowed condition of PV modules is analyzed. The results are evaluated by simulation and experimental implemented on a 300 W PV panel prototype. The simulation and hardware results show that ANFIS algorithm is more efficient than the INC algorithm.

Keywords MPPT · Cascaded H-bridge inverter (CHBMLI) · Selective harmonic elimination (SHE) PWM · Neuro-fuzzy inference system (ANFIS)

16.1 Introduction

The increase in the demand for electricity led to the need for new sources of energy which are cheaper and sustainable with less carbon emissions. Among all renewable energy sources, solar energy is most promising due to its abundance. The main

M. Muthuramalingam (✉)
Department of Electrical and Electronics Engineering, P.T.R College of Engineering and Technology, Madurai, Tamilnadu, India
e-mail: muthuramjaya@yahoo.in

P.S. Manoharan
Department of Electrical and Electronics Engineering, Thiagarajar College of Engineering, Madurai 625015, Tamilnadu, India
e-mail: psmeee@tce.edu

C. Kamalakannan et al. (eds.), *Power Electronics and Renewable Energy Systems*, Lecture Notes in Electrical Engineering 326, DOI 10.1007/978-81-322-2119-7_16

applications of PV systems are either stand-alone or grid-connected configurations [1]. In general, there is a unique point on the P–V or I–V curve, called the maximum power point (MPP), at which the entire PV system operates with maximum efficiency and produces its maximum output power. The performance of a PV module highly affected by the partial shaded condition [2]. Many MPPT techniques have been reported in the literature such as perturb and observation, incremental conductance, fuzzy logic based controller etc. [3–6]. In this paper INC and ANFIS MPPT algorithm being used to extract the maximum DC power from PV module by ISSBC. In recent times, multilevel inverter topologies have received more attention to the use in PV applications [7, 8]. However, this leads to harmonics in the output voltage and current of the multilevel inverter [9]. To overcome the difficulties, in this paper, single phase selective harmonic elimination ANN integrated modulation technique is proposed and verified.

16.2 PV Stand Alone and Array Modelling

The simulation diagram of the proposed topology for ISSBC and CHBMLI based stand alone PV system is shown in Fig. 16.1. Each H-bridge inverter is fed from an individual photovoltaic module through a DC-DC inverter integrated with INC and ANFIS MPPT algorithm. The output of the single phase SHE trained ANN unit has

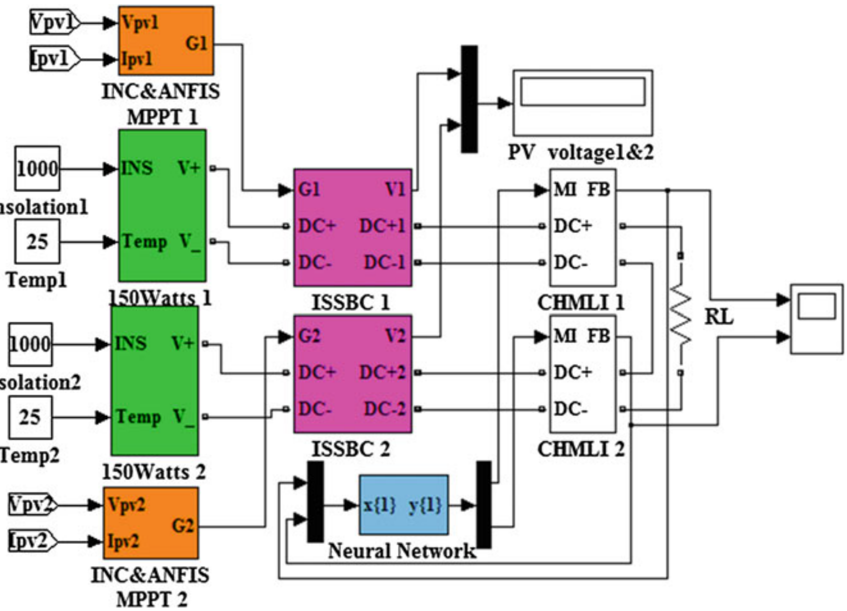

Fig. 16.1 Simulation system

been applied to the CHBMLI to achieve a balanced output with improved power quality even under non-ideal condition of PV module. The PV array used in the proposed system is 300 W solar panel. The basic current equation is given in Eq. (16.1).

$$I = I_{pv,cell} - I_{0,cell}\left[\exp\frac{qv}{akT} - 1\right] \tag{16.1}$$

$$I = I_{pv} - I_0\left[\exp\left[\frac{V + R_s I}{V_a}\right] - 1\right] - \frac{V + R_s I}{R_p}. \tag{16.2}$$

where $I_P Cell$ = current generated by the incident light (directly proportional to sun irradiation), $I_0 Cell$ = leakage current of the diode, q = electron charge 1.6021×10^{-19} C, k = Boltzmann constant (1.38×10^{-23} J/K), T = Temperature of the PN junction, a = diode ideality constant. Practically the PV array comprised with many PV cells connected in series and parallel. To develop embedded simulink model based on current equation and manufacturer's data sheet parameter.

16.3 MPPT Control Algorithms

The MPPT algorithm is used for extracting the maximum power from the PV module and passes it on to the load. A DC–DC inverter serves the purpose of transferring maximum power from the solar PV module to the load. By changing the duty cycle the load impedance, as seen by the source, is varied and matched at the point of the peak power with the source to transfer the maximum power.

16.3.1 INC MPPT Algorithm

The incremental conductance algorithm is derived by differentiating the PV array power with respect to voltage and setting the result equal to zero. This method based on the observation that, at the MPP it is $(dI_{PV}/dV_{PV}) + (I_{PV}/V_{PV}) =$ zero, where I_{PV} and V_{PV} are the PV array current and voltage, respectively [10]. When $(dI_{PV}/dV_{PV}) = -(I_{PV}/V_{PV}) =$ zero, at MPP, $(dI_{PV}/dV_{PV}) > -(I_{PV}/V_{PV})$, left of MPP, $dI_{PV}/dV_{PV}) < -(I_{PV}/V_{PV})$, right of MPP the algorithm knows that the maximum power point is reached and thus it terminates and returns the corresponding value of operating voltage for MPP. This method tracks rapidly changing irradiation conditions more accurately. One complexity in this method is that it requires many sensors to operate and hence is economically less effective.

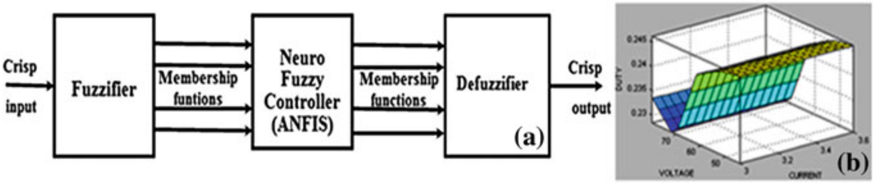

Fig. 16.2 **a** Adaptive neuro fuzzy control system **b** ANFIS surface view

16.3.2 ANFIS MPPT Algorithm

The ANFIS system is used to formulate the neural network architecture in the inference engine of a Fuzzy controller. The functional block diagram and structure of ANFIS is shown in Fig. 16.2a. The structure comprises of three distinct layers namely input layer, hidden layer and output layer.

The input membership functions are mapped to the output membership function by 49 rules through grid partitioning method using the FIS generator in MATLAB Simulink. The 250 data sets to train ANFIS is obtained from workspace from the previous INC MPPT algorithm model in which data's namely PV voltage and current and the corresponding modulation index (*MI*). The learning data trained through back propagation technique for 50 epochs for minimum error tolerance. The trained ANFIS connecting weights are adjusted in such a way that the estimated array voltage is identically equal to the MPP voltage [11]. The trained surface rule phase view shown in Fig. 16.2b, the trained data set exports the simulation and observes the performance different partial shading condition.

16.4 Soft Switching Boost Inverter

It serves as a suitable interface for PV cells to convert low voltage, high current input into a high voltage low current output. Figure 16.3a shows the functional diagram of an ISSBC, the interleaved boost inverter consists of two single phase boost inverters that are connected in parallel and inverters operating 180 degrees out of phase with 30 kHz switching frequency [12]. The input current is the sum of

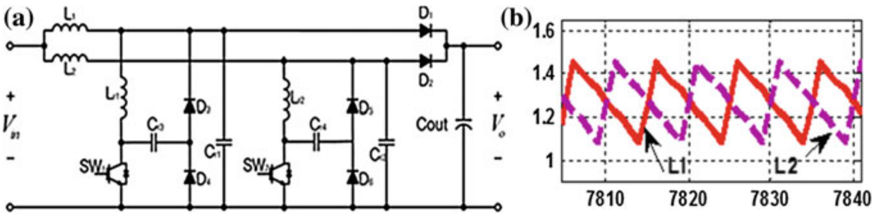

Fig. 16.3 **a** ISSBC **b** Main inductor current

the two-inductor currents, I_{L1} and I_{L2} shown in Fig. 16.3b. Because the inductor ripple currents are out of phase, they cancel each other and the input-ripple current reduce to 12 % of that of a conventional boost inverter [13].

16.5 Single Phase CHBML Inverter

As in the proposed topology of CHBMLI, each H-bride cell is fed from an individual PV module [14]. There is always a chance of voltage unbalance because of the partial shadow effect on any of the PV modules.

$$V_{ab}(\alpha) = \sum_{n=1,5,7,11\ldots}^{\infty} \left[\frac{4}{\pi . n} \cdot V_{pv1} \cos(n \cdot \alpha_1) + V_{pv2} \cos(n \cdot \alpha_2) \right] \tag{16.4}$$

In this paper selective harmonic elimination pulse with modulation technique is implemented to generate the switching duty cycle for CHB inverter. The Eq. (16.4) shows the contents of the output voltage at infinite frequencies, the module voltage $V_{pv1} - V_{pv2}$ are associated to their respective switching angle $\alpha_1 - \alpha_2$. These trigonometric transcendental equations can be solved by GA and implemented to find the switching angle (offline) for a set of predetermined modulation indices to get the required fundamental output voltage in a five level cascaded multi level inverter. The switching angles (α_1, α_2) lie in between 0 and $\pi/2$.

16.6 Simulation Results

The simulation validation of PV module and inverter results of the I–V and P–V characteristics of PV module as a function of irradiation and temperature under different partially shed condition shown in Fig. 16.4a, b. The simulation result is presented for the following configuration.

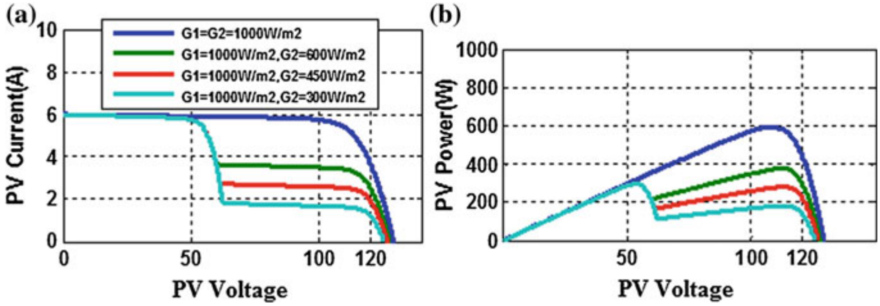

Fig. 16.4 **a** P–V curve at 25 °C **b** 11. I–V Curve at 25 °C

16.6.1 Effect of Partially Shaded Solar Irradiation

In order to verify the performances of the INC and ANFIS algorithm, the CHBMLI is connected to an RL load (R = 100 ohm and L = 20 mH) using switching frequency of 30 kHz in the ISSBC and SHE ANN modulated CHBMLI simulated both Partially shaded (unbalance) and un shaded (balanced) condition.

Under balanced condition both PV arrays receives constant solar irradiation of 1,000 W/m^2. The DC voltage input of two H-bridge inverter are $V_{dc1} = V_{dc2} = 59$ V and under unbalanced condition the two PV array irradiation of 1,000 W/m^2 and 750 W/m^2 respectively. The DC voltage input of two H-bridge inverter, for example, may become $V_{dc1} = 59$ V and $V_{dc2} = 47$ V respectively. The output of the step modulated inverter, voltage along with their harmonic spectrum up to 7.5 kHz under balanced condition for the INC and ANFIS algorithms are shown in Fig. 16.5a–c. The total harmonic distortion (THD) of the output with the INC model of control is 23.11 % and with the ANFIS model they are 20.11 % respectively. Similarly, under the unbalanced operating conditions of the PV panels both algorithms exhibit THD

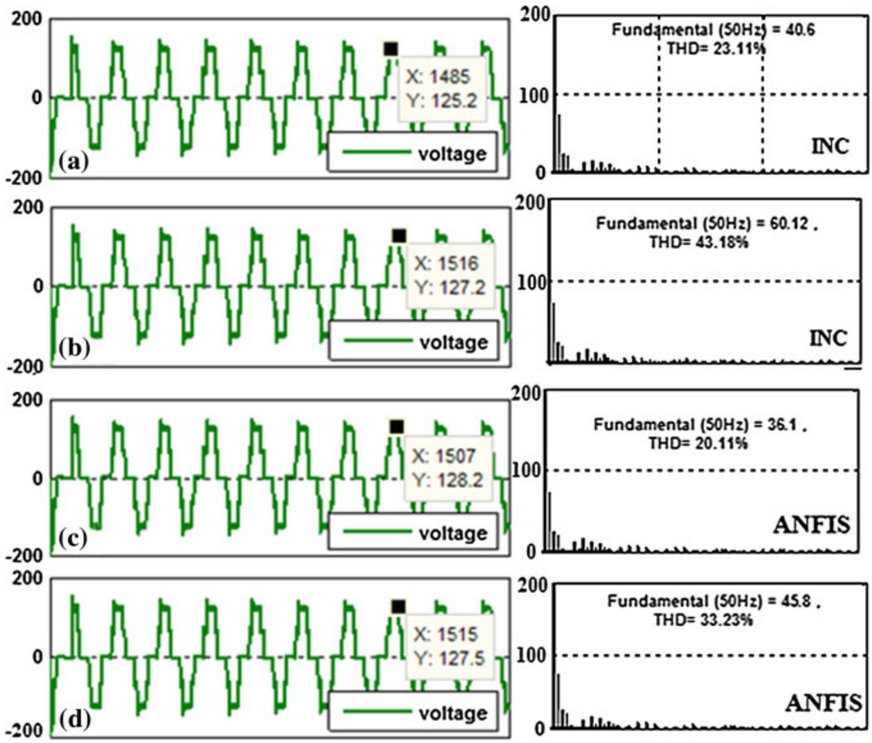

Fig. 16.5 Simulation results for output voltage and harmonic spectrum **a** INC under balanced condition **b** INC under unbalance condition **c** ANFIS under balance condition **d** ANFIS under unbalance condition

values for voltage as shown in Fig. 16.5b–d. The total harmonic distortion (THD) of the output voltage and current in the case of INC is 43.18 %. With the ANFIS model, the THD values for voltage and current are 33.23 %. It can be observed from the simulation results that for both balanced and unbalanced conditions, the percentage THD is less and more power extract in ANFIS algorithm as compared to the INC algorithm.

16.7 Experimental Validation

The simulation results were verified experimentally in the using the appropriate hardware built around the PIC 16F877A microcontroller. The MPPTs extracted power can be observed as an exposition of approximately 04:00 h range from 09:00 to 14:00 h with different PV insolation and cell temperature under partially shading condition. For that conditions are noted down and for the corresponding values of the PV. The current Vs voltage characteristics and power versus voltage characteristics are shown in Figs. 16.6 and 16.7. For the validation of maximum power point tracking control, the developed inverter is tested on at 12:30 PM. The irradiation and

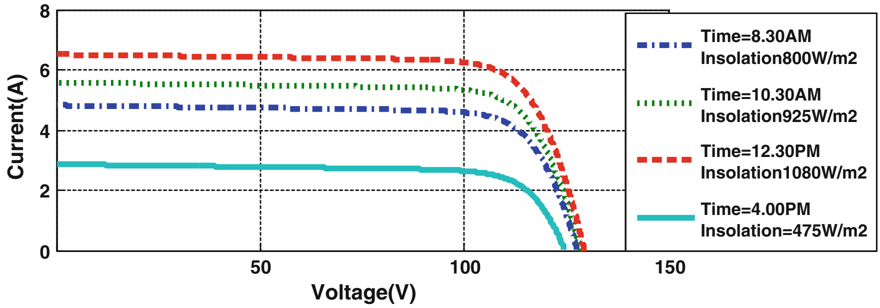

Fig. 16.6 V and I characteristics of PV module based on experimental data

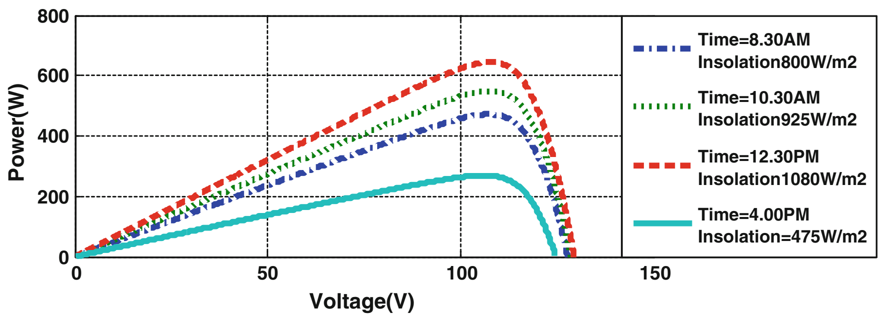

Fig. 16.7 P and V characteristics of PV module based on experimental data

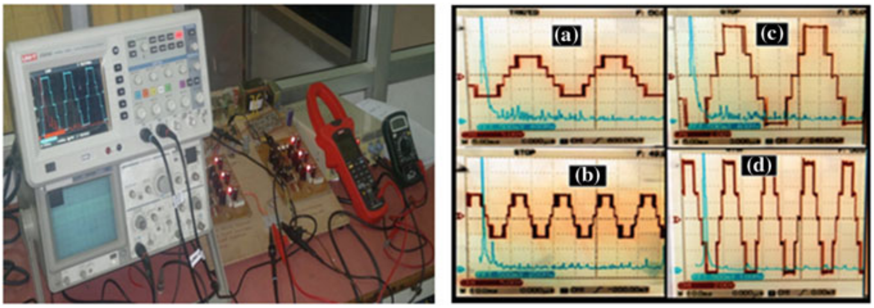

Fig. 16.8 Experimental setup and result for voltage and harmonic spectrum **a** balanced ANFIS **b** unbalanced ANFIS **c** balanced INC **d** unbalanced INC

temperature were measured as 1,050 W/m^2 and 32 °C respectively. During experimentation, both the PV modules in balanced condition with ANFIS and INC algorithm generates $V_{dc1} = V_{dc2} = 68.1$ V and $V_{dc1} = V_{dc2} = 69.8$ respectively. Similarly, under balanced operation the rms value of output voltage is found as 81.4 and 82.12 Volts respectively. Figure 16.8 Experimental setup and result of (a) and (c) shows the voltage and harmonic spectrum and the corresponding THDs which are found to be 22.3 and 20.3 % respectively. In order to test the algorithm for unbalanced condition, intentionally one of the PV modules was shaded by 25 %. Under this condition, the partially shaded module with ANFIS and INC algorithms are generating $V_{dc2} = 61.1$ V and $V_{dc2} = 63.8$ V respectively. The output voltage with their corresponding harmonic spectrums is shown in Fig. 16.8b, d. The rms value of output voltage 80.4 and 81.34 V and the corresponding THDs are found to be at 42.4 and 32.7%.

16.8 Conclusion

This paper analyzes the simulation and experimental performance of INC and ANFIS MPPT algorithms by stand-alone PV system. The configuration for the proposed system is designed and simulated using MATLAB/Simulink and implemented in 16F877A micro controlled prototype. Both unshaded and partially shaded condition, SHE-PWM trained ANN technique performs balanced output voltage. The ANFIS MPPT algorithm improves the voltage quality, power extraction, harmonics elimination as compared to the INC MPPT algorithm. The results obtained from ANFIS MPPT algorithm can gain importance in high performance applications such as PV standalone generation system.

References

1. Malla SG, Bhende CN, Mishra S (2011) Photovoltaic based water pumping system, the school of electrical sciences, Indian Institute of Technology Bhubaneswar, IEEE conference 2011, 978-1-4673-0136-7/11
2. Ishaque K, Salam Z (2013) A Deterministic particle swarm optimization maximum power point tracker for photovoltaic system under partial shading condition. IEEE Trans Indus Electron 60:3195–3206
3. Ben Salah C, Ouali M (2011) Comparison of fuzzy logic and neural network in maximum power point tracker for PV systems. Electr Power Syst Res 81:43–50
4. Esram T, Chapman PL (2007) Comparison of Photovoltaic array maximum power point tracking techniques. IEEE Trans Energy Convers 22(2007):439–449
5. Hohm DP, Ropp ME (2000) Comparative study of maximum power point tracking algorithms using an experimental, programmable, maximum power point tracking test bed. In: Proceedings of photovoltaic specialist conference 2000, pp 1699–1702
6. Mellit A, Kalogeria SA (2011) ANFIS-based modeling for photovoltaic power supply system. Renew Energy 36:250–258
7. Ravi A, Manoharan PS, Vijay Anand J (2011) Modeling and simulation of three phase multilevel inverter for grid connected photovoltaic systems. Sol Energy 85:2811–2819
8. Valan Rajkumar M, Manoharan PS (2013) FPGA based multilevel cascaded inverters with SVPWM algorithm for photovoltaic system. Solar Energy 87:229–245
9. Beser E, Arifoglu B, Camur S, Beser EK (2010) A grid-connected photovoltaic power conversion system with single-phase multilevel inverter. Sol Energy 84:2056–2067
10. de Brito MAG, Galotto L, Sampaio LP (2013) Evaluation of the main MPPT techniques for photovoltaic applications. IEEE Trans Indus Electron 60:1156–1167
11. Putri Ratna Ika, Rifa M (2012) Maximum power point tracking control for photovoltaic system using neural fuzzy. Int J Comput Electr Eng 4(2012):75–81
12. Jung DY, Ji YH, Park SH, Jung YC, Won CY (2011) Interleaved Soft-switching boost inverter for photovoltaic power-generation system. IEEE Trans Power Electr 26:1137–1145
13. Kim JH, Jung DY, Kim JH, Lee SW, Jung YC, Won CY (2008) Soft switching interleaved boost inverter for photovoltaic, power generation system, ICSET (2008), pp 257–262
14. Leon JI, Vazquez S, Watson AJ, Franquelo LG, Wheeler PW, Carrasco JM (2009) Feed forward space vector modulation for single-phase multilevel cascaded inverters with any DC voltage ratio. IEEE Trans Indus Electron 56:315–325

Chapter 17
Performance Comparison of D-STATCOM and SVC for Mitigation of Voltage Flicker in Electric Arc Furnace Using PSCAD/EMTDC

A. Pandiyarajan and S. Latha

Abstract Electric Arc Furnaces (EAF) are highly nonlinear load which causes power quality problems. Their nonlinearity and time varying characteristics generate harmonic distortion and voltage fluctuation. These effects are very harmful for the electric power supplying line and for other consumers. Utilities are concerned about these effects and try to take precautions to minimize them. In this project, an arc furnace model is developed and implemented. The main objective is to compare the performance of sinusoidal PWM voltage source converter based D-STATCOM control and SVC control for mitigation of voltage flicker caused by EAF. It is clear that STATCOM control has shown improved performance than SVC control. Moreover, the modeling and simulation of an IEC flicker meter are also performed to evaluate the severity of fluctuations in the simulated arc furnace voltage. Simulation and analysis are carried out in PSCAD/EMTDC environment. The reliability and robustness of the control scheme in the system response to the voltage disturbances due to EAF is obviously proved in the simulation results.

Keywords Electric arc furnace (EAF) · Static synchronous compensator (STATCOM) · Static var compensator (SVC) · Voltage source converter (VSC) · Proportional integral controller (PI) · Pulse width modulation (PWM)

A. Pandiyarajan (✉) · S. Latha
Department of Electrical and Electronics Engineering, Thiagarajar College of Engineering, Madurai 625015, Tamil Nadu, India
e-mail: pandiyarajan@tce.edu

S. Latha
e-mail: sleee@tce.edu

C. Kamalakannan et al. (eds.), *Power Electronics and Renewable Energy Systems*, Lecture Notes in Electrical Engineering 326, DOI 10.1007/978-81-322-2119-7_17

17.1 Introduction

The electric arc furnaces used for steel production are a main cause of voltage fluctuations in electrical networks, which may give rise to the flicker effect. AC and DC arc furnaces represent one of the most intensive disturbing loads in the sub-transmission or transmission electric power systems; they are characterized by rapid changes in absorbed powers that occur especially in the initial stage of melting, during which the critical condition of a broken arc may become a short circuit or an open circuit.

Voltage fluctuations, due to random arc-length variations during scrap melting, have typical frequencies in the range 0.5–35 Hz. Flicker consists of luminosity variations of lamps which may affect the human visual system, depending on their frequency and intensity. For example, voltage-amplitude variations of about 0.3 % about at frequency 10 Hz are sufficient to get over the mean human perceptivity threshold and also these are the nuisance to the neighboring customers who are all connected to the same point of common coupling. [1–3].

When the magnitude of the voltage flicker will be above threshold of irritation, lighting load (incandescent lamp) causes irritation to the eye [4].

Voltage flicker associated with an EAF is evaluated in two main ways around the world. The first is flicker meter, which is the IEC standard and has been established by the UIE. The other is meter, which is established by the Japanese Technical Committee [5].

Typically, a Static Var Compensator (SVC) or static synchronous compensator (STATCOM) is added to compensate for the reactive power fluctuation. The conventional SVC can only reduce part voltage fluctuation. However, the serious voltage flicker still occurs in EAF factories when the active power is very unstable. It cannot catch up the fast varying flicker (1–20 Hz) very well with the inherent limit of relatively low bandwidth. Hence, its dynamic performance for flicker mitigation is limited [6–8]. Therefore, it is necessary to develop control that can impact active and reactive power flows to mitigate electric arc furnace disturbances. STATCOM control that provides improved performance for flicker mitigation and power-quality (PQ) improvement for EAF applications. Specifically, the contributions of this paper are:

1. Modeling and analysis EAF voltage flicker
2. To design and Analysis of STATCOM control (PI MODE)
3. The application of STATCOM control to mitigate EAF flicker
4. A comparison with the conventional SVC control.

17.2 Test System

The Schematic diagram of the electrical distribution system feeding an Electric Arc furnace is shown in Fig. 17.1. The electrical network consists of a 115-kV generator and impedance is connected at the Point of Common Coupling (PCC) through step

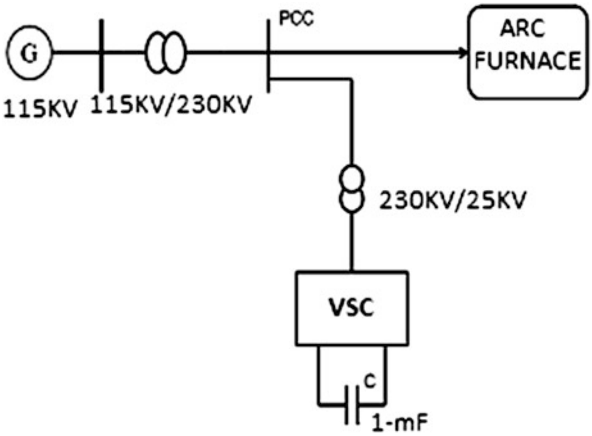

Fig. 17.1 Test system

up transformer (115/230 kV). The STATCOM is connected to the system through a 230/25-kV Star-Delta transformer.

17.2.1 Modeling of Electric Arc Furnace

Electric arc furnaces are typically used to melt steel and will produce current harmonics that are random. In addition to integer harmonics, arc furnace currents are rich in interharmonics. The flicker waveform has sub synchronous variations in the 5–35 Hz range. To synthesize the variations to the RMS waveform, an aperiodic waveform is generated by

$$R(t) = R_o + a_L \cos(\omega_L \mathrm{t} + \theta_L) + a_H \cos(\omega_H \mathrm{t} + \theta_\mathrm{H})\Omega \qquad (17.1)$$

where ω_L and ω_H are randomly generated frequencies in the range of interest and a_L and a_H are randomly generated positive scalars. At each zero crossing, a new set of parameters $[a_L \omega_L a_H \omega_H]$ is generated.

For arc furnace applications, the low frequency component ω_L should be centered about a frequency in the 5–35 Hz range. The high frequency component ω_H should be centered about an odd integer multiple of ω_L. For example, one such generated flicker waveform can be produced from the following parameters:

$\omega_L = 2\pi(1 + \rho 8)$ where $\rho \in [0, 1]$ is a random number
$\omega_H = 2\pi(10 + \rho 30)$
$a_L = 50\rho$
$a_H = 10\rho$
R_o = 130 Ω (phase a, b), R_o = 80 Ω (phase c)

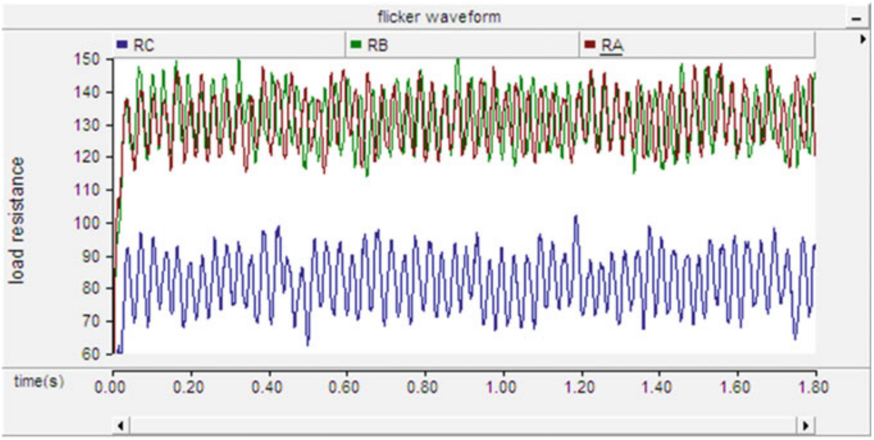

Fig. 17.2 Flicker waveform

Three phase set of variable resistive loads are generated by the Eq. (17.1) is shown in Fig. 17.2. This model is developed for simulating the dynamic performance of an electric arc furnace through the application of varying resistances. Each phase is randomly varying and potentially unbalanced. This model is implemented in PSCAD.

17.2.2 Flicker Mitigation Using SVC

The digital simulation is performed to study the voltage flicker mitigation with SVC connected at the PCC. The SVC consists of a thyristor controlled reactor and thyristor switched capacitor. The main objective of the SVC is to maintain the RMS voltage at the PCC within the limit. The block diagram of SVC control system is shown in Fig. 17.3. Here, The AC voltage control is achieved by filtering out the second harmonic and the low frequencies of the ac voltage which is compared with the reference voltage. The error voltage is given to the PI controller to obtain the firing angle. The voltage oscillations occurring due to EAF operation are eliminated by varying the firing angle of SVC.

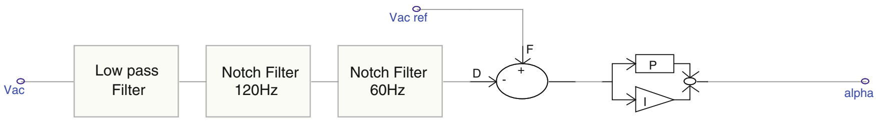

Fig. 17.3 SVC control system

17.2.3 Flicker Mitigation Using STATCOM

The D-STATCOM is composed of one Voltage Source Converter with energy storage capacitors on its dc side, inductances and a coupling transformer on its ac side, and a control system, and it is connected in parallel with the Electric Arc Furnace. The Voltage Source Converter converts the dc voltage across the storage device in a set of three-phase ac output voltages. These voltages are in phase and coupled with the ac system through the reactance of the coupling transformer. The STATCOM controls the reactive-power flow in the electric line, injecting or absorbing it. This reactive-power output of the converter is controlled by varying the amplitude of the output voltage.

17.2.3.1 Sinusoidal PWM Based Control

This section describes the PWM-based control scheme with reference to the D-STATCOM. The aim of the control scheme is to maintain constant voltage magnitude at the point where a sensitive load is connected, under system disturbances. The control system only measures the RMS voltage at the load point i.e., no reactive power measurements are required. The VSC switching strategy is based on a sinusoidal PWM technique which offers simplicity and good response.

Both m_a and δ are limited to bound the magnitude of the injected current and, therefore, limit the injected active and reactive powers. In this control, only the parameter must be tuned.

This control diagram of PI controller is shown in Fig. 17.4. The primary control targets of a D-STATCOM are to control the PCC root-mean-square (RMS) line voltage (Vrms) and the active power flow on the line.

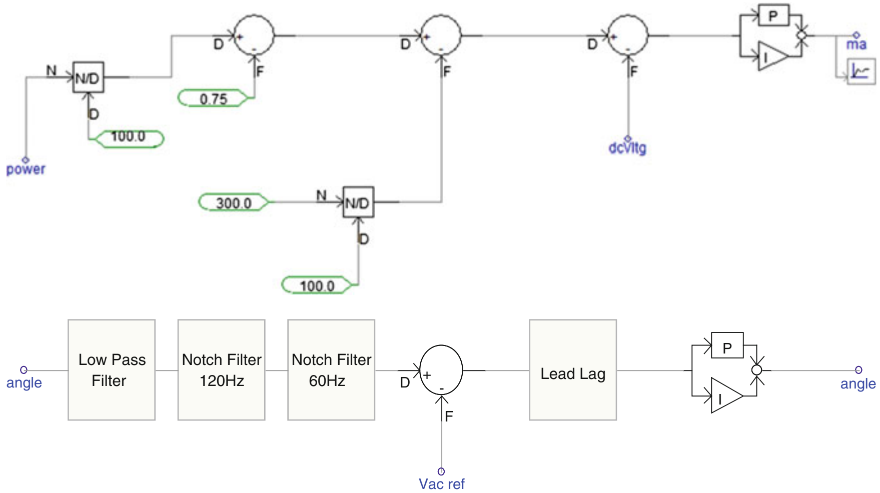

Fig. 17.4 PI control for STATCOM

The ac voltage control is achieved by filtering out the second harmonic and the low frequencies of the ac voltage and then a lead-lag and a PI controller are applied to the dc voltage error in order to obtain the modulation phase shift. The dc capacitor voltage error is put through a PI controller to provide the modulation index gain.

The D-STATCOM control system exerts voltage angle control as follows: an error signal is obtained by comparing the reference voltage with the RMS voltage measured at the load point. The PI controller process the error signal and generates the required angle δ to drive the error to zero, i.e., the load RMS voltage is brought back to the reference voltage. In the PWM generators, the sinusoidal $V_{control}$ signal is phase-modulated by means of the angle δ. The modulated signal $V_{control}$ is compared against a triangular signal (carrier) in order to generate the switching signals for the VSC valves.

17.3 Results and Discussion

The effectiveness of the controls presented earlier is assessed by using several quantitative assessments. The controllers are compared and contrasted for their performance in:

- maintaining the RMS voltage;
- Voltage balancing between phases;
- Reduction of total harmonic distortion (THD);
- Flicker mitigation.

17.3.1 Voltage Balancing and RMS Voltage

For unbalanced loads, the main problems that exist are harmonic generation on the dc side and consequent generation of low-frequency harmonics on the ac side. It will be shown that neither of these problems exists in the STATCOM control. Figure 17.5 shows the unbalance of voltages of the arc furnace load without, with SVC and with D-STATCOM. It clearly indicates that STATCOM control reduces the unbalances in the three phase voltages than SVC control and without control. Figure 17.6 shows the RMS value of with the unbalanced varying arc furnace load. Note that the SVC and STATCOM control improve the RMS voltage considerably, but the STATCOM control shows better performance than the SVC control and is able to control it better to the specified reference voltage (0.86 p.u.)

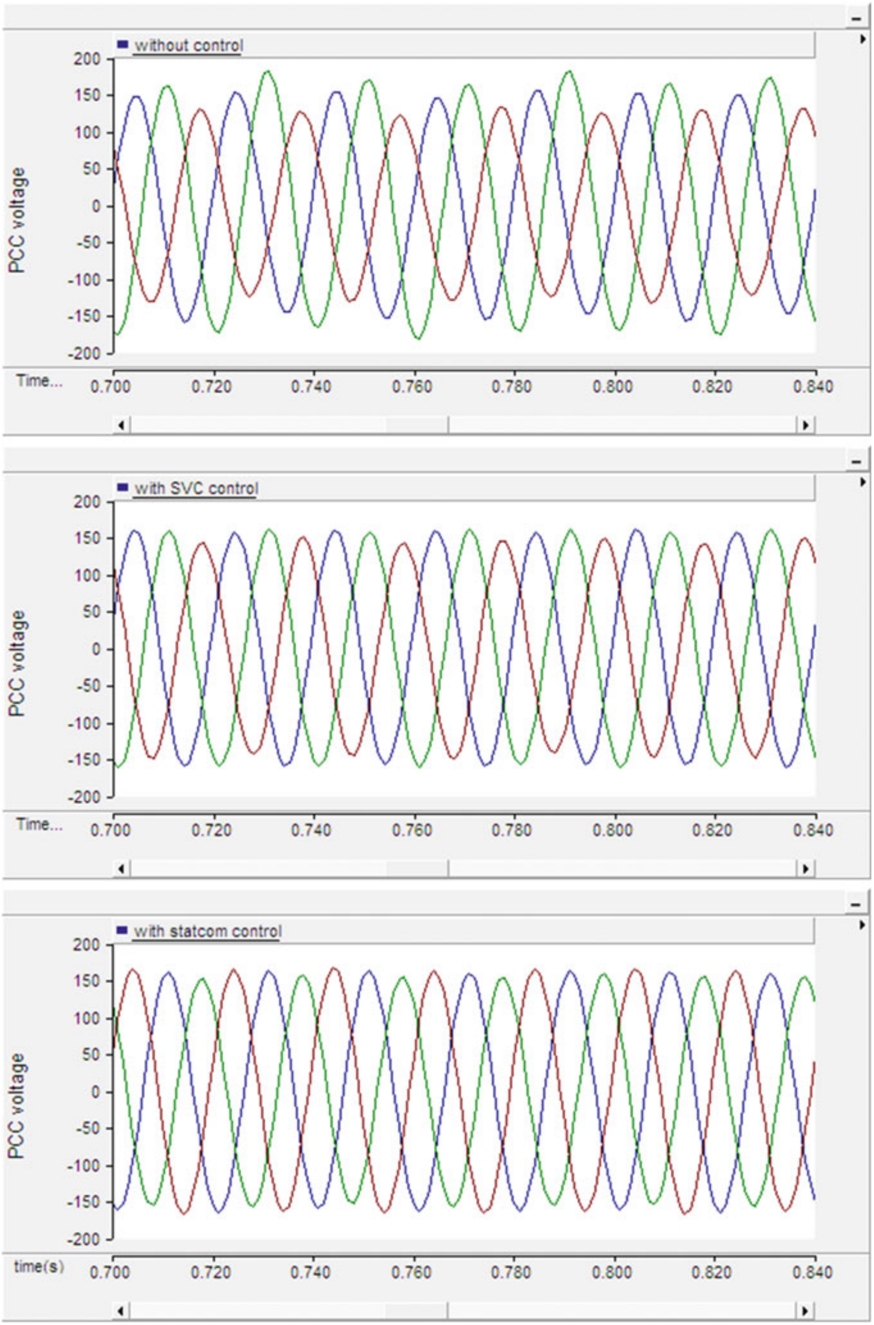

Fig. 17.5 Phase voltages at the PCC without, with SVC and with STATCOM control

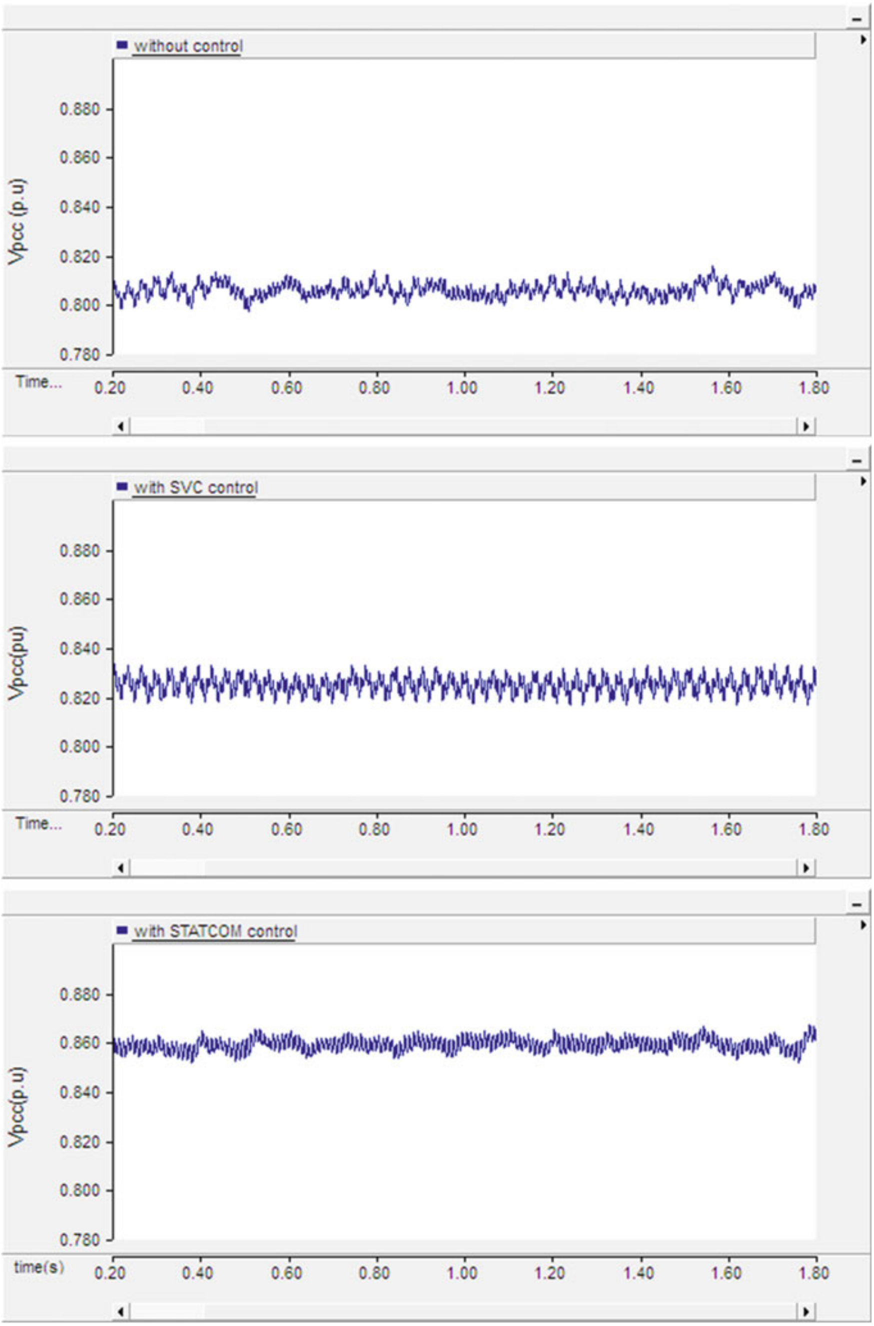

Fig. 17.6 RMS voltage at the PCC without, with SVC and with STATCOM control

17.3.2 The IEC Flicker Measurement Standard

The primary sources of flicker are industrial loads, usually arc furnaces, rolling mills, welding, and other manufacturing processes. The IEC 1000-4-15 Standard gives the specifics of a measurement approach for flicker that can be adapted to a wide variety of situations. The major portions of the flicker meter are (1) input processing, (2) "lamp-eye-brain" response, and (3) output processing.

The "lamp-eye-brain" characteristic is obtained from a mathematical derivation of (1) the response of a lamp to a supply voltage variation, (2) the perception ability of the human eye, and (3) the memory tendency of the human eye. The following transfer function:

$$\mathrm{H(s)} = \mathrm{G}\frac{\frac{S}{\omega_O}}{1 + 2z\frac{S}{\omega_O} + \frac{S^2}{\omega_O^2}} \tag{17.2}$$

is provided as a reasonable model for the human eye. The coefficients are given by the IEC for 230-V, 60-W incandescent lamps. The flicker meter is used to measure the flicker in the PCC voltage. This is modeled in PSCAD simulation software and is shown in Fig. 17.7.

The Flicker content of PCC voltages is shown in Fig. 17.8. Note that STATCOM control is significantly lower than SVC control and without control.

17.3.3 Total Harmonic Distortion (THD)

The THD has been calculated by using the THD module in PSCAD. For generality, only phase a is shown in the Fig. 17.9, but phases b and c are qualitatively similar although quantitatively different. Table 17.1 shows that the mean THD value is 1.1 % with STATCOM control. Mean THD is improved by 0.7 % as compared with the paper [1].

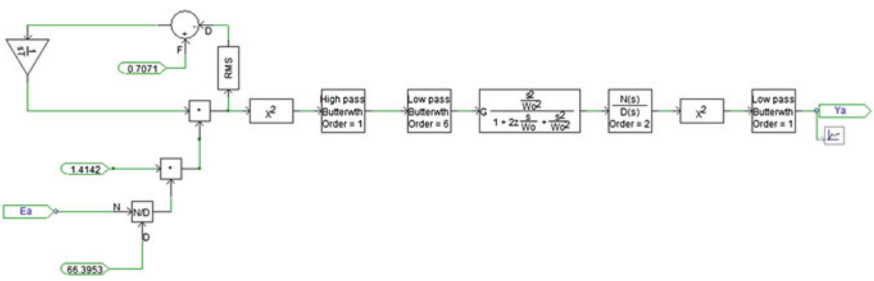

Fig. 17.7 Flicker measurement of the PCC voltage (phase a)

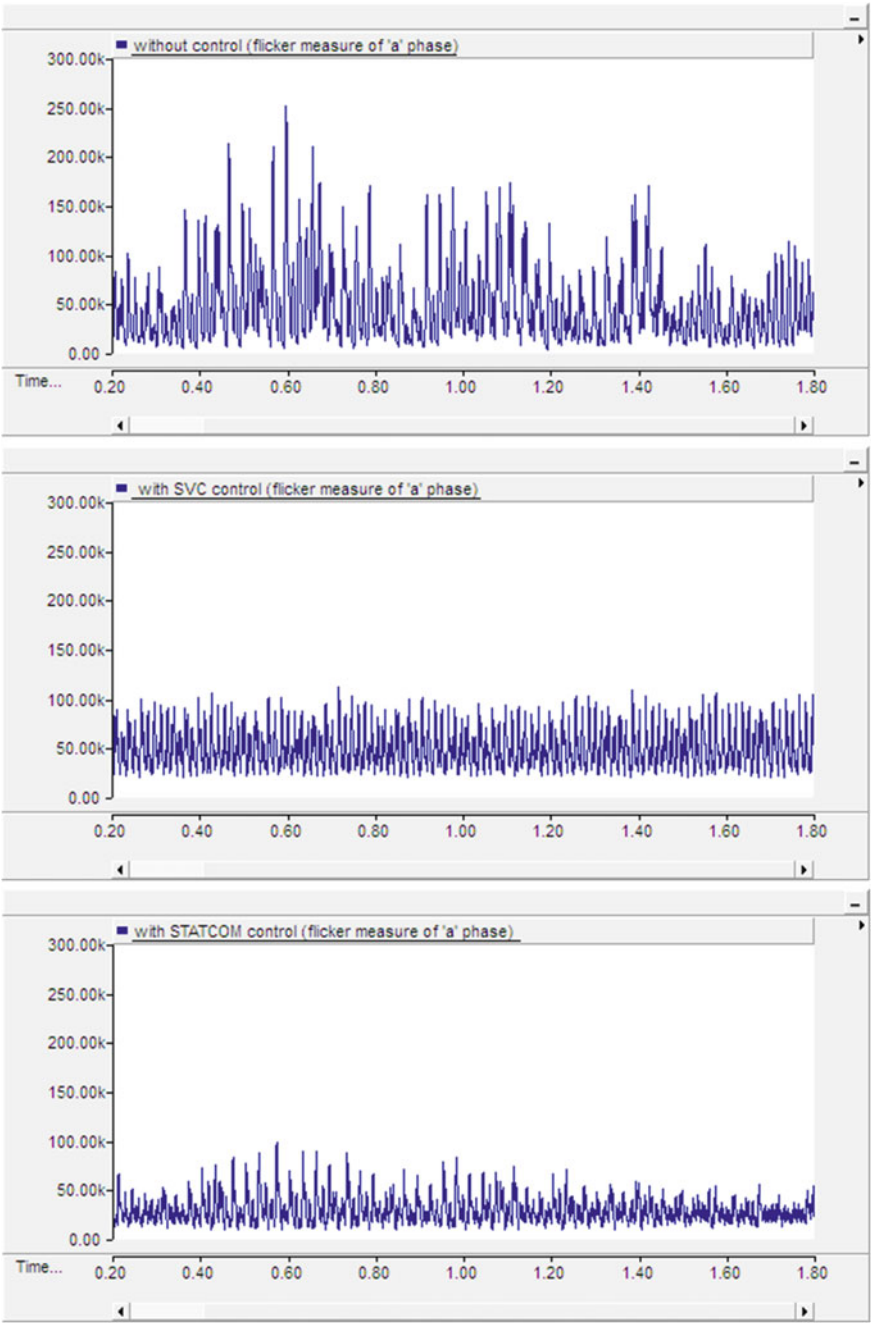

Fig. 17.8 Flicker measurement of the PCC voltage (phase a) without, with SVC and with STATCOM

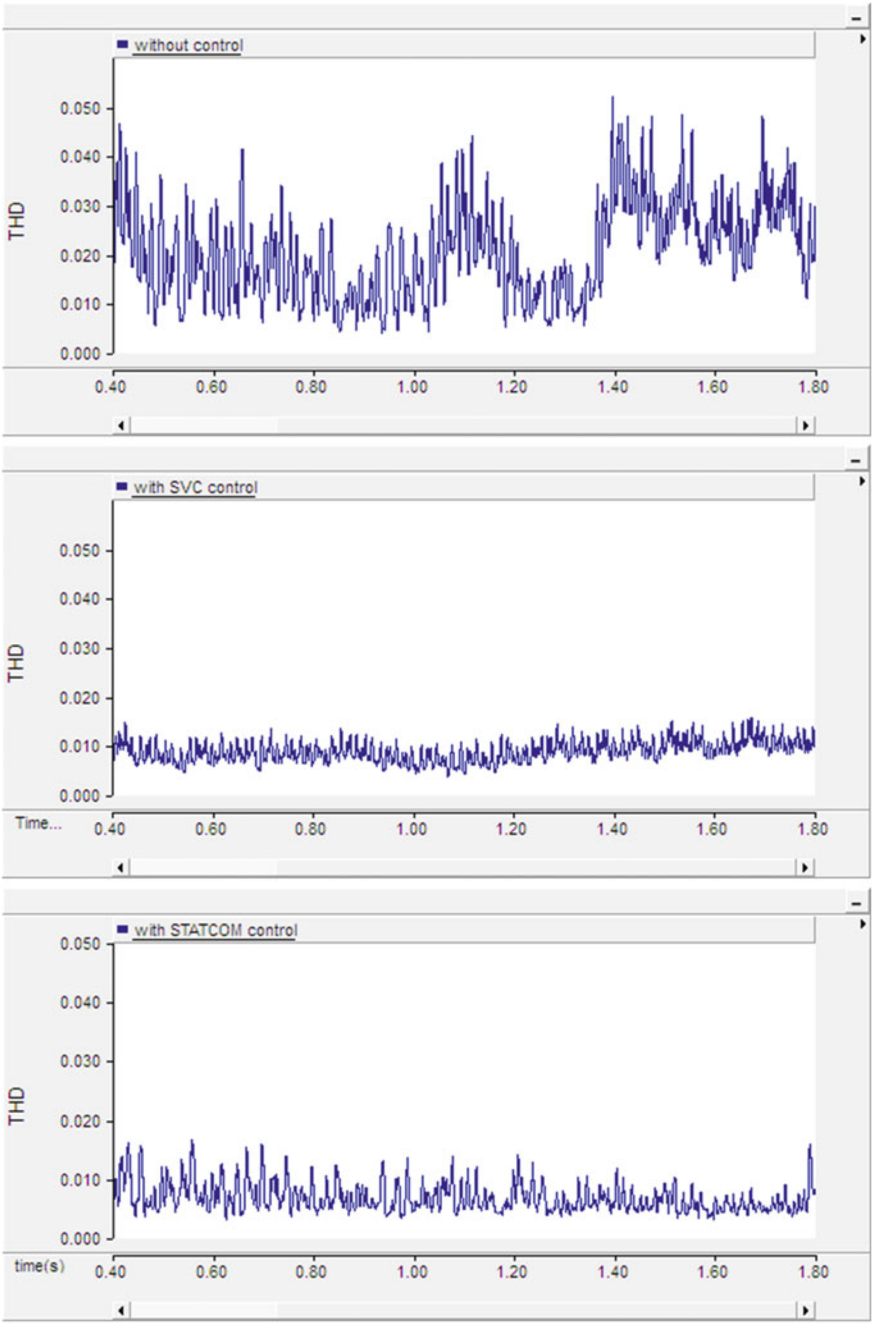

Fig. 17.9 THD of the PCC voltage (phase a) without, with SVC and with STATCOM

Table 17.1 Comparison of %voltage THD without with SVC and with STATCOM control

%voltage THD	Without control	With SVC control	With STATCOM control
Mean	3.7	1.5	1.1

17.4 Conclusion

This paper has compared the performance of Static Synchronous Compensator and Static Var Compensator for compensation of flicker caused by Electric arc furnaces. The applied load is randomly fluctuating and unbalanced. The STATCOM control is proposed to provide improved control for RMS voltage and line active power control. In addition, SVC control is compared against the STATCOM control in reducing total harmonic content, flicker, and phase imbalance. In all cases, the STATCOM control produced similar or improved results when compared with the SVC control.

Finally, the reduction in voltage flicker improves the voltage profile and increases the productivity of the Electric Arc Furnace [9, 10].

Acknowledgments The author would like to acknowledge the Management, Principal, HOD and Project Guide of EEE department, Thiagarajar college of Engineering, Madurai for their support in the project work.

References

1. Yazdani A, Crow ML, Guo J (2009) An improved nonlinear STATCOM control for electric arc furnace voltage flicker mitigation. IEEE Trans Power Delivery 24(4):2284–2290
2. García-Cerrada A, Garcia Gonzalez P, Collantes R, Tomás (2000) Comparison of thyristor-controlled reactors and voltage-source inverters for compensation of flicker caused by arc furnaces. IEEE Trans Power Delivery 15(4):1225–1231
3. Han Chong, Yang Zhanoning, Chen Bin, Huang Alex Q (2007) Evaluation of Cascade-Multilevel-Converter-Based STATCOM for Arc Furnace Flicker Mitigation. IEEE Trans Indus Appl 43(2):378–385
4. Miller TJE, Reactive power control in electric systems. Wiley, Inc.1982.ISBN 0-471-86933-3
5. Halpin SM, Bergeron R, Blooming T, Burch R, Conrad L, Key T (2003) IEEE power engineering society flicker task force—P1453, Voltage and lamp flicker issues: Should the IEEE adopt the IEC approach?. IEEE Trans Power Delivery 18(3):1088–1097
6. Sharmeela C, Uma G, Mohan MR, Karthikeyan K (2004) Voltage flicker analysis and mitigation—case study in AC electric arc furnace using PSCAD/EMTDC. Institute of Electrical Electronics Engineers International conference on industrial Technology, pp 207–212
7. Guan JL, Gu JC, Wu CJ (2005) A Novel Method for Estimating Voltage Flicker. IEEE Trans Power Deliv 20(1):242–247
8. Anaya-Lara O, Acha E (2002) Modeling and analysis of custom power systems by PSCAD/EMTDC. IEEE Trans Power Deliv 17(1):266–272

9. Mienski R, Pawelek R, Wasiak I (2004) Shunt compensation for power quality improvement using a STATCOM controller: modeling and simulation. Proc Inst Electr Eng Gen Transm Distrib 151(2):274–280
10. Gosh A, Ledwich G (2002) Power quality enhancement using custom power device. Kluwer Academic Publisher, Netherlands, p 460

Chapter 18
The Influence of Floor Tile Colour on Lighting and Energy Saving

P. Ganesan, S. Rajakarunakaran, M. Thirugnanasambandam and D. Devaraj

Abstract Selection of right building materials is a key factor in achieving the low energy and low emission buildings. In this paper, a model study is conducted to identify the energy saving potential in indoor lighting through different colour of floor tiles. The study revealed that the floor tile colour has the significant impact on electrical energy saving and lighting improvement. It is revealed that the minimum of 41 % and maximum of 70.9 % of light reflectance could be increased and saved by providing the white coloured tile. This study also proved that building materials can also contribute to the electrical energy saving. This strategy could be implemented to large commercial buildings, industrial buildings etc., to improve the lighting as well as energy saving without any additional investment and the payback is immediate.

Keywords Buildings · Energy saving · Floor tile colour · Indoor lighting · Light reflectance value

18.1 Introduction

Low energy and low emission buildings are the goals of worldwide researchers [1]. Lighting is an important issue in minimizing overall energy consumption of any building [2]. For the industrialized countries, lighting accounts for 5–15 % of the total electric energy consumption [3, 4]. The colour and texture of floor tile influences how much light energy it will absorb or reflect. Every colour reflects a certain amount of light while absorbing the rest as heat energy. The amount of reflected light is called the colour's light reflectance value. Dark colours with low light reflectance values tend to reflect little light while absorbing lots of heat energy, whereas light colours with high reflectance values reflect a lot of light and absorb little energy. The review

P. Ganesan (✉) · S. Rajakarunakaran · M. Thirugnanasambandam · D. Devaraj
Kalasalingam University, Anand Nagar, Krishnankoil 626126, Tamilnadu, India
e-mail: pganesanmech@gmail.com

C. Kamalakannan et al. (eds.), *Power Electronics and Renewable Energy Systems*,
Lecture Notes in Electrical Engineering 326, DOI 10.1007/978-81-322-2119-7_18

reveals that theoretical calculations, measurements in full-scale rooms and simulations with validated lighting programs indicate that an energy intensity of around 10 kWh/m^2 yr is a realistic target for electric lighting in future low energy buildings [1]. Keeping this in view, an experiment is conducted to identify the effect of colour of floor tile on indoor lighting and energy saving. The tile colours like white, grey, black, yellow and green are selected and experiments are conducted to identify the energy saving potential and possible improvement in interior lighting.

18.2 Experimental Setup and Procedure

18.2.1 Setup

The test bench is prepared and the colour's lux reflectance value is identified by following the guidelines given by the Alternative Energy Promotion Centre, Government of Nepal, Ministry of Environment, Science and Technology [5, 6]. A test bench of size 2 m length and 2 m height is prepared as shown in Fig. 18.1. The Fluorescent lamp (FTL) with electronic ballast is mounted on the test bench at a height of 2 m from the floor. The test bench is placed over the floor tiles of which the reflectance light value is to be measured. The Lux meter is fixed at 1 m above the floor to observe the light which is reflected by the floor tiles. The instruments used for this study is listed in Table 18.1.

18.2.2 Pre-test Requirements

The pre-test requirements are listed below [7] as per the guidelines of Bureau of Energy Efficiency (BEE):

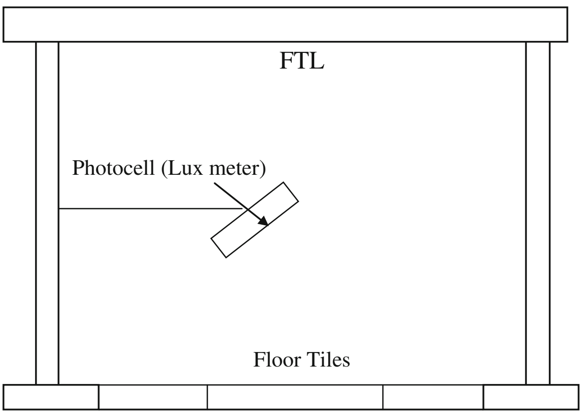

Fig. 18.1 Test bench

Table 18.1 Specification of the measuring instruments

Name of the instrument	Measurable parameters	Specification range	Accuracy
EXTECH make,3-phase clamp power analyzer with 2,000 A, model 382075	Volt, Amps, kW, pf, Hz	Up to 200 A, 2,000 A	±1.5 % for V and I, ±2 % for kW
EXTECH make, digital lux meter, model LT300	Lux, foot candles	Up to 200 klux, 20 kFc	±1.5 % for lux, ±1.5 % for Fc,
MECO make, ammeter	Amps	Up to 2 A	±1 %
MECO make, voltmeter	Volts	Up to 300 V	±1 %
DEVI ELECTRONIC CORPORATION make, auto transformer	–	Up to 240 V, Up to 5 A	±1 %

- The experiment should be carried out after dark/night time in order to avoid the natural light.
- The fluorescent lamps are to be switched ON for 30–45 min before the measurements to allow the lamps to be warmed up completely.
- Stray lights from surrounding rooms, spaces and through external window is minimized by the use of curtains and blinds etc.,
- Make sure that the Constant voltage supply is ensured using an auto transformer such that the output of the lamps is at full power and is not varied during the test.
- A second person is assigned to record the readings called out by the person reading the lux meter.
- Make sure that the photocell is not shadowed.

18.2.3 Data Collection

The different colour of floor tiles such as white, grey, black, yellow and green are selected for the light reflectance value test. The purpose of selecting these colours is of having less absorptivity and more reflectivity except black. But the exact lighting reflectance value of each colour is identified only through the experiment. The fluorescent lamps are to be switched ON for 30–45 min before the measurements to allow the lamps to be warmed up completely. The light which falls onto the floor tile is reflected and is captured with the help of photocell (lux meter). By capturing the light, it gives the value of light reflectance value in lux. The experiment is conducted by placing the different colours of flooring tiles one after another and the lighting reflectance value of each colour is noted.

The FTL's of 28 and 36 W is used for the study. For each FTL, all the colour of floor tiles is tested to identify the exact difference in lighting reflectance value between different colours of tiles. The lighting reflectance value for different colour of tile and for different wattage of FTL is presented in Table 18.2.

Table 18.2 Lighting reflectance value for different colour floor tiles

Tiles colour/wattage of FTL	28 W FTL with electronic ballast		36 W FTL with electronic ballast	
	LRV (lux) min.	LRV (lux) max.	LRV (lux) min.	LRV (lux) max.
Grey	8.58	8.72	9.36	9.4
White	21.98	22.61	23.9	24
Black	6.56	6.63	6.91	7.12
Green	7.25	7.28	7.72	7.81
Yellow	13.21	13.34	14.11	14.18

18.3 Results and Discussion

The experiment is conducted using five different colours of floor tiles and two different wattage of FTL's namely 28 and 36 W. The LRV for all the five colours of tiles are measured using a calibrated lux meter for each FTL. The LRV for different colours of tiles using 28 W is presented in Fig. 18.2. It is observed that the LRV for the white is large (21.98–22.61 lux) followed by the yellow colour tile (13.21–13.34 lux). The LRV is increased by 40.99 % in white coloured tile than in yellow for 28 W FTL and the same 41 % is increased for 36 W FTL too. This proves that the difference white and yellow coloured tile is 41 % at any case. These LRV values indicate that the light absorption value of the white coloured tile is very less followed by the yellow coloured tile.

Due to the increased reflectivity of the white, it absorbs less amount of light and produces less amount of heat energy.

Once the LRV value is less, it reflects more amount of light which comes from the FTL and in turn the room luminance is improved. The grey, green and black coloured tiles are having the maximum LRV as 8.72, 7.28 and 6.63 lux

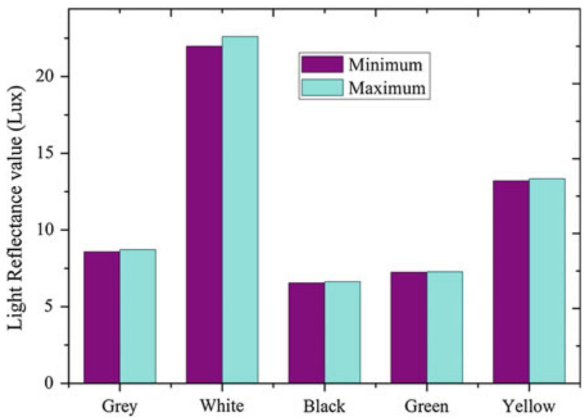

Fig. 18.2 Light reflection value of different tiles colour for 28 W FTL

Fig. 18.3 Light reflection value of different tiles colour for 36 W FTL

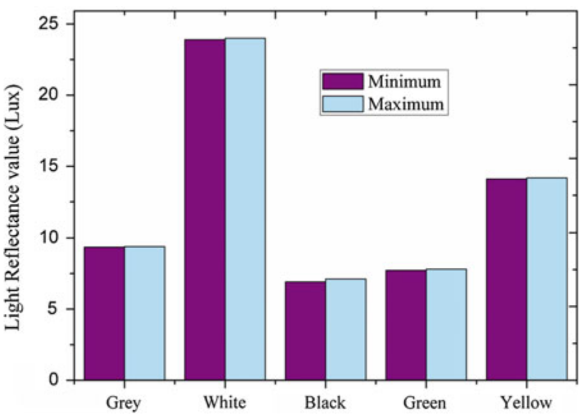

respectively. It is observed that the LRV for grey, green and black coloured tiles are lesser than the white and yellow colour. When comparing black and white colour, the white has the ability to create a 70.9 % LRV increase than black. The same trend is followed for the 36 W as presented in Fig. 18.3. But the LRV values of different coloured tiles are more for 36 W FTL than in 28 W FTL. This is due to the use of 36 W FTL. If a room is floored with grey coloured tile, it absorbs maximum of 13.89 lux and converts into heat energy than white, which means that the 13.89 lux of light energy is wasted and it could be saved with the provision of white coloured floor tile.

18.4 Conclusion

The floor tiles colour has the ability to create a significant amount of energy saving and increased luminance in the indoor lighting. Among the entire investigated floor tile colour, the white has the better LRV value. In turn, the room luminance is could be improved significantly and energy requirement to illuminate the room could be reduced. A sample study is conducted by considering single FTL If the same strategy is applied to commercial, Industrial and residential buildings where more number of lighting fixtures is used for lighting application then huge amount of energy could be saved by reducing the lighting energy consumed. This can be done by without any additional investment. It is revealed that the minimum of 41 % and maximum of 70.9 % of light reflectance can be increased and saved by providing the white coloured tile. Reduction of energy consumption in turn reduces the carbon released into the atmosphere. Selection of right colour for floor tile can create a positive impact towards low energy and emission buildings.

Acknowledgments The authors sincerely thank the Department of Science and Technology (DST), New Delhi, Government of India, for their financial grant (No. DST/IS-STAC/CO2-SR-92/11(G)) to carry out this research work under National Program on Carbon Sequestration Research (NPCSR).

References

1. Dubois M-C, Blomsterberg Å (2011) Energy saving potential and strategies for electric lighting in future North European, low energy office buildings: a literature. Int J Energy Build 43 (2011):2572–2582
2. EPB (2006) Energy performance of buildings—energy requirements for lighting. CEN, Brussels
3. Doulos L, Tsangrassoulis A, Topalis F (2008) Quantifying energy savings in daylight res ponsive systems: the role of dimming electronic ballasts. Int J Energy Build 40:36–50
4. Hanselaer P, Lootens C, Ryckaert WR, Deconinck G, Rombauts P (2007) Power density targets for efficient lighting of interior task areas. Int J Lighting Res Technol 39:171–184
5. Ganesan P, Rajakarunakaran S, Thirugnanasambandam M, Devaraj D (2013) Estimation of energy and carbon saving potential in industrial lighting system. Adv Mater Res 768:272–279
6. www.retsnepal.org/pdf/karnali_ujyalo%20.pdf (2011) accessed 11.09.2013
7. BEE (2006) BEE code—Lighting, Bureau of Energy Efficiency, Ministry of Power, Govt. of India

Chapter 19
Voltage Control of Fixed Speed Wind Farm Under Unbalanced Grid Faults Using DVR

B. Ashok Kumar, N. Kamaraj and C.K. Subasri

Abstract Increase of wind penetration in power system affects the power quality. This power quality problem causes nascent issue in power system. This work focus on the power quality problem due to injection of wind system into grid. Voltage sag occurs due to three phase to ground fault in wind generator. In the proposed scheme Dynamic Voltage restorer plays a major role to mitigate voltage sag and protect the power grid from disconnection of the wind generator. The proposed DVR control scheme is based upon Synchronous reference frame theory. The effectiveness of the proposed scheme makes the system to be in service even in the presence of fault. The study of DVR with wind energy generation system for power quality improvement has been proposed using MATLAB/SIMULINK software and better results are achieved.

Keywords Dynamic voltage restorer (DVR) · Voltage sag · Pulse width modulation (PWM)

19.1 Introduction

Renewable energy sources such as Solar, wind, tidal, hydro grow rapidly in the present scenario. Each sources supply enough energy to meet growing demand. Wind energy [1] grows very faster at present due to environmental impact and less supply of fossil fuels. To improve power production wind farm [2] is made to integrate with grid. Penetration of these large wind farms with power system results in power quality [3] issues. Power quality problem [4] which is caused due to the influence of power grid with wind turbine is voltage sag, voltage swell, harmonics, flicker etc. The major problem is voltage variation. In the fixed speed wind

B. Ashok Kumar (✉) · N. Kamaraj · C.K. Subasri
Department of Electrical and Electronics Engineering,
Thiagarajar College of Engineeering, Madurai, Tamilnadu, India
e-mail: ashokudt@tce.edu

C. Kamalakannan et al. (eds.), *Power Electronics and Renewable Energy Systems*,
Lecture Notes in Electrical Engineering 326, DOI 10.1007/978-81-322-2119-7_19

generator change in speed of wind affects torque, power which leads great damage to fluctuations of voltage. The transient fault causes nascent issue in the system which results in disconnection of power grid. Induction generator coupled with wind turbine starts to consume large reactive power from power grid. This causes shortage of reactive power which is the major reason for voltage dip/voltage sag. Sometimes active power in the system gets increases that may result in voltage swell. These voltage sag and voltage swell can be rectified with the help of Dynamic Voltage Restorer. The compensation capability of [5] DVR helps in maximum injection of voltage to the system and store the energy with the help of Restorer. This work focus on design of DVR with control strategy of synchronous reference frame transformation. Conventional controller using PI is implemented to reduce voltage error as fast as possible.

There are few techniques in [6–8] which are introduced to improve power quality without additional device in wind generator and also technology based on double fed based induction generator [9]. But in the proposed method additional device DVR based on fixed speed induction generator is used to maintain power quality in wind farm and make the system to be in service even under the fault condition. In general variable speed generator is used widely which has the disadvantage of cost and losses. In many countries fixed speed generator is used still which has less cost and easy maintenance with additional device using DVR [10]. Simulink model is developed for wind farm system with FACTS [11] device and analysis is presented with PI controller.

19.2 Dynamic Voltage Restorer

Dynamic Voltage Restorer [12] is device that can produce a sinusoidal voltage at fundamental frequency. It consists of Voltage Source converter, AC filter, and injection transformer etc (Fig. 19.1). The main function of the converter is to correct the voltage [13] which is accomplished by injection of the controlled voltage in series with the line through injection transformers. Here IGBT acts as switches. To remove harmonics [14] passive filter is used. Injection Transformer is used to step up low AC voltage to the required voltage level. There are different kinds of DVR which are ranked by [15].

In this work Wind farm coupled with induction generator is made to integrate with power grid. Induction generator used is of asynchronous type (Fig. 19.2). The wind turbine has three major components as generator speed, pitch angle and wind speed. Pitch angle is considered to be maintained at zero in order to attain maximum power. Pitch angle controller is not considered in many applications. The wind speed is kept as 12 m/s which are considered to be nominal value which may vary from 8 to 12 m/s according to fluctuations. The mechanical torque is produced from turbine which is made to couple with Induction Generator [16]. Load can be of ohmic or ohmic—inductive load. Wind farm is provided with three phase line to ground fault. The fault on wind farm side causes negative effect in power grid.

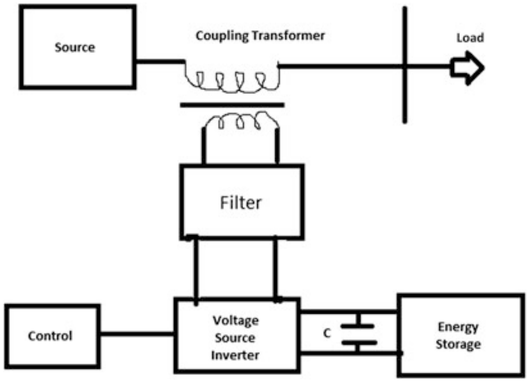

Fig. 19.1 Basic configuration of DVR

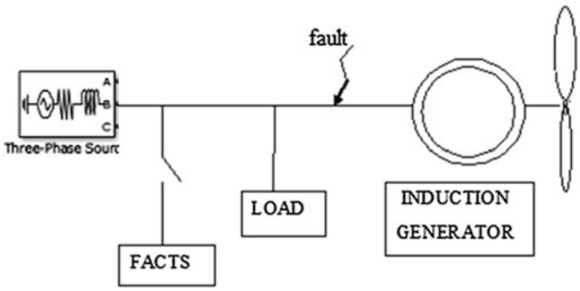

Fig. 19.2 Block diagram of wind farm interconnected with power grid

Due to fault, line voltage gets affected. The capacitor bank provided in each substation can support wind farm in faulty cases. But grid has to be protected. Hence DVR controller is installed across grid side to protect grid from negative effect caused by wind turbine. It has to meet the grid code requirement [17] that is voltage fluctuations has to be accepted as ±5 %.

Voltage sag occurs when three phases to ground fault occurs with time 0.03–0.08 s. Usually voltage sag occurs due to over speeding of generator, disturbances on load, three phases to ground fault. The RMS value of the grid voltage and the fluctuating voltage values are applied to the PI [18] control block. The output of the PI block is converted to the firing angles using PWM technique in which DVR acts according to signal thereby voltage sag [19] is rectified across grid and give protection.

19.3 Control Strategy

Control strategy is based upon Synchronous Reference Frame Theory. The synchronous frame method [20] uses Park's transformation to transform the three phase ac quantities into the synchronous rotating direct, quadrature and zero sequence

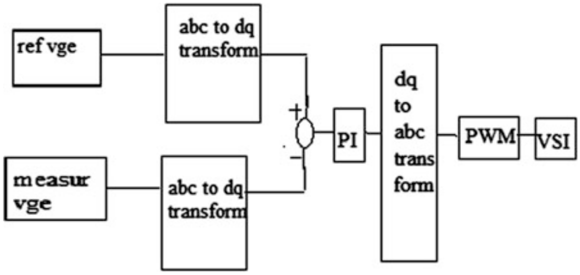

Fig. 19.3 Block diagram of controller

which are dc components and easy to analyze. This method is applicable especially in three phase system. Control algorithm is developed by comparing the reference voltage and fluctuating voltage. This compared signal is passed to PI controller and thus it minimizes the error signal. Therefore PI controller is required to achieve controller performance at very faster rate. According to reference frame transformation theory, reference signal detected [21] is made to transform from stationery frame [22] a-b-c to rotator frame d–q axis. PI controller is used to produce required signal for Pulse Width Modulation (PWM) from rotating frame signal. Before passing into PWM, the reference signal is produced by inverse transformation from rotating signal.

In PI controller the gain values are adjusted to get optimum performance. These gain values can be tuned based upon Ziegler Nichol's tuning or even by using Fuzzy controller. Proportional and integral controller helps to reduce error values as fast as possible. PWM is based on equal area theorem. This technique uses sinusoidal PWM. Figure 19.3 shows the basic control algorithm developed. In PWM technique suitable signal from PI controller has been generated as control signal which makes to produce desire reference signal so that corresponding carrier signal is produced. The carrier frequency is set in PWM block. So that appropriate pulse signal is created which acts as input to power switch and VSC. Pulse width Modulation is able to control switching device IGBT. Here reference signal is otherwise said to be modulating signal is made to compare with carrier triangular signal. Then according to that signal, ON-OFF pulse occurs simultaneously with corresponding delay due to synchronization.

19.4 Simulation Results

The parameters used in simulation are given in Table 19.1. It is used to verify the effectiveness of the DVR with PI controller. The simulations were accomplished using Matlab Simulink (Fig. 19.4).

Case 1: In the proposed system, the voltage sag occurs due to the three phase fault applied in the time interval of 0.03–0.08 s. Fault on the wind turbine side which is connected to grid. Figure 19.5 shows voltage sag in the grid side as this work mainly focus on grid side.

Table 19.1 Simulation parameters

Parameters	Values used in the simulation models
Main supply voltage	480 V
Line frequency	60 Hz
Source impedance	Ls = 16.59 mH
	Rs = 0.8928 Ω
Transformer turns	1:1
PI controller	$K_p = 0.1$, $K_i = 2$
Load	10 MW, 12 MVAR
Inverter	IGBT based 3 arms, 6 pulse, carrier frequency = 10,000 Hz
Asynchronous generator	Stator resistance = 0.016 Ohm
	Stator inductance = 0.05 H
	Nominal power 1 MW
	Voltage = 480 V
	Frequency = 60 Hz

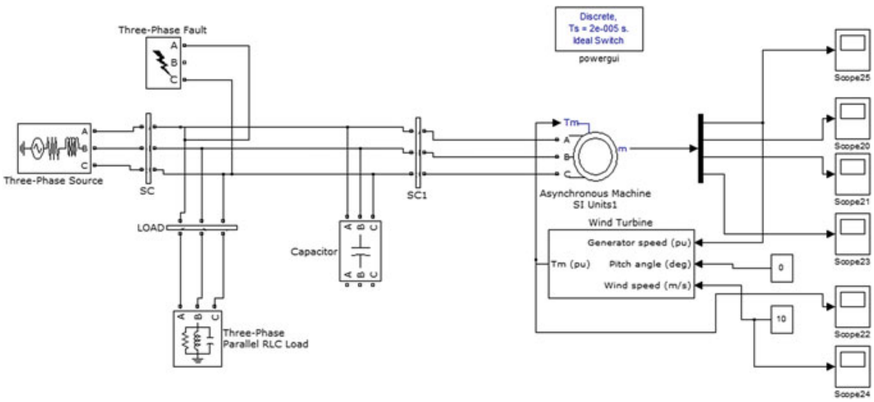

Fig. 19.4 Simulation diagram of wind farm connected to power grid with three phases to ground fault

Figure 19.6 represents real power across grid without compensation. During the fault time 0.03–0.08 s oscillations are high, at once fault time is cleared oscillations are decreased and curve starts to settle. At 0.02 s itself the machine starts to jerk due to severity effect of the fault.

Figure 19.7 represents that during fault time there is severe dip in reactive power across grid.

Case 2: The Fig. 19.8 shows the simulation carried out with compensation technique using DVR. In proposed system, the sag occurs due to the three phase fault applied in the time interval of 0.03–0.08 s in the wind turbine side which is connected to power grid. Here voltage sag is mitigated by reactive power compensation across power grid (Fig. 19.9).

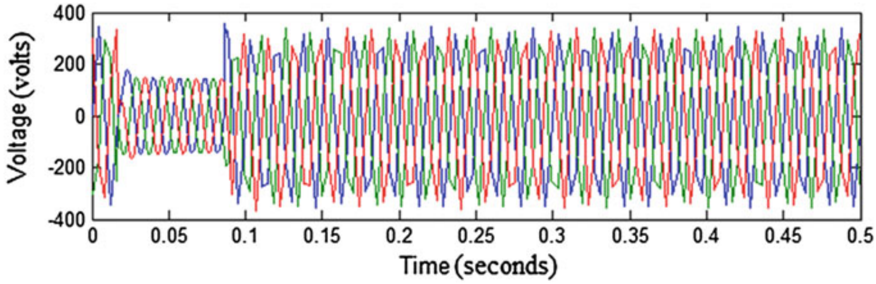

Fig. 19.5 Voltage sag due to three phase fault (0.03–0.08 s)

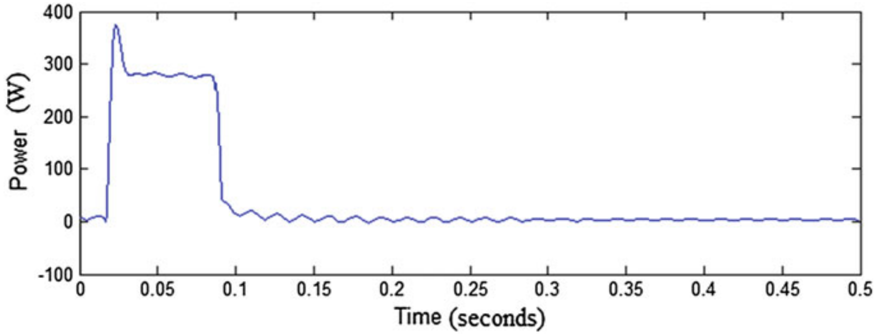

Fig. 19.6 Real power in grid during fault

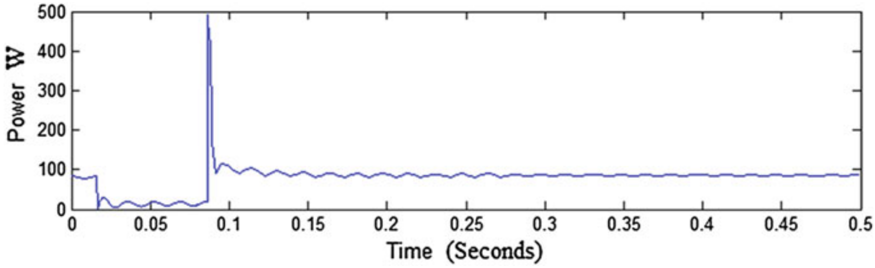

Fig. 19.7 Reactive power in grid during fault before compensation

The oscillation has been completely removed and Fig. 19.10 represents real power curve becomes smooth using PI controller after compensation even during fault time. Figure 19.11 represents reactive power in grid which gets compensated and curve is smooth during fault time.

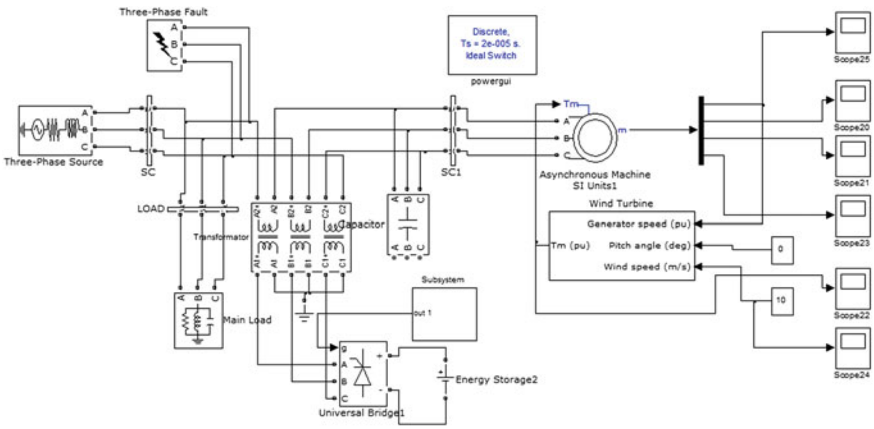

Fig. 19.8 Simulation diagram of wind farm connected to power grid with three phases to ground fault with DVR connected to system and voltage sag is mitigated using PI controller

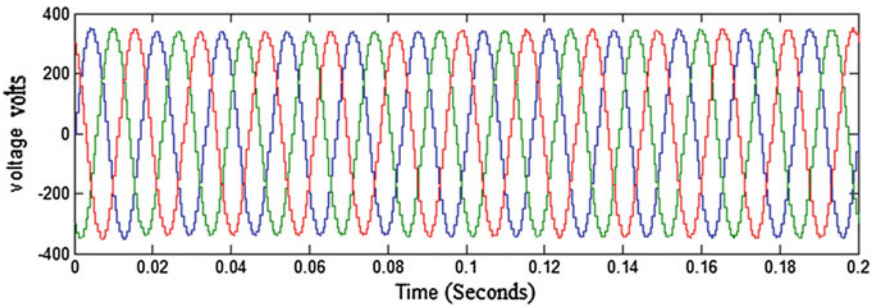

Fig. 19.9 Voltage sag mitigated by DVR

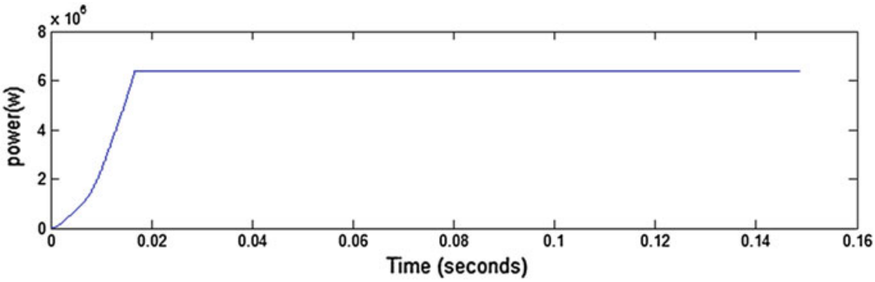

Fig. 19.10 Real power in grid after compensation

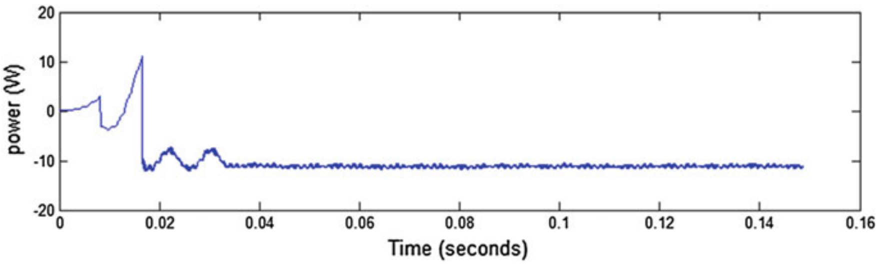

Fig. 19.11 Reactive power in grid after compensation using DVR

19.5 Conclusion

In this work, test system is developed using matlab/Simulink software. It is shown that power quality improvement is achieved successfully with the proposed DVR and voltage sag is mitigated in the wind farm interconnected with power grid. The simulation results shows that proposed system with PI controller can handle the system with fault and eliminate voltage sag. This study shows that DVR can compensate the voltage sag, provide support to stabilize the wind farm connected to grid and makes the system to be in service even under fault conditions without disconnection. If the system controller is replaced further with advanced control technology then other power quality problems such as harmonics, power factor can also be corrected.

Acknowledgments Authors like to thank the management, Principal and the faculty of EEE Department for the support and suggestions in this work.

References

1. Cardenas R, Molinas M, Rodriguez J (2011) Overview of multi-MW wind turbines and wind parks. IEEE Trans Ind Electron 58(4):1081–1095
2. Ackermann T (2008) Wind power in power systems. Wiley, Chichester
3. Tascikaraoglu A, Uzunoglu M, Vural B (2011) Power quality assessment of wind turbines and comparison with conventional legal regulations: a case study in Turkey. Appl Energy 88:1864–1872
4. Bollen HJ (2000) Understanding power quality problems. IEEE Press, New York
5. Blaabjerg F, Nielsen JG, Newman M, Nielsen H (2004) Control and testing of a dynamic voltage restorer (DVR) at medium voltage level. IEEE Trans Power Electron 19(3):806–813
6. Ning J, Gao W, Wang G (2009) Development of low voltage ride through control strategy for wind power generation using real time digital simulator. In: Power system conference and exposition, PES. IEEE/PES, pp 1–6
7. Basu KP, Hafidz SA (2008) Ride through capabilities of load during voltage sag/swell and power interruption with zigzag transformer. In: , IEEE conference on innovative technologies in intelligent systems and industrial applications, CITISIA, pp 119–122

8. Boynuegri AR, Tascikaraoglu A, Uzunoglu M, Vural B, Yumurtac R (2012) Voltage regulation capability of a prototype static VAr compensator for wind applications. Appl Energy 93:422–431
9. Zou H, Sun H, Zou J (2007) Fault ride through performance of wind turbine with doubly fed induction generator. In: 2nd IEEE conference on industrial electronics and applications, ICIEA, pp 1607–1611
10. Choi SS, Li BH, Vilathgamuwa DM (2002) Design and analysis of the inverter-side filter used in the dynamic voltage restorer. IEEE Trans Power Deliv 17(3):857–864
11. Hingorani NG, Gyugyi L (1999) Understanding FACTS. IEEE Press, New York
12. Boonchiam P, Mithulananthan N (2006) Understanding of dynamic voltage restorers through MATLAB simulation. Thammasat Int J Sci Tech 11(3):857–864
13. Chung I-Y, Moon I, Park JK, Won DJ (2003) The DC link energy control method in dynamic voltage restorer system. Electr Power Energy Syst 525–531:1–6
14. Newman J, Nielsen JG (2005) A dynamic voltage restorer (DVR) with selective harmonic compensation at medium voltage level. IEEE Trans Ind Appl 41(6):1744–1753
15. Blaabjer F, Nielsen. JG (2005) A detailed comparison system topologies for dynamic voltage restorers. IEEE Trans Ind Appl 41(5):1272–1280
16. Cidras J, Feijoo AE (2002) A linear dynamic model for asynchronous wind turbines with mechanical fluctuations. IEEE Trans Power Syst 17(3):681–687
17. Tsili M (2009) A review of grid code technical requirements for wind farms. IET Renew Power Gener 3(3):308–332
18. Kenan Dosoglu M (2012) Investigation of different load changes in wind farm by using FACTS devices. Appl Energy Convers 2012:422–431
19. Jowder FAL (2009) Design and analysis of dynamic voltage restorer for deep voltage sag and harmonic compensation. IET Gener Transm Distrib 3(6):547–560
20. Alepuz S, Busquets-Monge S, Bordonau J, Martinez-Velasco J, Pontt J, Rodriguez J (2009) Control strategies based on symmetrical components for grid-connected converters under voltage dips. IEEE Trans Ind Electron 56(6):2162–2173
21. Asiminoaei L, Hoffmann N, Lohde R, Thogersen P (2011) A review on fundamental grid-voltage detection methods under highly distorted conditions in distributed power-generation networks. In: Proceedings of IEEE ECCE, pp 3045–3052
22. Li YW, Blaabjerg F, Vilathgamuwa DM (2007) Design and comparison of high performance stationary-frame controllers for DVR implementation. IEEE Trans Power Electron 22 (2):602–612

Chapter 20
Smart Indian Railways: An Environment Friendly Model

Nitish Kumar Singh, Yashwant Singh Patel, Subnum Begum and Ananya Chatterjee

Abstract In recent years development of Indian railways took place rapidly, but still there are many issues related in the way of growth. The biggest issue is the creation of world's biggest open toilet. In every coach there is an open toilet system through which feces and urine of human is discharged directly on the tracks, which results corrosion of track components. Another issue of food waste on platforms and through the train canteens, which is another big headache for Indian railways. Several models of green toilets have been proposed for the purpose of improvement in the environment and hygiene like development of Controlled discharge toilet system (CDTS) built by DRDO based on train speed, development of Zero discharge toilets (ZDTS) by Research Designs and standards organization Lucknow and IIT Kanpur. These systems are tried by railway but rejected. These systems are not suitable for trains because of its infrastructure complexity, expensiveness and large number of people will use them. Therefore there is a requirement of proper sanitation in the Indian railways. In this paper a model is proposed which produces energy and fertilizers from toilet waste and food waste which can be used for thermal generation, electric generation, cooking, agriculture and some other purposes.

Keywords Biogas plant · Controlled discharge toilet system (CDTS) · Digester tank · Temporary collection box (TCB) · Waste indicator (WI) · Zero discharge toilets (ZDTS)

N.K. Singh (✉) · Y.S. Patel · S. Begum · A. Chatterjee
School of Computer Engineering, KIIT University, Bhubaneswar, Odisha, India
e-mail: nitishsingh49@gmail.com

Y.S. Patel
e-mail: yashwant.patelasct@gmail.com

S. Begum
e-mail: sqazis@gmail.com

A. Chatterjee
e-mail: ananyachatterjee18@gmail.com

C. Kamalakannan et al. (eds.), *Power Electronics and Renewable Energy Systems*,
Lecture Notes in Electrical Engineering 326, DOI 10.1007/978-81-322-2119-7_20

20.1 Introduction

Indian Railways (IRs) is known to be Asia's largest railway network. It uses moreover 40,000 coaches for passenger service, due to this IRs has to operate 1,60,000 toilets, round the clock, on coaches running at speeds of 100 kmph [1]. The toilets of Indian railways are small compartments and open type with hole through which human feces and urine are ejaculated on the tracks [2] and not only responsible for corrosion of tracks but also produces germs. These germs are source of various diseases like typhoid, cholera, diarrhea, hepatitis, parasite infections and other water-borne diseases. Many parasites are mainly spread through human waste like tapeworm, roundworm, hookworm and pinworm etc. Despite of these several issues, railway is creating an environmental hazard and promoting unsanitary situations. The railway's action flouts the Hazardous Wastes (Management and Handling) Rules, 1989, Environmental Protection Act, 1986, Indian Penal Code, 1860 and Code of Criminal Procedure, 1973 [3]. Even In railway stations public toilets, canteens are in poor conditions and lots of food is wasted through platforms and train canteens. These things are not only damaging environment but also creating a biggest environmental hazard. In this paper a model is proposed named as Smart Indian Railways that provides a solution for world's biggest open toilet and food wastage in platforms and trains. This approach will produce Biogas energy, which is an environment friendly in nature and will also produce fertilizers. Biogas energy and fertilizers can be used in cooking, agriculture, electric generation, thermal generation and some other purposes. In Sect. 20.2 of this paper related works are introduced. Section 20.3 discusses the working of Smart Indian Railway model. In Sect. 20.4 the proposed algorithm is discussed then in Sect. 20.5 paper is concluded.

20.2 Recent Works

Day to day large number of people is travelling in trains. This is creating a tough task for Indian railways to provide proper sanitation in train and stations. Several ideas and models were proposed to solve the Indian Railways open toilet problems.

Many technologies and model were developed for the purpose of Environment Friendly Toilets in trains. Zero Discharge Toilet System (ZDTS) is jointly developed by IIT Kanpur and Research Design & Standards Organization (RDSO), Lucknow [4]. This system uses a solid liquid separator which segregates solid waste and liquid waste. A box stores the Solid waste and treated with anaerobic bacteria. Then this box is to empty at stations. The liquid waste is to be used for flushing. These solid and liquid wastes are separated below the toilet seat itself. But removing Solid waste from tanks was a big problem for ZDTS [5].

Another system in this field is Controlled Discharge toilet System (CDTS). It discharges waste on the run only after the train speed reaches 30 kmph. Discharge takes place when train is away from the station for keeping stations clean. CDTS uses a sophisticated GPS system, which monitors if the train at a railway station or over water body and prevent the water bodies and terminals from pollution [1]. Several other technologies like vacuum toilet system of aircrafts are also on trials.

The proposed technologies were very costly, having a requirement of extra infrastructures at terminals and management of these systems is difficult. Controlled discharge toilet systems were expensive and costing around 6 lakh per piece. For ZDTS removing solid waste from tanks was a big problem and Vacuum toilet systems are prone to technical glitches [6].

20.3 The Proposed Model

In this section construction concept and working procedure are described. These two sub-sections of proposed model are described in this section one by one.

20.3.1 Construction Concept

In each railway coach vacuum toilets are installed with temporary collection boxes and each outlet of vacuum toilets is connected to the inlet of its temporary collection box. Waste indicator device is installed at the compartment of train's driver and driver of the train will have a control to perform discharge operation. In waste indicator, capacity of waste is indicated in the form of scale having values low, medium and high, as shown in Fig. 20.1. Coaches of the train are connected through different pipes. These pipes carry the faecal waste. Pipes between two coaches will be connected automatically at the time of discharge operation and will have an open and close mechanism. These pipes will build a pipeline at the time of

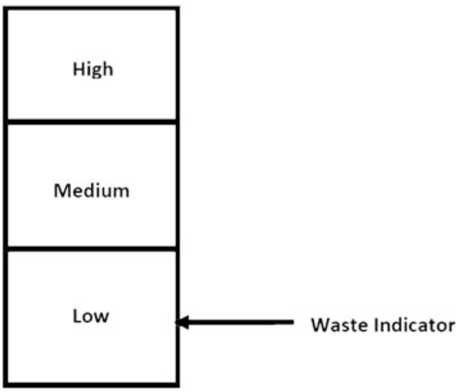

Fig. 20.1 Waste indicator

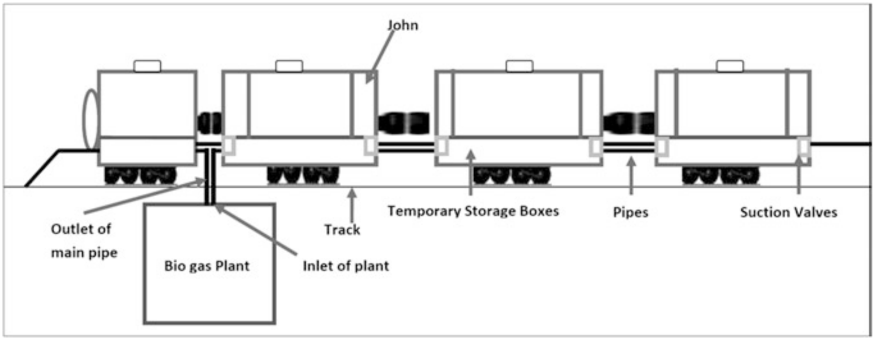

Fig. 20.2 Construction model

discharge and carry the faecal waste to the side of engine. Coaches having valves at the connecting points of these pipes. And these valves use a strong suction system to pull faecal waste at the time of discharge operation. Construction model, which is discussed above shown in Fig. 20.2.

20.3.2 Working Procedure

In this section working of proposed model is explained. After the successful installation of these devices it will be ready to use. Whenever people will use these toilets in their coaches, the waste like feces and urine will be collected in the TCB through outlet of vacuum toilets. Whenever train will arrive on junction, it will stop at the outlet point of biogas plant. Then the value of waste indicator will be checked if it is low this means TCB's are not filled completely so no action will be taken place. If it is medium then driver of the train will press the discharge button of waste indicator and the discharge operation will be performed. All pipes will be connected to each other and all valves will be opened automatically. With the help of a strong suction system all faecal waste will be pulled towards the engine. At the backside of the engine a main discharge pipe, which works like a piston will be connected to the outlet of biogas plant automatically. Discharge operation will check the value of stop time for a particular junction and discharge time. If the stop time is greater than or equal to discharge time then it will empty the faecal waste completely. Otherwise the discharge operation will be performed at the value of stop time. Stop time is an interval period of a train for a particular junction which is predefined by authority. After the discharge operation, all pipes will be closed automatically and the entrance of biogas plant will also be closed. Apart from the faecal waste of train toilets, toilets build in the junctions will also be connected to

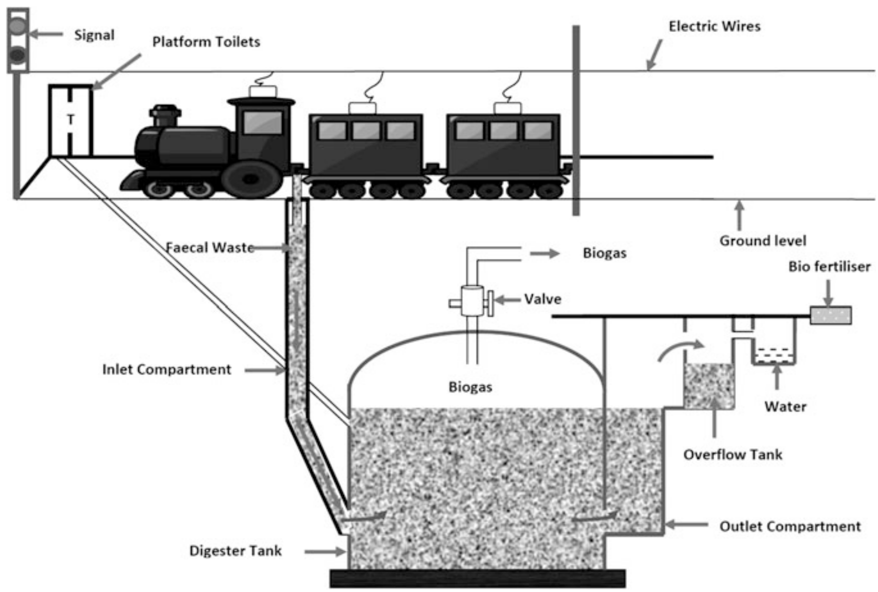

Fig. 20.3 Working model

this biogas plant through a common outlet system and send the faecal waste to the inlet of biogas plant. Working model which is discussed above is shown in Fig. 20.3.

In the canteens of the trains, Junctions lots of food and water are wasted. Food waste which is placed in the lands decomposed and form methane that can affect the climate badly [7]. Food waste can also be used to produce energy in the form of biogas. For this in the downside of train's canteen, a separated TCB will be used and the workers of the train will drop these waste to the inlet of the TCB. When the train will reach to the junction the workers will empty these boxes to the inlet of the food waste plant, which is build to a particular portion of the junction. And again they will fill fit the TCB in the canteen of the train. At the junction all the waste of food in the platform, in the dustbins will be collected and send to the inlet of the food waste plant. Food waste plant will produce the energy in the form of biogas and fertilizers as shown in Fig. 20.4. This can be used for some useful purposes like electricity generation, cooking, lighting in the stations etc.

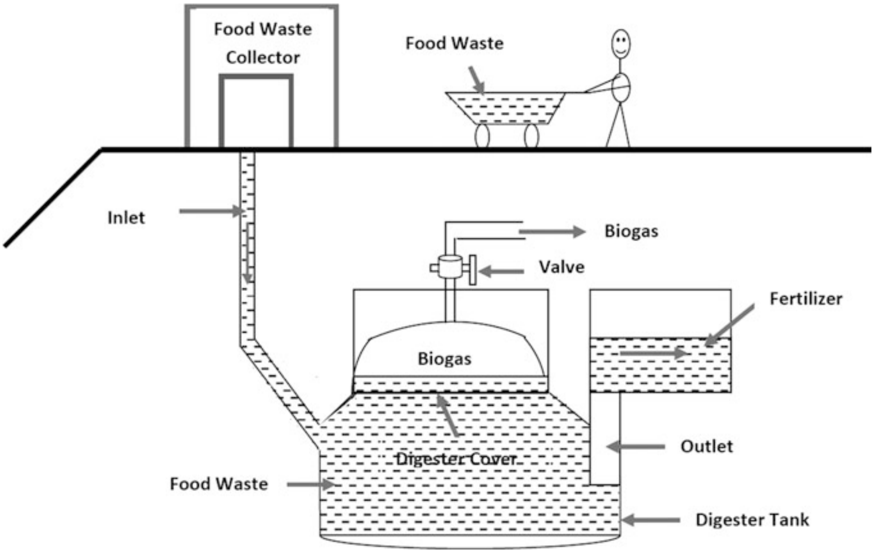

Fig. 20.4 Model for food waste

20.4 Proposed Algorithm

The proposed algorithm is described below:

20.4.1 Faecal Waste Indicator Algorithm

```
Check_faecal_waste_indicator_value ( )
{
   If (faecal_waste_indicator_value > = Medium && Junction_value = = true)
{
    Message ("Please press the discharge button")
    Discharge_operation ( );
 }
 Else
 {
        No action;
  }
 end
 }
```

20.4.2 Discharge_Operation ( )

```
{
        All_valve_value = open;
        If (stop_time > = discharge_time)   // discharge time is equal to time of
                                             normal faecal waste discharge operation
{
       Empty the storage tank;
 }
else
{
        Empty the storage tank = stop_time;
}
        All_valve_value = close;
        end
 }
```

20.5 Conclusion

Authorities of Indian Railway's have tried various models to improve the sanitation in Indian Railways. Open toilet system is a biggest problem for Indian Railways apart from this food wastage in platforms are very common.

Proposed model will convert the faecal waste as well as food waste to the energy in the form of biogas. This model will also produce fertilizers which can be used in the fields of agriculture. Approach used in this model will not only solve the problem of maintaining sanitation in Indian Railways but also produce various sources of energy.

Acknowledgments This work is partially supported by KIIT University, Bhubaneswar, India. Our sincere thanks to our seniors Virendra Kumar Yadav and Saumya Batham for their valuable suggestion that they have made during this work.

References

1. Environment Friendly Green Toilets on Indian Railways Passenger Coaches http://www.indianrailways.gov.in/railwayboard/uploads/directorate/mech_engg_pu/downloads/bkup/green/green_toilets.pdf
2. Hedaoo M, Hirde S, Khan A (2012) Sanitation in Indian railways premises: a great cause of concern. Int J Adv Eng Technol IJAET III(I):50–55
3. Rediff News (2007) Indian railways sued unhygienic waste disposal http://www.rediff.com/news/report/rail/20070128.htm (2007)
4. Development of green toilets on trains. http://indianrlys.wordpress.com/tag/zero-discharge-toilet-system-zdts/

5. Tare V, Balasundaram K, Mehrotra A (2009) A novel sanitation model based on EcoSan philosophy. In: 34th WEDC international conference, Addis Ababa, Ethiopia (2009)
6. The Times of India (November 28, 2012) "Railways needs a bug to keep toilets clean" http://articles.timesofindia.indiatimes.com/ 2012-11 28/chennai/35410640_1_toilet-system-discharge-toilets-indian-railways (2012)
7. Turning Food Waste into Energy at the East Bay Municipal Utility District (EBMUD) http://www.epa.gov/region9/waste/features/foodtoenergy/

Chapter 21
Grid Connected Multilevel Inverter and MPPT for Photovoltaic System

R. Santhiya, A. Senthilnathan, V. Kumar Chinnaiyan and R. Nithya Priya

Abstract This paper is based on the development of multilevel inverter for Photovoltaic (PV) system. It also depends on Improved Perturbation and Observation (IP&O) Maximum Power Point Tracking algorithm (MPPT). This algorithm is applied to a grid connected PV system through a seven level inverter with a novel pulse width modulated control scheme. The inverter used is seven level inverter and is capable of producing seven level output voltage from the DC supply voltage obtained from PV panels. Multilevel inverters offer improved sinusoidal output waveforms and lower THD. The results are verified through simulation using MATLAB/SIMULINK tools.

Keywords Improved perturbation and observation (IP&O) · Multilevel power converters · Maximum power point tracking algorithm (MPPT) · Total harmonic distortion (THD)

21.1 Introduction

Solar energy is one of the renewable resources of energy which is available at free of cost. Solar radiation is the most important natural energy resource because it drives all environmental processes acting at the surface of the earth. The conversion of solar energy into electrical energy has many application fields. Residential, vehicular, space and aircraft and naval applications are the main fields of solar energy [1]. A photovoltaic (PV) cell is used to convert sunlight into electricity, which reflects on a PV cell, may be reflected, absorbed, or passed however, only absorbed light generates electricity. A PV or solar cell is the basic building block of a PV (or solar electric) system. An individual PV cell is usually quite small, typically produces only a small amount of power.

R. Santhiya (✉) · A. Senthilnathan · V. Kumar Chinnaiyan · R. Nithya Priya
Dr. N.G.P. Institute of Technology, Coimbatore, India
e-mail: santhu2609@gmail.com

V. Kumar Chinnaiyan
e-mail: kumarchin@hotmail.com

C. Kamalakannan et al. (eds.), *Power Electronics and Renewable Energy Systems*,
Lecture Notes in Electrical Engineering 326, DOI 10.1007/978-81-322-2119-7_21

To boost the power output of PV cells, they have to be connected together to form larger units called modules. The modules, in turn, can be connected to form larger units called arrays, which can be interconnected to produce more power. By connecting the cells or modules in series, the output voltage can be increased. On the other hand, the output current can reach higher values by connecting the cells or modules in parallel.

PV solar electricity together with solar thermal has the highest potential of all the renewable energies since solar energy is a practically unlimited resource, available everywhere. The power delivered by the PV module depends on the irradiance, temperature, and shadowing conditions. The PV panel has a nonlinear characteristic, and the power has a Maximum Power Point (MPP) at a certain working point, with coordinates MPP voltage and MPP current. Since the MPP depends on solar irradiation and cell temperature, it is never constant over time thereby maximum power point tracking (MPPT) should be used to track its changes. The penetration of PV systems as distributed power generation systems has been increased dramatically in the last years. In parallel with this, MPPT is becoming more and more important as the amount of energy produced by PV systems is increasing.

When a conventional controller is charging a discharged battery, it simply connects the modules directly to the battery. The module works on the battery voltage but not on the ideal operating at which the modules are able to produce their maximum available power. But the MPPT controller calculates the voltage at which the module is able to produce maximum power. A high efficiency DC-to-DC power converter converts the module voltage at the controller input to battery voltage at the output. There are many algorithms available to find the maximum power point. A huge variety of concepts leads to an even larger variety of circuits and mechanisms for operating photovoltaic panels as close as possible to the point of maximum power. One such powerful algorithm is IP&O MPPT.

21.2 The Proposed System

The proposed system includes the photovoltaic cell, boost converter, seven level inverter, control schemes like IP&O MPPT, PWM control as shown in Fig. 21.1.

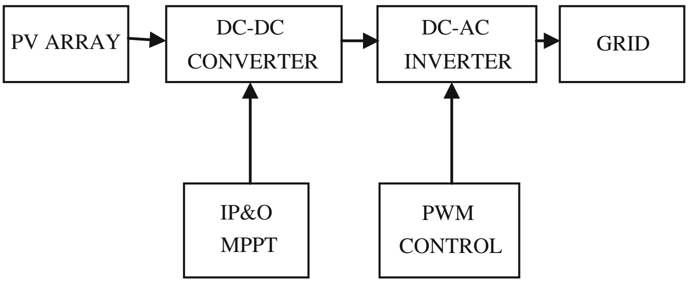

Fig. 21.1 Block diagram of the proposed system

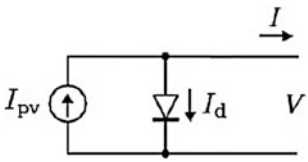

Fig. 21.2 Ideal model of PV cell

21.2.1 A PV Array

A simple PV cell from a modeling perspective is an ideal current source in parallel with an ideal diode as shown in Fig. 21.2. The two parameters used to model and characterize a PV cell are the open circuit voltage (V_{oc}) and the short circuit current (I_{sc}). The V_{oc} is the maximum voltage which a solar cell can provide at zero current. The I_{sc} is the maximum current which a solar cell can provide at zero voltage.

A single solar cell typically produces only about 0.5 V so they need to be connected in series forming what is known as the PV module. A PV panel is a collection of PV modules physically and electrically grouped together and finally a PV array is a collection of PV panels.

21.2.2 DC–DC

The MPPT algorithm is implemented in the dc–dc converter. The output of the MPPT is the duty-cycle function. A range of dc–dc switched mode converters are used to convert an unregulated dc input to a regulated dc output at a required voltage level. The voltage regulation can be achieved by varying the ON–OFF or duty ratio of the switching element. There are two main applications. One is to provide a dc power supply with adjustable output voltage, for general use. This application often requires the use of an isolating transformer. The other main application of dc–dc converters is to transfer power from a fixed dc supply. Basic PWM converter topologies, such as buck, boost, buck-boost, Cuk, and their versions with an isolation transformer, are most widespread in dc to dc conversion applications.

This converter occupies the main role in tracking the maximum power point from the solar panel. Among all the converter topologies, the grid connected system always needs a boost converter as shown in Fig. 21.3 because PV arrays had a voltage that is lower than the grid voltage. High dc bus voltages are necessary to ensure that power flows from the PV arrays to the grid. Boost converter operates both continuous and discontinuous conduction mode. A boost converter regulates the average output voltage at a level higher than the input or source voltage. For this reason the boost converter is often referred to as a step-up converter or regulator. The DC input voltage is in series with a large inductor acting as a current source.

Fig. 21.3 Boost converter

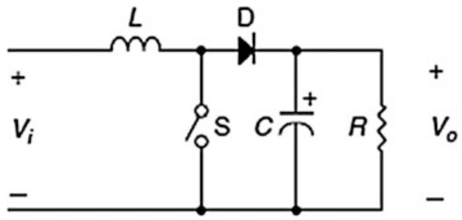

A switch in parallel with the current source and the output is turned off periodically, providing energy from the inductor and the source to increase the average output voltage.

21.2.3 Seven Level Inverter

The voltage source inverters produce an output voltage or current with levels either 0 or $\pm V_{dc}$. They are known as the two-level inverter. To produce a quality output voltage or a current wave form with less amount of ripple content, they require high switching frequency. In high-power and high voltage applications these two level inverters, however, have some limitations in operating at high frequency mainly due to switching losses and constraints of device ratings.

These limitations can be overcome by using multilevel inverters. The multilevel inverters have drawn tremendous interest in power industry. It may be easier to produce a high power, high voltage inverter with multi level structure because of the way in which the voltage stresses are controlled in the structure. The unique structure of multilevel voltage source inverters allows them to reach high voltages with low harmonics without the use of transformers or series connected synchronized-switching devices. Once the number of voltage level increases, the harmonic content of the output voltage waveform decreases significantly. There are three types of multilevel inverters Viz diode clamped multilevel inverter, flying capacitor multilevel inverter and cascaded multilevel inverter. These types of multilevel inverters require more number of components such as switches, clamping diodes and capacitors. As the number of voltage levels increases number of active switches increases. There are several types of multilevel inverters but the hybrid cascade multilevel inverter is considered in this work because of the advantages it possesses. In this, a seven-level inverter is used instead of conventional three-level inverter because it offer grater advantages, such as improved output waveform, smaller filter size, lower EMI and lower total harmonic distortion (THD). The new inverter topology offers an important improvement in terms of lesser component count and reduced complexity when compared with the other conventional inverters.

The proposed single phase seven level inverter is developed from the five level inverter. It comprises a single phase conventional H bridge inverter, two bidirectional switches, and a capacitor voltage divider formed by C_1, C_2, and C_3 which is

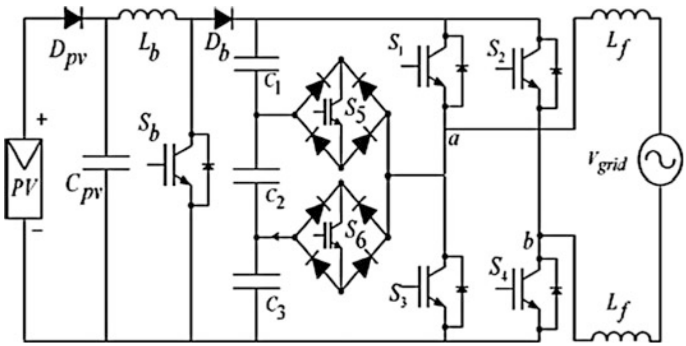

Fig. 21.4 Seven level inverter

shown in Fig. 21.4. The modified H-bridge topology is significantly advantageous over other topologies, i.e., less power switch, power diodes, and less capacitors for inverters of the same levels.

21.2.4 Control System

The control system comprises a MPPT algorithm, a dc bus voltage controller, reference current generation, and a current controller. The two main tasks of the control system are maximization of the energy transferred from the PV arrays to the grid, and generation of sinusoidal current with minimum harmonic distortion, also under the presence of grid voltage harmonics. The proposed converter utilizes the Improved Perturb and Observe algorithm but in common P&O algorithm the array terminal voltage is perturbed every MPPT cycle, therefore when the P&O is reached, the P&O algorithm will oscillate around it resulting in a loss of PV power, especially in cases of constant or slowly varying atmospheric conditions. This problem can be solved by improving the logic of the P&O algorithm which is called as IP&O. In IP&O parameters of two preceding cycles were compared in order to check when the P&O is reached, and bypass the perturbation stage.

In this technique, instead of utilizing the array voltage or current as the perturbed signal, the converter duty ratio is used. In order to improve the performance of P&O techniques, the modified calculation of the perturb value is utilized instead of the fixed values The improved P&O method is based on auto-tuning perturbation. The Improved perturbation and observation (IP&O) has the tracking response will be higher. It finds the real MPP under any working conditions. No oscillation during tracking and steady state operations. Low computational burden required.

The next important control is PWM switching control for inverter. In this dc link voltage V_{dc} is controlled in the dc–ac seven level PWM inverter, the change of the duty cycle changes the voltage at the output of the PV panels. A PID controller as shown in Fig. 21.5 is implemented to keep the output voltage of the dc–dc boost

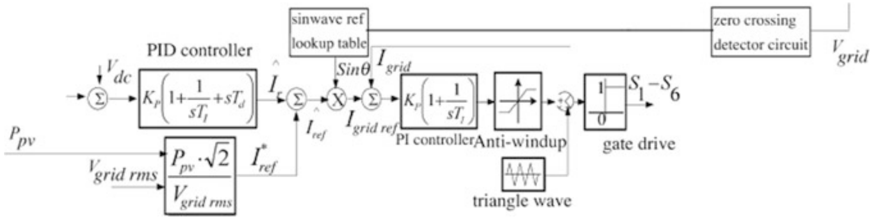

Fig. 21.5 PWM switching control scheme

Fig. 21.6 PWM switching signal generation

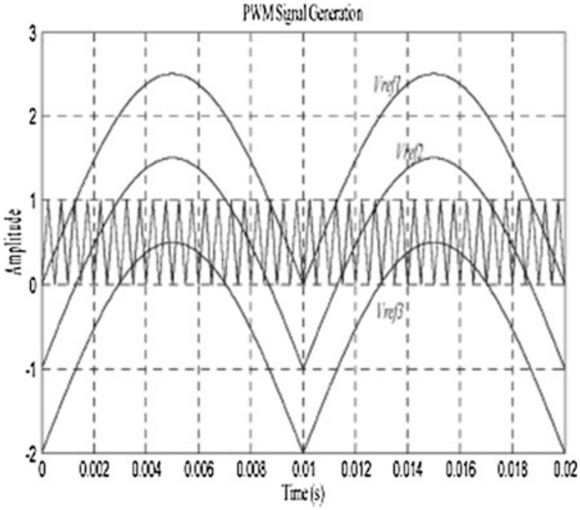

converter constant by comparing V_{dc} and $V_{dc\ ref}$ and feeding the error into the PID controller, which subsequently reduces the error. In this way, the V_{dc} can be maintained at constant.

The PWM switching patterns were generated by comparing three reference signals (V_{ref1}, V_{ref2}, and V_{ref3}) against a high frequency triangular carrier signal as shown in Fig. 21.6. Subsequently, the comparing process produced PWM switching signals for switches S_1–S_6 as shown in Fig. 21.6.

21.3 Simulation and Results

MATLAB SIMULINK software is used to simulate the configuration. In the proposed system the control scheme plays an important role. By controlling the modulation index (M_a), the desired number of levels of the inverter's output voltage can be achieved. The model used for simulation is shown in Fig. 21.7.

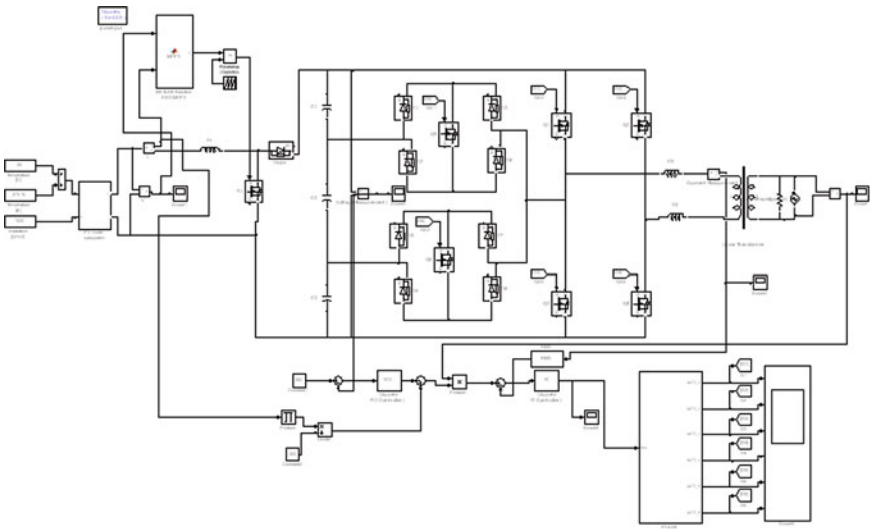

Fig. 21.7 Simulation block diagram of P&O MPPT with seven level inverter

The IP&O algorithm is implemented by calculating the power and comparing the voltage In this technique, instead of utilizing the array voltage or current as the perturbed signal, the converter duty ratio is used. The perturb step is fixed and designer dependent. The PI algorithm is used as the feedback current controller for the application. The current injected into the grid, also known as grid current I_{grid}, was sensed and fed back to a comparator that compared it with the reference current $I_{gridref}$. $I_{gridref}$ is the result of the MPPT algorithm as shown in Fig. 21.8.

The error from the comparison process of I_{grid} and $I_{gridref}$ is fed to the PI controller. The output of the PI controller, also known as $V_{ref,}$ goes through an antiwindup process before which is being compared with the high frequency triangular wave to produce the switching signals for S_1–S_6 as shown in Fig. 21.9.

21.4 Results and Waveforms

The response with Improved perturbation and observation (P&O) MPPT Technique has duty ratio of IP&O MPPT is shown in Fig. 21.10.

The dc bus voltage must always be higher than $\sqrt{2}$ times of V_{grid} to inject the current into the grid, or current will be injected from the grid into the inverter. Therefore, operation is recommended to be between $M_a = 0.66$ and $M_a = 1.0$. The output voltage comprises seven voltage levels. The current flowing into the grid is filtered to resemble a pure sinewave in phase with the grid voltage. The corresponding switching pulse for inverter and output voltage obtained is shown in Figs. 21.11, 21.12 and 21.13.

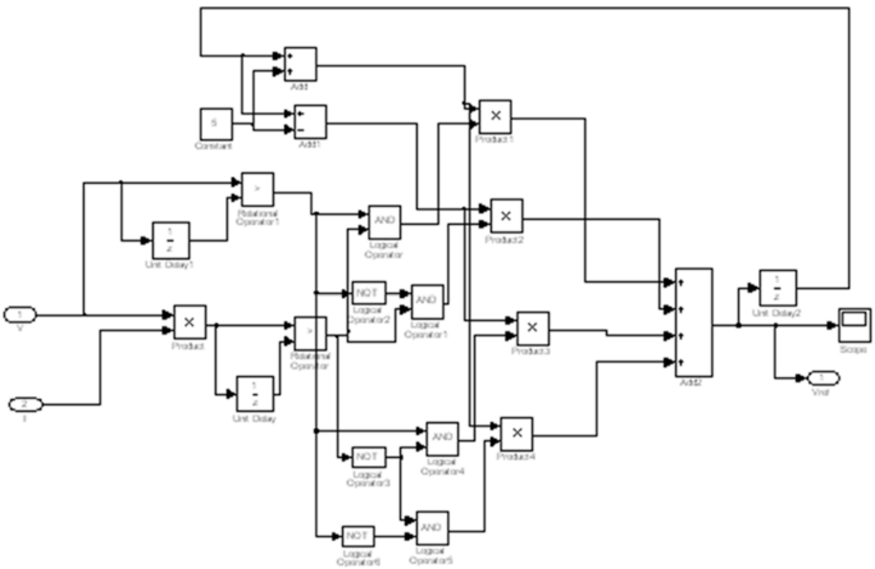

Fig. 21.8 MPPT algorithm

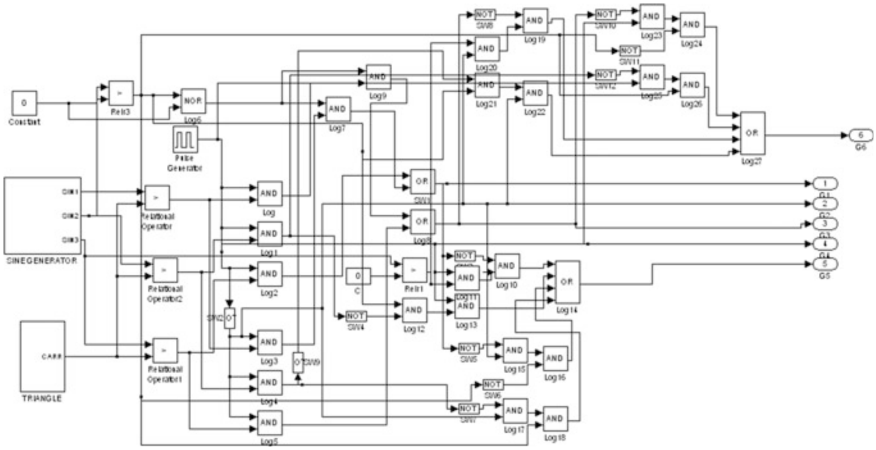

Fig. 21.9 PWM signals to switches

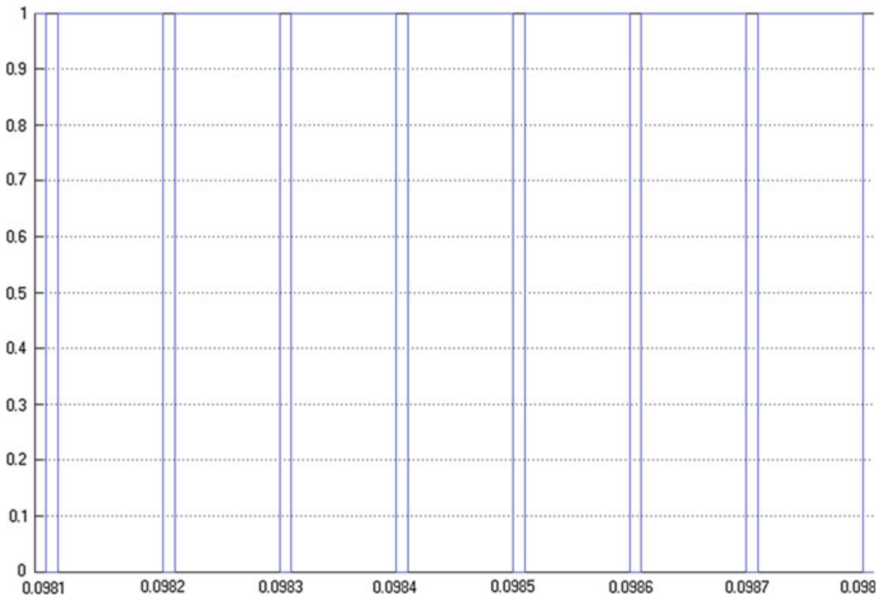

Fig. 21.10 Duty cycle of boost converter

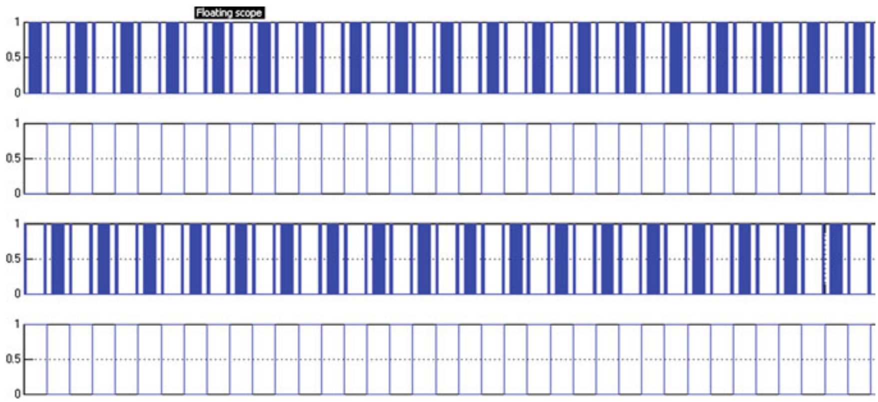

Fig. 21.11 Switching pulses for seven level inverter

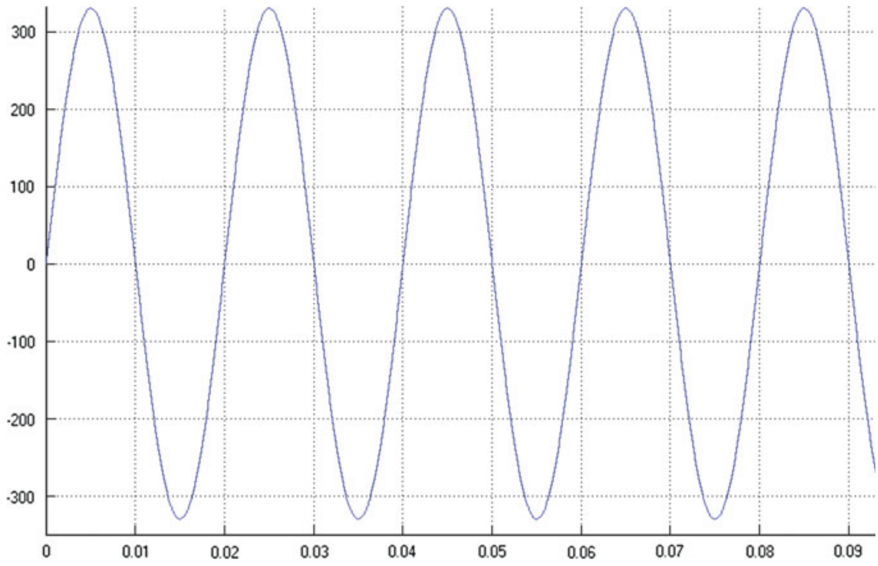

Fig. 21.12 Output voltage from inverter

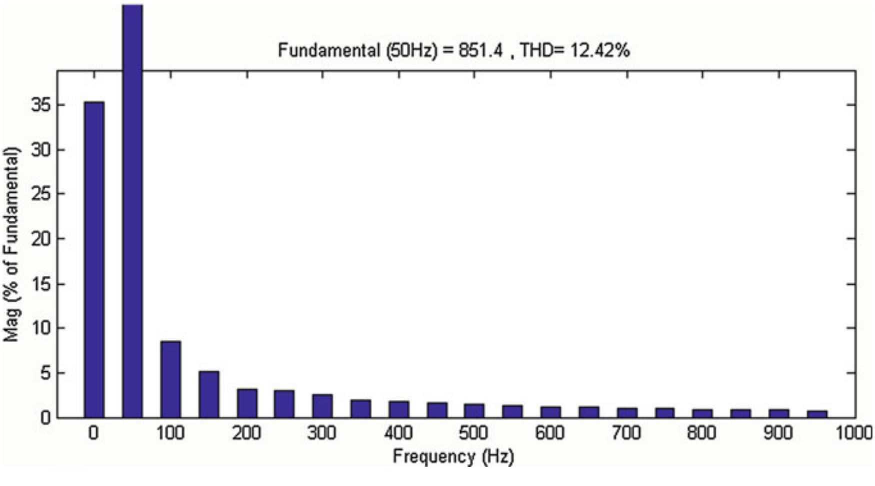

Fig. 21.13 THD

THD obtained is 12.42 % in case of seven level inverter as shown in Fig. 21.13 which is low compared to five level inverters.

21.5 Conclusion

In the proposed system, an Improved Perturb and Observe (IP&O) is used to track the maximum power point of PV system. It has a faster tracking speed, it exhibits zero oscillations at the MPP, it could locate the MPP for any environmental variations. On the other hand grid connected multilevel inverters offer improved output waveforms and lower THD. A novel PWM switching scheme is simulated for multilevel inverter. By controlling the modulation index, the desired number of levels of the inverter's output voltage can be achieved. The other advantage is that it can eliminate roughly half the number of switching devices, their gate drivers compared with the existing cascaded MLI counterparts. It is shown that due to lesser number of switches, the switching losses are also reduced.

References

1. Alexandru C, Pozna C (2010) Simulation of a dual-axis solar tracker for improving the performance of a photovoltaic panel. Proc Inst Mech Eng J Power Energy 224:B210–B215
2. Casadei D, Grandi G, Lega A, Rossi C (2008) Multilevel operation and input power balancing for a dual two-level inverter with insulated DC sources. IEEE Trans Ind Appl 44 (6):1815–1824
3. Esram T, Chapman PL (2007) Comparison of photovoltaic array maximum power point tracking techniques. IEEE Trans Energy Convers 22(2):439–449
4. Faranda R, Leva S, Maugeri V (2008) MPPT techniques for PV systems: energetic and cost comparison. Electrical Engineering Department Politecnico di Milano, Milano, Italy, pp. 1–6
5. Femia N, Petrone G, Spagnuolo G, Vitelli M (2009) A technique for improving P&O MPPT performances of double-stage grid-connected photovoltaic systems. IEEE Trans Ind Electron 56(11):4473–4482
6. Fortunato M, Giustiniani A, Petrone G, Spagnuolo G, Vitelli M (2008) Maximum power point tracking in a one-cycle-controlled single-stage photovoltaic inverter. IEEE Trans Ind Electron 55(7):2684–2693
7. González-Longatt FM (2005) Model of photovoltaic module in Matlab. In: 2do Congreso iberoamericano de estudiantes de ingenierıacute;a eléctrica, electrónica computación, ii cibelec, pp 1–5
8. Karpagam J, Nirmal Kumar A, Kumar Chinnaiyan V (2013) An experimental analysis of a single phase matrix converter for adjustable speed drives. Int Rev Modell Simul 6 (4):1071–1078
9. Khomfoi S, Tolbert LM (2007) Multilevel power converters. In: Rashid MH (eds) Power electronics handbook, 2nd edn. Elsevier, London. ISBN 978-0-12-088479-7, pp 451–482
10. Kumar Chinnaiyan V, Jerome J, Karpagam J (2010) Design and realization of a three phase cascaded multilevel inverter for industrial drives with reduced power quality issues. Int Rev Electric Eng 5(4):364–369
11. Oshiro M, Tanaka K, Senjyu T, Toma S, Yona A, Saber AY, Funabashi T, Kim CH (2011) Optimal voltage control in distribution systems using PV generators. Int J Electr Power Energy Syst 33(3):485–492
12. Rahim NA, Chaniago K, Selvaraj J (2011) Single-phase seven-level grid-connected inverter for photovoltaic system. IEEE Trans Ind Electron 58(6):2435
13. Rahim NA, Selvaraj J (2010) Multi-string five-level inverter with novel PWM control scheme for PV application. IEEE Trans Ind Electron 57(6):2111–2121

Chapter 22
Implementation of Anti-islanding Scheme for a Grid Connected Inverter

Arup Kumar Saikia and P.N. Kapil

Abstract As more PV systems join the utility grid the concern of undetected islanding operation increases. This concern is due to the safety hazards this phenomenon imposes on personnel and equipment. This paper discusses there different islanding schemes used and their features. As AFD method is the most popular method of islanding detection this paper proposes an improved method, where it uses AFD scheme for islanding detection but keeps the power quality high and the current THD less than 5 %. Also the paper shows the effectiveness in detecting island in less than 2 s according to IEEE standards.

Keywords Active islanding method · Active frequency drifts method · Distributed generation

22.1 Introduction

As more and more number of renewable energy sources are becoming popular due to fuel shortage in the future. As a clean energy source grid connected PV systems have been finding more and more applications around the world. In modern power systems, PV systems are becoming larger and more complicated. However due to larger PV systems the problem of stability still and power quality occurs in the adjacent utility [1]. The most issued problem is of islanding phenomenon in which the DG becomes isolated from the grid and independently supplies power to a portion of the utility, even when the portion is isolated from the rest of the utility source. This can cause safety problems for utility system include the non-islanding

A.K. Saikia
Power Electronics and Machine Drives, Nirma University, Ahmedabad, Gujarat, India
e-mail: 12meep01@nirmauni.ac.in

P.N. Kapil (✉)
Electrical Engineering Department, Nirma University, Ahmedabad, Gujarat, India
e-mail: p.n.kapil@nirmauni.ac.in

C. Kamalakannan et al. (eds.), *Power Electronics and Renewable Energy Systems*,
Lecture Notes in Electrical Engineering 326, DOI 10.1007/978-81-322-2119-7_22

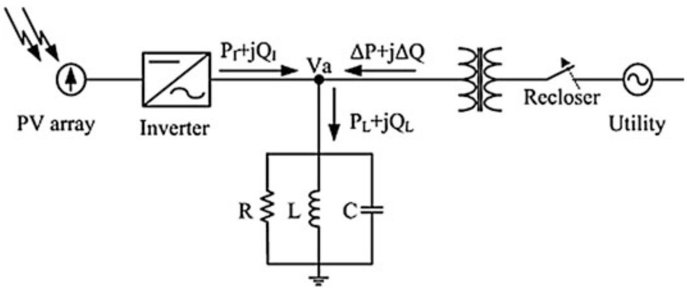

Fig. 22.1 An overview of islanding mode in a grid connected PV system [3]

inverter [2]. A general concept of islanding is illustrated in Fig. 22.1 [3]. During islanding mode, the utility circuit breaker is opened while the DG is still injecting power to supply the local load (i.e. section between utility and point of common coupling PCC) [3]. This phenomenon occurs when utility suffers from unpredictable interruption or abnormality, such as voltage shut down or short circuit or equipment failure [4].

To prevent islanding phenomenon various anti-islanding methods have been studied, which can be classified broadly into two categories namely local and remote islanding detection techniques [3]. The remote islanding detection technique relies on the communication between system utility grid and the DG. In the local methods come two categories namely passive and active methods as shown in Fig. 22.2.

22.2 Anti Islanding Methods

For better understanding of an islanding situation two key features has to be understood. The first feature is non-detection zone (NDZ) and the other one is quality (Q) factor [3]. Both the features are used as deciding parameters in evaluating the effectiveness of the anti-islanding methods. The NDZ represents the interval of islanding failed to be detected by the DG once islanding occurred. This region relates to the power mismatch between DG generating power and local load consuming power, therefore creating a real power variation (ΔP) and reactive power variation (ΔQ). For this reason the variation must be significant in order to detect the islanding within the stipulated time interval. Therefore, NDZ is defined as an evaluation index for an islanding detection technique.

The second feature which is the Q factor is defined as the two pi (π) times the ratio of the maximum storage energy to the energy dissipated per cycle at given frequency [3]. It demonstrates the relative amount of energy stored and energy dissipated in the RLC circuit. A high Q factor may hamper the effectiveness of an anti-islanding scheme, so the value Q factor is directly affected by potential load

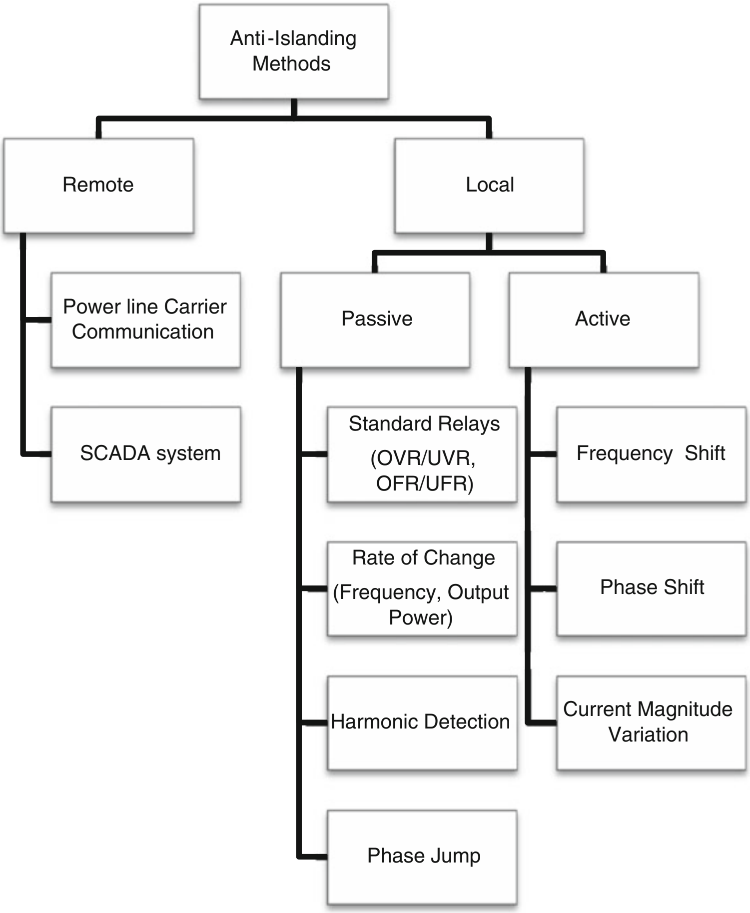

Fig. 22.2 Classification of different Anti islanding methods

inside the island. The load is modeled as parallel RLC load due to difficulty in islanding detection. Quality factor and NDZ are directly proportional so we have to keep both the factors as low as possible for an effective islanding technique.

As we have already classified different anti-islanding methods (AIM) above we will see the local methods which are active and passive methods.

22.2.1 Passive Methods

The passive methods just monitor the grid voltage and frequency protection and execute general protecting function such as under voltage or frequency protection or over voltage or frequency protection. They do not inject any disturbances into the system and hence the power quality remains unaffected. But they fail to detect small changes in voltage and frequency which are due to power balance between PV and load, hence also fail to detect islanding condition. Passive islanding method relies on the measurement of the system parameters (such as the variation in the voltage, frequency, harmonic distortion or the power) that causes the inverter to modify the output power in order to meet specific conditions during islanding conditions during islanding mode of operation. The boundary of the system parameters defines the NDZ. The parameters greatly vary at the point of common coupling (PCC) when the system is islanded. The difference between islanding condition and normal grid connected condition is based on threshold settings of system parameters. Extreme care should be taken while setting the value of threshold in order to differentiate islanding operation from other disturbances in controlled system. Passive methods have, therefore, large NDZ. Nevertheless, passive methods are conceptually simple and easy to implement. In general passive islanding detection techniques are fast and create no disturbance in the system however it has large NDZ which could fail islanding detection.

22.2.2 Active Methods

In order to reduce the NDZ in cases where the local loads are close in capacity to the DG system, active detection method is used [5]. Active islanding detection method is based on the injection of a small disturbance signal to certain parameters at the PCC. The concept of this method is that small disturbance signal will become significant upon entering the islanding mode of operation in order to help the inverter to cease power conversion. Hence, the values of system parameter will be varying during the cessation of power conversion, and by measuring the corresponding system parameters, islanding condition can be detected. In case when the PV inverter behaves as a current source, the current supplied to the utility is expressed by the following equation.

$$i_{\mathrm{PV\_inv}} = \mathrm{I}_{\mathrm{PV\_inv}}\sin(\omega_{\mathrm{PV}} + \varphi_{\mathrm{PV}}) \tag{22.1}$$

where I_{PV_inv} is the inverter current amplitude ($i_{PV\_inv} = I_{PV\_inv} + I_{disturbance}$), ω_{PV} is the frequency and φ_{PV} is phase angle. These three parameters can be varied and modified, or can be set as disturbance signals. Active islanding methods are more considered because of its minimal NDZ, especially in case where there is power balance between load and source. On the other hand, power quality and output generation for AIM can be impaired by perturbation because it changes the magnitude of frequency of output current [1]. However active methods require additional hardware of its working which makes it costlier but still it is an effective method and more commonly used.

Active AIMs are classified into three parts with respect to what the variation parameter is [6]. These parameters are current magnitude, frequency, and the start phase. More specifically they are described in detail as frequency shift methods, phase shift methods and the current magnitude variation method.

22.2.2.1 Frequency Shift Method

The typical frequency shift method is active frequency drift (AFD) method, which is easily implemented in PV inverter with the microprocessor based controller also adds essentially zero cost to such system [1, 4]. In this method and current wave form in injected into the islanded system which is distorted from the output current waveform. This distortion is increased above the tripping window of the system and islanding condition is prevented. In AFD method the key design parameter is chopping fraction (c_f) which is defined as the ratio of the zero time (T_z) to half of the period of the voltage waveform ($T_{util}/2$) as shown in following

$$C_f = \frac{2T_z}{T_{util}} \tag{22.2}$$

Unfortunately, the smaller NDZ obtained with AFD compared to passive methods comes at expense of increased THD which degrades the power quality provided by the grid tied converter [5]. The loss of power quality is inherent to AFD due to distortion injected to the current waveform. For AFD to be effective, c_f needs to be fairly large, which directly affects the THD of the current waveform [5]. Actually, AFD method has a difficulty to detect islanding when the generated reactive power by constant chopping fraction is cancelled by the local load power. Therefore, the enhanced AFD method has been developed such as Scandia frequency shift (SFS) method and AFD with pulsation of chopping fraction (AFDPF) [6, 7] (Fig. 22.3).

22.2.2.2 Phase Shift Method

One of the most famous phase shift method is, slip mode frequency shift method (SMS). SMS is the method forcing the phase of the inverter's output to be slightly miss-aligned with the grid to cause variation in the inverter current. This variation is sensed by a PLL and is increased significantly outside the normal operating frequency window. Hence island is detected and trips the source. While the SMS method uses a function of the frequency for current phase variation, the reactive power control method uses a function of time in order to vary the current phase [1].

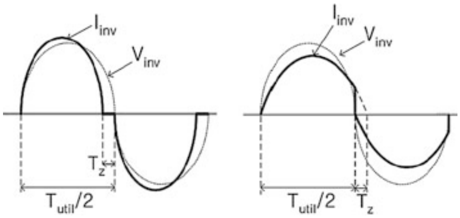

Fig. 22.3 Inverter voltage and current waveforms in AFD method, drift up with positive chopping fraction and drift down with negative chopping fraction

Frequency variation techniques increases the harmonics components of the current, and start phase variation method decreases the displacement power factor, which causes the lower power quality [2].

22.2.2.3 Current Magnitude Variation Method

Scandia Voltage Shift (SVS) method uses positive feedback technique to prevent islanding based on amplitude of the voltage at PCC. When utility grid is connected there will be small or no effect on the power of the system. But once the utility is disconnected, there is reduction in V_{PCC} can be detected by UVP or OVR.

The other method is periodic current magnitude variation (PCMV) method [2] is a current magnitude variation method with the same amount of increase and decrease. So the total average output power is maintained during current variation period. Time varying current magnitude variation makes the voltages variation when islanding occurs. One of the advantages for this method is high power quality without injecting harmonic signal or phase angle.

22.3 Proposed Method

The method proposed for AIM makes the magnitude current reference to be increased to K % higher than nominal value at first line cycle, and then makes that to be decreased to K % lower than the nominal value to the next line cycle. It makes the total average real power from PV to be constant between two consecutive line cycles without affecting the maximum power point tracking function of PV inverter. The operating principle of this scheme can be understood from the flowchart and the operational waveforms given in Figs. 22.4 and 22.5 respectively.

At the start of Co cycles, current magnitude is raised by K % for the first cycle and decreased by K % for second cycle. For the next C_1 cycles there is no change in the magnitude of current. Due to this current magnitude variation is employed but average power remains same. Thus power transferred is not affected. If this causes change in the rms value of the voltage beyond a specific threshold, the AFD method is injected and the frequency drift away from normal in case of islanding condition. The AFD injection is removed at the end of C_1 cycles. This maintains the power quality of the inverter when the active signals are not injected.

22.4 Simulation

In order to verify the proposed method, a single phase photo voltaic distributed generation with a local RLC load has been considered. The system parameters are listed in Table 22.1. The simulation of the proposed method was implemented in

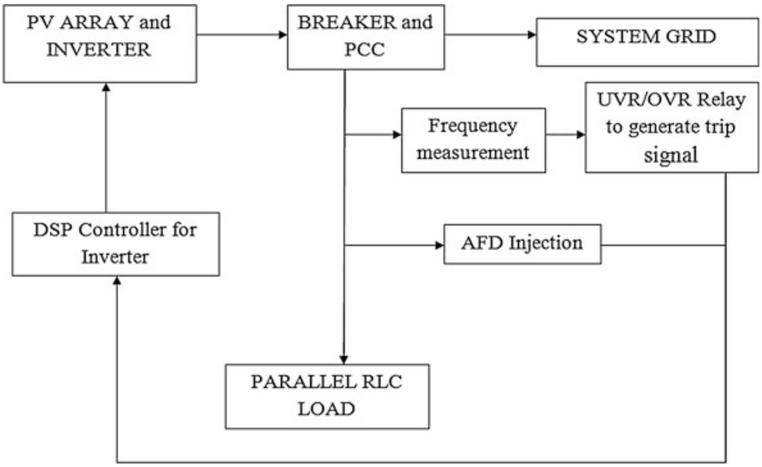

Fig. 22.4 Flowchart of the proposed method

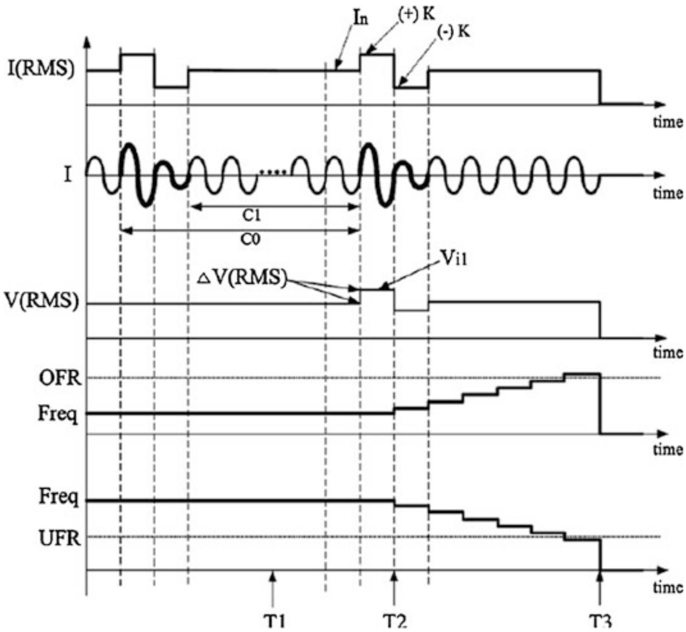

Fig. 22.5 Operational waveforms: inverter RMS command (*I(RMS)*), inverter current (*I*), and inverter RMS voltage (*V(RMS)*), frequency(*Freq*)

Table 22.1 Circuit parameters for simulation and experiments

Parameter	Value
Quality factor	2.5
Voltage (Volts)	220
Frequency (Hz)	50
K (%)	12
ΔV(rms), ref (Volts)	22
Chopping fraction (c_f) (%)	5
C_0 (cycles)	11
C_1 (cycles)	9
P_{inv} (kW)	3
Local inductive load Q_L (kVar, H)	0.77, 0.5
Local Capacitive load Q_c (kVar, nF)	0.77, 50.71

PSIM. Use of dll (dynamic link library) block is used and waveforms were obtained. The parallel RLC load was modeled. And calculations were done accordingly as follows.

As per given values of the parameters in above table we have [8]

Active Power P_i = 3 kW
Reactive Power Q_i = 0
Quality factor Q_f = 2:5
Gird Voltage rms V_{grid} = 220 V
Grid Frequency f = 50 Hz.
Load Resistance $R_o = \frac{V_{grid}^2}{P_i} = 16.1333336\ \Omega$
Load Inductance $L_o = \frac{V_{gird}^2}{2\pi f Q_f P_i} = 20.54 \times 10^{-3}$ H
Load Capacitance $C_o = \frac{Q_f P_i}{2\pi V_{grid}^2} = 493.2487 \times 10^{-6}$ F.

22.5 Results

The waveforms obtained from the simulation results are as shown below.

As shown in the Fig. 22.6d the AFD injection start signal goes to high when the rms value of the voltage crosses the set value of 22 V. Now, the AFD method will start. Due to the injection of active signal and the presence of islanding condition the frequency of the load voltage becomes 200 Hz which is undesirable yet it is outside the set trip window of 47–53 Hz. This condition generates a trip signal and the production of reference signal is stopped and hence the inverter voltage drops to zero. This phenomenon is shown in the Fig. 22.6e, f, for the above condition of islanding the time at which the AFD signal is injected is 0.68 s. The Trip signal is

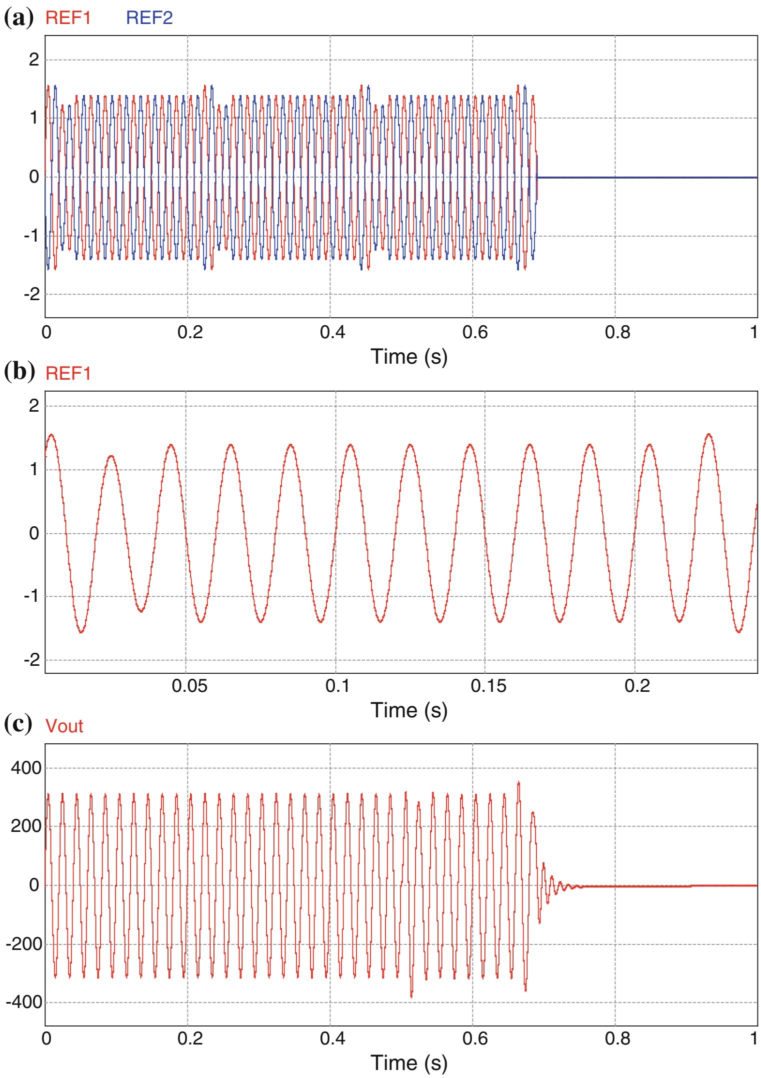

Fig. 22.6 Simulation results: **a** variation by K %, **b** output voltage, **c** RMS value of voltage, **d** RMS value of output voltage, **e** frequency, **f** AFD injection and inverter turn off signal, **g** output current

generated at 0.6910 s. At that instant at the output voltage starts decreasing to become zero. Thus, the total time taken to detect islanding is 0.110 s. This time is within the permissible limit set by the IEEE standard 1547 which is 2 s. The THD of the output current is also within IEEE standards i.e. less than 5 % which is 4.8 % in this case.

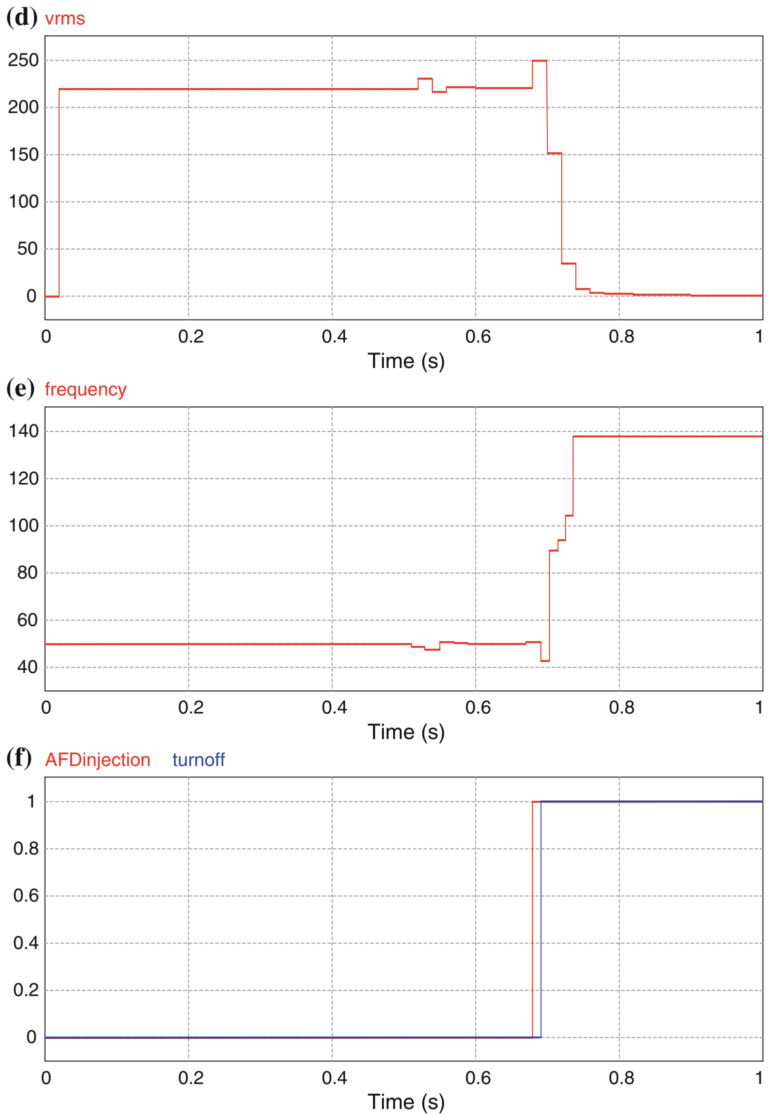

Fig. 22.6 (continued)

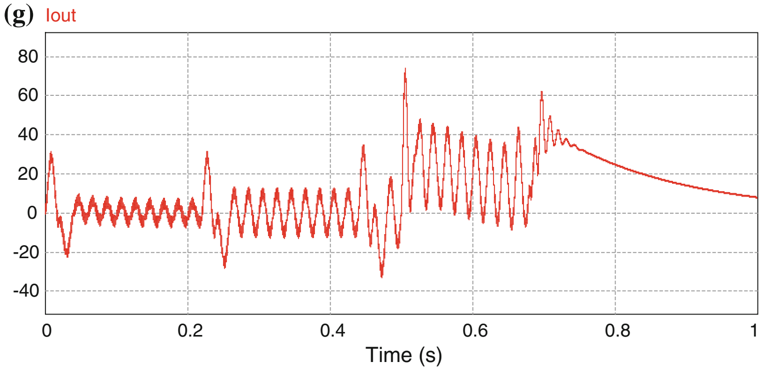

Fig. 22.6 (continued)

22.6 Conclusion

The paper has presented an effective method of islanding detection for grid connected PV system. The islanding was detected according to IEEE standards 1547, i.e. below 2 s which was 0.11 s. The paper proposes high power quality islanding method using effective power variation by varying periodically the magnitude of inverter current reference. The simulation results ensure the effectiveness of the method. Further improvements can be done in the system such as improving its current THD.

References

1. Yu B, Matsui M, Yu G (2010) A review of current anti-islanding methods for photovoltaic power system. Solar Energy J 84:745–754
2. Yu B, Matsui M, So J, Yu G (2008) A high power quality anti-islanding method using effective power variation. Solar Energy J 82:368–378
3. Teoh WY, Tan CW (2011) An overview of islanding detection methods in photovoltaic systems. World Acad Sci Eng Technol 58:674–682
4. Jung Y, Choi J, Yu B, Yu G, So J, Choi J (2005) A novel active frequency drift method of islanding prevention for the grid-connected photovoltaic inverter. In: Proceedings of power electronics specialists conference, pp 1915–1921
5. Yafaoui A, Wu B, Kouro S (2012) Improved active frequency drift anti-islanding detection method for grid connected photovoltaic system. IEEE Trans Power Electron 27(5):2367–2375
6. Ropp ME, Begovic M, Rohatgi A (1999a) Analysis and performance assessment of the active frequency drift method of islanding prevention. IEEE Trans Energy Convers 3:810–816
7. Ropp ME, Begoviv M, Rohatgi A (1999b) Prevention of islanding in grid-connected photovoltaic systems. Prog Photovolt Res Appl 7:39–59
8. Ye Z, Kolwalkar A, Zhang Y, Du P, Walling R (2004) Evaluation of anti-islanding schemes based on non detection zone concept. IEEE Trans Power Electron 19(5):1171–1176

Chapter 23
THD Analysis of One-Cycle and PWM Controlled Active Power Filters

Sravani Jennela and V. Raj Kumar

Abstract Nonlinear loads generate harmonics and reactive currents, which leads to poor power factor and harmful disturbance to other appliances. Active power filters are one of the viable solutions to eliminate the harmonic/reactive currents generated by non linear loads in power lines. In this paper an APF is connected in shunt with the nonlinear loads and functions as compensating current sources to eliminate the harmonic components in the source side so that the current flow into and from the grid is in phase with grid voltage. Here APF power converter is operated in dual boost converter mode with constant switching frequency by using one-cycle control method with vector operation and pulse width modulation control. The obtained simulation results were compared through which the best method has been concluded. All features are simulated in the MATLAB/SIMULINK environment.

Keywords Active powers filter (APF) · One-cycle control · Pulse width modulation (PWM) · Power quality control

23.1 Introduction

The harmonics are increased due to the increase in the non linear loads and distributed power sources which are connected to the grid such as Diode/Thyristor rectifiers with R, L, C loads and electronic appliances. As these non linear loads and sources generate the harmonics [1] which cause low power factor and harmful disturbances to the appliances the following are some of the techniques to eliminate the harmonics and improve the power factor, they are PFC technique, passive

S. Jennela · V. Raj Kumar (✉)
EEE Department, GITAM University, Visakhapatnam, India
e-mail: coolvrajkumar@gmail.com

S. Jennela
e-mail: jennelasravani@gmail.com

C. Kamalakannan et al. (eds.), *Power Electronics and Renewable Energy Systems*,
Lecture Notes in Electrical Engineering 326, DOI 10.1007/978-81-322-2119-7_23

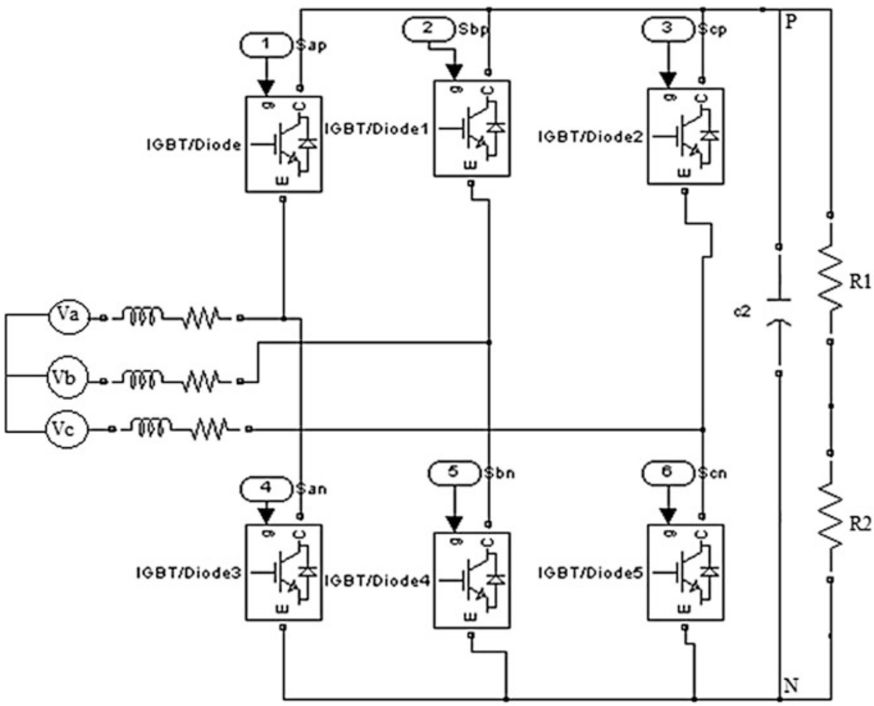

Fig. 23.1 Power stage of the three-phase APF with six switch bridge voltage-source converter

power filters, active power filters [2] which gives the suitable solutions to compensate the harmonics and improve the power factor. In PFC approach the PFC unit is usually connected in cascade in the power line which processes all the power and corrects the current to unity power factor. This kind of approach is suitable for low power i.e., less than 5 kVA. The APF can be connected either in series or shunt to the non linear load or sources and generate the harmonics and reactive power component to compensate the harmonics generated by the non-linear loads sources. To overcome the disadvantages due to passive filters, active power filters (APFs) have been presented [3] as a current-harmonic compensator for reducing the total harmonic distortion of the current and correcting the power factor of the input source. These kinds of approaches are applicable for low-power i.e., less than 5 kVA to high-power applications around 100 kVA. The active power filter used in this circuit as shown in Fig. 23.1 is comprised with three phase bridge converter with IGBT switches. Most previously reported control approaches need to sense the load current and calculate its harmonics and reactive components in order to generate the reference for controlling the current of a bridge converter. One among those approaches of control like PWM control [4] required the real time calculations for which we need to use different components which increase the complexity, cost of the equipment and the stability gets reduced.

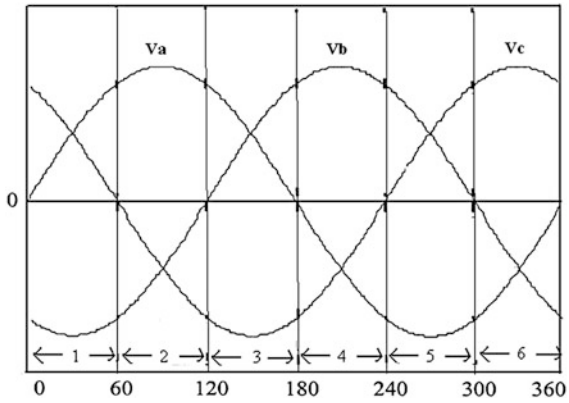

Fig. 23.2 Normalized three-phase grid voltage waveform

In this circuit all the switches are operated with switching frequency therefore, the switching losses are high. Reference [5] introduced a promising solution based on one cycle control which eliminates the need of calculations and use of multipliers and voltage sensors in the control loop which makes the circuit simple by introducing three phase APF with six-switch bridge converter with vector operation. It is found that this voltage source converter can be decoupled into a parallel-connected dual-boost converter with two-quadrant operation. Three-phase unity power factor can be achieved by controlling the parallel-connected dual-boost converter using One-Cycle control. The normalized three-phase grid voltage waveform is shown in Fig. 23.2.

23.2 One Cycle Control

The control is meant to achieve unity power factor at source side, that means source voltage and source current are in phase with each other and to reduce Total Harmonic Distortion (THD) in the line current, by operating Active Power Filter (APF) in the mode of dual boost converter with Vector operation by using One-Cycle Control in the form of closed loop control, such that APF would provide compensating currents into the power line.

The overall block diagram of the active power filter is shown in Fig. 23.3. Where Va, Vb, Vc are the three phase input source voltages, ia, ib, ic are the source currents ia_l, ib_l, ic_l are the nonlinear load currents. Due to load nonlinearity, it will introduce harmonic currents, so that the current wave form is distorted. Now our APF which is connected in shunt with nonlinear load will inject harmonic current into the AC system, of the same amplitude but reverse in phase to that of the load current harmonics.

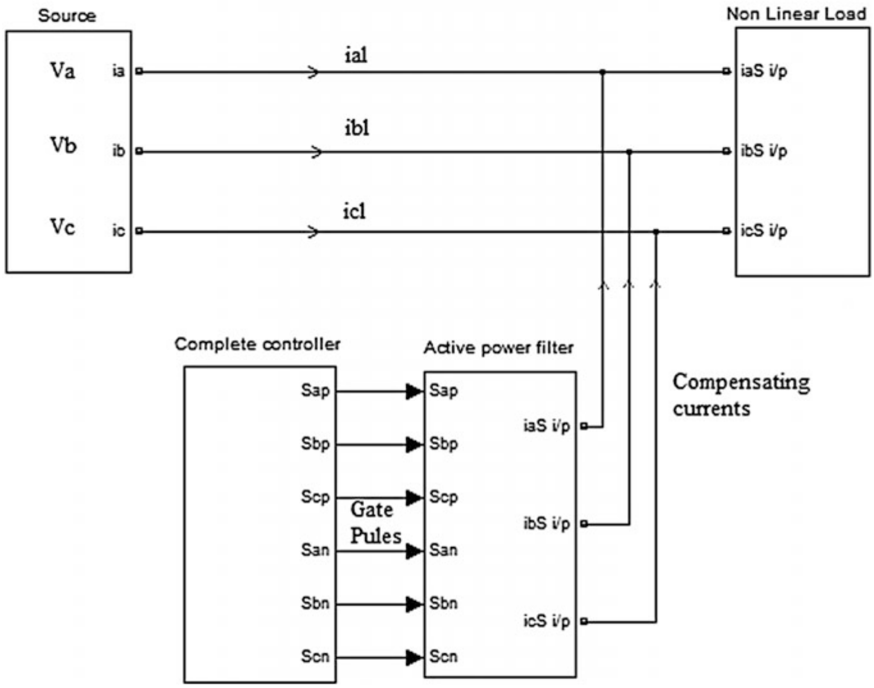

Fig. 23.3 One-cycle control of active power filter

This will thus result in sinusoidal line currents and unity power factor in the input power system. This APF is controlled by the gate pulses which are coming from the Vector controlled switching logic circuit, which is mainly controlled by the One-Cycle controller.

23.3 Concept of Parallel-Connected Dual-Boost Converter

The power stage of three phase active power filter is composed of voltage source converter with IGBT switches that is connected in parallel with a non linear load which could be several loads shown in Fig. 23.1. The normalized grid waveform is shown in Fig. 23.2.. During the region (0°–60°) the voltage V_b is negative dominant. In this case, switch S_{bn} conducts and switch S_{bp} is kept off during the whole 60° region, switches in the other two branches such as S_{an}, S_{ap}, S_{cn}, S_{cp} are controlled complementarily at switching frequency. The voltage source converter can be simplified to reduced convertor with four switches S_{ap}, S_{an}, S_{cp}, S_{cn}. This reduced convertor is converted to equivalent parallel-connected dual-boost converter with two grid voltages V_{ab}, V_{cb}. Where V_{ab}, V_{cb} are line to line voltages and E is the dc voltage of energy storage capacitor. The generalized parallel-connected dual-boost

Table 23.1 Cross reference of the circuit parameters and symbols between the bridge voltage-source converter and the dual boost converter

Region	V_p	V_n	i_p	i_n	L_p	L_n	L_t	T_p	T_n	$\overline{T}_p$	$\overline{T}_n$	T_t
0°–60°	V_{ab}	V_{cb}	i_a	i_c	L_a	L_c	L_b	S_{an}	S_{cn}	S_{ap}	S_{cp}	S_{bn}
60°–120°	V_{ab}	V_{ac}	$-i_b$	$-i_c$	L_b	L_c	L_a	S_{bp}	S_{cp}	S_{bn}	S_{cn}	S_{ap}
120°–180°	V_{bc}	V_{ac}	i_b	i_a	L_b	L_a	L_c	S_{bn}	S_{an}	S_{bp}	S_{ap}	S_{cn}
180°–240°	V_{bc}	V_{ba}	$-i_c$	$-i_a$	L_c	L_a	L_b	S_{cp}	S_{ap}	S_{cn}	S_{an}	S_{bp}
240°–300°	V_{ca}	V_{ba}	i_c	i_b	L_c	L_b	L_a	S_{cn}	S_{bn}	S_{cp}	S_{bp}	S_{an}
300°–360°	V_{ca}	V_{cb}	$-i_a$	$-i_b$	L_a	L_b	L_c	S_{ap}	S_{bp}	S_{an}	S_{bn}	S_{cp}

converter is of two categories. One is for the regions (0°–60°, 120°–180°, 240°–300°) and the other is for regions (60°–120°, 180°–240°, 300°–360°). Switch pairs T_p, $\overline{T}_p$ and T_n, $\overline{T}_n$ are controlled complementally. The current through the L_p and L_n increases when switches T_p and T_n are ON and decrease when they are OFF. The cross reference of the circuit parameters and symbols between the bridge voltage-source converters are shown in Table 23.1.

The objective of three phase APF is to control three phase grid currents to follow the three phase grid voltages, respectively. This can be achieved by controlling the equivalent parallel-connected dual-boost converter. This is obtained by doing interpolation i.e., for (0°–60°) Phase currents i_a, i_b replaced by i_p, i_n and phase voltages V_a, V_c replaced by V_p, V_n where $V_p = V_{ab}$ and $V_n = V_{cb}$. The control goal is given using ohms law V = IR.

23.4 Switching States of Parallel Connected Dual-Boost Converter

We have totally four switches in the equivalent circuit for every cycle. So we get four combinations as follows, switch state-I (T_p-ON, T_n-OFF, $\overline{T}_p$-OFF, $\overline{T}_n$-OFF) likewise we frame other four switch states. Considering switching state-I for Fig. 23.5 and by applying super position theorem and current division rule we obtain the voltages V_{lp}, V_{ln}, V_{lt} which was given in Table 23.2. For a three phase

Table 23.2 Control algorithm for the APF

Region	i_p	i_n	d_p	d_n	d_t	Q_{ap}	Q_{an}	Q_{bp}	Q_{bn}	Q_{cp}	Q_{cn}
0°–60°	i_a	i_c	d_{an}	d_{cn}	d_{bn}	$\bar{Q}_p$	Q_p	OFF	ON	$\bar{Q}_n$	Q_n
60°–120°	$-i_b$	$-i_c$	d_{bp}	d_{cp}	d_{ap}	ON	OFF	Q_p	$\bar{Q}_p$	Q_n	$\bar{Q}_n$
120°–180°	i_b	i_a	d_{bn}	d_{an}	d_{cn}	$\bar{Q}_n$	Q_n	$\bar{Q}_p$	Q_p	OFF	ON
180°–240°	$-i_c$	$-i_a$	d_{cp}	d_{ap}	d_{bp}	Q_n	$\bar{Q}_n$	ON	OFF	Q_p	$\bar{Q}_p$
240°–300°	i_c	i_b	d_{cn}	d_{bn}	d_{an}	OFF	ON	$\bar{Q}_n$	Q_n	$\bar{Q}_p$	Q_p
300°–360°	$-i_a$	$-i_b$	d_{ap}	d_{bp}	d_{cp}	Q_p	$\bar{Q}_p$	Q_n	$\bar{Q}_n$	ON	OFF

APF with a constant switching frequency, only two switching sequences are possible, i.e., I, II, IV (condition $d_p > d_n$ where d_p, d_n are the duty ratios of switches T_p, T_n, respectively) or I, III, IV is the other sequence which is possible. Based on the assumption that switching frequency is much higher than the line frequency, the inductor voltage-second balance is approximately valid, that is

$$\begin{aligned} V_p^* d_n + \left(V_p^* + \frac{1}{3}E\right) * \left(d_p - d_n\right) + \left(Vp^* - \frac{1}{3}E\right) * \left(1 - d_p\right) = 0 \\ V_n^* d_n + \left(V_n^* - \frac{2}{3}E\right) * \left(d_p - d_n\right) + \left(V_n^* - \frac{1}{3}E\right) * \left(1 - d_p\right) = 0 \\ V_t^* d_n + \left(V_t^* - \frac{1}{3}E\right) * \left(d_p - d_n\right) + \left(V_t^* - \frac{2}{3}E\right) * \left(1 - d_p\right) = 0 \end{aligned} \tag{23.1}$$

The following equation is true for a symmetrical three-phase system:

$$V_p^* + V_n^* - V_t^* = 0 \tag{23.2}$$

From the above two Eqs. (23.1) and (23.2) we obtain

$$\begin{bmatrix} \left(1 - d_p\right) \\ \left(1 - d_n\right) \end{bmatrix} = \begin{bmatrix} 2 & 1 \\ 1 & 2 \end{bmatrix} * \begin{bmatrix} \frac{V_p^*}{E} \\ \frac{V_n^*}{E} \end{bmatrix} \tag{23.3}$$

This equation gives a relationship between the duty cycle and the input, output voltage for the parallel-connected dual-boost converter. For the unity-power-factor three-phase APF, the control goal is to force the grid line current in each phase to follow the correspondent sinusoidal phase voltage, i.e.,

$$\begin{aligned} V_a = R_e * I_a \\ V_b = R_e * I_b \\ V_c = R_e * I_c \end{aligned} \tag{23.4}$$

where R_e is the emulated resistance that reflects the real power of the load and the control goal of three-phase APF can be rewritten as follows

$$V_p^* = R_e * i_p \tag{23.5}$$

$$V_n^* = R_e * i_n \tag{23.6}$$

Substituting Eqs. (23.5) and (23.6) into the Eq. (23.2) and considering the switch is ON for the entire 60° region, it is obtained as

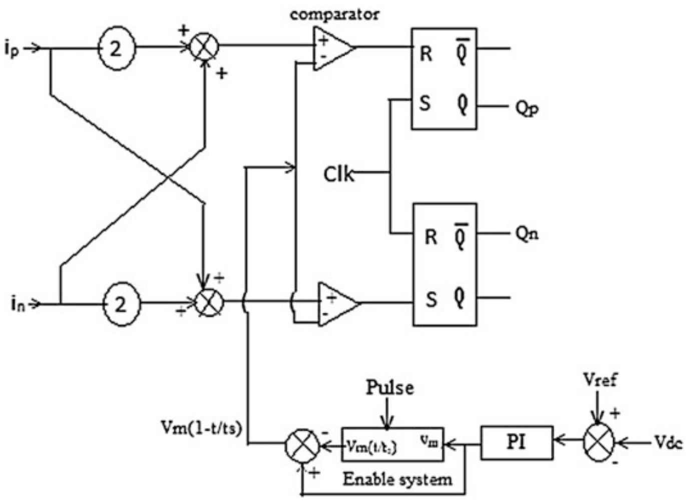

Fig. 23.4 Extended one-cycle control core

$$\begin{bmatrix} (1-d_p) \\ (1-d_n) \end{bmatrix} = \frac{R_e}{ER_s} * R_s * \begin{bmatrix} 2 & 1 \\ 1 & 2 \end{bmatrix} * \begin{bmatrix} i_p \\ i_n \end{bmatrix}_{d_t=1} \tag{23.7}$$

The control key equation obtained by substituting $V_m = ER_s/R_e$ in Eq. (23.7).

$$V_m * \begin{bmatrix} (1-d_p) \\ (1-d_n) \end{bmatrix} = R_s * \begin{bmatrix} 2 & 1 \\ 1 & 2 \end{bmatrix} * \begin{bmatrix} i_p \\ i_n \end{bmatrix}_{d_t=1} \tag{23.8}$$

By using the above Eq. (23.8) we design the one cycle controller as shown in Fig. 23.4.

So, now according to the operation of the dual boost converter the switching logic is being designed. For each switch of APF among six there will be six regions (0°–60°) to (300°–360°). The control algorithm for the APF is as follows in Table 23.2. According to the Table 23.2 we need to frame the logic block for switching the dual boost converter and inject the current in opposite direction to compensate the harmonics in the source side.

23.5 Pulse Width Modulation Control

As like in one cycle control the harmonics that are produced due to the non linear loads can be even compensated by using PWM controller [4]. PWM is a modulation technique that conforms the width of three pulses, formally the pulse duration, based on modulator signal information. Main features of PWM are the reference frame transformation and a digital low pass filter are used to compute the

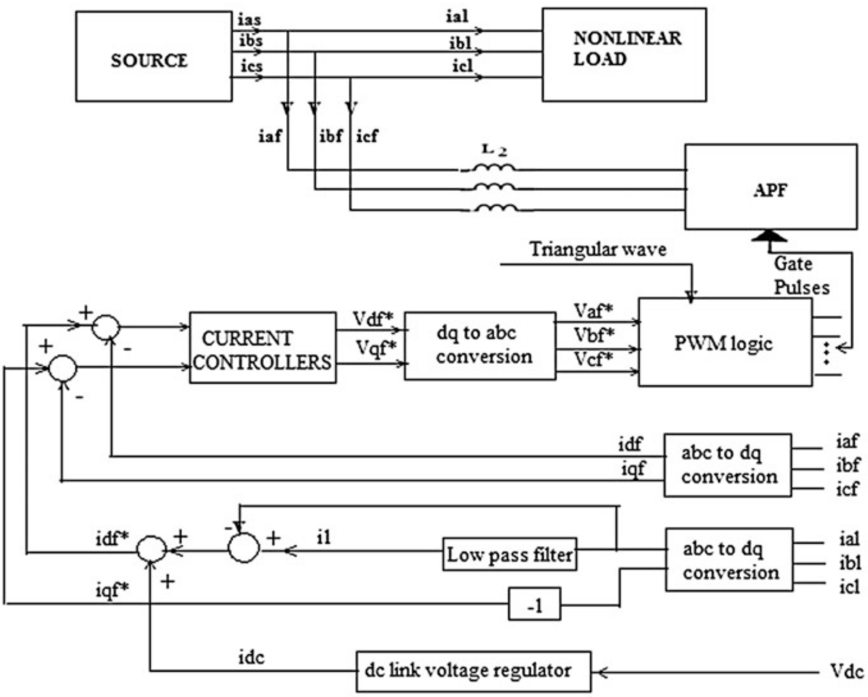

Fig. 23.5 Block diagram of PWM controlled APF

harmonic of the nonlinear load current, the voltage decouplers and pole zero cancellation methods are used in the current controllers of the APF to provide fast current harmonic compensation. In Fig. 23.5 i_{al}, i_{bl}, i_{cl} are load currents, i_{af}, i_{bf}, i_{cf} are filtering compensation currents, and V_{dc} is DC link capacitor voltage of the APF. Here filter currents and DC link capacitor voltages are taken as feedback.

After that load currents, and filter currents are transformed from abc model to dq model through reference frame transformation. I_{dl} current is passed through the low pass filter for getting fundamental current i_1, then by making (idl − i_1) gets total harmonic currents as reference. Here dc link voltage regulator current also taken into consideration for making direct axis filter reference current i_{df}^*.q-axis filter reference current i_{qf}^* is getting simply by making negative of that i_{ql}. Now these two currents are compared with the actual filter currents i_{df}, i_{qf} and produce the error. This error is now passed through the current controllers for getting reference voltages. Again these reference voltages are transformed into abc model. These three reference voltages are compared with the triangular wave, and by the method of bipolar voltage switching produce switching pulses for the APF power converter IGBT switches.

23.5.1 Design of Controllers

In PWM circuits the three phase voltage commands are compared with a triangular wave carrier of 10 kHz. The PWM output signals are used to switch ON or OFF the IGBT devices. The total control block as shown as below.

For the design of controllers [14], the system parameter used as follows:

$$V_m = 98\ \text{V} \quad \omega_e = 377\ \text{rad/s} \quad L_s = 0.4\ \text{mH}$$
$$V_c = 240\ \text{V} \quad L_2 = 0.25\ \text{mH} \quad R_2 = 0.03\ \Omega \quad C_2 = 4,800\ \mu\text{F}$$

Non linear load components are as follows:

Diode Bridge Rectifier with

$$\text{Ro} = 8.67\ \Omega, \quad \text{Co} = 3{,}300\ \mu\text{F}, \quad \text{Lo} = 3.1\ \text{mH}.$$

23.6 Experimental Results

A three phase APF with six switch bridge source converters was built to verify the concept of control by applying two methods named one cycle control and PWM control.

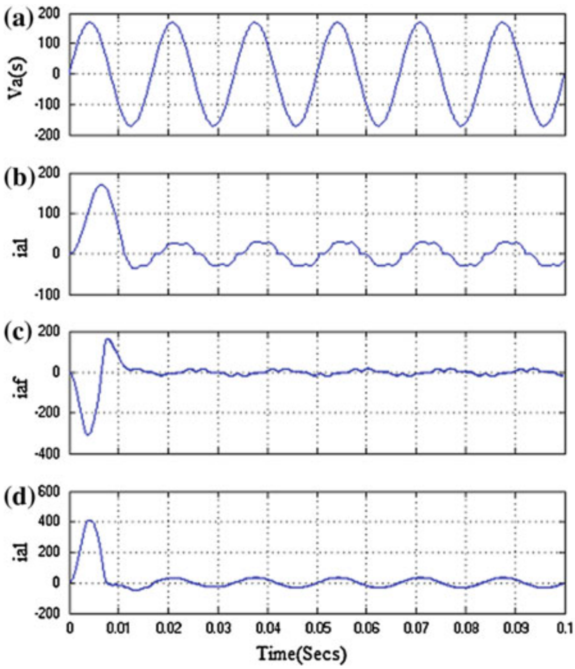

Fig. 23.6 Measured experimental waveforms for Phase A using one cycle control. **a** Is the phase voltage of the grid line, **b** is the distorted load current ial, **c** is the reactive component iaf, **d** is the compensated current ial which is free from harmonics

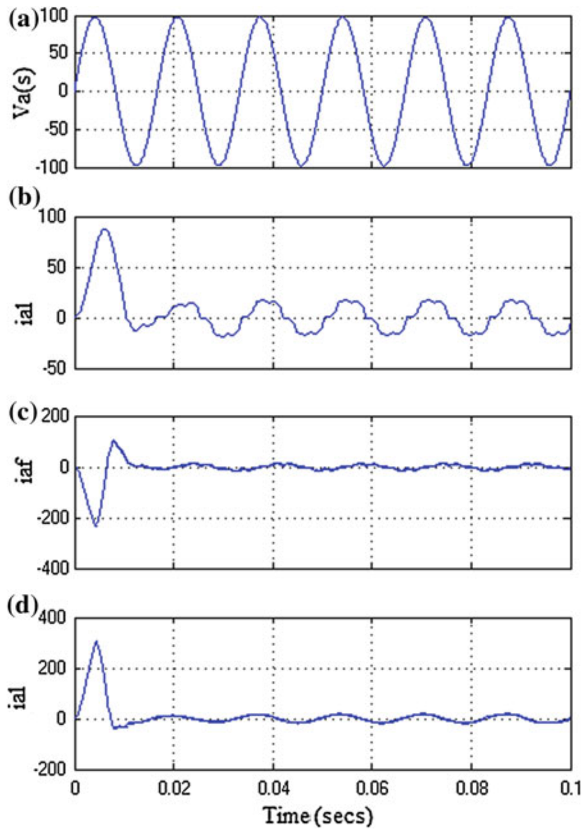

Fig. 23.7 Measured experimental waveforms for Phase A PWM control. **a** Is the phase voltage of the grid line, **b** is the distorted load current ial, **c** is the reactive component iaf, **d** is the compensated current ial which is free from harmonics

The experimental waveforms for one cycle control with and without APF are shown in Figs. 23.6 and 23.7. The applied phase voltage of gridline is shown in Figs. 23.6a and 23.7a due to nonlinear load whatever harmonic current is observed it is shown in Fig. 23.6b and 23.7b. This gets compensated by the reactive component of current shown in Figs. 23.6c and 23.7c which is provided by the active power filter and the resulted compensated current waveform is shown in Figs. 23.6d and 23.7d. The measured harmonic spectrum is shown in Figs. 23.8 and 23.9.

The experimental conditions of one cycle controlled APF are as follows: The phase voltage of the grid is 169.70 Vrms, the APF dc-link voltage is about 400 V; the input impedance is 0.4 mH; the filter inductance is 0.25 mH; the switching frequency is about 60 Hz. The THD of load current is about 16.02 %. After compensation, the THD of the line current decreased to 2.95 %. The same active power filter is verified by using PWM control. The THD of load current for PWM control is about 15.73 %. After compensation, the THD of the line current decreased to 7.81 %.

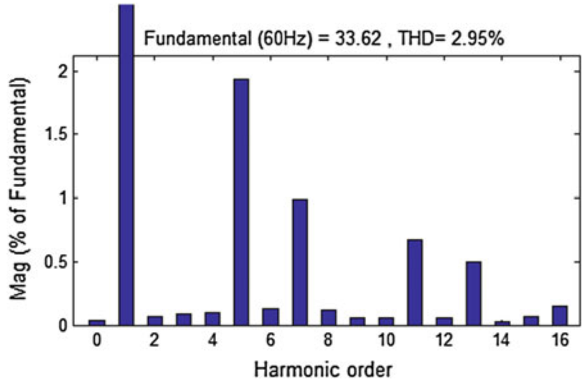

Fig. 23.8 Harmonic spectrum of phase A current using one cycle control

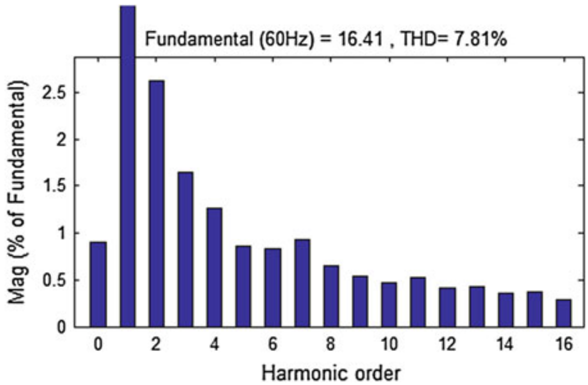

Fig. 23.9 Harmonic spectrum of phase A current using PWM control

From the results obtained, we can demonstrate that the one cycle controller is best compared to PWM controller can effectively cancels the harmonics of the load and improve the power factor. The comparison is shown in the Table 23.3.

Table 23.3 Performance comparison of PWM, one-cycle controlled APF

Controller type	THD without active filter (%)	THD with active filter (%)	Power factor
PWM controller	15.73	7.81	0.98
One-cycle controller	16.02	2.95	0.9996

23.7 Conclusion

In this paper, a three-phase shunt APF with extended one-cycle control has been used. The control approach senses only the mains current and the zero crossing of grid voltage. In addition to this, there is no need to calculate the reference for APF inductor current so that the complicated digital computation is eliminated. The control approach employs constant switching frequency modulation that is desirable for industrial applications. The control circuit contains one integrator with reset along with several logic and linear components to achieve unity power factor in all three phases. This APF is connected in shunt with the nonlinear load; so that it provides harmonics and reactive power to cancel the harmonics generated by the nonlinear load or sources. This APF compensates for systems with multiple loads therefore, it is a cost effective solution. The same controlling was done using PWM controller and the simulation results were compared to choose the best controller. The simulation results have demonstrated that the one cycle control of shunt active power filter can effectively cancels the reactive and harmonic component of the load compared to PWM, so that all the three-phase line currents are near sinusoidal.

References

1. Technical guide No. 6—Guide to harmonics with AC drives-Abb publications
2. Akagi H (2006) Modern active filters and traditional passive filters. Bull Pol Acad Sci Tech Sci 54(3):255–269
3. Fujita H, Akagi H (1991) A practical approach to harmonic compensation in power systems-series connection of passive and active filters. IEEE Trans Ind Appl 21(6):1020–1025
4. Kuo H-H, Yeh S-N, Hwang J-C (2001) Novel analytical model for design and implementation of three-phase active power filter controller. IEE Proc Electr Power Appl 148(4):369–383
5. Smedley K, Zhou L (2001) Unified constant-frequency integration control of single phase active power filter. U.S. Patent 6 249 108, 19 June 2001

Chapter 24
Simulation of PWM Controlled Double Half Bridge Inverter for Partly Coupled Induction Cooking System

Nagarajan Booma, Sathi Rama Reddy and Vishnuram Pradeep

Abstract This paper presents a double half bridge resonant inverter for induction heating (IH) system composed of two partly coupled coils. Induction coils are electrically characterized by their electrical equivalents, usually a series RL circuit, where the inductance is determined by the magnetic energy stored in the system and the resistance is associated with the power dissipated in the load. Pulse width modulation based control strategy for double half bridge resonant inverter based power supply circuit is presented. The aim of this work is to simulate and obtain the electrical equivalent of the inductor system for accurate power study with two concentric coils by considering the frequency dependent eddy current losses associated with both the pan and the coil. This paper gives an idea about the in new control modes taking advantage of the coupling between coils in order to provide the target output power. The performed analysis includes the description of the operation and principle of the control strategy. The power converter system is designed and the simulation results are presented to prove the performance of the double half bridge inverter for partly coupled induction heating coil.

Keywords Double half bridge resonant inverter · Induction heating coil · High frequency AC (HFAC) power supply

24.1 Introduction

High frequency induction heating is widely used in many industrial and domestic applications. It uses high frequency electricity to heat materials that are electrically conductive. A large number of inverter topologies have been developed for different applications with power levels ranging from hundreds of watts to several megawatts for domestic and industrial applications [1–3]. Among them voltage-fed half bridge

N. Booma (✉) · S. Rama Reddy · V. Pradeep
Department of Electrical and Electronics Engineering, Jerusalem College of Engineering, Chennai 600100, Tamil Nadu, India
e-mail: booma_nagarajan@yahoo.com

C. Kamalakannan et al. (eds.), *Power Electronics and Renewable Energy Systems*, Lecture Notes in Electrical Engineering 326, DOI 10.1007/978-81-322-2119-7_24

inverters are used in medium power applications and high power applications. High frequency AC (HFAC) power supply for IH equipment's have the advantages like energy saving, high reliability and low electromagnetic noise.

Domestic induction cookers are becoming one of the most popular appliances due to their high efficiency, speed, safety, and cleanliness compared with the other alternatives based on gas or electric heating [4–8]. Basically, an induction cooker consists of three or four burners in order to have the possibility of independent heating up this number of pots. The burners are composed of an inductor system fed up by a power converter, generally a single switch, a half-bridge or a full-bridge resonant inverter, in order to create an alternating current through the coil. The purpose of the inductor system is to create a variable electromagnetic field which heats up the pot placed above by means of eddy currents and hysteresis losses. Single coil inductor systems are electrically characterized by their equivalent impedance Z_{coil} which consists of the inductive term L_{coil} and the resistive contribution R_{coil}. The equivalent impedance is therefore represented as a series RL circuit [9]. However, the equivalent impedance $Z_{coil(\omega)}$ depends on the angular frequency ω of the current due to the properties of the induced current in the metallic work piece [10, 11]. In order to take into account of this phenomena, the electrical equivalent of a multi-coil system can be extended by means of the impedance matrix representation $Z_{coil(\omega)}$, where each term $Z_{ij(\omega)}$ establishes the relationship between the harmonic induced voltage $V_{coil,j(\omega)}$ in the coil j, and the amplitude of the harmonic intensity $I_{o,i(\omega)}$ carried by the coil I.

The above literature does not deal with the in phase and out of phase control of double half bridge inverter fed partly coupled induction cooking system. This paper presents the Simulink model for the above system. The paper discusses the power control of dual coil induction heating system using double half bridge inverter circuit. Power control of the load is achieved using the in phase and out of phase operation of the inverters.

This paper is organized as follows: The Sect. 24.2 presents modelling of induction heating load and Sect. 24.3 describes the system configuration and its operation. The basic control strategy is explained in Sect. 24.4. Finally the simulation results are given in Sect. 24.5 and conclusion of the paper is outlined in Sect. 24.6.

24.2 Modeling of IH Load

Single coil inductor systems are electrically characterized by their equivalent impedance constituting resistance depicting the power dissipation with respect to coil magnetically coupled with work piece and the inductance of the coil. The electrical equivalent of a multi-coil system can be extended by means of the impedance matrix representation $Z_{coil\ (\omega)}$. In the model of equivalent network, the diagonal terms are associated with the isolated coil equivalent impedances, as it is proposed in, whereas the equivalent networks of the off-diagonal terms correspond to the coupling terms relating non self-induced voltages with the current flowing through each coil.

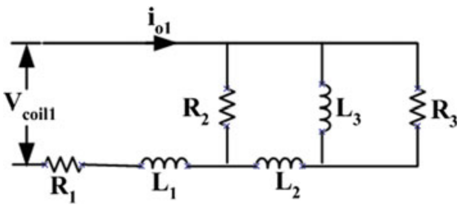

Fig. 24.1 Equivalent circuit of IH load

$$z_{coil}(\omega) = \begin{bmatrix} z_{coil,1}(\omega) & z_c(\omega) \\ z_c(\omega) & z_{coil,2}(\omega) \end{bmatrix} \tag{24.1}$$

The equivalent impedance matrix of the IH load is shown in Eq. 24.1 and respective equivalent circuit is shown in Fig. 24.1. Assuming the harmonic dependence at angular frequency of the signals, the impedance matrix establishes the relationship between the current values and the induced voltages in the coils, as it appears in the following expression

$$\begin{bmatrix} V_{coil,1}(\omega) \\ V_{coil,2}(\omega) \end{bmatrix} = \begin{bmatrix} z_{coil,1}(\omega) & z_c(\omega) \\ z_c(\omega) & z_{coil,2}(\omega) \end{bmatrix} * \begin{bmatrix} I_{a,1}(\omega) \\ I_{a,2}(\omega) \end{bmatrix}. \tag{24.2}$$

24.3 System Configuration and Circuit Description

24.3.1 System Configuration

Figure 24.2 shows the general block diagram of the induction heating power supply system, where it may be seen that the required input power is supplied by high

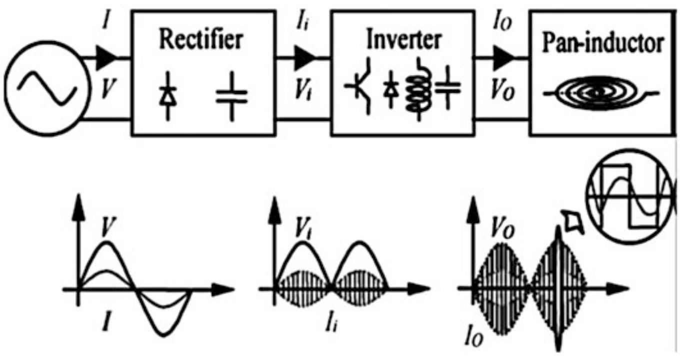

Fig. 24.2 Block diagram of the IH power supply system

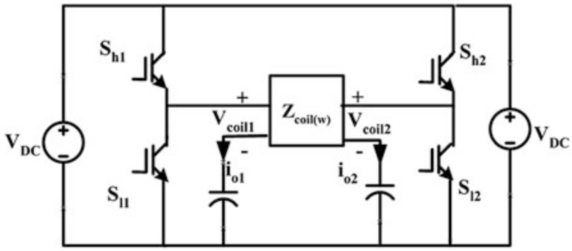

Fig. 24.3 Power circuit topology

frequency inverter which is of the voltage source load resonant type. Induction heater takes the energy from the mains which is rectified by diode bridge rectifier. Rectified DC is switched to high frequency AC through resonant inverter. The inverter supplies high frequency current to the coil.

24.3.2 Power Converter Topology

The circuit configuration of utility frequency to high frequency soft switching power conversion circuit for IH application is shown in Fig. 24.3. It may be seen that the output power is controlled by a double half bridge inverter and that the inverter is of the voltage source resonant type load. IGBTs are used as power switches in the inverters supplying two coils. The load is modeled as Z_{coil}.

24.4 Control Strategy

Power regulation is the important goal to be achieved in an induction heating load to maintain the required temperature. The power input to the working coil of IH load has to be controlled to control the heating of the work piece. It is achieved by control of both the inverters using the PWM technique in this paper. The output power *is* the mean instantaneous power during a switching period T_s. The instantaneous power is defined as the product between the output inverter voltage and the inverter current. Alternatively, the instantaneous power can be expressed as the product between the coil voltage and the output inverter current, because the resonant capacitors are assumed ideal devices without losses. The output powers inversely depends on the switching frequency in both inverters, but different outputs power are observed depending on the phase-shift ϕ between inverters because the output power is higher in the opposite-phase than in the in-phase. The output power also depends on the duty cycle of the pulses applied to the inverter, because the total power decreases when the duty is lower.

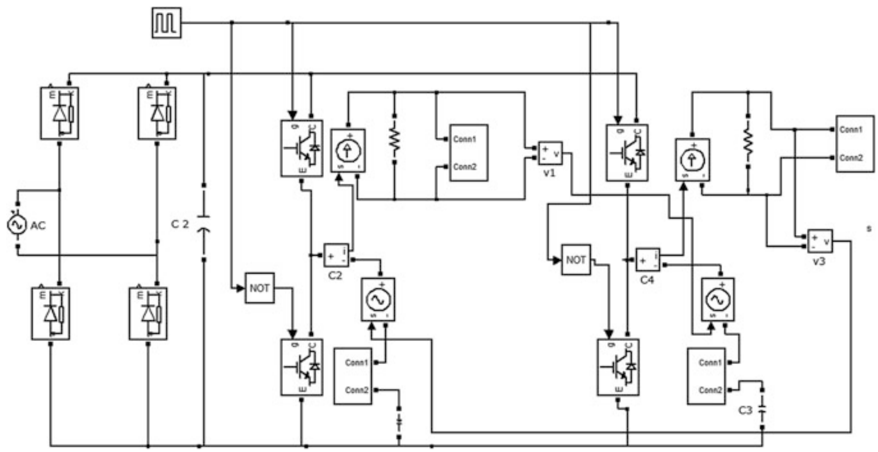

Fig. 24.4 Simulation circuit of the proposed converter topology

24.5 Results and Discussions

HFAC power conversion circuit is designed. Modeling is done using MATLAB Simulink. The simulation results are presented here to study the power control of inverter in in phase and out of phase operation.

24.5.1 In Phase Operation of the Inverters

The Simulink model of PWM controlled Double half bridge inverter is shown in Fig. 24.4. Simulation is carried out for an IH load of 3.4 kW with an input voltage of 230 V. The design parameters are as follows: $c_2 = 50\ \mu F$, $R_1 = 0.86\ \Omega$, $R_2 = 1.35\ \Omega$, $R_3 = 6.83\ \Omega$, $L_1 = 0.5$ mH, $L_2 = 3.13$ mH, $L_3 = 0.53$ mH.

Matlab results are shown in Fig. 24.5. The output AC voltage across two coils, current flowing through two coils and output power with respect to coil1 and coil2 and total output power of the simulation without phase difference between inverters are shown in Fig. 24.5a–d respectively. The output power obtained with PWM control for the high frequency power conversion circuit using double half bridge inverter is 3.4 kW, by considering the frequency dependent eddy current losses and the associated leakage flux with respect to both pan and coil.

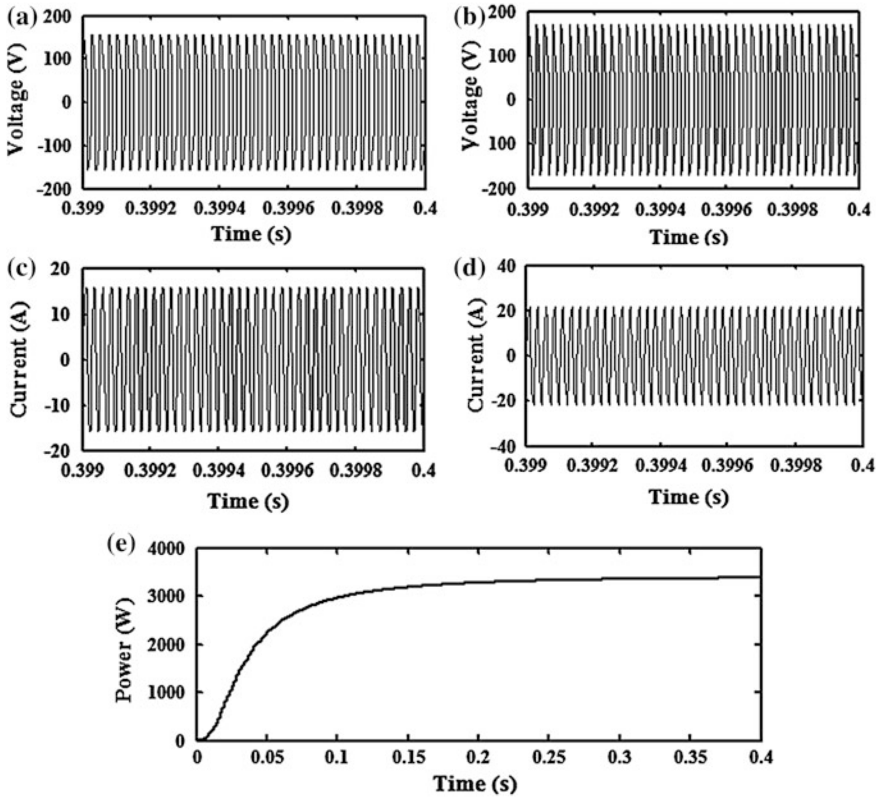

Fig. 24.5 Simulation results for inverter with in phase operation. **a** Output voltage across coil 1. **b** Output voltage across coil 2. **c** Output current through coil 1. **d** Output current through coil 2. **e** Total output power

24.5.2 Out of Phase Operation of the Inverters

The output power obtained with PWM control for the high frequency power conversion circuit using double half bridge inverter system with phase shift is found to be greater than the inverters in phase to each other. The simulation results shown in Fig. 24.6 are obtained for 50 % pulse width. If the pulse width increases obviously the output power increases.

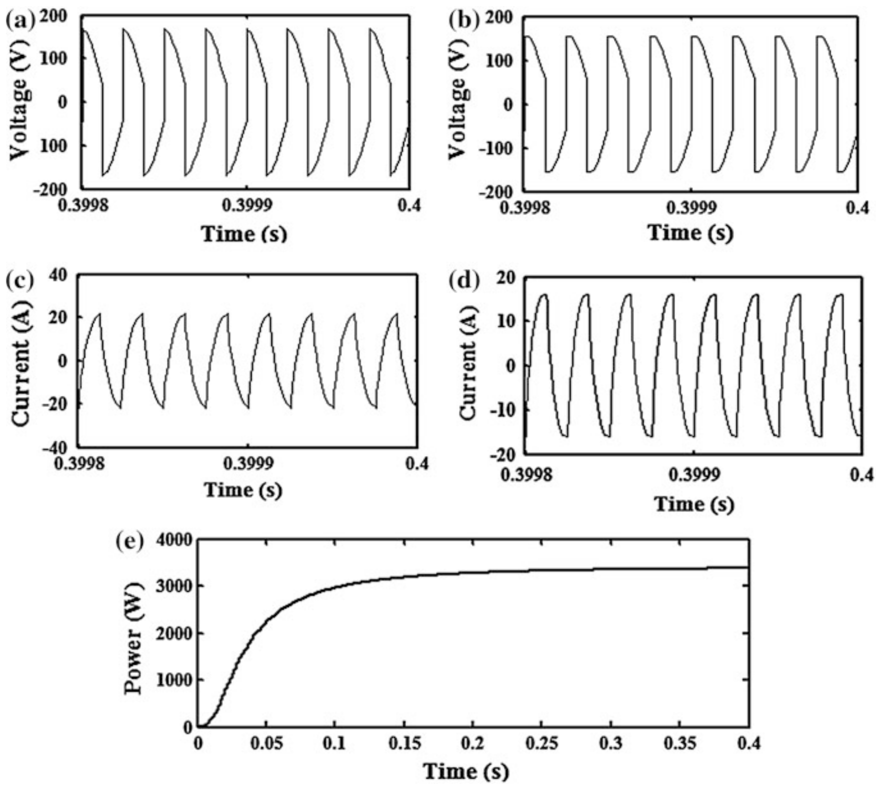

Fig. 24.6 Simulation results with out of phase operation. **a** Output voltage across coil 1. **b** Output voltage across coil 2. **c** Output current through coil 1. **d** Output current through coil 2. **e** Total output power

24.6 Conclusion

In this paper, the description of an inductor system composed of two partly coupled coils is performed. HFAC power supply circuit for induction heating has been designed and simulated. The power converter and the coupling of the inductors have been analytically studied for detailed output power analysis. The circuit topology and its control are very simple. The switches are operated in with the constant switching frequency. In addition to PWM control of inverter switches, the output power of the induction system is varied due to the out of phase operation of the half bridge inverters without varying the switching frequency. The simulation results are line with the predictions.

References

1. Acero J, Burdio JM (2009) Domestic induction appliances: an overview of recent research. IEEE Ind Appl Mag 16(2):39–47
2. Saha B, Kwon SK, Ahmed N, Omori H (2008) Commercial frequency AC to high frequency AC converter with boost active clamp bridge single stage ZVS-PWM inverter. Proc IEEE Trans Power Electron l23(1)
3. Sarnago H, Lucia O, Mediano A, Burdio JM (2014) Direct ac-ac resonant boost converter for efficient domestic induction heating applications. IEEE Trans Power Electron
4. Burdio JM, Garcia JR, Barragan LA (2005) A two output series resonant inverter for Induction heating cooking applications. Proc IEEE Trans Power Electron 20(4):815–822
5. Millian I, Acero J, Burdio JM, Lucia O, Llorente S (2011) Series resonant inverter with selective harmonic operation to all metal domestic induction heating. Proc IET Power Electron 4(5):587–592
6. Lucia O, Acero J, Carretero C, Burdio JM (2013) Induction heating appliances: towards more flexible cooking surfaces. IEEE Indus Electron Mag
7. Ogiwara H, Gamage L, Nakaoka M (2011) Quasi resonant soft switching PWM voltage-fed high frequency inverter using SIT for induction heating applications. IEEE Proc Electron Power Appl 148(5) 385–392
8. Ogiwara H, Itoi M, Nakaoka M (2011) ZCS High frequency inverter for induction heating applications. IEE Proc Electr Power Appl 150(2):185–192
9. Lucia O, Burdio JM, Millan I (2009) Load adaptive control algorithm of half-bridge series resonant inverter for domestic induction heating. IEEE Trans Ind Electron 56(8)
10. Sarnago A, Mediano A, Lucía O (2012) High efficiency ac-ac power electronic converter applied to domestic induction heating. IEEE Trans Power Electron 27(8):3676–3684
11. Kwon YS, Yoo SB, Hyun DS (2011) Half-bridge series resonant inverter for induction heating applications with load adaptive PFM control strategy. IEEE Trans Power Electron 20(4)

Author Biographies

Booma. N is a research scholar in Electrical and Electronics Engineering Department, center for collaborative research with Anna University Jerusalem College of Engineering. Her research interests include resonant inverters for induction heating and intelligent controllers.

Rama Reddy. S is professor in the Department of Electrical and Electronics Engineering, Center for collaborative research with Anna University, Jerusalem College of Engineering. His research interests include the areas of resonant converters and FACTS.

Pradeep. V is currently pursuing M.E degree in Power Electronics and Drives from Jerusalem college of Engineering, center for collaborative research with Anna University. His interests include resonant converters for induction heating, intelligent controllers and high Power factor rectifiers.

Chapter 25
Maximum Power Point Tracking of Photovoltaic System Using Two Input and Two Output Fuzzy System

Luckey Chouksey, P. Akash Pattanaik and R.K. Saket

Abstract This paper presents a new intelligent method to track the maximum power point of a photovoltaic system under variable irradiance and temperature conditions using Fuzzy control logic. The system mainly consists of a photovoltaic panel, boost converter and fuzzy controller. The fuzzy control used in the system uses a rate of change of power (error) and change in error as the inputs to get the optimum reference voltage and optimum duty cycle to track the maximum operating point. This method assures fast tracking of a maximum power point with a high accuracy and the results is verified by using simulation.

Keywords MPPT · Two input two output fuzzy controller · Photovoltaic panel

25.1 Introduction

Energy is the main concern of the modern life. As the fossil fuels are extinguishing rapidly from the earth, the demand of renewable energy is increasing day by day. The most effective among all renewable energy is the solar energy. Solar energy can be produced by using Photovoltaic panel but the major concern is the efficiency of producing the solar energy. Hence to overcome this problem and to get the maximum possible efficiency, the design of all the elements of the PV system has to be optimized.

L. Chouksey (✉) · P.A. Pattanaik · R.K. Saket
Department of Electrical Engineering, Indian Institute of Technology
(Banaras Hindu University), Varanasi 221005, Uttar Pradesh, India
e-mail: lcluckrock@gmail.com

P.A. Pattanaik
e-mail: akash.eee12@itbhu.ac.in

R.K. Saket
e-mail: rksaket.eee@itbhu.ac.in

C. Kamalakannan et al. (eds.), *Power Electronics and Renewable Energy Systems*,
Lecture Notes in Electrical Engineering 326, DOI 10.1007/978-81-322-2119-7_25

The Efficiency optimization is achieved by using the MPPT controllers. Therefore, these MPPT controllers are becoming the major integral part of PV system. Many MPPT techniques had been discussed in the past such as the incremental conductance technique or the perturbation and observation (P&O) technique [1, 2]. Currently many intelligent control techniques have been introduced. One of the most important intelligent technique i.e. Fuzzy Logic control technique is discussed in this paper for achieving the Maximum Power point.

25.2 Mathematical Modeling of PV Panel

PV Panel can be built by combining several solar cells in series and parallel and hence a solar cell is the basic element for building the PV panel. A single solar cell can be modeled by utilizing a current source, a diode and two resistors. The model shown in the Fig. 25.1 is known as a single diode model of solar cell [3–6].

The characteristic equation for a photovoltaic cell is given by Eqs. (25.1)–(25.6) [3].

$$I = (Iph^{*}Np) - Id - Ish \tag{25.1}$$

$$Id = Is\ [\exp\{(V + (I^{*}Rs))/(n^{*}c^{*}Vt^{*}Ns)\} - 1] \tag{25.2}$$

$$Ish = \{V + (I^{*}Rs)/Rp\} \tag{25.3}$$

$$Iph = Irr[Isc + \{Ki(Top - Tref)\}] \tag{25.4}$$

$$Irs = Isc/[\{\exp(Voc/(Vt\ ^{*}c^{*}Top)) - 1\}] \tag{25.5}$$

$$Is = \{(Top/Tref\ )3^{*}Irs\}^{*}[\exp\{(1/Top) - (1/Tref\ )\}^{*}\{(q2^{*}Eg\ )/(\ n^{*}K\ )\}] \tag{25.6}$$

where,

Iph: light generated photovoltaic current; Np: number of modules in parallel
Id: diode current; Ish: current through shunt resistor;

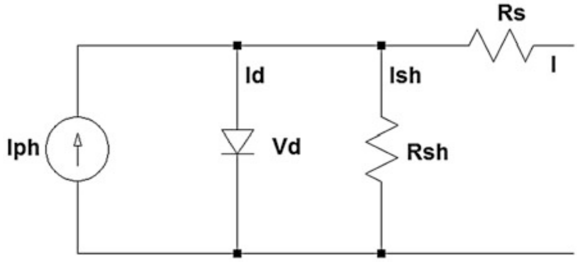

Fig. 25.1 Single diode model of a solar cell

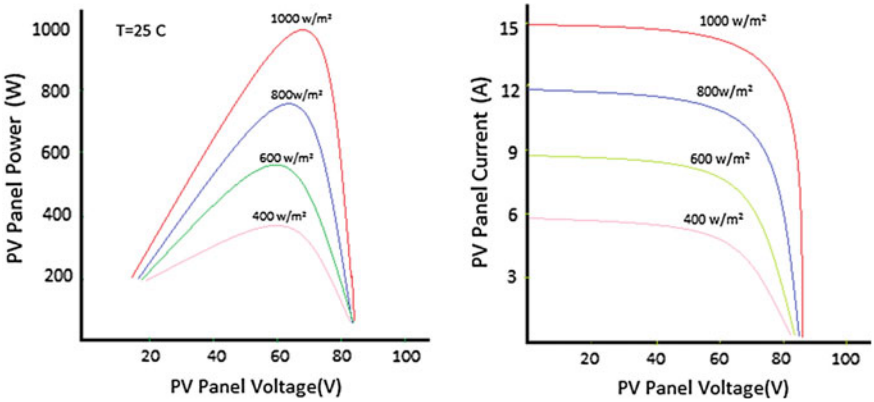

Fig. 25.2 PV and IV under varying irradiance conditions

Is: Reversed saturation current of diode; V: load or output PV voltage
I: load or output PV current; n: quality or ideality factor = 1.36 (1 ~ 2)
c: number of cells in a module = 36; Rs: series resistance; Rp: parallel resistance
Irr: ratio of irradiance; Ki: short circuit current temperature coefficient
Top: operational temperature; Tref: reference or standard temp. = (25 + 273.15) K
Isc: short circuit current; Voc: open circuit voltage
Vt: thermal voltage; c: number of cells in a module = 36
Irs: reverse saturation current at operational temperature;
q: charge of electron = 1.6×10^{-19} C; Eg: band energy gap for silicon = 1.12 eV
K: Boltzmann's constant = 1.38×10^{-23} J/K

The characteristics curve of PV Panel under different temperature and radiation is shown in the Figs. 25.2 and 25.3.

25.3 An Overview on DC–DC Boost Converter

Boost converter steps up the input voltage magnitude to a required output voltage magnitude without the use of a transformer. The main components of a boost converter are an inductor, a diode and a high frequency switch (MOSFET or IGBT). Due to high frequency switching and energy storage, power is supplied to the load at a voltage greater than the input voltage magnitude. The control strategy lies in the manipulation of duty cycle of the switch which causes the voltage to change [7, 8].

The output voltage is greater than the input voltage and is expressed as:

$$\mathrm{Vout} = \frac{1}{1 - \mathrm{D}} \mathrm{Vin} \tag{25.7}$$

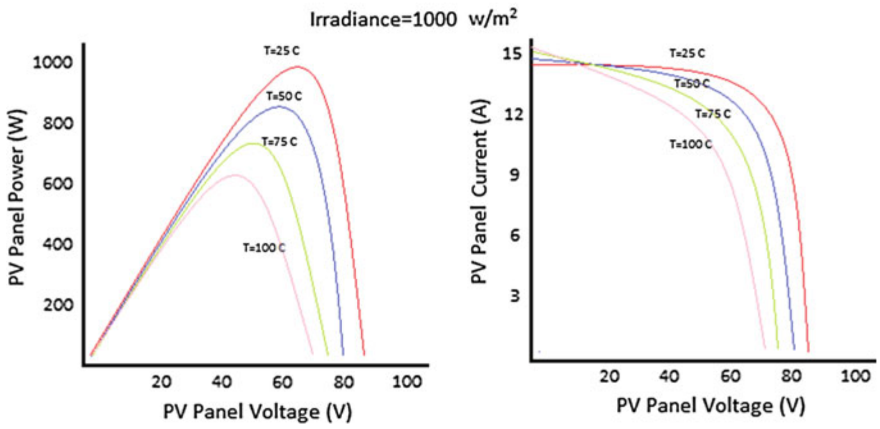

Fig. 25.3 PV and IV under varying temperature conditions

25.4 Maximum Power Point Techniques

The PV Panel has a non linear characteristics curve of Power versus voltage under varying conditions. As seen from the Figs. 25.2 and 25.3 that the maximum power point moves with the change in irradiance and temperature. To overcome this problem, it is obligatory to add an adaptation device, MPPT controller with a DC–DC Boost converter, between the load and the source. Many MPPT techniques have been evolved to conquer this problem [1, 2, 9, 10].

Maximum Power Point Techniques are Constant voltage control, Constant current control, Perturb and observe algorithm, Incremental conductance algorithm, parasitic capacitances, and artificial intelligent method. (Fuzzy logic control, neural network…)

25.5 Proposed MPPT Fuzzy Logic Controller

The Fuzzy logic controller is an intelligent controller which embeds the experience and hunch of a human plant operator. The conventional control technique depends upon the mathematical model, which in real life it is difficult to implement as the parameters changes abruptly. Hence a new Fuzzy Logic Controller is designed which uses the intelligent feedback concept to get a fast and precise output. In this MPPT technique a feedback reference voltage is given to the PV Panel so it can easily and quickly track the desired photovoltaic voltage and the duty cycle is feed to the boost converter so our PV panel operates at the MPPT point. Hence the two output of the fuzzy controller is change in reference voltage (ΔVref) and change in duty cycle (ΔD) and the input to the fuzzy controller is Error, E(k) and change in Error CE(k). The input variables for the Fuzzy Logic controllers can be calculated as

$$\mathrm{E(k)} = \frac{\Delta \mathrm{P}}{\Delta \mathrm{V}} \text{ or } \frac{\Delta \mathrm{P}}{\Delta \mathrm{I}}. \tag{25.8}$$

$$\mathrm{CE(k)} = \mathrm{E(k)} - \mathrm{E(k-1)} \tag{25.9}$$

where V is the output voltage from PV Panel, I is the output current from PV Panel and P is the output power from PV Panel

$$\mathrm{V} = \mathrm{V(k)} - \mathrm{V(k-1)} \tag{25.10}$$

$$\Delta \mathrm{I} = \mathrm{I(k)} - \mathrm{I(k-1)} \tag{25.11}$$

$$\Delta \mathrm{P} = \mathrm{P(k)} - \mathrm{P(k-1)} \tag{25.12}$$

The feedback reference voltage and duty cycle can be given as

$$\mathrm{Vref(k)} = \mathrm{Vref(k-1)} + \mathrm{Vref} \tag{25.13}$$

$$\mathrm{D(k)} = \mathrm{D(k-1)} + \mathrm{D} \tag{25.14}$$

The Fuzzy Controller is divided into three stages i.e. Fuzzification, Fuzzy Rule Base and Defuzzification [11–13].

25.5.1 Fuzzification

When the crisp set convert into the fuzzy set, the process is called the Fuzzification. Hence crisp values convert into the Linguistic variables. The membership function of input variables E(k) and ΔE(k) both have seven subsets. The membership function of output variable (ΔVref) and ΔD both have seven subsets. The Linguistic variables for Input and output variables such as BN (Big Negative), MN (Medium Negative), SN (Small Negative), Z (Zero), SP (Small Positive), MP (Medium Positive), BP (Big Positive) is basic fuzzy sets. The Membership function is denser at the centre in order to get the precise output at MPP. The linguistic variables for the Input and Output variables are shown in Figs. 25.4 and 25.5.

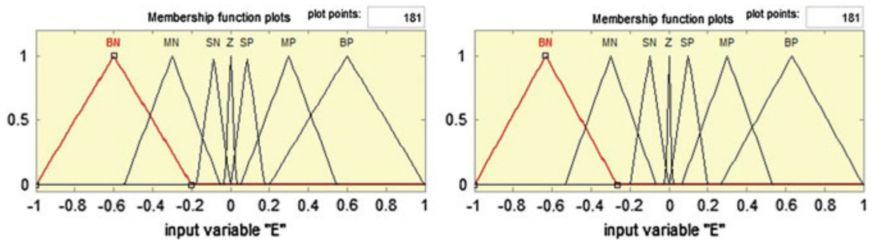

Fig. 25.4 Membership function of input variables ‘E’ and ‘CE’

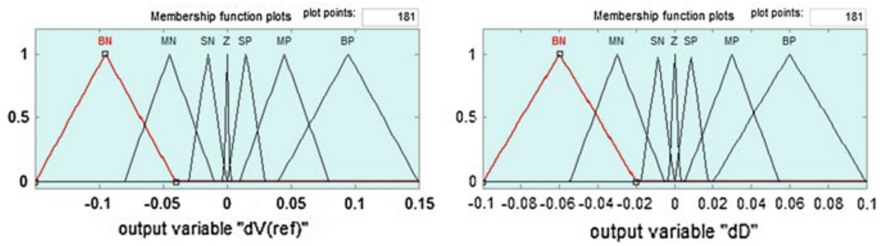

Fig. 25.5 Membership function of output variables ‘dVref’ and ‘dD’

25.5.2 Fuzzy Rule Base

By Using the Membership function a fuzzy rule base is developed such that it calculate the output Vref and D based on the magnitude of input variables E(k) and E(k) to operate PV Panel at MPP. The Rule base table for dVref and dD is given in Tables 25.1 and 25.2. The rule base is expressed as follows: “If (E is BN) and (CE is MN) then (dVref is BN) (dD is Z)”. Max–Min fuzzy combination operator of Mamdani’s fuzzy inference system (FIS) is used in this paper.

25.5.3 Defuzzification

The process of converting fuzzy sets into crisp single value is called Defuzzification. Many methods of Defuzzification are available such as bisector of area, mean value of maximum, smallest (absolute) value of maximum, largest (absolute) value of maximum but in this paper Centroid method is used.

Table 25.1 Rule base table for dVref

E CE	BN	MN	SN	Z	SP	MP	BP
BN	BP	BP	MP	Z	MN	BN	BN
MN	BP	MP	SP	Z	SN	MN	BN
SN	MP	SP	SP	Z	SN	SN	MN
Z	BN	MN	SN	Z	SP	MP	BP
SP	MN	SN	SN	Z	SP	SP	MP
MP	BN	MN	SN	Z	SP	MP	BP
BP	BN	BN	MN	Z	MP	BP	BP

Table 25.2 Rule base table for dD

E CE	BN	MN	SN	Z	SP	MP	BP
BN	Z	Z	SN	MN	MP	MP	BP
MN	Z	Z	Z	SN	SP	MP	BP
SN	Z	Z	Z	Z	SP	MP	BP
Z	BN	MN	SN	Z	SP	Z	Z
SP	BN	MN	SN	Z	Z	Z	Z
MP	BN	MN	SN	SP	Z	Z	Z
BP	BN	MN	SN	MP	Z	Z	Z

25.6 Simulation and Results

The Simulation of Fuzzy Logic Controller is shown in Fig. 25.6 and overall Simulation of PV system is shown in Fig. 25.7. The output plot of voltage and current is shown in the Fig. 25.8 under constant temperature (25 °C) while Irradiation changes from 1,000 to 600 W/m^2 at 0.5 s. In Fig. 25.9 the output curve of voltage and current is simulated for constant irradiation (1,000 w/m^2) while temperature changes from 25 to 125 °C at 0.5 s.

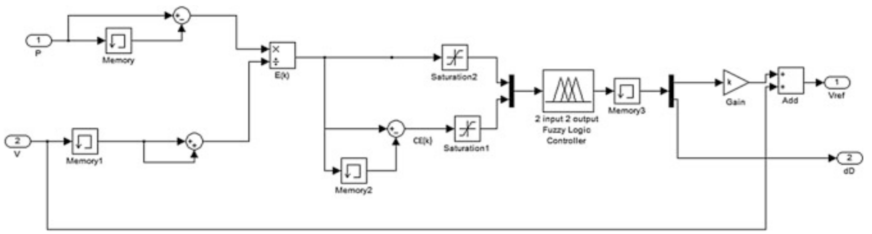

Fig. 25.6 Simulation of a two input two output fuzzy logic controller

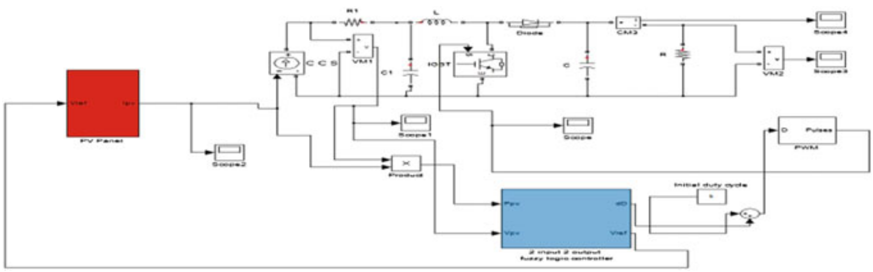

Fig. 25.7 Simulation of a PV system with two input two output fuzzy logic controller

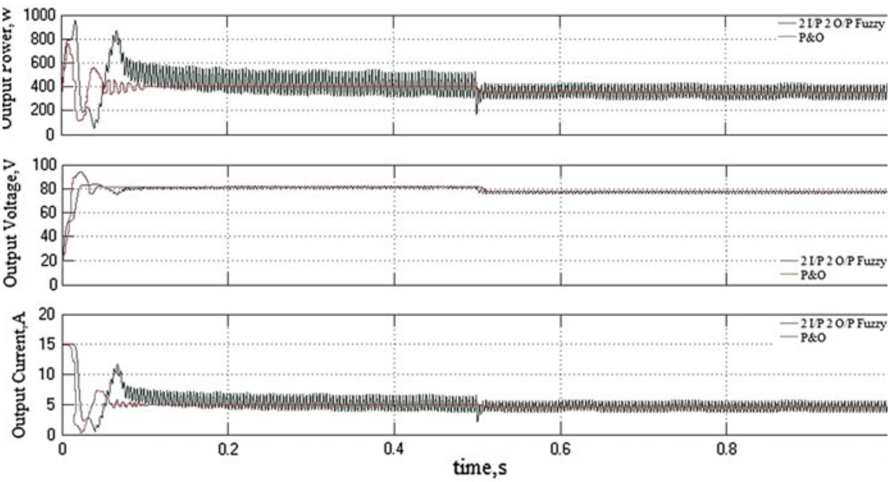

Fig. 25.8 Output of a two input two output fuzzy logic controller under varying irradiation

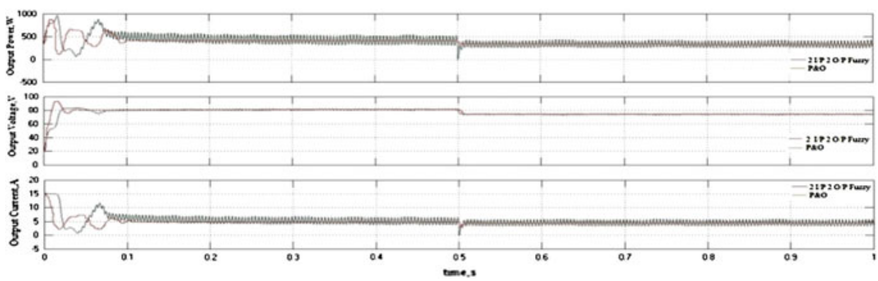

Fig. 25.9 Output of a two input two output fuzzy logic controller under varying temperature

25.7 Conclusion

In this paper, the new concept of two inputs and two outputs Fuzzy logic controller Maximum power point tracking is presented. The two inputs and two outputs fuzzy logic controller was formulated and tuned while the membership function for dVref and dD is designed using the Fuzzy Logic Toolbox in Matlab. Simulation results shows that due to feedback of reference voltage and the proper adjustment of duty cycle in two input two output Fuzzy logic controller. The oscillation present in the P&O method is removed and the stability is achieved.

References

1. Safari A, Mekhilef S (2011) Simulation and hardware implementation of IC MPPT with direct control method using Cuk Converter. IEEE Trans Ind Electron 58(4):1154–1161
2. Roshan R, Yadav Y, Umashankar S, Vijayakumar D, Kothari DP (2013) Modeling and simulation of incremental conductance MPPT algorithm based solar photo voltaic system using CUK converter. In: IEEE 2013: International conference on energy efficient technologies for sustainability (ICEETS)
3. Tsai HL, Tu CS, Su YJ (2008) Development of generalized photovoltaic model using MATLAB/SIMULINK. In: Proceedings of the world congress on engineering and computer science 2008 WCECS 2008, San Francisco, USA, 22–24 Oct 2008
4. Villalva MG, Gazoli JR, Ruppert E, (2009) Comprehensive approach to modeling and simulation of photovoltaic arrays. IEEE Trans Power Electron 25(5):1198–1208, ISSN 0885-8993
5. Ramos, Hernanz JA, Campayo Martín JJ, Zamora, Belver I, Larrañaga Lesaka J, Zulueta Guerrero E, Puelles Pérez E (2010) Modeling of PV module. In: International conference on renewable energies and power quality (ICREPQ'10) Granada (Spain), 23–25th Mar 2010
6. Sridhar R, Jeevananathan D, Selvan NT, Banerjee S (2010) Modeling of PV array and performance enhancement by MPPT algorithm. Int J Comput Appl (0975–8887) 7(5)
7. Verma AK, Singh B, Kaushik SC (2010) An isolated solar power generation using boost converter and inverter. In: Proceeding of national conference on recent advances in computational technique in electrical engineering, SLITE, Longowal, 19–20 Mar 2010
8. Kalirasu A, Dash SS (2010) Simulation of closed loop controlled boost converter for solar installation. Serb J Electr Eng 7(1):121–130
9. Ravikumar N, Kohila J (2013) Tracking maximum power point from photovoltaic system using fuzzy logic technique. In: Proceedings of 2013 IEEE conference on information and communication technologies (ICT 2013)
10. Esram T, Chapman PL (2007) Comparison of PV array maximum power point tracking techniques. IEEE Trans Energy Convers 22(2)
11. Bouchafaa F, Hamzaoui I, Hadjammar A (2011) Fuzzy logic control for the tracking of MPP of a PV system. Energy Procedia 6:633–642
12. Qiufeng J, Sujuan L, Hai-zhu Y (2010) Maximum power point tracking in photovoltaic system by using fuzzy algorithm. In: IEEE 2010: international conference on intelligent computing and cognitive informatics
13. Islam MA, Talukdar AB, Mohammad N, Khan PS (2010) Maximum power point tracking of photovoltaic arrays in matlab using fuzzy logic controller. In: Annual IEEE India Conference (INDICON)

Chapter 26
Performance of High Voltage Bushings Under Polluted Conditions

Avik Ganguly and R.S. Gorayan

Abstract Bushings are required for making transformer winding connections with the external circuit. Porcelain bushings are used upto 33 kV. The presence of a pollution layer on high voltage (h.v.) bushings is common in industrial and coastal regions. Flashover of bushings due to surface contamination is a major problem faced by power engineers. Because of these reasons, knowledge of Electric Field and Potential is important for its reliable performance in service. This paper presents the performance of h.v. bushings under polluted conditions. Integrated Engineering Software (IES) COULOMB, V8.0 has been used for carrying out the simulations.

Keywords Performance of high voltage bushings · Integrated engineering software (IES) COULOMB

26.1 Introduction

In the simplest form, a bushing consists of a current carrying conductor passing centrally through a hollow porcelain insulator. The space between the conductor and the insulator is filled with some dielectric, like oil or gas. One end of the bushing is fixed to the tank for mechanical reasons. Porcelain bushings are used upto 33 kV; and for higher voltages, the condenser bushing or oil-filled bushings are employed.

A lot of research [1–5] has been done on the pollution performance of suspension insulators. In this paper, the pollution performance of bushings has been

A. Ganguly (✉) · R.S. Gorayan
Department of Electrical Engineering, Indian Institute of Technology
(Banaras Hindu University), Varanasi 221005, Uttar Pradesh, India
e-mail: avikganguly2009@gmail.com

R.S. Gorayan
e-mail: rsgorayan.eee@itbhu.ac.in

C. Kamalakannan et al. (eds.), *Power Electronics and Renewable Energy Systems*,
Lecture Notes in Electrical Engineering 326, DOI 10.1007/978-81-322-2119-7_26

considered. The presence of a pollution layer on high voltage bushings is common in industrial and coastal regions. Such a layer of contamination becomes conductive when combined with moisture. Under this condition, a leakage current starts flowing. This causes heating effect, thus drying up some areas on the insulator surface leading to the formation of dry bands. High electric stresses across these dry bands cause the formation of arc and, finally leading to a flashover if the arc persists. Flashovers occur due to the distortion of Electric Fields and Potential around the bushing. Because of these reasons, computation of Electric Field and Potential is important. The performance of bushings under wet and contaminated conditions constitutes one of the guiding factors in the design and dimensioning of insulators.

Laboratory experiments may be helpful in calculating the Electric Field and Potential around h.v. bushings. However, computer simulation methods have become an essential tool, apart from laboratory methods, to do the same. There are certain numerical methods, with certain accuracy, like Charge Simulation Method, Boundary Element Method, Finite Element Method, Finite Difference Method, etc.

26.2 Pollution Severity of Insulators

The severity of contamination is expressed and classified in terms of the Equivalent Salt Deposit Density [5]. It is defined as the equivalent weight of dissolved salt in the wet contamination layer per unit area of the insulator surface. It's unit is mg/cm^2 (Tables 26.1 and 26.2).

Table 26.1 IEC 815 contamination severities

Pollution severity	Maximum ESDD (mg/cm^2)
(1) Light pollution	0.06
(2) Medium pollution	0.20
(3) Heavy pollution	0.60
(4) Very heavy pollution	Greater than 0.60

Table 26.2 Case studies

Case	Model	Description	Bushing details
A	A	The bushing sheds are absolutely horizontal	4 sheds, 0° inclination
B	B-1	Effect of inclination of the bushing shed at various angles with respect to the horizontal	Same as model "A", i.e., no inclination
	B-2		4 sheds, 15° inclination
	B-3		4 sheds, 30° inclination

26.3 Case Studies

In the present work, the pollution performance of a 33 kV transformer bushing has been studied and analyzed considering certain electrical and design aspects (Fig. 26.1).

26.3.1 Analysis of Model-A

The simple 2-D model is as follows. On the above model, certain critical points are marked as “A”, “B”, …, “N”. It is at these critical points wherein the study of

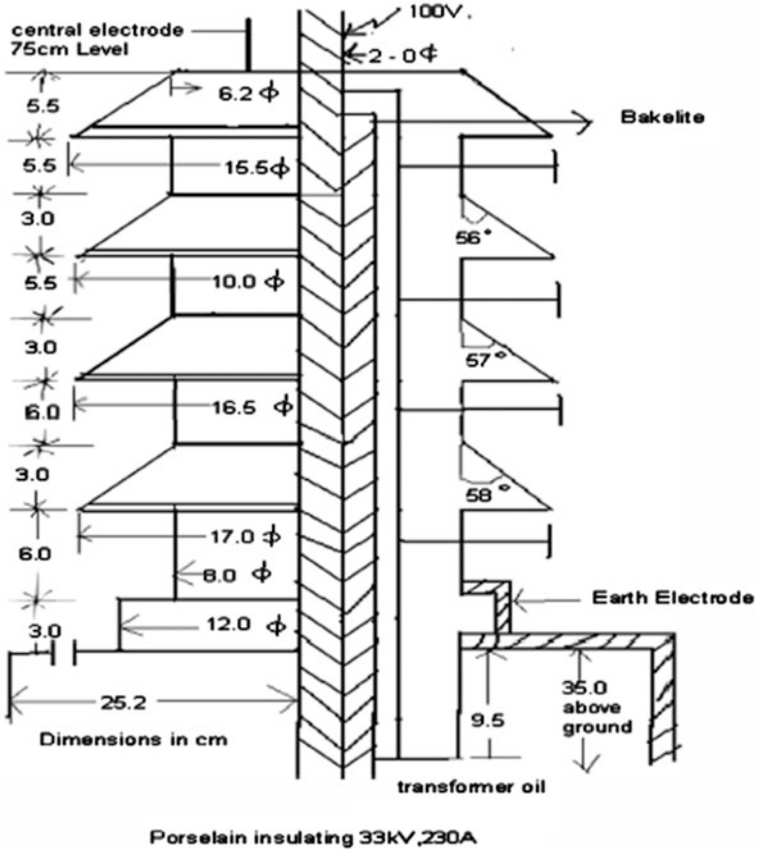

Fig. 26.1 Dimensions of the model used

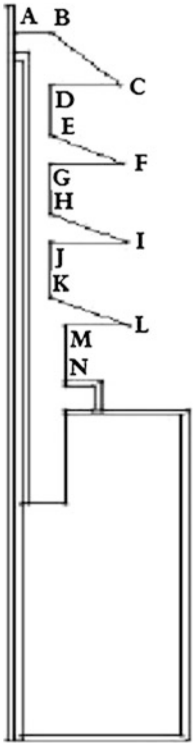

Fig. 26.2 Two-dimensional model developed in COULOMB software

Electric Field and Potential has been performed. The boundary condition is assigned in the following manner → 33 kV for the conductor, and 0 kV for the transformer tank (Figs. 26.2, 26.3 and 26.4).

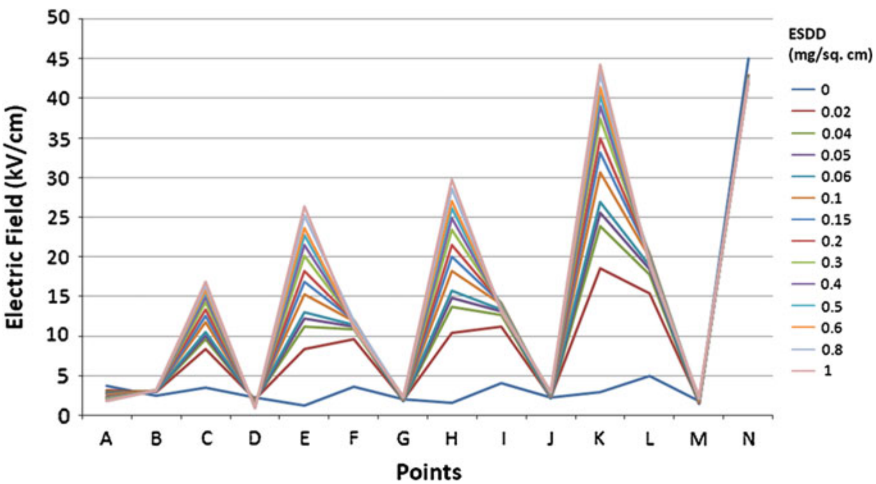

Fig. 26.3 Electric field along surface of model "A" for different pollution severities

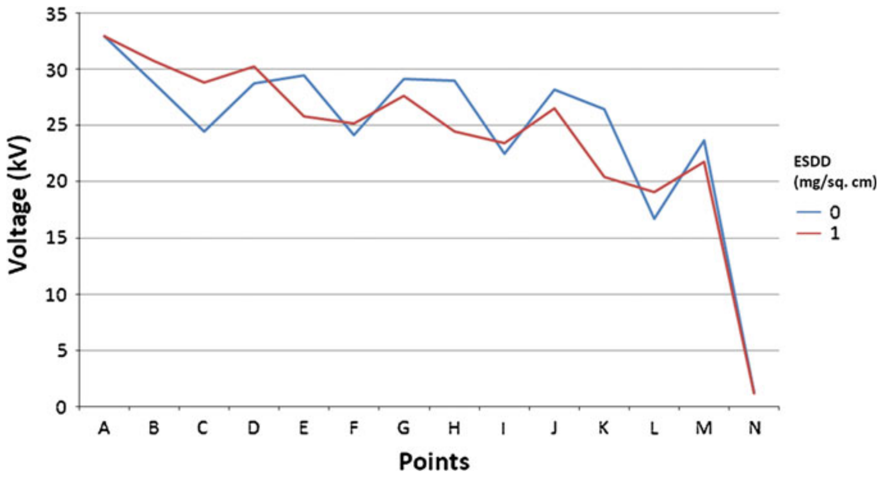

Fig. 26.4 Variation of Potential along surface for different pollution severities

It is seen that the maximum Electric Field occurs at point “N”. It is explained as follow. Electric Field (say, E) between 2 charged electrodes is related to their individual Potentials (say, V1 and V2) and the Distance (say, d) separating them by the equation:

$$E = (V1 - V2)/d, \tag{26.1}$$

Now, if the potential on one electrode is “V (kV)” while the other is grounded (i.e., 0 kV), then the electric field for the same spacing “d (cm)” will be:

$$E = V/d. \tag{26.2}$$

That is, for a constant value of “V”, the electric field is inversely proportional to the spacing between the 2 electrodes. In the model-A, among all the marked points, the spacing between the live conductor (of 33 kV) and the grounded transformer tank is the least at point “N”. Hence, the electric field at that point is the maximum.

26.3.2 Analysis of Model-B → Effect of Inclination of Sheds upon the Developed Electric Field

Herein, a design aspect of the transformer bushing has been considered. In the case of model-A, the undersurface of the bushing shed was modeled as horizontal. In this section, the effect of inclination of the undersurface of the bushing shed on the developed Electric Field has been studied. The critical points are still the same (Fig. 26.5).

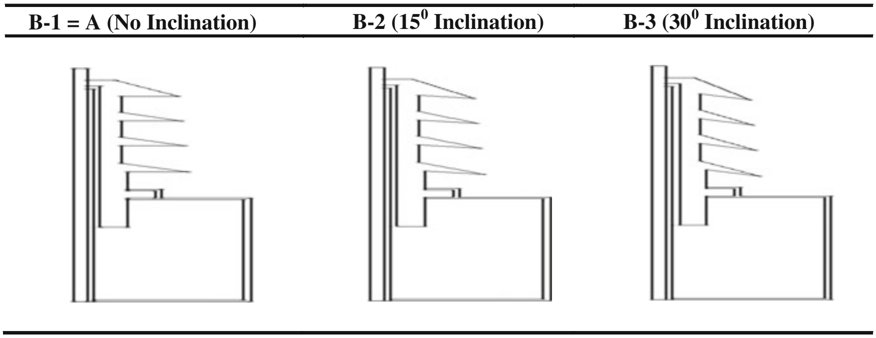

Fig. 26.5 Two-dimensional model developed in COULOMB software

Electric Field Analysis of Model "B-1"

The variation of electric field along the surface of model B-1 for different pollution severities will be the same as that for model "A", the reason is obvious.

Electric Field Analysis Of Model "B-2" (Fig. 26.6)

Electric Field Analysis Of Model "B-3" (Fig. 26.7).

26.4 Comparison of Various Models

Case: 1—No Pollution (ESDD = 0) (Fig. 26.8)

Case: 2—Light Pollution (ESDD = 0.04 mg/cm^2) (Fig. 26.9)

Case: 3—Medium Pollution (ESDD = 0.10 mg/cm^2) (Fig. 26.10)

Case: 4—Heavy Pollution (ESDD = 0.40 mg/cm^2) (Fig. 26.11)

Case: 5—Very Heavy Pollution (ESDD = 0.40 mg/cm^2) (Fig. 26.12).

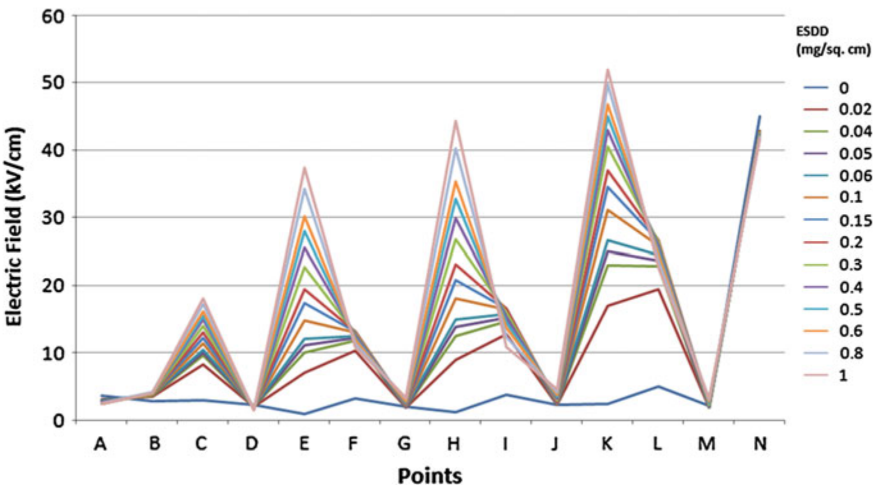

Fig. 26.6 Electric field along the surface of model "B-2" for different pollution severities

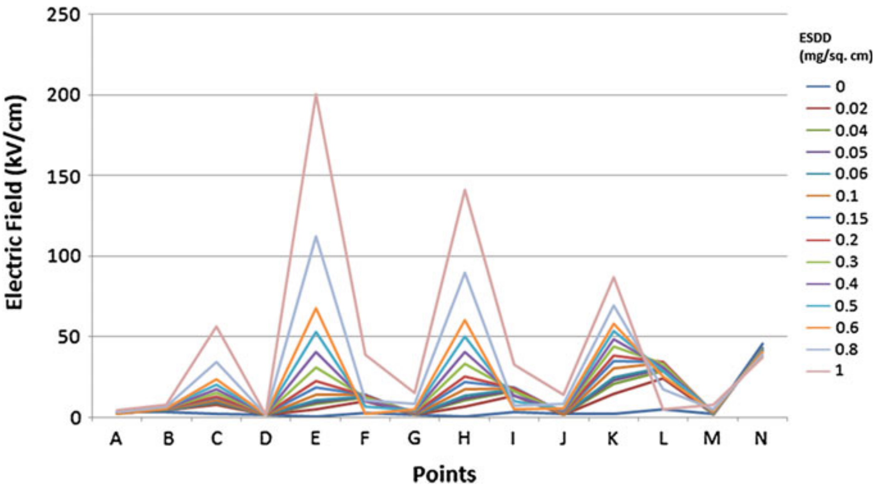

Fig. 26.7 Electric field along the surface of model "B-3" for different pollution severities

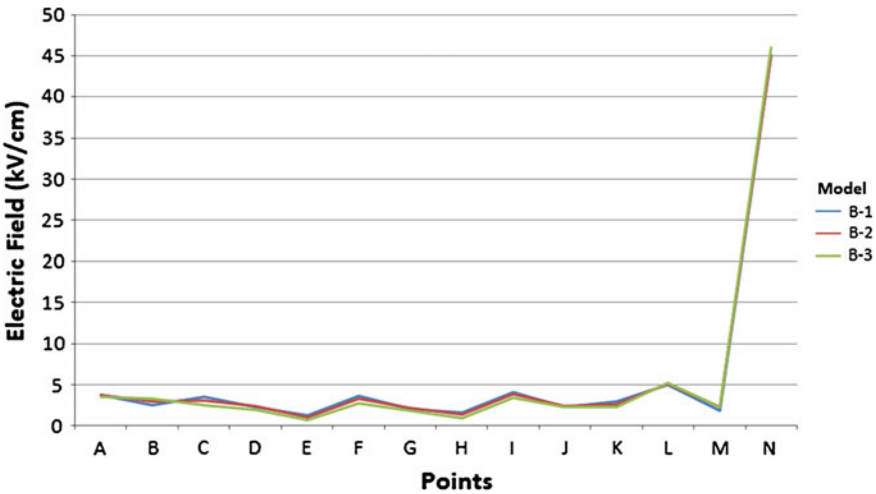

Fig. 26.8 Electric field along surface of various models when there is no pollution

From the above simulations and the comparison of various models, following points are noteworthy:

(a) There has been a substantial increase in the value of the electric field at point "K" (from around 2.5 kV/cm when there is no contamination to about

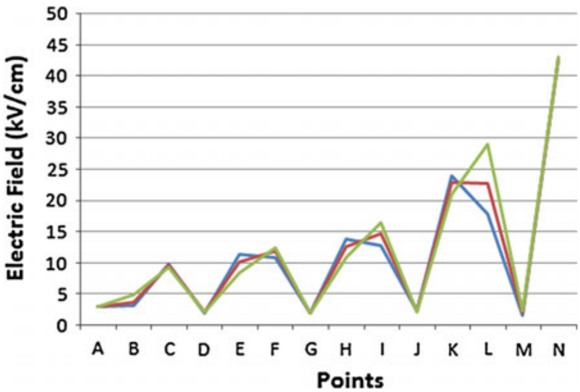

Fig. 26.9 Electric field along surface of various models for light pollution

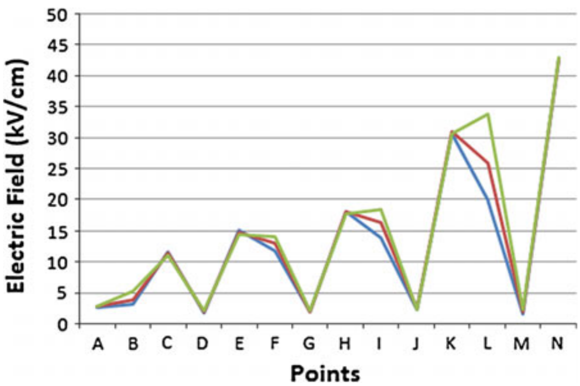

Fig. 26.10 Electric field along surface of various models for medium pollution

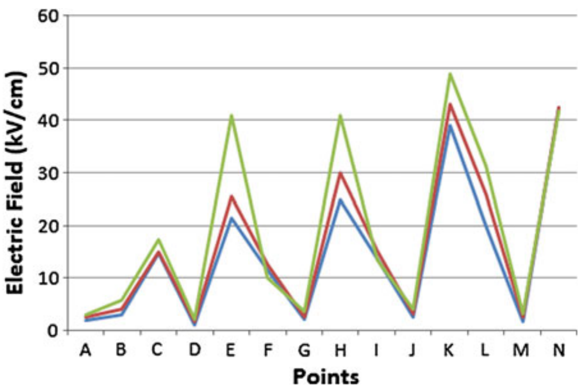

Fig. 26.11 Electric field along surface of various models for heavy pollution

75 kV/cm when there occurs very heavy pollution) and point "E" (from around 2 kV/cm to about 200 kV/cm). It is explained with reference to model "B-3".

At point "K", the voltage contour lines become closely packed as the contamination severity increases. The voltage contour plot actually represents the

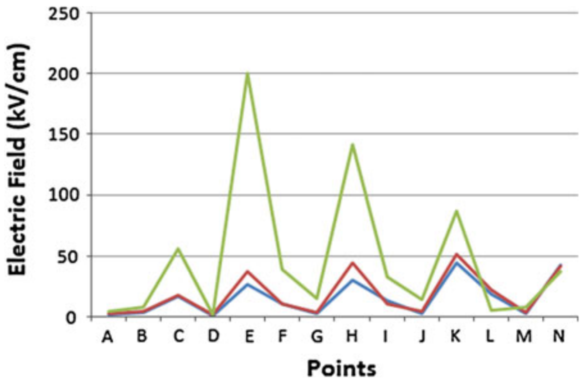

Fig. 26.12 Electric field along surface of various models for very heavy pollution

equipotential lines in and around the bushing. The Electric Field at any point, say "a", between 2 consecutive equipotential lines is given as:

$$E = -\Delta V/\Delta x. \tag{26.3}$$

Where $\Delta V \rightarrow$ voltage difference between the 2 lines near point "a".

$\Delta x \rightarrow$ distance between the 2 lines near point "a".

Referring to Fig. 26.13, it is seen that as the contamination severity increases, the equipotential lines becomes more closely packed successively. Thus, with the increase in contamination severity, the Electric Field at the above mentioned points increases.

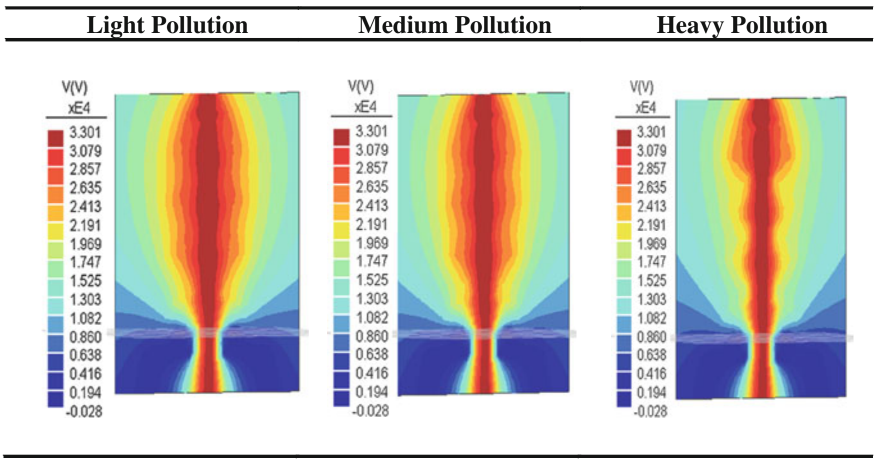

Fig. 26.13 Voltage contour plot of model B-3

(b) It is seen that at the same points, the developed Electric Field increases as the contamination severity increases.
(c) It is also seen that at the sharp points—C, F, I, and L—the Electric Field increases as the angle of inclination of the sheds increases. This is due to the increase in sharpness at these points.

26.5 Conclusion

In this work, the effect of contamination severity on the bushing surface has been simulated and analyzed for various models of bushings. The various results obtained are compared. These results depict the performance of h.v. bushings under polluted conditions—in terms of the maximum value of the electric field for a particular pollution severity, region experiencing maximum electric stress, etc.

Acknowledgments The authors are grateful to Dr. S. P. Singh, Professor and Head, Department of Electrical Engineering for providing necessary facilities for carrying out the research work.

References

1. Fazelian M et al (1989) A study on the profile of HVDC insulators, dc flashover performance. IEEE Trans Electr Insul 24(1):119–125
2. Ghosh PS, Chatterjee N (1996) Arc propagation over electrolytic surfaces under power frequency voltage. IEEE Trans Dielectr Electr Insul 3(4):529–536
3. Ghosh PS, Chatterjee N (1995) Polluted insulator flashover model. IEEE Trans Dielectr Electr Insul 2(1)
4. Mukherjee PK, Roy CK (1978) Computation of fields in and around insulators by fictitious point charges. IEEE Trans Electr Insul EI-13(1):24–31
5. Salam MA, Mohammad N, Nadir Z et al (2004) Measurement of conductivity and equivalent salt deposit density of contaminated glass plate 3:268–270. doi:10.1109/TENCON.2004.1414758

Chapter 27
Simulation of Static Var Compensator in IEEE 14 Bus System for Enhancing Voltage Stability and Compensation

M. Priyadhershni, C. Udhayashankar and V. Kumar Chinnaiyan

Abstract In this paper, a shunt flexible AC Transmission System (FACTS) device namely SVC (TSC-TCR type) is investigated. The modeling and simulation were carried out in MATLAB. Here the SVC is implemented in IEEE 5/14 bus system and the effects have been analyzed for various load conditions. Finally the results show that the SVC has accomplished the stability problems and considerable enhancement in voltage stability is achieved.

Keywords Static var compensator (SVC) · Flexible AC transmission systems (FACTS) · Thyristor switched capacitor · Thyristor controlled reactor · IEEE 5/14 bus · Voltage stability

27.1 Introduction

By switching the TCR's and TSC's in sequence, the output of the compensator can be controlled in steps. Rather than continuous control of reactors, stepwise switching can eliminate the need for harmonics filtering as part of the compensator scheme. A simple and easy design methodology of control namely, Proportional-Integral-Derivative (PID) controller, is used for significant improvements in system damping [1]. Based on the limit of minimum or maximum susceptance, SVC will behave as fixed capacitor or an inductor. By choosing the appropriate size of SVC, it finds prime importance in voltage stability enhancement applications. Figure 27.1 represents the single line diagram of SVC control scheme.

M. Priyadhershni (✉) · V. Kumar Chinnaiyan
Department of Electrical and Electronics Engineering, Dr. N.G.P. Institute of Technology, Coimbatore, Tamilnadu, India
e-mail: mpriya.ngpit@gmail.com

C. Udhayashankar
Department of Electrical and Electronics Engineering, Kumaraguru College of Technology, Coimbatore, Tamilnadu, India

C. Kamalakannan et al. (eds.), *Power Electronics and Renewable Energy Systems*, Lecture Notes in Electrical Engineering 326, DOI 10.1007/978-81-322-2119-7_27

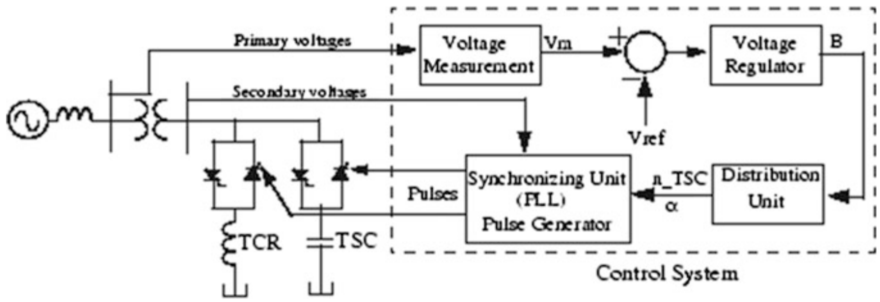

Fig. 27.1 SVC control structure

27.2 Test System Analysis

The test system consists of two synchronous machines. There are seven branches and five buses with four loads totaling 165 MW and 40 MVar [2]. The MATLAB Simulink diagram of IEEE 5 bus system without SVC is shown in Fig. 27.2.

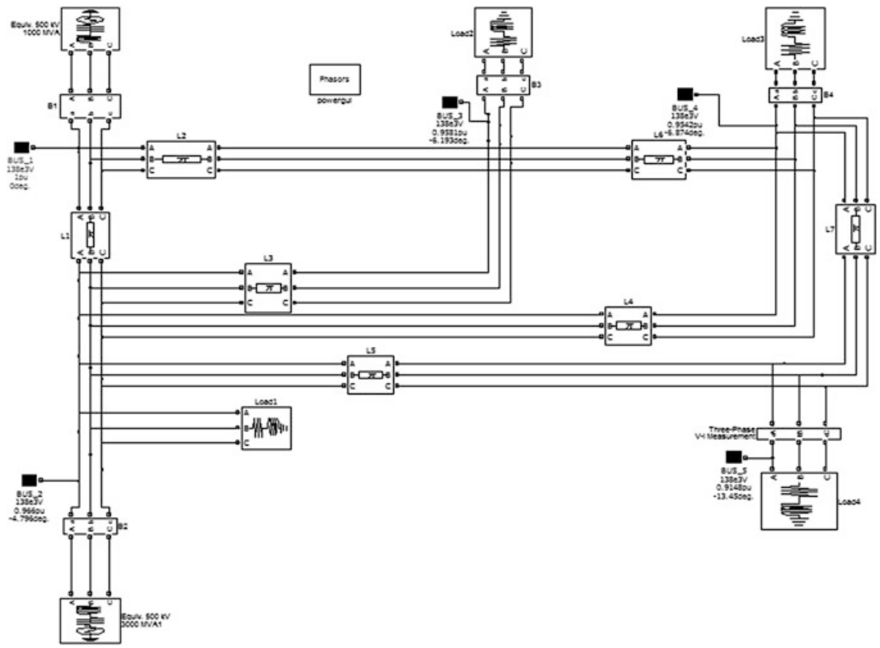

Fig. 27.2 MATLAB simulation diagram of IEEE 5 bus system

27.2.1 Load Flow Studies Without FACTS Device

In all the following cases only bus 5 is analyzed and discussed, since bus 5 is found to be the weakest bus [3, 4].

Case 1: In this case the real power and the reactive power are maintained the same. It is the normal condition and hence there is no change in voltage magnitude. Table 27.1 shows the load flow study of normal condition when no FACTS device is used.

Case 2: In this case the real power is increased from its original value to its maximum value whereas the reactive power is maintained the same. As a result, the voltage magnitude is dropped which is shown in Table 27.2.

27.2.2 Load Flow Studies with FACTS Device

SVC is connected for dynamic reactive power compensation in bus 5. It generates and absorbs reactive power whenever necessary. Now the improvement in voltage

Table 27.1 Normal condition

Bus no.	V (PU)	Delta (DEG)	P (MW)	Q (MVar)	Total generation P (MW)	Total generation Q (MVar)	Total losses P (MW)	Total losses Q (MVar)
1	1.000	0.00	125.20	−0.06	165.20	28.28	0.20	5.57
2	1.000	−1.13	40.00	28.34				
3	0.996	−2.10	0	0				
4	0.996	−2.22	0	0				
5	0.995	−2.55	0	0				

Magnitude = no change, P = 60 MW, Q = 10 Mvar

Table 27.2 When P is varied (P → Pmax; Q → Q)

Bus no.	V (PU)	Delta (DEG)	P (MW)	Q (MVar)	Total generation P (MW)	Total generation Q (MVar)	Total losses P (MW)	Total losses Q (MVar)
1	1.000	0.00	478.73	61.17	518.73	126.17	3.73	103.03
2	1.991	−4.83	40	64.65				
3	0.983	−6.17	0	0				
4	0.982	−6.83	0	0				
5	0.972	−13.04	0	0				

Bus no. = 5, P = 410 MW, Q = 10 Mvar

Table 27.3 Comparison table of voltage magnitude for with and without SVC

S. no.	Bus no.	Case		Voltage magnitude (p.u)	
		P (MW)	Q (Mvar)	Without SVC	With SVC
1	5	410	10	0.972	0.995
2	5	60	410	0.720	0.789
3	5	180	410	0.703	0.771
4	5	410	30	0.961	0.979
5	5	410	410	0.561	0.720

magnitude is listed in the table below. Table 27.3 compares the difference in voltage magnitude of all the above cases for both with and without SVC circuit [5].

Hence from the above table it is understood that voltage has been enhanced when SVC is connected to the bus. Figure 27.3 shows the comparison chart for with and without SVC. The MATLAB Simulation diagram of IEEE 5 bus system with SVC is shown in Fig. 27.4.

Figures 27.5a and 27.6a represents the Voltage magnitude comparison of actual voltage (V_{actual}) and SVC compensated voltage (V_{SVC}). Similarly, Figs. 27.5b to 27.6b represents Susceptance control comparison of actual (B_{actual}) and SVC (B_{SVC}).

Case 1: As seen earlier, when the real power is increased from its original value to its maximum value and the reactive power is kept the same, then the voltage magnitude was 0.972 p.u. By connecting SVC, the voltage magnitude is improved to 0.995 p.u.

Case 2: In this case when the reactive power is increased from its original value to the maximum allowable value and the real power is maintained the same then the voltage magnitude has been improved from 0.720 to 0.729 p.u.

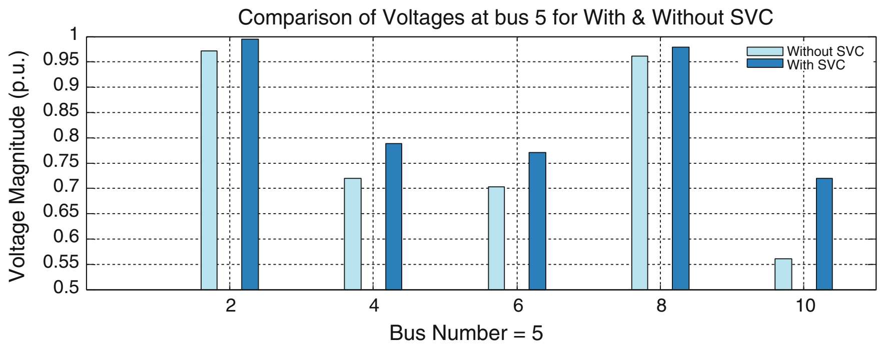

Fig. 27.3 Chart showing comparison of with and without SVC

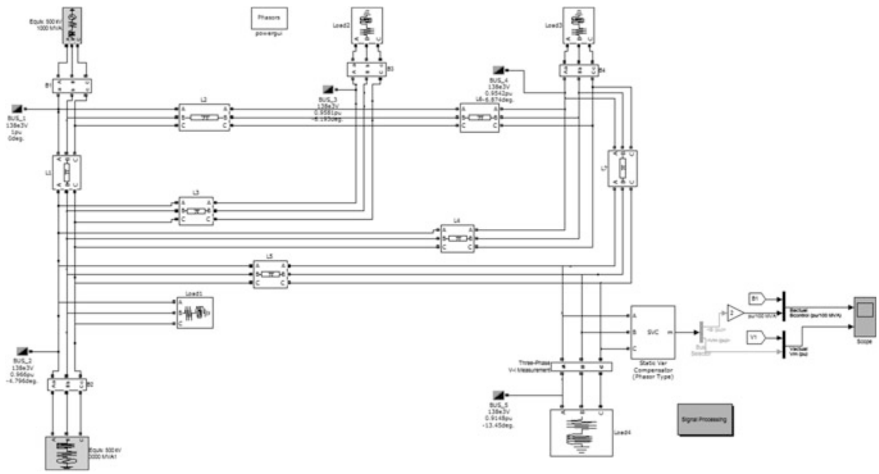

Fig. 27.4 IEEE 5 bus system simulation diagram with SVC

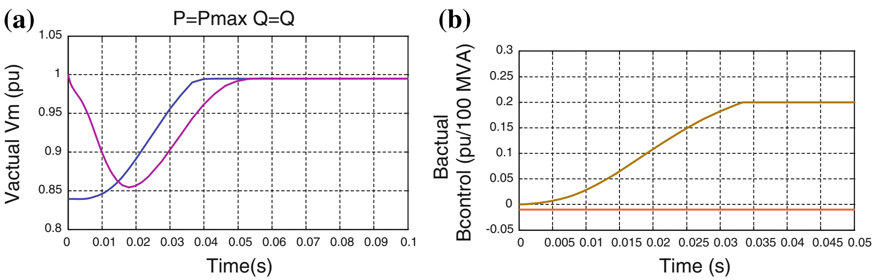

Fig. 27.5 **a** V_{actual} versus $V_{SVC.}$ **b** B_{actual} versus B_{SVC}

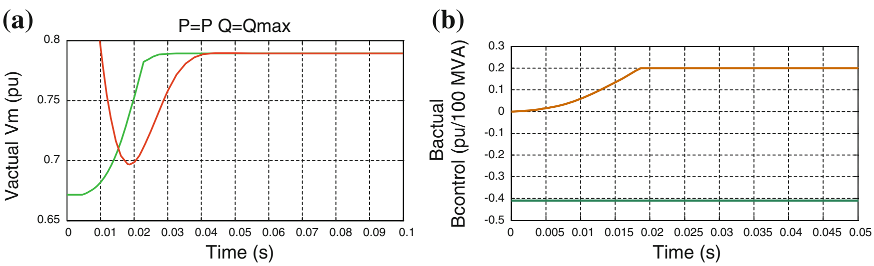

Fig. 27.6 **a** V_{actual} versus $V_{SVC.}$ **b** B_{actual} versus B_{SVC}

27.2.3 IEEE 14 Bus System

Figure 27.7 represents the MATLAB simulink diagram of IEEE 14 bus system without any FACTS devices.

In IEEE 14 bus system, among all 14 buses only bus number 12 is found to be the weakest bus and hence in all the following cases only twelfth bus is considered and analyzed. All the load variations are done in twelfth bus and the corresponding voltage variations are noted down and compared [6–8].

Case 1 (Table 27.4)

27.2.4 IEEE 14 Bus System Load Flow Studies with FACTS Device

Implementation of SVC in IEEE 14 bus system has improved the system performance by stabilizing voltage. The comparison results are shown below for many load variation cases and the improvement can be noted clearly. Figure 27.8 represents the MATLAB Simulink diagram of IEEE 14 bus system with SVC (Table 27.5).

Figures 27.9a and 27.10a shows the Voltage magnitude comparison of actual voltage (V_{actual}) and SVC compensated voltage (V_{SVC}). Similarly, Figs. 27.9b and 27.10b represents Susceptance control comparison of actual (B_{actual}) and SVC (B_{SVC}) [9, 10].

Case 1: P = Q = 1,200 (MW/MVar)

After implementing SVC in IEEE 14 bus system, the voltage magnitude has increased from 0.955 to 1.01 p.u.

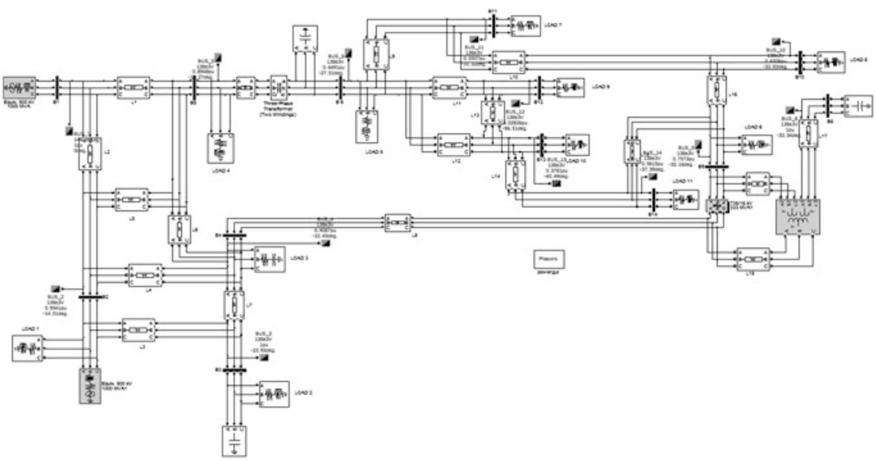

Fig. 27.7 IEEE 14 bus Simulation diagram

Table 27.4 Light variation in load

Bus no.	V (PU)	Delta (DEG)	P (MW)	Q (MVar)	Total generation P(MW)	Total generation Q (MVar)	Total losses P (MW)	Total losses Q (MVar)
1	1.000	0.00	1,422.15	1,512.90	1,462.15	1,502.90	6.26	262.32
2	1.051	−0.44	40.00	−10.00				
3	1.046	−0.78	0	0				
4	1.042	−0.93	0	0				
5	1.040	−1.00	0	0				
6	0.986	−3.83	0	0				
7	1.007	−2.56	0	0				
8	1.008	−2.84	0	0				
9	0.990	−3.71	0	0				
10	0.989	−3.74	0	0				
11	0.987	−3.79	0	0				
12	0.955	−3.42	0	0				
13	0.976	−4.40	0	0				
14	0.983	−4.03	0	0				

P = 1,200 MW Q = 1,200 MVar

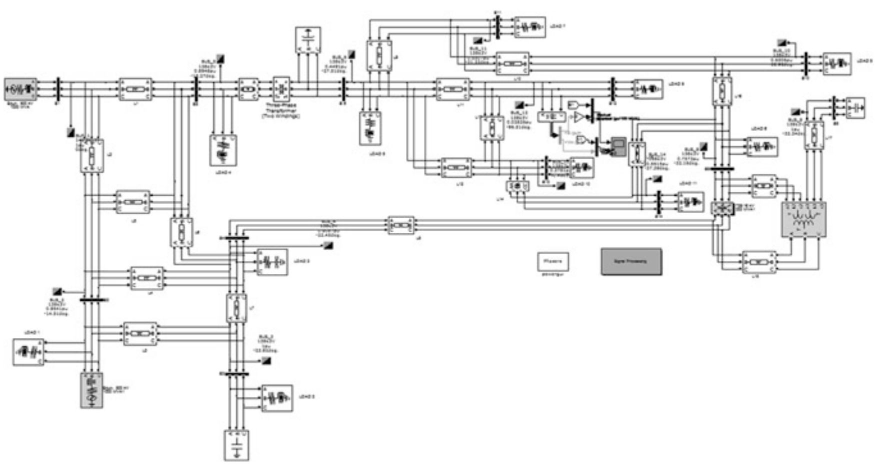

Fig. 27.8 IEEE 14 bus system with SVC-MATLAB model

Table 27.5 Voltage magnitude comparison table for with and without using SVC system

S. no.	Load variation	Bus no.	Case		Voltage magnitude (p.u)	
			P (MW)	Q (Mvar)	Without SVC	With SVC
1	Light	12	1,200	1,200	0.955	1.010
2	Moderate	12	1,200	1,700	0.900	1.005
3	High	12	2,100	2,100	0.846	0.998
4	Very High	12	2,500	2,500	0.776	0.996

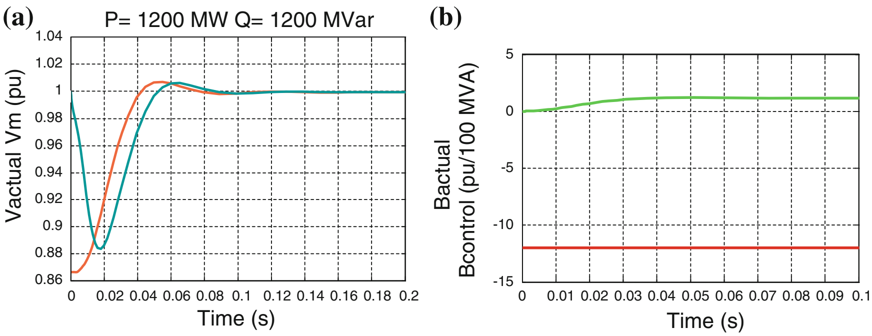

Fig. 27.9 **a** V_{actual} versus V_{SVC}. **b** B_{actual} versus B_{SVC}

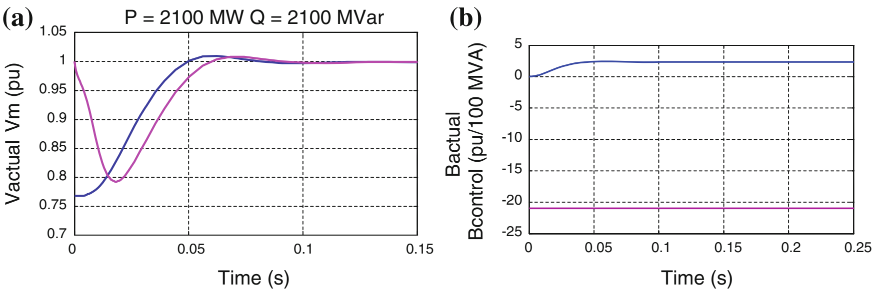

Fig. 27.10 **a** V_{actual} versus V_{SVC}, **b** B_{actual} versus B_{SVC}

Case 2: P = Q = 2,100 (MW/MVar)
The voltage level has increased to 0.998 from 0.846 p.u. in this case.

27.3 Conclusion

This paper elucidates the load flow study of IEEE 5 bus and 14 bus systems simulated using MATLAB. The paper clearly describes the usage of FACTS device (SVC) and their prime role in reactive power compensation, in the 5 and 14 bus systems. In a similar methodology, load flow studies using MATLAB Simulink can be extended for other high level buses. The location and positioning of SVC is relative important which determines the performance and effectiveness of SVC.

References

1. Acha E, Agelidis VG, Anaya-Lara O, Miller TJE (2002) Power electronic control in electrical systems (Chaps. 6 and 9). Newnes Publisher, London, 451 pp
2. Abdulla M, Ziyad S (1999) The effect of SVC's elements and power system's parameters on harmonic magnification: an experimental study. Electr Power Compon Syst 27(6):613–622
3. Ambriz-Perez H, Acha E, Fuerte-Esquivel CR (2000) Advanced SVC models for the Newton–Raphson load flow and Newton optimal power flow studies. IEEE Trans Power Syst 15(1):129–136
4. Ahmed T, Nishida K, Soushin K, Nakaoka M (2005) Static var compensator-based voltage control implementation of single-phase self-excited induction generator. IEE Proc Gener Transm Distrib 152(2):145–156
5. Farmer RG (2001) Power systems and dynamics stability. In: Electric power engineering handbook. CRC Press, Boca Raton
6. Gelen A, Yalc T (2010) Experimental studies of a scaled-down TSR-based SVC and TCR-based SVC prototype for voltage regulation and compensation. Turk J Elec Eng Comp Sci 18 (2):147–158
7. Hingorani NG, Gyugyi L (1999) Understanding FACTS: concepts and technology flexible AC transmission systems. IEEE Press, New York
8. Li X, Bao L, Duan X, He Y, Gao M (2000) Effects of FACTS controllers on small-signal voltage stability. IEEE Power Eng Soc. Winter Meeting, pp 2793–2799
9. Mathur RM, Varma RK (2002) Thyristor-based FACTS controllers for electrical transmission systems. IEEE Press, New York
10. Sharma PR, Kumar A, Kumar N (2007) Optimal location for shunt connected FACTS devices in a series compensated long transmission line. Turkish J Electr Eng Comput Sci 15 (3):321–328

Chapter 28
Study on Reflector Material Optimization of a Parabolic Solar Concentrator

A.B. Auti, D.R. Pangavane, T.P. Singh, M. Sapre and A.S. Warke

Abstract Increased demand of energy forced us to think about the non-conventional energy sources. Solar energy can be utilized for cooking by using solar cooker with a parabolic concentrator. Absorber located at the focal point of the parabolic concentrator receives sufficient energy to raise the temperature of food in reasonable time. The efficiency of the process depends on the reflectivity of the material of concentrator. The material used for solar concentrators needs to have high reflectivity, spectral physical properties to ensure long life of the system. The paper presents an experimental study for selection of cost effective reflective material with improved efficiency. Various materials are tested for cost effectiveness and better reflectivity and the material showing optimum results is selected for the experiment. Different designs in respect of size and material of absorber are tested at focal point of the concentrator and one of them showing most efficient result is selected.

Keywords Reflectivity · Absorber · Parabolic concentrator · Solar energy

28.1 Introduction

Fossil fuels have satisfied most of our energy needs in past centuries. Depletion and increasing cost of oil and coal based fuels have led to efforts to explore the use of other energy sources like wind energy and solar energy. Solar energy that is available in abundance can become a viable alternative for the conventional energy sources subject to its efficient and economic utilization. At present, the main problems availing these sources are high cost of equipment, low efficiency and storage. Researchers from different organizations are continuously working for

A.B. Auti (✉) · T.P. Singh · M. Sapre · A.S. Warke
Symbiosis International University, Pune 412115, Maharashtra, India
e-mail: autiabhijeet@sitpune.edu.in

D.R. Pangavane
Prestige Institute of Technology, Indore, India

C. Kamalakannan et al. (eds.), *Power Electronics and Renewable Energy Systems*, Lecture Notes in Electrical Engineering 326, DOI 10.1007/978-81-322-2119-7_28

developing technologies for harnessing this abundant resource economically. The sun has produced energy for billions of years. The sun's total energy output is 3.8×10^{20} MW and only a tiny fraction, 1.8×10^{11} kW, of the total radiation emitted is intercepted by the earth. However, it is estimated that, 30 min of solar radiation falling on earth is equivalent to the world energy demand for 1 year [1].

The study presented here is an attempt to improve the efficiency of a parabolic solar concentrator by choosing a proper reflector material. Solar concentrators of many shapes and materials have been tried and, parabolic concentrators showed highest thermal and optical efficiency [1–3]. A parabolic system consists of a parabolic dish concentrator that reflects solar radiation on a platform mounted at its focal point. Due to its low cost and high manufacturability, most common material used for reflectors is anodized aluminum. The aluminum reflectors have reflectivity in the range of 75–95 %. Unprotected aluminum degrades in a couple of years when exposed to atmosphere [4]. This degradation can be controlled. The anodized coating on aluminum protects the layer from further reaction due to atmospheric changes and can significantly improve the life of the reflectors.

In this paper, optimization is used for choosing a reflector material which has high reflectivity, low cost and desired efficiency. Different reflective materials were tested in a lab for their reflectivity. A parabolic concentrator of an existing design has been fabricated and tested for solar radiation, heat losses to the surrounding for different reflective material and absorber size and material [5]. By optimizing the results a reflective material and absorber of specific size and material has been chosen for concentrator and then the modified concentrator has been tested for efficiency. The results are compared with the results of existing designs.

28.2 Working Principle

The principle of a parabolic solar concentrator is based on reflecting infrared radiation emitted by the sun at a focal point, where the absorber is placed. For maximum utilization of solar energy, the parabolic concentrator is aligned with the sun rays. All sunrays parallel to parabolic axis, meet at focal point after reflection. As dark colors are good absorbers of heat and energy, the receiver ideally should be of black color in all exterior surfaces, and preferably dark on the inside as well, to absorb maximum solar radiations. The dark surface may be hard-anodized, non-stick, or of any other nontoxic, heat-resistant, and wear-resistant coating.

28.3 Parabolic Solar Cooker Design

In order to trace the parabolic curve, initially, the aperture diameter should be decided. Considering the energy requirement and heat losses in the surrounding over time and variations in the solar radiations, the system is designed for minimum

Table 28.1 Error in measurement for solar radiations using pyranometer

Average radiations (W/m^2) using			
Month	SPCTRAL2 (Theoretical)	Pyranometer (Experimental)	Error (%)
February	750	754	0.53
March	820	823	0.37
April	880	884	0.45
May	910	912	0.22

of 1,000 W. Heating equivalent of an induction cooker was taken as the basic input of the design. The average value of solar irradiance ($I_b r_b$) measured in good sunshine is in the range of 750–800 W/m^2. The solar radiations are measured using optical pyranometer. The values measured are compared with the theoretical values calculated using SPCTRAL2 [6]. This is an excel sheet which provides theoretical values of the solar radiations using latitude, longitude, time, day, and sunshine factor as an inputs. The values measured experimentally and theoretically per hour for each month and average radiations per month are shown in Table 28.1 with percent error. It is observed that error in the measurement using pyranometer is just 0.2–0.5 %. As a result readings taken from optical pyranometer are considered for experimental analysis.

Efficiency of solar concentrator is in the range of 30–35 % [7, 8]. The net heat input at the focal area (Q_{net}) is given by,

$$Q_{net} = I_b r_b \times A_e \times \eta, \tag{28.1}$$

where, A_e is the effective area of concentrator. For 1,000 W energy output, the area required will be,

$$\begin{aligned} 1{,}000 &= 750 \times A_e \times 0.3 \\ A_e &= 4.16\ m^2, \end{aligned} \tag{28.2}$$

For this area, the diameter of concentrator (d) requires will be, 2.3 m. The upward parabola symmetric about y axis is used with focal point (a) fixed at 0.5 m and the projected radius ($r = d/2$) is considered to be 1.15 m. For various values of radius (x), the height (y) is calculated using a standard equation of parabola $y = x^2/4a$ as shown in Table 28.2. Different (x, y) points are plotted on X–Y plane and the parabolic curve is traced using Table 28.2 [9].

Table 28.2 Values of x and y for curve tracing

Values of x (mm)	Values of y (mm)	Values of x (mm)	Values of y (mm)
1,150	660	−1,150	660
1,025	525	−1,025	525
875	380	−875	380
700	245	−700	245
575	165	−575	165
360	65	−360	65
150	10	−150	10
0	0	0	0

28.4 Selection of Reflective Material

The material used for solar concentrators needs to have high reflectivity and spectral physical properties to ensure long life of the system. Consideration must be given to the effect of accumulation of dust, stability of reflective coating, environmental effects, cleaning problem and cost. Among the metals, silver and aluminum are the best solar reflectors, with a weighted hemispherical reflectance of approximately 96 and 92 % respectively [10]. The main aim of this work is to study the reflectivity of commercially available reflectors and choose the optimum one with the best tradeoff between reflectivity and costs. Aluminum coated optical mirrors have good reflectivity (78–92 %) but has comparatively high cost of Rs. 2,475–5,380 per m^2 at current market prices, and cannot be fitted on the designed frame due to more weight and poor malleability [11].

After thorough search of reflective materials available in the market, used for solar application purpose, four anodized Aluminum reflector materials, are shortlisted for experimentation. These four materials A, B, C, D which are anodized Aluminum with extra bright surface and high reflectivity have a tensile strength between 160 and 200 MPa and yield strength of 140–160 MPa, Sample A is procured from a Germany based company that manufactures a variety of Aluminum grades. The cost of this sample is Rs. 1,722/- per m^2 [12]. Sample B is taken from a U.S company which is world's leading manufacturer of integrated Aluminum products. The cost of this sample is Rs. 2,260/- per m^2 [13]. Sample C is from an Indian company which is a manufacturer of Aluminum sheets. The cost of this sample is Rs. 1,937/-per m^2 [14]. Sample D is basic Aluminum sheet, taken from another Indian company which is Asia's largest integrated primary producer of Aluminum. The cost of this sample is Rs. 1,213/-per m^2 [15].

28.5 Reflectivity Testing

These four materials were submitted for reflectivity testing at University of Pune. The testing is done using JASCO UV-Vis-NIR spectrophotometer in the percentage reflectivity mode in the range of 400–2,000 μm. Before the reflectance spectra are

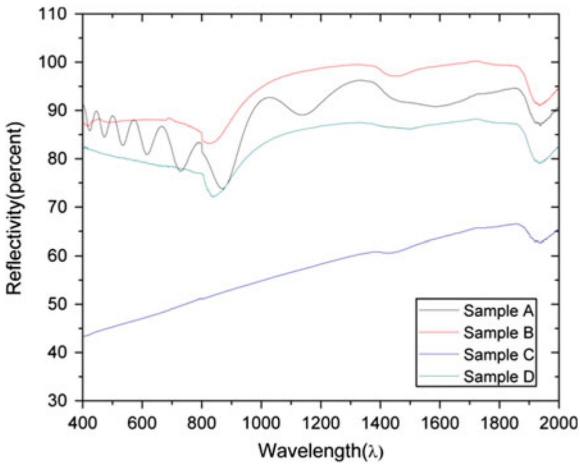

Fig. 28.1 Reflectivity graph for the four samples from 400 to 2,000 μm

measured, the samples are gently cleaned with soap and water to remove any depositions on the surface. Precaution is taken not to scratch the surface and no chemical solvents are used. The testing results are shown in Fig. 28.1.

The infrared rays having wavelength ranging from 750–1,000 μm are suitable for heating purposes [16]. On the basis of this wavelength range, it is observed material B shows reflectivity up to 90 % which is highest among all four materials. But the cost of this material is comparatively higher (Rs. 2,260/- per m^2). On the other hand, the reflectivity of Sample A is 88 % and its cost is Rs. 1,722/- per m^2 considering the cost factor and a minor difference in the reflectivity, sample A (MIRO 27) has been selected as suitable reflector material.

The total collector area is 4.16 m^2, hence the total cost of the sample B, MIRO 27 is Rs. 7,150 whereas the old system with sample A cost is Rs. 5,050. Hence spending Rs. 2,100, the reflectivity of material is improved from 60 to 88 %.

28.6 Absorber Design

Having selected the material, the next task is to design the absorber for improving the efficiency of the solar cooker. The first step in design is to determine the base diameter and height of the absorber. For this, a wooden ply board is taken and is kept at the designated focal area. Solar radiations incident on that point heated up a region on the ply board leading to the burning of board. After 5 min the ply board is removed. The burn marks on the ply board are then measured and are found to be 28–30 cm in diameter at focal point. The ply board is then kept vertical and positioned at the focal point perpendicular to the base of the stand of the absorber. The height of the burnt ply board is then found to be 23–25 cm. The procedure is repeated many times and the optimum diameter of the absorber is found to be 28 cm and height as 25 cm.

Hard anodized cookers with black coating of various sizes available in the market are checked for the available focal area. The hard anodized surface is non-toxic, non-staining and non-reactive with foods. High anodized surface is thermal-efficient, can withstand high temperature, is tough and durable and has a good corrosion resistance.

28.7 Testing and Results

To ascertain the efficiency and effectiveness of the new system, experiments are conducted with both the new concentrator and absorber as well as the old (existing system). Tests are conducted on old concentrator with basic Aluminum reflector and with normal vessel and the results are compared with the new reflector with black absorber. Table 28.3 shows the details of experimentations. In the first type the time of heating a predetermined mass of liquid up to predetermined temperature is noted while in the second case the time of heating is kept constant and the temperature attained of a predetermined mass is noted. The aim of conducting these two tests is to find reduction in the time for heating for achieving the task.

The readings of time, temperature and efficiency for 8 kg of water are given in Tables 28.4 and 28.5. To ascertain the efficiency and effectiveness of the new

Table 28.3 Details of Experimentations

Test	Details	Heated mass	System	Average value of irradiance (W/m^2)
1	Absorber is heated till the temperature reaches a predefined fixed value	8 kg mass is heated up to 95 °C	Conducted on both old and new system	820–880
2	The absorber is heated for a fixed time and the value of maximum temperature attended is measured	2 kg mass of liquid paraffin is heated for 65 min		800–860

Table 28.4 Results with 8 kg of water using old system

S. No.	t (min.)	Irradiance (W/m^2)	Temperature of water T_w (°C)	Heat utilization rate Q_u(W)	Heat supplied rate Q_i(W)	Efficiency η
1	13.00	864	38	–	–	–
2	13.10	861	53	837	3,582	0.24
3	13.20	877	66	726	3,648	0.23
4	13.30	868	81	837	3,610	0.23
5	13.40	820	95	782	3,411	0.23

Table 28.5 Results with 8 kg of water using new system

S. No.	t (min.)	Irradiance (W/m$^{2)}$	Temperature of water T_w (°C)	Heat utilization rate Q_u(W)	Heat supplied rate Q_i(W)	Efficiency η
1	13.00	865	38	–	–	–
2	13.10	862	56	1,005	3,586	0.29
3	13.20	872	74	1,061	3,628	0.30
4	13.32	870	95	1,116	3,619	0.31

system, experiments are conducted with new concentrator and absorber as well as with the old system. The temperature of water is measured after 10 min of time, t and the heat supplied to the water, Q_u is calculated as,

$$Q_u = \frac{mC_p dT}{time}, \tag{28.3}$$

The input energy Q_i is the product of radiations, $I_b r_b$ following over area, A_e. Efficiency of a system is the ratio of Q_u/Q_i and calculated by the formula,

$$\eta = \frac{\frac{mC_p dT}{time}}{I_b r_b \times A_e}, \tag{28.4}$$

The readings second test for the oil are shown in the Tables 28.6 and 28.7. For the same time interval, temperature rise of oil is noted using both the systems.

Table 28.6 Results with 2 kg of liquid paraffin using old system

S. No.	t (min.)	Irradiance (W/m^2)	Temperature of oil (°C)
1	11.30–11.45	810	74
2	11.45–12.00	830	99
3	12.00–12.15	852	135
4	12.15–12.30	862	168

Table 28.7 Results with 2 kg of liquid paraffin using new system

S. No.	t (min.)	Irradiance (W/m^2)	Temperature of oil (°C)
1	11.30–11.45	809	85
2	11.45–12.00	835	155
3	12.00–12.15	850	211
4	12.15–12.30	860	269

28.8 Result and Discussion

The system is designed, optimized and tested by performing theoretical and experimental analysis. It is observed from the experimental result that the efficiency of the system increases with the use of MIRO27 reflector and with designed absorber from 22 to 31 %. The required time to heat 8 kg of water is decreased using MIRO27 reflector and with futura 7 model absorber, from 40 to 32 min, as shown in Fig. 28.2. The maximum temperature for heating 2 kg of oil increased from 174 to 284 °C as shown in Fig. 28.3.

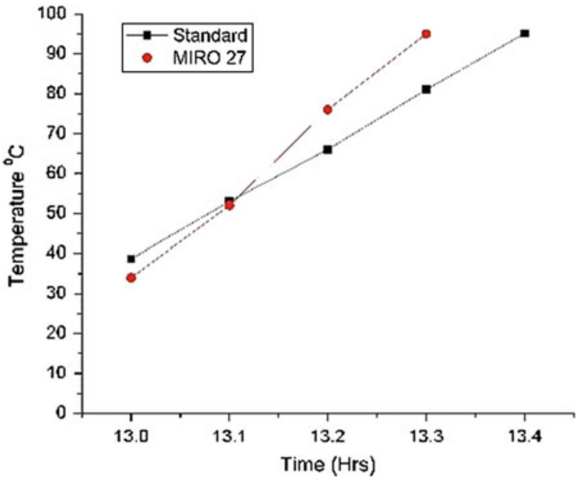

Fig. 28.2 Graph showing comparative variation in the time for 8 kg of water, between old and new system, when temperature is kept constant

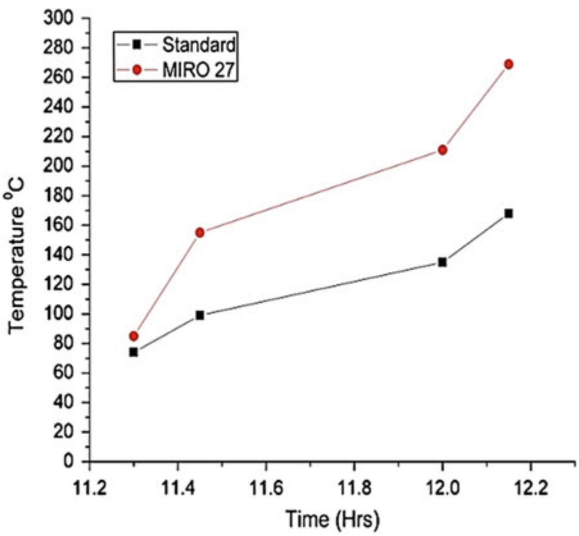

Fig. 28.3 Graph showing comparative variation in the temperature for 2 kg of oil, between old and new system, when time is kept constant

The readings of different parameters indicate that selection of MIRO27 reflector and new absorber has definitely reduced the time for heating and hence tracking. These experimental results signify that the efficiency of solar heater can be improved by proper design and fabrication and use of appropriate materials as reflector and absorber

28.9 Conclusion

The study demonstrates that a proper selection of reflecting material for parabolic concentrator and absorber compiled with proper design of the system carried out using theoretical concept followed by experimental validation can improve efficiency of the solar cooking system. As a result, system can also be used when the value of solar radiation is low. It can be considered from the study that solar energy can be effectively utilized for domestic and on large scale cooking by designing the system which is efficient, cost effective and reliable.

References

1. Swanson RM (2000) The promise of concentrators. Progress in Photovoltaics: Research and Applications, vol. 8. Wiley, New York, pp 93–111 (Millennium Special Issue)
2. Whitfield GR, Bentley RW, Burton JD (1995) Increasing the cost-effectiveness of small solar photovoltaic pumping systems. Renew Energy 6(5–6):469–475
3. Lovegrove K, Burgess G, Pye J (2011) A new 500 m^2 paraboloidal dish solar concentrator. Sol Eng 85:620–626
4. Badran AA, Mohammed HA (1998) Utilization of solar cooker energy for heating of fuel oil. Energy Convers Manage 39(1/2):105–111
5. Auti AB (2012) Domestic solar water desalination system. Elsevier Energy Procedia 14:1776–1778
6. Information on http://rredc.nrel.gov/solar/models/spectral/SPCTRAL2/SPCTRAL2.xls
7. Auti A, Singh TP, Pangavhane DR (2013) Thermal analysis of parabolic concentrator for finding optical efficiency by different methods with varying parameters. Int J Eng Technol 5 (2):1484–1488
8. le Roux WG Solar tracking for a parabolic dish used in a solar thermal Brayton cycle. Centre for renewable and sustainable energy studies
9. Brogren M, Karlsson B, Roos A, Werner A (2004) Analysis of the effects of outdoor and accelerated ageing on the optical properties of reflector materials for solar energy applications. Solar Energy Mater Solar Cells 82:491–515
10. Brogren M, Karlsson B, Roos A, Werner A (2004) Analysis of optical properties of outdoor and accelerated aged Reflector materials for solar energy applications. Solar Energy Mater Solar Cells 82:491–515
11. Harrison J (2001) Investigation of reflective materials for the solar cooker. Florida Solar Energy Center, pp 1–2

12. Information on http://alanod.com/opencms/opencms/en/products/
13. Information on http://www.alcoa.com/india/en/general/contact_alcoa.asp
14. Information on http://www.mirrorreflectors.com/contact.htm
15. Information on http://www.hindalco.com/contact_us/contact.htm
16. Information on http://science.hq.nasa.gov/kids/imagers/ems/infrared.html

Chapter 29
A New Approach for Torque Ripple Minimization of PMBLDC Motor Drive

J. Gayathri Monicka, V. Jamuna and K. Hemalatha

Abstract This objective of this paper is to minimize the torque ripple content of Permanent Magnet Brushless DC motors (PMBLDC) by using an Asymmetric Cascaded Multilevel Inverter (ACMI). Torque ripple reduction in BLDC motor has been main concern of the drive system. The BLDC motor is fed from the Asymmetric Cascaded Multilevel Inverter where the rotor position is the input. The proposed system is an effective replacement for the conventional method, which has a high torque ripple. The usage of BLDC enhances various performance factors ranging from higher efficiency, high power density, and low maintenance and less noise. This paper presents a mathematical model of BLDC motor and shows the values of various technical parameters using MATLAB/SIMULINK.

Keywords Permanent magnet brushless DC motor · Multilevel inverter · Torque ripples

29.1 Introduction

A motor that retains the characteristics of a DC motor but eliminates the commutator and the brushes is called a Brushless DC motor. Brushless DC (BLDC) motors can in many cases replace conventional DC motors. They are driven by dc voltage but current commutation is done by solid state switches i.e., the commutation is done electronically. Ideally, the BLDC motors have trapezoidal back-EMF waveforms and are fed with rectangular stator currents, which give a theoretically constant torque. A BLDC stator includes three coils, which can be simulated to reduce torque ripple and the rotor includes permanent magnets, composed of one to multiple pair of poles; Position of the rotor can be estimated using three hall sensors mounted on the stator. The BLDC motors have advantages over brushed DC motors

J. Gayathri Monicka (✉) · V. Jamuna · K. Hemalatha
Department of Electrical and Electronics Engineering, Anna University, Chennai, India
e-mail: monigaya2002@yahoo.com

C. Kamalakannan et al. (eds.), *Power Electronics and Renewable Energy Systems*,
Lecture Notes in Electrical Engineering 326, DOI 10.1007/978-81-322-2119-7_29

like higher efficiency, noiseless operation, higher speed range and higher dynamic response.

Torque ripples from BLDC motors are mainly due to fluctuation of the field distribution and armature mmf which in turn depends on the motor structure and voltage and current waveform. Due to a limited number of torque producing elements, the interior permanent magnets torque ripples become one of the disadvantage of BLDC motors. Torque ripples generated in commutation period is the main drawback of BLDC motor, however, which deteriorates the precision of BLDC motor. A different control strategy for BLDC machines were presented in [1]. New torque control method to reduce the torque ripple of BLDC motors, with un-ideal back EMF waveforms [2]. A torque ripple reduction, using repetitive current control method proposed [3]. Novel optimal current excitation schemes to minimize ripple torque based on the d–q–0 reference frame [4]. Multilevel DC link inverter, to reduce the current ripple in brushless permanent magnet motors, with very low inductance proposes [5]. The performance of BLDC drives under DTC and PWM current control compared [6].

Several methods have been studied to solve this problem. The torque ripple reduction was considered in the point of current control method if current can be control properly the motor does not produce torque ripple. The conventional methods proposed in the above literature use a six step inverter as an electronic commutator and there are several simulation models available for BLDC motor drives. Even though these models have made a great contribution to BLDC motor drives, there is no comprehensive model for the analysis of a motor using a multilevel inverter. In the BLDC motor, torque pulsations produce noise and vibrations in the system. Therefore, the minimization or elimination of noise and vibration is a serious issue in BLDC drives.

29.2 Analysis of BLDC Motor

The input to an Ideal BLDC motor is a constant source voltage and trapezoidal back EMF. The amplitude of the back EMF is proportional to the angular velocity of the motor and the shape is a function of the angular position $E = d\lambda_{r/}dt$. The source voltage allows the current to rise instantaneously to its steady state value, and the torque is produced without ripples. The current has a definite time constant, and cannot rise or fall to the steady state value instantaneously, and hence, produces a current ripple by the influence of inductance. The current ripple directly affects the torque ripple, which is primarily caused by commutation of the phase currents [7–10]. In order to minimize the torque ripples in Brushless DC machines, an analysis of the torque curves has to be performed. The constant current torque waveforms depend on many parameters, which are related to the design parameters. The commonly used commutation in a three phase BLDC motor consist of six-steps, in which each phase voltage is energized for an interval of 120 electrical degree, according to the rotor electrical position. In any sector, only one phase is energized as positive and one of the other phases is energized as negative, in order to maintain a current path. For controlling the BLDC motor, a typical three phase full bridge will be used to drive the motor. For the analysis of the commutation time, the commutations of the current through two phases are to be considered. Phase A will be switched off, and phase B will replace A phase, and the third phase C will remain conducting. Due to electronic commutation, the usage of high frequency switching of power devices and imperfections in the stator and the associated control system, the input supply to the motor contains various harmonics components. The commutation torque ripple exists due to the inductance of the windings, which restrict the current conduction through the phase, and make the current drawn during the interval. The performance of the system can be improved by reducing the ripple content using multilevel inverter.

The analysis is based on the following assumptions for simplification: Iron losses are negligible, motor is not saturated, semiconductor devices in the multilevel inverter are ideal and stator resistance of the entire winding are equal. The BLDC drive system is based on the feedback of the rotor position, which is obtained at fixed points, typically every 60 electrical degrees, for the six-step commutation of the phase currents through the winding. This developed drive system consists of the BLDC motor, multilevel inverter, rotor position sensor, and control circuit, as shown in Fig. 29.1.

The three phase windings use one Hall Sensor for each phase. It provides three overlapping signals, giving a 60° wide position range. Based on the decoded signal, precise firing pulses are generated to the MLI. This excites the stator winding to run the motor. The flux distribution in the PM brushless DC motor is trapezoidal; therefore the d-q rotor reference frames model developed for the PM synchronous motor, is not applicable. Given a non-sinusoidal flux distribution, it is prudent to derive a model of the PMBLDC motor in phase variable. The derivation of this model is based on the assumption that the induced currents in the rotor due to the stator harmonics fields are neglected, and the iron and stray losses are also neglected. Damper winding are not usually a part of the PMBLDC motor; damping is provided by the inverter control. The motor is considered to have three phases,

Fig. 29.1 Block diagram of PMBLDC drive

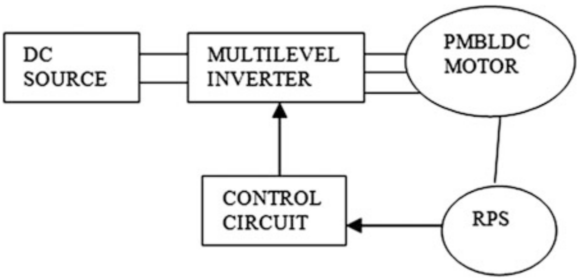

even though the derivation procedure is valid for any number of phases. A BLDC motor can be represented as

$$\begin{pmatrix} V_a \\ V_b \\ V_c \end{pmatrix} = \begin{pmatrix} R & 0 & 0 \\ 0 & R & 0 \\ 0 & 0 & R \end{pmatrix} \begin{pmatrix} i_a \\ i_b \\ i_c \end{pmatrix} + \begin{pmatrix} L-M & 0 & 0 \\ 0 & L-M & 0 \\ 0 & 0 & L-M \end{pmatrix} \frac{d}{dt} \begin{pmatrix} i_a \\ i_b \\ i_c \end{pmatrix} + \begin{pmatrix} e_a \\ e_b \\ e_c \end{pmatrix} \tag{29.1}$$

where e_a, e_b, and e_c are trapezoidal back EMFs. Rs is the phase resistance, v_a, v_b, v_c are phase voltages, L is the self-inductance, i_a, i_b, i_c are phase currents and M is the mutual inductance. Due to the interaction of the currents in stator windings, and the magnetic field from the rotor magnets, the electromagnetic torque of the BLDC motor is produced as follows

$$T_e = T_L + J\frac{d\omega_r}{dt} + B\omega_r \tag{29.2}$$

$$T_e = \frac{e_a i_a + e_b i_b + e_c i_c}{\omega_r} \tag{29.3}$$

where ω_r is the mechanical speed of the rotor. T_L is the load torque, B is the damping constant, J is the moment of inertia of rotor the shaft and load.

29.3 Asymmetric Cascaded Inverter with Unequal DC Sources

An asymmetric Cascaded Multilevel inverter is implemented, because this is more modular, has a simple construction, and eliminates the large number of bulky transformers. In order to lead the voltage imbalance among the dc sources, the numbers of dc sources required for the cascaded H-bridge multilevel inverter are reduced, and a method is proposed which uses lesser number of bridges. The nominal speeds powers driven by each inverter are different, where the high-voltage manages the major part of the output power [11].

The structure introduced in this work, is an Asymmetric cascaded multilevel inverter, which uses unequal DC Sources. The general function of this multilevel inverter is the same as that of the other two inverters. The multilevel inverter using an asymmetric cascaded-inverter provides a large number of output voltage levels, without increasing the number of full bridge units. This configuration provides higher voltage at a higher modulation frequency, due to which the topology can be employed for high power applications. Due to the reduction in the number of DC

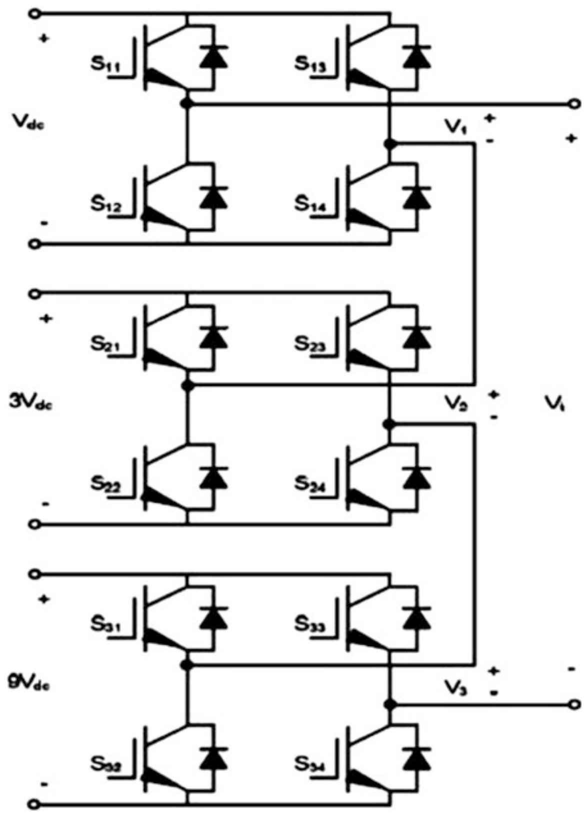

Fig. 29.2 Structure of asymmetric cascaded multilevel inverter

sources employed, the structure becomes more reliable, and the output voltage has a higher resolution, due to the increased number of steps. This configuration has recently becomes very popular in AC power supply and adjustable speed drive applications. This inverter can avoid extra clamping diodes or voltage balancing capacitors. An Asymmetric cascaded H-bridge inverter circuit is shown in Fig. 29.2.

In this proposed model, trinary DC voltage progressions of unequal DC sources of ACMLI are used. This is the most popular of unequal voltage progression with amplitude of DC voltage having a ratio 1:3:9:27; 81…. 3N and the maximum output voltage can reach [(3N − 1)/2] V_{dc}. The ACHB consists of three-bridges to generate 27 level output for the DC Sources of 9:3:1 ratio. The output waveform of 27 levels are $\pm$13 V dc … + 1 V dc and zero. By different combinations of the 12 switches, S1–S12, each inverter level can generate three different voltage outputs, $+V_{dc}$, $-V_{dc}$ and zero. Let the output, of H bridge-1 be denoted as V_1 (t), the output of H bridge-2 as V_2 (t) and the output of H bridge-3 as V_3 (t). Hence the output voltage is given by

$$\mathrm{V(t)} = \mathrm{V(t)} + \mathrm{V(t)} + \mathrm{V(t)}. \tag{29.4}$$

29.4 Result and Discussion

This section verifies the developed model for torque ripple reduction technique via simulation. A BLDC motor specification is shown in Table 29.1, the MATLAB simulation is done, and the results are presented.

The Simulink model for the three phase multilevel inverter fed PMBLDC motor drive is shown in Fig. 29.3. The Simulink model consists of three sub systems, each of which contains a MATLAB function, to issue firing pulses based on the decoded hall position signal. From the simulation, it is seen that the PMBLDC motor without any controller is used in this system. The phase voltages and phase currents in the winding of the motor are shown in Figs. 29.4 and 29.5. The electromagnetic torque waveform is shown in Fig. 29.6 and the percentage of the torque ripple is determined. The obtained results show the good dynamic performance and reduced torque ripples in the BLDC motor. The Performance parameters of proposed drive are shown in Table 29.2 (Fig. 29.7).

Table 29.1 BLDC motor specification

Parameters	Value
Stator resistance	2.875 Ω
Stator inductance	8.1e−3 H
Flux linkage	0.175 Wb
Rated torque	2 N-m
Rated speed	4,500 rpm

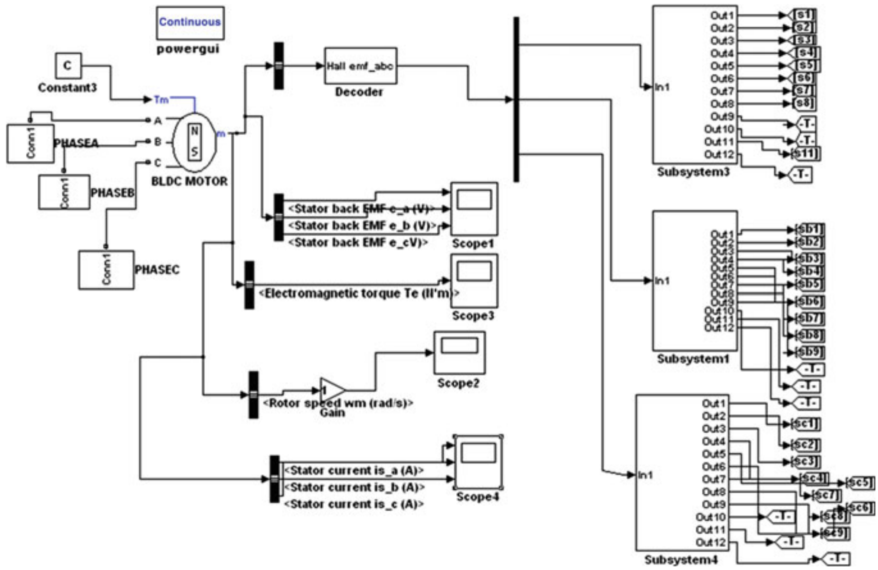

Fig. 29.3 Simulation model of the PMBLDC motor drive

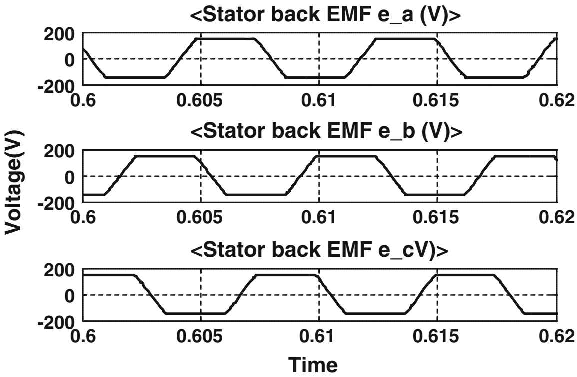

Fig. 29.4 Generated phase voltage waveforms

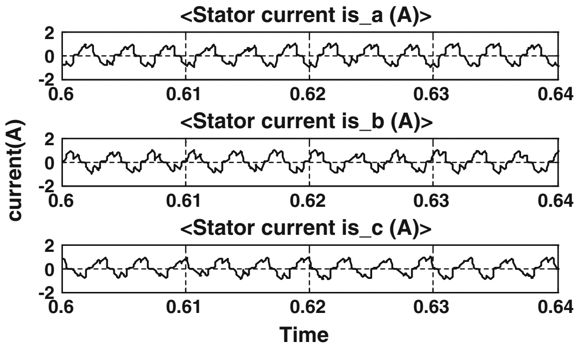

Fig. 29.5 Generated phase current waveforms

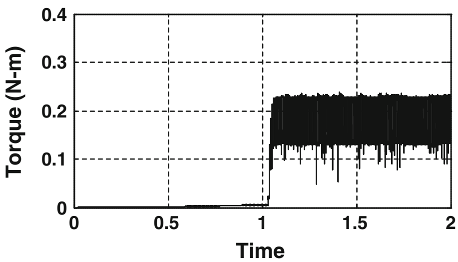

Fig. 29.6 Torque waveform

Table 29.2 Performance of proposed drive

Parameters	MLI fed drive
Back emf (V)	150
Stator current (A)	1
Speed (rpm)	2,000
Torque ripple	0.15

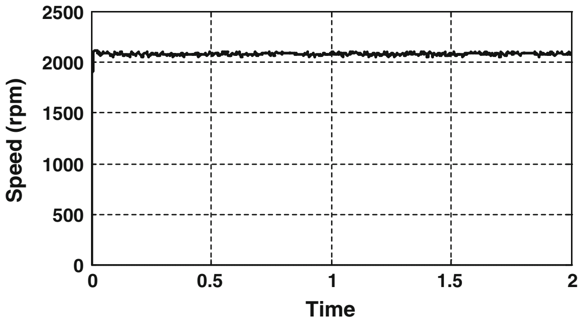

Fig. 29.7 Speed waveform in rpm

29.5 Conclusion

The Asymmetrical multilevel inverter fed PMBLDC motor drive has been proposed to the suppress commutation torque ripple of the Brushless DC motor is introduced in this paper. Asymmetrical multilevel inverter topology uses unequal DC sources with reduced number of bridges. The performance and feasibilities of the Permanent Magnet Brushless DC motor (PMLBDC) drive have been examined, by using the software package MATLAB SIMULINK, and its phase voltage, phase current, back EMF and torque waveform have been precisely analyzed. The simulated results show the improved performance of the reduction of the torque ripple using multilevel inverter. This model can be easily extended to the other control techniques, with a small change in the model. The proposed method enhances the performance of the BLDC motor drive and can be used for motor applications.

References

1. Ranjithkumar G, Prasad KNV (2012) Minimization of torque ripple content for BLDC motor by current controller using MLI. Int Conf Model Opt Comput Proc Eng 38:3113–3121
2. Lu H, Zhang L, Qu W (2008) A new torque control method for torque ripple minimization of BLDC motors with un-ideal back. IEEE Trans Power Electron 23:950–958
3. Mattavelli P (2005) Torque-ripple reduction in PM synchronous motor drives using repetitive current control. IEEE Trans Power Electron 20:1423–1431
4. Sung-In P (2003) An improved current control method for torque improvement of high-speed BLDC motor. APEC'03. Eighteenth Annual IEEE Appl Power Electron Conf Exposition 2003 1:294–299
5. Gui-Jia S, Adams DJ (2001) Multilevel DC link inverter for brushless permanent magnet motors with very low inductance in Industry Applications Conference, 2001. Thirty-Sixth IAS Annual Meeting. Conference Record of the 2001 IEEE, vol 2, pp 829-834
6. Zhu ZQ (2005) Comparison of performance of brushless DC drives under direct torque control and PWM current control. In: Proceedings of the eighth international conference on electrical machines and systems, ICEMS (2005), pp 1486–1491
7. Immaneni H (2013) Mathematical modeling and position control of brushless Dc motor. Int J Eng Res Appl 3:1050–1057

8. Vinod KR, Singh Patel, Pandey AK (2013) Modeling and performance analysis of PID controlled BLDC motor and different schemes of PWM controlled BLDC motor. Int J Sci Res Publ 3:1–14
9. Agarwal P, Bose A (2013) Brushless Dc motor speed control using proportional-integral and fuzzy controller IOSR. J Electr Electron Eng (IOSR-JEEE) 5:68–78
10. Viswanathan V, Jeevanantham S (2013) A novel space—vector current control method for commutation torque ripple reduction of brushless DC motor drive. Arab J Sci Eng 38:2773–2784
11. Rech C, Pinheiro JR (2007) Hybrid multilevel converters: unified analysis and design considerations. IEEE Trans Ind Electron 54:1092–1104

Chapter 30
Grid Integration of Hybrid Generation Scheme for Optimal Switching Pattern Based Asymmetrical Multilevel Inverter

G. Satyanarayana and K. Lakshmi Ganesh

Abstract Presently, (RES) Renewable Energy Systems are getting more widely preferred with accumulate of energy demand and concern for the environmental impact around the world. The Hybrid Generation Scheme (HGS) exerts fuel cell (FC) and photovoltaic (PV) sources are the main energy generation sources. Integration of hybrid generation system to grid has favorable advantages and integrated with the help of DC/DC converter because of maintains dc link voltage as a constant and interfacing to grid by using inverter model. Basic need of multilevel inverters has gained more attention in the area of distribution of energy and control due to its advantages in high power applications with low harmonics and also good quality of output voltage. This paper proposes a three-phase Asymmetrical Multilevel Inverter (AMLI) is more suitable converter for hybrid generation scheme, and also compared to the formal multilevel inverter contains need more switches for getting higher voltage levels, gate drive circuit and area of the requirement reduces. The Proposing AMLI produces 7–15 V levels by using 9 switches for this more levels THD goes to reduces. The proposed scheme is comprehensively evaluated with improved performance of AMLI using Matlab/Simulink Package.

Keywords CHB symmetrical and asymmetrical multilevel inverter (AMLI) · PV arrays · Total harmonic distortion (THD) · Hybrid generation scheme (HGS) · Fuel cell stacks

30.1 Introduction

Efficient, reliable, high-quality and low-cost power generation is one of the appreciable factors for improving and predication of very high standard and quality of life. The key necessitate in an optimized energy generation system are better

G. Satyanarayana (✉)
School of Management Studies, University of Hyderabad, Hyderabad, India
e-mail: gallasatya.eee@gmail.com

K. Lakshmi Ganesh
Vishnu Institute of Technology, Bhimavaram, India
e-mail: klganesh201@gmail.com

C. Kamalakannan et al. (eds.), *Power Electronics and Renewable Energy Systems*,
Lecture Notes in Electrical Engineering 326, DOI 10.1007/978-81-322-2119-7_30

system efficiency, high security, improved system reliability, low priced energy, enhanced power quality, very low environmental encroachment and integration of effective sustainable energy availability proposes in [1]. Nowadays, the generation of electricity faces expressive challenges from various avenues and more importance to update energy infrastructure, using renewable energy generation scheme will be vandalize to attempt climate changes as well as supporting viable growth of sustainable energy.

A hybrid generation scheme (HGS) extends splendid scalability and very high flexibility for energy management capability. Owing to safe, clean and eco-friendly specifications, the PV systems and fuel cells (FC) are extensively used as the main power generation sources [2]. FC stack have slow dynamic response, intermittent creation of PV, fast load changes will be impel the use as a energy storage system with prominent power density. Therefore, series hybrid FC/PV power source are used as individually in each power generation unit; the proposed HGS simultaneously secure the improvement of transient response, high modularity, and maintain quality power at grid, mostly in the aspect of unbalanced and nonlinear loads. Actually grid comprises of various energy generation units integrated to the system through power semiconductor converters [3]. In order to improve the performance of grid, employment of multilevel inverter in a generation scheme has been fascinated evolving attraction in present years. Due to ability and modularity to perform at higher levels with negligible THD, most of the multilevel inverters are CHB type which has more favour for high voltage and high power applications compared to other topologies [4].

The CHB MLI has some favorable advantages amongst of (DC) diode clamped type and (FC) flying capacitor type topologies because no need of extra clamping diodes and balancing sources, automatic voltage sharing [5], low dv/dt stress, switching redundancy. The symmetrical CHB MLI produces 7, 9, 11, 13 and 15 voltage levels by using 12, 16, 20, 24 and 28 switches. In this Symmetrical MLI produces more voltage levels, then number of switching devices, gate driving circuit and complexity goes to increases. The Asymmetrical CHB MLI produces 7 level output voltage by using 8 switches and 9, 11, 13 and 15 levels by using 12 switches. So, Asymmetrical CHB MLI has more advantages compare to the Symmetrical CHB MLI. This paper highlights a grid interfacing hybrid generation scheme using optimal switching pattern for three phased Asymmetrical MLI (AMLI) produces 7, 9, 11, 13 and 15 voltage levels by using 9 switches.

30.2 Hybrid Energy Generation Scheme

Each HGS is interfaced to dc link of a definite cell of the proposed inverter topology. The proposed HGS comprise of exchanging proton membrane of fuel cell stacks and PV arrays which together to form contribute the main power, which accumulates the fast transient response. Incremental of fuel saving to reduce the cost of the FC stacks, the PV power must serve the maximum imaginable portion of

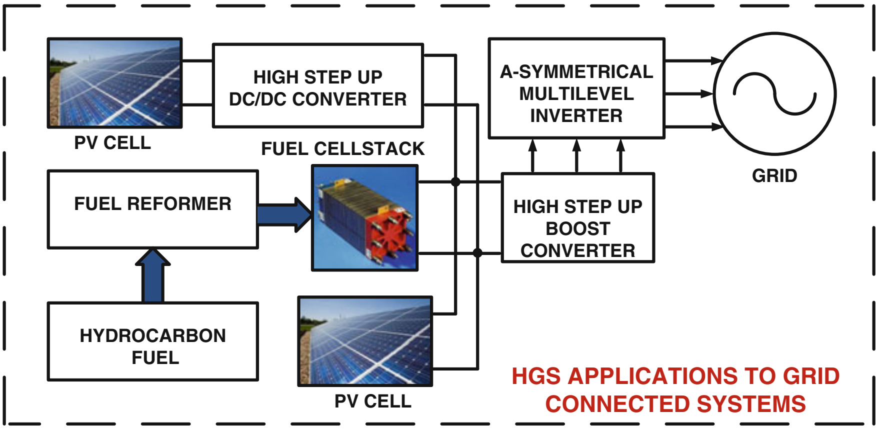

Fig. 30.1 Generalized equivalent model of hybrid energy generation scheme for grid applications

energy demand in spite of discontinuous nature [6]. Utilization of separate DC/DC converters in series facilitates to increase the high energy management capability and flexibility as well as overall performance of the HGS. The HGS controller is designed is able to convert and regulates dc-link voltage and accomplish the dc-link energy demand. In order to achieve high galvanic isolation, more efficiency the power sources of each HGS are interfaced to unidirectional conversion of the PV and FC units assemble to able smooth output current and regulation of output voltage at certain values [7]. Appropriate power point working model should be maintained for both the grid and the loads, so to extract the required power from the PV array, it is important to be persist stand for (MPP) maximum power point. And it is distinctive for each PV module, it may not constant point, it may change to effect based on request current for a distinct load changes. The MPPT is expected to accord the PV power to load challenge.

The generalized equivalent model of HGS as shown in Fig. 30.1; in this configuration, the PV/FC is integrated to drive the grid and maintain grid parameters to be standard with the importance of high rated converter configurations; the high power and high voltage conversion range is an imperative for interfacing the PV/FC source that operates as the input for grid interfacing inverter.

30.3 Grid Interfaced PV/FC with Proposed AMLI Technique

The Conventional Symmetrical and Asymmetrical CHB MLIs are shown in Fig. 30.2, Symmetrical CHB MLI produces 7-Level output voltage by using 12 switches with the help of same switches achieve 13 level by using asymmetrical CHB MLI topology as observed in above diagram [9]. Here proposed topology

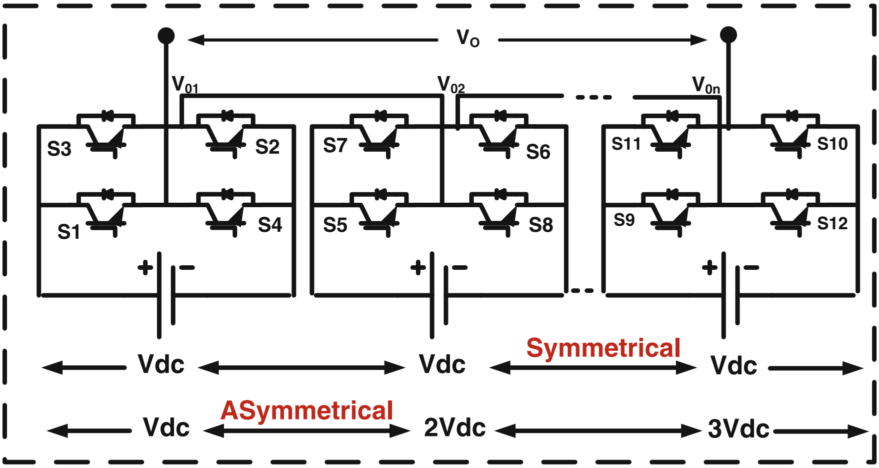

Fig. 30.2 Symmetrical and asymmetrical CHB MLI with equal and un-equal DC sources

going on same way for getting 15 levels requires 9 switches and have favorable advantages such as, reduced number of switching devices, gate driving circuit, complexity of the circuit, low space requirement and also THD reduction, enhancement quality voltage.

The newly proposed single phase AMLI topology is integrated to grid with HGS as shown in Fig. 30.3. Newly proposed single-phase AMLI topology produces several voltage levels such as 7, 9, 11, 13 and 15 levels by using 9 switches. With the

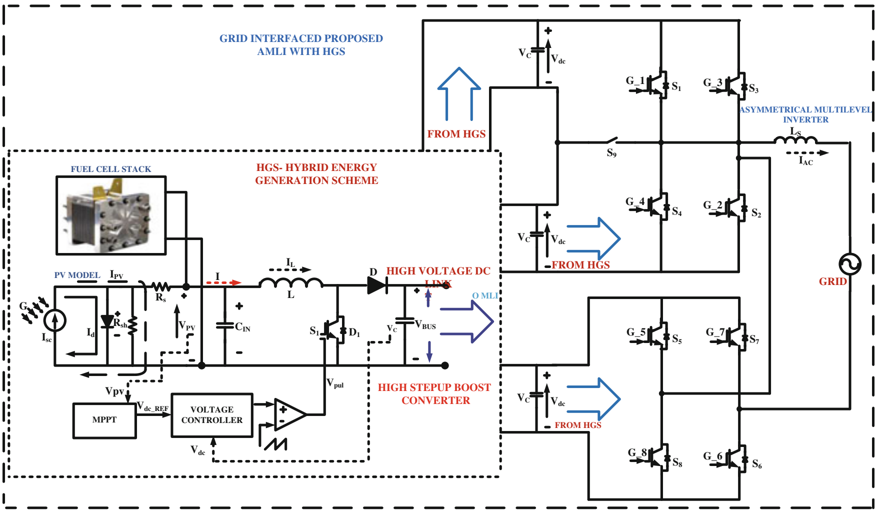

Fig. 30.3 Newly proposed topology of single-phase asymmetrical MLI interfaced to grid using HGS

Table 30.1 Number of switches required in comparison of proposed AMLI to CHB based symmetrical and asymmetrical MLI

Output voltage levels	Number of switches		
	Symmetrical CHB MLI	Asymmetrical CHB MLI	Proposing AMLI
7	12	8	9
9	16	8 or 12	9
11	20	12	9
13	24	12	9
15	28	12	9

usage of power semiconductor devices maintain dc link voltage such as high step up DC/DC converts, it converts variable dc coming from PV array to constant dc link voltage and with respect to high voltage gain and integrate to grid using AMLI.

As Table 30.1 represent the number of switches required in comparison of proposed AMLI to CHB Based symmetrical and asymmetrical MLI topologies, majorly minimization of switching devices in comparison of formal inverter topologies.

In the Table 30.2, switching configuration for production of 15 level output voltage by using newly proposed single phase AMLI with 9 switches only. In that switching states ‘1’ means switch is ‘ON’ and ‘0’ means switch is ‘OFF’.

Table 30.2 Switching pattern scheme for proposed AMLI

Vo	S_1	S_2	S_3	S_4	S_5	S_6	S_7	S_8	S_9
7Vs	1	1	0	0	1	1	0	0	0
6Vs	0	1	0	0	1	1	0	0	1
5Vs	1	0	1	0	1	1	0	0	0
4Vs	0	0	1	0	1	1	0	0	1
3Vs	0	0	1	1	1	1	0	0	0
2Vs	1	1	0	0	1	0	1	0	0
Vs	0	1	0	0	1	0	1	0	1
0	1	0	1	0	1	0	1	0	0
−Vs	0	0	1	0	1	0	1	0	1
−2Vs	0	0	1	1	1	0	1	0	0
−3Vs	1	1	0	0	0	0	1	1	0
−4Vs	0	1	0	0	0	0	1	1	1
−5Vs	1	0	1	0	0	0	1	1	0
−6Vs	0	0	1	0	0	0	1	1	1
−7Vs	0	0	1	1	0	0	1	1	0

30.4 Matlab/Simulink Modeling and Simulation Results

Figure 30.4 depicts the production of 11 level output voltage with the help of newly proposed single-phase AMLI with nine switches.

Figure 30.5 depicts the FFT Analysis of 11 Level Output Voltage of Proposed Single Phase AMLI. The fundamental voltage and THD value of 11 level output voltage produced by newly proposed single-phase 11 level AMLI are the fundamental component is 438 Volts and THD is 15.03 %.

Figure 30.6 depicts the production of 13 level output voltage with the help of newly proposed single-phase AMLI with nine switches.

Figure 30.7 depicts the FFT Analysis of 13 Level Output Voltage of Proposed Single Phase AMLI. The fundamental voltage and THD value of 13 level output voltage produced by newly proposed single-phase 13 level AMLI are the fundamental component is 520.8 Volts and THD is 14.28 %.

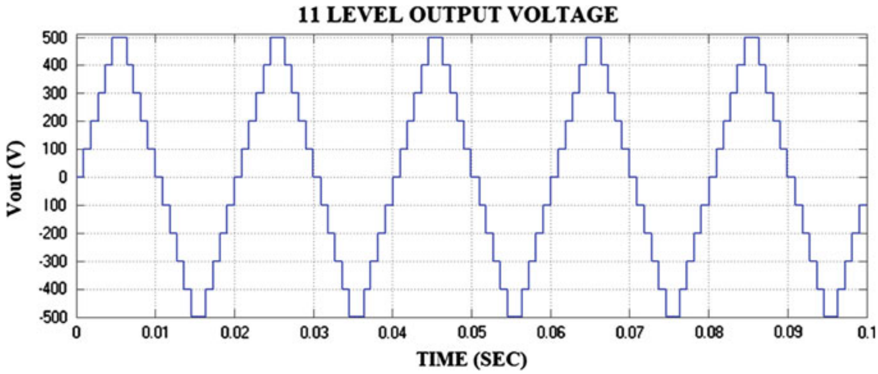

Fig. 30.4 Eleven level output voltage

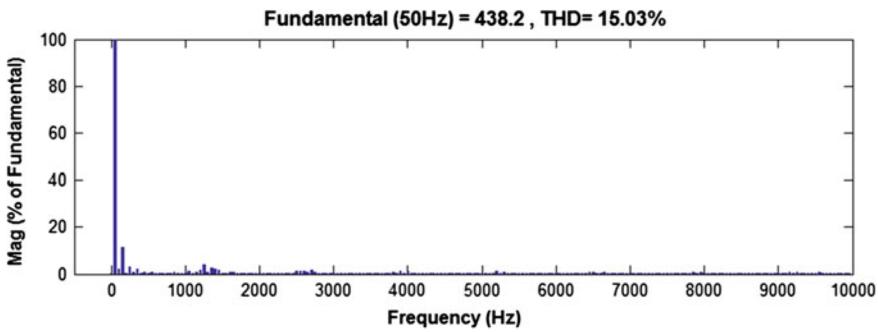

Fig. 30.5 FFT analysis of 11 level output voltage of proposed single phase AMLI

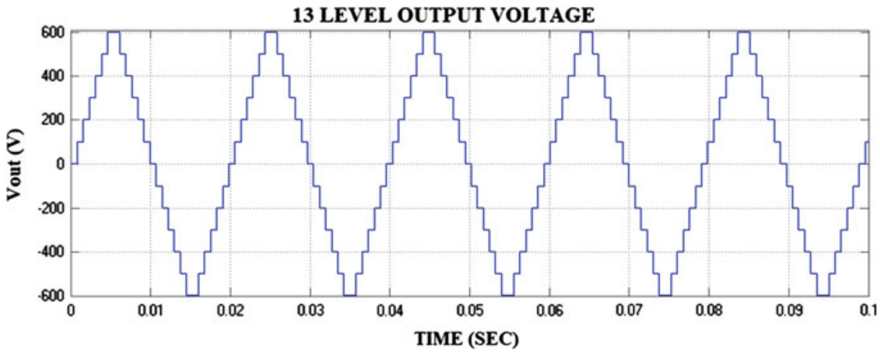

Fig. 30.6 Thirteen level output voltage

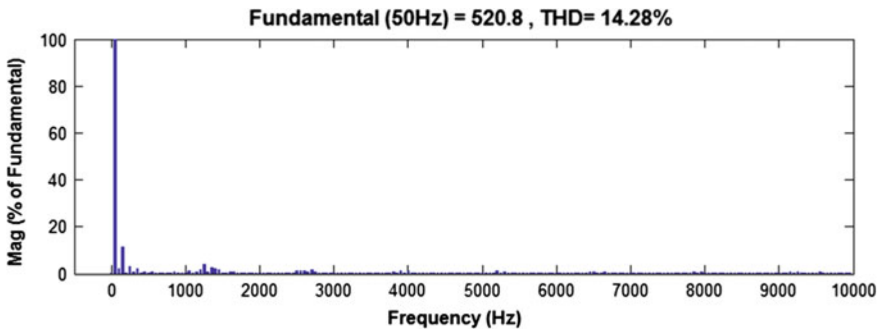

Fig. 30.7 FFT analysis of 13 level output voltage of proposed single phase AMLI

Figure 30.8 depicts the production of 15 level output voltage with the help of newly proposed three phased AMLI with 9 switches per phase.

Figure 30.9 depicts the FFT Analysis of 15 Level Output Voltage of Proposed Single Phase AMLI. The fundamental voltage and THD value of 15 level output

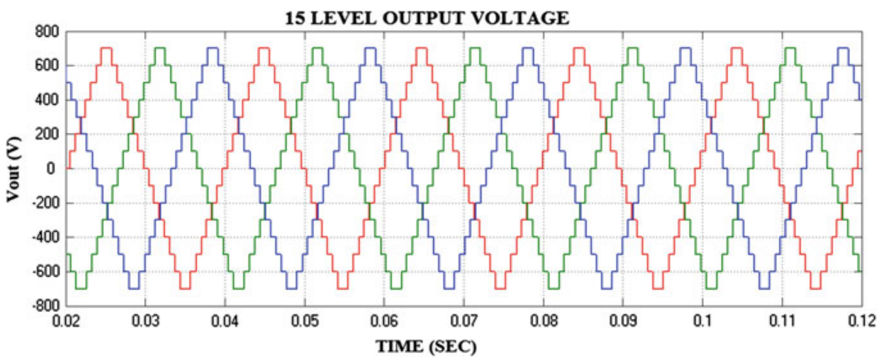

Fig. 30.8 Fifteen level output voltages

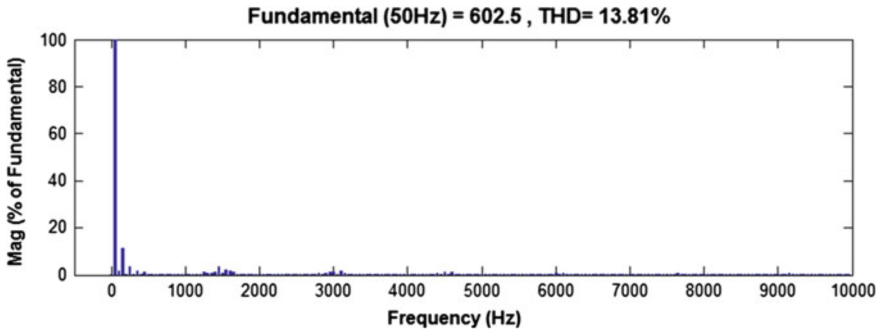

Fig. 30.9 FFT analysis of 15 level output voltage of proposed single phase AMLI

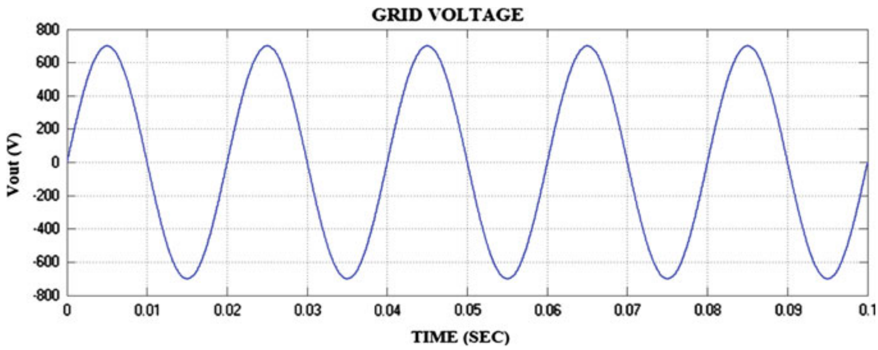

Fig. 30.10 Grid voltage

voltage produced by newly proposed single-phase 15 level AMLI are the fundamental component is 602.5 Volts and THD is 13.81 %.

Figure 30.10 depicts the grid voltage of Proposed Grid Interfaced Hybrid Generation Systems using AMLI Technique.

30.5 Conclusion

A Modern attitude to the proposed HGS strategy includes energy management of hybrid FC/PV energy generation scheme and a differential control scheme for the proposed asymmetrical multilevel inverter. The main features of the proposed HGS include high power density, high appearance and good transient response. Here proposed three phased AMLI for 7–15 levels have been evaluated by using Matlab/Simulink. The several conclusions are updated from the analysis of newly proposed three phase 15 level AMLI has less number of power devices, low space requirement, high flexible, low cost with low maintenance and may also comfort to interface with HGS to produce higher voltage levels. As more number of levels goes to increases, automatically THD content approximate to very small value as believe, thus it eradicate the needless of load side filter. The simulation results show that the proposed HGS strategy regulates the voltage at grid, reduces THD and improves power quality by using AMLI, enhancement of dynamic response at the grid beneath fast transient condition, express to balances the dc-link voltage, and meticulously manages the energy among the power sources in the HGS system.

References

1. Agelidis B, Calais M (1998) Multilevel converters for single-phase grid connected Photovoltaic systems-an overview. Proc IEEE ISIE 1:224–229
2. Kirubakaran A, Shailendra Jain, Nema RK (2009) A review on fuel cell technologies and power electronic interface. Int J Renew Sustain Energy Rev 13:2430–2440
3. Bhagwat PM, Stefanovic VR (1983) Generalized structure of a multilevel PWM inverter. IEEE Trans Ind Appl 1A–19:1057–1069
4. Bakhshai A, Jain P, Khajehoddi SA (2007) The application of the cascaded multilevel converters in grid connected photovoltaic systems. In: Proceedings IEEE EPC, Montreal, pp 296–301
5. Goyena SG, Sádaba OA (2009) Sizing and analysis of big scale and isolated electric systems based on renewable sources with energy storage. In Proceedings of IEEE PES/IAS conference sustainable alternative energy (SAE), Valencia pp 28–30
6. Correa P, Pacas M, Rodriguez J, Villanueva E (2009) Control of single phase cascaded H-bridge multilevel inverter for grid connected photovoltaic systems. IEEE Trans Ind Electron 56:4399–4406
7. Daher S, Schmid J, Antunes FLM (2008) Multilevel inverter topologies for stand-alone PV systems. IEEE Trans Ind Electron 55:2703–2712
8. Filho ER, Gazoliand J, Villalva MG (2009) Comprehensive approach to modeling and simulation of photovoltaic arrays. IEEE Trans Power Electron 24:1198–1208
9. Lai S, Rodriguez J, Peng GS (2002) Multilevel inverters: a survey of topologies, controls and applications. IEEE Trans Ind Electron 49:724–738

Chapter 31
Reactive Power Pricing Using Group Search Optimization in Deregulated Electricity Market

G. Kannan, D. Padma Subramanian and S. Siva Subramanian

Abstract This paper gives a Group Search Optimization (GSO) algorithm based reactive power pricing in deregulated electricity market. For the efficient transfer of the real power, reactive power flow must be adequate. The increased demand of the real power and insufficient reactive power forces the system to stressed operation. The real power loss is increased due to the voltage stability. This makes the Independent System Operator (ISO) to analyze and accept minimized total real power generation cost from the generating companies. The objective of the reactive power pricing is to minimize the total real power generation cost in a deregulated electricity market. The generator bus voltages, transformer tap settings, generator and capacitive reactive power compensation devices are determined for minimizing the real power generation cost in the system. This procedure is presented in IEEE 57 bus system.

Keywords Deregulated electricity market · Group search optimization · Reactive power pricing · Independent system operator

31.1 Introduction

The reactive power plays an important role in transferring the real power across the transmission system. It is a key tool for the secure and reliable operation of the power system. The main purpose of the reactive power pricing is to minimize the total real power generation cost by minimizing the real power loss in the deregulated electricity

G. Kannan (✉) · S. Siva Subramanian
Department of Electrical and Electronics Engineering, SMIT, Chennai, India
e-mail: ganapathykannan@yahoo.com

S. Siva Subramanian
e-mail: sssincredible@gmail.com

D.P. Subramanian
Faculty of Electrical and Electronics Engineering, Director-Centre for Renewable Energy and Robotic Automation, AMET University, Chennai, India
e-mail: jceprincipal2013@gmail.com

C. Kamalakannan et al. (eds.), *Power Electronics and Renewable Energy Systems*,
Lecture Notes in Electrical Engineering 326, DOI 10.1007/978-81-322-2119-7_31

market. Various conventional optimization techniques such as linear and non-linear programming were used on the proposed paper. But the time consumption was very high. Therefore, recently and naturally inspired algorithms have been used.

The power system leads to voltage collapse due to the insufficient reactive power support. For example in the report of US–Canada Power System Outage Task Force deficit reactive power was a cause in the August 2003 blackout, and has advocated strengthening of reactive power and voltage control practices in all North American Electric Reliability Council regions [1]. Therefore, the reactive power dispatch plays an important role in supporting the real power transfer across a large scale transmission system [2, 3]. The reactive power must procure from the suppliers since it cannot travel over long distances due to significant losses on the transmission lines [4–6]. The appropriate and accurate reactive power pricing is proposed which minimizes the total cost paid by the Independent System Operator (ISO) to the generators [7, 8].

The proposed paper uses Group Search Optimization method based on the animal searching behavior [9]. It is based on the producer-scrounger model, which assumes that the group members search for finding or joining opportunities. The animal scanning mechanisms are used for solving the optimization problem.

31.1.1 Deregulated Power System

In the past, the power system industry was under government control. The generation, transmission and distribution of power were done by a single entity. In the recent decades, the system underwent significant changes and went for restructuring in the electricity market known as deregulation. The aim of deregulation concept in the power system industry is to provide competition among the market participants there by giving a way to privatization. This system facilitates the consumers to have multiple choices to choose their desired electricity price from a number of generating companies [10].

Due to the deregulation in the electricity market, the power system industry is divided in three categories. They are generation, transmission and distribution systems. This lead to huge competition in the market where a number of market participants offer their bids to the Independent System Operator (ISO) of the transmission system. The ISO must analyze the system condition and accept the bid from the market participant having minimized cost.

31.2 Problem Formulation

The reactive power pricing problem is concerned with the minimization of the total real power generation cost paid by the ISO to the generating companies in deregulated electricity market subjecting to control constraints. GSO technique is adopted for solving this problem.

The objective function is to reduce the total real power generation cost which is given as follows:

$$\text{Total Cost Payment Min J} = \mathrm{Kp} \cdot \mathrm{P_{Loss}} \tag{31.1}$$

where

Kp	Cost per MW ($)
P_{Loss}	Real Power loss (MW)

Subject to

$$V_{i,min} \leq V_i \leq V_{i,max} \tag{31.2}$$

$$Q_{gi,min} \leq Q_{gi} \leq Q_{gi,max} \tag{31.3}$$

$$Q_{ci,min} \leq Q_{ci} \leq Q_{ci,max} \tag{31.4}$$

$$T_{i,min} \leq T_i \leq T_{i,max} \tag{31.5}$$

where

$Q_{ci,max}$ and $Q_{ci,min}$	the upper and lower limits of compensator reactive power output
$Q_{gi,max}$ and $Q_{gi,min}$	the upper and lower limits of generator reactive power output
$V_{i,max}$ and $V_{i,min}$	the upper and lower limits of bus voltage
$T_{i,max}$ and $T_{i,min}$	the upper and lower limits of transformer tap position

31.3 Group Search Optimization Algorithm

31.3.1 Introduction

Group Search Optimization is a newly developed algorithm inspired by animal behavioral ecology. It is a process of obtaining optimum solution in a search space. It consists of three types of members. They are producer, scrounger and ranger.

31.3.1.1 Producers

At each iteration, the candidate solution (Group member) conferring the best fitness value is chosen as producer. That member evaluates the search area for optimum position. Soon the producer will find a better position with the best fitness value. If that position has a better resource than the current position, then producer moves to that position or it will stay in current position and search for other optimal position.

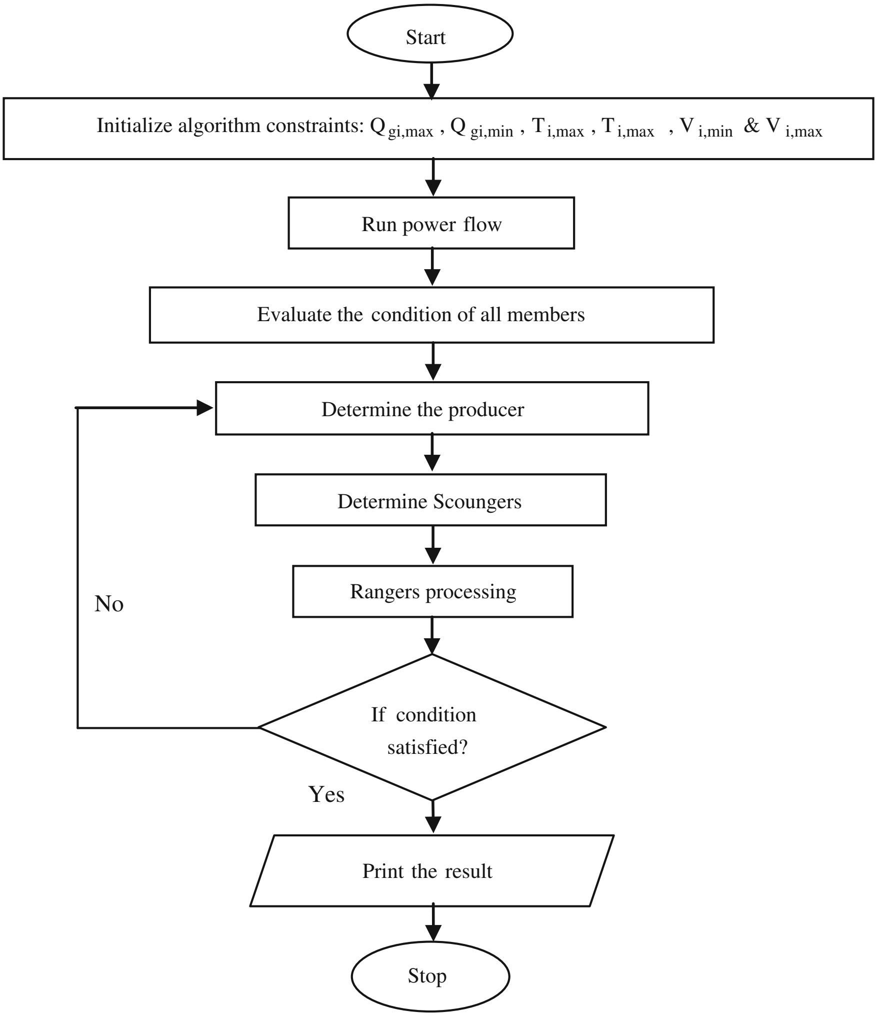

Fig. 31.1 GSO flowchart

If the producer cannot find a better position, it will retain back to its original position.

31.3.1.2 Scroungers

The job of the scroungers is keep track of the best fitness values obtained by the producers. In case, the current producer is unable to find better fitness value, it will be replaced by one of those scroungers having better fitness value next to producer.

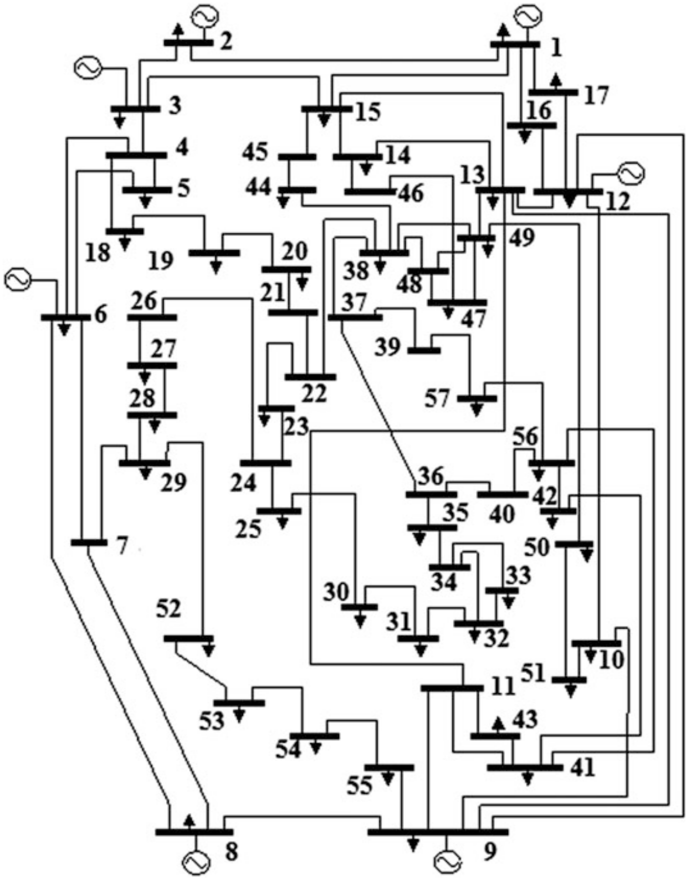

Fig. 31.2 IEEE 57 bus system

In case, if a scrounger finds better optimum position/area, it will be made as a producer in the following bout.

31.3.1.3 Rangers

The group other than producer and scroungers are the rangers. They are always less in population and do random walk in the search of better resource area. The flowchart for GSO is given in Fig. 31.1.

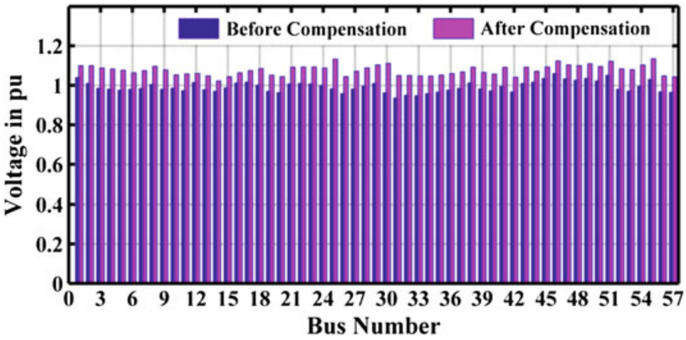

Fig. 31.3 Voltage profile comparison

Table 31.1 Limits for reactive power generation

Bus no.	1	2	3	6	8	9	12
$Q_{g\min}(MVAR)$	0	−40	−40	−40	−10	−6	−6
$Q_{g\max}(MVAR)$	10	50	50	40	40	24	24

Table 31.2 Initial values of the control variables

V_1	1.009	Q_{C25}	14.0779	T_{11-41}	0.955	T_{9-55}	0.94
V_2	1.008	Q_{C53}	10.6718	T_{15-45}	0.955	Q_{G1}	−16.1
V_3	1.003	T_{4-18}	0.97	T_{14-46}	0.9	Q_{G2}	50
V_6	1.026	T_{4-18}	0.978	T_{10-51}	0.93	Q_{G3}	60
V_8	1.044	T_{21-20}	1.043	T_{13-49}	0.895	Q_{G6}	25
V_9	1.004	T_{24-26}	1.043	T_{11-43}	0.958	Q_{G8}	62.1
V_{12}	0.992	T_{7-29}	0.967	T_{40-56}	0.958	Q_{G9}	2.2
Q_{C18}	10.897	T_{34-32}	0.975	T_{39-57}	0.98	Q_{G12}	128.5

31.4 Testing Cases, Results and Discussion

The IEEE 57 bus system is shown in Fig. 31.2. The number of control variables for IEEE 57 bus system is 32. The number of bus voltage limits is 7. The number of capacitive reactive power compensation device is 3. The number of generator reactive compensators is 7 and the number of transformer tap positions is 15. The load flow analysis of the IEEE 57 bus system is performed using Newton-Raphson power flow method in MATLAB. The base case real power cost is obtained as \$2,786.4. The total real power generation cost is reduced to \$2,481.81. Thus, the results obtained show that the Group Search Optimization has helped in the optimization of the reactive power pricing in IEEE 57 bus system, thus minimizing the total real power cost.

Table 31.3 Optimal values of the control variables obtained using GSO

V_1	1.1	Q_{C25}	14.0779	$T_{11–41}$	0.98121	$T_{9–55}$	0.973481
V_2	1.1	Q_{C53}	10.6718	$T_{15–45}$	0.95	Q_{G1}	8.16912
V_3	1.09393	$T_{4–18}$	1.04986	$T_{14–46}$	1.0151	Q_{G2}	36.8901
V_6	1.07365	$T_{4–18}$	1.00994	$T_{10–51}$	0.95	Q_{G3}	7.85802
V_8	1.9724	$T_{21–20}$	0.95	$T_{13–49}$	0.950007	Q_{G6}	32.9213
V_9	1.08889	$T_{24–26}$	0.950385	$T_{11–43}$	1.04986	Q_{G8}	31.1122
V_{12}	1.07376	$T_{7–29}$	0.95	$T_{40–56}$	0.95178	Q_{G9}	17.2714
Q_{C18}	10.897	$T_{34–32}$	0.95	$T_{39–57}$	0.975272	Q_{G12}	1.06576

Table 31.4 Limits for voltage and tap-setting (in p.u.)

V_G^{max}	V_G^{min}	V_{load}^{max}	V_{load}^{min}	T_k^{max}	T_k^{min}
1.1	0.95	1.1	0.95	1.05	0.95

Table 31.5 Comparison of simulated results for IEEE 57-bus system (real power cost minimization)

Cost	Initial condition	GSO
$/h	$2,786.4	$2,481.81

The voltage levels of the 57-buses before and after optimization are compared and it is seen that the voltage profile of the system has been improved after reactive power optimization using Group Search Optimization as shown in Fig. 31.3.

The limits for reactive power generation and voltage tap settings are given as shown in Tables 31.1 and 31.2 respectively. The control variables for IEEE 57 bus system are buses 1, 2, 3, 6, 8, 9 and 12 are shown in Table 31.3. The GSO is applied in order to obtain the optimal values of these control variables and the values obtained are shown in Table 31.4.

The total cost minimized after optimization using GSO algorithm is obtained to be $2,481.81. The optimized result is compared with that of the base case result and the result below as shown in Table 31.5.

31.5 Conclusion

In this paper, reactive power pricing using Group Search Optimization method is presented. Due to the increased demand of the real power and insufficient reactive power support, the power system operates under stressed condition. This leads to voltage instability and increased real power loss. This makes the Independent System Operator (ISO) to pay higher amount to the generators. The simulation results using MATLAB are carried out. From the result analysis, the total cost is minimized with the minimization of the real power loss (P_{Loss}). This algorithm is tested on IEEE-57 bus system for various control parameters of GSO. This proposed work minimizes the real power generation cost to the generating company for providing required reactive power support. This paper gives the reactive power dispatch model and re-scheduling of real power of generators exceeding its maximum limit of reactive power.

References

1. Sedighizadeh M, Rezazadeh A, Seyed Yazdi M (2010) Pricing of reactive power service in deregulated electricity markets based on particle swarm optimization. Int J Comput Electr Eng 2(6):pp 960–961
2. Singh A, Kalra PK, Chauhan DS (2009) A novel procurement market model approach of reactive power in deregulated electricity market. Int J Recent Trends Eng 2(5):363–365
3. Saadat H (1999) Power system analysis. McGraw-Hill Company, New York
4. Mahesh V, Deepeeha JR, Kamaraj N (2013) Reactive power dispatch and its pricing in re-structured electricity markets. In: International conference on power, energy and control (ICPEC), 2013, pp 378–379
5. El-Samahy I, Canizares CA, Bhattacharya K, Pan J (2007) An optimal reactive power dispatch model for deregulated electricity markets. In: Proceedings in IEEE power engineering society general meeting, June 2007, pp 1–5
6. Saunders JR, Wu QH (2006) A novel group search optimizer inspired by animal behavioural ecology. In: IEEE congress on evolutionary computation, 16–21 July 2006. Sheraton Vancouver Wall Centre Hotel, Vancouver, pp 4415–4418
7. Lee KY, Bai X (1995) Optimization method for reactive power planning by using a modified simple genetic algorithm. IEEE Trans Power Syst 10(4):1844–1847
8. US–Canada Power System Outrage Task Force. Final Report on the 14 Aug 2003, Blackout in the United States and Canada: causes and recommendations, issued April 2004
9. El-Samahy I, Battacharya K, Canizares CA, Anjos M, Pan J (2008) A procurement market model for reactive power services considering system security. IEEE Trans Power Syst 23:6–9
10. Canizares CA, Bhattacharya K, El-Samahy I, Haghighat H, Pan J, Tang C (2010) Re-defining the reactive power dispatch problem in the context of competitive electricity markets. IET Gener Transm Distrib 4:164–170

Chapter 32
Enhanced Controllers of DFIG with Unbalanced and Distorted Grid Voltage Conditions

A. Ramkumar, S. Durairaj and K. Dhivya

Abstract This project focuses on the enhanced and development of the controller of doubly fed induction generator (DFIG) with unbalanced and distorted grid voltage conditions. Real, reactive power and electromagnetic torque are improved by using the design and development of the proportional integral-dual frequency resonator (PI-DFR), Second order generalized integrator (SOGI), Frequency locked loop (FLL), multiple second order generalized integrator-frequency locked loop (MSOGI-FLL). Finally fundamental, fifth and seventh order harmonics are removed by using Fast Fourier transform (FFT) and also determine Total harmonic distortion (THD) and Individual harmonic distortion (IHD). The simulation result is exposed using power system computer aided design (PSCAD).

Keywords Direct torque controller · Doubly fed induction generator (DFIG) · Wind Power · Proportional integral-dual frequency resonator (PI-DFR) · Second order generalized integrator (SOGI)

32.1 Introduction

Wind energy is also known as a kind of clean and environmental energy. The Doubly fed induction generator (DFIG) system applied to wind power generation has gained substantial academic responsiveness and industrial application during the part 10 years. Voltage sag, Voltage distortion, Voltage imbalance and harmonics are occurred in previous work. This project using the doubly fed induction generator (DFIG) and some advantages are occurred in this system, so avoid voltage disturbances and harmonics. Doubly fed induction generator (DFIG) is used

A. Ramkumar · K. Dhivya (✉)
Department of EEE, Kalasalingam University, Srivilliputhur, Tamil Nadu, India
e-mail: dhivyakandeepan@gmail.com

S. Durairaj
Department of EEE, Kings College of Engineering, Tanjore, Tamil Nadu, India

C. Kamalakannan et al. (eds.), *Power Electronics and Renewable Energy Systems*,
Lecture Notes in Electrical Engineering 326, DOI 10.1007/978-81-322-2119-7_32

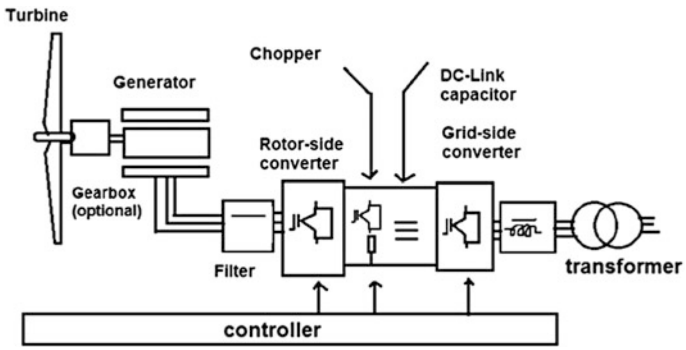

Fig. 32.1 DFIG configuration of wind turbine system rotor side converter (*RSC*) and grid side converter (*GSC*)

to enhance the uninterruptable capabilities of wind turbine system and variable speed wind turbine system. The efficiency of the doubly fed induction generator is high because rotor voltage and currents of the rotor circuit is controlled by a power electronic converter. This converter cost is low when compared with other variable speed solutions.

32.2 Block Diagram

A typical doubly fed induction generator (DFIG) configuration of a wind turbine is shown in Fig. 32.1. It consists of wind turbine, generator, rotor side converter (RSC), grid side converter (GSC) and a universal DC bus. Wind turbine connected to the doubly fed induction generator (DFIG). Here Rotor side converter (RSC) and Grid side converter (GSC) is connected in series. The Rotor side converter (RSC) provides the excitation of the induction machine rotor. With this Pulse width modulation (PWM) converter it is possible to control the torque hence the speed of the doubly fed induction generator (DFIG) and also power factor at the stator terminals. The rotor side converter provides an unpredictable excitation frequency depending on the wind speed conditions [1]. The grid side converter (GSC) controls the flow of real and reactive power toward the grid, throughout the grid interfacing inductance.

32.3 PI-DFR Controller

See Fig. 32.2.

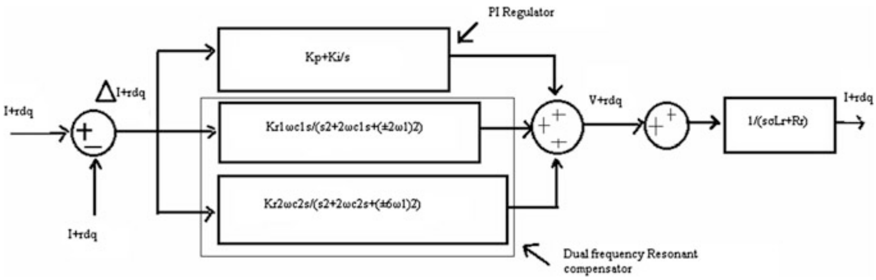

Fig. 32.2 Rotor current controller based on DFIG controller scheme

32.4 SOGI-FLL

The reassign task of the SOGI is given by,

$$SOGI(S) = \frac{V'}{k\varepsilon v(s)} = \frac{\omega' s}{s^2 + \omega'^2} \tag{32.1}$$

where the resonance frequency was called ω′ to difference it from the input frequency ω. The two in—quadrature output signals of the adaptive filter in Fig. 32.3. The bandwidth of the band pass filter exclusively set by the gain k and is independent of the center frequency ω′. The same happens with the low—pass filter of (4), in which the static gain only depends on k. Multiple second order generalized integrator-frequency locked loop (MSOGI-FLL) operation similar to the SOGI-FLL. Two or more SOGI connected in series, it is called as the MSOGI-FLL. Abbreviation of the FLL is frequency locked loop. Adaptive filters are including the FLL [2]. To give the input signal Era, Erb to a comparator and compare this signal

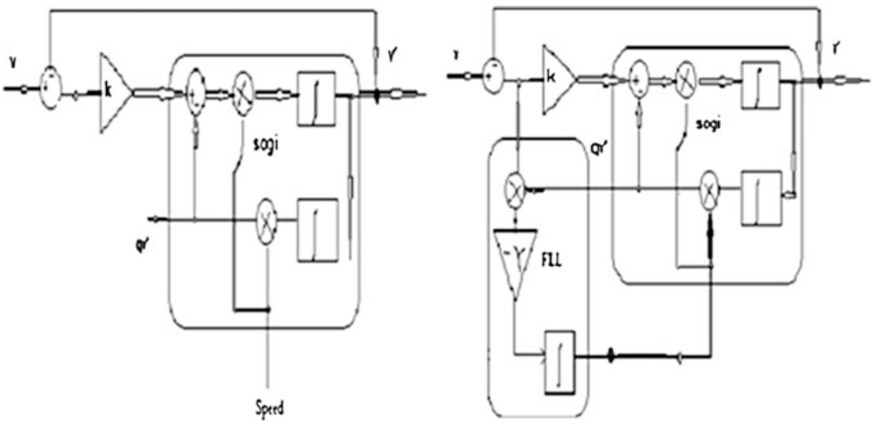

Fig. 32.3 Adaptive filter based on SOGI and SOGI-FLL

and this given to gain. Gain component adjust the gain value and to produce the accurate output voltage, it is the function of FLL [3].

32.5 DFIG Control Simulation Diagram

In this test system is shown in Fig. 32.4. The PI-DFR, SOGI, SOGI-FLL and MSOGI-FLL are added in the rotor circuit. The simulation results of DFIG with its controller are analyzed by PSCAD tool. The results are obtained from the following cases:

1. PI-DFR controller
2. SOGI
3. SOGI-FLL
4. MSOGI-FLL

This is doubly fed induction generator (DFIG) simulation diagram. These constructions are shown in Fig. 32.4. Wind turbine connected to the DFIG. This machine can be operated in either speed control (or) torque control mode. Normally, the machine is started in speed control mode with the 'w' input set to rated per—unit speed and then switched over to torque control after the initial transients at the machine die out. i.e., reaches steady—state [4]. This DFIG machine connected to the rotor side converter (RSC) and grid side converter (GSC). This principle and operations are already explained. Breaking capacitor connected to the main transmission line. The ON (closed) and OFF (open) resistance of the breaker must be specified along with its initial state. This element is proscribed through a named input signal, where the breaker logic is 0 = ON (closed) 1 = OFF (open).

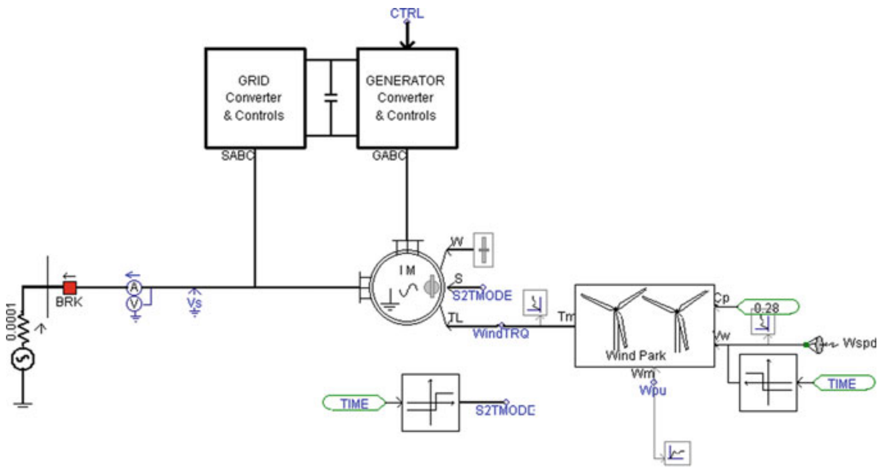

Fig. 32.4 DFIG simulation diagram using PSCAD

The output of timed fault logic is used specifically for controlling the fault state and duration of fault. Finally, produce the torque, real, reactive power and speed output waveform.

32.6 Simulation Results

32.6.1 PI-DFR Controller

Real power, reactive power, Electromagnetic torque, Speed, Capacitor voltage output waveform as shown in Fig. 32.5. To draw the graph between the speed versus time. Initially speed constant value increase the time, speed reaches the maximum value and speed values are decreased. Finally, speed is constant. To draw

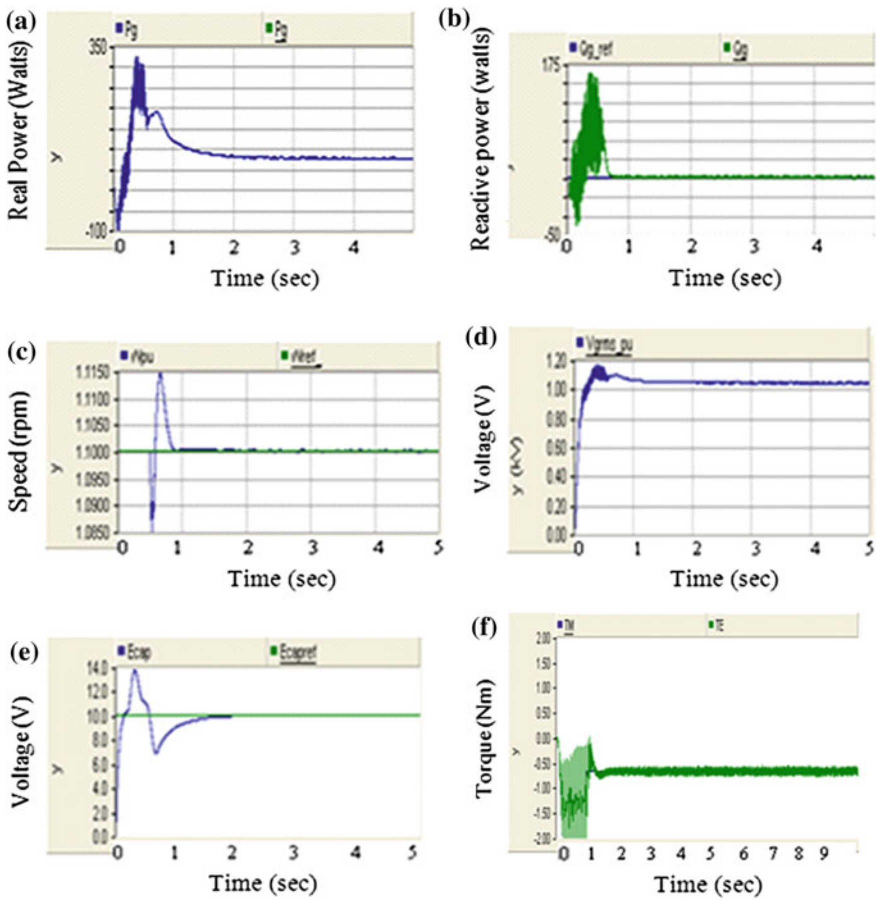

Fig. 32.5 **a** Reactive power, **b** real power, **c** speed, **d** breaking capacitor, **e** E-cap and **f** torque using PI-DFR controller

the graph between the power versus time. Initially, power decreases increases. To draw the graph between the speed versus time. Initially speed constant value increase the time, speed reaches the maximum value and speed values are decreased. Finally, speed is constant. To draw the graph between the power versus time. Initially, power decreases increase the simulation time, power reaches the maximum value, and after its decreases particular time power values are maintain the constant [5]. To draw the graph between the voltage and current versus time, here breaking capacitor voltage and DC current values are constant. To draw the graph between the voltage versus time. As simulation time increases voltage increases from zero to maximum value, and then its decreases and after sometime voltage is constant the simulation time, power reaches the maximum value, and after its decreases particular time power values are maintain the constant. To draw the graph between the voltage and current versus time, here breaking capacitor voltage and DC current values are constant. To draw the graph between the voltage versus time. As simulation time increases voltage increases from zero to maximum value, and then its decreases and after sometime voltage is constant. When SOGI controller added in the rotor circuit, simulation outputs are improved compare to the PI-DFR controller [6]. Compare the SOGI and SOGI-FLL output diagram, the outputs are improved by adding MSOGI-FLL in the rotor circuit.

Comparing the previous method real, reactive power and electromagnetic torque are improved by using the design and development of the proportional integral-dual frequency resonator (PI-DFR), Second order generalized integrator (SOGI), Frequency locked loop (FLL), multiple second order generalized integrator-frequency locked loop (MSOGI-FLL). Here, the PI-DFR, SOGI, SOGI-FLL and MSOGI-FLL controllers are used. SOGI controller added in the rotor circuit, compare the previous method outputs are improved. Figure 32.6a, b if input voltages are used evaluate

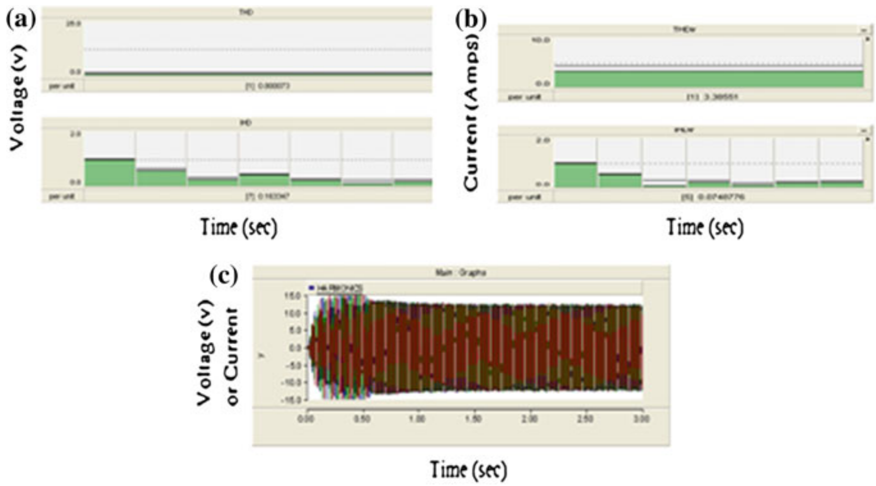

Fig. 32.6 Simulation diagram of Fast Fourier Transform

THD voltage and IHD voltage. To draw the graph between the voltage versus time. Here fundamental to seventh order harmonic spectrum displayed [7]. If you want to determine the THD and IHD values of any order, to click the respected columns.

32.7 Conclusion

In this paper enhanced and development of the controller of doubly fed induction generator (DFIG) with unbalanced and distorted grid voltage circumstances. Real, reactive power and electromagnetic torque are enhanced by using the design and development of the Proportional integral-dual frequency resonator (PI-DFR) i.e., resonant controller. Second order generalized integrator (SOGI), frequency locked loop (FLL), Multiple second order generalized integrator-frequency locked loop (MSOGI-FLL). As PI-DFR added in the rotor circuit, real reactive power and electromagnetic torque are improved. SOGI controller added in the rotor circuit, compare the previous method outputs are improved. Similarly, SOGI-FLL and MSOGI-FLL added in the rotor circuit, compare the previous method outputs are improved. Fundamental, fifth and seventh order harmonics are removed by using Fast Fourier transform (FFT) and also determine Total harmonic distortion (THD) and Individual harmonic distortion (IHD). For the future work real, reactive power and electromagnetic torque are improved and harmonics are removed by using the direct power, direct torque and direct controllers.

Acknowledgment The Authors thankfully acknowledge the management of Kalasalingam University, Krishnankoil, Tamil Nadu. India for their constant support and encouragement unmitigated during this research.

References

1. Liu C, Blaabjerg F, Chen W, Xu D (2012) Stator current harmonic control with resonant controller for doubly fed induction generator. IEEE Trans Power Electron 27(7):3207–3220
2. Okedu KE, Muyeen SM, Takahashi R, Tamura J (2012) Wind farms fault ride through using DFIG with new protection scheme. IEEE Trans Sustain Energy 3(2):242–254
3. Martinez MI, Tapia G, Susperregui A, Camblong H (2012) Sliding—mode control for DFIG rotor—side and grid—side converters under unbalanced and harmonically distorted grid voltage. IEEE Trans Energy Convers 27(2):328–339
4. Abdel-Baqi O, NasiriA (2010) A dynamic LVRT solution for doubly fed induction generators. IEEE Trans Power Electron 25(1):193–196
5. Liang S, Hu Q, Lee W-J (2012) A survey of harmonic emissions of a commercially operated wind farm. IEEE Trans Ind Appl 48(3):1115–1123
6. Rodriguez P, Pou J, Candela JI, Burgos RP, Boroyevich D (2007) Decoupled double synchronous reference frame PLL for power converter control. IEEE Trans Power Electron 22 (2):584–592
7. Rodriguez P, Luna A, Candela I, Mujal R, Teodorescu R, Blaabjerg F (2011) Multiresonant frequency—locked loop for grid synchronization of power converters under distorted grid conditions. IEEE Trans Ind Electron 58(1):127–138

Chapter 33
FPGA Controlled Power Conditioning System for Solar PV Fed PMDC Motor

Dogga Raveendhra, Padmanabh Thakur and Abhisekh Chauhan

Abstract In this paper, an appropriate power conditioning unit of 1.15 kWp solar array, for PMDC motor, is designed in MATLAB® and Xilinx system generator environment. The solar array consists of 7 modules in parallel configurations. Field Programmable Gate Array (FPGA) generated pulses are used to control the proposed power conditioning system with constant voltage method maximum power point method for all types of environmental circumferences. It is revealed that the characteristics of the proposed power conditioning unit, at maximum power point tracking (MPPT) condition, are in tune with the characteristics of PMDC motor and hence found proficient to drive it. Hence, the proposed power conditioning unit can be coupled to PMDC motor, suitable for water pumping application, to reduce the crisis of water shortage in rural areas.

Keywords PMDC motor · Field programmable gate array · PV system · Boost converter · Village water pumping

33.1 Introduction

Nowadays, shortage of electrical power and water has become a pressing issue, amongst the people, particularly in rural area. The huge demand of power and exhaustion of the conventional energy resources, make a leading concern amongst the researcher, to search for alternate sources of energy. The various types of alternate resources, for electric power generation, are now available to handle the strange consequence arising due to these issues. Among the available resources, the solar energy has received utmost attention, due to its external attributes [1–5]. Recently, the solar PV and water pumping systems coupled to it, have been drawn great attention among the researchers and industrial engineers, to reduce the scarcity

D. Raveendhra (✉) · P. Thakur · A. Chauhan
Department of EEE, Graphic Era University, Dehradun 248001, India
e-mail: doggaravi09@gmail.com

C. Kamalakannan et al. (eds.), *Power Electronics and Renewable Energy Systems*,
Lecture Notes in Electrical Engineering 326, DOI 10.1007/978-81-322-2119-7_33

of electrical power and shortage of water existing, specially, in villages [1–6]. The significant efforts were made by the researchers to develop a solar based pumping system using, semiconductor technology [5, 10–12, 15].

Generally, dc [1–8] and ac [9–14] powered water pumping systems fed by solar power, using various MPPT algorithms implemented in different controllers were reported in literatures. Variation of solar irradiation and average temperature has been investigated in [4] for the proper sizing of solar water pumping systems with more accuracy. Further, Four-Quadrant PWM converter driving the PMDC motor [5], optimization of system efficiencies [6], novel multi-input DC boost converter for brushless DC motor (BLDC) fed by photovoltaic (PV) array [7], design and performance analysis of a DC PV water pumping system in absence of battery and inverter [8], stand-alone PV water pumping system without battery [9–11], an induction-motor-pump fed by a PV generator and field-oriented control [12], low solar DC voltage comprises DC-AC converter with high-frequency DC-DC stage and machine-pump [13], PV water-pump control system based on digital signal processor [14] were investigated and documented in existing studies. Lot of computational efforts, issues related to memory usage for calculations, A/D and D/A conversions, clock frequencies of used controller and dynamic control are the major pitfalls of these aforementioned studies [1–15]. These shortcomings and inabilities, motivates the researchers to develop a holistic technique to reduce these inconsistencies.

Considering these shortfalls, this paper presents FPGA controlled DC powered solar power conditioning system for water pumping system being operated at the maximum operating point of solar array. It is proven that the proposed technique implemented in FPGA is found suitable for achieving MPPT, offers less quantization effects, on board A/D and D/A conversion, low controller design complexity, faster clock frequency and dynamic control.

33.2 Proposed System and Discussions on Simulation Results

The schematic of the proposed solar PV system is presented in Fig. 33.1, which runs a PMDC fed a centrifugal pump load for water pumping and treatment plants in rural areas. The proposed technique uses MPPT based DC-DC boost converter, controlled by the firing angle, generated from the FPGA, to obtain high and constant magnitude of voltage supply required by PMDC motor. The DC supply from FPGA controlled converter is found more compatible with less quantization effects, on board A/D and D/A conversions and fast dynamic response than the existing methods, and hence to drive the PMDC motor.

The data used to investigate the performance analysis of proposed technique are summarized in Table 33.1.

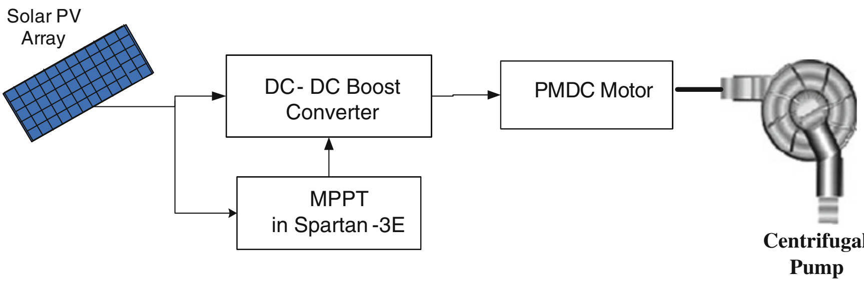

Fig. 33.1 Schematic diagram of the proposed system: PV array fed PMDC motor through DC storage

Table 33.1 Design specifications of solar PV module [16]

Data sheet values		Estimated parameters	
I_{sc}	7.36 A	I_{ph}	7.36
V_{oc}	30.4 V	I_o	0.104 μA
V_{mpp}	24.2 V	A	1.310
I_{mpp}	6.83 A	R_s	0.251 Ω
N_s	50	R_{sh}	1,168 Ω
Temperature coefficients			
K_i	0.057 %	K_v	−0.346 %

Here, I_{sc} = Short circuit current, I_{ph} = Photon current, V_{oc} = Open circuit voltage, Io = diode current, V_{mpp} = Voltage at maximum power, A = Diode factor, I_{mpp} = Current at maximum power, R_s = series resistance, N_s = No. of Series connected solar cells, R_{sh} = Shunt resistance, and Temperature Coefficients: K_i = Temperature Coefficient for current, K_v = Temperature Coefficient for voltage

The output voltage (in volts) and current (in Amps) of PV module waveforms, using data depicted in Table 33.1, Figs. 33.2 and 33.3. These figures are observed under different temperature (Varying from 20 to 40 °C) and irradiation level (varying from 900 to 1,000 W/m^2), results in variable dc voltage and currents at the output of the module.

Fig. 33.2 Solar module output voltage

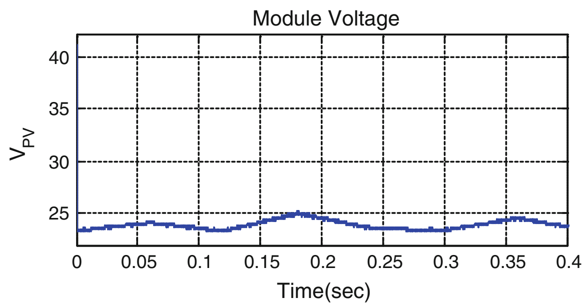

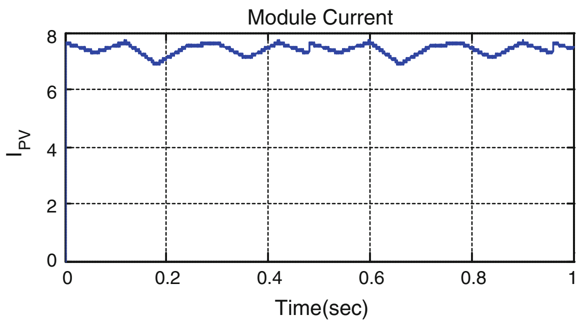

Fig. 33.3 Solar module output current

To make these voltages and currents constant and also to extract maximum power from the modules, Constant Voltage mode MPPT controlled boost converter is designed to drive PMDC motor for water pumping applications with following details.

Input voltage of the converter = 23–25 V (available voltage from module), the output voltage of the converter = 60 V (required by PMDC motor), output power of the converter = 165 W (at maximum power point condition, power from the module), assumed switching frequency to operate switch = 20 kHz.

Based above data, the key elements of the boost converter calculated as follows, Inductor = 700 μH, Capacitor C = 470 μF and their parasitic elements ESR of inductor = 0.019 Ω, ESR of capacitor = 0.111 Ω, internal on-state resistance of MOSFET = 0.18 Ω and on-state voltage drop of diode = 0.8 V. Designed dc-dc converter transfer function is shown in Eq. (33.1), and controlled with MPPT based voltage controller having transfer function shown in Eq. (33.2).

$$\text{Module based charge controller Transfer function } \frac{-0.7593s^2 - 1.112e^4 s + 6.578e^7}{s^2 + 536.3s + 4.386e^5} \tag{33.1}$$

$$\text{Controller transfer function for MPPT controller: } \frac{-0.14s + 174.2}{s} \tag{33.2}$$

Performance and robustness parameters of the controller are shown in following Table 33.2.

From the performance and robustness parameters of the controller, it is clear that

1. $W_{pc} > W_{gc}$, closed loop MPPT charge controller is stable,
2. Rise time reflects dynamic controlling,
3. Control technique is deployed into XilinxXC3S5000-FG900 Spartan-3 board and generated pulses in the Xilinx ISE environment are shown in Fig. 33.4.

Some of the key features of this board like Xilinx16Mbit Platform Flash configuration PROM, Xilinx64-macrocell XC2C64A Cool Runner CPLD, 64 MByte (512 Mbit) of DDRSDRAM, 40 MHz clock oscillator and socket for an auxiliary

Table 33.2 Performance and robustness parameters of controller

Time-domain specifications		Frequency-domain specifications	
Rise time Tr	0.00157	Gain margin	4.64 dB
Settling time Ts	0.0152	Phase margin	60°
Percentage peak overshoot %Mp	17.2	Phase crossover frequency W_{pc}	1,052 rad/s
		Gain crossover frequency W_{gc}	417 rad/s

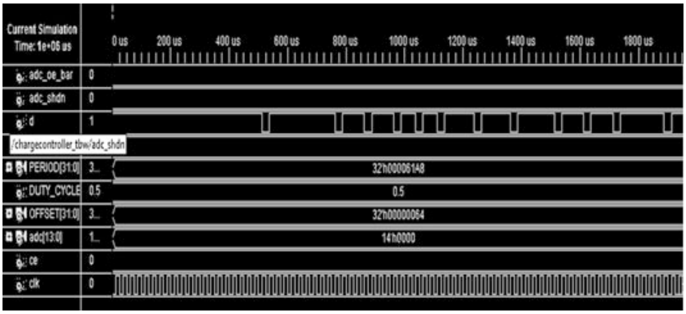

Fig. 33.4 Firing pulses from Xilinx ISE

crystal oscillator and On board add-on card (AD9240) with two14bit ADCs and two12bit DACs, provides sorting out the problems of quantization effects, A/D and D/A conversion, and controller design complexity, and low clock frequency.

MPPT based Solar PV modules of 7 numbers together in parallel mode, forms an MPPT based solar PV array, to meet power demand of PMDC motor, details shown in Table 33.3 and its output voltage and current waveform are shown in Fig. 33.5.

To test the performance of PMDC motor for water pumping applications, motor and centrifugal pump is modelled in MATLAB Simulink; data taken to model them are presented in Table 33.4. Modeled Simulink model of PMDC motor is connected to the output terminals of the PV array and observed following results shown in Figs. 33.6, 33.7 and 33.8. From these results, it is clear that required operating point in the characteristics of PMDC is achieved to drive the centrifugal pump at maximum operating condition of solar PV array.

Table 33.3 Details of solar PV array

	Module	After MPPT at module level	Array
Maximum voltage	24.2 V	60 V	60 V
Maximum current	6.83 A	2.75	19.25
Maximum power	165 W	160 W	1.15 kW

Fig. 33.5 PV array voltage and current

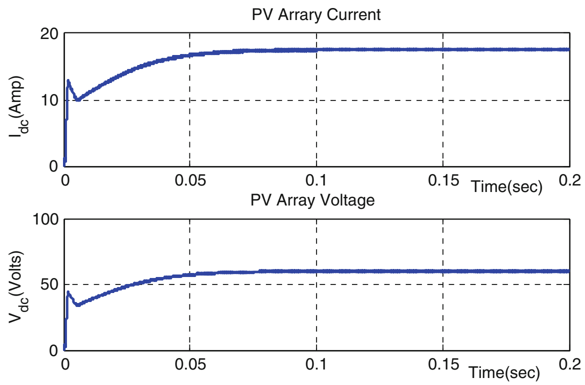

Table 33.4 Parameters of DC PM motor and load (manufactured by Kirloskar Electric Company, India) [1]

PMDC motor data		Load data	
V	60 V	J	0.024 kg-m^2
I	16.5 A	C	0.08 N-m
Ω	272.3 rad/s	D	0.0010 N-m/(rad/s)
R_a	0.8 Ω	T_L	$0.15 + 1.653 \times 10^{-5}\ \omega^2$
K_ϕ	0.175 V/(rad/s)		

V = rated motor Voltage, I = rated armature current, Ω = rated motor speed, R_a = Armature resistance, K_ϕ = Voltage and torque coefficient of dc PM motor, J = Moment of inertia, C = Torque constant for rotational losses, D = Viscous torque constant for rotational losses, T_L = Electromagnetic and centrifugal pump load torque

Fig. 33.6 Electromagnetic torque produced by PMDC motor

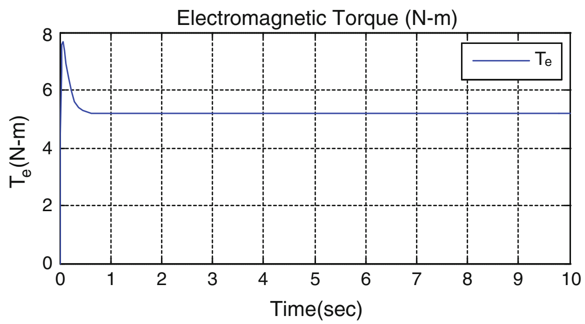

Fig. 33.7 Armature current of PMDC motor

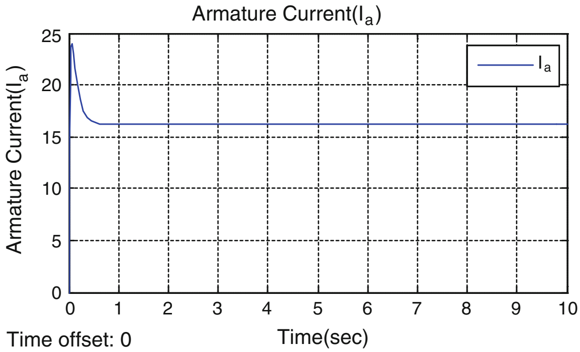

Fig. 33.8 PMDC motor speed

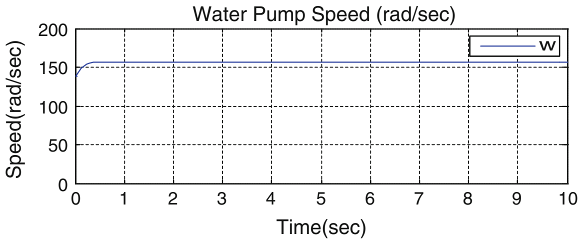

33.3 Conclusions

The proposed system computer simulations on Xilinx system generator interfaced MATLAB Simulink platform, assisted a lot for analyzing the system in t-domain and frequency domain, calculations of performance parameters of the controller and to investigate the feasibility of practical implementation. These results presented in this paper reveal the fact that, under different temperature (Varying from 20 to 40 °C) and irradiance (varying from 900 to 1,000 W/m^2) conditions always Wpc > Wgc, depicts that closed loop MPPT charge controller is stable under all atmospheric conditions. Time domain specifications presented in Table 33.2 reveals that designed controller offers very fast dynamic response. FPGA controlled MPPT algorithm offers high dynamic response, no quantization effects, no problems related to A/D and D/A conversion and low-complexity over conventional controllers.

References

1. Kolhe M, Joshi JC, Kothari DP (2004) Performance analysis of a directly coupled photovoltaic water-pumping system. In: IEEE Trans Energy Convers 19(3):613–618 (IEEE Press, New York)
2. Minai AF, Tariq A, Alam Q (2011) Theoretical and experimental analysis of photovoltaic water pumping system. In: 2010 India international conference on power electronics (IICPE), IEEE Press, New York, pp 1–8

3. Mokeddem A, Midoun A, Ziani N, Kadri D, Hiadsi S (2007) Test and analysis of a photovoltaic DC-motor pumping system. In: ICTON mediterranean winter conference. IEEE Press, New York, pp 1–7
4. Acakpovi A, Xavier FF, Awuah-Baffour R (2012) Analytical method of sizing photovoltaic water pumping system. In: IEEE 4th international conference on adaptive science and technology. IEEE Press, New York, pp 65–69
5. Sharaf AM, Yang L (2006) A novel maximum power tracking controller for a stand-alone photovoltaic DC motor drive. In: Canadian conference on electrical and computer engineering. IEEE Press, New York, pp 450–453
6. Dunlop JP (1988) Analysis and design optimization of photovoltaic water pumping systems. In: Conference record of the twentieth IEEE photovoltaic specialists conference. IEEE Press, New York, pp 1182–1187
7. Feyzi MR, MozaffariNiapour SAK, Nejabatkhah F, Danyali S, Feizi A (2011) Brushless DC motor drive based on multi-input DC boost converter supplemented by hybrid PV/FC/battery power system. In: 24th Canadian conference on electrical and computer engineering. IEEE Press, New York, pp 442–446
8. Khan MTA, Ahmed MR, Ahmed SI, Khan SI (2012) Design and performance analysis of water pumping using solar PV. In: 2nd international conference on the developments in renewable energy technology. IEEE Press, New York, pp 1–4
9. Malla SG, Bhende CN, Mishra S (2011) Photovoltaic based water pumping system. In: 2011 international conference on energy, automation, and signal (ICEAS). IEEE Press, New York, pp 1–4
10. Guo H, Xu Z, Li Y-C, Wang H (2005) A novel maximum power point tracking strategy for stand-alone solar pumping systems. In: IEEE/PES transmission and distribution conference and exhibition: Asia and Pacific. IEEE Press, New York, pp 1–5
11. Caracas JVM, Teixeira LFM, Farias GDC, Ribeiro LADS (2012) Implementation of a high efficiency and low cost converter for a photovoltaic water pumping system. In: Twenty-seventh annual IEEE applied power electronics conference and exposition. IEEE Press, New York, pp 2080–2086
12. Marouani R, Bacha F (2009) A maximum-power-point tracking algorithm applied to a photovoltaic water-pumping system. In: 8th international symposium on advanced electromechanical motion systems and electric drives joint symposium. IEEE Press, New York, pp 1–6
13. Mao M, Su J, Liuchen C, Zhang G, Lai J (2008) Research on the performance of induction-motor-based residential photovoltaic water pump system. In: Canadian conference on electrical and computer engineering. IEEE Press, New York, pp 1867–1870
14. Jiang D, Mo Y, Jiang W, Huang H, Zhang L, Xu P, Hu X (2011) Design of photovoltaic water-pump control system based on TMS320F2812. In: International conference on materials for renewable energy and environment. IEEE Press, New York, pp 147–150
15. Saggini S, Garcea G, Ghioni M, Mattavelli P (2005) Analysis of high-performance synchronous-asynchronous digital control for DC-DC boost converters. In: Twentieth annual IEEE applied power electronics conference and exposition. IEEE Press, New York, pp 892–898
16. Chatterjee A, Keyhani A (2011) Thevenin's equivalent of photovoltaic source models for MPPT and power grid studies. In: 2011 power and energy society general meeting. IEEE Press, New York, pp.1–7

Chapter 34
Genetic Algorithm Based Wind-Thermal Coordination Dispatch Including Transmission Losses

K. Dhayalini, S. Sathiyamoorthy and C. Christober Asir Rajan

Abstract In this paper Genetic Algorithm (GA) is used to solve wind and thermal dispatch problem with non-smooth fuel cost functions. Dispatch of wind and thermal system includes the determination of total cost of generation of all the units in the system which satisfies the load demand including line losses, equality and inequality constraints thereby minimizing the fuel cost. The unit minimum/maximum operational constraints, effects of valve-point loading and line losses are taken into consideration. To validate the results obtained, two test systems consisting of three and six units are considered. Solutions of the systems are obtained including and excluding transmission losses with non-smooth cost functions. Numerical simulation of the coordinated system reduces the total fuel cost.

Keywords Genetic algorithm · Wind-thermal coordination · Economic dispatch (ED) · Optimization

34.1 Introduction

In the present world demand for electrical energy is increasing. Generating electrical energy at low cost is very important. Alternative to fossil fuel and nuclear power is renewable energy technologies. Among the other renewable power sources, wind

---

K. Dhayalini (✉) · S. Sathiyamoorthy
J. J. College of Engineering and Technology, Trichy, India
e-mail: dhaya2k@gmail.com

S. Sathiyamoorthy
e-mail: sathyajeyam@gmail.com

C.C.A. Rajan
Pondicherry Engineering College, Pondicherry, India
e-mail: asir_70@pec.edu

C. Kamalakannan et al. (eds.), *Power Electronics and Renewable Energy Systems*,
Lecture Notes in Electrical Engineering 326, DOI 10.1007/978-81-322-2119-7_34

have recently experienced a rapid growth around the world. The main reason is, it brings diverse fuel sources that are free of cost, emission and pollution [1]. The wind energy stands out to be one of the most promising new sources of electrical power in the near term. The technology development and the resulting price decline have caught the interest of number of electric utilities to actively develop wind energy as one element of balancing resource. The environmental benefit is generally the primary contributing factor to the development of wind system. However the variability and unpredictable nature of wind resource challenge its integration in power system operation and responsibility to system operator. To determine the optimal generation to integrate wind penetration into the power system it requires a technique to bridge the gap between the operating dynamic constraints.

The importance of Economic Dispatch (ED) is to calculate the generation of all the generators in the system to satisfy the load demand yielding minimum fuel cost. The generation should also satisfy the equality and inequality constraints of the system [2]. In recent years, several methods and algorithms were analyzed to investigate the solution to perform ED on thermal systems. Where, dynamic programming, Lagrangian Relaxation [3] branch and bound [4], and Evolutionary Programming [5] could be used to solve the ED problems.

Normally in a wind thermal system the impact of wind power and total load is of prime importance. The integration of wind system into the power system reduces the thermal unit generation. To satisfy the load demand thermal generator should have sufficient capacity to meet the technical requirement of the operating reserve [6]. In wind thermal power system the operation of the thermal system, starting and stopping of thermal units and irregular wind power plays an important role for its economic evaluation [7].

In this paper the methodology used to find the solution to coordinate the wind and thermal system involves the Genetic Algorithm (GA). The test systems are solved considering the non smooth cost function and transmission losses. GA can provide near global optimum solution and less computation time.

34.2 Problem Formulation

Economic way of coordinating of wind and thermal system involves the distribution of generation between wind and thermal system such that the total production cost is minimized satisfying the constraints [3].

As there is no fossil fuel cost in wind power generation, the generation cost of wind power is initially eliminated during cost calculation and after evaluating the interrelation of the coordinated system the wind power cost will be added up to the total cost. The ED problem can be formulated as a classic mathematical optimization problem [3] of the form

$$F_T = \sum_{t=1}^{T} \sum_{i=1}^{NT} F_i(P_i(t)) \tag{34.1}$$

where,

n	Total number of generators in the system
F_T	Total cost of generation
$P_i(t)$	Power generated by ith unit

Generally, the cost of fuel of generators in thermal unit can be considered as a polynomial function with second order as

$$F_i(P_i) = a_i + b_i P_i + c_i P_i^2 \tag{34.2}$$

When nonlinear effect of valve is considered the fuel cost of a thermal will be a nonlinear function as (34.3)

$$F_i = a_i + b_i P_i + c_i P_i^2 \left[P_i^{\min} - P_i e_i * \sin\left\{ f_i \left(P_i^{\min} - P_i \right) \right\} \right] \tag{34.3}$$

where,

a_i, b_i, c_i	Cost function parameters of ith generating unit (Rs/MW 2 h, Rs/MWh, Rs/h).
e_i, f_i	Cost function parameters of ith generating unit considering valve point effects
$F_i(P_i)$	Production cost of thermal unit i at hour t
$P_i(t)$	Output power of thermal unit i at hour t

34.2.1 Constraints

34.2.1.1 Power Balance Constraint

$$\sum_{i=1}^{NT} U_i(t) * P_i(t) + P_{WT}(t) = P_L(t) + P_{LOSS} \tag{34.4}$$

where,

$U_i(t)$	Scheduled state of thermal unit i for hour t
$P_{WT}(t)$	Output power of wind unit at hour t
$P_L(t)$	Load demand of the system at hour t
P_{LOSS}	Transmission loss of the line

Transmission loss can be calculated using the Eq. (34.5)

$$P_{LOSS} = \sum_{i=1}^{m}\sum_{j=1}^{m} \mathrm{P_i B_{ij} P_j} + \sum_{i=1}^{m} \mathrm{B_{0i} P_i} + \mathrm{B_{00}} \tag{34.5}$$

where B_{ij}, B_{0i} and B_{00} are the transmission network power loss B-coefficients.

34.2.1.2 System Up/Down Spinning Reserve Requirements

$$\sum_{i=1}^{NT} U_i(t) * US_i(t) \geq USR_B + ASR_1(P_{WT}(t)) \tag{34.6}$$

$$\sum_{i=1}^{NT} U_i(t) * DS_i(t) \geq ASR_2(P_{WT}(t)) \tag{34.7}$$

34.2.1.3 Minimum/Maximum Thermal Plant Output Constraints

$$P_L(t) - P_{WT}(t) \geq ASR_2(P_{WT}(t)) + \sum_{i=1}^{NT} U_i(t) * P_i^{\min}(t) \tag{34.8}$$

$$\sum_{i=1}^{NT} U_i(t) * P_i^{\max}(t) + P_{WT}(t) \geq P_L(t) + USR_B + ASR_1(P_{WT}(t)) \tag{34.9}$$

where,

ASR_1	Up reserve requirement to be added considering wind power generation
ASR_2	Down reserve requirement to be added considering wind power generation
$US_i(t)$	Thermal unit up reserve contribution at hour t
$DS_i(t)$	Thermal unit down reserve contribution at hour t
$P_i^{max}(t)$	Maximum generation of unit i at hour t
$P_i^{min}(t)$	Minimum generation of unit i at hour t

34.2.1.4 Unit Capacity Constraint

$$P_i^{\min}(t) * U_i(t) \leq P_i(t) \leq P_i^{\max}(t) * U_i(t) \tag{34.10}$$

34.2.1.5 Ramp Rate Limit Constraints

Ramp rate is essentially the speed at which a generator can increase (ramp up) or decrease (ramp down) generation. The variations of output of thermal units are limited by their ramping capabilities. The ramp-rate limits are considered as inequality constraints and can be written as:

$$DR_i(t) = \min\left\{DR_i^{\max}, P_i(t) - P_{i,r}^{\min}\right\} \tag{34.11}$$

$$UR_i(t) = \min\{UR_i^{\max}, P_{i,r}^{\max} - P_i(t)\} \tag{34.12}$$

If there is an increase in generation

$$P_i(t) - P_i(t-1) \leq UR_i \tag{34.13}$$

If there is an decrease in generation

$$P_i(t-1) - P_i(t) \leq DR_i \tag{34.14}$$

where,

$P_i(t-1)$	Previous output power
UR_i	ith generator's up ramp limit (MW per time period)
DR_i	ith generator's down ramp limit (MW per time period)

34.3 Genetic Algorithms

The genetic algorithm is a search heuristics which mimics the process of natural selection and generate solutions to optimization and search problems. This algorithm is inspired by natural evolution such as inheritance, selection, crossover and mutation [8].

34.3.1 Implementation of GA

Implementation of Genetic Algorithm includes the following steps:

1. Construct an initial population (P) of chromosomes by random process.
2. Evaluate fitness of each chromosome.
3. Generate mating pool based on fitness function values.
4. Select mating pair of chromosomes called parent chromosomes from mating pool.

5. Create two child chromosomes from the parent chromosomes by applying genetic operators.
6. Repeat steps (4–5), till the child population of size P is generated.
7. Store the chromosome having the maximum fitness and also the corresponding objective function.
8. Repeat steps (2–7) until the specified numbers of genetic iterations are completed.
9. Return the chromosome with highest fitness function as the solution.

34.3.2 GA Based Coordination Dispatch

34.3.2.1 Initialization

The control variables are the generation power outputs. Therefore, an individual is a vector of 24 h output of n generation units.

34.3.2.2 Fitness Evaluation

Since not all the individuals are applicable, we must first define the fitness function to evaluate the fitness of each individual in the population. Thus, the fitness function is defined as the reciprocal of the sum of the generation cost function and the penalized demand and prohibited zone constraints.

34.3.2.3 Population Evolution

The evolution of the population takes place following the general GA principles through selection, crossover and mutation.

Selection: After the evaluation of the initial randomly generated population, the GA begins the creation of the new generation. Individual from the parent population are selected in pairs with a probability proportional to their fitness to replicate and form offspring individual. The selection scheme used is known as Roulette wheel selection.

Crossover: During crossover a new chromosome is produced by selecting the bits from the two set of parent chromosome. The probability of crossover is very high.

Mutation: Mutation provides an exploration source in selection. The probability of mutation is very low. Every parameter of the offspring undergoes a uniform mutation.

34.4 Numerical Simulation and Results

In order to demonstrated the performance of the proposed method two test systems with 3 and 6 thermal units are considered. The proposed algorithm is applied to the test systems with and without considering wind power. Also the analysis is made including/excluding transmission losses. The ranges for the parameters set in the GA are shown in Table 34.1 and used for performing the numerical simulation.

34.4.1 Case Study 1

Three-Unit System: This test system consists of 3 thermal generating units [9] with valve point effect and one wind farm of overall 50 MW capacity. The total demand on the system is 850 MW. Table 34.2 shows the cost characteristics of three generators while matrix B is the loss coefficient matrix for the considered system. The best results based on the proposed algorithm have been listed in Table 34.3. Figure 34.1 illustrates the convergence property of the proposed algorithm.

$$B = \begin{bmatrix} 0.000028 & 0.000017 & 0.000179 \\ 0.000093 & 0.000228 & 0.000017 \\ 0.000218 & 0.000093 & 0.000028 \end{bmatrix}$$

Table 34.1 GA parameters

Parameter	Value
Number of chromosome	3 and 6
Chromosome size	24 h × Number of generators
Maximum generation	1,000
Population size	500
Selection method	Roulette wheel
Type of crossover	Single point crossover
Crossover probability	0.85
Mutation probability	0.19

Table 34.2 Cost coefficients of three unit system

Unit	a_i	b_i	c_i	e_i	f_i	P_{imin}	P_{imax}
1	561	7.92	0.00156	300	0.0315	100	600
2	310	7.85	0.00194	200	0.0420	100	400
3	78	7.97	0.00482	150	0.0630	50	200

Table 34.3 Simulation results for three unit system with and without wind power using GA

Unit power output (MW)	Excluding transmission loss		Including transmission loss	
	Without wind	With wind	Without wind	With wind
P1	325	350	342	365
P2	375	370	368	330
P3	150	100	140	115
Wind power produced	–	30	–	40
Transmission loss	–	–	4.002	4.021
Total output	850	850	854.002	854.021
Total generation cost ($/h)	**8,236.25**	**8,234.35**	**8,243.65**	**8,241.45**

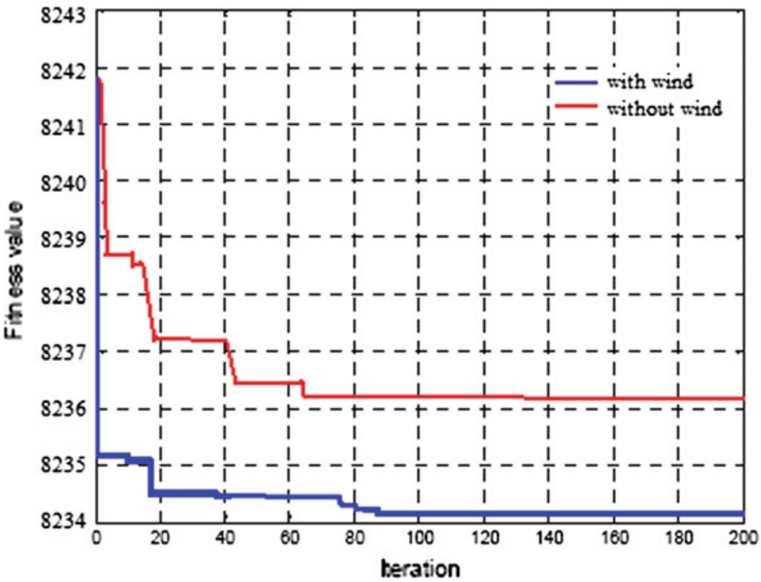

Fig. 34.1 Convergence characteristics of 3 unit system excluding transmission losses

$$B = \begin{bmatrix} 0.001700 & 0.001200 & 0.000700 & -0.00010 & -0.00050 & -0.00020 \\ 0.001200 & 0.001400 & 0.000900 & 0.000100 & -0.00060 & -0.00010 \\ 0.000700 & 0.000900 & 0.003100 & 0.000000 & -0.00100 & -0.00060 \\ -0.00010 & 0.000100 & 0.000000 & 0.002400 & -0.00060 & -0.00080 \\ -0.00050 & -0.00060 & -0.00100 & -0.00060 & 0.012900 & -0.00020 \\ -0.00020 & -0.00010 & -0.00060 & -0.00080 & -0.00020 & 0.015000 \end{bmatrix}$$

Table 34.4 Cost coefficients of six unit system

Unit	a_i	b_i	c_i	e_i	f_i	P_{imin}	P_{imax}
1	0.0070	7.0	240	300	0.035	100	500
2	0.0095	10.0	200	200	0.042	50	200
3	0.0090	8.5	220	200	0.042	80	300
4	0.0090	11.0	200	150	0.063	50	150
5	0.0080	10.5	220	150	0.063	50	200
6	0.0075	12.0	290	150	0.063	50	120

Table 34.5 Simulation results for six unit systems with and without wind power using GA

Unit power output (MW)	Excluding transmission loss		Including transmission loss	
	Without wind	With wind	Without wind	With wind
P1	474.8078	400.3752	472.2512	400.220
P2	178.7618	167.7021	180.1210	190.240
P3	262.2079	215.2312	260.7500	223.253
P4	133.4365	114.0125	135.1134	131.112
P5	141.9154	197.4521	142.3452	150.024
P6	71.8766	70.2615	72.4710	70.151
Wind power produced	–	97.9654	–	100.000
Transmission loss			11.002	12.003
Total output	1,263.0060	1,263.0000	1,274.0538	277.003
Total generation cost ($/h)	**15,464.3852**	**15,320.3086**	**15,530.225**	**15,514.431**

34.4.2 Case Study 2

Six-Unit System: This test system consists of 6 thermal generating units [10] with valve point effect and one wind farm of overall 165 MW capacity. The total demand on the system is 1,263 MW. Table 34.4 shows the cost characteristics while matrix B is the loss coefficient matrix for the considered system. The results for the overall cost with and without wind power are given in Table 34.5 and the convergence characteristics including transmission losses are shown in Fig. 34.2.

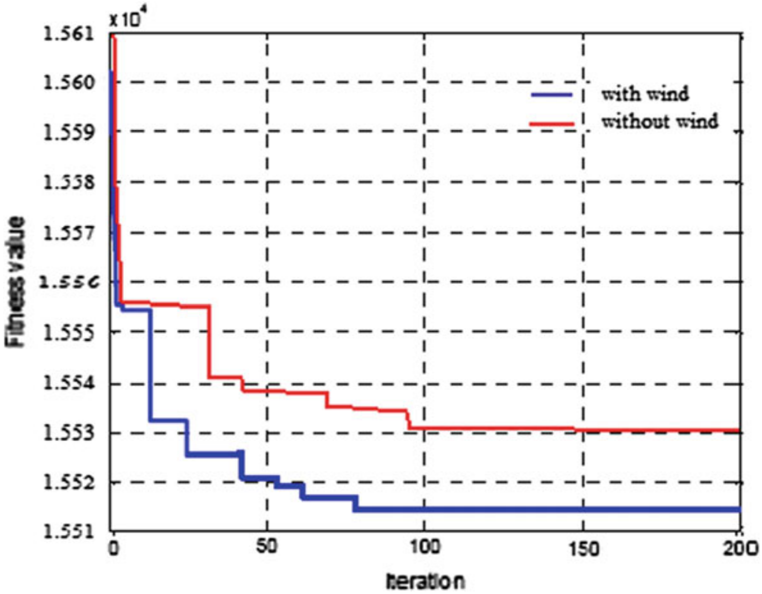

Fig. 34.2 Convergence characteristics of 6 unit system including transmission losses

34.5 Conclusion

In this paper GA is used for determining the total generation cost of a power system incorporating thermal power plant and wind power generation including transmission losses. It is evident from the results that the optimal total generation cost obtained by Genetic Algorithm is better than other optimization algorithms. Generator parameters which yield non linearity in the power system such as ramp rate limits, valve point zone and non smooth cost functions are considered for practical generator operation in the proposed method. The simulations performed using the proposed methodology proves that the operating costs and fossil fuel cost of the power systems are reduced by integrating wind power generation.

References

1. Ummels BC et al (2007) Impact of wind power on thermal generation unit commitment and dispatch. IEEE Trans Energy Convers Energy Policy 22:45–51
2. Bakirtzis AG, Dokopoulos PS (1988) Short term generation scheduling in a small autonomous system with unconventional energy sources. IEEE Trans Power Syst 3:1230–1236
3. Wood AJ, Wollenberg BF (2001) Power generation operation and control, 2nd edn. Wiley, New York

4. Chen CL, Wang SC (1993) Branch-and-bound scheduling for thermal generating units. IEEE Trans Energy Convers 8:184–189
5. Sinha N, Chakrabarti R, Chattopadhyay PK (2003) Evolutionary programming techniques for economic load dispatch. IEEE Trans Evol Comput 7:83–94
6. Chen CL (2008) Optimal wind thermal generating unit commitment. IEEE Trans Energy Convers 23:273–280
7. Chen Chun-Lung et al (2006) Optimal wind thermal coordination dispatch in isolated power system with large integration of wind capacity. Energy Convers Manag 47:3456–3472
8. Bakirtzis AG, Petridis V (1996) A genetic algorithm solution to the unit commitment problem. IEEE Trans Power Syst 11:83–92
9. Saadat H (1999) Power system analysis. McGraw Hill Companies, New York
10. Gaing ZL (2003) Particle swarm optimization to solve the economic dispatch considering the generator constraints. IEEE Trans Power Syst 18:1187–1195

Chapter 35
A Novel MLI Topology with Reduced Power Switches

N. Vinothkumar, V. Arunachalam and V. Kumar Chinnaiyan

Abstract The Multilevel inverter is a most attractive inverter in high power-medium voltage energy conversion. It can produce switched waveform with free of or reduced total harmonic distortion. It can produce most sinusoidal voltage with increase in number of output level. But increase in level that requires more number of switches which lead to increase the cost, space and complexity in control. In this paper, we proposed new multilevel inverter topology with reduced number of switches which reduce the size and cost considerably. Also the comparison of work with the existing types of multilevel inverter topologies is addressed. The validation of proposed inverter is verified with simulation result using MATLAB. The proposed method will reduce the limitation of multilevel inverter for real time application and viable as a commercial product.

Keywords MLI topology · Harmonic distortion

35.1 Introduction

The multilevel voltage source inverters are recently applied in many industrial applications such as ac power supplies static VAR compensators, drive systems, and Distributed Energy Resources area (DER). Especially in DER area, because several batteries, fuel cells, solar cell or rectified wind turbines or micro turbine can be connected through a multilevel inverter to feed a load or interconnect to the ac grid without voltage balancing problem [1]. In addition, multilevel inverters have a

N. Vinothkumar (✉) · V. Arunachalam
Central Power Research Institute, Bangalore, India
e-mail: nvk.cpri@gmail.com

V. Kumar Chinnaiyan
Dr. N.G.P Institute of Technology, Coimbatore, India

C. Kamalakannan et al. (eds.), *Power Electronics and Renewable Energy Systems*,
Lecture Notes in Electrical Engineering 326, DOI 10.1007/978-81-322-2119-7_35

lower switching frequency than the standard Pulse Width Modulation (PWM) inverters and thus reduced switching losses. The significant advantages of multilevel configuration are: the harmonic reduction in the output waveform without increasing switching frequency or decreasing the inverter power output [2]. The multilevel structure can ensure even voltage sharing, both statically and dynamically. Substantial reduction in size and volume is possible due to elimination of the bulky coupling transformers. Also it has advantages such as lower common mode voltage, lower voltage stress on power switches, lower dv/dt ratio to supply lower harmonic contents in output voltage and current [3]. Comparing two-level inverter topologies at the same power ratings, MLIs also have the advantages that the harmonic components of line-to-line voltages fed to load are reduced owing to its switching frequencies. The most common MLI topologies classified into three types are Diode Clamped MLI (DC-MLI), Flying Capacitor MLI (FC-MLI), and Cascaded H-Bridge MLI (CHB-MLI) [3, 4]. To produce more accurate sine wave and reduced Total Harmonic Distortion (THD) output, it is necessary to increase voltage level which requires more number of switches. Hence the voltage stresses and switching losses will increase and the circuit will become complex. The proposed method provides new multilevel inverter that requires the number of switches in comparison with existing methods and also provides generalized method for level. This attempt will make the multilevel inverter to be part in commercial solution. The circuit model is validated with the simulation results using MATLAB and result achieved is accepted as per standards.

35.2 Exiting Topologies

35.2.1 Diode Clamped Multilevel Inverter (DCMLI)

Diode clamp is called because of the diode is used to connect the neutral of point which clamps the DC voltage to achieve stepped output. These diodes only distinguish the circuit from conventional two level inverter. The capacitor C_1, C_2 splits Vdc into half Vdc across the devices to achieve 3 level output. A three level diode clamped inverter is shown in Fig. 35.1 and the Table 35.1 gives the required number of devices for this topologies. The advantages of this topology are that it has excellent reliability and availability and the converter can work like additional sine filter or high pulse transformer. It provides great flexibility and dynamic behavior [5]. The disadvantage are unsymmetrical semiconductor loss distribution [6] and need of sine filter [7]. The extension of level is limited due to blocking capacity or a series connection of semiconductor [8]. Finally it also limits the switching frequency into few hundred Hertz due to high switching losses.

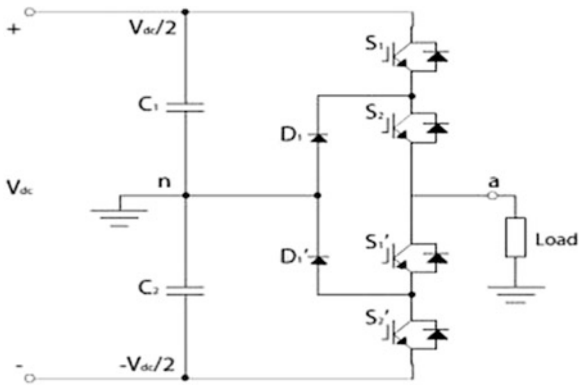

Fig. 35.1 Three level DCMLI

Table 35.1 Comparison of major components for different topologies

Topology	No. of voltage source	No. of power switches	No. of diodes	No. of capacitor
DCMLI	n − 1	2(n − 1)	(n − 1) (n − 2)	n − 1
FCMLI	n − 1	2(n − 1)	Nil	(n − 1)(n − 2)/2
CHB MLI	(n − 1)/2	2(n − 1)	Nil	Nil

35.2.2 Flying Capacitor Multilevel Inverter (FCMLI)

It is also called as capacitor clamped (CC) multilevel inverter. It is similar to diode clamped but with the difference that CC topology uses clamping capacitors instead of diodes. This topology has a ladder structure of dc side capacitor, where the voltage on each capacitor different from next capacitor and it assures the voltage stress on each device is equal and is $V_{dc}/(n-1)$. The Fig. 35.2 shows the basic

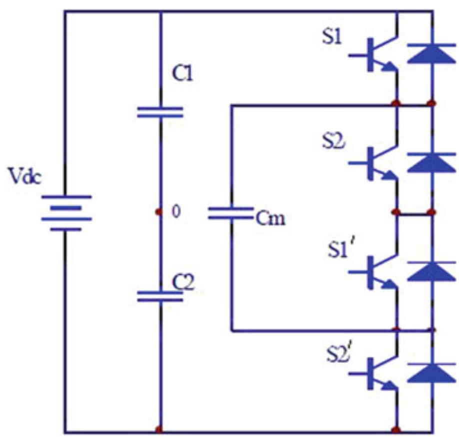

Fig. 35.2 Three level FCMLI

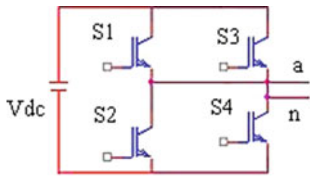

Fig. 35.3 Three level CHBMLI

structure of CCMLI for the Table 35.1 shows the required number of switches. The most important advantages of FC-MLI topology are preventing the filter demand, and controlling the active and reactive power flow besides phase redundancies. Although these advantages, the increment of n level will restrain the accurate charging and discharging control of capacitors, cost and size will be large due to increased number of capacitors. To maintain a steady state stability of the clamping capacitor voltage, the instantaneous duty cycles of the two switching cells must be equal to each other [9].

35.2.3 Cascaded H-Bridge Multilevel Inverter (CHBMLI)

The concept of the topology is that cascading the outputs of each module to get sine wave output. Each module consist of one full bridge inverter produces a three level output. In Fig. 35.3, one phase leg of a three level Cascaded Multilevel Inverter is shown and for the component requirement, the Table 35.1 is provided. The extension can be done by adding modules since each full-bridge can be seen as a module that builds up the CHBLI topology. CHBMLI can be divided into symmetric and asymmetric. In the symmetric topology, the values of all of the dc voltage sources are equal. In asymmetric the voltage sources are different to increase the voltage level [10]. The advantages of topology that requires the least number of components compared with other two topologies and higher reliability due to its modular topology.

35.3 Proposed Method

The proposed method is tried to achieve reduce no of switches of any level. The Fig. 35.4 shows the generalized structure of proposed multilevel inverter for any level of output. The bidirectional switches like MOSFET are used in this confirmation. There are two upper switches used for conducting positive and negative cycle respectively. For positive cycle, the Sw U1 is turned ON complete working half cycle and similarly Sw U2 is turned ON for negative half cycle. For step output, we need to turn ON two switches that is one from upper side and another is

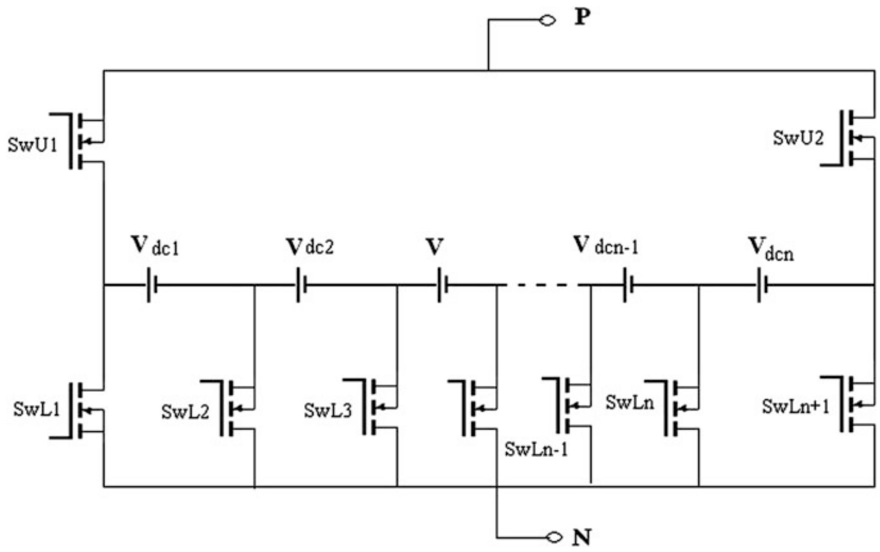

Fig. 35.4 Generalized structure for proposed MLI

from lower side. In this configuration, the addition of voltage sources is made by choosing proper switching of devices. For n level output the required number of DC sources and power switches are given in the Eqs. 35.1 and 35.2. Equation 35.3 gives the voltage equation for any level. Figure 35.5 shows seven level MLI with

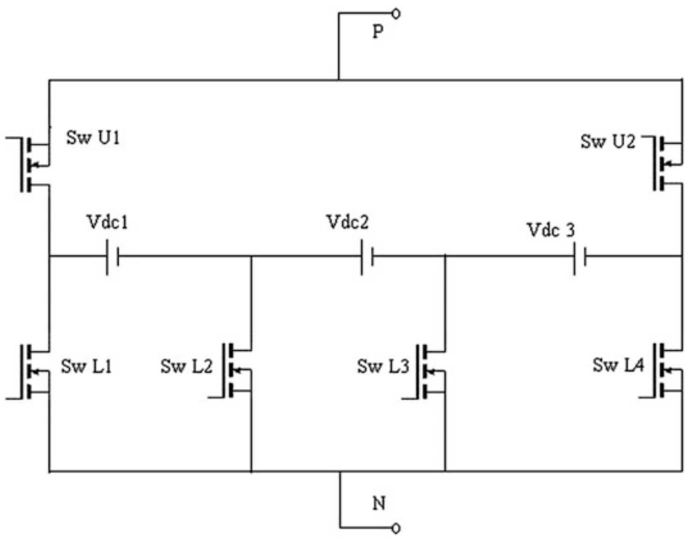

Fig. 35.5 Proposed seven levels MLI

Fig. 35.6 Switching pattern-seven level MLI

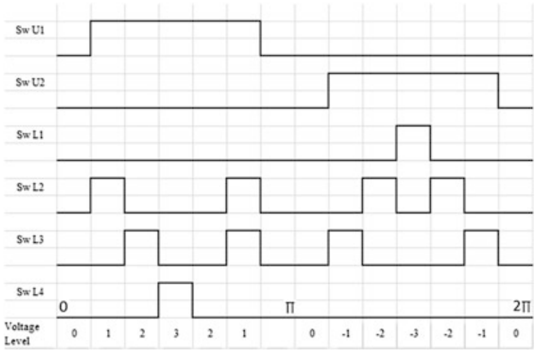

six switches and switching pattern is shown in Fig. 35.6. The number of switches required is six, the upper arm consists of two switches and the lower arm consists of four switches. The DC source required is three with equal voltages are connected in series with each other to add the voltages to achieve the required level. The extension of level can be easily varied by adding one DC source and a bidirectional power switch like MOSFET to the existing levels. This topology ensures the simple operation at each level and modular structure provides the reduced complexity in modulation and control techniques. This paper is paid attention to reduce the power switch and the control complexity. Modulation techniques can be applied any types to control the output and THD.

For n level output

$$\text{Number of DC sources required} = (\mathrm{n}-1)/2 \tag{35.1}$$

$$\text{Number of Power Switches required} = ((\mathrm{n}-1)/2)+3 \tag{35.2}$$

$$\mathrm{V}_{\mathrm{an}} = \mathrm{V}_{\mathrm{dc1}} + \mathrm{V}_{\mathrm{dc2}} + \cdots + \mathrm{V}_{\mathrm{dc(n-1)}} + \mathrm{V}_{\mathrm{dcn}} \tag{35.3}$$

35.4 Comparison with Other Existing Topologies

The proposed model has least number of power switches when compared with the existing works which is done for the same level of output voltage. The overall components reduction percent is shown Table 35.2 with existing topologies for seven level is 77 % in comparison with DCMLI, 66 % with FCMLI and 44 % with CHB MLI. Similarly reduction percent with existing topologies for eleven levels is 86 % in comparison with DCMLI, 78 % with FCMLI and 53 % with CHB MLI. It also assures that the components reduction percent will increase when the numbers of levels are increased. Hence reduction in switching losses, space, weight and finally implantation cost. There are some of attempts are made to reduce the number of switches and components in MLI topologies. The proposed method is foremost

Table 35.2 Comparison of major components of proposed seven level inverter with existing topology

Topology	No. of voltage source	No. of power switch	No. of diodes	No. of capacitor	No. of driver circuit	Total
Seven level						
DC MLI	6	12	30	6	12	66
FC MLI	6	12	Nil	15	12	45
CHB MLI	3	12	Nil	Nil	12	25
Proposed MLI	3	6	Nil	Nil	6	15
Eleven level						
DC MLI	10	20	90	10	20	150
FC MLI	10	20	Nil	45	20	95
CHB MLI	5	20	Nil	Nil	20	45
Proposed MLI	5	8	Nil	Nil	8	21

uses least number of switches for the same level with existing works. Kavitha et al. [11] used six switches and two DC sources for five level, the proposed method re requires only five switches and two. Gobinath et al. [12] proposed new model of multilevel inverter for seven level and obtained the results with seven switches and three dc sources, where as the said method requires only six switches and three DC sources, the results are shown. For Eleven level, Babaei [13] and Ebadpour et al. [14] proposed a new concept of reducing switches and achieved with twelve switches, ten switches respectively, our proposed work needs only eight switches. Kangarlu and Babaei [15] proposed new topology of sublevel concepts in MLI and the results are shown for thirteen level with sixteen number of switches and also [16] obtained the output with nineteen power switches for the same level, whereas the proposed method, the same level can be achieved with nine switches and six DC sources. The proposed concept in this paper required only least number of switches in comparison with existing topologies which required twelve switches for fifteen level [11]. Babaei [17] proposed a new topology for reducing the components; the seventeen and twenty one level is achieved with sixteen and twenty IGBT i.e. $n - 1$ switches for n level. Similarly [18] has proposed a simulation result for twenty one level with fourteen switches whereas the proposed topology requires only eleven and thirteen switches for seventeen level and twenty one level.

35.5 Simulation Results

This section deals with the simulation and validation of proposed inverter using Matlab software. The validation is done for both R and RL loads. The resistance and inductance for different values are verified. The results are as perfect as the inductance value varied from few mH to few hundred H. Figure 35.7 shows the simulation model and Fig. 35.9 shows output waveform for seven level and twenty one level proposed MLI. From that it is clearly proved that t required number of switch is less and it produces the waveform as per standards in comparison with existing works. Figure 35.8 shows the simulation of twenty one level MLI.

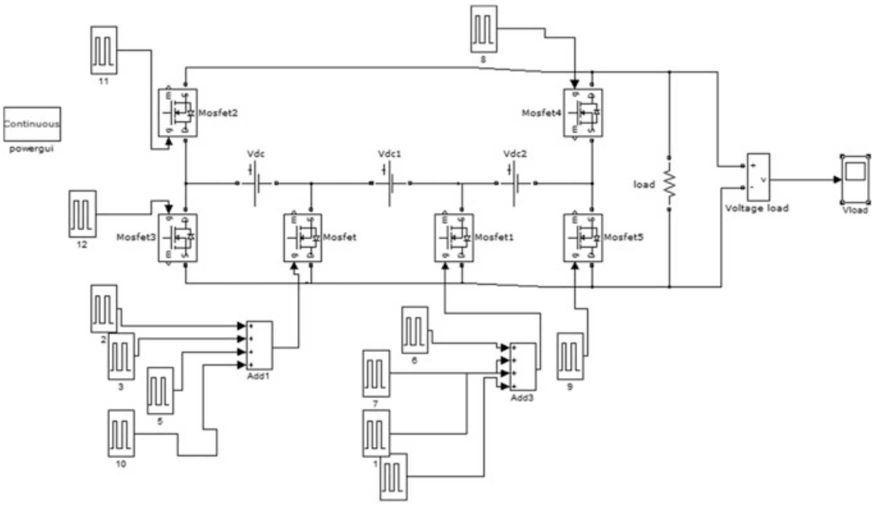

Fig. 35.7 Simulation model for seven level proposed MLI

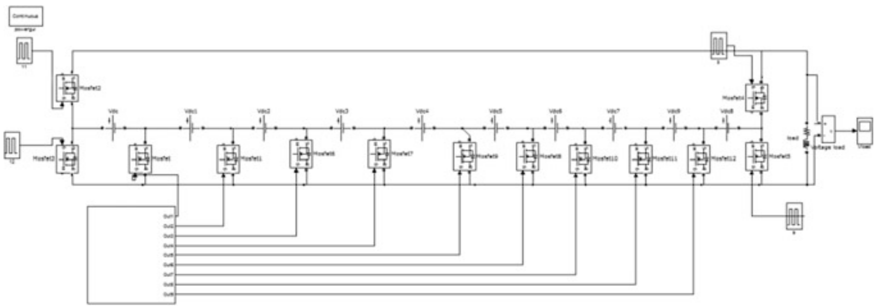

Fig. 35.8 Simulation model for twenty one level

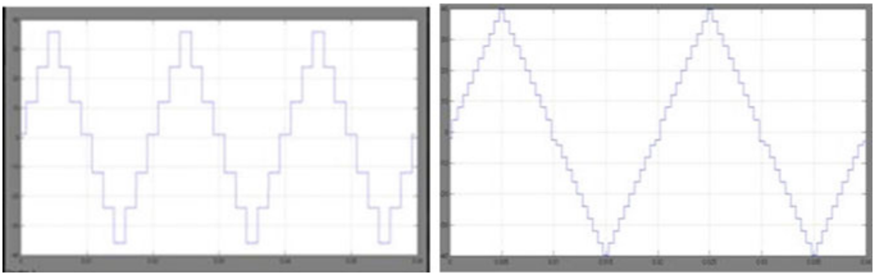

Fig. 35.9 Output waveform for seven and twenty one level

The validation of simulation can be experimented with hardware setup. In simulation model, the MOSFET is used and the wave forms are very symmetric and as per standards. THD and harmonics are not discussed in this paper.

35.6 Conclusion

The attempt is made to reduce the number of switches for any output level. The result shown in this paper clearly indicates that the main components like power switches, diodes, capacitors and DC sources are used is less in comparison with the existing topologies. The overall component reduction percent with CHB MLI is more than 40 % and it increases when levels are increased. The great reduction in components will ensure the reduction in switching losses, space and weight. Also complexity in working, driver circuits and the cost will be reduced considerably. The greatest limitation of multilevel inverter used in real time application is solved by reducing the number of components which assures of becoming a commercial product. The number of levels can be increased to higher number without any complexity is possible.

References

1. Tolbert LM, John N, Chiasson (2004) Harmonic optimization of multilevel converter using GA. IEEE Power Electron Lett 1–4
2. Kang FS, Cho SE (2005) Multilevel PWM inverters suitable for the use of stand-alone photovoltaic power system. IEEE Power Electron
3. Rodriguez J, Lai S (2002) Multilevel inverters: a survey of topologies, control and applications. IEEE Trans Industr Electron 49(4):724–738
4. Mittal N, Singh B, Singh SP, Dixit R, Kumar D (2012) Multilevel inverter: a literature survey on topologies and control strategies. In: 2nd international conference on power, control and embedded systems
5. Roidriguez J, Bernet S, Steimer PK, Lizama IE (2010) A survey on neutral-point-clamped inverters. IEEE Trans Ind Electron 57(7):2219–2230

6. Bruuml T, Bernet S (2001) Loss balancing in three-level voltage source inverters applying active NPC switches. In: Proceedings of IEEE power electron, special conference, pp 1135–1140
7. Bernet S (2000) Recent developments of high power converters for industry and traction applications. IEEE Trans Power Electron 15(6):1102–1117
8. Steimer PK, Apeldoorn O, Bernet S (2005) Very high power IGCT PEBB technology. In: Proceedings of IEEE power electronics and special conference, pp 1–7
9. Yuan XM, Stemmler H, Barbi I (2001) Self-balancing of the clamping-capacitor-voltages in the multilevel capacitor clamping inverter under sub-harmonic PWM modulation. IEEE Trans Power Electron 16:256–263
10. Manjrekar M, Lipo TA (1998) A hybrid multilevel inverter topology for drive application, vol 2. In: Proceedings of application power electronics and conference, pp 523–529
11. Kavitha M, Arunkumar A, Gokulnath N, Arun S (2012) New cascaded H-bridge multilevel inverter topology with reduced number of switches and sources. IOSR-JEEE 2(6):26–36
12. Gobinath K, Mahendran S, Gnanambal I (2013) New cascaded H-bridge multilevel inverter with improved efficiency. IJAREEIE 2
13. Babaei E (2008) A cascade multilevel converter topology with reduced number of switches. IEEE Trans Power Electron 23(6):2657–2664
14. Ebadpour M, Sharifian MBB, Hosseini SH (2011) A new structure of multilevel inverter with reduced number of switches for electric vehicle applications. Energy Power Eng 3(02:198–205
15. Kangarlu MF, Babaei E (2013) A generalized cascaded multilevel inverter using series connection of submultilevel inverters. IEEE Trans Power Electron 28(2):625–636
16. Hinago Y, Koizumi H (2010) A single phase multilevel inverter using switched series/parallel dc voltage sources. IEEE Trans Ind Electron 58(8):2643–2650
17. Babaei E, Hosseini SH, Gharehpetian GB, TarafdarHaque M, Sabahi M (2007) Reduction of dc voltage sources and switches in asymmetrical multilevel converters using a novel topology. Elsevier J Electr Power Syst Res 77(8):1073–1085
18. Jithin JI, Raj BS (2013) A new topology for a single phase 21 level multi level inverter using reduced number of switches. Int J Eng Res Technol (IJERT) 2(2):1–6
19. Banaei MR, Salary E (2011) New multilevel inverter with reduction of switches and gate driver. ELSEVIER 52:1129–1136
20. Rodriguez J, Bernet S, Pontt JO, Kouro S (2007) Multilevel voltage source converter topologies for industrial medium voltage drives. IEEE Trans Industr Electron 54(6):290–294
21. Wiechmann EP, Aqueveque P, Burgos R, Rodriguez J (2008) On the efficiency of voltage source and current source inverters for high power drives. IEEE Trans Ind Electron 55 (4):1771–1782
22. Khomfoi S, Tolbert LM (2007) Multilevel power converters. Chapter 17, power electronics handbook, 2nd edn. Elsevier, New York, pp 451–482
23. Oshiro M, Tanaka K, Senjyu T, Toma S, Yona A, Saber AY, Funabashi T, Kim C-H (2011) Optimal voltage control in distribution systems using PV generators Original Research Article. Int J Electr Power Energy Syst 33(3):485–492
24. Alexandru C, Pozna C (2010) Simulation of a dual-axis solar tracker for improving the performance of a photovoltaic panel. In: Proc Inst Mech Eng Part A: J Power Energy 210–215
25. Karpagam J, Kumar AN, Chinnaiyan VK (2013) An experimental analysis of a single phase matrix converter for adjustable speed drives. Int Rev Modell Simul 6(4):1071–1078
26. Kumar Chinnaiyan V, Jerome J, Karpagam J (2013) An experimental investigation on multilevel inverter for solar energy applications. Int J Electr Power Energy Syst 157–167 (Elsevier Publications)
27. Kumar Chinnaiyan V, Jerome J, Karpagam J (2013) An experimental investigation on multilevel inverter for solar energy applications. Int J Electr Power Energy Syst 157–167 (Elsevier Publications)
28. Kumar Chinnaiyan V, Jerome J, Karpagam J (2010) Design and realization of a three phase cascaded multilevel inverter for industrial drives with reduced power quality issues. Int Rev Electric Eng

Chapter 36
Optimal Placement and Sizing of Solar and Wind Based DGs in Distribution Systems for Power Loss Minimization and Economic Operation

Bibhudatta Patnaik, D. Sattianadan, M. Sudhakaran and S.S. Dash

Abstract The current challenge in the distribution system is regarding the proper placement and sizing of Distributed Generation (DG) that will further help in extracting their maximum benefits. This paper examines the role of optimal placement and sizing of different DGs based on minimization of power losses and also minimization of total cost of the system. The candidate locations for DG placement are identified based on distribution system load flow. A multi-objective function implementation, based on power loss and cost optimization, is done on radial networks using Genetic Algorithm (GA) and further implemented in MATLAB. It is applied to solar (PV) and wind (WTG) based DG and tested on IEEE 33-bus and IEEE 69-bus systems. The simulation results show the effectiveness and acceptable performance of the discussed method.

Keywords Distributed generation · Economic operation · Genetic algorithm · Optimal location and sizing · Radial distribution system

B. Patnaik (✉) · D. Sattianadan · S.S. Dash
SRM University, Chennai 603203, India
e-mail: bibhupatnaik91@gmail.com

D. Sattianadan
e-mail: sattia.nadan@gmail.com

S.S. Dash
e-mail: munu_dash_2k@yahoo.com

M. Sudhakaran
Pondicherry Engineering College, Puducherry 605014, India
e-mail: sudhakaran@pec.edu

C. Kamalakannan et al. (eds.), *Power Electronics and Renewable Energy Systems*,
Lecture Notes in Electrical Engineering 326, DOI 10.1007/978-81-322-2119-7_36

36.1 Introduction

The analysis of a distribution system is an important area of activity, as distribution systems provide the vital link between the bulk power system and the consumers. A distribution circuit normally uses primary or main feeders and lateral distributors. Radial distribution systems are popular because of their simple design and low cost. The high R/X ratio of the distribution lines results in large voltage drops, low voltage stability and power losses. Thus there is dire need to improve the overall efficiency of the system.

So the idea of using Distributed Generations (DGs) is now being included so as to reduce the losses in the system. The location and amount of power supplied from the DG into the distribution system have influence on the operation of the system. They can either increase or decrease the efficiency and stability of the system and even reverse the direction of power flow. Therefore, the suitable location and sizing of the DG is preferred.

In [1], the impact on operation and planning of distribution systems because of DG integration is discussed along with a detailed method of cost analysis of various DGs. In [2], analytical methods are discussed to determine the optimal location to place a DG in radial as well as networked systems to minimize the power loss of the system and improve the voltage stability of the analyzed system. In [3], nodal pricing to a model distribution network has been discussed, showing significant price differences between buses reflecting high marginal losses. Tan et al. [4], reviews the loss allocation schemes for multilateral trades based on a quadratic approximation of losses. It also includes the study of various methods which use various techniques viz. loss minimization, cost minimization, voltage stability index maximization, improving power stability index etc. References [5–8] primarily concentrate on optimal placement and sizing of multi-DG units based on constant and variation of loads. They also define modern methodologies and novel techniques for solving the optimization problems.

36.2 Distributed Generations

Distributed generation (DG) is defined as small generation units installed in distribution systems. DGs can significantly increase reliability, reduce losses and save energy while is cost effective, though it suffers from some disadvantages because of the isolated power quality functioning, and voltage control problems. DGs include diesel, combustion turbine, and combined cycle turbine, low-head hydro, fuel cells and renewable power generation methods such as wind and solar. Distributed generation resources are classified as:

Type 1 Active power producers like photovoltaic arrays and fuel cells which are connected to the grid by means of inverters. This type can only produce active power

Type 2 Active power producers and reactive power consumers (PQ) like fixed speed wind turbines, that use induction generator to produce electricity are placed in this type of DGs

Type 3 Active and reactive power producers (PV bus voltage regulator). This type of DG produces reactive power to maintain the voltage of the bus which they are connected to. Wind turbines which have converter and diesel generators are categorized in this type of DGs

Type 4 Reactive power (Q) producers like synchronous condensers which can only produce reactive power

However, according to [9], there is no specific definition for the capacity of the DG. They can be micro distributed generation (1 W–5 kW), small distributed generation (5 kW–5 MW), medium distributed generation (5–50 MW) and large distributed generation (50–300 MW).

Limitation of DG capacity taken into account in this paper depends on the total demand of a considered distribution system.

36.3 Load Flow for Distribution System

The load flow of a power network provides the steady state solution through which various parameters of interest like currents, voltages, losses etc. can be calculated and is important for the analysis of distribution system, to investigate the issues related to planning, design and the operation and control.

The method to carry out the load flow for the distribution system under balanced operating condition employing constant power load model is based on

- Equivalent current injection
- Formulation of BIBC matrix
- Formulation of BCBV matrix

At bus i, the complex power S_i is specified and the corresponding equivalent current injection at the kth iteration of the solution is computed as

$$S_i = P_i + jQ_i, \quad i = 1, 2, \ldots, N \tag{36.1}$$

$$I_i^k = I_i^r\left(V_i^k\right) + jI_i^i\left(V_i^k\right) = \left((P_i + jQ_i)/V_i^k\right)^*. \tag{36.2}$$

where, S_i is the complex power at ith bus, P_i is the real power at ith bus, Q_i is the reactive power at ith bus, V_i^k is the voltage at the kth iteration for the ith bus, I_i^k is the equivalent current injection at the kth iteration for the ith bus, I_i^r and I_i^i are the real and imaginary parts of the equivalent current injection at the kth iteration for the ith bus.

For formulation of BIBC matrix, the branch currents can then be formulated as functions of equivalent current injections. The relationship between the bus current injections and branch currents can be expressed as

$$[\mathrm{B}] = [\mathrm{BIBC}][\mathrm{I}]. \tag{36.3}$$

where, BIBC is the bus-injection to branch-current matrix.

The Branch-Current to Bus-Voltage (BCBV) matrix summarizes the relation between branch current and bus voltages. Using the same for all the buses, the Branch-current to Bus-voltage (BCBV) matrix can be expressed as

$$[\Delta\mathrm{V}] = [\mathrm{BCBV}][\mathrm{B}]. \tag{36.4}$$

Combining Eqs. (36.3) and (36.4), the relations between the bus current injections and bus voltages can be expressed as

$$[\Delta\mathrm{V}] = [\mathrm{DLF}][\mathrm{I}]. \tag{36.5}$$

where, [DLF] = [BCBV] [BIBC]

The solution for the load flow can be obtained by solving Eqs. (36.6), (36.7) and (36.8) iteratively which are given below

$$\mathrm{I}_i^k = \mathrm{I}_i^r\left(\mathrm{V}_i^k\right) + j\mathrm{I}_i^i\left(\mathrm{V}_i^k\right) = \left((\mathrm{P}_i + j\mathrm{Q}_i)/\mathrm{V}_i^k\right)^*. \tag{36.6}$$

$$\left[\Delta\mathrm{V}^{k+1}\right] = [\mathrm{DLF}]\left[\mathrm{I}^k\right]. \tag{36.7}$$

$$\left[\mathrm{V}^{k+1}\right] = \left[\mathrm{V}^0\right] + \left[\Delta\mathrm{Vk}^{+1}\right]. \tag{36.8}$$

The new formulation as explained uses only the DLF matrix to solve load flow problem.

36.4 Genetic Algorithms

Genetic Algorithms are probabilistic search approach, which are based on the ideas of evolutionary processes. As against traditional methods, Genetic Algorithms are suited for many real world problems which involve finding optimal parameters.

The advantages of using GA are that they require no knowledge or gradient information about the response surface; they are resistant to becoming trapped in local optima and they can be employed for a wide variety of optimization problems.

They constitute of various operators viz. selection, crossover and mutation. The selection procedure randomly selects individuals from current population for development of the next generation. Various types of selection procedures are available viz. Roulette-wheel selection, Generational selection, Hierarchical selection, Rank selection. The crossover procedure involves combining two selected individuals about a crossover point thereby creating two new individuals which represent the next generation. There are few types viz. single point crossover, multiple point crossovers, uniform crossover etc. The mutation procedure randomly modifies the genes of an individual subject to a small mutation factor, introducing further randomness into the population.

Genetic Algorithms can identify and exploit regularities in the environment, and converge on solutions that are globally optimal. This method is very effective at finding optimal or near optimal solutions to a wide variety of problems, because it does not impose limitations required by traditional methods such as gradient search, random search etc.

GA Program comprises three different phases of search:

Phase 1: creating an initial population;
Phase 2: evaluating a fitness function;
Phase 3: producing a new population.

These three phases are incorporated in programs and used iteratively to finally reach the set of individuals that give the most optimized result according to the defined problem.

36.5 Problem Formulation

The reduction in power losses is currently the primary objective of any study. The problem remains that the reduction in power loss increases the cost of installation of any DG and thus proper allocation and sizing of the DG needs to be done that reduces the cost and simultaneously keeps the losses at a lower level. The main objective of this paper is to observe and optimize the effect of placing and sizing of multi DG's in radial distribution system. The final objective function is the combination of two objective functions:

- minimizing the real power loss in the system
- minimizing the cost of installation of the system

The operation is thus multi-objective in nature. The objective functions used in the system are:

1. Real Power Loss:

$$f_1 = P_{loss} = I^2 \cdot R. \tag{36.9}$$

subject to,

$$\mathrm{V}_{\mathrm{i}}^{\min} < \mathrm{V}_{\mathrm{i}} < \mathrm{V}_{\mathrm{i}}^{\max}$$
$$\sum_{\mathrm{i}=1}^{\mathrm{N}}{}_{\mathrm{DG}} \sum_{\mathrm{k}=1}^{\mathrm{k}}{}_{\mathrm{DG}} \mathrm{DG}_{\mathrm{ik}} < \mathrm{DG}_{\max}$$

where, V is the voltage at the node

DG is the capacity of the distributed generation.

2. Cost Function:

$$C_{PV} = \sum_{j=1}^{S_n} \left(b_j p_j \frac{r_0(1+r_0)m}{(1+r_0)^m - 1} + om(p_j) + rep(p_j)\right) \tag{36.10}$$

$$C_{WT} = \sum_{j=1}^{W_n} \left(a_j p_j \frac{r_0(1+r_0)m}{(1+r_0)^m - 1} + om(p_j) + rep(p_j)\right) \tag{36.11}$$

where, C_{PV}, C_{WT} are the cost of PV and Wind Turbine systems, W_n, S_n are the number of wind generators, photovoltaic panels, a_i, b_j are the unit cost (Rs/kW), P_i, P_j is the power capacity, $om(P_i)$, $om(P_j)$ are the maintenance and operating costs, $rep(P_i)$, $rep(P_j)$ are the replacement costs corresponding to ith wind turbine, jth photovoltaic panels, m is the life span of the project and r_0 is the interest rate.

$$f_2 = C_{tot} = C_{PV} + C_{WT} \tag{36.12}$$

The discussed methodology is applied to the wind/PV hybrid energy systems in Jaipur, Rajasthan (India) and the corresponding data can be referred to from Table 36.1. Now the functions given by Eqs. (36.9) and (36.12) are the two objective functions that are to be used in the multi-objective GA so as to get a series of optimal solutions that are a compromise between P_{loss} and C_{tot}.

Table 36.1 Technical data sheet of hybrid energy system

Description		Data
PV	Capital cost (b_j)	200,000 Rs/kW
	Lifetime (m)	25 years
	Operation and maintenance cost ($om(P_j)$)	1,000 Rs/kW/year
	Replacement cost ($rep(P_j)$)	200,000 Rs/kW
WTG	Capital cost (a_i)	65,000 Rs/kW
	Lifetime (m)	25 years
	Operation and maintenance cost ($om(P_i)$)	1,000 Rs/kW/year
	Replacement cost ($rep(P_i)$)	65,000 Rs/kW

36.6 Results and Discussion

In this paper, IEEE-33 bus and IEEE-69 bus radial distribution test systems are used to study the performance of the discussed GA based method in MATLAB. The corresponding figures are shown in Figs. 36.1 and 36.2.

The method used in the paper is to first calculate the total cost of installation of the DG based on minimum power loss of the system (as a single objective) and then to include the cost function terms and solve as a multi-objective problem.

For 33-bus system, we have base voltage at 12.66 kV and base MVA at 100 MVA. The real power loss obtained was 232.288 kW.

For placing a solar (PV) DG in the system, the minimum total real power loss P_{loss} in the system was obtained as 209.8019 kW. The optimal DG placement was at site 31 and the corresponding DG size was 2.1653 MW. The total cost for placing the solar DG was rounded up to Rs. 52, 56, 93, 653 (approx).

For placing a wind DG in the system, the minimum real power loss in the system was obtained at 209.8021 kW. The optimal DG placement was at site 31 and the corresponding DG size was 188.5 kW. The total cost for placing the WTG was rounded up to Rs. 1, 82, 34, 152 (approx).

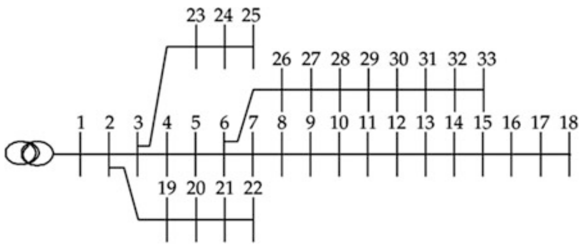

Fig. 36.1 IEEE-33 bus radial distribution system

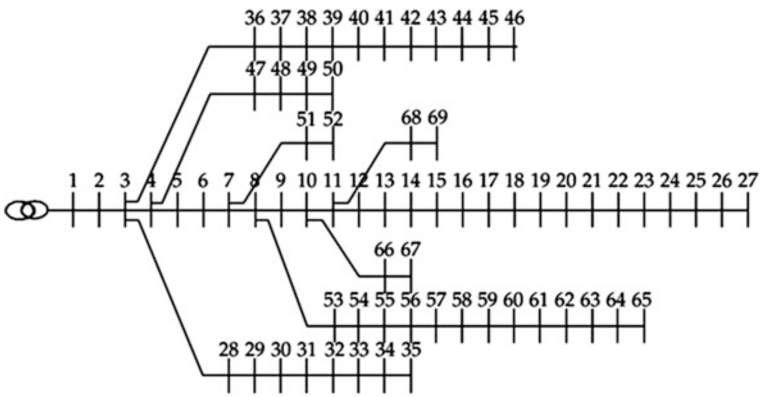

Fig. 36.2 IEEE-69 bus radial distribution system

The results obtained by simultaneous placement give a minimized power loss of 194.0458 kW. The location and size of PV and WTG are 31 and 7, 2.1834 MW and 179.1 kW, respectively and the total cost is Rs. 54, 30, 91, 305.

This result is better than the other types of DGs viz. type 1 and type 3 which have minimum power losses as 194.0484 kW and 218.2458 kW.

For 69-bus system, the real power loss without the placement of DG was obtained as 216.6168 kW.

For placing a solar (PV) DG in the system, the minimum total real power loss, P_{loss} in the system was obtained as 163.6652 kW. The optimal DG placement was at site 60 and the corresponding DG size was 4 MW. The total cost for placing the solar DG was rounded up to Rs. 98, 81, 05, 659 (approx).

For placing a wind DG in the system, the minimum real power loss in the system was obtained at 113.4301 kW. The optimal DG placement was at site 60 and the corresponding DG size was 589.9 kW. The total cost for placing the WTG was rounded up to Rs. 5, 43, 14, 387 (approx).

The results obtained by simultaneous placement give a minimized power loss of 112.5755 kW. The location and size of PV and WTG are 50 and 60, 3.883 MW and 569.1 kW, respectively and the total cost is Rs. 101, 44, 13, 493.

This result is better than the other types of DGs viz. type 1 and type 3 which have minimum power losses as 144.6395 and 213.6921 kW. This trend is what we have already observed in 33-bus system.

Following Tables 36.2 and 36.3, show the implementation of multi-objective problem on IEEE 69-bus system showing a compromise between cost and losses.

The results from the above sections show that without the placement of DGs, the real power losses in the system were higher as compared to the ones when the DGs

Table 36.2 Results for PV + PV (type 1 DG) using GA for multi-objective optimization

Sl. No.	P_{loss} (kW)	Cost (Rs) (approx)	PV_1 placement	PV_1 size (kW)	PV_2 placement	PV_2 size (kW)
1	129.105	1,372,883,827	60	3,988	61	3,993
2	215.690	19,327,839	34	54.8	61	59.5
3	152.613	715,283,927	60	1,489	61	3,575
4	140.940	1,127,267,938	60	3,357	61	3,001
5	133.283	1,237,336,933	60	3,471	61	3,885

Table 36.3 Results for PV + WTG (type 2 DG) using GA for multi-objective optimization

Sl. no.	P_{loss} (kW)	Cost (Rs) (approx)	PV placement	PV size (kW)	WTG placement	WTG size (kW)
1	216.467	5,368,025	60	9.73	36	30.5
2	163.699	992,938,405	60	3,997	36	47.7
7	175.199	752,393,736	60	3,003	36	108
4	202.462	256,373,027	60	950	36	215
5	178.006	689,374,928	60	2,773	36	44.1

were placed. Further placement of multiple DGs in the system reduced the system losses more than as compared to single DG placement but was subjected to the type of DGs. The cost of the DGs was inversely related to the real power losses occurring in the system and they were studied. Finally, the multi-objective optimization was carried out for both the test systems and a range of feasible values were shown.

36.7 Conclusion

The paper initially presents the objective to reduce the real power loss, P_{loss}, in the distribution system with the placement and size of multi-DGs by GA technique. The placement of multi-DGs (solar, wind, hybrid solar-wind) with the injection of real power, reactive power and the combination of real and reactive power has efficiently reduced the system real power loss satisfying the constraints. Further the cost of the system was also optimized. Again, it was found that the placement of multiple DGs in the system reduced the system losses more than as compared to single placement but were subjected to the type of DGs. Compared to solar or wind systems, hybrid systems gave a much better result. The work was carried on IEEE 33-bus and 69-bus radial distribution system in MATLAB and the results were compared.

References

1. Kumar R, Gupta RA, Bansal AK (2013) Economic analysis and power management of a stand-alone wind/ photovoltaic hybrid energy system using biogeography based optimization algorithm. Swarm Evol Comput 8:33–43
2. Kayal P, Chanda CK (2013) Placement of wind and solar based DGs in distribution system for power loss minimization and voltage stability improvement. Electr Power Energy Syst 53:795–809
3. Sotkiewicz PM, Mario VJ (2006) Nodal pricing for distribution networks: efficient pricing for efficiency enhancing DG. IEEE Trans Power Syst 21:1013–1014
4. Tan W-S, Hassan MY, Majid MS, Rahman Abdul H (2013) Optimal distributed renewable generation planning: A review of different approaches. Renew Sustain Energy Rev 18:626–645
5. Mohammadi M, Nafar M (2013) Optimal placement of multi-type DG as independent private sector under pool/hybrid power market using GA-based Tabu Search method. Electr Power Energy Syst 51:43–53
6. El-Zonkoly AM (2011) Optimal placement of multi-distributed generation units including different load models using particle swarm optimization. Swarm Evol Comput 1:50–59

7. Hasan D-M, Gharehpetian GB, Rastegar H, Olamaei J (2013) Optimal placement and sizing of DG (distributed generation) units in distribution networks by novel hybrid evolutionary algorithm. Energy 54:129–138
8. Moradi MH, Abedini M (2012) A combination of genetic algorithm and particle swarm optimization for optimal DG location and sizing in distribution systems. Electr Power Energy Syst 34:66–74
9. Esmaeilian HR, Darijany O, Mohammadian M (2000) Optimal placement and sizing of DGs and capacitors simultaneously in radial distribution networks based on voltage stability security margin. IEEE Proc Gen Transm Distrib 147(1):7–12

Chapter 37
Control of Three Phase to Three Phase Matrix Converter—A Direct Transfer Function Approach

A. Jamna, V. Jamuna and S. Rama Reddy

Abstract In recent years, Matrix converters have received enormous attention, due to their power control capability. They are capable of providing simultaneous transformation of amplitude and frequency of a three phase system. They are simple in structure and use bidirectional switches. In this paper the direct transfer function method is proposed to create variable voltage and variable frequency output and the same is simulated using MATLAB/SIMULINK simulation software.

Keywords Three phase matrix converter · Bi-directional switch · Direct transfer function method

37.1 Introduction

Application of power electronics based technology has rapidly increased due to the advancement of power semiconductor devices. Day by day the capability of these devices in terms of voltage rating, current rating, efficiency and reliability are increasing. A six- or twelve-pulse converter consumes the reactive power and it is very difficult to control the reactive power. High frequency switching of PWM converters produces harmonics, and filters are necessary to suppress them. Hence, it is necessary to go for a converter which overcomes these problems. Matrix converter, a direct converter, doesn't require any storage elements and hence the limitations of the two stage converters can be eliminated.

The concept of matrix converter was introduced in 1980 [1]. Matrix converter is a single stage ac-ac converter that uses bidirectional switch cells as the power controlling elements [2]. The bidirectional switches are created by assembling two

A. Jamna (✉)
MNM Jain Engineering College, Affiliated to Anna University, Chennai, India
e-mail: jamnaa@gmail.com

V. Jamuna · S. Rama Reddy
Jerusalem College of Engineering, Chennai 600100, India

C. Kamalakannan et al. (eds.), *Power Electronics and Renewable Energy Systems*,
Lecture Notes in Electrical Engineering 326, DOI 10.1007/978-81-322-2119-7_37

or four power switches and they are capable of allowing conduction of current in both directions and block any polarity of voltage [3, 4]. Due to the simplicity of construction, single stage voltage and frequency conversion, high efficiency, reliability and absence of dc link, makes this converter a better choice over a two stage or back to back converter [5, 6]. The matrix converter can be called a universal power converter as it promises diverse conversions like ac-dc, ac-ac, dc-ac and dc-dc [7]. There are various modulation strategies to improve the performance and efficiency of the converter [8, 9, 10]. The direct transfer function method is presented in this paper. The modulation algorithm using indirect transfer function is explained in [11, 12]. Improved modulation strategies have also been proposed to reduce output common mode voltage of converters [13, 14].

Since the output power, frequency and voltage fluctuate continuously with wind speed, the matrix converter can be employed as a powerful and efficient power converter in wind energy systems, to obtain a steady and constant output. The latest trends and configurations of wind energy systems are presented in [15, 16]. Grid connected wind turbines face many problems. Low voltage ride-through, the grid voltage imbalance and reactive power compensation are some of the issues [17, 18]. The other problem associated with wind power system is the overheating and torque pulsations due to the grid voltage imbalance [19, 20]. As a result, wind farms will be disconnected from the grid beyond a certain amount of imbalance. So it is a challenge to keep the output of the wind system constant.

In this paper, a direct transfer function method is developed, which offers a step up and step down frequency conversion along with controlling amplitude of the output voltage. The MATLAB/SIMULINK simulation results substantiate the behavior of the system.

37.2 Matrix Converter

Static converters have applications such as wind energy conversion systems, induction heating and general power supply system. The matrix converter is appropriate in ac systems, in which controlling of voltage and current is necessary, and bidirectional power flow is required [9, 12, 14, 17, 18].

The matrix converter is a forced commutated converter which uses an array of bidirectional switches as its main power conditioning elements. These power conditioning elements interconnects the input power supply to the output directly, without using any storage elements.

In Wind energy systems maintaining the output voltage and frequency is crucial and an efficient control algorithm is required to achieve the maximum power capture and thereby improve efficiency of the system. Various topologies of interfacing power electronic converters with the wind energy conversion system are discussed in literature [4, 12, 16, 17]. Among all the topologies, the two stage back-to-back converters are quite popular. But the wind energy conversion systems using these back-to-back converters include an ac-dc stage conversion, the bulky dc link (the filter) and then dc-ac conversion [12]. The use of matrix converter which is a single stage converter eliminates the use of the filter.

In the direct transfer function method, the output voltage matrix is calculated by multiplying the input voltage matrix by a modulation matrix. In this method, our main aim is to create a variable amplitude and frequency output voltage from a fixed input voltage of constant amplitude and frequency. To obtain the desired output, a time window is considered, in which the instantaneous values of the required output voltages are sampled. A signal is synthesized by using the instantaneous input voltages. The low-frequency component of the synthesized signal is the required output voltage. Both mathematical analysis and the simulation are presented.

37.3 Mathematical Model of the Matrix Converter

The basic H-bridge configuration of three phase matrix converter is shown in Fig. 37.1. It has an array of nine bidirectional switch cells. The switch cells are designed in such a way that it can allow the conduction of current in either direction and also to block the voltage. The switch cells connect and disconnect the input phase to the output phase in a particular fashion by applying appropriate switching pulses.

In order to generate the targeted output voltages, appropriate switching pulses have to be applied to each of the bidirectional switches of the Matrix Converter. From a constant amplitude and constant frequency input, an output of variable frequency and variable amplitude is obtained. This is achieved by considering a time window. The time window is created by sampling the instantaneous values of the output. To obtain the desired output voltage, a signal is synthesized by using the instantaneous values of the input voltage. The input phase voltages are V_M, V_N and V_O and the output phase voltages are V_m, V_n and V_o.

The input voltage can be written as,

$$\begin{pmatrix} V_M(t) \\ V_N(t) \\ V_O(t) \end{pmatrix} = \begin{pmatrix} V_{in}\cos\omega_i t \\ V_{in}\cos(\omega_i t + \frac{2\pi}{3}) \\ V_{in}\cos(\omega_i t + \frac{4\pi}{3}) \end{pmatrix} \tag{37.1}$$

The targeted output voltage can be written as,

$$\begin{pmatrix} V_m(t) \\ V_n(t) \\ V_o(t) \end{pmatrix} = \begin{pmatrix} V_{out}\cos\omega_O t \\ V_{out}\cos(\omega_O t + \frac{2\pi}{3}) \\ V_{out}\cos(\omega_O t + \frac{4\pi}{3}) \end{pmatrix} \tag{37.2}$$

By properly selecting the conduction states, the bidirectional switches connect or disconnect the input phase to the output phase of the load. The conduction states of the bidirectional switches are defined by switching function and it can be given as,

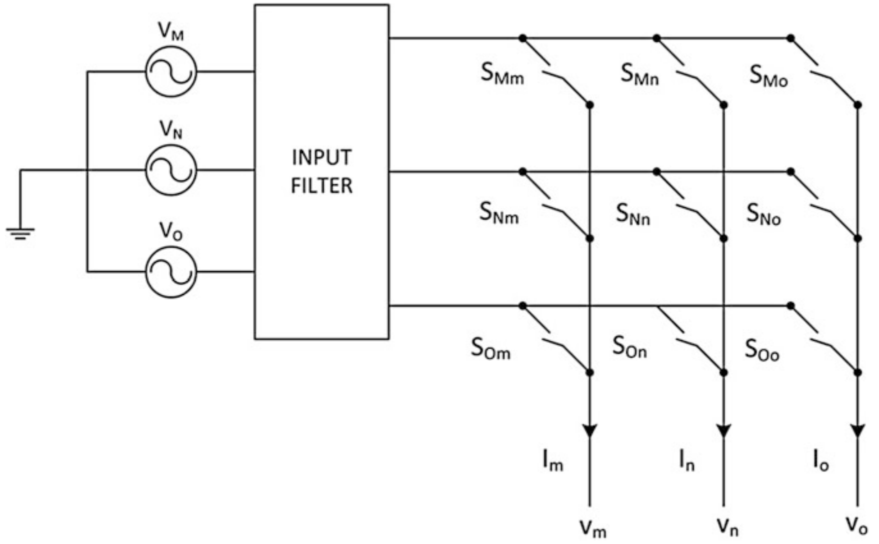

Fig. 37.1 H-bridge configuration of three phase matrix converter

$$S_{ij} = \begin{cases} 0, & \textit{if switch is off} \\ 1, & \textit{if switch is on} \end{cases} \tag{37.3}$$

It is important to note that two switches in the same input phases should not be on at the same time as it may cause a short circuit in the input and the destruction of converter. Similarly at least one switch in every output phase should be on.

Let us assume that the switch S_{ij} is 'ON' for duration of t_{ij} and the sampling interval is T. The low frequency component can be obtained as,

$$\mathrm{V_{jn}(t) = \big(t_{Mj}V_M(t) + t_{Nj}V_N(t) + t_{Oj}V_O(t)\big)/T} \tag{37.4}$$

We can also write,

$$\mathrm{T = t_{Mj} + t_{Nj} + t_{Oj}} \tag{37.5}$$

The duty cycle of each switch can be given as,

$$\mathrm{m_{Mj}(t) = t_{Mj}/T;\ m_{Nj}(t) = t_{Nj}/T;\ m_{Oj}(t) = t_{Oj}/T} \tag{37.6}$$

The modulation matrix M(t) can be obtained from the method suggested by Venturini and Alesina [2] as

$$M_{ij}(t) = 1/3[\frac{(1 + 2 * Vin * Vref)}{Vin^2}] \tag{37.7}$$

where i = {M, N, O} and j = {m, n, o}

$$[\mathrm{V_{OUT}}] = [\mathrm{V_{in}}] * [\mathrm{M(t)}] \tag{37.8}$$

Hence output voltage can be derived as follows,

$$\begin{pmatrix} V_{mN}(t) \\ V_{nN}(t) \\ V_{oN}(t) \end{pmatrix} = \begin{pmatrix} \mathrm{m_{Mm}(t)} & \mathrm{m_{Nm}(t)} & \mathrm{m_{Om}(t)} \\ \mathrm{m_{Mn}(t)} & \mathrm{m_{Nn}(t)} & \mathrm{m_{On}(t)} \\ \mathrm{m_{Mo}(t)} & \mathrm{m_{No}(t)} & \mathrm{m_{Oo}(t)} \end{pmatrix} \begin{pmatrix} V_M(t) \\ V_N(t) \\ V_O(t) \end{pmatrix} \tag{37.9}$$

37.4 Control Procedures for the Three Phase Matrix Converter

The following procedure is proposed to control the matrix converter.

Step 1 An input voltage sample V_{in} and a target output voltage sample V_{ref} should be obtained.

Step 2 The modulation matrix m(t) should be calculated by using the formula derived from Venturini modulation method given in the Eq. (37.7).

Step 3 m_{ij} (t) is then compared to a reference ramp signal and nine switching pulses of duration t_{ij} is calculated.

Step 4 The generated switching functions are used to switch on and switch off the bidirectional switch cells.

Figure 37.2 shows the switching functions of a jth output phase. From the figure it is been noted that the nine switching pulses should be generated according to this pattern to create the jth output phase.

At any instant, amplitude of the low frequency component of the output voltage cannot exceed the maximum available amplitudes and hence the output voltage can be a maximum of 0.5Vi. This is the limitation of the direct transfer function approach.

Fig. 37.2 Switching functions of a jth output phase

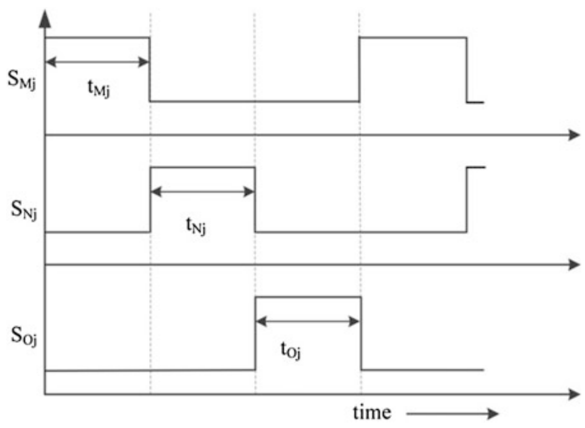

Table 37.1 Simulation parameters

Source voltage amplitude	230 V
Filter inductance	3 mH
Filter capacitance	25 μF
Filter resistance	1 Ω
Load inductance	30 mH
Load resistance	10 Ω

37.5 Simulation Details

The following parameters given in the Table 37. 1 are used for simulation of three phase matrix converter.

The MATLAB simulation circuit for the control of Matrix Converter is as shown in the Fig. 37.3. The input voltage and the targeted output voltage are used to create the switching functions in the converter. V_M, V_N and V_O are the input voltages and the corresponding output voltages are V_m, V_n and V_o.

The switching function can be given as,

$$S_{ij} = \begin{cases} 0, & s_{ij} \text{ is ON} \\ 1, & s_{ij} \text{ is OFF} \end{cases} \tag{37.10}$$

$$S_{Mm} + S_{Nm} + S_{Om} = 1 \tag{37.11}$$

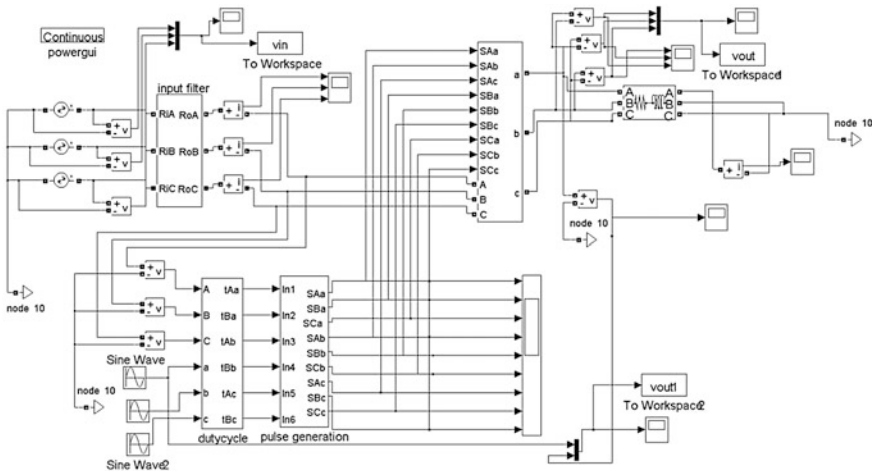

Fig. 37.3 Simulation circuit for proposed three phase matrix converter

The input voltage and reference voltage is used to create the switching function is given by,

$$m_{ij}(t) = (1 + 2V_{in}V_{ref})/\left(3 * V_{in}^2\right) \tag{37.12}$$

37.6 Results and Discussions

The simulations of direct three phase to three phase matrix converter is carried out using MATLAB/SIMULINK to produce a constant frequency output from a variable frequency input.

Figure 37.4 shows the duty cycle generation m_{ij}. Figure 37.5 shows the circuit diagram and Fig. 37.6 gives the graphical representation of the generation of pulses for the mth phase i.e. the switching pulses, S_{Mm}, S_{Mn} and S_{Mo}. The input voltage V_{in} and the reference output voltage V_{ref} are given as the input. t_{Mm} and t_{Mn} are compared with a ramp signal and the pulses are produced. From the two inputs t_{Mm} and t_{Mn} three pulses are generated and applied to the switches at the output phase m.

An input voltage waveform of 250 V, 50 Hz applied to the three phase matrix converter. Figure 37.7 shows corresponding output voltage waveform for 50 Hz.

Figure 37.8a, b show the output voltage of frequency 100 and 25 Hz, respectively, for an input voltage waveform of frequency 50 Hz.

Figure 37.9 shows the output voltage waveform with frequency 50 Hz for a corresponding input voltage waveform with frequency 100 Hz. Similarly, Fig. 37.10 shows the 50 Hz output voltage waveform for a corresponding 25 Hz input voltage.

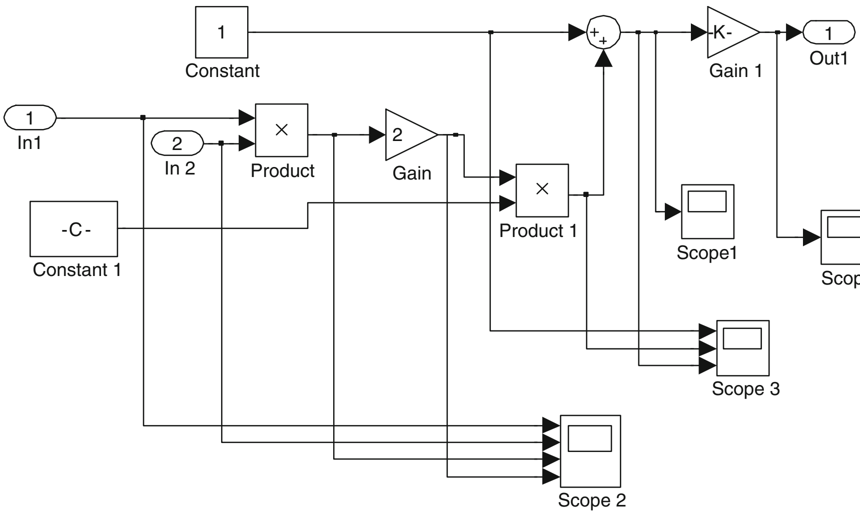

Fig. 37.4 Duty cycle generation m_{ij}

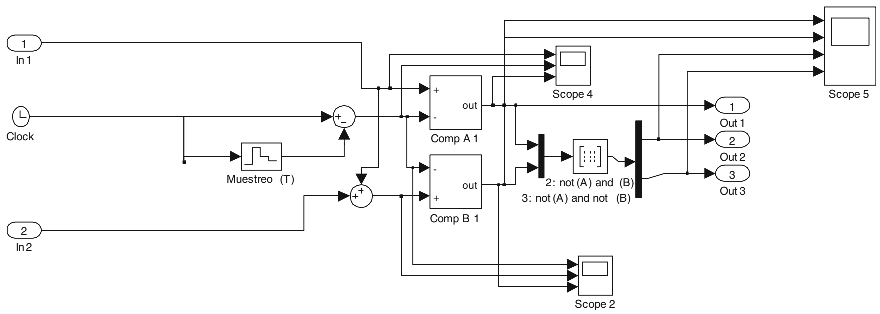

Fig. 37.5 Circuit for generation of pulses for mth phase

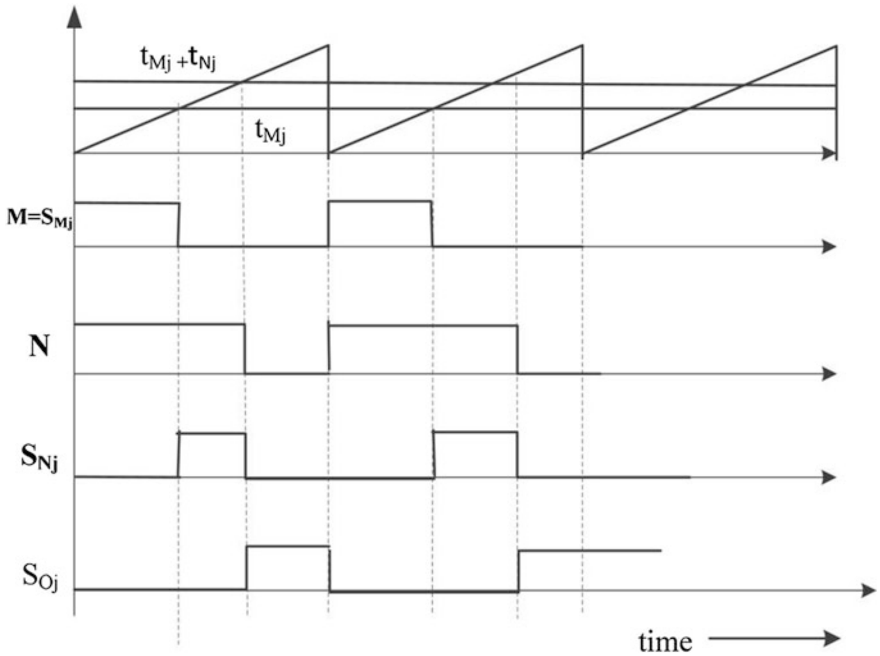

Fig. 37.6 Graphical representation of generation of pulses for the mth phase

37.7 Conclusion and Future Scope

The proposed topology can be implemented for a wind energy conversion system, where the input frequency varies with the speed of the wind. This topology and switching pattern ensure soft switching over a wide range of power control. The proposed commutation technique is very simple and can be implemented without any additional components. It is therefore possible to make a direct converter,

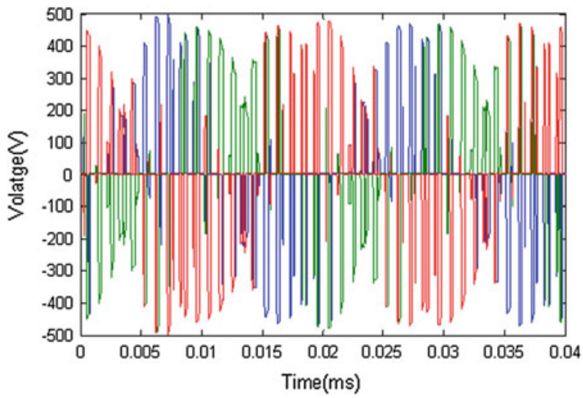

Fig. 37.7 Output voltage wave form for 50 Hz

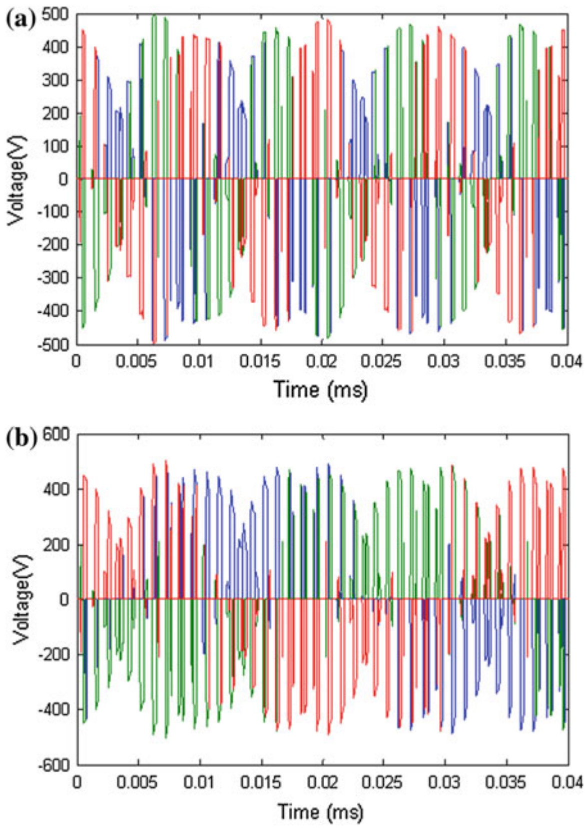

Fig. 37.8 **a** 100 Hz output voltage. **b** 25 Hz output voltage

without having any significant impact on the utility supply. Hence, with the advantages of single stage conversion of voltage and frequency, simple structure, low losses, high efficiency, reliability and absence of dc link makes the matrix converter a better proposition over a two stage converter.

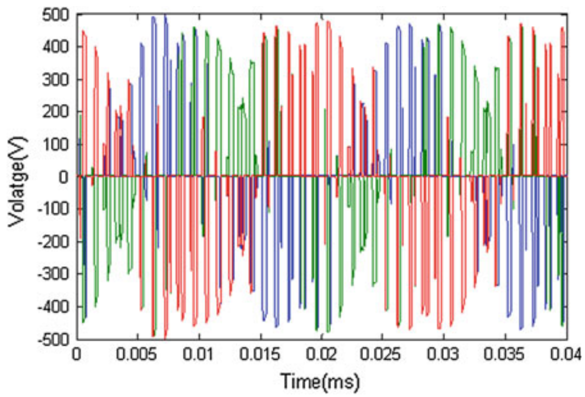

Fig. 37.9 50 Hz output voltage

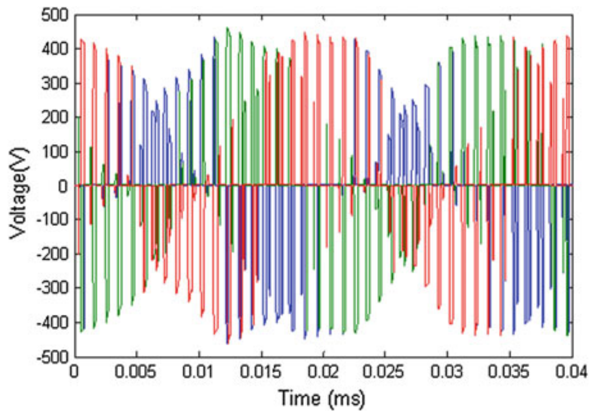

Fig. 37.10 50 Hz output voltage

The direct transfer function approach of the matrix converter along with the MATLAB simulation is explained in detail. A very good behavior of the matrix converter was produced and a variable voltage and variable frequency output was obtained from the constant voltage constant frequency input and the vice versa. The maximum output voltage ratio is 0.5. There is a possibility to cascade the two matrix converter to get the maximum voltage gain.

References

1. Venturini M (1980) A new sine wave in sine wave out conversion technique which eliminates eactive elements. In: Proceedings of POWERCON7, pp E3-1–E3-15
2. Alesina A, Venturini M (1988) Intrinsic amplitude limits and optimum design of 9-switches direct PWM AC-AC converters. In: Proceedings of IEEE PESC'88, pp 1284–1291
3. Deivasundari P, Jamuna V (2001) Single phase matrix converter as an 'all silicon solution'. In: Proceedings of 1st international conference on electrical energy systems (ICEES)

4. Itoh JI, Sato I, Odaka A, Ohguchi H, Kodachi H, Eguchi N (2004) A novel approach to practical matrix converter motor drive system with reverse blocking IGBT. In: IEEE 35th annual conference on power electronics, PESC04, vol 3, pp 2380-2385
5. Correa P, Rodríguez J, Rivera M, Espinoza JR, Kolar JW (2009) Predictive control of an indirect matrix converter," IEEE Trans Ind Electron 56(6):1847–1853
6. Friedli T, Kolar JW, Rodriguez J, Wheeler PW (2012) Comparative evaluation of three-phase AC–AC matrix converter and voltage DC-link back-to-back converter systems
7. Deivasundari PV, Jamuna A (2011) Z-source single phase matrix converter with safe commutation strategy. Int J Energy Environ 2(3):579–588 (Publisher: International Energy and Environment Foundation (IEEF), ISSN/EISSN: 20762895 20762909)
8. Huber L, Borojevic D (1995) Space vector modulated three-phase to three-phase matrix converter with input power factor correction. IEEE Trans IA 31:1234–1246
9. Neft CL, Schauder CD (1992) Theory and design of a 30-Hp matrix converter. IEEE Trans. IA 28:546–551
10. Zanchetta P, Wheeler PW, Clare JC, Bland M, Empringham L, Katsis D (2008) Control design of a three-phase matrix-converter-based AC–AC mobile utility power supply. IEEE Trans Ind Electron 55(1):209–217
11. Azib, Tazerart F, Metidji AB, Taib N, Ziane DJ, Rekioua T (2011) Matrix control algorithm dedicated to feed the double star induction machine. Int J Res Rev Comput Eng 1
12. Liu X, Loh PC, Peng FZ, Wang P (2010) Optimal modulation of indirect Z-source matrix converter. In: Proceedings of IPEC, pp 3049–3056
13. Hava AM, Ün E (2011) A high-performance PWM algorithm for common-mode voltage reduction in three-phase voltage source inverters. IEEE Trans Power Electron 26 (7):1998–2008
14. Renge MM, Suryawanshi HM (2010) Three-dimensional space-vector modulation to reduce common-mode voltage for multilevel inverter. IEEE Trans Ind Electron 57(7):2324–2331
15. Elizondo JJ, Macias ME, Mocheloud OM (2009) Matrix converters applied to wind energy conversion systems, technologies and investigation trends. In: 2009 electronics, robotics and automotive mechanics conference
16. Janssen W, Luetze H, Buecker A, Hoffmann T, Hagedorn R (2005) Low voltage ride through for wind turbine generators. U.S. Patent 6,921,985B2
17. Aghasi M, Faraji V, Khaburi DA, Kalantar M (2010) Direct power control for doubly-fed induction generator using indirect matrix converters. In: PSC international power system conference PSC
18. Muljadi E, Yildirim D, Batan T, Butterfield CP (1999) Understanding the unbalanced voltage problem in wind turbine generation. In Proceedings of industry applications conference, vol 2, pp 1359–1365
19. Ghousia SF (2012) A multilevel quasi matrix converter design for SRM drives in EV applications. Int J Power Electron Drive Syst (IJPEDS) 2(2):170–176 (ISSN: 2088-8694)
20. Wijekoon T, Klumpner C, Zanchetta P, Wheeler PW (2008) Implementation of a hybrid AC–AC direct power converter with unity voltage transfer. IEEE Trans Power Electron 23 (4):1918–1926

Chapter 38
Comparison of PI and PIR Regulators for DFIG During Unbalanced Grid Voltage Conditions

A. Ramkumar, S. Durairaj and N. Arun

Abstract This paper, offerings the control of a doubly fed induction generator (DFIG)-based wind power conversion and the two dissimilar classes of current regulators for a (DFIG) under unbalanced grid voltage conditions: proportional integral resonant (PIR) part and proportional integral (PI) regulator part. To verify the value of the proposed control strategy, simulation results with 500 MVA DFIG topology are presented and discussed in the paper. Finally, simulation studies are carried out on a 500 MVA wind-turbine driven DFIG system under unbalanced grid voltage conditions. All the results are validated by PSCAD simulation.

Keywords Doubly fed induction generator (DFIG) · Proportional integral (PI) · Proportional integral plus resonant (PI–R) · Unbalance voltage · Total harmonic distortion (THD)

38.1 Introduction

Renewable energy is attracting more attention all over the world to overcome the increasing power demand. At all the renewable energy sources, solar energy and wind energy are reliable energy sources. Now a day, wind power is gaining a lot of importance because it is cost effective, environmentally clean and safe renewable power source compared to fossil fuel and nuclear power generation. Recently, electricity production from multi megawatt (multi-MW) wind turbines arranged in wind parks has been the focus of considerable attention when it comes to the fulfillment of renewable-energy targets set by governments all over the world. A doubly-fed induction generator (DFIG) have some advantages due to variable

A. Ramkumar · N. Arun (✉)
Kalasalingam University, Srivilliputhur, TN, India
e-mail: arun.n89@gmail.com

S. Durairaj
Kings College of Engineering, Tanjore, TN, India

C. Kamalakannan et al. (eds.), *Power Electronics and Renewable Energy Systems*,
Lecture Notes in Electrical Engineering 326, DOI 10.1007/978-81-322-2119-7_38

speed operation and four quadrant active and reactive power capabilities compared with fixed speed induction generators and synchronous generators. The stator of DFIG is connected directly to the grid, and the rotor links the grid by a bidirectional converter; its rated power is much more minor than the DFIG rated power although the power converters used in squirrel cage induction or synchronous generators has to support the rated power of the machine. The rotor converter objective aims to the DFIG active and reactive power control between the stator and ac supply.

This paper proposes a PI and PIR control of a DFIG system under unbalanced grid voltage conditions by coordinating the control of the RSC and the GSC.

38.2 DFIG System Behavior with an Unbalanced Grid

For a DFIG-based wind generation system, the main task of the RSC is to control DFIG's stator output active and reactive power, whereas the GSC controls is common dc-link voltage. Complete models of both the RSC and GSC have been studied in [1, 2], thus essential description is only given in this paper.

38.2.1 RSC Model

The DFIG model considered is based on the stator-voltage orientation, when their mathematical equations given below.

The spatial relationship between the stationary $\alpha_s\beta_s$ frame, rotor $\alpha_r\beta_r$ frame rotating at the angular speed of ω_r, and dq^+ and dq^- frames rotating at the respective angular speeds of ω_s and $-\omega_s$. Vector F, for the transformations between different references frames are [3] (Fig. 38.1),

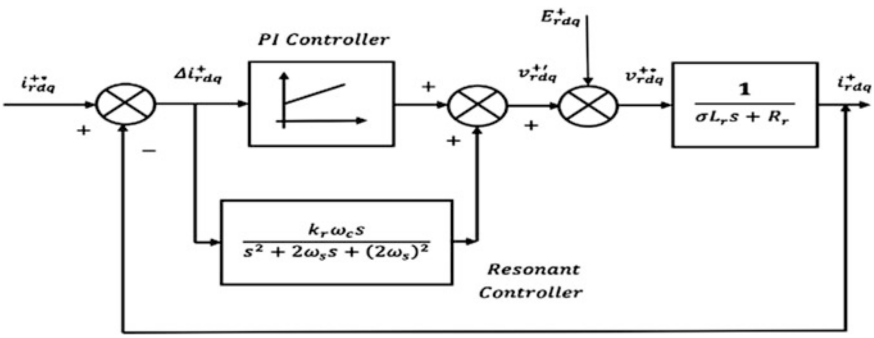

Fig. 38.1 Proposed PIR current controller for unbalanced loads

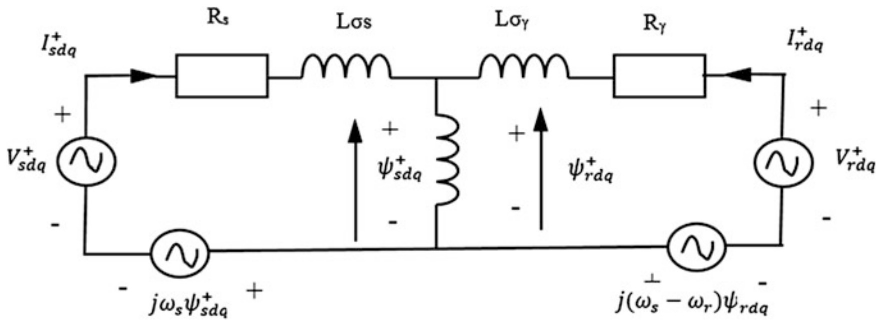

Fig. 38.2 DFIG equivalent circuit in the positive synchronous reference frame

$$F^{+}_{dq} = F\alpha_r\beta_r e^{-j\omega_{slip}} + t \tag{38.1}$$

$$F^{-}_{dq} = F\alpha_r\beta_r e^{j\omega_{slip}} - t \tag{38.2}$$

F can be expressed in terms of negative and positive sequence components in the respective positive and negative rotating synchronous frames as

$$F^{+}_{dq} = F^{+}_{dq+} + F^{+}_{dq-} = F^{+}_{dq+} + F^{-}_{dq-}e^{-j2\omega_s t} \tag{38.3}$$

Figure 38.2 shows the DFIG equivalent circuit in the positive dq^{+} reference frame. As in the rotor voltage in the dq^{+} reference frame can be expressed as

$$v^{+}_{r} = R_r I^{+}_{r}\sigma L_r \frac{dI^{+}_{r}}{dt} + \frac{L_m}{L_s}\frac{d\psi^{+}_{s}}{dt} + j\omega_{slip+}\left(\frac{L_m}{L_s}\psi^{+}_{s} + \sigma L_r I^{+}_{r}\right) \tag{38.4}$$

Under unbalanced grid voltage conditions, the instantaneous stator output active and reactive powers are expressed as,

$$\begin{aligned} P_s &= P_{s0} + P_{ssin\,2}\sin 2\omega_s t + P_{scos\,2}\cos 2\omega_s t \\ Q_s &= Q_{s0} + Q_{ssin\,2}\sin 2\omega_s t + Q_{scos\,2}\cos 2\omega_s t \end{aligned} \tag{38.5}$$

Similarly, the electromagnetic power is,

$$P_e = -\frac{3}{2}\mathrm{Re}j\omega_s\psi^{+}_{sdq} \times I^{+}_{sdq} \tag{38.6}$$

Neglecting copper losses, the rotor active power input is

$$P_r = P_s - P_e \tag{38.7}$$

Since the d^{+}-axis is fixed to the positive-sequence stator voltage, (38.6) and (38.7) can be further simplified by taking into account. $V_{sq+}^{+} = 0$.

38.2.2 GSC Model

Under unbalanced grid voltage conditions, the GSC can be decayed into positive and negative sequence components [4]. According to references, the instant active and reactive powers from the GSC to the ac network can be expressed by

$$\begin{aligned} P_g &= P_{g0} + P_{gcos\,2}\cos 2\omega_s t + P_{gsin\,2}\sin 2\omega_s t \\ Q_g &= Q_{g0} + Q_{gcos\,2}\cos 2\omega_s t + Q_{gsin\,2}\sin 2\omega_s t \end{aligned} \tag{38.8}$$

The common dc-link voltage to the GSC as

$$\mathrm{C}\frac{dV_{dc}}{dt} = (P_e - P_s) - \left(P_g - P_X\right) \tag{38.9}$$

where P_X is the active power across the coupling inductor L_g.

38.3 Current Regulation Using PI–R Control

The positive and negative system currents must be controlled just in order to meet the control objectives. Good current control depending on the accuracy of the *dq* components decoupling and the elimination of network voltage trouble. So that dazed these problems, the strategy accepted here is to have a PI–R current controller. The R regulator has been usually offered as an exciting alternative in the stationary frame to the use of synchronous PI controllers. This regulator commonly involves of a proportional and an integrator term, which covers an R pole, with the goal of finding an infinite gain at the R frequency [5]. In order to reduce the sensitivity toward possible grid frequency variation, a component with a cutoff frequency of ω_{c1} can be inserted into the R part to enlarge its frequency bandwidth.

38.3.1 RSC

During network imbalance, a DFIG system can be represented in the dq^+ reference frame without any decomposition of positive and negative sequence components, V_{rdq}^{+} is given as

$$V_{rdq}^{+} = \sigma L_r U_{rdq}^{+} + E_{rdq}^{+} \tag{38.10}$$

where U_{rdq}^{+} is the output from the PIR controller

$$U_{rdq}^{+} = \frac{d}{dt} I_{rdq}^{+} \tag{38.11}$$

E_{rdq}^{+} is the equivalent rotor back electromagnetic force acting as a disturbance to the PIR controller. The synchronous dq^+ frame to the rotor $\alpha_r\beta_r$ frame as

$$V_{r(\alpha_r\beta_r)} = V_{rdq}^{+} e^{j\omega_{slip}} + t \tag{38.12}$$

38.3.2 GSC

The GSC controls the usual common dc-link voltage which determines Pg0 and provides limited reactive power support to the grid, i.e., Qg0.

GSC under unbalanced supply voltage can be represented in the dq^+ frame as [6],

$$\frac{d}{dt} I_{rdq}^{+} = \left(V_{sdq}^{+} - R_g I_{gdq}^{+} - j\omega_s L_g I_{gdq}^{+} - V_{gdq}^{+} \right) / L_g \tag{38.13}$$

Where V_{gdq}^{+} control voltage by the GSC PIR controller.

Without the positive and negative sequence currents, V_{gdq}^{+} is designed as

$$V_{gdq}^{+} = -L_g U_{gdq}^{+} + E_{gdq}^{+} \tag{38.14}$$

An unbalanced grid control method based on proportional-integral (PI) controllers is shown in Fig. 38.3, which is a common control method for DFIGs. A 500 MVA DFIG is selected to be analyzed in this paper and the Base angular frequency is 376.99 rad/s. The DFIG's parameter values are listed in Table 38.1.

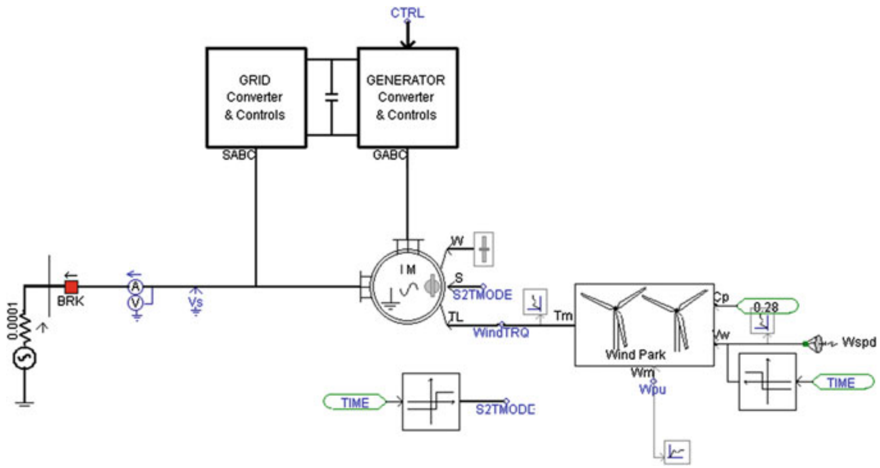

Fig. 38.3 DFIG control simulation diagram

Table 38.1 DFIG parameter values

Rated power	500.0 (MVA)
Rated voltage (L-L)	13.8 (kV)
Base angular frequency	376.99 (rad/s)
Stator resistance	0.0054 (pu)
Wound rotor resistance	0.00607 (pu)
Magnetizing inductance	4.362 (pu)

38.4 Simulation Results

Figure 38.4 shows the simulation results for the PI and PIR regulator for the (DFIG) under unbalanced grid voltage conditions. Figure 38.4a shows a PI control method voltage. Figure 38.4b shows a PIR control method voltage, comparison of the both voltage simulation results, it shows the PI control method voltage deviation is very high, compared to the PIR controller. In contrast, the PIR regulator provides unity gain and voltage stability at with in short duration.

In order to illustrate the impact of the R regulator on the current controller stability, as shown in the Fig. 38.5 Similarly, Fig. 38.5a shows a PI control method current, Fig. 38.5b shows a PIR control method current comparison of the both current simulation results, it shows the PI control method current deviation is very high, compared to the PIR controller. The current controllers with and without the R regulator can be seen, the R regulator has slight effect on the current control system, which, as a result, is as steady as with PI only.

By using PI controller the control of the rotor side converter was configured to control either the torque pulsations or the stator power oscillations. Figure 38.6 shows the torque simulation results for the PI and PIR regulator for the (DFIG)

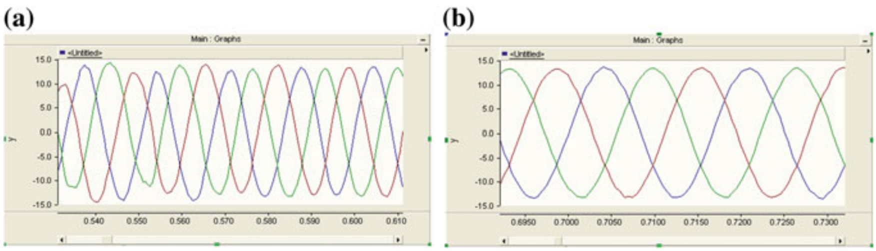

Fig. 38.4 PI and PIR control simulation results for voltage

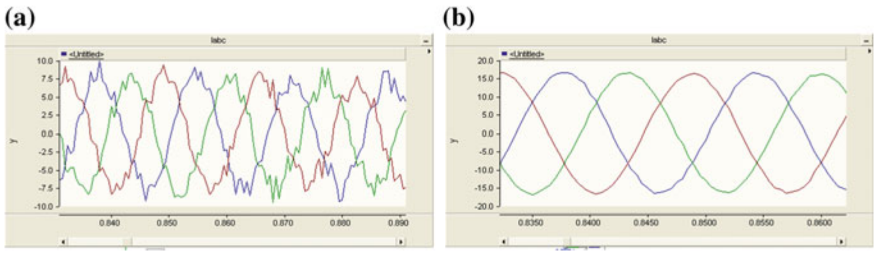

Fig. 38.5 PI and PIR control simulation results for current

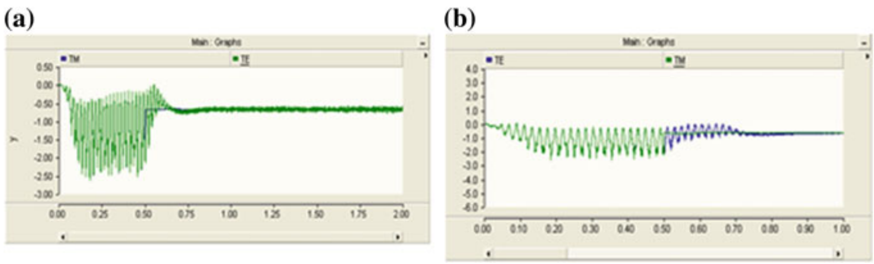

Fig. 38.6 PI and PIR control simulation results for torque

under unbalanced grid voltage conditions. Figure 38.6a shows a PI control method torque and Fig. 38.6b shows a PIR control method torque comparison of the both torque simulation results, it shows the PI control method torque oscillation is very high, compared to the PIR controller. In difference, the PIR regulator it offers unity gain and stability at with in short duration.

Similarly, Fig. 38.7a shows a PI control method real and reactive powers. Figure 38.7b shows a PIR control method real and reactive powers. Comparison of the both real and reactive powers simulation results, it shows the PI control method real and reactive powers is less, compared to the PIR controller. In contrast, the PIR regulator provides unity gain and system stability at with in short duration. The current controllers with and without the R regulator can be seen, the R regulator has

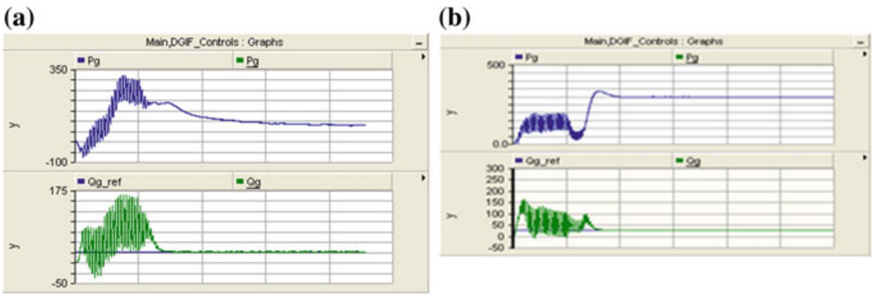

Fig. 38.7 PI and PIR control simulation results for real and reactive power

well efficient on the current control system. The PIR controller using DFIG control system has to be produce high amount of real and reactive power as shown in the PSCAD simulation results.

The measured harmonic frequency to be controlled by tuning the PI and PIR controllers. That is, the resonant controller is tuned to two times of the network frequency 2ω or to control third harmonics it is tuned to 3ω by controlling double frequency current oscillations resulting from asymmetric grid voltage. Figure 38.8 shows the total harmonic distortion (THD), simulation results for the PI and PIR regulator for the (DFIG) under unbalanced grid voltage conditions. Figure 38.8a shows a PI control method THD for i_b. Figure 38.8b shows a PIR control method THD for i_b comparison of the both harmonic distortion simulation results, it shows the PI control method THD is very high, compared to the PIR controller. In difference, the PIR regulator it offers low harmonic distortion in short duration.

In this above Fig. 38.9 shows the voltage THD for the DFIG system under unbalanced grid voltage conditions. The simulation results carried out the PI and PIR regulator for the (DFIG). Then the wind turbine's large inertia results in a larger mechanical time constant than the electrical one [6], the DFIG speed is assumed to be fixed for the initial simulation tests. Figure 38.9a shows a PI control method THD simulation results for voltage. Figure 38.9b shows a PIR control method DFIG system THD. For that simulation result comparison the PIR control voltage THD is less to the PI control method.

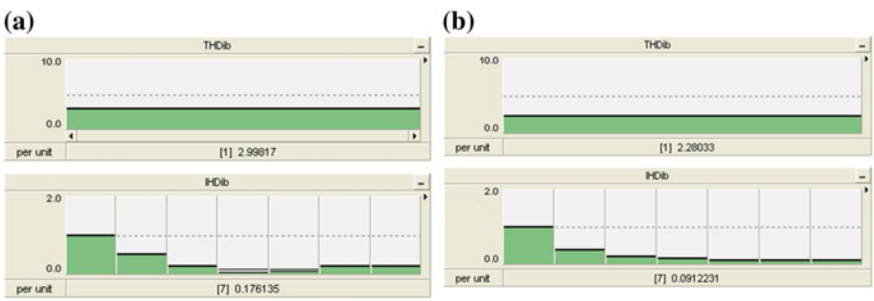

Fig. 38.8 PI and PIR control simulation results for THD value of i_b

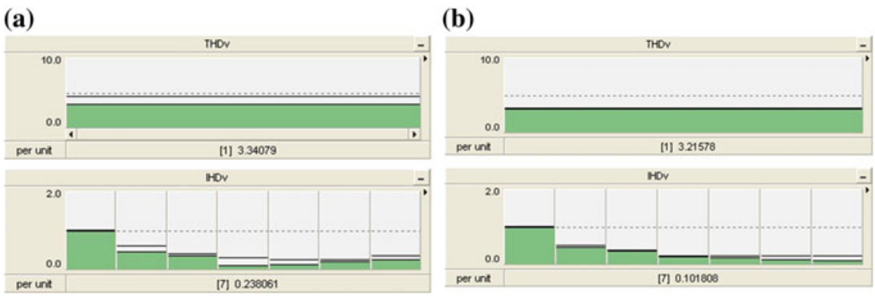

Fig. 38.9 PI and PIR control simulation results for THD value of voltage

Thus the Simulations of the proposed control strategy for a DFIG based wind power generation system were conducted using PSCAD/Simulation. The DFIG is rated at 500 MVA, with parameters listed in Table 38.1. Figure 38.7 shows the schematic diagram of the simulated system. The DFIG's power, torque, and currents shown in the above simulation results are all in per-unit (pu) term, where their rated values are defined as pu values.

38.5 Conclusion

This paper compares the PIR and PI regulators for DFIG operation control with unbalanced grid voltage using PSCAD software. The results are compared to the simulation results for compliance with the PI and resonant control. The Result Shows that Resonant control was well efficient after the comparison.

References

1. Hu J, Nian H, Xu H, He Y (2011) Dynamic modeling and improved control of DFIG under distorted grid voltage conditions. IEEE Trans Energy Convers 26(1):163–175
2. Xu L, Wang Y (2007) Dynamic modeling and control of DFIG based wind turbines under unbalanced network conditions. IEEE Trans Power Syst 22(1):314–323
3. Hu J, He Y, Xu L, Williams BW (2009) Improved control of DFIG systems during network unbalance using PI–R current regulators. IEEE Trans Ind Electron 56(2)
4. Xu L, Cartwright P (2006) Direct active and reactive power control of DFIG for wind energy generation. IEEE Trans Energy Convers 21(3):750–758
5. Liu C, Blaabjerg F, Chen W, Xu D (2012) Stator current harmonic control with resonant controller for doubly fed induction generator. IEEE Trans Power Electron 27(7)
6. Shang L, Hu J (2012) Sliding-mode-based direct power control of grid-connected wind-turbine-driven doubly fed induction generators under unbalanced grid voltage conditions. IEEE Trans Energy Convers 27(2)

Chapter 39
Implementation of Direct Torque Control for Matrix Converter Fed Induction Motor Drive Using Fuzzy Logic Controller

J. Karpagam, A. Nirmal Kumar, V. Kumar Chinnaiyan and M. Surya

Abstract Direct Torque Control (DTC) has emerged as a powerful tool to reduce the torque ripples. DTC is the strategy of selecting the proper stator voltage vectors to force the stator flux and developed torque within the prescribed band. However, the main disadvantage of conventional DTC is electromagnetic torque ripple. This paper aims to analyze the DTC to reduce the torque ripple in induction motor drive employing duty ratio fuzzy logic controllers. The DTC is combined with the Matrix Converter (MC) to give the advantages of the proposed method. Duty ratio controller is introduced to reduce the flux and torque ripples in place of hysteresis comparators. The simulations were carried out using Matlab/Simulink software package. Simulation result shows the effectiveness of drive performance, flux and torque responses.

Keywords Direct torque control · Induction motor drives · Matrix converters · Duty ratio fuzzy controller

39.1 Introduction

A matrix converter is a direct AC to AC converter in a single stage without any DC link. It consists of nine bidirectional switches. The advantages of MCs are inherent bidirectional power flow, sinusoidal input output waveforms, absence of dc link

---

J. Karpagam (✉) · V. Kumar Chinnaiyan
Dr. NGP Institute of Technology, Coimbatore, India
e-mail: sujisumi@rediffmail.com

V. Kumar Chinnaiyan
e-mail: kumarchin@hotmail.com

A. Nirmal Kumar
Karpagam College of Engineering, Coimbatore, India
e-mail: ankhod@gmail.com

M. Surya
Jansons Institute of Technology, Coimbatore, India
e-mail: surya_meyporul@yahoo.co.in

C. Kamalakannan et al. (eds.), *Power Electronics and Renewable Energy Systems*,
Lecture Notes in Electrical Engineering 326, DOI 10.1007/978-81-322-2119-7_39

reactive components and controllable input power factor [1]. The objective of the matrix converter is to generate variable amplitude and variable frequency ac supply from the fixed amplitude and frequency ac supply. The main condition is that any input phase should not be short circuited and any output phase should not be open circuited [2].

A different control technique is used to control the speed of the induction motor drive. A new class of control technique called direct torque control is introduced to reduce the electromagnetic torque ripples in drives. It is considered as an alternative to field oriented control technique [3]. DTC is the method used to directly control the torque and flux of a drive by the proper selection of the space vectors for converters. The main advantage of DTC is its simple structure, no coordinate transformations is required, no need for separate pulse width modulator, PWM generation are not required. The DTC method has become one of the high performance control strategies for AC machines to provide a very fast torque and flux control. For such advanced reasons, the combination of MC with DTC method is effectively possible. Even though, DTC has more advantages, it uses two hysteresis controllers for stator flux and torque which produces steady state ripple in flux and torque responses. To overcome this problem, hysteresis controller is replaced by duty ratio fuzzy logic controller.

The work presented in this paper mainly focuses on modeling of matrix converter fed induction motor drive and the design of fuzzy logic controller for torque and flux control with the corresponding membership functions [4]. Results are obtained for loaded conditions using Matlab/Simulink software to validate the performance of the proposed controller. The obtained results exhibit the better performance (reduced ripples) than that of the other methods.

39.2 Direct Torque Control

39.2.1 Conventional DTC

The principle of direct torque control is to directly select the voltage vectors according to the difference between reference and actual value of torque and flux linkage. The most opportune converter switching state is selected at any instant based on the output signals of a flux and torque comparators and with the knowledge of the position of the stator flux space vector [5].

The three phase quantities are treated using single equation known as space vector.

$$V_s = \frac{2}{3}[V_a(t) + V_b(t)e^{\frac{j2\pi}{3}} + V_c(t)e^{\frac{j2\pi}{3}}] \tag{39.1}$$

In the implementation of SVM, a rotating space vector will emulate a physical signal to determine each switching period to generate a time averaged sine wave

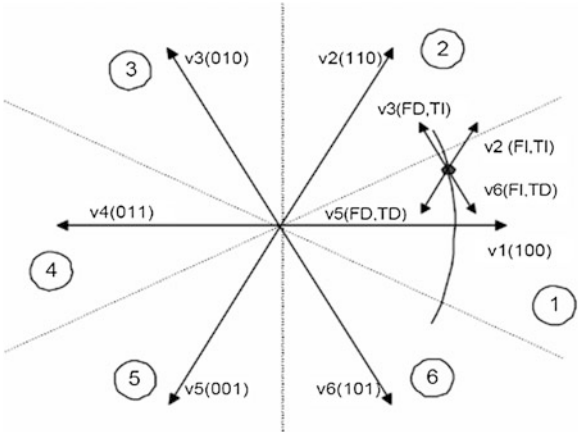

Fig. 39.1 Space vector representation of matrix converter

signal at the output of MC. The space vector travels through six sectors as shown in Fig. 39.1 each of which are 60°. Vectors 0 and 7 are on the origin called zero vectors and vectors 1–6 are called non-zero vectors.

The DTC technique allows to independently control the stator flux and the electromagnetic torque at the same time. If the reference value of the stator flux and torque are assumed, the estimated values are calculated from the stator currents and voltages. If the stator Ohmic drops are neglected, the stator voltage impresses directly the stator flux in accordance with the Eqs. (39.2)–(39.3) as follows:

$$V_s = \frac{d\psi_s}{dt} \tag{39.2}$$

$$d\psi_s = V_s dt \tag{39.3}$$

Therefore the variation of the stator flux space vector due to the application of the stator voltage vector V_s during a time interval of Δt can be approximated as in Eq. (39.4) and the electromagnetic torque in induction motor is expressed in Eq. (39.5),

$$\Delta\psi_s = V_s \Delta t \tag{39.4}$$

$$T_e = \frac{3}{2} P(\psi_{ds} i_{qs} - \psi_{qs} i_{ds}) \tag{39.5}$$

The decoupled control of the stator flux modulus and the torque is achieved by acting on the radial and tangential components respectively of the stator flux linkage in its locus. The radial component controls the stator flux vector amplitude while the tangential component controls the stator flux vector angular position and hence the torque. A good dynamic performance can be obtained by the selection of an appropriate inverter voltage vectors V_i and the reference values.

Table 39.1 DTC switching for voltage source inverter

Stator flux ($\theta\hat{}_s$)		1	2	3	4	5	6
$C_\psi = -1$	$C_T = -1$	$V_{2\text{-vsi}}$	$V_{3\text{-vsi}}$	$V_{4\text{-vsi}}$	$V_{5\text{-vsi}}$	$V_{6\text{-vsi}}$	$V_{1\text{-vsi}}$
	$C_T = 0$	$V_{7\text{-vsi}}$	$V_{0\text{-vsi}}$	$V_{7\text{-vsi}}$	$V_{0\text{-vsi}}$	$V_{7\text{-vsi}}$	$V_{0\text{-vsi}}$
	$C_T = 1$	$V_{6\text{-vsi}}$	$V_{1\text{-vsi}}$	$V_{2\text{-vsi}}$	$V_{3\text{-vsi}}$	$V_{4\text{-vsi}}$	$V_{5\text{-vsi}}$
$C_\psi = 1$	$C_T = -1$	$V_{3\text{-vsi}}$	$V_{4\text{-vsi}}$	$V_{5\text{-vsi}}$	$V_{6\text{-vsi}}$	$V_{1\text{-vsi}}$	$V_{2\text{-vsi}}$
	$C_T = 0$	$V_{0\text{-vsi}}$	$V_{7\text{-vsi}}$	$V_{0\text{-vsi}}$	$V_{7\text{-vsi}}$	$V_{0\text{-vsi}}$	$V_{7\text{-vsi}}$
	$C_T = 1$	$V_{5\text{-vsi}}$	$V_{6\text{-vsi}}$	$V_{1\text{-vsi}}$	$V_{2\text{-vsi}}$	$V_{3\text{-vsi}}$	$V_{4\text{-vsi}}$

The Conventional DTC (CDTC) has three main parameters such as stator flux (ψ_s), torque (T_e) and the position of stator flux ($\hat{\theta}_s$). There are two different loops corresponding to the magnitudes of the stator flux and torque. The DTC requires flux and torque estimations, which are performed by means of two different phase currents and the states of the inverter [6]. The torque and the stator flux are estimated and compared with the corresponding reference values before passing the hysteresis comparator. The resulting values of flux and torque are fed into the two level and three level hysteresis comparators respectively. The outputs from the comparators of the stator flux (C_ψ) and torque (C_T) comparators with the position of the stator flux are used as inputs of the look up Table 39.1. According to the DTC principle, the most suitable space vector is selected among eight vectors in order to maintain the torque and the flux values within the prescribed hysteresis band from Table 39.1.

The DTC for MC was developed from the CDTC for VSI. Based on the optimum inverter vector which is selected for CDTC from VSI and some other parameters, the corresponding switching pattern will be determined for MC. At any instance, the magnitude and direction of MC output vectors depends on the position of the input line voltage vectors V_i. Once the position of V_i is determined, then only two among six switching configurations, which have the same sector as V_i does in its space vector, are acceptable. The average value of $\sin\varphi_i$ (φ_i is the angle between the input current vector and the corresponding input line voltage vector) is employed as the third parameter to determined one final switching configuration. The hysteresis comparator directly controls this variable. The schematic of the DTC method using the matrix converter fed induction motor is represented in Fig. 39.2.

From the voltage vector selected in the Table 39.1, the $\sin\varphi_i$ and the sector of the input voltage, the corresponding voltage vector is selected from Table 39.2. For example, with $C_T = +1$, $C_\psi = -1$ and the stator flux in sector 1, the suitable voltage vector selected from Table 39.1 is $V_{6\text{-vsi}}$ for a given switching period. Then, with the chosen VSI voltage vector $V_{6\text{-vsi}}$, $C_\varphi = +1$ and the input voltage vector in sector 2, finally the opportune voltage vector selected from Table 39.2 is -5_{MC}.

The main drawback of the CDTC is torque ripple. The reason is that the selected voltage vector is applied for the complete switching period regardless of the magnitude of the torque error, resulting in a wide torque hysteresis band. A better drive performance can be achieved by varying the duration of applying the selected

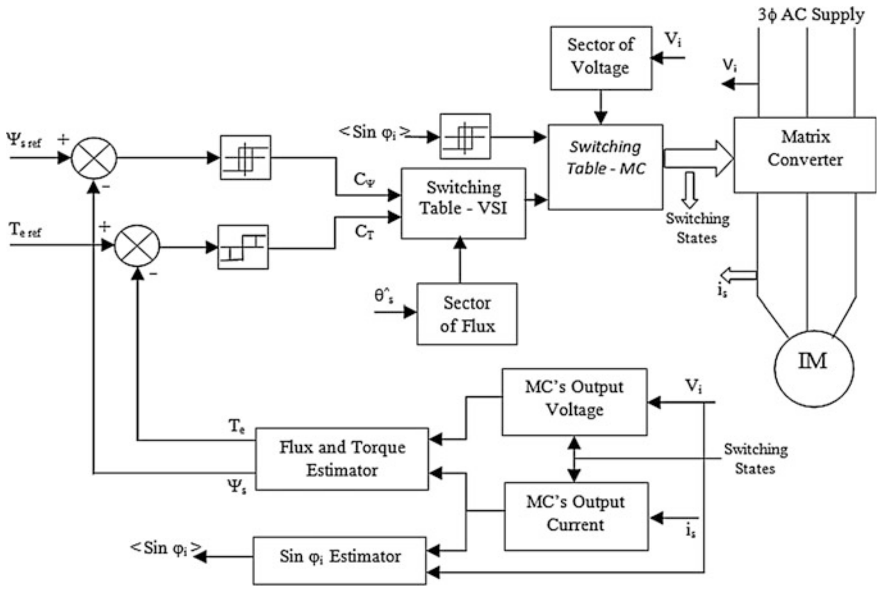

Fig. 39.2 Block diagram of direct torque control with MC

voltage vector during each switching period according to the magnitude of the torque error and the position of the stator flux, which will result in a small torque hysteresis band and hence lesser torque ripple [5]. Hence the selected non-zero voltage vector is applied for a part of the switching period and remaining period is with zero voltage vector. The ratio of the portion of the switching period for which a non-zero voltage vector is applied defined as duty ratio. Fuzzy logic is an appropriate choice for the design of the duty ratio controller.

39.3 Proposed Duty Ratio Fuzzy Logic Controller

The CDTC possess the good dynamic performance but shows quite poor performance in steady state since the crude voltage selection criteria gives rise to high ripple levels in flux linkage, torque and stator current. Fuzzy control is the best way for controlling the system without the need for knowing the mathematical model of the system [3]. The DTC performance can be improved by a complimentary use of fuzzy regulators are proposed. The two hysteresis controllers of CDTC are replaced with two fuzzy regulators.

From the observations obtained by examining the CDTC behavior, two sets of fuzzy rules were formulated; one when the flux magnitude is less than its reference value and the second when the flux magnitude is greater than the reference value. The inputs to each rule set are the magnitude of the torque error and the position of

Table 39.2 Switching table for DTC using matrix converter

V_i	1		2		3		4		5		6	
C_φ	+1	−1	+1	−1	+1	−1	+1	−1	+1	−1	+1	−1
$V_{1\text{-vsi}}$	-3_{mc}	$+1_{mc}$	$+2_{mc}$	-3_{mc}	-1_{mc}	$+2_{mc}$	$+3_{mc}$	-1_{mc}	-2_{mc}	$+3_{mc}$	$+1_{mc}$	-2_{mc}
$V_{2\text{-vsi}}$	$+9_{mc}$	-7_{mc}	-8_{mc}	$+9_{mc}$	$+7_{mc}$	-8_{mc}	-9_{mc}	$+7_{mc}$	$+8_{mc}$	-9_{mc}	-7_{mc}	$+8_{mc}$
$V_{3\text{-vsi}}$	-6_{mc}	$+4_{mc}$	$+5_{mc}$	-6_{mc}	-4_{mc}	$+5_{mc}$	$+6_{mc}$	-4_{mc}	-5_{mc}	$+6_{mc}$	$+4_{mc}$	-5_{mc}
$V_{4\text{-vsi}}$	$+3_{mc}$	-1_{mc}	-2_{mc}	$+3_{mc}$	$+1_{mc}$	-2_{mc}	-3_{mc}	$+1_{mc}$	$+2_{mc}$	-3_{mc}	-1_{mc}	$+2_{mc}$
$V_{5\text{-vsi}}$	-9_{mc}	$+7_{mc}$	$+8_{mc}$	-9_{mc}	-7_{mc}	$+8_{mc}$	$+9_{mc}$	-7_{mc}	-8_{mc}	$+9_{mc}$	$+7_{mc}$	-8_{mc}
$V_{6\text{-vsi}}$	$+6_{mc}$	-4_{mc}	-5_{mc}	$+6_{mc}$	$+4_{mc}$	-5_{mc}	-6_{mc}	$+4_{mc}$	$+5_{mc}$	-6_{mc}	-4_{mc}	$+5_{mc}$

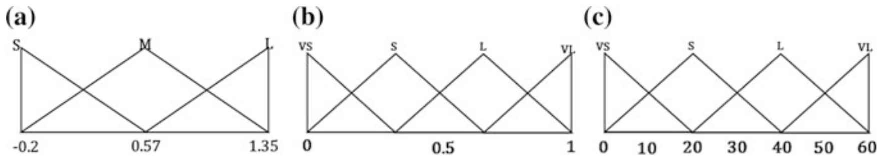

Fig. 39.3 Membership functions **a** torque error, **b** duty cycle, **c** flux angle

the stator flux; the output is the duty ratio [7]. Based on the universe of discourse of input and output membership functions such as very small, small, medium, very large and large as shown in Fig. 39.3, twelve rules are formulated in each set associated with the specific flux error sign.

With the selected three membership functions for torque error (input), four membership functions for flux angle (input) and duty ratio (output), the fuzzy rules are formed [7]. Generally the duty ratio is proportional to the torque error, since the rate of change of torque is proportional to the angle between the stator flux and the applied voltage vector, the duty ratio depends also on the flux position within each sector. The use of two fuzzy sets is due to the fact that when the stator flux is greater than its reference value a voltage vector that advance the stator flux vector by two sectors is applied which result in a higher rate of change of the torque compared to the application of a voltage vector that advance the stator flux vector by one sector when the stator flux linkage is less than its reference value.

39.4 Results and Discussion

CDTC and DTC with the duty ratio fuzzy control for the induction machine were simulated. The simulation was run at various switching frequencies and the optimum value is found as 5 kHz and results are presented for the same. MATLAB fuzzy logic toolbox was used in the implementation of the duty ratio fuzzy controller. The membership functions and the fuzzy rules were adjusted using the simulation until an optimal torque ripple reduction is achieved. In both the CDTC and FDTC, the dynamic response of torque, flux and stator current are analyzed. The stator flux trajectories were also obtained. To compare the above said parameters, the load torque is varied in steps.

Figure 39.4a, b shows the torque response of the motor using CDTC and fuzzy DTC for a step change of the reference torque of 40 Nm respectively. In both the methods, the starting torque is high. The torque response reaches its steady state value in 0.1 s. The torque ripple is around 15 Nm in CDTC, while with fuzzy DTC it is reduced to 4 Nm, neglecting the overshoot in the torque values at the beginning of the each voltage sector. In CDTC, higher ripples are produced. But in the proposed duty ratio controller reduces the torque ripples and exactly follows the set values. The obtained result proves that the proposed method is more effective than

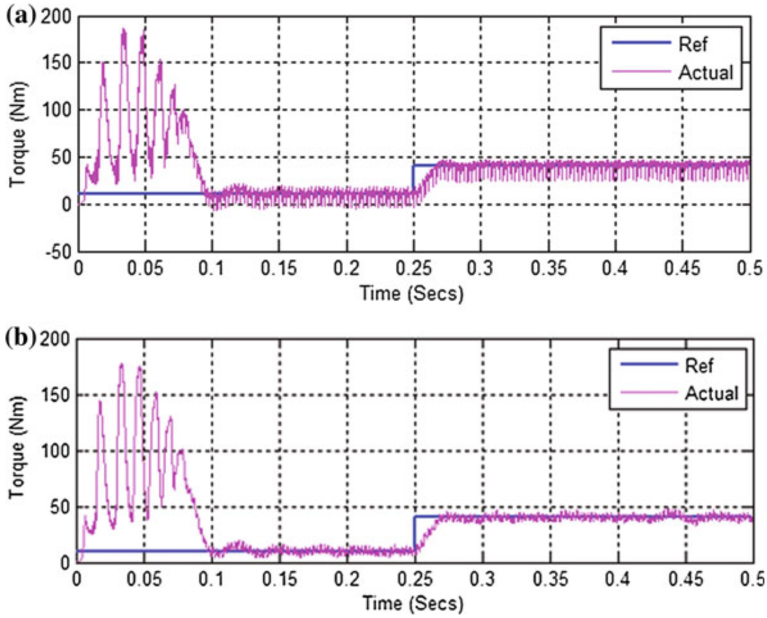

Fig. 39.4 Torque response of **a** conventional DTC, **b** fuzzy DTC

conventional method. Figure 39.5a, b shows the steady state stator current response of conventional and fuzzy DTC respectively. The fuzzy controller produces almost sinusoidal current waveform compared to conventional DTC which has more ripples. Figure 39.6a, b shows the stator flux for d and q axis of conventional and fuzzy DTC respectively. Similar to the current waveforms, stator flux is also sinusoidal when compared to conventional DTC.

Figure 39.7a, b shows the stator flux trajectory of conventional and fuzzy DTC for a step change in load torque. The flux vector describes that a trajectory is almost circular by keeping the torque and flux values are varied within their allowable tolerance band limits. While driving the motor in the projected stator flux paths, the torque ripples gets minimized and we can achieve the faster torque response. There is a dip in the stator flux magnitude at the beginning of the sector because the angle between the selected nonzero voltage vector and the stator flux is large when the stator flux vector lies in the beginning of the sector, so the selected vector does not act effectively in the longitudinal component of the flux vector to keep its magnitude close to its reference value.

The dynamic response of the proposed control scheme has been tested with sudden change in load torque such as decrease, increase and reversal for switching frequency of 5 kHz. It is observed that from Figs. 39.8 and 39.9, the torque shows a very good response and the current waveforms are almost sinusoidal immediately after the change in the torque command.

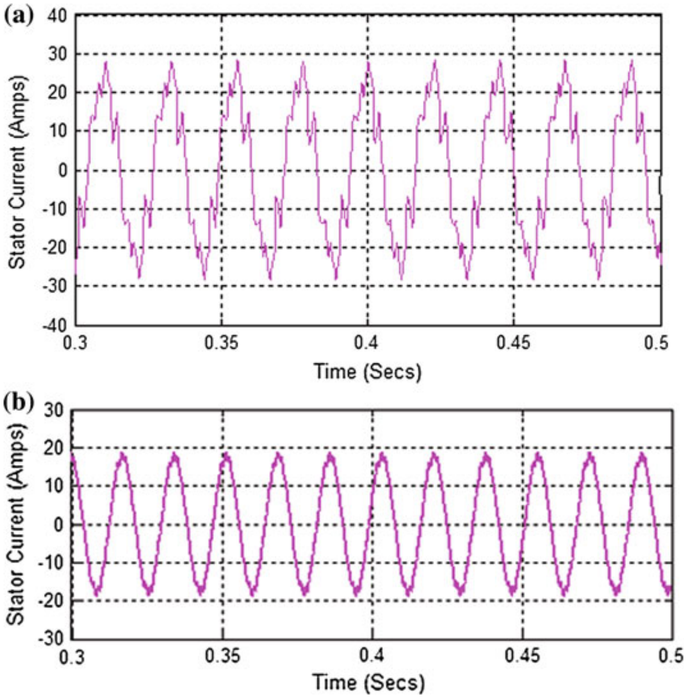

Fig. 39.5 Stator current of **a** conventional DTC, **b** fuzzy DTC

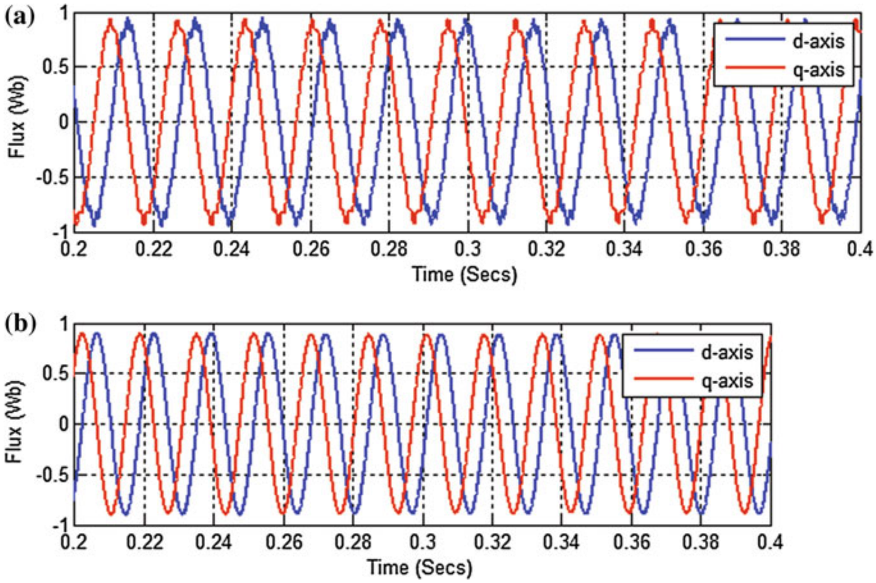

Fig. 39.6 Stator D and Q axis flux of **a** conventional DTC, **b** fuzzy DTC

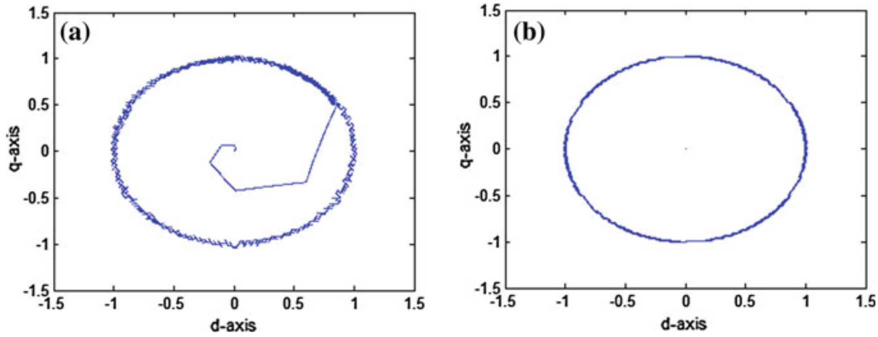

Fig. 39.7 Stator flux trajectory of **a** conventional DTC, **b** fuzzy DTC

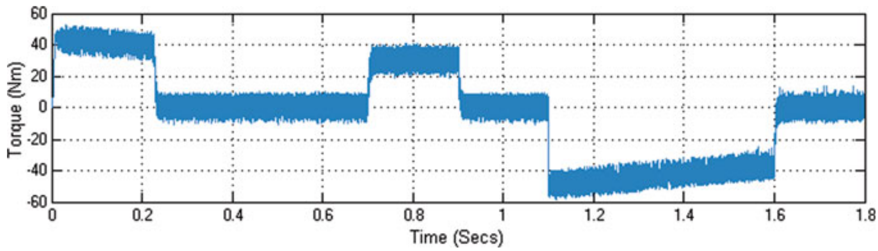

Fig. 39.8 Torque response of varying load torque

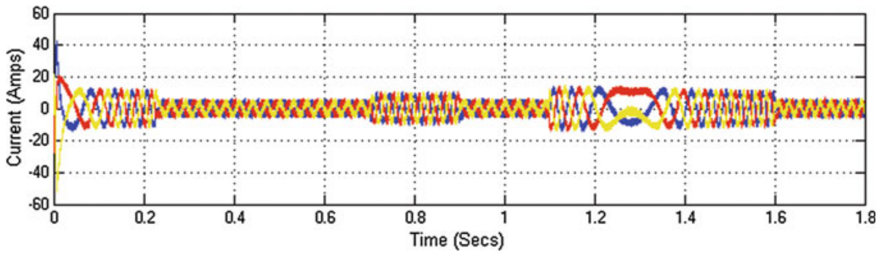

Fig. 39.9 Stator current

From the obtained results, it can be proved that the torque ripples are effectively reduced using the fuzzy controller. An improper selection of switching voltage vectors may results in undesired stator flux trajectory path, which increases the torque ripples. The simulation results suggest that proposed Fuzzy Logic Duty Ratio controlled DTC of induction machine can achieve precise control of the stator flux and torque. On comparison of results derived from simulation shows that Fuzzy Logic Duty Ratio DTC is superior to conventional DTC and minimizes the Torque ripple to large extent.

39.5 Conclusion

The MATLAB fuzzy logic toolbox is used in the implementation of the duty ratio fuzzy controller. Simulink is used to simulate the effect of the fuzzy controller on the performance of the DTC scheme and compare it to the conventional DTC. The use of fuzzy logic control reduces the computation burden by avoiding unnecessary complex mathematical modeling of the nonlinear systems and yields satisfactory results. The duty ratio fuzzy control improves the performance of the DTC at any given switching frequency without the need to change the frequency the terminals voltages, current and decides the voltage vector. The torque ripples are reduced by 26.2 % in fuzzy DTC compared to conventional DTC. The value of the duty ratio needs to be updated at each period in order to obtain the improved performance of the DTC drive. The duty ratio control reduces the stator current harmonics which intern reduces the torque ripple, the power losses and increase efficiency of the drive. The duty ratio control reduces the torque ripple in DTC induction motor drives and the same is verified by simulation results.

References

1. Wheeler PW, Rodriguez J, Clare J, Empringham L, Weinstein A (2002) Matrix converter: a technological review. IEEE Trans Ind Elect 49:276–287. doi:S 0278-0046(02)02895-2
2. Karpagam J, Kumar AN, Chinnaiyan VK (2013) An experimental analysis of a single phase matrix converter for adjustable speed drives. Int Rev Model Simul 6:1071–1078
3. Zidani F, Said RN (2005) Direct torque control of induction motor with fuzzy minimization torque ripple. J Elect Eng 56:183–188
4. Metidji B, Tazrart F, Azib A, Taib N, Rekioua T (2011) A new fuzzy direct torque control strategy for induction machine based on indirect matrix converter. Int J Res Rev Comp Eng 1:18–22
5. Lascu C, Boldea I, Blaabjerg F (2000) A modified direct torque control for induction motor sensorless drive. IEEE Trans. Auto Elect 36:122–130
6. Sudheer H, Kodad SF, Sarvesh B (2011) Improved direct torque control of induction motor using fuzzy logic based duty ratio controller. Int J Adv Eng Tech 1:473–479
7. Toufouti R, Meziane S, Benalla H (2007) Direct torque control for induction motor using intelligent techniques. J Theor Appl Info Tech 1:35–44

Chapter 40
Improvement of Power Quality in Distribution System Using D-STATCOM

Pravati Nayak, Amruta Pattnaik, Mihir N. Mohanty and Ranjan Kumar Mallick

Abstract Distribution system, as the name suggest, is the medium through which power is distributed among the end consumers. Power quality pollution at the load end is in the form of voltage/current waveform distortions, long/short duration voltage variations and poor load power factor. Amongst the various distribution FACTS controllers, distribution static compensator (D-STATCOM) is an important shunt compensator which has the potential to solve any power quality problems faced by distribution system. It provides effective **compensation to unbalance and non-linear loads by injecting** appropriate reactive power at the point of common coupling (PCC). In this paper we have designed two controllers. One is Synchronous Reference Frame based current controller and another one is Hysteresis Band Current Control to mitigate the harmonics due to unbalanced and nonlinear load. The investigation is carried out using MATLAB-SIMULINK power system block set.

Keywords D-STATCOM · Power quality · Hysteresis band current control · Sinusoidal PWM

40.1 Introduction

Supply of electricity plays an important role in the technological advanced world. The quality and reliability of power supplies relates closely to the economical growth of a country. However, power quality disturbances such as sags, swells, flicker, harmonics, voltage imbalance etc., create a lot of problem in achieving a

P. Nayak (✉) · A. Pattnaik · M.N. Mohanty · R.K. Mallick
ITER, Siksha O Anusandhan University, Bhubaneswar, Odisha, India
e-mail: pravatinayak@soauniversity.ac.in

M.N. Mohanty
e-mail: mihirmohanty@soauniversity.ac.in

R.K. Mallick
e-mail: rkm.iter@gmail.com

C. Kamalakannan et al. (eds.), *Power Electronics and Renewable Energy Systems*, Lecture Notes in Electrical Engineering 326, DOI 10.1007/978-81-322-2119-7_40

reliable and quality power supply. These power quality problems are very common in the electrical distribution systems.

The custom power term was proposed to designate a new generation of power quality improvement devices in distribution systems. It is dedicated to maintain and improve the quality and reliability of distribution level power. The Custom Power concept is to provide customer's solution through the utilities sector. Custom power devices can be classified as network configuring type and compensating type. The compensating type devices are used for active filtering; load balancing, power factor correction and voltage regulation. The family of compensating devices includes DSTATCOM (Distribution Static compensator), DVR (Dynamic voltage restorer) and Unified power quality conditioner (UPQC). DSTATCOM has a similar structure and function to STATCOM in the transmission system. It is connected in shunt with the power system. As DSTATCOM is a multifunctional device, the control algorithm plays a vital role for its application. Hence the design has to be flexible enough to exploit utmost multi-functionality. Many researchers have modeled with various techniques [1–3]. Also, some works have been done for control techniques [4–7].

Objective of the paper is to model the D-STATCOM in distribution system for load compensation of unbalance distribution system. Also, the performances of proposed controllers are compared with nonlinear loads.

The paper is organized as follows. Section 40.1 introduced the work; Sect. 40.2 explains the modeling of D-STATCOM. Section 40.3 proposes the design of controllers that follows Sect. 40.4 as the simulink model of it. Section 40.5 shows the result and Sect. 40.6 concludes the work.

40.2 Modeling of D-STATCOM

D-STATCOM connected to a three phase ac mains feeding three phase loads as shown in Fig. 40.1. Three phase loads may be of various kinds like, lagging power factor load, unbalance load, non-linear load, and linear load, mixed of these loads. For reducing ripple in the compensating currents interfacing inductors (L_f) are used at AC side of the voltage source converter (VSC).

It is used to operate the converter in such a way that the phase angle between the converter voltage and the line voltage is dynamically adjusted. The output voltage of the converter or VSC based IGBT inverter module, V_c is controlled in the same way as the distribution system voltage V_s.

The modeling of D-STATCOM is based on the Synchronous Reference Frame (SRF) method. Figure 40.2 shows the simplified diagram of the D-STATCOM comprising of a dc-link capacitor, IGBT based VSC, equivalent transformer and filter resistance, equivalent transformer and filter inductance and a three phase source.

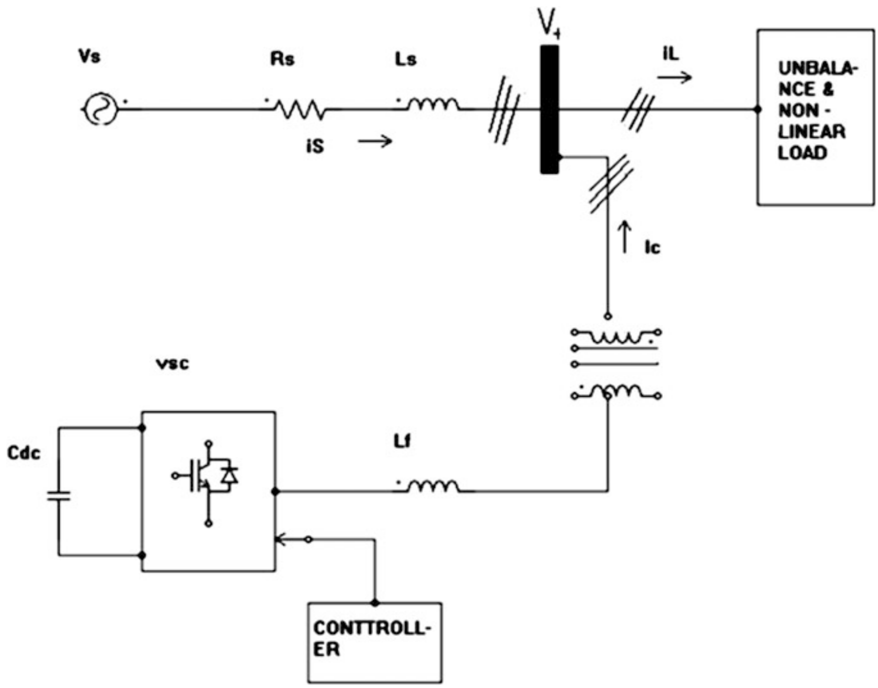

Fig. 40.1 Schematic Representation of D-STATCOM

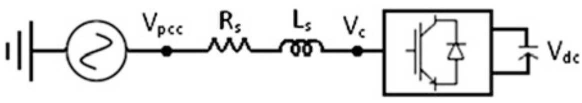

Fig. 40.2 Simplified Model of D-STATCOM

The relation between the point of common coupling (PCC) voltages and the inverter output voltage is illustrated as

$$R_s i_a + L_S[di_a/dt] = V_{pa} - V_{ca} \tag{40.1}$$

$$R_s i_b + L_S[di_b/dt] = V_{pb} - V_{cb} \tag{40.2}$$

$$R_s i_c + Ls[di_c/dt] = V_{pc} - V_{cc} \tag{40.3}$$

By transforming Eqs. (40.1–40.3) using park's transformation to SRF (synchronous reference frame) we obtain as,

$$L_s(di_d/dt) + R_s i_d = V_{pd} - mV_{dc}\cos\Theta + L_s w i_q \tag{40.4}$$

$$L_s\left(di_q/dt\right) + R_s i_q = V_{pq} + mV_{dc}\sin\Theta - L_s w i_d \tag{40.5}$$

where, w is the system frequency and m is the modulation index of the converter. These can be represented in state space from as in equation. i.e.,

$$\frac{d}{dt}\begin{bmatrix} id \\ iq \end{bmatrix} = \begin{pmatrix} -Rs/Ls & w \\ -w & -Rs/Ls \end{pmatrix}\begin{bmatrix} id \\ iq \end{bmatrix} + \frac{1}{Ls}\begin{pmatrix} Vpd - Vcd \\ Vpq + Vcq \end{pmatrix} \tag{40.6}$$

Neglecting the voltage harmonics we can rewrite as

$$m.Vdc\ \cos\ \theta = Vcd \tag{40.7}$$

$$m.Vdc\sin\theta = Vcq \tag{40.8}$$

Assuming the inverter is lossless circuit and as per the power balance theory, the instantaneous power at the ac-dc terminals of the inverter is

$$Vdc.idc = \frac{3}{2}(Vcd.id + Vcq.iq) \tag{40.9}$$

The dc side circuit equation is given as

$$idc = c.\frac{d(vdc)}{dt} = \frac{3}{2}.m.(id.\cos\theta - iq.\sin\theta) \tag{40.10}$$

Rearranging Eq. (40.10) and combining it with Eq. (40.6) yields

$$\frac{d}{dt}\begin{pmatrix} id \\ iq \\ Vdc \end{pmatrix} = F\begin{pmatrix} id \\ iq \\ Vdc \end{pmatrix} - \frac{1}{Ls}\begin{pmatrix} Vpd \\ 0 \\ 0 \end{pmatrix}$$

where F is given as

$$\begin{pmatrix} -Rs/Ls & w & -\frac{m}{Ls}\cos\theta \\ -w & -Rs/Ls & \frac{m}{Ls}\sin\theta \\ \frac{3}{2}\frac{m}{c}\cos\theta & -\frac{3}{2}\frac{m}{c}\sin\theta & 0 \end{pmatrix} \tag{40.11}$$

The instantaneous active and reactive power theory are described as

$$p = Vpd.id + Vpq.iq = Vpd.id = Vp.id \tag{40.12}$$

$$q = Vpq.id - Vpd.iq = -Vpd.iq = -Vp.iq \tag{40.13}$$

Based on Eqs. (40.12) and (40.13), the D-STATCOM performance can be controlled by controlling the Id and I_q values.

40.3 Controller Design

D-STATCOM model is with an outer loop consisting of ac and dc voltage controllers and the inner loop is the current controller whose output fires the IGBT Bridge. The reactive power control can be accomplished using both the controllers, either to achieve a unity power factor operation or to regulate the PCC voltage by compensating the losses in the distribution line. The ac voltage loop is activated to achieve voltage regulation. Current i_q* is the output of a PI controller, the input to which is the deviation of the PCC voltage Vpcc as compared to a reference V_{pcc}* [6–12]. The dc voltage loop is responsible for keeping constant the dc voltage through a small active power exchange with the ac network compensating the active power losses in the filter and the inverter. The current i_d* is responsible for unity power factor and harmonic mitigation operation in a D-STATCOM.

Once the decoupled references have been obtained, the inner current controller is activated. The implementation of linear/nonlinear current controllers is dealt with in the subsequent section. The objective of the control scheme is to force the currents in abc frame or d_{q0} frame to follow their respective reference signals and accordingly generate switching states for the switches in order to improve the tracking error. The desirable features in the control scheme should be:

- Ideal tracking to remove harmonic distortions.
- Fast response under various transient conditions.
- Limited switching frequency to avoid stressing of the Semiconductor switches.
- Good dc link utilization.

40.3.1 Sinusoidal PWM Controller

This controller operates in conjunction with the conventional PWM generator. The three line currents are transferred to d_{q0} frame as I_d and I_q. Three phase ac supply voltages and dc link voltage are sensed and fed to two pi controllers. The outputs of the amplitude will decide the reference reactive and active current. Comparisons of these amplitudes with the in phase and quadrature current yields the respective component of reference currents. When applying the algorithm for power factor correction and harmonic elimination, the quadrature component of reference current is made zero. The modulating signals for the rotating frame controller are given by as in [6–13],

$$V_{dref} = K_{p1}[I_{dref} - I_d] + K_{i1}\int [I_{dref} - I_d]\, dt$$

$$V_{qref} = K_{p2}\left[I_{qref} - I_q\right] + K_{i2}\int \left[I_{qref} - I_q\right]\, dt$$

where, K_{p1}, K_{i1}, K_{p2}, K_{i2} are the gains of the two current PI controllers respectively. The modulating signals are transferred back to the abc-frame. The modulating signal output of each phase is compared with a triangular carrier wave, which is common for all the three phases. A Phase Locked Loop (PLL) is used to synchronize the control loop to the ac supply so as to operate in the abc-to-d_{qo} reference frame.

Hysteresis current Controller has been analyzed due to the drawbacks like, the response time is slow as four PI controllers are used, PLL produces erroneous results in case of distorted mains. Complete harmonic suppression is not achieved in case of nonlinear loads. A larger filter inductance is required to filter the harmonics in the output converter current, but it reduces the var generating capability of the compensator.

40.3.2 Hysteresis Current Controller

This current controller is based on a non-linear feedback loop with two level hysteresis comparators. It decides the switching states for the devices of the PWM converter.

Three phase ac supply voltages and dc link voltage is sensed and fed to two PI controllers. The outputs will decide the amplitude of the reference reactive and active current. Comparisons of these amplitudes with the in-phase and quadrature current yield the respective component of reference currents. The summed direct and quadrature axis reference currents and the sensed line currents are fed to a carrier less hysteresis controller add a hysteresis band ± h around the calculated reference currents. The pulses are generated for the lower leg switches when Isabc ≥ Isabc_ref + h. For the upper leg switches, when Isabc ≤ Isabc _ref − h. The tracing becomes better if the hysteresis band is narrower, but at that moment the

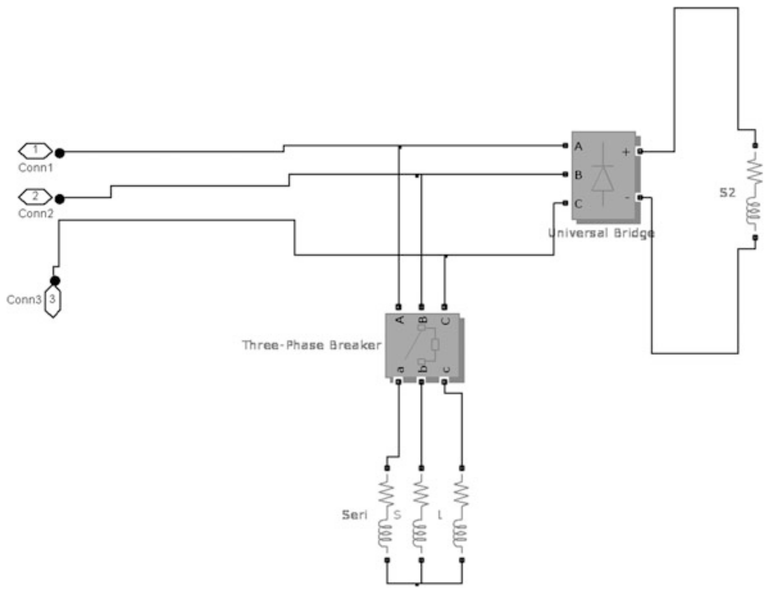

Fig. 40.3 Load connected to the distribution system

switching frequency is increased. That results in increased switching losses. Therefore the choice if hysteresis band should be a compromise between tracking error and inverter losses. It exhibits automatic current limiting characteristics [10–13].

40.4 Simulink Model

Figure 40.3 shows the test system implemented in simulink to carry out simulation for D-STATCOM. The test system comprises a 415 V distribution system. A 6-pulse D-STATCOM is connected in parallel with the system. The circuit parameter are Vs = 415 V, R = 1.7e3 Ω, L = 5.4e6 H, fs = 50 Hz, C = 10,000 μF. The system is connected with unbalance and non–linear load.

Simulations are carried out for both cases as D-STATCOM with connection and without connection. Figure 40.8 shows the un-balanced load and non-linear load (Fig. 40.4).

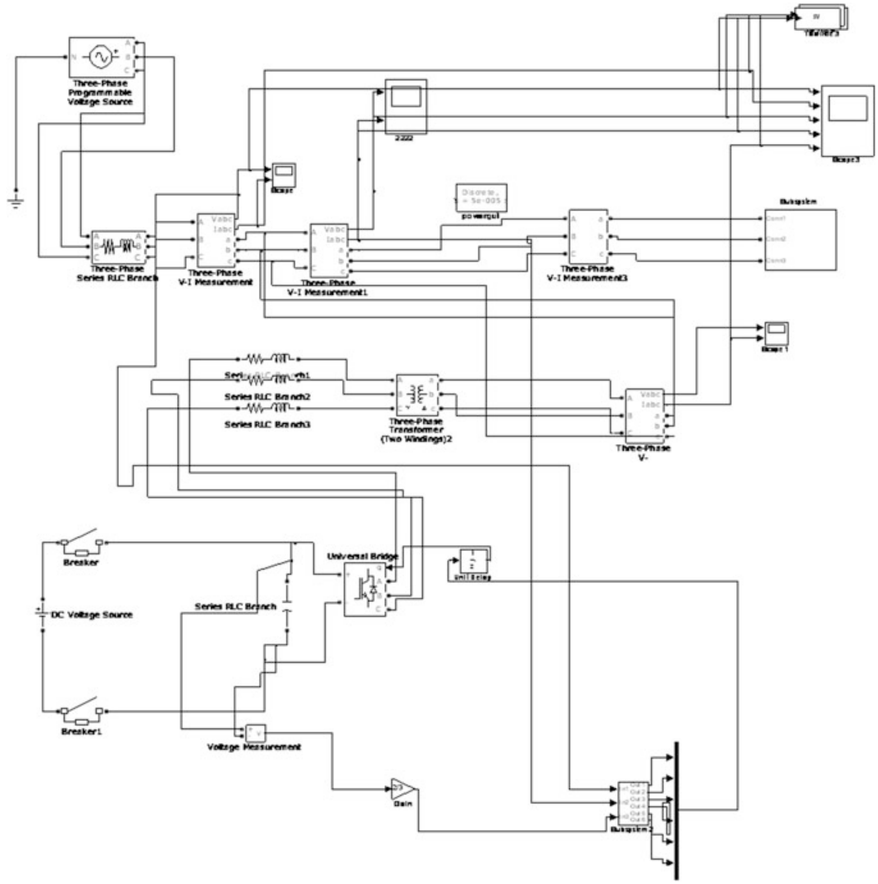

Fig. 40.4 Configuration of D-STATCOM

40.5 Results and Discussion

Case 1: Non-linear current control technique: It is based on PWM method. The result in Fig. 40.5 contains without D-STATCOM connected to the system. In Fig. 40.6 the source and load current drawn by load is of some magnitude, but contain harmonics of about 30.09 %. When the D-STATCOM is connected to the system the source current is sinusoidal as shown in Fig. 40.6 and the THD is reduced to 3.36 % as shown in Fig. 40.7b.

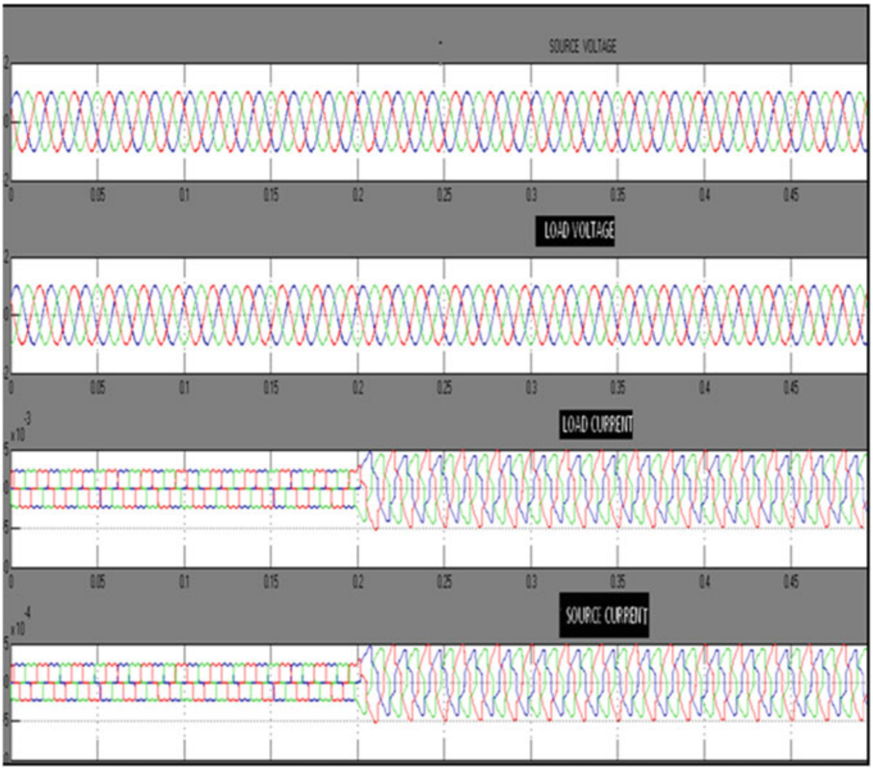

Fig. 40.5 Simulation results without D-STATCOM

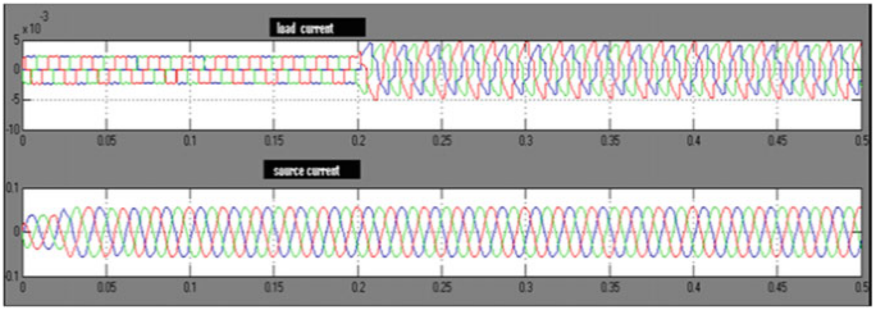

Fig. 40.6 Load current and source current with D-STATCOM

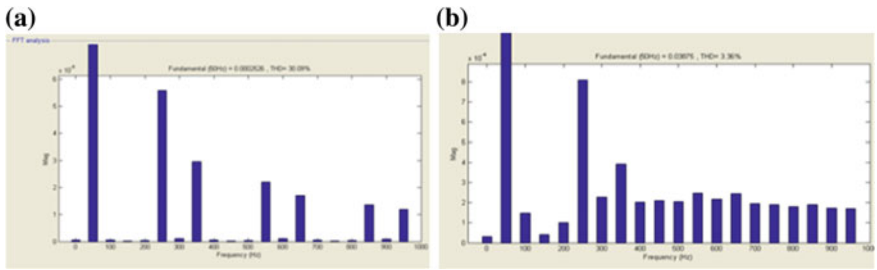

Fig. 40.7 Total harmonic distortions **a** without and **b** with D-STATCOM

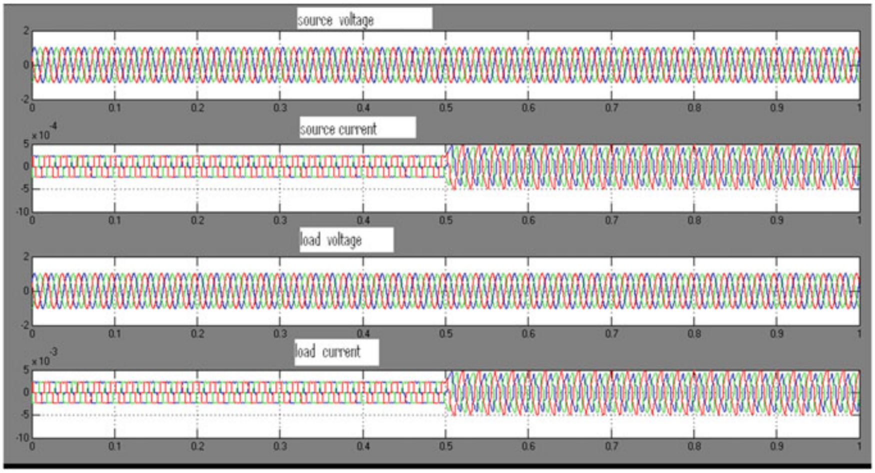

Fig. 40.8 Source voltage, source current, load voltage and load current without D-STATCOM

Case 2: Linear Current Control (sinusoidal PWM technique): Simulation results are shown from Figs. 40.8 to 40.10 for without and with D-STATCOM connected with load.

Figure 40.8 contains without D-STATCOM connected to the system result. The source and load current drawn by load is of some magnitude, but contain harmonics of about 30.09 %. When the D-STATCOM is connected to the system, the source current is sinusoidal as shown in Fig. 40.9 and the THD is reduced to 8.41 % as shown in Fig. 40.10b.

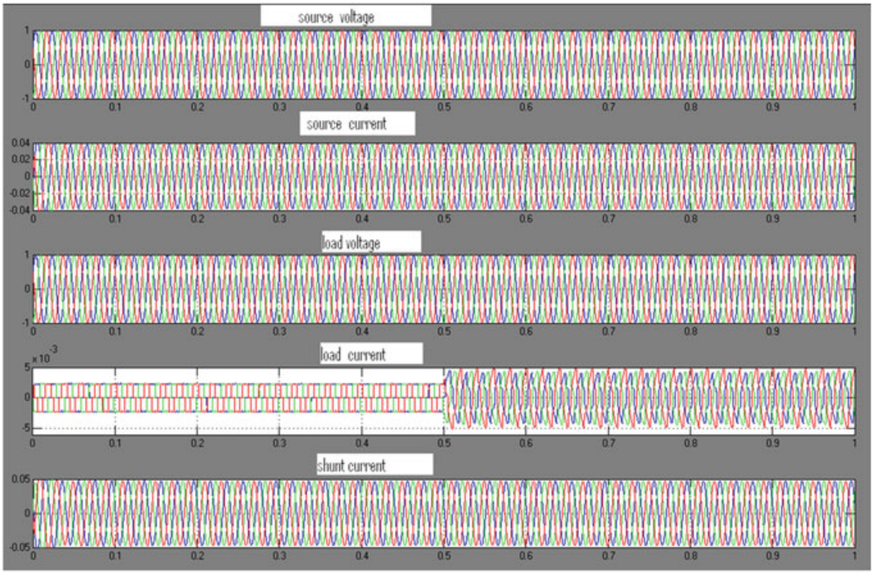

Fig. 40.9 Source voltage, source current, load voltage, load current and shunt current with D-STATCOM

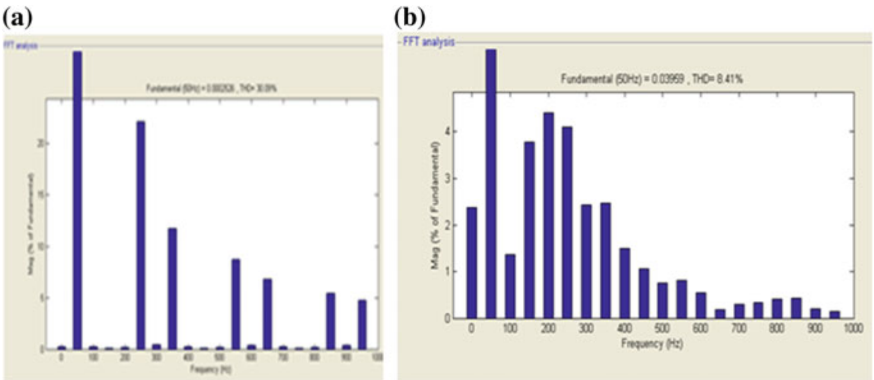

Fig. 40.10 Total harmonic distortions **a** with and **b** without D-STATCOM

40.6 Conclusion

This paper has described the design, modeling, implementation and performance of VSC based D-STATCOM with the simplest converter topology (2-level, 3-leg). Reactive power control is achieved by the indirect decoupled current and AC and DC bus voltage regulation and VSC harmonics are eliminated by the SRF based sinusoidal PWM and hysteresis band current control PWM technique. The paper also presents the comparative study of two control strategies used for the control of D-STATCOM. It can also be concluded that though conceptually similar to a STATCOM at the transmission level, a D-STATCOM control scheme should be such that in addition to complete reactive power compensation, power factor correction and voltage regulation of the harmonics are also checked, in order to achieve improved power quality levels at the distribution end.

References

1. Sen KK (1998) STATCOM theory, modeling & applications. IEEE conference 1998, pp 1177–1183
2. Giroux P, Sybille G, Le-Huy H (2001) Modelling and simulation of a distribution STATCOM using simulink's power system blockset. In: IEEE industrial electronics society, pp 990–994
3. Lara OA, Acha E (2002) Modeling and analysis of custom power systems by PSCAD/EMTDC. IEEE Trans Power Deliv 17(1):266–272
4. Akagi H, Kanazawa Y, Nabae A (1984) Instantaneous reactive power compensators comprising switching devices without energy storage components. IEEE Trans Ind Appl 20:625–630
5. Watanbe FH, Stephen RYI, Aredes M (1993) New concepts of instantaneous active and reactive powers in electrical system with generic loads. IEEE Trans Power Deliv 15 (2):697–703
6. Moran LA, Dixon JW, Wallaee RR (1995) A three phase active power filter with fixed switching frequency for reactive power and current harmonic compansator. IEEE Trans Ind Electron 42:402–408
7. Paserba JJ, Leonard DJ, Miller NW, Naumann ST, Lauby MG, Sener FP (1994) Coordination of a distribution level continuously controlled compensation device with existing substation equipment for long term VAR management. IEEE Trans Power Deliv 9(2):1034–1040
8. Kazmerkowski P, Malesani L (1998) Current control techniques for three phase voltage source PWM converters :a survey. IEEE Trans Ind Electron 45(5):691–703
9. Msigwa CJ, Kundy BJ, Mwinyiwiwa BMM (2009) Control algorithm for shunt active power filter using synchronous reference frame theory. World Academy of Science, Engineering and Technology
10. Singh B, Arya SR (2012) Design and control of a DSTATCOM for power quality improvement using cross correlation function approach. Int J Eng Sci Technol 4(1):74–86
11. Singh B, Solanki J (2009) A comparison of control algorithms for DSTATCOM. IEEE Trans Ind Electron 56(7):2738–2745
12. Reddy CVK, Veni KK, Das GT, Pulla S (2011) Performance analysis of D-STATCOM using control techniques for load compensation. Int J Adv Sci Tech Res 2(1), ISSN 2249-9954
13. Pillay K, Dahidah MSA, Mariun NB (2010) On comparing the performance of voltage source converters based D-STATCOM for voltage sag mitigation. In: IEEE International conference on power energy (PEcon2010), Kuala Lumpur, Malaysia, 29 Nov–1 Dec 2010

Chapter 41
Simulation and Optimization of Biomass Based Hybrid Generation System for Rural Electrification

M. Mahalakshmi and S. Latha

Abstract This paper focuses on the design and optimal sizing of hybrid Biomass-Solar Photovoltaic system for a particular load centre with the goal of minimizing Green House Gas (GHG) emissions. First, resource data has been collected from the existing Biomass project activity at Kadaneri village of T. Kallupati, Tamil Nadu, India. The selected region with 9.66°N Latitude and 77.79°E Longitude has an annual average solar insolation of 4.86 kWh/m^2 validated through NASA Surface Meteorology and Solar energy and the biomass fuels available in the region are Juliflora, Bagasse, Coconut shell, Paddy husk etc. estimated to be 265 tons per day on average. Then, based on the resource and load data, a comparative analysis of Grid alone, Biomass alone and PV-Biomass hybrid system using HOMER 2.81 (Hybrid Optimization Model for Electric Renewables) software is done for village panchayats in T. Kallupatti. In particular, the optimization of Biomass feedstock combination for maximum power output is carried out using Neural Network (NN) toolbox of Matlab 2010a. The results prove the effectiveness of the Stand-alone Solar-Biomass hybrid system for the chosen location in terms of cost and emissions.

Keywords PV/biomass hybrid system · Economic analysis · HOMER software · Optimization · Artificial neural network

41.1 Introduction

The increasing energy consumption day by day and the decreasing accessibility of conventional energy sources have led to the hike in the price of electricity. So the main aim of most of the countries in the world is to provide a reliable, cost effective,

M. Mahalakshmi (✉) · S. Latha
Department of Electrical and Electronics Engineering,
Thiagarajar College of Engineering, Madurai 625015, Tamil Nadu, India
e-mail: mmahalakshmi36@gmail.com

S. Latha
e-mail: sleee@tce.edu

C. Kamalakannan et al. (eds.), *Power Electronics and Renewable Energy Systems*,
Lecture Notes in Electrical Engineering 326, DOI 10.1007/978-81-322-2119-7_41

environmental friendly and affordable supply of electrical energy. Renewable Energy (RE) sources like wind, solar-PV, biomass and fuel cells are getting more prominent attention in the recent years. In India, solar, wind and Biomass are the most preferred renewable energy sources, particularly in Tamil Nadu because of enormous resource availability [1–3]. Tamil Nadu has reasonably high solar radiation (5.6–6.0 kWh/m^2) with around 300 clear sunny days in a year and has also announced its State Solar Energy Policy with a target of 3,000 MW till the year 2015. The estimated power generation potential from surplus biomass in Tamil Nadu is 487 MW, according to a district-level study carried out by Anna University and the Ministry of New and Renewable Energy Funding. There are a total of 17 biomass power plants in the state, each with a capacity of 7–10 MW. Nearly 130 MW is contributed by independent biomass generators.

During the past few years, a lot of literature has been analyzed regarding standalone and grid connected RE system in worldwide scenarios. HOMER tool has been used to analyze a hybrid electric supply system (Hydro/PV/Wind) and to find the optimum sizing of components for a diesel based RE system [4, 5]. Feasibility studies have been performed to foresee the suitability and cost effective application of hybrid RE system with energy storage technologies for a particular locality/region [6–9]. However, this paper analyses an economy scale solution for electrification of T. Kallupatti region, Tamil Nadu, based on Solar-Photovoltaic and Biomass hybrid system. Though the hybrid system involve high capital cost, they can be a viable option in the context of inadequate power generation in the state. The main focus of the paper lies in the comparative analysis of Grid alone and Standalone Solar-Biomass hybrid system using HOMER software tool, so that the agriculture prone area can be fed with continuous power supply. In the following sections, the resource potential assessment and economic analysis of the Solar-Biomass hybrid system is performed along with the biomass feedstock optimization using neural network toolbox of Matlab 2010a. The simulation and optimization results of the Biomass based System are presented.

41.2 Methodology

41.2.1 Availability of Renewable Resources

41.2.1.1 Potential of Solar Energy in the Region

The solar energy resource data for T. Kallupatti (9.66 *Latitude* and 77.79 *Longitude*) region in Madurai district is taken from NASA Surface Meteorology and Solar Energy [10] as seen in Table 41.1. From the table, it is obvious that the global solar irradiation is 4.86 kWh/m^2 on an average, which means that there is enough solar potential and considerable amount of solar energy can be obtained throughout the year.

Table 41.1 Monthly averaged insolation on a horizontal surface (kWh/m^2/day)

Lat 9.66 Lon 77.79	Jan	Feb	Mar	Apr	May	Jun	Jul	Aug	Sep	Oct	Nov	Dec	Annual average
22-year average	4.95	5.73	6.27	5.53	5.23	4.26	4.19	4.48	4.92	4.3	4.15	4.41	4.86

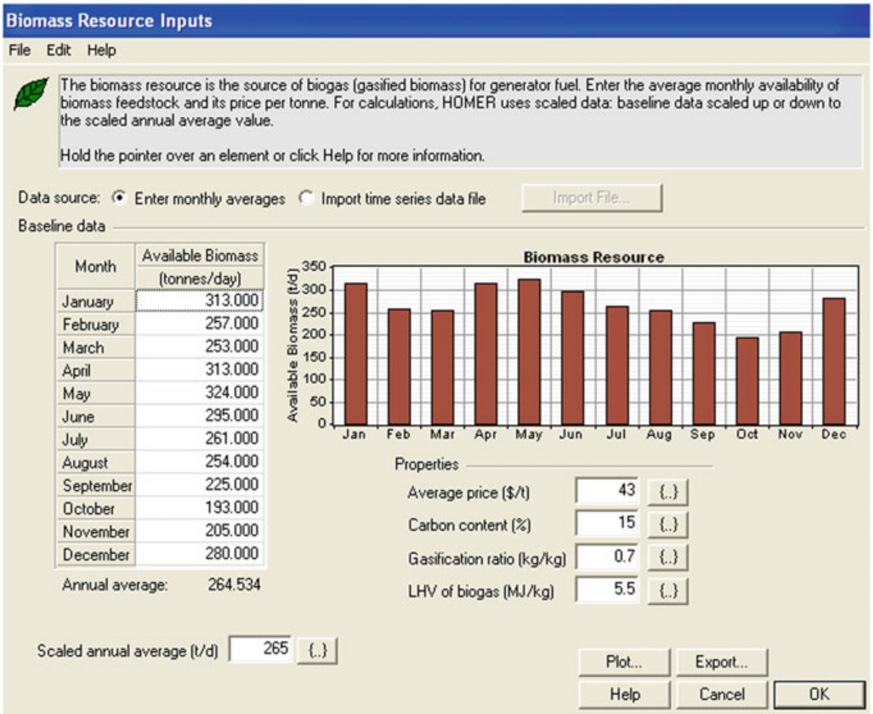

Fig. 41.1 Average monthly biomass feedstock availability

41.2.1.2 Potential of Biomass Resources

Agriculture is the highest grosser in and around T. Kallupatti. Cotton is a major crop here due to the presence of extensive black cotton soil. Rice is cultivated in the Western side of the town and there is also high level of Groundnut cultivation due to the presence of black soil. Juliflora, Bagasse, Ground Nut Shell, Paddy Husk, Plywood waste and Coconut Fibre are the fuels available that are purchased at the rate of Rs. 2,500–2,700 per ton by the Biomass Power Plant, M/s Auro Mira Bio Energy Madurai Limited (AMBEML) located in Kadaneri village of T. Kallupatti. The average biomass feedstock availability in AMBEML and the purchase price per ton of the feedstock during the year 2012 is entered as Biomass resource inputs in the HOMER tool as seen in Fig. 41.1.

Julia Flora, a plant known as Seemakaruvellai (Thorny tree) is available in abundance in the locality which ensures long-term sustainability of the Biomass based power projects [9].

Table 41.2 Load data of a typical remote village in T. Kallupatti

S. No.	Particulars of load	Watts	Quantity	Hours of operation	Energy consumption in kWh/day
1.	Domestic lighting	50	500	10	250
2.	Street lighting	50	100	12	60
3.	Water pumps	3,500	20	10	700
4.	Health centre	1,500	10	6	90
5.	Others (community halls, schools etc.)	50	100	12	60
Total					1,160 kWh/day

Using the above data, average daily load for the 42 villages is scaled to be 49 MWh with 4 MW peak and used as Load inputs in HOMER tool.

41.3 Load Profile of T. Kallupatti

T. Kallupatti is at the Crossroads of Madurai to Rajapalayam and Virudhunagar to Theni Highways making it a rural hub. **T. Kallupatti block** is a revenue block in the Madurai district of Tamil Nadu, India. It has a total of 42 panchayat villages and 65 % of the population depends on Agriculture. An approximate load data of a remote village in the chosen region is given in Table 41.2.

41.4 Optimal Hybrid System Modeling Using HOMER

HOMER is an optimization tool for hybrid RE system developed by the U.S. National Renewable Energy Laboratory (NREL), which provides optimized results of the hybrid system by performing thousands of simulations based on input parameters like solar irradiation, fuel price, renewable energy fraction and cost of the proposed hybrid system. HOMER tool requires data inputs of Solar, Biomass resource and economic inputs of RE System components. The cost assumptions are listed in Table 41.3.

Three scenarios are simulated and analyzed using HOMER software. The schematic diagram enumerating the system components for the three cases is shown in Fig. 41.2

Table 41.3 Component costs of the hybrid system

System (size)	Capital cost ($)	Replacement cost ($)	O and M cost
Photovoltaic (1 kW)	2,000	2,000	0 ($/year)
Biomass generator (1 MW)	1,000,000	850,000	0.010 ($/h)
Diesel generator (1 kW)	500	500	0.25($/h)

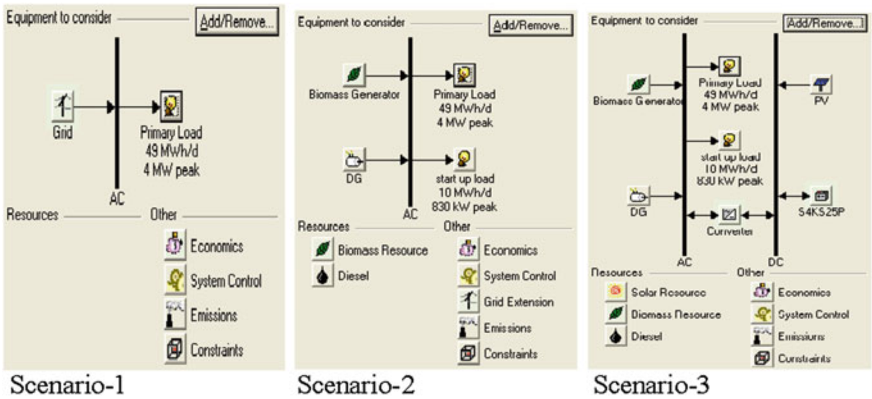

Fig. 41.2 Schematic diagram of the scenarios analyzed

41.5 Simulation and Analysis

41.5.1 Scenario-1: Grid Only System

The Grid only system is the conventional electric power supply system for the selected location. The system produces 17,702,504 kWh year^{-1} (100 %) of the total electricity with a net present cost of $18,556,392. But, CO_2 emissions are the highest about 15,047,128 kg/year for Grid only system as the conventional power plants are prone to GHG emissions.

41.5.2 Scenario-2: Biomass Only System

4 MW Biomass Generator has been modeled to supply the primary load of the village and Diesel Generator is used to meet the start up load requirements of the Biomass power system. The biomass feedstock consumption and price per ton are given as resource inputs in HOMER. The aim of this scenario is to meet the electricity utilization of the panchayat villages by Biomass only system. The system produces 23,134,520 kWh year^{-1} (100 %) of the total electricity with a net present cost of $32,676,046. The levelized cost of energy is 0.110 $/kWh as seen in Table 41.4.

Table 41.4 Cost and emission analysis

Parameters	Economic parameters and CO_2 emissions		
	Scenario 1	Scenario 2	Scenario 3
NPC ($)[a]	18,556,392	32,676,046	32,965,296
LCOE ($/kWh)[b]	0.082	0.110	0.111
Operating cost ($/year)	1,451,606	2,310,899	2,316,316
CO_2 emissions	15,047,128	10,327	10,299

[a] *NPC* net present cost; [b] *LCOE* levelized cost of energy

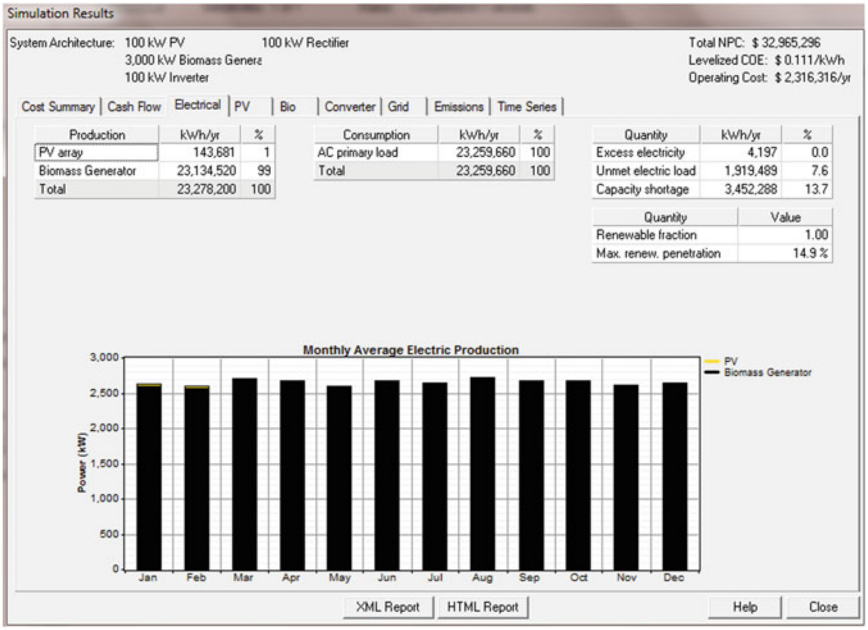

Fig. 41.3 Electrical energy production from the hybrid system

41.5.3 Scenario-3: Biomass–Solar Hybrid System

As there is enough potential for biomass and solar in the chosen area and subsidies are being provided by the Govt. for promoting such renewable sources, the feasibility of the hybrid system is analyzed for meeting the demand of the region. Domestic lighting load of the chosen area is around 250 kWh/day and the cost of battery back-up increases with the size of the PV arrays. So, the rating of the PV system is chosen as 100 kW with battery back-up. The electrical energy production from solar and Biomass generator is presented in Fig. 41.3.

As seen with Fig. 41.3, PV array and Biomass generator contribute to 1 and 99 % of the monthly average electrical energy production respectively.

41.6 Comparative Analysis of Grid Alone and Standalone Hybrid System

The cost and emission results for the scenarios are compared in Table 41.4. The total Net Present Cost is an important economic output of HOMER software.

From the table, it can be seen that the NPC of the hybrid system is $32,965,296, higher than the Grid only system and hence LCOE, due to the high capital cost of

Biomass and PV system. Also, the optimal PV-Biomass hybrid system produces the least CO_2 emissions of 10,299 kg/year compared to the conventional Grid system with 15,047,128 kg/year. With the advancement in technology, the price will be reduced and renewable sources will be the trend of the future.

41.7 Optimization of Biomass Feedstock Using ANN

The average price of Biomass fuel is around Rs. 2,500–2,700 per ton in the year 2013 and the fuel cost escalates by 5 % approximately year by year. So, optimal amount of fuel is to be used for maximum power output from the plant.

Using the data provided by AMBEML depicted in Table 41.5, optimization of the feedstock consumption is performed using the neural fitting tool of the Artificial Neural network (ANN) toolbox in Matlab 2010a. The Neural Network is based on the Levenberg–Marquardt algorithm incorporated in the back-propagation learning algorithm used to train the NN. The network is trained with 12 data set of fuel consumed, tested with 10 dataset and the optimized results for the 4 MW power generation has been obtained as displayed in Fig. 41.4.

The sum of the optimized values of each of the 6 fuel type is found to be 6,951 tons which is comparable with the amount of feedstock utilized in AMBEML as per the plant operator's experience.

Table 41.5 Consumption of biomass fuel types in AMBEML

Month/Year	Types of biomass fuel consumed (tons)						Gross generated (kWh)
	Juliflora	Bagasse	Paddy husk	Plywood waste	Groundnut shell	Coconut fibre	
Jan/2011	5,885.22	1,087.94	3,405.89	507.24	35.45	757.5	7,030,500
Feb/2011	4,288.04	2,049.00	2,651.67	549.23	51.99	759.52	6,398,800
Mar/2011	4,205.35	2,269.99	2,492.14	504.84	145.36	67.7	5,968,300
Apr/2011	4,856.16	1,401.79	2,255.35	96.899	347.79	486.67	5,889,700
May/2011	5,388.91	625.455	2,089.57	214.99	76.959	493.89	5,870,800
June/2011	4,846.07	455.69	3,257.12	472.92	16.474	916.57	6,582,800
July/2011	385.5	136.88	383.24	122.91	0.82	88.735	676,400
Aug/2011	1,236.83	767.07	828.298	13.625	0	367.42	2,143,900
Sep/2011	3,459.27	1,048.14	2,509.35	350.54	15.885	1,352.2	5,422,500
Oct/2011	3,114.41	369.535	1,640.65	141.54	26.49	1,553.5	3,603,800
Nov/2011	2,500.72	87.05	2,288.29	75.723	29.07	1,145.7	2,699,100
Dec/2011	4,428.89	271.995	1,736.54	32.51	12.3	1,347.2	3,875,000

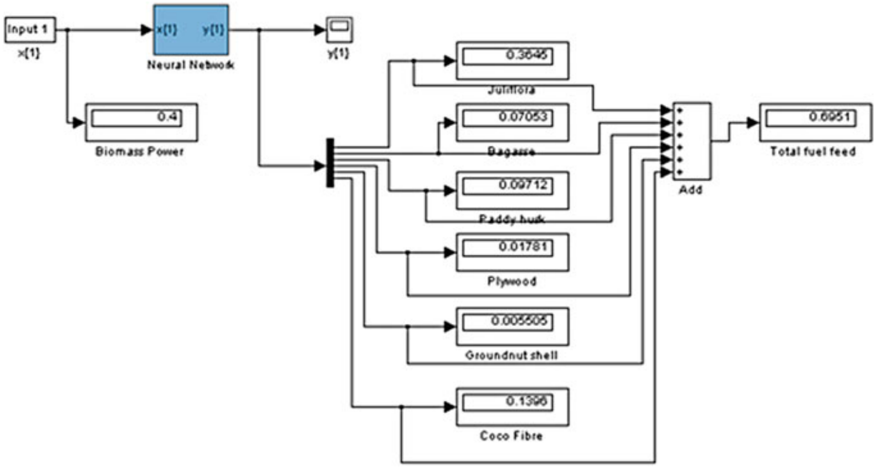

Fig. 41.4 Optimal fuel feed combination using ANN

41.8 Conclusion

In this work, the viability of PV/Biomass hybrid system for rural electrification in comparison with Grid only system is analyzed using HOMER in terms of cost and emissions for the chosen region T. Kallupatti of Madurai district. Also, the optimization of Biomass feedstock combination for maximum power output is presented using Neural Network toolbox. The following conclusions are drawn based on the simulation results:

- Biomass based hybrid system is the promising key of future for agriculture prone areas in India in the aspect of uninterrupted power supply to households and irrigational equipments. Also, CO_2 emissions are the least with biomass based RE system.
- In the economic point of view, currently biomass based electricity generation is a costlier solution compared to the conventional Grid system.

With successful technological up gradation in the future, the price of PV system will drop and the proposed hybrid Solar-Biomass power system will be the inevitable generation option for rural areas with potential Solar, Biomass resource availability.

Acknowledgments The authors express their sincere thanks to AMBEML's Vice president for providing the data of Biomass plant used for this research work and the Management of Thiagarajar College of Engineering, Madurai for supporting the research.

References

1. Singh R, Setiawan AD (2013) Biomass energy policies and strategies: harvesting potential in India and Indonesia. Renew Sustain Energy Rev 22:332–345
2. Khare V, Nema S, Baredar P (2013) Status of solar wind renewable energy in India. Renew Sustain Energy Rev 27:1–10
3. Ravindranath NH, Balachandra P, Dasappa S, UshaRao K (2006) Bioenergy technologies for carbon abatement. J Biomass Bioenergy 30:37–826
4. Bekele G, Tadesse G (2012) Feasibility study of small Hydro/PV/Wind hybrid system for off-grid rural electrification in Ethiopia. J. Appl Energy 97:5–15
5. Razak JA, Sopian K, Ali Y, Alghoul MA, Zaharim A, Ahmad I (2009) Optimization of PV-wind-hydro-diesel hybrid system by minimizing excess capacity. Europian. J Sci Res 25:663–671
6. Ashourian MH, Cherati SM, MohdZin AA, Niknam N, Mokhtar AS, Anwari M (2013) Optimal green energy management for island resorts in Malaysia. J Renew Energy 51:36–45
7. Aagreh Y, Al-Ghzawi A (2013) Feasibility of utilizing renewable energy system for a small hotel in Ajloun city, Jordan. J Appl Energy 103:25–31
8. Hafez O, Bhattacharya K (2012) Optimal planning and design of a renewable energy based supply system for microgrids. J Renew Energy 45:7–15
9. Buragohain B, Mahanta P, Moholkar VS (2010) Biomass gasification for decentralized power generation: The Indian perspective. J Renew Sustain Energy Rev 14:73–92
10. NASA Surface meteorology and Solar Energy. https://eosweb.larc.nasa.gov.cgi-bin/sse/grid.cgi

Chapter 42
Application of H-Bridge Converter Based Dynamic Voltage Restorer to Protect a Sensitive Load on Polluted Distribution Network

M.R.V. Murali and S. Latha

Abstract The growth in the use of power electronics has created a greater awareness of power quality. Power Quality (PQ) has been an issue is becoming increasingly pivotal in industrial electricity consumer's point of view in recent times. PQ has become important, especially, with the induction of sophisticated load, so such type of problems can eliminate by using custom power devices. One of these modern devices is Dynamic voltage restorer (DVR), which is a more efficient and effective modern custom power device. This paper presents the analysis and design of three phase H-bridge converter based DVR for protect sophisticated load, from polluted distributed network. The main objective of this paper is to save sophisticated load, from non linear voltages, currents and avoid PQ problem like voltage sag, swell conditions, in addition to the phase angle jump. Modeling and simulation of proposed DVR are implemented in PSCAD/EMTDC platform.

Keywords Dynamic voltage restorer (DVR) · H-bridge converter · Voltage sags · Power quality (PQ) · PSCAD/EMTDC

42.1 Introduction

Power quality importance (PQ) has risen over the last three decades due to a marked increase in the number of apparatus and machines which is sensitive to adverse PQ environments, the disturbances introduced by Non-linear loads, and the proliferation of renewable energy sources, among others [1]. At least 50 % of all Power quality problems are of the voltage quality type, where the interest is the study of any change

M.R.V. Murali (✉) · S. Latha
Department of Electrical and Electronics Engineering,
Thiagarajar College of Engineering, Madurai 625015, India
e-mail: rvmurali220@gmail.com

C. Kamalakannan et al. (eds.), *Power Electronics and Renewable Energy Systems*,
Lecture Notes in Electrical Engineering 326, DOI 10.1007/978-81-322-2119-7_42

or deviation of the voltage waveform from its ideal form. The well-known power quality disturbances or problems are voltage swells and sags, harmonic and inter-harmonic voltages, for three phase systems, voltage imbalances [3–7]. Voltage sag is normally caused by short-circuit faults in the power network or by the starting up of induction motors of large rating. The ensuing adverse effects are a reduction in the energy transfers of electric motors and the disconnection of sensitive equipment and industrial processes brought to a standstill [2].

The DVR is essentially a VSC (Voltage source converter) connected in series with the ac distribution network via an injecting transformer, which was originally conceived to mitigate voltage sags [2]. However, as shown in this paper work, its range of applicability can extended very considerably when provided with a suitable control scheme. The basic operating principle of the DVR is the injection of an in phase series voltage with the incoming supply to the load, sufficient enough to re-establish the voltage to its pre-sag state [2]. Its rate of success in combating voltage sags in actual installations is well cited, this being one of the logic why it continues to attract a great deal of interest in Higher and medium level companies and in academic circles.

This paper presents an H-Bridge cascaded converter avoid dissimilar device rating and uneven dc link voltage problems, in addition with power quality problems. In this paper, the electrical controller design and circuit design a consideration of an ac stacked using cascaded H-bridges is studied for DVR application.

42.2 Dynamic Voltage Restorer

To maintain a constant voltage value across a sophisticated load, Dynamic Voltage Restorer (DVR) is a series connected device designed. The DVR considered consists of: harmonic filter, an injection/series transformer, Voltage Source Converter (VSC), energy storage and control system.

The protection of sophisticated loads from voltage swells/sags coming from the network is the main function of a DVR. Therefore as shown in Fig. 42.1a, the DVR is located on approach of sophisticated loads. If a fault occurs or any nonlinear load connected with other lines, DVR inserts series voltage VDVR and compensates load voltage to a pre-fault value. The amplitudes of the three injected phase voltages are controlled such as to eliminate any detrimental effects of a bus fault to the load voltage VL. Any differential voltages caused by transient disturbances in the AC feeder will be compensated by an equivalent voltage generated by the converter and injected on the medium voltage level through the series transformer. The DVR works independently of the type of fault or any event that happens in the source side, for most practical cases, a more economical design can be achieved by only compensating the positive and negative sequence components of the voltage disturbance seen at the input of the DVR. This option is sensible because for a typical distribution bus configuration, the step down transformer will not allow the zero sequence part of a disturbance because of infinite impedance for this component.

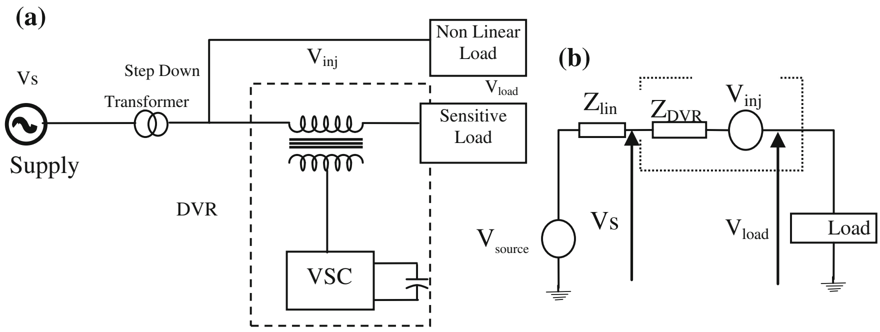

Fig. 42.1 **a** Schematic diagram of DVR configuration. **b** Equivalent circuit of DVR

The DVR has two modes of operation which are: standby mode and boost mode. In standby mode (VDVR = 0), the booster transformer's low voltage winding is shorted through the converter. Semiconductors switching is not occurs in this mode of operation, because the singular converter legs are triggered such as to establish a short-circuit path for the transformer connection. Therefore, only the comparatively semiconductors have low conduction losses in this current loop contribute to the losses. The DVR will work most of the time in this mode. In boost mode (VDVR > 0), the DVR is injecting a compensation voltage through the booster transformer due to a detection of a supply voltage disturbance [3].

Figure 42.1b show the equivalent circuit of DVR when the source voltages is drop and/or increase, a series voltage is injects by DVR V_{inj} through the injection transformer so that the desired load voltages magnitude V_L can maintained. Mathematical expressed the injection satisfies

$$V_L = V_S + V_{inj}. \tag{42.1}$$

where V_L is load voltage, V_S is supply voltage and V_{inj} is the voltage injected

$$S_L = V_L I_L \tag{42.2}$$

$$S_L = P_L + jQ_L = (P_S + jQ_S) + (P_{inj} + jQ_i) \tag{42.3}$$

42.3 Power Architecture

Although various topologies may be used to realize the VSC illustrated in Fig. 42.2i, at higher power levels H-bridge power converters are seen to have advantages in several aspects. First, converters can realize the higher power and high voltage using semiconductor switches of relative small ratings while avoiding the voltage sharing and current sharing problems associated with series and parallel connection of switches commonly employed in two-level converter realization. Second, converters

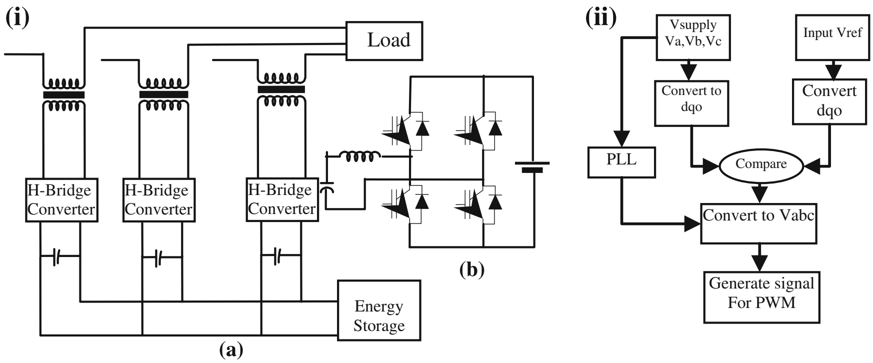

Fig. 42.2 **i** Proposed power architecture of the transformer coupled H-bridge converter applied to DVR. **ii** Flow chart of DVR operation

can integrate the output voltage with smaller steps and reduced harmonic content, while it resulting smaller potential thus lower electromagnetic interference (EMI). Third, compared with diode clamped multilevel topology, the H-bridge structure can avoid unequal device rating and unbalanced DC link voltage problems. When compared to flying-capacitor topology, the H-bridge multilevel converter has less storage capacitors and requires simpler control. Finally, it is worth noting that the modularity nature of the H-bridge cascaded converter makes an easier realization.

The power architecture of the series or boosting transformer coupled H-bridge converter is illuminated in Fig. 42.2i. Each phase is composed of three H-bridge inverters. The outputs of the converters are connected in series through transformers. This architecture fits with the DVR application, which automatically involves a series injection of the compensating voltage source. Furthermore, instead of using isolated dc link for each H-bridge inverter, a common dc link bus connects all H-bridge inverters dc ports in parallel. This is contrasting from the conventional H-bridge cascaded multilevel converter. This is also different from multiple six-pulse three- Switches (IGBT's) constituting the voltage source converter. The commutation pattern is generated by means of the sinusoidal pulse width modulation technique (SPWM); voltages are controlled through the phase modulation. The block diagram of the phase locked loop (PLL) is converters.

42.4 Control Philosophy

The basic purpose of a controller in a DVR are the detection of voltage swell/sag events in the system; computation of the correcting voltage, generation of trigger pulses to the sinusoidal PWM based DC-AC inverter, correction of any deviation in the series voltage injection and termination of the trigger pulses when the event has passed. The controller may also be used to shift the DC-AC inverter into a rectifier mode to charge the capacitors in the DC energy link in the absence of voltage swells/sags. The dqo transformation or Park's transformation [3] is used to control of DVR. The dqo method gives the sag depth and phase shift information with start and end times. The quantities are expressed as the instantaneous space vectors. Firstly convert the voltage from a-b-c reference frame to d-q-o reference.

Figure 42.2ii shows a flow chart of the FF (feed forward) dqo transformation for voltage swells/sags detection. The detection is carried out in each of the three phases. The error signal is used as a modulation signal that allows generating a commutation pattern for the power Illustrated in Fig. 42.4. The PLL circuit is used to generate a unit sinusoidal wave in phase with mains voltage.

$$\begin{bmatrix} V_d \\ V_q \\ V_o \end{bmatrix} = \begin{bmatrix} \cos\theta & \cos\left(\theta - \frac{2\pi}{3}\right) & 1 \\ -\sin\theta & -\sin\left(\theta - \frac{2\pi}{3}\right) & 1 \\ \frac{1}{2} & \frac{1}{2} & \frac{1}{2} \end{bmatrix} \begin{bmatrix} V_a \\ V_b \\ V_c \end{bmatrix} \tag{42.4}$$

Equation 42.4 defines the park transformation from three phase System rotating reference frames abc to dqo stationary frame. In this transformation, phase A is aligned to the d-axis that is in quadrature with the q-axis. The theta (θ) is defined by the angle between phase A to the d-axis.

42.5 Simulation Results and Discussions

A detailed simulation of control system for the DVR is performed using PSCAD/ EMTDC model as show in order to verify the operation. The parameter of the DVR system is shown in Table 42.1 (Fig. 42.3).

42.5.1 Non Linear Load with DVR

Figure 42.4ia shows voltage of source which is affected with non liner load connected in parallel to sophisticated load. Figure 42.4id, b show the voltage injected by DVR and corresponding load voltages with compensation of non linear voltage

Table 42.1 System data

S.No.	Parameters	Values used in the simulation models
1	Supply voltage	400 V
2	Series transformer turns ratio	1:1
3	DC link voltage	400 V
4	Filter inductance	1 mH
5	Filter capacitance	10 μF
6	Load resistance	0.01/phase
7	Load inductance	0.0024/phase

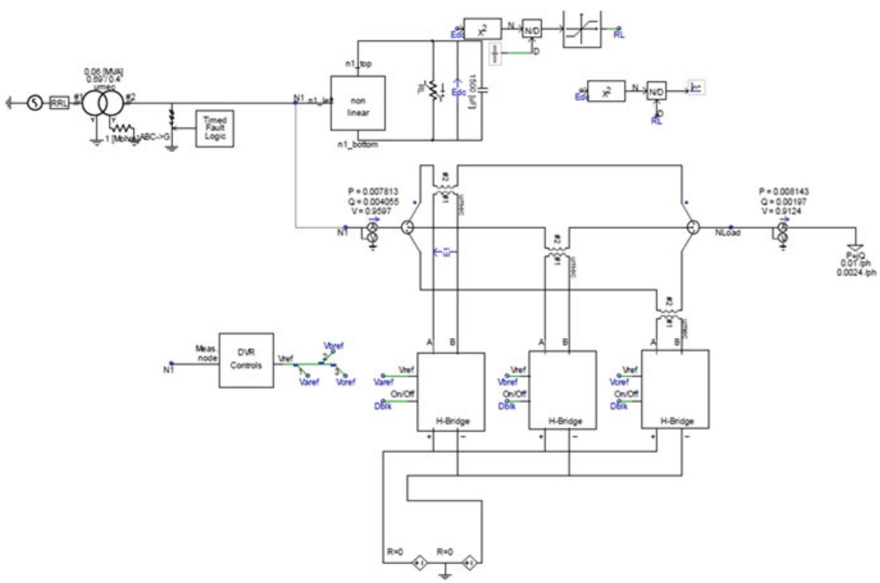

Fig. 42.3 A PSCAD/EMTDC model of proposed H-bridge converter based dynamic voltage restorer (DVR)

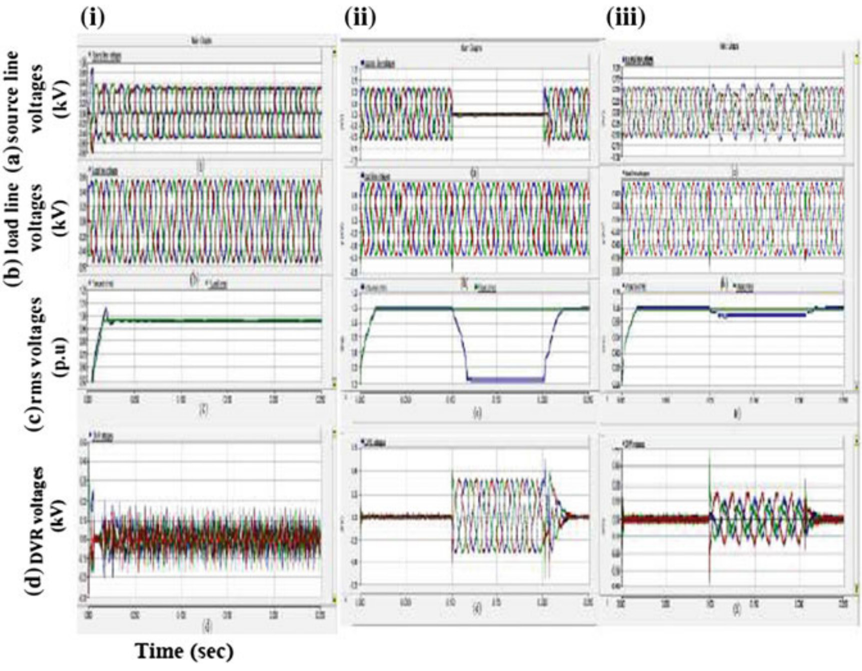

Fig. 42.4 **i–iii**: (*a*) source line voltages, (*b*) load line voltages, (*c*) rms voltages, (*d*) DVR voltages

into linear sinusoidal form. Figure 42.4id looks like disturbances but it the injecting voltages for compensating voltage. RMS voltages on both sides are equal.

42.5.2 Voltage Sags Without Non Linear Load

1. Three phase to ground fault

Figure 42.4iia shows voltage sag occurs on source at 0.1 s due to three phase to ground fault and it is kept 0.2 s, with total sag duration of 0.1 s. Figure 42.4iib, d shows the voltage injected by DVR and corresponding load voltages with compensation.

2. Double line fault

Figure 42.4iiia shows voltage unbalance occurs on source at 0.1 s due to Double line fault and it is kept 0.2 s, with total sag duration of 0.1 s. Figure 42.4iiib, d shows the voltage injected by DVR and corresponding load voltages with compensation.

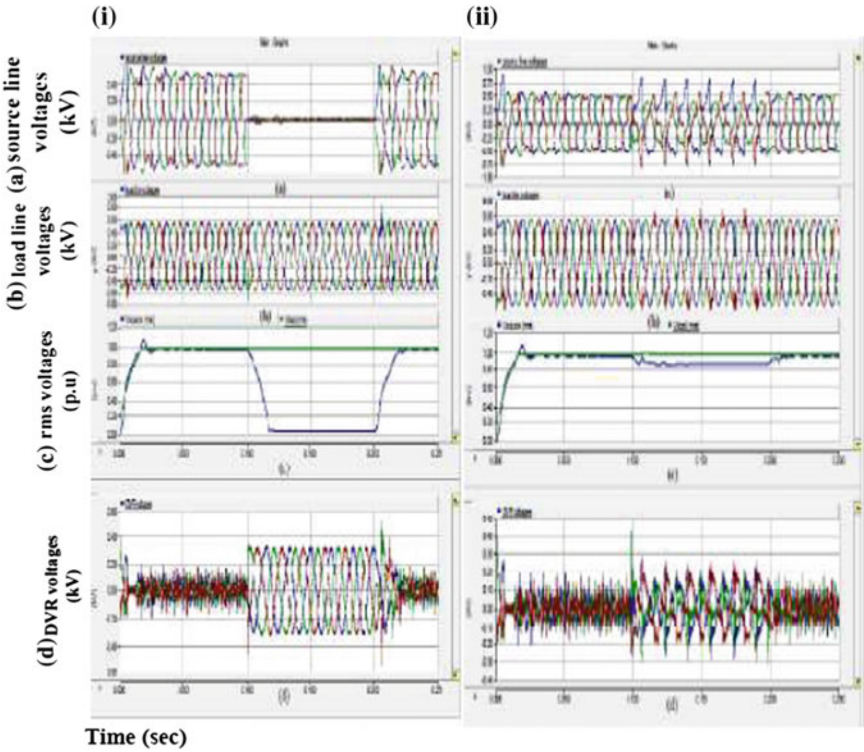

Fig. 42.5 **i** and **ii**: (*a*) source line voltage s, (*b*) load line voltages, (*c*) rms voltages, (*d*) DVR voltages

42.5.3 Voltage Sags with Non Linear Load and DVR

1. Three phase to ground fault

Figure 42.5ia shows voltage sag occurs on source at 0.1 s due to three phase to ground fault with non linear voltage and it is kept 0.2 s, with total sag duration of 0.1 s. Figure 42.5ib, d shows the voltage injected by DVR and corresponding load voltages with compensation.

2. Double line fault

Figure 42.5iia shows voltage unbalance occurs on source at 0.1 s due to Double line fault and it is kept 0.2 s, with total sag duration of 0.1 s. Figure 42.5iib, d shows the voltage injected by DVR and corresponding load voltages with compensation.

42.6 Conclusion

In this work, test system is developed using PSCAD/EMTDC software. This paper presents the features of DVR using converter with H-Bridges. H-Bridge cascaded converters avoid unequal device rating and unbalanced dc link voltage problems, in addition with power quality problems. The modeling and simulation of the proposed DVR using PSCAD/EMTDC had been presented. The simulation results shows that H-Bridge converter is protect the sophisticated load, form non liner voltage disturbances, Voltage sag and swell, and Voltage unbalance.

References

1. Woodley NH (2000) Field experience with dynamic voltage restorer (DVR™MV) systems. Proc. Singapore, IEEE Power Eng Soc Winter Meeting Conf, p 2864
2. Tolbert LM, Zheng PF, Habetler TG (1999) Multilevel converters for large electric drives. IEEE Trans Ind Appl 35(1):36
3. Hingorani NG (1995) Introducing custom power. IEEE Spectr 32(6):41
4. Nielsen JG, Newman M, Nielsen H, Blaabjerg F (2004) Control and testing of a dynamic voltage restorer (DVR) at medium voltage level. IEEE Trans Power Electron 19(3):806
5. Woodley NH, Morgan L, Sundaram A (1999) Experience with an inverter-based dynamic voltage restorer. IEEE Trans Power Delivery 14(3):1181
6. Kieferndorf R, Venkataramanan G, Manjrekar MD (2000) Power electronic transformer (PET) fed nine-level H-bridge inverter for large induction motor drives. In: Proceedings of IAS Annual Meeting, Rome, Italy, pp 2489–2495
7. Alepuz S, Busquets-Monge S, Bordonau J, Martinez-Velasco J, Silva C, Pontt J, Rodriguez J (2009) Control strategies based on symmetrical components for grid-connected converters under voltage dips. IEEE Trans Ind Electron 56(6):2162–2173

Chapter 43
Power Control of Wind Turbine Driven Permanent Magnet Synchronous Generator Using Maximum Power Point Tracking Algorithm

K. Devi Anusha and K.C. Jayasankar

Abstract The wind turbine generator considered in this work employs a direct-driven (Without gearbox) PMSG, which is directly coupled to the wind turbine and connected to the electric grid through the power conditioning system (PCS). The stator windings of the PMSG are directly connected to the PCS composed of a full-scale power converter built using a back-to-back AC/DC/AC power converter topology which includes a three-phase rectifier bridge (AC/DC conversion), a DC/DC converter and a grid-side converter with an intermediate DC link (DC/AC conversion). A maximum power point tracking algorithm is used to track the maximum power output to increase the power conversion efficiency in the system. Thus the generator produces the maximum power continuously.

Keywords PMSG · MPPT · Wind energy · Power conditioning system (PCS)

43.1 Introduction

Wind-powered machines have been used by humans for thousands of years. Until the 20th century the application of wind power is limited. Now-a-days wind energy is considered as feasible source of renewable energy. The reason is that it is considered inexhaustible and can be converted easily into electrical energy through various wind energy conversion systems.

Previously constant speed turbines are used for the conversion. Due to the fixed-speed operation for constant speed turbines, all the variations in the wind speed are transmitted as fluctuations in the mechanical torque and then as fluctuations in the electrical power grid. This can be avoided by the use of variable-speed wind turbine

K. Devi Anusha (✉) · K.C. Jayasankar
Department of Electrical and Electronics Engineering, Prathyusha Institute of Technology and Management, Chennai, Tamil Nadu, India
e-mail: devianusha88@gmail.com

C. Kamalakannan et al. (eds.), *Power Electronics and Renewable Energy Systems*,
Lecture Notes in Electrical Engineering 326, DOI 10.1007/978-81-322-2119-7_43

and also the increased energy capture, operation at maximum power point, improved efficiency, and power quality [1]. Because of this reason, the wind industry trend is to design and construct variable-speed wind turbines. In variable speed generation system, the power electronic converter controls the generator [2–4].

The gearbox couples the wind turbine and generator. It suffers from faults and requires regular maintenance. The reliability of the variable-speed wind turbine can be improved by the use of a direct-drive permanent magnet synchronous generator (PMSG). PMSG has many advantages like the property of self-excitation, which allows an operation at a high power factor and high efficiency and very high torque can be achieved at low speeds. Thus PMSG is widely used in case of wind turbines. For extracting maximum power from the fluctuating wind, variable-speed operation of the wind-turbine generator is necessary. It needs a control strategy for the generator. Maximum Power Point Tracking (MPPT) is a popular control strategy; optimum wind-energy utilization can be achieved using this. A maximum power point tracking (MPPT) algorithm increases the efficiency of the power conversion by regulating the turbine rotor speed with respect to actual wind speeds. This increases the efficiency and economics of wind energy conversion systems (WECS).

43.2 Wind Generator Model

Power available from the wind is given by

$$P = \frac{1}{2}\rho A V^3 \tag{43.1}$$

where,

ρ Density of air (1.225 kg/m^3)
A Rotor swept area
V Wind speed

Power can be derived using following equations
The kinetic energy available from the wind is given by

$$\mathrm{KE} = 1/2 * \mathrm{M} * \mathrm{V}^2 \tag{43.2}$$

Substitute for M $(\mathrm{M} = \rho * \mathrm{Vol})$ to obtain: $\mathrm{KE} = 1/2 * (\rho * \mathrm{Vol}) * \mathrm{V}^2$.
And Vol can be replaced by $\mathrm{A} * \mathrm{D}$ to give: $\mathrm{KE} = 1/2 * (\rho * \mathrm{A} * \mathrm{D}) * \mathrm{V}^2$.
And D can be replaced by $\mathrm{V} * \mathrm{T}$ to give: $\mathrm{KE} = 1/2 * (\rho * \mathrm{A} * \mathrm{V} * \mathrm{T}) * \mathrm{V}^2$
Leaving us with: $\mathrm{KE} = 1/2 * \rho * \mathrm{V}^3 * \mathrm{A} * \mathrm{T}$.

Power is just energy divided by time, so the power available from our air can be expressed as:

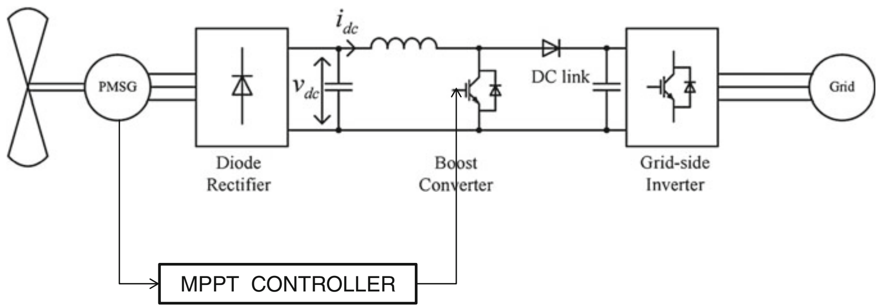

Fig. 43.1 Circuit diagram for overall scheme

$$P = KE/T = \left(1/2 * \rho * V^3 * A * T\right)/T = 1/2 * \rho * V^3 * A \tag{43.3}$$

where,

M Total Mass
Vol Volume
D Thickness of the pane

The output power from the wind turbine transfers through an ac–dc–ac stage, which consists of a diode bridge rectifier, a boost converter, and a grid-side inverter, which is connected to the grid. Due to the low cost and high reliability of diode bridge rectifier, it is used instead of a controlled rectifier. A boost converter controls the dc-side voltage and current for MPPT, and steps up the voltage for grid connection. Finally, the captured power is transferred to the grid via an inverter. The circuit diagram for overall scheme is explained in Fig. 43.1.

43.3 Power Point Tracking Methods

For obtaining the maximum amount of energy from the wind, the wind turbine must have a specific rotation speed to maintain the optimum tip-speed ratio. The purpose of the MPPT is to maintain the tip-speed ratio of the wind turbine as close as possible to the optimal tip-speed ratio. It is defined as the ratio between the rotor speed of the tip of a blade and the actual wind velocity.

Mainly, there are three types of MPPT algorithms, namely, TSR control and optimum relationship-based (ORB) control, perturb and observe (P&O) control (which is also known as hill-climbing searching control) [5, 6].

TSR control directly regulates the turbine speed to keep the TSR at an optimal value by measuring wind speed and turbine speed [5–9]. The control strategy is straightforward. An anemometer is required for this method. However, an accurate anemometer is expensive and adds extra cost to the system, especially for small-scale

WECSs. The fluctuations in the wind cannot be measured without the use of anemometer. ORB control uses MPPT with the aid of knowledge of optimum relationships between system parameters. The main disadvantage of this method is system pre-knowledge is required and also it needs lots of memory space.

P&O method is the proposed technique. In this only measured data and doesn't need any information about the CP curve, the optimum TSR, the wind speed or angular velocity [6]. The operating point can be on the positive slope, maximum point or negative slope. If the operating point on in the positive slope, the operating point must be moved to the right to obtain the maximum point. This can be achieved by reducing the load current. By reducing the load current the electromagnetic torque will be reduced, and the difference between the turbine torque and electric torque will accelerate the wind turbine. If the operating point is on the negative slope the load current must be increased to increase Te. If the torque developed by the turbine is smaller than Te and the losses caused by friction, the turbine will decelerate.

When the wind speed steps over the cut-in speed the controller will produce a perturbation. This perturbation will lead to power increase or decrease so the controller finds out on which side of the slope is the operation point at the given moment. After that the load is increased or decreased until the slope is zero. When the slope becomes zero the system has reached the maximum power point. A more advanced form of this method takes in account the slope for calculating the size of the step. The step is proportional with the slope. This will lead to a faster response. The tracking process is shown in Fig. 43.2.

This method has many advantages compared to other methods. It does not require an anemometer that is expensive especially for small-scale WECSs, does not require system pre-knowledge and has the ability of online updating. The flow chart for the proposed control method is shown in Fig. 43.3.

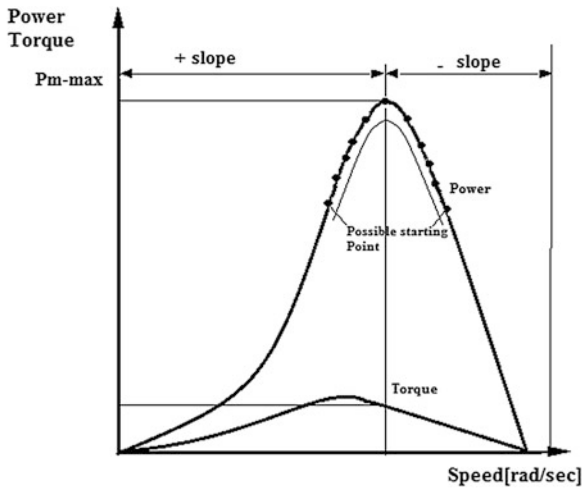

Fig. 43.2 MPPT process with P&O

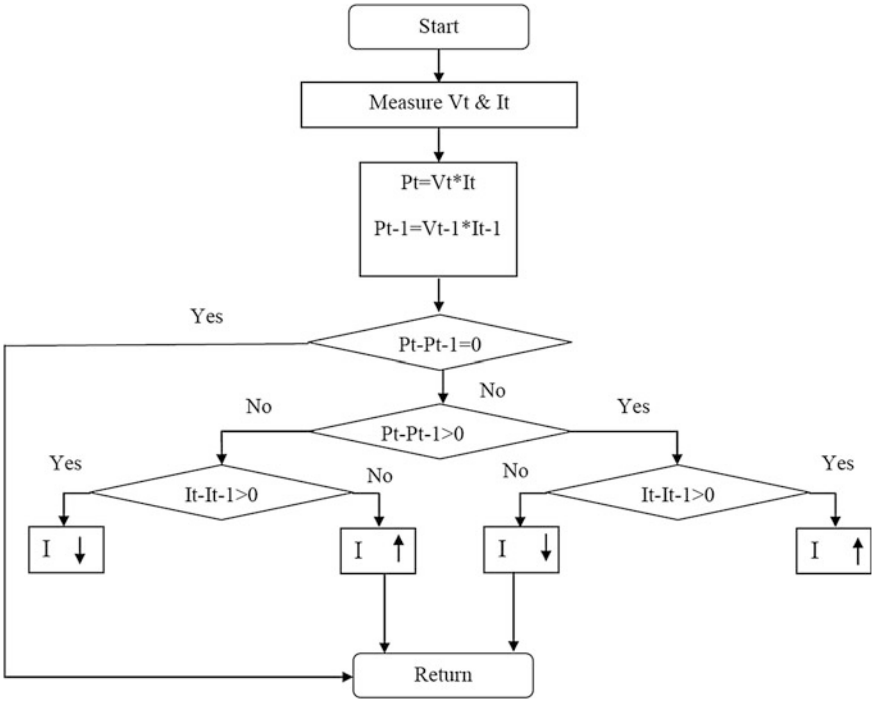

Fig. 43.3 Proposed MPPT technique control flow chart

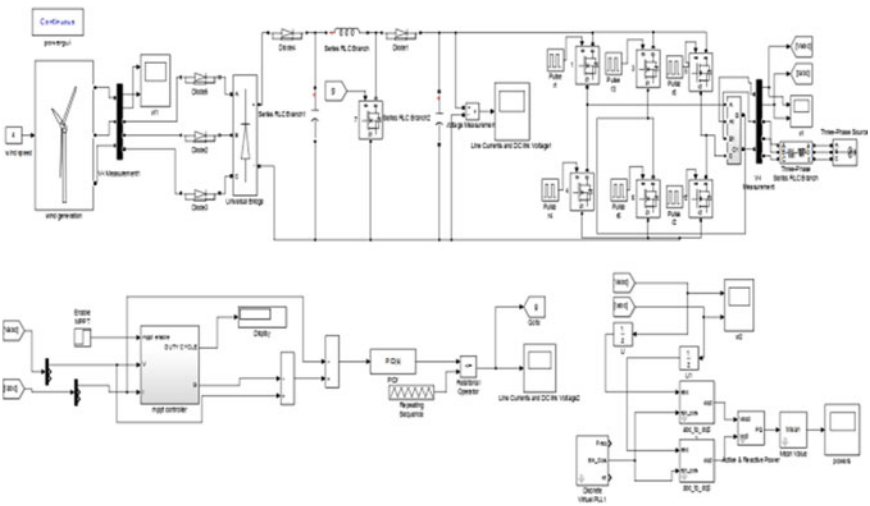

Fig. 43.4 The simulation diagram

43.4 Simulations and Results

The simulation diagram for proposed system is shown in Fig. 43.4. In this a permanent magnet synchronous machine works as a PMSG by changing its torque into negative. To the wind turbine model wind speed, pitch angle and generator speed is given as input. The output obtained is torque is feed to the mass drive train which acts as a shaft between wind turbine model and generator. The output waveforms from the wind turbine are shown in Figs. 43.5 and 43.6.

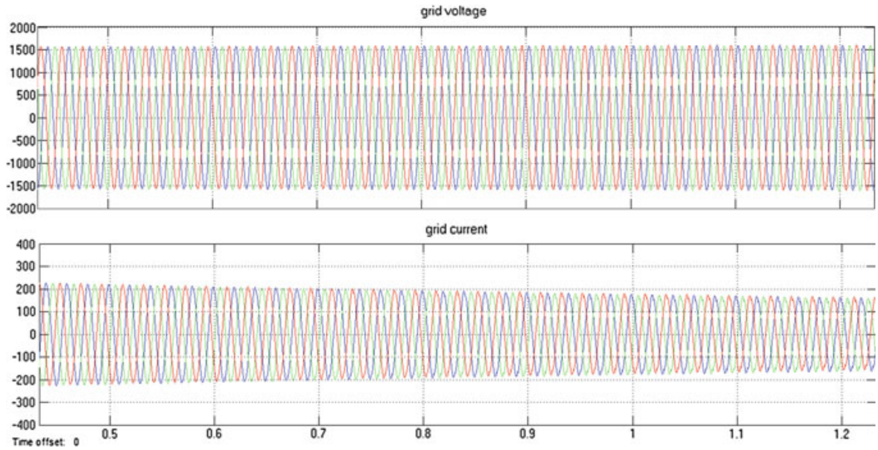

Fig. 43.5 The output waveforms from the wind turbine

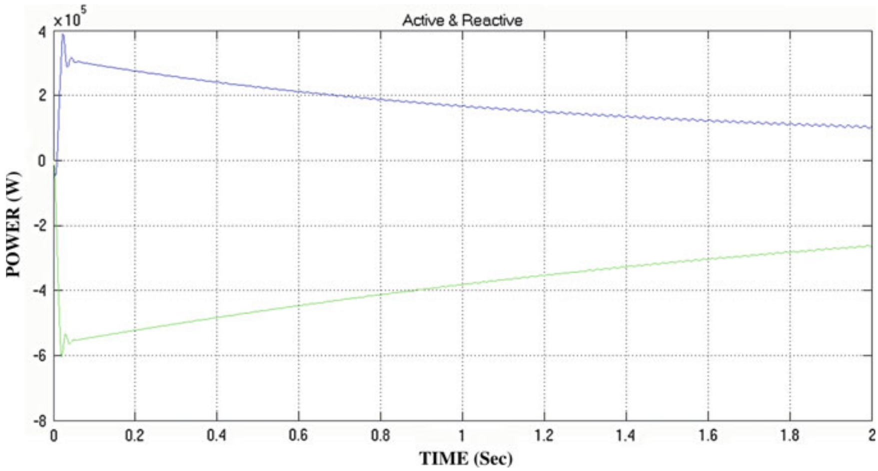

Fig. 43.6 The power output obtained from the system

43.5 Conclusion

The variable-speed wind energy conversion system using a permanent magnet generator has been discussed in this paper. The model consists of the wind generator model, an uncontrolled rectifier, an inverter. The model has been implemented in MATLAB/Simulink in order to validate it. The control strategy adopted is maximum power point tracking. Power-time characteristics have been obtained.

References

1. Benchagra M, Maaroufi M, Ouassaid M (2011) Study and analysis on the control of SCIG and its responses to grid voltage unbalance. In: Proceedings of international conference on multimedia computing and systems, IEEE ICMCS'11, pp 1–5
2. Buehring IK, Freris LL (1981) Control policies for wind energy conversion systems. Proc Inst Elect Eng C 128:253–261
3. Chedid R, Mrad F, Basma M (1999) Intelligent control of class of wind energy conversion systems. IEEE Trans Energy Convers 14:1597–1604
4. Errami Y, Ouassaid M, Maaroufi M (2011) Modelling and control strategy of PMSG based variable speed wind energy conversion system. In: Proceedings of IEEEICMCS', vol 11, pp 1–6
5. Hilloowala RM, Sharaf AM (1996) A rule-based fuzzy logic controller for a PWM inverter in a standalone wind energy conversion scheme. IEEE Trans Ind Appl 31:57–65
6. Johnson K, Fingersh L, Balas M, Pao L (2004) Methods for increasing region 2 power capture on a variable speed wind turbine. J Solar Energy Eng 126:1092–1100
7. Johnson KE, Pao LY, Balas MJ, Fingersh LJ (2006) Control of variable-speed wind turbines: Standard and adaptive techniques for maximizing energy capture. IEEE Control Syst Mag 26:70–81
8. Müller S, Deicke M, De Doncker RW (2002) Doubly fed induction generator system for wind turbines. IEEE Ind Appl Mag 8:26–33
9. Thiringer T, Linders J (1993) Control by variable rotor speed of a fixedpitch wind turbine operating in a wide speed range. IEEE Trans Energy Convers 8:520–526
10. Wang Q, Chang L-C (2004) An intelligent maximum power extraction algorithm for inverter-based variable speed wind turbine systems. IEEE Trans Power Electron 19:1242–1249
11. Chen Z, Guerrero JM, Blaabjerg F (2009) A review of the state of the art of power electronics for wind turbines. IEEE Trans Power Electron 24:1859–1875

Chapter 44
Performance Evaluation of Differential Evolution and Particle Swarm Optimization Algorithms for Optimizing Power Loss in a Worm Gear Mechanism

P. Sabarinath, M.R. Thansekhar and R. Saravanan

Abstract Optimal design of machine elements plays a vital role in reducing the cost of manufacturing the machine elements. Design optimization is an important task to achieve the above goal. Many optimization algorithms have been proposed and used in the past for design optimization and they are used to find the optimal set of design variables possibly subjected to a set of constraints. Still, there is a scope for efficient algorithms for the design optimization of machine elements. In this study, the design optimization of a worm gear mechanism is presented by using two non-conventional optimization algorithms namely Differential Evolution and Particle Swarm Optimization algorithms for minimizing the power-loss. The results obtained by using Differential Evolution and Particle Swarm Optimization algorithms are compared with that of genetic algorithm and analytical method. The results showed that both the algorithms are efficient in finding the optimal design values.

Keywords Optimal design · Worm and worm wheel · Differential evolution algorithm · Particle swarm optimization

44.1 Introduction

The successful functioning of any machine depends on the quality of the individual parts used to assemble the machine. The proper selection of material and suitable design of machine elements plays an important role. The design process involves the selection of suitable geometry and size of the component in order to withstand the stresses induced. Gear drives are important machine elements used for power

P. Sabarinath (✉) · M.R. Thansekhar
K.L.N. College of Engineering, Pottapalayam 630611, India
e-mail: jananisabari@gmail.com

R. Saravanan
Sri Krishna College of Technology, Coimbatore 641042, India

C. Kamalakannan et al. (eds.), *Power Electronics and Renewable Energy Systems*,
Lecture Notes in Electrical Engineering 326, DOI 10.1007/978-81-322-2119-7_44

transmission. Many types of gear drives are used in various applications such as spur gear drive, helical gear drive, bevel gear drive and worm gear mechanism. Worm gear mechanism is used in transmitting power at high speed ratio. Unlike other gear drives, worm gear mechanism uses a worm gear wheel and a worm screw to transmit power at a higher reduction rate. Hence the chances for power loss in maximum in worm gear mechanism than other gear drives. So, in this paper, minimizing power loss in a worm gear mechanism is addressed.

In design optimization, the criterion with respect to which the design is optimized is chosen first. It is known as objective function. It may be single or multi in nature. The ranges of design variables i.e., the maximum or minimum of design variables are assigned. The main aspect in design optimization is satisfying a certain set of specified requirements called constraints. Many methods involving mathematical programming have been developed in the past and are in use for design optimization. Differential evolution (DE) algorithm is one of the most powerful algorithms of evolutionary computation because of its excellent convergence characteristics and it uses only a few control parameters are required to be set by the users. Storn and Price [1] proposed this differential evolution algorithm, a simple and efficient heuristic shown effective for finding global optima for numerous unconstrained test functions. Differential evolution involves the evolution of a population of solutions with size NP using operators such as mutation, crossover, and selection. Particle swarm optimization (PSO) is a swarm intelligence computation technique developed by Kennedy and Eberhart [2]. Based on the animal behavior in groups such as bird flocking, fish schooling, and swarm theory, this PSO algorithm was developed. In this paper, we address the optimal design of worm gear mechanism with the objective of minimizing the power loss without compromising specified strength. Differential Evolution Algorithm and Particle Swarm Optimization, which are emerging as prominent meta-heuristics, have not been attempted in the past to the design optimization of worm gear mechanism problem. On this concern, this paper proposes DE and PSO algorithms to evolve best values of design variables so as to minimize the power loss. The performances of the proposed algorithms are analyzed and also compared with results by other algorithms like GA and analytical method.

44.2 Literature Review

Deb discussed the application of various traditional optimization techniques to solve many real world design optimization problems and its applications in real world design optimization from industrial point of view in [3]. Bhandari had solved many machine design problems in [4]. He proposed the procedure and the necessary steps to design various mechanical elements and transmission elements with design calculations. Gear design is a complicated process as it involves design variables in different forms such as discrete, integer and continuous variables. Since gear drives find applications in many fields involving power transmission, the optimal design of gear parameters becomes a challenging task for designers. Many traditional algorithms have been proposed in the past to optimize gear parameters. In recent years, many metaheuristic algorithms have been proposed in which genetic algorithms (GA) had been used by many researchers for optimizing the gear parameters for different types of gear drives. Gologlu and Zeyveli [5] used GA for minimizing the volume of a two-stage helical gear train. Caballero et al. [6] proposed GA for minimizing the weight of the cylindrical parallel gear train. Chong and Lee [7] developed a methodology involving GA for minimizing the geometric volume of two stage gear train and simple planetary gear train. Mendi and Baskal [8] used GA for reducing the volume of a gearbox. Since many high-performance power transmission applications (e.g., automotive, aerospace, machine tools, etc.) require low weight, Savsani et al. [9] solved weight minimization of spur gear drive using PSO and SA Algorithms. Weight minimization of the speed reducer involving spur gears subject to constraints on bending stress of the gear teeth and surface stress is attempted using ABC Algorithm in [10]. Padmanabhan et al. [11] had used modified Artificial Immune Algorithm for the weight minimization of worm gear drive. Mogal and Wakchaure [12] had used genetic algorithm for the multi objective design optimization of minimizing the volume of worm and worm wheel. This paper also considers other two objectives of minimizing the centre distance and minimizing the deflection of worm. Su and Peng [13] proposed a methodology which combines FEA, ANN and GA together to optimize the design variables of an involute cylindrical worm with a helical gear drive. Sabarinath et al. [14] had applied DE and PSO algorithms for finding the optimal design parameters of a belt pulley system. It is evident that lot of attempts has been made for single objective design optimization of basic machine elements such as bearings, pressure vessel, gear drives, welded joints, belt drives etc. using nontraditional optimization techniques. But very few attempts have been carried out to optimize the design of gears (i.e. Weight minimization), especially worm gear set. So in this work, power loss minimization of worm gear set is solved. The objective function of minimizing the power loss minimization of worm gear set is taken from [15] in which Yaman et al. used GA method to solve the optimal design of worm gear set. In this research paper, DE and PSO algorithms are used for solving the power loss minimization of worm gear set problem.

44.3 Problem Statement

The objective in this work is to minimize the power loss in a worm gear mechanism as shown in Fig. 44.1. The worm and worm wheel are used to transmit power and motion between two non-intersecting and non-parallel shafts. Mostly worm gear drives are positive drives and reverse motion is undesired. In this work, the worm shaft is the driving shaft. Bronze (GzSnBz12) and hardened steel (42CrMo4) are the materials used for the worm gear and worm respectively. In this application, the angle between the shafts is taken as 90°, gear ratio is 15:1; and the number of threads in the worm is three. As said earlier, the power loss in worm gear drive is

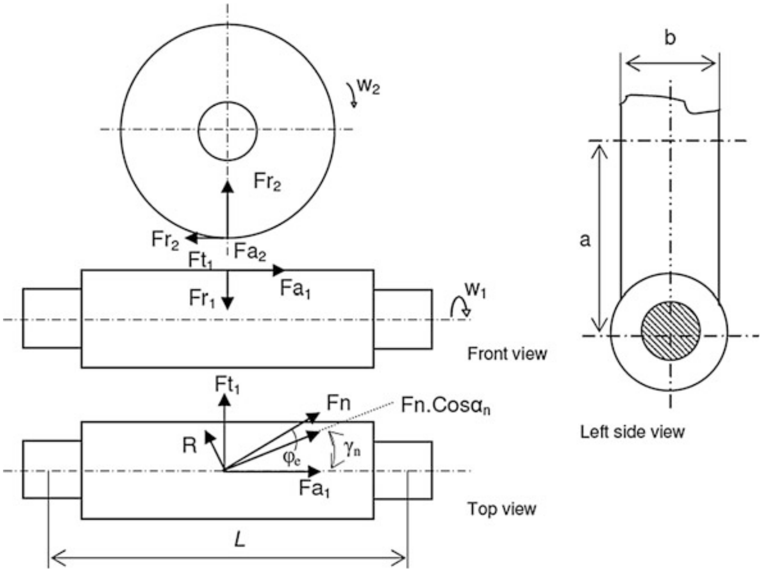

Fig. 44.1 Schematic representation of single enveloping worm gear set

high than other gear drives because of high friction. Here due to friction, heat is generated from the missing power. The objective function considered here is the power loss and the constraints are bending stress of gear tooth for acceptable deflection, linear pressure, acceptable deflection of worm shaft and worm gear tooth.

Power loss, ΔP, formulated as:

$$\Delta \mathrm{P} \ = \mathrm{P_i} - \ \mathrm{P}_o \tag{44.1}$$

where, P_i, input power, P_o, output power represented with Eq. (44.2).

$$P_o = F_n(\cos\alpha_n \cos\gamma_n - \mu \sin\gamma_n)\frac{m_a Z_g \omega_w}{2i} \tag{44.2}$$

where, F_n is normal force represented in Eq. (44.3), α_n is pressure angle, γ_n is helix angle, μ is friction coefficient, m_a is module, Z_g is number of gear tooth, ω_w is angular velocity of worm, and i is gear ratio.

$$F_n = \frac{F_{t1}}{(\cos\alpha_n \sin\gamma_n + \mu\cos\gamma_n)} \tag{44.3}$$

$$F_{t1} = \frac{2P_i}{\left(\frac{2\pi n}{60}\right)do_w} \tag{44.4}$$

where, F_{t1} is tangential force represented in Eq. (44.4). N is number of revolution tour of worm, do_w is worm diameter.

44.3.1 Objective Function

The objective function of minimizing the power loss in a worm gear mechanism is formulated as:

$$F_{obj} = F(Z_g, \gamma_n, \mu) = P_i - F_n(\cos\alpha_n \cos\gamma_n - \mu \sin\gamma_n)\frac{m_a Z_g \omega_w}{2i} \tag{44.5}$$

44.3.2 Design Variables and Parameters

The design variables vector consists of gear tooth number, friction coefficient, and helix angle.

$$\text{Gear tooth number } 21 \le Z_g \le 80 \tag{44.6}$$

$$\text{Friction coefficient } 0.03 \le \mu \le 0.05 \tag{44.7}$$

$$\text{Helix angle } 15 \le \gamma_n \le 25 \tag{44.8}$$

44.3.3 Constraints

The constraints considered for minimizing the power loss of worm gear mechanism are the following:

$$g_j(Z_g, \gamma_n, \mu) \le 0 \tag{44.9}$$

$$j = 1, \ldots NCON(\text{number of constraints}) \tag{44.10}$$

$$g_1(x) = \frac{F_{t2}}{bo_g m_a Z_g} 2.5 - 3.6 \le 0 \tag{44.11}$$

$$g_2(x) = \frac{F_{t2}}{\pi bo_g m_a} - 30 \le 0 \tag{44.12}$$

$$g_3(x) = \frac{df_w}{1{,}000} - \frac{F_{tR1} L^3}{48EI} \le 0 \tag{44.13}$$

where, $g_1(x)$ represents linear pressure of worm gear tooth, $g_2(x)$ is bending stress of gear tooth and $g_3(x)$ is acceptable deflection of worm shaft. F_{t2} is axial force of worm gear represented with Eq. (44.14), bo_g is width of worm gear represented with Eq. (44.15) and F_{tR1} is total radial force with Eq. (44.16).

$$F_{t2} = F_n(\cos\alpha_n \cos\gamma_n - \mu \sin\gamma_n) \tag{44.14}$$

$$bo_g = 0.45(do_1 + 6m_a) \tag{44.15}$$

$$F_{tR1} = \sqrt{\left(F_{t1}^2 + F_{r1}^2\right)} \tag{44.16}$$

where F_{r1} is radial force represented with Eq. (44.17).

$$F_{r1} = F_n \sin\alpha_n \tag{44.17}$$

44.4 Differential Evolution Algorithm

Differential evolution, a stochastic, simple yet powerful evolutionary algorithm, not merely possesses the advantage of a quite few control variables but also performs well in convergence was introduced to solve the global optimization by Storn and Price [1]. DE creates new candidate solutions by perturbing the parent individual with the weighted difference of several other randomly selected individuals from the same population. The parent will be replaced by a candidate only when the candidate gives better value than its parent. Thereafter, DE guides the population towards the vicinity of the global optimum through repeated cycles of mutation, crossover and selection.

44.5 Particle Swarm Optimization Algorithm

Particle swarm optimization (PSO) is a swarm intelligence computation technique developed by Kennedy and Eberhart [2]. PSO is initialized with a group of random particles (solutions) and then searches for optima by updating generations. Each particle is updated by two “best” values in every iteration. The first one is the best solution (fitness) it has achieved so far called pbest. Another “best” value is the best value obtained so far by any particle in the population. This best value is a global best and called gbest. The detailed step by step procedure to solve a problem using PSO algorithm is presented in [2].

44.6 Results and Discussion

The power loss minimization of worm gear set problem is solved by both DE and PSO algorithms. Both the algorithms are implemented using MATLAB 2009 to run on a PC compatible with Pentium IV, a 3.2 GHz processor and 2 GB of RAM (Random Access Memory). In this experiment, to start DE Algorithm, the population size is set to 20, the crossover constant is set to 0.8 and scaling mutation factor is set to 1. To start PSO approach, the population size is set to 20 particles, learning factors are set to 2 and inertia weight w is set based on a gradual decreasing from 0.9 to 0.4 with a linear decreasing rate. Static penalty method is applied for handling the constraints in both the algorithms. A total of 2,000 fitness function evaluations are made in each run for both the algorithms. The programs are executed 20 times for both the algorithms to see the convergence characteristics of both DE and PSO algorithms. The results obtained by the implementation of both the algorithms have been compared with the published results in Table 44.1. The result converges to 0.388 kW after 100 generations for DE algorithm and 0.369 kW after 60 generations for PSO algorithm and the best value obtained for both the algorithms is better than the published result of 1.362 kW obtained using analytical method and the result reported for GA i.e., 0.881 kW. In GA approach [15], binary coded string of length 27 is used to represent the chromosome that represents design variables. The population size is 85 and number of generations is 100. So a total of 8,500 fitness function evaluations were made with GA approach in each run whereas both DE and PSO Algorithms, implemented in the present work, use only 2,000 fitness function evaluations in each run. Also the statistical performance of the results obtained by 20 runs using both the algorithms implemented in this work clearly shows that the standard deviation is very small for both the algorithms in the range of 0.001. It clearly indicates that both DE and PSO algorithms performs well for the power loss minimization problem with minimum number of function evaluations and converges quickly to the global best solution than GA and analytical methods.

Table 44.1 Best result using DE and PSO algorithms for minimizing power loss of worm gear set

Method	Number of teeth of worm gear (Z_g)	Friction coefficient (μ)	Helix angle (γ_n)	Power loss (kW)
DE algorithm (present work)	45	0.0302	15.008°	0.388
PSO algorithm (present work)	45	0.0302	15.002°	0.369
GA [15]	46	0.0305	15.246°	0.881
Analytical method [15]	44	0.0390	16.280°	1.362

44.7 Conclusion

In this paper, two heuristic algorithms DE and PSO are proposed and applied to solve engineering design problem i.e., constrained optimization of input parameters to minimize the power loss of worm gear set. The simulation results presented in this paper demonstrate that both the algorithms tested are effective to improve the performance in preventing premature convergence to local minima. Both the proposed algorithms DE and PSO provide better and optimal solution than the results obtained by GA and previously published solutions for this problem. The simulation results show that both the algorithms converge to obtain solutions closer to the good solution and present a small standard deviation. In this work, PSO performs better in terms of accuracy and quicker convergence than DE. Also the problem can be converted into multiobjective optimization problem by adding one or two conflicting objective functions and the same can be solved using NSGA II as a future extension of the present work.

References

1. Storn R, Price K (1997) Differential evolution—a simple and efficient heuristic for global optimization over continuous spaces. J Global Optim 11:341–359
2. Kennedy V, Eberhart R (1995) Particle swarm optimization. In: Proceedings of the IEEE international conference on neural networks, pp 1942–1948
3. Deb K (1996) Optimization for engineering design: algorithms and examples. Prentice Hall, Englewood Cliffs
4. Bhandari VB (2010) Design of machine elements, McGraw Hill Education (India) Pvt Ltd
5. Gologlu C, Zeyveli M (2009) A genetic approach to automate preliminary design of gear drives. Comput Indus Eng 57:1043–1051
6. Caballero S, Colomerand V, Romero R (2008) Cylindrical parallel gear trains design by means of genetic optimization. In: Selected proceedings from the 12th international congress on project engineering, pp 150–160
7. Chong TH, Lee JS (2000) A design method of gear trains using a genetic algorithm. Int J Korean Soc Precis Eng 1(1):62–70
8. Mendi F, Baskal T (2010) Optimization of module, shaft diameter and rolling bearing for spur gear through genetic algorithm. Expert Syst Appl 37:8058–8064
9. Savsani V, Rao RV, Vakharia DP (2010) Optimal weight design of a gear train using particle swarm optimization and simulated annealing algorithms. Mech Mach Theory 45:531–541
10. Akay B, Karaboga D (2012) Artificial bee colony algorithm for large-scale problems and engineering design optimization. J Intell Manuf 23:1001–1014
11. Padmanabhan S, Chandrasekaran M, Srinivasa Raman V (2013) Worm gear drive optimization using modified artificial immune algorithm. J Curr Eng Res 3(1):48–51
12. Mogal YK, Wakchaure VD (2013) A multi-objective optimization approach for design of worm and worm wheel based on genetic algorithm. Bonfring Int J Man Mach Interface 3 (1):8–12

13. Su D, Peng W (2008) Optimum design of worm gears with multiple computer aided techniques. ICCES 6(4):221–227
14. Sabarinath P, Thansekhar MR, Saravanan R (2013) Performance evaluation of particle swarm optimization algorithm for optimal design of belt pulley system. Lecture notes in computer science, vol 8297, pp 601–616
15. Yaman M, Saruhan H, Mendi F (2006) Power loss optimization of a worm gear mechanism by using genetic algorithm. In: 11th international FIGES user conference for computer aided engineering and system modeling, Bolu, Turkey, 13–15 September, pp 1–7, ISBN 975-98408-2-0

Chapter 45
An Improved Buck Boost Converter Using Auxiliary Resonance for Photo Voltaic Based Dynamic Voltage Restorer

G. Ezhilarasan, Subhransu Sekar Dash and Chinmaya Samanta

Abstract Conventional Dynamic Voltage Restorers depend upon the grid for storing necessary energy that is required for sag and swell compensation. The objective of this work is to maximize the energy harvested from the PV cell using suitable DC–DC converter for maximization and stabilization of the energy harvested from the photovoltaic system. The maximization of energy harvested is done by increasing the efficiency of the dc–dc converter by using the concept of soft switching and resonance together. The converter discussed above was simulated using Power Sim software and it was compared with a laboratory setup.

Keywords DVR · Auxiliary resonant inverter · Sag · Swell

45.1 Introduction

Dynamic Voltage Restorer (DVR) provides the most cost effective solution to mitigate voltage sags, voltage swells by providing proper voltage quality level that is required by the sensitive loads. PV-DVR system has become a feasible solution for domestic and industrial loads [1].

The Converter proposed in this work is that might suitably fit for a DVR, since the DVR requires energy storage system and power DC–DC converters when fed

G. Ezhilarasan (✉)
Department of Electrical and Electronics Engineering, Saveetha University, Thandalam, Chennai 602105, India
e-mail: ezhil.power@gmail.com

S.S. Dash · C. Samanta
Department of Electrical and Electronics Engineering, SRM University, SRM Nagar, Kattankulathur, Kanchipuram 603205, India
e-mail: munu_2kdash@yahoo.com

C. Samanta
e-mail: chinmayasamanta99@gmail.com

C. Kamalakannan et al. (eds.), *Power Electronics and Renewable Energy Systems*,
Lecture Notes in Electrical Engineering 326, DOI 10.1007/978-81-322-2119-7_45

by renewable energy source like solar photovoltaic system [2]. The converters in this case has to be very efficient to maximize the energy harvested and suitably utilize the same for useful purpose. This in turn necessitates overall efficient system for the above.

The work is based on the following papers [3–6] where the concept of utilizing the DVR for mitigation of power quality problems without PV system is presented in [3]. Research work that been carried out on focusing the design and control of DVR [4]. In [6], Transients in DVR has been presented.

Form the above references it can be concluded that a DVR needs a high capacity DC storage system such as a battery storage system or using super capacitor. Using super capacitor as energy storage device for power quality improvement is presented in [2].

In the proposed work, a PV system with DC–DC boost converter is incorporated to function as a DC voltage source. The power for the entire DVR system is obtained through solar photovoltaic arrangement.

45.2 Description of the Switched Mode Power Supply for a DVR System

Recently, switch-mode power supplies has become smaller and lighter, because the switching frequency has increased. However, as the switching frequency has increased, the periodic losses at turn-ON/OFF have also increased. As a result, this loss brings down the efficiency. Therefore, to reduce these switching losses, a soft-switching method can be used, which involves an auxiliary circuit, instead of a hard-switching converter. A resonant converter as shown in Fig. 45.1 with auxiliary switch, main switch achieves soft-switching but auxiliary switch performs hard switching. Thus, these converters cannot improve the whole system efficiency owing to switching loss of auxiliary switch at normal frequency [7]. However during resonance, when the resonance current rises linearly, the load current gradually decreases. Thus, in order to reduce switching losses, the soft switching technology, which uses inductor and capacitor for resonance has been actively researched.

Fig. 45.1 Auxillary resonant Buck–Boost converter

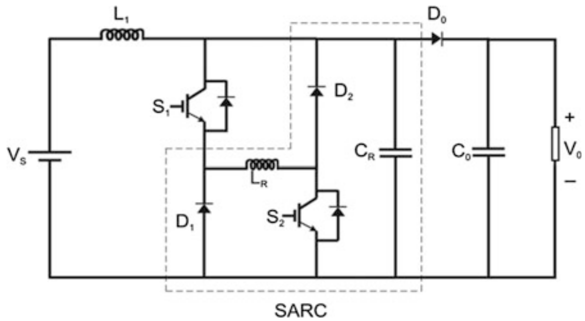

The proposed converter shown in Fig. 45.1, has an efficiency better than that of a conventional boost converter. Through this circuit, all of the switching devices performs soft-switching under zero-voltage and zero-current conditions. Therefore, the periodic losses occurring at turn-on and turn-off is decreased. The adopted soft switching boost converter was simulated by Power SIM (PSIM) software.

The auxiliary circuit discussed in [8] is composed of main switch (S_1), an auxiliary switch (S_2), a resonant capacitor (C_r), a resonant inductor (L_r), and two diodes (D_1 and D_2), as shown in Fig. 45.1. The operational principle of this converter can be divided into six intervals.

45.2.1 Interval-1 ($t_0 \leq t < t_1$)

In Fig. 45.1 of operating mode 1, Switches S1 and S2 are both in the OFF state, the current cannot flow through switches S_1 and S_2, and the accumulated energy of the main inductor is transferred to the load. In this interval, the main inductor current decreases linearly. During this time, the current does not flow to the resonant inductor, and the resonant capacitor has charged as output voltage.

After two of the switches have been turned-ON, interval-1 is over. These conditions are as follows:

$$v_L(t) = V_S - V_O \tag{45.1}$$

$$i_L(t) = i_L(t_0) - \frac{V_O - V_S}{V_L} t \tag{45.2}$$

$$\mathrm{i_{Do}(t) = i_L(t)} \tag{45.3}$$

$$i_{L_r}(t) = 0 \tag{45.4}$$

$$v_{Cr}(t) = V_O \tag{45.5}$$

45.2.2 Interval-2 ($t_1 \leq t < t_2$)

After turning on switches S_1, S_2, the current flows to the resonant inductor. At that time, two of the switches are turned-ON under zero-current condition. This is known as Zero-Current Switching (ZCS). Because the main and auxiliary switches implement ZCS, this converter has lower switch loss than the conventional hard switching converter. As the resonant current rises linearly, the load current gradually decreases. At t_2, the main inductor current equals the resonant inductor current, and the output diode current is zero. When the resonant capacitor voltage equals Vo, the output diode is turned-off, and interval-2 is over.

$$i_{L_r}(t_1) = 0 \tag{45.6}$$

$$V_{Lr}(t) = V_o \tag{45.7}$$

$$i_{Lr}(t) = (V_o/L_r)t \tag{45.8}$$

$$I_L(t) = I_{Lr}(t_2) \tag{45.9}$$

$$I_{\text{Do}}(t_2) = 0 \tag{45.10}$$

45.2.3 Interval-3 ($t_2 \leq t < t_3$)

The current that flowed to the load through output diode D_o no longer flows, since t_2 and the resonant capacitor C_r, and the resonant inductor L_r start a resonance. The current flowing to the resonant inductor is a combination of the main inductor current and the resonant capacitor current.

$$i_L(t) = I_{\min} \tag{45.11}$$

During this resonant period, the resonant capacitor C_r is discharged from V_o to zero. Resonant frequency and impedance are given by Eqs. (45.14) and (45.15). When the voltage of the resonant capacitor equals zero, the interval-3 is over.

$$v_{Cr}(t_2) = V_o \tag{45.12}$$

$$v_{Cr}(t_3) = 0 \tag{45.13}$$

$$\omega_r = \frac{1}{\sqrt{L_r C_r}} \tag{45.14}$$

$$Z_r = \sqrt{\frac{L_r}{C_r}} \tag{45.15}$$

45.2.4 Interval-4 ($t_3 \leq t < t_4$)

After the resonant period in interval-3, when the voltage of the resonant capacitor equals zero, interval-4 begins. In this interval, the freewheeling diodes of D_1 and D_2 are turned-ON, and the current of the resonant inductor is the maximum value. The resonant inductor current flows to the freewheeling diodes S1-Lr-D2 and S2-Lr-D1 along the feewheeling path.

$$\mathrm{i_{Lr}(t) = i_L(t) + i_{D1}(t) i_{D2}(t)} \tag{45.16}$$

$$i^{L}(t^{3}) = iL_r(t^{4}) = i^{L,\max} \tag{45.17}$$

During this time, the main inductor voltage equals the input voltage, and the current accumulating energy increases linearly

$$\mathrm{V_L(t) = V_S} \tag{45.18}$$

$$\mathrm{i_L(t) = I_{min} + (V_s/L)\,t} \tag{45.19}$$

45.2.5 Interval-5 ($t_4 \leq t < t_5$)

In interval-5, all of switches are turned-OFF under the zero voltage condition by the resonant capacitor. During this interval, the initial conditions of the resonant inductor current and resonant capacitor voltage are as follows:

$$i_{Lr}(t_4) = i_{Lr\max} \tag{45.20}$$

When all of the switches are turned-OFF, the resonant capacitor C_r is charged to the output voltage by two of the inductor currents. Until the resonant capacitor has been charged to V_o, the output diode is in the OFF state

$$i_{Lr}(t) = I_{\max} \tag{45.21}$$

45.2.6 Interval-6 ($t_5 \leq t < t_6$)

Interval-6 begins when the resonant capacitor equals the output voltage, and the output diode is turned-ON under the zero voltage condition. During this interval, the main inductor current i_L and the resonant inductor current iLr flow to the output through the output diode D_o

$$\mathrm{i_{D_o}(t) = i_L(t) + i_{Lr}(t)} \tag{45.22}$$

$$\mathrm{v_{Cr}(t) = V_o} \tag{45.23}$$

At that time, two of the inductor currents are linearly decreased, and the energy of the resonant inductor is completely transferred to the load. Then, the interval-6 is over

$$i_L(t) = \mathrm{I_{max}((V_o - V_s)/L_r)t} \tag{45.24}$$

45.3 Resonant Inductor and Capacitor

To satisfy the Zero-Voltage Switching (ZVS) condition [8], the resonant inductor current must exceed the main inductor current during the freewheeling interval of interval-4. For the maximum resonant current, the time of interval-3, which is the resonant time of the resonant inductor and capacitor, is defined as one-fourth of the resonant period. As a rule of thumb, the rising time of the resonant inductor current (intervals 2–3) can be set to 10 % of the min ON time.

$$t_2 - t_1 = L_r/V_o I_{min} \tag{45.25}$$

$$t_3 - t_2 = T_r/4 \tag{45.26}$$

$$(L_r/V_o)I_{min} + T_r/4 = 0.1DT \tag{45.27}$$

$$V_o/Z_r > \Delta\, i_L \tag{45.28}$$

45.4 Simulation Results

45.4.1 Open-Loop Circuit of Proposed Boost Converter

The adopted Soft-switching Boost Converter for input voltage of 200 V and switching frequency of 30 kHz is simulated using the PSIM software [3].

Figure 45.2 shows the voltage waveforms of the main switch. Via resonance of the resonant inductor and capacitor, ZVS and ZCS are achieved at turn-ON and turn-OFF.

Figure 45.3 shows the output voltage waveform in open loop which is obtained as follows: when the main switch is turned-ON, the energy of inductor is accumulated. When it is turned-OFF, this energy is transferred to the output.

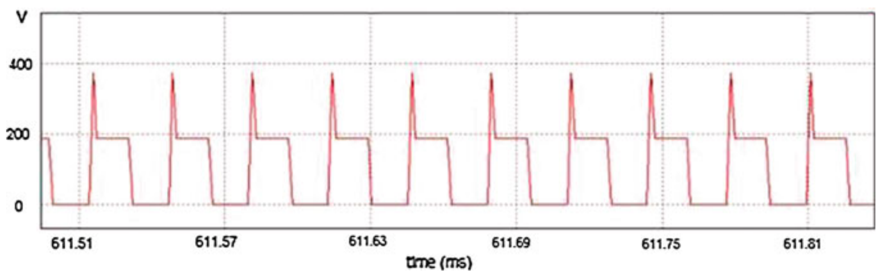

Fig. 45.2 Simulated waveforms of main switch voltage

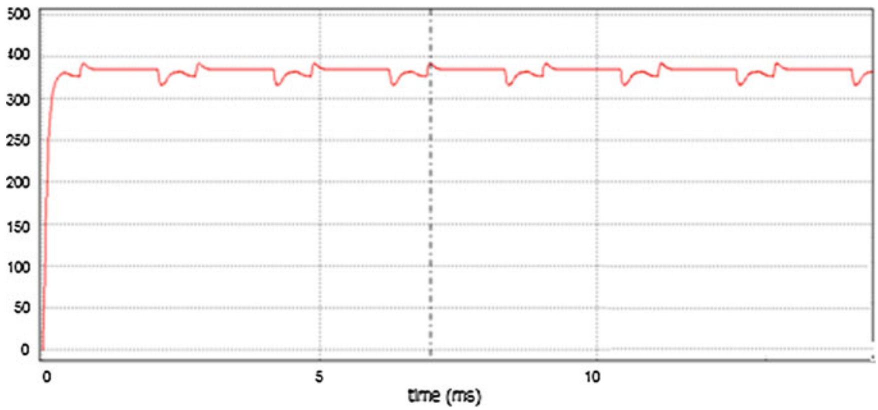

Fig. 45.3 Simulated waveform of output voltage in open-loop

45.4.2 Closed-Loop Circuit of Proposed Boost Converter

The Fig. 45.4 shows the output voltage of the closed-loop control of the boost converter shown in Fig. 45.1. In order to obtain a closed loop response, an electronic PI-controller with the use of op-amps is adopted here to control the output voltage for any change in the input voltage and the corresponding reference voltage.

The Proportional gain (K_p) and the Integral gain (K_I) are calculated by using Eqs. (45.29) and (45.30). The values of R1 = 1 K R2 = 2 K C = 0.1 μF were fixed by trial and error method

$$K_p = R_2/R_1 \tag{45.29}$$

$$K_i = 1/(R_2C) \tag{45.30}$$

45.4.3 Comparison Between Open-Loop and Closed-Loop Response

For the input voltage of 200 V and switching frequency of 30 kHz, the output voltage is compared with open-loop and closed-loop similar to comparison made in [4]. From the simulated waveform of output voltage in closed-loop as shown in Fig. 45.4, it is clearly noticed that the closed-loop has greatly improved the voltage profile, when compared with open-loop.

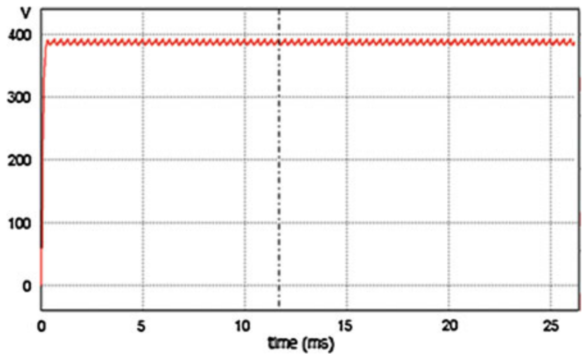

Fig. 45.4 Simulated waveform of output voltage in closed loop

Table 45.1 Comparison of response of the boost converters

Parameters	Basic boost converter	Resonant boost converter
Output voltage	398 V	401 V
Output current	8 A	8.4 A
Efficiency	93 %	95 %

45.5 Experimental Setup

This work was experimentally verified in the laboratory using discrete electronic components, first the basic boost converter was connected and its working performance was observed. The basic boost converter was then added with the resonant boost circuit and was tested in the open loop for its performance for the same load conditions used for basic boost converter. The PI controller was assembled as a separate circuit was added to the resonant boost converter and its performance was obtained. The results of the basic boost converter and the resonant boost converter is presented in Table 45.1.

45.6 Conclusion

A DC–DC converter for DVR system was designed and analyzed for the various operational modes in closed-loop control mode using Electronic PI- controller the comparison between soft switching and hard switching was experimentally validated. It can be observed that the efficiency of the resonant boost converter which uses soft switching techniques is more efficient compared to the hard switching based basic boost converter This soft-switching boost converter is easy to control because both the switches in the converter are controlled by the same gating signal. Moreover all the switching devices in this converter have achieved ZCS and ZVS conditions through the use of suitably designed resonant inductor and capacitor at turn-ON/OFF. As a result, the switching losses were reduced drastically. This Soft- switching Boost Converter is thus very much suitable for stand-alone and grid-connected PV systems.

References

1. Ashari M, Hiyama T, Pujiantara M, Suryoatmojo H, Hery Purnomo M (2011) A novel dynamic voltage restorer with outage handling capability using fuzzy logic controller. In: Proceedings of innovative computing, information and control conference, p 51
2. Moreno-Munoz A, de-la-Rosa JJG, Lopez-Rodriguez MA, Flores-Aries JM, Bellido-Outerino FJ, Ruiz-de-Adana M (2010) Improvement of power quality using distributed generation. Int J Electr Power Energy Syst 32(10):1069–1076
3. Boonchiam P, Mithulananthan N (2006) Understanding of dynamic voltage restorers through MATLAB simulation. Thammasat Int J Sic Tech 11(3):1–6
4. Ezoji H, Sheikholeslami A, Tabasi M, Saeednia MM (2009) Simulation of dynamic voltage restorer using hysteresis voltage control. Eur J Sci Res 27:152–166
5. Honrubia-Escribano A, Gomez-Lazaro E, Molina-Garcia A, Fuentes JA (2012) Influence of voltage dips on industrial equipment: analysis and assessment. Int J Electr Power Energy Syst 41:87–95
6. Ribeiro H, Marques H, Borges BV (2012) Characterizing and monitoring voltage transients as problem to sensitive loads. Int J Electr Power Energy Syst 43:1305–1317
7. Cha G-R, Park S-H, Won C-Y, Jung Y-C, Song S-H (2008) High efficiency soft switching boost converter for photovoltaic system. In: Proceedings of 13th EPE-PEMC, Sept 1–3, 2008, pp 383–397
8. Jain N, Jain PK, Joos G (2004) A zero voltage transition boost converter employing a soft switching auxiliary circuit with reduced conduction losses. Power Electr IEEE Trans 19 (1):130–139

Chapter 46
A Fuzzy Logic Controller Based Multi Converter UPQC to Enhance the Power Quality Problems

Paduchuri Chandra Babu, Subhransu Sekhar Dash, C. Subramani, Navya Tejaswini and Y. Sravan Kumar Reddy

Abstract A fuzzy logic controller based multiconverter unified power quality conditioner (MC-UPQC) to enhance the power quality issues. This newly designed controller is connected to a source in order to compensate voltage and current in the two feeders. In the proposed system the power can be conveyed from one feeder to another in order to mitigate the voltage sag, swell, interruption and transient response of the system. The control strategies of MC-UPQC are designed based on the MSRF theory with Fuzzy logic controller. The transient response of the fuzzy logic controller in dc-link voltage controller will be very fast. The relevant simulation and compensation performance analysis of proposed MC-UPQC with fuzzy logic controller is performed.

Keywords MC-UPQC · FLC · VSC · Power quality · MSRF theory

46.1 Introduction

An electrical power system consists of wide range of electrical and power electronic equipment in commercial and industrial applications. The quality of the power is effected by many factors like harmonic contamination, arc in arc furnace, sag and

---

P.C. Babu (✉) · S.S. Dash · C. Subramani · N. Tejaswini · Y. Sravan Kumar Reddy
Department of Electrical and Electronics Engineering, SRM University, SRM Nagar, Kattankulathur, Chennai 603203, India
e-mail: paduchuri.chandrababu@gmail.com

S.S. Dash
e-mail: munu_dash_2k@yahoo.com

C. Subramani
e-mail: csmsrm@gmail.com

N. Tejaswini
e-mail: knavya9@gmail.com

Y. Sravan Kumar Reddy
e-mail: sravan.yeee@gmail.com

C. Kamalakannan et al. (eds.), *Power Electronics and Renewable Energy Systems*, Lecture Notes in Electrical Engineering 326, DOI 10.1007/978-81-322-2119-7_46

swells due to the increment of non-linear loads such as large thyristor power converters, power electronics devices, voltage and current flickering, arc in arc furnaces and switching of loads respectively which also affects the sensitive loads to be fed from the system. In lightning strikes on transmission lines, the switching of capacitor banks and various network faults can also cause PQ problems. In order to meet PQ standard limits, it is necessary to include some sort of compensation [1]. The solutions can be found in the form of active rectification or active filtering [2]. The Shunt active power filter is suitable for the suppression of negative load influence on the supply network, supply voltage imperfections, a series active power filter may be needed to provide full compensation [3–8].

In all the above mentioned techniques PI controller is used for designed UPQC. In order to regulate the dc-link capacitor voltage, a conventional PI controller is used to maintain the dc-link voltage at the reference value. The conventional UPQC is also modified; with the new control techniques based on Modified Synchronous Reference Frame theory (MSRF) to overcome the power quality problems such as voltage current unbalance, harmonics, reactive power compensation, voltage sag, swell and interruptions.

46.2 Proposed System Description

46.2.1 Circuit Configuration

The MC-UPQC line diagram of a distribution system is shown in Fig. 46.1; two feeders connected to two different substations supply the loads Linear load $L1$, non linear load $L2$. The MC-UPQC is connected to two buses BUS1 and BUS2 with voltages of u_{t1} and u_{t2} and load L1 and L2 with a current of i_{l1} and i_{l2}. Sending end voltages are denoted by u_{s1} and u_{s2} while load voltages are u_{l1} and u_{l2}. Finally, feeder currents are denoted by i_{s1} and i_{s2}. The Bus voltages u_{t1} and u_{t2} are distorted and may be subjected to sag/swell.

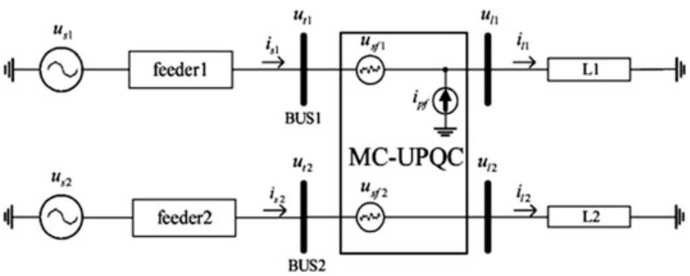

Fig. 46.1 Line diagram of a distribution system with an MC-UPQC

46.3 Design of Shunt and Series VSCs

46.3.1 The Control Scheme of the Shunt VSC

When compared to conventional method [2], the designed system of shunt VSC gives the better compensating of harmonics, reactive components of feeder one load current as well as to regulate the common dc-link capacitor voltage.

The three phase load currents for feeder one is transformed into load synchronous reference currents using Eq. (46.1).

$$\begin{bmatrix} i_{l-d} \\ i_{l-q} \\ i_{l-0} \end{bmatrix} = \begin{bmatrix} I_d \\ I_q \\ I_0 \end{bmatrix} \begin{bmatrix} i_{l-a} \\ i_{l-b} \\ i_{l-c} \end{bmatrix} \tag{46.1}$$

$$\begin{bmatrix} I_d \\ I_q \\ I_0 \end{bmatrix} = \frac{2}{3} \begin{bmatrix} \sin wt & \sin\left(wt - \frac{2\pi}{3}\right) & \sin\left(wt + \frac{2\pi}{3}\right) \\ \cos wt & \cos\left(wt - \frac{2\pi}{3}\right) & \cos\left(wt + \frac{2\pi}{3}\right) \\ 1/2 & 1/2 & 1/2 \end{bmatrix} \begin{bmatrix} I_a \\ I_b \\ I_c \end{bmatrix} \tag{46.2}$$

The fundamental direct axis component current is transferred into dc quantities using 2nd order LPF and it is added to the Fuzzy output to generate a new reference shunt feeder currents in Eqs. (46.3) and (46.4).

$$i_{f-d}^{ref} = \overline{i_{ld}} + \Delta I_{dc} \tag{46.3}$$

$$i_{f-q}^{ref} = i_{l-q} \tag{46.4}$$

The direct component of the feeder current is subjected to load direct dc components and quadrature components of the feeder current is subjected to zero. The new reference shunt feeder currents in Eqs. (46.3) and (46.4) are transformed back to the abc reference currents.

$$\begin{bmatrix} i_{f-a}^{ref} \\ i_{f-b}^{ref} \\ i_{f-c}^{ref} \end{bmatrix} = \begin{bmatrix} I_a \\ I_b \\ I_c \end{bmatrix} \begin{bmatrix} i_{f-d}^{ref} \\ i_{f-q}^{ref} \\ i_{f-0}^{ref} \end{bmatrix} \tag{46.5}$$

The shunt currents are added to the abc reference frame currents and it is sensed by the relay to control the currents.

46.3.2 The Control Scheme of the Shunt VSC

The MSRF based control algorithm for the shunt VSC block is shown in Fig. 46.2. When compared to conventional method [2], the proposed system of series VSC's gives the better compensation of voltage sag, swell and interruptions in feeder two alone. The series VSC block is based on the unit vector template by the new MSRF theory.

The three phase load voltages are transformed into load synchronous reference voltages using Eq. (46.6).

$$\begin{bmatrix} v_{l-d} \\ v_{l-q} \\ v_{l-0} \end{bmatrix} = \begin{bmatrix} v_d \\ v_q \\ v_0 \end{bmatrix} \begin{bmatrix} v_{l-a} \\ v_{l-b} \\ v_{l-c} \end{bmatrix} \tag{46.6}$$

$$\begin{bmatrix} v_d \\ v_q \\ v_0 \end{bmatrix} = \frac{2}{3} \begin{bmatrix} \sin wt & \sin\left(wt - \frac{2\pi}{3}\right) & \sin\left(wt + \frac{2\pi}{3}\right) \\ \cos wt & \cos\left(wt - \frac{2\pi}{3}\right) & \cos\left(wt + \frac{2\pi}{3}\right) \\ 1/2 & 1/2 & 1/2 \end{bmatrix} \begin{bmatrix} v_a \\ v_b \\ v_c \end{bmatrix} \tag{46.7}$$

The expected load Synchronous reference dqo voltages is subtracted to the V_{l-dqo} in Eq. (46.8) and its compensation reference feeder dqo voltages is transformed back to the synchronous reference feeder voltages using Eq. (46.9).

$$\begin{bmatrix} v_{f-d}^{ref} \\ v_{f-q}^{ref} \\ v_{f-0}^{ref} \end{bmatrix} = \begin{bmatrix} v_{l-d} \\ v_{l-q} \\ v_{l-0} \end{bmatrix} - \begin{bmatrix} v_{l-d}^{exp} \\ v_{l-q}^{exp} \\ v_{l-0}^{exp} \end{bmatrix} \tag{46.8}$$

$$\begin{bmatrix} v_{sf-a}^{ref} \\ v_{sf-b}^{ref} \\ v_{sf-c}^{ref} \end{bmatrix} = \begin{bmatrix} v_d \\ v_q \\ v_0 \end{bmatrix}^{-1} \begin{bmatrix} v_{f-d}^{ref} \\ v_{f-q}^{ref} \\ v_{f-0}^{ref} \end{bmatrix} \tag{46.9}$$

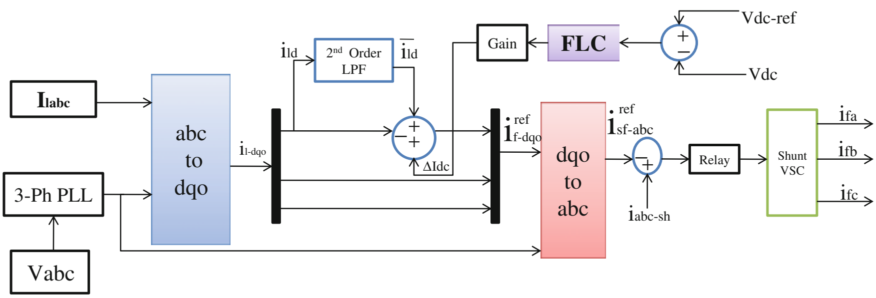

Fig. 46.2 SRF based control strategy of the shunt VSC

The output of the PWM generator compensation voltage is directly given to control part of series VSC.

46.4 Simulation Block Diagrams

The series VSC simulation control block diagram is shown in Fig. 46.3. In series VSC the measured load current is transformed into the synchronous dq0 reference frame by using Eq. 46.5. The reference current in (46.9) is then transformed back into the abc reference frame.

46.4.1 Design of Source Controller

The new source controller is designed using normal continuous sine wave. Changing the amplitude, angular frequency, phase sequence we can get the discrete sine wave form. The below Eqs. (46.10), (46.11), (46.12) shows the source of A, B, C for sine wave form.

$$\text{Source A} = [\text{sw}1 + (\text{sw}4 \times \text{t}1)] \times \text{Vp - p rms} \times \text{t}2 \tag{46.10}$$

$$\text{Source B} = [\text{sw}3 + (\text{sw}6 \times \text{t}1)] \times \text{Vp - p rms} \times \text{t}2 \tag{46.11}$$

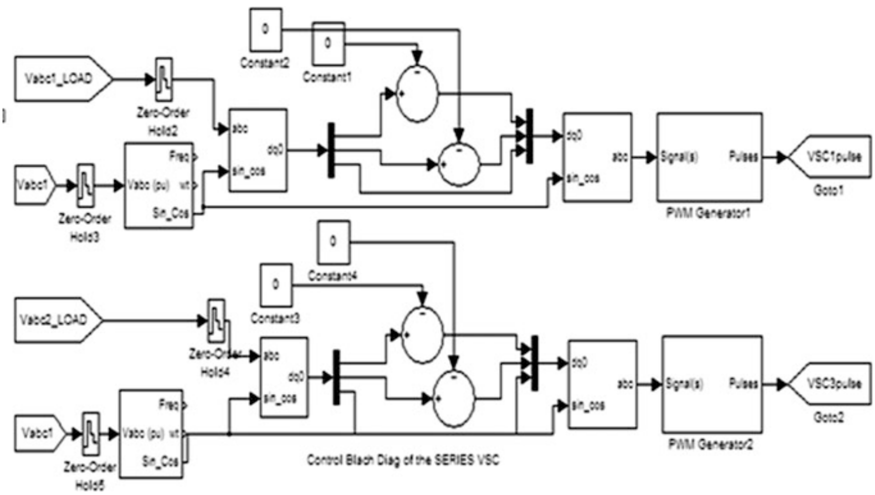

Fig. 46.3 Simulation control block diagram of the series VSC

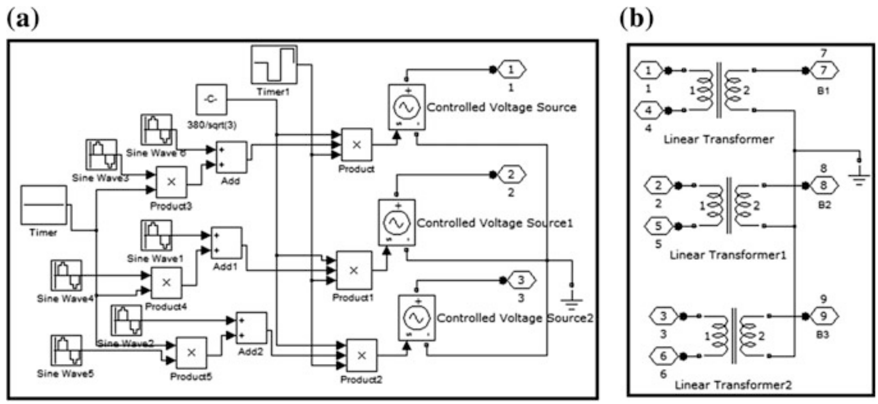

Fig. 46.4 Simulation circuit diagram of **a** pure sinusoidal supply voltage and **b** linear series transformer

Table 46.1 Active and reactive power for load and source side

	Without MC-UPQC		With MC-UPQC	
System	P (W)	Q (VAR)	P (W)	Q (VAR)
Source side	13.82	13.58	466.6	1,170
Load side	1.745	13.58	45.23	−4.827

$$\text{Source C} = [\text{sw5} + (\text{sw2} \times \text{t1})] \times \text{Vp - p rms} \times \text{t2} \tag{46.12}$$

Here Sw1 to Sw6 are the switches, t1 and t2 are the timer values, bias value is zero, phase degree is 120° phase shift. Using sample based sine wave type if numerical problems due to running for large time error. The simulation circuit diagram of pure sinusoidal supply voltage is shown in Fig. 46.4a and linear series transformer is shown in (b).

The load and source active and reactive powers are calculated without and with MC-UPQC is connected to system are shown in Table 46.1. The Simulation circuit diagram of Multi Converter-UPQC (MC-UPQC) is connected in a distribution system is shown in Fig. 46.5.

46.5 Simulation Results and Discussion

The simulation results of MC-UPQC are shown in below figures. In this section, calculating sag/swell, Harmonic for bus1, bus2, load side, source side in feeder1 and 2.

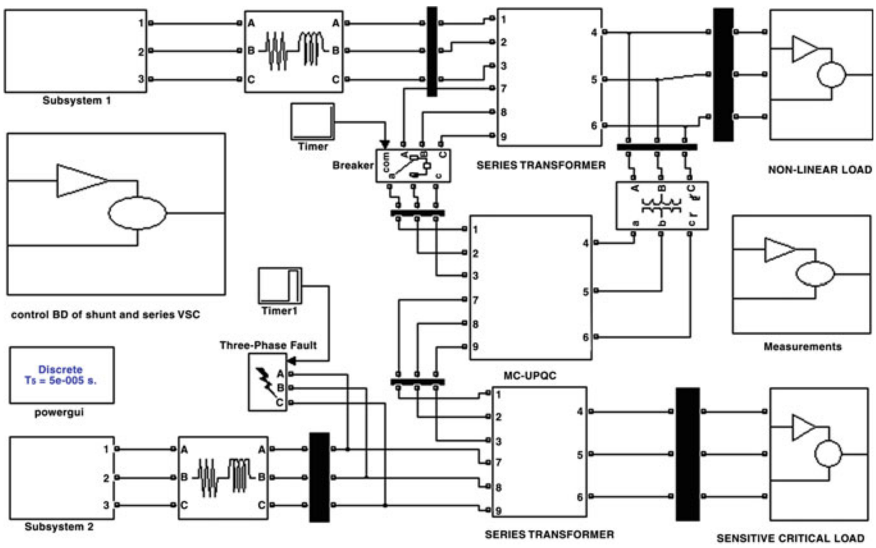

Fig. 46.5 Simulation circuit diagram of MC-UPQC is connected in a distribution system

46.5.1 The Bus Voltage on Distortion and Sag/Swell

The BUS1 voltage contains 37.50 % sag between 0.1–0.2 s and swells 134 % between 0.2–0.3 s. The BUS2 voltage contains 34 % sag between 0.15–0.2 s and swells 130 % between 0.25–0.3 s.

The MC–UPQC is switched on at t = 0.02 s. The BUS1 voltage and harmonic spectrum are shown Fig. 46.6, the corresponding compensation voltage injected by

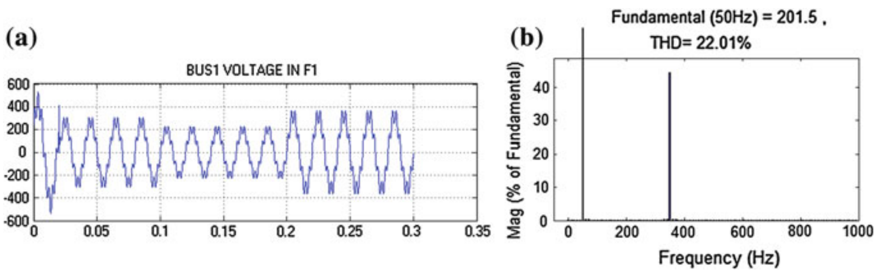

Fig. 46.6 Simulation results of **a** BUS 1 voltage in Feeder 1. **b** Harmonics spectrum for BUS 1 voltage

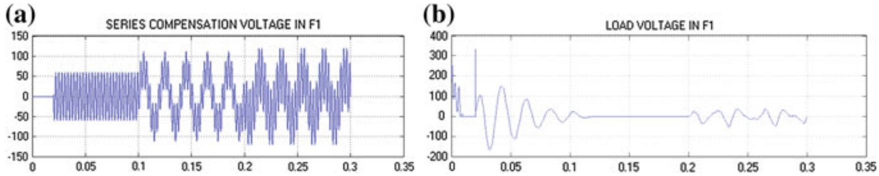

Fig. 46.7 Simulation results of **a** series compensating voltage in feeder 1 and **b** load voltage in feeder 1

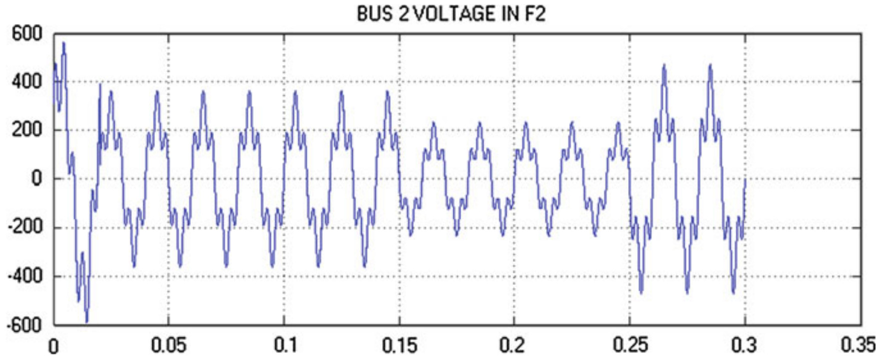

Fig. 46.8 Simulation results of bus 2 voltage in feeder 2

VSC1 is shown in Fig. 46.7a and load L1 voltage are shown in Fig. 46.7b. The distorted voltages of BUS1 and BUS2 are satisfactorily compensated for across the loads L1 and L2 with very good dynamic response. Similarly, the BUS2 voltage are shown in Fig. 46.8, corresponding compensation voltage injected by VSC3 is shown in Fig. 46.9a and the load L2 voltage are shown in Fig. 46.9b. Feeder1 current are shown in Fig. 46.10a. The distorted nonlinear load current is compensated and the THD of the feeder current is reduced from 14.68 to 3.49 % is shown in Fig. 46.10b. THD values for without and with MC-UPQC are shown in Table 46.2.

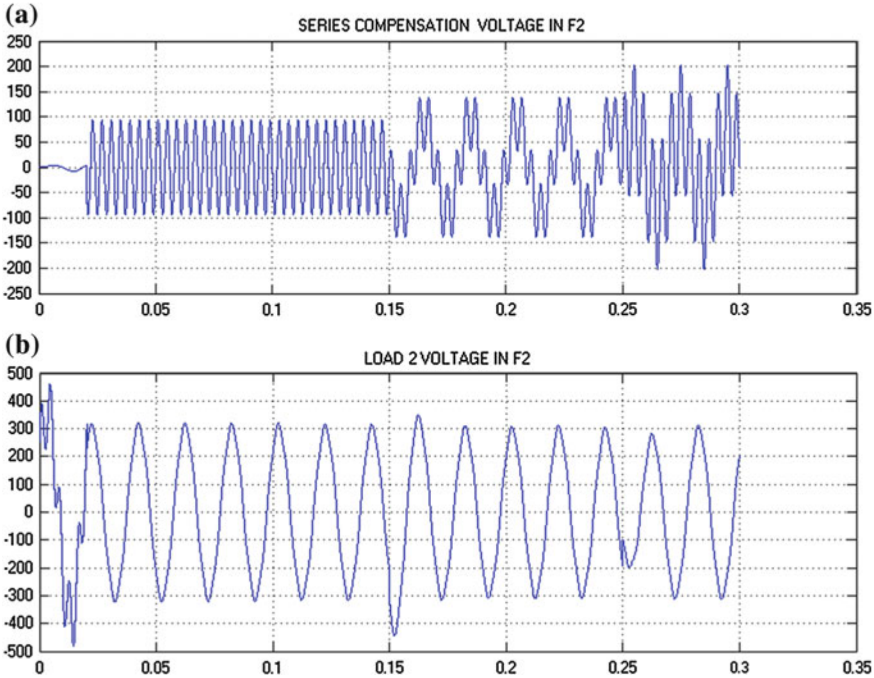

Fig. 46.9 Simulation results of **a** series compensating voltage in feeder 2 and **b** load voltage in feeder 2

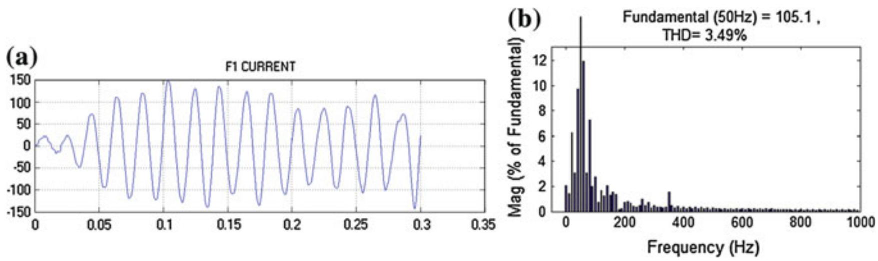

Fig. 46.10 Simulation results of **a** feeder 1 current and **b** harmonics spectrum for feeder 1 current

Table 46.2 Percentage THD values of without and with MC-UPQC

System voltage/current	Without MP-UPQC		With MP-UPQC	
	Percentage THD	Switching freq. (Hz)	Percentage THD	Switching freq. (Hz)
Bus1 voltage	21.92	327.6	22.01	201.5
Series compensation voltage	21.92	2674	65.91	67.2
Load 1 voltage	190.76	4.993	38.9	2.983
Bus 2 voltage	35.08	298.7	34.97	174.6
Series compensation voltage	14.11	8,004	64.92	94.1
Load 2 voltage	46.49	176.8	**4.30**	315.3
Non-linear load current	15.64	10.85	14.68	127.7
Shunt filter current	31.05	1.317×10^{-6}	17.62	106.8
Feeder 1 current	15.64	13.29	**3.49**	105.1

46.6 Conclusion

The design of a new source controller and Multi-Converter Unified Power Quality Conditioner (MC-UPQC) connected to 3P3 W system has been presented in this paper. By using FLC with MC-UPQC dc-link voltage controller it is observed that transient response is attained very fast. The distorted Non-linear load current is compensated very well. The harmonic components and unbalance of bus1 voltage are compensated for by injecting the proper series voltage.

References

1. Mohammadi HR, Varjani AY, Mokhtaria H (2009) Muti converter unified power-quality conditioning system: MC-UPQC. IEEE Trans Power Deliv 24(3):1679–1686
2. Babu PC, Dash SS (2012) Design of unified power quality conditioner (UPQC) to improve the power quality problems by using P-Q Theory. In: Proceedings of 2012 IEEE international conference on computer communication and informatics, ICCCI 2012, vol 3, no 1, pp 1–7, Jan 2012
3. Mokhtatpour A, Shayanfar HA (2011) Power quality compensation as well as power flow control using of unified power quality conditioner. In: Power and energy engineering conference (APPEEC), 2011 Asia-Pacific, pp 1–4: 25–28 Mar 2011
4. Rajasekaran D, Dash SS, Vignesh P (2011) Mitigation of voltage sags and voltage swells by dynamic voltage restorer. IET Semin Dig 2011(2):36–40
5. Leela S, Dash SS (2013) Modelling and simulation of SVM based DVR system for voltage sag mitigation. Res J Appl Sci Eng Technol 6(23):4424–4431
6. Premalatha S, Dash SS, Babu PC Power quality improvement features for a distributed generation system using shunt active power filter. Procedia Eng 64: 265–274

7. Babu PC, Dash SS (2012) Design of unified power quality conditioner (UPQC) to improve the power quality problems by using P-Q theory. In: 2012 International conference on computer communication and informatics, Jan 2012, pp 1–7
8. Reddy UV, Babu PC, Dash SS (2013) Space vector pulse width modulation based DVR to mitigate voltage sag and swell. In: 2013 International conference on computer communication and informatics, Jan 2013, pp 1–5

Chapter 47
Artificial Neural Network and Fuzzy Logic Controlled Single Phase Active Power Line Conditioner Under Non Sinusoidal Supply Condition: A Comparison

D. Kavitha, P. Renuga and V. Suresh Kumar

Abstract The harmonic reduction and power factor improvement are conflict to each other under non sinusoidal supply conditions. Optimization of total harmonic distortion (THD) and power factor subjected to power quality constraints for the evaluation of proposed APLC is carried out in this paper. Non dominated sorting genetic algorithm-II is used to obtain the reference source current to optimize both power factor and THD. The proposed APLC is evaluated using neural network and fuzzy logic. Neural network is trained from the samples obtained using conventional fixed frequency variable slope (FFVS) method. Fuzzy logic rule base is created from the same samples. Computer simulations of the proposed APLC have been performed using MATLAB and the results are encouraging. The results show that the proposed APLC can reduce the total harmonics distortion of a specific non-linear load from 13 % to about 3 % and improve the power factor close to unity under non sinusoidal conditions.

Keywords Non sinusoidal supply · Active power line conditioner · NSGA-II · Neural networks · Fuzzy logic · Harmonics · Power factor

D. Kavitha (✉) · P. Renuga · V. Suresh Kumar
Department of Electrical and Electronics Engineering,
Thiagarajar College of Engineeering, Madurai 625015, Tamilnadu, India
e-mail: dkavitha@tce.edu

P. Renuga
e-mail: preee@tce.edu

V. Suresh Kumar
e-mail: vskeee@tce.edu

C. Kamalakannan et al. (eds.), *Power Electronics and Renewable Energy Systems*,
Lecture Notes in Electrical Engineering 326, DOI 10.1007/978-81-322-2119-7_47

47.1 Introduction

The undesirable effects of harmonics are well identified and explained in literatures for the last 3 decades [1]. Hence harmonics has to be maintained within the limits [2]. The purpose of an active power line conditioner is to compensate the utility line current waveform so that it approximates a sine wave in phase with the line voltage when a nonlinear load is connected to the system. The APLC not only works as a harmonic compensator but also as a power factor corrector. The use of power electronic circuits in a wide range of applications has resulted in distorted current waveforms in the power system. This results in non-sinusoidal voltage drops across the transformers and transmission line impedances, resulting in a non-sinusoidal voltage supply at the point of common coupling. The requirements of harmonic free current waveforms and good power factor, under non- sinusoidal voltage conditions, are contradictory to each other [3]. Under these conditions, an optimum performance is the best one can achieve. This paper proposes a new scheme to compromise between the power factor and current distortion under non sinusoidal voltage conditions.

The conventional passive filters have the limitations of fixed compensation, large size and can also excite resonance conditions [4]. Hence shunt active power filters are introduced as a viable alternative to compensate harmonics and improve power factor [5]. In early APF designs, PWM based methods such as constant frequency control, sliding mode control, hysteresis control, and triangular waveform control are used to control the switches in the APF [6]. The main shortcoming of this method is that, in order to obtain optimum results, relatively high switching frequencies are needed, which subsequently leads to high switching losses. Neural network techniques were successfully applied to frequency domain APLC control [4].

In the artificial intelligence based APLC [7–9], a single objective function is considered to mitigate harmonics. The optimization of power factor while reducing the harmonics is not included. Harmonics is treated in a constraint where normally it is kept under the limit specified by IEEE standard. In practical situations, harmonics injecting loads are in abundance and definitely the limit will be violated if new additional loads are installed. Hence an attempt is made to compensate both power factor and harmonics. In this work, the harmonics in the load current is estimated using adaptive neural network [10]. Non dominated sorting genetic algorithm-II (NSGA-II) [11, 12] is used to optimize the compensation current tobe produced by the APLC to optimize the power factor and THD subjected to power quality constraints. Then the output (compensation current) of APLC is controlled using conventional FFVS method and neural network [11]. As the time taken by FFVS method is considerably large, it is not suitable for online operations. Hence a high speed neural network controller and fuzzy logic controller are proposed. The FFVS method is used to obtain the training samples for neural network and data base for fuzzy logic because of its accuracy.

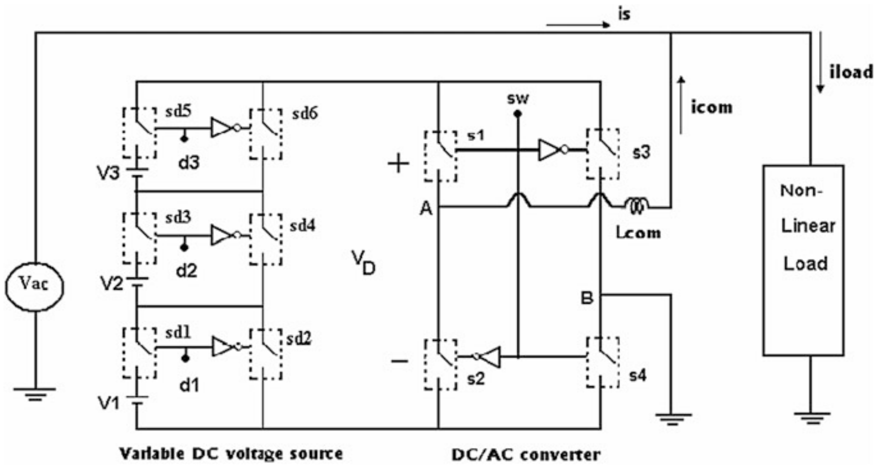

Fig. 47.1 Voltage type APLC

47.2 Active Power Line Conditioner (APLC)

The APLC is illustrated in Fig. 47.1 [8]. Basically it consists of two primary components, variable DC voltage source (VDVS) and DC/AC converter. Voltage V_{AB} has fifteen possible combinations of the four on-off control signals sw, d_1, d_2, d_3 [8].

Under non sinusoidal supply conditions, unity power factor is achieved by making the source current identical in phase and of identical shape as that of voltage, in all the phases. When the source current is made to have the same shape as voltage, current THD may rise beyond the acceptable limit. To obtain perfect harmonic compensation, current drawn from the source needs to be a perfect sine wave. However, in that case, unity power factor is not realized. Hence, there is a need to optimize the power factor, satisfying power demand and current harmonic limit, apart from achieving a balanced source current in the system. Initially the load current I_L is estimated using adaptive neural net [10]. The desired or reference source current $i_s^*(t)$ is obtained by solving the multi objective optimization problem using NSGA-II.

47.3 Estimation of Reference Current

The first objective function is to minimize the THD in the source current. The frequency components in the supply current and supply voltage should be identical and the corresponding phase angles should be zero to make power factor unity. But in this case the harmonic effect cannot be completely nullified. Hence there is a need of optimum reference current generation to mitigate the harmonics and to improve the power factor. The desired source current should be calculated in such a way that, it should supply the constant active power demanded by the load. As active power remains constant the only way to improve the power factor is to minimize the apparent power supplied from the source and it is considered to be the second objective function [3]. Let

$$I_{pi} = g_i V_{pi} \tag{47.1}$$

Then, Objective functions are:

$$\text{Minimize } THD^2 = \sum_{i=2}^{n} I_{pi}^2 / I_{p1}^2, \text{ and} \tag{47.2}$$

$$\text{Minimize } S^2 = \frac{1}{4} \sum_{i=1}^{n} V_{pi}^2 \sum_{i=1}^{n} I_{pi}^2 \tag{47.3}$$

Subject to constraints, Active power balance,

$$P = \frac{1}{2} \sum_{i=1}^{n} V_{pi} I_{pi} \tag{47.4}$$

$$P = \frac{1}{2} \sum_{i=1}^{n} g_i V_{pi}^2 \tag{47.5}$$

The other constraint of the problem is selective harmonic elimination.

$$\frac{I_{pi}}{I_{p1}} < SHL_i \tag{47.6}$$

The desired or reference source current for fundamental frequency of 50 Hz under non sinusoidal supply is given by

$$\mathrm{i}_{\mathrm{s}}^*(\mathrm{t}) = \sum_{\mathrm{i}=1}^{n} I_{pi} \sin(100\pi i t + \phi_i) \tag{47.7}$$

where ϕ_i is the phase angle of ith harmonic of estimated voltage. The compensation current $\mathrm{i}_{\mathrm{com}}^*(\mathrm{t})$ tobe injected by APLC is,

$$i_{com}^*(t) = I_L - \mathrm{i}_s^*(\mathrm{t}) \tag{47.8}$$

The task of the APLC is to produce an actual compensation current $\mathrm{i}_{\mathrm{com}}(\mathrm{t})$ that will be closely track $\mathrm{i}_{\mathrm{com}}^*(\mathrm{t})$.

47.4 Estimation of Switching Signals of APLC

In this paper, a suitable strategy is required to estimate the switching signals of APLC. In this work, neural network and fuzzy logic techniques are used independently to obtain the switching states of APLC.

47.4.1 Neural Network Based APLC

Multilayer perceptron with one hidden layer is used. One hidden layer consists of p neurons. The neural network is implemented in software and trained off line using the FFVS control scheme. Back propagation algorithm is used for training. The training data obtained with the FFVS method are built up from a collection of 400 typical nonlinear load current waveforms. Back propagation training produces optimum weight matrices for the neural network to be used in on line control. In this problem, the number of neurons in input, hidden and output layer is 32 each. These numbers are fixed based on number of switching to be given to APLC. For a 50 Hz system, the switching frequency is 50 × 32 = 1,600 Hz.

47.4.2 Fuzzy Logic Based APLC

Fuzzification converts input data into suitable linguistic values. Each sensed input is compared to a set of possible linguistic variables to determine membership. It is composed of seven triangular shaped membership functions with the relevant linguistic labels shown. The fuzzification function is given by $f:[-a, a] \rightarrow [0, 1]$ and is applied to the variable $I_{com}(T_{n+1}) - I_{com}(T_n)$ in order to approximate their measurement uncertainties with values between 0.0 and 1.0. By analyzing the knowledge base of the proposed APLC, the value of 'a' is taken as 45 in the considered high load current system. It consists of a database with the necessary linguistic definitions (rule set). Each rule has an antecedent statement with an associated fuzzy relation. Degree of membership for antecedent is computed. If (Antecedent) Then (Consequence).

Hence,

$$\{I_{com}(T_{n+1}) - I_{com}(T_n)\} + V_s(T_n) \propto V_{AB} \tag{47.9}$$

The variable to be determined is V_{AB}.

Let

$$T = V_{AB} - V_s(T_n) \tag{47.10}$$

Then,

$$I_{com}(T_{n+1}) - I_{com}(T_n) \propto T \tag{47.11}$$

From the knowledge of the characteristics of the system, fuzzy variable quantization and rule base is formed [8]. The Center of Gravity method is used to obtain the inferred (numerical) value of the control action.

Then,

$$V_{AB} = T + V_s(T_n) \tag{47.12}$$

47.5 Results and Discussions

The test system used in this work comprises of a two bus single phase system with nonlinear loads at the load bus. The voltage at the point of common coupling is made distorted by adding third and fifth order harmonics to a fundamental frequency supply of 50 Hz. The load current I_L is estimated using adaptive neural network up to 13th order and NSGA-II is used to solve the above stated optimization problem and computes the reference source current $i^*_s(t)$ using (47.8). The genetic parameters of NSGA-II are as follows: Number of population = 50; Number of generations = 250; Number of runs = 15; Simulated binary crossover with cross over index, $\zeta c = 5$, and mutation index, $\zeta m = 20$; Tournament selection and penalty less constraint handling method [12] is adopted. From the Pareto front obtained for various load cases considered from lower values of current to higher values of current, it is seen that the power factor can be better optimized when THD value is about 2 %. The Pareto front obtained for the sample case for 185 A and the load current is shown in Fig. 47.2. The objective function I in the Fig. 47.2 represents the

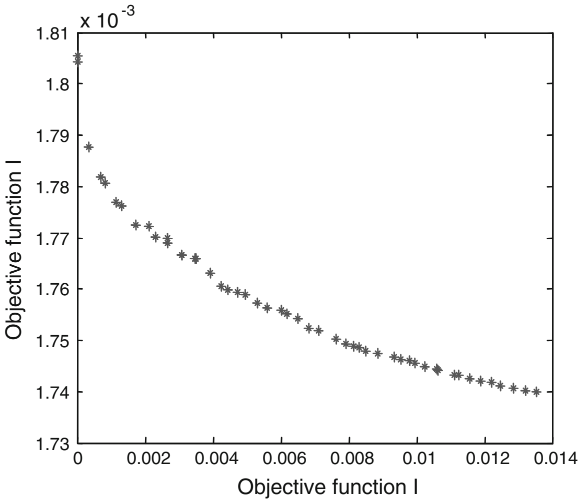

Fig. 47.2 Paretofront obtained from NSGA-II for 185 A

Table 47.1 Results obtained from Pareto front for case 1: 185 A

S. No	THD (%)	Power factor
1	0	0.97
2	2	0.9836
3	5	0.9896
4	7	0.9915
5	10	0.9951

square of THD and objective function II represents the normalized value of the square of apparent power delivered to the load. The objective function values are provided in Table 47.1. From the population of NSGA-II, the operating point is selected when THD is about 2 %. This selection ensures that THD will within limit of 5 % including the error in the injection of current from APLC. The values selected for simulation is L = 1 mH for high current load.

Case 1: In this case, the APLC output (compensation current) is generated using Neural network control technique. The conventional FFVS method is used to obtain the training samples for neural network because of its accuracy. By using FFVS technique, 400 training data are computed and neural net is trained. For on-line operation, the APLC monitors both the source current and the load current. When it determines that the source current THD is higher than allowable limit, the well trained NN controller takes a number of equally spaced samples from one 50 Hz cycle of the load current and produces control signals for the 10 switches in the APLC. APLC output states and the actual output current of the APLC compared with the reference compensation current are shown in Fig. 47.3. The source current before compensation is distorted, but the compensated line current is almost sinusoidal.

After injecting the compensation current through the APLC, the THD is reduced to about 2 % from 13 % and the power factor is improved from 0.82 to 0.9836. Table 47.2 shows the variation in the THD and power factor level for a non-sinusoidal supply conditions if the reference current is evaluated with and without optimization using NSGA-II for. From the results, it is seen that if the

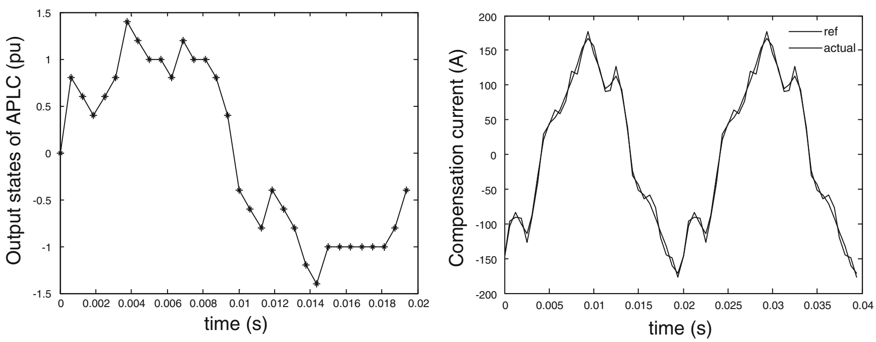

Fig. 47.3 APLC output states and comparison of reference and actual I_{com} for 185 A

Table 47.2 Results of neural network based APLC

Reference current	THD (%)		Power factor	
	Before compensation	After compensation	Before compensation	After compensation
Non-optimized	12.56	1.8	0.8205	0.968
Optimized	12.56	2.4	0.8205	0.981

reference current is obtained after optimizing the objective functions, the tradeoff between THD and power factor is achieved.

Case 2: In case 2, Fuzzy logic controller is designed for the same system. By using FFVS technique, 400 data are computed and fuzzy rule base [8] is formed. Error is calculated as the difference between actual output of APLC and reference value at each instant. Based on the values of present error and change in error, the decision of APLC output state is taken. After injecting the compensation current through the APLC, the THD is reduced to about 3 % from 13 % and the power factor is improved from 0.83 to 0.98. The harmonic spectrum of source current before and after compensation is shown in Fig. 47.4.

The numeric values of THD and power factor before and after compensation is given in Table 47.3 for the Fuzzy based APLC. It is evident from Tables 47.2 and 47.3 that the compensation for harmonics and power factor is better when APLC is controlled by NN based controller than fuzzy logic based method. Also time taken by NN based APLC is considerably less and it is well suitable for online operations.

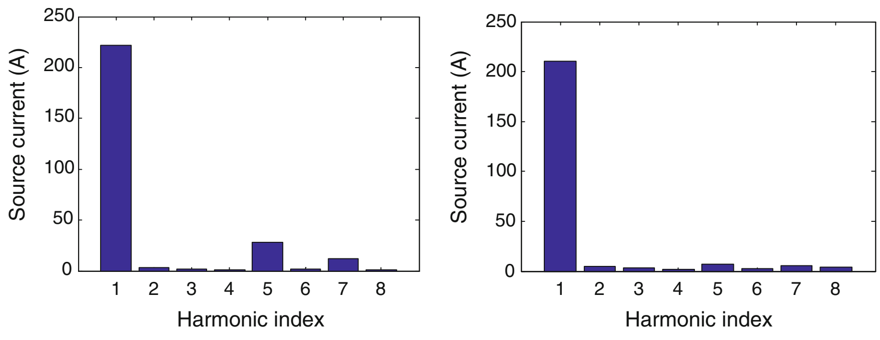

Fig. 47.4 Harmonic spectrum of current before and after compensation

Table 47.3 Results of fuzzy logic based APLC

	THD (%)	Power factor
Before compensation	12.56	0.82
After compensation	3.17	0.98

47.6 Conclusion

A flexible algorithm was proposed to limit the total and individual harmonic distortion and to improve the power factor under non-sinusoidal supply current conditions. The proposed APLC was controlled using neural network and fuzzy logic. They were used to estimate compensation current in on line accurately and previously NSGA-II algorithm was used to optimize the estimated line current in off line. Exhaustive simulations were carried out with different load conditions. Based on the simulation results, it is found that the proposed active power line conditioner perform satisfactorily, for the compensation of harmonics and reactive power. It makes the line current waveform as close as possible to a sinusoid and improves the power factor actually by reducing the apparent power supplied by the utility.

References

1. Owen EL (1998) History of harmonics in power system. IEEE Trans Ind Appl Mag pp 6–12
2. IEEE recommended practices and requirements for harmonic control in electrical power systems. ANSI/IEEE Std.519 (1992)
3. George S, Agarwal V (2008) Optimum control of selective and total harmonic distortion in current and voltage under nonsinusoidal conditions. IEEE Trans Power Delivery 23(2)
4. Au MT, Milanovic JV (2007) Planning approaches for the strategic placement of passive harmonic filters in radial distribution networks. IEEE Trans Power Delivery 22(1):347–353
5. Cheng P-T, Bhattacharya S, Divan D (2000) Experimental verification of dominant harmonic active filter for high-power applications. IEEE Trans Ind Appl 36(2):567–577
6. Battista HD, Mantz RJ (2000) Harmonic series compensators in power systems: their control via sliding mode. IEEE Trans Control Syst 8:939–947
7. Wang Y-J, O'connell RM (2000) Experimental evaluation of an active power line conditioner based on a neural control scheme. IEEE 2000, pp 493–497
8. Kirawanich P, O'connell RM (2004) Fuzzy logic control of an active power line conditioner. IEEE Trans Power Electron 19(6):1574–1585
9. Suresh Kumar V, Kavitha D, Kalaiselvi K, Kannan PS (2008) harmonic mitigation and power factor improvement using fuzzy logic and neural network controlled active power filter. J Electr Eng Technol 3(3):520–527
10. Suresh Kumar V, Kavitha D, Kalaiselvi K, Kannan PS (2007) Optimal estimation of harmonics in power system using intelligent computing techniques. In: Proceedings of IEEE neural networks conference, Orlando, USA
11. Srinivas N, Deb K (1994) Multi-objective optimization using non-dominated sorting in genetic algorithms. Evol Comput 2(3):221–248 (Fall 1994)
12. Deb K (2001) Multi-objective optimization using evolutionary algorithms. Wiley, New York

Chapter 48
Design and Implementation of SMR Based Bidirectional Laptop Adapter

M. Gowrinathan, V. Devi Maheswaran and V.T. Sreedevi

Abstract Rechargeable batteries are now widely used in many applications. The bidirectional adapter having the function of charging and discharging provides 230 V/50 Hz emergency output form the battery embedded in a UPS, Electrical Vehicles and other possible appliances. This bidirectional adapter having the function of for the forward mode providing the AC power and reverse mode providing a DC power from the battery to the critical power appliances. In forward mode, a front end DC/DC converter is equipped to establish a boosted DC link voltage from battery. This DC is inverted into emergency source for critical power appliances using H-Bridge converter. The output AC sinusoidal voltage obtained with inverter circuit. Conversely in charging mode, a Switch Mode Rectifier (SMR) based charger is formed using Intelligent Power Module. The two power stages are implemented using Intelligent Power Module. This Intelligent Power Module consists of one converter module and inverter module. In the proposed power module, the design and implementation of switch mode rectifier (SMR) based bidirectional laptop adapter is being simulated and the result are being presented [1, 2].

Keywords DC/DC Buck-boost converter · Emergency power · Inverter · Laptop computer · Intelligent power module · Battery · Power factor correction · Robust control

M. Gowrinathan (✉) · V. Devi Maheswaran
Rajalakshmi Engineering College, Thandalam, Chennai, India
e-mail: gowrinathan2009@gmail.com

V. Devi Maheswaran
e-mail: devimaheswaran.v@gmail.com

V.T. Sreedevi
Vellore Institute Technology, Chennai, India
e-mail: sreedevi.vt@vit.ac.in

C. Kamalakannan et al. (eds.), *Power Electronics and Renewable Energy Systems*,
Lecture Notes in Electrical Engineering 326, DOI 10.1007/978-81-322-2119-7_48

48.1 Introduction

Electricity is most essential part required for the basic needs of the human and the growth of any nation. The new generation people are focusing on renewable energy particularly in solar power and wind power generation. The solar power and battery based converter circuit is formulated for the bidirectional adapter because of low cost high efficiency. Battery used as main source of energy for the various applications, such as personal digital assistance (PDA), uninterruptible power supply (UPS), electrical vehicles (EVS), and cellular phone [2]. It is also commonly used for energy storage devices. Most of the renewable energy is produces a DC power which can be utilized for various applications. The DC power is stored in battery using solar panel. When the AC power is not available, during that period we can use the battery power. These three input sources are used to convert the DC-DC Buck-Boost converter topology. Hence this paper is motivated to develop a bidirectional adapter for the charging mode and discharging mode for the emergency purpose. The DC voltage is given in the H-bridge inverter circuit; the DC power is inverted into the AC sinusoidal power for all application. This is the charging mode or forward direction of the of DC-DC converter [1, 2].

In discharging mode the H-bridge converter is used to convert the AC to DC power. The DC-DC converter is achieved by variable DC into fixed DC power. This stored DC power is used for the emergency purpose. The bidirectional adapter is useful for today trend scenario, and also used for various applications. The power is demand for the various applications like an industrial and commercial purpose, due to power demand all are focusing on the inverter and renewable energy sources like a solar power and wind power. The battery power is used for critical power appliances [2, 3].

48.2 Working Principle of Battery and Solar Powered Buck-Boost Converter

Charging a battery with solar power has becomes very popular. A solar cell typical voltage is 0.7 V that is derived from the data sheet. The number of single solar cell is connected in series and parallel combination to achieve a required DC power. The growing market for the solar energy technology has resulted in a rapid growth in the power electronics. The PV system is the conversion of sun ray's into usable electricity form. The solar power provides the consumer application like lighting and water pumping, refrigeration, telecommunication [3, 4].

Battery is the energy storage devices used as emergency purpose. Battery means a single electrochemical unit which exhibits a voltage differential across its two terminals. The differences in chemistry among various battery types result in different charge requirements. Li-Ion batteries are charged with a constant-voltage, constant-current. The charge current is usually expressed as C-rate. The C-rate describes the battery capacity in Ampere-Hours. It measures how much current is required to fully charge the battery within 1 h, assuming no losses. Because batteries are not 100 % efficient in converting charge current into stored charge, it takes longer than 1 h to fully charge the battery at 1C rate. For any energy system requires the battery to store the DC power to meet the power demand during the period of low solar irradiation [4, 5].

48.3 Traditional Circuit

The traditional circuit of the bidirectional adapter is one input source, using in front side of bidirectional. The DC input source to the converter circuit is not compensate for the all-time, when the power is not present it has disadvantage of this adapter. The buck-boost converter circuit is used to convert fixed DC power into variable DC power. The forward mode of operation it is acting as boost mode, and reverse direction acts as the buck mode to store the DC power to the battery. This is achieved by DC-DC converter topology techniques. The stored DC power is using for emergency purpose [2–5] (Fig. 48.1).

48.4 Working Principle of Proposed Circuit Model

The proposed circuit with bidirectional adapter has the solar power and buck-boost converter circuit and energy storage devices act as battery which is using in emergency purposes. The SMR based bidirectional laptop computer adapter is used

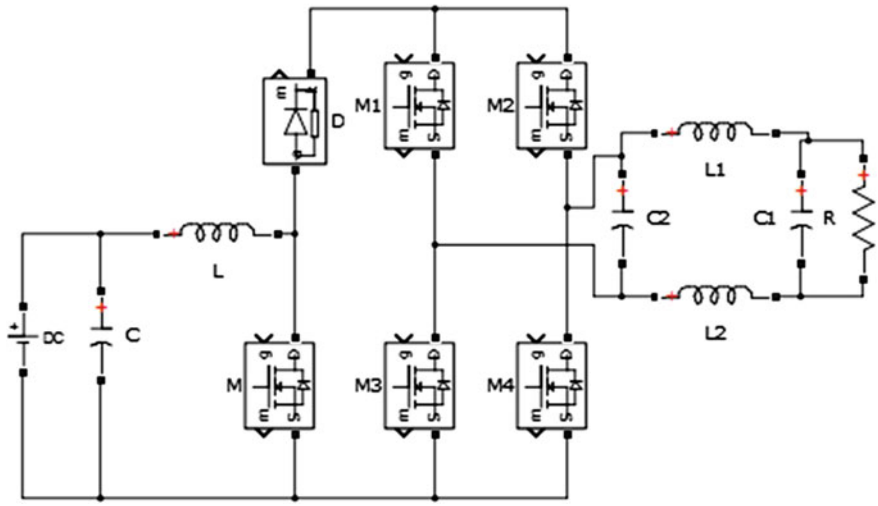

Fig. 48.1 Traditional circuit

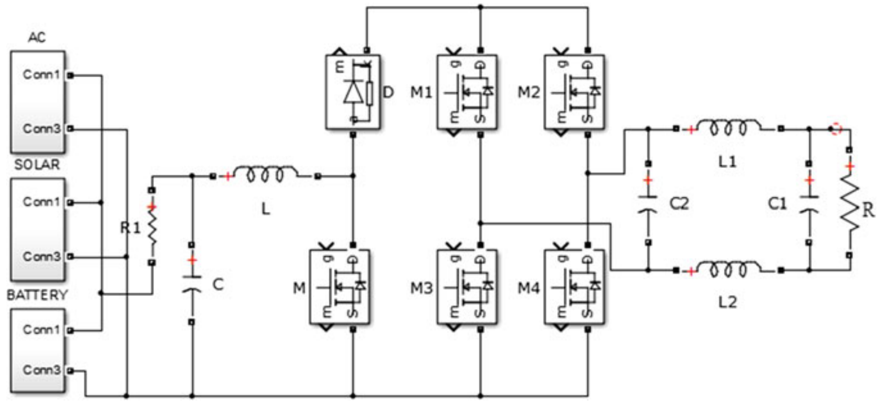

Fig. 48.2 Circuit diagram

to utilize the power in both directions. The two or three input source is using based upon the switch mode rectifier (SMR) based converter. First input is AC source we can use directly. The sun shines at noon time peak energy production (Fig. 48.2).

The third input is battery source when power is not present we can utilize the power from battery using inverter circuit. The input source is used to convert the (Buck-Boost converter) fixed DC to variable DC for giving required gate pulse to the pulse generator. That variable DC power is again inverted into AC power using H-bridge inverter circuit that is used for application. The inverted power not pure sine wave power some ripple and harmonics will be presented. This ripple and harmonics will be filtered out using filter circuit. The consumer appliance used to provide the services such as lighting water pumping refrigeration, telecommunication [2–7].

48.5 Design Specification of Buck/Boost Converter

K should be greater than 0.5 (Table 48.1)

Let k = 0.75 and F = 500 kHz.

$$\mathrm{V_{out}} = \frac{V_s \mathrm{k}}{(1-\mathrm{K})} \tag{48.1}$$

$$= \frac{(0.66 * 24)}{(1-0.66)} \tag{48.2}$$

$$\mathrm{V_{out}} = 47.58. \tag{48.3}$$

Table 48.1 Component specification

Parameter	Values
Maximum power	18 W
AC input voltage (Vs)	230 V
Solar voltage (Vs)	24 V
Output current (Io)	0.350 mA
Output voltage (Vo)	47 V
Inductor (L)	0.18 mH
Capacitor (C)	5,000 μF
Resistor (R)	50 Ω

$$\mathrm{L} \;= \frac{V_s \mathrm{k}}{(\Delta \mathrm{I} * \mathrm{F})} \tag{48.4}$$

ΔI is the ripple current that is 20–30 % of output current.

$$\Delta \mathrm{I} = 0.2 * (\frac{48}{50}). \tag{48.5}$$

$$\Delta \mathrm{I} = 0.96. \tag{48.6}$$

$$\mathrm{L} = \frac{(24 * 0.75)}{(0.96 * 500{,}000)} \tag{48.7}$$

$$\mathrm{L} = 0.18\,\mathrm{mH}. \tag{48.8}$$

$$\text{Required capacitance value(C)} \;= \frac{(I_o * \mathrm{K})}{(\Delta \mathrm{v} * \mathrm{F})} \tag{48.9}$$

Δv is the ripple current that is 20–30 % of output voltage.

$$\Delta \mathrm{V} = 0.2 * (\frac{48}{50}). \tag{48.10}$$

$$\Delta \mathrm{V} = 0.96. \tag{48.11}$$

$$\mathrm{C} \;= \frac{(0.96 * 0.75)}{(0.2 * 500{,}000)} \tag{48.12}$$

$$\mathrm{C} = 5{,}000\,\mu\mathrm{F}. \tag{48.13}$$

$$\text{Efficiency} \;= \frac{(\text{output power})}{(\text{input power})} \tag{48.14}$$

$$= \frac{(48 * 0.423)}{(24 * 0.01)} \tag{48.15}$$

$$\text{Efficiency} = 82.6\,\%. \tag{48.16}$$

48.6 Simulation Circuit Result

48.6.1 Forward Direction

The switch is on condition by giving the proper gate pulse to the switch. In this mode the energy is stored in inductor by using input voltage of 24 V. The switch is off condition by removing the gate pulse to the switch, the stored energy is transferred from inductor to the capacitor. This is forward mode or boost mode of operation. This boosted variable DC is given to the H-bridge inverter circuit. The H-bridge inverter circuit is used to convert the DC voltage to AC voltage. This Ac source is not pure one this will be given to the LC filter. This LC is used to filter the harmonics and ripple content in the AC source, and gives pure sinusoidal wave form. This sinusoidal AC source is using in application such mobile charging, and commercial purpose [5–7] (Fig. 48.3).

48.6.2 Reverse Direction

The input source is AC sinusoidal voltage source. This 48 V of AC source is given to the H-bridge inverter circuit and inverter circuit is used to convert the AC source

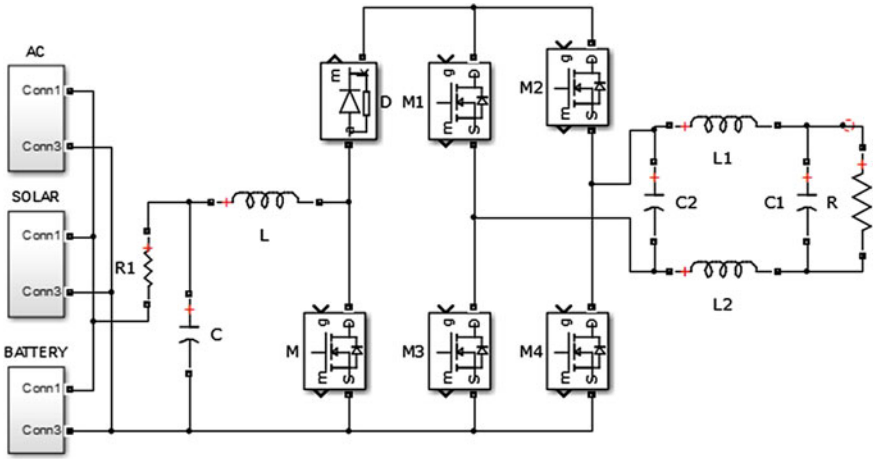

Fig. 48.3 Forward direction

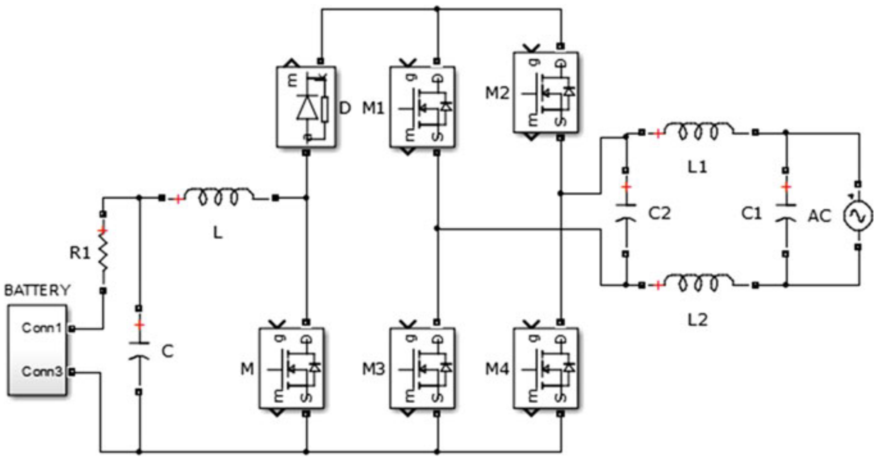

Fig. 48.4 Reverse direction

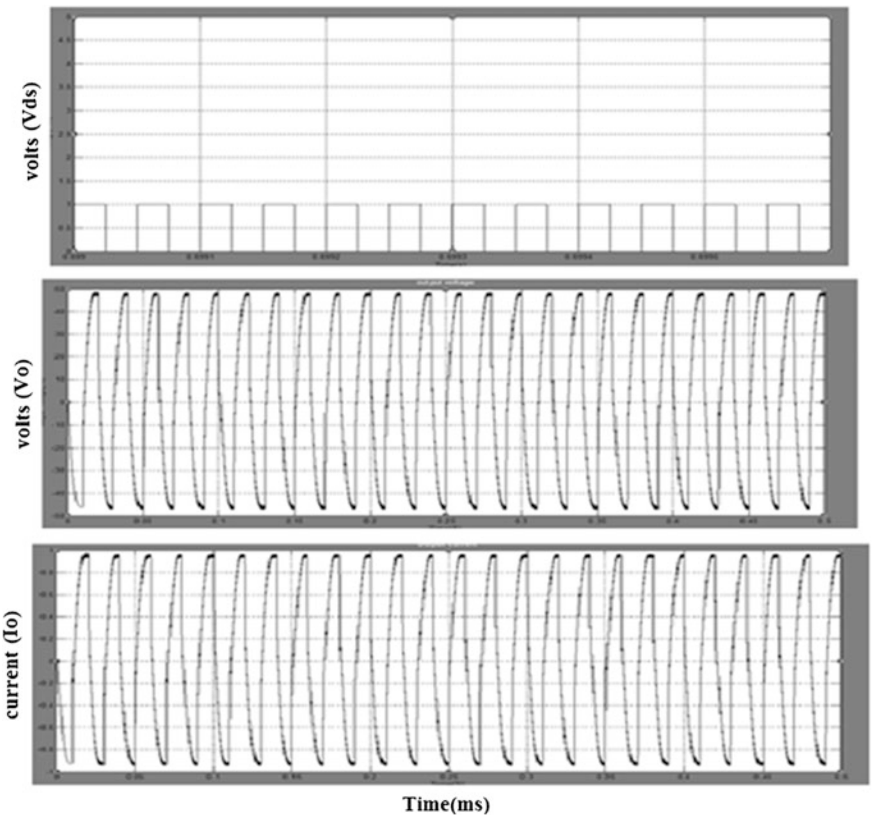

Fig. 48.5 Switching pulse and output voltage current

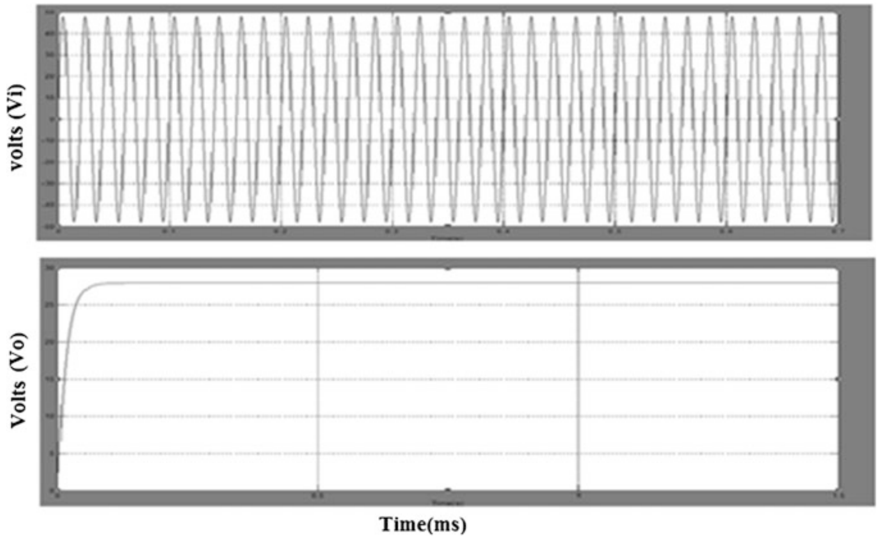

Fig. 48.6 Input and output voltage

into DC variable source. This DC variable source is not required to store the battery. It will be convert the variable DC source into fixed DC voltage by using Buck converter. Here the switch is on condition by giving proper gate pulse to the switch. This is turn on the switch and battery is charged from capacitor. The switch is off condition by removing the gate pulse to switch, at the time the diode is on condition and freewheeling action can take place, and energy is transferred from inductor to the battery. The battery stores the DC power and when the power is not present we can utilize the power from the battery and also used in emergency purpose [6, 7] (Fig. 48.4).

48.7 Simulation Wave Form for Forward Mode

See Fig. 48.5.

Table 48.2 Simulation results

Parameter	Values
Input voltage	24 V
Output voltage	47 V
Output current	0.42 mA
Output power	18.47 W
Input power	24 W
Efficiency	82.6 %

48.8 Simulation Wave Form for Reverse Direction

See Fig. 48.6 and Table 48.2.

48.9 Conclusion

Hence the simulation circuit of bidirectional adapter for, solar panel and battery with Buck Boost converter circuit is simulated. The circuit wave form for the converter circuit of both buck and boost mode of the operation was simulated. The bidirectional adapter with forward mode of operation, AC power will be utilizing and for the reverse mode of operation DC power can be stored in battery. When power is not available the DC power can be used in emergency purpose. The power circuit is analyzed; designed and implemented the simple robust control scheme is also developed. The SMR operation based characteristics of the entire converter and inverter circuit is performed. The miniaturization, efficiency improvement, and commercialization for the developed bidirectional adapter can easily be accomplished by the industries [6–8].

References

1. Hu K-W, Liaw C-M (2014) On a bidirectional adapter with G2B charging and B2X emergency discharging functions. IEEE Trans Ind Electron 61(1):243–257
2. Jain M, Daniele M, Jain PK (2000) A bidirectional DC–DC converter topology for low power application. IEEE Trans Power Electron 15(4):595–606
3. Jang M, Agelidis VG (2011) A minimum power-processing-stage fuel-cell energy system based on a boost-inverter with a bidirectional backup battery storage. IEEE Trans Power Electron 26 (5):1568–1577
4. Bialasiewicz JT (2008) Renewable energy systems with photovoltaic power generators: operation and modeling. IEEE Trans Ind Electron 55(7):2752–2758
5. Rodriguez C, Amaratunga GAJ (2008) Long-lifetime power inverter for photovoltaic ac modules. IEEE Trans Ind Electron 55(7):2593–2601
6. Cao J, Emadi A (2011) Batteries need electronics. IEEE Ind Electron Mag 5(1):27–35
7. Kjaer SB, Pedersen JK (2005) A review of single-phase grid connected inverters for photovoltaic modules. IEEE Trans Ind Appl 41(5):1292–1306
8. Duryea S, Islam S, Lawrence W (2001) A battery management system for stand-alone photovoltaic energy systems. IEEE Ind Appl Mag 7(3):67–72

Chapter 49
Analysis of Different Current Commutation Technique in Matrix Converter

S.K. Das and P. Syam

Abstract Matrix converter is an alternative topology for a solid state frequency changer without any reactive elements like inductors and capacitors. One of the major obstacles of this topology is the complex commutation of the bi directional switches in absence of natural free wheeling path for the inductive currents. A detailed study has been made here to understand the limitations and possible improvement of the existing current commutation techniques in this paper. A universal and synchronous commutation scheme for all the IGBTs is devised so that commutation can smoothly take place as and when required within the minimum possible time depending on the switching time of the IGBT used. The different aspects of this commutation are verified through MATLB simulink. Possibility of step less current commutation is explored.

Keywords Matrix converter · Current commutation

49.1 Introduction

Power frequency changer is an integral part of ac drive applications. From power quality point of view, it is desirable to use a direct frequency changer to provide sinusoidal output voltages with varying amplitude and frequency, while drawing sinusoidal input currents with unity power factor from the ac source. Matrix converter is an array of controlled bi-directional switches that connects directly a three-phase source to a three phase load (Fig. 49.1). This topology, which has progressively developed over the last two decades, offers a nearly all semiconductor

S.K. Das (✉)
Department of EEE, HIT, Bhubaneswar, Odisha, India
e-mail: saratkrdas89@gmail.com

P. Syam
Department of EE, BESU, Shibpur, Howrah, West Bengal, India
e-mail: prasidsyam@yahoo.co.uk

C. Kamalakannan et al. (eds.), *Power Electronics and Renewable Energy Systems*,
Lecture Notes in Electrical Engineering 326, DOI 10.1007/978-81-322-2119-7_49

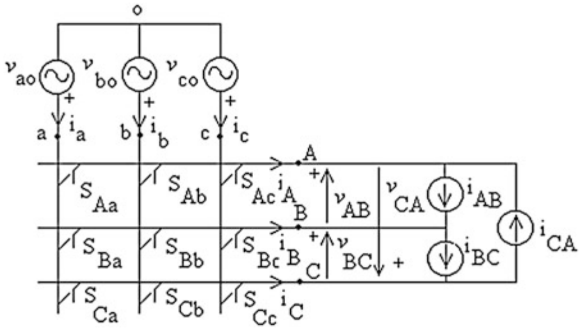

Fig. 49.1 Matrix converter circuit

solution for AC-to-AC power conversion. Despite being equipped with some of the most desirable features for any power converter, commercial exploitation of this topology has been held back due to some practical limitations. One of these issues has been the problem of current commutation, which, of late has been the focus of considerable attention and many schemes have been proposed to address this issue [1–7].

49.2 Current Commutation

The process of turning off a conducting semiconductor and transferring the current to another switch is known as "commutation". Current commutation is an integral part of a matrix converter realization where load current needs to be transferred in any one of the three input phases depending on the modulation logic through one of the three different bi-directional switch cells connecting a output phase to the input phases as shown in Fig. 49.1. A switch cell is generally constructed using IGBTs and diodes in various configurations for medium power applications [2].

The general rule that has to be adhered to while considering any control strategy for a matrix converter is that each output phase must have only one switch cell connected to an input phase at any time at steady state. This prevents the input from being short-circuited and at the same time provides continuous current through the inductive load at output Whenever there is a requirement of changing the input phase connected to a particular output phase, the current flowing through the output phase needs to be transferred from outgoing input phase to incoming input phase instantaneously without any disruption of the output current considering the load is inductive. Reliable current commutation between switch cells of matrix converters is more difficult to achieve than in conventional VSIs due to the absence of natural freewheeling paths. The commutation needs to be actively controlled all the time with respect to the switching rule stated above and illustrated in Fig. 49.2. To attenuate the high frequency component in the input current L-C filters are used in the input. The output inductances signifies that, during switching, the output load is considered as constant current load [2].

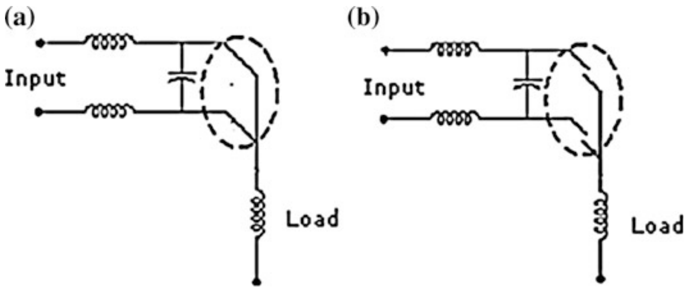

Fig. 49.2 Unwanted switching: **a** short circuit at input lines **b** open circuit at output lines

Different schemes are in use for commutation [5]. The schemes follow the switching constraints and also take into account the finite switching times of the semiconductor devices and sensor delays. Some of these rely on the output current direction, while others rely on relative magnitudes of input voltages to activate the commutation stages. However, the disadvantages of relative voltage based commutation method outweighs its advantages as has been pointed out in [5] where the commutation time has been shown to be greater than the methods relying on output current directions. The main disadvantage of output current detection based commutation is that the offset errors make erroneous signals for commutation logic for which output may be open circuited causing over voltage. However, this is of no major concern because of a clamp circuit connected between the input and output terminals [2] can be used to effectively counter this problem. The over voltages can appear from the input side, originated by line voltage perturbations. Also, dangerous over voltages can appear from the output side, caused by an over current fault. When the switches are turned off following an over current fault, the current in the inductive load is suddenly interrupted. The energy stored in the motor inductance has to be discharged without creating over voltages.

Therefore, the method using output current direction information has been considered here for further improvement in commutation time. The output current direction can be sensed by using either output current sensors or by measuring the voltages across each device in a bi-directional switch cells which was proposed and had been covered in details in [6]. The process allows the current to commutate from one switch to another without causing a line-to-line short circuit or a load to be open circuited. This commutation is known as “semi-soft” commutation since 50 % of the switching is by devices that are reverse biased. This implementation is asynchronous. In this method data transfer is not based on predetermined timing pattern and is limited by frequent interactions between the sensor circuits during the commutation process. This adds unwanted delays of the sensing devices to the commutation process. The total time taken by the commutation process cannot be estimated quantitatively. A large number of sensing circuitry (one voltage sensor per IGBT device) has to be used to implement the method. The sensors need to interact in between themselves as well as the gate driver during the commutation process.

This makes the control scheme complicated and offsets the other advantages of two-step commutation using voltage measurements across the switching devices.

In this paper, a generalized, synchronous switching logic for current commutation based on output current direction [7] is considered for detail study and further improvement. The advantages of this schemes are (1) entire process of commutation is a synchronous one, (2) is not affected by delays from current sensor circuits and (3) commutation time can be conveniently estimated and fixed for any commutation requirement occurring any time and anywhere in the circuit. This time is also programmable depending on the switching times of the semiconductor devices. The commutation time used here (1.6 μs) for four-step commutation considering a particular type of IGBTs [8]. This is negligible compared to the sampling period of pulse width modulation of 20 kHz (1.6 ≪ 50 μs). However, for subintervals of the duty cycles, this commutation time may be significant. But this limit should be adhered to for safe commutation. The commutation sub-intervals are general and hence, are applicable for all switching devices including IGBTs. The commutation process is described in the following section.

49.3 Generalised Synchronous Current Direction Based Commutation Method

The commutation scheme is explained with the help of a two-phase to single phase matrix converter is shown in Fig. 49.3. The two phase to single phase matrix converter is considered to make the analysis simple but rigorous. The two ac voltage sources of same magnitude and phase but with phase differences are the two input supply phases to the matrix converter. Two bi-directional switch cells connect those two phases to the single phase load. The switch cells are composed of two emitter-coupled back to back IGBTs with inverse parallel connected diodes. The modulation pulses for these switches obeys the constrains of switching i.e. at any instant of time either of the switch cells must get switch-on gating pulse when the other receives switch-off gating pulse.

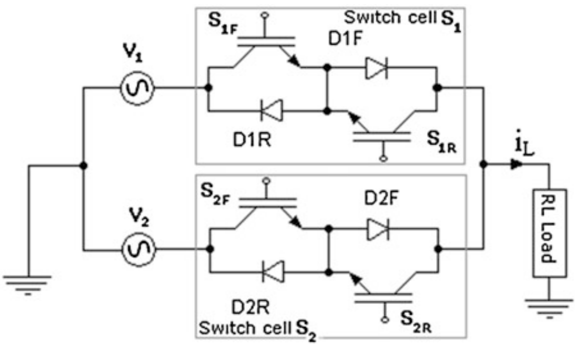

Fig. 49.3 Two phase to single phase matrix converter considered in the scheme

Width In an active cell, two unidirectional devices are connected in such a way so that current in both the direction can flow. In conducting state, both of the devices in the active cell are gated to allow both directions of current flow. At a particular instant of time, one of the devices is taking the current. The other device in the same cell is reverse biased by the forward biased diode connected across it as shown in Fig. 49.3. This is required because IGBTs considered here cannot block reverse voltage. This device can be said to stay at "OFF" condition, although it has the turning-on gate voltage.

49.3.1 Four Step Commutation

We consider the circuit shown in Fig. 49.3. It is assumed that at the instant of time considered, the load current (iL) is in the direction shown and that the upper bi-directional switch S1 is closed i.e. active. When a commutation to S2 is required, the current direction is used to determine which device in the active cell is not conducting. This device (in this case, S1R) is then turned off first. The device that will conduct the current in the incoming switch is then gated (S2F in this example) after a time duration t_{C1}. The load current begins to divert to the incoming device. The outgoing device (S1F) is turned off just after the incoming device S2F (time interval t_{C2}) starts sharing the load current. The load current is completely transferred to the incoming device after certain time depending on the incoming voltage and circuit parameters. The remaining device in the incoming switch (S2R) is turned on after time duration t_{C3} assuming the outgoing device will turn-off completely after this time interval. This will allow current reversals in steady state. This precaution is taken to prevent input short circuit. The process is illustrated by the timing diagram as shown in Fig. 49.4.

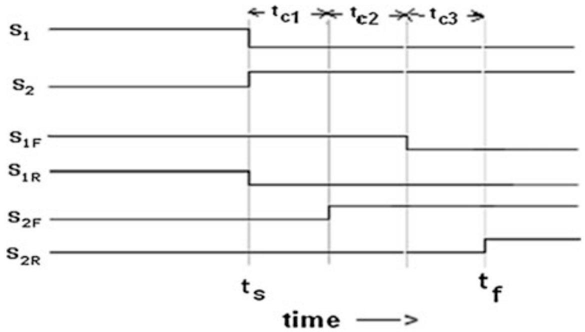

Fig. 49.4 Four step current commutation

49.3.2 Three Step Commutation

In the case of a three step commutation method, S2F and S1F has to be turned on and off at the same instant. The corresponding timing diagram is shown in the Fig. 49.5. Since turn off time of an IGBT is greater than the turn on time under all operating conditions, both the switching transitions can take place without violating the output open circuit switching constraint and this will further reduce the overall commutation time. There will be a definite problem at low current level due to offset in the current sensors for which the output current direction might be erroneously indicated. Then the conducting IGBTs may be switched off causing output voltage spike. For example, if S1R is turned off at first by wrongly sensing the current direction as positive, the excessive voltage will occur across the switches. The snubbers (R-C) across IGBTs can reduce the voltage spike. For a large capacity IGBTs, resistance for the snubber must be set low to reduce heat dissipation and turn-on losses. For frequent change in the voltages across snubber, losses in snubber itself are quite large. So, it is not suitable for high frequency pulse modulated matrix converter. However, this spike is reduced by a diode bridge clamp

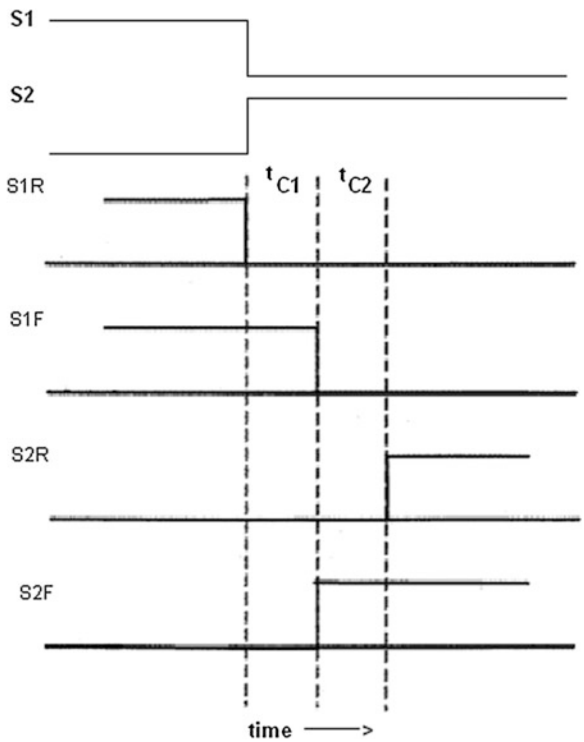

Fig. 49.5 Three step commutation

circuit commonly Connected between output and input terminals as an extra protection circuit which clamps the output voltage level within the input voltage magnitude [2].

49.3.3 Step Less Current Commutation

In the case of a step less commutation method, S1F, S1R are turned off by reverse bias gate voltage according to the modulation signal and at the same instant of time, S2F and S2R get the turned-on gate pulses. The corresponding timing diagram is shown in Fig. 49.6. The turn-off gate pulses make the outgoing conducting IGBT S1F to be turned off after the turn-off time and make the non-conducting IGBT S1R turned-off quickly (will take less time than the conducting IGBT because of absence of tailing current effect and no storage charge in the drift region). The turn-on gate pulses for the incoming switch cell S2 make the incoming IGBT S2F turned-on within the turn-on time of the IGBT and make the non-conducting IGBT S2R turned-on. There is a possibility of short circuit current for a very short duration when both the IGBT S1F and S1R are in their turning-off and turning –on phase respectively. But this duration is negligibly small because the other incoming IGBT S2F while begins to share the load current make the diode across the IGBT S2R in forward conducting mode. The forward voltage drop across this diode set reverse voltage across the collector emitter of the IGBT S2R making it OFF. Usually the IGBTs are rated to withstand this small duration short circuit current and the input L-C filter reduces the level of this short circuit current. The step less commutation has advantage of not sacrificing the modulation pulse width for commutation. There is no requirement of current sensors also [7].

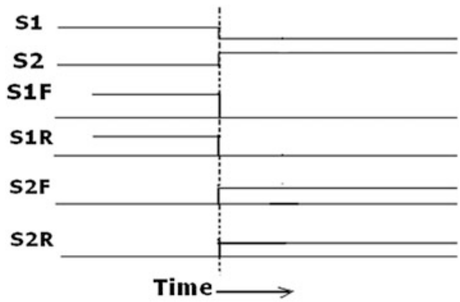

Fig. 49.6 Step less current commutation

49.4 Simulation Result

The MATLAB Simulation results of four-step current commutation are shown in Fig. 49.7a for output current direction is towards load as shown in Fig. 49.3. Similarly, for the three-step current commutation, the waveforms are shown in Fig. 49.7b. There is no problem of input short circuit and output open circuit as evident from the simulation result.

In step less commutation, only the block containing the shift register and multiplexer is modified. The corresponding block with changed configuration is shown in Fig. 49.8a. Those changes should be made for four such control blocks to get the gating signals for the four IGBTs. It is evident from the control logic that the gating signals of all the IGBTs will go for transition at the same instant of time and it will occur at the same instant when modulation signal goes for transition. The results are shown in Fig. 49.8b.

As soon as there is a change in modulation signal, the gate pulses of the respective IGBTs are generated to facilitate single step commutation. This has been observed that commutation will generate voltage spikes in the output. This magnitude of these spikes increases with increase in output current magnitude for a particular value of load inductance. For a very short duration, at the instant of start of commutation, the incoming switch cell takes finite time (in the order of 100 ns) to turn on. Until the switch is completely turned-on, the load circuit resistance

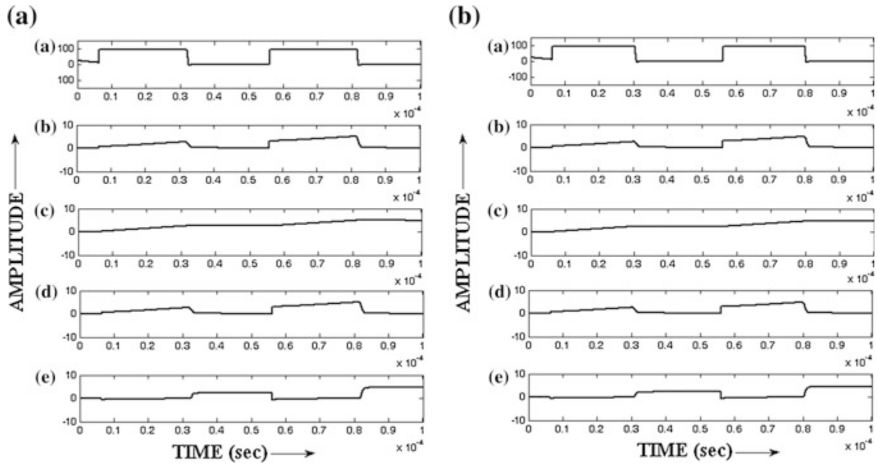

Fig. 49.7 Voltage and current in different parts: **a** Four step commutation and **b** three step commutation: *a* Output load voltage across the R-L branch, *b* current flowing in the input supply line connected to switch cell 1, *c* current flowing in the R-L branch, *d* current flowing through switch cell 1, *e* current flowing through switch cell 2

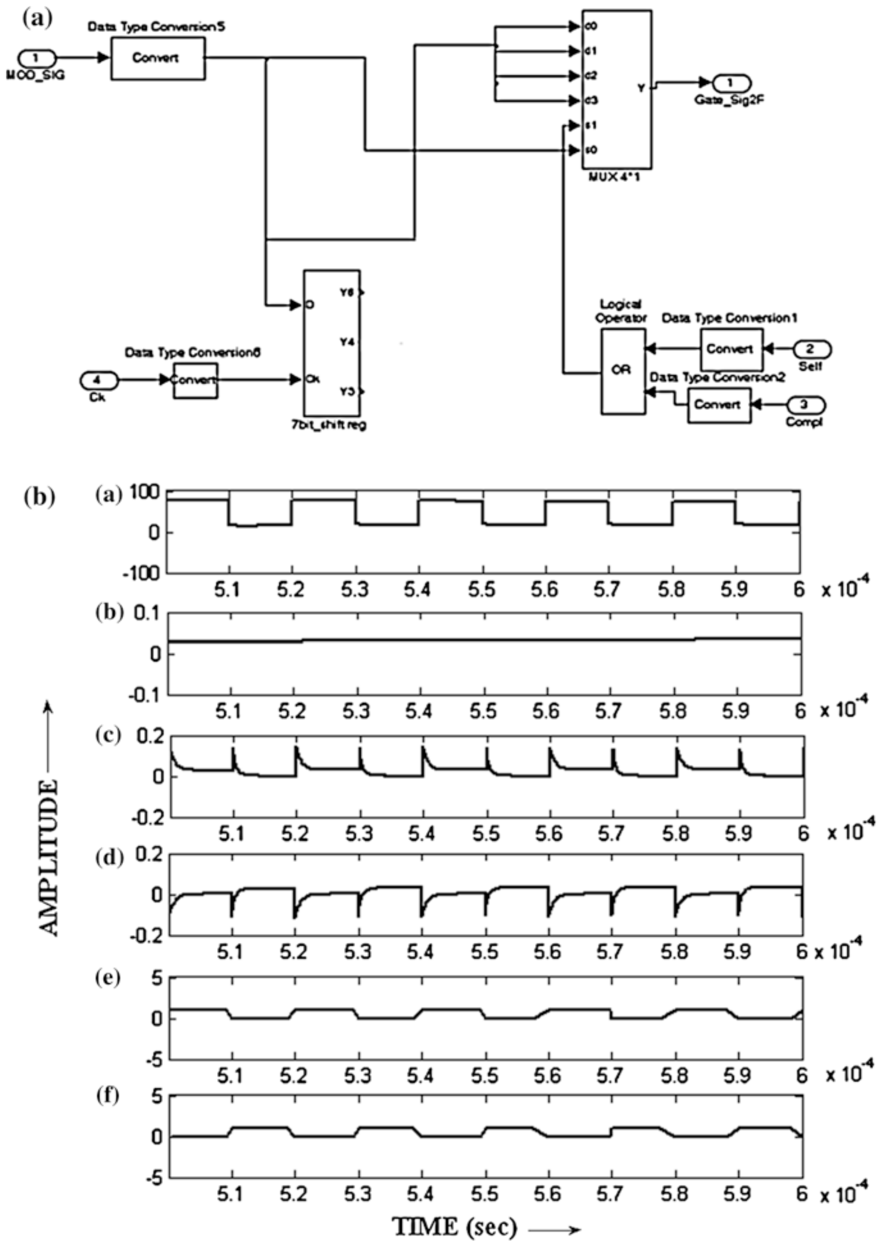

Fig. 49.8 **a** Necessary changes in the control block for step less commutation and **b** step less commutation (voltage and current in different parts) without using source impedance *a* output load voltage across the R-L branch, *b* current flowing in the R-L branch, *c* current flowing in the input supply line connected to switch cell 1, *d* current flowing in the input supply line connected to switch cell 2 *e* modulation signal connected switch cell 1, *f* modulation signal connected switch cell 2

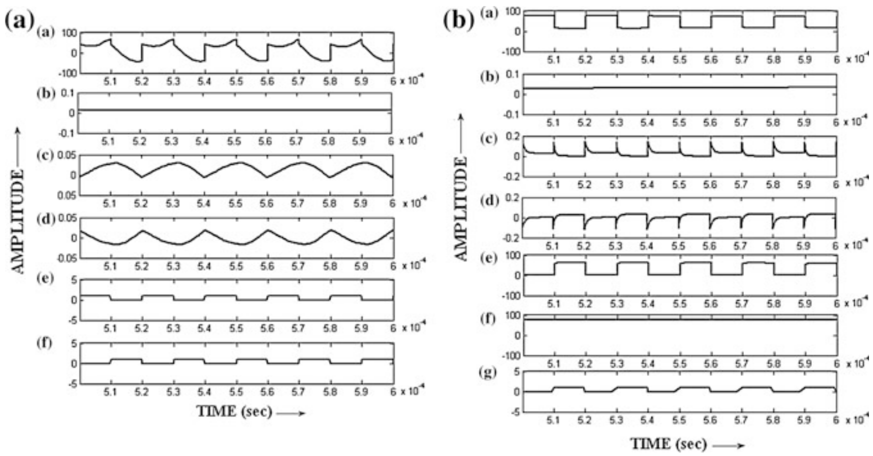

Fig. 49.9 Step less commutation (voltage and current in different parts) **a** without using source impedance and **b** with source impedance and filter capacitors *a* output load voltage across the R-L branch, *b* current flowing in the R-L branch, *c* current flowing in the input supply line connected to switch cell 1, *d* current flowing in the input supply line connected to switch cell 2 *e* modulation signal connected switch cell 1, *f* modulation signal connected switch cell 2

jumps to a high value causing voltage spikes as shown in Fig. 49.9a. However, the voltage spikes are small. Although these voltage spikes can be attenuated to a safe level by using a clamp circuit which allows path for the inductive current for very small duration of time when both the two switch-cells are off at the start of commutation instant.

49.4.1 Effect of Source Impedance

Source impedance consisting of 1 ohm resistance in series with 10 mH inductance is connected to each supply source to see the effect of source impedance on the performance of the converter. Two ac voltage sources having frequency 50 Hz, phase difference of 120° and peak magnitude 100 V are used. The load is a R-L load where R = 5 ohm, L = 800 mH. Two pulse generators are used to provide modulation signals of frequency 50 kHz. The modulation signals are phase displaced by 10 μs to maintain the switching constraint. The results are shown in Fig. 49.9b. Since, at the time of commutation the two switch cells are getting simultaneously on-off pulses, the output inductive load is always connected to one of the input sources except the starting instants of commutation. The output voltage waveform mostly follows the corresponding input supply waveform which is connected to the load by the conducting switch cell. There is short circuit current as evident from the source current waveforms at the starting instant of commutation. This short circuit current magnitude depends on the instantaneous difference of the input voltage sources and the equivalent impedance of the two switch cells when both the switches are in conduction at the starting instant of commutation. This duration is very small but the short circuit current can destroy the devices if it exceeds the limit of the peak current capability of the devices. The source impedance, if any, can attenuate this short circuit current and also the input filter connected to reduce the high frequency harmonic current can also attenuate this short circuit current to an acceptable level. If source impedance connected at input supply, the load voltage does not follow exactly the input source voltage waveform due to the effect of source impedance. The two switch cells are always in conduction (as evident from the input source current waveforms) irrespective of the gating pulses to allow inductive current (due to source inductance). Due to this flow of short circuit current (although limited by the source inductance) the output voltage deviates largely from the expected waveform of a matrix converter. The input source voltage also shoots up due to the presence of source inductance when the connected switch cell is intended to make off. This also generates around twice the supply voltage across the non-conducting switch cell. The comparison between different waveforms with and without connecting source impedance are shown in Figs. 49.8b and 49.9a respectively.

49.4.2 Improvement of the Output Voltage Waveform by Connecting Capacitors to the Input of the Switch Cells

Additionally capacitors (3 μF) are connected to the input of the each switch cells. The output voltage waveform looks similar Fig. 49.9b to the desired converter waveform.

The capacitors connected at the input gives path for the source inductance stored energy. Therefore, even if for the non-conducting switch-cell, the voltage across it is the just difference between the two input supply source. The capacitor connected in the input smooth any supply voltage ripple at the input of the converter. The short circuit current will stay for very small duration at the start of commutation and its magnitude is tolerable.

49.5 Conclusion

In this paper, a generalized and synchronous implementation of a widely used current commutation strategy in matrix converter through MATLAB simulink is presented. Output Current based different commutation techniques are studied in depth. The reduction of input short circuit current, output voltage overshoot and commutation intervals are the major objectives of the commutation techniques.

Near zero current the commutation scheme can fail, causing output voltage notches. Simulation results establish that it is possible to realize step less commutation by the filter circuit capacitance usually provided in input current filter. Simulation results are to be verified experimentally as a future extension of this work.

Acknowledgments We would like to express our deepest and most sincere gratitude to Dr. Tirupati Panigrahi, Hon'ble Chairman and Prof (Dr.) R.N. Satpathy, Principal, Hi-Tech. Institute of Technology, Bhubaneswar, Odisha.

References

1. Burany N (1989) Safe control of four quadrant switches. In: Conference of Rec. industry application society annual meeting (Oct 1989), San Diego CA, vol 1, pp 1190–1194
2. Wheeler P, Rodriguez J, Clare J, Empringham L, Weinstein A (2002) Matrix converters: a technology review. IEEE Trans Ind Electron 49:276–289
3. Huber L, Borojevic D (1995) Space vector modulated three phase to three phase matrix converter with input power factor correction. IEEE Trans Ind Appl 31:1234–1246
4. Wheeler P, Grant D (1997) Optimisation input filter design and low-loss switching techniques for a practical matrix converter. IEE Proc Electric Power Appl 144(1):53–60
5. Wheeler P, Clare J, Empringham L (2004) Enhancement of matrix converter output waveform quality using minimized commutation times. IEEE Trans Ind Electron 51:240–244
6. Wheeler P, Clare J, Empringham L, Bland M, Apap M (2002) Gate drive level intelligence and current sensing for matrix converter current commutation. IEEE Trans Ind Electron 49:382–389
7. Dasgupta A, Mukherjee S, SenGupta M, Syam P, Chattopadhyay AK (2006) Implementation of Universal Logic system of generating commutating pulses in matrix converters using FPGAs. In: Proceedings in CDROM, IEEE-ICIT'06, Mumbai (Dec 2006), pp 1436–1441
8. Munzer M (2001) EconoMac—The first all in one IGBT module for matrix converters. In: Proceedings of drives and control conference, sec 3, London, UK. CD-ROM

Chapter 50
Performance Comparison of DC to DC Boost Converters for Solar Power Installation System

A. Kalirasu, Subhransu Sekhar Dash and M.V. Muthukumar

Abstract The main objective of this work is to find the high efficiency DC to DC boost converter for solar power installation system. This paper mainly focuses the modeling of high gain with high efficiency DC to DC boost converter for photovoltaic system under wide input voltage range. The modeling and Matlab simulink simulation of an interleaved and a cascaded DC to DC boost converters are presented. An interleaved and a cascaded DC to DC boost converters are analyzed in open loop and closed loop condition. These converters provide the constant output voltage even the output voltage of the PV panel is continuously varying. The performance of these converters is compared. Based on the comparison result the cascaded boost converter is implemented using PIC microcontroller. This comparison reveals that the cascaded boost converter system has the advantages like reduced number of switching component, low ripple content and high efficiency.

Keyword Boost converter · Cascaded boost converter · Interleaved boost converter · Dc to dc converter · Closed loop · Solar installation · Solar converters · PV cells · Photovoltaic system · Matlab · Simulation

A. Kalirasu (✉)
Department of Electrical and Electronics Engineering, Sathyabama University, Chennai, India
e-mail: akalirasu@yahoo.co.in

S.S. Dash
Department of Electrical and Electronics Engineering, SRM University, Chennai, India
e-mail: munu_dash_2k@yahoo.com

M.V. Muthukumar
Department of Electrical and Electronics Engineering, VEC, Chennai, India
e-mail: mvmuthukumar88@gmail.com

C. Kamalakannan et al. (eds.), *Power Electronics and Renewable Energy Systems*, Lecture Notes in Electrical Engineering 326, DOI 10.1007/978-81-322-2119-7_50

50.1 Introduction

Now a day's most of the countries in the world face the power demand problem. The economy of the country is mainly related with the electric power generation capacity of the country. Today, all countries encourage their researchers in the field of renewable energy. In different kinds of renewable energy, solar energy has the greatest potential. PV cell is directly converting the solar energy to DC electricity. Solar cell or PV cell is similar to that of a diode. The equivalent circuit of a PV cell under illumination is shown in Fig. 50.1. The PV cell output current equation is given below

$$I = I_{PV} - I_D - I_{sh} \tag{50.1.1}$$

Here, I_{PV} represents the light-generated current in the cell, I_D represents the voltage-dependent current lost to recombination, I_{sh} represents the current lost due to shunt resistances, I and V are cell output current and voltage [1].

Under a specific illumination level and temperature the power is maximized at a unique point on the I-V curve [2]. The change in temperature mainly affects the PV output voltage, while the irradiation changes mainly affect the PV output current. To match the PV panel output voltage with the load voltage, the PV panel output voltage either to be stepped up or stepped down using the efficient DC to DC converter. Many researchers have been investigated different types of modified step-up converter topologies to increase the conversion efficiency. An alternate soft switching scheme is applied to the conventional boost converters using lower source voltages is presented [3]. A high voltage gain using a switched capacitor circuit in DC to Dc converter is reported in [4, 5]. High-power applications such as power factor correction, hybrid electric vehicles, and fuel cell power conversion systems new soft-switched Continuous Conduction Mode (CCM) boost converter is much suitable [6]. New topology of a non-isolated boost converter for the solar installation system is discussed [7–9]. For renewable energy system a novel DC to DC converter conversion systems with PV solar cell or fuel cell stack input is presented [10, 11]. This converter is based on a boost converter and a voltage-doubler configuration with a coupled inductor to achieve high step up voltage conversion ratio.

The above literatures do not deal with the comparison and implementation of a cascaded DC to DC boost converter. The limitations of the boost converters are

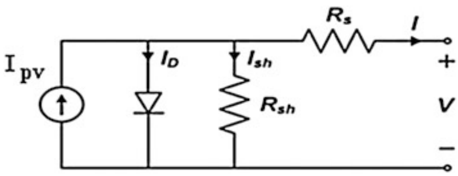

Fig. 50.1 Equivalent circuit of PV cell

analyzed and the conceptual solution for high step-up conversion is proposed in this paper. This work makes an attempt to implement embedded based cascaded boost converter using PIC controller.

50.2 Interleaved Boost Converter

The MATLAB SIMULINK simulation diagram for obtaining the electrical characteristics of PV cell is shown in Fig. 50.2. The I-V and P-V characteristic of a PV module under different values of Insolation (200, 400, 600, 800, 1,000 W/m^2) is shown in Fig. 50.3.

Any switching converter draws a source current with some amount of superimposed ripple. The amplitude of the ripple can be reduced by operating the converter in high frequency. The increase in frequency increases the switching losses. Using interleaved boost configuration, this problem can be avoided. The equations used to design the interleaved boost converter are given below.

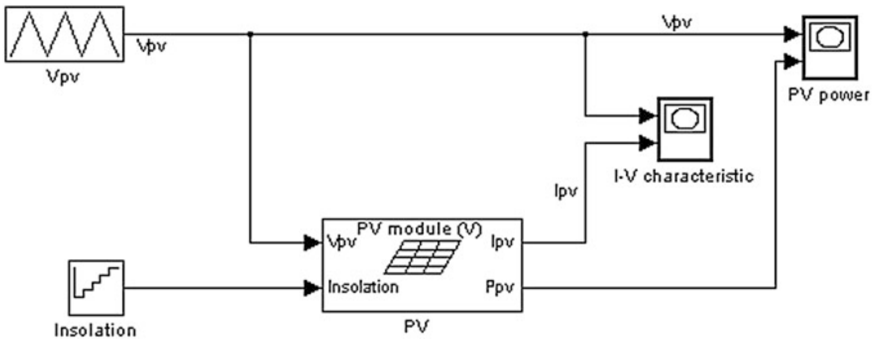

Fig. 50.2 Simulink circuit for PV module characteristics

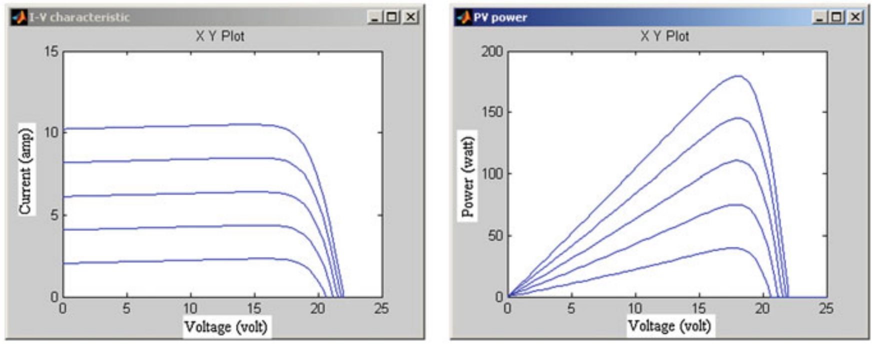

Fig. 50.3 I-V and P-V characteristic of the PV module for different insolation levels

The current ripple

$$\Delta I_L = V_{pv}\left(\frac{V_o - V_{pv}}{f_s \times L \times V_o}\right) \tag{50.2.1}$$

where $L_1 = L_2 = L$

The inductor

$$L = \left(\frac{V_{pv} \times \delta}{\Delta I_L \times f_s}\right) \tag{50.2.2}$$

The capacitor

$$C = \frac{I_o \times \delta}{f_s \times \Delta V_c} \tag{50.2.3}$$

where ΔI_L is the inductor ripple current, V_{pv} is the solar panel output voltage, δ is the duty cycle ratio, f_s is the switching frequency, I_o is output current, ΔV_c is the capacitor ripple voltage and L, C are value of inductor and capacitor. Matlab/Simulink model of an interleaved DC to DC boost converter shown in Fig. 50.4, results are presented. The following parameters are considered for the simulation of an interleaved boost converter. V_{in} = 12–15 V, V_o = 60 V, duty cycle ratio δ = 65 % and load resistance R_L = 25 Ω.

The driving pulses of the MOSFET are shown in Fig. 50.5. PV panel output voltage of 12 V is applied as input voltage. For the applied voltage of 12 V, the interleaved boost converter produces the output voltage of 56.6 V, output current of 2.25 A and the output power of 126.33 W. The input and output voltage waveform is shown in Fig. 50.6.

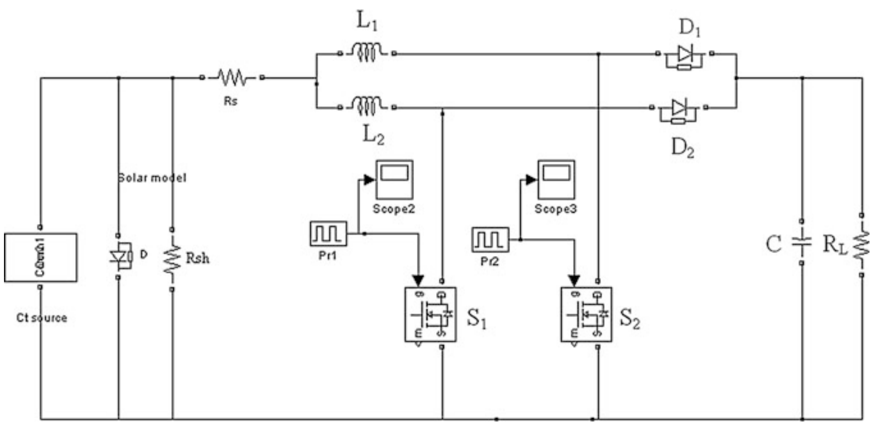

Fig. 50.4 Simulink model of interleaved DC to DC boost converter

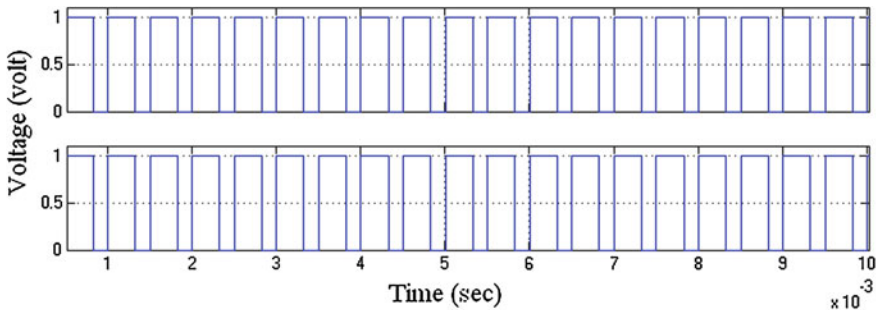

Fig. 50.5 Driving pulses for MOSFET

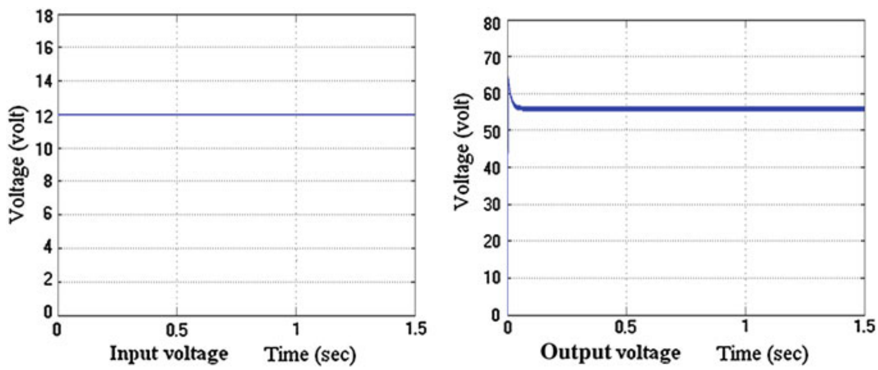

Fig. 50.6 DC input and output voltage of interleaved boost converter

The closed loop system with step change in input voltage is shown in Fig. 50.7. The closed loop system is designed to give constant output voltage for a step change in output voltage. The input and output voltages of the closed loop converter with step change in voltages are shown in Fig. 50.8. Till 0.5 s, the output voltage of the converter is 56.2 V for the input of 12 V. At 0.5 s, the input voltage increases from 12 to 15 V due to the step change in voltage. Hence the output voltage increases to 84 V.

The closed loop system consists of comparator and PI controller. The output voltage of the converter is sensed and it is compared with a reference voltage. The error signal is applied to a PI controller. The output of the PI controller is given to the MOSFET. The different values of proportional gain K_p and integral gain K_i are selected for tuning the PI controller. Then, the error is processed by properly tuning the PI controller. The output of PI controller generates the pulses to maintain the constant output voltage of 60 V. Thus the output voltage reduces and reaches the steady state set value of 60 V at 0.65 s. In closed loop system at 0.5 s, the output current increases beyond the 2.248 A and reaches the steady state constant value of

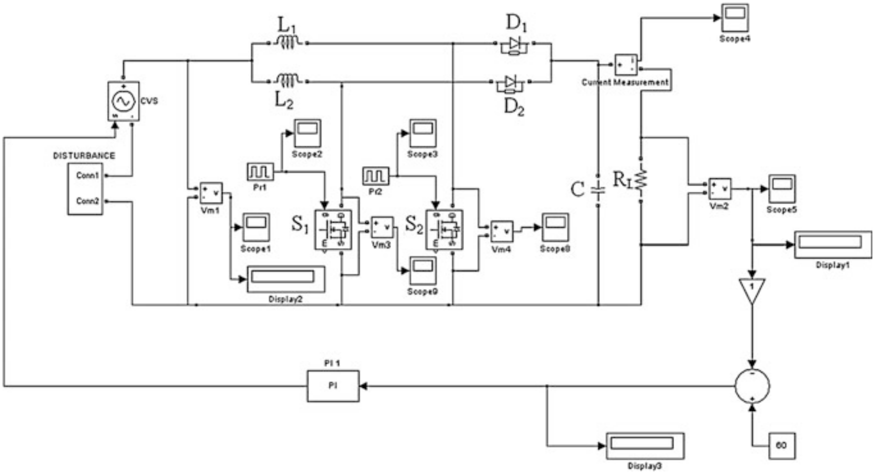

Fig. 50.7 Closed loops interleaved DC to DC boost converter with step change in input voltage

2.248 A at 0.65 s which is shown in Fig. 50.8. The response of the closed loop system is very faster than the response of the open loop system. It reaches its steady state very quickly.

50.3 Cascaded Boost Converter

Under the super lift electronic circuits design technique the positive output cascade boost converters are categorized. One of these circuits is the two stages positive output cascade boost converters. By using additional components the gain limitation problem is overcome [8]. The operation of this cascaded boost converter circuit can be simply explained by stating that the current flowing through inductor L_2 increases with voltage V_1 during the switching ON period δT and decreases with voltage $-(V_o - V_1)$ during the switching OFF period $(1 - \delta)T$. As a result the voltage across capacitor C_2 is charged to V_0. The following equations were used to design the cascaded boost converter.

Output voltage

$$V_o = V_{in}/(1 - \delta)^2 \tag{50.3.1}$$

The current of the first inductor is

$$I_{L1} = I_o/(1 - \delta)^2 \tag{50.3.2}$$

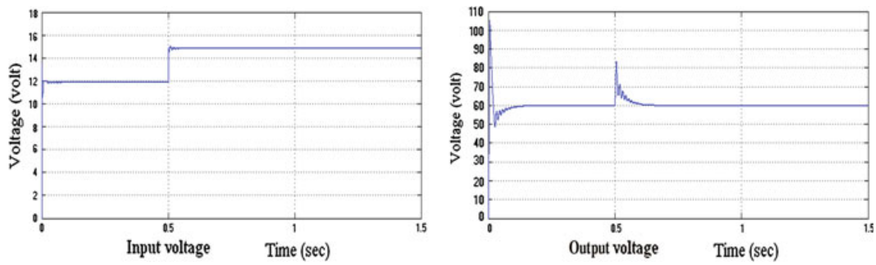

Fig. 50.8 Input and output voltage for the step change in input voltage of closed loop system

And the current of the second inductor is

$$I_{L2} = I_o/(1-\delta) \quad (50.3.3)$$

Simulation of the cascaded DC to DC boost converter is done using Matlab/Simulink and the results are presented and Matlab/simulink model is shown in Fig. 50.9. The following parameters are considered for the simulation of the cascaded boost converter. V_{in} = 12–15 V, V_o = 60 V, duty cycle ratio δ = 65 % and load resistance R_L = 25 Ω.

PV panel output voltage of 12 V is applied as input voltage. For the applied voltage of 12 V, the cascaded boost converter produces the output voltage of 65.5 V, output current of 2.49 A and the output power of 154.25 W. The input and output voltage waveform is shown in Fig. 50.10.

The closed loop system with step change in input voltage is shown in Fig. 50.11. The closed loop system is designed to give constant output voltage for a step change in output voltage. The input and output voltages of the closed loop cascaded boost converter with step change in voltages are shown in Fig. 50.12. Till 2.5 s, the

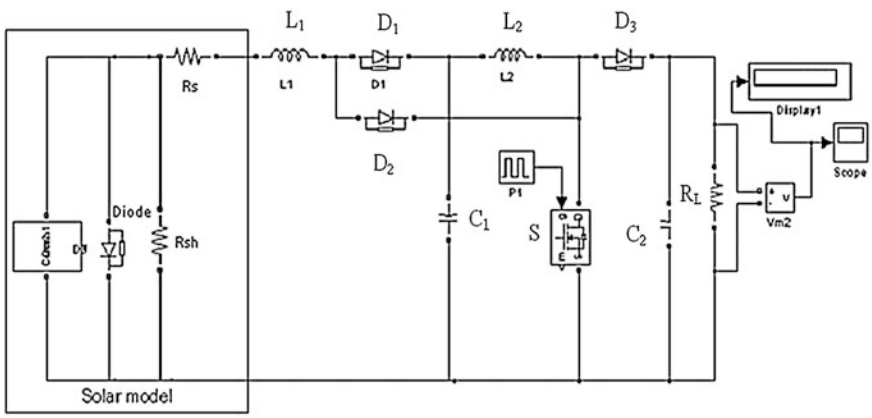

Fig. 50.9 Simulink model of cascaded DC to DC boost converter

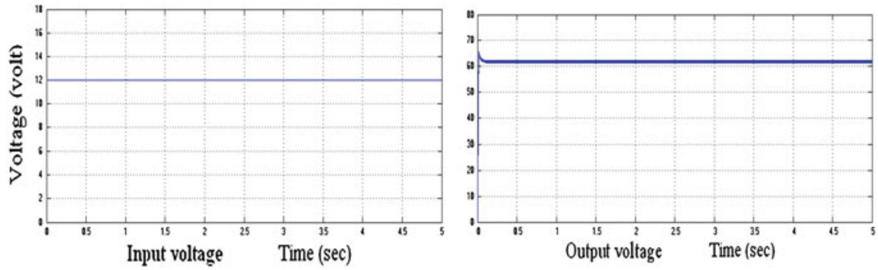

Fig. 50.10 Input voltage of cascaded boost converter

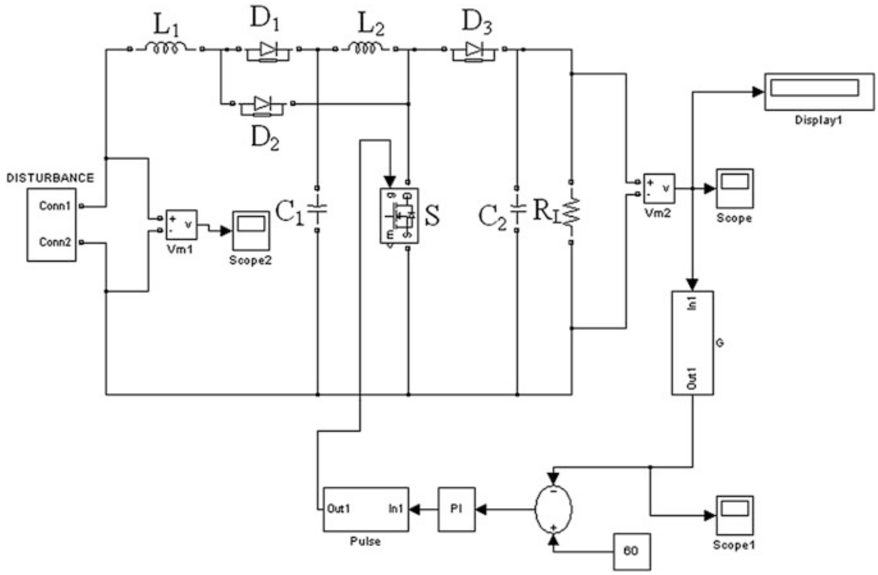

Fig. 50.11 Closed loop cascaded DC to DC boost converter with step change in input voltage

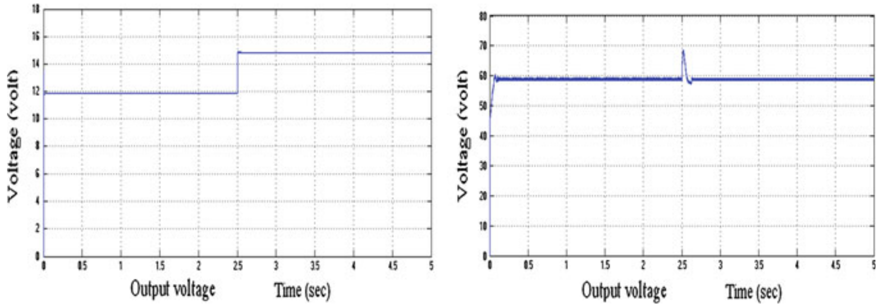

Fig. 50.12 Output voltage for the step change in input voltage of closed loop system

output voltage of the converter is 62.5 V for the input of 12 V. At 2.5 s, the input voltage increases from 12 to 15 V due to the step change in voltage. Hence the output voltage increases beyond 60 V. The output voltage of the converter is sensed and it is compared with a reference voltage. Then the PI controller generate the pulse for maintain the constant output voltage. This converter reaches the constant steady state voltage of 60 V at 2.65 s, which is shown in Fig. 50.12. At 2.5 s, the output current increases beyond the 2.482 A and reaches the steady state constant value at 2.65 s.

50.4 Performance Comparison Analysis and Experimental Results

The performance of the interleaved converter is compared with the performance of the cascaded boost converter and the comparison is presented in Table 50.1. The interleaved and cascaded DC to DC boost converter performances in open loop system are analysed for different input voltages. However, in closed loop system the converter maintains a constant output voltage for step change in input voltage.

For the input of 12 V, interleaved boost converter can deliver an output power of 126.33, but the cascaded boost converter can deliver an output power of 154.25 W. This is almost 27.92 W higher than the interleaved boost converter output power. For the same input of 12 V, the efficiency of the interleaved boost converter is 77.64 but the cascaded boost converter can give an efficiency of 91.21 %. This is almost 13.57 % higher than the interleaved boost converter efficiency. The above results confirm that the cascaded DC to DC boost converter has better performance efficiency and gives fastest response than interleaved DC to DC boost converter.

In order to verify the circuit operation and confirm the simulation results, cascaded DC to DC boost converter has been built and lab tested which is shown in Fig. 50.13. The solar panel input is applied to the cascaded DC to DC boost converter circuit. The switches are turned on and turned off by the pulse driver circuit. The PIC16F84A controller generates the driving pulses applied to the MOSFET to maintain the constant output voltage across the load. The output voltage of cascaded DC to DC boost converter is 68.7 V for the input of 13.53 V, which is closely in line with the simulation result.

Table 50.1 Performance comparison

Name of the boost converter	Input voltage (V)	Output voltage (V)	Output current (A)	Input power (W)	Output power (W)	Efficiency (%)
Interleaved boost converter	12	56.2	2.25	162.7	126.33	77.64
Cascaded boost converter	12	62.15	2.49	169.1	154.25	91.21

Fig. 50.13 Hardware setup of the cascaded DC to DC boost converter

50.5 Conclusion

In this paper, an interleaved and a cascaded DC to DC boost converter is designed, developed and its performances are compared. In closed loop system both converters maintained the constant output voltage. The cascaded boost converter system performances are good compared to the interleaved boost converter system in terms of its output current, output power and efficiency. The proto type model of cascaded boost converter has been built and lab tested. The obtained simulation results are in close conformity with the obtained experimental results. Hence the cascaded DC to DC boost converter is the better choice to maintain the constant output voltage under non-linear and step change in input voltages for the solar power installation system with high efficiency. It is observed that the cascaded boost converter system has the advantages like high efficiency, low ripple content, reduced number of switching component and fastest response.

References

1. Tafticht T, Doumbia ML, Chériti A (2008) An improved maximum power point tracking method for photovoltaic systems. Renew Energy 33(11):1508–1516
2. Enrique JM, Duran E, Sidrach de Cardona M, Andujar JM, Bohorquez MA, Carratero J (2005) A new approach to obtain IV and PV curves of photovoltaic modules by using DC/DC converters. In: Record of the IEEE photovoltaic specialist conference, pp 1769–1722
3. Bagaewadi MD, Fernandes BG, Subrahmanyan RVS (2000) A novel soft switched boost converter using a single switch. In: Power electronics and motion control conference, pp 412–416
4. Abutbul O, Gherlitz A, Berkovich Y, Ioinovici A (2003) Step-up switching-mode converter with high voltage gain using a switched capacitor circuit. IEEE Trans Circuits Syst I Fundam Theory Appl 50(8):1098–1102
5. Tseng KC, Liang TJ (2004) Novel high efficiency step up converter. IEE Proc Electr Power Appl 151(2):182–190

6. Sungsik P, Sewan C (2010) Soft switched CCM boost converters with high voltage gain for high power applications. IEEE Trans Power Electron 25(45):1211–1217
7. Kalirasu A (2012) Non isolated soft switching DC-DC converter for solar installation. Lap Lambert Academic Publishing GmbH & Co, Germany
8. Kalirasu A, Dash SS (2012) Embedded controlled high gain cascaded boost converter for solar installation system. Eur J Sci Res 89(1):109–120
9. Kalirasu A, Dash SS (2013) A novel high gain improved boost converter system for solar installation system. IUP J Electr Electron Eng 6(1):57–73
10. Lee CS, Oh YJ, Na KY, Kim YS, Kim NS (2013) Integrated BiCMOS control circuits for high performance DC-DC boost converter. IEEE Trans Power Electron 28(5):2596–2603
11. Lin BR, Dong JY (2012) New zero voltage switching DC-DC converter for renewable energy conversion systems. IET Power Electron 5:393–400

Chapter 51
DC-DC Converter Based on Cockcroft-Walton for High Voltage Gain

D. Parameswara Reddy, V. Suvitha and K. Somasekhar

Abstract This paper proposes a high step-up DC-DC converter based on Cockcroft-Walton (CW) voltage multiplier without using step up transformer. The low input DC voltage is boost up by inductor (Ls) in DC-DC converter and the proposed circuit performs the inverter operation. The five-stage CW-voltage multiplier is applying low input AC voltage to high output DC voltage. It provides continuous input current with low ripple, high voltage gain, reduced switching losses, low voltage stress on the switches, diodes and capacitors and improving efficiency of the converter. Finally the proposed converter is validated by Matlab simulation.

Keywords Cockcroft-Walton (CW) voltage multiplier · Voltage gain · Boost converter

51.1 Introduction

The extensive use of electrical equipment has imposed severe demands for electrical energy and this trend is constantly growing. The conventional boost DC-DC converter can provide a very high voltage gain by using an extreme high duty cycle [1]. The step-up DC-DC converters have been proposed to obtain high voltage ratios without extreme high duty cycle by using isolated transformers or coupled inductors [2]. The current fed converters are providing low input current ripple and high voltage ratio. The step-up DC-DC converters without step-up transformers and

D. Parameswara Reddy (✉) · V. Suvitha · K. Somasekhar
Department of Electrical and Electronics Engineering, Prathyusha Institute of Technology and Management, Chennai 602025, Tamil Nadu, India
e-mail: dpreddy38@gmail.com

V. Suvitha
e-mail: suvithakarunakaran@yahoo.co.in

K. Somasekhar
e-mail: sekharkesani@gmail.com

C. Kamalakannan et al. (eds.), *Power Electronics and Renewable Energy Systems*,
Lecture Notes in Electrical Engineering 326, DOI 10.1007/978-81-322-2119-7_51

coupled inductors were presented [3]. The conventional Cockcroft-Walton voltage multiplier is very popular among high voltage DC applications. Replacing the step-up transformer with the boost type structure, the proposed converter provides higher voltage ratio than that of the conventional CW voltage multiplier [4]. The proposed converter operates in continuous conduction mode, so that switch stresses, the switching loss, and EMI noise can be reduced [5].

51.2 Steady State Analysis of Proposed Converter

The proposed converter is supplied by a low-level dc source, such as battery, PV module or fuel cell sources. The proposed converter consists of one boost inductor L_s, four switches (S_{m1}, S_{m2}, S_{c1}, and S_{c2}), and one n-stage CW voltage multiplier. S_{m1} (S_{c1}) and S_{m2} (S_{c2}) operate in complementary mode, and the operating frequencies of S_{m1} and S_{c1} are defined as f_{sm} and f_{sc}, respectively. In this paper, f_{sm} is set much higher than f_{sc}, and the output voltage is regulated by controlling the duty cycle of S_{m1} and S_{m2}, while the output voltage ripple can be adjusted by f_{sc}. As shown in Fig. 51.1, in an n-stage CW voltage multiplier, there are N (=2n) capacitors and N diodes.

51.2.1 Circuit Operating Principle

As shown in Fig. 51.1, the proposed converter is an integration of a boost converter with a CW voltage multiplier. S_{m1} (S_{c1}) and S_{m2} (S_{c2}) operate in complementary mode, and the operating frequencies of S_{m1} and S_{c1} are defined as f_{sm} and f_{sc}, respectively.

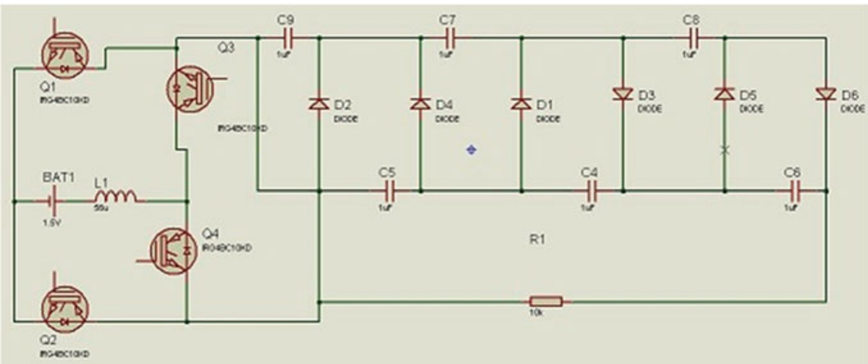

Fig. 51.1 Proposed converter with N-stage CW voltage multiplier

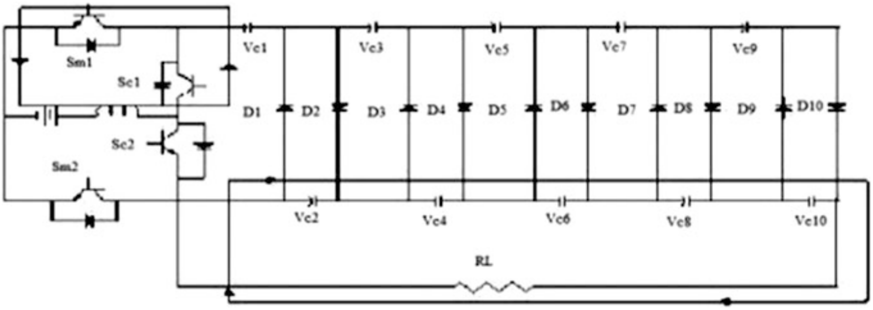

Fig. 51.2 Mode-1

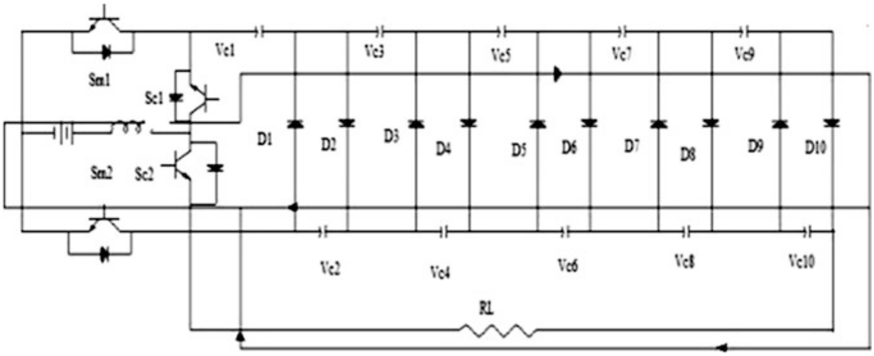

Fig. 51.3 Mode-2

The proposed converter and the characteristic behavior of each mode in both positive and negative-half cycles are presented as follows:

Mode-1: The boost inductor is charged by the input DC source, the odd-group of capacitors C_1, C_3, C_5, C_7, C_9 are Floating, and the even-group of capacitors C_2, C_4, C_6, C_8, C_{10} and are Supply the load as shown in Fig. 51.2.
Mode-2: D_8 is conducting and D_1 to D_9 are not conducting, thus, the even-group capacitors C_2, C_4, C_6, C_8, C_{10} Charged and the odd-group capacitors C_1, C_3, C_5, C_7, C_9, and C_9 are discharged by i_γ (Fig. 51.3).
Mode-3: D_8 is conducting, thus, C_2, C_4, C_6, C_8, C_{10} are charged while C_1, C_3, C_5, C_7, C_9 are discharged by i_γ (Fig. 51.4).
Mode-4: D_{10} is conducting, thus, C_2, C_4, C_6, C_8 and C_{10} are charged while C_1, C_3, C_5, C_7 and C_9 are discharged by i_γ (Fig. 51.5).
Mode-5: D_8 is conducting, thus, C_2, C_4, C_6 and C_8 are charged while C_1, C_3, C_5 and C_7 are discharged by i_γ (Fig. 51.6).
Mode-6: D_6 is conducting, thus, C_2, C_4 and C_6 are charged while C_1, C_3 and C_5 are discharged by i_γ (Fig. 51.7).

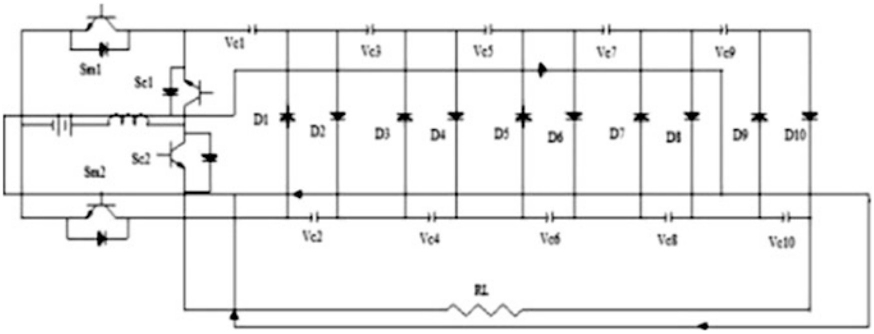

Fig. 51.4 Mode-3

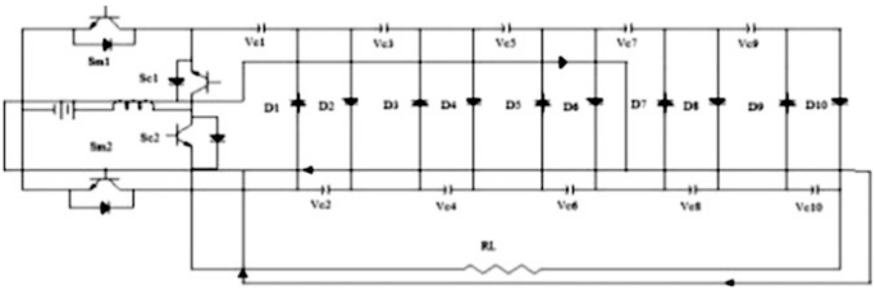

Fig. 51.5 Mode-4

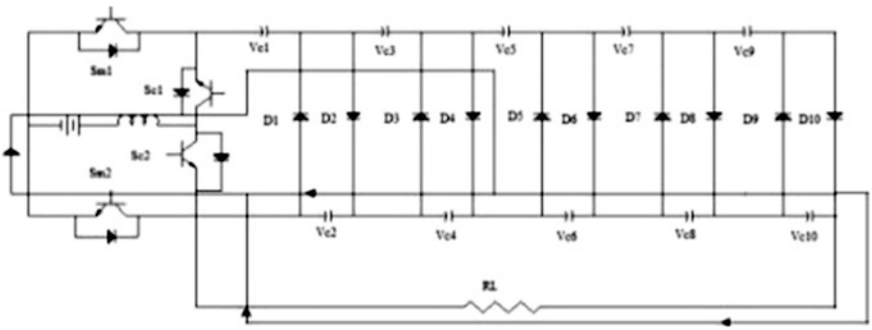

Fig. 51.6 Mode-5

Mode-7: D_4 is conducting, thus, C2 and C_4 are charged whileC_1 and C_3 are discharged by i_γ (Fig. 51.8).
Mode-8: D_2 is conducting, thus, C_2 is charged while C_1 is discharged by i_γ (Fig. 51.9).

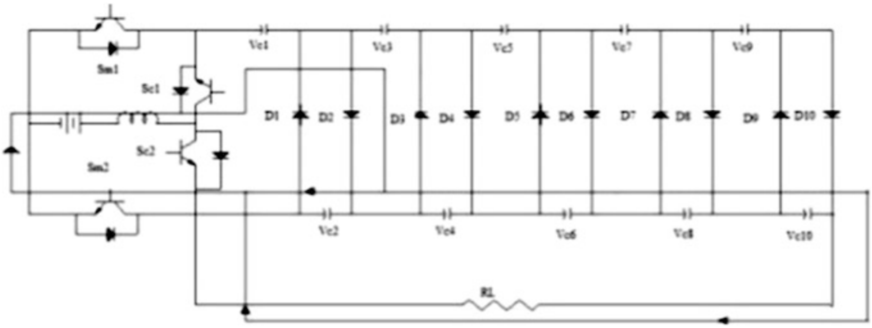

Fig. 51.7 Mode-6

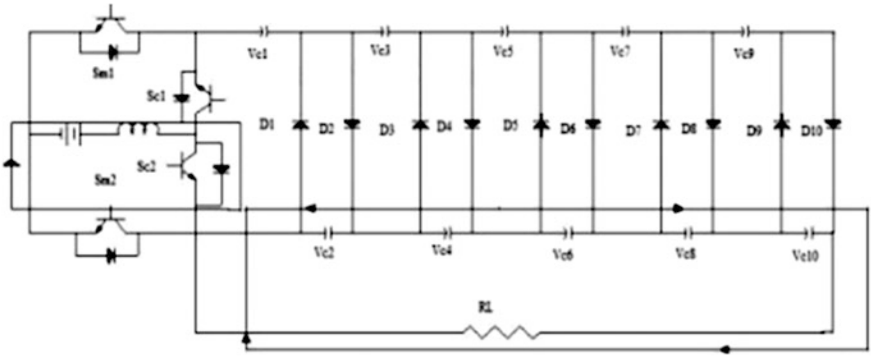

Fig. 51.8 Mode-7

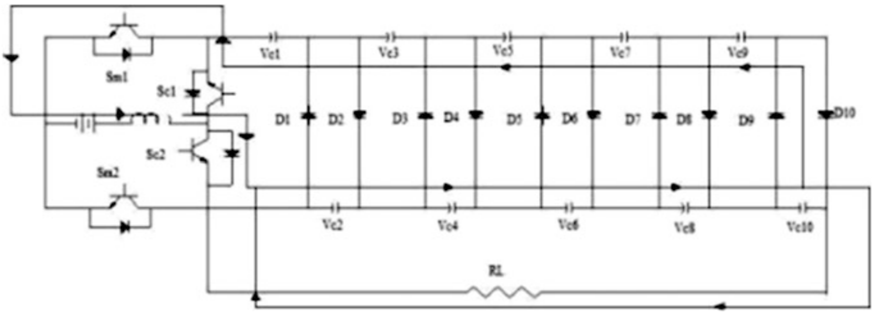

Fig. 51.9 Mode-8

Mode-9: S_{m2} and Sc_2 are turned on, S_{m1}, Sc_1 and all CW diodes (D_1 to D_{10}) are not conducting. The boost inductor is charged by the input DC source, the even-group capacitors C_2, C_4, C_6, C_8 and C_{10} are supply the load, and the odd-group capacitors C_1, C_3, C_5, C_7 and C_9 are floating (Fig. 51.10).

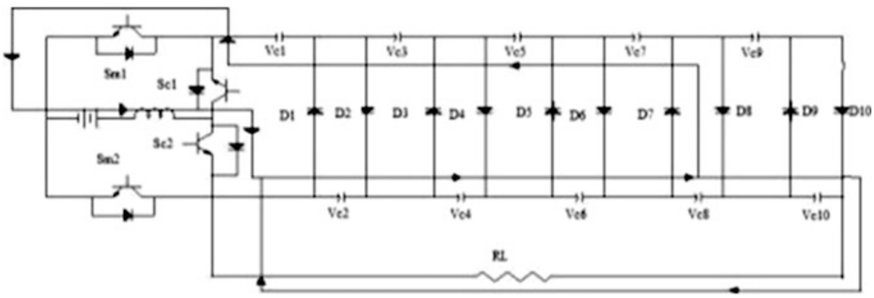

Fig. 51.10 Mode-9

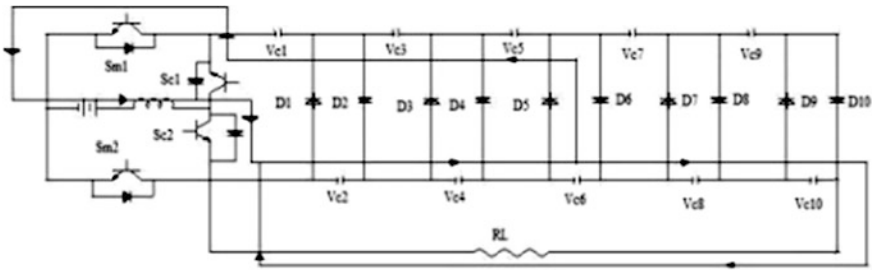

Fig. 51.11 Mode-10

Mode-8: D_9 is conducting, thus, the even-group capacitors C_2, C_4, C_6, C_8 and C_{10} are discharged and the odd-group capacitors C_1, C_3, C_5, C_7, and C_9 are charged by i_γ as shown in Fig. 51.2 (Fig. 51.11).
Mode-9: D10 is conducting, thus, C_2, C_4, C_6, C_8, C_{10} and C_{12} are discharged and C_1, C_3, C_5, C_7 and C_9 are charged by i_γ, C_{14} is supply load current and C_{13} is floating as shown in Fig. 51.2 (Fig. 51.12).
Mode-10: D_9 is conducting, thus, C_1, C_3, C_5, C_7 and C_9 are charged by i_γ, while all even capacitors C_2, C_4, C_6, C_8 and C_{10} are discharge (Fig. 51.13).
Mode-11: D_7 is conducting, thus, C_2, C_4, C_6 and C_8 are discharged and C_1, C_3, C_5 and C_7 are charged by i_γ, C_{10} are supply load current and C_9 are floating.
Mode-12: D_5 is conducting, thus, C_1, C_3 and C_5 are charged by i_γ, while all even capacitors C_2, C_4 and C_6 are Discharge, C_8, C_{10} are supply load current, and C_7, C_9 are floating.

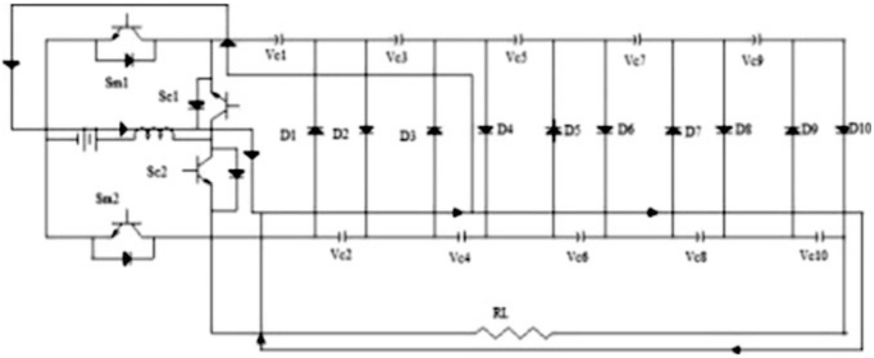

Fig. 51.12 Mode-11

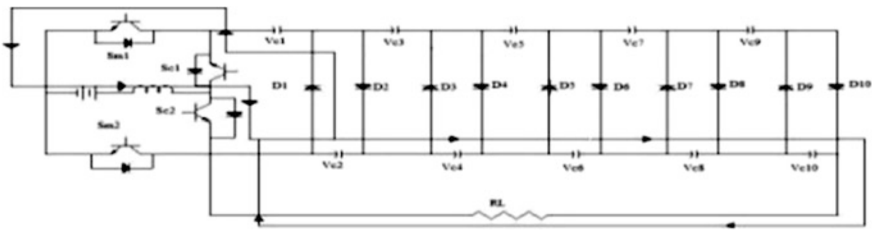

Fig. 51.13 Mode-12

51.2.2 Cockcroft Walton Voltage Multiplier

The Cockcroft Walton (CW) voltage multiplier is constructed by a cascade of n-stage with each stage containing two capacitors and two diodes. The CW-voltage multiplier having both capacitors and diodes are divided into odd group and even group according to their suffixes.

According to the polarity of current is i_γ, the operation of the proposed converter can be divided into two parts: positive conducting interval for $i_\gamma > 0$ and negative conducting interval for $i_\gamma < 0$. The switching pulse waveforms are shown in Fig. 51.14. In modes-2, 3, 4, 5, 6, 7 and 8, S_{m2} turns on, and the inductor transfers energy to the CW circuit through D_{10}, D_8, D_6, D_4, and D_2 respectively.

51.3 Simulation Circuit

The simulation circuit is separated into two parts; they are DC-DC boost converter with inverter and five stages of Cockcroft Walton voltage multiplier circuit. The proposed converter is supplied by a low-level DC source such as battery. The simulation circuit of proposed converter with five-stage CW voltage multiplier is shown in Fig. 51.15.

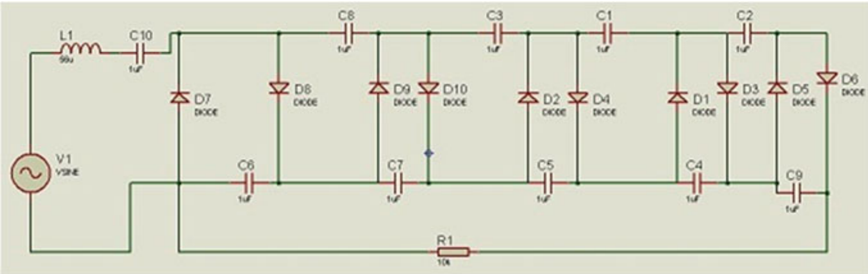

Fig. 51.14 Five-stage CW voltage multiplier circuit

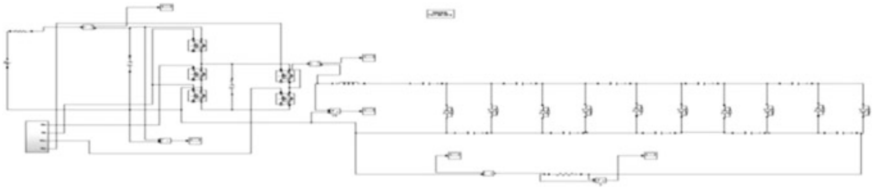

Fig. 51.15 Simulation circuit of proposed converter with five-stage CW voltage multiplier

Table 51.1 System specification of the prototype

Parameters	Ratings
Input DC voltage, Vin	12 V
Output voltage, Vo	119 V
Modulation frequency, fsm	52 kHz
Alternating frequency, fsc	1 kHz
Resistive load, RL	1 kW
Stage numbers, n	5
Capacitors, C1–C2	470 µF

The frequency fsm (60 kHz) is set much higher than fsc (1 kHz), and the output voltage is regulated by controlling the duty cycle of Sm1 and Sm2, while the output voltage ripple can be adjusted by fsc in Sc1 and Sc2. The system specification of the prototype designs is shown in Table 51.1.

51.4 Design Considerations of Proposed Converter

In this section, the voltage and current stresses on each capacitor, switch, and diode will be considered. Moreover, the values of inductor and capacitors will be discussed as well.

51.4.1 Capacitor Voltage Stress

In steady-state condition, assuming that all capacitors are large enough, then each capacitor in an n-stage CW voltage multiplier, theoretically it has the same voltage except the first one, which has one half of the others. It can be seen that the capacitor voltage of the proposed converter only depends on the input voltage and duty cycle, while the capacitor voltages of the others are dependent on the number of the cascade stages, thus the determination of the capacitor rating is easier for the proposed converter.

51.4.2 Capacitance of CW-Voltage Multiplier

In steady-state condition, assuming that all capacitors are large enough, then each capacitor in an n-stage CW voltage multiplier, theoretically it has the same voltage except the first one, which has one half of the others. It can be seen that the capacitor voltage of the proposed converter only depends on the input voltage and duty cycle, while the capacitor voltages of the others are dependent on the number of the cascade stages, thus the determination of the capacitor rating is easier for the proposed converter.

51.4.3 Formula and Mathematical Representation

The individual stages are:

C1 = C′1 = C2 = C′2 = Cn = C′n

$$\Delta V_n = \left(\frac{q}{C}\right)n \tag{51.1}$$

$$\Delta V_{n-1} = \left(\frac{q}{C}\right)[2n + (n-1)] \tag{51.2}$$

By summation and with q = I/f

$$\Delta V_0 = \frac{1}{fc}\left(\frac{2n^2}{3} + \frac{n^2}{2} - \frac{n}{6}\right) \tag{51.3}$$

- $V\ out = 2n * V\ ac.$ (51.4)

  - n = Number of Stags.
  - V ac = Peak input AC voltage.

- V out = 2(5)*11.95.
- V out = 119.5V.

51.5 Simulation Results and Waveform Analysis

The system specifications and the waveform explain in detail the operation of proposed DC-DC boost converter with five-stage Cockcroft Walton voltage multiplier. Components of the prototype are summarized in Tables 51.1 and 51.2, respectively. Moreover, Matlab/Simulink is applied to simulate the mathematic model and control strategy of the proposed converter. Some selected waveforms of the proposed converter at $Vin = 12$ V and $Vo = 119$ V for both simulation and experiment. The experimental waveforms of the switching signals, vo, iL, $v\gamma$, and $i\gamma$. Obviously, the simulation results well agree with experimental results.

51.5.1 Simulation and Experimental Results

The output waveform of the boost converter of DC input voltage is shown in Fig. 51.16. Some selected waveforms of the proposed converter Vin = 12 V, and Vout = 119 V for both simulation and experiment. The upper part of the switching signals of simulation for the four switches, which Sc1and Sc2 are operated at fsc, and Sm1 and Sm2 are operated at fsm.

The simulation of switching pulse waveforms in DC-DC boost converter is shown in Fig. 51.17. The simulation of output voltage waveform is shown in

Table 51.2 Component list for the prototype

Components description	Symbol	Value/part no.
Control IC	–	PIC16F788A
CPLD	–	LC4, 256 V
Boost inductor	Ls	1.5 mH
Power switches	Sm1, Sm2, Sc1, Sc2	IRF640
Capacitors	C1–C2	470 μF
Diodes	D1–D2	SF20L60U
Gate driver	–	HCPL-3120

Fig. 51.16 Simulation of boost converter of DC input voltage waveform

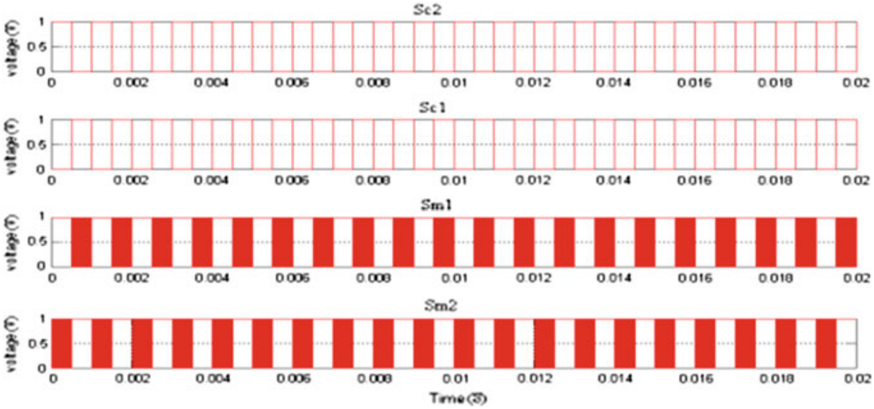

Fig. 51.17 Simulation of gate switching pulse waveforms

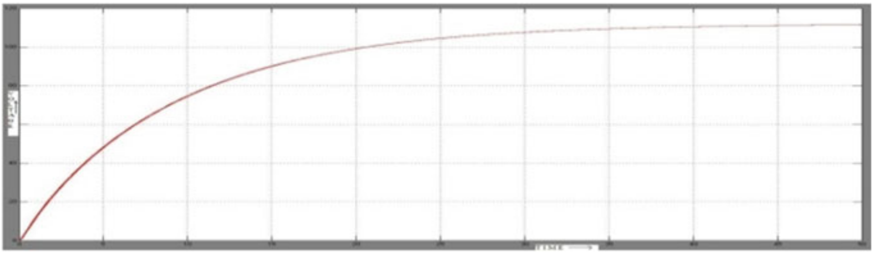

Fig. 51.18 Simulation of output voltage waveform

Fig. 51.18. The results also influence the terminal voltage Vγ and current iγ of the CW voltage multiplier.

Thus the simulation of the DC-DC boost converter using Cockcroft Walton voltage multiplier was successfully carried out using MATLAB Simulink software and the output waveforms were observed (Fig. 51.19).

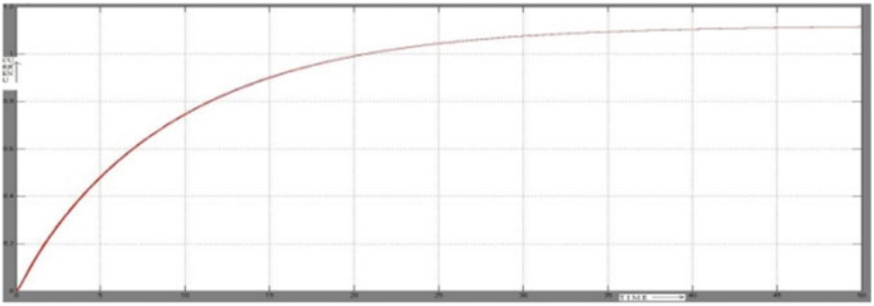

Fig. 51.19 Simulation of output current waveform

51.6 Conclusion

In this paper, a high step-up DC-DC converter based on CW voltage multiplier without a line or high-frequency step-up transformer was presented to obtain a high voltage gain. Finally, the simulation and experimental results proved the validity of theoretical analysis and the feasibility of the proposed converter. In future work, the influence of loading on the output voltage of the proposed converter will be derived for completing the steady-state analysis. Thus the design, simulation and analysis of proposed DC-DC boost converter with five-stage Cockcroft Walton voltage multiplier was done.

References

1. Hwang F, Shen Y, Jayaram SH (2006) Low-ripple compact high-voltage DC power supply. IEEE Trans Ind Appl 42(5):1139–1145
2. Kobougias C, Tatakis EC (2010) Optimal design of a half-wave Cockcroft-Walton voltage multiplier with minimum total capacitance. IEEE Trans Power Electron 25(9):2460–2468
3. Yang LS, Liang TJ, Chen JF (2009) Transformer less DC-DC converters with high step-up voltage gain. IEEE Trans Ind Electron 56(8):3144–3152
4. Abutbul O, Gherlitz A, Berkovich Y, Ioinovici A (2003) Step-up switching-mode converter with high voltage gain using a switched-capacitor circuit. IEEE Trans Circuits Syst I, Fundam Theory Appl 50(8):1098–1102
5. Malesani L, Piovan R (1993) Theoretical performance of the capacitor- diode voltage multiplier fed by a current source. IEEE Trans Power Electron 8(2):147–155
6. Axelrod B, Berkovich Y, Ioinovici A (2008) Switched-capacitor/switched-inductor structures for getting transformer less hybrid DC-DC PWM converters IEEE Trans Circuits Syst. I Regular Papers 55(2):687–696
7. Bellar MD, Watanabe EH, Mesquita AC (1992) Analysis of the dynamic and steady-state performance of Cockcroft-Walton cascade rectifiers. IEEE Trans Power Electron 7:526–534
8. Li W, He X (2011) Review of nonisolated high-step-up DC-DC converters in photovoltaic grid-connected applications. IEEE Trans Ind Electron 58(4):1239–1250

9. Wai RJ, Lin CY, Duan RY, Chang YR (2007) High-efficiency DC-DC converter with high voltage gain and reduced switch stress. IEEE Trans Ind Electron 54(1):354–364
10. Kobougias IC, Tatakis EC (2010) Optimal design of a half-wave Cockcroft-Walton voltage multiplier with minimum total capacitance. IEEE Trans Power Electron 25(9):2460–2468

Chapter 52
New Direct Torque Control Algorithm for High Performance Induction Motor

S. Srinivasan and A. Sabari Raja

Abstract This paper presents a new Direct Torque Control algorithm for high performance Induction motor with the information obtained from only one shunt resistor. The objective here is to develop low cost and high efficient induction motor drive using an algorithm in which the stator currents are remade to obtain the electromagnetic torque and motor flux using the DC link currents. A modified look up table is obtained by analyzing the theoretical background of the direct torque control. The current access table is designed for phase current reconstruction. Simulation results are shown for the proposed scheme of DTC using induction motor drive in order to validate the concept.

Keywords Direct torque control algorithm · Induction motor · Discrete space vector modulation (DSVM)

52.1 Introduction

The Direct Torque Control also known as direct self control was introduced in the mid 1980s particularly for voltage fed PWM inverter drives. This technique gives the same performance as given by the vector controlled drives and hence widely used in industrial applications due to its simple control structure. DTC uses wide area of application used in machines like PMSM, PMBLDC and also in reluctance motor. In this paper we propose low cost DTC algorithm for high performance induction motor. The stator flux vector and the electromagnetic torque are directly calculated from the voltage and current derived from single dc-link voltage sensor (voltage divider) and a single dc-link current sensor (shunt resistor). The phase

S. Srinivasan (✉) · A.S. Raja
Department of Electrical and Electronics Engineering, Hindustan University, Chennai, India
e-mail: srinivasan@hindustanuniv.ac.in

A.S. Raja
e-mail: sabari87mtech@gmail.com

C. Kamalakannan et al. (eds.), *Power Electronics and Renewable Energy Systems*,
Lecture Notes in Electrical Engineering 326, DOI 10.1007/978-81-322-2119-7_52

currents are estimated by two dc-link current measurements processes. Stator currents and dc-link voltages are required for DTC scheme to estimate the values of stator flux and electromagnetic torque. The current feedback for the closed loop control is usually obtained by sensing phase current by current sensors. Typically at least two output of the power converter to provide current feedback signals. These Sensors though gives good results, suffers with the disadvantage of high cost, encumbrance with non-linearity. The latest development in this is to use Single current sensor to reconstruct phase current from the dc link current sensor [1].

Some methods adjusts the pulse width modulation (PWM) signals to ensure the two-phase Currents. DTC technique for induction motor and PMSM are dealt only in few papers in which the algorithm works in two steps. The stator currents are initially obtained from a model of the motor which is adjusted to get the corrected value later by sensing the dc-link current. This algorithm suffers with the following drawbacks 1. It requires additional computation to do and 2. The necessity of knowing the stator transient inductance. In the proposed method, a DTC scheme for Induction motor is proposed with a low cost single shunt current sensor which overcomes the above stated problems.

To summarise the rest of the paper, in Sect. 52.2, the basic DTC structure and its working is given. The control strategy and the control algorithm is given in Sects. 52.3 and 52.4 respectively. The simulation results are shown in Sect. 52.5. Finally conclusion is given in Sect. 52.6.

52.2 How DTC Works?

The advanced scalar control technique DTC directly control the stator torque and flux using the inverter voltage space vector selection through a look up table [2]. The instantaneous stator flux and output motor torque are calculated by measuring the current and voltage values. The flux and torque are brought to its rated value over a given period are possible with the help of control algorithm based on flux and torque hysteresis controllers. The fundamental functional blocks used to implement the DTC scheme are represented in Fig. 52.1.

Here the equation for stator flux vector and the torque of the motor, $T_{em,}$ can be calculated by the Eqs. (52.1) and (52.2) respectively. These necessities the applied voltage vector V_s and the measured stator current $\mathrm{I_S}$, measured stator resistance R_s and the number of Poles P

$$\varphi_{\mathrm{s}} = \int (V_s - R_s I_s)\ \mathrm{dt} \tag{52.1}$$

$$I_{em} = y_z\, with \underset{y}{\rightarrow} = \frac{3}{2} p(\varphi_s \times I_s) \tag{52.2}$$

The switching table is derived from applied voltage vectors using a hysteresis control. This is possible only when the magnitude of electromagnetic torque and

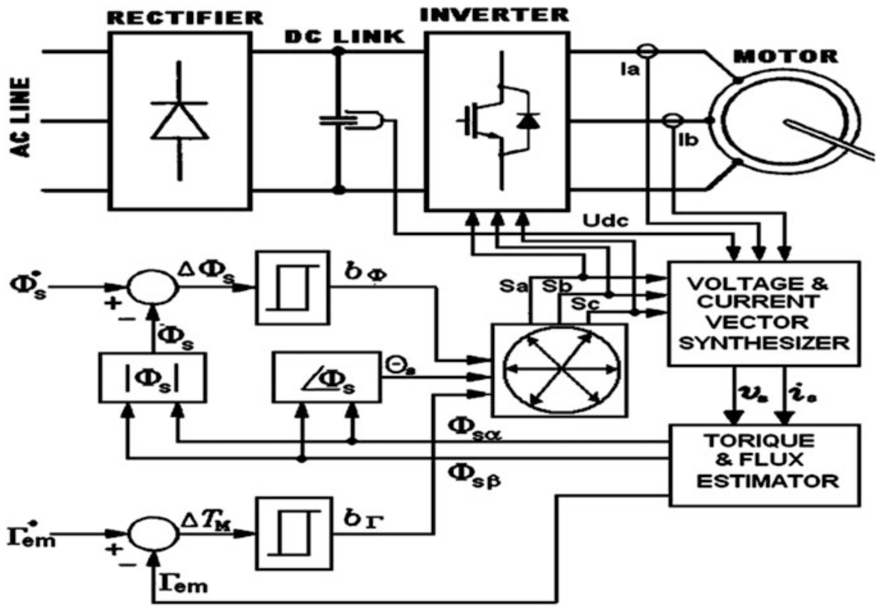

Fig. 52.1 Block diagram of DTC

stator flux are known. From the measured dc-link voltage U_{dc} Eqs. (52.3) and (52.4) can be obtained which gives the polar components of stator voltage on perpendicular reference frame where the switching states S_a, S_b *and* S_c are given by [2, 3].

$$V_{s\alpha} = \sqrt{\frac{2}{3}} U_{dc} \left(S_a - \frac{1}{2}(S_b + S_c) \right) \tag{52.3}$$

$$V_{s\beta} = \frac{1}{\sqrt{2}} U_{dc} (S_b - S_c) \tag{52.4}$$

And Stator current components are given by,

$$I_{s\alpha} = \sqrt{\frac{3}{2}} I_a \tag{52.5}$$

$$I_{s\beta} = \frac{1}{\sqrt{2}} (I_b - I_c) \tag{52.6}$$

The stator resistance R_s can be assumed constant. The voltage vector applied to the motor will be constant during a switching period. The EMF can be integrated to get the stator flux and is given by

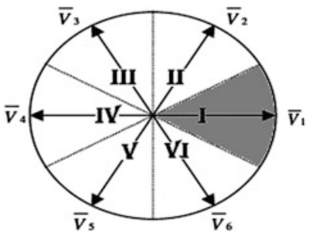

Fig. 52.2 DTC vectors and inverter voltage vectors

$$\varphi_{s\alpha} = \int (V_{s\alpha} - R_s I_{s\alpha})dt \tag{52.7}$$

$$\varphi_{s\beta} = \int \left(V_{s\beta} - R_s I_{s\beta}\right)dt \tag{52.8}$$

The switching period is constant during the switching period and Eqs. (52.7) and (52.8) can be written as

$$\varphi_{s\alpha} = \varphi_{s\alpha} + (V_{s\alpha} - R_s I_{s\alpha})T_s \tag{52.9}$$

$$\varphi_{s\beta} = \int \left(V_{s\beta} - R_s I_{s\beta}\right)dt \tag{52.10}$$

where T_s represents the control loop period.

The magnitude of the stator flux can be given by

$$\varphi_s = \sqrt{\left(\varphi_{s\alpha}^2 + \varphi_{s\beta}^2\right)} \tag{52.11}$$

and hence the electromagnetic torque

$$T_{em} = \frac{3}{2}p(\varphi_{s\alpha} - \varphi_{s\beta}I_{s\alpha}) \tag{52.12}$$

The switching combination is chosen for inverter operation such that it has six equally spaced vectors have same amplitude and two zero voltage vectors as shown in Fig. 52.2.

52.3 Control Strategy

The DTC method proposed in this paper requires only one shunt resistor for dc link current measurement as shown in Fig. 52.3 where as it is two in the basic DTC scheme.

By using Discrete Space Vector Modulation (DSVM) technique, it is possible to get new voltage vectors with respect to the basic scheme [4]. Out of the 12 new voltage vectors, only six are used in the proposed scheme as shown by red line in Fig. 52.4.

The new look up table for the new scheme is given for the modified DTC in Table 52.1.

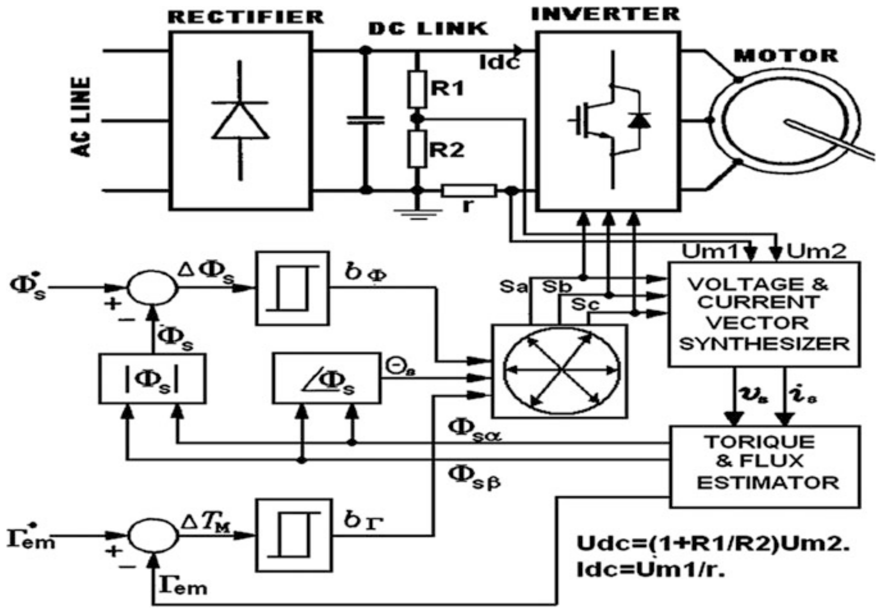

Fig. 52.3 Proposed DTC scheme

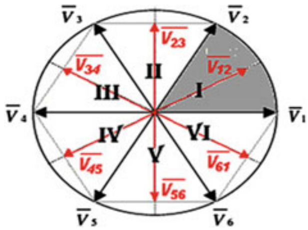

Fig. 52.4 Proposed DTC sectors and inverter voltage vectors

Table 52.1 Proposed DTC switching table for sensing dc-link current and stator current reconstruction

bΦ	b_r	Sect I	Sect II	Sect III	Sect IV	Sect V	Sect VI
1	1	v_{56}	V_{61}	V_{12}	V_{23}	V_{34}	V_{45}
	0	V_{34}	V_{45}	V_{56}	V_{61}	V_{12}	V_{23}
0	1	V_{61}	V_{12}	V_{23}	V_{34}	V_{45}	V_{56}
	0	V_{23}	V_{34}	V_{45}	V_{56}	V_{6I}	V_{12}

52.4 Control Algorithm

One of the most important purposes for single-shunt three phase reconstruction is to reduce the cost. This, in turn, simplifies the sampling circuit to one shunt resistor and some other electronic components. Moreover, the single-shunt algorithm allows the use of power modules that do not provide, for each phase, individual ground connection. Another single-shunt measurement advantage is that the same circuit is being used to sense all three phases. For all measurements, the gains and offset will be the same, which eliminate the software calibration of each phase measurement structure.

52.4.1 DC Current Measurement

Figure 52.5 explains how the dc current is sensed using only one shunt resistor in an voltage source Inverter. A measurement shunt resistor is placed between the lower side power switches emitter terminals and the negative dc bus rail that is connected to the ground. The voltage drop across the shunt resistor is amplified and level shifted. In the case of nonisolated grounds between control circuit and power circuit, the signal is sent directly to the analog-to-digital converter (ADC) inputs of a digital signal controller (DSC), where control algorithm for motor is implemented and executed in real time. For more protection, a linear photo isolator amplifier used to isolate the control circuit from power circuit.

52.4.2 Phase Current Reconstruction

In the basic DTC scheme, there is one current flowing in the dc link for every active voltage vector, where as it is measured in two intervals in the new scheme according to the switch states. The relationship between the dc-link current and the phase currents for the two schemes are shown in Tables 52.2 and 52.3.

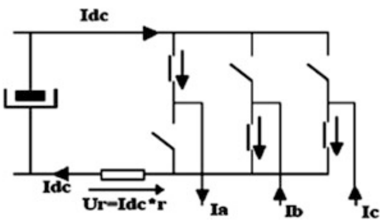

Fig. 52.5 DC current sensing in inverter

Table 52.2 Basic DTC voltage vector phase current measurement

Active voltage vector	DC-link Current
V_1	la
V_2	−Ic
V_3	lb
V_4	−la
V_5	Ic
V_6	−lb

Table 52.3 Proposed DTC voltage vector phase current measurement

Active voltage vector	1st interval DC-link current	2nd interval DC-link current
V_{12}	la	−Ic
V_{23}	−Ic	lb
V_{34}	lb	−la
V_{45}	−la	Ic
V_{56}	Ic	−lb
V_{61}	−lb	la

By using the two-interval discrete space vector modulation, for each one of the new six active vectors, we can reconstruct the three-phase motor currents. It is clear that by knowing the inverter switch position in two intervals of each period the actual currents for two phases can be obtained without further computing process. Assuming that, *I*dc1 is the dc-link current measured at the end of the first interval and *I*dc2 is the one measured at the second half interval, are summarized in Table 52.4, the three-phase motor currents *Ia*, *Ib*, and *Ic*are given in function of voltage vector and the dc-link current. A phase-current reconstruction time.

Table 52.4 Phase current reconstruction relationship for each voltage vector

Voltage vector	Ia	Ib	Ic
V_{12}	Idc_1	$Idc_2 - Idc_1$	$-Idc_2$
v_{23}	$Idc_1 - Idc_2$	Idc_2	$-Idc_1$
V_{34}	$-Idc_2$	Idc_1	$Idc_2 - Idc_1$
V_{45}	$-Idc_1$	$Idc_1 - Idc_2$	Idc_2
V_{56}	$Idc_2 – Idc_1$	$-Idc_2$	Idc_1
V_{61}	Idc_2	$-Idc_1$	$Idc_1 - Idc_2$

52.4.3 Motor Speed Range

In two-interval DSVM, the sampling period is divided into two equal time intervals and each of them is supplied with one VSI voltage vectors. In this way it is possible to generate 14 vectors. The proposed low-cost DTC algorithm uses only six voltage vectors out of them which can be used for phase-current reconstruction. The magnitude of the generated voltage vector V_1 using the basic DTC algorithm can be written as

$$|\mathrm{V}_1| = 2/3U_{dc} \tag{52.13}$$

The generated voltage vector $V12$ using the proposed DSVM. DTC algorithm is given by

$$|\mathrm{V}_{12}| = \frac{2}{3}U_{dc}\cos\frac{\pi}{6} = \frac{1}{\sqrt{3}}\,U_{dc} \tag{52.14}$$

The vector voltage magnitude ratio is given by

$$\mathrm{r} \;=\; |\mathrm{V}_{12}|/\,|\mathrm{V}_1| = \sqrt{3}/2 \tag{52.15}$$

Speed control is achieved by means of variable frequency. Apart from frequency, the applied voltage needs to be varied because the stator flux magnitude is kept constant by the DTC.

Neglecting the stator resistance drop, we can consider that the voltage magnitude, in steady state, is given by

$$V_{sn} = \varphi_{snw_s} \tag{52.16}$$

Reducing the voltage maximum magnitude will reduce the Rotational components of the back EMF, leading to a reduction in the maximum stator pulsation and hence to the speed range. The Maximum motor speed with the proposed algorithm is limited to 86 % compared to the original DTC control algorithm.

52.5 Simulation Results

The DTC scheme proposed for the high performance induction motor is simulated in the MATLAB environment (Figs. 52.6, 52.7, 52.8 and 52.9).

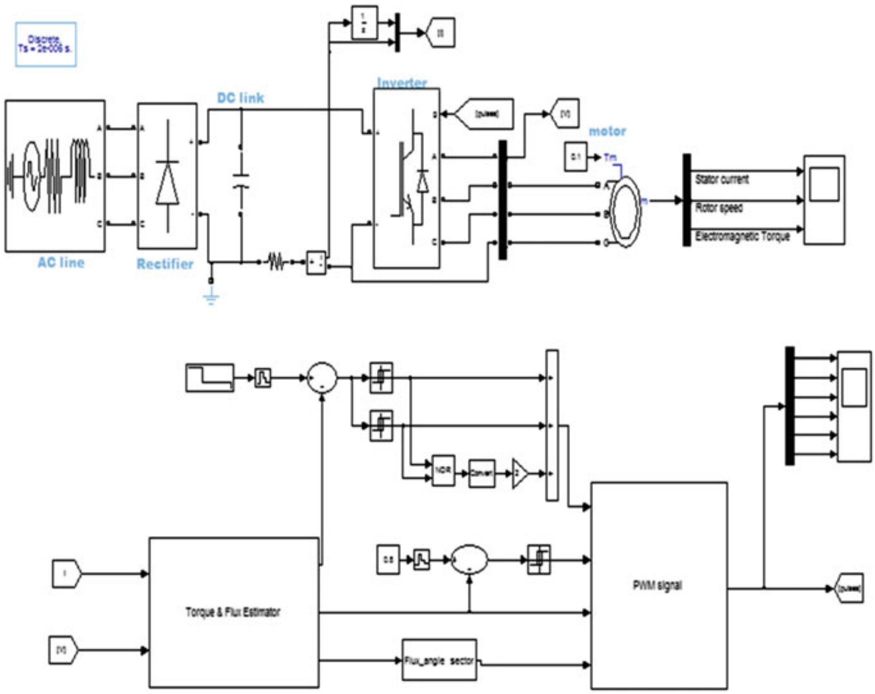

Fig. 52.6 Proposed DTC scheme simulation diagram

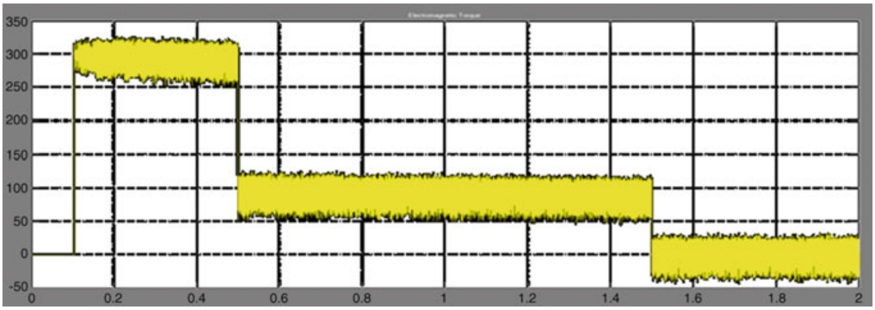

Fig. 52.7 Torque waveform

In the simulations, a sample frequency of 10 kHz is used. The dc-bus voltage V_{dc} equals 300 V and the desired grid rms voltage V_g equals 163 V with a fundamental frequency of 50 Hz was verified for a RL load with R = 10 ohms and L = 123 mH.

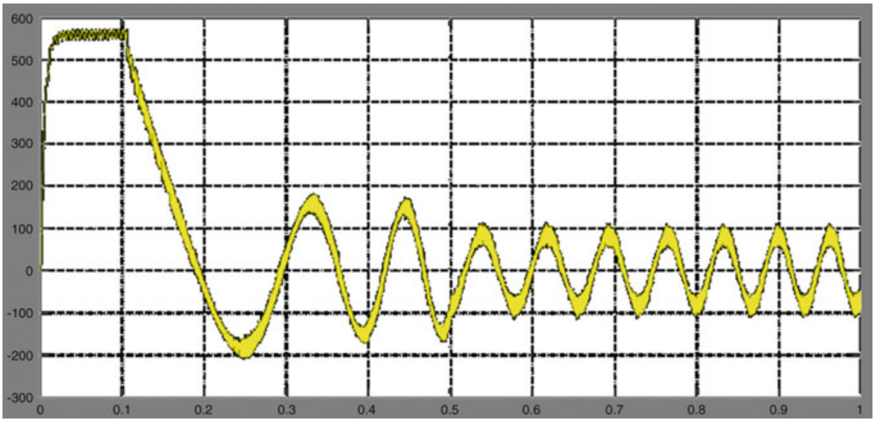

Fig. 52.8 Output current waveform

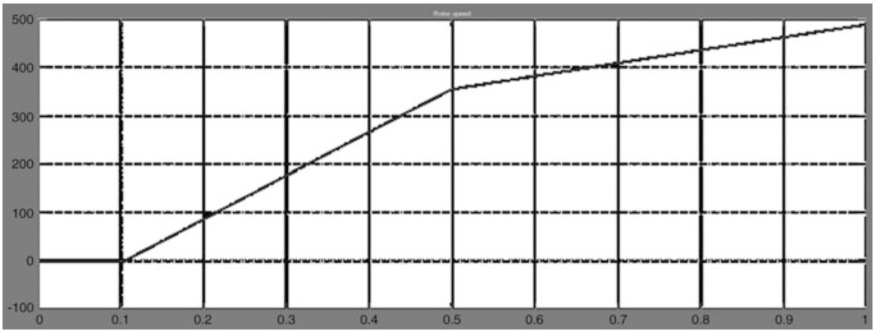

Fig. 52.9 Output speed waveform

52.6 Conclusion

In this paper, a new and low-cost direct torque control algorithm for IM drives has been presented where the phase-current reconstructed by having only one shunt resistor connected in the dc-link path. By using Discrete Space Vector Modulation (DSVM) technique with two equal time interval in the proposed method, there are twelve new voltage vectors are generated out of which only six are used for stator currents reconstruction to estimate the stator flux magnitude and the electromagnetic motor torque, by means of a simple modification in the basic DTC scheme; 30° zone shift strategy is applied. Hence the proposed scheme of DTC with single current sensor reduces the overall cost of the sampling circuit and other electronic devices compared to the existing method. Finally simulation results are shown to pave support to the proposed scheme.

References

1. Green TC, Williams BW (1989) Derivation of motor line-current waveforms from the dc-link current of an inverter. Proc IEE Elect Power Appl 136(4):196–204
2. Takahashi I, Noguchi T (1986) A new quick-response and high-efficiency control strategy of an induction motor. IEEE Trans Ind Appl, IA- 22(5):820–827
3. Zaid SA, Mahgoub OA, El-Metwally K (2010) Implementation of anew fast direct torque control algorithm for induction motor drives. IET Electr Power Appl 4(5):305–313
4. Metidji B, Taib N Rekiou T Bacha S (2012) Low cost direct-torque control algorithm for induction motor without AC phase current sensors. IEEE Trans Power Electr 27(9)

Chapter 53
Performance Analysis of Induction Generator Using Computational Technique

R. Gopikaramanan, R. Sridevi and C. Kumar

Abstract This paper probe about the performance analysis of the Self Excited Induction Generator feeds to linear load for various operating speed condition, capacitance and load condition using Particle swarm optimization (swarm intelligence) which has the advantage of reduced complexity and improved accuracy in solving the equations, the swarm intelligence is investigated for comparing that with the conventional method and Genetic algorithms in order to evaluate the performance of SEIG.

Keywords SEIG · Particle swarm optimization · Swarm intelligence · GA

53.1 Introduction

The self-excited induction generators (SEIG) or squirrel cage induction generator which plays a major role in industrial application and its versatile properties such as low maintenance and high efficiency have been made SEIG as a suitable one for energy conversion for remote locations to be incorporated with wind energy system better suits even for standalone application [1, 2]. These type of isolates setup along with SEIG has the capability to generate the power which can meet local demand of remote areas.

Where grid is unavailable or the laying the transmission line to such a remote village may cost too high in order to overcome this we can go for standalone system [3]. SEIG has many advantages such as DC power supply act as excitation is not

R. Gopikaramanan (✉) · R. Sridevi · C. Kumar
S.K.P.Engineering College, Thiruvannamalai, Tamil Nadu, India
e-mail: ps.er.gopi@gmail.com

R. Sridevi
e-mail: srisuhar06@gmail.com

C. Kumar
e-mail: drchkumararima@gmail.com

C. Kamalakannan et al. (eds.), *Power Electronics and Renewable Energy Systems*,
Lecture Notes in Electrical Engineering 326, DOI 10.1007/978-81-322-2119-7_53

required in the case of SEIG, simple and rugged in construction, reduced maintenance cost, Self capability of short circuit protection capability, no need of carbon brushes and no synchronizing problem which are the major concerns to concerned while we using synchronous generator. For past few years self excited induction generator has drawn considerable attention among the researcher due to its versatile quality and adoptability in many renewable energy application such as a standalone generator, applicable for variable speed application along with power electronic converter circuits and using conventional and non conventional energy sources [4]. This paper probe about the implementation of soft computing technique (swarm intelligence Algorithms), such as Particle swarm optimization, which is used to analyze the performance of the SEIG and got better results when compared to existing Evolutionary algorithm technique.

53.2 Analysis of SEIG and Problem Formulation

The steady state operating characteristics of the SEIG can be successfully analyzed using the equivalent circuit representation shown in the below Fig. 53.1.

R_S, R_R, R_L are the Resistances of Stator, Rotor, and Load respectively. X_S, X_R, X_M, X_C are the Reactance of Stator, Rotor, Magnetizing and Excitation parameter respectively. Y_S, Y_R, Y_M, Y_L, Y_C notated for Admittance value of Stator, Rotor, Magnetizing, Load and Excitation parameters respectively. F is the frequency in P. U. v is the ratio between rotor speed and synchronous speed which is expressed in P.U . I_S, I_R, I_L, are the current of stator, rotor and load parameters respectively. V_g, V_T, E_1 are the air gap, Terminal, air gap voltage at rated frequency expressed in P.U respectively [5, 6].

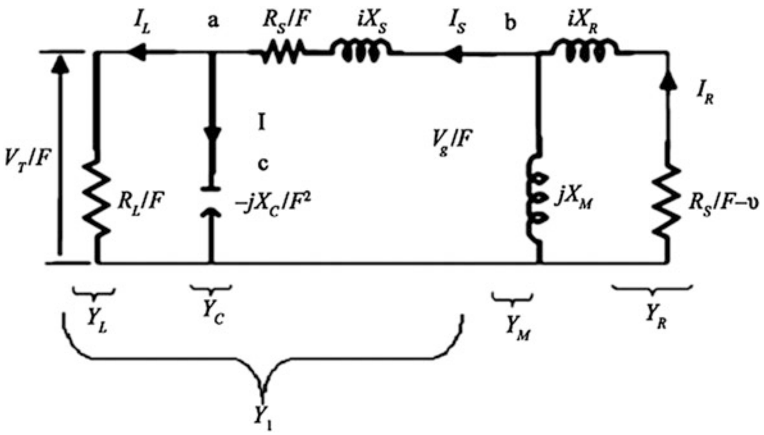

Fig. 53.1 Per phase equivalent circuit of SEIG

From the perphase equivalent circuit diagram shown above total current at node A can be given by the following Eq. (53.1)

$$E_1(Y_R + Y_M + Y_1) = 0 \tag{53.1}$$

During the condition of self excitation we have $E \neq 0$ which interprets that, the summation of all the admittances connected across the air gap have to be zero for the given value of the rotating shaft speed, excitation capacitance, generator parameters and load impedance, solution to the Eq. (53.4) gives the value of frequency F in P.U.

For the value of F which was obtained by solving Eq. (53.4) Corresponding Magnetizing reactance can be calculated by solving the Eq. (53.5) After solving the Eqs. (53.4) and (53.5) and determining the values of F and X_M, from the Magnetization curve obtained experimentally air gap voltage E_1 can be determined which relates V_g/F and X_M. Applying mesh current analysis was applied to the per phase equivalent circuit of the SEIG shown in Fig. 53.1, the stator current (I_S) and the current of the load (I_L) can be determined successfully from the following Eq. (53.6)

$$\begin{gathered} Y_1 = \frac{(Y_C + Y_L)Y_S}{Y_C + Y_L + Y_S} \quad Y_L = \frac{1}{(R_L/F)} \\ Y_M = \frac{1}{jX_M} \quad Y_C = \frac{1}{(-jX_C/F.\verb|^|2)} \\ Y_S = \frac{1}{(R_S/F) + jX_S} \quad Y_R = \frac{1}{\frac{R_R + (F-V)jX_R}{F-V}} \end{gathered} \tag{53.2}$$

$$Y_R + Y_M + Y_1 = 0 \tag{53.3}$$

$$\text{Real}\ (Y_R + Y_M + Y_1) = 0 \tag{53.4}$$

$$\text{Imag}(Y_R + Y_M + Y_1) = 0 \tag{53.5}$$

$$\begin{gathered} I_S = \frac{E_g/F}{(R_S/F) + jX_S - ((jX_C R_L)/(F\verb|^|2R_L - jFX_C))} \\ I_L = \frac{-jX_C I_S}{R_L F - jX_C} \qquad V_g = I_L R_L \end{gathered} \tag{53.6}$$

Subjected to Constraints

$$0.9 < F < 0.99$$
$$100 < Xm < 200$$

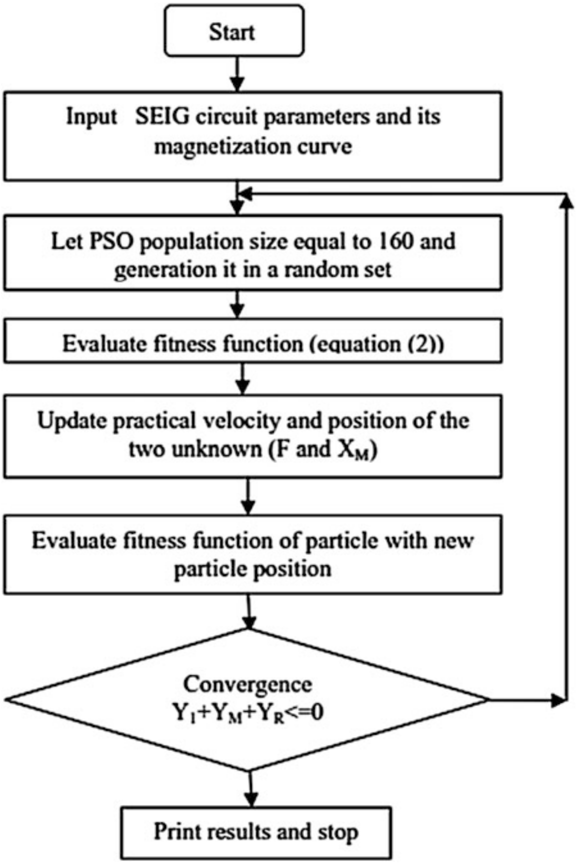

Fig. 53.2 Flow chart for the PSO analysis of SEIG

53.3 Particle Swarm Optimization

Optimization technique inspired from swarm behavior of the birds and fishes, how they search their food and how they communicating with the adjacent nodes about the information of the food to reach the food is observed and programmed [7, 8].

Particle swarm optimization based Analysis of SEIG The objective function and the constraints of the problem is same and it is solved using PSO algorithm to show the effectiveness of the PSO (Fig. 53.2).

53.4 System Results and Simulation

The simulation is carried out in the mat lab simulation package and the results are obtained by using PSO (Swarm intelligence) for the specification of the machine given in the appendix section, shown details in the Table 53.1 are for each set taken

Table 53.1 The input data (N, C, R)

Set no.	Speed (rpm)		C (μF)	R (Ω)	No. of samples
	From	To			
1	1,435	1,570	36	160	6
2	1,275	1,435	51	160	6
3	1,410	1,565	36	220	6
4	1,290	1,425	51	220	6

from the test machine in the range of speed and value of terminal capacitance have been chosen in such a way to supply power to the tapped load at rated voltage since resistive loads are not sensitive to the changes occur in frequency the values of load resistance chosen arbitrarily. Figures 53.3 and 53.4 depicts the variation of terminal voltage and generated frequency in different operating condition i.e. different shaft rotating speed values with capacitance (36 μF) and different value of resistive load (160 Ω, 220 Ω), from the Graphical analysis it is cleat that the value of terminal voltage and generated frequency increases with the increasing shaft speed of the generator.

Figures 53.3 and 53.4 shows V versus N at C = 36 μF and R = 160 Ω and 220 Ω respectively, we used the same input data into compare our result with them. We get this result after the average cumulative change in value of the fitness function over

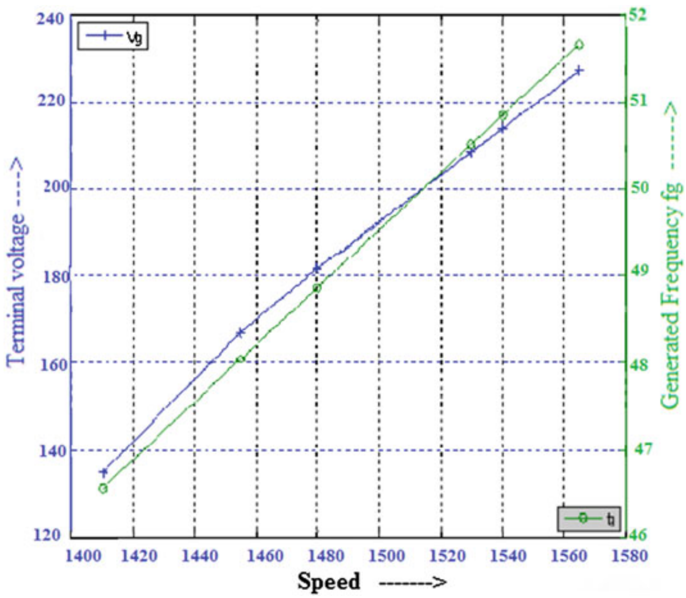

Fig. 53.3 Terminal voltage, generated frequency versus speed at C = 36 μF and R = 120 Ω

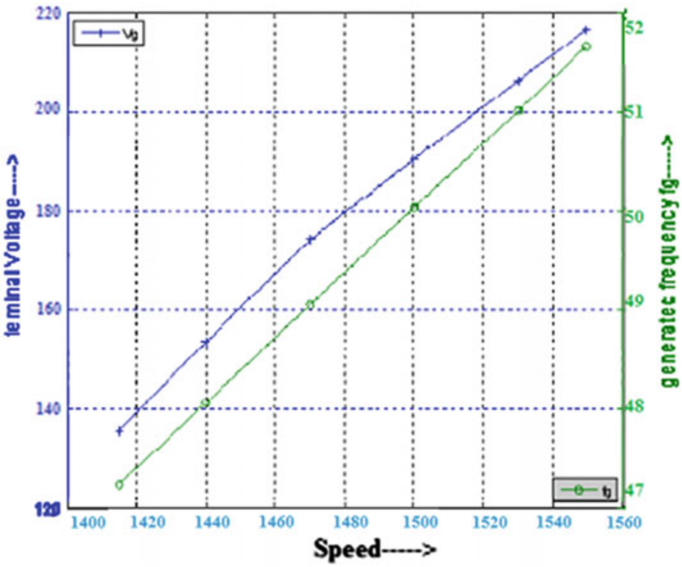

Fig. 53.4 Terminal voltage, generated frequency versus speed at C = 36 μF and R = 260 Ω

50 generations, less than 1e-006 and constraint violation less than 1e-006, after 102 generations.

Figure 53.5 shows the initial and final position of the particles position, from the figure the initial position of the particle swarm spread all over the graph but after many iteration the particle swarm settled and cumulative in definite position between 0.94 and 0.95 of the number of initial population range. Figure 53.6 shows

Fig. 53.5 Mean score, best score versus generation

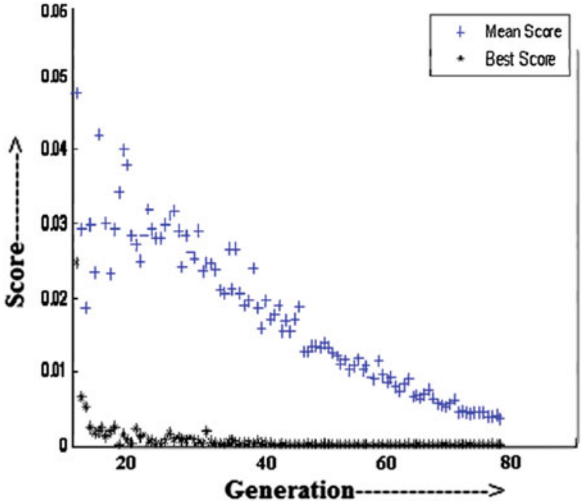

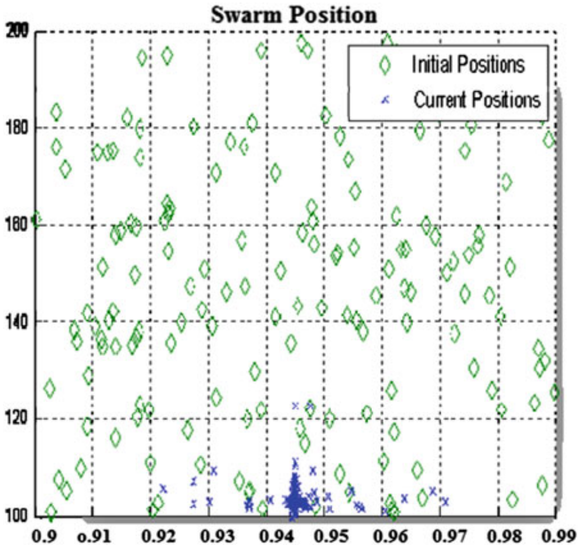

Fig. 53.6 Initial position, current position of swarm position

a histogram of the scores at each generation. The individual is any point to which one can apply the fitness function. From the result we found it so close to the result in. Moreover, the PSO method is fast, easy and more accurate than the method in.

The various characteristics curve of the SEIG can be traced by solving the objective function framed clearly from the perphase equivalent circuit of the SEIG using swarm intelligence algorithm for different possible values of a particular parameter, the above graphs shows the accuracy of the PSO swarm intelligence algorithm.

53.5 Comparison for GA and PSO in Analysis of SEIG

For the machine specification given in appendix for c = 36 μF, R = 160 Ω and N = 1,435 rpm the optimization is carried out in both GA and PSO (Table 53.2).

From the above table itself is a testimony for the particle swarm optimization has the better efficiency when compared to the Genetic algorithm and the below figure evident that PSO has the better convergence characteristics When compared to GA (Fig. 53.7).

Table 53.2 Comparison between GA and PSO

Algorithm	Frequency P.U	Magnetizing reactance Ω
Genetic algorithm	0.9451	102.8225
Particle swarm optimization	0.9021	101.6733

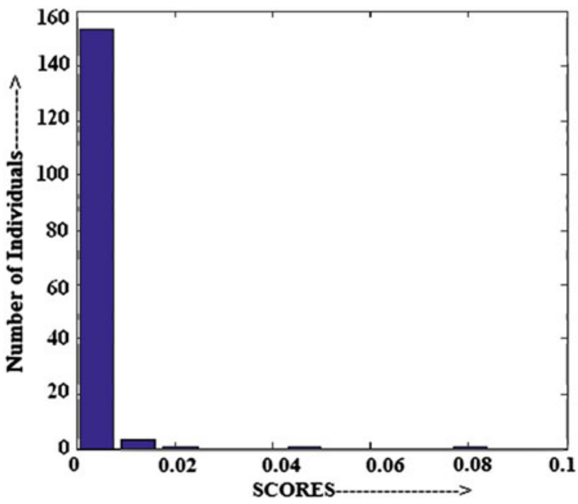

Fig. 53.7 Number of individuals in each generation

53.6 Conclusion

In this paper we presented that swarm Intelligence has the better accuracy and simple in evaluating the performance of the Self Excited induction generator for different operating speed, capacitance for Unity power factor load i.e. Resistive load. Simulation results are evident to prove that PSO is better to evaluate the performance of SEIG compared to the conventional techniques.

Appendix

SEIG Specification

3 phase, 50-Hertz, 2.2 kW/3.0H.P, 4 pole, 230 V, 8.6 Amp Delta connected squirrel cage Induction machine.

Machine parameters

$Rs = 3.35\ \Omega$, $R_R = 1.76\ \Omega$, $Xs = 4.85\ \Omega$, $X_R = 4.85\ \Omega$

Magnetizing characteristics of machine for determination of Air gap voltage

$E1 = 344.411-1.610X_M$, $X_M < 82.292$; $E1 = 465.120-3077X_M$, $95.569 > X_M \geq 82.292$

$E1 = 579.897-4.278X_M$, $108.00 > X_M \geq 95.569$; $E1 = 0$, $X_M > 108$

References

1. Joshi D, Sandhu K, Soni M (2009) Voltage control of self excited induction generator using genetic algorithm. Turk j Electr Eng Comput Sci 17(1):87–97
2. Sandhu K, Joshi D (2008) A simple approach to estimate the steady state performance of self excited induction generator. Wseas Trans syst control 3(3):208–218
3. Vadhera S, Sandhu K (2010) Genetic algorithm toolbox based investigation of terminal voltge and frequency of self excited induction generator. Int j Adv Eng Appl 1(1):243–250
4. Mahlev S, Chauhan Y (2008) Steady state analysis of three phase self excited induction generator Thesis, Department of power system and electric drives. Thappar university, Patiala
5. Vadhera S, Sandhu K (2008) Constant voltage operation of self excited induction generator using optimization tools. Int J Energy Environ 2(4):191–198
6. Alolah AL, Alkanhal MA (2000) Optimization based steady state analysis of three phase self-excited induction generator. IEEE Trans Energy Convers 15(1):61–65
7. Cao Y, Wu Q (1999) Teaching genetic algorithm using matlab. Int J Electr Eng Educ 36 (2):139–153
8. Ibrahim HEA, Metwaly M, Serag M (2010) Analysis of self excited induction generator using symbolic toolbox and artificial neural network. Ain Shams J Electr Eng 3(8):17–28

Chapter 54
Performance Analysis of Efficiency Enrichment Technique for SPVPGS: An Experimental Assessment

K.R. Chairma Lakshmi

Abstract The electrical performance and reliability of Solar PV Power Generation System (SPVPGS) is strictly influenced by irradiance, elevated solar PV cell operating temperature, dust and wind. In order to utilize solar PV power and increase SPVPGS efficiency, it is necessary to keep both the solar PV cell temperature and reflection as low as possible. This article presents a new technique to improve solar photovoltaic (PV) panel efficiency. In this work, the efficiency of SPVPGS is enhanced by maintaining solar PV panel temperature as minimum using sprayer arrangement. Water-cooling system is implemented using a chilled water source and a perforated tube which is fitted on the top of the solar PV panel. The cooling water directly wets the solar PV panel active surface, thereby decreasing the temperature of the panel at the same time which decreasing the light reflection loss and cleaning the solar PV panel surface. Experimental results show that the efficiency of solar PV panel is increased 2–4 % more than traditional stand alone SPVPGS by reducing thermal loss, dust effect and reflection loss.

Keywords Efficiency · LabVIEW · Temperature cooling system · SPVPGS

54.1 Introduction

Energy crisis and the unavailability of enough resources to meet the power demand using the conventional energy sources have enforced to develop the renewable energy resources. Solar electricity is one of the most promising technologies for our future electricity supply. The solar photovoltaic module allows the direct conversion of solar energy into electrical energy with maximum efficiency at around 9–12 %, depending on the type of solar PV cell [1]. More than 80 % of the solar irradiation reaching the solar PV cell is not converted into electricity [2]; it is

K.R. Chairma Lakshmi (✉)
R.M.K Engineering College, Kavaraipettai, Tamil Nadu, India
e-mail: chermalakshmi@gmail.com

C. Kamalakannan et al. (eds.), *Power Electronics and Renewable Energy Systems*,
Lecture Notes in Electrical Engineering 326, DOI 10.1007/978-81-322-2119-7_54

reflected or converted into thermal energy. The heat generated induces an increase in the solar PV cell temperature and consequently a decrease in the conversion efficiency of SPVPGS. The open circuit voltage decreases significantly with solar PV cell's increasing temperature. The electrical efficiency and hence the power output of a solar PV panel depend on the operating temperature, which decrease in solar PV cell temperature, so their conversion efficiency decreases by about 0.4–0.5 % per degree rise in temperature. In this experimental study, we analyze the behavior of solar PV panels at high temperature whilst using the temperature cooling system. The advantages of this temperature cooling system are decreasing temperature of the solar PV panels and obtaining better electrical efficiency due to decreasing the reflection loss because of using water as a cooling medium [3]. It also eliminates the dust loss in SPVPGS [4–6].

54.2 Experimental Model

The experimental analyses are obtained by using 40 W poly crystalline solar PV panel. The specification of solar PV panel is shown in Table 54.1. The solar PV panel is tested in laboratory condition using light source which is shown in Fig. 54.1. The design and construction of temperature cooling system could be separated into three main parts which are mentioned below.

(a) Temperature Sensor unit
(b) Temperature Controlling unit (LabVIEW)
(c) Water Pump and Water sprayer arrangement

Thin film PT-100 RTD is used as a temperature sensor to measure the solar PV panel's outer glass temperature which is placed on the edge of solar PV panel. The RTD sensor converts the change in temperature into a change in resistance. This resistance will be converted into a voltage (0–5 V) by using an external circuit like voltage divider or Wheatstone bridge circuit or instrumentation amplifier etc. Here, the voltage divider circuit with RTD sensor is used to convert the change in temperature into a change in voltage. The LabVIEW temperature controlling program measures the temperature of the solar PV panel using the temperature sensor unit, compares it to a desired set point or reference point, and issues the proper control signal to operate the final control element (i.e. Pump). The control signal acts as ON/OFF signal to control the operation of the water pump through relay circuit for cooling purpose. Screenshot of the temperature controlling program is shown in Fig. 54.2. This pumping system consists of a high efficient 13 W submersible pump at a flow rate of 800 m^3/h. The water feeding pipe installed on the top end of the solar PV panel provides the water free flow on the front side of the solar PV panel. The cooling water flowed from 6 nozzles lined up over the 12.7 mm diameter water feeding pipe. This configuration utilized less amount of the pumped water for cooling and the rest could be used directly, e.g., for irrigation. The SPVPGS system with temperature cooling system is shown in Fig. 54.1.

Table 54.1 Hardware description

Parameters	Characteristics
Solar PV panel	Peak power (PP) = 42.071 W
	Voltage at peak power (VP) = 21.725 V
	Current at peak power (IP) = 2.607 A
	Short circuit current (ISC) = 2.741 A
	Open circuit voltage (VOC) = 21.492 V
Current sensor (WCS2702)	Measure the output current of solar PV panel
	Manufacturer: Winson
	Range: 0–2.0 A
	Sensitivity: 1 mV/mA
Thin film RTD	Measure the temperature of the solar PV panel
	Manufacturer: lab facility limited
	Range: −50 to 400 ℃
	Tolerances: ± 0.3 ℃ + 0.005 t
	Acquire input voltage from sensors
Analog input DAQ card (NI 9205)	Manufacturer: national instruments
	No. of input channels: 32
	Resolution: 16 bits
	Range: −10 to 10 V
	Generate output signal
Analog output DAQ card (NI 9263)	Manufacturer: national instruments
	No. of output channels: 4
	Resolution: 16 bits
	Range: −10 to 10 V

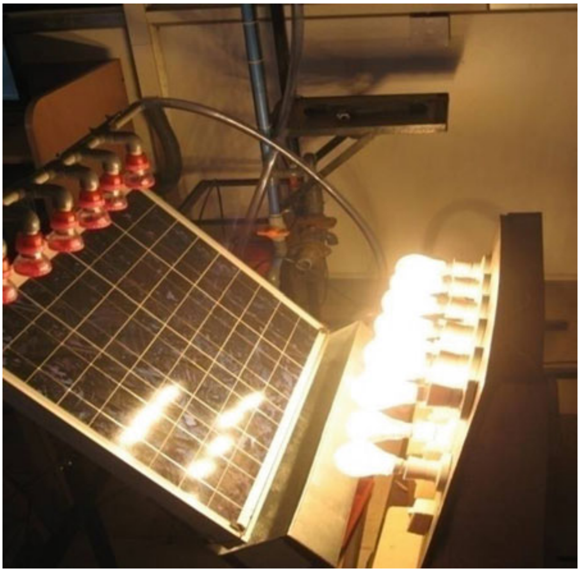

Fig. 54.1 Hardware implementation of SPVPGS

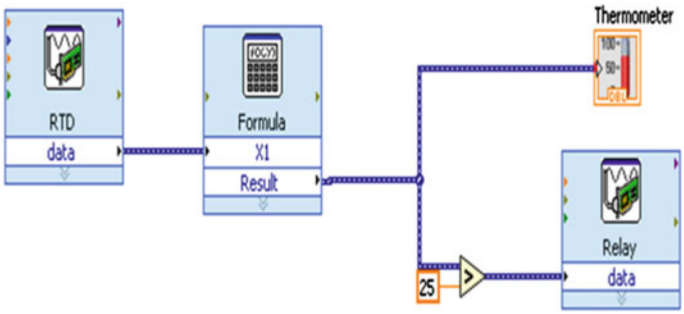

Fig. 54.2 Screenshot of LabVIEW block diagram for temperature cooling system

Solar PV Panel temperatures at different points, Solar PV Panel output voltage, and output current are measured to understand the solar PV panel behavior under different irradiance conditions and to compare the behavior of solar PV panel with and without temperature cooling system.

54.3 Description of the Instrumentation Used

The main features of the sensors used in the hardware installation are shown in Table 54.1. The solar PV panel temperatures are measured with three thin film resistance temperature detectors (RTD), which are attached to the edge of the solar PV panel. The average of these three sensors considers as temperature of solar PV panel. Hall Effect Base Linear Current Sensor (WCS2702) is used to measure solar PV panel output current. The electrical variables are measured using a variable load or a rheostat to achieve the characteristic curves (I–V and P–V) of the solar PV panel. The LUX meter measures the solar irradiance emitted from the light source. All data are acquired, registered and recorded by means of a DAQ card using LabVIEW software.

54.4 Experimental Analysis

To study the impact of solar PV panel temperature in efficiency of SPVPGS and solar PV panel characteristics, several experimental cases have been made for different configurations. The specification of solar PV panel used throughout our research is mentioned in Table 54.1. The analysis carried out at different angular position with respect to the light source and solar PV panel and different irradiance levels.

The efficiency loss due to temperature is shown in Figs. 54.3, 54.4 and 54.5 under various angles and solar irradiance condition. Figures 54.3, 54.4 and 54.5 shows that the experimental results of efficiency of SPVPGS under various

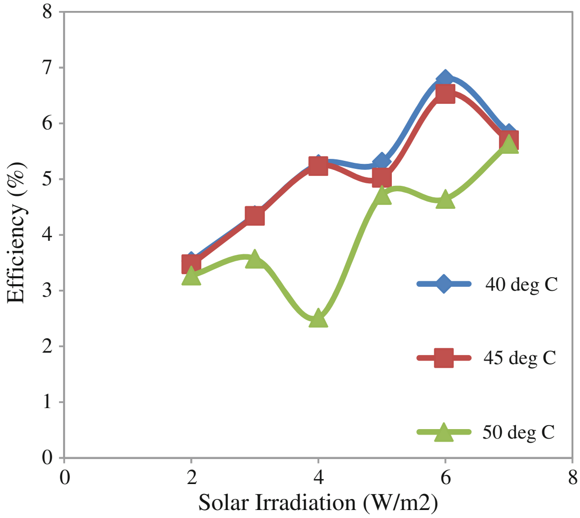

Fig. 54.3 Efficiency versus solar irradiation at 90° incident angle

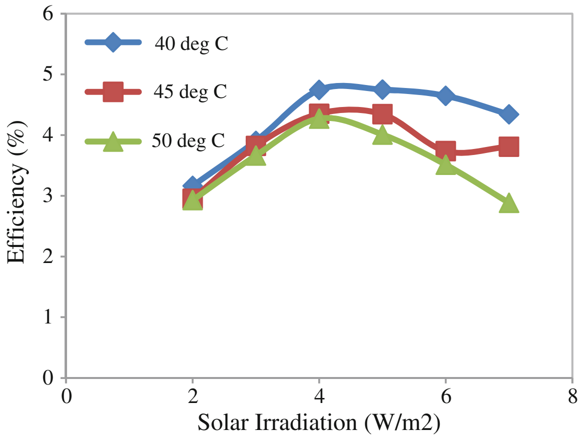

Fig. 54.4 Efficiency versus solar irradiation at 45° incident angle

irradiance and 90°, 60° and 30° incident angle respectively. From the analysis, the SPVPGS affects heavily by temperature variation, it means that to obtain maximum efficiency from SPVPGS, the solar PV panel temperature should maintain at low.

54.4.1 Results Collected for Solar PV Panel with Maximum Solar Irradiance with Temperature Cooling System

From Figs. 54.3, 54.4 and 54.5, results proved that the efficiency of SPVPGS is best at maximum irradiance with 90° angle only. Due to the maximum irradiance, the

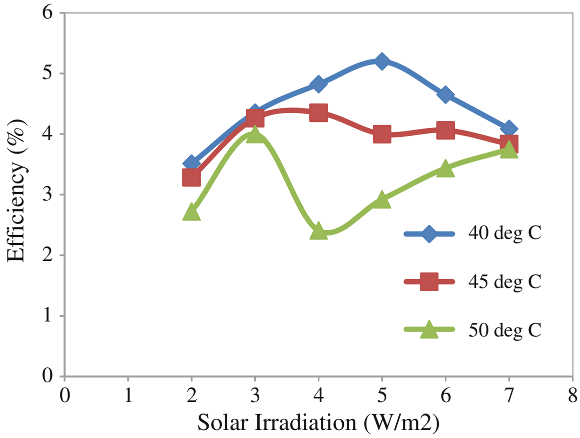

Fig. 54.5 Efficiency versus solar irradiation at 30° incident angle

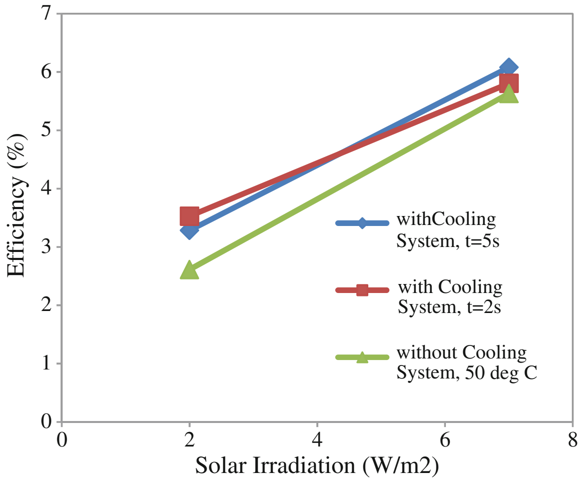

Fig. 54.6 Efficiency versus solar irradiation when the cooling water flows over solar PV panel for particular time

thermal loss is increasing consequently. On account of thermal loss; the efficiency of the solar PV panel is reduced even though the solar PV panel operates at maximum irradiance condition.

The experimental results obtained from SPVPGS with and without cooling system are shown in Fig. 54.6. From the results, the efficiency of SPVPGS is increased when the cooling system is on for 5 s than other conditions. From Fig. 54.6, we prove that the continuous temperature cooling is necessary for the SPVPGS for extract maximum power.

54.5 Conclusion

This work describes the performance of SPVPGS under different loss like irradiation effect, temperature effect and incident angle effect. The efficiency of SPVPGS is loss due to the increasing temperature of solar PV panel which can be reduced by heat removal from the front surface of solar PV panel by spraying water across the solar cells. This study examines the performance of a 40 W SPVPGS under 7 W/m^2 irradiance condition with water spray over the solar PV panel. It is found that spraying water over the solar PV panel strongly improves the system efficiency. Since when the modules are working closely on the temperature of maximum power generation, the load can receive most of the solar PV panel power. It is shown that, the temperature cooling system increases the solar PV panel conversion efficiency at 2–4 % more than stand alone SPVPGS. The efficiency of SPVPGS is affected by irradiance and the incident angle effect also. It is shown that, the loss due to irradiance and the incident angle effect is reduced then the efficiency of SPVPGS is increased 4–5 % and 2–5 % respectively. The overall efficiency of the SPVPGS is increased up to 14 % when the irradiance, temperature and incident angle is eliminated. The experimental results prove that the efficiency of solar PV power generation system is improved up to 8–14 % by proposed efficiency improvement techniques. The testing and analysis are conducted in laboratory environment only, if it is accessed in outdoor environment the results may change but it also in the tolerable range only.

References

1. Daoud A, Midoun A (2008) Single sensor based photovoltaic maximum power point tracking technique for solar water pumping system. Electr Power Q Utilization J XIV(2):69–72
2. Baras A, Bamhair W, Al Khoshi Y, Al Odan M, Engel-Cox J (2012) Opportunities and challenges of solar energy in Saudi Arabia. In: Proceedings of the world renewable energy forum, Denver, Colorado
3. Krauter S (2004) Increased electrical yield via water flow over the front of photovoltaic panels. Solar Energy Mater Solar Cells 82(1):131–137
4. Sulaiman SA, Hussain HH, Leh NSHN, Razal MSI (2011) Effects of dust on the performance of PV panels. World Acad Sci Eng Technol 58:558–593
5. Benatiallah A, Ali AM, Abidi F, Benatiallah D, Harrouz A, Mansouri I (2012) Experimental study of dust effect in mult-crystal PV solar module. Int J Multi Sci Eng 3(3):3
6. Zorrilla-Casanova J, Piliougine M, Carretero J, Bernaola P, Carpena P, Mora -López L, Sidrach-de-Cardona M (2011) Analysis of dust losses in photovoltaic modules. In: World renewable energy congress 2011, Sweden, pp 2985–2992

Chapter 55
Cable Laying Precautions in Offshore Wind Farms with Reactive Power Compensation

Ahmed M. Atallah, Almoataz Y. Abdelaziz, Mohamed Ali, R.K. Saket and K.S. Anand Kumar

Abstract This paper combines both analytic and practical aspects of submarine power cable to transmit offshore wind energy to grid. Factors should be considered during laying submarine cable are shortly presented. Cable design, laying and compensation of its reactive power are also presented. Cable laying costs [1–3] times of the cable cost itself. Compensation of reactive power to both unity power factor and near unity but more economic is performed and tabulated. Three cases are performed in Zaafarana, Egypt. The results are compacted and simulated.

Keywords Offshore wind farm · Submarine cable · Cable laying · Reactive power compensation

Symbols and Abbreviations

f	Power supply frequency
w	is the pulsation (2πf)
ε_i	dielectric constant of the insulation material
r_o	The inner radius of the metallic sheath of the cable. The metallic sheath is grounded

A.M. Atallah (✉) · A.Y. Abdelaziz · M. Ali
Electrical Power and Machines Department, Faculty of Engineering,
Ain Shams University, Cairo, Egypt
e-mail: almoatazabdelaziz@hotmail.com

M. Ali
e-mail: mohamed_ali_mohamed_ali86@yahoo.com

R.K. Saket
Department of Electrical Engineering, Indian Institute of Technology,
Banaras Hindu University, Varanasi, Uttar Pradesh, India
e-mail: rksaket.eee@iitbhu.ac.in

K.S. Anand Kumar
National Aerospace Laboratory, Bangalore, Karnataka, India
e-mail: anand_kumarks@nal.res.in

C. Kamalakannan et al. (eds.), *Power Electronics and Renewable Energy Systems*,
Lecture Notes in Electrical Engineering 326, DOI 10.1007/978-81-322-2119-7_55

r_i	The conductor radius
Q_{Lcomp}	is the module of the inductive reactive power
$\lvert I_L \rvert$	is the module of the current through the inductive component
$\lvert X_L \rvert$	is the module of the inductive impedance

55.1 Introduction

The generated reactive power by cable capacitance during active power transmission from the offshore wind farm (OWF) identifies the ability of the transmission system to transmit the generated power along the transmission length. This study is about improving the transmission efficiency of the submarine power cable by using reactive power compensation to improve power factor (P.F), reduce current, reduce conduction losses and increase transmission distance. Also this paper presents shortly some important precautions to be considered for OWF cable laying.

55.2 Lesson Learned from Previous Experiences

The entire lesson learned and previous accidents with submarine cables in OWFs or oil and gas platforms should be studied and taken into consideration to avoid the occurrence of same accidents in future and to provide more reliability and availability of OWFs.

Laying cost is 1–3 times of the cable cost depending on the site conditions, burial depth, length, etc. Cables themselves cost between US$90/m and $130/m for medium voltage cables, and in the range of $200/m for 145 kV, not including transportation.

Choose the optimum cable design which provides minimum losses, adequacy of power carrying and mechanical strength of the cable to stand all risks. In past cables were designed according to standards but that isn't suitable for OWFs. Cable's overall jacket polymer (to avoid corrosion and erosion of the cable) is chosen according to the selected route, seabed characteristics, sediments, water currents, wind speed and water salinity. The armor is designed (single or double layer, in S or Z direction) according to navigation risks, scour events, unsupported length along the cable route and the laying direction.

Choose the optimum cable route which secures the cable along its length, provides lower installation cost, best cable protection, and availability of installation vessels. Installation vessels which lay, bury the cable and backfill trench according to pre-performed surveys on the route and seabed characteristics. Selecting installation vessel with suitable size to ensure its ability to handle and lay the cable with its cross section area (C.S.A) with recommended laying tension. That planning and survey processes could take 2 years.

Table 55.1 Cable bending radius, failure rate and repair plan [1]

Voltage (kV)	132	220	400	275	400
Cable type	3C	3C	3C	SC	SC
Diameter (mm)	172	254	273	151	162
Weight (kg)	62	112	124	62.9	69.2
Bending diameter (m)	4.3	6.35	6.82	3.8	4.1
Failure rate (failure/year)	0.25	0.46	0.67	0.15	0.22
Planned number of repairs in 20 years	30	27	26	18	13

There are many factors should be considered during the J-tube design: The bending radius according to manufacturer data as shown in Table 55.1. The J-tube inner surface must be smooth and free of any snags that could cut the cable during pulling process into the J-tube and coating the inner surface of anti corrosion material. J-tube spacing must provide enough space for heat dissipation usually 2.5 of the cable diameter.

Usually rock dumping is used due to high water currents, high wind velocity and high tides. The seabed around turbine foundations and offshore platform moves and seabed characteristics change that known by scour. The scour leads to cable exposure for a distance up to 8 m and cable will be subjected to navigation risks and high water currents apply extra mechanical strength on it.

In advance repair plan should be set. Repair vessels, jointers and experienced H.V electricians should be available. To identify fault location, cable recovery, jointing and cable reburying that takes 2/3 time required for installing new cable. The availability of spare cable will identify if replacing will be more effective than repairing or not. A pre-calibrated reflecto-meter is used to identify the fault location.

Typically failure rate for 3 core submarine cables is 0.1 failure/100 km/year with mean repair time 2 months and changes due to site conditions [3]. For single core cable failure rate 0.024 failures/100 km/year and joint failure rate 0.01 per 100 components per year [4]. Divers or ROV (remotely operated vehicles) to track cable during burial and laying process should be used.

Vessels traffic, their types, anchors types, their dragging depth and their penetration to seabed should be known to calculate navigation risks on the cable and probability of damage due to anchors and take the required steps for protection.

Choose optimum burial depth to protect the cable from navigation risks, animal bits. Usually burial depth of a minimum 1 m for HVAC extending to 2 m for HVDC cable, if burial depth increases the heat dissipation reduces and current capacity reduces (in Scorby sand OWF burial depth chosen to be 3 m because of sand waves [5, 6].

In shallow water; although there are neither navigation risks nor anchors nor fish gear risks on the laid cable but it is recommended to continue burying to mitigate the induced EMF (electro-magnetic field) effect. Using floats and towing system on the shore is the method used to lay the cable in shallow water, where installation vessels can't reach because vessels impellers could hit the seabed and damage the vessel.

Monitoring the tension on the cable by cable awareness programs during installation and pulling into the J-tube is required to ensure that cable won't be damaged.

55.3 Cable Capacitance (C)

The special design of the submarine cable (to meet the environmental conditions) makes the cable has high capacitive component. The capacitance is determined by:

$$C = \frac{2\pi\varepsilon_o\varepsilon_i}{\ln\frac{r_o}{r_i}} \, {}^{F}\!/_{m} \tag{55.1}$$

can be simplified to

$$C = \frac{\varepsilon_i}{17.97 \times \ln\frac{r_o}{r_i}} \ \mu F/km \tag{55.2}$$

The required charging current in the capacitance could be calculated from Eq. (55.3), the reactive current increases with the capacitance increase and the active current transmission capability of the cable reduce ($I_{reactive} \alpha \frac{1}{I_{active}} \alpha C$)

$$I_{ch} = \frac{|V|}{X_c} = 2\pi fcV \tag{55.3}$$

Table 55.2 shows the different values of dielectric constants for submarine cables insulators.

55.3.1 *Capacitive Component Effect on the Transmission System [8]*

The capacitance and transmitted power are distributed along the cable length. The charging/discharging reactive current of the capacitance will reduce the cable ability to transmit the required active power. The actual current flows through the cable will be:

Table 55.2 Relative permittivity of polymer at 50 Hz [7]

Material	PVC	PE	XLPE	EPR
Permittivity	8	2.3	2.3	3.5

Table 55.3 Characteristics of the submarine cables

Cable	Vn (kV)	In (A)	Ra.c (Ω/km)	L (mH/km)	C (μF/km)	$I_{reactive}$ (A/km)	Q_c (MVAR/km)
1	36	911	0.0341	0.294	0.331	2.16	0.134
2	150	1,088	0.0205	0.352	0.233	6.339	1.647

$$|I| = \sqrt{I_{active}^2 + I_{reactive}^2} \tag{55.4}$$

The conductor's C.S.A, conductor's and insulation's thermal characteristics are limitations of the total actual transmitted current. The distance of OWF to shore is the only limitation of the AC transmission. As cable length increases, cable capacitance increases, more reactive current flows in the cable, lower active current and transmission system efficiency will be low.

Q_c is the generated reactive power in the cable capacitance and its value doesn't depend on the current changes because the capacitance is a shunt component in the cable.

$$Q_c = \frac{|V|^2}{x_c} \tag{55.5}$$

For different cables types and with the previous equations, the reactive current/power as shown in Table 55.3, the cable capacitance, reactive current, reactive power and overall current increase with the cable length increase. In contrast the active power transmission efficiency and P.F reduce. The transmission voltage level affects on the reactive power generated by the cable capacitance. To get the transmission P.f = cosφ

$$\tan\varphi = \frac{Q}{P} \tag{55.6}$$

From Eq. 55.6, P.F depends on the cable generated reactive power which depends on cable length.

55.4 Case Study: 1

A proposed OWF near Zaafarana, generates 150 MW, is placed at different locations (50, 100, 200 km) from shore, assumed transmission voltage level is 150 kV, the cable number 2 in Table 55.3 is used in calculations. The P.F and overall current |I| carried by the cable will be discussed and simulated (Fig. 55.1).

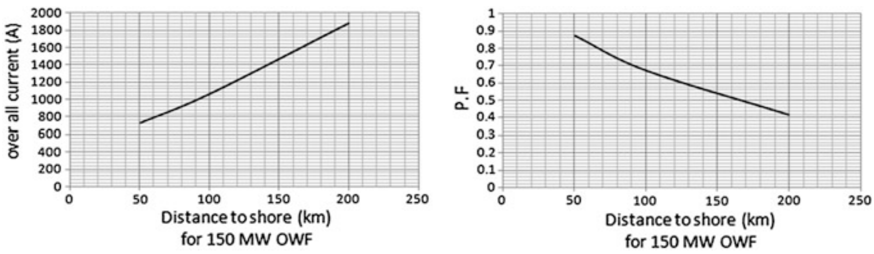

Fig. 55.1 The variation of P.F and cable overall current against distance to shore

55.5 Types of Reactive Power Control

As a high reactive power will flow in the cable ability to transmit the active power is reduced so a larger C.S.A cable will be required to transmit the generated power to the onshore substation which is not economical, so the reactive power compensation is required. Also at most of grid codes P.F should be close to unity at least at point of common coupling (PCC). The reactive power compensation can be divided into:

55.5.1 The Location of the Reactive Power Compensation [8]

Injection of the inductive reactive power at one end or at both ends. If the reactive power compensation at onshore end. Advantage of this method; (1) Cheap because only onshore compensation inductance required and its installation at the onshore end is cheaper than installing it at the offshore platform, (2) The P.F. at PCC is nearly unity. Disadvantage of this method; (1) Low active power transmission, (2) The transmission length is limited by the amount of the reactive power generated by the cable capacitance, (3) No control on the reactive power generated by cable capacitance.

Cable capacitance is distributed along the cable; the compensation inductance can't be distributed along the cable because it is impossible to install compensation inductance along the buried cable, expensive cost of installing the compensation inductance on offshore platforms. The other solution will be connecting the compensation inductance at both ends, at offshore central collecting point (CCP) and at PCC. Advantage of this method, (1) P.F at the PCC will be nearly unity and the conduction power will be lower, (2) Higher active power transmission, (3) Longer distance for power transmission, (4) Controlled reactive power. Disadvantage of this method is expensive.

The half of the inductive reactive power is injected at onshore PCC and the other half is injected at CCP. The half of inductive power at CCP will cancel the effect of the capacitive reactive power at this half. The other half of the inductive compensator at the onshore side will improve P.F at PCC. Improving P.F at CCP reduces conduction losses the current will be minimum in the middle and maximum

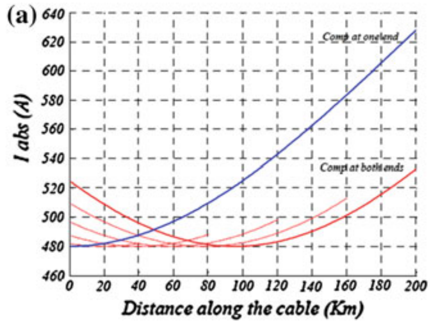

Fig. 55.2 Total current along the submarine cable depending on cable length, compensation at both ends (*red*) and onshore compensation only (*blue*). **a** 30 MW–36 kV and **b** 150 MW–150 kV

at both ends that is because of the distributed capacitance along the cable and cable parameters distribution.

From Fig. 55.2, for compensation at both ends, the reactive current flows in the cable will be 150 A at distance 50 km; it is nearly the half value of the reactive current without compensation in Table 55.4. As a result the cable ability to carry a higher active power is increased in case of both ends compensation.

55.5.2 Static or Dynamic Control of the Compensation

As we discussed before the generated reactive power by the cable capacitance depends on the transmission voltage level and the capacitance value. The cable inductance which is series component, its reactive power depends on the flowing active power (active current).

$$Q_L = |I_L|^2 X_L \tag{55.7}$$

Q_L is the reactive power absorbed by cable inductance. Q_L reduces the effect of Q_C and reduces total reactive power generated as in Eq. (55.8). In dynamic controlled compensation; the compensation inductance changes with the variation of the active power flow. Controlling the reactive power means controlling P.F and active power. The variation of the cable loading (transmitted active power) affects the compensation inductance value. Moreover, the cable loading changes with the wind speed variation [10].

$$Q_{comp} = Q_c - Q_L \tag{55.8}$$

Studying the required compensation for OWF in case 1 in Table 55.4. The generated power versus the wind speed as shown in Ref. [9]. The wind velocity profile for Zaafarana; the daily wind speed is shown in Ref. [11] and monthly wind

Table 55.4 Variation of overall current flowing and P.F in the cable with changing distance to shore

Case	Distance (km)	P_{gen}	Transmission voltage (kV)	$I_{reactive}$ (A)	Q_c (MVAR)	P.F	|I| (A)	Notes
1	50	150	150	316.95	82.35	0.877	730.65	$<I_n$
2	100	150	150	633.9	164.7	0.673	1,066.3	$<I_n$
3	200	150	150	1,267.8	329.4	0.414	1883.6	$>I_n$

speed shown in Ref. [12], The variable speed WTs have back-to-back converters which convert the generated power to the required voltage, so at any speed there is a generated power at constant voltage and frequency but the current is variable.

As shown in Ref. [11, 12] the wind speed is almost uniform, the mean annual wind speed in this location is 8 m/s and the wind direction is almost constants.

From Figs. 55.3 and 55.4 the inductance will be within range of 0.87–0.89 H which is narrow range for control. A 0.89 shunt compensator is required for rated output power.

Finally the compensation inductance depends on: (1) Insulation characteristics (material, thickness and dielectric constant) and cable characteristics (capacitance, inductance). (2) Transmission voltage level. (3) Transmission frequency. (4) Distance between the OWF and the onshore substation. (5) Active power generated by the OWF which depends on the wind speed. (6) Although the cable inductance has small influence on the compensation calculations but it still varies with the cable loading.

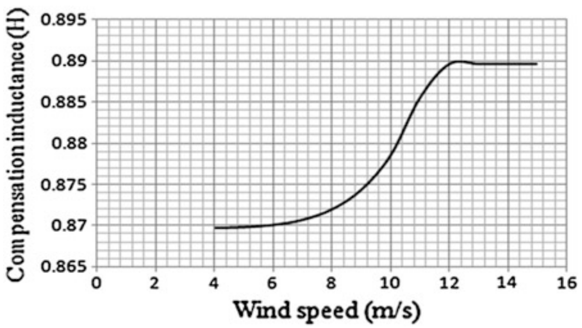

Fig. 55.3 The compensation inductance variation with wind speed variation

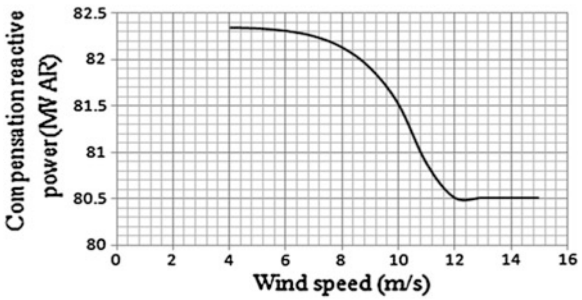

Fig. 55.4 The compensation reactive power variation with wind speed variation

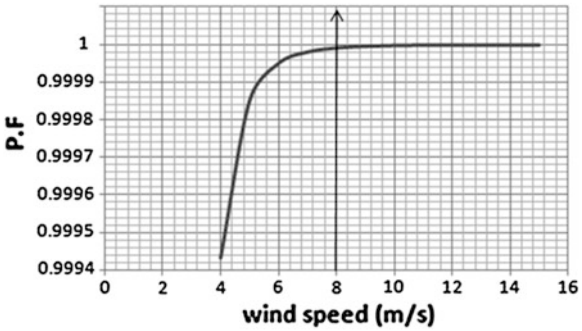

Fig. 55.5 P.F variation with wind speed variation (constant compensation inductance)

55.6 Most Economical Solution

A 0.872 H fixed compensation inductance is installed (at most frequent wind speed 8 m/s). P.F almost unity. Economically cheaper and practically guarantee stable system operation (Fig. 55.5).

55.7 Conclusion

Cable laying costs more than the cable price itself. Getting use of the previous knowledge of cable laying and their problems will help us to decrease the overall cost of submarine cable and OWFs. Aggregating this knowledge has been done in this paper.

From cases 1, 2, 3; eliminating reactive power from submarine cable will decrease overall current, decrease losses, decrease cable temperature and decreasing cable C.S.A.

Therefore, to perform the management of the reactive power flowing through the transmission line, there are two different options:

1. Adjusting compensation onshore at PCC with constant compensation calculated at the most frequent wind speed and rated power. In this case, P.F will vary due to change of wind speeds.
2. Connecting two compensations, one is constant and the other is varying to guarantee unity P.F through all wind speeds.

References

1. Hagerman G (2001) Southern new England wave energy resource potential. In: Building energy 2001 conference, Medford Massachusetts
2. Rademakers L, Braam H (2002) O&M aspects of the 500 MW offshore wind farm at NL7. DOWEC 10080 Rev 2

3. http://www.nationalgrid.com/NR/rdonlyres/CC4994A2-83C5-4990-9E0CF8CE04DCA588/43378/Appendices2010_Final.pdf
4. Ericsson A, Thunwall B, Gustafsson A, Svahn J (2003) Qualification of a highly electrically and mechanically stressed AC cable system. In: Proceedings JICABLE
5. http://www.lorc.dk/offshore-wind-farms-map/scroby-sands
6. Warne DF Advances in high voltage engineering. Institution of Electrical Engineers
7. Mason JH (1971) Basic requirements for electric insulation: part one. Insul Engr, Elec Electr (GB) 1(5):9–14
8. Chondrogiannis S, Barnes M (2006) Technologies for integrating WFs to the grid DTI
9. http://cleantechnica.com/2012/07/23/offshore-wind-turbines-uk/
10. Gasch R, Twele J (2001) Wind power plants: fundamentals, design and operation. Solar praxis AG, Germany
11. http://www.windfinder.com/weatherforecast/zafarana
12. Theoretical investigation and mathematical modeling of a wind energy system case study for Mediterranean and Red Sea (2008) Technischen Universität Berlin zur Erlangung des akademischen Grades

Chapter 56
Single Phase Soft Switching Techniques Power Factor Correction Converter

P. Anjappa, K. Naresh, V. Ramesh, P. Lakshmipathi and K. Reddy Swathi

Abstract This paper proposes a dual mode used to control a single phase soft switching boost power factor correction converter (PFC) developed with a new active snubber circuit. The soft switched boost power factor correction converter has merits of less voltage and current stresses, improved efficiency and reduced switching losses. Thus the cost and complexity of the converter is reduced. The dual mode controller combines both continuous conduction mode (CCM) and critical conduction mode (CRM). The simulation results declare high efficiency and optimum power factor for wide range of varying loads.

Keywords Power factor correction · Soft switching · Critical conduction

56.1 Introduction

This proposed PFC converter has simple structure, low cost, and easy of control as well. Boost converters operating in continuous conduction mode (CCM) have become particularly popular because reduced electromagnetic interference (EMI)

P. Anjappa (✉) · P. Lakshmipathi · K. Reddy Swathi
Department of Electrical and Electronics Engineering, GVIC Engineering, Madanapalli, Andhra Pradesh, India
e-mail: anji_abhi@yahoo.co.in

P. Lakshmipathi
e-mail: plp.826@gmail.com

K. Reddy Swathi
e-mail: reddyswathik777@gmail.com

K. Naresh · V. Ramesh
Department of Electrical and Electronics Engineering, K L University, Guntur, Andhra Pradesh, India
e-mail: knaresh@kluniversity.in

V. Ramesh
e-mail: rameshvaddi6013@kluniversity.in

C. Kamalakannan et al. (eds.), *Power Electronics and Renewable Energy Systems*, Lecture Notes in Electrical Engineering 326, DOI 10.1007/978-81-322-2119-7_56

levels result from its utilization. Within this context, this work deals with a comprehensive review of some of the most relevant ac-dc single phase boost converters for PFC applications [1, 2]. The cause of having low PF and high THD for a diode-capacitor type of rectifiers is related to nonlinearity of the input current. Method of re-shaping the input current waveform to be similar pattern as the sinusoidal input voltage is done by the Boost converter and the related controls that act as a Power Factor Correction (PFC) circuit [3]. The results of the designed system were compared against with and without PFC control.

56.2 Soft Switching Power Factor Correction Converters

56.2.1 Operation Stages and Analysis

The proposed circuit diagram for PFC converter is shown in Fig. 56.1. In this circuit, V_i is input ac voltage, V_o is output L_F is source inductance, output capacitor C_o act as a filter circuit and resistance R act as Load, the two switches S_1 and S_2 are main and auxiliary switches respectively, and D_F is the main diode. The main switch consists of a main switch S_1 and its body diode D_{S1}. C_S is the sum of the parasitic capacitors of the main switch. L_{R1} and L_{R2} are upper and lower snubber inductances, C_R is snubber capacitor. The diodes D_1, D_2, D_3, and D_4 are act as an auxiliary diodes. L_m is the magnetization inductance, the transformer has a leakage inductances of L_{il} and L_{ol} respectively [4]. In Fig. 56.1 i_s is input current, I_i is

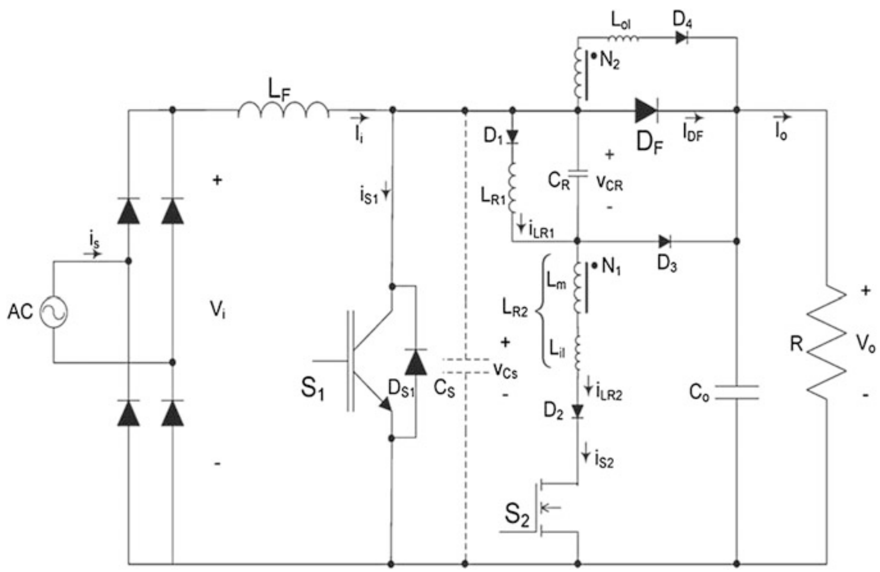

Fig. 56.1 Circuit scheme of the proposed new power factor converter

current flowing through main inductance and i_{S1} is current in main switch, i_{LR1} is L_{R1} inductance current, i_{LR2} is L_{R2} inductance current, i_{S2} is current in auxiliary switch, i_{DF} is main diode current, and I_o is output current. V_{CS} and V_{CR} are voltage across capacitance C_S and C_R respectively.

For one switching cycle, the following assumptions are made in order to simplify the steady-state analysis of the circuit shown in Fig. 56.1. Output voltage V_o and input current I_i are constant for one switching cycle, and all semiconductor devices and resonant circuits are ideal [5]. Furthermore, the reverse recovery times of all diodes are not taken into account (Fig. 56.2).

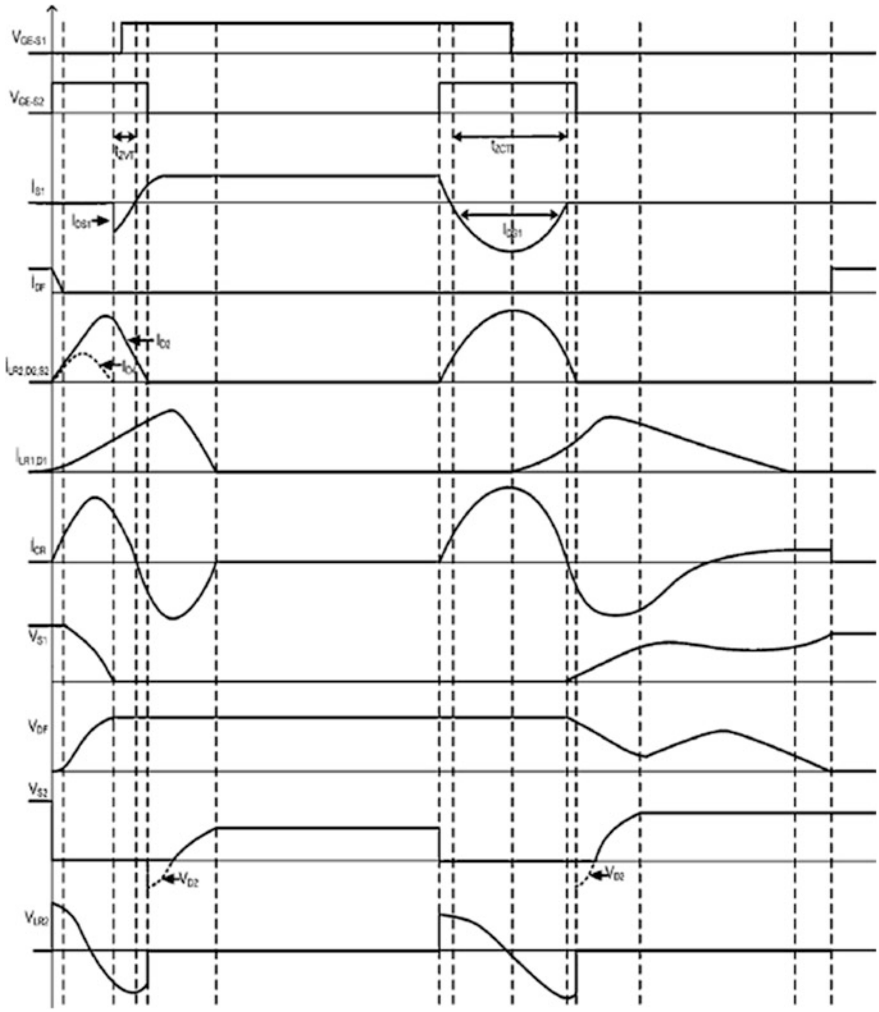

Fig. 56.2 Key waveforms concerning the operation stages in the proposed converter

56.3 Converter Features

The proposed PFC converter is equipped with ZVT–ZCT–PWM active snubber circuit to combine most of the desirable features of both the ZVT and ZCT converters [4]. The proposed converter overcomes most of the drawbacks of these converters and also provides PFC.

- All semiconductors work with SS in the proposed converter. The main switch is turned ON with ZVT and is turned OFF with ZCT, the auxiliary switch is turned ON and OFF with ZCS. Other components of the converter also work with SS.
- There is no extra current or voltage stress on the main switch.
- There is no extra current or voltage stress on the main diode.
- The circulating energy is quite small in this converter and the sum of the transient time intervals is very small for part of the one switching period.
- Due to the main and the auxiliary switches have a common ground, the converter can easily control.
- The proposed new active snubber circuit can be easily applied to the other basic PWM converters and to all switching converters.
- The new presented active snubber circuit can be adapted to the other dc–dc converters.
- At light-load conditions, in the ZVT process, the main switch voltage falls to zero earlier due to decreased interval time t_{01} and that does not make a problem in the ZVT process for the main switch.
- At light-load conditions, in the ZCT process, the main switch's body diode ON-state time is increased when the input current is decreased. However, there is no effect on the main switch turn-OFF process with ZCT.
- Reverse recovery problems of the main and the auxiliary diodes are prevented by using silicone carbide (SIC) diodes in the proposed PFC converter.

56.4 Soft Switching Conditions

In order to achieve SS for the main and the auxiliary switches, the following conditions should be satisfied in the Circuit.

56.4.1 Main Switch Turn ON with ZVT

While the main switch is in OFF state, the control signals applied to the auxiliary switch. The parasitic capacitor of the main switch should be discharged completely and the main switch's anti parallel diode should be turned ON [6]. The ON-state time of the ant parallel diode is called t_{ZVT} and in this time period, the gate signal of the main switch should be applied. So, the main switch is turned ON under ZVS and ZCS with ZVT.

56.4.2 Main Switch Turn OFF with ZCT

While the main switch is in ON state and conducts input current, the control signal of the auxiliary switch is applied. When the resonant starts, the resonant current should be higher than the input current to turn ON anti parallel diode of the main switch. The ON-state time of the anti parallel diode (t_{ZCT}), has to be longer than the main switch's fall time ($t_f s_1$) [7]. After all these terms are completed, while anti parallel diode is in ON state, the gate signal of the main switch should be cutoff to provide ZCT for the main switch.

56.4.3 Auxiliary Switch Turn ON with ZCS

The auxiliary switch is turned ON with ZCS because the coupling inductance limits the current rise speed. The current pass-through the coupling inductance, should be limited to conduct maximum input current at the end of the auxiliary switch rise time ($t_r s_2$). So, the turn-ON process of the auxiliary switch with ZCS is provided.

56.4.4 Auxiliary Switch Turn OFF with ZCS

To turn OFF the auxiliary switch with ZCS, while the auxiliary switch is in ON state, the current pass through the switch should fall to zero with a new resonant. Then, the control signal could be cutoff. If C_S is neglected, L_{R1} value should be two times more than L_{R2} to fall the auxiliary switch current to zero. Because the current cannot stay at zero as long as the auxiliary switch fall time (t_{fs2}), the auxiliary switch is turned OFF nearly with ZCS.

56.5 Simulation Results

See (Figs. 56.3, 56.4, 56.5, 56.6 and 56.7).

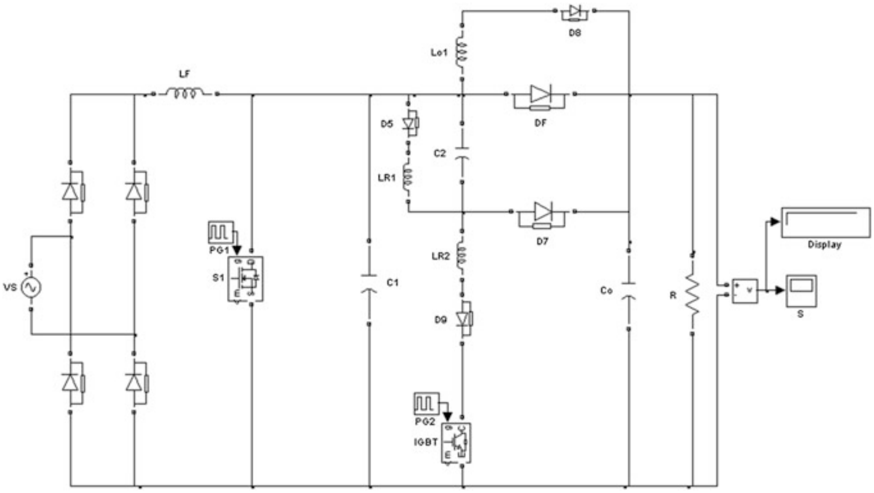

Fig. 56.3 Open loop circuit diagram

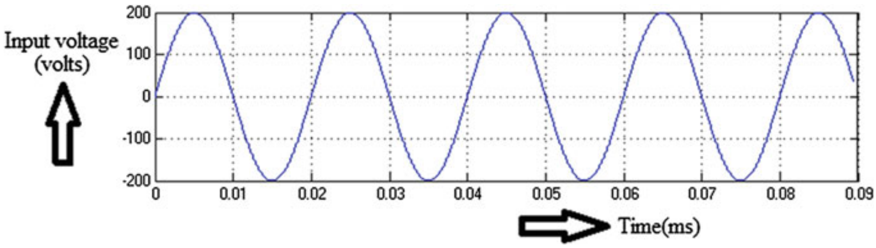

Fig. 56.4 Input voltage waveform

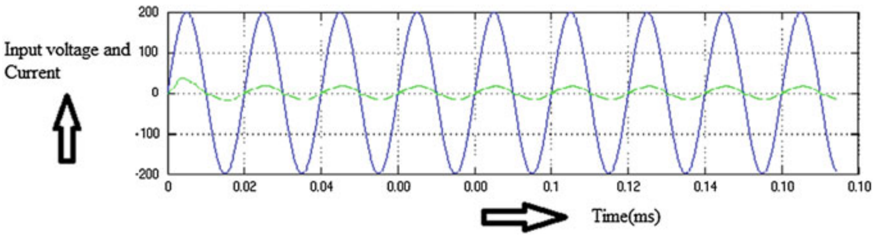

Fig. 56.5 Input voltage and current waveforms

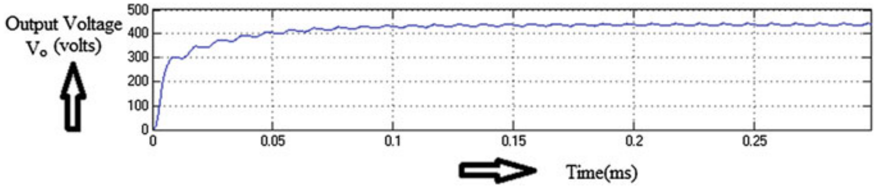

Fig. 56.6 Gate and drain for source voltage waveform

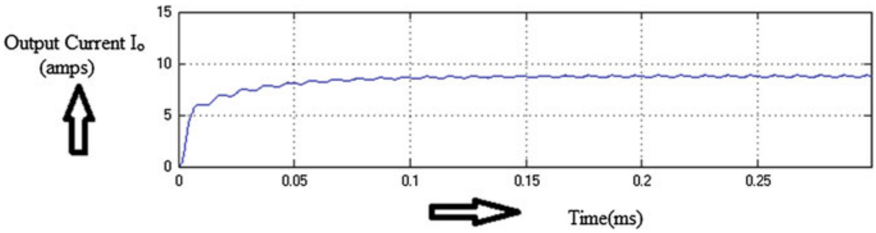

Fig. 56.7 Output current waveform

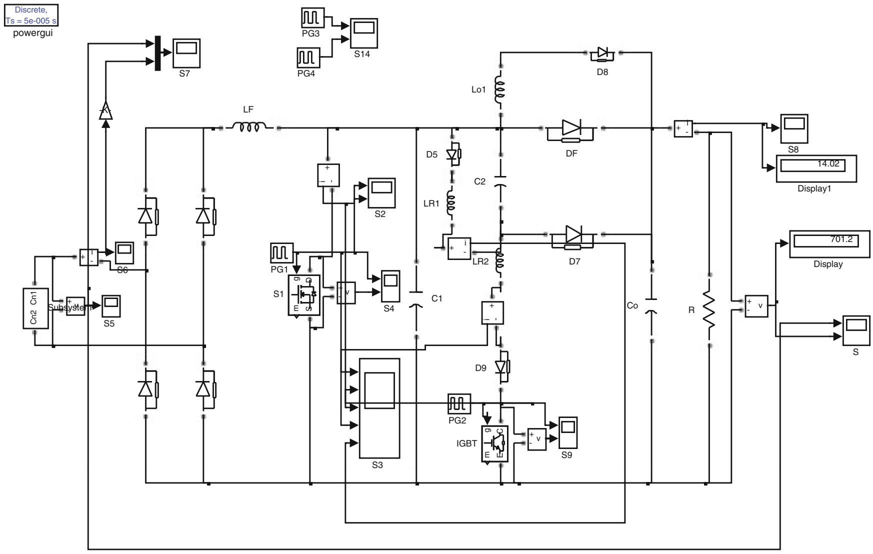

Fig. 56.8 Circuit diagram with disturbance

56.5.1 Circuit Diagram with Disturbance

See (Figs. 56.8, 56.9, and 56.10).

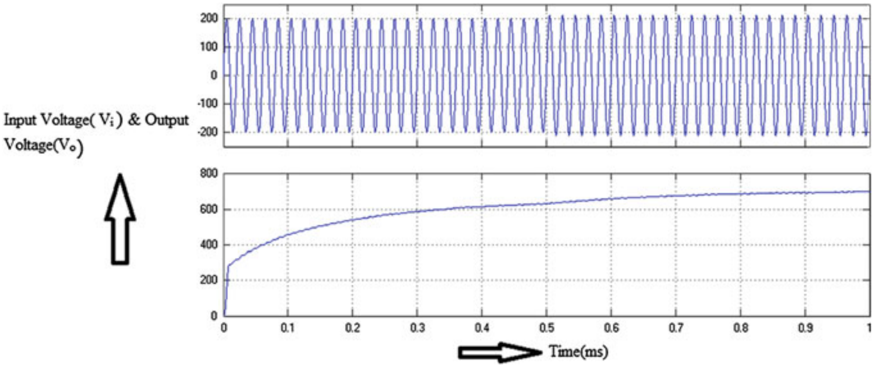

Fig. 56.9 Input and output voltage

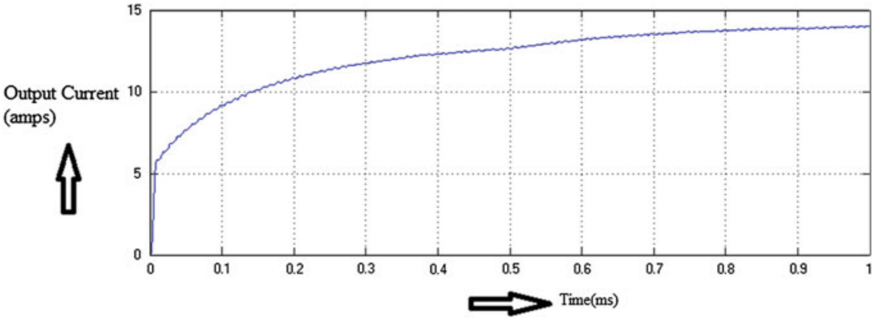

Fig. 56.10 Output current

56.6 Conclusions

In this paper a new power factor correction technique is proposed. The main switch and other semiconductor devices are operated by using ZVT and ZCT methods. The main switch is turned ON with ZVT and turned OFF with ZCT, the auxiliary switch is turned ON and turned OFF with ZCS. A part of the current on the auxiliary switch is transferred to the output load by the coupling inductance to improve the efficiency of the converter. The diode is added serially to the auxiliary switch path to prevent the incoming current stresses from the resonant circuit to the main switch. There are absolutely no current or voltage stresses on the main switch and auxiliary switches.

References

1. Hua G, Yang EX, Jiang Y, Lee FC (1994) Novel zero-current-transition PWM converters. IEEE Trans Power Electron 9(6):601–606
2. Lin RL, Zhao Y, Lee FC (1998) Improved soft-switching ZVT converters with active snubber, in Appl. Power Electr Conf Exposition IEEE 2:1063–1069
3. Hua G, Leu CS, Jiang Y, Lee FC (1994) Novel zero-voltage-transition PWM converters. IEEE Trans Power Electron 9(2):213–219
4. Umamaheswari K, Venkatachalam V (2013) Single phase converters for power factor correction with tight output voltage regulation. Int J Emerg Technol Adv Eng (ISSN 2250-2459, ISO 9001:2008 Certified J 3(2) February):516–521
5. Gotfryd M (2000) Output voltage and power limits in boost power factor corrector operating in discontinuous inductor current mode. IEEE Trans Power Electron 15(1):51–57
6. Singh K, Al-Haddad K, Chandra A (1999) A review of active filters for power quality improvement. IEEE Trans Ind Electron 46(5):960–971
7. Akin B, Bodur H member IEEE (2011) A new single-phase soft switching power factor correction converter. IEEE Trans. Power Electr 26(2):436–454

Chapter 57
Cuckoo Search Algorithm for Short Term Hydrothermal Scheduling

Hari Mohan Dubey, Manjaree Pandit and B.K. Panigrahi

Abstract This paper presents a novel nature inspired cuckoo search algorithm (CSA) to solve short term hydrothermal scheduling problems. The effectiveness of CSA algorithm is examined on three different test cases considering quadratic cost with and without prohibited discharge zones (PDZ), quadratic cost with prohibited discharge zones and valve point loading (VPL) effect in thermal unit. The outcome of simulation were compared with other recent reported approaches demonstrates the superiority of CSA algorithm.

Keywords Cuckoo search algorithm (CSA) · Prohibited discharge zones (PDZ) · Hydrothermal scheduling

57.1 Introduction

In the modern power system, efficient scheduling of available energy resources to satisfy the load demand is inevitable. Hydrothermal Scheduling (HTS) problem is a complex constrained non linear dynamic optimization problem. The idea of integrated operation is for proper utilization of all available energy resources such that the fuel cost is minimized along with minimal use of fossil fuel in addition

H.M. Dubey (✉) · M. Pandit
Department of Electrical Engineering, Madhav Institute of Technology and Science Gwalior, Gwalior, India
e-mail: harimohandubey@rediffmail.com

M. Pandit
e-mail: manjaree_p@hotmail.com

B.K. Panigrahi
Department of Electrical Engineering, Indian Institute of Technology Delhi, Delhi, India
e-mail: bkpanigrahi@ee.iitd.ac.in

C. Kamalakannan et al. (eds.), *Power Electronics and Renewable Energy Systems*, Lecture Notes in Electrical Engineering 326, DOI 10.1007/978-81-322-2119-7_57

minimizing the environmental damage. The key objective of short term HTS is to determine the optimal sharing of hydro and thermal generators in order to fulfill the load demand while satisfying the operating constraints in a schedule horizon of time interval. Various researchers have been investigating the HTS problem with different constraints and complexity since last few decades. Mathematical approaches like Dynamic Programming (DP) [1], Linear programming (LP) [2], may not perform satisfactory due to the highly non linear characteristics of HTS problem and associated constraints.

On the other hand population based optimization approach Genetic Algorithm (GA) [3], Evolutionary Programming (EP) [4], Particle swarm optimization (PSO) [5], improved PSO (IPSO) [6], adaptive particle swarm optimization (APSO) [7], Differential Evolution (DE) [8], modified differential evolution (MDE) [9], Modified hybrid differential evolution (MHDE) [10], Teaching learning based optimization (TLBO) [11] have been successfully employed to solve the HTS problem.

In this paper CSA is employed to solve three different cases of hydrothermal scheduling considering complex operating constraint. CSA is a novel evolutionary approach proposed by Yang et al. [12], Yang and Deb [13] and inspired from obligate brood parasitism of some cuckoo species by laying their egg in the nest of other host bird of other species. When the host bird discover an alien egg in their nest they can either throw it away or simply abandon their nest and build a new one elsewhere. The structure of CSA combines two main operations, a direct search based on Levy flights and a random search based on the probability for a host bird to discover an alien egg in its nest. With the combination of two operations, the CSA become more powerful search approach to solve complex optimization problems.

The remainder of paper is organized as follows: the problem formulation of short term hydrothermal scheduling (HTS) of power system with cascade reservoirs is described in Sect. 57.2. Section 57.3 explains the CSA method and Implementation process to solve short term HTS problem. Section 57.4 presents the simulation results and conclusions are presented in Sect. 57.5.

57.2 Problem Formulation

The key objective of short time hydrothermal scheduling problem is to minimize the total thermal generation cost without any violating constraint associated with hydro and thermal plant such that all load demand over a generation schedule horizon are satisfied.

57.2.1 Objective Function

$$\begin{aligned} \text{Min} \quad FC(PT) = \sum_{i=1}^{n_t} \sum_{j=1}^{NH} a_i \times PT_{i,j}^2 + b_i \times PT_{i,j} + c_i \\ + \left| e_i \times \sin(f_i \times (PT_i^{\min} - PT_{i,j})) \right| \end{aligned} \tag{57.1}$$

57.2.2 Constraints

(1) Power balance constraints

$$\sum_{i=1}^{n_h} PH_{i,j} + \sum_{i=1}^{n_t} PT_{i,j} = P_{D_j} + P_{L_j} \tag{57.2}$$

The hydroelectric generation is a function of water discharge rate and reservoir water head which in turn, is a function of storage. Mathematically,

$$PH_{i,j} = c_{1,i}V_{i,j}^2 + c_{2,i}Q_{i,j}^2 + c_{3,i}V_{i,j}Q_{i,j} + c_{4,i}V_{i,j} + c_{5,i}Q_{i,j} + c_{6,i} \tag{57.3}$$

(2) Generation limits constraints

$$PH_i^{\min} \le PH_{i,j} \le PH_i^{\max} \quad i = 1, 2, \ldots, n_h; \quad j = 1, 2, \ldots, NH \tag{57.4}$$

$$PT_i^{\min} \le PT_{i,j} \le PT_i^{\max} \quad i = 1, 2, \ldots, n_t; \quad j = 1, 2, \ldots, NH \tag{57.5}$$

(3) Water dynamic balance

$$V_{i,j} = V_{i,j-1} + I_{i,j} - Q_{i,j} - S_{i,j} + \sum_{k=1}^{u_i} (Q_{k,j-D_{k,i}} + S_{k,j-D_{k,i}}) \tag{57.6}$$

(4) Reservoir storage volume limit

$$V_i^{\min} \le V_{i,j} \le V_i^{\max} \quad i = 1, 2, \ldots, n_h; \quad j = 1, 2, \ldots, NH \tag{57.7}$$

(5) Discharge rates limit

$$Q_i^{\min} \le Q_{i,j} \le Q_i^{\max} \quad i = 1, 2, \ldots, n_h; \quad j = 1, 2, \ldots, NH \tag{57.8}$$

57.3 Cuckoo Search Algorithm

Cuckoo search algorithm (CSA) is developed by Yang and Deb in 2009 [12]. The idea behind CSA is inspired by the obligate brood parasitism of few cuckoo species in combination of the Levy flight behavior of some bird and fruit flies. It has three idealized rules for CSA as below [13]:

- Each cuckoo lays one egg (a design solution) at a time and dumps its egg in random chosen nest among the fixed number of available host nests.
- The best nests with a high quality of egg (better solution) will be carried out for next generation.
- As the number of available hosts nests is fixed, and the egg laid by a cuckoo is discovered by the host bird with a probability $P_a \in [0,1]$. In this case it can simply either throw the egg away or abandon the nest and find a new location to built a completely new one.

Based on three above rules, a general precise model for CSA algorithm is presented in references [12, 13].

57.3.1 Implementation of CSA

Step: 1 In short term HTS problem, the dependent variables like water discharge rate of all plants for number of hours and generation of thermal units for all time intervals are selected randomly within the operating limits. The storage volume of each reservoir is evaluated using (57.6), generation of hydro plants is computed using (57.3). Afterwards, the thermal power generation is calculated using (57.2). The population of host nest N_P is expressed as $X = \left[X_1, X_2, \ldots, X_{Np}\right]^T$, where each nest X_i is formulated as:

$$X_i = \begin{bmatrix} Q^i_{1,1} & \ldots & Q^i_{1,j} & \ldots & Q^i_{1,n_h}, & P^i_{s_{1,1}} & \ldots & P^i_{s_{1,j}} & \ldots & P^i_{s_{1,n_i}} \\ \ldots & \ldots & \ldots & \ldots & \ldots & \ldots & \ldots & \ldots & \ldots & \ldots \\ Q^i_{k,1} & \ldots & Q^i_{k,j} & \ldots & Q^i_{k,n_h}, & P^i_{s_{k,1}} & \ldots & P^i_{s_{k,j}} & \ldots & P^i_{s_{k,n_i}} \\ \ldots & \ldots & \ldots & \ldots & \ldots & \ldots & \ldots & \ldots & \ldots & \ldots \\ Q^i_{NH,1} & \cdots & Q^i_{NH,j} & \cdots & Q^i_{NH,n_h}, & P^i_{s_{NH,1}} & \cdots & P^i_{s_{NH,j}} & \cdots & P^i_{s_{NH,n_i}} \end{bmatrix} \quad (57.9)$$

Step: 2 Set the generation count

Step: 3 Calculate the objective function using (57.1). With constraints equation, various constraints violation is determined. After this, improved fuel cost is computed as given below:

$$FC(PT)^{*} = FC(PT) + \sum_{k=1}^{TC} \lambda_k \times Vio_k^2 \tag{57.10}$$

where TC represents the total number of constraints, λ_k is the penalty value for kth constraint and Vio_k is the amount of violation of kth constraint.

Step: 4 The new solution is generated via Levy flights. Here, calculation of new solution is based on the previous best nest via Levy flights. In this method, the optimal path for the levy flights is calculated using the Mantegna's algorithm [14]. The new solution is given as:

$$X_i^{new} = Xbest_i + \alpha \times rand_2 \times \Delta X_i^{new} \tag{57.11}$$

where $\alpha > 0$ is the updated step size, $rand_2$ is a normal distributed stochastic number and ΔX_i^{new} is calculated as below:

$$\Delta X_i^{new} = \upsilon \times \frac{\sigma_x(\beta)}{\sigma_y(\beta)} \times (Xbest_i - Gbest) \tag{57.12}$$

$$\upsilon = rand_x / \left| rand_y \right|^{1/\beta} \tag{57.13}$$

where $rand_x$ and $rand_y$ are two normally distributed stochastic variables with standard deviation $\sigma_x(\beta)$ and $\sigma_y(\beta)$ are given by

$$\sigma_x(\beta) = \left[\Gamma(1+\beta) \times \sin(\pi\beta/2) / \Gamma(\frac{1+\beta}{2}) \times \beta \times 2^{\left(\frac{\beta-1}{2}\right)} \right]^{1/\beta} \tag{57.14}$$

$$\sigma_y(\beta) = 1 \tag{57.15}$$

where β is the distribution factor, $0.3 \le \beta \le 1.99$ and $\Gamma(.)$ is the gamma distribution function. The obtained new solution must satisfy its all associated constraints.

Step: 5 The action of discovery of an alien egg in a nest of a host bird with the probability of p_a also creates a new solution for the problem similar to the Levy flights. The new solution is calculated as follows:

$$X_i^{dis} = Xbest_i + k \times \Delta X_i^{dis} \tag{57.16}$$

where k is the updated coefficient determined based on the probability of a host bird to discover an alien egg in its nest:

$$k = \begin{cases} 1 & \textit{if } rand_3 < p_a \\ 0 & \textit{otherwise} \end{cases} \tag{57.17}$$

The increased value ΔX_i^{dis} is determined by

$$\Delta X_i^{dis} = rand_3 \times [randp_1(Xbest_d) - randp_2(Xbest_d)] \tag{57.18}$$

where $rand_3$ is the distributed random number in [0, 1], $randp_1(Xbest_i)$ and $randp_2(Xbest_i)$ are the random perturbation for positions of nests in $Xbest_i$. Again for the newly generated solution, its upper and lower limits must satisfy the unit's limit. The best value is updated for each nest $Xbest_d$ and the nest corresponding to best fitness function is determined by *Gbest.*

Step: 6 The algorithm stops when the current generation reaches the maximum number of generations.

57.4 Simulation Result

To examine the applicability and performance of CSA, the test system has been adopted from [3, 4]. It consists of a multi-chain cascade of four hydro plants and a number of thermal units represented by an equivalent thermal plant. The schedule period of 24 h, with 1 h time intervals is considered for simulation. The problem under consideration is classified into three cases based on types of their fuel cost functions and operational constraints. The present work has been executed in Matlab 7.0 for solution of HTS problem and system configuration is Pentium dual core processor with 2.80 GHz and 1 GB RAM. After various runs with different values of CSA control parameter, the key control parameter selected are Population (Np) = 100, maximum iteration = 500 and value of probability (P_a) = 0.7.

Case 1 (*HTS Problem with Quadratic Cost Functions*) Here cost functions of thermal units of hydrothermal systems are to be quadratic and there is no prohibited discharge zone. The optimal hydro discharge, hydro power generations along with minimum cost obtained by CSA algorithm are listed in Table 57.1. Comparisons of

Table 57.1 Hourly plant discharge, generation schedule and thermal generations for case 1

Hour	Hydro plants								Total thermal generation (MW)	Thermal generation cost ($)
	Discharge (10^4 m^3)				Generation (MW)					
	Plant 1	Plant 2	Plant 3	Plant 4	Plant 1	Plant 2	Plant 3	Plant 4		
1.	7.2562	9.0926	18.9556	13.0050	70.9469	67.3881	45.7012	200.1325	985.8313	2.5182e+004
2.	8.7258	6.9601	20.0507	15.7406	80.3896	55.5083	37.3153	205.5375	1.0112e+003	2.5753e+004
3.	10.2087	6.0448	25.0797	14.5386	87.2354	50.9982	1.0102	180.1370	1.0406e+003	2.6417e+004
4.	12.7420	7.5652	18.9510	13.0085	93.1717	61.9636	37.1412	151.0414	946.6822	2.4306e+004
5.	5.8504	6.0332	16.2425	15.0333	58.4572	52.7990	47.0867	171.1764	960.4807	2.4614e+004
6.	8.2975	6.1301	22.8478	19.4340	74.9174	53.9594	18.7147	195.5441	1.0669e+003	2.7013e+004
7.	8.7876	9.2893	24.0307	13.0087	77.3847	71.5315	7.3983	172.9409	13207e+003	3.2923e+004
8.	10.2983	11.6653	19.1860	15.4396	84.0417	79.0656	33.5496	195.9012	1.6074e+003	3.9905e+004
9.	5.0259	10.1283	28.4860	14.4612	52.0119	71.2678	0	191.1609	1.9256e+003	4.8038e+004
10.	9.6340	6.2069	14.1243	13.0566	83.6087	50.3874	45.1115	191.8085	1.9491e+003	4.8656e+004
11.	6.1964	8.3380	29.5441	14.4955	63.3387	64.3001	0	214.9765	1.8874e+003	4.7041e+004
12.	5.0001	6.3997	11.9586	13.1066	54.0476	53.0508	45.7794	209.9452	1.9472e+003	4.8606e+004
13.	10.2474	13.5863	18.6077	13.1787	90.2896	83.1289	31.5582	226.5621	1.7985ef003	4.4740e+004
14.	7.5254	8.2941	16.5557	13.0625	75.2566	61.9723	38.4585	226.5149	1.7978e+003	4.4723e+004
15.	12.2096	10.0941	19.9685	16.1900	98.9438	70.4874	25.2853	267.0506	1.6682e+003	4.1428e+004
16.	13.3230	11.2928	10.1522	13.7207	100.7011	73.2053	47.7971	243.9003	1.6044e+003	3.9830e+004
17.	8.2175	11.2262	17.6255	17.1383	79.2115	69.8128	42.0254	274.0087	1.6649e+003	4.1345e+004
18.	8.0948	7.4779	14.2836	14.0354	78.3981	50.3289	52.6886	250.5567	1.7080e+003	4.2433e+004
19.	5.2124	8.6721	14.7847	13.5199	56.3587	55.8549	53.7080	251.3791	1.8227e+003	4.5364e+004

(continued)

Table 57.1 (continued)

Hour	Hydro plants								Total thermal generation (MW)	Thermal generation cost ($)
	Discharge (10^4 m^3)				Generation (MW)					
	Plant 1	Plant 2	Plant 3	Plant 4	Plant 1	Plant 2	Plant 3	Plant 4		
20.	5.4702	6.5541	11.8750	17.4596	58.7109	44.3526	56.6433	278.0379	1.8423e+003	4.5870e+004
21.	5.9073	9.9037	13.0345	14.6194	62.6086	62.3151	57.3135	257.9028	1.7999e+003	4.4776e+004
22.	5.3301	7.4514	13.9114	16.6266	57.8391	50.4675	57.5317	272.4876	1.6817e+003	4.1767e+004
23.	10.1407	6.9278	10.0088	17.1498	91.2280	47.9704	55.6730	274.0513	1.3811e+003	3.4365e+004
24.	5.2987	6.6659	12.5509	19.0809	57.7903	47.1950	58.9036	279.1934	1.1469e+003	2.8849e+004

Total cost of thermal generator ($\Day): 913,945.87885582

Table 57.2 Comparison of optimal costs obtained by different algorithms for case 1

Method	Best fuel cost ($/day)	Avg. fuel cost ($/day)	Worst fuel cost ($/day)	Method	Best fuel cost ($/day)	Average fuel cost ($/day)	Worst fuel cost ($/day)
FEP [4]	930,267.92	930,897.44	931,396.81	EGA [5]	934,727.00	936,058.00	937,339.00
CEP [4]	930,166.25	930,373.23	930,927.01	PSO [5]	928,878.00	933,085.00	938,012.00
IFEP [4]	930,129.82	930,290.13	930,881.92	EPSO [5]	922,904.00	923,527.00	924,808.00
IPSO [6]	922,553.49	–	–	MDE [9]	922,555.44	–	–
APSO [7]	926,151.54	–	–	TLBO [11]	922,373.39	922,462.24	922,873.81
MAPSO [7]	922,421.66	922,544.00	923,508.00	CSA	*913,945.87*	917,624.024	921,994.25

Table 57.3 Hourly plant discharge, generation schedule and thermal generations for case 2

Hour	Hydro plants								Total thermal generation (MW)	Thermal generation cost (S)
	Discharge (10^4 m^3)				Generation (MW)					
	Plant 1	Plant 2	Plant 3	Plant 4	Plant 1	Plant 2	Plant 3	Plant 4		
1.	7.8667	13.3173	28.2230	14.5190	74.8878	81.0560	0	211.1155	1.0029e+003	2.5566e+004
2.	7.5564	6.1004	16.6759	13.2328	73.2233	47.6415	47.0834	187.6298	1.0344e+003	2.6277e+004
3.	5.5923	11.9923	18.1283	13.6253	58.7776	76.2506	40.5194	175.7465	1.0087e+003	2.5696e+004
4.	10.0442	62.366	28.5493	14.8192	87.2286	48.4454	0	164.3546	989.5713	2.5275e+004
5.	6.5706	8.2735	11.1451	13.7370	65.8710	61.0832	49.6371	176.1875	937.2213	2.4095e+004
6.	7.5453	8.0736	10.3057	13.0001	72.6861	59.2313	52.6891	174.5519	1.0504e+003	2.6640e+004
7.	7.2033	10.6097	15.0329	14.5542	70.5450	68.6551	52.8177	191.7684	1.2662e+003	3.1632e+004
8.	12.3777	6.0009	15.4495	14.5864	94.2343	43.6336	52.8443	211.8912	1.5974e+003	3.5655e+004
9.	5.3854	6.2883	15.1416	14.3186	56.6214	46.7355	53.6331	202.8888	1.8801e+003	4.6852e+004
10.	12.3949	8.2873	12.4114	13.4647	95.6459	59.6594	57.8311	192.1400	1.5147e+003	4.7755e+004
11.	5.2788	8.7480	29.1634	20.2880	56.5721	62.3630	0	227.2261	1.8838e+003	4.6949e+004
12.	12.5215	8.8087	28.7245	13.0073	97.6448	62.1352	0	184.8786	1.5653e+003	4 5084e+004
13.	11.2777	8.6454	18.6467	13.4803	93.5639	60.8166	39.9592	190.8766	1.8448e+003	4.5935e+004
14.	5.6824	9.1701	29.3756	13.2882	60.5595	63.4499	0	188.2091	1.8878e+003	4.705 le+004
15.	9.3864	9.7945	14.5375	13.7443	87.0488	65.9433	50.6719	210.1617	1.7162e+003	4.2640e+004
16.	6.1709	6.4305	18.8360	15.5093	65.2932	47.7750	39.4366	241.5531	1.6755e+003	4.1612e+004
17.	5.7032	9.7359	16.5597	13.1782	61.5047	64.8301	46.8176	224.6736	1.7322e+003	4.3046e+004
18.	6.7926	6.0968	13.0910	13.6936	70.7451	43.6313	53.5894	244.7155	1.7269e+003	4.2912e+004
19.	6.7483	8.4563	17.2841	13.5715	70.4089	57.2031	46.1595	248.2262	1.8180e+003	4.5243e+004

(continued)

Table 57.3 (continued)

Hour	Hydro plants								Total thermal generation (MW)	Thermal generation cost (S)
	Discharge (10^4 m^3)				Generation (MW)					
	Plant 1	Plant 2	Plant 3	Plant 4	Plant 1	Plant 2	Plant 3	Plant 4		
20.	5.5732	6.5016	16.5483	13.1469	60.4206	46.4028	48.4164	245.3877	1.8794e+003	4.6832e+004
21.	5.3746	11.7827	10.0000	19.0951	58.6430	71.0571	52.3690	291.6537	1.7663e+003	4.3916e+004
22.	13.8450	6.0965	13.3762	22.0656	105.0274	43.7380	54.5985	297.1273	1.6191e+003	4.0197e+004
23.	5.7936	10.2191	10.0042	14.6563	62.3452	65.4497	53.4984	251.7983	1.4169e+003	3.5228e+004
24.	12.3150	6.3340	10.5319	21.6476	101.3071	44.5878	56.5751	292.4226	1.0943e+003	2.7640e+004

Total cost of thermal generator ($/day): 917,727.86084471 costs are made with TLBO [11], MDE [9], MAPSO [7], PSO [5], EGA [5] and others in Table 57.2, which shows CSA capitulates better result in term of thermal generation cost 913,945.878 ($) then TLBO [11], MDE [9], PSO [5], IFEP [4] and others while satisfying all associated constraints.

Case 2 (*HTS Problem with Quadratic Cost Functions and PDZ*) The optimal hydrothermal schedule with minimum thermal generation cost as 917,727.86 ($) is obtained without VPL effect and with PDZ by CSA. The optimal hydro discharge, hydro and thermal power generations along with corresponding cost obtained by CSA for 24 h are listed in Table 57.3. The comparison of costs obtained by CSA made with most recent reported TLBO [11] and IPSO [6] algorithm as in Table 57.4.

Case 3 (*HTS Problem with Valve Point Effect and Prohibited Discharge Zone*) To validate feasibility for practical system, VPL effect of the thermal generator is considered in this case along with PDZ constraints of hydro plants. The optimal hydro discharge, hydro and thermal power generations along with corresponding cost obtained by CSA for 24 h are listed in Table 57.5. The statistical result in term of cost obtained by different methods available in literature are shown in Table 57.6, which depicts the superior search capability of CSA in comparison to other method for problem under consideration. Figure 57.1 shows the cost convergence of proposed method for this case.

Table 57.4 Comparison of optimal costs obtained by different algorithms for case 2

Method	Best fuel cost ($/day)	Average fuel cost ($/day)	Worst fuel cost ($/day)
IPSO [6]	923,443.17	–	–
TLBO [11]	923,041.91	923,174.58	923,463.16
CSA	917,727.86	920,900.98	922,868.24

Table 57.5 Hourly plant discharge, generation schedule and thermal generations for case 3

Hour	Hydro plants								Total thermal generation (MW)	Thermal generation cost (S)
	Discharge (10^4 m^3)				Generation (MW)					
	Plant 1	Plant 2	Plant 3	Plant 4	Plant 1	Plant 2	Plant 3	Plant 4		
1.	5.1533	6.3950	18.2274	13.6236	54.7806	52.7038	48.4113	204.8083	1.0093e+003	2.6156e+004
2.	9.1997	14.6696	16.5866	14.1719	83.5203	84.2562	50.4691	195.2159	976.5385	2.5203e+004
3.	9.8479	6.2152	20.2692	13.1066	86.2526	49.1408	33.7386	172.1947	1.0187e+003	2.5994e+004
4.	9.0221	6.0285	13.6186	13.3135	81.3544	49.6086	52.8366	156.2493	949.9511	2.4743 e+004
5.	6.3941	6.4333	29.6719	13.2243	64.0476	53.3468	0	162.2964	1.0103e+003	2.6131e+004
6.	13.2341	8.3998	15.2077	13.8035	93.6660	64.8454	51.6044	170.4917	1.0294e+003	2.6758e+004
7..	7.5733	6.2402	18.4129	14.4898	70.6824	51.0537	42.4356	183.2653	1.3026e+003	3.3038e+004
8.	12.3373	6.9771	27.7341	13.3787	90.3661	56.0371	0	175.0331	1.6786e+003	4.1931e+004
9.	6.0277	9.1229	20.5431	15.3165	59.8504	67.9392	29.7246	207.9938	1.8745e+003	4.7097e+004
10.	5.0066	9.6174	17.4268	13.2208	52.8050	70.0450	43.0349	193.8507	1.9603e+003	4.9650e+004
11.	7.8766	6.3156	20.4584	13.4636	75.7979	52.1437	28.3530	201.7168	1.8720e+003	4.6900e+004
12.	13.5569	6.0291	10.2632	14.0370	97.8612	51.2555	49.3763	222.0257	1.8895e+003	4.7765e+004
13.	9.8542	10.4603	20.8224	13.6658	86.3218	75.4150	29.2344	226.0906	1.8129e+003	4.5811e+004
14.	13.8423	6.2698	18.5056	14.0721	97.9796	53.1081	41.0255	233.1822	1.7747e+003	4.483 1e+004
15.	5.2570	6.1724	16.3414	14.6701	56.0228	53.9810	48.3282	244.3075	1.7274e+003	4.3349e+004
16.	7.9403	6.0525	21.2547	13.8866	77.0597	54.1575	31.6855	233.7393	1.6734e+003	4.2057e+004
17.	5.8969	6.5450	14.1669	13.2302	62.2902	57.8696	53.1793	235.0747	1.7216e+003	4.2890e+004
18.	6.2456	10.5007	10.0005	15.5045	65.4148	77.7904	53.1681	258.3422	1.6853e+003	4.2010e+004
19.	5.8033	6.8676	17.9779	14.1419	61.8570	57.6732	45.5961	248.5646	1.8263e+003	4.5705e+004

(continued)

Table 57.5 (continued)

Hour	Hydro plants								Total thermal generation (MW)	Thermal generation cost (S)
	Discharge (10^4 m^3)				Generation (MW)					
	Plant 1	Plant 2	Plant 3	Plant 4	Plant 1	Plant 2	Plant 3	Plant 4		
20.	5.2451	6.0057	14.0932	20.2942	57.0076	52.8050	53.4619	294.4286	1.8223e+003	4.5806e+004
21.	11.8418	9.6352	11.5005	14.1005	97.0566	74.5968	55.2824	249.1471	1.7639e+003	4.426 le+004
22.	5.2841	12.7563	10.0680	15.6365	57.1571	84.8382	54.3354	257.0131	1.6667e+003	4.2074e+004
23.	5.6489	14.5347	11.7213	18.1929	60.7129	84.6248	57.6832	275.5596	1.3714e+003	3.4812e+004
24.	6.9109	13.7561	10.8209	15.8374	71.4488	78.5578	57.4011	256.6338	1.1260e+003	2.8505e+004

Total cost of thermal generator ($/day): 923,477.35457270

Table 57.6 Comparison of optimal costs obtained by different algorithms for case 3

Method	Best fuel cost ($/day)	Avg. fuel cost ($/day)	Worst fuel cost ($/day)	Method	Best fuel cost ($/day)	Avg fuel cost ($/day)	Worst fuel cost ($/day)
FEP [4]	935,021.93	942,262.75	951,524.37	DP [6]	935,617.76	–	–
CEP [4]	934,713.18	938,801.47	946,795.20	DE [6]	928,236.94	–	–
IFEP [4]	933,949.25	938,508.87	942,593.02	NLP [6]	936,709.52	–	–
IPSO [6]	925,978.84	–	–	MDE [9]	925,960.56	–	–
APSO [7]	925,991.35	–	–	TLBO [11]	924,550.78	924,702.43	925,149.06
MAPSO [7]	924,636.88	926,496	927,431	*CSA*	923,477.35	926,412.93	931,702.22

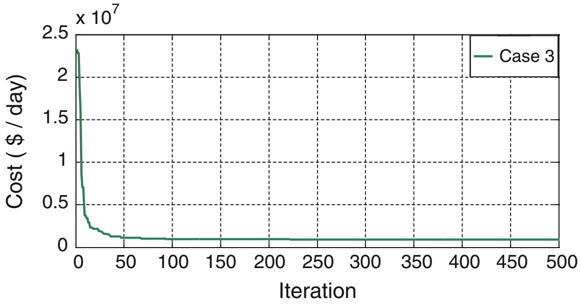

Fig. 57.1 Cost convergence characteristic of CSA for case 3

57.5 Conclusion

In this paper the CSA has been efficiently implemented to solve short term HTS problem. Its applicability and validity were investigated on a hydrothermal system having four hydro units and a thermal plant for 24 h of time horizon with 1 h time intervals. In all three different cases under simulation studies, the production costs obtained by CSA is found to be much better as compared to other reported existing methods reported in literature. Therefore CSA is a promising method which can be extended to solve other complex constraint large scale optimization problem faced by the utilities.

References

1. Yang JS, Chen N (1989) Short-term hydrothermal coordination using multi-pass dynamic programming. IEEE Trans Power Syst 4(3):1050–1056
2. Mohan MR, Kuppusamy K, Khan MA (1992) Optimal short-term hydro-thermal scheduling using decomposition approach and linear programming method. Int J Electr Power Energ Syst 14(1):39–44
3. Orero SO, Irving MR (1998) A genetic algorithm modeling framework and solution technique for short-term optimal hydrothermal scheduling. IEEE Trans Power Syst 13(2):501–518
4. Sinha N, Chakrabarti R, Chattopadhyay PK (2003) Fast evolutionary technique for short-term hydrothermal scheduling. IEEE Trans Power Syst 18(1):214–220
5. Yuan X, Wang L, Yuan Y (2008) Application of enhanced PSO approach to optimal scheduling of hydro system. Energ Convers Manag 49(11):2966–2972
6. Hota PK, Barisal AK, Chakrabarti R (2009) An improved PSO technique for short-term optimal hydrothermal scheduling. Electr Power Syst Res 79(7):1047–1053
7. Amjady N, Soleymanpour HR (2010) Daily hydrothermal generation scheduling by a new modified adaptive particle swarm optimization technique. Electr Power Syst Res 80 (6):723–732
8. Mandal KK, Chakraborty N (2008) Differential evolution technique-based short-term economic generation scheduling of hydrothermal systems. Electr Power Syst Res 78 (11):1972–1979

9. Lakshminarasimman L, Subramanian S (2006) Short-term scheduling of hydrothermal power system with cascaded reservoirs by using modified differential evolution. IEE Proc Gener Transm Distrib 153(6):693–700
10. Lakshminarasimman L, Subramanian S (2008) Modified hybrid differential evolution for short-term scheduling of hydrothermal power system with cascaded reservoirs. Energ Convers Manag 49(10):2513–2521
11. Roy PK (2013) Teaching learning based optimization for short-term hydrothermal scheduling problem considering valve point effect and prohibited discharge constraint. Electr Power Energy Syst 53:10–19
12. Yang XS, Deb S (2009) Cuckoo search via Lévy flights. In: Proceedings of world congress on nature and biologically inspired computing (NaBIC). IEEE Publications, USA, pp 210–214
13. Yang XS, Deb S (2010) Engineering optimization by Cuckoo search. Int J Math Model Numer Optim 1(4):330–343
14. Mantegna RN (1994) Fast accurate algorithm for numerical simulation of Levy stable stochastic processes. Phys Rev E 49(5):4677–4683

Chapter 58
Performance of Phase-Shift Control Using High-Efficiency Switched-Capacitor-Based Resonant Converter

K. Naresh, K. Kareemulla Khan, V. Ramesh, Mohan Bukya and K. Chaitanya Kumar

Abstract Performance of a switched-capacitor-based resonant converter (SCRC) using a phase-shift control method realizes zero-voltage switching operation, and thus achieves high conversion efficiency. A theoretical analysis shows that the SCRC can reduce its inductor volume compared with a conventional buck converter when the output voltage range is within 19–81 % of its input voltage. Experimental results verify the operating characteristics of the proposed method and show the improved conversion efficiency of more than 99 %. Switched-capacitor technology is widely used in low power DC–DC converter, especially in power management of the integrated circuit. These circuits have a limitation: high pulse currents will occur at the switching transients, which will reduce the efficiency and cause electromagnetic interference problems. This makes it difficult to use this technology in high-power-level conversion. The new design method for DC–DC converter with switched-capacitor technology. The proposed converter has no requirement for magnetic components and can achieve peak efficiency at full load. The experimental results verify the analysis and demonstrate the advantages.

Keywords Switched-capacitor technology · Resonant converter · Zero-voltage switching (ZVS) · Electromagnetic interference (EMI)

K. Naresh (✉) · K.K. Khan · V. Ramesh · M. Bukya · K.C. Kumar
Department of Electrical and Electronics Engineering, K L University, Guntur, Andhra Pradesh, India
e-mail: knaresh@kluniversity.in

K.K. Khan
e-mail: kareemmusfi@hotmail.com

V. Ramesh
e-mail: rameshvaddi6013@kluniversity.in

M. Bukya
e-mail: mohanbukya@kluniversity.in

K.C. Kumar
e-mail: chaitu5678@gmail.com

C. Kamalakannan et al. (eds.), *Power Electronics and Renewable Energy Systems*, Lecture Notes in Electrical Engineering 326, DOI 10.1007/978-81-322-2119-7_58

58.1 Introduction

Various types of DC–DC converters are widely applied to dc power supplies, battery chargers, voltage regulators for photovoltaic's and fuel cells, etc. Most of the DC–DC converters include magnetic components, such as inductors and/or transformers for stepping up/down or smoothing the current/voltage. The magnetic components, however, occupy a large volume and weight in the converter, and also produce non-negligible losses [1]. Switched-capacitor converters (SCC) have been used as a simple and low-cost DC–DC converter in small power applications. The advantage of the SCC is its small volume because it needs no inductor or transformer. Recently, resonant power converters consisting of an SCC and a small-rated resonant inductor have been proposed to reduce the switching loss and electromagnetic interference (EMI). The resonant converters have an additional small inductor connected in series with the switched capacitor, leading to soft-switching operation with a low-switching loss [2]. The inductor used in the resonant converters is much smaller than that in a conventional buck converter because the converter mainly stores the electrical energy in the switched capacitor similarly to the SCC. As a consequence, the resonant converter seems to be more suitable for a high-power application than the SCC. A circuit configuration using synchronous rectification has been proposed to reduce the conduction loss and the mitigation of the conducted EMI is also reported. Switched-capacitor technology has been used in DC–DC power conversion for a very long time [3]. The well known one is the charge pump circuits. They are widely used in low power DC–DC converter, especially in power management of the integrated circuits. Usually, they use high-frequency switching actions and only use capacitors to transfer the energy. These traditional circuits have a limitation: high pulse currents will occur at the switching transients, which will reduce the efficiency and cause electromagnetic interference (EMI) problems [4]. This makes it difficult to design the converter with the switched-capacitor technology in high-power-level conversion.

58.1.1 Problem Formulation

The major concerns of these studies including to reducing the switching loss and electromagnetic interference (EMI). A circuit configuration using synchronous rectification has been proposed to reduce the conduction loss and the mitigation of the conducted EMI is also reported. The resonant converters have an additional small inductor connected in series with the switched capacitor, leading to soft-switching operation with a low-switching loss. The output voltage error is caused by the input voltage fluctuations, and the voltage drops in the switching devices and the passive components. Some feedback control methods have been proposed to regulate the output voltage by adjusting the blanking time [5]. A new voltage-regulation method has proposed for SCRCs, which adjusts a phase-shift angle. The control method realized a current amplitude control by adjusting the phase difference among gate signals [6]. The method makes the SCRC not only decrease the output voltage, but also increase it continuously, resulting in a more flexible voltage regulation. The SCRC can continue zero-voltage switching (ZVS) even if the output voltage is changed.

58.2 DC–DC Converters

The DC–DC converters are widely used in regulated switch mode dc supplies and in dc motor drive applications. The input to these converters is often an unregulated dc voltage, which is obtained by rectifying the line voltage and therefore it will fluctuate due to changes in the line voltage magnitude. Switch mode DC–DC converters are used to convert the unregulated dc input into a controlled dc output at a desired voltage level. Most of the DC–DC converters include magnetic components, such as inductors and/or transformers for stepping up/down or smoothing the current/voltage. The magnetic components, however, occupy a large volume and weight in the converter, and also produce non-negligible losses. Switched-capacitor converters have been used as a simple and low-cost DC–DC converter in small power applications [7]. The advantage of the SCC (Switched capacitor converter) is its small volume because it needs no inductor or transformer. Resonant power Converters consisting of an SCC and a small-rated resonant inductor have been proposed to reduce the switching loss and electromagnetic interference (EMI). The resonant converters have an additional small inductor connected in series with the switched capacitor, leading to soft-switching operation with a low-switching loss.

58.2.1 Control of DC–DC Converters

In DC–DC converters, the average dc output voltage must be controlled to equal a desired level, though the input voltage and the output load may fluctuate. Switch MODE DC–DC converters utilize one or more switches to transform dc from one level to another. In a DC–DC converter with a given input voltage, the average output voltage is controlled by controlling the switch on and off durations. One of the methods for controlling the output voltage employs switching at a constant frequency and adjusting the on duration of the switch to control the average output voltage. In this method, called pulse-width modulation (PWM) switching, the switch duty ratio, which is defined as the ratio of the on duration to the switching time period, is varied [5]. The other control method is more general, where both the switching frequency (and hence the time period) and the on duration of the switch are varied. This method is used only in DC–DC converters utilizing force-commutated thyristors. Variation in the switching frequency makes it difficult to filter the ripple components in the input and output waveforms of the converter and the peak of the saw-tooth waveform, the switch duty ratio can be expressed as

$$D = \frac{t_{on}}{T_S} \tag{58.1}$$

58.2.2 Electromagnetic Interference

As the name suggests, it is related with the disturbance caused due to electromagnetic waves to the operation of the DC–DC converter or any other electronic circuit. Because of the rapid changes in voltages and currents within a switching converter, power electronic equipment is a source of electromagnetic interference with other equipment as well as with its own proper operation. The electromagnetic interference is transmitted in two forms: radiated and conducted. The switching converters supplied by the power lines generate conducted noise into the power lines that is usually several orders of magnitude higher than the radiated noise into free space. Metal cabinets used for housing power converters reduce the radiated component of the electromagnetic interference. Conducted noise consists of two categories commonly known as the differential mode and the common mode.

58.3 Switched Capacitor Based Resonant Converters

Switched capacitor based resonant converter Fig. 58.1, shows a circuit configuration of a SCRC. This circuit acts as a step-down converter and feeds the output voltage Vout to a load. The SCRC consists of two half-bridge inverters with four switching devices S1–S4 and a series resonant circuit Lr and Cr. Addition of the small inductor Lr is the difference from a conventional SCC in the circuit

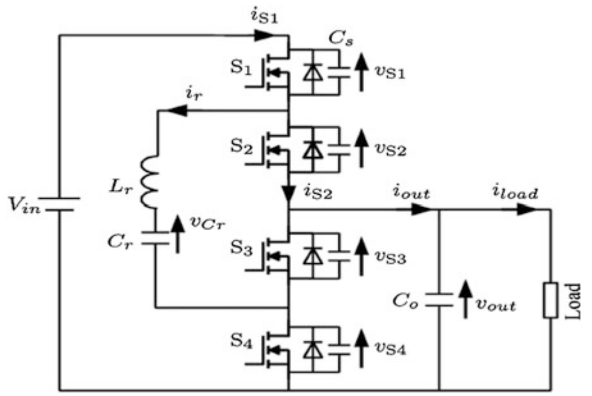

Fig. 58.1 Switched capacitor based resonant converter

configuration, resulting in a great suppression of spike currents, power losses, and EMI issues. The configuration is the same as that in [8] except for addition of four snubber capacitors Cs.

58.3.1 Configuration and Operation

Switched capacitor based resonant converter shows a circuit configuration of a SCRC. This circuit acts as a step-down converter and feeds the output voltage Vout to a load. The SCRC consists of two half-bridge inverters with four switching devices S1–S4 and a series resonant circuit Lr and Cr. Addition of the small inductor Lr is the difference from a conventional SCC in the circuit configuration, resulting in a great suppression of spike currents, power losses, and EMI issues. The configuration is the same as that in [8] except for addition of four snubber capacitors Cs.

58.3.2 Phase-Shift Control

SCRC consisting of four switching modes. Four switching modes exist because the SCRC consists of two half-bridge inverters. Figure 58.1 illustrates the switching sequence and waveforms of the phase-shift control. These waveforms are drawn under the condition of a power flow from the voltage source Vin to the load. In addition, the output voltage is assumed to be Vout = Vin/2. The switching frequency f_{SW} should be set at a higher frequency than the resonant frequency of the series resonant circuit (Fig. 58.2).

$$f_r = \frac{w_r}{2\pi} = \frac{1}{2\pi\sqrt{LC}} \tag{58.2}$$

58.3.3 Control Scheme

The block diagram (Fig. 58.3) of the output voltage controller for the SCRC. The output voltage Vout can be regulated by applying voltage feedback with proportional and integral (PI) gains. The reference of the averaged output current I*out is given as follows: (from Fig. 58.3)

$$I^*_{out(s)} = \left(K_p + \frac{K_i}{s}\right)\{V^*_{out(s)} - V_{out(s)}\} \tag{58.3}$$

where K_p is a proportional gain, K_i is an integral gain, and is a reference of the output voltage. The proposed feedback control realizes an accurate voltage regulation in

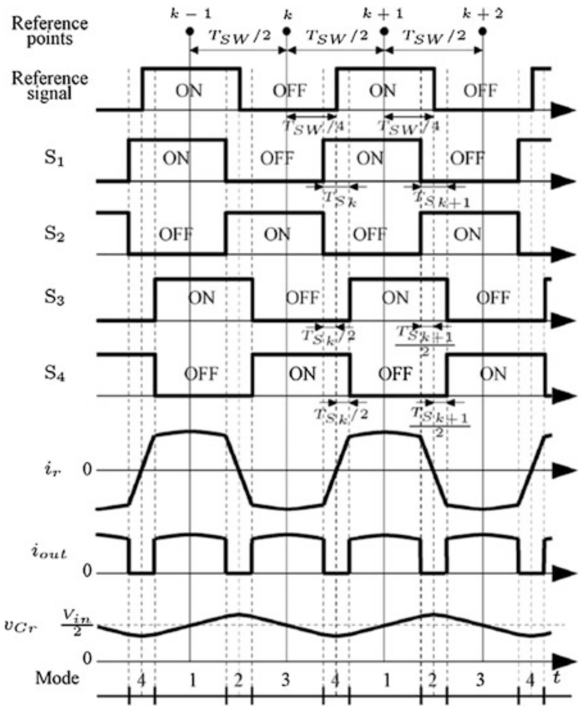

Fig. 58.2 Switching sequence in the phase shift control

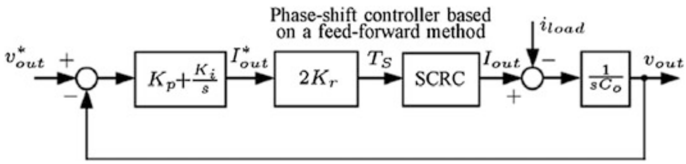

Fig. 58.3 Block diagram of the output voltage controller

spite of the input voltage fluctuation and/or voltage drops in devices. According to the above relation, T_s is calculated from the reference value of the output current I*out as follows:

$$T_s = 2K_r I_{out}^* \tag{58.4}$$

where Kr is a control gain depending on circuit parameters, given by

$$K_r = \frac{Z_r T_{sw}}{2V_{in}\tan\left(\frac{wrT_{sw}}{4}\right)} \tag{58.5}$$

This control method simply decides Ts to be in proportion to the I*out, and do not need any current sensor.

58.4 Simulation Results

58.4.1 Switched Capacitor Based Resonant Converter

See (Fig. 58.4).

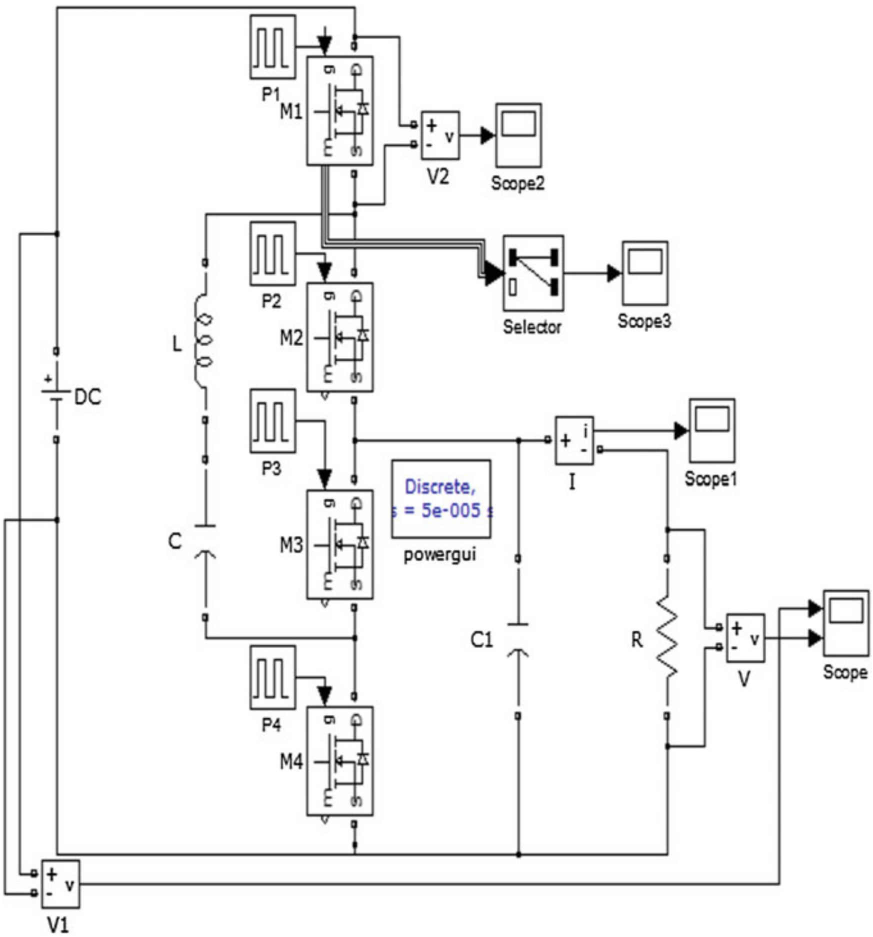

Fig. 58.4 Simulation of switched capacitor based resonant converter

58.4.2 Simulation Results for Switched Capacitor Based Resonant Converter

See (Figs. 58.5, 58.6 and 58.7).

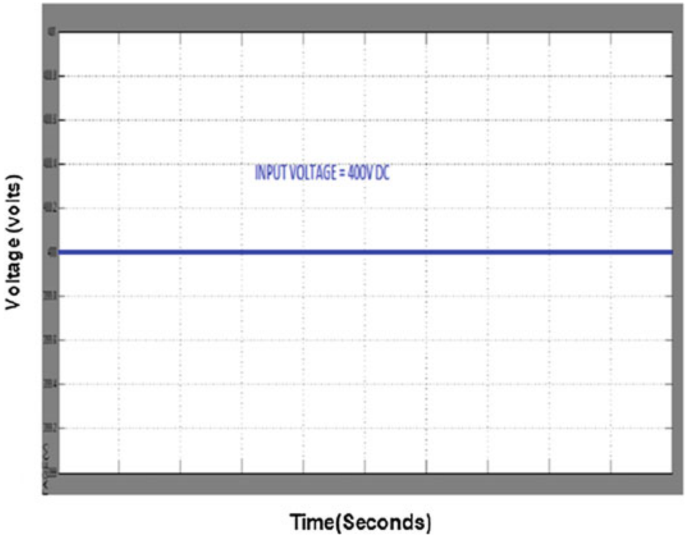

Fig. 58.5 Input voltage of switched capacitor based resonant converter

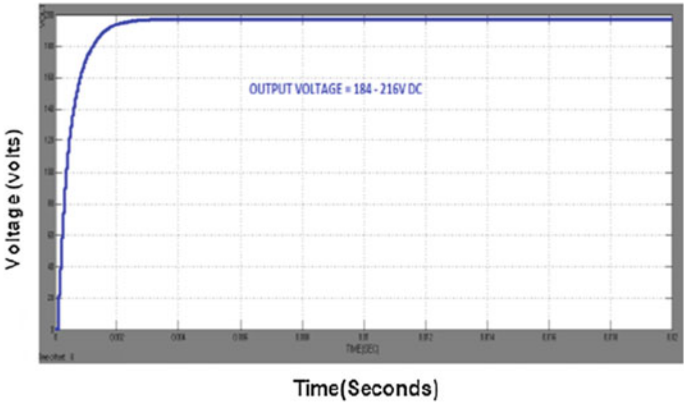

Fig. 58.6 Output voltage of switched capacitor based resonant converter

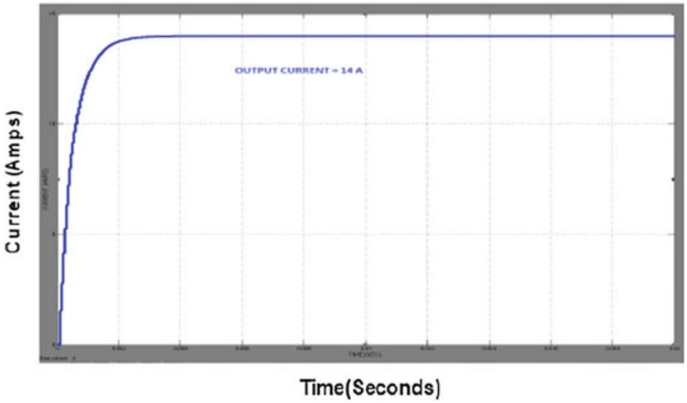

Fig. 58.7 Output current of switched capacitor based resonant converter

58.5 Conclusion

The output voltage regulation characteristics, the inductor volume, and the efficiency of the SCRC using a phase-shift control method were verified. A control method and soft switching operation of the SCRC was explained. The analysis of the stored energy in the inductor revealed that the inductor volume of the SCRC is smaller than the conventional converter when the converter is operated in a range of 19–81 % in voltage conversion ratio. The analysis also showed that the SCRC has a significant advantage in inductor volume in case the voltage conversion ratio is around 0.5. The efficiency of the experimental setup reached more than 99 %. The experimental results showed that the SCRC has a significant advantage in efficiency in case the voltage conversion ratio is around 0.5.

References

1. Sano K, Fujita H (2011) Performance of a high-efficiency switched-capacitor-based resonant converter with phase-shift control. IEEE Trans Power Electron 26(2):280–289
2. Zhang F, Du L, Peng FZ, Qian Z (2008) A new design method for high-power high-efficiency switched-capacitor DC–DC converters. IEEE Trans Power Electron 23(2):832–840
3. Shen M, Peng FZ, Tolbert LM (2008) Multilevel DC–DC power conversion system with multiple dc sources. IEEE Trans Power Electron 23(1):420–426
4. Cao D, Peng FZ (2009) Zero-current-switching multilevel modular switched-capacitor DC–DC converter. In: Proceedings of IEEE ECCE 2009, pp 3516–3522
5. Yeung YPB, Cheng KWE, Ho SL, Law KK, Sutanto D (2004) Unified analysis of switched-capacitor resonant converters. IEEE Trans Ind Electron 51(4):864–873
6. Sano K, Fujita H (2008) Voltage-balancing circuit based on a resonant switched-capacitor converter for multilevel inverters. IEEE Trans Ind Appl 44(6):1768–1776

7. Yu W, Qian H, Lai J-S (2010) Design of high-efficiency bidirectional–DC converter and high-precision efficiency measurement. IEEE Trans Power Electron 25(3):650–658
8. Inoue S, Akagi H (2007) A bidirectional DC–DC converter for an energy storage system with galvanic isolation. IEEE Trans Power Electron 22(6):2299–2306

Chapter 59
Single Stage High Voltage Gain Boost Converter for Battery Charging Using PV Panels

P.M. Midhun

Abstract One of the major concerns in the Renewable Energy applications is need of a high DC voltage which is necessary to supply inverters, UPS, etc. This paper reports a novel high voltage gain boost converter topology for battery charging using PV panels at a reduced number of conversion stages. The proposed topology aims to reduce the number of conversion stages, thus increasing the converter efficiency and simplifying the control system. The simulation studies are performed using MATLAB/SIMULINK.

Keywords Boost converter · Voltage gain · Renewable energy

59.1 Introduction

Renewable Energy attracts interest for power generation since the non-renewable energy like petrol, diesel, etc. are diminishing and energy crisis is an important issue in most of the nations. Energy production using solar energy could be a solution for the increasing power demands. The photovoltaic generation systems can either be operated as isolated systems or connected to the grid as a part of an integrated system. One of the major advantages of PV technology is that it has no moving parts; it has a long lifetime and low maintenance requirements and most importantly it is one solution that offers eco-friendly power. The solar energy is directly converted into the electric energy by the Photovoltaic (PV) module.

As generally acknowledged, the high-gain DC–DC converter is widely used in the sustainable energy system as the front-stage of the DC–AC converter. Therefore, it is indispensable for low voltage to be boosted to high voltage. In general, the boost converter or the buck-boost converter is widely used in such applications. However, it is not easy for such converters to achieve high voltage ratio [1].

P.M. Midhun (✉)
Department of EEE, SNS College of Engineering, Coimbatore, India
e-mail: midhun_pan@yahoo.com

C. Kamalakannan et al. (eds.), *Power Electronics and Renewable Energy Systems*,
Lecture Notes in Electrical Engineering 326, DOI 10.1007/978-81-322-2119-7_59

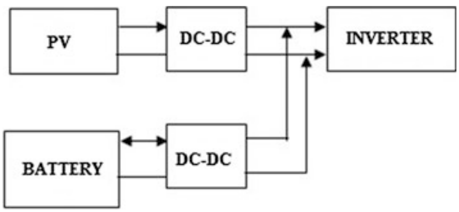

Fig. 59.1 Existing system architecture

A novel high voltage gain boost converter topology for battery charging using PV panels and a reduced number of conversion stages is presented in this project [2]. The presented converter operates in Zero Voltage Switching (ZVS) mode for all switches. By using the new concept of single-stage approaches, the converter can generate a DC bus with a battery bank or a photovoltaic (PV) panel array, allowing the simultaneous charge of the batteries according to the radiation level.

Nowadays, many systems use an AC power supply and a low voltage inverter associated with a low frequency transformer to provide a sinusoidal voltage waveform with the appropriated voltage level (Fig. 59.1).

However, this solution presents high weight and appreciable losses owing to the high currents processed by the inverter and owing to the low frequency transformer [3]. Thus, an additional stage is necessary to step the low level voltage up from the battery bank (12, 24, or 48 V) to the higher voltage level of the inverter DC link (200 or 400 V). As traditional step-up converters are not feasible for providing such high voltage gain, typical solutions use one high frequency isolated stage to achieve the high step-up voltage gain. Recently, non-isolated DC–DC converters with high voltage gain capability were successfully introduced. However, in systems where photovoltaic panels and battery banks are required, two DC–DC stages are still necessary [4].

59.2 Single Stage High Voltage Gain Boost Converter

In the low voltage side, the bidirectional characteristic of the topology allows the MOSFET Bridge to be supplied by either the battery or the PV array. Besides, the use of resonant capacitors in the full-bridge capacitors provides Zero Voltage Switching (ZVS) of the switches. The integrated topology resulting from the boost converter and the three-state switching cell is shown below [5]. The main advantage of this topology is the low voltage stress across the active switches, low input current ripple, and simplicity, and higher efficiency (Fig. 59.2).

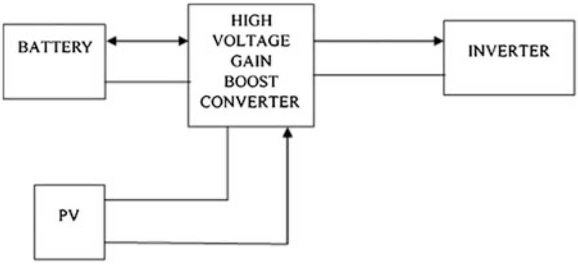

Fig. 59.2 Proposed architecture

59.3 Circuit Diagram

The proposed converter has two operation regions, which work analogously. The duty cycle is applied to the lower switches of each leg (S2 and S4), which operate in opposite phase. The converter behavior and the operation region are defined by the applied duty cycle. If the duty cycle is higher than 50 %, the lower switches work in overlapping mode. However, if the duty cycle is lower than 50 %, then only the upper switches are in overlapping mode. As the operation principle regarding the switches is analogous, only the case for D > 50 % is selected. The converter presents six operation stages. As it can be observed, the current through the input inductor has a frequency which is twice higher than the switching frequency, which characterizes the three-state commutation cell behavior (Fig. 59.3).

59.4 Mathematical Modelling

Considering that the duty cycle is applied to the lower switches, there are two possible operation modes. For Duty cycle >50 %, there is an overlapping period for the lower switches, which remain turned on simultaneously during a certain time interval [6]. On the other hand, for Duty cycle <50 %, there is an overlapping period of the upper switches.

59.4.1 Static Gain for Duty Cycle >50 %

The equivalent circuits from which were derived equations are shown in Figure.

The output voltage can be obtained as:

$$V_O = V_{C1} + V_{C2} + V_{C3} + V_{C4} \tag{59.1}$$

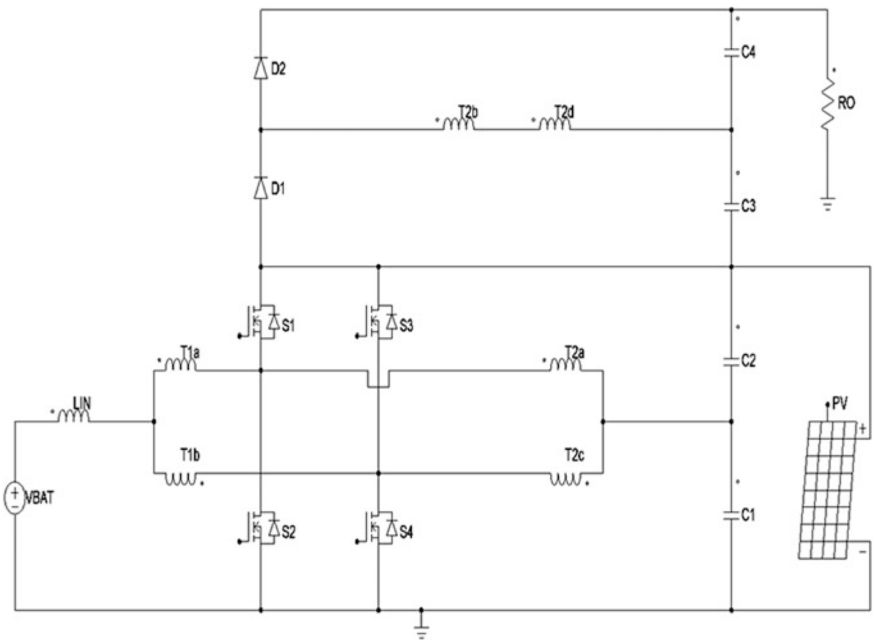

Fig. 59.3 Proposed circuit diagram

where,

$$V_{C3} = V_{C4} = n \cdot (V_{P1} + V_{P2}) \tag{59.2}$$

VP1 and VP2 represent the transformer secondary voltage reflexed on primary side. Since the voltage across the capacitor C is equal to the voltage across the battery bank, VC1 and VC2 can be obtained as:

$$V_{C1} = V_{BAT} \tag{59.3}$$

From the equations of the currents through the inductors LS1 and LS2 is given as:

$$I_{LS1} = I(0) - \left(\frac{V_{C1} + V_{C2}}{L_S}\right) \cdot t \tag{59.4}$$

$$I_{LS2} = -I(0) + \left(\frac{V_{C1} - V_{C2}}{L_S}\right) \cdot t \tag{59.5}$$

$$I_{LS1}(0) = I_{LS2}(0) = 0 \tag{59.6}$$

Table 59.1 Parameters

Switching frequency	f_s = 25 kHz
Input voltage	V_{IN} = 24 V
Output voltage	V_{out} = 200 V
Input inductance	L_{IN} = 200 μH
Leakage inductance	L_K = 0.5 μH
Output capacitors	C1, C2, C3 and C4 = 1,000 μF
Turns ratio for the transformer	(1:4)

$$I_{LS1} = \left(\frac{V_{C1} + V_{C2}}{L_S}\right) \cdot t \tag{59.7}$$

$$I_{LS2} = \left(\frac{V_{C1} - V_{C2}}{L_S}\right) \cdot t \tag{59.8}$$

From the previous equations, the static gain can be obtained as:

$$G_{D>50\,\%} = \frac{V_0}{V_{BAT}} = \frac{1}{(1-D)} + \frac{2 \cdot n}{[(1-D) + \alpha]} \tag{59.9}$$

$$V_0 = V_{BAT}\left[\frac{1}{(1-D)} + \frac{2 \cdot n}{[(1-D) + \alpha]}\right] \tag{59.10}$$

The static gain depends exclusively on the duty cycle ‘D’, the transformer turns ratio ‘n’, and the normalized load current ‘α’ (Table 59.1).

Where,

$$\alpha = \frac{4 \cdot n \cdot I_0 \cdot L_S}{V_{BAT} \cdot T_S}$$

59.5 Simulation Results

The proposed high voltage gain boost converter with high voltage gain is implemented using MATLAB. The efficiency of the proposed converter at different output powers is very high than conventional converters. Since the low input is applied in this energy conversion system, the input of proposed converter should suffer very high current ripple which result much conduction loss during the switch on period (Fig. 59.4).

The proposed converter uses only one active switch for the energy conversion, which also suffers very low current ripple during the switch on period [7].

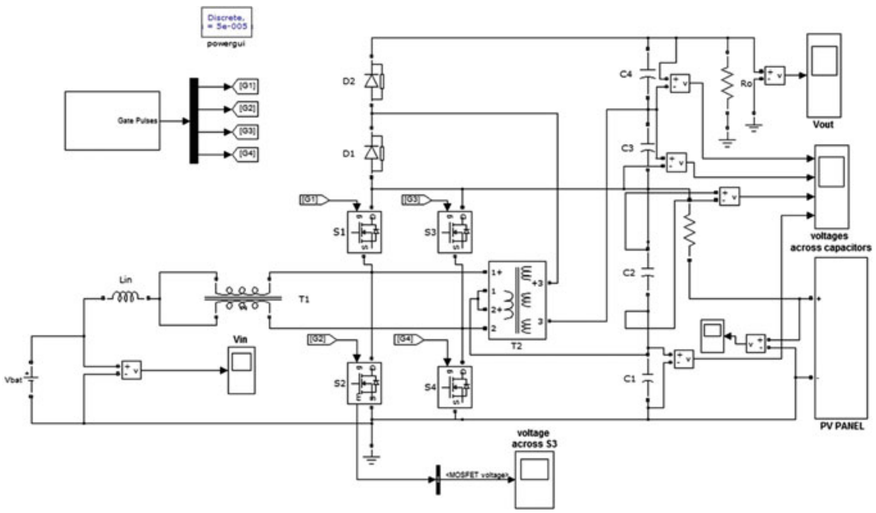

Fig. 59.4 Simulink diagram

The low and middle power applications are suitable for this proposed converter. The switches connected in parallel are usually for the high current issue to improve efficiency and to reduce conduction losses.

The simulation of the converter is done with output voltage is obtained as the sum of four capacitor voltages and the high voltage gain is obtained. As the voltage across the switches is not an over voltage, so the converter operates in soft-switching, with ZVS mode at the switches turn-on. The voltage across capacitor C3 is obtained as 4 times that of C1 and similarly the voltage across C4 is 4 times that of C2 [8].

Figure 59.5 shows the Simulink model for high voltage gain boost converter. The proposed topology is formed by one input inductor Lin, four controlled power

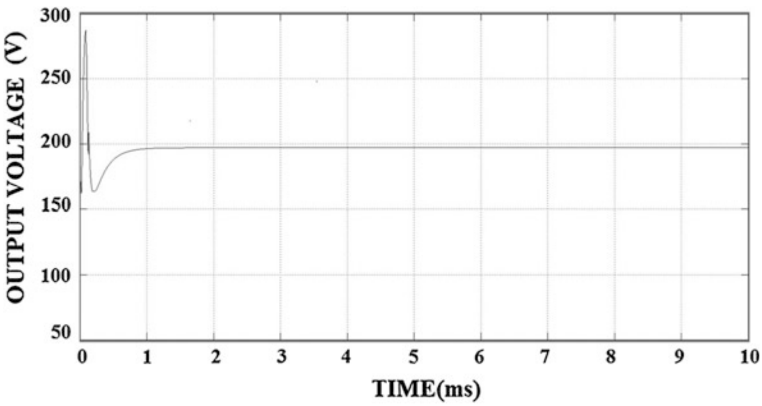

Fig. 59.5 Waveform of output voltage

switches S1 to S4, two diode rectifiers D1 and D2, two transformers T1 and T2 and four output capacitors C1 to C4. Even though additional components are included, the current sharing is maintained between S1, S2, T1a, T2a and S3, S4, T1b, T2c. Then, besides the reduced current stress through the component, the instantaneous current during the turn off of the switches is significantly reduced for D > 50 %, thus leading to minimize the switching losses [9].

Output voltage is shown in Fig. 59.6. The voltage reaching is the 200 V mark after a transient state. So when the output voltage of the proposed converter is 200 V. It must be observed that the ripple on the output voltage is inside the 10 % range [10].

Voltage across the output capacitors is shown in Fig. 59.7 where it can be seen that sum of such quantities gives the output voltage. This result also shows better voltage sharing across the output capacitors.

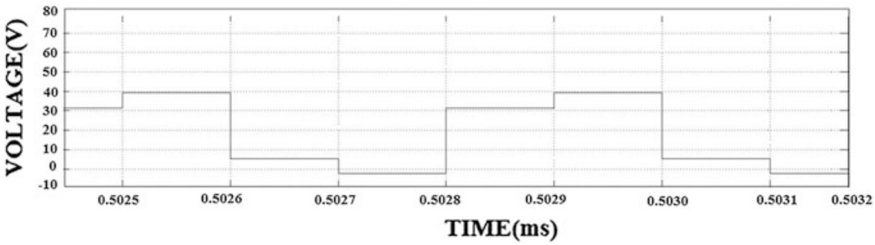

Fig. 59.6 Voltage across diode D1

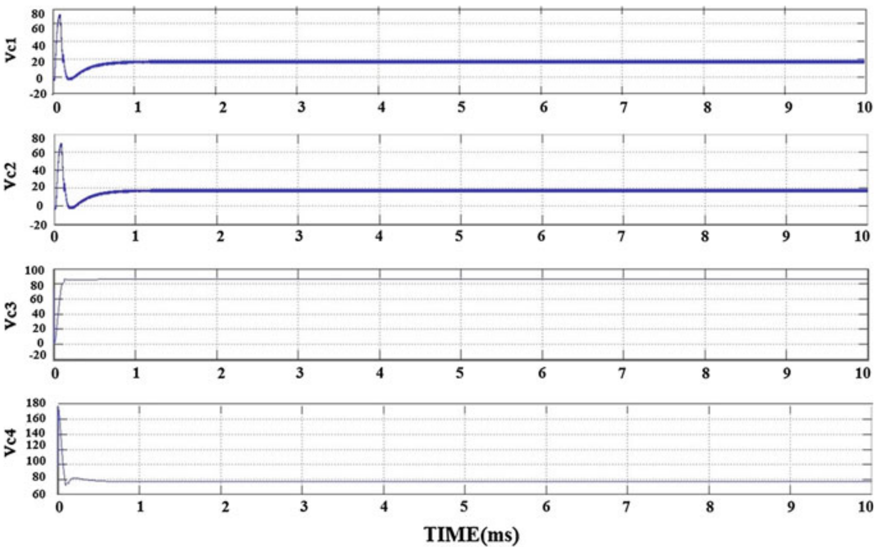

Fig. 59.7 Voltage across switch capacitors

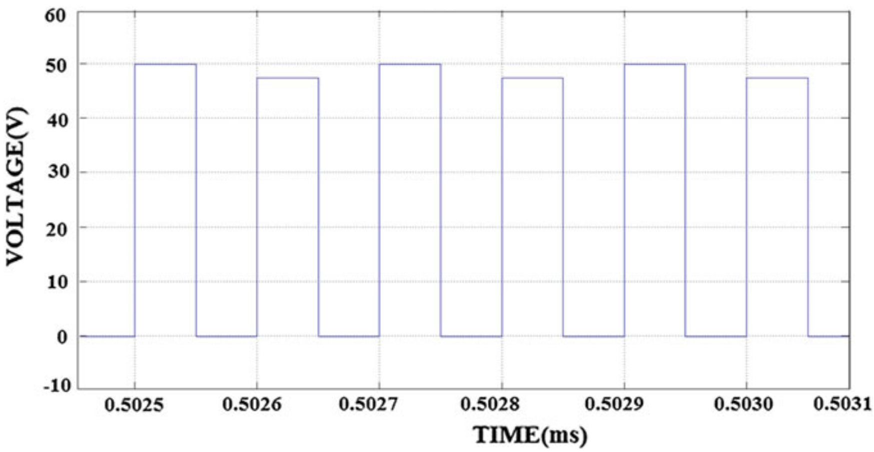

Fig. 59.8 Voltage across switch S1

Figure 59.8 indicates the voltages across the diode S1, which operate in a complementary way, while the voltages are compared to approximately 50 V, that is, there is no over-voltage [11]. The operation of S2 is complementary to S1. It can be seen that S2 operates in ZVS mode. Also, the current at the instant of the turning off is reduced what favors the turning off behavior [12].

59.6 Conclusion

A boost converter with high voltage gain was implemented. The modelling of the converter is performed. The simulation studies were carried out using MATLAB/Simulink. The output voltage, voltage across capacitors, and the voltage across the switches are observed for the converter. The simulation results obtained from the system have validated the concept, with high voltage gain over a wide load range and high efficiency at the rated condition. The promising concept of integrated converters in a single-stage approach leading to the proposal of additional topologies feasible to photovoltaic and fuel cell applications.

References

1. Barreto LHS, Praça PP, Oliveira Jr DS, Bascopé RPT (2011) Single-stage topologies integrating battery charging, high voltage step-up and photovoltaic energy extraction capabilities. Electron Lett (IET) 47:49
2. Barreto LHSC, Praça PP, Henn GAL, Câmara RA, Ranoyca NALS, Oliveira DS (2011) High voltage gain boost converter battery charger applied to PV systems. Applied power electronics conference and exposition (APEC), Twenty-sixth annual IEEE, March 2011, pp 1526–1531

3. Barreto LHSC, Praca PP, Henn GAL, Silva RNAL, Oliveira DS (2012) Single stage high voltage gain boost converter with voltage multiplier cells for battery charging using photovoltaic panels. Applied Power Electronics Conference and Exposition (APEC), Twenty-seventh annual IEEE, Feb 2012, pp 364–368
4. Yang B, Li W, Wu J, Zhao Y, He X (2008) A grid-connected PV power system with high step-up ZVT interleaved boost converter. 34th annual conference of IEEE industrial electronics, IECON 2008, pp 2082–2087
5. Chen SM, Liang TJ, Yang LS, Chen JF (2010) A cascaded high step-up DC–DC converter with single switch for microsource applications. IEEE transactions on power electronics, vol 99
6. Cheung CK, Tan SC, Tse CK, Ioinovici A (2012) On energy efficiency of switched-capacitor converters. IEEE transactions on power electronics, vol 99, p 1
7. Hong CM, Yang LS, Liang TJ, Chen JF (2009) Novel bidirectional DC–DC converter with high step-up/down voltage gain. Energy conversion congress and exposition (ECCE 2009), pp 60–66
8. Colling IE, Barbi I (2001) Reversible unity power factor step-up/step-down AC–DC converter controlled by sliding mode. IEEE Trans Power Electron 16(2):223–230
9. Garcia LS, de Freitas LC, Buiatti GM, Coelho EAA, Farias VJ, Freitas LCG (2012) Modeling and control of a single-stage current source inverter with amplified sinusoidal output voltage. Applied power electronics conference and exposition (APEC 2012) twenty-seventh annual IEEE, 5–9 Feb 2012, pp 2024–2031
10. Gules R, Pfitscher LL, Franco LC (2003) An interleaved boost DC–DC converter with large conversion ratio. IEEE international symposium on industrial electronics, ISIE ‘03, 9–11 June 2003, vol 1, pp 411–416
11. Henn GAL, Silva RNAL, Praça PP, Barreto LHSC, Oliveira DS (2010) Interleaved-boost converter with high voltage gain. IEEE Trans Power Electron 25(11):2753–2761
12. Jovcic D (2009) Step-up DC–DC converter for megawatt size applications. Power Electron (IET) 2(6):675–685

Chapter 60
Performance Assessment of Photovoltaic Predicated Dynamic Voltage Restorer Using PI and Fuzzy Logic Controller

Greeshma Govind, R. Suresh Kumar and M. Maheswari

Abstract In this paper, a photovoltaic based dynamic voltage restorer (DVR) is proposed to compensate voltage sag using a fuzzy logic controller. It also operates as an uninterruptable power supply (UPS) when the utility grid fails to supply. It also reduces the usage of utility power. A high step up DC–DC converter with high voltage gain is used which reduces the size of the series injection transformer and also reduces the number of batteries used. The fuzzy logic controller takes the two inputs, error and change in error maintains the load voltage by detecting voltage variations using dq transformation technique. The PI controller utilizes the error signal from the comparator to trigger the switches of an inverter using a sinusoidal PWM scheme. Simulation results prove the ability of the proposed DVR to mitigate the voltage sag.

Keywords Dynamic voltage restorer (DVR) · Fuzzy logic controller · Sinusoidal PWM · Boost converter

60.1 Introduction

The Dynamic Voltage Restorer as a means of series compensation for mitigating the effect of voltage sag has become established as a preferred approach for improving power quality at sensitive load locations. The PV-DVR is a solution where substantial amounts of insolation is available and frequent power interruptions are more. The dynamic voltage restorer is fast, flexible and efficient solution

G. Govind (✉) · R.S. Kumar · M. Maheswari
Department of EEE, SNS College of Engineering, Coimbatore 641107, Tamil Nadu, India
e-mail: yodelkukku@gmail.com

R.S. Kumar
e-mail: sureshramasamy8@gmail.com

M. Maheswari
e-mail: maheswarikgd@gmail.com

C. Kamalakannan et al. (eds.), *Power Electronics and Renewable Energy Systems*,
Lecture Notes in Electrical Engineering 326, DOI 10.1007/978-81-322-2119-7_60

for the voltage sag problem. It can restore the load voltage in a few milliseconds. The Dynamic Voltage Restorer (DVR), also referred to as the Serial Voltage Booster (SVB) or the Static Series Compensator (SSC), is a device that utilizes solid state or static power electronic components, and it is serially connected to the utility primary distribution circuit. The DVR provides three phase controllable voltage, whose vector that is, magnitude and angle is added to the source voltage to restore the load voltage to pre-sag conditions.

A voltage sag or voltage dip is a short duration reduction in rms voltage which can be caused by a short circuit, overload or starting of electric motors. A voltage sag happens when the rms voltage decreased between 10 and 90 % of nominal voltage for one half cycle to 1 min. According to the IEEE 519-1992 and IEEE 1159-1195 standards, a typical duration of voltage sag is 10 ms to 1 min [1–3]. Voltage Sag is a reduction of AC voltage at a given frequency for the duration of 0.5 cycles to 1 min time. The concept of utilizing the DVR for voltage sag and outage mitigation without PV system is presented in [4]. The rating and design of series injection transformer of the DVR are presented in [5]. Many research works have been carried out focusing on the design and control of DVR [6–9].

A super capacitor as an energy storage device is used to support the DVR without PV system for power quality improvement in electrical distribution systems as presented in [10]. The detection of voltage disturbances can be done in many ways as presented in [11, 12]. In [13], PV operated DVR has been presented to compensate the voltage sag of the system. It does not provide any monetary benefit to the customers. To overcome the demerits of the above mentioned conventional DVRs, a new concept for optimal utilization of PV solar system inverter as a DVR for voltage sag has been proposed.

In this paper, a new coordinating logic is proposed to operate the PV solar system as a DVR, utilizing the rated inverter capacity during night time and inverter capacity remaining after excess or equal real power generation of the PV system. This allows full utilization of expensive assets of the PV system over a 8 h period. This has additional financial benefits over the conventional DVRs used in the past. It also eliminates the need of UPS and stabilizers for the individual equipment. In order to attain the optimal utilization of PV system, a simple DC–DC converter associated with a function called MPPT is introduced between the PV array and battery. A MATLAB simulation results and experimental results are presented to validate the proposed method.

60.2 Proposed DVR

The block diagram of the proposed PV based DVR is shown in Fig. 60.1. The proposed system mainly consists of a photovoltaic array, low and high power DC/DC boost converters, battery, PWM inverter, series injection transformer, and semiconductor switches S_1, S_2, S_3, R_1 and R_2 [14].

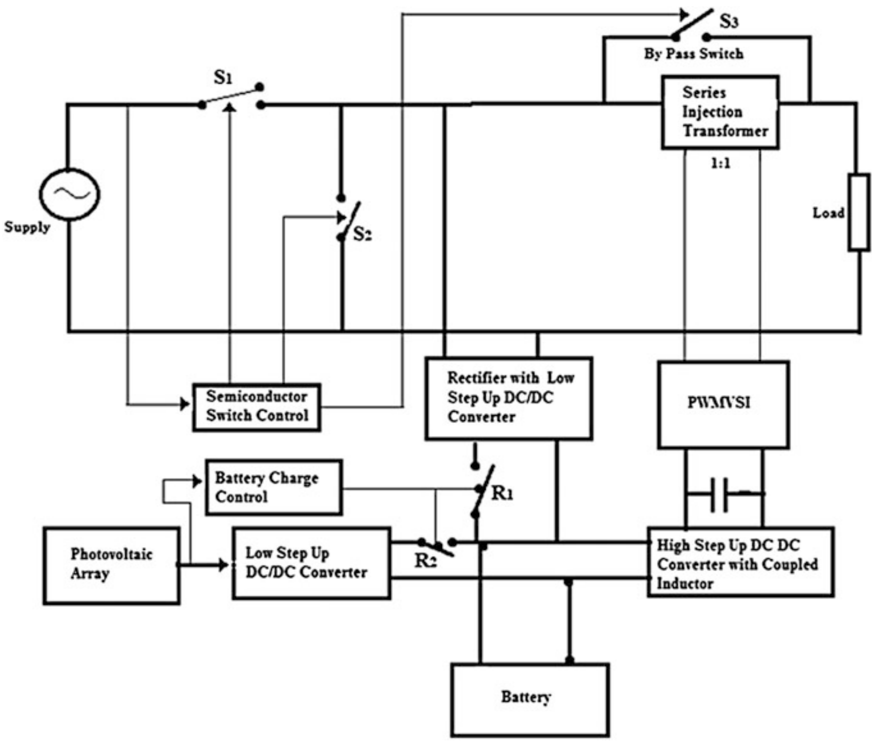

Fig. 60.1 Structural block diagram of the proposed system

Table 60.1 Control signals for S1, S2 and S3

S. no	Supply voltage in (%)	Control signals			Mode of operation
		S_1	S_2	S_3	
1	90–100	1	0	1	Ideal
2	<90	1	0	0	DVR
3	>110	1	0	0	DVR
4	0	0	1	0	UPS

Tables 60.1 and 60.2 show the control signals of the semiconductor switches S_1, S_2, S_3 and R_1, R_2 respectively. When the grid voltage is normal the switches S_1 and S_2 are normally closed and S_2 is normally open. When the grid fails or when the PV array generates excess power the switches are activated and the inverter supplies the load. An injecting transformer is connected in series with switches S_1, S_2 and S_2 for handling outages and switches R_1 and R_2 used for battery charging control. The proposed PV DVR acts in four modes of operation. They are compensation mode, UPS mode, energy conservation mode and idle mode [5].

Table 60.2 Battery charging control

S. no	PV voltage in (V)	Control signals		Battery charging unit
		R_1	R_2	
1	>14	0	1	PV array
2	<14	1	0	Rectifier

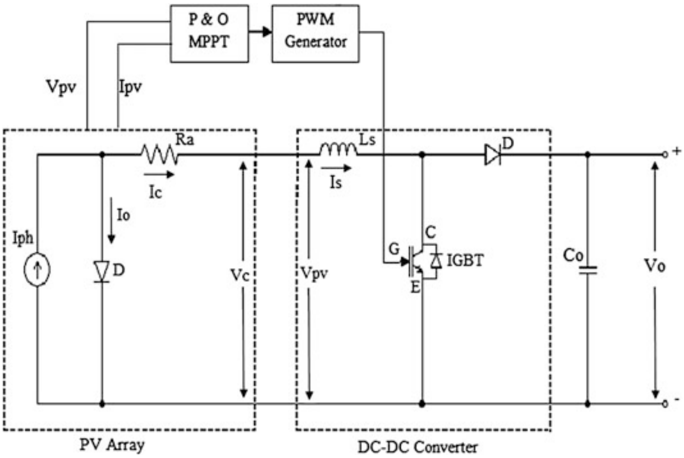

Fig. 60.2 PV modeling with low step up boost converter

60.3 Photovoltaic Array Modelling

PV array is a system which uses two or more solar panels to convert sunlight into electricity. PV array is a linked collection of solar cells. The use of new, efficient photovoltaic solar cells has emerged as an alternative source of renewable green energy conversion. In the proposed DVR, PV array provides a DC source for the DVR. The electrical system powered by the PV array requires DC–DC converter due to the varying nature of the generated solar power, resulting from sudden changes in weather conditions which change the solar irradiation level as well as cell operating temperature.

The PV array is designed and modeled with a low step-up DC–DC converter to charge the batteries or to handle the load. An equivalent circuit model of photovoltaic cell with low step-up DC–DC converter is shown in Fig. 60.2.

60.4 DC/DC Converter

The output voltage level of the low power DC–DC converter and batteries are low. Hence, it is not sufficient to inject the required amount of voltage to load to mitigate voltage sags, swells and outages. For that a high step up DC–DC converter is used

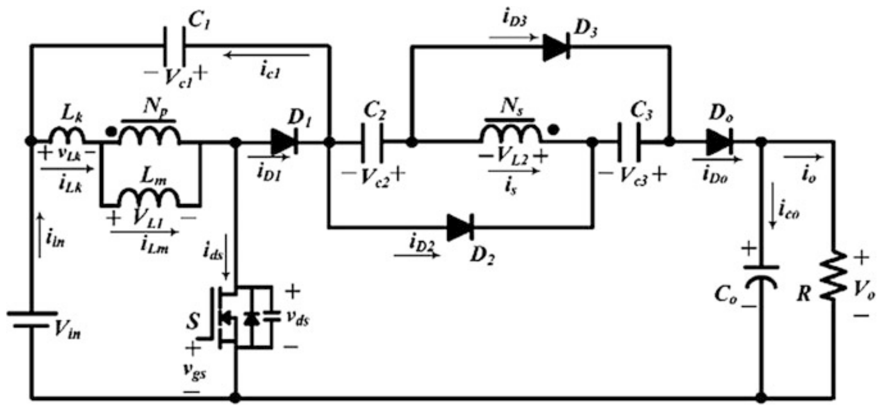

Fig. 60.3 High step up DC–DC converter

to step up the low power DC to high power DC. It is connected in between batteries and PWM voltage source inverter. The main operating principle of this converter is that when the switch S is turned on, the coupled inductor induces voltage on the secondary side and magnetic inductor Lm is charged by V_{in}. The induced voltage in the secondary makes V_{in}, V_{C1}, V_{C2} and V_{C3} to release energy to the load in the series. When the switch S is turned off, the energy stored in the magnetic inductor L_m is released via the secondary side of coupled inductor to charge the capacitors C_2 and C_3 in parallel. The proposed converter operation can be divided into five modes of operation. The circuit diagram of the converter is shown in Fig. 60.3.

The output equation of high step up DC–DC converter is shown below.

$$V_o = V_{in} + V_{C1} + V_{C2} + V_{L2}^{II} + V_{C3} \tag{60.1}$$

The secondary of the coupled inductor can charge capacitors in parallel and discharge them in series with the load. This converter combines the concept of the coupled inductor and switched capacitor techniques. The secondary of the coupled inductor, charges the capacitors C2 and C3 when the switch (*S*) is turned off and are discharged in series by the secondary side of the coupled inductor when the switch is turned on.

60.5 Controller Design

60.5.1 PI Controller

The control scheme used to maintain a constant voltage magnitude at the load point, under system disturbance, is shown in Fig. 60.4. In the proposed controller, a discrete single phase PLL is used to track the phase angle of the source voltage to

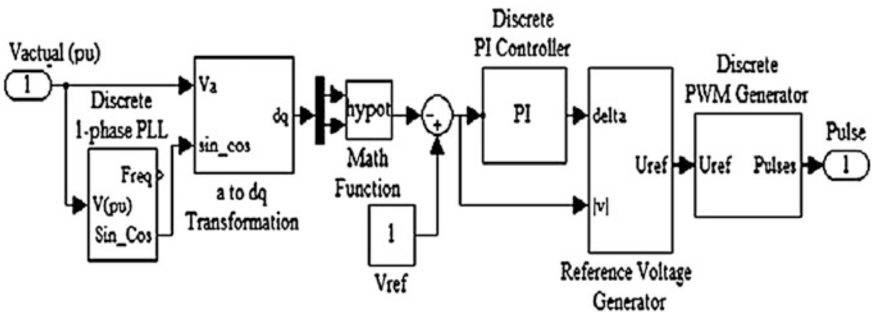

Fig. 60.4 Control structure of PI controller

perform the park's transformation on the measured single phase voltage [15]. The measured p.u. value of supply voltage is converted into |Vs|, and the error is obtained from the difference of $|V_s|$ and reference voltage (V_{ref}). The PI controller designed by the Ziegler–Nichols tuning method processes the error and generates required angle d to drive the error to zero. The modulating angle d is applied to the reference voltage generator to generate the V_{ref} for the Sinusoidal Pulse Width Modulation (SPWM).

60.5.2 Fuzzy Logic Controller

The control loop for a PWM voltage source inverter is designed using a fuzzy logic controller. The control structure for proposed DVR is shown in Fig. 60.5. Here a discrete single phase PLL is used to track the phase angle of the source voltage and generates a reference signal with a magnitude of unity, locked to supply frequency. The supply voltage is then converted into pu value which should be transformed using the sag detection method to give input to the fuzzy logic controller. The fuzzy logic controller for the proposed PV based DVR has two inputs, named error and change in error. The membership functions of the error and change in error inputs are triangular. The triangular membership function is used here because the steady state error is minimum under this condition. The steady state error is reduced for membership functions with the reduced value of the nucleus.

For a triangular membership function the nucleus is a single point and it is the height. It is very easy to implement a triangular membership function. The input signals are fuzzified and represented in fuzzy set notations by membership functions. There are 49 rules utilized here to produce the optimum control signal. The rules provide a functional mapping between the input and the output using linguistic variables.

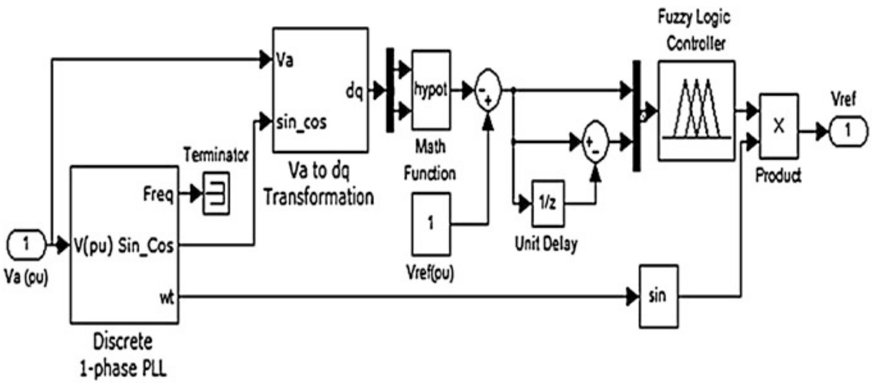

Fig. 60.5 Control structure of fuzzy logic controller

60.6 Simulation Results and Discussions

The proposed PV-DVR is tested for its capability using a low voltage single phase distribution system. The model is simulated by MATLAB Simulink to reduce the energy consumption and to compensate voltage sag. At first a voltage sag is created by giving a heavy load controlled by a circuit breaker with external monitoring. It is implemented with an AND logic controller. Two step input is given with a step time of 0.25 and 0.45 respectively. A heavy load of power 20 KW is given. The total simulation period is 1 s. Using the facilities available in MATLAB the DVR is simulated to be in operation, only when the supply voltage differs from its nominal value or the generated power in the PV array is greater than or equal to the load demand. The Fig. 60.6 shows the source voltage, injected voltage and the load voltage of the DVR injection (Figs. 60.7 and 60.8).

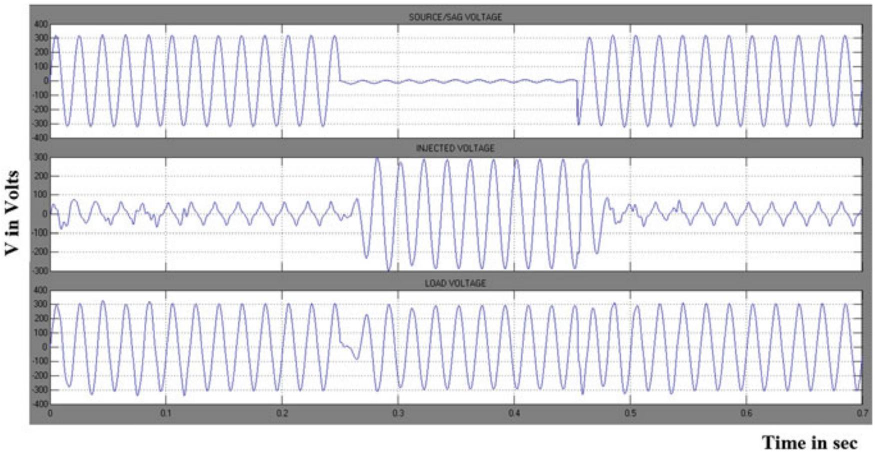

Fig. 60.6 Simulation output of the DVR injection

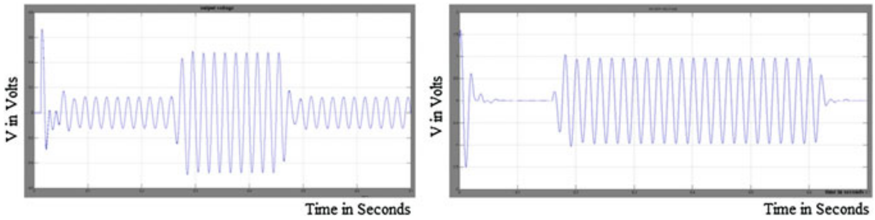

Fig. 60.7 Simulation output from PI and fuzzy logic controller

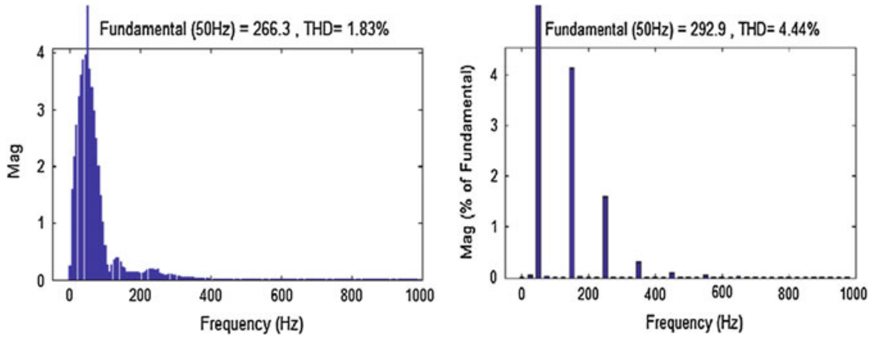

Fig. 60.8 THD % of PV-DVR with PI and fuzzy logic controller

60.7 Conclusion

The most common problems faced by electricity consumers are voltage sags and swells. Many industries produce their products by using the electric power from the raw materials. So if these problems are solved their production cost can be reduced. In this project a novel application of utilizing a PV solar system as a DVR for voltage sag compensation is considered. A photovoltaic based DVR with energy saving capability using a fuzzy logic controller has been developed and tested for power quality.

Design of DVR incorporates a PV array module with low and high power boost converters. Modelling and simulation of proposed DVR obtained by MATLAB Simulink. Voltage sag is created by switching on the heavy load of 25 KW, which results in 40 % sag creation in the supply voltage. The total simulation period is about 0.7 seas and a heavy load is switched ON during the interval 0.25–0.45 s. to compensate the voltage sag occurred, proposed DVR utilizes the energy drawn from the PV array and utility source during normal operation and stored in batteries. The stored voltage of 12 V is converted into 325 V using a high power boost converter.

The PI and fuzzy logic controller utilize the error and change in error in voltage and voltage reference is produced as output. This is given to the PWM generator to trigger the switches of the inverter. Inverter converts 325 V DC into 230 V and supplies the load. Thus the output nominal voltage after compensation will be 230 V AC as required to supply the load. Total harmonic distortion percentage acquired is about 4.44 % for PI controller and 1.83 % for the Fuzzy Logic controller and it is considered to be abruptly below 5 % as specified by IEEE standard for harmonics 519.

References

1. Ezoji H, Sheikholeslami S, Tabasi M, Saeednia M (2009) Simulation of dynamic voltage restorer using hysteresis voltage control. Eur J Sci Res 27:152–166
2. Ribeiro H, Marques H, Borges BY (2012) Characterizing and monitoring voltage transients as problem to sensitive loads. Int J Electr Power Energy Syst 43:1305–1317
3. Honrubia-Escribano A, Gomez-Lazaro E, Molina-Garcia M, Fuentes JA (2012) Influence of voltage dips on industrial equipment: analysis and assessment. Int J Electr Power Energy Syst 41:87–95
4. Ashari M, Hiyama T, Pujiantara M, Suryoatmojo H, Hery Purnomo M (2007) A novel dynamic voltage restorer with outage handling capability using fuzzy logic controller. In: Proceedings of ICICIC'07, pp 51–58
5. Sasitharan S, Mishra MK, Kalyan Kumar B, Jayashankar V (2010) Rating and design of DVR injection transformer. Int J Power Electron 2:143–163
6. Jowder FAL (2009) Modeling and simulation of different system topologies for dynamic voltage restorer using Simulink. In: Proceedings of EPECS'09, pp 1–6
7. Strzelecki R, Benysek G (2008) Control strategies and comparison of the dynamic voltage restorer. In: Proceedings of PQ'08, pp 79–82
8. Boonchiam P, Mithulananthan N (2006) Understanding of dynamic voltage restorers through MATLAB simulation. Thammasat Int J Sci Tech 11(3):1–6
9. Nielsen JG, Newman M, Nielsan H, Blaabjerg F (2004) Control and testing of a dynamic voltage restorer (DVR) at medium voltage level. IEEE Trans Power Electron 19(3):806–813
10. Omar R, Rahim NA (2012) Voltage unbalanced compensation using dynamic voltage restorer based on super capacitor. Int J Electr Power Energy Syst 43:573–581
11. Gencer O, Ozturk S, Erfidan T (2010) A new approach to voltage sag detection based on wavelet transform. Int J Electr Power Energy Syst 32:133–140
12. Fitzer C, Barnes M, Green P (2004) Voltage sag detection technique for a dynamic voltage restorer. IEEE Trans Ind Appl 40(1):203–212
13. Al-Mathnani AO, Mohamed A, Mohd Ali MA (2007) Photovoltaic based dynamic voltage restorer for voltage sag mitigation.: In: Proceedings of 5th student conference on research and development, pp 1–6
14. Ramasamy M, Thangavel S (2013) Experimental verification of PV based dynamic voltage restorer (PV-DVR) with significant energy conservation. Electr Power Energy Syst 49:296–307
15. Lira J, Nunez C, Flota M, Alvarez R (2006) A control strategy to improve voltage sag ride through in single phase multilevel active rectifier. In: Proceedings of electrical and electronics engineering, pp 1–4

Chapter 61
Multiple Winding Linear Transformer for Interleaved Step-up ZVT Converter

Nidhin Antony and K. Karthikeyan

Abstract In this paper, the concept of three winding linear transformer based voltage multiplier cell is derived to generate an interleaved high step-up converter. The switch duty cycle and the transformer turns ratio can be employed as two controllable parameters to increase the voltage ratio flexibly. The power device voltage stress can also be reduced to improve the circuit performance and the active clamp scheme is adopted to recycle the leakage energy, absorb the switch turn-off voltage spikes, and achieve zero-voltage switching (ZVS) operation for all active switches. The linear transformer based voltage multiplier cell is composed of three transformer windings, two voltage multiplier diodes, and two voltage multiplier capacitors. The voltage multiplier capacitors are charged and discharged alternatively to double the voltage gain. Meanwhile, the diode reverse recovery problem is alleviated by the leakage inductance of the built-in transformer. All these factors benefit the circuit performance improvements in the high step-up and large current applications. It can also reduce input current ripple, output voltage ripple and size of passive components. Soft switching technique is used to reduce the switching loss.

Keywords Zero-voltage switching (ZVS) · Voltage multiplier · Interleaved high step-up converter

61.1 Introduction

In conventional interleaved boost converters only switch duty cycle is varied to regulate the voltage gain. But it possess large peak current and switching losses. The switched capacitor based converter switch suffer high transient current and conduction losses are higher [1]. The interleaved concept presented in this paper is

N. Antony (✉) · K. Karthikeyan
SNS College of Engineering, Coimbatore, Tamil Nadu, India
e-mail: nidhinantony86@gmail.com

C. Kamalakannan et al. (eds.), *Power Electronics and Renewable Energy Systems*,
Lecture Notes in Electrical Engineering 326, DOI 10.1007/978-81-322-2119-7_61

mainly depend on the transformer turns ratio and switch duty ratio accordingly. Also the built-in transformer concept or the illustrated three winding transformer.

The voltage gain can also be increased and input ripple current is reduced. Voltage multiplier cell increases the voltage gain and active clamping scheme is adopted to decrease the switching losses [2, 3]. The number of phases is determined such that the input current is reduced to a great extent and also consider the cost details. The other considerations are the switching frequency. By increasing the switching frequency the switching losses are also increased. Soft switching suppresses EMI in the converters. So for making switching losses to zero either current or voltage across the switch are to be made zero [4].

By using the zero voltage switching we can avoid RCD snubbers from the circuit. Gate pulses of the switches of two phases are shifted by 360°/n. Here the level is selected as two, so gate pulses are shifted by 180°. Switching ripple voltage is reduced to a great extend [5]. Thus the efficiency can be improved.

Two phase soft switching step-up converter is used as an interfacing to reduce the switching loss and ripples. In this project two phase soft switching step-up converter is used as power conversion device [6–8]. The input current ripple and stress on power devices are decreased because the input current is divided into two parallel inductors. Two phase boost converter is used for high power application.

The current rating of switching device is reduced by interleaved method which distributes the input current to each phase [9, 10]. In a two-phase converter, there are two output stages that are driven 180° out of phase. By splitting the current into two power paths, conduction (I2R) losses can be reduced, increasing overall efficiency compared to a single-phase converter. Because the two phases are combined at the output capacitor [11], effective ripple frequency is doubled, making ripple voltage reduction much easier.

61.2 Proposed Converter and Operational Principle Analysis

By inserting two pairs of diodes and capacitors to compose two voltage multipliers with the linear built-in transformer, the proposed ZVT interleaved high step-up converter with linear built-in transformer voltage multiplier cell is obtained as shown in Fig. 61.1. The equivalent circuit is also similar to Fig. 61.1 where L_1 and L_2 are the input filter inductors, S_1 and S_2 are the main switches, D_{o1} and D_{o2} are the output diodes, C_o is the output capacitor.

S_{c1} and S_{c2} are the active clamp switches, C_{c1} and C_{c2} are the clamp capacitors, D_{d1} and D_{d2} are the voltage multiplier diodes, C_{d1} and C_{d2} are the voltage multiplier capacitors, C_{s1} and C_{s2} are the parallel capacitors, including the parasitic capacitors of the main switches, and L_a, L_b, and L_c are the primary, secondary, and third windings of the linear built-in transformer, respectively. L_{lk} is the total reflected leakage inductance; V_{in} and V_{out} are the input and output voltages, respectively. N is defined as the turn's ratio n_2/n_1.

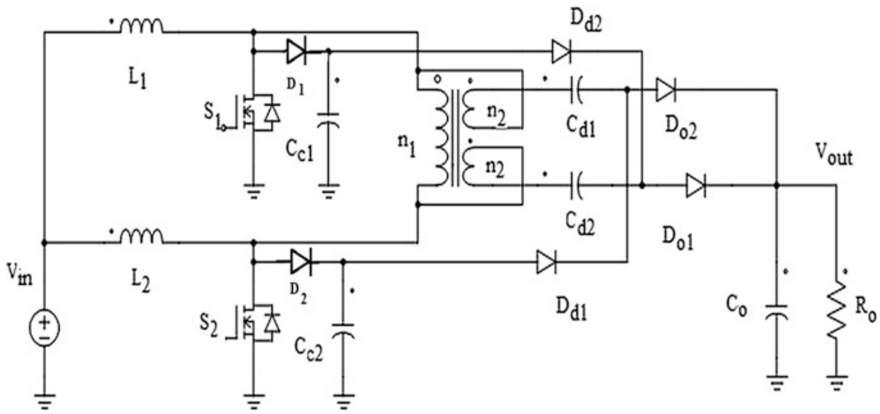

Fig. 61.1 Proposed converter

ZVS soft-switching performance is achieved for both the main and the clamp switches during the whole switching transition, which reduces the switching losses greatly. The ZVS turn-off of the main switches and the clamp switches is realized due to the parallel capacitors C_{s1} and C_{s2}. The ZVS turn-on of the clamp switches is realized naturally because their antiparallel diodes are in conduction state before their turn-on gate signals come.

Meanwhile, the falling rates of the output diode and the voltage multiplier diode are controlled by the leakage inductance of the linear built-in transformer, which alleviates their reverse-recovery problem, reduces the electromagnetic interference (EMI) noise, and improves the circuit efficiency.

61.3 Design Considerations

The design considerations of various circuit components and different parameter selection are given as follows. This paper utilizes two phases of converter since the ripple content reduces with increase in the number of phases.

61.3.1 Design of an Input Inductor

The current ripple can be set 40 % of each input inductor current in the proposed converter due to the interleaved configuration, which results in only 20 % of the total input current. Hence, input inductor is determined by

$$L_r = \frac{5 * V_{in} * D * T_s}{I_{in}} \tag{61.1}$$

61.3.2 Selection of Duty Cycle

The voltage gain can be extended greatly without an extreme duty cycle as the turns ratio of the linear built-in transformer increases, which makes the converter suitable for high step-up and high power conversion. Duty cycle can be directly obtained from the basic boost converter equation given by,

$$V_o = \frac{V_{in}}{(1 - D)} \tag{61.2}$$

61.3.3 Calculation of Input Ripple Current

The current ripple can be set 40 % of each input inductor current in the proposed converter. Due to interleaved configuration, which results in only 20 % of the total input current

$$\Delta I = \frac{V_{in}(V_o - V_{in})}{f * L_r * V_o} \tag{61.3}$$

61.3.4 Input Current Calculation

Due to the symmetry of the interleaved circuit, input current is divided to both inductors at the input side equally. The input current is approximately derived as shown below.

$$I_{in} = \frac{2(N + 1)V_o}{(1 - D)R_o} \tag{61.4}$$

61.3.5 Delay Time

Delay time should be less than 10 % of the switching period. Switching period is 10^{-5} s. So the delay time should ranges from 0.01 * 10^{-5} to 0.10 * 10^{-5} s. Delay time is given only for the second MOSFET. Parallel capacitance is generally selected as small as 1.1 nF.

$$T_d \geq I_{in} * \frac{L_r}{2V_o} + \frac{\pi}{2} * \sqrt{L_r * C_s} \tag{61.5}$$

61.3.6 Output Voltage Ripple Calculation

The amount of ripple content in the output voltage can be determined for checking the quality of the interleaved converter. it can be calculated by the given formula,

$$\Delta V_o = \frac{V_o * D^2 * T_s}{2 * R_o * C_o} \tag{61.6}$$

61.3.7 Clamp Capacitor

The capacitor is selected by considering the voltage ripple on the capacitor. According to this principle, the clamp capacitor can be chosen as

$$C_c = \frac{(N+1) * I_o * T_s}{4\Delta V_{Cc}} \tag{61.7}$$

61.3.8 Voltage Gain Expression

Assuming the three winding linear transformer is well coupled and the leakage inductance is zero, from the steady analysis in previous section, it can be drawn that the input filter inductor is charged by the input voltage during the switch turn-on period and discharged by the voltage of the clamp capacitor voltage minus the input voltage during the switch turn-off period.

Voltage gain expression can be obtained from all the values from the simulation diagram designed. Voltage Gain Curves Versus Turns Ratio and Duty Ratio is shown in Fig. 61.2

$$\begin{aligned}
\frac{V_o}{V_{in}} &= \frac{2(N+1)/(1-D) - 2V_d/V_{in}}{1+A+B} \\
A &= [2(N+1)R_L + (2N+D+1)R_{ds}]\frac{N+1}{(1-D2)R_o} \\
B &= \left[(4N+3)\left(N+\frac{1}{2}\right)R_{ds} + 2N(N+1)R_1 + R_2 + R_d\right]\frac{1}{(1-D)R_o}
\end{aligned} \tag{61.8}$$

Fig. 61.2 Voltage gain curves versus turns ratio and duty ratio

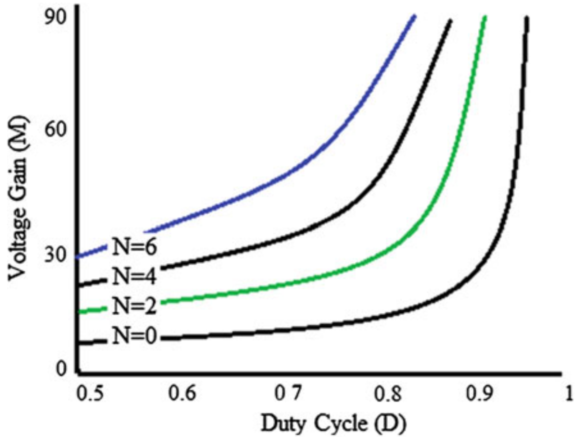

61.3.9 Turns Ratio of Linear Built-in Transformer

Change in number of turns of the linear built-in transformer also determines the output voltage of the converter. When the duty ratio, input voltage and output voltage are determined, the turns ratio of the built-in transformer can be obtained by,

$$N = \frac{n_2}{n_1} = \frac{(1-D)V_o}{2V_{in}} - 1 \tag{61.9}$$

The primary winding RMS current is given by

$$I_{La-RMS} = 2NI_o\sqrt{\frac{2}{3(1-D)}} \tag{61.10}$$

The primary winding RMS voltage is given by

$$V_{La-RMS} = V_{in}\sqrt{\frac{2}{1-D}} \tag{61.11}$$

The apparent power processed by the built-in transformer is derived by,

$$\begin{aligned} S &= V_{La-RMS}.I_{La-RMS} \\ &= \frac{4NV_{in}I_o}{\sqrt{3}(1-D)} \\ &= \frac{2NV_{in}I_{in}}{\sqrt{3}(N+1)} \end{aligned} \tag{61.12}$$

61.3.10 Voltage and Current Stress Analysis

The voltage stresses of the main switch S_1 and S_2 and the active clamp switches S_{c1} and S_{c2} are equal to that of clamp capacitors C_{c1} and $C_{c2.}$

$$V_s = V_{Sc} = V_{Cc} = \frac{V_{in}}{(1-D)} = \frac{V_o}{2(N+1)} \tag{61.13}$$

It is represented by,

$$I_{RMS-Sc} = \frac{I_o(N+1)}{\sqrt{3(1-D)}} \tag{61.14}$$

61.4 Simulation Results

The main aim of this paper is to increase the voltage gain of interleaved step-up converter with the help of linear built-in transformer and voltage multiplier cells and voltage multiplier diodes. Active clamp scheme is adopted to recycle leakage energy. The simulation work is done in MATLAB-SIMULINK. The output voltage obtained across the load resistor is as given in Fig. 61.3. It is 380 V.

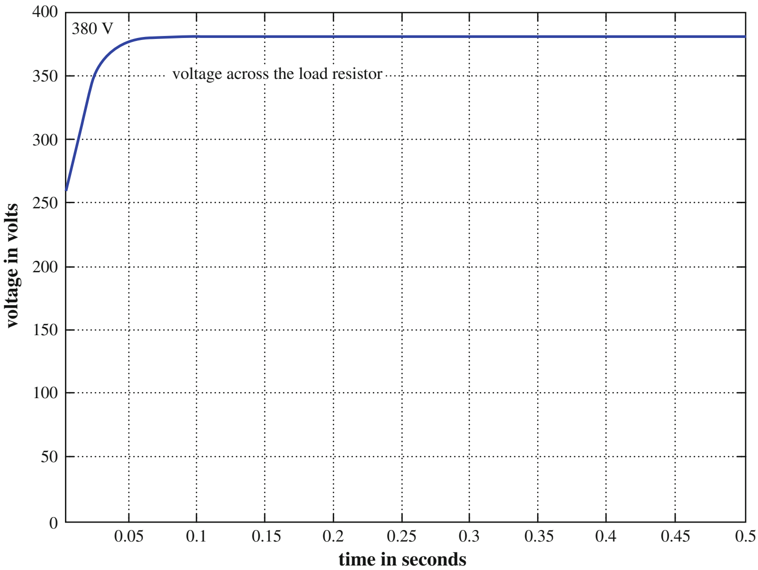

Fig. 61.3 Output voltage across load resistor

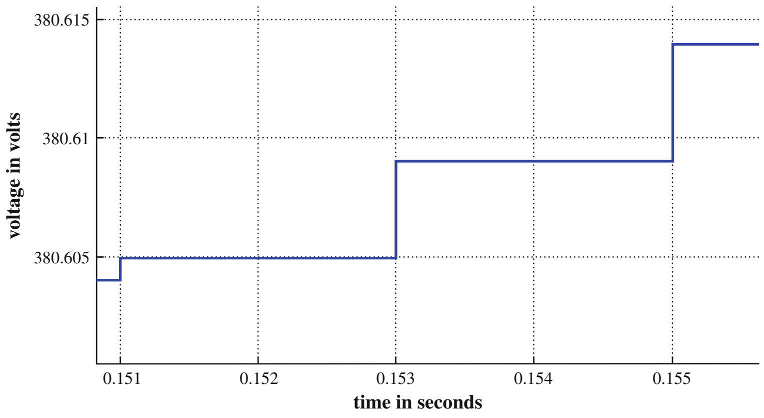

Fig. 61.4 Output voltage ripple

In the conventional boost converters output voltage ripple is around 0.040–0.050 V which reduces the performance of the converter. In this converter the output voltage is reduced to 0.011 V. The output voltage ripple of the interleaved high step-up ZVT converter is shown in Fig. 61.4.

The output current through the capacitor is 2.63 A and it is shown in the Fig. 61.5. Output current calculation is done in the mathematical modelling. That is during the first time interval, both the main switches S_1 and S_2 conduct (Table 61.1).

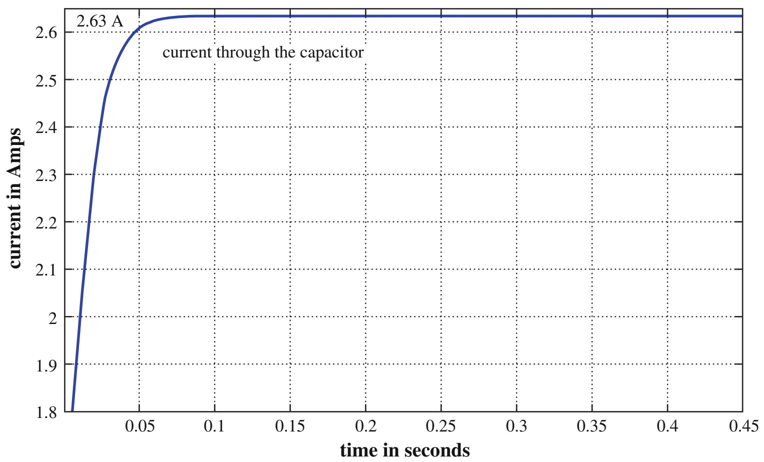

Fig. 61.5 Current through the capacitor

Table 61.1 Simulation parameters and results

Converter parameters	Range
Input voltage	40 V
Input current	35.08 A
Output voltage	380 V
Output current	2.63 A
Output power	1 kW
Input inductor	50 μH
Output capacitor	470 μF
Output resistor	144.4 Ω
Clamp capacitor	4.7 μF
Voltage multiplier cell	4.7 μF

61.5 Conclusion

A ZVT interleaved high step-up converter with linear built-in transformer voltage multiplier cell is presented in this paper. ZVS soft-switching performance is achieved for both the main and clamp switches during the whole switching transition, which reduces the switching losses. The turn-off current falling rates of the output diode and the voltage multiplier diode are controlled by the leakage inductance of the built-in transformer, which alleviates the reverse recovery problem and reduces the reverse-recovery losses. By employing the built-in transformer voltage multiplier cell, the voltage gain can be greatly extended and the switch voltage stresses far lower than the output voltage, which makes the low voltage-rated, low on-resistance, and high-performance MOSFETs available to reduce the conduction losses in the high output voltage applications. Finally, the proposed converter has been designed to show the converter performance and the experimental result.

References

1. Yang B, Li W, Wu J, Zhao Y, He X (2008) A grid-connected PV power system with high step-up ZVT interleaved boost converter. Industrial electronics, IECON 2008. 34th annual conference of IEEE. pp 2082–2087
2. Cheung CK, Tan, SC, Tse CK, Ioinovici A (2012) Energy efficiency of switched-capacitor converters. IEEE Trans Power Electron (28):2, pp 862–876
3. Erickson RW, Maksimovic D (2001) Fundamentals of power electronics, 2nd ed. Kluwer, Norwell
4. Henn GAL, Silva RN, Praça PP, Barreto LHSC, Oliveira DS (2010) Interleaved-boost converter with high voltage gain. IEEE Trans Power Electron 25(11):2753–2761
5. Jovcic D (2009) Step-up DC-DC converter for megawatt size applications. IEEE Trans Power Electron 2(6):675–685
6. Li W, He X (2011) Zero-voltage transition interleaved high step-up converter with built-in transformer. IEEE Trans Power Electron 4(5):523–531

7. Li W, Zhao Y, Wu J, He X (2012) Interleaved high step-up converter with winding-cross-coupled inductors and voltage multiplier cells. IEEE Trans Power Electron 27(1):133–143
8. Genc N, Iskender I (2008) An improved zero-voltage-transition interleaved boost converter with high power factor
9. Oliveira DS Jr, Bascopé RP, Silva CEA (2006) Proposal of a new high step-up converter for UPS applications. IEEE Int Symp Ind Electron 2:1288–1292
10. Qun Z, Lee FC (2003) High-efficiency, high step-up DC-DC converters. IEEE Trans Power Electron 18(1):65–73
11. Sravan C, Narasimharao D (2012) An interleaved boost converter with zero-voltage transition for grid connected PV system 2(2). ISSN 2249-6149

Chapter 62
Embedded Based PFC Converter for an Air Conditioner with BLDC Motor

Tinu Francis and P. Gokulakrishnan

Abstract This paper deals with PFC based speed control of PMBLDC motor. PFC is done by means of an embedded based Cuk dc-dc converter. A voltage source inverter with properly controlled switches will acts as commutator for PMBLDC motor. Embedded based switch control is implemented in both inverter and converter. Optimum air-conditioning is obtained by means of speed control. DC link voltage which is proportional to speed is controlled properly to attain this aim. The proposed PMBLDCM drive is designed and modeled, and its performance is evaluated in Matlab–Simulink environment. Simulated results are presented to demonstrate an improved power quality at ac mains of the PMBLDCMD system in a wide range of speed and input ac voltage. Test results of a developed controller are also presented to validate the design and model of the drive.

Keywords BLDC motor · PFC converter · Optimum air-conditioning

62.1 Introduction

Popularity of BLDC motors is increasing due to their performance advantages over induction motor and brushed DC (BDC) motors due to their high efficiency, wide speed range and low maintenance [1]. Compared to a DC motor, the BLDC motor uses an electronic commutation, replacing the mechanical Commutator and making it more reliable than the dc motor. In BLDC motors, rotor magnets generate the rotor's magnetic flux, allowing BLDC motors to achieve higher efficiency. BLDC motors have a relatively flat speed-torque characteristic [2]. This enables the motor to operate at lower speeds without compromising torque when the motor is loaded. The ratio of output power to frame size is higher in BLDC motors. This reduces the size and weight of the product. This also saves the cost of motor mounting and

T. Francis (✉) · P. Gokulakrishnan
SNS College of Engineering, Coimbatore, India
e-mail: tinufp@gmail.com

C. Kamalakannan et al. (eds.), *Power Electronics and Renewable Energy Systems*,
Lecture Notes in Electrical Engineering 326, DOI 10.1007/978-81-322-2119-7_62

shipping expenses. In BLDC motors, rotor magnets generate the rotor's magnetic flux, allowing BLDC motors to achieve higher efficiency. Therefore, BLDC motors may be used in high-end white goods such as refrigerators, washing machines, dishwashers, etc., high-end pumps, fans, and other appliances that require high reliability and efficiency [3].

The Air-Con system with PMBLDCM has low running cost, long life, and reduced mechanical and electrical stresses compared to a single-phase induction motor-based Air-Con system operating in "on/off" control mode. Comparing to induction motor BLDC motor have better efficiency and power factor and therefore 20–50 % greater output power can be obtained [4, 5]. The commutation in a PMBLDCM is accomplished by solid state switches of a three-phase Voltage Source Inverter (VSI). Its application to the compressor of an air-conditioning system results in an improved efficiency of the system if operated under speed control while maintaining the temperature in the air conditioned zone at the set reference consistently. The Air-Con exerts constant torque, i.e., rated torque, on the PMBLDCM while operated in speed control mode.

The PMBLDCMD is fed from a single-phase ac supply through a Diode Bridge Rectifier (DBR) followed by a capacitor at dc link. It draws a pulsed current with a peak higher than the amplitude of the fundamental input current at ac mains due to an uncontrolled charging of dc link capacitor. This results in poor Power Quality (PQ) at ac mains in terms of poor power factor (PF) of the order of 0.728, high Total Harmonic Distortion (THD) of ac mains current at the value of 81.54 %, and high crest factor (CF) of the order of 2.28. Therefore, a PF converter among various available converter topologies is almost inevitable for a PMBLDCMD.

62.2 Proposed System Control Scheme

Figure 62.1 shows the proposed embedded based speed control scheme for an air compressor. Speed of the motor is directly proportional to dc link voltage. Thus speed control of this system is obtained by controlling DC link voltage. Embedded

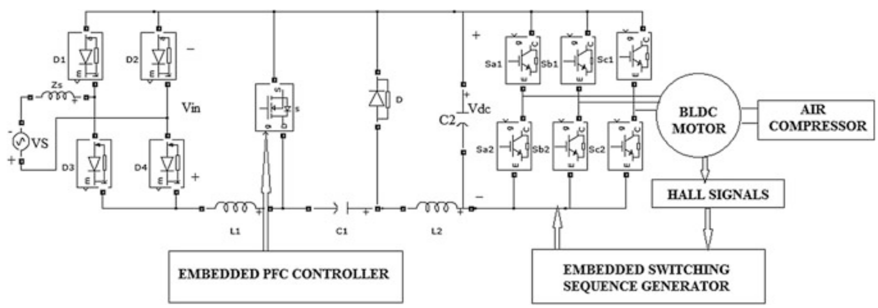

Fig. 62.1 Proposed speed control scheme for embedded based Cuk PFC fed VSI based PMBLDCM

Table 62.1 Electronic commutation table

Switching sequence	Seq. no	Position sensor			Switch closed		Phase current		
		H1	H2	H3			A	B	C
0	0	0	0	0	–	–	Off	Off	Off
0–60	1	0	0	1	Sc1	Sb2	Off	−	+
60–120	3	0	1	0	Sb1	Sa2	Off	−	+
120–180	3	0	1	1	Sc1	Sa2	−	+	Off
180–240	4	1	0	0	Sa1	Sc2	−	Off	+
240–300	5	1	0	1	Sa1	Sb2	+	Off	−
300–360	6	1	1	0	Sb1	Sc2	+	−	Off
360	7	1	1	1	–	–	Off	Off	Off

based control of Metal Oxide Semiconductor Field Effect Transistor (MOSFET) switch of Cuk converter is employed to control the DC link voltage. DC voltage is fed to the PMBLDCM by means of VSI. PMBLDC make use of hall sensor based commutation. Switching of VSI corresponding to each hall sensor states is done according to the switching table (Table 62.1) by using an embedded switching sequence generator. VSI uses IGBT switches because of its operation at lower frequency compared to PFC converter.

Embedded based controllers are employed in this system. PFC controller and Switching Sequence Generator for commutation are the controllers of the system. Matlab based programs forms the basis of the controllers. Program based controllers can be controlled in different ways with required modifications at different instants. Thus making the system control easier.

Embedded PFC Controller controls MOSFET switch of Cuk converter. Duty ratio decides the ON-OFF time of the converter. Ratio of output voltage to the sum of input and output voltages gives the duty ratio. So output and input voltages are continuously monitored and any change in its set value is corrected by a factor added to the duty ratio. Thus the DC link voltage, output of Cuk converter, is kept constant by adjusting the duty ratio. Matlab functioning program helps as to achieve this goal.

Appropriate switching sequence for VSI is made based on six states of hall signals. Six possible Hall Effect states and the switch which remains "ON" at each state and also the polarity of each phases of BLDC motor is given in the Table 62.1. As per the table data switching sequence is generated and output of switch sequence generator, Commutator, can generate gate pulses for switches of VSI. PWM signals for switches in VSI are obtained by using 'embedded switching sequence generator'. Hall signals is having six possible combinations representing six states as shown in the Table 3.1. Switches which remains ON during each state is also given in the Table 3.1.

62.3 Design of PFC Cuk Converter Based PMBLDCMD

The proposed PFC Cuk dc–dc converter controls the dc link voltage using the equation

$$V_{dc} = \frac{V_{in} D}{1 - D} \tag{62.1}$$

where V_{in} is the average output of the DBR for a given ac input voltage (V_s) related as

$$V_{in} = \frac{2\sqrt{2}}{\pi} V_s \tag{62.2}$$

The Cuk converter uses a boost inductor (L_i) and a capacitor (C_1) for energy transfer. Their values are given as

$$L_{in} = \frac{D V_{in}}{f_s (\Delta I_{Lin})} \tag{62.3}$$

$$C_{in} = \frac{D I_{dc}}{f_s \Delta V_{cin}} \tag{62.4}$$

where ΔI_{Lin} is a specified inductor current ripple, ΔV_{c1} is a specified voltage ripple in the intermediate capacitor ($C1$), and I_{dc} is the current drawn by the PMBLDCM from the dc link. A ripple filter is designed for ripple-free voltage at the dc link of the Cuk converter. The inductance (Lo) of the ripple filter restricts the inductor peak-to-peak ripple current (ΔI_{Lo}) within a specified value for the given switching frequency (fs), whereas the capacitance (Cd) is calculated for the allowed ripple in the dc link voltage (ΔV_{Cd}) [5, 6]. The values of the ripple filter inductor and capacitor are given as

$$L_{out} = \frac{(1 - D) V_{dc}}{f_s \Delta I_{lout}} \tag{62.5}$$

$$C_d = \frac{I_{dc}}{2\omega \Delta V_{cd}} \tag{62.6}$$

The PFC converter is designed for a base dc link voltage of $V_{\mathrm{dc}} = 298$ V at $V_s = 220$ V for $f_s = 40$ kHz, $I_s = 4.5$ A, $\Delta I_{\mathrm{Li}} = 0.45$ A (10 % of I_{dc}), $I_{\mathrm{dc}} = 3.5$ A, $\Delta I_{\mathrm{Lo}} = 3.5$ A ($\approx I_{\mathrm{dc}}$), $\Delta V_{\mathrm{Cd}} = 4$ V (1 % of V_o), and $\Delta V_{\mathrm{C1}} = 220$ V ($\approx V_s$). The design values are obtained as $L_i = 6.61$ mH, $C_1 = 0.3$ μF, $L_o = 0.82$ mH, and $C_d = 1{,}590$ μF.

62.4 PMBLDCMD

The PMBLDCMD consists of an electronic commutator, a VSI, and a PMBLDCM.

62.4.1 Electronic Commutator

In BLDC motor, the rotor position was guided by the electronic switches which is to ensure proper commutation and thus the motor rotates. Thus the detection of the rotor position is crucial in order for the BLDC motor to work properly. Generally, the Hall sensor is used to sense the rotor position and placed 120° apart [7]. In every 60° of rotation, the Hall sensor changed its state and each combination of hall sensors states represents a specific rotor position. The electronic commutator uses signals from Hall-effect position sensors to generate the switching sequence for the VSI as shown in Table 62.1.

62.4.2 Voltage Source Inverter

The BLDC motor uses six step inverter operation to replace the commutator part. Six-step commutation is a cost-effective due to its simple and relatively inexpensive feedback and drive dives.

The output of VSI to be fed to phase "a" of the PMBLDC motor is calculated from the equivalent circuit of a VSI-fed PMBLDCM shown in Fig. 62.2 as When Sa1 = 1,

$$V_{a0} = \frac{V_{dc}}{2} \tag{62.7}$$

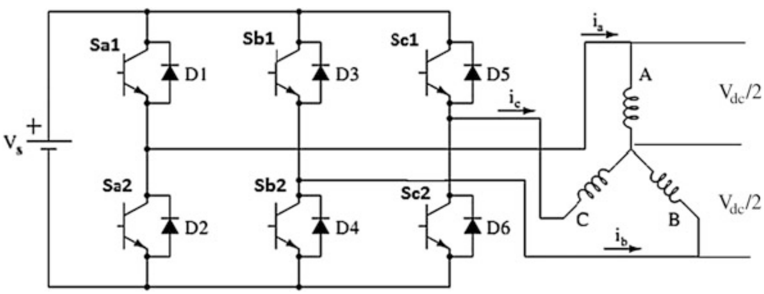

Fig. 62.2 Equivalent circuit of VSI fed PMBLBCM

When Sa2 = 1,

$$V_{a0} = -\frac{V_{dc}}{2} \tag{62.8}$$

When Sa1 = Sa2 = 0,

$$V_{a0} = 0 \tag{62.9}$$

where v_{ao}, v_{bo}, v_{co}, and v_{no} are the voltages the three phases (a, b, and c) and neutral point (n) with respect to the virtual midpoint of the dc link voltage shown as "o" in Fig. 62.2. The voltages v_{an}, v_{bn}, and v_{cn} are the voltages of the three phases with respect to the neutral terminal of the motor (n), and V_{dc} is the dc link voltage. The values 1 and 0 for S_{a1} or S_{a2} represent the "on" and "off" conditions of respective IGBTs of the VSI. The voltages for the other two phases of the VSI feeding the PMBLDC motor, i.e., v_{bo}, v_{co}, v_{bn}, and v_{cn}, and the switching pattern of the other IGBTs of the VSI.

62.4.3 PMBLDCM

Differential equations governing PMBLDC is given as

$$V_{an} = Ri_a + p\lambda_a + e_{an} \tag{62.10}$$

$$V_{bn} = Ri_b + p\lambda_b + e_{bn} \tag{62.11}$$

$$V_{cn} = Ri_c + p\lambda_c + e_{cn} \tag{62.12}$$

where $\lambda_{a,}$ $\lambda_{b,}$ λ_c are flux linkages and they are given by

$$\lambda_a = L_s i_a - M(i_b + i_c) \tag{62.13}$$

$$\lambda_b = L_s i_b - M(i_a + i_c) \tag{62.14}$$

$$\lambda_c = L_s i_c - M(i_b + i_a) \tag{62.15}$$

where Ls indicates self-inductance and M indicates mutual inductance of PMBLDC motor windings.

Torque developed by motor is given by the equation

$$T_e = \frac{(e_a n i_a + e_b n i_b + e_c n i_c)}{\omega_r} \tag{62.16}$$

62.5 Simulation and Results

Proposed PMBLDC drive is designed with Air compressor load and the system is designed in matlab Simulink environment. Efficient control of the proposed circuit is done by means of embedded controllers. A 0.816-kW rating PMBLDCM is used to drive the air-conditioner, the speed of which is controlled effectively by controlling the dc link voltage. The complete model of proposed PFC based BLDC motor system can be divided into two parts, Cuk Converter for PFC and VSI Fed BLDC motor.

Matlab Simulation diagram for the proposed circuit is shown in Fig. 62.3. Simulation diagram of PFC Cuk converter is separately shown in Fig. 62.4. Controlled DC voltage is given into the PMBLDCM drive. Here DC voltage is controlled with respect to the compared speed because of the proportionality relation between speed and voltage. Switching pulses to the Cuk converter is controlled by comparing voltage and input AC current. So that power factor correction for the system is achieved successfully by the switching sequence generation by the switching sequence generation.

Figure 62.5 illustrates the Proposed system has used a Cuk converter for power factor correction and obtained power factor which is around unity shown in Fig. 62.5a. Output characteristics of the PMBLDC motor. Figure 62.5e shows that proposed system can attain a constant torque characteristics by BLDC motor at varying speed ranges. Controllers of the system is properly designed such that the Fig. 62.5 waveforms shows that the voltage is correspondingly increased as per the increase in speed and accordingly current in the system is decreased.

Smoothening of input AC current with increase in speed with improvement in THD value is shown in Fig. 62.6. THD value of input AC current is 2.52 % for the proposed drive at its rated speed. Variation of THD value according to speed variation is shown in Fig. 62.7.

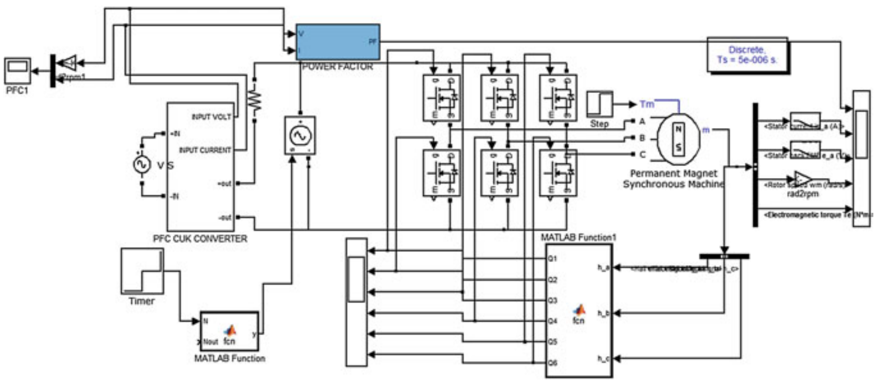

Fig. 62.3 Simulation diagram of the proposed system

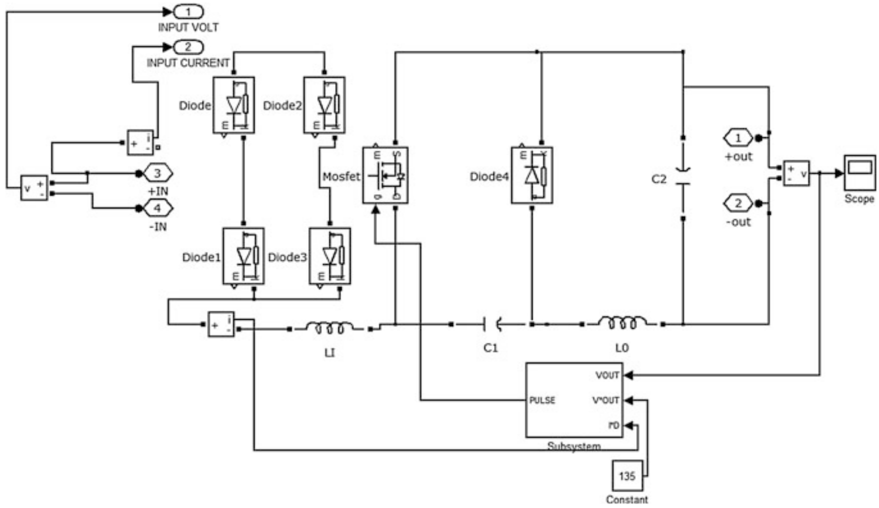

Fig. 62.4 Simulation diagram of PFC Cuk converter

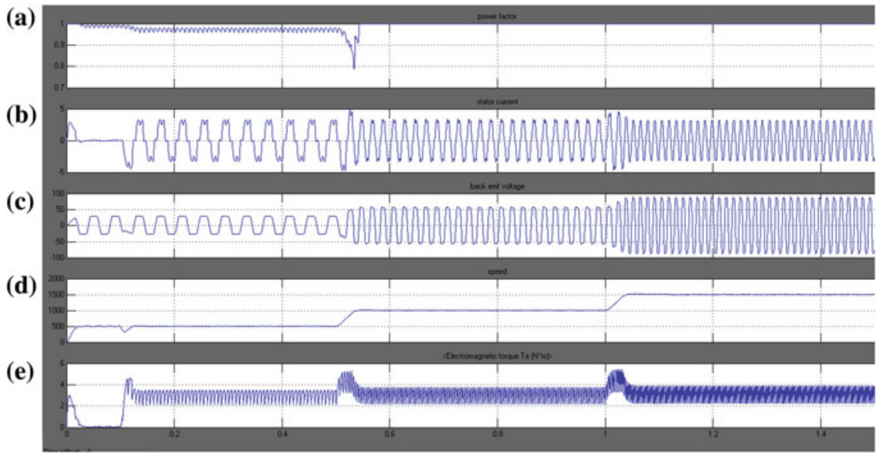

Fig. 62.5 Output characteristics of PMBLDCM (a) PF, (b) stator current, (c) back emf, (d) speed, (e) Torque

Evaluation of motor under different speed results in constant torque for the above system also a constant speed is maintained by the system under varying torque conditions. Stator current value, the electrical input to the system, is giving almost constant value indicating the efficient operation of PMBLDC motor. Electrical input and mechanical output of BLDC motor in this proposed system is able to maintain constant value indicating stable operation of motor.

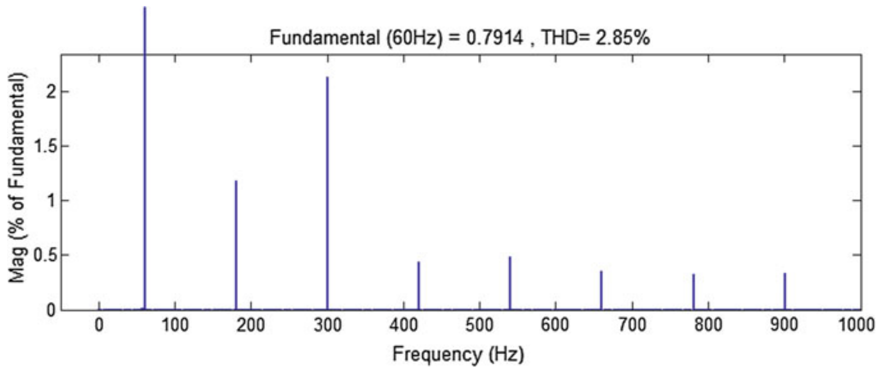

Fig. 62.6 THD value of input AC current THD = 2.52 %

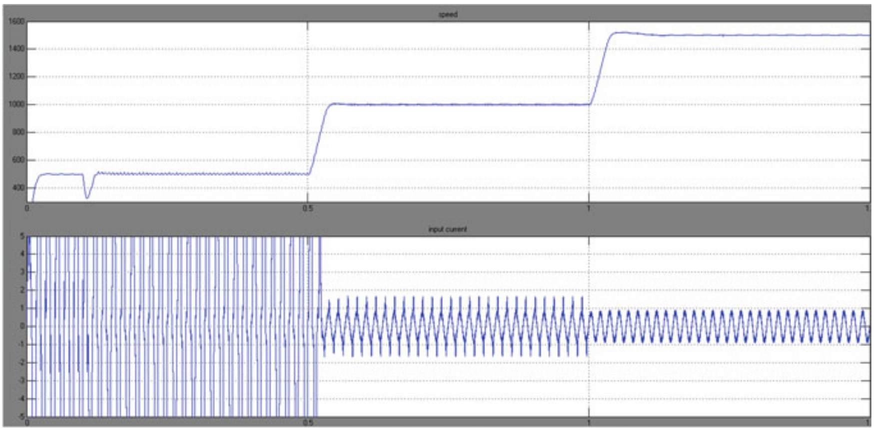

Fig. 62.7 Variation of input current with speed

Table 62.2 shows that the proposed circuit has attained an efficient power factor of around unity at all speeds. Also THD of the system is below 5 % thus satisfying the IEC standards. THD of the system is observed as 2.52 %. Power factor correction is one of method by which PQ at the AC mains can be improved. This indicates that proposed system is able to solve PQ problems caused by PMBLDCM to some extends. Thus helping in efficient utilization of available energy in a power system.

Table 62.2 THD and PF analysis at 220 V input AC mains

V_{dc} (V)	Speed (rpm)	THD (%)	PF
159.5	700	4.37	0.9987
176.5	800	3.76	0.9988
194	900	3.12	0.9989
211.5	1,000	2.57	0.9990
229	1,100	2.31	0.9991
246	1,200	2.47	0.9991
263.5	1,300	2.56	0.9991
281	1,400	2.55	0.9991
298	1,500	2.52	0.9991

62.6 Conclusion

A new control strategy for speed control of PMBLDCMD has been developed such that a wide range of speed control can be achieved by means of this system. Proposed system has reference speed as an equivalent dc link voltage designed for an air conditioner with Cuk PFC converter. The speed of PMBLDCM has been found to be proportional to the dc link voltage thereby, a wide and smooth control of speed is observed while controlling the link voltage. DC link voltage control and commutator action control has been successfully achieved by means of embedded control blocks. PFC converter designed here has enabled the circuit to attain a unity PF at the AC main at rated speed. Also a THD of 2.85 % has been attained at AC mains. Thus PQ indices of the proposed PFC drive are in conformity to the International Standard IEC 61000-3-2.

Here PFC based air conditioner is designed by using a PMBLDCD by using hall sensor based commutation. Sensorless control can be incorporated in the above system to attain more Compact and cost effective control to make the system more reliable.

References

1. Singh B, Singh BN, Chandra A, Al-Haddad K, Pandey A, Kothari DP (2003) A review of single-phase improved power quality ac–dc converters. IEEE Trans Ind Electron 50(5):962–981
2. Hung C-W, Chen J-H, Chang L-S, Li C-H (2000) A simple strategy of power factor correction based on low-end MCU. In: 5th IEEE conference on industrial electronics and applications
3. Fazil M, Rajagopal KR (2010) Development of external rotor single-phase PM BLDC motor based drive for ceiling fan. Power electronics, drives and energy systems (PEDES) and 2010 power india IEEE conference, pp 1–4. ISBN:978-1-4244-7782-1
4. George GJ, Rakesh R, Arun N (2012) PMBLDC motor drive with power factor correction controller. In: Computing, electronics and electrical technologies (ICCEET) international conference, pp 63–68
5. Kenjo T, Nagamori S (1985) Permanent magnet brushless dc motors. Clarendon, Oxford

6. Kasim R, Ismail KA, Jidin A, Bahari N (2012) Modeling and simulation of brushless dc machines. IC-GWBT2012, Ahmad Dahlan University, 23–24 March 2012
7. Gamazo-Real JC, Vázquez-Sánchez E, Gómez-Gil J (2010) Position and speed control of brushless dc motors using sensorless techniques and application trends. Sensors 10:6901–6947. ISSN 1424-8220. doi:10.3390/s100706901

Chapter 63
Photovoltaic Power System Application Using Energy Stored Quasi Z Source Inverter

S. Aysha and P. Selvakumar

Abstract The quasi-Z-source inverter (QZSI) is a single stage power converter derived from the Z-source inverter topology, employing an impedance network which couples the source and the inverter to achieve voltage boost and inversion. The quasi-Z-source inverter (qZSI) with battery operation can balance the stochastic fluctuations of photovoltaic (PV) power injected to the grid/load. This paper proposes a new topology of the energy-stored qZSI to overcome the discontinuous conduction mode during battery discharge. A new carrier based pulse width modulation (PWM) strategy for the (QZSI) which gives a significantly high voltage gain compared to the traditional PWM techniques is implemented. This technique employs sine wave as both carrier and reference signal, with which the simple boost control for the shoot-through states is integrated to obtain an output voltage boost. The conventional triangular wave carrier used in simple boost control technique is replaced by sine wave, which improves the shoot-through duty ratio for a given modulation index. The conventional perturb and observe maximum power point tracking algorithm is replaced by ANFIS based MPPT algorithm.

Keywords Quasi-Z-source inverter (QZSI) · Pulse width modulation (PWM) · MPPT · ANFIS

63.1 Introduction

The worldwide installed photovoltaic (PV) power capacity shows nearly an exponential increase due to decreasing costs and to improvements in solar energy technology. Power converter topologies employed in the PV power generation systems are mainly characterized by two- or single-stage inverters [1].

S. Aysha (✉) · P. Selvakumar
SNS College of Engineering, Coimbatore, Tamil Nadu, India
e-mail: aysharain@gmail.com

C. Kamalakannan et al. (eds.), *Power Electronics and Renewable Energy Systems*,
Lecture Notes in Electrical Engineering 326, DOI 10.1007/978-81-322-2119-7_63

The single-stage inverter is an attractive solution due to its compactness, low cost, and reliability. However, its conventional structure must be oversized to cope with the wide PV voltage variation derived from changes of irradiation and temperature [2]. The two-stage inverter topology applies a boost dc/dc converter to minimize the required kilo volt ampere rating of the inverter and boost the wide-range input voltage to a constant desired output value [3].

However, the switch in the dc/dc converter will increase the cost and decrease the efficiency. The Z-source inverter (ZSI) presents a new single-stage structure to achieve the voltage boost/buck character in a single power conversion stage, which has been reported in applications to PV systems [4]. This type of converter can handle the PV dc voltage variations over a wide range without overrating the inverter. As a result, the component count and system cost are reduced, with improved reliability due to the allowed shoot through state [5]. Recently proposed quasi-Z-source inverters (qZSIs) have some new attractive advantages more suitable for application in PV systems.

63.2 Quasi Z Source Inverter Topology

The quasi z-source inverter (QZSI) is a single stage power converter derived from the Z-source inverter topology, employing a unique impedance network [6]. The conventional VSI and CSI suffer from the limitation that triggering two switches in the same leg or phase leads to a source short and in addition, the maximum obtainable output voltage cannot exceed the dc input, since they are buck converters and can produce a voltage lower than the dc input voltage [7]. Both Z-source inverters and quasi-Z-source inverters overcome these drawbacks; by utilizing several shoot-through zero states [8]. A zero state is produced when the upper three or lower three switches are fired simultaneously to boost the output voltage.

Sustaining the six permissible active switching states of a VSI, the zero states can be partially or completely replaced by the shoot through states depending upon the voltage boost requirement. Quasi-Z-source inverters (QZSI) acquire all the advantages of traditional Z source inverter [9]. The impedance network couples the source and the inverter to achieve voltage boost and inversion in a single stage. By using this new topology, the inverter draws a constant current from the PV array and is capable of handling a wide input voltage range [10]. It also features lower component ratings, reduces switching ripples to the PV panels, causes less EMI problems and reduced source stress compared to the traditional ZSI.

63.3 Energy Stored Quasi Z Source Inverter

The intermittent and unscheduled characteristics of solar power limit the applicability of PV systems. The addition of an energy storage system (ESS) to work in conjunction with PV power generation, make its output power continuous, stable,

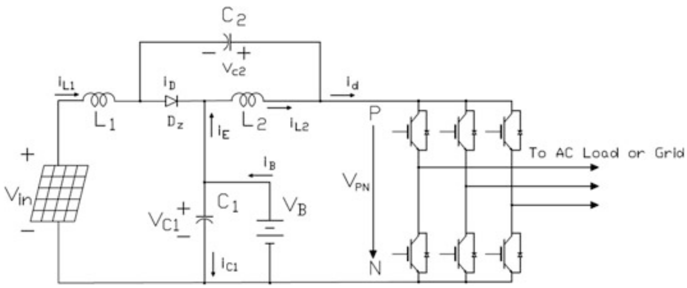

Fig. 63.1 Energy stored QZSI

and smooth. Most of the existing ESS technologies employ a bidirectional dc/dc converter to manage the batteries which makes the system complex, increases its cost, and decreases its reliability. Without the requirements of any additional dc-dc converters or components the quasi Z source inverter can be developed by connecting a battery in parallel with capacitor C1 as shown in the Fig. 63.1

This system is able to do the following simultaneously:

(1) Produce the desired output ac voltage to the grid/load;
(2) Regulate the battery state of charge (SOC);
(3) Control the PV panel output power (or voltage) to maximize energy production.

They have common points: (1) there are three power sources/consumers, i.e., PV panels, battery, and the grid/load, (2) As long as controlling two power flows, the third one automatically matches the power difference, according to the power equation

$$P_{in} - P_{out} + P_B = 0 \tag{63.1}$$

P_{in}, P_{out}, P_B are the PV panel power, the output power of the inverter, and the battery power respectively. The power Pin is always positive because the PV panel is single directional power supply, *PB* is positive when the battery delivers energy and negative when absorbing energy, and *P*out is positive when the inverter injects power to the grid.

63.4 Operating Principle and Equivalent Circuit of QZSI

63.4.1 Active Mode

In the non-shoot through mode, the switching pattern for the QZSI is similar to that of a VSI. The inverter bridge, viewed from the DC side is equivalent to a current source, the input dc voltage is available as DC link voltage input to the inverter,

Fig. 63.2 Equivalent circuit of active mode

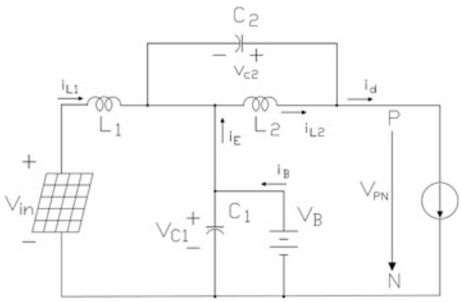

which makes the QZSI behave similar to a VSI. This mode will make the inverter operate in one of the six active states and two traditional zero states, which is referred to as the non-shoot-through state.

A continuous current flows through the diode D_z and its equivalent circuit is shown in Fig. 63.2.

During this time interval the circuit equations are

$$C\frac{dV_{c2}}{dt} = i_{L2} - i_d \tag{63.2}$$

$$L\frac{di_{L1}}{dt} = V_{in} - V_{c1} \tag{63.3}$$

63.4.2 Shoot Through Mode

In the shoot through mode, switches of the same phase in the inverter bridge are switched on simultaneously for a very short duration. The source however does not get short circuited when attempted to do so because of the presence LC network, while boosting the output voltage. The DC link voltage during the shoot through states, is boosted by a boost factor, whose value depends on the shoot through duty ratio for a given modulation index. This mode will make the inverter short circuit via any one phase leg, combinations of any two phase legs, and all three phase legs, which is referred to as the shoot through state. As a result, the diode *Dz* is turned off due to the reverse-bias voltage. Its equivalent circuit is shown in Fig. 63.3.

During this time interval the circuit equations are presented as follows:

$$L\frac{di_{L1}}{dt} = V_{in} + V_{c2} \tag{63.4}$$

$$C\frac{dV_{c2}}{dt} = -i_{L1} \tag{63.5}$$

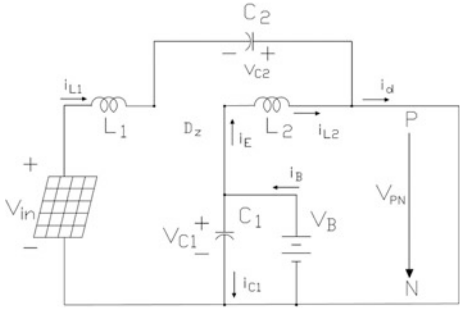

Fig. 63.3 Equivalent circuit of active mode

63.5 ANFIS Based MPPT

Artificial intelligence (AI)-based methods are increasingly used in renewable energy systems due to the flexible nature of the control offered by such techniques. The AI techniques are highly successful in nonlinear systems due to the fact that once properly trained they can interpolate and extrapolate the random data with high accuracy. Voltage and current are taken as the input to the ANFIS controller. This technique utilizes the weather information the input to the ANFIS. The ANFIS integrates the neural network and fuzzy logic, thus this synergy offers the most powerful artificial intelligence technique. An ANFIS technique is used to determine the maximum power capability of a PV module for variable solar irradiance and temperature conditions.

The inputs to the ANFIS are given as environmental conditions, i.e., the solar irradiance and temperature. There are two control variables for this qZSI control system, i.e., the shoot-through duty (D) and modulation index (M).

The control scheme with ANFIS based MPPT is shown in Fig. 63.4.

The overall neuro-fuzzy structure shown in Fig. 63.5 is a five-layer network. The structure shows two inputs of the solar irradiance and the cell temperature, which is translated into appropriate membership functions, three functions for the solar irradiance and three functions for temperature. The membership function’s shape varies during the training stage and the final shape obtained after the completion of the training they are termed as “low,” “medium,” and “high.”

63.6 SPWM Control Strategy

A PWM control technique for QZSI, with modified carrier for active and shoot through states is presented. While the zero states of traditional VSI are replaced by shoot through states, the active states should remain unaltered, for the shape of output voltage waveform to be preserved. This technique uses sine wave as both reference and carrier. The simple boost control method used here employs two constant voltage envelopes which are compared with the sine carrier wave.

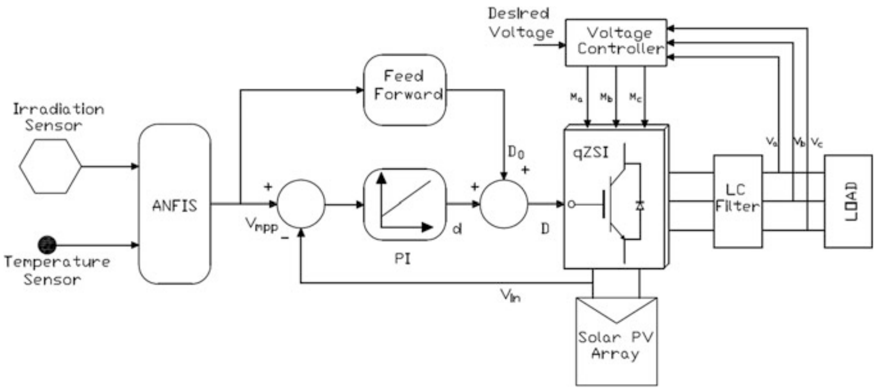

Fig. 63.4 Control scheme of ANFIS based MPPT

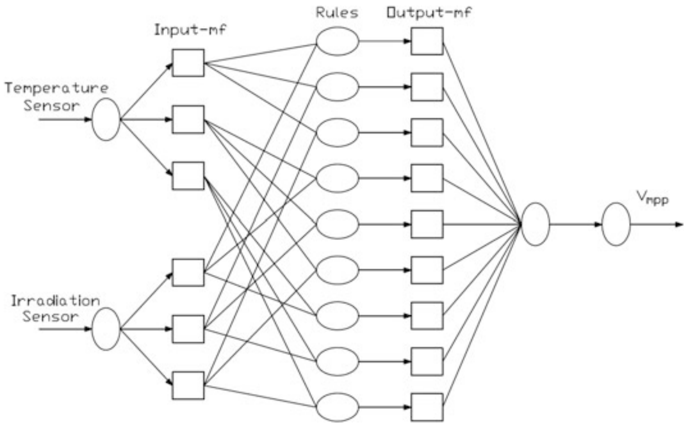

Fig. 63.5 Neuro fuzzy structure

Whenever the magnitude of sine carrier wave becomes greater than or equal to the positive constant magnitude envelope (or) lesser than or equal to the negative constant magnitude envelope, pulses are generated and they control the shoot through duty ratio *Do*. These pulses serve as firing signals for the switches in the inverter.

The voltage gain *G* of QZSI is given by,

$$\mathrm{G} = \frac{\text{Output peak ac voltage}}{\text{DC link voltage}}$$

$$V_{link} = \frac{V_s}{2} \tag{63.6}$$

$$V_{ac} = MB \times \frac{V_s}{2} \tag{63.7}$$

where

V_{link}	is the DC link voltage of inverter
V_{ac}	is the peak ac voltage
B	is the boost factor
M	is the modulation index

$$D_0 = \frac{T_0}{T} = 1 - \frac{2}{\pi}\sin^{-1} M \tag{63.8}$$

It is observed that sine carrier PWM gives high shoot through duty ratio compared to triangular carrier, for the same modulation index, which reduces the voltage stress on the device and gives high peak output voltage. The simple boost control method has shoot through states spread uniformly which makes output free of low frequency ripples.

The use of sine carrier wave has also resulted in reduction of THD in output voltage, improved fundamental component.

63.7 Simulation Results

The PV panel output is shown in the Fig. 63.6. It is obtained as 85 V. The active and reactive power for the circuit is shown in Fig. 63.7. The active power is obtained as positive and the reactive power value is obtained as negative (Fig. 63.8).

Using SPWM technique the voltage and current feeding to the grid is obtained nearly in phase with each other.

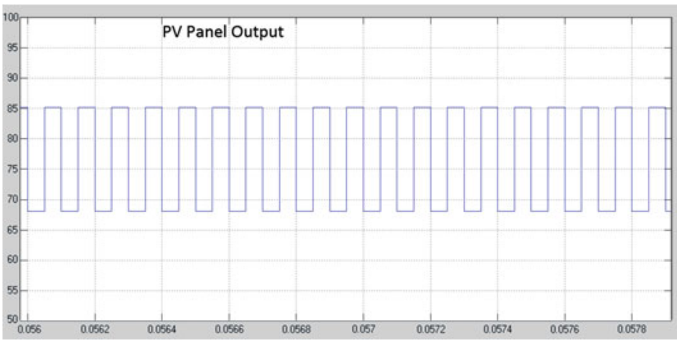

Fig. 63.6 PV panel output

Fig. 63.7 Active and reactive power

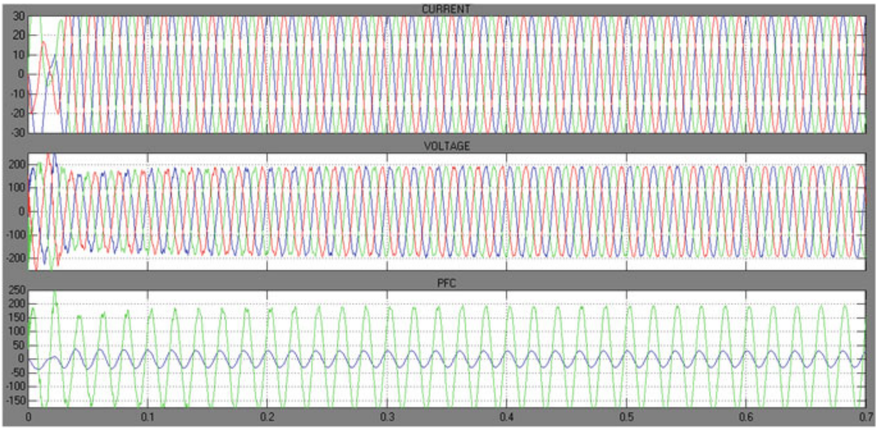

Fig. 63.8 Output waveform of inverter in grid synchronized operation

63.8 Conclusion

A novel topology for an energy-stored qZSI has been discussed to overcome the shortcoming of the existing solutions in PV power system. PV array has been simulated and integrated to the QZSI with maximum power point tracking algorithm (ANFIS BASED). QZSI has been simulated with sine pulse width modulation and the results have been compared. The proposed QZSI inherits all the advantages of the ZSI and features its unique merits. It can realize buck/boost power conversion in a single stage with a wide range of gain that is suited well for application in PV power generation systems. Furthermore, the proposed QZSI has advantages of continuous input current, reduced source stress, and lower component ratings when compared to the traditional ZSI. The voltage gain with sine carrier is greater than the voltage gain with triangular carrier. While using sine pulse width modulation technique the voltage and current feeding to the grid is somewhat in phase with each other. Also the power factor of the active power is nearly unity.

References

1. Anderson J, Peng FZ (2008) A class of quasi-Z-source inverters. In: Conference record IEEE IAS annual meeting, Edmonton, AL, Canada, Oct 2008, pp 1–7
2. Abu-Rub H, Iqbal A, Ahmed SM, Peng FZ, Li Y, Baoming G (2013) Quasi-Z-source inverter-based photovoltaic generation system with maximum power tracking control using ANFIS. IEEE Trans Sustain Energy 4(1):11–20
3. Bradaschia F, Cavalcanti MC, Ferraz PEP, Neves FAS, dos Santos EC, da Silva JHGM (2011) Modulation for three-phase transformerless Z-source inverter to reduce leakage currents in photovoltaic systems. IEEE Trans Ind Electron 58(12):5385–5395
4. Bratcu AI, Munteanu I, Bacha S, Picault D, Raison B (2011) Cascaded DC–DC converter photovoltaic systems: power optimization issues. IEEE Trans Ind Electron 58(2):403–411
5. Beltran H, Bilbao E, Belenguer E, Etxeberria-Otadui I, Rodriguez P (2013) Evaluation of storage energy requirements for constant production in PV power plants. IEEE Trans Ind Electron 60(3):1225–1234
6. Chavarria J, Biel D, Guinjoan F, Meza C, Negroni J (2013) Energy balance control of PV cascaded multilevel grid-connected inverters for phase-shifted and level-shifted pulse-width modulations. IEEE Trans Ind Electron 60(1):98–111
7. Rani BI, Ilango GS, Nagamani C (2013) Control strategy for power flow management in a PV system supplying DC loads. IEEE Trans Ind Electron 60(8):3185–3194
8. Femia N, Petrone G, Spagnuolo G, Vitelli M (2009) A technique for improving P&O MPPT performances of double-stage grid-connected photovoltaic systems. IEEE Trans Ind Electron 56(11):4473–4482
9. Cintron-Rivera JG, Li Y, Jiang S, Peng FZ (2011) Quasi Z source inverter with energy storage for PV generation systems. In: Applied power electronics conference and exposition (APEC), 2011 twenty-sixth annual IEEE, pp 401–406
10. Kadri R, Gaubert J, Champenois G (2011) An improved maximum power point tracking for photovoltaic grid-connected inverter based on voltageoriented control. IEEE Trans Ind Electron 58(1):66–75

Chapter 64
Power Management of a Grid Connected PV/Battery

Chinmaya Samanta, Subhransu Sekhar Dash, G. Ezhilarasan and N.K. Rayaguru

Abstract This paper presents the modelling and analysis of a grid connected photovoltaic and battery hybrid system to achieve the desired power sharing amongst the PV array, battery and grid for constant load supply with full utilization of photovoltaic generation and maintaining a constant DC link voltage. This hybrid system mainly consists of a PV array coupled through a unidirectional boost converter to a DC link. This DC link is further connected to the AC grid through an inverter and a coupling transformer. A storage device in the form of battery is connected to the DC link through a bidirectional converter for charging and discharging. The composite system is available for safe operation in on-grid as well as off-grid mode satisfying voltage and power balance constraints. Four different modes of operation have been demonstrated to verify and validate the desired power management amongst the various sources. MATLAB/SIMULINK software is used for simulating the composite model.

Keywords Power management · Hybrid system · MPPT · Grid

64.1 Introduction

Now-a-days the demand of Electrical power is increasing day by day and the reserve of coal and fossil fuels are diminishing at a faster rate. So the importance of hybrid systems consisting of renewable energy (RE) sources has increased

C. Samanta (✉) · S.S. Dash · G. Ezhilarasan
Department of Electrical and Electronics Engineering, SRM University, Chennai, India
e-mail: Chinmaya.samanta99@gmail.com

S.S. Dash
e-mail: munu_dash_2k@yahoo.com

N.K. Rayaguru
Veltech Multitech Dr Rangarajan Dr Sakunthala Engineering College, Chennai, India
e-mail: nkrayaguru29@gmail.com

C. Kamalakannan et al. (eds.), *Power Electronics and Renewable Energy Systems*,
Lecture Notes in Electrical Engineering 326, DOI 10.1007/978-81-322-2119-7_64

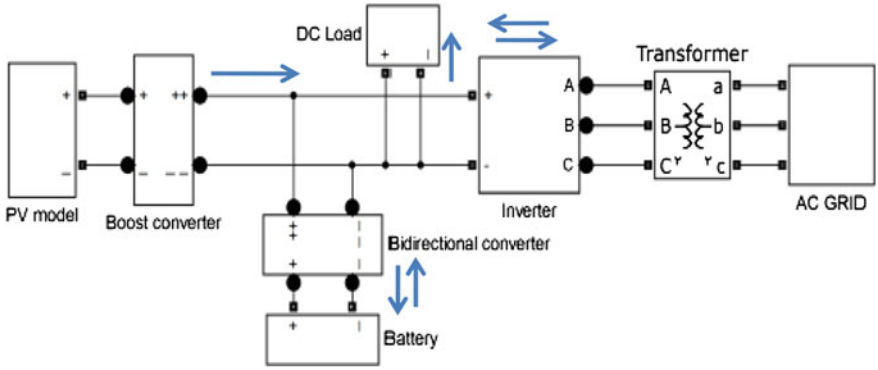

Fig. 64.1 Overall arrangement of grid connected PV and battery

significantly as they appear to be the effective solution for a clean and distributed energy production. Hybrid power system consists of a combination of RE sources such as photovoltaic (PV), wind generators, fuel cells along with energy storage devices such as battery, ultra-capacitors etc. At present, PV generation is assuming increased importance as a renewable energy source application because of several distinctive advantages such as simple configuration, high availability of sunlight, absence of fuel cost, low maintenance and absence of noise and wear owing to the absence of rotating parts and also it is 100 % eco friendly [1, 2, 9].

However, the disadvantage of PV generation is that it is characteristically unstable, heavily being dependent on weather conditions. Thus, energy storage element is necessary to facilitate stable and reliable power from PV system for loads or AC grid and thus improve both steady state and dynamic behaviour of the whole generation system. Because of its nature of technology, low cost and high efficiency, battery energy storage system (BESS) is extensively used in distribution generation. BESS can be integrated into PV generation system to form a hybrid PV/Battery generation system [1, 2, 9]. This paper presents a grid-connected PV/Battery generation system consisting of a PV array, battery, power conditioning converters, filter, various controllers, DC load and AC grid as shown in Fig. 64.1.

64.2 Model Analysis

64.2.1 Model Parameters

This composite system consists of a hybrid model of 5,000 W, 240 V PV array connected via a DC/DC boost converter to a 320 V DC link and a 250 V, 11 Ah battery connected via a bidirectional DC/DC buck/boost converter to the DC link. This DC link is further synchronized to a 33 kV grid via a three phase three-level DC/AC inverter and a coupling transformer.

The entire simulation is carried out with PV array delivering a maximum power of 5,000 W at 850 (W/m^2) solar irradiance (G) and working temperature (T) of 313 (K) with G and T being kept constant at these values for all the four modes of experiment.

A 4.5 kHz boost converter is used for connecting PV to DC link which increases PV generation voltage of 240 V DC at maximum power point to 320 V DC. A 3-level 3 phase DC/AC inverter of 1,980-Hz (33 × 60) is used for AC grid connection of the composite model. This bidirectional inverter can either convert the 320 V DC to 320 V AC at unity power factor or vice versa. A 7 kVA 320 V/33 kV three phase coupling transformer is used for AC grid connection. AC grid block consists of 33 kV distribution lines and 132 kV transmission and generation system. Filter is a high pass filter of 500 VAR rating for filtering harmonics produced by inverter. A 250 V, 11 Ah battery from Matlab library is used.

PV array: The 5,000 W PV array consists of 5 strings of 4 series connected modules connected in parallel (5 × 4 × 255 W = 5,100). Each module consists of 81 no. of series-connected cells, open-circuit voltage (Voc) is 61.2 V, Short-circuit current (Isc) is 4.53 A, voltage and current at maximum power: V_{MPP} = 51.3 V, I_{MPP} = 4.97 A.

DC/DC boost converter: R-L branch: R = 1,000 Ω, L = 20 mH, Cbus1 = 100 μF

Bidirectional DC/DC converter for battery: R-L branch1: R = 900 Ω, L = 19 mH, Cbus1 = 100 μF, R-L branch2: R = 900 Ω, L = 19 mH, Cbus2 = 50 μF

DC side filter: Cp1 = 1.2 μF, Cn1 = 1 μF, Cp2 = 0.7 μF, Cn2 = 0.6 μF, R = 0.11 Ω, L = 6 mH.

64.2.2 Various Operating Modes of the Composite System

See Table 64.1.

Table 64.1 Various operating modes of the composite system

Mode	Composite system status	PV status	Battery status	Inverter status
I	On-grid	MPPT	Charging/off	Injecting power to AC grid
II	On-grid	MPPT	Charging/off	Drawing power from AC grid
III	Off-grid	MPPT	Discharging	Off
IV	Off-grid	MPPT	Charging	Off

64.2.3 Modelling of PV Arrays

The mathematical equations that describe the V–I characteristic of the ideal photovoltaic cell [3–5, 9] are:

$$I = I_{pvcell} - I_d \text{ and, } Id = I_{0cell}[\exp(qV/akT) - 1] \tag{64.1}$$

where I_{pvcell} (A) is the current generated by the incident light (it is directly proportional to the solar irradiation), I_d is the Shockley diode equation, I_{0cell} (A) is the reverse saturation or leakage current of the diode, q is the electron charge ($1.60217646 \times 10^{-19}$ C), k is the Boltzmann constant ($1.3806503 \times 10^{-23}$J/K), T (K) is the working temperature of the p-n junction, and a is the diode ideality factor.

$$I = I_{pv} - I_0[\exp[(V + R_s I)/(aV_t)] - 1] \tag{64.2}$$

where I_{pv} (A) and I_0 (A) are the photovoltaic and saturation currents of the array and $V_t = (N_s kT)/q$ is the thermal voltage of the array with N_s cells in series. R_s and R_p are the equivalent series and parallel resistance of the array.

$$I_{pv} = \left(I_{pvn} + K_I \Delta T\right) \times (G/G_n) \tag{64.3}$$

where I_{pvn} (A) is the light-generated current at the nominal condition (usually 25 °C and 1,000 W/m^2), $\Delta T = T - T_n$ [T and T_n are the actual and nominal temperatures (K)], G (W/m^2) and G_n (W/m^2) are the operating and nominal irradiation, K_I is current/temperature coefficient in A/K.

The diode saturation current I_0 mainly depends on temperature given by,

$$I_0 = (I_{scn} + K_I \Delta T)/[\exp\{(V_{ocn} + K_V \Delta T)/(aV_t)\} - 1] \tag{64.4}$$

where I_{scn} (A) is nominal short circuit current, V_{ocn} (V) is the nominal open circuit voltage and K_V is voltage/temperature coefficient in V/K.

If photovoltaic array is composed of N_{ser} series and N_{par} parallel modules then

$$I = I_{pv} N_{par} - I_0 N_{par}\left[\exp\left\{\left\{V + R_s\left(N_{ser}/N_{par}\right)I\right\}/(aVtN_{ser})\right\} - 1\right] \tag{64.5}$$

Array maximum power output is given by

$$P_{MPP} = V_{MPP} \times I_{MPP} \tag{64.6}$$

64.2.4 MPPT Control

The role of MPPT in PV systems is to automatically track the voltage V_{MPP} or current I_{MPP} at which a PV array should operate to obtain the maximum power output P_{MPP} under a given operating temperature and irradiance. Most MPPT techniques respond to changes in both irradiance and temperature. In the present

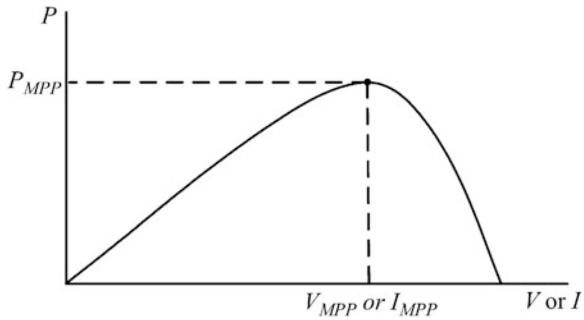

Fig. 64.2 Incremental conductance algorithm P–V/P–I characteristic

work incremental conductance (INC) method is used in which the problem of tracking peak power under fast varying atmospheric condition is resolved. The INC method is based on the fact that the slope of the PV array power is zero at the MPP, positive on the left of the MPP, and negative on the right as shown in Fig. 64.2 [6].

So, $\Delta I/\Delta V = -I/V$ at MPP, $\Delta I/\Delta V > -I/V$ on left of MPP, $\Delta I/\Delta V < -I/V$ on right of MPP. The MPP can thus be tracked by comparing the instantaneous conductance (I/V) with the incremental conductance ($\Delta I/\Delta V$) [6].

64.2.5 DC/DC Converter

The boost converter steps up the DC voltage from 240 to 320 V. This converter uses the INC based MPPT system which automatically varies the gate pulse of the GTO in order to generate the required voltage to extract maximum power [7–9] as shown in Fig. 64.3.

250 V battery is connected to the 320 V DC link through a bidirectional buck/boost converter [7–9]. This converter steps up the voltage from 250 to 320 V during discharging mode and vice versa during charging mode as shown in Fig. 64.4.

64.2.6 Inverter and Battery Control

PV array and the battery are connected to the AC grid through a common DC/AC inverter and coupling transformer. This inverter is responsible for regulating the DC link voltage and maintaining a bidirectional power flow to achieve the desired power sharing between DC link and AC grid as required during on-grid mode of operation. Inverter control circuit has 4 blocks. PLL and transformation block produces the measured d and q components of voltage and current V_{dmes}, V_{qmes} and I_{dmes}, I_{qmes}. Voltage controller block produces I_{dref} and I_{qref} corresponding to V_{dc} and V_{dcref}. A current controller block produces intermediate d and q components V_{dr} and V_{qr} using V_{dmes}, V_{qmes}, I_{dref} and I_{qref}. The final block generates the signal

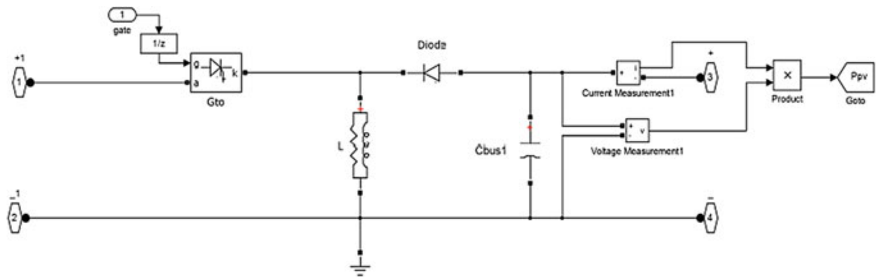

Fig. 64.3 DC/DC boost converter for PV

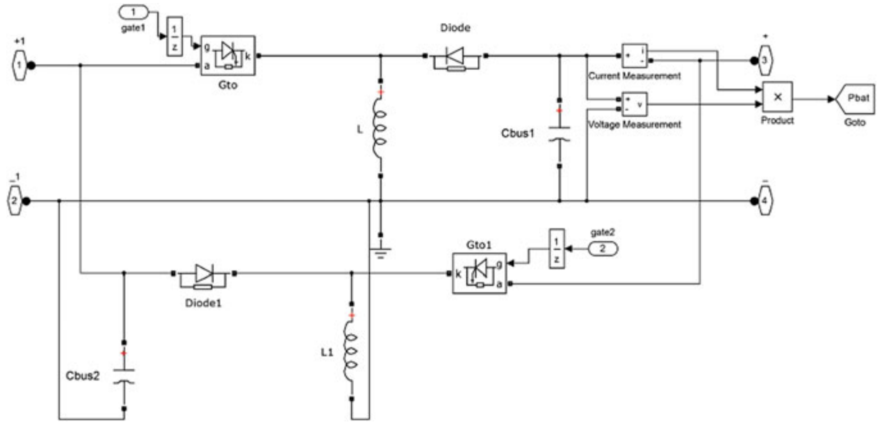

Fig. 64.4 DC/DC bidirectional converter for battery

for the PWM using V_{dr}, V_{qr}, V_{dcref}, LV side voltage of coupling transformer and PWM generates the pulses for the 3 phase three level bridge circuit for AC grid synchronization [7–9] (Fig. 64.5).

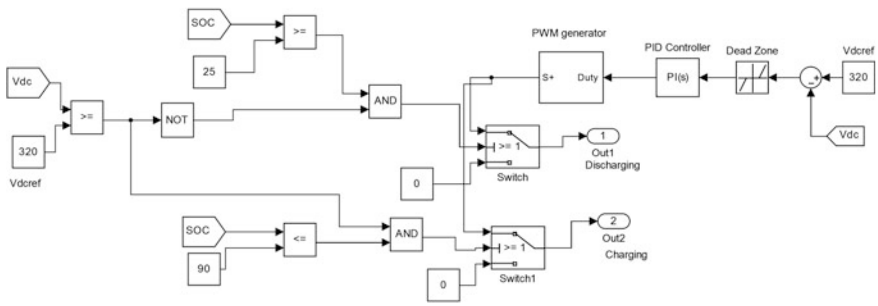

Fig. 64.5 Charging and discharging control for battery

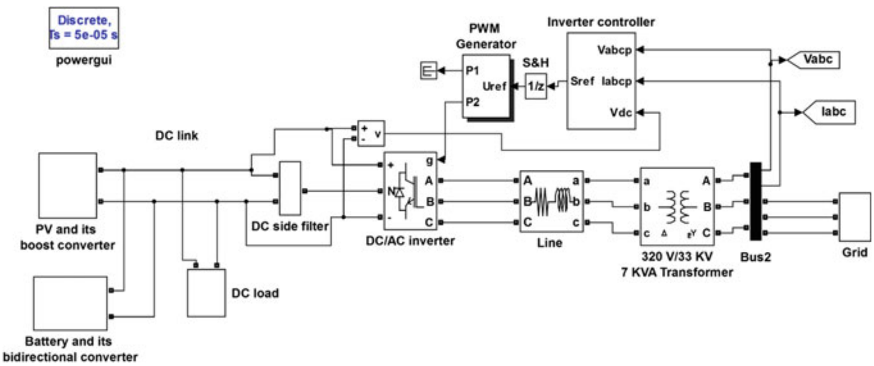

Fig. 64.6 Detailed model

64.3 Simulation Result Analysis

The detailed model of the PV/Battery hybrid system is shown in Fig. 64.6. The variation of DC load power (P_{load}), PV output power (P_{pv}), power being supplied to/drawn from AC grid (P_{grid}), Battery charging/discharging power (P_{batt}), DC link voltage (V_{dc}) and PV output voltage (V_{pv}) in various modes of simulation for 3 s are shown in Figs. 64.7, 64.8, 64.9 and 64.10.

64.3.1 Mode-I (On-Grid)

Since P_{pv} (5,000 W) > [P_{load} (2,000 W) + P_{batt} (2,000 W)], so surplus power of PV is injected to the AC grid. So P_{grid} becomes 1,000 W. Positive sign of P_{grid} indicates that power is being injected to the AC grid. V_{pv} is maintained at 240 V and V_{dc} is maintained around 320 V. Negative sign of P_{batt} indicates the charging power of battery (Fig. 64.7).

64.3.2 Mode-II (On-Grid)

Since [P_{load} (7,400 W) + P_{batt} (2,000 W)] > P_{pv} (5,000 W), so additional power required is drawn from the AC grid. So P_{grid} becomes −4,400 W. Negative sign of P_{grid} indicates that power is being drawn from the AC Grid. V_{pv} is maintained at 240 V and V_{dc} is maintained around 319 V. Negative sign of P_{batt} indicates the charging power of battery (Fig. 64.8).

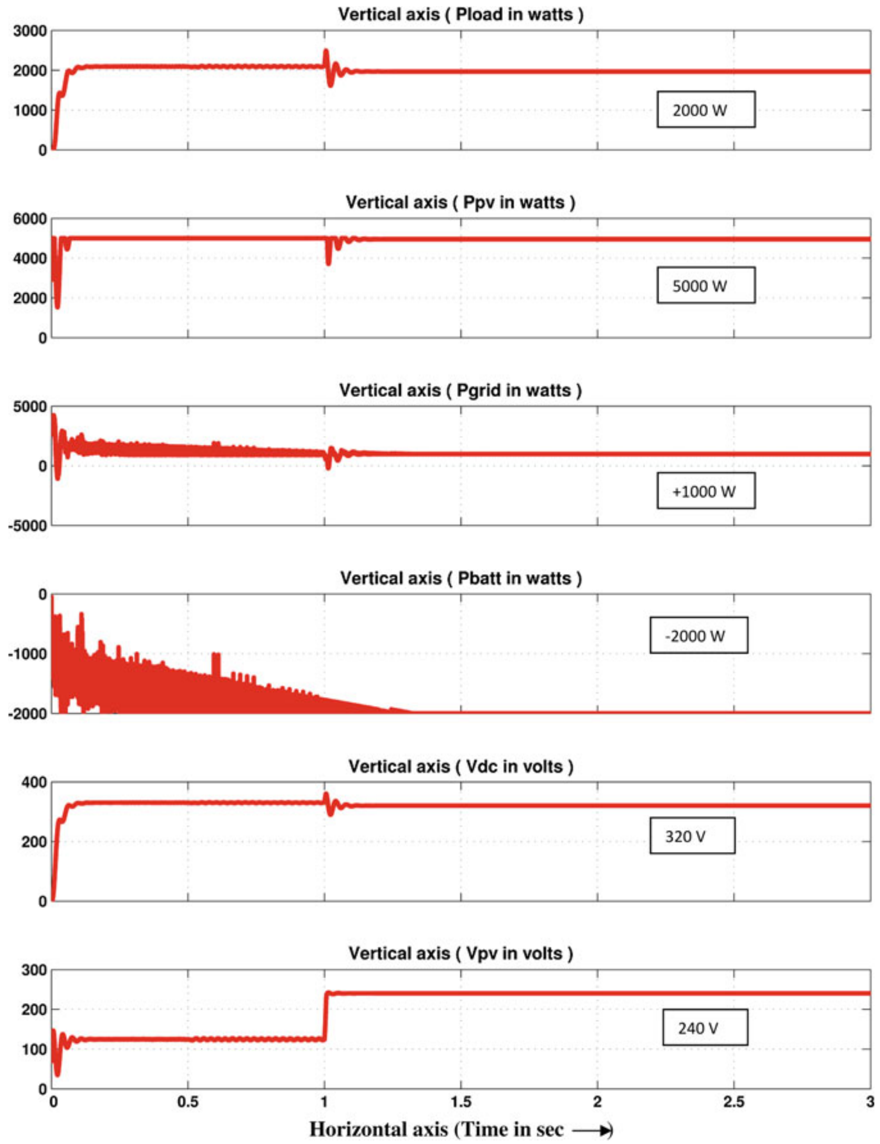

Fig. 64.7 Mode-I injecting power to grid

64.3.3 Mode III (Off-Grid)

Since P_{load} (6,100 W) > P_{pv} (5,000 W), additional power required by the load is supplied by battery operating in discharging mode with the assumption that battery is close to full charge. Power balance is managed by battery, so P_{batt} is 1,100 W and

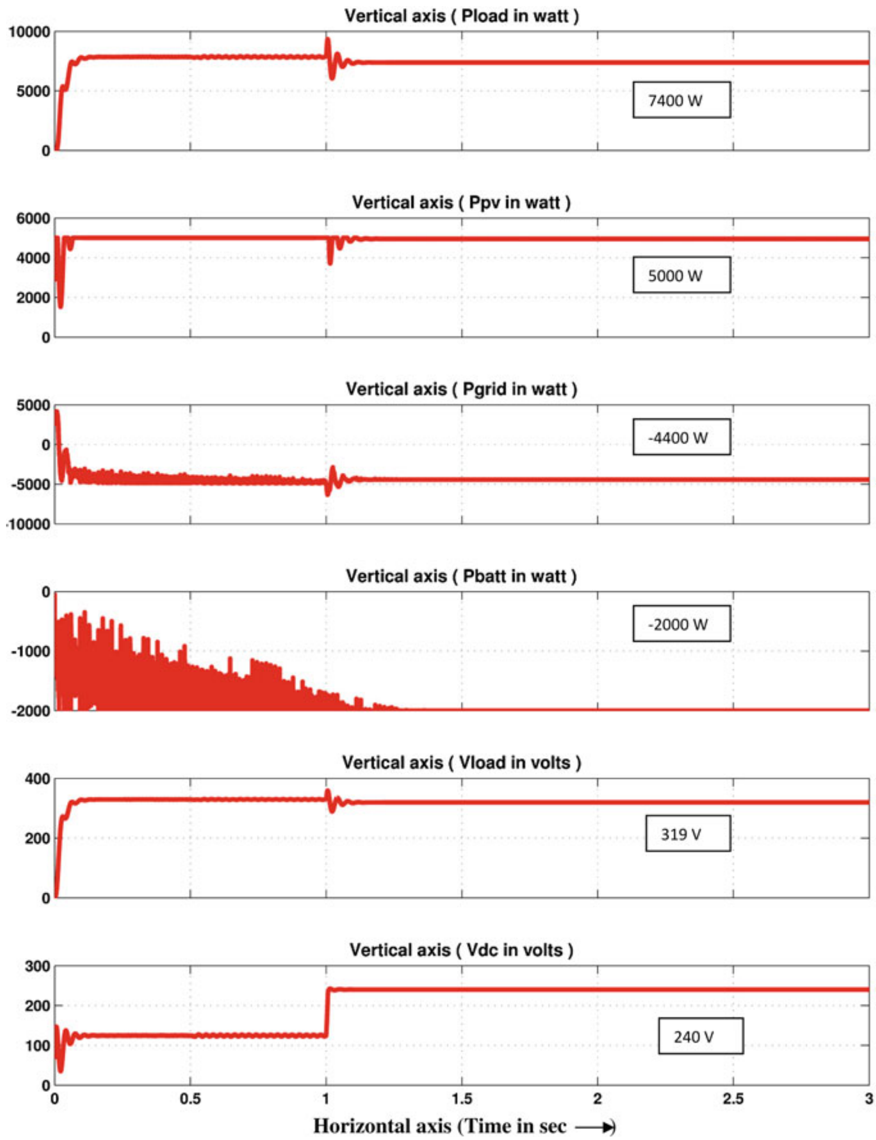

Fig. 64.8 Mode-II drawing power from grid

$P_{load} = P_{batt} + P_{pv}$ equation is satisfied. V_{pv} is maintained at 240 V and V_{dc} is maintained around 315 V. Positive sign of P_{batt} indicates the discharging power of battery (Fig. 64.9).

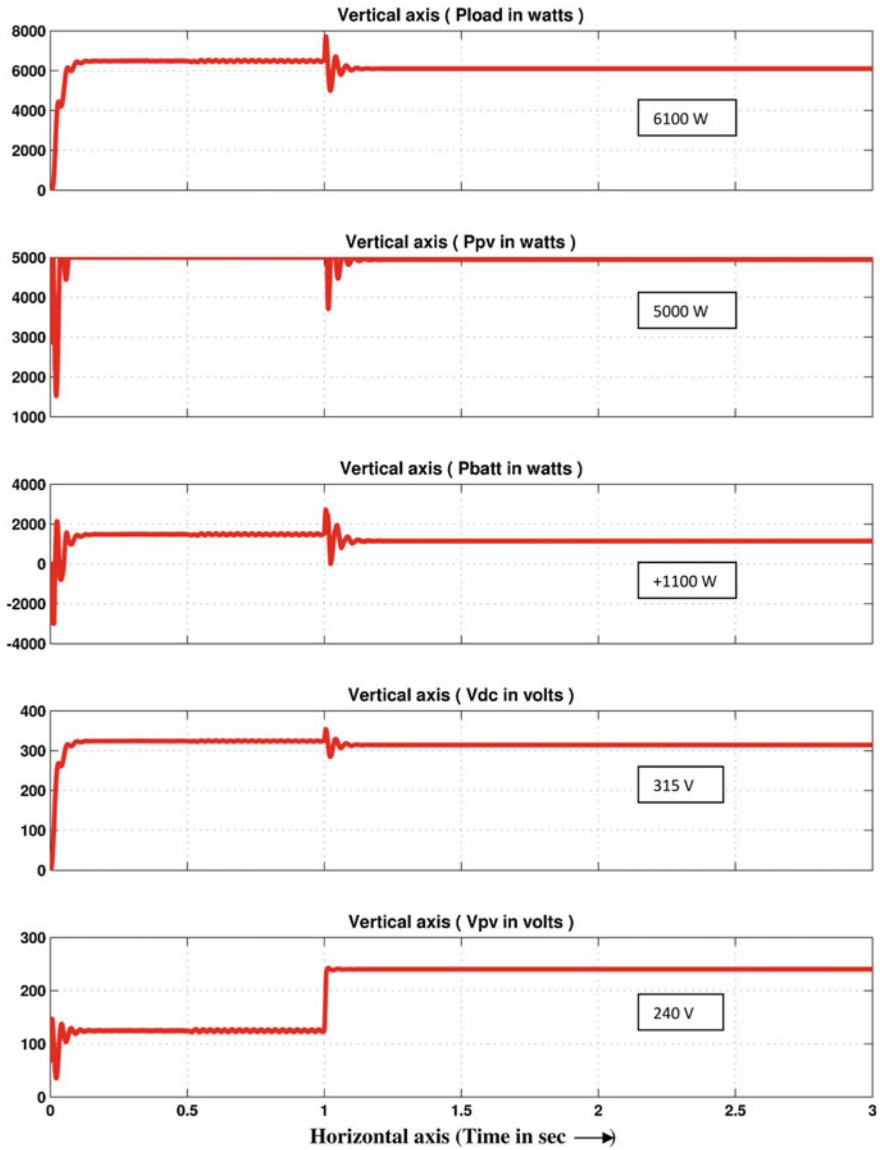

Fig. 64.9 Mode-III off-grid with battery discharging

64.3.4 Mode IV (Off-Grid)

Since P_{load} (3,500 W) < P_{pv} (5,000 W), so surplus power of PV is used for battery charging assuming that battery is partially charged. Power balance is managed by

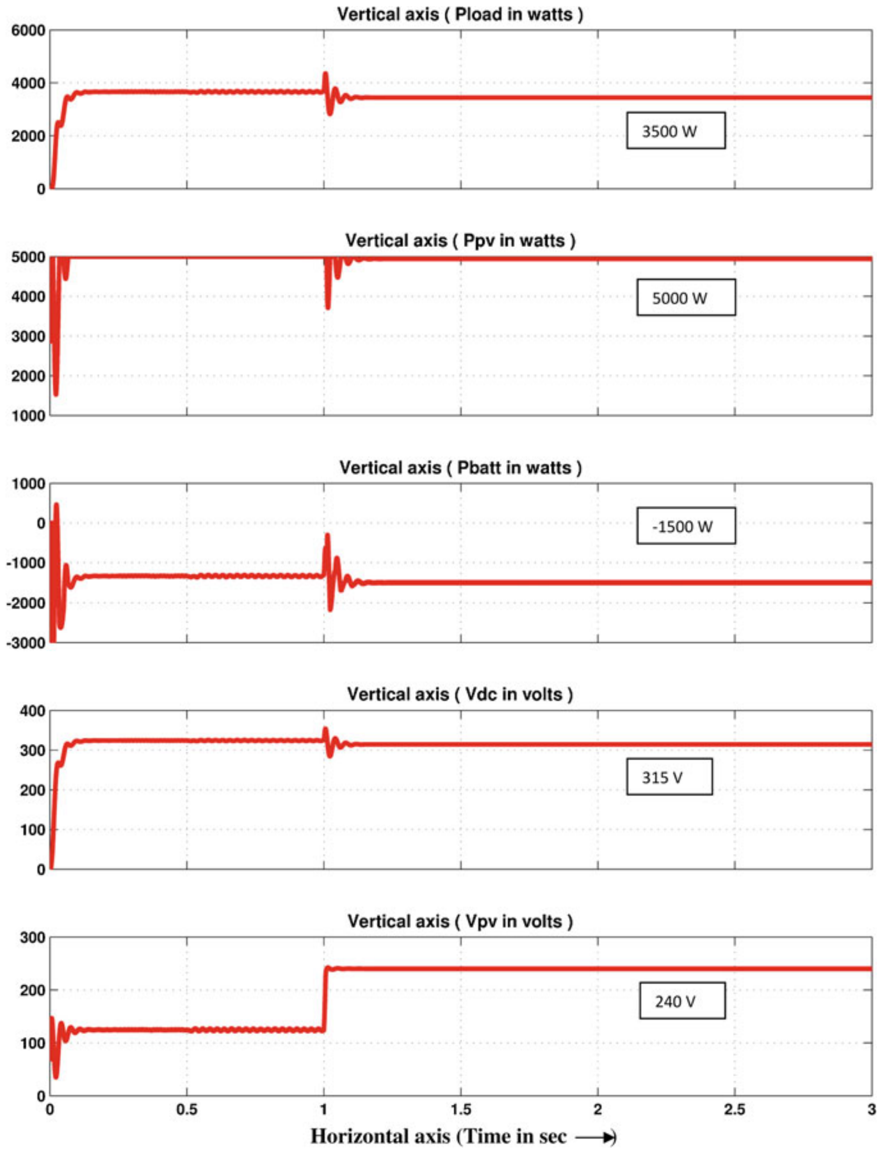

Fig. 64.10 Mode-IV off-grid with battery charging

battery so P_{batt} is −1,500 W and $P_{load} + P_{batt} = P_{pv}$ equation is satisfied. V_{pv} is maintained at 240 V and V_{dc} is maintained around 315 V. Negative sign of P_{batt} indicates the charging power of battery (Fig. 64.10).

64.4 Conclusion

From the simulation result it can be validated that the power management strategy of the designed composite model for a grid connected PV array and battery works for both on-grid as well as off-grid mode of operation maintaining constant DC voltage, achieving desired power sharing between the various sources and DC load with full utilization of PV power in all the four operational cases.

References

1. Shimakage T, Sumita J, Uchiyama N, Kato T, Suzuoki Y (2008) Supply and demand control of distributed generators in a microgrid. In: Proceedings of the 2008 IEEE telecommunications energy conference, pp 1–5
2. Lasseter RH, Paigi P (2004) Microgrid: a conceptual solution. In: Proceedings of the 2004 IEEE power electronics specialists conference, vol 6, pp 4285–4290
3. Rauschenbach HS (1980) Solar cell array design handbook. Van Nostrand Reinhold, New York
4. Lasnier F, Ang TG (1990) Photovoltaic engineering handbook. Adam Hilger, New York
5. Khouzam K, Koh CK, Ly C, Yong Ng P (1994) Simulation and real-time modelling of space photovoltaic systems. In: IEEE 1st World conference on photovoltaic energy conversion. Conference record of the 24th IEEE photovoltaic specialists conference, vol 2, pp 2038–2041
6. Esram T, Patrick L (2007) Comparison of photovoltaic array maximum power point tracking techniques. IEEE Trans Energy Convers 22(2):439–449
7. Bimbhra PS (2012) Power electronics, 4th edn. Khanna, New Delhi, pp 127–198
8. Mohan N, Undeland TM, Robbins WP (2010) Power electronics, converters, applications and design, 2nd edn. Wiley, New York
9. Samanta C, Dash S, Rayaguru NK (2014) Control scheme of PV-battery integrated in a DC/AC Micro Grid. ICREU-2014, Coimbatore, p 69

Chapter 65
Design and Comparative Analysis of Diode Clamped Multilevel Inverter for Eliminating Total Harmonics Using High Switching Frequency Techniques

P.K. Dhal and C. Christober Asir Rajan

Abstract This paper is purposed the total harmonic distortion in multilevel inverter. Conventional two level multilevel inverter using pulse width modulation generates harmonic which is very harmful in electric drives applications. Multilevel inverter technology has been developed to overcome in solid state switching device. So it can be applied in high power medium voltage energy control. The multilevel voltage source inverter is a unique topology allows them to reach high voltage with low harmonics without use of transformers. Novel control techniques are used in Diode Clamped Inverter with SPWM and SVM in Quasi three, five level operation. It is analyzed in MATLAB/SIMULINK and developed modulation techniques to reduce total harmonic distortion.

Keywords Multilevel inverter · Total harmonic distortion · SPWM and SVM

65.1 Introduction

Multilevel inverter plays important role in field of power sector and industries. The medium voltage motor drives and utility application are required medium and megawatt power. In the medium voltage grid, it is connected only one power semiconductor switch directly. As a result which multilevel power inverter structure has been introduced as an alternative in high power and medium voltage. So multilevel inverter is not only achieving high power rating but also enables the use of renewable energy sources. Renewable energy sources such as photovoltaic, wind and fuel cells can be easily interfaced to a multilevel inverter system for a high

P.K. Dhal (✉)
Department of EEE, Veltech Dr. RR and Dr. SR Technical University, Chennai, India
e-mail: pradyumna.dhal@rediffmail.com

C.C.A. Rajan
Department of EEE, Pondicherry Engineering College, Puducherry, India

C. Kamalakannan et al. (eds.), *Power Electronics and Renewable Energy Systems*,
Lecture Notes in Electrical Engineering 326, DOI 10.1007/978-81-322-2119-7_65

power application [1, 2]. However the elementary concept of a multilevel inverter is to achieve higher power which is used a series of power semiconductor switches with several lower voltage dc sources to perform the power conversion by synthesizing a staircase voltage waveform. The commutation of the power switches aggregate these multiple dc sources in order to achieve high voltage at the output. However the rated voltage of the power semiconductor switches depends only the rating of the dc voltage sources to which it is connected. The multilevel inverter have the following characteristics: (a) the level of inverters are easy to increase (b) when the number of levels are high, the harmonic content is low (c) there is no need to use filters (d) inverter efficiency is high because all devices are switched at the fundamental frequency (e) the control strategy is simple.

65.2 Multilevel Inverter Topology

A continuous increase energy demand is developed higher voltage and higher current power semiconductors to drive high power systems. The multilevel inverters are good solutions for power applications due to the fact they can achieve high power using medium power semiconductor technology. Multilevel inverters present great advantages compared with conventional two level inverters. So voltage source inverter consists of a turn-off device connected in anti-parallel with a diode which has lowest reverse leakage current with the anode of turn-off device connected to the positive side of DC side. In order to show the improved quality of the output voltages of a multilevel inverter, the output voltage of a single phase two-level inverter is compared to the three-level and seven level etc. the power inverter output voltage improves its quality as the number of levels increases and reducing the total harmonic distortion (THD) of the output wave forms [3, 4]. It has a great efforts trying to improve multilevel inverter performances such as the control simplification and the performance of different optimization algorithms in order to enhance the THD of the output signals, the balancing of the dc capacitor voltage and the ripple of the currents. The most common multilevel inverter topologies are the neutral-point clamped (NPC) inverter, flying capacitor (FC) inverter and cascaded H-bridge (CHB) inverter as shown in Fig. 65.1.

65.3 Diode-Clamped Multilevel Inverter

The multilevel inverter is commonly used as diode clamped multilevel inverter. The diode is used as the clamping device to clamp the dc bus voltage. So as to achieve steps in the output voltage. The main concept of this inverter is to use diodes to limit the power devices voltage stress. The voltage over each capacitor and each switch is V_{dc}. A n level inverter needs $(n - 1)$ voltage sources, $2(n - 1)$ switching devices and $(n-1)(n-2)$ diodes. The numbers of voltage levels are increased, the

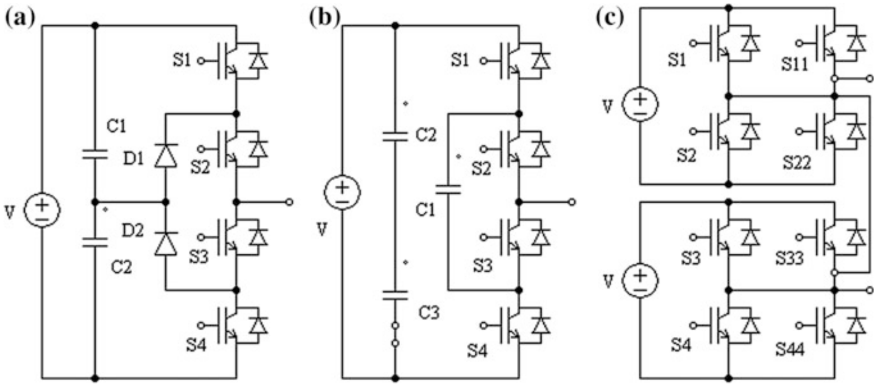

Fig. 65.1 Multilevel inverter topologies **a** DCMI **b** FCMI **c** MMCI

quality of the output voltage is improved and the voltage waveform becomes closer to sinusoidal wave form as shown in Fig. 65.2.

65.3.1 Five Level Diode-Clamped Multilevel Inverter

Figure 65.3 shows a five level diode clamped inverter in which the dc bus consists of four capacitors C_1, C_2, C_3, C_4 and dc bus voltage V_{dc}. The voltage across each capacitor is $\frac{V_{dc}}{4}$ and each device voltage stress is limited to one capacitor voltage level $\frac{V_{dc}}{4}$ through clamping diodes. The staircase voltage is synthesized from Fig. 65.2. The neutral point n is considered as the output phase voltage w.r.t 0 point. There are five switch combinations to synthesize the five level voltages across a and n. from the Fig. 65.3 (a) the voltage level $V_{an} = \frac{V_{dc}}{2}$, It is turned on all upper switches S_1 to S_4 (b)

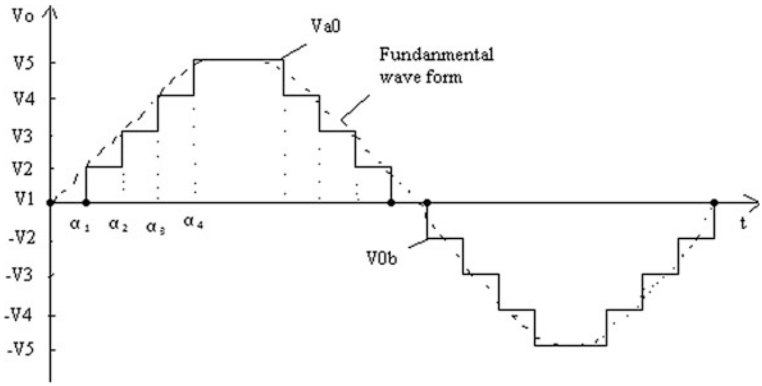

Fig. 65.2 Phase and fundamental voltage waveforms of a five level inverter

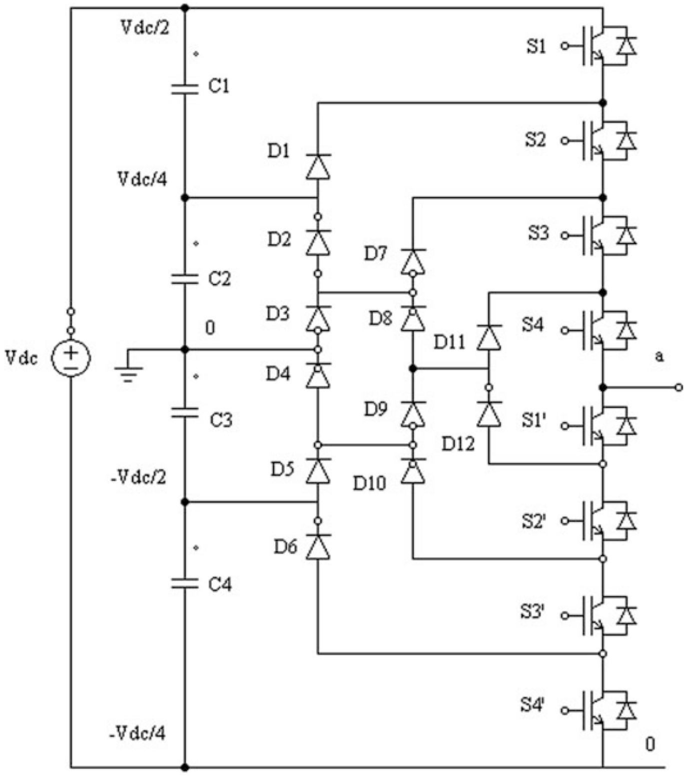

Fig. 65.3 Five level diode clamped multilevel inverter

the voltage level $V_{an} = \frac{V_{dc}}{4}$, it is turned on three upper switches S_2 to $S_4$and one lower switch $S_1^{'}$ (c) the voltage level $V_{an} = 0$, it is turned on two upper switches S_3, S_4 and two lower switches S_1' and S_2' (d) the voltage level $V_{an} = \frac{-V_{dc}}{4}$, it is turned one upper switch S_4 and three lower switches S_1' to S_3' (e) the voltage level $V_{an} = \frac{-V_{dc}}{2}$, it is turned on all lower switches S_1' to S_4'. In this Fig. 65.3 the complementary switch pairs exist in each phase. The four complementary pairs are $(S_1, S_1'), (S_2, S_2'), (S_3, S_3'), (S_4, S_4')$. Each active switching device is required to block a voltage level of $\frac{V_{dc}}{(K-1)}$ where k is the number of steps of the phase voltage with respect to the negative terminal of the inverter [5] (Table 65.1).

Each active switching device is required to block a voltage level of $\frac{V_{dc}}{(K-1)}$. So the clamping diodes have different voltage ratings for reverse voltage blocking. If each blocking diode voltage rating is the same as the active device rating, then the number of diodes are required foe each phase $(k-1)(k-2)$. This number is represented a quadratic increase in k. When k is sufficient high, the number of diodes are required to make the system impractical to implement.

Table 65.1 Switching states of five level inverter topology

Output voltage V_{a0}	Switching states							
	S_1	S_2	S_3	S_4	S_{11}	S_{22}	S_{33}	S_{44}
V_5	1	1	1	1	0	0	0	0
V_4	0	1	1	1	1	0	0	0
V_3	0	0	1	1	1	1	0	0
V_2	0	0	0	1	1	1	1	0
V_1	0	0	0	0	1	1	1	1

65.4 Control and Modulation Technique for Multilevel Inverter

In industrial applications, it is required to control the output voltage of inverters. It is necessary to cope with the variations of dc input voltage, to regulate inverters. So it is satisfied the constant volts and frequency control requirement. There are various techniques are required to vary the inverter gain. The output voltage is to incorporate PWM control within the inverters. So the modulation methods are used in multilevel inverters which can be classified according to switching frequency. The methods of work with high frequencies have many commutations for the power semiconductor device during one cycle of the output voltages. It is generated a staircase waveform. The popular method in industrial applications is the carrier based sinusoidal PWM (SPWM) that uses the phase shifting technique to reduce the harmonics in the load voltage [6, 7].

65.4.1 Sinusoidal Pulse Width Modulation (SPWM)

The sinusoidal pulse width modulation techniques have been developed to reduce the distortion in multilevel inverters. It is based on the classical SPWM with triangular carriers. The SPWM compares a high frequency triangular carrier with three sinusoidal reference signals. It is called as modulating signals to generate the gating signals. The smallest distortion is obtained when the carriers are shifted by an angle of $\theta = \frac{360^\circ}{N_c} = 120^\circ$. In common practice the multilevel inverter is injected a third harmonic in each cell to increase the output voltage. So the effective switching frequency of load voltage is three times switching frequency of each cell. It is determined by carrier signals. It reduces the switching losses. When it is used in diode clamped multilevel inverter with n number of voltage levels, $(n - 1)$ number of triangular carrier waves is used. These carrier waves have the same frequency. It is arranged on top of each other. It will produce maximum output voltage to minimum output voltage as shown in Fig. 65.3.

From Fig. 65.1 is analyzed that multilevel inverter can produce a quarter wave symmetric voltage waveform. It is synthesized by several DC voltages. By applying Fourier series analysis, the output voltage can be written as

$$V(t) = \sum_{n=1,3,5}^{\infty} \frac{4V_{dc}}{n\pi}[\cos(n\theta_1) + \cos(n\theta_2) + \cdots + \cos(n\theta_s)] \sin(n\omega t) \qquad (65.1)$$

where s is the number of DC sources and V_{DC} is the voltage of each DC level.

The switching angles must satisfy the condition $0 \prec \theta_1 \prec \theta_2 \prec \cdots \theta_s \prec \frac{\pi}{4}$.

It is to minimize harmonic distortion and to achieve adjustable amplitude of the fundamental component up to $(s-1)$ harmonic contents which can be removed from the voltage waveform [8].

65.4.2 Space Vector Modulation

The space vector modulation technique can be extended to all multilevel inverter. The vector diagrams are universal types and used in five level diode clamped multilevel inverter [9]. The adjacent three vectors can synthesize a desired voltage vector by computing the duty cycle $((S_j, S_{j+1} \text{ and } S_{j+2})$ for each vector.

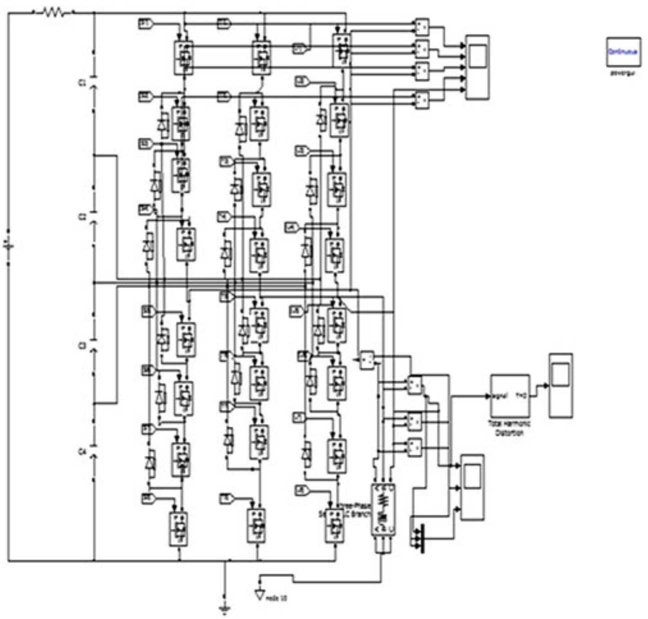

Fig. 65.4 Circuit diagram for SPWM operation of five level diode clamped inverter

$$V^{*} = \frac{(S_j V_j + S_{j+1} V_{j+1} + S_{j+2} V_{j+2})}{S} \tag{65.2}$$

The SVM methods have following advantages: good utilization of DC link voltage, low current ripple and ease hardware implementation by digital signal processor. When number of level increases, switching state are needed. So the selecting switching state increases dramatically as shown in Fig. 65.9 (Figs. 65.4, 65.5, 65.6, 65.7, 65.8, 65.10, 65.11, 65.12, 65.13, 65.14, 65.15, 65.16 and 65.17).

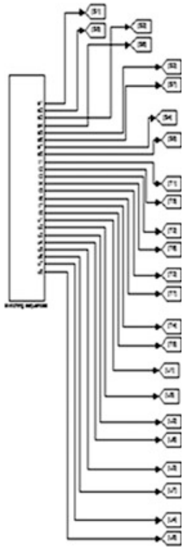

Fig. 65.5 Control circuit of diode clamped inverter for SPWM operation scheme

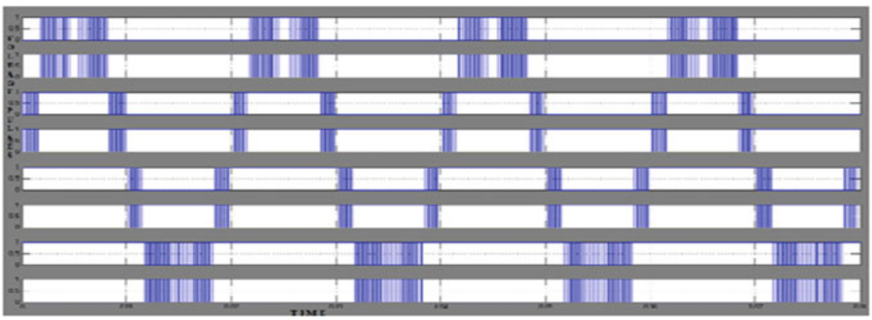

Fig. 65.6 Input pulses for a five level diode clamped inverter with SPWM

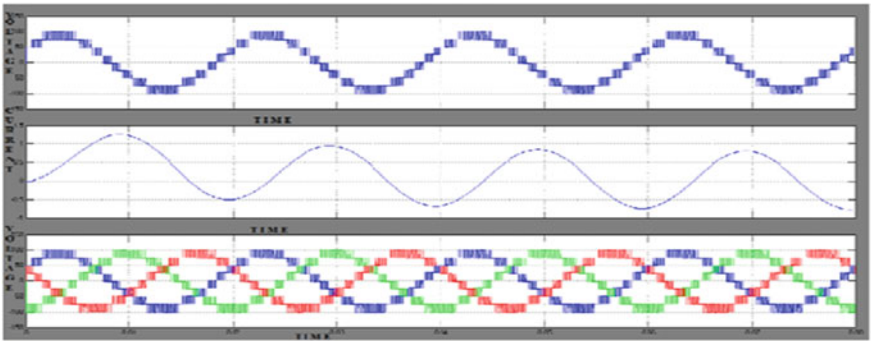

Fig. 65.7 Phase voltage, output current and output voltage of diode clamped inverter for SPWM

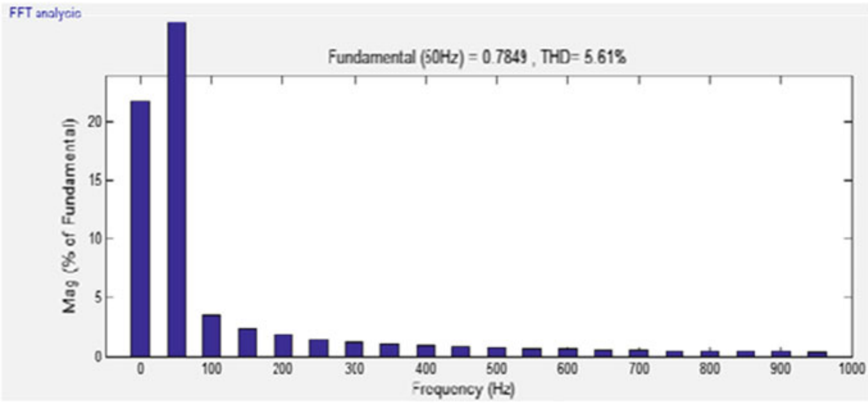

Fig. 65.8 THD spectrum for a five level diode clamped inverter in SPWM

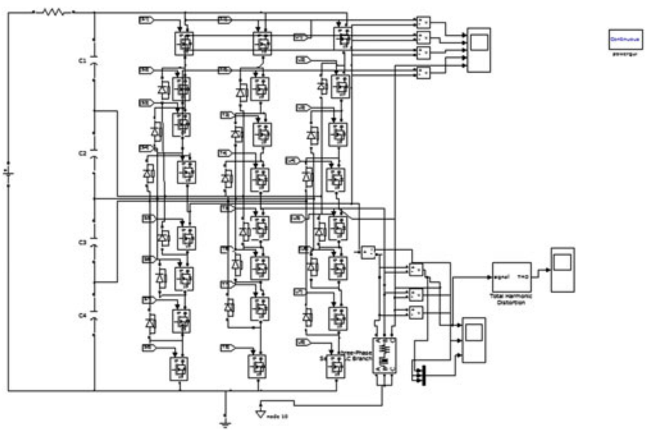

Fig. 65.9 Circuit diagram for SVM operation of five level diode clamped inverter

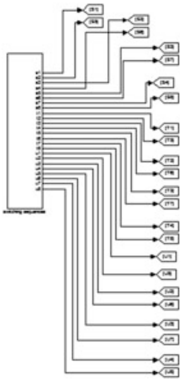

Fig. 65.10 Control circuit of diode clamped inverter for SVM operation scheme

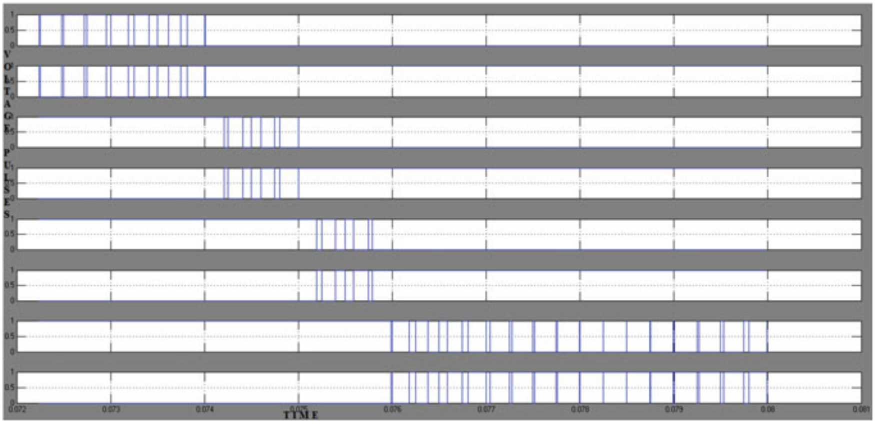

Fig. 65.11 Input pulses for diode clamped inverter for SVM

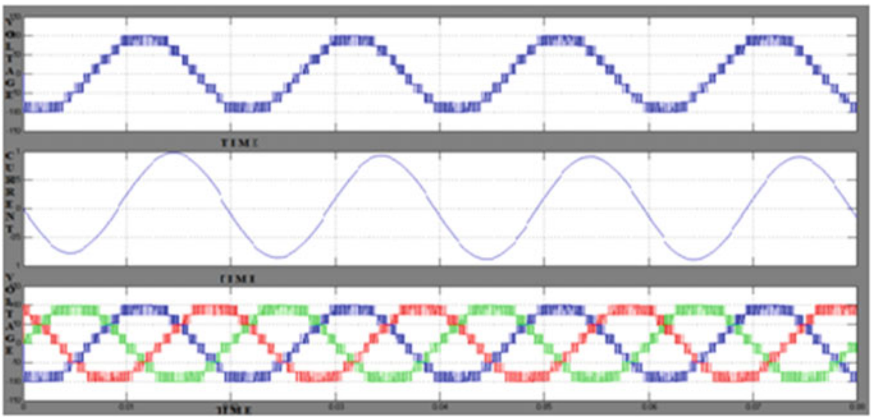

Fig. 65.12 Phase voltage, output current and output voltage of diode clamped inverter for SVM

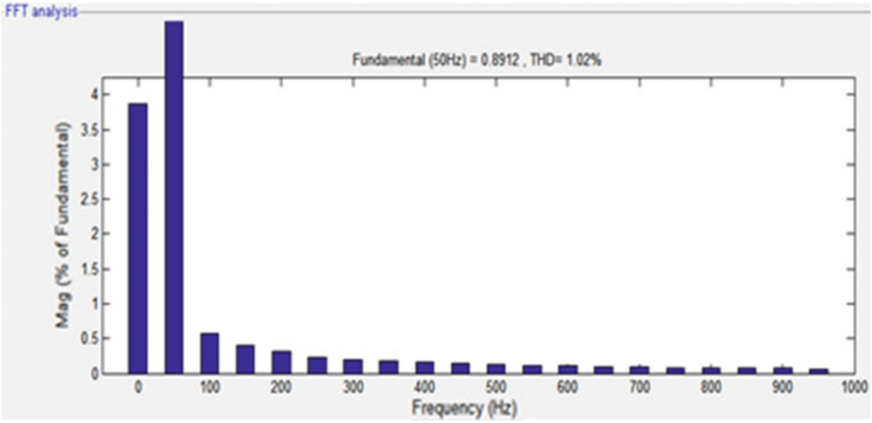

Fig. 65.13 THD spectrum for five level diode clamped inverter in SVM

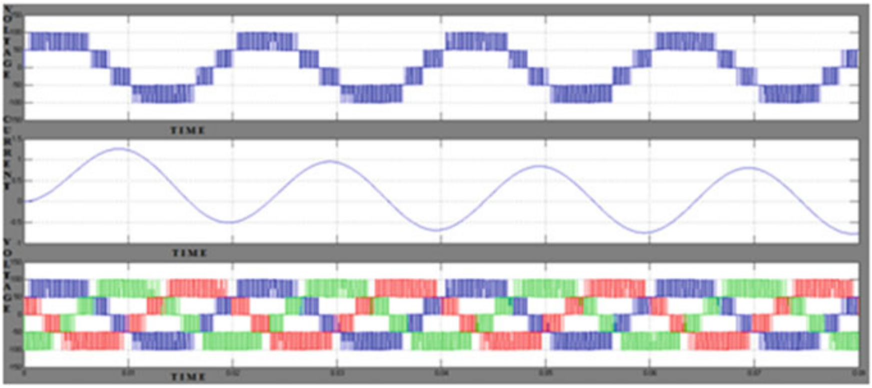

Fig. 65.14 Phase voltage, output current and output voltage in quasi three level using SPWM for diode clamped inverter

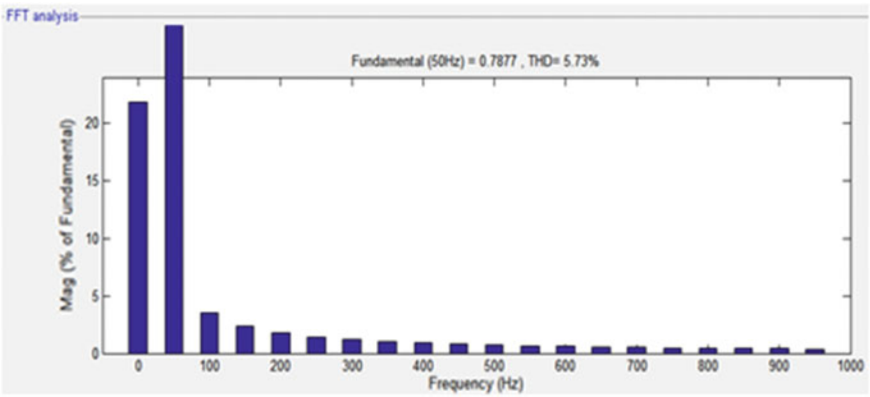

Fig. 65.15 THD spectrum for quasi three level operation using SPWM

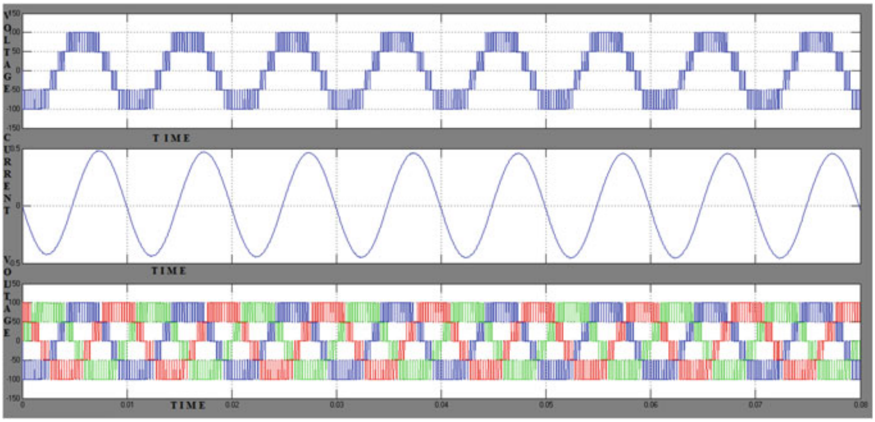

Fig. 65.16 Phase voltage, output current and output voltage in quasi three level using SVM for diode clamped inverter

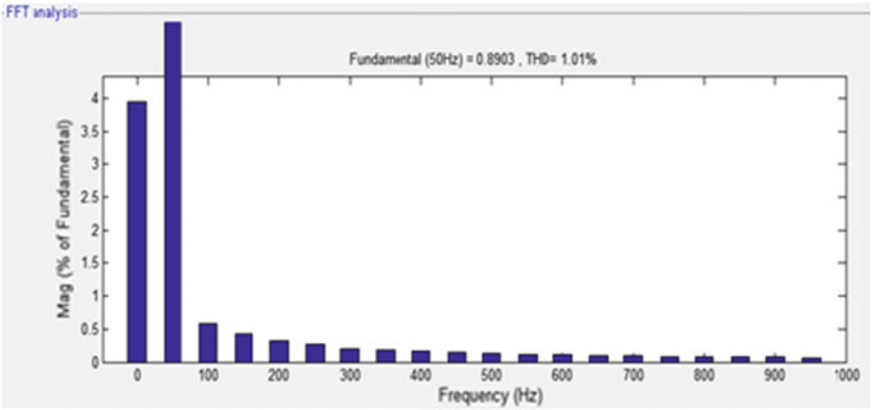

Fig. 65.17 THD spectrum for quasi three level operation using SVM

65.5 Quasi Level Operation Using SPWM and SVM

Figure 65.2 shows one phase of a five level diode clamped inverter. This diode clamped circuit ensures the voltage across the switching devices. It is clamped diodes which are limited to one capacitor voltage and eliminates series connection of clamping diodes [10]. In general diode clamped inverter is operated in quasi two-level mode, the dc link nodes are utilised to generate intermediate voltage levels in order to get a stepped between the voltages $\frac{+V_{dc}}{2}$ and $\frac{-V_{dc}}{2}$. The intermediate voltage levels are held for minimum dwell time. The step wave form approaches within each switching cycle. It allows the inverter switching devices to operate based on the principle of minimum switching losses. However the effective switching frequency per switch is the same as two level and three level. The three level diode clamped inverter is only possible when number of levels is odd. The advantages of quasi level operation is to improve the dc link voltage. It will avoid dc link capacitor voltage imbalanced associated with standard multilevel inverter [11]. The intermediate nodes of the dc link capacitors are utilised to generate intermediate voltage levels. These voltage levels are used to achieve smooth transition between voltage levels 0 to V_{dc}. The intermediate dc link nodes are used only for short durations. The energy is drawn from the dc link capacitors which is much smaller than with full multilevel operation. So the capacitor voltage balancing issues are reduced [12].

65.6 Simulation Results of Diode Clamped Multilevel Inverter

The experimental results are presented for different levels of diode clamped multilevel inverter (Table 65.2).

Table 65.2 Comparison table for diode clamped inverter for different techniques

Level of operation	Modulation techniques	% THD
Five level operation	SPWM	5.16
Five level operation	SVM	1.02
Quasi three level operation	SPWM	5.73
Quasi three level operation	SVM	1.01

65.7 Conclusion

The classical three techniques are proposed for five level diode clamped multilevel inverter. The main feature of the modulation technique lies in its ability to eliminate the total harmonic in the five level inverter output voltages. The design and analysis of the useful techniques, the mechanism of the THD with increase in level of inverter employing SPWM, SVM and Quasi three level are discussed. The quasi three levels are useful compared to other two techniques.

References

1. Kedareswari M (2013) Reduction of THD in diode clamped multilevel inverter employing SPWM technique. Int J Sci Res Publ 3(6):1–4
2. Shukla A, Ghosh A, Joshi A (2010) Flying-capacitor-based chopper circuit for DC capacitor voltage balancing in diode-clamped multilevel inverter. IEEE Trans Ind Electron 57:2249–2261
3. Farid B, Farid B (2009) A study of new techniques of controlled PWM inverters. Eur J Sci Res 32(1):77–87. ISSN 1450-216X
4. Srinivas S (2009) Uniform overlapped multi-carrier PWM for a six-level diode clamped inverter. In: World Academy of Science, Engineering and Technology 3:208–213
5. Fujita H, Yamashita N (2008) Performance of a diode-clamped linear amplifier. IEEE Trans Power Electron 23(2):824–831
6. Renge MM, Suryawanshi HM (2008) Five-level diode clamped inverter to eliminate common mode voltage and reduce dv/dt in medium voltage rating induction motor drives. IEEE Trans Power Electron 23(4):1598–1607
7. Bouhali O, Francois B, Berkouk EM, Saudemont C (2007) DC link capacitor voltage balancing in a three-phase diode clamped inverter controlled by a direct space vector of line-to-line voltages. IEEE Trans Power Electron 22(5):1636–1648
8. Brükner T, Holmes DG (2005) Optimal pulse-width modulation for three-level inverters. IEEE Trans Power Electron 20(1):82–89
9. Chiasson JN, Tolbert LM, McKenzie KJ, Du Z (2004) A complete solution to the harmonic elimination problem. IEEE Trans Power Electron 19(2):491–499
10. Wang J, Wei R, Ge Q, Li Y (2003) The harmonic selection elimination of multilevel converters. IEEE Int Conf Electr Mach Syst 1:419–422
11. Seo JH, Choi CH, Hyun DS (2001) A new simplified space-vector PWM method for three-level inverters. IEEE Trans Power Electron 16(4):545–550
12. Yuan X, Barbi I (2000) Fundamentals of a New Diode Clamping Multilevel Inverter. IEEE Trans on Power Electron 15(4):711–718

Chapter 66
PID Control of SAPF for Elimination of Harmonics in Power System Based on DQ Reference Frame Theory

Pradeep Katta, Arun, D. Atul Kumar Mishra and H. Vignesh

Abstract Active Power Filters are widely used in power quality applications such as harmonic elimination. Reduction in the cost of signal processors and power electronic semiconductor devices has increased the market for active power filters (APF). Other advantages of APF are ease of design and control operation, compactness and less power consumption etc. The paper utilizes the Synchronous Reference Frame Theory to generate reference current for operating the Voltage Source Convertor (VSC) of a Shunt Active Power Filter (SAPF). This method is based upon the performance of a Proportional-Integral-Derivative (PID), to achieve a better control action of SAPF. The reference signal thus generated is transformed from the stationary a-b-c frame to the rotating 0-d-q frame, using the Reference Frame Transformation. The PID controller controls the reference signal in 0-d-q rotating frame to obtain the reference signal as required for the Pulse Width Modulation.

Keywords Active power filters (APF) · Voltage source convertor (VSC) · Proportional-integral-derivative (PID)

66.1 Introduction

Harmonic pollution due to extensive usage of non-linear loads has become a matter of serious concern and with the increase of power semiconductor rectifiers and cycloconverters in industrial applications and transmission/distribution systems. Due to a finite supply impedance, the harmonic currents from non-linear loads results in voltage distortion at the point of common coupling [1]. Harmonic filtering can be achieved by either passive filters or active power filters. Passive filters were

P. Katta (✉) · Arun · D. Atul Kumar Mishra · H. Vignesh
EEE Department, Vel Tech High Tech Dr. Rangarajan Dr. Sakunthala Engineering College, Chennai 600062, Tamil Nadu, India
e-mail: pradeep.2048@gmail.com

C. Kamalakannan et al. (eds.), *Power Electronics and Renewable Energy Systems*,
Lecture Notes in Electrical Engineering 326, DOI 10.1007/978-81-322-2119-7_66

conventionally used for reducing power system harmonics. A proposed alternative is active power filter, adequate enough to mitigate power system harmonics as well as compensation of reactive power [2]. Passive filters consisting of high/low/band pass tuned LC have been traditionally used for power factor improvement and for absorption of power system harmonics, because of their simplicity and low cost. A tuned LC circuit/filter should exhibit lower impedance at the tuned harmonic frequency as compared to the supply frequency, so that most of the harmonic current, which is at the harmonic frequency is filtered by the LC filter. In theory, a passive filters filtering characteristics is determined by the ratio of impedances of the supply and the passive filter. Hence, it is a difficult task for a passive filter installed near a harmonic producing load that is connected to a stiff ac supply, to satisfy the above mentioned design criteria. Current harmonics elimination, reactive power compensation and improvement of voltage regulation are the some important functions of active power filters for the enhancement of power quality [3]. However, the passive power filters have the following limitations:

- The passive filter may get overloaded due to the utility supply side background voltage distortion. In worst case, it may fall into a series resonance with the impedance of the supply.
- At a particular frequency, the filter may fall into a parallel resonance with supply impedance, due to which harmonic current is amplified.

Active filters are classified into shunt and series. They have undergone serious researches in the field of reactive power compensation, harmonics and/or flicker, negative-sequence etc. in industrial as well as domestic power systems since their basic working principles were proposed during the 1970s. However, during that time, there were almost nil advances in the area of active filters except for the laboratory testing stage as the circuit technology at that time was too poor to implement those compensation principles in practice [1]. Recent progress and advancement in the voltage/current rating as well as the switching frequency of power semiconductor devices such as GTO thyristors and IGBTs has encouraged the interest in the study of APFs with the goal of practical applications [4]. Sophisticated PWM convertor technology, along with the "pq-theory", has made them to flourish in the commercial market stage [5–7].

66.2 Converter for Shunt APF

Voltage Source Converters operating at relatively high speed are used in Active Power Filters to generate power signal, which is then used for nullifying lower order harmonic waves present in the power system. With the Shunt Active Power Filter (SAPF), shown in Fig 66.1a crucial step involved is the generation of the reference signal which is used to produce gating signal/pulses for the VSC. As compared to the Current Source Converters, the Voltage Source PWM Converter are of higher efficiency, lower cost, and lesser physical size. The advancement and

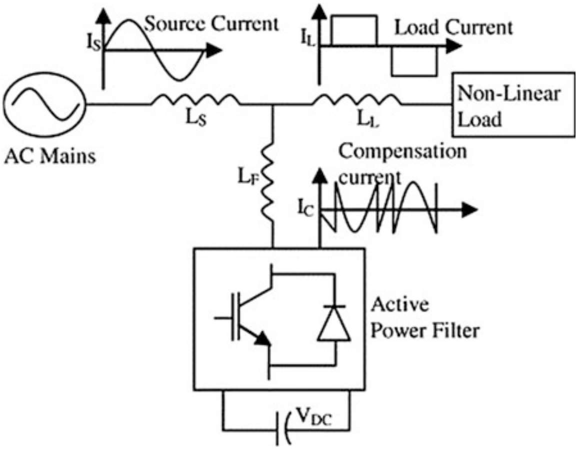

Fig. 66.1 Shunt active power filter

accessibility of high frequency power semiconductor switches like the IGBTs also have a preference for VSC because of the freewheeling diode that is connected in anti-parallel with IGBT. Further the switching stress problems in the Voltage Source Converters are very less in comparison with those in the Current Source Converter [2].

66.3 Reference Plane Transformation

The term Reference frame transformation implies to the transformation of a-b-c to d-q-0 coordinate system. Coordinate transformation from the three- phase stationary a-b-c coordinate system to the rotating d-q-0 coordinate system is shown in Fig. 66.2. Here a-b-c is initially converted to alpha-beta coordinates and then the alpha-beta coordinated to d-q-0. Two transformation matrices namely the Clarks Transformation and the Parks Transformation are employed for this purpose. These transformation matrices are depicted below in Eq. 66.1 [2, 8].

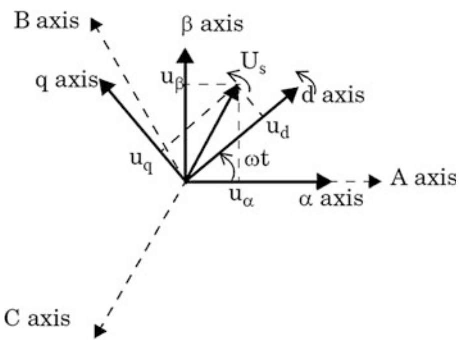

Fig. 66.2 Reference frame transformation

$$x_{dq0} = Kx_{abc} = \sqrt{\frac{2}{3}} \begin{bmatrix} \cos\theta & \cos(\theta - 2\pi/3) & \cos(\theta + 2\pi/3) \\ -\sin\theta & -\sin(\theta - \frac{2\pi}{3}) & -\sin(\theta + \frac{2\pi}{3}) \\ 1/\sqrt{2} & 1/\sqrt{2} & 1/\sqrt{2} \end{bmatrix} \begin{bmatrix} x_a \\ x_b \\ x_c \end{bmatrix} \quad (66.1)$$

In synchronous reference frame PID based controller, integrators are used to eliminate the steady state error of the DC components of the 0-d-q coordinates of the reference signals. In accordance to the 0-d-q frame theory, the current harmonics are represented as DC components in their corresponding reference frame and the integrators eliminate the steady state error of each harmonic component [5].

The reference signals are initially converted from a-b-c rotating frame to 0-α-β stationery frame using the Clarks Transformation, and then to 0-d-q rotating frame by using the Park transformation. The PID controller eliminates the steady state error, and helps achieve the controlled reference signal, as required. The algorithm is carried a step forward further, where inverse Park and Clark transformation are applied to the voltage reference signal in 0-d-q rotating frame and alpha-beta frame respectively to obtain back the a-b-c stationery frame, the reference signal for generating the Pulse Width Modulation (PWM).

66.4 System Design

66.4.1 Reference Voltage Generation

The harmonic components present in the mains current is calculated/extracted by using the Synchronous reference frame method. Three phase supply current and voltage vectors are transformed into the q (quadrature) and d (direct) frames rotating at fundamental frequency ω1 by implementing the Clark and Park transformations. By this, the fundamental frequency component of the main current gets converted to a DC signal and all the harmonic components which still remains as AC signals keeps on rotating with respect to the reference frame [9]. A second order high pass filter of 20 Hz cut-off frequency is used to extract the Harmonic current components. The Harmonic components so extracted are then converted into harmonic current components in a-b-c frames, by applying the inverse Clark and Park transformations. To obtain a voltage reference for each phase, each harmonic component is then amplified by a gain factor K [3].

Moreover, an additional feed forward control loop has been used for the elimination of 5th harmonic current component as the feedback gain K is limited to only certain values, due to the stability problems of the system. The 250 Hz components of the load current (5 times fundamental frequency) are used to generate the reference voltages in the proposed feed forward control.

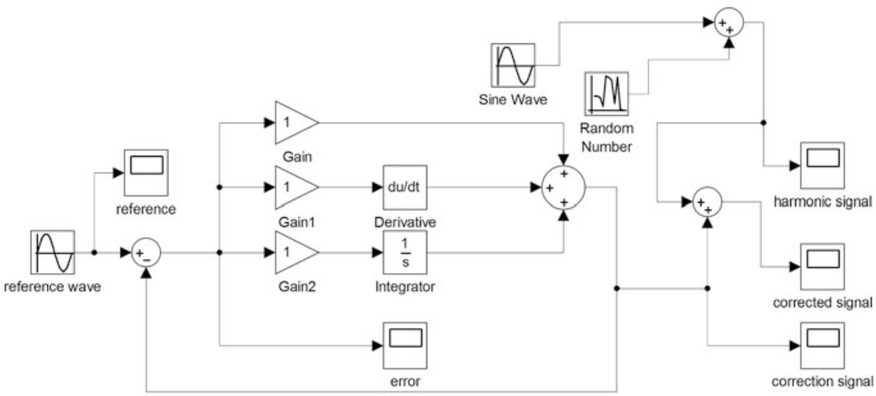

Fig. 66.3 Simulink model for PID controller

66.4.2 Modulation Method

The modulation method employed is the Sinusoidal Pulse Width Modulation (SPWM) method. The sinusoidal PWM gating signals for the semiconductor switches are obtained by comparing the voltage references (Va*, Vb*, Vc*) obtained from the feedback loop, feed forward loop and the DC link voltage with a triangular carrier wave of 12.5 kHz frequency [3].

66.5 PID Control

The PID feedback control block for demonstrating the function of SAPF action of Harmonic suppression and its response is shown in Figs. 66.3 and 66.4.

66.6 Simulink Model and Simulation Results

Simulation of the Shunt Active Power Filter is done and observations are shown as various graphical responses. The block diagram of shunt APF in Simulink is shown Fig. 66.5 as well as the Gate pulse for the Voltage Source Converter in Simulink model is shown in Fig. 66.6.

Below is the response of PID controlled SAPF is shown in the Figs. 66.7 and 66.8. The diagram in Fig. 66.7 represents the supply current variation with time and

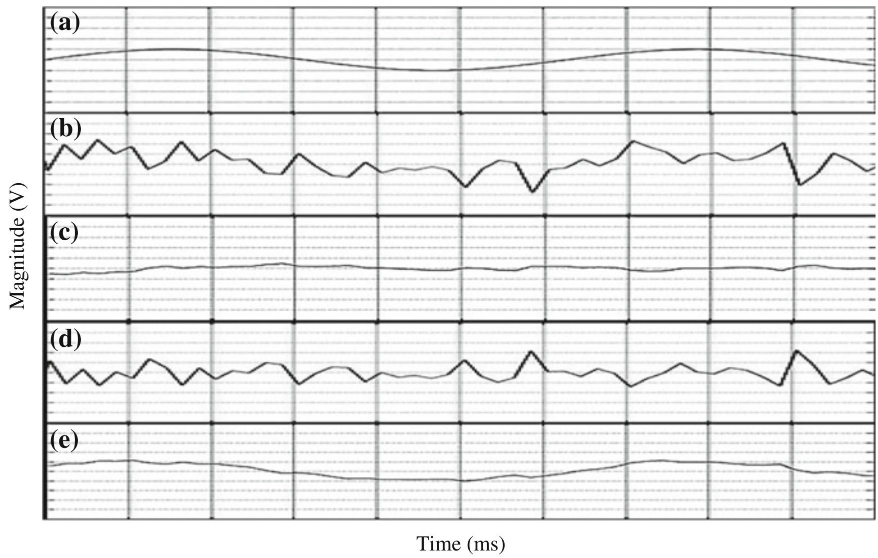

Fig. 66.4 PID response for correcting a harmonic wave. **a** Reference signal, **b** wave with harmonics, **c** error signal, **d** correction signal, **e** wave with harmonics suppressed

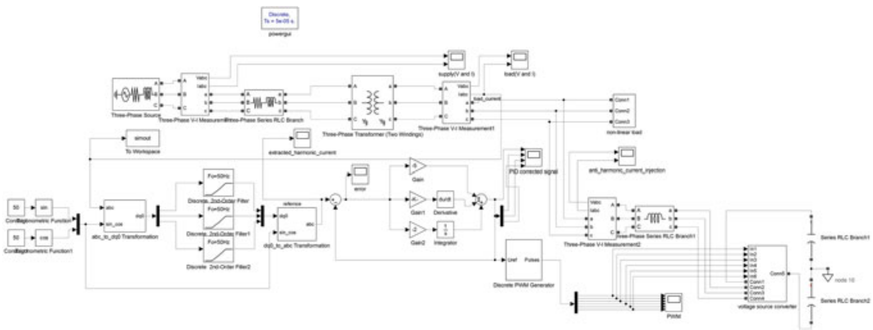

Fig. 66.5 Shunt APF simulink model

THD of various harmonic order without PID control. The diagram in Fig. 66.8 represents the supply current variation with time and THD of various harmonic order with PID control. It can be seen clearly that the fifth order harmonic which is more prevalent is suppressed.

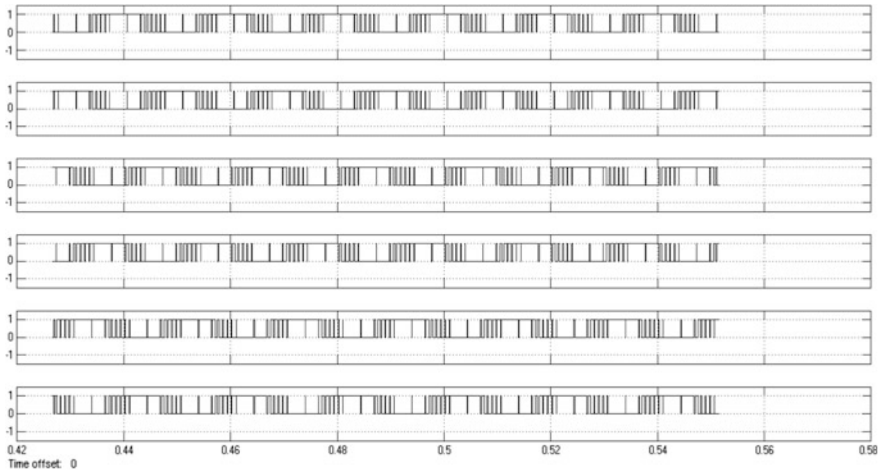

Fig. 66.6 Gating pulses for the voltage source converter in simulink model

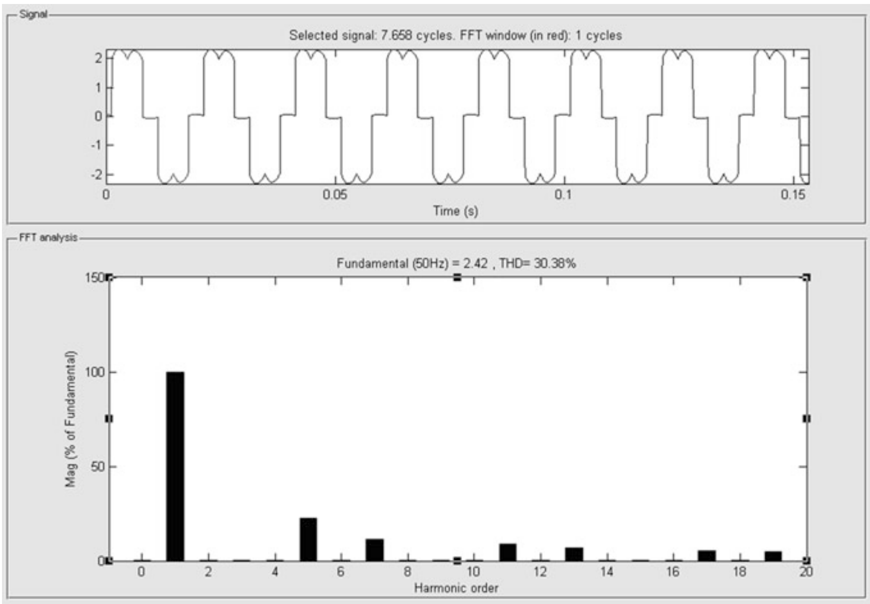

Fig. 66.7 Supply current and harmonic order bar chart without compensation

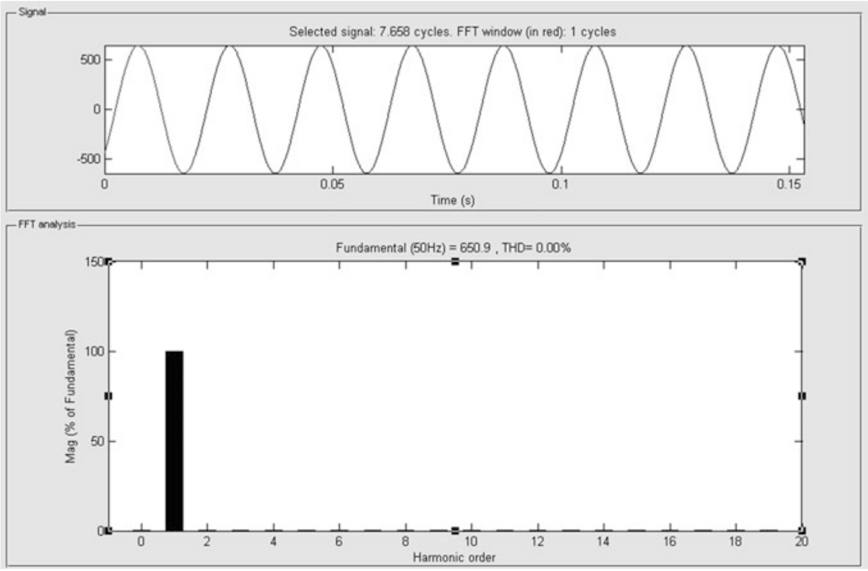

Fig. 66.8 Supply current and harmonic order bar chart with compensation

66.7 Conclusion

This paper has implemented the PID (Proportional Integral and Derivative) control of SAPF for harmonic suppression in Power system due to non-linear loads. The performance of the proposed system for the generation of reference current for controlling the Shunt Active Power Filter was verified using Simulation Model with the help of MATLAB SIMULINK software. This method was found to be more effective in active filtering of harmonics than the conventional PI (proportional Integral).

References

1. Akagi H, Fujita H (1995) A new power line conditioner for harmonic compensation in power systems. IEEE Trans Power Deliv 10(3):1570–1575
2. Sunitha M, Kartheek BN (2013) Elimination of harmonics using active power filter based on DQ reference frame theory. Int J Eng Trends Technol (IJETT) 4(4):781–785
3. Ucak O, Kocabas I, Terciyanli A (2008) Design and implementation of a shunt active power filter with reduced DC link voltage. http://www.emo.org.tr/ekler/815a62bc723a1c2_ek.pdf
4. Bose BK (1992) Evaluation of modern power semiconductor devices and future trends of converters. IEEE Trans Ind Appl, 28(2)
5. Akagi H, Nabae A, Atoh S (1986) Control strategy of active power filters using multiple voltage-source PWM converters. IEEE Trans Ind Appl IA-22(3):460–465
6. Kawahira H, Nakamura T, Nakazawa S (1983) Active power filters. IEEE/PES Winter Meeting, 1977, A77026-8. pp 625–630, 1984. IEEJ IPEC-Tokyo, pp 981–992

7. Takeda M, Ikeda K, Tominaga Y (1987) Harmonic current compensation with active filter. IEEE/IAS Ann Meet 1:808–815
8. Pottker FP, Ivo B (2000) Single-phase active power filters for distributed power factor correction. PESC
9. Gu HJ, Gyu HC (1998) New active power filter with simple low cost structure without tuned filters. 29th annual IEEE power electronics specialists conference, vol 1, pp 217–222

Chapter 67
Power Quality Improvement in Distribution System Using Unified Power Quality Conditioner

D. Rajasekaran, Subhransu Sekhar Dash, C. Subramani, Arun Bhaskar Mayilvaganan and Yarralinganagari Venkatesh

Abstract The major power quality issues are voltage sag, voltage swell and voltage harmonics in distribution system. These power quality issues are solved by custom power conditioning devices such as Dynamic Voltage Restorer (DVR), Distributed Static Compensator (DSTATCOM) and Unified Power Quality Conditioner (UPQC). This paper presents the ability of Unified Power Quality Conditioner to mitigate voltage sag, voltage swell and voltage harmonics in distribution system. UPQC is modeled in MATLAB_SIMULINK environment with Fuzzy Logic (FL), Neural Network (NN) controllers. The performances of UPQC with two controllers are compared.

Keywords UPQC · Fuzzy logic · Neural network · THD · Voltage sag

67.1 Introduction

Voltage sag, voltage swell and voltage harmonics are the most important power quality problem. Sensitive equipments used in industries and domestic are not tolerating these power quality issues [1, 2]. UPQC is a combination of series and shunt active power filters (APF) connected to a common DC link voltage as shown in Fig. 67.1. UPQC is modeled either with voltage-source inverter or current source

D. Rajasekaran (✉)
Department of EEE, R.M.D. Engineering College, Chennai, Tamil Nadu, India
e-mail: drajasekaran73@gmail.com

S.S. Dash · C. Subramani · Y. Venkatesh
Department of Electrical and Electronics Engineering,
SRM University, Chennai, Tamil Nadu, India
e-mail: munu_2kdash@yahoo.com

A.B. Mayilvaganan
Department of EEE, Velammal Engineering College, Chennai, Tamil Nadu, India

C. Kamalakannan et al. (eds.), *Power Electronics and Renewable Energy Systems*,
Lecture Notes in Electrical Engineering 326, DOI 10.1007/978-81-322-2119-7_67

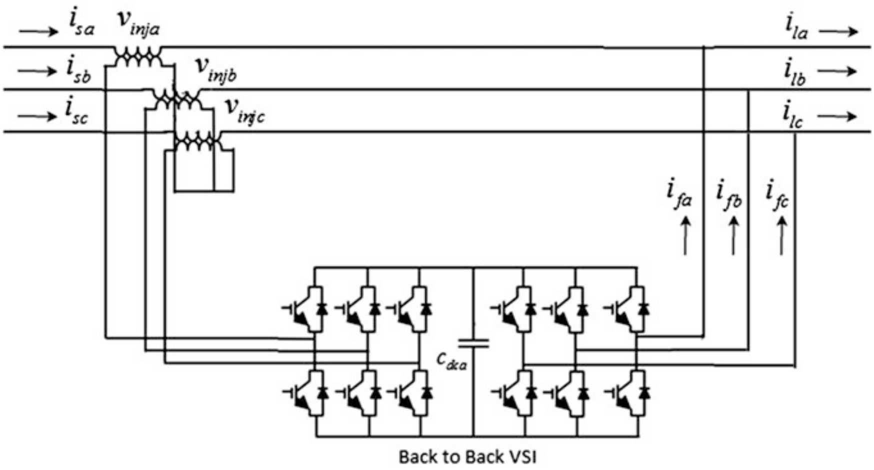

Fig. 67.1 Block diagram of UPQC

inverter [4]. In this paper UPQC is modeled by using voltage source inverters (VSIs). To make input current sinusoidal, shunt APF inject a compensating harmonic current and the series APF inject a compensating voltage to make load voltage sinusoidal [5]. This paper investigates the ability of UPQC with FL, and NN to mitigate voltage sag, swell and harmonics. UPQC with two controllers are modeled in MATLAB-SIMULINK environment. The performances of UPQC with two controllers are compared.

67.2 Distribution System Under Study with UPQC

Figure 67.2 shows distribution system under study with UPQC. The UPQC is connected in-between the source and load, to protect the load from voltage sag, swell and harmonics. Voltage sag, swell and harmonics are realized using RL load, RC load and Rectifier type load respectively. Two different controllers such as FL and NN are used for UPQC to mitigate the above mentioned issues. Each controller is discussed in detail as follows.

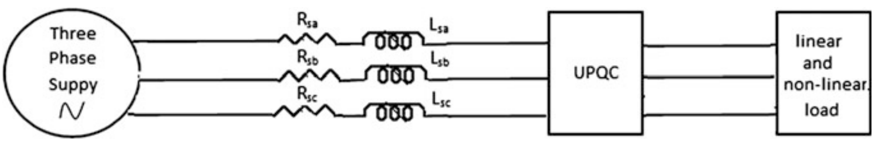

Fig. 67.2 Distribution system under study with UPQC

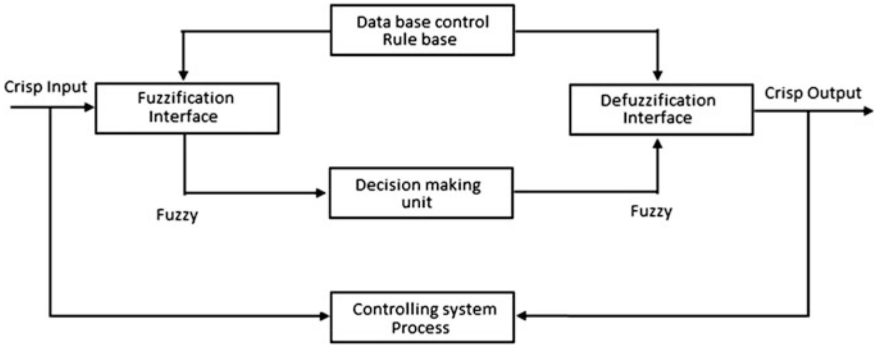

Fig. 67.3 Fuzzy logic controller

67.2.1 The Fuzzy Logic Controller

Figure 67.3 shows the block diagram of FL controller [6]. Fuzzy rules are framed by expert experience or knowledge database [3]. The fuzzy rule base is shown in Table 67.1 [7].

67.2.2 The Neural Network Controller

NN controller consists of three neuron layers. The three layers are input layer, the hidden layer and the output layer. The output from NN is received by comparator and finally the output from comparator is applied to PWM generator to trigger VSI as shown in Fig. 67.4.

67.3 Simulation Results and Discussion

67.3.1 System Without UPQC

Initially for 0–0.05 s the load voltage is not find any issues such as sag, swell and harmonics. At 0.05 s RL and rectifier type load is connected which leads to voltage

Table 67.1 Fuzzy rule Base

E/ΔE	NB	NM	NS	Z	PS	PM	PB
NB	NB	NB	NB	NB	NM	NS	Z
NM	NB	NB	NB	NM	NS	Z	PS
NS	NB	NB	NM	NS	Z	PS	PM
Z	NB	NM	NS	Z	PS	PM	PB
PS	NM	NS	Z	PS	PM	PB	PB
PM	NS	Z	PS	PM	PB	PB	PB
PB	Z	PS	PM	PB	PB	PB	PB

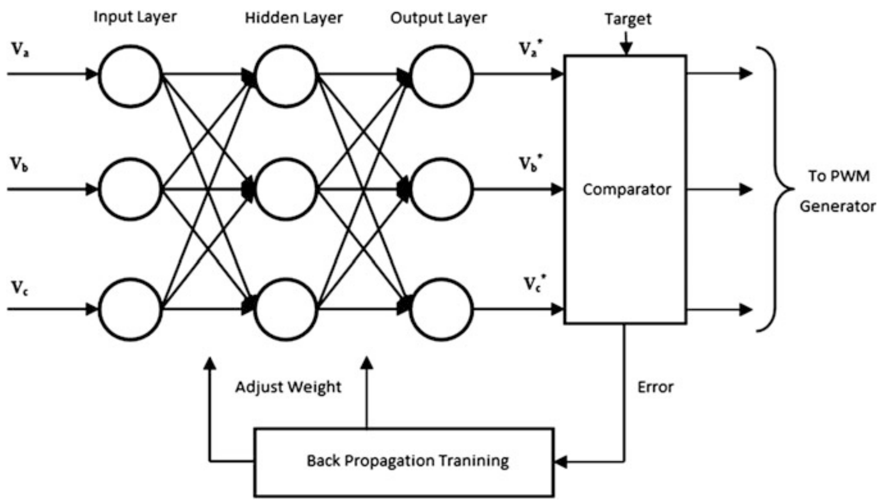

Fig. 67.4 Neural network controller

sag. When load is removed suddenly at 0.05 s from system, the system voltage rise i.e., voltage swell occurs. Figures 67.5, 67.6 and 67.7 shows source voltage, load voltage with sag and load voltage with swell respectively. The voltage sag and voltage swell occurs from 0.05 to 0.15 s.

Figures 67.8, 67.9 and 67.10 shows FFT analysis of source voltage, load voltage with sag and load voltage with swell respectively. The THD values of source voltage, voltage sag and voltage swell are 0.04, 43.21 and 26.08 % respectively. The THD value of system without UPQC is given in Table 67.2.

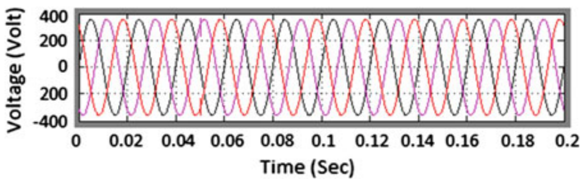

Fig. 67.5 Source voltage

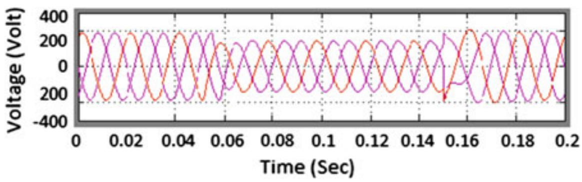

Fig. 67.6 Load voltage with sag

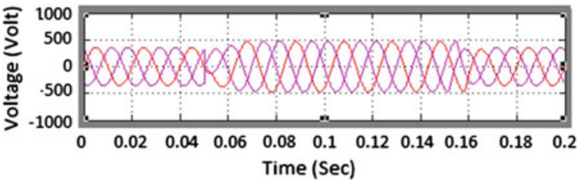

Fig. 67.7 Load voltage with swell

Fig. 67.8 FFT analysis source voltage

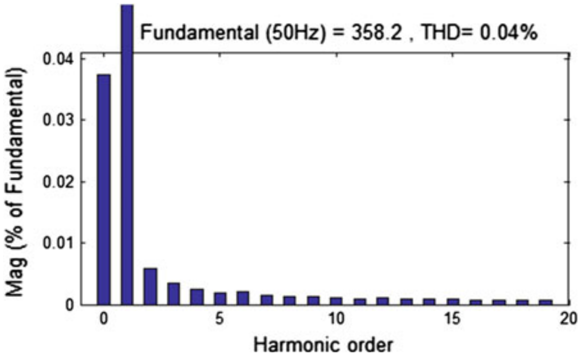

Fig. 67.9 FFT analysis of load voltage with sag

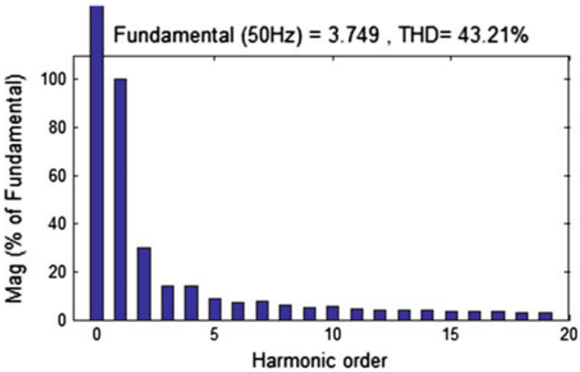

Fig. 67.10 FFT analysis of load voltage with swell

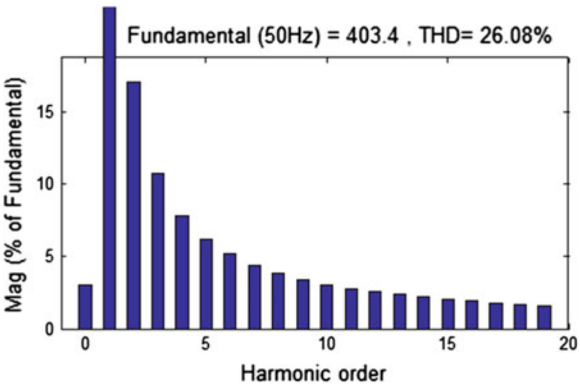

67.3.2 Voltage Sag, Voltage Swell and Harmonics Mitigation by UPQC with Fuzzy Logic Controller

Figures 67.11 and 67.12 shows load voltage after mitigation for voltage sag and voltage swell respectively by UPQC with FL controller. FFT analyses of mitigated voltages are shown in Figs. 67.13 and 67.14. The THD values of mitigated load voltage for voltage sag and voltage swell are 0.62 and 0.33 % respectively. The THD values of load voltage without and with mitigation by UPQC with FL controller are given in Table 67.3.

Table 67.2 THD values of the system without UPQC

THD	
Without UPQC	
Load voltage with sag	Load voltage with swell
43.21 %	26.08 %

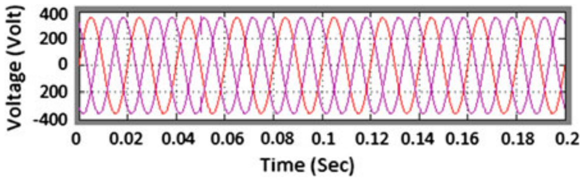

Fig. 67.11 Load voltage after sag mitigation by UPQC with FL controller

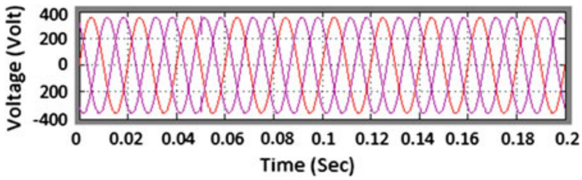

Fig. 67.12 Load voltage after swell mitigation by UPQC with FL controller

Fig. 67.13 FFT analysis of load voltage after sag mitigation by UPQC with FL controller

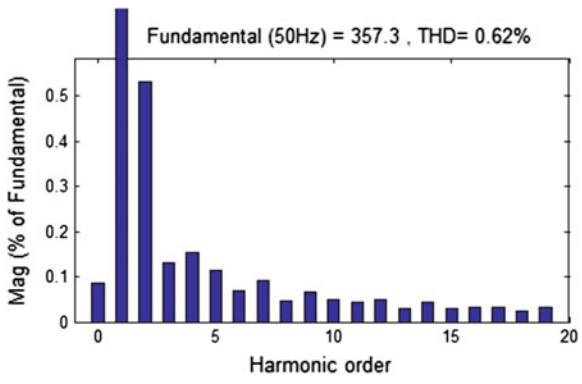

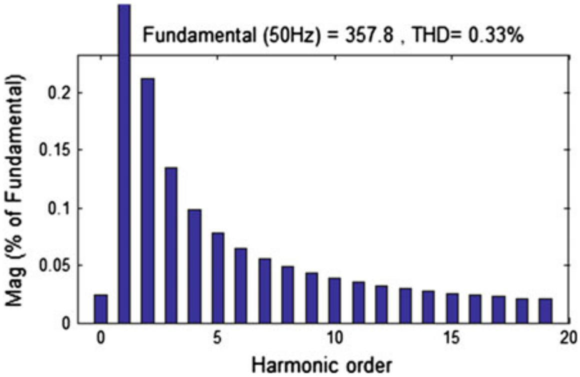

Fig. 67.14 FFT analysis of load voltage after swell mitigation by UPQC with FL controller

Table 67.3 THD values of load voltage without and with mitigation by UPQC with FL controller

THD			
Without UPQC		With UPQC	
Load Voltage with sag	Load voltage with swell	Sag mitigated load voltage	Swell mitigated load voltage
43.21 %	26.08 %	0.62 %	0.33 %

67.3.3 Voltage Sag, Voltage Swell and Harmonics Mitigation by UPQC with Neural Network Controller

Figures 67.15 and 67.16 shows load voltage after mitigation for voltage sag and voltage swell respectively by UPQC with NN controller. FFT analyses of mitigated voltages are shown in Figs. 67.17 and 67.18. The THD values of mitigated load voltage for voltage sag and voltage swell are 0.45 and 0.29 % respectively. The THD values of load voltage without and with mitigation by UPQC with NN controller are given in Table 67.4.

67.3.4 Comparison of UPQC with Fuzzy Logic and Neural Network Controllers

Performance of UPQC with FL and NN controllers for voltage sag and voltage swell mitigation and THD are compared and given in Table 67.5. The simulation results show UPQC with NN controller effectively mitigates voltage sag, voltage swell and voltage harmonics in distribution system.

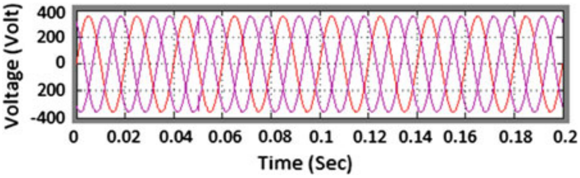

Fig. 67.15 Load voltage after sag mitigation by UPQC with NN controller

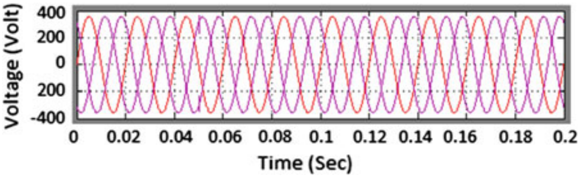

Fig. 67.16 Load voltage after swell mitigation by UPQC with NN controller

Fig. 67.17 FFT analysis of load voltage after sag mitigation by UPQC with NN controller

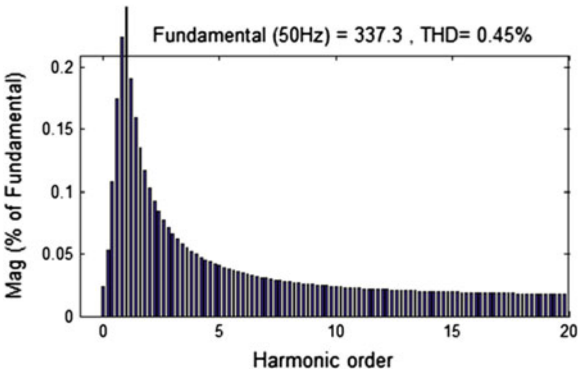

Fig. 67.18 FFT analysis of load voltage after swell mitigation by UPQC with NN controller

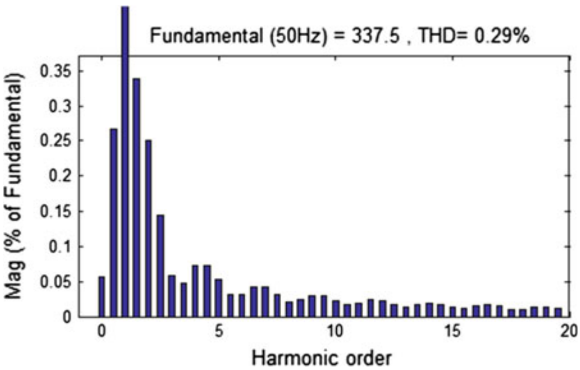

Table 67.4 THD values of load voltage without and with mitigation by UPQC with NN controller

THD			
Without UPQC		With UPQC	
Load voltage with sag	Load voltage with swell	Sag mitigated load voltage	Swell mitigated load voltage
43.21 %	26.08 %	0.45 %	0.29 %

Table 67.5 Comparison of UPQC with FL and NN controller

Factor	FL controller (%)	NN controller (%)
Load voltage THD after sag mitigation	0.62	0.45
Load voltage THD after swell mitigation	0.33	0.29
Load voltage after mitigation	377	375
Error in load voltage after mitigation	0.03	0.05

67.4 Conclusion

Unified Power Quality Conditioner (UPQC) is used to mitigate voltage sag, swell and harmonics in distribution system. Two different controllers such as Fuzzy Logic and Neural Network (NN) are used. UPQC is simulated with FL and NN in MATLAB-SIMULINK environment. The performances of UPQC with two controllers are compared (Table 67.5). The simulation results show UPQC with Neuro Network (NN) controller effectively mitigates voltage sag, swell and harmonics in distribution system.

References

1. Dugan RC, MacGranaghan MF, Beaty HW (2003) Electrical power systems quality, 2nd edn. McGraw-Hill, New York. ISBN 10:007138622X, pp 528
2. Singh GK (2009) Power system harmonics research: a survey. Eur Trans Elect Power 19:151–172. doi:10.1002/etep.201
3. Saad S, Zellouma L (2009) Fuzzy logic controller for three-level shunt active filter compensating harmonics and reactive power. Electr Power Syst Res 79:1337–41. http://dx.doi.org/10.1016/j.epsr.2009.04.003
4. Pal Y, Swarup A, Singh B (2010) Performance of UPQC for power quality improvement. IEEE
5. Ravi Kumar KS, Sastry SVAR (2011) Application of PI, fuzzy logic and ANN in improvement of power quality using unified power quality conditioner. IJCSET 1(5):214–217
6. Mikkili S, Panda AK (2011) RTDS hardware implementation and simulation of 3-phase, 4-wire SHAF for mitigation of current harmonics with p–q and I_d–I_q control strategies using fuzzy logic controller. Int J Emerg Electr Power Syst 12(5). http://dx.doi.org/10.2202/1553-779X.2758 (Article 5)
7. Mikkili S, Panda AK (2012) Real-time implementation of PI and fuzzy logic controllers based shunt active filter control strategies for power quality improvement. Electr Power Energy Syst 43:1114–1126

Chapter 68
Hybrid Power System Based Load Sharing and Maintaining the DC Voltage in UPS System

R. Jaiganesh and S. Sharmila

Abstract Power interruption is the major problem in many sectors, to overcome this issue Uninterruptible Power Supply is used. During emergency situation it is a reliable source. During backup time batteries are more efficient when supplied to low load. In case of connecting to heavy load, Pulsated power is extracted. This greatly reduces the lifetime of the battery and alters the battery cycle due to frequent charging and discharging. To overcome this issue ultra capacitors are used. The proposed method has a variable speed wind turbine using a permanent magnet synchronous generator (PMSG), integrated with the grid system. This combination will be reducing the wind turbine fluctuation and voltage variation. The design is simulated by using MATLAB Simulink. Results show that this method efficiently eliminates the battery stress and improve the power quality.

Keywords Permanent magnet synchronous generator (PMSG) · Load sharing · Uninterruptible power supply · Grid system

68.1 Introduction

In recent years, power variations and frequent power out have been the main reason behind developing Uninterruptible Power Supply (UPS) system [1, 2]. In many sectors, high reliability power supply is required for heavy loads. Uninterruptible Power Supplies (UPS) improve the power quality and guarantee the reliability of backup power [3, 4].

R. Jaiganesh (✉) · S. Sharmila
Department of Electrical and Electronics Engineering, SNS College of Engineering, Coimbatore, Tamil Nadu, India
e-mail: Jaiganesh2406@gmail.com

S. Sharmila
e-mail: sharmilaurfriend@gmail.com

C. Kamalakannan et al. (eds.), *Power Electronics and Renewable Energy Systems*,
Lecture Notes in Electrical Engineering 326, DOI 10.1007/978-81-322-2119-7_68

However, there are disadvantages associated with batteries such as limited charge/discharge cycles. Moreover, extracting pulsed power instead of average power from the battery can alter the cycle and decrease the lifespan.

In this paper, ultracapacitor (UC) is used to overcome the disadvantage. Ultracapacitors represent one of the newest innovations in the field of electrical energy storage and will find their place in many applications where energy storage can help to the smoothing of strong and short time power interruption of a distribution network.

An ultracapacitor [5] is a double-layer electrochemical capacitor which can store thousand times more energy than an ordinary capacitor. It has both the characteristics of batteries and conventional capacitors and has more energy density than a battery. Moreover, they have almost negligible losses and long lifespan. They possess a large number of charge and discharge cycles compared to few thousand cycles for lead-acid batteries and can supply much higher currents than batteries.

Batteries are mostly efficient when used to supply low power levels. Ultracapacitor leakage rate and series resistance are quite small. The power sharing between ultracapacitors, and batteries is a promising solution for improving system performance due to the dynamic behavior of the SCs and their long life. Renewable Energy Systems (RES) are also an independent power producer.

Bi-directional converters are used in connecting energy storage systems like ultracapacitors and battery banks to wind power systems. Permanent-magnet synchronous generator is coupled with the wind turbine, with this interfacing RES based output is controlled, load shared and maintained in the UPS system. An applications of ultracapacitor and battery tie is used in pure battery powered electric vehicle, hybrid electric vehicle [6] and in escalators. Simulation results are provided for maintaining the load and sharing the DC voltage to UPS system and reducing the stress in battery to show the effectiveness of the proposed system.

68.2 Proposed Topology

The proposed topology is shown in Fig. 68.1. The rectifier is connected to the wind generator, it converts AC to DC and its output is variable. The load is connected to the grid, the battery and supercapacitor tie is connected to bi-directional converter and it is controlled by PI controller. Normally when there is a demand power and wind generator doesn't meet the demand, the battery acts as a backup. But when heavy load acts, the battery backup power is greatly reduced and it's under heavy stress. To overcome this issue UC is used, it reduces the high drawing power from the battery at start by instantly giving the demanded power. The UC is charged by battery when UC gets discharged.

In the proposed method, permanent magnet synchronous generator is coupled with wind generator, which is the renewable energy source. The output is filtered by

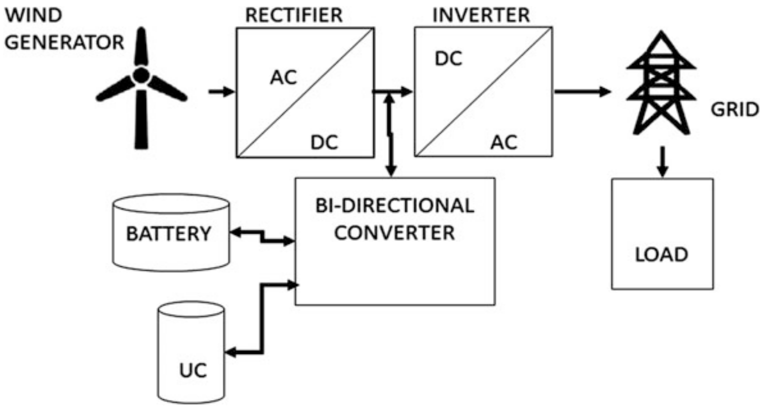

Fig. 68.1 Topology of the UPS system

RLC filter, they are rectified and DC voltage is given to the bidirectional converter. The battery and ultracapacitor is integrated with bi-directional converter and IGBT inverter. Overall it is controlled by the current control system and DC voltage to UPS system is maintained, load sharing between heavy load and low load is controlled and reduces the stress in battery. The switching between heavy load and low load is controlled using circuit breaker. When the demand is high and heavy load acts, the ultracapacitor produces the pulsated power for a short period of time, then the battery gives the backup power until the interruption is rectified. Then supercapacitor gets charged from the battery. The effectiveness of the proposed system is clearly analyzed.

68.3 System Description

68.3.1 Permanent Magnet Synchronous Generator

Permanent magnet synchronous generator (PMSG) belongs to Horizontal-axis wind turbines (HAWT) and they are the major commercial energy source [7]. Excitation to the generator is provided by excitation field instead of coil. The mechanical output energy of turbine like steam, hydro, gas and wind energy are converted into electrical power using this generator for the grid. The induced voltage, frequency (f) in the rotor and armature conductors, is directly proportional to the number of permanent magnet stator poles (p), so they are called synchronous generators. The constant of proportionality is $\frac{P}{120}$ and P is magnetic poles and RPM is the revolutions per minute of the rotor (or angular speed) $f = \frac{RPM}{120}P$.

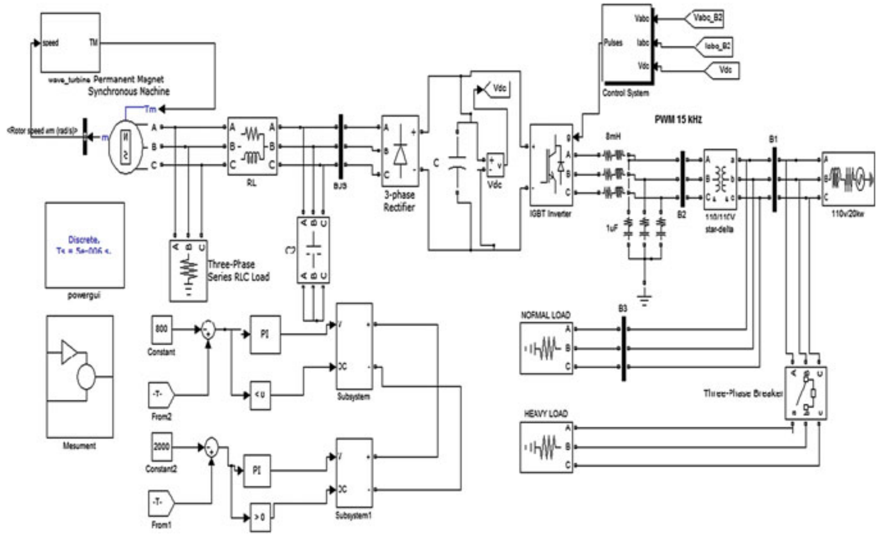

Fig. 68.2 MATLAB simulation for RES based control of load sharing and maintaining the dc voltage to UPS system

68.3.2 *Uninterruptible Power Supply*

The integrated ultracapacitor and battery is the Uninterruptible Power Supply used in the proposed system shown in Fig. 68.2.

The ultracapacitor produces the necessary pulsated power when heavy load acts, this increases the lifetime of the battery and its stress are greatly reduced. The ultracapacitor works purely on physical phenomena rather than through a chemical reaction and a highly reversible process, which result in high power life cycle, shelf life and maintenance issues are low [6]. Modeling of ultracapacitor and battery is same while the control system slightly varies (Figs. 68.3 and 68.4).

68.4 Performance Analysis of Proposed System

The proposed system is designed with MATLAB, Simulink environment. Efficient control of the proposed circuit is analyzed by using a circuit breaker for load controlling when heavy load acts the ultracapacitor gives the necessary pulsated power to the load. The simulation parameters are showed in Table 68.1.

The output generated by Permanent magnet synchronous generator is shown in Fig. 68.5. Individual analysis of the battery and supercapacitor is compared in Figs. 68.6 and 68.7.

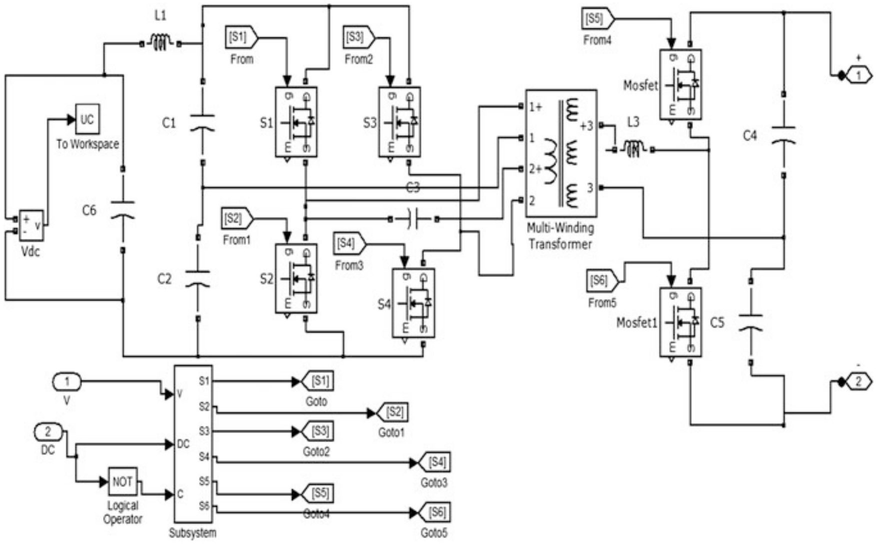

Fig. 68.3 Modelling block of ultracapacitor with bi-directional converter

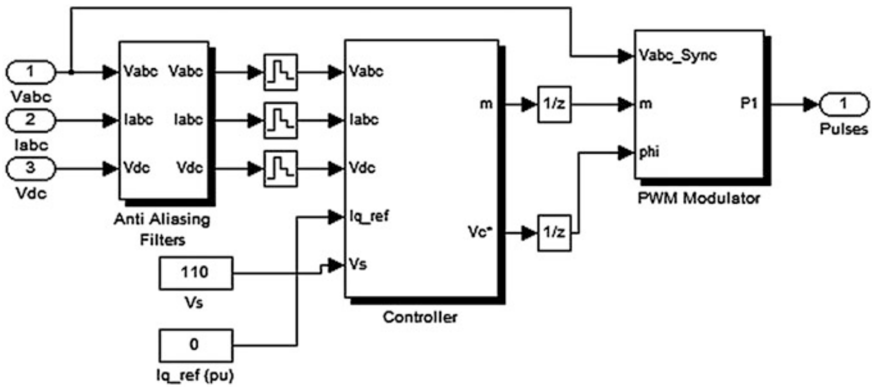

Fig. 68.4 Current control system block

The fall in signal of Fig. 68.6 shows there is demand for source power and the battery gives necessary power for the grid. The fall in signal of Fig. 68.7 shows there is demand for source power and the ultracapacitor gives necessary power for the grid, while the peak shows it gets charged from battery (Fig. 68.8).

Table 68.1 Simulation parameters

S. No	Parameters	Ratings
1	Fundamental frequency	50 Hz
2	Capacitance of super capacitor	10 F
3	Capacitor voltage	12 V
4	C1–C5	0.0495 µf
5	Battery voltage	24v
6	Rated capacity	20 Ah
7	Initial state of charge	60 V
8	Active power of normal load	1,000 W
9	Active power of heavy load	20,000 W
10	Transition time of heavy load	0.8 and 1.4 s

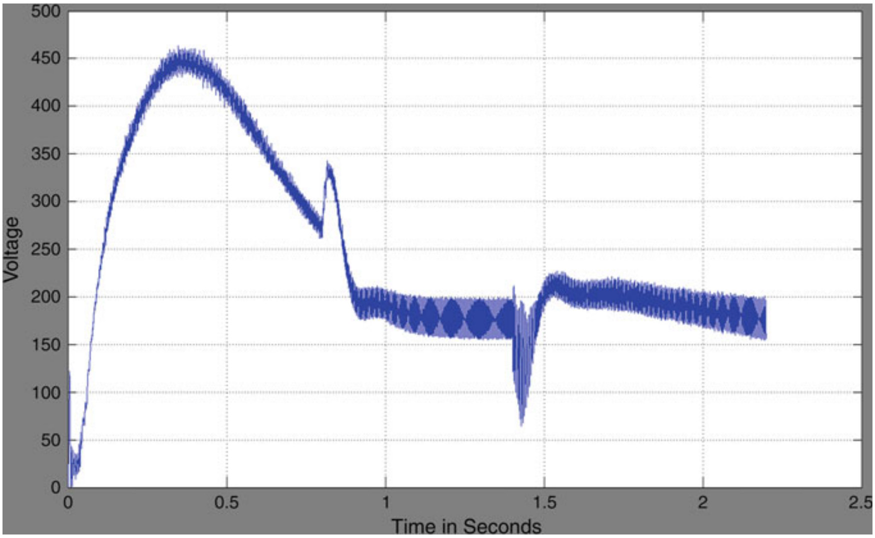

Fig. 68.5 Wind generator output

In Fig. 68.9, the peak of source power shows the demand and in inverter power the fall in peak shows the power demand is given by Uninterruptible Power Supply.

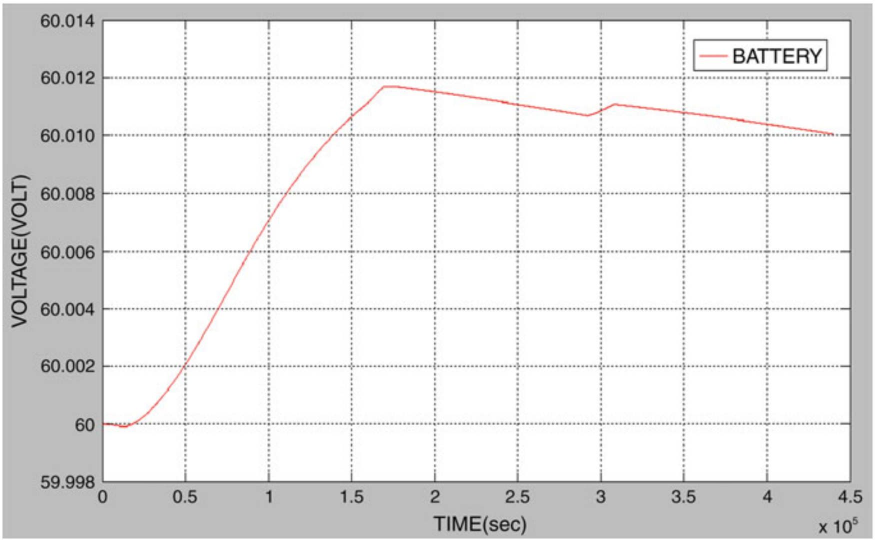

Fig. 68.6 Battery output

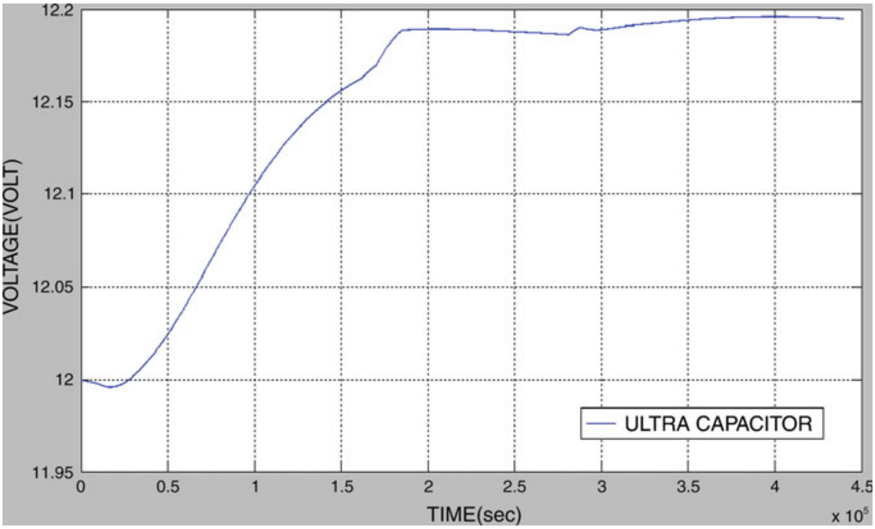

Fig. 68.7 Ultracapacitor output

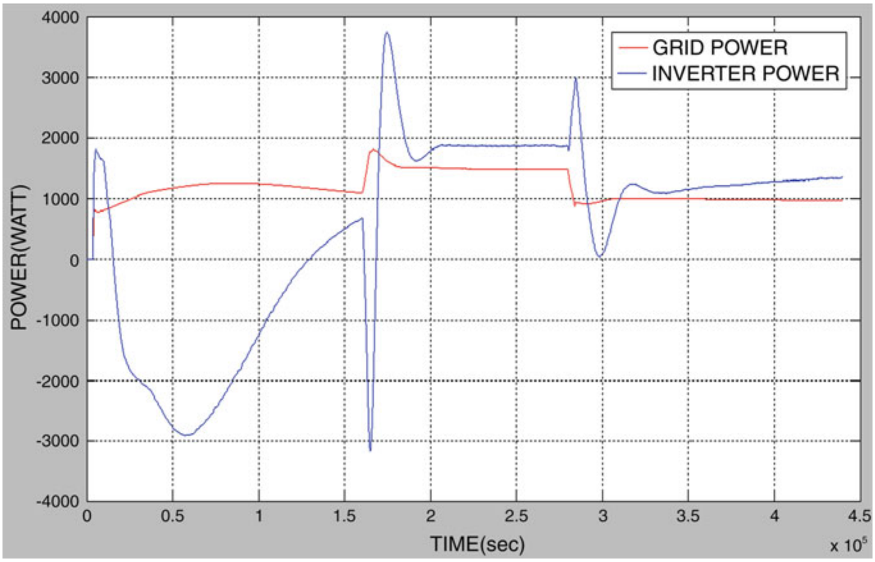

Fig. 68.8 Comparison between ultracapacitor and battery

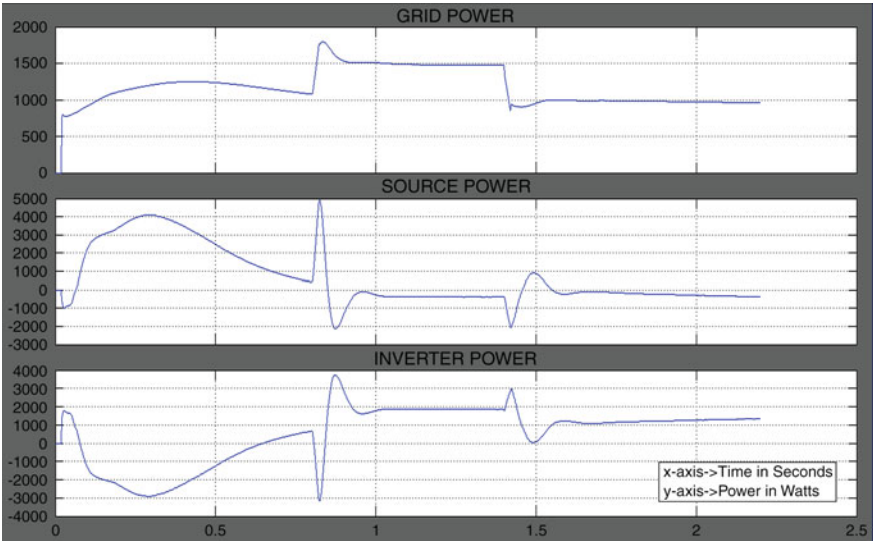

Fig. 68.9 Source power versus inverter power

68.5 Conclusion

The design of battery—supercapacitor combination has been presented. A control concept of the hybrid system is developed using normal load and heavy load. The integration of the batteries and the supercapacitor in the storage system and integration of wind generation in the grid system is explained. The reduction in battery stress has been discussed. The supercapacitor meets the high power demand and reduces the battery stress during backup time. The supercapacitor and the battery are simulated using MATLAB/Simulink system. Simulation technique shows that this technique reduces the battery stress and increases its lifetime.

References

1. Chlodnicki Z, Koczara W, Al-Khayat N (2008) Hybrid UPS based on supercapacitor energy storage and adjustable speed generator. Electr Power Qual Utilis. J XIV(1):13–24
2. Guerrero JM (2007) Uninterruptible power supply systems provide protection. IEEE Ind Electron Mag 1:28–38
3. Camara MB, Gualous H, Gustin F, Berthon A (2008) Design and new control of DC/DC converters to share energy between supercapacitors and batteries in hybrid vehicles. IEEE Trans Veh Technol 57(5):2731–2735
4. Casadei D, Grandi G, Rossi C (2002) A supercapacitor-based power conditioning system for power quality improvement and uninterruptible power supply. In: Proceedings of IEEE international symposium industrial electronics, vol 4. pp 1247–1252
5. Zubieta L, Bonert R (2000) Characterization of double-layer capacitors for power electronics applications. IEEE Trans Ind Appl 36(1):199–205
6. Dougal RA, Liu S, White RE (2002) Power and life extension of battery–ultracapacitor hybrids. IEEE Trans Compon Packag 25(1):120–131
7. Song S, Kang S, Hahm N (2003) Implementation and control of grid connected AC–DC–AC power converter for variable speed wind energy conversion system. In: Proceedings of 18th Annual IEEE APEC, vol 1. pp 154–158

Chapter 69
Analysis of Full Bridge LCC Resonant Converter for Wide Load Variations

M. Santhosh Rani, Subhransu Sekhar Dash and Julie Samantaray

Abstract A full-bridge LCC Resonant Converter for wide load variations is presented, which gives a stable output voltage and high circuit efficiency. The novel full bridge topology used for resonant converter has higher efficiency and reduced losses as compared to other conventional topologies. In the adopted DC/DC converter, a full-bridge inverter with fixed frequency is used to achieve zero current switching for active power switches and regulate the output voltage. The operating waveforms and design of the proposed converter are presented. An experimental result of a prototype is shown in order to verify the operation of the converter. The detailed circuit operation, mathematical analysis and design of the converter are presented. The proposed converter exhibits higher conversion efficiency more than 75 % for wide load conditions. Experimental results are presented to verify the performance of the adopted circuit.

Keywords FBLCC · ZCS · ZVS · MOSFET

69.1 Introduction

In recent years, the resonant converter has become more and more popular in isolated DC-DC applications due to its high power density, high efficiency and long hold up time capability. With the development of power conversion technology, power density and efficiency of converter have become the major challenging factors. In recent decade, research on DC-DC converters with power factor correction and low THD is consistently enjoying increasing interests.

The resonant based converters are capable of providing high efficiency and compact size power supplies due to their operation with near lossless switching [1–7]. Research on resonant converter is one of the hot spots due to its efficiency

M. Santhosh Rani (✉) · S.S. Dash · J. Samantaray
SRM University, Kattankulathur, Chennai 603203, Tamil Nadu, India
e-mail: brsr68@gmail.com

C. Kamalakannan et al. (eds.), *Power Electronics and Renewable Energy Systems*,
Lecture Notes in Electrical Engineering 326, DOI 10.1007/978-81-322-2119-7_69

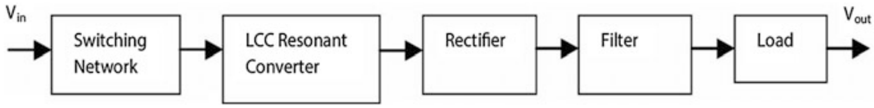

Fig. 69.1 Block diagram of resonant converter

and high power density. Generally, resonant converters are switching converters that include a tank circuit that actively participate in determining input-to-output power flow. The family of resonant converters is extremely vast and it is not an easy task to provide comprehensive picture. They are based on a "resonant inverter", i.e. a system that converts a dc voltage into a sinusoidal voltage (more generally, into a low harmonic content ac voltage), and provides ac power to a load. To do so, a switch network which typically produces a square-wave voltage is applied to a resonant tank tuned to the fundamental component of the square wave. In this way, the tank will respond primarily to this component and negligibly to the higher order harmonics, so that its voltage and/or current, as well as those of the load, will be essentially sinusoidal or piecewise sinusoidal [8].

DC power to a load can be obtained by rectifying and filtering the ac output of a resonant inverter. The general block diagram of a resonant converter is shown in Fig. 69.1.

Resonant converters eliminate most of the switching losses encountered in PWM converters. The major drawback of the DC-DC converters is the reverse recovery losses in the secondary rectifier diodes and the high voltage ringing due to the resonance between diode parasitic capacitance and transformer leakage inductance. Current fed topologies with capacitive output filter inherently minimizes diode rectifier ringing since the transformer leakage inductance is effectively placed in series with the supply side inductor [8–10]. In this paper a high efficiency full bridge LCC resonant DC-DC converter is presented which has a LCC tank circuit on the primary side of a HF transformer. The converter which is an hybrid converter has become more popular in DC-DC applications recently due to its high power density, high efficiency and long hold up time capability [7, 11, 12]. The proposed converter which is a subset of DC-DC converters can be operated either with Zero Voltage turn on(above resonant frequency) or Zero Current turn off (below resonant frequency) to eliminate the turn on and turn off losses of semiconductor vices [13]. The ZCS (Zero Current Switching) condition is very important for the primary switches of a DC-DC converter [13]. The active device is switched with either zero current switching (ZCS) or zero voltage switching (ZVS) at its terminals. When current through the switch is made zero, it is turned on/off, it is known as zero current switching and voltage across the switch is made zero, it is turned on/off, it is known as zero voltage switching. In the proposed converter illustrated in Fig. 69.2, control of output voltage at no load is achieved by proper selection of parallel capacitor in the input side of HF Transformer. Also the ripple content in the output dc filter capacitor is eliminated thus maintaining good efficiency. The full bridge

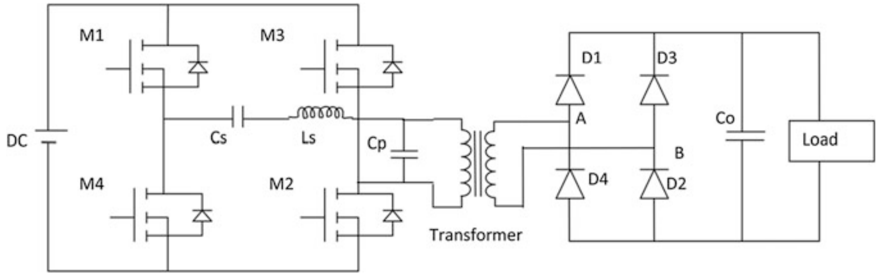

Fig. 69.2 Schematic diagram of full-bridge LCC resonant converter

LCC resonant converter has the ability to regulate the output voltage from no load to full load, line regulation, load regulation, response time and stability obtained depends on the design and specifications of the resonating elements.

69.2 Design of Full Bridge LCC Resonant Converter

Figure 69.2 shows the schematic of a Full Bridge LCC Resonant Converter (FBLCC). The circuit comprises of a full-bridge inverter, resonant tank circuit, bridge rectifier, filter circuit a resistive load. The resonant circuit consist of series inductance (L_s), series capacitor(C_s) and parallel capacitor(C_p). M1–M4 are switching devices having base/gate turn on and turn off capability. Anti-parallel diodes are present across these switching devices. The MOSFET and its anti parallel diode act as a bi-directional switch. The gate pulses for M1 and M2 are in phase but 180° out of phase with the gate pulses for M3 and M4. The positive portion of switch current flows through the MOSFET and negative portion flows through the anti-parallel diode. The voltage across the points AB is rectified and fed to load through low pass filter Co. In the analysis, it is assumed that the converter operates in continuous conduction mode and the semiconductors have ideal characteristics. The parameters for resonant converter are Ls = 65 μH, $C_s = C_p = 0.188$ μF, $V_s = 48$ V, Output voltage = 14 V.

Discontinuous conduction mode is not very effective in achieving a high power throughput and one inverter leg ceases to have ZVS conditions. Hence the proposed converter is developed for continuous conduction mode (CCM) being switched at a frequency higher than its resonant frequency as shown in Fig. 69.4.

Referring to Fig. 69.3a, during Interval T0–T1, switches M1 and M2 are on and M3 and M4 are off. This is a power transfer interval and the primary current flows through M1, transformer primary, resonant inductor (Ls) and M2. The rate of rise of the current (di/dt) through Ls is proportional to the difference between the input voltage Vin and the output voltage Vo. During this mode power flows to the output through rectifier diodes D3 and D4 and also energy is stored in Ls. Battery is chosen as load in Fig. 69.3.

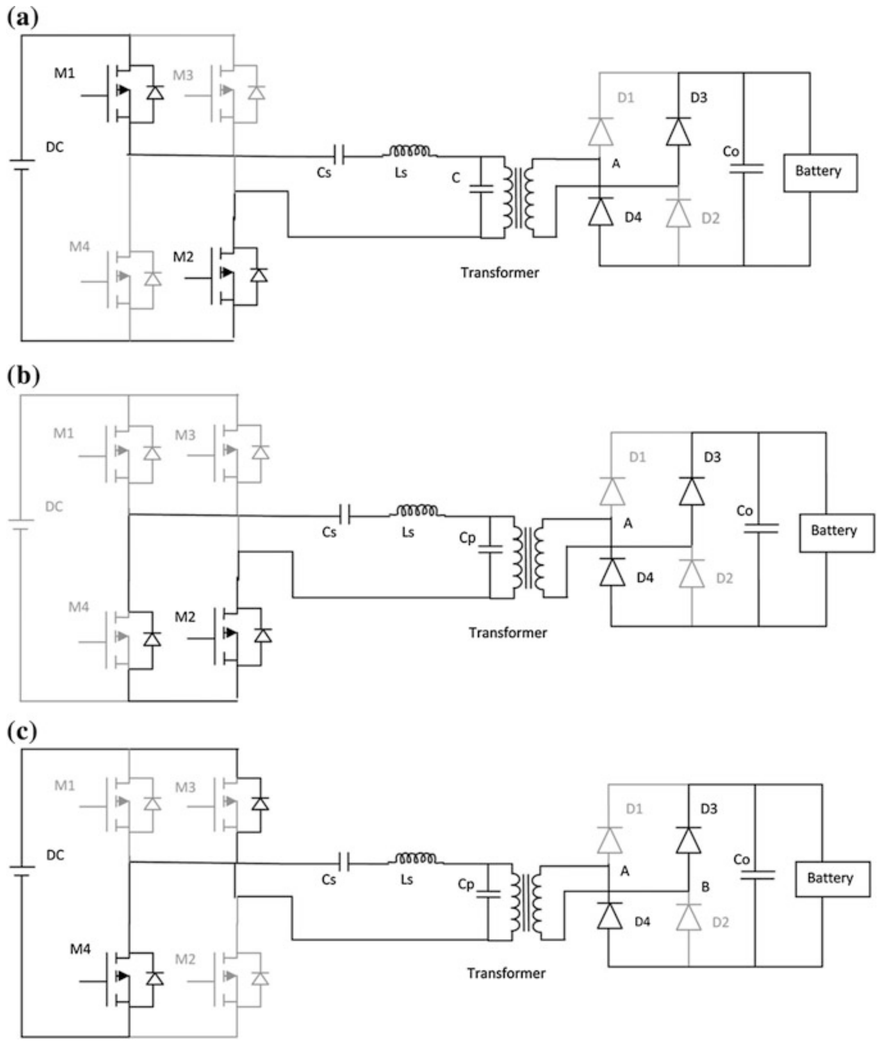

Fig. 69.3 Modes of operation for intervals T0–T3. **a** Refers interval T0–T1, **b** refers interval T1–T2 and **c** refers interval T2–T3

During the interval T1–T2, the energy stored in L_r is transferred to the output as shown in Fig. 69.3b. The primary resonant inductor (L_s) maintains the current, which circulates around the path of D4, transformer primary, resonant inductor (L_s) and M2. The rate of the downslope of the current through Ls is proportional to the output voltage V_o. At T2 the entire energy stored in L_s is transferred to the output.

During the interval T2–T3, at T2, M4 and M2 toggle as shown in Fig. 69.3c. The actual timing of this toggle is dependent on the resonant delay which occurs prior to M3 turning on. When M4 and M2 toggle, the primary resonant inductor current that

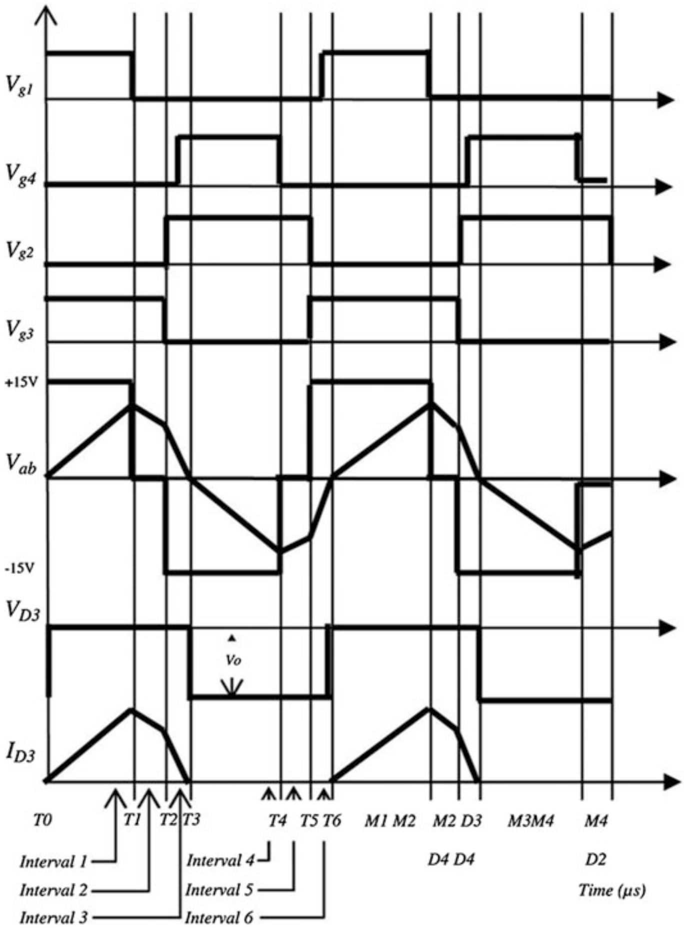

Fig. 69.4 Operation of ZVS full bridge converter in CCM

was flowing through M2 finds an alternate path by charging/discharging the parasitic capacitances of switches M2 and M4 until the body diode of M3 is forward biased. If the resonant delay is set properly, switch M3, can be turned on with ZVS. At T3 the entire energy stored in Lr is transferred to the output and the current becomes zero and the rectifier diodes D3 and D4 turn off. Intervals T3–T4, T4–T5 and T5–T6 are the negative equivalents of intervals T0–T1, T1–T2 and T2–T3 respectively. Operation of ZVS full bridge converter in CCM is shown in Fig. 69.4.

The gain frequency characteristic curves of Fig. 69.5, it is desirable to select the converter components so that full load Q is in the neighbourhood of 4–5. For these values of Q the converter appears essentially as a series resonant converter and the circulating current will decrease as the load resistance increases.

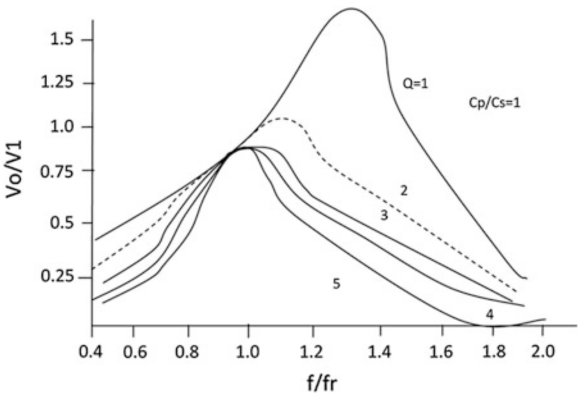

Fig. 69.5 Gain frequency characteristic curves

As the load decreases further, the converter takes on the characteristics of a Parallel resonant converter and the circulating current no longer decreases with load.

The proposed converter works satisfactorily for wide variation of supply voltage and load current. In the proposed circuit, it is assumed that

$$\frac{C_s}{C_p} = 1; \quad Q_s = 4; \quad \frac{\omega}{\omega_s} = 1.1$$

where $Q_s = \frac{\omega L_s}{R_L}$ *and* $\omega_s = 2\pi f_s = \frac{1}{\sqrt{L_s C_s}}$

$$\textit{resonant frequency} f_r = \frac{1}{2\pi\sqrt{LC_e}} \tag{69.1}$$

where $C_e = \frac{C_s C_p}{C_s + C_p}$

L_s is the series inductor, C_s and C_p are series and parallel capacitors respectively. The resonant frequency of the proposed circuit is 64.2 kHz. The switching Frequency of the MOSFET is 50 kHz.

69.3 Simulation Results

The performance of the converter designed in Sect. 69.2 is evaluated using MATLAB (version R2012a) as shown in Fig. 69.6. Simulations are run for various load values. Circuit parameters of simulation are listed in Table 69.1 for an input voltage of 48 V. Figure 69.7a–c provides output voltage, output Current, Gate pulses for the switch pairs M1–M4, input and output Voltage of the HF Transformer for the proposed Converter.

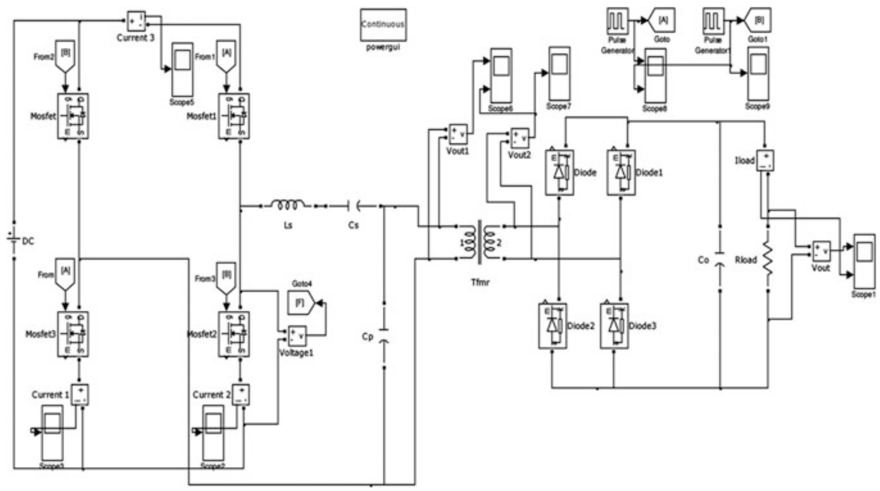

Fig. 69.6 Simulated circuit of proposed converter

Table 69.1 Simulation circuit parameters

S.No	Parameter	Values
1	Input voltage (V_s)	48 V
2	Switching frequency (f_s)	50 kHz
3	Resonant frequency (f_r)	64.2 kHz
4	Resonant inductor (L_s)	65.0 μH
5	Series resonant capacitor (C_s)	0.18 μF
6	Parallel resonant capacitor (C_p)	0.18 μF
7	Filter capacitor (Co)	1 mF
8	Output voltage (Vo)	14 V

69.4 Parameters of Proposed Topology

The circuit parameters used for simulation and efficiency calculation are given in Table 69.2 respectively. Hardware values of FBLCC are presented in Table 69.3. Figure 69.8 shows the Prototype circuit with output voltage, the driving pulses for M1–M4.

It can be observed from Table 69.2 and Fig. 69.9 that the proposed LCC Converter has good efficiency from light to heavy loads. Figure 69.10 shows the THD of the pro-posed converter (2.89 %) which is well within the limits. It overcomes the disadvantages of both Series Resonant converters and Parallel Resonant converters. This makes it more suitable for applications involving light to heavy loads.

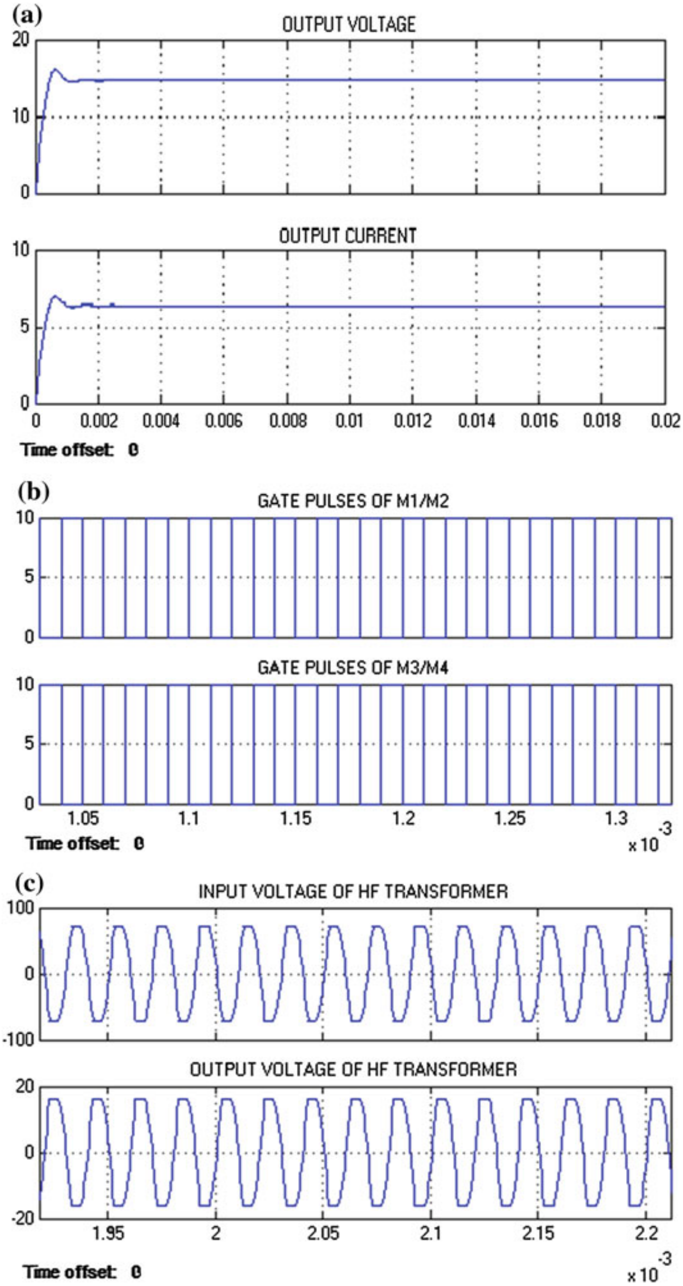

Fig. 69.7 **a** Output voltage and output current. **b** Driving pulses for M1/M2 and M3/M4. **c** Input and output voltage waveform

Table 69.2 Efficiency calculation

Input voltage (V)	Load (Ω)	Input power (W)	Output voltage (V)	Output power (W)	Efficiency (%)
48	0.78	300	14.12	255.6	85.2
48	2	125.76	14.6	106.4	84.7
48	10	30.2	15.51	24.05	79.5
48	15	21.7	15.75	16.5	76

Table 69.3 Hardware circuit parameters

S.No	Parameter	Values
1	Input voltage (V_s)	48 V
2	Switching frequency (f_s)	50 kHz
3	Resonant frequency (f_r)	64.2 kHz
4	Resonant inductor (L_s)	2.2 µH
5	Series resonant capacitor (C_s)	33 pF
6	Parallel resonant capacitor (C_p)	33 pF
7	Filter capacitor (Co)	1 µF
8	Output voltage(Vo)	14 V

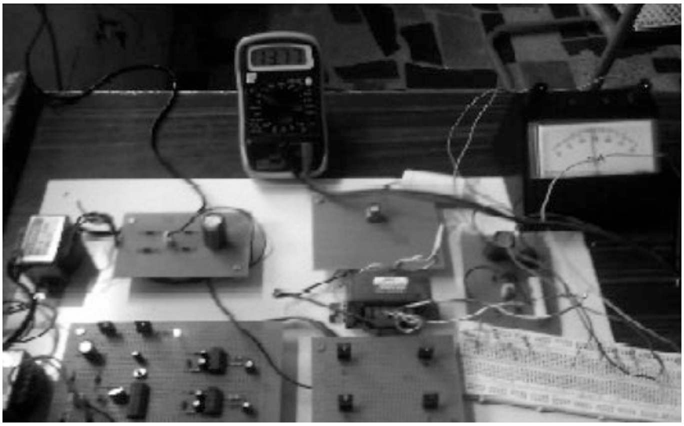

Fig. 69.8 Prototype circuit of FBLCC

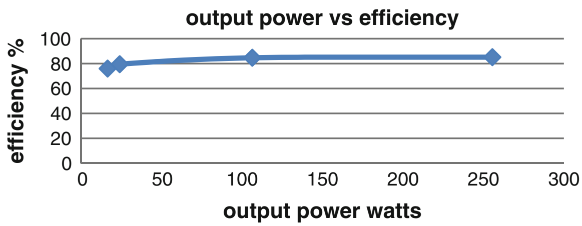

Fig. 69.9 Output power vs Efficiency

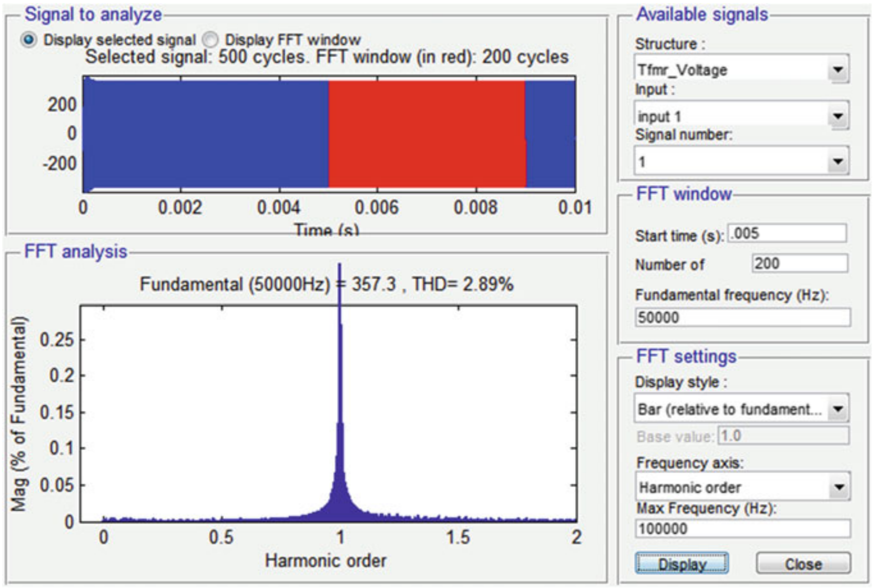

Fig. 69.10 THD of FBLCC converter

69.5 Conclusion

This work presents the implementation of FBLCC Resonant Converter. The simulation and experimental results closely match. This makes FBLCC Converter more suitable for applications involving light loads to heavy loads. The efficiency is above 85 % for light loads and is maintained above 75 % for heavy loads. THD is 2.89 %. The experimental results demonstrate the effectiveness of the proposed topology. The circuit structure is simpler and cheaper than other control mechanisms which require many components.

References

1. Steigerwald RL (1988) A comparison of half-bridge resonant converter topologies. IEEE Trans Power Electron 3(2)
2. Bhat AKS (1990) Analysis, optimization and design of a series parallel resonant converter. In: Proceedings of the IEEE applied power electronics conference, Los Angeles, CA, 11–19 Mar 1990, pp 155–164
3. Bhat AKS (1994) Analysis and design of LCL type series resonant converter. IEEE Trans Ind Electron 41(1):118–124
4. Koo GB, Moon GW, Youn MJ (2005) New zero-voltage-switching phase-shift full-bridge converter with low conduction losses. IEEE Trans Ind Electron 52(1):228–235
5. Li X, Bhat AKS (2010) Analysis and design of high frequency isolated dual bridge series resonant DC/DC converter. IEEE Trans Power Electron 23(4):850–862
6. Lo YK, Lin CY, Hsieh MT, Lin CY (2011) Phase shifted Full bridge Series-resonant DC-DC converters for wide load variations. IEEE Trans Ind Electron 58.6
7. Jafari M, Imanieh M, Malekjamshidi Z (2011) Design, simulation and implementation of a full bridge series parallel resonant DC-DC converter using ANN controller. In: International Siberian conference on control and communications SIBCON 2011, pp 97–103
8. Zhao C, Wu X, Yao W, Qian Z (2008) Synchronous rectified soft-switched phase-shift full-bridge converter with primary energy storage inductor. In: IEEE applied power electronics conference and exposition, APEC
9. Zhao C, Wu X, Yao W, Qian Z (2008) Optimum design considerations for soft- switched phase-shift full-bridge converter with primary-side energy storage inductor. Presented at the IEEE power electronics specialist conference, PESC
10. Jala S (2009) High frequency transformer isolated soft-switched hybrid phase modulated DC-to-DC converters. MA Sc Thesis, Department of ECE, University of Victoria
11. Ivensky G, Bronshtin S, Abramovitz A (2011) Approximate analysis of resonant LLC DC-DC converter. IEEE Trans Power Electron 26(11):3274–3284
12. Beiranvand R, Zolghadri MR, Rashidian B, Alavi SMH (2011) Optimizing the LLC-LC resonant converter topology for wide output voltage and wide output load applications. IEEE Trans Power Electron 26(11):3192–3204
13. Sivakumaran TS, Natarajan SP (2006) Development of fuzzy control of series—Parallel loaded resonant converter-simulation and experimental evaluation. In: Proceedings of India international conference on power electronics, pp 360–364

Chapter 70
Power Quality Improvement Using Multilevel Inverter Based Dynamic Voltage Restorer with PI Controller

M. Maheswari, S. Thangavel, R. Suresh Kumar and C. Vivekanandan

Abstract With the invasion of power electronic based devices in all sectors in the recent past, not only in industry but also in domestic, the quality of power is degraded considerably and need to be addressed as the power quality has direct economic impact. Out of several power quality issues, voltage sag and swells in the medium and low voltage distribution grids are considered in this paper, as their occurrence is more frequent in the grids and it is necessary to protect sensitive loads against such disturbances. Among a variety of solutions proposed to handle this issue, Dynamic Voltage Restorer (DVR) is considered to be the most efficient and effective solution and hence, a twenty seven levels cascaded multilevel inverter based DVR is proposed in this paper to compensate the voltage under balanced voltage sags in a distribution system. Simulations are carried out using MATLAB/SIMULINK to estimate the performance of the proposed method and the results show considerable improvement in the power quality terms of harmonics.

Keywords Dynamic voltage restorer (DVR) · Power quality · Multilevel inverter · PI controller

M. Maheswari (✉) · R. Suresh Kumar · C. Vivekanandan
SNS College of Engineering, Coimbatore, India
e-mail: maheswarikgd@gmail.com

R. Suresh Kumar
e-mail: sureshramasamy8@gmail.com

C. Vivekanandan
e-mail: vivekanandan.cit@gmail.com

S. Thangavel
K.S. Rangaswamy College of Technology, Tiruchengode, India
e-mail: golds71@yahoo.com

C. Kamalakannan et al. (eds.), *Power Electronics and Renewable Energy Systems*,
Lecture Notes in Electrical Engineering 326, DOI 10.1007/978-81-322-2119-7_70

70.1 Introduction

Almost all the modern industrial processes and advanced equipments introduced recently are based on a large number of electronic devices such as programmable logic controllers, adjustable speed drives and related configurations which have degraded the quality of power to a major extend in terms of harmonics, voltage swells, voltage sags and the like. In addition, the performance of sophisticated electronic devices is very sensitive to the quality of power supply and hence less tolerant to power quality problems such as voltage dips, voltage swells, and harmonics [1–4].

In a 50 Hz supply system, a change in the amplitude of voltage from 10 to 90 % lasting for 10 ms–1 min is called as voltage sag, where as an increase in rms voltage or current at the power frequency for durations from 0.5 cycle to 50 cycles with typical magnitudes between 1.1 pu and 1.8 pu is known as voltage swell [1, 5]. In a distribution system both swell and sag can cause sensitive equipment to fail, or shutdown, as well as create a large current unbalance that could blow fuses or trip breakers leading to minor quality variations to production downtime and equipment damage and may be prohibitively costlier [2–4, 6–8]. However, voltage swells are less common compared to voltage sags and hence, latter need to be addressed more seriously.

Earlier to protect sensitive loads from the impact of voltage sags custom power devices are connected in series with the load and presently both Static Synchronous Series Compensator (SSSC) and Dynamic Voltage Restorer (DVR) are commonly used for series voltage sag compensation. SSSC compensates the sag by injecting the required voltage in series whereas DVR compensates the unbalance in supply voltage of different phases by injecting the active power with the help of DC energy storage with required reactive power generated internally without any means of DC storage. In general, DVR is installed on a critical load feeder, in series between the load and the supply voltage, and can compensate voltage at both transmission and distribution sides by supplying the voltage difference i.e. voltage difference between the normal value and the value during sag. Under normal conditions i.e. when there is no sag DVR operates in a low loss standby mode and said to be in steady-state [2–4]. During abnormal condition, i.e. when the supply voltage deviates from nominal value due to disturbance, DVR supplies voltage for compensation of sag and is said to be in transient state. [2–4, 6–9].

70.2 Conventional DVR System

A DVR consists of two basic circuits viz. power circuit and control circuit in which the power circuit generates the voltage to be injected into the system by proper control of switches, for which the control circuit is used generate the required control signal [6–9]. DVR basically consists of a voltage injection/series transformer, an output filter, an energy storage device, a voltage source inverter (VSI)

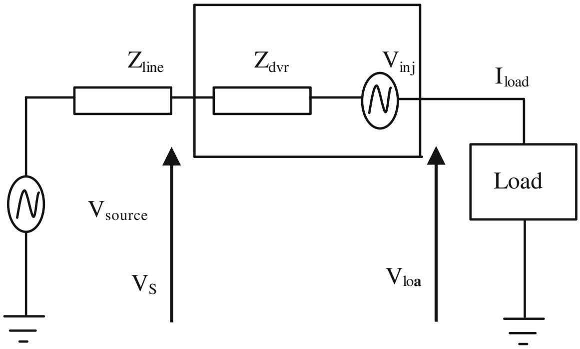

Fig. 70.1 Equivalent circuit of DVR

and a control circuitry. DVRs are preferably installed very closer to sensitive loads as the main objective of installing a DVR is to protect those loads from voltage sags/swells, flowing from the network, as a consequence of disturbances by injecting a series voltage V_{inj} through the boost-transformer so as to eliminate any detrimental effects of a bus-fault to the load voltage V_{load}.

During most of the time DVR is in standby mode with $V_{inj} = 0$, during which no switching of semiconductors takes place and hence the low voltage winding of the series transformer is shorted through the converter resulting relatively low conduction losses in semiconductors. Once the disturbance in supply voltage is sensed DVR enters into boost-mode and compensates the shortfall in voltage by injection through booster transformer with $V_{inj} > 0$ [6–9].

Figure 70.1 shows the equivalent circuit of DVR. When the source voltage drops or increases, the DVR injects a series voltage V_{inj} through the injection transformer so that the desired load voltage magnitude V_{load} can be maintained. The expression for load voltage can be written as

$$V_{load} = V_s + V_{inj} \tag{70.1}$$

where,

V_{load} is the desired load voltage magnitude
V_s is the source voltage during sag/swell
V_{inj} is voltage injected by DVR

The load current I_{load} is given by,

$$I_{load} = (P_{load} + jQ_{load}) / V_{load} \tag{70.2}$$

70.3 Proposed DVR

VSI is the main component of DVR which converts the DC capacitor voltage into AC voltage of required magnitude and phase which will be injected for compensation and a multilevel inverter is used as VSI in this work. Multilevel inverters are

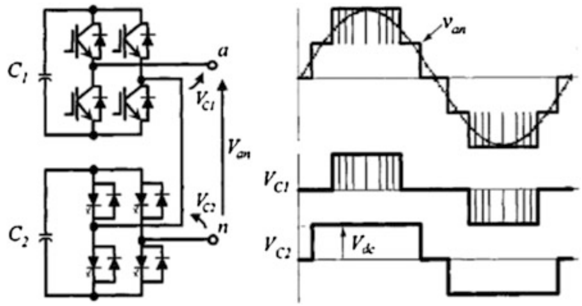

Fig. 70.2 Cascaded multi cell inverter

realized using three different topologies viz. diode clamped, capacitor clamped and cascaded multi cell inverter (CMCI) with separate DC sources [10, 11] and the third topology is preferred in this work in view of its less complexity and relatively better performance. The minimum configuration of multilevel starts with three and as the amount of harmonics in the injected voltage depends on number of levels of inverter, a 27 level inverter is selected in this work to reduce the harmonics level appreciably [10–14] and the 27 levels of voltage is realized using 13 cascaded H-Bridge modules with the minimum and maximum voltages are −13 and +13 V and the in between levels are in steps of V.

To illustrate the advantage of multilevel, a five level inverter is depicted in Fig. 70.2 involving two full-bridge configurations. By turning on/off the devices properly in each leg of a bridge, three levels of voltage +V, 0 and −V can be realized and the output voltage of the inverter is the sum of output voltages of the two bridges and hence, five levels of voltages 2 V, V, 0, −V and −2 V can be achieved where V is the voltage across the capacitors C_1 and C_2. Hence, it may be stated that if the number of levels is denoted by 'm' and that of full-bridge modules is 'S' then the maximum output voltage is ((m − 1)/2) V = SV and the minimum voltage is ((m − 1)/2) (−V) = −SV. CMCI is capable delivering full DC-bus voltage in both positive and negative directions where as it is only half of DC-bus voltage in other topologies. Further, CMCI configuration is scalable and it is possible to operate every full-bridge module with different voltages.

70.4 Control Method

A PI based closed-loop control is suggested in this work and the entire control strategy is designed and simulated using MATLAB-Simulink as shown in Fig. 70.3. The control unit consists of a sensor, a sequence analyzer, a magnitude comparator, a PI module and a pulse-width modulation unit.

The supply voltage is continuously measured which is simulated using V-I measurement block and the measured three phase voltage is converted into equivalent d-q-0 quantities through sequence analyzer using Park's transformation

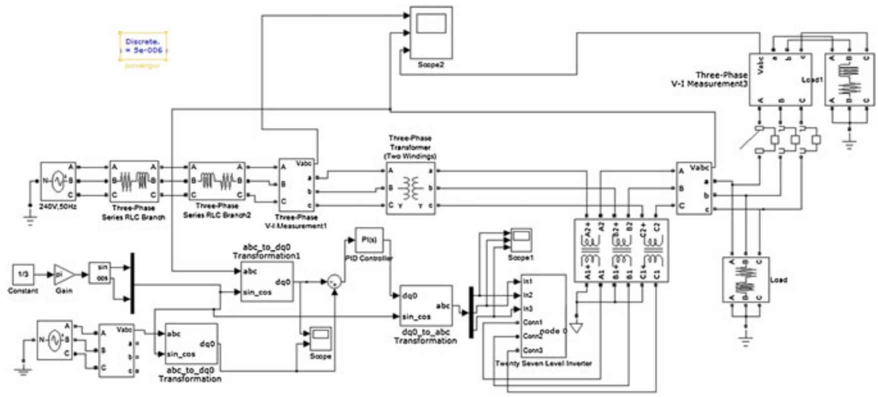

Fig. 70.3 Simulink model of DVR test system for voltage sag

[15, 16]. The magnitude of the d-q-0 component is compared with the input reference, the representative of nominal voltage. The output of the comparator is fed to a PI controller, whose output is the modulating signals for PWM pulse generator. The other input to PWM pulse generator is high frequency carrier wave in triangular form symmetrical about time axis [17]. The carrier frequency chosen in this work is 20 kHz. PWM generates the gate pulses for the inverter module in such a way that the inverter output is a three phase 50 Hz sinusoidal voltage in correct magnitude and proper phase sequence to compensate the voltage sag [16, 18]. The output voltage of the inverter is injected into the line using booster transformer as shown in Fig. 70.3.

A temporary single-line-to-ground fault is forced using three fault module at 0.3 ms so that it results in voltage sag between 0.3 and 0.8 ms as shown in Fig. 70.4. The magnitude component of d-q-0 equivalent of the supply voltage

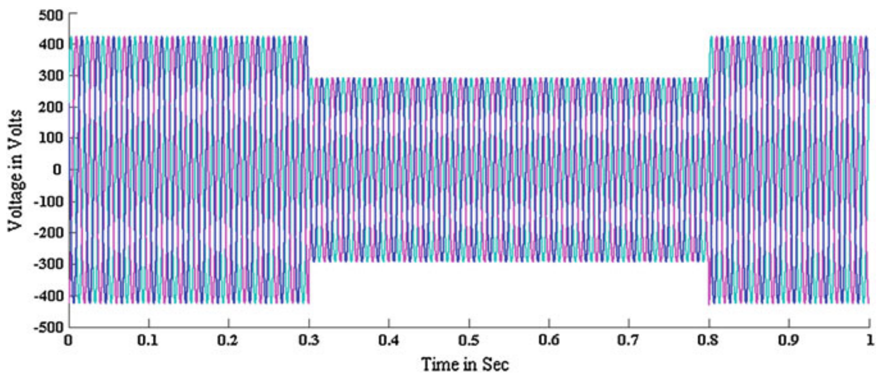

Fig. 70.4 Supply voltage with sag

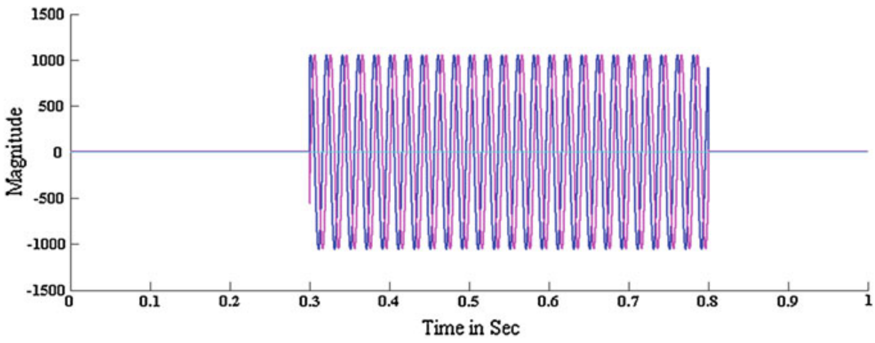

Fig. 70.5 Output of PI controller

compared with the reference voltage V_{ref}, the error is fed to the PI controller and the signals generated by the controller for PWM generator is shown in Fig. 70.5. The switching pulses generated by PWM generator for the full-bridge modules.

70.5 Simulation Results

The source voltage selected for simulation is three phase 415 V, 50 Hz. The load is assumed to be of 10 kW with negligible reactive component. The transmission line parameters are chosen as 0.01 + j0.005. The waveform of supply voltage is given in Fig. 70.4 with and without sag. The output of the PI controller and PWM module are given in Figs. 70.5 and 70.6 respectively. The output of the inverter and the compensated voltage applied to load is given in Figs. 70.7 and 70.8. It is observed

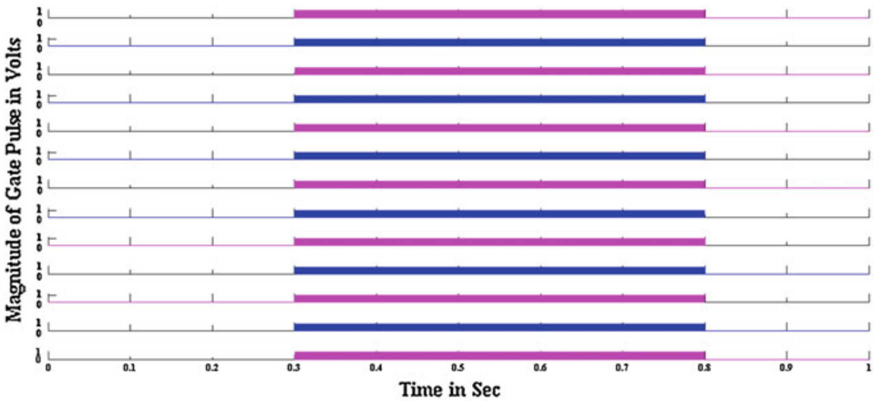

Fig. 70.6 Gate pulses for multilevel inverter

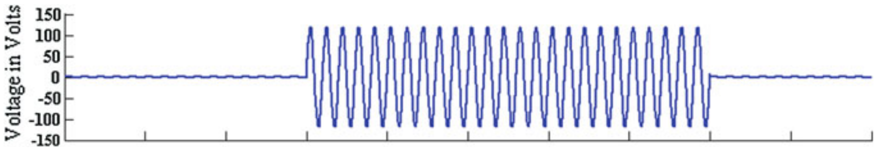

Fig. 70.7 Multilevel inverter output voltage

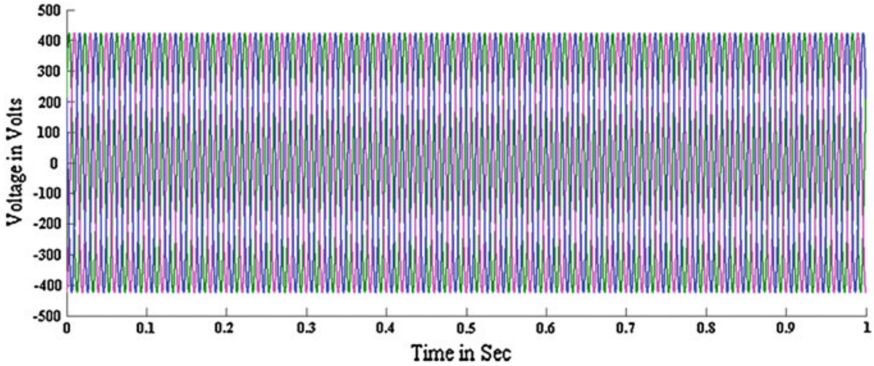

Fig. 70.8 Compensated voltage to load

that the performance of the 27 level CMCI is appreciable. It generates the required compensating voltage in proper phase sequence and magnitude once the sag occurs and continues this till the existence of the sag. The inverter output becomes zero once the sag disappears which is evident from the graphs shown in Fig. 70.7. Figure 70.9 shows the harmonic analysis of the proposed DVR, from which it is observed that the total harmonic distortion (THD) improves appreciably and is well below the maximum value specified by IEEE 519-1992 standard.

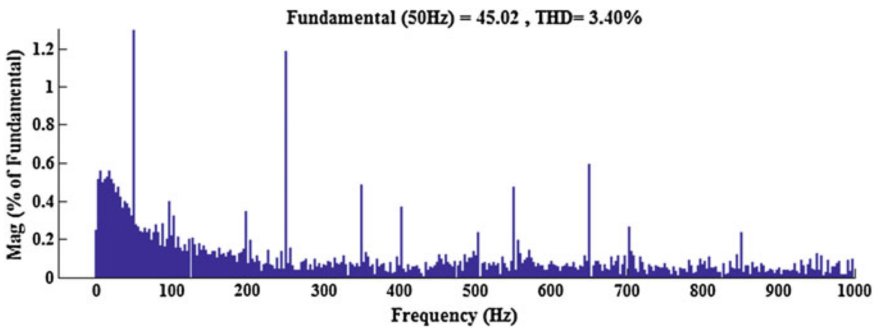

Fig. 70.9 Total harmonic distortion

70.6 Conclusion

In this paper, a PI controlled twenty-seven level CMCI based DVR is proposed in mitigating voltage sag and its performance is analyzed using MATLAB/Simulink. The PI controller is suggested to improve the performance of the DVR during the sag and it is observed that during sag the compensating voltage is injected exactly in phase and magnitude. The simulation results show appreciable improvement in the quality of the power delivered. The improvement in THD is obvious as THD with normal VSI based DVR is 13.8 and that of the proposed configuration is 3.4. Hence, it may be concluded that the proposed DVR configuration is better than its present counterparts. In this work only sag is considered and the performance of the proposed DVR may be evaluated for voltage swells and interruptions.

References

1. Ghosh A, Ledwich G (2002) Power quality enhancement using custom power devices. Kluwer Academic Publishers, Berlin
2. Omar R, Rahim N, Sulaiman M (2006) Modelling and simulation for voltage sags/swells mitigation using dynamic voltage restorer. J Theor Appl Inf Technol 464–470
3. Gupta SK, Tiwari HP, Pachar R (2010) Study of major issues and their impact on DVR system performance. Int J Comput Electr Eng 2(1):105–110
4. Ravi Kumar SV, SivaNagaraju S (2007) Simulation of D-STATCOM and DVR in power systems. ARPN J Eng Appl Sci 2(3):7–13
5. Dugan RC, McGranaghan MF, Santoso S, WayneBeaty H (2008) Electrical power systems quality, 3rd edn. The McGraw-Hill Companies, New York
6. Boonchiam P, Mithulananthan N (2006) Understanding of dynamic voltage restorers through MATLAB simulation. Thammasat Int J Sci Technol 11(3):1–6
7. Benachaiba C, Ferdi B (2009) Power quality improvement using DVR. Am J Appl Sci 6 (3):396–400
8. Singh M, Tiwari V (2009) Modelling analysis and solution of power quality problems. Int J Comput Electr Eng 58–64
9. Zhan C, Ramachandramurthy VK, Arulampalam A, Fitzzer C, Barnes M, Jenkins N (2002) Control of a battery supported dynamic voltage restorer. IEEE Proc Transm Distrib 149:533–542
10. Rodriguez J, Bernet S et al (2007) Multilevel voltage-source-converter topologies for industrial medium-voltage drives. IEEE Trans Ind Electr 54(6):2930–2945
11. Nabae A, Takahashi I, Akagi H (1981) A new neutral point clamped PWM inverter. IEEE Trans Ind Appl IA-17:518–523
12. Rodriguez J, Lai JS, Peng FZ (2002) Multilevel inverters: a survey of topologies, controls, and applications. IEEE Trans Ind Electr 49(4):724–738
13. Lai JS, Peng FZ (1996) Multilevel converters—a new breed of power converters. IEEE Trans Ind Appl 32:509–517
14. Hammond P (1997) A new approach to enhance power quality for medium voltage ac drives. IEEE Trans Ind Appl 33:202–208
15. Ganesh SNV, Ramesh Reddy A, Shankar Ram BV (2009) A neuro: control strategy for cascaded multilevel inverter based dynamic voltage restorer. Int J Electr Power Eng 3 (4):208–214

16. Manojkumar P, Sumanth Y, Ganesh SNV (2010) Improving the power quality by MLCI type DSTATCOM. Int J Comput Appl 10(1):36–40
17. Perera K, SalomonSon D, Atputharaj A, Alakakoon S (2006) Automated control technique for a single phase dynamic voltage restorer. IEEE Xplore Digit Libr 63–68
18. Venkateshwarlu S, Muni BP, Rajkumar AD, Praveen J (2008) Direct power control strategies for multilevel inverter based custom power devices. World Acad Sci Eng Technol 39:205–213

Chapter 71
Design and Implementation of Fractional Order Proportional Integral Controller for the Control of Aircraft Pitch Dynamics

Abdul Wahid Nasir and U. Sabura Banu

Abstract Fractional calculus has gained attraction in the recent past in various fields. But the control design techniques available for the fractional order system suffer from lack of systematic approaches. In this paper, fractional order Proportional Integral Controller is designed to improve the performance and robustness for Aircraft pitch dynamic system which is governed by a Type 1 second order system open loop unstable process. Frequency domain specifications such as phase margin specification, gain margin specification and robustness to parameter variations are considered for the design purpose. From the simulation studies, it is clear that the proposed controller works efficiently even under parameter variations.

Keywords Aircraft pitch dynamic system · Proportional integral controller · Frequency domain specifications

71.1 Introduction

Fractional calculus uses derivatives and integrals of arbitrary real or complex order which finds application in various fields. Even though, conventional integer order PID controller can be applied to a Single-Input-Single-Output and Linear Time Invariant system, it is the widely used due to is structural simplicity. Integer order PID controller considers only three specifications at a time since it has three dependent variables to tune. Providing slight advancements in the PID, by considering fractional order Integrator and differentiator, the integer order PID can be extended to Fractional order PID. A fractional PID controller is the generalization

A.W. Nasir (✉) · U. Sabura Banu
Department of Electronics and Instrumentation Engineering, B.S. Abdur Rahman University, Vandalur, Chennai 600048, India
e-mail: awonasir@gmail.com

U. Sabura Banu
e-mail: sabura.banu@bsauniv.ac.in

C. Kamalakannan et al. (eds.), *Power Electronics and Renewable Energy Systems*, Lecture Notes in Electrical Engineering 326, DOI 10.1007/978-81-322-2119-7_71

of a standard PID controller giving more flexibility to the controller as it involves five parameters. The parameters include proportional gain, integral gain, derivative gain, order of integrator and order of differentiator. Many researchers have contributed to the tuning rules for integer order PID tuning. Straight forward PID tuning techniques are available since the tunable parameters are three. Whereas, fractional order PID controller involves five parameters complicating the controller design. Fraction order $PI^{\lambda}D^{\mu}$ controller tuning [1] have been proposed by many modern-day researchers, to name a few Zeigler Nichols' tuning rule by Valerio and Da Costa [2] and MIGO [3] based FOPI controllers by Chen et al. [4] which needs reduction of higher order process to FOPDT form [2, 4], which will not be sufficient to describe the complex dynamic behavior of the higher order plant. Tuning of FOPI/FOPD controller parameters considering phase margin, gain margin and robustness specifications [5–7] for controlling integer order systems have been discussed in [8, 9]. Luo et al. has extended the same strategy for fractional order models [10, 11]. Sensitivity and complimentary sensitivity function based frequency oriented optimization was been proposed by Monje et al. [12] and Dorcak et al. [13]. Pole placement time domain tuning [14, 15] and time domain based optimal tuning minimizing integral performance indices are discussed. The aforementioned technique doesn't guarantee closed loop stability of the process. Dominant pole placement technique based tuning is proposed by Type 0 second order system is proposed by Biswas et al. [14] and Maiti et al. [15]. But when the type of the system is increased leading to a open loop unstable system, satisfactory results are not obtained. In addition the technique gives inferior closed loop performance and often unstable response for time delay systems, since the Pade approximation of delay term effectively raises the order of the overall system. Multi-objective optimization with the objective function as maximum overshoot, rise time, settling time, steady-state error, Integral of Absolute Error (IAE), squared control signal, inverse of phase margin and gain margin was proposed by Zamani et al. [16]. Optimal tuning based on minization of Time multiplied Absolute Error (ITAE) and Integral of Square Error (ISE) by Lee and Chang [17] to find out the optimal set of controller parameters. An optimization based controller tuning by minimizing matrix norms as the cost functions has been proposed by Bouafoura and Braiek [18]. Few time domain and frequency domain specifications are tuned for first order system by Castillo et al. [19]. Bhambhani et al. [20] proposed a multi-objective optimization based FOPI controller tuning methodology for Networked Control Systems (NCS) which simultaneously minimizes ITAE of the closed loop system and maximizes the jitter margin. In the proposed work, an attempt has been made to design and implement a fractional order PI controller for the aircraft pitch control which is Type 1 second order system. Section 71.2 discusses the process dynamics of Aircraft Pitch, Sect. 71.3 follows the fractional order PI controller design, followed by Sect. 71.4 with the analysis of results and finally by the conclusion section.

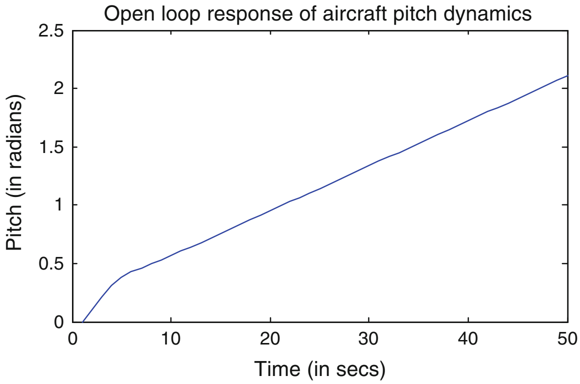

Fig. 71.1 Open loop response of aircraft pitch dynamics

71.2 Process Dynamics of Aircraft Pitch

In the present case under study, mathematical model for Boeing's commercial aircraft is used [21]. The output of the process under study is the aircraft pitch angle and the manipulated variable is the elevator deflection angle. The reference to the system is 0.2 radians (11°). Figure 71.1 shows the open loop response of the system given by Eq. (71.1). On investigation of the transfer function, the system is a Type 1, second order system which is open loop unstable process. The open-loop transfer function of the aircraft pitch dynamics is given by:

$$P(s) = \frac{1.151s + 0.1774}{s^3 + 0.739s^2 + 0.921s} \tag{71.1}$$

71.3 Fractional Order PI Controller for Aircraft Pitch Dynamics

71.3.1 Fractional Order PI Controller and the Tuning Constraints

The motivation of this section is to design a fractional order PI controller of the form

$$C(s) = K_p + \frac{K_p K_i}{s^{\lambda}} \tag{71.2}$$

where

K_p is the Proportional Gain,
K_i is the Integral Gain,
λ is the order of the integrator.

Let ω_{gc} is the gain crossover frequency. The design of the controller parameters are performed as per the specifications given as follows:

1. Phase margin constraint

$$\mathrm{Arg}[\mathrm{G}(\mathrm{j}\omega_{gc})] = Arg[C(\mathrm{j}\omega_{gc})P(\mathrm{j}\omega_{gc})] = -\pi + \phi_m \tag{71.3}$$

2. Gain crossover frequency constraint

$$\left|\mathrm{G}(\mathrm{j}\omega_{gc})\right|_{db} = \left|C(\mathrm{j}\omega_{gc})P(\mathrm{j}\omega_{gc})\right|_{db} = 0 \tag{71.4}$$

3. Robustness to parameter variation, which is obtained by equating the phase derivative with respect to the frequency as zero, i.e. the phase plot of the Bode around the gain crossover frequency ω_{gc} is flat.

$$\left|\frac{\mathrm{d}(\mathrm{Arg}(\mathrm{G}(\mathrm{j}\omega)))}{d\omega}\right|_{\omega=\omega_{gc}} = 0 \tag{71.5}$$

71.3.2 *Fractional Order PI Controller Tuning for the Aircraft Pitch Dynamics*

The procedure adopted to tune the FOPI controller parameters for the aircraft pitch model is given as under:

Consider Eq. (71.1) and put s = jω and simplify, then

$$P(j\omega) = \frac{1.151j\omega + 0.1774}{j(0.921\omega - \omega^3) - 0.739\omega^2} \tag{71.6}$$

The magnitude of the above $P(j\omega)$ is given by:

$$|P(j\omega)| = \frac{\sqrt{1.324\omega^2 + 0.03147}}{\omega\sqrt{(\omega^4 - 1.296\omega^2 + 0.848)}} \tag{71.7}$$

And the phase angle is given by:

$$Arg(P(j\omega)) = \tan^{-1}(6.488\omega) - \tan^{-1}\left(\frac{\omega^2 - 0.921)}{0.739\omega}\right) \tag{71.8}$$

For the system defined by Eq. (71.1), the transfer function of the fractional order PI controller is given by:

$$C(s) = K_p + \frac{K_p K_i}{s^\lambda} = K_p\left(1 + \frac{K_i}{s^\lambda}\right) \tag{71.9}$$

Putting s = jω, in the above equation we have:

$$C(j\omega) = K_p\left(1 + K_i(j\omega)^{-\lambda}\right) \tag{71.10}$$

Since, we know that:

$$j^{-\lambda} = \cos\frac{\lambda\pi}{2} - j\,\sin\frac{\lambda\pi}{2} \tag{71.11}$$

Substituting this value $j^{-\lambda}$ and rearranging in Eq. (71.10), we get:

$$C(j\omega) = \left(K_p + K_p K_i \omega^{-\lambda}\cos\frac{\lambda\pi}{2}\right) - j\left(K_p K_i \omega^{-\lambda}\sin\frac{\lambda\pi}{2}\right) \tag{71.12}$$

Thus the magnitude of $C(j\omega)$ is given by:

$$|C(j\omega)| = K_p\sqrt{1 + K_i^2\omega^{-2\lambda} + 2K_i\omega^{-\lambda}\cos\frac{\lambda\pi}{2}} \tag{71.13}$$

And the phase angle of $C(j\omega)$ is given by

$$Arg(C(j\omega)) = \tan^{-1}\left(\frac{-K_i\omega^{-\lambda}\sin\frac{\lambda\pi}{2}}{1 + K_i\omega^{-\lambda}\cos\frac{\lambda\pi}{2}}\right) \tag{71.14}$$

For phase margin specification from Eq. (71.3):

$$Arg[G(j\omega_{gc})] = Arg[C(j\omega_{gc})P(j\omega_{gc})] = -\pi + \phi_m$$

Substituting the phase and taking tan on both sides

$$\tan\left(\tan^{-1}\left(\frac{-K_i\omega_{gc}^{-\lambda}\sin\frac{\lambda\pi}{2}}{1+K_i\omega_{gc}^{-\lambda}\cos\frac{\lambda\pi}{2}}\right)+\pi\right) = \tan\left(\tan^{-1}\left(\frac{\omega_{gc}^2-0.921)}{0.739\omega_{gc}}\right)-\tan^{-1}(6.488\omega_{gc})+\phi_m\right) \tag{71.15}$$

Since ω_{gc} and ϕ_m are known desired specifications and constants, so taking the RHS of Eq. (71.15) as A:

$$A = \tan\left(\tan^{-1}\left(\frac{\omega_{gc}^2-0.921)}{0.739\omega_{gc}}\right)-\tan^{-1}(6.488\omega_{gc})+\phi_m\right) \tag{71.16}$$

Replacing this value of A in Eq. (71.15), and simplifying following is obtained:

$$\tan\left(\tan^{-1}\left(\frac{-K_i\omega_{gc}^{-\lambda}\sin\frac{\lambda\pi}{2}}{1+K_i\omega_{gc}^{-\lambda}\cos\frac{\lambda\pi}{2}}\right)+\pi\right) = A \tag{71.17}$$

Simplifying above equation using tan(a + b) formula:

$$\frac{\tan\left(\tan^{-1}\left(\frac{-K_i\omega_{gc}^{-\lambda}\sin\frac{\lambda\pi}{2}}{1+K_i\omega_{gc}^{-\lambda}\cos\frac{\lambda\pi}{2}}\right)\right)+\tan\pi}{1-\tan\left(\tan^{-1}\left(\frac{-K_i\omega_{gc}^{-\lambda}\sin\frac{\lambda\pi}{2}}{1+K_i\omega_{gc}^{-\lambda}\cos\frac{\lambda\pi}{2}}\right)\right)\cdot\tan\pi} = A \tag{71.18}$$

Substituting the value $tan\pi = 0$, will result in:

$$\Rightarrow \frac{-K_i\omega_{gc}^{-\lambda}\sin\frac{\lambda\pi}{2}}{1+K_i\omega_{gc}^{-\lambda}\cos\frac{\lambda\pi}{2}} = A \tag{71.19}$$

Solving for K_i from above equation, finally:

$$K_i = \frac{-A}{\omega_{gc}^{-\lambda}\left(\sin\frac{\lambda\pi}{2}+A\,\cos\frac{\lambda\pi}{2}\right)} \tag{71.20}$$

Similarly for gain crossover frequency specification from Eq. (71.4):

$$|G(j\omega_{gc})| = |C(j\omega_{gc})P(j\omega_{gc})| = 1$$

Substituting the magnitude of $C(j\omega_{gc})$ and $P(j\omega_{gc})$ in above equation:

$$\frac{K_p\sqrt{1+K_i^2\omega_{gc}^{-2\lambda}+2K_i\omega_{gc}^{-\lambda}\cos\frac{\lambda\pi}{2}}\sqrt{1.324\omega_{gc}^2+0.03147}}{\omega_{gc}\sqrt{\left(\omega_{gc}^4-1.296\omega_{gc}^2+0.848\right)}} = 1 \tag{71.21}$$

Taking cross multiplication:

$$K_p\sqrt{1+K_i^2\omega_{gc}^{-2\lambda}+2K_i\omega_{gc}^{-\lambda}\cos\frac{\lambda\pi}{2}} = \frac{\omega_{gc}\sqrt{\left(\omega_{gc}^4-1.296\omega^2+0.848\right)}}{\sqrt{1.324\omega_{gc}^2+0.03147}} \tag{71.22}$$

Since the RHS of Eq. (71.22) is constant, so considering it as B i.e.:

$$\frac{\omega_{gc}\sqrt{\left(\omega_{gc}^4-1.296\omega^2+0.848\right)}}{\sqrt{1.324\omega_{gc}^2+0.03147}} = B \tag{71.23}$$

So the Eq. (71.22) becomes:

$$K_p\sqrt{1+K_i^2\omega_{gc}^{-2\lambda}+2K_i\omega_{gc}^{-\lambda}\cos\frac{\lambda\pi}{2}} = B \tag{71.24}$$

Solving for K_p, following solution for K_p is obtained:

$$K_p = \frac{B}{\sqrt{1+K_i^2\omega_{gc}^{-2\lambda}+2K_i\omega_{gc}^{-\lambda}\cos\frac{\lambda\pi}{2}}} \tag{71.25}$$

Finally for robustness to gain variation of the plant from Eq. (71.5) we have:

$$\frac{d\left(\tan^{-1}\left(\frac{-K_i\omega_{gc}^{-\lambda}\sin\frac{\lambda\pi}{2}}{1+K_i\omega_{gc}^{-\lambda}\cos\frac{\lambda\pi}{2}}\right)\right)}{d\omega} + \frac{d\left(\tan^{-1}\left(6.488\omega_{gc}\right)\right)}{d\omega} - \frac{d\left(\tan^{-1}\left(\frac{\omega_{gc}^2-0.921)}{0.739\omega_{gc}}\right)\right)}{d\omega} = 0 \tag{71.26}$$

After differentiating the above equation and substituting $\omega = \omega_{gc}$:

$$\frac{\left(\lambda K_i \omega_{gc}^{-\lambda-1} \sin\frac{\lambda\pi}{2}\right)}{\left(1 + K_i^2 \omega_{gc}^{-2\lambda} + 2K_i \omega_{gc}^{-\lambda} \cos\frac{\lambda\pi}{2}\right)} = \frac{0.739\omega_{gc}^2 + 0.68062}{\omega_{gc}^4 - 1.296\omega_{gc}^2 + 0.848} - \frac{6.488}{1 + 42.094\omega_{gc}^2} \tag{71.27}$$

Taking the RHS of Eq. (71.27) as C, i.e.:

$$C = \frac{0.739\omega_{gc}^2 + 0.68062}{\omega_{gc}^4 - 1.296\omega_{gc}^2 + 0.848} - \frac{6.488}{1 + 42.094\omega_{gc}^2} \tag{71.28}$$

Substituting the value of Eq. (71.28) in Eq. (71.27), will lead to:

$$\frac{\left(\lambda K_i \omega_{gc}^{-\lambda-1} \sin\frac{\lambda\pi}{2}\right)}{\left(1 + K_i^2 \omega_{gc}^{-2\lambda} + 2K_i \omega_{gc}^{-\lambda} \cos\frac{\lambda\pi}{2}\right)} = C \tag{71.29}$$

Simplifying the above equation

$$K_i^2\left(C\omega_{gc}^{-2\lambda}\right) + K_i\left(2C\omega_{gc}^{-\lambda}\cos\frac{\lambda\pi}{2} - \lambda\omega_{gc}^{-\lambda-1}\sin\frac{\lambda\pi}{2}\right) + C = 0 \tag{71.30}$$

Now substituting the value of K_i from Eqs. (71.20) to (71.30), we obtain:

$$\begin{gathered}\left(\frac{-A}{\omega_{gc}^{-\lambda}\left(\sin\frac{\lambda\pi}{2} + A\,\cos\frac{\lambda\pi}{2}\right)}\right)^2\left(C\omega_{gc}^{-2\lambda}\right) + \left(\frac{-A}{\omega_{gc}^{-\lambda}\left(\sin\frac{\lambda\pi}{2} + A\,\cos\frac{\lambda\pi}{2}\right)}\right)\\ \left(2C\omega_{gc}^{-\lambda}\cos\frac{\lambda\pi}{2} - \lambda\omega_{gc}^{-\lambda-1}\sin\frac{\lambda\pi}{2}\right) + C = 0\end{gathered} \tag{71.31}$$

$$\Rightarrow \sin^2\left(\frac{\lambda\pi}{2}\right)\left(\frac{A\lambda}{\omega_{gc}} + A^2C + C\right) = \left(-\frac{A^2\lambda}{2\omega_{gc}}\right)\sin\lambda\pi \tag{71.32}$$

71.3.3 Computation of the Controller Parameters Graphically

The graphical method used to get Kp, Ki and λ is given by

1. From equation no (71.32), we infer that it contains only one variable i.e. λ and all the other parameters are known quantities. So Eq. (71.32) can be solved

Fig. 71.2 Graphical computation of λ

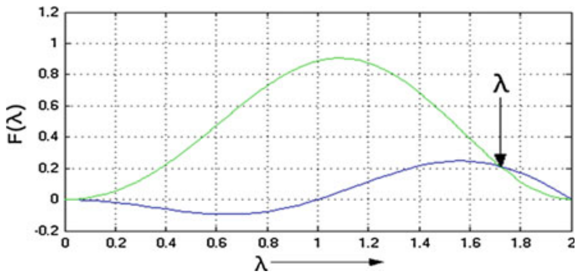

graphically to get the value of λ by considering LHS as one function of λ i.e. $F_1(\lambda)$ and RHS as another function of λ i.e. $F_2(\lambda)$. Plot the graphs of $F_1(\lambda)$ and $F_2(\lambda)$ and find the intersection of both the curve to have the solution of λ. Also keep in mind that select that value of λ such that it should lie between 0 and 2 i. e. $\lambda \in (0, 2)$.

$$F_1(\lambda) = \sin^2\left(\frac{\lambda\pi}{2}\right)\left(\frac{A\lambda}{\omega_{gc}} + A^2C + C\right) \tag{71.33}$$

and,

$$F_2(\lambda) = \left(-\frac{A^2\lambda}{2\omega_{gc}}\right)\sin\lambda\pi \tag{71.34}$$

Graphical solution for λ is shown in Fig. 71.2 with ω_{gc} = 2.05 rad/s and φ_m = 60°.

The controller parameters λ obtained from the graph is λ = 1.7257.

2. Substitute the value of λ in Eq. (71.20), the parameter K_i is obtained as 8.516.
3. Substitute the value of λ and K_i in Eq. (71.25), K_p is obtained as 1.676.

71.4 Performance Analysis of the FOPI Controller for Aircraft Pitch Dynamics

The Bode plot for the FOPI controller for Aircraft pitch control system is shown in Fig. 71.3. From the graph, it is evident that the plot is flat at ω_{gc} = 2 rad/s and phase margin of 60°, based on the proposed design. Figure 71.4 shows the servo response of the proposed controller for the aircraft pitch dynamics. Under parameter

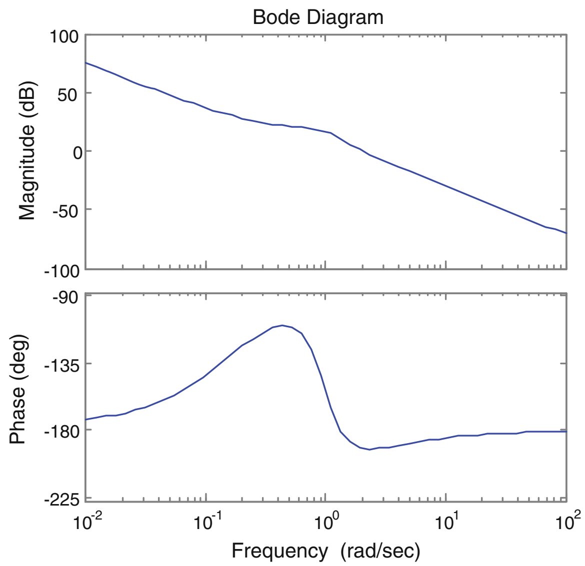

Fig. 71.3 Bode diagram of FO-PI control for Aircraft pitch

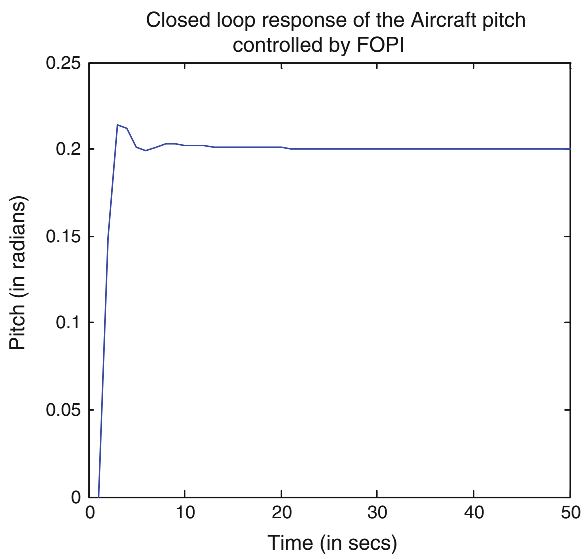

Fig. 71.4 Servo response of the FOPI controller for Aircraft pitch control

variations (Process gain changes ±10 %), the controller tracks the set point exactly reproducing the dynamics under no parameter change. Figure 71.5 shows the servo response under parameter variations.

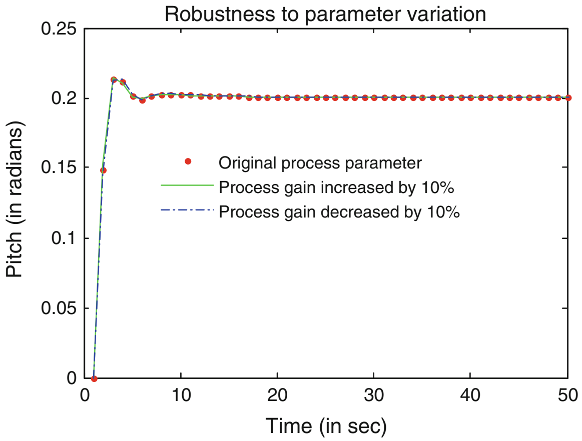

Fig. 71.5 Servo response under variations in process gain

71.5 Conclusion

A fractional order Proportional Integral controller is proposed for an Aircraft Pitch control system which is a Type 1, second order system. This method is simple one as only design specifications need to be fed into the equations to obtain the tuning parameters. Even though the process considered is open loop unstable, the proposed control tracks the set point making it stable in the closed loop. The response shows the robustness to process gain variations of ±10 %.

References

1. Igor P (1999) Fractional-order systems and $PI^{\lambda}D^{\mu}$ controllers. IEEE Trans Autom Control 44 (1):208–214
2. Valerio D, Da Costa JS (2006) Tuning of fractional PID controllers with Ziegler–Nichols-type rules. Sig Process 86(10):2771–2784
3. Astrom KJ, Hagglund T (2004) Revisiting the Ziegler–Nichols step response method for PID control. J Process Control 14(6):635–650
4. Chen YQ, Bhaskaran T, Xue D (2008) Practical tuning rule development for fractional order proportional and integral controllers. ASME J Comput Nonlinear Dyn 3(2):021403
5. Ho WK, Hang CC, Cao LS (1995) Tuning of PID controllers based on gain and phase margin specifications. Automatica 31(3):497–502
6. Shantanu Das (2008) Functional fractional calculus for system identification and controls. Springer, Berlin
7. Chen YQ, Moore KL (2005) Relay feedback tuning of robust PID controllers with iso-damping property. IEEE Trans Syst Mach Cybern 35(1):23–31
8. Monje CA, Calderon AJ, Vingre BM, Chen YQ, Feliu V (2004) On fractional PI^{λ} controllers: some tuning rules for robustness to plant uncertainties. Nonlinear Dyn 38(1–2):369–381
9. Li HS, Luo Y, Chen YQ (2010) A fractional order proportional and derivative (FOPD) motion controller: tuning rule and experiments. IEEE Trans Control Syst Technol 18(2):516–520

10. Luo Y, Chen YQ (2009) Fractional order [proportional derivative] controller for a class of fractional order systems. Automatica 45(10):2446–2450
11. Luo Y, Chen YQ, Wang CY, Pi YG (2010) Tuning fractional order proportional integral controllers for fractional order systems. J Process Control 20(7):823–831
12. Monje CA, Vinagre BM, Feliu V, Chen YQ (2008) Tuning and auto-tuning of fractional order controllers for industry applications. Control Eng Practices 16(7):798–812
13. Dorcak L, Terpak J, Papajova M, Dorcakova F, Pivka L (2007) Design of the fractional-order $PI^{\lambda}D^{\mu}$ controller based on the optimization with self-organizing migrating algorithm. ACTA Montanist Slovaca 12(4):285–293
14. Biswas A, Das S, Abraham A, Dasgupta S (2009) Design of fractional-order $PI^{\lambda}D^{\mu}$ controllers with an improved differential evolution. Eng Appl Artif Intell 22(2):343–350
15. Maiti D, Chakraborty M, Acharya A, Konar A (2008) Design of a fractional-order self-tuning regulator using optimization algorithms. In: Proceedings of 11th international conference on computer and information technology, pp. 470–475
16. Zamani M, Karimi-Ghartemani M, Sadati N, Parniani M (2009) Design of a fractional order PID controller for an AVR using particle swarm optimization. Control Eng Practices 17 (12):1380–1387
17. Lee C-H, Chang F (2010) Fractional-order PID controller optimization via improved electromagnetism-like algorithm. Expert Syst Appl 37(12):8871–8878
18. Bouafoura MK, Braiek NB (2010) $PI^{\lambda}D^{\mu}$ controller design for integer and fractional plants using piecewise orthogonal functions. Commun Nonlinear Sci Numer Simul 15(5):1267–1278
19. Castillo FJ, Feliu V, Rivas R, Sanchez L (2010) Design of a class of fractional controllers from frequency specifications with guaranteed time domain behavior. Comput Math Appl 59 (5):1656–1666
20. Bhambhani V, Han Y, Mukhopadhyay S, Luo Y, Chen Y (2010) Hardware-in-the-loop experimental study on a fractional order networked control system testbed. Commun Nonlinear Sci Numer Simul 15(9):2486–2496
21. http://ctms.engin.umich.edu/CTMS

Chapter 72
Retracted: An Independent Reconstruction Error Using Randomized Quantization

S. Arunadevi and S. Sathya

Abstract The analyze of optimal randomized quantization is the existence of an optimal (minimum distortion) randomized quantizer having a fixed output distribution under various conditions. For source with densities and the mean square distortion measure, This optimum can be attained by randomizing quantizer. The source achieve an independent quantization error. The reconstruction error is deterministic function which is never render the quantization error independent of source. Also implement the optimal quantizer from conventional uniform quantizer. The dither signal is matched to the uniform quantization interval while maintaining independence of the source. The propose dithering in the companded domain. The derivation of the closed form necessary conditions for optimality of the compressor and expander mappings for both fixed and variable rate randomized quantization. In numerically optimize the mappings by iteratively imposing these necessary conditions. The experimental results show that optimal quantizer performance for both fixed and variable rate and correlation of reconstruction error.

Keywords Conventional · Compander · Dither · Mapping · Minimum distortion · Optimal

72.1 Introduction

Dithered quantization is a randomized quantization method introduced. A central motivation for dithered quantization is its ability to yield quantization error that is independent of the source which can be achieved if certain conditions, determiner

The erratum of this chapter can be found at DOI 10.1007/978-81-322-2119-7_157

S. Arunadevi (✉) · S. Sathya
Department of Electronics and Communication Engineering, Dhanalakshmi Srinivasan Engineering College, Perambalur, Tamilnadu, India
e-mail: arunadevi.s90@gmail.com

C. Kamalakannan et al. (eds.), *Power Electronics and Renewable Energy Systems*, Lecture Notes in Electrical Engineering 326, DOI 10.1007/978-81-322-2119-7_72

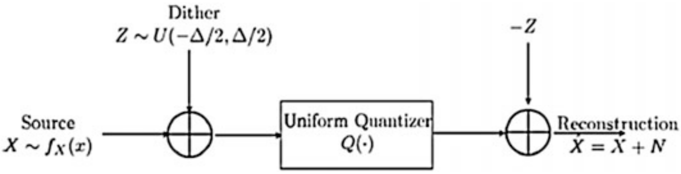

Fig. 72.1 The basic structure of dithered quantization

by schuchman, are met. The conventional dithered quantization framework involves a uniform quantizer, with step size Δ, and a dither signal uniformly distributed over $\left(-\frac{\Delta}{2}, \frac{\Delta}{2}\right)$ matched to the quantizer interval as shown in Fig. 72.1. A uniformly distributed dither signal is added before quantization and the same dither signal is subtracted from the quantized value at the decoder side, while in non-subtractive dithering decoder does not have access to the dither signal. Subtractive dithering renders the quantization error independent of the source. We consider only subtractive dithering in this paper, while noting that the basic ideas are also applicable to non-subtractive.

On the more theoretical side, randomized (dithered) quantizers have been studied in the past due to important properties that differentiate them from deterministic quantizers, and were employed to characterize rate-distortion bounds for universal compression. The continued interest in dithered quantizers is due to their statistical properties. Zamir and Feder provide extensive studies of the properties of dithered quantizers. The results of these studies, entrophy as, specifically the fact that the dithered lattice quantizer at asymptotically high dimension realizes the Gaussian test channel, have led to the wide use of entropy coded dithered lattice quantization as a "structured method" to achieve fundamental bounds obtained via random (unstructured) coding arguments.

A main application area of dithered quantization in complex system, due its simplicity in modeling quantization errors. For instance, Goyal recently investigated the performance of a collection of subtractively—dithered uniform scalar quantizers with the same step size, used in parallel as a model for the randomly varying uniform conventional quantizers. It is useful in analog-digital converters in general, particularly in delta-sigma modulators where statistics of the quantization error is an important consideration. Many filter/system optimization problems in practical compression settings, such as the "rate-distortion optimal filter bank design" problem, or low rate filter optimization for DPCM compression of Gaussian autoregressive processes, assume quantization noise that is independent of the source.

In this paper, consider a generalization to enable effective dithering of non-uniform quantizers. To the best of our knowledge, this paper is the first attempt to consider dithered quantization in a non-uniform quantization framework. One immediate problem with non-uniform dithered quantization is how to apply dithering to unequal quantization intervals. The propose dithering in companded domain. Derive the closed form necessary conditions for optimality of the compressor and expander mappings for both fixed and variable rate randomized quantization.

The paper is organized as follows: In Sect. 72.3, present the proposed non-uniform randomized quantizers, along with its extension to constrained randomized quantizer that renders the quantization error orthogonal to source. In Sect. 72.4, derive the necessary conditions of optimality for the deterministic quantizer that generates reconstruction error uncorrelated with the source. In Sect. 72.5, study the asymptotic results, and show that for a Gaussian source. Experimental results that compare the proposed quantizers are presented in Sect. 72.4. Discuss the results and summarize the contributions in Sect. 72.7.

72.2 Review of Dithered Quantization

72.2.1 Notation and Preliminaries

Let R and R^{+}denote the respective sets of real numbers, and positive real numbers.

The mutual information between two random variables X and Y with marginal densities $f_X(x)$ and $f_Y(y)$ and a joint density $f_{XY}(x, y)$ is given by

$$I(X, Y) = \iint f_{X,Y}(x, y) \log \frac{f_{X,Y}(x, y)}{f_X(x) f_Y(y)} dxdy \tag{72.1}$$

72.2.2 Dithered Quantization

A quantizer is defined by a set of reconstruction points and a partition. The scalar uniform quantizer, with reconstructions $\{\pm\Delta, \pm 2\Delta, \ldots, T\Delta\}$, is a mapping Q: R $\rightarrow$ R such that

$$\mathrm{Q(x)} = \mathrm{i}\Delta \ \mathrm{for}\ \mathrm{i}\Delta - \mathrm{i}\Delta/2 < \mathrm{x} \le \mathrm{i}\Delta + \Delta/2. \tag{72.2}$$

72.3 Non-uniform Dithered Quantizer

The main idea is to circumvent the main difficulty due to unequal quantization intervals by performing uniform dithered quantization in the companded domain (Fig. 72.2). The source X is transformed through compressor g(·) before undergoing dithered uniform quantization. At the decoder side, the dither is subtracted to obtain Y. Since we perform uniform dithered quantization in the companded domain, it is easy to show that Y = g(x) + N, where N is uniformly distributed over $(-\Delta/2, \Delta/2)$ and independent of the source. The reconstruction is obtained by applying the expander $\hat{X} = \mathrm{w}(Y)$. The objective is to optimal compressor and expander mappings g(·), w(·) that minimize the expected distortion under the rate constraint. The MSE distortion can be written as:

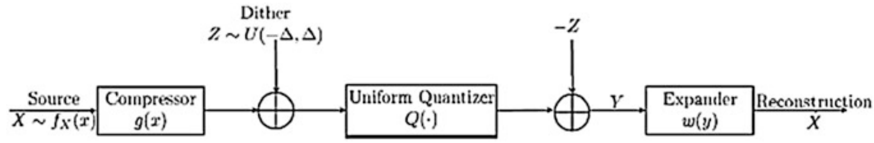

Fig. 72.2 The proposed non-uniform dithered quantizer

$$\mathrm{D} = \iint \left[x - w(g(x) + n)\right]^2 fX(x) f_N(n) dxdn\right] \tag{72.3}$$

where $f_N(\mathrm{n})$ is uniform over $(-\Delta/2, \Delta/2)$.

72.3.1 Optimal Expander

The conditional expectation $\mathrm{E}\{\mathrm{X} \backslash Y = y\}$ minimizes MSE between the source and the estimate, the optimal expender can be written, in terms of known quantities as

$$w(y) = \frac{\int_{-\infty}^{\infty} x f_X(x) f_N(y - g(x)) dx}{\int_{-\infty}^{\infty} f_X(x) f_N(y - g(x)) dx} \tag{72.4}$$

72.3.2 Optimal Compressor

Unlike the expander, the optimal compressor cannot be written in closed form. Thus, a locality optimal compressor g(·), for a given expander w(·), requires that the functional derivative of the total cost, J, along the direction of any admissible variation function $n(\cdot)$. Vanishes, i.e.,

$$\frac{\partial}{\partial \varepsilon}\Big|_{\varepsilon=0} J[g(x) + \varepsilon\eta(x)] = 0, \tag{72.5}$$

a.e. in x, for all admissible perturbation functions n(·).

72.3.3 Design Algorithm

The basic idea is to iteratively alternate between the imposition of individual necessary conditions for optimality, and thereby successively decrease the total cost. By design, the Lagrangian cost decreases monotonically as the algorithm proceeds iteratively. The update for the compressor is stated generically as

$$g_{i+1}(\mathrm{x}) \ = g_i(\mathrm{x}) - \mu \nabla J[g] \tag{72.6}$$

where i is the iteration index, $\nabla J[g(\cdot)]$ is the directional derivative and μ is the step size. The precise expressions for $\nabla J[g]$ for fixed and variable rates.

72.4 Reconstruction Error Uncorrelated with the Source

We propose two quantization schemes (one deterministic, one randomized) that satisfy the constraint that reconstruction error be uncorrelated with the source.

72.4.1 Constrained Deterministic Quantizer

A deterministic quantizer cannot yield quantization noise independent of the source. However, it is possible to render the quantization noise uncorrelated with the source.

72.4.2 Constrained Randomized Quantizer

Due to the effect of companding, the non-uniform randomized quantizer does not guarantee reconstruction error uncorrelated with the source even though it builds on the (conventional) dithered quantizer whose quantization error is independent of the source.

72.5 Asymptotic Analysis

72.5.1 Rate-Distortion Functions

We define two rate-distortion functions in which we respectively constrain the reconstructions error to be (i) uncorrelated with the source: $R_U(\mathrm{D})$, and (ii) independent of the source: $R_I(\mathrm{D})$. The source compression under the constraints that reconstruction error is uncorrelated with or independent of the source. i.e., $R_U(\mathrm{D}) = R_U^*(D)$ and $R_I(\mathrm{D}) = R_I^*(\mathrm{D})$.

72.5.2 Gaussian Vector Source with MSE Distortion

The reconstruction error for the Gaussian source subject to the uncorrelated error constraint is independent of the source. No deterministic quantizer can render the quantization noise independent from the source by definition; hence, the optimal quantizer is a randomized one.

72.6 Simulation Results

We compare the proposed quantizers to the conventional (uniform) dithered quantizer and to the optimal quantizer, for a standard unit variance scalar Gaussian source. In this paper, we proposed three new quantizers:

Quantizer 1: Unconstrained randomized quantizer. This quantizer does not render the reconstruction error uncorrelated with the source.

Quantizer 2: Constrained randomized quantizer which render the quantization error uncorrelated with the source.

Quantizer 3: Constrained deterministic quantizer which renders the quantization error uncorrelated with the source.

Figures 72.3 and 72.4 demonstrate the performance comparisons among quantizers for fixed and variable rates respectively. Note that for both fixed and variable rate, the optimal randomized quantizer performs very close to the optimal quantizer.

Note that for fixed rate, conventional (uniform) dithered quantization suffers significantly from the sub optimality of having equal quantization intervals irrespective of the rate region. However, at variable rate, the difference between the proposed and conventional dithered quantizer diminishes at high rates, while at low

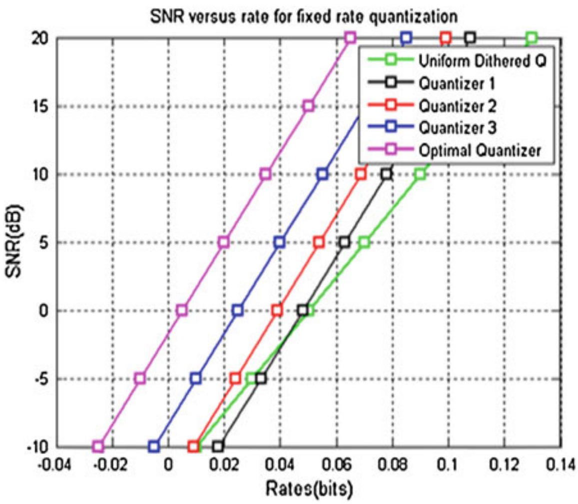

Fig. 72.3 Performance comparison in terms of SNR versus rate for fixed rate quantization

rates difference is quite significant. This is theoretically anticipated since at high rates, the optimal variable rate quantizer is very close to uniform, hence there is not much to gain from using a non-linear compressor-expander. While both of them perform significantly better than the conventional dithered quantizer (Figs. 72.5 and 72.6).

An additional benefit of the proposed random quantizers pertains of the correlation of the reconstruction errors when correlated sources are quantized. The conventional dithered quantizer renders quantization error independent of the source hence, when two correlated sources are quantized with a dithered quantizer, the reconstruction errors are uncorrelated.

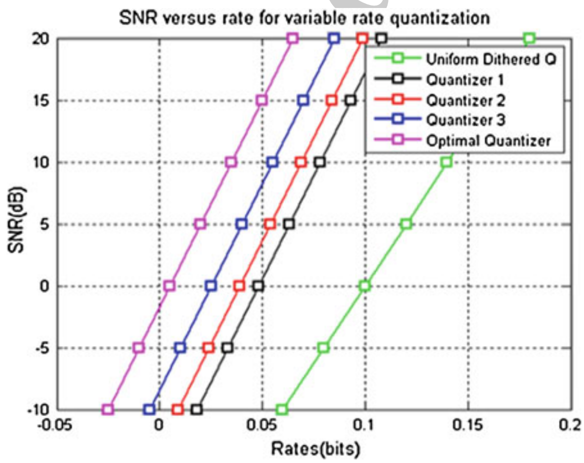

Fig. 72.4 Performance comparison in terms of SNR versus rate for variable rate quantization

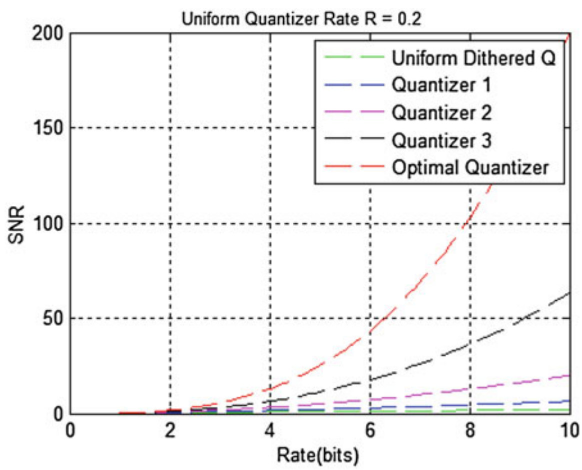

Fig. 72.5 Performance of SNR Versus Rate (Bits) At R = 0.2

Fig. 72.6 Correlation of the reconstruction error versus correlation for fixed and variable rate R = 1.4 bits/ sample

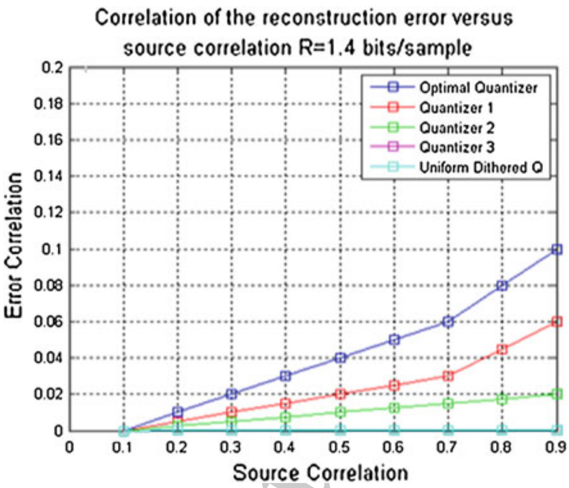

72.7 Conclusion

In this paper, the proposed a non-uniform randomized quantizer where dithering is performed in the companded domain to circumvent the problem of matching the dither range to varying quantization intervals. The optimal compressor and expander mappings that minimize the mean square error are found via a novel numerical method. The proposed constrained randomized quantization outperforms conventional dithered quantization and also the constrained deterministic quantizer proposed in this paper, while still satisfying the requirement that the reconstruction error be uncorrelated with the source. Moreover, the proposed randomized quantizers significantly reduce the correlations across reconstruction errors when correlated samples. The design complexity of proposed non-uniform dithered scalar quantizers is not significantly different from that of the optimal conventional quantizers. And also showed that at asymptotically high dimensions, the MSE optimal vector quantizer designed for a vector Gaussian source, which renders the reconstruction error uncorrelated with the source, must be a randomized quantizer.

References

1. Wannamaker RA, Lipshitz SP, Vanderkooy J, Wright JN (2000) A theory of nonsubtractive dither. IEEE Trans Signal Process 48(2):499–516
2. Li M, Klejse J, Kleijn WB (2010) Distribution preserving quantization with dithering and transformation. IEEE Signal Process Lett 17(12):1014–1017
3. Saldi N, Linder T, Yuksel S (2013) Randomized quantization and optimal design with a marginal constraint. In Proceedings of IEEE international symposium information theory (ISIT), 2013

4. Ostergaard J, Zamir R (2009) Multiple-description coding by dithered delta-sigma quantization. IEEE Trans Inf Theory 55(10):4661–4675
5. Zamir R, Kochman Y, Erez U (2004) Achieving the Gaussian rate-distortion function by prediction. IEEE Trans Inf Theor 50(10):2293–2314
6. Pamarti S, Welz J, Galton I (2007) Statistics of the quantization noise in I-bit dithered single-quantizer digital delta-sigma modulators. IEEE Trans Circuits Syst I Reg Papers 54(3):493–503
7. Boyd S, Ghosh A, Prabhakar B, Shah D (2006) Randomized gossip algorithms. IEEE Trans Inf Theor 52(6):2508–2530

Chapter 73
Mitigation of Power Quality Issues in Three-Phase Four-Wire Distribution System Employing Four-Leg DSTATCOM

C.K. Sundarabalan, K. Selvi and P. Shirley Vaz

Abstract An increasing growth of non-linear load in the three-phase four-wire distribution system, results in various power quality problems in the distribution system. Custom power devices (CPD) have been evolved to solve the power quality problems in the distribution system. Among the various custom power devices, Distribution Static Compensator (DSTATCOM) is one of the effective solutions for solving the power quality problems. This paper reveals about Distribution static compensator (DSTATCOM) for balancing of source currents, harmonic mitigation and neutral current compensation in three-phase four-wire distribution system. A synchronous reference frame (SRF) theory is projected for the control of DSTATCOM. Four-leg voltage source converter (VSC) with a dc capacitor is used as four-wire DSTATCOM. Here DSTATCOM is operated in load compensation mode. The first three-legs are used for balancing of source current and harmonic mitigation and the fourth leg is used for neutral current compensation. The compensation performance of DSTATCOM using the proposed control strategy is demonstrated using simulation results obtained from MATLAB/SIMULINK.

Keywords Custom power device · Distribution static compensator (DSTATCOM) · Synchronous reference frame (SRF) theory · Voltage source converter (VSC)

73.1 Introduction

With the development of power electronic technology, CPD plays an important role in bringing unique efficiency improvement and cost effectiveness in modern electrical power systems [1, 2]. They root excessive neutral currents, overheating of

C.K. Sundarabalan (✉) · K. Selvi · P.S. Vaz
Department of Electrical and Electronics Engineering,
Thiagarajar College of Engineering, Madurai, India
e-mail: ckseee@tce.edu

C. Kamalakannan et al. (eds.), *Power Electronics and Renewable Energy Systems*,
Lecture Notes in Electrical Engineering 326, DOI 10.1007/978-81-322-2119-7_73

electrical apparatus, poor power factor, voltage distortion, high levels of neutral-to-ground voltage, and interference with communication systems [3, 4]. The literature reports the progress of different CPD to mitigate the above power quality problems by injecting voltages/currents or both into the system [5–7]. The shunt-connected custom power device, called the distribution static compensator (DSTATCOM), injects current at the point of common coupling (PCC). So that harmonic filtering, power factor correction, and load balancing can be achieved. The custom power is a relatively emerging concept designed at achieving high power quality, operational flexibility and controllability of the electrical power systems [8]. The DSTATCOM is one of the CPD that received much awareness for improving power system performance during steady state, dynamic stability, voltage regulation and better power quality [9]. Most of the commercial and industrial loads own non-linear characteristics. Among the different control techniques applied to the three-phase four-wire compensators, the SRF theory is suitable for the control of DSTATCOM [10]. The instantaneous reactive power theory (p–q theory), SRF theory, power balance theory, space vector pulse width modulation technique [11, 12] etc. have been proposed to control DSTATCOM for three-phase four-wire systems. However, SRF theory is considered superior than p-q theory in the three-wire system owing to reduced computation and directly using the currents only. In this paper, four-leg VSC employing fast switching insulated gate bipolar transistor (IGBT) with a dc bus capacitor is mainly engaged for the required compensation. The first three legs are used for balancing of source current and harmonic mitigation and the fourth leg is used for neutral current compensation.

73.2 Proposed System

A VSC based DSTATCOM is coupled to a three-phase source feeding three-phase linear/non-linear load through impedance connected between them, which is exposed in Fig. 73.2. The performance of DSTATCOM depends upon the accuracy of harmonics current detection and reference current generation. Interfacing inductors are connected at ac output of the VSC for reducing ripples in the compensating current. Ripple filter is used for reducing the high frequency switching noise of the VSC. The DSTATCOM currents are injected as required compensating currents to cancel the harmonics of the load current, so that harmonics is reduced on the distribution system. The data used in three-phase four-wire distribution system is given in appendix. The dc bus voltage is calculated as follows:

$$V_{dc} = 2\sqrt{2}V_{LL}/\sqrt{3}m \tag{73.1}$$

where m is the modulation index considered as 1 and the V_{LL} is line to line voltage.

Thus V_{dc} is obtained as 677.69 V for V_{LL} of 415 V and it is selected as 680 V. The dc capacitor is calculated as

$$0.5C_{dc}\left[\left(V_{dc}^2\right) - \left(V_{dc1}^2\right)\right] = 3V(aI)t \tag{73.2}$$

where V_{dc} is the reference dc voltage and V_{dc1} the minimum voltage level of dc bus, a the overloading factor, V the phase voltage, I the phase current, and t the time by which the dc bus voltage is to be recovered. Considering V_{dc} = 680 V, V_{dc1} = 700 V, V = 415/√3 = 239.6 V, I = 5.13 A, t = 350 μs and a = 1.2, the calculated value of C_{dc} is 2600 μF. So C_{dc} the chosen to be 3,000 μF. Among various theories SRF theory is used for the exploration of three-phase four-wire DSTATCOM. A block diagram of the control scheme is given in Fig. 73.1. The feedback signals are sensed from the load currents, PCC voltages and dc bus voltages of DSTATCOM. The load currents from the a-b-c frame are first transformed to α-β-0 frame and then to d-q-0 frame [13].

Each current component has an average value of dc component referred as I_{d1} and an oscillating value or ac component as I_{d2}.

$$I_d = I_{d1} + I_{d2} \tag{73.3}$$

Similarly in quadrature component, average value of dc component is referred as I_{q1} and oscillating quantity as I_{q2}.

$$I_q = I_{q1} + I_{q2} \tag{73.4}$$

The output of PI controller at the dc bus voltage of DSTATCOM is considered as the current (i_{loss}) for meeting its losses.

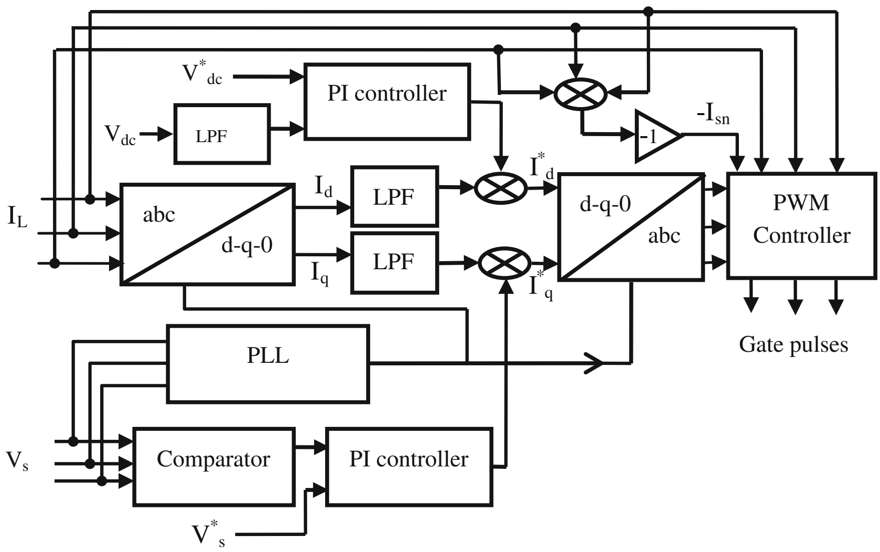

Fig. 73.1 DSTATCOM controller

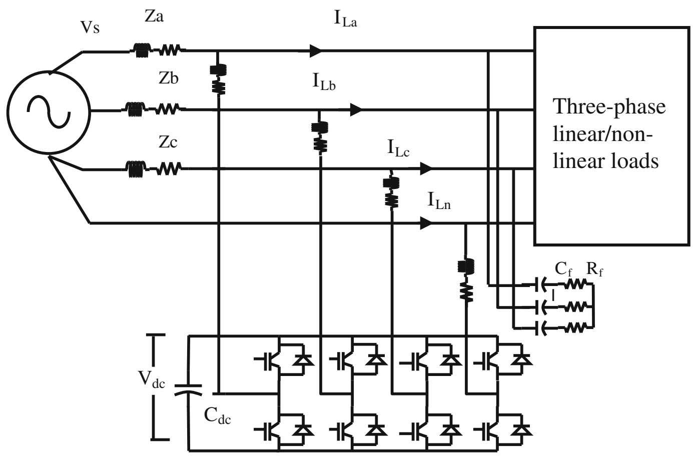

Fig. 73.2 Schematics of proposed system

$$I_{loss(n)} = I_{loss(n-1)} + K_{pd}\left(V_{de(n)} - V_{de(n-1)}\right) + K_{id}V_{de(n)} \tag{73.5}$$

where $V_{de(n)}$ is the error between reference and sensed dc voltage at the nth sampling instant. K_{pd} and K_{id} are the proportional and integral gains. Therefore the reference source current is,

$$I_d^* = I_{d1} + I_{loss} \tag{73.6}$$

The reference source current in the a–b–c frame is obtained by reverse transformation of the current vector.

73.2.1 Neutral Current Reduction

The novelty of the proposed system lies in neutral current reduction. Here the fourth leg of the inverter is used for neutral current compensation. The gating pulse for the two switches in the fourth leg of VSC of the DSTATCOM are obtained from the error signal by comparing sensed (i_{sn}) and reference (i_{sn}^*) neutral currents. The estimated signals of neutral current are obtained as

$$I_{sn} = -I_{sa} - I_{sb} - I_{sc} \tag{73.7}$$

73.3 Results and Discussions

The entire control algorithm and the compensation techniques has been carried out in the system shown in Fig. 73.2.

73.3.1 Performance of DSTATCOM with Linear Load for Load Balancing

The dynamic performance of DSTATCOM for linear load is shown in Fig. 73.3. At 0.1–0.2 s the load is changed to two phase loads and again to single phase loads at 0.2–0.3 s. The amplitude of the PCC voltage is maintained in its reference value under all disturbances. All the three-phases in source current are equal in magnitude even when the load is unbalanced.

73.3.2 Performance of DSTATCOM with Non-linear Load for Load Balancing and Harmonic Reduction

The dynamic performance of DSTATCOM for non-linear load is shown in Fig. 73.4. At 0.2–0.3 s the load is changed to two phase loads. The amplitude of the PCC voltage is maintained in its reference value under all disturbances. The source current in all the three-phases are equal in magnitude even when the load is unbalanced. This shows the effectiveness of compensation and also the dc bus voltage is maintained in its reference value. Also the harmonics is reduced in the source current.

73.3.3 Neutral Current Compensation

Due to the presence of unbalanced load in the distribution system there will be a flow of current in the neutral. Also due to effective compensation, the neutral current is nearly zero as shown in Fig. 73.5.

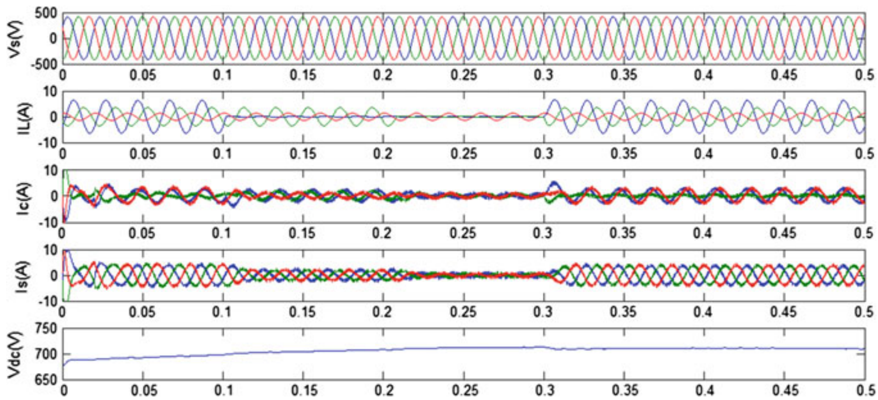

Fig. 73.3 Performance of DSTATCOM for load unbalancing

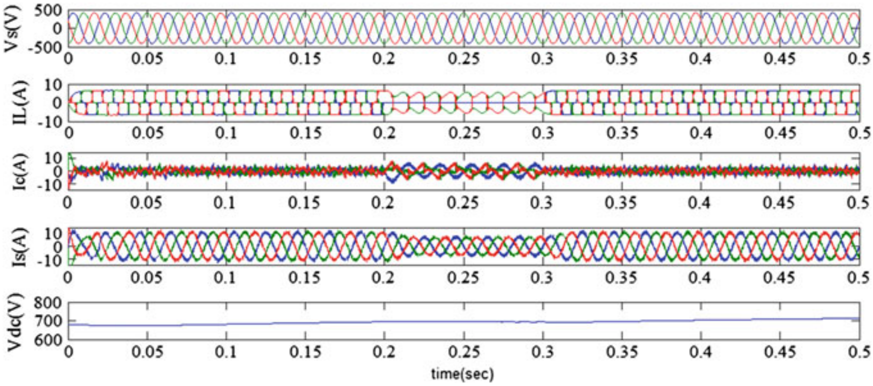

Fig. 73.4 Performance of DSTATCOM for harmonic mitigation

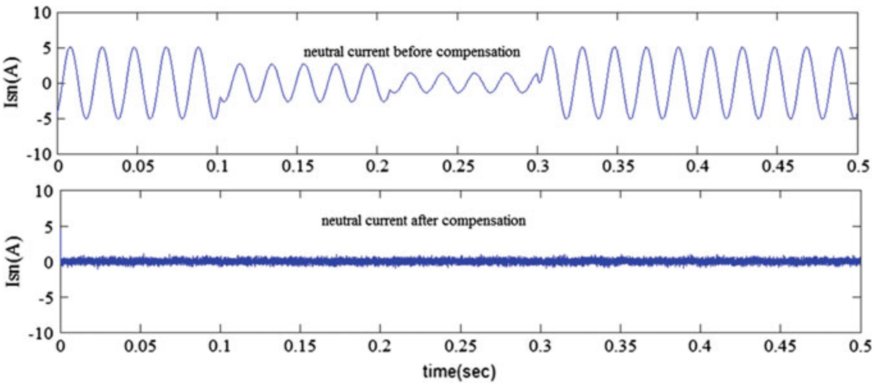

Fig. 73.5 Performance of DSTATCOM for neutral current compensation

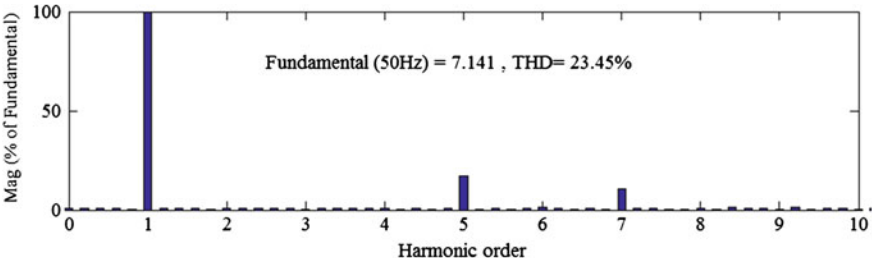

Fig. 73.6 Harmonic spectrum of source current before compensation

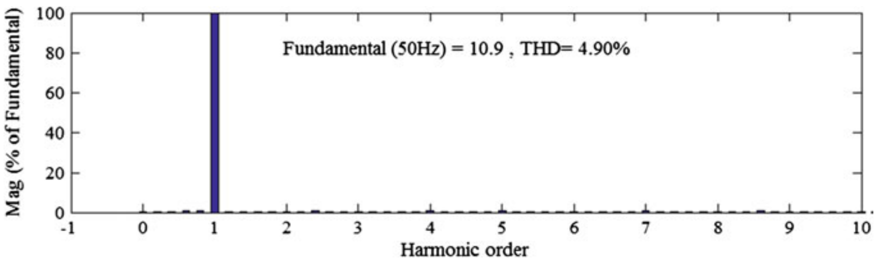

Fig. 73.7 Harmonic spectrum of source current after compensation

73.3.4 Harmonic Mitigation

It can be observed from Fig. 73.6 and 73.7 the DSTATCOM compensate the THD of source current from 23.45 % to 4.90 % respectively.

73.4 Conclusion

The performance of three-phase four-wire DSTATCOM for the mitigation of power quality issues like neutral current compensation, source harmonic reduction and load unbalancing are extensively simulated in MATLAB/SIMULINK.SRF theory has been presented for load unbalancing, source harmonic reduction, and neutral current compensation. First three leg of VSC are used for the compensation of unbalanced source current and harmonic current and the fourth leg of VSC is used for the compensation of neutral current due to the unbalanced load in the distribution system. The DSTATCOM injects current in such a way, to cancel out the excess neutral current, harmonic current and injection of reactive component, so that source current gets balanced. Pulse width modulation technique is used for pulse generation. It is observed that the THD (Total Harmonic Distortion) of the source current is reduced from 23.45 to 4.90 %.

A.1 73.5 Appendix: System Parameters of Proposed System

3-phase AC line voltage: 415 V, 50 Hz

Line impedance: Rs = 0.01 Ω, Ls = 2 mH per phase.

Ripple filter: $R_f = 5\ \Omega$, $C_f = 5\ \mu F$

DC bus capacitor of DSTATCOM: 3,000 μF

DC bus voltage: 680 V

Reference DC bus voltage: 700 V

DC bus voltage PI controller: $K_p = 0.025$, $K_i = 0.14$

PCC voltage PI controller: $K_p = 0.2$, $K_i = 0.5$
Linear load: $R_a = 30\ \Omega$, $L_a = 0.07$ H, $R_b = 60\ \Omega$, $L_b = 0.1$ H, $R_c = 120\ \Omega$, $L_c = 0.4$ H
Non-linear load: rectifier with RL loads 2,000 kVA, 0.707 pf lag.

References

1. Hingorani NG, Gyugyi L (2000) Understanding FACTS concept and technology of flexible AC transmission system. IEEE Press, New York
2. Olimpo AL, Acha E (2002) Modelling and analysis of custom power systems by PSCAD/EMTDC. IEEE Trans Power Deliv 17(1):266–272
3. Bollen MHJ (2001) Understanding power quality problems: voltage sags and interruptions. IEEE Press, New York
4. Grady WM, Santoso S (2001) Understanding power system harmonics. Proc. IEEE Power Eng Rev 21(11):8–11
5. Ghosh A, Ledwich G (2002) Power quality enhancement using custom power devices. Kluwer, Norwell
6. Dinavahi V, Iravani R, Bonert R (2004) Design of a real-time digital simulator for a D-STATCOM system. IEEE Trans Ind Electron 51(5):1001–1008
7. Vilathgamuwa D, Wijekoon HM, Choi SS (2006) *A* novel technique to compensate voltage sags in multiline distribution system and the interline dynamic voltage restorer. IEEE Trans. Ind. Electron 55(5):1603–1611
8. Crow ML (2004) Power quality enhancement using custom power devices. IEEE Power Energ Mag 2(2):50–53
9. Yu Q, Li P, Liu W, Xie X (2004) Overview of STATCOM technologies. Proceedings of IEEE international conference on electric utility deregulation, restructuring and power technologies, pp 647–652
10. Milanes MI, Cadaval ER, Gonzalez FB (2007) Comparison of control strategies for shunt active power filters in three-phase four-wire systems. IEEE Trans Power Electr 22(1):229–236
11. Kim H, Blaabjerg F, Jensen BB, Choi J (2002) Instantaneous power compensation in three-phase systems by using p-q-r theory. IEEE Trans Power Electron 17(5):701–709
12. Zaveri Tejas, Bhalja Bhavesh, Zaveri Naimish (2012) Comparison of control strategies for DSTATCOM in three-phase, four-wire distribution system for power quality improvement under various source voltage and load conditions. Electr Power Energy Syst 43:582–594
13. Kamatchi kannan V, Rengarajan N (2012) Photovoltaic based Distribution Static Compensator for power quality improvement. Electr Power and Energy Syst 42:685–692

Chapter 74
Performance Investigation of Fuzzy Logic Controlled MPPT for Energy Efficient Solar PV Systems

C.K. Sundarabalan, K. Selvi and K. Sakeenathul Kubra

Abstract This paper deals with the mathematical way of modeling solar panels involving mathematical equations for the calculation of solar panel current. Along with the conventional inputs series and shunt resistances are taken as additional inputs. Maximum Power Point Tracking (MPPT) algorithms implementing Perturb and Observe (P&O) and fuzzy logic techniques having the same voltage and current variables as inputs are implemented and their efficiencies are checked. A standard configuration of the boost converter employing a MOSFET device as a switch is implemented to obtain a constant DC output voltage. The MPPT algorithms identify the duty cycle at which the gating pulses have to be given to the switching device so that triggering occurs at the maximum power point thereby delivering maximum power to the load. Simulation results are obtained in MATLAB Simulink environment based on the mathematical and electrical models developed.

Keywords Boost converter · Fuzzy logic · MPPT · Perturb and observe · Solar PV array

74.1 Introduction

Solar energy production is one of the fastest growing renewable energy productions as the energy utilized is the light energy which comes from the sun which is inexhaustible. There are specific types of materials which generate current upon absorbing light. Those materials are called as photovoltaic materials. This voltage can be effectively utilized by series and parallel combination of cells [1]. The energy produced by the solar panels cannot be delivered efficiently to the load. Maximum power point controllers are modeled to extract the maximum power from

C.K. Sundarabalan (✉) · K. Selvi · K. Sakeenathul Kubra
Department of Electrical and Electronics Engineering, Thiagarajar College of Engineering, Madurai, India
e-mail: ckseee@tce.edu

C. Kamalakannan et al. (eds.), *Power Electronics and Renewable Energy Systems*, Lecture Notes in Electrical Engineering 326, DOI 10.1007/978-81-322-2119-7_74

the solar panels. Throughout the literature studies many authors have concentrated in the modeling of solar panels. Also many types of algorithms have been implemented in many papers. In [2], a fuzzy logic based controller is used to track the maximum power and the results are compared for various types of solar modules. In [3–6], a grid connected solar panel is modeled and [5] the controllers are developed to sense the grid active and reactive power. In [3], a buck boost converter is designed and a microcontroller is used to control the converter for maximum power transfer. In [7], simulation models for solar cells are developed in simelectronics environment. In [8], analytical techniques are used for modeling non-linear DC-AC switching converter for PV systems under islanding conditions. In [9, 10], a new algorithm is proposed to extract maximum power from the radiation. A detailed study is made for the solar energy in [1, 11]. In [12], solar based thermo electric generators are developed. The performance of PID controller and Fuzzy Logic controller are compared for various operating conditions in [13]. In this work, mathematical modeling of solar panels is done. Along with the conventional inputs such as insolation and temperature, series and shunt resistances are taken as additional inputs. The solar panel characteristic curves are checked for various input variables such as temperature, irradiation, series resistance and shunt resistance. To track the maximum power, MPPT controllers employing P&O type and also a fuzzy logic controller is implemented along with the boost converter. The performances of the MPPTs are compared with each other.

74.2 Mathematical Modeling of Solar Panel

The Fig.74.1 shows the equivalent circuit of the PV panel and it's represented by a current source in parallel with a conventional diode. Since an average solar cell produces less than 2 W, the cells must be added in series and parallel in order to get a higher voltage [2].

74.3 Maximum Power Point Tracking Algorithm

The voltage obtained for loads such as battery, DC motors, resistors could be enhanced with a better efficiency if the operating points are kept near the knee of the P-V and I-V curves. The devices used to maintain such a constant voltage are maximum power point trackers. A fuzzy logic MPPT controller tracks the maximum power when compared to other methods. The flowchart shows the algorithm for the implementation of fuzzy logic based algorithm for MPPT. In this algorithm, PV input voltage and current are taken as inputs. The duty cycle of the converter is taken as output [13] (Fig. 74.2).

The equations associated for the calculation of error and changes in error are as below.

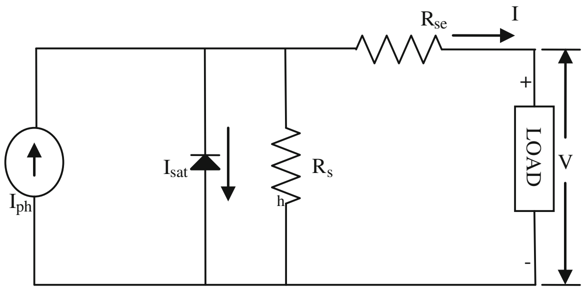

Fig. 74.1 Equivalent circuit of a PV cell

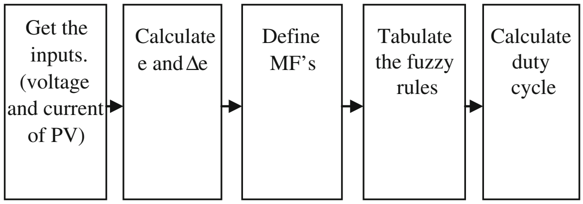

Fig. 74.2 Flowchart for the fuzzy logic controller implemented

$$E(K) = \frac{I}{V} + \frac{\Delta I}{\Delta V} = \frac{\Delta P}{\Delta I} = \frac{\Delta P}{\Delta V}. \tag{74.1}$$

$$CE(K) = E(K) - E(K-1). \tag{74.2}$$

$$\Delta I(K) = I(K) - I(K-1). \tag{74.3}$$

$$\Delta V(K) = V(K) - V(K-1). \tag{74.4}$$

$$\Delta P(K) = P(K) - P(K-1). \tag{74.5}$$

where, E(K)—error value, CE(K)—change in error value, ΔI(K)—change in current value, ΔV(K)—change in voltage value, ΔP(K)—change in power value [13]. The function of the fuzzy logic controller is to maintain a constant duty cycle for varying output voltage at the load so that power transfer is maximum.

74.3.1 Membership Functions

In this work five triangular and two trapezoidal shaped membership functions are selected. Their ranges are calculated based on the oscillation of each signal. The inputs are error and change in error. The output is the duty cycle given to the boost converter. The degree of membership function ranges from 0 to 1.

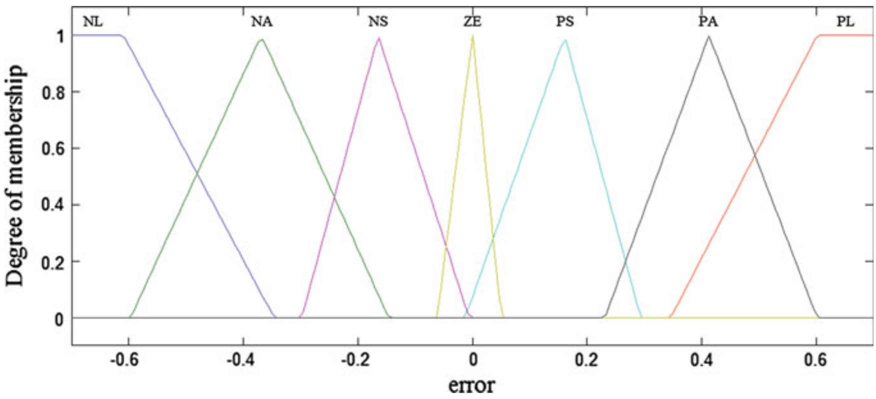

Fig. 74.3 Membership function plot for error

Figures 74.3, 74.4 and 74.5 are the membership function plot for error, change in error and duty cycle respectively. Each of the variables has seven membership functions. Thus a total of fourteen membership functions are used for input variables and seven membership functions are used for output variables.

74.3.2 Rule Settings for Fuzzy Controller

Different subsets can be used for tuning the rules for fuzzy logic controller. The subset used for this work consists of 49 rules which have been tuned. These rules give better accuracy and dynamic response although their tuning is difficult. The fuzzy rules are given in Table 74.1.

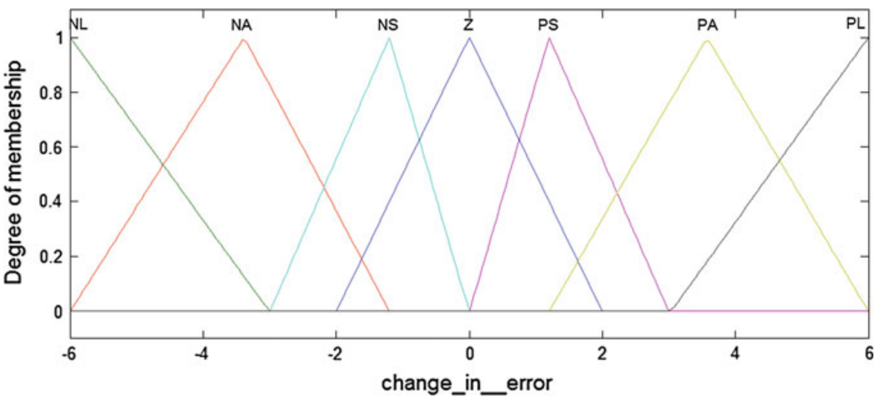

Fig. 74.4 Membership function plot for change in error

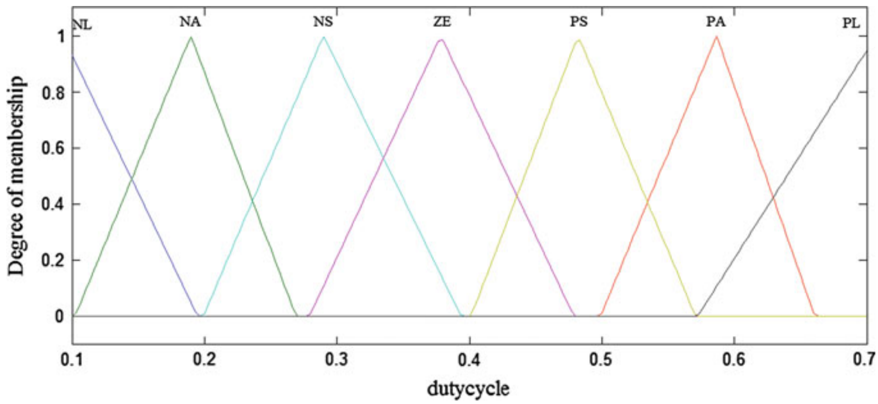

Fig. 74.5 Membership function plot for duty cycle

Table 74.1 Fuzzy rules formulation

E	CE						
	NL	NA	NS	ZE	PS	PA	PL
NL	ZE	ZE	ZE	NL	NL	NL	NL
NA	ZE	ZE	ZE	NA	NA	NA	NA
NS	NS	ZE	ZE	NS	NS	NS	NS
ZE	NA	NS	ZE	ZE	ZE	PS	PA
PS	PA	PS	PS	PS	ZE	ZE	ZE
PA	PA	PA	PA	ZE	ZE	ZE	ZE
PL	PL	PL	PL	ZE	ZE	ZE	ZE

74.3.3 Perturb and Observe Type of MPPT

Perturb and observe type is the simplest and the most common method. The input variables taken are change in current, voltage and power. The output variable is the change in power. The flowchart implemented in the algorithm is shown [11]. The flowchart make uses the voltage perturbation as shown in Fig. 74.6. An alternative method uses the same input variables to perturb the duty cycle. This method is not used in the project as the duty cycle perturbations are random in this method and not accurate.

74.4 Operation and Design of the Boost Converter

Figure 74.7 shows the basic circuit configuration of a boost converter, where V_{in} is the dc input voltage, L is the boost inductor, S is the controlled switch, D is a diode, C is a filter capacitor, and R_L is the load resistance. Boost converter works in two

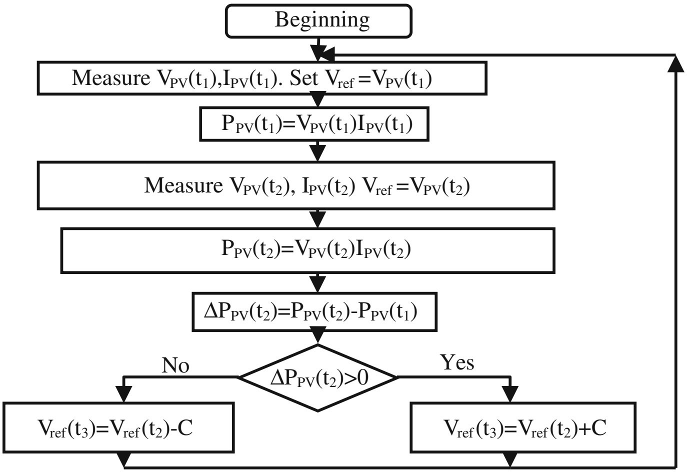

Fig. 74.6 Flowchart of the P&O algorithm implemented

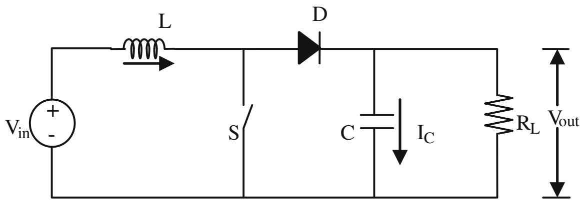

Fig. 74.7 Circuit diagram of the implemented boost converter

states. When the switch S is open, current in the boost inductor increases linearly, and the diode D is off at that time. When the switch S is closed, the energy stored in the inductor is released through the diode to the output R_L circuit.

74.5 Results and Discussions

74.5.1 Variation of I-V and P-V Curves with Series Resistance

Addition of series resistance reduces the voltage which reduces the slope of the curves and the maximum power point is also reduced as seen in Figs. 74.8 and 74.9. Thus it is evident that with the increase in series resistance, the efficiency of the solar panel reduces.

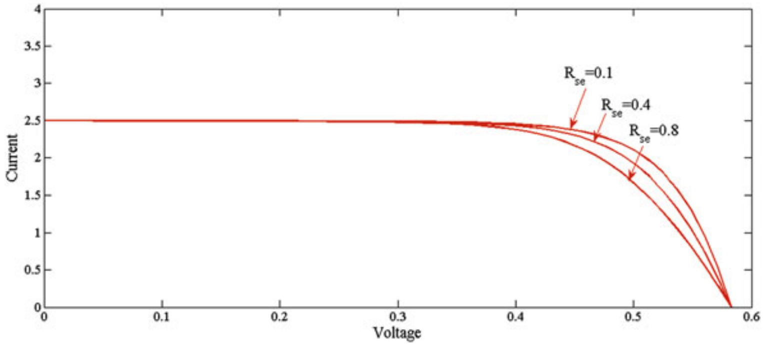

Fig. 74.8 Effect of variation of I-V and P-V curves with series resistance

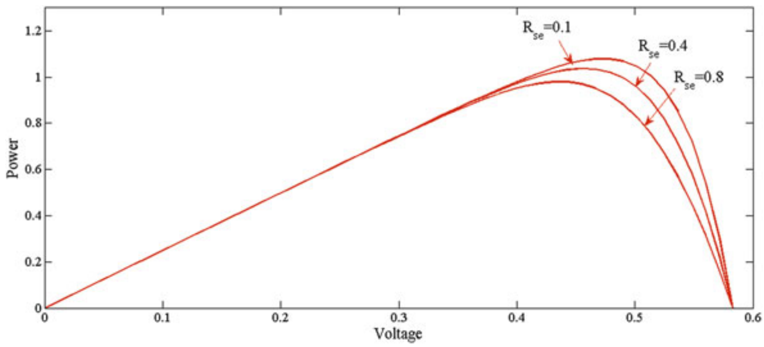

Fig. 74.9 Effect of variation of I-V and P-V curves with series resistance

74.5.2 Variation of I-V and P-V Curves with Shunt Resistance

The shunt resistance for a PV cell should be high. Lower value of shunt resistance leads to a steeper collapse of the curves which lowers the fill factor which is shown in Figs. 74.10 and 74.11.

74.5.3 Duty Cycle Obtained by FLC and P&O Controller

Figures 74.12 and 74.13 show the duty cycle waveform obtained by both the controllers. It can be seen that the fuzzy logic controller used tracks a constant duty cycle whereas the perturb and observe controller used does not track the duty cycle as efficiently as fuzzy logic controller.

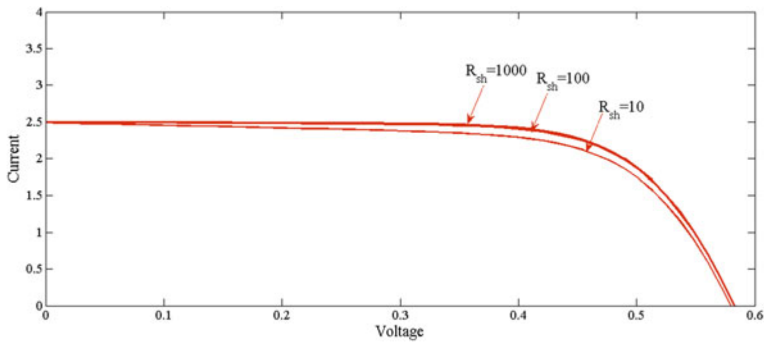

Fig. 74.10 Effect of variation of I-V and P-V curves with shunt resistance

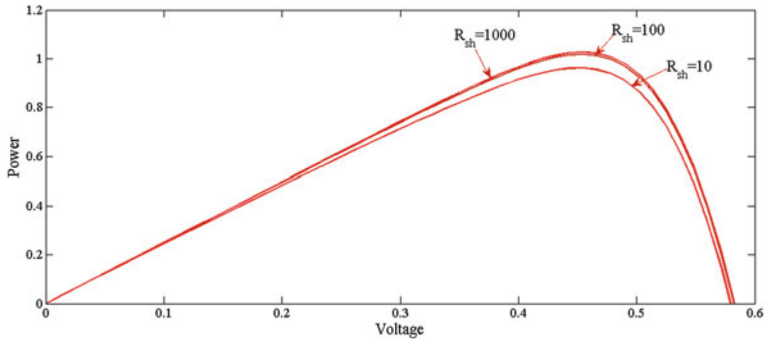

Fig. 74.11 Effect of variation of I-V and P-V curves with shunt resistance

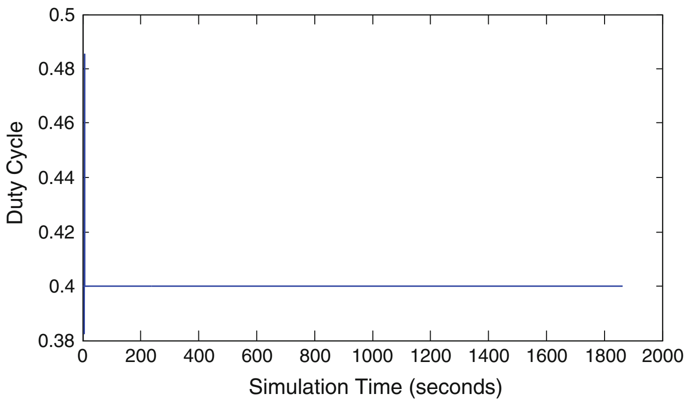

Fig. 74.12 Duty cycle tracked by the fuzzy logic controller and P&O controller

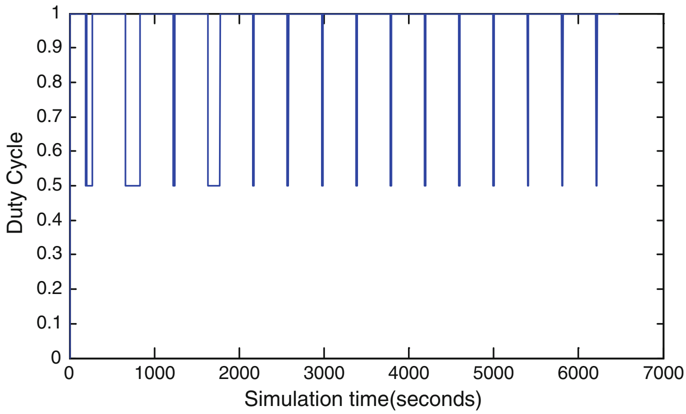

Fig. 74.13 Duty cycle tracked by the fuzzy logic controller and P&O controller

A constant duty cycle is achieved at the beginning of the simulation whereas the P&O MPPT controller does not track a constant duty cycle for a very long time. The fuzzy logic controller shows an efficient operation when compared with the P&O controller.

74.6 Conclusion

The solar PV array is successfully modeled and the characteristics curves are observed for the change in irradiation, temperature, series and shunt resistances. Maximum power point controllers based on P&O and fuzzy logic controllers are modeled. The duty cycle curves for both the controllers are noted and it is evident that the fuzzy logic controller proves to be the best in comparison with the P&O MPPT controller. Thus the robustness of the fuzzy logic controller is justified. The simulation is done in MATLAB simulink environment (R2011).

Appendix

Parameters taken for simulation	Values
Switching frequency	100 kHz
Solar PV array temperature	25 °C
Irradiation	600 W/m2
No. of solar cells in series	65
No. of rows solar cells in parallel	4

(continued)

(continued)

Parameters taken for simulation	Values
Series resistance	0.016 Ω
Shunt resistance	10 Ω
Resistance of the load	300 Ω
Voltage step used in P&O algorithm	0.01
Capacitance of the boost converter	0.626 μF
Inductance of the boost converter	3.7 mH

References

1. Masters GM (2004) Renewable and efficient electric power systems. Wiley, New Jersey
2. Mahamudul H, Saad M, Ibrahim Henk M (2013) Photovoltaic system modelling with fuzzy logic based maximum power point tracking algorithm. Int J Photoenergy. doi:10.1155/2013/762946
3. Ahmed KT, Datta M et al (2013) A novel two switch non-inverting buck-boost converter based maximum power point tracking system. Int J Electr Comput Eng 3(4):467–477. ISSN:2088-8708
4. Manohar K, Sobha Rani P (2012) MPPT and simulation of grid connected photvoltaic systems. Int J Eng Sci 1(2):158–166
5. Ropp ME, Gonzalez S (2008) Development of a MATLAB/simulink model of a single-phase grid connected photovoltaic system. Energy Convers IEEE 24(1):195–202. doi:10.1109/TEC.2008.2003206
6. Chowdhury P, Koley I, Sen S, Saha PK, Panda GK (2013) Modelling, simulation and control of grid connected non conventional solar power generation system using matlab. Int J Adv Res Electr Electron Instrum Eng 2(4):1183–1191
7. Khanna V, Das BK et al (2013) MATLAB/SIMELECTRONICS models based study of solar cells. Int J Renew Energy Res 3(1):30–34
8. Chayawatto N, Kirtikara K, Monyakul V, Jivacate C, Chenvidhya D (2009) DC-AC switching converter modelings of a PV-grid connected system under islanding phenomena. Renew Energy 34(12):2536–2544. doi:10.1016/j.renene.2009.05.002
9. Armstrong S, Hurley WG (2010) A new methodology to optimise solar energy extraction under cloudy conditions. Renew Energy 35(4):780–787. doi:10.1016/j.renene.2009.10.018
10. Noguchi T, Matsomoto H (2007) Maximum power point tracking of photovoltaic using only single current sensor. doi: 10.1002/eej.20275
11. Garg HP (1982) Treatise on solar energy. In: Fundamentals of solar energy, vol I. Wiley, New York
12. Leon MTD, Chong H, Kraft M (2012) Design and modelling of SOI based solar thermoelectric generators. Proc Eng 47:76–79. doi:10.1016/j.proeng.2012.09.088
13. Mahammad Ak, Saon S, Chee WS (2013) Development of optimum controller based on MPPT for photovoltaic system during shading condition. Proc Eng 53:337–346. doi:10.1016/j.proeng.2013.02.044

Chapter 75
Identification of the Fractional Order First Order Plus Dead Time Parameters of Two Interacting Conical Tank Process Using Bee Colony Optimization Technique Minimizing Root Mean Square Error

S.K. Lakshmanaprabu, U. Sabura Banu and N. Sivaramakrishnan

Abstract Mathematical Model of two interacting conical tank process is derived and the second order process transfer function resulted is reduced to Fractional Order First Order Plus Dead Time (FOFOPDT) system. Normally, any higher order process can be reduced to first order plus dead time. With the recent advancements of fractional calculus in the field of process modeling and control, an attempt has been taken to model fractional order FOPDT system for the process. Identification of the process parameters is not an easy job. Recently, swarm intelligence techniques are used to identify model parameters. The model reduction is obtained using bee colony optimization minimizing root mean square error.

Keywords Fractional order first order plus dead time (FOFOPDT) system · Bee colony optimization · Time domain

75.1 Introduction

Fractional calculus, the branch of math investigating differentiation and integration operators of non-integer order, has become a valuable tool for scientists and engineers. It has emerged that fractional order models can often describe the behaviour of certain physical processes (among which anomalous diffusion, visco-elastic phenomena, etc.) in a more accurate way than using classical integer order

S.K. Lakshmanaprabu (✉) · U. Sabura Banu · N. Sivaramakrishnan
Department of Electronics and Instrumentation Engineering, B.S. Abdur Rahman University, Vandalur, Chennai 600048, India
e-mail: prabusk.leo@gmail.com

U. Sabura Banu
e-mail: sabura.banu@bsauniv.ac.in

C. Kamalakannan et al. (eds.), *Power Electronics and Renewable Energy Systems*, Lecture Notes in Electrical Engineering 326, DOI 10.1007/978-81-322-2119-7_75

models. In recent years there has been an increasing attention paid to fractional-order processes, which are really useful to represent the different stable physical phenomena with anomalous decay both from the academic and control engineers for the modeling and control issues because they can be provide more flexibility and advancement in the computation power, which allows the adequate precision for both the simulation and implementation of these processes. It is clear that fractional calculus (i.e., the fractional integro-differential operator) is a generalized of the integration and differential to the non-integer order of integrals and derivatives, which is obtained from the ordinary calculus by extending the ordinary differential equations (ODE) to fractional-order differential equations (FODE). Fractional calculus is gaining popularity in recent past in control areas [1] for the control of integer order systems [2, 3] and fractional order systems [4]. Fractional calculus generalize the integer order derivatives and integrals to rational order introduced by L'Hospital followed by Leibnitz. Non-integer order system, the fractional order systems finds application in various fields of science such as electrochemistry, thermal engineering, biomedical engineering, acoustic, etc. [5, 6]. They are characterized by long memory transients and infinite dimensional structure. Modeling of fractional system is required for simulation, identification and control applications [7, 8]. Normally any higher order system can be approximated to First order plus dead time. In the proposed study, an attempt will be made to approximate a second order system to Fractional Order First Order Plus Dead Time (FOFOPDT) system. The available conventional technique for finding the parameters of the FOFOPDT system is mostly an approximation model. Swarm intelligence techniques like Bee colony optimization, Ant Colony Optimization, Bacterial Foraging, etc. are used for getting the global optimal solution in the recent past. Bee colony optimization technique is an attractive method which gives an optimal global search optimization for the tuning of the filter constant λ. Colonies of social insects such as ants and bees have instinct ability known as swarm intelligence [9, 10]. This highly organized behavior enables the colonies of insects to solve problems beyond capability of individual members by functioning collectively and interacting primitively amongst members of the group. In a honey bee colony, this behavior allows honey bees to explore the environment in search of flower patches (food sources) and then indicate the food source to the other bees of the colony when they return to the hive. Such a colony is characterized by self organization, adaptiveness and robustness. Seeley [11] proposed a behavioral model of self organization for a colony of honey bees. In the model, foraging bees visiting flower patches return to the hive with nectar as well as a profitability rating of respective patches. The collected nectar provides feedback on the current status of nectar flow into the hive. The profitability rating is a function of nectar quality, nectar bounty and distance from the hive. The feedback sets a response threshold for an enlisting signal which is known as waggle dance, the length of which is dependent on both the response threshold and the profitability rating. The waggle dance is performed on the dance floor where individual foragers can observe. The foragers can randomly select a dance to observe and follow from which they can learn the location of the flower patch and leave the hive to forage. This self organized model enables proportionate feedback on goodness of food sources. Bee colony optimization is used for optimizing the parameters of FOFOPID mode.

75.2 Two Interacting Conical Tank Process Description

The proposed system consists of two conical tanks which are in the shape of an inverted cone fabricated from a sheet metal. The height of the process tank is 50 cm and the top end, tapering end diameters are 40 and 14 cm. The two tanks are connected through an interacting pipe with valve (HV1). The interaction of process can be changed by position of this valve (HV1). It has a reservoir to store water and this is supplied through the pumps to the tanks. Provisions for water inflow and outflow are provided at the top and bottom of the tank respectively. Gate valves, one at the outflow of the tank1 and the other at the outflow of the tank2 are connected to maintain the level of water in the tanks. Variable Speed pump work as actuator and it is used to discharge the water from reservoir tank to process tanks. The speed of pump directly propositional to the input voltage. It consists of differential pressure transmitter for measuring the bottom pressure created by water level and it gives height in terms of milliamps (Fig. 75.1).

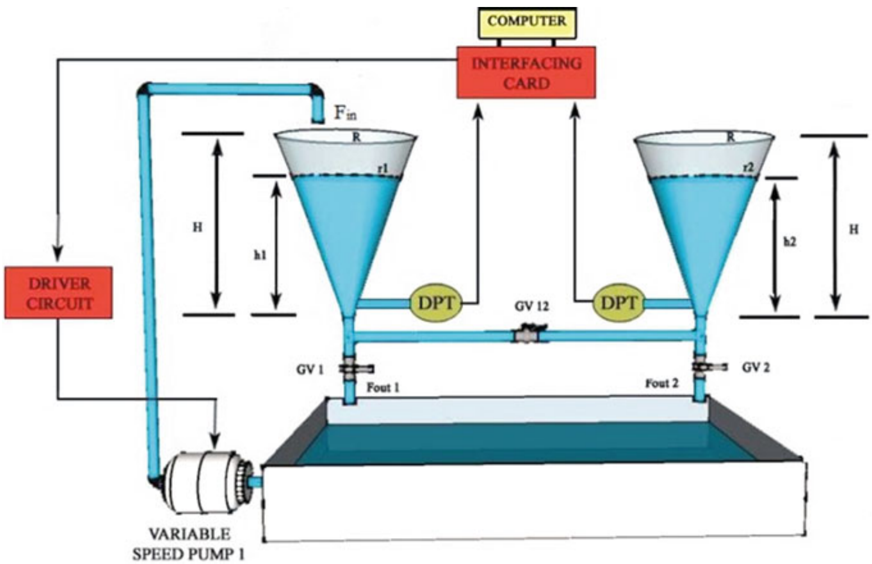

Fig. 75.1 Schematic diagram of two interacting *conical* tank with F_{in1} as the manipulated variable and h_2 as the process output

75.2.1 Mathematical Modeling

Mathematical models of system were developed for many reasons. They may be constructed to assist in the interpretation of experimental data, to predict the consequences of changes of system input or operating condition, to deduce optimal system or operating conditions and for control purposes. But the main problem in modeling is the process dynamics should be captured otherwise no use in modeling the process. The dynamic model of the process has been derived from the application of fundamental physical and chemical principles to the system, using a conventional mathematical modeling approach.

$$\frac{dh_1}{dt} = \frac{F_{in} - sign(h_1 - h_2)K_{12}\sqrt{(h_1 - h_2)}}{A_1 h_1^2} \tag{75.1}$$

$$\frac{dh_2}{dt} = \frac{sign(h_1 - h_2)K_{12}\sqrt{(h_1 - h_2)} - K_2\sqrt{h_2}}{A_2 h_2^2} \tag{75.2}$$

The nominal values of the parameters and variables are tabulated in Table 75.1.

75.2.2 Open Loop Data

The open loop data was generated in the conical tank system by varying the inflow rate F_{in} in tank1 and noting down the respective level h_1 and h_2. Figures 75.2 and 75.3 shows the I/O characteristics and linearized region of the two conical tank process.

Thus the piece wise Linearization method is used to separate the whole nonlinear region into various regions. The characteristics are divided into different region. The operating points are found out for each region.

Table 75.1 Nominal values of the parameters used

Parameter	Description	Value
R	Top radius of conical tank	20 cm
H	Maximum height of tank1, tank2	50 cm
F_{in}	Maximum inflow to tank1	200 cm^3/s
β_{12}	Valve co-efficient of Mv12	1
β_2	Valve co-efficient of Mv2	0.50
a_1, a_{12}, a_2	Cross section area of pipe	1.2272 cm^2

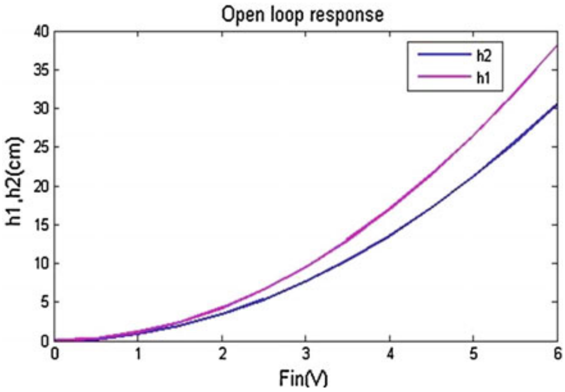

Fig. 75.2 I/O characteristics of the conical tank process

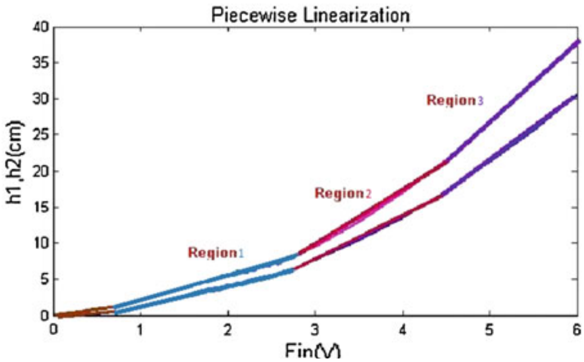

Fig. 75.3 Linearized region from the I/O characteristics

75.2.3 State Space Model

The linearized state space model can be represented as

$$\dot{X}' = AX' + BU' \tag{75.3}$$

$$Y' = CX' + DU' \tag{75.4}$$

where

$$X' = X - X_s \tag{75.5}$$

$$U' = U - U_s \tag{75.6}$$

$$Y' = Y - Y_s \tag{75.7}$$

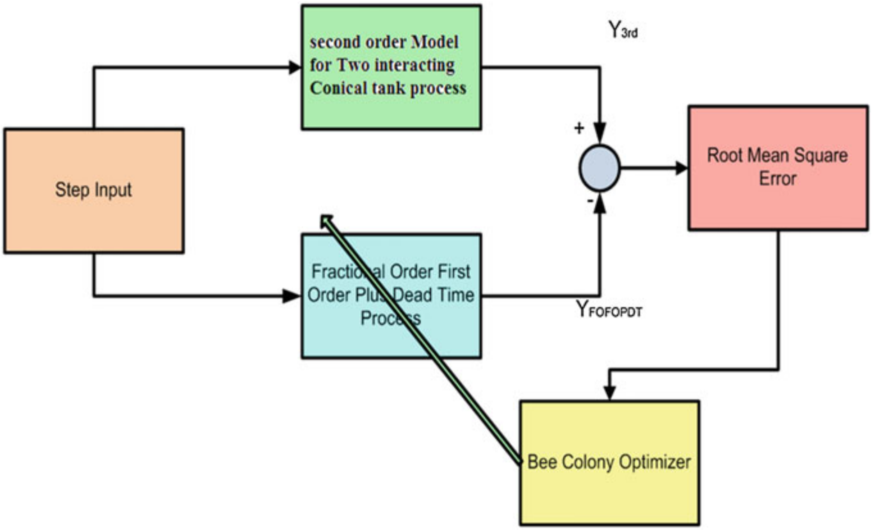

Fig. 75.4 Block diagram of the fractional order FOPDT system approximation using bee colony optimization

where X—state vector $[h_1,\ h_2,\ h_3]$, Y—Output vector $[h_1,\ h_2,\ h_3]$,

U—Input vector $[U_1, U_2]$, X′—State (in terms of deviation variable)

U′—Control input (in terms of deviation variable),

Y′—Output (in terms of deviation variable), X_s—State variable's steady state operating point, Y_s—Output's operating point, U_s—Input's operating point.

State space model for the two interacting tank process is obtained by linearizing the entire nonlinear region into two linear regions by Jacobian approximation and substituting the operating conditions. Table 75.2 shows the operating conditions and the corresponding models for each region.

$$A = \begin{bmatrix} \frac{-2}{A}\left(\frac{F_{1s}}{h_{1s}^3}\right) - \frac{K_{12}}{A}\left[\frac{-1}{2{h_{1s}}^2\sqrt{h_{1s}-h_{2s}}} - \frac{-2\sqrt{(h_{1s}-h_{2s})}}{h_{1s}^3}\right] & \frac{K_{12}}{A}\left[\frac{-1}{2{h_{1s}}^2\sqrt{h_{1s}-h_{2s}}}\right] \\ -\frac{K_{12}}{A}\left[\frac{-1}{2{h_{1s}}^2\sqrt{h_{1s}-h_{2s}}}\right] & \frac{K_{12}}{A}\left[\frac{-2\sqrt{h_{1s}-h_{2s}}}{h_{2s}^3} - \frac{1}{2{h_{1s}}^2\sqrt{h_{1s}-h_{2s}}}\right] + \frac{3K_2}{2A{h_{2s}}^2\sqrt{h_{2s}}} \end{bmatrix};$$

$$B = \begin{bmatrix} \frac{1}{A{h_{1s}}^2} \\ 0 \end{bmatrix};\ C = [0\ 1];\ D = [0\ 0] \tag{75.8}$$

Table 75.2 Operating conditions and the conventional state space and transfer function model of the interacting conical tank process

Region	Operating points	State space	Transfer function matrix G(s)
$h_1 = 2.5 - 6.5$ $h_2 = 2 - 5.5$	$F_{in1s} = 2.1$ $h_{1s} = 4.66$ $h_{2s} = 3.73$	$A = \begin{bmatrix} -2.5833 & 2.5802 \\ 4.0272 & -5.0273 \end{bmatrix}$ $B = \begin{bmatrix} 2.2888 \\ 0 \end{bmatrix}$ $C = [0 \quad 1]; D = [0 \quad 0]$	$\frac{9.217}{s^2 + 7.611s + 2.596}$
$h_1 = 6.5 - 21.5$ $h_2 = 5.5 - 17$	$F_{in1s} = 3.58$ $h_{1s} = 13.55$ $h_{2s} = 10.85$	$A = \begin{bmatrix} -0.162 & 0.162 \\ 0.253 & -0.317 \end{bmatrix}$ $B = \begin{bmatrix} 0.250 \\ 0 \end{bmatrix}$ $C = [0 \quad 1]; D = [0 \quad 0]$	$\frac{0.06342}{s^2 + 0.4788s + 0.01027}$
$h_1 = 21.5 - 38$ $h_2 = 17 - 30.5$	$F_{in1s} = 4.8$ $h_{1s} = 24.37$ $h_{2s} = 19.49$	$A = \begin{bmatrix} -0.025 & 0.025 \\ 0.039 & -0.049 \end{bmatrix}$ $B = \begin{bmatrix} 0.056 \\ 0 \end{bmatrix}$ $C = [0 \quad 1]; D = [0 \quad 0]$	$\frac{0.002213}{s^2 + 0.07421s + 0.0002466}$

75.2.4 *Transfer Function for the Two Interacting Conical Tank Process*

From the transfer function matrix, the transfer function between F_{in1} and h_2 is considered in the present work which is a second order over damped single input single output system. To obtain the interacting second order process, the inflow to tank2 is shut down and input to the process is considered to be the inflow to tank1 and the output from the process is the height of the second tank.

Table 75.3 Original second order transfer function, FOPDT system, fractional order FOPDT system transfer function for different regions

Region	Conical transfer function	First order plus dead time system transfer function	Fractional order FOPDT system transfer function
I	$\frac{9.217}{s^2 + 7.611s + 2.596}$	$\frac{3.55146}{2.80331s + 1} e^{-0.133846s}$	$\frac{3.5381}{2.8167s^{0.8685} + 1} e^{-0.1372s}$
II	$\frac{0.06342}{s^2 + 0.4788s + 0.01027}$	$\frac{6.177}{44.58s + 1} e^{-2.12765s}$	$\frac{6.1955}{44.5137s^{0.5994} + 1} e^{-2.1327s}$
III	$\frac{0.002213}{s^2 + 0.07421s + 0.0002466}$	$\frac{8.97656}{287.752s + 1} e^{-13.7278s}$	$\frac{8.981}{287.75s^{0.9575} + 1} e^{-13.811s}$

75.3 Approximation of the Second Order Transfer Function to Fractional Order First Order Plus Dead Time Model for the Two Interacting Process Using Bee Colony Optimization Technique

Any higher order process can be approximated to first order plus dead time. Analysis and controller design will be easy if higher order system is approximated to a FOPDT system. With the growing advancements of fractional calculus in the field of modeling and automation, an attempt has been made to approximate the second order process to fractional order FOPDT system. Bee colony optimization is used for the approximation process.

75.3.1 Objective Function for the Approximation

The Fractional Order FOPDT system takes the form

$$G_{FOFOPDT}(s) = \frac{K}{\tau s^{\alpha} + 1} e^{-Ls} \tag{75.9}$$

where K is the Process Gain, τ is the time constant, α is the order of the first order transfer function and L is the dead time. The objective function for the identification process, Root Mean Square Error (RMSE) is given by

$$RMSE = \sqrt{\frac{(Y_{2nd} - Y_{FOFOPDT})^2}{N - 1}} \tag{75.10}$$

where Y_{second} is the output response of the second order two interacting tank process and the $Y_{FOFOPDT}$ is the output response of the Fractional Order FOPDT system. The objective function for the Bee colony optimizer is the root mean square error. The parameters to be optimized are K, τ, α and L.

75.3.2 Bee Colony Optimization

The ways of communication of the bee for find the food sources are very interesting. In the bee hive, the worker bees are responsible for food collection. The worker bees in a honey bee colony are grouped as food-storer, scout and forager. The food collection is organized by the colony by recruiting bees for different jobs. The recruitment is managed by the forager bees which can perform dances to communicate with their fellow bees inside the hive and recruit them. The scouts are sent to different directions in search of honey. Each bee visits a number of flowers. The floral findings are communicated to the other bees through dancing. At the entrance of the hive is an area called the dance-floor, where dancing takes place. Algorithm for Bee colony optimization for model approximation:

1. Initialize the population of solutions $x_{i,j}$
2. Evaluate the population
3. Cycle = 1
4. Repeat
5. Produce new solutions (food source positions) $v_{i,j}$ in the neighbourhood of $x_{i,j}$ for the employed bees using the formula

$$v_{i,j} = x_{i,j} + \phi_{ij}(x_{i,j} - x_{k,j}) \tag{75.11}$$

where k is the solution in the neighbourhood of i, ϕ is a random number and evaluate them

6. Apply the greedy selection process between x_i and v_i
7. Calculate the probability values P_i for the solutions x_i by means of their fitness values using

$$P_i = \frac{fit_i}{\sum_{i=1}^{SN} fit_i} \tag{75.12}$$

The fitness values of solutions are calculated as

$$fit_i = \left\{ \begin{array}{ll} \frac{1}{1+f_i} & \text{if } f_i \geq 0 \\ 1 + \text{abs}(f_i) & \text{if } f_i < 0 \end{array} \right\} \tag{75.13}$$

Normalize P_i values into [0, 1]

8. Produce the new solutions (new positions) v_i for the onlookers from the solutions x_i, selected depending on Pi and evaluate them
9. Apply the greedy selection process for the onlookers between v_i and x_i
10. Determine the abandoned solution (source) if exists and replace it with a new randomly produced solution x_i for the scout using

$$x_{ij} = \min_j + \ \text{rand}(0,1) * \left(\max_j - \min_j\right)$$

11. Memorize the best food source position (solution) achieved so far
12. Cycle = cycle + 1, Until cycle = Maximum cycle Number

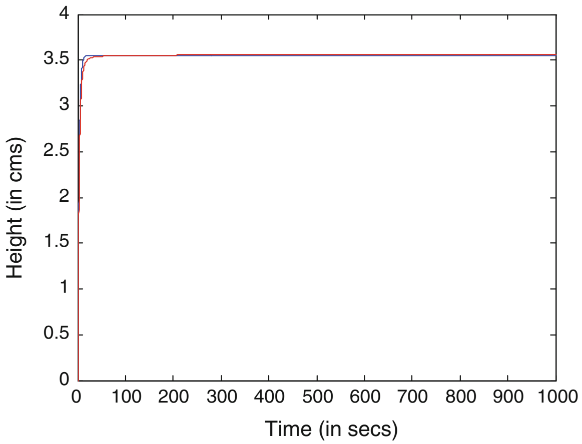

Fig. 75.5 Comparison of the step response of the second order system, FOPDT system and fractional order FOPDT system for the first region

The termination criterion can be in two ways: either by ending the program when objective function value reaches a reasonably low value or after a finite number of iterative steps. In the present case, the program was terminated after 100 iterations.

75.3.3 Fractional Order Model Approximation of the Second Order System Using Bee Colony Optimization

Figure 75.4 shows the block diagram for the optimal fractional order model approximation of the second order system. The process and the fractional order model both are given the same step input. The fractional order parameters are optimally identified using bee colony optimizer with root mean square error as the objective function. Table 75.3 shows the transfer function of FOPDT model and fractional order FOPDT model.

75.4 Time Domain Comparison

Step input is applied for the second order transfer function, FOPDT system and Fractional Order FOPDT system for the different regions and performance compared in Figs. 75.5, 75.6 and 75.7. The response coincides stating that the approximated model is a perfect replica of the second order process. Root mean square error computed between the second order process and the approximated model. RMSE for the first region is 0.0492, second region is 0.27372 and for the third region is 0.246.

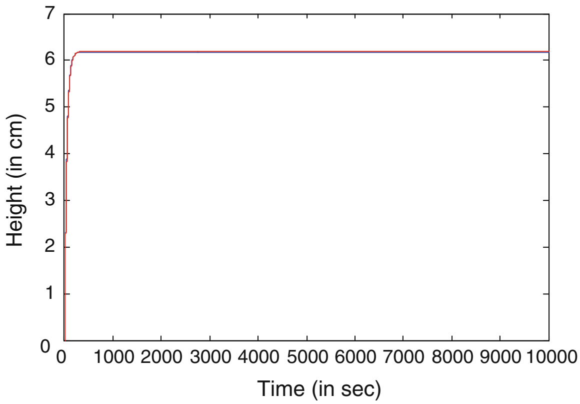

Fig. 75.6 Comparison of the step response of the second order system, FOPDT system and fractional order FOPDT system for the second region

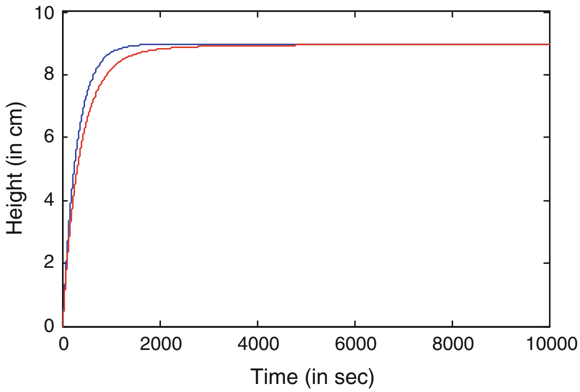

Fig. 75.7 Comparison of the step response of the third order system, FOPDT system and fractional order FOPDT system for the second region

75.5 Conclusion

In this paper, the second order two interacting conical tank process which exhibits a nonlinear dynamic behavior is approximated to a FOPDT system and Fractional Order FOPDT system. On analysis of the RMSE between the higher order system and approximated Fractional Order FOPDT system, it is evident that the values are minimum specifying that the approximation closely resembles the original model. The phase and gain margin also closely matches with the higher order system.

References

1. Podlubny I (1999) Fractional Order systems and $PI^{\lambda}D^{\mu}$ controller. IEEE Trans Autom Control 44(1):208–214
2. Xue D, Zhao C, Chen YQ (2006) Fractional order PID control of a DC motor with elastic shaft: a case study. In: Proceeding of the American control conference, Minnesota, USA, pp 3182–3187
3. Monje CA, Vinagre BM, Feliu V, Chen YQ (2008) Tuning and auto-tuning of fractional order controllers for industry appilcations. Control Eng Practices 16:798–812
4. Xue D, Zhao C, Chen YQ (2005) A fractional order PID tuning algorithm for a class of fractional order plants. In: Proceedings of the IEEE/ICMA, Niagara Falls, Canada, pp 216–221
5. Ichise M, Nagayanagi Y, Kojima T (1971) An analog simulation of non-integer order transfer functions for analysis of electrode processes. J Elect Chem Interfacial Electrochem 33:253
6. Matingnon D, d' Andrea Novel B, Depalle P, Oustaloup A (1994) Viscothermal losses in wind instrument: a non-integer model. In: System and networks: mathematical theory and applications, vol 2. Akademie Verlag, Berlin
7. Lin J, Poinot T, Trigeassou JC, Coirault P (2001) Parameter estimation of fractional systems: application to heat transfer. In: ECC 2001, European control conference, Porto, Portugal, pp 2644–2649
8. Lin J, Poinot T, Trigeassou JC, Ouvrard R (2000) Parameter estimation of fractional system: application to the modeling of lead acid battery. In: SYSID 2000, 12th IFAC symposium on system identification, USA
9. Nakrani S, Tovey C (2004) On honey bees and dynamic allocation in an internet server colony. Adapt Behav 12(3–4):223–240
10. Teodorovic D, Dell'orco M (2005) Bee colony optimization - A cooperative learning approach to complex transportation problems. In: Advanced OR and AI methods in transportation, pp 51–60
11. Seeley TD (1995) The Wisdom of the Hive. Harvard University Press, p 302

Chapter 76
Real Time Simulation of Single Machine Infinite Bus System Using dSPACE Controller Board

R. Ramya and K. Selvi

Abstract This paper presents a linear mathematical model of a Synchronous Generator with excitation system for small signal stability analysis and it proposes a dynamic simulator that is used to simulate a Synchronous power plant in real time. The state space model of the Synchronous Machine is developed using MATLAB/SIMULINK. Using Real Time Interface, the model is executed in Digital Signal Processor of dSPACE hardware, a platform for real time simulation. The model is analyzed for its performance under real time changes in input mechanical torque and reference voltage. An experimental installation of a real time platform of a Synchronous Generator thus developed facilitates its control design also.

Keywords Synchronous generator · State space model · Real time simulation · dSPACE

76.1 Introduction

The quality of power supply must meet certain minimum standards with regard to the following factors: (a) constancy of frequency, (b) constancy of voltage and (c) level of reliability. The function of the excitation control is to regulate generator voltage and reactive power output [1]. Modeling of Synchronous machine is well established in Power Systems. For a Synchronous machine, an equivalent circuit model based on Park's equation can be developed, and its parameters can be identified by relatively less information. In [1], the flux linkage model is developed from the basis of magnetic circuit analysis. The system parameters have also been

R. Ramya (✉)
University College of Engineering, Ariyalur, Tamil Nadu, India
e-mail: rramyame@gmail.com

K. Selvi
Department of Electrical and Electronics Engineering,
Thiagarajar College of Engineering, Madurai, Tamil Nadu, India
e-mail: kseee@tce.edu

C. Kamalakannan et al. (eds.), *Power Electronics and Renewable Energy Systems*,
Lecture Notes in Electrical Engineering 326, DOI 10.1007/978-81-322-2119-7_76

expressed in terms of operational impedance. The simulations using personal computers have been done for the synchronous machine in [2]. In [3], the equivalent circuit model has been developed and simulated using Matlab/Simulink for various operating conditions of the power system. Reference [4] proposes a model and simulates a salient-pole synchronous generator using a modified winding function theory. Appropriate model of synchronous generator for low-frequency harmonic studies are presented in reference [5]. This model is developed using detailed "dq0" representations of the synchronous machine. In [6], the synchronous generator with excitation system is modeled using state space technique, where the current and flux linkage are used as state variables. Thus, an efficient methodology to achieve better stability and excitation control for synchronous generator is an active research area. In this paper, a steady state model for synchronous generator is developed to analyze the performance characteristics. The effect of magnetic saturation is included in the design.

It is usually recognized that, studying and experimenting with simulation models, students can experiment with systems that are impossible to work with in a laboratory, being potentially dangerous or huge dimensions or very expensive processes. In this way, it is possible to obtain some knowledge about its modeling, operation or stability aspects without being in actual contact with the plant. But, at the same time, this is the major drawback of this approach: being in contact with the real process and its associated hardware is an important issue concerning Engineering education. Even if it were possible to have a laboratory process, to design and build the electronic circuitry required for its measurement and control would require a lot of time. A different approach is possible using real time simulation tools, and it is also possible to develop laboratory applications in short time, using a PC, a hardware simulator and its associated software [7]. Therefore, the challenge is how to use a suitable implementation medium for the model, so that, the Synchronous machine model must be accurate enough to simulate different transients. This requires the real time simulation of the machine to which the new equipment will be added. Hence, a user friendly man-machine interface which mimics the actual operating environment of Synchronous machine including interactive setting of several parameters and real-time data presentation is developed in this work. This real time platform allows simulation and verification environments to be created from Simulink models. To test the control devices in virtual environments, dSPACE simulator can be equipped with this software that simulates the real controlled system.

76.2 Mathematical Model

The equations of central importance in power system stability analysis are the rotational inertia equations describing the effect of unbalance between the electromagnetic torque and the mechanical torque of the individual machines. The usual conventions are adopted in this work.

Mechanical Equations

The acceleration equations are

$$\Delta\dot{\omega}_r = \frac{1}{2H}(T_m - T_e - K_D\Delta\omega_r) \tag{76.1}$$

$$\dot{\delta} = \omega_o\Delta\omega_r \tag{76.2}$$

Electrical Equations

$$\Delta T_e = K_1\Delta\delta + K_2\Delta\psi_{fd} \tag{76.3}$$

$$\Delta\psi_{fd} = \frac{K_3}{1 + pT_3}\left[\Delta E_{fd} - K_4\Delta\delta\right] \tag{76.4}$$

$$\Delta E_t = K_5\Delta\delta + K_6\Delta\psi_{fd} \tag{76.5}$$

$$\Delta\dot{v}_1 = \frac{K_5}{T_R}\Delta\delta + \frac{K_6}{T_R}\Delta\psi_{fd} - \frac{1}{T_R}\Delta v_1 \tag{76.6}$$

Linear model of SMIB

By linearizing the above equations on at operating point we have the state variable model of a single machine to infinite bus as

$$\begin{aligned} \dot{x} &= Ax + Bu \\ y &= Cx + Du. \end{aligned} \tag{76.7}$$

A fourth-order model is considered for the synchronous generator. The system matrix A is function of the system parameters, which depends on the operating conditions. The perturbation matrix B depends on the system parameters only. The perturbation signal u is ΔT_m. The output matrix C relates the desired output signals vector y to the state variables vector x.

$$\begin{bmatrix} \Delta\dot{\omega}_r \\ \Delta\dot{\delta} \\ \Delta\dot{\psi}_{fd} \\ \Delta\dot{v} \end{bmatrix} = \begin{bmatrix} \frac{-K_D}{2H} & \frac{-K_1}{2H} & \frac{-K_2}{2H} & 0 \\ \omega_0 & 0 & 0 & 0 \\ 0 & \frac{-\omega_0 R_{fd}}{L_{fd}} m_1 L'_{ads} & \frac{-\omega_0 R_{fd}}{L_{fd}}\left[1 - \frac{L'_{ads}}{L_{fd}} + m_1 L'_{ads}\right] & \frac{-\omega_0 R_{fd}}{L_{adu}} KA \\ 0 & \frac{K_5}{T_R} & \frac{K_6}{T_R} & \frac{-1}{T_R} \end{bmatrix} \begin{bmatrix} \Delta\omega_r \\ \Delta\delta \\ \Delta\psi_{fd} \\ \Delta v_1 \end{bmatrix} + \begin{bmatrix} \frac{1}{2H} & 0 \\ 0 & 0 \\ 0 & \frac{\omega_0 R_{fd}}{L_{adu}} \\ 0 & 0 \end{bmatrix} [\Delta T_m]$$

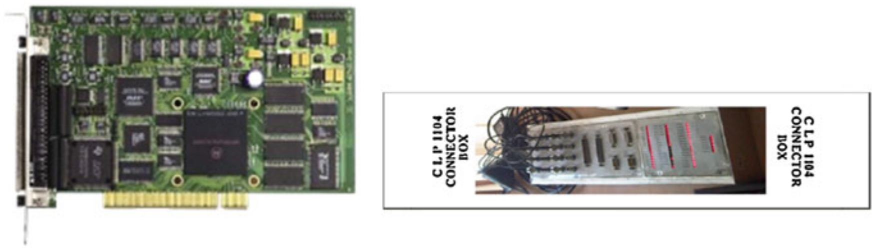

Fig. 76.1 TMS320F240 DSP microcontroller and CLP1104 connector box

76.3 dSPACE (DS1104)—Real Time Software

The DS1104 R&D controller board is a standard board that can be plugged into a PCI slot of a PC. The DS1104 is specifically designed for the development of high speed multivariable digital controllers and real time simulations in various fields. It is a complete real time control system based on a 603 power PC floating point processor running at 250 MHz. For advanced I/O purposes, the board includes a slave-DSP subsystem based on the TMS320F240 DSP microcontroller (Fig. 76.1).

For purpose of rapid control prototyping (RCP), specific interface connector and connector panel like CP1104 provide easy access to all input and output signals of the board. External devices can be individually connected, disconnected or interchanged without soldering via BNC connectors and Sub-D connectors. In addition to the CP1104, the CLP1104 Connector/LED panel provides an array of LEDs indicating the states of the digital signals. This simplifies system construction, testing and troubleshooting. Thus, the DS1104 R&D controller board is the ideal hardware for rapid control application [8].

76.4 MATLAB-dSPACE Interface

dSPACE real time simulation systems, which is a set of hardware and software platforms is developed by German company dSPACE for control system development and plant simulation. It has the characteristics of high reliability and favorable scalability. It is intended to greatly simplify the task of acquiring signals and generating specific waveforms in the laboratory, thus facilitating teaching and research. The dSPACE platform used in this paper is single board hardware—DS1104 R&D controller board and its block diagram is shown in Fig. 76.2.

The I/O connections to the real world systems are added to the Simulink model from the RTI library. RTI ensures the control over each individual variable immediately after the implementation process. C code written on the DSP hardware performs the real-time simulation.

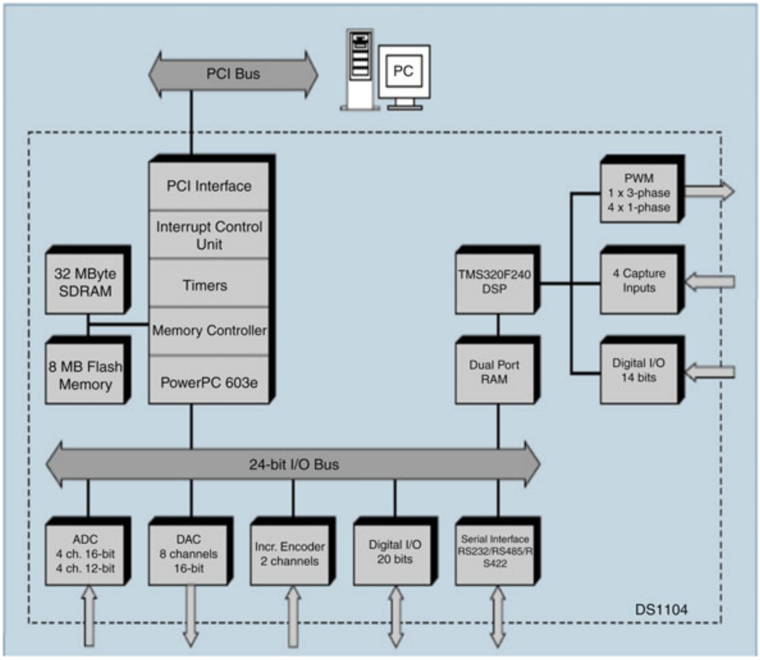

Fig. 76.2 Block diagram of DS1104 R&D controller board

The real time simulation can be controlled from the PC with the Control Desk program software, a graphical user interface for conveniently changing parameters and monitoring signals online—without regenerating the code during an experiment. Thus there is smoother transition from offline to real time implementation as shown in Fig. 76.3.

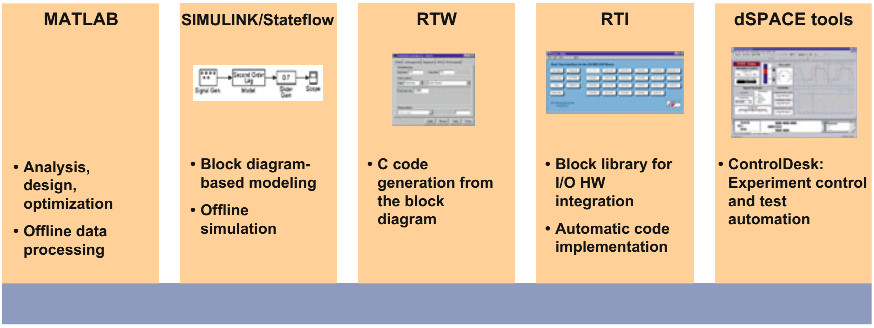

Fig. 76.3 MATLAB-dSPACE interface

76.5 Real Time Implementation

A dynamic model of a power system, Fig. 76.4 a single machine infinite bus (SMIB) power system [1] is considered as a test model in this paper. The Simulink model for single machine connected to infinite bus is developed as shown in Fig. 76.5. After the model is tested in Simulink, one needs to prepare it for implementation on the real time hardware. The plant model is replaced by I/O blocks from the RTI I/O library that form the interfaces to the real controlled system.

As shown in Fig. 76.5, keeping the excitation voltage E_f constant, Synchronous Generator model gets the values for the mechanical power P_{mech}, as physical input signals and is read in by a ADC block.

From the input values, the model can calculate the electrical output torque T_e, the air-gap fluxes Φ_m, the armature winding currents i_m (m = a, b, c), generated real and reactive powers P_{gen}, Q_{gen}, rotor angle etc. in real time in DSP of the simulator and can be obtained as physical signals through D/A converters. A better understanding of how the machine model reacts under sudden large disturbances in real time can be achieved by varying its input signals in real time as in Fig. 76.6.

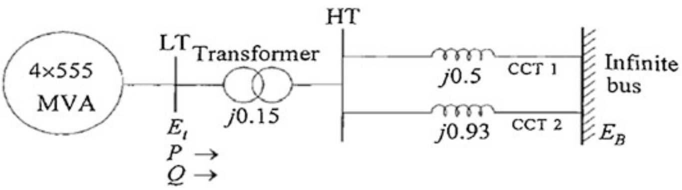

Fig. 76.4 Single machine connected to an infinite bus through transmission lines

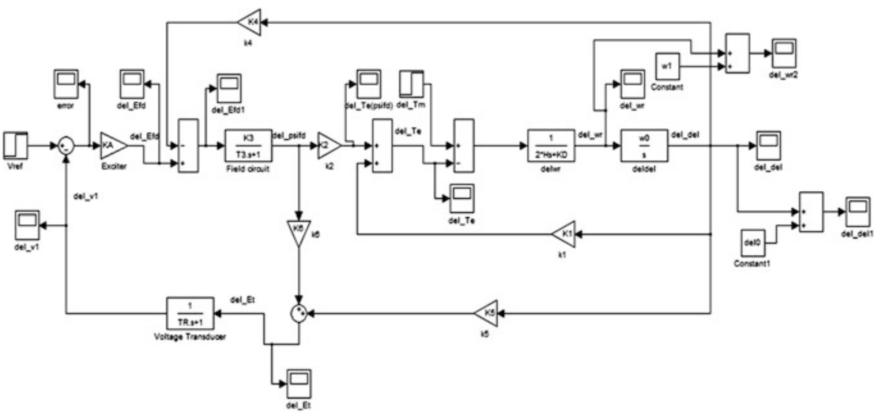

Fig. 76.5 Block diagram representation of synchronous generator model

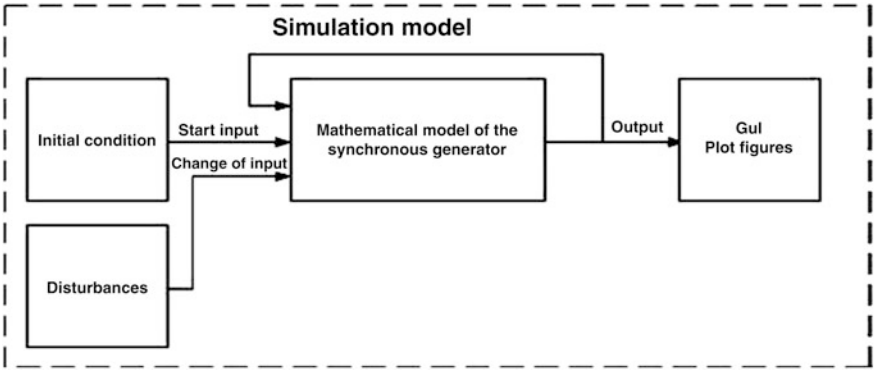

Fig. 76.6 Real time simulation of synchronous generator

76.6 Test Results

In this work, DS 1104 having MPC 8240 processor with PPC603e core and TMS320F240 DSP is used. Fixed step continuous solver ode5—Dormand Prince Formula with step size of 0.0001 is specified in the configuration parameters pane. Comparison is presented by the way of offline simulation in MATLAB/SIMULINK and implementation is realized using DS1104. A 2220 MVA, 24 kV, 2 poles, 60 Hz rated machine as shown in Fig. 76.4 is taken as a test system. Under steady state, the generator delivers one per unit power at unity power factor to the bus of voltage magnitude at one per unit. The rotor rotates at the synchronous speed $w_{r.}$ The machine is tested for its electrical performance with the following cases in real time:

Case (i) Changes in input mechanical torque
Case (ii) Changes in reference voltage

Case (i): The input reference voltage is held constant throughout this run. The machine is driven by an externally applied mechanical torque T_{mech}. A sharp variation of T_{mech} in real time is given using Control Desk instrument of dSPACE as shown in Fig. 76.7. At t = 50 s, the mechanical input is increased abruptly from 1 p.u to 1.2 p.u. Figure 76.7 depicts the variation of electromagnetic torque for the changes in mechanical torque. The electromagnetic torque T_{em} will be negative when the machine is generating and is positive when it is motoring. The machine response of terminal voltage E_t, real power P, reactive power Q and many other parameters are recorded during this real time variation of externally applied $T_{mech.}$ On which the response of terminal voltage, deviations in rotor speed and rotor angle are shown in Fig. 76.8.

Obviously, the terminal voltage remains constant at 1 p.u with slight oscillations after the variation in the input. Figure 76.8 also shows the deviation in rotor speed and rotor angle changes for case (i). It is observed from the rotor angle curve that

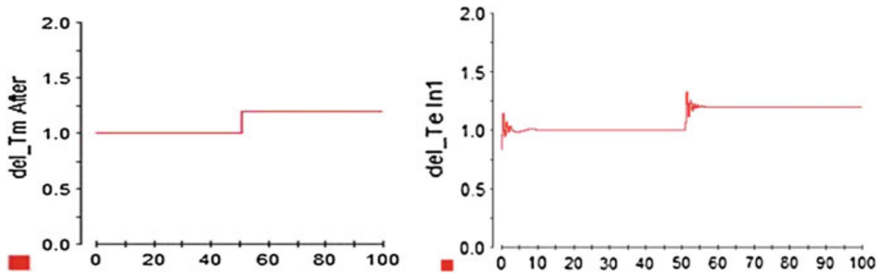

Fig. 76.7 Variations of mechanical torque and electrical torque in real time

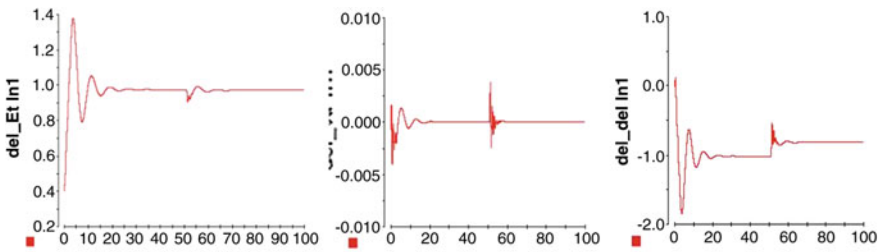

Fig. 76.8 Response of terminal voltage, deviation in rotor speed and rotor angle

the synchronous machine is stable for the applied sharp variations in the mechanical input.

Case (ii): Keeping the mechanical input constant, the simulations are also done for decrease in reference voltage by 20 % in real time. At t = 50 s, the reference voltage is decreased from 1 p.u to 0.8 p.u as shown in Fig. 76.9.

The response of Terminal Voltage is also shown in Fig. 76.9. It shows that the terminal voltage is settled to 0.8 p.u. after the variation in input reference voltage (V_{ref}). The response of machine such as field voltage, deviation in rotor speed and

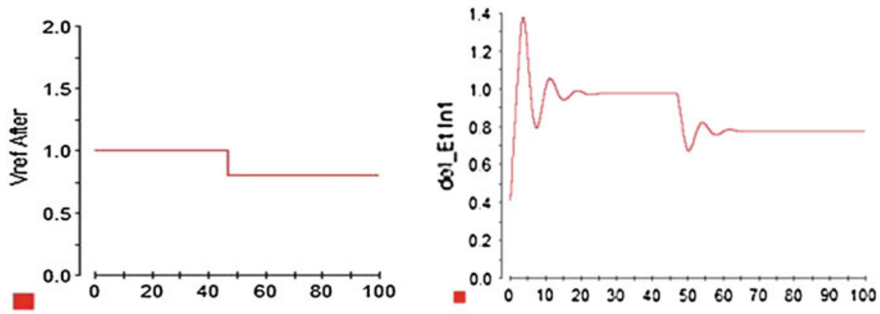

Fig. 76.9 Variations in reference voltage and terminal voltage

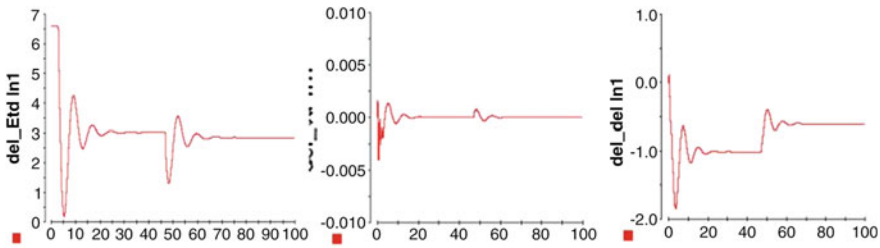

Fig. 76.10 Field voltage, deviation in rotor speed and rotor angle

rotor angle for decrease in reference voltage is shown in Fig. 76.10. It proves that the machine comes to steady state even after the perturbation occurs in the system in real time.

76.7 Conclusion

A linear model of a synchronous generator including the oscillation of rotor caused by changes in its inputs is realized on a real-time hardware. More realistic results are obtained when the actual pieces of equipment are used in the simulation. The real-time dSPACE simulator behaves like an actual power plant and can provide signals to the controller in real-time. Therefore, it is possible to build a closed-loop system consisting of an excitation device as device under test and the simulated synchronous generator as test tool, which offers the opportunity for setting-up, testing and designing excitation devices. In such case, the model can read the excitation voltage from the excitation device and calculates in real-time the stator voltages and currents as output values depending on the parameters applied mechanical power and voltage of the supply network. This type of real time analysis is helpful for future expansion of installed power system and development of new power system.

References

1. Kundur P (1994) Power system stability and control. Tata Mc Graw-Hill, New Delhi
2. Anderson PM, Fouad AA (1981) Power system control and stability. GalGotia Publications, New Delhi
3. Ong CM (1998) Dynamic simulation of electric machinery—using matlab simulink. Prentice Hall, Englewood Cliffs
4. Tabatabaei I et al (2004) Modelling and simulation of a salient-pole synchronous generator with dynamic eccentricity using modified winding function theory. IEEE Trans Magn 40 (3):1550–1555

5. Singhvi V, Halpin SM (2007) Synchronous machine modeling for low- frequency harmonic studies. In: 39th southeastern symposium on system theory, Mercer University, Macon, March 2007, pp 228–231
6. Mon TW, Aung MM (2008) Simulation of synchronous machine in stability study for power system. World Acad Sci Eng Technol 39:128–133
7. Jackson G et al (2005) A real time platform for teaching power system control design. In: International conference on power systems transients in montreat, Canada on 19–23 June
8. dSPACE Catalog (2009) DS1104 R&D controller board hardware installation and configuration for DS1104. Paderborn, Germany

Chapter 77
RGA Based Fractional Order PI Controller Design for Speed Control of IPMSM

A. Shakila Banu and R.S.D. Wahidabanu

Abstract This paper discusses the application of Real coded Genetic Algorithm (RGA) in fractional order PI controller design for speed control of Interior Permanent Magnet Synchronous Motor (IPMSM). Real coded Genetic Algorithm used for finding the optimal fractional order PI controller parameters by minimizing the performance index such as Integral Absolute Error (IAE) of speed in IPMSM. The performance of the RGA based fractional order PI controller is compared with the RGA based integer order PI controller. The simulation results demonstrated that the RGA based fractional order PI controller performance is better than RGA based Integer order PI controller.

Keywords Genetic algorithm · Interior permanent magnet synchronous motor (IPMSM) · Integral absolute error (IAE) · PI controller

77.1 Introduction

Permanent Magnet Synchronous Motor (PMSM) are AC motors which are used in the applications like actuators, machine tools and robotics and electrical vehicle due to its high power-density, efficiency, reduced volume and weight, low noise and robustness [1]. Electrically excited field windings are replaced by Permanent Magnets because of their advantages like elimination of brushes, slip-rings and rotor copper losses that yields high efficiency and also these magnets produce constant flux [1]. Hence, a precise speed control is needed for IPMSM, due to the nonlinear coupling along with its winding currents the rotor speed and torque [2, 3]. Many possible control methods like non-linear, adaptive, intelligent control exist in

A.S. Banu (✉)
Department of ICE, Sethu Institute of Technology, Viruthunagar 626115, Tamil Nadu, India
e-mail: banushakila_a@yahoo.co.in

R.S.D. Wahidabanu
Government College of Engineering, Salem 636011, Tamil Nadu, India
e-mail: drwahidabanu@gmail.com

C. Kamalakannan et al. (eds.), *Power Electronics and Renewable Energy Systems*,
Lecture Notes in Electrical Engineering 326, DOI 10.1007/978-81-322-2119-7_77

the market of electrical drives and control [4, 5]. But a simple and sophisticated control system is needed in speed control of IPMSM.

Among the various Artificial Intelligence techniques, Fuzzy Logic Controller (FLC) is commonly used for speed control of high performance PMSM drive [6, 7]. FLC is based on the rules which are set by the engineer. The robustness of the FLC due to plant parameter variations and environmental changes is questionable and implementation as well as modification of FLC is complicated in real time. Now days, PID controller is widely used in industrial applications because of its simplicity and performance and robustness [8]. Also, most research is done to improve the performance of PID controller by modifying the structure. Recently fractional calculus is employed in the PID structure to improve the performance of the PID controller [8]. Many researchers showed the fractional order in the Integrator part in PI controller gives the good performance than Integer order PI controller [9].

In this paper, the performance of RGA based fractional order PI controller is compared with the RGA based Integer order PI controller. Most common representation GA is binary. The chromosomes consist of only binary values {0, 1} [10]. However, in the problems in continuous domain represents the gene to real numbers. Davis (1991) and Michalewicz (1992) are extensively worked in the real coded numerical optimization for continuous domain problem. Here, speed control of IPMSM is in continuous domain. Hence, a real coded Genetic algorithm (RGA) is chosen for this problem. RGA finds the optimal controller parameter (for both integer order PI and fractional order PI) by minimizing Integral Absolute Error (IAE) of the IPMSM's motor speed.

The rest of the paper is organized as follows, Sect. 77.2 has the Mathematical model of IPMSM; Sect. 77.3 describes the control principle and controller in speed control of IPMSM; Sect. 77.4 defines the objective function; Sect. 77.5 describes the steps in Real coded Genetic Algorithm. Section 77.6 has Simulation results and Discussion. Conclusion is on Sect. 77.7.

77.2 Mathematical Model of IPMSM

The objective in IPMSM speed control is to runs in mechanical load at desired speed (ω_{ref}). The current controllers in the IPMSM drive systems are used for maintaining the current rate in the closed loop. The mathematical model of PMSM in d–q synchronously rotating frame of reference can be obtained from synchronous machine model can be represented by the set of following nonlinear [11] differential equations.

$$v_{sd} = r_s i_{sd} + p\lambda_{sd} - \omega_e \lambda_{sq} \tag{77.1}$$

$$v_{sq} = r_s i_{sq} + p\lambda_{sq} - \omega_e \lambda_{sd} \tag{77.2}$$

$$\lambda_{sd} = L_d i_{sd} + \lambda_m \tag{77.3}$$

$$\lambda_{sq} = L_q i_{sq} \tag{77.4}$$

$$T_e = \frac{3}{2}\frac{P}{2}[\lambda_m i_{sq} + (L_d - L_q) i_{sd} i_{sq}] \tag{77.5}$$

$$T_e = J\frac{2}{P}\frac{d\omega_e}{dt} + B\frac{2}{P}\omega_e + T_l \tag{77.6}$$

$$\omega_e = P\omega_r/2 \tag{77.7}$$

$$p\theta_r = \frac{2}{P}\omega_e \tag{77.8}$$

where v_{sq}, v_{sd}, i_{sq}, i_{sd} are d–q axis voltages and currents respectively. L_d, L_q are d–q axis inductances, λ_{sd} λ_{sq}, are d–q axis flux linkages, ω_e and r_s are electrical speed of motor and stator resistance respectively. T_e is the electromagnetic torque and T_l is the load torque. P represents number of poles, þ is the differential operator, B is the damping coefficient, θ_r is the rotor position, ω_r is the rotor speed, and J_m is the moment of inertia.

The PMSM motor drive shown in Fig. 77.1 and consist of two control loops. The two control loops are 1. Speed control loop 2. Current control loop. The speed control loop has the PI controller responsible for closed loop speed control of IPMSM. The current loop controller has two PI controllers which are responsible for the limit the current in the IPMSM drive. The two current loop controllers are tuned statically using trial and error and the parameters of the current PI controllers

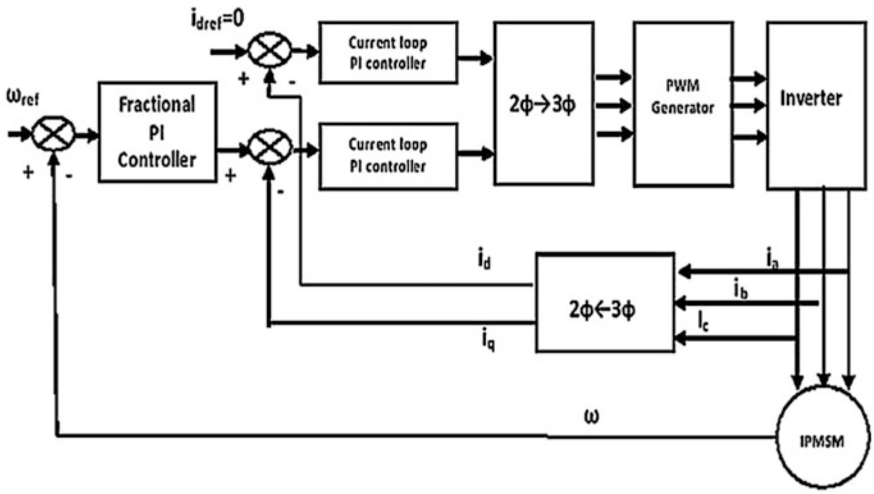

Fig. 77.1 Block diagram of PMSM drive

are $K_{pc} = 2$; $K_{ic} = 1$; Speed loop has two inputs such as reference speed, measured speed. The Error between reference speed and measured speed is the taken as the performance index (i.e. IAE) and Genetic Algorithm gives the optimal controller parameters by minimizing the error. The output of the speed loop PI controller is reference current of i_q*. The two currents i_d and i_q are converted to Three phase current using inverse park transformation. The three phase current is fed to the PWM inverter containing IGBT switches and PWM generator. The three phase current signal is compared with a carrier signal to generate 3 pulse width modulated pulses for motor supply. These pulses are used to trigger the upper IGBT switches in the three arms and the pulse to the upper switch in the arm is inverted and given to the lower switch in the arm. From this inverter three phase voltage is taken out for motor supply.

77.3 Control Principle

The tuning of both fractional order PI and Integer order PI controller is offline and independently. GA is the population based optimization algorithm which generates the NP number of solutions (i.e. controller parameters) and simulate the IPMSM model with the populated solutions. Based on objective comparison (i.e. IAE) it selects the best solution for the next generation. The steps in Genetic Algorithm described in the Table 77.1. Block diagram of controller tuning is shown in Fig. 77.2.

77.3.1 *Fractional Order PI Controller*

Fractional Calculus (FC) is the branch of Mathematics, having 300 years of history. Recently this theory was applied to many fields of science and engineering [9, 10, 12, 13]. FC is a generalization of ordinary differential calculus which considers the possibility of taking real number power of differential and integration operator. There are many ways to describe fractional-order integrals and derivatives. The main concept of FC lies in developing a functioning operator D which is known as

Table 77.1 RGA initial parameters

Parameter	Size
Population size	100
Maximum function evolution	1,000
Maximum generation	10
η_c (SBX parameter)	5
η_m (Polynomial mutation parameter	20
P_c (Crossover probability)	0.8
P_m (Mutation probability	0.5

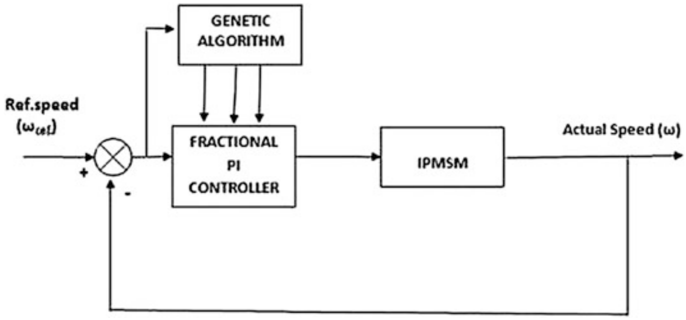

Fig. 77.2 Block diagram for controller tuning

differ-integrator operator, according to Riemann-Liouville definition it is mathematically defined as

$$ {}_aD_t^\alpha f(t) = \frac{1}{\sqrt{(m-\alpha)}}\left(\frac{d}{dt}\right)^m \int_a^t \frac{f(\tau)}{(t-\tau)^{1-(m-\alpha)}} d\tau \tag{77.9} $$

The generalized form of fractional order PI controller is the PI controller, which involves an fractional integrator of order l. In this paper Speed error (e(t)) is taken as input to Fractional order PI controller and output is taken to the system. The controller signal u(t) can then expressed in time domain as given in Eq. (77.10).

$$ u(t) = K_p e(t) + \frac{K_i}{s^\lambda} e(t) \tag{77.10} $$

where

e(t)	is the difference between actual and reference speed of IPMSM at time t
K_p	is the proportional gain of the controller,
K_i	is the integral gain of the controller,
$0 \leq \lambda \leq 1$	is the fractional order in the controller.

The transfer function of fractional order PI controller is given as follows.

$$ K(s) = K_p + \frac{K_I}{s^\lambda} \tag{77.11} $$

If $\lambda = 1$ then the fractional order controller in Eq. (77.11) automatically converted to integer order PI controller. GA finds the fractional order PI controller parameters (i.e. k_p, k_i, λ) by minimizing IAE of IPMSM speed.

77.4 Objective Function

There are various performance criteria for design of controllers, of which some are integral absolute error (IAE), integral squared error (ISE) and Integral Time Absolute Error (ITAE). In this paper, Integral Absolute Error (IAE) is chosen as a performance index for the design of fractional order PI controller in IPMSM speed control. The objective function to be minimized is described as follows.

$$J = \int e(t)dt \tag{77.12}$$

The performance of the drive depends on the fractional order PI controller parameters which indeed depend on the objective function to be minimized. RGA gives the optimal set of parametric values for KP, KI, and λ to meet the user defined specifications for a given process call for real parameter optimization in three-dimensional hyperspace.

77.5 Real Coded Genetic Algorithm

Genetic algorithms (GAs) are randomized generated population based algorithms which is based on the concepts of biological evolution [12]. Genetic Algorithm starts with a population of randomly generated chromosomes and by using genetic operators such as crossover and mutation the new chromosomes are generated for every generation. During the generations, the chromosomes are move towards the optimal solutions based on their objective value (i.e. selection procedure). The steps followed in RGA are as follows.

Step 1: Generate randomly N × n number of parent solutions (i.e. controller parameters K_p, K_i, λ and n is the dimension of the problem).

Step 2: Simulate IPMSM drive with the parent solution and compute the objective value J as in the Eq. (77.12).

Step 3: Create a new population of solutions by repeating following steps until the new population is complete.

Step 3.1: Select a two solution from the parent population using tournament selection.

Step 3.2: Recombine the parent solutions using SBX crossover to form a new child solution with crossover probability [10].

Step 3.3: Mutate the new child solution using polynomial mutation with a mutation probability [12, 13].

Step 4: Compute the objective value with child solution. Select the best solution based on the objective value.

Step 5: Check if the objective is minimized or satisfied the stopping criteria. If not go to step 2. If the condition is satisfied stop the algorithm. The algorithm is stopped when the function evaluation reaches maximum function evaluation which is set as per in the Table 77.1.

77.6 Results and Discussion

All the simulations are done in MATLAB R2009a in core2duo processor with 2 GB RAM. The initial parameters of GA are set as in the Table 77.1. The same parameters are set for both the fractional order and integer order PI controller design. The genetic algorithm based fractional order PI controller is given in Eq. (77.13).

$$K(s) = 0.08 + \frac{2.2}{s^{0.2}} \tag{77.13}$$

and GA based integer order PI controller as in the Eq. (77.14).

$$K_{\text{integer}}(s) = 0.12 + \frac{2}{s} \tag{77.14}$$

Figure 77.3 shows the IPMSM's closed loop speed response of both integer order and fractional order controller. From Fig. 77.3 Integer order PI controller has large peak overshoot than fractional order PI controller. Table 77.2 shows the time

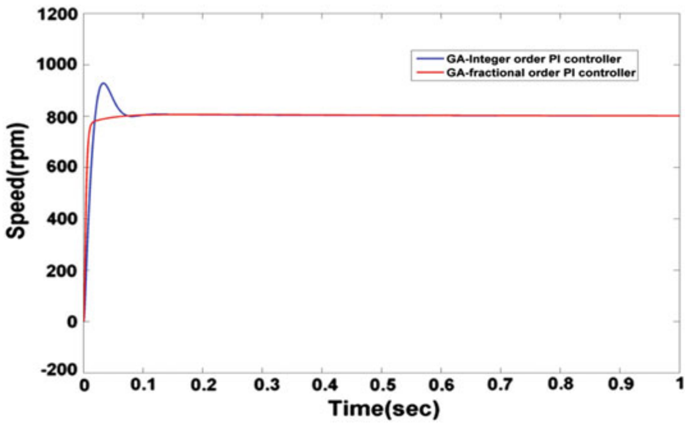

Fig. 77.3 IPMSM speed response of both fractional and integer order controllers

Table 77.2 Time domain specifications of the controllers

Parameters	Integer order PI controller	Fractional order PI controller
Rise time	0.0141	0.0074
Settling time	0.0629	0.0260
Overshoot	15.8849	0.6491
Undershoot	0.1438	0.0986
Peak time	0.0333	0.1798

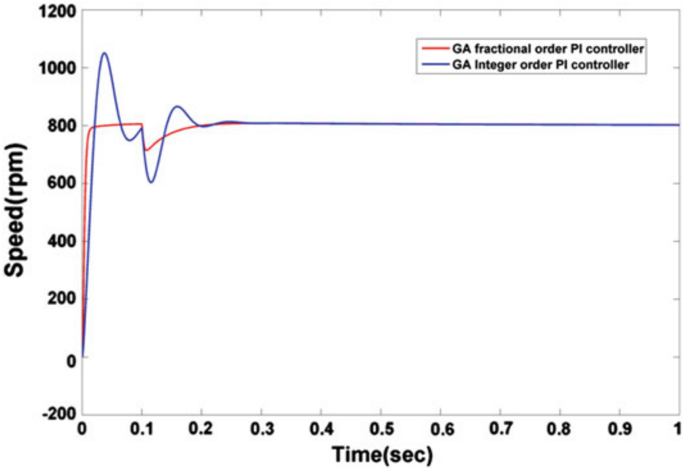

Fig. 77.4 IPMSM speed response of both fractional and integer order controllers with load torque

domain specifications data for both fractional order and Integer order controller. From table fractional orders PI controller gives quick response (i.e. less rise time) and quickly reach the steady state than Integer order PI controller.

Figure 77.4 shows the speed response of IPMSM under unit step change in load torque at 0.1 s time. Form Fig. 77.4 fractional order PI controller can manage the load torque but the integer orders PI controller oscillate more to reach steady state and has more peak overshoot than the nominal response as in the Fig. 77.3.

Figure 77.5 shows the convergence graph of RGA for both fractional and integer order controllers. As seen in Fig. 77.5, RGA for fractional order controller converges quickly to minimum objective value.

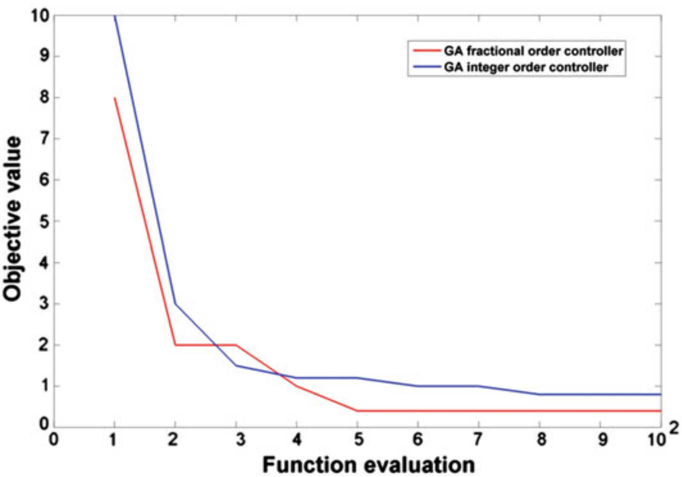

Fig. 77.5 Convergence of RGA for both fractional order and integer order controller

77.7 Conclusion

In this paper fractional order PI speed loop controllers are designed for Interior Permanent Magnet Motor (IPMSM) using real coded Genetic Algorithm (RGA). The performance of the fractional order PI controller is compared with the RGA designed Integer order PI controller. From the simulation results, fractional order PI controller has good command tracking performance and also can able to tolerate load torque, efficiently than the integer order PI controller. Hence, fractional order PI controller works better and it is useful for the precise control of IPMSM.

References

1. Vas P (1998) Sensorless vector and direct torque control, 1st edn. Oxford University Press, Oxford
2. Rahman MF, Zhong L, Lin KW (1998) A direct torque-controlled interior permanent magnet synchronous motor drive incorporating field weakening. IEEE Trans Ind Appl 34 (6):1246–1253
3. Uddin MN, Radwan TS, Rahman MA (2002) Performance of interior permanent magnet drive over wide speed range. IEEE Trans Energy Convers 72(1):79–84
4. Slotine JJ, Li W (1991) Applied nonlinear control. Pearson Education, Englewood Cliffs
5. Jain LC, De Silva CW, Jain LC (1998) Intelligent Adaptive Control. Industrial Applications. CRC, Boca Raton
6. Guney I, Yuksel, O, Serteller F (2001) Dynamic behaviour model of permanent magnet synchronous motor fed by PWM inverter and fuzzy logic controller for stator phase current, flux and torque control of PMSM. International Electric Machines and Drive Conference, pp 479–485

7. Dogan M, Dursun M (2012) Application of speed control of permanent magnet synchronous machine with PID and Fuzzy Logic Controller. Energy Educ Sci Technol Part A Energy Sci Res 28(2):925–930
8. Astrom KJ, Hugglund T (2001) The future of PID control. Control Eng Pract 9:1163–1175
9. Chen YQ, Xue D, Dou H (2004) Fractional calculus and biomimetic control. In: Proceedings of the first IEEE international conference on robotics and biomimetics (RoBio04), Shengyang, IEEE
10. Goldberg DE (1989) Genetic algorithms in search, optimization and machine learning. Addison-Wesley, New York
11. Pillay P, Krishnan R (1989) Modeling, simulation, and analysis of permanent-magnet motor drives, part I: the permanent-magnet synchronous motor drive. IEEE Trans Ind Appl 25 (2):265–273
12. Willjuice Iruthayarajan M, Baskar S (2009) Evolutionary algorithms based design of multivariable PID controller. Expert Syst Appl 36:9159–9167
13. Blanco A, Delgado M, Pegalajar MC (2001) A real-coded genetic algorithm for training recurrent neural networks. Neural Netw 14:93–105

Chapter 78
Optimization of Photovoltaic Power Using PID MPPT Controller Based on Incremental Conductance Algorithm

B. Ashok Kumar, M. Srinivasa Venkatesh and G. Mohan Muralikrishna

Abstract This work proposes a method of designing a optimum controller based maximum power point tracking (MPPT) control for a photo voltaic system (PV) using proportional integral and derivative (PID) controller. The proposed methodology is two stage controller which uses PID with incremental conductance algorithm to extract maximum power from PV system. The proposed PID controller is used to vary the duty cycle of the boost converter. Here PV system is tested under various environmental conditions. The proposed work is simulated using MATLAB SIMULINK. The SIMULINK results are compared with conventional methods such as Perturb and observe (P&O) and Incremental conductance method, results show that the power extracted is utmost for PID MPPT controller.

Keywords Photovoltaic · Maximum power point tracking · PID controller · Boost converter · Incremental inductance

78.1 Introduction

The present power scenario is in great need of renewable energy source. Among existing renewable sources PV suits for many climatic conditions around the world. The PV system has high initial cost but has the advantage of good life time. The power that is extracted is highly non linear and difficult to estimate, also it has one more intricacy that the voltage and current depends on the irradiance and temperature, which themselves are non linear. In order to extract utmost power the PV has to operate in an optimal operating point called as maximum power point (MPP). MPP is a point which satisfies the maximum power transfer theorem. The optimum power point can be tracked with various methods [1–3]. Some of the most common methods used are Perturb and observe (P&O), Incremental conductance, fuzzy logic [4] and neural network based [5].

B. Ashok Kumar (✉) · M. Srinivasa Venkatesh · G. Mohan Muralikrishna
Department of Electrical and Electronics Engineering, Thiagarajar College of Engineering, Madurai, Tamil Nadu, India
e-mail: ashokudt@tce.edu

C. Kamalakannan et al. (eds.), *Power Electronics and Renewable Energy Systems*, Lecture Notes in Electrical Engineering 326, DOI 10.1007/978-81-322-2119-7_78

P&O is the most commonly used controlling process because of its simple algorithm and easy implementation. It works on principle that the rates of change of power will me minimum around MPP. P&O has disadvantage of oscillation around the MPP. Incremental conductance is another most commonly used algorithm which is based on the truth that the slope of the P–V curve will approaching zero as system reaches the MPP. In order to find the operating point the change in current and change of voltage are considered. It provides better MPPT even in rapidly varying atmospheric conditions. The oscillations are also less compared to P&O. The limitation of this system is in choosing the incremental step size.

Intelligent controls like fuzzy logic [6–8], and neural network [9], can be used to gain the advantage of directly varying the duty cycle of the converter connected to the system, which solves the problem of fixed step perturbation. The working of fuzzy logic depends on the rules designed, which intern depends on the designer experience. So the basic disadvantage is there is no unique methodology. The neural network method requires more accurate data to test and train. The quality of a data is the major prerequisite here which is more difficult to obtain. The most widely used controllers in the industrial control processes are the PID controllers due to their simple construction, ease of application, low cost and robust performance in a wide range of operating conditions. The selection of a PID as an MPPT controller satisfies most of the above aspects. The design of such a PID controller which requires the determination of three parameters: proportional gain, integral time constant and derivative time constant is discussed in brief in this paper.

78.2 Methodology

The major things that have to be considered in development of MPPT controller are PV module modelling, DC to DC converter and algorithm.

78.2.1 PV Module Modelling

The PV module characteristic is a non linear characteristic which depends on the reverse saturation current of the diode in parallel to the photo current source. The photon current is produced because of the photovoltaic action. As per the load requirement the specification of the PV panel used here are (Table 78.1).

78.2.2 DC to DC Converter

The usage of the DC/DC converter is essential for achieving MPPT as it is the element which is driven by the controller in order to move the operating point of a

Table 78.1 Parameter specifications of 110 W PV module

Parameter	Variable	Value
Maximum power	Pm	110 W
Maximum voltage	Vm	33.6 V
Current at maximum power	Im	3.5 A
Open circuit voltage	Voc	41.6 V
Short circuit current	Isc	3.74 A

PV source to be coincident to MPP. The boost converter is widely used to pinpoint the ultimate point of power of the PV array. Here the boost converter and resistive load are connected in parallel with the PV module. These elements form the power circuit. The boost converter can operate in continuous conduction mode along with discontinuous conduction mode. The mode of conduction depends of the capacity for storage of energy along with the relative timeframe of the switching. The output voltage is depends on the duty cycle and it is adjusted by the maximum power controller. The relation of the output voltage with the input voltage as function of duty cycle is given by

$$\frac{Vo}{Vi} = \frac{1}{1 - \mathrm{D}} \tag{78.1}$$

Vo = average output voltage, Vi = the input voltage, PV voltage and D = duty cycle.

The design the boost converter [11, 12] mainly includes the coupling capacitor on the input side, capacitor on the output side of converter and the inductor. The Vin and Vout are 33.6 and 54 V respectively depending on which capacitor and inductor values varies. The values are shown in the Table 78.2.

78.3 Proposed MPPT Controller Design

78.3.1 PID Controller

PID controller as the name indicates is proportional integral and derivative controller. The PID controller acts in such a way that it tries to minimize the error which is given as input to the controller [13]. The continuous PID equation is depends on the K_p, K_i and K_d values. In order to calculate the proportional, integral

Table 78.2 Boost converter specifications

Parameters	Ratings
Switching frequency	10 kHz
L Boost	1.93 mH
Cout	69.1 μF
Cin	141 μF
R load	24 Ω

Table 78.3 PID controller parameters

Parameter	Value
K_p	0.14
K_I	70
K_d	0.00007

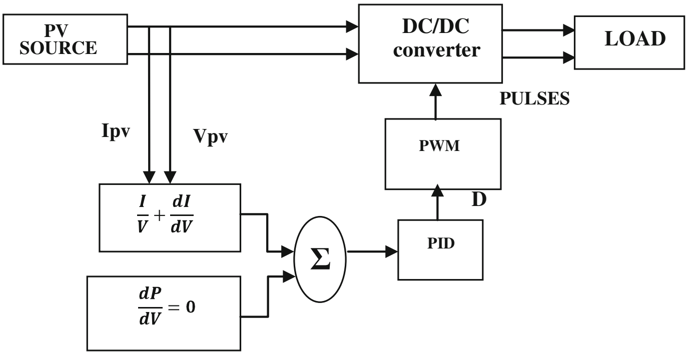

Fig. 78.1 Block diagram of PID MPPT for PV system

and derivative gains of PID controller, the Zeigler Nicholas method is applied. The values of the K_p, K_i and K_d values use here are tabulated (Table 78.3).

The incremental conductance method it tracks the maximum power point, by comparing the solar array incremental and instantaneous conductance. The algorithm is based on the fact that the slope tangent of the characteristic p–v is zero in MPP, the calculation of this slope is given by:

$$\frac{dP}{dV} = \frac{d(VI)}{dV} = I + V\frac{dI}{dV} = 0 \tag{78.2}$$

$$\frac{I}{V} + \frac{dI}{dV} = 0 \tag{78.3}$$

In proposed system the PID controller takes the Eq. 78.3 as error signal and tries to reduce it. The PID used in this simulation is used to reduce the error between the PV slope to reference value, and controls the switching of boost converter. The overall block diagram of the proposed MPPT with PV system is shown in Fig. 78.1.

78.4 Simulation and Results

The Fig. 78.2 shows the major simulation diagram that consists of PV module connected to load through the DC-DC converter. The Fig. 78.3 shows the simulation results for PID for various atmospheric conditions. The comparison for various parameters of all three methods are listed below.

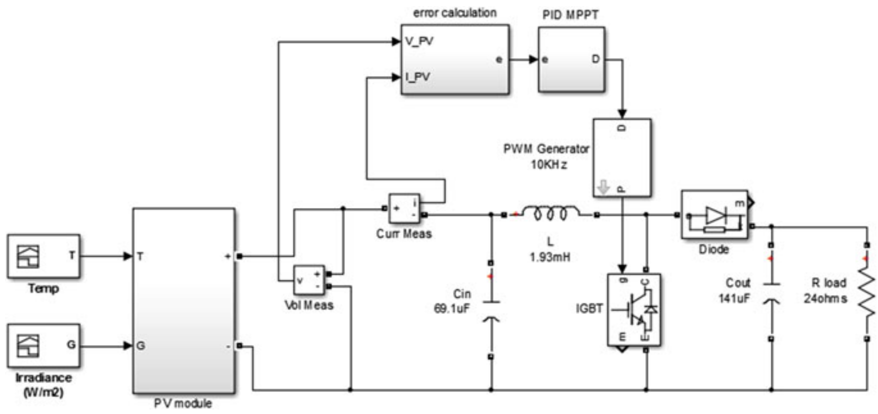

Fig. 78.2 Simulation diagram for PID controlled PV system

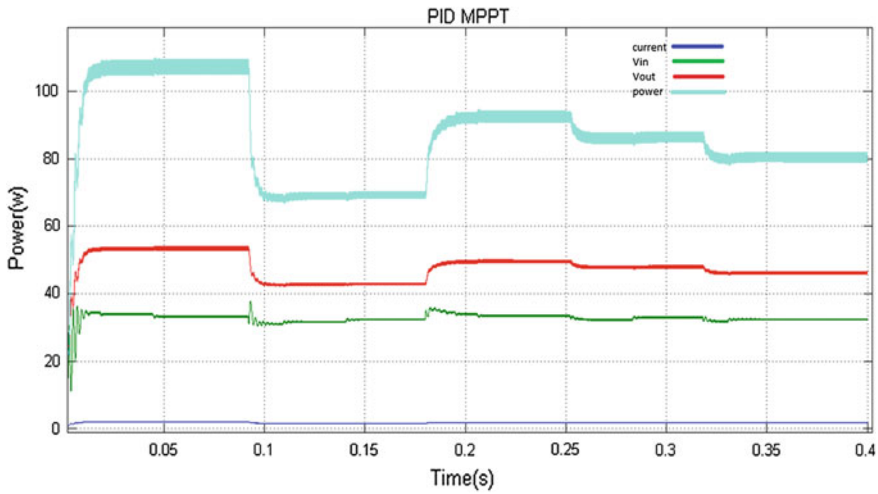

Fig. 78.3 Simulation results for PID controller

Table 78.4 Performance analysis for different methods

Parameters	P&O	INC COND	PID
Pmax	108.21	108.51	109.45
Vmax	53.64	53.72	53.91
Imax	2.01	2.019	2.03
Tmax	0.045	0.045	0.019
Efficiency	95.71	96.13	97.44

The Table 78.4 gives the comparison for various methods where we can observe that the PID MPPT tracking can yield more power and the max values are attained higher through this method. The time at which this maximum value reached is also less for PID method, which shows that the response time is fast.

78.5 Conclusion

In the proposed work a PV module of 110 W and DC to DC boost converter with coupling capacitors and inductor are designed. The algorithm followed tuning of K_p K_i and K_d with zigler Nicholas method. The results obtained from the simulation are clear that the PID results are effective and efficient than the conventional methods. There was improvement in the output power. The results of the proposed method show that the time taken by the PID method to reach the optimal point is very less compared to P&O and incremental. Also the values of voltage, current and power are better in PID MPPT method. The oscillations are will also be reduced through this control strategy. The efficiency of the PV system with PID controller is found to gain more than the other two techniques.

References

1. Esram T Chapman PL (2007) Comparison of photovoltaic array maximum power point tracking techniques. IEEE Trans Energy Convers 22:439–449
2. Carlos AP, Tavares1, Karla T. F. Leite2, Walter I. Suemitsu3, Maria D. Bellar (2009) Performance evaluation of photovoltaic solar system with different MPPT methods. IEEE Trans pp 719–724, 978-1-4244-4649
3. Li J, Wang H (2009) A novel stand-alone PV generation system based on variable step size INC MPPT and SVPWM control. IEEE 6th international power electronics and motion control conference, 2009. IPEMC '09. pp 2155–2160
4. Yang YR (2010) A fuzzy logic controller for maximum power point tracking with 8-bit microcontroller. IEEE. pp 2895–2900, ISBN 978-1-4244-5226-2/10
5. Liu YH, Liu C, Huang JW, Chen JH (2013) Neural-network-based maximum power point tracking methods for photovoltaic systems operating under fast changing environments. Sci Direct Solar Energy 89:42–53
6. Islam MA, Talukdar AB, Mohammad N, Shadhu Khan PK (2010) Maximum power point tracking of photovoltaic arrays in matlab using fuzzy logic controller. Annual IEEE India conference (INDICON) pp 1–4, ISBN 978-1-4244-9074-5/10
7. Mohamed A, Hannan MA (2010) Hardware implementation of fuzzy logic based maximum power point tracking controller for PV systems. The 4th international power engineering and optimization conference (PEOCO2010), IEEE, Subiyanto, IEEE. pp 435–439, ISBN 978-1-4244-7128-7/10
8. Punitha K, Devaraj D, Sakthivel S (2012) Development and analysis of adaptive fuzzy controllers for photovoltaic system under varying atmospheric and partial shading condition. Sci Direct Appl Soft Comput 13:4320–4332

9. Liu YH, Liu CL, Huang JW (2013) Neural-network-based maximum power point tracking methods for photovoltaic systems operating under fast changing environments. Sci Direct Solar Energy 89:42–53
10. Xiao W, Lind M, Dunford W, Capel A (2006) Real-time identification of optimal operating points in photovoltaic power systems. IEEE Trans Ind Electron 53(4):1017–1026
11. Ortiz-Rivera EI (2008) Maximum power point tracking using the optimal duty ratio for DC-DC converters and Load matching in photovoltaic application. Applied power electronics conference and exposition, 2008. APEC 2008. Twenty-Third Annual IEEE, pp 987–991
12. Hasaneen BM, Elbaset Mohammed AA (2007) Design and simulation of DC/DC converter. 12th international middle-east, power system conference, MEPCON 2008, pp 335–340
13. Fengwen C, Yiwang W (2010) Variable universe adaptive fuzzy-PI compound control applied in maximum power point tracking for photovoltaic energy generation system. Proc ICIC 2010:514–519

Chapter 79
Development of a Universal Controller for Converter Based Switched Reluctance Motors

P. Avirajamanjula and P. Palanivel

Abstract This dissertation covers the design procedure of a 8/6 switched reluctance motor from the first principles. The methodical approach to designing the machine is one of the major objectives of this paper. The calculation of the unaligned inductance follows the basic principles of electromagnetic. The procedure for calculating voltage, current, speed and losses for various rotor positions has been developed. A detailed procedure to calculate the eddy-current losses was described. The process of finding the hysteresis losses does not rely on approximate flux profiles. Instead accurate flux plots are used to find the hysteresis losses. The calculation and documentation of the iron loss is one of the significant objective of this paper. The dissertation describes the design procedure for a SRM drive using the new voltage source inverter configuration. The design procedure was verified with computer simulations and experimental verifications of the drive have been done. A SRM drive to PID control has been developed. The dissertation shows the implementation of SRM drives using a DSP based controller and a single converter configuration.

Keywords Switched reluctance motor (SRM) · Current controller · Speed controller · PID controller · DSP controller

79.1 Introduction

Switched Reluctance Drive (SRD) is a step less speed regulation system, which is composed of SRM, converter and controller. For producing the maximum torque from a motor in the given speed, the combination of power converter—motor can

P. Avirajamanjula (✉)
Periyar Maniammai University, Thanjavur, India
e-mail: avmanjula@pmu.edu

P. Palanivel
MAM College of Engineering, Trichy, India
e-mail: palaniveleee@mamce.org

C. Kamalakannan et al. (eds.), *Power Electronics and Renewable Energy Systems*,
Lecture Notes in Electrical Engineering 326, DOI 10.1007/978-81-322-2119-7_79

be defined. However, control strategy, converter's topology and optimized design of SRM have crucial influence on performance of SRD. The suitable control of the SRM is not completed adequately. The natural nonlinearity of a SRM makes torque production greatly dependent on the geometry of the poles, which is described by the dependence on both rotor position current and rotor position [1, 2].

79.2 Proportional Integral Derivative Control

The PID algorithm is the most well-known feedback controller used in the manufacturing industries. It is a forceful easily understood algorithm that can provide first-rate control performance despite the varied active manufacturing of process plant (Fig. 79.1).

PID controllers classically use control loop feedback in industrial and method systems applications. The controller first evaluates a value of error as the subtraction of the measured process variable and preferred set-point. It tries to reduce the error by varying the control inputs to the progression, so that process variable change closer to the set point [3].

The mathematical representation is,

$$\frac{mv(s)}{e(s)} = k_c\left[1 + \frac{1}{T_{is}} + T_D s\right] \tag{79.1}$$

(or)

$$Mv(t) = MV_{ss}\left[e(t) + \frac{1}{T_i}\int e(t) + T_D\frac{de(t)}{dt}\right] \tag{79.2}$$

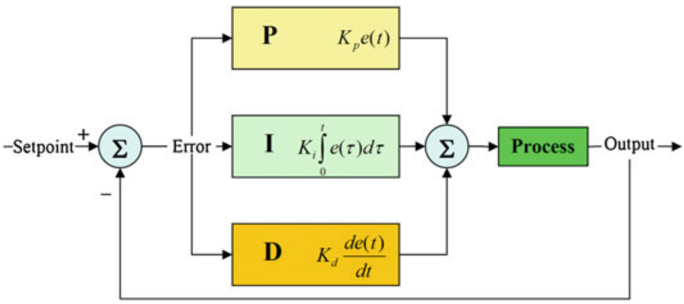

Fig. 79.1 PID controller block diagram

Imitative action (also called derivative or pre-act) *anticipates* where the process is heading by looking at the time rate of change of the controlled variable (its derivative). T_D is the 'rate time' and this characterizes the derivative action (with units of minutes). The problem of harmonic signals makes the use of imitative action un defendable. Derivative action depends on the slope of the error, disparate P and I. If the error is persistent derivative action has no effect.

79.3 Ziegler Nichols Closed Loop Method

First fix the controller to P mode only. Next, fix the gain of the controller (k_c) to a minimum value. Make a small set point (or load) change and observe the response of the controlled variable. If kc is low the response should be inactive. Rice k_c by a influence of two and make another small change in the set point or the load. Keep rising k_c until the result turn into oscillatory. Finally, fine turn k_c up to a response is obtained that produces continuous variations (Table 79.1).

79.4 Digital Signal Processor

The strategic objective and description were met in the following elevated speed DSP based digital controller. The system reaches good speed enactment by using a fast DSP and fast data attainment hardware [4].

A schematic of the DSP connections and hardware for clock generation, power-on reset, and input/output (I/O) space decoding. A 50 MHz clock oscillator with a CMOS level output is used to drive the external clock input of the DSP. This 50 MHz clock is divided by two by a toggle flip-flop to provide a 25 MHz reference for use elsewhere in the system. To cause a reset on power-up, a simple RC network drives a pair of Schmitt's triggers which control the reset input of the DSP. On power-up, the RC circuit asserts reset for approximately 400 ms, allowing the clock oscillator to stabilize and the DSP to reset [5, 6] (Fig. 79.2) (Table 79.2).

Table 79.1 PID controller parameter

Controller	Kc	Ti	TD
P	ku/2	–	–
PI	Ku/2.2	Pu/1.2	–
PID	Ku/1.7	Pu/2	Pu/8

Fig. 79.2 Flow chart

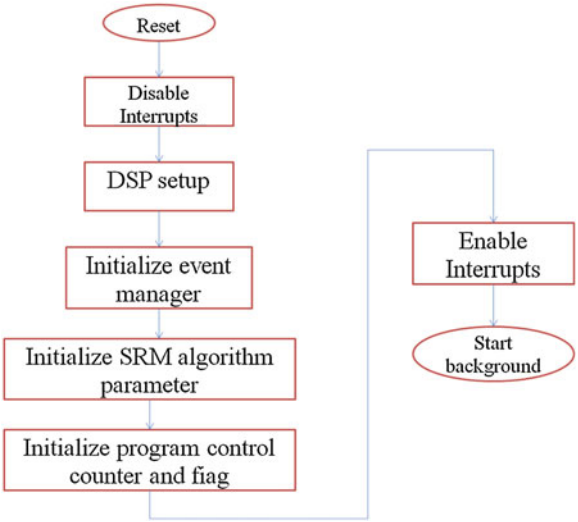

Table 79.2 Input and output port map with wait-states

I/P port	Input functions	Wait	Output functions	Wait
0	Digital In	0	Digital out, ADC select	0
1	S/P/D speed time	0	PWM1, PWM0	0
2	S/P/D Pos, Dir	0	PWM3, PWM2	0
3	Digital position	0	PWM5, PWM4	0
4	Unused	0	PWM7, PWM6	0
5	ADC data	1	ADC start	0
6	Unused	0	S/P/D divider	0
7	Unused	0	PWM divider	0
8–15	Serial	5	Serial	5

79.5 Power Electronic Converters for SRM Drives

The most resourceful SRM converter topology is the prototype bridge converter topology shown in Fig. 79.3a, suitable for powering a 3-phase motor. Note that the uneven bridge converter requires 2q power switches and 2q power diodes for a q-phase motor, reminiscent of the standard ac motor drives. Think through Phase a. The voltage given to the phase winding is $+V_{DC}$ when the upper arm and lower arm transistors T1 and T2 are turned on. Phase current i_a then increases through the switches. If one switch is off while the other is still on, the winding voltage will be zero. Phase current then reduces slowly by freewheeling through transistor and one

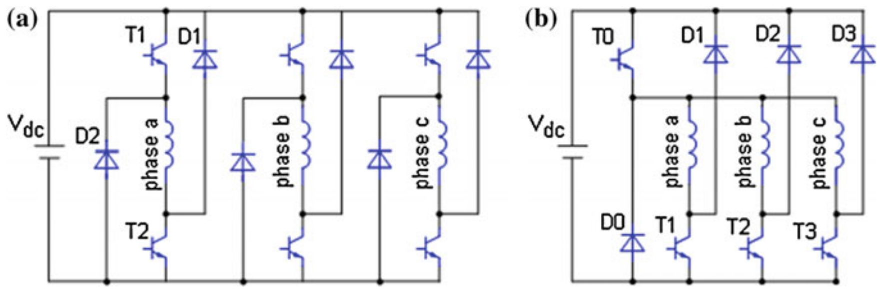

Fig. 79.3 Converter topologies of a 3-phase asymmetric half-bridge converter

diode. When both transistors are off, the phase winding will experience $-V_{DC}$ voltage. Phase current then rapidly decreases through both diodes. By suitably matching the above three switching states, the SRM phase current can be controlled [7].

In Fig. 79.3b the circuit has been modified. The existing converter circuit requires (q + 1) power switches for a q-phase machine. Firing a transistor T1…T4 selects which phase winding is excited. For all the phases Transistor T0 is the common switch. Here the number of switches are required for per phase winding is reduced. At any time the motor winding is series with the three devices which decreases the voltage applied to the winding and increase the conduction losses to the winding.

79.6 Generalized Equation of Motor

Through careful derivation, one can find the voltage equation of every particular phase as,

$$V = ri + \frac{dy}{dt} \tag{79.3}$$

where,

$$\mathrm{y} \;= \mathrm{Li} = \mathrm{Nj} \tag{79.4}$$

r = winding resistance, L = Nonlinear equivalent inductance; r = 0

$$V = L\frac{di}{dt} + i\omega\frac{dL}{dq} \tag{79.5}$$

79.7 Development of Torque

The expression for per phase torque produced at the given rotor position is,

$$Td = [\frac{d\omega'}{dq}]i = const \tag{79.6}$$

Since W′ = Co-energy = $\frac{1}{2}Ff = \frac{1}{2}NIj$

This equation shows that input electrical power partly increases the stored magnetic energy $\frac{1}{2}L^{*}i^{2}$ and partly provides mechanical output power $\frac{i^2}{2} \times \frac{dL}{dq} \times \omega$ the output power being related with the rotational e.m.f. in the stator circuit.

Neglecting saturation non-linearity, L = Inductance = $\frac{NF}{I}$

$$T_d = \frac{1}{2}i^2\frac{dL}{dq} \tag{79.7}$$

it depends on magnitude of current & direction of dL/dθ.

$$\text{Te} = \ \text{SN} \tag{79.8}$$

$$\text{i} = 1\ T_d = T_L + B\omega + J\frac{d\omega}{dt} \tag{79.9}$$

where, Te is the sum of the torque developed by all phases, N is the number of phases, and J and B denote the total inertia moment and the total damping ratio respectively.

79.8 Current Controller

Current is regulated by fixed frequency PWM signal with varying duty cycle.

$$P = \frac{Clock\ frequency}{PWM\ frequency} - 1$$

PWM frequency of 20 kHz is used.

The dynamic performance of current loop band width to cross over frequency 370 Hz

$$\begin{aligned}\theta_{LOSS} &= \omega\tau \\ \theta_{LOSS} &= 2\pi \times 370 \times (100 \times 10^{-6}) \\ &= 0.232\ rad = 13.3^{0}\end{aligned}$$

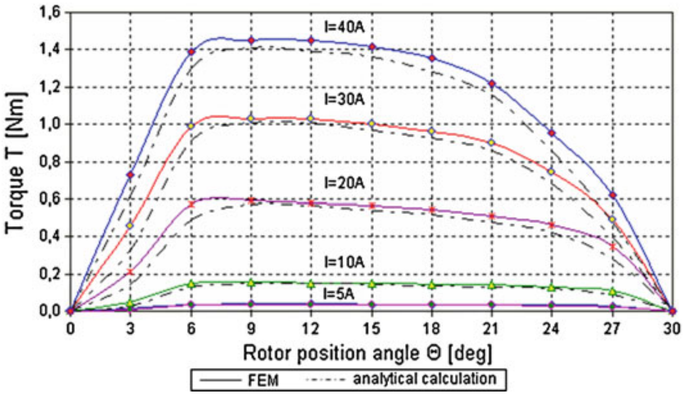

Fig. 79.4 Torque characteristics of the gear SRMIII for different current values

Assuming that the processing delay is equal to 50 % of a loop cycle the open-loop magnitude occurs at 370 Hz, then the resulting phase margin in the loop will be about 64° [8].

79.9 Calculation Results

At first, the electromagnetic torque is presented as a function of the rotor position angle for different current values. It can be seen in Fig. 79.4 that the desired value of approx. T = 1 Nm can be achieved with a current of I = 40 A. The largest contribution to rising the torque building capability is making a larger radius in the stator slots to increase the winding area. of course, that leads to a greater flux density in the stator core where the radius is increased (see Fig. 79.4) and therefore higher core losses and local heat sources. The developed torque is nearly constant in the range between 6 and 25° up to a current of approximately I = 10 A. For higher current values, the iron starts to saturate, which leads to a stronger decrease of the torque characteristic towards the aligned position (θ = 30°).

79.10 Conclusion

The PID compensator using a linearzed small-signal mode for SRM current loop is proposed. Based on the derived loop transfer function for the duty cycle to control output, the PID compensator can be designed with sufficient stability margin. The performances with open-loop Hysteresis and the proposed closed-loop PWM current controllers are compared with computer simulation. Through the frequency spectrum analysis, we can see that the noise spectra in audible range with conventional Hysteresis current controller is disappeared with the fixed switching frequency PWM controller. The results indicate that the PWM current controller achieves numerous advantages: (1) constant switching frequency, (2) low audible noise, (3) small current ripple, and (4) smooth torque production. A DSP controller based SRM drive system was then implemented to verify the proposed technique. Experimental results agree with the simulation very well. Torque ripple and acoustic noise prevent SRM from high performance application.

References

1. Latchman T, Mohamad TR, Fong CH (2004) Nonlinear modeling of switched reluctance Motors using artificial Intelligence techniques. IEE Proc Power Appl 151:1–2
2. Lu W, Keyhani A, Klode H, Proca A (2003) Modelling and parameter identification of switched reluctance motors from operating data using neural networks. IEEE proceedings (2003), pp 1709–1713
3. Akhtar HE, Sharma V, Chandra A, Al-Haddad K (2003) Modelling, simulation and performance analysis of switched reluctance motor operating with optimum value of fixed turn-on and turn-off switching angles. IEEE proceeding (2003), pp 397–402
4. Kim CC, Hur J, Hyun DS (2002) Simulation of a switched reluctance motors using matlab/M file. IEEE proceedings (2002), pp 1066–1071
5. Chancharoensook P, Rahman MF (2002) Dynamic modelling of a four-phase 8/6 switched reluctance motor using current and torque look-up tables. IEEE proceedings, (2002), pp 491–496
6. Shanshan L, Zhao Z (2002) A nonlinear analytical model for switched reluctance motor. IEEE proceedings, (2002), pp 2034–2037
7. Faiz J, Raddadi J, Finch JW (2002) Magnetics: spice-based dynamic analysis of switched reluctance motor with multiple teeth per stator pole. IEEE Trans 38:1780–1788
8. Wang X, Lai JS (2002) Small signal modelling and control for PWM control of switched reluctance motor drives. IEEE proceedings (2002), pp 546–551

Chapter 80
PSO Based Social Welfare Maximization of Wind Thermal Coordinated System in a Deregulated Power Market

R. Manimegalai, S. Visalakshi and Lucina Joseph

Abstract This paper presents maximization of social welfare in a wind thermal coordinated, deregulated wholesale power market using Particle Swarm Optimization algorithm. As the real power demand is always variable in nature, power generators can be rescheduled to meet the demand with the objective of maximizing the social welfare. In the proposed approach, wind turbine speeds are generated for various values of demand and the generators are rescheduled accordingly with the objective of maximization of social welfare using Particle Swarm Optimization algorithm. The proposed method is tested on Modified WSCC-9 bus system, where one of the generators is treated as thermal unit while the other two generators are wind power generators. Simulations are done with MATLAB 10.0 version.

Keywords Wind thermal coordinated · Deregulated · Maximization · Optimum power generation

80.1 Introduction

Deregulation in the power industry has changed the monopoly into oligopoly in the generation and trading sectors. Deregulation is expected to draw private investment, increase efficiency, promote technical growth and improve customer satisfaction as

R. Manimegalai (✉) · L. Joseph
Department of Electrical and Electronics Engineering, St. Joseph's College of Engineering, Chennai, India
e-mail: manimegalaiananthan@gmail.com

L. Joseph
e-mail: lucinajoe@gmail.com

S. Visalakshi
Department of Electronics and Instrumentation Engineering, Valliammai Engineering College, SRM Nagar, Kattangalathur, Chennai 603203, India
e-mail: visalakshivenkat@rediffmail.com

C. Kamalakannan et al. (eds.), *Power Electronics and Renewable Energy Systems*,
Lecture Notes in Electrical Engineering 326, DOI 10.1007/978-81-322-2119-7_80

different parties compete with each other to win and to remain in competition [1]. However the rapid depletion of fossil fuels due to the increased energy requirements of the increasing population has necessitated the search for renewable energy sources. Wind energy is a source of renewable energy that helps in reducing the carbon—dioxide released to the atmosphere. The wind resource is inexhaustible, freely available and the conversion process is environment friendly. Even though it is capital intensive, it has low operating costs. Now a days wind turbines have become more efficient, and their capital costs have gone down, several countries are subsidizing wind energy [7]. However, as wind technologies advance, wind energy is becoming more competitive and subsidies will eventually be significantly reduced or even halted.

The competitive short-term electricity markets require that energy producers submit day-ahead schedules to the system operator. System operator works out for balancing the supply and demand. Then he applies penalty for the producers not meeting their energy schedules. Because wind is stochastic and day-ahead wind forecast is highly uncertain [2], wind traders are exposed to high risks due to generation-schedule mismatch. Such risks can be minimized by the coordinated operation of wind and thermal generators [3]. Therefore the determination of optimal wind power generation, which can be integrated into the emerging power system is very important. In this paper the wind turbine speed has been optimized using particle swarm optimization (PSO) technique [4] for maximizing the social welfare in the deregulated power market. According to the variable demand the wind power production is adjusted by controlling its turbine speed with the available wind speed.

80.2 Wind Turbine Model

The basic components of a wind turbine are tower structure, rotor with two or three blades attached to the hub, shaft with mechanical gear, electrical generator, Yaw mechanism, such as the tail vane, sensors and control. Various modeling techniques are developed by researchers to model components of wind system. Performance of individual component is either modeled by deterministic or probabilistic approaches [6]. Wind turbines are manufactured in sizes ranging from a few kW to a few MW depending on the application for utility—scale power generation. Large wind turbines being installed today are of variable speed design incorporating pitch control and power electronics. Small machines, on the other hand, must have simple, low—cost power and speed control.

The rotor speed must be controlled for three reasons:

- To capture more energy
- To protect the rotor, generator, and power electronic equipment from overloading during gusty winds
- When the generator is disconnected from the electrical load, accidentally or for a scheduled event. Under this condition, the rotor speed may run away, destroying it mechanically, if it is not controlled.

80.3 Problem Formulation

The objective function is to maximize Social Welfare (SW) as given below:

$$\text{Maximize SW} = \sum_{j} B_j(d_j) - \sum_{i} C_i(d_i) \tag{80.1}$$

where

$$B_j(d_j) = \frac{1}{2} m_d d_j^2 + b_j d_j \tag{80.2}$$

$$C_i(g_i) = \frac{1}{2} m_g g_i^2 + b_i g_i \tag{80.3}$$

The $C_i(g_i)$ and $B_j(d_j)$ are the production costs and customer benefits respectively.

$$P_i = b_i + m_g g_i \quad \text{for i} = 1, 2, \ldots, \text{I} \tag{80.4}$$

where
b_i is the intercept ($b_i > 0$) in €/MWh
m_g is the slope ($m_g > 0$) in €/MW^2h
P_i is the price at which producer 'i' is willing to supply in €/MWh,
g_i is the supply in MW.

$$P_j = b_j + m_g d_j \quad \text{for j} = 1, 2, \ldots, \text{J} \tag{80.5}$$

where
b_j is the intercept ($b_j > 0$) €/MWh,
m_d is the slope ($m_d < 0$) in €/MW^2h,
P_i is the price at which consumer j is willing to pay in €/MWh,
d_j is the demand in MW.

80.3.1 Constraints

- Equality constraints

$$0 = \sum_{i=1}^{NG} P_{gi} - \sum_{j=1}^{NLoad} P_{dj} - P_{loss} \tag{80.6}$$

where *NG* and *NLoad* are the total number of wind turbines and loads, respectively. P_{loss} is the total active power loss.

- Inequality constraints
  Active power constraint

$$P_b^{\min} \le P_b \le P_b^{\max} \tag{80.7}$$

- Thermal constraint

$$S_F - S_F^{\max} \le 0 \tag{80.8}$$

- Wind turbines' active power constraint

$$0 \le P_g \le P_g^{\max} \tag{80.9}$$

80.4 Uncertainty Modeling

The wind speeds are unpredictable. They have a random probability distribution or pattern that may be analyzed statistically. The same is the case with load demand. Hence the stochastic nature of, both the wind speeds as well as the load demands, have to be modeled mathematically.

80.4.1 Modeling Wind Speed

In spite of various wind speed regimes in different places, wind speed varies over a wide range in different geographical locations. The power thus generated by the wind turbines rely on the wind speeds that is stochastically varying. Here Weibull probability distribution function is used to model the random variations in wind speeds [5]. Wind speed frequency distributions follow the Weibull probability distribution. The Weibull probability distribution function has two parameters 'k' and 'c', where 'k' is the shape coefficient and 'c' is the scale coefficient. The speed 'v' is distributed as Weibull and its probability distribution function is given by:

$$f(v) = \frac{k}{c}\left(\frac{v}{c}\right)^{k-1} e^{\left(-v/c\right)^k} \quad (\mathrm{k} \ > 0, \mathrm{v} \ > 0, \mathrm{c} \ > 1). \tag{80.10}$$

80.4.2 Modeling Wind Turbine Output Power

The output power is calculated from the power curve [4]. A wind turbine is designed such that it starts producing power at the cut in speed, V_{cin}, reaches its rated power, P_r at the rated speed, V_r, and beyond that, inspite of the increasing wind speed, the power remains constant at P_r up to the cut out speed, V_{co}. The mathematical expression of the power curve is as follows:

$$P_{WT} = \begin{cases} 0 & v < v_{cin} \\ P_r \frac{v^3}{v_r^3} & v_{cin} \le v \le v_r \\ P_r & v_r \le v \le v_{co} \end{cases}. \tag{80.11}$$

80.5 Modeling Wind Turbine Output Power

Recently, evolutionary computation techniques are attractive for many researchers. They are useful for optimizing problem solutions when the traditional approaches become extremely complex [3]. These techniques generally differ from traditional search in three main ways:

- They utilize a population of points in their search
- They use direct fitness which can be calculated directly from the objective function
- Information instead of function derivatives or other related knowledge and they use behavior of stochastically generated particles (points), rather than deterministic, transition rules.

Hence, evolutionary computation is suitable to solve this optimization problem. In this paper, Particle Swarm Optimization (PSO), one of the evolutionary computation techniques is employed. PSO is a stochastic optimization technique. Due to multiple path search procedure, the optimal solution can be achieved in less number of iterations.

The proposed methodology comprises of four components as follows:

80.5.1 Initialization

The population of particles is randomly initialized within the operating range. In this paper the wind turbine speed is randomly generated using Weibull.

80.5.2 Fitness Evaluation

Fitness has been evaluated by considering social welfare maximization and thermal limit violation.

80.5.3 Selection and Updating

The current iteration particles are compared with the previous iteration particles; according to their fitness values, particles are chosen and termed as particle best (Pbest). The particle with the best fitness value of all the particles is chosen as global best (gbest).

Particles' velocity and position is updated using the following equations.

$$v[] = w * v[] + C_1 * rand() * (pbest[] - present[]) + C_2 * rand() * (gbest[] - present[]). \tag{80.12}$$

$$w = \frac{(w_{\max} - w_{\min})}{iter\max} \times iter. \tag{80.13}$$

$$present[] = present[] + v[]. \tag{80.14}$$

The weight factor 'w' in the velocity equation is given by the Eq. (80.13). Where $v[]$is the velocity vector; C_1 and C_2 are learning factors.

80.5.4 Termination Criteria

The proposed algorithm will be stopped when it reaches maximum number of iterations.

80.6 Test System Description

The following analyses are carried out based on the power flow data of the network built on the WSCC 9-bus 3-generator system [7]. One of the generators is treated as thermal power producer and the remaining are treated as wind power producer.

80.7 Results and Discussion

The proposed method has been applied on the above mentioned system.

It can be seen from Tables (80.1) and (80.2), the social welfare is maximized by obtaining optimum wind turbine speed using PSO technique. For the optimum turbine speed wind generators produces power and the demand is met with wind and thermal units.

Table 80.1 Optimum power generation

Sl. No	Power demand (MW)	Thermal	Power generation (MW)	
			Wind farm-1	Wind farm-2
1	250	116.035	63.8011	70.1638
2	300	173.4880	61.4781	65.0338
3	350	218.3376	61.2590	70.4034
4	400	266.2644	70.3243	63.4113

Table 80.2 Maximized social welfare by Optimum turbine speed

Sl. No.	Wind farm-1			Wind farm-2		
	Demand (MW)	Wind speed (m/s)	Turbine speed (rpm)	Wind speed (m/s)	Turbine speed (rpm)	Social welfare €/MWh
1	250	7.5171	19.8548	7.7591	22.0705	342.3
2	300	7.4247	19.6108	7.5652	21.5189	601.1
3	350	7.4159	19.5875	7.7679	22.0955	1,028.8
4	400	7.7650	20.5096	7.5017	21.3384	1,563.7

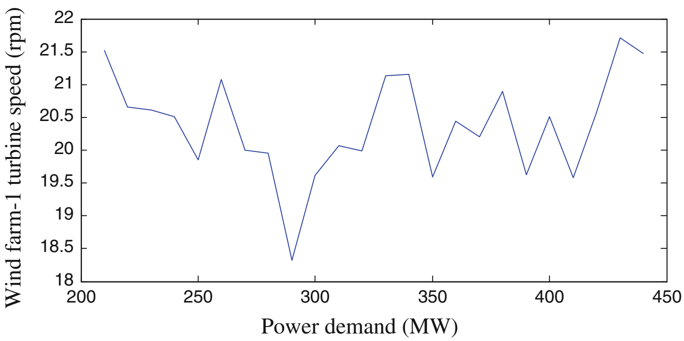

Fig. 80.1 Turbine speed variation of wind farm-1

Wind turbine speed variations for maximized social welfare in wind farms 1 and 2 are shown in Figs. 80.1 and 80.2 respectively.

The wind turbine speed variations are considered for variable demand and wind speeds. The PSO convergence pattern for a load of 310 MW is as sown in Fig. 80.3.

The probabilistic social welfare for variable demand is shown in Fig. 80.4. We can find the variations in social welfare with variable load demand.

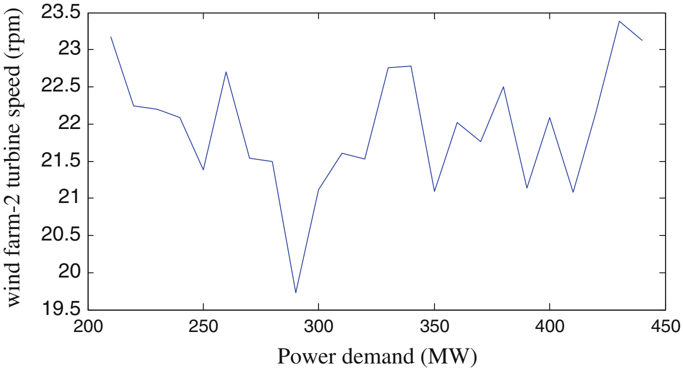

Fig. 80.2 Turbine speed variation of wind farm-2

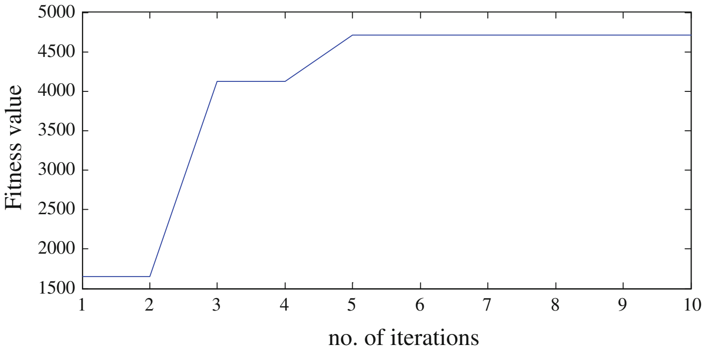

Fig. 80.3 PSO convergence pattern for 310 MW load

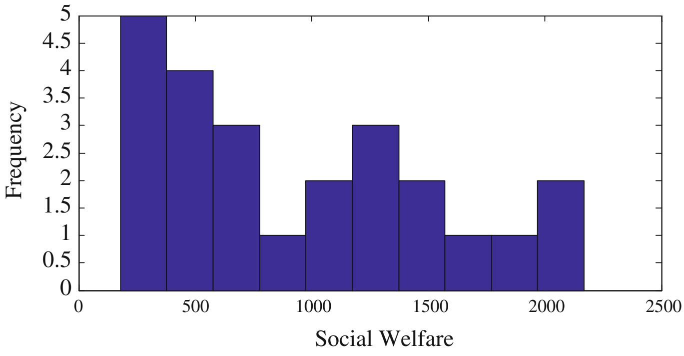

Fig. 80.4 Probabilistic social welfare for variable demand

80.8 Conclusion

This paper proposes a methodology for the wind power producers to increase their benefits by controlling the wind turbine in accordance with the varying load demands and wind speeds. The idea of maximizing social welfare of the wind thermal coordinated system is explained for variable demand.

In the future work, practical system may be considered with additional constraints.

References

1. Singh SN, Erlich I (2006) Wind power trading options in competitive electricity market. In: Power engineering society general meeting, IEEE
2. Wangdee Wijarn, Billinton Roy (2006) Considering load-carrying capability and wind speed correlation of WECS in generation adequacy assessment. IEEE Trans Energy 21(3):734–741
3. Chen C-L (2008) Optimal wind-thermal generating unit commitment. IEEE Trans Energy Convers 23(1):273–280
4. Albadi MH, El-Saadany EF (2012) Comparitive study on Impacts of power curve model on capacity factor estimation of pitch regulated turbines. TJER 9(2):36–45
5. Li Gong, Shi Jing (2012) Agent-based modeling for trading wind power with uncertainty in the day-ahead wholesale electricity markets of single-sided auctions. Appl Energy 99:13–22
6. Mokryani Greev, Siano Pierluigi (2013) Combined monte carlo simulation and OPF for wind turbines integration into distribution networks. Electr Power Syst Res 103:37–48
7. www.iwea.org

Chapter 81
Microcontroller Based BLDC Motor Drive for Commercial Applications

Shanmugam Sathishkumar, R. Meenakumari, Eswaramoorthi Jobanarubi, Pattu John Samuel Anitta and Premkumar Ravikumar

Abstract Brushless DC (BLDC) motors are now a days becoming popular in battery operated vehicles, fuel pumps, medical equipments, printers and in many applications because of its light weight, high operating speed and excellent speed-torque characteristics. However, BLDC motor requires complex and expensive high speed drives and converter circuits to perform electronic commutation and suitable control circuits for implementing control technique. Since the conventional drive circuits are expensive, bulky and more complex, this paper proposes a low cost, compact, high performance BLDC drive system employing solar module with DC–DC converters and Pulse Width Modulation (PWM) control strategy. The proposed drive consists of a solar module, charge controllers, batteries, SEPIC converter and BLDC motor, henceforth developed into the Solar Powered BLDC motor drive and solar powered equipments and three phase inverter containing six MOSFET switches. A microcontroller or DSP will be used to control the overall system. This project explains the study of designing a Solar Powered BLDC Motor Drive which is one of the solutions for the oncoming crisis. The approach of selecting the appropriate components for this application is studied and each of them is simulated.

Keywords Brushless DC (BLDC) motors · Pulse width modulation (PWM) · SEPIC converter

S. Sathishkumar (✉) · E. Jobanarubi · P.J.S. Anitta · P. Ravikumar
Department of EEE, Jansons Institute of Technology, Coimbatore, Tamilnadu, India
e-mail: sat_meae2k5@rediffmail.com

E. Jobanarubi
e-mail: jobanarubi@gmail.com

P.J.S. Anitta
e-mail: anittapattu@gmail.com

P. Ravikumar
e-mail: eroderavi@gmail.com

R. Meenakumari
Kongu Engineering College, Erode, Tamilnadu, India

C. Kamalakannan et al. (eds.), *Power Electronics and Renewable Energy Systems*,
Lecture Notes in Electrical Engineering 326, DOI 10.1007/978-81-322-2119-7_81

81.1 Introduction

Brushless DC Motor is a rotating electric machine where the stator is a classic three phase stator like that of an induction motor and the rotor has surface mounted permanent magnets. The BLDCM is driven by rectangular strokes coupled with the given rotor position [1, 2]. The generated stator flux interacts with the rotor flux, which is generated by a rotor magnet that defines the torque and the speed of the motor. The voltage strokes must be properly applied the two phases of three phase winding system, so that the angle between the stator flux and rotor flux is kept close to 90°. BLDC motors are a type of synchronous motor. This means the magnetic field generated by the stator and the magnetic field generated by the rotor rotates at the same frequency. BLDC motors do not experience the slip that is normally seen in Induction motors [1]. Even though conventional DC motors are highly efficient, it had some drawbacks due to commutator and brushes which need proper maintenance. But in BRUSHLESS DC MOTOR when the functions of commutator and brushes were implemented by solid- state switches, maintenance free motors were realized. Instead of commutating the armature current by using brushes, here electronic commutation is used. This eliminates the problems associated with the brush and the commutator arrangement, thereby, making a BLDC more rugged as compared to a DC motor [3, 4]. BLDC motors are come in single phase, 2-phase and 3-phase configurations. Corresponding to its type, the stator has the same number of windings. Out of these, 3-phase motors are the most popular and widely used. Three-phase motors have a number of slots (and teeth) that are evenly divisible by three. A phase is an individual group of windings with a single terminal accessible from outside the motor. Most of the brushless motors are available in three-phase motor.

In this paper three phase BLDC motor drive is designed for commercial applications which is controlled by using proportional and integral controller. Power converter in the BLDC motor drives system consists of two parts, which is a rectifier and 3-phase full bridge inverter. Control schemes for this motor drives typically a PWM waveform driving the inverter [3]. A suitable switching technique is needed to generate pulses to drive the power device circuit. To produce the desired output, PWM switching technique will be used to generate the pulses for power device via microcontroller. Factors to be considered in designing the converter for the BLDC motor drives in order to meet the requirement includes a suitable switching technique and controlling switching angles for the BLDC motor rotation and controllable magnitude and frequency of the output voltage.

81.1.1 BLDC Motor Equation

When DC supply is switched on to the motor the armature winding draws a current. The current distribution within the stator armature winding depends upon rotor position and the device is turned on. An EMF perpendicular to permanent magnet field is set up. Then the armature conductors experience a force. The reactive force develops a torque in the rotor. If this torque is more than the opposing frictional and load torque, the motor starts. It is a self starting motor. The voltage equation of the BLDC motor is given as

$$V\,dc = 2[Rs\,Ia + (L - M)d\,Ia/dt] + e1 - e2 = Ra\,Ia + La\,d\,Ia/dt + e1 - e2 \tag{81.1}$$

The electromagnetic torque is proportional to stator current and is given by

$$Te = Kb\;I\;a. \tag{81.2}$$

$$V\,dc = Ra\,Ia + La\,dia/dt + Kb\omega \tag{81.3}$$

The load torque which varies with motor speed is given by

$$TL = K\;T\omega. \tag{81.4}$$

The mechanical equation of the rotor is

$$Te - TL = J\,d\omega/dt + B\omega. \tag{81.5}$$

Substituting Eqs. (81.3) and (81.4) into Eq. (81.5) we get

$$Kb\,Ia - K\,T\,\omega = Jd\,\omega/dt + B\omega \tag{81.6}$$

81.1.2 Functional Block Diagram of BLDC Motor Drive

The Brushless DC Motor is a combination of a Permanent Magnet AC Motor and an Electronic Commutator. In BLDC motor inverter has to replace the commutator of a conventional DC motor. The commutator acts like a three phase frequency converter. The commutation of a brushless DC motor depends upon the position of the rotor. The angle between the magneto—motive force of stator and magneto—motive force of rotor is fixed to 90° (electrical) (Fig. 81.1).

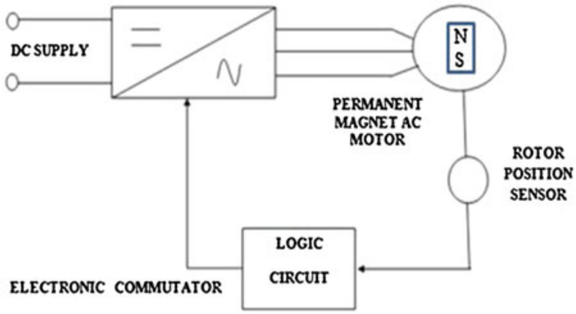

Fig. 81.1 Functional block diagram of BLDC motor

There are several methods to convert DC to AC. They differ mainly in their approximation to a perfect sinusoidal signal. As one would expect the best approximation yields the best transfer of power to a device that expects a sinusoidal signal. The applied DC voltage is supplied to the inverter block an thereby it converts DC to AC. The function of an inverter is to change a DC input voltage to AC output voltage of desired frequency and magnitude. In case of 3-phase inverter, the inverter circuit changes DC input voltage to a symmetrical AC output voltage of desired magnitude and frequency [5, 3]. Output voltage could be fixed or variable at a fixed or variable frequency. Variable output voltages are obtained by varying the input DC voltage with maintaining the gain of the inverter constant.

Rotor Position Sensor is used to sense the position of the rotor of the BLDC motor. Hall Effect sensor is a transducer that varies its output voltage in response to a magnetic field. Hall Effect sensors are used for proximity switching, positioning, speed detection, and current sensing in BLDC motor drive. Hall sensors are commonly used to time the speed of wheels and shafts, such as for internal combustion engine ignition timing, tachometers and anti-lock braking systems. They are used in brushless DC electric motors to detect the position of the permanent magnet. Hall sensors can be used to operate as a switch. It's cost is less than other mechanical switches. It is also used in the brushless DC motor to sense the position of the rotor and to switch the transistor in the right sequence [3].

81.1.3 Circuit Diagram of BLDC Motor

Figure 81.2 shows the block diagram for a 3-phase BLDC drives, which consists of a 3-phase inverter and a BLDC motor. The 3-phase inverter uses a signal generated by the microcontroller to trigger the power device to produce necessary current in the motor winding for rotor shaft rotation.

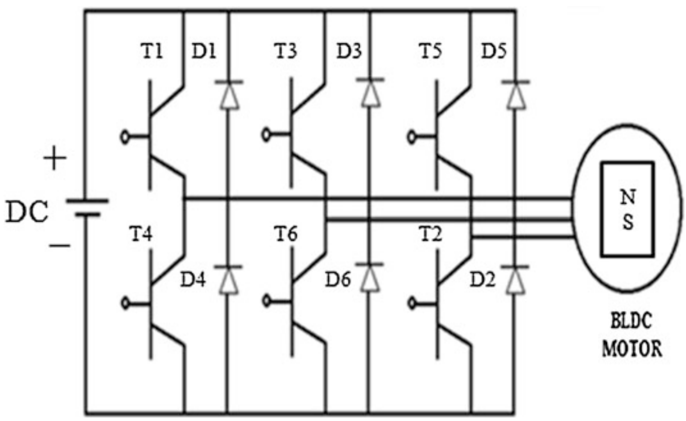

Fig. 81.2 BLDC motor circuit

The inverter is controlled by PWM switching schemes to drive the BLDC motor. The gating signals of MOSFET are shifted by 60º by each gate to obtain a 3-phase balanced fundamental voltage with 120º phase shift. The setting of the conduction period is done by programming the desired on time of the MOSFET onto the microcontroller. The power semiconductor chosen for BLDC motor drive is MOSFET. It requires continuous operation of a gate-source voltage of appropriate magnitude in order to be in the on state. The switching time is very short, that is in range of nanoseconds to picoseconds depending on the device type. However, because of the switching speed is very fast, the switching losses can be very small. So the switching power loss in a semiconductor varies linearly with the switching frequency and the switching times. The three phase inverter which is used to drive the BLDC motor consists of six switches (MOSFET). Depending upon the control power supply capability, the motor with the correct voltage rating of the stator can be chosen. 48 V, or less than that voltage rated motors are used in automotive, robotics, small arm movements etc. Motors with 100 V or higher than that rating are used in appliances, automation and in industrial applications [5, 3]. BLDC motors have come to dominate many applications, particularly devices such as computer and hard drives, CD/DVD. Small cooling fans in electronic equipment are powered exclusively by BLDC motors. They can be found in cordless power tools where the increased efficiency of the motor leads to longer periods of use before the battery needs to be charged. Low speed, low power BLDC motors are used in direct-drive turntables for gramophone records. BLDC motors are commonly used as pump, fan and spindle drives in adjustable speed drives.

81.2 Modeling of BLDC Motor

Computer simulation plays a great role in research to analyze the behavior of new circuits, which leads to improved understanding of the circuit. In industry, they are used to shorten the overall design process, since it is usually easier to study the influence the parameter on the system behavior in simulation, as compared to accomplishing it in the laboratory on the hardware breadboard. The simulation is used to calculate the circuit waveform, the dynamic and steady state performance of the system, voltage and current rating of various components [6]. Simulink is an interactive tool for modeling, simulating and prototyping analog and mixed signal system using the block sets rather than the line of code. It works as an integral part of the MATLAB environment. MATLAB/Simulink platform is being used in industries also to simulate algorithms and evaluate alternatives early in the design process and convenient tool for monitoring simulation results [7] (Fig. 81.3).

The BLDC motor has to be equipped with a position sensor which informs the controller what the position of the rotor magnetic pole is, with respect to the particular stator phase winding. The above figure shows the simulation model of BLDC Motor drive and the mathematical equations that are modeled are incorporated in the SIMULINK block diagram and the characteristics of the motor are

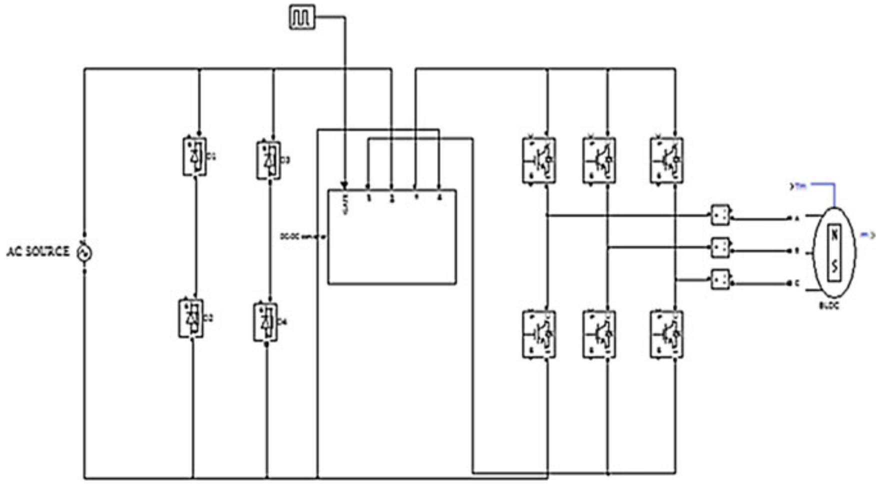

Fig. 81.3 Simulation model of BLDC motor

studied from the output waveforms of simulation. Since BLDC motor drive is a special machine, an inverter is required for its operation. A typical BLDC drive consists of a Voltage source inverter, BLDC motor and rotor position sensors for finding the rotor position after every switching sequence of the inverter. The induced voltages and currents in a BLDC motor drive are trapezoidal in nature. The BLDC motor fed from a DC source through a standard three phase inverter bridge. Two switches should be conducting for every pattern, one from lower leg and another from upper leg resulting in alternate excitation of two phases at a time out of three phases which facilitates continuous rotation of the rotor. PI is a feedback controller which drives the plant to be controlled with a weighted sum of the error and the integral of that value [6]. PI controllers are widely used in industrial application, due to their simplicity, low cost and robustness. These controllers can also be implemented easily through analog components. The general operation of PI can be represented by the following equation.

$$M(t) = Kp\,e(t) + Ki \int e(t)dt \tag{81.7}$$

where,

e(t) is the speed error
M(t) is the output of the controller
Kp is the proportional constant and
Ki is the integral constant

Here the controller provides an appropriate feedback to the system based on the error signal. This feedback takes account of the magnitude as well as its rate of change and integral effect. Filter is widely used in power electronics to reduce harmonic components at the output waveform. It is also used for smoothing the voltage wave of a load fed from a rectifier in reducing the harmonic content of an inverter output, preventing unwanted harmonic component being reflected into AC system. Output of the inverter is a "chopped DC voltage with zero DC components" [6, 2]. In some applications such as AC motor drives, filtering is not required. Besides, with PWM switching schemes algorithm, elimination of certain harmonic can be done without using external filter circuit on the converter system.

81.3 BLDC Motor Powered by Solar Module

The below figure shows the SEPIC converter based drive for *BLDC* motor. *Front-end single-ended primary inductance converter (SEPIC) and a switch in series with each phase is proposed for driving a permanent magnet brushless dc (BLDC) motor with unipolar currents* (Fig. 81.4).

A DC to DC converter is an electronic circuit which converts a source of direct current (DC) from one voltage level to another. DC to DC converters are important in portable electronic devices, which are supplied with power from batteries primarily. Such electronic devices often contain several sub circuits, each with its own voltage level requirement different from that supplied by the battery or an external supply (sometimes higher or lower than the supply voltage). Most DC to DC converters also regulate the output voltage [2]. In these DC-to DC converters, energy is periodically stored into and released from a magnetic field in an inductor by adjusting the duty cycle of the charging voltage (that is, the ratio of on/off time), the amount of power transferred can be controlled. Usually, this is applied to control the output voltage, though it could be applied to control the input current, the output current, or maintain a constant power [4]. Chopper systems are characterized by high efficiency, fast response and regeneration operation capability.

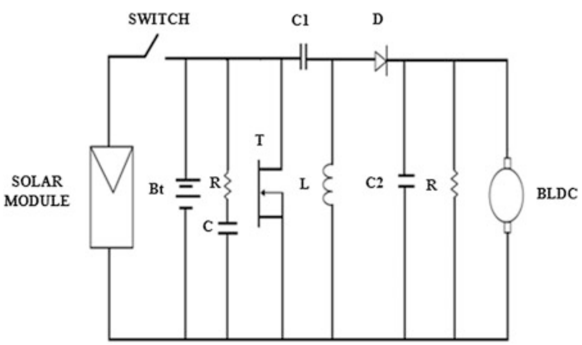

Fig. 81.4 Circuit diagram of SEPIC converter along with BLDC motor

81.3.1 SEPIC Converter

The DC to DC converter here used is SEPIC converter Single-ended primary-inductor converter (SEPIC) is a type of DC–DC converter allowing the electrical potential (voltage) at its output to be greater than, less than, or equal to that at its input; the output of the SEPIC is controlled by the duty cycle of the control transistor [7]. A SEPIC is similar to a traditional buck-boost converter, but has advantages of having non-inverted output (the output has the same voltage polarity as the input), using a series capacitor to couple energy from the input to the output (and thus can respond more gracefully to a short-circuit output), and being capable of true shutdown: when the switch is turned off, its output drops to 0 V. In SEPIC converter the voltage drop and switching time of diode is critical to a SEPIC's reliability and efficiency. The diode's switching time needs to be extremely fast in order to not generate high voltage spikes across the inductors, which could cause damage to components. Fast conventional diodes or Schottky diodes may be used.

81.3.2 Solar Module

Solar modules use light energy (photons) from the sun to generate electricity through the photovoltaic effect. The structural (load carrying) member of a module can either be the top layer or the back layer. Cells must be protected from mechanical damage and moisture. Most solar modules are rigid, but semi-flexible ones are available, based on thin-film cells. These early solar modules were first used in space in 1958. Electrical connections are made in series to achieve a desired output voltage and/or in parallel to provide a desired current capability [2]. The requirements for residential and commercial are different in that the residential needs are simple and can be packaged so that as solar cell technology progresses, the other base line equipment such as the battery, inverter and voltage sensing transfer switch still need to be compacted and unitized for residential use (Fig. 81.5).

The usage of solar energy is used to power up for commercial appliances. In order to achieve the required voltage, the Photo Voltaic (PV) Module may be connected either in parallel or series, but it's costlier. Thus to make it cost effective, power converters and batteries are been used. The electrical charge is consolidated from the PV panel and directed to the output terminals to produce low voltage

Fig. 81.5 Schematic approach of proposed system

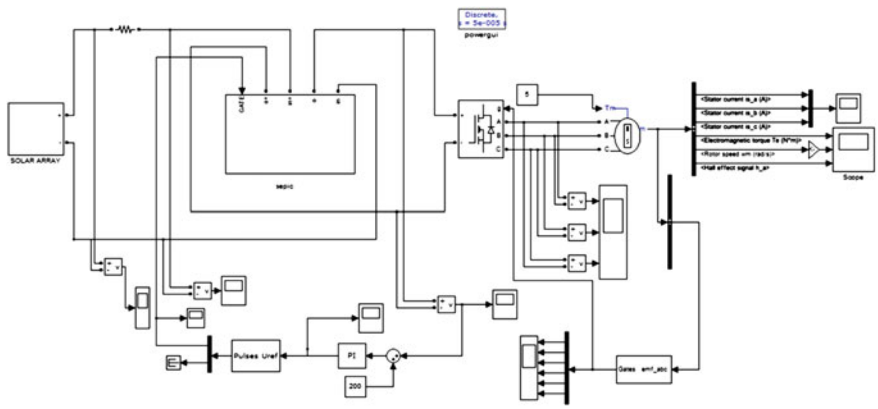

Fig. 81.6 Simulation diagram of proposed system

(Direct Current). The charge controllers direct this power acquired from the solar panel to the batteries. According to the state of the battery, the charging is done, so as to avoid overcharging and deep discharge. The voltage is then boosted up using the SEPIC power converter, ultimately running the BLDC motor which is used as the drive motor for our commercial application. In the course work, the characteristic features of the components are required for the commercial applications were studied and also were modeled individually using MATLAB/SIMULINK and the complete hardware integration of the system is tested to meet up the application's requirement.

81.4 Simulation of Proposed System

The simulation of the proposed BLDC motor drive was done using the software package MATLAB/SIMULINK (Fig. 81.6).

81.5 Simulation Results and Discussions

After running the simulation, the speed, torque, current, input and output power waveforms were recorded and analyzed using m-file. The below figures show the waveforms of the electrical and mechanical quantities after the stator was supplied with a desired sinusoidal voltage and frequency. From the simulation results we can obtain the stator current, rotor speed, electromagnetic torque and hall effect signal waveforms are plotted in Figs. 81.7, 81.8, 81.9 and 81.10 [6, 5].

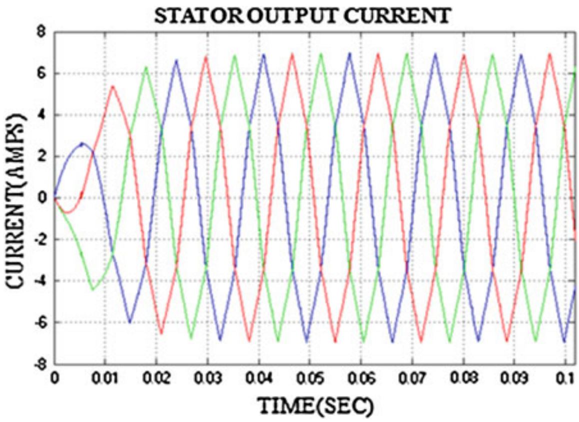

Fig. 81.7 Stator current waveform

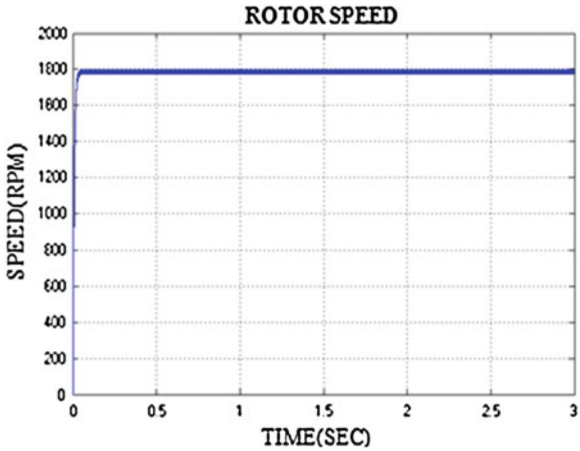

Fig. 81.8 Rotor speed waveform

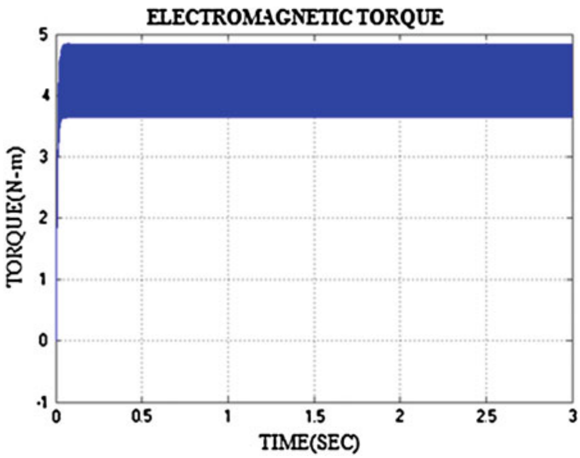

Fig. 81.9 Torque waveform

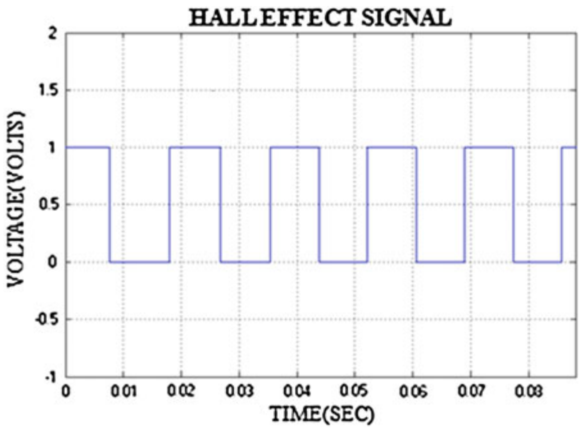

Fig. 81.10 Hall effect signal waveform

81.5.1 Stator Current

Stator current of the proposed system is nearly about 5 ampere. The stator current wave form is as shown in the Fig. 81.7. This waveform can be obtained from MATLAB/SIMULINK.

81.5.2 Rotor Speed

The Fig. 81.8 shows the speed of the Proposed BLDC motor drive. The speed of motor is 1,800 rpm. This rotor speed waveform can be done by using MATLAB/SIMULINK. It can be plotted between speed and time.

81.5.3 Electro Magnetic Torque

The figure shows the electromagnetic torque waveform of the proposed BLDC motor drive. It is plotted between torque and time.

81.5.4 Hall Effect Signal Waveform

The Hall Effect signal waveform is shown in the Fig. 81.10. It is plotted between voltage and time.

The easiest way to know the correct moment to commutate the winding currents is by means of a position sensor. Many BLDC motor manufacturers supply motors

Table 81.1 BLDC motor specifications

S.no	Parameter	Specifications
1.	Power	25
2.	Rated voltage	48 V
3.	Rated current	0.5 A
4.	Rated speed	4,000 rpm

with a three-element Hall Effect position sensor. Each sensor element outputs a digital high level for 180 electrical degrees of electrical rotation, and a low level for the other 180 electrical degrees. The three sensors are offset from each other by 60 electrical degrees so that each sensor output is in alignment with one of the electromagnetic circuits (Table 81.1).

81.6 Conclusions

This paper discusses the simulation of microcontroller based BLDC motor drive and their results. We designed and simulated the solar powered BLDC motor drive using SEPIC converter has been done in MATLAB/SIMULINK. In this paper the speed control is achieved by using PI controller which is best choice for small scale BLDC motor applications like cooling fans in air conditioner, exhaust fans in kitchen, ceiling exhaust fans etc. The PI controller provides a better performance in terms of low ripples, high efficiency. The BLDC motor along with SEPIC converter provides a better performance in term of overshoot limitation, fast operation and smooth response. The dynamic performance of BLDC is analyzed by simulation in MATLAB/SIMULINK environment. Simulation results will be verified by hardware implementation in future. Hardware Implementation is done using PIC 16F877A. The PIC Microcontroller generates high-resolution PWM outputs in order to get high efficiency and high response. The rotor position is obtained from the Hall Effect Position Sensing Unit. Hence the closed loop control technique is easily achieved by using PI controller.

References

1. Wu H, Cheng S, Shu-mei C (2005) A controller of brushless DC motor for electric vehicle. IEEE Trans Magn 41(1):509–513
2. Alphonse I, Thilagar H, Singh FB (2007) Design of solar powered BLDC motor driven electric vehicle. Int J Renew Energy Res 2(3):456–462
3. Khopkar R, Madan SM, Hajiaghajani M, Toliyat HA (2002) A low-cost BLDC motor drive using buck-boost converter for residential and commercial applications. In: IEEE transaction on power electronics
4. Park JS, Seo J-M, Choi J-H (2012) Development of BLDC motor and drive module for automotive application. In: IEEE vehicle power and propulsion conference

5. Ali M, Orabi M (2010) Design consideration of modified SEPIC convert for LED lamp driver. In: IEEE international symposium on power electronics for distributed generation systems
6. Mingji L, Hanjin G, Meihong S, IEEE member (2012) Ripple torque analysis and simulation of BLDC motor. In: International power electronics and motion control conference
7. Naithani V, Tiwari AN, Dobhal S (2009) Simulation of SEPIC converter FED LEDs. Int J Eng Sci Technol 4(3):1015–1020

Chapter 82
Forecasting India's Electricity Consumption Using Particle Swarm Optimization

S. Saravanan, R. Nithya, S. Kannan and C. Thangaraj

Abstract This paper uses Particle Swarm Optimization (PSO) technique to estimate the electricity consumption in India, based on economic indicators. The data used to estimate the consumption are non-linear. An exponential model is developed and applied to forecast the electricity consumption based on the economic indicators such as population, per capita Gross Domestic Product (GDP), import and export data. The available data are partly used for training the model (1975–2000) and remaining used for testing the model (2000–2010). Mean Absolute Percentage Error (MAPE) is used as an evaluation criterion for finding the future electricity consumption up to the year 2025. The results are compared with the 18th Electric Power Survey of India.

Keywords Particle swarm optimization (PSO) · Mean absolute percentage error (MAPE) · Electricity consumption

82.1 Introduction

Electricity is an important source for many activities and it plays an essential role in the economic development [1]. Electricity consumption has become a concern due to rapid development of India's population, growth in per capita income and

S. Saravanan (✉) · R. Nithya · S. Kannan
Kalasalingam University, Krishnankoil, Tamil Nadu, India
e-mail: s.saravanan@klu.ac.in

R. Nithya
e-mail: nithya8591@gmail.com

S. Kannan
e-mail: kannaneeeps@gmail.com

C. Thangaraj
Anna University of Technology, Chennai, India
e-mail: thangaraj.vc@gmail.com

C. Kamalakannan et al. (eds.), *Power Electronics and Renewable Energy Systems*,
Lecture Notes in Electrical Engineering 326, DOI 10.1007/978-81-322-2119-7_82

urbanization. It has increased from 316.60 Tera Watt hours (TWh) in 2000 to 694.392 TWh in 2010 with compounded growth rate of 9.09 %, i.e., the consumption has increased more than double in a decade [2]. Most of the authors used population, per capita GDP, import and export as inputs [2–12].

Long term forecasting of electricity consumption based on realistic indicators is a prerequisite to power system planning. Having adequate installed capacity with required reserve is essential to become a developed country with high living standards. Overestimating the energy consumption may lead to unnecessary investment, while underestimating may cause serious energy crisis [6]. In this paper, a model using particle swarm optimization (PSO) is developed to forecast the electricity consumption of India. In Sect. 82.2, the literature survey is presented. In Sect. 82.3, the concept of swarm intelligence and the basic PSO algorithm are presented. In Sect. 82.4, electricity consumption forecasting model developed and future estimations for three different scenarios are presented. Finally, the study is concluded in Sect. 82.5.

82.2 Literature Survey

Electricity consumption estimation is a subject of wide-spread present interest, among practitioners and academicians concerned with problems of energy production and consumption [8]. In the early 1970s, various studies of energy consumption had been undertaken using various estimation methods, which can be broadly classified into five groups, namely Econometric approach, Artificial intelligence approach, Hybrid model, Grey theory forecasting model and Long range Energy Alternatives Planning System (LEAP) model [1]. Two forms of the electricity consumption forecasting model using PSO were developed and three scenarios proposed to forecast Turkey's energy consumption [6]. PSO-Genetic Algorithm electricity demand estimation model was developed. The effect mechanism of China's energy consumption is investigated in detail by using the path-coefficient analysis [1]. Two forms linear and quadratic model were developed to meet the fluctuations of economic indicators [8]. They are compared with Ant colony optimization and PSO models. A Tribal PSO to design the Functional link based neuro-fuzzy inference system (FLNIS) for prediction applications was proposed in [13].

82.3 Swarm Intelligence

Swarm intelligence is an attempt to design algorithms or distributed problem solving devices inspired by the collective behavior of social insects and other animal societies. Ant colony optimization and PSO are the most popular optimization frameworks based on the original notion of swarm intelligence. They are based on the repeated sampling of solutions to the problem at hand, which means each agent provides a solution [6]. PSO is a population-based stochastic optimization technique developed in 1995 by Kennedy and Eberhart, which is inspired by social behavior of bird flocking. To apply PSO successfully, one of the key issues is to find how to map the solution of the problem into the PSO particle, which directly affects its feasibility and performance [6].

Each agent in PSO is a particle-like data structure which contains the coordinates of the current location in the optimization landscape, the best solution point visited so far, the subset of other agents seen as neighbors [6]. The system is initialized with a population of random solutions (particles) with uniform distribution and searches iteratively through the d-dimensional problem space for optima by updating iterations. Each agent knows its best value so far (pbest) and its XY position. This information is analogy of personal experiences of every agent. Also, each agent knows the best value in the group (gbest) among pbest. This information is analogy of knowledge of how the other agents around them have performed. Each agent in the model tries to modify its position using the following information:

- the present positions (x, y),
- the present velocities (v_x, v_y),
- the distance between the present position and *pbest*,
- the distance between the present position and *gbest*.

An algorithm model for the PSO method is presented as follows:

1. Set t, n, c_1, c_2 values
2. Find initial parameters (I) of $Y_{\text{exponential}}$ according to standard exponential model
3. Determine positions randomly for all particles in the neighborhood of I.
4. While (the end criterion is not met) do

   (a) $t = t + 1$;

   (b) Find the fitness value for each particle;

$$\mathrm{f(x)} = \sum_{i=1}^{k} \frac{(E_{observed} - Epredicted)^2}{E_{observed}};$$

   (c) for i = 1: n

   $\mathrm{pbest_i} = \min\{\mathrm{f(x)it}\}$
   next$i$;

$$g\mathrm{best_i} = \min_{i=1}^{n}\{\mathrm{pbest_i}\}$$

5. End while.

82.4 Estimation of Electricity Consumption

The four indicators namely population, per capita GDP, import and export are used in electricity consumption estimation model. These indicators are commonly used in the literature [2–12] since as the electricity consumption of a country is mostly affected by them. Population, per capita GDP, import, export and electricity consumption of India have increased 387.02, 67.64, 2653.05, 3684.51 and 641.05 % respectively between 1975 and 2010 years. In this study, the estimation of electricity consumption based on economic indicators was modeled by using exponential form. Exponential form can be expressed as,

$$\mathbf{E_{exponential}} = \mathrm{w}_1 + \mathrm{w}_2 X_1^{\mathrm{w3}} + \mathrm{w}_4 X_2^{\mathrm{w5}} + \mathrm{w}_6 X_3^{\mathrm{w7}} + \mathrm{w}_8 X_4^{\mathrm{w9}} \tag{82.1}$$

where,

X_1 is the population, X_2 is the per capita GDP, X_3 is the import
X_4 is the export, w_1, w_2, w_3, ..., w_n are the weighting parameters.

In estimating electricity consumption, the main task is to find the appropriate model to the data. The fitness function f(v) of the model is given by,

$$\mathrm{Min}\,\mathrm{f}(\mathrm{v}) = \sum_{r=1}^{R} \left(\mathrm{E}_r^{\mathrm{observed}} - \mathrm{E}_r^{\mathrm{predicted}}\right)^2 \tag{82.2}$$

where $\mathrm{E}_r^{\mathrm{observed}}$ and $\mathrm{E}_r^{\mathrm{predicted}}$ are the actual and predicted electricity consumption, respectively, R is the number of observations.

Statistical experiments based on a general factorial design are performed in order to find the best parameter set of the PSO-Electricity demand forecasting models. Three important factors such as particle number (n), maximum iteration (t) and learning factors ($c1$, $c2$) are considered. As a result of the statistical analysis, the parameter values are set as n = 80, t = 500 and $c1$, $c2$ are two positive numbers usually $c1 = c2 = 2$.

In the exponential form of the PSO (PSO-EXP), coefficients obtained are given below:

$$\begin{aligned}\mathrm{Y_{Exponential}} = {} & 17.5963 - 4.0646 X_1^{-5.3880} + 4.0905 X_2^{1.3387} + 2.3659 X_3^{-7.7910} \\ & - 30.8004 X_4^{-16.5986}\end{aligned}$$

The data related to the design parameters of India's population, per capita GDP, import and export are obtained from the World Bank data [14] and trend line values are found shown in Fig. 82.1a–d. The performance of the PSO model for the testing period is given in Table 82.1. The lowest average MAPE (2.6102) is in the exponential form of PSO model.

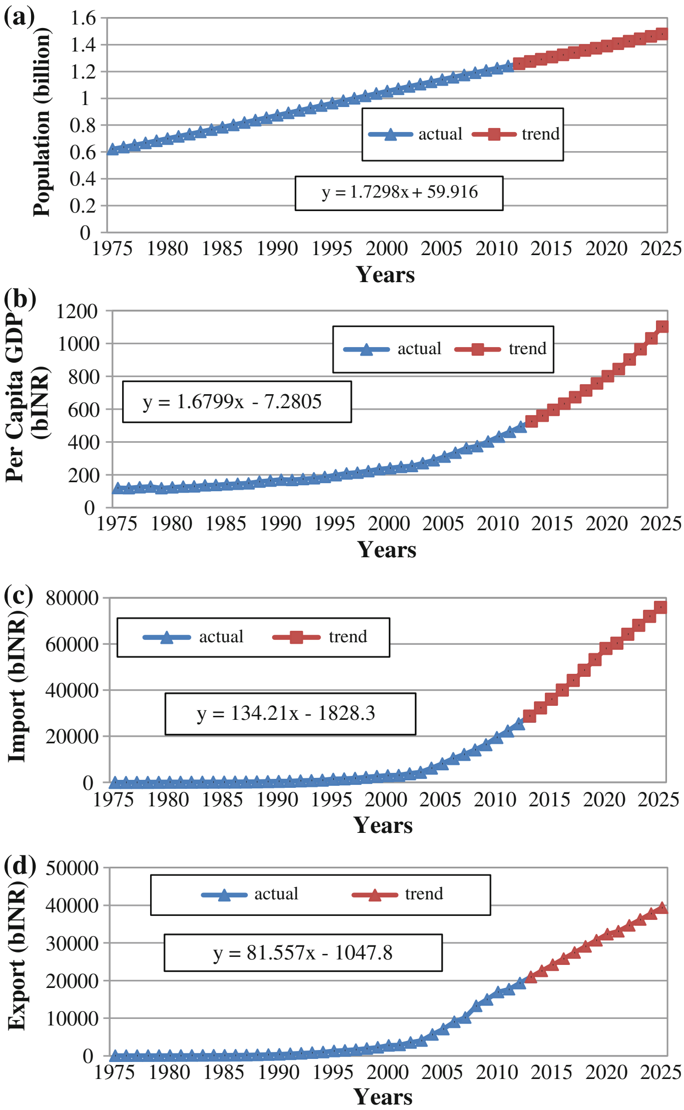

Fig. 82.1 **a** Trend line values and actual data of population. **b** Trend line values and actual data of per capita GDP. **c** Trend line values and actual data of import. **d** Trend line values and actual data of export

An observation from the result shows that the growth rate of India's population, per capita GDP, import and export have been increasing between 1.2–1.6 %, 6–9 %, 8–10 % and 6–9 %, respectively, in the last 10 years from 2001 to 2010. So three scenarios are assumed.

Table 82.1 MAPE between observed and estimated values for electricity consumption

Year	Electricity consumption (TWh)		Error (%)
	Actual	Estimated	
2001	322.459	319.440	0.936
2002	339.598	328.021	3.409
2003	360.937	356.116	1.336
2004	386.134	386.489	0.092
2005	411.887	424.921	3.164
2006	455.749	467.260	2.526
2007	501.977	517.499	3.092
2008	553.995	540.680	2.403
2009	612.645	594.432	2.973
2010	694.392	651.545	6.170
		MAPE	2.6102

82.4.1 Low Growth Scenario

It is assumed that the average growth rate of population is 1.2 %, per capita GDP is 6 %, import is 8 % and export is 6 % during the period of 2015–2025 (see Fig. 82.2). The exponential form of PSO model is extended to estimate the future electricity consumption. As can be seen from Fig. 82.2, the estimated value for the exponential PSO model and 18th Electricity power Survey of India are given for low growth scenario. The electricity consumption in 2023 with the PSO_{exp} for low growth scenario will be about 1727.6 TWh.

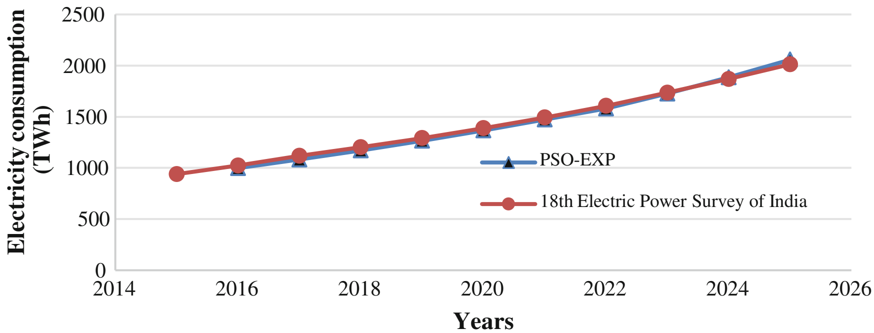

Fig. 82.2 Electricity consumption estimation for India—low growth scenario

82.4.2 High Growth Scenario

It is assumed that average growth rate of population is 1.6 %, per capita GDP is 9 %, import is 10 % and export is 9 % during the period of 2015–2025 (see Fig. 82.3). The exponential form of PSO model results are compared with the 18th Electricity Power Survey of India for high growth scenarios. The electricity consumption in 2023 with PSO_{exp} for high growth scenario will be about 1734 TWh.

82.4.3 Trend Line Model Scenario

To predict the electricity consumption in India, the individual variables (per capita GDP, population, import, export) should be analyzed and their trends for the future should be forecasted first (Fig. 82.1a–d). Future electricity consumption for the year 2015–2025 (see Fig. 82.4) was calculated with estimated per capita GDP, population, import and export. The "18th electric power survey of India", prepared by Central Electricity Authority, Government of India, predicted the electricity

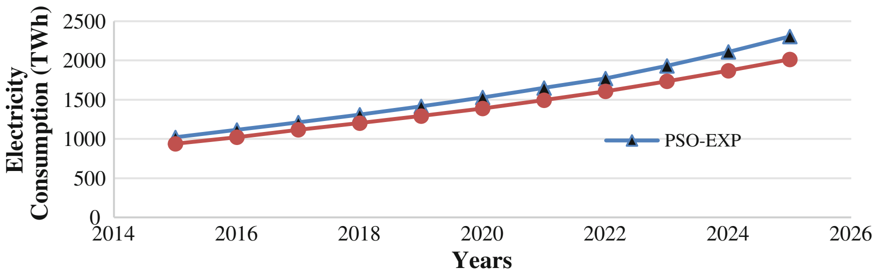

Fig. 82.3 Electricity consumption estimation for India—high growth scenario

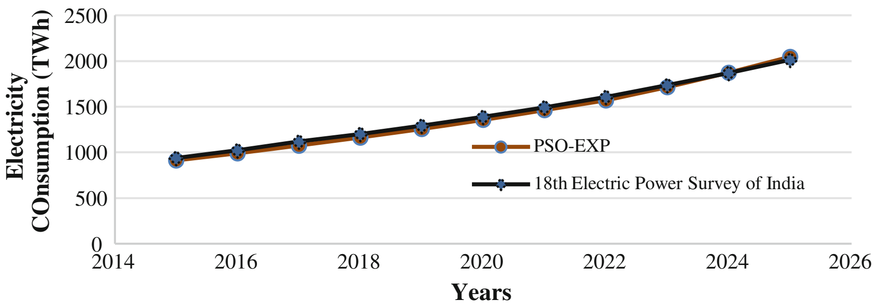

Fig. 82.4 Electricity consumption estimation for India—trend line model scenario

consumption by using Partial end use method (i.e., time series and end use methodology) and the results are validated by econometric model.

The 18th electric power survey of India, predicted the electricity consumption for the year 2020 as 1388.819 TWh, whereas PSO predictions are 1480.1 TWh for low growth; 1481.9 TWh for high growth; and 1357.4 TWh for trend line method. The results by PSO are closer to the results obtained by 18th electric power survey of India. The future electricity consumption of India may vary between 1734 and 1736.2 TWh in the year 2022 depending on low/high growth. It can be seen that, prediction of input variables; Per capita GDP, population, import and export by regression and electricity consumption prediction using PSO are much closer to the results of 18th Power Survey of India.

82.5 Conclusion

The relation between the economic development of a country and its energy consumption is considered a key issue and it involves many economic, social and technological analysis. In this study the forecasting of India's energy consumption based on Per capita GDP, population, import and export is studied. Since the model is nonlinear in form, PSO model is used to achieve a better value. The exponential form of the PSO model is developed using a 27-set data (1975–2010). Three scenarios are proposed to forecast India's energy consumption for a period between 2015 and 2025. The range of scenarios developed and their associated energy consumptions are quite small, but we hope they will provide a useful set of inputs into future energy system modeling. Forecasting of energy consumption can also be investigated with other heuristic algorithms.

Acknowledgments The authors gratefully acknowledge the Management of Kalasalingam University, Krishnankoil, Tamilnadu, India for their constant support and encouragement extended during this research. They are also thankful to the Department of Science and Technology, New Delhi, for its support through the project: SR/S4/MS/364/06.

References

1. Yu S, Zhu K, Zhang X (2012) Energy consumption projection of China using a path-coefficient analysis and PSO-GA approach. Energy Convers Manag 53:142–153
2. Saravanan S, Amosedinakaran A, Kannan S, Thangaraj C (2014) India's electricity demand estimation using genetic algorithm. IEEE Int Conf Circuit Power Comput Technol 02:97–101
3. Assareh E, Behrang MA, Assari MR, Ghanbarzadeh A (2010) Application of PSO (particle swarm optimization) and GA (genetic algorithm) techniques on consumption estimation of oil in Iran. Energy 35:5223–5229
4. Kankal M, Akpınar A, Komurcu M, TS Ozsahin (2011) Modeling and forecasting of turkey's energy consumption using socio-economic and demographic variables. Appl Energy 88:1927–1939

5. Geem ZW, Roper WE (2009) Energy consumption estimation of South Korea using artificial neural network. Energy Policy 37:4049–4054
6. Unler A (2008) Improvement of energy consumption forecasts using swarm intelligence: the case of Turkey with projections to 2025. Energy Policy 36:1937–1944
7. Kıran MS, Ozceylan E, Gunduz M, Paksoy T (2012) Swarm intelligence approaches to estimate electricity energy consumption in Turkey. Knowl Based Syst 36:93–103
8. Kıran MS, Ozceylan E, Gunduz M, Paksoy T (2012) A novel hybrid approach based on particle swarm optimization and ant colony algorithm to forecast energy consumption of Turkey. Energy Convers Manag 53:75–83
9. Kavaklioglu K, Ceylan H, Ozturk HK, Canyurt OE (2009) Modeling and prediction of Turkey's electricity consumption using artificial neural networks. Energy Convers Manag 50:2719–2727
10. Ceylan H, Ozturk HK (2004) Estimating energy consumption of Turkey based on economic indicators using genetic algorithm approach. Energy Convers Manag 45:2525–2537
11. Yu S, Wei YM, Wang K (2012) China's primary energy consumptions in 2020: predictions from an MPSO–RBF estimation model. Energy Convers Manag 61:59–66
12. K Kavaklioglu (2011) Modeling and prediction of Turkey's electricity consumption using Support Vector Regression. Appl Energy 88:368–375
13. Chen CH, Liao YY (2014) Tribal particle swarm optimization for neurofuzzy inference systems and its prediction applications. Commun Nonlinear Sci Numer Simul 19:914–929
14. Input variable. http://api.worldbank.org/datafiles/IND_Country_MetaData_en_EXCEL.xls

Chapter 83
Frequency Regulation of Isolated Hybrid Wind/Diesel, Power Generation with Fuel Cell System

Shailendra Singh, Munendra Singh, S. Chanana and S. Semwal

Abstract This paper presents frequency fluctuation analysis of an isolated hybrid power system. Hybrid system includes Wind, Diesel-Engine Generator (DEG) and Fuel Cell (FC) system. This hybrid system is connected to the local utility point and it may connect to the local electric grid. The impact of the FC system on the frequency stability of an isolated hybrid system has been analyzed. Due to limited storage capacity, the limits of hydrogen volume have also been incorporated. Simulation results show that the FC system can give better performance for stabilizing the frequency of the system in comparison to conventional distributed sources like DEG, FC system contribution is extremely useful in both cases when the load rises and also when the load drops.

Keywords Hybrid system · Regulation · Fuel cell · Load demand

83.1 Introduction

In modern scenario, energy is playing a vital rolein technical and economical growth of any country. Economic growth of a modern nation depends on the availability of energy for the long term from sources that are sustainable, reliable, affordable and eco-friendly [1]. High fuel prices and high carbon contain have forced to researchers, engineers to think about new and renewable, cheaper alternatives to reach their energy demands [2, 3]. Among all renewable, wind renewable technology having high popularity due to its benefits such as availability of resources, efficiency of generations, operation and maintenance [4]. Production of electricity through wind power is spread across over one hundred countries worldwide. So far, it is at the apex in Asia, North America and Western Europe.

S. Singh (✉) · M. Singh · S. Semwal
Graphic Era University, Dehradun, India
e-mail: singh.shail1986@gmail.com

S. Chanana
National Institute of Technology, Kurukshetra, India

C. Kamalakannan et al. (eds.), *Power Electronics and Renewable Energy Systems*,
Lecture Notes in Electrical Engineering 326, DOI 10.1007/978-81-322-2119-7_83

When the instability is caused by fluctuations in connected load, the DG can also used to retain the frequency within the local distribution system [5]. Despite increasing interest in distributed generation the concern for frequency stability is a new and important issue [6]. The introduction of multiple power generating sources in the distribution system the instability in frequency may occur. There is variation among the frequencies of various power generation sources, the synchronism may lose [7]. DG and energy storage system plays vital role in hybrid system to improve their system performances, fuel cell system is a kind of power source which can used as DG and storage device. It stored energy in the form of hydrogen energy. Hydrogen is used as fuel in, fuel cell system for electrical power production [8, 9]. Fuel cells are fundamentally fossil- fueled batteries. Continuation supply of hydrogen and air into fuel cell system, they certainly not terminate the flow of energy [10]. Fuel cell system having quit incredible fuel efficiencies—up to 50–70 % including with by producing thermal energy that tends to increase the plant efficiency of the system [11]. In this paper, the impact of fuel cell operation on the frequency stability under isolated condition has been discussed. The complete fuel cell system comprises of fuel cell, electrolyzer and a Hydrogen storage Facility. Modeling of wind speed to wind power is also incorporated.

83.2 Fuel Cell System

The fuel cell is an electrochemical device that transfers chemical energy into electrical energy. It generates DC power directly by method of different chemical reactions without an intermediary transfer into mechanical power/energy. Full cell system has facilities of fuel cells, electrolyzer and hydrogen storage [11–13].

The role of electrolyzer is splitting water into hydrogen (H_2) and oxygen (O_2) by providing of DC supply to its electrodes. Approximately 4–6 % of the H_2 production comes from the electrolysis. In electrolysis plants, alkaline electrolyzer uses alkaline electrodes, so they called as alkaline electrolyzer. Conventionally alkaline electrolyzers have designed for continuous H_2 production rates. Proton exchange membrane (PEM) electrolyzer is used for inconsistent rate of H_2 production.

Produced hydrogen (H_2) through an electrolyzer can be stored in various forms such as in gas as compressed gas, in solids such as metal hydrides, carbon materials and in liquid as a cryogenic liquid, H_2 carriers inform as methanol and ammonia [13].

83.3 Wind Speed to Power Conversion Model

It is assumed that wind speed is the combination of following four components: average speed (V_{wa}), wind speed ramp (V_{wr}), wind gust (V_{wg}) and wind turbulence (V_{wt}) [14]. The resultant wind speed is given by:

$$V_w(t) = V_{wa}(t) + V_{wr}(t) + V_{wg}(t) + V_{wt}(t) \quad (83.1)$$

This composite wind model is firstly discussed by Wasnczuk, Anderson and Bose [15, 16]. The relevant equations for computational analysis of various wind speed components have been discussed in Refs. [9, 14, 17]. In this work, variation of wind speed with for typical day has been analyzed.

The power produced by a wind turbine can be represented by using subsequent equation:

$$P_w = c_p(\lambda, \beta)\frac{\sigma}{2}\pi r^2 V_w^3 \quad (83.2)$$

where c_p is the power coefficient of wind turbine which is function of λ and β.

83.4 Hybrid System Model

Consider an isolated hybrid power system as shown in Fig. 83.1 Wind, DEG and fuel cell system are supplying power to variable load. Plants output is mainly an energy source for electricity and by product heat, as well as for splitting water into hydrogen and oxygen in the electrolyzer. H_2 stored in hydrogen storage system, which is use as fuel in FC system. Power conditioning systems, converts fuel cell DC output to AC power, which has supplied with the system generation. If the electricity consumers are connected to the utility point or the local grid, then system can be used for both import and export power.

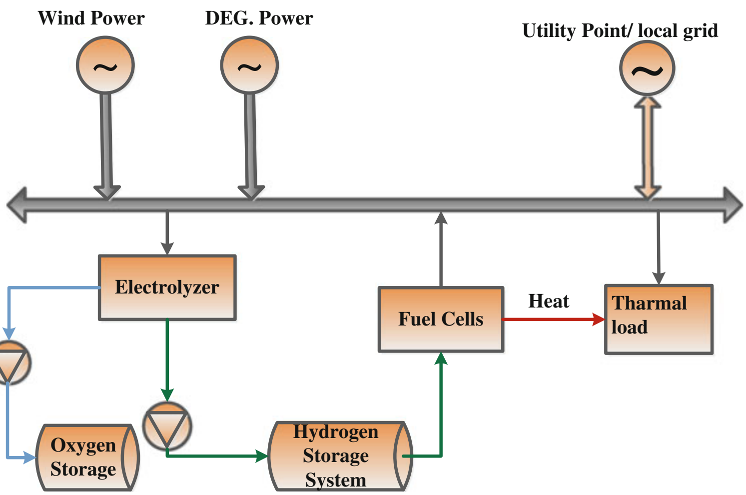

Fig. 83.1 Schematic diagram of a hybrid wind power, DEG- fuel cell system

83.4.1 Mathematical Analysis of Hybrid System

Transfer function based mathematical analysis of proposed hybrid power generation system has discussed here To maintain a stable operation of a hybrid system, the total power generation must be effectively controlled and properly dispatched to meet the total power demand of the connected loads. Control approach has determined by the difference between power demand ΔP_D and change in total generation:

$$\Delta P_T = \Delta P_w + \Delta P_{FC} + \Delta P_{DEG} - \Delta P_E \tag{83.3}$$

whereas ΔP_w, ΔP_{FC}, ΔP_{DEG}, ΔP_E are the change in- Wind power generation, diesel power generation, fuel cell power and power consumption by the electrolyzer in per units.

$$\Delta P_S = \Delta P_T - \Delta P_D \tag{83.4}$$

where the ΔP_S is net power deviation.

The system frequency variation ΔF is calculated by:

$$\Delta F = \frac{K_{PS}}{1 + T_{PS}} \Delta P_S \tag{83.5}$$

Since an inherent time delay exists between system frequencies so the transfer function for system frequency variation to per unit power deviation can be expressed by:

$$\Delta F = \frac{1}{D + sM} . \Delta P_S \tag{83.6}$$

where M and D are, respectively, the equivalent inertia constant a damping constant in per unit of the hybrid power system. Consider 2 MW power generations as the base value of the complete system.

Transfer Function Equation of Fuel Cells. The transfer function for system frequency variation in per unit fuel cell power is expressed by

$$\Delta P_{FC} = \frac{K_{FC}}{1 + sT_{FC}} . \Delta F \tag{83.7}$$

Transfer Function Equation of Electrolyzer. Some part of the generated power is feed to the electrolyzer to generate available H_2 for the fuel cell. The transfer function of the electrolyzer is expressed by:

$$\Delta P_E = \frac{K_E}{1 + sT_E} \cdot \Delta F \tag{83.8}$$

Transfer Function Equation of Diesel Engine Generator. The transfer function equation of diesel power generation expressed by

$$\Delta P_{DEG} = \frac{K_{DEG}}{1 + T_{DEG}} \cdot \frac{\Delta F}{R} \tag{83.9}$$

R is speed regulation. DEG automatically starts up with proper control.

Transfer Function of Hydrogen Storage. Change in hydrogen volume can be finding by the following transfer function equation:

$$\Delta V_E = \frac{\eta_E}{HHV} \cdot \frac{\Delta P_E}{s} \tag{83.10}$$

where ΔV_E is net change H_2 volume due to processing of electrolyzer and η_E is the electrical efficiency of electrolyzer, HHV is the higher heating value.

Similarly change in hydrogen volume due to working of fuel cell is defined by following transfer function equation:

$$\Delta V_{FC} = \frac{1}{HHV \cdot \eta_{FC}} \cdot \frac{\Delta P_{FC}}{s} \tag{83.11}$$

where ΔV_{FC} net change in hydrogen volume due to operation of FC and η_{FC} is the electrical efficiency of the FC including power conversion losses. By this equation the fuel cell power can also determine if ΔV_{FC} is known.

From above equations net H_2 volume stored in the tank is determined by following equation:

$$[V_H] = V_H^0 + \Delta V_E - \Delta V_{FC} \tag{83.12}$$

where V_H is net H_2 volume stored in tank and V_H^0 is initial H_2 volume of the tank.

83.5 Operation Strategy

A flow chart, which describes the operating strategy of plant model discussed in has shown Fig. 83.2. Change in frequency depends upon change in load demand so whenever load demand increases system frequency decreases and vice versa. So, for this to make a change in frequency to be zero power supply should be adjusted that means whenever an increase in load demand power supply is increased and when the load demand is decreases power should be reduced. On this basis in plant proceeds as when the change in frequency becomes a negative fuel cell system is

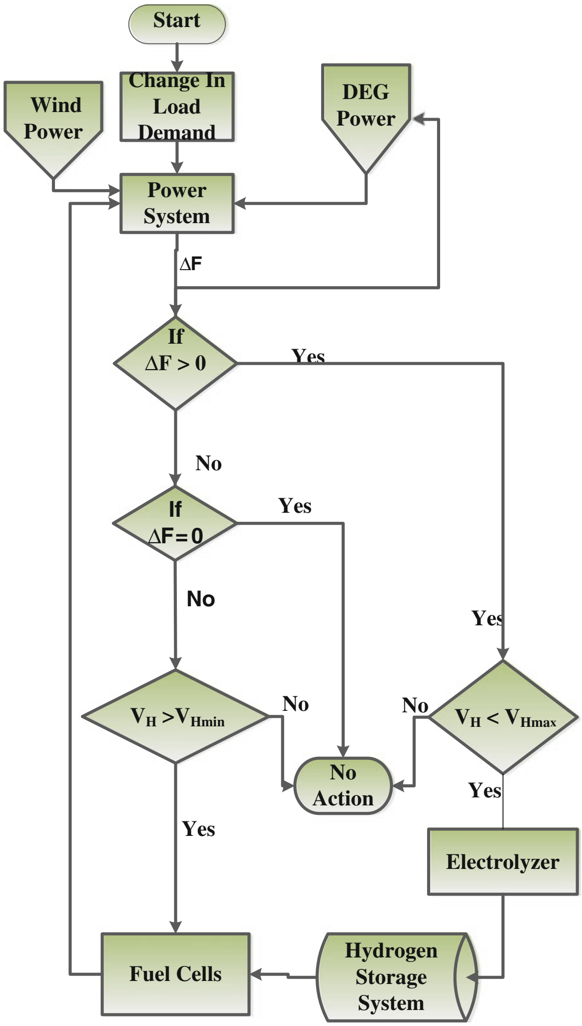

Fig. 83.2 Illustration of the operational strategy

supplying the power to the system but before operating of fuel cell it must undergo that process where hydrogen volume of the tank is compared to its minimum volume if hydrogen volume is greater than the minimum volume than fuel cell system run and supply to power to the system otherwise fuel cell do not produce power. In another case when the change in frequency is positive fuel cell do not supply the power and to reduce the power. Some of the excess power supply to the electrolyzer system before running the electrolyzer hydrogen volume of the tank has compared to its maximum hydrogen volume. If the hydrogen volume of the tank is less than its maximum volume, then electrolyzer run and producing H_2 and O_2 that are stored in their tanks and this H_2 is used in fuel cell, otherwise electrolyzer will stop (Table 83.1).

Table 83.1 Parameter and rating of the hybrid power system

K_{FC} = 0.1, and T_{FC} = 0.03 s	System power rating—2 MW
K_{DEG} = 1, and T_{DEG} = 0.05 s, R = 0.5	Fuel cell power = 80 KW, DEG. Power = 250 KW, Wind Power = 200 KW, Electrolyzer power = 80 KW
K_E = 0.1, and T_E = 0.05 s	H_2 max. volume = 500 Nm^3, H_2 min. volume = 60 Nm^3, Initial H_2 vol. = 250 Nm^3
M = 0.12, and D = 0.1	$\eta_E = 85\,\%$, $\eta_{FC} = 50\,\%$, HHV = 3.509 Kwh/Nm^3, Frequency 50 Hz

83.6 Simulation Results and Analysis

Real time performance of the hybrid system has simulated for a typical day in Matlab/Simulink environment. Variations in load demand with respect to real-time load demand have shown in Fig. 83.3a, b shows the change in wind power generation. Time domain simulated responses of the system are observed mainly two cases of disturbances occurred in load demand.

83.6.1 Case-I

Increase in load demand. Sudden rise in load demand results fall in system frequency so there is need to increase to power production to maintain the frequency stability of the system. For stability concern DEG power can be increased to feed the power to the system, up to its rated capacity. But power supplied by DEG is not sufficient to full the need. So to compensate the load demand FC system starts feeding the power in the system as shown in Fig. 83.3c. Due to functioning of fuel cell hydrogen volume has consumed. Due to that net change in hydrogen volume has shown in Fig. 83.3d.

83.6.2 Case-II

Decrease in load Demand. Due to drop in load demand, there is rise in system frequency, for constant frequency operation there should be reduction in power supply by shutting down DEG power and fuel cell power, but surplus power is still more than load demand so for balancing the load and power generation, some of total power is fed to electrolyzer and its response shown in Fig. 83.4a. Due to the functioning of Electrolyzer, H_2 volume of the tank will also rise, so its response is shown in Fig. 83.3d.

Fig. 83.3 Variation in **a** Load demand. **b** Fuel cells power. **c** Wind power. **d** Hydrogen volume in storage tank

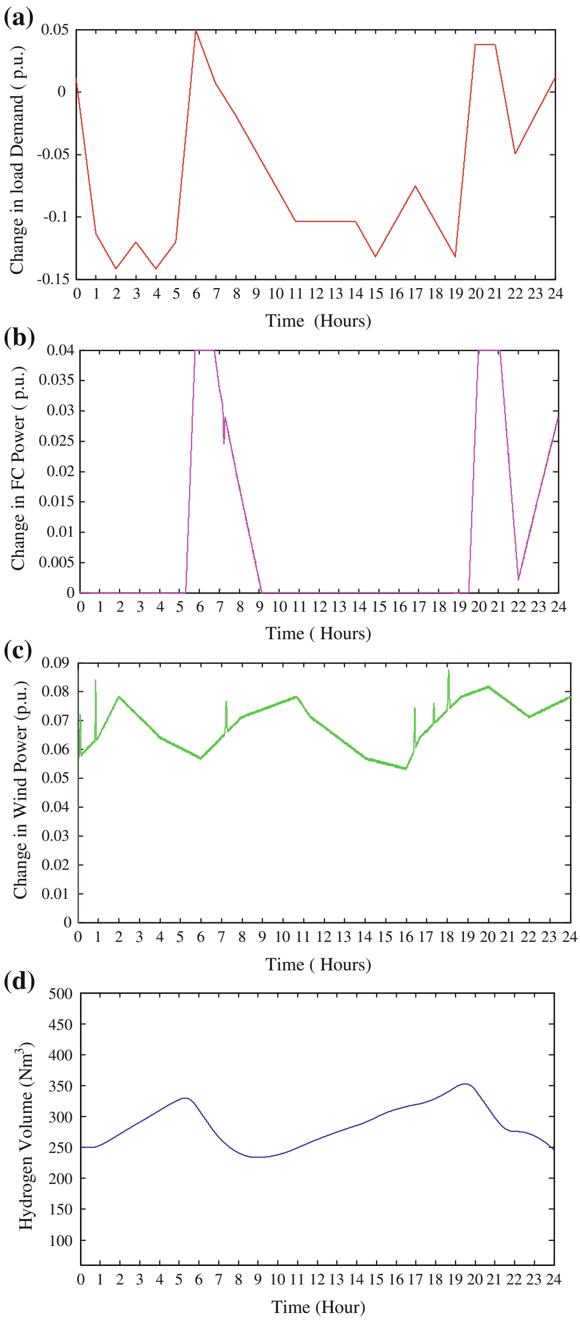

Fig. 83.4 **a** Power consumed by Electrolyzer. **b** Variation in Frequency of the system

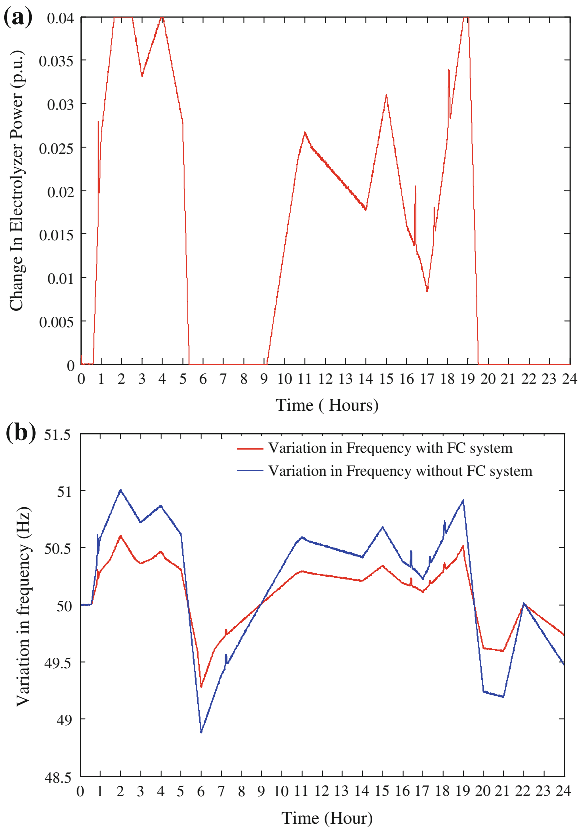

From above cases, it can be concluded that fluctuation in frequency decreases by adding the fuel cell system with wind-DEG power system Fig. 83.4b show the complete variations in system frequency with and without the FC system.

83.7 Conclusion

This paper discussed the operation and control of an isolated hybrid system. The role of DG sources like wind, diesel and fuel cell in controlling grid/system frequency have analyzed. A fuel cell based model for responding to system frequency oscillations has been developed. From simulation results it can be observed that a collective fuel cell and diesel generator gives better performance in controlling the frequency variation in comparison to the only diesel generator. Due to the operation of the electrolyzer, it is performing two functions simultaneously first one the significant fuel saving for Fuel cell, as the volume of hydrogen is replenished in the storage tank and another controlling of frequency when it upswing due to drop in load demand. By addition of other renewable with hybrid system is extremely useful.

References

1. Lee D-J, Wang L (2008) Small-signal stability analysis of an autonomous hybrid renewable energy power generation/energy storage system, part I: time-domain Simulations. IEEE Trans Energy Convers 32:311–320
2. Osman H, Negnevitsky A-M, Haque M Md, Gargoom A (2013) A Novel operation and control strategy for a standalone hybrid renewable power system. IEEE Trans Sustain Energy 4:402–413
3. Toshiro H, Hirofumi M (2012) Standalone hybrid wind-solar power generation system applying dump power control without dump load. IEEE Trans Indus Electron 59:988–998
4. Kabouris J, Kanellos FD (2010) Impact of large-scale wind penetration on designing and operation of electric power systems. IEEE Trans Sustain Energy 1:107–115
5. Vinicius F, Martins LT, Carmen B (2011) Active distribution network integrated planning incorporating distributed generation and load response uncertainties. IEEE Trans Power Syst 26:2164–2172
6. Argiento R, Faranda R, Pievatolo A, Tironi E (2012) Distributed interruptible load shedding and micro-generator dispatching to benefit system operations. IEEE Trans Power Syst 27:840–848
7. Celli G, Ghiani E, Mocci S, Pilo F (2005) A multi-objective evolutionary algorithm for the sizing and siting of distributed generation. IEEE Trans Power Syst 20:750–757
8. Singh, S., Singh, A., K.., Chanana, S.: Operation and control of a hybrid Photovoltiac, diesel - fuel cell system connected to micro grid, IEEE Fifth POWER INDIA Conference, Delhi National Capital Region(2012) 1- 6
9. Singh S, Singh M, Chanana S, Raveendhra D (2013) Operation and control of a hybrid wind-diesel-battery energy system connected to micro-grid. In: 2013 international conference on control, automation, robotics and embedded systems pp 1–6
10. Ellis MW, Von Spakovsky MR, Nelson DJ (2001) Fuel cell systems: efficient, flexible energy conversion for the 21st century. Proc IEEE 89:1808–1818
11. Ramos-Paja CA (ed) (2009) Minimum fuel consumption strategy for PEM fuel cells. IEEE Trans Indus Electron 56:685–696
12. Puranik VS, Ali K, Farshad K (2010) State-space modeling of proton exchange membrane fuel cell. IEEE Trans Energy Convers 25:804–813
13. Magnus K, Holen T (2006) Operation planning of hydrogen storage connected to wind power operating in a power market. IEEE Trans Energy Convers 21:742–749
14. Chanana S, Kumar A (2011) Operation and control of BESS using frequency-linked pricing in real-time market with high wind penetration. Int J Energy Sector Manag 5:585–602
15. Wasnczuk O, Man DT, Sullivan JP (1981) Dynamic behaviour of a class of wind turbine generators during random wind fluctuation. IEEE Trans Power Appratus Syst 100:2837–2845
16. Anderson PM, Bose A (1983) Stability simulation of wind turbine systems. IEEE Trans Power Apparatus Syst 12:3791–3795
17. Slootweg JG, de Haan SWH, Polinder H, Kling WL (2003) General models for representing variable speed wind turbines in power dynamics simulations. IEEE Trans Power Syst 18: 144–151

Chapter 84
Residential Load Signature Analysis for Their Segregation Using Wavelet—SVM

Munendra Singh, Sanjeev Kumar, Sunil Semwal and R.S. Prasad

Abstract The unique power consumption pattern of each appliance or a combination of appliances can be analyzed using their load signatures which can be acquired from a single point. It is quite difficult to disaggregate the similar kind of home appliances because of their similar characteristics. Wavelet coefficients of load signature have been chosen as the feature vectors which reflected the edge over other features. These coefficients serve as input data for the classifier. By considering various classification algorithms a comparison has been made and the best algorithm was investigated which is the linear Support Vector Machine (SVM) for the selected similar appliances. The results of laboratory experiment promise a new application for smart meters.

Keywords Load disaggregation · Load signature · Wavelet · SVM · NILM

84.1 Introduction

It is well known to us that the day by day the energy demand will exponentially increase. The question is, are we ready to full fill this demand? At least not by the generation only. Although everyone is aware to save the wastage electricity and try to use appliances as their requirement but it is not sufficient because how much we

M. Singh (✉) · S. Kumar · S. Semwal · R.S. Prasad
Department of Instrumentation and Control Engineering, Graphic Era University, Dehradun, India
e-mail: munendra107@gmail.com

S. Kumar
e-mail: Sanjeev.rgec@rediffmail.com

S. Semwal
e-mail: Sunil.111213@gmail.com

R.S. Prasad
e-mail: drsachpd@yahoo.com

C. Kamalakannan et al. (eds.), *Power Electronics and Renewable Energy Systems*, Lecture Notes in Electrical Engineering 326, DOI 10.1007/978-81-322-2119-7_84

are and can be really conscious? A study suggests in [1] that maximum energy saving can be achieved by real-time appliance level consumption information as opposed to monthly bills, weekly advice on energy usage. This study motivates researchers to develop the smart meter which have capabilities of online billing on a daily basis, dynamic charges according to on peak and off peak timings, control the appliances etc. To achieve this, the appliance load monitoring system must be employed in the smart meters. There are two major approaches to monitor the appliance load; one is Intrusive Load Monitoring (ILM) and other Non-Intrusive Load Monitoring (NILM). In the first method, each appliance is connected through a dedicated sensor which detects the load profile of the connected load. This technique is reliable but costly as one sensor is associated with each appliance. The second method NILM having some practical advantages like low cost and less number of the required sensors [2], consists of the following steps: (i) Acquisition of current signature, (ii) Extraction of features and events, and (iii) Classification of features and events. The today's complex electrical loads have complex signatures that depending on their state and mode of use leads the challenges in NILM method to improve the understanding of these signatures with the help of signal processing, artificial intelligence and machine learning techniques.

Some attempts have already been made to disaggregate the appliance using load signature study. To classify the load signatures some of its features are responsible like current waveform (CW), active/reactive power (PQ), harmonics (HAR), instantaneous admittance waveform (IAW), instantaneous power waveform (IPW), eigenvalues (EIG), and switching transient waveform (STW). In most of the work, a combination of some features have been used [3, 4] although one feature is also sufficient to classify most of the appliances [5, 6] but classification accuracy is still an issue. The classification accuracy affected by selection of features as well as on the classification algorithm. Artificial Neural Network (ANN) classifier is a good classifier [5, 7] in order to obtain accurate results but this nonlinear classifier is sensitive to over train the data. Regardless of this technique some researchers correlated event detection for residential appliance identification [8, 9] this method takes relatively long time to acquire the data. SVM [10] has been used to find the type of power system disturbances [11] but till date application of SVM has not been reported for load appliance segregation. In this paper wavelet based features have been used for the classification and suggested the effectiveness of different classification algorithms for nonlinear—similar type (Category B) appliances.

The first step to process any signal is to filter the noise for this purpose filter can be used after decomposing the signal. After denoising the signal, it is used to extract the features. As discussed earlier various features of an electrical signal may possible but the amplitude spectrum of Fast Fourier Transform (FFT) [4, 6] and wavelet based features [11] are the potential features for the classification. The classifier is selected according to the input data, if the randomness within the class is less, classifier based on non Gaussian distribution preferred over the Gaussian. The experimental data have good separability among different classes the linear SVM has an edge on other SVM techniques and the techniques based on iterative

Fig. 84.1 Load signature of Category ‘A’ appliances **a** Bulb, **b** Room Heater

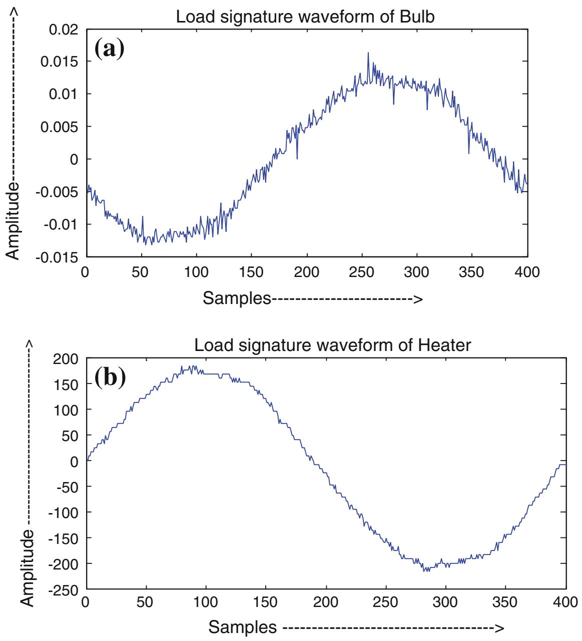

Mean Square Error (MSE) optimization. This paper organized as follows: proposed signal processing followed by the experimental set up for load signature acquisition and finally we discuss the results before conclusion.

84.2 Platform Design

Home appliances can be categorized in Category-A: electrical type which consists of passive networks and Category-B: electronic type, consist of passive as well active networks. Clearly diverse load signatures as seen in Figs. 84.1 and 84.2 provides good inter category disaggregation but the intra category appliance disaggregation is quite difficult because of same characteristics especially for category B appliance. This problem may severe for very similar type use appliances like Laptop, CPU, LCD, TV etc. In cat-B, we chose most commonly used appliances Laptop, CPU and LCD for the disaggregation to test the feasibility of classification algorithms.

84.2.1 Experimental Setup

Figure 84.3 shows the overall block diagram of the home appliance identification system. A current sensor has been installed in the main phase wire which comes out

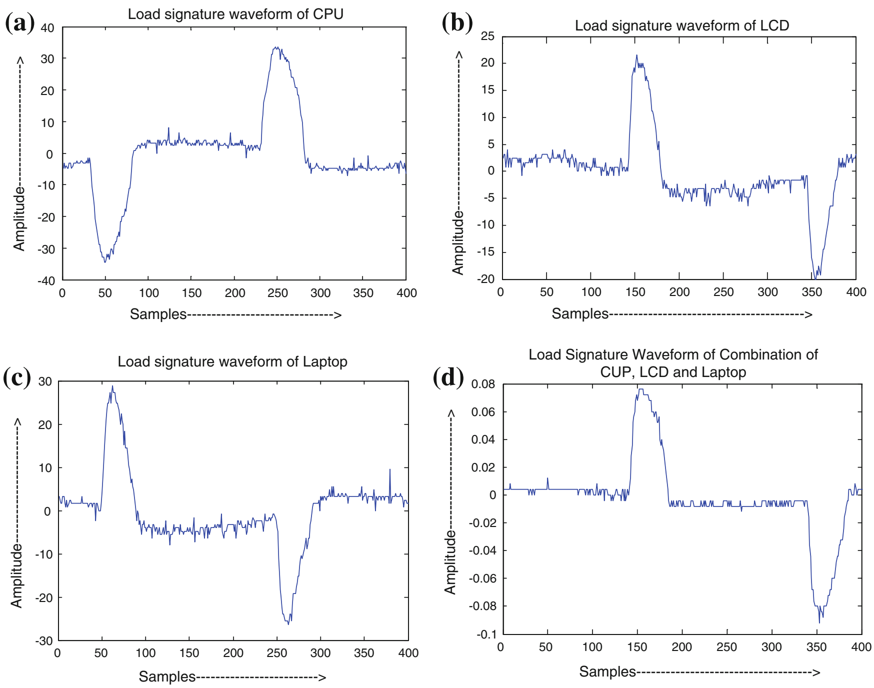

Fig. 84.2 Load signature of category 'B' appliances **a** CPU **b** LCD **c** Laptop and **d** combination of CPU, Laptop and LCD

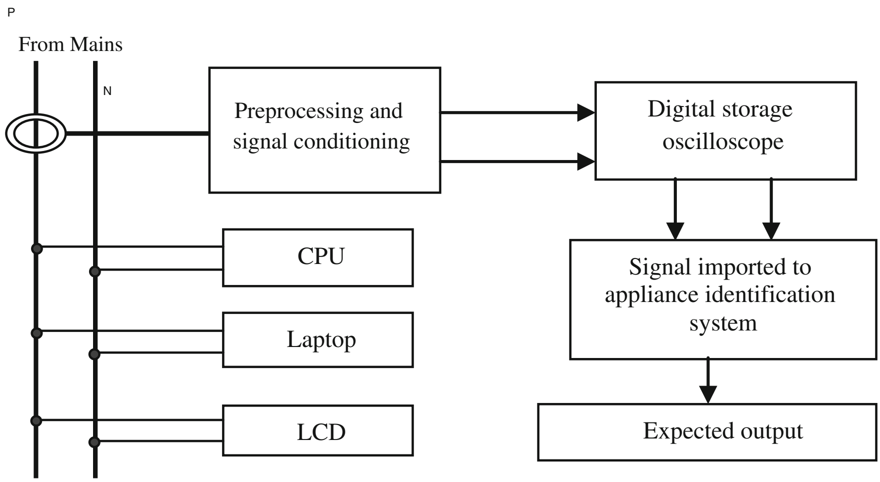

Fig. 84.3 Block diagram of home appliance identification system

Table 84.1 Combination of appliances and their respective classes

Sr.	Class	Appliances
1	Class 1	CPU
2	Class 2	Laptop
3	Class 3	LCD
4	Class 4	CPU + Laptop
5	Class 5	CPU + LCD
6	Class 6	Laptop + LCD
7	Class 7	CPU + Laptop + LCD

from the main distribution box. This current sensor gives output in very low current rating and this current gives the voltage droop across a resistor and this voltage is acceptable as the input signal for the Digital Storage Oscilloscope (DSO). The waveform appears on the DSO screen is the load signature which has been stored for further signal processing. The individual appliance load signature has been acquired and then the load signature of each possible combination (the total possible combinations of load signature became 7, say total 7 classes) as shown in Table 84.1. For each of the class 20 samples have been collected which gave total 140 samples.

84.2.2 Feature Extraction

Load signature may have many features as we already discussed but we must choose the features which lead to minimum classification error with less execution time as well includes all the important properties. Coefficient of Fourier transform contains the physical meanings of a signal, Fast Fourier Transform is a technique to calculate these coefficients and these coefficients can be taken as the features after preprocessing. Generally some of primary coefficients are chosen for this purpose. If a signal having sudden small changes, the primary coefficients lost this information and may not sufficient features, whereas Wavelet consider this spatial information. Thus we use the coefficients of Discrete Wavelet Transform as the features for the classification.

84.2.3 Classification

A classifier identifies the classes of testing data. The accuracy of classifier's mainly depends on the best selection of classifier for the type of data set. The solution of this difficult problem which is based on knowledge of input vector as well classifier's strategy. Here we tried to scrutinize the practicability of various classifiers and

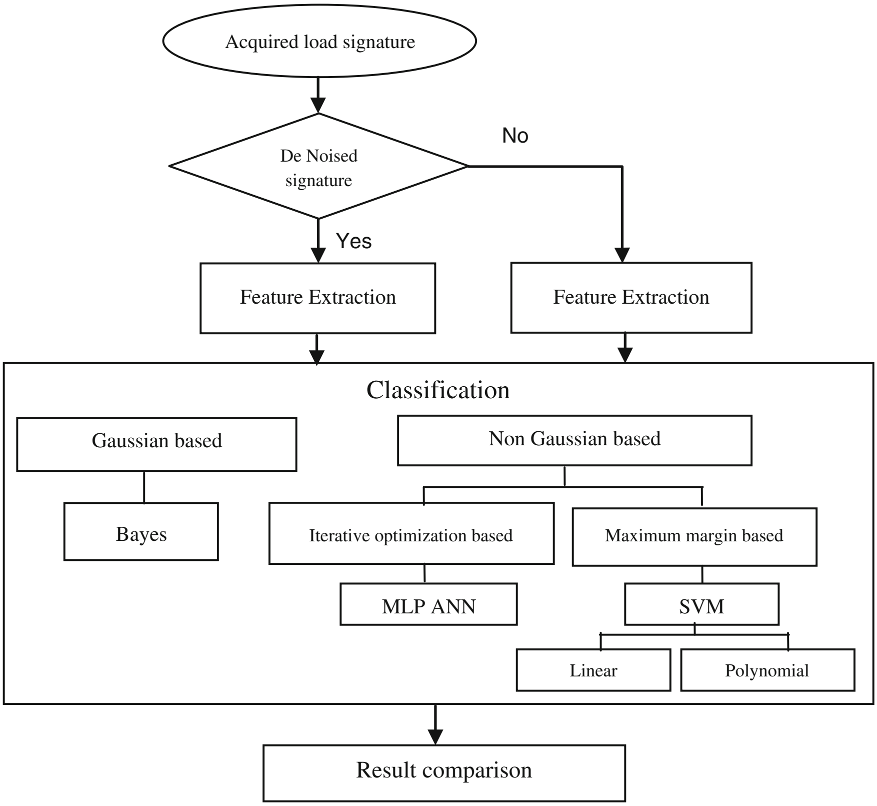

Fig. 84.4 Signal processing and pattern recognition framework for load signature

the best classifier for the chosen home appliances has been driven. Features of the load signatures are the input vector for the classifier. These input vectors has been fed to classifier based on Gaussian distribution i.e. Bayes and non—Gaussian i.e. MLP-ANN (Multilayer Perceptron Artificial Neural Network), SVM to calculate the classification accuracy. Finally a decision has been taken by observing the results which is the best classifier for the experimental data and it was observed that the intuitive knowledge has been confirmed by the decision. This framework has been shown in Fig. 84.4.

84.3 Results and Discussion

There were seven classes and each of the classes had 20 samples; these samples were divided into two groups one is 'Train' (Actual or Target group) and another is 'Test' (Predicted or output group). When the data has been tested using Bayes

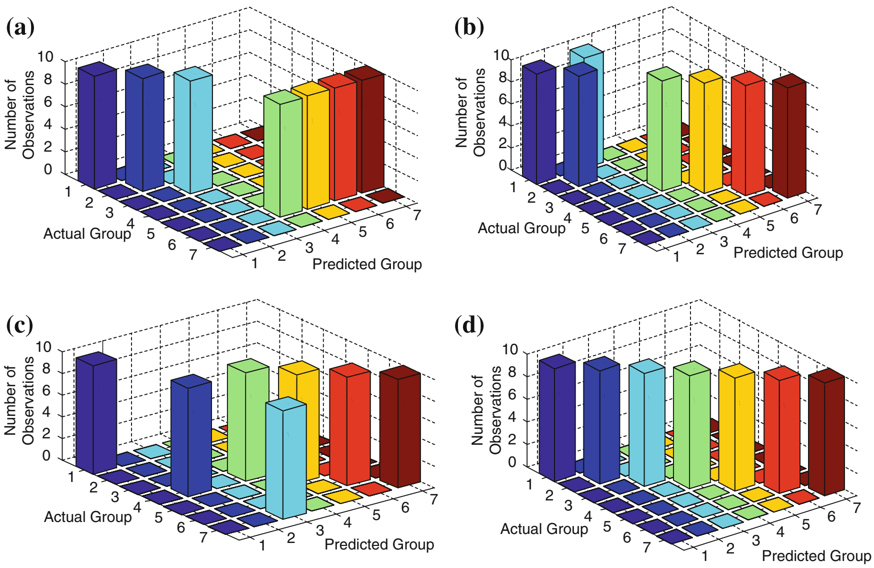

Fig. 84.5 Confusion bar plot of classifires: **a** Bayes **b** MLP-ANN **c** Polynomial 3rd order SVM and **d** linear SVM

classifier, it can be seen in the obtained confusion matrix, shown in Fig. 84.5a, which describes that the classes 1, 2, 3, and 6 are correctly classified, whereas classes 4, 5, 7 are misclassified into class 6 which turned out to be poor classification Fig. 84.5b represents the confusion matrix for MLP-ANN classifier, this time the classes 1, 2, 4, 5, 6, 7 are correctly classified, whereas class 3 is misclassified into class 1.

Figure 84.5c revealed the polynomial (3rd order) SVM in which the classes 1, 4, 5, 6, 7 are correctly classified into their actual groups whereas class 2 misclassified to 4, and class 3 misclassified into class 7. All these classifiers lead to poor classification results of closely related home appliances. Linear SVM is the best classifier for this kind of data which can be seen by the obtained results shown in Fig. 84.5d where all the classes are correctly classified into their actual class. In Table 84.2 all the results are summarized for all approaches to classify the home appliances considered in the experiments. Types of input data which were load signatures and Wavelet transforms are responsible for providing the best results by linear SVM because the data has very good interclass variance, whereas polynomial SVM, and MLP-ANN increased the complexity during the classification and Bayes' is more suitable because there is very less variance within the class.

Figure 84.5b represents the confusion matrix for MLP-ANN classifier, this time the classes 1, 2, 4, 5, 6, 7 are correctly classified whereas classes 3 is misclassified into class 1. Figure 84.5c revealed the polynomial (3rd order) SVM in which the classes 1, 4, 5, 6, 7 are correctly classified into their actual groups whereas class 2 misclassified to 4 and class 3 misclassified into 7. These all classifiers lead poor

Table 84.2 Comparison of different classification techniques

Appliances	Accuracy of different classifiers			
	Bayes (%)	ANN (MLP) (%)	SVM	
			Polynomial (%)	Linear (%)
Class 1	100	100	100	100
Class 2	100	100	0	100
Class 3	100	0	0	100
Class 4	0	100	100	100
Class 5	0	100	100	100
Class 6	100	100	100	100
Class 7	0	100	100	100
Average accuracy	57.14	85.71	71.42	100

classification results of closely related home appliances. Linear SVM is the best classifier for this kind of data which can be seen by the obtained results shown in Fig. 84.5d where all the classes are correctly classified into their actual class. In Table 84.2 all the results are summarized for all approaches to classify the considered home appliances. Type of input data which were load signatures and Wavelet transform are responsible for providing the best results by linear SVM because the data has very good interclass variance whereas polynomial SVM, and MLP-ANN increased the complexity during the classification and Baye's is more suitable because there is very less variance within the class.

84.4 Conclusion

We succeeded in the disaggregation of similar kind of home appliances whereas inter category appliance disaggregation was relatively easy so it was not considered. It was observed that the results are highly dependent on the adopted feature extraction and classification methodology. Instead of calculating some set of features which was time taking a technique or FFT based features, Wavelet coefficients were proposed the potential features. Baye's classifier, MLP-ANN, polynomial SVM and linear SVM were the worth considering choice for classification. Comparative study showed that the linear SVM is the best suited classifier for the similar kinds of home appliances. This result can be concluded without investigating the optimal numbers of features for each of the classifiers because linear SVM yielded 100 % classification accuracy. After recognition, online controlling of particular appliance will be our further research motivation which will help to manage and save the energy.

References

1. Ehrhardt-Martinez K, Donnelly KA, Laitner S (2010) Advanced metering initiatives and residential feedback programs: a meta-review for household electricity-saving opportunities. Am Council Energy-Eff Econ, Washington DC
2. Hart GW (1992) Nonintrusive appliance load monitoring. In: Proceedings of the IEEE, New York, USA, vol 80, pp 1870–1891
3. Figueiredo M, Almeida AD, Ribeiro B (2012) Home electrical signal disaggregation for non-intrusive load monitoring (NILM) systems. Neurocomputing 96:66–73
4. Prasad RS, Semwal S (2013) A simplified new procedure for identification of appliances in smart meter applications. In: Systems Conference (SysCon). IEEE, Orlando, USA, pp 339–344
5. Liang J, Ng SKK, Kendall G, Cheng J (2010) Load signature study—part I: basic concept, structure and methodology. IEEE Trans Power Delivery 25:551–560
6. Srinivasan D, Ng WS, Liew AC (2006) Neural-network-based signature recognition for harmonic source identification. IEEE Trans Power Deliv 21:398–405
7. Chang HH, Chien PC, Lin LS, Chen N (2011) Feature extraction of non-intrusive load-monitoring system using genetic algorithm in smart meters. In: International conference on e-business engineering (ICEBE). Coventry, UK, pp 299–304
8. Shaw SR, Leeb SB, Norford LK, Cox RW (2008) Nonintrusive load monitoring and diagnostics in power systems. IEEE Trans Instrum Meas 57:1445–1454
9. Dong M, Meira PCM, Xu W, Freitas W (2012) An event window based load monitoring technique for smart meters. IEEE Trans Smart Grid 3:787–796
10. Boser BE, Guyon IM, Vapnik VN (1992) A training algorithm for optimal margin classifiers. In: Proceedings of the fifth annual workshop on Computational learning theory. ACM, New York, USA, pp 144–152
11. Erişti H, Uçar A, Demir Y (2010) Wavelet-based feature extraction and selection for classification of power system disturbances using support vector machines. Electr Power Syst Res 80:743–752

Chapter 85
Fuzzy-Based Torque Ripple Optimization and Digitalized Sector Selection in DTC Scheme

D. Deenadayalan and I. Alexandar Beski

Abstract This paper presents an efficient method of torque ripple optimization in Direct Torque Control (DTC) scheme for an induction motor drive (IMD), where the optimization has been done by varying the bandwidth of the torque hysteresis comparator (band adaption) online using fuzzy controller and also here a simple Digital Logic Circuit (DLC) has been presented, which reduces the computation burden on the DSP to evaluate the sector number of the flux linkage space vector and so the proposed DTC scheme does not require any high speed/high cost DSP in order to attain the fast and precise control. In order to test the performance of the proposed DTC scheme, a complete simulation model for both the conventional and proposed DTC are developed using MATLAB/Simulink.

Keywords Direct torque control (DTC) · Optimization · Fuzzy controller · Hysteresis controller

85.1 Introduction

Direct torque control (DTC) is the most advanced ac drive technology developed by any manufacturer in the world. Now a day's one third of electric power consumed by electric drives. This electric drives are mainly AC and DC drives. During last four decades AC drives are become more and more popular, especially induction motor Drives (IMD), because of robustness, high efficiency, high performance, and rugged structure ease of maintenance so widely used in industrial application, such as paper miles, robotics, steel miles, servos, transportation system, elevators, machines tools alternative energy vehicles (AEVs) [1], etc.

D. Deenadayalan (✉)
Anna University, Coimbatore, Tamil Nadu, India
e-mail: ddayalan.eee@gmail.com

I. Alexandar Beski
Prathyusha Engineering College, Chennai, Tamil Nadu, India
e-mail: alexandarbeski001@gmail.com

C. Kamalakannan et al. (eds.), *Power Electronics and Renewable Energy Systems*, Lecture Notes in Electrical Engineering 326, DOI 10.1007/978-81-322-2119-7_85

The merits of DTC can be summarized as fast torque response, simple structure (no need of complicated coordinate transformation, current regulation, or modulation block), and robustness against motor parameter variation [2–6]. The major problem in a DTC-based motor drive is the presence of ripples in the Motor-developed torque and stator flux. Induction motors are of complex, highly non-linear, time varying dynamics system and also inaccessibility of exact measurements of output leads to a challenging problem for controlling but these problems can be solved by use of the torque and flux control techniques, because they are sensitive to drive parameter variations. Intelligent controllers are considered as potential candidates for such an application, because their designs do not depend on accurate mathematical model of the system and they can handle nonlinearity of arbitrary complexity. Here fuzzy based Adaptive intelligent techniques are applied to achieve high performance torque control. In this paper, a simpler practically feasible FLC is designed that selects the appropriate bandwidth for the torque hysteresis controller to optimize the ripple level in the developed torque and, hence, to improve the motor speed response.

In addition conventionally, the determination of the sector number of the stator flux-linkage space vector for the DTC scheme involves a trigonometric function (tangent). The microprocessor evaluates the trigonometric function by using time-consuming complex calculations as compared to normal arithmetic relations [7]. The requirement for the working of the DTC scheme is only the sector number, in which the stator flux-linkage space vector is positioned and not its accurate position. Therefore, in this paper presents a simpler efficient logical circuit was designed to determine the stator flux-linkage sector without using any trigonometric or complex function. Hence, the proposed work reduces the calculation burden for the processor. The need of relatively high speed/high cost digital signal processors which limit their use to high-end drives where the controller cost may be only a small fraction of the overall drive cost is avoided since the computational burden on DSP have been reduced enormously. In addition overall delay in program execution time severely limits the achievable PWM frequency of the inverter and thus there will be ripple in motor flux, current and torque. Here the reduced computational time will reduce the ripples effectively. A complete simulation model for the proposed drive is developed using MATLAB/Simulink. The effectiveness of the proposed drive is verified at different dynamic operating conditions by simulation.

85.2 Modeling of IM for DTC

85.2.1 Stator Voltage

The block diagram for the conventional DTC scheme of an induction motor drive is shown in Fig. 85.1. Generally DTC considered three input (torque hysteresis controller's output, flux linkage hysteresis controller output and position or sector

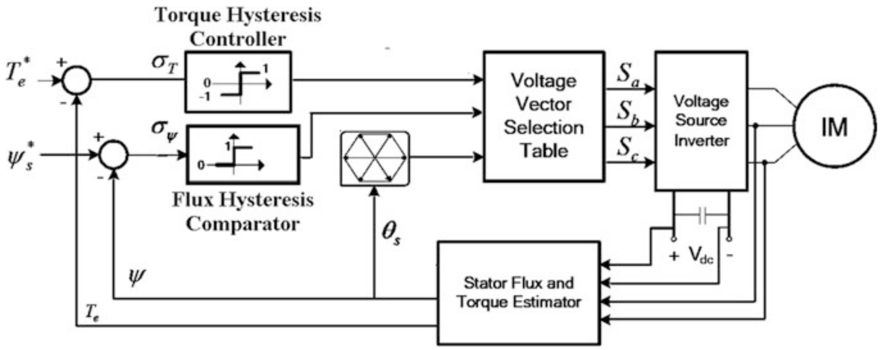

Fig. 85.1 Conventional DTC scheme for IM drive

number where the stator flux linkage located). These three inputs are referred to the switching table as shown in the figure which produces respective logical signals $S_{a,}$ S_b, S_c, which trigger the switches of the three phase voltage source inverter. Thus the output voltage from the VSI is fed to the induction motor which is given by

$$V_{sa} = (V_{dc}/3)\,(2S_a - S_b - S_c) \tag{85.1}$$

$$V_{sb} = (V_{dc}/3)\,(2S_b - S_c - S_a) \tag{85.2}$$

$$V_{sc} = (V_{dc}/3)\,(2s_c - S_a - S_b) \tag{85.3}$$

By using the Concordia transformation, the above can be transformed into real ($V_{s\alpha}$) and imaginary ($V_{s\beta}$) component of voltage vectors, similarly the current vectors of $I_{s\alpha}$ and $I_{s\beta}$ can be obtained and from which the flux components of $\phi_{s\alpha}$ and $\phi_{s\beta}$ can be computed.

85.2.2 Flux and Torque Analysis

In the DTC scheme, the motor-developed torque and stator flux linkage are estimated as

$$Te = {}^3\!/_2[\Phi s\alpha Is\beta - \Phi s\beta Is\alpha] \tag{85.4}$$

$$\Phi s = \sqrt{(\Phi^2\, s\beta + \Phi^2\, s\alpha)} \tag{85.5}$$

where Isα and Isβ are the direct and quadrature components of stator current, respectively. The estimated values of torque and flux are compared with the corresponding command/reference values, and the error signals are delivered to the respective hysteresis controllers. On the basis of the magnitude of the error signals and allowable bandwidth, each hysteresis controller produces a digit. Then, the position of the stator flux-linkage space vector is evaluated as

$$\theta s = \tan^{-1}(\Phi s\beta/\Phi s\alpha) \tag{85.6}$$

Using this angle, the flux sector number (1–6 as stated in Fig. 85.2) is determined. Therefore, two digits produced by hysteresis controllers and one by flux position are collectively used to trigger the switches of the VSI which selects the appropriate voltage vector by using the classical DTC lookup table [8]. In order to maintain the torque and flux remain within their respective band limits.

Under the influence of any active VSI voltage vector, the motor torque keeps on increasing or decreasing until it touches the boundary defined by torque hysteresis bands. If bandwidth decreases ripple content also will decrease but, the VSI switching frequency increases, which proportionally increases its switching losses and a too small band may result in the selection of reverse voltage vector instead of zero vector to reduce the torque. The selection of reverse voltage vector may then cause torque undershoots which leads torque ripple higher than those specified by the hysteresis controller band limits. Hence so the bandwidth must be optimized in such as a way that the torque ripple level and switching frequency of the inverter are within acceptable limits [9].

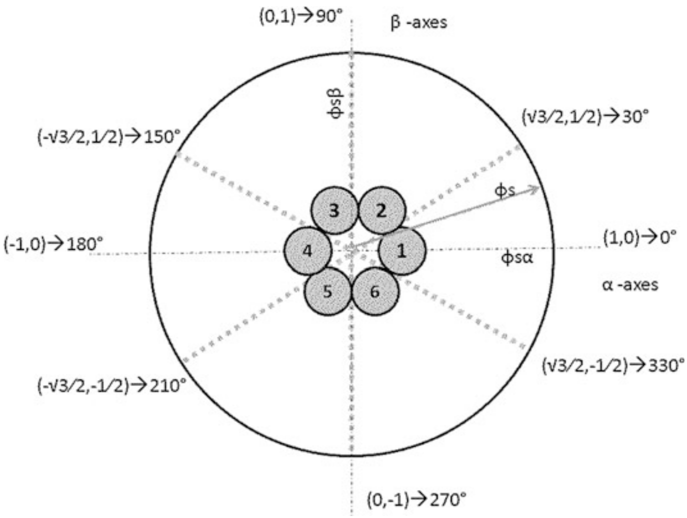

Fig. 85.2 Stator flux-linkage vectors with six sectors

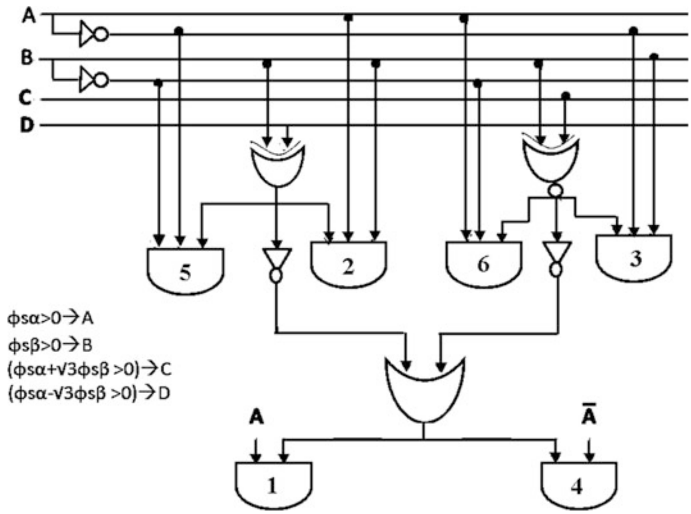

Fig. 85.3 Sector selector based on digital logical circuit

85.3 Proposed Flux Linkage Algorithm

According to the DTC control, the flux sector position is enough to determine the sector number at where the flux linkage vector is located. Let assume the amplitude of the stator flux-linkage vector is unity, if so the stator flux-linkage space vector with its coordinates in complex plane at the boundary of each sector can be shown as in Fig. 85.2, by using these boundary coordinates the sector number are classified easily. The above discussion replaces the trigonometric relation based selection of the sector number to the logical based selection of sector number, because it is considered the stator flux travels under circular trajectory and also it is found for the proper selection of voltage vector, the location of the stator flux in six dividend sector is enough and there is not necessary a perfect position of the stator flux. On framing the logical equations for each and individual sector leads to the logical circuit as shown in the Fig. 85.3.

85.4 Design of FLC for Torque Ripple Optimization

A fuzzy controller seems to be a reasonable choice to evaluate and approximate the amplitude of torque hysteresis band according to the torque ripple level controller in order to keep the torque ripples minimum, since it is an universal function approximator [10]. Based on the Faraday's electromagnetic theory for coil wound on unsaturated magnetic material (linear range of magnetizing curve), the stator flux linkage is proportional to the stator current. Therefore, the motor-estimated torque

(85.7) variation (dT_e) and stator current variation (dI_s) over a sampling period are chosen as inputs to the FLC which can be defined by the following equations

$$\mathrm{dT_e} = \mathrm{T_e[k] - T_e[k-1]} \tag{85.7}$$

$$\mathrm{dI_s} = \mathrm{I_s[k] - I_s[k-1]} \tag{85.8}$$

where Te[k] and Te[k − 1] present the present and previous samples of motor-estimated torque, respectively. The magnitude of the stator current is defined a

$$Is = \sqrt{I\alpha s^2 + I\beta s^2} \tag{85.9}$$

The crisp output ΔH (incremental amplitude of torque hysteresis band) is integrated in such way that the updated upper and lower bandwidths of the torque hysteresis controller are obtained as

$$HB^n_{TU} = HB_{TU} - K_U\, \Delta\, HB_T \tag{85.10}$$

$$HB^n_{TL} = HB_{TL} - K_L\, \Delta\, HB_T \tag{85.11}$$

where HB_{TU} and HB_{TU} are the base fixed upper and lower bandwidths of the torque hysteresis comparator. K_U and K_L are the scaling factors. The fuzzy controller design is based on intuition and simulation. For different values of motor torque and current, the values which reduce torque ripple were found and these values used to extract the table rule. The block diagram of FLC is shown in Fig. 85.4. The fuzzy rules employed are shown in the Table 85.1. Here for the inputs, we use triangular/trapezoidal membership functions in order to reduce the computational burden.

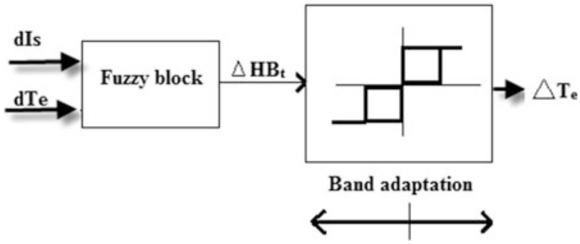

Fig. 85.4 Torque hysteresis controller adapted band

Table 85.1 Fuzzy rules of torque hysteresis controller

FIS	dT_e	NH	NL	ZE	PL	PH
dI_s	ΔHB_t					
N		NH	NH	ZE	PL	NH
Z		NH	NH	ZE	PH	PH
P		NH	NL	ZE	PH	PH

However, Gaussian membership functions are chosen for the output so that the hysteresis bandwidth will be changed smoothly.

The motor mechanical equation, neglecting the friction coefficient, can be written as

$$T_e - T_L = J\frac{d\omega r}{dt} \tag{85.12}$$

The above equation leads to the conclusion that reducing the motor torque ripples directly reduces the motor speed ripple as well.

Here shown in the Table 85.1 represents the fuzzy inference table, where the linguistic variables will be assigned as PH: positive high, NH: negative high, PL: positive low, NL: negative low, ZE: zero error, the input variables are $dTe_{,}$ dI_s and the output variable will be the crisp output $\Delta HB_{t.}$

85.5 Simulation Results

The performance of the proposed FLC-based DTC scheme for IM drive has been investigated extensively at different operating conditions. Sample simulations results are presented below. The Figs. 85.5 and 85.6 show the various IM drive responses for step change in motor load from 4 to 12 N m. The change in load is applied at a time of 0.3 s. Figure 85.5 shows the simulated speed response of the conventional and the proposed DTC schemes, where it is clearly found that the speed ripples are negligible in the proposed work as compared to the conventional. The average speed ripples with the conventional DTC scheme are approximately 0.05 RPM, respectively. The Fig. 85.6 presents the corresponding torque response of the two DTC schemes. It can be compared that, in the steady state, the torque

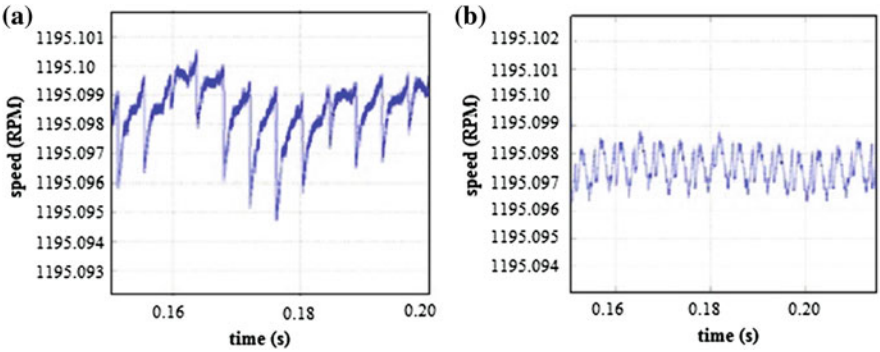

Fig. 85.5 Steady-state speed responses of the IM drive for a step change in load from 4 to 12 N m at 0.8 p.u (RPM). **a** Conventional DTC. **b** FLC-based DTC

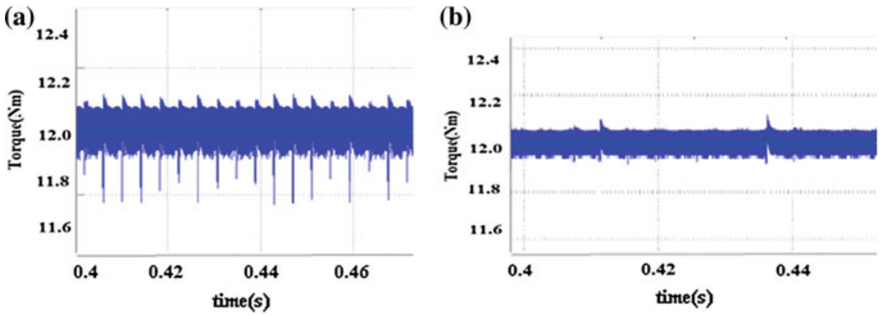

Fig. 85.6 Developed torque responses of the IM drive for a step change in load from 4 to 12 N m at speed of 0.8 p.u (RPM). **a** Conventional DTC. **b** FLC-based DTC scheme

ripple in the conventional scheme is approximately 0.1 N m while, in the proposed scheme, it is only 0.05 N m, which proves the superiority of the proposed DTC scheme over the conventional one.

85.6 Conclusion

Here FLC-based DTC scheme for IM drive has been presented in this paper. This controller optimizes the desired amplitude of torque hysteresis band to improve the dynamic performance. It is shown that the proposed scheme results in improved performance with optimal torque ripple and speed responses under steady state condition. Comparative results show that the torque ripple of the proposed drive has considerably been reduced. The dynamic speed response of the proposed FLC-based DTC scheme has also been found better as compared to the conventional DTC scheme.

References

1. Chen CC, Bouscayrol A, Chen K (2010) Electric, hybrid, and fuel-cell vehicles: Architectures and modeling. IEEE Trans Veh Technol 59(2):589–598
2. Blaschke F (1971) A new method for structural decoupling of AC induction machines. In Conference Rec IFAC, Duesseldorf, Oct 1971, pp 1–15
3. Takahashi I, Noguchi T (1985) A new quick-response and high-efficiency control strategy for an induction motor. In Conference Rec IEEE IAS Annual Meeting, pp 495–502
4. Zhang Y, Zhu J (2011) Direct torque control of permanent magnet synchronous motor with reduced torque ripple and commutation frequency. IEEE Trans Power Electron 26(1):235–248
5. Casadei D, Serra G, Tani A (1998) Improvement of direct torque control performance by using a discrete SVM technique. In Proceedings of 29th Annual IEEE Conference on Power Electronics Specialist Record, 1998 (PESC 98) vol 2 (17–22 May 1998) pp 997–1003

6. Buja GS, Kazmierkowski MP (2004) Direct torque control of PWM inverter-fed AC motors—a survey. IEEE Trans Ind Electron 51(4):744–757
7. Fowkes AE (1993) Hardware efficient algorithm for trigonometric functions. IEEE Trans Comput 42(2):235–239
8. Abdul Wahab HF, Sanusi H (2008) Simulink model of direct torque control of induction machine. Am J Appl Sci 5(8):1083–1090
9. Casadei D, Grandi G, Serra G, Tani A (1994) Effects of flux and torque hysteresis band amplitude in direct torque control of induction machines. Proc IEEE IECON 1:299–304
10. Lee CC (1990) Fuzzy logic in control systems: fuzzy logic controller—Part I. IEEE Trans Syst Man Cybern 20(2):404–418

Chapter 86
A Mobile Based Novice Detection of Driver's Fatigue Level and Accident Reporting Solution

Jay Lavanya and R. Essaki Raj

Abstract The lives are made easier because of rapid growth of technology and infrastructure. The technology has increased, so the road accident take place frequently which causes huge loss of life and property because of the poor emergency facilities so this project deals with intelligent car system which is used to provide critical information of real time situations such as accidents and fatigue disorders. The status of the victims such heart rate is determined using sensor and GPS sends accident location coordinates by message to the rescue team with the help of the GSM module. This will help to reach the rescue service in time and save the valuable human life. Fatigue symptoms are also determined by eye blink sensor which continuously monitors the iris if it is not recognised for more than 5 s then the driver is sleepy, in that case a buzzer is operated and the speed of the vehicle is controlled automatically. If the driver is found to have alcohol in the breath, it warns by buzzer and then turns the ignition off. Proteus software is used here do the simulation where all sensors are coordinated with the ARM processor and the simulation is done. It is found to be accurate, robust and reliable.

Keywords Driver safety · ARM 7 · Sensors · GSM technology · GPS receiver

86.1 Introduction

Every year, vehicular accidents cause generous waste of money and loss of human lives. The proposed system will automatically identify the accident, then immediately transmit the location of the accident and the status of the physiological

J. Lavanya (✉) · R. Essaki Raj
Rajalakshmi Engineering College, Chennai, Tamil Nadu, India
e-mail: lavanyajaychandran@gmail.com

R. Essaki Raj
e-mail: essakiraj.r@rajalakshmi.edu.in

C. Kamalakannan et al. (eds.), *Power Electronics and Renewable Energy Systems*,
Lecture Notes in Electrical Engineering 326, DOI 10.1007/978-81-322-2119-7_86

parameters of the victim's heartbeat to the emergency care centre phone number through short message service [1].

Accelerometer senses the collision of the vehicle and sends the information to a hospital. Real time vehicular tracking system incorporates a hardware device installed in the vehicle. The location information is sent to server using GSM by SMS [2]. Tracking server also has GSM modem that receives vehicle location information, stores the information and it is available to authorized users of the system [3].

Microcontroller is the Central Processing Unit which has an In-Vehicle unit whose all operations are controlled by the microcontroller. These instructions are provided to microcontroller by writing the software into flash memory and perform the action as required by instruction [4].

Driver drowsiness is one of the major causes of traffic accidents to detect fatigue symptoms in drivers and control the speed of vehicle to avoid accidents [5]. Designing of an eye blink sensor which continuously monitors the iris if it is not for more than 5 the driver is sleepy, in that case a buzzer is operated. In fatigued state, the eye blink frequency increases beyond the normal rate. The fraction of periods of sleep lasts for 3–4 s which are the good indicator of the fatigued state [6].

Real time sensors like gas, eye blink, alcohol, impact sensors are used. MQ-3 gas sensor has high sensitivity to Alcohol. This sensor is used to detect alcohol. If the driver is found to have alcohol in the breath, it warns and then turns the ignition off. The system assumes very little processing and communication requirements on the sensor [7, 8].

86.2 Block Diagram

(Figure 86.1).

86.3 Overall Design of the System

The vehicular system (VS) includes hardware that consists of an ARM 7 TDMI core processor, Accelerometer, Eye blink sensor, Alcohol sensor, Heart beat sensor, GPS module, GSM module, l6 × 2 LCD. The 5 V dc regulated power supply is used for whole VS to work. The UART1 of ARM processor is the GPS receiver module that is to be interfaced to provide speed and location information. All this information are shown on LCD that is interfaced with a GPIO and send it to a care centre by GSM module wirelessly that is interfaced with UART0 of ARM processor. The module requires GSM SIM (Subscriber Identity Module). The event is stored in a program and when collision/accident occurs that is sense by an Accelerometer which is interfaced to ADC0 of ARM processor.

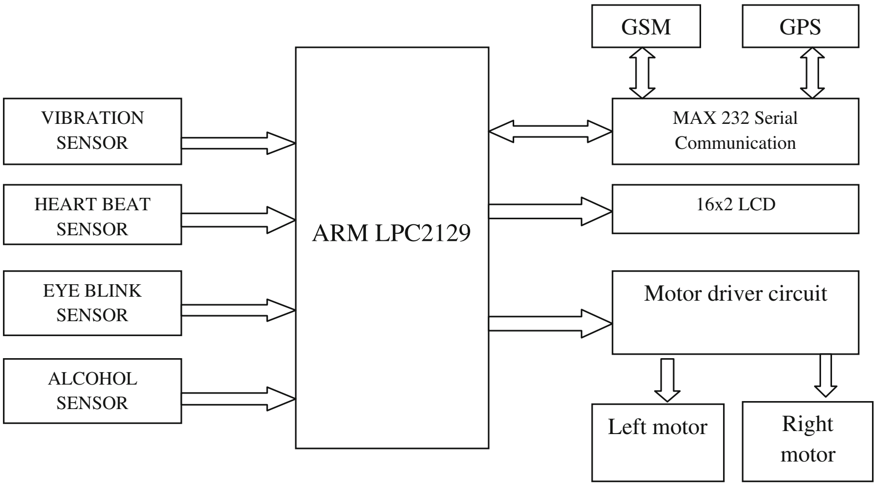

Fig. 86.1 Architecture of the accident identification and reporting system

86.4 System Architecture

86.4.1 Alcohol Sensor

The system is started and it gets displayed on the LCD monitor. If the driver has consumed alcohol it is detected by MQ-3 sensor. When the alcohol content is sensed it stops the engine and will not start until the value comes to predefined limit. This unit can be easily incorporated into an alarm unit to sound an alarm or give a visual indication. This sensor is placed near to steering wheel to analyze the alcohol content in driver's breath.

86.4.2 Eye Blink Sensor

The eye-blink sensor works by illuminating the eye with infrared sensor CNY 70 on the iris if it is not detected for 5 s then the driver is sleepy. If any abnormal situation arises the vehicle is stopped with an alarm indication.

86.4.3 Accident Identification Module

Then the vibration sensor works when the vehicle is collided with any obstacle it detects whether the vibration is within the range of 23 km/h or not, if it is sensed then it waits for 15 s to confirm the accident. If the driver presses the switch then the driver is safe or else the geographical coordinates are transmitted to care centre. For this operation the impact sensors are placed in front and sides of the vehicle. After the accident has occurred the live, accurate heart rate is determined by the speed of the blood, the emergency situation is determined after the accident and it is alerted. It is placed in the seat belt provided in the vehicle. The signal from the heart is fed to the GPS unit, both low and high unusual heart rate is transmitted to the care unit.

86.4.4 ARM Processor

The conventional 8 and 16 bit Microcontrollers has its deficiencies when compared with 32 bit microcontroller. ARM architecture uses Reduced Instruction Set Computer (RISC). The instruction set are much simpler than those of micro programmed Complex Instruction Set Computers which results in a high instruction throughput and fast real-time interrupt response. The Philips LPC2148 32 bit ARM7 TDMI core supports real time simulation. When ARM processor used with RTOS timing constraint can be realized for the data acquisition and transmission of data with high precision.

86.4.5 GSM Module

Interfacing of GSM module with ARM Processor on UART1 Global System for Mobile communications (GSM) is the most popular wireless standard for mobile phones. GSM module allows transmission of Short message service (SMS) in two modes: TEXT mode and PDU mode. The design uses SIM 300 GSM module in text mode that provide 900/1800/1900 MHz Tri-band. The module operates on AT (Attention Command) command over TTL interface. The abbreviation AT is always used to start a command line to be send from TE (Terminal Equipment) to TA (Terminal Adaptor). The information contains speed, longitude, latitude, of the vehicle that is transmitted to the monitoring station by the SMS through the GSM. The Module works on 12 V, 2 A power supply and is configured at 9,600 baud rate.

86.4.6 GPS Module

Global Position System (GPS) is a space-based satellite navigation that provides location and time information anywhere on or near the Earth. Cirocomm uses GPS Receiver MT3318 Module which is used to have an active patch antenna which tracks 51 satellites simultaneously. The module is mounted on the PCB along with the 3.3 V low drop voltage regulator, transmit, receive and power indication LEDs, Schmitt trigger based buffer for 5–3.3 V. The GPS receiver gives −157 dBm tracking sensitivity. The module is configured at 9,600 baud rate. Module requires a 5 V supply and can be interfaced with the 5 V TTL/CMOS logic.

86.5 Simulation Results

The schematic representation of the Accident Reporting System is designed by using the Proteus software and the code is done through compiler software. Here the result is represented as eight figures, (1) Normal condition (Fig. 86.2), (2) Alcohol consumed state (Fig. 86.3), (3) Driver fatigue condition (Fig. 86.4), (4) Accident occurred state but the driver is safe (Fig. 86.5), (5) Severe accident has occurred (Fig. 86.6), (6) Heart rate of the victim is high (Fig. 86.7), (7) Heart rate of the victim is low level (Fig. 86.8). The representation of figures are shown below.

86.6 Results and Comparisons

This paper gives a different way of approaching the problem. The accident location can be located easily and the detection of accident is precise unlike the prior approaches. In this approach the accident is detected by the vibration sensor and

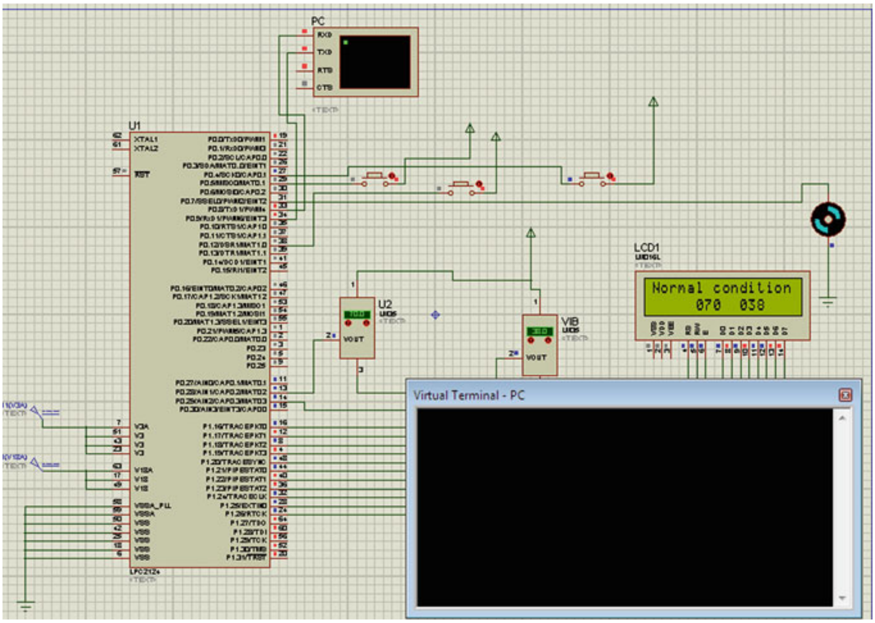

Fig. 86.2 Normal condition of the vehicle system

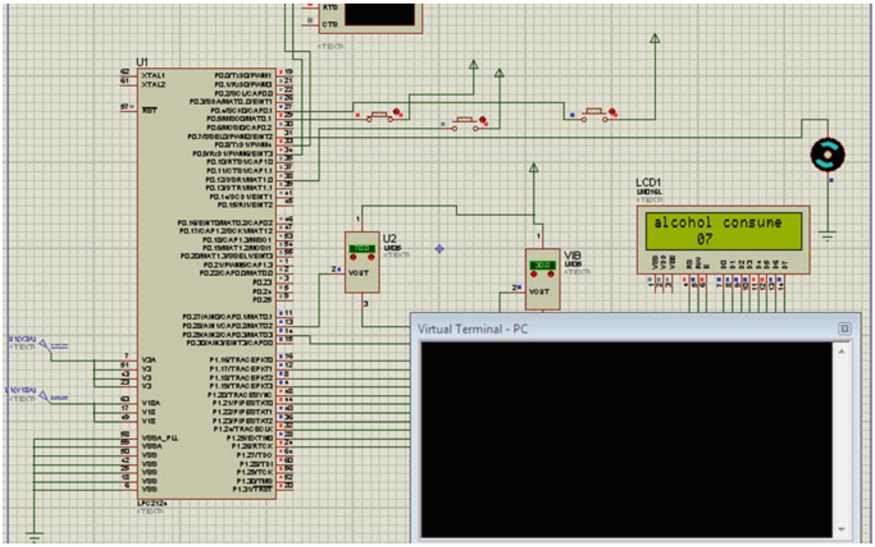

Fig. 86.3 Status indicating the alcohol consumption of driver

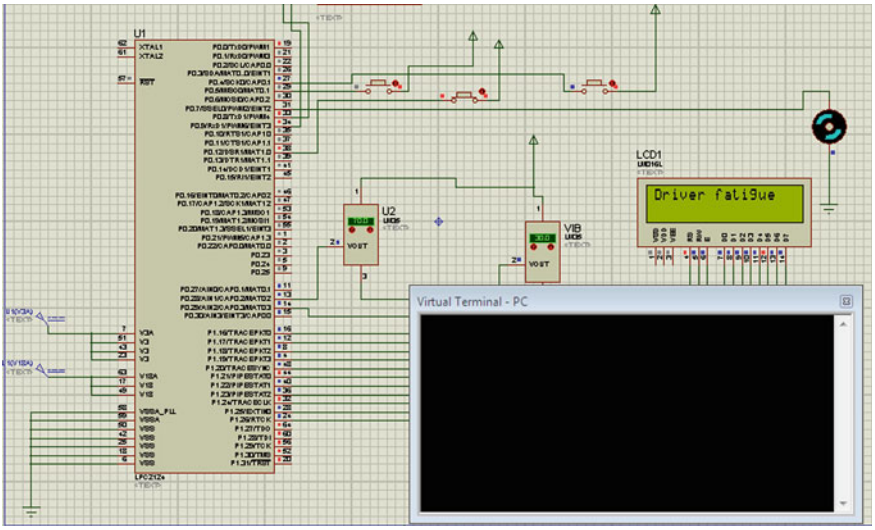

Fig. 86.4 Status indicating the driver fatigue condition

there is an alternative way provided to stop the whole process of messaging through a switch. Whereas the other approaches provide only one way of detecting the accident. Hence this paper has an edge over the other earlier approaches.

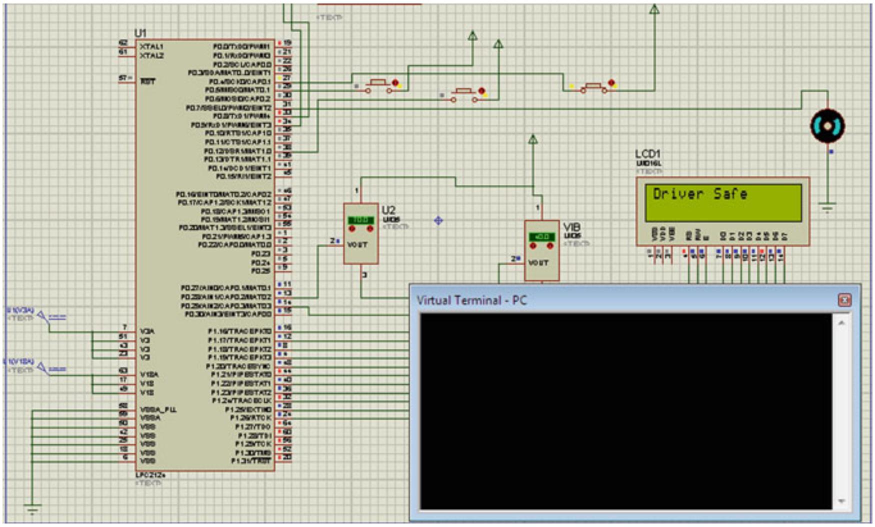

Fig. 86.5 Status of the driver that he is in safe condition after the accident

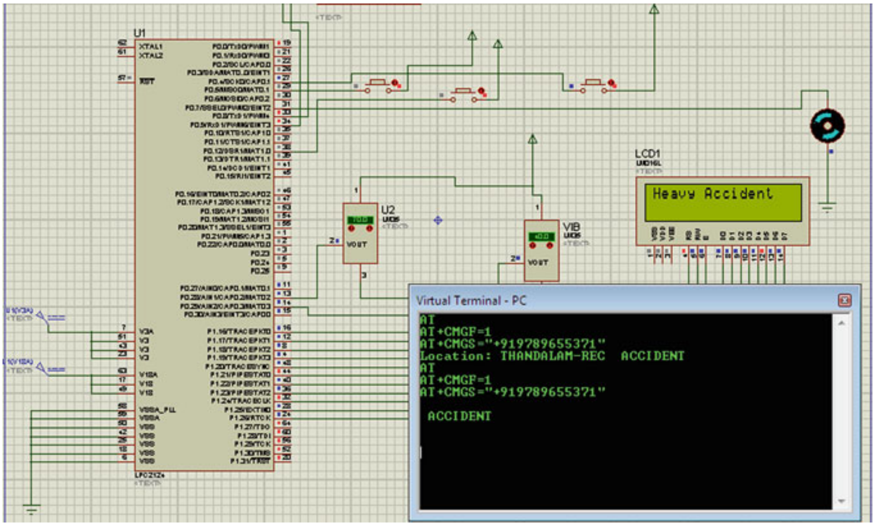

Fig. 86.6 Status of the system when heavy accident is determined

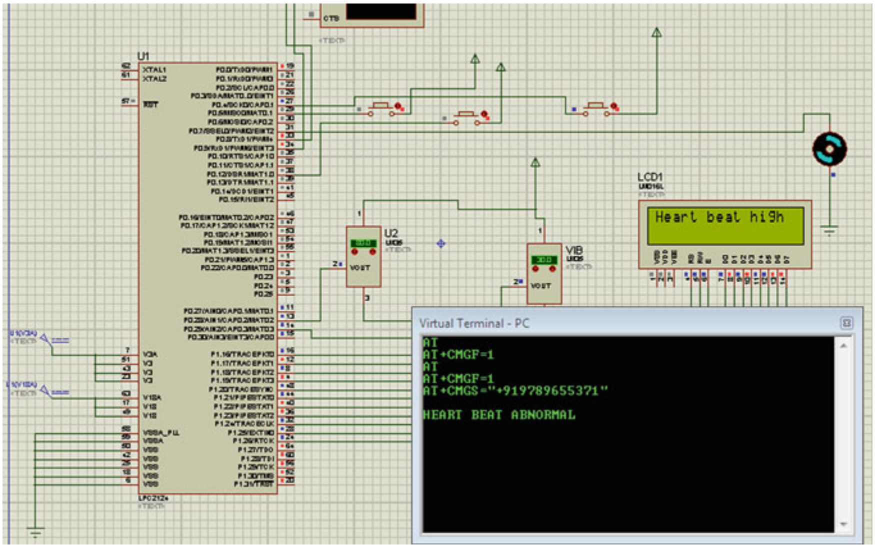

Fig. 86.7 Status of the victim's heart rate when it is high

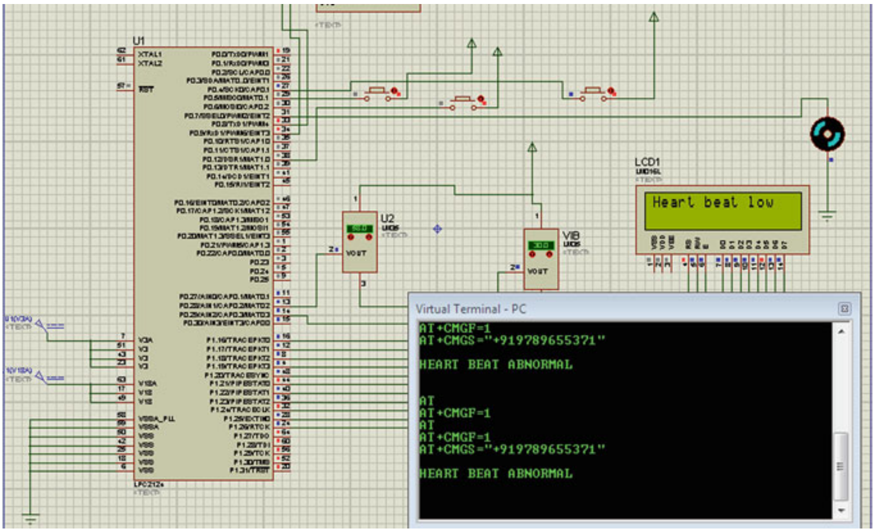

Fig. 86.8 Status of the victim's heart rate when it is low

86.7 Conclusion

With the advent of science and technology in every walk of life the importance of vehicle safety has increased and the main priority is being given to reduce the alarming time when an accident occur, so that the rescue team can attend the wounded lives in lesser time. The design provides low cost, portability, small size and easy expansibility. The Vibration sensor, GPS and GSM interfacing with ARM platform shortens the alarm time to a large extent and locate the site of accident frequently. The system overcomes the problem of lack of automated system for accident detection. The searching time of the location is reduced and the person can be treated as soon as possible. The controller will process the data, as soon as input is received, the alarm is ON and message is sent through the GSM module. The latitude and longitudinal coordinates and the accident site are detected by the GPS module. An alternate solution is done by pressing a switch to interrupt the system from sending the message in case of no casualty; this will help to save time of medical rescue team and unnecessary alarming in unusual conditions. The automatic detection of accident location will help us to provide security to the vehicles and to the lives of the people. Here the accident determining sensors are used to determine the abnormal condition of driver. Therefore, the paper provides a feasible and easy solution to traffic hazards and it gives security to vehicle and reduces loss of valuable lives and property.

References

1. Bhumkar SPB, Deotare VV, Babar RV (2012) Intelligent car system for accident prevention using ARM-7. Int J Emerg Technol Adv Eng
2. Kodavati B (2012) GSM and GPS based vehicle location and tracking system. Int J Eng Res Appl
3. Ariffin AAB, Aziz NHA, Othman KA (2011) Implementation of GPS for location tracking. IEEE Control Syst Grad Res
4. Simoes ND, Goncalves JL, Caciro ML, . Boavida ML, Cardoso FD (2011) Zigbee/GPS tracking system for rowing races
5. Zhang W, Cheng B, Lin Y (2012) Driver drowsiness recognition based on computer vision technology. TSINGHUA Sci Technol
6. Varma AR, Arote SV, Bharti C (2012) Accident prevention using eye blinking and head movement. Int J Comput Appl
7. Chandrasekaran SS (2013) Automated control system for air pollution detection in vehicles. IEEE Trans
8. Gurram SK, Conrad JM (2011) Implementation of can bus in an autonomous all-terrain vehicle. IEEE Trans

Chapter 87
Analysis and Position Control of Switched Reluctance Motor Drives by Using Fuzzy Logic

K.S. Srikanth, L.V. Narasimha Rao, D. Ravikrishore, K. Naresh and V. Ramesh

Abstract This paper presents modeling, simulation of Switched Reluctance motor. A Matlab/Simulink environment to simulate switched reluctance motor is described. The SRM drive operates over the entire speed range and provides low torque ripple. This low torque ripple is achieved by controlling the firing angles through simple formulas so as to minimize the current pulses in the commutation region. The smooth transition is attained since the conditions that determine the firing angles of one operating mode are derived from the conditions of the other operating mode. This is important since the position precision is highly influenced from the motor torque ripple. For obtaining better torque ripples we used Advanced proportional–integral and Fuzzy controllers. And also A gain-scheduling technique is used for providing high dynamic performance and precise position control.

Keywords Switched reluctance motor · Fuzzy controllers · Proportional–integral · TSF method

K.S. Srikanth (✉) · L.V. Narasimha Rao · D. Ravikrishore · K. Naresh · V. Ramesh
Department of Electrical and Electronics Engineering, K L University, Greenfields, Vaddeswaram, India
e-mail: Sri_anth.dsd@gmail.com

L.V. Narasimha Rao
e-mail: Lvnrao1964@gmail.com

D. Ravikrishore
e-mail: dravikrishore@gmail.com

K. Naresh
e-mail: knaresh@kluniversity.in

V. Ramesh
e-mail: sitamsramesh@gmail.com

C. Kamalakannan et al. (eds.), *Power Electronics and Renewable Energy Systems*, Lecture Notes in Electrical Engineering 326, DOI 10.1007/978-81-322-2119-7_87

87.1 Introduction

The last years and several papers have been published introducing the Switched Reluctance Machines (SRMs) as a strong-candidate [1]. The SRM can operate as a motor as well as a generator by adjusting the firing angles. At low speeds, the torque is limited by the current which is controlled either by voltage-PWM or current regulation (PWM mode). At high speeds, the available voltage is insufficient to regulate the current and the torque is controlled by the duration of the current pulses (single pulse mode). Although the SRMs have some very attractive characteristics, their acceptance by the industry for variable speed applications is very slow. The torque ripple remains a serious problem for servo drive applications. Significant effort has been made over the past decades to overcome this problem by improving the magnetic design of the machine or by introducing sophisticated control techniques. In recent years, SRMs have attracted renewed interest due to the tendency to shift from the complex design and precise manufacturing to the highly effective and more sophisticated control [2]. The improvement in control algorithms and techniques can extract good performance from a simple SRM drive and result in increasing the penetration of the SRM drives in highly demanding applications [3]. This can give new trends in motor drive applications and open new horizons in the existing field of advanced motor drive engineering. In the problem of rotor position sensing has been investigated, and several sensor less control techniques for speed control operation have been proposed. Basic four-quadrant sensor less configurations for SRM drives have been described curves is not required. The optimization criteria of TSF for torque-ripple reduction in SRM, providing the low copper losses with acceptable drive performance, are discussed in this paper [4]. The novel, well adapted to the low copper losses, family of TSFs is proposed. Each TSF from the family provides that the phase currents flow through the whole region where positive torque production is possible. Several simulation results from a SRM drive model developed in Simulink environment are presented to validate the theoretical.

87.2 SRM Operating Principles

The optimization criteria of TSF for torque-ripple reduction in SRM, providing the low copper losses with acceptable drive performance, are discussed in this paper. The novel, well adapted to the low copper losses, family of TSFs is proposed. Each TSF from the family provides that the phase currents flow through the whole region where positive torque production is possible.

The voltage equation for each phase j is given by

$$\mathrm{uj} = \mathrm{Rjij} \; + (\mathrm{d}\lambda\mathrm{j}(\mathrm{i}, \theta))/\mathrm{dt} \tag{87.1}$$

and the rate of change of the flux linkage, at constant speed, is

$$\frac{d\lambda_i}{dt} = \frac{\partial \lambda_i}{\partial i}\frac{d_i}{dt} + \frac{\partial \lambda_i}{\partial \theta}\omega_r = \mathrm{Lj}(\mathrm{i},\ \theta)\frac{d_i}{dt} + \mathrm{e_j} \tag{87.2}$$

where $Lj(i, \theta) = \partial\lambda j/\partial i$ is the incremental inductance (slope of the magnetization curve at the position θ), e_i is the back electromotive force (EMF), u_j is the applied voltage, ij is the phase current, $\mathbf{R_i}$ is the winding resistance per phase, λj is the phase flux linkage, and θ is the mechanical angle (87.1).

The electromagnetic torque for SRM is produced by each phase is given defined by

$$\mathrm{Tj}(\mathrm{i}, \theta) = \frac{\partial Wej(i, \theta)}{r\theta} \quad \text{where i is constant} \tag{87.3}$$

where

$$\mathrm{W}_{\mathbf{ci}} = \int_0^i \lambda j(e, \theta) \quad \text{where is } \theta \text{ is constant} \tag{87.4}$$

The total electromagnetic torque is obtained by the sum of the individual phase torques of all three phases

$$\mathrm{Te} = \sum_{j=1}^{m} \mathrm{Tj}(\mathrm{i}, \theta) \tag{87.5}$$

where m is the number of SRM phases (87.5).

In the most popular control approaches for torque-ripple minimization, the static T-i-θ characteristics are stored in 3-D lookup tables. During the motor operation, these data are used to determine the command current for each phase from the information of the rotor position and the torque requirement. The magnetic nonlinearities of the machine can be taken into account through the appropriate modeling of the nonlinear flux–current–angle (λ−i−θ) characteristics.

87.3 Defining the Turn-on and Turn-off Angle Conditions for Smooth Torque Control

TSF method provides a low torque-ripple operation of an SRM drive. However, the copper losses in an SRM drive depend on the type of TSF (i.e., choice of f_{rise} and consequently f) and TSF parameters such as angles θ_{on}, θ_{off}, and θ. As the copper losses are directly related to the drive efficiency and drive torque capability, the type and parameters of TSF should be carefully chosen. Furthermore, the choice of TSF affects the range of speed with acceptable low torque-ripple and also the peak phase current requirement (Fig. 87.1).

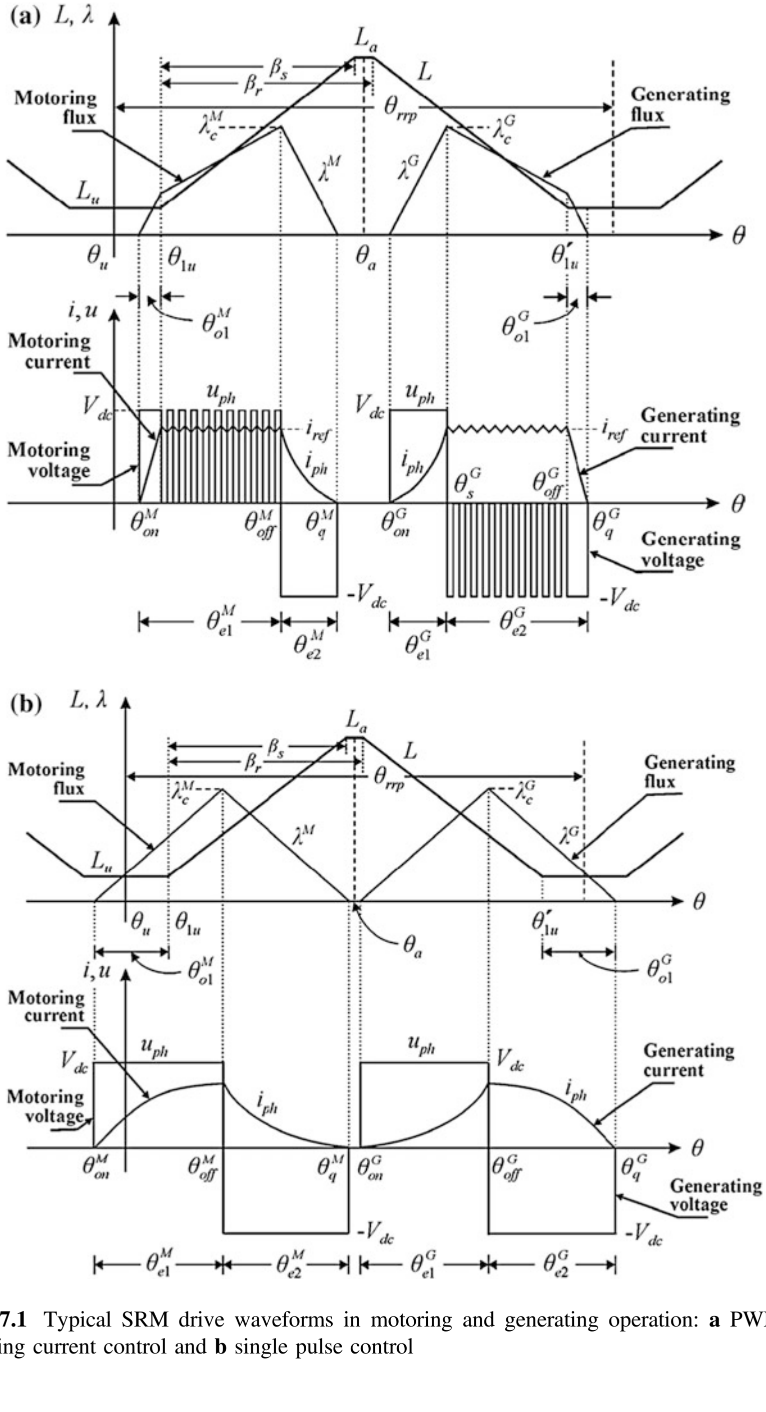

Fig. 87.1 Typical SRM drive waveforms in motoring and generating operation: **a** PWM soft chopping current control and **b** single pulse control

87.4 Design and Implementation of the Control System

The feedback system with the speed and position controllers is shown in Fig. 87.2. The transfer function Gp(s) represents the SRM and the power converter. In the speed PI controller, an anti windup protection is used in order to avoid low-frequency oscillations that may lead to instability. This is realized by applying inner negative feedback to the integral action of the controller. The Simulink diagram of

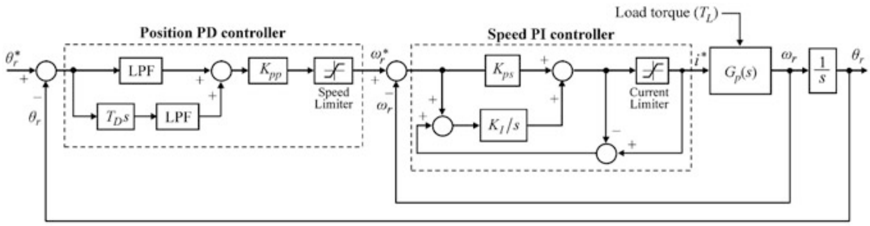

Fig. 87.2 Model configuration of the advanced speed and position controllers

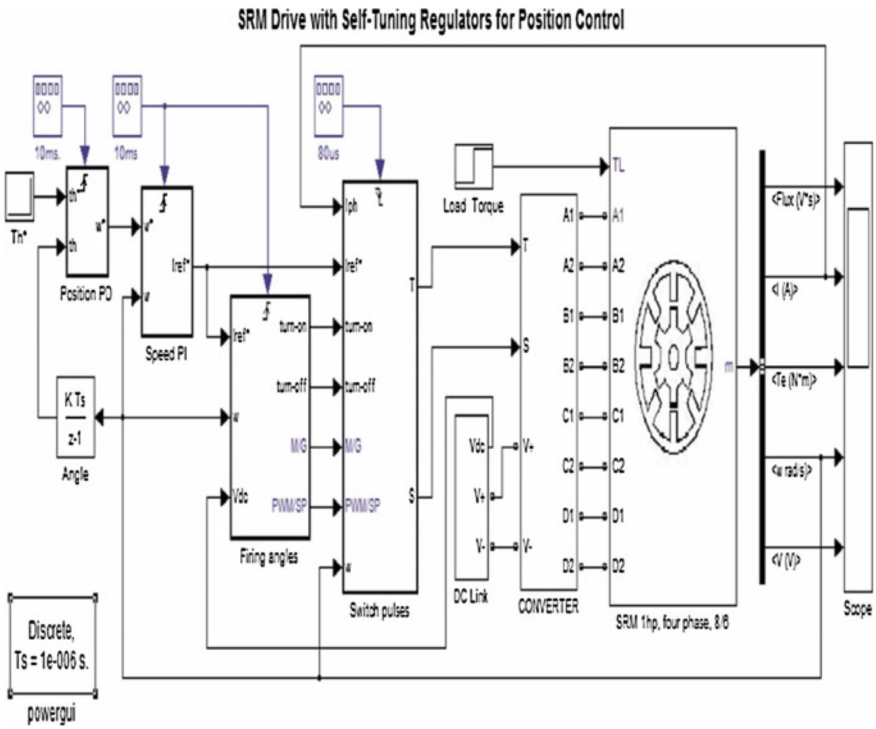

Fig. 87.3 Simulink diagram of the SRM drive with advanced speed PI and position PD controllers

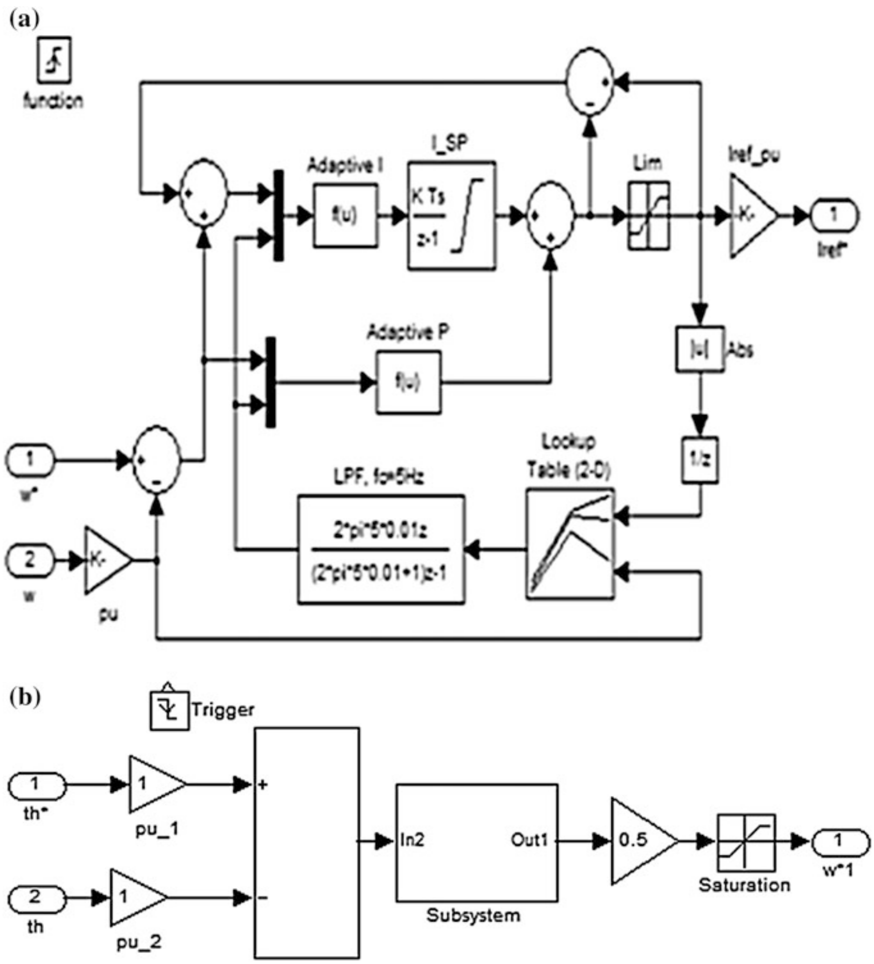

Fig. 87.4 **a** Speed PI control. **b** Fuzzy PD control

the SRM drive that is used in simulations is shown in Fig. 87.3. The same controller model, in combination with the I/O interface blocks provided by the board supporting software, was used for programming the DSP controller board. Figure 87.4a and b shows the Simulink diagrams of the advanced speed and fuzzy position controllers of the SRM drive, respectively. The block "Firing angles" determines the command turn-on and turn-off angles, i.e., (θ^*_{on} and θ^*_{off}), respectively, through the conditions presented in Sect. 87.3. The block "Switch pulses" generates the control pulses for the SRM power converter switches. In the low-speed region, the phase current is regulated by a hysteresis-band PWM control technique. The block "Speed PI" determines the reference phase current i^* through the speed error $(\omega * r - \omega r)$. The gains KI and Kps of the PI controller are online adapted.

87.5 Simulation Results

The simulation is done for an 8/6 SRM drive was used to validate the developed position control system. Figure 87.5 shows the variation of torque ripple factor as defined by ripple coefficient

$$\mathbf{K_{rip}} = \frac{t_{\max} - t_{\min}}{T_{\text{avg}}} \tag{87.6}$$

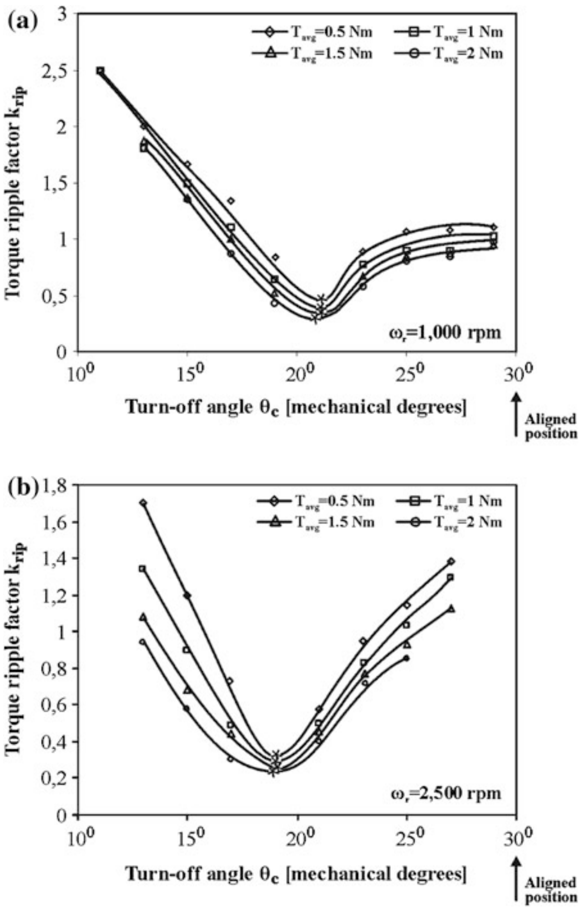

Fig. 87.5 Variation of torque ripple factor, as defined in Chap. 29, for various speeds and load torque values, in a four-phase 1-hp 8/6 SRM-drive. **a** PWM operation. **b** Single-pulse operation

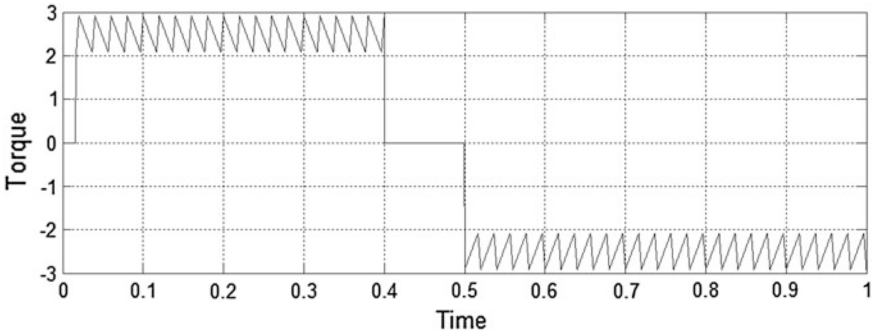

Fig. 87.6 Torque graph when it changes from Motoring mode to Breaking mode

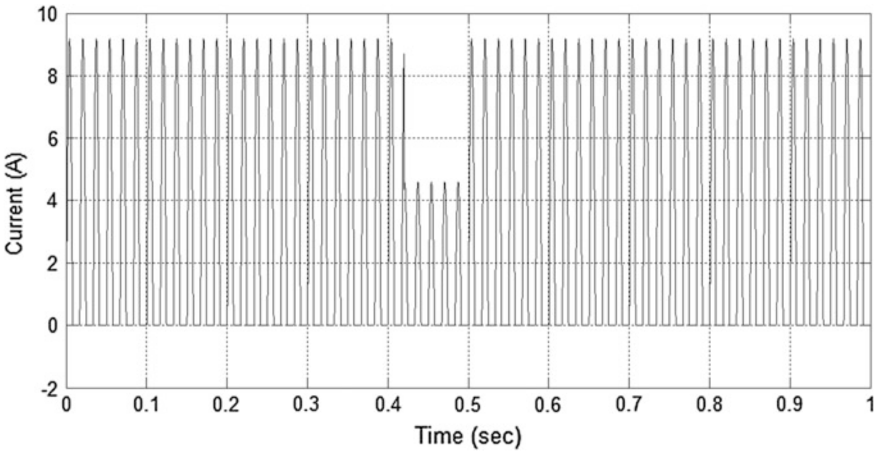

Fig. 87.7 Current graph when it turns from motoring to braking operation

where T_{min} and T_{max} are the minimum and maximum instantaneous torques, respectively, for each given SRM speed, while T_{avg} is the average torque. Figure 87.5a corresponds to a PWM operation, while Fig. 87.5b corresponds to a single-pulse operation. All points noted by asterisk correspond to operating points obtained with the firing angle conditions of Sect. 87.3. It can be seen that, in these points, minimum torque ripple is achieved (Figs. 87.6, 87.7, 87.8, 87.9, 87.10, and 87.11; Table 87.1).

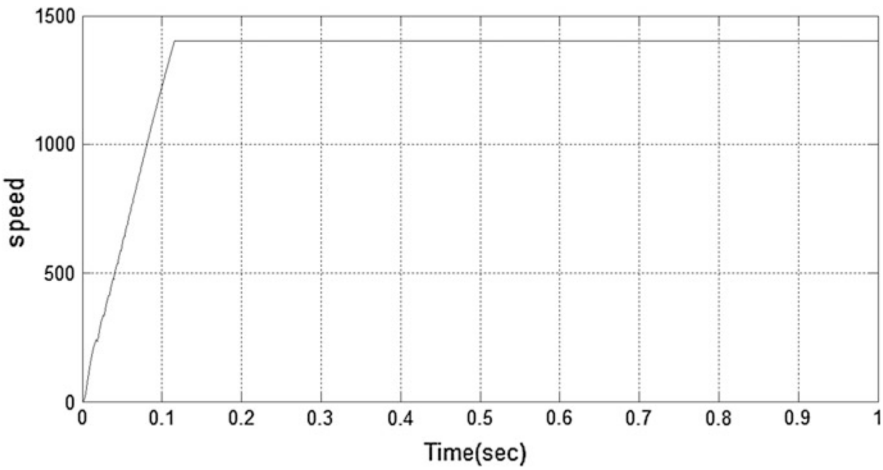

Fig. 87.8 Speed graph

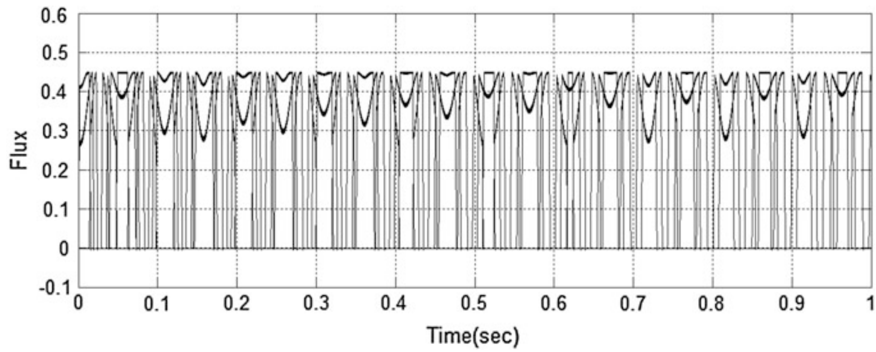

Fig. 87.9 Flux graph

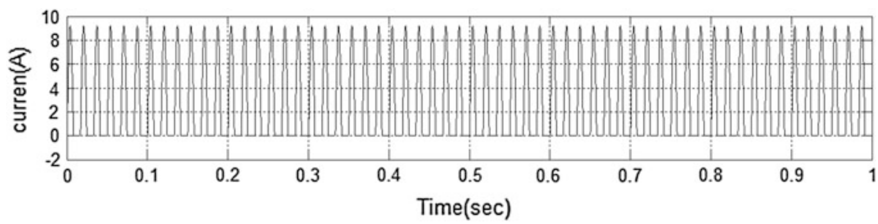

Fig. 87.10 Current in motoring operation

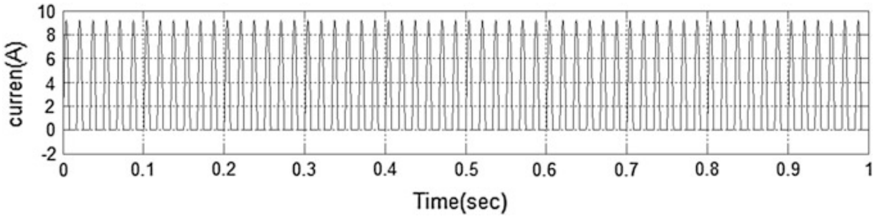

Fig. 87.11 Current in breaking operation

Table 87.1 Four-phase 1-hp 8/6 SRM

Output power 1-hp at 4,000 rpm (motoring operation)	
Inertia 0.0004 kg m^2	
$m = 4$	$\beta_s = 23°$
$N_s/N_r = 8/6$	$\beta_r = 23.4°$
$\theta_{rrp} = 2\pi/N_r = 60°$	$R_{ph} = 1.3\ \Omega$
$L_a = 52.7$ mH	$L_u = 9.1$ mH

87.6 Conclusion

In this paper, the procedure for optimization of TSFs for reduction of torque ripple is described. The simple SRM model is used to identify the optimal parameters of TSF in order to provide the torque-ripple minimization with maximal SRM drive efficiency and retaining an acceptable torque-speed capability. In addition, a novel family of TSFs that can simultaneously be concerned with operating efficiency, peak phase current, and torque-speed capability has been proposed. The two optimal TSFs have been extracted from the family: one intended to maximize the theoretical torque-ripple-free speed range, and the other one intended to maximize torque-speed capability of the SRM drive several simulation results are presented to validate the feasibility of the proposed control scheme.

References

1. Mademlis C, Kioskeridis I. Gain-scheduling regulator for high-performance position control of switched reluctance motor drives
2. Mademlis C, Kioskeridis I. Four-quadrant smooth torque controlled switched reluctance machine drives. In: Proceedings
3. Pan J, Cheung NC, Yang J (2005) High-precision position control of a novel planar switched reluctance motor. IEEE Trans Ind Electron 52(6):1644–1652
4. Husain I, Ehsani M (1994) Error analysis in indirect rotor position sensing of switched reluctance motors. IEEE Trans Ind Electron 41(3):301–307

Chapter 88
Assessment of Six Phase Synchronous Generator Using Fuzzy Controller

N. Rathika, A. Senthil Kumar and S. Rahul

Abstract This paper describes the Matlab/Simulink model of Six Phase Synchronous Generator and the exploration of Fuzzy controlled synchronous generator united to a wind turbine for diverse renewable energy generation. It has portrayed that the synchronous generator is well suited to supply two three phase loads which are independent in operation. Fuzzy Controller is implemented to control the output of Synchronous generator. Various resistive loadings are taken and evaluated the controller output.

Keywords Six phase synchronous generator (SPSG) · Renewable energy generation · Fuzzy controller

88.1 Introduction

Although three-phase electric machines are still leading in number in industrial applications, machines with more than three phases can provide more settlement in some applications, such as lower per-phase current rating, current ripple, torque pulsation, dc-link voltage ripple, and higher reliability [1], which are particularly smart for high power applications. Alternate energy sources are typically located in isolated areas where utility supply is not available or is frequently interrupted, thereby frequently placing the energy source in isolation to supply the load. Such situation requires that alternate energy power generating system perform the voltage

N. Rathika (✉) · S. Rahul
SKP Engineering College, Tiruvannamalai, Tamilnadu, India
e-mail: n_rathikaa@yahoo.co.in

S. Rahul
e-mail: rahulsatheesh21@yahoo.com

A. Senthil Kumar
Velammal Engineering College, Chennai, Tamilnadu, India
e-mail: vastham@gmail.com

C. Kamalakannan et al. (eds.), *Power Electronics and Renewable Energy Systems*,
Lecture Notes in Electrical Engineering 326, DOI 10.1007/978-81-322-2119-7_88

regulation function by providing a source not only for real power to the load but also reactive power. It is well known that an induction machine may generate voltage if capacitor is connected to its stator terminals while its rotor is driven by a prime mover [2]. With the development of high power devices, synchronous machine are supplied by voltage source inverter. But the limitations on the gate-turn-off lead to the high current and torque ripple. To overcome this problem, synchronous machine has fed by multilevel inverter. Another way is to apply the power segmentation on both inverter and machine. The most common structure consist in using of double star synchronous machine whose winding are spatially phase shifted by 30°, supplied with source voltage inverters.

Six phase synchronous machine possess several advantages over conventional three phase. These include increasing the inverter output power, reducing the amplitude of torque ripple, lowering the dc link current harmonics and improve the reliability; the motor can start and run since the loss of one or many phase. Many industry segments today are increasingly asking for medium-large motor solutions with traditional demands of high efficiency, high power density, reliability and superior control aspects for variable speed operations along with a new demand of redundancy. In recent times, because of several benefits of multi-phase AC machine, interest has re-emerged in the usage of multiphase generators in combination with different prime mover systems [3]. The research in this area is still at an early stage although the findings reported in the available literatures indicate general feasibility of multi-phase machines for various generating systems [4]. Modern work shows the possibility of SPSG for standalone renewable energy system in aggregation with hydro power plant [5]. Synchronous Generator is tied with converter system for most of the solicitation purposes, further it is fed into dc system. Operational modes are the factors which enviable the huge pulse count in the derivation of dynamic mediocre models [6]. It signposts that it is proficient of Supplying supplementary power in the same edging [7, 8]. Systematic scrutiny has been conceded to evaluate the transient and dynamic performance of the machine [9, 10].

88.2 Mathematical Model of the SPSG

Two sets of three-phase windings (with displaced coils of 120° between) are provided to build the desired six phase synchronous generator. These two arrangements are displaced by 30°. The internal structure presents two sets of three-phase windings, branded as *abc* and *xyz*, correspondingly. Figure 88.1 signs the constructive standard of the machine under exploration. The reference axes *abc*, *xyz* and the *dq* reference are represented in the Fig. 88.1. To attain the representative expressions for the machine, the first step comprises of ruling the equations for the inductances. These must take into account the magnetic coupling between each pair of windings and that dependent on the rotor position for salient pole machines.

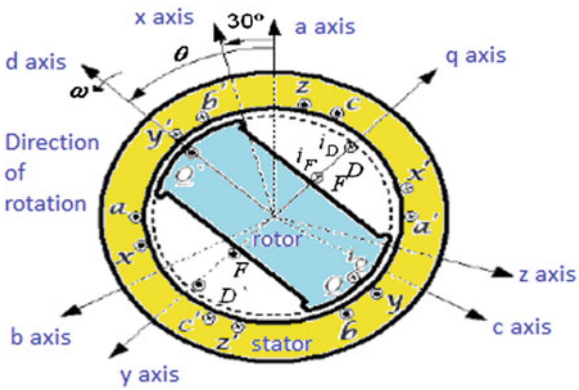

Fig. 88.1 Physical arrangement for the six-phase generator

Thus, expression (88.1), generically, defines the behavior of the self-inductance of a single phase of the stator:

$$L_{ii} = (Ls_{1+}Ls_2) + L_m \cdot \cos 2(\theta + \alpha_i) \tag{88.1}$$

L_{ii} self-inductance of each phase of the stator, where sub index *ii* must assume the values of *a*, *b*, *c*, *x*, *y* and *z*, for *i* = *i*; L_{s1}—constant parcel of the self-inductance;
L_{s2} coil leakage inductance;
L_m amplitude of the variable term of the self-inductance;
θ Angle that defines the rotor position;

The mutual inductance between any two phases of the stator can be represented by the following expression:

$$L_{ik} = -M_s - L_m \cdot \cos(2(\theta + \alpha_{ik})) \tag{88.2}$$

where:
L_{ik} mutual inductance between two phases of the stator, where subindex *ii* must assume: *a*, *b*, *c*, *x*, *y* and *z*, for $i \neq k$, and $L_{ik} = L_{ki}$;
M_s average value of the mutual inductance;
L_m amplitude of the variable term of the mutual inductance;
θ Angle that defines the rotor position;
α_{ik} angle where the mutual inductance is maximum in relation to the reference.

The general expression that describes the mutual inductance between a phase of the stator and the rotor is:

$$L_{ik} = Mk \cdot \cos(\theta + \alpha_{ik}) \tag{88.3}$$

L_{ik} mutual inductance between a generic phase of the stator and with any coil of the rotor, where the sub index *ik* must assume *i* = *a*, *b*, *c*, *x*, *y* and *z*, and *k* = *F*, *D* and *Q*, and *Lik* = *Lki*;
M_k amplitude of the variable term of the mutual inductance;
θ Angle that defines the rotor position;
α_{ik} angle between the axis of the phase in analysis and the reference.

With regard to the self-inductance of the rotor, it is given by Eq. (88.4).

$$L_{ii} = L_{i1} + L_{i2} \tag{88.4}$$

where:
L_{ii} self-inductance of a given rotor coil, where sub index *ii* assumes: *F*, *D* and *Q*, for *i* = *i*;
L_{i1} coil self-inductance;
L_{i2} coil leakage inductance

The general expression for the mutual inductance between the pertaining rotor coils can be written as:

$$L_{ik} = L_{i1} \tag{88.5}$$

where:
L_{ik} mutual inductance between the circuits under analysis, where the sub index *ik* assumes: *F*, *D* and *Q*, for $i \neq k$

These equations are, in a general form, given by expression (88.6).

$$[\lambda] = [L][i] \tag{88.6}$$

where:
$[\lambda]$ vector of the concatenated flux;
$[L]$ matrix of the machine's inductances;
$[i]$ array of currents in the windings of the machine.

In function of the previous definitions it is possible, from (88.6), to obtain the equations for the concatenated flux for all the windings of the six-phase synchronous machine.

The electromagnetic torque can be obtained from the principle of energy conservation. The result of the application of this fundament law leads to:

$$T_e = \frac{P}{2}\sum_{i}\sum_{K} i_i i_K \frac{dL_{ik}}{d\theta} \tag{88.7}$$

Seeing that:

T_e electromagnetic torque developed by the generator;

p Number of poles of the generator;

i Currents in the windings of the generator, where I and k assumes: a, b, c, x, y, z, F, D, Q.

The dynamics of the movement of the synchronous machine can be given by:

$$J\frac{d^2\theta}{dt^2} = T_T - T_E. \tag{88.8}$$

where:

T_T primary drive torque (wind turbine);

T_e electromagnetic torque;

J Inertia moment

$$\mathrm{v} = \mathrm{e} - \mathrm{r}\cdot\mathrm{i} \tag{88.9}$$

where:

v Terminal voltage in the winding;

r Resistance of the winding;

i Winding current;

e Electrometric force produced in the winding and given by:

$$\mathrm{e} = -\mathrm{d}(\mathrm{Li})/\mathrm{dt} \tag{88.10}$$

Substituting (88.10) in (88.9):

$$v = -r\cdot i - \frac{d\lambda}{\mathrm{dt}} \tag{88.11}$$

Therefore, to obtain the voltage equations, (88.11) must be applied to each winding in the machine under consideration.

88.3 Description of Simulation Set up

The schematic diagram of the basic two pole six-phase synchronous generator is shown in Fig. 88.1. The stator has six distributed phase windings a, b, c and x, y, z, and are connected in a set to form two stars with isolated neutral, to prevent the flow of physical fault and triplen harmonics between the two winding sets i.e. '*abc*' and '*xyz*' set. The magnetic axes of the two three phase sets are displaced by an angle of 30° electrical degree. It is assumed that the windings of each set are sinusoidally distributed and have their axes displaced by 120° apart. The rotor side has a field

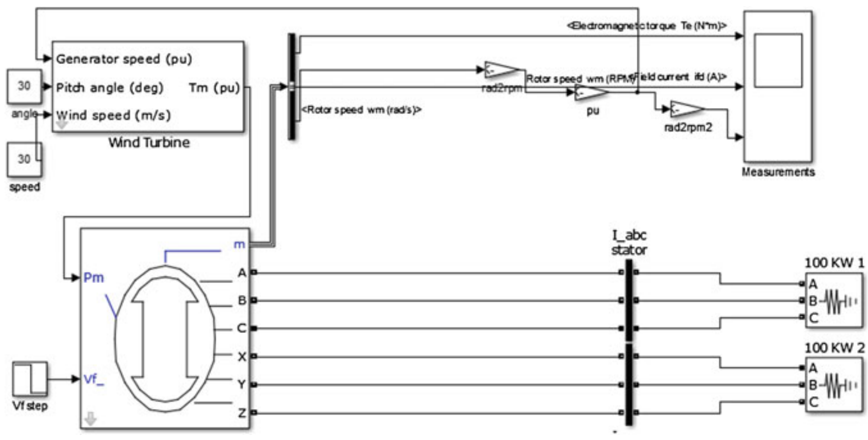

Fig. 88.2 Six phase synchronous generator under independent three phase loads

winding (f_d) along the polar axis and two circuited windings (Kd and Kq) each along polar and inter polar axes respectively. The short circuited windings are representing the effects of physical damper windings.

At the instant of time shown in Fig. 88.1, the d-axis coincides with the axis of phase '*a*'. SPSG is coupled with two independently operated three phase loads and it is analyzed. Then the output parameters are controlled with the conventional techniques. Check the results with bar graphs and analyses the voltages and current and it is controlled with the help of converters. Conventional techniques like PI and PID are checked after that Fuzzy controlling techniques are implemented [11, 12] (Fig. 88.2).

88.4 Fuzzy Controller Structure

At the controlling complex systems highly non-linear have shown to be very challenging using conventional control theory. In artificial intelligence fuzzy logic was chosen. Following blocks: fuzzification, Knowledge base, Inference engine, defuzzification constitute to form the complete fuzzy control system. A Fuzzy logic controller can be represented by Fig. 88.3. The shape fuzzy sets can be triangular, trapezoidal, etc.

A fuzzy control essentially embeds the consciousness and skill of a designer and researcher [7, 13]. Fuzzification—convert classical data or crisp data into fuzzy data or Membership Functions (MFs). Fuzzy Inference Process—combine membership functions with the control rules to derive the fuzzy output. Defuzzification—use different methods to calculate each associated output and put them into a table: the lookup table. Pick up the output from the lookup table based on the current input during an application. Any physical variable may contain some

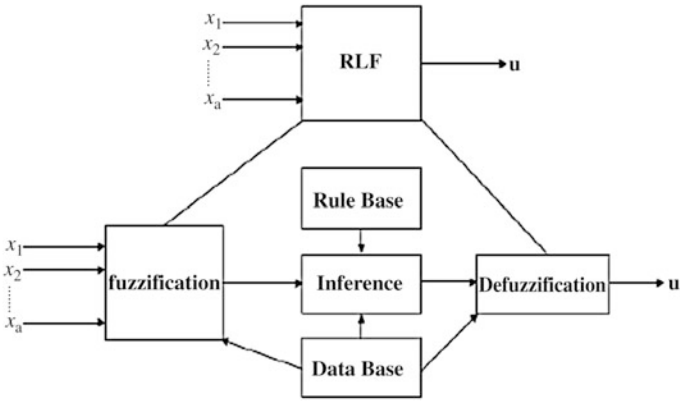

Fig. 88.3 Fuzzy logic controller

other components. For instance, if someone says: the temperature here is high. This high temperature contains some middle and even low temperature components. From this point of view, fuzzy control uses universal or global components, not just a limited range of components as the classical variables did [13]. With the rapid development of fuzzy technologies, different fuzzy control strategies have been developed based on different classical control methods, such as PID-fuzzy control, sliding-mode fuzzy control, neural fuzzy control, adaptor fuzzy control and phase-plan mapping fuzzy control. More and more new fuzzy control strategies or combined crisp and fuzzy control techniques are being developed and will be applied to many areas in our society in the future [14, 15].

By this controlling technique best performances are achieve through desired trajectory tracking. The fuzzy controller discards the load disturbance rapidly with no overshoot and with a negligible steady state error [16]. For the voltage control, instead of PI and PID voltage controller fuzzy logic controller is used. From simulation results are obtained parameters of the fuzzy logic controller [17]. PI or a PID fuzzy control structure has highlighted the necessity of on-line re-tuning of those controllers parameter in the case of processes with diverse dynamic behaviors related to the functioning management. These kinds of processes are represented by power systems, exemplified by a synchronous generator [18, 19].

88.5 Results

Input signal is truly an error signal, which is the set point or difference between the measured value and the desired value. The output voltage is measured through DC power and the fuzzy controller is goes to the boost converter (Figs. 88.4, 88.5 and 88.6).

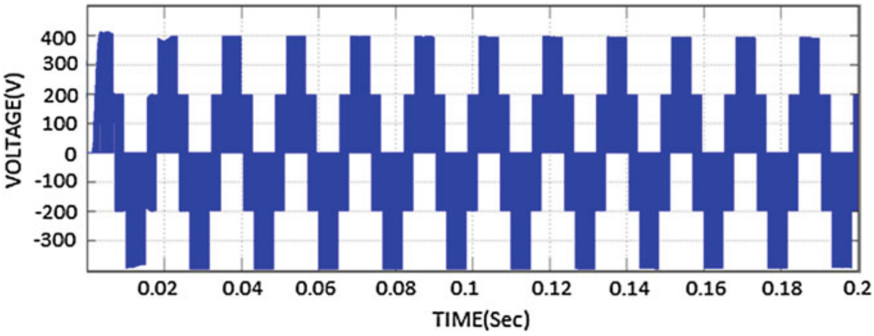

Fig. 88.4 Fuzzy logic control of load

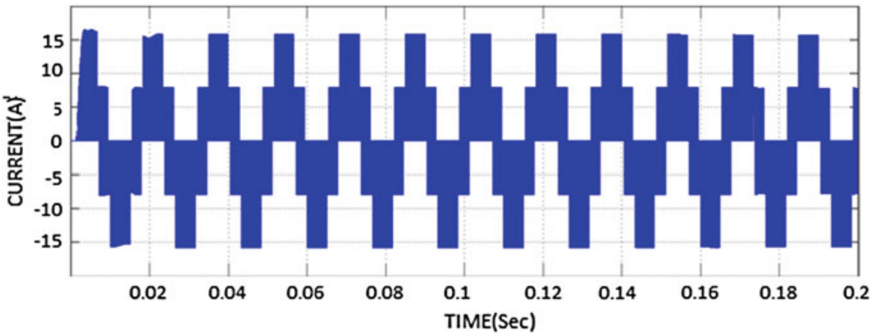

Fig. 88.5 Current measurement

Fig. 88.6 Fuzzy control voltage wave from measurement

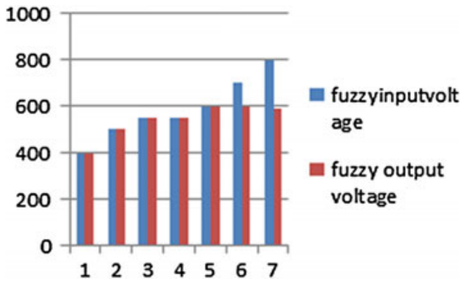

The boost converter is used to keeps the voltages nearly constant over the whole wind speed and step up the voltage level. The diodes are used for freewheeling purpose and the IGBT's are acts as Switches and PWM inverters are used to eradicate the harmonics and advance the reliability. Using Matlab/Simulink fuzzy controlled load voltage and load currents are measured and checked for various readings.

88.6 Conclusion

The functionality of Fuzzy controller is implemented in MATLAB/Simulink. Hence six-phase synchronous generator provides greater consistency and it feeds two liberated loads [20]. There is collaboration amid the two sets as the load on one part alters the working environments of the other set. Hence Fuzzy controller technique is one of the best methods compared to PID like conventional technique for computing controlled output voltage in six phase synchronous generator.

References

1. Jahns TM (1980) Improved reliability in solid state AC drives by means of multiple independent phase drive units. IEEE Trans Ind Appl 1A–16(3):321–331
2. Singh GK, Senthil Kumar A, Saini RP (2011) Performance evaluation of series compensated self-excited six-phase induction generator for stand-alone renewable energy generation. Energy 33:1688–1699
3. Singh GK, Senthil Kumar A, Saini RP (2011) Performance analysis of a simple shunt and series compensated six phase self-excited induction generator for standalone renewable energy generation. Energy Convers Manage 1688–1700
4. Singh GK (2008) Modeling and experimental analysis of a self-excited six phase induction generator for standalone renewable energy generation. Renew Energy 33:1605–1621
5. Singh GK (2011) A six phase synchronous generator for standalone renewable energy generation; experimental analysis. Energy 36:1768–1775
6. Grabic S (2008) Permanent magnet synchronous generator cascade for wind turbine application. IEEE Trans Power Electron 23(3):1136–1142
7. Cirsteea M, Dinu A, Khor JG, McCormick M (2002) Neural and fuzzy logic control of drives and power systems. Newness, Oxford
8. Singh GK (2011) Modelling and analysis of six phase synchronous generator for standalone renewable energy generation. Energy 36:5621–5631
9. Khan K (2004) Comparative analysis of multiphase machines. Master's thesis, international masters program in electric power engineering
10. Locment F, Semail E, Piriou F (2006) Design and study of a multiphase axial-flux machine. IEEE Trans Magn 42(4):1427–1430
11. Schiferl R, Ong C (1983) Six phase synchronous machine with AC and DC stator connections —part 1 2. IEEE Trans Power Appar Syst 102:2685–2693
12. Badr MAL (2005) A self-tuning PID voltage regulator for synchronous generator. Electr Eng J Can 8(1):18–27 Department of Electrical Engineering, Ain Shams University, Cairo, Egypt
13. Bose BK (1994) Expert system, fuzzy logic, and neural network applications in power electronics and motion control. Proc IEEE 82(8):1303–1321
14. Kim YT, Bien Z (2000) Robust self-learning fuzzy controller design for a class of nonlinear MIMO system, soft computing in intelligent systems and information processing. In: Proceedings of the 1996 Asian 111, 61–66
15. Spooner JTM, Ordonez M, Passino R (2002) Stable adaptive control and estimation for nonlinear system. Neural Fuzzy Approximator Tech, Willey-Interscience, pp 266–280
16. GhaniAissaoui A (2007) Mohamed Abid.: a fuzzy logic controller for synchronous machine. J Electr Eng 58(5):285–290

17. Sumina D, Erceg G, Idzotic T (2011) Comparison of the excitation control of a synchronous generator with fuzzy logic controller and PI voltage controller. In: Electrical engineering and computing, Croatia, pp 1–5
18. Filip I, Proştean O, Vasar C, Szeidert I (2011) Adaptive fuzzy controller for synchronous generator. Department of automation and applied informatics, Faculty of automation and computer sciences, "Politehnica" University, Timisoara, pp 1–10
19. Yuan C (2002) Research on PID parameters optimization of synchronous generator excitation control system. In: Key laboratory of power system protection and dynamic security monitoring and control, Electric Power University, Beijing, China, pp 1–5
20. Singh GK (2011) Self excited induction generator research-a survey. Department of electrical engineering, IIT Roorkee, pp 107–114

Chapter 89
Power Loss Minimization in Presence of Distributed Generation by DSM

S. Sambath and P. Palanivel

Abstract This paper is an intent to quantify and analyses the impact and roll of distributed generation (DG) in Tamil Nadu, India to examine what the benefits of decentralized generation would be for demand side management. Use load flow analysis to simulation over a quantify the loss reduction and system improvement by having decentralized generation available line conditions for actual rural feeders in Tamil Nadu, India. In order to realize the energy efficiency potential, and upscale the implementation of DSM program by utility, load research should be the starting point. One of the key objectives of load research is to understand and analyses the utility's system load profile and Peak clipping. This helps utilities to better plan their system in Demand side Management.

Keywords Distributed generation · Load flow analysis · Loss reduction

89.1 Introduction

India is witnessing a tremendous growth in the demand of electricity. This increased demand has outpaced supply, leading to significant overall energy and peak shortages. Energy and peak shortages across India stood at 8.8 and 9.9 % respectively in 2012–2013. Increasing supply is an option, but inadequate capacity additions in the past and associated environmental concerns merit the promotion of energy efficiency and Demand Side Management (DSM) as an important strategy to reduce the peak demand, our approach in this study how that DG will help for DSM and improve the power quality. Distributed generation technologies have emerged against bad environment and energy crisis, and they have been developed well in

S. Sambath (✉)
Periyar Maniammai University, Thanjavur, India
e-mail: yeses.eng@gmail.com

P. Palanivel
MAM Engineering College, Trichy, India

C. Kamalakannan et al. (eds.), *Power Electronics and Renewable Energy Systems*,
Lecture Notes in Electrical Engineering 326, DOI 10.1007/978-81-322-2119-7_89

recent years. In addition to emphasizing the importance of DGs in DSM, paper demonstrates the importance and necessity of DGs and DSM's coordinated operation in the smart grid [1].

89.2 Demand Side Management

89.2.1 DSM in India

The historic problems of the Indian power sector can be traced to three root issues —unacceptably high T&D losses, large commercial losses due to poor billing, metering, collection and energy theft, and, low end-use efficiency of energy use specifically in agriculture. The irrigation pumping electricity use is at the heart of the subsidy issue and along with electricity theft and T&D losses, comprise the root cause for the sector's financial crisis [2].

89.2.2 DSM in Tamil Nadu

Tamil Nadu Electricity Board (TNEB) was functioning as a vertically integrated utility responsible for generation, transmission, and distribution of electricity until 2010. In 2010, it was restructured into a holding company, viz., TNEB Ltd, and two subsidiary companies—TANGEDCO responsible for generation and distribution and Tamil Nadu Transmission Corporation Limited (TANTRANSCO) responsible for transmission of electricity. The utilities are under the regulatory purview of the Tamil Nadu Electricity Regulatory Commission (TNERC). The policies and guidelines for power sector development are framed by the Department of Energy, Government of Tamil Nadu (GoTN). In addition, there are agencies such as Electrical Inspectorate Department responsible for electrical safety and energy conservation and Tamil Nadu Energy Development Agency (TEDA) responsible for renewable energy development in the state.

The total installed capacity in Tamil Nadu is about 10,124 MW as on 31st March 2013 (including share from Private generators and central generating stations), of which thermal constitutes the highest share (46 %), followed by renewable (37 %), hydro (14 %), and nuclear (3 %). Of the total installed capacity in the state, TANGEDCO's own capacity is to the tune of 5,750 MW As on 31st March 2013, Tamil Nadu ranks first in wind-installed capacity of 4,101 MW contributing around 47 % of the country's total share. In terms of the sector-wise breakup, the private sector contributes the highest share of installed capacity (44 %), followed by the state and central sector with a share of 37 and 19 %, respectively [3].

Electricity supply in rural area of Tamil Nadu India has been lagging in terms of service (measured by hours of supply) as well as penetration. The demand-supply gap is currently 28 % of average load and 38.5 % of peak demand at current prices, which are heavily subsidized, on average. In order to bridge this gap and meet anticipated growth, it is necessary to double the present capacity, i.e., install an additional generation capacity of 10,000 MW by 2017. This would require an investment of Rs. 75,000 crore (approximately) for generation and Rs. 90,000 crore including investments in transmission and distribution. The average cost of supply is Rs. 5.97/kWh and the average revenue is only Rs. 3.78/kWh [4, 5].

For reducing the peak demands and losses the TNEB implementing various methods with the fund of Rural Electric corporation (REC) and Power Finance Corporation (PFC) like, Network Reconfiguration, link lines, Strengthening of conductor, Capacitor installation, increase the HT:LT Ratio, Erection of Distribution Transformer at load center, Load Balancing, Adoption of HVDS, Energy Conservation and Energy Efficiency, Rural load management system, But duet to some more reasons the peak demands and line losses not yet reduced as per the standard (below 10 %) [6, 7].

The present policies of building large centralized generation and extended distribution networks are clearly unlikely to solve the problems of rural electricity supply, at least in the near future. Decentralized power generation close to the rural load centers using renewable sources appears to have the potential to address at least some of the problems including reduction of line losses and reduce the peak demand in rural electrification described in the earlier section.

89.2.3 DSM Techniques

DSM works to reduce electricity consumption in homes, offices, and factories by continually monitoring and actively managing how appliances consume energy. It consists of DR programs, smart meters, dynamic electricity pricing, smart buildings with smart appliances, and energy dashboards. DSM manipulates residential electricity usage to reduce cost by altering the system load shape.

Common techniques used for load shaping are peak clipping, valley filling, load shifting, strategic conservation, strategic load building, and flexible load shape as shown in figure (Papermanns).

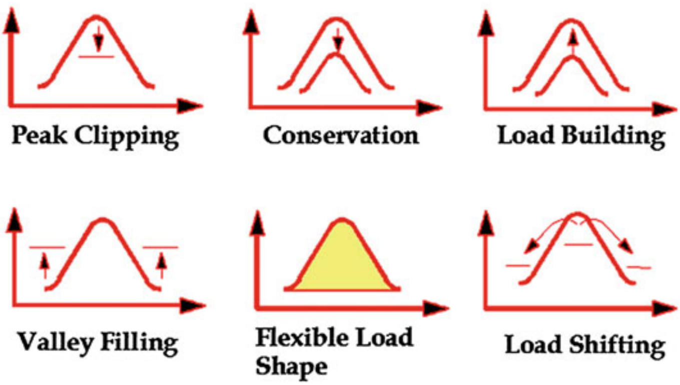

89.3 DSM and Power Quality

The improvement in power quality and hence energy efficiency has major socio-political implications. A subject of considerable political sensitivity is that associated with tariff increases for power supply to agriculture and the urban poor. DSM and energy efficiency has the inherent potential to mitigate the rising impact of such politically sensitive tariffs through an integrated program of metering, installation of energy conservation devices and efficient system operation and maintenance.

Importance of Renewable Energy Resources is increasing with every passing day. The International Renewable Energy Agency (IRENA) is an intergovernmental organization for promoting the adoption of renewable energy worldwide. It aims to provide concrete policy advice and facilitate capacity building and technology transfer and promote DG [8].

The Peak clipping is one of the method for reduction of grid load mainly during peak demand periods. Our aim is by optimization of distributed generation in the rural feeder and analyses how the peak demand and losses will be reduced.

89.4 Distributed Generation

89.4.1 Rationale for Distributed Generation

Distributed Generation (DG) systems are small-scale power generation technologies (typically in the range of 3–10,000 kW) used to provide an alternative to or an enhancement of the traditional electric power system. The usual problem with distributed generators is their high cost Distributed generation is currently being used by many customers to provide some or all of their electricity needs. The vast majority of DG units are operated to provide emergency back-up and are unlikely to ever operate in parallel with the distribution system. There are also some customers that use DG to reduce their demand charges, and others that use DG to provide premium power or reduce the environmental emissions from their power supply [9].

89.4.2 Planning for Decentralized Generation

The conventional wisdom has indicated that large generation stations offer significantly better economies of scale. However, such calculations must be recalibrated when faced with the state of the power grid in many emerging economies in the states in India, viz., large distributed (rural) load, high T&D losses (including theft), limited capacity availability, and dramatically poor supply conditions. In such cases, a thorough analysis should be made for the policies, technical specifications, and economic analysis behind use of DG [10].

89.4.2.1 Current System

The utilities interconnect with the renewable DG generators at high voltages (>110, >33 or, >11 kV, depending on the state lowest "transmission" voltage level). This gives the utility the flexibility to divert the power in the grid. However, the local area does not benefit significantly from decentralized generation and moreover, there is no discernible improvement in the power supply and reduction of peak demand or in utility's revenues even though the utility purchases expensive power from the DG units. The generator pays for the wiring necessary to connect to the nearest sub-station [11, 12].

89.4.2.2 Proposed System

The utilities' policy for DG units appears to be one-sided and overlooks the possible benefits of decentralized power generation in remote rural feeders. In this paper we examine the opportunities with decentralized power generation in rural areas and attempt a more rational basis for framing utilities' policies towards the DG units. In particular, we address the following issues:

1. Impact of DG on the voltage profiles and technical distribution losses.
2. Peak clipping approach to reduce peak demand.

89.5 Simulation and Analysis

89.5.1 Methodology

The approach of this study is to conduct a three-phase AC load flow analysis (TANGEDCO) of a rural distribution feeder (Koraiyaru feeder) in Tiruvarur district of Tamilnadu in Fig. 89.1. This is representative of a typical rural distribution feeder and the results will therefore have a wider applicability.

The feeder begins with a 110/11 kV sub-station Mannargudi. There are 120 buses out of which there are 75 load buses, each roughly supplying a village or hamlets. Each load bus has a step-down transformer for 415 V/240 V and the transformer ratings are 25, 63, or 100 KVA. The distance between the sub-station and the tail end bus is about 17 km and the peak demand is 7.6 MW (Table 89.1). The feeder's load is mostly agriculture pumps and motors that are inductive and often operate at power factor as low as 0.70.

The buses are numbered in a sequential manner, but due to the branching of the network, higher numbered nodes are not necessarily further away from the sub-station. The present annual consumption of the feeder is 57 Lakhs Units (kWh). There are four main categories of consumers: Domestic, commercial, industrial and agricultural (irrigation pumps). The kWh consumed by the first three categories are metered and they are charged on a per kWh basis, while agricultural consumers are

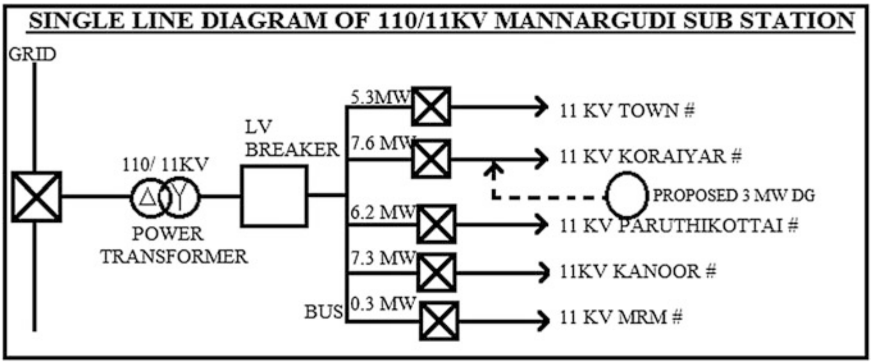

Fig. 89.1 *Single line* diagram of 110/11 kV sub-station Mannargudi in Thiruvarur district, Tamilnadu (peak demand 27 MW)

Table 89.1 Details of the Koraiyaru distribution feeder

Substation transformer	110/11 kV
Total no. of buses	115
No. of load buses	70
Peak load	3 MW
Transformer in the feeder	25, 63, 100 KVA

not metered and they pay on a flat rate basis (Rs. 1,750//HP/Annum). Since Agriculture pumps are not metered, there is no data available on their annual power consumption and it is estimated by sample metering.

$$\text{Total KWh}_{\text{feeder}} = \text{KWh}_{\text{Metered}} + \text{KWh}_{\text{Unmetered}} + \text{Losses} \tag{89.1}$$

where Losses = T&D losses + Theft.

The only known quantities in (89.1) are the total kWh at the feeder level in substation and the kWh consumed by the metered consumers. It is therefore impossible to know precisely the three unknowns from a single equation. The recent tariff order of the Tamilnadu Electricity Regulatory Commission (TNERC) explains a rough procedure adopted by the utilities to estimate these numbers. The utility makes an assumption of the annual kWh consumed by an Agriculture pumps by sampling a few predominantly agricultural feeders (clearly this is a crude exercise at best). This results in an estimate of the total losses technical losses and theft.

89.5.2 AC Load Flow Study

The approach is to conduct a three-phase AC load flow analysis for this feeder using the Gauss-Seidel algorithm. It was first carried out a base case scenario

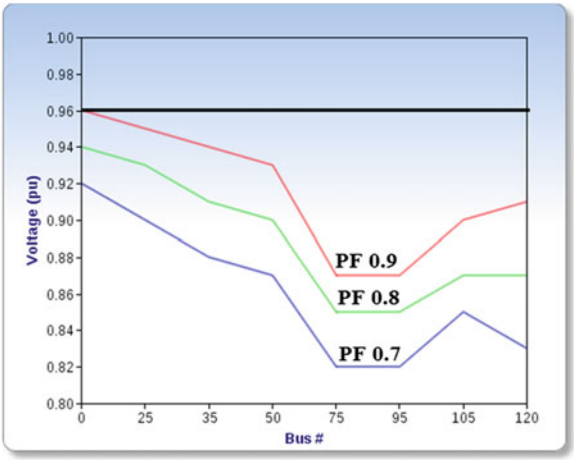

Fig. 89.2 The voltage profiles (per unit basis, or *pu*) under heavy load conditions (75 %) with a theft of 13 %, with the power factor varying between 0.7 and 0.9

Table 89.2 Assumptions for the three-phase AC load flow analysis

Variable	Value or range
On line load	40–80 % of the sanctioned load
Theft	13 % of on-line load
Power factor	0.70–0.90 lagging

(without DG) to obtain the voltage profiles, distribution losses and then considered the impact of a DG installed in the feeder (Fig. 89.2).

For simplicity, the following assumptions are made (Table 89.2).

89.6 Results

89.6.1 Peak Demand and Distribution Losses

89.6.1.1 Current System

Figure 89.3 shows the current system the decentralized power generation source placed in the beginning of the feeder i.e. at sub-station the calculated distribution losses as a function of the power factor under moderate loading condition of 60 with 14 % theft. Depending on the power factor, the technical distribution losses are between 8.5 and 12.5 %. In most rural feeders, the power factor is 0.75–0.8 and therefore distribution losses are likely to be at least 10 % under normal loading conditions.

Fig. 89.3 Technical distribution losses (I^2R) in the feeder under moderate loading of 60 % as a function of the overall power factor. The losses are 8–12 %

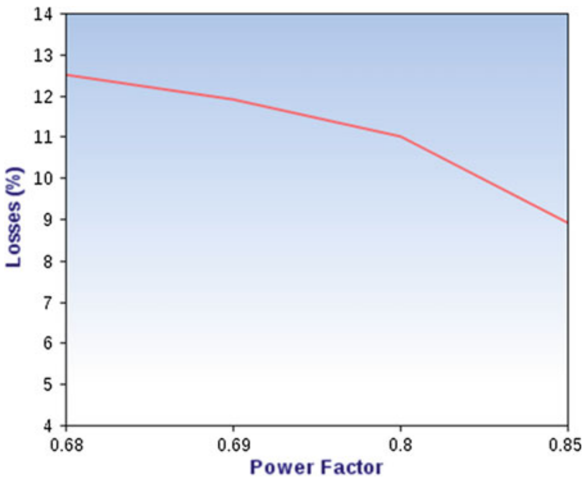

89.6.1.2 Proposed System

Figure 89.4 shows the impact of a decentralized power generation source placed in the feeder at Bus # 60. The choice of the bus was made on the basis of it being centrally located in the feeder, and almost equidistant from all the branches. The generator power varied from 0 to 4 MW with a power factor of unity.

The voltage of the system under study will increased when the DG is connected in the middle of the feeder .Hence the feeder load is 7.6 MW. When we connect 4 MW DG in the middle of the feeder is optimum to maintain the feeder voltage within the accepted level.

Fig. 89.4 Impact of a decentralized generator placed centrally at Bus # 60 on the voltage profiles. The generator is varied from 1 to 4 MW

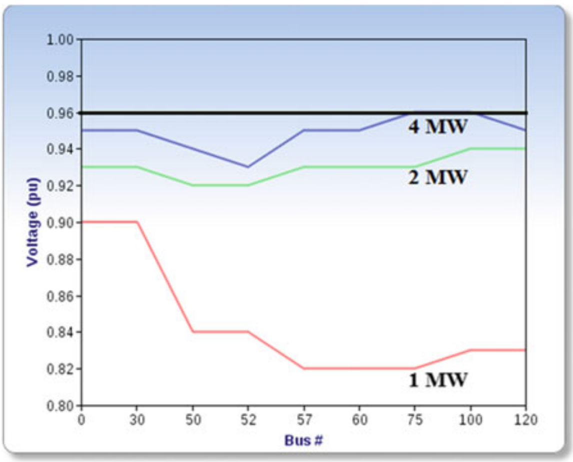

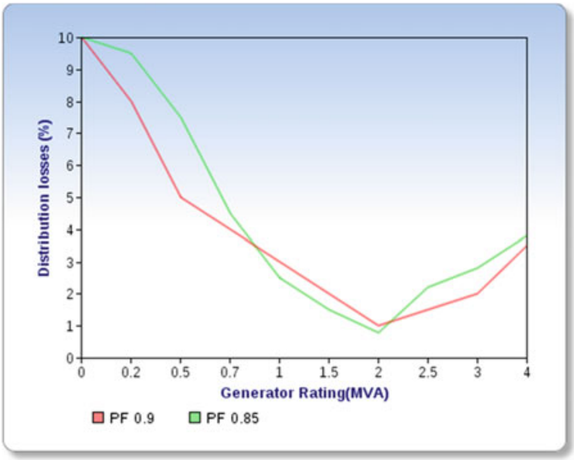

Fig. 89.5 Technical distribution losses for different MVA ratings of the generator (1–4 MVA) and for two generator power factors of 0.80 and 0.95

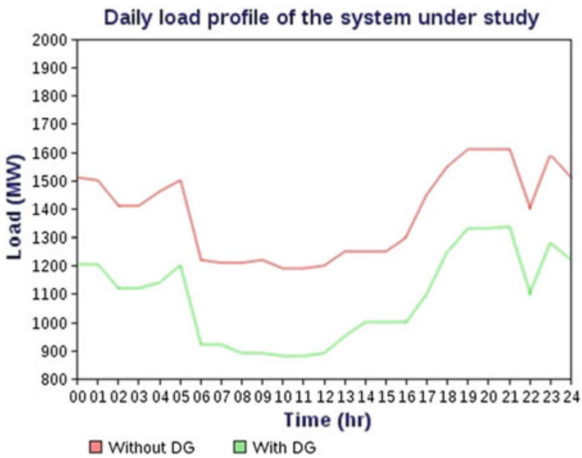

Fig. 89.6 Daily load profile of 120 bus feeder in Koraiyar, Mannargudi substation Tamil Nadu. Peak reduction of 30 % achieved with DG

Figure 89.5 shows the technical distribution losses as a function of the generator MVA rating. There is a dramatic reduction in the losses from the base case of 10 % without the decentralized generator. Figure 89.6 shows how the peak demand reduced with the DG.

Therefore, appropriate sizing and locating a decentralized generator improves the quality of power supplied to the feeder and also reduces the distribution losses. Using photovoltaic generation and wind power, other researchers have reported similar results that reduce distribution losses [13]. The above discussion suggests that distributed generation close to the rural load centers benefits both the local consumers (improved power quality) as well as the utility (lower losses) and helps to reduce peak demands.

89.7 Conclusion

In this paper we examined opportunities for distributed power generation in rural Tamil Nadu India. The results obtained show that power losses of the system is considerably reduced, the power quality enhanced and peak load reduced by finding optimum location of a decentralized power generator. There is a significant improvement in the voltage profiles and reduction of technical distribution losses. This creates a possibility of setting up rural micro-grids or rural electricity cooperatives with Gas based and non conventional power generators. From the experimental and practical implemented proposed system, clearly identified that the percentage reduction in line loss, voltage improvements and peak clippings were achieved. Our study is limited to only in Tamil Nadu state in India. In future work our study will be expanded to all states in India using the above techniques for demand side management in whole country and increase the revenue of the utilities.

References

1. Tan QY, Wang SR, Cheng SJ (2005) Demand side management review. Relay 33(17)
2. Nezhad HG, Sarkar A (1997) Demand-side management: a policy model for India. In: Proceedings of the 20th annual international energy conference of the international association for energy economics, New Delhi, India, Jan 1997, vol II, pp 448–458
3. Annual Report 2012–13 of Tamilnadu Electricity Board (TNEB), Chennai India
4. Indian Electricity scenario (2013) Ministry of power (MOP), India
5. DSM action plan for Tamil Nadu (2012) The energy and resource institute (ERI), New Delhi, India
6. Tariff Order (2012) Tamil Nadu electricity regulatory commission (TNERC), Chennai, India
7. Ramesh L, Chowdhury SP, Chowdhury S, Natarajan AA (2008) Voltage stability analysis and real power loss reduction in distributed distribution system. In: IEEE transmission and distribution conference and exposition, T&D, IEEE/PES 21–24 Apr 2008
8. Ieadsm (2010) Integration of demand side management, distributed generation, renewable energy sources
9. Caamano-martin E et al (2008) Interaction between photovoltaic distributed generation and electricity networks. Res Appl 16:629–643
10. Gonzlez-Longart FM Impact of distributed generation over power losses on distribution system
11. Grunbaum R, Halvarsson B, Wilczynski W (1999) FACTS and HVDC light for power systems interconnections. In: Power delivery conference, Madrid, Spain
12. Annual Report (2012–2013) Ministry of non-conventional energy sources (MONCES). Government of India, New Delhi
13. Ramesh L, Chowdhury SP, Chowdhury S, Natarajan AA (2008) Distribution feeder restructuring for better voltage regulation and line loss reduction. In: IEEE Powercon 2008
14. Distributed generation: definition, benefits and issues Papermans G, K.U. Leuven Energy Institute
15. Datas collected from various sources in TANGEDCO training institutes and LD centre, Chennai

Chapter 90
Comparative Study of Prototype and Simulation of SVC for Transmission Congestion Management

Khatavkar Vrushali, Redekar Abhijeet and Dharme Anjali

Abstract In deregulated/restructured power system, congestion of electrical power is a major problem. The solution includes the management methodologies namely technical and pricing methods. The technical methods suggest the use of FACTS controllers to reduce the congestion without considering the economic matters. This work deals with designing a prototype of Static VAR Compensator (SVC). This SVC prototype comprises of 440 kV, 300 km modular transmission line model which operates on lab voltage i.e. 400 V, 50 Hz, and compensator consisting of three delta connected capacitors together with three delta connected air gap type linear inductors along with two anti-parallel thyristors. Modelling has been done considering two modes of thyristor i.e. when thyristor is ON and second when thyristor is OFF. Both modes are characterised by the time duration. With these two modes, two second order differential equations are derived and finally converted into second order state space model. This state space model will be helpful to predict the load voltage behaviour. SVC is modelled in MATLAB Simulink and simulation results are compared with the prototype results to validate the controller design parameters. The aim of this work is to enhance voltage stability and increase power transfer capability of the long transmission line using FC-TCR configuration of Static VAR Compensator.

Keywords Static VAR compensator (SVC) · Fixed capacitor thyristor controlled reactor (FC-TCR) · PID controller

K. Vrushali (✉) · R. Abhijeet
Department of Electrical Engineering, Modern College of Engineering, Pune, India
e-mail: vrushali_4@rediffmail.com

R. Abhijeet
e-mail: abhijeetredekar@ieee.org

D. Anjali
Department of Electrical Engineering, College of Engineering, Pune, India
e-mail: aad.elec@coep.ac.in

C. Kamalakannan et al. (eds.), *Power Electronics and Renewable Energy Systems*, Lecture Notes in Electrical Engineering 326, DOI 10.1007/978-81-322-2119-7_90

90.1 Introduction

For many years the electric power industry was characterized by a vertically integrated structure (Bundled Power System), consisting of power generation, transmission/distribution and trading [1]. The liberalization process has resulted in the unbundling of this organizational structure. Now generation and trading are organized as separate business entities, subject to competition, while the transmission/distribution business remains a natural monopoly. The electric transmission network has a fixed structure consisting of different voltage levels; the higher levels are for transmission purposes whereas the lower levels are used for the distribution tasks. Each network element has a finite power transmission capacity, limiting the amount of electricity to be transported or distributed. Open access electricity market activities and a growing demand for electricity have led to heavily stressed power systems. This requires operation of the networks closer to their stability limits. Therefore Power system operation is affected by stability related problems, leading to unpredictable system behaviour. Cost efficient solutions are preferred over network extensions. In many countries, permits to build new transmission lines are hard to get, which means the existing network has to be enforced to fulfil the changing requirements [2]. This increasingly unpredictable system behaviour requires innovative equipment to handle such situations successfully. Innovative operational equipment based on power electronics offer new and powerful solutions commonly described by the term ‘Flexible AC Transmission Systems’ or ‘FACTS devices’ [3]. FACTS-devices can be utilized to increase the transmission capacity, improve the stability and dynamic behaviour or ensure better power quality in modern power systems. Their main capabilities are,

1. Reactive power compensation
2. Voltage control
3. Enhancing active power flow

Transmission line parameters like R, L, and C, are taken as scaled down parameter per km basis. Paper [4] deals with microprocessor based static VAR compensator. This paper gives the details of closed loop control strategy and procedure of compensating power calculation of SVC and long transmission line which is suitable for laboratory experiments. Simple software strategy for PD/PID control is introduced. The output of hardware presented as receiving end voltage and three phase power transferred to load. The controller demonstrated with resistive load, which is for system compensation only [5]. Binary capacitor bank instead of using one capacitor bank, has made this type of compensation scheme deals with the performance evaluation of SVC through analytical studies and practical implementation on an existing system. The SVC consists of Thyristor Binary Compensation (TBC) and Thyristor Controlled Reactor (TCR). A fast acting error adaptive controller is developed using micro controller 89C51 with PI control strategy for contactor switched capacitors and Thyristor switched capacitors. The controller is kVAR based i.e. kVAR sensed at Point of Common Coupling (PCC) and fed back to the controller. In the result PCC voltage, voltage regulation, and load capacity are shown. Work presented in [6] compares SVC compensation with fixed capacitor compensation for active, reactive power and voltages at R.E. bus. It is possible to increase the power transfer capability of line with FC (Fixed Capacitor), but the voltage control is not satisfactory. The power deals with the simulation of SVC on PSCAD/EMTDC. For SVC the TSC-TCR (Thyristor Switched Capacitor–Thyristor Controlled Reactor) scheme is used with bus voltage as a sensing parameter.

90.2 Experimental Study

The individual performance of prototype and simulation circuit has been compared in the presented work.

This SVC prototype comprises of 440 kV, 300 km modular transmission line model which operates on lab voltage i.e. 400 V, 5 A, 50 Hz, and compensator consisting of three delta connected capacitors (2.4 kVAR) together with three delta connected air gap type linear inductors (2.6 kVAR) along with two anti-parallel thyristors. Figure 90.1 shows SLD of Transmission line with its parameters, as well as a capacitor bank and Thyristor Controlled Reactor (TCR) connected at receiving end bus (Load bus). Fixed capacitor Thyristor Controlled Reactor (FC-TCR) is one

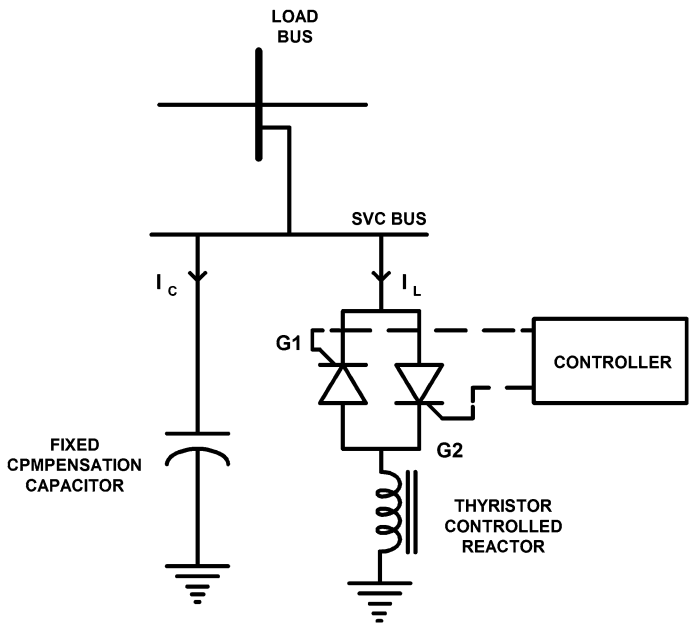

Fig. 90.1 Prototype study system

Table 90.1 Observations of simulations

Sr. no.	Load step	Before compensation			After compensation	
		Vs (V)	Vr (V)	Active power transferred Pr (W)	Vr (V)	Active power transferred Pr (W)
1	1	300	275	295	300	340
2	2	300	269	560	300	690
3	3	300	260	800	290	850

of the configurations of SVC. In the prototype, generator bus is connected to a.c. supply and static balanced R-L load is connected al load bus. From Table 90.1, it is clear that between the sending-end and the receiving-end voltages, a magnitude variation. The most significant part of the voltage drop in the line is due to the reactive component of the load current and the line parameters for each pi unit as given in Fig. 90.1. In the experimental set-up the sending end voltage is adjusted to specified value as shown in the observation table. Star connected variable R-L Load is connected to Load bus. Load is gradually increased in steps from step 1 to step 3 and observations are taken without compensation and with compensation.

90.3 State Space Model of SVC

When analysing the steady state operation of the SVC circuit of Fig. 90.2, two modes of operation can be noted. The time location of the two modes of operation is shown in Fig. 90.2.

Mode I: Characterized by a time duration for an interval, $\pi - \alpha < \omega t < \alpha, and$ $2\pi - \alpha < \omega t < \pi + \alpha$. Its dynamic equation is represented in second order differential equation as,

Fig. 90.2 Operation mode locations

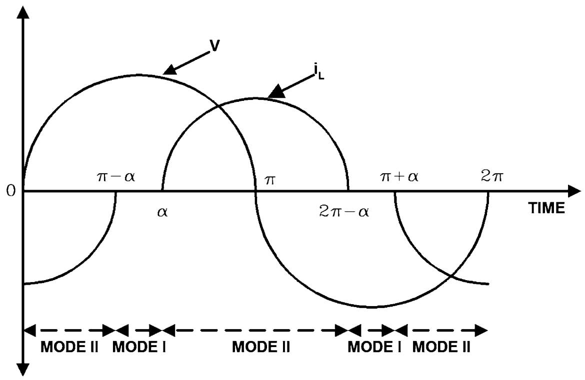

$$V_s = L_t C \frac{d^2 v}{dt^2} + \frac{L_t}{R}\frac{dv}{dt} + v \tag{90.1}$$

where α represents the firing angle and ω is the angular velocity of the supply voltage (Vs). In such a mode, the two thyristors are not conducting and thus the SVC inductor can be omitted.

Mode II: Characterized by a time duration for an interval, $0 < \omega t < \pi - \alpha$, $\alpha < \omega t < 2\pi - \alpha$, and $2\pi - \alpha < \omega t < 2\pi$. Its dynamic equation is represented in second order differential equation as,

$$V_s = \frac{L_t}{L} + L_t C \frac{d^2 v}{dt^2} + \frac{L_t}{R}\frac{dv}{dt} + v \tag{90.2}$$

These are presented through a single equivalent dynamic representation, valid for both Modes as,

$$x = Ax + bu \tag{90.3}$$

$$\begin{bmatrix} \frac{dv}{dt} \\ \frac{di}{dt} \end{bmatrix} = \frac{1}{L_t C}\begin{bmatrix} 0 & L_t C \\ -(1 + m\frac{L_t}{L}) & \frac{-L_t}{R} \end{bmatrix}\begin{bmatrix} v \\ i \end{bmatrix} + \frac{1}{L_t C}\begin{bmatrix} 0 \\ 1 \end{bmatrix} V_s \tag{90.4}$$

90.4 Simulink Model of SVC

The SVC is modelled in Simulink using four main components viz: Source, Transmission line, Controller, and Static load. The main function of a SVC is to inject a controlled capacitive or inductive current so as to maintain or control mainly load bus voltage. A well-known configuration of SVC, the Fixed Capacitor (FC) with Thyristor Controlled reactor (TCR) is implemented. The SVC is typically modelled using a variable reactance with maximum inductance and capacitance, which directly correspond to the limits in the firing angles of the thyristors. In addition to the main function of the SVC controller to control the SVC bus voltage (Fig. 90.3).

In controller model the PID control block is selected but only K_p and K_i parameter are required. So here K_d factor is always set as zero to keep off the effect of derivative controller. Therefore only PI controller is used. As shown in Fig. 90.4 the addition of K_p, K_i, and K_d gain blocks are fed to the saturation function. The saturation function feeds signals to the PWM generator. This generates pulses to trigger anti parallel thyristors as shown in Fig. 90.4.

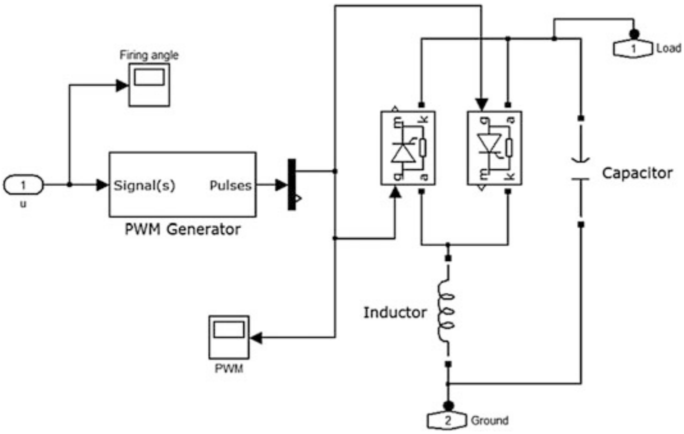

Fig. 90.3 FC-TCR Simulink model

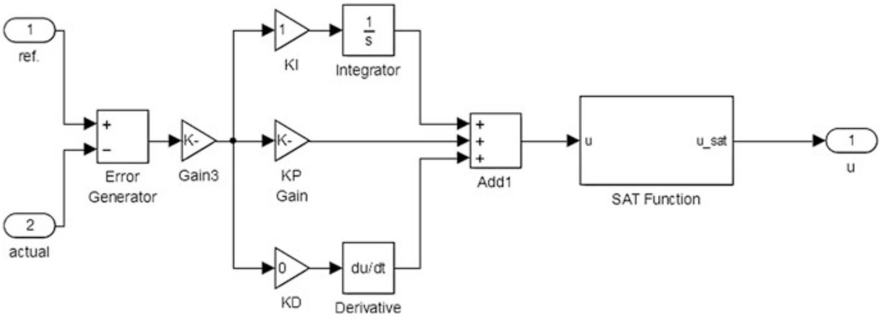

Fig. 90.4 Controller Simulink model

90.5 Performance of Prototype and Simulation

We are interested in load bus voltage and active power transferred at load side, so observations were taken with and without compensation from both systems. In prototype model RMS value of voltage and current are measured so for comparison purpose we have to connect RMS block in Simulink model. Each Figs. 90.5, 90.6, and 90.7 shows the simulation results of load bus voltage and active power transferred for three loading steps.

From prototype model we can get results from voltmeter and watt-meter which is connected at load bus. This is shown in Table 90.2.

The effect on the power transferred and load bus voltage to the load is also clearly understood from the Table 90.3. If the voltage at the receiving end is maintained high, larger power can be delivered to the load. Figure 90.8 shows percentage increase in power transferred and bus voltage at each loading condition.

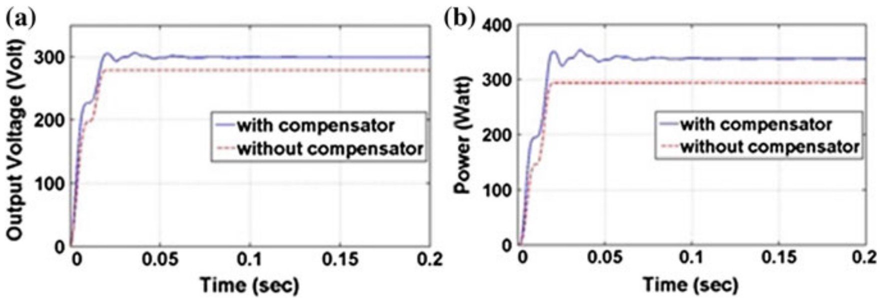

Fig. 90.5 **a** Simulation result for bus voltage at first loading condition. **b** Simulation result for active power transferred at first loading condition

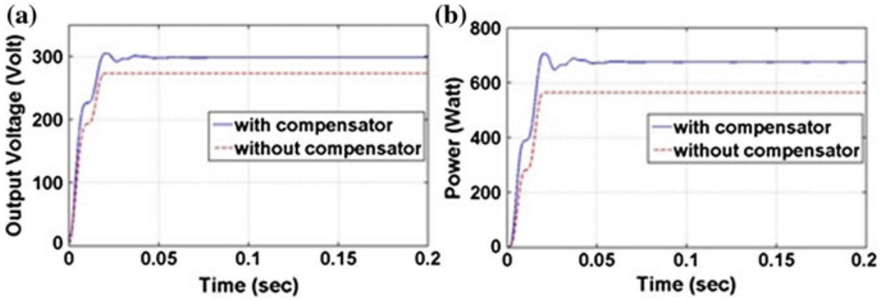

Fig. 90.6 **a** Simulation result for bus voltage at second loading condition. **b** Simulation result for active power transferred at second loading condition

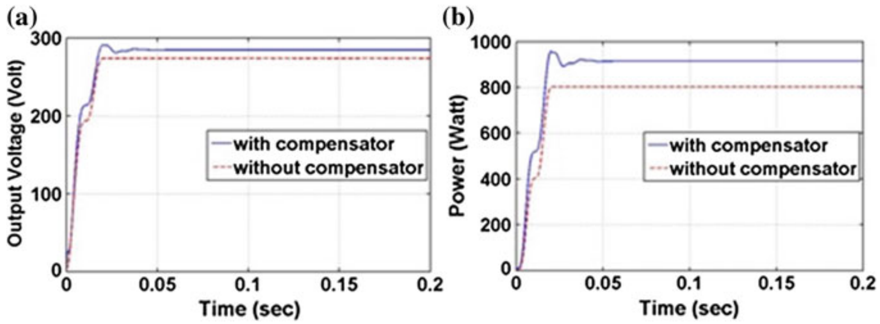

Fig. 90.7 **a** Simulation result for bus voltage at third loading condition. **b** Simulation result for active power transferred at third loading condition

Table 90.2 Observations of prototype

Sr. no.	Load step	Vs (V)	Before compensation			After compensation		
			Vr (V)	Active power transferred Pr (W)	Power factor (lag)	Vr (V)	Active power transferred Pr (W)	Power factor (lag)
1	1	300	270	281	0.8	300	328	0.99
2	2	300	260	537	0.75	300	674	0.99
3	3	300	255	787	0.7	290	838	0.98

Table 90.3 Percentage improvement of load bus voltage and power transferred

Sr. no.	Load step	By simulation		By prototype	
		R.E. bus voltage (%)	Power transferred (%)	R.E. bus voltage (%)	Power transferred (%)
1	1	9.1	15.25	11.11	16.72
2	2	11.52	23.21	15.38	25.51
3	3	11.53	6.25	13.72	6.48

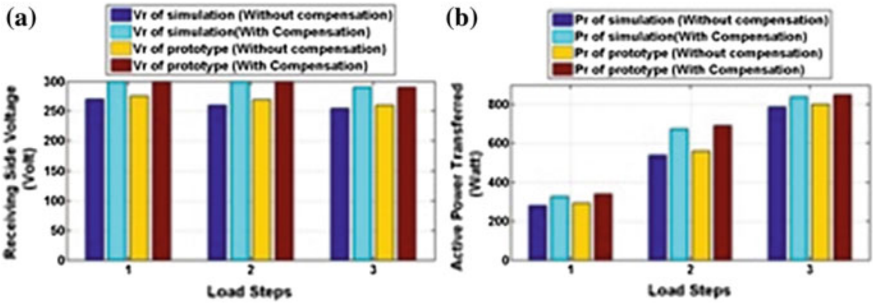

Fig. 90.8 Percentage improvement by simulation and prototype method. **a** Load bus voltage. **b** Power transferred

90.6 Comparison of Simulation and Experimental Results

Finally comparison of active power transferred by simulation and by experimentation is shown in Table 90.4. The percentage deviations between the two methods do not exceed 4 %. The dotted line in graph shows before compensation results and continuous line shows after compensation results (Fig. 90.9).

Table 90.4 Comparison of simulation and experimental results

Sr. no.	Load step	Power transferred (W)	Load bus voltage (V)	Percentage deviations between two methods
1	1	340	328	3.5
2	2	690	674	2.3
3	3	850	838	1.4

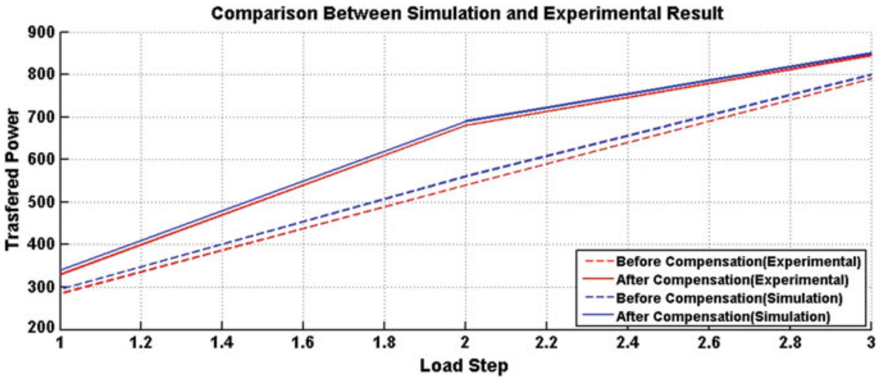

Fig. 90.9 Comparisons between simulation and experimental result

90.7 Conclusion

A laboratory model representing static VAR compensator using FC-TCR configuration was constructed. It was demonstrated that use of SVC could effectively control bus voltage and increases active power transfer capacity. The rise in active power transferred helps to relieve the congestion. The difference between the implemented SVC model in MATLAB-Simulink and the prototype is less than 3.5 %. Moreover, more accurate results are obtained by increasing the load; also the disturbance introduced by load resistance can be overcome within 1 s.

Acknowledgement The authors gratefully acknowledge management of Bharati Vidyapeeth College of Engineering Pune, Modern College of Engineering Pune, College of Engineering Pune, and Mr. D.M. Tagare, Madhav Capacitors Pvt. Ltd. Pune for providing us facility to carry out research work efficiently.

Appendix

The value of each loading step is given as follows

- Load step1—(480 − j450) Ω,
- Load step2—(820 − j748) Ω, and
- Load step3—(1,044 − j876) Ω

PI Controller: Kp: 12.0, Ki: 1
T.F. of controller:

$$Gc = \frac{S + 12}{S}$$

References

1. Khaparde SA, Abhyankar AR (2002) Deregulation in power industry. In: Continuing education programme, IIT Mumbai
2. Singh SN (2002) Role of FACTS devices in competitive power market. In: Continuing education programme, IIT Mumbai
3. Mathur RM, Varma RK (2002) Thyristor-based FACTS controllers for electrical transmission systems. IEEE Press, New York
4. Paul S, Basu SK, Mondal R (1992) A microcomputer controller static VAR compensator for power system laboratory experiments. IEEE Trans Power Syst 7(1):371–376
5. Patil DR, Gudaru U (2012) The experimental studies of transient free digital SVC controller with thyristor binary compensator at 125 kVA distribution transformer. London, U.K, 4–6 Jul 2012, vol II
6. Chopade P, Bikdash M, Kateeb I, Kelkar AD (2011) Reactive power management and voltage control of large transmission system using SVC (static VAR compensator). IEEE, Mar 2011, pp 85–90

Chapter 91
Design Aspects of Blade Shape and Position for the MAGLEV Vertical Axis Wind Turbine

G.P. Ramesh and C.V. Aravind

Abstract Due to its low power generation capabilities, the Vertical Axis Wind Turbine is highly conducive for standalone applications. The operational range limits the power generating capability in wind turbines and is highly influenced through the blade shape and angle of attack. Recently maglev concept is introduced to increase the velocity of rotational mass and thereby the power generation capability. A maglev design incorporated with the optimized wind turbine is presented in this work. Initial investigation on three different wind profiles and the suitable airfoil provide the degree of impact at angle of 30° to have the highest lift coefficient for the chosen airfoil structure. The power generation is further influenced by the choice of the high torque density electric generator is used for evaluations of the design.

Keywords Vertical axis wind turbine · Maglev design · Optimize · Airfoil · Computational fluid dynamics (CFD)

91.1 Introduction

Adopting horizontal wind turbine production is challenging with the positioning of Malaysia in the global map. An annual wind velocity 2–3 m/s adopting the technology for horizontal wind turbine are challenging [1]. However vertical axis type wind turbine generates electricity even at low wind speed [2, 3], mostly for low power utility due to its inability to support wind force from all directions. The turbine efficiency can be improved with the optimal choice and design of the blades as the

G.P. Ramesh
St. Peter's University, Chennai, India
e-mail: rameshgp@yahoo.com

C.V. Aravind (✉)
CIARC, Taylor's University, Subang Jaya, Selangor, Malaysia
e-mail: aravindcv@ieee.org

C. Kamalakannan et al. (eds.), *Power Electronics and Renewable Energy Systems*,
Lecture Notes in Electrical Engineering 326, DOI 10.1007/978-81-322-2119-7_91

cut-in speed is proportional to the amount of wind power generated. The efficiency improvement is feasible with the use of magnetic bearing instead of mechanical bearing, a concept of magnetic levitation as introduced in [4]. The technological advancement in machine design and fabrications, the decrease of price material such as magnets, this type of maglev-assisted turbine offer great advantage in the market [4–6]. With lesser vibrations and inertia the maintenance is easier comparatively [5]. An approach to the choice on the blade shape and position for such Maglev assisted vertical turbine is investigated in this work. With the improvement on the rotor blade of the proposed turbine, the increase in the wind harvest is initiated, thereby increasing the efficiency. This paper presents the implementation of such designed structure for small renewable energy supply network.

91.2 Air-Foil Design Concepts

Wind technology uses either lift or drag principles as in both the Vertical Axis Wind Turbine (VAWT) and Horizontal Axis Wind Turbine (HAWT). The structure of VAWT is that the rotor rotates the shaft in the same axis of the generator [7]. Furthermore it does not derive any intensive cost in the installations. The operating efficiency depends on the amount of wind that it can harvest in either of the technology approach. The maximum amount of kinetic energy that can be extracted is only 59.3 %, based on the Betz limitation under ideal condition [1].

The design on the shape of the air-profile, the number of blades and the position of the blades are important for the operational efficiency of the turbine. Figure 91.1a shows the general aerodynamic that is acting on the rotor blades. The separation of the vertical components at various positions is critical in the power output from the turbine. The design on the turbine blades and the positions with respect to the wind flow is also critical in enhancing the output power. Also this depends on the mechanical

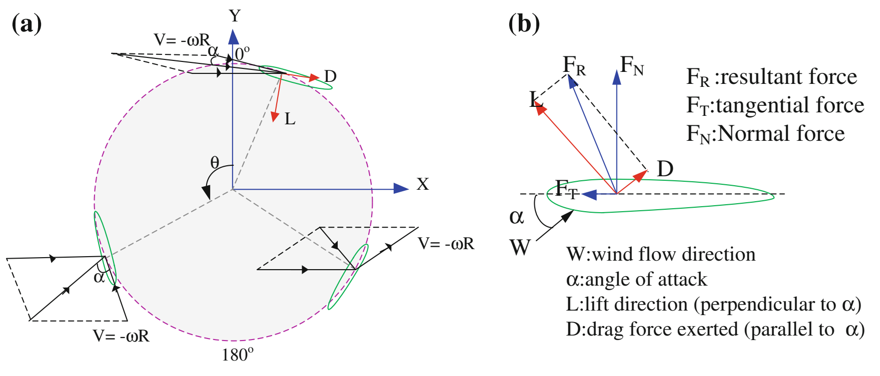

Fig. 91.1 Aero-dynamic forces at the Blade Vertex. **a** General aero-dynamic forces. **b** Force acting on a blade

characteristics of the turbine, the size of the turbine, the number of blades. When the wind hits the blade, drag and lift force are produces. The efficiency of the airfoil highly depends on the lift force produce from the airfoil. Figure 91.1b shows the force acting on a blade. The momentum of force that course the lift and drag derive the machine to be either lift based turbine or drag force turbine [4]. Figure 91.2 shows the flowchart representations of the analysis using the Computational Fluid Dynamics (CFD). National Advisory Committee for Aeronautics (NACA) developed aircraft wings, as NACA airfoils are the various structures generally used for the design of blades [7]. There are three different types of blade shapes namely NACA0012, NACA4212 and NACA8612 are used for the analysis for the design of VAWT as it provide better solidity for VAWT [4]. For the same solidity, different number of blade and chord size will affect the performance of the VAWT [8–10]. Figure 91.3a shows the characteristics of the NACA 0012 designed model. The lift co-efficient reach about 1.2 with the position of the blade about 16°. This is due to the symmetry of the profile about its horizontal axis. Figure 91.3b show the characteristics of the designed NACA 4212 with the lift co-efficient improvement about 1.48. NACA 88612 reveals better lift coefficient due to the change in the ratio of the vortex inside its structure as seen in Fig. 91.3c.

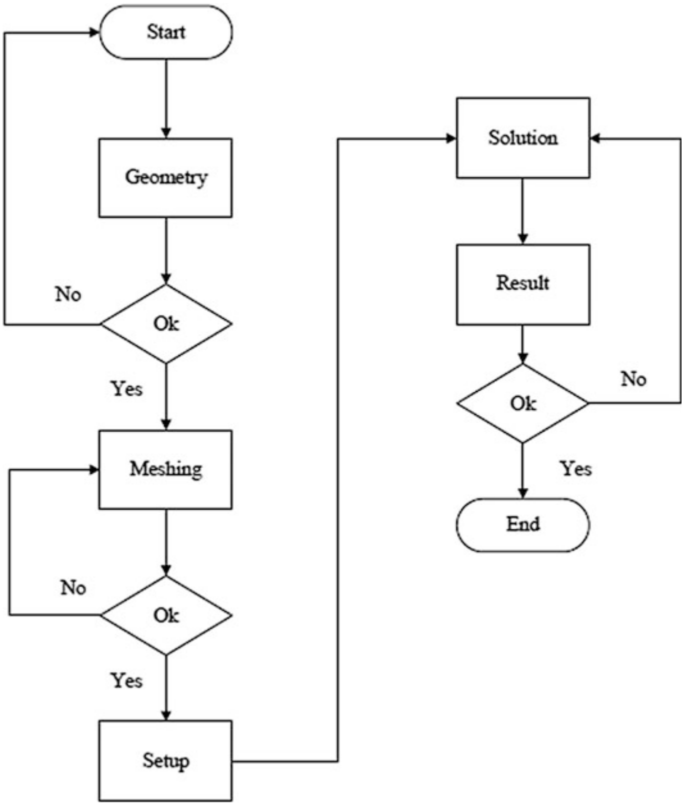

Fig. 91.2 Flowchart for the analysis using CFD

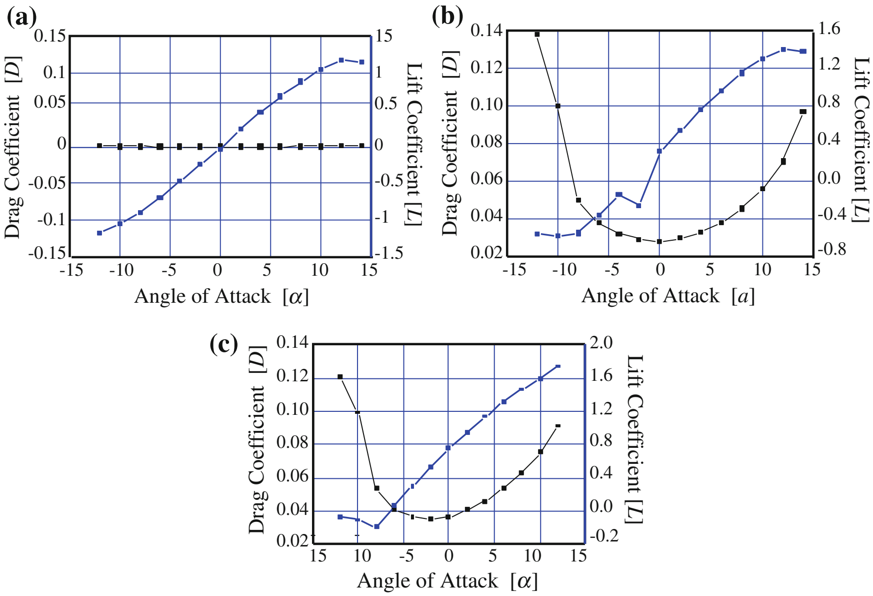

Fig. 91.3 Characteristics of airfoil under investigations. **a** NACA 0012. **b** NACA 4212. **c** NACA 8612

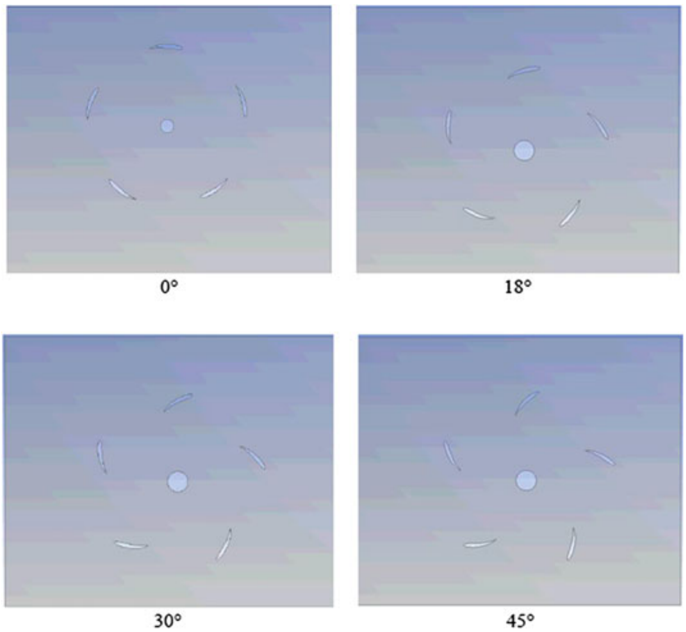

Fig. 91.4 Position analysis of the airfoil design (shown for NACA 8612)

91.3 Results and Discussions

A five blade structure is used for the analysis to determine the best position of the blade structure. In this case of analysis the degree of the blade structure as a whole is varied until the maximum output is developed with respect to the static wind profile. Figure 91.4 shows the lift coefficient for various degree of impact. It is

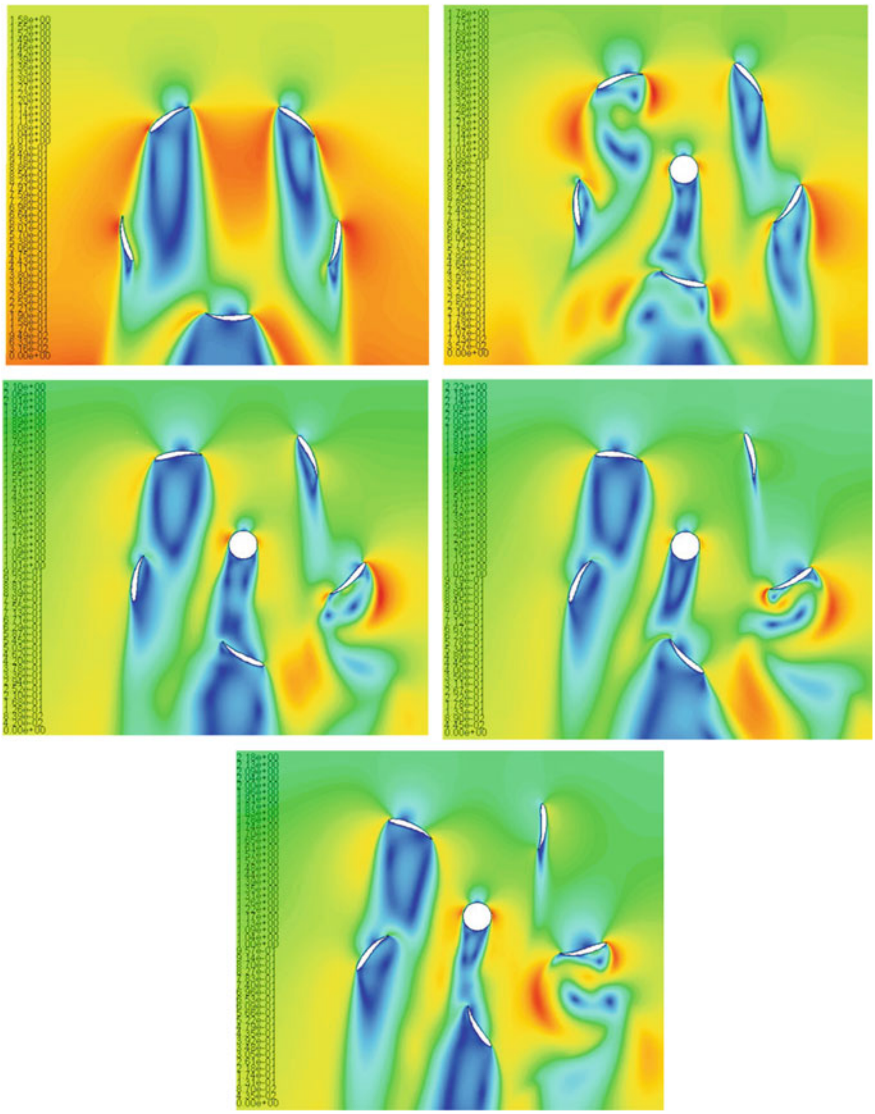

Fig. 91.5 Lift coefficient of NACA 0012, NACA 4212 and NACA 8612

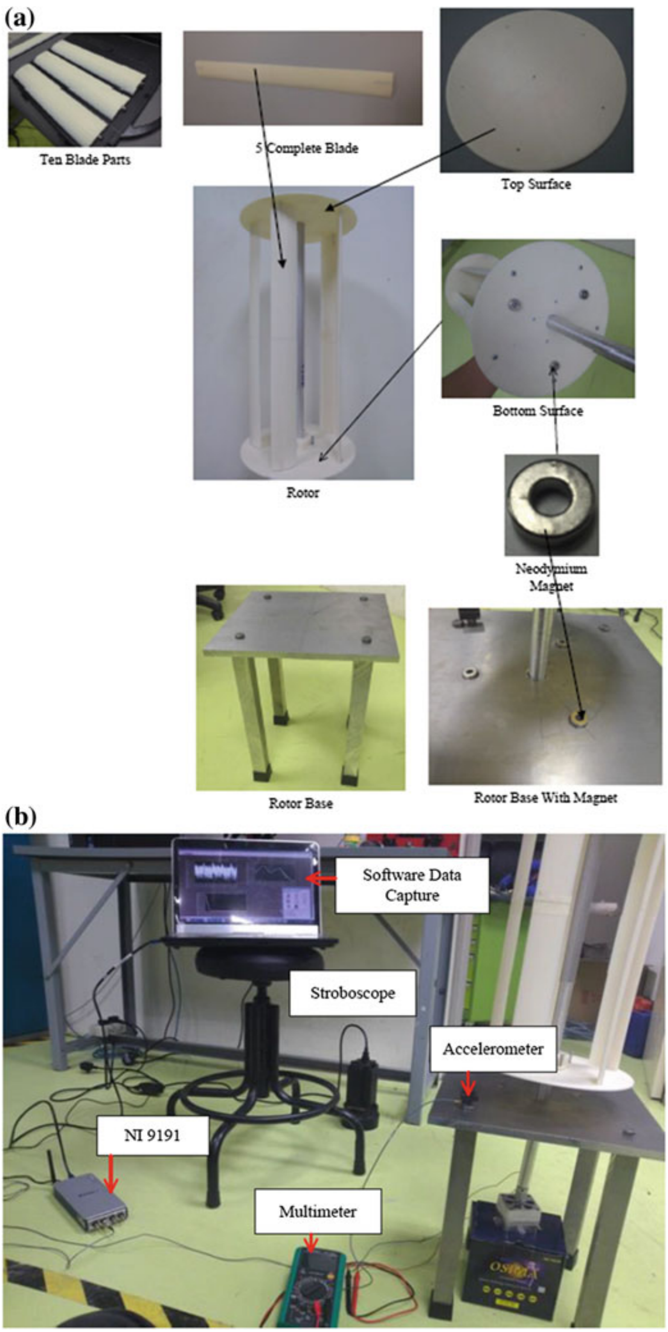

Fig. 91.6 Prototype of the designed system. **a** Components of the designed prototype. **b** Experimental set-up for testing

Table 91.1 NACA profile under investigations for various angle of attack

Angle of Attack	NACA 0012	NACA 4212	NACA 8612
2	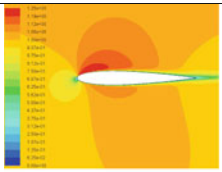	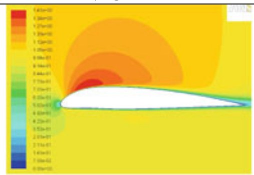	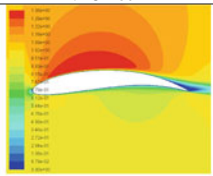
8	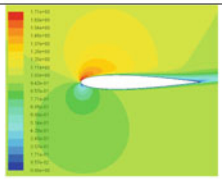	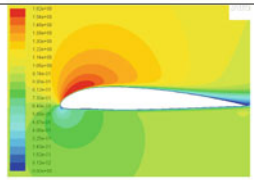	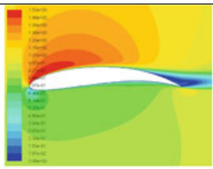
14	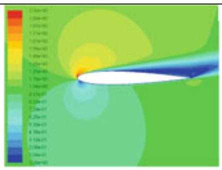	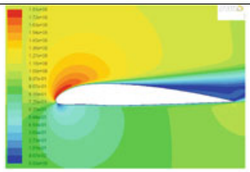	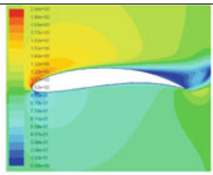
16	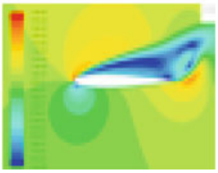	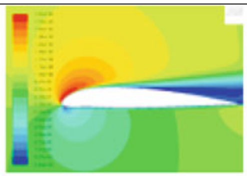	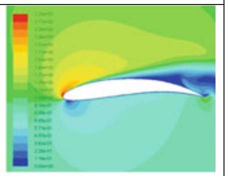

observed that at 30° is the most suitable because of the highest lift coefficient. In order to have the airfoil to have a high lift coefficient the pressure below the airfoil has to be larger than on the top of the airfoil [7]. Figure 91.5 shows the simulation results obtain from the analysis of the five blade positioning. From the comparison, it is shown that at the angle of attack of 30°, the lift coefficient is the highest. Figure 91.6 shows the designed blade and the integrated blades to the turbine structures. Table 91.1 shows a comparison of three blade structure for various angle of attack.

91.4 Conclusions

The ability of the rotor to harvest more wind is analysed on the three blade design and for the blade position. Computational fluid dynamics based finite element approach is used for the analysis on the blade design and the positioning of the blade on the rotor. The lift and drag characteristic of the airfoil is investigated using the FEA tool. Among the blade analyzed the NACA 8612 exhibit better lift coefficient which is 1.79. The positioning of the five blade structure on the rotor is done at various angles and is found that optimal angle is at 30° with respect to the wind approach. The experimental setup produced better power output with the use of low speed high power generator the results would be documented in subsequent work.

References

1. Siti MRS, Norizah M, Syafrudin M (2011) The evaluation of wind energy potential in Peninsular Malaysia. Int J Chem Environ Eng 2:4–5
2. Shahrukh Adnan Khan Md, Rajprasad KR, Rajparthiban KR, Aravind CV (2013) Performance analysis of a 20 Pole 1.5 KW three phase permanent magnet synchronous generator for low speed vertical axis wind turbine. Sci Res Energy Power Eng
3. Rigoberto C, Samuel G, Joseph T (2011) Wind power technologies: a need for research and development in improving VAWT's airfoil characteristics. J Ind Technol 27:4
4. Aravind CV, Rajparthiban R, Rajprasad R, Wong YV, Stanley GI (2013) A novel magnetic levitation assisted vertical axis wind turbine—design procedure and analysis. In: Proceedings 8th international colloquium on signal processing and applications, Kualalumpur, 22–23 Mar 2012
5. Sandra E, Hans B, Mats L (2006) Evaluation of different turbine concepts for wind power. Renew Sustain Energy Rev 12:10–11
6. Alex S (2010) Aerodynamic forces acting on an airfoil. The College of Wooster, May 2010
7. Moran J (2003) An introduction to theoretical and computational aerodynamics. Dover, p 7. ISBN 0-486-42879-6
8. Carringan TJ (2010) Aerodynamic shape optimization of a vertical axis wind turbine. University of Texas
9. Wahab AA, Mohd S, Dahalan MN, Mat S, Chong WT, Ismail MH, Abas MF, Muslimen R (1986) Eqwin turbine—the break through for wind energy implementation in Malaysia. In Proceedings of ICME
10. Aravind CV, Rajparthiban R, Rajprasad R, Wong YV (2012) A novel magnetic levitation assisted vertical axis wind turbine–design procedure and analysis. EURECA 2013 Taylor's University Malaysia

Chapter 92
Placement and Sizing of D-STATCOM Using Particle Swarm Optimization

S. Devi and M. Geethanjali

Abstract This paper addresses the improvement of power quality using distribution Static Compensator in radial distribution systems. The major factors to improve the quality of power are voltage profile improvement and total loss reduction of the system. Compensation of reactive power decreases the total power loss of the distribution systems. The main objective of this work is to reduce the total loss of the radial distribution system with voltage profile improvement. Particle Swarm Optimization technique has been used in this work for the placement and sizing of DSTATCOM in radial distribution systems. Also, the test results are compared with the results obtained from the analytical method. The proficiency and significance of the proposed work have been instigated on 12, 34 and 69 bus radial distribution system consisting of 11, 33 and 68 sections respectively.

Keywords Particle swarm optimization (PSO) · Radial distribution systems (RDS) · Distribution static compensator (DSTATCOM)

92.1 Introduction

The advent of FACTS devices for fast dynamic voltage, impedance, and phase angle control on high-voltage ac lines has given rise to a new family of power electronic equipment to control and optimize the power system dynamic performance, e.g., Static Synchronous Compensator (StatCom), Static Synchronous Series Compensator (SSSC), and Unified Power Flow Controller (UPFC). The application of this technology has paved way for new and better opportunities for an appropriate transmission and distribution control. The series and shunt power systems

S. Devi (✉)
Department of EEE, National College of Engineering, Tirunelveli, India
e-mail: devi_balasubramanian@yahoo.com

M. Geethanjali
Department of EEE, Thiagarajar College of Engineering, Madurai, India

C. Kamalakannan et al. (eds.), *Power Electronics and Renewable Energy Systems*,
Lecture Notes in Electrical Engineering 326, DOI 10.1007/978-81-322-2119-7_92

compensation handles reactive power to maintain the bus voltages close to their nominal values for reducing line currents and system losses [1]. Flexible AC Transmission System (FACTS) was initially developed for transmission networks but at present the same has been applied for distribution systems too. Also for the protection of sensitive loads from the voltage sag, FACTS devices are becoming more popular [2]. Nowadays in the distribution systems, the reactive loads such as pumps, fans and induction motor consumes more power. A power electronics converter that has been used in industries and domestic devices also draws more reactive power from the supply. This creates voltage distortion to the loads coupled at the same point and increases the loss in the distribution feeder. A Static Compensator (STATCOM) is a Flexible AC Transmission System (FACTS) controller, which can either absorb or deliver reactive power to a power system. Therefore DSTATCOMs have been connected with the distribution systems to improve the voltage stability and to compensate the reactive power [3]. The DSTATCOM is a power electronic-based Synchronous Voltage Generator (SVG) capable to supply rapid and uninterrupted capacitive and inductive reactive power supply [4]. For Power Quality improvements distribution static synchronous compensator (D-STATCOM) is a fast response, solid-state power controller. It provides flexible voltage control at the point of connection to the utility distribution feeder. Therefore, by absorbing/supplying the reactive power, DSTATCOM regularizes the voltage. Optimal location and sizing of shunt FACTS controllers such as SVC or STATCOM is very important to protect the system from voltage collapse and to provide better voltage profile [5]. Distribution STATic COMpensator (D-STATCOM) is proposed for compensation of reactive power and unbalance caused by various loads in distribution system. A D-STATCOM injects a current into the system to correct the voltage sag, swell and power factor. Distribution Static Synchronous Compensator (D-STATCOM) is an effective measure to maintain voltage stability and improve power quality of distribution line. Particle Swarm Optimization (PSO) is also a bio-mimetic optimization technique developed by Eberhart and Kennedy in 1995, which was inspired by the social behavior of bird flocking and fish schooling. The critical concept of PSO is the velocity change of each particle toward its individual best location and global best location among the individual at each step. The balance between the global and local search throughout the run makes PSO a successful optimization algorithm. In past several years, PSO has been successfully applied in many research and application areas [6]. Therefore, in this proposed work PSO technique has been used for the placement and sizing of radial distribution systems. By comparing the results with the analytical method, the effectiveness of this work has been proved.

92.2 Static Compensator (STATCOM)

Power quality problems such as unbalanced load, voltage sag, voltage fluctuations and voltage unbalance are compensated by Distribution STATCOM (DSTATCOM) which is a shunt connected voltage source converter [7].

92.2.1 Mathematical Calculation

The relationships between voltage and current between bus 'i' and 'j' can be written as

$$V_{oj}\angle\alpha_0 = V_{oi}\angle\delta_0 - (R + jX)I_{oL}\angle\theta_o \tag{92.1}$$

where, $V_{oj}\angle\alpha_o$—Voltage of bus j before compensation, $V_{oi}\angle\delta_0$. Voltage of bus i before compensation, $Z = R + jX$. Impedance between buses i and j, $I_{oL}\angle\theta_0$—Current flow in line before compensation. In the steady state condition, the changes occur in all node voltages, especially the neighboring nodes of DSTATCOM location and the branch current of the network is changed by installing the DSTATCOM in RDS. The schematic diagram of buses 'i' and 'j' of the distribution system, when DSTATCOM is installed for voltage regulation in bus 'j', is shown in Fig. 92.1. Voltage of bus j changes from V_j to V_{jnew} when DSTATCOM is used.

$$\begin{gathered}\angle I_{DSTATCOM} = (\pi/2) + \alpha_{new}, \\ \alpha_{new} < 0\end{gathered} \tag{92.2}$$

$$V_{jnew}\angle\alpha_{new} = Vi\angle\delta - (R + jX)I_L\angle\theta - (R + jX)I_{DSTATCOM}\angle((\pi/2) + \alpha_{new}) \tag{92.3}$$

where, $I_{DSTATCOM}\angle((\pi/2) + \alpha_{new})$ Injected current by DSTATCOM, $V_{jnew}\angle\alpha_{new}$ Voltage of bus j after compensation, $Vi\angle\delta$ Voltage of bus i before compensation, $I_L\angle\theta$ Current flow in line after DSTATCOM installation.

Voltage $Vi\angle\delta$ and current $I_L\angle\theta$ are derived from the direct load flow analysis.

Injected power by DSTATCOM can be written as

$$jQ_{D-STATCOM} = V_{jnem}(I_{D-STATCOM})^* \tag{92.4}$$

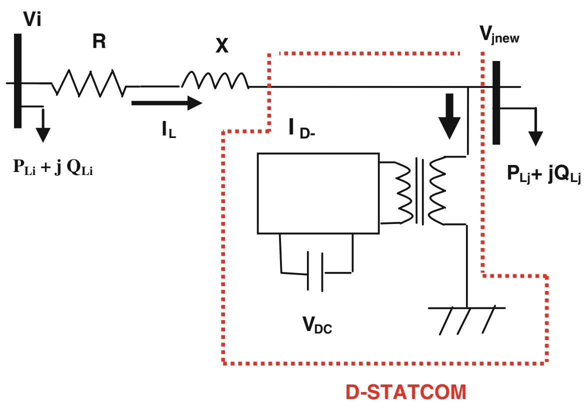

Fig. 92.1 Single line diagram of two buses of a distribution system with consideration of DSTATCOM

where,

$$V_{jnew} = V_{jnew} \angle \alpha_{new} \tag{92.5}$$

$$I_{D-STATCOM} = I_{D-STATCOM} \angle((\pi/2) + \alpha_{new}) \tag{92.6}$$

92.3 Problem Formulation

The objective of DSTATCOM placement in the distribution system is to minimize the reactive power of the system, subjected to certain operating constraints. Mathematically, the objective function of the problem is described as:

$$\min f = \min(T_{Loss}) \tag{92.7}$$

where, T_{Loss} is the total power loss of the radial distribution system.

Constraints:
Equality Constraint:
Angle difference between V_{jnew} and $I_{D\text{-}STATCOM}$ = 90°
Inequality Constraints:
Voltage constraints:

$$V_{i\min} \geq V_i \geq |V_{i\max}|, i = 1, 2, \ldots N \tag{92.8}$$

Current constraints:

$$|Ii| \leq |I i\max|, i = 1, 2, \ldots N \tag{92.9}$$

V_{imin} and V_{imax} are the minimum and maximum voltages of the ith bus respectively. Similarly, I_{max} is the maximum value of the branch current. The above mentioned equality and inequality constraints (Eqs. 92.8 and 92.9) can be used to minimize the total real power loss. In this paper PSO algorithm is analyzed and the placement and sizing of DSTATCOM is optimized.

92.4 Load Flow Analysis

The traditional load flow methods used in transmission systems, such as the Gauss-Seidel, Newton-Raphson and fast decoupled methods cannot be used to find the voltages and line flows in distribution systems because of high R/X ratio. In this paper direct load flow analysis has been used [8].

92.5 Particle Swarm Optimization (PSO)

Particle Swarm Optimization (PSO) is also a population based algorithm that was developed in 1995 [9]. The randomly generated population is called a swarm and it consists of individuals named particles. Every particle in the swarm indicates a probable explanation of the optimization problem. With a random velocity, each particle moves through a D-dimensional search space [10]. Each particle's velocity and position is updated using Eqs. (92.10 and 92.11).

$$V_i^{k+1} = c * [\omega V_i^k + C_1 rand1 * (Pbest - S_i^k) + C_2 rand2 * (Gbest - S_i^k)] \quad (92.10)$$

$$S_i^{k+1} = S_i^k + V_i^{k+1} \quad (92.11)$$

$$\omega = \omega_{\max} - \frac{[(\omega_{\max} - \omega_{\min}) * current\,generation\,number]}{Maximum\,generation\,number} \quad (92.12)$$

where, $\omega_{\max}$ Initial value of the inertia weight, $\omega_{\min}$ Final value of the inertia weight

$$c = \frac{2}{(2 - \phi - \phi 1)} \quad (92.13)$$

$$\phi 1 = \sqrt{\phi^2 - 4\phi} \quad (92.14)$$

where S^k is current searching point, S^{k+1} is modified searching point, v^k is current velocity, v^{k+1} is modified velocity of agent i, C_1 and C_2 are weight coefficients for each term, ω is weight function for velocity of the agent, and rand1, rand2 are the random value generated between [0, 1]. Constriction coefficient 'c' is calculated from the values of the acceleration coefficient limits φ and φ_1. Here φ is varied between $\varphi_{\min}$ and $\varphi_{\max}$.

92.6 Simulation Results

The proposed work has been evaluated using three different test systems (12, 34 and 69 bus) [11].

92.6.1 Test System-1 (12 Bus System)

Table 92.1 shows the final results of DSTATCOM sizing and placement in 12 bus radial distribution system. From Table 92.1 it is inferred that, the total loss obtained from analytical method and PSO are 0.01395 and 0.009933 MW respectively.

Table 92.1 DSTATCOM placement for 12 bus test system using analytical method and PSO technique

Parameter	Without DSTATCOM	With DSTATCOM	
	DLF	Analytical	PSO
Total load (MVA)	0.43 + 0.4i	0.43 + 0.4i	0.43 + 0.4i
Total loss (MW)	0.0207	0.01395	0.009933
Bus number	8	8	8
Voltage (p.u)	0.9754	0.98	0.9799
Size of DSTATCOM (MVar)	–	0.4312	0.2497

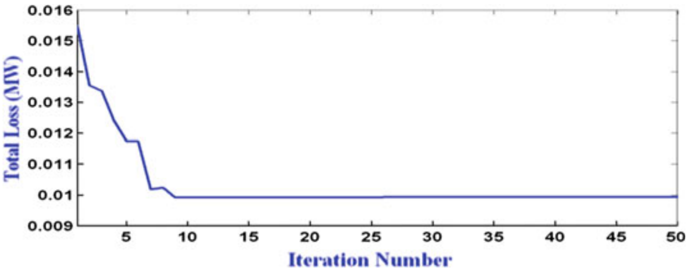

Fig. 92.2 Evolution of the objective function (total loss) with respect to number of iterations for bus no. 8 in 12 bus distribution test system

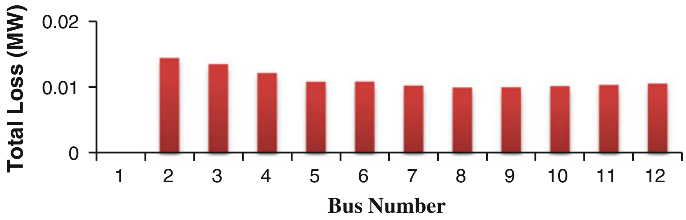

Fig. 92.3 Total loss after the placement of DSTATCOM for 12 bus system using PSO

The total loss is reduced after the placement of DSTATCOM. The size of DSTATCOM attained from the analytical method and PSO is 0.4312 and 0.2497 MVar respectively. Also, the optimal placement of DSTATCOM obtained from the analytical method and PSO is 8th bus.

Figure 92.2 shows the evolution of the objective function (total loss) with respect to number of iterations for bus no. 8 in 12 bus distribution test system. The voltage before the placement of DSTATCOM is 0.9754 p.u and after the placement of DSTATCOM using PSO is 0.97799 p.u. From Fig. 92.3, it is inferred that the total loss is minimum in bus number 8 after placement of DSTATCOM when compared with other buses. The voltage profile improvement is shown in Fig. 92.4. From

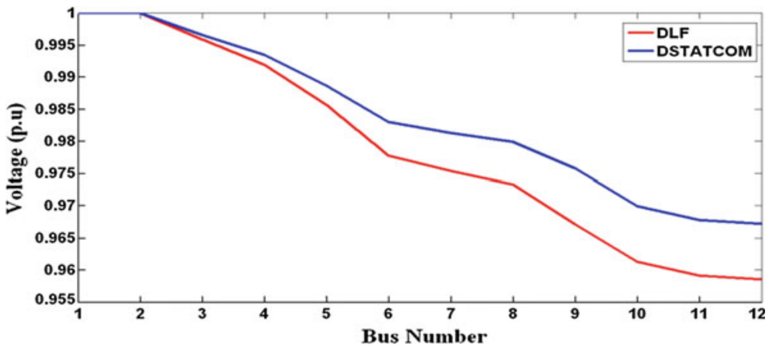

Fig. 92.4 Voltage profile improvement of each bus in 12 bus system after the placement of DSTATCOM using PSO

Table 92.2 DSTATCOM placement for 34 bus test system using analytical method and PSO technique

Parameter	Without DSTATCOM	With DSTATCOM	
	DLF	Analytical	PSO
Total load (MVA)	4.6 + 2.8i	4.6 + 2.8i	4.6 + 2.8i
Total loss (MW)	0.1638	0.1476	0.13356
Bus number	21	21	21
Voltage (p.u)	0.9663	0.97	0.9711
Size of DSTATCOM (MVar)	–	1.4862	1.8021

Fig. 92.4, it is inferred that the voltage has been improved after the placement of DSTATCOM using PSO when compared with the results obtained from DLF analysis.

92.6.2 Test System-2 (34 Bus System)

The final results of DSTATCOM sizing and placement in 34 bus radial distribution system are tabulated in Table 92.2. From Table 92.2, the total loss obtained from the analytical method and PSO are 0.1476 and 0.13356 MW respectively. Here also after the placement of DSTATCOM the total loss is reduced. The size of DSTATCOM attained from the analytical method and PSO are 1.4862 and 1.8021 MVar respectively. Figure 92.5 shows the evolution of the objective function (total loss) with respect to number of iterations for bus no. 21 in 34 bus distribution test system. From Fig. 92.6 it is understood that the total loss is minimum when DSTATCOM is placed at the 21th bus. So the optimal placement of DSTATCOM obtained from the analytical method and PSO is 21st bus in the 34 bus test system.

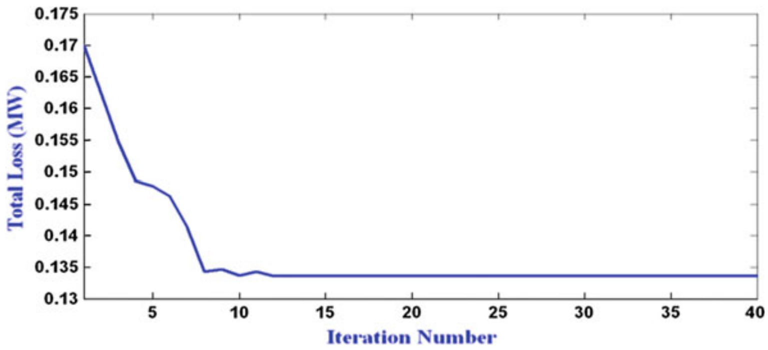

Fig. 92.5 Evolution of the objective function (total loss) with respect to number of iterations for bus no. 21 in 34 bus distribution test system

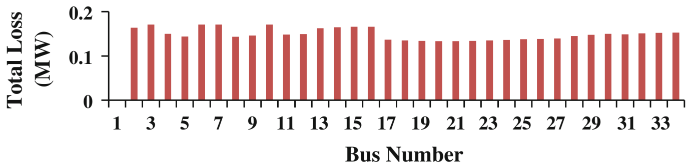

Fig. 92.6 Total loss after the placement of DSTATCOM for 34 bus system using PSO

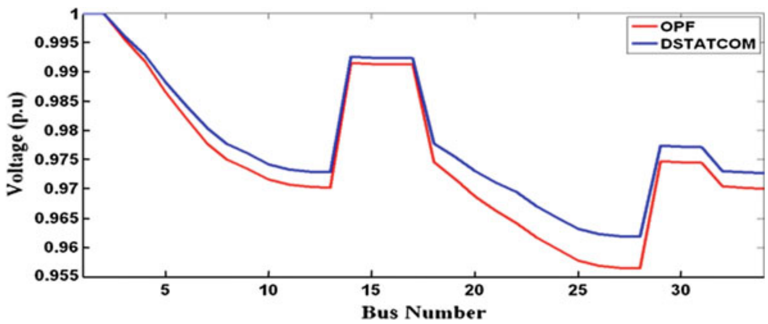

Fig. 92.7 Voltage profile improvement of each bus in 34 bus system after the placement of DSTATCOM using PSO

The voltage before the placement of DSTATCOM is 0.9663 p.u, after the placement of DSTATCOM using PSO it is 0.9711 p.u. Figure 92.7 shows the voltage profile improvement of 34 bus test system. From Fig. 92.7 it is inferred that, after the placement of DSTATCOM, the voltage has been improved when compared with the results obtained from DLF analysis. This analysis shows that the results obtained from PSO gives better results than the analytical method.

Table 92.3 DSTATCOM placement for 69 bus test system using analytical method and PSO technique

Parameter	Without DSTATCOM	With DSTATCOM	
	DLF	Analytical	PSO
Total load (MVA)	3.8 + 2.69i	3.8 + 2.69i	3.8 + 2.69i
Total loss (MW)	0.24479	0.1744	0.1685
Bus number	61	61	61
Voltage (p.u)	0.9196	0.98	0.94245
Size of DSTATCOM (MVar)	–	1.4464	1.4616

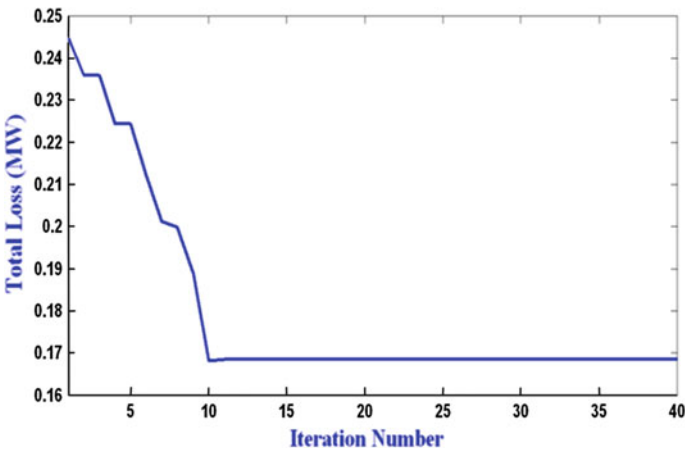

Fig. 92.8 Evolution of the objective function (total loss) with respect to number of iterations for bus no. 61 in 69 bus distribution test system

92.6.3 *Test System-3 (69 Bus System)*

The results obtained from DSTATCOM sizing and placement in 69 bus Radial Distribution System is tabulated in Table 92.3. From Table 92.3, it is inferred that the total loss calculated from the analytical method and PSO 0.1744 and 0.1679 MW respectively. The size of DSTATCOM attained from the analytical method and PSO 1.4464 and 1.4616 MVar respectively. Also it shows that the placement of DSTATCOM reduces the total loss. Figure 92.8 shows the evolution of the objective function (total loss) with respect to number of iterations for bus no. 61 in 69 bus distribution test system. Figure 92.9 shows the total loss in each bus. From Fig. 92.9 it is understood that the total loss is minimum when DSTATCOM is placed at the 61th bus. So the optimal placement of DSTATCOM obtained from the analytical method and PSO technique is at the 61th bus in 69 bus test system. Before placing the DSTATCOM, the voltage at the 61th bus is 0.9196 p.u, after the

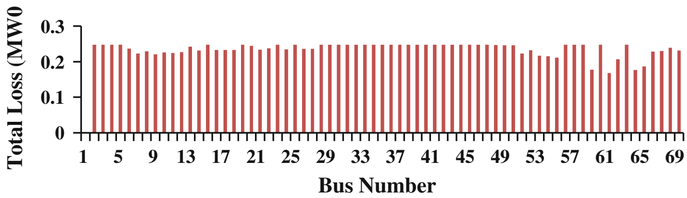

Fig. 92.9 Total loss after the placement of DSTATCOM for 69 bus system using PSO

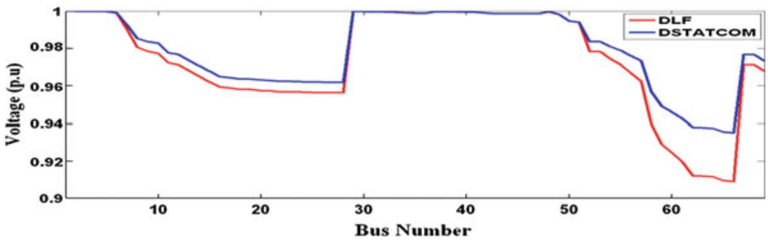

Fig. 92.10 Voltage profile improvement of each bus in 69 bus system after the placement of DSTATCOM using PSO

placement of DSTATCOM using PSO it is 0.94245 p.u and using the analytical method it is 0.98 p.u. Figure 13 shows the voltage profile improvement of 69 bus test system.

Figure 92.10 shows, after the placement of DSTATCOM the voltage has been improved in all the nodes when compared with the results obtained from DLF analysis. This analysis also shows that, the results obtained from the PSO gives better results than the results obtained from the analytical method in location and sizing of DSTATCOM, reduction of total loss and improvement of voltage profile in Radial Distribution Systems.

92.7 Conclusion

This paper proposes the improvement of power quality using the optimal placement and sizing of DSTATCOM in Radial Distribution Systems. To improve the quality of power, the two important factors such as reduction of total loss and improvement of voltage profile has been considered. This work has been done on three test systems (12, 34 and 69 bus) using analytical method and Particle Swarm Optimization Algorithm. The results show that the final values obtained from the two methods are approximately equal. Implementation of PSO algorithm is very easy when compared with the equations used in the analytical method. PSO does not require any complex differential equation. Therefore, using PSO the placement and sizing can be done effectively. Also, it shows that the placement and sizing of DSTATCOM in Radial Distribution System reduces the total loss and improves the voltage profile, thereby improving the power quality.

References

1. Valderrábano Antonio, Ramirez Juan M (2010) DStatCom regulation by a fuzzy segmented PI controller. Electr Power Syst Res 80:707–715
2. Goswami AK, Gupta CP, Singh GK (2011) Minimization of voltage sag induced financial losses in distribution systems using FACTS devices. Electr Power Syst Res 81:767–774
3. Zaveri Tejas, Bhalja Bhavesh, Zaveri Naimish (2012) Comparison of control strategies for DSTATCOM in three-phase, four-wire distribution system for power quality improvement under various source voltage and load conditions. Electr Power Energy Syst 43:582–594
4. Valderrábano Antonio, Ramirez Juan M (2010) DStatCom regulation by a fuzzy segmented PI controller. Electr Power Syst Res 80:707–715
5. Phadke AR, Fozdar M, Niazi KR (2012) A new multi-objective fuzzy-GA formulation for optimal placement and sizing of shunt FACTS controller. Electr Power Energy Syst 40:46–53
6. Eberhart RC, Shi YH (2001) Particle swarm optimization: developments, applications and resources. In: CEC 2001: proceedings of the IEEE congress on evolutionary computation, Seoul Korea, May, 2001. IEEE, New Jerssey pp 81–86
7. Hosseini M, Shayanfar HA, Fotuhi-Firuzabad M (2007) Modeling of D-STATCOM in distribution systems load flow. J Zhejiang Univ Sci A 8(10):1532–1542
8. Teng Jen-Hao (2003) A direct approach for distribution system load flow solutions. IEEE Trans Evol Comput 18(3):882–887
9. Kennedy J, Eberhart R (1995) Particle swarm optimization. In: Proceedings of the IEEE international conference on neural networks
10. Abdelsalam AE (Student Member, IEEE), El-Hawary ME (Life Fellow, IEEE) (2010) Optimal capacitor placement and sizing in unbalanced distribution systems with harmonics consideration using particle swarm optimization. IEEE Trans Power Deliv 25(3)
11. Gozel T, Hocaoglu MH (2009) An analytical method for the sizing and siting of distributed generators in radial systems. Electr Power Syst Res 79:912–918

Chapter 93
Fault Tolerant Soft Starter Control for Induction Motors

V. Jaikrishna, Linss T. Alex, Subhranhsu Sekhar Dash and Susanta Kumar Gachhayat

Abstract This thesis presents a fault-tolerant soft starter capable of operating in a two-phase mode in the event of a thyristor/SCR open-circuit or short-circuits switch-fault in any one of the phases using closed-loop control scheme. This soft starter fault-tolerant control will reduce starting motor torque pulsations and reduced inrush current magnitudes. Faults occurring in soft starters do not cause immediate permanent damage to the motor-soft starter system. But the impact of a fault on both the soft starter and the motor will gradually evolve into a severe damage stage if the fault is left unattended. A DSP controller is used to give the triggering pulses to the thyristors connected in antiparallel. This thesis includes the simulation of fault tolerant closed loop control of induction motor with SCR switch fault.

93.1 Introduction

Polyphase induction motors were the main prime movers for industrial and manufacturing processes as well as numerous propulsion applications. But whenever an induction motor is started, the electrical system experiences a current surge and torque surge [1]. With line voltage applied to the motor, the current can be anywhere between five to seven times the motor full load current. The magnitude of

V. Jaikrishna (✉) · L.T. Alex · S.S. Dash · S.K. Gachhayat
Deptartment of EEE, SRM University, Kattankulathur, Chennai, Tamil Nadu, India
e-mail: jaikrishnavijay@gmail.com

L.T. Alex
e-mail: linsstalex@gmail.com

S.S. Dash
e-mail: munu_dash_2k@yahoo.com

S.K. Gachhayat
e-mail: gachhayatsusantakumar@yahoo.in

C. Kamalakannan et al. (eds.), *Power Electronics and Renewable Energy Systems*,
Lecture Notes in Electrical Engineering 326, DOI 10.1007/978-81-322-2119-7_93

torque that the driven equipment will have is also very large [2]. These Current and torque surges can be reduced substantially by reducing the voltage supplied to the motor during starting. Using soft starters for reducing high starting currents is a low cost means in comparison to modern ASDs if speed-torque control is not required.

In vital and critical applications, the reliability of soft starters is of paramount importance in ensuring a continuous, almost disturbance-free operation and a gentle, judder-free soft starting, respectively, under various possible faulty conditions [3, 4]. Accordingly, such fault tolerant capabilities will entail the reduction in maintenance costs, downtimes, and more importantly the avoidance of unnecessary soft starter failures, with their potential costly or even perhaps catastrophic consequences.

For fault-tolerant soft starter to be practical and feasible, both hardware and software must be developed to perform the following tasks: (1) fault detection, (2) fault diagnosis, (3) fault isolation, and (4) remedial action. It is essential to carry out this sequence in the minimum possible time after the onset of a fault, in order to avoid the occurrence of secondary failures and this fault has to be cleared in minimum time [5].

Faults occurring in soft starters do not cause immediate permanent damage to the motor-soft starter system. However, the impact of a fault on both the soft starter and the motor will gradually evolve into a severe/damaging stage if the fault is left unattended [6]. Therefore, by monitoring the behavior of the three-phase currents during starting, one could detect and diagnose the type of switch fault. Hence, the core of this dissertation is centered on developing "limp-home" strategies for both the soft starters and the standard adjustable-speed PWM drives.

93.2 Soft Starting

Soft starter technology is widely employed as effective and low-cost means, as compared to modern PWM adjustable-speed drives, to reduce high starting currents and torque pulsations of medium voltage and large ac motors in numerous critical industrial, manufacturing, and transportation applications through use of thyristor-based voltage control. The circuit topology and its control scheme are simple and easy to implement, which will be described in the following subsection.

93.2.1 Principles of Operations

The most common control strategy employed by the soft starter of Fig. 93.1 is the open loop voltage control. Such control approach is widely adopted in commercially available soft starters, as well as soft starter designs reported in the literature. The voltage control is implemented by adjusting either the delay angle, α, or the hold-off angle, γ. The thyristors are then selectively fired to conduct current in the appropriate phase, and naturally commutate off when the current reaches zero.

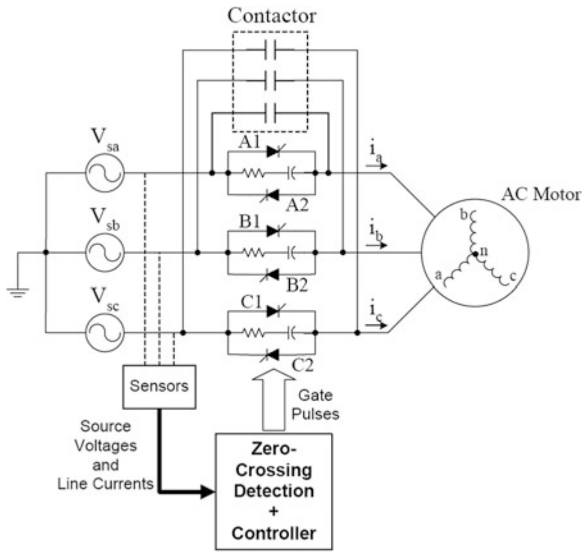

Fig. 93.1 Three-phase soft starter topology

The larger the delay angle, α, or the hold-off angle, γ, the larger the notch width in the applied motor voltage, which consequently reduces the effective or RMS value of such voltage impressed upon the motor. However, improper control of the α or γ firing angles may result in relatively high starting torque and current oscillations. Therefore, optimum starting profiles of the α or γ firing angles have been extensively investigated to produce smooth starting torque and current profiles.

93.2.2 Analysis of Failure Modes and Effects

Two distinct types of failure modes considered in this work are: (1) short-circuit SCR fault, and (2) open-circuit SCR faults, occurring only in one phase of the soft starter. A short-circuit SCR fault can happen in situations such as loose wire in the circuit or breakdown in the snubber circuit. Conversely, an open-circuit SCR fault can occur due to malfunctions either in the gate driver or the pulse generator of the controller.

During a short-circuit SCR fault, the motor terminal of phase-*c* is connected directly to the utility grid. As a consequence, the problem of voltage unbalances impressed upon the motor windings arises during starting. This is due to the fact that the motor phase winding without the SCR connection experiences a full applied voltage at its terminal, whereas the other two phases experience reduced voltages impressed upon them during starting. It is well known that voltage unbalances introduce negative sequence components in the stator currents, which consequently lead to average torque reduction and torque pulsations during the starting transients.

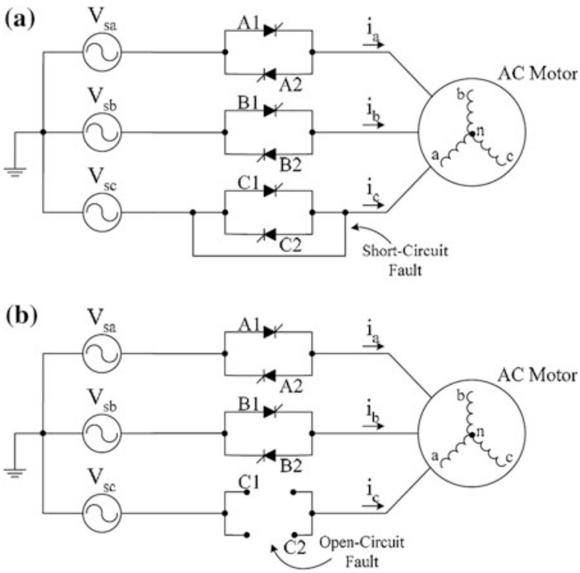

Fig. 93.2 Failure modes in soft starter circuit. **a** Short-circuit fault. **b** Open-circuit fault

An open-circuit fault in the SCR switches can happen when there is a malfunction in the gate driver or the controller that prevents gating of the SCR switches. One common type which is under consideration in this work is depicted in Fig. 93.2b, where both the SCR switches of one phase are inactive. A fault of this nature results in either 2-phase or 1-phase conduction mode during soft starting. Clearly, in the event of 1-phase conduction mode, the motor is incapable of starting since there is no complete path for the current to flow.

93.3 Fault Tolerant Soft Starters

The main concerns in designing and constructing a fault tolerant system are the potential added cost and feasibility issues. The most cost-effective means is to modify the existing control algorithm to accommodate the impact of a fault while still providing acceptable performance. Such a measure usually involves hardware modifications to the soft starter which need to be performed in a modest and cost effective manner.

In this work, the proposed fault tolerant soft starter system is designed with minimum hardware modifications to the soft starter. The control algorithm was implemented in a closed-loop form which is more dynamic, effective, and robust in so far as controllability and performance issues are concerned. In fact, by adopting the proposed control technique, a low-cost soft starter with only two-phase switching mode can be developed.

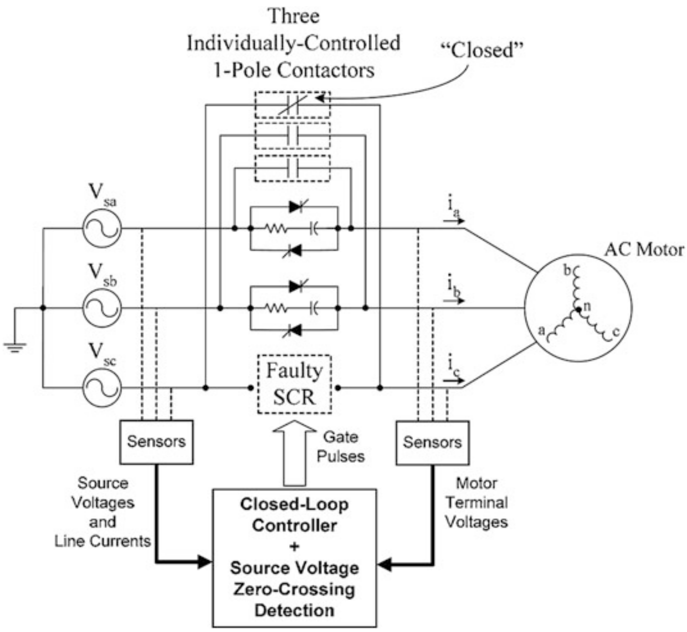

Fig. 93.3 Post-fault soft starter configuration

93.3.1 Topology

The vital part of realizing the fault tolerance of the soft starter through integrating the proposed control algorithm is the amendment of its hardware configuration. The first modification from the conventional soft starter is the addition of a set of three-phase voltage sensors at the motor end of the soft starter to measure the motor terminal voltages. The reason for having these sensors is that the motor terminal voltage measurement will be employed as one set of the feedback signals for the present closed loop control scheme. The second modification is the replacement of the existing 3-pole synchronously-controlled modular contactor with three individually-controlled 1-pole contactors, one pole per phase. The main purpose of this modification is such that the contactor of the corresponding SCR phase can be closed in the event of an open-circuit SCR switch fault. This is in order to isolate the faulty SCR phase, as depicted in Fig. 93.5. Accordingly, the soft starter can function in a two-phase switching mode using the present two-phase control approach. In the event of a short-circuit SCR fault, the corresponding motor phase is automatically connected directly to the utility mains, and hence the soft starter is already in its two-phase switching mode.

Due to the asymmetry of the post-fault two-phase thyristors configuration shown in Fig. 93.3, the problem of voltage unbalances impressed upon the motor windings arises during starting. This is due to the fact that the motor phase winding without

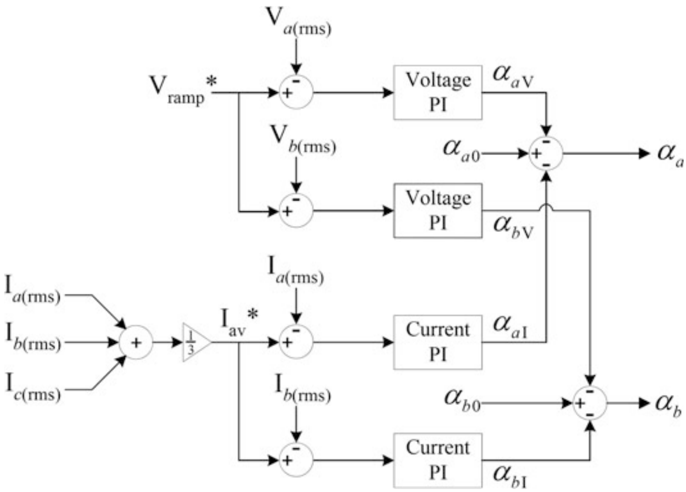

Fig. 93.4 Present closed-loop two-phase control for fault tolerant soft starter

the SCR connection experiences a full applied voltage, whereas the other two phases experience reduced voltages impressed upon them during starting. Therefore, the control strategy has to be adjusted to control the firing of the thyristors in the remaining two phases independently. This is in order to generate nearly balanced three-phase stator currents during the soft starting period, so that the starting torque pulsations can be alleviated.

93.3.2 A Resilient Closed-Loop Two-Phase Control Scheme

In order to control the firing of the thyristors in the remaining two healthy phases independently, a new set of firing angles for each of the two phases has to be defined. It is not easy to achieve using open-loop control, since the firing angle profile will vary with different horsepower motors as well as load conditions. Therefore, closed-loop type of control was adopted here, which will inherently generate the appropriate firing angle profile for the thyristors of each of the two phases under different horsepower motor ratings and different types of load conditions.

The present closed-loop two-phase control scheme is graphically depicted in Fig. 93.4. In this control method, there are two types of feedback control loops, namely a voltage loop and a current loop for each of the remaining two healthy phases. The outputs of these feedback loops represent the changes in the firing angles that will be used to compute the resulting firing (delay) angles, which is defined as follows:

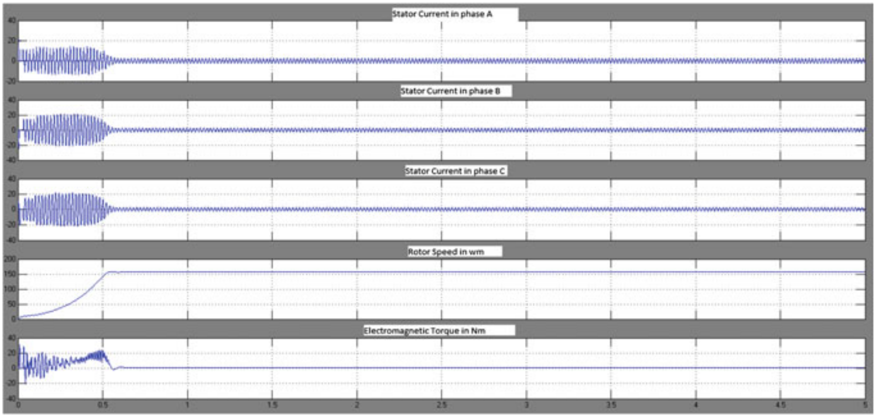

Fig. 93.5 Simulink results open loop soft starting with any fault

$$\begin{aligned}\alpha_a &= \alpha_{a0} - \alpha_{aV} - \alpha_{aI} \\ \alpha_b &= \alpha_{b0} - \alpha_{bV} - \alpha_{bI}.\end{aligned} \tag{93.1}$$

where α_{aV} and α_{bV} are the outputs of the voltage feedback loop, α_{aI} and α_{bI} are the outputs of the current feedback loop, and α_{a0} and α_{b0} are the initial firing (delay) angles for phase-*a* and phase-*b*, respectively. The resulting firing (delay) angles, α_a and α_b computed are used to generate the gate pulses for triggering the thyristors of the two controlled phases.

With only the voltage feedback loop, the motor will still exhibit unbalanced starting currents, and consequently significant starting torque pulsations. Accordingly, in order to ensure nearly balanced three-phase motor currents during starting, a current feedback loop is utilized. The effective (rms) values of the three-phase motor currents, $I_{a(\mathrm{rms})}$, $I_{b(\mathrm{rms})}$, and $I_{c(\mathrm{rms})}$, are measured and the average value of these currents, I^*_{av}, is used as the current reference command for the current controller, which is expressed as follows:

$$I^*_{av} = \left(I_{a(\mathrm{rms})} + I_{b(\mathrm{rms})} + I_{c(\mathrm{rms})} \right)/3. \tag{93.2}$$

The average current, I^*_{av}, is compared with the measured effective (rms) motor currents of the two controlled phases, $I_{a(\mathrm{rms})}$ and $I_{b(\mathrm{rms})}$, and the errors are conditioned by a set of current PI regulators. Here, the outputs of the PI regulators represent the second part of the firing angles, α_{aI} and α_{bI}, for phase-*a* and phase-*b* firing angles, α_a and α_b, respectively. By regulating the rms values of the two controlled phase currents, $I_{a(\mathrm{rms})}$) and $I_{b(\mathrm{rms})}$ to be near the average current value, I^*_{av}, the rms value of the third phase current, $I_{c(\mathrm{rms})}$, is automatically adjusted to be the average current, I^*_{av}, so as to satisfy the condition of (93.2). As a result, a nearly balanced three-phase current condition is realized through this approach, which will in turn provide reduced starting torque transients.

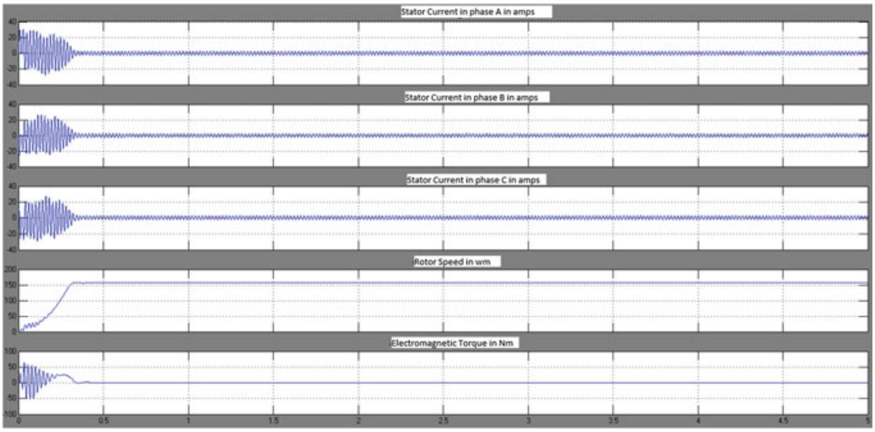

Fig. 93.6 Simulink results open loop soft starting with short circuit fault

93.4 Circuit Simulations of Fault Tolerant Soft Starter

The open loop and the closed-loop under healthy and faulty conditions were verified here using dynamic simulations that were carried out using a commercial circuit simulation software package, namely Matlab-Simulink. A 2.2 kW, 415-V, 4-pole, three-phase induction motor was used as the target for these verification efforts, providing valuable results that raise confidence in the accuracy and value of the analytical results. Meanwhile, motor performance under fault tolerant control operations was also evaluated here using simulations. The simulation work indicates promising results that illustrate reduced starting torque pulsations under SCR switch fault condition through using the present two-phase control technique.

The first three waveforms represent the stator current in phase A, phase B and phase C. When using a soft starter there are no sudden rise in current in all the phases. The fourth waveform represents the rotor speed (Fig. 93.5).

In open loop with fault condition the value for α is set at 110° at the beginning and it is gradually reduced using S—Function Builder. A short circuit SCR fault in phase A i.e. the source V_a is directly connected to the motor terminal A (Fig. 93.6).

In closed loop soft starter control without fault a voltage feedback loop is used. The voltage feedback loop is used to control the starting acceleration profiles of the motor currents and torque. The input to voltage feedback loop is the phase voltage. The voltage across the motor terminals are measured and converting it to the phase value (Fig. 93.7).

In closed loop soft starter control with SCR short circuit fault voltage and current feedback loops are used. With only the voltage feedback loop, the motor will still exhibit unbalanced starting currents, and consequently significant starting torque pulsations. So in order to ensure nearly balanced three-phase motor currents during starting, a current feedback loop is used (Fig. 93.8).

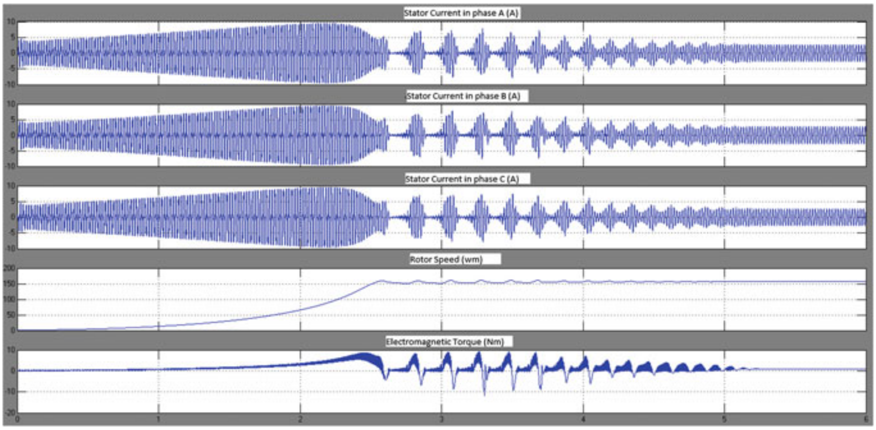

Fig. 93.7 Simulink results for closed loop soft starting without any fault

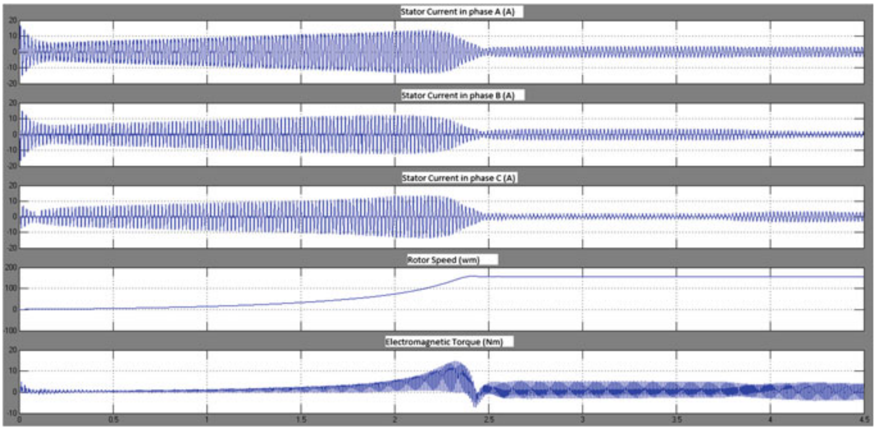

Fig. 93.8 Simulink results for closed loop soft starting with short circuit fault

In open loop when a fault occurs the resulting current will be 6 or 7 times higher than the rated value. Then the closed loop method has been checked when all the thyristors are working. It has been done using a voltage feedback loop. The voltage at the motor terminals are measured and given as inputs to voltage feedback loop. The two phase closed loop control mode gives better results when compared with open loop mode with SCR fault.

93.5 Conclusions

A deep study of soft starter control of induction motor using thyristorised voltage control method was done and a complete Matlab simulation of open loop and closed loop control of induction machine with and without faults were done. From simulation it was observed that closed loop soft starter is far better than open loop control. And it was also observed that performance of induction machine improve with closed loop control.

References

1. Sundareswaran K, Jos BM (2005) Development and analysis of novel soft-starter/energy-saver topology for delta-connected induction motors. Proc Inst EEE Power Appl 152(4):922–932
2. Zenginobuz G, Cadirci I, Ermis M, Barlak C (2001) Soft starting of large induction motors at constant current with minimized starting torque pulsations. IEEE Trans Ind Appl 37 (5):1334–1347
3. Zenginobuz G, Cadirci I, Ermis M, Barlak C (2004) Performance optimization of induction motors during voltage-controlled soft starting. IEEE Trans Energy Conserv 19(2):278–288
4. de Araujo Ribeiro RL, Jacobina CB, E. R. C. da Silva, and A. M. N. Lima, “Fault-tolerant voltage-fed PWM inverter ac motor drive systems,” IEEE Transactions on Industrial Electronics, Vol. 51, No. 2, pp. 439-446, Apr. 2004
5. Kastha D, Majumdar AK (2000) An improved starting strategy for voltage-source inverter fed three phase induction motor drives under inverter fault conditions. IEEE Trans Power Electron 15(4):726–732
6. Yeh CC, Demerdash NAO (2009) Fault tolerant soft starter control of induction motor with reduced transient torque pulsations. IEEE Trans Energy Convers 24(4)
7. Jacobina CB, de Araujo Ribeiro RL, Lima AMN, da Silva ERC (2003) Fault-tolerant reversible AC motor drive system. IEEE Trans Ind Appl 39(4):1077–1084
8. de Rossiter Corrêa MB, Jacobina MB, da Silva ERC, Lima AMN (2001) An induction motor drive system with improved fault tolerance. IEEE Trans Ind Appl 37(3):873–879
9. Mendes AMS, Lopez-Fernandez XM, Cardoso AJM (2007) Thermal behavior of a three-phase induction motor fed by a fault-tolerant voltage source inverter. IEEE Trans Ind Appl 43 (3):724–730
10. Kim GT, Lipo, TA (1996) VSI-PWM rectifier/inverter system with a reduced switch count. IEEE Trans Ind Appl 32(6):1331–1337

Chapter 94
A Novel Soft Switched Positive Output Super Lift Luo Converter for Li-Ion Battery Charging

Winnie Raghu and T.S. Saravanan

Abstract Positive output super lift Luo converter is a recent topology in a DC/DC converter with a high voltage transfer gain. The modified soft switching technique for positive output super lift Luo converter is proposed, designed and simulated to show the mitigation of the limitations of high voltage gain super lift Luo converter. The modes of operation, equivalent circuit, dynamic equations and steady state differential equations of the soft switched super lift Luo converter under different time instants were derived to compute the resonant values. This proposed converter is simulated for both resistive load and Li-Ion battery charging. To charge Li-Ion battery, the classical Constant Current Constant Voltage (CCCV) charging method is used. The simulation results clearly show the elimination of switching losses for the resistive load, the battery charging profile with the state of the charge and transition from CC to CV.

Keywords Lithium-Ion · Constant current constant voltage · State of charge · Depth of discharge

94.1 Introduction

The utilization of renewable energy resources can help mitigate the issues with fossil fuels. The energy storage systems can be used to complement renewable energy resources in order to optimize energy use [1]. But the major problem faced while designing a converter for energy storage system is that its efficiency has to be

W. Raghu (✉) · T.S. Saravanan
Department of Electrical and Electronics Engineering, Rajalakshmi Engineering College Affiliated to Anna University, Chennai, India
e-mail: winnieraghu@gmail.com

T.S. Saravanan
e-mail: saravanan.ts@rajalakshmi.edu.in

C. Kamalakannan et al. (eds.), *Power Electronics and Renewable Energy Systems*,
Lecture Notes in Electrical Engineering 326, DOI 10.1007/978-81-322-2119-7_94

optimized during application. Li-Ion batteries needs special care as overcharging and undercharging leads to permanent failure of the battery [2].

The circuits proposed in [3, 4] use an alternative switch to implement soft switching in the main switch. The circuits proposed in [5, 6] does not any auxiliary switch but the number of devices the devices are more. The circuit proposed in [6] offers reduced voltage and current stresses and the duty cycle limitations can be reduced by coupling between main and auxiliary circuit inductors. The circuit proposed in [7] does not use extra switch, is simple but device count is high. The circuit proposed in [8] does not uses any alternative switch and it has been implemented in boost converter. This paper offers an alternate scheme for soft switching of the positive output super-lift Luo converter. The proposed circuit consists of a simple auxiliary circuit with passive components and uncontrolled switches for achieving zero voltage turn off and zero current turn on of the main switch and it do not use any extra switch or coupled inductors.

94.2 Principle of Operation

The proposed circuit is shown in Fig. 94.1. The switch S_1, L_1, C_1, C_2, D_1 and D_4 are the main super-lift Luo converter components. Inductor L_2, L_3, D_2, D_3, and Cr, form the auxiliary circuit for accomplishing the soft switching of S_1. Inductors L_2 and L_3 are much smaller than L_1, and C_r is much smaller than C_1 and C_2. The duration of modes 1, 2, 5 and 6 being quite small i_{LI}, V_{C1} and V_{C2} are assumed

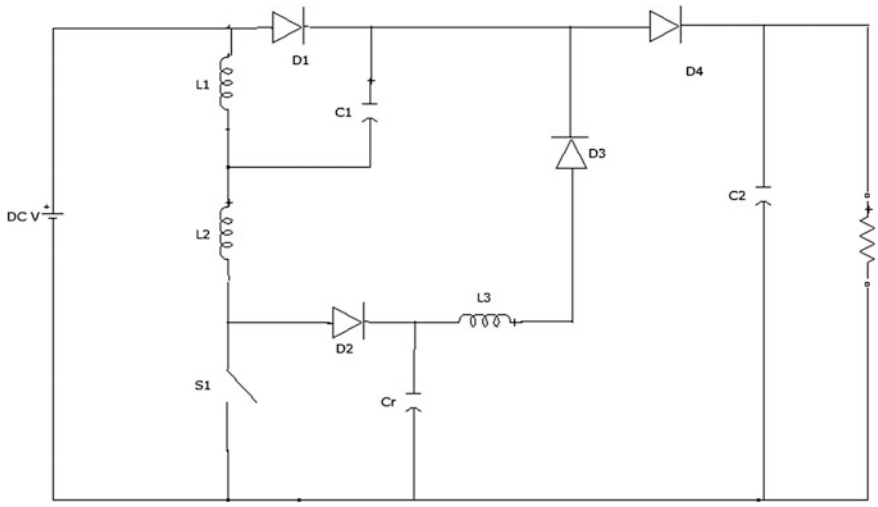

Fig. 94.1 Proposed soft switched positive output super lift Luo converter

constant at I_1, zero and V_I for modes 1 and 2, and I_2, V_S and V_2 for modes 5 and 6 respectively. The mode wise analysis of the circuit is as follows.

94.2.1 Operation of Mode 1 (T_0–T_1)

This mode begins with the turn on of S_1. Initial conditions on L_2, L_3 and C_1 are zero. Capacitor Cr is previously charge to $V_{Cr}(t_0)$ and C_2 charged to V_1. At the end of this mode the current through inductor L_2 becomes $i_{L2}(t) = i_{L3}(t_1) + I_1$. This mode comes to an end when D_4 stops conduction. The steady state expressions for current through L_2, L_3 and voltage through C_r are given as follows.

$$i_{L2(t)} = \frac{V_s t}{L_2} \tag{94.1}$$

$$V_{Cr(t)} = \left[V_1 - V_{Cr(t0)}\right][1 - \cos\omega_1 t] + V_{Cr(t0)} \tag{94.2}$$

$$i_{L3(t)} = \frac{[V_{cr(t0)} - V_1]\sin\omega_1 t}{\omega_1 L_3} \tag{94.3}$$

$$\omega_1 = \frac{1}{\sqrt{L_3 C_1}}$$

94.2.2 Operation of Mode II (T_1–T_2)

The initial conditions on L_2, L_3 and Cr are $i_{L3}(t_1) + I_1$, $i_{L3}(t_1)$ and $V_{Cr}(t_1)$ respectively attained at the end of mode1. In this mode, C_1 completely discharges and its reverse charging is arrested by D_1. This mode comes to an end when V_{Cr} reaches zero at t_2. The expressions for i_{L2}, i_{L3} and V_{Cr} are as follows.

$$V_{cr(t)} = [V_{Cr}(t_1) - V_{C1}(t_1)]\cos\omega_2 t - \frac{i_{L3}(t_1)}{\omega_2 Cr}\sin\omega_2 t + V_{C1}(t_1) \tag{94.4}$$

$$i_{L3}(t) = i_{L3}(t_1)\cos\omega_2 t + \frac{V_{Cr}(t_1) - V_{C1}(t_1)}{\omega_2(L_2 - L_3)}\sin\omega_2 t \tag{94.5}$$

$$i_{L2}(t) = i_{L3}(t_1)\cos\omega_2 t + I_1 + \frac{V_{Cr}(t_1) - V_{Cr}(t_1)}{\omega_2(L_2 + L_3)}\sin\omega_2 t \tag{94.6}$$

$$\omega_2 = \frac{1}{\sqrt{(L_2 + L_3)C_1}}$$

94.2.3 Operation of Mode III (T_2–T_3)

The initial condition on L_2, L_3 and V_{Cr} are $i_{L2}(t_2)$, $i_{L3}(t_2)$ and zero. This mode comes to an end at t_3 when i_{L3} reaches zero. Reversal of i_{L2} is arrested by D_2. The current through L_3 is given by the following equation.

$$i_{L3}(t) = -\frac{V_{C1}(t_2)t}{L_2 + L_3} + i_{L3}(t_2) \tag{94.7}$$

94.2.4 Operation of Mode IV (T_3–T_4)

At the end of this mode, $i_{L1}(t)$ attains a value of I_2 and voltage across C_2, reaches V_2. This mode comes to an end when S_1 is turned off at zero voltage at t_4. The current through L_2 is given by the following equation.

$$i_{L2}(t) = \frac{[V_s - V_{c1}(t_3)]t}{L_2} + i_{L2}(t_3) \tag{94.8}$$

$$V_{C2}(t) = V_1 e^{\left(\frac{1}{RC_2}\right)} \tag{94.9}$$

94.2.5 Operation of Mode V (T_4–T_5)

This mode begins with the turn off of S_1 at zero voltage at t_4. The initial condition on i_{L2} for this mode is I_2. The expressions for i_{L2}, i_{L3} and V_{Cr} for this mode are as follows.

$$V_{Cr(t)} = K_3 \cos \omega_3 t + K_4 \sin \omega_3 t + \frac{V_2 - V_s}{L_2 \omega_3^2 C_r} \tag{94.10}$$

$$i_{L3(t)} = \frac{K_3}{L_3 \omega_3} \sin \omega_3 t + \frac{K_4 (\cos \omega_3 t - \sin \omega_3 t)}{L_3 \omega_3} + \frac{K_1}{L_2} \tag{94.11}$$

$$i_{L2(t)} = \frac{V_s t}{L_2}\left(\frac{1}{L_2 \omega_3^2 C_r} - 1\right) - \frac{K_3 \sin \omega_3 t}{L_2 \omega_3} + \frac{K_4 \cos \omega_3 t}{L_2 \omega_3} + \frac{K_1}{L_2} \tag{94.12}$$

$$\omega_3 = \frac{1}{\sqrt{\frac{L_2 L_3}{L_2 + L_3} C_r}}, K_1 = I_2 - \frac{K_4}{L_2 \omega_3}$$

$$K_3 = \frac{[V_s - V_2]L_3}{L_2 - L_3}$$

$$K_2 = \frac{K_4}{\omega_3}, K_4 = \frac{I_2}{\omega_3}\left(\frac{1}{Cr} + 1\right)$$

94.2.6 Operation of Mode VI (T_5–T_6)

In this mode i_{L3} reduces to zero. This mode comes to an end at t_6 when i_{L3} becomes zero. The expression for i_{L3} and V_{Cr} for this mode are as follows.

$$i_{L3}(t) = (V_{Cr}(t_5) - V_2 + V_s)\omega_1 C_r \sin \omega_1 t + i_{L3}(t_5) \cos \omega_1 t \tag{94.13}$$

$$V_{Cr}(t) = V_{Cr}(t_5) \cos \omega_1 t + (V_2 - V_s)(1 - \cos \omega_1 t) - \frac{i_{L3}(t_5)}{C_r \omega_1} \sin \omega_1 t \tag{94.14}$$

$$\omega_1 = \frac{1}{\sqrt{L_3} Cr}$$

94.2.7 Operation of Mode VII (T_6–T_7)

In this mode i_{L2}, i_{L3} are zero. This mode comes to an end at t_7 when S_1 is turned on at zero current. This is the normal mode of positive output super-lift Luo converter. At the end of this mode, inductor current i_{L1} reaches I_1, V_{C2} reaches V_1 and V_{C1} reaches zero.

$$i_{L1}(t) = \frac{V_s t}{L_1} + i_{L1}(t_6) \tag{94.15}$$

$$V_{C1}(t) = \frac{V_s}{C_1 R} - \frac{V_1}{C_1} + V_{C1}(t_6) \tag{94.16}$$

94.3 Simulations

MATLAB simulation software package was used to these converters to verify the design and calculation results. The simulation results of soft switched Positive Output super-lift Luo converter with resistive load and with battery load are shown separately.

94.3.1 Simulation Results of Soft Switched Positive Output Super Lift Luo Converter with Resistive Load

The data inputs were V_{in} = 12 V, f = 50 kHz, k = 0.5, L_1 = 1 mH, L_2 = 0.1 μH, L_3 = 0.5 μH, C_r = 5 nF, C_1 = C_2 = 50 μF, R = 44 Ω.

The soft switching waveforms, inductor current, output current and inductor ripple current along with input and output voltage are shown separately. The waveforms are as shown in Fig. 94.2b, c.

The waveforms of current through the switch, voltage across switch, Current through L_3, Trigger pulse are indicated above. The simulation results clearly shows Zero Current turn on and Zero Voltage turn off of the switch.

94.3.2 Simulation Results of Soft Switched Positive Output Super Lift Luo Converter with Battery Load

The data inputs were R = 0.11 Ω, Battery type = Li-Ion, Battery voltage = 19.8 V, State of Charge = 40 %. The CCCV charging algorithm is implemented by a current control loop that is dependent on the battery voltage via a hyperbolic tangent function [4]. This function is given by Eq. (94.17).

$$I_{bat} = A \cdot \tanh(V_{ref} - V_{bat})/S \tag{94.17}$$

where A is a scaling factor to scale the current to the battery capacity, V_{ref} the end of charge voltage reference, V_{bat} the battery voltage and S a variable to determine the voltage where the charge current starts to decrease.

Figure 94.3b shows a plot of this function with A set to 0.45, the end of charge voltage set to 19.8 V and S set to 0.05. The output of this function provides a reference for the charge current. From Fig. 94.3b, it is clear that the charging current maintains maximum charging current of 0.45 A up to 95 % SoC of battery and after that it decreases. The charging current reaches minimum value when the SoC reaches 99.99 %. Figure 94.3c shows the charging development of Li-Ion battery from 40 to 99.99 %.

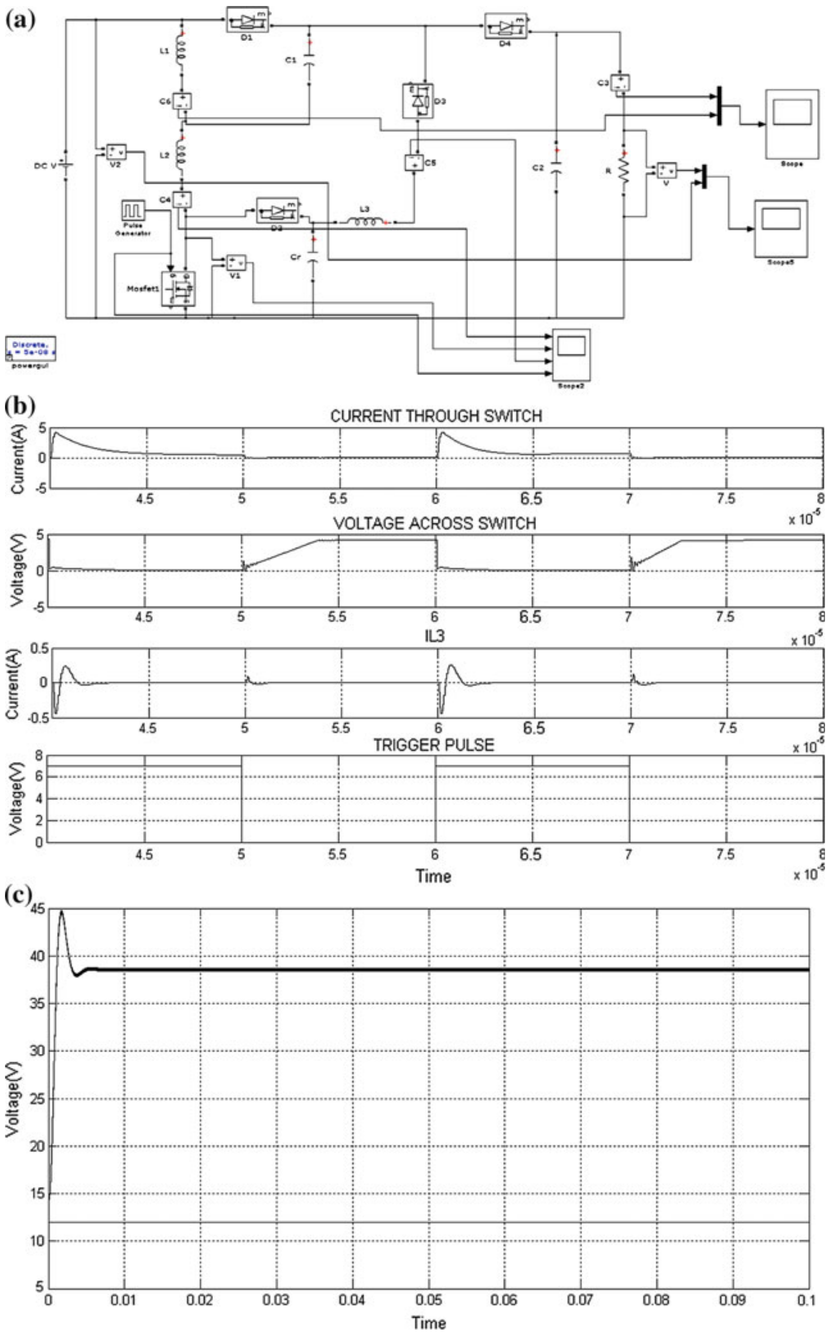

Fig. 94.2 **a** Simulation circuit of soft switched positive output super lift Luo converter. **b** Soft switching waveforms. **c** Input and output voltage waveforms

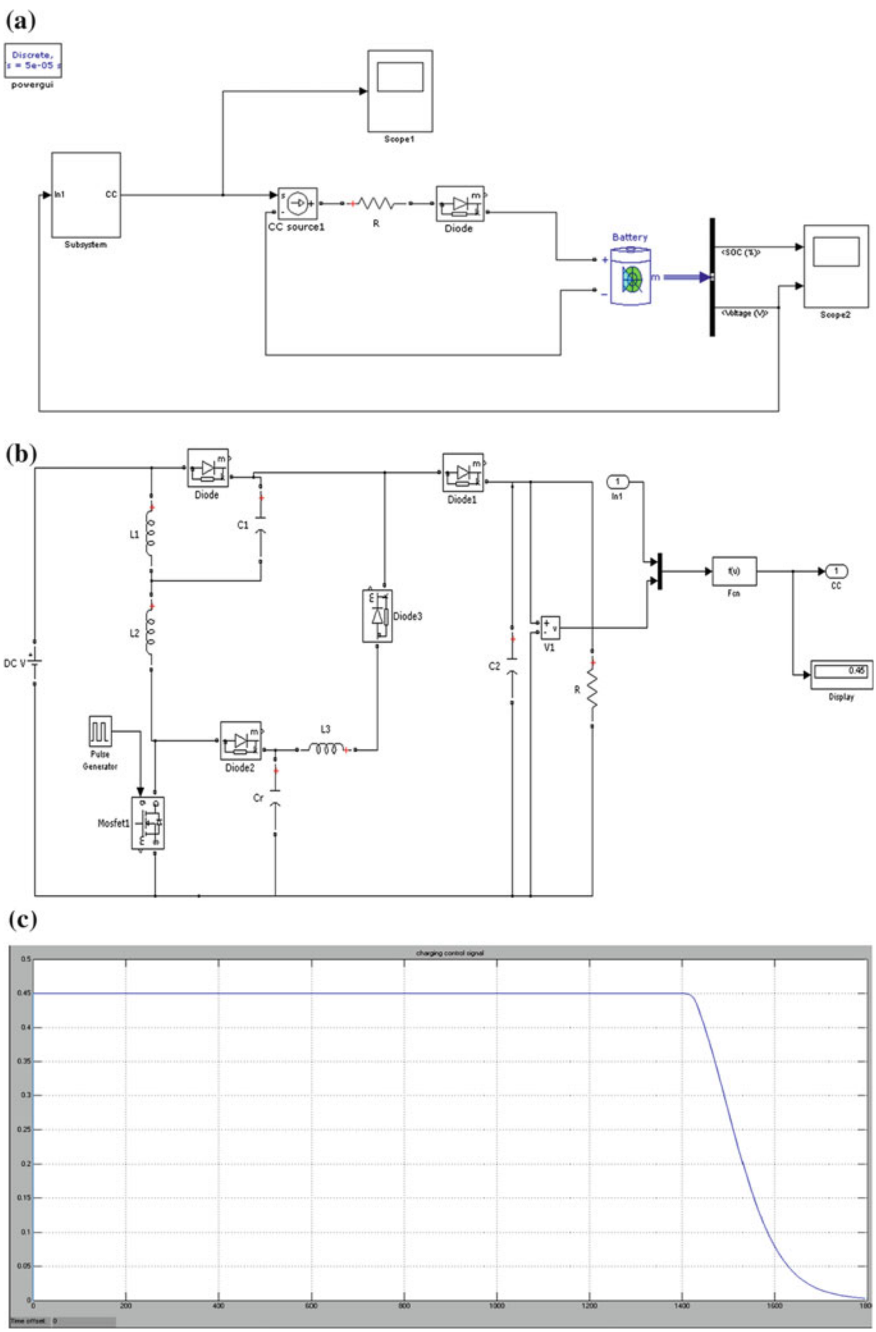

Fig. 94.3 **a** Simulation circuit of Li-Ion battery charger. **b** Battery charging control function integrated with soft switched positive output super lift Luo converter. **c** CCCV control and battery charge development profile

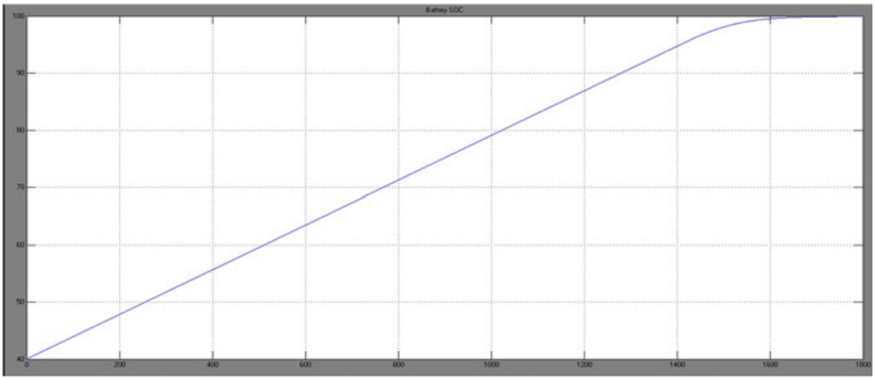

Fig. 94.3 (continued)

94.4 Conclusion

This proposed converter is simulated for both resistive load and Li-Ion battery charging. The simulation results of the proposed converter with resistive load were found to be matched with theoretical analysis. The results clearly show the elimination of switching losses for the resistive load, the battery charging profile with the state of the charge and transition from CC to CV. The efficiency of the Luo converter has decreased when it is implemented for battery charging. This is because the capacitive voltage drops which will be prominent when output resistance is very low.

References

1. Huang AQ, Crow ML, Heydt GT, Zheng JP, Dale SJ (2011) The future renewable electric energy delivery and management (freedm) system: the energy internet. Proc IEEE 99:133–148
2. Valle BD, Wentz CT, Sarpeshkar R (2011) An area and power efficient analog Li-Ion battery charger circuit. IEEE Trans Biomed Circuits Syst 5:131–137
3. Liu YH, Hsieh CH, Luo YF (2011) Search for an optimal five step charging Pattern for Li-ion batteries using consecutive orthogonal arrays. IEEE Trans Energy Convers 26:654–661
4. Elasser A, Torry DA (1996) Soft switching active snubber for DC/DC converters. IEEE Trans Power Electron 11:710–722
5. Ba-Tunya AS, Pillai SK, Prasad D (1998) Certain novel synchronised topologies for achieving soft switching DC/DC boost and flyback converters with minimum voltage stress across switches. IEEE PESC Conf 682–688
6. Lambert JA (1999) Boost PFVM converter with low voltage and current stresses. IEEE Trans Power Electron 13:26–35
7. Tseng CJ, Chen CL (1998) Passive lossless snubbers for DC/DC converters. Proc IEEE PESC 1049–1054
8. Bagaewadi MD, Fernandes BG, Subrahmanyan RVS (2000) A novel soft switched boost converter using a single switch. In: Proceedings of 3rd international power electronics and motion control conference, vol 1, pp 412–416

Chapter 95
Reduction in Ripples Using Interleaved Soft Switching Boost Converter for Hybrid Power Generation System

A. Alice Hepzibah, A. Senthil Kumar and R. Joylin Rini

Abstract An interleaved soft switching boost converter for a hybrid power generation system is proposed. Hybrid renewable energy systems plays an important role in remote area power generation. Here the hybrid system is the combination of photovoltaic module and fuel cell. Whenever there is a failure in the Photo Voltaic module, due to less insolation or any other fault in the module, then fuel cell is used in generation of power. The output voltage of this hybrid system is very low. To increase the output voltage boost converter is required. In this, interleaved soft-switching boost converter is connected which helps in the reduction of ripples in the output voltage. The main advantage of this is interleaved soft-switching boost converter is that, it minimizes the switching losses by adopting a resonant soft switching method.

Keywords Soft switching method · Boost converter · Hybrid · Fuel cell

95.1 Introduction

Hybrid renewable energy systems plays an important role in the generation of power especially in remote areas. Hybrid system is the combination of two or more power generation system. The selection of proper combination is important in hybrid power generation. Based on the availability and requirement, the combination is selected. Of the all renewable energy, solar is the most abundant

A. Alice Hepzibah (✉) · R. Joylin Rini
Rajalakshmi Engineering College, Chennai, India
e-mail: alice030979@yahoo.co.in

R. Joylin Rini
e-mail: joylinrini@gmail.com

A. Senthil Kumar
Vellamal Engineering College, Chennai, India
e-mail: vastham@gmail.com

C. Kamalakannan et al. (eds.), *Power Electronics and Renewable Energy Systems*,
Lecture Notes in Electrical Engineering 326, DOI 10.1007/978-81-322-2119-7_95

renewable energy and it is used in most of the hybrid power generation system. There are various advantages in using the solar energy. Some of which are reduced pollution, reduces the energy exhaustion caused due to increase in the consumption of energy. But the power generation from solar module is possible only when there is light insolation. So, a backup power generation system must be combined with this solar generation system. Fuel cell are considered to be one of the most promising future energy devices due to their energy efficiency and environmental friendliness [1]. Therefore Fuel cell can be used for this purpose. The reason for this is that combining a fuel cell with other system, the efficiency of the combined system can be increased. The advantage of fuel cells is that it produce very low emissions and it has very high operating efficiencies.

Therefore, Fuel cell can be combined with solar module for power generation. Fuel cell and solar panel can be combined in such a way that, whenever there is a failure or reduced power generation in solar panel due to less insolation, then fuel cell is used in the generation of power. The output voltage of this hybrid system is varying. In order to increase the output efficiency a DC/DC converter is required. In this paper a comparison between the converters is done based on ripples in the output voltage.

95.2 Hybrid Power Generation System

Solar panel and fuel cell are combined in this hybrid system. Comparison of output voltage ripples in boost converter, interleaved boost converter and interleaved soft switching boost converter is done for best selection of converter for this hybrid power generation system.

95.2.1 Solar Module

Solar modules use light energy from the sun to generate electricity through the photovoltaic effect. Solar module is number of solar cells connected in series or parallel. Current and voltage rating of a module can be modified by varying number of cells connected in series and number of cells connected in parallel. The equivalent circuit of a solar cell is given in Fig. 95.1.

Module photo-current:

$$I_{ph} = [I_{scr} + K_i(T - 298)] * \frac{\lambda}{1{,}000} \tag{95.1}$$

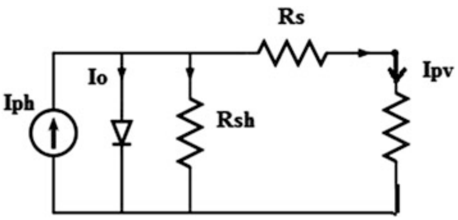

Fig. 95.1 Equivalent circuit of solar cell

Module reverse saturation current:

$$I_{rs} = \frac{I_{scr}}{\left[\exp\left(\frac{qV_{oc}}{N_s kAT}\right) - 1\right]} \tag{95.2}$$

The module saturation current I_o varies with the cell temperature, which is given by

$$I_o = I_{rs}[\frac{T}{T_r}]^3 \exp\left[\left(\frac{qE_{go}}{Bk}\right)\left\{\frac{1}{T_r} - \frac{1}{T}\right\} - 1\right] \tag{95.3}$$

The current output of PV module is

$$I_{pv} = N_p * I_{ph} - I_o * N_p\left[\exp\left\{q * \frac{V_{pv} + I_{pv}R_s}{N_s AkT}\right\} - 1\right] \tag{95.4}$$

As per the equations, the design of solar module is done in MATLAB software with the reference of [2, 3].

95.2.2 Fuel Cell

Fuel cell is the device used for converting chemical energy into electrical energy with the help of electrochemical cell. Proton exchange membrane fuel cell is most commonly used fuel cell for vehicular application. Hydrogen and oxygen is continuously supplied at the anode and cathode respectively. The protons formed will permeate through the membrane and electrons will move through an external circuit, thus causing a current. At cathode, this proton will combine with oxygen to form water as byproduct. A single fuel cell output voltage can be calculated by the following equation,

$$\mathrm{V_{fc}} = \mathrm{E_{nerst}} - \mathrm{V_{act}} - \mathrm{V_{ohm}} - \mathrm{V_{conc}} \tag{95.5}$$

where V_{fc}—voltage of fuel cell (V), E_{nerst}—Nernst voltage (V), V_{act}—Actual voltage (V), V_{ohm}—Ohmic voltage drop (V), V_{conc}—Concentration Voltage (V).

The reversible voltage of fuel cell is calculated by the following equation,

$$E_{nerst} = 1.229 - 0.85 \times 10^{-3}(T - 298.15) + 4.31 \times 10^{-5} + \left[\ln(PH_2) + \frac{1}{2}\ln t(PO_2)\right] \tag{95.6}$$

where T—Temperature (K), PH_2—partial pressure of the Hydrogen (N/m^2) and-PO_2—partial pressure of the oxygen (N/m^2).

Activation potential, V_{act} can be calculated by the following equation

$$V_{act} = -[\varepsilon_1 + \varepsilon_2 T + \varepsilon_3 T\ln(co_2) + \varepsilon_4 \ln(I_{stack}) \tag{95.7}$$

The ohmic loss is calculated by the following equation,

$$V_{ohmic} = I_{stack}(R_m + R_c) \tag{95.8}$$

where R_c—resistance of the membrane to the transfer of protons (0.0003 Ω), R_m—resistance to the electron flow of the membrane (6.39 μΩ).

The voltage drop due to mass transport is calculated by following equation,

$$V_{conc} = -B\ln\left(1 - \frac{J}{J_{max}}\right) \tag{95.9}$$

where B(V)—parametric coefficient (A/cm) − 0.016, J—Current density [A/m^2] (500), J_{max}—Maximum current density [A/m^2] (1,500). The equations for determining the E_{nerst} and V_{act} is implemented in separate subsystem.

95.2.3 Interleaved Softswitching Boost Converter (ISSBC)

An interleaved boost converter combines two or more boost converters in parallel. When two boost converters are connected in parallel, then the second converter is triggered after 180°. Similarly, when three converters are connected in parallel, the signal difference is 120° and so on. Thus, this helps in the reduction of ripples in output voltage. Various circuits with soft switching were analysed. The circuit discussed in [4] zero voltage switching is achieved using a series connected transformers. The circuit discussed in [5] has common soft switching circuit for two switches. The circuit in [6] is used for high power applications and it has more number of cells. While comparing circuits the circuit with single soft switching circuit would be a better option. Figure 95.2 represents an interleaved boost converter with common soft switching circuit.

It has a common soft-switching circuit. This circuit consists of the resonant inductor L_r, resonant capacitor C_r, capacitors C_{Sa} and C_{Sb}, and an auxiliary switch

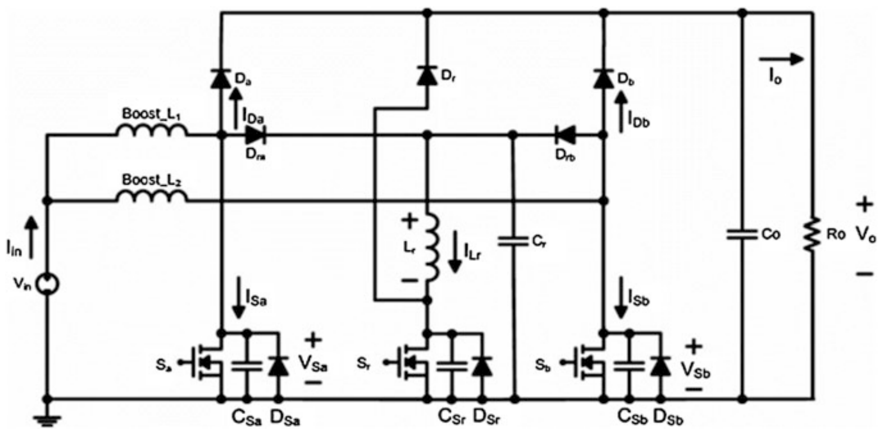

Fig. 95.2 Circuit diagram of ISSBC

S_r to b achieve ZVS and ZCS conditions [7]. There are two operating modes based on the duty cycle given to the switches.

(1) Duty cycle less than 50 %
Switch Sr is used in soft switching. Initially the switches Sa and Sb are in off state. Sr is turned on and the diode Dr is in off state. Since the switch Sr is in on, the inductor charges. When this inductor value reaches the peak value, the voltage across the switch reduces to zero. At that time the switch Sa can be turned on to achieve zero voltage switching. Then the switch Sr is turned off. Then the energy stored in the inductor L_1 is transferred to load.

(2) Duty cycle greater than 50 %
Initially all the switches are in on state. The rectifier diodes are turned off. The main switch currents is less than zero. So, when current reaches zero, the switch can be turned off achieving zero current switching. The switch Sb is turned off. The diode Dr is turned on. Then the stored energy in the inductor (Lr) is transferred to the load. The switch Sr is turned on. The resonant inductor current increases while the rectifier diode current decreases to zero. When the resonant inductor current increases to the peak value, the voltage decreases due to resonance. At that time the switch Sb is turned on achieving the zero voltage and zero current turn on simultaneously.

The equations governing interleaved soft switching boost converter is given below. Let, D_1—duty cycle of switch S_a, D_2—duty cycle of switch S_b, D_r—dutycycle of switch S_r

where $D_r = D_{rv} + D_{rc}$, Output voltage equation when D > 50 %

$$V_o = \frac{V_{in}}{1 - (D_1 + D_{rv})} \tag{95.10}$$

Output voltage equation when D < 50 %

$$V_o = \frac{V_{in}}{1 - (D_1 + D_{rc} + 2D_{rv})} \tag{95.11}$$

The minimum boost inductor when D > 50 %

$$L_{min} = \frac{(D_1 + D_{rv})(1 - (D_1 + D_{rv}))^2 R_{max}}{f_s} \tag{95.12}$$

The minimum boost inductor when D < 50 %

$$L_{min} = \frac{(D_1 + 2D_{rv})(1 - (D_1 + 2D_{rv}))^2 R_{max}}{f_s} \tag{95.13}$$

95.3 Hybrid System with Different Converter Topology

95.3.1 Hybrid System with Boost Converter

Depending on the light insolation solar module or fuel cell is included. Here the output of solar is designed for 12 V. This output voltage is boosted to 50 V. Therefore, inductance and capacitance required is 9.12 mH and 0.01266 mF respectively. The simulation of this circuit is shown in Fig. 95.3.

The output voltage is measured and ripples in the output voltage is determined. The output voltage waveform of hybrid system with boost converter is shown in Fig. 95.4.

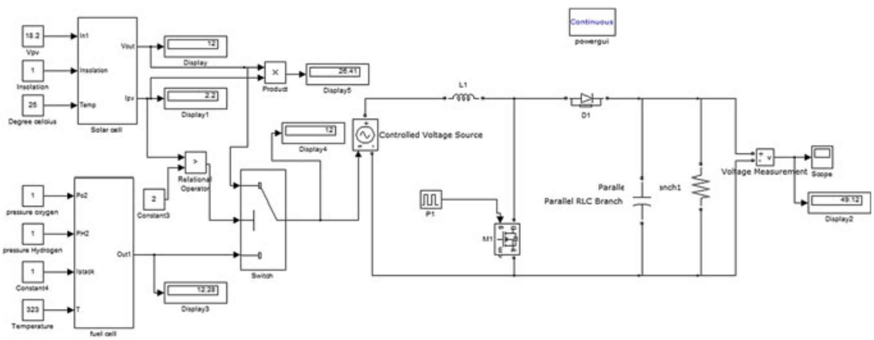

Fig. 95.3 Simulation of hybrid system with boost converter

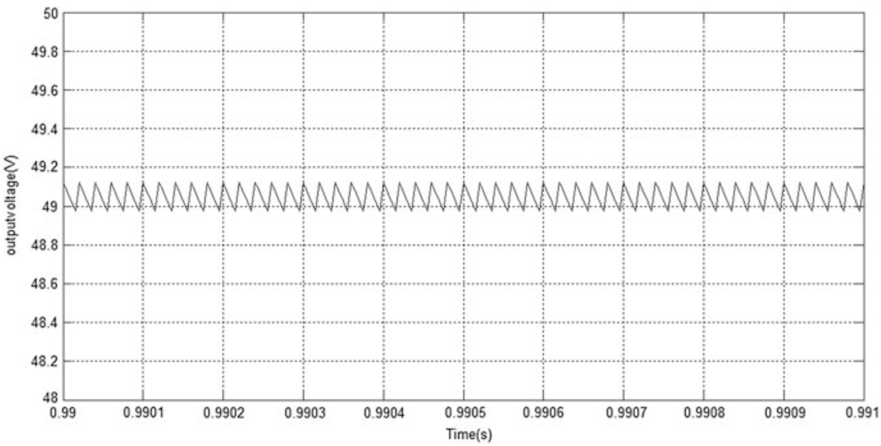

Fig. 95.4 Output voltage waveform

95.3.2 Hybrid System with Interleaved Boost Converter

Interleaved boost converter is the two boost converter connected in parallel. The firing of two boost converters are made in such a way that, second converter is fired at the phase shift of 180°. The simulation of this circuit is shown in Fig. 95.5. The values of inductance and capacitance is same as that of boost converter.

The output voltage waveform of interleaved boost converter is shown in the Fig. 95.6.

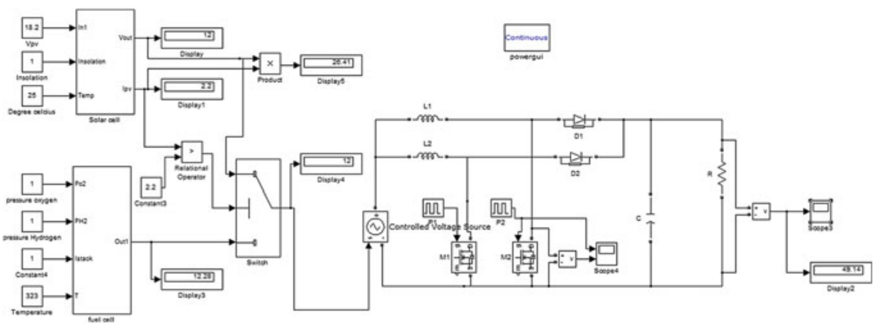

Fig. 95.5 Simulation of hybrid system with interleaved boost converter

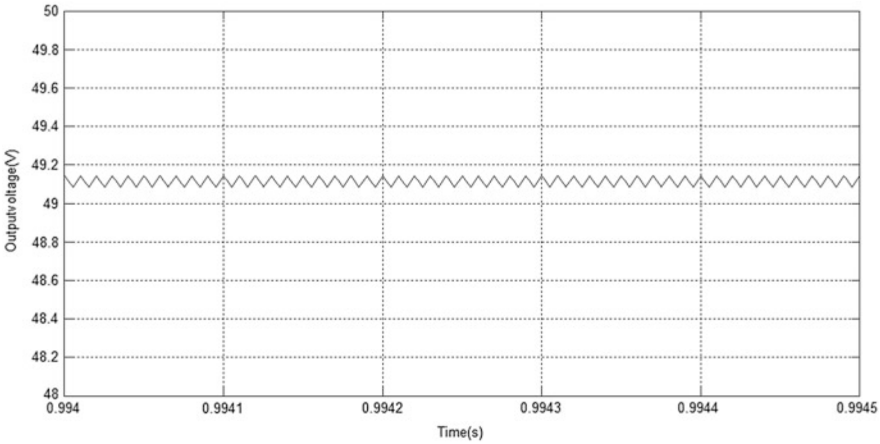

Fig. 95.6 Output voltage waveform

95.3.3 Hybrid System with ISSBC

The Design of interleaved soft switching boost converter is based on the equations discussed above. The designed values are shown in the Table 95.1.

Using this designed values the simulation is carried out which is shown in the Fig. 95.7.

The output voltage waveform of interleaved soft switching boost converter is shown in the Fig. 95.8.

Soft switching is nothing but the turn on and turn off of the switch either at zero voltage or zero current. The waveforms regarding switch S_a is shown in the Fig. 95.9. It is clear that turn on of the switch is achieved during zero current and turn off of the switch during zero voltage. Similarly, turn on at zero current and turn off at zero voltage is achieved for switch $S_{b.}$

Table 95.1 Designed values of ISSBC

Desired output voltage	50 V
Inductance L_1, L_2	9 mH
Capacitance C_0	400 μF
L_r	10 μH
C_r	1.5 nF
C_{sa}, C_{sb}	0.3 μF
C_{sr}	5 nF

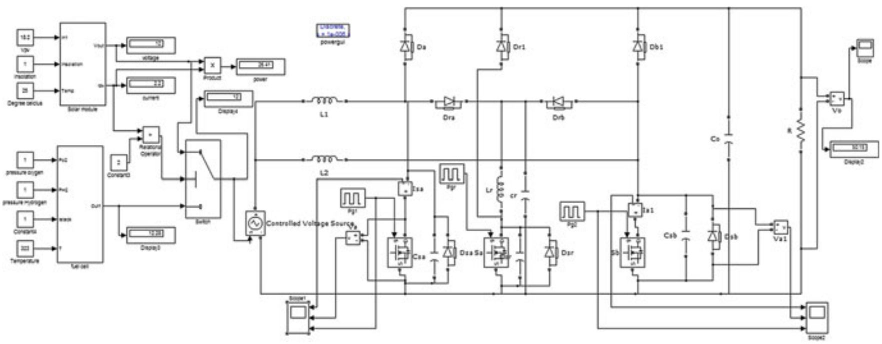

Fig. 95.7 Simulation of hybrid system with interleaved soft switching boost converter

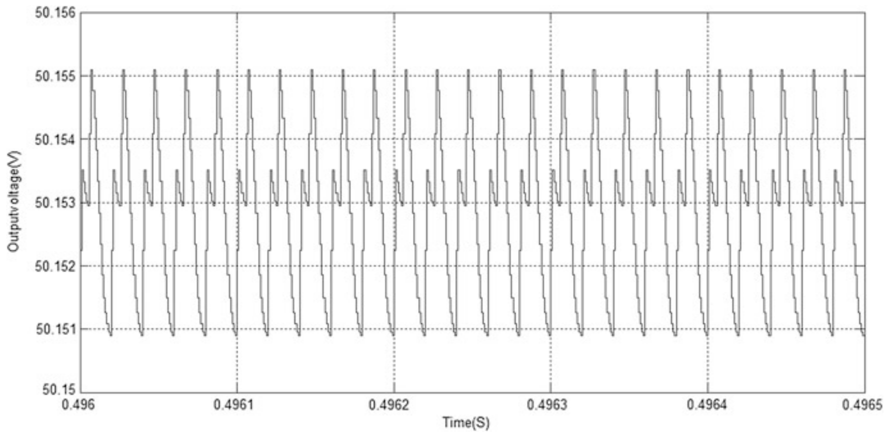

Fig. 95.8 Output voltage waveform

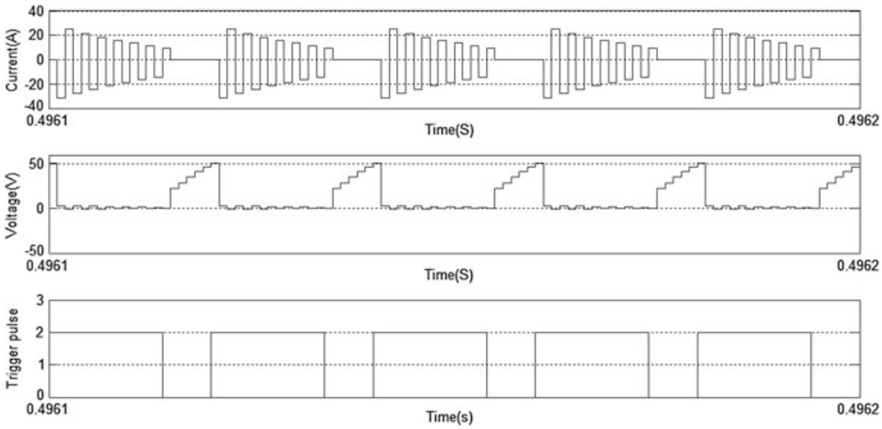

Fig. 95.9 Waveforms related to switch S_a

Table 95.2 Output voltage ripples in different converters

Converter	Ripples (V)
Boost converter	0.19
Interleaved boost converter	0.04
Interleaved soft switching boost converter	0.004

95.4 Conclusion

The output voltage waveforms of boost converter, interleaved boost converter and interleaved soft switching boost converter is analyzed. Output voltage ripple in converters is shown below in Table 95.2. It is clear from the simulation that ripple in output voltage is minimum in case of interleaved soft switching boost converter when compared with other two converters.

Also soft switching is achieved, that is turn on at zero current and turn off at zero voltage is achieved. From this it can be concluded that, Interleaved soft switching boost converter is better option for hybrid power generation system.

References

1. Liu C, Johnson A, Lai JS (2005) A novel three-phase high-power soft-switched DC/DC converter for low-voltage fuel cell applications. IEEE Trans Ind Appl 41
2. Pandiarajan N, Muthu R (2011) Mathematical modeling of photovoltaic module with simulink. In: International Conference on Electrical Energy Systems (ICEES), January 2011, pp 3–5
3. Natarajan P (2012) Performance improvement of PV module at higher temperature operation, IRACST Eng Sci Technol Int J 2(5). ISSN: 2250-3498

4. Lin BR, Chao CH (2013) Analysis of an interleaved three-level ZVS converter with series-connected transformers. IEEE Trans Power Electron 28(7)
5. Jung DY, Hyokji Y, Park SH, Jung YC, Won CY (2011) Interleaved soft-switching boost converter for photovoltaic power-generation system. IEEE Trans Power Electron 26(4)
6. Park S, Park Y, Choi S, Choi W, Lee KB (2011) Soft-switched interleaved boost converters for high step-up and high-power applications. IEEE Trans Power Electron 26
7. Chen YT, Shiu SM, Liang RH (2012) Analysis and design of a zero-voltage-switching and zero-current-switching interleaved boost converter. IEEE Trans Power Electron 27(1)

Chapter 96
Implementation of Reactor and Capacitor in Adjustable Speed Drive for Power Quality Problem

R. Suganthi, V. Kumar Chinnaiyan and M. Gopinath

Abstract Third order input harmonics of Adjustable Speed Drive (ASD) is reduced by the AC line reactor, DC ink reactor and shunt capacitor. Effectiveness of these reactors depends on many factors such as loading factor and source impedance. Under variable load conditions such factors are analyzed and performance of system also analyzed. In this paper simulated and hardware is done by inserting such factor which also suggested for future real time applications.

Keywords AC line reactor · DC link reactor · Input harmonics · Powerfactor · Shunt capacitor · Source inductance

96.1 Introduction

Due to wide applications of nonlinear loads produces the harmonic at the input side of adjustable speed drive which affects the performance of ASD. Like rectifiers, inverters, variable speed drives are contribute to a decreasing the power quality due to harmonic distortion. Harmonic current producing loads cause additional losses in power cables, transformers and capacitors. They induce harmonic Voltage drops at the supply transformers. Due to this harmonic distortion sensitive loads may be disturbed or even damaged, which also cause problems ranging from interference in telephone transmission to conductors degradation and failure of insulating material in motors and transformers. In the past, different harmonic power filter topologies have been installed and successfully operated keeping the harmonic distortion within acceptable limits, which are shunt active filter, hybrid active filter, switching techniques which are some techniques used for harmonic mitigation [1–8]. Among that AC line reactor, link reactor, shunt capacitor are the simplest way to reduce the harmonics present in the AC source. Line reactors are used at line side or input side

R. Suganthi (✉) · V. Kumar Chinnaiyan · M. Gopinath
Dr.N.G.P Institute of Technology, Coimbatore, India
e-mail: suganthirvk@gmail.com

C. Kamalakannan et al. (eds.), *Power Electronics and Renewable Energy Systems*, Lecture Notes in Electrical Engineering 326, DOI 10.1007/978-81-322-2119-7_96

of adjustable frequency drive, here it is used at input side and link reactor connects the diode rectifier and inverter circuit of adjustable speed drive. In addition that in industrial installations powerfactor correction circuitries is often used to compensate reactive power. Typically, switched capacitor banks are connected in parallel to inductive loads. In this paper for the simulation purpose third order harmonics are generated at input side. Voltage distortion is directly proportional to source impedance of the line, electrical apparatus are designed to work within 5 % of harmonic limits from stand by equipments [3]. With the use of non-linear loads on the rise globally, isolation for poor quality distribution systems and mitigation of harmonics will become increasingly important. The limits as per IEEE Std 519. As a result, THD on certain power systems could be much higher, especially considering the difficulty in attaining harmonic measurements. The APT line of programmable AC power sources isolates electronic equipment from a distorted mains supply while maintaining low THD during testing and measurement [9]. AC line reactors are used to reduce the harmonic present in AC supply source line without changing any driver circuit internally. The inductor value is as low as possible the total system impedance as 3 % for cost effectiveness. DC link reactors are used is kept small to reduce the losses and system as compact one.

When applying the reactors and capacitors in ASD mainly two factors get affected which are (i) loading factor of adjustable speed drive (ii) power system source impedance.

96.2 ASD Loading Factor

ASD loading factor consists of an important role in harmonic current distortion level at the ASD input. 430 V, the following factors are assumed for the simulation. The input supply is three phase, 430 V, and load is three phase adjustable speed drive subjected to different loading conditions from 25 to 100 %. The power system source impedance of 5 % is used in simulation, which is typical value for 1MVA, 430 V, 50 Hz power system with line source inductance and line resistance are Ls is 0.033 mH and 0.01 Ω respectively.

96.3 Simulated Performance Analysis

In this paper harmonics in industrial load is get analysed. Supply frequency of the lab load is 50 Hz, single phase, 430 V. Basically two types of THD are available in supply line, (i) Voltage harmonic, (ii) current harmonic. Input supply side Voltage and current harmonic content is 3.11 and 5.2 %. Usually current harmonic content is always higher than Voltage harmonic. After the inverter and rectifier circuit harmonic content of supply to ASD gets increased.

In three methods harmonic content get analysed, (i) Line reactor, (ii) link reactor, (iii) shunt capacitance (Figs. 96.1, 96.2 and 96.3).

In which 6 pulse diode rectifier is used for converting three phase AC supply to DC supply, link reactor is used to connect rectifier circuit and inverter circuit. Pulse Width Modulation (PWM) Current Source Inverter (CSI) is used as inverting circuit for speed control of induction motor drive. Medium power applications CSI fed ASD are used instead of Voltage Source Inverter (VSI). For low power applications VSI fed drive is used for ASD. Wide range of speed control is not possible in VSI fed drive.

PWM current source inverter equipped with IGBT switch in parallel with freewheeling diode to block the reverse break down Voltage, IGBT switch is used to operate at above 3 kHz

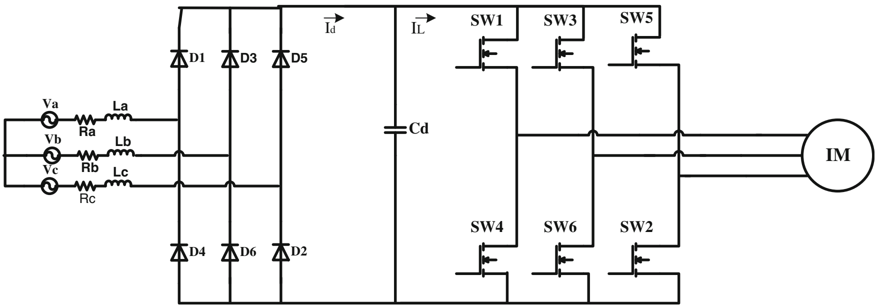

Fig. 96.1 Typical ASD design configuration with Line reactor

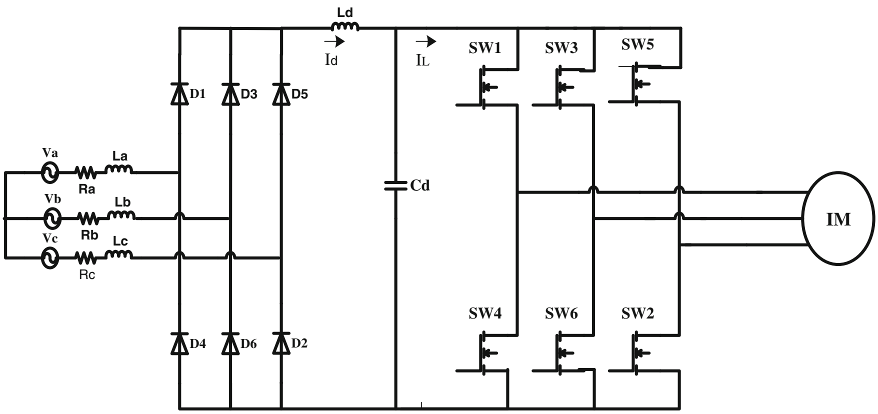

Fig. 96.2 Typical ASD design configuration with link reactor

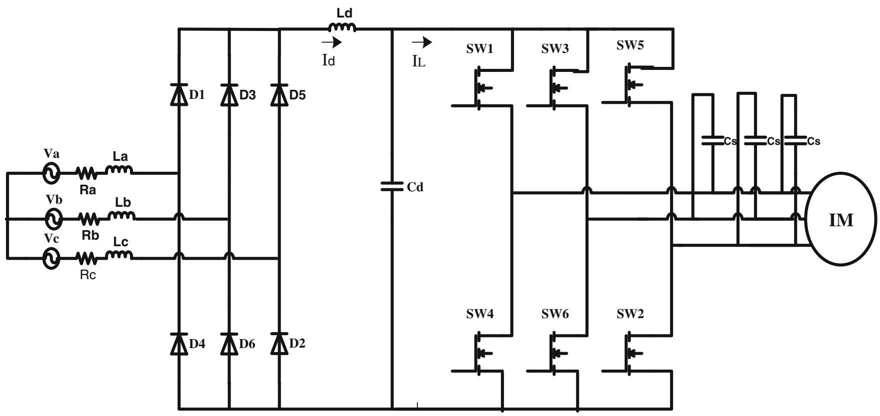

Fig. 96.3 Typical ASD design configuration with shunt capacitance

$$Z_{eff} = \frac{2 * \sqrt{3} * f * L * I_{fnd}}{V_{LL}} * 100 \tag{96.1}$$

Above equation Z_{eff} (total effective impedance), f (supply frequency), L (line inductance), I_{fnd} (fundamental phase current), V_{LL} (phase Voltage of supply) is used for calculate the total effective impedance of the source, among that 6 % of the reactance is used for calculate the filter reactance In which 5 % of reactance is used as AC line reactance and 3 % of reactance is used as DC link reactance. AC line inductance and DC link inductance can be chooses as same value. For 3 % of AC line inductance harmonic value get reduced 83 % for 25 % loading and 41 % for 75 % loading. For 3 % of DC link reactance the harmonic value get reduced 92 % for 25 % loading and 48 % for 100 % loading. The AC line reactor is 3 % and DC link reactor chosen as 5 % for effective value of THD reduction in ASD.

96.3.1 Limiting Current Ripple

For steady state behaviour, the mean value of the mains and machine side DC link Voltages has to be equal when neglecting losses. The inductance in the DC link has to smooth the DC link current to the determined ripple value to render regular drive operation Reactance value will be more effective at heavier load drive condition compare to that of lesser load condition that means THD reduction rate increases with increasing in load. In this AC line reactor is more effective than DC link reactor. The value of inductance in this paper is in milliHenries. The reduction rate of DC link reactor is small as compared to AC line reactor. The reduction rate of ASD drive of the loading is calculated by using below formula

$$\text{THD reduction rate} = \frac{\text{THD without reactor} - \text{THD with AC or DC reactor}}{\text{THD without reactor}} \quad (96.2)$$

For 4 % of AC line reactance the DC link inductance value will be 7.3 %, so DC link reactance value will be equal to 1.65 times of AC line reactance value. The individual harmonic depends on the source inductance and loading of the ASD.

In Fig. 96.4, with AC line reactor the total harmonic distortion is reduced from 86.4 to 39.58 % and also powerfactor varies from 0.5–0.78 under different loading conditions. i.e. from 30 to 100 %. Although the lower order harmonics are present in adjustable speed drive system.

In Fig. 96.5 simulated wave form consists of input Voltage in that third harmonic are generated at input side and outputs are analysed.

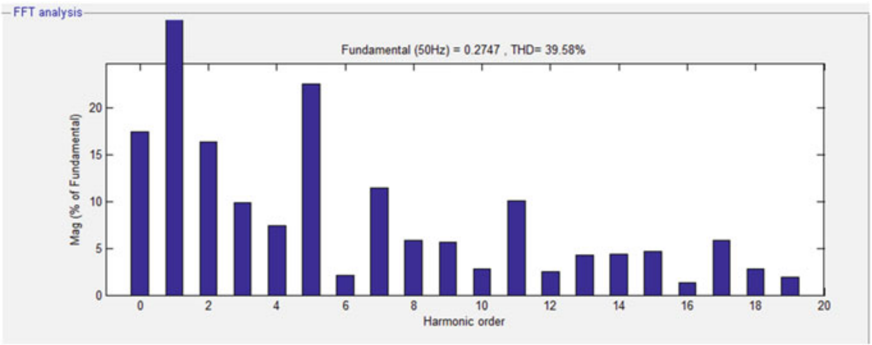

Fig. 96.4 FFT analysis of AC Line reactor in ASD

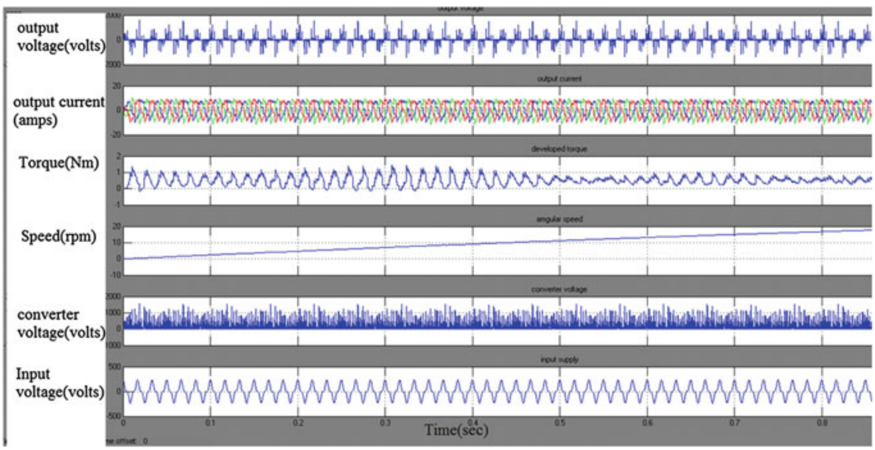

Fig. 96.5 Simulated waveform for AC line reactor

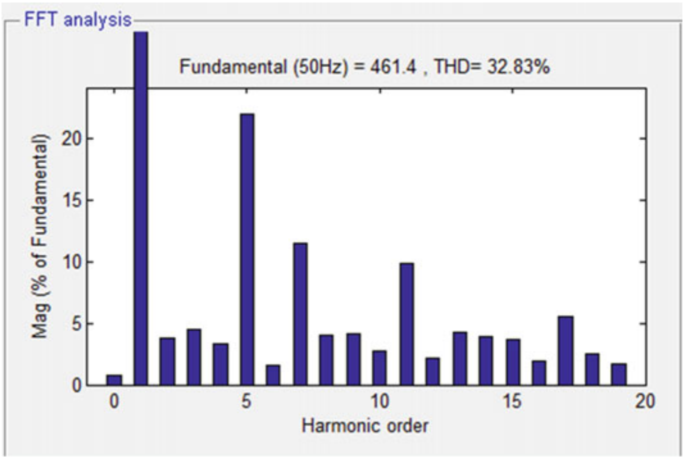

Fig. 96.6 FFT analysis of DC link reactor in ASD

In Fig. 96.6 shows FFT analysis of ASD with DC link reactor, In this DC link reactor reduces harmonic from 82.3 to 32.83 % and powerfactor varies from 0.64 to 8.6 %, compare to AC line reactor total harmonic distortion get reduced and powerfactor get improved compare than DC link reactor.

Increasing value of DC link reactor reduces the value of total harmonic distortion and increases performance of the adjustable speed drive, which also protects the inverter drive from Voltage sags and swells and other power quality problem.

In Fig. 96.7 output waveform consists output wave form which that distortion is more loss than AC line reactor with ASD.

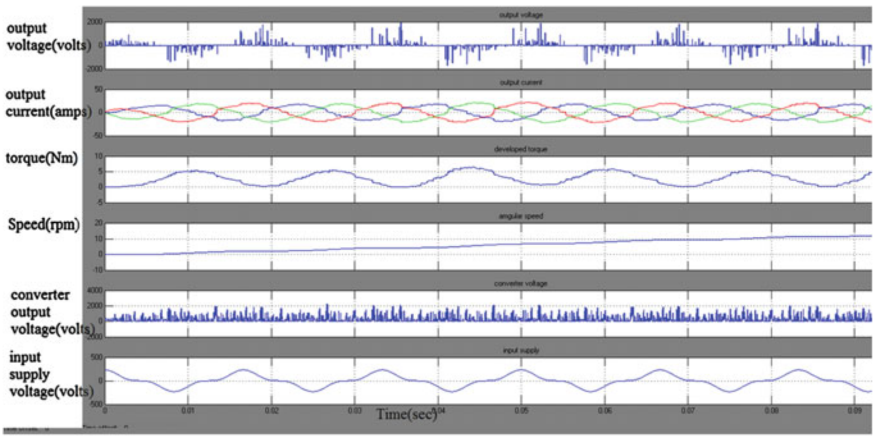

Fig. 96.7 Simulated waveform for DC link reactor

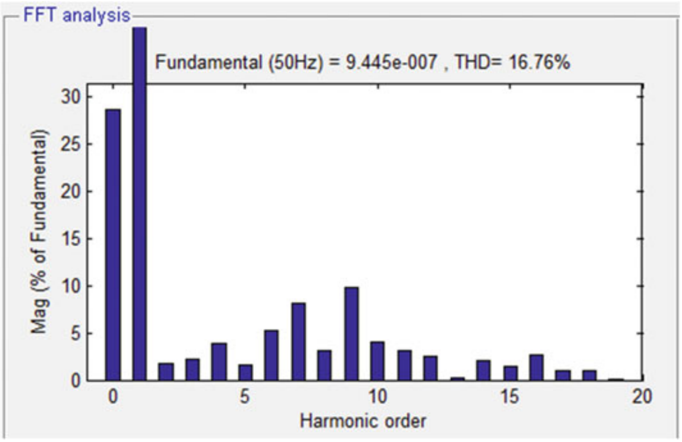

Fig. 96.8 FFT analysis with reactor and capacitor in ASD

In Fig. 96.8 shows FFT analysis of ASD with reactor and capacitor filter, compare to AC line and DC link reactor, combination of this reactor and capacitor reduces the harmonic from 39.58, 32.83 to 16.76 %, lower order harmonics are drastically reduced by this filter, powerfactor get improved from 0.5–0.78, 0.64–0.85 to 08–0.93. In this type of filter is best suited for input side harmonic elimination in adjustable speed drive at industrial applications compare than other filter, but cost of filter is high from AC and DC link reactor and comparatively low from other shunt and hybrid active filters. Due to this power losses are reduced from 30 to 40 % from total power loss, and windings of machines also safe in operation.

Figure 96.9 shows the final analyzed simulated wave form of ASD with reactor and inductor. Input supply waveform of ASD gets reduced in harmonic level (Table 96.1).

The lower order harmonic 5th to 13th order harmonics get affected due to source inductance and driving load, harmonic 17th to 49th are insensitive to them. 5th and 7th harmonics are dominant to six pulse ASD drive and significantly affected by drive loading and inductance of the reactors. So for effective six pulses ASD either AC line reactor or DC link reactor get added to the drive configuration.

For 12 pulse ASD drive dominant characteristic harmonic are 11th and 13th order harmonics. It's found that without reactor 11th and 13th order harmonics are quit sensitive. By adding small amount of reactor in ASD drive circuit 11th and 13th order harmonics are insensitive. For 12 pulse ASD drive adding phase transformer in front of driving unit reduces the harmonic of source inductance, which not required AC or DC line and link reactance, but cost of the phase shifting transformer is high.

For 18 pulses ASD, characteristics form 17th order, but the ASD loading and source inductances are insensitive to system. So AC line reactance and DC link reactance are not necessary to add in Add in that Adjustable frequency drive for 18 pulse other high pulse drive, but switching loss and cost of high pulse drive are high.

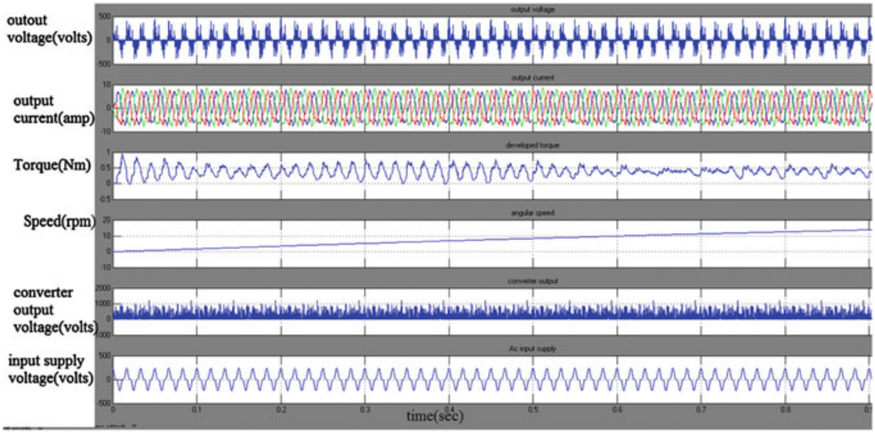

Fig. 96.9 FFT analysis of reactor and capacitor in ASD

Table 96.1 Comparative analysis of THD and powerfactor

Sl. no.	Parameter	THD (%)	Powerfactor
1	AC line reactor	39.58	0.5–0.78
2	DC link reactor	32.83	0.64–0.85
3	Reactor and capacitor	16.76	0.8–0.93

96.4 Hardware Performance Analysis

Third order harmonic control circuit is designed with the help of proteus software for DFT analysis, in which processor is used for harmonic measurement at input side and activate the filter circuit depending on the harmonic level. Hardware designed with lab loads which as three phase induction machine (Vs = 430 V, F = 50 Hz, P = 3500 watts, L_S = 0.033 mH, R_S = 0.01 mH) (Fig. 96.10).

Hardware setup of ASD shows converter circuit, control circuit, inverter circuit, filter circuit, induction machine, fluke meter (Fig. 96.11).

AC line reactor is air core inductor is used, which reduces the total harmonic distoriton level up to 33.6 %, from the value of THD 82 %. Compare to simulated output wave form the THD value is 6.3 % is higher in hardware.

Figure 96.12 shows fluke meter result of ASD with AC line reactor and DC link reactor, in which the same air core inductor is used for AC line and DC link reactor. Numerical value of these reactors is stated in above simulated result.

Figure 96.13 shows fluke meter result of ASD with reactor and capacitor, in which air core inductor is used for reactor and electrolytic capacitor is used for capacitor. In fig shows comparative analysis of level of the third order harmonics. In which third order harmonics at input side of ASD get reasonably reduced.

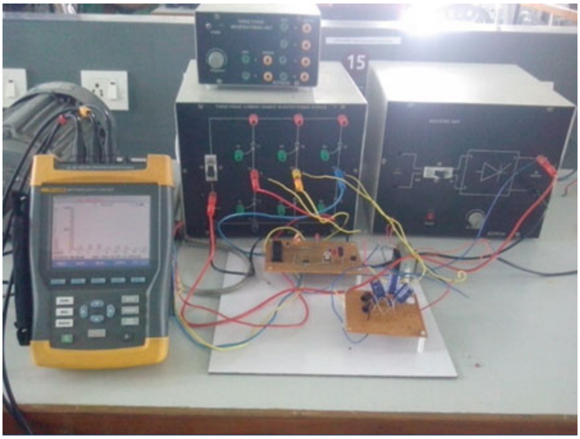

Fig. 96.10 Hardware implementation of ASD with filter

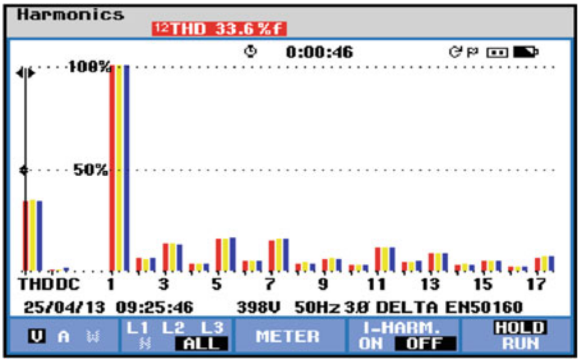

Fig. 96.11 Fluke meter output of ASD with line reactor

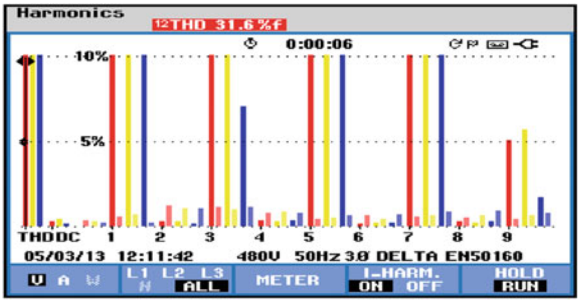

Fig. 96.12 Fluke meter output of ASD with AC line and DC link reactor

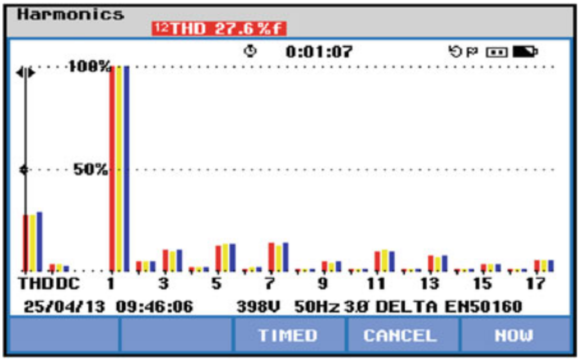

Fig. 96.13 Fluke meter output of ASD with reactor and capacitor

96.4.1 Factor 2: Power Systems Source Impedance

The source impedance of power systems in the form of a series source resistance and a series source inductance, which represents the equivalent system impedance seen from the input of a ASD, could have considerable effectiveness of AC line or DC link reactors in the drive package. The simulated using a six-pulse ASD is done with different source impedances reflecting possible system conditions in the real life. A fixed source resistance equal to 0.01 Ω is used for all simulation cases, while the source inductances are 0.01, 0.033 (typical), 0.05, 0.07, and 0.09 mH for a 1 MVA 480 V 50 Hz rated power source, which corresponds to 1.8, 6 (typical), 9.1, 12.7, and 16.4 %, respectively. The loading of ASD is also treated as a variable in the simulation. The simulated THDs at the ASD input under 100 and 30 % drive loadings using AC line and DC link reactors. The source impedance of the power system is equivalent to an additional AC line reactor to the ASD package, larger source inductance results in a lower THD at the drive input under a specific drive loading condition.

96.5 Conclusion

Based on the simulation and result in this paper, the following conclusions are drawn. Usually, the AC line reactors or DC link reactors or shunt capacitor are required for six-pulse ASDs, but they are not necessary for 12-pulse, 18-pulse, and other higher pulse VFDs for the input harmonics reduction purpose. Two factors significantly affect the THDs at the drive input which are loading of the drive and the source impedance of the power system at the VFD input. A larger source inductance results in lower THDs at the drive input for a specific drive loading condition. For the case in which the power system source impedance is unknown, the typical source impedance (Ls = 6 %). Although AC line reactors and DC link reactors both appear to be effective, the inductance of a DC link reactor should be about 1.7 times of the inductance of an AC line reactor to obtain the similar harmonic reduction effect at the ASD input for a specific drive loading, for shunt capacitor bank typical value had been chosen. Inverter capacitor is used to improve the powerfactor at load side, and reduces the THD compare to the AC line and DC link reactor. Capacitor reactance is the 6 % of the total System load impedance value. This capacitor also improves the system performance of adjustable speed drive.

References

1. Liang X, Ochonwu O, Lim J (2011) Influence of reactors on input harmonics of variable frequency drives. IEEE Trans Indus Appl 47(5):2195–2197
2. IEC/TR61000-3-6:2008, Electromagnetic Compatibility (EMC)—Part 3–6: Limits—Assessment of emission limits for the connection of distorting installations to MV, HV and EHV power systems, April 2008
3. de Oliveira Filho ME, Gazoli JR, Sguarezi Filho AJ, Ruppert Filho E (2008) A control method for voltage source inverter without DC link capacitor, 2008 IEEE vol 978-1-4244-1668-4/08/
4. Lee K, Jahns TM, Lipo TA, Venataramanan G, Berkopec WE (2008) Impact of input Voltage sag and unbalance on dc-link inductor and capacitor stress in adjustable-speed drives. IEEE Trans Ind Appl 44(6):1825–1833
5. Fuchs FW, Kloenne A (2004) DC link and dynamic performance features of PWM IGBT current source converter induction machine drives with respect to industrial requirements. In: Proceedings of 4th IPEMC, 2004, vol 3, pp 1393–1398
6. Detjen D, Jacobs J, De Doncker RW, Mall H-G (2001) A new hybrid filter to dampen resonance sand compensate harmonic current industrial power systems with powerfactor correction equipment. IEEE Trans Power Electron 16(6):821–827
7. Sladky R, Gilmore T, Frazier G, Jaszkowski D (1995) Distribution system disturbances and its effects on Voltage source inverter drives. In: Rockwell automation, standard drives business unit, power group, Allen-Bradley Co., July 18, 1995
8. IEEE Std. 519-1992 (1993) IEEE recommended practices and requirements for harmonic control in electrical power systems
9. Fuchsand FW, Mueller-Hellmann A (1983) Control methods for reducing the inductance in the DC link of current source inverters. IEEE Trans Ind Appl 1A-19(5):699–707

Chapter 97
Yaw Control of Wind Turbine Using Fuzzy Logic Controller

R. Bharani and K.C. Jayasankar

Abstract Wind power generation need some advancement in tracking the direction of high wind speed to generate maximum power all through the day. This paper explains about the maximum wind speed direction tracking using fuzzy logic controller. As the maximum wind speed and direction is sensed using anemometer and wind vane respectively. The present direction of the wind turbine head is sensed, the present wind direction is considered as reference then the error is calculated. The error signal is given to the fuzzy controller to rectify the error and make the wind turbine head to turn towards the direction of the maximum wind. Thus the generator generates maximum power.

Keywords Fuzzy controller · Wind turbine · Yaw control · PID controller

97.1 Introduction

Wind energy is accepted as a carbon-emission-free source of renewable energy. Wind blows all throughout the day. It is available in abundance for converting them into electrical energy. In fact, the wind power production spreading, also aided by the transition from constant to variable speed operation, that represents one of the significant factors in the development of wind turbines, involves the development of efficient control systems in order to improve the effectiveness of wind systems [1]. Wind is converted into electrical energy effectively by tracking the maximum wind point to get maximum power output all through the day. The conversion process uses the basic aerodynamics of lift to produce a net positive torque on a rotating shaft. From the point of view of wind energy, the most striking characteristic of the wind resource is its variability. The amount of wind power crucially depends on the speed of the wind, as the power is proportional to the cube of the wind speed. Hence, small

R. Bharani (✉) · K.C. Jayasankar
Department of Electrical and Electronics Engineering, Prathyusha Institute of Technology and Management, Chennai 602025, Tamil Nadu, India
e-mail: bharanikrishnakumar@gmail.com

C. Kamalakannan et al. (eds.), *Power Electronics and Renewable Energy Systems*, Lecture Notes in Electrical Engineering 326, DOI 10.1007/978-81-322-2119-7_97

differences in the wind speed result in significant differences in the produced power [2]. The wind is highly variable, both geographically and temporally [3]. At a particular wind velocity the wind turbine speed attains maximum to get maximum power. Thus we are going for variable speed wind turbine to produce the electrical power. In fact, variable speed operation increases the energetic efficiency and reduces the drive train torque and generated power fluctuations [4]. Therefore, to control the turbine blade direction few innovative solutions based on soft computing methodology is needed. Thus, we are going for fuzzy system to control the direction of wind turbine towards the direction of the wind. Fuzzy logic theory have found a great variety of applications in control engineering, power systems, telecommunication, consumer electronics, information processing, pattern recognition, signal processing, machine intelligence and so on. The fuzzy control algorithm basically consisted of a set of heuristic control rules and fuzzy sets [4]. The IF-THEN rules play a main role in developing fuzzy rules. The fuzzy control “IF–THEN” rules are often obtained based on an operator’s control action or knowledge [4]. To provide a better tracking effect for system, an approach of fuzzy rule is adopted, which PID parameter is adjusted by fuzzy rule when Wind Turbine Generator is operating [5]. Adjusting of PID parameter will improve the PID controller performance only. To improve the resolution the fuzzy controller is used to control the servo motor to turn the turbine head. The fuzzy rules are developed using MATLAB toolbox and the fuzzy controller is designed and developed. As the number of rules increases the resolution of rotating angle of the wind turbine head too increases. Thus, the turbine head faces the maximum wind direction all the time. The basic block diagram of yaw controller is shown in Fig. 97.1.

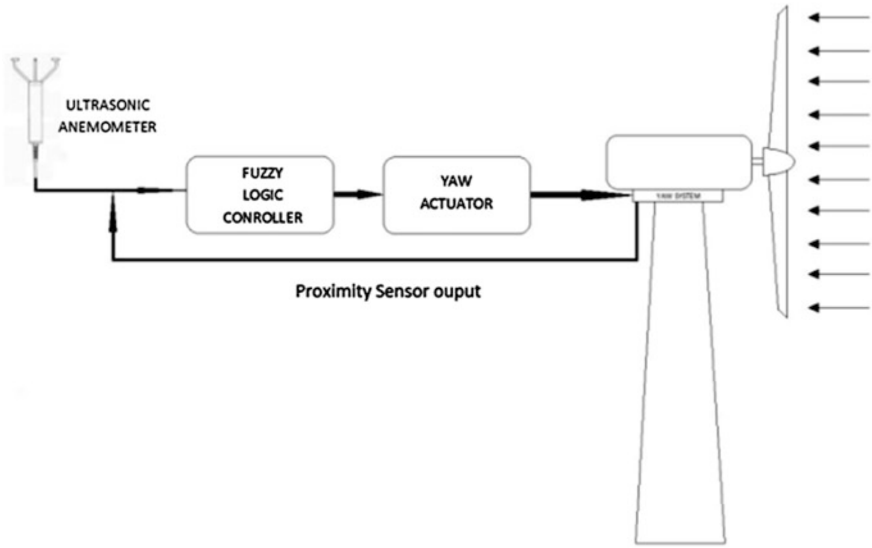

Fig. 97.1 Basic block diagram

97.2 Materials and Methods

97.2.1 Selection of Wind Turbine

The power output from the wind turbine is given by following equation

$$P = \frac{1}{2} C_p \rho A U^3 \quad (97.1)$$

where,

ρ	Density of air (1.25 kg/m^3)
C_p	Power coefficient
A	Rotor swept area
U	Wind speed

As by varying the power coefficient and rotor swept area modest increase in power output can be achieved. Instead, to increase the output power drastically the wind turbine should be located on the site with higher wind speed. The basic driving force of air movement is a difference in air pressure between two regions. This air pressure is described by several physical laws. One of these is Boyle's law, which states that the product of pressure and volume of a gas at a constant temperature must be a constant, or

$$p1V1 = p2V2 \quad (97.2)$$

The wind speed at heights of 20–120 m above ground is very desirable in selecting the type of wind turbine to be installed according to the power to be generated. The capacity of the wind turbines selected is large wind turbines ranging from 1.5 MW to 5 MW. The synchronous generator is used to generate the power output, which is used to measure the maximum output power produced using yaw control system.

97.2.2 Wind Energy Measurement

Wind energy measurements are associated with wind speed, wind turbine rotational speed and electrical signal including voltage, current or collective electrical power. Ultrasonic anemometer is used to measure the wind direction and cup type anemometer is used to measure the wind speed. An ultrasonic anemometer in the nacelle supplies the reference angle to the controller, which sends a signal to the yaw actuators to move the nacelle towards the wind direction [6]. The cup type air speed measurement is used for free air. The present position of the nacelle is detected by the induction potentiometers. To determine electrical energy output it

Table 97.1 Electrical energy measurement

Quality	Symbol	Unit of measurement
Current	I	Amp
Voltage	V	Volt
Resistance	R	Ohm
Power/Energy	E	Watt

can be measured either directly as energy in kWh or indirectly by measuring voltage current output of the wind turbine. The lists of electrical energy measuring quantity are listed in Table 97.1.

97.2.3 Yaw System

Yaw system consists of two main systems as yaw control system and yaw drive system. Horizontal wind turbines employs yaw mechanism to keep the turbine headed into the wind. Yaw angle is the system of change of tracking the wind direction. It usually turns at a constant speed. Thus, a very simple configuration consisting of several motors working together is enough to position the nacelle. The present position of the nacelle is detected is compared with the direction of the wind at present, an error signal is generated to compensate the difference in angle. This is a closed loop control system to compensate the error. The yaw motor is rotated in clockwise direction to rotate the missile in anticlockwise direction vice versa. The yaw ring gear and yaw induction gears rotation are shown in Fig. 97.2.

Fig. 97.2 Yaw gears

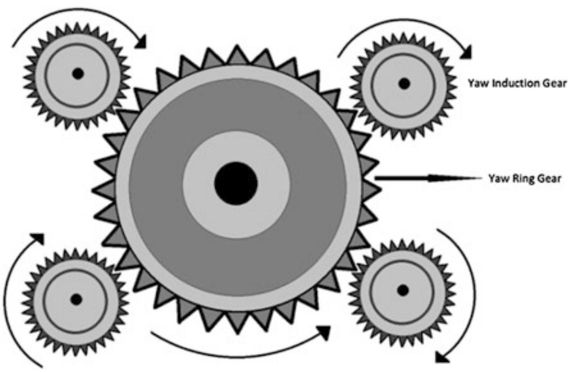

97.3 Theory and Calculation

97.3.1 Fuzzy Controller and Algorithm

The fuzzy control is used to solve complex, nonlinear and multivariable models. They do not need any mathematical model of the plant. It is basically an adaptive and nonlinear control, which gives performance for a linear or nonlinear plant with parameter variation. The fuzzy control algorithm basically consist of a set of heuristic control rules, fuzzy sets and fuzzy logic were used to represent linguistic terms and to evaluate the control rules called conventional fuzzy control or Mamdani-type fuzzy control [4]. The tracking of wind direction is controlled by using Mamdani-type fuzzy controller. The primary benefit of fuzzy systems theory is to approximate system behavior where analytic functions or numerical relations do not exist. Hence, fuzzy systems have high potential to understand the very systems that are devoid of analytic formulations: complex systems [7]. The fuzzy controller is designed and simulated using MATLAB R2013a toolbox. The fuzzy system consists of input set and output set interfaced by the fuzzy inference process. The fuzzy inference process consists of three major steps as

- Fuzzification
- Rule base evaluation
- Defuzzification

97.3.1.1 Fuzzification

Fuzzification is the process of finding the membership degrees to which input data belong to the fuzzy sets in the antecedent part of a fuzzy rule [8]. A membership function (MF) is a curve that defines how each point in the input space is mapped to a membership value (or degree of membership) between 0 and 1. Wind direction and turbine head direction are the two analog input variables ranging from 0° to 359° and 0° to 359° respectively. There corresponding fuzzy set are in the range of 0 to 5 V and 0 to 30 V respectively. The output variable is torque of yaw actuators to rotate the turbine head. The inputs and outputs are determined by the degree to which they belong to each of the appropriate fuzzy sets via membership functions (Fig. 97.3).

97.3.1.2 Rule Base Evaluation

The rules are expressed in conventional antecedent-consequent form. The type of fuzzy Interface System used is ‘Mamdani’. Mamdani is one of the pioneers in the application of fuzzy logic in control system. This is the most commonly used implication method [9]. The two input variables have their own membership

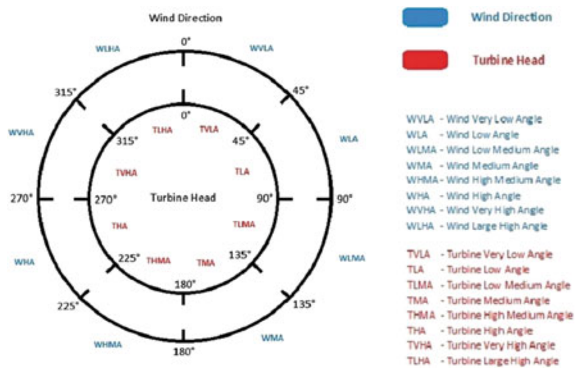

Fig. 97.3 Fuzzy membership functions

functions. The rules are evaluated using IF-TEHN rules. The flow chart of the rules is shown in Fig. 97.4. Totally of 64 rules has been has been developed. Some of the samples are shown below

1. IF Wind Direction is WVLA (Wind Very Low Angle) AND Turbine Head is TLMA (Turbine Low Medium Angle) THEN Torque is ACT (Anti Clockwise Torque)
2. IF Wind Direction is WLA (Wind Low Angle) AND Turbine Head is TLHA (Turbine Large High Angle) THEN Torque is CT (Clockwise Torque)
3. IF Wind Direction is WLMA (Wind Low Medium Angle) AND Turbine Head is TLMA (Turbine Low Medium Angle) THEN Torque is ZT (Zero Torque)
4. IF Wind Direction is WHMA (Wind High Medium Angle) AND Turbine Head is TVLA (Turbine Very Low Angle) THEN Torque is CT (Clockwise Torque)
5. IF Wind Direction is WHA (Wind High Angle) AND Turbine Head is TLA (Turbine Low Angle) THEN Torque is ACT

The rules are evaluated with AND (min) operation of the fuzzy operation set. The Degree of Fulfillment (DOF) of the rule is

$$DOF_1 = \mu_{WVLA}(X) \wedge \mu_{TLMA}(Y) \tag{97.3}$$

where $\bigwedge$ is minimum operator and μ_{WVLA} and μ_{TLMA} are the membership functions of Wind Direction (X) and Turbine Head (Y), respectively. The DOF of the remaining rules are

$$DOF_2 = \mu_{WLA}(X)\mu\wedge_{TLHA}(Y) \tag{97.4}$$

$$DOF_3 = \mu_{WLMA}(X)\mu\wedge_{TLMA}(Y) \tag{97.5}$$

$$DOF_4 = \mu_{WHMA}(X)\mu\wedge_{TVLA}(Y) \tag{97.6}$$

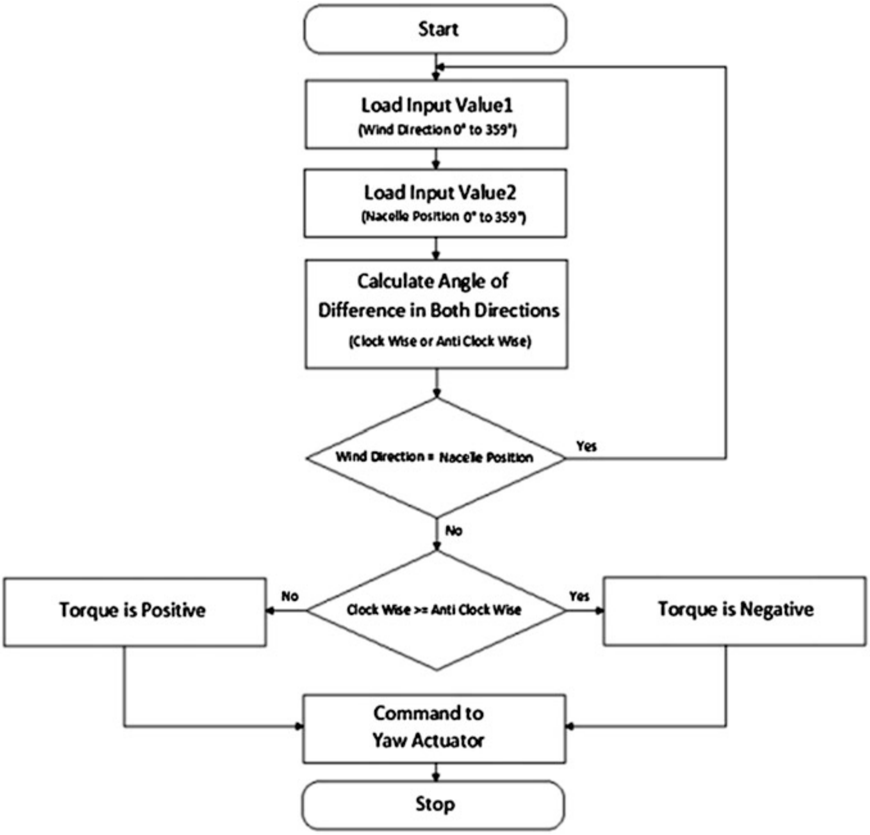

Fig. 97.4 Flow chart

$$DOF_5 = \mu_{WHA}(X)\mu\wedge_{TLA}(Y) \tag{97.7}$$

The rule output is given by the truncated membership function. The total fuzzy output is the union (OR) of all the component membership functions.

$$\mu_{OUT}(Z) = \mu_{WVLA'}(Z)\vee\mu_{TLMA'}(Z)\vee\mu_{WLA'}\ldots\mu_{WLMA'}(Z) \tag{97.8}$$

where $\vee$ is maximum operator and $\mu_{x\prime}$ are the membership functions for total fuzzy output. It is the union of all component membership function of the universe.

97.3.1.3 Defuzzification

As the fuzzy number is determined by the membership function, to achieve the purpose of ranking, the sort of fuzzy numbers is to construct various order

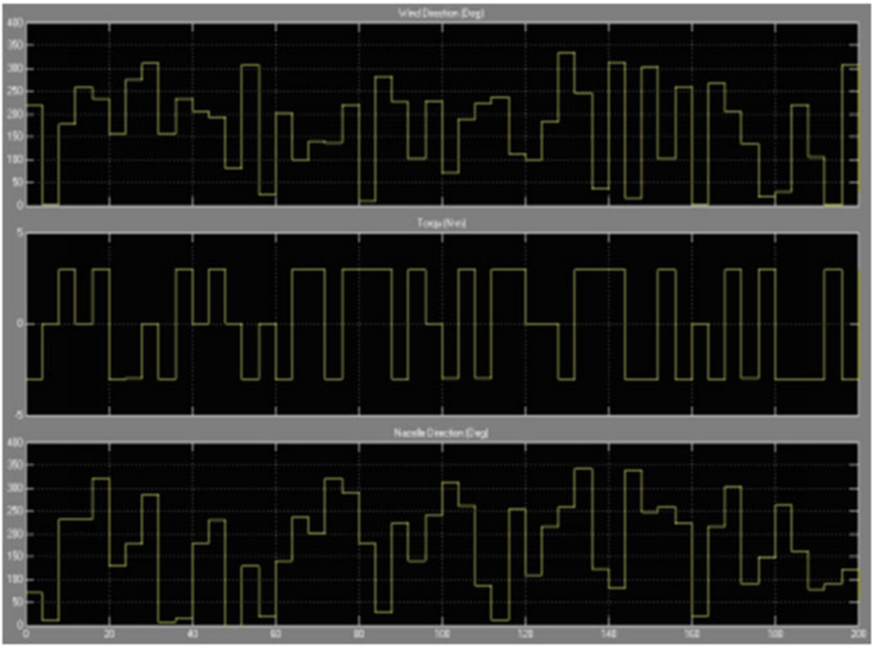

Fig. 97.5 Torque output

relationships from the standpoint of membership function to some extent. Practically, the centroids of fuzzy numbers are some properties of fuzzy numbers which are extracted from geometric aspects [10]. The centroid method is used here for defuzzifing fuzzy output functions. This procedure (also called center of area, center of gravity) is the most prevalent and physically appealing of all the defuzzification methods [11, 12], it is given by the algebraic expression

$$Z^{*} = \frac{\int \mu_c(z).zdz}{\int \mu_c(z).dz} \tag{97.9}$$

where $\int$ denotes an algebraic integration. The calculation of defizzified value using centroid method is converted into analog data.

97.4 Simulation Result

The two inputs parameters are given as wind direction and nacelle position as a signal to fuzzy controller. As the two inputs are same the torque produced should be zero. That is, as the missile is pointing in the direction of wind there is no torque (Zero) needed rotate the missile. If the direction of wind changes from the present

Fig. 97.6 Surface view

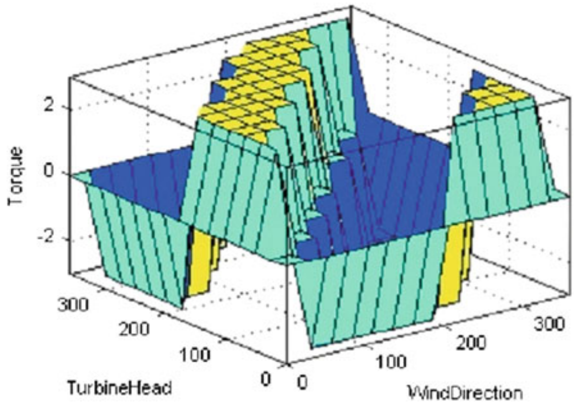

position the error is created, can be compensated using fuzzy controller and makes the nacelle to rotate in clockwise or anticlockwise direction (Fig. 97.5). A detailed description of the control systems for both the converters and the yaw angle command can be found in reference MathWorks [13]. The Fuzzy Logic Toolbox allows you to do several things, but the most important thing it lets you do is create and edit fuzzy inference systems. You can create these systems by hand, using graphical tools or command-line functions, or you can generate them automatically using either clustering or adaptive neuro-fuzzy techniques. The fuzzy toolbox is used to develop this controller for the wind power plant. The three dimensional representation of the output is surface viewer (Fig. 97.6).

97.5 Conclusion

A wind turbines yaw control using fuzzy controller is modeled and simulated. The system components namely, the wind turbine, yaw system and fuzzy controller have been modeled and brought together for wind energy conversion. Control of overall yaw system has been achieved by fuzzy logic controller. The high quality extracted power from the wind and electrical energy implies that the fuzzy controller has reflected its advantages to the system. Tracking the wind direction and regulating the power output is achieved by yaw system control. The positive or negative torque of the yaw motors drives the yaw ring gears towards the direction of maximum wind speed. The presented simulation results demonstrate that the proposed yaw control is feasible and has certain advantages.

References

1. Calderaro V, Galdi V, Piccolo A, Siano P (2008) A fuzzy controller for maximum energy extraction from variable speed wind power generation systems. Electr Power Syst Res 78:1109–1118
2. Kramer O, Gieseke F, Satzger B (2013) Wind energy prediction and monitoring with neural computation. Neurocomputing 109:84–93
3. Burton T, Jenkins N, Sharpe D, Bossanyi E (2011) Wind energy handbook, 2nd edn. Wiley, Hoboken (2011)
4. Feng G, Series editors frank l. Lewis, shuzhi sam ge (2010) Analysis and synthesis of fuzzy control systems. Taylor and Francis Group, Boca Raton
5. Torabi A, Tarsaii E, Mashhadi SKM (2014) Fuzzy controller used in yaw system of wind turbine noisy. J Math Comput Sci 8:105–112
6. Mathew S, Philip GS (2011) Advances in wind energy conversion technology. Springer Heidelberg
7. Timothy J (2004) Ross: fuzzy logic with engineering applications. Wiley, England
8. Kasabov NK (1998) Foundations of neural networks, fuzzy systems, and knowledge engineering. Congress Cataloging-in-Publication
9. Bose BK (2002) Modern power electronics and AC drives. Prentice Hall PTR, USA
10. Saneifard R, Saneifard R (2011) A method for defuzzification based on centroid point. Official J Turk Fuzzy Syst Assoc 2:36–44
11. Sugeno M (1986) An introductory survey of fuzzy control. Inf Sci 36:59–83
12. Lee C (1990) Fuzzy logic in control systems: fuzzy logic controller, parts I and II. IEEE Trans Syst Man Cybern 20:404–435
13. The MathWorks, SimPowerSystems For Use with Simulink, User's Guide Version 4

Chapter 98
Overload Protection and Speed Monitoring of Induction Motor Using ZigBee Wireless Sensor Networks and GSM Technology

P.E. Elavenil and R. Kalaivani

Abstract This paper is for monitoring the speed, torque and protection of three phase induction motor from overload by implementing ZigBee based wireless sensor network. The design of the system maintains security, provides high reliability and also protect from many types of faults. The system has transmitter and receiver section which are controlled by PIC16F877A microcontroller. The communication between those sections are made by ZigBee transmitter and receiver section. The parameters such as voltage, current, speed and torque of induction motor were monitored. The monitored values are displayed in PC and as SMS in mobile through GSM technology. If overload condition occurs, relay driver circuit will open and makes the motor to turn OFF. Thus input values are maintained within the limit and speed of the motor will be in a controlled manner.

Keywords GSM technology · Induction motor · Overload protection · Speed monitoring · WSN (wireless sensor networks) · ZigBee transmitter and receiver

98.1 Introduction

It is becoming very popular the utilization of three phase induction motors when compared to single phase induction motors for many of the applications because of its simple design, rugged performance and easy maintenance. The advancement of power electronics technology and the cost makes this utilization possible.

P.E. Elavenil (✉) · R. Kalaivani
Rajalakshmi Engineering College, Chennai, Tamil Nadu, India
e-mail: elavenil.263@gmail.com

C. Kamalakannan et al. (eds.), *Power Electronics and Renewable Energy Systems*,
Lecture Notes in Electrical Engineering 326, DOI 10.1007/978-81-322-2119-7_98

The obtained parameters from the motor while operation are sent to the monitoring unit through wireless sensor networks (WSN) [1, 2] provide self-organisation and local processing capability and will be displayed in PC (Personal Computer) [1]. LM-35 sensor is used for temperature sensing of the motor [1]. Therefore this appears as flexible and inexpensive solution for building industrial monitoring and control systems. ZigBee wireless sensor network is used here which allows the formation of a large network of sensors in various industrial segments. In comparison with the other standards such as IEEE 802.11 (Wi-Fi) and IEEE 802.15.1 (Bluetooth), the ZigBee standard has advantages related to energy consumption, low cost and scalability [3, 4].

The speed performance of induction motor is checked first without controller and then with the help of PID (Proportional Integral Derivative) controller. The software simulation model for this speed monitoring of three phase induction motor is developed by using MATLAB simulink software [5, 6]. The fault period for the particular simulation is to be given in the three phase fault circuit. Thus the speed of the motor decreases, if the load increases. The parameters such as settling time and rise time were compared and finally conclude that PID controller gives the better performance of speed characteristics.

The overload protection of the motor is checked by using the parameter called voltage which is varied through potentiometer and then the results are displayed in LCD (Liquid Crystal Display) as well as in the virtual terminal of GSM (Global System for Mobile communication) block. The software simulation model for this overload protection of motor is developed by using Proteus 7.2 software.

98.2 ZigBee WSN

ZigBee is a specification for a suite of high level communication on protocols using small, low-power based on an IEEE 802 standard. This network is often used in mesh network form to transmit data over longer distances, passing data through intermediate devices to reach more distant ones [3]. ZigBee specifies operation in the unlicensed 2.4 GHz (worldwide), 915 MHz (Americas and Australia) and 868 MHz (Europe) ISM bands. Transmission range is between 10 and 75 m (33 and 246 feet) and up to 1,500 m for ZigBee PRO.

ZigBee is used in the lighting control, sensor networks, smart energy management systems. ZigBee is not intended to support power line networking but to interface with it at least for smart metering and smart appliance purposes. Because ZigBee nodes will go from sleep to active mode in 30 ms or less and responsive [4].

98.3 Experiment Methodology

The schematic of protection and monitoring system is shown in the Fig. 98.1. The workbench was designed to obtain the speed and torque parameters of the induction motor. It has a nominal rotation speed of 1,500 RPM. Proximity sensor senses the speed performance of the induction motor which is fixed in front of the shaft. The heat sensor called LM-35 is used to measure the temperature of the motor for each of the rotation. Then the signals from the sensor are transferred to the embedded unit. The PIC16F877A microcontroller controls both the transmitter and receiver section. The read datas are sent to the wireless ZigBee (a pair of ZigBee module can act as a transmitter and as a receiver) transmitter and then to the ZigBee receiver through the serial communication using RS 232 port. Thus the speed and torque values were obtained and transmitted to the monitoring unit through ZigBee. Those values were getting displayed in PC (Personal Computer) as well as in mobile as SMS (Short Message Service) through GSM technology. The potential transformer and current transformer is used to find out the voltage and current of the induction motor which can withstand high voltages.

If the overload condition occurs, the system makes the relay circuit in open condition. Thus the common switch of relay is in contact with Normally Open (NO) switch which makes the induction motor to turn OFF. Thus the overload condition is prevented by using relay driver circuitry. The input to drive the motor will be given in the keypad. The overload condition will be displayed in the LCD (Liquid Crystal Display) as a message called "motor overload". The buzzer produces a beep sound at this time of overload which indicates that the motor turns into OFF condition.

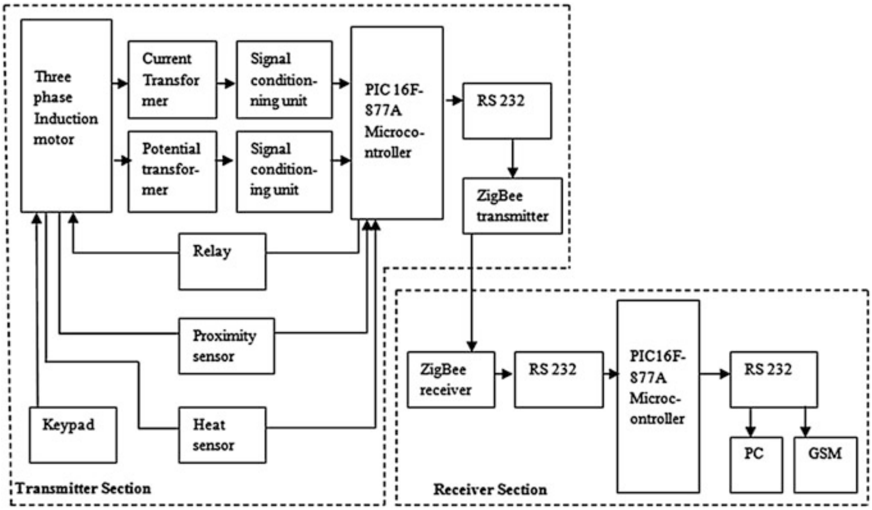

Fig. 98.1 Schematic of embedded system integrated into WSN

98.4 Development of Simulation Blocks

98.4.1 Speed Monitoring of Motor Using MATLAB Simulink

The simulation model with and without controller for speed monitoring of three phase induction motor are shown in the Figs. 98.2 and 98.3. This model has IGBT (Insulated Gate Bipolar Transistor) which converts the DC (Direct Current) to AC (Alternating Current). The converted AC current is fed to the motor through three legs of the IGBT transistors and three phase V-I measurement block [5]. This V-I measurement block is used to produce the voltage and current of the motor. The resulting speed will be RPS (Rotation Per Second) which is converted into RPM (Rotation Per Minute) through gain block. The particular fault period for the occurrence of fault is given in the three phase fault circuit. This system is designed for both the model with PID (Proportional Integral Derivative) controller and without controller. The obtained speed after the transition time is compared with the set speed value and the error is minimised by PID controller [6].

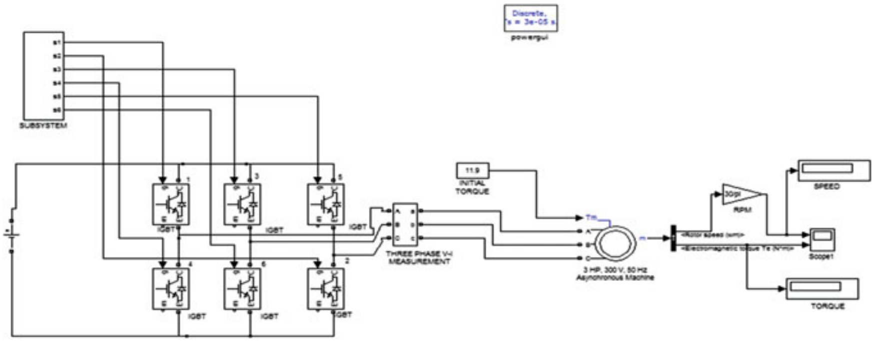

Fig. 98.2 Developed simulink model without controller

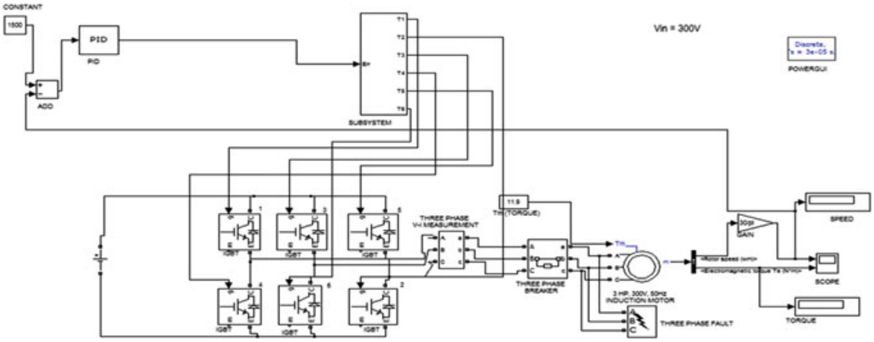

Fig. 98.3 Developed simulink model with PID controller

98.4.2 Overload Protection of a Motor Using Proteus 7.2

The simulation circuit for overload protection of the motor is designed using Proteus 7.2 software which is shown in the Fig. 98.4. The required components are picked form the library block of Proteus design schematic and placed in the model. The pins from PIC16F877A microcontroller are interconnected with the 16 × 2 LCD display, GSM module and motor. The voltage produced from the potentiometer is given as the input to PIC16F877A microcontroller. The baud rate set for GSM module is 9,600. Two conditions are verified here. First, what happens to the motor, if the set input voltage is getting exceeded. Second, what happens to the motor, if the set input voltage is not getting exceeded. This input voltages are specified in the program which is written in embedded C language. The tool used here is the MP lab software to convert the original code into hex file. The converted hex file is dumped into the PIC16F877A microcontroller in the Proteus design suite. Then the simulation is to be compiled and verify the conditions by increasing or decreasing the voltages in the positive and negative terminals of the potentiometer.

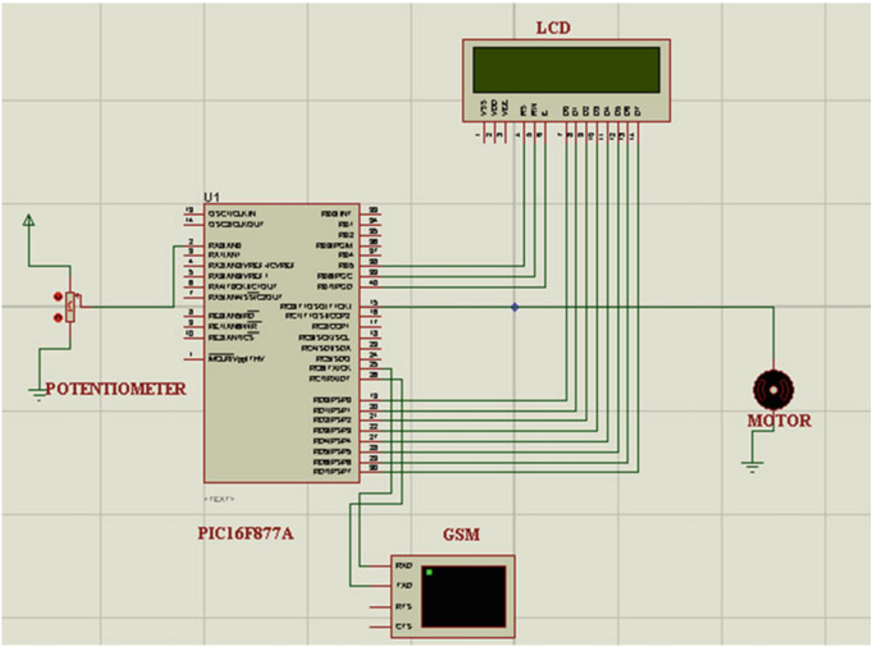

Fig. 98.4 Developed proteus model for overload protection of the motor

98.5 Simulation Results

98.5.1 Simulation Result for the Overload Protection of Motor

Simulation for overload protection of the motor is carried out in Proteus environment and the results are verified. The whole system is compiled by the "Run" button. The overload is checked by increasing or decreasing the voltage through potentiometer's positive and negative terminals in which it displays the message as "motor ON" and "motor OFF" for the corresponding changes. The set input voltage which is written in program using embedded C language is 100 V. If the limit exceeds 100 V, the motor turns off automatically by sending message as "motor overload" through GSM block and LCD screen. If the limit does not exceeds 100 V, the motor operates in normal manner. Thus the motor stops its rotation and the overload to the motor is minimized which is shown in the Fig. 98.5.

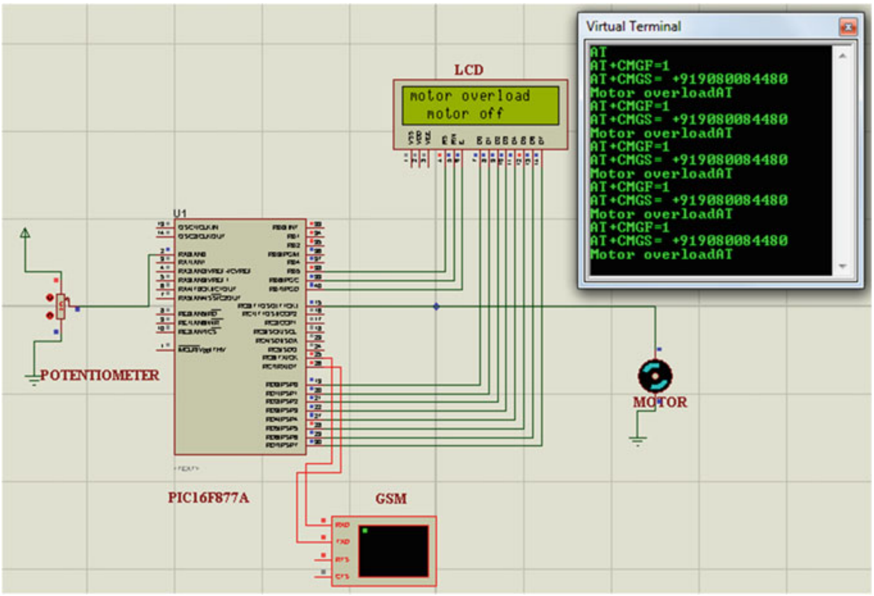

Fig. 98.5 Simulink output for overload condition

98.5.2 Simulation Results for Speed Monitoring of the Motor

Simulation results for speed monitoring of the motor are carried out in MATLAB environment and the results are verified for the speed v/s time characteristics. The speed response of induction motor is checked for the models of without controller and with PID controller [5]. When the simulation is compiled for the give transition time, the respective speed and torque values are obtained which is displayed in the scope as well as waveforms in the output screen of both the models [6]. The speed and torque waveforms are obtained with some distortion and without distortion which are shown in the Figs. 98.6a, b and 98.7a, b.

98.6 Comparative Results

See (Figs. 98.8, 98.9 and Table 98.1).

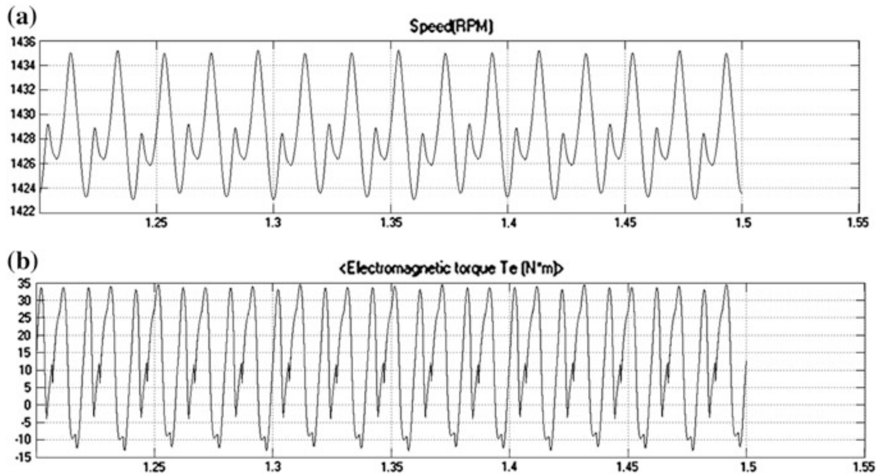

Fig. 98.6 Plot for speed and torque without controller. **a** Speed. **b** Torque

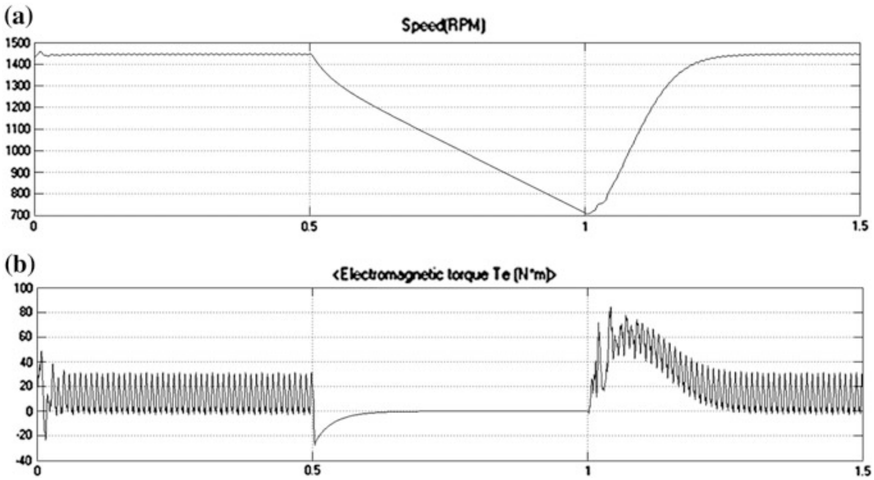

Fig. 98.7 Plot for speed and torque with PID controller. **a** Speed. **b** Torque

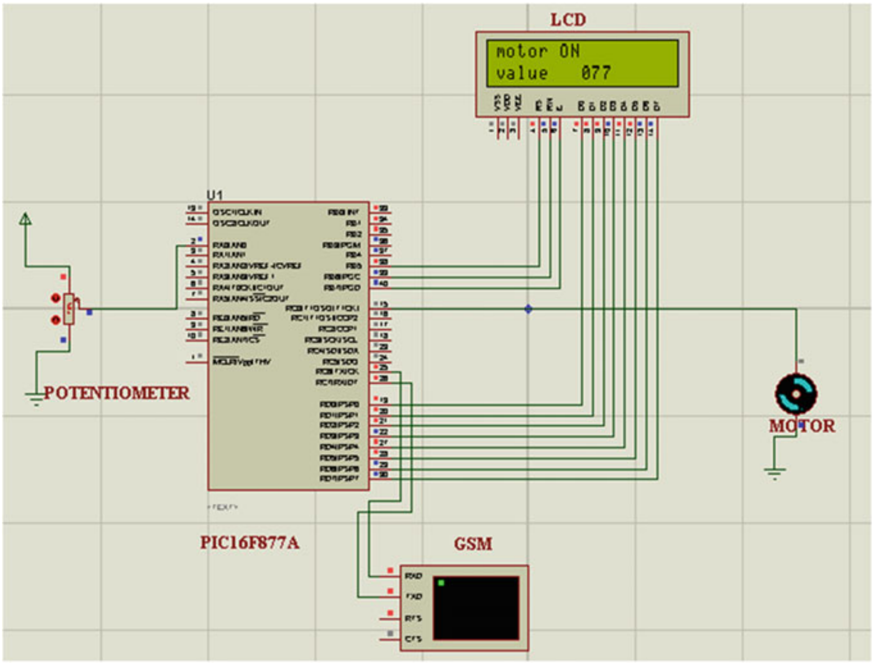

Fig. 98.8 Simulation output for below threshold value (100 V)

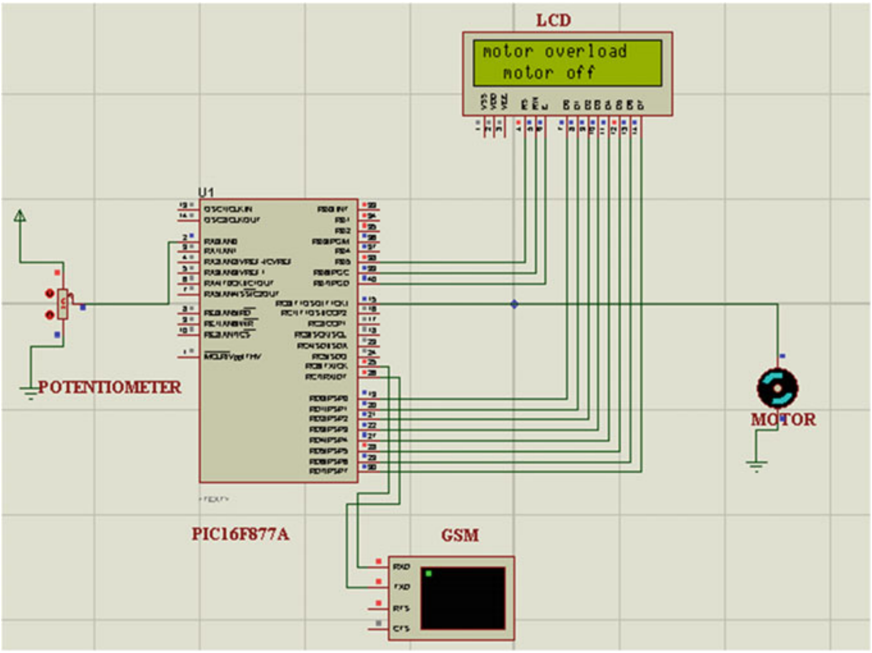

Fig. 98.9 Simulation output for above threshold value (100 V)

Table 98.1 Comparative results for with and without a controller

Parameters	Without controller	With controller
Set speed	1,500 RPM	1,500 RPM
Set torque	11.9 Nm	11.9 Nm
Settling time	Not settled	0.02
Rise time	1.21	0.001

98.7 Conclusion

Thus this paper presents the integration of embedded system with a ZigBee wireless sensor networks technology for the speed and torque monitoring of three phase induction motor. Relay driver unit is used to turn off the motor if the overload condition exists. The speed performance is maintained in a better manner by using PID controller. The fault period is set in the three phase fault circuit so that the speed of the motor decreases. After the clearance of the fault period, the speed maintains constantly without any distortion. The software simulations are done by using MATLAB simulink and Proteus 7.2 software for the speed monitoring and overload protection of three phase induction motor.

References

1. Bayindir R, Sefa I, Colak I, Bektas A (2008) Fault detection and protection of induction motors using sensors. IEEE Trans Energy Convers 23(3):734–741
2. Reddy PN (2013) Microcontroller based speed control of induction motor using wireless technology. Int J Emerg Sci Eng (IJESE) 1(9), ISSN: 2319–6378
3. Simoes ND, Goncalves JL, Caeiro ML, Boavida MJ, Cardosco FD (2010) ZigBee/GPS tracking system for rowing races. In: International conference on advances in mobile computing and multimedia, Paris, France, Nov 2010
4. The ZigBee protocol Alliance, Zigbee Specification, http://www.zigbee.org, June 2005
5. Mhaisgawali ML (2012) Induction motor speed control using PID controller. Int J Technol Eng Sci 1(2):151–155
6. Chabre M, Meoufel A, Bendaha Y (2011) Speed control of induction motor using genetic algorithm-based PID controller. Acta Polytech Hung 8(6):141–153

Chapter 99
Thermal Analysis of Switched Reluctance Machine Under Steady State and Transient Conditions Using Finite Element Method

E. Annie Elisabeth Jebaseeli and S. Paramasivam

Abstract In developing electrical machines, temperature limits is a key factor which affects the efficiency of the overall design. Since it is expensive to load and find temperature in an electrical machine conventionally, the estimation of temperature rise by various techniques became increasingly important. In the present paper, temperature rise is estimated using finite element method. A 2-D steady state analysis is carried out on an 8/6 Switched Reluctance Machine to observe the temperature distribution and maximum temperature. For the transient thermal analysis, the load corresponding to maximum temperature is taken as initial condition. From the transient analysis, heat distributions at various load steps are observed. Simulation results are presented under steady state and transient conditions and are validated experimentally. Comparisons with experimental results obtained with a 2 H.P. Switched Reluctance Machine show the effectiveness of the developed model to predict the temperature rise for a range of operating conditions.

Keywords Losses · Finite element method · Switched reluctance machine · Temperature

99.1 Introduction

An electrical machine is a complex engineering system consisting of different materials with different thermal properties and heat sources [1]. To design energy saving electrical machines, it has become necessary to carry out thermal analysis along with the traditional Electromagnetic field analysis. In an electric machine heat

E.A.E. Jebaseeli (✉)
Faculty of Electrical and Electronics Engineering, Sathyabama University,
Chennai, India
e-mail: anniejebaseeli@gmail.com

S. Paramasivam
R&D Head, ESAB Group, Chennai, India

C. Kamalakannan et al. (eds.), *Power Electronics and Renewable Energy Systems*,
Lecture Notes in Electrical Engineering 326, DOI 10.1007/978-81-322-2119-7_99

is generated by the electric currents and friction. This increases the temperature of different parts of the machine which could cause deterioration of insulation in windings [2], thermal stress, efficiency reduction and may lead to motor failure. Also under high loads, temperature rise influences the machine electrical and magnetic parameters [3]. It is therefore necessary to limit the temperature of the machine components within permissible limits for safety operation [4]. So the temperature rise analysis of Switched reluctance machine is implemented in this paper.

This paper in its Sect. 99.2 deals with Switched Reluctance Machine and finite element analysis along with machine model is discussed in Sect. 99.3. The simulation results under steady state and transient conditions are presented in Sect. 99.4 for a 8/6 Switched Reluctance Machine. Developed Model is validated with experimental results in Sect. 99.5. Section 99.6 includes the conclusive remarks.

99.2 Switched Reluctance Machine

Switched Reluctance Machines (SRM) have attracted increasing attention of electrical machine researches due to their simplicity, robustness, high torque density and low cost in its manufacture and maintenance. All the active parts of the machine namely the windings are present only in the stator. Hence they can have a relatively simpler cooling system since it is often sufficient to cool the stator where all the copper loss and most of the iron loss exist. This causes SRM to be applied in some harsh working environment like high speed and high ambient temperature [5]. Also the speed-torque characteristics of switched reluctance motor can be tailored to suit any desired application, [6] so the popularity of its dive has been increased.

In this electrical machine, torque is developed by the tendency of the rotor to occupy a position so that the reluctance of the magnetic path of the excited stator phase winding is minimum [7]. A two dimensional (2-D) finite element model of an 8/6 Switched Reluctance Machine is shown in Fig. 99.1 whose specifications are given in Table 99.1.

The two main components of electromagnetic losses in Switched reluctance Machine are core loss in the laminations and copper loss in the windings which form the heat source in a thermal analysis [8].

For any motor the copper loss can be calculated from the I^2R products, where R is the effective resistance of one phase winding. Core loss in switched reluctance machine are relatively low but in high speed applications they become the dominant component of the total loss. It is therefore important to estimate the power loss in the machine analytically or numerically under various loaded conditions in order to use them as input parameters for thermal analysis.

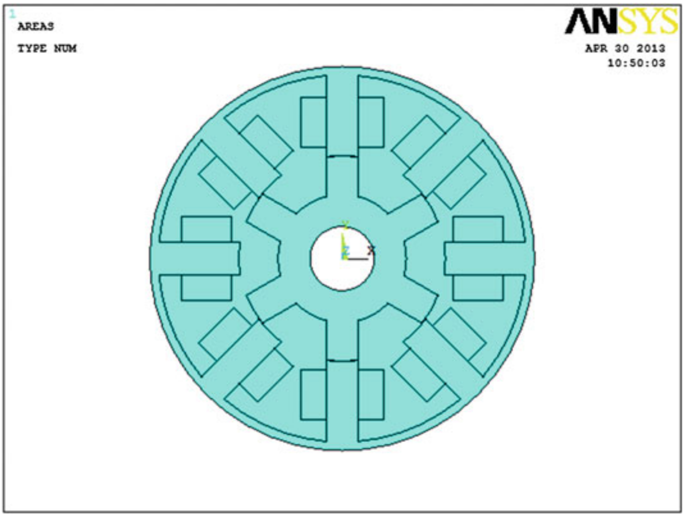

Fig. 99.1 Finite element model of 8/6 SRM

Table 99.1 Machine specifications

No. of. stator poles	8
No. of. rotor poles	6
Stator outer diameter	180 mm
Stator inner diameter	96.5 mm
Stator pole width	17 mm
Stator pole height	29.6 mm
Rotor outer diameter	96 mm
Rotor inner diameter	40 mm
rotor pole width	18.5 mm
rotor pole height	18.7 mm
Stack length	110 mm
Body length	225 mm

99.3 Thermal Analysis of Switched Reluctance Machine

Electric motor thermal analysis necessity has been increased with the increasing requirements for miniaturization, energy efficiency and cost reduction. Modern thermal analysis techniques can be classified into two basic methods [9] namely Lumped parameter thermal model method and Numerical method.

In Lumped thermal model method, thermal problem is solved using thermal networks analogous to electrical circuits. The result shows only the overall distribution of the temperature of the motor but does not indicate the point of internal temperature [10]. Also the procedure has to be modified virtually on a case-to-case basis.

Table 99.2 Thermal parameters

Material	Thermal conductivity (W/m K)	Density (Kg/m3)
Copper	380	8,940
Steel	40	7,850
Air	0.024	1.165

Numerical analysis is one of the most promising technologies. Most commercially available numerical analysis computer programs use finite element method. No assumptions are made regarding flux path or related empirical factors. A field solution can be obtained even with time-variable fields and with materials that are non-homogeneous, anisotropic or non linear. Hence this method has proved to be more flexible, reliable and effective and a general tool for the thermal analysis of electrical machines.

In this paper amount of heat generated due to losses is calculated and 2-Dimensional steady state and transient analysis are carried out. Corresponding to the physical dimensions given in Table 99.1 and from the core and copper loss of the machine, quantity of heat generation is calculated for different parts like stator core and coils. A finite element heat run [11] is simulated with this value which is the main heat source.

Analysis is carried out with Thermal parameters listed in Table 99.2 which are required for the prediction of the temperatures in the electrical machine [12].

99.4 Simulation Result Analysis

99.4.1 Steady State Thermal Analysis

In steady state analysis, various boundary conditions for conductive heat transfer is obtained from the Fourier law of conduction as given in Eq. 99.1.

$$\frac{1}{r}\frac{\partial}{\partial r}\left(kr\frac{\partial T}{\partial r}\right)+\frac{1}{r^2}\frac{\partial}{\partial \theta}\left(k\frac{\partial T}{\partial \theta}\right)+\frac{\partial}{\partial Z}\left(k\frac{\partial T}{\partial Z}\right)+\dot{q}=0 \tag{99.1}$$

Liquid and gas particles near heated body become lighter and rise, giving way to cooler particles which in turn gets heated and rise. Natural convection takes place due to changes in fluid density. This takes place on the external housing of the machine. In modern machines heat is removed by forced convection. The usual method is by blasting air on heating surfaces.

In convection the rate at which heat is removed is governed by Newton's Law

$$\frac{P}{A}=h(T_1-T_2) \tag{99.2}$$

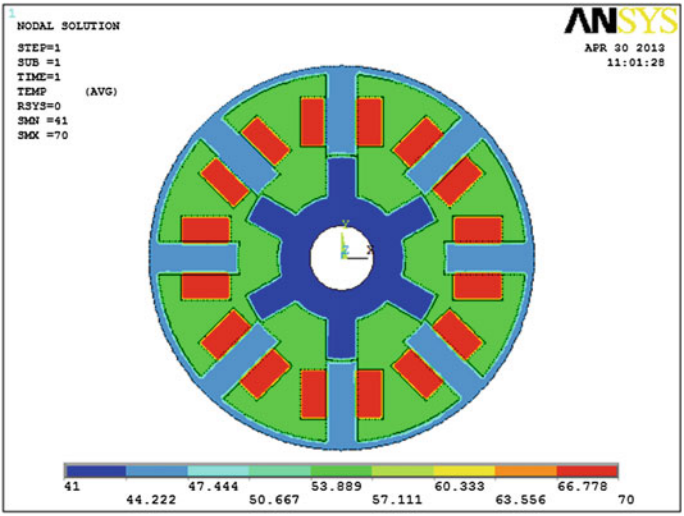

Fig. 99.2 Steady state temperature distribution at 1,500 rpm

where $(T_1 - T_2)$ is the temperature difference between the surface being cooled and the cooling medium. The value of convection heat transfer coefficient *h* depends on various factors like viscosity, thermal conductivity, specific heat and other properties of the coolant. With the help of empirical expressions, an estimation of the coefficients is possible.

The ambient temperature was set as 33 °C which is the room temperature when the real time measurement is carried out. Based on this a steady state analysis with the heat generation at full load condition is carried out. By analysing the temperature distribution presented in Fig. 99.2, it is clearly seen that at steady state, the temperature rises due to copper loss which depends on the current passing through the coil and the convective coefficients. Thus at full load the highest temperature of 70 °C occurs in the winding area. This area is most sensitive to possible thermal damages and hence it is considered as a benchmark for validation of the model.

99.4.2 Transient Thermal Analysis

In Transient thermal analysis, temperature varies with respect to time [13]. In a hollow cylinder containing heat source, Conductive heat transfer with various boundary conditions is obtained from the Fourier law [14] in cylindrical coordinate as

$$\frac{1}{r}\frac{\partial}{\partial r}\left(kr\frac{\partial T}{\partial r}\right) + \frac{1}{r^2}\frac{\partial}{\partial \theta}\left(k\frac{\partial T}{\partial \theta}\right) + \frac{\partial}{\partial Z}\left(k\frac{\partial T}{\partial Z}\right) + \dot{q} = \rho c\frac{\partial T}{\partial t} \qquad (99.3)$$

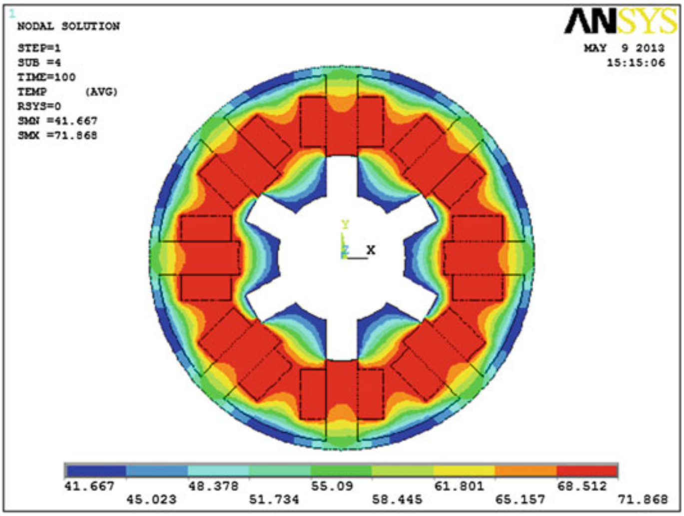

Fig. 99.3 Temperature distribution after 100 min

where $\dot{q}$ is the heat source which is substituted by the losses. Also, the boundary conditions are conductive heat transfer from the body and the axial shaft at two ends. Natural Convection is considered on stator external surface. Internal surfaces are subjected to [15] have forced convection due to the rotation of the rotor.

The boundary conditions considered are at t = 0, the machine has atmospheric temperature and at t > 0, the temperature increases due to heat generation in the machine. The time taken by the machine to reach steady state temperature can be found out using Transient thermal analysis. Figure 99.3 represents the results of transient thermal analysis. It shows that steady temperature is reached after 100 min. Thus heat distribution within the components of the machine with respect to time can be analysed accurately with transient thermal analysis.

99.5 Thermal Testing and Model Validation

Thermal testing involves inserting Resistance temperature Detectors into the selected parts of the machine. Then the machine is operated under loaded condition until the temperature reach their steady state value. The experimental setup used here for the model validation is shown in Fig. 99.4. A 2 H.P four phase 8/6 SRM was tested in the laboratory to observe the temperature rise in different locations. Figure 99.5 shows the variation of temperature in the winding with respect to time.

The accuracy of the thermal model described in Sect. 99.3 has been evaluated by comparing the results obtained numerically with the finite element model and the practical measurements in the corresponding conditions. Based on these, the

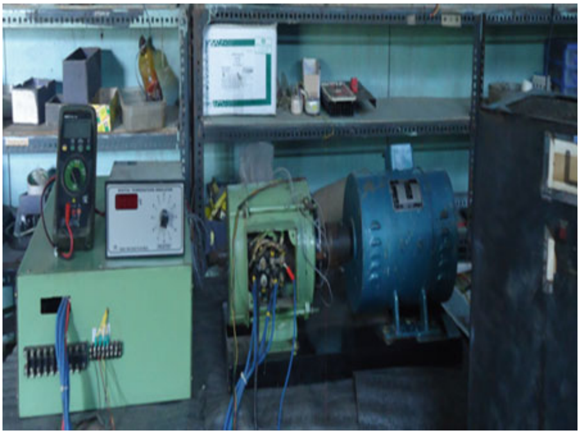

Fig. 99.4 Experimental setup for the temperature measurement

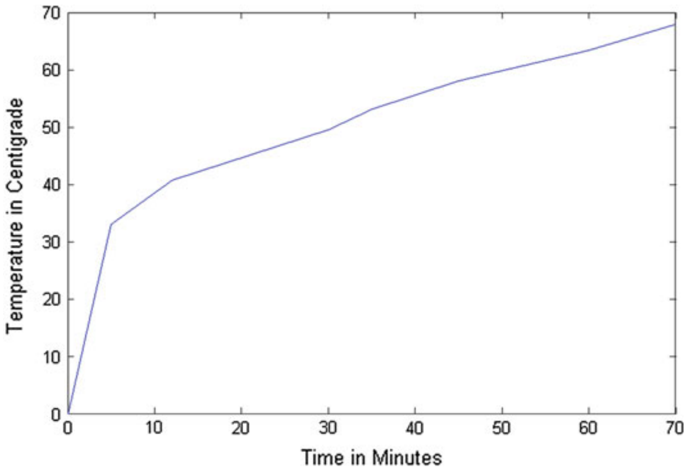

Fig. 99.5 Temperature measurement by resistance temperature detector at full load condition

results clearly demonstrate that over a wide range of operating conditions, the temperature distribution in any Electrical Machine can easily be obtained using finite element method effectively. Hence wastage of power required for conventional loading is minimised.

99.6 Conclusion

In electrical machines, the insulation life time varies inversely with the working temperature. Hence to improve the machine performance and its reliability, a thermal analysis is carried out by 2-D finite element analysis under steady state and transient conditions. It is observed that a maximum temperature of 70 °C is obtained in the winding area. The effectiveness of this approach is validated by comparison with the results of real time measurement. It can be concluded that this technique has a guiding significance in testing the motor for long term stability.

References

1. Huai Y, Melnik RVN, Thogersen PB (2003) Computational analysis of temperature rise phenomena in electric induction motors. Appl Therm Eng 23(7):779–795
2. Inamura S, Sakai T, Sawa K (2003) A temperature rise analysis of switched reluctance motor due to the core and copper loss by FEM. IEEE Trans Magn 39(3):1554–1557
3. Balamurugan S, Sumathi P (2004) Analysis of temperature rise in switched reluctance motor due to the core and copper loss by coupled field finite element analysis. In: International conference on power system technology—POWERCON 2004, pp 630–634
4. Fonseca DSB, Cabrita CMP, Calado MRA (2006) Thermal modelling and characterization of electrical machines and calculation of current ratings. In: Fourth IET conference on power electronics, machines and drives, pp 475–479
5. Li GJ, Ojeda J, Hoang E, Lecrivain M, Gabsi M (2011) Comparative studies between classical and mutually coupled switched reluctance motors using thermal-electromagnetic analysis for driving cycles. IEEE Trans on Magn 47(4):839–846
6. Srinivas KN, Arumugam R (2003) Dynamic characterization of switched reluctance motor by computer-aided design and electromagnetic transient simulation. IEEE Trans on Magn 39(3): 1806–1812
7. Vijayakumar K, Karthikeyan R, Sathishkumar GK, Arumugam R (2008) Two dimensional magnetic and thermal analysis of high speed switched reluctance motor using soft magnetic composite material. In: Proceedings of IEEE Region10 conference, TENCON, pp 1–5
8. Vijayakumar K, Karthikeyan R, Paramasivam S, Arumugam R, Srinivas KN (2008) Switched reluctance motor modeling, design, simulation, and analysis: a comprehensive review. IEEE Trans Magn 44(12):839–846
9. Boglietti A, Cavagnino A et al (2009) Evolution and modern approaches for thermal analysis of electrical machines. IEEE Trans on Ind Electr 56(3):871–880
10. Sun H, Gao J, Dong Y, Zheng Y (2008) Analysis of temperature field in switched reluctance motor based on finite-element. In: 11th international conference on electrical machines and systems, pp 597–601
11. Srinivas KN, Arumugam R (2001) Thermal characterization through finite element analysis of the switched reluctance motor. In: IEEE region 10 international conference on electrical and electronics technology, vol 2, pp 819–823
12. Wu W, John BD, Stephen JC, Bruce AK (2003) Design optimization of a switched reluctance motor by electromagnetic and thermal finite-element analysis. IEEE Trans Magn, 39(5): 3334–3336
13. Srinivas KN, Arumugam R (2005) Analysis and characterization of switched reluctance motor: part II-flow, thermal, and vibration analyses. IEEE Trans Magn, 41(4)

14. Rouhani H, Jawad F, Caro L (2007) Lumped thermal model for switched reluctance motor applied to mechanical design optimization. J Math Comput Model, pp 625–638
15. Annie EJE, Paramasivam S (2012) Steady state and transient thermal analysis of switched reluctance machine. Int J Comput Electr Eng, 4(5):794–798

Chapter 100
Design and Analysis of Three Phase Four Wire Shunt Active Filter with Neural Network Controller for Different Loading Conditions

V.V. Karthikeyan, S. Thangavel, Sreedendu and R. Sasikala

Abstract Non-linear loads draw harmonic current and propagate them through the supply line. These current affect both the consumers and utility. To eliminate harmonics shunt active filters are widely used. In this paper three phase four wire shunt active filter is analyzed for the mitigation of power quality problem. Task of an active filter is to make the supply current waveform as close as possible to a sinusoid in phase with the supply voltage. I_d and I_q control strategy is used to extract three phase reference current. Output of the PI controller tuned by neural network controller and result is compared. Design, simulation development and study of shunt active filter is accomplished using MATLAB Simulink power system tool box.

Keywords Active filter · Neural network · PI controller · Hysteresis current control

100.1 Introduction

In various sectors power quality is decreasing due to temperature rise in conductors and generators, high level voltage and current, and harmonic overloads. For the above disturbances are well understood and directly related to the loads consuming non-sinusoidal current, referred as non-linear loads. These loads is used for the conversion, variation and regulation of electrical power in commercial purpose. Use of non-linear loads either single phase or three phase has been increase loads employ solid state power conversion and draw non-sinusoidal current [1]. It also

V.V. Karthikeyan (✉) · Sreedendu · R. Sasikala
SNS College of Engineering, Coimbatore, India
e-mail: karthi.maharaja.@gmail.com

S. Thangavel
K.S. Rangasamy College of Technology, Thiruchangode, India

C. Kamalakannan et al. (eds.), *Power Electronics and Renewable Energy Systems*,
Lecture Notes in Electrical Engineering 326, DOI 10.1007/978-81-322-2119-7_100

cause harmonics and reactive power burden. So the efficiency increased and results interference to nearby communication network [2].

Use of power electronic based equipment have significant impacts on the quality of supplied voltage and increased the harmonic in distribution system.

Solution is suitable for power conditioning methodology such as passive filtering and active filtering to suppress harmonics in power system [3, 4]. Passive filters have been traditionally for mitigating the distortion due to harmonic current in industrial power system. But these filters have many drawbacks compared to active filter [5]. Dependency of their performance on the system impedance, resonance problem, absorption of harmonic current of non-linear load in passive filter. This could lead to further harmonic propagation through the power system.

Performance of shunt active filter is validated using controlling DC link voltage and three phase source current [6]. In this two control loops are used to generate gate signals. Fuzzy logic controller based compensation scheme is used to eliminate voltage and current harmonics with good dynamic performance [7]. Reference current for shunt active filter is calculated by dq transformation in [8]. In this scheme integrator control was proposed to improve the active power filter performance.

Neural network is applied to several components of shunt active for several purpose [9] denotes the advantages of processing speed, system stability and precision and maintenance of constant temperature. For the improvement of convergence and reduced computational requirement ANN based PWM controller is used [10]. This control strategy regulate the DC link voltage in the APF followed by adalline-based THD minimization technique. In this work both PI [11] and neural network controlled shunt active power filter for the harmonics and reactive power compensation of a nonlinear load are implemented. Both controllers performance under certain conditions and different system parameters is studied.

100.2 Proposed Topology

100.2.1 Operation of Shunt Active Filter

Injection of harmonic current is the basic principle of shunt active filter which is in equal in magnitude and opposite in phase. Load current is controlled in a closed loop manner to shape the load current and is shown in Fig. 100.1. The filter performance is studied under balanced supply condition for a three phase four wire shunt active filter.

Here the non-linear load is consisting of diode bridge rectifier with R-L load. Harmonic currents generated is increased by increasing loads and may become very significant. As a viable solution recent years voltage source inverter based shunt active filter has been used [12]. By sensing line current required compensating currents are determined. Filter generated harmonics of same amplitude but opposite in phase in that of load current harmonics injected in point of common coupling.

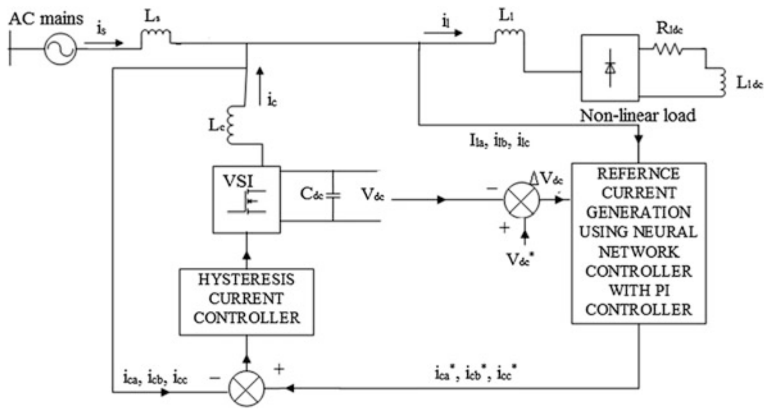

Fig. 100.1 Circuit diagram of shunt active filter

100.2.2 Park's Transformation

To simplify the three phase circuits direct–quadrature–zero (dq0) transformation or zero–direct–quadrature (0dq) transformation is used [13]. The dq0 transform is often referred as Park's transformation. PQ method is replaced by the instantaneous active and reactive current component ($i_d - i_q$) method which brings down the total harmonic distortion (THD) in supply current below 5 % so as to satisfy the IEEE-519 standards. The entire reference current generation scheme has been illustrated in Fig. 100.2.

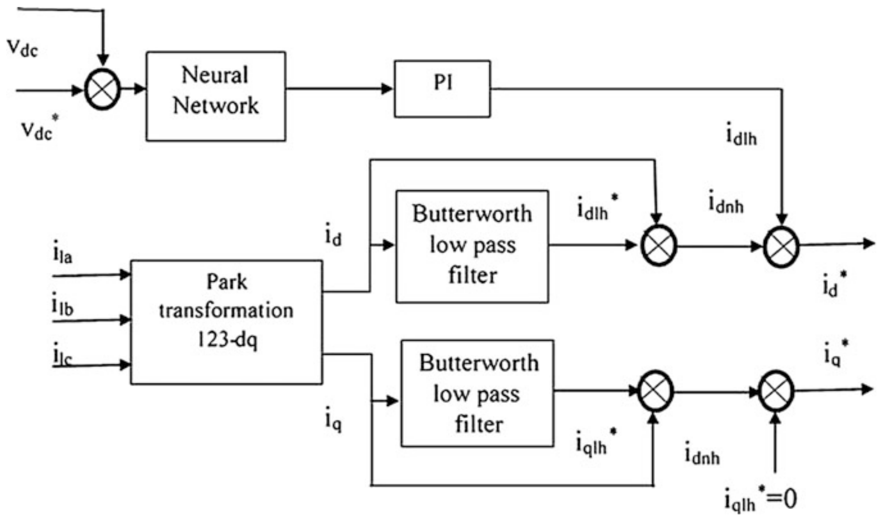

Fig. 100.2 Compensation current extraction using DQ control strategy

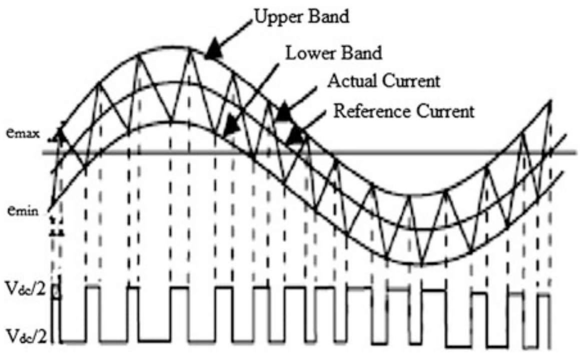

Fig. 100.3 Hysteresis current controller

100.2.3 Hysteresis Current Controller

Diagram of Hysteresis Current Control (HCC) is shown in Fig. 100.3. HCC is utilized independently for each phase and directly generates the switching signals for three-phase voltage source inverter. An error signal e(t) is the difference between the desired current $i_{ref}(t)$ and the actual current $i_{actual}(t)$.

If the error current exceeds the upper limit of the hysteresis band, the upper switch of the inverter arm is turned OFF and the lower switch is turned ON. As a result, the current start to decay. If the error current crosses the lower limit of the hysteresis band, the lower switch of the inverter arm is turned OFF and the upper switch is turned ON

100.3 Simulink Model of Shunt Active Filter

Simulink model of shunt active filter with neural network controller is shown in Fig. 100.4 modelled in MATLAB/SIMULINK. In this three phase balanced supply is given to the non-linear load.

Three phase source is connected to a RL load with diode bridge rectifier. Diode bridge rectifier in parallel with RL load act as non-linear load. Chosen the R = 20 Ω and L = 25 mH. Voltage Source Inverter (VSI) is built with universal bridge of IGBT. VSI act as shunt active filter for injecting compensation current at point of common coupling. DC link voltage is provided by split capacitors of C_1 and C_2 of 1,500 μF.

Gate pulse for VSI is produced by PI controller. And the PI controller is tuned using neural network controller. Three phase load current is taken and given to abc to dq0 transformation block which produce i_{Ld} and i_{Lq} current.

Capacitor link voltage is compared with DC reference voltage and the error is given to the neural network controller with a delay. The neural network controller is formed by using MATLAB program.

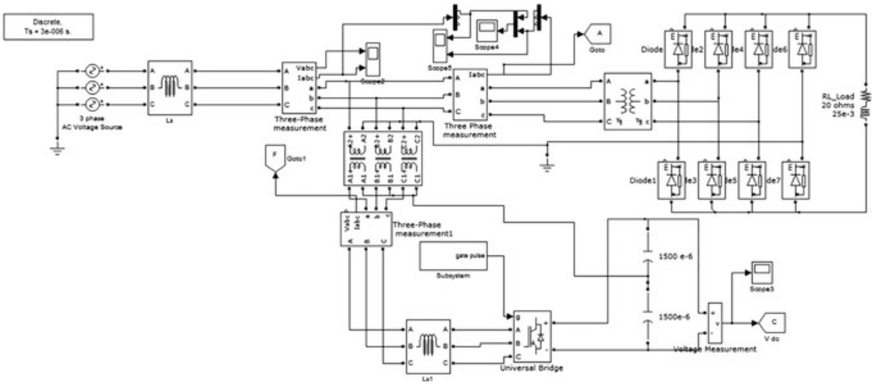

Fig. 100.4 Three phase four wire shunt active filter using neural network controller for balanced non-linear load

For developing the program two inputs are considered. DC voltage error and delayed error. The output of the neural network controller is dc voltage error which is given to PI controller as its input. Non-linear load produces harmonics which will not make any severe impact on source voltage, but sometimes it cause magnitude variation in source voltage. Figure 100.5 shows the source voltage before compensation.

Harmonics in the non-linear load makes distortions in the load current. This harmonic current flows through the line and affect the source current. Figure 100.6 shows three phase source current before compensation which is distorted. Analysing the THD value for this system by FFT analysis. THD value of source current was 30.48 %, which is greater than IEEE allowable limit of 5 %.

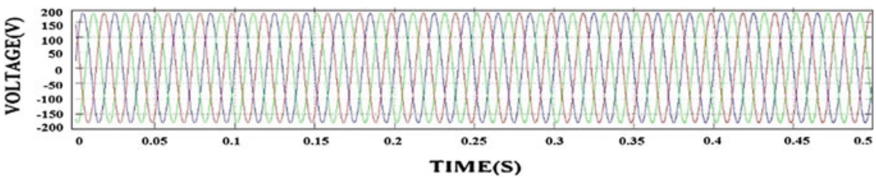

Fig. 100.5 Source voltage before compensation

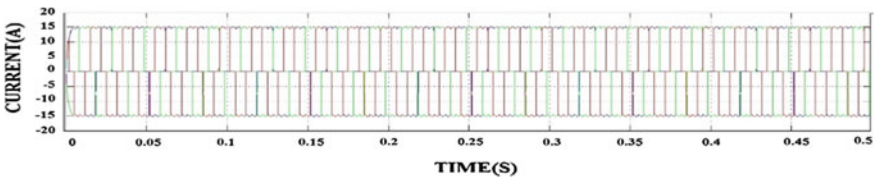

Fig. 100.6 Source current before compensation

This THD value describes low quality of power. For the improvement of power quality shunt active filter is used. The task of shunt active filter is to make line current waveform as close as possible to a sinusoid in phase with the line voltage by injecting the compensation current. So the three phase load current is given to dq0 transformation block for further control and analysis. Three phase load current is transformed into dq0-axis current. The d axis current and q axis current separated into positive and negative axis current.

The dq0 transformation is selected for the harmonic detection because of the fast calculation time in which it is suitable for the real time application. Further dq axis current is comparing with PI controller output.

To eliminate the waveform distortions and to get better waveform Butterworth filter is used. Separated d and q axis current is given to butterworth filter which gives small phase shift in harmonics and sufficiently high transient response. I_d axis with butterworth filter is shown in Fig. 100.7 and for q axis current filtered is shown in Fig. 100.8.

Filtered current is compared with PI controller output where PI is tuned using neural network controller. And the output of comparator is again converted as three phase currents shown in Fig. 100.9. Hysteresis current controller compare this reference current with measured filter current. By this comparison it produce a gate pulses for VSI (Fig. 100.10).

By analysing the waveform, there is a sudden increase in current up to 35 A for 0.01 s. This indicates the delay time for the compensation current injection in PCC by shunt active filter. So the components under zero crossing is not working properly.

Bar chart of THD analysis before compensation, after compensation with PI controller and with PI controller and Neural Network controller is shown in Figs. 100.11, 100.12 and 100.13 respectively.

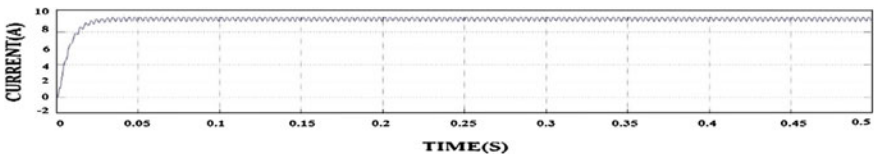

Fig. 100.7 I_d with Butterworth filter

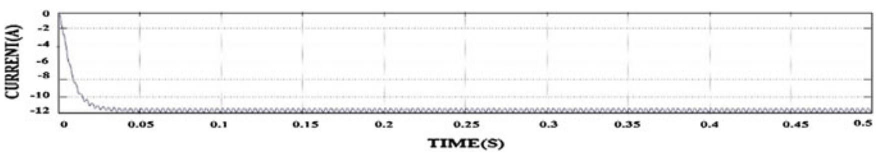

Fig. 100.8 I_q with Butterworth filter

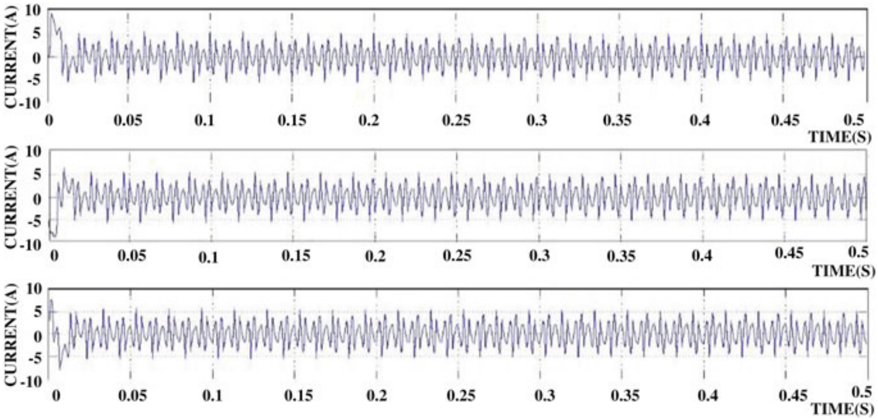

Fig. 100.9 Compensation currents

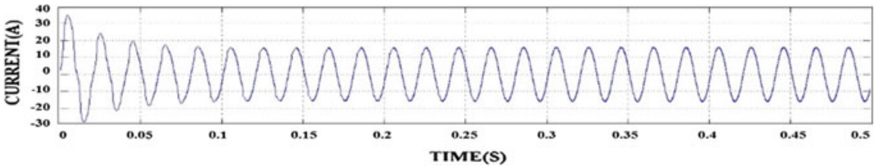

Fig. 100.10 Waveform of source current after compensation

Fig. 100.11 THD analysis before compensation

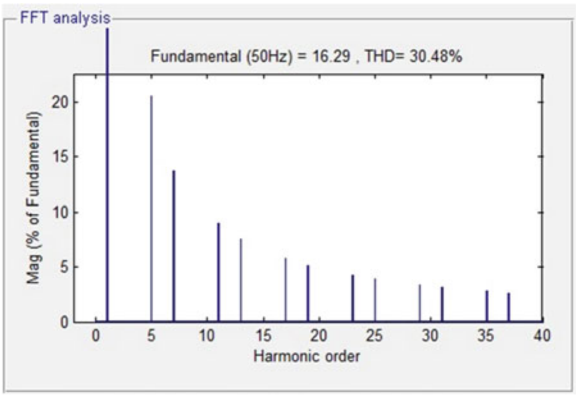

Performance comparison of SAF with and without neural network controller is described in Table 100.1. Before compensation the THD value is highly greater than IEEE allowable THD limit.

Using Shunt Active Filter with PI controller, equal and opposite harmonic current is injected. And the THD become lower and nearly to the IEEE limit. Shunt Active Filter with Neural Network controller, source current THD become 1.59 %.

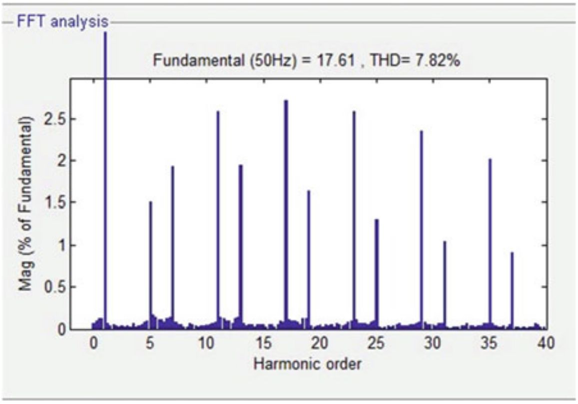

Fig. 100.12 THD analysis after compensation with PI controller

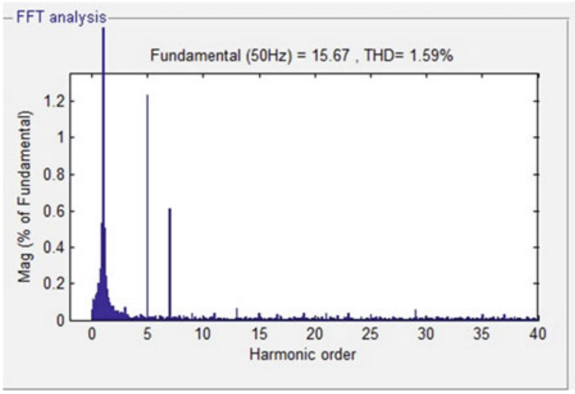

Fig. 100.13 THD analysis after compensation with PI and neural network controller

Table 100.1 Comparison of THD Values

Conditions	THD_i (%)
Before compensation	30.48
SAF with PI controller	7.78
SAF with PI controller and neural network	1.59

100.4 Conclusion

The effective solution to power quality problem using three phase for wire Shunt Active Filter with neural network controller is modelled. It is a better solution for current harmonic compensation than the conventional approach based on PI controller. The system is developed and verified using MATLAB. Under the control of Neural Network Controller PI and Hysteresis Current Controllers extract reference current from the distorted source current to reduce harmonic current. Simulation results were compared with conventional PI controller tuning. Further the THDs of the source current have improved significantly, which indicates the elimination of harmonics. The use of PI controller and Neural Network controller improves the THD up to 1.59 % is good and the main objective of the work is fulfilled.

References

1. Mahalekshmi T (2010) Current harmonic compensation and power factor improvement by hybrid Shunt active power filter. Int J Comput Appl (0975–8887), vol 4(3), pp 9–13
2. Litran P, Salmeron P, Vazquez JR, Flores JL (2005) Compensation of voltage unbalance and current harmonics with a series active power filter. Renew Energy Power Qual J 27 (6):1022–1029
3. Fujita H, Akagi H (1991) Design strategy for the combined system of Shunt passive and series active filters. In: Industry applications society annual meeting, vol 2(1), pp 175–180
4. Karthik K, Quaicoe JE (2000) Voltage compensation and harmonic suppression using series active and Shunt passive filters. In: Electrical and computer engineering, Canadian conference, vol 1, pp 582–586
5. Charles S, Bhuvaneswari G (2010) Comparison of three phase Shunt active Z power filter algorithms. Int J Comput Electr Eng 2(1):175–180
6. Areerak KL, Santiprapan P (2010) Performance improvement of harmonic detection using synchronous reference frame method. In: International conference on advances in energy engineering (ICAEE 2010), Beijing, China, 19–20 June 2010, pp 52–55
7. Singh M, Tiwari V (2008) Modeling analysis and solution of power quality problems. Natl Level Conf Probl Pract Prospects Power Distrib Syst Oper Control 27(6):1020–1025
8. Rao RVDR, Dash SS (2010) Enhancement of power quality by using unified power quality conditioner with PID and fuzzy logic controller. Int J Comput Appl (0975–8887), vol 5(7), pp 21–27
9. Tarapatla MR, Sridhar M, Raj Gopal ANVJ (2012) Shunt active power filter implementation using source voltage and source current detection. Int J Eng Res Appl (IJERA), vol 2. ISSN: 2248-9622
10. Dehini R, Bassou A, Ferdi B (2009) Artificial neural networks application to improve Shunt active power filter. Int J Comput Inf Eng 3(4): 254
11. Karuppanan P, Mahapatra K (2010) PLL with PI, PID and fuzzy logic controllers based Shunt active power line conditioners. In: International conference on power electronics, drives and energy systems at IIT-Delhi, vol 32(12), pp 1010–1012
12. Litran SP, Salmeron P, Vazquez JR, Herrera RS (2007) Different control strategies applied to series active filters. IEEE Trans Power Qual Eng 21(14):1020–1025
13. Watanabe EH, Aredes H (2008) Instantaneous P-Q power theory for compensating non-sinusoidal systems. In: Proceedings of international conference: INSCC 2008, Lagow, June 10–13, pp 1–10

Chapter 101
MPPT Measurement of Photovoltaic System Under Partial Shading Condition Using DPSO Algorithm

D. Gokilapriya and S. Barvin Banu

Abstract Renewable energy is generally defined as energy that comes from resources which are naturally replenished on a human timescale such as sunlight, wind, rain, tides, waves and geothermal heat. Solar energy is a vital untapped resource in a tropical country like ours. The main hindrance for the penetration and reach of solar PV systems is their low efficiency and high capital cost. Solar cell panels are exposed to sunlight at different angles and with variable intensity, therefore the resulting output power varies depending on the illumination angle as well as the light intensity of each panel. The MPPT is responsible for extracting the maximum possible power from the photovoltaic and feed it to the load via the buck-boost converter which steps up the voltage to required magnitude. The main aim will be to track the maximum power point of the photovoltaic module so that the maximum possible power can be extracted from the photovoltaic. This project investigates in detail the concept of DPSO algorithm under partial shading condition which significantly increases the efficiency of the solar photovoltaic system. To evaluate the idea, the algorithm is implemented on a buck-boost converter and compared to the conventional PSO method.

Keywords Maximum power point tracking (MPPT) · Partially shaded · Particle swarm optimization (PSO) · Photovoltaic (PV) systems

101.1 Introduction

Solar power is the conversion of sunlight into electricity, either directly using Photovoltaics (PV), or indirectly using concentrated solar power (CSP). Concentrated solar power systems use lenses or mirrors and tracking systems to focus a large area of sunlight into a small beam. To ensure the optimal utilization of large PV arrays, maximum power point tracker (MPPT) is employed in conjunction with the

D. Gokilapriya · S. Barvin Banu (✉)
SNS College of Engineering, Coimbatore 641107, India
e-mail: barvinsickandhar@gmail.com

C. Kamalakannan et al. (eds.), *Power Electronics and Renewable Energy Systems*, Lecture Notes in Electrical Engineering 326, DOI 10.1007/978-81-322-2119-7_101

power converter (dc-dc converter and/or inverter). However, due to the varying environmental condition such as temperature and solar radiation, the *P–V* characteristics curve exhibit inconsistent MPP, posing a challenge to the tracking problem. The situation becomes more complicated when the array is subjected to partial shading, that is a condition when a part or the whole module of the PV array receives non uniform radiation. During partial shading, the *PV* curves are characterized by multiple peaks—several local and one global peak (GP). particle swarm optimization (PSO) is the method to track the GP during the partial shading. However, in all these PSO methods, random numbers are used. The main disadvantage of this approach is that the randomness tends to reduce the searching efficiency significantly. In view of these drawbacks, this paper introduces a deterministic PSO (DPSO) to improve the tracking capability of the conventional PSO algorithm. The main idea is to remove the random number in the accelerations factor of the PSO velocity equation. The buck–boost DC/DC converter topology is the only one which allows the follow-up of the PV module maximum power point regardless of temperature, irradiance and connected load and also the connection of a buck–boost DC/DC converter in a photovoltaic panel output could be a good practice to improve performance. The DPSO algorithm implemented along with P&O MPPT technique. P&O technique is the general MPPT technique used to track the maximum possible power from the PV array. P&O technique is mostly preferable for the PV array normal condition. Maximum power point tracking (MPPT) plays an important role in photovoltaic systems because it maximize the power output from a PV system for a given set of conditions, and therefore maximize the array efficiency and minimize the overall system cost. Since the maximum power point (MPP) varies, based on the irradiation and cell temperature, appropriate algorithms must be utilized to track the (MPP) and maintain the operation of the system in it. This paper proposes a MPPT method that is capable of tracking the GP under partially shaded conditions.

101.2 PV Array Characteristics Under Partial Shading Condition

101.2.1 PV Cell

Photovoltaic power generation employs solar panels composed of a number of solar cells containing a photovoltaic material. Materials presently used for photovoltaics include monocrystalline silicon, polycrystalline silicon, amorphous silicon, cadmium telluride, and copper indium gallium selenide/sulfide. Copper solar cables connect modules (module cable), arrays (array cable), and sub-fields. Because of the growing demand for renewable energy sources, the manufacturing of solar cells and photovoltaic arrays has advanced considerably in recent years. Photovoltaic power capacity is measured as maximum power output under standardized test conditions (STC) in “Wp” (Watts peak). The actual power output at a particular point in time may be less than or greater than this standardized, or “rated,” value,

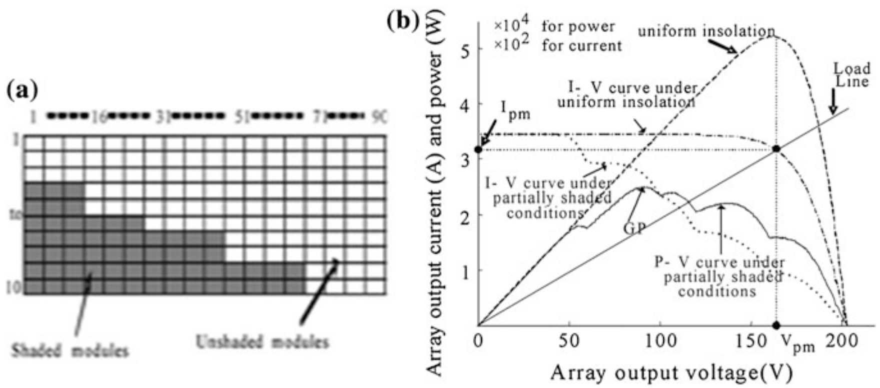

Fig. 101.1 *P–V curves* for the PV array under partially shaded conditions. **a** PV array with insolation of 1,000 W/m^2 on the unshaded modules and *lower* insolation on shaded modules. **b** Shaded modules with 100 W/m^2

depending on geographical location, time of day, weather conditions, and other factors (Fig. 101.1).

The basic equation of PV cell is determined by the following equation

$$I = I_{ph} - I_0[\exp(q(V + R_s I)/AK_B T) - 1] \tag{101.1}$$

$$R_s = -\, dV/dI_{VOC(T1)} - 1/X_V \tag{101.2}$$

$$X_V = [I_{0(T1)} \times q \times \exp(qV_{OC(T1)}/nkT_1)]\ nkT \tag{101.3}$$

V and I are the PV cell's output voltage and current. I_{Ph} is the Photo current. I_0 is the saturation current. A is the diode ideality factor. q is the charge (1.6012×10^{-19} C). K_B is the Boltzmann's constant (1.38×10^{-23} J/K). T is the junction temperature. R_s is the series resistance. Rsh is the shunt resistance.

PV array consists of two types of diodes (Fig. 101.2a). First is the bypass diode that is connected in parallel with each PV module to protect modules. The second is the blocking diode connected at the end of each PV from hotspot. This problem usually occur when a number of the series PV cells/modules are less illuminated and behave as a load string. It protects the array from being affected by the current imbalance between the strings.

101.2.2 Optimization Algorithm of PSO Method

Steps involved in the PSO algorithm

(1) Initialize the swarm from the solution space
(2) Evaluate the fitness of each particle
(3) Update individual and global best

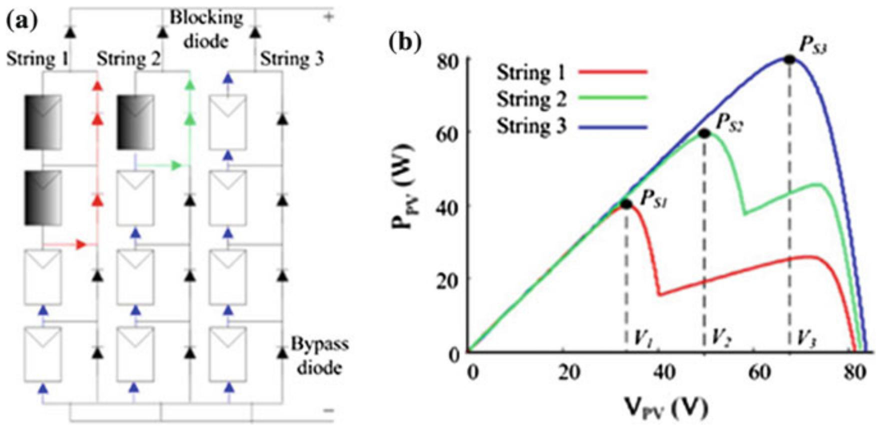

Fig. 101.2 **a** PV array under shading **b** PV *curves* for each string

(4) Update velocity and position
(5) Go to step 2 and repeat until termination condition

Velocity and position of the particle can be calculated by following equation
Velocity update equation

$$v_i^{t+1} = Wv_i^t + \varphi_1 r_1\{(p_{besti}) - x_i^t\} + \varphi_2 r_2\{(g_{best}) - x_i^t\} \tag{101.4}$$

v_i^{t+1}	Inertia
$\varphi_{1,}\varphi_2$	Acceleration constant
$\varphi_1 r_1\{(p_{besti}) - x_i^t\}$	cognitive component
$\varphi_2 r_2\{(g_{best}) - x_i^t\}$	social component

Pbest is the personal best position. Gbest is the best position of the particle.
Position update equation

$$x_i^{t+1} = x_i^t + v_i^{t+1} \tag{101.5}$$

The Application of PSO algorithm are

(1) Electronics and Electromagnetics
(2) Signal, image and video processing.

101.3 Proposed DPSO Method

The Tracking capability of MPPT technique can be improved by the DPSO algorithm. It remove the random number in the PSO velocity Equation and also the maximum change in the velocity restricted into particular value which determined based on the critical study of Photovoltaic characteristics.

101.3.1 Working Principle of DPSO Algorithm

Figure 101.3 shows the complete flow chart of the proposed method that covers the operation in both global and local modes. In this flow diagram, if ΔP is greater than a certain threshold value (Pthr), then the tracking process starts to search for the new GP (in the main program). The sudden variations in insolation are usually small in magnitude and occurs within 1 s. Moreover, the initial duty cycles for the power converter are selected between dmin and dmax. However, as stated earlier, the position of the duty cycle signals should be able to detect the staircase *P–V* curves during partial shading.

101.4 Result and Discussion

101.4.1 Simulink Model of MPPT Technique

The MPPT tracking scheme can be simulated by the matlab simulink model. The Fig. 101.4 shows the overview of MPPT method. PV panel and buck boost converter are combined together to form the MPPT method conjuction with the buck boost converter. The DPSO and PSO algorithm are linked with the simulink model.

101.4.2 Simulink Model of PV Panel

The Fig. 101.5 shows the simulink model of PV panel. It consists of three strings. Each string consists of three PV modules. The voltage of each string is 35 V. The maximum current is 9 A. Partial shading and uniform insolation are determined by the duty cycle value. During the Partial shading the duty cycle value called from the workspace.

101.4.3 Simulink Model of Buck Boost Converter

The Fig. 101.6 shows that the MPPT technique of perturb and observation, DPSO and PSO algorithm are implemented on the buck boost converter. In the case of normal condition P&O algorithm are activated and the corresponding output are fed into buck boost converter. In the case of partial shading condition duty cycle value from DPSO and PSO algorithm are fed into buck boost converter.

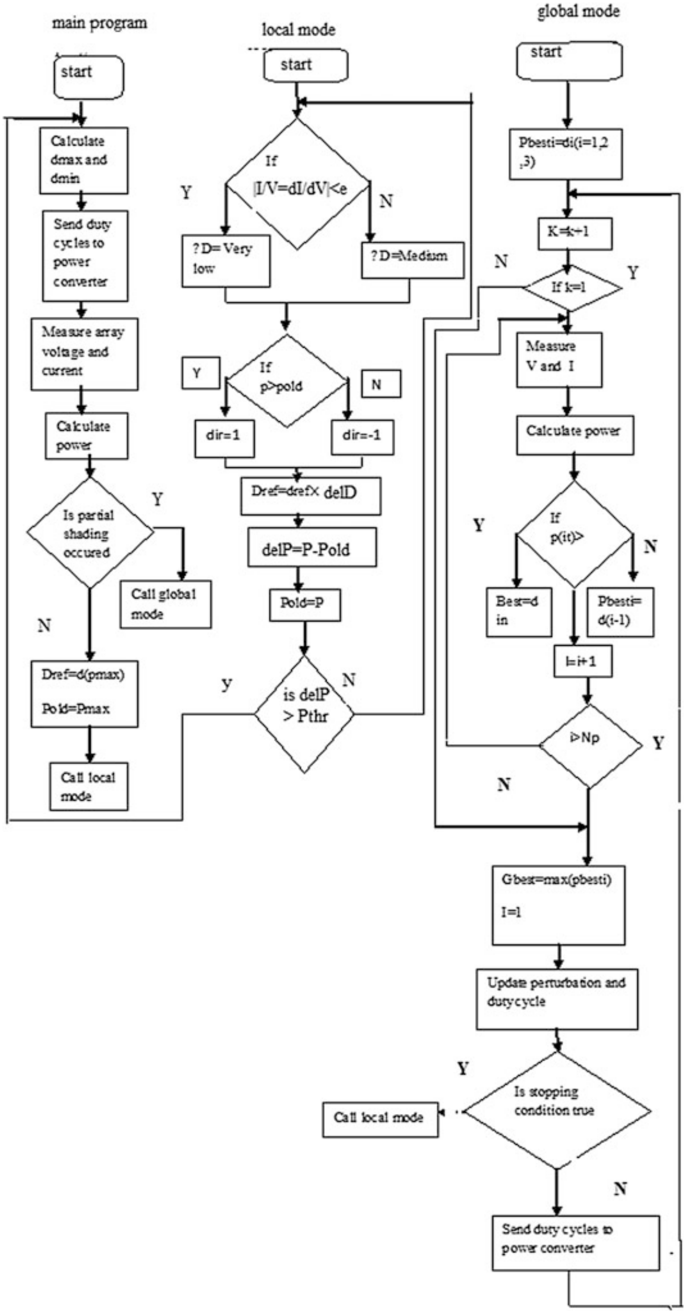

Fig. 101.3 Flow chart of the proposed method

Fig. 101.4 simulink model of MPPT technique

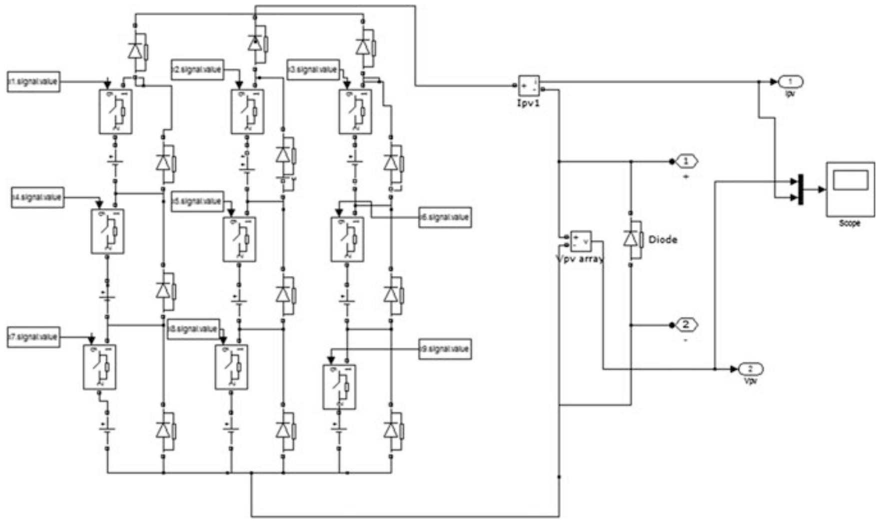

Fig. 101.5 Simulink model of PV panel

101.4.4 Simulation Result of Normal Condition Using P&O Technique

Figure 101.7 shows the simulation result of normal condition. if the PV panel is in normal conditions the MPPT technique utilizes the P&O method Duty cycle value initialize into zero. The result indicates the maximum power is 17.012 kW (Tables 101.1 and 101.2).

101.4.5 Simulation Result of Partial Shading Using PSO and DPSO Method

Figure 101.8 shows the simulation result of partial shading using PSO and DPSO method. In that case for each PV module the duty cycle value called from the

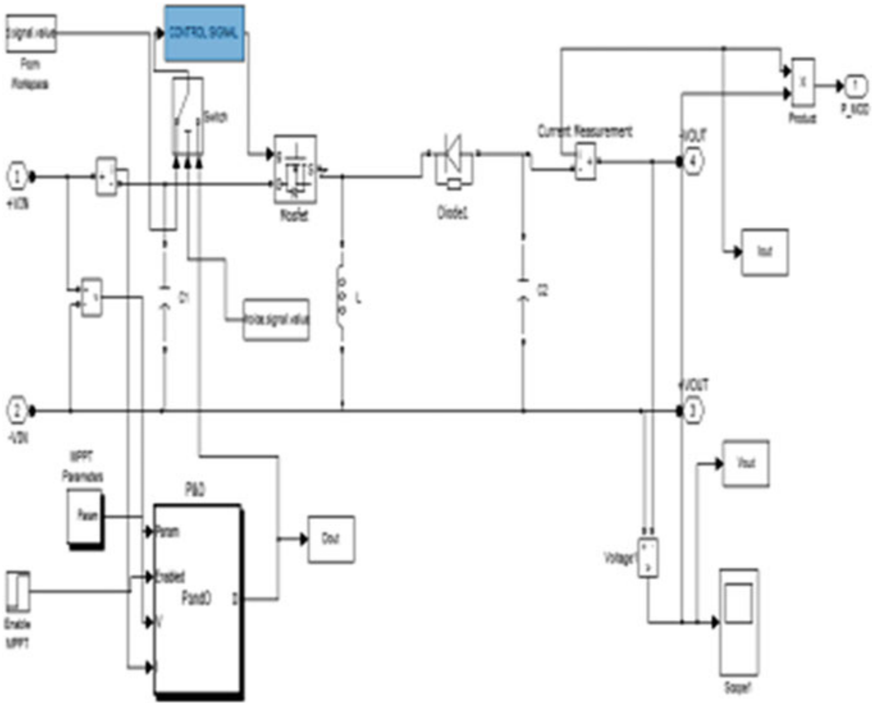

Fig. 101.6 Simulink model of buck boost converter

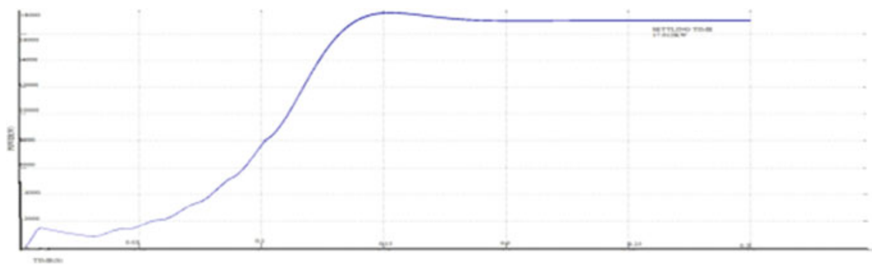

Fig. 101.7 Plot of normal condition

Table 101.1 Difference between PSO and DPSO in terms of iteration

Parameter	Iteration level
PSO	7 (high)
DPSO	4 (low)

Table 101.2 Comparison of PSO, DPSO, P&O MPPT technique

PV panel condition	MPPT technique	Energy
Normal	P&O method	17.012 kW
Partial shading	DPSO, PSO	1.7421 kW

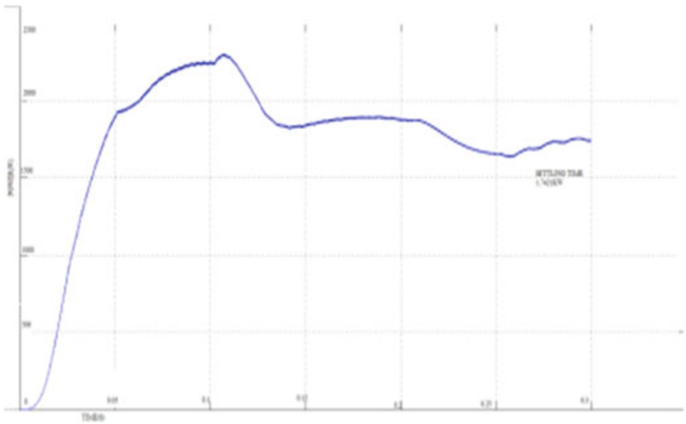

Fig. 101.8 Plot of partial shading

workspace. In the Simulink model each PV module designed into choice signal value. In the case of partial shading condition the corresponding signal value is fed into the buck boost converter by the use of switch mode. The result indicates the maximum power is 1.7421 kW.

101.5 Conclusion

The DPSO and PSO method was proposed along with P&O technique to track the MPP of a PV system. P&O concern with the normal condition. PSO and DPSO concern with the partial shading condition. The DPSO greatly simplifies the control structure of the MPPT by removing the random number and acceleration coefficient factors of the conventional PSO. Simulation result of PSO and DPSO are compared. The number of iteration required for DPSO partial shading condition is greater than the PSO partial shading condition to track the MPP peak of the PV curve. This Project demonstrate that the buck boost DC/DC converter is able to manage the facility to follow the photovoltaic panel maximum power point at all times, regardless of cell temperature, solar global irradiation and connected load.

References

1. Gastli A, Masmoudi A, Bouzguenda M, Salmi T (2012) Matlab/simulink based modelling of solar photovoltaic cell. Int J Renew Energy Res 2(2):213–218
2. Stallon D, Kumar K (2013) Simulation of high step-up Dc–Dc converter for photovoltaic module application using matlab/simulink. Int J Intell Syst Appl 5(7):72
3. Enrique JM, Dura'n E, Sidrach-de-Cardon M (2006) Theoretical assessment of the maximum power point tracking efficiency of photovoltaic facilities with different converter topologies. Solar Energy 81:31–38
4. Farand R, Dolara A, Leva S (2009) Energy comparison of seven MPPT techniques for PV systems. J Electromagn Anal Appl, pp 152–162. doi:10.423
5. Petrone G, Femia N, Spagnuolo G (2009) A technique for improving P&O MPPT performances of double-stage grid-connected photovoltaic systems. IEEE Trans Ind Electr 56:11
6. Kim H-J, Ahmad J (2009) A voltage based maximum power point tracker for low power and low cost photovoltaic applications. World Acad Sci Eng Technol 60:712–715
7. Kondawar SS, Vaidya U (2012) A comparison of two MPPT techniques for PV system in matlab simulink. Int J Eng Res Dev 2(7):73–79

Chapter 102
Cascaded Dual Buck Inverter with Sensorless Current Control Method for Grid Connected Photovoltaic Systems

Sumith Surendran and R.B. Selvakumar

Abstract This paper presents a grid connected cascade dual buck inverter with Sensorless current control method to utilize the present renewable energy structure. Active and reactive power flow capability in a wide range for renewable energy and distributed generation sources using a cascaded dual buck inverter is proposed for grid tie control system. A cascaded two switch dual buck inverter with two power MOSFETs and two fast recovery diodes is used as grid connected inverter. It eliminates the dead time issues and has no shoot through concerns. The freewheeling current flows through independent fast recovery diodes, which reduces the reverse recovery loss of the diodes. A digital current mode controller mechanism implemented by utilizing a sensorless current control method. The current mode loop is Sensorless and it depends on constants and internal loop states. It avoids the need to sense controlled voltages or current for inner loop.

Keywords Dual buck inverter · Renewable energy · MPPT · Digital control

102.1 Introduction

The concept of PV module, integrated with multilevel voltage level inverters is an important topology in grid-tie control system. Among different renewable resources, Photovoltaic (PV) system is having advantages such as absence of fuel cost, low maintenance cost and no wear and tear due to absence of moving parts. In multilevel structures, 'n' number of PV modules is connected in series to supply the inverter with an input voltage within its operating range. The output power of a PV panel depends on the operating terminal voltage. The maximum power generated by the system

S. Surendran (✉) · R.B. Selvakumar
SNS College of Engineering, Coimbatore, India
e-mail: sumiths32@gmail.com

R.B. Selvakumar
e-mail: 2rbsk.snsce@gmail.com

C. Kamalakannan et al. (eds.), *Power Electronics and Renewable Energy Systems*,
Lecture Notes in Electrical Engineering 326, DOI 10.1007/978-81-322-2119-7_102

depends upon changes in insolation and temperature. For obtaining the maximum increased voltage PV panel operates at maximum power point (MPP). A simple boost converter is used to obtain a constant dc voltage. In this paper three strings of PV arrays connected to their own dc–dc boost converter is used. To convert power from dc to ac, an inverter must be integrated to the PV installation.

In conventional bridge type voltage source inverters, shoot through problems and dead time related issues exists. The elimination of the shoot-through problems, which is the major failure of traditional voltage source inverters, is the main advantage. It does not need dead time, which fully utilizes the pulse width modulated (PWM) voltage and transfers total desired energy to the load. In two switch dual buck inverter, high-voltage power MOSFETs without the complexity of soft-switching assisting circuit are used to improve the system efficiency. The dual buck inverter has the same input-voltage utilization rate as a full-bridge inverter. At each half line cycle, one diode and one switch operate in high frequency. The free-wheeling current flows through the independent freewheeling diodes instead of the body diodes of the switches, so reverse-recovery loss of the diodes can be reduced.

Current-mode controllers are considered to be superior to voltage mode controllers, due to the fast inner current loop and its improved dynamics resulting in a more robust control scheme. The need for current sensing components increases system cost, and reduces reliability. Sensorless current mode control overcomes these problems. By using equations, constants and internal loop states, the current mode loop is made sensorless, removing the need to sense controlled voltages or current for inner loop.

102.2 Topology and System Block Diagrams

102.2.1 System Structure

Figure 102.1 shows the topology of proposed cascade dual buck half-bridge inverter. The grid-tie control system will be based on this topology. It consists of three strings of PV arrays connected to their own dc–dc boost converter. Each PV source is connected to individual unit of cascaded dual-buck inverter through dc–dc converter. The output port 1P and NN can be connected to the grid through the commonly used inductor–capacitor–inductor (LCL) filter.

102.2.2 PV Cell Model

Combinations of PV strings are used as the input voltage sources. The modeling of a PV panel is derived from the physics of the PN junction and is used to obtain characteristic behavior of the cell. The array cell static characteristics, as a function of light intensity and temperature, are given by the equations.

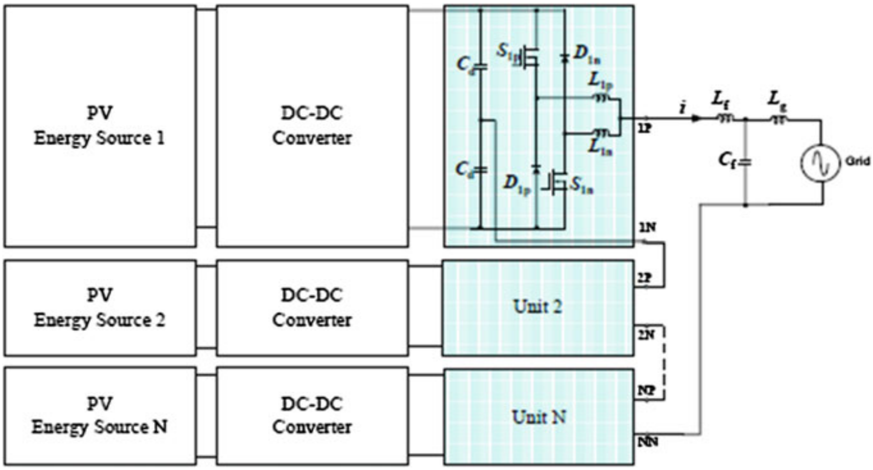

Fig. 102.1 System structure

$$I = I_{ph} - I_s\left(\exp\frac{q(V + IR_s)}{NKT} - 1\right) - \frac{V + IR_s}{R_{sh}} \tag{102.1}$$

$$I_0 = I_{or}\left[\frac{T}{T_r}\right]^3 \exp\left[\frac{qE_{G0}}{BK}\left\{\frac{1}{T_r} - \frac{1}{T}\right\}\right] \tag{102.2}$$

$$I_{LG} = [I_{SCR} + K_1(T_C - 28)]\lambda/100 \tag{102.3}$$

where
Iph is the short circuit current,
Is is the reverse saturation current of diode (A),
q is the electron charge (1.602×10^{-19} C),
V is the voltage across the diode (V),
K is the Boltzmann's constant (1.381×10^{-23} J/K),
T is the junction temperature in Kelvin (K),
N Ideality factor of the diode,
Rs is the series resistance of diode,
Rsh is the shunt resistance of diode.

By solving above equations an equivalent circuit can be determined and a simulation model is developed. The equivalent circuit of a solar cell is a current source in parallel with a diode. The output of the current source is directly proportional to the light falling on the cell (photocurrent Iph) (Fig. 102.2).

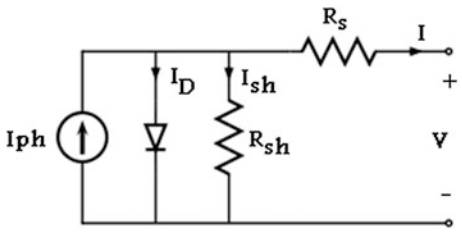

Fig. 102.2 PV cell circuit model

102.2.3 Maximum Power Point Tracking

During changes in direction of sun, solar insolation and temperature the output power of the solar PV module changes. If there is a good irradiance condition, the photovoltaic system can generate maximum power efficiently while an effective PPT algorithm is used with the system. The perturbation and observation method offers the main advantage of providing high efficiency under rapidly changing atmospheric conditions, so it has been employed in the proposed model.

102.2.4 Perturb and Observe Algorithm

MPPT can effectively improve the solar energy conversion efficiency of PV systems. In this paper, Perturb-and-observe (P&O) method is used to achieve this function [7]. The perturb and observe (P&O) algorithm is also known as the "hill climbing" method. In this algorithm the operating voltage of the PV module is perturbed by a small increment, and the resulting change of power, ΔP, is observed. If the ΔP is positive, then it is supposed that it has moved the operating point closer to the MPP. Thus, further voltage perturbations in the same direction should move the operating point toward the MPP. If the ΔP is negative, the operating point has moved away from the MPP, and the direction of perturbation should be reversed to move back toward the MPP.

102.2.5 DC/DC Converters

In order to achieve low cost, easy control, high efficiency, and high reliability, a simple boost dc–dc converter using minimal devices is introduced to interface the low-voltage PV module. A boost converter comprised of three cascaded connected boost converters introduced in the output of each of the PV panel. The main advantage of this topology is that it can meet the requirements of generating a high output voltage with a relatively high efficiency. Due to its high-voltage-gain, cascade topology can be attractive for large-scale PV system. Additionally, the converters can be operated with high switching frequency to improve power density.

102.2.6 Cascaded Two-Switch Dual Buck Inverter

The single-unit dual-buck inverter has two basic forms, dual-buck half-bridge inverter and dual-buck full-bridge inverter. The proposed cascade dual buck inverter is cascade dual-buck half-bridge inverter. The three dual-buck half-bridge inverters is connected in series output to obtain higher voltage. In the cascading inverter, separate dc power supplies are used for each cell and shares the same filter components. The output port 1P and NN can be connected to the grid through the commonly used inductor–capacitor–inductor (LCL) filter (Fig. 102.3).

Figure 102.5 shows the topology of the proposed cascade dual-buck half-bridge inverter. It consists of N units of single dual-buck half-bridge inverter. Each unit is composed of two power MOSFETs and two fast recovery diodes. Each unit has two output ports, *i*P and *i*N (i = 1, 2, …, N). To realize the cascade topology, connect the *i*N port of the *i*th unit with the ($i + 1$)P port of the ($i + 1$)th unit, and use port 1P and NN as the output ports. Sip and Dip are a working pair, and operate at the positive half-cycle of output current i. Sin and Din are another working pair, and operate at the negative half-cycle of output current i.

102.2.7 Sensorless Current Control Method

A digital current-mode controller for cascaded dual buck inverter is introduced. The current-mode loop is sensorless, relying on constants and internal loop states, removing the need to sense controlled voltages or currents for the inner loop. The instantaneous error between the grid current and the desired reference current will be reduced to zero after a specified number of cycles.

Figure 102.4 shows the control block diagram of system. The input of the cascaded inverter is given by the output of the boost converter. The mean-value dc bus control loop with PI compensator *G*v will generate the current reference for inner current loop, which produces the equivalent duty cycle *deq*. Each individual unit has its own dc bus controller. The outputs of mean-value loop and individual loop are fed into individual duty cycle generation block.

If the individual dc bus is not controlled by cascade inverter we can assign

$$\mathrm{d_1 = d_2 = \cdots = d_n = d_{eq}} \tag{102.4}$$

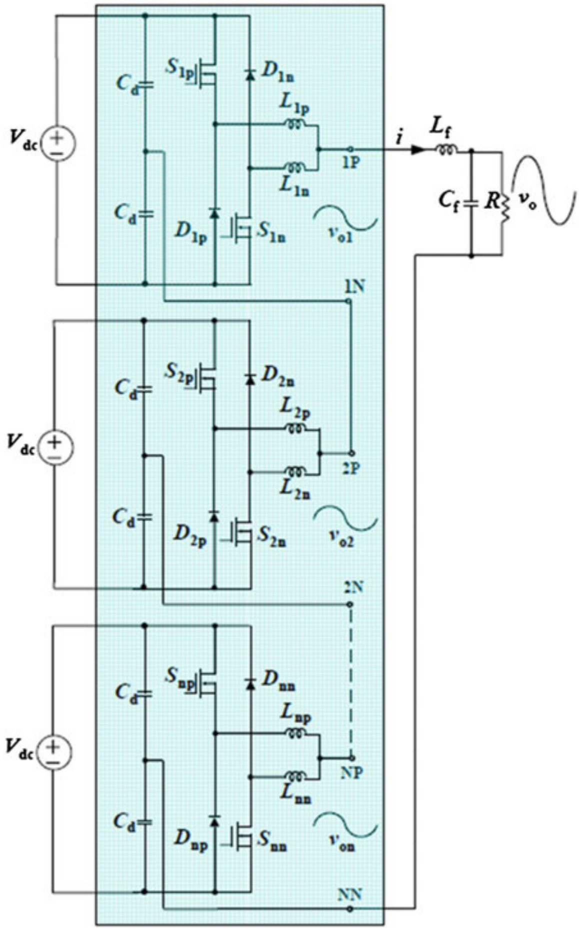

Fig. 102.3 Topology of cascaded dual-buck half bridge inverter

Then we have the following relation

$$d_1\frac{V_{dc1}}{2}+d_2\frac{V_{dc2}}{2}+\cdots+d_n\frac{V_{dcn}}{2}=d_{eq}\frac{(V_{dc1}+V_{dc2}+\cdots+V_{dcn})}{2}=d_{eq}\frac{nV_{dc}}{2} \tag{102.5}$$

where V_{dc} is the mean value of the sum of each individual dc bus voltage. We can derive the equivalent average model of cascade dual-buck inverter where $j = 1\ 2\ n$

$$\begin{aligned} \Sigma L_j &= L_1+L_2+\cdots+L_n \\ d_{eq}(t)\cdot\frac{nV_{dc}}{2}-v(t) &= L\frac{di(t)}{dt} \end{aligned} \tag{102.6}$$

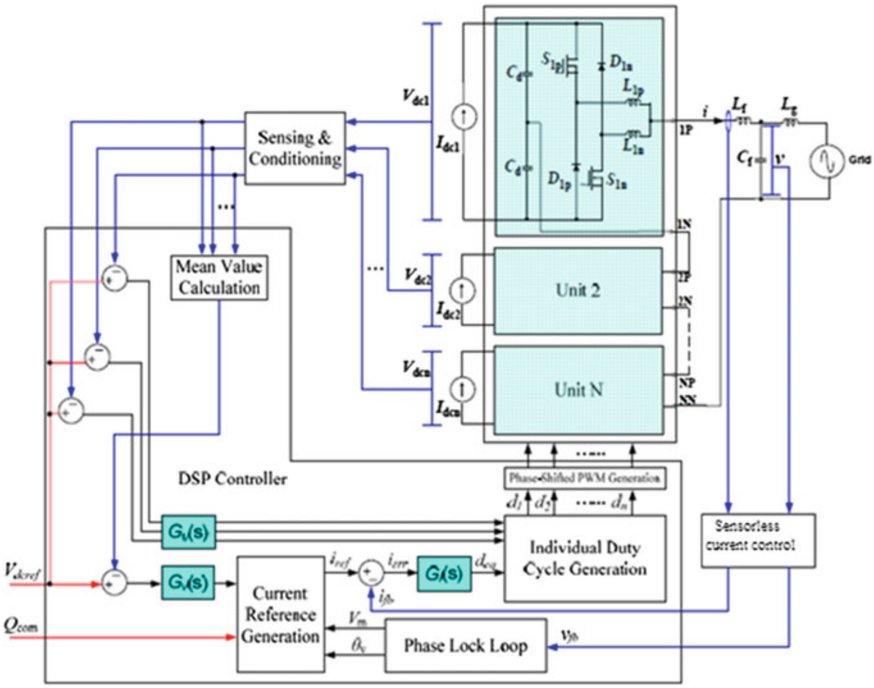

Fig. 102.4 Sensorless current control closed loop system

Transfering to *s* domain, we have

$$i(s) = \frac{1}{sL}(d_{eq}(s) \cdot \frac{nV_{dc}}{2} - v(s)) \tag{102.7}$$

So the transfer functions from *d*eq to current *I* and voltage *v* to current *I* are as follows

$$\begin{aligned} G_{id}(s) &= \frac{i(s)}{d_{eq}(s)} = \frac{\frac{nV_{dc}}{2}}{sL} \\ G_{iv}(s) &= \frac{i(s)}{v(s)} = \frac{1}{sL} \end{aligned} \tag{102.8}$$

where $G_{id}(s)$ is the control-to-output transfer function and $G_{iv}(s)$ is an uncontrolled feed forward term. In the equivalent dc bus voltage is *V*dc, and thus the outcome of admittance compensation term is the reciprocal of *V*dc. The equivalent dc bus voltage for the cascade dual-buck inverter is $\frac{nV_{dc}}{2}$. Therefore, the admittance compensation transfer function is obtained as follows

$$G_{AC}(s) = \frac{1}{\frac{nV_{dc}}{2}} \tag{102.9}$$

Through PLL, the grid voltage magnitude V_m and phase angle θ_v can be tracked down, and are used for admittance compensation and current reference generation. The active power and reactive power command can be used to calculate the apparent power command S_{com} and power factor angle φ as follows

$$S_{com} = \sqrt{P_{com}^2 + Q_{com}^2} \tag{102.10}$$

$$\varphi = \tan^{-1}\left(\frac{Q_{com}}{P_{com}}\right) \tag{102.11}$$

The current reference magnitude *I*m can be obtained by

$$I_m = \frac{S_{com}}{\frac{V_m}{2}} \tag{102.12}$$

102.3 Simulink Model and Results

The entire proposed system is simulated in the Matlab-Simulink environment to study its performance under given conditions (Figs. 102.5, 102.6, 102.7 and 102.8).

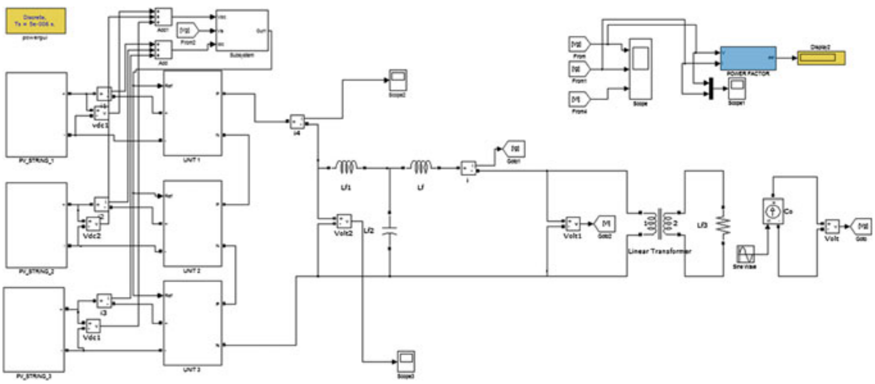

Fig. 102.5 System simulation diagram

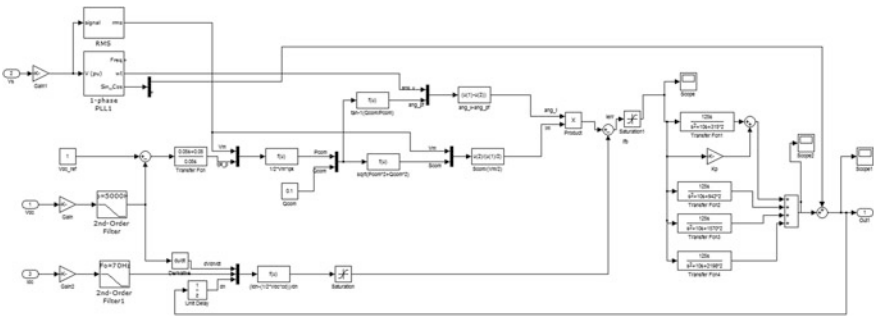

Fig. 102.6 Sensorless current control closed loop

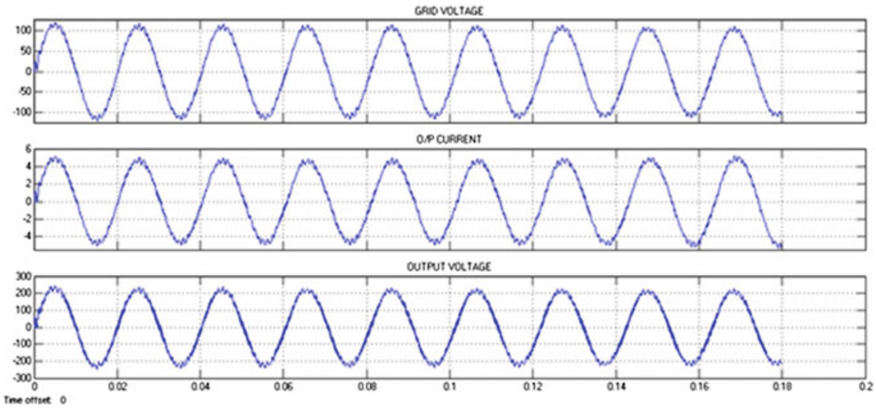

Fig. 102.7 Simulation output

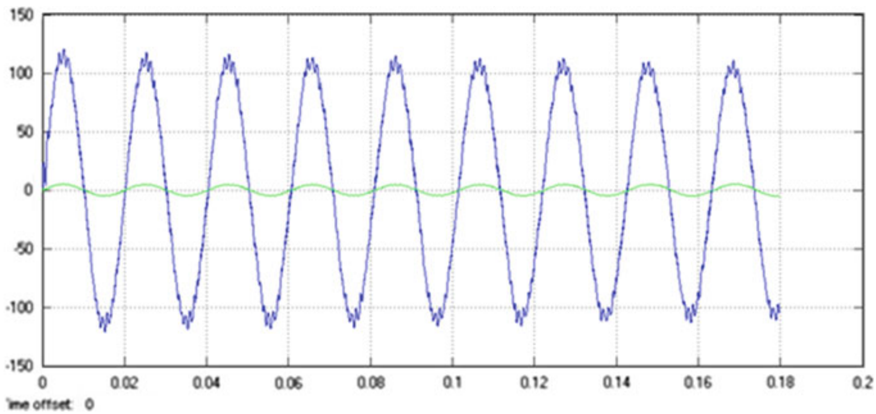

Fig. 102.8 In phase output voltage and current

102.4 Conclusion

The paper presented grid-tie control of cascade dual buck inverter for renewable energy systems. The control system ensures wide range power flow capability from pure active power to pure reactive power delivery. In this paper sensorless closed loop current control was designed using matlab and the simulation output obtained fulfill the objectives. By using a sensorless current control the cost of the circuit has been considerably reduced. The variations in the input are tracked easily and the controlling is done at a faster rate. The output in phase current and voltage are obtained, that is the power factor is nearer to unity. An inverting current of 5 A for a 120 V grid has been obtained. A reduction of total harmonic distortion below the IEEE 519 standard (limit of 5 %) is achieved. By implementing 3-unit cascade dual buck inverters, the viability and advantages of the cascade dual buck inverter are validated.

References

1. Villanueva E, Correa P, Rodriguez J, Pacas M (2009) Control of a single phase cascaded H-bridge multilevel inverter for grid-connected photovoltaic systems. IEEE Trans Ind Electron 56(11):4399–4406
2. Blabbjerg F, Chen Z, Kjaer SB (2004) Power electronics as efficient interface in dispersed power generation systems. IEEE Trans Power Electron 19(5):1184–1194
3. Bialasiewicz JT (2008) Renewable energy systems with photovoltaic power generators: operation and modeling. IEEE Trans Ind Electron 55(7):2752–2758
4. Carrasco JM, Franquelo LG, Bialasiewicz JT, Galván E, Portillo Guisado RC, Prats Ma ÁM, León JI, Moreno-Alfonso N (2006) Power-electronic systems for the grid integration of renewable energy sources: A survey. IEEE Trans Ind Electron 53(4):1002–1016
5. Malinowski M, Gopakumar K, Rodriguez J, Perez MA (2010) A survey on cascaded multilevel inverters. IEEE Trans Ind Electron 57(7):2196–2206
6. Sun P, Liu C, Lai JS, Chen CL (2012) Grid-tie control of cascade dual-buck inverter with wide-range power flow capability for renewable energy applications. IEEE Trans Power Electron 27(4)1839–1849
7. Midya P, Krein PT, Greuel MF (2007) Sensorless current mode control-an observer-based technique for DC-DC converters. IEEE Trans Power Electron 16(4):522–526
8. Gupta R, Ghosh A, Joshi A (2008) Switching characterization of cascaded multilevel-inverter-controlled systems. IEEE Trans Ind Electron 55(3):1047–1058
9. Bojoi RI, Limongi LR, Roiu D, Tenconi A (2011) Enhanced power quality control strategy for single-phase inverters in distributed generation systems. IEEE Trans Power Electron 26 (3):798–806
10. Yao Z (2009) Two switch dual-buck grid connected inverter. In: IEEE 6th international conference power electronics and motion control, IPEMC '09

Chapter 103
Steady State Analysis and Open Loop Modeling of Permanent Magnet Stepper Motor

S. Vijaya, A. Senthil Kumar and R. Suganya

Abstract A stepper motor is an incremental actuator that can operate when driven by a digital pulse train. Of all the types of stepper motor the permanent magnet stepper motor (PMSM) is widely preferred due to it being the cheapest and its parameters such that the enhancement of its performance characteristic is still an upcoming area of research. Existing literature review shows that the determination of the transient rather than steady-state performance is in existence. In this paper linear differential equations of the PMSM are obtained from review and the steady-state equations of the PMSM in constant torque mode for a single step is resolved using numerical integration. The results are validated with the simulation carried out using MATLAB-Simulink in open loop for micro-step. It is observed that the speed of the stepper motor is dependent on the frequency of the input pulse train and the load torque.

Keywords Micro stepping · Open loop · Permanent magnet stepper motor · Steady state · Sine PWM

103.1 Introduction

The stepper motors can be commanded digitally to hold a step without any feedback sensor. The performance of the stepper motor is strongly dependent on the control of the driver circuit. Various power drivers have been developed to improve

S. Vijaya (✉) · R. Suganya
S.K.P Engineering College, Tiruvannamalai, India
e-mail: srinivasavijayaa@gmail.com

R. Suganya
e-mail: r.suganyatharani@gmail.com

A. Senthil Kumar
Velammal Engineering College, Chennai, Tamil Nadu, India
e-mail: vastham@gmail.com

C. Kamalakannan et al. (eds.), *Power Electronics and Renewable Energy Systems*,
Lecture Notes in Electrical Engineering 326, DOI 10.1007/978-81-322-2119-7_103

the torque-angle characteristics of the stepper motor. They are broadly classified into three basic forms. They are the constant voltage, constant current and constant torque or micro-step drive [1–3]. With the advancement in electronics, ICs are being widely used to give better rated torque at each step, thus making the microstep drive more preferable for higher speeds. Micro stepping was invented by Durkos in 1974. When two phases of a PMSM were energized by currents of different magnitude the resultant vector drives the rotor to the next step position [4]. The step size of stepper motor in this mode is usually less than 1.8° which is suitable for certain applications such as machine tool drives, plotters, turn tables and robotics where the step size is usually met by using gears. The major advantage of this mode of operation is that the resolution is very high i.e. 1/8, 1/16, 1/256, 1/51,200 etc. But this is not the only reason for consumers to go for micro stepping. The microstepping gives the definite advantage of reduced mechanical noise and low speed ripple [5].

The contributions to this paper are summarized as follows. Sections 103.2 and 103.3 presents the mathematical model and the steady-state analysis. Section 103.4 compares the open loop PMSM driver utilizing two level sine PWM with the three level sine PWM and Sect. 103.5 provides the simulation results and discussions.

103.2 Modelling of Permanent Magnet Stepper Motor

This section re-examine the various modus operandi on modelling of PMSM. The documents [6–8] commonly used transfer function modelling to obtain the response of the PMSM for a step input. In this method of modelling both the current and the voltage was maintained constant and a relation between the step position and motor parameters were obtained. Kuo et al. exploited state space to analyze the PMSM in 1978 [9, 10]. This method is convenient and easy to functionalize in dynamic equations. From the Kuo model the electromechanical equations representing the system are written down, neglecting the effect of magnetic coupling between the phases, the equations in its linear form are as follows:

$$\frac{dI_a}{dt} = \frac{1}{L}(V_a - RI_a + K_m\omega \sin(N_r\theta)). \tag{103.1}$$

$$\frac{dI_b}{dt} = \frac{1}{L}(V_b - RI_b + K_m\omega \cos(N_r\theta)). \tag{103.2}$$

$$\frac{d\omega}{dt} = \frac{1}{J}(-K_m I_a \sin(N_r\theta) + K_m I_b \cos(N_r\theta) - B\omega - T_l). \tag{103.3}$$

$$\frac{d\theta}{dt} = \omega. \tag{103.4}$$

where V_a, V_b and I_a, I_b are the voltages and currents in the two phases A, B respectively, ω is the angular velocity in (Rd/s), R and L are the electrical circuit constants in ohms (Ω) and Henry (H) respectively. J and B are the mechanical constants of rotor inertia and viscous friction in Kg m^2 and (Kg m^2/s) and K_m is the motor torque constant in (Nm/A), T_l is the load torque in Nm, N_r is the number of rotor teeth. The motor torque is proportional to the current, position and velocity. The dynamics of the system, Eqs. (103.1)–(103.4) are represented in phase variable form as (103.5)–(103.8).

$$\dot{I}_a = \frac{1}{L}(V_a - RI_a + K_m\omega\sin(N_r\theta)). \tag{103.5}$$

$$\dot{I}_b = \frac{1}{L}(V_b - RI_b - K_m\omega\cos(N_r\theta)). \tag{103.6}$$

$$\dot{\omega} = \frac{1}{J}(-K_m I_a\sin(N_r\theta) + K_m I_b\cos(N_r\theta) - B\omega - T_l). \tag{103.7}$$

$$\dot{\theta} = \omega. \tag{103.8}$$

103.3 Steady State Analysis

The steady-state investigation of the PM stepper motor can be attained when the derivatives of the state variables in the Eqs. (103.5)–(103.7) converge to zero. The differential equations can now be written down as auxiliary Eqs. (103.9)–(103.11)

$$(V_a = RI_a - K_m\omega\sin(N_r\theta)). \tag{103.9}$$

$$(V_b = RI_b + K_m\omega\cos(N_r\theta)). \tag{103.10}$$

$$\omega = \frac{1}{B}(-K_m I_a\sin(N_r\theta) + K_m I_b\cos(N_r\theta) - T_l). \tag{103.11}$$

At steady state, the inputs V_a, V_b is a step value applied for a time interval $t_1 - t_2$ and the disturbance applied i.e. load torque T_l is zero. Now the auxiliary equations can be solved to get the variables of interest speed ω and its relation with the step angle θ by numerical integration of Eq. (103.8).

$$\left(\theta = \int_{t_1}^{t_2} \omega\ .\ dt\right). \tag{103.12}$$

Equating (103.11) and (103.12)

$$\frac{I_aR - V_a}{K_m \sin N_r\theta_0} = \frac{V_b - I_bR}{K_m \cos N_r\theta_0}$$
$$\theta_0 = \frac{1}{N_r}\tan^{-1}\left(\frac{I_aR - V_a}{V_b - I_bR}\right). \tag{103.13}$$

103.3.1 Case A

If $V_a = V_b =$ constant, $\theta = \theta_0$, then substituting $I_a = I_b = I$, in Eqs. (103.9) and (103.10) we get the step position at which the rotor is in equilibrium is $\theta_0 = \frac{\pi}{4N_r}$. Now the motor speed ω is zero since the torque developed in the two phases being equal and opposite.

103.3.2 Case B

If two step inputs are applied simultaneously such that $V_a \neq V_b$, $= \theta_0$, then $I_a \neq I_b$. This can be proved by assuming the controversy that $V_a = V_b$ in (103.13).

Consider

$$\theta = \theta_0 = (2n+1)\frac{\pi}{N_r}.$$
$$(2n+1)\frac{\pi}{N_r} = \frac{1}{N_r}\tan^{-1}\left(\frac{I_aR - V_a}{V_b - I_bR}\right).$$
$$(2n+1)\frac{\pi}{N_r} = \frac{1}{N_r}\tan^{-1}\left(\frac{I_aR - V_a}{V_a - I_bR}\right).$$
$$(2n+1)\frac{\pi}{N_r} \neq \frac{\pi}{4N_r}.$$

Hence proved that $V_a \neq V_b$.

The Eqs. (103.14–103.19) show that the currents and motor speed ω is a constant for various values of step angle θ.

(i) For $\theta_0 = (2n+1)\frac{\pi}{N_r}$ where n = 0, 1, 2, 3…

$$I_a = \frac{V_a}{R}.$$
$$I_b = \frac{V_bB}{BR + K_m^2}. \tag{103.14}$$
$$\omega = -\frac{K_mI_b}{B}.$$

$$\theta = -\frac{K_m V_b}{BR}\int_{t_1}^{t_2} dt - \frac{K_m^2}{BR}\omega\int_{t_1}^{t_2} dt. \quad (103.15)$$

(ii) For $\theta_0 = \frac{2n\pi}{N_r}$ where n = 1, 2, 3…

$$\begin{aligned} I_a &= \frac{V_a}{R}. \\ I_b &= \frac{V_b B}{BR + K_m^2}. \\ \omega &= \frac{K_m I_b}{B}. \end{aligned} \quad (103.16)$$

$$\theta = \frac{K_m V_b}{BR}\int_{t_1}^{t_2} dt - \frac{K_m^2}{BR}\omega\int_{t_1}^{t_2} dt. \quad (103.17)$$

(iii) For $\theta_0 = (2n+1)\frac{\pi}{2N_r}$ where n = 0,1,2,3

$$\begin{aligned} I_a &= \frac{V_a B}{BR + K_m^2}. \\ I_b &= \frac{V_b}{R}. \\ \omega &= -\frac{K_m I_a}{B}. \end{aligned} \quad (103.18)$$

$$\theta = -\frac{K_m V_a}{BR}\int_{t_1}^{t_2} dt - \frac{K_m^2}{BR}\omega\int_{t_1}^{t_2} dt. \quad (103.19)$$

The Eqs. (103.14–103.19) can give the value of motor speed ω and step angle θ for each step by numerical integration.

103.4 Open Loop Stepper Motor Drive

Literature review of papers [1, 3–11] reveals the various topologies for a simple open loop stepper motor driver in micro stepping mode. The proposed open loop driver shown in Fig. 103.1 uses sinusoidal pulse width modulation (sine PWM) and phase shifted sine PWM for exciting the phase windings A,B respectively of the PMSM. The switching pulses can be generated by two methods.

In the former the instantaneous output voltage of the driver i.e. voltage input to the motor windings has two levels $\pm V_{dc}$ where V_{dc} is the source for the H-bridge as shown in Fig. 103.2a. Hence this approach is named 'Two level PWM'. In this technique the PWM signals of one phase may be reversed and used for the other. In

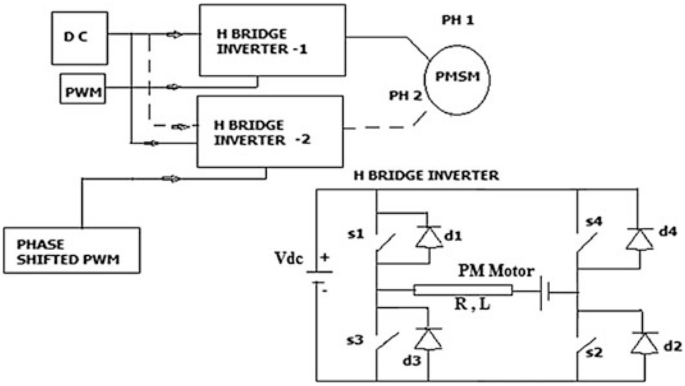

Fig. 103.1 Proposed open loop PM stepper motor drive

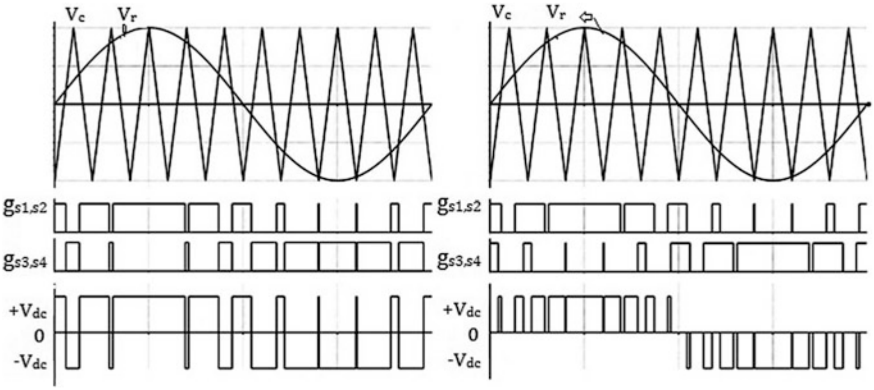

Fig. 103.2 **a** Two level sine PWM and **b** Three level sine PWM [12]

the latter two reference signals $V_r, -V_r$ are compared with bi-directional carrier signal to produce the switching pattern for the switches s1, s2 and s3, s4. The instantaneous load voltage has three levels (+V_{dc}, 0, $-V_{dc}$) as shown in Fig. 103.2b. However the switches in top leg and bottom leg should not be allowed to conduct simultaneously. So this method is not easy to implement and an alternative is comparing a uni-directional triangular carrier wave with a single sinusoidal reference. This generates the same 'Three level PWM' output.

The following equations of m, D govern the output voltage of the H-Bridge.

Modulation Index lies between 0 to 1 i.e. $\mathrm{m} = \frac{V_r}{V_c}$; The over modulation is generally avoided because it introduces low frequency harmonics, non-linearity between magnitude of modulating signal and fundamental voltage output by the inverter. Duty cycle $D = T_{on} f_s$ where T_{on} is the conduction time of the switches, f_s is switching frequency.

103.5 Simulation Results and Discussion

The simulation of the H-bridge bipolar driver with PMSM is carried out in MATLAB-Simulink/SimPowersystem tool. The driver output voltage waveform for Two level PWM is shown in Fig. 103.3 and for Three level PWM is shown in Fig. 103.4. The driver current waveforms in Fig. 103.5 show that the currents in the windings are orthogonal to each other.

The overall total harmonic distortion (THD) in the load current using two level PWM is compared with (THD) in the load current using three level PWM as shown in Table 103.1.

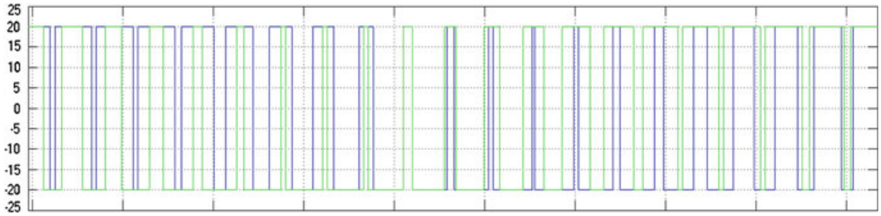

Fig. 103.3 Simulation (two level) output of voltage per phase versus time

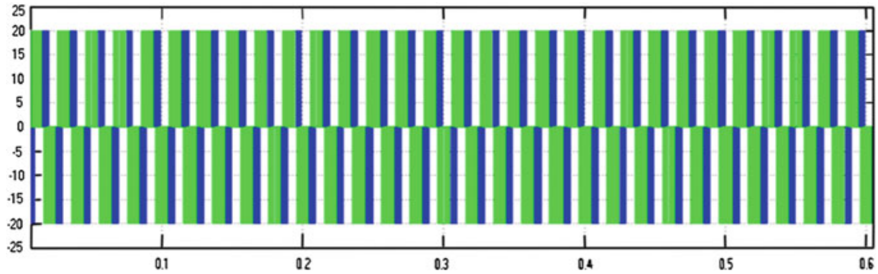

Fig. 103.4 Simulation (three level) output of voltage per phase versus time

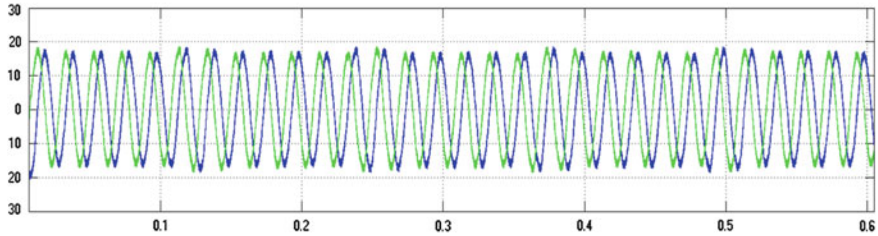

Fig. 103.5 Simulation output of current per phase versus time

Table 103.1 %THD comparison chart

	Two level PWM	Three level PWM
%THD	1.17	1.78

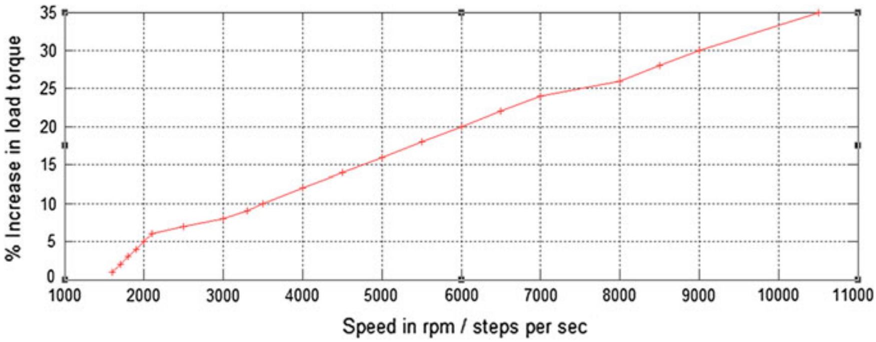

Fig. 103.6 Speed of PMSM in steps per sec versus % increase in load torque

Table 103.2 Speed regulation

Percentage increase in T_l (%)	T_l	T_m	Speed regulation
1	0.02	2	0.0625
3	0.06	2	0.166
5	0.1	2	0.25
7	0.14	2	0.4
9	0.18	1.5	0.545
12	0.24	1.5	0.625
14	0.28	1.5	0.66
16	0.32	1.5	0.7
18	0.36	1.4	0.727
20	0.4	1.5	0.75
22	0.44	1.5	0.76
24	0.48	1.5	0.78
26	0.52	1.3	0.8125
28	0.56	1.2	0.823
30	0.60	1.2	0.83
35	0.7	1.2	0.857

The rotor will make a single micro step movement only if the torque developed due to excitation is greater than the algebraic sum of the friction torque, torque due to moment of inertia of motor and load, detent torque and load torque in Nm. If the motor direction is to be reversed, the incremental torque must now compensate an additional holding torque in the case of PMSM. The variations in the motor torque due to the increase in the load torque are measured and the speed regulation is obtained as shown in Fig. 103.6 and Table 103.2.

103.6 Conclusion

In this paper the PMSM is described in state variable form and the steady state calculation for like and unlike input voltage, current to the phases A,B of the stepper motor is carried out. The steady state analysis for the PMSM which does not exist in the literature survey gives the correlation between step angle and speed. Micro stepping is applied to enhance the resolution and attain smooth operation. The dynamic equations governing the electro-mechanical system are modelled using the classical approach. The Table 103.1 shows that the %THD in the load current is greater in three level PWM when compared to the two level PWM. A simple solution to this problem is adding a Low Pass filter to remove the ripples in the current waveform. The steady-state and dynamic performance of the modelled PM stepper motor for varying speeds is obtained by applying a disturbance input after 3 s. The sampling time used is 51 µs which is the compromise between computation time and accuracy of the result.

Acknowledgments The paper work was carried out at S.K.P Engineering College. The author (s)[1,3] express their gratitude to the management for providing the necessary support and guidance for successful completion of the work.

A.1 103.7 Appendix

Simulation Parameters of Stepper Motor Drive:

Phase winding Resistance R = 0.7 Ω, Phase winding Inductance L = 4.6 mH.
Motor Torque constant K_m = 0.252 N m/A, Detent Torque constant K_d = 0.12 N m.
EMF constant K_e = 0.464 N m/A, No. of rotor teeth N = 50,
Motor inertia J = 6.98×10^{-4} kg m^2, Vis.friction co-eff. B = 1×10^{-4} N m s/Rd.

References

1. Rahman MF, Poo AN (1988) An application oriented test procedure for designing microstepping step motor controllers. IEEE Trans Ind Electron 35:542–546
2. Athani VV (1997) Stepper motors: fundamentals applications and design. New Age International Publishers

3. Hopkins T (2002) AN1495 application note: microstepping stepper motor drive using peak detecting current control
4. Jones DW (1998) Chapter 5-microstepping of stepping motors. http:/www.cs.iowa.edu/jones/step/micro.html
5. Bodson M (2006) Spontaneous speed reversals in stepper motors. IEEE Trans Control Syst Technol 14(2):369–273
6. Kieburtz N (1964) The step motor—the next advance in control systems. IEEE Trans Autom Control 9:98–104
7. Robinson DJ, Taft CK (1969) A dynamic analysis of magnetic stepping motors. IEEE Trans Ind Electron Control Instrumentation volume IECI-16 2:111–125
8. Ellis PJ (1971) Analysis and control of the permanent magnet stepper motor. Radio Electron Eng 4:302–308
9. Kuo BC, Tal J (1978) The incremental motion step motors and control systems, vol II. SRL Publishing
10. Kenjo T (1984) Stepping motors and their microprocessor control. Clarendon Press, New York
11. Le NQ, Jeon JW (2007) An open-loop stepper motor driver based on FPGA. In: International conference on control, automation system
12. Bellini C, Concari C, Franceschini G, Toscan A (2007) Mixed-mode PWM for high performance stepping motors. IEEE Trans Ind Electron 54:3167–3177

Chapter 104
Reliability Evaluation of Tamil Nadu Power Grid for the Year 2012

K. Karunanithi, S. Kannan and C. Thangaraj

Abstract Reliability is a key aspect of power system planning. The objective of this study is to calculate the reliability indices, Loss of Load Probability (LOLP) and Energy Not Served (ENS) for Tamil Nadu, an Indian State, for the year 2012 using a state-of the art computer model, the Wien Automatic System Planning (WASP-IV) package. During the year 2012, the peak load of the state was approximately 12,000 MW. The peak load shortage of approximately 3,500–4,000 MW though the installed capacity is 17,936 MW. Tamil Nadu faced severe power cuts and break downs. The additional capacity required to get the standard LOLP of 0.1, i.e., one day in ten years, one day in one year and one day in one month are calculated. The results of the computer model analysis shows an additional capacity requirement to meet the proposed LOLP varies between 4,054 and 5,723 MW.

Keywords Power grid · Loss of load probability (LOLP) · Wien automatic system planning (WASP-IV) package

104.1 Introduction

Power is one of the critical inputs necessary for the sustained growth of any economy. Its demand has been continuously growing in industrialized and urbanized regions due to varied reason. Moreover, there is no convenient method to store electric energy in large quantities and hence it is compulsory to maintain a

K. Karunanithi (✉) · S. Kannan
Kalasalingam University, Krishnankoil, Virudhunagar 626126, Tamil Nadu, India
e-mail: kkkarunanithi@yahoo.com

S. Kannan
e-mail: kannaneeeps@gmail.com

C. Thangaraj
Anna University of Technology, Chennai, India
e-mail: thangaraj.vc@gmail.com

C. Kamalakannan et al. (eds.), *Power Electronics and Renewable Energy Systems*,
Lecture Notes in Electrical Engineering 326, DOI 10.1007/978-81-322-2119-7_104

continuous and almost instantaneous balance between production and consumption of electricity. Some additional generation capacity is kept as reserve margin to satisfy the variations in demand. If the supply system is not able to meet the demand, load shedding is unavoidable. The increased installed capacity can reduce the power shortage. However, overinvestment and high operating costs may lead to increased energy cost and may reflect in the bill paid by the consumer. On the other hand, underinvestment and low generation margins may lead to unavailability of power and poor reliability to consumers.

Southern region of India has the highest peak shortage of 14.5 % and energy shortage of 10.5 Million Units (MU) [1]. Tamil Nadu is one of the states in southern region. Over the last few years, Tamil Nadu has been facing massive power deficits due to varied reasons. As a result, the state is now facing huge power cuts. This power shortage affects the industries, leading to loss in efficiency, production and loss of income. In order to substitute the power during the power cuts, most of the domestic consumers are using the Uninterrupted Power Supply (UPS) system, commercial consumers are using mini Diesel/Kerosene generators and industrial consumers are using large diesel generators. Hence the estimation of reliability indices in terms of LOLP and EENS is of critical importance.

The performance of various plants in Tamil Nadu was analyzed for the period 2004–2008 and the potential for wind, solar and biomass was discussed in [2]. The incorporation and impact of Wind Energy Conversion System (WECS) in Generation Expansion Planning (GEP) using WASP-III was analyzed in [3]. The different version of WASP model was used in (i) Iranian power grid (ii) Pakistan's Power Plants and (iii) Oman power grid [4–6].

In this paper, WASP-IV package [7] has been used to analyse the reliability in terms of LOLP and ENS of Tamil Nadu Power Grid. The reliability study is carried out for the year 2012. The rest of the paper is organized as follows: Sect. 2 describes the overview of Tamil Nadu power scenario and Sect. 3 describes implementation of the problem in WASP-IV. Section 4 provides results and discussion and Sect. 5 concludes.

104.2 Power Sector in Tamil Nadu-An Overview

Tamil Nadu, the eleventh largest state in India, covers 130,058 m^2 (50,216 sq. miles) and has a coastline of about 910 km (600 miles). In terms of population, it is the seventh most populous state with a population of about 72 million, nearly 6 % of India's population (census 2011). Tamil Nadu has the highest level of urbanization in India, which accounts for 9.6 % of India's urban population. The state has the distinction of having two monsoon seasons: south-west monsoon from June to September and the north-east monsoon from October to December. This distinctive feature has helped Tamil Nadu to become a favored wind power destination because the monsoon winds contribute to the bulk of the annual wind power generation. Tamil Nadu has an installed capacity of 6,700 MW of wind power. The total installed generation capacity of Tamil Nadu in the year 2012 was 17,936 MW [8]. Table 104.1 shows technology and the existing installed capacity of the state in the year 2012.

At present, about one-third of the installed capacity of renewable sources in India exists in Tamil Nadu alone. Out of 17,936 MW installed capacity, thermal contributes 45.6 % and renewable powers contribute 54.4 % (Wind 37.35 %, Biomass 4.85 % and Hydro 12.2 %). The generation mix in the year 2012 is shown in Fig. 104.1.

Though the installed capacity 17,936 MW was sufficiently higher than the peak demand of 12,000 MW, the system was not able to fulfill the demand due to the following reasons:

(i) Scheduled or unscheduled maintenance of generating units and its auxiliaries
(ii) Uncertainty in availability of wind power and hydro power
(iii) Units are working less than their rated capacity due to aging, i.e., many units crossed their lifetime.

In order to overcome the power shortage, the TANGEDCO adopts the following countermeasures [8]

- Forty percent (40 %) cut on base demand and energy for high-tension (HT) industrial and commercial consumers.
- HT industrial and commercial consumers can draw less than 10 % of power from the grid during evening peak hours.

Table 104.1 Installed generation capacity (MW) in Tamil Nadu

S. no.	Name of the plant	Type of fuel	No. of units	Cap./unit (MW)	Cap. (MW)	FOR (%)	Maint. sche. (days/year)
1	Ennore	Coal	3	150	450	3	30
2	Tuticorin	Coal	4	210	840	7	26
3	Mettur	Coal	5	210	1050	10	21
4	Nr. Chennai	Coal	3	210	630	10	34
5	Biomass	–	3	290	870	25	30
6	Wind farm	–	100	67	6700	81.4	10
7	TANGEDCO	Gas	5	103	515	3	20
8	IPP	Gas	10	118	1180	3	20
9	Kalpakkam	Nuclear	2	165	330	3	25
10	Others	Diesel	10	65	650	10	30
11	Share from Central	Lignite	5	506	2530	10	30
12	Hydro	–	33	–	2191	–	–
Total					17,936	–	–

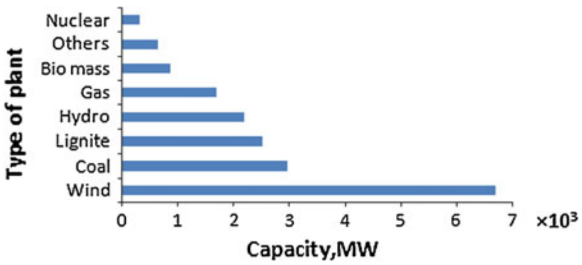

Fig. 104.1 Generation mix of Tamil Nadu in the year 2012

- Introduction of power holiday to all the HT, low tension (LT) and low-tension current transformer (LTCT) industries for one day between Monday and Saturday on staggered basis.
- All HT industries are required to declare Sunday as a weekly holiday.
- All HT industries can procure power through both inter-state and intra-state open access.
- A nine-hour (six hours during day time and three hours during night) three-phase supply for agricultural services.
- For domestic consumers daily two-hour load shedding (i.e., partial loads disconnected) in the state capital Chennai and its suburbs, and four hours in urban and rural feeders in other areas.

104.3 Implementation in WASP-IV

WASP-IV is one of the popular application software package used for Generation Expansion Planning (GEP) studies. WASP-IV calculates reliability indices LOLP and ENS for every year of planning study. In this study, WASP-IV is used to evaluate the Tamil Nadu power in terms of reliability indices and additional capacity required to achieve the same.

104.3.1 Load Data

The detailed load data for Tamil Nadu for every month of the year 2012 is available in [9]. The number of periods (seasons) per year considered as four. Peak load ratio for each season is the ratio of each seasonal peak load divided by peak load of that year. The load duration curve for the year 2012 is shown in Fig. 104.2.

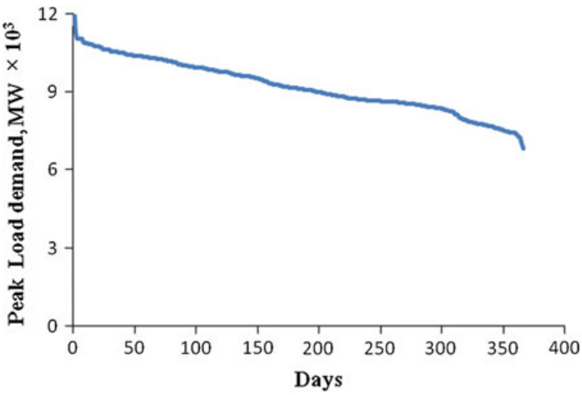

Fig. 104.2 Load duration *curve* of Tamil Nadu for the year 2012

104.3.2 Wind Plant Modeling in WASP

There are several ways to model wind plant in WASP [6] and all have some kind of approximation. In the present study, a wind turbine is modeled as a thermal plant with high FOR (81.4 %).

104.4 Results and Discussions

The minimum demand was 8,052 MW and maximum demand was 12,000 MW in the year 2012. The load factor was 81.51 %. The energy demand in the year 2012 was 85,687.4 GWh and shown in Table 104.2.

The season wise energy generations are as shown in Tables 104.3, 104.4, 104.5 and 104.6. During the first period of study, the energy demand was 20,395.9 GWh and generated energy was only 18,523.5 GWh, the energy shortage was 1,890.9 GWh. The LOLP in this period was 93.52 %. The higher value of LOLP was due to inadequacy of power generation. During the second period, the energy demand was 21,084.3 GWh and generation was 19,323.4 GWh. The energy deficit in this period was 1,760.9 GWh. The LOLP was 76.25 %, which is less than the previous period. During the third period, the highest energy demand occurred as 23,549.8 GWh among the four periods and energy generated was 20,983.3 GWh. The energy shortage was 2,566.6 GWh. The LOLP was still higher as 93.39 %. During the fourth period, the energy demand was 20,657.4 GWh and generation

Table 104.2 Max. and min. load demand, energy demand, load factor in 2012

Year	Max. demand (MW)	Min. demand (MW)	Total energy demand (GWh)	Load factor (%)
2012	12000	8052	85687.4	81.51

Table 104.3 Summary of all four periods

S. No.	Periods	Capacity (MW)	Gen. (GWh)	Peak load (MW)	Energy demand (GWh)	ENS (GWh)	LOLP (%)
1	1	15978.6	18523.5	10800.0	20395.9	1870.9	93.5215
2	2	15995.0	19323.4	11160.0	21084.3	1760.9	76.2566
3	3	16214.4	20983.3	11760.0	23549.8	2566.6	93.3904
4	4	15995.0	19982.5	12000.0	20657.4	674.9	34.0460
Total			78,812.7	–	85,687.4	6873.3	–

Table 104.4 Energy generation of year 2012-Period 1

S. No.	Name of the plant	No. of units	Peak cap. (MW)	Total cap. (MW)	Energy (GWh)	Cap. factor (%)
1	HYRDO	33	194.8	233.6	500.0	10.4
2	ENN	3	150	450	956.1	97.0
3	TUTI	5	210	1050	2093	91.0
4	METT	4	210	840	1683.4	91.5
5	NR.C	3	210	630	1262.4	91.5
6	BIO	3	290	870	957.6	50.3
7	WECS	100	67	6700	2729.2	18.6
8	TANGEDCO	5	103	515	1089.5	96.6
9	IPP	10	118	1180	2507.1	97.0
10	KALP	2	165	330	476.3	65.9
11	OTHE	10	65	650	888.2	62.4
12	CENT	5	506	2530	3380.7	61.0
Total					18523.5	–

was 19,982.5 GWh (Table 104.7). The energy not served was 674.9 GWh. The LOLP was 34.04 %. The LOLP has drastically reduced because of lower value of ENS compared with other periods. In the fourth period, all plants were in service. The total energy produced by all plants in the year 2012 was 78,812.62 GWh and total energy demand was 85,687.4 GWh and shown in Table 104.8. The overall energy shortage in the year 2012 was 6,874.78 GWh. The overall LOLP was 74.30 % (271.208 days/year).

In order to get standard/accepted LOLP of one day in ten years (0.02739 %), we have to add additional generation capacity of 5,723 MW. Table 104.9 shows the additional capacity requirement from the plants. With the addition of 5,723 MW capacity, the total energy generation will increase from 78,812.7 GWh to

Table 104.5 Energy generation of year 2012-Period 2

S. No.	Name of the plant	No. of units	Peak cap. (MW)	Total cap. (MW)	Peak energy (GWh)	Energy (GWh)	Cap. factor (%)
1	HYDRO	33	211.2	250	415.0	500.0	10.4
2	ENN	3	150	450	478.0	955.9	97
3	TUTI	5	210	1050	71.2	1494.7	65
4	METT	4	210	840	61.6	1294.5	70.4
5	NR.C	3	210	630	60.1	1262.4	91.5
6	BIO	3	290	870	936.2	1429.0	75
7	WECS	100	67	6700	2607.0	2729.2	18.6
8	TANGEDCO	5	103	515	83.5	716.0	63.5
9	IPP	10	118	1180	442.1	1918.5	74.2
10	KALP	2	165	330	219.2	657.7	91
11	OTHE	10	65	650	916.3	1323.6	93
12	CENT	5	506	2530	1056.2	5042.0	91
Total					7346.4	19323.5	–

Table 104.6 Energy generation of year 2012-Period 3

S. No.	Name of the plant	No. of units	Peak cap. (MW)	Total cap. (MW)	Peak energy (GWh)	Energy (GWh)	Cap. factor (%)
1	HYDRO	33	396.3	469.4	840.0	1000.0	20.8
2	ENN	3	150	450	320.8	641.5	65.1
3	TUTI	5	210	1050	99.6	2092.5	91
4	METT	4	210	840	80.2	1683.2	91.5
5	NR.C	3	210	630	37.7	791.5	57.4
6	BIO	3	290	870	936.2	1429.0	75
7	WECS	100	67	6700	2607.0	2729.2	18.6
8	TANGEDCO	5	103	515	136.1	1086.6	96.3
9	IPP	10	118	1180	594.3	2506.1	97
10	KALP	2	165	330	219.2	657.7	91
11	OTHE	10	65	650	916.5	1323.8	93
12	CENT	5	506	2530	1056.2	5042.0	91
Total					7843.8	20983.1	–

Table 104.7 Energy generation of year 2012-Period 4

S. No.	Name of the plant	No. of units	Peak cap. (MW)	Total cap. (MW)	Peak energy (GWh)	Energy (GWh)	Cap. factor (%)
1	HYDRO	33	211.2	250	415.0	500.0	10.4
2	ENN	3	150	450	477.6	955.5	97
3	TUTI	5	210	1050	99.6	2092.5	91
4	METT	4	210	840	80.2	1683.2	91.5
5	NR.C	3	210	630	60.1	1262.4	91.5
6	BIO	3	290	870	936.2	1429.0	75
7	WECS	100	67	6700	2607.0	2729.2	18.6
8	TANGEDCO	5	103	515	47.4	453.4	40.2
9	IPP	10	118	1180	331.6	1868.5	72.3
10	KALP	2	165	330	219.2	657.7	91
11	OTHE	10	65	650	902.8	1309.1	92
12	CENT	5	506	2530	1056.2	5042.0	91
Total					7232.9	19982.5	–

Table 104.8 Summary of result for the year 2012

S. No.	Name of the plant	Cap./unit (MW)	No. of units	Cap. factor (%)	Energy (GWh)
1	HYDRO	–	33	13.03	2500.00
2	ENN	150	3	89.02	3509.12
3	TUTI	210	5	84.5	7772.71
4	METT	210	4	86.22	6344.30
5	NR.C	210	3	82.97	4578.80
6	BIO	290	3	68.81	5244.50
7	WIND FARM	67	100	18.6	10916.71
8	TANGEDCO	103	5	74.16	3345.46
9	IPP	118	10	85.14	8800.29
10	KALP	165	2	84.73	2449.28
11	OTHE	65	10	85.08	4844.66
12	CENT	506	5	83.5	18506.79
Total					78812.62

Table 104.9 Results for reliability indices-various scenarios

S. No.	Additional capacity required (MW)	Total energy generated (GWh)	LOLP	ENS (GWh)	Contribution of RES
1	4054	85,592.3	One day in one month	95.2	51.59%
2	5153	85677.9	One day in one year	9.2	51.16%
3	5723	85683.6	One day in ten years	3.8	48.80%

85,683.6 GWh and ENS will be 3.8 GWh. Now total installed capacity becomes 23,659 MW. The contribution of renewable power will be 9,356 MW, approximately 39.54 %. In order to get approximately LOLP of one day in one year, we have to add additional generation capacity of 5,153 MW. With the addition of 5,153 MW capacities, the total energy generation will increase to 85,677.9 GWh and ENS will be 9.2 GWh. Now total installed capacity becomes 23,089 MW. In order to get approximately LOLP of one day in one month, we have to add additional generation capacity of 4,054 MW. With the addition of 4,054 MW capacities, the total energy generation will increase to 85,592.3 GWh and ENS will be 95.2 GWh. Now total installed capacity becomes 21,990 MW.

104.5 Conclusion

In this paper, reliability evaluation of Tamil Nadu power grid for the year 2012 was studied. The LOLP for the year was 74.3 % and approximately 271 days/year. In other words during the year 2012, the generation (available) was not being able to meet the demand approximately for nine months. This value is very high, even though total installed capacity was 17,936 MW and nearly 6,000 MW higher than that of peak demand. The higher value of LOLP is due to high wind power installed capacity since it is intermittent in nature and poor capacity adequacy. The result shows that additional capacities of 5,723 MW, 5,153 MW and 4,054 MW needs to be installed from various resources to get LOLP of one day in ten years, one day in one year and one day in one month.

References

1. Rallapalli SR, Ghosh S (2012) Forecasting monthly peak demand of electricity in India-A critique. Energy Policy 45:516–520
2. Jayabalan (2009) Study on power scenario in Tamil Nadu centre for Asia studies. http://www.asiastudies.org/file/publication/balan/TNEB%20paper.pdf. Accessed 10 Feb 2013

3. Schenk KF, Chan S (1981) Incorporation and impact of wind energy conversion system in generation expansion planning. IEEE Trans Power Apparatus Syst 100:4710–4718
4. Noshad Bahram et al (2012) Generation expansion planning for Iranian power grid aiming at providing reliability by comparing WASP-IV program and proposed algorithm by dynamic programming. Indian J Sci Technol 5:2961–2965
5. Shinwari Muhammad Fahad et al (2012) Optimization model using WASP-IV for Pakistan's power plants generation expansion plan. J Elect Electron Eng 3:39–49
6. Malik Arif S, Kuba Cornelius (2013) Power generation expansion planning including large scale wind integration: a case study of Oman. J Wind Energy 2013:1–8
7. Wien automatic system planning package version-IV (2001) User's manual. International Atomic Energy Agency, Vienna
8. Tamil Nadu Energy department Policy Note (2013). http://cms.tn.gov.in/sites/default/files/documents/energy7.pdf. Accessed 10 Feb 2013
9. Southern regional power committee Bangalore, progress report from January to December (2012) http://www.srpc.kar.nic.in/html/all uploads.html. Accessed 10 Feb 2013

Chapter 105
Implementation of Low Cost Single Switch Based Switched Reluctance Motor Drive

S. Rajagopal and S.S. Dash

Abstract Switched Reluctance motor has gained much popularity for low and medium power variable speed drives because of high starting torque, efficiency and reliability. While using switched reluctance motors with conventional converters it is seen that stored energy in the winding is recovered, temporarily stored in the capacitor during commutation, circulated in the DC link capacitor and then injected into the winding. As there is appreciable energy loss, it is proposed in this new convertor that energy recovered from the winding of the motor during commutation is retained and directly utilized in the motor. This paper deals with design, simulation and implementation of single switch based reluctance motor drive. The drive is powered from asymmetric two phase switched reluctance motor. The modeling is done using the elements of Simulink and it is simulated using matlab. The hard ware is fabricated and tested in the laboratory. The obtained experimental results are compared with simulation results.

Keywords Switched reluctance motor · Commutation · Pulse width modulation PWM

105.1 Introduction

Squirrel cage induction motors are used in industrial applications due to robustness and easy maintenance. It is found that core losses and copper losses are increasing heavily while operating squirrel cage induction motors at high frequencies. While using DC motors for variable speed drives, many problems arise due to sparking

S. Rajagopal (✉)
Sathyabama University, Chennai, India
e-mail: rajagopalavit@yahoo.in

S.S. Dash
Department of EEE, SRM University, Chennai, India
e-mail: munu_dash_2k@yahoo.com

C. Kamalakannan et al. (eds.), *Power Electronics and Renewable Energy Systems*,
Lecture Notes in Electrical Engineering 326, DOI 10.1007/978-81-322-2119-7_105

during commutation. Further use of DC motors is also limited due to their low voltage operations (<650 VDC) and low speed (<6,000 rpm) conditions. In addition to that efficiency and overload capacity of DC motors are also low.

Due to the above mentioned problems in using squirrel cage induction and DC motors in industrial applications nowadays switched reluctance motors are preferred for variable speed requirements. Switched reluctance motors have many advantages like high efficiency, high torque/weight ratio and high starting torque.

Any fault in one phase of stator winding will not affect other phases as they are electrically separated from each other. Mutual coupling between them is negligible. Further uninterrupted operation of the system with reduced output is possible in case of failure of one phase winding of switched reluctance motors.

The switched reluctance motor drive requires an electronic power converter for its operations. The converter has to supply square wave currents to windings. This condition requires that the current supply has to be regulated during conduction time and commutation from one winding to another must be also be as fast as possible. Quick commutation is limited due to the high inductance values of the windings and energy stored in them is also more.

To retrieve the stored energy and reduce the current fall time some of the following solutions have been considered. (a) The stored energy is dissipated in a resistor. (b) The stored energy is temporarily reserved in a capacitor and injected into the dc link and then to the following phase winding.

Instead of the above two methods the energy recovered from the main winding is retained and utilized with in the motor in the new converter system presented in this paper. Due to this improvement losses in the retrieved energy are reduced, size of dc link is made smaller, obtained decrease in cost and finally life time of the converter is increased.

The above literature does not deal with comparison of results of simulation and experimentation of single controlled switched reluctance motor drive. This paper deals with simulation and implementation of single switch based switched reluctance motor drive.

105.2 Converter System

The motor used in the proposed converter has asymmetric main and auxiliary windings. Main winding produces main torque and auxiliary winding provides self starting and reversal of speed (Figure 105.1).

The important features of the new converter system are as follows.

1. A bridge rectifier with a filter capacitor C1 form a DC link to supply energy to the main winding.
2. During commutation of the main phase current flows through the capacitor C_2 to charge it and a small amount of current also flows through the auxiliary winding.

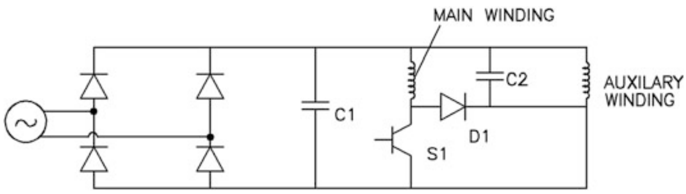

Fig. 105.1 Proposed converter

3. In the new converter voltage across the main winding is equal to $-V_{C2}$.
4. Commutation time depends upon the size of the capacitor C_2 and parameters of main and auxiliary winding as both phases are tightly coupled with C_2 during commutation.

105.3 Modes of Operation

Figures 105.2, 105.3, 105.4, 105.5 and 105.6.

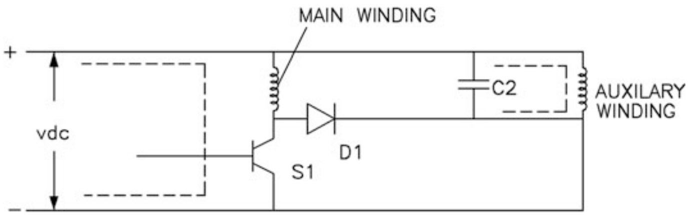

Fig. 105.2 Mode1. When S_1 is turned on main winding is energized with energy from DC link. The auxiliary winding is also energized from C_2 if there is a charge in the capacitor

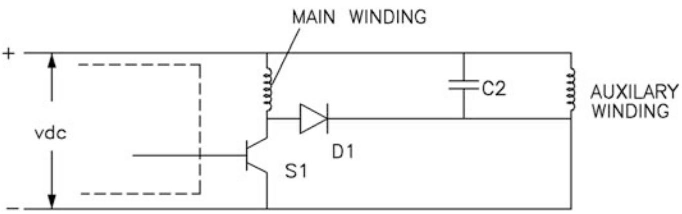

Fig. 105.3 Mode 2. S_1 is still in on condition. The main winding continues to be energized. C_2 is completely discharged and there is no current flow from the capacitor

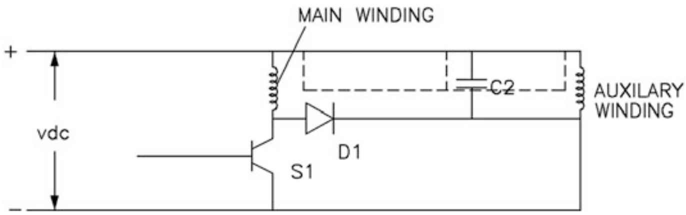

Fig. 105.4 Mode 3. When S_1 is turned off the current in the main winding flows through diode D to the auxiliary winding transforming energy partly to the capacitor and auxiliary winding

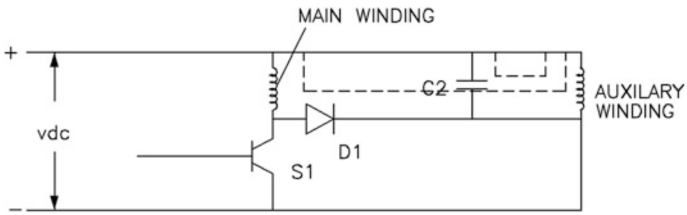

Fig. 105.5 Mode 4. S_1 is in turned off condition. Both the main winding and capacitor C_2 supply current to the auxiliary winding

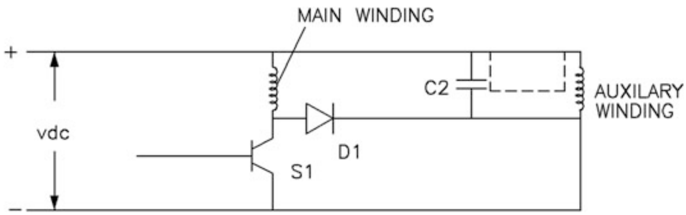

Fig. 105.6 Mode 5. S_1 is in turned off condition. Capacitor C_2 supply current to the auxiliary winding

105.4 Simulation Results

The design was done and the circuit is modeled using the elements of MATLAB. The simulation is done and the results are presented here. The simulation model of drive system shown in Fig. 105.7a. AC input is converted into DC using an uncontrolled rectifier. The even harmonics in the output are absorbed by the capacitor. The pulses required by the SRM are generated by using the MOSFET.

AC input voltage is shown in Fig. 105.7b. the PWM pulses given to the MOSFET are shown in Fig. 105.7c. Gate voltage and drain to source voltage are shown in Fig. 105.7d. The voltage across main winding and auxiliary winding are shown in Fig. 105.7e. The current through main winding and auxiliary winding are shown in Fig. 105.7f. The currents are displaced by 180°.

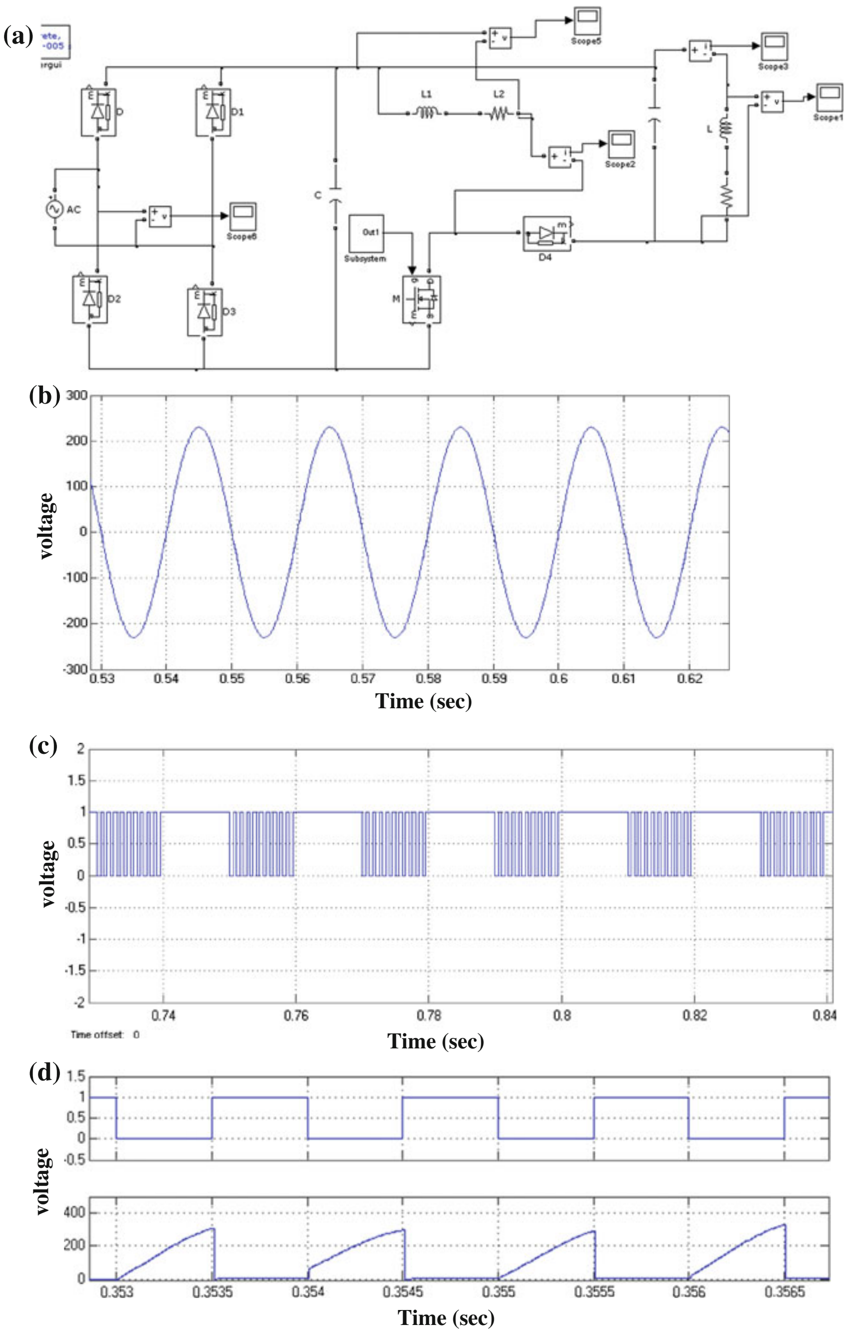

Fig. 105.7 **a** Circuit diagram. **b** AC input voltage waveform. **c** Switching pulse (M). **d** Gate voltage and drain to source voltage waveforms. **e** Main winding and auxiliary winding voltage waveforms. **f** Main winding and auxiliary winding current waveforms

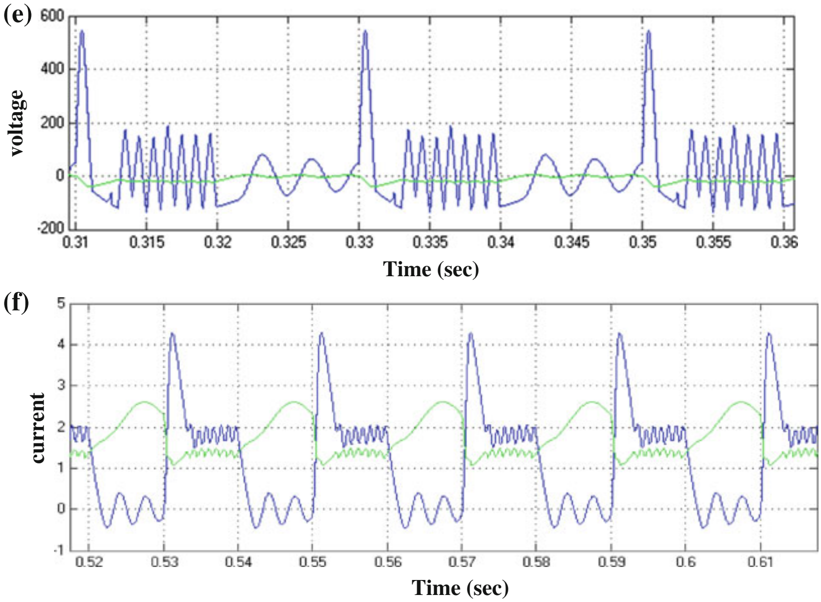

Fig. 105.7 (continued)

105.5 Experimental Verification

The hardware is fabricated and tested in the laboratory. The hardware system comprises of power circuit and control circuit. The power circuit consists of rectifier, power MOSFET, and filter. The control circuit uses PIC 16F84 to generate the pulses. These pulses are amplified by using twin driver IC IR 2110. The experimental set up is shown in Fig. 105.8. AC input voltage is shown in Fig. 105.9. The pulses generated by the micro controller are shown in Fig. 105.10.

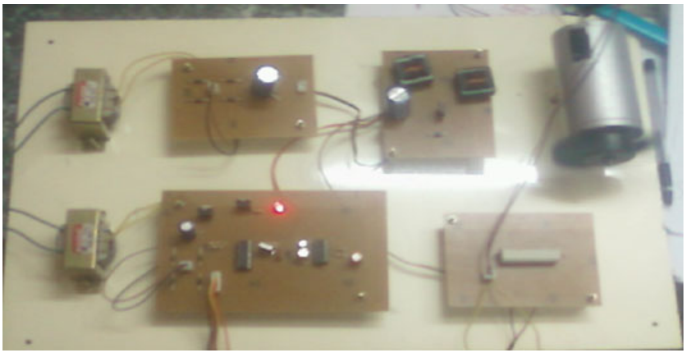

Fig. 105.8 Hardware snap shot

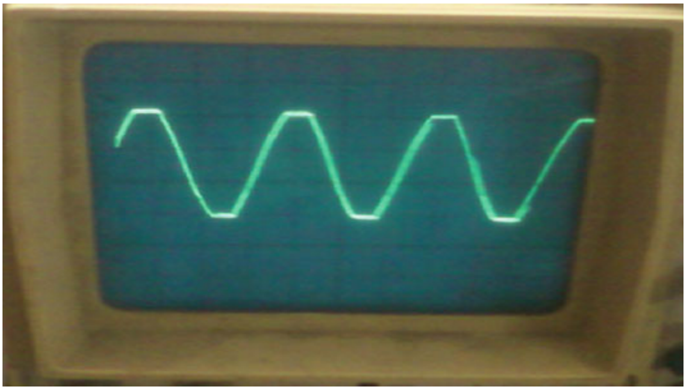

Fig. 105.9 Input voltage

The switching pulse and voltage across MOSFET are shown in Fig. 105.11. The voltage across main winding is shown in Fig. 105.12. The voltage across auxiliary winding is shown in Fig. 105.13.

Fig. 105.10 Switching pulse

Fig. 105.11 Switching pulse and vds

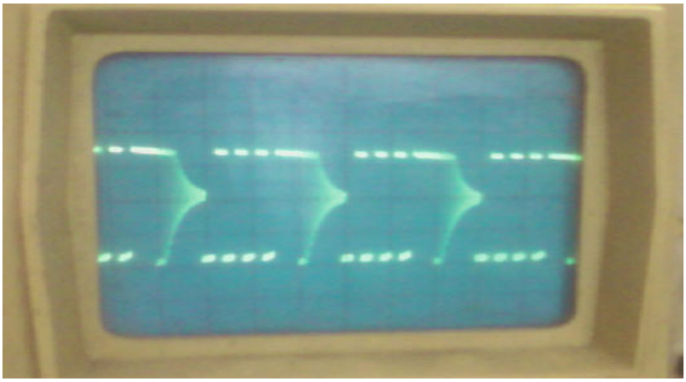

Fig. 105.12 Main winding voltage

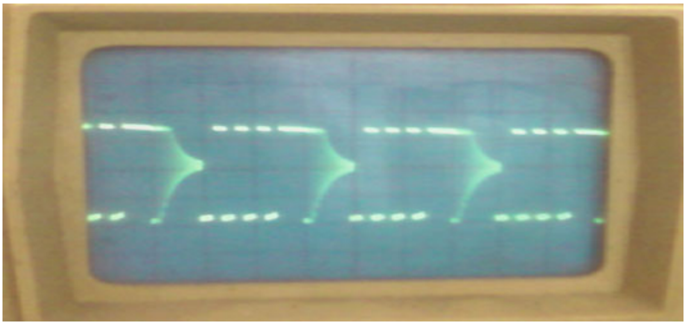

Fig. 105.13 Auxiliary winding voltage

105.6 Conclusion

Single switch based switched reluctance motor drive is simulated using MATLAB and it is implemented successfully. The speed of the motor is controlled by controlling the switching frequency. The cost of the system is reduced since it is controlled by a low cost microcontroller. Advantages of this drive is flexibility in programming, standardized hardware variable speed operation and reduced cost. The experimental results closely agree with the simulation results.

References

1. Krishnan R (1997) A novel single—switch-per-phase converter topology for four—quadrant pm brushless dc motor drive. IEEE Trans Ind Appl 33(5):1154–1161
2. Jaehyuck Kinm, "Single – Controllable – Switch – Based Switched Reluctance Motor Drive for Low Cost, Variable Speed Applications"

3. Lawrenson PJ, Stephenson JM, Blenkinsop PT, Corda J, Fulton NN (1980) Variable speed reluctance motors. Proc. IEEE. Part B 127:253–265
4. RayWF Lawrenson PJ, Davis RM, Stephenson JM, Fulton NN, Blake RJ (1986) High-performance switched reluctance brushless drives. IEEE Trans Ind Appl IA-22:722–730
5. Bass JT, Ehsani M, Miller TJE (1987) Simplified electronics for troque control of sensorless switched reluctance motor. IEEE Trans Ind Electron IE-34:234–239
6. Miller TJE, Bower PG, Becerra RC, Ehsani M (1988) Four-quadrant brushless reluctance motor drive. In Proc IEE Conf Power Electron CP-291:273–276
7. Chomat M, Lipo TA (2003) Adjustable-speed single-phase im drive with reduced number of switches. IEEE Trans Ind Appl 39(3):819–825
8. Welchko B, Lipo TA (2001) A novel variable-frequency three-phase induction motor drive system using only three controlled switches. IEEE Trans Ind Appl 37(6):1739–1745
9. Yang G, Deng Z, Cao X, Wang X (2008) Optimal winding arrangements of a bearingless switched reluctance motor. IEEE Trans Power Electron 23 (6)3056–3066

Author Biographies

S. Rajagopal has obtained B.E. degree from Madurai University and M.E. degree from Satyabama University in the years 1972 and 2005 respectively. He has 11 years of teaching and 23 years of industrial experience. He is presently a research scholar at Satyabama University. He is a life member of ISTE. He is working as a Professor in the Electrical and Electronics Engineering Dept at Aarupadai Veedu Institute of Technology, Paiyanoor, Chennai.

Dr. S.S. Dash is working as a Professor in SRM University, Chennai, India. He has 16 years of teaching and research experience. He has received Ph.D., degree in Electrical Engineering from Anna University in the year of 2006. His current research includes FACTS and Drives.

Chapter 106
A Novel Block-Based Selective Embedding Type Video Data Hiding Using Encryption Algorithms

P. Saravanan and K.K. Thyagarajan

Abstract Video data hiding continues to be an important research topic as a result of the design complexities involved. The process of embedding information into a host medium is a information concealment. In general, as a result of their wide presence and also the tolerance of human sensory activity systems involved visual and aural media are most popular. The strategies vary looking on the nature of such media and also the general structure of data hiding process doesn't rely on the host media sort. However, most of the video information concealment strategies utilize uncompressed video information. Recent video information hiding techniques are focused on the characteristics generated by video pressing standards. We have a tendency to propose a new video information concealment method that makes use of correction capability of repeat accumulate codes and superiority of forbidden zone information concealment (FZDH). FZDH is used for no alteration is allowed while information hiding process. The framework is tested by all reasonably videos like .mp4, .3gp, .avi etc., and gets triple-crown output for all video information concealment process.

Keywords Embedding · Forbidden zone data hiding · QIM · Video data hiding · Robust

P. Saravanan (✉)
Department of Information Technology,
Mailam Engineering College, Mailam, India
e-mail: saravana36@gmail.com

K.K. Thyagarajan
Department of Computer Science and Engineering,
RMD Engineering College, Chennai, India
e-mail: kkthyagharajan@yahoo.com

C. Kamalakannan et al. (eds.), *Power Electronics and Renewable Energy Systems*,
Lecture Notes in Electrical Engineering 326, DOI 10.1007/978-81-322-2119-7_106

106.1 Introduction

As Information Technology and Communication (ITC) grows speedily, multimedia is used widely so as to have flexibility in expression and conjointly communication. This led to security problems over web. This expedited the need for new information hiding technologies for having secret communication. Cryptography is one such technique that scrambles messages or converts message into construe able format while another technology by name steganography hides information in such the simplest way that it can't be viewed by adversaries. Property such as digital media like video, audio, pictures are distributed, manipulated and reproduced over IT systems. Copyright protection in this situation could be a difficult issue. Towards this finish watermarking technology came into existence. This technology is supposed for distinguishing the owner of the media. This is achieved by cryptography some form of hidden data for copyright protection. It is in distinction with encryption as it may be part of media permanently and protects copyrights while encryption just restricts information access lawlessly. As another to encryption, information hiding inside cowl media came into existence. The quilt media includes video, image and audio. This sort {of information of knowledge of information} concealment may also be called as steganography wherever data is hidden in unused and undetectable bytes of the select host media. It provides superior security when put next with cryptography. The process of data concealment in numerous cover media has important similarities. However, the info concealment method in video demands more advanced styles [1, 2].

There is a unit two main ways during which information hiding in video takes place. They are data-level and bit stream-level. The bit stream—level information concealment exploits redundancy in compression standards. Its encoders have freedom to settle on numerous options for the purpose of data concealment based on the structure of the bit stream. This makes the technique fragile and it can't stand up to any kind of format conversion though perceptual quality may be preserved. So it is not appropriate to all or any applications except some fragile applications like authentication. On the other hand, information-level approach to data concealment is more robust to security attacks. This makes it appropriate for big selection of applications. In spite of their fragility, the bit stream-level information concealment techniques area unit still attractive solutions for information concealment as represented in [3–5]. In [3] redundancy in block size selection is used while in [4] DCT coefficients area unit changed in the bit-stream level. In [5] QIM (Quantization Index Modulation) technique is used to low frequency DCT coefficients based on the parameters of videos of kind MPEG-2. They modified implant rate based on the type of video frame resulting in de-synchronization of erasures and insertions that happen at the decoder. They processed each frame individually since the parameters area unit used based on the type of frame.

In this paper, we propose a replacement block-based selective embedding kind information concealment framework that encapsulates impermissible Zone information concealment (FZDH) [6] and RA codes in accordance with an extra temporal synchronization mechanism. FZDH could be a sensible information hiding methodology that is shown to be superior to the standard quantization Index Modulation (QIM) [7]. RA codes area unit already utilized in image [3] and video [2] information concealment because of their hardiness against erasures. This hardiness permits handling a synchronism between embedded and decoder that happens as a result of the variations within the chosen coefficients. So as to include frame synchronization markers, we have a tendency to partition the blocks into 2 teams. One cluster is employed for frame marker embedding and therefore the different is employed for message bits. By means of easy rules applied to the frame markers, we have a tendency to introduce sure level of hardiness against frame drop, repeat and insert attacks. We have a tendency to utilize systematic RA codes to encipher message bits and frame marker bits. Every bit is related to a block residing in an exceedingly cluster of frames. Random interleaving is performed spatio-temporally; therefore, dependency to native characteristics is reduced. Host signal coefficients used for information concealment area unit chosen at four stages. First, frame choice is performed. Frames with ample variety of blocks area unit chosen. Next, just some preset low frequency DCT coefficients area unit allowable to cover information. Then the typical energy of the block is anticipated to be larger than a preset threshold. Within the finish, the energy of every constant is compared against another threshold.

106.1.1 Problem Domain

The major disadvantage of host activity primarily based ways is that the host activity collected from every stepping stone is usually not trustworthy. Since the wrongdoer is assumed to own full management over every stepping stone, it will simply modify, delete or forge user login info. This defeat the power to correlate supported host activity.

106.1.2 Existing Methods

In special domain, the hiding method like least important bit (LSB) replacement, is completed in special domain, whereas remodel domain methods; hide information in another domain like rippling domain.

- Least significant bit (LSB) is that the simplest type of Steganography. LSB relies on inserting information within the least important little bit of pixels that result in a small amendment on the quilt image that's not noticeable to human eye. Since this methodology
- LSB methodology has intense affects on the applied mathematics info of image like bar graph. Attackers may be awake to a hidden communication by simply checking the bar graph of a picture. An honest resolution to eliminate this defect was LSB matching. LSB-Matching was a good discovery in Steganography ways and plenty of others get ideas from it.

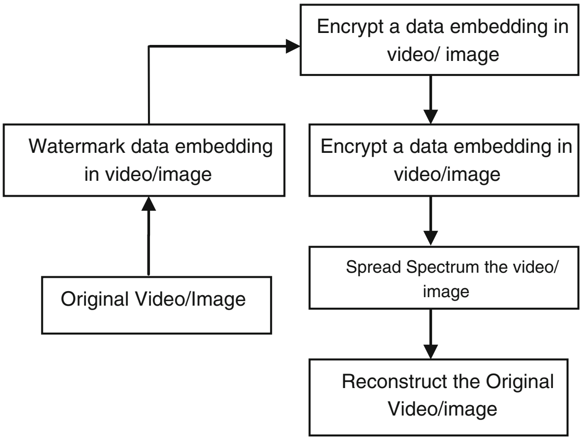

Fig. 106.1 Block diagram of the new block-based selective embedding type data hiding framework

106.1.3 Proposed Methods

- Data concealment in video sequences is performed in 2 major ways: bit stream-level and data-level.
- In this paper, we have a tendency to propose a brand new block-based selective embedding kind information concealment framework that encapsulates forbidden Zone data hiding (FZDH).
- By suggests that of easy rules applied to the frame markers, we have a tendency to introduce sure level of hardiness against frame drop, repeat and insert attacks.

Advantages

- User cannot find the original data.
- It is not easily cracked.
- To increase the Security.
- To increase the size of stored data

Block Diagram (Fig. 106.1).

106.2 Forbidden Zone Data Hiding

Forbidden zone data hiding (FZDH) is introduced in [6]. The method depends on the forbidden zone (FZ) concept, which is defined as the host signal range where no alteration is allowed during data hiding process. FZDH makes use of FZ to adjust the robustness-invisibility tradeoff.

106.2.1 Proposed Video Data Hiding Framework

A block based mostly accommodative video information concealing technique that includes FZDH that is shown to be superior to QIM and competitive with DC-QIM

[6], and erasure handling through RA Codes. We tend to utilize selective embedding to work out that host signal coefficients are employed in information concealing as in [3]. Not like the strategy in [3], we tend to use block choice (entropy choice selection [3]) and constant choice (selectively embedding in coefficients theme [3]) along. The de-synchronization thanks to block choice is handled via RA Codes as in [2, 3]. The de-synchronization thanks to constant choice is handled by exploitation multi-dimensional sort of FZDH in variable dimensions. In [2], the frames square measure processed severally. it's ascertained that [8] intra and lay frames don't yield important variations. Therefore, so as to beat native bursts of error, we tend to utilize 3-D interleaving the same as [4], that doesn't utilize selective embedding, however uses the full LL sub band of distinct riffle rework. Moreover, as in [4], we tend to equip the strategy with frame synchronization markers so as to handle frame drop, insert, or repeat attacks. Hence, it may be explicit the first contribution of this paper is to plan a whole video information concealing technique that's immune to de-synchronization thanks to selective embedding and strong to temporal attacks, whereas creating use of the prevalence of FZDH.

106.2.1.1 Framework

The embedding operation for one frame is shown in Fig. 106.2. Y-channel is employed for information embedding. Within the initiative, frame choice is performed and therefore the hand-picked frames are processed block wise. For every block, solely one bit is hidden. Once getting 8×8 DCT of the block, energy check is performed on the coefficients that are predefined in a very mask. Selected coefficients of variable length are wont to hide information bit m. m could be a member of message bits or frame synchronization markers. Message sequence of every cluster is obtained by victimization RA codes for T consecutive frames. Every block is allotted to at least one of those teams at the start. Once the inverse rework host frame is obtained.

Decoder is that the twin of the embedded, with the exception that frame choice isn't performed. Figure 106.3 shows the flow chart for one frame. Marked frames area unit detected by victimization frame synchronization markers. Decoder employs equivalent system parameters and determines the marked signal values which will be fed to information extraction step. Non-selected blocks area unit handled as erasures. Erasures and decoded message information probabilities (om) area unit passed to RA decoder for T consecutive frames as a full so the hidden information is decoded.

106.2.1.2 Selective Embedding

Host signal samples, which can be used in information hiding, are determined adaptively. The selection is performed at four stages: frame selection, frequency band determination, block selection, and coefficient selection.

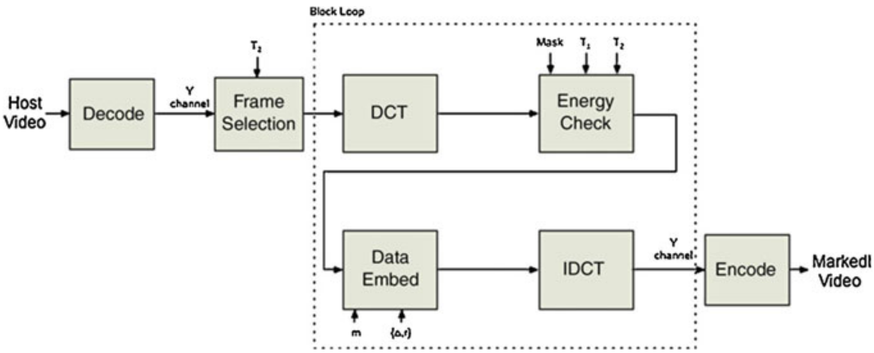

Fig. 106.2 Embedded flowchart of the proposed video data hiding framework for a single frame

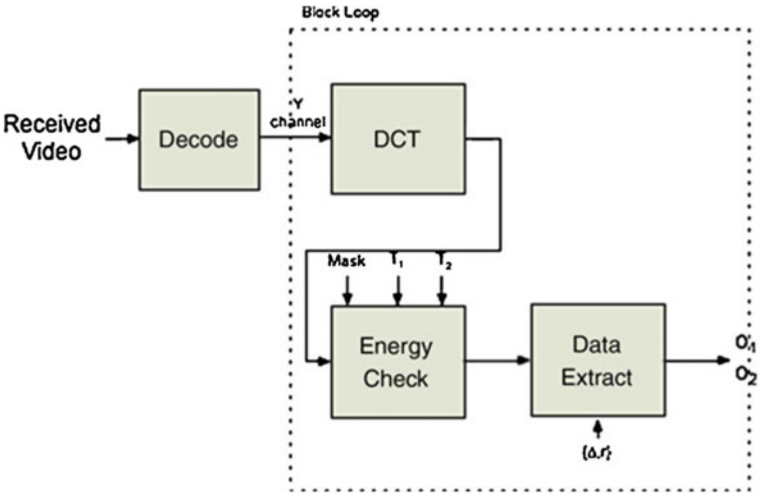

Fig. 106.3 Decoder flowchart of the proposed video data hiding framework for a single frame

1. Frame selection: selected number of blocks within the whole frame is counted. If the ratio of selected blocks to all blocks is above a certain price (T0) the frame is processed. Otherwise, this frame is skipped.
2. Frequency band: only sure DCT coefficients square measure utilized. Middle waveband of DCT coefficients shown in Fig. 106.3 is used like [2].
3. Block selection: energy of the coefficients within the mask is computed. If the energy of the block is above a certain price (T1) then the block is processed. Otherwise, it's skipped.
4. Coefficient selection: energy of each coefficient is compared to a different threshold T2. If the energy is above T2, then it's used throughout information embedding in conjunction with different selected coefficients within the same block.

106.3 Modules

In this paper, we divided into four modules. They are

- Input Module
- Encryption Module
- Decryption Module
- Security Module-Umaram

106.3.1 Input Module

The Input Module is meant intrinsically the way that the projected system should be capable of handling any form of information formats, like if the user needs to cover any image format then it should be compatible with all usual image formats like jpg, gif, bmp, it should be also compatible with video formats like .avi, .flv, .wmf etc. And also it should be compatible with varied document formats, so that the user may be able to user any formats to cover the key information.

106.3.2 Encryption Module

In Encryption module, it consists of Key file part, where key file can be specified with the password as a special security in it. Then the user can type the data or else can upload the data also though the browse button, when it is clicked the open file dialog box is opened and where the user can select the secret message. Then the user can select the image or video file through another open file dialog box which is opened when the cover file button is clicked. Where the user can select the cover file and then the Hide button is clicked so that the secret data or message is hidden in cover file using Forbidden Zone Data Hiding Technique.

106.3.3 Decryption Module

This module is the opposite as such as Encryption module where the Key file should be also specified same as that of encryption part. Then the user should select the encrypted cover file and then should select the extract button so that the hidden message is displayed in the text area specified in the application or else it is extracted to the place where the user specifies it.

106.3.4 Security Module

UMARAM: The UMARAM was designed by Ramesh G and R.Umarani in the year 2010. This algorithm uses a key size of 512-bits to encrypt a plaintext of 512-bits during the 16-rounds. In this Algorithm, a series of transformations have been used depending on S-BOX, different shift processes, XOR-Gate, and AND-Gate. The S-Box is used to map the input code to another code at the output. It is a matrix of $16 \times 16 \times 16$. The S-Box consists of 16-slides, and each slide having 2-D of 16×16. The numbers from 0 to 255 are arranged in random positions in each slide [9].

106.4 Implementation and Experimental Results

106.4.1 Implementation

Implementation is the stage of the project when the theoretical design is turned out into a working system. Thus it can be considered to be the most critical stage in achieving a successful new system and in giving the user, confidence that the new system will work and be effective. The implementation stage involves careful planning, investigation of the existing system and it's constraints on implementation, designing of methods to achieve changeover and evaluation of changeover methods. For more security provides by RSA Encryption is the act of encoding text so that others not privy to the decryption mechanism (the "key") cannot understand the content of the text. Encryption has long been the domain of spies and diplomats, but recently it has moved into the public eye with the concern of the protection of electronic transmissions and digitally stored data. Standard encryption methods usually have two basic flaws:

(1) A secure channel must be established at some point so that the sender may exchange the decoding key with the receiver; and
(2) There is no guarantee that sent a given message. Public key encryption has rapidly grown in popularity (and controversy, see, for example, discussions of the Clipper chip on the archives given below) because it offers a very secure encryption method that addresses these concerns.

In a classic cryptosystem in order to make sure that nobody, except the intended recipient, deciphers the message, the people involved had to strive to keep the key secret in a public-key cryptosystem. The public key cryptography solves one of the most vexing problems of all prior cryptography: the necessity of establishing a secure channel for the exchange of the key. The RSA algorithm, named for its creators Ron Rivest, Adi Shamir, and Leonard Adleman, is currently one of the favorite public key encryption methods. Here is the algorithm (Fig. 106.4).

Fundamentally UMARAM performs only two operations on its input, bit shifting, and bit substitution. The key controls exactly how this process works. By

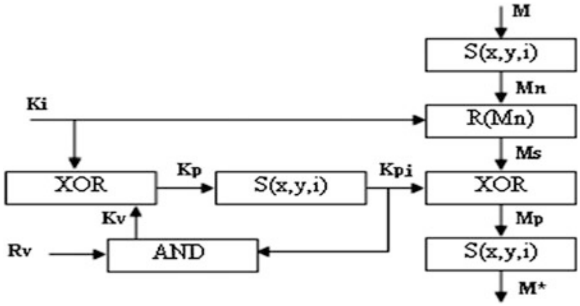

Fig. 106.4 Encryption process in each round of UMARAM encryption algorithm

doing these operations repeatedly and in a non-linear manner you end up with a result which cannot be used to retrieve the original without the key. Those familiar with chaos theory should see a great deal of similarity to what UMARAM does. By applying relatively simple operations repeatedly a system can achieve a state of near total randomness. Consult one of the references in the bibliography for details.

106.4.2 Experimental Results

In Secret file, we can upload our video file with any format then to select which file used to hide in this by using cover file.

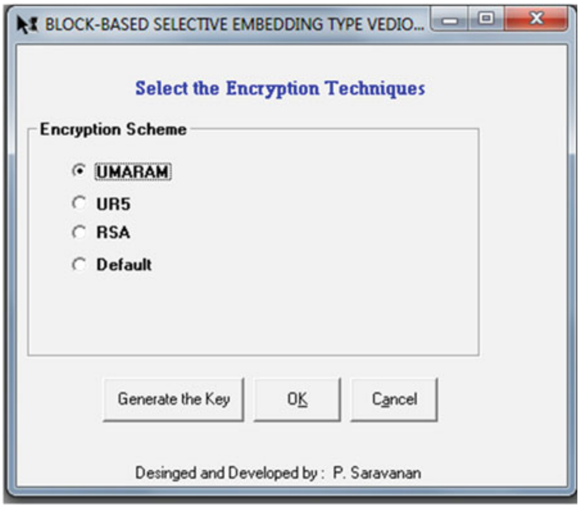

Finally to select the destination path to store our hidden file with password. When we retrieve the original file that time to provide same password. In this initial stage, while hiding the video data by choose any one of the encryption techniques.

106.5 Conclusion

A new video data hiding framework that produces use of erasure correction capability of RA codes and superiority of FZDH. The method is additionally robust to frame manipulation attacks via frame synchronization markers. First, we have a tendency to compared FZDH and QIM as the data hiding method of the planned framework. Web served that FZDH is superior to QIM, especially for low embedding distortion levels. The frame work was tested with MPEG-2, H.264 compression, scaling and frame-rate conversion attacks. Typical system parameters area unit reported for error-free secret Writing. The results indicate that the framework can be with success used in video data hiding applications.

References

1. Wu M, Yu H, Liu B (2003) Data hiding in image and video: I. Fundamental issues and solutions. IEEE Trans Image Process 12(6):685–695
2. Wu M, Yu H, Liu B (2003) Data hiding in image and video: II. Designs and applications. IEEE Trans Image Process 12(6):696–705
3. Kapotas SK, Varsaki EE, Skodras AN (2007) Data hiding in H-264 encoded video sequences. In Proceedings of IEEE 9th workshop multimedia signal process, pp 373–376
4. Wong K, Tanaka K, Takagi K, Nakajima Y (2009) Complete video quality-preserving data hiding. IEEE Trans Circuits Syst Video Technol 19:1499–1512
5. Sarkar A, Madhow U, Chandrasekaran S, Manjunath BS (2007) Adaptive MPEG-2 video data hiding scheme. In proceedings of 9th SPIE security steganography watermarking multimedia contents, pp 373–376
6. Wu M, Yu H, Liu B (2003) Data hiding in image and video II: Designs and applications. IEEE Trans Image Process 12:696–705
7. Esen E, Alatan AA (2006) Forbidden zone data hiding. In IEEE international conference on image processing, pp 1393–1396
8. Chen B, Wornell GW (2001) Quantization index modulation: a class of provably good methods for digital watermarking and information embedding. IEEE Trans Inf Theor 47:1423–1443
9. Skoric B, Vladimirova TU, Celik M, Talstra JC (2008) Tardos fingerprinting is better than wethought. IEEE Trans Inf Theor 54(8):3663–3676

Author Biographies

Mr. P. Saravanan obtained his M.C.A., degree from Mailam Engineering College (Anna University) and received his M.E., degree in computer Science from Manila Engineering College (Anna University). He has served at Mailam Engineering College. Since August 2008, he is the Asst.Prof of Mailam Engineering College. He has published 4 National Conference Papers, One International Conference and One International Journal.

Dr. K.K. Thyagharajan obtained his B.E., degree in Electrical and Electronics Engineering from PSG College of Technology (Madras University) and received his M.E., degree in Applied Electronics from Coimbatore Institute of Technology in 1988. He also possesses a Post Graduate Diploma in Computer Applications from Bharathiar University. He obtained his Ph. D. degree in Information and Communication Engineering (Computer Science) from College of Engineering Guindy, Anna University. He has served at various Educational Institutions. He has 25 years of teaching experience. Since September 2012 he is the Dean (Academic) of R.M.D. Engineering College.

He has written 5 books in Computing including “Flash MX 2004” published by McGraw Hill (INDIA) and it has been recommended as text and reference book by universities and Polytechnics. He has published more than 60 papers in National and International Journals and Conferences. His current research interests are Multimedia Networks, Content Based Multimedia Retrieval, Mobile Computing, e-learning, Image Processing. He is reviewer for many International Journals and Conferences. He is a recognized supervisor for Ph.D. by Anna University Chennai, MS University, JNTU and Sathyabama University, and now 10 students are doing Ph.D. under his Guidance.

Chapter 107
General Regression Neural Network for Software Effort Estimation of Small Programs Using a Single Variable

S.K. Pillai and M.K. Jeyakumar

Abstract Software development effort estimation always remains a challenging task for project managers. New techniques are applied to estimate effort. Predicting effort for small programs in educational setting is a difficult task. Minimum number of independent variables should be used to reduce data collection effort. Evaluation of accuracy is a major activity as many methods are proposed in the literature. Here, we have applied General Regression Neural Network (GRN) and compared the results with Linear Least Squares Regression (LSR) for one and two independent variables. Results are evaluated using statistical tests and effect size. The results show that accuracy of GRN and LSR with one and two variables are not different for small programs.

Keywords Software development effort estimation · Least squares regression · Statistical tests · Effect size · Neural network

107.1 Introduction

One of the major activities in software project management is software development effort estimation (SDEE). Recently machine learning methods and data mining techniques are getting more attention [1, 2]. Among the model based techniques regression is most frequently used. In comparing different methods regression is used as a default method. Problems of comparing one method with another arise as there

S.K. Pillai (✉)
Electrical and Electronics Department, Noorul Islam University,
Kumaracoil, Tamil Nadu, India
e-mail: skpillai50@gmail.com

M.K. Jeyakumar
Computer Applications Department, Noorul Islam University,
Kumaracoil, Tamil Nadu, India
e-mail: jeyakumarmk@yahoo.com

C. Kamalakannan et al. (eds.), *Power Electronics and Renewable Energy Systems*,
Lecture Notes in Electrical Engineering 326, DOI 10.1007/978-81-322-2119-7_107

are many criteria for accuracy evaluation. Accuracy also depends on the data used for evaluation as well as the criteria. Generally one can classify SDEE into four groups:

(i) Analogy based methods
(ii) Expert estimation, Delphi and Wideband Delphi
(iii) Model based such as COCOMO, SLIM, etc.
(iv) Artificial Intelligence (AI) methods such as neural networks, fuzzy logic, genetic algorithms or combinations there of

Past projects data are used directly or indirectly in all the methods. Analogy based methods compare the current project with past project which is close to it. In expert estimation, opinion of experts is sought for effort values. In model based methods, relationship between effort and project parameters are obtained using historical data. Among the AI methods neural networks are most commonly used [3]. Here we have used General Regression Neural Network (GRN) which is easy to implement with only one parameter to be tuned and its performance compared with classical Linear Least Squares Regression (LSR).

Section 107.2 gives related work followed by estimation problem and measurement data in Sect. 107.3. LSR and GRN are explained in Sects. 107.4 and 107.5 respectively. Comparative results are provided in Sect. 107.6. Section 107.7 provides conclusions and future research. References are listed at the end. We have followed the empirical software engineering approaches given in [4, 5].

107.2 Related Work

Software development effort estimation continues to be a hot topic in spite of many persons across many countries doing research. The major problems are related to input data, algorithm, and accuracy evaluation criteria. One needs to consider all these three factors to arrive at a conclusion. Boehm et al. [6] suggest that no one technique should be relied upon for SDEE. Instead multiple methods should be compared for decision making. Also when students learn estimation and apply in a college setting it becomes easy for any organization to implement SDEE. As discussed earlier, SDEE is a function of input where size of software projects play an important role. For small projects effort required is also small. Lopez-Martin [7] used fuzzy logic model based on two independent variables New and Changed (N&C) code and Reused (R) code. He has compared the performance of fuzzy model with multiple regression model. The results indicate that there is no difference between these two models. Two fuzzy logic models Mamdani and Takai-Sugeno are studied in [8]. The evaluation of these methods with linear regression showed that Takai-Sugeno fuzzy system performs better. Here only New and Changed code is used as independent variable. GRN is used to predict effort of industrial projects [9]. It is proved using statistical tests ANOVA and Kruskal-Wallis that GRN is an alternative to regression model. None of the above works compares SDEE using one and two independent variables. It is suggested to report effect size in statistical testing of all randomized algorithms [5].

107.3 Estimation Problem and Measurements

SDEE generally consists of two stages viz. model building and model evaluation. These are also known as verification or training and validation or testing. A part of the measurements is used to build the model and the remaining data are used to validate the model. Here we have used the data for verification and validation given in [7]. This consists of Actual Effort (AE), N&C code (N&C) and Reused code (R) for small projects in an academic setting. Effort is the dependent variable or response and the two independent variables or predictors are N&C code and R code. For training 163 projects are used and for testing 68 projects are used. Table 107.1 summarizes both training and testing data (N&CT, RT, AET). Pearson correlation coefficients of different variables are given in Table 107.2. It can be observed that the linear correlation of Reused code with Actual Effort is small compared with New and Changed code correlation. More details of the data are available in [7].

The estimation problem aims at finding a relationship between dependent and independent variables using training data. Then the test data is used to validate the developed model. We have used General Regression Neural Network (GRN) [10] and compared the results with Linear Least Squares Regression (LSR) for one and two independent variables. The accuracy is evaluated by magnitude of error relative to prediction (MER) with respect to each project and for each model. It has been strongly suggested not to use magnitude of error with respect to prediction (MRE) [11]. Also the error, (Actual effort_i − Predicted effort_i), known as residual in statistics literature is uncorrelated to Predicted effort. For each project:

$$\text{MER}_i = \text{abs}(\text{Actual effort}_i - \text{Predicted effort}_i)/\text{Predicted effort}_i$$

The aggregate for all the n projects is: $\text{MMER} = (1/n)\ \Sigma\ \text{MER}_i$.

Table 107.1 Characteristics of training and testing data

Variable	Mean	Stdev	Minimum	Median	Maximum	Skewness	Kurtosis
N&C	35.56	26.60	10.00	27.00	137.00	1.67	2.45
R	41.82	30.86	4.00	34.00	149.00	1.41	1.88
AE	77.07	37.81	19.00	67.00	195.00	0.85	0.04
N&CT	44.93	21.28	12.00	41.00	104.00	0.54	−0.10
RT	35.43	23.71	1.00	30.00	100.00	0.95	0.29
AET	79.16	26.47	11.00	78.00	144.00	0.22	−0.14

Table 107.2 Pearson correlation coefficients of different variables

N&C versus R	N&C versus AE	R versus AE	N&CT versus RT	N&CT versus AET	RT versus AET
0.114	0.747	−0.032	−0.175	0.307	0.190

107.4 Linear Least Squares Regression (LSR)

107.4.1 Using Two Independent Variables (N&C, R)

We have used MINITAB® to obtain the following results. The least squares method fits training data in the two variables as AE = 44.7 + 1.08 N&C − 0.146 R.

The contribution of Reused code is one tenth of New and Changed code. The coefficient signs are intuitively correct.

$$\text{R - Sq} = 57.2\,\% \quad \text{R - Sq(adj)} = 56.6\,\% \quad \text{R - Sq(pred)} = 55.43\,\%$$

The R-Sq value indicates that the predictors explain 57.2 % of the variance in Actual Effort. The R-Sq(adj) is 56.6 %, which accounts for the number of predictors in the model. The R-Sq(pred) value is 55.43 %. Because the predicted R value is close to the R-Sq and adjusted R-Sq(adj) values, the model does not appear to be over fit.

The *P*-value, 0.000, in the Analysis of Variance table (Table 107.3) shows that the model estimated by the regression procedure is significant at an α-level of 0.05. This indicates that at least one coefficient is different from zero.

The *P*-values for the estimated coefficients of N&C and R are both less than 0.05, indicating that they are significantly related to AE. The residuals plots for model validation are shown in Fig. 107.1. The normal probability plot shows an

Table 107.3 Analysis of variance for two variables

Source	DF	SS	MS	F	P
Regression	2	132,382	66,191	106.74	0.000
Residual error	160	99,214	620		
Total	162	231,596			

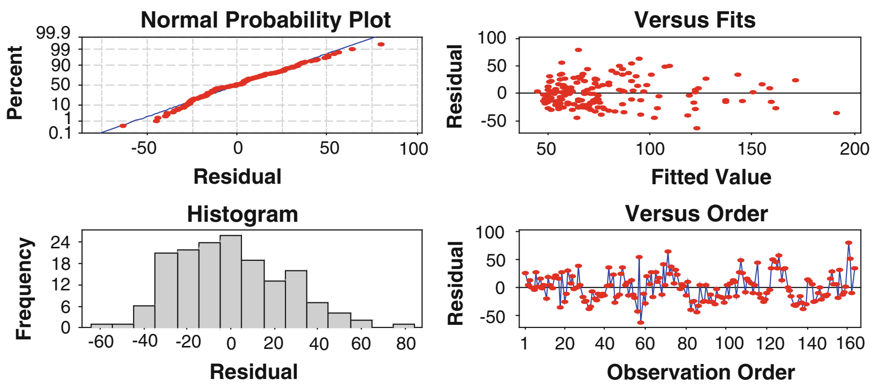

Fig. 107.1 Residual plots for training data for two variables

Table 107.4 Coefficients table for two variables

Predictor	Coef	SE Coef	T	P
Constant	44.723	4.032	11.09	0.000
N&C	1.08075	0.07403	14.60	0.000
R	−0.14568	0.06382	−2.28	0.024

approximately linear pattern consistent with normal distribution. The plot of residuals versus the fitted values shows that the residuals are distributed on both sides of the reference line. The graphs do not show any abnormality. From both graphical and tabular data analysis, we can accept the regression equation for two variables. The accuracy in term of MMER for training and testing are 0.274 and 0.287 respectively.

107.4.2 Using One Independent Variable (N&C)

Since the correlation of Reused code with AE is small we have used only N&C. The regression equation is

$$\text{AE} = 39.3 + 1.06\ \text{N\&C}$$
$$\text{R - Sq} = 55.8\,\% \quad \text{R - Sq(adj)} = 55.5\,\% \quad \text{R - Sq(pred)} = 54.63\,\%$$

These values are not much different from two variables results. Both ANOVA and coefficient table (not shown) (Table 107.4) indicate the significance of regression and coefficient. Residuals plots also do not show any problem. One interesting observation no residual is more than three sigma value where as for two variables case one observation (160) is outside three sigma. The accuracy in term of MMER for training and testing are 0.272 and 0.276 respectively.

107.5 General Regression Neural Network (GRN)

The GRN is a type of neural network which can be used to perform regression on a continuous data [10]. It can learn fast compared to standard back propagation multilayer perceptron as the output is obtained using a single pass. Also GRN needs only one parameter, spread, to be tuned. This network can be used for any regression problem including assumption of no linearity. We have used MATLAB® for GRN application. Figure 107.2 gives the architecture of GRN. The network contains one radial basis layer (Hidden) and one linear layer (Output). Radial basis layer activation function is exponential and its spread needs to be adjusted empirically for a particular problem. We need to find two optimal spreads one for two variable case and another for one variable input.

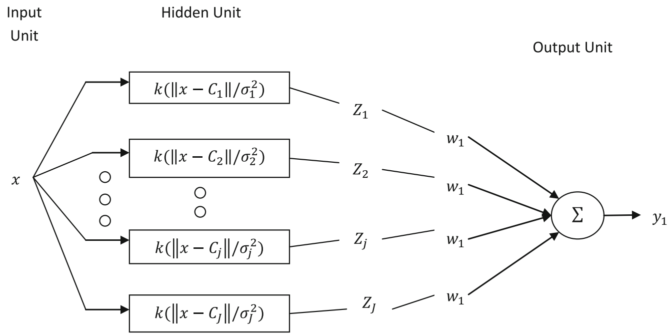

Fig. 107.2 Generalized regression neural network architecture

The spread is varied in steps of 0.01 from 0.01 to 1.0. The input and output are scaled from 0 to 1. For two variables, N&C and R, input it is found that at spread equal to 0.22, training and testing MMER are nearly equal. MMER for training is 0.2976 and for testing is 0.2986. For one variable case, N&C, input it is found that at spread equal to 0.08, training and testing MMER are nearly equal. MMER for training is 0.2725 and for testing is 0.2733. Although the accuracy is better (reduced error) for one variable, we need to validate statistically.

107.6 Comparative Analysis

We have used MINITAB® for testing the equality of two means and two medians. Two sample t test is used for the former as it is robust to moderate departures from normality assumptions. A non-parametric test, which does not require any distribution assumption, Mann-Whitney (M-W) test, is applied for comparing medians. As suggested in [5], we give *P* values for both tests. It is also required to give effect size as it is possible to obtain statistically significant results for large samples with *t*-test and M-W test. Here we report non-parametric effect size measure A_{12} given in [5].

$A_{12} = \{R1/m - (m + 1)/2\}/n$, where R1 is the rank sum of the first data group, m is the number of observations in first data sample, n is the number of observations in second data sample. Given a performance measure, M, the A_{12} statistics measures the probability that running algorithm one yields higher M values than running second algorithm. Table 107.5 provides comparison of mean, median and standard deviation of MER for LSR and GRN for one variable and two variables for testing and training data. The differences are small and we want to confirm by statistical tests. Results, *P* values, for different statistical tests for LSR and GRN are given in Table 107.6. It can be seen from t test and M-W test that for all cases *P* values are more than 0.05. We can conclude that GRN performs equal to LSR for one or two variables and for training and testing. Effect size for all the four cases is near 0.5, we

Table 107.5 Comparison of statistical parameters for LSR and GRN

	LSR				GRN			
	One variable (N&C)		Two variables (N&C, R)		One variable (N&C)		Two variables (N&C, R)	
	Training	Testing	Training	Testing	Training	Testing	Training	Testing
Mean	0.272	0.277	0.274	0.287	0.272	0.273	0.298	0.299
Median	0.251	0.271	0.249	0.287	0.262	0.269	0.288	0.279
Stdev	0.193	0.184	0.194	0.186	0.192	0.190	0.217	0.182

Table 107.6 Comparison of statistical tests for LSR and GRN

	One variable (N&C)		Two variables (N&C, R)	
	Training	Testing	Training	Testing
t-test, *P* values	0.965	0.921	0.312	0.715
Mann-Whitney test, *P*	0.923	0.833	0.513	0.726
Effect size	0.497	0.511	0.479	0.482

Table 107.7 Comparison of statistical tests for one (N&C) and two variables (N&C, R)

	LSR		GRN	
	Training	Testing	Training	Testing
t-test, *P* values	0.891	0.743	0.269	0.431
Mann-Whitney test, *P*	0.835	0.729	0.410	0.418
Effect size	0.507	0.517	0.526	0.540

can conclude that LSR and GRN perform equally well. Table 107.7 compares the performance of one and two variables. As expected *P* values for *t*-test and M-W test are greater than 0.05. Also effect size values are close to 0.5. We can conclude that there is no performance difference between one or two variables for LSR or GRN.

107.7 Conclusions

Software effort estimation accuracy of GRN is equal to LSR for small projects for the MMER criteria. Software effort estimation accuracy using one variable is equal to two variables for small projects for the MMER criteria for both algorithms. It is recommended to use one variable, N&C, for estimation of small projects. Research needs to be carried out to theoretically justify the same performance of GRN and LSR.

References

1. Dejaeger K, Verbeke W, Martens D, Baesens B (2012) Data mining techniques for software effort estimation: a comparative study. IEEE Trans Softw Eng 38:375–397
2. Wen J, Li S, Lin Z, Hu Y, Huang C (2012) Systematic literature review of machine learning based software development effort estimation models. Inf Softw Technol 54:41–59
3. Dave VS, Dutta K (2012) Neural network based models for software effort estimation: a review. In: Artificial intelligence review, Springer, Berlin (online)
4. Kitchenham BA, Pfleeger SL, Pickard LM, Jones PW, Hoaglin DC, Emam KE, Rosenberg J (2007) Preliminary guidelines for empirical research in software engineering. IEEE Trans Softw Eng 28:721–733

5. Arcuri A, Briand L (2011) A practical guide for using statistical tests to assess randomized algorithms in software engineering. ICSE'11, Honolulu, USA, 21–28 May 2011
6. Boehm B, Abts C, Chulani S (2000) Software development cost estimation approaches: a survey. Ann Soft Eng 10:177–205
7. Lopez-Martin C (2011) A fuzzy logic model for predicting the development effort of short scale programs based upon two independent variables. Appl Soft Comput 11:724–732
8. Garcia-Diaz N, Lopez-Martin C, Chavoya A (2013) A comparative study of two fuzzy logic models for software development effort estimation. Procedia Technol 7:305–314
9. Lopez-Martin C, Isaza C, Chavoya A (2012) Software development effort prediction of industrial projects applying a general regression neural network. Empirical Softw Eng 17:738–756
10. Specht DF (1991) A general regression neural network. IEEE Trans Neural Netw 2:568–576
11. Foss T, Stensrud E, Kitchenham B, Myrtveit I (2003) A simulation study of the model evaluation criterion MMRE. IEEE Trans Softw Eng 29:985–994

Chapter 108
EBRP: Evolutionary Backup Routing Protocol for Mobile Ad Hoc Networks

A. Samuel Chellathurai and E. George Dharma Prakash Raj

Abstract Evolutionary backup routing protocol for mobile Ad hoc network is developed by adding backup routes and efficient route discovery mechanism. This paper utilizes Genetic Algorithm to find the optimal path from the route discovery. These optimal paths are not only shortest paths, it is the shortest end to end delay path and that can transmit more amount of data in the network with maximum packet delivery ratio and minimum packet loss. Moreover alternate paths can be used from the backup paths in case of link failure occurrence and it avoids reroute discovery process.

Keywords Ad hoc network · Genetic algorithm · Optimal path · Backup route

108.1 Introduction

Wireless network enables communication between computers using standard network protocols, without network cabling. There are two kinds of wireless networks viz. Access point and Ad hoc networks [1]. In access point, wireless network uses an access point or base station, which acts as hub providing connectivity between two different nodes, wired and wireless LAN, a node and wireless LAN [2], etc., In ad hoc networks, direct communication between nodes are possible by using

A.S. Chellathurai (✉)
Department of Information Technology, James College of Engineering and Technology, Nagercoil, India
e-mail: samuelbhc@yahoo.com

E.G.D.P. Raj
Department of Computer Science and Engineering, Bharathidasan University, Tiruchirappalli, India
e-mail: georgeprakashraj@yahoo.com

C. Kamalakannan et al. (eds.), *Power Electronics and Renewable Energy Systems*, Lecture Notes in Electrical Engineering 326, DOI 10.1007/978-81-322-2119-7_108

wireless network interface cards, without any access points. Mobile ad hoc network (MANET) is a flexible, self organizing wireless network containing wireless mobile nodes [3] which has no centralized control or any specific infrastructure. Every node that participates in the network acts as both systems and routers. The communication is achieved through either through single-hop transmission if the source node is within the transmission range of source node, or the relaying through intermediate nodes. Each movement of the host affects the topology of the network and the route of transmission [2]. This paper is organized as follows: Sect. 108.2 provides a discussion on work related to the existing routing protocols and working of genetic algorithm and its features. Section 108.3 provides proposed new protocol, Evolutionary Backup Routing Protocol and its working. Section 108.4 provides implementation and result analysis. Section 108.5 gives the conclusions.

108.2 Related Work

108.2.1 Conventional Routing Protocols

Routing protocols can be broadly classified into two types. They are proactive and reactive routing protocols [4]. Proactive or table-driven protocols try to maintain routes to all the nodes in the network at all times by broadcasting routing updates. On the other hand, reactive or on demand protocols attempt to find a route to the destination, only when the source has a packet to send to the destination. Proactive protocols maintain the routing information of one node to the other using routing tables. Whenever there is a need for the route to the destination, it is readily available incurring minimum delay. But, at the same time, they may lead to a lot of wastage of the network resources if a majority of these available routes are never used [5]. Reactive protocols are usually associated with less control traffic in a dynamic network.

108.2.2 Genetic Algorithmic Approach

In Genetic Algorithm (GA), the paths obtained from route discovery phase are considered as initial chromosomes [6]. For an obtained solution, quality can be evaluated accurately with the help of fitness function [7]. The goal of using GA is to find the shortest path, and lowest throughput between source and destination.

108.3 Evolutionary Backup Routing Protocol

In this paper a new protocol called Evolutionary Backup Routing Protocol (EBRP) is proposed for MANET. It is developed by adding backup routes [8] and efficient route discovery process with the help of GA [9]. It discovers multiple routes from source to destination in order to store a backup route [10], which can be used in case of link or node failure, which avoids the reroute discovery phase. AODV [11] protocol is used as the source protocol for the proposed system. This proposed protocol has optimum path and backup path as two main modules.

108.3.1 Optimum Path

GA can be used to find the optimal path from the available multiple paths. The optimal path will be identified by considering three parameters; they are shortest path, maximum packet delivery ratio and minimum packet loss. The shortest path can be identified by considering the number of intermediate nodes. A routing path consists of sequence of nodes in network. A routing path is encoded by a string of positive integers that indicating the IDs of the nodes in the network. The length of the string should not be more than the number of nodes present in the network. In GA each chromosome represents a potential solution and this can contain more than one solution initially. The paths obtained from route discovery phase are considered as initial chromosomes. The quality of an obtained solution can be evaluated with the help of fitness function [7].

The topology of multihop networks can be specified by the directed graph G = (N, A), where N is a set of nodes (vertices), and A is a set of its links (edges). There is a cost C_{ij} associated with each link (I_{ij}). The costs are specified by the cost matrix C = [C_{ij}], where C_{ij} denotes a cost of transmitting a packet on link (I_{ij}). Source and destination nodes are denoted by S and D, respectively. Each link has the link connection indicator denoted by I_{ij}, which plays the role of a chromosome map (masking) providing information on whether the link from node i to node j is included in a routing path or not. Iij is 1, if the link from node i to node j exists in the routing path, otherwise it is 0. The fitness function can be formulated as,

$$\mathrm{F}(x) = \sum_{i=S}^{D} \sum_{\substack{i = S \\ i \neq j}}^{D} \mathrm{C_{ij}} \cdot \mathrm{I_{ij}} \tag{108.1}$$

The selection of chromosome is done on the result of fitness function. Crossover is done to find the better solution from current one. Since chromosomes are used as path structure, every time two chromosomes can be chosen for crossover. Selected chromosomes should have at least one common node. Now two sub paths from each chromosome can be exchanged with respect to the common node [9].

108.3.2 Backup Path

Backup path is used to choose the alternate path to be used in case of optimal path failure. The alternate path will be next best path when compared to the optimal path. There are many reasons for the link failure like node stability, low bandwidth, node failure and network allocation and it will be too costly for the reroute discovery again. An alternate path can be used in case of link failure instead of doing route discovery again. Hence this will provide more effective routing process even in the case of link failure [12] as shown in Fig. 108.1.

Fig. 108.1 Backup path selection

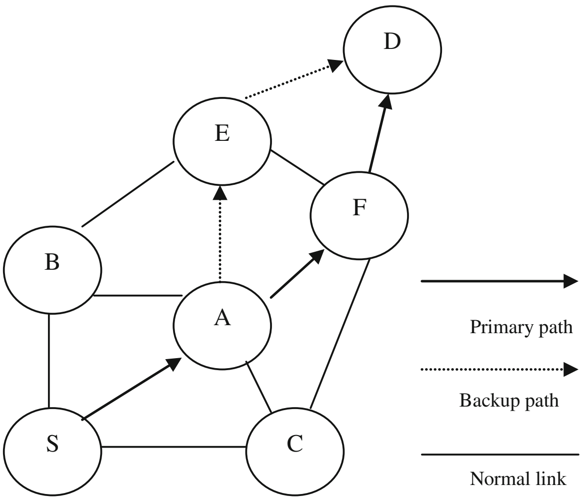

The proposed algorithm EBRP is given below to find out optimum and backup path.

Input: Source_Node, Destination_Node
Output: Path_weight

```
Step 1: [Initialization]
        For i ←0 to n-1 do
           ch[i].Gene[i] ← Node_Name;
           ch[i].Gene[i].← Weight;
Step 2: [Fitness Function]
        For i←0 to m-1 do
           For j ←0 to n-1 do
              Fittest[i] ← ∑_{i=S}^{D} ∑_{i=S, i≠J}^{D} Cij.Iij
Step 3: [Crossover]
        For i←0 to n-1 do
           For j←0 to n-1 do
              IF (ch1.gene[i] = = ch2.gene[j]) Then
                 Cross_point = i;
                 Break;
        For i←0 to n-1 do
           IF (ch1.gene[i] < = Cross_point) Then
              Tmp1.ch.gene[i] = ch1.gene[i];
              Count1++;
           Else
              Tmp2.ch.gene[i] = ch1.gene[i]
              Count2++;
           IF (ch2.gene[i] < = Cross_point) Then
              Tmp3.ch.gene[i] = ch2.gene[i];
              Count2++;
           Else
              Tmp4.ch.gene[i] = ch2.gene[i];
              Coun1++;
        For i←0 to Count1 do
           IF (Tmp1.ch.gene[i] < = Cross_point) Then
              ch3.gene[i] = Tmp1.ch.gene[i]
           Else
              ch3.gene[i] = Tmp4.ch.gene[i];
        For i←0 to Count2 do
           IF (Tmp3.ch.gene[i] < = Cross_point) Then
              ch4.gene[i] = Tmp3.ch.gene[i]
           Else
              ch4.gene[i] = Tmp2.ch.gene[i]
Step 4: [Optimal Path]
        For i←1 to m do
           For j←0 to n-1 do
              ch[i].Weight  = ∑_{i=0}^{n-1} ch[i].gene[j];
           IF (ch[1].weight < ch[2].weight && ch[1].weight<
           ch[3].weight && ch[1].weight<ch[4].weight) Then
              Path_weight= ch[1].weight;
           IF (ch[2].weight <ch[3].weight && ch[2].weight <
           ch[4].weight) Then Path_weight = ch[2].weight;
           IF (ch[3].Weight < ch[4].weight) Then
              Path_weight = ch[3].weight;
           Else
              Path_weight = ch[4].weight;
           IF (∑_{i=0}^{n-1} ch[j].gene[i] = = path_weight) Then
              Optimal_Path[i] = ch[j].gene[i];
Step 5: [Backup Path]
        For i←0 to Destination_Node do
           Source_Node ← Optimal_Path[i];
        IF (Source_Node! = Error) Then
           IF (Source_Node = = Destination_Node) Then
           Break;
        Else
           For j←1 to m do
              For i←0 to n-1 do
                 IF (ch[j].gene[i] = = Source_Node-1) Then
                    Source_Node ←ch[j].gene[i];
```

Table 108.1 Simulation parameters

Parameter	Value	Description
Simulator	NS2	Simulator tool
Simulation time	300 s	Maximum execution time
Simulation area	500 m × 500 m	Simulation area
Number of nodes	20	Number of nodes
Transmission range	100 m	Transmission range
Max speed	0,5,10,15,20 m/s	Max speed
CBR flows	20	CBR flows
Data payload	512 bytes	Data payload
Sending rate	4 packets/s	Sending rate
Movement model	Random waypoint	Movement model

108.4 Implementation and Result Analysis

To implement the proposed protocol by using NS-2, the initial simulation parameters have to be initialized before entering the simulation phase as shown in Table 108.1.

The parameters declared here are to be used in the design of network, where the protocol is going to be simulated. The protocol performance can be analyzed by considering parameters like packet delivery ratio and packet drop against time. Since the XGraph tool [13] is used, the proposed protocol EBRP is compared against the AODV protocol.

Initially Packet delivery ratio is taken as the metric and XGraph tool is used to compare two protocols. It is observed from the result that the packet delivery ratio of evolutionary backup routing protocol is high when compared to AODV protocol as shown in Fig. 108.2.

Finally Packet drop is taken as the metric and XGraph tool is used to compare the two protocols. It is observed from the result that the packet drop of evolutionary backup routing protocol is less than AODV protocol as shown in Fig. 108.3.

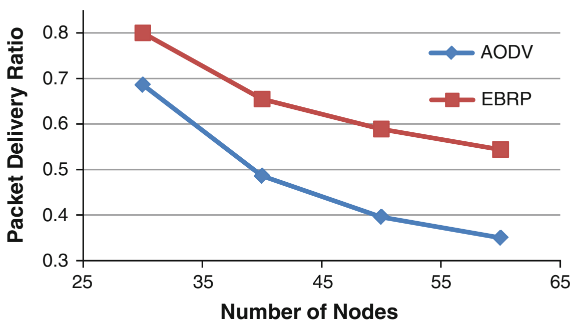

Fig. 108.2 Packet delivery ratio

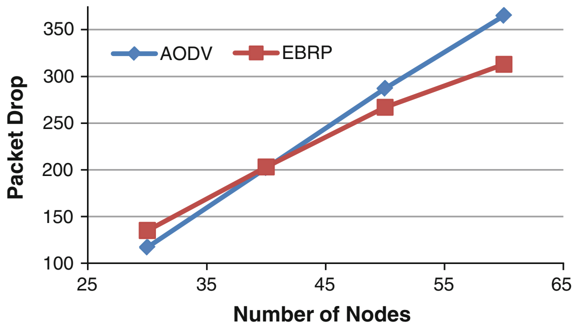

Fig. 108.3 Packet drop

108.5 Conclusion

The proposed scheme utilizes the genetic algorithm to find the optimal path from the route discovery. These optimal paths are not only shortest paths. They can also transmit more amount of data in the network with less packet loss. The alternate paths are used in case of link failure occurence and it avoids reroute discovery. Thus an efficient routing protocol has been developed for Mobile Ad hoc network. The proposed protocol is simulated using NS2 and results are obtained. From the results, it is concluded that the performance of the proposed protocol is better than existing one.

The future work of this research is to improve the performance in various aspects and to consider more number of parameter to improve the performance of the proposed genetic algorithm in order to find more accurate optimal path.

References

1. Schiller JH (2001) Mobile communications. Pearson Education, India
2. Murthy CSR, Manoj BS (2007) Ad hoc wireless networks, architectures and protocols, 2nd edn. Pearson Education, Delhi
3. Stallings W (2000) Wireless communications and networks. Prentice Hall, Englewood Cliffs
4. Royer EM, Toh CK (1999) A review of current routing protocols for Ad hoc mobile wireless networks. IEEE Pers Commun 6(2):46–55
5. Yu KM, Yu CW, Yan SF (2011) An ad hoc routing protocol with multiple backup routes. Wirel Pers Commun 57(4):533–551
6. Sumathy S, Harsha ES, Yuvaraj B (2012) Beegala survey of genetic based approach for multicast routing in MANET, vol 4, No 6, pp 474–485, Dec 2012–Jan 2013
7. Yang S, Cheng H, Wang F (2010) IEEE: genetic algorithms with immigrants and memory schemes for dynamic shortest path routing problems in mobile ad hoc networks. Proc IEEE Trans Syst Man Cybern-Part C: Appl Rev 40(1):52–63
8. Lee K (2011) A backup path routing for guaranteeing bandwidth in ad Hoc networks for multimedia applications. In: Proceedings of multimedia tools applications, 11 Jan 2011. Springer, Berlin

9. Kumar PS, Ramachandram S (2008) Genetic zone routing protocol. J Theor Appl Inf Techol 789–794
10. Huang TC, Huang SY, Tang L (2010) AODV-based backup routing scheme in mobile ad hoc networks. In: Proceedings of IEEE 2010 international conference on communications and mobile computing. IEEE
11. Chao L, Ping'an L (2010) An efficient routing approach as an extension of the AODV protocol. Proc IEEE 1:95–99
12. Lavanya G, Kumar C, Macedo arokiaraj AR (2010) Secured backup routing protocol for Ad hoc networks, In Proceedings of IEEE 2010 international conference on signal acquisition and processing, pp 45–50
13. XGraph homepage. url:www.isi.edu/nsnam/xgraph

Chapter 109
A QCP Approach for Bandwidth Reallocation in Integrated Cellular Network

C.P. Maheswaran and C. Helen Sulochana

Abstract Integrated Cellular Networks (ICNs), as part of heterogeneous networks, are usually constructed by adding ad hoc overlay on cellular networks to solve present issues and improve network performance. Routing plays an important role in such systems. In some cases, Origin nodes are unknown by the system, and need to be pre-decided prior to a route discovery process. Quasi-source Chosen Procedure (QCP) are proposed for routing process in ICNs. By evaluating the performance of QCP, a routing protocol in ICNs can choose one according to its own design purposes.

Keywords QCP · ICN · Bandwidth reallocation · Routing

109.1 Introduction

Now a day, wireless networks have made incredible progress with both the worldwide upgrade of cellular networks to support wide-area network and the widespread deployment of IEEE 802.11-based local area networks. However, there are quite a few important differences between the current local-area wireless networks and wide-area. First, while wide-area wireless networks provide large cell coverage (limit up to 20 km), the cell coverage in local-area wireless networks is limited up to 250 m for IEEE 802.11. Third, while wide-area wireless networks

C.P. Maheswaran (✉)
Department of Computer Science and Engineering, Noorul Islam Centre for Higher Education, Thuckalay, Kanyakumari, Tamil Nadu, India
e-mail: maheswaran_ncp@yahoo.co.in

C. Helen Sulochana
Department of Electronics and Communication and Engineering, St. Xavier's Catholic College of Engineering, Chunkankadai, Kanyakumari, Tamil Nadu, India
e-mail: helenrajan@yahoo.com

C. Kamalakannan et al. (eds.), *Power Electronics and Renewable Energy Systems*,
Lecture Notes in Electrical Engineering 326, DOI 10.1007/978-81-322-2119-7_109

operate in infrastructure mode with fixed base stations serving mobile users, local area wireless networks can operate in ad hoc mode where mobile clients relay packets for each other over multi-hop wireless links.

The capacity of a cellular network can be enhanced by creating a larger number of smaller cells, each of which houses an expensive base station (BS). The benefit of such an approach is the increased spatial reuse of the spectrum. Alternatively, in order to improve spatial reuse, cellular networks may be augmented with ad hoc wireless connectivity; this is attractive as compared to the former approach in terms of the incurred cost. The major drawbacks of present cellular networks encourage people to integrate current cellular networks with other network systems like ad hoc networks, iCAR (Integrated Cellular and Ad Hoc Relaying System) [1] and MADF (Mobile-Assisted Data Forwarding) [2]. To setup relaying routes, routing protocols has to accommodate the heterogeneous network architecture (such as DARP in [3]).

Although several routing protocols [4] for heterogeneous networks have been proposed [1, 2], the source selection in heterogeneous network routing needs to take further steps for improving the performance of ICNs. Before the start of a route discovery process, a source needs to be identified. And a proper choice of such a source node plays a critical role. This paper proposes Quasi-source Chosen Procedure QCP and investigates their performance under different network circumstances.

109.2 Preliminary

iCAR-FA is proposed to solve congestion problems in hot cells. Similar to iCAR, iCAR-FA deploys TDS's in managed locations [5] so that MH's in a hot cell can utilize the bandwidth from a cold cell by accessing to TDS's and through relaying routes (which are constructed by TDS's and MH's). For a more efficient use of out-of-band frequencies, TDS's should prefer communicating through A interface rather than through C-interface. Besides, relaying routes in iCAR-FA are composed of both TDS's and MH's with A-interface, not just TDS's. By this means, the number of TDS's added in iCAR-FA can be reduced, and relaying routes could be constructed more easily and flexibly.

In iCAR-FA [6, 7], if a MH in a hot cell is within the transmission range of a TDS, it can directly access to the TDS and makes a call by utilizing the bandwidth from a cell with enough free bandwidth through a relaying route. However, due to the limited number and transmission range of TDS's, MH's within the area uncovered by TDS's are not able to directly divert their calling traffic through relaying routes. In this situation, the home BS (BS1) chooses a pseudo source to release its occupied bandwidth for the use of the original source (MH1) just after the pseudo source starts diverting traffic through a discovered relaying route. Pseudo sources are those MH's within the coverage of TDS's. Whereas, the presence of more than one pseudo sources requires that the home BS chooses only one pseudo source to start a route discovery and divert its traffic, because many pseudo sources could cause a heavy routing overhead brought by the route discovery process. Hence, QCP need to be applied to choose a reasonable pseudo source from lots of available pseudo sources.

109.3 System Model

This section discusses the process of reallocating the bandwidth (Resource) released by the Quasi-source and the operation of conventional Method. In a congested cell, in order to allocate a bandwidth for the use of a MH uncovered by TDS's, a quasi-source is chosen by the home BS to release its occupied bandwidth without interrupting the present communication of the quasi-source.

Suppose assume that a MH in congested cell is uncovered by any TDS's, it sends a Quasi-Source Request (QS_REQ) to the home BS as trying to make a call. After receiving a QS_REQ, the home BS broadcasts a MH List Request Packet (MHL_REQ) to all TDS's within the home cell. Once a TDS receives a MHL_REQ, it broadcasts a Adjacent Node Detection Request Packet (AND_REQ) to all MH's within its coverage, which respond Adjacent Node Reply Packets (AN_REP) to the TDS. Then, the TDS return a list of MH's to the home BS by sending a MH List Reply Packet (MHL_REP), which contain the TDS bandwidth status. After receiving the MHL_REP's from the TDS's entire upper bounded to a timeout, the home BS applies a rational QCP to analyze the information included in MHL_REP's so as to choose a proper quasi-source. Following this, the home BS sends a Quasi-Source Reply Packet (QS_REP) to the decided quasi-source so that the quasi-source begins a route detection process by broadcasting Path Request Packets (PREQ). After receiving Path Reply Packets (PREP), the quasi source releases its occupied bandwidth and starts diverting its calling traffic through a relaying path. Finally, the home BS reallocates the released bandwidth to the original source.

109.3.1 Resource Reallocation via QCP

As mentioned above, QCP's are modeled to execute in BS's. The goal of QCP is to decide quasi-sources to improve the overall performance of the system. Additionally, the operation of QCP depends on the information contained in MHL_REP packets (contains the free Bandwidth info, TDS Identifier, MH ID List) (Fig. 109.1).

After receiving MHL_REP packets, the home BS gets a giant list of MHs. In fact, a source node should satisfy the requirements that a source node is an MH within the transmission range of the home cell, and a source node should be covered by at least one TDS. Hence, the home BS chooses all the MHs, which fulfill the basic requirements, to build up a table of available source nodes. Then,

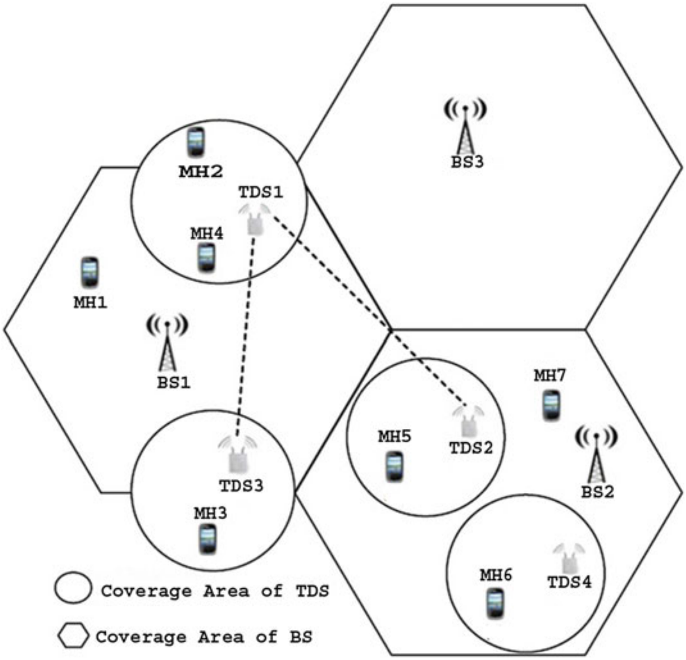

Fig. 109.1 Physical and route layout of ICN

the home BS chooses a final source node to divert its traffic according to a QCP procedure.

As shown in Table 109.1, MH_i indicates Mobile Host Address, TDS_{ij} is the address of a reachable TDS of MH_i, TDS^D_{ij} indicates the Demand Denial Rate DDR of TDS, B_{ij} refers offered bandwidth of reachable TDS_{ij} *of* MH_i, N_i indicate the reachable TDS. In order to compute the weight factors $W_i(P^R_{MH_i}$ *and* $B_{MH_i})$ of quasi source, the following procedure are as follows:

Step 1: **Intialization**—Assume that the DDR probability of TDS^D_{ij} is P^D_{ij} $\left(0 \le P^D_{ij} \le 1\right)$. DDR of MH$_1$ and MH$_2$ is $P^D_{MH_1} = P_{11}$ and $P^D_{MH_2} = P_{21}P_{22}P_{23}$, when the value of of $P^D_{ij} \le 1$. In general DDR of MH$_1$ can be represented as $P^D_{MH_i} = P_{i,1\ \le\ j\ \le No\ of\ reachable\ TDS}$

Table 1 Status of MHL_REP Packet

BS /TDS	BW status	Coverage node	Visitor node
BS$_1$	B_{BS1}	MH_1, MH_4	MH_2, MH_3
TDS$_1$	B_{TDS1}	MH_2, MH_4	–
TDS$_3$	B_{TDS3}	MH$_3$	–
BS$_2$	B_{BS2}	MH_5, MH_6, MH_7	–

Step 2: **Constraints**—Suppose if the value of P_{11}, P_{21}, $P_{22}\, and\, P_{23}$ are equal then it indicates that $P^D_{MH_1} \geq P^D_{MH_2}$ and if $TDS_{MH_i} = N_i$ then $P^D_{MH_i} = P_{i1}P_{i2}\ldots P_{iN}$. This step focuses on finding source nodes with maximum number of reachable TDSs, but may cause that diversion traffic floods some TDSs and lets the bandwidth of other TDSs unused. Since the current diversion traffic in the home cell is the difference between the current traffic load in a certain cell and the maximum traffic load that a BS can burden without traffic diversion (Current traffic load should be greater than Maximum load in Source) then

$$if\ \ T_{Needed} - T_{maximum} \leq \sum_{i=\omega}^{N} T_{TDS}\, N_i \quad then\ N_a = \omega \tag{109.1}$$

$$if\ \ T_{Needed} - T_{maximum} \geq \sum_{i=\omega}^{N} T_{TDS}\, N_i \quad then\ N_a = 0 \tag{109.2}$$

where T_{Needed} indicates current traffic in a certain cell, $T_{maximum}$ indicates maximum traffic that a BS can burden without traffic diversion, T_{TDS} indicates the number of TDSs covering MHs with i reachable TDSs and N_i indicates the maximum traffic that a TDS can burden.

Step 3: **Computation**—In order to find the average bandwidth of all reachable TDS of an offered quasi-source is

$$B_{MH_i} = \frac{\left(\sum_{j=1}^{N-1_i} B_{N-1_{ij}} + B_{N_{ij}}\right)}{No\ of\ reachable\ TDS\,(N_i)} \tag{109.3}$$

Step 4: **Integration**—Finally Integrated factors of Weight $W_i = \left(1 - P^D_{MH_i}\right) * B_{MH_i}$ where $\left(1 - P^D_{MH_i}\right)$ denotes the successful discovery of relaying route. The above mentioned computation can be reduced as follows: First arrange the MH in terms of reachable TDS and then in terms of average bandwidth of reachable TDS in descending order. Finally the combined weight factor of MH_i is simplified as $W_i = \rho_{TDS}\, \rho_{BW}$.

After applying Integration process, more than one quasi-source may still exist. A final source node still could not be specified because some MHs may have the same value of weight during obtain the calculation of Integration process. Therefore after Integration process, the mobility [8] and location information (Selection Process) of MHs could be taken into consideration for the further selection of source node.

Step 5: **Selection**—The main idea of Selection process is to choose MHs with the most possibility of moving out of the home cell during call time, because MHs will automatically release its occupied bandwidth and use the bandwidth from the adjacent BSs as they move to the neighbor cells. To simplify the analysis, we assume that the shape of the home cell is a circle with a transmission radius as R (instead of a hexagon with a centre-to-vertex distance as R). Also, the moving field of an MH is assumed as a circle with a radius r, which indicates that the MH moves

Fig. 109.2 Mobility analysis based on quasi-source

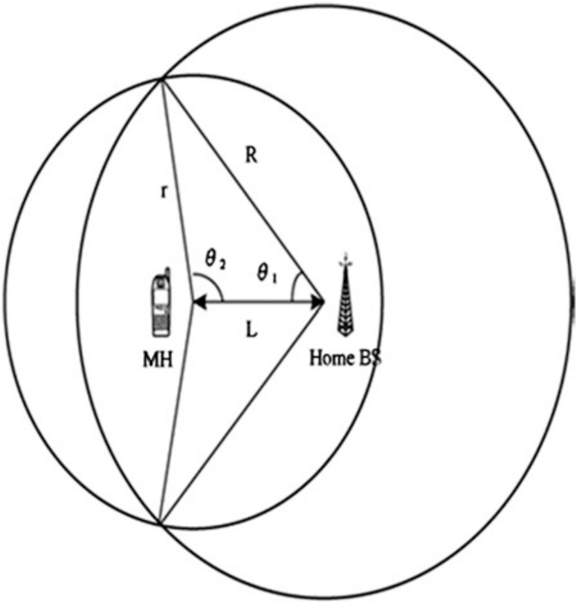

under a random direction model. As shown in Fig. 109.2, L indicates the distance between the home BS and an MH. By analyzing Fig. 109.2, the probability of MH_i moving outside the home cell (P_{M_i}) equals to the area of the MH_i's moving field outside the home cell (A_{out}) divided by the overall area of the MH_i's moving field (A_m), namely

$$P_{M_i} = {}^{A_{out}(MH_i)}\!/_{A_m(MH_i)} \tag{109.4}$$

Also, the moving radius of MH_i (r) is the speed of MH_i (S_i) multiplied by the average call time (T_C). In fact, T_C is a statistical value calculated by BS's [8]. For example, T_C could be the average value of last N_{call} calls, namely

$$T_C = \frac{\sum_{i=1}^{N_C} T_i}{N_{call}} \tag{109.5}$$

The speed of MH_i could be also calculated as the result of the moving distance of MH_i during a period from t_1 to t_2 ($D = \sqrt{(\Delta x)^2 + (\Delta y)^2}$) divided by the moving period (Δt) [7], namely $S_i = {}^{D}\!/_{\Delta t}$. Where ($x_1$, y_1) is the location of MH_i at t_1 and (x_2, y_2) is the location of MH_i at t_2. The location information [9, 10] of a certain MH can be obtained by many ways, such as [11]. Hence, L could also be computed according to the locations of MH's and BS's. According to P_{M_i} and T_C we have $A_m = \pi r^2$ where$r = S_i T_C$. In terms of A_{out}, it can be equal to the result of (A_m)

minus the area of the MH_i's moving field inside the home cell. As shown in Fig. 109.2.

$$\theta_1 = \cos^{-1}\left(\frac{R^2 + L^2 - r^2}{2RL}\right) \, and \, \theta_2 = \cos^{-1}\left(\frac{r^2 + L^2 - R^2}{2rL}\right) \tag{109.6}$$

Then

$$A_{in} = \theta_1 R^2 + \theta_2 r^2 - (R^2 \sin\theta_1 \cos\theta_1 + r^2 \sin\theta_2 \cos\theta_2) \tag{109.7}$$

Finally, we have

$$P_{M_i} = 1 - \frac{A_{in}}{\pi r^2} \tag{109.8}$$

where $r^2 = S_i^2 T_C^2$. According to the formula given above, the probability of MH_i moving out (P_{M_i}) can be calculated. Thus, MHs with maximum P_{M_i} are chosen as source nodes. If the number of MHs with maximum P_{M_i} is still more than one, MHs with the farthest distance from the home BS are chosen as quasi-sources. Alternatively, we could also randomly choose one of the MHs left after all selections.

If a network has a low overloaded traffic, or the number and the bandwidth of TDSs are enough, we can use Step 1 and 2 (Integration and Constraints) to choose quasi-sources. In contrast, Steps 3 (Computation) is suitable for networks with limited number of TDSs and high overloaded traffic. Step 4 (Integration) could be applied to networks with intermediate overloaded traffic.

109.4 Performance Evaluation

We considered the QCP in terms of the average DDR of the overall network and the signaling overhead both in home BS and TDSs. The numerical model is built using NS2. The coordinates and bandwidth values for both 'home BS' and 'TDS' are pre-allocated. Each MH is organized randomly, and the demanded bandwidth of every call is identical. For our convenience here we consider eight TDSs organized in the home BS. The maximum traffic that a BS can carry without traffic diversion is $T_{\max} = 100$ Erlangs. The maximum traffic that a TDS can burden is $T_{TDS} = 10$ Erlang. The average traffic of each call is 1 Erlang. The average DDR of TDSs is P = 0.5. The average number of MHs within the transmission range of TDSs is 15.

Because the DDR in QCP (Integration) fluctuates stuck between a maximum and a minimum value, we only compute the average value of QCP (Integration) during the evaluation. Considering the signaling overhead analysis, we calculate the average signaling overheads required for one successful bandwidth re-allocation at each certain traffic level, and the amount of signaling overheads is only related to the number of TDSs and MHs without the consideration of collision. Because QCPs that run in home BS are centralized algorithms, the signaling overheads introduced by QCPs are used to collect the network information for the decision of quasi-sources. Hence, the signaling overheads in QCP (Step 1, 2 and 3) are identical due to the same method used for collecting the network information.

According to Fig. 109.3, the average DDR in QCP—Computation Process remains stable (at 0.20 in this case), because source nodes are chosen only according to the bandwidth status of TDSs, not according to the number of reachable TDSs. Supposing the average DDR of TDSs is 0.5 as designed above and all neighbor cells have enough free bandwidth to support diversion traffic, the DDR of a call is only related to the number of its reachable TDSs. If a TDS has some free bandwidth unused, it can still divert traffics from MHs. When the diversion traffic is low, the DDR in QCP (Step 1, 2 and 4) stays at a low level (at 0.13 in this case), compared with that in QCP Step 3. However, as the traffic diversion in the home cell goes up, the average DDR in Step 4 jumps to an intermediate stage (at around 0.21 in Fig. 109.3) because the bandwidth balancing among the TDSs causes QCP Step 3 to choose source nodes with less number of reachable TDSs. In QCP Step 1 and 2, with the increase in the diversion traffic, more and more TDSs are blocked due to the partial selection of TDSs. The congestion of TDSs causes a high average RRR of TDSs. Thus, the DDR in QCP Step 1 and 2 increases rapidly with increase in the diversion traffic (from 30 to 60 Erlangs). In addition, the DDR in both QCP step 3 and 4 only rises sharply as the diversion traffic increases to a very high level (at around 72 Erlangs in this case), because the balance of the bandwidth consumption of TDSs results in only very high diversion traffic congesting TDSs. As more TDSs become congested, the average DDR increases accordingly. Hence, if TDSs have limited available bandwidth, QCP Step 3 and 4 could be used to choose quasi-sources to avoid congesting TDSs. If the diversion traffic in a network is not high, QCP Step 1 and 2 can be adapted to achieve a low DDR of the system.

Fig. 109.3 DDR analysis

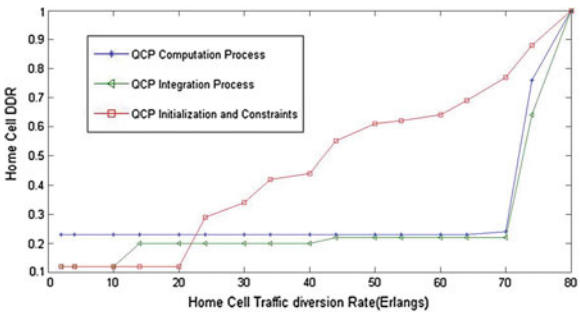

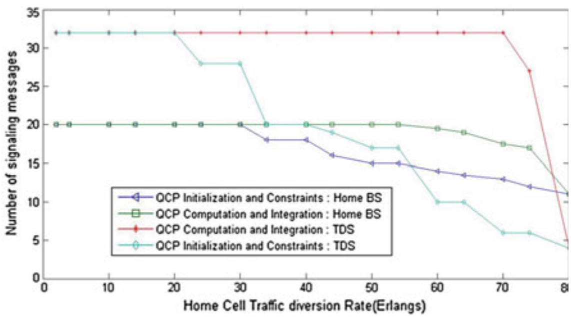

Fig. 109.4 Signaling overheads (both in home BS and TDS)

In respect of the signaling overhead, the number of signaling messages which home BS in QCP Step 1 and 2 needs to process decreases as the diversion traffic increases (Fig. 109.4). This is because more diversion traffic from the Home BS could cause more TDSs being congested due to the lack of bandwidth balance among TDSs in QCP Step 1 and 2, and more congested TDSs lead to more dropping of signaling messages and as such less signaling messages being eventually transmitted. However, because both Step 3 and 4 of QCP can balance the consumption of bandwidth among TDSs, the number of signaling messages decreases only when diversion traffic goes very high (at around 72 Erlangs as in Fig. 109.4). As mentioned above, as signaling overheads are only related to the number of TDSs or MHs, the overheads drop only when the number of available TDSs or MHs goes down. Then, the signaling messages which home BS in QCP Step 3 or 4 needs to process decreases only when the amount of the diversion traffic is very high. In normal cases, the numbers of neighbor MHs are more than the number of TDSs. To achieve a small amount of signaling overheads, QCP step 1 and 2 can be applied, but this may cause a higher request rejection rate, compared with Step 3 and Step 4 of QCP.

109.5 Conclusion

This paper mainly focuses on the QCP part of routing protocols in ICNs. QCP algorithm is designed to execute in BSs to choose quasi-sources to divert their calling traffic. QCPs aim to choose source nodes that have the maximum possibility of successfully detecting relaying routes. Moreover, the source node selection in QCPs also tries to stabilize the bandwidth of TDSs, which is used for traffic diversion. Based on the quantity and bandwidth of TDSs, network planners can choose a reasonable QCP to achieve a relatively low call block rate. Alternatively, by estimating the amount of overloaded traffic, planners can choose a QCP to reduce the number of TDSs deployed in each cell.

References

1. Cavalcanti D, Agarwal D (2001) Issues in integrating cellular networks WLAN's & MANET's. IEEE Wirel Commun
2. Cavalcanti D, Cordeiro CM, Agrawal DP, Xie B, Kumar A (2007) Issues in integrating cellular networks, WLANs, and MANETs: A futuristic heterogeneous wireless network. IEEE Wirel Commun Mag 12(3):30–41
3. Wu H, Qiao C, De S, Tonguz O (2008) Integrated cellular and ad hoc relaying systems: iCAR. IEEE J Sel Areas Commun 19(10):2105–2115
4. Carbone B (2006) Routing protocols for interconnecting cellular and ad hoc networks. Universite Libre De Bruxeles, Faculte des Sciences, Department 'd Informatique, 2006. Tavel, P. 2007 modeling and simulation design. AK Peters Ltd
5. Hu W, Qiao C, De S, Tonguz O (2009) Integrated cellular and ad hoc relaying systems: iCAR. IEEE JSAC 19(10):2105–2115
6. Samad BM, Ibrahim C, Kazi Ahmed (2010) A review of routing protocols of heterogeneous networks. Int J Comput Appl 58–66
7. Ko Y, Vaidya NH (2009) Location-aided routing (LAR) in mobile ad hoc networks. In: Proceedings of the ACM/IEEE international conference on mobile computing and networking (mobilcom). pp 66–75
8. Wu Y, Yang K (2006) An adaptive routing protocol for an integrated cellular and ad-hoc network with flexible access. IWCMC 2006 conference, Vancouver Canada, 3–6 July 2006
9. George A, Kumar A, Cavalcanti D, Agrawal PD (2008) Protocols for mobility management in heterogeneous multihop wireless networks, published in pervasive and mobile computing, science direct, pp 92–116
10. Hightower J, Borriello G (2001) A survey and taxonomy of location systems for ubiquitous computing. Technical report UW-CSE 01 Aug 03, 24 Aug 2001
11. Xiao Y, Pan Y, Li J (2004) Design and analysis of location management for 3G cellular networks. IEEE Trans Parallel Distrib Syst 15(4)

Chapter 110
A Grade Prediction Methodology for Astrocytoma Using Modified K-Clustering Network

M. Monica Subashini, Sarat Kumar Sahoo, S. Prabhakar Karthikeyan and I. Jacob Raglend

Abstract The proposed method predicts the grade of astrocytoma based on certain features extracted from magnetic resonant images. MR brain images of three views namely Axial, Sagittal and Coronal are considered for perfect grade evaluation of astrocytoma. Gray level co-occurrence matrix is utilized for feature extraction. The extracted features are subjected to classification through a classifier which predicts the grade. Fuzzy logic classifier and K-Clustering network are the most used classifiers for prediction of grades among many available. The performances of the techniques are evaluated through discussions with neuroradiologist to find their accuracies. A modified K-Clustering network is developed to give a better diagnosis for predicting the grades of astrocytoma.

Keywords Brain MR images · Gray level co-occurrence matrix · Feature extraction · Classifiers · Grade prediction

110.1 Introduction

Artificial neural networks are applied for the analysis of medical images (MRI). They are efficiently used in tumor detection, classification of cancer, tissue classification, pattern recognition, face recognition and many more applications. In the

M. Monica Subashini (✉) · S.K. Sahoo · S. Prabhakar Karthikeyan
School of Electrical Engineering, VIT University, Vellore, Tamil Nadu, India
e-mail: monicasubashini.m@vit.ac.in

S.K. Sahoo
e-mail: sksahoo@vit.ac.in

S. Prabhakar Karthikeyan
e-mail: spk25in@yahoo.co.in

I. Jacob Raglend
NI University, Kumarakovil, Thuckalay, Kanyakumari, Tamil Nadu, India
e-mail: jacobraglend@rediffmail.com

C. Kamalakannan et al. (eds.), *Power Electronics and Renewable Energy Systems*,
Lecture Notes in Electrical Engineering 326, DOI 10.1007/978-81-322-2119-7_110

proposed work, the problem taken was to predict the grade of astrocytoma (glioma). Glioma is a tumor that originates from glial cells in brain [1]. Glioma is treatable and curable if detected at the earliest stages. A thorough physical examination would be the first step and it is followed by neurologic exam, a CT scan, Magnetic Resonant Image which shows the presence of a tumor, angiogram, skull x-ray, spinal tap (test on cerebrospinal fluid), myelogram and finally biopsy. Biopsy would confirm the tumor as malignant or benign.

Several automated methods as shown in [2–4] are available for the detection and grade prediction of tumors and every day some new technique has been applied for improving the accuracy of performance measures in tumor assessment with the aid of magnetic resonant brain tumor images [5]. Classifiers are developed based on artificial neural networks as in [6, 7] which generally yield accurate results. Some advanced techniques like machine learning and fuzzy logic are applied for better prediction of grades in tumors and it is proved in [8, 9]. Astrocytoma grade detection and prediction involves feature extraction, feature selection and classification. GLCM is a technique which extracts features from MR brain images and the features that showed major variation between grades are selected. In the first phase, the selected features are the inputs to fuzzy logic classifier and K-Clustering network. Depending on the feature values, tumor grades are predicted as per the rules assigned. The accuracy of prediction was analyzed with the help of neuroradiologist. In the second phase, based on their (physicians) feedback and suggestion, a modified K-Clustering network was developed to grade the brain MR images accurately from normal to all other grades (I/II/III/IV).

110.2 Proposed Methodology for the Grade Prediction Process

The objective of the proposed work is to predict the grade of astrocytoma and to differentiate normal brain from abnormal MR image. The images are preprocessed to enhance the quality of the magnetic resonant brain images which is followed by feature extraction. A normal brain image shows considerable difference when compared with diseased brain image. This difference deflects in the extracted features too. The feature values are different for each grade. This could be utilized for grade prediction. The extracted features are then subjected to classification. Figure 110.1 shows the process involved in grade prediction.

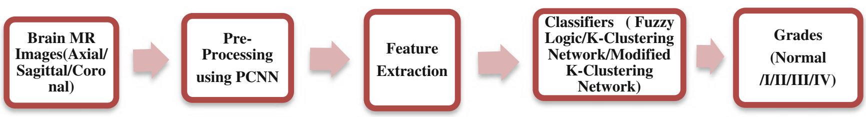

Fig. 110.1 Grade prediction process

Table 110.1 Testing input images

Grade	Plane (view)	No. of images collected
Pilocytic astrocytoma	Axial	5
	Sagittal	5
	Coronal	5
Low Grade Astrocytoma	Axial	5
	Sagittal	5
	Coronal	5
Anaplastic astrocytoma	Axial	5
	Sagittal	5
	Coronal	5
Glioblastoma Multiforme	Axial	5
	Sagittal	5
	Coronal	5
Normal	Axial	5
	Sagittal	5
	Coronal	5

110.2.1 Dataset

The magnetic resonance images were downloaded from MedPix [10], an online image database and a dataset had been developed which comprises of normal and abnormal (astrocytoma) T1/T2 images.

The abnormal set comprises of 60 patients' brain images as shown in Table 110.1. Figure 110.2a–c, shows the Grade I astrocytoma images. Similarly, the database consists of Grade II, Grade III and Grade IV diseased MR images.

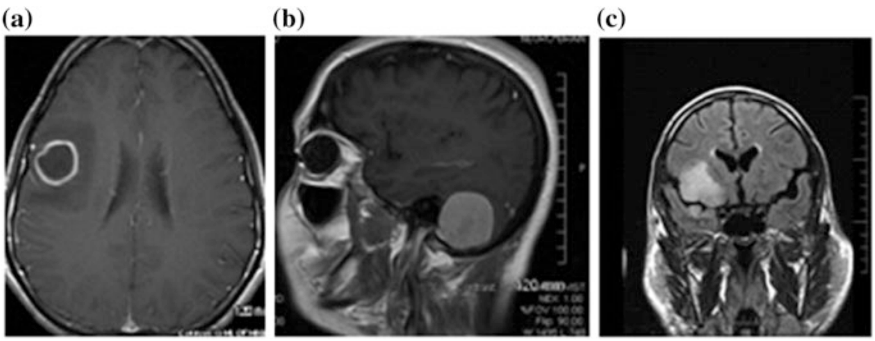

Fig. 110.2 Grade I (pilocytic astrocytoma). **a** Axial view, **b** sagittal view, **c** coronal View

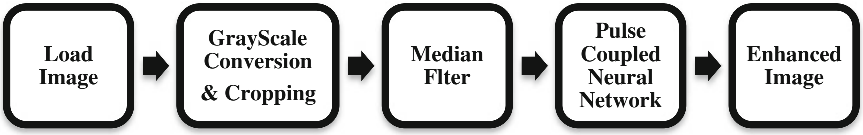

Fig. 110.3 Preprocessing procedure

110.2.2 Pre-processing

The dataset has to be processed to remove the header which contains patient detail. The loaded brain MR image from the dataset is converted to binary and subjected to cropping. A median filter and Pulse coupled neural network are utilized in noise removal [11] and image enhancement [12]. The process is highlighted in Fig. 110.3: Preprocessing Procedure.

110.2.3 Feature Extraction

Feature extraction is a very important task in the grade prediction because the classifier would depend only on the features for clustering the data into groups. Gray-level co-occurrence matrix (GLCM) is a statistical method [13] to examine and extract the features that considers the spatial relationship of the pixels. The GLCM functions which is programmed in MATLAB, characterize the texture of an image by calculating the number of times pairs of pixel with specific intensity (i) values and in a specified spatial relationship with a value (j) occur in an image, creating a GLCM, a matrix and then extracting statistical measures from this matrix. The number of rows and columns is equivalent to the number of gray level denoted by G. P(i, j) is the relative frequency. 'μ' is the mean value of P.

Six statistical features are extracted using GLCM and among them two features were selected which are more prominent in differentiating the images. The features are first order statistical textural features and are termed as variance, Skewness, Homogeneity, Entropy, Energy and Contrast. The statistical features extracted from normal, grade I, grade II, grade III and grade IV Coronal view MR brain images are consolidated in Table 110.2. The brain MR images (diseased/undiseased) vary from each other in their values (variance, skewness, entropy, energy, contrast and homogeneity). As been discussed earlier, the features are extracted with respect to axial, sagittal and coronal views.

Table 110.2 Features extracted from coronal T1-weighted images

Features	Normal images and tumor grades (I/II/III/IV)				
	Normal	Pilocytic astrocytoma	Low grade astrocytoma	Anaplastic astrocytoma	Glioblastoma multiforme
Variance	1,058	0	1,458	$3.87e^{+03}$	11,552
	2,450	98	1,682	5,832	17,298
	4,050	8,978	2,592	5,202	18,050
	8,192	512	512	648	$1.01e^{+04}$
	1,250	3,872	1,690	968	$1.19e^{+04}$
Skewness	3.45587713	2.853314	6.796607	3.135177	11.73153573
	2.04309916	3.010955	4.04737	2.298387	10.88323816
	1.95959551	4.402298	5.154393	1.406711	10.3976464
	3.99794703	3.040886	2.221032	7.311923	2.992517765
	2.23902412	4.184637	4.04837	6.264903	3.481429383
Entropy	**7.03233896**	**6.820662**	**6.990879**	**7.060418**	**6.330436241**
	6.91451956	**6.741877**	**6.711181**	**7.238955**	**6.1981448**
	6.98300189	**6.856218**	**7.071194**	**7.295703**	**6.166665685**
	6.99804007	**6.864345**	**7.176773**	**6.594138**	**$3.42e^{+05}$**
	7.26011186	**6.613638**	**6.718111**	**6.687096**	**6.863931304**
Energy	**0.2567**	**0.214**	**0.2155**	**$2.26e^{-01}$**	**0.2501**
	0.2242	**0.27**	**0.2915**	**0.1766**	**0.2532**
	0.2028	**0.2458**	**0.2183**	**0.1663**	**0.255**
	0.2078	**0.293**	**0.1622**	**0.254**	**0.2555**
	0.1696	**0.3376**	**0.2899**	**0.2551**	**0.2541**
Contrast	0.1851	0.1801	0.1856	0.213	0.1315
	0.1836	0.1645	0.1449	0.3548	0.129
	0.2779	0.1928	0.2	0.3329	0.1333
	0.2297	0.1689	0.4538	0.1811	0.1956
	0.1914	0.2677	0.1451	0.1677	0.1447
Area	$4.57e^{+05}$	$4.84e^{+05}$	160,521	$1.70e^{+05}$	195,888.125
	$4.40e^{+05}$	$4.74e^{+05}$	157,553	$1.90e^{+05}$	$2.39e^{+05}$
	$1.97e^{+05}$	$3.84e^{+05}$	$1.60e^{+05}$	$1.99e^{+05}$	2,49,652
	$3.67e^{+05}$	$4.61e^{+05}$	$4.94e^{+04}$	162,160	$3.42e^{+05}$
	$2.46e^{+05}$	345,698	156,992	$1.64e^{+05}$	$3.72e^{+05}$

110.2.4 Findings

Energy, Contrast and Entropy does not show much variation. Variance, Skewness and Area showed good variation in their values. Practically all the features would not support classification. Hence effort has to be taken to select parameters which show considerable differences. A suitable classifier has to be developed considering features that show significant difference.

110.3 Classifiers

Artificial Neural networks, evolutionary algorithms, fuzzy logic as in are generally applied for grade prediction and classification problems. In the proposed method, fuzzy logic and K-Clustering networks are utilized for the grade prediction. These networks depend on the textural features for classification.

110.3.1 Fuzzy Logic Classifier

Fuzzy logic deals with reasoning; it provides a simple way to end up with a definite conclusion based on approximate input parameters. Fuzzy logic provides a simple methodology to arrive at a quick and accurate decision. A fuzzy logic object was created with multiple inputs to perform the grade identification. The inputs are the features extracted through GLCM. Hence six inputs representing the image parameter values namely variance, skewness, energy, entropy, contrast and area are provided for the fuzzy object. Each feature input has been assigned a membership function plot representing parameter ranges. The membership function plot is named and assigned with feature ranges.

110.3.1.1 Fuzzy Rules to Assign Membership Function

1. If the input feature lies within the membership function plot range, the corresponding membership function assumes a value of ‘1’.
2. If the feature value lies outside the range specified by the membership function plot, the function assumes a value of ‘0’.

The classification is based on the ranges of six parameters instead with a single parameter. A combination of membership plot value ranges are assigned with respect to each parameter values. The individual membership function binary values are concatenated using ‘OR’ and ‘AND’ conjunctions. The grade of the tumor is labeled corresponding to each rule. The assigning of membership plots and rules are developed using FIS object editor. Matlab is eminent software and the entire programming and classifications are done using the same. The steps followed in fuzzy logic classification are given below.

- Input (Axial, Sagittal and Coronal views) images are loaded.
- Preprocessing of images (PCNN).
- Features Extracted (GLCM).
- FIS object evaluation.
- Grade Identification and classification.

110.3.1.2 Accuracy of Fuzzy Logic Classifier

The grade prediction problem could be solved only with the aid of extracted features. Table 110.2; clearly show that there are certain features which overlap in values. This creates a problem while separating the range for membership function plot. The classifier depends on membership function and hence accuracy is very less. The second challenge was weights assigning to individual features. The accuracy in classification is obviously less. The results depicted that increasing weights to certain features would definitely increase the accuracy of the classifier. A suitable network to accomplish this task is a K-Clustering network.

110.3.2 K-Means Clustering Networks

K-Means Clustering Networks generate a group of specified clusters which are disjoint, non-hierarchical. This method is an unsupervised, iterative technique. The computations are fast even if large numbers of variables are present.

$$J = \sum_{j=1}^{K} \sum_{n \in S_j} \left| x_n - \mu_j \right|^2 \tag{110.1}$$

Mathematically, the method is expressed as shown in Eq. (110.1). ‘n’ data points are chosen to be clustered into K subsets (disjoint). S_j contains the data points to be partitioned which perform the minimization of the sum-of-squares. ‘x_n’ represents the nth data point; μ_j represents the geometric centroid of the data points.

110.3.2.1 Challenges in K-Clustering Network

The k-Clustering network is not suitable with non-globular clusters. Since the feature ranges are similar, there is a possibility of forming new clusters. K-Clustering network can be used when we need to classify an image after extracting multiple parameters, a combination of which determines the category under which the image lies. The range of separation did not aid the prediction of grades. The network has to be modified according to the needs of a perfect classifier. In this regard, a modified K-Clustering network has to be developed since the extracted features do not show sufficient range separation to aid the classification of grades.

110.3.3 Modified K-Clustering Network

110.3.3.1 Motivation

The method aims to construct a classifier which accepts input images and segregates into five clusters representing normal and the four stages of astrocytoma respectively. A combination of parameters with adequate range separation was taken into account for accurate classification. The 'kmeans' function partitions the points in the n-by-p data matrix into K–clusters, based on the net closeness of values.

110.3.3.2 Procedure

1. 'n' is the number of images and 'p' is the number of parameters obtained by feature extraction.
2. The value of K is set to 5 in order to segregate the images into 5 clusters representing normal and the 4 stages of astrocytoma.
3. The value of n is set to 10 representing the number of input images.
4. The proposed method was tested with 10 images and the number of input images can be increased and the value of 'n' could be altered.
5. The required matrix may be formed by mentioning the p parameters associated with each of the n images in which case the value of p assigned will be 6 representing the number of image parameters, namely variance, skewness, energy, entropy, contrast and area. The rows of input image parameter matrix contain the extracted parameters in the same order.

110.3.3.3 Importance of Iterative Partitioning

The iterative partitioning performed by the inbuilt 'kmeans' function after accepting the image parameter matrix minimizes the sum, over all clusters, of the within-cluster sums of point-to-cluster-centroid distances, thereby organizing the images into clusters where the images have the most proximity with respect to values of all parameters. The 'kmeans' function returns a 10-by-1 vector containing the cluster indices of each image. From this vector, the index of the cluster under which each image is organized may be obtained. The vector thereby yields information about the grouping of images into clusters by the k-means function. The ‘kmeans’ function also returns the cluster centroid locations in a 5-by-6 matrix which yields information about the mean value of each parameter in each of the 5 clusters. However, the method of forming the image parameter matrix by including all the extracted parameters in each of the rows suffers from major drawbacks.

110.3.3.4 Challenges with Extracted Features

In the case of feature extraction with the given set of parameters, the values of the different parameters do not lie in the same range or even have comparable values. As a result, the ‘kmeans’ function does not consider parameters having lower values while performing the classification and the classification is done on the basis of the values of parameters having higher values alone. In order to overcome this problem, the values of parameters must be normalized so that parameters having greater values are not given unduly high weightage.

110.3.3.5 Solution

To perform this, the image parameter matrix is broken down column wise to form six new image parameter matrices representing each of the image parameters, namely variance, skewness, energy, entropy, contrast and area. In this modified method, shown in Fig. 110.4, the images were segregated into clusters based on individual parameters by applying the ‘kmeans’ function to each of the six new image parameter matrices. The vectors which return the cluster indices corresponding to each image can be operated upon to yield the weighted mean clustering indices.

110.3.4 Implementation

This is done by computing the weighted mean of cluster indices of each image from the vectors returned by the ‘kmeans’ function corresponding to each of the image parameter matrices. Variance, skewness and area were assigned greater weights as they showed better parameter separation. The weighted mean clustering indices still do not show enough range separation to classify the image easily through conditional statements. The classification of a particular image is found to be a function of both the weighted mean clustering index and the value of its extracted features. To obtain a measure of its extracted parameters, the average normalized value of the extracted image parameters is computed. Since the values of the extracted parameters are not comparable, each of the parameter values is divided by a value such that the resultant value lies between 0 and 2, thereby assigning equal weights to all the parameters.

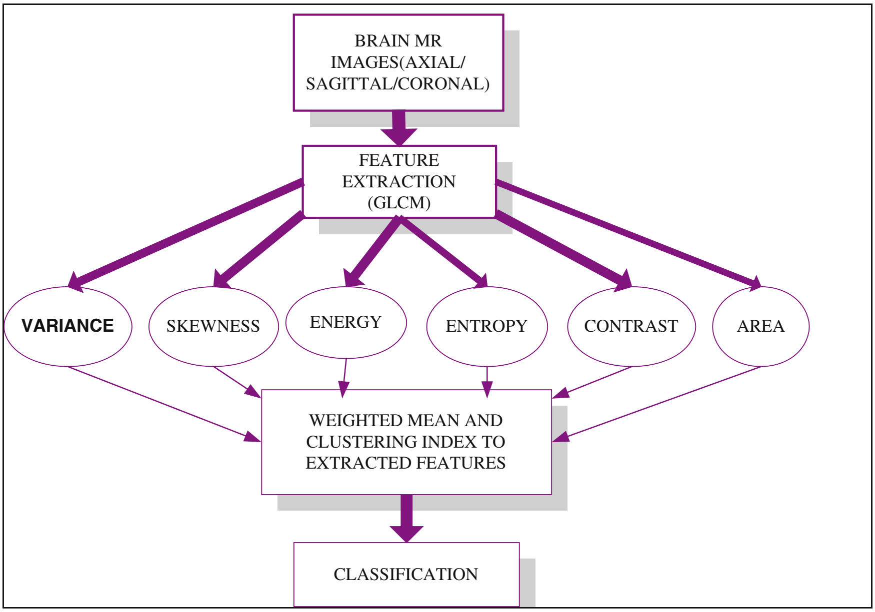

Fig. 110.4 Modified K-Clustering network

110.4 Discussion and Results

While constructing the classifiers based on the feature extraction, it was noticed that no single feature gave perfect range separation between different stages for any of the three views. Hence it was necessary to use combination of parameters to determine the stage of astrocytoma. Before constructing classifiers, the ranges for parameters were assigned which would determine the grade of tumor. The assigned parameter ranges for four grades were verified using programs with conditional statements. As the parameter ranges varied for all the three views, there had to be a program for each of the three views. Through rigorous testing and discussion with neuroradiologist, a program was developed which supported all the three views. In this modified method, Entropy and Energy values are not considered while computing the average normalized value of the image parameters because they do not show sufficient variation and taking them into account will decrease the sensitivity of the method.

To obtain a single quantity which can be used to determine the classification of the image, the product of the weighted mean clustering index and the average normalized value of the image parameters were taken. Now the image can be classified based on the range in which this quantity lies. These ranges are assigned on the basis of the values of the quantity for the test images belonging to each category. 75 images were tested and the results provided 94 % percent accuracy. The Accuracy and Performance analysis of the developed classifiers are highlighted in Table 110.3 and in Chart 110.1.

Table 110.3 Classifier results

Classifier	Number of input images	Number of rightly classified images	Number of misclassified images	Accuracy in astrocytoma grade prediction (%)
Fuzzy logic	75	60	15	80
K-Clustering network	75	62	13	83
Modified K-Clustering network	75	70	5	94

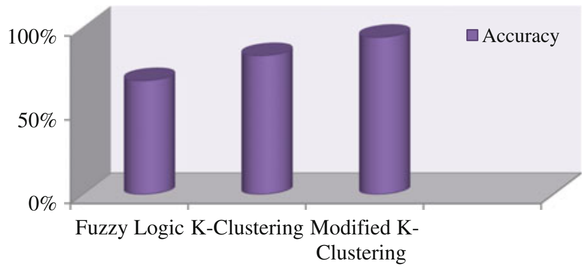

Chart 110.1 Performance analysis

110.5 Conclusion

Glioma is a type of tumor which originates from glial cells. The tumor grows gradually and it can be graded as Grade I (Pilocytic Astrocytoma), Grade II (Low Grade Astrocytoma), Grade III (Anaplastic Astrocytoma) and Grade IV (Glioblastoma Multiforme). Sagittal, Coronal and Axial views of tumor (Glioma) MR Images are subjected to pre-processing and feature extraction. Median Filter and Pulse coupled neural network is applied for image enhancement. GLCM is utilized for feature extraction. The extracted features are the key for the classification. Fuzzy logic and k-Clustering network were initially utilized and later based on the discussions with neuroradiologist; a modified method of K-Clustering network was developed to provide accurate grade prediction. This modified method of K-Clustering network is more reliable and conclusive because obtained quantity shows sufficient range separation between each category of images and there is no overlap of features which is the most important criteria for grade prediction. This method performs the classification considering each of the parameters, allowing greater weights for parameters that show better range separation. Thus the proposed work is a medical aid for physicians when huge number of data is received for grade prediction.

Acknowledgments This work has been supported by School of Electrical Engineering, VIT University and Krishna Advanced MRI & CT Scan Centre, Vellore.

References

1. Louis DN, Ohgaki H, Wiestler OD, Cavenee WK, Burger PC, Jouvet A, Scheithauer BW, Kleihues P (2007) The 2007 WHO classification of tumours of the central nervous system. Acta Neuropathol 114:97–109
2. Gondal AH, Naeem M, Khan A (2013) A review of fully automated techniques for brain tumor detection from mr images. Int J Mod Educ Comput Sci 2:55–61
3. Lin CY, Yin J-X, Ma L-H, Chen J-Y (2006) Fuzzy bayesian network-based inference in predicting astrocytoma malignant degree. In: Proceedings of the 6th world congress on intelligent control and automation (WCICA),vol 2. Article number 1714008, pp 10251–10255
4. Resmi SA, Thomas T (2012) A semi-automatic method for segmentation and 3D modeling of glioma tumors from brain MRI. J Biomed Sci Eng 5:378–383
5. Neuner I, Kaffanke JB, Langen K-J, Kops ER, Tellmann L, Stoffels G, Weirich C, Filss C, Scheins J, Herzog H, Shah NJ (2012) Multimodal imaging utilising integrated MR-PET for human brain tumour assessment. Eur Radiol 22:2568–2580
6. Li G-Z, Yang J, Ye C-Z, Geng D-Y (2004) Degree prediction of malignancy in brain glioma using support vector machines. Preprint submitted to Comput Biol Med 27
7. Xingyue J, Daoying G, Tianzhen S (2004) Predicting the malignant degree of astrocytoma with use of artificial neural networks: Pilot Study J China Med Comput Imaging 10 (4):217–220
8. Zacharaki EI, Wang S, Chawla S, Soo Yoo D, Wolf R, Melhem ER, Davatzikos C (2009) Classification of brain tumor type and grade using MRI texture and shape in a machine learning scheme. Magn Reson Med 62(6):1609–1618
9. Javed U, Riaz MM, Ghafoor A, Cheema TA (2013) MRI brain classification using texture features, fuzzy weighting and support vector machine. Prog Electromagnet Res B 53:53–73
10. MedPix online image database: http://rad.usuhs.mil/synapse/cow.html
11. Jiang J, Shen J (2010) An effective adaptive median filter algorithm for removing salt & pepper noise in images. In: Proceedings in IEEE of symposium on photonics and optoelectronics (SOPO)
12. Monica Subashini M, Sahoo SK (2014) Pulse coupled neural networks and its applications. Expert Syst Appl 41:3965–3974
13. Zulpe N, Pawar V (2012) GLCM textural features for brain tumor classification. IJCSI Int J Comput Sci Issues 9(3)

Chapter 111
Simulation and Application on Power System Reliability for Bulk Electrical System

N. Mahiban Lindsay and A.K. Parvathy

Abstract Power system reliability investigation is an important activity in both vertically incorporated and unbundled electric power utilities. New planning criteria with broader engineering consideration of transmission entrée and reliable risk assessment must be explicitly addressed. This research work introduces the concept of applying reliability index probability distributions to measure mass electric system risk. Bulk electric system reliability recital index probability distributions are used as integral elements in a performance based regulation method. The system well-being notion presented in this paper is a probabilistic framework that incorporates the accepted deterministic N − 1 security criterion, and provides precious information on what the degree of the system susceptibility might be under a particular system condition using a quantitative elucidation of the degree of system security and insecurity. An overall reliability investigation framework taking into accounts both adequacy and security perspectives are projected. The system planning process using combined adequacy and security considerations offers a supplementary reliability-based dimension.

Keywords System reliability · Sequential simulation · Chronological simulation · PBR · IEEE-RTS

111.1 Introduction

Electric power systems all through the world are undergoing substantial change in regard to structure, operation and regulation. Technological developments and evolving customer prospect are among the driving factors in the new electricity

N.M. Lindsay (✉) · A.K. Parvathy
Department of Electrical and Electronics, Hindustan University, Chennai, India
e-mail: nmlindsay@hindustanuniv.ac.in

A.K. Parvathy
e-mail: akparvathy@hindustanuniv.ac.in

C. Kamalakannan et al. (eds.), *Power Electronics and Renewable Energy Systems*,
Lecture Notes in Electrical Engineering 326, DOI 10.1007/978-81-322-2119-7_111

hypothesis. The probability of the occurrence of worst possible scenarios must also be documented in the criteria and acceptable risk levels incorporated in the decision making process [1]. The basic function of an electric power system is to supply its customers with electrical energy as reasonably as possible and with a sensible degree of continuity and quality [2]. Power system engineers, therefore, attempt to achieve a satisfactory level of system reliability in their forecast, design and operation within the existing economic constraints. In order to resolve the conflict between the economic and consistency constraints, a wide range of techniques and criteria has been developed and used in the system design, planning and functioning phases. It is alleged that the application of reliability concepts in electric power system planning and operation will continue to increase in the future in both regulated and deregulated utility environments. The delivery function associated with transmission and distribution is still a synchronized, control business due to its natural characteristics [3]. A Power Exchange (PX) is an organization somewhat like a stock exchange where the buyers and sellers of extensive electricity are allowed to buy and sell electric energy as a service. Retail energy services companies are retailers of electric power who buy power from a power market and sell it directly to customers [3]. The ISO is an entity entrusted with the responsibility of ensuring the reliability and security of the bulk electric system consisting of the generation and transmission amenities. It is an independent authority who does not contribute in the electricity market trades nor own generation services for business (except for owning some capacity for emergency use) [4]. In the framework of power systems, reliability in general terms is related to the ability of the system to supply electric power to its consumers under both static and active conditions, with a mutually acceptable assurance of continuity and quality [5]. The term “system reliability” can be subdivided into the two primary aspects of system adequacy and system security [1]. In system security considerations, the analysis can be further classified into two types elected as transient (dynamic) and steady-state (static). Transient stability evaluation consists of determining if the system oscillations following an outage or a fault will cause loss of synchronism between generators. The purpose of steady-state security testing is to determine whether, following the incident of a contingency, there exists a new steady-state secure operating point where the troubled power system will settle after the dynamic oscillations have damped out. The essential objective of this research work is to take advantage of the sequential imitation technique to create reliability index prospect distributions, which indicate the annual variability of reliability indices and the likelihood of specific values being exceeded from both the sufficiency and steady-state security perspectives. An inherent benefit of the sequential representation used in chronological simulation is the opportunity to investigate the impact on bulk electric system reliability of sporadic energy resources such as wind power.

111.2 Sequential Simulation

In sequential simulation, each subsequent system state sample is related to the earlier set of system states. A sequential time evolution of system performance is created which enables a wide range of reliability indices to be assessed. The sequential simulation approach is very useful when the system to be analyzed is past-reliant, i.e. the state of the system at any given time is partially resolute by the historical time evolution of the system. Sequential simulation is particularly useful when the operating system is the past reliant or time correlated. Sequential simulation can incorporate realistic and complicated load models that incorporate the sequential characteristics inherent within each customer sector and the customer mix at each bulk system supply point. If the functioning life of the system is simulated over a long period of time, it is possible to study the activities of the system and to obtain a clear picture of possible deficiencies that the system may endure. The recorded information can be used to compute the expected values of selected reliability indices together with an appreciation of the dispersal of these indices. There is recurrently a need to know the likely range of reliability indices, the likelihood of certain values being exceeded, and similar parameters. These can be accessed from a acquaintance of the probability distribution associated with the expected value. At the present time, sequential simulation is the only realistic option existing to investigate the distributional aspects associated with system index mean values.

111.3 Chronological Simulation Approach

The sequential simulation process described above is briefly illustrated using the simple system composed of two parallel superfluous components shown in Fig. 111.1. This system is in the failed state when both components are in the botched state at the same time.

The sequential component state transition processes of the two components obtained using three simulation years are illustrated in Fig. 111.2. The sequential system state transition process is obtained by combining the sequential component state alteration processes as shown in the bottom of Fig. 111.2. There is no system crash in the first simulation year and there are one and two failures in the second

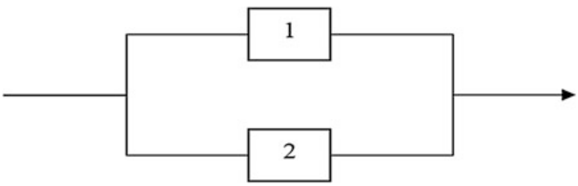

Fig. 111.1 A simple parallel system

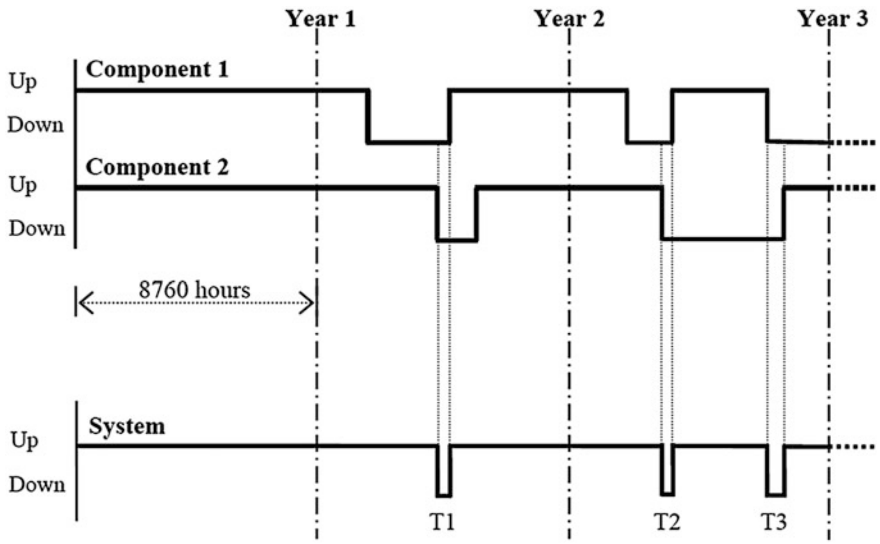

Fig. 111.2 Sequential component and system state transition process

and third simulation years respectively. If the desired reliability index $\Phi(S)$ is the system failure frequency index, the expected value $E(\Phi)$ based on the three imitation years can be calculated as follows using Eq. (111.1)

$$E(\Phi) = \frac{(\Phi)(S_{f1}) + (\Phi)(S_{f2}) + (\Phi)(S_{f3})}{3} \tag{111.1}$$

$$E(\Phi)\frac{(0) + (1) + (2)}{3} = 1.0\frac{occurrence}{Year} \tag{111.2}$$

111.4 Reliability Analysis Using Chronological Simulation

The reliability analysis normally involves the elucidation of the network configuration under random outage situations. There is a wide series of adequacy indices which can be calculated at the individual delivery points and for the overall mass electric system. These indices are helpful for overall system adequacy supervision. Adequacy indices are computed using the primary parameters of frequency, duration and magnitude of power outage events. The magnitude of an outage event depends on the components on outage, their relative consequence and their location in the network. Chronological simulation can be used to estimate the indices by simulating the actual sequential process and random behaviour of the system in fixed distinct time steps.

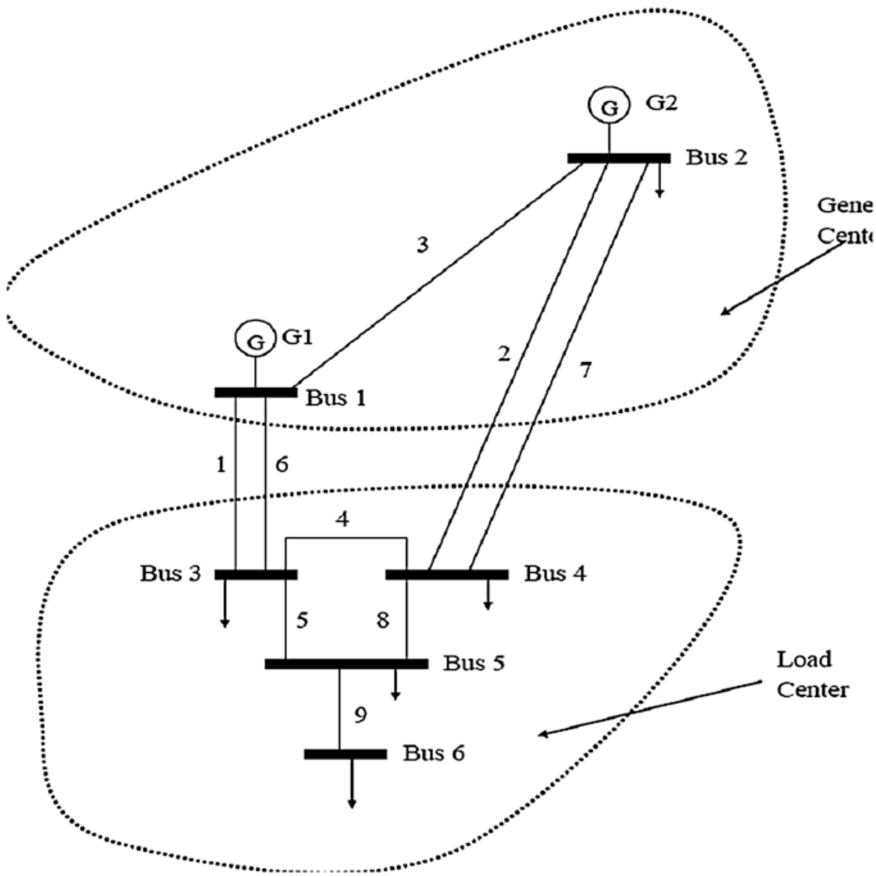

Fig. 111.3 The single line diagram of the RBTS

111.4.1 Illustration

Consider the RBTS 6 bus system composed of 2 generator buses, 5 load buses, 9 transmission lines and 11 generating units. The system peak load is 185 MW and the total generation is 240 MW. A single line diagram of the RBTS is shown in Fig. 111.3.

There are two basic types of reliability indices. They are designated as annualized indices when derived using a constant peak load, and annual indices when calculated using a load period curve or a sequential load model.

The ENLC shown in Table 111.1 is a surrogate or approximate value for the more accurate frequency index obtained using the chronological method. When a constant load is used, the annualized ENLC obtained using the non-sequential method is a high estimate of the annualized EFLC obtained using the chronological approach. It is important to note, however, that both techniques provide quite

Table 111.1 Annualized system indices for the RBTS

Annualized indices	Non-sequential	Sequential
ENLC	5.4	–
EFLC	–	2.7
EENS	0.0102	0.00098
Computation time (s)	0.14	15.1

similar estimates for other reliability indices such as the PLC and EENS, which are not frequency-related indices. The EENS index is used in a wide range of power system reliability studies and is often absolute to estimate the usual customer outage expenses using an interrupted energy assessment rate.

111.5 Competence and Inert Security Indices

There is a wide range of mass electric system reliability indices. Although all the reliability indices have their own idea and worth, presenting them all in an overall framework involves a voluminous set, predominantly when considering both competence and inert security aspects.

It is important to highlight that bulk electric system reliability indices associated with the at jeopardy state in system well-being analysis are identical to the predictive reliability indices related to load curbing in adequacy evaluation. These relationships are as follows:

The probability of the at risk state is equivalent to the Probability of Load Curtailment

$$\mathrm{Prob}\{\mathrm{R}\} = \mathrm{PLC} \tag{111.3}$$

The frequency of the at risk state is equivalent to the Expected Frequency of Load Curtailment

$$\mathrm{Freq}\{\mathrm{R}\} = \mathrm{EFLC} \tag{111.4}$$

The reliability indices selected to estimate the severity of system failure based on a competence perspective are as follows:

$$\mathrm{DPUI} = \text{Delivery point unreliability index (system minutes)}$$
$$\mathrm{ECOST} = \text{Expected customer interruption cost (dollars/year)}$$

These two competence indices together with the six safety indices described earlier provide a sufficient and effective overall framework that includes both adequacy and static safety considerations.

The case studies are presented in the following sections using two basic scenarios. The first scenario is focused on bulk electric systems with generation deficiencies. The second scenario is focused on bulk systems with transmission deficiencies. The IEEE-RTS is used as the test systems.

111.5.1 Generation Deficient Systems

The original IEEE-RTS is used in this study. The total generation is 3,405 MW and the system peak load is 2,754.75 MW. The original IEEE-RTS has a very strong transmission network and a feeble generation system. The combined system reliability indices considering both competence and safety for the original IEEE-RTS with different system peak demands are shown in Table 111.2. The load shedding philosophy is based on the bypass policy. Table 111.2 shows that the overall system reliability indices mortify as the system peak load progressively increases. As discussed earlier, the system peak demand levels shown prohibit transmission losses. The total system utilization in each case is therefore slightly higher than that shown in Table 111.2. In a similar the adequacy indices of DPUI and ECOST increase dramatically at the high peak loads while the security indices of Prob{H} and Prob{M} gradually depreciate. Generation deficiencies have a important undesirable effect on the system adequacy indices as the harshness of supply interruptions increase rapidly as the system peak load increases. Generation lacking environments, however, tend to have relatively less effect on the system safety indices than on the system adequacy indices.

111.5.2 Transmission System Reinforcements

The primary task in transmission planning is to develop the system as economically as possible while maintaining a satisfactory reliability level. The deterministic N − 1 criterion has been widely accepted and used by system planners in transmission forecast practice for many years. This proposed safety cost is designated as the

Table 111.2 Overall system reliability indices of IEEE-RTS system

System indices	System peak load (MW)				
	2,650	2,730	2,790	2,830	2,860
Prob{H}per year	0.978	0.958	0.946	0.898	0.899
Prob{M}per year	0.028	0.039	0.058	0.068	0.079
Prob{R}per year	0.001	0.004	0.004	0.007	0.009
DPUI	65	98	135	200	280
ECOST(M$.year)	13.33	19.006	30	41.87	60.12

expected potential insecurity cost (EPIC) and is obtained using the multiplication of the prospect of the marginal state (Prob{M}) and the expected customer interruption cost (ECOST), as shown in Eq. (111.5).

$$\text{Expected Potential Insecurity Cost (EPIC)} = \text{Prob}\{\text{M}\} \times \text{ECOST} \qquad (111.5)$$

The ECOST is the expected economic impact on customers due to supply failures and is normally used in the competence evaluation domain. The Prob{M} indicates the potential system diffidence if a specified element based on the $\text{N} - 1$ criterion fails and results in load curtailments. The total economic loss in the combined reliability framework is designated as the expected overall reliability cost (EORC) as shown in Eq. (111.6).

$$\text{Expected Overall Reliability Cost (EORC)} = \text{ECOST} + \text{EPIC} \qquad (111.6)$$

The deterministic cost (EPIC) can be considered as an augmentation of the overall reliability cost (EORC).

111.6 Conclusions

This paper is focused on complex generation and transmission system reliability evaluation using sequential simulation. Chronological simulation can be used to reasonably represent most contingencies and the complex operating characteristics intrinsic in a bulk electric system and also provide a comprehensive range of reliability indices in both competence and steady-state safety analyses. Two significant advantages when utilizing sequential simulation are the ability to obtain exact frequency and duration indices, and the opportunity to synthesize the reliability index probability distributions associated with the mean values. Reliability worth evaluation methodologies for bulk electric systems are presented. The results obtained using this method therefore can also serve as benchmarks in the development of more fairly accurate methods required due to the absence of detailed information in many real life situations. Actual historical data and simulated bulk electric system reliability performance indices are applied to theoretical PBR frameworks. A discussion of the potential utilization of the PBR protocol for overall bulk electric systems is presented. A system planning process using combined competence and security considerations offers an additional reliability-based measurement. The proposed process is illustrated by considering a series of possible reinforcement alternatives in the test system using reliability cost worth considerations.

References

1. Billinton R, Allan RN (1996) Reliability evaluation of power systems, 2nd edn. Plenum Press, New York
2. Lindsay NM, Parvathy AK (2013) Enhancing power system reliability using multiple FACTS devices. NASA Digit Libr 4:141–145
3. Bulk electricity system: delivery point interruptions and significant power interruptions 1999–2003 report. Canadian Electricity Association, Dec 2004
4. Billinton R, Wangdee W, Bulk electricity system reliability performance assessment. In: IX symposium of specialists in electric operational and expansion planning (SEPOPE), Rio de Janeiro, Brazil, 23–27 May 2004
5. Billinton R, Satish J (1994) Predicting assessment of bulk system reliability performance indices. IEE Proc Gener Transm Distrib 14(5):466–472
6. Billinton R, Fotuhi-Firuzabad M, Bertling L (2001) Bibliography on the application of probability methods in reliability evaluation 1996–1999. IEEE Trans Power Syst 16 (4):595–602
7. Billinton R, Li W (1991) Hybrid approach for reliability evaluation of composite generation and transmission systems using monte carlo simulation and enumeration technique. IEE Proc-C 138(3):233–241
8. Pereira MVF, Maceira MEP, Oliveira GC, Pinto LMVG (1992) Combining analytical models and monte carlo techniques in probabilistic power system analysis. IEEE Trans Power Syst 7 (1):265–272
9. Billinton R, Li W (1993) A system state transition sampling method for composite system reliability evaluation. IEEE Trans Power Syst 8(3):761–771
10. Billinton R, Sankarakrishnan A (1994) A system state transition sampling technique for reliability evaluation. Reliab Eng Syst Saf 44:131–134
11. Rubinstein RY (1981) Simulation and the monte carlo methods. Wiley, New York
12. Ubeda R, Allan RN (1992) Sequential simulation applied to composite system reliability evaluation. IEE Proc-C 139(2):81–86
13. Allan RN, Roman J (1989) Reliability assessment of generation systems containing multiple hydro plant using simulation techniques. IEEE Trans Power Syst 4(3):1074–1080
14. Billinton R, Allan RN (1996) Reliability evaluation of power systems, 2nd edn. Plenum Press, New York
15. Philipson L, Willis HL (1999) Understanding electric utilities and deregulation. Marcel Dekker, New York

Chapter 112
Intelligent Load Shedding Using Ant Colony Algorithm in Smart Grid Environment

V. Margaret, K. Uma Rao and G.G. Ganeshprasad

Abstract For every country which is expecting a large growth in power demand in the near future or facing a power crisis, an effective load control and power distribution strategy is a necessity. Load shedding is done whenever power demand is more than power generation in order to sustain power system stability. The current load shedding strategies fails to shed exact amount of load as per the system requirement and does not prioritize loads which are being shed. Given the dimension of the problem, it would not be feasible computationally, to use regular optimization techniques to solve the problem. The problem is typically suited for application of meta-heuristic algorithms. This paper proposes a new scheme for optimizing load shedding using ant colony algorithm in a smart grid platform considering loads at utility level. The algorithm developed considers each electrical connection from Distribution Company as one lumped load and provides an effective methodology to control the load based on various constrains such as importance of load and time of load shedding.

Keywords Intelligent load shedding · Ant colony algorithm · Smart grid · Optimization · Grading of loads

112.1 Introduction

In any power system, load shedding becomes necessary when there is a mismatch in power demand and power generation. When there is a power crisis or large growth in power demand is expected in next few years, the strategies to improve power

V. Margaret (✉) · G.G. Ganeshprasad
Faculty of Engineering, Electrical and Electronics Department,
Christ University, Bangalore, India
e-mail: vijaya.margaret@christuniversity.in

K.U. Rao
Electrical and Electronics Department, R.V. College of Engineering, Bangalore, India
e-mail: umaraok@rvce.edu.in

C. Kamalakannan et al. (eds.), *Power Electronics and Renewable Energy Systems*,
Lecture Notes in Electrical Engineering 326, DOI 10.1007/978-81-322-2119-7_112

generation and to utilize the available power effectively plays a vital role. If the load shedding is unavoidable, it is better to implement a methodology to reduce the impact of load shedding from the perspective of the distribution company as well as the consumer. Intelligent load shedding methods which optimize the load shedding based on various perspectives, improve the power distribution and consumer participation in demand management [1].

Whenever there is a power deficiency, the Load Dispatch Center (LDC) which is responsible for allotment of available power, sends intimation to the substations to reduce a particular amount of load. In current load shedding strategy, loads are disconnected from the supply in a ‘Round robin’ manner for duration of half an hour or 1 h at the feeder level in the substation. This method fails to shed exact amount of load as per the system requirement and it does not consider the type and importance of load which is being shed and the revenue that would have generated from the load. As selective load shedding is not possible at consumer level, high priority loads such as hospitals, data-centers, industries etc. connected to a feeder are declined power while feeding low priority loads such as domestic loads in another feeder. The method fails to distribute the available power effectively and to reduce the impact of load shedding.

112.1.1 Load Shedding in Smart Grid Environment

In smart grid environment each electrical connection from the distribution company is considered as a lumped load [2]. Each lumped load is remotely controlled by the control center. The control center communicates with the load and gets the real time data such as power consumption, voltage, power factor etc. which is processed and control action on the load is performed. This method allows selective load shedding at consumer level as individual utility can be controlled remotely by control center. It provides unique opportunity to shed the exact amount of load as per system requirement. There is a flexibility to choose individual loads based on the importance of load, time of load shedding and profitability to the distribution company. The method improves the efficacy of power distribution and improves consumer satisfaction.

112.1.2 Grading of Loads

Grading of the loads is a strategy to differentiate the various type of loads connected to a feeder so that selective control of the loads is possible, by some sort of prioritization of the loads [3, 4]. Loads connected to the feeder can be classified on following considerations.

1. Priority time of the load.
2. Number of units of power consumption.

3. Social impact of load shedding.
4. Revenue loss and discomfort to the consumer.
5. Revenue loss to the power distribution company.
6. Any other consideration by the power distribution company.

Grade point is mere a number which is assigned to each load which tells about the relative importance of that particular load at a particular duration of time. Grade points are dynamic and flexible and can be defined to include any other considerations apart from those mentioned above [3, 4].

The priority time is an option open to the consumer to define the time of the day crucial for the consumer, when the customer does not want the load to be shed. Grade points are chosen such that a high priority is assigned to critical loads such as hospitals, data centers, government offices, industries at their priority time. Grade point and priority time are assigned to a load on mutual agreement of the consumer and the distribution company. This technique identifies the priority consumer and provides power to him at right time. It allows the consumer to manage the loads within the utility and also provides opportunity to implement availability based tariff and dynamic billing.

112.2 Ant Colony Algorithm

Ant colony algorithm is one of the popular algorithms in swarm intelligence. It is a metaheuristic algorithm which simulates the behavior of ants while searching for food. Ants travel in random direction in search of food. They lay trails called pheromone on the path they travel which evaporate with time. Ant which travelled in the minimum distance path comes back to the original location in minimum time traversing the path twice. The pheromone trails are more in the least distance path as pheromone update happens twice and evaporation of pheromone is less as time taken to traverse the path is less. Next set of ants chose the path to food source based on the pheromone trails on the path. More ants take least distance path and pheromone update further increases. After certain duration ants converge on the minimum distance path. The algorithm is most popular in routing problems [5–7].

112.2.1 Basic Assumptions

For the application of Ant colony algorithm to load shedding problem following assumptions were made:

1. Each electrical connection from the distribution company or one utility is considered as a lumped load.
2. The utility is assumed to be able to communicate continuously with the control center and data of the load is stored and available for processing.

3. Based on the amount of power deficiency the load dispatch center sends intimation to substation regarding the amount of load which has to be reduced by that substation.
4. The substation does load shedding in the blocks of 1 h duration.
5. Substation feeds the current power consumption of each load, grade points assigned to each load, load shedding requirement to the algorithm.
6. Based on the results obtained from the algorithm substation performs suitable control action for load shedding for the next hour.

112.2.2 Implementation of Algorithm

1. A test system with different types of load is considered for load shedding.
2. For simplicity Grade points in a range of 0–100 is assumed for each load which varies with time of load shedding.
3. Power consumption of each load is assumed and preloaded from the database (Fig. 112.1).
4. A binary bit '1' represents load should be disconnected from the supply. '0' otherwise.
5. The objective of the algorithm is to minimize the error between the load to be shed and load being shed. And to minimize the sum of grade points of all the loads being shed. Which ensures correct amount of load is being and shed by selecting loads which have least priority at that time.

   $$\text{Load shedding error} = \text{amount of load to be shed} - \text{amount of Load being shed.}$$
   $$\text{Cost of load shedding} = \text{sum of grade points of all the loads being shed}$$

   Inverse of sum of objective functions is taken as distance so that solution with less error gives higher values of pheromone.
6. Ratio of load to be shed to the total load at that time is assigned as the attractiveness function to the '1' to favor load shedding.
7. At each load an ant chooses either one or zero based on the pheromone value.
8. After certain iterations probability of choosing a particular path will tend to path tend to one. The path is taken as final solution.

112.2.3 Advantages of Ant Colony Algorithm

Major advantage of using Ant colony algorithm is it is a 'metaheuristic' algorithm. The transition from one state to another is partially probabilistic and partially deterministic [7, 8]. This nature of the algorithm provides flexibility for the designer to guide the search to a particular path in search space. Algorithm can be designed

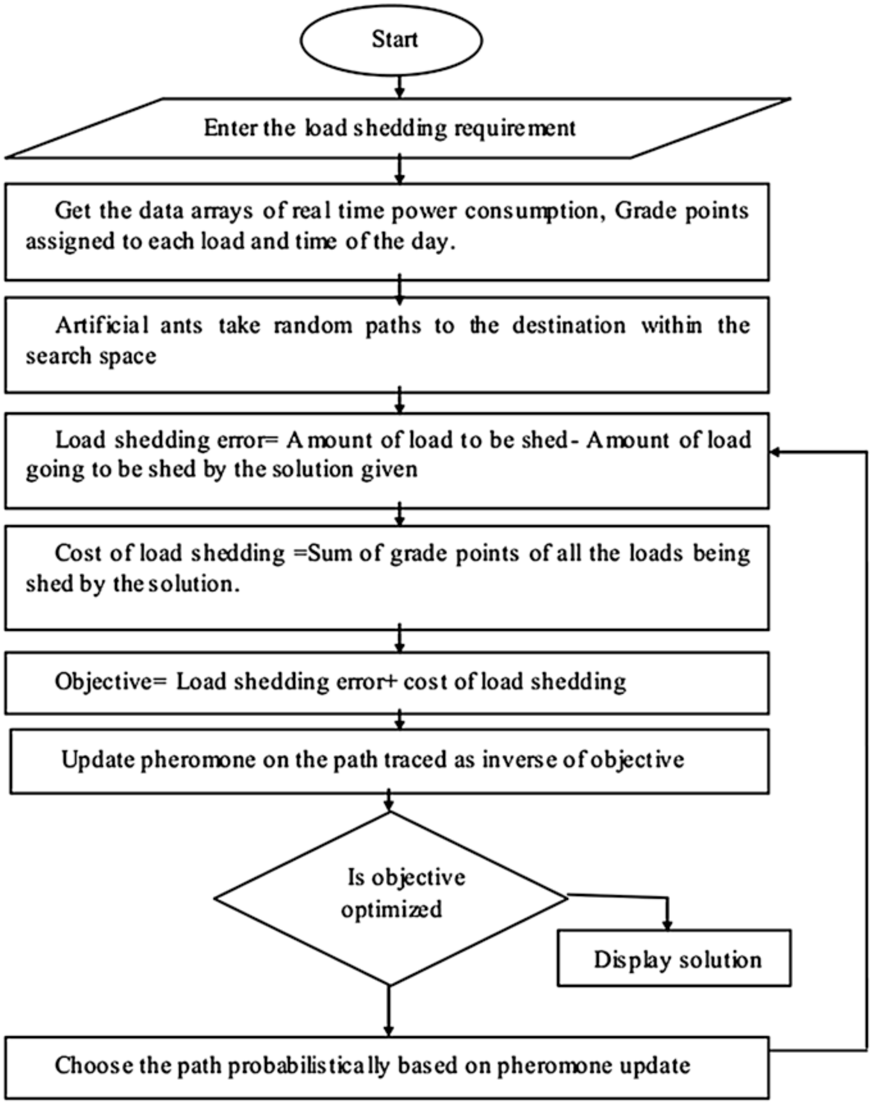

Fig. 112.1 Flow chart of ant colony algorithm

to meet several constrains with minimum iterations. For example, if we want to exclude the loads which are disconnected in the previous load shedding duration we can easily do it by assigning vary less attractiveness coefficients to those loads. This cannot be done so easily with a purely probabilistic algorithm. The algorithm is capable of handling dynamic variations. That is if the power generation increase or power demand increase suddenly in the middle of a search it can easily account for the change and provide suitable solution. Most of the purely probabilistic gives best result if solution is at the center of a search space and fails at the corners. For example, if total power consumption in a substation is 2 MW, most of the algorithm gives best solutions in less time if the load shedding value is within 400–1,600 kW. Algorithms take more time to converge if the load to be shed is less than 400 kW or more than 1,600 kW i.e. at the corners of search space. But the ant colony algorithm can be made to converge faster at the corners by limiting the search to the corner region. In some of the algorithms which are single point or multi point search techniques the convergence time depends upon the initial guess [5]. But convergence time in ant colony algorithm does not depend upon initial path chosen. Any other algorithm solution evolved depends upon best combination appeared in the transition but in this algorithm best part of each transition is taken to constitute a solution. So Ant colony algorithm applied load shedding is very powerful.

112.3 Case Studies and Results

A test system of 100 loads is used for testing the algorithm efficiency. System is generated based on the real time data from the R.K. Nagar substation of Chamunadeshwari electric supply corporation Mysore. Loads and their power consumption are taken proportionally based on the tariff scheme of distribution company [9]. E.g. LT2 represents Low tension non commercial loads such as domestic loads, schools etc., with maximum power consumption 5 kW. Power consumption assumed for each load at the time of load shedding is as given in the Table 112.1. Each column gives power consumption of a lumped load. Number of loads taken in one tariff category is proportional to substation data.

Case 1: Load Shedding of 400 KW at 9.00 a.m.

Load shedding requirement of 400 kW at 9.00 a.m. is considered for testing algorithm. Power consumption of loads is taken from Table 112.1. The grade points assumed for each load is as shown in Table 112.2. Solution given by the ant colony algorithm is as given in Table 112.3.

The solution tells that the loads corresponding to the columns marked as one have to be shed and others should be kept in operation to meet load shedding requirement and to maximize revenue generation and consumer satisfaction. It can be observed that the loads which have minimum grade points at the time of load shedding are considered for shedding.

In this case for the same condition of load shedding algorithm does not consider the loads which are shed in previous run. The solution in Table 112.4 shows for the same conditions, loads which are marked as 1 (loads shed) are not considered for shedding and next set of loads with minimum grade points are shed.

The results show that algorithm optimizes load shedding based on priority assigned to each load. The algorithm developed can handle dynamic constraints assigned.

Table 112.1 Power consumption of each load in kilo Watt

LT1	LT2(A1)			LT2(A2)		LT2B	LT3		LT4	LT5	LT6	LT7	HT1	HT2	HT3
0.9	1.62	0.04	1.5	0.63	3.89	3.63	13.28	9.61	6.58	74.51	21.16	35.42	56.46	68.26	80.36
0.95	1.5	1.84	0.46	1.62	3.06	4.46	12.4	7.82	13.58	33.01	24.39		79.24	102.36	130.58
	0.24	1.3	0.12	1.58	4.99	3.77	11.96	12.44		72.27	18.54			138.25	
	1.05	1.86	1.53	1.7	2.67	3.56	12.50	13.88		30.82	19.1				
	0.65	0.32	1.34	1.01	3.96	4.58	9.06	6.24		60.77	24.84				
	1.09	1.84	1.43	1.27	3.82	4.02	10.94			65.56					
	0.8	1.58	1.28	1.9	3.16	4.49	10.6			54.03					
	0.83	1.15	0.84	0.88	2.42	4.08	10.24			69.84					
	0.36	0.88	0.78	2.18	2.08		8.0			70.46					
	0.51	0.52	1.63	4.60	3.26		7.98			58.16					

Total power consumption of 100 loads is 1.74 MW

Table 112.2 Grade points of load at 9.00 a.m.

LT1	LT2(A1)			LT2(A2)		LT2B	LT3		LT4	LT5	LT6	LT7	HT1	HT2	HT3
10	53	49	51	31	41	54	35	84	44	46	11	58	39	64	86
10	40	44	55	47	37	55	45	73	49	58	20		31	40	73
	56	46	50	36	50	46	57	72		47	67			58	
	40	52	52	44	41	46	64	59		60	49				
	45	46	12	31	43	46	52	70		53	50				
	49	48	49	39	35	27	39			43					
	58	57	27	46	19	28	58			43					
	45	47	38	42	17	29	54			31					

Table 112.3 Load shedding solution for 400 kW at 9.00 a.m.

LT1	LT2(A1)			LT2(A2)		LT2(B)	LT3		LT4	LT5	LT6	LT7	HT1	HT2	HT3
1	0	0	1	0	1	0	1	0	1	1	1	0	1	0	0
1	0	1	0	0	0	0	1	0	0	0	0		1	1	0
	0	1	0	1	0	0	1	0		0	1			0	
	1	1	1	0	0	0	0	0		1	0				
	1	1	1	1	1	0	0	0		1	0				
	1	0	0	0	1	0	1			0					
	0	0	0	0	1	1	1			1					
	0	1	1	1	0	0	1			0					
	1	0	0	1	1		1			0					
	1	0	0	0	0		0			0					

The time taken by the algorithm is 0.593 s
Error in load shedding value 0.12 kW

Table 112.4 Solution for load shedding excluding the loads which are shed in previous hour

LT1	LT2(A1)			LT2(A2)		LT2(B)	LT3		LT4	LT5	LT6	LT7	HT1	HT2	HT3
0	0	0	0	0	0	0	0	0	0	0	0	0	0	0	0
0	0	0	1	0	1	0	0	0	1	0	0		0	0	0
	0	0	1	0	0	1	0	0		1	0			1	
	0	0	0	1	1	1	1	1		0	1				
	0	0	1	0	1	0	1	0		0	0				
	0	1	0	1	0	1	0			1					
	0	1	1	0	0	0	0			1					
	1	0	0	1	1	1	0			1					
	0	1	0	0	0		0			0					
	0	1	0	0	1		0			0					

The time taken by the algorithm is 0.765 s
Error in load shedding value 2.31 kW

Table 112.5 Grade points of load at 2.00 p.m.

LT1	LT2(A1)			LT2(A2)		LT2(B)	LT3		LT4	LT5	LT6	LT7	HT1	HT2	HT3
10	17	19	21	11	11	50	66	88	31	37	11	39	54	73	80
10	16	14	17	15	21	43	68	83	32	69	20		59	76	74
	15	16	14	11	10	55	69	87		70	36			86	
	11	23	12	11	12	60	66	65		63	56				
	11	10	17	15	15	56	66			55	52				
	14	16	15	13	12	52	50			68					
	17	13	13	26	37	55	68			66					
	13	14	10	13	27	59	60			60					
	10	12	27	11		52	85			66					
	11	17	36	14		58	89			65					

Time taken by the algorithm is 0.493 s
Load shedding error is 0.23 kW

Table 112.6 Solution given by the ant colony algorithm

LT1	LT2(A1)			LT2(A2)		LT2(B)	LT3		LT4	LT5	LT6	LT7	HT1	HT2	HT3
1	0	0	1	0	1	1	1	0	1	1	1	0	1	0	0
1	0	1	0	0	0	0	1	0	0	0	0		1	1	0
	0	1	0	1	0	0	1	0		0	1			0	
	1	1	1	0	0	0	0	0		1	0				
	1	1	1	1	1	0	0			1	0				
	1	0	0	0	1	0	1			0					
	0	0	1	0	1	1	1			1					
	0	1	1	1	0	0	1			0					
	1	0	0	1	1		1			0					
	1	0	0	0	0		0			0					

Case 2: Load shedding of 400 KW at 2.00 p.m.

Load shedding requirement of 400 kW at 2.00 p.m. is considered for testing algorithm. Power consumption of loads is taken from Table 112.1. The grade points of the loads at 2.00 p.m. are as shown in Table 112.5. Solution is as given in Table 112.6.

Grade points are varied with time to include time priority for each load. Since algorithm optimizes grade points, loads are shed based on time priority. Hence the algorithm sheds load with minimum amount of excess load shedding considering time of importance of consumer and value of the consumer. The algorithm used is open to handle larger set of constraints based on the requirement. The algorithm effectively optimizes the cost of load shedding and error in load shedding value in any case is less than 0.5 % of the load shedding requirement. Time taken by the algorithm to give an effective solution is less than 0.5 s in the normal run.

112.4 Conclusions

Ant colony algorithm applied for intelligent load shedding is a new approach which very efficiently handles a large number of loads in a substation. Ant colony algorithm applied for load shedding in smart grid environment provides a unique opportunity to treat an individual utility as single lumped load and efficiently minimizes the error in load shedding value and also minimizes the cost of load shedding. The algorithm tries to minimize the impact of load shedding to the possible extent by considering time priority of each load and the grade points assigned to each load. Ant colony algorithm is particularly helpful as it is a faster algorithm for optimization which can easily handle 50,000–1,00,000 loads expected in a substation. It allows the user to define any constrains which increases the efficiency of the power distribution. Ant colony algorithm is capable of handling constraints dynamically. It also provides a unique opportunity to change the constraints of the algorithm based on the situation. The algorithm is highly flexible and easily modified to give a best solution in the given situation. The algorithm encourages customer participation in load management by assigning grade points and time priority to each load and assuring the power to the customer at his priority time. The algorithm increases the efficacy of power distribution by routing the power to the right consumer at right time. The algorithm ensures maximum usability and profitability of available power.

References

1. Shokooh S, Khandelwal T, Shokooh F, Tastet J, Dai JJ (2005) Intelligent load shedding need for a fast and optimal solution. IEEE PCIC Eur
2. Mayne D (2010) How the smart grid will energise the world-white paper. Digi International Inc

3. Rao KU, Bhat SH, Jayaprakash G, Ganeshprasad GG, Pillappa SN (2013) A novel grading scheme for loads to optimize load shedding using genetic algorithm in a smart grid environment. IEEE ISGT Asia 2013 1569809675
4. Rao KU, Bhat SH, Jayaprakash G, Ganeshprasad GG, Pillappa SN (2013) Time priority based optimal load shedding using genetic algorithm. Fourth international conference on advances in power electronics and instrumentation engineering, PEIE
5. Maniezzo V, Gambardella LM, Luigi FD (2004) New optimization techniques in engineering studies in fuzziness and soft computing, vol 141, pp 101–121
6. Maniezzo V, Carbonaro A (2001) Ant colony optimization: an overview. In: Ribeiro C (ed) Essays and surveys in metaheuristics. Kluwer, Berlin, pp 21–44
7. Dorigo M. Ant colony optimization web page, http://iridia.ulb.ac.be/mdorigo/ACO/ACO.html
8. Xing L, Chen Y, Yang K (2009) Simulation model of ant colony optimization for the FJSSP. In: Khosrow-Pour M (ed) Encyclopedia of information science and technology, 2nd edn. Information Science Reference, Hershey, pp 3468–3474. doi:10.4018/978-1-60566-026-4.ch551
9. http://www.cescmysore.org
10. National Center for Biotechnology Information, http://www.ncbi.nlm.nih.gov

Chapter 113
Design of ANFIS Controller for Power System Stability Enhancement Using FACTS Device

G.Y. Sree Varshini, S. Charles Raja and P. Venkatesh

Abstract Artificial Neuro Fuzzy Inference System (ANFIS) is applied to design static synchronous series compensator based damping controller for the improvement of small signal stability. The proposed controller is implemented in the single machine system. The generated database from conventional static synchronous series compensator based damping controller is used for training the ANFIS. Bacterial foraging optimization algorithm (BFOA) is employed for optimal controller parameter selection. Simulation is done for four cases namely single machine without damping controller, with SSSC and without damping controller, with SSSC based damping controller and with SSSC based ANFIS controller. Simulation results shows that the SSSC based ANFIS controller provide efficient damping and improves the small signal stability of power system when compared to conventional damping controller.

Keywords ANFIS · BFOA · SSSC · Damping controller · Stability

113.1 Introduction

During power exchange of power systems interconnected by weak tie lines, low frequency oscillations are observed. These oscillations leads to islanding if no adequate damping is provided. Static Synchronous Series Compensator (SSSC) is

G.Y. Sree Varshini (✉) · S.C. Raja · P. Venkatesh
Department of Electrical and Electronics Engineering, Thiagarajar College of Engineering, Madurai, Tamil Nadu, India
e-mail: gysreevarshini90@gmail.com

S.C. Raja
e-mail: charlesrajas@tce.edu

P. Venkatesh
e-mail: pveee@tce.edu

C. Kamalakannan et al. (eds.), *Power Electronics and Renewable Energy Systems*,
Lecture Notes in Electrical Engineering 326, DOI 10.1007/978-81-322-2119-7_113

one of the member of FACTS family [1] which can be installed in series in the transmission line. An auxiliary stabilizing signal superimposed on the power flow control function of the SSSC so as to improve power system oscillation stability [2]. The influence of degree of compensation and mode of operation of SSSC on small disturbance and transient stability is reported in the literature [3, 4]. In recent years, new artificial intelligence-based approaches have been proposed to design a FACTS-based supplementary damping controller due to its robustness and less memory requirement when compared to conventional controllers [5].

In this paper the small signal stability of a power system is improved by SSSC based ANFIS controller where the controller parameters are optimally selected using BFOA. The performance of the proposed controller is evaluated for single-machine system which has efficient damping for local mode of oscillations under three phase to ground fault. To minimize the power system oscillations due to the disturbances the SSSC based damping controller [6, 7] is designed in order to improve stability of the system. The oscillations results in deviations of power angle, rotor speed and tie-line power. Minimizing any one of the above deviation is taken as the objective function. In this paper, the speed deviation is taken as the objective function for single machine system. Even though there is a delay in obtaining the remote signal, the control action is better than choosing the power angle deviation of local signal. Moreover the local signal is not highly observable and controllable [8, 9]. Therefore speed deviation of remote signal is considered as the objective function where

$$\Delta\omega = \frac{1}{H}(P_e - P_m) \tag{113.1}$$

$\Delta\omega$ is the speed deviation of rotor,
H is the rotor inertia,
P_e is the electrical power,
P_m is the mechanical power.

113.2 General System Description

The single line diagram (Fig. 113.1) shown above consists of a generator connected to a three phase transformer, a Series FACTS controller called SSSC is placed at midpoint of the transmission line and the load. In the proposed system, three phase to ground fault is applied in the time interval of 50–60 s in the transmission line (Table 113.1).

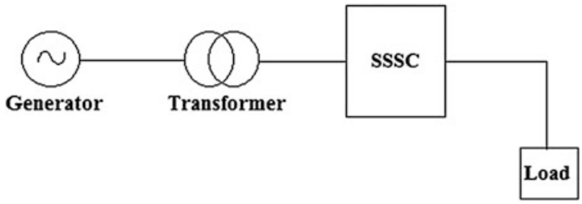

Fig. 113.1 Single line diagram of the proposed system

Table 113.1 Parameters of the proposed system

Elements	Rating
Generator	Sb = 10 MVA, H = 3.7 s, Vb = 13.8 kV, f = 60 Hz, xd = 1.305, xd′ = 0.296, xd″ = 0.252, xq = 0.243, xq′ = 0.18, xq″ = 0.18
Transformer	10 MVA, step up voltage is 13.8/50 kV, f = 60 Hz, R1 = R2 = 0.02, L1 = 0, L2 = 0.12, delta/star connection, Rm = 500, Lm = 500
Transmission line	3-ph, 60 Hz, Length = 5 km, R1 = 0.02546 ohm/Km, L1 = 0.9337e−3H/Km, L0 = 4.1264e−3H/Km, c1 = 12.74e−9F/Km, c0 = 7.751e−9F/Km
Load	V = 50 kV, P = 50 MW, Q = 15 MVAR, f = 60 Hz
Converter rating	DC Voltage regulator gains: Kp = 0.1 × e−3, Ki = 20e−3, Vq = 0.1(pu), Snom = 10 MVA, Vnom = 50 kV, f = 60 Hz, Vqref = 3pu/s, R = 0.00533, L = 0.16, Vdc = 40 kV, C = 375 × e−6F

113.2.1 Objective Function

The objective function for the single machine system is expressed as follows,

$$J = \int_{t=0}^{t=tsim} \Delta w.t.dt \tag{113.2}$$

where Δw is the speed deviation, t_{sim} is the time range of the simulation. For objective function calculation, the time-domain simulation of the power system model is carried out for the simulation period. It aims to minimize this objective function in order to improve the system response in terms of the settling time and overshoots. Therefore, the design problem can be formulated below.

Minimize J, subject to the constraint

$$K_i^{\min} \le K_i \le K_i^{\max}$$
$$T_{1i}^{\min} \le T_{1i} \le T_{1i}^{\max}$$
$$T_{2i}^{\min} \le T_{2i} \le T_{2i}^{\max}$$
$$T_{3i}^{\min} \le T_{3i} \le T_{3i}^{\max}$$
$$T_{4i}^{\min} \le T_{4i} \le T_{4i}^{\max}$$

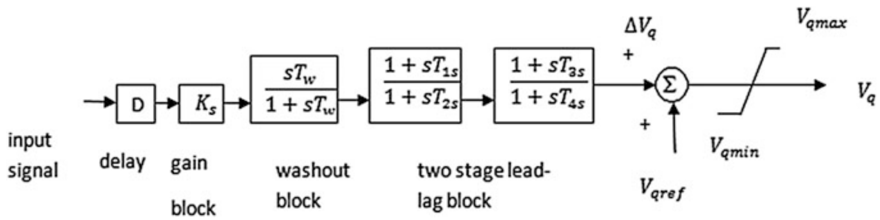

Fig. 113.2 Block diagram of SSSC based damping controller

113.3 Methodology

113.3.1 Damping Controller

It consist of delay block, gain block, signal washout block and two-stage phase compensation block. Depending on the type of signal at the input the time delay is introduced in the delay block. The gain block is used to dampen the oscillations [10]. The washout block act as a high-pass filter, with the time constant Tw and it is high enough to allow signals associated with oscillations in input signal to be pass unchanged which may be in the range of 1–20 s .Phase compensation blocks (time constants T1s, T2s and T3s, T4s) which provide the phase-lead characteristics in order to compensate for the phase lag takes place between input and the output signals and used to modulate the injected quadrature voltage. Quadrature reference voltage namely Vqref as desired by the steady state power flow control loop. Here the Vqref is assumed to be constant during the disturbance period.

$$V_q = V_{qref} + \Delta V_q \tag{113.3}$$

According to the change in the SSSC-injected voltage which is added to Vqref, the desired value of compensation is obtained (Fig. 113.2).

During dynamic conditions the series injected quadrature voltage is modulated to damp the system oscillations.

113.3.2 Bacterial Foraging Optimization Algorithm

It is used for multi optimal function optimization [11]. The gain and four Time constants of damping controller are optimally determined using this algorithm. It involves determination of minimum of function $J(\alpha)$ where α determines bacteria position in high dimensional space. A negative value of $J(\alpha)$ implies that the bacterium is in nutrient environment, a zero value implies a neutral environment and a positive value implies a noxious environment. Thus the objective is to move the bacteria to nutrient environment and avoid noxious and neutral environment. Basic steps are,

- Initialize the parameters
- Set the elimination and dispersal loop $l = l + 1$
- Reproduction loop: $k = k + 1$
- Chemotaxis loop: $j = j + 1$
- Compute fitness function, $J\ (i, j, k, l)$.
- For tumbling, generate a random vector with each element $\Delta_m(i), m\ 1, 2, \ldots, p$, a random number on [−1, 1].
- Move the bacterium up to the swim length and Compute $J\ (i, j + 1, k, l)$
- If j < Nc, repeat step 4
- Perform reproduction and sort the bacteria and chemotactic parameters
- For i = 1, 2…, S, eliminate and disperse each bacterium. If a bacterium is eliminated, disperse another one to a random location on the optimization domain. If $l < N_{ed}$, then go to the step 2.

113.3.3 ANFIS (Artificial Neuro Fuzzy Inference System) Controller

There are 7 membership functions and 49 rules in the ANFIS controller. Depending on the input variables the fuzzy membership function compute the quadrature voltage of the SSSC. Since the conventional controller have delays in implementing the control action [5]. Therefore ANFIS controller is used which provide faster control and also robust when compared to conventional damping controller

Design steps of ANFIS controller in MATLAB/SIMULINK:

- Draw the SIMULINK model with the conventional damping controller namely SSSC based damping controller and simulate it.
- After simulation, collect the data from the conventional damping controller which is used for training the ANFIS.
- The two inputs for training data are the speed deviation and change in speed deviation and the output is quadrature voltage injected by the SSSC.
- After loading the training data, generate the FIS with gaussian bell membership functions which gives the least error during training.
- Then train the collected data with the generated FIS up to a particular number of epochs (iterations).
- Test the trained data using the same procedure as done in training.
- Save the FIS file which is nothing but the ANFIS.

113.4 Results and Discussions

The proposed system has been developed using SIM Power System (SPS) Toolbox in MATLAB/SIMULINK environment and BFOA program has been written (in .m file). For objective function calculation, the developed model is simulated. Then the objective function value is evaluated and used in BFOA program. The transfer of objective function value from the SIMULINK model to .m file has been realized by using 'To Workspace'.

Case 1: Without SSSC Based Damping Controller

Without any controller the overshoot of oscillation is very high and also draws high current at load side as shown in Fig. 113.3.

Case 2: With SSSC and Without Damping Controller

The overshoot of oscillation for load current is reduced after implementing SSSC due to injection of quadrature voltage (Figs. 113.4 and 113.5).

Case 3: With SSSC Based Damping Controller

Figure 113.6 shows that the oscillations are reduced due to implementation of damping controller in SSSC. The current is controlled to 50 A compare to previous case of SSSC without damping controller (Fig. 113.7).

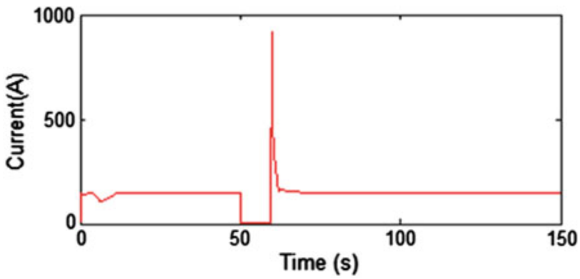

Fig. 113.3 Load current response

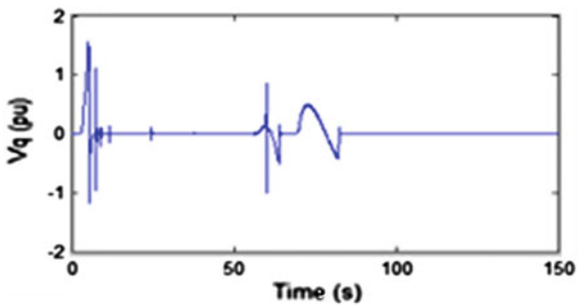

Fig. 113.4 Quadrature voltage

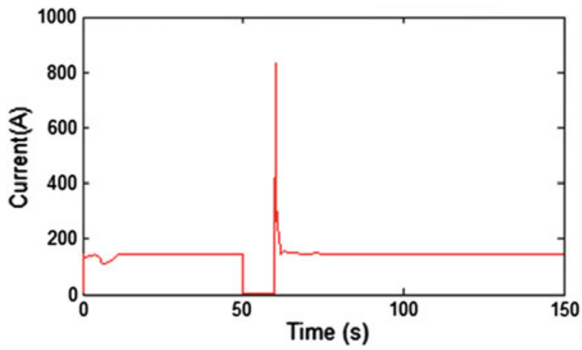

Fig. 113.5 Load current response

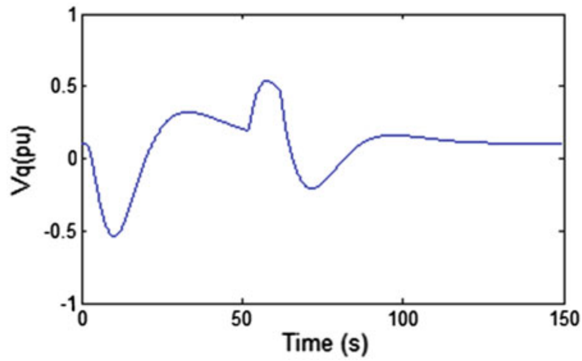

Fig. 113.6 Quadrature voltage

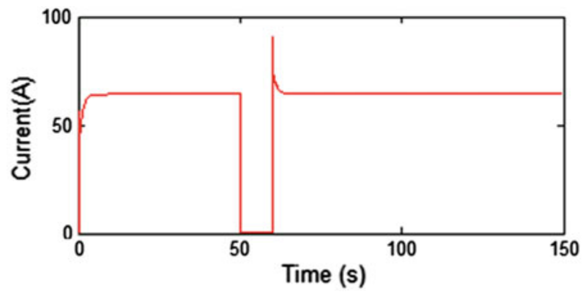

Fig. 113.7 Load current response

Case 4: With SSSC Based ANFIS Controller

The oscillation are highly reduced in quadrature voltage waveform compared to conventional damping controller and also no overshoot of oscillation at load current response (Fig. 113.8).

The local mode of oscillation in the single machine system is well damped by SSSC based ANFIS controller as shown in the Fig. 113.10 The overshoot of the oscillation is very high in the first case of without any controller. By using SSSC the overshoot of oscillation is slightly reduced. Whereas by implementing the

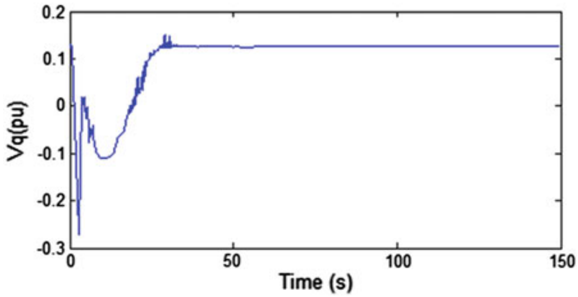

Fig. 113.8 Quadrature voltage

damping controller in SSSC, the overshoot is reduced higher than the previous case. Since the conventional damping controller has delay in control action which is overcome by ANFIS controller. Therefore SSSC based ANFIS controller provide higher damping of oscillation due to quick response.

113.5 Conclusion

Thus the designed ANFIS Controller is found to exhibit better performance characteristics therefore reducing speed deviation compared to other three cases.

From Fig. 113.9, the characteristics of current has no overshoot of the oscillation after implementing ANFIS controller. From Fig. 113.10 the settling time of first case without any controller takes more time to settle at zero speed deviation. It is observed that the designed ANFIS controller quickly react for the change in operating conditions and recover the system to steady state within few seconds when compared to conventional damping controller. The proposed ANFIS controller provide much better damping characteristics to low frequency oscillations under three phase to ground fault and improve the small signal stability by modulating the SSSC injected quadrature voltage.

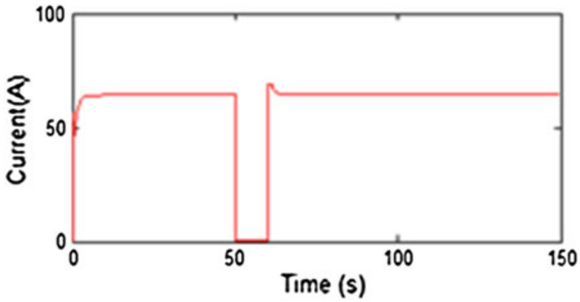

Fig. 113.9 Load current response

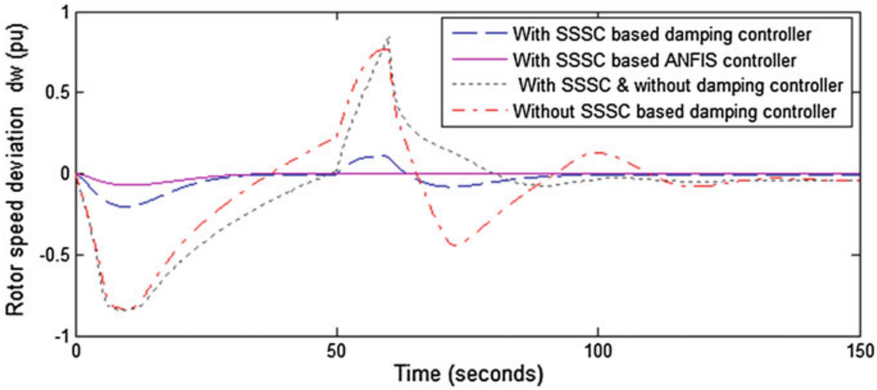

Fig. 113.10 Speed deviation characteristics for four cases

Acknowledgments The authors would like to acknowledge the support of the Thiagarajar college of management, principal and all faculty of EEE department for suggestion and commands.

References

1. Kundur P (1994) Power system stability and control. Mc-Grall Hill, New York
2. Wang HF (2000) Static synchronous series compensator to damp power system oscillations. Electr Power Syst Res 54:113–119
3. Jowder FAL (2005) Influence of mode of operation of the SSSC on the small disturbance and transient stability of a radial power system. IEEE Trans Power Syst 20:935–942
4. Castro MS, Ayres HM, da Costa VF, da Silva CLP (2007) Impacts of the SSSC control modes on small-signal transient stability of a power system. Electr Power Syst Res 77:1–9
5. Khutia SR, Sidhartha panda S (2013) ANFIS approach for SSSC controller design for the improvement of transient stability performance. Math Comput Model 57:289–300
6. Sen KK (1998) SSSC-static synchronous series compensator: theory, modeling, and application. IEEE Trans Power Delivery 13(1):241–246
7. Taheri H, Shahabi S, Taheri S, Gholami A (2009) Application of synchronous static series compensator (SSSC) on enhancement of voltage stability and power oscillation damping. IEEE Trans Power Syst 533–539
8. Panda S, Yegireddy NK, Mohapatra SK (2013) Hybrid BFOA–PSO approach for coordinated design of PSS and SSSC based controller considering time delays. Electr Power Energy Syst 49:221–233
9. Panda S, Swain SC, Rautray PK, Malik RK, Panda G (2010) Design and analysis of SSSC-based supplementary damping controller. Simul Model Pract Theory 18:1199–1213
10. Hingorani NG, Gyugyi L (2000) Understanding FACTS: concepts and technology of flexible ac transmission systems. IEEE Press, New York
11. Das S, Bacterial foraging optimization algorithm: theoretical foundations, analysis, and applications

Chapter 114
Application of Bacterial Foraging Optimization for Elimination of Lower Order Harmonics in Seven Level Inverter

W. Razia Sultana, Sarat Kumar Sahoo, S. Prabhakar Karthikeyan, I. Jacob Raglend, A. Chandrashekar and A. Syam Pradeep

Abstract This paper presents the Bacterial Foraging Optimization (BFO) for elimination of harmonics in a cascaded H-bridge multilevel inverter (MLI). The main aim is to eliminate the dominant lower-order harmonics which is done by solving nonlinear transcendental equations, while maintaining the maximum fundamental component. In this paper, the BFOA algorithm which basically deals with the food foraging behavior of bacteria is applied to a 7-level cascaded MLI for solving these equations. The performance of the BFO is evaluated and the graphs between Switching Angles and Total Harmonic Distortion (THD) with various Modulation Indices (MI) shows that the proposed method gives best optimal solution between MI in the range of 0.7–0.8. The results show that 5th and 7th harmonics are reduced and are maintained minimum.

Keywords Cascaded H-bridge MLI · Bacterial foraging optimization · Selective harmonic elimination · Switching angles · THD · MI

114.1 Introduction

Multilevel inverter is attaining increasing attention in the past few years because of its high voltage and therefore high power capability [1, 2]. There are various modulation methods which includes sinusoidal PWM (SPWM) and space-vector

W. Razia Sultana (✉) · S.K. Sahoo · S.P. Karthikeyan · A. Chandrashekar · A. Syam Pradeep
VIT Universty, Vellore 632014, Tamil Nadu, India
e-mail: wraziasultana@vit.ac.in

S.K. Sahoo
e-mail: sarata1@rediffmail.com

S.P. Karthikeyan
e-mail: spk25in@yahoo.co.in

I.J. Raglend
NI University, Kumaracoil, Thuckalay, Kanyakumari, Tamil Nadu, India
e-mail: jacobraglend@rediffmail.com

C. Kamalakannan et al. (eds.), *Power Electronics and Renewable Energy Systems*,
Lecture Notes in Electrical Engineering 326, DOI 10.1007/978-81-322-2119-7_114

modulation (SVM) to control the output voltage and to reduce unwanted components in multilevel inverters. Selective Harmonic Elimination (SHE) is a technique choosing the switching times so that specific lower order dominant harmonics such as 5th, 7th, and 11th and so on are suppressed in the output voltage connected to the load [3, 4]. The SHE technique involves solving the nonlinear transcendental equations characterizing the harmonic contents, which offers multiple solutions. These equations can be solved through optimization techniques effectively [5]. There are several optimization algorithms such as GA (Genetic algorithm) which emulates the process of biological evolution [6], PSO (Particle Swarm Optimization) inspired by social behavior of bird flocking [7], ACO (Ant Colony Optimization) emulating the foraging behavior of ant colonies [8], Artificial Bee Colony Algorithm (ABC) mimicking foraging behavior of swarm of honey bees [9] have been used extensively for the solving the non-linear equations. In this paper, BFOA is realized to minimize lower-order harmonics, and to maintain the desired fundamental component.

114.2 Cascaded Multilevel Inverter

Among the different topology structures of MLI, Cascaded H-bridge topology has gained more prominence due to their simplicity of its structure and control, modularity and flexibility. The cascaded MLI consists of a series connected H bridge inverter units. Each of the individual cell (full bridge unit) can generate three different output voltage levels: +Vdc, 0, and −Vdc. All the H Bridges connected in series can produce staircase waveform. A 7 level cascade MLI is shown in Fig. 114.1. The level of the output phase voltage in a cascaded MLI is 2V + 1, for V number of dc voltage sources. The phase voltage waveform for a 7-level cascaded multilevel inverter with three separate dc sources (V = 3) is shown in Fig. 114.1. Each H-bridge cell produces a quasi-square waveform by shifting the phase of the switching timings of both of its phase legs.

114.3 Selective Harmonic Elimination PWM

A 7-level MLI waveform shown in Fig. 114.2 has three variables θ_1, θ_2, and θ_3, where all the isolated voltage sources Vdc1, Vdc2, and Vdc3 are equal. The Fourier series expansion of the output phase voltage waveform, is written as the following equation,

$$V(\omega t) = \sum_{n=1}^{\infty} V_n \sin(n\omega t) \tag{114.1}$$

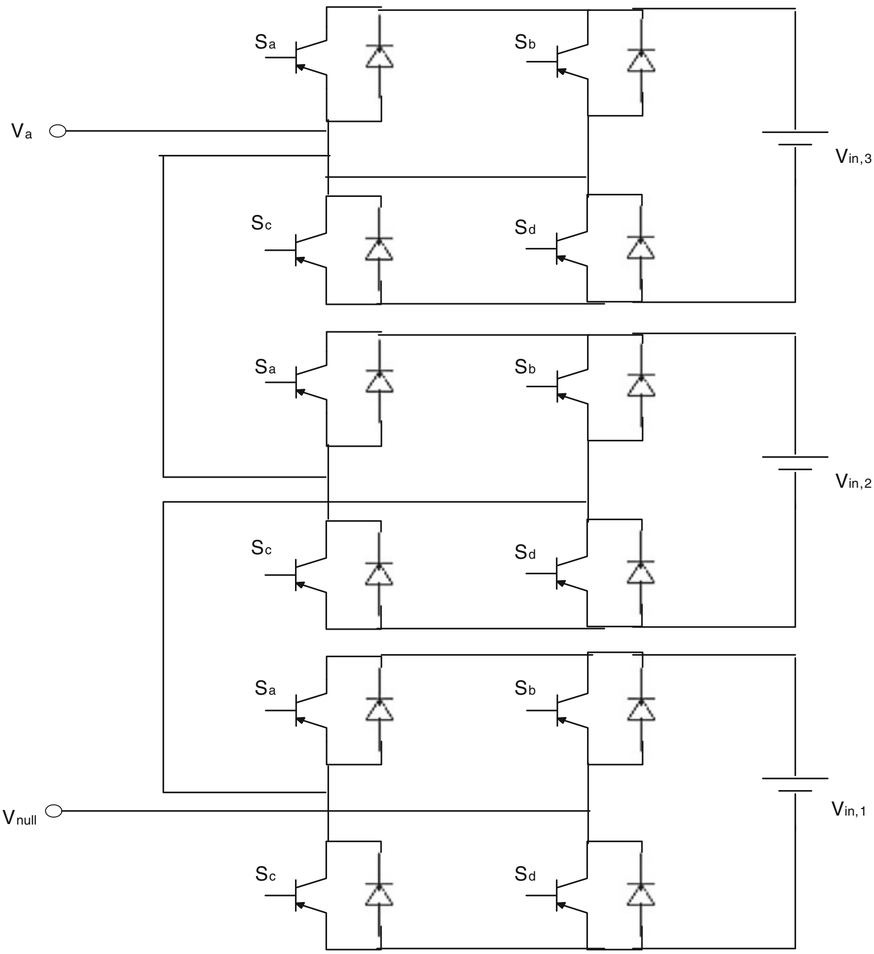

Fig. 114.1 7 level cascaded multilevel inverter

Fig. 114.2 Output voltage waveform of a 7-level MLI

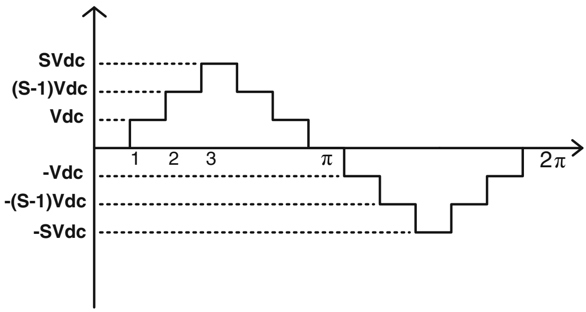

where V_n is the *n*th harmonic component amplitude. The angles of the switches should be restricted between 0 and $\pi/2$ ($0 \le \theta < \pi/2$). Because of odd quarter-wave symmetry, even order harmonics become zero.

The objective of SHEPWM is to eliminate the lower order dominant harmonics. In a 7-level Cascaded MLI the 5th and 7th dominant lower order harmonics are to be eliminated because 3rd harmonic will be eliminated in 3 phase systems. So, in order to obtain the desired fundamental harmonic and to eliminate 5th and 7th harmonics, three non-linear equations with three switching angles are shown in Eq. (114.2),

$$\left.\begin{aligned} V_1 &= \frac{4V_{dc}}{\Pi}[\cos\theta_1 + \cos\theta_2 + \cos\theta_3] \\ V_5 &= \frac{4V_{dc}}{5\Pi}[\cos 5\theta_1 + \cos 5\theta_2 + \cos 5\theta_3] \\ V_7 &= \frac{4V_{dc}}{7\Pi}[\cos 7\theta_1 + \cos 7\theta_2 + \cos 7\theta_3] \end{aligned}\right\} \tag{114.2}$$

In (114.2), V_5 and V_7 are set to zero in order to eliminate 5th and 7th harmonics, respectively. In order to obtain various switching angles a titled modulation index, new index, is defined to be a representative as:

$$MI \triangleq \frac{V_1}{12V_{dc}/\prod}(0 \le MI \le 1) \tag{114.3}$$

Here, *MI* is between 0 and 1 in order to cover various values of V_1. Thus, by replacing Eq. (114.3) in Eq. (114.2) we get the following equations

$$\left.\begin{aligned} MI &= \frac{1}{3}[\cos\theta_1 + \cos\theta_2 + \cos\theta_3] \\ 0 &= [\cos 5\theta_1 + \cos 5\theta_2 + \cos 5\theta_3] \\ 0 &= [\cos 7\theta_1 + \cos 7\theta_2 + \cos 7\theta_3] \end{aligned}\right\} \tag{114.4}$$

Now, the three different switching angles, namely $\theta 1$, $\theta 2$, and $\theta 3$, can be found with respect to the range of *MI*.

114.4 Bacterial Foraging Optimization Algorithm

In recent years BFOA has been recognized as global optimization algorithm and is applied to many fields [10, 11]. BFOA is inspired by food foraging behaviour of Escherichia coli bacterium. Flagella in bacterium help in its two basic operation which are to swim or to tumble, at the time of searching of food (foraging). The foraging is sub-divided into four behaviour's namely chemo taxis, swarming, reproduction, and elimination and dispersal [11, 12].

114.4.1 Chemo Taxis

The foraging behaviour of bacteria is simply defined in two steps i.e. swimming and tumbling, together known as chemo taxis. Depending on the rotation of flagella movement the chemo taxis is defined. If the bacterium is moving in clock-wise rotation then it is swimming and if it is in counter clock-wise, it is tumbling. Suppose θ^a(b, c, d) a denotes a-th bacterium at b-th chemotactic, c-th reproductive and d-th elimination and dispersal step. C(a) is the step size taken in the random direction specified by the tumble [9]. Then the bacterium movement may be represented by

$$\theta^a(b+1,c,d) = \theta^a(b,c,d) + C(a)\frac{\Delta(a)}{\sqrt{\Delta^T(a) * \Delta(a)}} \tag{114.5}$$

where Δ represents a vector in random direction.

114.4.2 Swarming

E. coli bacterium has special sensing and decision making technique. They release unique attractant to make other bacterium to swarm towards them. In the same manner they can warn by repellent.

The mathematical representation for swarming can be represented by

$$\left.\begin{aligned} J_{cc}(\theta, P(a,b,d)) &= \sum_{a=1}^{S} J_{cc}^{a}(\theta, \theta^a(b,c,d)) \\ &= \sum_{a=1}^{S}[-d_{attract}\exp\{-W_{attract}\sum_{m=1}^{P}(\theta_m - \theta_m^a)^2\}] \\ &\quad + \sum_{a=1}^{S}[-h_{repellent}\exp\{-W_{repellent}\sum_{m=1}^{P}(\theta_m - \theta_m^a)^2\}] \end{aligned}\right\} \tag{114.6}$$

where J_{cc} (θ, P (b, c, d) is the value of the cost function required to be added to the real function to be made minimum which presents the cost function varying with time. $d_{attract}$, $\omega_{attract}$, $h_{repelent}$, and $\omega_{repelent}$ are different coefficients which needs to be selected carefully.

114.4.3 Reproduction

After several stages of chemo tactic steps, original group of bacteria attains the reproduction stage. The finest group of bacterium is divided into two groups; the least healthy bacterium is replaced with replica of healthier bacterium. This makes population bacterium constant.

114.4.4 Elimination and Dispersal

When there is some noxious environment. The bacteria are dispersed and eliminated to some arbitrary positions in the optimization territory according to the probability. Because of this elimination-dispersal event the bacterium does not get trapped into local optima

114.5 Implementation

For obtaining the switching angles, the BFOA program code is written using MATLAB software. The parameters to be initialized are number of bacteria required for searching which are initialized as 26 and number of iterations to be undertaken, taken here as 100. The fitness function that is used is given below

$$f = 100\left[\frac{V_1^* - V_1}{V_1^*}\right]^4 + \sum_{S=2}^{S}\frac{1}{h_s}\left[50\frac{V_{h_s}}{V_1}\right]^2 \tag{114.7}$$

V_1^* desired fundamental voltage
V_1 fundamental voltage
h_s order of sth harmonic
V_{h_s} voltage of sth harmonic

The switching angles thus found eliminate the low-order harmonics (5th and 7th) while retaining the maximum fundamental component

114.6 Simulation Results

The software implementation is carried out in MATLAB/SIMULINK environment, for a 7 level cascaded MLI, to validate the results obtained. The voltage of the dc link for all the H-bridge cells used is 100 V and simulation is carried out for various MI. The Switching Angle at MI = 0.8 is found to be optimum as THD is less (Table 114.1).

For these optimum angles the FFT analysis window of output phase voltage of 7 level Cascaded MLI is shown in Fig. 114.3.

Table 114.1 The optimum switching angles, %5th harmonic, %7th harmonic and %THD

MI	θ_1 (degrees)	θ_2 (degrees)	θ_3 (degrees)	% 5th harmonic	% 7th harmonic	% THD
0.1	79.1	87.24	89.43	69.4	76.1	87.2
0.2	52.51	81.3	89.2	66.2	56.12	71.3
0.3	45.21	79.41	88.51	14.4	18.2	44.32
0.4	42.21	64.25	86.35	16.1	11.1	23.5
0.55	28.467	54.28	72.14	3.4	2.4	18.01
0.65	30.12	51.185	68.124	1.4	3.8	16.8
0.7	21.2	45.24	60.82	1.3	2.2	15.01
0.77	13.3548	39.4587	59.3587	0.88	0.94	12.04
0.8	10.4191	31.2453	57.0338	0.61	0.87	11.71
0.82	11.7423	26.4190	54.2139	0.59	0.86	11.82

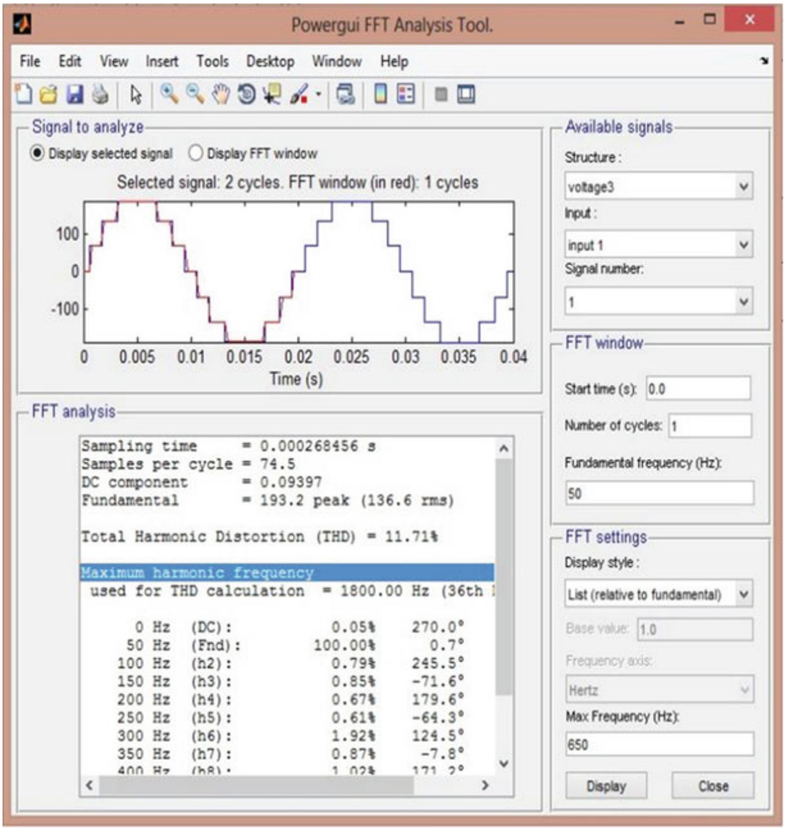

Fig. 114.3 FFT analysis of the output voltage of a 7 level cascade MLI

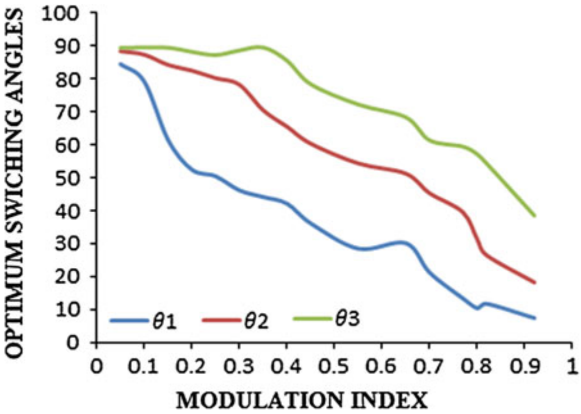

Fig. 114.4 Modulation index versus optimum switching angles

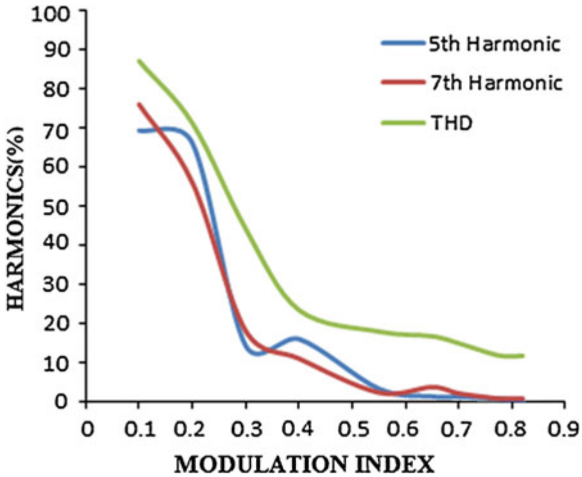

Fig. 114.5 Modulation index versus percentage of lower order harmonics and THD

In Fig. 114.3 we can observe that percentage of 3rd harmonic is 0.85, percentage of 5th harmonic is 0.61 and percentage of 7th harmonic is 0.87.

The algorithm was run for 10 different spells and the best result obtained based on the least obtained fitness function is selected. Figure 114.4 shows the graph between the optimum angles (θ_1, θ_2, θ_3) and the range of MI from 0 to 1 with the step-size of 0.01 and Fig. 114.5 shows the percentage of lower order harmonics and THD versus MI. From the results it can be seen that for the MI of 0.8 the THD obtained is minimum

114.7 Conclusion

Bacterial Foraging Optimization has been successfully applied to the SHE-PWM for a 7 level Cascaded MLI. Simulation results provided for this inverter to validate the accuracy of this algorithm, shows that undesired 5th and 7th harmonics has been efficiently minimized in the output voltage waveform of inverter. The graph between Switching Angles and THD with various MI shows that the suggested method gives the best optimal solution between MI in the range of 0.7–0.8. This work can be further extended by comparing this technique with other optimizing techniques and evaluating the performance of both the techniques.

References

1. Rodríguez J, Lai J, Peng FZ (2002) Multilevel inverters: a survey of topologies, controls and applications. IEEE Trans Ind Electron 49(4):724–738
2. Malinowski M, Gopakumar K, Rodriguez J, Perez MA (2010) A survey on cascaded multilevel inverters. IEEE Trans Ind Electron 57(7):2197–2206
3. Du Z, Tolbert LM, Chiasson JN (2006) Active harmonic elimination for multilevel converters. IEEE Trans Power Electron 21(2):459–469
4. Tang T, Han J, Tan X (2006) Selective harmonic elimination for a cascade multilevel inverter. Proc IEEE Int Symp Ind Electron 2:977–983
5. Mishra S, Bhende CN (2007) Bacterial foraging technique-based optimized active power filter for load compensation. IEEE Trans Action Power Delivery 22(1)
6. Tolbert LM, Chiasson JN, McKenzie K, Du Z (2003) Elimination of harmonics in a multilevel converter with non-equal DC sources. In: Proceedings of IEEE applied power electronic conference, Miami, FL, pp 589–595
7. Salehi R, Farokhnia N, Abedi M, Fathi SH (2011) Elimination of low order harmonics in multilevel inverter using genetic algorithm. J Power Electron 11(2):132–139
8. Sundareswaran K, Jayant K, Shanavas TN (2007) Inverter harmonicelimination through a colony of continuously exploring ants. IEEE Trans Ind Electron 54(5):2558–2565
9. Kavousi A, Vahidi B, Salehi R, Bakhshizadeh MK, Farokhnia N, Hamid Fathi S (2012) Application of the bee algorithm for selective harmonic elimination strategy in multilevel inverters. IEEE Trans Power Electron 27(4):1689–1695
10. Vahedi H, Hosseini SH, Noroozian R (2010) Bacterial foraging algorithm for security constrained optimal power flow. In: 2010 7th international conference on the european energy market (EEM), pp 1, 6, 23–25 June 2010
11. Passino KM (2002) Biomimicry of bacterial foraging for distributed optimization and control. IEEE Control Syst 22(3):52, 67
12. Salehi R, Vahidi B, Farokhnia N, Abedi M (2010) Harmonic elimination and optimization of stepped voltage of multilevel inverter by bacterial foraging algorithm. J Electr Eng Technol 5 (4):545–551

Chapter 115
Affine Invariant Shape Descriptor Using Object Area Normalization

P. Arjun, T.T. Mirnalinee, S. Sindhuja and G. Bharathi Raja

Abstract Shape features play vital role in computer vision applications. The object silhouettes provide more evident properties for shape matching, and analysis. This paper presents contour and region based affine invariant shape descriptor based on object area normalization. The continuous contour is normalized by dividing total object area into equal part areas using sector area approach. This forms the 1-D feature vector to represent image object characteristics. The correlation coefficient and Euclidean distance are the metrics used for similarity measurement. The proposed method is validated on MPEG-7 CE Shape-1 Part-B dataset images and its affine variants. From the experimental results, it is observed that normalization based on area of the sector is more accurate in representing contour and region information than triangle area method. Moreover, this work can be adapted in object recognition and image retrieval tasks.

Keywords Object matching · Affine enclosed area · Object area normalization · Feature extraction · Contour normalization

P. Arjun (✉) · G. Bharathi Raja
CSE, University College of Engineering, Villupuram, India
e-mail: arjun_ucev@ymail.com

G. Bharathi Raja
e-mail: bharathirajaag@gmail.com

T.T. Mirnalinee
CSE, SSN College of Engineering Chennai, Chennai, India
e-mail: mirna123@gmail.com

S. Sindhuja
CSE, VRS College of Engineering and Technology, Villupuram, India
e-mail: sindhuja.vrs@gmail.com

C. Kamalakannan et al. (eds.), *Power Electronics and Renewable Energy Systems*,
Lecture Notes in Electrical Engineering 326, DOI 10.1007/978-81-322-2119-7_115

115.1 Introduction

An image is an entity that carry rich amount of information than other kind of data. Every day millions of images are generated from consumer digital camera, medical field, engineering designs, animated images, biometric images, barcode images, satellite images etc. The growth of image data generated is exponential order since last two decades because rapid developments in computers and internet. It is very much essential to develop appropriate image processing and retrieval techniques for handling and efficient processing of digital images.

This work focuses on shape feature extraction and the shape provides powerful clues for object identification. From the Ref. [1] it is found that 71 % of image users are interested in shape based retrieval because shape is considered the most promising for the identification of objects in an image.

The affine transformation gets influence in applications in which the object shape is subject to change, due to movement of object or camera viewpoint changes with respect to the object, the resulting boundary of the object will be deformed. This deformation can be approximated by general affine transformations like translation, scaling, rotations, shearing etc.

In this paper, a sector area based affine invariant shape descriptor is proposed to represent the shape information. This method is evaluated with MPEG-7 CE Shape-1 Part-B dataset images using Euclidean distance and correlation coefficient against the affine variants of the query image.

The reminder of this paper is organized as follows. Section 115.2 presents study on shape feature extraction. Section 115.3 presents detailed explanation about working principles of Object Area Normalization. Section 115.4 discusses experimental results. Finally Sect. 115.5 concludes this paper.

115.2 Literature Review

Shape feature extraction methods are broadly classified into region based and contour based [2]. The region based methods account all pixels present inside the object shape e.g. Zernike moments, shape matrix etc. In contour based approaches, shape is defined by (x, y) coordinates of its boundary points e.g. CSS, polygonal approximation, chain code etc. Contour based methods are further divided into transform domain (e.g. Fourier Descriptor) and spatial domain (e.g. CSS, Chain code).

A good shape descriptor satisfies many of the following quality parameters [3, 1]: completeness, compactness, simplicity, accessibility, large scope, uniqueness, stability, high discrimination capability, computational efficiency, robustness to distortion and noise.

To date, numerous shape feature extraction works published. Some of the notable shape feature extraction methods discussed by Yang et al. [3] are Bounding

Box, Convex Hull, Shape Context, Chord Distribution, Shock Graphs, Zernike Moments, Radial Chebychev Moments, Homocentric Polar-Radius Moment, Curvature Scale Space (CSS), Intersection Points Map, R-Transform, Edge Histogram Descriptor etc.

Simple and fast one dimensional binary shape object features are Area, Centroid, Axis of Least Inertia, Eccentricity, Perimeter, Thinness Ratio, Irregularity, Aspect Ratio, Euler Number etc. The classical image retrieval system Query By Image Content (QBIC) combines many of the above statistical one dimensional features for image retrieval [4].

The affine enclosed area based equal area normalization by Yang et al. [5] works better than equidistant vertices normalization using arc length parameter [6]. The object contour is normalized to 'N' points. The normalized points are obtained by split the shape area into equal area parts with respect to object centroid. This shape descriptor satisfies affine invariance property and robust to shape deformations and noise on shapes.

Alajlan et al. [1] proposed a triangle area representation (TAR) method for shape retrieval. Arica et al. [7] proposed a shape descriptor called Beam Angle Statistics (BAS). The object contour is normalized into N boundary points.

A shape descriptor developed by Bernier and Landry [8] for representing and matching natural objects shapes using boundary points of an object with their distances and centroid provides better results for irregular closed contour shapes. Similarly a shape representation method designed by Lin et al. [2] works in polar coordinate form, they describes feature vector as contour point-centroid distance and angle (d, θ).

Abbasi et al. [9] proposes Curvature Scale Space (CSS) descriptor. The contour is normalized by arc-length parameter, in which the boundary is resembled and represented by fixed number of equally distant points.

Simple and fast shape descriptors are in need today. Following are the common challenges of shape feature extraction: viewpoint changes, recognition from cluttered scenes, recognition from occluded objects and recognition from object shape deformed image. Primary challenge is to recognize the object with varying viewpoints.

The proposed work is based on Equal Area Normalization published by Yang et al. [5]. The goal of this work is to recognize object shape with viewpoint changes and various deformations. In the proposed work the object shape is represented by 1-D feature vector composed of equal part area segments using area of the sector approach. This Object Area Normalization is a contour based affine invariant shape feature extraction method works only on closed contour objects. The number of segments is of user's choice. The proposed method performs well for recognizing arbitrary shape objects and non-rigid shaped objects and satisfies affine invariance property. The area of the sector approach preserves contour and region information of the shape. For similarity measurement the Euclidean distance and correlation coefficient are used. This proposed idea can be adapted for object recognition systems, video surveillance, object tracking and monitoring, and CBIR systems.

115.3 Object Area Normalization

Object area normalization is a curve normalization technique; it takes only boundary pixels of the object to describe the object shape. The continuous contour is normalized into fixed (N) number of vertices. The parametric equation of closed curve is:

$$\Gamma(\mu) = [x(\mu),\ y(\mu)] \tag{115.1}$$

where $\mu \in \{1, 2, \ldots N\}$. The arc length, enclosed area, centroid distance, centroid angle are the parameters used to describe an object shape. The complete system diagram of the work is shown in Fig. 115.1 which includes three major steps: image preprocessing, shape feature extraction and similarity matching.

Image Preprocessing. The image preprocessing step makes the input image suitable for further steps. In this work zero padding, holes removal, edge smoothing operations are applied.

Zero Padding. If the object boundary touches border of the image, it produces discontinuities while extracting the contour pixels. Zero padding prevents this problem by adding zero valued pixels on all sides of the image.

Holes removal. We are only using object contour information for shape feature extraction, other details are not necessary. This step removes small details and not closed edges present inside object shape.

Edge Smoothing. The contour curve is smoothening by Gaussian filter. It closes narrow isthmuses and eliminating thin protrusions.

Shape Feature Extraction. After preprocessing, the object boundary pixels are extracted from a specified starting point in clockwise or anti-clockwise direction. The starting point is chosen as farthest contour point from the centroid. The shape feature extraction is described in the following steps:

Step 1. Extract the contour pixels in sequence using Moore-edge following algorithm [10] and represented it as ($\Gamma_{\mu+i}$, $i \in \{0, 1, 2, \ldots m-1\}$ and 'm' is number of boundary pixels) and find centroid (G), total object area (S) and equal part area (S_{part}).

Centroid. To represent a shape for affine invariance, the centroid is calculated. Centroid is the geometric centre of a plane object. It is the reference point in a plane area such that the moment of the area, about any axis, through that point is zero.

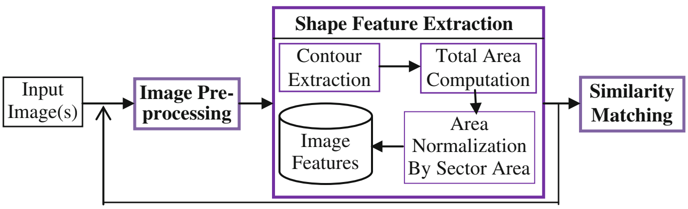

Fig. 115.1 Schematic diagram of object area normalization

The centroid of an image is rotationally invariant. The centroid for the object shape with 'n' pixels is calculated using formula given below:

$$G_x = \sum_{i=1}^{n} \frac{x_i}{n} \quad \text{and} \quad G_y = \sum_{i=1}^{n} \frac{y_i}{n} \qquad (115.2)$$
$$\text{Centroid (G)} = (G_x, G_y)$$

For easy computation, the centroid is transformed to origin that is $(G_x, G_y) = (0, 0)$.

Total Object Area and Equal Part Area. The total area S of the object shape is calculated using summation of all white pixels enclosed within object boundary. Divide the object area into 'N' equal parts. Approximate area of each part is computed using $S_{part} = S/N$.

Step 2. Object area normalization is performed. After normalization, the new points obtained are represented by ($P_{\mu+i,}$ $i \in \{0,1,2,\ldots N-1\}$ and m > N). The diagrammatic representation of object area normalization is shown in Fig. 115.2.

Select the starting point in normalized contour as $P_\mu = \Gamma_\mu$. From the point P_μ follow on the adjacent pixels ($\Gamma_{\mu+i}$, and $i \in \{0, 1, 2, \ldots m-1\}$) of the continuous contour to compute the area of the segment $(P_{\mu,} \Gamma_{\mu+i,} G)$ is given in Eq. 115.3 and compared with S_{part}.

$$Sector\ Area\,(P, \Gamma, \mathrm{G}) = \frac{1}{2} \times \left(\frac{r_P + r_\Gamma}{2}\right)^2 \times \theta \qquad (115.3)$$

where (r_p, r_Γ)—distance from G to P and Γ, and θ—angle between r_p and r_Γ.

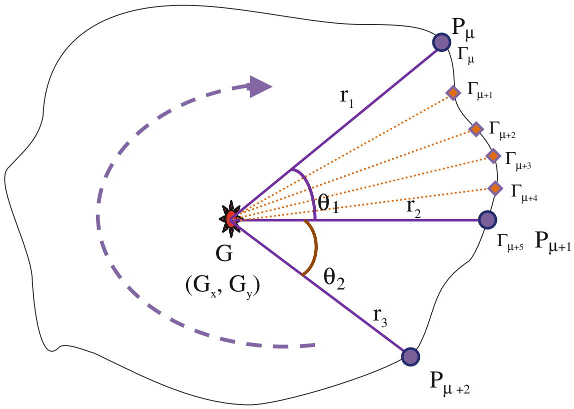

Fig. 115.2 Illustration of object area normalization. P_μ is a starting point and centroid is assumed G = (0,0). The actual contour points of the shape are $(\Gamma_\mu, \Gamma_{\mu+1}, \Gamma_{\mu+2} \ldots \Gamma_{\mu+n-1})$ in sequence, and $(P_\mu, P_{\mu+1}, P_{\mu+2} \ldots P_{\mu+N-1})$ are normalized contour points

$$r_p = ((P_x - G_x)^2 + (P_y - G_y)^2)^{1/2}$$
$$r_\Gamma = ((\Gamma_x - G_x)^2 + (\Gamma_y - G_y)^2)^{1/2}$$
$$\theta = \tan^{-1}\left|\frac{M_P - M_\Gamma}{1 + M_P \cdot M_\Gamma}\right|$$

where M_P, M_Γ—slope of lines (P, G), and (Γ, G).

$$M_P = \frac{P_y - G_y}{P_x - G_x},\ M_\Gamma = \frac{\Gamma_y - G_y}{\Gamma_x - G_x}$$

When the computed area of the segment is equal to S_{part}, mark this pixel coordinates as $P_{\mu+1}$. Now the current point $P_{\mu+1}$ as starting point and the same procedure is applied to find the points $P_{\mu+2}$, $P_{\mu+3}\ldots P_{\mu+N-1}$. The first and last points are same, $P_\mu = P_{\mu+N}$. The final set of points $\{P_\mu, P_{\mu+1}, P_{\mu+2}\ldots P_{\mu+N-1}\}$ are normalized contour points. At the end of this normalization N numbers of equal part area values form an equal part area vector (*f*) of size N. Normalized equal part area vector is obtained by $f = f/S$.

Similarity Matching. This step compares feature vectors of query and affine transformed images to show degree of closeness with different shape deformations. According to Bai et al. [11] measuring the similarity between two shapes often can be done in two ways: (1) computing direct difference in features extracted from shape contours, which are invariant to the choice of starting points and robust to certain degree of deformation; (2) performing matching to find the detailed point-wise correspondences to compute the differences, it is computationally expensive. Here the feature vectors of query image f_q and affine version of that image f_a, and a $\in \{1, 2, \ldots n\}$ using Euclidean distance and correlation coefficient.

115.4 Experimental Results

This shape descriptor is tested on MPEG-7 CE Shape-1 Part-B dataset described by Latecki [12], which contains 1,400 GIF format binary images with 70 classes and each class with 20 different images. The experiments are conducted on subset of images from this dataset contains closed contour shapes. For illustration, the complete sets of experiments are done on an image object shape and its affine variants to show the effectiveness of the object area normalization. End of this section evaluates the experimental results for ten different category object shapes.

The affine transformed images are created from the input image with the linear scale factor 1.1 to 2.0, rotated for every 15° and shearing factor is −1.7 to +1.7. Figure 115.3 shows the experiment is applied to "tree-5" image from the dataset and its affine variants.

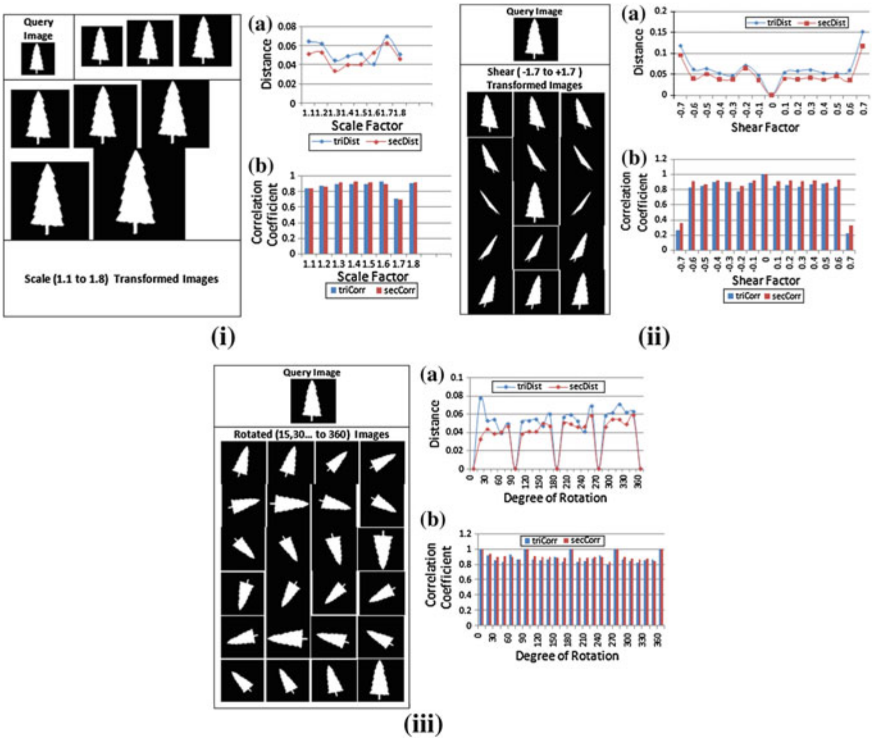

Fig. 115.3 Euclidean distance and correlation coefficient results for “tree-5” image and its affine transformed images. **i** Scale transformation. **ii** Shearing transformation. **iii** Rotation transformation

From the Fig. 115.3, the graph results along with affine transformed images are shown for “tree-5” image. The Euclidean distance results (a) are shown in line chart and correlation coefficient results (b) are shown in bar chart. Among different affine transformations, the sector area approach performs good for all cases in shearing transformation, for rotation transformations out of 24 rotated images the sector area method gives higher correlation results on 21 images and for scale transformations out of 8 images sector area method performs better on 6 images. All of the above graph results show the effectiveness of sector area method. More than 85 % of comparison results of Euclidean distance and correlation coefficient values favor area normalization using sector area method.

The above experiment is applied to other images present in the dataset. In the following Table 115.1, the experimental results for ten different category object shapes are shown. The average Euclidean distance values using triangle area and sector area are denoted by TA_D_E and SA_D_E respectively. Similarly the average correlation coefficient values for triangle area and sector area are represented by TA_r and SA_r respectively. For each query image and its 50 affine versions the following comparison is prepared. Assume the contour is normalized by N = 80 points.

Table 115.1 Experimental results for ten different categories of object shapes

Query image name	TA_D_E	SA_D_E	TA_r	SA_r
Cellular_phone-6	0.0590	0.0464	0.8687	0.9227
Classic-9	0.0513	0.0405	0.9158	0.9190
Device0-8	0.0412	0.0290	0.9348	0.9249
Dog-3	0.0715	0.0304	0.9266	0.9540
Flatfish-12	0.0398	0.0327	0.9043	0.9253
Fork-13	0.1001	0.0485	0.8419	0.8780
Guitar-1	0.0638	0.0572	0.8099	0.8464
Personal_car-15	0.0426	0.0439	0.8967	0.9067
Shoe-20	0.0323	0.0327	0.9262	0.9276
Teddy-09	0.0545	0.0503	0.8887	0.9047

For all the category of shapes mentioned in the Table 115.1, the SA_D_E value is smaller than TA_D_E for all images except personal_car-15 and shoe-20. The SA_r value is greater than TA_r for all images except device0-8 image. Most of the cases correlation coefficient value is above 90 % for object area normalization using sector area method. From these results, it is observed that sector area based shape descriptor is invariant to all affine transformations and it preserves contour and region information of the shape.

115.5 Conclusions

By using contour information, an affine invariant shape descriptor based on object area normalization is proposed. The continuous contour is normalized by dividing total object area into equal part areas using sector area approach. This shape representation is a simple and fast one dimensional feature vector consists of normalized equal part area values. The limitations are it works on closed contour objects and fixed starting points. The MPEG-7 CE Shape-1 Part-B dataset is used for experiments. From the experimental results, it is observed that sector area method works superior than triangle area approach. This shape descriptor can be used for object recognition and CBIR systems design. Optimal selection of number equal part areas (N) is one of the feature directions of this work.

References

1. Alajlan N, El Rube I, Kamel MS, Freeman G (2007) Shape retrieval using triangle-area representation and dynamic space warping. Pattern Recogn (Elsevier) 40:1911–1920
2. Lin HJ, Kao YT, Yen SH, Wang CJ (2004) A study of shape-based image retrieval. In: Proceedings of the 24th international conference on distributed computing systems workshops, pp 118–123

3. Yang M, Kpalma K, Ronsin J (2012) Shape-based invariant feature extraction for object recognition. In: Advances in reasoning-based image processing, analysis and intelligent systems: conventional and intelligent paradigms, version 1, pp 1–60
4. Ashley J, Barber R, Flickner M, Hafner J, Lee D, Niblack W, Petkovic D (1994) Automatic and semiautomatic methods for image annotation and retrieval in QBIC. In: Proceedings of storage and retrieval for image and video databases (SPIE) III, vol 2420, pp 24–35
5. Yang M, Kpalma K, Ronsin J (2007) Affine invariance contour descriptor based on the equal area normalization. IAENG Int J Appl Math 36(5)
6. Tieng QM, Boles WW (1997) Wavelet-based affine invariant representation: a tool for recognizing planar objects in 3D space. IEEE Trans Pattern Anal Mach Intell 19(8):846–857
7. Arica N, Vural F (2003) BAS: a perceptual shape descriptor based on the beam angle statistics. Pattern Recogn Lett 24
8. Bernier T, Landry JA (2003) A new method for representing and matching shapes of natural objects. Pattern Recogn 36:1711–1723
9. Abbasi S, Mokhtarian F, Kittler J (1999) Curvature scale space image in shape similarity retrieval. Multimedia Syst (Springer) 467–476
10. http://www.imageprocessingplace.com/downloads_V3/root_downloads/tutorials/contour_tracing_Abeer_George_Ghuneim/moore.html
11. Bai X, Wang B, Yao C, Liu W, Zhuowen T (2012) Co-transduction for shape retrieval. IEEE Trans Image Process 21(5):2747–2757
12. Latecki LJ, Lakamper R, Eckhardt U (2000) Shape descriptors for non-rigid shapes with a single closed contour. In: IEEE conference on computer vision and pattern recognition (CVPR), pp 424–429

Chapter 116
Automatic Classification of CC View and MLO View in Digital Mammograms

K. Vaidehi and T.S. Subashini

Abstract Digital mammography is the reliable method to detect breast cancer in the benign stage. Mammograms are taken in different views for examining the breast. Mammogram view classification is a preliminary step in content based mammogram retrieval system and this study aims at automatic classification of mammogram based on the standard mammographic views namely CC view and MLO view. The proposed methodology is tested with 320 images, which includes CC view and MLO view mammograms of both right side and left side breasts. In this work, connected component labeling is used for artifact removal. Angle and length features are used as key features for classification. K-means clustering and KNN classifiers are used for classification. The result demonstrates that K-means clustering outperforms the KNN classifier with an accuracy rate of 96.69 %.

Keywords Mammograms · CC view · MLO view · View classification

116.1 Introduction

Breast cancer is one of the leading cancers in the world. There are about 1.4 million new cases of breast cancer worldwide annually, and it comprises 10 % of all cancers, making it the second most common cancer in the world [1]. Additionally, studies have shown that Indian women develop breast cancer roughly decade earlier than women in western countries. The Indian Cancer Society has declared 2013 as Breast Cancer Awareness Year and is taking various necessary actions to increase awareness in people. Mammogram is the X-ray image of the human breast and is a

K. Vaidehi (✉) · T.S. Subashini
Department of Computer Science and Engineering, Annamalai University, Annamalai Nagar, Chidambaram, India
e-mail: vainakrishna@gmail.com

T.S. Subashini
e-mail: rtramsuba@gmail.com

C. Kamalakannan et al. (eds.), *Power Electronics and Renewable Energy Systems*,
Lecture Notes in Electrical Engineering 326, DOI 10.1007/978-81-322-2119-7_116

visual aid to the radiologist to detect early breast cancer and to increase treatment options and survival rate [2]. A computer-aided detection (CAD) system can assist the radiologist to detect the breast cancer in the benign stage and helps to improve the accuracy of detection. The CAD systems act as a second reader and the final decision is made by the expert radiologist.

There are two primary mammogram views such as craniocaudal (CC) view and mediolateral oblique (MLO) view and are most commonly used for screening and diagnostic mammographic examinations. A craniocaudal view is a top to bottom view and it show as much as possible of glandular tissue (ducts and lobes), the surrounding fatty tissue and the outermost edge of chest wall muscle. Nipple will be shown in a profile. The craniocaudal view cannot capture much of the breast tissue that is in armpit and upper chest. A mediolateral oblique view is a side view taken at an angle. It will show glandular as well as fatty tissue and it covers a larger area than a CC view [3]. Left and right CC view and MLO view images are shown in Fig. 116.1.

A standard views namely MLO view and CC view and numerous additional views are explained in [4]. A CAD system used for detecting breast cancer in digital mammograms is given in [5]. Current status and future perspectives of CAD schemes using CBIR approaches have been investigated and developed for detecting abnormalities depicted on mammograms are discussed in [6]. CAD scheme for detecting the suspicious mass regions in mediolateral oblique views and craniocaudal views is given in [7]. High intensity artifacts present in the mammogram is eliminated by applying connected component labeling in our previous works [8, 9]. In [10] CC views and MLO views were manually separated for the analysis of content based mammogram image retrieval. In this paper it is proposed to automate classification of mammograms based on the CC views and MLO views and this is the first step towards creating a CBIR system.

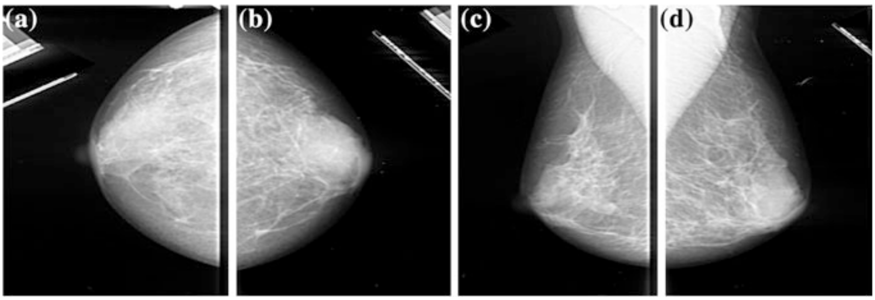

Fig. 116.1 **a** *Left* CC view; **b** *Right* CC view; **c** *Left* MLO view; **d** *Right* MLO view

116.2 Proposed Method

The various phases of the proposed method are shown in Fig. 116.2.

116.2.1 Data Source

The proposed work was done using the Digital Database for Screening Mammography (DDSM) database, which is freely available for download at [11, 12].

116.2.2 Preprocessing

A mammogram image may contain radio opaque artifacts which may hinder further processing and lead to misclassification results. So in this work as a preprocessing step artifact removal is done. Artifact is defined as any variation in mammographic density not created by true attenuation differences in the breast [13]. Otsu's thresholding method is used to binarize the mammogram before applying connected component labeling. Larger component namely the breast region is retained eliminating the other smaller components which contains artifacts and other labels. An original mammogram image and the obtained artifact less mammogram images are shown in Fig. 116.3a, b.

116.2.3 Feature Extraction

The feature extraction phase consists of two steps: (1) Identifying the breast side and flipping it if right side. (2) Finding the orientation of the breast.

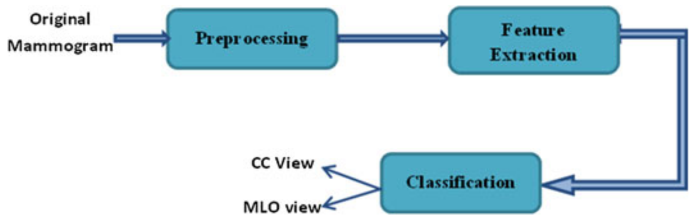

Fig. 116.2 Various phases of the proposed method

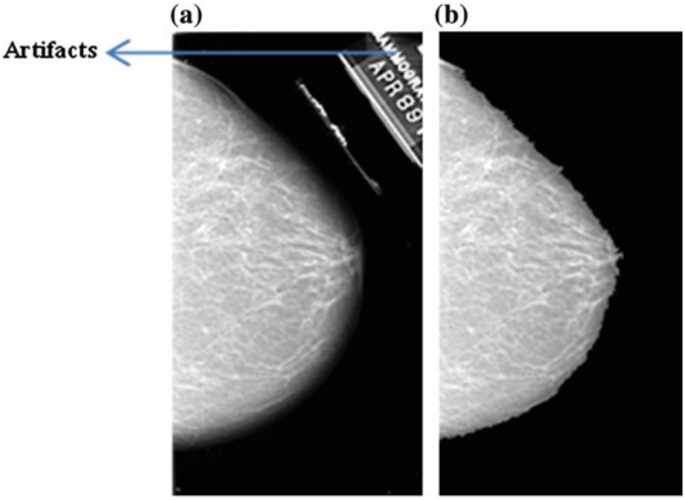

Fig. 116.3 **a** Original mammogram image with artifacts; **b** Artifact removed mammogram image

116.2.3.1 Identifying the Breast Side

Normally, two views namely CC and MLO view are performed both on the left and right side breasts while taking mammograms. The proposed methodology aims to automatically identify the views in both right and left mammograms. This will be useful for automatic annotation of the mammogram for CBIR. For identifying the breast side, raster scanning is done from the right corner to left corner on each row and the pixel which is lying in the breast region are detected, counted and stored. This process is repeated for all the rows and the row which has the maximum count value is marked as AB and is shown in Fig. 116.4a.

Now the sum of non-zero pixels (intensities of all the pixels) lying in first 5 columns starting at the column location of point A is found out and it is denoted as SUM (A). Similarly the sum of number of non-zero pixels (intensities of all the pixels) lying in last 5 columns ending at the column location of point B is find out and denoted as SUM (B). If SUM (B) is greater than SUM (A), it indicates that the given image is left side breast else it is right side breast. SUM (A) and SUM (B) is shown in Fig. 116.4b, c. To make computation easy the right side breast is first flipped to left side.

116.2.3.2 Finding the Orientation of the Breast

To find the orientation of the breast point C is now found out by scanning the column represented by point B moving row by row upwards starting from point B till the first white or black pixel is encountered. The pixel at the penultimate row in that column is marked as point C. Figure 116.5 shows the triangle ABC.

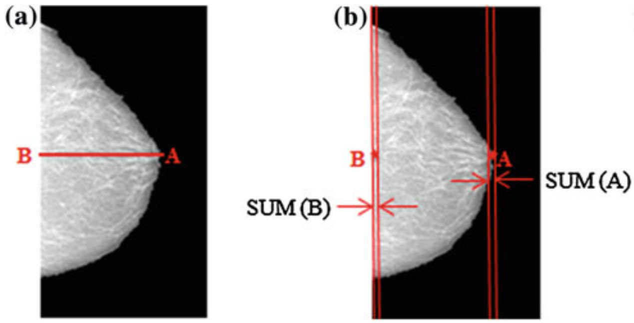

Fig. 116.4 **a** Line BA marked (*largest length line*) mammogram image; **b** Calculating SUM (A) and SUM (B) in a *right* breast; **c** *Right side* breast flipped into *left side* (SUM (B) > SUM (A) hence flipped)

Fig. 116.5 Points *A*, *B*, *C*, *D* and angle are marked

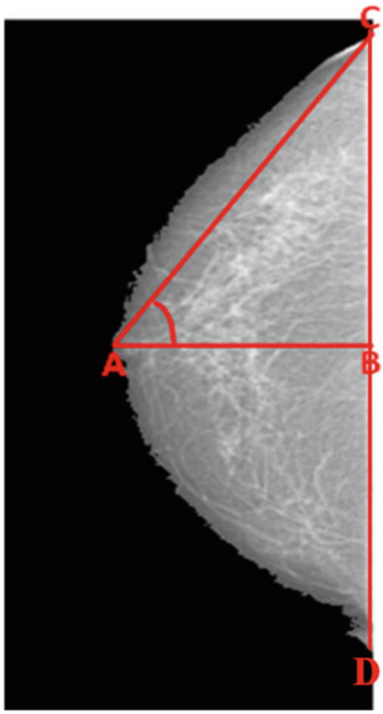

In this work for classifying the breast based on 4 features (angle and 3 length features) are calculated. The steps to determine the angle ∠BAC is given below.

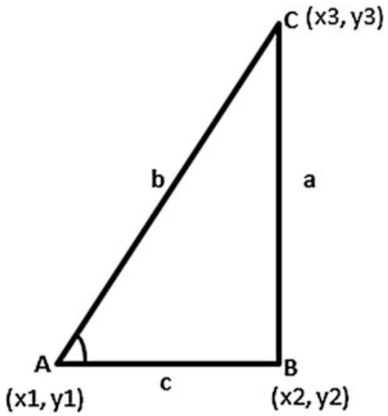

Step 1: Distance between the three sides are found out by using the expressions given in Eqs. (116.1), (116.2) and (116.3).

$$AB = c = \sqrt{(x2 - x1)^2 + (y2 - y1)^2} \tag{116.1}$$

$$BC = a = \sqrt{(x3 - x2)^2 + (y3 - y2)^2} \tag{116.2}$$

$$CA = b = \sqrt{(x1 - x3)^2 + (y1 - y3)^2} \tag{116.3}$$

Step 2: Then the angle is calculated using expressions (116.4) and (116.5)

$$\cos A = \frac{b^2 + c^2 - a^2}{2bc} \tag{116.4}$$

$$A = \cos^{-1}\left(\frac{b^2 + c^2 - a^2}{2bc}\right) \tag{116.5}$$

The length BC and length BD are considered as a second and third feature respectively. Finally, the length ACis taken as a fourth feature. In this work, 160 MLO view and 160 CC view mammograms were taken and 4 dimension feature vectors was obtained for the 320 images, which will be fed to the K-means and KNN for view identification.

116.3 Results

Two volume of DDSM database namely Normal_01 and Normal_02 is used for this study. 160 images of both views and both sides are taken from each volume. 4 features namely angle, BC, BD and AC are extracted from each image to obtain 320

Table 116.1 Accuracy of mammogram views classification using K-means clustering and KNN

K-means				KNN		
No. of features used	CC view (%)	MLO view (%)	Overall accuracy (%)	CC view (%)	MLO view (%)	Overall accuracy (%)
4	92.85	90.90	91.87	92.30	88.88	90.59
2	96.43	96.96	**96.69**	99.99	88.88	**94.43**

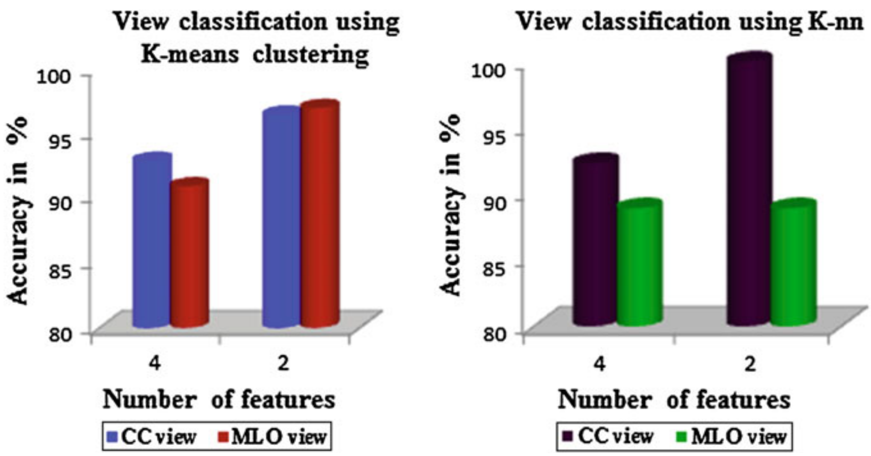

Fig. 116.6 Accuracy of mammogram view classification using K-means clustering and KNN

four dimension feature vectors. These feature vectors are used for classification using K-means clustering and KNN classifiers and the accuracy obtained is 91.87 and 90.59 % respectively.

Then it was experimented with the two features angle and length BC alone and the performance was improved with 96.69 and 94.43 % using K-means and KNN respectively. Angle and length BC is the most predominant features among the 4 features extracted and it was able to classify the views with better accuracy rate. When compared with KNN, K-means clustering offers a better performance of 96.69 %. Table 116.1 shows the obtained results. Figure 116.6 shows the accuracy rate of the proposed system for K-means and KNN using 2 and 4 features respectively. Figure 116.7 compares the overall accuracy obtained using 2 and 4 features using K-means and KNN. It can be seen that K-means gives better performance than KNN for using 2 and 4 features.

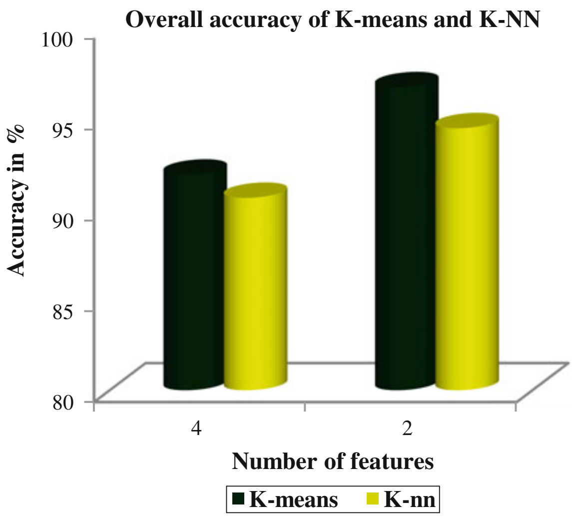

Fig. 116.7 Overall accuracy of K-means and KNN classifiers

116.4 Conclusion

A new method for CC view and MLO view classification is proposed in this paper. Totally 320 images were taken up for the study from DDSM database. The accuracy achieved was 96.69 and 94.43 % using K-means clustering and KNN classifier respectively. The orientation is a important factor for classifying the CC view and MLO view mammogram images. The view classification is the preprocessing step for content based mammogram image retrieval and annotation of mammographic images. In our future work, the method may be extended to automate the detection of other views for improving the CAD results.

Acknowledgments The authors would like to thank Dr. M.K. Sivakkolunthu, Professor of Radiology, Raja Muthiah Medical College Hospital, Annamalai Nagar for his valuable help and comments in carrying out this work. The work has been done under University Grants Commission (UGC) Major Research Project. The financial support of UGC is greatly acknowledged with appreciation.

References

1. Bailey L (2013) The growing problem of breast cancer in India. University of Michigam, USA
2. Ehresman LK, Shratter LA (2013) Encyclopedia of surgery mammography
3. Stephan P (2012) Mammogram views for routine and diagnostic screening. Breast Cancer
4. Kruger G, Radswiki et al. Mammography views. radiopedia.org/articles/mammography-views
5. Kim SJ, Moon WK, Cho N, Cha JH, Kim SM, Im J-G (2006) Computer-aided detection in digital mammography: comparison of craniocaudal, mediolateral oblique, and mediolateral views. Radiology 241(3):695–701

6. Zheng B (2009) Computer-aided diagnosis in mammography using content-based image retrieval approaches: current status and future perspectives. Algorithms 2(2):828–849
7. Van Engeland S, Timp S, Karssemeijer N (2006) Finding corresponding regions of interest in mediolateral oblique and craniocaudal mammographic views. Med Phys 33:3203
8. Subashini TS, Ramalingam V, Palanivel S (2010) Automated assessment of breast tissue density in digital mammograms. Comput Vis Image Underst 114(1):33–43
9. Vaidehi K, Subashini TS (2013) Automatic Identification and elimination of pectoral muscle in digital mammograms. Int J Comput Appl 75(14):15–18
10. Kinoshita SK, de Azevedo-Marques PM, Pereira RR Jr, Rodrigues JAH, Rangayyan RM (2007) Content-based retrieval of mammograms using visual features related to breast density patterns. J Digit Imaging 20(2):172–190
11. Bowyer K, Kopans D, Kegelmeyer WP, Moore R, Sallam M, Chang K, Woods K (1996) The digital database for screening mammography. In: Proceedings of the third international workshop on digital mammography, Chicago. http://marathon.csee.usf.edu/Mammography/Database.html
12. Heath M, Bowyer K, Kopans D, Moore R, Kegelmeyer P (2001) The digital database for screening mammography. In: Yaffe MJ (ed) Proceedings of the fifth international workshop on digital mammography. Medical Physics Publishing, ISBN 1-930524-00-5, pp 212–218
13. Otsu N (1979) A threshold selection method from gray-level histograms. IEEE Trans Syst Man Cybern 9(1):62–66

Chapter 117
Power Quality Improvement in a Wind Farm Connected to Grid Using FACTS Device

C.K. Subasri, S. Charles Raja and P. Venkatesh

Abstract This paper presents the method to mitigate voltage sag in wind farms interconnected with power grid. Flexible Alternate Current Transmission System plays a major role to overcome the power quality problems. Power quality problem is great issue with the increasing of wind penetration in power system. Among the power quality problem voltage sag is one of the most challenging problem faced by power system engineers. These voltage fluctuations can be eliminated with the help of advanced reactive power compensator SVC. The controller is designed based on Synchronous Reference Frame theory. The performance is analyzed with the help of PI controller and Fuzzy logic technique. The simulation studies have demonstrated the effective influences of the SVC on the improvement of voltage profile during the penetration of wind power in power grid using MATLAB simulink. It also shows that fuzzy logic controller gives better result when compared to PI controller.

Keywords Static var compensator (SVC) · Flexible AC transmission system (FACTS) · Pulse width modulation (PWM) · Proportional integral (PI) controller

117.1 Introduction

Renewable energy sources like solar, wind, tidal, hybrid each contribute major amount of power to generate electricity. Earlier days fossil fuels are used largely to extract electricity. Today due to shortage of fuels and environmental pollution

C.K. Subasri (✉) · S. Charles Raja · P. Venkatesh
Department of Electrical and Electronics Engineering, Thiagarajar College of Engineeering, Madurai, Tamil Nadu, India
e-mail: ssmk.2013@gmail.com

S. Charles Raja
e-mail: charlesrajas@tce.edu

P. Venkatesh
e-mail: pveee@tce.edu

C. Kamalakannan et al. (eds.), *Power Electronics and Renewable Energy Systems*, Lecture Notes in Electrical Engineering 326, DOI 10.1007/978-81-322-2119-7_117

caused by green house gases, renewable energy has come to an effect. Among these renewable energy sources, wind energy plays an important role in present scenario [1]. However, connection of large wind farms to power grid [2] may result in power quality problems. This power quality problem causes a nascent issue in wind farms and collapses the entire systems especially when it is connected to weak electric grids [3]. The fault caused on wind turbine affects the power grid and makes the system unstable. Sometimes wind farm gets disconnected and voltage of the system gets affected [4]. Induction Generator coupled with wind farm starts to consume large amount of reactive power from the power grid. Shortage of reactive power takes place which in turn affects line voltage of the system. This causes voltage in the line to decrease or increase simultaneously. So, voltage sag is considered mainly in this study as a major power quality problem. Simple compensator is used to eliminate such power quality problem. Due to advancement with rapidly varying voltage it is difficult to improve power quality with simple compensator.

Advanced reactive power compensators with fast control and power electronics [5] have emerged to supersede the conventional reactive compensators. SVC helps in improving voltage in electrical network connected with grid [6]. Few techniques using Double Fed Induction generator was introduced which is able to provide system stability during fault without help of external controller [7, 8]. But due to cost and easy maintenance fixed speed Induction Generator is mostly used even in many countries still [9].

This work focus on comprehensive of proposed system with controller PI has been carried out in MATLAB environment using simulink. PI controller plays important role in reducing error signal and give suitable signal to PWM. Simulation result showed that the proposed SVC with conventional Controller is efficient in mitigating voltage sags. The ultimate objective of compensation is to increase power transmission of the system by maintaining the voltage across the grid using SVC which should meet grid code requirements. This code is standard for operation and is accepted for its safe operation [10]. The conventional PI controller is replaced by Fuzzy logic controller [11] and better results were obtained.

117.2 SVC

Static Var Compensator is a shunt compensating device widely used to decrease voltage fluctuations in an efficient manner. It is classified to three types as Thyristor Controlled Reactor (TCR), Thyristor Switched Reactor (TSR) and Thyristor Switched Capacitance (TSC). Among these, thyristor controlled reactor is used here as it has a major advantages such as either it will supply or extract reactive power and also injects voltage to avoid voltage collapse. Figure 117.1 depicts the basic configuration of SVC (FC-TCR) type. A basic single-phase TCR comprises an anti-parallel connected pair of thyristor valves with a linear air core reactor connected in series. Firing angle of thyristor can be varied from 90 to 180° to achieve smooth variation of reactive power. Here the capacitor is fixed and the current through

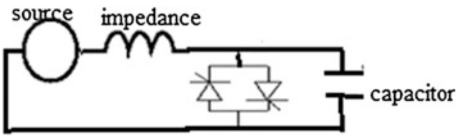

Fig. 117.1 Configuration of SVC

reactor changes according to the input pulse signal. According to the input pulse signal, thyristor is fired and starts to act.

Based upon the voltage condition it can operate in inductive and capacitive mode. If the voltage gets increases then firing angle is decreased, to make the voltage attain its reference value. Similarly, if the voltage gets decreased then firing angle is increased to maintain voltage at its reference value, then it is said to be in capacitive mode. In inductive mode the reactor plays a dominant role. The effective value of the voltage applied to the reactor circuit and accordingly the reactor current may be adjusted to any desired value continuously with respect to the requirement by varying the firing angle of the thyristor. The magnitude of the voltage is compared to a reference value and the firing angle is adjusted according to the comparison. These are few methods to regulate bus voltage by SVC investigated in previous papers. With the help of this Var dispatch and slope setting technology, voltage is said to be controlled using SVC [12]. Static Var Compensator (SVC) is used further to control the reactive power injection according to the thyristor firing with the nodal voltage magnitudes and angles of the power network for iterative solutions to regulate the bus voltage [13].

In this work Wind farm coupled with induction generator is made to integrate with power grid. Induction generator used is of asynchronous type. The wind turbine has three major components as generator speed, pitch angle and wind speed. Pitch angle is considered to be maintained at zero in order to attain maximum power. Pitch angle controller is not considered in many applications. The wind speed is kept as 12 m/s which are considered to be a nominal value which may vary from 8 to 12 m/s according to fluctuations. The mechanical torque is produced from turbine which is made to couple with Induction Generator. Load can be of ohmic or ohmic—inductive load. Wind farm is provided with three phase line to ground fault [14]. The fault on wind farm side causes negative effect in power grid. Due to fault, line voltage gets affected. The capacitor bank provided in each substation can support wind farm in faulty cases. But grid has to be protected. So in such cases additional equipment is necessary to maintain line voltage and for grid protection. Hence SVC [15] device emerge at a very faster rate to meet such requirements. This FACTS controller is installed across grid side to protect grid from negative effect caused by wind turbine. It has to meet the grid code requirement in which voltage fluctuations in range of ±5 %.

117.3 Control Strategy

Control strategy is based upon Synchronous Reference Frame Theory. The synchronous frame method [16] uses Park's transformation to transform the three phase ac quantities to the synchronous rotating direct, quadrature and zero sequence which are DC components and easy to analyze. This method is applicable especially in three phase system. Control algorithm is developed by comparing the reference voltage and fluctuating voltage. This compared signal is passed to PI controller and thus it minimizes the error signal [17]. Therefore PI controller is required to achieve controller performance at very faster rate. According to reference frame transformation theory, reference signal detected [18] is made to transform from stationery frame a-b-c to rotator frame d-q axis. PI controller is used to produce required signal for Pulse Width Modulation (PWM) from rotating frame signal. Before passing into PWM, the reference signal is produced by inverse transformation from rotating signal. In PI controller the gain values are adjusted to get optimum performance. These gain values can be tuned based upon Ziegler Nichol's tuning or even by using Fuzzy controller. PWM is based on equal area theorem. The equal area theorem can be applied to realize any shape of waveforms. Figure 117.2 shows the basic control algorithm developed. It briefly describes about the importance of reference frame theory and PI controller. In Pulse Width Modulation technique, suitable signal from PI controller has been generated as control signal which makes to produce desire reference signal so that corresponding carrier signal is produced. The carrier frequency is set in PWM block. So that appropriate pulse signal is created which acts as an input to power switch and Voltage Source Converter. Pulse width Modulation is able to control the switching device IGBT. Here reference signal is otherwise said to be modulating signal which is made to compare with carrier triangular signal. Then according to that signal, ON-OFF pulse occurs simultaneously with corresponding delay due to synchronization.

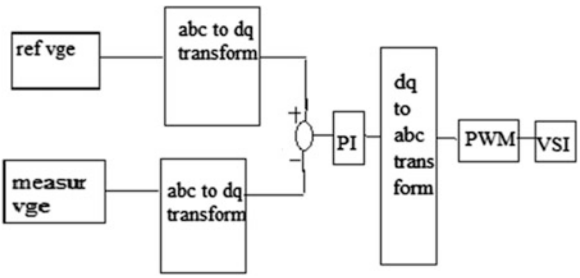

Fig. 117.2 Block diagram of controller

117.3.1 Fuzzy Logic Technique

The fuzzy logic controller [19] is used by replacing PI controller. Better performance can be observed using fuzzy logic controller for power quality improvement [20]. The following steps involved in control algorithm are given below.

Stage 1: Error Calculation
Error is calculated on the basis of difference between reference and fluctuated voltage. Error rate is calculated as Vref − Vfluctuated.

Stage 2: Fuzzification
Fuzzification is the process where the crisp quantities are converted to fuzzy. It converts non fuzzy (numeric) input variables to fuzzy set (linguistic variable). The membership functions is defined as error and change in error as Positive Big (PB), Positive Small (PS), Positive Medium (PM), Zero, Negative Small (NS), Negative Medium (NM), Negative Big (NB).

Stage 3: Decision Making
The set of rules for fuzzy are represented below: There are 49 rules for fuzzy controller. The output is based on the evaluation of rules by the fuzzy sets and fuzzy logic operation.

Stage 4: Defuzzification
Defuzzification means conversion of fuzzy set to crisp value. It can be achieved using defuzzification process. Centroid method is used in this simulation study.

Stage 5: Signal Processing
The outputs of FLC process [21] are the control signals that are used in generation of switching signals of the PWM inverter by comparing with a carrier signal (Fig. 117.3).

Voltage sag occurs when three phases to ground fault occurs with time 0.03–0.08 s. The RMS value of the grid voltage and the fluctuating voltage values are applied to the PI control block. The output of the PI block is converted to the firing angles using PWM technique in which SVC acts according to signal thereby voltage sag is rectified across grid and give protection.

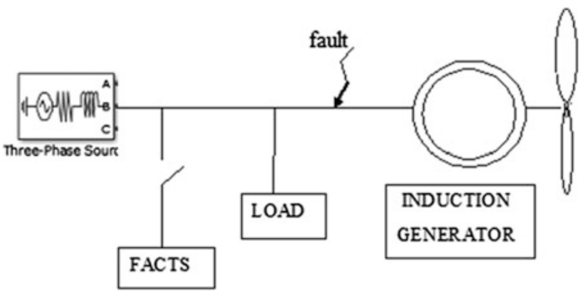

Fig. 117.3 Overall block diagram of wind farm connected with power grid

Table 117.1 Simulation parameters

Parameters	Values used in the simulation models
Main supply voltage	480 V
Line frequency	60 HZ
Source impedance	Ls = 16.59 mH
	Rs = 0.8928 Ω
Transformer turns	1:1
PI controller	$K_p = 0.1$, $K_i = 2$
Load	10 MW, 12MVAR
Asynchronous generator	Stator resistance = 0.016 Ω
	Stator inductance = 0.05 H
	Frequency = 60 HZ

117.4 Simulation Results

The parameters used in simulation are given in Table 117.1. It is used to verify the effectiveness of the SVC with PI controller and fuzzy logic technique. The simulations were accomplished using Matlab Simulink.

Case 1: Figure 117.4 shows voltage sag in the grid side as this work mainly focus on grid side (Fig. 117.5).

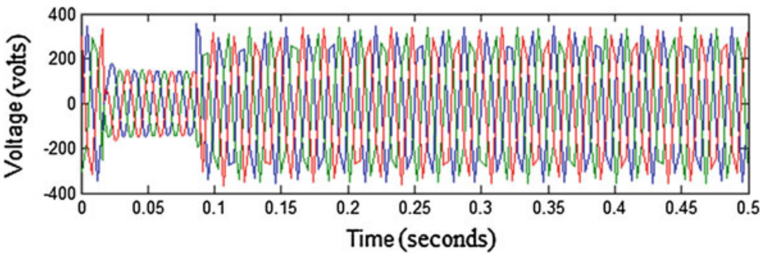

Fig. 117.4 Voltage sag due to three phase fault (0.03–0.08 s)

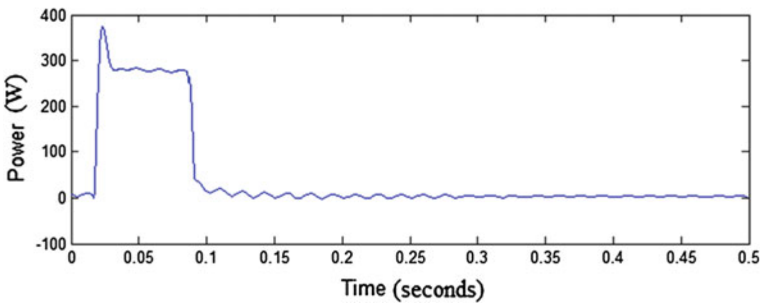

Fig. 117.5 Real power in grid during fault

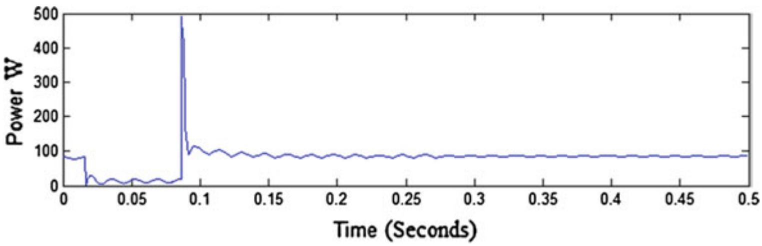

Fig. 117.6 Reactive power in grid during fault before compensation

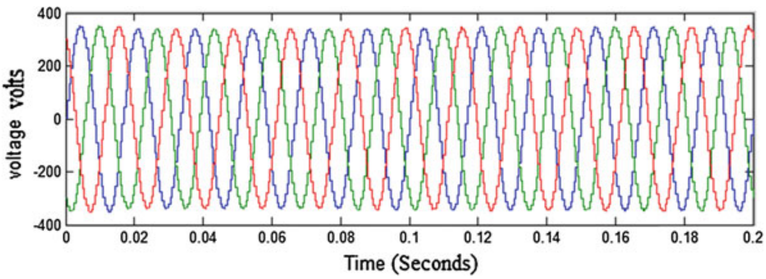

Fig. 117.7 Voltage sag mitigated by SVC

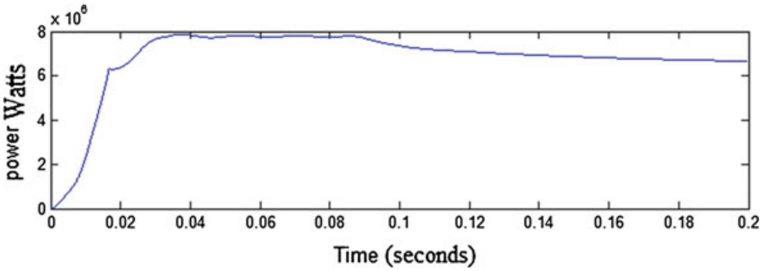

Fig. 117.8 Real power in grid after compensation

Figure 117.6 represents that during fault time there is severe dip in reactive power along grid.

Case 2: In Fig. 117.7 the simulation is carried out with compensation technique using PI Controller. The mitigated output waveform is shown below. After compensation of SVC with PI Controller voltage has been increased up to 338 V (Figs. 117.8 and 117.9).

Case 3: The simulation is carried out using FUZZY LOGIC technique and the improvement has been achieved by replacing PI controller. The voltage waveform is increased to about 440 V (Figs. 117.10 and 117.11).

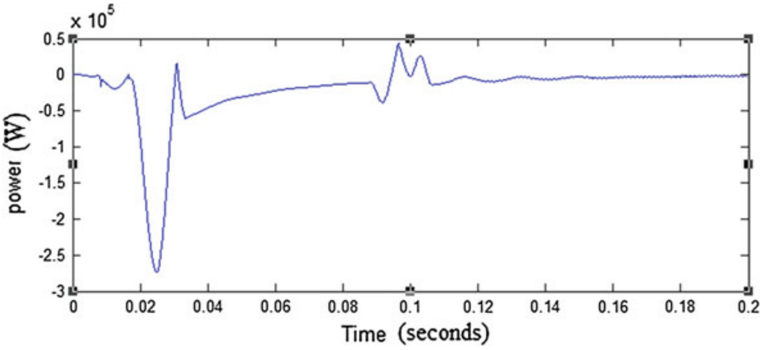

Fig. 117.9 Reactive power in grid after compensation using SVC

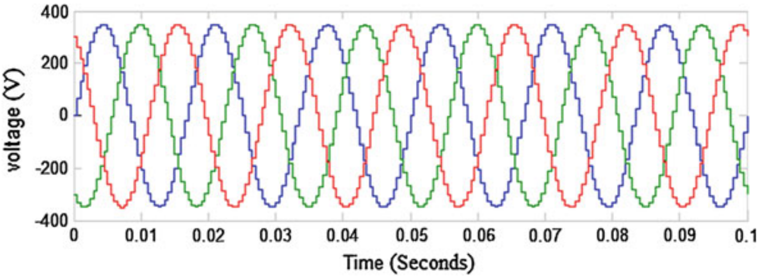

Fig. 117.10 Voltage in grid using fuzzy logic technique

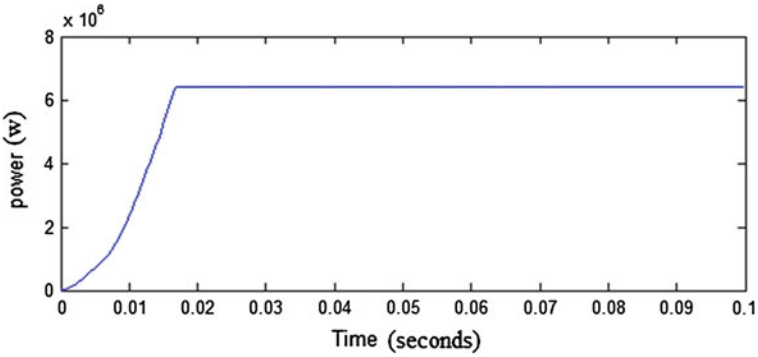

Fig. 117.11 Real power in grid using fuzzy logic technique

The real power curve becomes smooth and oscillations have been decreased when compared to PI controller (Fig. 117.12).

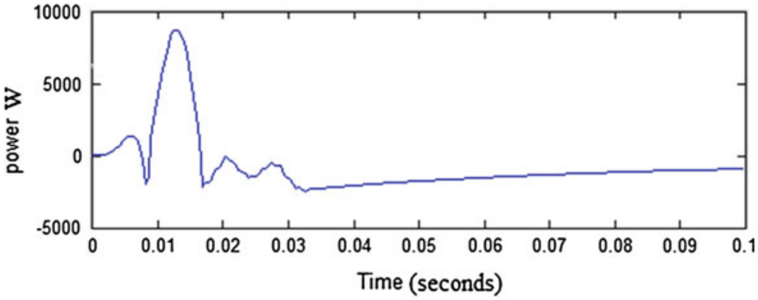

Fig. 117.12 Reactive power in grid using fuzzy logic controller

117.5 Conclusion

In this work, test SVC system is developed using matlab Simulink software. It is shown that power quality improvement can be achieved successfully with SVC. The proposed system with PI controller can handle the system with fault to eliminate voltage sag by reactive power compensation. The control scheme is improved further by using Fuzzy logic controller and voltage sag is further minimized. Better results are achieved with Fuzzy controller when compared to PI controller. The simulation results proves that SVC based Fuzzy logic technique improves the voltage profile of the system and oscillations has been reduced. If the controller is replaced further by advanced technique then Harmonics, power factor can also be corrected.

Acknowledgments Authors like to thank the management, Principal and the faculty of EEE Department for the support and suggestions in this work.

References

1. Ackermann T (2008) Wind power in power systems. Wiley, Chichester
2. Tande JOG (2003) Grid integration of wind farms. Wind Energy 6:281–295
3. Tande JOG (2000) Exploitation of wind energy resources in proximity to weak electric grids. Energy Convers 65(1-4):395–401
4. Boulaxis NG, Papathanassiou SA, Papadopoulos MP (2002) Wind turbine effect on the profile of distribution networks. Renew Energy 25(3):401–415
5. Molinas M, Suul JA, Undeland T (2000) Low voltage ride through of wind farms with cage generators: STATCOM versus SVC. IEEE Trans Power Electron 23(3):1104–1117
6. Maharani NA, Aouzellag D, Mendel B (2009) Contribution to the improvement of voltage profile in electrical network with wind generator using SVC. Renew Energy
7. Ramachandramurthy VK (2010) Fault ride through and voltage regulation for grid connected wind turbine. Appl Renew Energy 36(1):206–215

8. Jiaxin W, Ning J (2009) Development of low voltage ride through control strategy for wind power generation using real time digital simulator. Power system conference and exposition. IEEE/PES
9. Cidras J, Feijoo AE (2002) A linear dynamic model for asynchronous wind turbines with mechanical fluctuations. IEEE Trans Power Syst 17(3):681–687
10. Tascikaraoglu A, Uzunoglu M, Vural B (2011) Power quality assessment of wind turbines and comparison with conventional legal regulations. IEEE Trans Appl Energy 88:1864–1872
11. Al-Kandari AM, Soliman SA, Alammari RA (2006) Power quality analysis based on fuzzy estimation algorithm: voltage flicker measurements. Electr Power Energy Syst 28 (10):723–728
12. Li S, Ding M, Wang J, Zhang W (2009) Voltage control capability of SVC with var dispatch and slope setting. Electr Power Syst 79(5):818–825
13. Mendil B (2010) Contribution to the improvement of voltage profile in electrical network with wind generator using SVC device. Appl Renew Energy 35(1):243–248
14. Fuchs F, Molinas M (2011) Voltage control of a statcom at a fixed speed wind farm under unbalanced grid faults. In: Proceedings of 37th IEEE, pp 979–984
15. Kazemi A, Badrzadeh B (2004) Modeling and simulation of SVC and TCSC to study their limits on maximum loadability point. Electr Power Energy Syst 26:381–388
16. Alepuz S, Busquets-Monge S, Bordonau J, Martinez-Velasco J, Silva C (2009) Control strategies based on symmetrical components for grid-connected converters under voltage dips. IEEE Trans Ind Electron 56(6):2162–2173
17. Boynuegri AR, Tascikaraoglu A, Uzunoglu M, Yumurtac R (2012) Voltage regulation capability of a prototype Static VAr compensator for wind applications. Appl Energy 93:422–431
18. Hoffmann N, Lohde R, Thogersen P (2011) A review on fundamental grid-voltage detection methods under highly distorted conditions in distributed power-generation networks. In: Proceedings of IEEE ECCE, pp 3045–3052
19. Al-Kandari AM, Soliman SA (2006) Power quality analysis based on fuzzy estimation algorithm: voltage flicker measurements. Electron Power Energy Syst 28(10):723–728
20. Sivanandam SN, Sumathi S (2007) Introduction to fuzzy logic using MATLAB. Springer, Berlin Heidelberg
21. Miranda V (2007) An improved fuzzy inference system for voltage/VAR control. IEEE Trans Power Syst 22(4):2013–2020

Chapter 118
Development of Power Backup Device Using Solar Energy Harvesting for Real Time Industrial Applications

K. Janakiraman, D. Manivannan and R. Winnie Beulah

Abstract Depletion of renewable energy sources leads to more stress on finding out methods to overcome the issues of scarcity of electrical energy. Electrical energy is the prime need for running out industrial process, commercial applications and mainly it is the criteria that decide the economic wealth of any nation in today world. Solar energy is an important resource which finds an increasing use in real world because of its convincing advantages over other sources. The proposed system prototype takes the solar energy as the key aspect and efficiently harvesting the power to be used as a remote backup device in the real time applications. The major factors that makes the prospective model over the existing system is the portability and considerably smaller in size. The system can function with high degree of performance as an external power supply device for industrial utilization and in remote and harsh environments such as surveillance applications. To obtain the energy in accessible form as needed by the load or grid where problems such as voltage fluctuations and ripples may be the disturbances. To overcome this, in the proposed work the processors LPC 2148 and ATMega-8L are used. The processor typically achieves by the usage of inherent PWM channels as modified for the above mentioned by means of algorithms. In addition to which a suitable monitoring provision is given in the hardware model by integrating components for displaying status. The ultimate goal of this prototype is to satisfy factors such as reliability, scalability and maintenance which are successfully accomplished.

Keywords Photovoltaic array · Atmega-8L · LPC 2148 · MOSFET · Grid

K. Janakiraman (✉) · D. Manivannan · R. Winnie Beulah
School of Computing, SASTRA University, Tirumalaisamudram, Thanjavur 613401, Tamil Nadu, India
e-mail: kjanakiraman1984@gmail.com

D. Manivannan
e-mail: dmv@cse.sastra.edu

R. Winnie Beulah
e-mail: winnie.beulah@gmail.com

C. Kamalakannan et al. (eds.), *Power Electronics and Renewable Energy Systems*, Lecture Notes in Electrical Engineering 326, DOI 10.1007/978-81-322-2119-7_118

118.1 Introduction

The electrical energy demand increases sequentially leading to an intensified stress of scarcity in meeting out the demands of fast and furious world. Statistically speaking many people in rural areas has access to deceptive electricity networks. The importance of energy is analyzed critically [1] when it is seen the basic criteria of development. The existing non-renewable sources are becoming depleted and efficient harvesting of the alternative sources should be given priority. The major hurdles in implementing new projects in electricity sector are execution and management, assuring the availability of fuel resources, environmental impacts, and shortage of coal and natural gas resources owing to high cost. Electricity can be typically generated from any form of source [2] such as mechanical, wind energy and other non-conventional sources. The conventional energy sources like coal meets a number of disputes such as increasing cost of fuels due to its exhaustible nature since it is a non-renewable energy resource and increasing environmental changes correlated with generation of power using fossil fuels. Due to these issues faced by the conventional energy sources governments, many business administrators, consumers and even researchers are increasingly supporting the development of alternative energy sources and new technologies for electricity generation. One such a renewable source is the solar energy. Solar energy [3] poses to be the demandable energy resource in the near future for the generation of electricity. Solar energy being a pollution free, inexhaustible resource, and its distribution all over the world, made it as very useful and effective energy resource. The increasing demand for clean energy due to recent issues like global warming, drastic climatic changes and the largely unexploited potential of the sun as an energy source made it as increasingly important especially the solar energy conversion technology. The electrical energy obtained from the solar energy can be used for numerous purposes such as lighting, pumping, household appliances and small businesses by fixing solar panels on their roof which is significant in industrial applications such asremote terminal and surveillance units, telecommunication networks. The amount and timing of sunlight will vary with respect to the day, season and year and therefore a system should be designed to regulate the voltage obtained from the solar panels through sunlight before using in real time applications [4].

This paper focuses on developing the system which utilizes the potential benefits of solar system by overcoming the challenges like transportation cost in electricity sector, unreliability in hazardous environment, non-compactness and high cost [5]. The efficiency is achieved in prototype by integrating a photovoltaic array with battery for power storage, voltage fluctuations overcome by using ATMega-8L [6] and higher end processor for achieving optimization in code and physical implementation and finally supplying power to the load. Firstly, in this proposed system the methodology it can be implemented in remote areas where it is way too expensive to extend the electricity power grid [4], this is overcome in the proposed prototype. Secondly compact in size and cost effective where in 20 % of the total cost is reduced by this prototype thus concluding the high reliability and profitability in this system. Normally the PV source current- voltage [7] features is extremely nonlinear. Voltage fluctuations occur when an input voltage and load is connected which in turn leads to ripples and noise, so voltage regulation should be done before connecting it load or any other applications which is successfully accomplished by regulating the voltage obtained from Photo Voltaic array by a series of conversion using ATMega-8L and LPC2148 [8] and also a provision for seeing solar panel and load connection, battery charging statuses using LCD display providing efficient system.

118.2 Related Works

The sun light is efficiently harnessed by means of photovoltaic (PV) array [2] for generation of electrical energy to meet out the commercial and residential demands. An inverter is used for conversion of the DC power supplied by photovoltaic array to AC power used by real time applications in sense refer to loads. The lithium battery is incorporated in the prototype to store the voltage drawn out from the panel. ATMega8 [6] microcontroller is used to drive the MOSFET of the DC-DC converter for PWM generation with reference to the voltage and current obtained from the sensors. For efficiency 3 ATMega8 [6] microcontrollers are used for DC-AC conversion where in ATMega8 has only PWM channel. Each stage of voltage regulation uses one ATMega8. The voltage and current feedback received from the grid and LCD output is fed to microcontroller 1. The result thus obtained from the microcontroller 1 after processing the inputs is supplied to microcontroller 2 to change the duty cycle of PWM pulse in adjustable with the frequency of inverter with the grid voltage. When there are no fluctuations in voltage between grid and inverter, an interrupt from microcontroller 3 is given to microcontroller 1 [1]. On reception of interrupt signal, first microcontroller that is numbered 1 will provide a signal to second microcontroller for generating PWM signal with same duty cycle and given to inverter which in turn fed to grid. Microcontroller 3 also regulates the voltage at the inverter side. The voltage from inverter is fed to microcontroller 3 through voltage sensors. The PWM signal is generated and used to drive the MOSFET of DC-DC converter to regulate the voltage given to inverter. LCD display is used for showing the current status of the operating system. At the solar side one LCD is used to display the voltage received with the help of solar panel. Another LCD display is used at the load side for displaying details about the load. The above features describe the existing methodology poses certain flaws such as increased use of microcontrollers leading to expensive in terms of cost, larger size of the physical hardware unit and no ease of debugging the errors which is taken as key aspects to be overcome in this prospective model. In the proposed method the 3 ATMega-8L microcontrollers in DC-AC conversion stage are replaced by a single higher end processor LPC 2148 [8] which has 6 PWM channels. The key aspect of making the replacement of 3 ATMega-8L with a single LPC 2148 relies on the fact it leads to easier troubleshooting, optimized code size, debugging of error is accessible and in case collapsing of a microprocessor pose a threat to the reliability of the system. Considering these points the LPC 2148 is the trusted entity where the reliability and durability of the system is considerably increased for any critical remote applications.

118.3 System Prototype

Scarcity of electricity is the major concern of all government sectors [1] for research oriented analysis. Alternate energy sources are the primary need and efficient harvesting of energy from the non-renewable energy sources find an increasing commitment. Solar energy [2] is the quickest solution to meet out the energy deficit. Solar energy functions typically by converting the sun light into electrical energy as required by the load or grid. The implementation takes place by a photovoltaic array which is a provision of solar synthesizing components to provide electricity in the usable form. To obtain considerable amount of solar energy a large number of solar cells is connected in series and parallel according to the requirements. The proposed method is represented pictorially in Fig. 118.1 and its specifications are discussed in the following section. The photovoltaic array [2] output is a voltage which needs to be regulated or fixed for battery powered applications. The charging of battery is done under certain conditions considering the voltage, within acceptable limit. Considering the fact that the voltage obtained from the solar panel changes according to the variation in the radiant power received by unit area of solar panel surface and temperature of the panel.

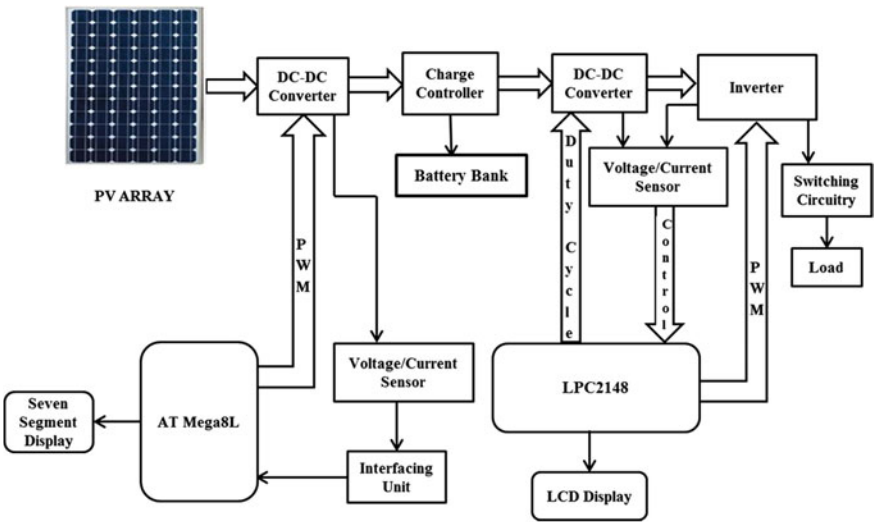

Fig. 118.1 Block diagram of proposed model

To get a constant voltage, the voltage obtained from the photovoltaic array [9] is sent to Buck-Boost converter for the mentioned purpose. The buck–boost converter is a series of DC-DC converter that has an output voltage which is either greater than or less than the input voltage magnitude depending upon the duty ratio [10] given to switch which is an outstanding feature for highly efficient for PV and standalone applications. The voltage and current sensors are used for continuous sensing of the voltage and current from the DC-DC converter and is fed to the ADC of ATmega-8L microcontroller. The input voltage from the solar panel is in the range of 0–600 V according to panel specifications. This voltage range is scaled into 0–5 V range with the help of 10 bit ADC. The PWM signals [1] are generated by the ATmega-8L [6] microcontroller according to the sensed input which is used to trigger the MOSFET of the converter. When the output voltage is greater than the battery voltage, enabling the control of the switching of MOSFET is done and at the same time, minimization of the percentage of duty cycle to control the output current to the battery limits and in the reverse when output voltage is less than battery voltage the control mechanism is done by rising the percentage of duty cycle which technically means boosting up of voltage to the acceptable range. Such a restriction allows the output to be fixed, which is in the required form to be stored in battery. A suitable provision for displaying the voltage in the solar panel is given through an inclusion of seven segment display and with the help of a LCD, which displays the details of load, battery charging, and also about solar panel whether it is connected or not to provide a better monitoring system. The DC current is stepped up for providing usable AC power as required by the load or grid by means of DC-AC converters. The specification of the Boost converter used in this prototype is 12–230 V DC where in the inversion process is typically the conversion from 230 V DC to 230 V AC. In case of steady environment stipulation, the boost converter amplified the [10] PV array voltage into expected level. By the usage of boost converter, the PV arrays voltage is lower [11] compare with the grid voltage. The DC-AC inverter input typically ranges around 12 V or 24 V battery power source and the output will be 230 AC and 50 Hz frequency. The inversion process is of two stages. Firstly, the conversion of low voltage DC power to a high voltage DC source and secondly, the conversion of the high DC source to an AC power. For enhanced performance and optimization, a higher end processor LPC 2148 [12] is preferred for the above mentioned conversion process. LPC 2148 also uses 10 bit ADC which produces resolution of about 0.22 V, while scaling an input range of 0–230 V into 0–5 V. The value thus obtained will be compared with reference value. According to the error or variation the processor will vary the ON-OFF duration of the PWM. The vital feature of LPC 2148 ARM processor [12] is that it consists of 6 PWM channels. Both the converters use separate PWM channel and vary the percentage of the duty cycle of the PWM signal according to the sensed inputs from converters which are in turn driven to MOSFETs of corresponding converters. The voltage and current from both the DC-DC converter and Inverter sensed by voltage and current sensors respectively is fed to processor via ADC through feedback system. Pseudo code for generation of PWM is given below.

118.3.1 Pseudocode

```
BEGIN

        Set the general input and output pin for register
        Initialize inbuilt PWM in LPC2148
        Initialize A/D conversion in LPC2148

OutputVal

        while the ADC conversion is set
        do

            Read the data register to the variable Val
            Declare delay between the conversions

        End while

    If the variable Val is not equal to old Val

        Set the PWM match register to the Val, the duty cycle
        Enable the PWM
    End if

END
```

The output of the inverter can be either fed to power grid, from which the power get transmitted to consumer ends at high voltage or directly supply the load through switching circuitry. One of the issues while connecting the output voltage with either grid or load is the voltage spikes and Electro Magnetic Interference, especially while switching of AC mains. This can be controlled by microcontrollers with the help of zero crossing detectors, and there is the possibility of reduction in noise. In order to reduce the error between frequency of the inverter and grid, output of zero crossing detectors is given as interrupt to EINT0 pin of ARM processor [12] to measure the frequency of the grid voltage which will be compared with incoming frequency of the inverter voltage. Voltage spike and electrical noise are minimized if the switching occurs whenever the voltage is zero which means at the beginning or end of cycles. A zero-crossing detector controls the switching so that it occurs at close to zero voltage of the cycle. Implementation is done by an algorithm in LPC 2148. So the regulation of voltage obtained from the Photo Voltaic array is automatic in the system, which leads to voltage stabilization which is of major concern these days.

As seen above all the three stages of conversion uses single LPC 2148 [8] in place of 3 ATMega8 [6] microcontrollers which increases the portability, and also the system becomes less complex. Using a higher end processor also increases the overall performance of the system, since it reduces the Electromagnetic Interference (EMI), which will be higher while using more number of controllers. Conducted EMI is produced due to the noise signal generated from the electrical paths such as wires. While using 3 ATmega8 controllers, each controller need 5.5 V which will increase EMI for sure, and apparently when single processor is used, EMI is reduced. The voltage required to operate the LPC 2148 processor [8] is just 3.3 V which is considerably small. Since power for these controllers also acquired from the solar panel itself, it will be energy efficient if energy consumed by the system is less. Using ARM LPC 2148 processor which optimizes the code, and evidently reduces the memory space thereby increases the speed and efficiency of the processor.

118.4 Hardware Setup

The proposed methodology gives a clear picture of the basic components used to achieve the required reliable output implemented through the hardware prototype. Figure 118.2 shows the whole experimental setup of the proposed system in the idle state. In Fig. 118.3 load of 4 W is connected and powered by the battery charged through inverter in the absence of solar panel.

The LCD connected displays the current status. In this case there is no solar energy and load connected, which is displayed.

In Fig. 118.4 solar panel is connected and battery is charging by a constant voltage obtained through converter. The voltage obtained from the solar panel is displayed using a seven segment display.

In this voltage obtained was 10.78 V which was boosted using converter and stored in the battery. The load of 4 W is connected and receives power from battery through inverter. In this case the LCD displays as battery charging and load connected.

Fig. 118.2 Experimental setup of the proposed model

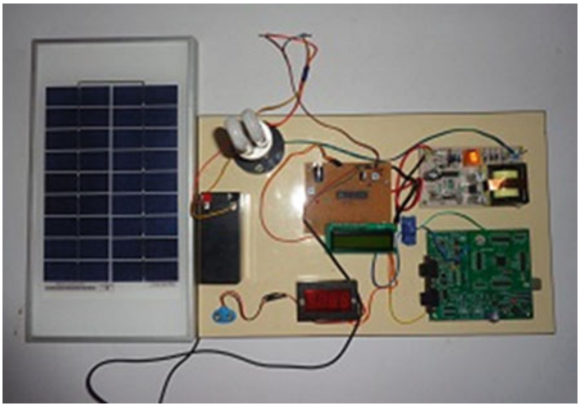

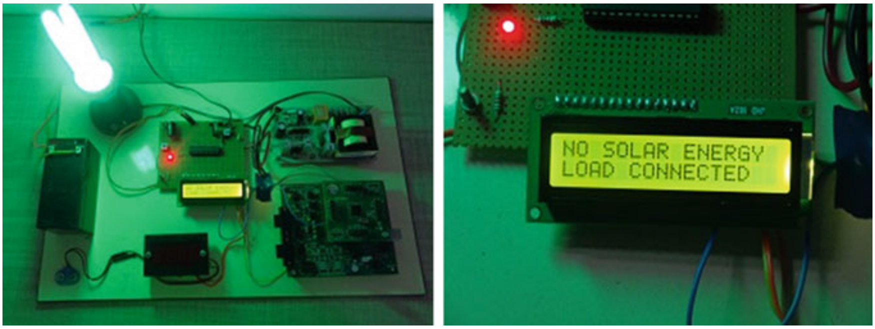

Fig. 118.3 Load powered by the charge stored in the battery

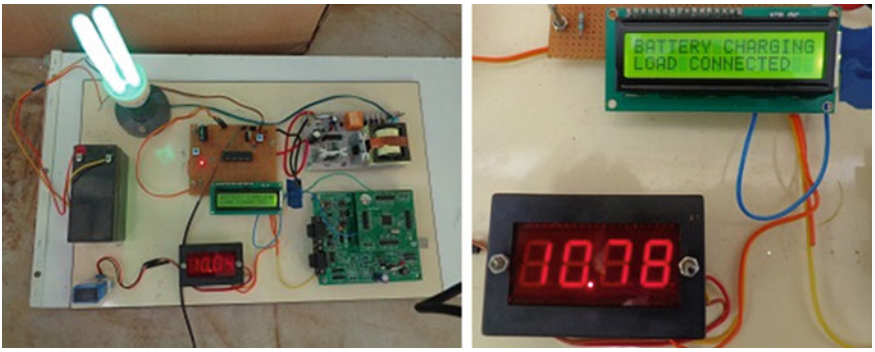

Fig. 118.4 Load powered by the battery which is charged by solar panel (10.78 V)

118.5 Result Analysis

The output efficiency of each stage is depicted in terms of waveform patterns. The Fig. 118.5 represents the voltage obtained from the photovoltaic array before it undergoes conversion in the buck-boost converter. Figure 118.6 is the snapshot of the voltage that is stored in the battery after the voltage from the solar panel is boosted through the converters.

The Figures below indicate the voltage obtained from the output terminal of the inverter and the PWM waveform obtained by the variation in the duty cycle depending on the variation in the signals. As illustrated in Fig. 118.7 clearly depicts a voltage value of 229.5 V AC approximately equal to 230 V AC as supplied to the grid and the PWM duty cycle variation (Fig. 118.8).

The expected output is 230 V AC which is 229.5 V AC obtained marginally close which proves in terms of the reliability aspects. The illustration thus emphasis the solar power obtained in the range 0–12 V DC can be supplied to the industrial

Fig. 118.5 Voltage obtained from solar panel

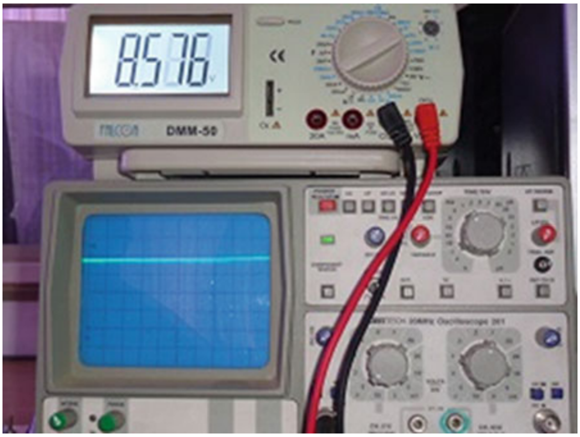

Fig. 118.6 Voltage stored in battery

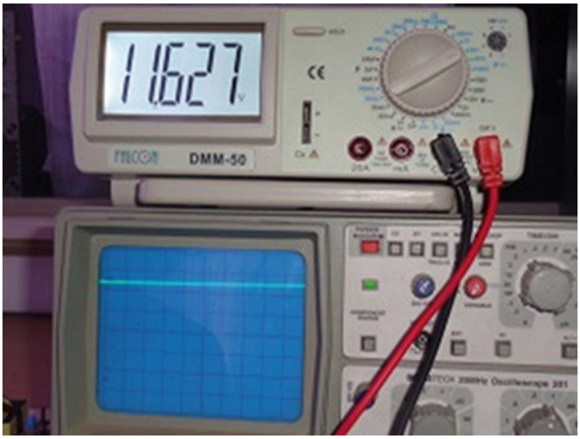

Fig. 118.7 Alternating voltage waveform

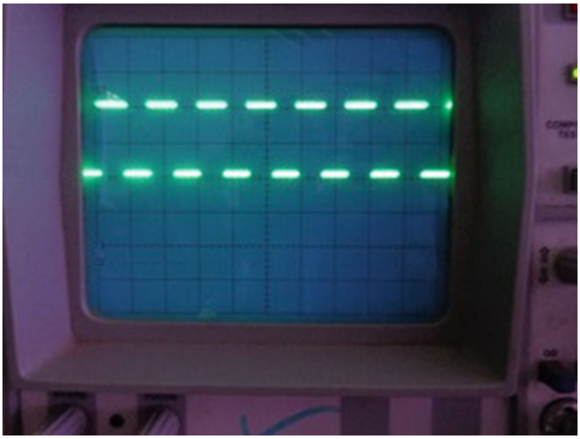

Fig. 118.8 Enabling the PWM due to fluctuation of voltage

requirements ranging from 0–230 V AC efficiently backing up as a power device for real time industrial applications where in it includes triggering of a single phase unit. Single phase motors are used in multifariousness of diligence like remote applications, households (commercial ventilation systems), small industrial measuring system, adaptable—speed AC drives and uninterruptible power supplies.

118.6 Conclusion

The major concern today is lack of renewable energy resources [4] which is the prime area of research. To meet out the demands of electrical production and consumption related issues, solar power is considered as the optimal solution. The mission of today technologically progressing world is to sort out these issues by the use of non-conventional energy source. Energy harvesting is efficiently done and the power obtained is changed to usable form by the load or grid. The process is accomplished in the proposed method by integrating the high end and low end processors. The proposed methodology is tardily to enforce and necessitate only a little amount of trashy elements is in compact size. The reliability of the system is highly functional in the remote areas where a dependence on an external energy supply is not significant. Such a system is adequate to sort out to the energy supply needs of wireless networks which find an increasing application and key aspects in research areas. In case of power failures in industries, the system acts as the backup device to cater out to the needs of real time electrical consumers expectations with a high degree of dependability, suitable for any environmental conditions irrespective of their nature and also cost-effective.

References

1. Hossain MI, Khan SA, Shafiullah M, Hossain MJ (2011) Design and implementation of MPPT controlled grid connected photovoltaic system. In: IEEE symposium on computers and informatics, pp 284–289
2. Desai HP, Patel HK (2007) Maximum power point algorithm in PV generation: an overview. In: International conference on power electronics and drive systems (PEDS07), Thailand, pp 637–641, 27–30 Nov 2007
3. Matsuo H, Kurokawa F (1984) New solar cell power supply systemusing a boost type bidirectional DC-DC converter. IEEE Electron 31:51–55
4. Zahedi A (1994) Energy, people, environment, development of an integrated renewable energy and energy storage system, an uninterruptible power supply for people and for better environment. In: The international conference on systems, man, and cybernetics. ‘Humans, information and technology’, vol 3, pp 2692–2695
5. Bull SR (2001) Renewable energy today and tomorrow. IEEE Proc 89(8):1216–1226
6. ATMega8x Atmel user manual. Rev. 2486AA–AVR–02/2013
7. Dahmane M, Bosche J, EI-Hajjaji A (2013) Robust control approach for photovoltaic conversion system. IEEE
8. LPC214x user manual. Rev. 3–4. nxpb.v. Oct 2010
9. Arai J, Iba K, Funabashi T, Nakanishi Y, Koyanagi K, Yokoyama R (2008) Power electronics and its applications to renewable energy in Japan. IEEE Circ Syst Mag 8(3):52–66
10. Chowdhury ASK, Shehab MS, Awal MA, Razzak MA (2013) Design and implementation of a highly efficient pure sine-wave inverter for photovoltaic applications. IEEE
11. Christopher IW, Ramesh R, Parthiban J, Saravanan B, Kumar R, Pallavan S (2012) Microcontroller based single-phase simplified seven-level inverter for PV system. IEEE
12. Reddy NM, Nagabhushanraju K, Pavan C, Chandra D, Reddy S (2013) Design and development of arm processor based solar tracking system using DC motor. IJESAT 3 (3):106–110

Chapter 119
An Image Watermarking Scheme Resilient to Geometric Distortions

D. Vaishnavi and T.S. Subashini

Abstract In this article, a robust watermarking scheme is proposed to lighten the problem of geometric distortion using Lifting Wavelet Transform (LWT). Initially, the host image is normalized to make it as invariant to affine distortion. Then LWT is applied and LD subband is divided into 8 × 8 non overlapping blocks. The first element of each block is retrieved to form a matrix to apply Singular Value Decomposition (SVD). The watermark is embedded in these singular values after applying Arnold scrambling to enhance the security of the watermark. Robustness of the proposed scheme are estimated using the metric Peak Signal to Noise Ratio (PSNR) and Structural Similarity (SSIM). The experimental results are compared and it exemplifies that the proposed method generates good robustness for geometric distortion.

Keywords Image watermarking · Robustness · Scrambling · Normalization

119.1 Introduction

A digital image watermarking technique must be robust against the various kinds of attacks. The geometric attacks are not easy to deal with than the other kinds of attacks. It mostly initiates the synchronization errors between the encoder and decode and even if the watermark is present, the detector is not able to extract it. Rather, the content-preserving image processing operations (such as the addition of noises, common compression and filtering operations) do not initiate synchronization problems. A relative number of geometric invariant watermarking schemes has been proposed. In [1], normalized host image is jumbled using chaotic map and

D. Vaishnavi (✉) · T.S. Subashini
Department of Computer Science and Engineering, Faculty of Engineering and Technology, Annamalai University, Chidambaram, Tamilnadu, India
e-mail: vaishume11@gmail.com

T.S. Subashini
e-mail: rtramsuba@gmail.com

C. Kamalakannan et al. (eds.), *Power Electronics and Renewable Energy Systems*, Lecture Notes in Electrical Engineering 326, DOI 10.1007/978-81-322-2119-7_119

the watermark is inserted using the logistic map. In [2], the Rotation, Scaling and Translation invariant descriptors are determined from the complex moments of host image's Radon Transform and watermark is embedded using the DCT. In [3], Harris feature points are extracted from normalized host image to generate some non-overlapped circular regions and which is classified using DCT to embed or extract the watermark. In [4], both the normalized host image and watermark image is divided into 8×8 sized block and DCT is applied on each block of host image. Then each watermark block is embedded on the transformed block of host image respectively. The work in [5], concatenates the first SVs of adjacent blocks of the normalized image to form a singular value (SV) block and in which DCT is carried out. A watermark is embedded in the high frequency band of SVD-DCT block. In [6], Blind Normalization Algorithm is used to achieve affine invariant wavelet transform. The normalized cover image is wavelet decomposed and block based DCT is applied to embed the watermark in DC coefficients. In [7], visually significant feature points are extracted by end-stopped wavelet to find non-overlapping circular images to embed the watermark. The watermark embedding process is performed by modifying low-frequency coefficients of DCT transformed blocks, which are randomly selected using a secret key. In this article, a robust watermarking method is proposed to alleviate the problem of distortion for geometric attacks using the image normalization, LWT, SVD and Arnold scrambling. The rest of this paper is constituted as follows: Sect. 119.2 delivers the concepts of algorithms used, Sect. 119.3 illustrates the proposed methodology, Sect. 119.4 demonstrates the results and discussion and finally Sect. 119.5 concludes the paper.

119.2 Background Details

119.2.1 Lifting Wavelet Transform

The lifting wavelet is used to build another wavelet with the aspects based on a simple wavelet. The reconstruction of image by lifting wavelet is faultless because, it increases the smoothness and reduces aliasing effects. It reduces the information loss thus; it increases the reliability of embedded watermark which aids to increase the robustness. It reduces the setup execution time by half while comparing general wavelets [8, 9]. The algorithm involves in three steps:

#	Steps	Equations	Operations
1.	Split	$x_e(n) = x(2n),\ x_o(2n+1)$	Splits an input signal $x(n)$ into even and odd samples
2.	Predict	Detail signal $d(n) = x_o(n) - P[x_e(n)]$	Takes difference between prediction values of $x_e(n)$ and original values of odd signals. It denotes high frequency components of $x(n)$
3.	Update	Approximate signal $c(n) = x_e(n) + U[d(n)]$	Updates the even samples using $d(n)$ and it denotes low frequency components of $x(n)$

119.2.2 Singular Value Decomposition

It bundles the maximum signal energy into few of coefficients. An image of a real matrix with the size of $m \times n$ can be decomposed as: $A = U * S * V^T$ where U is $m \times m$ unitary matrix, S is $m \times n$ matrix with nonnegative numbers on the diagonal and zeros on the off diagonal which represents the luminance value and V^T denotes the conjugate transpose of V of $n \times n$ unitary matrix. The matrix U and V represents the geometry of an image [10]. The main features of SVD are: (1) The quality of the reconstructed image will not degrade, even if ignoring the small SV's in the reconstruction of image. (2) SVD has a capacity to well represent the intrinsic algebraic properties of an image, where singular vectors reflect geometry properties of an image. (3) When a small annoyance is added to an image, its SVs do not vary rapidly.

119.2.3 Arnold Transform

It is used as preprocessing step to embed the watermark, which reduces the spatial relationship between the pixels and makes the meaningful image as meaningless [11]. The 2-dimensional Arnold scrambling algorithm is defined as:

$$\begin{bmatrix} x' \\ y' \end{bmatrix} = \begin{bmatrix} 1 & 1 \\ 1 & 2 \end{bmatrix} \begin{bmatrix} x \\ y \end{bmatrix} \bmod N x, y \in \{0, 1, 2, \ldots, N-1\}$$

wherein, x, y is the pixel coordinates of the original space: x', y' is the pixel coordinates after iterative computation scrambling; N is the size of the image.

119.2.4 Image Normalization

The end goal of normalization is to increase the robustness for geometrical deformation. Normalization is used to perform watermark embedding and extraction in its original coordinate system by computing the affine transformation parameters from the geometric moment of the image. So that, it is invariant to any affine s of the image and it will guarantee the reliability of watermark embedded in the normalized host image. The normalization procedure composed of the following steps [12, 13].

1. To obtain the translation invariance, shifting the cover image to its central point, image center for $f(x, y)$ is determined by the equation $\begin{pmatrix} x_a \\ y_a \end{pmatrix} = A \cdot \begin{pmatrix} x \\ y \end{pmatrix} - d$ where, $A = \begin{pmatrix} 1 & 0 \\ 0 & 1 \end{pmatrix}$ and vector $d = \frac{d_1}{d_2}$ with: $d_1 = \frac{m_{10}}{m_{00}}, d_2 = \frac{m_{01}}{m_{00}}$ where m_{10}, m_{01}

and m_{00} are the moments of $f(x, y)$ and let $f_1(x, y)$ denotes the resulting center image.

2. Apply shearing transform on $f_1(x, y)$ in the X-direction with matrix denoted $A_x = \begin{pmatrix} 1 & \beta \\ 0 & 1 \end{pmatrix}$ by $f_2(x, y) = A_x[f_1(x, y)]$. The value of β can be calculated using following equation $\mu_{30} = \mu_{30} + 3\beta\mu_{21} + 3\beta^2\mu_{12} + \beta^3\mu_{03}$.
3. Apply shear transform to $f_2(x, y)$ in the Y-direction with the matrix is denoted $A_y = \begin{pmatrix} 1 & 0 \\ \gamma & 1 \end{pmatrix}$ by $f_3(x, y) = A_y[f_2(x, y)]$. The value of γ can be calculated using following equation $\mu_{11} = \gamma\mu_{20} + \mu_{11}$. Thus, the parameter γ has a unique solution.
4. Apply scale $f_3(x, y)$ in both X and Y directions such that $A_s = \begin{pmatrix} \alpha & 0 \\ 0 & \delta \end{pmatrix}$ and the resulting image is denoted by $f_4(x, y) = A_s[f_3(x, y)]$. The parameters α and δ are determined by its moments $\mu_{50} > 0, \mu_{05} > 0$ respectively. This eliminates the scaling distortion.

119.3 Proposed Scheme

119.3.1 Watermark Embedding

A normalization procedure is applied to the host image which makes it as invariant to affine distortions. Now the LWT is applied to decompose the normalized image into LA, LH, LV and LD. The LD sub band is divided into 8 × 8 non overlapping blocks. The first element of each block is retrieved to form a matrix and singular values of S matrix are obtained using the $U * S * V^T$. The 32 × 32 size of gray scale watermark is scrambled using Arnold map and which is embedded in the singular value of the host image using the scaling factor. The image is reconstructed using the $R = U * S1 * V^T$ and the first element of each block of LD is replaced with each elements of R and all the blocks are combined as single block LD matrix. The watermarked image is constructed by taking inverse LWT to modify LD with three unmodified sub bands. Finally the watermarked image is placed in its original position and orientation by applying the inverse normalization procedure.

119.3.2 Watermark Recovery

A normalization procedure is applied to watermarked image and LWT is applied to get LD sub band. Then it is divided into 8 × 8 non overlapping blocks and first element of each block is retrieved to get the singular values of matrix by applying

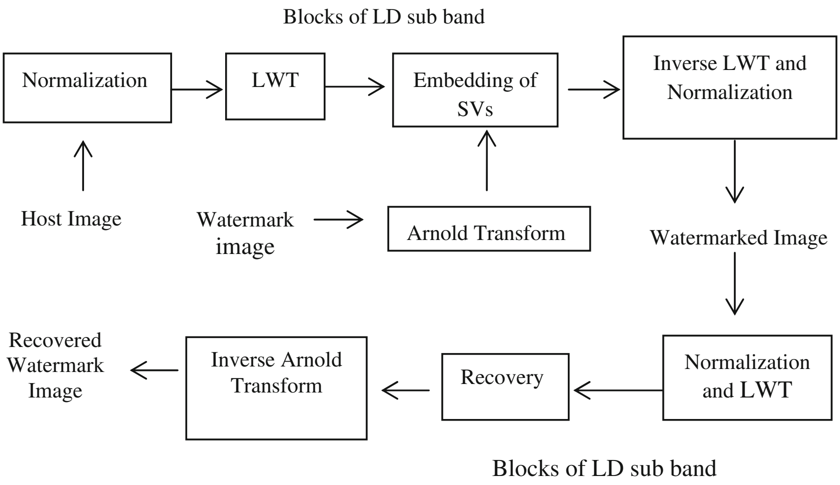

Fig. 119.1 Proposed watermarking scheme

the SVD. The scrambled watermark is recovered from the singular values and watermark is obtained by reordering the coefficients to its original coordinate position using inverse Arnold transform. The entire process of proposed watermarking scheme is shown in the Fig. 119.1.

119.4 Results and Discussion

The experimental setup was done using Math works MATLAB 12. The sample host image is a gray scale of resolution 256 × 256. Figure 119.2 shows the sample host and watermark images. To experimentally ascertain the invisibleness and robustness, the metric Peak Signal to Noise Ratio (PSNR) is used by equation given below:

$$PSNR = 10\log_{10}\left(\frac{255^2}{MSE}\right), \quad MSE = \frac{\sum_{M,N}[I_1(m,n) - I_2(m,n)]}{M \times N}$$

Figure 119.3 shows the watermarked image with rotation, translation, scaling, X-direction shearing and Y-direction shearing attack. Figure 119.4 shows recovered watermark from watermarked image after subjecting it the above attacks respectively.

The invisibleness of the proposed scheme has a PSNR value of 38.6441. Table 119.1 shows the robustness (PSNR value) of proposed method for various attacks with scaling factor 0.1, 0.5 and 1. It shows that PSNR value is much increasing while increasing the scaling factor and it also found that quality of

Fig. 119.2 Sample host and watermark images

Fig. 119.3 Watermarked image subjected to various attacks. **a** Rotation, **b** Translation, **c** Scaling, **d** X-Shearing, **e** Y-shearing

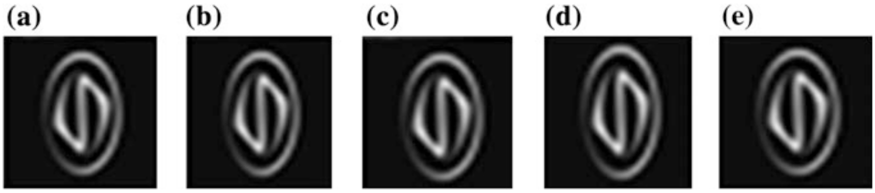

Fig. 119.4 Recovered watermark after subjecting it to various attacks. **a** Rotation, **b** Translation, **c** Scaling, **d** X-Shearing, **e** Y-Shearing

recovered watermark is high for the scaling factor 1. In order to justify the proposed scheme, the LWT based robust watermarking scheme [9] is also implemented. The robustness of the schemes was evaluated by the metric Structural Similarity (SSIM) using the equation given below:

$$SSIM(x, y) = \frac{(2\mu_x\mu_y + c_1)(2\sigma_{xy} + c_2)}{(\mu_x^2 + \mu_y^2 + c_1)(\sigma_x^2 + \sigma_y^2 + c_2)}$$

Table 119.1 Robustness (PSNR) of proposed method

Scaling factor / Attacks	0.1	0.5	1
Rotation	33.9272	48.7976	56.8988
Translation	33.3773	47.5669	53.8968
Scaling	33.9231	47.8960	53.7042
X-sh	36.8325	49.8977	52.1141
Y-sh	30.5170	44.3494	50.2842

where, μ_x, μ_y: The average of x, y respectively, σ_x^2, σ_y^2: The variance of x, y respectively, $\sigma_{x,y}$: The covariance of x and y, $c_1 = (k_1 L)^2, c_2 = (k_2 L)^2$: Two variables to stabilize the division with weak denominator, L the dynamic range of the pixel-values $k_1 = 0.01$ and $k_2 = 0.03$ by default.

The comparative analysis for rotation, translation and scaling attacks for the gain factor 0.1 and 0.5 is given in the Table 119.2. It shows that robustness of the proposed system is highly robust to geometric attacks. And it depicts that the robustness of proposed scheme is much increased for the scaling factor 0.1. Figure 119.5 graphically shows the robustness of proposed system for the scaling factor 0.1, 0.5 and 1. Figure 119.6 shows that the comparison of proposed system with existing LWT method [9] for the scaling factor value of 0.1.

Table 119.2 Comparison of robustness (SSIM) for proposed method with existing method [9]

Scaling factor	Existing method		Proposed method	
Attacks	0.1	0.5	0.1	0.5
Rotation	0.8331	0.9789	0.9997	0.9998
Translation	0.7447	0.9785	0.9985	0.9999
Scaling	0.9692	0.9896	0.9997	0.9998

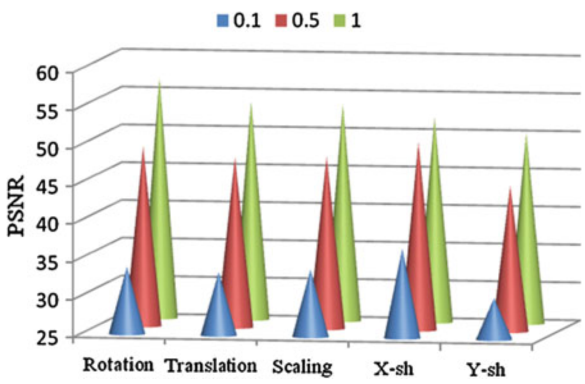

Fig. 119.5 Robustness of proposed scheme

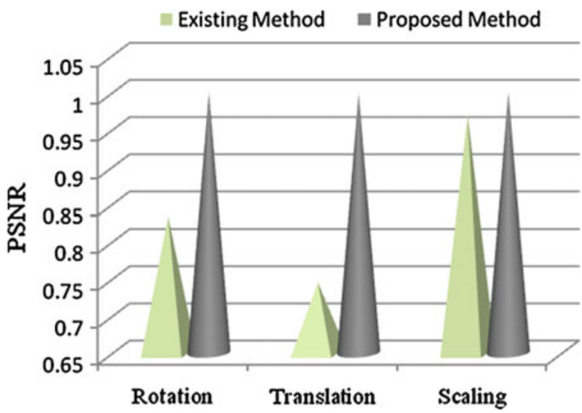

Fig. 119.6 Comparison of proposed method

119.5 Conclusion

A robust watermarking technique for geometric distortion using image normalization was implemented. The watermark image is embedded in the LWT of LD sub band. The security of watermarking scheme is increased by displacing the watermark image coefficients using the chaos theory of Arnold Scrambling. The experimental results proves that the proposed system has good robustness for geometric attacks and a comparisons was made with [9]. The study proves that the proposed system is highly resilient than the existing method.

References

1. NesaKumari GR, Maruthuperumal S (2012) Normalized image watermarking scheme using chaotic system. Int J Inf Netw Secur 1:255–264
2. Zhu H, Liu M, Li Y (2010) The RST invariant digital image watermarking using radon transforms and complex moments. Digit Signal Process 20:1612–1628
3. Na W, Yamaguchi K, Cedillo-Hernández M, Miyatake MN, Pérez-Meana H (2010) Robust image watermarking using feature points and image normalization. In: Electronics, robotics and automotive mechanics conference (CERMA), 2010, pp 313–318
4. Kumar A, Luhach AK, Pal D (2013) Robust digital image watermarking technique using image normalization and discrete cosine transformation. Int J Comput Appl 65:5–13
5. Foo SW, Dong Q (2010) A normalization-based robust image watermarking scheme using SVD and DCT. Acad Sci Eng Technol V6 N 4
6. Sridevi T, Kumar VV (2011) A Robust Watermarking Algorithm Based on Image Normalization and DC Coefficients. Int J Comput Sci Issues 8
7. Nasir I, Khelifi F, Jiang J, Ipson S (2012) Robust image watermarking via geometrically invariant feature points and image normalisation. Image Process. IET 6:354–363
8. Sweldens W (1996) The lifting scheme: a custom-design construction of biorthogonal wavelets. Appl Comput Harmonic Anal 3:186–200
9. Vaishnavi D, Subashini TS (2013) A novel approach to improve invisibleness and robustness of a digital watermark in copyright protection. Int J Comput Appl 71:7–13

10. Chandra DS (2002) Digital image watermarking using singular value decomposition. In: The 2002 45th Midwest symposium on circuits and systems, 2002. MWSCAS-2002, vol 3, pp 3–264
11. Venkata Rama Prasad RKV (2010) Secure image watermarking in frequency domain using Arnold scrambling and filtering. Adv Comput Sci Technol 3:236–244
12. Dong P, Brankov JG, Galatsanos NP, Yang Y, Member S, Member S, Davoine F (2005) Digital watermarking robust to geometric distortions. IEEE Trans Image Process 14:2140–2150
13. Mohamed FK, Abbes R (2007) RST Robust watermarking schema based on image normalization and DCT decomposition. Malaysian J Comput Sci 20:77

Chapter 120
Intensification of Available Transfer Capability Via Real Coded Biogeography Based Optimization

A. Ramesh Kumar and L. Premalatha

Abstract Decisive challenge for giving economical electricity to the end users in the restructured and rivalry electricity open market can be solved by the resolution and augmentation of Available Transfer Capability (ATC). In this paper, real coded biogeography based optimization (RCBBO) is used to scrutinize prevail of FACTS devices like TCSC and SVC in order to relieve congestion as well as boost the transferring of power at both normal and abnormal circumstances. And hence to improve the voltage profile in the system and reduces the transmission losses. The consequences have been concluded for whole and line contingency cases without and with FACTS device. The proposed technique aims to improve the real coded searing ability, avoid the prematurity of solution, improve the convergence characteristics and enhance the population diversity of the biogeography based optimization algorithm by using adaptive Gaussian mutation. The suggested algorithm will to provide a new way for Biogeography Based Optimization (BBO) to solve multi-objective optimization problems, have been tested on IEEE 30-bus and IEEE 118-bus system and the comparative results are made with existing population based methods.

Keywords ATC · RCBBO · TCSC · SVC · IEEE 30-bus · IEEE 118-bus system

120.1 Introduction

The electrical power transmission network in the open market has become very influential. The increase in the custom of electricity has pilot the market to restructured and deregulated environment. This novelty enhanced the scholars to

A. Ramesh Kumar (✉)
Anna University, Chennai, Tamilnadu, India
e-mail: a_rameshkumar@live.com

L. Premalatha
Anand Institute of Higher Technology, Chennai, Tamilnadu, India
e-mail: premaprak@yahoo.com

C. Kamalakannan et al. (eds.), *Power Electronics and Renewable Energy Systems*,
Lecture Notes in Electrical Engineering 326, DOI 10.1007/978-81-322-2119-7_120

afford finest optimization techniques to endow with slightest outlay energy with better quality service [1].

It is possible for customers to buy a reduced amount of electrical energy from secluded location with the overture of contest in the convenience industry. As a consequence, power transactions taking place over long distances in different areas need to be scrutinized and synchronize by the system operators. Hence, it becomes essential to evaluate multi-area ATC, and a novel method for determining multi-area ATC has been offered in the journal [2].

It is necessary to enhance the ATC to spotlight on the potential ways to prevail over the uncertainties like weather condition and non-availability of generation voltage variations and stability problems [3]. NERC (North American Electrical Reliability Council has recognized a structure for formative ATC of the interconnected networks for the extensive market [4]. Continuation power flow, repeated power flow based approaches were used by various researchers to determine ATC [5–8].

The system operator gets valuable information regarding the proficiency of an interconnected network to consistently transfer bulk power between two nodes or between different areas of the network without causing threat to system reliability by the evaluation of ATC.It is well demonstrated through number of case studies, that the location of the devices and their control parameters significantly affect the ATC which can be overcome by utilization of FACTS devices. The transmission system capability is increasing with FACTS technology [9–14]. Different evolutionary algorithms are used to identify the optimal location and size of FACTS devices and hence available transfer capability is improved that have been reported in recent literature genetic algorithm [15], for complex and large scale power systems, a hybridization of real coded genetic algorithm (RCGA) is applied in [16], and hybrid mutation particle swarm optimization is applied in [17].

The endeavor of presenting this paper is to intensify ATC by the utilization of FACTS controllers like TCSC and SVC with real coded biogeography based optimization technique. Active and reactive power control, as well as adaptive voltage magnitude control and regulating all the three variables simultaneously, can be achieved by RCBBO. The suggested method has been tested on IEEE 30-bus and IEEE 118-bus system.

120.2 Real Coded Biogeography-Based Optimization

The Biogeography-based Optimization (BBO) technique, which is proposed by Simon [18] is a comprehensive algorithm for solving optimization problems and is based on the study of geographical distribution of species. Real Coded Biogeography-based Optimization (RCBBO) is an extension of BBO where individuals are directly encrypted by a floating point for the continuous optimization problems which is discussed in [19], where probabilistic based mutation operator is used which affects the convergence characteristics. In this paper, Gaussian adaptive mutation is applied to prevent premature convergence and produce a smooth convergence.

120.2.1 Migration Operator

Migration is the process that probabilistically modifies each individual in the habitat by sharing information with other individual solution. Geographical areas with high Habitat Suitability Index (HSI) are said to be well suitable for biological species. Suitability Index Variables (SIVs) are the variables that characterize the habitat of the species. Geographical areas with high HSI tends to have a large number of species, high emigration rate and low immigration rate. Therefore, habitats with high HSI tends to be more static in their species distribution compared to low HSI habitats. A habitat with high HSI is analogous to a good solution and a habitat with low HSI is analogous to a poor solution. The sharing of features of individuals in the habitat is done based on the migration rate. The immigration rate, λ_k and the emigration rate, μ_k are functions of the number of species in the habitat. When there are no species in a habitat, the immigration rate of the habitat is maximal. The immigration rate, λ_k can be formulated as:

$$\lambda_k = I\left(1 - \frac{k}{n}\right) \tag{120.1}$$

where I is maximum possible immigration rate, k is number of species of kth individual and n is maximum number of species. The emigration rate, μ_k can be formulated as:

$$\mu_k = E\left(\frac{k}{n}\right) \tag{120.2}$$

where E is maximum possible emigration rate.

120.2.2 Mutation Operator

The process of mutation tends to increase diversity among the individuals in the habitat to get better solution.

$$X_i(j) = X_i(j) + N_j(\mu, \sigma_1^2) \tag{120.3}$$

where $X_i(j)$ is the jth decision variable of individual X_i, and $N_j(\mu, \sigma_i^2)$ represents the Gaussian random variable with mean μ and variance σ^2

$$\sigma_i = \beta_S * \left[\frac{F_i}{f_{min}}\right] * \left(P_{Gi}^{max} - P_{Gi}^{min}\right) \tag{120.4}$$

where β_s is the scaling factor or mutation probability, F_i is the fitness value of ith individual, f_{min} is the minimum fitness value of the generation, and P_{Gi}^{max} and P_{Gi}^{min} are the maximum and minimum limits of ith individual. The algorithm of RCBBO is given below

Generate the initial population randomly
Evaluate the fitness value for each individual
While The halting criterion is not satisfied **do**

Sort the population from best to worst based on their fitness value
For each individual, map the fitness value to the number of species
Calculate the immigration rate and the emigration rate for each individual
Modify the population with the migration operator
Update habitat with modified individual
Sort the population from best to worst
Mutate the worst half of individuals from the habitat using mutation operator
Update the habitat with mutated individuals
Evaluate the fitness for each individual

End while

120.3 Problem Formulation

In this paper, intensification of ATC problem is designed as a multi-objective optimization problem. The problem is expressed as to find the best location and size of FACTS devices. The objective function comprises the minimization of fuel cost for thermal generating units, the enhancement of available transfer capability, the improvement of the voltage profile and minimization of transmission power losses.

$$F = optimize\{FC, ATC, V_m, P_L\} \tag{120.5}$$

120.3.1 Minimization of Fuel Cost

$$FC = \sum_{i=1}^{Ng} \left(a_i + b_i(P_{Gi}) + c_i\left(P_{Gi}^2\right)\right) \tag{120.6}$$

where FC is the total fuel cost, N_g is the number of generating units. P_{Gi} is the generated active power and a_i, b_i and c_i are the fuel cost coefficients of the ith unit.

120.3.2 Enhancement of Available Transfer Capability

Available transfer capability in the tie lines connected between inter zones is calculated by according to the North American Electric Reliability Council (NERC) procedure, ATC is the difference between Total Transfer Capability (TTC) and the summation of the Existing Transmission Commitment (ETC), the Transmission Reliability Margin (TRM) and the Capacity Benefit Margin (CBM) [4].

TTC is the thermal limit of transmission line. ETC is calculated from base case power flow analysis. TRM is taken as a constant percentage (i.e. 10 % of the TTC). CBM can be taken from the market value between energy contractors. CBM is referred for IEEE 30-bus from [20] and CBM is not considered for IEEE 118-bus system. ATC can be computed by

$$\mathrm{ATC} = \mathrm{TTC} - (\mathrm{ETC} + \mathrm{TRM} + \mathrm{CBM}) \tag{120.7}$$

$$\%\ of\ ATC\ improvement = \frac{ATC_2 - ATC_1}{ATC_1} \times 100 \tag{120.8}$$

where ATC_1 and ATC_2 are available transfer capability in the tie lines before and after placement of FACTS devices respectively.

120.3.3 FACTS Device Constraints

$$-100\,MVAr \le Q_{SVC} \ge 100\,MVAr \tag{120.9}$$

$$-0.8X_L \le X_{TCSC} \ge 0.2X_L \tag{120.10}$$

where X_{TCSC} is the reactance added by placing thyristor controlled series compensator (TCSC), XL is the reactance of the line where TCSC is connected and Q_{svc} is the reactive power injected at the bus by connecting SVC.

120.4 Results and Discussions

The proposed real coded biogeography-based optimization for enhancement of ATC has been applied to the IEEE 30-bus and IEEE 118-bus test system. The details of bus data and line data are taken from MATPOWER package [21]. The numerical results are presented in this section. The results obtained by the proposed approach are compared with the results found by alternative population-based algorithms reported in the literature recently. Power flow calculations by Newton–Raphson method were performed using the software package MATPOWER 4.1 [21].

120.4.1 IEEE 30-Bus System

The system consists of 6 generator buses, 24 load buses and 4 tap changing transformer. Bus 1 is taken as slack bus. This system is modified for the purpose of area split up. Total number of tie lines between areas is 5.

Case A: Line outage
A transmission line connecting buses 1 and 2, 2 and 6 are congested due to line outage between buses 1 and 3. A set of FACTS devices are connected in optimal location and hence congestions are relieved.

120.4.2 IEEE 118-Bus System

The system consists of 54 generators, 99 loads and 12 tap changing transformer. Bus 69 is taken as slack bus. This system is modified to create three areas and each areas are connected through set of tie lines. Total number of tie lines in the system is 12.
Case B: Generator outage
A transmission line connecting buses 8 and 30 is congested due to generator 5 outage at bus 10. Two set of FACTS devices are connected in optimal location and hence congestion is relieved.

The results obtained for base case (without contingency) optimal power flow (OPF) for IEEE 30-bus and IEEE 118-bus system are presented in Tables 120.1 and 120.2 respectively. Active power flow in congested line before and after connecting FACTS device is presented in Table 120.3. The optimized multi-objective function values by different methods are presented in Tables 120.4 and 120.5.

Table 120.1 OPF results shown for IEEE 30-bus system by different methods

Parameter	RCBBO	BBO	PSO	GA
Fuel cost ($/Hr)	802.1168	802.1191	802.1538	802.1233
ATC (MW)	154.1149	154.0042	154.7861	154.0043
Mean of voltage (p.u)	1.0242	1.0242	1.0242	1.0242
Active power loss (MW)	9.4536	9.4271	9.5401	9.4015

Table 120.2 OPF results shown for IEEE 118-bus system by different methods

Parameter	RCBBO	BBO	PSO	GA
Fuel cost ($/Hr)	130,190	130,320	131,550	133,460
ATC (MW)	2,080.4	2,095.5	2,123.1	2,219.1
Mean of voltage (p.u)	0.9861	0.9861	0.9861	0.9861
Active power loss (MW)	88.8784	89.4525	84.3091	81.0222

Table 120.3 Line flows in congested lines

Cases	Congested line	Line flow before placement of FACTS	Line flow after placement of FACTS (MW)			
			RCBBO	BBO	PSO	GA
Case A	1–2	180.8350	106.979	106.630	104.2833	106.8348
	2–6	66.6878	47.2064	46.7720	46.8846	48.1972
Case B	8–30	231.0474	73.2112	72.3139	42.8984	115.6798

Table 120.4 Results obtained for enhancement of ATC—Case A

Method	Object function			SVC		TCSC	
	Fuel cost	% of ATC improvement	Active power loss	Bus location	Capacity	Line location	Level of compensation
RCBBO	850.9881	7.3856	7.2970	15	11.1203	12	0.6
BBO	852.2749	6.4682	7.2093	24	7	12	0.6
PSO	857.4385	5.2391	7.0744	5	28.1106	12	0.6
GA	851.5923	6.4525	7.4348	11	17	12	0.6

Table 120.5 Results obtained for enhancement of ATC—Case B

Method	Object function			SVC		TCSC	
	Fuel cost	% of ATC improvement	Active power loss	Bus locations	Capacity	Line locations	Level of compensation
RCBBO	135,280	17.9640	54.8405	28, 13	5.1168, 15.4291	38, 7	0.6, 0.6
BBO	135,310	17.8985	54.5587	11, 13	17.128, 14.7474	7, 38	0.6, 0.6
PSO	140,090	16.0815	57.2773	13, 3	45.22, 52.794	21, 14	0.3158, 0.4830
GA	137,460	17.1755	58.3516	18, 13	64.00, 79.00	7, 19	0.0, 0.6

120.5 Conclusion

In this paper, a real coded biogeography based optimization algorithm is improved by adaptive Gaussian mutation operation and successfully applied to solve multi-objective functions including minimization of fuel cost, enhancement of ATC, maintenance of magnitude of voltage and transmission loss. This algorithm is very influential with restructured electricity market, to identify the optimal location and size of FACTS devices for improvement of available transfer capability. This approach is shown its effectiveness using the IEEE 30-bus and IEEE 118-bus system under both normal and contingency situations. The results obtained from the RCBBO approach are compared with other population based algorithms like BBO, PSO and GA. The superiority and solution quality of the proposed method are found better than other techniques. According to the results obtained, the RCBBO algorithm has a simple framework, smooth and quick convergence characteristic, therefore, can be used to solve the multi-objective function in large-scale power systems with several thousands of buses utilizing the strength of parallel computing.

References

1. Song YH, Wang X (2003) Operation of restructured power systems. Operation of market-oriented power system, Chap. 1. Springer, Berlin, pp 1–2
2. Manikandan BV, Raja SC, Venkatesh P, Kannan PS (2008) Available transfer capability determination in the restructured electricity market. Electr Power Compon Syst 36(9):941–959
3. Wunderlich S, Wu T, Fischl R, O'Connell R (1995) An inter-area transmission and voltage limitation (TVLIM) program. IEEE Trans Power Syst 10(3):1257–1263
4. North American Electric Reliability Council (NERC). (1996) Available transfer capability definitions and determination. NERC, report, June 1996
5. Ejebe GC, Tong J, Waight JG, Frame JG, Wang X et al (1998) Available transfer capability calculations. IEEE Trans Power Syst 13(4):1521–1527
6. Ajjarappu V, Christy C (1992) The continuation power flow: a tool for steady state voltage stability analysis. IEEE Trans Power Syst 7(1):416–423
7. Ou Y, Singh C (2002) Assessment of available transfer capability and margins. IEEE Trans Power Syst 17(2):463–468
8. Gao B, Morison GK, Kundur P (1996) Towards the development of a systematic approach for voltage stability assessment of large-scale power systems. IEEE Trans Power Syst 11 (3):1314–1324
9. Xiao Y, Song YH, Liu C-C, Sun YZ (2003) Available transfer capability enhancement using FACTS devices. IEEE Trans Power Syst 18(1):305–312
10. Sawhney H, Jeyasurya B (2004) Application of unified power flow controller for available transfer capability enhancement. Electric Power Syst Res 69(2):155–160
11. Ghawghawe ND, Thakre KL (2009) Computation of TCSC reactance and suggesting criterion of its location for ATC improvement. Int. J Electr Power Energy Syst 31(3):86–93
12. Mathur RM, Varma RK (2012) Thyristor-based FACTS controllers for electrical transmission systems
13. Xiao Y, Song YH, Sun YZ (2001) Application of unified power flow controller to available transfer capability enhancement. IEEE Power Eng Rev 72:66–68
14. Xiao Y, Song YH, Liu CC, Sun YZ (2003) Available transfer capability enhancement using FACTS devices. IEEE Trans Power Syst 18(1):305–312
15. Rashidinejad M, Farahmand H, Fotuhi-Firuzabad H, Gharaveisi AA (2008) ATC enhancement using TCSC via artificial intelligent techniques. Electric Power Syst Res 78:11–20
16. Nireekshana T, Kesava Rao G, Siva Naga Raju S (2012) Enhancement of ATC with FACTS devices using real-code genetic algorithm. Electric Power Energy Syst 43:1276–1284
17. Farahmand H, Rashidinejad M, Mousavi A, Gharaveisi AA, Irving MR, Taylor GA (2012) Hybrid mutation particle swarm optimization method for available transfer capability enhancement. Electric Power Energy Syst 42:240–249
18. Simon D (2008) Biogeography-based optimization. IEEE Trans Evol Comput 12:702–713

19. Gong W, Cai Z, Ling CX, Li H (2010) A real-coded biogeography-based optimization with mutation. Appl Math Comput 216(9):2749–2758
20. Gnanadass R, Padhy NP, Manivannan K (2004) Assessment of available transfer capability for practical power systems with combined economic emission dispatch. Electric Power Syst Res 69(3):267–276
21. Zimmerman RD, Murillo-Sanchez CE, Thomas RJ (2011) MATPOWER: steady-state operations, planning and analysis tools for power systems research and education. IEEE Trans Power Syst 26(1):12–19

Chapter 121
Application of SRF Algorithm and SVPDM Concept in Power Electronic Transformer

T. Ruban Deva Prakash and R. Shiju Kumar

Abstract Increasing power demand, carbon emission from fossil fuel based generation, depletion of resources, unreliability of power system, poor power quality, low energy efficiency, high transmission losses are the driving factors to move towards smart grid. Smart grid is the integration of electrical grid with information and communication technology and comprises of several micro grid. The micro grids are integrated with main utility grid at point of common coupling using transformers. Such transformer should be of small size for indoor substations. The transformers should have features like bidirectional power flow, real and reactive power flow control and power quality control. Power electronic transformers (PET) are best suited for this application. This paper deals with matrix converter based power electronic transformer which has three phase matrix converter, STATCOM, bilateral converter, dc link capacitor, and voltage source inverter. The main problems of matrix converter based transformers are low input power factor and harmonics. Input power factor and input current harmonic problems are rectified by adding a STATCOM at the input side of matrix converter. Novel space vector based pulse density modulation is designed to obtain harmonic free output voltage in output side of PET. Additionally, the proposed PET performs typical functions and has advantages such as voltage regulation, voltage sag and swell elimination and voltage flicker mitigation. In addition, it has other benefits such as bidirectional power flow, light weight, low volume and no toxic dielectric coolants. Performance of the proposed power electronic transformer is validated by simulation studies.

Keywords PET · STATCOM · CPP · Matrix converter · RES · SVPDM

T.R.D. Prakash (✉)
Sree Narayana Gurukulam College of Engineering, Kollenchery, Kerala, India
e-mail: mahiruban2006@yahoo.co.in

R.S. Kumar
Sathyabama University, Chennai, Tamil Nadu, India
e-mail: r.shijukumar@hotmail.com

C. Kamalakannan et al. (eds.), *Power Electronics and Renewable Energy Systems*,
Lecture Notes in Electrical Engineering 326, DOI 10.1007/978-81-322-2119-7_121

121.1 Introduction

Electricity is the most versatile form of energy and its global demand is increasing day by day. The present generation in India is not sufficient to meet the increasing demand. The electric power system was built up more than 150 years and its efficiency and reliability are very less. A smarter grid is definitely needed to satisfy both the increasing demand for power and the need to reduce carbon dioxide emissions, in a sustainable, reliable and economic way. A smarter grid will provide greater control over energy costs, a more reliable energy supply for consumers, integration of more renewable power sources, and reduced CO_2 emissions and other pollutants. Smart grids possess demand response capacity to help balance electrical consumption with supply as well as the potential to integrate new technologies to enable energy storage devices. Smart grid is composed of cluster of smart micro-grids. A micro-grid is a mini grid comprising of low voltage generators, mostly renewable generators integrated with energy storage devices, plug-in electric vehicles and loads. Micro-grid integrated with information and communication technology to incorporate smart features like automatic fault and disturbance detection with self healing ability, cost reduction, energy saving, CO_2 emission reduction and regulating energy demand is called smart micro-grid. The micro grid has Custom Power Park (CPP) which has highly unbalanced, nonlinear load along with distributed generation using renewable energy sources (RESs). High penetration of RESs and CPP leads to several power quality issues in micro grid. Hence measures have to be taken to mitigate power quality issues. Micro grids are connected to the utility grids at the point of common coupling (PCC) through a transformer.

Power transformers are an integral part of micro grid. Recently steps are taken to reduce the size and weight of transformer. The size of transformers can be reduced by replacing the power transformers with high frequency transformers. For use of high frequency transformer in power systems, first the low frequency voltages are converted to high frequency by a power electronic converter and then it is stepped up or down by the high frequency transformer and finally the high frequency voltage is converter to low frequency by a second power electronic converter. The whole system is termed as power electronic transformer (PET).

Several topologies of PET are available in literature [1]. Adding intelligent features to transformers are under development [2]. Less attention is paid to the areas of the circuit topologies [3, 4]. Sabahi et al. [5] proposed a new modular flexible power electronic transformer (FPET). The proposed FPET is flexible enough to meet future needs of power electronic centralized systems. Iman-Eini et al. [6] proposed a modular power electronic transformer (PET) for feeding critical loads. The above topologies use more number of power electronic switches and switching losses are more. Controls of such topologies are complicated. Matrix converter based power electronic transformer gains attention recently [7]. Vector quantized spread spectrum pulse density modulation for 4-level inverter is proposed for reducing output voltage harmonics [8] in 2011. A novel topology of power electronic transformer is proposed in [9]. In the design process, the AC/DC, DC/AC, AC/AC converters and high frequency transformer have been used. One matrix converter operates as AC/AC converter in power electronic transformer. The above power electronic transformer performs typical functions and has advantages such as power factor correction, voltage sag and swell elimination, voltage flicker reduction and protection capability in fault situations.

Power flow control features are incorporated in PET. Optimal regulator-based control of electronic power transformer for distribution systems is proposed in [10]. Pulse density modulation control using space vector modulation is recently applied to single-phase to three-phase indirect matrix converter [11]. A power electronic transformer based on matrix converters (MC) with open ended primary is proposed recently [12]. The open ended primary of the transformer is fed from two power converters MC1 and MC2. These two converters are matrix converters with three bi-directional switches removed, one from each leg. The secondary of the transformer is connected to a third matrix converter MC3. The control is complicated and the number of power electronic switches is more. The proposed PET consists of input matrix converter, shunt voltage source inverter, high frequency transformer, bilateral converter, dc link capacitor and output Voltage Source Inverter (VSI).The ac side of shunt VSI is connected at the input side of matrix converter and dc side with dc link in secondary side of PET. This filters the input current harmonics produced by matrix converter and improves input power factor. It acts like a power conditioner and performs typical functions and has advantages such as voltage regulation, voltage sag and swell elimination and voltage flicker reduction. A novel Space Vector based Pulse Density Modulation (SVPDM) is designed for output VSI to reduce the output voltage harmonics.

121.2 Circuit Topology of the Proposed PET

Basically the proposed topology comprises of three IGBT based three arm converter, a matrix converter, high frequency transformer and two dc link capacitors. The block diagram of proposed PET is shown in Fig. 121.1. It has three phase to three phase matrix converter, high frequency transformer, bilateral AC/DC converter, output voltage source inverter and STATCOM. The STATCOM is connected in the input side of the matrix converter. Power frequency ac is converted to high frequency ac using matrix converter. The high frequency ac is stepped up/down using high frequency transformer which provides galvanic isolation between the primary and secondary voltage sources. The resulting high frequency ac in the secondary is converted to dc using bilateral AC/DC converter. The bilateral AC/DC converter has the same structure as VSI, but it acts in rectifier mode. The dc link has energy storage capacitor. The dc is converted back to power frequency ac by a voltage source inverter. The voltage source inverter output is a stepped wave having harmonics. Space vector pulse density modulation control is used to reduce the harmonics in the output voltage of inverter. The proposed device has added features

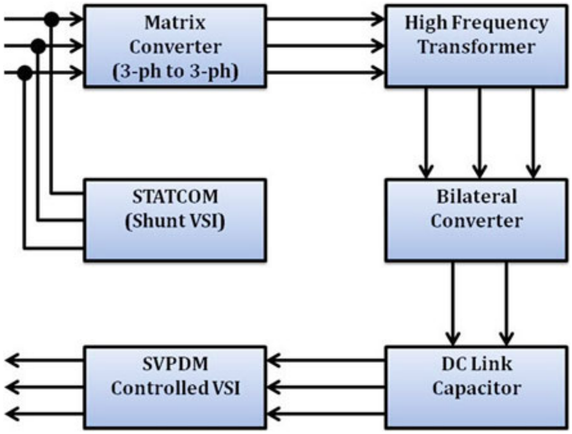

Fig. 121.1 Block diagram of proposed PET

like voltage regulation, power factor correction and power conditioning. The control unit is used to generate switching pulses for all the four converters. The control unit has d-q based control for generating reference current signal for STATCOM and hysteresis control is used to generate switching pulses. A simple pulse generation control technique is used for matrix converter. The proposed PET supports bidirectional power flow.

121.3 Matrix Converter and Its Control

The 3-ph to 3-ph matrix converter has nine bidirectional switches. Each bidirectional switch is realized using four diodes and an IGBT. The switch will conduct in both positive and negative half cycles, if switching pulse is given to the IGBT. During positive half cycle, the diodes D1 and D4 are forward biased. Hence the current flows from input side to output side of switch through D1, S and D2, if the switching pulse is applied to 'S'. During negative half cycle, the diodes D2 and D3 are forward biased. Each output phase of converter is connected with all the three input phases through bidirectional switches. But only one input phase has to be connected with one output phase at a time and the remaining two switches of the same output phase should be OFF to prevent short circuit between phases. Thus by proper switching any desired output frequency can be obtained by matrix converter irrespective of the input frequency. Hence matrix converter can be used as a frequency regulator. The structure of matrix converter shown in Fig. 121.2. The control strategy of matrix converter has a comparator to compare the phase voltages with a rectangular wave. The rectangular wave is generated with the desired output frequency of matrix converter. During the positive half cycle of rectangular wave,

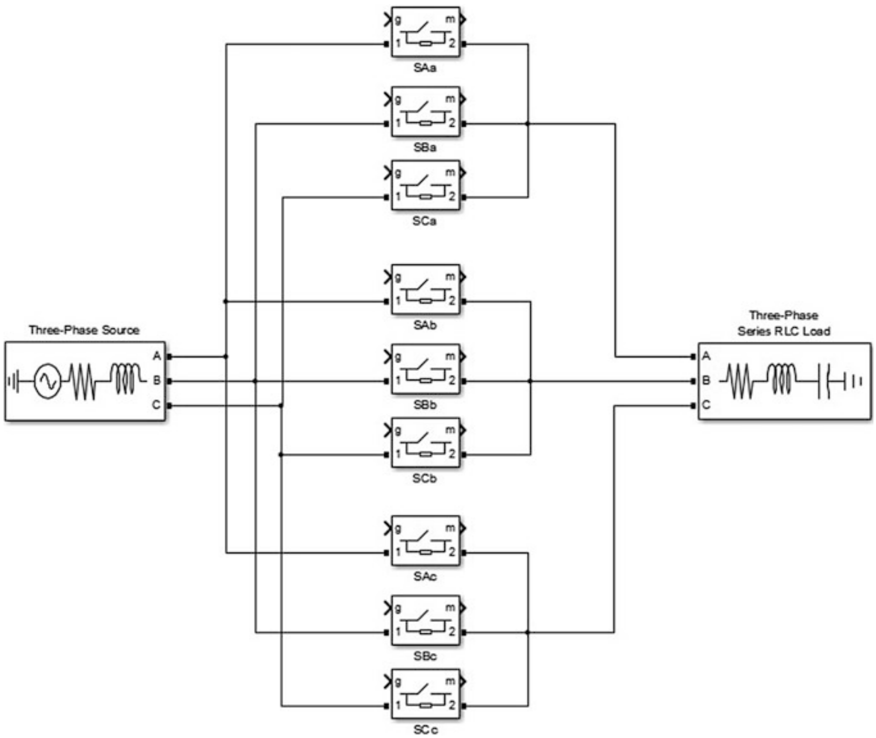

Fig. 121.2 Structure of matrix converter

gating pulse for IGBT based bipolar switch is produced when the corresponding phase voltages are greater than rectangular wave. During the negative half cycle of rectangular wave, gating pulse for IGBT based bipolar switch is produced when the corresponding phase voltages are lesser than rectangular wave. Which has AND, OR and NOT gates.

121.4 High Frequency Transformer

The power frequency transformer is bulky, occupies large space and heavy. The near future in electric grid is smart grid comprising of micro-grids. Substation transformer at the point of common coupling of micro-grid and utility grid should be compact for indoor installations. Hence high Frequency Transformer (HFT) gains importance due to its reduced size and weight. The core of HFT is made up of nano crystalline material like FINEMET and hence core is small. It has the added advantage of high energy efficiency. In PET the HFT gives galvanic isolation and transforms voltage levels to any desired value depending on the design. The core loss of FINEMET built HFT is approximately 1/11th of the core loss of 50 Hz power transformer and the size of HFT is approximately 1/150th of that of 50 Hz power transformer. The potential use of high frequency transformer is at very high frequencies starting from 10 kHz, which is a desirable characteristics since higher the frequency smaller is the weight and volume of the transformer. FINENET is a promising material in terms of reducing core loss manufactured by HITACHI.

121.5 Bilateral AC/DC Converter and DC Link Capacitor

The structure of bilateral ac to dc converter has six IGBT switches connected in three arms. It acts in rectifier mode and converts the high frequency ac output of HFT to dc. It can act in inverter mode when the direction of power flow has to be reversed. Bilateral converter is used to impart bidirectional feature to the PET. If the ac input wave is less than zero, the gate signal to corresponding IGBT in the upper arm is logic 1 and the complementary control signal is given to the IGBT at the lower arm to avoid short circuit. The output side of bilateral converter has dc link capacitor which acts as smoothening filter to reduce voltage ripples in the dc side. The same act as energy storage element and continue to supply output even with momentary interruption or voltage sag in the input supply side of PET. Hence power quality disturbances in the primary side are not carried over to the secondary side. The capacitor rating is selected as 120 microfarad per kVA.

121.6 VSI and Proposed Modified SVPDM Control

The six pulse Voltage Source Inverter (VSI) with Pulse Width Modulation (PWM) control and Space Vector Pulse Width Modulation (SVPWM) suffers from the drawback of high output voltage harmonics. Hence in order to reduce the Total Harmonic Distortion (THD), Pulse Density modulation (PDM) control and Space Vector Pulse Density Modulation (SVPDM) are proposed. This paper proposes a modified SVPDM approach which has much simplified control algorithm when compared to the existing techniques. The filter has low pass module which filters all the higher order harmonics and three, single tuned shunt filters for filtering 3rd, 5th and 7th harmonics which are the dominating harmonics. The control signal block generates sine wave with frequency, magnitude and phase same as that of the desired output from the VSI. The control signals are transformed from three phase abc axis to two phase m-n axis. The m-n axes are similar to alpha-beta axis but the two axes are phase shifted by 60° instead of 90°. The transformation formula is given in Eqs. (121.1)–(121.3).

$$V_m = \sqrt{\frac{2}{3}}\left(V_a - \frac{1}{2}V_b - \frac{1}{2}V_c\right) \tag{121.1}$$

$$V_n = \sqrt{\frac{2}{3}}\left(\frac{1}{2}V_a + \frac{1}{2}V_b - V_c\right) \tag{121.2}$$

$$V_0 = \sqrt{\frac{2}{3}}\left(\frac{1}{\sqrt{2}}V_a + \frac{1}{\sqrt{2}}V_b + \frac{1}{\sqrt{2}}V_c\right) \tag{121.3}$$

The filtered output from VSI is also converted from abc to m-n. The error between the desired output and actual output are computed in m-n domain and integrated using digital integrator. This is similar to delta-sigma modulation in PDM technique. The output from delta-sigma modulation stage is converted once again to abc as shown in Fig. 121.10 using inverse transform of Eqs. (121.1)–(121.3). The transformed output is fed to hexagonal quantizer. The hexagonal quantizer has angle calculation sub-block which converts the signal from abc to alpha-beta using Eqs. (121.4) and (121.5).

$$V_{alpha} = \sqrt{\frac{2}{3}}\left(V_a - \frac{1}{2}V_b - \frac{1}{2}V_c\right) \tag{121.4}$$

$$V_{beta} = \sqrt{\frac{2}{3}}\left(0.V_a + \frac{\sqrt{3}}{2}V_b - \frac{\sqrt{3}}{2}V_c\right) \tag{121.5}$$

Then angle is calculated using Eq. (121.6).

$$\theta = \tan^{-1}\frac{V_{beta}}{V_{alpha}} \tag{121.6}$$

The sector selection block selects the sector based on the angle as per Table 121.1 and its simulink implementation is shown in Fig. 121.3. The switching pulses generation block generates switching pulses for the IGBTs in upper side of the corresponding phase arms and the NOT gate output of the same is applied to IGBTs in the lower part of the arm to avoid short circuit between phases. Switching pulses corresponding to each sector are also given in Table 121.1 and its simulink implementation is shown in Fig. 121.4. The information stored in subatomic block ‘sector 1’ alone is shown at the side and the other subatomic sector blocks also has similar information as per Table 121.1. This modified SVPDM is simple and suitable for digital implementation.

Table 121.1 Sector selection and corresponding switching pulses

Angle	Sector	Switching pulses		
		S_a	S_b	S_c
−30 to 30	1	1	0	0
30 to 90	2	1	1	0
90 to 150	3	0	1	0
150 to −150	4	0	1	1
−150 to −90	5	0	0	1
−90 to −30	6	1	0	1

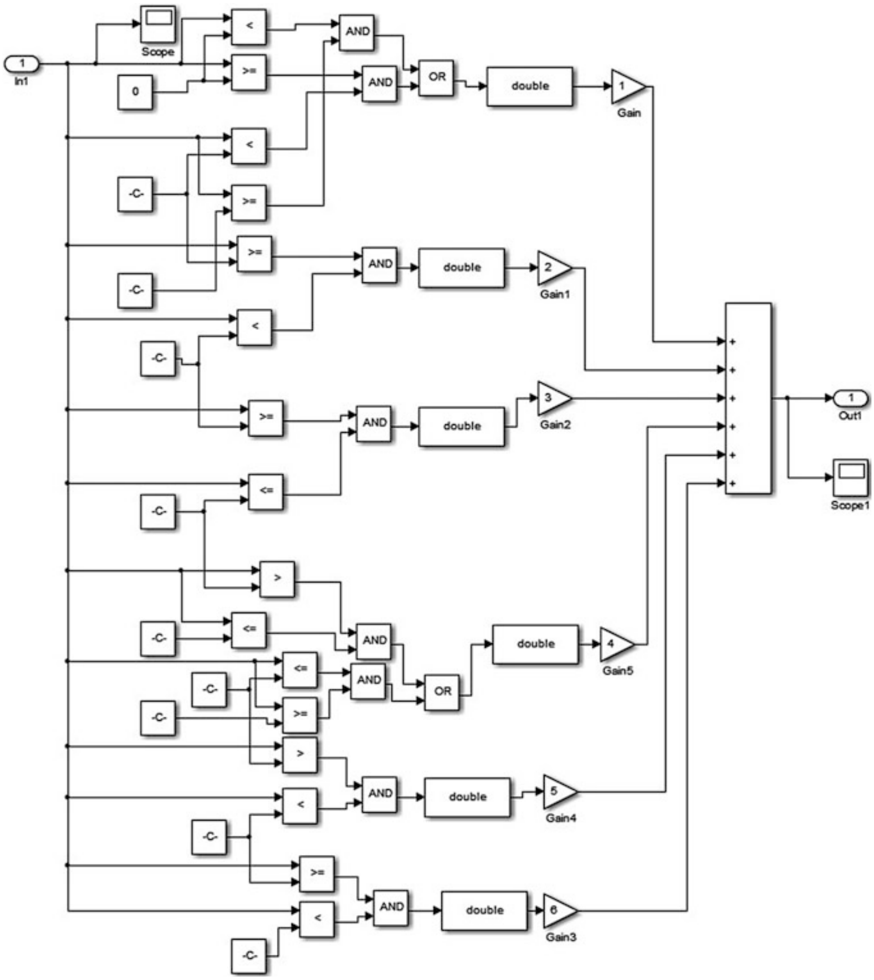

Fig. 121.3 Sector selection block

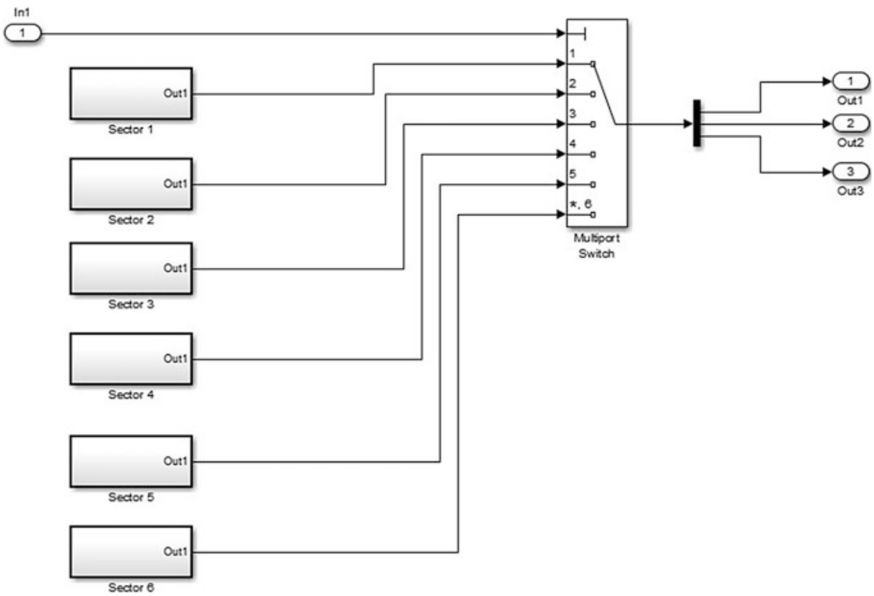

Fig. 121.4 Switching pulse generation block

121.7 Power Conditioning

The input side of PET has matrix converter which has low input power factor and high input current harmonics. This problem is overcome by connecting a VSI in shunt at the input side. The dc side of VSI is connected to dc link capacitor which makes its configuration similar to STATCOM. This structure draws current from the mains whose magnitude is same as harmonic components but at 180° out of phase. It also draws a component of current same as the reactive component of load current but at 180° out of phase which means leading current. Thus input current harmonics are eliminated and system power factor is maintained at unity. Input side of shunt VSI has inductance. The 1,200 μF dc link is maintained at 15.5 kV by a PI controller. The controller uses Synchronous Reference Frame (SRF) algorithm. In SRF algorithm three phase voltages are converted to alpha-beta using abc to alpha-beta conversion as per Eqs. (121.4) and (121.5). Angle θ calculation is done using (121.6). Similarly, three phase currents are converted to alpha, beta and zero using Eqs. (121.7), (121.8) and (121.9).

$$I_{alpha} = \sqrt{\frac{2}{3}}\left(I_a - \frac{1}{2}I_b - \frac{1}{2}I_c\right) \tag{121.7}$$

$$I_{beta} = \sqrt{\frac{2}{3}}\left(0.I_a + \frac{\sqrt{3}}{2}I_b - \frac{\sqrt{3}}{2}I_c\right) \tag{121.8}$$

$$I_0 = \sqrt{\frac{2}{3}}\left(\frac{1}{\sqrt{2}}I_a + \frac{1}{\sqrt{2}}I_b + \frac{1}{\sqrt{2}}I_c\right) \tag{121.9}$$

The current is converted again from alpha-beta to d-q using angle θ and Eqs. (121.10) and (121.11).

$$I_d = \left(I_{alpha}\cos\theta + I_{beta}\sin\theta\right) \tag{121.10}$$

$$I_q = \left(-I_{alpha}\sin\theta + I_{beta}\cos\theta\right) \tag{121.11}$$

The voltages are of 50 Hz and θ is calculated from voltages, hence 50 Hz component of currents are converted to dc in d-q domain. The oscillating components correspond to current harmonics. The oscillating components are separated using high pass filter and used as harmonic reference. In order to correct power factor, the reactive power requirement of load is supplied from STATCOM. Since I_q corresponds to reactive component of current, it has to be included along with the reference signal. Thus the reference current generated corresponds to harmonics and reactive component of current drawn by the load, which is converted back from d-q to alpha-beta and then to abc using inverse transformation. The reference current is compared with the actual current supplied by the compensator and the error is used to generate switching pulses in hysteresis controller. The hysteresis controller changes switching state, when the error crosses the upper and lower tolerance limit (hysteresis band).

121.8 Results and Discussion

The simulink model of the proposed PET with all controllers is shown in Fig. 121.5. The simulation parameters are given in Table 121.2. Simulation type is discrete with 5 μs sampling time. Variable step ode23tb solver is used for simulation. The input voltage and current of PET before connecting shunt VSI module is shown in Fig. 121.6. Fast Fourier Transform (FFT) tool shows that the THD of current is 78.17 % as shown in Fig. 121.7. The harmonic magnitudes are given in amps.

The input current of PET after connecting shunt VSI module and its FFT analysis is shown in Figs. 121.8 and 121.9. The THD has reduced from 78.17 to 22.37 %. The output of bilateral converter is shown in Fig. 121.10. The output voltage is constant around 320 V. But the ripples are due to the fluctuations in high frequency input. DC link capacitor of 1,200 μF is used and the ripple level can be reduced by further increasing the rating. The output voltage of VSI with the proposed modified SVPDM is shown in Fig. 121.11. The FFT analysis result is shown in Fig. 121.12. The output voltage of PET after passive filter is shown in Fig. 121.13 and its FFT analysis is shown in Fig. 121.14. The THD is found to be

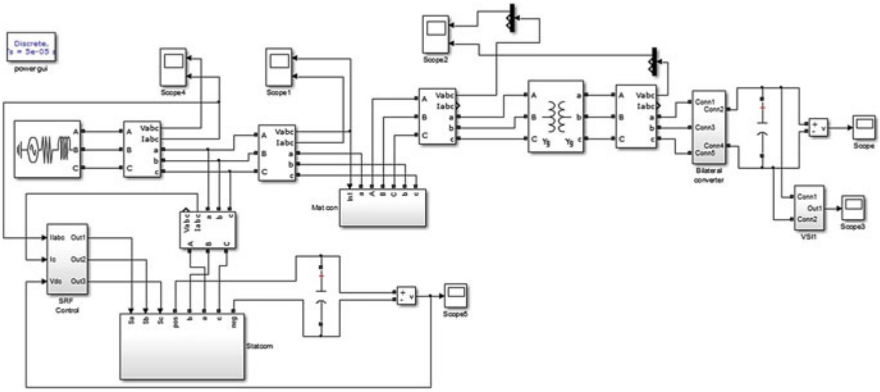

Fig. 121.5 Simulink model of proposed PET with controllers

Table 121.2 Simulation parameters

Simulation parameters	Values
Generator voltage, frequency, resistance, inductance	11 kV, 50 Hz, 0.28 Ω, 6.58 mH
HFT connection, voltage, kVA rating, frequency, R_{pu}, L_{pu}, R_{mpu}, L_{mpu}	Yg/Yg, 11 kV/415 V, 25 kVA, 2.5 kHz, 0.002, 0.08, 500, 500
Load	100 Ω
DC link capacitor at secondary side of HFT	1,200 μF, 450 V
DC link capacitor at STATCOM	1,200 μF, 16,000 V
DC link voltage of STATCOM	15,500 V
Filter at STATCOM	0.4 Ω, 2.5 mH
IGBT/diode R_{on}, R_s, C_s	0.001 Ω, 100 kΩ, inf
Diode R_{on}, L_{on}, V_f, R_s, C_s	0.001 Ω, 0, 0.8 V, 500 Ω, 0.25 μF

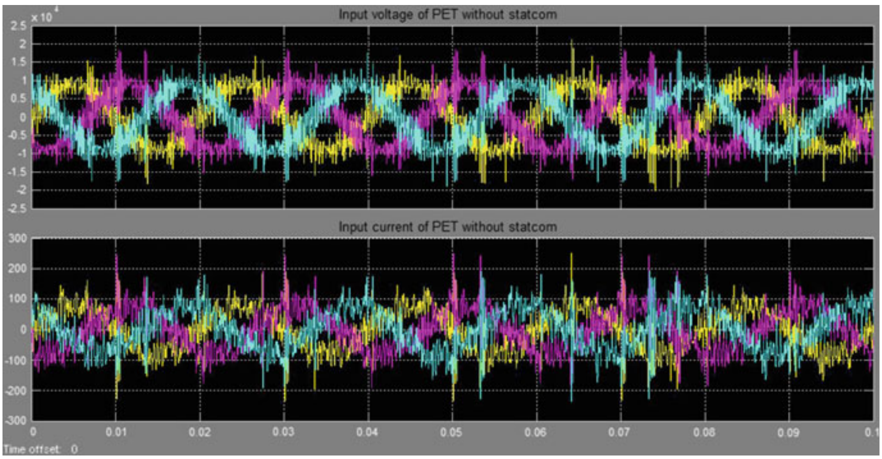

Fig. 121.6 Input voltage and current without statcom

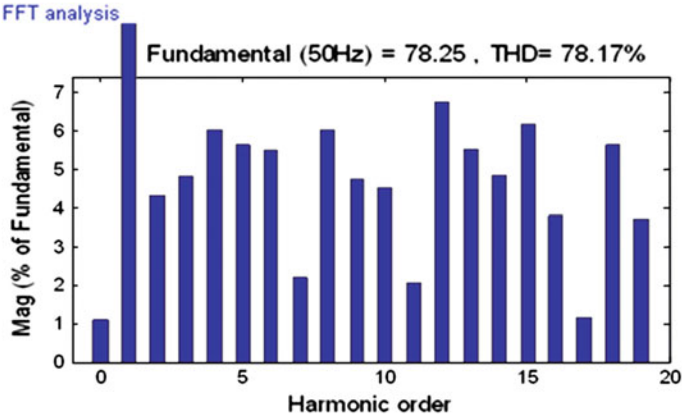

Fig. 121.7 FFT of input current without statcom

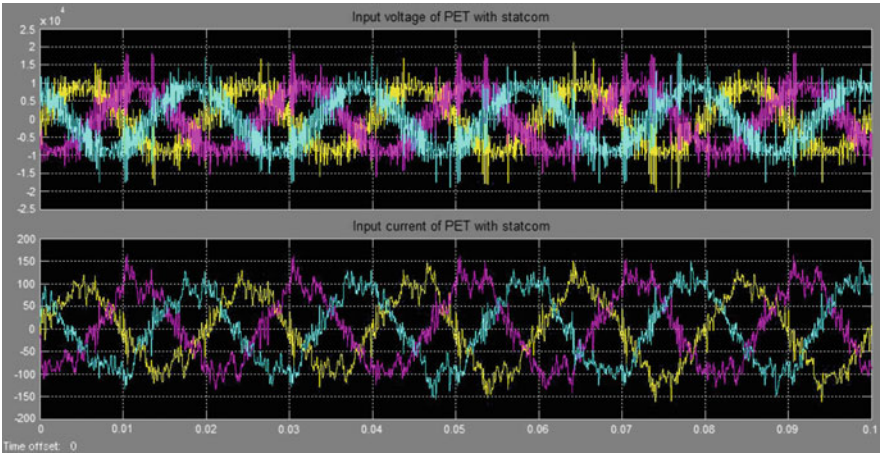

Fig. 121.8 Input voltage and current with statcom

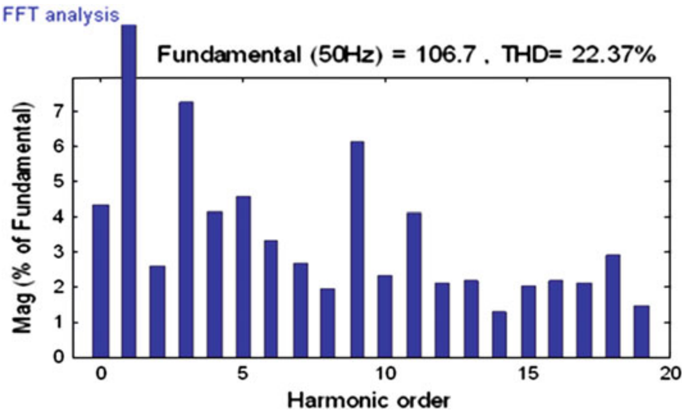

Fig. 121.9 FFT of input current with statcom

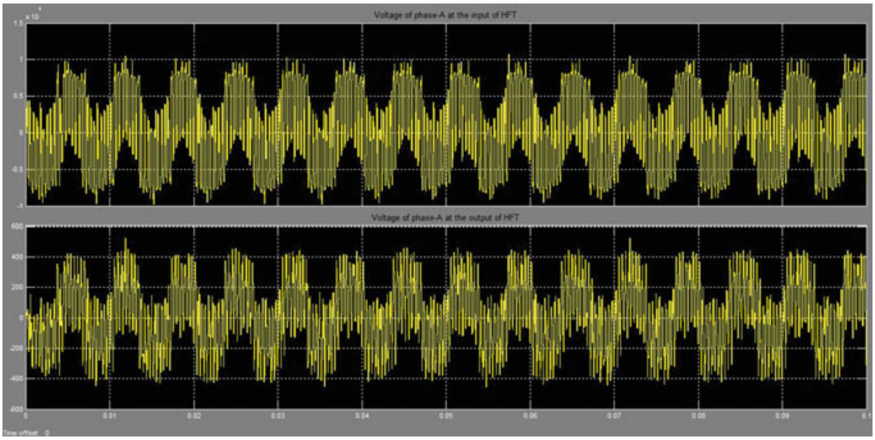

Fig. 121.10 Line voltages at the input and output side of HFT

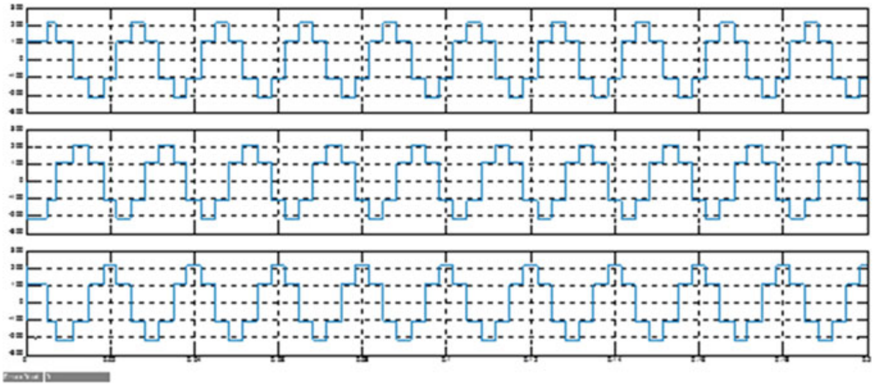

Fig. 121.11 Output voltage of PET before filter

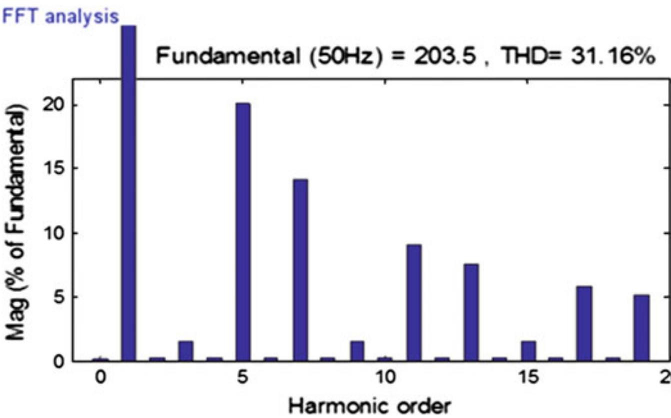

Fig. 121.12 FFT of output voltage of PET before filter

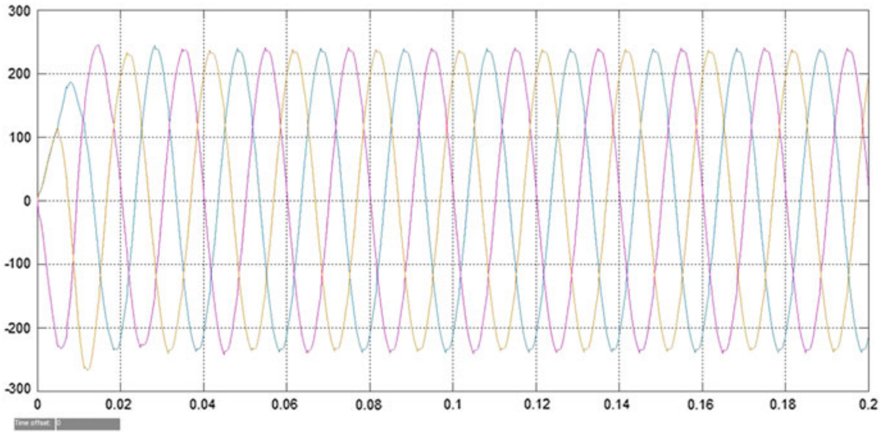

Fig. 121.13 Output voltage of PET

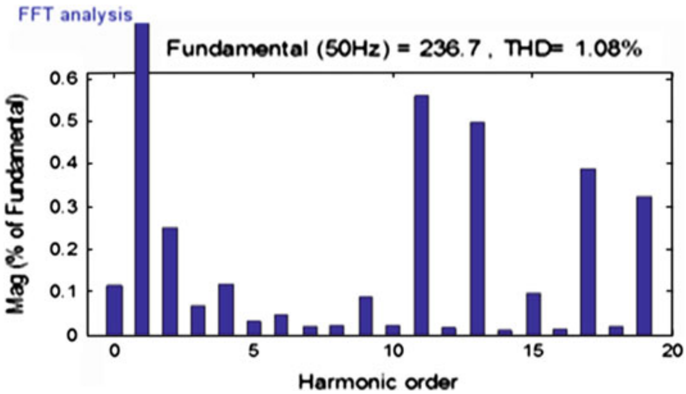

Fig. 121.14 FFT of output voltage of PET

1.08 % which is much below IEEE limit of 5 %. The dc link voltage of statcom is maintained constant at 15.5 kV.

121.9 Limitation and Future Scope

The proposed PET topology has high input power factor but the input current harmonics are high. The total harmonic distortion in current amounts to 22.37 % which is very high when compared to IEEE limits. In order to reduce output voltage harmonics modified SVPDM is proposed. But still the output voltage has THD of

31.16 % without passive filter which is also very high. Hence modified SVPDM can be developed for matrix converter to reduce input current harmonics. Multi-level converter topologies can be tried for reducing output voltage harmonics. The number of switches used in this topology is more and attention can be given to meet the desired objective with less number of power electronic switches.

121.10 Conclusion

Matrix converter based power electronic transformer with dc link in secondary side is proposed in this paper. The proposed PET has three phase matrix converter, STATCOM, bilateral converter, dc link capacitor, and voltage source inverters. The main problems of matrix converter based transformers are low input power factor and harmonics. The above problem is rectified by adding a STATCOM at the input side of matrix converter. Novel space vector based pulse density modulation is designed to obtain harmonic free output voltage in output side of PET. Additionally, the proposed PET performs typical functions and has advantages such as voltage regulation, voltage sag and swell elimination and voltage flicker mitigation. Due to the presence of dc link in secondary side of PET, the above power quality problems are not pronounced in the load side. In addition, it has other benefits such as bidirectional power flow, light weight, low volume and no toxic dielectric coolants. Performance of the proposed power electronic transformer is validated by simulation studies.

References

1. Falcones S, Mao X, Ayyanar R (2010) Topology comparison for solid state transformer implementation. Power and energy society general meeting, IEEE 25–29 Jul 2010, pp 1–8
2. Viktor B, Indrek R, Tõnu L (2011) Intelligent transformer: possibilities and challenges. Sci J Riga Tech Univ, Power Electr Eng, vol 29
3. Aijuan J, Hangtian L, Shaolong L (2006) A new high-frequency AC link three-phase four-wire power electronic transformer. In: Proceedings of IEEE conference on industrial and electronic applications, May 2006, pp 1–6
4. Krishnaswami H, Ramanarayanan V (2005) Control of high-frequency AC link electronic transformer. IEE Proc Elect Power Appl 152(3):509–516
5. Sabahi M, Goharrizi AY, Hosseini SH, Sharifian MBB, Gharehpetian GB (2010) Flexible power electronic transformer. IEEE Trans Power Electron 25(8):2159–2169
6. Iman-Eini H, Farhangi S, Schanen J-L, Khakbazan-Fard M (2009) A modular power electronic transformer based on a cascaded H-bridge multilevel converter. Electr Power Syst Res 79:1625–1637
7. Basu K, Gupta RK, Nath S, Castelino GF, Mohapatra KK, Mohan N (2010) Research in matrix-converter based three-phase power-electronic transformers. International power electronics conference (IPEC), Jun 2010, pp 2799–2803

8. Jacob B, Baiju MR (2011) Vector quantized spread spectrum pulse density modulation for four level inverters. 6th IEEE conference on industrial electronics and applications (ICIEA), Jun 2011, pp 674–679
9. Banaei MR, Salary E (2011) Power quality improvement based on novel power electronic transformer. 2nd power electronics, drive systems and technologies conference, 2011, pp 286–291
10. Liu H, Mao C, Lu JM, Wang D (2009) Optimal regulator-based control of electronic power transformer for distribution systems. Electric Power Syst Res 79:863–870
11. Nakata Y, Itoh J (2012) Pulse density modulation control using space vector modulation for a single-phase to three-phase indirect matrix converter. IEEE energy conversion congress and exposition (ECCE), 2012, pp 1153–1159
12. ShabariNath, K. K. Mohapatra and Ned Mohan (2009) Output voltage regulation in matrix converter fed power electronic transformer for power systems application in electric ship. IEEE electric ship technologies symposium, 20–22 Apr 2009, pp 203–206

Chapter 122
Investigations on the Dynamics of Seven Level Inverter Fed Induction Motor Drive with Neural Based Rotor Resistance Estimator

A. Chitra and S. Himavathi

Abstract Inverter fed induction motor drive dynamics is greatly dependent on the input voltage pattern. Indirect field oriented control (IFOC) is of industrial standard which is highly sensitive to motor parameter variations. This paper attempts to address the above cited issues. To ensure the quality of the input voltage multilevel inverter (MLI) is employed to feed the motor. Amongst all the motor parameters rotor resistance is of paramount important as it varies with temperature, frequency and skew effects and also the exact value of rotor resistance is required for the unit vector generation and slip calculation in an IFOC scheme. Hence neural network learning based model reference adaptive system (NN-MRAS) for the on-line estimation of rotor resistance (R_r) is utilized. The Neural learning algorithm determines the estimation speed, stability, weight convergence, accuracy of estimation, speed of tracking and ease of implementation. This work proposes a new neural learning strategy for R_r estimation. The entire system is modeled and simulated in Matlab/Simulink. The MLI fed drive is compared with the conventional inverter fed drive. Also the MLI fed drive dynamics are presented with and without the proposed estimator.

Keywords IFOC · MLI · NN-MRAS · ASD · CHBMLI · PWM

122.1 Introduction

Induction motors are the commonly used machines in the industry due to their low cost, size, reliability, versatility, ruggedness, simplicity and less maintenance. Induction motors have been used, for a long time, in low performance drives. The

A. Chitra (✉)
School of Electrical Engineering, Department of Electrical and Electronics Engineering, VIT University, Vellore, India
e-mail: chitra.a@vit.ac.in

S. Himavathi
Pondicherry Engineering College, Pondicherry, Pudhucherry, India
e-mail: himavathi@pec.edu

C. Kamalakannan et al. (eds.), *Power Electronics and Renewable Energy Systems*, Lecture Notes in Electrical Engineering 326, DOI 10.1007/978-81-322-2119-7_122

early motor drive control techniques for induction motors are of the scalar type and based on steady-state models, e.g., the Volts/Hertz technique that provides poor dynamic performance [1]. As it involves complex speed control methods to provide good dynamic response. The recent advancement in power electronics and digital processors have made this possible to achieve more efficient speed control strategies for induction motor drives [2].

The traditional adjustable speed drives (ASD) system is based on the voltage source inverter (VSI). It suffers from common limitations such as: high harmonics, low reliability, and huge filter requirements. Multilevel inverter (MLI) is preferred to feed induction motors because of its superior performance compared to the normal three phase inverter [3]. Three major topologies are available for MLI namely: Cascaded H Bridge, Diode clamped and Flying Capacitor. The Cascaded H Bridge MLI (CHBMLI) is probably the only kind of multilevel inverter wherein the inputs can be isolated energy sources (capacitors, batteries, PV arrays, etc.) and hence is best suited for renewable energy systems [4–6].

A three phase seven level CHBMLI is used to feed the induction motor [7, 8]. Each phase of the inverter contains Three H Bridges Each H Bridge contains four switches and is supplied from a separate DC source. Pulse Width Modulation (PWM) techniques are used to achieve better sinusoidal output with reduced total harmonic distortion [9]. Various PWM techniques include sine PWM, space vector PWM, selective harmonic elimination etc. In this work, multicarrier level shifted sine PWM is employed.

In the IFOC scheme, the unit vectors are generated by using the measured rotor speed and the calculated slip frequency. The calculation of slip speed depends on the rotor resistance which changes significantly with temperature. An error in the calculation of slip speed produces an error in the unit vectors, resulting in coupling between the flux and torque-producing currents due to axis misalignment [10, 11]. This results in a sluggish torque response with possible overshoot or undershoot and a steady-state error. It is, therefore, necessary to track the changes in the rotor resistance with a parameter identifier. There are several classes of parameter identifier used in the problem of rotor resistance estimation [12–14]. In this work an online neural based rotor resistance estimator is used because of its advantages over the other conventional methods such as less computation and easy implementation.

The paper is organized as follows: NN-MRAS based online R_r estimator with the proposed constraint based back propagation algorithm is dealt in Sect. 122.2. Indirect vector controlled drive is explained in Sect. 122.3. The simulation results for the drive scheme are exhaustively presented in Sect. 122.4. Section 122.5 concludes this paper.

122.2 Neural Network Learning Based Model Reference Adaptive System (NN-MRAS) with the Proposed Learning Strategy

This section presents the NN-MRAS based method of estimation for the rotor resistance of the induction motor in the IFOC drive. A simple two layered feed forward neural network trained by proposed constraint based back propagation technique is used for the estimation. Two models of the state variable estimation are used, one provides the actual induction motor output and the other gives the neural model output. The total error between the desired and actual state variables is then back propagated.

The rotor flux of the induction motor estimated with a classical voltage model is the key input of the rotor resistance estimator. The flux estimated with this voltage model will be correct irrespective of the variations in R_r since voltage model equations are independent of R_r and this provides the desired state variable. The another state model is the neural model which is based on current model equations and this provides the actual output of the induction motor since the current model equations are dependent on rotor resistance of the induction motor. The rotor resistance of an induction motor is estimated using the neural network system illustrated in Fig. 122.1. Two independent estimators are used to estimate the rotor flux vectors of the induction motor. Equation based on stator voltages and currents called as voltage model equation and are given in Eq. (122.1).

$$\begin{bmatrix} \frac{d\lambda dr}{dt} \\ \frac{d\lambda qr}{dt} \end{bmatrix} = \frac{Lr}{Lm}\left[\begin{bmatrix} vds \\ vqs \end{bmatrix} - \begin{bmatrix} Rs + s\sigma Ls & 0 \\ 0 & Rs + s\sigma Ls \end{bmatrix}\begin{bmatrix} ids \\ iqs \end{bmatrix}\right] \tag{122.1}$$

Equation based on stator currents and rotor speed called as current model equations. The discrete current model equations are given as

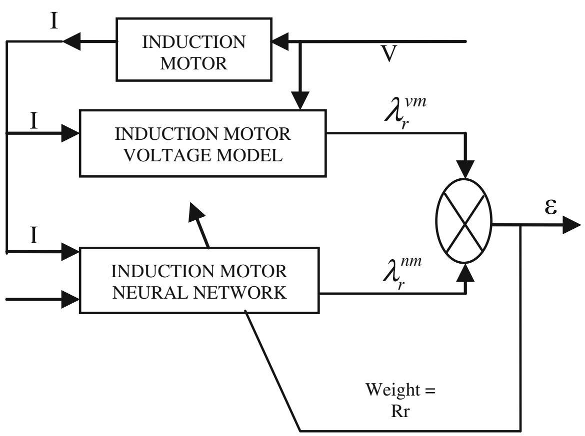

Fig. 122.1 Structure of neural network system for R_r estimation

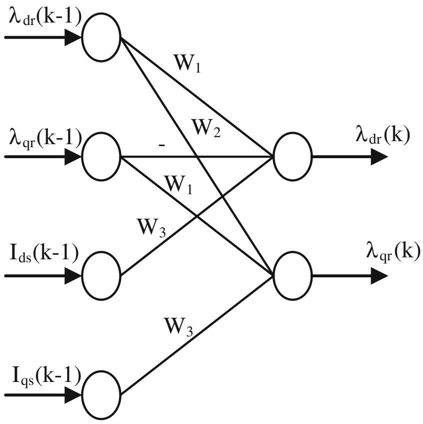

Fig. 122.2 Neural network structure

$$\lambda_{dr}(k) = W_1 \cdot \lambda_{dr}(k-1) - W_2 \cdot \lambda_{qr}(k-1) + W_3 \cdot i_{ds}(k-1) \tag{122.2}$$

$$\lambda_{qr}(k) = W_1 \cdot \lambda_{qr}(k-1) + W_2 \cdot \lambda_{dr}(k-1) + W_3 \cdot i_{ds}(k-1) \tag{122.3}$$

The neural model represented by Eqs. (122.2) and (122.3) is shown in Fig. 122.2, where W_1, W_2, W_3 represent the weights of the two layer neural network used to estimate rotor resistance and they are given by the Eq. (122.4).

$$\left.\begin{aligned} W_1 &= 1 - \frac{T}{Tr} \\ W_2 &= \omega r \cdot T \\ W_3 &= \frac{T \cdot Lm}{Tr} \end{aligned}\right\} \tag{122.4}$$

Here T is the sampling period, T_r is the rotor time constant, ω_r is electrical rotor angular velocity, λ_{dr} and λ_{qr} are d-axis and q-axis rotor fluxes, I_{ds} and I_{qs} are d-axis and q-axis stator currents and σ is called leakage coefficient. Among the three weights W_2 is already known and W_1 and W_3 need to be updated. The weights between neurons, W_1 and W_3 are trained, so as to minimize the energy function *E*. The energy function is given by Eqs. (122.5) and (122.6) is used to find the error in d-axis $\varepsilon_d(k)$ and q-axis $\varepsilon_q(k)$ at the kth iteration.

$$E = \frac{1}{2}\left[\lambda_{\mathrm{r}}^{vm} - \lambda_{\mathrm{r}}^{nm}\right] = \frac{1}{2}\left[\varepsilon_d(k)^T \varepsilon_q(k)\right] \tag{122.5}$$

$$\begin{aligned} \varepsilon_d(k) &= \lambda_{dr}^{vm}(k) - \lambda_{dr}^{nm}(k) \\ \varepsilon_q(k) &= \lambda_{qr}^{vm}(k) - \lambda_{qr}^{nm}(k) \end{aligned} \tag{122.6}$$

The rotor resistance can be calculated from either W_1 or W_3 from the Eqs. (122.7) and (122.8)

$$R_r = \left(\frac{L_r * W_3}{L_m * T}\right) \tag{122.7}$$

$$R_r = \frac{L_r}{T}(1 - W_1) \tag{122.8}$$

The change in weight updates for the proposed constraint based back propagation algorithm is coded as m-File in Matlab. The voltage model equations are implemented in simulink model file. The neural model estimator is updated at a sampling frequency of 10 kHz, so the sampling period for on-line rotor resistance estimator is T = 0.0001 s.

In this algorithm the back propagation learning technique is used to update the weight W_3 and the weight W_1 is found from the value of W_3. Here the initial transients are reduced in the estimation and also this shows excellent tracking performance. The update laws for the constraint based back propagation algorithm are given below in Eqs. (122.9), (122.10).

$$W_3(\mathrm{k}) = W_3(\mathrm{k}-1) + \Delta W_3(\mathrm{k}) + \alpha * \Delta W_3(\mathrm{k}-1) \tag{122.9}$$

$$W_1(\mathrm{k}) = 1 - (W_3(\mathrm{k})/\mathrm{Lm}) \tag{122.10}$$

The advantages of constraint based back propagation are

(a) Superior tracking performance
(b) Less rigorous computation.

122.3 Indirect Rotor Field Oriented Control of MLI Fed Induction Motor Drive

The block diagram of the IFOC drive is shown in Fig. 122.3. The complete drive scheme has been modeled using SIMULINK. The speed controller generates the input to the i_{qs} controller. The flux controller generates the reference to the i_{ds} controller. The currents i_{ds} and i_{qs} are controlled in synchronously rotating reference frame. Here the three phase seven level CHBMLI is used to feed the induction motor. The torque command is generated as a function of the speed error signal, generally processed through a PI controller. The torque and flux command are processed in the calculation block. The three phase reference current generated is compared with the actual current in the hysteresis band current controller and the controller takes the necessary action to produce PWM pulses. The PWM pulses are used to trigger the seven level CHBMLI to drive the Induction motor.

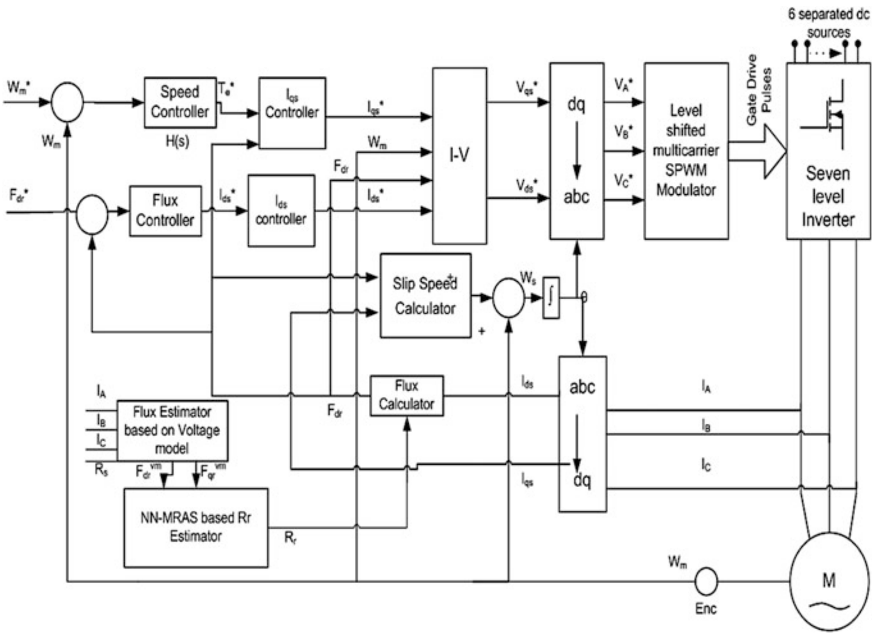

Fig. 122.3 Block diagram of MLI fed IFOC induction motor drive with proposed R_r estimator

In indirect Field Orientation of induction motors, the major problem is the variation in the rotor resistance which is affected by change in rotor temperature. The practical temperature excursion of the rotor is approximately 130 °C above ambient. This increases the rotor resistance by 100 % over its ambient or nominal value. When this parameter is incorrect in the controller, the calculated slip frequency is incorrect and the flux angle is no longer appropriate for field orientation. This results in instantaneous error in both flux and torque which can excite a second order transient characterized by an oscillation frequency equal to the command slip frequency. Thus the IFOC scheme demands an online R_r estimator for its enviable operation. The IFOC scheme is designed and developed with both conventional VSI and seven level CHBMLI. As the CHBMLI fed drive surpass the conventional VSI scheme the further results are presented for the CHBMLI case.

122.4 Results and Discussion

The induction motor has been modeled using T-model equations in Matlab simulink to incorporate the variations in rotor resistance as in the practical case.

The simulation results for the rotor resistance Estimation using proposed NN-MRAS based R_r estimator is studied for the following cases.

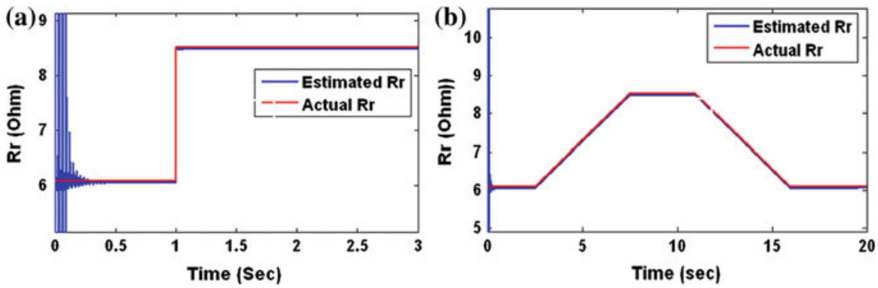

Fig. 122.4 Estimation of R_r using constraint based BP. **a** With 40 % step change in R_r. **b** With 40 % trapezoidal change in R_r

1. With 40 % step change in Rotor Resistance
2. With 40 % trapezoidal change in Rotor Resistance

The performance of the NN-MRAS based rotor resistance estimator using proposed learning strategy is shown in the Fig. 122.4. The results for tracking step change and trapezoidal change using the proposed learning technique constraint based back propagation are explored.

The proposed learning algorithm exhibits good tracking profile with less estimation time and error. Also it has the added advantage less computations which makes it feasible for implementation in digital processors. The IFOC drive performance has been analyzed under steady state and dynamic operating conditions. The linear change in rotor resistance due to gradual variation in temperature can be considered as ramp change and sudden change in rotor resistance due any rotor bar breakage because of excessive temperature can be considered as step change. The proposed learning algorithm exhibits good tracking profile with less estimation time and error. Also it has the added advantage less computations which makes it feasible for implementation in digital processors. The IFOC drive performance has been analyzed under steady state and dynamic operating conditions. The linear change in rotor resistance due to gradual variation in temperature can be considered as ramp change and sudden change in rotor resistance due any rotor bar breakage because of excessive temperature can be considered as step change. The simulation results are taken for step and trapezoidal changes in rotor resistance.

The simulation results are taken under steady state with a reference speed of 100 rad/s and reference flux of 0.9 wb. The drive system is operated with a constant load torque of 7.5 Nm. In this case the R_r is considered to be constant.

122.4.1 Variable Speed, Constant Load Operation and Constant R_r

The simulation results are taken with a step reference speed of 100–80 rad/s at 4 s, with a constant load torque of 7.5 Nm and a reference flux of 0.9 wb. Simulation results are observed for speed, stator currents, and torque and rotor flux. With the assumption of R_r constant the satisfactory performances of the drive are presented where the reference speed and reference flux are tracked with minimal oscillations. As a comparative analysis the IFOC drive performance with the conventional VSI and with the 7-level CHBMLI are presented. The results reveal that the drive exhibits superior performance with 7-level CHBMLI. The torque ripples and the current ripples are reduced in the 7-level CHBMLI fed drive scheme. Also the overall system efficiency is increased with reduction in current and voltage total harmonic distortion (THD). The utility of CHBMLI in addition reduces the filter size and cost along with reduced electromagnetic interferences due to possible low switching frequencies.

The performance of the IFOC drive is presented in the Fig. 122.5 for variable speed application. The speed and the flux responses are as in Fig. 122.5a. The torque and the stator current waveforms are in the Fig. 122.5b.

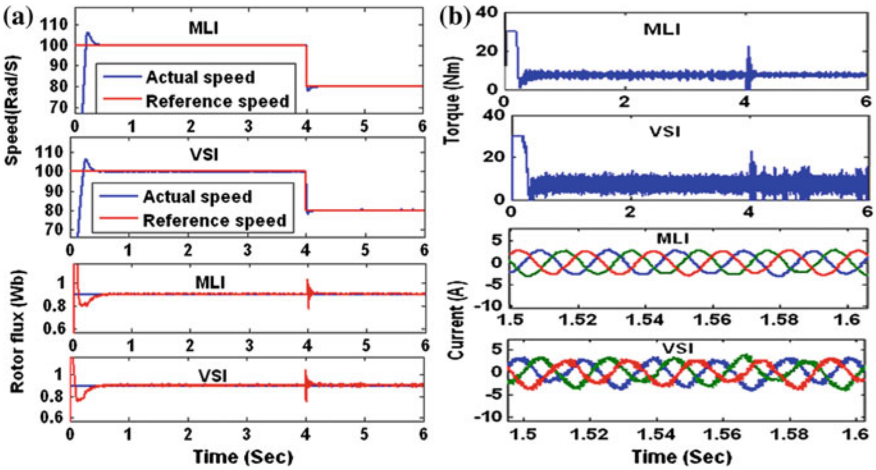

Fig. 122.5 Response of IFOC drive with VSI and MLI. **a** Speed and flux response of IFOC drive. **b** Torque and current response of IFOC drive

122.4.2 Constant Speed, Variable Load Operation and Variation in R_r

In the previous study the rotor resistance is assumed to be constant. But practically the rotor resistance is subjected to variations due to changes in operating conditions. Hence the performance of the drive system for changes in rotor resistance has been studied through simulation.

The results for the drive scheme without online R_r estimator operating with a reference speed of 100 rad/s, rotor flux reference of 0.9 wb, and with a dynamic load torque of 6–5.5 Nm at 2 s are observed when the rotor resistance of the machine is changed from 6.085 to 8.519 Ω at 2.5 s and are shown in Fig. 122.6. In this case study the results of the 7-level CHBMLI fed IFOC drive scheme alone has been presented as it is superior which is concluded in the previous case study. Here the changing rotor resistance is not updated in the controller and hence the machine and the controller will be working with different values of R_r.

From the results it can be observed that the performance of the drive deteriorates because of the detuning effect. The mismatch in the value of R_r between the machine and the controller results in detuning. The effect of detuning can be observed from the results shown in Fig. 122.6a. The responses shown in Fig. 122.6a can be concluded as follows. The speed response is observed to track the reference with some oscillations. The actual torque of the motor deviates from the reference torque which is generated by the speed controller. The rotor flux increases from the command value. Thus from the above observation it can be concluded that the response of the drive scheme is not satisfactory when the rotor resistance changes

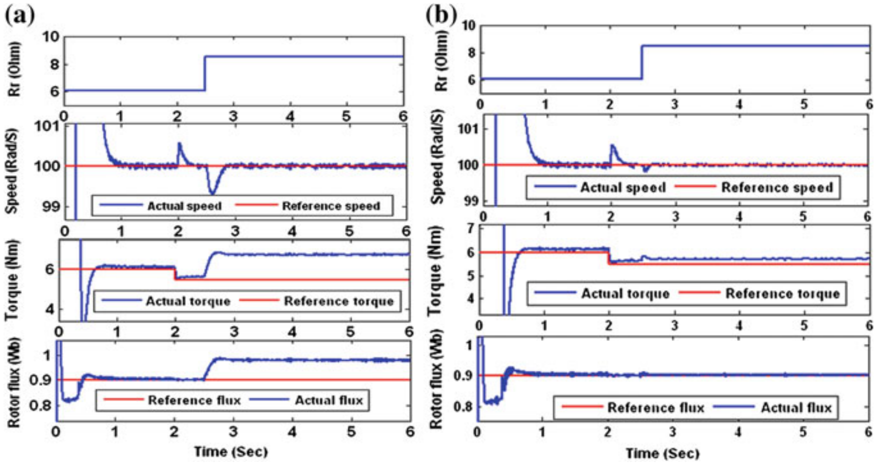

Fig. 122.6 **a** 40 % step change in R_r, speed, torque and flux response of the 7-level CHBMLI fed drive without the proposed R_r estimator. **b** Speed, torque and flux response of the 7-level CHBMLI fed drive with the proposed R_r estimator

and the controller has no adaptation of the changing R_r. To give acceptable results, the drive system demands the knowledge of exact value rotor resistance which can be provided with online estimator.

The results for the drive scheme with the proposed online NN-MRAS R_r estimator operating conditions as before are shown in Fig. 122.6b. The enhanced results of the drive scheme can be observed from the results shown in Fig. 122.6b. The speed response is observed to track the reference without any oscillations. The actual torque of the motor tracks the reference torque. The rotor flux tracks the command value.

122.5 Conclusion

The IFOC drive scheme is built and analysed with conventional VSI and 7-level CHBMLI. The 7-level CHBMLI fed drive outperforms the conventional drive in terms of torque ripples, current ripples, THD, and switching losses. This is well illustrated with the results. As the IFOC scheme is sensitive to R_r variation, NN-MRAS based online estimator is developed in Simulink and trained with a new learning strategy namely constraint based back propagation coded in m-file. Also performance of the IFOC drive scheme has been studied for various operating conditions with and without online rotor resistance estimator. Without R_r estimator the instantaneous torque control is lost, the rotor flux increases from the command value and also the decoupled control is missing. Thus from the results it can be concluded that the performance of the drive is satisfactory with the proposed neural based estimator.

A.1 Appendix

Induction motor parameters: $R_s = 6.03\ \Omega$, $R_r = 6.085\ \Omega$, $L_m = 0.4893$ H, f = 50 Hz, p = 6, J = 0.19 Kgm^2, B = 0.0027 kg/ms, $L_r = 0.5192$ H, $L_s = 0.5192$ H, T = 0.0001 s, $V_s = 415$ V, DC Voltage (Each H-bridge cell) = 140 V.

References

1. Leonhard W (1986) Microcomputer control of high dynamic performance ac-drives—a survey. Automatica 22:1–19
2. Chehimi H, Said SH, Msahil F (2013) A predictive controller for induction motors using an unknown input observer for online estimation and an update technique for load torque. J Control Theory Appl, vol 11
3. José Rodríguez, Jih-Sheng Lai, Fang Zheng Peng (2002) Multilevel inverters: a survey of topologies, controls, and applications. IEEE Trans Ind Electron, vol. 49

4. Du Z, Ozpineci B, Tolbert LM, Chiasson JN (2009) DC–AC cascaded H-bridge multilevel boost inverter with no inductors for electric/hybrid electric vehicle applications. IEEE Trans Ind Appl, vol 45
5. Daher S, Schmid J, Antunes FLM (2008) Multilevel inverter topologies for stand-alone PV systems. IEEE Trans Ind Electron, vol 55
6. Vitorino MA, Maurício Beltrão de Rossiter Corrêa M, Jacobina CB, Lima AMN (2011) An effective induction motor control for photovoltaic pumping. IEEE Trans Ind Electron, vol 58
7. José Rodríguez (2007) High-performance torque and flux control for multilevel inverter fed induction motors. IEEE Trans Power Electron, vol 22
8. Kamel S, Mark S, Greg A (2012) Sensorless control of induction motors using multi-level converters. IET Power Electron, vol 5
9. Zhong Du, Leon M. Tolbert, Burak Ozpineci, and John N. Chiasson (2009) Fundamental frequency switching strategies of a seven-level hybrid cascaded H-bridge multilevel inverter. IEEE Trans Power Electron, vol 24
10. Yahia K, Zouzou S, Benchabane F (2012) Induction motor variable speed drives diagnosis through rotor resistance monitoring. Front Energy, vol 6
11. Jayakrishnan VK, Sarin MV, Archana K, Chitra A (2013) Performance analysis of MLI fed Induction motor drive with IFOC speed control. Annual IEEE India conference
12. Escalante MF, Vannier JC, Arzandé A (2002) Flying capacitor multilevel inverters and DTC motor drive applications. IEEE Trans Ind Electron, vol 49
13. Singh GK, Singh DKP, Nam K, Lim SK (2005) A simple indirect field-oriented control scheme for multiconverter-fed induction motor. IEEE Trans Ind Electron, vol 52
14. Kenné G, Simo RS, Lamnabhi-Lagarrigue F, Arzandé A, Vannier JC (2010) An online simplified rotor resistance estimator for induction motors. IEEE Trans Control Syst Technol, vol 18

Chapter 123
Comparison of Single Layer and Multilayer Feed-Forward Architecture for On-line Economic Load Dispatch Problem

C.S. Boopathi, Subhransu Sekhar Dash, A. Venkadesan, C. Subramani and G.V. Anilkumar

Abstract This paper compares the single layer and multi layer feed forward architecture for on line Economic Load Dispatch (ELD) problem. The economic load dispatch (ELD) is an important problem for real time power system planning and Operation. The conventional methods used for economic load dispatch are iterative techniques and takes longer time for computation. Neural Network (NN) provides an alternate solution for on-line Load Dispatch. The on-line Load Dispatch requires the NN model to be accurate, simple and structurally compact to ensure faster execution time for effective load dispatch. This in turn to a large extent depends on the type of Neural Architecture. In this paper, single layer feed-forward (SLFF) and multilayer feed-forward (MLFF) neural architecture are designed for on-line economic load dispatch problem. Their performance is compared in terms of accuracy and structural compactness. The results are validated for IEEE 26 Bus system. The promising results obtained are presented.

Keywords Feed-forward neural architecture · SLFF-NN · MLFF-NN · Artificial neural network · Economic load dispatch

C.S. Boopathi (✉) · S.S. Dash · A. Venkadesan · C. Subramani · G.V. Anilkumar
Department of EEE, SRM University, Chennai, India
e-mail: boopathi.cs@ktr.srmuniv.ac.in

S.S. Dash
e-mail: munu_dash_2k@yahoo.com

A. Venkadesan
e-mail: Venkadesan.a@ktr.srmuniv.ac.in

C. Subramani
e-mail: subramani.c@ktr.srmuniv.ac.in

G.V. Anilkumar
e-mail: anileee207@gmail.com

C. Kamalakannan et al. (eds.), *Power Electronics and Renewable Energy Systems*,
Lecture Notes in Electrical Engineering 326, DOI 10.1007/978-81-322-2119-7_123

123.1 Introduction

In recent years, economic load dispatch (ELD) is an important problem in power system planning and Operation [1, 2]. ELD solutions are found by solving the conventional load flow equations while at the same time minimizing fuel costs [3–5]. Lambda iteration method is popularly used Conventional method to solve ELD problems. The lambda iteration method is an iterative technique. It takes longer time for computation and hence may not be suitable for online applications.

Neural Network (NN) based estimators provide an alternate solution for on-line economic load dispatch. The nonlinear dynamic system mapping capability of neural network was well proven in the literature [6]. It is computationally less rigorous as compared to conventional method. It is suitable for on-line economic load dispatch problem. Many neural network based methods for economic load dispatch are available in literature. Single-layer and multilayer feed-forward Artificial Neural Networks are used to solve the Economic and Emission dispatch problem [7]. Optimal Economic dispatch of electrical power plants using single-layer feed-forward networks is proposed [8]. Radial basis neural network is used to solve economic and emission dispatch problem [9]. Various learning algorithms for drives applications are investigated and presented [10].

Thus, NN has got excellent potential for on-line economic load dispatch problem in power system applications. The major issues in NN based on-line load dispatch are; the NN model should be accurate, simple and structurally compact to ensure faster execution time in real time implementation. This in turn to a large extent depends on the type of neural architectures for on-line load dispatch.

This paper carries out a comparison between single layer and multi layer neural architecture. The two architectures are trained using Levenberg-Marquardt (LM) learning algorithm and their performance is compared in terms accuracy, structural compactness and computational complexity.

123.2 Economic Dispatch

In an interconnected power system, the objective is to find the real and reactive power scheduling of each power plant in such a way as to minimize the operating cost. This means that the real and reactive powers are allowed to vary within certain limits, so as to meet a particular load demand with minimum fuel cost. The ED problem is formulated using Lagrange dynamics. The objective of the optimization problem is to minimize the total fuel generation cost function, so that the objective function is

$$Minimize\ F_T = \sum_{i=1}^{n_g} F_i(P_i) \tag{123.1}$$

where F_T is the total generation fuel cost and it is given by $F_T = F_1 + F_2 + F_3 + \cdots + F_{ng}$, F_i is the generation cost, P_i is the power generated of each unit i, n_g is the number of generating units.

The objective function for the ELD reflects the costs associated with generating power in the system. The quadratic cost model is used. The objective function for the entire power system can then be written as the sum of the quadratic cost model for each generator:

$$F_i(P_i) = a_i + b_i p_i + c_i p_i^2 \tag{123.2}$$

where a_i, b_i and c_i are the fuel cost coefficients of the generating unit i.

123.2.1 Equality Constraints

The generation-demand equality constraint implies that the sum of the generated power is equal to the total load demand plus the transmission losses so that

$$\sum_{i=1}^{n_g} (P_i) = P_D + P_{Loss} \tag{123.3}$$

where P_D is the total active load demand, P_{Loss} is the transmission losses. The transmission losses is given in terms of Kron's loss formula is

$$P_L = \sum_{i=1}^{N} \sum_{j=1}^{N} P_i B_{ij} B_j + \sum_{j=1}^{N} P_i B_{oi} B_{oo} \tag{123.4}$$

where B_{ij}, B_{oi} and B_{oo} are the transmission network power losses coefficients.

The B-loss coefficients represent the transmission line loss.

123.2.2 Inequality Constraints

Each generating unit has minimum and maximum generation capacities so that

$$P_i^{\min} \le P_i \le P_i^{\max} \tag{123.5}$$

where $P_i^{\min}$ and $P_i^{\max}$ are the designed minimum and maximum generated power capacities of each unit i, respectively.

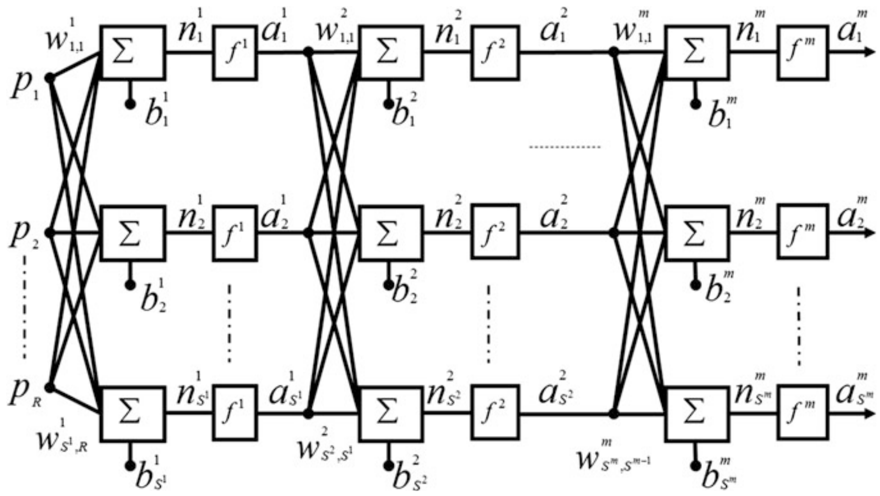

Fig. 123.1 Feed-forward architecture with R inputs and M layers (M)

123.3 Feed Forward Architecture

Feed forward architecture consists of a set of sensory units (source nodes) that constitute the input layer, one or more hidden layers and output layer. Feed-forward architecture with R inputs and M layers (M) is shown in Fig. 123.1 [11]. The input signal propagates through the network in a forward direction, on a layer-by-layer basis. Feed-forward architecture with one hidden layer is called as Single Layer Feed Forward Neural Network (SLFF-NN) and when multiple layers are used it is called Multilayer Layer Feed Forward Neural Network (MLFF-NN).
where, w_{ij}^{m}-Interconnection weight of neuron 'i' of layer 'm' for input from neuron 'j' of layer '(m − 1)'.

The structure of the FF-NN architecture is denoted as $S^0 - S^1 - \cdots - S^M$.

123.4 Design of Feed Forward Architecture for On-line Economic Load Dispatch Problem

The popular single layer and multilayer feed-forward architecture are designed for on-line economic load dispatch problem. The IEEE 26 Bus system is considered for investigation. There are totally six generators. Around 120 data sets are obtained using Lambda iteration method for various load demands (100 for training and 20 for testing). The input to NN Model is power demand (P_D). The outputs are the real power generation of six generators (P_{G1}, P_{G2}, P_{G3}, P_{G4}, P_{G5}, P_{G6}), loss (P_L), cost (C). The activation function for hidden and output layers is chosen as tan-sigmoid and pure linear function respectively. For comparison, both the NN architectures are trained with the same input/output data using the Levenberg-Marquardt algorithm for the target accuracy of 1×10^{-7}. The structure obtained for single layer and multilayer feed-forward is 1-68-8 and 1-15-15-8 respectively. The designed two architectures are used to solve economic load dispatch problem. The performance of both the architectures is compared in terms of accuracy and compactness.

123.5 Results and Discussions

The designed SLFF-NN model and MLFF-NN model are compared in terms of accuracy. 20 data sets are used for testing the SLFF-NN and MLFF-NN. The sample results for loss and cost along with error curve for both the architectures are presented in Figs. 123.2 and 123.3 respectively. From the results obtained, it is found that the outputs obtained from multilayer architecture are found to closely match with the conventional method as compared to SLFF-NN architecture. The average error for

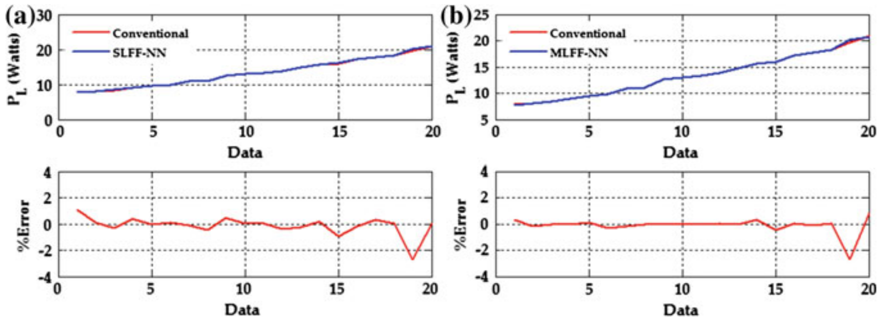

Fig. 123.2 Power loss. **a** SLFF-NN. **b** MLFF-NN

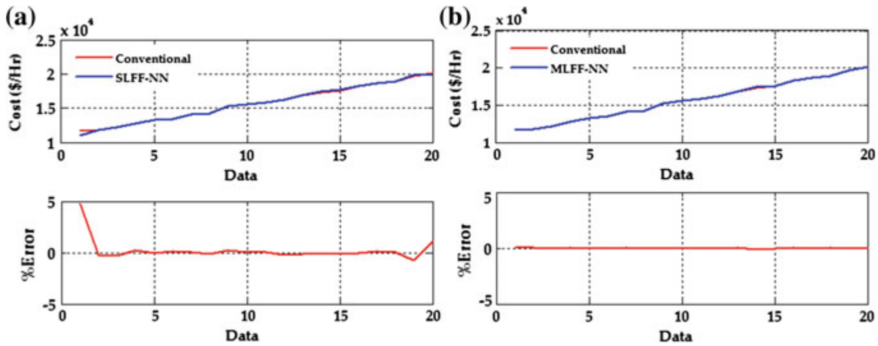

Fig. 123.3 Cost ($/Hr). **a** SLFF-NN. **b** MLFF-NN

Table 123.1 Average error for SLFF-NN and MLFF-NN

Outputs	% average error		Outputs	% average error	
	Single layer	Multi layer		Single layer	Multi layer
P_{G1}	−0.0169	*0.008662*	P_{G5}	−0.0598	*−0.01938*
P_{G2}	0.0127	*0.001407*	P_{G6}	−0.0142	*−0.00373*
P_{G3}	−0.0481	*−0.03735*	P_L	−0.124	*−0.11677*
P_{G4}	−0.0418	*−0.00842*	Cost	0.233	*−0.00829*

single and multi layer architecture is consolidated and presented in Table 123.1. From the Table 123.1, it is observed that the average error for multi layer is lesser as compared to the single layer architecture. This is due to the high degree of non-linear mapping capability of the multilayered structure.

The performance of SLFF-NN and MLFF-NN is compared in terms of structural compactness and computational complexity which assumes importance for real time on-line economic load dispatch problem. The number of parameters for the feed-forward architecture can be calculated using the formula (123.6). As SLFF-NN is a special case of MLFF-NN with one hidden layer, the same formula (123.6) suits both type of FF-NN [12].

$$P_{MLFF} = \underbrace{\sum_{m=1}^{M} S^{m-1} S^{m}}_{weights} + \underbrace{\sum_{m=1}^{M} S^{m}}_{biases} \tag{123.6}$$

The number of parameters and neurons required for SLFF-NN and MLFF-NN are presented in Table 123.2. In terms of compactness, multilayer network requires lesser number of neurons as compared to single layer network. The total number of parameters required for multilayer feed-forward architecture is lesser as compared to single layer architecture.

The Multilayer feed-forward architecture is approximately 2 times more compact as compared to single layer architecture. The multilayer feed-forward neural Network model provides the required accuracy with lesser number of neurons/parameters as compared to single layer feed-forward neural network. Thus multilayer architecture is more compact and gives required accuracy. Hence it is concluded that the MLFF-NN is found to be more suitable for on-line Load dispatch.

Table 123.2 Performance comparison of NN Models in terms of compactness and complexity

NN architecture	FF-NN architecture	Computational complexity	
		No. of neurons	No. of parameters
SLFF	1-68-8	76	688
MLFF	*1-15-15-8*	*38*	*398*

123.6 Conclusion

This paper carries out a new type of investigation on the neural architectures for on-line load dispatch which is the major contribution of this paper. The popular SLFF-NN and MLFF-NN architecture are considered for investigation. The two architectures are trained with same input/output data using LM algorithm for the same target accuracy. The results are validated for IEEE 26 bus system. From the results obtained, the MLFF-NN is found to result in the most compact architecture with much lesser number of neurons/parameters as compared to SLFF-NN. Thus it is concluded that the MLFF-NN is compact, accurate and suitable for on-line economic Load Dispatch problem.

References

1. Long RW, Barrios JR (1967) A parametric equations approach to the economic dispatch problem. IEEE Trans Power Appar Syst 86(2):141–149
2. Ozyon S, Durmuş B, Yaşar C, Temurtaş H, Kuvat G (2012) Solution to non-convex economic power dispatch problems with generator constraints by charged system search algorithm. Int Rev Electr Eng (IREE) 7(5):5840–5853
3. Subramanian R, Thanushkodi K (2013) Solving economic load dispatch problems by novel TANAN's algorithm (NTA). Int Rev Model Simul 6(3):814–818
4. Sulaiman MH (2013) An application of differential search algorithm in solving non-convex economic dispatch problems with valve-point effects. Int Rev Model Simul 6(4)
5. Wood AJ, Wollenberg BF (1996) Power generation, operation and control. Wiley, New York
6. Narendra KS, Parthasarathy K (1990) Identification and control of dynamical systems using neural networks. IEEE Trans Neural Networks 1(1):4–27
7. Kar B, Mandal KK, Pal D, Chakraborty N (2005) Combined economic and emission dispatch by ANN with back prop algorithm using variant rate and momentum coefficient. In: IEEE 7th power engineering conference, Singapore, pp 1–235
8. Panta S, Permrudeepreechacharan S, Nuchprayoon S, Dechthummarong C, Janjommanit S (2007) Optimal economic dispatch for power generation using ANN. In: IEEE international power engineering conference, pp 1343–1348
9. Huang CM, Wang FL (2007) Radial basis neural network for OLS and EPSO algorithms for real-time power dispatch. IEEE Trans Power Syst 22(1):96–104
10. Venkadesan A, Himavathi S, Muthuramalingam A (2012) Suitability of learning algorithm for neural network based on-line flux estimator in sensor-less vector controlled induction motor drives. IUP J Electr Electron Eng 5(4):24–38
11. Venkadesan A, Himavathi S, Muthuramalingam A (2010) Design of feed-forward neural network based on-line flux estimator for sensor-less vector controlled induction motor drives. Int J Recent Trends Eng Technol 4(3):110–114
12. Venkadesan A, Himavathi S, Muthuramalingam A (2013) Performance comparison of neural architectures for on-line flux estimation in sensor-less vector controlled IM drives. Springer J Neural Comput Appl 22(7–8):1735–1744

Chapter 124
Prediction of India's Industrial Sector Electricity Consumption Using ANFIS

S. Saravanan, S. Kannan and C. Thangaraj

Abstract The objective of this study is, to predict the industrial sector electricity consumption in India, using the Adaptive Neuro Fuzzy Inference System (ANFIS). ANFIS technique is more suitable for uncertain and ambiguous data. Gross National Product (GNP), imports and exports are selected as the input variables. The electricity consumption of industrial sector is the predicted output variable. A 29 year data set is used to train the network and 9 years data set is used to test the network. Mean Absolute Percentage Error (MAPE) is used as performance evaluation criteria. The prediction is carried out for the period 2014–2021.

Keywords ANFIS · GNP · MAPE · ANN and fuzzy systems

124.1 Introduction

Electric energy is an important input for technical, social and economic development of any country. Electricity is used in all kinds of human activities, such as industrial production, residential, agriculture, transportation, lighting and heating [1–4]. The development of a country is characterized by the per capita electricity consumption, which is a direct measure of the standard of life in that country. The identification and the analysis of energy development and the issues of energy policy options such as consumption, distribution and planning are most important for today [5].

S. Saravanan (✉) · S. Kannan
Kalasalingam University, Krishnankoil, Virudhunagar 626126, Tamil Nadu, India
e-mail: s.saravanan@klu.ac.in

S. Kannan
e-mail: kannaneeeps@gmail.com

C. Thangaraj
ACCESS Institute, Virudhunagar, India
e-mail: thangaraj.vc@gmail.com

C. Kamalakannan et al. (eds.), *Power Electronics and Renewable Energy Systems*,
Lecture Notes in Electrical Engineering 326, DOI 10.1007/978-81-322-2119-7_124

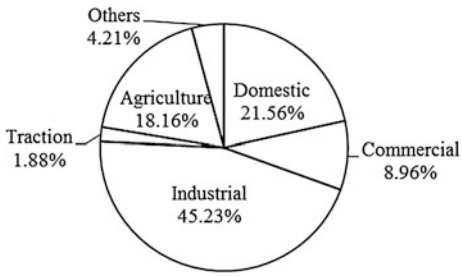

Fig. 124.1 Sector wise electricity consumption in the year 2011

India's net electricity consumption has increased at an average rate of 7.3 % annually from 2000 to 2012. The electricity consumption was 43.724 Tera Watt hour (TWh) in 1970 and has increased to 772.603 TWh in 2011. Since 1970, much of the growth in electricity consumption of India has taken place in the industrial sector. This is due to the increasing number of applications of electricity intensive technologies in industrial sector. The electricity consumption in Industrial sector has increased from 29.579 TWh in 1970–1971 to 346.469 TWh in 2011–2012. An annual average growth rate of for industrial sector electricity consumption was 12.56 % between the years 2002 and 2011. The sector wise electricity consumption for the year 2011 is shown in Fig. 124.1.

Normally electricity consumption has an increasing trend. The prediction of electricity demand is very important, since the further projection of electric supply system is based on this prediction [4]. Gross National Product (GNP) is a measure of all economic activities, increasing GNP means improved living standards and thus increased energy use [6]. Imports and exports for India are related to manufacturing processes and therefore strongly affect the industrial electricity consumption. The electric load forecasting can be divided into short, medium and long term forecasting and they range from 1 h to 1 week, 1 month to 1 year and 1 year to decades respectively [2, 3, 7]. Long term forecasting is needed to plan the size, type and location of power plant and the required investments.

In recent studies artificial intelligent techniques are frequently used as a predicting tool to electricity demand forecast. To forecast the industrial sector electricity demand for Turkey, Genetic Algorithm [6], ANN [8] and structural time series analysis [4] were used. Though many studies have been conducted on electricity demand/consumption forecasting [9–15], the application of Adaptive Neuro Fuzzy Inference System (ANFIS) approach for forecasting industrial electricity demand is still unexplored.

In this paper, an ANFIS network is used with GNP, imports and exports as input variables and industrial sector electricity consumption as the predicted output variable. In the following section, a brief description of ANFIS is given. In Sect. 124.3, Industrial sector electricity consumption forecasting model, which is developed for India and future projections are presented. Finally, the study is concluded in Sect. 124.4.

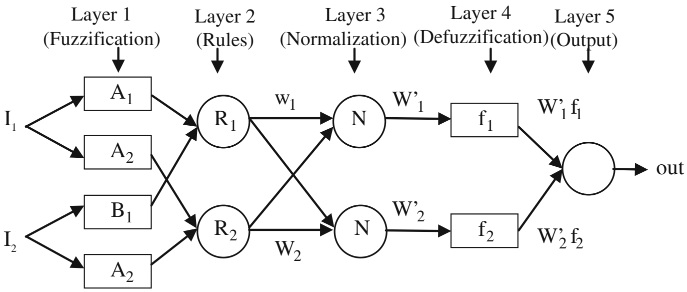

Fig. 124.2 Structure of ANFIS model

124.2 ANFIS

In recent year's artificial intelligence techniques, such as ANNs, Fuzzy logic and ANFIS have been successfully applied to solve many engineering problems. ANN provides effective learning from scratch by adjusting the interconnections between layers and fast computations. Fuzzy inference system (FIS) is a popular computing framework based on the concept of fuzzy set theory. It allows thinking and reasoning capability for the fuzzy logic. The learning usually applies to the membership function (MF) of the IF-THEN rules of the fuzzy systems [16]. ANFIS is a multilayer feed-forward network which is applied to map an input space to an output space using a combination of neural network learning algorithms and fuzzy reasoning [17]. The structure of ANFIS model is shown in Fig. 124.2. ANFIS can overcome the drawbacks of fuzzy logic such as: significant time to recognize the correct MF and rules as well as poor generalization capability and that of neural networks such as: difficulty in determining proper size and optimal structure of the neural net and in manipulating parameters for learning and convergence [18]. In other words, by combining ANN and FIS in ANFIS, it is possible to bring the computational power and learning of neural networks into FIS. Thus, ANFIS has the capability of fast and accurate learning, extension of capacity, excellent explanation facilities in the form of semantically meaningful fuzzy rules and the ability to adopt both data and existing expert knowledge [19]. ANFIS, as a hybrid intelligent system that enhances the ability to automatically learn and adapt, is being used by researchers in various engineering systems.

124.3 Results and Discussion

ANFIS modeling involves different parameter adjustments such as finding suitable number, type of MF and rules, selection of proper input parameters, linear coefficients and so on. The fuzzy part of ANFIS is mathematically expressed in the form of MF. By increasing the number of MFs per input, the number of rules increases [20].

Table 124.1 Correlation coefficient between input variables and output variable

Parameters	Correlation coefficient (R^2)
GNP	0.9744
Imports	0.9498
Exports	0.9501

Selection of input variables may decide the accuracy in ANFIS model. To evaluate the influence of each input variable correlation coefficients between Industrial sector electricity consumption and input variables are estimated and given in Table 124.1. These coefficients provide a measure of the linear relation between any one of the input variables and output variable (Industrial sector electricity consumption).

The variables are normalized in the range of (0–1). It is essential (i) to prevent larger numbers from overriding smaller ones and (ii) to prevent premature saturation of hidden nodes, which impedes the learning process [21]. The experimental data is randomly divided for training and testing. The training data are used to approximate the network parameters and the testing data are used to evaluate the predictive ability of the developed model. The type, numbers and parameters of MF are tested to determine the appropriate model [19]. This structure is obtained by trying different types and number of MF for input variables. The best architecture is selected based on the MAPE, which is computed according to the Eq. 124.1.

$$\mathrm{MAPE} = \left(\frac{1}{n}\sum_{i=0}^{n}\left|\frac{(A_i - P_i)}{A_i}\right|\right) \times 100 \tag{124.1}$$

where P_i, A_i were the predicted and actual values, and 'n' denoted the total number of data in the testing set.

The trial and error procedure is followed for deciding the optimal number of MF and the four kinds of MF such as Gaussian combination MF ('gauss2mf'), generalized bell MF ('gbellmf'), triangular MF ('trimf') and pi MF ('pimf'). The MFs are varied from 2, 2, 2 to 4, 4, 4 and results are given in Table 124.2. Out of all the combinations, Table 124.2 shows the number of MFs whose MAPE is less than 8 % for selecting 'gbellmf', 10 % for 'gauss2mf' and 'trimf' and 12 % for 'pimf'. Those MFs having higher MAPE are neglected. From Table 124.2, it is evident that the 'gbell' with number of MF 2, 3, 3 is found to have a superior performance.

Table 124.2 Test results with different MFs

gbellmf		gauss2mf		trimf		pimf	
NMF[a]	MAPE	NMF[a]	MAPE	NMF[a]	MAPE	NMF[a]	MAPE
2,3,2	2.0730	3,3,2	7.5765	2,2,2	6.5981	3,2,2	10.4420
2,3,3	6.5842	3,2,3	8.8993	2,3,2	9.0471	3,3,2	11.2535
3,3,2	7.5911	2,3,3	9.4508				

NMF[a] Number of membership function

Table 124.3 Optimum structure and specifications of the proposed ANFIS model

Parameters	Specifications
Input MF type	'gbell'
Number of MF	2, 3, 2
Output MF type	Linear
Number of nodes	44
Number of linear parameters	48
Number of nonlinear parameters	21
Total number of parameters	69
Number of fuzzy rules	12
Number of epochs	10

Table 124.4 Industrial electricity sector electricity consumption actual versus predicted

Year	Actual (bkWh)	Predicted (bkWh)
1976–1977	41.606	42.166
1999–2000	106.728	104.618
2000–2001	107.622	106.360
2001–2002	107.296	110.607
2003–2004	124.573	120.801
2004–2005	137.589	140.944
2005–2006	151.557	156.389
2007–2008	189.424	188.087
2009–2010	236.752	232.690
MAPE		2.073

The other parameters of ANFIS optimum structure and specifications of the proposed model are given in Table 124.3.

In this study, the implementation of the proposed ANFIS model, computer program written using MATLAB software Version 7.10 is used. The simulation results for ANFIS model with minimum MAPE and comparison between actual and predicted Industrial electricity consumption results are given in Table 124.4. The electricity consumption is given in billion kilo Watt hours (bkWh).

From the results in Table 124.4, the actual value of industrial sector electricity consumption in the year 1976–1977 was 41.606 bkWh and in the year 2007–2008 is 189.424 bkWh. The industrial sector electricity consumption calculated using ANFIS is 42.1664 bkWh (year 1976–1977), and 232.690 bkWh (year 2009–2010). The results for the remaining years are also presented in Table 124.4. From these results, ANFIS appears to have similar trend between actual and predicted data though there exist a small discrepancy.

To forecast the industrial sector electricity consumption, the input variables (GNP, imports and exports) should be analyzed and their trends for the future

Table 124.5 Predicted input variables

Year	GNP (bINR)	Imports ((bINR)	Exports (bINR)
2014–2015	102,536.225	4,036.105	3,552.975
2015–2016	115,895.311	4,848.062	4,258.022
2016–2017	130,994.906	5,823.364	5,102.978
2017–2018	148,061.774	6,994.870	6,115.606
2018–2019	167,352.224	8,402.053	7,329.178
2019–2020	189,155.960	10,092.323	8,783.570
2020–2021	213,800.428	12,122.631	10,526.570
2020–2021	241,655.737	14,561.383	12,615.448

Table 124.6 Future industrial sector electricity consumption (bkWh) of India

Year	Predicted (bkWh)
2014–2015	265.52
2015–2016	283.29
2016–2017	303.79
2017–2018	326.61
2018–2019	351.99
2019–2020	380.71
2020–2021	413.89
2021–2022	452.93

should be predicted first. The prediction has been made based on the historical data from 1975 using a Regression method. The forecasted results based on historical data are given in Table 124.5. The units of input variable such as GNP, imports and exports data are given in billion Indian Rupees (bINR).

Using the predicted input variables, the industrial electricity sector consumption has been predicted with the same number and type of MF for the period of 2014–2015 to 2021–2022 and the results are given in Table 124.6.

124.4 Conclusion

Modeling and prediction of Industrial sector electricity consumption has a significant importance in developing sustainable energy policies. Accurate prediction of industrial sector electricity consumption is vital, when demand grows faster. This is the first study using ANFIS to predict the industrial sector electricity consumption for India, based on the input variables GNP, imports and exports. The ANFIS network has excellent forecasting capability with minimum MAPE (2.0730).

The obtained results show that the unique features of the proposed ANFIS model are consistent, fast and suitable for complex and uncertain data because they are composed of both ANN and fuzzy systems. The predicted industrial sector electricity consumption increases approximately 7.93 % annually from 2014 to 2021. The policy makers of the Indian electric energy system may use the forecasts by ANFIS approach to plan timely investments.

Acknowledgments The authors gratefully acknowledge the management of Kalasalingam University, Krishnankoil, Tamilnadu, India for their constant support and encouragement extended during this research. They are also thankful to the Department of Science and Technology, New Delhi, for its support through the project: SR/S4/MS/364/06.

References

1. Azadeh A, Ghaderi SF, Sohrabkhani S (2008) Annual electricity consumption forecasting by neural network in high energy consuming industrial sectors. Energy Convers Manag 49:2272–2278
2. Saravanan S, Kannan S, Thangaraj C (2012) India's electricity demand forecast using regression analysis and artificial neural networks based on principal components. ICTACT J Soft Comput 2:365–370
3. Akdemir B, Cetinkaya N (2012) Long-term load forecasting based on adaptive neural fuzzy inference system using real energy data. Energy Procedia 14:794–799
4. Bilgili M, Sahin B, Yasar A, Simsek E (2012) Electric energy demands of Turkey in residential and industrial sectors. Renew Sustain Energy Rev 16:404–414
5. Azadeh, Faiz ZS (2011) A meta-heuristic framework for forecasting household electricity consumption. Appl Soft Comput 11:614–620
6. Zahedi G, Azizi S, Bahadori A, Elkamel A, Wan Alwi RS (2013) Electricity demand estimation using an adaptive neuro-fuzzy network: a case study from the Ontario province-Canada. Energy 49:323–328
7. Cunkas M, Altun AA (2010) Long term electricity demand forecasting in Turkey using artificial neural networks. Energy Sour Part B: Econ, Plann, Policy. 5:279–289
8. Ozturk HZ, Kemal H, Ceylan H (2005) Forecasting total and industrial sector electricity demand based on genetic algorithm approach: Turkey case study. Int J Energy Res 29:829–840
9. Dilaver Z, Hunt LC (2011) Industrial electricity demand for Turkey: a structural time series analysis. Energy Econ 33:426–436
10. Ekonomou L (2010) Greek long-term energy consumption prediction using artificial neural network. Energy 35:512–517
11. Kandananond K (2011) Forecasting electricity demand in Thailand with an artificial neural network approach. Energies 4:1246–1257
12. Kermanshahi B, Iwamiya H (2002) Upto year 2020 load forecasting using neural networks. Electr Power Energy Syst 24:789–797
13. Akpinar A, Kankal M, Komurcu MI, Ozsahin TS (1939) Modeling and forecasting of Turkey's energy consumption using socio-economic and democratic variables. App Energy 88 (2011):1927–1939
14. Azadeh A, Ghaderi SF, Sohrabkhani S (2007) Forecasting electricity consumption by integration of neural network, time series and ANOVA. Appl Math Comput 186:753–1761

15. Kavaklioglu K, Ceylan H, Kemal H, Ozturk HK, Canyurt OE (2009) Modeling and prediction of Turkey's electricity consumption using artificial neural networks. Energy Convers Manag 50:2719–2727
16. Karimi G, Sedaghat SB, Banitalebi R (2013) Designing and modeling of ultra low voltage and ultra low power LNA using ANN and ANFIS for bluetooth applications. Neurocomputing 120:504–508
17. Khoshnevisan B, Rafiee S, Omid M, Mousazadeh M (2014) Prediction of potato yield based on energy inputs using multi-layer adaptive neuro-fuzzy inference system. Measurement 47:521–530
18. Khoshnevisan B, Rafiee S, Omid M, Mousazadeh H, Clark S (2013) Environmental impact assessment of tomato and cucumber cultivation in greenhouses using life cycle assessment and adaptive neuro-fuzzy inference system. J Cleaner Prod:1–10
19. Heidari E, Ghoreishi SM (2013) Prediction of supercritical extraction recovery of EGCG using hybrid of adaptive neuro-fuzzy inference system and mathematical model. J Supercrit Fluids 82:158–167
20. Karami A, Afiuni-Zadeh S (2012) Sizing of rock fragmentation modeling due to bench blasting using adaptive neuro-fuzzy inference system. Int J Min Sci Technol 22:459–463
21. Basheer IA, Hajmeer M (2000) Artificial neural networks: fundamentals, computing, design, and application. J Microbiol Method 43:3–31

Chapter 125
Enhancing the Security of AES Algorithm in Wireless Network

R. Velayutham, E. Siva Ganesh and D. Manimegalai

Abstract A secure transmission of information among wireless network is a crucial challenge in the communication technology of the present circumstances. In this concern, a successful data transfer requires a vital cryptographic algorithm to guard the data or information from the intruders. To overcome this state, the improvement and implementation of new techniques to authenticate the confidentiality of the information. It has been one of the emphases in the wireless communication research community. A wireless network is fragile when the intruders can supply a counterfeit data reports through compromised nodes and it may lead to a data leakage against valid information. The Advanced Encryption Standard (AES) algorithm is renowned in cryptographic algorithm. The goal of this proposed work is to provide a concrete AES algorithm along with the new Non-linear structure of the S-box to justify the validity of the information in wireless networks. The proposed scheme is designed for wireless sensor network communication to maintain the integrity, authentication and confidentiality of the transmitted data.

Keywords AES · S-box · Non-linearity

125.1 Introduction

A Wireless Sensor Network (WSN) is one of the important technologies in the current network infrastructure. In the real time mechanism, the wireless sensor networks have been successfully implemented and effectively used in many cam-

R. Velayutham (✉) · E. Siva Ganesh
Department of CSE, Einstein College of Engineering, Seethaparpanallur, Tamilnadu, India
e-mail: rsvel_kumar@yahoo.co.uk

E. Siva Ganesh
e-mail: sivag87@gmail.com

D. Manimegalai
Department of IT, National Engineering College, Kovilpatti, India
e-mail: megalai_nec@yahoo.co.in

C. Kamalakannan et al. (eds.), *Power Electronics and Renewable Energy Systems*,
Lecture Notes in Electrical Engineering 326, DOI 10.1007/978-81-322-2119-7_125

puses and enterprise networks [1]. Data transfer between nodes in wireless sensor network involves a great challenge among the users to maintain the integrity, confidentiality and authenticity of the transferred data. In this circumstance the sender, receiver and the transmitter is to be autonomously monitored.

To impart security in wireless sensor network, many of the cryptographic algorithms consequently developed for the purpose of encrypting and decrypting the transferring data and also to defend against the intruders. It is anticipated that this secured data transfer is to become the accepted means of encrypting digital information like financial data, telecommunications and government data.

125.2 Advanced Encryption Standard

The working process of AES algorithm involves Shift Rows, Mix Columns, Add Round Keys and Substitution Bytes all the stages contains inverse process. In which the Substitution Bytes and Add Round Key stages depends on the choice of the S-box. The stated default S-box is arranged in a liner manner, which can be easily breakable by the attackers. Substitution Bytes and Add Round Keys are explained as follows (Fig. 125.1).

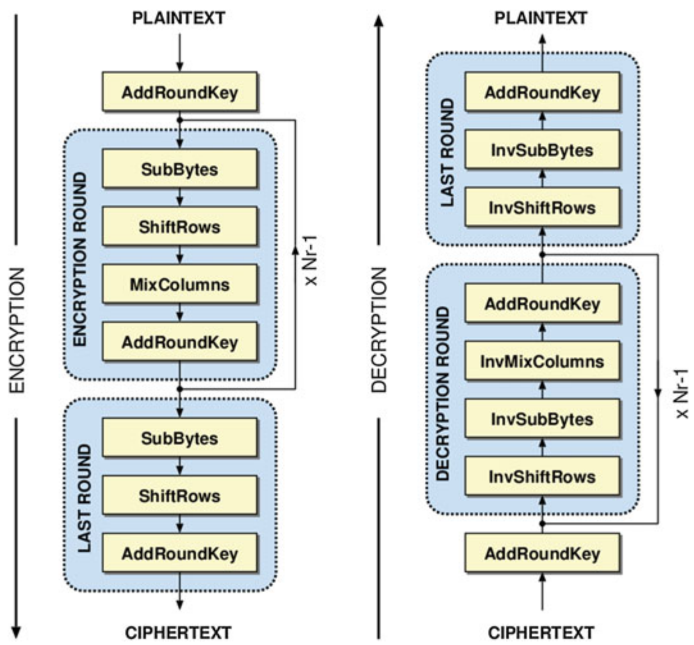

Fig. 125.1 AES block diagram

125.3 Existing System

The confidentiality of the secure information processed through the wireless communications is one of the focused research methodologies for the researchers in today's cryptographists. AES is based on the evaluation of the key generation between the sender and receiver. The key generation depends on the hexadecimal table that is called Substitution box (S-box). It is perceivable to people from all known cryptographist, so we have to endurance the S-box by using some Non-linear transformation. In the key expansion phase every transformation affects all bytes of the state.

In AES algorithm the predefined S-box is used for the encryption and decryption process. The S-box is implied in Substitution bytes transformation and Add round key transformation, in both the phases linear arrangement S-box is used. Some internal properties in the design of AES algorithm pose a threat to its security. The strength of the AES algorithm is the S-box and Inverse S-box. The design of the S-box is Public and it may lead an advantage to the attackers also interference in data traffic.

125.4 Proposed System

By various researches in AES algorithm, the Non-linear arrangement of Substitution box is vital to turn the entire algorithm stronger. In AES algorithm the major phase is the Key Expansion which depends on the S-box. After come across various researches it has been discovered that there is some lacuna in the structure of the available S-box. In order to bring more complex in the design of S-box structure, this approach deals with a new dynamic Non-linear S-box without disconcerting the originality of the AES S-box [2]. This Non-linear AES S-box can be very well resisting against various cryptanalysis attacks. Enhancing the default S-box by this new Non-linear approach, through the mathematical operations on the 16×16 hexadecimal S-box by finding the 1's complement of the binary values of those hexadecimal numbers and imply a XOR operation. This same methodology works on alternating the 1's complement into 2's complement.

125.5 Methodology

In the Non-linear implementation three S-boxes are being used. During encryption, the input value is first plotted towards the Default S-box (Pre-defined S-box), which is the original AES S-box and this value undergoes a XOR process with the new derived S-box which is the one's complement or Two's Complement of the actual S-box to generate the virtual S-box. Thus for each different input value, the virtual

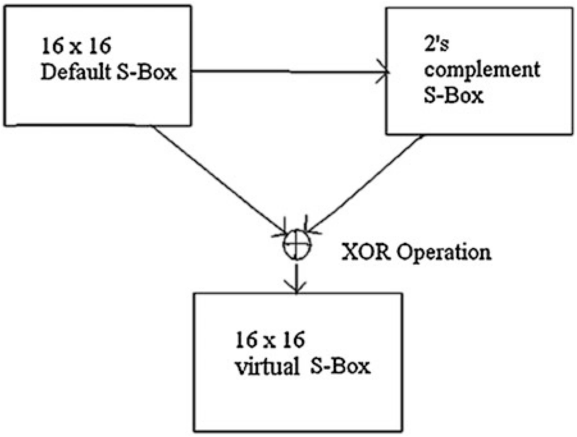

Fig. 125.2 Creation of dynamic S-box

S-box will be dynamically generated [3]. Similarly, for the decryption, the reverse process will take place using the inverse virtual S-box. Figure 125.2 shows the creation of dynamic S-box.

The construction of the S-box is made strong by replacing the existing S-box into a Non-linear structure. The Non-linear agreement of S-box would be derived by substituting a random hexadecimal number to the actual S-box value. The original or default S-box Hexadecimal value is plotted to a random hexadecimal number that is obtained during the encryption phase through the proposed system. The obtained random number is inversed in the decryption process and plotted towards the actual inverse S-box.

In this propose scheme the design of the dynamic S-box that is highly secure. In the Non-linear implementation three different S-box structures is being used. The first one is the default S-box. Every values in the default S-box is converted to one's complement values and it is worked with Two's complement conversion also and stored as one's complement or Two's complement S-boxes, after this the default S-box values and one's complement or Two's complement S-boxes undergoes a XOR operation and finally these values are stored as a virtual S-box or Non-linear S-box. Since Non-linearity is applied to the S-box, the key is also protected. The key could not be known to the attackers due to the dynamic formulation of the S-box. Thus it will provide an enhanced security.

In the encryption process, every input state values will be plotted to the dynamically produced S-box and then these values will be plotted to the conventional AES S-box to create the encrypted consequence (Fig. 125.3).

Similarly in the decryption process, the input state value will be plotted towards the original AES S-box and then this value will be plotted towards the virtually created Inverse S-box to yield the decrypted original result. The similar procedure is used in the formation of dynamic S-box concept also used for the creation of one's complement and two's complement Non-linear S-box also (Fig. 125.4).

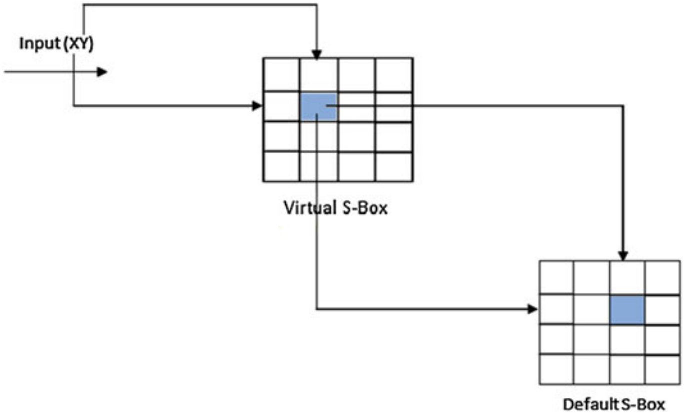

Fig. 125.3 Encryption process

Fig. 125.4 System architecture

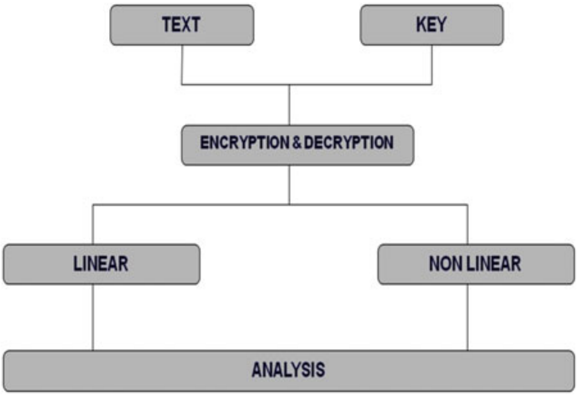

125.6 Results and Discussion

In our analysis, the sensor nodes are grouped based on the message id range and the number of nodes per cluster. The specific cluster group will be having unique characteristics associated with the cluster head, which is capable of receiving the multicast data from the corresponding sensor nodes. The locations of the static sensors are fixed in such a way that the cluster head is capable of receiving the encrypted data from each of its associated sensor node in a single-hop/multi-hop. Similarly all the cluster heads will be sending the encrypted data to the base station in a single-hop (Fig. 125.5).

In the graph the evaluation of time analysis among the data transfer and execution time of linear S-box as well as 1's complement and 2's complement S-box operation. In the time analysis graph, the x-axis has the time consumption in

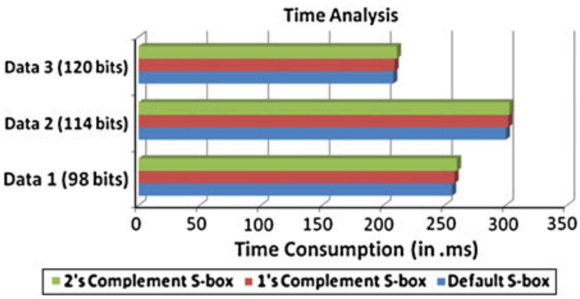

Fig. 125.5 Performance analysis

milliseconds and in the y-axis has the different size of data in bits. The time comparison results of linear S-box (blue), 1's complement (red), 2's complement S-box (green).

125.7 Conclusion

This implementation scheme safe guard the data from the intruders and major goal of this work is the Non-linearity implementation does not affect the originality of the AES algorithm, based on the time analysis the originality not affected as well the Non-linear agreement made the algorithm stronger. The scheme of the implementation is feasible in the networking environment, and has an acceptable speed of data encryption and decryption. This implementation presents a new Non-linear transformation for AES S-box to enhance the complexity of the S-box structure. The enhanced S-box structure provides a strong and expanded security.

References

1. Mozaffari-Kermani M, Student Member, IEEE, Reyhani-Masoleh A, Member, IEEE (2011) A lightweight high-performance fault detection scheme for the advanced encryption standard using composite fields
2. Velayutham R, Manimegalai D (2011) Enhancing confidentiality and integrity in IEEE 802.11i wireless networks using AES-CCMP. Euro J Sci Res ISSN 1450-216X 55(1):117–124
3. Sivaganesh E, Velayutham R, Manimegalai D (2012) A secure software implementation of non linear AES S-box with the enhancement of biometrics. In: International conference on ICCEET 2012, 927–932 © IEEE
4. Carlet C (2008) Recursive lower bounds on the non-linearity profile of boolean functions and their applications. IEEE Trans Inf Theory 54(3):1262–1272
5. Wong MM, Wong MLD, Nandi AK, Hijazin I (2012) Construction of optimum composite field architecture for compact high-throughput AES S-boxes. Very Large Scale Integr (VLSI) Syst, IEEE Trans 20(6):1151–1155
6. Rachh RR, Anami BS Ananda Mohan PV (2009) Efficient implementations of S-box and inverse S-box for AES algorithm 978-1-4244-4547 © IEEE

7. Li X, Chen J, Liu W, Wan W (2010) An improved AES encryption algorithm. IEEE
8. Chun Y, Yanxia G (2009) A research and improvement based on Rijndael algorithm
9. Kalbasi A, Alomar O, Hajipour M, Aloul F Wireless Security in UAE: A Survey Paper, by Department of Computer Engineering, American University of Sharjah (AUS), UAE @ aus.edu
10. Liu H, Darabi H, Banerjee P, Liu J (2007) Survey of wireless indoor positioning techniques and systems. IEEE Trans Syst, Man, Cybern-Part C: Appl Rev 37(6)

Chapter 126
Effect of Grid Impedance Variation on the Control of Grid Connected Converters with Synchronous Reference Frame Controllers in Micro-Grids

A. Vijayakumari, A.T. Devarajan and N. Devarajan

Abstract This paper presents an investigation on the effect of grid impedance variation on the control of grid connected voltage source converter when they are controlled using synchronous reference frame (SRF) current controllers in micro-grid applications. Mutual coupling terms introduced between the d and q control loops in SRF PI controller which are normally decoupled using the grid impedance through a feed-forward control to achieve independent control of active and reactive powers. But if the configurations change in systems like micro-grids due to intermittent nature of renewable energy sources then the feed forward decoupling becomes inadequate. A practical micro-grid and its parameters are taken for the investigation and the analysis is extended through simulation studies. The effectiveness of decoupling and the system stability under configuration change in micro-grids were investigated. The loss of independency of power control and stability analysis is presented to justify the need for a dynamic intelligent controller.

Keywords Grid impedance · Synchronous reference frame · Micro-grid · Decoupled d-q control · Current control

A. Vijayakumari (✉) · A.T. Devarajan
Department of Electrical and Electronics Engineering, Amrita Vishwa Vidyapeetham University, Amrita Nagar, 641112 Coimbatore, India
e-mail: a_vijayakumari@cb.amrita.edu

A.T. Devarajan
e-mail: at_devarajan@cb.amrita.edu

N. Devarajan
Department of Electrical and Electronics Engineering, Government College of Technology, 641013 Coimbatore, India
e-mail: profdevarajan@yahoo.com

C. Kamalakannan et al. (eds.), *Power Electronics and Renewable Energy Systems*,
Lecture Notes in Electrical Engineering 326, DOI 10.1007/978-81-322-2119-7_126

126.1 Introduction

A micro-grid approach plays an enormous role in the increased penetration of renewable energy resource into the grid thus reducing the emissions due to large coal fired power plants [1]. A micro-grid considers the local generation and the local loads as a subsystem. Usually there are Power electronic interfaces through which the local generators are connected to the system enable these control capabilities for the micro-grids [2, 3]. The generators may be wind, Solar PV, diesel generators etc. The power electronic interfaces are normally, single or multi-stage power electronic converters. These converter systems are developed with the following control capabilities viz. (i) Independent control of active and reactive powers (ii) synchronization to grid, (iii) meeting the harmonics standards, (iv) control under healthy and fault grid conditions and (v) islanding detection and isolation, (vi) Galvanic isolation between the source and the utility especially under grid fault condition.

The power delivered by the converter is controlled by current control [4, 5]. Simple regulators like PI is frequently used and recently the PR control is promoted [6, 7]. The selection of controller is based on the steady state and transient state performance requirements to meet the power quality standards. PR controllers are very sensitive to the grid frequency fluctuations causing the system to go to unstable conditions. On the other hand, linear PI regulators are first order controllers with large phase margin which best suits for many control systems, where high dynamics are to be accounted. Moreover, they are industry accepted and time tested. Only dc quantities can be handled by PI regulators as they have infinite gain only for zero frequency. However, in grid connected systems the ac currents injected to the grid are to be controlled for active-reactive power control. So, the ac quantities are first transformed into dc quantities using synchronously rotating reference frame transformations i.e. *abc*-*dq* transformations [8–10] so as to derive a dc control loop to track the ac quantities with zero steady state error.

Due to the *abc*-*dq* transformation a cross coupling term is introduced between the control loops, which links the active and reactive power control loops due to the presence of the impedance between inverter and grid [8–10]. This cross coupling results in the loss of independency in the control of active reactive powers. Meaning that when active power reference is changed, it not only changes the active power delivered but also the reactive power delivered as well. This may lead to tripping of the feeder, mal functioning of the relay circuits etc. This cross coupling is removed by feed forward and feedback based controllers as reported in the literature [11–14]. They use impedance values in a decoupling term, which removes the cross coupling effect. Also, when the grid impedance changes the plant transfer function changes which may result an unstable operation as the PI compensator's gains are normally fixed constant. But in micro-grids the grid impedance is not constant. It varies when the generation/load pattern changes.

This paper presents a study and investigation of the effect of grid impedance variations on the active-reactive power decoupling and the on the system stability within a micro-grid. An existing laboratory model of micro-grid is used in the study and the results are presented for the change in grid impedances.

126.2 Synchronous Reference Frame Current Controllers for Grid Connected Voltage Source Inverters (VSI)

Grid connected VSIs were controlled in synchronous reference frame (SRF) [8–10], in which the controlled parameters, the phase current delivered by the inverter are converted using the SRF transformation to make it appear as dc quantities in the control loop. The control action is accomplished with simple PI controllers. Figure 126.1 shows the circuit diagram of a three phase grid connected VSI. u_a, u_b *and* u_c are the inverter pole voltages, e_a, e_b and e_c are the grid phase voltages, L_i is the filter inductance and L_g is the grid inductance. The currents injected into the grid in each phase are i_a, i_b and i_c. The differential equation for the system shown in Fig. 126.1 is

$$L\left[\frac{di}{dt}\right]_{abc} = [u]_{abc} - [e]_{abc} - R[i]_{abc} \tag{126.1}$$

where L is the total inductance from the inverter to the mains, i.e. $L = L_i + L_g$. If $\omega = 2\pi f$, where f is the grid frequency, then Eq. (126.1) is written in synchronously rotating reference frame [12, 15].

$$u_{dq} = L\frac{di_{dq}}{dt} + (R + j\omega L)i_{dq} + e_{dq} \tag{126.2}$$

Resolving Eq. (126.2) to its real and imaginary parts results,

$$u_d = L\frac{di_d}{dt} - Ri_d - \omega Li_q + e_d \tag{126.3}$$

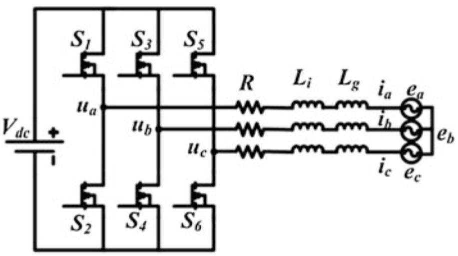

Fig. 126.1 Three phase grid connected VSI

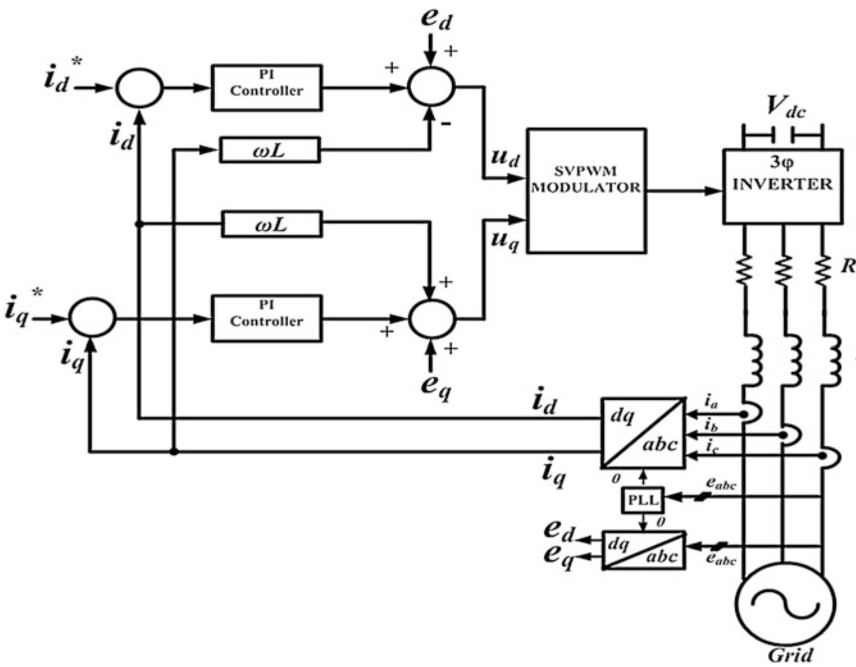

Fig. 126.2 General block diagram of current control of VSI in synchronous reference frame

$$u_q = L\frac{di_q}{dt} - Ri_q + \omega Li_d + e_q \tag{126.4}$$

Based on Eqs. (126.3) and (126.4) the control block diagram for the grid connected VSI in synchronous reference frame is obtained as shown in Fig. 126.2, where $i_d{}^*$, $i_q{}^*$ are d and q axes reference currents respectively. The active and reactive powers in the SRF is expressed as $P = 3/2u_d i_d$, $Q = 3/2u_d i_q$; thus, the active and reactive powers can be controlled by controlling the d and q axis currents. Though there are many advantages for PI controllers like large phase margines, first order etc., there are few shortcomings like inferior dynamic performance, loss of independence in the control of P&Q due to the presence of cross coupling. For meeting the adequacy of an accurate control the cross couplings are to be cancelled.

126.3 Decoupling the Dependency of Active and Reactive Powers on Each Other

In Eqs. (126.3) and (126.4), u_d and u_q are the reference voltages of the inverter in d and q axes respectively and forces the output of the inverter to follow these quantities upon a change in the active or reactive power references. Due to the

Fig. 126.3 Current control with an inner decoupling loop

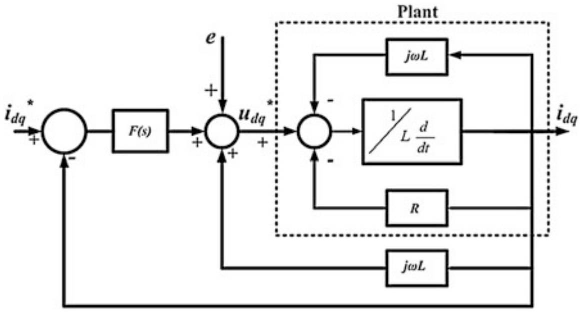

existence of the term $j\omega Li$ in Eq. (126.2), the d axis control voltage u_d not only depends on the d axis current but also on the q axis current and vice versa, i.e. two first order systems, are interacting with each other resulting a cross couplings. The removal of cross coupling [11, 12] is done by cancelling the complex drop due to the inductance by selecting a control voltage u_{dq} as

$$u_{dq} = u_{dq}{}^{*} + j\omega Li_{dq} \tag{126.5}$$

By substituting u_{dq} from Eq. (126.5) in Eq. (126.2) and obtaining control equation for the decoupled system as

$$L\frac{di_{dq}}{dt} = u_{dq}{}^{*} - Ri_{dq} - e_{dq} \tag{126.6}$$

Now it can be observed that there is no cross coupling in Eq. (126.6) as there is no complex valued coefficients as in Eqs. (126.3) and (126.4). Equation (126.5) is modeled as the inner feedback loop and a current regulator having its output as $u_{dq}{}^{*}$ is designed as an outer loop for the decoupled system. The block diagram of the decoupled control system with the new control voltage as in Eq. (126.5) is given in Fig. 126.3, where i_{dq} is the reference current vector. The transfer function of the decoupled system from $u_{dq}{}^{*}$ to i_{dq} is expressed as $G'(s) = 1/(sL + R)$. Now it is converted as a first order complex valued system but has no interacting terms. A PI controller with transfer function as $F(s) = kp + ki/s$ is used as a feed-back regulator.

126.4 Configuration Changes in Micro-Grids and Its Effect on Grid Impedance

A micro-grid consists of a group of loads and generating sources operating as a single controlled section that powers a local area [2, 3]. This arrangement brings down the generation-demand control to local control station, thus the need for central load dispatch is eliminated providing more reliable power to the consumers. Various types of generations are available in micro-grids with a utility interconnection point for continuity of supply during non-renewable generation periods. But, these micro-grids can operate with or without the utility connection, depending on the mode of operation, the availability of generation, the required load demand, presence of the utility etc. When the VSI is feeding power to large utility network, then the control is relatively simple compared to when it feeds into a micro-grid. Because in micro-grids, most of the generators are nature driven like, wind, solar etc. which are always intermittent. So, any generator may come into or go out of generation at any point of time during the operation. Such a switching in and switching out of one or more generators will cause the configuration of the network to get altered frequently.

An attempt is made to investigate the variation in the configuration of a micro-grid due to switching in and switching out of generators and load. Studies and experiments are carried out on a scaled down model of a micro-grid available in the department laboratory. The micro-grid model has various distributed generators and loads represented in a single line diagram with the indicated parameters of the transmission lines as shown in Fig. 126.4. Assuming the generator output voltages are regulated using automatic voltage regulators (AVRs), the electrical equivalent circuit of the micro-grid when all the generators and loads are present is shown in Fig. 126.5a.

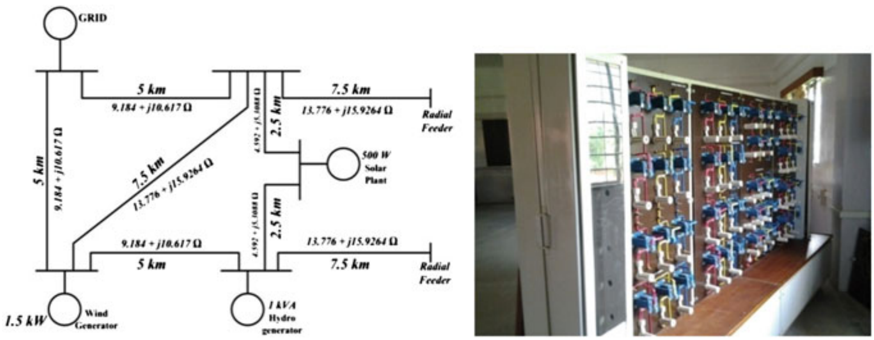

Fig. 126.4 The *single line* diagram and snapshot of the scaled down laboratory model of micro-grid

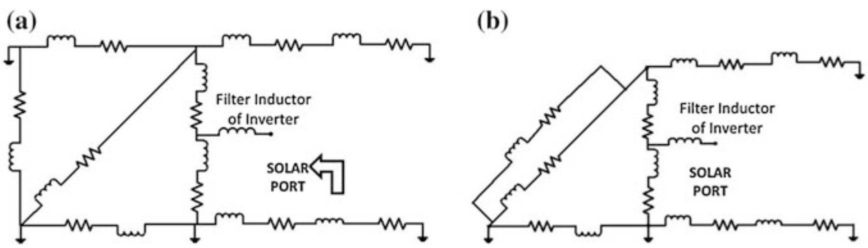

Fig. 126.5 Equivalent circuit of the micro-grid **a** under all generators and load present condition **b** when the grid failure condition

Table 126.1 The impedance presented by the micro-grid at the solar port

Grid	Wind	Hydro	Load 1	Load 2	Impedance seen at solar inverter (Ω) (By experiment)	Impedance seen at solar inverter (Ω) (By simulation)
1	1	1	1	1	3.094 + j 4.531	3.124 + j 4.583
0	1	1	1	1	3.262 + j 4.731	3.297 + j 4.782
1	0	1	1	1	3.144 + j 4.59	3.187 + j 4.608
1	1	0	1	1	5.334 + j 7.192	5.375 + j 7.201
1	0	0	1	1	7.041 + j 9.288	7.093 + j 9.292
0	0	1	1	1	3.61 + j 5.146	3.99 + j 5.189
1	0	0	0	1	7.486 + j 9.742	7.504 + j 9.799

The configuration of Fig. 126.5a is applicable only, when the above mentioned condition exists in the system. For example if the grid/utility connection is lost during the operation the configuration is modified as shown in Fig. 126.5b. Similarly every combination of generators-loads, results a unique configuration. Simulations and experiments are carried out on the laboratory model to measure the range of impedances which results due the configuration change in the micro-grid as it is essential for the decoupling process.

As an example, at the solar PV converter bus the range of impedance variation felt by the inverter controller when different generators and loads switches in and out of the network is measured through simulation and by experiment. The results of this study are listed in Table 126.1. The entry as "1" in Table 126.1, represent the presence of the respective generator/load and a "0" entry represent its absence. It is observed that the inductive reactance is varying between j4.531 Ω to j9.742 Ω, which is +63 to −73 % from its average value of j7.135 Ω.

126.4.1 The Effect of Grid Impedance Change on Decoupling

The decoupling as explained in Sect. 126.2 is very important in grid connected VSIs not only to control the active and reactive powers independently also for the obtaining system stability. But the effectiveness of decoupling solely depends on the accuracy of impedance used in the control loop. i.e. how close the actual impedance in the line as seen by the inverter is to the impedance value used in the control loop for decoupling. Generally a nominal value of impedance is used in the control loop for obtaining the decoupling in a grid connected inverter system [7, 8, 10, 11], as they are feeding power to the utility whose impedance is constant as the utility being a very stiff power generator. However, in micro-grids the variation of impedance can be quite high as shown in Table 126.1. To demonstrate the effect of source inductance variations on the decoupling the system shown in Fig. 126.2 has

Table 126.2 Parameters for simulation

Parameters	Values
DC bus voltage	680 V
Inverter PWM frequency	4 kHz
Output filter inductance L_f	11 mH, 0.23 Ω
Load power	1 kW
Grid specifications	230 V (rms), 50 Hz
PI controller constants	$K_p = 24$, $K_i = 505$

been set up in MATLAB/Simulink with the specifications of Table 126.2. A nominal value of *j*7.135 Ω is used for ωL, in the control loop and the micro-grid is configured with the highest and lowest value of actual inductive reactance from Table 126.1 viz. j4.531 Ω and j9.742 Ω.

A step change in the active power reference (P_{ref}) is introduced keeping the reactive power reference (Q_{ref}) constant at zero. The power references are introduced in terms of reference current i_d^* calculated from the required P_{ref}. Figure 126.6 shows the simulation results of the active and reactive power delivered by the inverter for step changes in their references. It is evident from Fig. 126.6 that the step changes in P_{ref} and Q_{ref} is causing a change in the reactive and active powers delivered during a considerable transient period inspite of their references being kept constant. Though the feedback controller regulates these quantities at their reference values, it requires a considerable transient period as seen from the figures; consequently results a system which is not dynamics free.

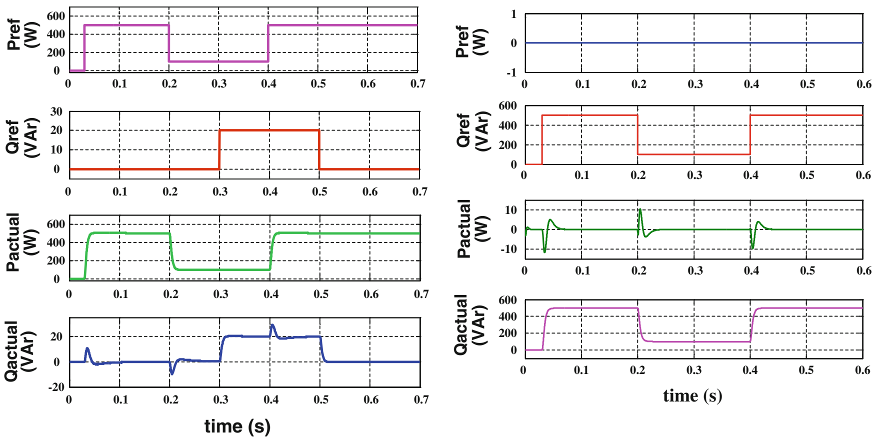

Fig. 126.6 Effect of step change in P_{ref} on reactive power and Q_{ref} on active power

126.4.2 The Effect of Grid Impedance Change on the Micro-Grid System Stability

In the design of a reliable control system, it is often obligatory to investigate the performance of a system when one or more parameters of the system vary over a known range. Here, the stability of the control loops under various configurations of the micro grid is investigated with constant PI controller coefficients fixed constant at a value as specified in Table 126.2. These values are chosen based on loop shaping method of tuning proposed in [12, 15].

Conventional techniques for stability analysis like root locus and the Bode plot were used with the original designed PI controller gains. Figure 126.7 shows the Root locus and the Bode plot of the micro-grid for condition 1 of Table 126.1. It can be observed from Fig. 126.7, that the trajectory of the roots for the entire range of gain lies well within the left half of the S-plane resulting a stable control loop. Also it is confirmed from the Bode plot showing a stable loop with ample phase margin of almost 90°.

Figure 126.8 shows the Root locus and Bode plot of the same micro-grid system when the configuration is being altered corresponding to the last row of Table 126.1, one of the extreme operating condition of the micro-grid. It can be observed that the trajectories of the roots are now on the imaginary axis and moving to the right half of the S-plane leading to unstable regions. From the corresponding Bode plot it can be found that the phase margin falling to a low value of 2° which may lead to an oscillatory loop. Thus it is very important to understand that the decoupling and the system stability is not always perfect unless the system is controlled with some sophisticated, fool proof, dynamic controller to track these configuration changes for micro-grids.

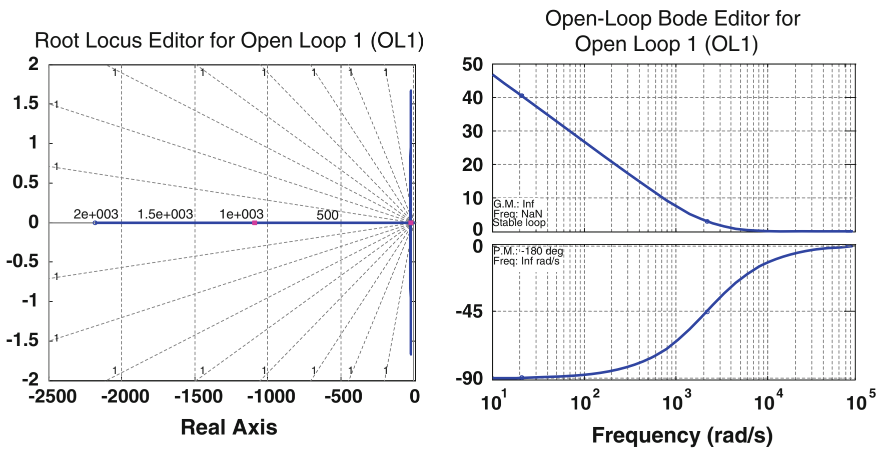

Fig. 126.7 Root locus and Bode plot with the basic design PI controller constants

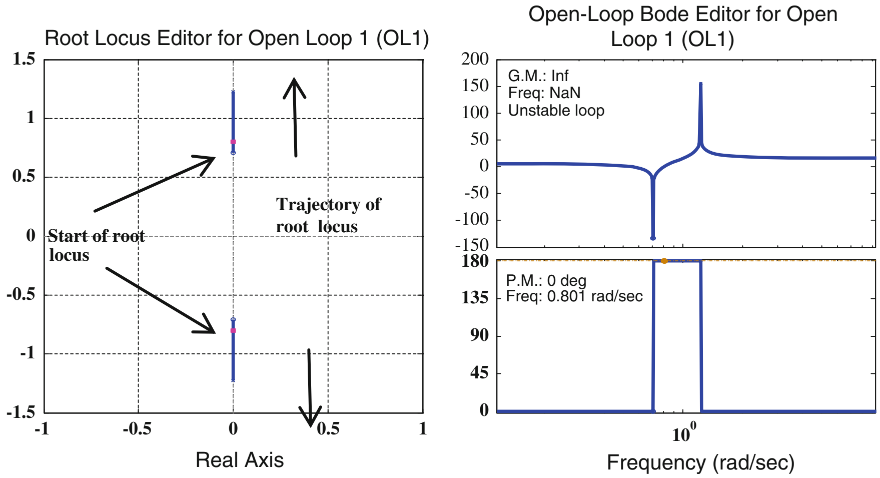

Fig. 126.8 Root locus Bode plot of the micro-grid system under altered configuration

126.5 Conclusion

This paper presented an investigation on the effect of grid impedance variation on the control of grid connected voltage source converter when they are controlled using synchronous reference frame (SRF) current controllers in micro-grid applications. The removal of the cross coupling terms in SRF-PI control using the grid impedance through a feed-forward control is presented. A practical micro-grid is considered for this work and its parameters are taken for the investigation and the analysis is extended through simulation studies. The influence of the configuration change on the grid impedance value and subsequently on the system performance is shown through simulation studies. The findings from the investigations are categorised in two streams. The first one is the dependency of the active and reactive powers on each other. It is concluded that when active power reference is varied, the reactive power delivered is also getting altered for a considerable transient period when the decoupling is not accurate. Next the influence of the grid impedance changes on the micro-grid system stability is analysed through traditional control system methods and the results are presented. It has been observed that the micro-grid systems become unstable under extreme operating conditions with SRF-PI controllers. The investigations conclude that the SRF-PI current controller is inadequate in addressing the active reactive power decoupling problem and also lead to an unstable system when they are used under micro-grid environment. The loss of independency of power control and stability analysis justifies the need for a dynamic intelligent controller with evolutionary algorithms which can track these configuration changes and modifies the controller capabilities accordingly when used in micro-grids.

References

1. International Energy Agency (IEA)'s (2011) Emissions from coal fired Power Generation. Available from: www.iea.org/media/workshops/2011/cea/Ito.pdf
2. Lasseter RH, Piagi P (2004) Microgrid-a conceptual solution, PESC'04, Germany (2004), pp 20–25
3. Beidou FB, Morsi WG, Diduch CP, Chang L (2010) Smart grid: challenges, research directions and possible solutions. 2010 2nd IEEE international symposium on power electronics for distributed generation system, IEEE
4. Blaabjerg F, Teodorescu R, Liserre M, Timbus AV (2006) Overview of control and grid synchronization for distributed power generation systems. IEEE Trans Ind Electron 53 (5):1398–1409
5. Bahrani B, Karimi A, Rey B, Rufer A (2013) Decoupled DQ-current control of grid-tied voltage source converters using nonparametric models. IEEE Tran Ind Elect 60(4):1356–1366
6. Teodorescu R, Blaabjerg F, Liserre M, Loh PC (2006) Proportional-resonant controllers and filters for grid connected voltage source converters. IEE Proc Electr Power Appl 153 (5):750–762
7. Liu B, Wu JJ, Li J, Dai JY (2013) A novel PFC controller and selective harmonic suppression. Intl J Electr Power Energy Syst 44(1):680–687
8. Kadri R, Gaubert JP, Champenois Gerard (2011) An improved maximum power point tracking for photovoltaic grid-connected inverter based on voltage-oriented control. IEEE Trans Ind Electron 58(1):66–74
9. Peng Q, Pan H, Liu Y, Xiang L (2013) Dual-loop control strategy for grid-connected inverter with LCL filter. Energy Power Eng 5:97
10. Al-Saedi W, Lachowicz SW, Habibi D, Bass O (2013) Power flow control in grid-connected microgrid operation using particle swarm optimization under variable load conditions. Intl J Electr Power Energy Syst 49:76–85
11. Milosevic M (2006) Decoupling control of d and q current components in three-phase voltage source inverter. Power systems conference and exposition (PSCE), Atlanta
12. Stefan Ö (2008) Electrical machines and drives. Course compendium KTH
13. Bahrani B, Kenzelmann S, Rufer A (2011) Multivariable PI-based dq current control of voltage source converters with superior axis decoupling capability. IEEE Trans Ind Electron 58(7):3016–3026
14. Bahrani B, Vasiladiotis M, Rufer A (2014) High-order vector control of grid-connected voltage source converters with LCL-filters. IEEE Trans Ind Elec 61(6):2767–2775
15. Harnefors L, Nee HP (2002) Control of variable-speed drives applied signal processing and control. Mälardalen University, Västeras

Chapter 127
Application of SVM as Classifier in Estimating Market Power Under Deregulated Electricity Market

S. Prabhakar Karthikeyan, I. Jacob Raglend, K. Sathish Kumar, Sarat Kumar Sahoo and B. Priya Esther

Abstract This paper presents an approach to the application of Support Vector Machines (SVM) in estimating market power with the perspective of generation companies (Gencos). By choosing proper attributes and criterion for classification, SVM can be effectively used as a tool for market power estimation in the deregulated electricity market. In this paper, an analysis has been made to infer how effective the SVM technique is in predicting whether market power can be exercised by an entity or not. The person who is handling the technique i.e. Gencos decides the attributes chosen and the classifying criterion. Nodal Must Run Share Index is used in estimating market power. A simple three bus system with two generators and one load/two loads is chosen for the study. Performance of both linear and non-linear kernels is also compared.

Keywords SVM · Gencos · Nodal Must Run Share Index · Linear and non-linear kernels

127.1 Introduction

127.1.1 Support Vector Machines

SVM is basically used in all Engineering applications which require classification and regression. A SVM is a concept in statistics and computer science for a set of related supervised learning methods that analyze data and recognize patterns, used for classification and regression analysis. A version of SVM for regression was proposed in 1996 by Vladimir N. Vapnik, Harris Drucker, Christopher J. C. Burges,

S. Prabhakar Karthikeyan (✉) · K. Sathish Kumar · S. Kumar Sahoo · B. Priya Esther
School of Electrical Engineering, VIT University, Vellore, Tamil Nadu, India
e-mail: spk25in@yahoo.co.in

I. Jacob Raglend
NI University, Thakkalai, Nagercoil, Tamil Nadu, India

C. Kamalakannan et al. (eds.), *Power Electronics and Renewable Energy Systems*,
Lecture Notes in Electrical Engineering 326, DOI 10.1007/978-81-322-2119-7_127

Linda Kaufman and Alexander J. Smola [1]. This method is called Support Vector Regression (SVR). The model produced by support vector classification (as described above) depends only on a subset of the training data, because the cost function for building the model does not care about training points that lie beyond the margin. Analogously, the model produced by SVR depends only on a subset of the training data, because the cost function for building the model ignores any training data close to the model prediction (within a threshold ϵ). Another SVM version known as least squares support vector machine (LS-SVM) has been proposed in Suykens and Vandewalle.

127.1.2 Market Power

Consumers enjoying a deregulated electricity market, meaning they have the power to choose their electricity provider. Market Power can be measured using market power indices. These indices have their own significance and portrait the market power within their limitations. Study on market power indices shows that the definition of the market power was varying with time and problem of interest. In [2, 3], various market power indices and their advantages are discussed elaborately. In [2], Nodal must run share (NMRS) index is proposed and its importance are illustrated with an IEEE 24 bus RTS under various system conditions. NMRS is used as an index in this paper for determining the market power of a generation company.

127.2 Problem Formulation

In the deregulated electricity market, the sole objective of the system is to create a healthy and competitive environment among the players (within power producers and power consumers) by which the whole society gets benefited. Owing to various constraints on the system, the power producers get an opportunity to exercise their market power on the power consumers. So it is quite worthy for the utilities and the ISO to estimate or to predict the market power existence which affects the environment.

In this paper, SVM is used as a classifier for determining whether market power can be exercised or not by a Genco. This solely depends upon the utility who is utilizing this technique and their objective. Here assuming a Genco which is interested in finding out the point where it gets profit by taking the amount of generation for a given load as an attribute is using this tool. Similarly a Disco can come out with a point where market power is exercised on them or not by taking the amount of generation from a particular Genco as an attribute. An ISO (market regulator can use it to check whether a particular transaction leads to undue advantage of one entity over other.

127.3 Algorithm

Step 1 Scaling: Enter training data and output data in data matrix
Step 2 Classify training data as X and output as Y
Step 3 Kernel selection: Select the kernel to be used to calculate SVM (e.g. linear, radial basis function)
Step 4 The parameters like the penalty term C, which determines the tradeoff between minimizing the training error and minimizing model complexity and Gamma, the term defines non-linear mapping from input space to high dimensional feature space are suitably selected.
Step 5 Train the SVM using the kernel using the input variables and the output data. RBF kernel requires more number of training data for better accuracy unlike linear kernel.
Step 6 Error checking: A definite set of sample input variables are taken to check how accurate the plot is.

127.4 Simulation and Results

A sample three bus system, shown in Fig. 127.1 with two generators and one load is taken to illustrate the problem. The load is assumed to be inelastic. All the line reactances are taken to be j0.2p.u. The cost functions of both the generators are taken to be $F(Pg_i) = 0.02Pg_i^2 + 2Pg_i$ (where $c_i = 0$). It is to be noted that this simple system is sufficient to understand the proposed methodology of estimation and classification of market power using SVM.

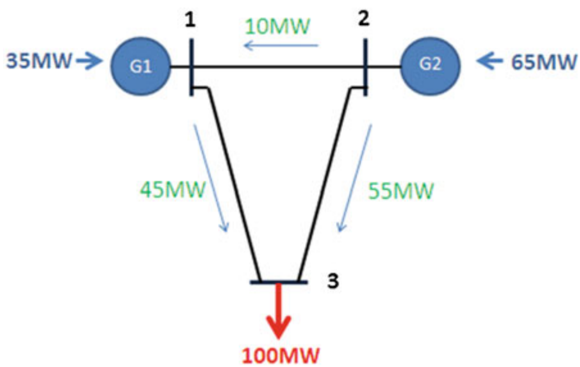

Fig. 127.1 Sample three bus system with transmission line constraint

127.4.1 With Transmission Line Limit

When the transmission line between bus 1 and bus 3 is constrained with the limit of 45 MW as shown in Fig. 127.1, generator 2 gets an advantage because most of the power of generator 1 will flow through this constrained line and hence its generation is reduced.

It is inferred that MRG of both the generators cannot be 100 MW as this would violate the transmission constraint. So MRG of both the generators are calculated using linear programming. It is found to be 65 MW for generator 2 and that of the generator 1 is 0 MW. i.e. for the given market condition, generator 2 can run without depending on generator 1. Hence the MRS and the NMRS values of generator 2 have gone up from 0 to 0.65. Since there is only one load, the MRS and the NMRS are same.

127.4.2 SVM as a Linear Classifier: Genco's Perspective

Let us assume the transmission constraint still exists on the same line. As a Genco, generator 1 can change only its maximum generation and the bid which is submitted to ISO (i.e. P_{max} and b_i). Hence 40 random points for generator 1 are chosen and the training points are generated. The conditions for classification are the NMRS of generator 2 and the profit incurred by the generator 1. The NMRS of generator 2 is chosen because due to the existence of the transmission constraint, the NMRS of the generator 1 is always zero. The classification conditions are NMRS of generator 2 should not exceed 0.7 and the profit incurred by the generator 1 should not be less than Rs. 20. The 40 random values (training points) are generated for which market power is determined.

In Fig. 127.2, P_{max1} and B_2 (one of the cost co-efficients) are the variables chosen to reflect G1's and G2's behaviour respectively. Genco's variables are selected as this analysis is on behalf of gencos' perspective. In order to check the performance of the classifier, 12 more random test points are chosen. The Y values (which represents the existence of market power, +1 when market power exists and −1 when market does not exists) of the 12 points are predicted using the training data and they are compared to the original values. The test points, their predicted values and the original values are tabulated below in Table 127.1. In Fig. 127.2, the red points represent Y = −1 and blue points represent Y = +1.

As the system is simple, the linear classification is effective. In order to verify the effectiveness of the other kernels, the sample system is slightly modified as shown in Fig. 127.3.

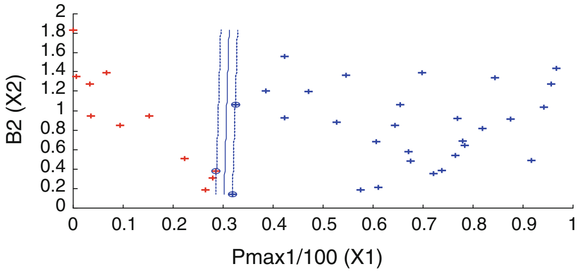

Fig. 127.2 SVM as linear classifier

Table 127.1 Test points for Sect. 127.4.2

P_{max} (X1)	B (X2)	Y_{pred}	Y_{orig}
10	0.5	1	−1
20	0.55	1	1
40	0.7	1	1
60	0.6	1	1
80	0.5	1	1
80	0.55	1	1
80	0.45	1	1
85	0.6	1	1
90	0.6	1	1
95	0.65	1	1
87.5	0.6	1	1
84	0.55	1	1

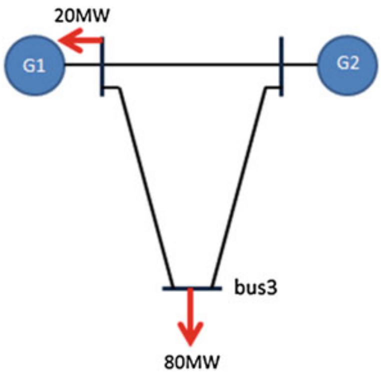

Fig. 127.3 Modified sample three bus system

127.4.3 SVM as a Linear Classifier: Genco's Perspective for the Modified Sample System

Figure 127.3 shows a three bus system with a load at bus 3 and bus 1. The cost functions, the maximum and minimum generations of the generators are assumed to be same. The loads are assumed to be inelastic.

Like in the Sect. 127.4.2, when there is no transmission constraint, no generator enjoys market power and hence the MRG, MRS and NMRS are zero. When the line connecting bus 1 and bus 3 is imposed by the constraint of 35 MW, generator 2's MRG, MRS and NMRS on bus 3 increases. The impact is not seen on bus 1 and this is due to the direct connection of generator 1 at bus 1. The flow details with the transmission constraint are shown in Fig. 127.4.

The classifying constraints are NMRS of the generator 2 on load at bus 1 and bus 3 and the profit of the generator 1. The value of Y will be −1 if the NMRS of generator 2 over load at bus 1 is greater than 0.2 and that over load at bus 3 is greater than 0.7 and if the profit of the generator 1 is less than Rs. 20. Training points and the Y values as discussed earlier in case 1 are determined for case 2 with the transmission line constraint. The results of linear classification are shown in Fig. 127.5 in which green points represents the test points (Table 127.2).

The percentage of accuracy of prediction for the given test points is 75 %.

127.4.4 SVM as a Non linear [Radial Basis Kernel (P1 = 1)] Classifier: Genco's Perspective for the Modified Sample System

In this case, the percentage of accuracy of prediction for the given test points is 83.33 %. From Fig. 127.6 and from Table 127.3, it is observed that with the complexity of the kernel, the accuracy of the prediction increases.

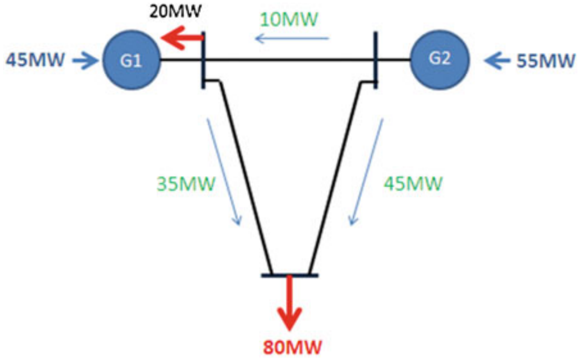

Fig. 127.4 Modified sample three bus system with transmission line constraint

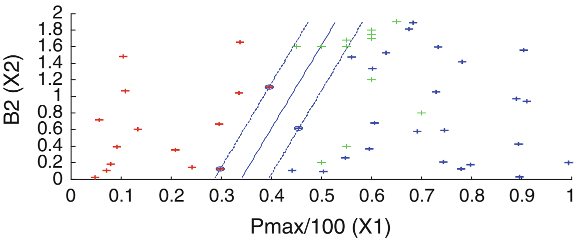

Fig. 127.5 SVM as a linear classifier for Sect. 127.4.3 with transmission line constraint

Table 127.2 SVM as a linear classifier-sample results

P_{max}	B	Y_{pred}	Y_{orig}
50	0.2	1	−1
55	0.4	1	−1
70	0.8	1	1
60	1.2	1	1
50	1.6	1	1
55	1.6	1	1
45	1.6	−1	1
60	1.7	1	1
60	1.8	1	1
65	1.9	1	1
60	1.75	1	1
55	1.68	1	1

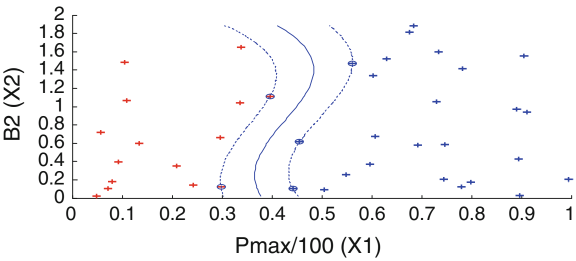

Fig. 127.6 SVM as Non linear classifier (rbf with $p_1 = 1$)

Table 127.3 SVM as non linear classifier (rbf with $p_1 = 1$) for Sect. 127.4.4-sample results

P_{max}	B	Y_{pred}	Y_{orig}
50	0.2	1	−1
55	0.4	1	−1
70	0.8	1	1
60	1.2	1	1
50	1.6	1	1
55	1.6	1	1
45	1.6	1	1
60	1.7	1	1
60	1.8	1	1
65	1.9	1	1
60	1.75	1	1
55	1.68	1	1

127.5 Conclusions

In this paper, the application of SVM as a classifier in estimating market power is discussed. The attributes chosen and the classifying criterion are based on the utility that is using the technique. Since NMRS is an efficient market index, it is used as the classifying criterion in all the cases discussed above. SVM has been used as a classifier with the perspective of gencos. Only two attributes have been chosen in all the examples of classification so that the results can be visualized on a 2-Dimensional plot. It is inferred that the predication or classification is more accurate when non-linear kernels are used. But the main disadvantage of non-linear kernels is that it requires more number of training points. The nature and the order of the kernels have to be manually chosen by the user in-order to classify or fit the data points in an effective manner. The results obtained are quite encouraging and can be useful for the researchers to estimate market power through SVM technique for strategic bidding by gencos or discos and to regulate market by ISOs. SVM can also be used as a part of a multistep optimization process that requires a rough estimate of the market power that can be exercised by an entity over another in a market, with the minimum information possible.

Acknowledgments The authors acknowledge the support rendered by VIT University, Tamil Nadu for carrying out this work. The authors also sincerely thank them for their technical support throughout the period of their study.

References

1. Burges CJ, Kauffman L, Smola A, Vapnik V, Mozer MC, Jordan JI, Petscbe T (eds) (1997) Support vector regression machine, neural information processing systems vol 9. MIT Press, Cambridge, pp 155–161. http://ece.ut.ac.ir/classpages/F83/PatternRecognition/Papers/SupportVectorMachine/support-vector.pdf
2. Peng W, Xiao Y, Yi D (2004) Nodal market power assessment in electricity markets. IEEE Trans Power Syst 19(3):1373–1379
3. Prabhakar Karthikeyan S, Jacob raglend I, Kothari DP (2013) A review on market power in deregulated electricity market. Int J Electr Power Energy Syst 48:139–147

Chapter 128
Optimal Capacitor Placement in Radial Distribution System to Minimize the Loss Using Fuzzy Logic Control and Hybrid Particle Swarm Optimization

S. Joyal Isac and K. Suresh Kumar

Abstract Shunt capacitors installation at suitable locations will reduce the power loss and increase the voltage profile. The objective function includes cost of power loss, energy loss and capacitor banks. Constraints include voltage limits, number and location of installed capacitors. Fuzzy Expert system is used to find the place where the capacitors have to be installed. Optimal size is found using Particle Swarm Optimization and it is compared with Hybrid Particle Swarm Optimization. The proposed method is applied to 15 bus and 34 bus radial distribution system. Comparative study was done for the system without capacitor and with optimally placed capacitors with and without voltage constraint. Results show robustness of proposed method in solving this difficult task.

Keywords Radial distribution systems · Shunt capacitors · Fuzzy expert system · Hybrid particle swarm optimization · Savings in capitals

128.1 Introduction

Electrical power systems networks are typically composed of four main parts namely generation, transmission, distribution, and loads. In order to maintain voltage profile and to reduce the power loss in the distribution system, shunt capacitors are to be installed at suitable locations in a large distribution system.

Distribution systems have high R/X ratio, significant voltage drop that could cause power loss in the feeders. Totally 13 % of the generated power is consumed as loss at the distribution level.

S. Joyal Isac (✉) · K. Suresh Kumar
Department of EEE, Saveetha Engineering College,
Chennai, Tamil Nadu, India
e-mail: joyalisac25@gmail.com

K. Suresh Kumar
e-mail: sureshbarath@gmail.com

C. Kamalakannan et al. (eds.), *Power Electronics and Renewable Energy Systems*,
Lecture Notes in Electrical Engineering 326, DOI 10.1007/978-81-322-2119-7_128

By placing capacitors optimally, we can thereby do power flow control, improve system stability, power factor correction, voltage profile management and thereby reduction in active energy losses.

Many methods are there to solve optimal capacitor placement problem such as Genetic algorithm, Ant colony algorithm, and simulated annealing based on fuzzy logic and other intelligence techniques. In this paper fuzzy logic control is used to solve the problem. This problem is suited only for fundamental frequency signal. The sizing of capacitors is modeled by the objective function to obtain maximum savings using Particle Swarm Optimization and Hybrid Particle Swarm Optimization. To illustrate the applicability of the algorithm, this method is applied to IEEE 15 bus and 34 bus radial distribution system. This can be extended to three phase system with non-linear load and unbalanced load [5].

128.2 Framework of Approach

This complete framework of this approach is to solve for optimal capacitor allocation problem. It includes use of some computational procedures, to find out the total power loss and voltage level in the radial distribution system and then the coupling of fuzzy expert system to find out the candidate sensitivity index. A modified Newton Raphson program is used to calculate power loss reduction in the test system.

There are some simplifies approach for the load flow program in the radial system, Ref. [1].

An efficient method for load flow solution in radial distribution system is also there, Ref. [8].

A new approach is established for capacitor placement in radial distribution feeders [6].

Incorporating both the power loss index (PLI) and per unit voltage in fuzzy expert system which will determine sensitivity index and thereby the most sensitive nodes for placing capacitors.

Particle Swarm Optimization and Hybrid Particle Swarm Optimization is used to find the optimal capacitor sizing to reduce the cost [2] (Fig. 128.1).

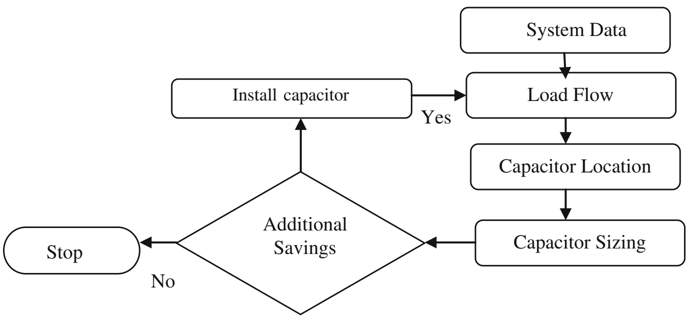

Fig. 128.1 Framework of approach [4]

1. Read the given data for the radial distribution system.
2. Perform load flow and base case total active power loss.
3. By means of reactive power injection each node (expect source node), run load flow and calculate active power loss.
4. Calculate power loss reduction and power loss index using this equation,

$$\mathbf{PLI(t) = [\{X(t)-Y\} / \{Z-Y\}]\ ¥\ t = 2,3,4\ldots.,n}$$

X Loss reduction
Y Minimum reduction
Z Maximum reduction

5. Select candidate nodes where PLI > tolerance.
6. Calculate the optimal size of the capacitor by PSO and HPSO.
7. Find the additional savings by placing the optimal size of the capacitor.
8. Install the capacitor.
9. Stop.

128.3 Problem Formulation and Implementation

Radial Distribution System
Feeder test specification:
Radial Feeder: 11 kV, 15 bus system
Load: 1.0 P.U
Number of Load level: 1
Load duration: 8,760 h
Number of capacitor location: 5 (15 bus system)
Number of capacitor location: 7(34 bus system)

Consider a IEEE 15 bus distribution system and IEEE 34 bus distribution system. The single line diagram of such a feeder comprising a branches and node is shown in the Fig. 128.2.

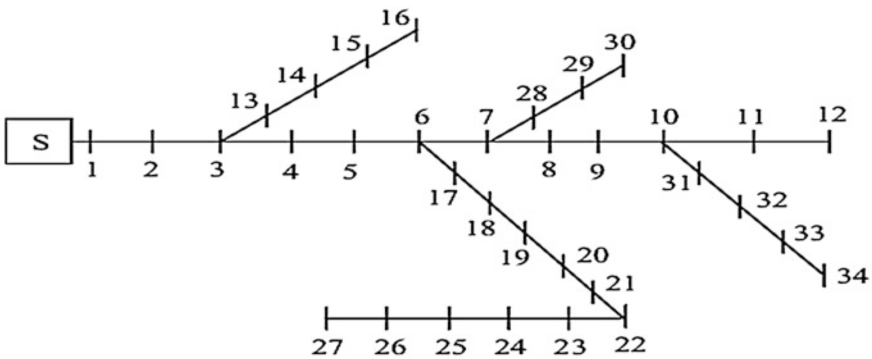

Fig. 128.2 34 bus distribution network

128.4 Distribution System

Radial Distribution System provide link between the high voltage transmission system and the consumers. The circuit starts from a substation and it passes through the major load centres. There will be laterals and sub-laterals in this distribution system. Lateral feeder connects all the load points with main feeder connected with many lateral and sublaterals are called Radial Distribution System. Since the design in simple and they are generally low cost they are popular.

128.4.1 Features of Radial Distribution System

(a) Many nodes and branches.
(b) Wide range of resistance and reactance values.
(c) Unbalanced load and unbalanced operations.
(d) Radial network structure.

128.4.2 Some Advantages and Benefits

(a) Line loss reduction.
(b) Reduced environmental impacts.
(c) Improved system stability.
(d) Improved feed voltage conditions.

Bus data and Line data are given as inputs to the load flow program by Newton-Raphson method. This gives power loss and voltage of each of the bus which is used for further analysis.

128.5 Fuzzy Expert System (FES) Implementation

The FES contains a set of rules, which are developed from qualitative descriptions. In a FES, rules may be fired with some degree using fuzzy inferencing, whereas, in a conventional expert system, a rule is either fired or not fired. For the capacitor allocation problem, rules are defined to determine the suitability of a node for capacitor installation. For determining the suitability of capacitor placement at a particular node, a set of fuzzy rules has been established. The rules are summarized in the fuzzy decision matrix [1]. These fuzzy variables described by linguistic terms are represented by membership functions. The membership functions are graphically shown in Figs. 128.3 and 128.4.

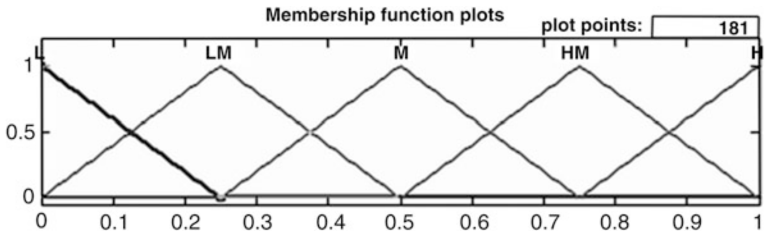

Fig. 128.3 Input variable-power loss index (PLI)

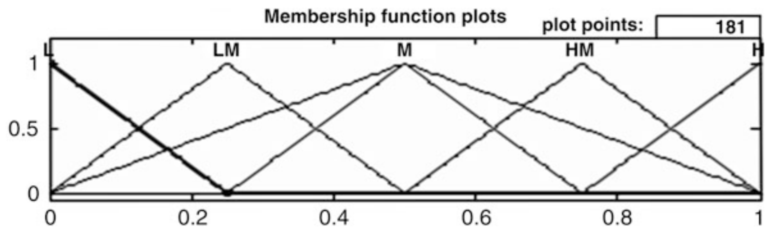

Fig. 128.4 Input variable-per unit voltage (V)

128.5.1 Fuzzy Expert System: Output-15 and 34 Bus System

In the fuzzy expert system two inputs and one output type is selected in Mamdani type fuzzy interference system, Power loss index and per unit voltage are selected as input and the output obtained is candidate sensitivity index. The two inputs are given to the fuzzy interference system to obtain the candidate sensitivity index. Only triangular membership function is selected for power loss index considering that the loss will increase to the peak and then It will be reduced to the lower value. Five functions are selected for power loss index. All the membership functions are tried and found that triangular function shows best result and it is shown here.

Both triangular and trapezoidal membership function are tried and found it to be best. Here also five membership functions are selected and it is enough to explain the concept. The result is shown below.

The output membership function is shown here. Only triangular membership functions are obtained. The sensitivity should be there or it shouldn't be there. So only triangular function is selected. The output obtained is found to be perfect and checked for different functions. The values are then obtained using program written in Matlab M-file.

The functions selected for the rules are classified as low, low medium, medium, high medium, high.

128.5.2 Inference-15 Bus System and 34 Bus System

From the above result it is found that for 15 bus system the sensitivity index is more in 4, 6, 7, 11, 15 buses. But placing the capacitors in all the 5 buses will increase the total cost to a higher level. So the bus where the sensitivity is peak is selected as the node for placing the capacitor. They are 11, 15 buses.

For 34 bus system the sensitivity index is more in, 8, 9, 11, 18, 19, 20, 21, 22, 23, 24, 25, 26 buses. But placing the capacitors in all the 5 buses will increase the total cost to a higher level. So the bus where the sensitivity is peak is selected as the node for placing the capacitor. They are 19, 20, 21, 22, 23, 24, 25 buses.

128.6 Capacitor Sizing: PSO

PSO optimizes a problem by having a population of candidate solutions, here dubbed particles, and moving these particles around in the search-space according to simple mathematical formulae over the particle's position and velocity. Particle swarm optimization is originally attributed to Kennedy, Eberhart [7].

Step 1. Initialize a population of particles (pp) with random positions.
Step 2. Calculate the fitness value for the given objective function for each particle.
Step 3. Set present particles as "Pbest".
Step 4. Initialize velocity (V_{old}) for initial particles.
Step 5. Find fitness value for each new set of particles.
Step 6. Compare each particle's fitness value to find new "Pbest" between the two set of particles.
Step 7. Find minimum fitness value by comparing two set of particles and corresponding particle is "Gbest".
Step 8. Update velocity and position for next iteration using the below formula,

$$V_{new} = w * V_{old} + [a\ (P_{best} - pp) + b(G_{best} - pp)]$$
$$pp_{new} = pp_{old} + V_{new}$$

Step 9. The iteration is repeated until the convergence is made.

128.6.1 Objective Function

$$\text{Min } S = ke\sum_{j=1}^{L} TjPj + \sum_{i=1}^{ncap} (Kcf + KcQci) + \lambda\left(V^{l}_{min} - V^{s}_{min}\right)^2$$

P_j	Power loss at *j*th load level
Q_{ci}	Reactive power injection from capacitor to node i
S	Savings in '\$'
T_j	Load Duration (8,760 h)
N_{cap}	Number of Capacitor locations
L	Number of Load level
K_e	Capacitor Energy Cost of Losses (0.06\$/kWh)
K_{cf}	Capacitor Installation Cost (1,000\$)
K_c	Capacitor Marginal Cost (3\$/kVAr)
$V^l_{\min}$	Minimum voltage limit
$V^s_{\min}$	Voltage of the system
λ	Constant multiplier

128.6.2 Capacitor Sizing: HPSO

For the positions of children:

$$\begin{aligned}\mathrm{Child_1(x_i)} &= \mathrm{p_i \times\ parent_1(x_i) + (1 - p_i) \times parent_2(x_i)}\\ \mathrm{Child_2(x_i)} &= \mathrm{p_i \times parent_2(x_i) + (1 - p_i) \times parent_1(x_i)}\end{aligned}$$

For the velocity of the children:

$$\begin{aligned}\mathrm{Child_1(v)} &= \frac{\mathrm{(parent_1(v) + parent_2(v)) \times \mid parent_1(v) \mid}}{\mathrm{\mid Parent_1(v) + parent_2(v) \mid}}\\ \mathrm{Child_2(v)} &= \frac{\mathrm{(parent_1(v) + parent_2(v)) \times \mid parent_2(v) \mid}}{\mathrm{\mid Parent_1(v) + parent_2(v) \mid}}\end{aligned}$$

128.6.3 FES Output-15 Bus System

Bus no.	FES inputs		FES output
	Power loss index (p.u)	Voltage (p.u)	Candidate sensitivity index
1	0	1	0.08
2	0.1779	0.9713	0.2373

(continued)

(continued)

Bus no.	FES inputs		FES output
	Power loss index (p.u)	Voltage (p.u)	Candidate sensitivity index
3	0.4294	0.9567	0.4203
4	0.954	0.9509	0.75
5	0.3158	0.9499	0.3254
6	0.8365	0.9582	0.75
7	0.8773	0.956	0.75
8	0.4422	0.957	0.4307
9	0.3141	0.968	0.3483
10	0.2063	0.9669	0.2423
11	0.9862	0.95	0.75
12	0.551	0.9458	0.5613
13	0.3602	0.9445	0.3631
14	0.5094	0.9486	0.5135
15	1	0.9484	0.75

128.6.4 Power Loss Comparison-15 Bus System

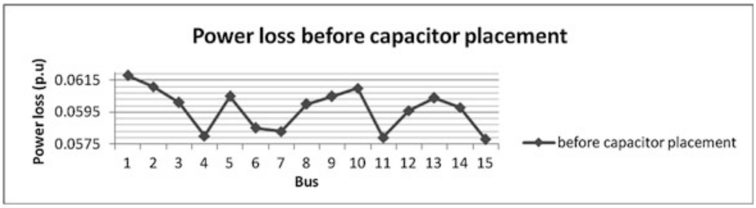

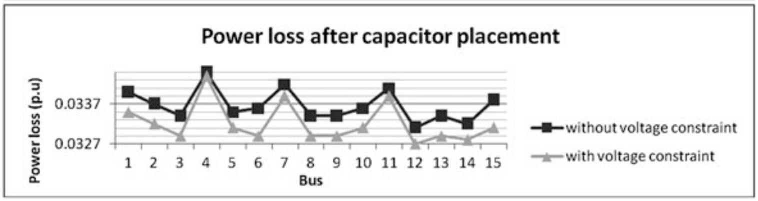

128.7 Average Power Loss and Voltage Comparison

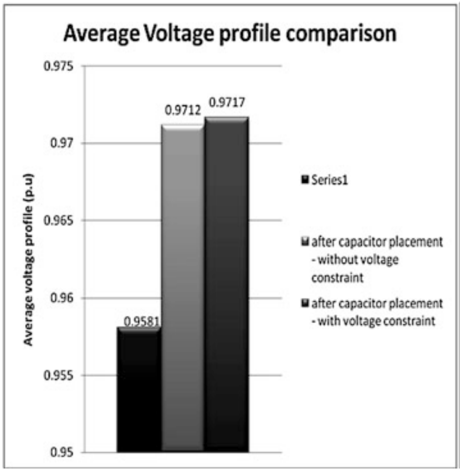

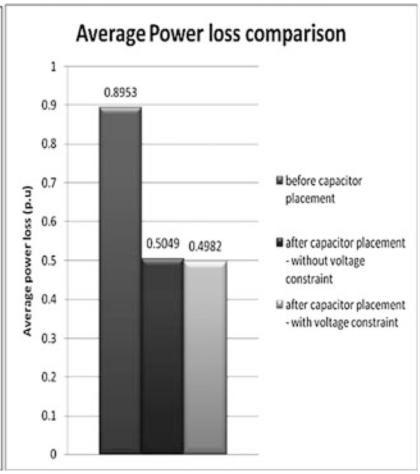

128.8 Savings

$$\text{Max} \cdot S = KP + KF + KE - KC$$

Released demand KP = ΔKP * CKP * IKP	Released feeder capacity KF = ΔKF * CKF * IKF
Savings in energy KE = ΔKE * r	Cost of installation of capacitor KC = Qc * ICKC * IKC

1. ΔKP—Reduced Demand.
2. CKP—Cost of Generation($200/kW).
3. IKP—Annual rate of Generation cost (0.2).
4. CKF—Cost of feeder ($3.43/kVA).
5. ΔKE—Savings in energy.
6. r—Rate of energy ($0.06/kWh)
7. Qc—Total kVar
8. ICKC—Cost of Generator ($4/kVar)
9. IKC—Annual rate of cost of capacitor (0.2).

128.9 Conclusion

Algorithm based on fuzzy logic is developed for capacitor placement in radial distribution system to minimize the line loss. Fuzzy expert system determines the candidate nodes for capacitor placement by striking a compromise between the possible loss reduction from capacitor installation and voltage levels. Simulation study was carried out on sample 15 bus and 34 bus systems, comparative study was done for the system without capacitor and with optimally placed capacitors and the following inferences were made.

1. Locations for optimal capacitor placement were identified.
2. Significant loss reduction is observed.
3. Considerable voltage improvement is achieved.

The voltage constraint is taken into account in this paper which distinguishes this present work, when compared to previous published work.

128.10 Problems Associated with Above Technique

(a) Capacitor siting and sizing is performed under sinusoidal conditions only.
(b) Improvement in stability constraints is not guaranteed at each iteration.
(c) Applied method is not practical for the analysis of real networks due to their great number of calculations.
(d) Over voltage and under voltage once capacitor bank is installed.
(e) Actual power loss being differ from the calculated value.
(f) Optimal placement may not be practically feasible for capacitor placement.

References

1. Masoum MAS, Jafarian A, Ladjevardi M, Fuchs EF, Grady WM (2004) Fuzzy approach for optimal placement and sizing of capacitor banks in the presence of harmonics. IEEE Trans Power Del 19(2):822–829
2. Eajal AA, El-Hawary ME (2010) Optimal capacitor placement and sizing in unbalanced distribution systems with harmonics consideration using particle swarm optimization. IEEE Trans Power Deliv 25(3):1734–1741
3. Abou-Ghazala A (2003) Optimal capacitor placement in distribution systems feeding nonlinear loads. In: Proceedings of IEEE Bologna power technical conference, pp 97–103
4. Muthukumaran E, Karthick Raja T, Praveen Kumar K, Kannan SM (2011) Analysis of capacitor allocation in radial distribution feeder using PSO with voltage constraint. In: 2011 1st international conference on electrical energy systems
5. Carpinelli G, Varilone P, Di Vito V, Abur A (2005) Capacitor placement in three-phase distribution systems with nonlinear and unbalanced loads. Proc Inst Elect Eng Gen Trans Distrib 152(1):47–52

6. Hamada MM, Wahab MAA, El-Sayed AHM, Ramadan HA (2006) A new approach for capacitor allocation in radial distribution feeders. Online J Electron Electr Eng (OJEEE) 1 (1):24–29, Reference Number: W09-0006
7. Masoum MAS, Ladjevardi M, Jafarian A, Fuchs EF (2004) Optimal placement, replacement and sizing of capacitor banks in distorted distribution networks by genetic algorithms. IEEE Trans Power Del 19(4):1794–1801
8. Ghosh S, Sherpa KS (2008) An efficient method for load flow solution of radial distribution networks. World Acad Sci Eng Technol 45:700–707

Chapter 129
Vector Control Based Dynamic Voltage Restorer for Fault Ride Through of Doubly Fed Induction Generator

G. Sivasankar and V. Suresh Kumar

Abstract This work presents a control strategy of a dynamic voltage restorer (DVR) to improve the reliability of doubly fed induction generator (DFIG) based wind turbine in case of grid voltage fault. Since wind power contribution is in predominant percentage, maintaining its stability becomes an important issue. The proposed strategy is to use dynamic voltage controller (DVR) to compensate the grid voltage disturbances. The DVR can compensate the faulty line voltage and aid the DFIG wind turbine for a stable operation as demanded in actual grid codes.

Keywords DVR · DFIG · FSIG · Grid fault · Compensation

129.1 Introduction

The wind power integration with power grid has increased significantly. DFIG based wind turbine offer several advantage over fixed speed induction generator FSIG [1, 2]. Advantage includes variable-speed operation, independent control of active and reactive power and its partially rated power converter [3, 4]. It has low converter costs and reduced power losses.

An important problem with induction generator based wind farm is the inability to stay connected to the grid during a fault due to its low voltage ride through capability. Any disturbance such as dip may lead to wind generators outage [5]. In the past the wind power penetration was low in percentage, hence any outage may not affect the system stability [6]. But in recent years wind generation is in rapid expansion and its contribution to grid is as do conventional generation plant. Hence

G. Sivasankar (✉) · V. Suresh Kumar
Department of Electrical and Electronics Engineering, Thiagarajar College of Engineering, Anna University Chennai, Madurai 625015, Tamilnadu, India
e-mail: g.sivasankar@live.in

V. Suresh Kumar
e-mail: vskeee@tce.edu

C. Kamalakannan et al. (eds.), *Power Electronics and Renewable Energy Systems*,
Lecture Notes in Electrical Engineering 326, DOI 10.1007/978-81-322-2119-7_129

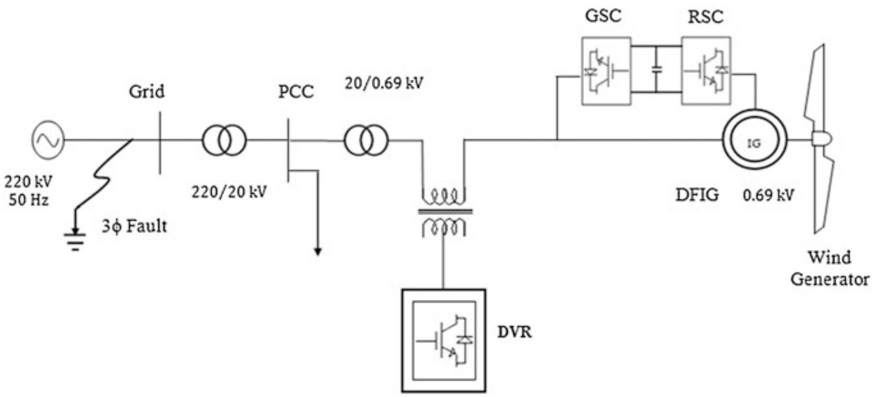

Fig. 129.1 Wind generator connected to grid with DVR protection

any outage of wind generators may lead to power shortage and collapse the stability [7]. The proposed strategy is to use dynamic voltage restorer (DVR) for voltage dip compensation by series voltage injection. Figure 129.1 shows the schematic diagram of DVR protected DFIG-based wind turbine. Vector-controller is used to achieve dynamic control of DVR to improve system performance. It generates continuous control signals for instantaneous current and voltage values to be controlled in a system. This scheme is very efficient in detecting the fault very earlier for proper control and protection.

129.1.1 DFIG

A DFIG is a wound-rotor induction generator, the stator is connected to the grid, and the Rotor windings are fed by a partially rated variable frequency ac/dc/ac converter (VSC). It can handle around 25 % of the machine rated power and the range of the speed variation is 33 % around the synchronous speed [8]. The VSC consists of a rotor-side converter (RSC) and a grid-side converter (GSC) connected back-to-back by a dc-link capacitor. Independent control of both active and reactive powers using the vector control is possible [9]. Both the stator and the rotor in DFIG are able to supply active power.

129.2 Control of the DVR

The considerations for control of the DVR include: reference voltage generation, control of injection voltage, real and reactive power exchange and protection of DVR. A high performance control is required for a grid integration system [10].

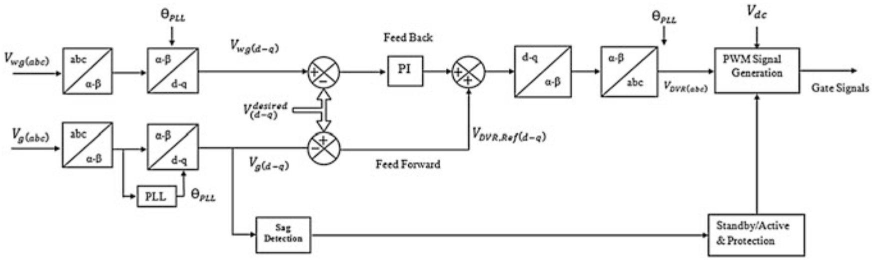

Fig. 129.2 Vector control in the rotating dq reference frame

Hence vector control scheme is employed for control of the DVR as shown in Fig. 129.2.

129.2.1 Reference Voltage Generation

The controller has to generate a accurate reference voltage for successful compensation. The control scheme uses Park (dq0) transformation to obtain d-q component, which is a widely used transformation. It is applied for time-dependent arbitrary three-phase system which is used to decouple variables and refer to common reference frame. The grid voltage may contain negative and zero-sequence components due to unbalanced voltage. For categorizing the sequence components the system voltage is transformed into the synchronous *dq0* reference frame.

The control of injection voltage is done by the combination of grid voltage feed-forward and PI d-q wind generator voltage feedback. Due to the inverter's output filter, there is a difference between the voltage generated with the inverter and the voltage actually injected in series with the line, so a PI regulator is used for equalization. The regulator output is added to DVR reference, serving as feed forward to improve the system response speed and uses the dc-link voltage to calculate the required modulation depth to inject the difference between grid voltage and the reference voltage. Finally, a sinusoidal pulse width modulation (SPWM) is used for the inverter switching.

129.2.2 Real and Reactive Power Exchange

The fault ride through capability of wind generator not only affect by voltage disturbance but also due to power dearth. The proposed DVR is capable of providing real and reactive power support. The uncontrolled shunt rectifiers are used to maintain a strong dc link which acts as a source to meet the real power demand. The reactive power compensation is done by switching the series converter in appropriate phase angle.

129.2.3 DVR Protection System

The series connected DVR inverter may face severe problem due to transients or fault current in the grid. And there is a chance of high in-rush of current reflects into DVR, if the dip is not completely compensated. A proper protection of DVR inverter is one of the important aspects of the design which can be done using the design scheme presented in [11].

129.3 Simulation Result and Discussion

129.3.1 Three-Phase-to-Ground Fault and Mitigation

A three-phase-to-ground fault is evolved near the grid which starts at 500 ms and lasts for about 100 ms causing voltage dip of 60 % at grid is shown in Fig. 129.3a.

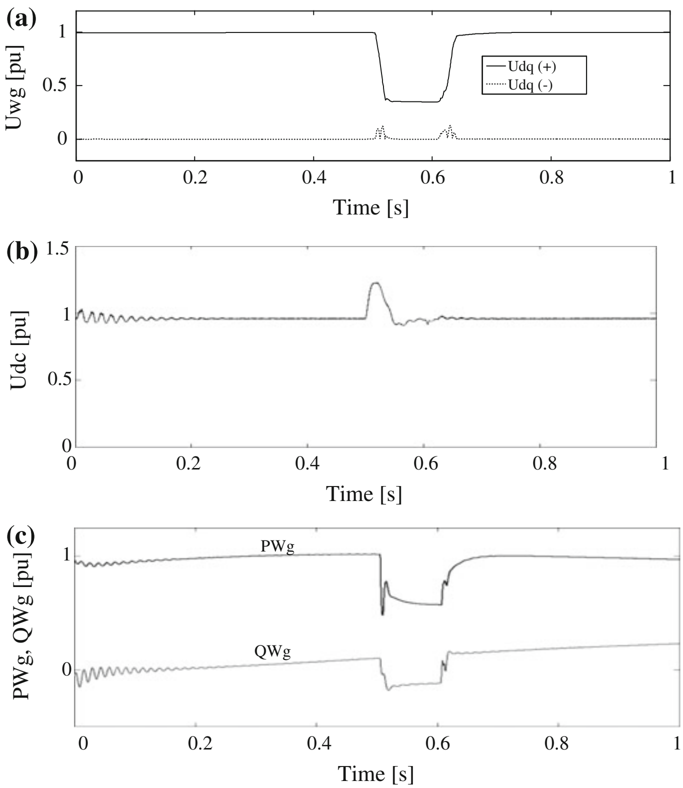

Fig. 129.3 The grid connected wind generator during three- phase-to-ground fault **a** voltage dip **b** Dc voltage of DFIG converter **c** active and reactive power at wind generator

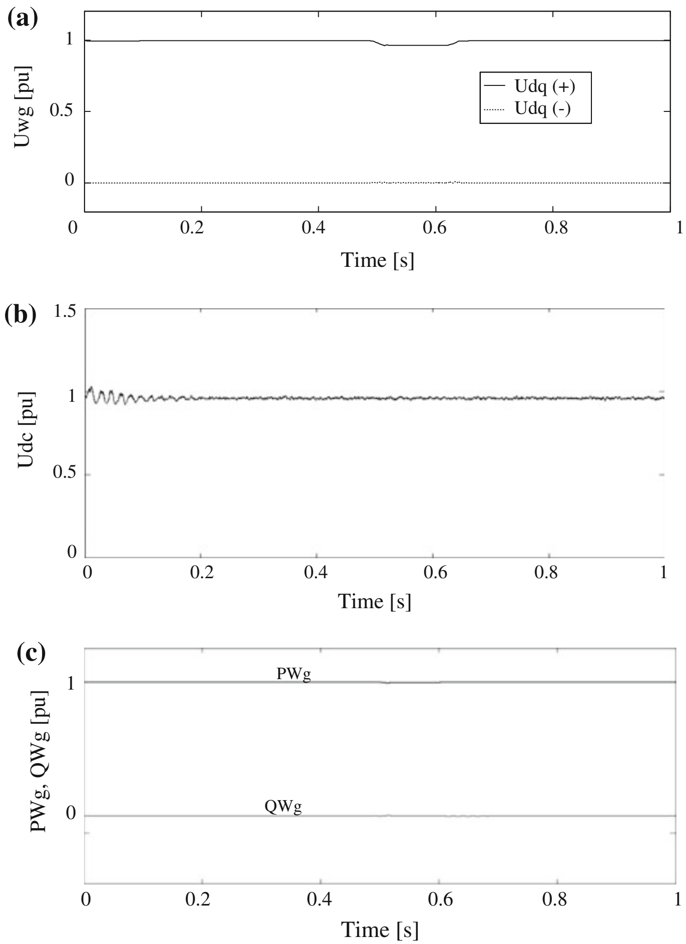

Fig. 129.4 The three- phase-to-ground fault compensation **a** compensated voltage **b** compensated dc voltage **c** active and reactive power at wind generator

The effect of fault on dc link voltage of DFIG converter is as depicted in Fig. 129.3b. The real and reactive power at wind generator side is shown in Fig. 129.3c. Using the vector control strategy, voltage dip magnitude was calculated and DVR compensation voltage is generated as shown in Fig. 129.4a. The dip is compensated by an in-phase insertion of voltage in series with the line. The Fig. 129.4b shows the compensated voltage of the wind generator. The real and reactive power at wind generator bus after compensation of three- phase-to-ground fault is depicted in Fig. 129.4c.

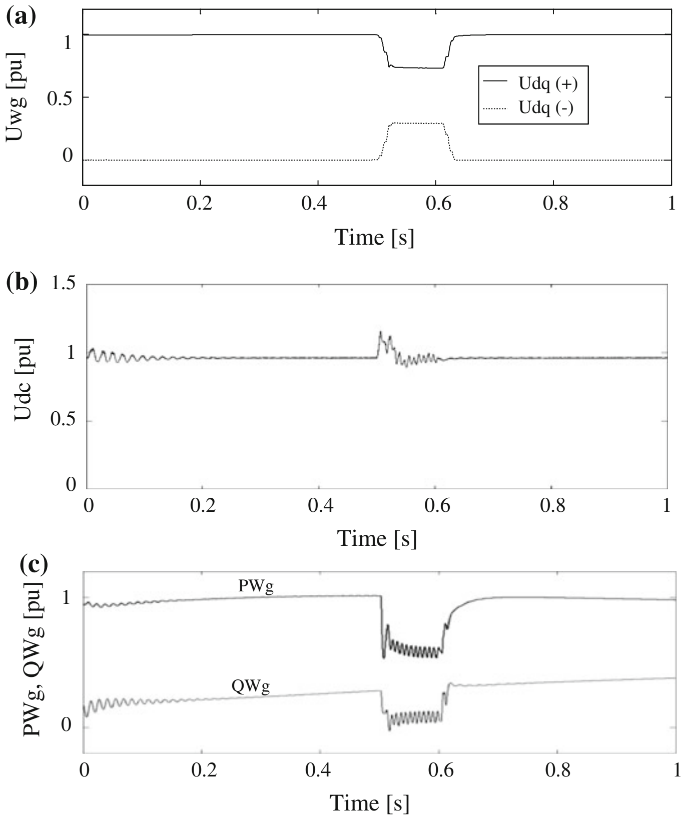

Fig. 129.5 The grid connected wind generator during phase-to-phase fault **a** voltage dip **b** Dc voltage of DFIG converter **c** active and reactive power at wind generator

129.3.2 Phase-to-Phase Grounded Fault and Mitigation

Unbalanced dip is realized using phase-to-phase grounded fault near grid. The voltage variation at wind generator is as shown in Fig. 129.5a. The dc link voltage of DFIG converter is as depicted in Fig. 129.5b. The Fig. 129.5c shows the real and reactive power at wind generator bus during the fault. The compensation algorithm was same as the previous section and compensated voltage is shown in Fig. 129.6a. The Fig. 129.6b shows the dc voltage level after the compensation. Real and reactive power at wind generator bus after compensation of phase-to-phase ground fault is show in Fig. 129.6c.

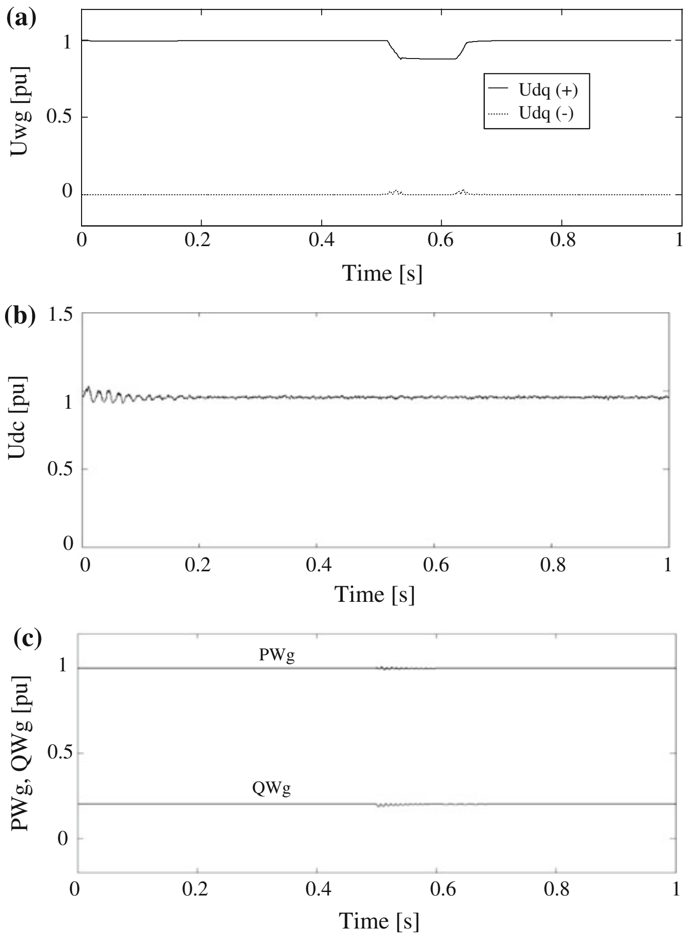

Fig. 129.6 The grid connected wind generator after phase-to-phase fault compensation **a** compensated voltage **b** compensated dc voltage **c** active and reactive power at wind generator

129.4 Conclusion

The proposed DVR can recover the wind generator from voltage disturbances and grid fault. Hence fault ride through capability of the DFIG based wind farm is improved with the aid of a DVR. The wind generator is able to remain connected to the grid without loss of stability and guarantee the reliability of the system. It affords the stable operation for the DFIG wind turbine system under different types of grid faults. The proposed control scheme can also limit the fault current and protect the wind generator from destruction. The matlab results of DFIG model and a DVR control strategy demonstrates the viability of the proposed scheme.

The results show that the control technique is very effective and yield excellent compensation for voltage dip and associated problems.

References

1. Muller S, Deicke M, De Doncker RW (2002) Doubly fed induction generator systems for wind turbines. IEEE Ind Appl Mag 8(3):26–33
2. Pena R, Clare JC, Asher GM (1996) Double fed induction generator using back-to-back PWM converter and its application to variable speed wind-energy generation. Proc Inst Elect Eng B 143(3):231–241
3. Yamamoto M, Motoyoshi O (1991) Active and reactive power control for doubly-fed wound rotor induction generator. IEEE Trans Power Electron 6(4):624–629
4. Kayikci M, Milanovic J (2007) Reactive power control strategies for DFIG based plants. IEEE Trans Energy Convers 22(2):389–396
5. Sun T, Chen Z, Blaabjerg F (2003) Voltage recovery of grid-connected wind turbines after a short-circuit fault. In: Proceedings of IEEE international symposium industrial Electronics, Roanoke, Virginia, pp 2723–2728
6. Nunes MVA, Lopes JAP, Zurn HH, Bezerra UH, Almeida RG (2004) Influence of the variable-speed wind generators in transient stability margin of the conventional generators integrated in electrical grids. IEEE Trans Energy Convers 19(4):692–701
7. Bollen MHJ, Häger M (2005) Impact of increasing penetration of distributed generation of the number of voltage dips experienced by end-customers. In: Presented at the 18th international conference electricity distribution, Turin, Italy, June 6–9 2005
8. Tapia A, Tapia G, Ostolaza JX, Saenz JR (2003) Modeling and control of a wind turbine driven doubly fed induction generator. IEEE Trans Energy Convers 18(2):194–204
9. Lei Y, Mullane A, Lightbody G, Yacamini R (2006) Modeling of the wind turbine with a doubly fed induction generator for grid integration studies. IEEE Trans Energy Convers 21 (1):257–264
10. Nielsen JG, Newman M, Nielsen H, Blaabjerg F (2004) Control and testing of a dynamic voltage restorer (DVR) at medium voltage level. IEEE Trans Power Electron 19(3):806–813
11. Newman MJ, Holes DG (2002) An integrated approach for the protection of series injection inverters. IEEE Trans Ind Appl 38(3):679–687

Chapter 130
Design of PSO-Fuzzy MPPT Controller for Photovoltaic Application

J. Prakash, Sarat Kumar Sahoo, S. Prabhakar Karthikeyan and I. Jacob Raglend

Abstract This paper focus on modeling and simulation of Photovoltaic (PV) system by using improved mathematical model. Improved mathematical model which is used to study the changes in different parameter and effects on the PV array such as operating temperature and solar irradiation level improved. In this paper PSO-Fuzzy algorithm is proposed for MPPT control. The proposed algorithm will find the suitable duty ratio in order to maximize the power output of DC-DC converter. The proposed PSO-Fuzzy MPPT controller can work in the maximum power point for the complete range of solar data (temperature and solar irradiance level).

Keywords Photovoltaic (PV) · Maximum power point tracking (MPPT) · Particle swarm optimization (PSO)

130.1 Introduction

The output characteristics of PV Panel depend upon surrounding temperature and illumination intensity. Each output characteristic has a unique Maximum Power Point (MPP) where the maximum power. The purpose of a maximum power point

J. Prakash (✉)
Department of Electrical and Electronics Engineering, R.M.K. College of Engineering and Technology, Chennai, Tamil Nadu, India
e-mail: prakash_ies@yahoo.co.in

S.K. Sahoo · S.P. Karthikeyan
School of Electrical Engineering, VIT University, Vellore, Tamil Nadu, India
e-mail: sksahoo@vit.ac.in

S.P. Karthikeyan
e-mail: spk25in@yahoo.co.in

I.J. Raglend
NI University, Kanyakumari, Tamil Nadu, India
e-mail: jacobraglend@rediffmail.com

C. Kamalakannan et al. (eds.), *Power Electronics and Renewable Energy Systems*, Lecture Notes in Electrical Engineering 326, DOI 10.1007/978-81-322-2119-7_130

tracker (MPPT) is to make certain photovoltaic panel runs at its maximum efficiency by keeping it operating at the MPP, regardless of changes in external conditions. An MPPT system consists of a buck or boost DC-DC converter to regulate the voltage and current at the load. It can be achieved by various conventional MPPT algorithms [1, 2].

In practical PV system, the MPPT Control is widely used the Perturb-and-observe (P&O) method for maximum power tracking due to its high reliability, simple implementation, and best tracking efficiency [3–6]. But the main demerit of this P&O method is operating the system by slow trial and error process at the maximum power point, and thus the PV arrays is not fully utilize the solar energy. However, other MPPT algorithms have use extensive calculations, online sensed data or special circuit configurations.

The proposed PSO-Fuzzy algorithm is a simplify version of MPPT algorithm it is to track global MPP even under any change in environmental conditions. The main advantage of proposed PSO-Fuzzy algorithm is to find the global MPP to maximize the generated power from the PV source. It is applicable to large scale PV system.

130.2 Modeling of Photo Voltaic Arrays

In practical arrays consist of number of photovoltaic cells which is connected in series and parallel. To get a maximum current the cells are connected in parallel similarly in order to maximize the output voltage the cells are connected in series. The basic equation requires additional parameters by the observation of the characteristics at the terminals of the photovoltaic array. So it can be expressed [2, 7, 8, 9] as

$$I = I_{\mathrm{pv}} - I_o\left[e^{\left(\frac{V+R_sI}{V_ta}\right)} - 1\right] - \frac{V+R_sI}{R_p} \tag{130.1}$$

The characteristic of the PV devices depends on the internal characteristics of the device (R_s, R_p) and on peripheral influences such as temperature and irradiation level [9]. It can be expressed in Eq. (130.2).

$$I_{\mathrm{pv}} = \left(I_{\mathrm{pv,n}} + K_I\Delta T\right)\frac{G}{G_{\mathrm{n}}} \tag{130.2}$$

where,

I_{pv} is the PV current at the nominal condition (at 25 °C and 1,000 W/m^2)

$$\Delta T = T - T_n$$

[T and T_n the actual and nominal temperatures (K)]
G is the irradiation on the device surface (W/m^2), and
G_n is the nominal irradiation (W/m^2).

130.2.1 Simulation Model of PV Array

The equivalent circuit model of photovoltaic array can be simulated by using MATLAB/simulink environment (Fig. 130.1). In the system considered, there are 48 numbers of solar array (TITANS6_60) for 1 kW power generation. The panels are arranged in two parallel combination of Nss = 6 (series) and Npp = 4 (parallel) manner to get a required current and voltage ratings. The parameters of solar panel are given as input to the simulink model to plot and analyse the output characteristics of proposed system.

Simulation results shown in Figs. 130.2 and 130.3 represents I-V and P-V curve for different temperature levels at 1,000 W/m^2.

I-V and P-V Curve shown in Figs. 130.4 and 130.5 are plotted for different irradiation levels at 25 °C. These figures clearly show how the dependency of output current I and output voltage V on temperature and insolation translate into a dependency of the output power on the same two parameters. These simulation results provide the knowledge of designing the MPPT controller with the proposed algorithm.

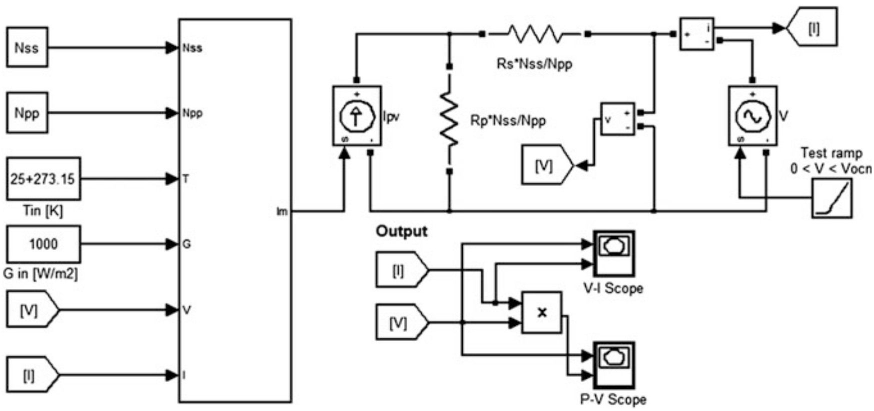

Fig. 130.1 Generalized simulation model of a PV system

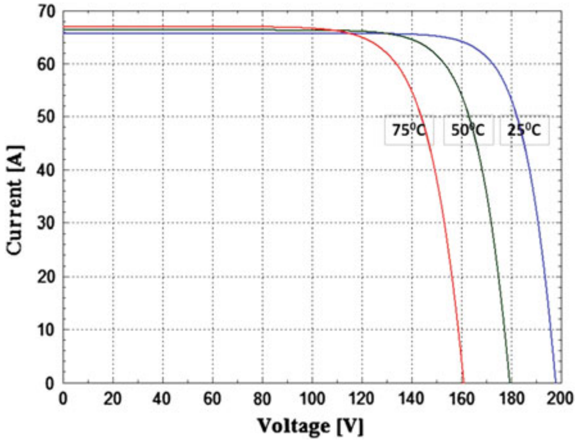

Fig. 130.2 I-V curve for different temperature level at 1,000 W/m^2

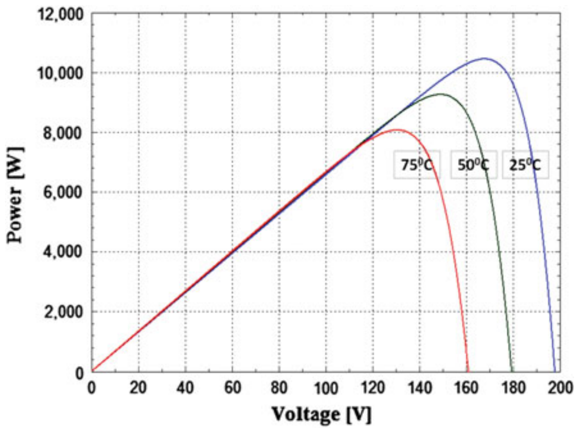

Fig. 130.3 P-V curve for different temperature levels 1,000 W/m^2

130.3 Boost Converter Design

The typical DC-DC boost converter is shown in Fig. 130.6 where the input voltage variation V_{in}(min) = 50 V is obtained when the system connected with load as indicated in Table 130.1 and V_{in}(max) = 74 V of open circuit value from experimental data of a proposed system configuration. Nominal output voltage (V_{out}) and maximum output current (I_{out}) of a Boost converter is to be fixed as 230 V and 5 A respectively.

Minimum and maximum duty ratio for the boost converter switch (SW) D(min) is 66.36 % and D(max) is 77.27 % are determined from Eqs. (130.3) and (130.4).

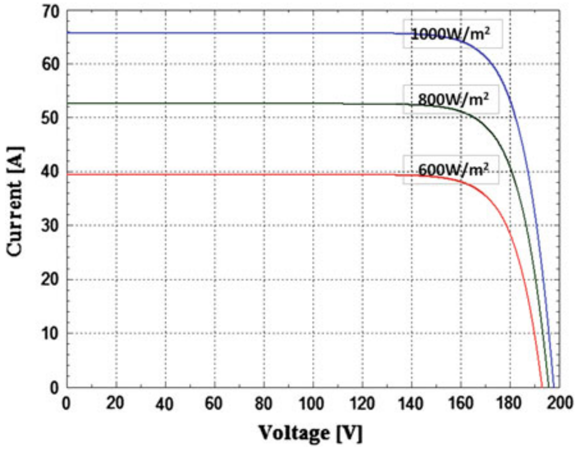

Fig. 130.4 I-V curve for different irradiation levels at 25 °C

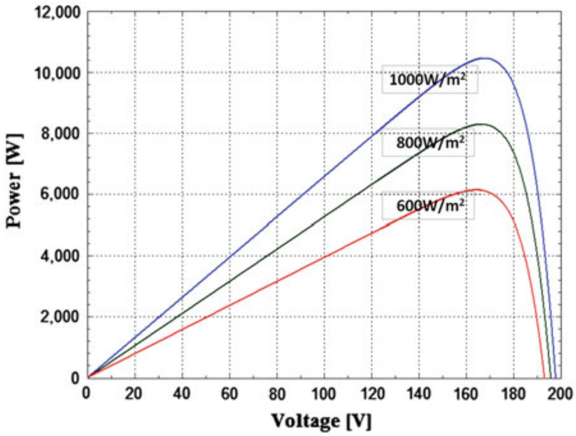

Fig. 130.5 P-V curve for different irradiation levels at 25 °C

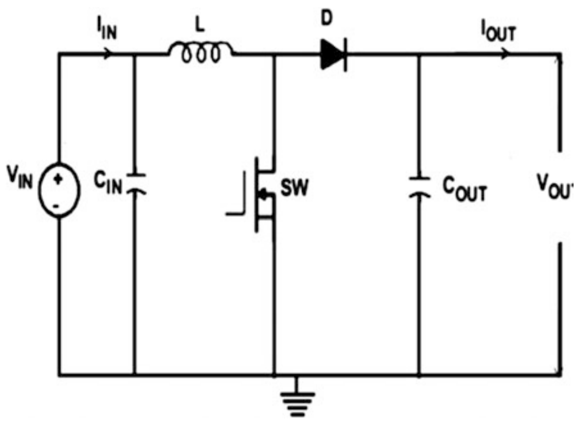

Fig. 130.6 DC-DC boost converter

Table 130.1 Experimental data of 1 kW PV system

Temp (°C)	Irradiation (W/m^2)	Panel output voltage (V)
26.3	250	61.5
27.2	520	66.2
28.6	630	69.4
28.9	640	63.4
29.0	650	57.1
29.8	570	54.6

The nominal switching frequency of the converter switch is considered as f_{sw} = 20 kHz.

$$D(\min) = 1 - \left(\frac{V_{i\max}}{V_{0\min}}\right) \tag{130.3}$$

$$D(\max) = 1 - \left(\frac{V_{i\min}}{V_{0\max}}\right) \tag{130.4}$$

130.4 Implementation of PSO-Fuzzy Algorithm

130.4.1 Particle Swarm Optimization

Particle Swarm optimization method is a meta-heuristic optimization algorithm which is proposed for multidimensional functions. PSO algorithm need not required any objective or error function it can be obtain the best solution by itself.

The PSO algorithm has predefined restriction in order to fly a swarm of particles on the search space. To evaluate the performance of each particle by using objective function and also considering the minimization problem, for this case, the more performance is given for the particle with lower value. From the iterations, the best performance of each particle is stored in its memory and called personal best (P_{best}). It is determines the global best (G_{best}). By using the concept of P_{best} and G_{best}, the velocity of each particle is updated in (130.4). About PSO and Fuzzy control method is discussed in [10–12].

$$V_i^{k+1} = w \times V_i^k + C_1 \times R_1 \times \left(P_{best} - P_i^k\right) + C_2 \times R_2 \times \left(G_{best} - P_i^k\right) \tag{130.4}$$

where,

Vi^{k+1}	Particle velocity at current iteration (k + 1)
Vi^k	Particle velocity at iteration k
R_1, R_2	random number between [0, 1]
C_1, C_2	acceleration constant

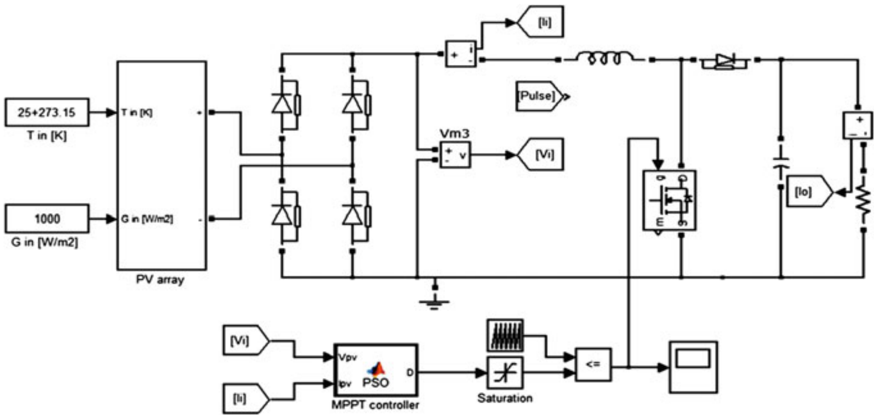

Fig. 130.7 Simulation model of PV array with PSO-Fuzzy MPPT controller

After this, particles fly to a new position:

$$P_i^{k+1} = P^k + V_i^{k+1}$$

130.4.2 Design of PSO-Fuzzy MPPT Controller

The Proposed PV system with PSO-Fuzzy algorithm is tested using MATLAB/ Simulink as shown in Fig. 130.7. The output of the PV array is given as input to the PSO-Fuzzy controller. The proposed controller will calculate the actual power input to the converter. The algorithm is effectively the changes the duty ratio of the converter from 66.36 to 77.27 % according to the load variation and also to the changes in physical parameters such as temperature and irradiation levels. It operates the converter around the maximum power point. It improves the efficiency of the boost converter as well as overall performance of the PV system.

The proposed PSO-Fuzzy MPPT controller is operating the system around Maximum power point. The simulation results shown in Figs. 130.8 and 130.9 indicate the remarkable operating points of a proposed PV system at 25 °C and 1,000 W/m^2.

130.5 Results and Discussions

The proposed PSO-FUZZY MPPT is shown in Fig. 130.11. The controller tracks the maximum power of the Panel under fast varying climate conditions. The results show the effectiveness of the PSO-Fuzzy algorithm. It tracks the MPP of the panel with in 10 µs. The result is presented in Figs. 130.10 and 130.11.

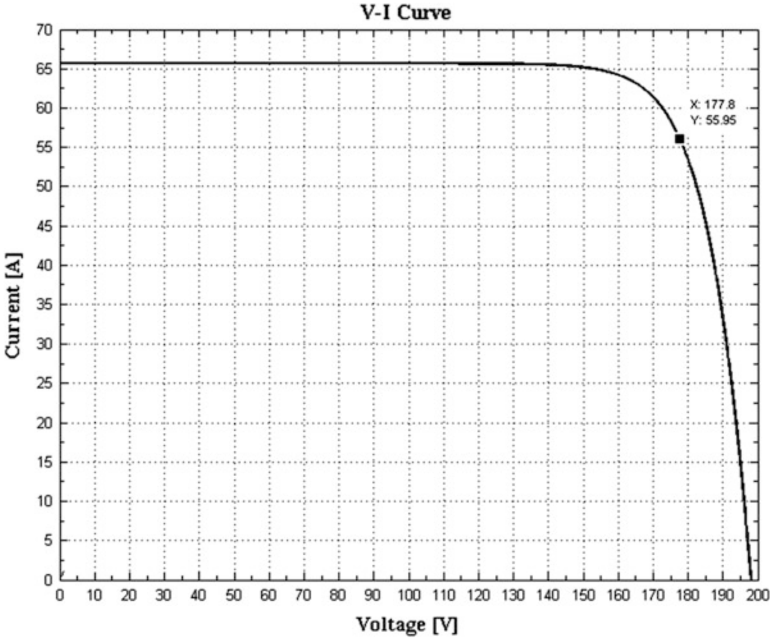

Fig. 130.8 I-V curve at 25 °C and 1,000 W/m^2

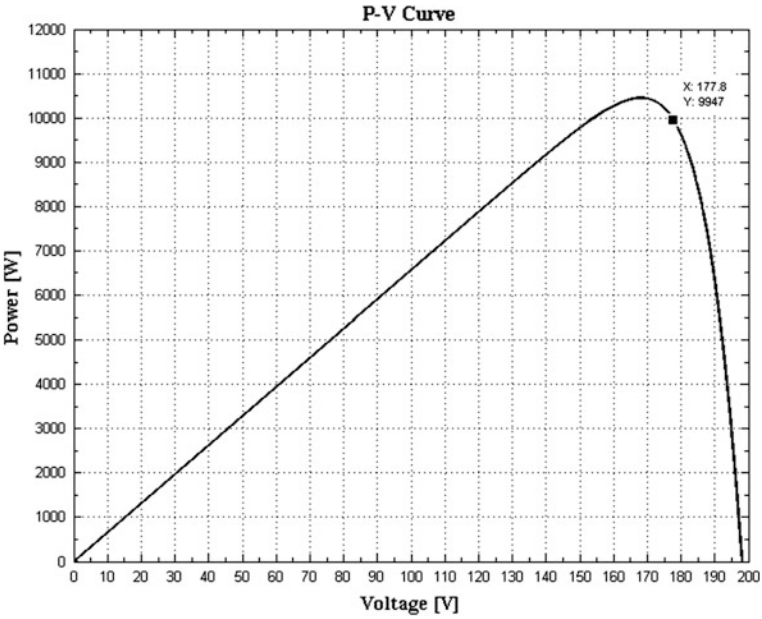

Fig. 130.9 P-V curve at 25 °C and 1000 W/m^2

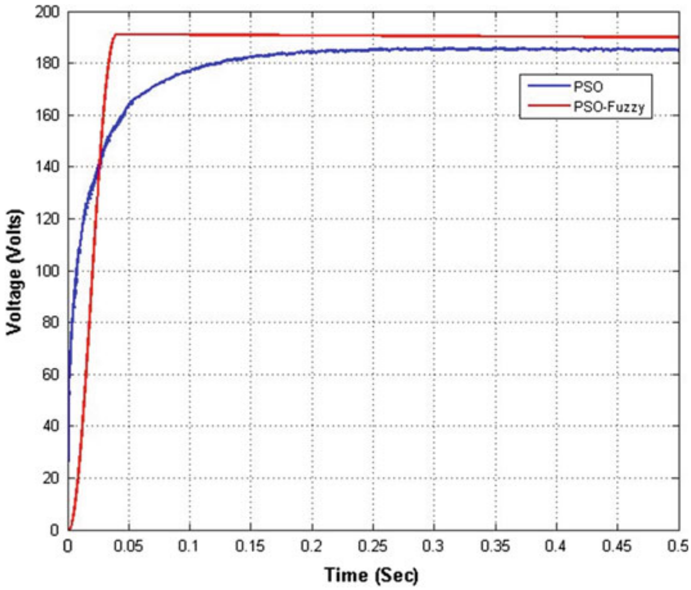

Fig. 130.10 Output voltage of the proposed converter under 250 W/m^2

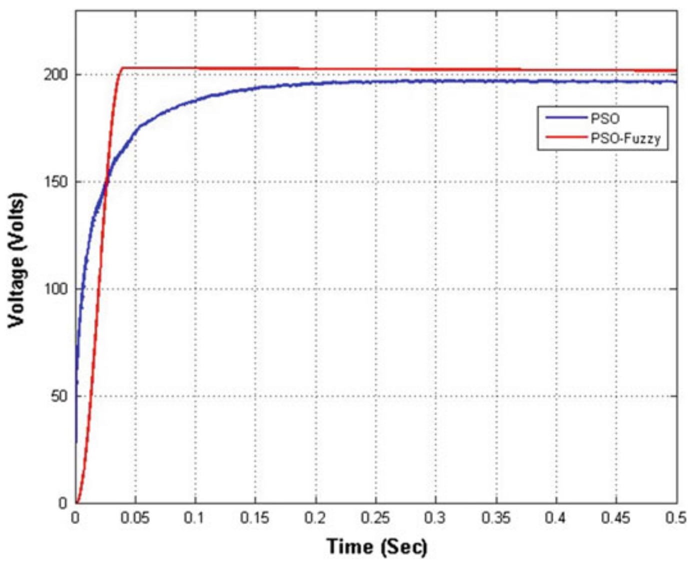

Fig. 130.11 Output voltage of the proposed converter under 500 W/m^2

130.6 Conclusion

This paper proposes generalized simulation model for photo voltaic array to be used in MATLAB-Simulink GUI environment. The proposed model has a common structure. So the model has been used to develop a 10 kW power generation along with boost converter and PSO-Fuzzy MPPT controller. The output power characteristic of PV module is thoroughly investigated. The method is very simple and the experimental results show that proposed PSO-Fuzzy MPPT method is able to considerably increase the efficiency of the PV system during rapidly changing irradiance. It shows the effectiveness of the algorithm around MPP. This will improve the overall performance of the photovoltaic system under different temperature and irradiation levels. This model will be used to study the influence of PV array as a part of proposed hybrid power system which consist of PV and Wind with batteries as a storage device.

References

1. Ahmed EM, Shoyama M (2011) Variable step size maximum power point tracker using a single variable for stand-alone battery storage PV systems. J Power Electron 11(2):218–227
2. Sridhar R, Jeevananathan, Selvan NT, Banerjee S (2010) Modeling of PV array and performance enhancement by MPPT algorithm. Int J Comput Appl 7(5):35–39
3. Hernanz JAR, Martín JJC, Belver IZ, Lesaka JL, Guerrero Z, Puelles Pérez E (2010) Modeling of photovoltaic module. In: International conference on renewable energies and power quality (ICREPQ'10), 23 Mar 2010
4. Jiang Y, Qahouq JAA, Batarseh I (2010) Improved solar PV cell matlab simulation model and comparison. In: Proceedings of IEEE international symposium on circuits and systems, Paris, pp 2770–2773
5. Mahdi AJ, Tang WH, Wu QH (2010) Improvement of a MPPT algorithm for PV systems and its experimental validation. In: International conference on renewable energies and power quality (ICREPQ'10), Granada (Spain), 23–25 Mar 2010
6. Al-Diab A, Sourkounis C (2010) Variable step size P&O MPPT algorithm for PV systems. In: 12th international conference on optimization of electrical and electronic equipment, OPTIM 2010
7. El Shahat A (2005–2010) PV cell module modeling and ann simulation for smart grid applications. J Theor Appl Inf Technol 9–20
8. Ren B, Sun X, Tong X, Zhong Y (2010) Maximum power point tracking method based on the intermittent step-varied search for PV array 978-1-4244-4813-5/10/2010 IEEE
9. Villalva MG, Gazoli JR, Filho ER (2009) Comprehensive approach to modeling and simulation of photovoltaic arrays. IEEE Trans Power Electron 24(5):1198–1208
10. Fu Q, Tong N (2011) A new fuzzy control method based on PSO for maximum power point tracking of photovoltaic system. In: International conference on computer science and network technology (ICCSNT-2011), vol 3. ISBN no: 978-1-4577-1586-0, 24–26 Dec 2011
11. Bogaraj T, Kanakaraj J (2012) Development of MATLAB/SIMULINK models for PV and wind systems and review on control strategies for hybrid energy systems. Int Rev Model Simul 5(4):1701
12. Zaraki A, Othman MFB (2009) Implementing particle swarm optimization to solve economic load dispatch problem. In: International conference on soft computing and pattern recognition 2009

Chapter 131
Voltage Control of a STATCOM at a Fixed Speed Wind Farm Under Unbalanced Grid Faults Using Fuzzy Logic Technique

B. Ashok Kumar, N. Kamaraj and C.K. Subasri

Abstract Wind farms equipped with squirrel cage induction generator can be improved with the help of Flexible Alternate Current Transmission System device. Power quality problems will arise with increasing wind power penetration in power system. Voltage sag is an important power quality issue is reduction of RMS voltage lasting for very short duration which may cause serious problems to the system. These voltage fluctuations can be eliminated using advanced reactive power compensator devices. In this work one such Static Compensator (STATCOM) device is analyzed for wind farms using Synchronous Reference Frame theory. The performance of the wind farm system is verified using PI controller and Fuzzy logic controller. The proposed system is analyzed using MATLAB and simulation studies show the effective influences of the STATCOM on the improvement of voltage profile and make the wind farm system to be in service even under fault conditions. It also shows that fuzzy logic controller gives better result when compared to PI controller.

Keywords STATCOM · PI controller · Fuzzy logic controller · Voltage sag · Power quality

B.A. Kumar (✉) · N. Kamaraj · C.K. Subasri
Department of Electrical and Electronics Engineering,
Thiagarajar College of Engineeering, Madurai, Tamil Nadu, India
e-mail: ashokudt@tce.edu

N. Kamaraj
e-mail: nkeee@tce.edu

C.K. Subasri
e-mail: ssmk.2013@gmail.com

C. Kamalakannan et al. (eds.), *Power Electronics and Renewable Energy Systems*,
Lecture Notes in Electrical Engineering 326, DOI 10.1007/978-81-322-2119-7_131

131.1 Introduction

Renewable energy sources grow rapidly in the present scenario. Solar, wind, tidal, hydro each sources supply energy to meet growing demand. Due to environmental impact and less supply of fossil fuels, wind energy [1] grows very faster at present. To improve power production, wind farm is made to integrate with grid. Penetration of these large wind farms in power system results in power quality [2] issues. Power quality problem [3] which is caused due to the influence of power grid with wind turbine is voltage sag, voltage swell, harmonics, flicker etc. In the fixed speed wind generator, change in speed of wind affects torque, power which leads great damage to fluctuations of voltage. Induction generator coupled with wind turbine starts to consume large reactive power from power grid. This causes shortage of reactive power which is the major reason for voltage dip/voltage sag. Sometimes active power in the system gets increases that may result in voltage swell. Third generation is based upon Voltage Source Converter devices such as STATCOM. As SVC is thyristor based devices it has more switching losses, so STATCOM [4] is proposed as control scheme in wind generator integrated with power grid. STATCOM is defined as Static Synchronous Compensator static means solid state switching device with no rotating components, synchronous means an ideal synchronous machine with three phase voltage sinusoidal at fundamental frequency.

To improve efficiency, robustness and to meet grid code requirements [5] Fuzzy logic technique has been implemented and better results are obtained when compared to conventional PI technique.

There are few techniques in [6–9] which are introduced to improve power quality without additional device in wind generator and also double fed based induction generator (DFIG) [10]. It is kind of variable speed generator which is used widely but has the disadvantage of high cost and more losses. So in many countries fixed speed generator is used still which has less cost and easy maintenance with additional device using STATCOM [11]. Matlab/simulink model is developed for wind farm system and analysis is presented with PI and Fuzzy logic controller [12, 13].

131.2 STATCOM

Static Synchronous Compensator is made up of a shunt transformer, a voltage source converter (VSC), a dc capacitor, a magnetic circuit, and a controller. It generates a set of balanced three phase sinusoidal voltages at the fundamental frequency, with rapidly controllable amplitude and phase angle. The objective of the STATCOM is to regulate the voltage [14] at the PCC rapidly in the desired range and keep its dc link voltage constant. It can enhance the capability of the wind turbine to ride through transient disturbances in the grid [15]. STATCOM with wind turbine driven Induction Generator connected directly to the grid. STATCOM is widely used in grid

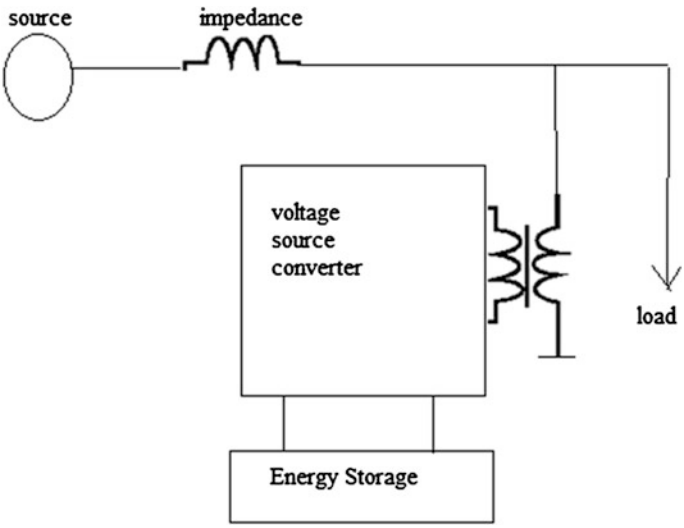

Fig. 131.1 Schematic diagram of STATCOM

connected wind turbine for power quality improvement [16]. The VSC converts the dc voltage across the storage device into a set of three-phase ac output voltages. Figure 131.1. Clearly describes the basic structure of STATCOM.

The negative sequence effect caused by wind turbine on grid can be eliminated by voltage control capability of STATCOM [17]. PI controller [18] is used as conventional technique and comparison is made with fuzzy logic controller [19].

131.3 Control Strategy

Control strategy is based upon Synchronous Reference Frame Theory. The synchronous frame method [20] uses Park's transformation to transform the three phase ac quantities into the synchronous rotating direct, quadrature and zero sequence which are dc components and easy to analyze. This method is applicable especially in three phase system. Control algorithm is developed by comparing the reference voltage and fluctuating voltage. This compared signal is passed to PI controller and thus it minimizes the error signal [21]. Therefore PI controller is required to achieve controller performance at very faster rate. According to reference frame transformation theory, reference signal detected [22] is made to transform from stationery frame a-b-c to rotator frame d-q axis. PI controller is used to produce required signal for Pulse Width Modulation (PWM) from rotating frame signal.

In PI controller the gain values are adjusted to get optimum performance. These gain values can be tuned based upon Ziegler Nichol's tuning or even by using Fuzzy controller [23]. This technique uses sinusoidal PWM. Figure 131.2 shows the

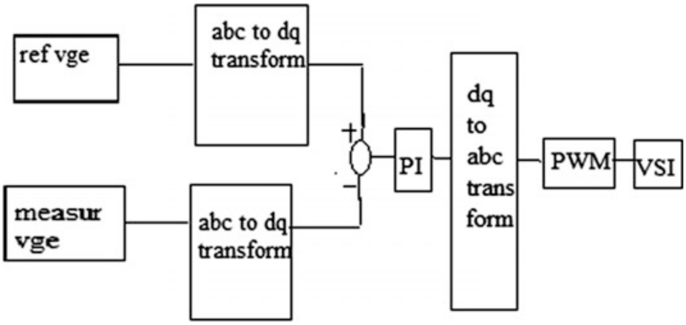

Fig. 131.2 Block diagram of controller

basic control algorithm developed. It briefly describes about importance of reference frame theory and PI controller. In Pulse Width Modulation technique, suitable signal from PI controller has been generated as control signal which makes to produce desire reference signal so that corresponding carrier signal is produced. So that appropriate pulse signal is created which acts as input to power switch and Voltage Source Converter.

131.3.1 Fuzzy Logic Control

The fuzzy logic controller is used by replacing PI controller. It is a tool which deals with uncertainty and provides a technique to deal with imprecision (Fig. 131.3).

Stage 1: Error Calculation

Error is calculated as difference between reference and fluctuated voltage. Error rate is denoted as Vref–Vfluctuated.

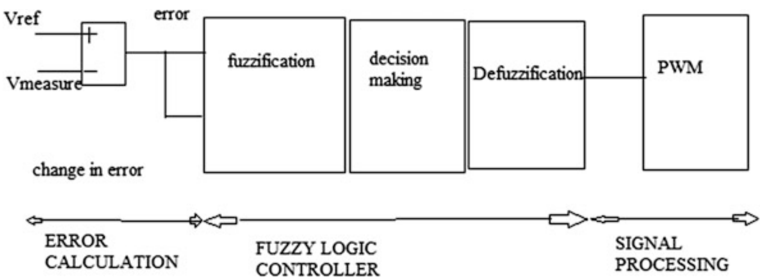

Fig. 131.3 Block diagram of fuzzy logic controller

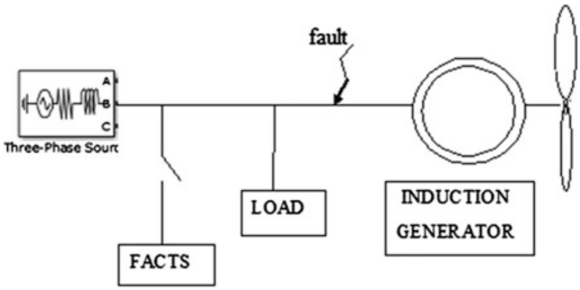

Fig. 131.4 Block diagram of wind farm interconnected with power grid

Stage 2: Fuzzification

In Fuzzification the crisp quantities are converted to fuzzy. The membership functions is defined as error and change in error as Positive Big (PB), Positive Small (PS), Positive Medium (PM), Zero, Negative Small (NS), Negative Medium (NM), Negative Big (NB).

Stage 3: Decision Making

There are 49 rules for fuzzy controller. The output is based on the evaluation of rules by the fuzzy sets and fuzzy logic operation.

In this work Wind farm coupled with induction generator is made to integrate with power grid (Fig. 131.4). The wind speed is kept as 12 m/s which are considered to be nominal value. The mechanical torque is produced from turbine which is made to couple with Induction Generator [24]. The fault on wind farm side causes negative effect in power grid. STATCOM [25] controller is installed across grid side to protect grid from negative effect caused by wind turbine.

131.4 Simulation Results

The parameters used in simulation are given in Table 131.1. It is used to verify the effectiveness of the STATCOM with PI and fuzzy logic controller.

Case 1: Figs. 131.5, 131.6 and 131.7 shows voltage sag in the grid side as this work mainly focuses on grid side.

Figure 131.7 represents that during fault time there is severe dip in reactive power along grid.

Case 2: The figure shows the simulation carried out with compensation technique using STATCOM. In the proposed system, the sag occurs due to the three phase fault applied in the time interval of 0.03–0.08 s.

Figure 131.8 depicts STATCOM provides reactive power compensation and make the system to maintain voltage even under fault condition.

Figures 131.9 and 131.10 represents real power and reactive power across grid after compensation with the help of STATCOM. The curve becomes smooth after fault clearing time about 0.08 s.

Table 131.1 Simulation parameters

Parameters	Values used in the simulation models
Main supply voltage	480 V
Line frequency	60 Hz
Source impedance	Ls = 16.59 mH
	Rs = 0.8928 Ω
Transformer turns	1:1
PI controller	$K_p = 0.1$, $K_i = 2$
Load	10 MW, 12 MVAR
Inverter	IGBT based 3 arms, 6 pulse, Carrier frequency = 10,000 Hz
Asynchronous generator	Stator resistance = 0.016 Ω
	Voltage = 480 V, Frequency = 60 Hz

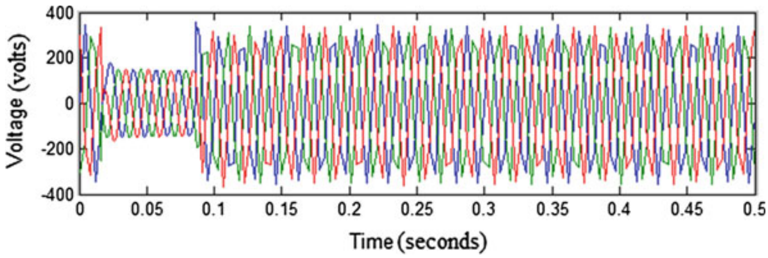

Fig. 131.5 Voltage sag due to three phase fault (0.03–0.08 s)

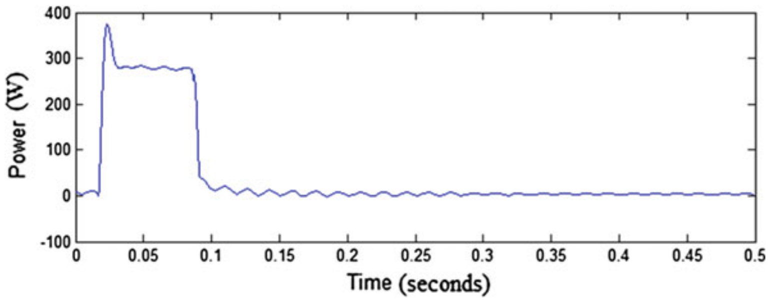

Fig. 131.6 Real power in grid during fault

Case 3: The simulation is carried out using FUZZY LOGIC technique and the improvement has been achieved by replacing PI controller (Figs. 131.11 and 131.12).

Due to its easy and fast adaptive nature in fuzzy the oscillations has been completely removed and better real power is achieved than PI controller (Fig. 131.13).

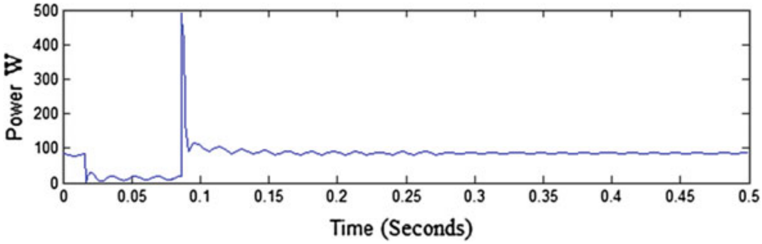

Fig. 131.7 Reactive power in grid during fault before compensation

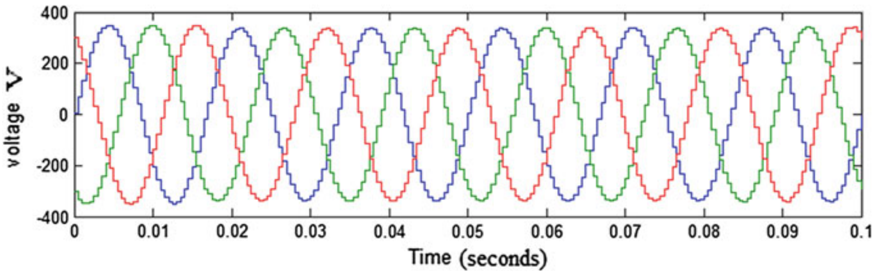

Fig. 131.8 Grid voltage after compensation using STATCOM

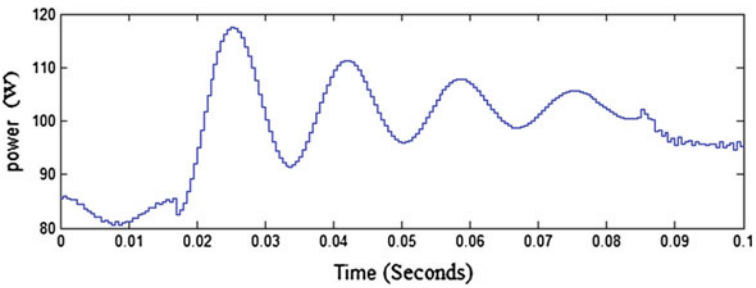

Fig. 131.9 Real power in grid after compensation using STATCOM

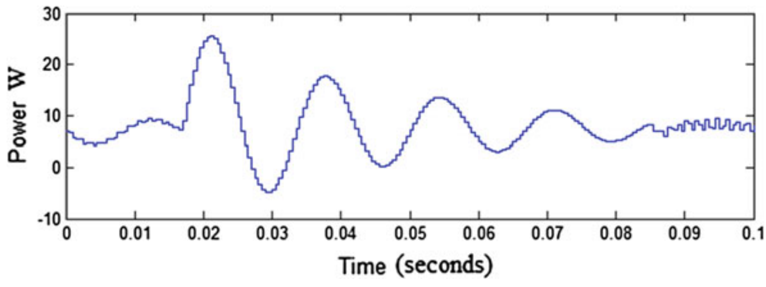

Fig. 131.10 Reactive power in grid after compensation using STATCOM

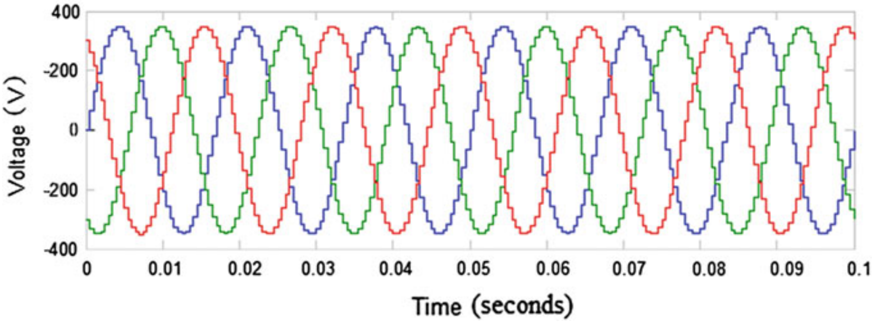

Fig. 131.11 Voltage in grid using fuzzy logic technique

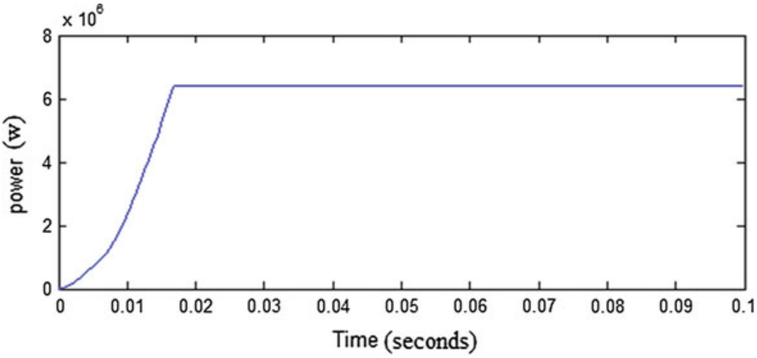

Fig. 131.12 Real power in grid using Fuzzy logic technique

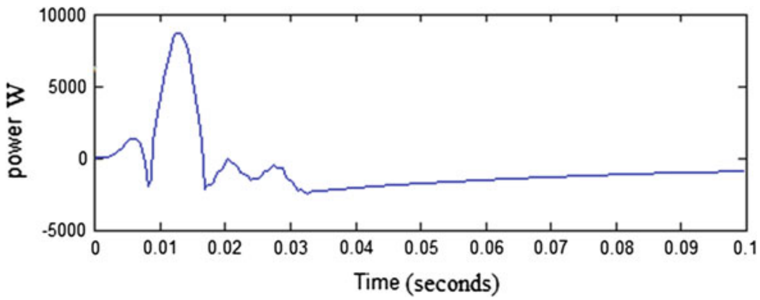

Fig. 131.13 Reactive power in grid using fuzzy logic controller

131.5 Conclusion

In this work, test system is developed using MATLAB Simulink software. The proposed system with PI controller can handle the system with fault and eliminate voltage sag by reactive power compensation. The simulation result shows that STATCOM can compensate the voltage sag and support to stabilize the wind farm connected to grid. In the proposed system, FACTS device with PI controller are designed to decrease voltage fluctuations and to improve power quality. The control scheme is further improved by using Fuzzy logic controller and voltage sag is further minimized.

Acknowledgments Authors like to thank the management, Principal and the faculty of EEE Department for the support and suggestions in this work.

References

1. Cardenas R, Molinas M, Rodriguez J (2011) Overview of multi-MW wind turbines and wind parks. IEEE Trans Ind Electron 58(4):1081–1095
2. Tascikaraoglu A, Uzunoglu M, Vural B (2011) Power quality assessment of wind turbines and comparison with conventional legal regulations: a case study in Turkey. Appl Energy 88:1864–1872
3. Bollen HJ (2000) Understanding power quality problems. IEEE Press, New York
4. Molinas M, Soul JA, Undeland T (2008) Low voltage ride through of wind farms with cage generators, STATCOM versus SVC. IEEE Trans Power Electron 23(3):1104–1117
5. Papathanassiou S (2009) A review of grid code technical requirements for wind farms. IET Renew Power Gener 3(3):308–332
6. Ning J (2009) Development of low voltage ride through control strategy for wind power generation using real time digital simulator. In: Power system conference and exposition. IEEE/PES
7. Basu KP, Hafidz SA (2008) Ride through capabilities of load during voltage sag/swell and power interruption with zigzag transformer. In: Innovative technologies in intelligent systems and industrial applications. IEEE conference
8. Li S, Ding M, Wang J, Zhang W (2009) Voltage control capability of SVC with var dispatch and slope setting. Electr Power System 79(5):818–825
9. Mendil B (2010) Contribution to the improvement of voltage profile in electrical network with wind generator using SVC device. Appl Renew Energy 35(1):243–248
10. Zou H, Sun H, Zou J (2007) Fault ride through performance of wind turbine with doubly fed induction generator. In: Industrial electronics and applications, 2nd IEEE conference
11. Molinas M, Fuchs FW (2013) StatCom control at wind farms with fixed speed induction generators under asymmetrical grid faults. IEEE Trans Ind Electron 60(7):2864–2873
12. Al-Kandari AM, Soliman SA (2006) Power quality analysis based on fuzzy estimation algorithm: voltage flicker measurements. Electron Power Energy Syst 28(10):723–728
13. Sivanandam SN, Sumathi S (2007) Introduction to fuzzy logic using MATLAB. Springer, Berlin
14. Murthy GBS (2006) STATCOM-based voltage regulator for self-excited induction generator feeding nonlinear loads. IEEE Trans Electron 53(5):1437–1452
15. Fuchs F, Molinas M (2011) Voltage control of a statcom at a fixed speed wind farm under unbalanced grid faults. In: Proceedings of 37th IEEE, November 2011, pp 979–984

16. Mohod SW, Aware MV (2010) A STATCOM-control scheme for grid connected wind energy systems for power quality improvement. IEEE Syst J 4(3):346–352
17. Ortiz A, Ostrem T, Sulkowski W (2011) Indirect negative sequence voltage control for STATCOM supporting wind farms directly connected to the grid. In: Proceedings of IEEE 37th IECON, November 2011, pp 1903–1908
18. Dosoglu K (2012) Investigation of different load changes in wind farm by using FACTS devices. Appl Energy Convers 93:422–431
19. Ghafori A, Zolghadri MR (2001) Fuzzy controlled STATCOM for improving the power system transient stability. In: IEEE international conference on power system, pp 1178–1185
20. Alepuz S, Busquets-Monge S, Bordonau J, Martinez-Velasco J, Silva C (2009) Control strategies based on symmetrical components for grid-connected converters under voltage dips. IEEE Trans Ind Electron 56(6):2162–2173
21. Boynuegri AR, Tascikaraoglu A, Uzunoglu M, Yumurtac R (2012) Voltage regulation capability of a prototype static VAr compensator for wind applications. Appl Energy 93:422–431
22. Hoffmann N, Lohde R, Thogersen P (2011) A review on fundamental grid-voltage detection methods under highly distorted conditions in distributed power-generation networks. In: Proceedings of the IEEE ECCE, September 2011, pp 3045–3052
23. Benachaiba C, Dib S, Dehini R (2010) Adaptive PI control of dynamic voltage restorer using fuzzy logic. J Electr Eng Theory Appl 1(3):165
24. Cidras J, Feijoo AE (2002) A linear dynamic model for asynchronous wind turbines with mechanical fluctuations. IEEE Trans Power Syst 17(3):681–687
25. Luna A, Medeiros G, Tedorescu R (2010) Control of STATCOM in wind power plants based on induction generators during asymmetrical grid faults. In: Proceedings of the IPEC, June 2010, pp 2066–2073

Chapter 132
Evaluation and Prediction of Contamination Level in Insulators Based on the Leakage Current Characteristics Using Neural Network

A. Sheik Sidthik, A. Raymon and L. Seenivasagam

Abstract This effort demonstrate the serious issues of coastal, industrial and polar region pollutions on insulator surface and their Leakage Current (LC) and flashover voltage on insulator. The disc type porcelain insulator is tested under normal and abnormal conditions for the surface defect near HV electrode and far from HV electrode, with different pollutants such as marine, industrial and polar. The cavity size, location and pollution level decides the flashover performance of the insulator. The test is performed using the standard IEC60507 at artificial test chamber and leakage current is continuously recorded. Finally the recorded leakage current is given as input to Back Propagation Neural Network (BPNN) to predict the level of contamination severity and the test results are compared with normal and abnormal condition.

Keywords LC · BPNN · IEC60507 · ANN · ESDD · NSDD

132.1 Introduction

Generally, the term insulator is used explicitly to refer the insulating supports used to attach electric power distribution or transmission lines to utility poles and transmission towers [1]. Almost in every parts of power system, insulators are the vital part that governs the mechanism of insulation. The major functions of insulators are; to

A.S. Sidthik (✉) · A. Raymon · L. Seenivasagam
Department of EEE, Renganayagi Varatharaj College of Engineering, Sivakasi 626128, Tamil Nadu, India
e-mail: mail2sidthik@gmail.com

A. Raymon
e-mail: raymonrfengineer@gmail.com

L. Seenivasagam
e-mail: seenivasagamhve@gmail.com

C. Kamalakannan et al. (eds.), *Power Electronics and Renewable Energy Systems*,
Lecture Notes in Electrical Engineering 326, DOI 10.1007/978-81-322-2119-7_132

provide sufficient insulation and mechanical support [2]. The optimum performance of power system is attributed using the following parameters; continuity in service and faults incurred in the insulator. In analogous to the faults developed in the insulator, the internal and external defects are archived on the stability criteria of the insulator and the performance can be evaluated by the severity of pollution formed on the insulator surface [3]. The severity of pollution on the insulator depends on the region at which it is implied for service [4, 5]. The different pollution regions like coastal, industrial, polar, agricultural and desert affects the performance of the insulator. The suspected pollutants like salt, cement, ash, sand and dust are transferred and deposited on the insulator surface by wind. This deposition is succeeded by the formation of heavy contamination layer on the insulator surface. The flashover due to contamination layer is influenced by factors like environmental changes, contamination severity, voids, cavity, surface defects and operating voltage [2, 6–9]. In this work, disc type porcelain insulator is selected for investigation. The test results are carried out from light pollution level and the results are used to determine the moderate and heavy pollution level using ANN technique.

132.2 Experimental Setup

The test insulators are suspended inside the test chamber (dimension: 80 × 80 × 80 cm) in vertical manner, which is shown in Fig. 132.1. The test transformer (TEO 100/20) rated voltage is 2 × 0.22/100/0.22 kV. The high voltage end is connected to an AC capacitive voltage divider which records the applied voltage during test.

Fig. 132.1 Experimental setup

Fig. 132.2 Porcelain test insulators. **a** Without defect. **b** Defect near HV. **c** Defect far from HV. The disc type porcelain insulators with the range of 11 kV are involved in artificial pollution test

132.2.1 Test Samples

In this work, three porcelain insulators were subjected based on defect for investigation. The Fig. 132.2 shown the three categories of insulator based on defect, they were made insulator without defect, insulator with surface defect near HV electrode and insulator with defect far from HV electrode.

132.2.2 Test Methodology

An Artificial solid layer pollution test is carried out in the high voltage laboratory based on IEC 60507 standard [7]. In the beginning of test, the distilled water and clean clothes are used to remove the dust and water content from the surface of the test insulator by washing and cleaning process. The artificial pollutions are prepared by mixing kaolin and NaCl with above mentioned ratio for coastal region pollution test and the cement is used for industrial pollution test. Initially the weight of the kaolin, NaCl and cement were measured by the weight gauge. This mixture was coated on the separate insulator surface and allowed to dry for 24 h. For experiment artificially polluted insulator is hanged inside the test chamber (Fig. 132.1) by means of testing support. To measure the leakage current and flashover voltage the contaminated insulator's cap is connected with high voltage terminal and other terminal connected to ground. During the test, the constant voltage is applied on the 11 kV insulator for 2 min and the leakage current is measured before the flashover. After the process of leakage current measurement on polluted insulators the samples are collected from the marked unit area of the surface shown in Fig. 132.3 and collected pollution sample is dissolved in the 150 ml distilled water. The test is conceded with the magnetic stirrer and the sample is stirred for 30–40 min and conductivity is measured.

Fig. 132.3 **a** Coastal pollution on the surface of the porcelain insulator. **b** Industrial pollution on the surface of the porcelain insulator. **c** Polar pollution on the surface of the porcelain insulator

Table 132.1 Description of pollution range

S. No.	ESDD (mg/cm^2)	Kaolin (gm)	NaCl (gm)
1	0.02	1.5	20
2	0.04	2.5	20
3	0.06	3.5	20
4	0.07	4	20

132.3 Importance of Pollution Measurement

The ESDD and NSDD are used to determine the contamination severity on insulator surface which is measured by NaCl mg/cm^2 and cement mg/cm^2. The ESDD and NSDD values afford the pollution severity for coastal, industrial and polar zones. The speed of wind and location of the insulator are considered for the safety margin of insulators [10]. The wind transmits such pollutants on the surface of the insulator and hence in this region the insulators are easily damaged and frequent replacement is mandatory [10]. The various pollution ranges of insulator in terms of ESDD are given in Table 132.1.

In the industrial region the power line insulators are affected by the deposition of cement, ash and carbon dust on the surface of the insulator. Air pollutants generated by the cement manufacturing process consist primarily of alkaline particulates from the raw and finished materials [7–10]. Similarly ice accumulates on the windward face of the outdoor insulator, which can lead to a considerable reduction in its electrical performance [9]. In many cold climate regions, overhead transmission lines and their insulators are subjected to ice loading. The presence of a water film on the insulator surface is the cause of flashover [6, 10]. The Fig. 132.3a–c represents the polluted insulator with salt, cement and ice (manually formed).

132.3.1 Determining ESDD and NSDD

The conductivity of the solution containing the pollutants are measured. The measurements are made after enough stirring of the solution (distilled water with sample). The conductivity correction shall be made using the Eq. (132.1) and corresponding ESDD is found using Eq. (132.2). (This calculation is based on Clause 16.2 and Clause 7 of IEC Standard 60507) [3]. After measuring LC, some of the non-soluble samples are collected from marked area and then the weights of collected samples are measured using electronic balancer, the NSDD is calculated using the Eq. (132.3).

$$\sigma_{20} = \sigma_\theta[1 - b(\theta - 20)] \tag{132.1}$$

$$ESDD = \frac{Sa \times V}{A} \tag{132.2}$$

$$\text{NSDD} = \frac{\text{Weight of the sample (g)}}{\text{Area of the insulator surface for collecting pollutants }(\text{cm}^2)} \tag{132.3}$$

For region involving mixed pollution the sample is subjected to ESDD and NSDD measurements. The ESDD measurement is followed by residual filtration using weighed Whatman filter paper and measurement of non-soluble pollutants.

132.3.2 Artificial Neural Network (ANN)

Learning is an important process in ANN to adapt the parameters through the network stimulation. In Neural Network, the weights are adjusted by neurons to obtain the desired outputs. This process is called as learning or training, that are categorized into supervised and unsupervised learning. In supervised Learning the control is provided externally. Each results delivers desired response to the input signals therefore overall information is required during the learning process. In this learning process the objective is to determine the weights at which the error rate gets minimized. The Least Mean Square (LMS) convergence is the most commonly used learning paradigms [3]. The Back propagation is the powerful algorithm to allocate the responsibility of error through output neurons by weights adjustment. The Delta rule is employed in back propagation to calculate the error at output nodes. It is the powerful algorithm but expensive in terms of computational requirements for the training process [5].

In most application the output layer will either be a single output node or even number of input nodes. The recorded performances of the coastal region pollution test on normal insulator readings are carried out using the above tool. The first step is to load the data into the MATLAB workspace. In Back Propagation Neural Network the LC is given as the input and the target is the ESDD and the network is trained. (For training the default Levenberg-Marquardt algorithm is used). Here TRAINLM is the training function and LEARNGDM is the adaption learning function. After the network training the unknown LC values are simulated by this network. The Neural Network train tool box is shown in the Fig. 132.4a. The network training is the process of adjust the data according to its error. Validation is

Fig. 132.4 **a** Neural network train tool. **b** Plot performance

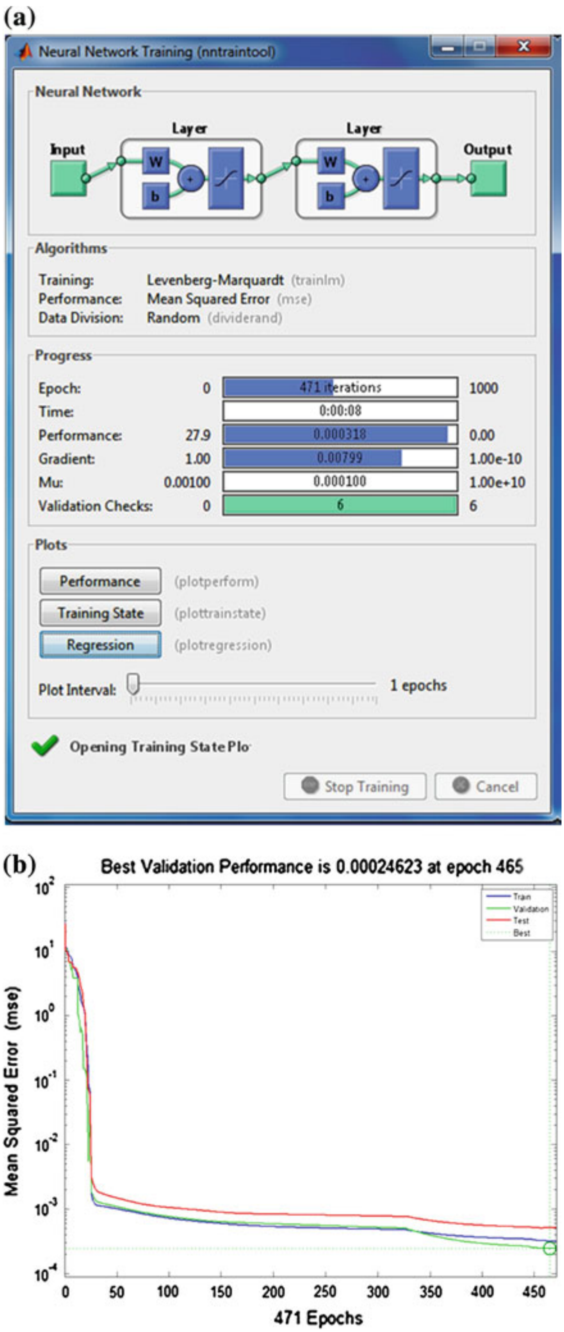

used to measure network generalization, and to halt training when generalization stops improving. Validation vectors are used to stop training early if the network performance on the validation vectors fails to improve or remains the same for *max_fail* epochs in a row. Test vectors are used as a further check that the network is generalizing well, but do not have any effect on training. This training stopped when the validation error increased for six iterations, which occurred at iteration 471. The performance in the training window, a plot of the training errors, validation errors, and test errors appears, are shown in the Fig. 132.4a.

132.4 Results and Discussion

Based on the test conducted under three different conditions of insulators and under three different types of pollutions such normal condition, insulator with defect near HV and insulator with defect far to HV and coastal, industrial and polar and the test results were shown in Table 132.2. Based on the observation, in normal insulator

Table 132.2 Comparison between simulated and measured ESDD at normal insulator, simulated and measured ESSD at defect near to the high voltage electrode and simulated and measured ESSD at defect far to the high voltage electrode for various pollutions

Actual ESDD (mg/cm^2)			Simulated ESDD (mg/cm^2)			Difference		
No defect	Defect near HV	Defect near LV	No defect	Defect near HV	Defect near LV	No defect	Defect near HV	Defect near LV
For coastal pollution								
0.02	0.02	0.02	0.02	0.02	0.02	0.00	0	0
0.03	0.03	0.03	0.02	0.029	0.03	0.00	0.00	0
0.04	0.04	0.04	0.04	0.040	0.040	0.00	0.00	0.00
0.05	0.05	0.05	0.05	0.049	0.05	0.00	0.00	0.00
0.06	0.06	0.06	0.05	0.060	0.059	0.00	0.00	0.00
0.07	0.07	0.07	0.06	0.069	0.069	0.00	0.00	0.00
For industrial pollution								
0.010	0.02	0.02	0.010	0.022	0.02	0.000	0.002	0
0.015	0.03	0.03	0.015	0.029	0.028	0.00	0.000	0.0010
0.020	0.04	0.04	0.02	0.040	0.042	0	0.000	0.0020
0.025	0.05	0.05	0.024	0.051	0.051	0.00	0.001	0.0011
0.030	0.06	0.06	0.030	0.06	0.062	0.00	0	0.0023
For polar pollution								
0.02	0.02	0.02	0.020	0.020	0.020	0.000	0.000	0.0001
0.03	0.03	0.03	0.029	0.031	0.029	0.000	0.001	0.0000
0.04	0.04	0.04	0.039	0.039	0.041	0.000	0.000	0.0001
0.05	0.05	0.05	0.050	0.049	0.052	0.000	0.000	0.0001
0.07	0.07	0.07	0.07	0.069	0.07	0	0.000	0.0001

Table 132.3 Predicted ESDD values under normal conditions, defect near HV and LV for coastal, industrial and polar pollutions

Normal insulator		Defect near HV		Defect near LV	
Mean LC	Predicted ESDD	Mean LC	Predicted ESDD	Mean LC	Predicted ESDD
For coastal pollution					
34.2	0.0709	36.2	0.0715	39.3	0.0717
34.6	0.073	36.7	0.0752	39.6	0.0735
35	0.0755	37.3	0.0793	40	0.0757
35.5	0.0781	37.5	0.0808	40.5	0.0786
36	0.0807	38	0.0844	41	0.0816
For industrial pollution					
34.80	0.0407	38.00	0.0812	40.20	0.0825
35.00	0.04115	38.30	0.0830	40.50	0.0850
35.50	0.04255	38.80	0.0871	41.00	0.0890
36.00	0.04395	39.00	0.0883	41.50	0.0931
36.50	0.0454	39.50	0.0925	42.00	0.0972
For polar pollution					
23.33	0.0707	26	0.0706	28.87	0.07084
23.83	0.0718	26.5	0.0719	29.37	0.0722
24.23	0.0727	27	0.0732	29.87	0.0737
24.7	0.0738	27.5	0.0746	30.27	0.075
25.3	0.0752	28	0.076	30.57	0.076

the impact of pollutant on the insulator surface is less when compare to the defect near and far to HV. The predicted results are published in Table 132.2 and the test results are compared with simulated results which are shown in Table 132.3. The cement mainly contains gypsum, which are tiny particles deposited on the surface of the insulator near cement industries. The deposition leads to higher absorption of moisture and hence reduces the hydrophobicity and flashover voltage of the insulator. Similarly for insulator with defect far to HV, higher deposition of pollutants on defect is accounted and but LC range is very less compare to the insulator with defect near HV electrode.

132.5 Conclusion

The leakage current in test insulators are measured with different contamination levels and are compared with respect to the dielectric strength of the insulators. The test results show that the leakage current depends upon atmospheric condition around the insulators and the surface condition of the insulator. The insulator is affected by factors such as aging, mechanical defects and natural pollution, which pilots the leakage current through the surface. For on-site measurement of insulator during the maintenance it is very difficult to find the contamination level of all the insulators, therefore contamination level prediction is necessary for the quality checkers and anti-contamination designers. The solid layer pollution test is carried out under light and moderate pollution level and the values are evaluated by using the Back Propagation Neural Network technique. The difference in the actual ESDD/NSDD and simulated ESDD/NSDD value shows accuracy of the NN tool. Thus the surface defect far from the HV electrode produce rapid flashover voltage because of short leakage current path compared to the other samples.

References

1. Kumagai S, Yoshimura N (2004) Leakage current characterization for estimating the conditions of ceramic and polymeric insulating surfaces. IEEE Trans Dielectr Electr Insul 11:681–690
2. Han S, Hao R, Lee J (2009) Inspection of insulators on high-voltage power transmission lines. IEEE Trans Power Deliv 24:2319–2327
3. Sidthik AS, Kalaivani L, Iruthayarajan MW (2013) Evaluation and prediction of contamination level in coastal region insulators based on leakage current characteristics. IEEE international conference on circuits, power and computing technologies, pp 132–137
4. Li J, Sima W, Sun C, Sebo SA (2010) Use of leakage currents of insulators to determine the stage characteristics of the flashover process and contamination level prediction. IEEE Trans Dielectr Electr Insul 17:490–501
5. Jiang X, Shi Y, Sun C, Zhang Z (2010) Evaluating the safety condition of porcelain insulators by the time and frequency characteristics of LC based on artificial pollution tests. IEEE Trans Dielectr Electr Insul 17:481–489
6. Jiang X, Chen L, Zhang Z, Sun C, Hu J (2010) Equivalence of influence of pollution simulating methods on DC flashover stress of ice-covered insulators. IEEE Trans Power Deliv 25:2113–2120
7. Jiang X, Yuan J, Zhang Z, Hu J, Sun C (2007) Study on AC artificial-contaminated flashover performance of various types of insulators. IEEE Trans Power Deliv 22:2567–2574
8. Chandrasekar S, Kalaivanan C (2009) Investigations on leakage current and phase angle characteristics of porcelain and polymeric insulator under contaminated conditions. IEEE Trans Dielectr Electr Insul 16:574–583
9. Farzaneh M, Li Y, Zhang J, Shu L, Jiang X, Sima W, Sun C (2004) Electrical performance of ice-covered insulators at high altitudes. IEEE Trans Dielectr Electr Insul 11:870–880
10. Fernando MARM, Gubanski SM (2010) Ageing of silicone rubber insulators in coastal and inland tropical environment. IEEE Trans Dielectr Electr Insul 17:326–333

Chapter 133
A Hybrid PSO-SFS-SBS Algorithm in Feature Selection for Liver Cancer Data

S. Gunasundari and S. Janakiraman

Abstract Feature selection is an essential one in building high performance classification systems with the maximum classification accuracy. In this paper Particle Swarm Optimization (PSO) hybridized with Sequential Forward Selection (SFS) and Sequential Backward Selection (SBS) algorithm is proposed for improving the performance of the classification system. The feature subsets are extracted from the pattern under classification using First Order Statistics (FOS) combined with the Co-occurrence based features for different distance and degrees. Binary Particle Swarm Optimization (BPSO) is applied to the feature subset. After some iteration the 30 % of the worst particles in PSO is replaced by the best feature subset of SFS and SBS algorithm. The proposed algorithm improves search ability and investigates two types of hybridization (1) PSO-SFS and (2) PSO-SFS-SBS with two options (1) velocity reset of all particles and (2) velocity reset of only worst particles. This hybrid system is applied to liver cancer data to reduce the features and to classify the liver disease as benign or malignant. Liver diseases like Hepatic Cellular Carcinoma (HCC), hemangioma, Focal Nodular Hyperplasia (FNH) and cholangiocarcinoma are classified. The Region of Interest (ROI) is cropped from an abdominal CT. The results obtained from different hybridized feature selection methods are examined. Experimental results show that the proposed methods select the 40 % of features as best features to train the Probabilistic Neural Network (PNN) classifier with insignificant time to categorize the disease to give the accuracy of 96.4 % for data set-1 and 92.6 % for data set-II.

Keywords BPSO · SFS · SBS · Feature selection · Co-occurrence features · PNN

S. Gunasundari (✉) · S. Janakiraman
Pondicherry University, Pondicherry, India
e-mail: gunapondyuniv@gmail.com

S. Janakiraman
e-mail: jana3376@yahoo.co.in

S. Gunasundari
Velammal Engineering College, Chennai, India

C. Kamalakannan et al. (eds.), *Power Electronics and Renewable Energy Systems*,
Lecture Notes in Electrical Engineering 326, DOI 10.1007/978-81-322-2119-7_133

133.1 Introduction

Liver cancer is one of the significant causes of death in several countries. CT is often the favored method for identifying many different liver diseases. Computer Aided Diagnostic systems have been developed to help doctors to diagnose precisely. Tumors can be benign or malignant. Benign tumors are not cancer cells, whereas malignant tumors are cancer cells and can invade and damage nearby tissues and organs. In pattern recognition system numbers of features involved are more. To improve their performance with a small feature subset, feature selection has to be done. A famous swarm intelligence algorithm is the Particle Swarm Optimization (PSO) algorithm which is very capable to search large solution spaces. In our work, the Binary Particle Swarm Optimization (BPSO) algorithm hybridized with SFS and SBS as a feature selector and PNN as a classifier is incorporated effectively. The selected best features from hybridized algorithm are fed to PNN classifier to characterize the liver diseases.

Liver texture analysis methods for reliable liver tissue classification have been proposed and surveyed in the past [1]. Support Vector Machine (SVM) was used to characterize liver diseases. Kernel-based Classifier is implemented [2] for classification of cyst, hepatoma and cavernous hemangioma. The features derived from the co-occurrence matrix, shape descriptors, etc. are used to train the SVM for classification. Mala et al. [3] and Gunasundari and Anandhi [4] concluded that the performance of PNN is good when it is compared with other neural networks. Orthogonal moments [5] are used to classify the liver diseases from abdominal CT. Logistic maps and tent maps [6] are embedded in BPSO to find out the inertia weight of the BPSO. Chaotic binary particle swarm optimization is proposed to implement the Feature Selection (FS). Catfish binary particle swarm optimization [7] is proposed in which the catfish effect is applied. This effect is the introduction of catfish particles into the search space, which replaces particles with the worst fitness. A novel FS method for the categorization of high dimensional cancer microarray data is designed which used filtering technique such as signal-to noise ratio (SNR) score and PSO [8]. A novel method for hepatitis disease diagnosis is designed [9], which is based on Rough Set, PSO and SVM. The proposed method is tested on the multi-core platform. Different spectral features are analyzed from transrectal ultrasound images for prostate cancer recognition [10]. A novel FS and classification method for hyperspectral images by combining the global optimization ability of PSO algorithm and SVM is reported [11]. Global optimal search performance of PSO is improved by using a chaotic optimization search technique. Granularity based grid search strategy is used to optimize the SVM model parameters. A combination of Integer-Coded Genetic Algorithm and PSO is coupled with the neural-network-based Extreme Learning Machine, is used for gene selection and cancer classification [12]. Semi supervised Ellipsoid ARTMAP algorithm combined with the PSO to distinguish tumor tissues with more than two categories through analyzing gene expression profiling is implemented [13]. NR-PSO algorithm (Neighborhood-redispatch-PSO) [14] is proposed to find the optimal solution for UWB antenna design. Feature selection is improved using BPSO [15] to classify liver disease. The rest of the paper is organized as follows. Section 133.2 briefly presents the BPSO. Section 133.3 describes the hybridized algorithm. Section 133.4 discusses the implementation and results. Section 133.5 concludes the work.

133.2 Binary Particle Swarm Optimization

PSO is an evolutionary computation technique that was proposed by Kennedy and Eberhart [16]. It is initialized with a population of random solutions, called particles which fly around in the search space to find the best solution. Each particle in PSO should consider the current position, the current velocity, the personal best solution, pbest, and the gbest, to modify its position. The particles are manipulated according to the following equation:

$$v_i^{t+1} = wv_i^t + c1 \times rand \times (pbest_i - x_i^t) + c2 \times rand \times (gbest - x_i^t) \tag{133.1}$$

$$x_i^{t+1} = x_i^t + v_i^{t+1} \tag{133.2}$$

where v_i^t is the velocity of particle i at iteration t, w is a inertia weight, c1 and c2 are acceleration constant, rand is random number between 0 and 1, x_i^t is the current position of particle i at iteration t, pbesti is the best solution that the i-th particle has obtained so far, and gbest indicates the best solution the particle has obtained so far. The PSO starts with randomly placing the particles in a problem space. At each pass, the velocities of particles are computed using Eq. (133.1). After defining the velocities, the position of particles can be computed using Eq. (133.2). The process of changing particles' positions will continue until satisfying an objective function. In designing the binary version of PSO, some basic concepts of the velocity and position updating process must be modified. In binary space the position updating process cannot be performed using Eq. (133.2). A transfer function is necessary to map velocity values to probability values for updating the positions. The original BPSO was proposed by Kennedy and Eberhart [17] to allow PSO to operate in binary problem spaces. The roles of velocities are to present the probability of a bit taking the value 0 or 1. A sigmoid function as in Eq. (133.3) was employed to transform all real values of velocities to probability values in the interval [0, 1].

$$T(v_i^k(t)) = \frac{1}{1 + e^{-v_i^k(t)}} \tag{133.3}$$

Where $v_i^k(t)$ indicates the velocity of particle i at iteration t in k-th dimension. After changing velocities to probability values, position vectors could be updated with the probability of their velocities as in Eq. (133.4):

$$x_i^k(t+1) = \begin{cases} 0 \quad if \quad rand \quad < T(v_i^k(t+1)) \\ 1 \quad if \quad rand \quad > T(v_i^k(t+1)) \end{cases} \tag{133.4}$$

133.3 Hybridized PSO-SFS and PSO-SFS-SBS Feature Selection Methods

The Haralick [18] based features and First Order Statistics features (FOS) are extracted from the ROI. The extracted features are given to the hybridized PSO-SFS-SBS algorithm with two different options velocity reset of all particles and velocity reset of only worst particles algorithm. The hybridized algorithms in detail are given in Table 133.1.

133.4 Implementation and Results

The proposed algorithm is tested for the classification of liver diseases. From the website "ctisus.org" the abdominal CT image is downloaded which is created and maintained by The Advanced Medical Imaging Laboratory (AMIL). The total number of different image slice considered for evaluation is 108. It includes 47 hepatoma, 11 Cholangiocarcinoma, 12 hemangioma and 38 FNH images. The input is partitioned into two data sets. First data set (DS-I) contains 85 slices which includes the diseases FNH and hepatoma whereas DS-II contains all 108 slices. The Region of Interest is cropped from an abdominal CT using MATLAB Simulink. The segmentation output for some images is shown in Table 133.2.

In FOS, the mean, standard deviation, variance, kurtosis and skewness are derived from the ROI. Spatial Gray Level Dependence Matrix (SGLDM) is constructed for the given lesion by varying the distance (d = 4, 6 and 8) and degree (0, 45, 90 and 135). For all co-occurrence matrices, 13 features like energy, Contrast, Correlation, Sum of Variances, Inverse Difference Moment, Sum Average, Sum Variance, Sum Entropy, Entropy, Difference Variance, Difference Entropy, Information Measures Correlation1 and Information Measures Correlation2 were extracted. For each distance, 4 degrees are used to construct feature set for an image. So total no of features extracted are 52 (13×4). Including FOS the no of features to represent an image are 57. The features are given to PNN for classification. 60 slices are considered for training and 25 images are considered for testing for DS-I. 70 images are considered for training and 38 images are considered for testing for DS-II. The training sets of both DS-I and DS-II produced the accuracy of

Table 133.1 Hybridized PSO-SFS and PSO-SFS-SBS algorithm with 2 options

• **Hybridized PSO/SFS/SBS – velocity reset of all particles Algorithm**
 	
Input:
Np: the number of particles
Nd: the number of dimension
c1=2, c2=2: positive acceleration constants
wMax =0.9and wMin=0.4: Maximum and minimum value of inertia weight
local_Nl: Number of local iterations
n_Replacement: No of replacement
Output: gBestPosition: Best features
Step 1: // Initialize the particle positions
for i = 1 to Np do
for j = 1 to Nd do
position[i][j] = random binary number
enddo
enddo
Step 2: // Initialize the particle velocities
for i = 1 to Np do
for j = 1 to Nd do
velocity[i][j] = 0
enddo
enddo
Step 3: // Initialize the global and particle best
gBest = inf;
for i = 1 to Np do
pBest[i] = inf
enddo
Step 4: // Loop for finite number of local iterations
for k = 1 to local_Nt do
// Calculate the fitness of each particle
fitness = calculate _fitness (position)
// Update the particle best and its position
for i = 1 to Np do
if (fitness(i) < pBest(i))
pBest[i] = fitness(i)
for j = 1 to Nd do
pBestPosition[i,j] = position (i,j)
enddo
endif
enddo
// Update the global best and its position
[minimum, index] = min (fitness (I))
if (minimum <gBest)
gBest = minimum
for j = 1 to Nd do
gBestPosition[j] = position (index,j)
enddo
endif
//update inertia weight
w=wMax-k*((wMax-wMin)/local_Nt);
// Update the particle position
for i = 1 to Np do
for i = 1 to Nd do
r1 = uniform random number
	• **Hybridized PSO/SFS – velocity reset of all particles Algorithm**
	
	Step1- Step 4 and Step 6 is similar to Hybridized PSO/SFS/SBS – velocity reset of all particles Algorithm
	
	Step 5:// Find and update 15% of worst particles
	for l= 1 to n_Replacement do
	Let m = 15% of Np
	Call SFS for m times to get the m set of the best features
	Identify the 15% of worst particles which is having very less pBest value
	Replace the 15% of worst particles by the best features obtained from SFS
	Repeat steps 2-4
	Enddo// Number of replacements
	
	• **Hybridized PSO/SFS/SBS – velocity reset of only worst particles Algorithm**
	
	Step1- Step 4 and Step 6 is similar to Hybridized PSO/SFS/SBS – velocity reset of all particles Algorithm
	
	Step 5:// Find and update 30% of worst particles
	for l= 1 to n_Replacement do
	Let m = 15% of Np
	Call SFS for m times to get the m set of the best features
	Call SBS for m times to get the m set of the best features
	Identify the 30% of worst particles which is having very less pBest value
	Replace the 30% of worst particles by the best features obtained from SFS and SBS
	// Update velocity, pBest of worst particles alone
	Set velocity = 0 for all worst particles
	Set pBest = inf for all worst particles
	Repeat step 4
	enddo// Number of replacements

(continued)

Table 133.1 (continued)

r2 = uniform random number
velocity[i][j] = w*velocity[i][j] + c1*r1*(pBestPosition[i][j] - position[i][j])+ c2*r2*(gBestPosition[j] - position[i][j])
//Apply transfer function
T(velocity[i][j])=Compute_S1(velocity[i][j])
//Update the particle velocity
r3 = uniform random number
If (r3 < T(velocity[i][j]))
position[i][j] = 0
else
position[i][j] =1
endif
enddo
enddo
enddo // Number of local_Nt
 	
Step 5:// Find and update 30% of worst particles
for l= 1 to n_Replacement do
Let m = 15% of Np
Call SFS for m times to get the m set of the best features
Call SBS for m times to get the m set of the best features
Identify the 30% of worst particles which is having very less pBest value
Replace the 30% of worst particles by the best features obtained from SFS and SBS
Repeat steps 2-4
enddo// Number of replacements
Step 6: // List the best features
Output the gBest and gBestPosition
	• **Hybridized PSO/SFS – velocity reset of only worst particles Algorithm**
	
	Step1- Step 4 and Step 6 is similar to Hybridized PSO/SFS/SBS – velocity reset of all particles Algorithm
	
	Step 5:// Find and update 15% of worst particles
	for l= 1 to n_Replacement do
	Let m = 15% of Np
	Call SFS for m times to get the m set of the best features
	Identify the 15% of worst particles which is having very less pBest value
	Replace the 15% of worst particles by the best features obtained from SFS
	
	// Update velocity, pBest of worst particles alone
	Set velocity = 0 for all worst particles
	Set pBest = inf for all worst particles
	Repeat step 4
	enddo// Number of replacements

Table 133.2 Segmentation output

Input Image	Segmented ROI	Input Image	Segmented ROI	Input Image	Segmented ROI
 Hepatoma		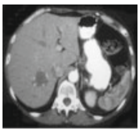 Hemangioma	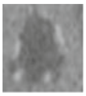	 Chlongiocarcinoma	

100 %. The accuracy of PNN classifier using FOS and SGLDM feature for various distances and degrees is 87.5 % for DS-I 82.4 % for DS-II.

The FOS + SGLDM features are given to the hybridized feature selection methods to fetch the best feature set individually. In BPSO the Number of particles

Table 133.3 Performance of PSO-SFS and PSO-SFS-SBS for DS-I

Accuracy/Number of best features selected						
d	Without PSO	PSO (20runs)	Velocity reset of all particles		Velocity reset of worst particles alone	
			PSO/SFS/SBS (20 runs)	PSO/SFS (20 runs)	PSO/SFS/SBS (20 runs)	PSO/SFS (20 runs)
4	87.5/57	94.1/17	94.1/20	94.1/18	94.1/24	94.1/22
6	87.5/57	91.7/19	96.4/23	96.4/22	**96.4/20**	96.4/28
8	87.5/57	90.5/28	91.7/28	92.9/26	91.7/28	94.1/17

Table 133.4 Performance of PSO-SFS and PSO-SFS-SBS for DS-II

Accuracy/Number of best features selected						
d	Without PSO	PSO (20runs)	Velocity reset of all particles		Velocity reset of worst particles alone	
			PSO/SFS/SBS (20 runs)	PSO/SFS (20 runs)	PSO/SFS/SBS (20 runs)	PSO/SFS (20 runs)
4	82.4/57	89.8/23	92.6/23	**92.6/21**	92.6/28	92.6/29
6	82.4/57	88.8/21	91.6/28	90.7/25	88.8/26	88.8/22
8	82.4/57	85.1/26	87.0/26	87.9/25	87.0/21	87.0/26

(Np) = 30 and c1, c2 = 2. The Number of dimensions (Nd) is 57, No of replacement n_Replacement is 2. The number local iteration is tried for 30, 50 and 100. The number of runs is 20. The Fitness function considered is the misclassification rate of PNN classifier. The reduced feature set is given as input to PNN for classification of disease and for analyzing the performance. The training sets produced the accuracy of 100 %, whereas the testing set produces the maximum accuracy of 96.4 % with 20features for DS-I and 92.6 % for DS-II. Four different hybridized algorithms are employed for features to analyze the performance. From the Tables 133.3 and 133.4 it is clearly understood that PSO-SFS-SBS features are giving maximum performance for d = 6 for DS-I. PSO-SFS algorithm works well for DS-II and gives the accuracy of 92.6 % for d = 4 with 21 feature subset.

133.5 Conclusion

The new Hybrid PSO-SFS-SBS and PSO-SFS algorithms are proposed and it is implemented successfully for two data sets using MATLAB for the classification of benign and malignant lesion from an abdominal CT. The FOS and co-occurrence based features are extracted from the segmented ROI. The best features are selected using hybridized algorithms. The best features are given as input to a PNN classifier to classify hepatoma and cholangiocarcinoma as malignant and hemangioma and FNH as benign. The hybridized algorithms are analyzed based on their performance. In comparison hybrid PSO-SFS-SBS algorithm gives the very minimal best features to PNN for classification, which yields better result with the accuracy rate of 96.4 % for DS-I and PSO-SFS yields 92.6 % for DS-II. In future, it will be tested on a different type of data sets. The proposed algorithm is executed sequentially; in future it will be tested in a distributed computing environment.

References

1. Gunasundari S, Janakiraman S (2013) A study of textural analysis methods for the diagnosis of liver diseases from abdominal computed tomography. Int J Comput Appl 74(11):7–12
2. Lee CC, Chiang YC, Tsai CL, Chen SH (2007) Distinction of liver disease from CT images using Kernel-based classifiers. ICMED 1(2):113–120
3. Mala K, Sadasivam S (2010) Classification of fatty and cirrhosis liver using wavelet-based statistical texture features and neural network classifier. Int J Softw Inform 4(2):151–163
4. Gunasundari S, Ananthi MS (2012) Comparison and evaluation of methods for liver tumor classification from CT datasets. Int J Comput Appl 39(18):46–51
5. Bharathi VS, Ganesan L (2008) Orthogonal moments based texture analysis of CT liver images. Pattern Recogn Lett 29:1868–1872
6. Chuang LY, Yang CH, Li JC (2011) Chaotic maps based on binary particle swarm optimization for feature selection. Appl Soft Comput 11:239–248
7. Chuang LY, Tsai SW, Yang CH (2011) Improved binary particle swarm optimization using catfish effect for feature selection. Expert Syst Appl 38:12699–12707
8. Sahu B, Mishra D (2012) A novel feature selection algorithm using particle swarm optimization for cancer microarray data. Procedia Eng 38:27–31
9. He F, Yang HM, Wang G, Cui GD (2012) A novel method for hepatitis disease diagnosis based on RS and PSO. In: Proceedings of international conference of 4th electronic system-integration technology conference, pp 1289–1292
10. Mohamed SS, Salama MA (2008) Prostate cancer spectral multi feature analysis using TRUS images. IEEE Trans Med Imaging 27(4):549–556
11. Yang HC, Zhang SB, Deng KZ, Du PJ (2007) Research into a feature selection method for hyperspectral imagery using PSO and SVM. J China Univ Min Technol 17(4):0473–0478
12. Saraswathi S, Sundaram S, Sundararajan N, Zimmermann M, Hamilton MN (2011) ICGA-PSO-ELM approach for accurate multiclass cancer classification resulting in reduced gene sets in which genes encoding secreted proteins are highly represented. IEEE/ACM Trans Comput Biol Bioinf 8(2):452–463
13. Xu R, Anagnostopoulos GC, Wunsch DC II (2007) Multiclass cancer classification using semisupervised ellipsoid ARTMAP and particle swarm optimization with gene expression data. IEEE/ACM Trans Comput Biol Bioinf 4(1):65–77
14. Li YL, Shao W, You L, Wang BZ (2013) An improved PSO algorithm and its application to UWB antenna design. IEEE Antennas Wirel Propag Lett 12:1236–1239
15. Gunasundari S, Janakiraman S (2013) Improved feature selection based on particle swarm optimization for liver disease diagnosis. In: Panigrahi BK et al (eds) Proceedings of SEMCCO 2013, part II, LNCS, vol 8298, pp 214–225
16. Kennedy J, Eberhart RC (1995) Particle swarm optimization. In: Proceedings of the IEEE international conference on neural networks, vol 4, USA, pp 1942–1948
17. Kennedy J, Eberhart RC (1997) A discrete binary version of the particle swarm algorithm. In: Proceedings of the IEEE international conference on computational cybernetics and simulation
18. Haralick RM, Shanmugam K, Dinstein I (1973) Texture features for image classification. IEEE Trans Syst Man Cybern SMC 3(6):610–621

Chapter 134
Heart Disease Prediction System Using Intelligent Network

R. Chitra and V. Seenivasagam

Abstract Heart Disease is one of the most common causes of death all over the world. This paper presents on developing a Intelligent Prediction System as an artificial second cardiologist using Neural Network. The major advantage of using Intelligent Network is they are supposed to possess humanlike expertise within a specific domain. The prediction system is developed using Feed Forward Neural Network and Cascaded Correlation Neural Network in the proposed work and their performance is analyzed.

Keywords Heart disease · Neural network · Prediction system · Intelligent network

134.1 Introduction

Heart disease (HD) is a term that refers to more than one disease of the circulatory system including the heart and blood vessels, whether the blood vessels are affecting the lungs, the brain, kidneys or other parts of the body. Heart diseases are the leading cause of death in adult men and women. In recent years, Soft Computing and Intelligent algorithms are gaining more importance and giving promising results in medical applications. These issues motivate in applying intelligent and soft computing paradigms for analyzing and improving the performance of detection and classification of abnormal and normal condition of Heart Disease.

R. Chitra (✉)
Department of Computer Science and Engineering, Noorul Islam Centre for Higher Education, Kanyakumari, India
e-mail: jesi_chit@yahoo.co.in

V. Seenivasagam
Department of Computer Science and Engineering, National Engineering College, Thoothukudi, India
e-mail: yespee1094@yahoo.com

C. Kamalakannan et al. (eds.), *Power Electronics and Renewable Energy Systems*, Lecture Notes in Electrical Engineering 326, DOI 10.1007/978-81-322-2119-7_134

As with many labor-intensive occupations, cardiologists use computer-aided detection systems that can identify potential on heart disease dataset. Currently, the best practice for reducing human mortality rates caused by complex diseases is to detect their symptoms at early stages. Through the early recognition of symptoms one can get the most effective clinical treatment for the best outcome [1]. Helmy et al. [2] proposed ensemble and hybrid intelligent techniques such as Support Vector Machine, Function Network and Fuzzy Logic to classify bioinformatics datasets. Deepika et al. [3], proposed Association rule for classification of Heart-attack patients. The significant patterns were extracted from the heart disease warehouse and association rule is used to classify the normal and abnormal patterns. Prediction System for heart disease used system contains huge amount of data, used to extract hidden information for making intelligent medical diagnosis. Shouman et al. [4] proposed k-means clustering with the decision tree method to predict the heart disease. In their work they suggested several centroid selection methods for k-means clustering to increase efficiency. 13 input attributes were collected from Cleveland Clinic Foundation Heart disease data set. Srinivas et al. [5], proposed Application of Data Mining Technique in Healthcare and Prediction of Heart Attacks. The potential use of classification based data mining techniques such as Rule based, Decision tree and Naive Bayes were applied to healthcare data. For data pre-processing and effective decision making one dependency augmented Naive Bayes classifier and naive creedal classifier were used. The main objective of the proposed system is to build Intelligent Heart Disease Prediction System that gives diagnosis of heart disease using historical heart database. HD risk factors never occur in isolation but they are correlated to each other [6]. To develop the system, medical terms such as sex, blood pressure, and cholesterol like 13 input attributes are used for prediction. The prediction system is developed by using two different intelligent network Feed Forward Neural Network (FFNN) and Cascaded Correlation Neural Network (CCNN) and the performance are compared.

134.2 Heart Disease Dataset

Heart attack dataset is obtained from UCI (University of California, Irvine C.A) centre for machine learning and intelligent systems [7]. The Cleveland heart disease data was obtained from V.A. Medical Center, Long Beach and Cleveland Clinic Foundation from Dr. Robert Detrano. This database contains 76 attributes, but all published experiments refer to using a subset of 14 of them. The data have been collected from 270 patients are used for proposed work. The digitized data has 150 normal and 120 abnormal cases. In this dataset first 13 attributes describes the risk factors of heart disease and last attribute describes the output class. There are two output classes for the diagnosis of heart attack. In the selected dataset, class 0 specifies the absence of heart attack and class 1 specifies the presence of heart disease. The dataset contains the data in the age range between 25 and 75 and it also contains the data of women as well as men. The 13 input attributes used in the HD dataset are age, gender, resting blood pressure, blood sugar, cholesterol, Chest Pain Type, resting electrocardiographic results, maximum heart rate achieved, exercise induced angina, the slope of the peak exercise ST segment, ST depression induced by exercise relative to rest, number of major vessels (0–3) colored by fluoroscopy in angiogram test and thallium test result.

Normalization is one of the data transformation technique used to scale attribute values to fall within a specified range. In this work prediction system is designed based on intelligent technique and the tool used is neural network. Because neural networks work internally with numeric data, binary data and categorical data must be encoded in numeric form. Additionally, experience has shown that in most cases numeric data, such as a person's age, should be normalized. In the proposed work neural network is trained with back propagation algorithm. When using back propagation networks, depending on the activation function of the neurons, it will be necessary to perform some pretreatment of data used for training. Supposing that logistic sigmoid are used, the interval of variation of the output variables has to be accommodated to the maximum output range of the sigmoid, that is from zero to one. An adequate normalization, not only for the network output variables but also for the input ones, previous to the training process is very important to obtain good results and to reduce significantly calculation time. Hence the input attributes in the HD dataset are normalized before classification. The Min-max normalization is used in the proposed work and it performs a linear alteration on the original data. The values are normalized within zero and one.

134.3 Intelligent Heart Disease Prediction

The intelligent HD prediction system with ANN is explained in this section. In the proposed work FFNN and CCNN are used and the performance of both network are compared.

134.3.1 Heart Disease Detection Using (FFNN)

An artificial neuron is a computational model inspired in the natural neurons. Artificial Neural Network's (ANN) are weighted directed graphs in which neurons are nodes and directed edges (with weights) are connected between neuron outputs and neuron inputs. The multi-layer feed forward neural network consists of multiple layers. The architecture of this class of network has input layers, output layers and have one or more intermediary layers called the hidden layers. Multilayer feed forward neural networks can be well applied to non-linear classification problems by introducing more hyper planes. The multilayer feed forward neural network used is a three layer network with one hidden layer. The input layer corresponds to the mixed feature vector of each attribute and the output layer corresponds to abnormal or normal. Each neuron in a particular layer is connected with the other neurons in the next layer. The connection between *i*th and *j*th neuron is characterized by the weight coefficient and the *i*th neuron by a threshold coefficient. The weight coefficient reflects the degree of importance of the given connection in the neural network. Sigmoid activation function is used to train the patterns, which is given as,

$$f(x) = \frac{1}{1 + e^{-x}}$$

Generally Back propagation algorithm [8] is used for training the FFNN. Back propagation algorithm is a gradient descent algorithm in which the input vectors and its corresponding target vectors are used to train a network until it can approximate a function. The goal of the training process is to obtain a desired output when certain inputs are given. Since the error is the difference between the actual and the target output, the error depends on the weights, and weights have to be adjusted in order to minimize the error. Mean square error function used in the neural network training and the error function for the output of each neuron is defined as,

$$E = \frac{1}{n}\sum_{i=1}^{n}(y_i - t_i)^2$$

The gradient of the error function is computed and used to correct the initial weights, so that the error function gets minimized. The weights are adjusted using the gradient descendent,

$$\Delta w_{ij}(t + 1) = -\eta\frac{\partial E}{\partial w_{ij}} + \alpha\Delta w_{ij}(t)$$

Where is the error signal. is the momentum factor and is the learning rate.

The input data to FFNN need to be normalized as NN only work with data represented by numbers in the range between 0.001 and 0.999. Three layers FFNN were used in this study for model calibration. The number of input neurons depends on the input attributes and there is only one neuron in the output layer. In the proposed work 13 input neurons and one output neuron for prediction of heart disease is used. FFNN was trained and tested with standard heart disease dataset and real world dataset. The training and testing is performed for 270 data obtained from standard dataset.

134.3.2 Heart Disease Detection Using (CCNN)

Cascaded Correlation Neural Network (CCNN) was developed by Fahlman and Libiere [9]. Cascade correlation neural networks are "self organizing" networks and are similar to traditional networks in that the neuron is the most basic unit. Training the neurons however is novel. The CCNN is a supervised learning architecture that builds a near-minimal multilayer network topology in the course of training. Initially the network contains only inputs, output units, and the connections between them. This single layer of connections is trained using the Quickprop algorithm [10] to minimize the error. Cascade-correlation eliminates the need for the user to guess in advance the network's size, depth, and topology. A reasonably small (though not minimal) network is built automatically Cascade correlation network training is quite robust, and good results usually can be obtained with little or no adjustment of parameters. The network begins with only input and output neurons. During the training process, neurons are selected from a pool of candidates and added to the hidden layer. A cascade correlation neural network has three layers: input unit, hidden unit and output unit. The network begins with an input and the output unit and no hidden units. The number of inputs (I_p) and the output (O_p) is defined by the problem, which is defined as, $I_p = \{i_1, i_2, \ldots, i_p\}$ and $O_p = \{o_1, o_2, \ldots, o_p\}$.

Every input is connected to the output unit with the weights obtained from the BP algorithm. There is also a bias which is set to +1. The hidden units are added to the network one by one until the error is minimized or the stopping criterion is reached. Each new hidden unit receives a connection from each of the network's original inputs and also from every pre-existing hidden unit. The hidden unit's input weights are frozen at the time the unit is added to the net; only the output connections are trained repeatedly. Each new unit therefore adds a new one-unit "layer" to the network, unless some of its incoming weights happen to be zero. This leads to the creation of very powerful high-order feature detectors. To create a new hidden unit, we begin with a *candidate unit* that receives trainable input connections from all of the network's external inputs and from all pre-existing hidden units. The goal of this adjustment is to maximize S,

$$S = \Sigma_o |\Sigma_p (V_p - \overline{V})(E_{p,o} - \overline{E}_o)|$$

Where o, is the output unit, p, number of patterns in the training set, is the candidate units value at p, is the residual error of all the training pattern at the output unit. and are the values of V and E_o averaged over all patterns.

The residual error is calculated using,

$$E_{p,o} = (Y_{p,o} - T_{p,o})$$

Where the actual output at the output unit o is, is the desired output at the output unit o. The training is done using backprop algorithm. Backprop uses a gradient descent method to update the weights.

The number of input neurons used in CCNN is 13 (I_p = 13) and the number of output neurons used is 1 (O_p = 1). The maximum epochs is set to 150. In cascaded correlation neural network the epochs got stopped when the desired accuracy got the system will stop immediately. CCNN was trained and tested with standard heart disease dataset and real world dataset. The training and testing is performed for 270 data obtained from standard dataset.

134.4 Result Analysis and Discussion

The FFNN and CCNN is trained and tested with the data obtained from UCI repository standard dataset. The training and testing set performance are shown in Table 134.1. In the proposed heart disease prediction system obtained results are evaluated by the performance metrics sensitivity, specificity, and accuracy. The work focus on binary classification problems and the classifier yields two results: positive and negative. In a binary classification, there are four possible outcomes. When a positive instance is correctly classified as positive, it is counted as a true positive (TP); if it is incorrectly classified as negative, it is counted as false negative (FN). If the instance is negative and has been classified correctly, it is counted as a true negative (TN), otherwise it is counted as a false positive (FP). Sensitivity, specificity and accuracy are the commonly used statistical measures to analyze the medical diagnostic test to enumerate how the test was good and consistent. Sensitivity evaluates the diagnostic test correctly at detecting a positive disease. The performance metric is analyzed for both intelligent networks and it is listed in Table 134.2. Accuracy measures correctly figured out the diagnostic test by eliminating a given condition and it is defined as

Table 134.1 Training and testing performance metrics

Dataset	Performance metric	Training set	Testing set
FFNN	Accuracy	88.4	90.8
	Sensitivity	87.54	90.42
	Specificity	89.62	90.64
CCNN	Accuracy	83.76	87.435
	Sensitivity	80.89	84.45
	Specificity	87.321	89.739

Table 134.2 Performance metrics for proposed intelligent network

Measures	FFNN	CCNN
True positive	0.84	0.83
True negative	0.88	0.87
False positive	0.16	0.17
False negative	0.12	0.13
Accuracy	0.854	0.85
Sensitivity	0.833	0.83
Specificity	0.866	0.87

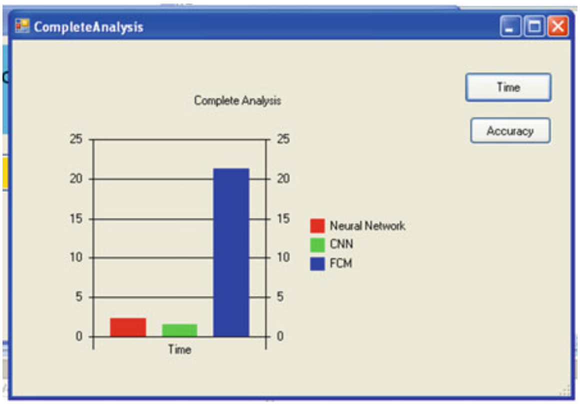

Fig. 134.1 Analysis by time (seconds)

The time taken for training is compared with multilayer feed forward network and fuzzy C means clustering is shown in Fig. 134.1. From the figure it is proved that the time taken for prediction using CNN is less compared with other techniques.

The training and testing set accuracy it is proved that the proposed prediction systems out performs the other existing statergies in the literature. Moreover, it is observed that the proposed classifeier achieved comparable performance over the testing and training set of all the patient records. In CCNN the epochs got stopped when the desired accuracy got the system will stop immediately. The time taken to train the neural network with backpop algorithm is 2 s where as the ANN with backpropagation algorithm requires 4 s for training. Analysis based on time complexity proves that Cascaded Neural Network takes minimum amount of time for training and testing compared to FFNN. From the performance analysis the performance of both networks are almost same but the time complexity of FFNN is high compared to CCNN. But in real time HD prediction system the training is done in offline and no need to consider the time complexity. The FFNN is a novel ANN technique and whereas CCNN special ANN network. Hence FFNN can be used for prediction in real time application.

134.5 Conclusion

In the present study a FFNN and CCNN is used to develop an Intelligent Prediction System for Heart Disease. The offline training and testing is performed in both networks using standard Heart Disease dataset. From the performance analysis it is proved that the time complexity is less in CCNN whereas the design complexity is less in FFNN. Hence both intelligent networks are significantly good for the design of classifier and the accuracy is same.

References

1. Sullivan F (2009) Preparing for an aging society: challengers faced by healthcare system in European Union, Japan and United States
2. Helmy T, Al-Harthi MM, Faheem MT (2012) Adaptive ensemble and hybrid models for classification of bioinformatics datasets. Int J Technol Optim vol 3
3. Deepika N, Chandra shekar K (2011) Association rule for classification of heart attack patients. Int J Adv Eng Sci Technol 11(2):253–257
4. Shouman M, Turner T, Stocker R (2012) integrating decision tree and k-means clustering with different initial centroid selection methods in the diagnosis of heart disease patients. In: Proceedings of international conference on data mining, pp 24–30
5. Srinivas K, Kavitha Rani B, Govrdhan A (2011) Application of data mining techniques in healthcare and prediction of heart attacks. Int J Comput Sci Eng 02(02):250–255
6. Stamler J, Vaccaro O, Neaton JD, Wentworth D (1993) Diabetes, other risk factors, and 12-yr cardiovascular mortality for men screened in the multiple risk factor intervention trial. Diabetes Care 16:434–444
7. Murphy, PM, Aha DW (2004) UCI machine learning databases repository Irvine C. A, University of California, Department of Information and Computer science
8. David E, Rumelhart D, McClelland JL (1987) Parallel distributed processing. MIT Press, Cambridge
9. Fahlman SE, Lebiere C (1990) The cascade-correlation learning architecture. In: Touretzky DS (ed) Advances in neural information processing systems, Morgan Kaufmann, vol 2, pp 524–532
10. Fahlman SE (1988) Faster-learning variations on back-propagation: an empirical study. In Proceedings of the 1988 connectionist models summer school, Morgan Kaufmann, pp 38–51

Chapter 135
Performance Comparison of AI Controllers for DC Link Voltage of SAPF System for Power Quality Enhancements

P.M. Balasubramaniam and S.U. Prabha

Abstract In this article, an artificial intelligent controller based mammalian limbic system and an emotional process is presented in DC Link voltage control for three phase shunt active power filter. A novel approach of the intelligent techniques, for control and decision making processes, was introduced that is based on the emotion processing mechanism in the brain, and is essentially an active selection, which is based on sensory inputs and emotional cues. In this work, a model of shunt compensation system for improving power quality by using the artificial intelligent control system, which control the DC link voltage spike during the transient period accurately and maintains quick settling time during step changing of load. And also it does not require any conventional controllers. In this proposed method BELBIC controller is used, the response of the DC link voltage is compared with PI and Fuzzy Gain scheduling controller. This generation of intelligent controllers that has high auto learning speed with simple structure shows excellent error free environment for industrial applications.

Keywords DC link voltage · BELBIC controller · PI and fuzzy gain scheduling controller · APF · HCC

135.1 Introduction

Increasing applications of nonlinear loads results in a variety of undesirable phenomena in the power transmission and distribution systems. Especially in the small rating stand alone power grids, such as ships, oil field, etc., the equivalent short

P.M. Balasubramaniam (✉)
Sri Shakthi Institute of Engineering and Technology, Coimbatore, Tamilnadu, India
e-mail: mebalu3@gmail.com

S.U. Prabha
Bannari Amman Institute of Technology, Erode, Tamilnadu, India
e-mail: drsuprabha@gmail.com

C. Kamalakannan et al. (eds.), *Power Electronics and Renewable Energy Systems*,
Lecture Notes in Electrical Engineering 326, DOI 10.1007/978-81-322-2119-7_135

circuit impedance of the system is large, so harmonic current, voltage distortion and frequency fluctuations are common conditions. Traditionally, passive filters have been used to attenuate the harmonic distortion and compensate the reactive power. However passive filter may resonate with the supply impedance. The usage of passive filter is becoming extinct. The use of nonlinear loads such as diode and thyristor rectifiers, consumer electronics, uninterruptible power supplies and adjustable speed drive results in the distorted current waveforms in the electrical distribution systems. These harmonic currents can cause the voltage and current distortion throughout the system, which can result in additional losses, measurement errors and malfunctions of protection devices. The active power filter (APF) is a popular approach for cancelling the harmonics in power system. The active power filters have good performance into compensation not only for current harmonics but also for reactive power and the unbalance of nonlinear and fluctuating loads, they are studied and applied widely, and great development has taken place in the theory and application of shunt active power filters. The Shunt Active Power Filter has two major parts, one is reference current extraction from the distorted line current, and another is the current modulator to generate switching patterns for converter. The Hysteresis Current Controller (HCC) method attracts researcher's attention due to unconditional stability and simple implementation. The performance of SAPF strictly depends on the features of the current control algorithms using the DC link voltage controller. Bhende et al. [1] and Kumar and Mahajan [2] analyzed the performance of SAPF using PI and Fuzzy logic controllers. Here a current control scheme of SAPF with fuzzy gain scheduling and BELBIC are proposed for harmonic elimination under steady state and transient state, power factor correction and reducing transients in current during a sudden change in load.

The shunt active power filter for power system with nonlinear load is analyzed by many authors for various configurations like single phase system, three phase three wire system and three phase four wire system were analyzed the performance of various configurations of active power filters such as shunt active, series active, hybrid shunt filter and hybrid series filter. It is proved in this analysis SRF provides better performance than IRPT. The THD during steady state is decreased to 2.53 from 25.38 %, during transient state is decreased to 2.48 from 25.32 % using Fuzzy Logic Controller. Cascaded voltage source inverter proposed in this system increases the number of switching devices and complicates the control circuit. Choi et al. [3] proposes synchronous reference frame based phase locked loop for harmonic control. It requires an additional controller to tune gains of the controller. The system is not analyzed in terms of power factor and reactive power. Mikkili and Panda [4] proposes I_d–I_q Control Strategy for 3 Phase 4 Wire Shunt Active Filters. The system is analyzed with balanced and unbalanced voltage. The THD of the system is reduced to 2.34 %. The system is not analyzed in terms of power factor and reactive power. Belaidi et al. [5] proposes the reference current computation of the shunt APF is based on the instantaneous reactive power theory. The proposed controllers are used in DC link voltage control. FLC is giving better performance than conventional PI controller in terms of V_{dc} settling time, reactive power compensation and THD. FLC provides reduced THD to 3.21 from 26.67 %.

The system is analyzed only during steady state. Hamad et al. [6] Active power filter (APF) performance is affected by the system delay introduced in the reference signals and the actual injected current. This study introduces an artificial intelligent controller based technique using a neural network control strategy for a shunt active power filter. In this analysis Band pass filter is used in SRF, it requires optimum selection of cutoff frequency to reduce harmonics. Steady state performance of non linear load is not analyzed which is the main cause of harmonics. From the above literatures, it can be observed that only a few studies have been made on PI with fuzzy, artificial neural network controller for DC link voltage control. It does not control the voltage stress on the capacitor and transients in the source current during a change in load. Hence the present work is with the BELBIC becomes necessary to study the DC link voltage control in shunt active power filter.

A MATLAB program has been developed to simulate the system operation. The simulation results provide the validation of the Synchronous reference frame based SAPF system to meet IEEE Standard 519. It is the recommended harmonic standards for different rated nonlinear loads under balanced supply conditions.

135.2 Control Algorithm for Shunt Active Filter

The synchronous reference frame theory is based on time domain reference signal estimation techniques. It performs the operation in steady state or transient state as well as for generic voltage and current waveforms. The synchronous reference frame based SAPF is shown in Fig. 135.1 Initially the three phase line currents i_a, i_b, and i_c are transformed from three phase (abc) reference frame to two phase (dq) stationary reference frame currents I_d and I_q using park transform. The dq transformation output signals depend on the load current (fundamental and harmonic components) and the performance of the Phase Locked Loop (PLL). Harmonic current references can be obtained by performing the inverse transform of parks synchronized with network frequency [6]. The PLL circuit provides the rotation speed of the rotating reference frame, where ωt is set as a fundamental frequency

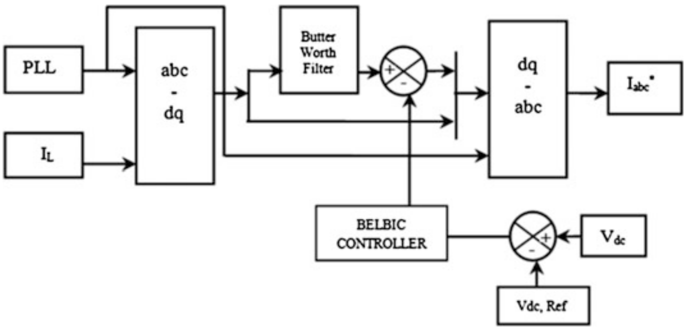

Fig. 135.1 Current control scheme for SAPF system

component. The i_d–i_q current are sent through second order butter worth low pass filter (LPF) for filtering the harmonic components of the load current, which allows only the fundamental frequency components.

The Butterworth characteristic provides a very flat amplitude response in the pass band and a roll-off rate of −20 dB/decade. Furthermore, it maintains the capacitor voltage is nearly constant. The DC link capacitor voltage of PWM voltage source inverter is sensed and compared with desired reference voltage for calculating the error voltage. This error voltage is passed through a BELBIC controller. The BELBIC controller is used to eliminate the steady state error of the DC component of the d axis reference signals.

135.3 Simulation Model

The SRF theory based shunt active power filter is simulated using MATLAB/Simulink R 2011b. The specifications of the system analyzed are 100 V, 12A and frequency of $\omega = 100\ \pi$. Initially the performance of the system is analyzed with conventional Proportional and Integral (PI) Controller. The Ziegler Nicholas method has been employed to tune gains of PI controller. To verify the performance of the system during transient state a sudden change in load was applied at the time of 0.5 s. Here considering the transient period is 0.5–0.6 s and after this time system comes to steady state. The THD during transient state is 3.02 %, steady state is 2.32 % and the overall system THD is 2.54 %. The SRF based SAPF system improves power factor in the range of 0.98, whereas it is 0.86 before compensation. But the hitch of this controller is it produces transients in capacitor DC link voltage and long settling time because the control gains are constant irrespective of error. Therefore it necessitates a controller to tune the gains of the controller during runtime.

135.4 Fuzzy Gain Scheduling Controller Based SAPF

The fixed value of K_p and K_i in a PI controller produces the sudden drop in capacitor voltage and high harmonics in the source current. Online tuning of K_p and K_i in a PI controller can conquer this problem. In order to implement the fuzzy logic control algorithm of an active power filter in a closed loop, the DC bus capacitor voltage is sensed and then compared with the desired reference value Fei et al. [7]. The error DC voltage and its derivative are given as inputs using Min-Max method of Fuzzification. Fuzzification is the process of converting crisp value input into linguistic values. The proportional gain K_p the integral gain K_i are produced as fuzzy outputs by the centroid method of defuzzification. This reference current takes care of the active power demand of the non linear load for harmonics and reactive power compensation. It improves the performance of the system compared to the PI controller in terms of harmonics, transient in current and rise in capacitor voltage during transient. But the hitch in it is the drop in DC link voltage is increased compared. So it is essential to control the voltage stress on the capacitor. It necessitates an advanced artificial intelligent controller with very fine tuning.

135.5 Brain Emotional Learning Based Intelligent Controller (BELBIC) Based SAPF

A Novel Artificial Intelligent technique of Brain Emotional Learning Based Intelligent Controller has been introduced in SAPF to reduce voltage transients caused by the PI and Fuzzy PI controller is an oscillation in a power system. BELBIC is proposed for its dual feedback system for fine tuning. It is based on the architecture of the "Limbic System" of the human brain suitable for control and decision making in linear and nonlinear system. BELBIC consists of an internal feedback in a controller it can produce smoothen output. Figure 135.2a, b shows the sectional view of human brain structure and block diagram of BELBIC controller Jafari et al. [8], Daryabeigi et al. [9]. BELBIC is a simple composition of the sensory input, Emotional cue, and Amygdala and orbitofrontal cortex.

A DC link voltage error is given as input to sensory input which produces peak reference $I_{max.}$ Sensory cortex is formed by PI controller. The output of Sensory cortex is again fine tuned to produce a constant voltage in capacitor using Amygdala and orbitofrontal cortex. Amygdala and orbitofrontal cortex decides the output of controller as shown in Fig. 135.4 and corresponding shown in Eq. (135.1).

$$\mathrm{MO} = \mathrm{A} - \mathrm{OC} \tag{135.1}$$

where MO is Model Output, A is Amygdala Output, OC is orbitofrontal Cortex. Internal feedback system Emotional cue in Eq. (135.2) formed using present error and model output.

$$\mathrm{EC} = \mathrm{MO}(\mathrm{W}_1(\mathrm{e} \times \frac{\mathrm{de}}{\mathrm{dT}}) + \mathrm{W}_2(|\mathrm{e}|)) \tag{135.2}$$

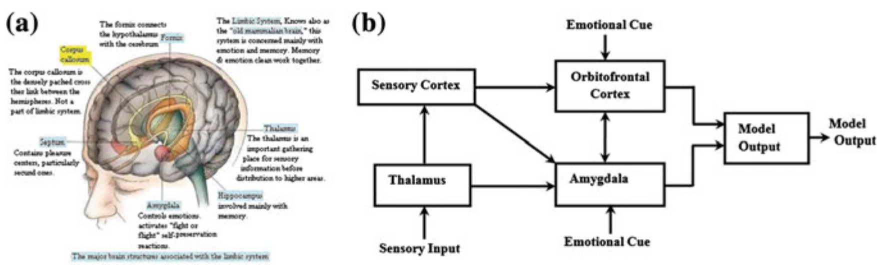

Fig. 135.2 **a** Sectional view of the human; **b** Block diagram of BELBIC

where EC is the EC Emotional cue, W_1 and W_2 are the weights, and e is the DC link voltage error. EC fine tunes the A in Eq. (135.3) and O Eq. (135.4) value in the rate of α and β as shown in Eqs. (135.5) and (135.6).

$$A = G_A \times SC \tag{135.3}$$

$$O = G_{OC} \times SC \tag{135.4}$$

$$\frac{dG_A}{dT} = \alpha \times SC(ES - A) \tag{135.5}$$

$$\frac{dG_{OC}}{dT} = \beta \times SI(A - O - ES) \tag{135.6}$$

where α is Learning rate of Amygdala, G_A is Gain for Amygdala, the G_{OC} is Gain or orbitofrontal Cortex Rouhani et al. [10].

Based on the above equations mathematical model of BELBIC is formed. The Figs. 135.3 and 135.4. Shows the emotional cue and model output of BELBIC fine tuned peak reference I_{max}.

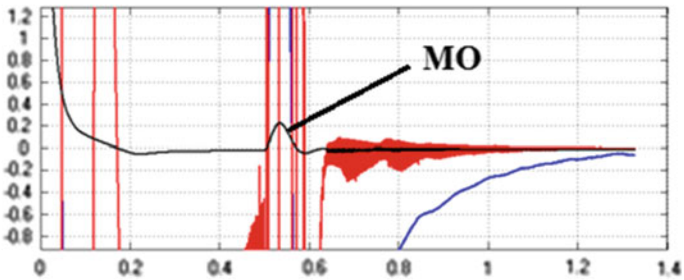

Fig. 135.3 Output of MO

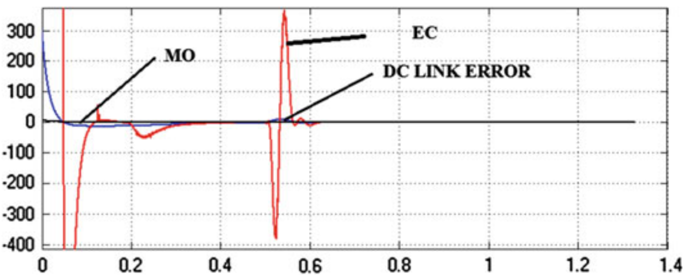

Fig. 135.4 Output of emotional cue and model output

135.6 Simulation Results

In order to evaluate this emotional controller and hence, to assess the effectiveness and control capability of the proposed BELBIC scheme, the performance of the proposed control scheme is investigated in simulation test scrutiny at different operating conditions. Digital computer simulations have been performed using MATLAB/Simulink. The Fig. 135.5 shows that, here the highly non linear loads has connected. Then the load 1 is switched to load 2 with the interval time of 0.5 s, the harmonics are presented in the output wave form and it would affect the source current. Eventually, the source current is deviated from the fundamental sinusoidal current.

The load currents can be converted from a–b–c to d–q–0 by park transformation. The '0' sequence component gets nullified, finally d–q currents are obtained with higher order harmonics. It can be removed by second order butter worth filter. The

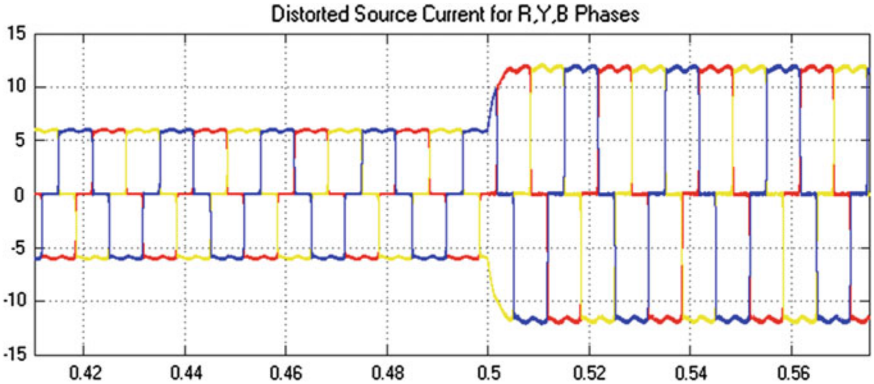

Fig. 135.5 Source current with harmonics

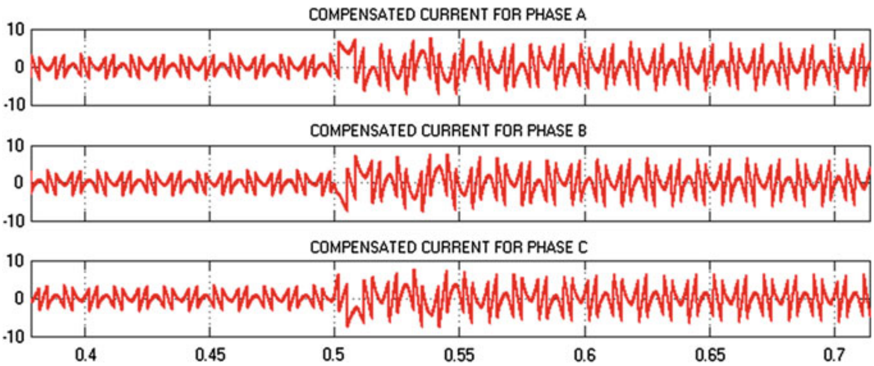

Fig. 135.6 Compensation current

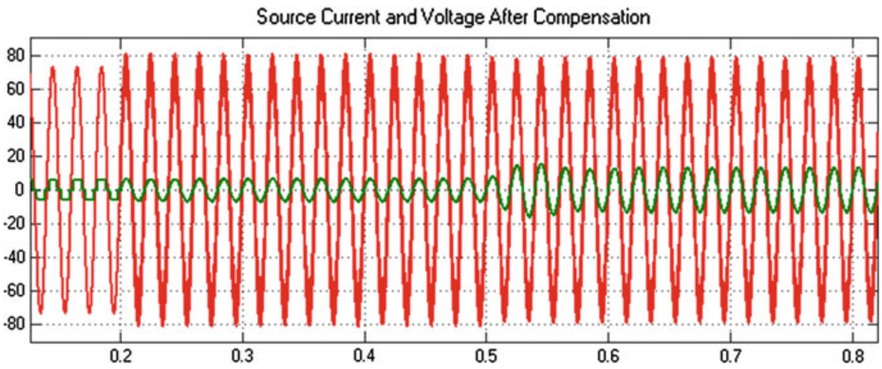

Fig. 135.7 Compensated source current in phase with the source voltage

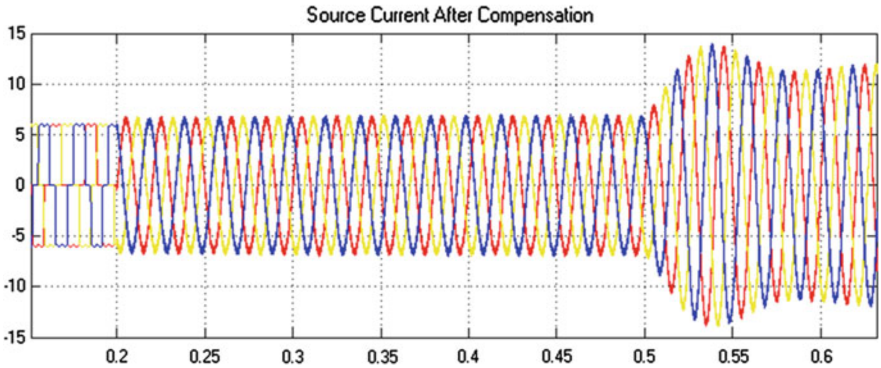

Fig. 135.8 Compensated source current

Figs. 135.6 and 135.7 represents the required compensation currents, which could be injected but opposite in phase to the common coupling point. The Fig. 135.8 shows sources current are in phase with the source voltage. The reference current already fixed the DC link voltage is measured and compared with the reference voltage. Then the error voltage is given to the BELBIC controller, which makes the DC capacitor voltage to maintain a constant level. The Fig. 135.9 Shows the DC link voltage of SAPF with BELBIC controller.

135.6.1 (a) Steady and Transient State

In steady state condition the simulation time is taken as t = 0. 6–t = 0. 99 s with two sets of load. Here consider at 0.5 s load has been changed, for the particular time the current increased, then after 0.6 s it comes to settle. During the steady state period,

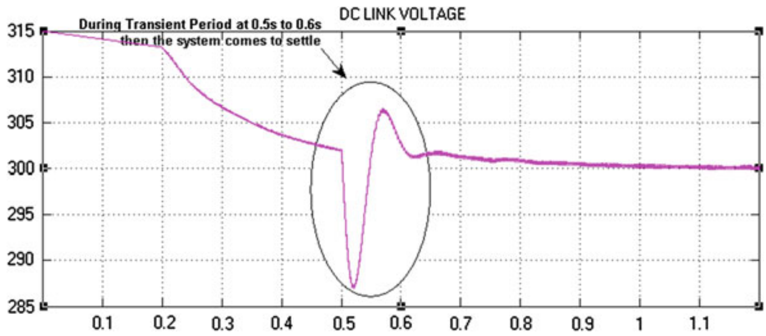

Fig. 135.9 DC link voltage

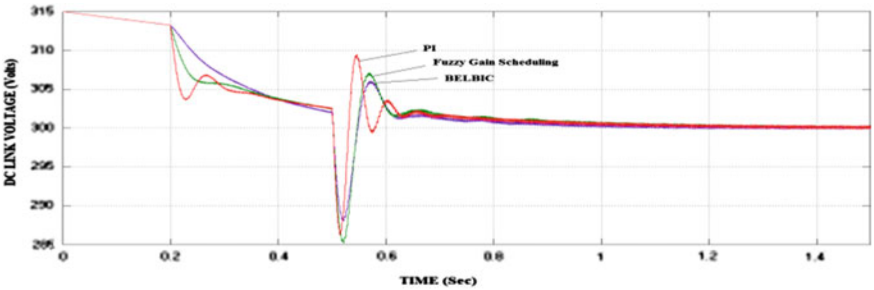

Fig. 135.10 Comparative analyses of various controllers

the current is noted. During the period t = 0.5–t = 0.6 s R, L parameters of the nonlinear load are set as 40 Ω and 80 mH respectively. At 0.5 s the load parameters are changed to 55 Ω and 100 mH respectively. The corresponding waveforms obtained are shown in the Fig. 135.10.

The Fig. 135.10 shows the performance of AI controller during step changing the load.

The Table 135.1 shows the SAPF system operates with various controllers during transient and steady state instants.

Table 135.1 Performance comparison of various controllers

Controller	I_S THD during In %	I_S THD during E_{ss} In %	C_{Stress} during transient	I_S rise during load changing	Ts in (Sec)	THD
PI	3.03	2.54	7.33	24.06	1.2	2.54
FGS	2.72	2.36	7	9.03	1.1	1.95
BELBIC	2.57	2.08	6	8.9	0.885	1.85

135.7 Conclusion

The article describes advanced artificial intelligent controllers based on brain emotional processes in limbic system achieved good results. According to given description in this article about advanced intelligent controllers based on brain emotional processes in limbic system has reduced ripple of dc link voltage of shunt active power filter during transient and steady state conditions. It has reduced overshoot of DC capacitor voltage during step changing of load and maintains quick settling time. So that we can say that BELBIC based SAPF system has been achieved good power quality with IEEE 519 standard. And also the proposed emotional controller has some gains, which give good desired responses in terms of overshoot, settling time, steady state error and smoothness. These make the emotional controller effective and flexible in high performance for industrial applications. Moreover, simple structure, fast auto learning and high tracking potency of BELBIC have been made to present a new control plant that is independent of SAPF parameters and controls steady state error simultaneously and eliminated conventional controllers.

References

1. Bhende CN, Mishra S, Jain SK (2006) TS-Fuzzy-controlled active power filter for load compensation. IEEE Trans Power Deliv 21(3):1459–1465
2. Kumar P, Mahajan A (2009) Soft computing techniques for the control of an active power filter. IEEE Trans Power Deliv 24(1):452–461
3. Choi H-J, Song S-H, Jeong S-G, Choi J-Y, Choy I (2011) Enhanced dynamic response of SRF-PLL system for high dynamic performance during voltage disturbance. J Power Electron 11(3):369–374
4. Mikkili S, Panda AK (2011) PI and fuzzy logic controller based 3-phase 4-wire shunt active filters for the mitigation of current harmonics with the Id-IQ control strategy. J Power Electron 11(6):914–921
5. Belaidi R, Haddouche A, Guendouz H (2012) Fuzzy logic controller based three phase shunt active power filter for compensating harmonics and reactive power under unbalanced mains voltages. Energy Procedia 18:560–570
6. Balasubramaniam PM, Prabha SU (2013) A practical approach to harmonic compensation in industrial power systems—using shunt active power filter. Aust J Basic Appl Sci 7 (11):393–403
7. Hamad MS, Gadoue SM, Williams BW (2012) Harmonic compensation of a six-pulse current source controlled converter using neural network-based shunt active power filter. IET Power Electron 5(6):747–757
8. Fei J, Ma K, Zhang S, Yan W, Yuan Z (2013) Adaptive current control with PI-fuzzy compound controller for shunt active power filter. Math Probl Eng 2013:1–11
9. Jafari M, Shahri AM, Shuraki SB (2013) Speed control of a digital servo system using brain emotional learning based intelligent controller. In: Power electronics, drive systems and technologies conference (PEDSTC), pp 311–314

10. Daryabeigi E, Sadeghi H, Arab Markadeh GR, Lucas C (2010) Speed control of brushless DC Motors using emotional intelligent controller. In: Annual conference on IEEE industrial electronics society, pp 2911–2916
11. Rouhani H, Jalili M, Araabi BN, Eppler W, Lucas C (2007) Brain emotional learning based intelligent controller applied to neurofuzzy model of micro-heat exchanger. Expert Syst Appl 32:911–918

Chapter 136
Online Fuzzy Supervised Learning of Radial Basis Function Neural Network Based Speed Controller for Brushless DC Motor

K. Premkumar and B.V. Manikandan

Abstract In this paper, Online Fuzzy Logic Supervised Learning of Radial Basis Function Neural Network (RBFNN) based speed controller for Brushless DC (BLDC) motor is presented. The Fuzzy PID controller is acting as supervisor for RBFNN controller. Dynamic speed response is analyzed for BLDC motor with conventional PID controller and proposed controller. Rise time, peak overshoot, recovery time and steady state error are measured and analyzed for above controller. From the results, the proposed controller outperforms than PID controller.

Keywords BLDC motor · PID controller · Fuzzy PID controller · Online radial basis function neural network controller

136.1 Introduction

Brushless DC motor becomes a replacement for DC motor because it overcomes the limitation of a brushed DC motor. They incorporate high efficiency, high torque per weight, increased reliability, reduced noise, a lower susceptibility of the commutator assembly to mechanical wear and longer lifetime. It has come to govern countless applications, particularly in transport, heating and ventilations, motion control systems, positioning and actuation systems, model engineering and radio controlled cars [1, 2]. In the last two decades, many numbers of intelligent controllers was developed based non linear model of BLDC motor [3–12]. In [3], Proportional Integral (PI)

K. Premkumar (✉)
Pandian Saraswathi Yadav Engineering College, Sivagangai, Tamil Nadu, India
e-mail: prem.kamaraj@gmail.com

B.V. Manikandan
Mepco Schlenk Engineering College, Sivakasi, Tamil Nadu, India
e-mail: bvmani73@yahoo.com

C. Kamalakannan et al. (eds.), *Power Electronics and Renewable Energy Systems*,
Lecture Notes in Electrical Engineering 326, DOI 10.1007/978-81-322-2119-7_136

based speed controller is designed for three base BLDC motor. Proportional Integral controller based current controller is proposed for BLDC motor [4]. In the speed response, PI controller produces uncertainty due to load variations and set speed variations. Fuzzy logic based speed controller is discussed for brushless AC motor [5]. In [6], hybrid Fuzzy-PID controller is implemented for BLDC motor. As a result, fuzzy logic controller outperforms the PID controller. In [7], adaptive speed controller based on the fuzzy logic system is implemented for BLDC motor. The effectiveness of the fuzzy logic controller is analyzed and superior for variable speed drives. But it required expert, who know the system to be modelled. In [8], educational tool for neural network and it is presented for Brushless DC Motor. In [9], Radial Basis Function Neural Network is used for learning the maximum of system unknown loads and external disturbances for BLDC motor. Genetic algorithm optimized RBFNN based speed controller is presented for BLDC motor in [10]. A neural network approach for the identification and control of a separately excited direct DC motor driving a centrifugal pump load is applied in [11]. In [12], speed control of DC motor of neural network is presented. And neural networks are trained by Levenberg-Marquardt back propagation algorithm. In [3–12], the neural network is trained by off line learning algorithm. In this paper, an online learning algorithm is used to train the RBFNN. The Fuzzy logic controller is used for supervisor to train the RBFNN in online. And it is applied to control the speed of the BLDC motor. Dynamic speed response is analyzed and compared with the conventional PID controller. Control system parameter, i.e., Rise time, peak overshoot, recovery time and steady state error for speed response is measured and compared to both PID controller and proposed controller.

136.2 The Design Approach of Online Fuzzy Supervised Learning of Radial Basis Function Neural Network Controller

In this section, the design approach of online fuzzy supervised learning of neural network is presented for BLDC motor. Figure 136.1 shows the online fuzzy supervised learning of RBFNN based speed controller for BLDC motor.

Rotor position sensor and speed sensor used to measure the actual rotor position and the speed of the motor. The speed error (e) is obtained by comparing reference speed with actual speed. The rate of change of speed error (Δe) is produced by differentiating the speed error. The e and Δe is the input to the online supervised RBFNN controller. This controller also receives the supervised error (e_s) by comparing the Fuzzy PID supervised algorithm output (U_F) and output of the controller (U_a). Based on this supervised error, the parameter of RBFNN is updated in the network. The switching logic and PWM inverter are receiving the signal from the controller and rotor position sensor. The switching logic circuit provides the PWM signal for inverter based on controller output and rotor position. The speed of

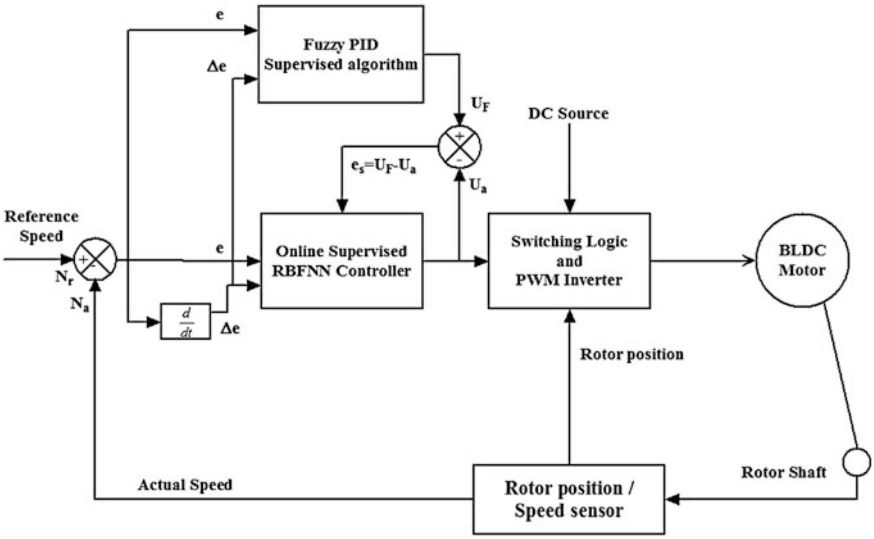

Fig. 136.1 Online Fuzzy supervised learning of RBFNN based speed controller for BLDC motor

the motor is controlled by controlling the DC bus voltage by means of triggering the switches in PWM inverter.

136.2.1 Development of Fuzzy PID Supervised Algorithm

In this section, the development of Fuzzy PID Supervised Algorithm is presented for RBFNN. Figure 136.2 shows the basic block diagram for Fuzzy supervised PID Algorithm.

Fuzzy logic PID controller consists of three main functions that are fuzzification, fuzzy rule base and defuzzification. In fuzzification, the crisp value is converted into a fuzzy variable. It receives the inputs and inputs are distributed by using membership function. In fuzzy rule base, the inputs and outputs are connected with if then rules. It has provided the relation between inputs and outputs. In defuzzification, output fuzzy value is converted into crisp value. The Fuzzy PID supervisor is modeled by Takagi-Sugeno (T-S) type system. Fuzzy PID has two inputs that are e and Δe and output (U_F). Each input has three triangular membership functions and provided in the Eq. (136.1).

$$
\begin{aligned}
\mu A_i(e, a_i, b_i, c_i) &= e - a_i/b_i - a_i \quad \text{for } a_i \le e \le b_i; \\
&\quad c_i - e/c_i - b_i \quad \text{for } c_i \le e \le b_i \\
\mu B_i(\Delta e, a_i, b_i, c_i) &= \Delta e - x_i/y_i - x_i \quad \text{for } x_i \le \Delta e \le y_i; \\
&\quad z_i - \Delta e/y_i - z_i \quad \text{for } z_i \le \Delta e \le x_i
\end{aligned}
\tag{136.1}
$$

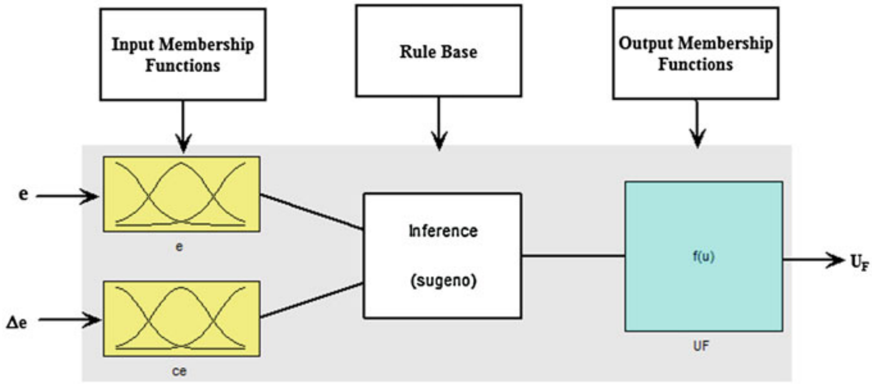

Fig. 136.2 Block diagram for fuzzy PID supervised algorithm

where a, b, c, x, y and z are adjustable location of the triangular membership functions. Output has nine constant values. The if then rules for the T-S system is given in the Eq. (136.2).

$$\begin{aligned}
&\text{Rule 1: IF e is } A_1;\ \Delta e \text{ is } B_1; \quad \text{then } f_1 = s_1\\
&\text{Rule 2: IF e is } A_1;\ \Delta e \text{ is } B_2; \quad \text{then } f_2 = s_2\\
&\vdots\\
&\text{Rule } j-1\text{: IF e is } A_i;\ \Delta e \text{ is } B_{i-1}; \quad \text{then } f_{j-1} = s_{j-1}\\
&\text{Rule } j\text{: IF e is } A_i;\ \Delta e \text{ is } B_i; \quad \text{then } f_j = s_j
\end{aligned} \tag{136.2}$$

where s is the output constant value of T-S fuzzy inference system. Figure 136.3 shows the rule base for Fuzzy PID supervised algorithm.

The weighted average defuzzification method is used in the fuzzy logic controller and given in the Eq. (136.3). Where W_j is the weight of the output membership functions.

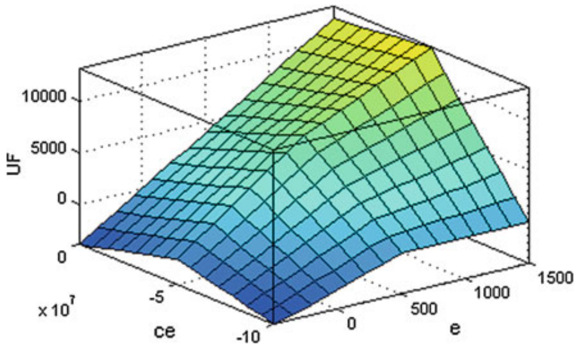

Fig. 136.3 The rule base for fuzzy PID supervised algorithm

$$U_F = W_j * f_j / \Sigma W_j \tag{136.3}$$

136.2.2 Development of Online Supervised Radial Basis Function Neural Network

In this section, development of Radial Basis Function Neural Network is described. Figure 136.4 shows the Architecture of Four Receptive Field Radial Basis Function Neural Network. In general, it combines the interpolation and approximation theory.

Consider a Gaussian basis function of centered u_i with a width parameter σ; the activation level of the ith receptive field unit or hidden layer is given in the Eq. (136.4),

$$W_i = R_i(\|x - u_i\|) = \exp\left(-(x - u_i)^2 / 2\sigma_i^2\right) \tag{136.4}$$

where x is the input multidimensional vector. Each training input (U_F) from Fuzzy PID supervised algorithm serves as a center for the basis function (R_i), the Gaussian interpolation RBFNN is given in the Eq. (136.5),

$$d(x) = \left(\sum_{i=1\ldots n} \left(c_i \exp\left(-(x - U_F)^2 / 2\sigma_i^2\right)\right)\right) / \left(\sum_{i=1\ldots n} W_i\right) \tag{136.5}$$

where c_i is the linear function of the inputs. Center and output of RBFNN are changed based upon supervised error (e_s).

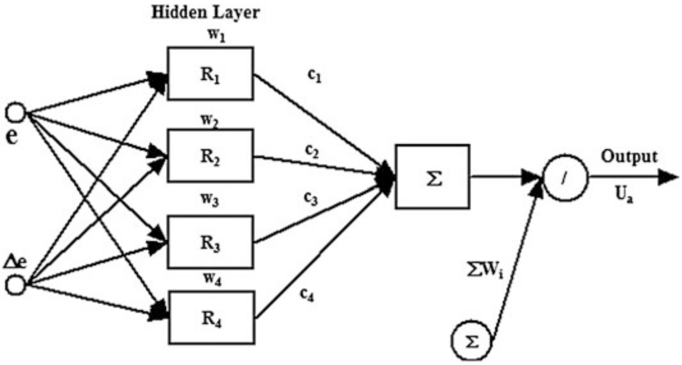

Fig. 136.4 The architecture of four receptive field radial basis function neural network

136.3 Simulink Model and Simulation Results

In order to validate the proposed controller, The Simulink model is created by MATLAB/Simulink Toolbox. And speed response is obtained for varying load conditions and varying set speed conditions. Figure 136.5 shows a Simulink model of proposed controller. The specification for the BLDC motor are follows, Nominal Power-50 Watts, Rated Current-2.5 Amps, Input Voltage-28 V DC, Rated Speed-1,500 rpm, Rated Torque-0.38 N-m.

136.3.1 Speed Response Under Varying Load Condition

Result of simulation of varying load condition under PID and proposed controller is shown in Fig. 136.6. Here, we considered two cases. Case 1, the load is varied from no load to full load at 0.2 s. Case 2, the load is varied from full load to no load at 0.4 s. The control system parameters are measured for speed response and tabulated in Table 136.1. From the results in Table 136.1, it is revealing that the performance index of all vital parameter i.e., Rise time, peak overshoot and steady state error are in favor of proposed controller only.

136.3.2 Speed Response Under Varying Set Speed Conditions

Result of simulation in varying set speed conditions under PID and proposed controller is shown in Fig. 136.7. Here, we considered two cases. Case 1, the set

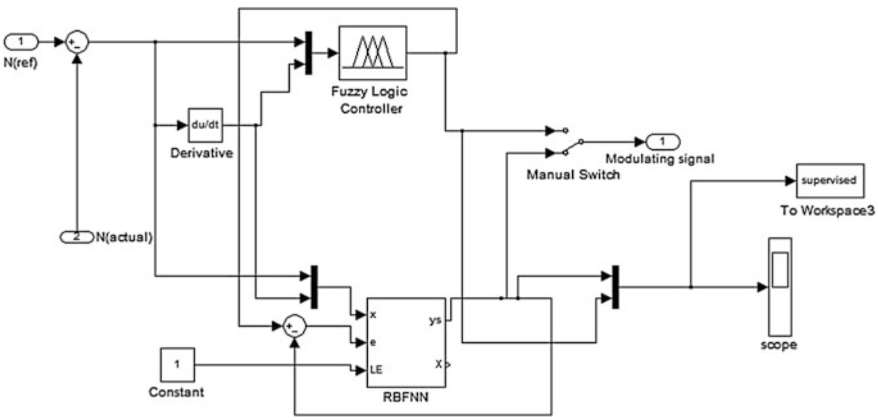

Fig. 136.5 The simulink model of online fuzzy supervised learning of radial basis function neural network

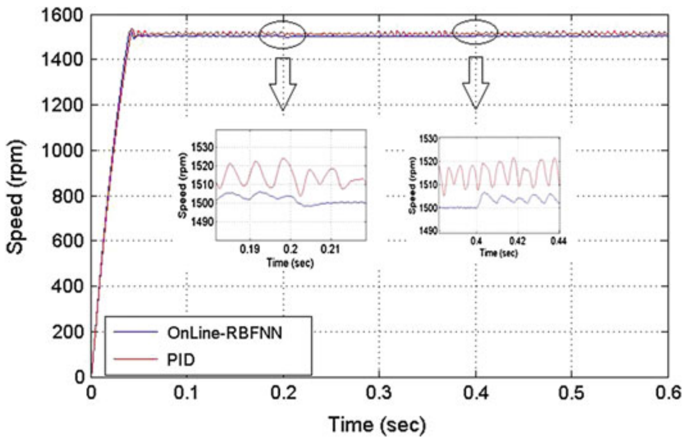

Fig. 136.6 Speed response of BLDC motor under varying load condition with PID and proposed controller

Table 136.1 Control system parameters under varying load conditions

Controller	Rise time (s)		Peak over shoot (%)		Steady state error (rpm)	
	Case 1	Case 2	Case 1	Case 2	Case 1	Case 2
PID	0.04	–	2.6	1.46	12	15
Online RBFNN	0.035	–	1.5	0.33	0.5	3.5

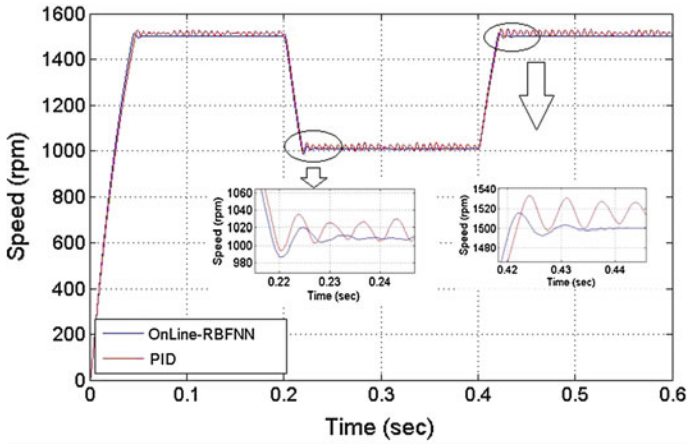

Fig. 136.7 Speed response of BLDC motor under varying set speed condition with PID and proposed controller

Table 136.2 Control system parameters under varying set speed conditions

Controller	Recovery time (s)		Peak over shoot (%)		Steady state error (rpm)	
	Case 1	Case 2	Case 1	Case 2	Case 1	Case 2
PID	0.30	0.50	3.5	3.2	15	17
Online RBFNN	0.22	0.43	2.0	1.5	8	0.5

speed is varied from 1,500 to 1,000 rpm at 0.2 s. Case 2, the set speed is varied from 1,000 to 1,500 rpm at 0.4 s. The control system parameters are measured for speed response and tabulated in Table 136.2.

From the results in Table 136.2, it is revealing that the performance parameters are in favor of proposed controller only.

136.4 Conclusion

An online fuzzy supervised learning of RBFNN is proposed and simulated for BLDC motor. The aim of this paper is to develop an online learning algorithm for RBFNN. The Fuzzy PID supervised algorithm is applied to the RBFNN and it is compared with PID control. In case of PID controller, produces more oscillation in the speed response and has large steady state error. In case of proposed controller, produces less oscillation and has less steady state error when compared to PID control. From the results, proposed controller outperforms than PID controller under varying load and set speed conditions.

References

1. Wang HB, Liu HP (2009) A novel sensorless control method for brushless DC motor. IET Electr Power Appl 3(3):240–246
2. Singh B, Singh S (2010) Single-phase power factor controller topologies for permanent magnet brushless DC motor drives. IET Power Electron 3(2):147–175
3. Joice CS, Paranjothi SR, Kumar VJS (2013) Digital control strategy for four quadrant operation of three phase BLDC motor with load variations. IEEE Trans Indus Info 9 (2):974–982
4. Karthikeyan J, Dhana Sekaran R (2011) Current control of brushless DC motor based on a common DC signal for space operated vehicles. Electr Power Energy Syst 33(10):1721–1727
5. Shen JX, Zhu ZQ, Howe D, Buckley JM (2005) Fuzzy logic speed control and current-harmonic reduction in permanent-magnet brushless AC drives. IEE Proc Electr Power Appl 152(3):437–446
6. Rubaai A, Castro-Sitiriche MJ, Ofoli AR (2003) DSP-based laboratory implementation of hybrid fuzzy-PID controller using genetic optimization for high-performance motor drives. IEEE Trans Indus Appl 44(6):1977–1986

7. Premkumar K, Manikandan BV (2013) Adaptive fuzzy logic speed controller for brushless DC motor. In: IEEE international conference on power, energy and control, pp 290–295
8. Gokbulut M, Tekin A (2006) An educational tool for neural network control of brushless DC motors. Int J Eng Educ 22(1):197–204
9. Cheng Z, Hou C, Wu X (2009) Global sliding mode control for brushless DC motors by neural networks. IEE Proc Art Intell Comp Intell 4:3–6
10. Wang Y, Xia C, Zhang M (2007) Adaptive speed control for brushless DC motors based on genetic algorithm and RBF neural network. In: IEE Proceeding of Con and Auto, pp 1219–1222
11. Feilat EA, Maaitab EK (2012) RBF neural network approach for identification and control of DC motors. Tech J Electr Res 9(2):80–89
12. Atri A, Ilyas M (2012) Speed control of DC motor using neural network configuration. Int J Adv Res Comp Sci Soft Eng 2(5):209–212

Chapter 137
Modeling of Wind Turbine Power Curves Using Firefly Algorithm

N. Karthik, R. Arul and M.J. Hari Prasad

Abstract Wind turbine power curve portrays the relationship between the wind speed and output power of the turbine. Wind speed values ranging between cut-in speed and cut-out speed acquire the most vital role for estimating wind power curve models. All wind turbines have different cut-in and cut-out speed limits and generation of electricity could be accomplished in a definite interval that could be termed as affective interval. This paper presents the development of parametric model of wind turbine power curves. An evolutionary strategy algorithm is used to build a nonlinear parametric model to monitor the performance of wind turbine. The parameters of these logistic expressions have been solved using firefly algorithm. The wind turbine power curve is constructed using historical wind turbine data obtained from three different wind turbine manufacturers.

Keywords Power curve modeling · Firefly algorithm (FFA) · Root mean squared error (RMSE) · Mean absolute error (MAE)

137.1 Introduction

A well-designed and optimum energy system will be cost effective, reliable and in addition, would perk up the quality of life of its consumers. Accurate modeling of all the components of any system is a decisive step for its optimization. Obviously, knowledge of all the factors which manipulate the performance of that system is a prerequisite for accurate modeling. The power curve establishes the basic correlation between the wind speed at a site and the power produced by a specific wind

N. Karthik (✉)
Department of Electrical and Electronics Engineering, Hindustan University, Chennai, India
e-mail: snkarthik3@gmail.com

R. Arul · M.J.H. Prasad
Department of EEE, ARM College of Engineering and Technology, Maraimalainagar, Chennai, India

C. Kamalakannan et al. (eds.), *Power Electronics and Renewable Energy Systems*,
Lecture Notes in Electrical Engineering 326, DOI 10.1007/978-81-322-2119-7_137

turbine. Performance of a single wind turbine can be exemplified by a power curve —a graphical representation of the turbine electric power output as a function of the wind speed. With such a curve, turbine power output and energy production can be visualized without detailed knowledge of turbine operations and its control schemes. Developing nonlinear parametric models characterizing the power generating process is a challenge for power monitoring of wind turbines. There are three key points on this curve: (1) cut-in speed below which the turbine will not produce power; (2) rated speed at which the rated power of the turbine is produced; and (3) cut-off speed beyond which the turbine is not allowed to deliver power.

The theoretical power obtained from wind is given by

$$P = 0.5\rho\pi R^2 C_p(\lambda, \beta)u^3 \tag{137.1}$$

where P is the theoretical power captured by the rotor of a wind turbine, ρ is the air density, R is the radius of the rotor determining its swept area, C_p is the power coefficient, λ is the tip-speed ratio, and u is the wind speed [1]. The air density ρ at the turbine's hub height remains more often than not constant over a long-time horizon. The power coefficient specifies the efficiency of a turbine capturing the wind energy. Wind turbine power curves principally designate the performance of turbines. As the wind turbine power curves under normal conditions are made available by the turbine manufacturers, any irregularities can be effectively detected by monitoring them. An accurately modeled power curve can serve as a tool for wind forecast too. Since wind energy is stochastic in nature, prediction models for forecasting wind power are required. Wind turbine power curves can be used as a reference for predicting the output power of a turbine if the forecasted wind speed is available. Power curves represented for many turbines can help in simulation of planned expansions in a power system with wind power [2]. A parametric wind turbine power curve which could be used for prediction, control, monitoring and optimization of wind farm performance has also been developed in [2]. Accurately modeled wind turbine power curves can also serve as a basis of comparison between the performances of available turbines, serving the customers to make a proper option based on their requirements. Wind turbine power curve models can be classified into parametric and nonparametric models. The parametric least squares model and the nonparametric nearest neighbor model illustrated greater accuracy than the other models in [3]. A critical analysis of a variety of methods used for modeling of wind turbine power curves like weibull distribution, method of least squares, and cubic spline interpolation have been compared in [3]. Parametric models of the wind turbine power curve have been evolved using advanced algorithms like genetic algorithm, particle swarm optimization, evolutionary programming and differential evolution in [4]. Nonparametric models of the power curve also have been developed using neural networks, fuzzy c-means clustering and data mining in [4]. In [5], data mining and evolutionary computation algorithm for power optimization of wind turbines based on a data driven approach have been presented. The best results were obtained when the fuzzy logic modeling was

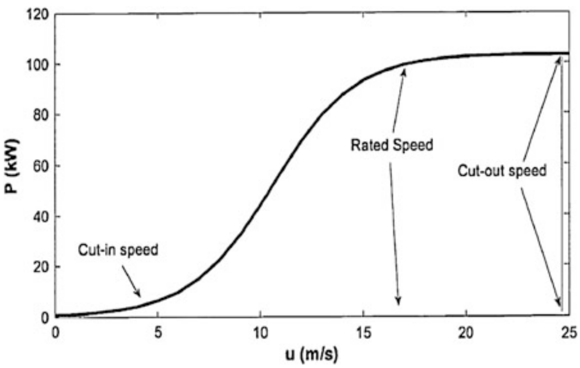

Fig. 137.1 Wind turbine power curve

implemented. A probabilistic model to illustrate the dynamics of the output power of wind turbine has been discussed in [6] (Fig. 137.1).

This paper has exploited the advantages offered by the modern nontraditional optimization technique for modeling of wind turbine power curve. This paper presents the implementation of firefly algorithm for modeling of wind turbine power curves. Nonparametric model of wind turbine power curves have been developed and their accuracy has been determined using the root mean squared error (RMSE) and mean absolute error (MAE) as performance metrics. The models are developed using five sets of data.

137.2 Power Curve Models

The wind turbine power curve can be modeled using parametric and nonparametric methods. In statistics, a parametric model is a family of distributions that can be described using a finite number of parameters. These parameters are usually composed together to form a single-dimensional parameter vector. In order to find out the value of the single-dimensional vector parameter, the modeling of the power curve using a four-parameter logistic expression can be defined as an optimization problem as follows:

Minimize Objective function

$$\sum_{i=1}^{N} [P_e(u_i) - P_a(i)]^2 \tag{137.2}$$

The shape of the power curve can be approximated using a logistic expression with four parameters [7]. The four-parameter logistic function is given by

$$P_e(u_i) = f(u_i, \theta) = d + (a - d)/(1 + \left(\frac{u_i}{c}\right) b) \tag{137.3}$$

where $\theta = (a, b, c, d)$ is the parameter vector of the four parameter logistic function.

The estimated power is calculated by $P_e(u_i) = d + (a - d)/(1 + (\frac{u_i}{c})b)$

The following are the constraints:

$$\left.\begin{array}{l} a_{min} \le a \le a_{max},\ b_{min} \le b \le b_{max} \\ c_{min} \le c \le c_{max},\ d_{min} \le d \le d_{max} \end{array}\right\} \quad (137.4)$$

137.3 Estimating Parameters with the Firefly Algorithm

The firefly algorithm is a meta heuristic algorithm, inspired by the flashing behavior of fireflies. The primary purpose for a firefly's flash is to act as a signal system to attract other fireflies. The intensity (I) of flashes decreases as the distance (r) increases and thus most fireflies can communicate only up to several hundred meters. In the implementation of the proposed firefly algorithm, the flashing light is formulated in such a way that it gets associated with the objective function to be optimized.

In firefly algorithm, there are three idealized rules:

1. All fireflies are unisexual, so that one firefly will be attracted to all other fireflies;
2. Attractiveness is proportional to their brightness, and for any two fireflies, the less bright one will be attracted by (and thus move to) the brighter one; however, the brightness can decrease as their distance increases;
3. If there are no fireflies brighter than a given firefly, it will move randomly.

Based on these three rules the pseudo code of the Firefly algorithm can be prepared.

PSEUDO CODE OF THE FFA:

Objective function of f(x), where x = $(x_1,\ldots,x_d)$
Generate initial population of fireflies;
Formulate light intensity I;
Define absorption coefficient γ;
While (t < MaxGeneration)
For i = 1 to n (all n fireflies);
For j = 1 to n (all n fireflies)
If $(I_j > I_i)$, move firefly i towards j;
End if
Evaluate new solutions and update light intensity;
End for j;
End for i;
Rank the fireflies and find the current best;
End while;
Post process results and visualization;
End procedure;

The brightness should be associated with the objective function. FA has two major advantages over other algorithms: automatic subdivision and the ability of dealing with multimodality. First, FA is based on attraction and attractiveness decreases with distance. This leads to the fact that the whole population can automatically subdivide into subgroups, and each group can swarm around each mode or local optimum. Among all these modes, the best global solution can be found. Second, this subdivision allows the fireflies to be able to find all optima simultaneously if the population size is sufficiently higher than the number of modes. Mathematically, $1/\sqrt{\gamma}$ controls the average distance of a group of fireflies that can be seen by adjacent groups. Therefore, a whole population can subdivide into subgroups with a given, average distance. In the extreme case when $\gamma = 0$, the whole population will not subdivide. This automatic subdivision ability makes it particularly suitable for highly nonlinear, multimodal optimization problems.

137.4 Results and Analysis

The modeling of the wind turbine power curve has been carried out using five sets of data from three different wind turbine manufacturers. The first five datasets were obtained from the wind turbine manufacturer GE Wind Energy India [10]. The second five datasets were obtained from the wind turbine manufacturer Suzlon Energy Limited [10]. The third five datasets were obtained from the wind turbine manufacturer Vestas Wind Technology Private Limited [10]. The performance of the parametric model has been evaluated using the performance metrics MAE and RMSE which are characterized as follows:

$$\mathrm{MAE} = \frac{1}{N}\sum_{i=1}^{N}|P_e(u_i) - P_a(i)| \tag{137.5}$$

$$\mathrm{RMSE} = \sqrt{\frac{1}{N}\sum_{i=1}^{N}(P_e(u_i) - P_a(i))^2} \tag{137.6}$$

The RMSE is a measure of the differences between values predicted by a model or an estimator and the values actually observed. Basically, the RMSE corresponds to the sample standard deviation of the differences between predicted values and observed values. It is a quadratic scoring rule which measures the average magnitude of the error. Expressing the formula in words, the difference between forecast and corresponding observed values are each squared and then averaged over the sample. Finally, the square root of the average is taken. Since the errors are squared before they are averaged, the RMSE gives a relatively high weight to large errors. This means the RMSE is most useful when large errors are particularly undesirable. The MAE measures the average magnitude of the errors in a set of forecasts, without considering their direction. It measures accuracy for continuous variables. The equation is given in the library references. Expressed in words, the MAE is the average over the verification sample of the absolute values of the differences between forecast and the corresponding observation. The MAE is a linear score which means that all the individual differences are weighted equally in the average. The MAE and the RMSE can be used together to diagnose the variation in the errors in a set of forecasts. The RMSE will always be larger or equal to the MAE; the greater difference between them, the greater the variance in the individual errors in the sample. If RMSE equals MAE, then all the errors are of the same magnitude. The optimized values of the four parameters have been tabulated in Table 137.1 for all the datasets of three different wind turbine manufacturers. The four parameters are optimized using firefly algorithm such that the difference between MAE and RMSE is reduced to a minimum. The MAE and RMSE values have been tabulated in Table 137.2 for all the datasets. The number of datasets considered was 60 for GE Wind Energy India and 30 for Suzlon Energy Limited and Vestas Wind Technology Private Limited. The proposed firefly algorithm has been ranked based on their error measures in Table 137.3 for each dataset obtained from different wind turbine manufacturers. When the RMSE and MAE measure is considered, Dataset 2

Table 137.1 Parameters of 4-parameter logistic function

GE Wind Energy India				
	A	B	C	D
Dataset 1	40.871	43.274	7.653	1186.290
Dataset 2	18.515	17.067	8.853	1178.041
Dataset 3	20.516	60.734	10.574	1077.998
Dataset 4	16.674	29.370	23.202	1056.000
Dataset 5	24.310	34.477	8.549	1629.538
Suzlon Energy Limited				
Dataset 1	4.325	8.853	7.995	197.479
Dataset 2	6.859	7.658	7.953	675.701
Dataset 3	11.004	8.575	8.062	696.963
Dataset 4	10.478	11.227	8.873	705.254
Dataset 5	0.085	10.295	7.955	709.591
Vestas Wind Technology Private Limited				
Dataset 1	1.499	7.415	8.026	155.564
Dataset 2	3.460	8.685	10.576	157.253
Dataset 3	0.132	9.796	9.391	342.060
Dataset 4	−0.085	24.178	146.290	363.803
Dataset 5	3.221	7.616	8.006	455.905

Table 137.2 Determination of RMSE and MAE

	GE Wind Energy India		Suzlon Energy Limited		Vestas Wind Technology Private Limited	
	RMSE	MAE	RMSE	MAE	RMSE	MAE
Dataset 1	541.400	190.35	66.805	47.08	47.966	35.670
Dataset 2	526.438	171.965	211.204	168.38	62.374	50.290
Dataset 3	676.222	376.656	211.76	158.85	113.414	90.40
Dataset 4	1051.912	725.256	221.276	179.31	398.935	282.63
Dataset 5	859.630	289.006	216.043	172.14	140.331	105.50

Table 137.3 Analysis of results

	GE Wind Energy India		Suzlon Energy Limited		Vestas Wind Technology Private Limited	
	RMSE	MAE	RMSE	MAE	RMSE	MAE
Dataset 1 rank	2	2	1	1	1	1
Dataset 2 rank	1	1	2	3	2	2
Dataset 3 rank	3	4	4	2	3	3
Dataset 4 rank	5	5	5	5	5	5
Dataset 5 rank	4	3	3	4	4	4

is ranked 1 for the wind turbine data obtained from GE Wind Energy India and Dataset 1 is ranked 1 for the wind turbine data obtained from Suzlon Energy Limited and Vestas Wind Technology Private Limited.

137.5 Conclusion

The wind turbine power curve has been modeled using firefly algorithm in this paper. A nonlinear parametric model of the wind turbine power curve was constructed with an evolutionary computation algorithm. Since the wind turbine power curve is one of the important indicators of its performance, precisely modeled power curves will definitely improve the wind turbine performance and contribute enormously in renovating a wind farm into a wind power plant. The wind turbine power curve model developed using firefly algorithm can be used to examine the online performance of the wind turbine and also for developing wind power forecasting models.

Acknowledgments The author wish to thank the Management of Hindustan University, Padur Chennai for their support and encouragement to carry out this work.

References

1. Kusiak A, Zheng H, Song Z (2009) On-line monitoring of power curves. J Renew Energy 34 (6):1487–1493
2. Kusiak A, Zheng H, Song Z (2009) Models for monitoring wind farm power. J Renew Energy 34(3):583–590
3. Thapar V, Agnihotri G, Sethi VK (2011) Critical analysis of methods for mathematical modeling of wind turbines. J Renew Energy 36(11):3166–3177
4. Lydia M, Immanuel Selvakumar A, Suresh Kumar S, Edwin Prem Kumar G (2013) Advanced algorithms for wind turbine power curve modeling. IEEE Trans Sustainable Energy 4 (3):827–835
5. Kusiak A, Zheng H, Song Z (2010) Power optimization of wind turbines with data mining and evolutionary computation. J Renew Energy 35:695–702
6. Jin T, Tian Z (2010) Uncertainty analysis for wind energy production with dynamic power curves. In: Proceedings of 2010 international conference probabilistic methods applied to power systems, pp 745–750
7. Gottschalk PG, Dunn JR (2005) The five parameter logistic: a characterization and comparison with the four-parameter logistic. J Anal Biochem 343(1):54–65
8. Lydia M, Suresh Kumar S (2010) Wind Farm Power Prediction: An Overview. In: Proceedings of 2010 international symposium on computational wind engineering, Chapel Hill
9. Lydia M, Suresh Kumar S, Immanuel Selvakumar A, Edwin Prem Kumar G (2014) A comprehensive review on wind turbine power curve modeling techniques. J Renew Sustain Energy Rev 30:452–460
10. http://www.inl.gov/wind/software

Chapter 138
An Innovative Classification Model for CAD Dataset Using SVM Based Iterative Linear Discriminant Analysis

G. Nalini Priya and A. Kannan

Abstract Data mining plays an important role in medical data analysis. It considers large datasets and is capable of discovering interesting patterns that help to represent and use the nature of medical data. Moreover, these data patterns are useful for the medical practitioners for making effective decisions since it collects the necessary temporal information from large data repositories by applying intelligent data mining techniques. In this paper,a statistical technique is proposed for performing effective decision making in medical application, screening and manipulating the training samples with little bit of Gaussian distribution random values (GDRV) before using the data for training the neural network. This paper present, a way to improve the performance of a neural network based classification model through the proposed algorithm which has been evaluated with the coronary artery disease (CAD) data sets taken from University California Irvine (UCI). The scope of this paper is to present an iterative LDA based classification method for the classification of multivariate data sets. The performance of the proposed iterative LDA based classifier will be evaluated with standard metrics.

Keywords CAD · Heart disease · Classification · Multivariate data · SVM · ANN · LDA random values

138.1 Introduction

Representation and analysis of temporal data pertaining to medical diagnosis systems is gaining importance recently. This helps to perform temporal analysis, where temporal databases are created using knowledge representation models. These

---

G.N. Priya (✉)
Department of Information Technology, Saveetha Engineering College, Anna University, Chennai, India
e-mail: nalini.anbu@gmail.com

A. Kannan
Department of Information Science and Technology, Anna University, Chennai, India

C. Kamalakannan et al. (eds.), *Power Electronics and Renewable Energy Systems*, Lecture Notes in Electrical Engineering 326, DOI 10.1007/978-81-322-2119-7_138

models provide features for temporal rules extraction, which may be further used for decision support system. Clustering, Classification and other data mining algorithms play major role in designing [1, 2] such pervasive computing environments in smart hospitals. For instance, classification algorithms are often useful in patient activity classification [3, 4] and the diagnosis of a disease using a multivariate clinical data, which were acquired from the hospital environment using different [5, 6] technologies. This data may be the combination of different types.

Development of computer methods for the diagnosis of heart disease attracts many researchers [1]. At the earlier time, the use of computer is to build knowledge based decision support system which uses knowledge from medical experts and transfers this knowledge [7–9] into computer algorithms manually. This process is time consuming and really depends on medical expert's opinion which may be subjective. To handle this problem, machine learning techniques have been developed in this work to gain knowledge automatically from examples or raw data.

138.1.1 Coronary Artery Disease (CAD)

CAD is a chronic disease in which the coronary arteries gradually hardens and narrow. It is the most common form of cardiovascular disease and the major cause of heart attacks in all countries. Moreover, cardiovascular disease is the leading killer of while considering other diseases. The data generally used for diagnosing the CAD will be multivariate in nature. Having so many factors to analyze to diagnose the heart diseases, physicians generally make decisions by evaluating the current test results of the patients. The previous decisions made on other patients with the same condition are also examined by the physicians. These complex procedures are not easy when considering the number of factors that the physician has to evaluate. So, diagnosing [10] the heart disease of a patient involves experience and highly skilled physicians. In the last few decades computational tools have been designed to improve the experiences and abilities of physicians for making decisions about their patients.

138.1.2 Classification Using LDA

Linear Discriminant Analysis (LDA) is a classification method originally developed in 1936 by R. A. Fisher. It is simple, mathematically robust and often produces models whose accuracy is as good as more complex methods.LDA is based upon the concept of searching for a linear combination of variables (predictors) that best separates two classes (targets). To capture the notion of separability, Fisher defined the following score function.

A new point is classified by projecting it onto the maximally separating direction and classifying it as c1 if

$$\beta^T\left(x-\left(\frac{\mu_1+\mu_2}{2}\right)\right) > \log(\frac{p(c_1)}{p(c_2)})$$

where

β^T	is the coefficients vector,
X	is the data,
$\left(\frac{\mu_1+\mu_2}{2}\right)$	is the mean vector,
$\log\left(\frac{p(c_1)}{p(c_2)}\right)$	is the class probability

In practical classification problems, the class means and covariance are not known. They can, however, be estimated from the training set. Either the maximum likelihood estimate or the maximum a posteriori estimate may be used in place of the exact value in the equations.

138.1.3 Problem Definition

The clinical data which will be used to diagnose a disease will be a mixed type of data, which contains different types of attributes. Classification of a data can be solved by using a lot of methods from simple methods such as nearest neighbor method to complex methods such as decision trees, neural networks and genetic algorithms. However, it is known that classification of multivariate data are a difficult problem because of several reasons. Generally, this kind of medical data or multivariate data will contain an error and missing values and will not always be pure. Further, the mutual dependence of attributes or variables causes distortion of the space. Due to an effect called "boundary effect", the nearest points seem to be rather far and farther points near and this causes considerable error in distance calculation during the clustering or classification process. Hence most of the algorithms which are used for classification cannot be applied on multivariate data.

Motivated by the need of such an expert system, this paper, we propose a hybrid model for improving the performance of machine learning based classification system. In this paper, we address a simple methods for improving the training performance and make the algorithm to provide a constant performance in terms of accuracy and little a bit improvement in accuracy itself. For achieving this statistical technique is used for screening and manipulating the training samples along with the neural network.

138.2 Classification Methods Under Evaluation

Classification is the process of grouping a set of physical or abstract objects into classes of similar objects. A cluster is a collection of data objects that are similar to one another with the same cluster and are dissimilar to the objects in other clusters. This has been widely used in numerous applications, including pattern recognition, data analysis, image processing, and market research, etc. Classification is a very important application area but widely interdisciplinary in nature, that makes it very difficult to define its scope.

138.2.1 Supervised Learning Methods

In the Training a neural network [11, 12] model essentially means selecting one model from the set of allowed models (or, in a Bayesian framework, determining a distribution over the set of allowed models) that minimizes the cost criterion. There are numerous algorithms available for training neural network models; most of them can be viewed [5, 13, 14] as a straightforward application of optimization theory and statistical estimation. Most of the algorithms used in training artificial neural networks are employing some form of gradient descent.

138.2.2 Support Vector Machines (SVM)

Support vector machine is a pattern classification algorithm developed by Vapnik. SVM originally designed to solve problems [5, 15, 16, 17] where data can be separated by a linear decision boundary. By using kernel functions, SVMs can be used effectively to deal with problems that are not linearly separable in the original space. Some of the commonly used kernels include Gaussian Radial Basis Functions (RBFs), polynomial functions, and sigmoid polynomials whose decision [13, 18] surfaces are known to have good approximation properties. Relying on the fact that the training data set is not linearly separable, a Gaussian Radial Basis Function (RBF) kernel is selected in this paper. The RBF kernel performs usually better for the reason that it has better boundary response as it allows for extrapolation.

138.2.3 The Proposed Iterative Model Search _LDA (IMS_LDA) Algorithm

Let D_{train} be the set of healthy records and sick records to be normally trained with the support vector machine.

$$\text{Dtrain} = \{\ \text{h1},\ \text{h2},\ \text{h3}\ldots\text{hm},\ \text{s1},\ \text{s2},\ \text{s3}\ldots\ \text{sn}\}$$

$$\text{H} = \{\text{h1},\ \text{h2},\ \text{h3}\ldots\ \text{hm},\}$$

be the separated set of healthy records

$$\text{S} = \{\text{s1},\ \text{s2},\ \text{s3}\ldots\text{sn}\}$$

be the separated set of sick records

//Separate N, records with Statistically insignificant distance

```
N={}
for i=1 to m {
    for j= i to n {
        dij = (( h1 - s1 ) 2)1/2
        if dij < dmin {
N← N∪{ h1 , s1 }
        }
    }
}
Amax← 0
For I=1: Imax {
      Lpredict ← LDA_classify(Dtrain, N, LN)
      AI ← Accuracy(Ltrain, Lpredict)

   if  AI > Amax {
   Mopt ← N
 Amax ← AI
  }
     D1 ← Dtrain ∩ N
     N ← N + η
     Dtrain ← D1 ∪ N
}

Ltest← LDA_classify (Dtest, Mopt, LN)
```

where

m	is the total number of healthy records
n	is the total number of sick records
d_{ij}	is the Euclidean distance between two records
d_{min}	is a minimum expected distance between healthy and sick records
N	is the set of more Statistically insignificant records which should not be directly used to train the network (from the healthy and sick records)
D_1	is the set of more significant records which can be directly used to train the network
I_{max}	is the Maximum Iterations
M_I	is the Model arrived at Ith Iteration

$L_{predict}$ is the predicted labels of Training records using the Model M_I at Ith Iteration
A_I is the Prediction Accuracy at Ith Iteration
R is the random noise added
M_{opt} is the optimum model which will be used for classifying the testing data
η is a set of small random values of the same size of set N

But, set N will contain records which are pair of records which will be statistically much similar to one another. We believe that this insignificant difference between the records of two different categories will lead to poor training in any machine learning based models as well as any classification method.

To improve the training performance and recognition rate, we propose the a little bit of random noise on the statistically weak set of data N.

$$D_2 = N + \eta$$

where η is a set of random values (between −1 and 1) of the same size of the set individual attributes of the set N and will be added to the corresponding individual attributes set of N records.

This set of noise values can be guessed randomly or based on the previous experience of training. The addition of this random noise in the statistically very similar records will make them statistically different from one another, at least with a minimum significance.

138.3 Implementation and Evaluation

To evaluate the proposed algorithm, a suitable and standard multivariate data set is needed. A suitable UCI data set called "cleveland.data" [10, 19], concerning heart disease diagnosis is used for the evaluation of the algorithms under consideration. This data was originally provided by Cleveland Clinic Foundation. This database contains 303 records with 13 attributes which have been originally extracted from a larger set of 75 attributes and a class attribute among the 303 records, 164 belongs to healthy and remaining are from diseased. As far as the proposed Clevend data set is concerned, only few of the records contained missing values. We just removed them; so that the total records become 297. Almost all the classification algorithms will work good if the input data is in normalized form. In out proposed evaluation system, after loading the CAD data, the data will be normalized by dividing each value of the attribute with the maximum value of that particular attribute (or column). This will lead to values between 0 and 1 which will be suitable for almost all the classification algorithm.

138.3.1 Metrics Considered for Evaluation

Three metrics such as sensitivity, specificity and accuracy has been considered in this work. Sensitivity measures the proportion of actual positives which are correctly identified as such (e.g. the percentage of sick people who are correctly identified as having the condition). Specificity measures the proportion of negatives, which are correctly identified (e.g. the percentage of healthy people who are correctly identified as not having the condition). Accuracy of a measurement system is the degree of closeness of measurements of a quantity to its actual (true) value.

138.4 The Results of the Evaluation

We have successfully implemented the proposed algorithms under Matlab and repeated the experiments with different set of parameters to obtain optimum performance with the proposed model. The following table is showing the performance of the normal SVM based algorithm along with the proposed algorithm. The experiments were repeated for different set of randomly shuffled samples and the significant results were tabulated (Table 138.1).

On the randomly selected traing sets and the testing sets. It was observed that the performance of IMS_LDA method was high and better than all other methods. In terms of accuracy, the proposed IMS-LDA Method as well as the other proposed methods performed better than all other earlier works.

In this research work, IMS-LDA have been proposed and implemented for classifying two Coronary Artery Disease (CAD) data sets namely Cleveland and Stat log from UCI repository. From the experiments carried out in this work, it has been observed that the proposed classification algorithms provide better accuracy when they are compared with decision tree and SVM due to the application of temporal constraints. But most of the existing algorithms (SVM-BT,SVM-IMS) were not giving ideally good classification results while applying them on multivariate CAD dataset to meet the challenges of accurate classification in the multivariate heart datasets.

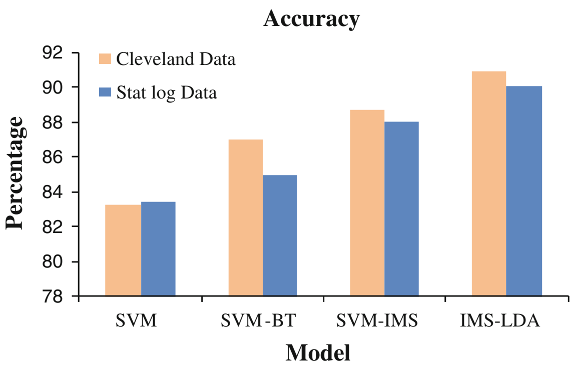

Table 138.1 The average performance of Cleveland and Stat log dataset

	Cleveland dataset			Stat log dataset		
Method	Sensitivity	Specificity	Accuracy	Sensitivity	Specificity	Accuracy
SVM	76.82	89.11	83.26	89.99	75.42	83.42
IMS_LDA	81.37	90.78	90.91	91.30	82.86	90.01

In this work iterative model search LDA based (IMS-LDA) classification model have been proposed to provide accurate classification. The experiments were repeated for different set of randomly shuffled data sets. This algorithm is mathematically robust and often produces models whose accuracy is as good as more complex methods.

138.5 Conclusion

In this paper, we propose a IMS–LDA method for enhancing the accuracy of classification algorithms for the diagnosis of coronary artery disease. The results obviously show the complex nature of data set restricts these algorithms from achieving better accuracy if we directly train the SVM with the data. It was realized that the reason for this poor classification is due to the insignificant difference between some of the records of the two classes under classification. The statistically indistinguishable records were separated from the training set and a Gaussian Distribution Random values were added to them to make them somewhat distinguishable from one another. This lead to better performance in terms of accuracy of classification. In this implementation, we used simple Euclidean distance based metric for isolating the problematic or statistically indistinguishable records from the original training data set. Finally a temporal classifier which can handle uncertainty of medical dataset accurately can be developed as a further work.

References

1. Setiawan NA, Venkatachalam PA, Hani AFM (2009) Diagnosis of coronary artery disease using artificial intelligence based decision support system. In: Proceedings of the international conference on man-machine systems (ICoMMS), Malaysia, Oct 2009
2. Deng Z (2010) Robust relief-feature weighting, margin maximization, and fuzzy optimization. IEEE Trans Fuzzy Syst 18(4):726–744
3. Wei J-M, Wang S-Q et al (2010) Ensemble rough hypercuboid approach for classifying cancers. IEEE Trans Knowl Data Eng 23(3):381–389
4. Sahbi H (2011) Context-dependent kernels for object classification. IEEE Trans Pattern Anal Mach Intell 33(4):699–708
5. Windeatt T (2011) Embedded feature ranking for ensemble MLP classifiers. IEEE Trans Neural Netw 22(6):907–968

6. Dutta H, Kargupta H, Datta S, Sivakumar K (2003) Analysis of privacy preserving random perturbation techniques further explorations. In: Proceedings of the 2003 ACM workshop on privacy in the electronic society, pp 31–38, New York, USA, ACM 2003
7. Grinblat Guillermo L et al (2011) Solving nonstationary classification problems with coupled support vector machines. IEEE Trans Neural Netw 22(1):37–51
8. Masud MM et al (2011) Classification and novel class detection in concept-drifting data streams under time constraints. IEEE Trans Knowl Data Eng 23(6):859–874
9. Cheng H et al (2010) Efficient algorithm for localized support vector machine. IEEE Trans Knowl Data Eng 22(4):381–389
10. Ince T, Kiranyaz S, Pulkkinen J, Gabbouj M (2010) Evaluation of global and local training techniques over feed-forward neural network architecture spaces for computer-aided medical diagnosis. Elsevier—Expert Syst Appl 37(12):8450–8461
11. Wang B (2011) ELITE: ensemble of optimal input-pruned neural networks using TRUST-TECH. IEEE Trans Neural Netw 22(4):96–107
12. Gutiérrez PA (2011) Logistic regression by means of evolutionary radial basis function neural networks. IEEE Trans Neural Netw 22(2):246–278
13. Khan SS, Kant S (2007) Computation of initial modes for K-modes clustering algorithm using evidence accumulation, IJCAI
14. Yang J-B (2011) Determination of global minima of some common validation functions in support vector machine. IEEE Trans Neural Netw 22(4):656–678
15. Windeatt T (2011) Embedded feature ranking for ensemble MLP classifiers. IEEE Trans Neural Netw 22(6):907–968
16. Alvarez G, Coiera E (2005) Interuptive communication patterns in the intensive care unit ward round. J Med Informatics 74(10):779–781
17. Yang J-B et al (2011) Determination of global minima of some common validation functions in support vector machine. IEEE Trans Neural Netw 22(4):654–659
18. Yang Jian-Bo (2011) Determination of global minima of some common validation functions in support vector machine. IEEE Trans Neural Netw 22(4):656–678
19. Das R, Turkoglu I, Sengur A (2009) Effective diagnosis of heart disease through neural networks ensembles. Elsevier—Expert Syst Appl 36(4):7675–7680

Chapter 139
Phenotypic Evolutionary Programming for Economic Operation of Thermal—Wind Coordination

W.A. Augusteen, R. Rengaraj and N.B. Muthu Selvan

Abstract This paper aims to solve Economic Dispatch (ED) problem involving conventional thermal generators with wind generation. This co-ordinated ED problem is solved by the application of Phenotypic Evolutionary Programming (PhEP) with correlated mutation. In the recent past it has become necessary to utilize renewable energy generation as an alternative for thermal energy power generation due to its depletion nature. This paper considers wind power generation as renewable generation. The main advantage of wind power generation is that it produces cleaner electrical power without introducing harmful environmental pollutants. The incorporation of wind generation into conventional ED problem modifies to a higher degree of non-linear problem. Hence this paper attempts to solve this wind integrated ED problem through PhEP algorithm with correlated mutation. The proposed algorithm has been tested with standard 3, 13 and 40 unit test systems and implemented through matlab.

Keywords Economic dispatch · Wind energy · Evolutionary programming

139.1 Introduction

The Economic Dispatch (ED) problem is one of immense importance that dominates the researchers conducted in the field of power systems. ED is to acquire minimum production cost from available generated power to the system connected

W.A. Augusteen (✉) · R. Rengaraj · N.B.M. Selvan
Department of Electrical and Electronics Engineering, SSN College of Engineering, Anna University, Chennai, India
e-mail: augusteen@rocketmail.com

R. Rengaraj
e-mail: rengaraj81@gmail.com

N.B.M. Selvan
e-mail: nbmselvan@gmail.com

C. Kamalakannan et al. (eds.), *Power Electronics and Renewable Energy Systems*, Lecture Notes in Electrical Engineering 326, DOI 10.1007/978-81-322-2119-7_139

loads [1]. Specifically in solving ED gives optimal allocation of the available generators facilities to produce energy at the lowest cost. To achieve this lowest operating cost becomes highly non linear.

Previously to overcome these non linearity various methods and optimization techniques have been applied those include the lambda—iteration method [1] which the conventional method of performing ED but the problem is to find global solution for larger number of units takes time and complex. Dynamic Programming (DP) [2] is classical approach to solve dynamic ED but it may lead to loss of optimal solution and become complex. In recent decades the advent of Stochastic search algorithms like genetic algorithms (GAs) [3–5], Evolution strategies (ESs) [6, 7], evolutionary programming (EP) [8, 9], simulated annealing (SA) [10], and PSO [11] has been an effective methodology in solving nonlinear ED problems without any restrictions on the shape of the cost curves. Even though these heuristic methods do not always guarantee discovering the globally optimal solution in finite time, they often provide a fast and reasonable solution (near-globally optimal). In practice GA and EP search algorithms are based on the simulated evolutionary process of natural selection. These heuristic methods are more flexible and robust than conventional calculus-based methods. EP differs from traditional GAs in two aspects: EP uses the control parameters only in real values, and it relies primarily on mutation and selection, but not on crossover. The ED problem conventionally involves thermal energy power generators, which utilizes the fossil fuels as resources [12]. For the future it has become necessary for alternatives to thermal energy power generation, and one of the possible source of energy more widespread use is the wind energy. The major reimbursement of wind energy is that, once the initial land and capital costs, there is essentially no cost involved in the production of power from wind energy conversion systems (WECS). In addition, the impacts of WECS are generally considered to be environmentally friendly than the impacts of thermal energy sources. By developing ED model that incorporates both thermal and wind energy leads to high non linear problem, moreover the task will become much more complex. To solve this high non linearity problem require a methodology to provide nearer to global optimal solution.

139.2 Problem Formation

The objective function of the wind integrated ED problem to obtain minimum operating cost including the probabilities wind varying with the Weibull distribution function [12] is given by:

$$\min\left[\begin{array}{r}\sum_{i}^{M} C_i(P_i) + \sum_{i}^{N} C_{wi}(w_i) + \sum_{i}^{N} C_{p,w,i}(W_{i,av} - w_i) \\ + \sum_{i}^{N} C_{r,w,i}(w_i - W_{i,av})\end{array}\right] \tag{139.1}$$

Subject to:

$$P_{i,min} \le P_i \le P_{i,max} \tag{139.2}$$

$$0 \le w_i \le w_{r,i} \tag{139.3}$$

$$\sum_{i=1}^{M} P_i + \sum_{1}^{N} w_i = D \tag{139.4}$$

where, M: The number of conventional power generators; N: The number of wind power generators; C_i: Cost function of ith generator; P_i: The power output from the ith conventional generator; C_{wi}: The cost functions for the ith wind-powered w_i generator; The scheduled wind power from the ith wind-powered generator; $C_{p,w,i}$: The underestimation penalty cost function for the ith wind-powered generator; $W_{i,av}$: The available wind power from the ith wind-powered generator and it is a random variable, with a value range of $0 \le W_{i,av} \le w_r$ with the probabilities varying with the Weibull distribution function; $C_{p,w,i}$: The overestimation reserve cost function for the ith wind-powered generator; $W_{r,i}$: The rated wind power from the ith wind-powered generator, D: The system load and its losses.

The first term of the objective function is the sum of the fuel costs of the conventional generators. The second term describes the direct cost of the power derived from the wind-powered generators. The third term accounts for the price to be paid for underestimation of the available wind power. Lastly, the fourth term relates to the price that must be paid for over-estimation of the available wind power with the assumption that a reserve is available if all the available wind power is not sufficient to cover the scheduled wind power at a given period of time. A linear cost function is assumed for the wind generated power is given by

$$C_{w,i}(w_i) = d_i, w_i \tag{139.5}$$

where, d_i: The direct cost coefficient for the ith wind generator. However, there is always a penalty to be included with the WES as the available wind power is not utilized completely [13]. The penalty cost that is incurred due to the underestimation of the wind power is linearly related to the difference between the available wind power and the actual wind power used and is given by:

$$C_{p,w,i}(W_{i,av} - w_i) = k_{p,i}(W_{i,av} - w_i) = k_{p,i} \int_{w_i}^{w_{r,i}} (w - w_i) f_w(w) dw \tag{139.6}$$

where, $k_{p,j}$: Underestimation penalty cost coefficient for the ith wind generator, $f_W(w)$: The WECS power probability distribution function, It is known that the wind speed profile at a given location can be obtained using the Weibull distribution function whose probability distribution function (PDF) is given by [15]. Once the uncertain nature of the wind is characterized as a random variable, the output of WES power is obtained through a transformation from wind speed to generate power—output. Neglecting minor non-linearity, with a given wind speed Generated output power of the WES is given by:

$$w = \begin{cases} 0, & \text{for } v < v_i \text{ and } v > v_0 \\ w_r \frac{(V - V_i)}{(V_r - V_i)}, & \text{for } v_i \leq v \leq v_r \\ w_r, & \text{for } v_r \leq v \leq v_0 \end{cases} \tag{139.7}$$

w: The WECS output power (kilowatt or megawatt); w_r: The WECS rated power, v_i: The cut-in wind speed (miles/hour or miles/second); v_r: The rated wind speed, v_0: The cut-out wind speed; v: Wind speed (a realization of the wind speed is random variable).

139.3 Phenotopic Evolutionary Programming (PhEP)

In this proposed work phenotype [14] results from the expression of an organism's genes as well as the influence of environmental factors and the interactions between the two. When two or more clearly different phenotypes exist in the same population of a species, it is called polymorph. In [14] Mendel states that, "Not all organisms with the same genotype look or act the same way because appearance and behavior are modified by environmental and developmental conditions." Based on this concept the phenotypic behavior can be applied to EP. This modified PhEP algorithm accelerates the convergence time towards the global optima.

139.3.1 Phenotypic

For natural selection process to occur, the phenotypic variation [14] becomes a fundamental prerequisite. It is the living organism as a whole that contributes (or not) to the next generation, so natural selection affects the genetic structure of a population indirectly via the contribution of phenotypes. Without phenotypic variation, there would be no evolution by natural selection. The interaction between genotype and phenotype has often been conceptualized by the following relationship:

$$\text{Genotype (G)} + \text{Environment (E)} \rightarrow \text{Phenotype (P)} \tag{139.8}$$

where, G: Genotype as the required demand D in MW, E: Environmental aspects, P: Phenotype, the dominant initial population.

139.3.2 Evolutionary Programming

Natural Evolution is a population-based process produces the best solution with lesser number of generations. Also a probabilistic search technique, which generates uniformly distributed initial parent vectors within the limits and obtains global optimum solution over number of iterations. The main stages of this technique are initialization, creation of offspring by mutation and competition and selection of best vectors to evaluate best fitness solution [15].

139.3.3 Initialization

The initial-population (number of parent vectors) is generated with phenotypic parent vectors are real—power outputs of generating units distributed uniformly between their minimum and maximum limits. Let $P_i = P_1, P_2, P_3, \ldots P_N$ be the individual population of M thermal generating units subjected to their respective constraints. $W_i = W_1, W_2, \ldots W_N$ be the individual population of the N wind generated units.

139.3.4 Mutaion and Creation of Offspring

The purpose of mutation is to introduce a slight perturbation to increase the diversity of trial individuals preventing trial individuals from clustering and causing premature convergence of solution. In conventional techniques a random number is added to the parent so that there is a slight disturbance. However, this method requires constant adaptation of probability values so as to obtain an optimal solution. Self-adaptation (SA) is a process which overcomes these difficulties [15, 16]. SA makes the parameters of mutation vary simultaneously with the decision variables. However in this approach employs correlated mutation. An offspring is created from every parent and a small distribution of mean zero and standard deviation one is added to the parent. Another parameter called as the learning parameter is also added which decides varies automatically as the algorithm proceeds to obtain the optimal solution in the quickest, possible time. In correlated mutation both the rotation angle and the covariance of the individual solution is varied in order to vary the mutation strength [17]. This leads to better solutions being obtained in the smallest number of iterations.

$$\sigma_i^{(t+1)} = \sigma_i^{(t)} p\left(\tau' N(0,1) + \tau N_i(0,1)\right) \tag{139.9}$$

$$\alpha_i^{(t+1)} = \alpha_i^{(t)} + \beta_\alpha N_i(0,1) \tag{139.10}$$

$$x_i^{(t+1)} = x_i^{(t)} + N\left(0, C\left(\sigma^{(t+1)}, \alpha^{(t+1)}\right)\right) \tag{139.11}$$

where σ is the mean step size, τ and τ': The learning parameter, have been commonly set to $\left(\sqrt{2\sqrt{2n}}\right)^{-1}$ and $\left(\sqrt{2n}\right)^{-1}$; N(0,1): The normalized random distribution with mean of 0 and standard deviation 1, x_i: The parent for ith iteration, $C\left(\sigma^{(t+1)}, \alpha^{(t+1)}\right)$: The covariance between $\sigma^{(t+1)}$ and $\alpha^{(t+1)}$.

139.3.5 Competition and Selection

The parent vectors and their corresponding offspring will compete with each other for survival in a competing pool based on their cost. The best vector having minimum cost is selected for the new parent for the next generation. Initialization and mutation are repeated until there is no appreciable improvement in the fitness value.

139.4 Case Studies

139.4.1 Wind Energy Systems

PhEP was employed to solve standard 3, 13 and 40 respectively. The population size for the PhEP is taken as 25 [18]. Wind Cut-in Speed (V_i) speed has been taken as 3 m/s. Rated wind power output of the wind unit 1 (W_{r1}) as 3 MW, Rated wind power output of the wind unit 2 (W_{r2}) as 3 MW, Velocity of the wind (V_1), for the unit 1 as 6 m/s, Velocity of the wind (V_2), for the unit 2 as 10 m/s, Rated Wind Speed (V_r) as 13 m/s, Number of iteration taken as 100, Population as 50, β_α as 0.0873(5°) (Fig. 139.1).

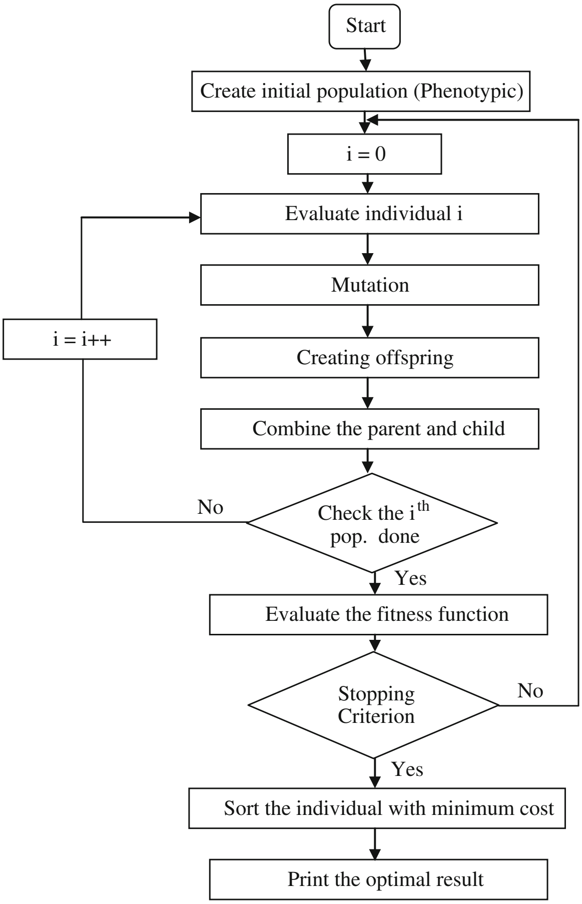

Fig. 139.1 Flow chart of phenotypic evolutionary programming

139.4.2 Three Uint System

The quadratic cost function incorporating the effects of valve-point loadings as a test case of [19]. The overall load demand is taken as 850 MW. It has been computed for a 100 iteration with a population size of 25. Table 139.1 shows that the PhEP performance proves the better than GAB, CEP, IFEP of [19]. And also shows that the execution time had been improved to obtain global optimum solution. Figure 139.2a represents the convergence characteristics of 3 units system without incorporating wind energy. Table 139.2 Shows the by incorporating the wind energy of two wind powered generator with maximum generation of 1.5 MW of W_1 and W_2 respectively shows the better production cost than the conventional economic dispatch, where the dynamics of wind energy not incorporated [18, 20, 21]. Figure 139.2b represents the convergence characteristics of 3 units system incorporating 2 wind generator of total 3 MW.

Table 139.1 Results of test case 3 units system with demand of 850 MW

Evaluation method	Mean time (sec.)	Best time (sec.)	Mean cost [$]	Maximum cost [$]	Minimum cost [$]
GAB	35.80	32.46	–	–	8,234.08
CEP	24.65	23.03	–	–	8,234.07
IFEP	6.78	6.11	8,234.16	8,234.54	8,234.07
PhEP	3.4	2.3	8,355.72	8,460.03	8,221.31

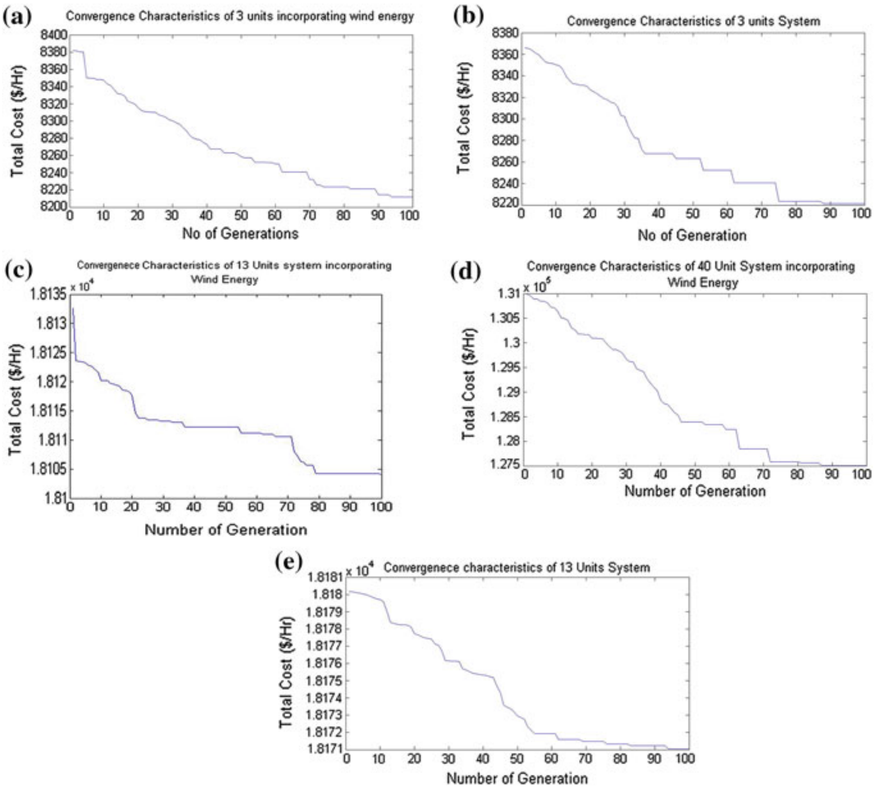

Fig. 139.2 **a** Convergence characteristics of 3 units without incorporating wind energy, **b** convergence characteristics of 3 units incorporating wind energy, **c** 13, and 40 units systems, convergence characteristics of 13 units without incorporating wind energy, **d** convergence characteristics of 13 units incorporating wind energy, **e** convergence characteristics of 40 units incorporating wind energy

Table 139.2 Results of test case 3 units incorporating wind energy with demand of 850 MW

Unit	Maximum MW	Minimum MW	Without wind MW	With wind MW
1	100	600	349.5061	347.9474
2	100	400	399.8996	398.8632
3	50	200	100.5943	100.1893
W1 MW	–	–	–	1.5
W2 MW	–	–	–	1.5
Total	–	–	850	850
Cost [$]	–	–	8,221.314	8,200.995

139.4.3 13 Units System

The quadratic cost function incorporating the effects of valve-point loadings as a test case of [19]. The overall load demand is taken as 1,800 MW. It has been computed for 100 iteration with a population size of 25. Table 139.3 shows that the PhEP perform near optimal solution by incorporating the wind energy of two wind powered generator with maximum generation of 1.5 MW of W_1 and W_2 respectively. And also shows the better production cost than the conventional economic dispatch, where the dynamics of wind energy not incorporated [18]. Figure 139.2c, d represents the convergence characteristics of 13 units system with and without incorporating wind energy.

Table 139.3 Results of test case 13 units incorporating wind energy with demand of 1,800 MW

Unit	Minimum MW	Maximum MW	Without wind MW	With wind MW
1	00	680	487.3940	472.1856
2	00	360	297.4156	184.0683
3	00	360	195.6164	212.6365
4	60	180	151.8420	118.4392
5	60	180	99.7463	124.3095
6	60	180	76.1080	77.10793
7	60	180	60.1046	144.3532
8	60	180	83.5362	147.3456
s9	60	180	141.2012	102.4521
10	40	120	43.6196	43.64635
11	40	120	42.6891	50.21172
12	55	120	61.7807	58.87784
13	55	120	58.9415	61.3661
W1 MW	–	–	–	1.5
W2 MW	–	–	–	1.5
Total MW	–	–	1,800	1,800
Cost [$]	–	–	18,170.34	18,147.34

139.4.4 40 Units System

The quadratic cost function incorporating the effects of valve-point loadings as a test case of [19]. The overall load demand is taken as 10,500 MW. It has been computed for 100 iteration with a population size of 25. Table 139.4 shows that the PhEP perform near optimal solution by incorporating the wind energy of two wind powered generator with maximum generation of 1.5 MW of W_1 and W_2 respectively. And also shows the better production cost than the conventional economic dispatch, where the dynamics of wind energy not incorporated [18]. Figure 139.2e represents the convergence characteristics of 40 units system incorporating wind energy.

Table 139.4 Results of test case 13 units incorporating wind energy with demand of 10,500 MW

Unit	Minimum MW	Maximum MW	Without wind MW	With wind MW
1	36	114	100.518	80.45551
2	36	114	88.7658	87.17793
3	60	120	101.4703	107.647
4	80	190	185.6081	166.7659
5	47	97	71.67035	89.615
6	68	140	120.115	103.1272
7	110	300	297.213	288.2549
8	135	300	189.2948	250.3643
9	135	300	280.6165	264.6959
10	130	300	273.7082	272.4049
11	94	375	182.7462	354.095
12	94	375	374.4679	323.8081
13	125	500	370.1543	460.2788
14	125	500	420.2419	462.1299
15	125	500	325.3093	326.2391
16	125	500	408.7549	178.618
17	220	500	487.0913	494.8038
18	220	500	451.9958	436.1165
19	242	550	369.3288	545.6515
20	242	550	528.6578	459.5271
21	254	550	510.0597	524.9721
22	254	550	532.5022	335.0309
23	254	550	485.9392	402.478
24	254	550	546.9986	483.2182
25	254	550	381.0186	541.1359
26	254	550	516.6629	522.6379
27	10	150	39.32057	43.1658

(continued)

Table 139.4 (continued)

Unit	Minimum MW	Maximum MW	Without wind MW	With wind MW
28	10	150	27.96271	12.700023
29	10	150	49.77531	32.28681
30	47	97	88.10134	96.4944
31	60	190	183.3216	189.3632
32	60	190	101.251	139.8501
33	60	190	116.5889	158.6096
34	90	200	199.4089	197.8432
35	90	200	145.7016	140.297
36	90	200	186.113	187.4323
37	25	110	56.73997	106.4155
38	25	110	95.18179	91.6852
39	25	110	75.04535	41.60203
40	242	550	534.8462	497.9744
W1 MW	–	–	–	1.5
W2 MW	–	–	–	1.5
Total MW	–	–	10,500	10,500
Cost [$]			127,510.5138	127,093.4144

139.5 Conclusion

This paper has explained in detail the application of phenotypic-EP using correlated mutation for solving ED problem incorporating wind energy systems. The proposed algorithm has been tested on standard 3, 13 and 40 units systems and with two wind energy systems. From the results obtained it is inferred that phenotypic-EP with correlated mutation obtains the best optimal solution with lesser number of iterations thereby reducing the execution time. Thus the proposed algorithm gives a promising future to solve other power system problems incorporating wind energy.

References

1. Wood AJ, Wollenberg BF (1996) Power generation, operation and control, 2nd edn Wiley, New York
2. Grainger JJ, Stevenson WD Jr (1994) Power system analysis. McGraw-Hill, New York
3. Swarup KS, Yamashiro S (2002) Unit commitment solution methodologies using genetic algorithm. IEEE Trans Power Syst 17:87–91
4. Song H, Wang GS, Wang PY, Johns AT (1993) Environmental/economic dispatch uing fuzzy logic controlled genetic algorithms. Proc Inst Elect Eng C 144:377–381
5. Walter DC, Sheble GA (1993) Genetic algorithm solutions of economic dispatch with valve point loading. IEEE Trans Power Syst 8:1325–1332

6. Fogel DB (1994) An introduction to simulated evolutionary optimization. IEEE Trans Neural Network 5:3–14
7. Fogel DB (1995) Evolutionary computation toward a new philosophy of machine intelligence. IEEE Press, Piscataway
8. Chellapilla K (1998) Combining mutation operators in evolutionary programming. IEEE Tans Evol Comput 2:91–96
9. Fogel, DB (1992) An analysis of evolutionary programming. In: Proceedings of 1st annual conference on evolutionary programming, CA, pp 43–51
10. Wong KP, Fung CC (1992) Simulated annealing based economic dispatch algorithm. Proc Inst Elect Eng C 140:544–550
11. Park JB, Lee KS, Shin JR, Lee KY (2005) A particle swarm optimization for economic dispatch with nonsmooth cost function. IEEE Trans Power Syst 20(1):34–42
12. Hetzer J, Yu DC, Bhattarai K (2008) An economic dispatch model incorporating wind power. IEEE Trans Energy Convers 23(4):603
13. Miranda D, Hang PS (2005) Economic dispatch model with fuzzy wind constraints and attitudes of dispatchers. IEEE Trans Power Syst 20(4):2143–2145
14. Mahner M, Kary M (1997) What exactly are genomes, genotype and phenotypes. J Theor Biol 186:55–63
15. Sinha N, Chakrabarti R, Chattopadhyay PK (2003) Evolutionary programming techniques for economic load dispatch. IEEE Trans Evol Comput 7:83
16. Chenguang Z, Qiang H, Maihuan Z, Fengwei T (1994) Economical operation of hydro power plant based on self-adaptive mutaion evolutionary programming. In: 5th world conference on intelligent control and automation 15th June 1994
17. Tinos R, Yang S (2007) Self-adaptation of mutation distribution in evolutionary algorithms. In: IEEE confernece on evolutionary computation, 25th Sept 2007
18. Warsono DJ, King KS, Bradly DA (2007) Economic load dispatch of renewable energy in power system using genetic algorithm. In: IEEE Proc Power Tech 531:2174–2179
19. Wong KP, Wong YW (1995) Thermal generator scheduling using hybrid genetic/simulated arming approach. IEEE Proc C 142:372–380
20. Chen PH, chang HC (1995) Large-scale economic dispatch by genetic algorithm. IEEE Trans Power Syst 10:1919–1926
21. Venkatesh P, Gnanadass R, Padhy NP (2003) Comparison and application of evolutionary programming techniques to combined economic emission dispatch with line flow constraints. IEEE Trans Power Systems 18(2):688–697

Chapter 140
Mathematical Modeling of BLDC Motor Using Two Controllers for Electric Power Assisted Steering Application

G.R. Puttalakshmi and S. Paramasivam

Abstract The improvement in the field of engineering and technology over last decades made BLDC Motor application possible in the automotive industry. This paper deals with one such application. This paper gives a steering control system using two controllers namely a hysteresis controller and a PID controller. This system reduces the noise and it is more accurate than the mechanical system which is used presently in the vehicles. The controller uses two reference techniques to estimate torque and speed of BLDC motor. The controller was simulated for various load side disturbances and found to exhibit better controlling capability than existing methods.

Keywords Simulation · PID control · Electric power steering

140.1 Introduction

Nowadays as the technology improved, the steering which is hydraulic previously was changed to electric power steering. Previously the motor used for electric power steering is DC servo motor. Because of the advantages of the BLDC motor, the DC servo motors are overruled in the electric power steering application. BLDC motors usage started in this application. BLDC motor in its construction mainly consists of stator and rotor. Stator is having a 3 phase winding housed in the slots. Rotor is made up of the permanent magnet. The permanent magnet motors are classified as PM Synchronous motor and PM Brushless DC Motor depending on the back emf produced. If the back emf produced is sinusoidal then it is called as

G.R. Puttalakshmi (✉)
Sathyabama University, Chennai, India
e-mail: grplakshmi@gmail.com

S. Paramasivam
ESAB, Chennai, India

C. Kamalakannan et al. (eds.), *Power Electronics and Renewable Energy Systems*,
Lecture Notes in Electrical Engineering 326, DOI 10.1007/978-81-322-2119-7_140

PM Synchronous motor and if the back emf is trapezoidal then it is called as PM Brushless DC motor [1, 2].

140.2 Mathematical Modeling

The BLDCM is very similar to the standard wound rotor synchronous machine except that the BLDCM has no damper windings and excitation is provided by a permanent magnet instead of a field winding. Since the rotor is made up of permanent magnet, saturation of magnetic flux linkage is same as that of synchronous machines. The stator is having three phases winding and fed with the three phase source [3, 4]. Therefore the stator can be modeled by using the following equations. The voltage equation of BLDC motor can be represented as

$$\begin{bmatrix} V_a \\ V_b \\ V_c \end{bmatrix} = \begin{bmatrix} R & 0 & 0 \\ 0 & R & 0 \\ 0 & 0 & R \end{bmatrix} \begin{bmatrix} i_a \\ i_b \\ i_c \end{bmatrix} + \begin{bmatrix} L & 0 & 0 \\ 0 & L & 0 \\ 0 & 0 & L \end{bmatrix} \frac{d}{dt} \begin{bmatrix} i_a \\ i_b \\ i_c \end{bmatrix} + \begin{bmatrix} e_a \\ e_b \\ e_c \end{bmatrix} \tag{140.1}$$

where,

R	Phase resistance
L	Phase inductance
V_a, V_b, V_c	Phase voltages
i_a, i_b, i_c	Phase currents
e_a, e_b, e_c	Back EMFs

The torque equation of the BLDC motor is as represented as in Eq. 140.2.

$$T = \frac{e_a i_a + e_b i_b + e_c i_c}{\omega} \tag{140.2}$$

where ω is motor angular velocity.

The equation of the mechanical system is given by

$$T_e - T_1 = J\frac{d\omega_m}{dt} + B\omega \tag{140.3}$$

where,

T_1	load torque [N-m]
J	Inertia of rotor [kg m^2]
B	Damping constant [N ms rad^{-1}]

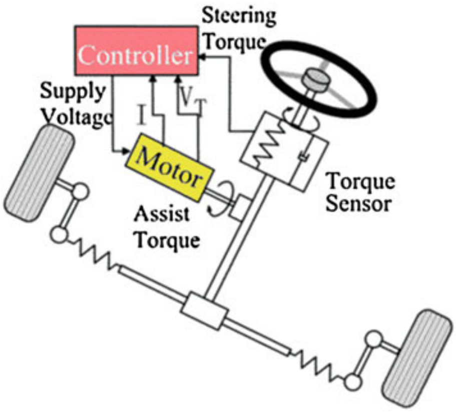

Fig. 140.1 Electrically assisted power steering

140.3 Electric Power Steering

The reduction of steering effort on vehicles by using external source to assist in turning the wheels is known as power steering. The steering effort is increased with higher vehicle mass and wider tires. For modern vehicles it is difficult to manage at low speeds during parking without assistance. Electric power steering systems have an advantage in fuel efficiency because there is no hydraulic pump constantly running. The electrically assisted power steering system consists of BLDC motor. Electrically assisted power steering is shown in Fig. 140.1. It needs several parts such as torque sensor, engine speed sensor, vehicle speed sensor, steering column, torsion bar and electronic control unit.

140.4 Proposed Techniques

Two controllers are used in the proposed technique. The inner controller is Hysteresis controller and the outer controller is the PID controller. The values of the proportional, integral and differential constants are $K_p = 20$, $K_i = 0.8$, $K_d = 10$. The general equation of the PID controller is given by

$$u(t) = MV(t) = K_p e(t) + K_i \int_0^t e(\tau) d\tau + K_d \frac{de(t)}{dt} \tag{140.4}$$

where

K_p Proportional gain, a tuning parameter
K_i Integral gain, a tuning parameter
K_d Derivative gain, a tuning parameter
e Error

t Time or instantaneous time (the present)
τ Variable of integration; takes on values from time 0 to the present *t*

The DsPIC controller is used to control the speed of the motor and the motor can be rotated in both the directions [5]. There are two types of torque required to move the locomotive. They are namely static torque and dynamic torque. The static torque is the torque required to move the locomotive parts without any accelerating force. The torque of the cars drive axle down the highway is taken as rotating static torque. But in the cars engine both the torques is produced and they are differentiated depending on where it is measured. The dynamic torque is the torque produced with the acceleration. For specific vehicle the static torque required with electronic power steering is 2.4–3.4 N-m, dynamic torque is 2.0–3.0 N-m and for hydraulic steering the static torque is 5.37 N-m and the dynamic torque is 4.5 N-m. In [6–8] the motor used for the power steering is of lesser rating it may not possible to produce that much torque required for moving the locomotive. Therefore in this paper higher rating motor is used which can produce the torque required for the movement of the locomotive. In [9] the DSP is used as controller. In [10] IPMSM is used for the power steering and in [11] the direct back emf sensing method is used for the feedback. We are using BLDC Motor and taking speed as feedback signal.

140.5 Simulation

The simulation of the BLDC Motor with the controller is done by using the Matlab environment. The 1 kW, 1,500 rpm BLDC Motor is used for simulation. The simulation circuit is as shown in Fig. 140.2. Various load side disturbances are given and the performances are observed. The simulation outputs for the different load side disturbances are taken such as step input, constant input and ramp input. The corresponding graphs of back emf, speed and torque are shown in Figs. 140.3, 140.4, 140.5, 140.6, 140.7, 140.8 and 140.9.

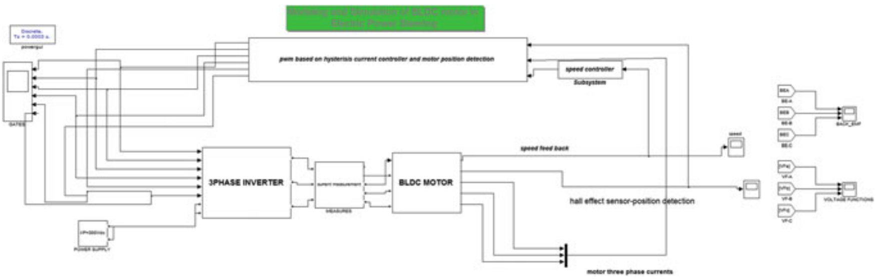

Fig. 140.2 Simulation diagram of BLDC motor

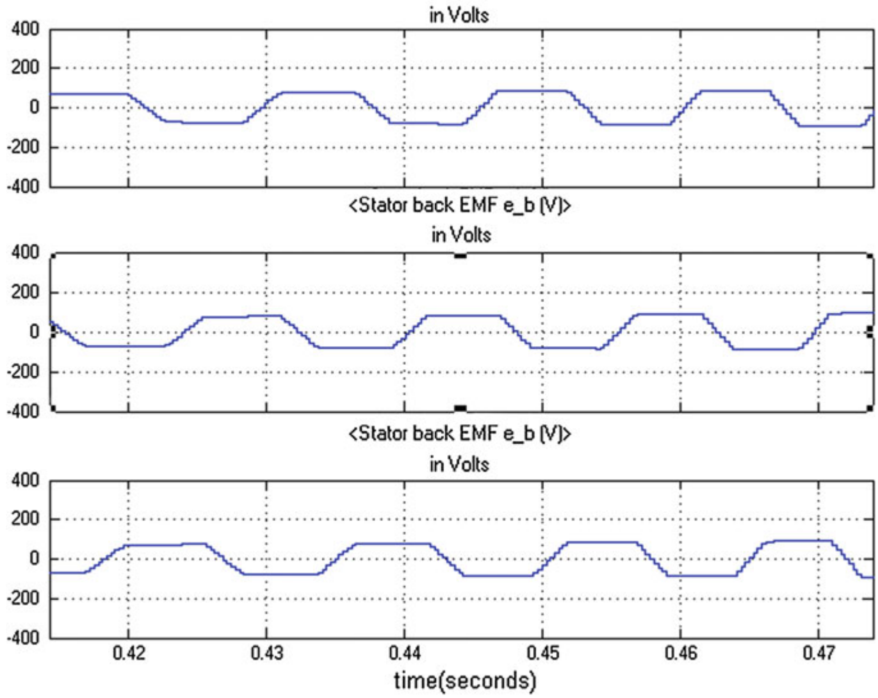

Fig. 140.3 The back emf of the three phases

Fig. 140.4 The speed *curve* of the BLDC motor for step load disturbance

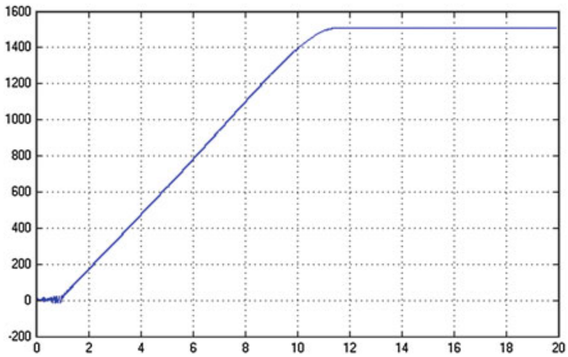

From the simulation outputs it is clear that for the load disturbances like step, constant and ramp, the torque wave form is disturbed for duration of 0.2 s and settles down. The speed reaches to rated speed within 10 s.

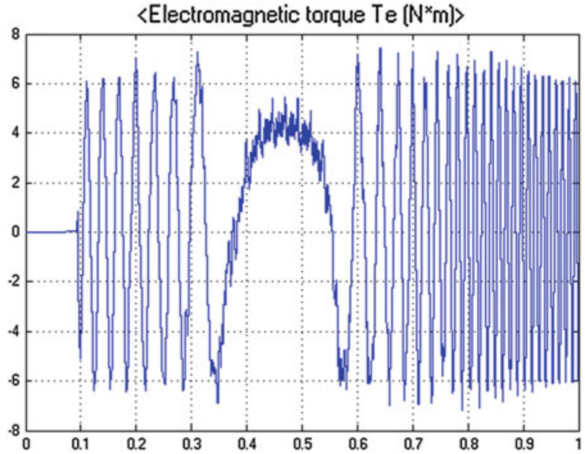

Fig. 140.5 Torque wave form for the step load disturbance of the BLDC motor

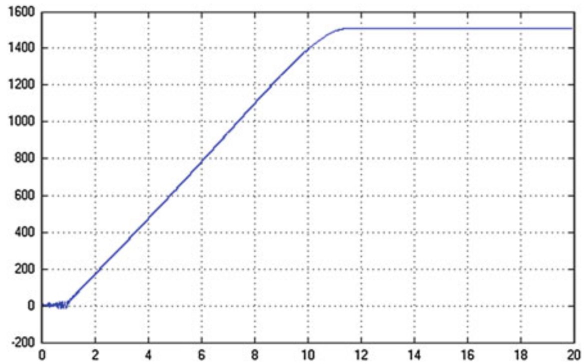

Fig. 140.6 The speed *curve* of the BLDC motor for constant load disturbance

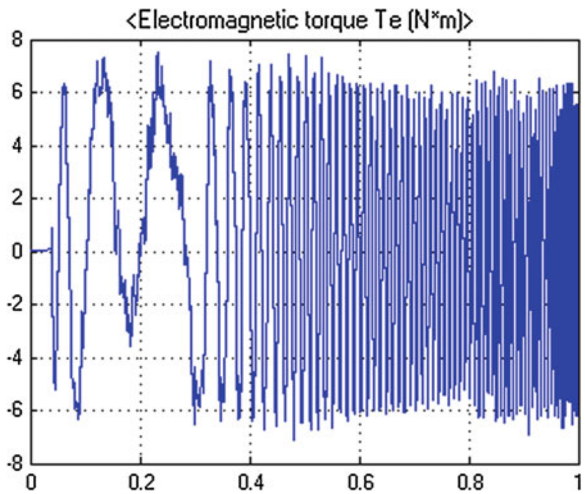

Fig. 140.7 The torque wave form for constant load disturbance of the BLDC motor

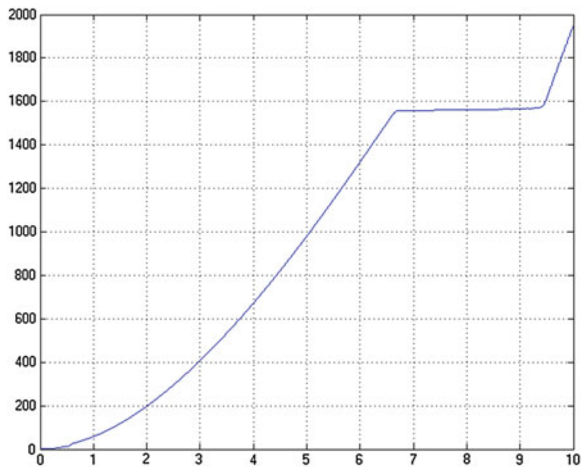

Fig. 140.8 The speed *curve* of the BLDC motor for load disturbance of ramp

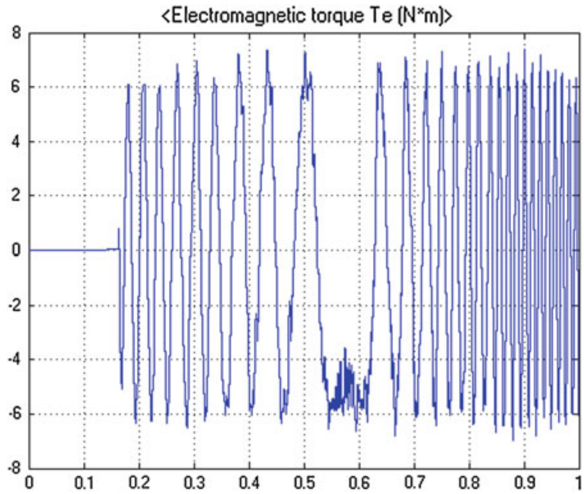

Fig. 140.9 The torque wave form of the BLDC motor for Ramp load disturbance

140.6 Conclusion

The mathematical modeling and simulation of the BLDC Motor is done by using the Matlab simulink environment. In this paper the controller was subjected simulated to various load side disturbances such as constant, step, and ramp. For these load side disturbances, the disturbance in the torque waveform settles within 2 s which shows that the motor controller is suitable for the electric power steering. The torque developed by the motor in the simulation output of the motor is around 7 N-m. This amount of torque is necessary to run the light locomotive which requires around 2.0–4.0 N-m.

References

1. Pragsen P, Krishnan R (1989) Modeling, simulation and analysis of permanent-magnet motor drives. II. The brushless DC motor drive. IEEE Trans Ind Electron 25(2):274–279
2. Yedamale P (2003) Brushless DC(BLDC) motor fundamentals. Microchip Technol Inc, p 20
3. Sun ZMRRC, An Y (2010) The mathematical simulation model of brushless DC motor system In: Proceedings of international conference on computer application and system modeling (ICCASM 2010) vol 12, pp v12-625–v12-629
4. Sun D, Cheng X, Xia X (2010) The research of novel modeling and simulation approach of brushless DC motor control system In: Proceedings of international conference on E-product E-service and E-Entertainment, (ICEEE), 2010, pp 1–5, 7th–9th Nov 2010
5. Lakshmi GRP, Paramasivam S (2013) DsPIC based power assisted steering using BLDC motor. Amer J Appl Sci pp 1419–1426
6. Cai C, Zhang H, Liu J, Gao Y (2010) Modeling and simulation of BLDC motor in electric power steering. In: The proceedings of Asia-Pacific power and energy engineering conference (APPEEC), pp 1–4
7. Fujita K (2001) Development of control method for hydraulic—electro power steering system using brushless D.C. Motors. KOYO Eng J Engl (edn no 159E), 44–49
8. Rahman MF Electric power assisted steering system for automobiles. In: Electrical engineering, vol III. UNESCO-EOLSS
9. Murugan R, Nandakumar S, Mohiyodeen MS (2008) DSP-based electric power assisted steering using BLDC motor. Sadhana 33(5):581–590
10. Hur J (2008) Characteristics analysis of interior permanent—magnet synchronous motor in electro hydraulic power steering systems. IEEE Trans Ind Electron 55(6):2316–2323
11. Shao J (2006) An improved micro controller-based sensorless brushless DC motor drive for automotive applications. IEEE Trans Ind Appl 42(5):1216–1221

Chapter 141
Comparison and Simulation of Various PFC Boost Converters

K. Mohanraj, C. Danya Bersis and Subhransu Sekhar Dash

Abstract This paper demonstrates various PFC Boost Converters. In general PFC Boost converters are used to increase the output voltage. This paper compares Pseudo Totem pole Bridgeless PFC Boost converter, Totem pole Bridgeless PFC Boost converter and ZVS Interleaved PFC Boost converter. Simulation result shows that Power Factor of the various PFC Boost converters are nearer to Unity. By using these PFC Boost converters voltage drop get reduced.

Keywords PFC boost converters · Pseudo totem pole · ZVS interleaved PFC boost converter · Power quality

141.1 Introduction

There are various Power Factor Correction techniques are used to control power quality problems. In general, Continuous Conduction Mode (CCM) Boost converters are used as power factor correction. In general, PFC Boost converters are used to decrease conduction losses by reducing number of switches present in the circuit and increase the efficiency of the circuit. Totem pole Bridgeless PFC Boost converters are usually requires complex control method. Power Factor Correction (PFC) is one of the major research topics in power electronics and drives. Power Factor is defined as the angle by which the load current lags or leads the supply voltage. When they (voltage and current) are in phase power factor is unity. When they (voltage and current) are in out of phase power factor is zero. If the power factor is poor, supply

K. Mohanraj (✉) · C. Danya Bersis · S.S. Dash
Department of EEE, SRM University, Chennai 603203, India
e-mail: mohanraj.k@srmuniv.ac.in

C. Danya Bersis
e-mail: danyabersis@gmail.com

S.S. Dash
e-mail: hod.eee@ktr.srmuniv.ac.in

C. Kamalakannan et al. (eds.), *Power Electronics and Renewable Energy Systems*,
Lecture Notes in Electrical Engineering 326, DOI 10.1007/978-81-322-2119-7_141

voltage drop and efficiency get reduced. So power factor should be increased towards unity or nearer to unity. The high power non linear loads and low power loads are used to produce harmonics which leads to poor power factor operation [1–5]. Power factor is to increase the input line current as well as performing voltage regulation i.e. regulate over and under voltage. In general, the CCM Boost converter topology has been widely used in PFC converter. Since it has high power capability and simple design [6–8]. ZVS interleaved Boost converters are used to increase the power factor which is used in Plug –In Electric Vehicles. In general, PFC techniques are used in low power applications and Active Power Factor Correction techniques are used in many applications. Boost converters like Buck, Boost and Buck Boost converters are used in Active Power Factor Correction techniques [9–16]. Bridgeless PFC Boost converters are also used to improve the Power Factor. In this, diode-bridge is not used. It has less conduction losses and high efficiency [17–20]. High performance single phase rectifier also used to improve the power factor [21–23]. This paper compares various PFC Boost converters like Pseudo totem-pole bridgeless PFC Boost converter, Totem-pole bridgeless PFC Boost converter, ZVS Interleaved PFC Boost converter.

141.2 Various PFC Boost Converters

Figure 141.1 shows pseudo totem-pole bridgeless PFC Boost converter. During the positive half cycle L_1–S_A–D_3 will conduct. During the negative half cycle L_2–S_B–D_4 will conduct. This circuit requires complex control technique and drive circuit.

Figure 141.2 shows Totem-pole bridgeless PFC Boost converter. In this, diode D_A and D_B are slow recovery diodes. During the positive half cycle Diode D_B and switch S_A will conduct through inductor L_1. During the negative half cycle Diode D_A and S_B will conduct.

Figure 141.3 shows ZVS Interleaved PFC Boost converter. In this diode-bridge is used. Few kilo watt power MOSFET's are used. Two inductors are used to increase the output voltage. Output capacitor is used to remove the ripples present the circuit.

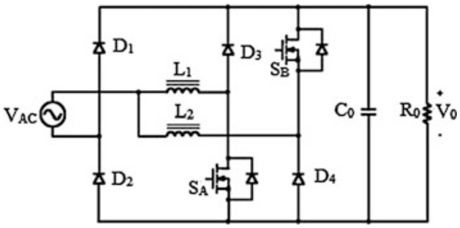

Fig. 141.1 Pseudo totem-pole bridgeless PFC boost converter

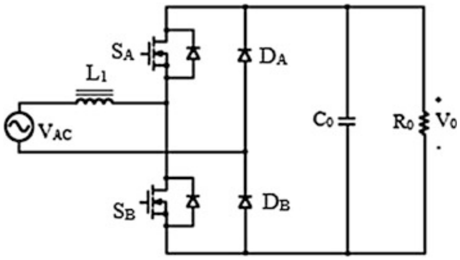

Fig. 141.2 Totem-pole bridgeless PFC Boost converter

Fig. 141.3 ZVS interleaved PFC Boost converter

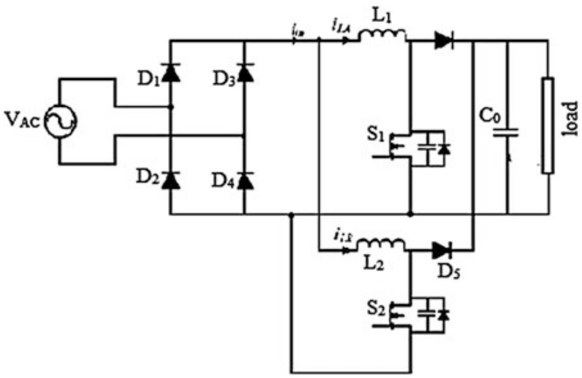

141.3 Simulation of Various PFC Boost Converters

Figure 141.4 shows simulation circuit of Pseudo totem-pole bridgeless PFC Boost converter. Power factor obtained is 0.9622.

Figure 141.5 shows output voltage waveform of Pseudo totem-pole bridgeless PFC Boost converter. Input voltage given is 250 V. Output voltage obtained is 305 V.

Figure 141.6 shows output current waveform of Pseudo totem-pole bridgeless PFC Boost converter. Output current obtained is 6 A.

Figure 141.7 shows simulation circuit of Totem-pole Bridgeless PFC Boost converter. Power factor obtained is 0.9846. Compared to Pseudo totem-pole bridgeless PFC Boost converter its power factor is high.

Figure 141.8 shows output voltage waveform of Totem-pole bridgeless PFC Boost converter. Input voltage given is 250 V. Output voltage obtained is 313 V. Compared to Pseudo totem-pole bridgeless PFC Boost converter its output voltage is high.

Figure 141.9 shows output current waveform of Pseudo totem-pole bridgeless PFC Boost converter. Output current obtained is 9 A.

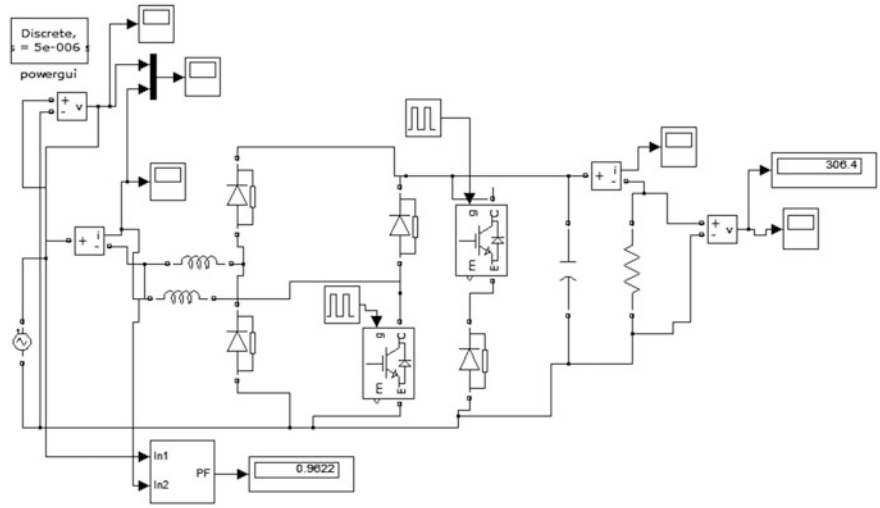

Fig. 141.4 Simulation circuit of pseudo totem-pole bridgeless PFC boost converter

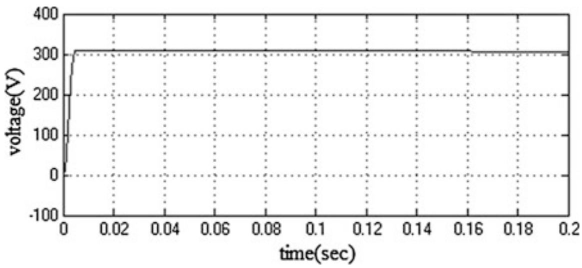

Fig. 141.5 Output voltage waveform of pseudo totem-pole bridgeless PFC boost converter

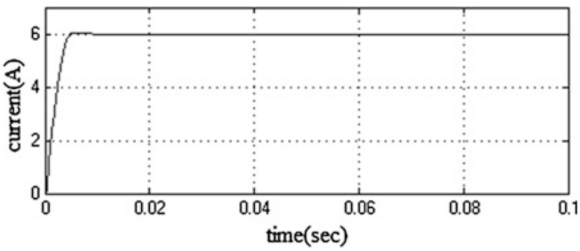

Fig. 141.6 Output current waveform of pseudo totem-pole bridgeless PFC boost converter

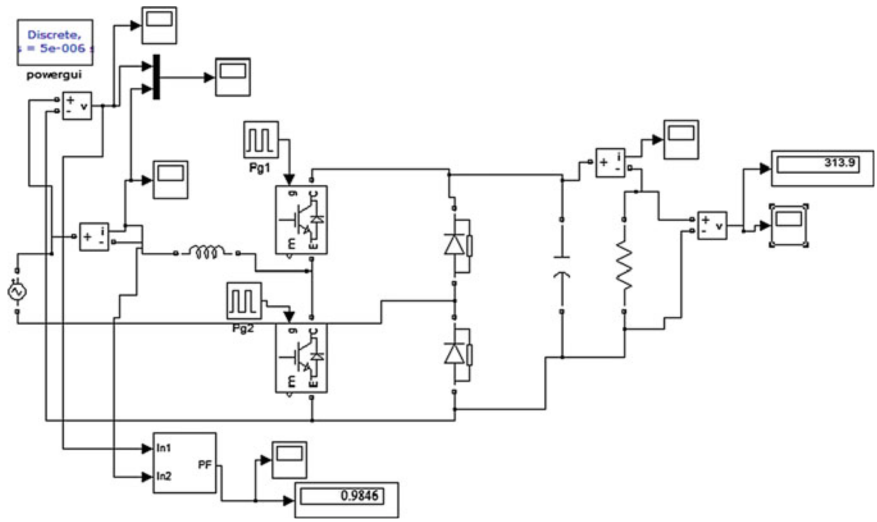

Fig. 141.7 Simulation circuit of totem-pole bridgeless PFC boost converter

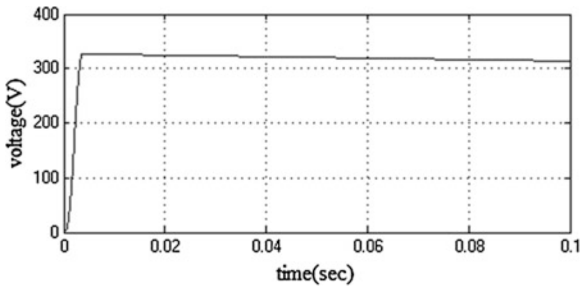

Fig. 141.8 Output voltage waveform of totem-pole bridgeless PFC boost converter

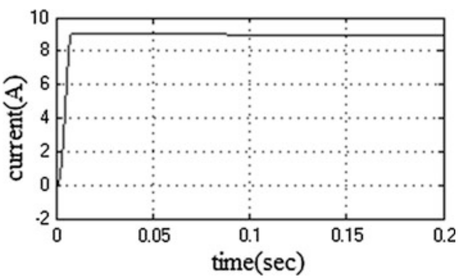

Fig. 141.9 Output current waveform of totem-pole bridgeless PFC boost converter

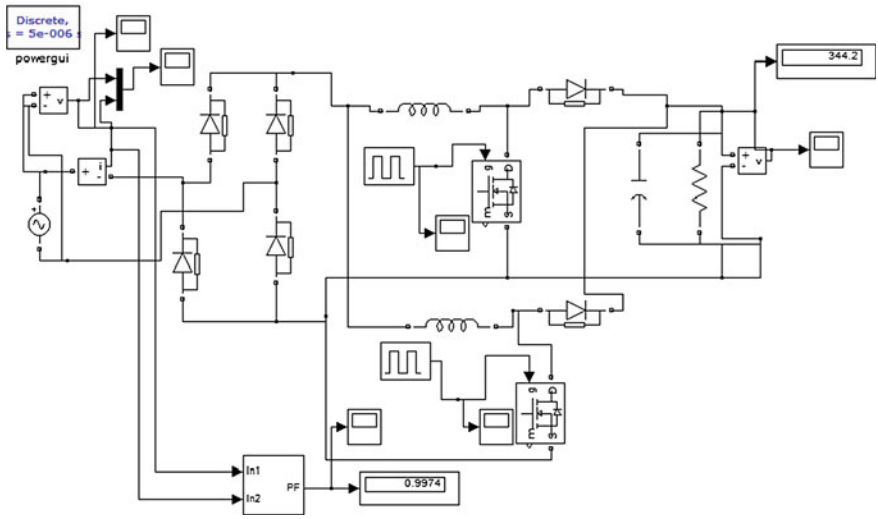

Fig. 141.10 ZVS interleaved PFC boost converter

Figure 141.10 shows simulation circuit of ZVS Interleaved PFC Boost converter. Power factor obtained is 0.9974. It gives high power factor. So the efficiency of the circuit has greatly increased and also the performance of the converter gets increased.

Figure 141.11 shows output voltage waveform of ZVS Interleaved bridgeless PFC Boost converter. Input voltage given is 250 V. Output voltage obtained is 345 V.

Figure 141.12 shows output current waveform of ZVS Interleaved bridgeless PFC Boost converter. Output current obtained is 11 A.

Various PFC Boost converter parameters are shown in Table 141.1. ZVS Interleaved PFC Boost converter gives high output voltage and current and also it has high efficiency. Since it gives more power factor.

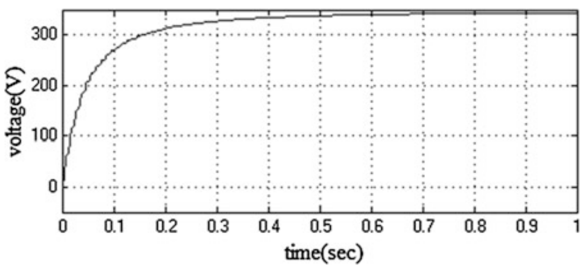

Fig. 141.11 Output voltage waveform of ZVS interleaved PFC boost converter

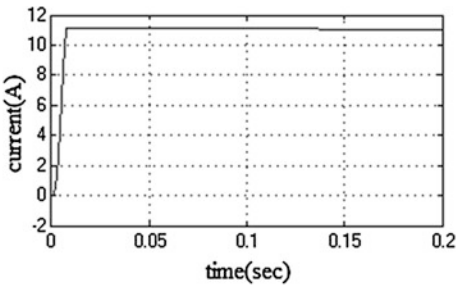

Fig. 141.12 Output current waveform of ZVS interleaved PFC boost converter

Table 141.1 Various parameters of PFC boost converters

Various bridgeless PFC boost converters	Output voltage	Output current (A)	Power factor
Pseudo totem-pole	305 V	6	0.9622
Totem pole	313 V	9	0.9846
ZVS interleaved	345 A	11	0.9974

141.4 Conclusion

Various PFC Boost converters like Pseudo totem-pole bridgeless PFC Boost converter, Totem-pole Bridgeless PFC Boost converter and ZVS Interleaved PFC Boost converter are simulated by using MATLAB/SIMULINK and the results are observed. It is noted that high output voltage can be obtained by using various PFC Boost converters and the power factor obtained is nearer to unity.

Acknowledgments We thank to the entire EEE department faculty members and supporting staff for their good support for completing my project in successful manner. We thank the authors whose research papers helped us in developing this system.

References

1. Gopinath M (2011) Bridgeless PFC converter for power factor correction. Int J Adv Eng Sci Technol 9:1049–1054
2. Carbone R, Corsonello P (2003) A new passive power factor corrector for single phase bridge diode rectifier. In: IEEE Power electronics specialist conference (PESC 03), 15–19 June 2003
3. Pahlevaninezhad M, Das P, Drobnik J, Jain PK, Bakhshai A (2012) A ZVS interleaved boost AC/DC converter used in plug-in electric vehicles. IEEE Trans Power Electron 27 (8):3513–3529
4. Moriconi U. (2002) A bridgeless PFC configuration based on L 4981 PFC controller. Application note an 1606, ST microelectronics, 1/18–18/18
5. Anitha U, Boini SK (2012) AC to DC conversion using Active PFC. Proc Int J Modern Eng Res 2(6):4220–4223

6. Jaya Kumar MS, Ajeesh G (2012) A high efficient high input power factor interleaved boost converter. Proc Int J Electr Comp Eng 2(3):339–344
7. Huber L, Jang Y, Jovanovic MM (2008) Performance evaluation of bridgeless PFC boost rectifies. IEEE Trans Power Electron 23(3)
8. Park S, Choi S (2010) Soft-switched CCM boost converters with high power application. IEEE Trans Power Electron 25(5):1211–1217
9. Martinez R, Enjeti PN (1996) A high-performance single-phase rectifier with input power factor correction. IEEE Trans Power Electron 11(2):311–317
10. Vijaya Prasana P, Rama Rao JBVG, Lakshmi ChM (2013) Improvement in power factor and THD using dual boost converter. Int J Eng Res Appl 2:2368–2376
11. Scappatura CA (2004) A high efficiency power factor correction for single phase bridge diode rectifier. In: IEEE conference ESE, 4 June 2004, Aachen, Germany
12. Lu B, Brown R, Soldano M (2005) Bridgeless PFC implementation using one cycle control technique. In: IEEE applied power electronics (APEC) conference proceeding, pp 812–817
13. Maswood AI, Liu F (2011) A unity power factor front and rectifier with hysteresis current control. IEEE Trans Energy Convers 21(1):153–160
14. Kin ID, Choi SH, Nho EC, Ahn JW (2007) A simple ZVT PWM single-phase rectifier with reduced conduction loss and unity power factor. Proc J Power Electron 7(1):1–7
15. de Souza AF, Barbi I (1995) A new ZVS—PWM unity power factor rectifier with reduced condition losses. IEEE Trans Pow Elec 10(6):746–752
16. Salmon JC (1992) Circuit topologies for single-phase voltage-doubler boost rectifies. In: Proceedings of IEEE applied power electronics conference, March 1992, pp 549–556
17. Erno T, Frisch M (2004) Second generation of PFC solutions. Power Electron Eur 7:33–35
18. Liu J, Chen W, Zang J, Xu D, Lee FC (2001) Evaluation of power losses in different CCM mode single-phase boost PFC converters via simulation tool. In: IEEE industry applications conference (IAS) record session, high frequency power conversion, paper 4
19. Rossetto L, Spiazzi G, Tenti P (2000) Boost PFC with 100 Hz switching frequency providing output voltage stabilization and compliance with EMC standard. IEEE Trans Ind Appl 36:188–193
20. Rossetto L, Buso S, Spiazzi G (2000) Conducted EMI Issues in a 600 W boost PFC Design. IEEE Trans Ind Appl 36(2):578–585
21. Daut Ismail, Ali Rosnazri, Taib Soib (2006) Design of a single-phase rectifier with improved power factor and low THD using Boost converter technique. Amer J Appl Sci 37:1902–1904
22. Kong P, Wang S, Lee FC (2006) Common mode EMI noise suppression in bridgeless boost PFC converter. In: CPES power electronics conference proceeding, pp 65–70
23. Wang CM (2003) A novel zero-voltage switching PWM boost rectifier with high power factor and low conduction losses.In: International telecommunication energy conference (INTELEC) proceeding, pp 224–229

Chapter 142
Modified LBP Based Region Growing Segmentation of MR Brain Images

K.S. Angel Viji and J. Jayakumari

Abstract MRI segmentation of brain tumor is a complex process and it plays a vital role in treatment planning, monitoring and efficiency examination. Insufficiency of reliable ground truth also makes the process critical. Deformation of brain tissue due to tumor mass effect, infiltration caused due to swelling of tumor, ambiguity of the structural boundaries between the tumor and healthy tissues are some of the troublesome factors exhibiting in segmenting MRI brain tumor. Region growing segmentation is purely based on image region. It takes intensity as a limitation to segment images into regions. But it does not meet the above factors. So a texture and intensity based region growing (TIBRG) segmentation algorithm was proposed. Here the region is grown only if intensity and texture constraints are met. The texture constraint is obtained from Local Binary Pattern (LBP) calculation. It was implemented in MATLAB. The method shows satisfactory simulation results.

Keywords SSC · MRI segmentation · Fuzzy c-mean clustering · First order statistics · GLCM

142.1 Introduction

Automatic brain tumor segmentation has always been a fundamental problem in medical diagnosis and treatment planning. The manual segmentation of MRI images by medical experts are tedious and time consuming. A wide variety of

K.S. Angel Viji (✉)
Department of Computer Science and Engineering, Noorul Islam Center for Higher Education, Kumaracoil, Kanyakumari, India
e-mail: angelhevin@yahoo.com

J. Jayakumari
Department of Electronics and Communication Engineering, Noorul Islam Center for Higher Education, Kumaracoil, Kanyakumari, India
e-mail: jkumaribharat@yahoo.com

C. Kamalakannan et al. (eds.), *Power Electronics and Renewable Energy Systems*, Lecture Notes in Electrical Engineering 326, DOI 10.1007/978-81-322-2119-7_142

algorithms have been developed by researchers to solve image segmentation problem. Active contour model is one method of segmenting images. This method start with a curve around the object. The curve traverse interiorly and depending on the energy minimization model it stops when the actual boundary is reached. But it is sensitive to initial conditions. An efficient local Chan-Vese model for image segmentation was proposed by Xiao-Feng et al. It was purely based on curve evolution technique, local statistics and level set method. This method will segment images with intensity in-homogeneity effectively. The re-initialization step that is adopted in earlier level set methods is time consuming and it was entirely eliminated by including a new penalizing energy. But the energy functional of local Chan-Vese model include three terms namely global term, local term and regularization term [1].

Deformable model include shape and appearance characteristics. For a weak low-level appearance information, in order to get accurate segmentation, shape plays a vital role. The shape prior model using sparse shape composition (SSC) has low run time efficiency. So it will not supply the medical requirements. Hence a deformable segmentation via sparse representation and dictionary learning was proposed by Shaoting et al. It improves overall accuracy and the computational complexity was reduced significantly. However it is time consuming [2]. A general, robust and comprehensive sparse shape model and active shape model also improve image segmentation. Even though this methods recover the detailed information, they are not satisfactory in training data.

The two cell segmentation approaches are parametric models and implicit models. Parametric models represent objects explicitly. Implicit models increase cell segmentation accuracy with the help of level sets [3]. Growth in Tumor and edema growth may occur concurrently. The processes involved in growth model are biomechanics, nutrient distribution, and metabolic processes [4]. In brain MRI presence of diffuse lesions of white matter is a disease. These lesions are formed in the cell due to some tension and diabetes. Also these lesions are inhomogeneous and are not sharp. But their intensity values vary from neighbouring healthy tissues [5]. In the method used by Alamgir Nyma et al., vector median filtering is used to remove impulse noise. The homogeneous regions are determined using Otsu's thresholding. Partitioning of brain MRI into several segments is done using suppressed fuzzy c-mean clustering [6].

Efficacy was systematically investigate for different types of features including texture, level-set shape and intensity for segmentation of tumors [7]. In noisy images detecting accurate boundary is a complex task. It takes intensity gradient feature through vector image model and texture feature through Laws model. Texture values and intensity values from T1 and T2 weighted and FLAIR MRI images will train the classifier. Machine learning techniques are used to increase segmentation performance of brain tumor [8]. Kavitha et al. [9], has proposed a modified region growing technique using orientation constraint in addition to intensity constraint. Here a new modified region growing algorithm with texture constraint in addition to intensity constraint has been proposed.

The organization of this paper is as follows: Sect. 142.2 explains the overall methodology. Sections 142.3 and 142.4 shows the experimental results and performance evaluation and Sect. 142.5 concludes the paper.

142.2 Methodology

The proposed technique pass on through four stages namely preprocessing, feature extraction, classification and segmentation. Gaussian filtering is used for preprocessing the input image. Feature extraction is the process by which certain features of interest within an image are detected and represented for further processing. The statistical texture analysis features such as first order statistics (FOS) and gray level co-occurrence matrix (GLCM) features are extracted for our analysis. Then the artificial feed forward neural network classifier will classify the image into normal or a pathological one. In the new modified region growing segmentation, the region is grown iff the intensity and texture constraints are met and the segmentation performance is analyzed. Texture constraint is obtained from LBP calculation. The overall process is shown in Fig. 142.1.

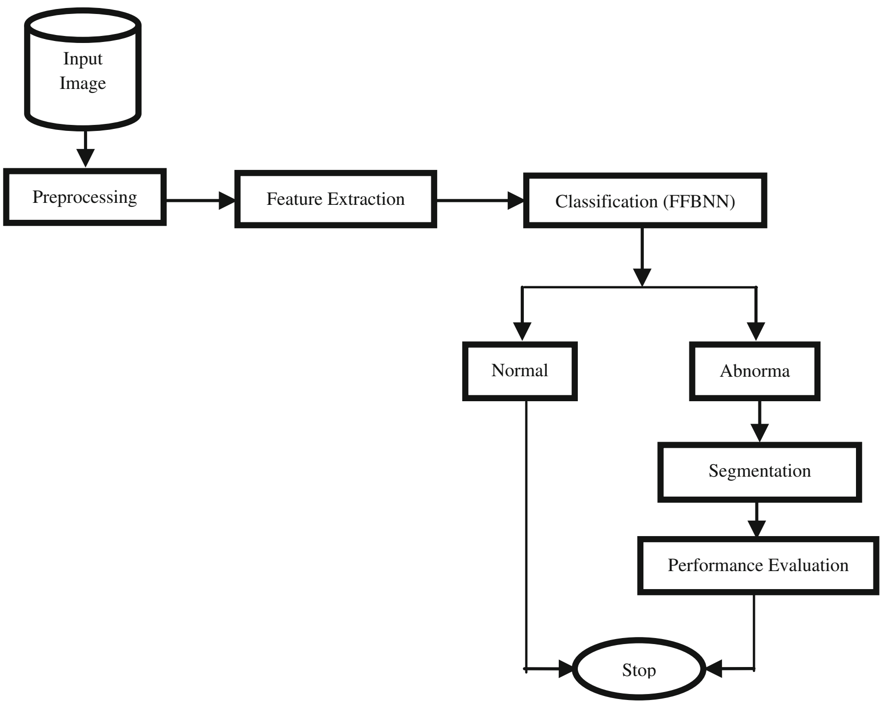

Fig. 142.1 The overall methodology

142.2.1 Preprocessing

The image is first acquired and it is preprocessed using Gaussian filters. The MRI image dataset that we have utilized in image segmentation technique is taken from the publicly available sources. As Gaussian filters have minimum possible group delay and as they reduce the rise and fall time they are used for preprocessing. Mathematically this filter convolutes the input signal using a Gaussian function. This function is a sequence of integral transforms. This is a continuous function but not discrete. The ratio between sample rate f_s and standard deviation σ is called the cut-off frequency (f_c) and is defined as:

$$f_c = \frac{f_s}{\sigma} \tag{142.1}$$

During preprocessing by passing the input image through Gaussian filter, reduces the noise present in the input image and also makes the image fit for further processing. Image quality is also increased using Gaussian filter [9].

142.2.2 Feature Extraction

Feature extraction is the process by which certain features of interest with in an image are detected and represented for further processing. It is a critical step in most computer vision and image processing solutions. The resulting representation can be subsequently used as an input to a number of pattern recognition and classification techniques, which will then label, classify, or recognize these mantic contents of the image or its objects. A feature vector is a n × 1 array that encodes then features (or measurements) of an image or object. Mathematically, a numerical feature vector x is given by

$$X = (x_1, x_2, \ldots, x_n)^T \tag{142.2}$$

Where n is the total number of features and T indicates the transpose operation. Histogram-based features are also called the First Order Statistics (FOS) features. FOS provides different statistical properties of the intensity histogram of an image. The main advantage of this approach is its simplicity through the use of standard descriptors (e.g. mean) to characterise the data. Mean, standard deviation, entropy, skewness and kurtosis are the FOS features used. Histogram-based texture descriptors are limited by the fact that the histogram does not carry any information about the spatial relationships among pixels. Gray-Level Co-occurrence Matrix (GLCM) introduced by Haralick et al. (1973) is a popular and robust statistical tool for extracting second-order texture information from images. A GLCM indicates the probability of grey-level i occurring in the neighbourhood of grey-level j at a distance d and direction θ. GLCMs can be computed from texture images using different values of d and θ and these probability values create the co-occurrence matrix $G(i, j|d, \theta)$. GLCM is also known as the gray-level spatial dependence matrix. The GLCM functions characterize the texture of an image creating a GLCM, and then extracting statistical measures from this matrix. Important steps include (1) Creating a gray-level co-occurrence matrix, (2) specifying the offsets and (3) deriving statistics from a GLCM.

(1) *Creating GLCM and specifying the offsets*: The method of creating a GLCM and specifying the offset values are shown in Fig. 142.2.

In the output GLCM, element (1, 1) contains the value 1 because there is only one instance in the input image where two horizontally adjacent pixels have the values 1 and 1, respectively. glcm (1, 2) contains the value 2 because there are two instances where two horizontally adjacent pixels have the values 1 and 2. GLCM is created in matlab using *graycomatrix* function.

(2) Deriving Statistics from a GLCM: After creating GLCM, several statistics can be derived using *graycoprops* function in MATLAB. The features extracted in our work are contrast, correlation, energy and homogeneity. *Contrast* returns a measure of intensity between a pixel and its neighbour over the whole image. Contrast is 0 for a constant image. For two neighboring pixels i and j the contrast is calculated as:

Fig. 142.2 The method of creating a GLCM. **a** input Image, **b** GLCM

(a)

1	1	5	6	8
2	3	5	7	1
4	5	7	1	2
8	5	1	2	5

(b)

	1	2	3	4	5	6	7	8
1	1	2	0	0	1	0	0	0
2	0	0	1	0	1	0	0	0
3	0	0	0	0	1	0	0	0
4	0	0	0	0	1	0	0	0
5	1	0	0	0	0	1	2	0
6	0	0	0	0	0	0	0	1
7	2	0	0	0	0	0	0	0
8	0	0	0	0	1	0	0	0

$$C = \sum_{i,j} |i,j|^2 p(i,j) \tag{142.3}$$

Correlation returns a measure of how correlated a pixel to its neighbour over the whole image. Correlation is 1 or −1 for perfectly positively or negatively correlated image. Correlation is NaN for constant image. The correlation is given by:

$$Corr = \sum \frac{(i, \mu i)(j, \mu j)p(i,j)}{\sigma_i \sigma_j} \tag{142.4}$$

Where $\mu \; and \; \sigma$ are mean and standard deviation respectively. The sum of squared elements in the GLCM is its energy and is computed as:

$$E = \sum_{i,j} p(i,j)^2 \tag{142.5}$$

Energy is 1 for a contrast image. A value that measures the closeness of the distribution of elements in the GLCM to the GLC diagonal is homogeneity. Homogeneity is defined as:

$$H = \sum_{i,j} \frac{p(i,j)}{1 + |i - j|} \tag{142.6}$$

142.2.3 Classification

Neural network is a suitable tool for image classification. We use neural network to model real world relationships because they are non linear models. Neural networks are nonlinear models, which makes them suitable in modelling real world intricate relationships. Neural networks are able to approximate the subsequent probabilities, which offer the basis for setting up classification rule and performing statistical analysis. Initially the neural networks are trained by the features that are extracted in the previous step. A feed forward neural network classifier is used to classify the input MRI images into tumor or normal. The three layers of the neural network includes (1) input layer, (2) hidden layer and (3) output layer. Features are extracted and the neural networks are trained by those features. We took around 25 images of which 20 are tumorous and 5 non tumor.

Consider a single Feed Forward Back Propagation Neural Network (FFBNN) that is trained using the features extracted from each and every image in the database. The extracted features are given to neural network for training and classification purpose. The neural network is well trained using these extracted features. The structure of the FFBNN is given as below in Fig. 142.3. Weights are assigned randomly to all the neurons except input neurons. The bias function and activation function for the neural network is described below in (142.7) and (142.8).

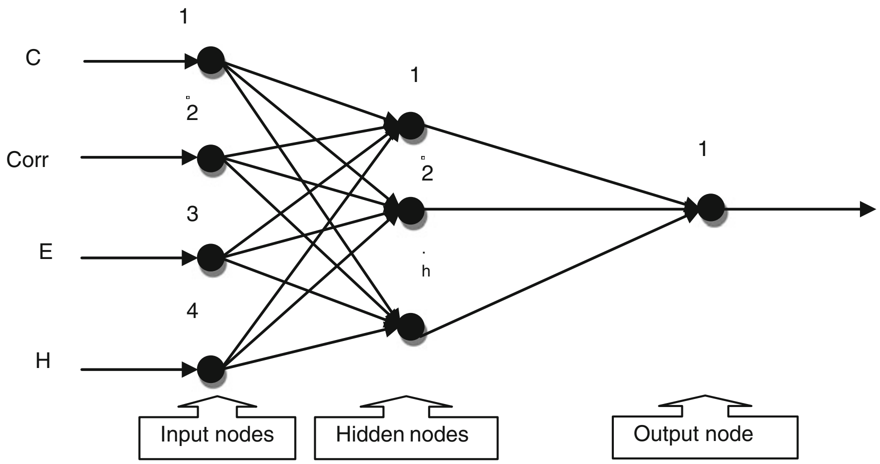

Fig. 142.3 Structure of FFBNN

$$X(t) = \beta + \sum_{q=0}^{h-1} \left(w_{tq}c_{tq} + w_{tq}corr_{tq} + w_{tq}E_{tq} + w_{tq}H_{tq} \right) \tag{142.7}$$

$$X(a) = \frac{1}{1 + e^{-X(t)}} \tag{142.8}$$

In bias function, c_{tq}, $corr_{tq}$, E_{tq} and H_{tq} are the contrast, correlated, energy and homogeneity features respectively. The w_{tq} is the randomly assigned weight of each neurons. Then the learning error is calculated using the formula (142.9).

$$E = \frac{1}{h}\sum_{q=0}^{h-1} d_q - a_q \tag{142.9}$$

E is the FFBNN learning error, d_q *and* a_q are the desired and actual outputs and h is the total number of neurons in the hidden layer. Finally the classifier will classify the images into normal or abnormal.

142.2.4 Segmentation

The abnormal images are subjected to segmentation process. A texture based segmentation algorithm have been proposed. It make use of texture constraint from lbp image in addition to intensity constraint for the purpose of growing the region. Also it is applied for the input image that leaves the gridding concept used in [10]. The problem with this method is it lacks correctness measure. The algorithm is given below:

Procedure: TIBRG
Input: Pre-processed Image
Output: Regions

Step 1: Start
Step 2: Apply *LBP* operator to the image to get the *texture image*.
Step 3: Set the *intensity threshold* T_I and *texture threshold* T_T.
Step 4: For the image I do

a. Perform histogram equivalization (denoted as *Hist*) of all pixel P_j.
b. Extract the most frequent histogram of the image and denote it as $Freq_{Hist}$.
c. Choose any pixel P_j corresponding to the $Freq_{Hist}$ and assume that pixel as seed point SP with intensity I_P.
d. If the intensity of neighboring pixel is I_N and if texture value is T_N, then check for intensity constraint $\|I_P - I_N\| \leq T_I$ and texture constraint $\|T_P - T_N\| \leq T_T$.
e. If both(intensity and texture) the constraints are satisfied, grow the region to neighboring pixel. In all the other case the region is not grown to the neighboring pixel.

Step 5: Stop.

142.3 Experimental Results

Experiment was conducted for 25 images of which 20 are tumorous and 5 non tumor. The MRI image dataset that we have utilized in image segmentation technique is taken from the publicly available sources. The proposed MRI abnormality detection and tissue segmentation technique is implemented in the working platform of MATLAB (version 7.12). The input, ground truth, preprocessed, region growing (RGW) segmentation and TIBRG images are given in Fig. 142.4.

142.4 Performance Evaluation

The resemblance among two objects in the midst of logically distinct variety of data is termed as a similarity coefficient measure. If a represents the number of features of A that is absent in B, b represents the number of features of B that is absent in A, c denotes the number of features common to both A and B and d denotes number of features absent from both A and B, for two objects A and B then *c* and *d* measure the present and the absent matches, respectively, i.e., similarity; while *a* and *b* measure the corresponding mismatches, i.e., dissimilarity. Similarity between the ground truth (manual) and region growing(automatic) segmented images are calculated and are shown in Tables 142.1 and 142.2.

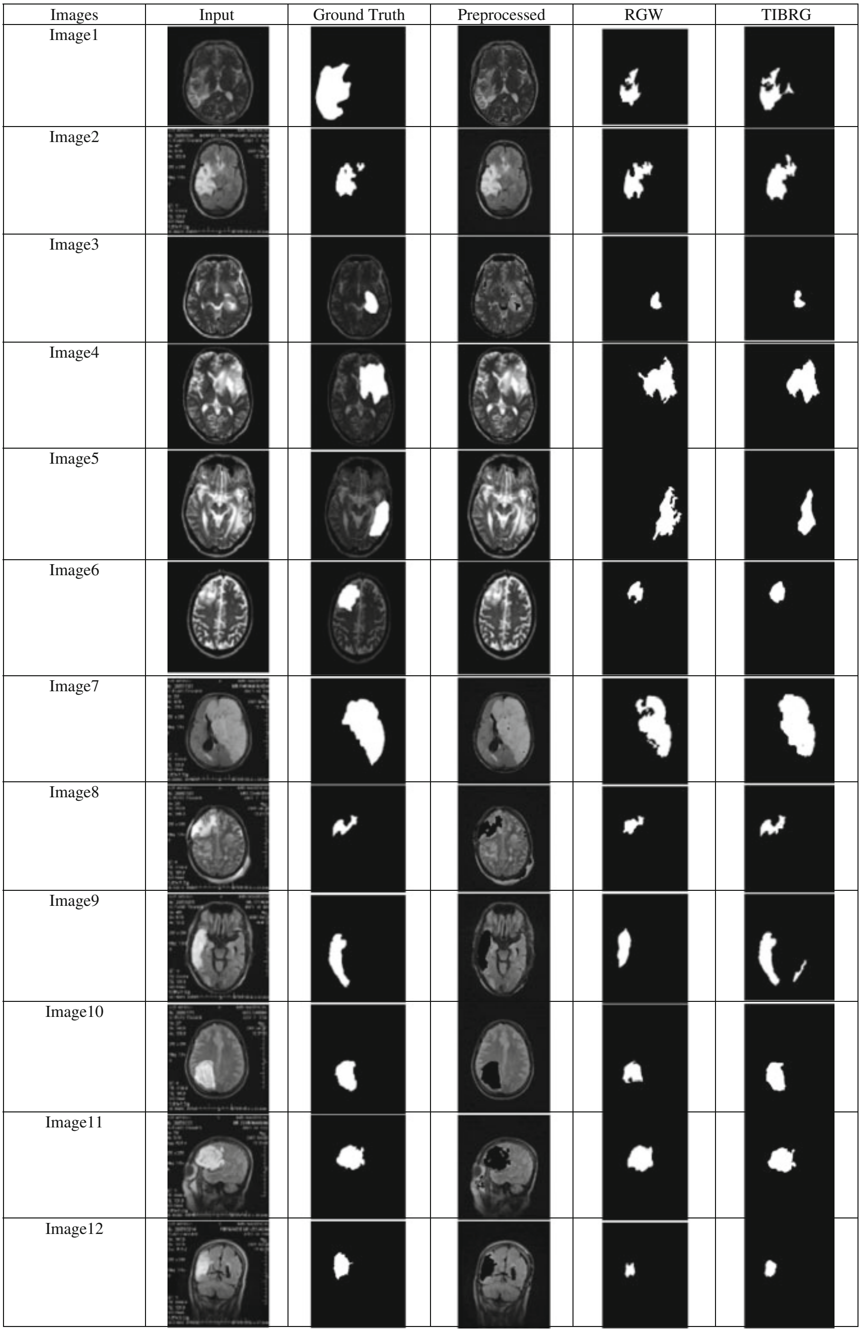

Fig. 142.4 Segmentation results

Table 142.1 Coefficient of similarity (ε)

Method	Coefficient of similarity (ε)											
	Image 1	Image 2	Image 3	Image 4	Image 5	Image 6	Image 7	Image 8	Image 9	Image 10	Image11	Image12
RGW	0.730	0.776	0.691	0.821	0.843	0.754	0.738	0.786	0.723	0.745	0.906	0.685
TIBRG	0.837	0.926	0.701	0.853	0.843	0.851	0.795	0.816	0.915	0.904	0.947	0.754

Table 142.2 Spatial overlap (£)

Method	Spatial overlap (£)											
	Image 1	Image 2	Image 3	Image 4	Image 5	Image 6	Image 7	Image 8	Image 9	Image 10	Image 11	Image12
RGW	0.736	0.766	0.684	0.828	0.835	0.732	0.749	0.785	0.728	0.751	0.914	0.685
TIBRG	0.842	0.919	0.719	0.846	0.849	0.843	0.781	0.827	0.908	0.909	0.932	0.757

Coefficient of similarity (ε) is calculated using the formula as

$$\varepsilon = 1 - \frac{|manual - automatic|}{automatic} \tag{142.10}$$

Spatial overlap(£) is calculated as

$$£ = \frac{2 \times intersection}{manual + automatic} \tag{142.11}$$

For the proposed method the coefficient of similarity and spatial overlap is better for images 2, 9, 10 and 11. It is average for 1, 4, 5, 6 and 8. However it is less for images 3, 7 and 12 images. Image 11 got the value as 0.9478. The average coefficient of similarity obtained is 0.7670 % for RGW and 0.8456 % for TIBRG. Spatial overlap is 0.9329 for image 11. The average spatial overlap is 0.7665 % for RGW and 0.8447 % for TIBRG. Comparison between images in terms of coefficient of similarity and spatial overlap is shown in Figs. 142.5 and 142.6.

Fig. 142.5 Coefficient of similarity

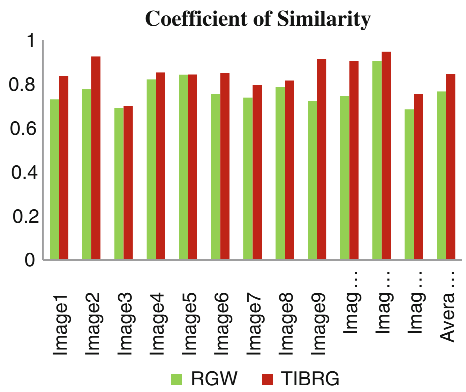

Fig. 142.6 Spatial overlap

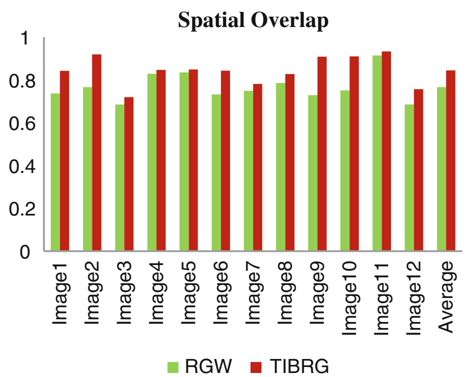

142.5 Conclusion

In this paper a new medical image segmentation technique was presented. In the preprocessing step, we utilized Gaussian filtering to reduce the influence of noise. We then performed classification using FFBNN with the extracted features. To obtain well-segmented images, we finally used TIBRG algorithm of the proposed approach. Experimental results showed that the proposed method outperforms the RGW algorithm in terms of coefficient of similarity and spatial overlap. It is 0.8456 and 0.8447 % for TIBRG algorithm respectively.

References

1. Wang XF, Huang DS, Xu H (2010) An efficient local Chan–Vese model for image segmentation. Pattern Recogn 43:603–618
2. Zhang S, Zhan Y, Metaxas DN (2012) Deformable segmentation via sparse representation and dictionary learning. Med Image Anal 16:1385–1396
3. Bergeest JB, Rohr K (2012) Efficient globally optimal segmentation of cells in fluorescence microscopy images using level sets and convex energy functional. Med Image Anal 16:1436–1444
4. Prastawa M, Bullitt E, Gerig G (2009) Simulation of brain tumors in MR images for evaluation of segmentation efficacy. Med Image Anal 13:297–311
5. Kruggel F, Paul SJ, Gertz HJ (2008) Texture-based segmentation of diffuse lesions of the brain's white matter. NeuroImage 39:987–996
6. Nyma A, Kang M, Kwon YK, Kim CH, Kim JM (2012) A hybrid technique for medical image segmentation. J. Biomed Biotechnol 10:1–7
7. Ahmed S, Iftekharuddin KM, Vossough A (2011) Efficacy of texture, shape, and intensity feature fusion for posterior-fossa tumor segmentation in MRI. IEEE Trans Inf Technol Biomed 15:206–213
8. Shen S, Sandham W, Granat M, Sterr A (2005) MRI fuzzy segmentation of brain tissue using neighborhood attraction with neural-network optimization. IEEE Trans Inf Technol Biomed 9:459–467
9. Kavitha A, Chellamuthu C, Rupa K (2012) An efficient approach for brain tumor detection based on modified region growing and neural network in MRI images. In: International conference on computing, electronics and electrical technologies (ICCEET), pp 1087–1095
10. Viji KS, Jayakumari J (2013) Texture based segmentation of MRI brain tumor images. IRECOS 8:2051–2057

Chapter 143
A Novel Reference Current Generation Algorithm for Three Phase Shunt Active Power Filter

Deepthi Joseph, N. Kalaiarasi and K. Rajan

Abstract Reference current generation algorithms for shunt active power filters have always been associated with increased computational tasks. In this paper we present a method to reduce the computational task and thereby increase the processing speed of the filter. We suggest a new fundamental current extraction method which involves peak value calculation of the distorted signal. The method is achieving the same compensation level as that of the conventional method which has been verified by MATLAB/SIMULINK software.

Keywords Discrete Fourier transform approach · Synchronous detection method · PLL · UDCS · Current extraction method

143.1 Introduction

The growth of power electronics industry has demanded improvements in the quality of power in terms of magnitude, frequency etc. because of the increased usage of nonlinear loads. A pure harmonic free supply current at the point of common coupling has always kept the power loss at a premium. Since many nonlinear loads which distort the supply current operate at a time, using a harmonic

D. Joseph (✉)
EEE Department, Vel Tech High Tech Dr. Rangarajan Dr. Sakunthala Engineering College, Chennai, India
e-mail: deepths@gmail.com

N. Kalaiarasi
R.M.K. College of Engineering Technology, Chennai, India
e-mail: kalaiarasi_n69@hotmail.com

K. Rajan
Vel Tech Engineering College, Chennai, India
e-mail: rajanharry@yahoo.com

C. Kamalakannan et al. (eds.), *Power Electronics and Renewable Energy Systems*,
Lecture Notes in Electrical Engineering 326, DOI 10.1007/978-81-322-2119-7_143

filter can significantly reduce the losses and increase the efficiency of the whole power system.

Conventionally passive filters and capacitor banks are used to eliminate the harmonics and other power quality related problems [1]. The passive filters seems to be bulky and may introduce resonance related issues. Moreover they may not work effectively with dynamic loads. Therefore shunt active filtering has been adopted to mitigate the above mentioned issues [2–4]. Shunt active filtering consists of two main parts. Out of this one is to generate the reference current for the three phase inverter and the other is to resynthesis the same.

There are various topologies to extract the harmonic content in a distorted signal like Instantaneous Reactive power theory [5, 6], Discrete Fourier Transform approach [7], Synchronous Detection Method [8, 9] etc. In this paper, we compare Synchronous Reference Frame algorithm and the suggested method to analyse the computational burden and simplicity of the algorithms.

The second part is resynthesising the extracted harmonics using a voltage source inverter which is nothing but the Active Filter. Since the filter is connected in parallel to the power system, it is referred as shunt active power filter. Harmonics can be resynthesised by using different current control techniques like Hysteresis method [10], ramp method [9] etc. The filter is a pulse width modulated filter which is capable of injecting equal and opposite phase harmonic current to the point of common coupling. The main components of the Active Power Filter are the Voltage Source Inverter (VSI) and the DC capacitor [10].

The block diagram of an APF connected to a three phase source in parallel to a nonlinear load is shown in Fig. 143.1.

Implementation of a less computational based algorithm for reference current generation will be advisable if it results in reduced processing speed and programming memory requirement of the filter while maintaining the same level of compensation. The method proposed satisfies the above mentioned conditions and the results of both conventional and proposed method have been analysed and compared using MATLAB/SIMULINK software.

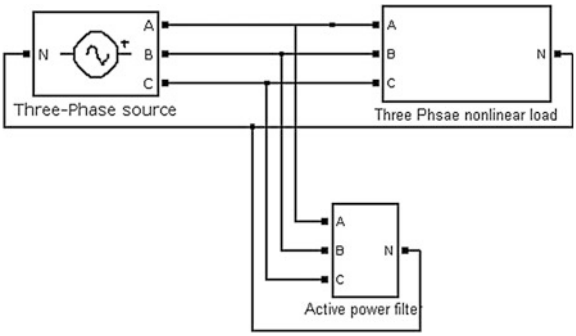

Fig. 143.1 Simulink block of shunt APF connected to a three-phase four wire system

143.2 Reference Current Generation Process for APF

There are diverse methods for producing the current reference for shunt APFs. The elementary methods consist of the sensing of source voltages and load currents. These methods are not quite computational intensive. In this paper, the current reference for APF is generated using root mean square (r.m.s.) method. This method is apt under balanced and un-balanced source conditions. This method is quite uncomplicated because it has a lesser number of computations than conservative techniques.

143.2.1 Root Mean Square Method

In this method, the distorted source currents are sensed. The r.m.s. value of the waveform is found out by using the basic r.m.s equation which is given below.

$$I_{rms} = \sqrt{I/T \int_{0}^{T} f^2(t)dt} \quad (143.1)$$

Here f(t) is the distorted source current. Once the r.m.s. value is calculated, the peak value is obtained by dividing the result by 1.414. Now the peak value of DC link voltage is found by the same method which has already been proposed in the literatures. The peak value of DC voltage is used to divide the source voltage to obtain a unit sine wave, which in turn is multiplied by the peak value of distorted source current to obtain the fundamental component. This fundamental current has been subtracted from the distorted current to obtain the harmonic current which is nothing but the reference current.

The method yields the same T.H.D. as that of conventional method on the other hand with less computational task.

143.2.2 Conventional Synchronous Reference Frame Method

In this method, the nonlinear currents are sensed and is transformed to d-q reference frame by means of Park's transformation. The d-q frame revolves with the fundamental angular frequency that sorts the fundamental signal to give the impression as dc component. The angle information is given from a Phase Locked Loop (PLL). The output of reference frame will still have a ripple factor which can be filtered by a low pass filter. Now the output of low pass filter will be pure dc component and

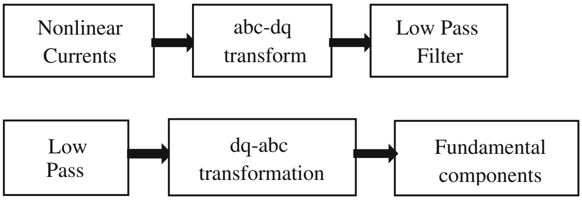

Fig. 143.2 Block diagram of SRF method

hence an inverse Park's transformation will yield the fundamental component of the source current. Figure 143.2. shows the block diagram of conventional method.

$$\begin{bmatrix} I_d \\ I_q \end{bmatrix} = \begin{bmatrix} \cos\theta & \cos(\theta - \frac{2\Pi}{3}) & \cos(\theta + \frac{2\Pi}{3}) \\ \sin\theta & \sin(\theta - \frac{2\Pi}{3}) & \sin(\theta + \frac{2\Pi}{3}) \end{bmatrix} \begin{bmatrix} I_a \\ I_b \\ I_c \end{bmatrix} \tag{143.2}$$

$$\begin{bmatrix} I_a \\ I_b \\ I_c \end{bmatrix} = \begin{bmatrix} \cos\theta & \sin\theta \\ \cos(\theta - \frac{2\Pi}{3}) & \sin(\theta - \frac{2\Pi}{3}) \\ \cos(\theta + \frac{2\Pi}{3}) & \sin(\theta + \frac{2\Pi}{3}) \end{bmatrix} \begin{bmatrix} I_d \\ I_q \end{bmatrix} \tag{143.3}$$

$$I_{ca} = I_{La} - I_{sa} \tag{143.4}$$

$$I_{cb} = I_{Lb} - I_{sb} \tag{143.5}$$

$$I_{cc} = I_{Lc} - I_{sc} \tag{143.6}$$

I_{La}, I_{Lb}, and I_{Lc} are the currents strained by the load from the source, which have been sensed at the point of common coupling, and I_{sa}, I_{sb}, I_{sc} are fundamental current components obtained from the transformations. I_{ca}, I_{cb} and I_{cc} are the currents generated using this method. These currents are given as reference to the inverter to generate the suitable gating pulses [9].

The advantage of SRF method is that selective harmonic compensation is possible. But as we observed above transformations are involved which makes the algorithm slightly computational intensive.

143.3 Compensation Current Generation Using User-Defined Constant Switching Frequency Scheme

A constant switching frequency scheme is implemented in place of conventional hysteresis control method of active power filters to control the switching frequency of the voltage source inverter. Even though hysteresis method is considered as the best method to generate the compensation current, the issues regarding variable

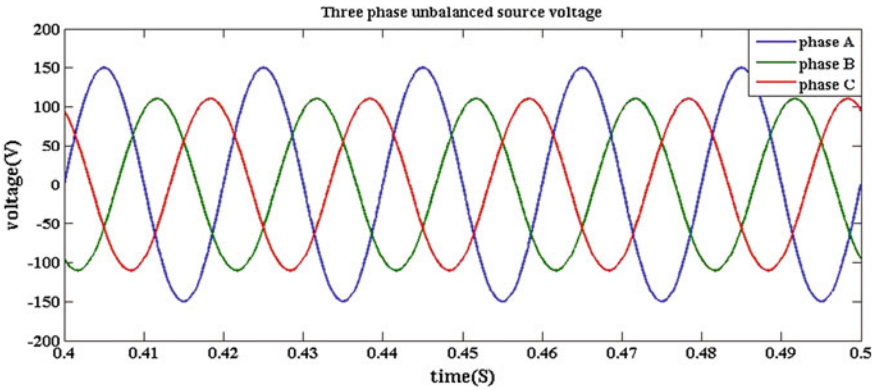

Fig. 143.3 Unbalanced source voltages

switching frequency is much of a concern at present. The variable switching frequency pattern causes high switching loss, sub harmonics, etc. These problems can be reduced if we go for a constant switching frequency pattern. The user-defined constant switching frequency scheme (UDCS) for a four-leg voltage source inverter-based active filter is implemented as shown in Fig. 143.3. Here the hysteresis current controller is employed in the generation of switching pulses S_1, S_2, S_3, S_4, S_5, and S_6 for the voltage source inverter to track the filter currents. A square pulse of a user-defined frequency is given to the fourth leg to generate the pulses Z_1 and Z_2, which produce and control the zero states that lead to the reduction and constancy in switching frequency [11].

In traditional methods, we are unable to foresee the zero states and its duration even if the zero states are identified. In this method of switching, two zero states are persuasively generated in every switching cycle. By allowing the variation of duty cycles of signals of other three legs, a constant switching frequency is obtained. Here two zero states are available where zero switching state 1 is the state in which all the upper switches are ON and all the lower switches are OFF and zero switching state 2 is the state in which all the upper switches are OFF and all the lower switches are ON [12].

In the UDCS scheme, the user defines the switching frequency and makes the other three legs also to operate in that frequency. This helps to obtain the constant switching frequency. Switching frequencies can be reduced by choosing a lower frequency switching pulse. During the zero states, the dc capacitor gets disconnected from the Voltage Source Inverter (VSI). So appropriate current synthesis does not take place; this reasons the filter currents to violate the band. Here it will work as an adjustable hysteresis band, whereby the band variation is accomplished by the user-defined switching frequency [12].

143.4 Simulation Studies

The simulation is performed in a three-phase four-wire system. It has been done by keeping the source voltage non-stiff. A three-phase diode bridge rectifier is kept as the non-linear load. The software used for simulation is MATLAB/SIMULINK. The simulation parameters are given in Table 143.1.

The root mean square method works quite satisfactorily even when the source is non-stiff. The source voltage is kept unbalanced throughout the simulation by increasing the voltage in one phase. Figure 143.3. Shows the unbalanced source voltage.

The unbalance in simulation can be achieved by giving different value of voltage to one of the phases. The distorted source current due to non-linear load is also shown in Fig. 143.4. The non-linear load used is a three-phase bridge rectifier.

The reference currents are generated by using the Eq. (143.1). The reference currents generated when the source is non-stiff is shown in Fig. 143.5. It is generated by implementing the equation of root mean square value. The three phase currents which act as the reference currents are shown in figure.

The pulses generated while using the UDCS frequency is shown in Fig. 143.6. The frequency of the user-defined pulse is 2.57 kHz. It can be observed that the frequency of the other legs of the filter is also getting confined to the user-defined frequency. The frequency of conventional hysteresis switching technique is a variable frequency that ranges from 3 to 2.8 MHz.

Table 143.1 Simulation parameters

Sl no.	Parameters	Value
1.	Source	Unbalanced condition Voltage phase A—150 V Voltage phase A—110 V Voltage phase A—110 V Freq—50 Hz
2.	Load	Three phase diode bridge Phase A resistance and inductance—20 Ω, 3e −3H Phase B resistance and inductance—10 Ω, 3e −3H Phase C resistance and inductance—10 Ω, 3e −3H
3.	Switching frequency	2.57 kHz
4.	Hysteresis band	0.24
5.	Interface inductance and resistance	0.07 H, 200 Ω
6.	DC link capacitor	2, 200 μF

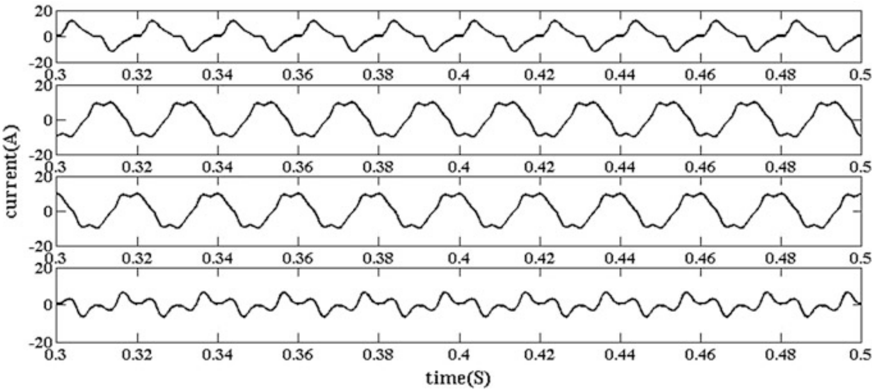

Fig. 143.4 Distorted source current due to nonlinear load

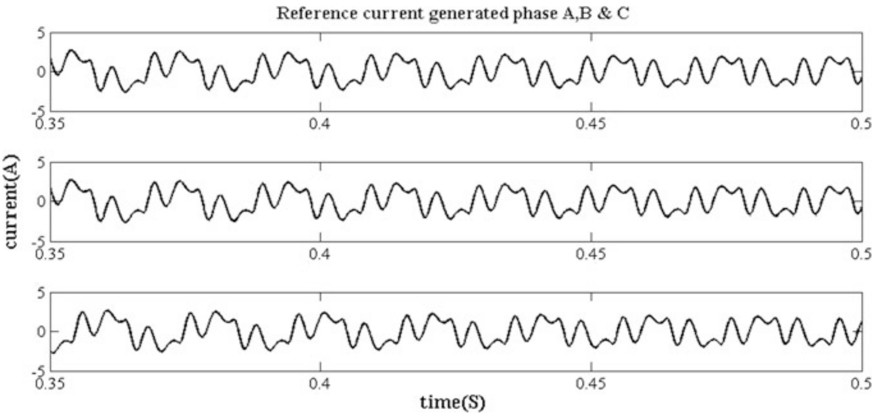

Fig. 143.5 Extracted harmonic currents of phases A, B & C

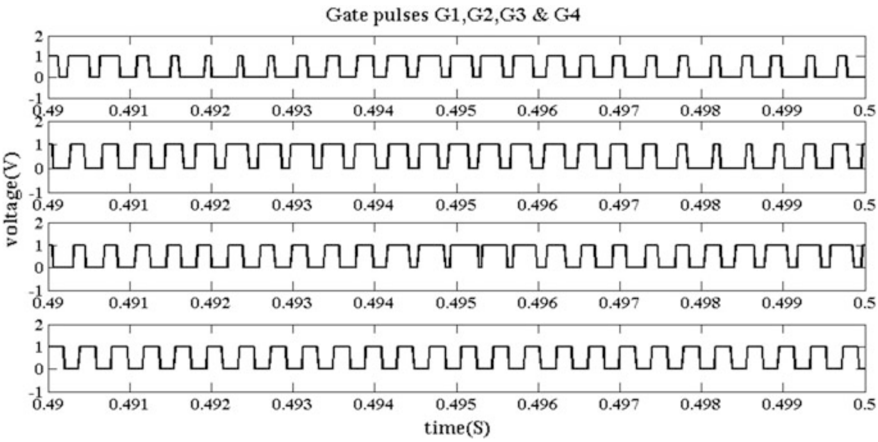

Fig. 143.6 Constant frequency pulses generated while using UDCS scheme

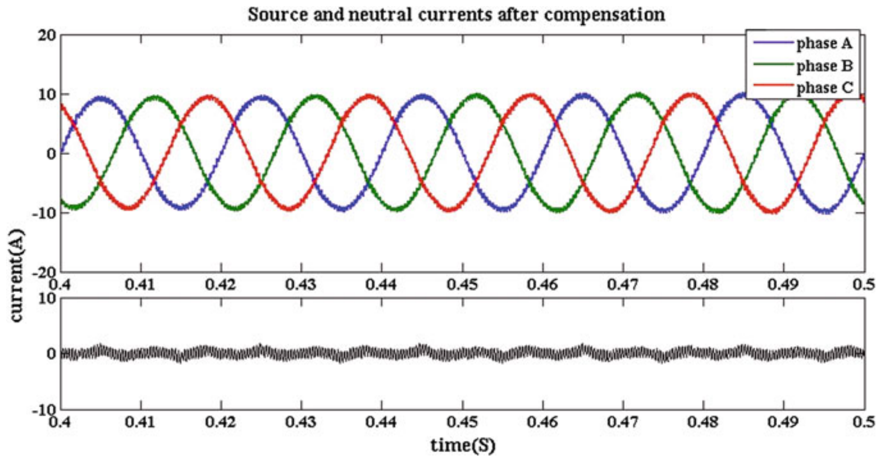

Fig. 143.7 Phases A, B and C compensated source currents and neutral current

The constant frequency gating signals switch the inverter to synthesis the compensating current. By injecting this compensating current from the filter back to the source, the source currents get compensated [9]. The compensated source currents and neutral current are shown in Fig. 143.7.

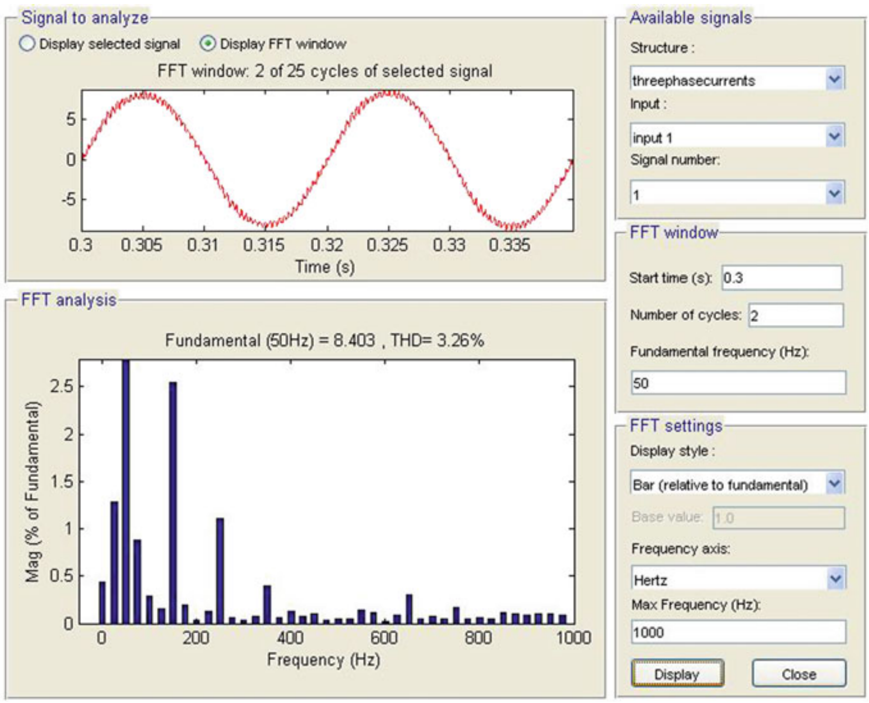

Fig. 143.8 THD of source current after compensation

143.5 Conclusion

Here a shunt APF using synchronous reference frame method is described. The total harmonic distortion is reduced from 34.93 to 3.26 %. This is shown by the bar diagram in Fig. 143.8. The suggested Root Mean Square method is seemed to be simple and less computational intensive. The method involves only one equation, which saves the computation time. The switching frequency has been reduced to a constant frequency of 2.57 kHz from a range of variable frequency of 3 to 2.8 MHz. The problems with conventional hysteresis control is been given prior importance, and a method to control the switching frequency is discussed. The simulation work has been done under a non-stiff source condition. By using UDCS scheme, the switching frequency became fixed. This causes very low switching losses compared to other methods. Since only load currents are sensed, the numbers of sensors are reduced and hence the cost of the filter is reduced considerably. The simulation study has been done using MATLAB/SIMULINK environment. The solver used is Variable step, ode 45.

References

1. MacGregor SD (1998) An overview of power quality issues and solutions. IEEE/PCA Cement Industry technical conference, pp 57–64, 1998
2. Akagi H (1996) New trends in active filters for power conditioning. IEEE Trans Ind Appl 32 (6):1312–1322
3. Bhattacharya S, Frank TM, Divan DM, Banerjee B (1998) Active filter system implementation. IEEE Ind Appl Mag 4(5):47–63
4. Akagi H (2005) Active harmonic filters. IEEE Proc 93(12):2128–2141
5. Montero MIM, Cadaval ER, Gonzalez FB (2007) Comparison of control strategies for shunt active power filters in three-phase four wires systems. IEEE Trans Power Electron 22 (1):229–236
6. Buso S, Malesani L, Mattavelli P (1998) Comparison of current control techniques for active filter applications. IEEE Trans Ind Electron 45(5):722–729
7. Ginn HL, Chen GD (2008) Flexible active compensator control forvariable compensation objectives. IEEE Trans Power Electron 23(6):2931–2941
8. Bhattacharya S, Frank TM, Divan DM, Banerjee B (1998) Active filter system implementation. IEEE Ind Appl Mag 4(5):47–63
9. Li H, Zhuo F, Wu L, Lei W, Liu J, Wang Z (2004) A novel current detection algorithm for shunt active power filters in harmonic elimination, reactive power compensation and three phase balancing. In: 35th Annual IEEE power electronics specialists conference
10. Anand V, Srivastava SK (2012) Performance investigation of shunt active power filter using hysteresis current control method. Int J Eng Res Technol (IJERT) 1(4). ISSN:2278-0181
11. George V, Mishra MK, Sridharan S (2008) A novel constant frequency strategy for a three leg DSTATCOM. In: Proceedings of 21st Canadian conference on electrical and computer engineering, 4–7 May 2008, Canada
12. Alex A, George V (2009) A constant switching frequency DSTATCOM operating under non stiff source conditions. In: 10th National conference on technological trends (NCTT09) 6–7 Nov 2009

Chapter 144
Mathematical Model of Brushless Doubly Fed Induction Generator Based Wind Electric Generator

Anjana Suresh, R. Resmi and V. Vanitha

Abstract Electric power generated from renewable source of energy is generally referred to as "Green power". There has been a renewed interest in wind energy in recent years because it is a potential source for electricity generation with minimal environmental impacts and with no cost of fuel. Nowadays, the main challenge in a Doubly Fed Induction Generator (DFIG) based wind electric conversion system is the proper maintenance of slip rings and brushes. Due to wear and tear, the slip rings and brushes of generator have to be frequently changed, which will be quite expensive. Also it will be very difficult to access them in the case of offshore wind farm. So, Brushless Doubly-Fed Induction Generator (BDFIG) was proposed to replace the traditional DFIG. Besides eliminating the slip rings and brushes, BDFIG has other advantages such as the improvement of reliability and cost effectiveness. This paper deals with mathematical modelling of BDFIG based Wind Electric Generator (WEG). Modelling is done for 50 kW WEG with the help of mathematical equations governing each component using MATLAB Simulink and the results are presented.

Keywords Green power · DFIG · Brushless doubly-fed induction generator · Wind electric generator · Variable frequency converter

A. Suresh (✉) · R. Resmi · V. Vanitha
Electrical and Electronics Department, Amrita Vishwa Vidyapeetham University, Coimbatore, India
e-mail: anjanasuresh2009@gmail.com

R. Resmi
e-mail: resmidhun2010@gmail.com

V. Vanitha
e-mail: v_vanitha@cb.amrita.edu

C. Kamalakannan et al. (eds.), *Power Electronics and Renewable Energy Systems*,
Lecture Notes in Electrical Engineering 326, DOI 10.1007/978-81-322-2119-7_144

144.1 Introduction

Doubly-Fed Induction Generators (DFIG) are one of the most common and famous in the family of Wind Electric Generators (WEG). This is because these generators employ partially rated power electronic converters which are rated around 30 % of the power rating of the generator for a ±25 % speed range making them suitable for wind power applications. DFIG suffers from several disadvantages. One of the major disadvantage is that these generators employ slip rings and carbon brushes in order to recover slip power from the rotor and deliver it to the grid. Carbon brushes are known to have limited life span and therefore are replaced every couple of months. Carbon dust is conducting in nature and when trapped in the generator windings it will increase the risk of sparking between the winding conductors which could result in the weakening of the insulation and therefore a reduction of system reliability. Due to these factors, overall maintenance costs are increased especially for offshore wind turbines. Due to aforementioned reasons, it is of vital importance that the doubly-fed generators are designed in a manner so as to recover slip power utilizing more reliable means than carbon brushes and slip rings. Due to these limitations of DFIG, it is replaced by **B**rushless **D**oubly **F**ed **I**nduction **G**enerator (**BDFIG**), a machine without brushes and slip rings and hence achieving higher reliability and lower operational cost.

144.2 BDFIG Configuration

Brushless Doubly Fed Induction Machine is an AC electrical machine which can operate as both generator and a motor. As the name implies, the machine requires two AC three phase stator windings and either a squirrel cage rotor winding or a wound rotor winding. Since no electric terminals are taken from rotor, it removes the use of slip rings and brushes. It is a single frame induction machine with two stator windings of different pole numbers. Typically, the two stator windings are of different frequencies, one a fixed frequency connected to the grid, and the other a variable frequency derived from a power electronic frequency converter. Stator winding which is connected directly to the grid is called the Power Winding (PW), and the other connected to a variable voltage, variable frequency converter is called the Control Winding (CW) [1]. Different pole numbers are chosen to avoid the direct coupling between two stator windings. Figure 144.1 shows the schematic diagram of BDFIG based WEG. As shown in Fig. 144.1, PW is directly connected to grid where the major part of active and reactive power pass through this winding. CW is connected to grid by a fractional sized bidirectional converter consisting of two back to back converters. The synchronous speed ω_r of the machine is given by Eq. (144.1)

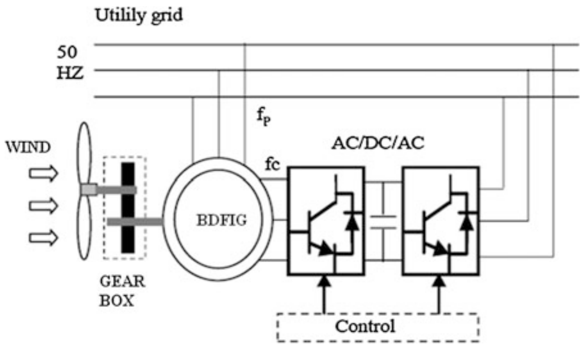

Fig. 144.1 Schematic diagram of BDFIG based WEG

$$\omega_{\mathrm{r}} = \frac{\omega_p \pm \omega_c}{P_p + P_c} \tag{144.1}$$

where ω_p and ω_c are the electrical angular frequencies of PW and CW voltages respectively. P_P and P_C are the respective pole pair numbers.

In synchronous mode, two stator windings are connected to the supply as shown in Fig. 144.1 and the rotor rotates at certain speed, which enables it to couple the two stator windings magnetic fields. It should be noted that the two stator windings do not have any direct coupling with each other because of different pole numbers. Advantage is that precise open loop speed control can easily be obtained [2].

144.3 Modelling of WEG

All analysis in the engineering sciences starts with the formulation of appropriate models. A model in power system analysis invariably means a mathematical model, which is a set of equations, which appropriately describes the interactions between different quantities in the time frame studied and with the desired accuracy of the physical system. Like the power system components, WEGs also consist of a wide range of time constants. So in order to study the behavior of BDFIG based WEG, its mathematical model is developed in this paper [3]. The modelling of each component is done in MATLAB Simulink.

144.3.1 Wind Turbine Model

A wind turbine is a rotating machine that converts the kinetic energy of wind into mechanical energy. The turbine power (P_t) is given by the Eq. (144.2)

$$\mathrm{P_t} = \frac{\rho A C p v^3}{2} \tag{144.2}$$

where P_t is the power output from the wind turbine in watts, ρ is the air density, A is the turbine swept area and Cp is the performance coefficient or power coefficient of the wind turbine. Tip Speed Ratio (TSR) of a wind turbine, which is defined as the ratio of turbine speed at its tip to wind speed [4].

$$\lambda = \frac{2\pi NR}{v} \tag{144.3}$$

Where λ is the TSR is given in the Eq. (144.3) and R is the radius of turbine swept area, N is the rotational speed of turbine in rps, v is the wind speed in m/s. Using all these equations, wind turbine model can be developed. Figure 144.2 shows the simulink model of Wind turbine.

144.3.2 Drive Train Modelling

Neglecting the stiffness and damping factor, one-mass model for the drive train obtained is given by

$$\mathrm{T_{gen}} - \mathrm{T_{wtr}} = \mathrm{J_{ech}}\frac{\mathrm{d}\omega_r}{\mathrm{dt}}. \tag{144.4}$$

where $\mathrm{T_{gen}}$ is the generator torque given in Eq. (144.4)

ω_r is the generator speed.

Equivalent moment of inertia is given in the Eq. (144.5)

$$\mathrm{J_{ech}} = \mathrm{J_{gen}} + \frac{\mathrm{J}}{\mathrm{Kgear}^2} \tag{144.5}$$

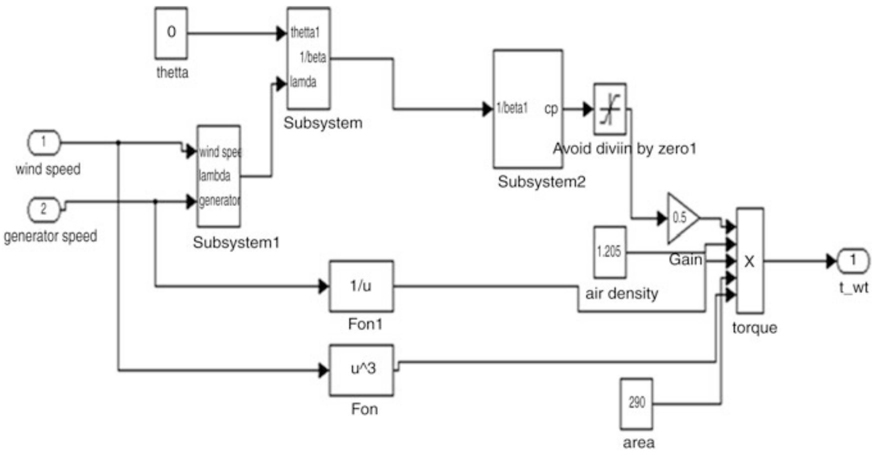

Fig. 144.2 Simulink model of wind turbine

The Simulink model for the Drive train is shown in Fig. 144.3 using the datas from [4].

144.3.3 BDFIG Modelling

Using Electrical Machine Analysis theory, Dynamic model of BDFIG can be obtained in dq reference frame [5, 6]. Voltage Equations for two stator windings and one rotor winding in dq frame are given by the following Eqs. (144.6–144.11)

$$\mathrm{V_{dp}} = \mathrm{R_p i_{dp}} + \frac{d\lambda \mathrm{dp}}{dt} - \omega_p \lambda \mathrm{pq} \tag{144.6}$$

$$\mathrm{V_{dq}} = \mathrm{R_p i_{qp}} + \frac{d\lambda \mathrm{qp}}{dt} + \omega_p \, \lambda \mathrm{dp} \tag{144.7}$$

$$\mathrm{V_{dc}} = \mathrm{R_c i_{dc}} + \frac{d\lambda \mathrm{dc}}{dt} - (\omega_p - (\mathrm{P}p + Pc)\omega_r)\lambda \mathrm{qc} \tag{144.8}$$

$$\mathrm{V_{qc}} = \mathrm{R_c i_{qc}} + \frac{d\lambda \mathrm{qc}}{dt} + (\omega_p - (\mathrm{P}p + Pc)\omega_r)\lambda \mathrm{dc} \tag{144.9}$$

$$\mathrm{V_{dr}} = \mathrm{R_r i_{dr}} + \frac{d\lambda \mathrm{dr}}{dt} - (\omega_p - \mathrm{P}p\,\omega_r)\lambda \mathrm{qr} \tag{144.10}$$

$$\mathrm{V_{qr}} = \mathrm{R_r i_{qr}} + \frac{d\lambda \mathrm{qr}}{dt} + (\omega_p - \mathrm{P}p\,\omega_r)\lambda \mathrm{dr} \tag{144.11}$$

The active and reactive power through PW are given by Eqs. (144.12) and (144.13) respectively

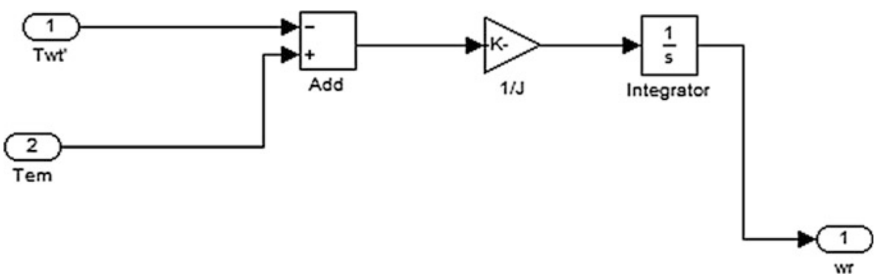

Fig. 144.3 Simulink model of drive train

$$P_p = \frac{3}{2}\left(V_{dp} i_{dp} + V_{qp} i_{qp}\right) \tag{144.12}$$

$$Q_p = \frac{3}{2}\left(V_{qp} i_{dp} - V_{dp} i_{qp}\right) \tag{144.13}$$

The active and reactive power through CW are given by Eqs. (144.14) and (144.15)

$$P_c = \frac{3}{2}\left(V_{dc} i_{dc} + V_{qc} i_{qc}\right) \tag{144.14}$$

$$Q_c = \frac{3}{2}\left(V_{qc} i_{dc} - V_{dc} i_{qc}\right) \tag{144.15}$$

Using all above equations, BDFIG model is developed using specifications from [7]. Figure 144.4 shows the simulink model of BDFIG (Fig. 144.5).

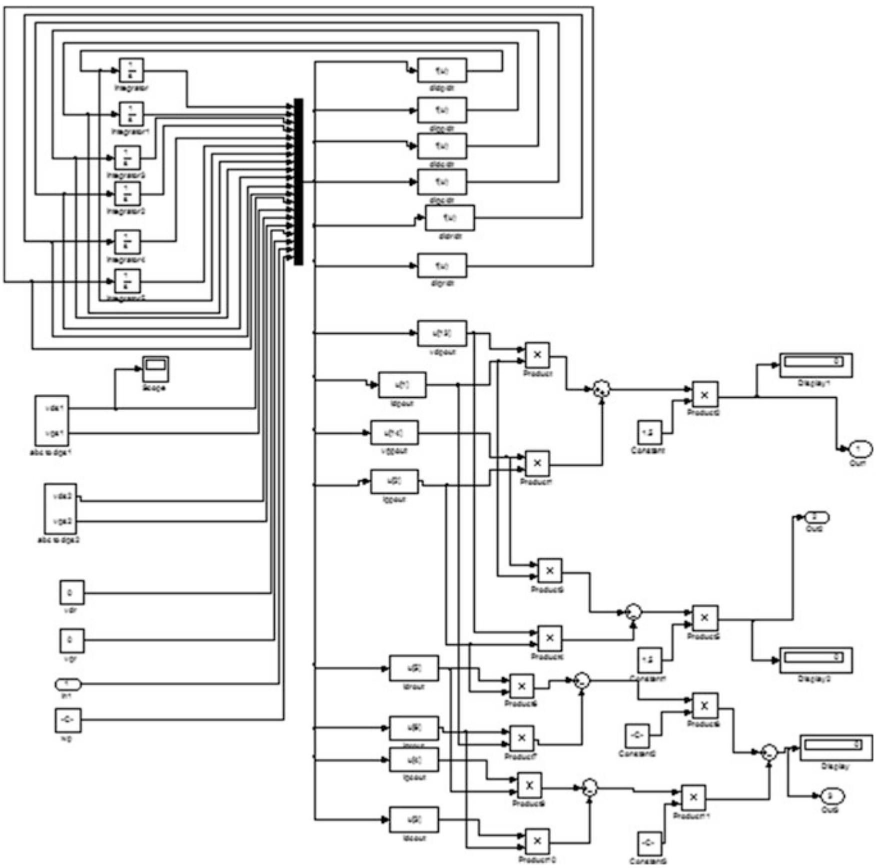

Fig. 144.4 Simulink model of BDFIG

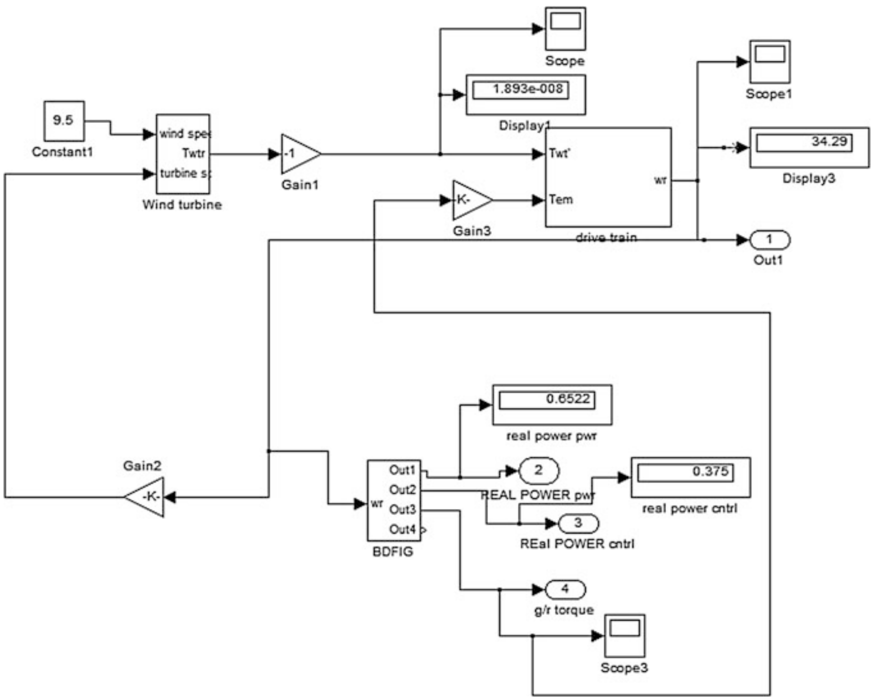

Fig. 144.5 Complete simulink model of BDFIG based WEG

144.4 Simulation Results

144.4.1 Wind Turbine and Drive Train Model

The Wind turbine torque obtained is −104.5 Nm and generator speed of 34.29 rad/s for wind speed of 9.5 m/s (Figs. 144.6 and 144.7).

144.4.2 Brushless Doubly Fed Induction Generator

Figure 144.8a shows the Voltage waveform applied to Power Winding. Figure 144.8b shows the voltage waveform in dq axis. The voltage V_d obtained is 1 p.u and V_q obtained is 0 p.u.

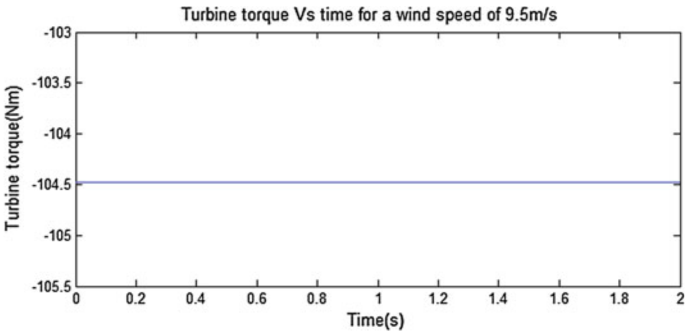

Fig. 144.6 Wind turbine torque

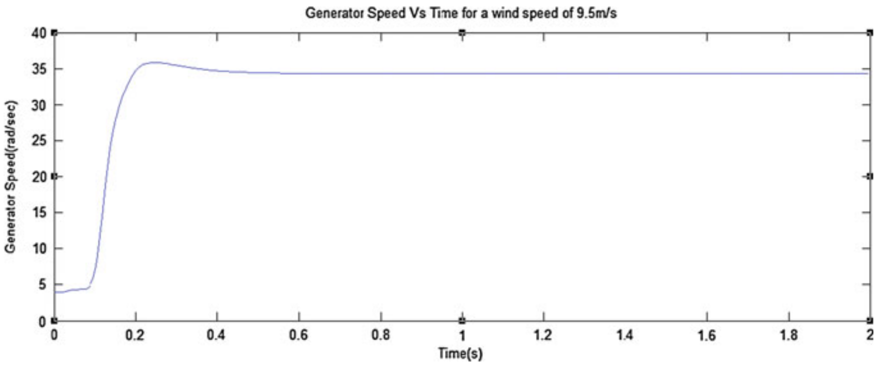

Fig. 144.7 WEG speed characteristics

Figures 144.9 and 144.10 shows the BDFIG Real Power through the Power Winding (PW) and Control Winding (CW) respectively. The real power through Power Winding obtained is 0.65 p.u and Control Winding power obtained is 0.35 p.u for a wind speed of 9.5 m/s.

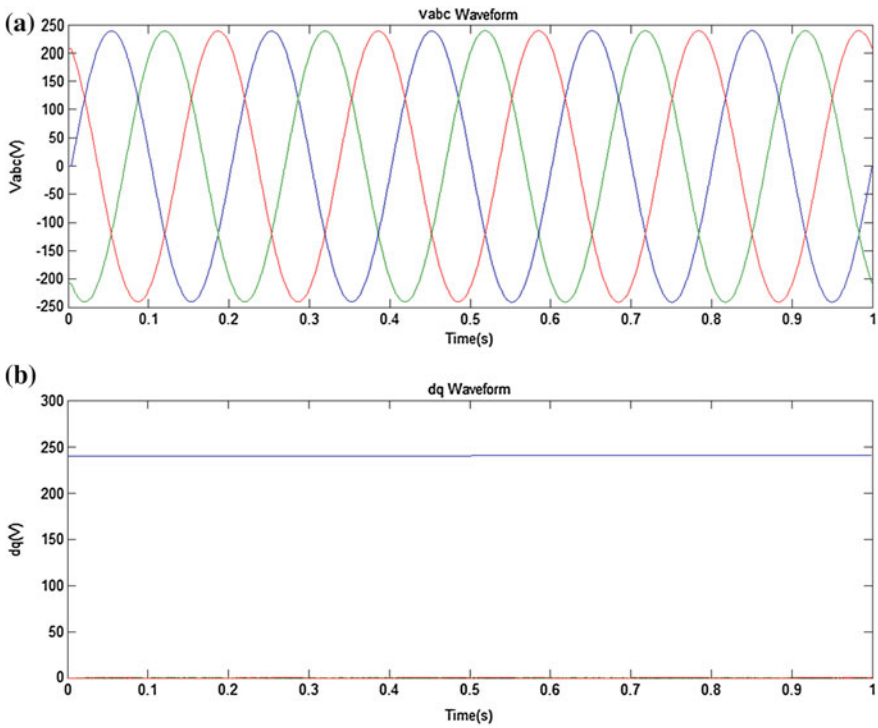

Fig. 144.8 **a** Voltage waveform. **b** dq axis waveform

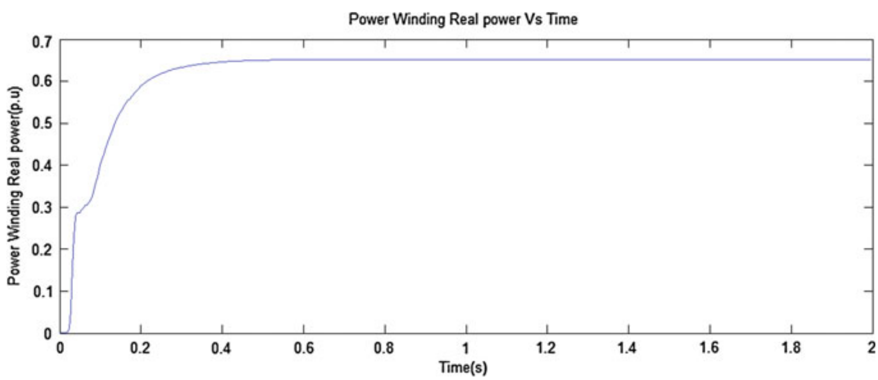

Fig. 144.9 Power winding real power

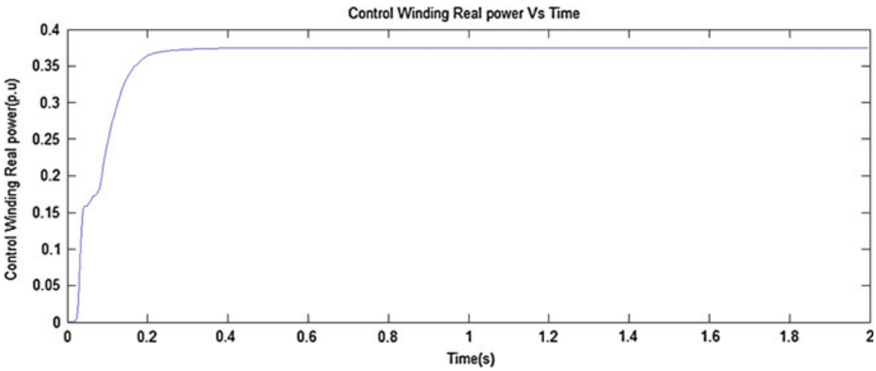

Fig. 144.10 Control winding real power

144.5 Conclusions

In this paper, general constructional features of BDFIG are studied. Advantages of BDFIG over conventional DFIG are also studied. Nowadays, offshore wind farms are becoming more popular which necessitates to prefer BDFIG over conventional DFIG. This paper has presented the complete model of BDFIG based WEG. Mathematical Modelling of each component is implemented in MATLAB Simulink. Simulation results are presented in the paper. This model forms the basis of the more complicated model with converter control of BDFIG with variable speed wind turbine to track maximum power from wind turbine for the given wind speed.

References

1. Gorginpour H, Oraee H, McMahon RA (2011) Performance description of brushless doubly-fed induction machine in its asynchronous and variable speed synchronous modes. J Electromagn Anal Appl 3(12):490
2. Wei Z, Wang X, Chen X, Kan C (2009) Research on brushless doubly-fed machine with a new wound rotor and its generating system. In: Progress in electromagnetics research symposium proceedings, Moscow, Russia, Aug 2009
3. Protsenko K, Xu D (2008) Modelling and control of brushless doubly-fed induction generators in wind energy applications. IEEE Trans Power Electron 23(3):1191–1197
4. Rodríguez AGG, Rodríguez AG, Payán MB (2001) Estimating wind turbines mechanical constants. Department of Electrical Engineering, University of Jaen, Spain, 2001
5. Serhoud H, Benattous D (2012) Maximal wind energy tracing of brushless doubly-fed generator under flux oriented vector control. Int J Renew Energy Res 2(2): 243–249
6. Liu H, Xu L (2010) Design and performance analysis of a doubly excited brushless machine for wind power generator application. In: Power electron for distributed generation systems, pp 597–601

7. Shao S, Abdi E, Barati F, McMahon R (2009) Stator-flux-oriented vector control for brushless doubly fed induction generator. IEEE Trans Ind Electron 56(10): 4220–4228
8. Logan T, Warrington J, Shao S, McMahon R (2009) Practical deployment of the brushless doubly-fed machine in a medium scale wind turbine. In: Power Electronics and Drive Systems, pp 470–475

Chapter 145
Design of Wideband Widescan Linear Tapered Slot Antenna for an Active Electronically Scanned Array Antenna

Babu Saraswathi K. Lekshmi and Jacob I. Raglend

Abstract A wideband linear tapered slot antenna is designed for widescan active phased array antenna. The results of computation and simulation show how the antenna has very high simultaneous bandwidth over X-band and widebeam scanning capabilities up to ±60°. The reflection coefficient is less than −10 dB over the operating frequency band. A Vivaldi notch antenna element is fed by stripline and may be coupled electromagnetically by tapered transitions. Stripline-fed Vivaldi antennas are comprised of: (1) a stripline-to-slotline transition; (2) a striplinestub and a slotline cavity; and (3) a tapered slot. The radiation characteristics, return loss, beamwidth and scan angle are achieved through the use of a commercially available electromagnetic simulation software HFSS by ANSYS.

Keywords Lineartapered slot antenna · Stripline to slotlinetransition · Widescan wideband · Vivaldi antenna

145.1 Introduction

The use of tapered slot antenna (TSA), often called notch or Vivaldi antenna, for wide-band/widescan phased arrays was proposed more than two decades ago [1, 2]. These arrays offer one of the best opportunities for realizing wide-bandwidth, wide-scanning phased arrays. This paper attempts to design TSA by providing information about achievable performance and relationships between specific antenna parameters and performance using the full wave simulation tool high frequency structure simulator (HFSS). A parameter study of tapered slot antenna shows the

B.S.K. Lekshmi (✉) · J.I. Raglend
Electrical and Electronics Engineering, Noorul Islam University,
Kumaracoil, Thuckalay, India
e-mail: kavitha20012@gmail.com

J.I. Raglend
e-mail: jacobraglend@rediffmail.com

C. Kamalakannan et al. (eds.), *Power Electronics and Renewable Energy Systems*,
Lecture Notes in Electrical Engineering 326, DOI 10.1007/978-81-322-2119-7_145

key features that affect the wide-band and widescan performance of this antenna. The overall performance can be optimized by judiciously choosing a combination of parameters. The design guideline is introduced, and the antenna parameters including Voltage Standing Wave Ratio (VSWR), radiation patterns and gain are investigated.

Phased arrays have been required to operate over wide bandwidths and wide scan angle to support multifunction operation in both telecommunication and radar applications [3, 4]. Phased array antennas are attractive for applications that require rapid scanning of the beam or multiple simultaneous beams [5, 6]. In response to that need, the design of a wideband widescan tapered slot antenna with striplinefeed network has been designed. This antenna can operate from 8 to 15 GHz and scan angle up to ±60°. The simulation results are shown to certificate the performance of the proposed antenna. Vivaldi antenna gives significant advantages of efficiency, high gain, wide bandwidth and simple geometry [7].

A tapered slot antenna has a slotline flare from a small gap (50 Ω) to a large opening (377 Ω), matching to free space wave impedance. TSA is larger than a half wavelength to achieve the desired performance [8]. TSAs have moderately high directivity and narrow beamwidth because of the travelling wave properties and almost symmetric E-plane and H-plane radiation patterns over a wide frequency band as long as antenna parameters like shape, total length, dielectric thickness and dielectric constant are chosen properly. Other important advantages of TSAs are that they exhibit broadband operation, low sidelobes and ease of fabrication. TSA has the unique characteristics of symmetrical patterns in two planes, high gain (7–10 dB) in addition to having wide bandwidth characteristics in terms of radiation performance and impedance characteristics [9, 10].

145.2 Design Parameters of a Vivaldi Notch-Antenna

The schematic of the three layers forming the complete linear tapered slot antenna (Vivaldi notch-antenna) assembly viz., namely; bottom layer, top layer and the middle layer (stripline feed) is shown in Fig. 145.1. The design parameters of a linear tapered slot antenna with square cavity tapered slot and radial stub stripline feed are defined in Fig. 145.2. The parameters of the antenna geometry can be classified into two categories: substrate parameters (relative dielectric constant ε_r, and thickness t) and antenna element parameters, which can be subdivided into the stripline/slotline transition, the tapered slot, and the stripline stub and slotline cavity.

The model illustrates two substrates back to back consisting of radiating flare geometries on the two opposite faces. One of the substrate is etched completely on the opposite side of the flare and the other substrate consists of stripline feed being printed and sandwiched between the two substrates containing the flares. The RT-Duroid dielectric substrate used for this design with ε_r = 2.2 and t = 1.27 mm). The flares act as an impedance transformation network between free space and the

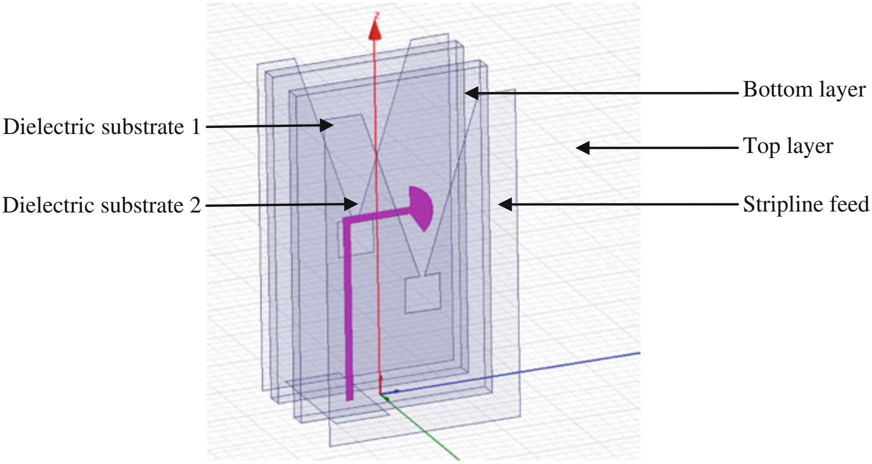

Fig. 145.1 Exploded view of stripline-feed Vivaldi notch antenna

Fig. 145.2 Definition of parameters of linearly tapered slot antenna with square cavity linearly tapered slot and radial stub stripline feed

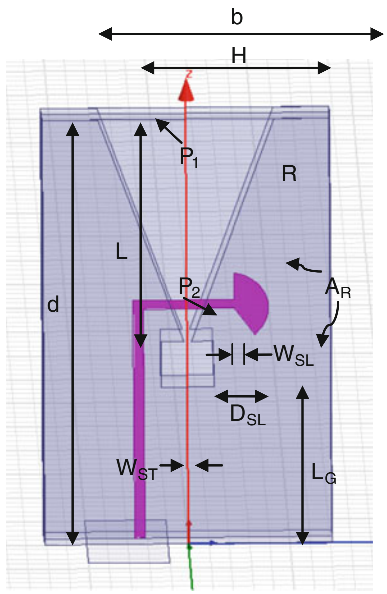

stripline feed. Radiation from the antenna occurs when the slotline impedance is matched to the impedance of free space.

The stripline/slotline transition is specified W_{ST} (stripline width) and W_{SL} (slotline width). The exponential taper profile is defined by the opening rate R and two points $P_1(z_1,y_1)$ and $P_2(z_2,y_2)$

$$y = c_1 e^{Rz} + c_2 \tag{145.1}$$

where

$$c_1 = \frac{y_2 - y_1}{e^{Rz2} - e^{Rz1}}$$
$$c_2 = \frac{y_1 e^{Rz2} - y_2 e^{Rz1}}{e^{Rz2} - e^{Rz1}}$$

The taper length L is $z_2 - z_1$ and the aperture height H is $2(y_2 - y_1) + W_{SL}$. In the limiting case where opening rate R approaches zero, the exponential taper results in a so-called linearly tapered slot antenna (LTSA) for which the taper slope is constant and given by $s_o = (y_2 - y_1)/(z_2 - z_1)$. For the exponential taper defined by (145.1), the taper slope s changes continuously from s_1 to s_2, where s_1 and s_2 are the taper slope at $z = z_1$ and $z = z_2$, respectively, and $s_1 < s < s_2$ for $R > 0$. The taper flare angle is defined by $\alpha = \tan^{-1}s$. The flare angles, however, are interrelated with other defined parameters, i.e. H, L, R and W_{SL}.

In this study ε_r = 2.2, Distance from the transition to the taper (L_{TA}) and Distance from the transition to the slotline cavity (L_{TC}) are taken as zero (otherwise L_{TA} and L_{TC} should be large enough to accommodate the stubs of the transition). The Radius of radial stripline stub (R_r = 2.02 mm) and square slotline cavity (D_{sl} = 2.6 mm × 2.6 mm) are investigated in this parametric study.

It will be convenient to discuss the feeding technique to be used as the first step of the design. Electromagnetically coupled transitions are more advantageous compared with direct coupling due to ease of implementation. Microstrip to slotline and antipodal slotline transitions are unbalanced electromagnetically coupled feeding techniques. These kinds of transitions are unable to produce a spatially symmetric structure leading to perfectly linear polarization in the principal planes unlike the balanced transitions. Besides, microstrip to slotline transition limits the wide bandwidth of Vivaldi antenna whereas antipodal slotline transition limits the wide bandwidth of Vivaldi antenna whereas antipodal slotline transition produces unacceptable cross polarization levels. Stripline to slotline transitions show symmetry owing to their balanced structures. However, the beamwidth of this type of transition increases with increasing frequency which is unacceptable when the beamwidth requirement of the design is too strict. Thus stripline to slotline transition will be the most convenient choice with its beamwidth characteristic and fairly enough bandwidth performance.

The stripline to slotline transition bandwidth is improved using nonlinear stubs, radial or circular stubs. The bandwidth of the antenna is improved with non-uniform stubs and also noted that radial stub was more advantageous regarding the overlapping between stripline and slotline stubs. The stripline feeding increased the antenna bandwidth compared with the microstrip feeding. The Table 145.1 depicts the antenna parameters considered for the LTSA.

Table 145.1 LTSA design parameters

Parameters	Specifications (in mm)
Aperture height (H)	8.5
Taper length (L)	14.2
Taper depth (d)	25.7
Antenna width (b)	14.2
Radius of radial stripline stub (R_r)	2.02
Angle of radial stripline stub (A_R)	130°
Square slotline cavity (D_{sl})	2.6 × 2.6
Slotline width (W_{SL})	0.2
Stripline width (W_{ST})	0.5
Length of slotline cavity from ground plane (L_G)	8.9

145.3 Results, Discussion and Performance

The simulated S-parameter plot (Fig. 145.3) shows the return loss (RL) is less than −10 dB for an isolated LTSA element over the desired operating band frequency and at 12.2 GHz frequency the maximum return loss is -23 dB. Figure 145.4 shows the voltage standing wave ratio of LTSA, it is clearly seen that the VSWR is below 2.5 for frequency band 10.5–15 GHz.

The simulated radiation pattern of active element is shown in Fig. 145.5 and the polar plot of LTSA is shown in Fig. 145.6. The results of radiation pattern for the H-plane cuts (Φ = 0°) illustrating the achieved 3-dB beamwidth (Half Power

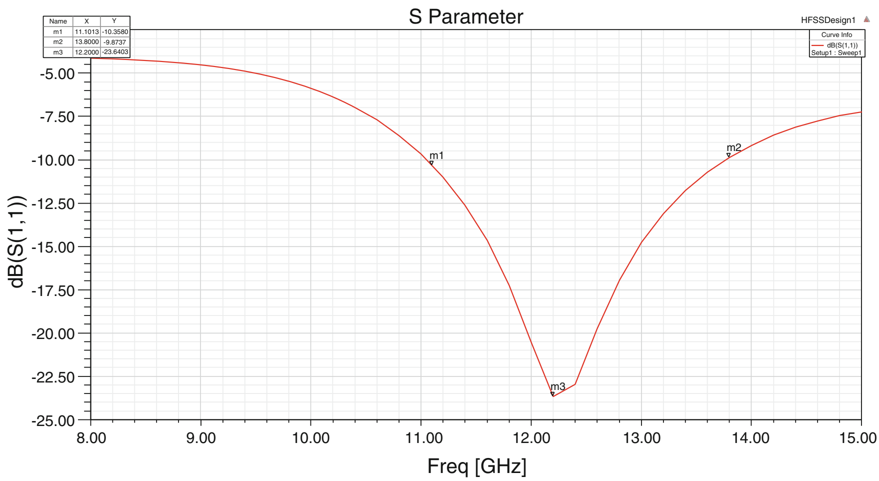

Fig. 145.3 Simulated S-parameter plot of an isolated linearly tapered slot antenna element

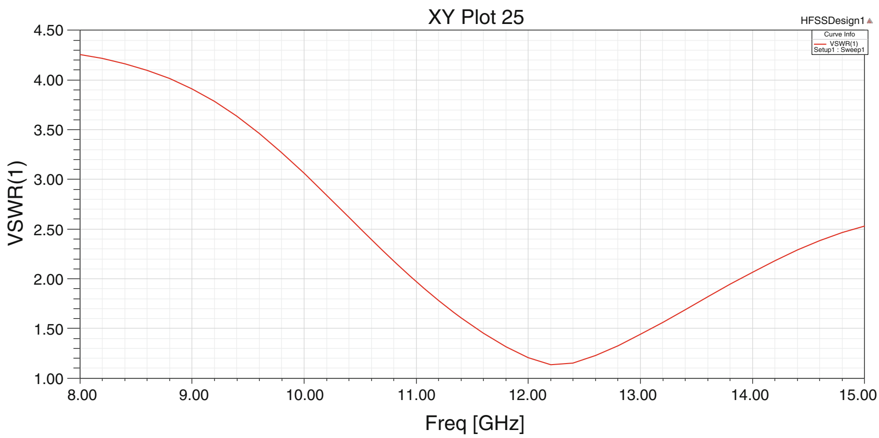

Fig. 145.4 Voltage standing wave ratio (VSWR) plot of an isolated LTSA element

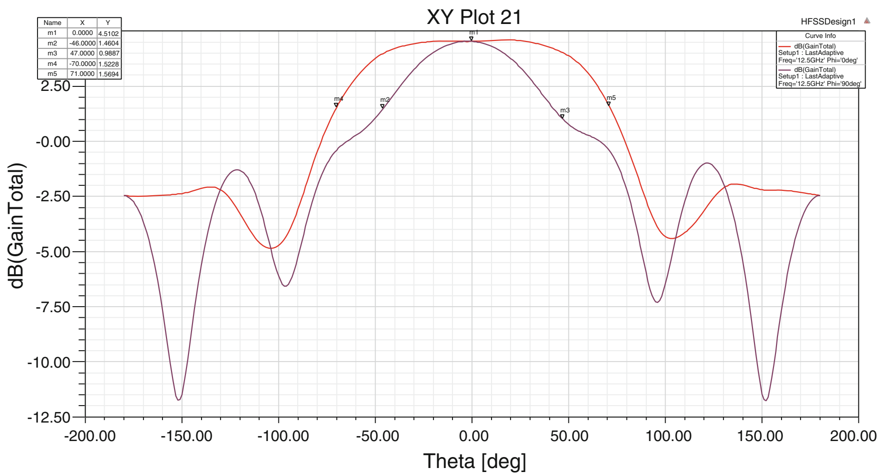

Fig. 145.5 Radiation patterns of linear tapered slot antenna in E-plane and H-plane

Beamwidth—HPBW) greater than 120° and E-plane cuts (Φ = 90°) illustrating the achieved 3-dB beamwidth (HPBW) greater than 90°. The 3-D polar plot of LTSA (see Fig. 145.7) depicts the gain of LTSA is 4.59 dB over full X-band operating frequency. The proposed antenna is vertical placed and operating by horizontal polarization which means the 3 dB beamwidth of H-plane decides the scan angle. The results are demonstrated that the linear tapered slot antenna has good performance for widescan phased array covering X and Ku band.

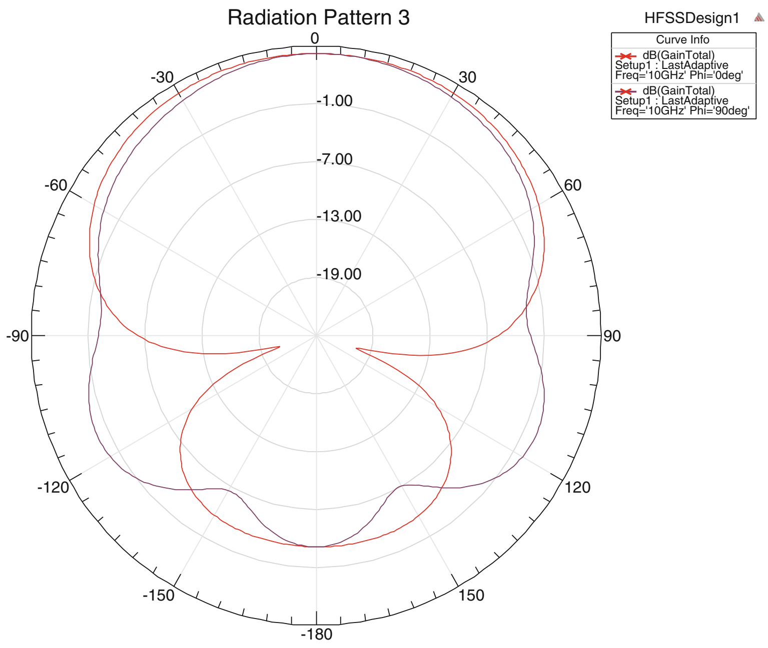

Fig. 145.6 Radiation patterns in polar plot of linearly tapered slot antenna in E-plane and H-plane

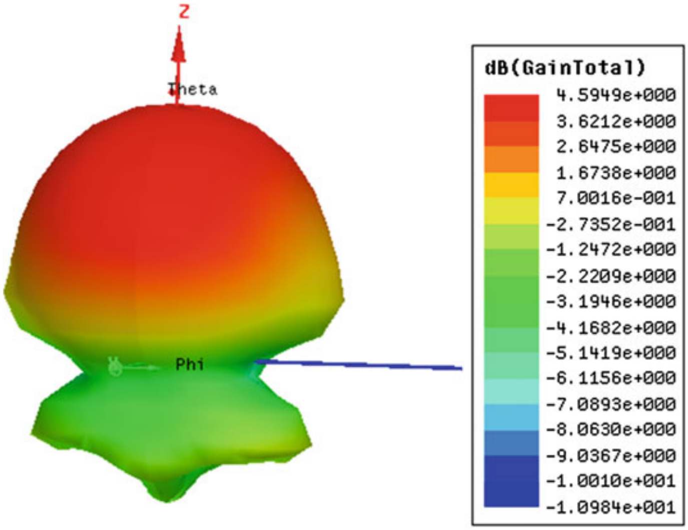

Fig. 145.7 Three dimensional polar plot of linear tapered slot antenna element with gain of 4.59 dB

145.4 Conclusion

A wide band linearly tapered slot antenna is designed with gain of 4.5 dB. The simulated S-parameter return loss for an isolated linear tapered slot antenna element achieved is less than −10 dB for the operating frequency 11–13.8 GHz range. The wide scan angle (±60°) performance is achieved in H-plane and E-plane over the X-band operating frequency. The voltage standing wave ratio of LTSA is below 2.5 for frequency band 10.5–15 GHz. Thus, the designed linear tapered slot antenna is promising candidate for the airborne active phased array radars and other similar applications.

References

1. Gibson PJ (1979) The Vivaldi aerial. In: Proceedings of the 9th European microwave conference Brighton, UK, pp 101–105
2. Shin J, Schaubert DH (1999) A parameter study of stripline-fed Vivaldi notch antenna arrays. IEEE Trans Antennas Propag 47:879–886
3. Skolnik MI (1981) Introduction to radar systems. Book Company, McGraw Hill
4. BabuSaraswathiKavitha L, Jacob Raglend I (2013) A wide-scan phased array antenna for a small AESA antenna—a review. In: Proceedings of IEEE international conference on circuit, power and computing technologies (ICCPCT 2013), art.no.652910, pp 1008–1016
5. Hemmi C, Dover RT, German F, Vespa A (1999) Multifunction wideband array design. IEEE Trans Antenna Propag 47(3):425–431
6. Balanis CA (2008) Modern antenna handbook. Wiley, London
7. Ebnabbasi K, Busuioc D, Birken R, Wang M (2012) Taper design of Vivaldi and co-planar tapered slot antenna (TSA) by Chebyshev transformer. IEEE Trans Antennas Propag 60 (5):2252–2259 (Student Member, IEEE)
8. Kedar A, Beenamole KS (2011) Widebeam tapered slot antenna for wide angle scanning phased array antenna. Prog Electromagnet Res 27:235–251
9. Chio T-H, Schaubert DH (2000) Parameter study and design of wide-band wide-scan dual-polarized tapered slot antenna arrays. IEEE Trans Antennas Propag 48(6):879–886
10. Yao Y, Liu M, Cheb W, Feng Z (2010) Analysis and design of wideband widescan planar tapered slot antenna array. IET Microw Antennas Propag 4(10):1632–1638

Chapter 146
Energy Efficient Decoder Design for Non-binary LDPC Codes

T. Yasodha, I. Jocobraglend and K. Meena Alias Jeyanthi

Abstract Increased SNR and Reduced BER is being the aim of wireless CDMA systems. Coding plays a major role in achieving the target. LDPC codes are being the desired ones in achieving reduced area and power input. This paper presents a high performance error detection and correction for non-binary low density parity check codes (LDPC). Check node processing is formulated by using Euclidean graph decoding architecture. The proposed decoding method reduces the number of iterations and achieves reduction in area and power. EG-Decoder with Q-ary sum product algorithm is implemented in log domain and reduced power of 0.6080 mW and area of 2.17 MB is achieved.

Keywords Non-binary LDPC codes · Euclidean graph · Q-ary sum product algorithm

146.1 Introduction

Binary low-density parity-check (LDPC) codes are becoming more and more popular in applications because of their performance approaching capacity. In terms of performance, binary LDPC codes start to show their weaknesses when the

T. Yasodha (✉)
Department of Electronics and Communication Engineering,
Christian College of Engineering and Technology, Oddanchatram,
Tamil Nadu, India
e-mail: yasrams@gmail.com

I. Jocobraglend
Department of Electrical and Electronics Engineering,
Noorul Islam University, Nagercoil, Tamil Nadu, India
e-mail: jacobraglend@rediffmail.com

K. Meena Alias Jeyanthi
Department of Electronics and Communication Engineering,
PSNA College of Engineering and Technology, Dindigul, Tamil Nadu, India
e-mail: meena.jeyanthi@gmail.com

C. Kamalakannan et al. (eds.), *Power Electronics and Renewable Energy Systems*,
Lecture Notes in Electrical Engineering 326, DOI 10.1007/978-81-322-2119-7_146

codeword length is small or moderate or when higher order modulation is used for transmission. For these cases, non binary LDPC (NB-LDPC) codes over high-order Galois fields have shown great potential. NB-LDPC codes of moderate length outperform binary codes with the same equivalent lengths over binary input additive white Gaussian noise (AWGN) channel as well as QAM-AWGN channel.

In 1948, Shannon proved that for any channel there exist families of block codes that achieve arbitrarily small probability of error at any communication rate up to the capacity of the channel. We will refer to such code families as “very good” codes. By “good” codes we mean code families that achieve arbitrarily small probability of error at nonzero communication rates up to some maximum rate that may be less than the capacity of the given channel. By “bad” codes we mean code families that can only achieve arbitrarily small probability of error by decreasing the information rate to zero [1].

Convolutional codes (which can be viewed as block codes with memory) can approach the Shannon limit as their constraint length increases but the complexity of their best known decoding algorithms grows exponentially with the constraint length. The best practical decoding algorithm that is known for these codes appears to be prohibitively costly to implement, and algebraic- geometry codes do not appear to be destined for practical use.

Gallager’s low-density parity-check codes are defined in terms of a very sparse random parity- check matrix “MN codes” are also defined in terms of very sparse random matrices, and were first presented in. (MN stands for MacKay–Neal; MacKay and Neal generalized MN codes to Gallager codes, then realized that they had rediscovered Gallager’s work.) MN codes are unconventional in that redundancy can be incorporated in the transmitted code words not only by using a generator matrix with transmitted block length greater than the source block length, but also by using a source that is itself redundant. These code families both have two important properties.

First, because the codes are constructed from sparse matrices, they have simple and practical decoding algorithms which work, empirically, at good communication rates. Second, we prove that in spite of their simple construction these codes are “very good” that is, sequences of codes exist which, when optimally decoded, achieve information rates up to the Shannon limit of the binary-symmetric channel. We further prove that the same codes are in fact good for any ergodic symmetric channel.

Non-binary low-density parity-check codes are robust to various channel impairments. However, based on the existing decoding algorithms, the decoder implementations are expensive because of their excessive computational complexity and memory usage [2]. Low latency variable processing node together with the low latency min-sum check processing node for non-binary LDPC codes achieve excellent error correcting performance with better throughput [3]. Shift-message structure is proposed by using memories concatenated with variable node units to enable efficient partial-parallel decoding for cyclic NB-LDPC codes.

Extended Min-Sum (EMS) algorithm based on trellis representation of inputting messages to the check node reduces the decoding complexity by choosing only n_m

most reliable values and by introducing the idea of configuration sets conf(n_m, n_c), where n_c is the number of deviations from the most reliable output configuration [4].

Compared to previous designs based on the Min-max decoding algorithm, these decoders have at least tens of times lower complexity with moderate coding gain loss [5].

146.1.1 Features of LDPC

- Excellent error-correcting capability close to the Shannon limit with soft-decision information
- Inherently parallelizable decoding scheme that can lead to very high decoding throughput
- The error performance of LDPC decoding is closely related to the precision of LLR information.

146.1.2 Features of EG-LDPC

- A class of finite geometry (FG) LDPC codes
- Good error-correcting performance, fast convergence
- Cyclic or quasi cyclic codes that allows efficient implementation
- Redundant parity-checks give additional improvement in error performance
- No harmful trapping sets with the size smaller than their minimum weights.

Binary LDPC codes can achieve near-capacity performance when the code length is long. However, when the code length is small or moderate, binary LDPC codes reveal a disadvantage compared to non-binary LDPC codes. Non-binary LDPC codes can achieve a coding gain of about 1 dB compared to their binary counter parts. However, a straight forward implementation of the Q-ary LDPC decoder results in a high decoding complexity, which is a drawback of non-binary LDPC codes. The QSPA can be viewed as an extension of the sum-product algorithm (SPA) for binary LDPC codes. Since it is sensitive to quantization effects and a complicated multiplication operation is required, it is not easy to implement QSPA in the probability domain. In addition to the multiplication operation, a normalization factor is not needed in Log-QSPA.

This paper presents a high performance error detection and correction for non-binary low density parity check codes (LDPC). Check node processing is formulated by using Euclidean Graph decoding. This decoding method reduces the number of iterations and achieves the reduction in area and power. Q-ary sum product algorithm is implemented in log domain, it replaces the complicated multiplication by addition. Compared to decoders used in existing method the proposed decoder can achieve better throughput.

The main Objective of this work is to achieve the reduction in area and power consumption and increase the speed by reducing the number of iterations using Euclidean graph decoding.

146.2 Research Work

Shuffled schedule (SS) of the min-max decoding algorithm is used for non binary low-density parity-check (LDPC) codes. To increase the throughput and reduce the memory requirement, a modified SS (MSS) with much simpler check node processing is also proposed, based on a new shuffled merge algorithm. Numerical simulations for three LDPC codes with different lengths and rates over GF(32). Both the SS and MSS have a slightly better error performance and converge faster than the flooding schedule. Significantly reducing the complexity of the CNP, the MSS leads to higher throughput [6].

A high-throughput memory-efficient decoder architecture for low-density parity-check (LDPC) codes is proposed based on a novel turbo decoding algorithm. Memory overhead problem in current day decoders is reduced by more than 75 % by employing a new turbo decoding algorithm for LDPC codes that removes the multiple check to-bit message update bottleneck of the current algorithm. Simulations demonstrate that the proposed architecture attains a throughput of 1.92 Gb/s for a frame length of 2,304 bits, and achieves savings of 89.13 and 69.83 % in power consumption. A scalable memory architecture and message-transport networks have been proposed that constitute the main building blocks of a generic LDPC decoder architecture [7].

The high complexity is mainly caused by the complicated computations in the check node processing and the large memory requirement. In this paper, a novel check node processing scheme and corresponding VLSI architectures are proposed for the Min-max NB-LDPC decoding algorithm. The proposed scheme first sorts out a limited number of the most reliable variable-to-check (v-to-c) messages, then the check-to-variable (c-to-v) messages to all connected variable nodes are derived independently from the sorted messages without noticeable performance loss. Compared to the previous Min-max decoder architecture, the proposed design for a (837, 726) code can achieve the same throughput with only 46 % of the area. Efficient architectures have been designed for the sorter and path constructor, and the computation scheduling has been optimized to further reduce the overall area and latency [8].

Efficient multi-standard low density parity-check (LDPC) decoder architecture using a shuffled decoding algorithm, where variable nodes are divided into several groups. In order to provide sufficient memory bandwidth without the need for using registers, a FIFO-based check-mode memory, which dominates the decoder area, is used. This decoder supports 133 codes, occupies an area of 5.529 mm, and achieves an information throughput of 1.956 Gbps. Multi-standard decoder can support a larger number of standards, and achieves a higher throughput and comparable TAR compared to the multi-standard LDPC decoders described in previous literature. The paper is organized as follows. The proposed architecture and the Description of the proposed algorithm is shown in Sect. 146.3. The Simulation results and comparison is shown in Sect. 146.4 and conclusion of the proposed work is discussed in Sect. 146.5 [9].

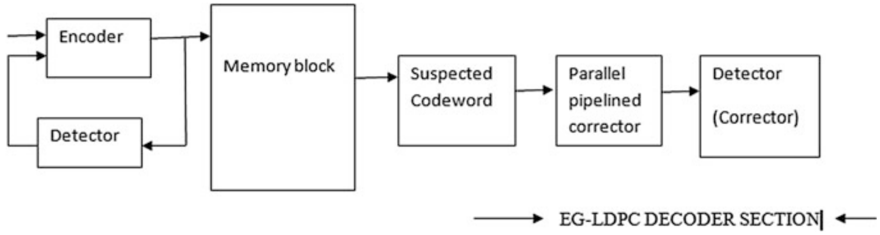

Fig. 146.1 Overview of the proposed architecture

146.3 Proposed Architecture

(Figure 146.1).

146.3.1 Architecture Overview

As shown in Fig. 3.1, the Information bits are fed into the encoder section to perform encoding operation. Encoded bits are forward to detector to check the coding operation. If the detector detects any error then encoding operation must be redone. Corrected Codewords are stored in memory block, Similar to the encoder unit, a fault-secure detector monitors the operation of the corrector unit. All the units shown in Fig. 3.1 are implemented in fault-prone, nanoscale circuitry; the only component which must be implemented in reliable circuitry are two OR gates that accumulate the syndrome bits for the detectors. Data bits stay in memory for a number of cycles and, during this period, each memory bit can be upset by a transient fault with certain probability.

Therefore, transient errors accumulate in the memory words over time. In order to avoid accumulation of too many errors in any memory word that surpasses the code correction capability, the system must perform memory scrubbing. Memory scrubbing is the process of periodically reading memory words from the memory, correcting any potential errors, and writing them back into the memory.

Code words are susceptible to transient faults during transmission. so in detector side parallel pipelined detector is used to correct the retrieved code words. Corrector (detector) in the receiver side monitors the decoding operation. Parallel operation increases the speed of decoding (Fig. 146.2).

146.3.2 Fault Secure Detector

The core of the detector operation is to generate the syndrome vector, which is basically implementing the following vector matrix multiplication on the received

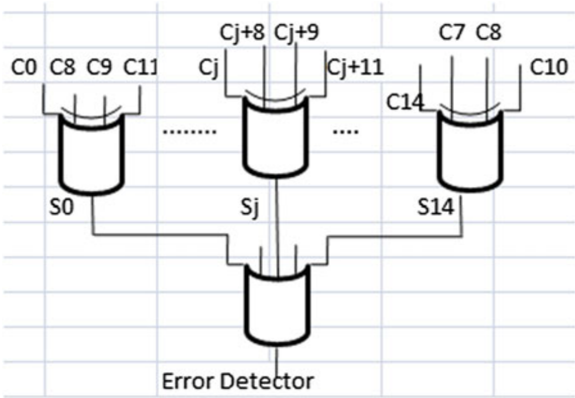

Fig. 146.2 Fault-secure detector operation

encoded vector c and parity-check matrix H: s = c × HT, and therefore each bit of the syndrome vector is the product of the following vector-vector multiply: si = c hi T, where hi T is the transposed of the ith row of the parity-check matrix. The above product is a linear binary sum over digits of c where the corresponding digit in hi is 1. This binary sum is implemented with an xor gate. Since the row weight of the parity-check matrix is P, to generate one digit of the syndrome vector we need a P-input xor gate, or (P − 1) 2-input xor gates in a tree structure. For the whole detector, it takes n(P − 1) 2-input xor gates. An error is detected if any of the syndrome bits has a nonzero value. The final error detection signal is implemented by an or function of all the syndrome put of this n-input or gate is the error detector signal.

146.3.3 Parallel Corrector

For high error rates, the corrector is used more frequently and its latency can impact the system performance. Therefore we can implement a parallel one-step majority corrector, which copies the single one-step majority-logic corrector. All the memory words are pipelined through the parallel Corrector (Fig. 146.3).

This way the corrected memory words are generated every cycle. The detector in the parallel case monitors the operation of the corrector, if the output of the corrector is erroneous, the detector signals the corrector to repeat the operation. Note that faults detected in a nominally corrected memory word arise solely from faults in the detector and corrector circuitry and not from faults in the memory word. Since detector and corrector circuitry are relatively small compared to the memory system, the failure rate of these units is relatively low (Fig. 146.4).

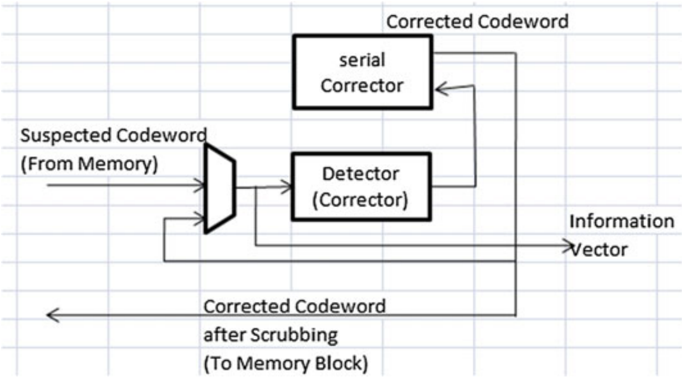

Fig. 146.3 Operation of the parallel corrector

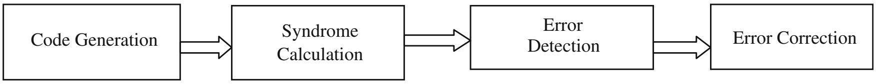

Fig. 146.4 EG LDPC decoder operation

146.3.4 EG LDPC Decoder

The proposed decoder has four blocks code generation block converts signal into binary information. Output of encoder is given as input of the code generation block. Syndrome calculation unit check whether error is present or not. If it detects any error then Error detection unit find the position of error in 64 bit binary information. Complement operation is performed in error detection unit which means that error bit is complemented to correct the error (Fig. 146.5).

Input received by EG-LDPC Decoder is the output of encoder unit. The binary information from encoder have no error means it is directly passed to output of decoder. This state is represented by error out 00 (Fig. 146.6).

The binary information from encoder unit contains error then EG-LDPC decoder find the position of error and performs complement (NOT) operation to rectify the correct codeword. Error detection and correction state is represented by 01.

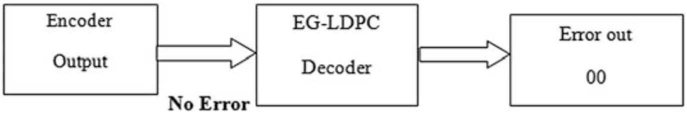

Fig. 146.5 Operation of decoder without error

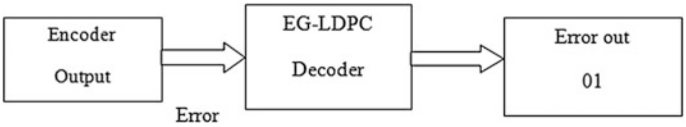

Fig. 146.6 Operation of decoder with the presence of error

146.3.5 Q-Ary Sum Product Algorithm

1. Initialization
2. Check node Processing
3. Variable node Processing
4. Normalization are the steps in the Q-ary Sum-Product Algorithm

Let $I_c(m)$ be the index set of neighboring variable nodes connecting to check node, and $I_R(n)$ be the index set of neighboring check nodes connecting to variable node. If we let C = (C0,C1,…CN − 1) be a codeword, where C_n € GF(q), 0 ≤ n < N we can write a parity-check equation for check node, where 0 ≤ m < M as follows:

$$\sum_{n \in I_c(m)} h_{mn} C_n = 0 \tag{146.1}$$

only addition and max* operations are used. The definition of max* operations for K variables (real numbers) $x_1, x_2, \ldots x_k$ is as follows

$$\max(x_1, x_2, \ldots, x_k) \equiv \ln(e^{x_1} + e^{x_2} + \cdots + e^{x_k}) \tag{146.2}$$

In algorithm, $L_n(a)$ denotes the channel value of variable node n for symbol a, where a € GF(q). In addition $R^{(k)}_{mn}(a)$ denotes the check to variable (c2v) messages from check node m to variable node n, $Q^{(k)}_{mn}(a)$ denotes the (variable to check) message from variable node n to check node m, and $Q^{(k)}_{n}$ denotes the posteriori probability (APP) of variable node n for symbol a produced during the kth iteration. Note that $L_n(a)$, $Q^{(k)}_{mn}(a)$, and $Q^{(k)}_{n}$ are log-likelihood ratio (LLR). The LLR for a = β, where β € GF(q), is defined by

$$L(a = \beta) = \ln\left(\frac{\Pr(a = \beta)}{\Pr(a = \beta')}\right) \tag{146.3}$$

where β € GF (q), denotes the reference symbol.

146.4 Results and Discussion

Speed is increased by reducing the number of iterations and parallel detector also increases the speed. Area is reduced by half when compared to existing decoder. Q-ary sum product algorithm is implemented in log domain, so complicate multiplication is replaced by addition. Euclidean Geometry based decoder increases the speed and throughput compared to Trellis based decoding architecture (Figs. 146.7, 146.8, 146.9 and Table 146.1).

$$\mathbf{Power} = \mathbf{0.712} \times \mathbf{84.6/100} = \mathbf{0.602\,mW}$$

The above comparison chart shows that the proposed EG-Decoder outperforms the existing Trellis decoder in terms of Speed, throughput, area and power.

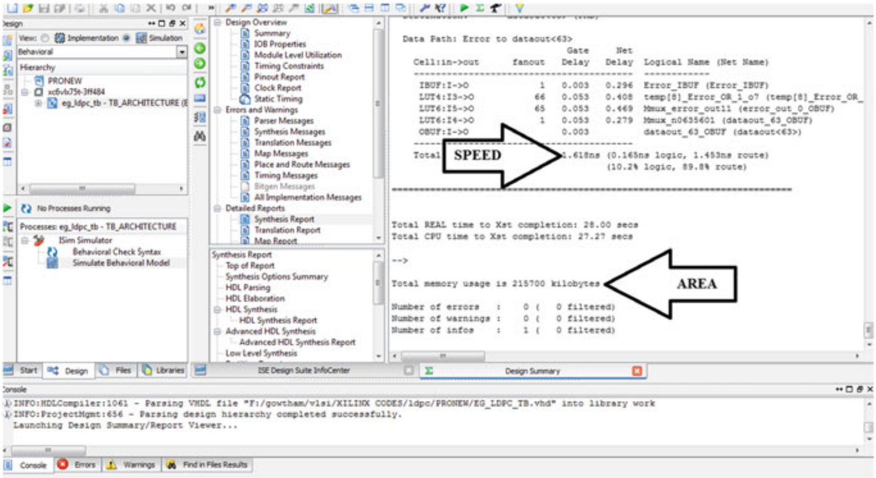

Fig. 146.7 Implementation of area-speed in vertex 6 family

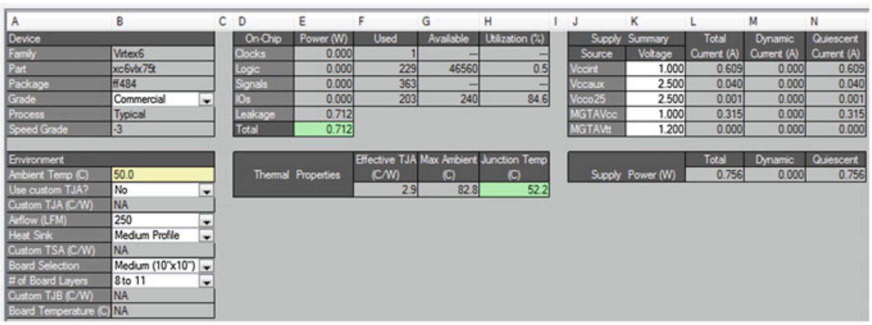

Device	
Family	Virtex6
Part	xc6vlx75t
Package	ff484
Grade	Commercial
Process	Typical
Speed Grade	-3

Environment	
Ambient Temp (C)	50.0
Use custom TJA?	No
Custom TJA (C/W)	NA
Airflow (LFM)	250
Heat Sink	Medium Profile
Custom TSA (C/W)	NA
Board Selection	Medium (10"x10")
# of Board Layers	8 to 11
Custom TJB (C/W)	NA
Board Temperature (C)	NA

On-Chip	Power (W)	Used	Available	Utilization (%)
Clocks	0.000	1	---	---
Logic	0.000	229	46560	0.5
Signals	0.000	363	---	---
IOs	0.000	203	240	84.6
Leakage	0.712			
Total	0.712			

Thermal Properties	Effective TJA (C/W)	Max Ambient (C)	Junction Temp (C)
	2.9	82.8	52.2

Supply Summary Source	Voltage	Total Current (A)	Dynamic Current (A)	Quiescent Current (A)
Vccint	1.000	0.609	0.000	0.609
Vccaux	2.500	0.040	0.000	0.040
Vcco25	2.500	0.001	0.000	0.001
MGTAVcc	1.000	0.315	0.000	0.315
MGTAVtt	1.200	0.000	0.000	0.000

	Total	Dynamic	Quiescent
Supply Power (W)	0.756	0.000	0.756

Fig. 146.8 Design and power summary of the circuit

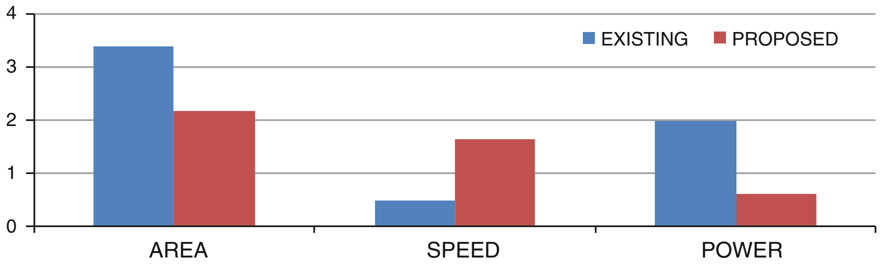

Fig. 146.9 Comparison with the existing system

Table 146.1 Comparison of the parameters between the existing and proposed decoder design

S.no	Design parameters	Existing method [10]	Proposed method
1	Decoder design	Trellis based decoder	EG-LDPC decoder
2	Area	3.3957 MB	2.17 MB
3	Speed	0.469 ns	1.618 ns
4	Power	1.964 mW	0.6080 mW
5	Throughput	62.696 GHz	152.51 GHz

146.5 Conclusion

In this paper, Euclidean Graph based decoder architecture is proposed for Log-QSPA. Parallel detector is used to reduce decoding latency. Speed is increased by reducing the number of iterations and parallel detector also increases the speed. Area is reduced by half when compared to existing trellis decoder. Q-ary sum product algorithm is implemented in log domain, so complicate multiplication is replaced by addition. Euclidean Geometry based decoder increases the speed to 1.61 ns and throughput to 152.51 GHz compared to Trellis based decoding architecture. Reduced area and power of 2.17 MB and 0.60 mW respectively is achieved using the proposed architecture.

References

1. Ryan WE, Lin S (2009) Channel codes: classical and modern. Cambridge University Press, Cambridge, UK
2. Wang C-L, Chen X-H, Li Z-W, Yang S-H (2013) A simplified min-sum based decoding algorithm for non-binary LDPC codes. IEEE Trans Commun 61(1):24–32
3. Tao Y, Park YS, Zhang Z (2012) High-throughput architecture and implementation of regular $(2,d_c)$ nonbinary LDPC decoders. Presented at the IEEE international symposium circuits system (ISCAS), Seoul, Korea
4. Li E, Declercq D, Gunnam K (2012) Trellis-based extended min-sum algorithm for non-binary LDPC codes and its hardware structure. IEEE Trans Signal Process 60(8):4387–4402

5. Zhang X, Cai F, Lin S (2012) Low-complexity reliability-based message passing decoder architectures for non-binary LDPC codes. IEEE Trans VLSI Syst 20(11):1938–1950
6. Lin J, Yan Z Efficient shuffled decoder architecture for nonbinary quasi-cyclic LDPC codes. IEEE Trans Very Large Scale Integr (VLSI) Syst, preprint. doi:10.1109/TVLSI.2012.2218839
7. Mansour MM, Shanbhag NR (2003) High-throughput LDPC decoders. IEEE Trans Very Large Scale Integr (VLSI) Syst 11(6):976–996
8. Zhang X, Cai F (2011) Reduced-complexity decoder architecture for non-binary LDPC codes. IEEE Trans Very Large Scale Integr (VLSI) Syst 10(7):1229–1238
9. Ueng Y-L, Yang B-J, Yang C-J, Lee H-C, Yang J-D (2013) An efficient multi-standard LDPC decoder design using hardware-friendly shuffled decoding. IEEE Trans Circ Syst I Reg Pap 60 (3):743–756
10. Ueng Y-L, Liao K-H, Chou H-C, Yang C-J (2013) A high-throughput trellis-based layered decoding architecture for non-binary LDPC codes using max-log-QSPA. IEEE Trans Signal Process 61(11):2940–2951

Chapter 147
Automated Segmentation of MR Images by Implementing Multi SVM Technique

G. Paul, Tinu Varghese, K.V. Purushothaman and Albert Singh

Abstract In this paper, we present an automated SVM segmentation scheme for the MR images for the early diagnosis of neurodegenerative diseases. This method consists of three steps. In the first method we undergo the preprocessing part which removes the skull and the unwanted areas, and then the features are extracted. The third step, the multiple SVM is used to segment the MR images into Gray Matter (GM), White Matter (WM), and Cerebro Spinal Fluid (CSF). The SVM technique is a powerful discriminator is able to handle nonlinear classification problems. The proposed method is used to segment GM, WM and CSF from real magnetic resonance imaging (MRI) in south Indian population. The automated segmented brain tissues are then evaluated by comparing it with the corresponding ground truth set by the radiologist.

Keywords Gray matter (GM) · White matter (WM) · Cerebro-spinal fluid (CSF) magnetic resonance imaging (MRI) · Support vector machines (SVM)

G. Paul (✉)
Department of ECE, St Thomas Institute for Science and Technology,
Thiruvananthapuram, Kerala, India
e-mail: geenub@yahoo.com

T. Varghese
Noorul Islam University, Kumara coil, Thuckalay, Tamil Nadu, India
e-mail: tinuannevarghese@gmail.com

K.V. Purushothaman
Department of ECE, Heera College of Engineering and Technology,
Thiruvananthapuram, Kerala, India
e-mail: kvpuru@hotmail.com

A. Singh
Noorul Islam University, Kumara coil, Thuckalay, Tamil Nadu, India
e-mail: albertsingh@rediffmail.com

C. Kamalakannan et al. (eds.), *Power Electronics and Renewable Energy Systems*,
Lecture Notes in Electrical Engineering 326, DOI 10.1007/978-81-322-2119-7_147

147.1 Introduction

When there is a change in the cellular environment of the bran, it means that there is a degenerative disease. The variation in the factors like shape, size and volume varies from one disease to another. Accurate segmentation of three-dimensional anatomical brain magnetic resonance imaging (MRI) plays an essential role in both clinical and medical research fields. This can potentially help in the diagnosis, disease monitoring and evaluation of possible treatments of neurodegenerative diseases especially multiple sclerosis and Alzheimer disease. Characterizing morphological differences between subjects based on volumetric analysis of gray matter (GM), white matter (WM) and cerebro-spinal fluid (CSF).

Segmentation of MRI Images is one of the most difficult tasks in the image processing field. A production of meaning full image due to segmentation for easy analysis is the main purpose. Hence, the fact that many applications depend on accurate, robust and cost-effective brain segmentation has inspired much work for developing automatic brain segmentation tools.

In this study, we are proposing a segmentation method called the Support Vector Machine (SVM). SVM is a supervised learning method that is used for classification and regression based on kernel methods. A standard segmentation problem within MRI is the task of labeling boxes according to their tissue type that are White Matter, Gray Matter and Cerebro-spinal Fluid. Image segmentation provides volumetric quantification of cortical atrophy and thus helps in the diagnosis of Neuro degenerative diseases such as Alzheimer's disease. The proposed SVM method can provide the capability to reliably detect and identify general and specific structural abnormalities of the brain and monitoring the progression of the neurodegenerative disease. The detection of changes in brain tissues that reflect the pathological processes of the disease that would prevent or postpone the disease progression. It can be diagnosed at an early stage and effectively intervened, and then it is possible to reduce the advanced damages.

147.2 Literature Review

There are many techniques that are being proposed for manual, semi-automatic or automatic segmentation of brain tissues as CSF, WM, and GM. On observing the future existing works we can see that there are several papers with segmentation works. Statistical based segmentation, [1–4] geometrical-based segmentation, [5, 6] atlas-based segmentation [7] and learning-based segmentation methods [8]. The atlas based brain tissue segmentation starts by registering the brain atlas to the input image. The tissue class labels provided by registered brain atlas are used for the initial brain tissue segmentation. A Maximum Likelihood (ML) or Maximum A Posteriori (MAP) approach and the Expectation- Maximization (EM) algorithm is used in the optimization process, here the statistical model parameters are usually estimated. Alternatively to statistical parametric methods, unsupervised non-parametric schemes have been recently proposed for adult brain MRI segmentation.

In this study, we are proposing a supervised multilayer SVM [9, 10] method that is used for classification and regression based on kernel methods. Recently, SVM has become a popular machine learning tool since it has shown excellent performance in many real world applications such as a classification problem [11–13]. In contrast to linear classification methods, SVM maps the original parameter vectors into a higher (possibly infinite) dimensional feature space through a non-linear kernel function. Then, it tries to find an optimal hyper plane that minimizes the discrimination error for the training data. In comparison to other machine learning methods (e.g. Bays and ANN), SVM can transform the problem into a quadratic programming (QP). On the other hand, SVM aims to obtain the optimal solution under the circumstance of small sample size, instead of infinite sample size. Thus, SVM provides a better generalization ability that can handle nonlinear classification problems such as brain tissue segmentation [14].

In recent years, Artificial Neural Networks (ANN) has been used in MR image segmentation and promising results were obtained [9]. ANNs uses the connection perspectives of the human brain. It is the simplified version. Multilayer Perceptron (MLP) is the simplest neural network architecture for the segmentation procedure. Some previous studies had successfully implemented a three-layered Perceptron to segment the gray tones [15, 16]. ANNs are the simplified version of the human brain that utilizes connectionist perspectives. The ANN network is composed of a topology of neurons; they are capable of performing parallel computing.

The aim of the present research is to propose an effective automated method for the segmentation using the SVM supervised method to classify them as GM, WM, and CSF, In this method, skull stripping is done in the preprocessing section and then feature extraction is done prior to the implementation of segmentation using the SVM technique for classification of brain tissues as GM, WM, and CSF.

147.3 Proposed Methods and System Model

The Fig. 147.1; shows the proposed method and its block diagram. It consists of different block which performs its own functions the functions of each block are explained below.

In our proposed method the first step is selection of input MR images. The proposed study using T1 weighted axial MR images for the segmentation purposes. The next step involves preprocessing. In this study, skull stripping techniques based on the mathematical morphology and the image is enhanced and smoothed using Gaussian filters. Next the features are extracted and selected and finally classify the MR images into GM, WM and CSF. The block diagram of the proposed system is shown in Fig. 147.1. The proposed system has 3 stages; they are Pre-processing, Feature extraction and classification.

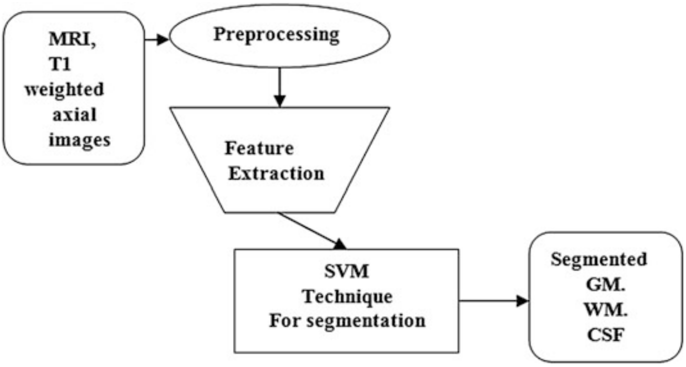

Fig. 147.1 Block diagram of proposed system

147.3.1 MRI Parameters

T_1 weighted axial view of the DICOM MR Images was used as test images. MRI scanning was performed on a 1.5 Tesla Siemens' Magneto—Avanto, SQ MRI scanner. In all subjects, MR images of the entire brain were obtained using a three dimensional T_1 weighted, spin echo sequence with the standard parameters (TR = 11 ms, TE = 4.95, flip angle = 150, slice thickness = 1 mm and matrix size = 256 × 256).

147.3.2 Pre-processing

These test images were undergone through the process called Pre-processing. The obtained MR images undergo changes due to the interference of the noise. We undergo various filtering transactions for enhancing the MR images. This gives information about the edges and at the same time avoids blurring. There are cortical tissues and non cortical tissues, for volumetric analysis of the brain we have to segment each separately. The unwanted tissues during segmentation are non cordial we have to remove it. The process of removing these non cortical tissues is called skull stripping.

Mathematical morphological operations are applied to the MR images for skull striping applications. This technique removes the skull, scalp, fat, skin, eyeball, etc. Is the parts that are not required to be segmented, i.e. they come under the category of non brain tissues. The skull removed tissues of the MR image is used for further classification of brain tissues into White matter, gray matter and cerebro-spinal fluid. This can be differentiated using the primary colors such as Red, Green and Blue. To smooth the original image, Gaussian filters are used. By subtracting pixel wise the smoothed-image of the contrast-enhanced image, the background is strongly attenuated and the classifications are more accentuated.

147.3.3 Feature Extraction

One of the fundamental principles of conventional image segmentation is the use of attribute characteristics of text, image, and background objects. These distinctions, henceforth referred to as features, are extracted during image processing stages to identify text, image, and background objects by means of various well known techniques such as wavelet transform, segmentation, or feature extraction [15]. On employing employs two simple and straightforward statistical features, namely, mean and standard deviation of block pixel gray scale level to distinguish those objects from one another. The principles rest on the observation that image pixel colors are lighter than those of background in gray scale level. In addition, every pixel feature values belonging to the same object block are relatively close to those of its neighbors.

In the proposed study, feature extraction is the process in which texture features were extracted from the skull stripped MR image. The foundation of texture classification is the earlier knowledge of texture category with an observed image. Image texture is a significant visual marker of both spatial discrepancy and the display of the central image elements. The spatial discrepancy most often visualized as gray level values and texture features have to be derived from these gray tones of the image [17]. From this analysis textural properties are derived from a 2D convolution kernel. To generate the Texture Energy Measures (TEM) at each pixel, these masks are convolved with the image pixel. The texture descriptions used are level (L), edge (E), spot (S), wave (W) and ripple (R). L5 = (1, 4, 6, 4, 1), E5 = (−1, −2, 0, 2, 1), S5 = (−1, 0, 2, 0, −1), W5 = (−1, 2, 0, −2, −1), R5 = (1, −4, 6, −4, 1).

147.3.4 Support Vector Machine Segmentation

SVM as a subcategory of supervised learning methods is generally used for both classification and regression problems. In SVM classifier, as introduced by Vapnik, a decision boundary is defined to classify a set of objects or features by generating input–output mapping functions using a set of labeled training data. The basic idea behind SVM is to use a set of kernels to map original feature space into a high dimensional feature space. Hence, it builds a non-linear discrimination boundary, i.e. Complex curve, in the original space through creating an optimal linear discriminating boundary in the high dimensional feature space. Practical expressions are formulated in the dual space in terms of the related kernel function and the solution follows a (convex) QP problem. The LS version of the SVM classifier has been first proposed by Suykens and Vandewalle. The aim of LS-SVM is to construct function y = f (x), which represents the dependence of the scalar output *Yi* on the input vector xi given a set of N training data $\{(x, y)\}N_{I=1}$. The SVM takes the following form in the feature space:

$$\begin{aligned} y &= \sum_{i=1}^{h} w_i \varphi_i(x) + b = w^T \varphi(x) + b; \\ w &= [w_1, w_2, \ldots w_h]^T, \varphi = [\varphi_1, \varphi_2, \ldots, \varphi_h]^T \end{aligned} \tag{147.1}$$

where b is a bias term and (x) is a non-linear mapping function which maps the input data into a higher dimensional feature space whose dimensionality can be infinite. In the SVM, the optimization problem is defined by the following equations:

$$\min_{w,b,e} J_P(w, e) = \frac{1}{2} w^T w + \frac{1}{2} \gamma \sum_{i-1}^{N} e_i^2 \tag{147.2}$$

With constraints *due = with* (xi) + b + *EI*. The e_i is the error in the ith training sample and g is the penalty factor, which is the trade-off parameter between a smoother solution and the training error. A larger g usually results in higher training accuracy, which may cause to over fit the training data. Equation (147.2) shows two modifications in Comparison to the Vapnik formulation: (1) The inequality constraints are replaced with equality constraints, (2) a squared loss function is taken for this error variable. The Lagrangian form to solve the constrained optimization problem (Eq. 147.2) in feature space (primal space) is as follows:

$$L(w, b, e; \alpha) = J_P(w, e) - \sum_{i=1}^{h} \alpha_K \{ w^T \varphi(X_i) + b + e_i - y_i \} \tag{147.3}$$

where α k values are the Lagrange multipliers. The solution for the constraint optimization problem in the dual space results in the following solution:

$$y(x) = \sum_{(i=1)}^{h} \alpha_i K(x, x_i) + b \tag{147.4}$$

Function K (xi, xj) is the kernel defined as K (x i, x j) = (x i) T (x j) which performs the nonlinear mapping implicitly. The output of the SVM is converted to a posteriori probability, i.e. rang [0, 1], using the sigmoid function.

147.4 Experimental Results

The performance of a supervised SVM segmentation method, which has been applied on real brain MR datasets, has been presented here. The Fig. 147.2 represents the Segmentation of MR brain images using SVM clustering techniques.

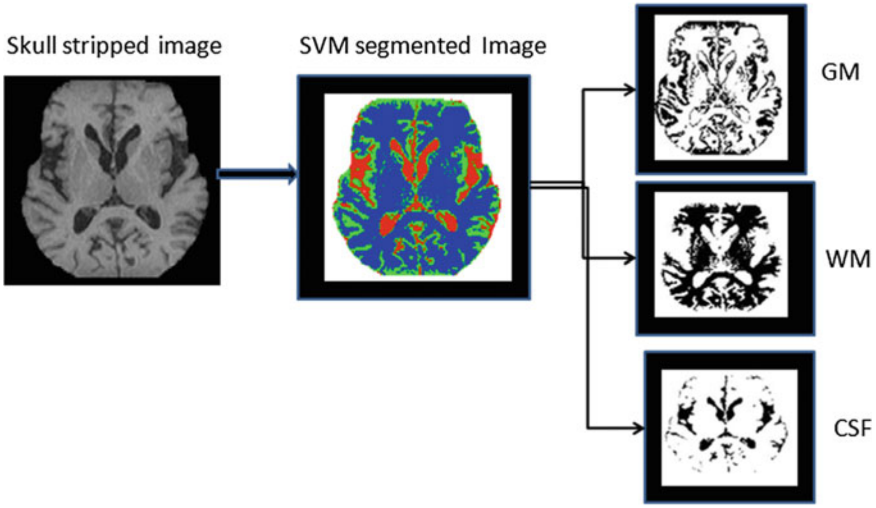

Fig. 147.2 Proposed work model

SVM clustering, segments all the brain tissues into GM, WM and CSF. On observing the segmented output we can observe the degeneration of the area of WM, GM and CSF. The figure shown represents the segmentation results using SVM of a real axial T1 weighted MR Image. Since images from the MRI database are commonly used for brain tissue segmentation assessment here real brain MRI images are being used for extracting volumetric data from patients' MR brain images, relating them to reference data would aid diagnostic readers in classifying neurodegenerative disease. Volumetric anatomical information extracted from brain images using automatic segmentation can support diagnostic decision making. The results presented in this paper are preliminary and further clinical evaluation is required. Segmented images are then differentiated with colors of red, blue and green. The segmentation output of images after the Skull stripping is shown in Fig. 147.2.

The results of both skull stripping and segmentation were validated quantitatively by two expert neuroradiologists. On further, we are planning to analyze the Performance evaluations of multi SVM have been done on the basis of Accuracy, Sensitivity, Specificity and Youden index parameter measures.

147.5 Conclusion and Future Work

On studying the segmented image, the reduction in the GM in the brain image indicates the presence of degenerative disease. To understand the disease progress in the early stage, both quantitative and qualitative analysis is important. As there is a reduction in GM there will be an increase in the volume of CSF. We can say that the theoretical value that give the volume of WM, GM, and CSF makes it more easy to find out the changes that has occurred even those who are not expert in this field. The conclusion of this study is that volumetric results can support diagnostic decision making in imaging of neurodegenerative disease. This also gives an idea for the doctor on the factor of deciding the effect of candidate treatment this is the most valuable single part of it.

A more advanced and prompt study can be developed in the future. An advanced technique can be adapted for the automated segmentation as it may improve the accuracy of the volumetric analysis.

References

1. Bezdek JC, Hall LO, Clarke LP (1993) Review of MR image segmentation techniques using pattern recognition. Med Phys 20:1033–1048
2. Held K, Kops ER, Krause BJ, Wells WM III, Kikinis R, Muller Gartner HW (1997) Markov random field segmentation of brain MR images. IEEE Trans Med Imaging 16:878–886
3. Liew AW, Yan H (2009) An adaptive spatial fuzzy clustering algorithm for 3-D MR image segmentation. IEEE Trans Med
4. Wells WM, Grimson WE, Kikinis R, Jolesz FA (1996) Adaptive segmentation of MRI data. IEEE Trans Med Imaging 15:429–442
5. Li C, Kao CY, Gore JC, Ding Z (1996) Minimization of region-scalable fitting energy for image segmentation. IEEE Trans Image Process C 17:1940–1949
6. Wang L, Chen Y, Pan X, Hong X, Xia D (2010) Level set segmentation of brain magnetic resonance images based on local Gaussian distribution fitting energy. J Neurosci Methods 188:316–325
7. Collins DL, Holmes CJ, Peters TM, Evans AC (1995) Automatic 3D model-based neuroanatomical segmentation. Hum Brain Mapp C 3:190–208
8. Hall LO, Bensaid AM, Clarke LP, Velthuizen RP, Silbiger MS, Bezdek JC (1992) A comparison of neural network and fuzzy clustering techniques in segmenting magnetic resonance images of the brain. IEEE Trans Neural Netw 3:672–682
9. Wu Y, Guo L (2006) Multi-layer support vector machine and its application. In: International conference IEEE transactions on machine learning and cybernetics, pp 3627–3631
10. Cristianini N, Shawe-Taylor J (2000) An introduction to support vector machines. Cambridge University Press, Cambridge, UK
11. Osuna E, Freund R, Girosi F (1997) Training support vector machines: application to face detection. In: Proceeding computer vision and pattern recognition conference proceedings. IEEE Computer Society, pp 130–136
12. Pontil M, Verri A (1998) Support vector machines for 3D object recognition. IEEE Trans Pattern Anal Mach Intell 20:637–646
13. Scholkopf B, Kah-Kay S, Burges CJ, Girosi F, Niyogi P, Poggio T et al (1997) Comparing support vector machines with Gaussian kernels to radial basis function classifiers. IEEE Trans Signal Process 45:2758–2765
14. Guo L, Liu X, Wu Y, Yan W, Shen X (2007) Research on the segmentation of MRI image based on multi-classification support vector machine. Conf Proc IEEE Eng Med Biol Soc 6020–6023
15. Deepa N, Aruna Devi B (2011) A survey on artificial intelligence approaches for medical image classification. Indian J Sci Technol 4(11):1583–1595
16. Desikan SR, Howard JC (2009) Automated MRI measures identify individuals with MCI and AD. Brain 132:2048–2057
17. Dheeba J (2012) Tamil Selvi: an improved decision support system for detection of lesions in mammograms using differential evolution optimized wavelet neural network. J Med Syst 36 (5):3223–3232

Chapter 148
Implementation of ARM Processor Based Online Learning Neural Network Controller for Buck-Boost Converter

M.V. Mini and L. Padma Suresh

Abstract This paper proposes an implementation of a DC-DC buck boost converter using an ARM processor. This design uses back propagation algorithm using Online Learning Neural Network control system (OLNNC). This controller design is efficient enough to maintain steady output voltage and also improves performance during line and load variation. The experiment proves that this controller gives enhanced results during line and load variation.

Keywords DC-DC buck boost converter · OLNNC · PID controllers · Hybrid neuro-fuzzy control · PWM

148.1 Introduction

There is a steady increase in popularity for DC-Power Supply that in the past was limited to electronic devices. A DC-Power Supply is essential for electric vehicles and is being widely used for aerospace applications. A DC-DC converter is indispensable to satisfy the DC voltage source level requirements of the DC power supply load. Likewise, the DC-DC converter is vital in applications such as power conditioning of the photovoltaic-alternative electrical energy, wind generator as well as fuel cell systems. For these reasons, DC-DC converter applications are going to be highly prevalent in the future.

Primarily, the DC-DC converter consists of power semiconductor devices which operate as electronic switches. All such DC-DC converters including a Buck-Boost converter functions as switching devices that ascribe them to have inherently non-

M.V. Mini (✉) · L. Padma Suresh
Department of Electrical and Electronics Engineering, Noorul Islam University, Kumaracoil, Kanyakumari, Tamil Nadu, India
e-mail: mvmini2007@gmail.com

L. Padma Suresh
e-mail: suresh_lps@yahoo.com

C. Kamalakannan et al. (eds.), *Power Electronics and Renewable Energy Systems*,
Lecture Notes in Electrical Engineering 326, DOI 10.1007/978-81-322-2119-7_148

linear characteristics. For this reason, a converter requires a controller with a high degree of dynamic response. Traditionally, Proportional-Integral-Differential (PID) controllers are usually applied to the converters because of their minimalism. However, by implementing this control method to the nonlinear power converters will have a dynamic response of the converter's output voltage regulation. It is commonly observed that a PID controller produces long rise time as the overshoot in output voltage decreases.

Use of various Intelligent controllers like Neural network control, Fuzzy logic control and Hybrid Neuro-fuzzy control methods to improve dynamic response in DC-DC converters was reported in [1–8]. Applications of the fuzzy logic controller to buck converter and power stage DC-DC converter using microcontroller have been verified in [2, 3] respectively. Basically, while developing a fuzzy logic controller, the fuzzy logic method utilizes linguistic variable and general rule without requiring exact model. Hence, this technique has exhibited potential in handling the nonlinear system to achieve voltage regulation in DC-DC converter [4].

Despite the fact that the fuzzy logic controllers have attained many practical triumphs, it has not yet been considered as proven science owing to lack of formal analysis and synthesis techniques [4]. Consequently, many researches were done to develop adaptive fuzzy logic controllers. Use of neural methods in developing adaptive fuzzy logic controls like hybrid neuro-fuzzy controller for DC-DC converter application can be sighted in [4, 5].

The Neural Network Controls (NNC) can update the internal controller parameters when compared to intelligence controls. A computer simulation model designating implementation of the NNC for DC-DC converter has been proposed in [6]. Investigational verification of the NNC for the DC-DC converter has been developed successfully in [7]. In similar lines, the NNCs have also been applied for numerous others power electronic devices and drive applications [8]. Attempts have been made to develop online learning scheme of the NNC with an objective of improving performance.

In this paper, it is contemplated to adopt online learning neural network control (OLNNC) method for Buck-Boost converter. The resulting OLNNC can adapt and modify its own controller parameters with negligible steady state error. It was found to be adapting to external disturbance and internal variation of the converter keeping minimum overshoot and output voltage rise time.

After this introduction, this paper will follow the following organization: In Sect. 148.2 focus is on the basic concept of Buck-Boost converter. The structure and learning schemes of online learning neural network control is described in Sect. 148.3. While the experimental results are detailed in Sect. 148.4, the conclusions and inferences are outlined in Sect. 148.5.

148.2 Buck Boost Converter

A Buck-Boost converter is a step-down and step-up DC-DC converter. Output of the Buck-Boost converter is regulated according to the duty cycle of the Pulse Width Modulation (PWM) input at fixed frequency. As long as the duty cycle (d) remains lesser than 0.5, the output voltage of the converter will be lower than the input voltage. However, as the duty cycle gets beyond 0.5 the converter output voltage will be higher than the input voltage. The basic power stage of a Buck-Boost converter is depicted in Fig. 148.1 where V_I is input voltage source, Vo is the output voltage, Sw is switching component, D is diode, C is the capacitance, L is inductance and R is load resistance.

The converter contains two independence ac inputs, the control $\hat{v}(s)$ and line $\hat{v}_I(s)$ and one output, $\hat{v}_o(s)$.

The converter contains two independence ac inputs, the control $\hat{d}(s)$ and line $\hat{v}_I(s)$ and one output, $\hat{v}_o(s)$.

The control-to-output transfer function(G_{vd}) is derived from small signal model of the converter as

$$G_{vd}(s) = \left(-\frac{V_I - V_o}{D'^2}\right)\frac{\left(1 - s\frac{LI}{V_I - V_o}\right)}{1 + s\frac{L}{D'^2R} + s^2\frac{LC}{D'^2}} \tag{148.1}$$

Plug in numerical values illustrated in Table 148.1 is substitute in (12)

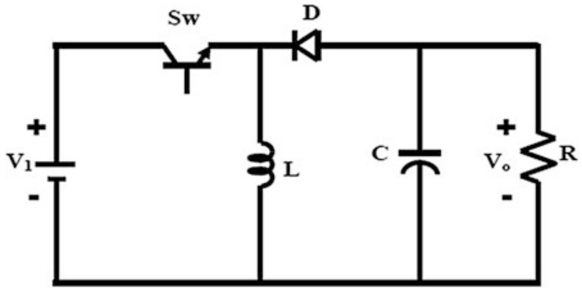

Fig. 148.1 Circuit diagram of a buck boost converter

Table 148.1 Parameters of buck boost converter

Symbol	Parameter	Values
L	Inductance	220 μH
C	Capacitance	220 μF
R	Load resistance	20 Ω
V_I	Input voltage	12 V
V_o	Output voltage	−24 V

$$G_{vd}(s) = 2.5\frac{(1 - 16.28\, s)}{0.3 \times 10^{-6}\, s^2 + 68.7 \times 10^{-6}\, s + 1} \tag{148.2}$$

148.3 Neural Network Structures and Learning Scheme

148.3.1 Structures of ONNC

It is important to have some information about the plant before proceeding with the design of the neural network control. The number of input and output signals of the system will be same as that of input and output neurons in each layer. The structure of the proposed neural network control of a buck boost converter can be found in Fig. 148.2.

Depending upon the number of neurons in each layer of the proposed OLNNC architecture, the network can be claimed to have a 2-3-1 structure. The input layer consists of two input neurons. The first input neuron forms the error signal between actual signal and desired signal. The second input neuron has the difference between previous error signal and current error signal.

At mth layer, the connections weight parameter between jth and ith neuron is given by w_{ij}, and at ith neuron the bias parameter of this layer is represented by b_i^m. Then, the transfer function of the network at ith neuron in mth layer is defined as

$$n_i^m = \sum_{j=1}^{s^{m-1}} w_{ij} a_j^{m-1} + b_i^m \tag{148.3}$$

The output function of neuron at mth layer is given by

$$a_i^m = f^m(n_i^m) \tag{148.4}$$

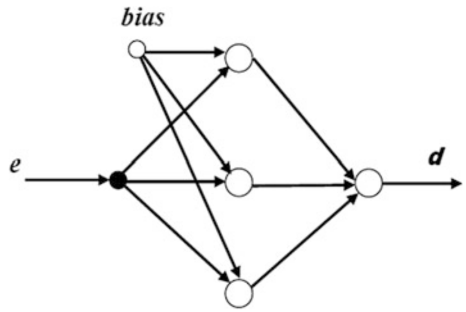

Fig. 148.2 Proposed neural network controller architecture

where $\boldsymbol{f}$ is the activation function of the neuron. In this design, the activation function for the output layer is a unity activation function and the hidden layer has a tangent hyperbolic function. The activation function of the hidden layer is represented as

$$f^m(n_i^m) = \frac{2}{1 + \mathrm{e}^{-2n_i^m}} - 1 \tag{148.5}$$

The updating of the connection weight and bias parameters are given in (148.6 and 148.7)

$$w_{ij}^m(k+1) = w_{ij}^m(k) - \alpha \frac{\partial F(k)}{\partial w_{ij}^m} \tag{148.6}$$

$$b_i^m(k+1) = b_i^m(k) - \alpha \frac{\partial F(k)}{\partial b_i^m} \tag{148.7}$$

where $\boldsymbol{k}$ is sampling time, $\boldsymbol{\alpha}$ is learning rate, and $\boldsymbol{F}$ is performance index function of the network.

148.3.2 BPEOC Online Learning Algorithm

Once the neural network architecture is modeled, the next stage is to define the learning model to update network parameters. The training process through an optimization method curtails the error output of the network. Generally, in OLNNC it is required to have sufficient training input-output mapping data of the converter.

Updates of the network parameters are carried out following the first order optimization scheme. The sum of square error performance index is given by

$$F(k) = \frac{1}{2}\sum_i e_i^2(k) \tag{148.8}$$

$$e_i(k) = t_i(k) - a_i(k) \tag{148.9}$$

where $\boldsymbol{t_i}$ is target signal and $\boldsymbol{a_i}$ output signal on last layer.

The gradient descent of the performance index against to the connection weight is given by:

$$\frac{\partial F}{\partial w_{ij}^m} = \frac{\partial F}{\partial n_i^m} \frac{\partial n_i^m}{\partial w_{ij}^m} \tag{148.10}$$

The sensitivity parameter of the network is defined as

$$S_i^m = \frac{\partial F}{\partial n_i^m} \tag{148.11}$$

$$S_i^m = \frac{\partial F}{\partial a_i^m}\frac{\partial a_i^m}{\partial n_i^m} \tag{148.12}$$

Gradient of the transfer function again to the connection weight parameter is given by

$$\frac{\partial n_i^m}{\partial w_{ij}^m} = a_i^{m-1} \tag{148.13}$$

From substituting Eqs. (148.11) and (148.12) into (148.6) the updating connection parameter is given by:

$$w_{ij}^{m-1}(k+1) = w_i^{m-i}(k) - \alpha s_i^m(k) a_i^{m-1}(k) \tag{148.14}$$

With the same technique the updating bias parameter is given by:

$$b_i^{m-1}(k+1) = b_i^{m-i}(k) - \alpha s_i^m(k) \tag{148.15}$$

The DC input is given to the buck-boost converter. The difference in measured output and V_{ref} (error) is send to the neural network. Based on the error the neural network will adjust the duty cycle of the converter.

148.4 Experimental Results

To investigate the effectiveness of the proposed controller, is implemented by using ARM processor. Block diagram of the proposed OLNNC for the buck-boost converter is show in Fig. 148.3.

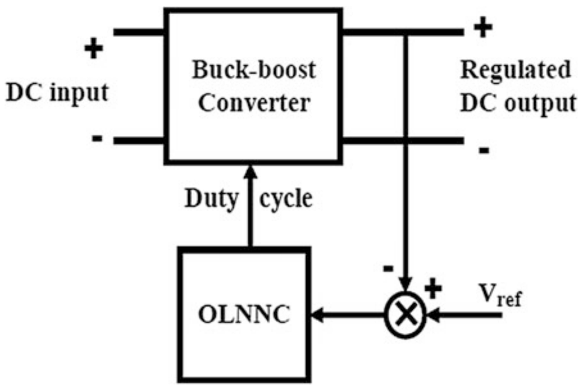

Fig. 148.3 Block diagram of the proposed OLNNC control of buck-boost converter

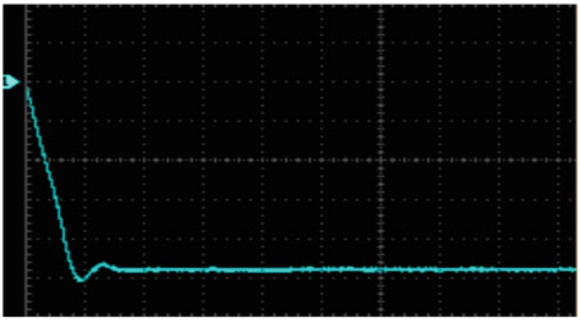

Fig. 148.4 The output voltage transient response of the converter during starting-up (5 V/div and 1 μs/div)

For the experiment, the prototype buck boost converter's input voltage was 12 V, the output voltage was −24 V, and the nominal duty cycle was 66 %. Startup transient response with input voltage variation from 12 to 30 V was evaluated. Load transient response for 100 % load increase (from 0.48 to 0.96 A) and 50 % load decrease (from 0.96 to 0.48 A) were also evaluated.

Figure 148.4 shows the transient response of the buck-boost converter during the staring up. During the starting up converter settling time is 1.6 μs and it have very less amount of steady state error.

Figure 148.5 shows the Transient response of the load variation. Load is increased 50–100 % disturbance is produce in the output then it become stable. Again the load is decreasing from 100–50 % it produce a disturbance in the output voltage then it become stable.

Figure 148.6 shows the output voltage transient response of line variation. The channel 1 represents the input and channel 2 represents the output voltage. The input voltage varying from 12 to 24 V but the controller control the output and maintain in the −24 V as desired voltage.

It is evident from Figs. 148.6 and 148.7 that under the line and load variations, the proposed OLNNC has a enhanced transient response.

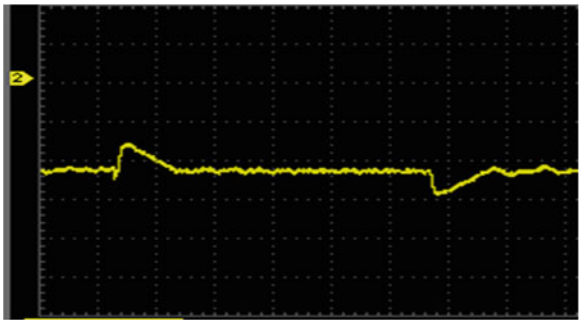

Fig. 148.5 Transient response to load variation (10 V/Div)

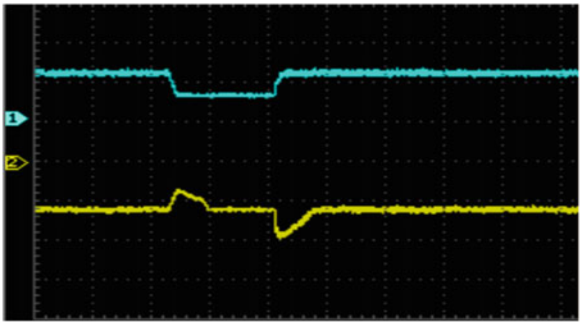

Fig. 148.6 The output voltage transient response of line variation (20 V/Div, 1 µs/Div)

148.5 Conclusion

In the increasing industrial use of DC Power Supply, it is always essential to identify opportunity to maintain steady output even during line and load variation. This study on OLNNC enabled with back propagation algorithm empirically proves that its use in a DC-DC Buck-Boost converter will have a better Transient response. The experimental results also prove that the OLNNC has a fast response to a track desired output voltage and is also effective in decreasing overshoot, oscillation and settling time.

References

1. Mattavelli P, Rossetto L, Spiazzi G, Tenti P (1997) General-purpose fuzzy controller for DC–DC Converters. IEEE Trans Power Electron 12(1):79–86
2. Gupta T, Boudreaux RR, Nelms RM, Hung JY (1997) Implementation of a fuzzy controller for DC-DC converters using an inexpensive 8-b microcontroller. IEEE Trans Ind Electron 44 (5):661–669
3. Ofoli AR, Rubaai A (2006) Real-time implementation of a fuzzy logic controller for switch-mode power-stage DC–DC converters. IEEE Trans Ind Appl 42(6):1367–1374
4. Rubaai A, Ofoli AR, Burge L, Garuba M (2005) Hardware implementation of an adaptive network-based fuzzy controller for DC-DC converters. IEEE Trans Ind Appl 41(6):1557–1565
5. Kuo-Hsiang Cheng C-F, Hsu Chih-Min, Lin Tsu-Tian Lee, Li C (2007) Fuzzy-neural sliding mode control for dc–dc converters using asymmetric gaussian membership functions. IEEE Trans Ind Electron 54(3):1528–1536
6. Leyva R, Martinez-Salamero L, Jammes B, Marpinard JC, Guinjoan F (1997) Identification and control of power converters by means of neural networks. IEEE Trans Ind Appl 44(8):735–742
7. Mahdavi J, Nasiri MR, Agah A, Emadi A (2005) Application of neural networks and State-space averaging to DC/DC PWM converters in sliding-mode operation. IEEE Trans Mechatron 10(1):60–67
8. Elbuluk ME, Chan HW, Husain I (1998) Neural network controllers for power factor correction of AC/DC switching converters. In: Proceedings of industry applications conference, pp 1617–1624

Chapter 149
A Control Strategy for Harmonic Reduction in a Single Phase High Step up AC–DC Converter Based on Matrix Converter and Cockcroft-Walton Voltage Multiplier with PFC for Low Power Applications

S. Anuraj, M.R. Rashmi and A. Suresh

Abstract A high-performance transformer-less single-stage high step-up AC–DC matrix converter based on Cockcroft–Walton (CW) voltage multiplier is presented in this paper. This topology deploys a four bidirectional switch matrix converter between the ac source and CW circuit. This configuration offers high quality of line conditions, adjustable output voltage and low output ripple. The matrix converter is operated with two independent frequencies: one of which is associated with Power Factor Correction (PFC) control and the other is used to set the output frequency of the matrix converter. The relationship among the latter frequency, line frequency, and output ripple are also discussed. A 120 V/100-W converter is simulated for the analysis purpose. At full-load, with closed loop control the power factor and the system efficiency are improved and output voltage ripple is reduced. The simulated results presented in this paper demonstrate the high performance of the proposed converter.

Keywords Cockcroft-Walton (CW) voltage multiplier · Matrix converter · High step-up AC-DC converter · Power factor correction

---

S. Anuraj
Amrita Vishwa Vidyapeetham, Bangalore, India

M.R. Rashmi (✉)
Amrita School of Engineering, Bangalore, India
e-mail: rashmi.power@gmail.com

A. Suresh
SMK Fomra Institute of Technology, Chennai, India
e-mail: asuresz@yahoo.com

C. Kamalakannan et al. (eds.), *Power Electronics and Renewable Energy Systems*,
Lecture Notes in Electrical Engineering 326, DOI 10.1007/978-81-322-2119-7_149

149.1 Introduction

High voltage dc power supplies are widely applied to industries, science, medicine, military, such as test equipment, X-ray systems, dust-filtering, insulating test, electrostatic coating etc. The conventional Cockcroft–Walton voltage multiplier is a popular option for high voltage dc applications [1]. It offers high voltage ratio, low voltage stress on the diodes and capacitors and is compact and cost effective. The CW voltage multiplier is constructed by cascading a number of diode–capacitor stages with each stage containing two capacitors and two diodes. Theoretically, an n-stage CW voltage multiplier provides dc voltage with the value of $2n$ times of the magnitude of the ac voltage source under no load condition [2–4]. In practice, the CW has a number of drawbacks. As the number of stages increased, the voltage at the higher stages begin to sag, primarily due to the AC impedance of the capacitors in the lower stages and when supplying an output current, the voltage ripple rapidly increases as the number of stages are increased. For these reasons, CW multipliers with large number of stages are used only where relatively low output current is required [5]. These effects can be partially compensated by increasing the capacitance in the lower stages, by increasing the frequency of the input power. By driving the CW voltage multiplier from a high frequency source, such as an inverter, the overall physical size and weight of the CW power supply can be substantially reduced. Taking the advantages of the high frequency switching technologies, many modified CW circuits have been developed for saving the volume of the transformers, smoothing the output ripple, and regulating the output voltage. In [6–8], some voltage-fed modified CW topologies, which provide not only high voltage gain but also simplicity of implementation, were proposed. Nevertheless, among these topologies, the high frequency transformer with high turns ratio causes high leakage inductance, this leads to high voltage and current stresses and higher switching losses in the switches. Moreover, operating in Discontinuous Conduction Mode (DCM), these topologies incur more stress, losses, and electromagnetic interference (EMI) problems.

Few cascaded single switch step up dc–dc converters without step up transformer were also proposed by Luo and Ye [10], Axelrod et al. [11], which provides high voltage gain with advantages of simplicity and cost efficiency. Prudente et al. [12] proposed a modified topology with integrated multiphase boost converter and voltage multiplier for high step up conversion and high power applications as well. In this topology, all capacitors in the voltage multiplier had identical voltage rating. The diode reverse recovery current problem is minimized. For converters supplied by AC, power factor correction (PFC) techniques have to be applied to the front stage; otherwise, the converter will exhibit poor line quality. The arrangement of the four bidirectional switches can be seen as a single-phase matrix converter deployed between the ac source and the CW circuit. With the help of the boost structure in the proposed converter, not only the voltage gain can be higher than that of the conventional one but also the PFC technique is applied to the matrix converter to achieve high quality of line conditions and dc output regulation.

149.1.1 The AC-DC Converter—Description and Design Consideration

The block diagram of the scheme is shown in Fig. 149.1. The topology is mainly composed of a single phase matrix converter cascaded with a traditional *n*-stage CW voltage multiplier. The single-phase matrix converter which is shown in Fig. 149.2, consists of four bidirectional switches that are divided into two sets denoted as (*Sc* 1, *Sc* 2) and (*Sm*1, *Sm*2). The converter is energized by a line-frequency ac source with a series inductor for boost operation. Two anti-series Insulated Gate Bipolar Transistors (IGBT) with freewheel diode are used as a bidirectional switch.

The matrix converter employs two independent frequencies. One of the frequencies applies to two of the four switches to perform PFC function, and the other applies to the rest of the two switches to determine the output frequency of the matrix converter. The latter frequency determines the output frequency of the matrix converter and then, can be used to smooth the ripple voltage in the dc output. Voltage control loop and an inner current control loop are added to the proposed converter which modifies the original switching signal to trigger the four bidirectional switches appropriately.

Two stage CW voltage multiplier used with the AC-DC converter is shown in Fig. 149.2. All the capacitors in the CW voltage multiplier are sufficiently large and the voltage drop and ripple of each capacitor can be ignored under a reasonable load

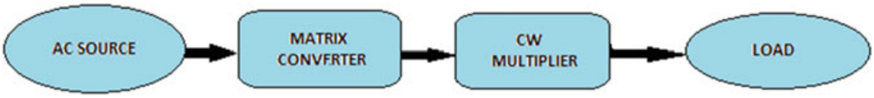

Fig. 149.1 Block Diagram of the proposed converter

Fig. 149.2 Two stage AC-DC converter with CW voltage multiplier and matrix converter

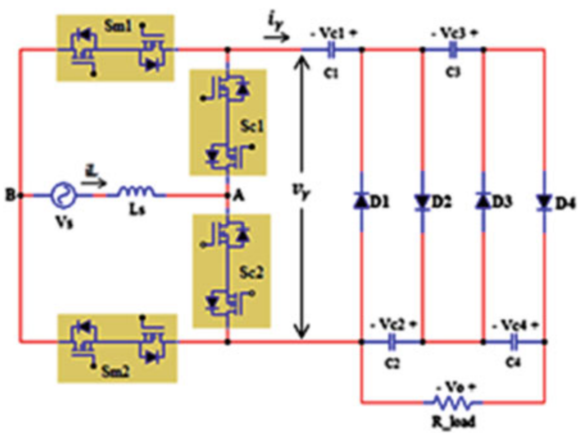

condition. Thus, the voltages across all capacitors are equal, except the first capacitor whose voltage is one half of the others. The proposed converter operates in Continues Conduction Mode and under steady state condition.

Each capacitor voltage in the CW voltage multiplier is given by

$$V_{ck} = \begin{cases} \dfrac{V0}{N} & for \quad k = 1 \\ \dfrac{2V0}{N} & for \quad k = 2, 3, \ldots N \end{cases} \tag{149.1}$$

where V_{ck} is the voltage of the Kth capacitor, V_c the maximum peak value of terminal voltage of the CW voltage multiplier under steady state condition, and $N = 2n$.

For an n-stage CW voltage multiplier, the steady state output voltage is equal to the total voltage of all even capacitors, which can be expressed as

$$V_0 = \mathrm{NV_c} V_c \tag{149.2}$$

According to the polarity of the ac source and the switching state of $Sc1$, there are four operating modes, denoted as Modes I–IV. Moreover, combining with boost operation, each mode has two states. Figure 3.1 shows the two states of Mode I, which provides positive i_γ during positive-half cycle of the ac source and Fig. 3.2 shows the two states of Mode II, which provides negative during negative-half cycle of the ac source. Similarly modes III and IV are obtained by changing the directions of and from Figs. 3.1 and 3.2, respectively. Switches $Sm1$ and $Sm2$ works as boost switches while $Sc1$ and $Sc2$ control the direction of. Basically, $Sc1$ ($Sm1$) and $Sc2$ ($Sm2$) should be operated in complimentary mode and the operating frequencies of $Sc1$ and $S1$ are defined as and respectively, where is called alternating frequency and is called as modulation frequency is taken as 3.75 kHz and =60 kHz.

149.2 Design Considerations

The current ripple in the line current is used to design the value of the boost inductor and the output ripple voltage caused by both line frequency and alternating frequency is used to determine the value of the capacitance. The voltage and current stresses on capacitors, switches and diodes are also considered. The converter specifications for simulation are summarized in Table 149.1.

The ideal static voltage gain of the converter is

$$M_v = \frac{V_o}{|V_s|} = \frac{N}{1 - D} \tag{149.3}$$

Table 149.1 Specifications of the prototype

Output power P_o	100 W
Output voltage V_o	120 V
Input line voltage V_s	24 V
Line frequency f_s	50 Hz
Modulation frequency f_m	60 kHz
Alternating frequency f_c	3.75 kHz
Load resistance R	150 Ω
Number of stages n	2

149.3 Simulation Results

The designed converter for 120 V/100-W is simulated using PSIM software. The simulation specifications are listed in Table 149.2.

Figure 149.3 shows the open loop simulation diagram. The AC input voltage is applied to the Matrix converter which operates with two independent frequencies. The output from Matrix converter is applied to a conventional two stage Cockcroft Walton voltage multiplier. The output voltage is observed across the resistive load.

Table 149.2 Component list for simulation

Component specification	Symbol	Value/specification
Input voltage	V_s	24 V AC
Output voltage	V_o	120 V DC
Boost inductor	L_s	700 μH
Capacitors	C_1–C_4	1,000 μF/200 V
Diodes	D_1–D_4	200 V/10 A
Load resistor	R_L	150 Ω

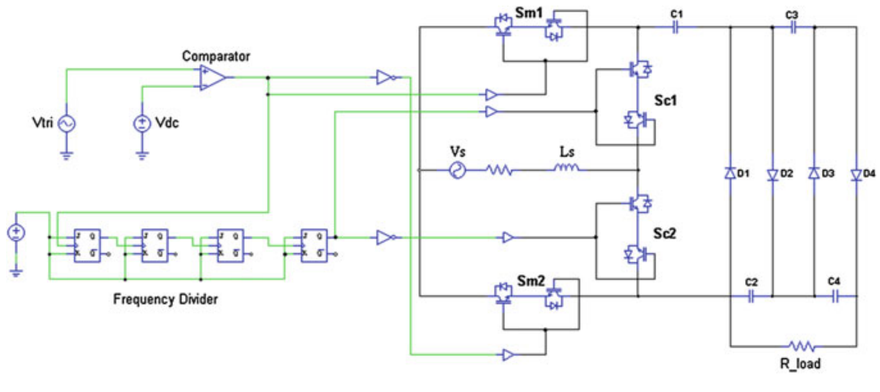

Fig. 149.3 PSIM model of the converter for n = 2

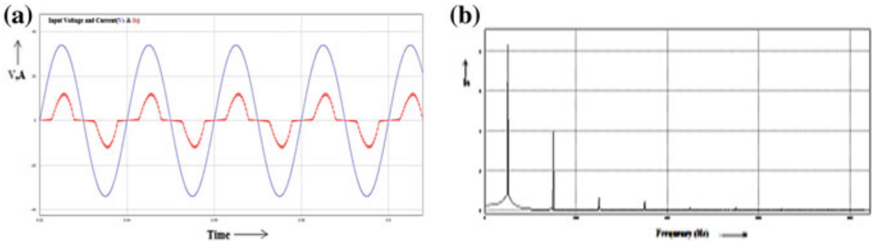

Fig. 149.4 **a** Input voltage and current. **b** Harmonic spectrum of input current

The input voltage is 24 V (RMS). The input voltage and current waveforms are shown in Fig. 149.4a and Harmonic spectrum of input current is shown in Fig. 149.4b. The output voltage and current are shown in Fig. 149.5.

From the simulation results it is observed that DC output voltage = 120 V and output current = 0.8 A. Input power factor = 0.80, Total Harmonic distortion = 37.23 %, Supply peak current = 10 A.

For comparison, a conventional two-stage voltage source CW multiplier with the identical input voltage and power is simulated along with the new converter topology. An ac voltage of 24 is applied to the conventional CW circuit. Figure 149.6 shows the simulated waveforms of source voltage V_s and line current of the conventional CW circuit and the proposed converter at = 3.75 kHz. Figure 149.7a, b shows the variation of output voltage for conventional and proposed CW multiplier respectively for an alternating frequency of 938 Hz. The output voltage of the proposed converter for alternating frequencies of 938, 1,875 and 3,750 Hz are shown in Fig. 149.7b–d respectively.

From the simulation results in Fig. 149.7a, b it is observed that the conventional CW circuit incurs high distorted line current, poor power factor and high ripple in

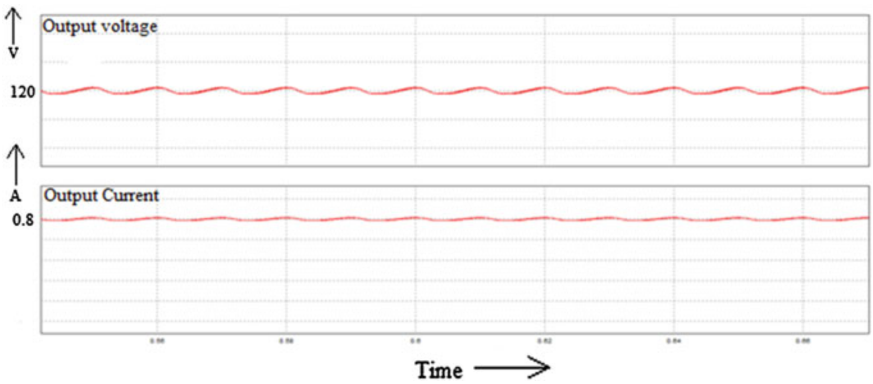

Fig. 149.5 Output voltage and current

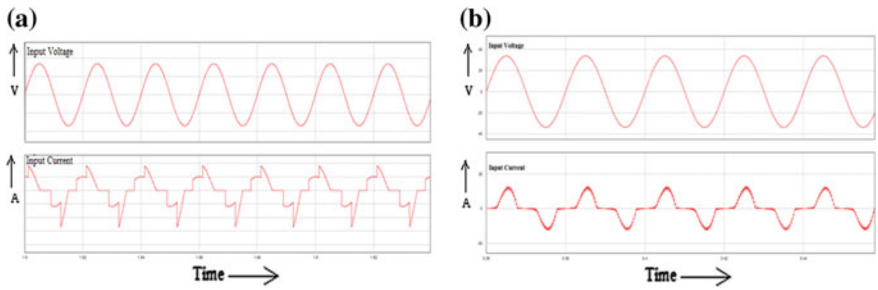

Fig. 149.6 Simulated waveforms of V_s and for **a** Conventional CW multiplier, and **b** proposed converter

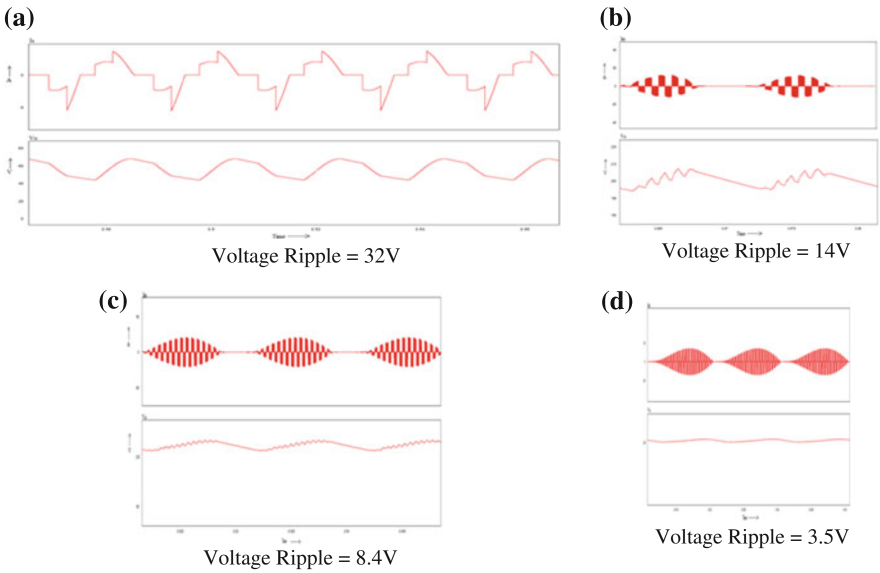

Fig. 149.7 The output voltage of the proposed converter for alternating frequency **a** = 50 Hz, **b** = 938 Hz, **c** = 1,875 Hz, and **d** = 3,750 Hz

the output voltage, while the proposed converter provides significantly good line conditions and rather low output ripple. From Fig. 149.7c, d, it is observed that for = 1,875 Hz, the ripple in output voltage is 8.4 V and for = 3,750 Hz the voltage ripple is 3.5 V. When was increased above 3,750 Hz, it was observed that the ripple was increasing. Hence f_c is set at 3,750 Hz at which the ripple in the output voltage was found to be minimum.

149.4 Closed Loop Simulation

Figure 149.8 presents the block diagram of the control system for the converter, which includes a proportional-integral (PI) controller, to regulate the output voltage. The reference value i_{L_ref} for the inner current loop is obtained from the multiplication between the output of the voltage controller and the absolute value $|Vs(t)|$. A hysteresis controller provides a fast control for the inductor current i_L, resulting in a practically sinusoidal input current. The harmonics in the input current can be reduced by shortening the hysteresis width. Figure 149.9 shows the complete closed loop circuit diagram of the converter. The load is increased by 10 %, the corresponding output voltage and load current waveforms with respect to the new load are shown in Fig. 149.10. Input Voltage and current are shown in Figs. 149.11 and 149.12 show FFT Spectrum of input current.

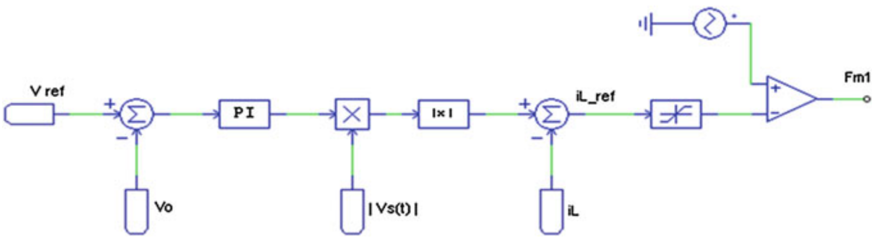

Fig. 149.8 Control circuit

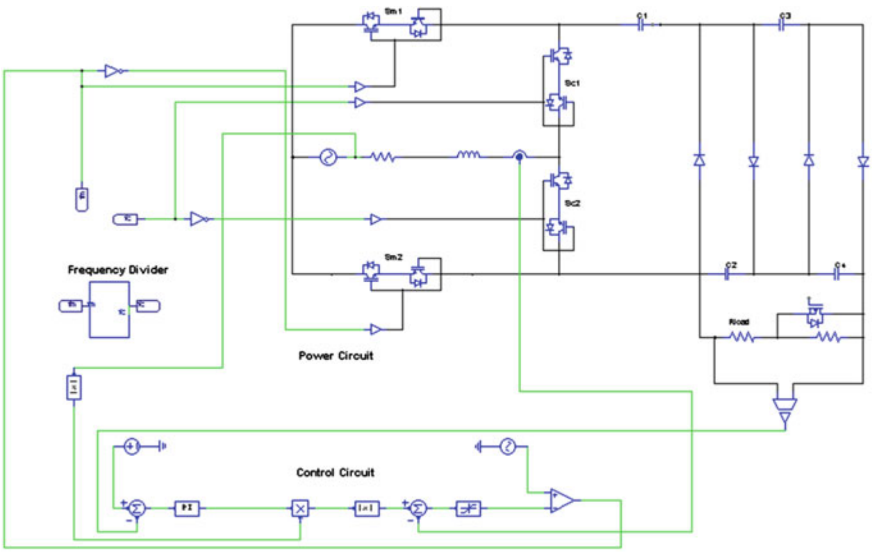

Fig. 149.9 Closed loop circuit diagram of the converter

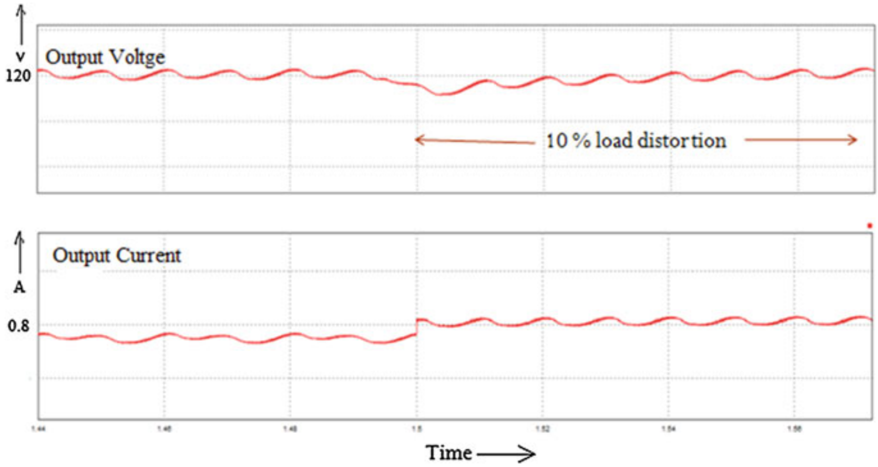

Fig. 149.10 10 % load change

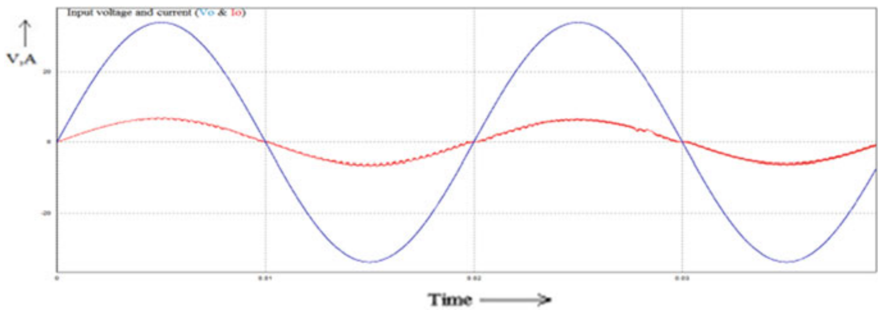

Fig. 149.11 Input voltage and current

Fig. 149.12 FFT spectrum of input current

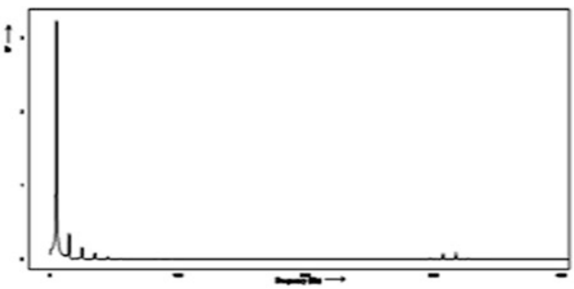

Table 149.3 Simulation results

<table>
<tr><th colspan="3">Parameter converter</th><th>Input power factor</th><th>THD (%)</th><th>Output voltage ripple (V)</th></tr>
<tr><td colspan="3">Conventional CW voltage multiplier</td><td>0.38</td><td>76.5</td><td>32</td></tr>
<tr><td rowspan="4">Converter based on CW voltage multiplier and matrix converter</td><td rowspan="3">Open loop</td><td>f_c = 938 Hz</td><td>0.75</td><td>40.18</td><td>14</td></tr>
<tr><td>f_c = 1,835 Hz</td><td>0.78</td><td>38.12</td><td>8.4</td></tr>
<tr><td>f_c = 3,750 Hz</td><td>0.798</td><td>37.23</td><td>3.5</td></tr>
<tr><td colspan="2">Closed loop (f_c = 3,750 Hz)</td><td>0.925</td><td>7.25</td><td>3.5</td></tr>
</table>

From the simulation results it is observed that with closed loop control, for 10 % increase in load at 1.49 s. The output voltage dipped to 102 V and at 0.5 s, it attains original value 120 V, with a ripple of 3.5 V. Supply power factor is found to be 0.925, with Peak supply current as 7 A. From the FFT analysis, it is found that the third order harmonic is reduced by 75 % and the THD is found to be 7.25 %. The simulation results are tabulated in Table 149.3.

149.5 Conclusion

A 120 V/100 W AC to high voltage DC converter based on matrix converter and Cockcroft-Walton voltage multiplier was designed and simulated. From the simulation results it is observed that the ripples in the output voltage are very much reduced to 3.5 V as compared to a conventional CW voltage multiplier in which the output voltage ripple was 32 V. The power factor which was 0.798 in open loop was improved to 0.925 with closed loop control in which both voltage and current controls are adapted. The closed loop controller consisting of PI controller and hysteresis current controller provides a fast control of the inductor current resulting in a practically sinusoidal input current with improved power factor. From FFT spectrum it is found that third order harmonic is reduced by 75 %. The proposed control scheme helps in reducing the THD of the converter.

References

1. Young CM (Member, IEEE), Chen MH (Member, IEEE), Yeh SH, Yuo KH (2012) A single-phase single-stage high step-up AC–DC matrix converter based on Cockcroft–Walton voltage multiplier with PFC. IEEE Trans Power Electron 27(12)
2. Bellar MD, Watanabe EH, Mesquita AC (1992) Analysis of the dynamic and steady-state performance of Cockcroft-Walton cascade rectifiers. IEEE Trans Power Electron 7 (3):526–534

3. Kobougias IC, Tatakis EC (2010) Optimal design of a half-wave Cockcroft-Walton voltage multiplier with minimum total capacitance. IEEE Trans Power Electron 25(9):2460–2468
4. Weiner MM (1969) Analysis of Cockcroft-Walton voltage multipliers with an arbitrary number of stages. Rev Sci Instrum 40(2):330–333
5. Tanaka J, Yuzurihara I (1988) The high frequency drive of a new multistage rectifier circuit. In: Proceedings of IEEE Power Electronics Specialists Conference (Apr 1988) pp 1031–1037
6. Sbenaty SM, Ventrice CA (1991) High voltage DC shifted RF switch mode power supply system design for gas lasers excitation. In: Proceedings of Applied Power Electronics Conference Exposition (Mar 1991) pp 173–177
7. Maranesi PG, Raina F, Riva M, Volpi G (2000) Accurate and nimble forecast of the HV source dynamics. In: Proceedings IEEE Power Electronics Specialists Conference (June 2000) pp 539–543
8. Belloni F, Maranesi P, Riva M (2004) Parameters optimization for improved dynamics of voltage multipliers for space. In: Proc. IEEE Power Electronics Specialists Conference (June 2004) pp 493–443
9. Johnson SD, Witulski AF, Erickson RW (1988) Comparison of resonant topologies in high-voltage DC applications. IEEE Trans Aerosp Electron Syst 24(3):263–274
10. Luo FL, Ye H (2004) Positive output cascade boost converters. Proc IEE Electric Power Appl 151(5):590–606
11. Axelrod B, Berkovich Y, Ioinovici A (2008) Switched capacitor/switched-inductor structures for getting transformer less hybrid DC–DC PWM converters. IEEE Trans Circuits Syst I Reg Papers 55(2):687–696
12. Prudente M, Pfitscher LL, Emmendoerfer G, Romaneli EF, Gules R (2008) Voltage multiplier cells applied to non-isolated DC–DC converters. IEEE Trans Power Electron 23(2):871–887

Chapter 150
Classification of ECG Signal Using Hybrid Feature Extraction and Neural Network Classifier

K. Muthuvel, L. Padma Suresh, T. Jerry Alexander and S.H. Krishna Veni

Abstract The heart is one of the crucial parts of a human being. The heart produces electrical signals and these cycles of electrical signals are normally called as cardiac cycles. The graphical recording of the cardiac cycles is known as Electrocardiogram (ECG) signal. The Electrocardiogram signal is used to diagnose the irregularity in heart beat which in turn can be used to identify heart problems. Automatic classification of ECG signals has applications in human-computer interaction, as well as in clinical application such as detection of key indicators of the onset of the certain illness. In this work, we have developed an algorithm to detect the five abnormal beat [2, 3] signals includes Left bundle branch block beat (LBBB), Right bundle branch block beat (RBBB), Premature Ventricular Contraction (PVC), Atrial Premature Beat (APB) and Nodal (junction) Premature Beat (NPB) along with the normal beat. In order to prepare an appropriate input vector for the neural classifier several pre processing stages have been applied. For efficient feature extraction we use hybrid feature extractor. The hybrid feature extraction is done in three steps, (i) Morphological based feature extraction (ii) Haar wavelet based feature extraction (iii) Tri-spectrum based feature extraction. The classification is done using Forward Feed Neural Network. Finally, the MIT-BIH [4] database is used to evaluate the proposed

K. Muthuvel (✉) · L.P. Suresh · S.H.K. Veni
Noorul Islam University, Kanyakumari, Tamil Nadu, India
e-mail: er.muthuvel@gmail.com

L.P. Suresh
e-mail: suresh_lps@gmail.com

S.H.K. Veni
e-mail: veni_shk@ymail.com

T.J. Alexander
Sathyabama University, Chennai, Tamil Nadu, India
e-mail: tjerry_2k@gmail.com

C. Kamalakannan et al. (eds.), *Power Electronics and Renewable Energy Systems*,
Lecture Notes in Electrical Engineering 326, DOI 10.1007/978-81-322-2119-7_150

algorithm. The beat classification hybrid system (Hybrid + FFBN) based gives an accuracy is achieved 78 %, (Morp + FFBN) is achieved 62 %, (wavelet +FFBN) is achieved 65 %, (Spect + FFBN) is achieved 70 %, (Morp + Wavelet + FFBN) is achieved 62 %, (Morp + spect + FFBN) is achieved only 73 %.

Keywords Hybrid feature extraction · Haar wavelet · Tri spectrum · Neural network · ECG classification

150.1 Introduction

The ECG is a diagnosis tool that reported the electrical activity of heart. It is a noninvasive technique which means, the signal is measured on the surface of the human body. This signal is used to identify the heart diseases [1]. Any disorder of heart rate of rhythm, or change in morphological pattern, is an indication of cardiac arrhythmia, which could be detected by analysis of the recorded ECG wave form. The typical ECG wave form is shown in Fig. 150.1 records the electrical activity of the heart, where each heart beat is displayed as a series of electrical waves characterized by peaks and valleys. Normally, the frequency range of an ECG signal is of 0.05–100 Hz and its dynamic range of 1–10 mV [5]. One cardiac cycle in an ECG signal consists of P-QRS-T waves. Most of the clinically useful information in the ECG is found in the intervals and amplitudes as defined by its features [6].

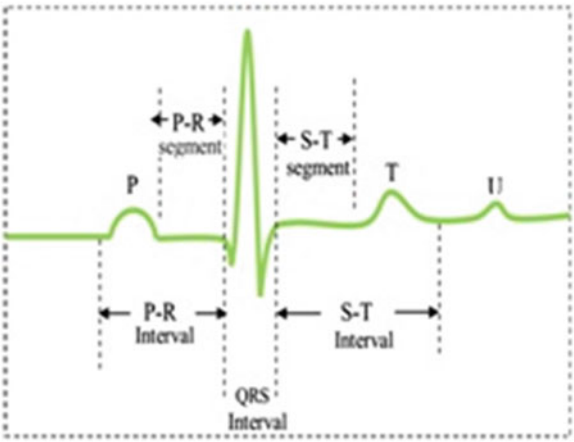

Fig. 150.1 ECG wave form

150.2 Hybrid Feature Extraction and Classification

After pre-processing step, the input, in MatLAB file format are given for feature extraction for PQRST detection. After we point out P, Q, R, S and T points of ECG signal based on the peak value.

Morphological feature extraction is done in three steps. First find the standard deviation of RR interval, PR interval, PT interval, ST interval, TT interval, QT interval. Second the maximum values of P, Q, R, S, T peaks are obtained and finally the number of R peaks count is taken.

The Haar wavelet [8, 9] is a smooth and quickly vanishing oscillating function with a good localization in both frequency and time. In wavelet transform the feature extractions were made in two steps, (1) Depending on distinct frequency sub bands the ECG beat signals are decomposed. (2) The disintegrated beat signals at distinct frequency sub bands are evaluated using numerous resolutions.

For the ECG beat signal $e(t)$ the wavelet transform is given as

$$W(p,q) = \int_{-\infty}^{\infty} e(t).\Psi p, q(t)dt \tag{150.1}$$

where $\Psi p, q(t)$ is the wavelet function.

In proposed technique two dimensional Haar wavelet transform is used because it reduces the computational time and also it extracts more features. For the t input beat signal u_t the Haar wavelet transform v_t is given as

$$v_t \ = H_t u_t \tag{150.2}$$

Tri spectrum can also obtain by taking Fourier transform for fourth cumulant function of random process u_n [10]. Let v1, v2, v3 be the three frequencies then the Tri spectrum of three frequencies is given as

$$T_s(v_1, v_2, v_3) = E[U(v_1)U(v_2)U(v_3)U * (v_1 + v_2 + v_3) \tag{150.3}$$

where

v	is the frequency
$U(v)$	is the Fourier transform of random process u_n
$E[]$	is the expectation factor
$*$	is the complex conjugation.

In the Trispectrum method [7], expectation of the frequency is obtained by taking the average of the three frequencies. It is a three dimensional structure. The resultant image is obtained in 512 * 512 pixels. The Trispectrum was applied to obtain a Trispectrum plot and magnitude Trispectrum.

(i) By using the number of pixel present in the row, column, and both diagonals we can calculate the centre point of the pixel.
(ii) The properties of the region nearer to the centre point of tri-spectrum can be calculated by using the region props function in the MatLAB. The region props function helps to evaluate the orientation, eccentricity, solidity, extents and perimeter values of the region.

By using tri spectrum based feature extraction, it extracts 12 features from the input ECG beat.

After extracting the features from ECG beat signal Forward Feed Neural Network (FFNN) classifier is used to classify the ECG beat signal.

For training the neural network [11, 12] 24 features extracted from the hybrid feature extraction is given as input layer. After optimizing the weights used in the hidden layer the six beats of ECG beat signals are get grouped in the output layer.

For testing the selected solution from the training is taken as input to the feed forward neural network. In this step the ECG beat signal is compared with the trained beat signal and classified based upon the feature.

150.3 Result and Discussion

In this section we discuss the result obtained from the propose technique.

In our proposed work we have chosen MIT-BIH Arrhythmia Database. The source of the ECG beat signal in the database is taken from 25 men aged from 32 to 89 years and 22 women aged from 23 to 89 years. The Arrhythmia Database contains almost 109,000 beats. We have taken six beats including normal beat, abnormal beat such as Left bundle branch block beat (LBBB), Right bundle branch block beat (RBBB), Premature Ventricular Contraction (PVC), Atrial Premature Beat (APB) and Nodal (junctional) Premature Beat (NPB). For our proposed work we have taken 45 beat signals in the dataset.

The evaluation of proposed ECG beat classification technique in MIT-BIH Arrhythmia Database are carried out using the following metrics as suggested by below equations,

Sensitivity: The sensitivity of the feature extraction and the feature classification is determined by taking the ratio of number of true positives to the sum of true positive and false negative. This relation can be expressed as.

$$S_t = \frac{T_p}{T_p + F_n} \tag{150.4}$$

where S_t is the Sensitivity, T_p is the True positive, F_n is the False negative.

Specificity: The specificity of the feature extraction and the feature classification can be evaluated by taking the relation of number of true negatives to the combined true negative and the false positive. The specificity can be expressed as

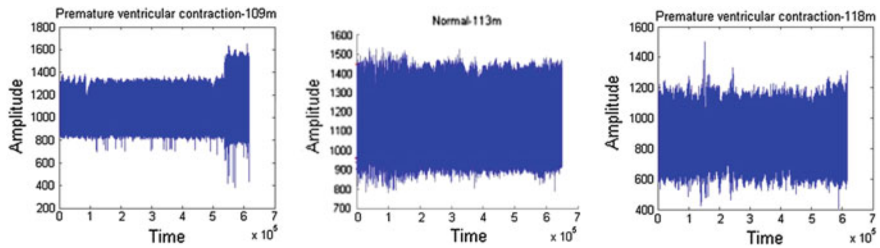

Fig. 150.2 Input ECG beat signal

$$S_p = \frac{T_n}{T_n + F_p} \quad (150.5)$$

where S_p is the Specificity, T_n is the True negative, F_p is the False positive.

Accuracy: The accuracy of feature extraction and the feature classification can be calculated by taking the ratio of true values present in the population. The accuracy can be described by the following equation

$$A = \frac{T_p + T_n}{T_p + F_p + F_n + T_n} \quad (150.6)$$

where A is the accuracy, T_p is the true positive, T_n is the true negative, F_p is the false positive, F_n is the false negative.

For hybrid feature extraction we use three extraction techniques. The Fig. 150.2 shows the three sample input ECG beat signals taken for classification. Figure 150.3 shows the marked P, Q, R, S, T for input beat signal. The tri spectrum plot of the input beat signal is shown in the Fig. 150.4.

We have compared our proposed technique with the existing techniques such as (Hybrid + FFBN), (Morp + FFBN), (wavelet + FFBN), (Spect + FFBN) (Morp + Wavelet + FFBN), (Morp + spect + FFBN). The evaluation graphs of the accuracy, the sensitivity, and the specificity and the accuracy graph are shown in Figs. 150.5, 150.6 and 150.7. From the figure the proposed ECG beat classification

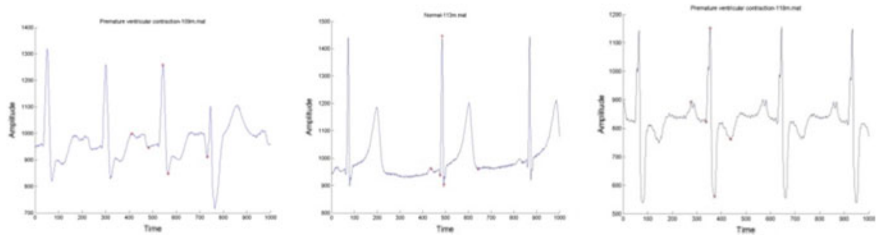

Fig. 150.3 Labeled P, Q, R, S, T for input beat signal

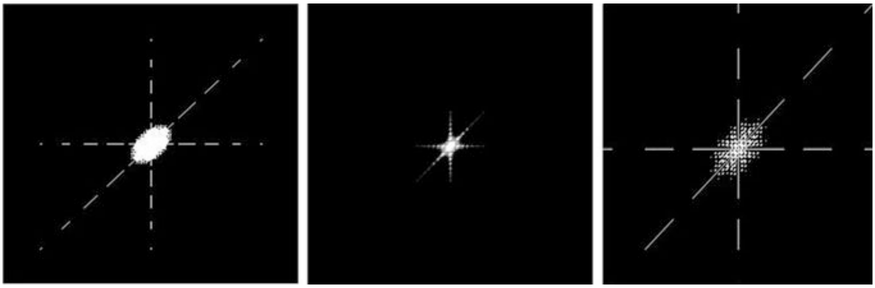

Fig. 150.4 Tri spectrum plot

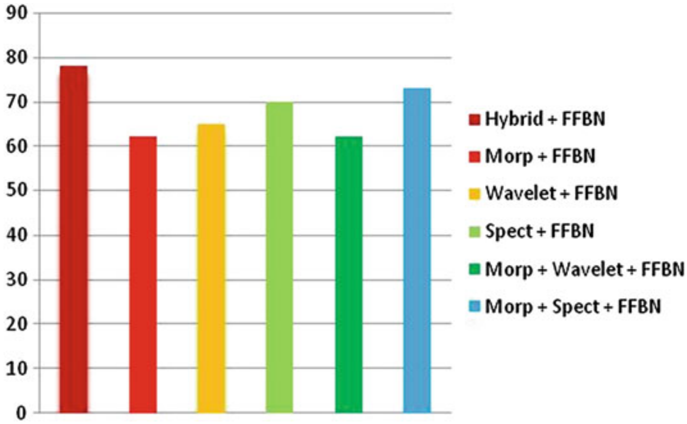

Fig. 150.5 Comparative analysis graph for accuracy

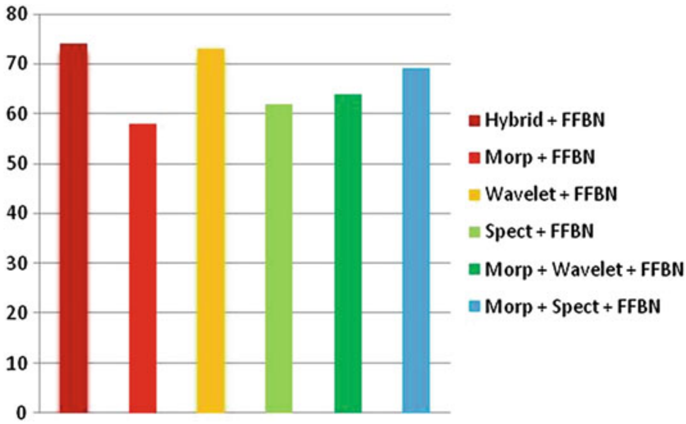

Fig. 150.6 Comparative analysis graph for sensitivity

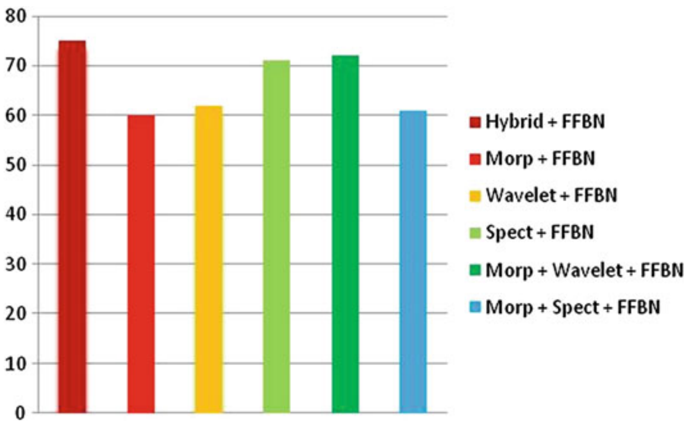

Fig. 150.7 Comparative analysis graph for specificity

technique achieved the overall accuracy value of 78 % which is high compared with the accuracy of existing systems such as (Morp + FFBN) is achieved 62 %, (wavelet + FFBN) is achieved 65 %, (Spect + FFBN) is achieved 70 %, (Morp + Wavelet + FFBN) is achieved 62 %, (Morp + spect + FFBN) is achieved only 73 %.

150.4 Conclusion

In this paper, Harr based neural network technique for the classifications of ECG signals are proposed. Here algorithm to detect the five abnormal beat signals includes Left bundle branch block beat (LBBB), Right bundle branch block beat (RBBB), Premature Ventricular Contraction (PVC), Atrial Premature Beat (APB) and Nodal (junction) Premature Beat (NPB) along with the normal beats are classified and collected from MIT-BIH data base and these sample signals are extracted. This extracted sample signals are plotted by using mat lab. The final decisional output is obtained by using the MatLAB software package. The ECG beat classification system using only morphological information resulted in an accuracy of 62 %, wavelet information resulted in an accuracy of 65 %, trispectrum information resulted in an accuracy of 70 %, combined morphological with wavelet information resulted in an accuracy of 62 %, combined morphological with tri-spectral information resulted in an accuracy of 73 %. However, the combined information led to an accuracy of 78 %, sensitivity value of 74 % and specificity value of 75 %.

References

1. Afonso VX, Tompkins WJ, Nguyen TQ, Luo S (1999) ECG beat detection using filter banks. IEEE Trans Biomed Eng 46:192–202
2. Kohler BU, Hennig C, Orglmeister R (2002) The principles of software QRS detection. IEEE Eng Med Biol Mag 21:42–57
3. Signals getting from Data base-http://www.physionet.org/physiobank/
4. Eddie Filho BL, Rodrigues NM, da Silva EA, de Carvalho MB, de Faria SM, da Silva VMM (2009) On ECG beat signal compression with 1-D multiscale recurrent patterns allied to preprocessing techniques. IEEE Trans Biomed Eng 56(3):896–900
5. Tompkins WJ (1995) Biomedical digital signal processing. Prentice Hall, New Jersey
6. Anuradha B, Reddy VCV (2008) ANN for classification of cardiac arrhythmias. J Eng Appl Sci 3(3)
7. Mallat S (2008) A wavelet tour of signal processing 3rd edn. Academic Press, Waltham
8. Chang CC, Chuang JC, Hu YS (2004) Similar image retrieval based on wavelet transformation. Int J Wavelets Multiresolut Inf Process 2(2):111–120
9. Ge D, Srinivasan N, Krishnan SM (2002) Cardiac arrhythmia classification using autoregressive modeling. Biomed Eng OnLine 1(5)
10. Khadra L, Al-Fahoum AS, Binajjaj S (2005) A quantitative analysis approach for cardiac arrhythmia classification using higher order spectral techniques. IEEE Trans Biomed Eng 52 (11)
11. Setiono R, Liu H (1996) Symbolic representation of neural networks. IEEE Comput 29(3)
12. Anagnostou T, Remzi M, Lykourinas M, Djavan B (2003) Artificial neural networks for decision-making in urologic oncology. Eur Urol 43(6):596–603

Chapter 151
Power Flow Constrained Unit Commitment Problem Using Improved Shuffled Frog Leaping Algorithm

J. Mary Anita and I. Jacob Raglend

Abstract This paper presents the application of improved SFLA to solve the unit commitment problem including operational and power flow constraints to ensure system security. The SFLA combines both memetic and social behavior of genetic PSO techniques. It includes both deterministic and random techniques for effective use of the search space. The introduction of cognitive component speeds up the local search process by widening the search space. In this proposed model the optimal power flow is carried out for every frog to obtain the minimal operating cost generator scheduling while satisfying the operational and network constraints. Gaussian random noises are introduced for hourly load variations. The proposed algorithm has been applied for IEEE 6 bus and IEEE 30 bus test systems for 24 h. The proposed algorithm is simulated using MATLAB'11 software and the results are quite encouraging because of its excellent convergence.

Keywords Shuffled frog leaping algorithm · Frogs · Unit commitment · Economic dispatch · Local search · Integer coded unit commitment · Cognitive component · Optimal power · Optimal power flow · Newton Raphson

151.1 Introduction

Operating under the present competitive and vibrant environment, UC is essential since a significant amount of savings can be obtained by a sound UC decision. The main objective of the UC is to determine the schedule of the generating units to meet the forecasted demand to minimize the total operating cost over a scheduling horizon of between 24 and 168 h (1–7 days). If the UC schedule satisfies only the operational constraints it may lead to an insecure operation of power system.

J. Mary Anita (✉) · I. Jacob Raglend
Noorul Islam University, Kanyakumari, Tamil Nadu, India
e-mail: anitajayaseelan@rediffmail.com

I. Jacob Raglend
e-mail: jacobraglend@rediffmail.com

C. Kamalakannan et al. (eds.), *Power Electronics and Renewable Energy Systems*,
Lecture Notes in Electrical Engineering 326, DOI 10.1007/978-81-322-2119-7_151

The system security is still most important and cannot be compromised. Mathematically, UC along with PFC is a large scale, complex, non-convex and non-linear mixed integer optimization problem. Traditional and conventional techniques like PL DP, MIP, LR, branch and bound method, and interior point method are available in literature [1–3]. The stochastic search methods such as Genetic Algorithm (GA), [4–6], Particle Swarm Optimization (PSO) [7], Ant colony optimization, and Bacterial foraging (BF) [8] are available. These methods are capable of handling complex nonlinear constraints to provide a high quality solution. The combination of EA's along with a local search process was named as memetic algorithms (MA's). They are found to be more successful and effective than traditional EAs for some specific complex problem domain.

SFLA is one among the available memetic algorithm. Eusuff and Lansey introduced SFLA [9, 10] in 2003. This method is based on the behavior of group of frogs searching for the location that has the maximum amount of available food. Possible solutions are randomly generated to create the initial population of frogs. And these frogs are grouped into memeplexes. Memetic evolution step (local search) is carried out within every memeplex and a shuffling is done between the memeplexes. This process is repeated till the required convergence is reached. This algorithm has been successfully applied for several engineering optimization problems. In original SFLA, the search space is limited to a linear segment which limits the optimal frog within the segment. Hence, a cognition component is introduced to widen the search space which speed up the search process.

The integer coded UC [11] is used. The minimum up/down constraints are directly coded hence there is no need for any penalty function for these constraints. In order to obtain a physically feasible solution, network security constraints are to be added along with the operational constraints. Several techniques have been discussed in literature for including the network constraints.

Murrillo-Sanchez [12] incorporates AC power flow constraints to thermal unit commitment using lagrangian relaxation and variable duplication algorithm. Qing Zia [13] decomposed the SCUC into two sub problems; one with integer commitment variables and the other with continuous variables of real power dispatch among the committed units. Bo and Shahidehpour [14] solved SCUC along with ac constraints by decomposing the SCUC problem into a master problem by optimizing the UCP with operational constraints and the sub problem by minimizing the network violations. In this algorithm, initially frogs are generated satisfying the operational constraints. Optimal Power Flow (OPF) is carried out for every frog over the scheduling horizon. The frog which does not satisfy the OPF constraints at all intervals is penalized. The optimal frog thus gives the optimal schedule with minimum cost and minimum network violations.

The organization of this paper is as follows. In Sect. 151.2 the mathematical model of the UCP is presented. In Sect. 151.3 details the idea of improved shuffled frog leaping algorithm and the introduction of cognitive component to modify the leaping rule. In Sect. 151.4 the implementation of improved SFLA for UCP with security constraints along with their mathematical equations is discussed. In Sects. 151.5 and 151.6 the simulation results and conclusion are discussed respectively.

151.2 Mathematical Modeling of UC

The main objective of UC is to minimize the total operating cost which includes fuel cost, startup cost and shut down cost. The fuel costs are normally expressed in a quadratic equation of real power output of each generator at each hour determined by Economic Dispatch (ED) among committed units.

$$F_c(P_i) = A_i + B_iP_i + C_iP_i^{\,2} \tag{151.1}$$

where A_i, B_i, C_i are coefficients of cost matrix. The total fuel cost for the entire scheduling horizon 'T' for a power system with N generators is given by

$$\Sigma_{t-1}^{T}\Sigma_{i=1}^{N}F_cP_i * X_i(t) \tag{151.2}$$

where $X_i(t)$ is the status of ith unit at tth hour. Startup cost is the cost involved in bringing the thermal unit online. Startup costs is expressed as a function of the number of hours the units has been shut down (exponential when cooling and linear when banking). Shut down costs are defined as a fixed amount for each unit/shutdown. However it is not taken into account in this paper. A simplified startup cost model is used as follows.

$$SUC_i = \begin{cases} HSC_i, if\ MDT_i \le DT_i < MDT_i + CSH_i \\ CSC_i, if\ DT_i > MDT_i + CSH_i \end{cases} \tag{151.3}$$

System power balance, system spinning reserve requirements, min up/down time and Maximum/Minimum power limits of generating units, ramp rate constraints and power flow equality are the constraints that must be satisfied by the UCP.

The power flow constraints are very important to ensure system security. The real and reactive power generated by the generators should satisfy the following equality and inequality constraints (151.4). The voltage (151.5) and phase angle (151.6) of the load and generator buses should be within the limit. The MVA flow (151.7) on each line should be within the limit

$$\begin{gathered} P_{Gi}^{min} \le P_{Gi} \le P_{Gi}^{max}, \mathrm{i} = 1, 2, \ldots N_G \\ Q_{Gi}^{min} \le Q_{Gi} \le Q_{Gi}^{max}, \mathrm{i} = 1, 2, \ldots N_G \end{gathered} \tag{151.4}$$

$$\left|\overline{V}_i^{min}\right| \le \left|\overline{V}_i\right| \le \left|\overline{V}_i^{max}\right|, \mathrm{i} = 1, 2, \ldots N_B \tag{151.5}$$

$$\phi_i^{min} \le \phi_i \le \phi_i^{max}, \mathrm{i} = 1, 2, \ldots N_B \tag{151.6}$$

$$MVA\, f_{ij} \leq MVA\, f_{ij}^{max}, \mathrm{i} = 1, 2, \ldots N_{TL} \tag{151.7}$$

151.3 Improved Shuffled Frog Leaping Algorithm

SFLA is a metaheuristic optimization method which combines the GA's memetic evolution and PSO's social behavior. It is a combination of deterministic and random strategies. The deterministic approach allows the algorithm to use the search space effectively to guide its heuristic search and the random approach ensures flexibility and robustness of the search process. SFLA mainly based on the behavior of group of frogs searching for the location that has the maximum amount of available food. The most promising benefit of this algorithm is its faster convergence speed.

The SFLA involves a population of possible solutions defined by a set of virtual frogs. This set of virtual frogs is partitioned into subsets known as memeplexes. Within each memeplex each frog holds different ideas and the idea of each frog can be used to infect the ideas of other frogs.

In the original SFL algorithm, every frog updates its position according to the best solution because of the influence of the local best solution. According to the frog leaping rule used in SFLA the leaping of the frog to its new position is restricted between the worst and the best frog position, and not beyond the best frog position. It may restrict the search space of the local search algorithm. This may lead to slower convergence and convergence within local optimal point. The above mentioned problem is overcome by the introduction of the cognitive component. The ability and stability of the algorithm is improved by the introduction of the cognition component. Introduction of this component allows the frog to adjust its position according to the thinking of the frog itself along with best frog within the memeplex or the global best frog of the population. The coordinates of current position of each frog is entered into the formulas for the measure of error of the estimate of target values, and it is moved towards the new position. This is repeated for a defined number of times. While moving towards the multivariate space, the individuals compare their current error value with the best error value they have attained at any point up to that iteration. The lowest error value is termed as the best error value $Pbest_j$, and the position where the $Pbest_j$ is evaluated is termed as P_j. The difference Pi-X_i indicates the distance between the individual's previous and current position. Each element of the above distance vector is weighted by a positive random number in the range [0 1]. Because of the introduction of this component the frog is not restricted to move along the line segment. Now, the leaping of the frog takes place in a widened search space avoiding premature convergence (i.e.) definitely beyond the best frog, the global optimal point. The mathematical equation of the new modified frog leaping rule is given by the Eq. (151.15). Figure 151.1 represents the modified frog leaping rule.

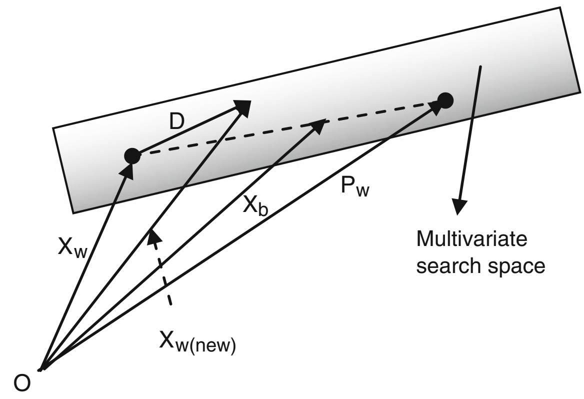

Fig. 151.1 Modified leaping rule

$$D_i = rand(1) * (P_w - X_w) + rand(1) * (X_b - X_w) \tag{151.8}$$

$$X_w = X_w + D_i,\ D_{i\min} < |D_i| < D_{i\max} \tag{151.9}$$

The process of passing information between the frogs of a memeplex is known as local search or memetic evolution step. After a defined number of memetic evolution step the virtual frogs are reorganized so that the quality of memeplex is improved. Shuffling enhances the meme quality after infection and ensures the cultural evolution towards any particular interest. The process of memetic evolution and shuffling are repeated unit a required convergence is reached.

151.4 Implementation of SFLA to Security Constrained UCP

The following steps are involved in implementing this algorithm for UC problem including operational and security constraints.

Step: 1 *Generation of Random frogs*

The population size (P) is chosen initially. The position of a frog in integer coded SFLA for UCP consists of a sequence of alternatively signed integers representing the duration of ON/OFF cycles of units during the scheduling horizon. A positive integer in the frog vector represents the duration of continuous ON state of a unit whereas the negative integer represents the duration of continuous OFF state of a unit. The size of a frog is decided by the no of units (N) and no of cycles (C). No of cycles (C) is determined by the load peaks and minimum up and down time of units.

For a 10 unit, 5 cycle system the size of the frog for a 1 day scheduling is 1 × 10 × 5. The sample frog for a 5 unit 5 cycle system is given in Table 151.1.

Table 151.1 Commitment schedule of 6bus system for case:1(Base case)

	Operating cost=$83122																							
Unit / Hour	1	2	3	4	5	6	7	8	9	10	11	12	13	14	15	16	17	18	19	20	21	22	23	24
1	1	1	1	1	1	1	1	1	1	1	1	1	1	1	1	1	1	1	1	1	1	1	1	1
2	0	0	0	0	0	0	0	0	1	1	1	1	1	1	1	1	1	1	1	1	1	1	0	0
3	0	0	0	0	0	0	0	0	0	0	0	0	0	1	1	1	1	1	1	1	1	1	0	0

151.4.1 Creating Initial Population

A part of a frog representing the operating schedule of a particular unit during the scheduling horizon should be formed such that the values of T_i^c of the initial population is randomly generated.

Step: 2 *Network security check*

From the economic view point the frogs obtained in the previous step provides a set of possible cost effective generator schedule. But it cannot ensure system security as violations on transmission line flow and bus voltages may exist. The economic operation may schedule the cost effective generators to supply the load through long transmission lines. This may cause the bus voltage at the load side to be very less. These under voltages can be restricted by increasing the generation of units near the load centre, even though it is costly.

Also the violations of transmission line flow can be restricted by re dispatching the generation on buses corresponding to which the transmission line is connected to and at the hour of violation.

Before checking for any security violations it is essential to check the convergence of power flow equations. Since, a converged power flow itself indicates that the real and reactive power mismatches are within the allowable limit. In this algorithm, the Newton Raphson method of solving power flow is used.

Steps involved in mitigating the violated line flows.

1. Economic Dispatch is performed using lambda iterative method among the committed units.
2. Check the frog for convergence of power flow using the values of power dispatched at each hour. Newton Raphson based power flow is performed in this algorithm. The bus data is modified according to the commitment schedule.
3. If it is not converged, it not the feasible frog and it is penalized (Π_{pf}) with a high value and go to step: 7
4. If the power flow of a frog for each hour is converged, perform optimal power flow analysis, then check the transmission line flows and bus voltages for violations.
5. If any violation presents, change the cycle duration of the frog on violated duration of violated units.

6. Check for violations and repeat step 5 for a fixed no of times (say about 5 times). If the violation is not mitigated in certain no of iterations add a penalty (Π_{pf}) as this frog is not feasible.
7. Compute fitness function [discussed in step (3)] including penalty if any.

Step: 3 *Computation of fitness function*

The objective function of UC using SFLA has two terms, and they are the total operation cost and the penalty functions for violating system constraints (spinning reserve, power balance and power flow violation)

$$\text{xxx} \tag{151.10}$$

The penalty function has three terms. The first term for spinning reserve violation and is given by

$$\text{xxx} \tag{151.11}$$

The second term for excessive capacity is given by

$$\text{xxx} \tag{151.12}$$

where 'ω' depends on maximum operating cost of the system over a scheduling period 'T'

$$\text{xxx} \tag{151.13}$$

where α is a constant. The third term is for network violation. Π_{pf} is usually chosen as a large value around 10^5. Now the objective is to minimize the fitness function

$$Fitness = A/(TC + \Pi_{res} + \Pi_{cap} + \Pi_{pf}) \tag{151.14}$$

$A = 10^8$. 'A' is a system dependent constant added for avoiding the fitness value from obtaining too small values. This should be of the order of the system maximum operating cost.

Step: 4 *Grouping of Frogs into Memeplexes*

The entire population of 'P' frogs are grouped into 'M' memeplexes, and each memeplex is formed so that each memeplex consists of 'N' no of frogs (P = MXN). The partitioning of memeplexes is done so that each memeplex have frogs with lower and higher fitness values. For this the first frog goes to 1st memeplex, the second frog goes to 2nd memeplex, the mth frog to mth memeplex and m + 1th frog goes to 1st memeplex.

Step: 5 *Local search process* (*Memetic evolution step*)

i. Within each memeplex, the frogs with worst (X_w) and best (X_b) fitness values are identified. Also the frog with global fitness X_g is also identified.
ii. The frog with worst fitness is leaped towards the best frog by a random vector which is given by

$$D_i = rand(1) * (P_w - X_w) + rand(1) * (X_b - X_w) \tag{151.15}$$

$$X_w = X_w + D_i,\ D_{imin} < |D_i| < D_{imax} \tag{151.16}$$

iii. The fitness of the new leaped worst frog is calculated. If there is no improvement in fitness, the leaping vector is calculated with X_g

$$D_i = rand(1) * (P_w - X_w) + rand(1) * \left(X_g - X_w\right) \tag{151.17}$$

$$X_w = X_w + D_i,\ D_{imin} < |D_i| < D_{imax} \tag{151.18}$$

iv. The fitness of the new leaped worst frog is calculated. If there is no improvement, then *Xw* is replaced with a new random frog.
v. The steps (i)–(iv) are repeated for some specific number of iterations.
After all the above corrections are carried out, on X_w, the step 2 (optimal power flow) should be carried out for each hour of scheduling horizon for all committed units. Then the fitness value is calculated as discussed in step 3.

Step: 6 *Shuffling Process*

After local search in every memeplex is completed shuffling of memeplex is done, and the frogs are reorganized in descending order of fitness values and again grouped into memeplex and local search process is carried out.

Step: 7 *Checking for Convergence*

(i) The relative change in the fitness of the global frog within a number of consecutive shuffling iterations is less than a pre-specified tolerance.
(ii) The maximum predefined numbers of shuffling iterations have been reached.

The above all steps I, II, III, IV are repeated until

151.5 Simulation Results and Discussions

The proposed improved shuffled frog leaping algorithm has been simulated on MATLAB'11 environment. The test cases taken are standard 6 bus system, IEEE 30 bus system. The load and generator data of all the test systems are taken form reference [14]. The reserve requirement is taken as 10 % of the hourly load. The initial population size for improved SFLA has been taken as 200 frogs. Grouping of 200 frogs is done between 20 memeplexes each with 10 frogs. Memetic evolution step is done for 10 iterations before each shuffling process. To discuss the efficiency of the proposed approach and to analyze the effect of transmission loss on the operating cost, we have considered two cases.

Case: 1 Base case with only operational constraints and no network constraints.
Case: 2 SCUC case including both operational and network constraints.

151.5.1 Six Bus System

This system consists of 3 generators and 5 transmission lines with 2 tap changing transformers. The data is taken from the Ref. [15].

Case 1: Table 151.1 gives the optimal frog and the commitment schedule for the base case. The optimal frog is obtained in 5 shuffling iterations. The optimal operational cost is $83,122. The expensive units G2 and G3 are not committed at certain intervals to ensure economic operation. The generator dispatch is not physically feasible even though it is economical. The Newton Raphson based power flow is carried out for each hour. It shows that there is a violation of transmission power flow on line 3–6. The allowable power flow is 100 MW but the actual power flow is 129.5 MW at hour 8. Also there is a violation of voltages at hours 20, 21 at bus 4. The allowable bus voltage is 1.05 p.u but it is 1.0515 p.u.

Case 2: The SCUC has mitigated the transmission power flow at line 3–6 by committing unit 2 at hour 8. The voltage violation is overcome by de-committing units 2 and 3 between hours 20–22 and maintaining it to meet the min up and down time constraints. The optimal frog is obtained in 6 shuffling iterations. The operational cost is $83,720.6 which is 0.72 % higher than the base case. The commitment schedule is listed in Table 151.2.

Table 151.2 Commitment schedule of 6bus system for case:2 (SCUC case)

	Operating cost=$83720																							
Unit / Hour	1	2	3	4	5	6	7	8	9	10	11	12	13	14	15	16	17	18	19	20	21	22	23	24
1	1	1	1	1	1	1	1	1	1	1	1	1	1	1	1	1	1	1	1	1	1	1	1	1
2	0	0	0	0	0	0	0	1	1	1	1	1	1	1	1	1	1	1	1	1	1	1	0	0
3	0	0	0	0	0	0	0	0	0	0	0	0	1	1	1	1	1	1	1	0	0	0	0	0

Table 151.3 Comparison of optimal cost for 6 bus system between various methods

Sl. no.	Method	Optimal operational cost for base case ($)	Optimal operational cost for SCUC case ($)
1	SDP [15]	83,429.10	84,268.70
2	Parallel hybrid EIGA [16]	83,406.08	84,262.80
3	Improved shuffled frog leaping algorithm	83,122.00	83,720.60

151.5.2 IEEE 30 Bus System

The base case result gives an optimal operating cost of 12,491 $. But it is not ensuring system security. The security constrained UCP gives an optimal cost of 13,836$ which is 10.8 % higher than the base case. But the dispatch of real power at all scheduling intervals is satisfying the load flow equations and all the line MVA flows are within the limit. Also the improved SFLA based UCP has a better convergence and the optimal results are obtained in 5–7 shuffling iterations for both the cases. The results obtained are quite satisfactory. The optimal operating cost of the 6 bus system is much better than the results obtained using SDP [15] and Parallel Hybrid EIGA [16]. This is detailed in Table 151.3.

151.6 Conclusion

In this proposed algorithm, the transmission power flow, bus voltages and the interaction between the real and reactive power which exist in power system operation. The generator schedule obtain from this result is physically feasible for power system operation. Since it ensures system security, it is one of the best among the available options. The proposed improved SFLA gives a promising result with better convergence. It does not encounter any inherent limitations such as relaxation of variables and excess decomposition. But traditional methods like DP, LR, Branch and bound, GA suffer with those inherent limitations. The proposed algorithm has been tested for several test systems like IEEE 6Bus, IEEE30 Bus for 24 h and the results are satisfactory. Even though the inclusion power flow constraints increase the optimal cost, the schedule of generating units can be guaranteed to be a physically feasible solution.

References

1. Wood AJ, Wollenberg BF (1984) Power generation operation and control. Wiley, New York
2. Kothari DP, Dhillon JS (2011) Power system optimization. Prentice Hall of India Pvt. Ltd., New Delhi

3. Virmani S, Adrian EC, Imhof K (1989) Implementation of a Lagrangian based Unit commitment problem. IEEE Trans Power Syst 4(4):1373–1380
4. Kazarlis SA, Bakitris AG, Petridis V (1996) A Genetic algorithm solution to the unit commitment problem. IEEE Trans Power Syst 11(1):83–92
5. Swarup KS, Yamashiro S (2002) Unit commitment solution methodology using genetic algorithm. IEEE Trans Power Syst 17(1):87–91
6. Arroyo JM, Conejo AJ (2002) A parallel repair genetic algorithm to solve unit commitment problem. IEEE Trans Power Syst 17(4):1216–1224
7. Xiong W, Li MJ, Cheng Y (2008) *An* improved particle swarm optimization algorithm for unit commitment problem. In: Proceedings of ICICTA
8. Eslamian M, Hosseinian SH, Vahidi B (2009) Bacterial foraging based solution to the unit commitment problem. IEEE Trans Power Syst 24(3):1478–1488
9. Eusuff MM, Lansey KE, Pasha F (2006) Shuffled Frog leaping: a memetic meta-heuristic for discrete optimization. Eng Optimiz 38(2):129–154
10. Zhang X, Hu X, Cui G, Wang Y, Niu Y (2008) An improved shuffled frog leaping algorithm with cognitive behavior. In: Proceedings of 7th world congress, intelligent control and automation
11. Damousis IG, Bakirtzis AG, Dokopolous PS (2004) A solution to unit commitment problem using integer coded genetic algorithm. IEEE Trans Power Syst 19(2):1165–1172
12. Murrillo-Sanchez CE, Thomas RJ (2000) Parallel processing implementation of the unit commitment problem with full ac power flow constraints. In: Proceedings of the 33rd Hawaii international conference on system sciences
13. Qing Xia YH, Song Boming Zhang, Kang Congqng, Xiang Niande (2000) Effective decomposition and co-ordination algorithms for unit commitment and economic dispatch with security constraints. Electr Power Syst Res 53:39–45
14. Bo L, Shahidephour M (2005) Unit commitment with flexible generating units. IEEE Trans Power Syst 20(2):1022–1034
15. Bai X, Wei H (2009) Semi-definite programming-based method for security constrained unit commitment with operational and optimal power flow constraints. IET Genrn Trans Distr 3 (2):182–197
16. Columbus C, Simon SP (2012) Parallel hybrid enhanced inherited GA based SCUC in a distributed cluster. Artif Intel Res 1(1):96–106

Chapter 152
Investigation and Control of Principal Axes of Aircraft Using Robust Method

V. Rajeswari and L. Padma Suresh

Abstract The development of automatic control systems has played an important role in the growth of civil and military aviation. Modern aircraft include a variety of automatic control systems that aid the flight crew in navigation, flight management and augmenting the stability characteristics of the airplane. In this paper, autopilots were designed to control the lateral and longitudinal axis of the aircraft using modern controllers. The effectiveness of the controller were studied and verified using MATLAB and the simulation results are presented in time domain.

Keywords Autopilot · Lateral and longitudinal dynamics · LQR · Principal axes

152.1 Introduction

The fast growth of aircraft designs from the less capable airplane to the present day high performance military, commercial and general aviation aircraft required the development of many technologies. The automatic control systems play an important role in monitoring and controlling of many of the aircraft's subsystems, for which an autopilot is designed that controls the principal axes of the aircraft leading to the safe landing of the aircraft during adverse weather conditions [1]. Generally the aircraft is free to rotate around the three axes which are perpendicular to each other. Rotation about the vertical axis is the yaw which passes through the plane from top to bottom and the longitudinal axis passes through the plane from nose to tail and the rotation about this axis is pitch. The lateral axis passes through the plane from wing tip to wing tip and rotation about this axis is roll [2]. The pitch,

V. Rajeswari (✉)
ICE Department, G. Narayanamma Institute of Technology and Science, Hyderabad, India
e-mail: rajiviswanath28@gmail.com

L.P. Suresh
EEE Department, Noorul Islam University, Kanyakumari, India
e-mail: suresh_lps@yahoo.co.in

C. Kamalakannan et al. (eds.), *Power Electronics and Renewable Energy Systems*,
Lecture Notes in Electrical Engineering 326, DOI 10.1007/978-81-322-2119-7_152

roll and yaw are then controlled by the elevators, ailerons and rudder respectively. By moving the elevator up, the downward force on the horizontal tail is raised so that the nose of the aircraft is lifted up. The ailerons cause the rolling of aircraft by creating an unbalanced side force component of the wing lift force that makes the aircraft to take a curved path [3]. Yaw changes the direction of aircraft's nose to point left or right. This is a 3rd order non-linear system which is linearized about the operating point. In this paper, a control system design for pitch, roll and yaw control are presented. An optimal and robust controller (LQR) is developed for controlling the three axes of the aircraft. The performances of this controller are investigated and the simulation results for the response of the controller are presented in time domain.

152.2 Modeling of Dynamic Equations of Aircraft

For an aircraft, there are two types of dynamic equations: Lateral dynamic equations of motion which represents the lateral axis and longitudinal equations of motion that represents the longitudinal axis. The equations governing the motion of aircraft are a set of six non-linear differential equations which can be decoupled and linearized into longitudinal and lateral equations. Figure 152.1 shows the aerodynamic forces, moments and velocity components in body axis system. In Fig. 152.1, X_B, Y_B and Z_B emphasize a body fixed axis system. L, M, N represents the aerodynamic moments and p, q, r shows the angular velocities roll, pitch and yaw respectively [2]. By applying Newton's second law to the rigid body, the equations of motion of aircraft can be established in terms of the translational and angular accelerations. Assuming that the aircraft is steady state cruise at constant altitude and velocity so that the thrust and drag cancel out each other and lift and weight balance out each other. The change in pitch, roll and yaw angles does not change the speed of aircraft.

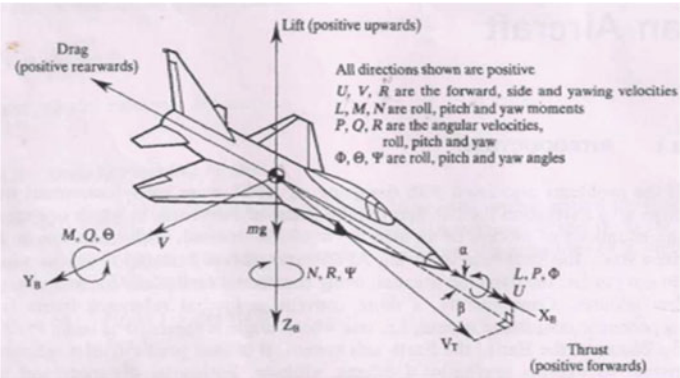

Fig. 152.1 Aerodynamic forces, moments and velocity components

152.2.1 Lateral Dynamic Equation of Motion of Aircraft

Figure 152.2 shows the angular orientation and velocities of gravity vector relative to body axis. This is expressed depending on the angular velocity of the body axes about the vector 'mg'. With respect to Fig. 152.2, the equation of motion can be expressed as

$$Y + mg\,\cos\theta\,\sin\varphi = m[\dot{v} + ru - pw] \tag{152.1}$$

$$L = I_{xx}\dot{p} - I_{xz}\dot{r} + qr(I_{zz} - I_{yy}) \tag{152.2}$$

$$N = -I_{xz}\dot{p} - I_{zz}\dot{r} + pq\left(I_{yy} - I_{xx}\right) + I_{xz}qr \tag{152.3}$$

The above equations are nonlinear and simplified by considering the aircraft to comprise two components: a mean motion that represents the equilibrium or trim conditions and a dynamic motion which accounts for the perturbations about the mean motion. Thus every motion variable is considered to have two components.

$$\begin{aligned} &U \triangleq U_o + \Delta u, \quad \triangleq Q_o + \Delta q, \quad R \triangleq R_o + \Delta r, \quad M \triangleq M_o + \Delta m, \\ &Y \triangleq Y_o + \Delta y, \quad P \triangleq P_o + \Delta p, \quad L \triangleq L_o + \Delta l, \quad V \triangleq V_o + \Delta v, \\ &\delta \triangleq \delta_o + \Delta\delta \end{aligned} \tag{152.4}$$

The reference flight condition is assumed to be symmetric and the propulsive forces are assumed to be constant.

$$\mathrm{v_o} = \mathrm{q_o} = \mathrm{u_o} = \mathrm{r_o} = \varphi_{\mathrm{o}} = \Psi_{\mathrm{o}} = 0 \tag{152.5}$$

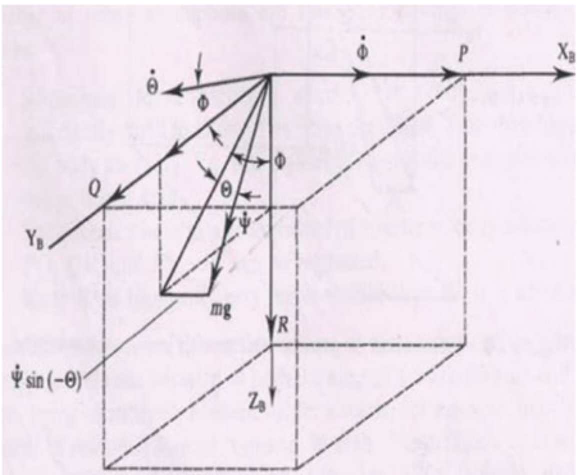

Fig. 152.2 Angular orientation and velocities of gravity vector

The complete linearised equations of motion are obtained as below where sideslip angle is used.

$$\left(\frac{d}{dt} - Y_v\right)\Delta v - Y_p\Delta p + (u_0 - Y_r)\Delta r - (g\,\cos\theta_0)\Delta\varphi = Y\delta r \cdot \Delta\delta r \tag{152.6}$$

$$-L_v\Delta v + \left(\frac{d}{dt} - L_p\right)\Delta p - L_r\Delta r = L\delta r \cdot \Delta\delta r + L\delta a \cdot \Delta\delta \tag{152.7}$$

$$-N_v\Delta v + \left(\frac{d}{dt} - N_r\right)\Delta r - N_p\Delta p = N\delta r \cdot \Delta\delta r + N\delta a \cdot \Delta\delta \tag{152.8}$$

Substituting, $\Delta v = \Delta\beta$, $Y_v = Y_\beta$, $L_v = L_\beta$, $N_v = N_\beta$ and $\Delta_\beta = \Delta_v/u_o$

$$\left(\frac{Y_\beta}{u_o}\right)\Delta\beta + \frac{Y_p}{u_o}\Delta p - \left(1 - \frac{Y_r}{u_0}\right)\Delta r + \frac{(g\,\cos\theta_0)}{u_0}\Delta\varphi = \frac{Y\delta r}{u_0} \cdot \Delta\delta r \tag{152.9}$$

$$-L_\beta\Delta\beta + \left(L_p\right)\Delta p + L_r\Delta r = L\delta r \cdot \Delta\delta r + L\delta a \cdot \Delta\delta a \tag{152.10}$$

$$-N_\beta\Delta\beta + \left(N_p\right)\Delta p + N_r\Delta r = N\delta r \cdot \Delta\delta r + N\delta a \cdot \Delta\delta a \tag{152.11}$$

Using the Eqs. (152.9), (152.10), and (152.11) the state space model for the roll and yaw control problem can be formulated.

$$\begin{bmatrix} \dot{\Delta}_\beta \\ \dot{\Delta}_p \\ \dot{\Delta}_r \\ \dot{\Delta}_\varphi \end{bmatrix} = \begin{bmatrix} \frac{Y_\beta}{u_o} & \frac{Y_p}{u_o} & -\left(1 - \frac{Y_r}{u_0}\right) & \frac{g\,\cos\theta_0}{u_0} \\ L_\beta & L_p & L_r & 0 \\ N_\beta & N_p & N_r & 0 \\ 0 & 1 & 0 & 0 \end{bmatrix} \begin{bmatrix} \Delta\beta \\ \Delta p \\ \Delta r \\ \Delta\varphi \end{bmatrix} + \begin{bmatrix} 0 & \frac{Y\delta r}{u_o} \\ L\delta a & L\delta r \\ N\delta a & N\delta r \\ 0 & 0 \end{bmatrix} \begin{bmatrix} \Delta\delta a \\ \Delta\delta r \end{bmatrix} \tag{152.12}$$

The roll control problem has the input as the aileron deflection angle with the output as roll angle of the aircraft. Similarly, the yaw control problem has the input as rudder deflection angle and output as change in the yaw angle of aircraft. For this study, the data of the General Aviation airplane Navion is considered [1]. The lateral stability derivatives [4] are tabulated in Table 152.1.

The values from Table 152.1 are considered for the roll and yaw control schemes of the aircraft. For the roll control problem, the rudder deflection is neglected and for yaw control the aileron deflection is neglected in Eq. (152.12). Equations (152.13) and (152.14) gives the state space representation for roll and yaw control problem respectively.

Table 152.1 Lateral stability derivatives

Lateral derivatives	Components		
	X-force derivatives	Rolling moment derivatives	Yawing moment derivatives
Pitching velocities	$Y_v = 0.254$	$L_v = -0.091$	$N_v = 0.025$
Sideslip angle	$Y_\beta = -44.6$	$L_\beta = -15.84$	$N_\beta = 4.3$
Rolling rate	$Y_p = 0$	$L_p = -8.349$	$N_p = -0.342$
Yawing rate	$Y_r = 0$	$L_r = 2.086$	$N_r = -0.76$
Rudder deflection	$Y_{\delta r} = 12.43$	$L_{\delta r} = -2.67$	$N_{\delta r} = -4.79$
Aileron deflection	$Y_{\delta a} = 0$	$L_{\delta a} = -28.68$	$N_{\delta a} = -0.216$

$$\begin{bmatrix} \Delta\dot{\beta} \\ \Delta\dot{p} \\ \Delta\dot{r} \\ \Delta\dot{\varphi} \end{bmatrix} = \begin{bmatrix} -0.254 & 0 & -1 & 0.184 \\ -15.84 & -8.349 & 2.086 & 0 \\ 4.3 & -0.342 & -0.76 & 0 \\ 0 & 1 & 0 & 0 \end{bmatrix} \begin{bmatrix} \Delta\beta \\ \Delta p \\ \Delta r \\ \Delta\varphi \end{bmatrix} + \begin{bmatrix} 0 \\ -28.68 \\ -0.216 \\ 0 \end{bmatrix} [\Delta\delta a] \tag{152.13}$$

$$\begin{bmatrix} \Delta\dot{\beta} \\ \Delta\dot{p} \\ \Delta\dot{r} \\ \Delta\dot{\varphi} \end{bmatrix} = \begin{bmatrix} -0.254 & 0 & -1 & 0.184 \\ -15.54 & -8.349 & 2.086 & 0 \\ 4.3 & -0.34 & -0.76 & 0 \\ 0 & 1 & 0 & 0 \end{bmatrix} \begin{bmatrix} \Delta\beta \\ \Delta p \\ \Delta r \\ \Delta\varphi \end{bmatrix} + \begin{bmatrix} 0.07 \\ -2.67 \\ -4.79 \\ 0 \end{bmatrix} [\Delta\delta r] \tag{152.14}$$

152.2.2 Longitudinal Dynamic Equations of Motion

From Fig. 152.2, the equation of motion can be expressed as [2],

$$\mathrm{x} - \mathrm{mg}\sin\theta = m(\dot{u} + qw - rv) \tag{152.15}$$

$$\mathrm{z} + \mathrm{mg}\cos\theta\cos\varphi = m(\dot{w} + pv - qu) \tag{152.16}$$

$$M = I_{yy}\dot{q} + qr(I_{xx} - I_{zz}) + I_{xz}(p^2 - r^2) \tag{152.17}$$

Taking all assumptions as in Eqs. (152.4) and (152.5), the complete linearized equations of motion is obtained as below:

$$\left(\frac{d}{dt} - X_u\right)\Delta u - X_u\Delta w + (g\cos\theta_0)\Delta\theta = X\delta e \cdot \Delta\delta e \tag{152.18}$$

Table 152.2 Longitudinal stability derivative

Longitudinal derivatives	Components		
	X-force derivatives	Z-force derivatives	Pitching moment
Yawing velocities	$X_w = 0.254$	$Z_w = -2$	$M_w = -0.05$
	$\dot{X}w = 0$	$\dot{Z}w = 0$	$\dot{M}w = -0.051$
Rolling velocities	$X_u = -0.04$	$Z_u = -0.37$	$M_u = 0$
Angle of attack	$X_\alpha = 0$	$Z_\alpha = -355$	$M_\alpha = -8.8$
	$\dot{X}\alpha = 0$	$\dot{Z}\alpha = 0$	$\dot{M}\alpha = -0.898$
Pitching rate	$X_q = 0$	$Z_q = 0$	$M_q = -2.05$
Elevator deflection	$X_{\delta e} = 0$	$Z_{\delta e} = -28.15$	$M_{\delta e} = -11.88$

$$-Z_u\Delta u + [(1 - Z_w)\frac{d}{dt} - Z_w]\Delta w + [(u_0 - \dot{Z}_q)\frac{d}{dt} - g\ \sin\theta_0]\Delta\theta = Z\delta e \cdot \Delta\delta e \tag{152.19}$$

$$-M_u\Delta u - \left(\dot{M}_w\frac{d}{dt} + M_w\right)\Delta w + \left(\frac{d^2}{dt^2} - M_q\frac{d}{dt}\right)\Delta\theta = M\delta e \cdot \Delta\delta e \tag{152.20}$$

The longitudinal stability derivatives are tabulated in Table 152.2 [5] from where the transfer function can be obtained [6].

$$\text{Transfer function is } \frac{\Delta\theta(s)}{\Delta\delta e(s)} = \frac{11.7s + 22.5}{s^3 + 4.96s^2 + 12.9s} \tag{152.21}$$

152.3 Design of LQR

Linear quadratic optimization [7, 8] is a basic method for designing controllers of dynamical systems. LQR is a powerful method for designing flight control systems. This method is based on the manipulation of the equations of motion in state space and the system can be stabilized using full state feedback system. Consider the state and output equations describing the longitudinal and lateral equations of motion.

$$\begin{aligned} \dot{X}(t) &= Ax(t) + Bu(t) \\ y(t) &= Cx(t) + Du(t) \end{aligned} \tag{152.22}$$

In the LQR design, the LQR function in MATLAB can be used to determine the value of the vector ‘K’ which is used to find the feedback control law.

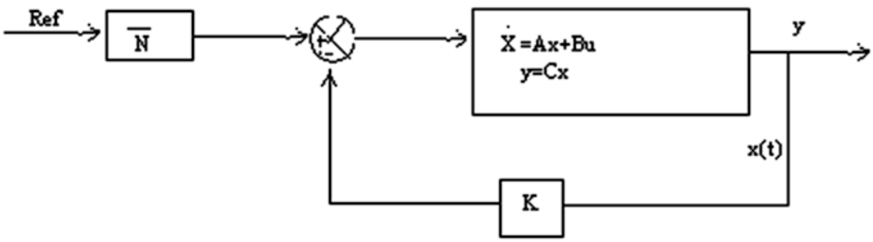

Fig. 152.3 Full state feedback controller

$$u(t) = -kx(t) + \Delta\delta e.N \tag{152.23}$$

This control law has to minimize the performance index, $J = \int_0^\infty (X^T QX + u^T Ru)dt$ where, Q-state cost matrix, R-performance index matrix. Here R = 1 and $Q = C^T C$.

Figure 152.3 shows the full state feedback controller with reference input. For the present study, the value of 'K' is to be determined.

152.4 Simulation and Results

A Control system for the roll, yaw, and pitch axes is simulated using LQR and the results of simulation are analyzed and presented. To investigate the performance of the control strategy, the time domain specifications are analyzed. The values of K for the yaw, roll and pitch control problems are obtained as

K = [5.299 −3.1065 −0.9996 −38.68] and $\bar{N} = -38.7298$ with weighting factor x = 1,500

K = [0.528 −0.538 −0.0917 −8.6567] and $\bar{N} = -8.6567$ with weighting factor x = 75

K = [−0.5670 1.69 22.36] and $\bar{N} = 22.36$ with weighting factor x = 500 respectively.

Figure 152.4a, b, c shows performances of the controller for the roll, yaw and pitch axes in time domain respectively.

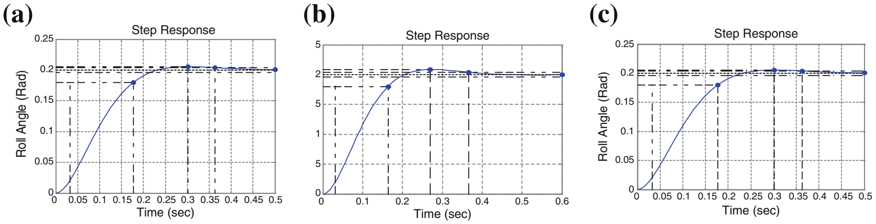

Fig. 152.4 Performances of controller **a** response of roll, **b** yaw and **c** pitch axes respectively

Table 152.3 Performance characteristics of controller in three axes

Time domain specifications	Yaw control	Roll control	Pitch control
Overshoot (%)	4.12	2.77	4.3
Settling time (s)	0.804	0.363	0.36
Rise time (s)	0.256	0.145	0.133

Table 152.3 shows the time domain specifications analyzed from the response of the controller.

From Fig. 152.4a, b, c and the specifications in Table 152.3. It is observed that the LQR controller gives a fast and robust response by handling the effect of disturbances in the system.

152.5 Conclusion

The work emphasizes the design of an autopilot for controlling the three principal axes of aircraft which was done using LQR on the MATLAB environment. The controller was designed and the responses were analyzed and verified in time domain. From the result of simulation it is observed that the controller gives optimal performance in controlling the three axes efficiently by handling the effect of disturbances in the system.

References

1. Nelson RC (1998) Flight stability and automatic control, 2nd edn. McGraw Hill, New York
2. Mclean D (1990) Automatic flight control systems. International series in systems and control engineering. Prentice Hall, Englewood Cliffs
3. www.nasa.gov (01.03.2011)
4. Seckel E, Moris JJ (1971) The stability derivatives of the Navion aircraft estimated by various methods and derived from flight test data. Federal Aviation Administration, Systems Research and Development Service
5. Struett RC (2012) Empennage sizing and aircraft stability using MATLAB. American Institute of Aeronautics and Astronautics
6. Wahid N, Hassan N, Rahmat MF, Mansor S (2011) Application of intelligent controllers in feedback control loop for aircraft pitch control. Aust J Basic Appl Sci
7. Kirk DE (1970) Optimal control theory: an introduction. Prentice Hall, Englewood Cliffs
8. Hespanha P (2007) Undergraduate lecture notes on LQR/LQG controller design

Chapter 153
Secret Key Sharing in Networks Using Classical Cryptography Based Quantum Stratagem Approach

R. Sarath, A. Shajin Nargunam and R.P. Sumithra

Abstract The abstract should summarize the contents of the paper and should. A new approach for implementing BB84 protocol is proposed in this paper there by introducing a new technique for secret sharing of key in networks. BB84 protocol has practical weakness like single photon generation, lack of authentication and many real time implementation problems. This paper explains how the drawback of BB84 protocol is eliminated by combining classical cryptography and quantum techniques. The usage of dual channel technique and programmable polarizer are analyzed which ensure the way to remove the practical difficulties of quantum cryptography and their combination result in feasibility of authentication, entanglement and hacker identification there by introducing a novel method for key transmission.

Keywords Classical cryptography · Quantum cryptography · Quantum bit error rate · Programmic polarizer · Secure communication

153.1 Introduction

This Secure communication has become the topmost priority of modern society. In classical cryptography the sender and receiver need to share a secret sequence of random numbers, we call it as key. In classical cryptography, key is exchanged by

R. Sarath (✉)
Department of EIE, Noorul Islam Centre for Higher Education, Kumaracoil, Thuckalay, India
e-mail: sarathraveendran@gmail.com

A.S. Nargunam
Department of CSE, Noorul Islam Centre for Higher Education, Kumaracoil, Thuckalay, India
e-mail: ashajin@yahoo.com

R.P. Sumithra
Department of CSE, Ponjesly College of Engineering, Nagercoil, India
e-mail: r.p.sumithra@gmail.com

C. Kamalakannan et al. (eds.), *Power Electronics and Renewable Energy Systems*,
Lecture Notes in Electrical Engineering 326, DOI 10.1007/978-81-322-2119-7_153

physical means. No one can assure the security of the key that is send by physical means. This leads to the major failure in classical cryptography [1]. Quantum cryptography overcomes this disadvantage by sending the key in the form of photon using quantum channel [2]. The most important aspect of Quantum cryptography is that quantum system has *qubits* which not only has two states i.e. '0' and '1' bit but also a superposition of both. Various protocols have been proposed in quantum cryptography such as BB84, B92, and EIR [3]. BB84 protocol was first proposed by Bennett and Brassard. According to this protocol two channels are required for key transfer one quantum channel and one public channel. Sender measures the photons on the basis of information obtained through public channel and makes raw key. Quantum cryptography is theoretically strong but has lot of practical difficulties [1, 4]. Few drawbacks of Quantum Cryptography [5, 6] are implementing authentication schemes, generating single photon, possibility of change in polarization of photons. But the major drawback of quantum cryptography is that it is very difficult for long distance photon transmission. Hence both the cryptographic technique does not provide solution for key transfer.

The basic objective of this paper is to put forth a new technique by combining the advantages of Quantum cryptography and Classical cryptography there by introducing a new technique for secret key transmission.

153.2 BB84 Protocol

BB84 [7] allows a secret key to be agreed between two communications parties without having two parties meet face to face. BB84 allows receiver and sender, to establish a secret common key sequence using polarized photons. According to this protocol, two channels are required for key transfer one quantum channel and one public channel. BB84 protocol coding scheme uses four non-orthogonal polarization state (0°, 90°, 45° and −45°) that will polarize each of the photon that will be transmitted. Each of these photons is in a state denoted by one of the four following symbols: —, |, ⁄, \, BB84 Protocol consists of three steps: raw key extraction, key error correction, and privacy amplification.

To exchange a secret key in BB84 protocol, Sender and receiver must do as follow:

Sender creates a binary random number and sends it to receiver using randomly the two different bases + (rectilinear) and × (diagonal): Receiver simultaneously measures the polarization of the incoming photons by randomly using the different bases. Here the receiver does not know which of his measurements are deterministic. Later, the sender and receiver communicate the list of the bases they used via public channel. This communication carries no information about the value of the measurement, but allows sender and receiver to know which values were measured by receiver correctly.

Receiver and sender keep only those bits that were measured deterministically and will discard those sent and measured in different bases. If the 50 % of the bases are same then the receiver agree with sender bits and, hence they can reconstitute the random bit string. In other case they may think that the information channel was eavesdropped.

Error may appear during the raw key generation because of long distance travel. The transmission length, the data rate, and the quantum bit error rate are the three important factors of quantum key distribution. According to Quantum Bit Error Rate (QBER) and raw key rate a general formula could be arrived. Key rate is the product of pulse rate υ, average no of photons per second μ, the transfer efficiency η_t, and detector efficiency η_d

$$R_{\text{raw}} = \frac{1}{2}\upsilon\eta_t\eta_d \tag{153.1}$$

Tancevski [8] has estimated the fraction of bit loss due to error correction as

$$\mathrm{r}_{\mathrm{ec} = \mathrm{QBER}}\left(\frac{7}{2} - l_2^{\mathrm{QBER}}\right) \tag{153.2}$$

And the fraction of bit loss due to privacy amplification as

$$r_{pq} = 1 + \log_2\left(\frac{1 + 4QBER - 4QBER^2}{2}\right) \tag{153.3}$$

So the final bit rate is

$$\mathrm{R}_{\text{final}} = (1 - \mathrm{r}_{\mathrm{ec}})(1 - \mathrm{r}_{\mathrm{pq}})\mathrm{R}_{\text{raw}} \tag{153.4}$$

As the transmission distance increases the quantum transmission efficiency decreases. Presence of disturbances in the channel decreases receiving efficiency. More over single photon generation is very difficult. Practical implementation of quantum key distribution has lot of hurdles like long distance transmission, and high QBER. Hence a new method has been proposed.

153.3 Novel Method

Extracting the advantages of both Quantum cryptography and Classical cryptography a new concept has been introduced. This method uses three channels Channel A, B and C (Fig. 153.1).

Channel A and B are the dedicated channel between sender and receiver. Channel C is the open channel (e.g.) internet. Data is then made to pass through the programmic polarizer. In programmic polarizer there are two bases one bases representing rectilinear polarization and other representing diagonal polarization. Rectilinear polarization has two states (0°, 90°) for representing 0° state, binary value of S is selected and for 90° state complement of S is selected. Also in

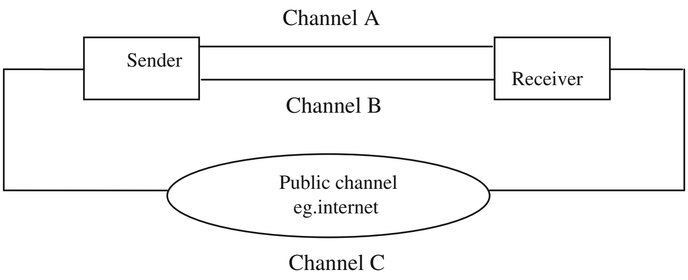

Fig. 153.1 Simple architecture of proposed method

diagonal polarization there are two states (45°, 135°.). For representing 45° state binary value of P is selected and for 135° state complement of P is selected. For each bit sender can select any one of the bases depending on his choice (Table 153.1).

After selecting the base the sender can select any one of the state. If sender select the rectilinear base, then the data along with the state, is then send through the channel A. If sender selects the diagonal base, then the data along with the state is then send through the channel B. Receiver will receive the data from both the channel. Receiver will generate its own choice of bases and corresponding states. And send the states to sender through the dedicated channel. This whole process is known as raw key extraction (Table 153.2).

Receiver will compare each states. If both the states matches that bits will be selected. Then the bits will be compared. Same bit will be selected. Otherwise that bit will be discarded. This process is known as key error correction. Receiver will send the error corrected data in encrypted form to the sender using any of the public key cryptographic technique through the dedicated channel and receiver will

Table 153.1 Key generation in transmission section

Step	Bit sequence	1	2	3	4	5	6	7	8	9
1	Sender logic sequence	000	001	010	011	101	110	111	100	1,001
2	After passing through senders filter	S	P	S	S	S	P	P	S	S
3	Sender state	S000	P001	S010	S011	S101	P110	P111	S100	S1001
4	Datas through channel A	S000		S010	S011	S101			S100	S1001
5	Datas through channel B		P001				P110	P111		

Table 153.2 Key generation in receiving section

Step	Bit sequence	2	2	3	3	5	5	7	7	9
1	Sender logic sequence	001	001	010	010	101	101	111	111	1001
2	After passing through receiver filter	S	S	S	S	S	S	P	P	P
3	Senders state	S001	S001	S010	S010	S101	S101	P111	P111	P1001
4	Datas through channel A	S001	S001	S010	S010	S101	S101			
5	Datas through channel B							P111	P111	P1001

announce the public key through the public channel. During the error correction process total no of bit matches is taken as the private key. Thus the sender and receiver will have the private key. Sender can now decrypt the data using the private key. This decrypted data is the secret key generated (Table 153.3).

The transmission length, the data rate, and the bit error rate (BER) are the three important factors of novel key distribution. Tancevski has estimated the fraction of bit loss due to error correction as

$$\mathrm{r_{ec}} = \mathrm{BER}\left(\frac{7}{2} - l_2^{\mathrm{BER}}\right) \tag{153.5}$$

Table 153.3 Generation of raw key

Step	Data received through channel A and B	S000	P001	S010	S011	S101	P110	P111	S100	S1001
1	Data generated in receiving section	S001	S001	S010	S010	S101	S101	P111	P111	P1001
2	Comparison of states	Yes	No	Yes	Yes	Yes	No	Yes	No	No
3	Comparison of data from selected state	*	*	√	*	√	*	√	*	*
4	Selected data			010		101		111		
5	Generated key			3		5		7		

Table 153.4 Comparison table for features of various cryptographic algorithm

Features	Classical cryptography algorithm	BB84	Novel method
Authentication	Yes	No	Yes
Need dedicated channel	No	Yes	Yes
Distance transmission	Longer	Short	Longer
Bit rate error	Lower	Higher	Lower
Key transfer	Insecure	Secure	Secure

And there is no fraction of bit loss due to privacy amplification. So the final bit rate is (Table 153.4)

$$R_{final} = (1 - r_{ec})R_{raw}. \tag{153.6}$$

153.4 Conclusion

We have proposed a simple scheme for quantum key distribution utilizing two quantum channels. Dual channel implementation helps in implementing authentication in quantum BB84 protocol. We combined the advantages of quantum techniques and classical techniques and tried to implement a novel technique to ensure secure communication.

References

1. Vignesh RS, Sudharssun S, Kumar KJJ (2009) Limitations of quantum and the versatility of classical cryptography: a comparative study. In: Second international conference on environmental and computer science ICECS'09, vol 28–30, Dec 2009, pp 333–337
2. Bennet CH, Brassard G (1984) Quantum cryptography: public key distribution and coin tossing. In: Proceedings of IEEE international conference on computer system and signal processing, Bangalore, India, Dec 1984, pp 175–179
3. Kurochkin VL (2011) Protocols for quantum cryptography. In: International conference and seminar of young specialists on micro/nanotechnologies and electron devices (EDM), 30 June 2011–4 July 2011, pp 114–115
4. Wooters WK, Zurek WH (1982) A single quantum cannot be cloned. Nature 299:802–803
5. US NIST (2001) Secure hash standard, draft FIPS PUB 180–2, May 2001

6. Barlett S (2003) Lecture on quantum computing, NITP Summer School, Adelaide
7. Nielsen MA, Chuang IL (2002) Quantum computation and quantum information. Cambridge University Press, Cambridge
8. Tancevski L, Slutsky B, Rao R, Fainman S (1997) Evaluation of the cost of error correction protocol in quantum cryptographic transmission. In: Proceedings SPIE, vol 3228, pp 322–331

Chapter 154
Cuckoo Search Based Color Image Segmentation Using Seeded Region Growing

M. Mary Synthuja Jain Preetha, L. Padma Suresh and M. John Bosco

Abstract A new meta-heuristic algorithm is proposed in this paper for color image segmentation. Initial seeds are selected based on the threshold which is optimized using cuckoo-search optimization algorithm. Regions are grown from the initial seed point by combining neighboring pixels that are similar with respect to intensity level. Texture characterization is performed by local entropy computation. This obtained texture information and the region growth map of the fully grown regions are considered for merging procedure to merge regions with similar characteristics.

Keywords Color image segmentation · Seeded region growing · Threshold optimization · Texture characterization

154.1 Introduction

Image segmentation is a very significant and complex task in image processing applications. To extract the useful information from any given image, we need to segment the image as either foreground or background. For this purpose image segmentation is the right task in image processing application. Image segmentation can be done based on thresholding, Boundary-based, region based or any hybrid technique.

M.M.S.J. Preetha (✉)
ECE, Noorul Islam Centre for Higher Education, Kumaracoil, India
e-mail: johnsynthuja@gmail.com

L.P. Suresh
EEE, Noorul Islam Centre for Higher Education, Kumaracoil, India
e-mail: suresh_lps@yahoo.co.in

M.J. Bosco
EEE, St. Xavier's Catholic College of Engineering, Chunkankadai, India
e-mail: johnmbosco2004@gmail.com

C. Kamalakannan et al. (eds.), *Power Electronics and Renewable Energy Systems*,
Lecture Notes in Electrical Engineering 326, DOI 10.1007/978-81-322-2119-7_154

Many segmentation algorithms have been proposed in the literature. Many segmentation algorithms have been proposed to segment gray-scale images [1, 2]. Thresholding is a method which is mainly used to segment gray scale images [3–5]. The basic objective of image thresholding is to differentiate the pixels as either a pixel corresponding to an object or those that corresponds to the background. Nowadays segmentation of colour images become essential and to extract meaningful information from color images various method have been proposed. Color images can be segmented by Boundary-based, Region-based or any Hybrid method. Boundary based segmentation is based on the assumption that there will be a sudden change in the pixel properties such as intensity, color or texture in different regions [6–8]. Region-based segmentation is based on similarities (i.e.) they assume that the neighboring pixels in a region share similar properties like color, texture or intensity [9–16]. Hybrid methods combine the advantages of both boundary based and region based to provide better segmentation results [17–19].

In this paper, we propose a color image segmentation algorithm based on seeded region growing. Initial seeds are selected based on threshold generated from the histogram of the gradient map. To improve the segmentation efficiency the generated threshold is optimized using cuckoo search optimization algorithm. After the selection of initial seed, regions are grown based on the intensity. Texture characterization is done to obtain the information of the patterns within the image. Final segmentation map is obtained by combining initial segmentation and the texture image.

154.2 Proposed Method

Figure 154.1 shows the general block diagram of our proposed algorithm. In order to overcome the problems in image segmentation we have proposed an image segmentation technique in which the threshold is generated for initial seed selection is optimized using cuckoo search algorithm. Our proposed work comprises of three phases: (1) Initial seed generation for region growing. (2) Texture Characterization. (3) Region Merging.

154.2.1 Gradient Image

This proposed algorithm uses an edge detection phase that provides the intensity of edges. Edge detection provides the basic shape information of edges. Edges are vector variables with high gradient values. The edge detection procedure defined by Lee and Cok [21], using the magnitude of the gradient for the 3D image is described as,

Fig. 154.1 Block diagram for the proposed algorithm

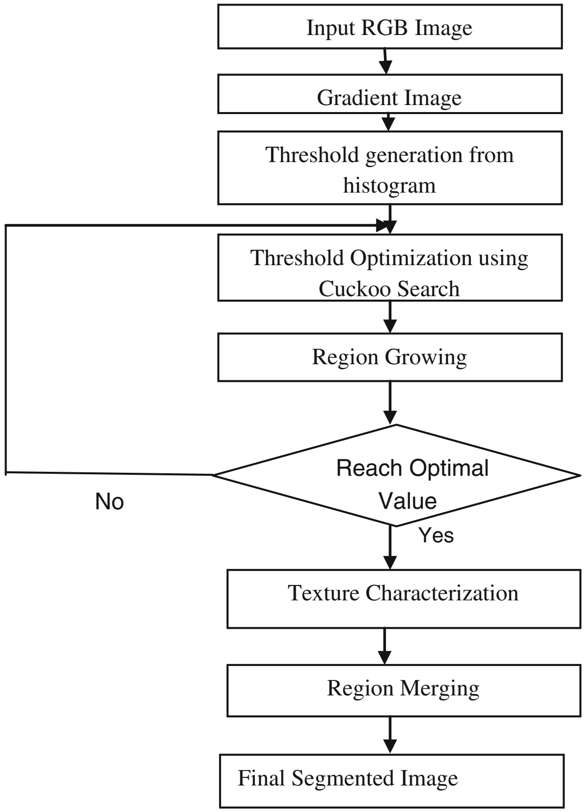

Let x, y, z denote three color channels and i, j denote the spatial co-ordinates of a pixel. The following variables are defined to find the corresponding gradient values in each location:

$$q = \left(\frac{dx}{di}\right)^2 + \left(\frac{dy}{di}\right)^2 + \left(\frac{dz}{di}\right)^2 \tag{154.1}$$

$$r = \left(\frac{dx}{di}\frac{dx}{dj}\right) + \left(\frac{dy}{di}\frac{dy}{dj}\right) + \left(\frac{dz}{di}\frac{dz}{dj}\right) \tag{154.2}$$

$$s = \left(\frac{dx}{dj}\right)^2 + \left(\frac{dy}{dj}\right)^2 + \left(\frac{dz}{dj}\right)^2 \tag{154.3}$$

The gradient matrix D for the vector field f can be defined as

$$D = \begin{bmatrix} \frac{dx}{di} & \frac{dx}{dj} \\ \frac{dy}{di} & \frac{dy}{dj} \\ \frac{dz}{di} & \frac{dz}{dj} \end{bmatrix} \tag{154.4}$$

The distance from a given point with a unit vector u in the spatial domain $d = \sqrt{u^T D^T Du}$ corresponds to the distance travelled in color domain. The largest eigen value of the matrix $D^T D$ gives the maximum distance travelled. The matrix $D^T D$ is given by

$$D^T D = \begin{bmatrix} q & r \\ r & s \end{bmatrix} \tag{154.5}$$

The largest eigen value λ is $\lambda = \frac{1}{2}(q + s + \sqrt{(q + h)^2 - 4(qs - t^2)})$. The gradient value in each location is $G = \sqrt{\lambda}$.

Image gradient is a direction change in the intensity or color in an image. At each pixel point, the gradient vector points in the direction of largest possible intensity increase. Image gradients can be used to extract information from images. After computing the gradient values pixels with large gradient values become possible edges.

154.2.2 Initial Seed Selection

Region growing is a method in which neighboring pixels are compared and grouped with the seed pixel based on some similarity conditions like color, gray level, texture or pixel intensity to form a distinct region. Hence to initiate the growing process we need a seed pixel. The quality of the final segmentation is highly dependent on the initial seed selection. In our work, the seed selection procedure searches for regions where the gradient (edge) map displays no edge.

154.2.3 Threshold Generation

The gradient values are generated as explained in Sect. 154.2.1. Initial thresholds are generated from the histogram plot of the gradient image. For images in which a large percentage of gradient values spread over a narrow range, a high threshold is chosen and for images in which large percentage of gradient values spread over a wide range, a low threshold value is chosen [19]. The threshold T is chosen such

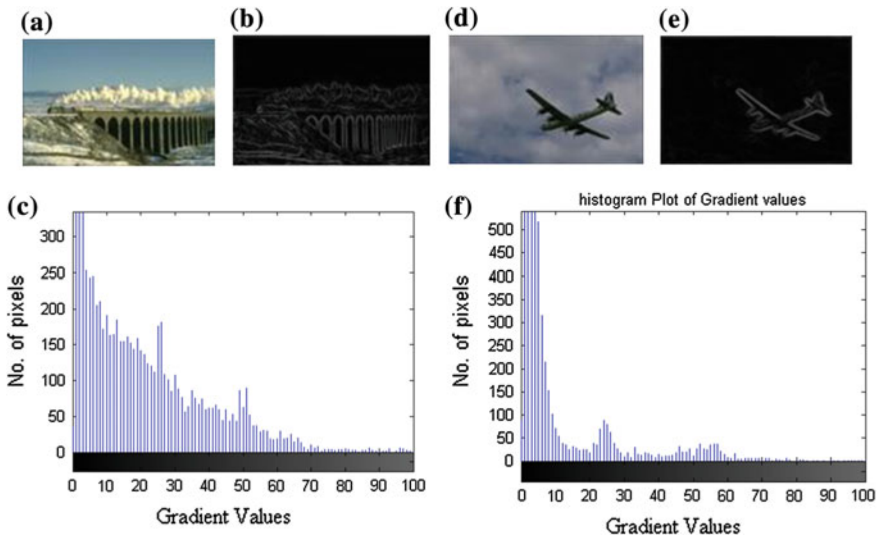

Fig. 154.2 Threshold selection **a** input image **b** edge map of **a**, **c** (T = 10 case) histogram for input **a**, **d** input image, **e** edge map of **d**, **f** (T = 5 case) histogram for input **d**

that all low gradient regions are taken as the initial seed. Hence, regions with low gradient values are chosen as the initial seed. As given in GSEG algorithm [19], we choose the low threshold value as 5 and the high threshold value as 10. Figure 154.2 shows the histogram plot for two different images.

154.2.4 Region Growing

Region growing is a type of image segmentation in which regions are grown by combining neighboring pixels with the seed based on the chosen predicate (color, texture, intensity). In our method we chose intensity as the predicate for region growing. After the selection of initial seed pixels these are labeled as seed pixels and there are several other unlabeled pixels which are to be grouped with the initial seed pixel to form a region.

Let the initial seed pixels are named as grouped pixels and the neighboring pixels are named as ungrouped pixels. Let P_g be a grouped pixel and P_u be a ungrouped pixel. The difference in intensity between the two pixels is calculated. If this difference is greater than the threshold (T) it is discarded and if it is less it is grouped with the seed pixel. This process is carried out until all ungrouped pixels are added to any one of the region. Figure 154.3 shows the initial seed map for the generated threshold.

Fig. 154.3 **a** Input image, **b** edge map, **c** initial seed

154.3 Threshold Optimization Using Cuckoo Search Algorithm

Cuckoo search algorithm is a meta-heuristic algorithm which was inspired by the breeding behavior of cuckoos.

154.3.1 Cuckoo Breeding

Cuckoos are brood parasite. They lay their eggs mostly in the nest of other host birds. If a host bird found that the egg in the nest is not their own, they will either destroy the eggs by throwing away or they will build a new nest elsewhere. Some cuckoo species can imitate the color and pattern of the eggs of the chosen nest. This mimicry will reduce the probability of cuckoo eggs being abandoned and therefore increases their re-productivity. Cuckoo search can be described by three generalized rule [20]: (1) Each cuckoo lays one egg at a time, and dump its egg in randomly chosen nest; (2) The best nests with high quality of eggs will carry over to the next generations; (3) The number of available host nests is fixed, and the egg laid by a cuckoo is discovered by the host bird with a probability pa 2 [0, 1]. In this case, the host bird can either throw the egg away or abandon the nest, and build a completely new nest. For an optimization problem the fitness is proportional to the value of objective function.

154.3.2 Implementation

The population of the host nest n = 1, 2…m, is randomly initiated. From this population, the first host nest (n = 1) is chosen and the fitness function of that particular nest is calculated using Eq. (154.1)

$$\mathrm{F} = \max(\mathrm{PR}) \tag{154.6}$$

To measure the quality of segmentation result, we have chosen the evaluation metric PR as the fitness function. PR is the Probabilistic Rand Index. This PR allows comparison of a test segmentation result with a ground truth segmentation image [19].

The Probabilistic Rand Index is defined as

$$PR(S_{test}, S) = \frac{1}{\binom{N}{2}} \sum_{\substack{i,j \\ i<j}} [p_{ij}^{c_{ij}} (1 - p_{ij})^{1-c_{ij}}] \tag{154.7}$$

Where C_{ij} is the information about each pair of pixel (x_i, x_j), S_{test} is the test segmentation image and S is the ground truth image. This index takes values between 0 and 1, where 0 means 0 % similarity and 1 means 100 % similarity.

Hence to get the fitness value (F), the region growing process described in sec is carried out for the initially selected threshold (T). The fitness value of this image compared with its ground truth is calculated. The worst nests are discarded and the best solutions are identified based on the fitness function. This best solution is the optimal solution and the optimal thresholds are obtained for seeded region growing.

154.4 Texture Characterization and Region Merging

Texture analysis refers to the characterization of regions in an image by their texture content. The presence of regions that contain textures is the great source of problem in image segmentation. By evaluating the randomness present in various regions of an image, we can obtain the information of patterns within an image. Entropy is a statistical measure of randomness that can be used to characterize the texture of the input image. Entropy is maximum in textured areas.

Let S be a random group of pixels from an image with the possible values {a1, a2, …, an}. Let $P(a_i)$ be the probability for a specific value a_i, then $P(a_i)$ is said to contain $I(a_i)$ units of information which is defined as

$$I(ai) = \log \frac{1}{P(ai)} \tag{154.8}$$

Thus the information I(ai) for the pixel set S is found and the entropy for that block set is calculated using the equation

$$E(s) = -\sum_{i=1}^{n} P(a_i) \log P(a_i) \tag{154.9}$$

Thus the texture feature for the given image is obtained.

In region merging process the region grown image using cuckoo search optimization and the textured image are combined together to form the final segmented image. Merging of regions by considering the texture allows us to merge regions that have been separated due to small texture differences and occlusion. In region merging, the distance between each pixel of the region grown image and the textured image are calculated distance evaluation is carried out by Euclidean distance measure. If this distance is less than a particular threshold we set the particular pixel as 0 and otherwise, the pixel values are set as 1. Thus the same pixel regions are merged based on the pixel distance calculation. In our experiment we choose 10 as the threshold for region merging process.

154.5 Results and Discussion

We have evaluated our proposed segmentation algorithm in the color images taken from the publically available Berkeley dataset. The results of our proposed algorithm at different stages are presented in Fig. 154.4a–f.

The input RGB image is shown in Fig. 154.5a and its edge Map is shown in Fig. 154.5b. The initial seed map and the region grown image is shown in Fig. 154.5c and d respectively. The texture image is given in Fig. 154.5e. The final segmented image after region merging is shown in Fig. 154.5f. Figures 154.6 and 154.7 provides some additional results for our proposed algorithm.

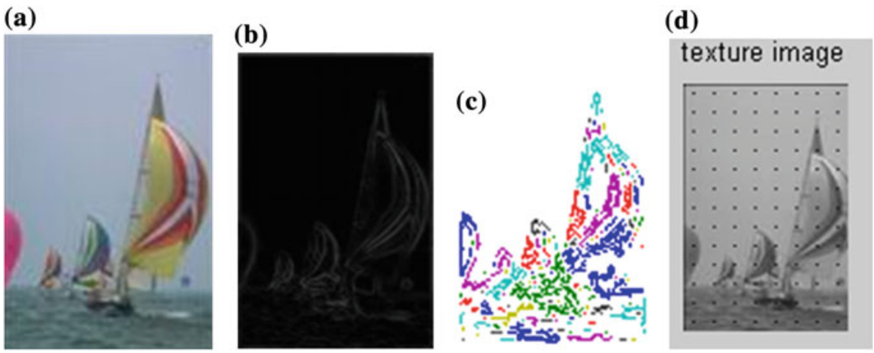

Fig. 154.4 **a** Input image, **b** edge map of **a**, **c** initial seeds, **d** texture image

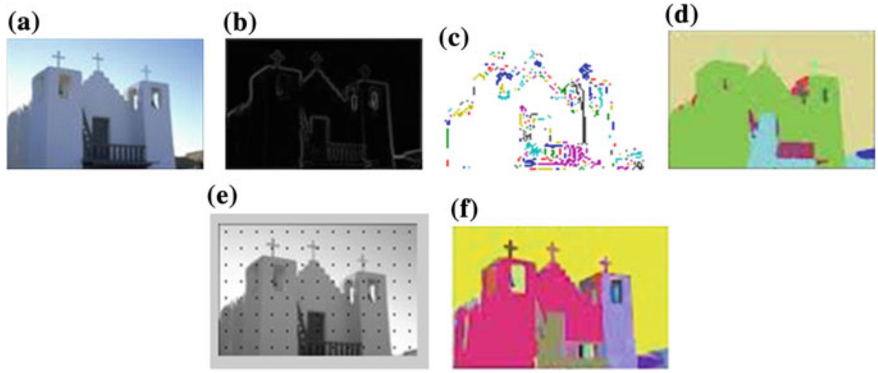

Fig. 154.5 **a** Input image, **b** edge map, **c** initial seeds, **d** seeded region, **e** texture image, **f** final segmented image after region merging

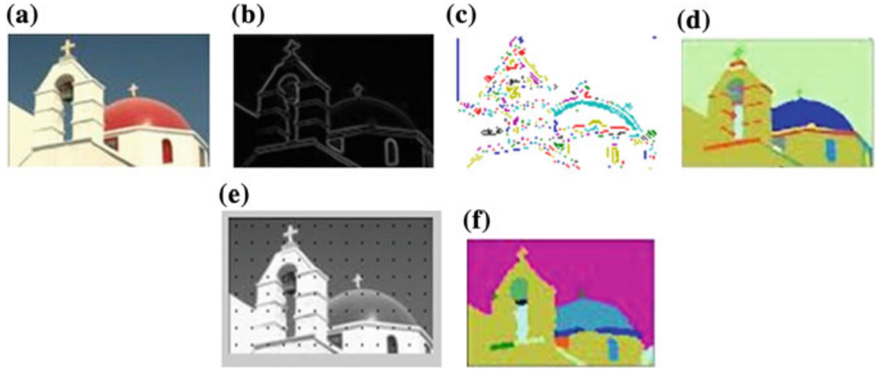

Fig. 154.6 **a** Input image, **b** edge map, **c** initial seeds, **d** seeded region, **e** texture image, **f** final segmented image after region merging

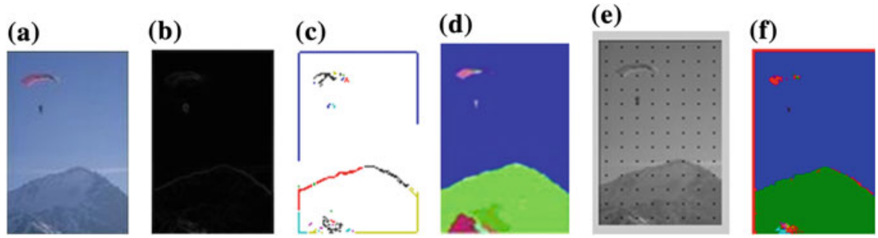

Fig. 154.7 **a** Input image, **b** edge map, **c** initial seeds, **d** seeded region, **e** texture image, **f** final segmented image after region merging

154.6 Conclusion

In this paper we proposed a new meta-heuristic color image segmentation algorithm based on cuckoo-search optimization. This algorithm is based on the threshold optimization for initial seed selection, region growing and region merging. This algorithm has been tested in publicly available Berkeley dataset. Experimental results show that our proposed algorithm is robust to various color images and can produce reasonably good results. By changing the fitness function this algorithm can be used for medical image segmentation.

References

1. Cheng H, Jiang X, Sun Y, Wang J (2001) Color image segmentation: advances and prospects. Pattern Recogn 34(12):2259–2281
2. Sahoo PK, Soltani S, Wong AKC (1988) A survey of thresholding techniques. Comput Vis Graph Image Process 41:233–260
3. Otsu N (1979) A threshold selection method from gray-level histogram. IEEE Trans Syst Man Cybern 9(1):62–66
4. Wong AKC, Sahoo PK (1989) A gray-level threshold selection method based on maximum entropy principle. IEEE Trans Syst Man Cybern 19(4):641–647
5. Cheng HD, Chen CH, Chiu HH, Xu H (1998) Fuzzy homogeneityapproach to multilevel thresholding. IEEE Trans Image Process 7(7):1084–1088
6. Basak J, Chanda B (1994) On edge and line linking with connectionist model. IEEE Trans Syst Man Cybern 24(3):413–428
7. Marteli A (1976) An application of heuristic search methods to edge and contour detection. Graph Image Process 19(2):73–83
8. Nalwa VS, Pauchon E (1987) Edgel aggregation and edge description. Comput Vis Graph Image Process 40(1):79–94
9. Tremeau A, Bolel N (1997) A region growing and merging algorithm to color segmentation. Pattern Recogn 30(7):1191–1203
10. Shih FY, Cheng S (2005) Automatic seeded region growing for color image segmentation. Pattern Recogn 23:877–886
11. Garcia Ugarriza L, Saber E, Vantaram SR, Amuso V, Shaw M, Bhaskar R (2009) Automatic image segmentation by dynamic region growth and multiresolution merging. IEEE Trans Image Process 18(10):2275–2288
12. Wan S, Higgins W (2003) Symmetric region growing. IEEE Trans Image Process 12 (9):1007–1015
13. Fan J, Yau DKY, Elmagarmid AK, Aref WG (2001) Automatic image segmentation by integrating color-edge extraction and seeded region growing. IEEE Trans Image Process 10 (10):1454–1466
14. Pavlidis T, Liow YT (1990) Integrating region growing and edge detection. IEEE Trans Pattern Anal Mach Intell 12(3):225–233
15. Chu C, Aggarwal JK (1993) The integration of image segmentation maps using region and edge information. IEEE Trans Pattern Anal Mach Intell 15(2):1241–1252
16. Haddon JF, Boyce JF (1990) Image segmentation by unifying region and boundary information. IEEE Trans Pattern Anal Mach Intell 12(10):929–948

17. Chen J, Pappas T, Mojsilovic A, Rogowitz B (2002) Adaptive image segmentation based on color and texture. In: Proceedings of international conference image process, vol 3, pp 777–780
18. Chen J, Pappas T, Mojsilovic A, Rogowitz B (2005) Adaptive perceptual color-texture image segmentation. IEEE Trans Image Process 14(10):1524–1536
19. Garcia Ugarriza L, Saber E, Vantaram SR, Amuso V, Shaw M, Bhaskar R (2009) Automatic image segmentation by dynamic region growth and multiresolution merging. IEEE Trans Image Process 18(10):2275–2288
20. Yang XS, Deb S (2009) Cuckoo search via Lévy flights. In: Proceedings of world congress on nature and biologically inspired computing (NaBIC 2009, India), pp 210–214
21. Lee H, Cok D (1991) Detecting boundaries in vector field. IEEE Trans Signal Process 39 (5):1181–1194

Chapter 155
Comparative Study of PI and PID Controller for Non Linear MIMO System

S. Anitha Janet Mary, L. Padma Suresh, Rini Valsa Mathew and N. AlbertSingh

Abstract There are lot of controllers in process control such as on-off, PI, PD and PID controllers. But commonly used controllers in industrial control applications are proportional-integral (PI) and proportional-integral-derivative (PID) controllers. A PI controller is used when fast response of the system is not required. PID controller has the advantage of high stability and reliability. The PID controller is having the accurate and efficient tuning of parameters. Generally, most industrial processes are multivariable systems. It is difficult to tune the gains of PI and PID controllers because many industrial plants are often burdened with problems like high order, time delays, poor damping, nonlinearities, and time-varying dynamics etc. That means, the proper design of multi-loop PID control for multivariable process is a challenging task. In this paper, PI and PID controllers are designed for multi-input multi-output system. To validate the performance of PI and PID control design, binary Wood-Berry distillation column which is a multivariable, non linear process with strong interactions with input and output pairs is taken and compared their performances.

Keywords PI controller · PID controller · MIMO · Wood-Berry distillation column

S.A.J. Mary (✉) · L.P. Suresh · R.V. Mathew
Department of EEE, Noorul Islam University,
Kumaracoil, Tamil Nadu, India
e-mail: ani27_simon@yahoo.com

L.P. Suresh
e-mail: suresh_lps@yahoo.co.in

R.V. Mathew
e-mail: rinivls811@gmail.com

N. AlbertSingh
BSNL, Nagercoil, India
e-mail: albertsingh@rediffmail.com

C. Kamalakannan et al. (eds.), *Power Electronics and Renewable Energy Systems*,
Lecture Notes in Electrical Engineering 326, DOI 10.1007/978-81-322-2119-7_155

155.1 Introduction

The most widely about 95 % of control loops are PID, with a wide range of applications [1] since PID controllers have simple structure and the meaning of three parameters, which can be easily understood by process operators. Optimal tuning of PID control parameters are needed for the best performance of the system. Various tuning methods such as Ziegler and Nichols [2], Cohen and Coon [3], gain phase margin methods are used. These methods are based on trial and error and process reaction curve. In this paper PI and PID controllers are designed based on Z-N method for a binary Wood-Berry distillation column which is a highly nonlinear, multivariable process with strong interactions with input and output pairs and the performance are compared. This paper is structured as follows. In Sect. 155.2, a description of binary distillation column is given. Section 155.3 presents the design of PI and PID controller. Section 155.4 explains tuning method. Simulation results are presented and discussed in Sect. 155.5. Finally, Sect. 155.6 outlines a brief conclusion about this study.

155.2 Process Description

Distillation is defined as a process in which a liquid or vapour mixture of two or more substances is separated into its component fractions of desired purity, by the application and removal of heat. Distillation columns are used to get this separation efficiently. Distillation can contribute to more than 50 % of plant operating costs. The way of reducing operating costs of existing units is to improve their efficiency and operation via process optimization and control. The Wood and Berry distillation column process is chosen for study. Wood and Berry model is a 2 × 2 process (2 inputs and 2 outputs) that separates methanol and water [4]. It's a binary column with feed contains only two components. It's tray column consist of 8 trays where trays of various designs are used to hold up the liquid to provide better contact between vapour and liquid, hence better separation. The composition of the top and bottom products expressed in weight percentage of methanol is the controlled variables. The manipulated inputs are reflux and reboiler steam flow rates expressed in lb/min. The transfer function of distillation column has first order dynamics with time delays. The transfer function model of this process is given by

$$\begin{bmatrix} y_1(s) \\ y_2(s) \end{bmatrix} = \begin{bmatrix} \frac{12.8e^{-s}}{16.7s+1} & \frac{-18.9e^{-3s}}{21.0s+1} \\ \frac{6.6e^{-7s}}{10.9s+1} & \frac{-19.4e^{-3s}}{14.4s+1} \end{bmatrix} \begin{bmatrix} u_1(s) \\ u_2(s) \end{bmatrix} + \begin{bmatrix} \frac{3.8e^{-8.1s}}{10.9s+1} \\ \frac{4.9e^{-3.4s}}{13.2s+1} \end{bmatrix} D$$

where input signals are the reflux flow rate u1 and steam flow rate u2, the output signals are the top product composition y1 and bottom product composition y2 in mole fraction. The feed flow rate D is act as process disturbance. The linear model is valid around the set point y1 = 0.96 and y2 = 0.02 [5]. The time sampling is 1 min. The block diagram of distillation column is shown in Fig. 155.1

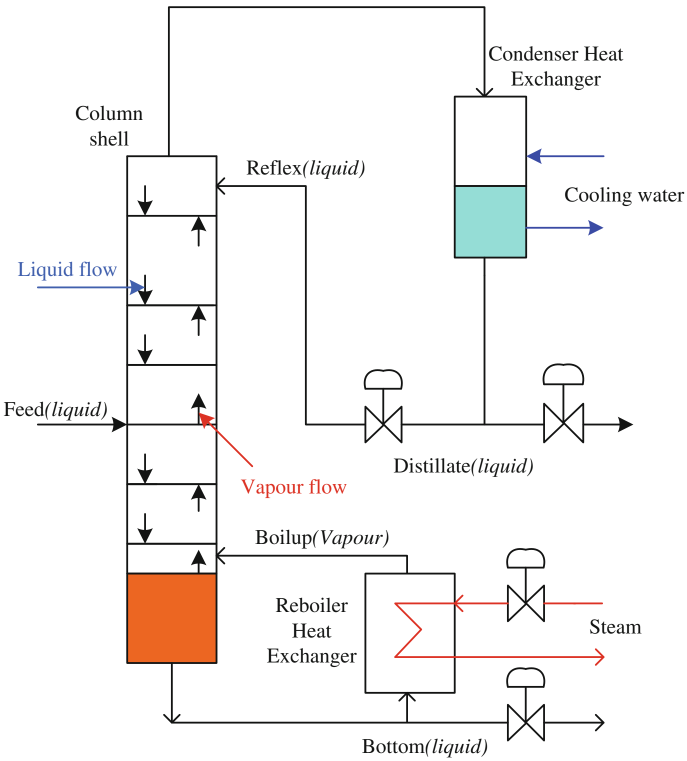

Fig. 155.1 Block diagram of distillation column

155.3 Design of Controllers

In this paper PI and PID controllers are designed. PID controller parameters consist of three separate terms: proportional, integral and derivative values denoted by Kp, Ki, and Kd. The appropriate setting of these parameters will improve the dynamic response of a system, reduce overshoot, eliminate steady state error and increase the stability of the system [6]. The transfer function of a PID controller is

$$C(s) = \frac{U(s)}{E(s)} = K_p + \frac{K_i}{s} + K_d s \tag{155.1}$$

The fundamental structure of PID controller is shown in Fig. 155.2. Once the set point has been changed, error will be computed between the set point and actual output. The error signal E(s), is used to generate the proportional, integral and derivative control actions, with the resulting signals weighted and summed to form the control signal U(s) applied to the plant model M. New control signal, U(s), will be sent to the plant M. This process will run continuously until steady state [7].

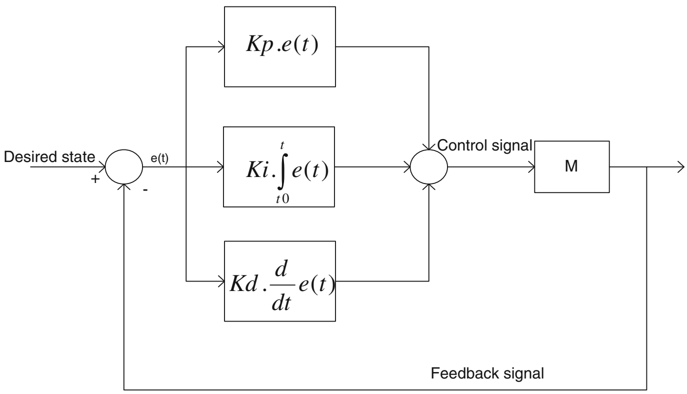

Fig. 155.2 Structure of PID controller

In PI controller the derivative term is absent. The transfer function of PI controller is

$$C(s) = \frac{U(s)}{E(s)} = K_p + \frac{K_i}{s} \tag{155.2}$$

155.4 Tuning Method

The diagram of multivariable controller design is given in Fig. 155.3. It consists of error detector, PI or PID controller, plant (distillation column). The error signal generated by the error detector is the difference between input signal and feedback signal. The controller modifies and amplifies error signal to produce better control action. This modified error signal is fed to the plant (distillation column) to correct its output.

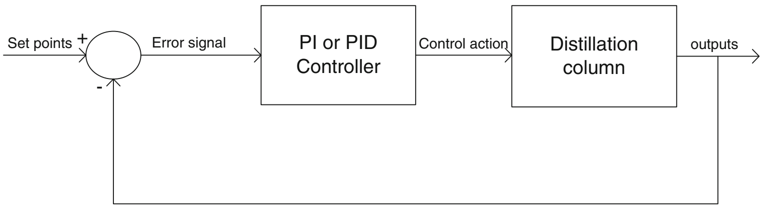

Fig. 155.3 Diagram of multivariable controller design

Table 155.1 Tuning values

Controller parameters	PI controller	PID controller
$K_{p,1}$	1.9866	1.9866
$K_{i,1}$	0.2643	0.4643
$K_{d,1}$	–	1.0242
$K_{p,2}$	−0.2254	−0.2254
$K_{i,2}$	−0.0701	−0.1008
$K_{d,2}$	–	−0.4123

155.5 Simulation Results

In the design of PI and PID controller, the controller parameters such as Kp, Ki, Kd are obtained using one of the conventional method called Ziegler and Nichols [2]. The parameter values are tabulated in Table 155.1. This calculated controller parameter values are applied to the chosen process and results are compared.

The control action of PI and PID controller for top product is reflux flow rate u1 and bottom product is stream flow rate u2. That control actions are shown in Figs. 155.4 and 155.5.

The servo and regulatory responses of top and bottom products are given in Figs. 155.6 and 155.7. The disturbance is given at time 120 s.

The performance analysis of the process for top and bottom products of PI and PID controller are tabulated in Table 155.2.

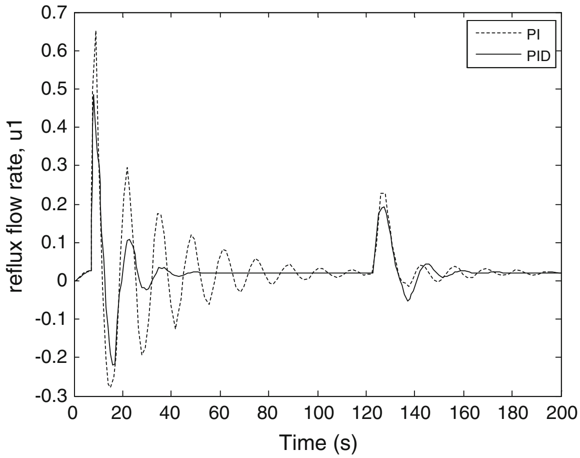

Fig. 155.4 Control action of top product

Fig. 155.5 Control action of bottom product

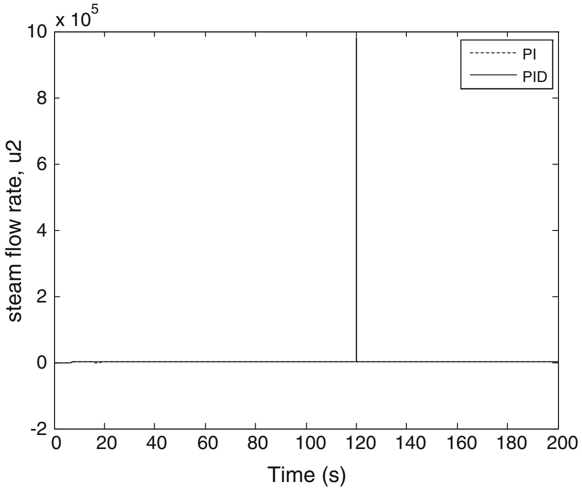

Fig. 155.6 Output response of top product

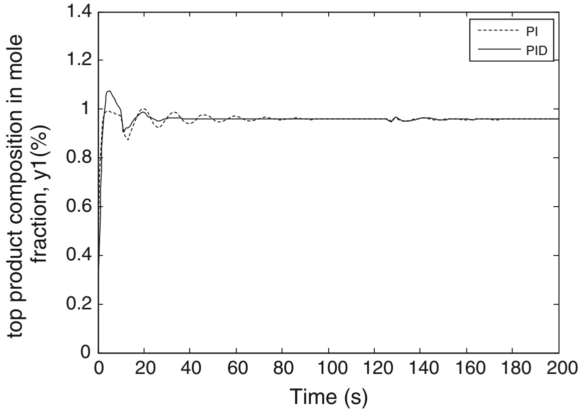

Fig. 155.7 Output response of bottom product

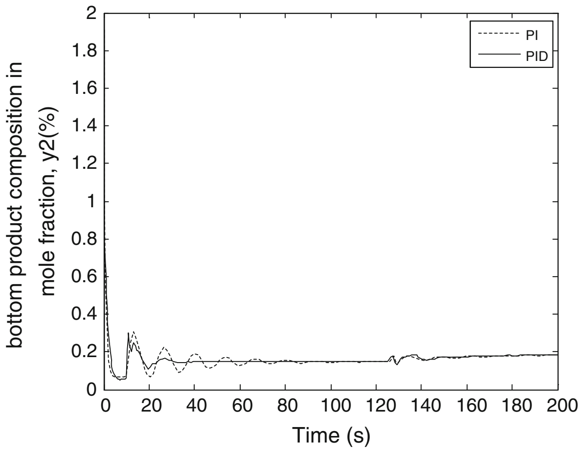

Table 155.2 Performance analysis of top and bottom products

Criteria	Top product		Bottom product	
	PI	PID	PI	PID
Rise time	3.0604	7.1862	3.0747	7.9310
Settling time	45.1788	52.4701	119.8083	191.8750
Overshoot	4.2030	11.9081	3.2950e+003	2.2913e+003
Undershoot	0	0	1.4508e+003	1.0819e+003

155.6 Conclusion

In this paper two input two output distillation column process was studied, analyzed and simulated. The PI and PID controllers are designed independently to control the process. The PI controller outputs are oscillating but PID controller outputs are settling in a good manner. In PID time taken is also less to respond. Therefore while comparing PI and PID controller, PID controller is giving best result. All the simulations are done by MATLAB tool in windows 7 operating system.

155.7 Future Work

Distillation column is a multivariable process it has many non linearity. Linearization of distillation column is a very vast field to work. If we talking about Optimization of distillation column, it would be an interesting field to work on.

References

1. Åström KJ, Hägglund T (1995) PID controllers: theory, design and tuning, 2nd edn. Instrument Society of America, Research Triangle Park, North Carolina
2. Ziegler JG, Nichols NB (1942) Optimum setting for automatic controllers. Trans ASME 64 (8):759–768
3. Cohen GH, Coon GA (1953) Theoretical consideration of retraded control. Trans ASME 75:827–834
4. Wood RK, Berry MW (1973) Terminal composition control of a binary distillation column. Chem Eng Sci 28(9):1707–1717

5. Aceves-López A, Aguilar-Martin J (2006) A simplified version of mamdani's fuzzy controller: the natural logic controller. IEEE Tran Fuzzy Syst 14(1):16–30
6. Xiong Q, Cai WJ, He MJ (2007) Equivalent transfer function method for PI/PID controller design of MIMO processes. J Process Control 17(8):665–673
7. Chang DW (2007) A multi-crossover genetic approach to multivariable PID controllers tuning. Expert Syst Appl 33(3):620–626

Chapter 156
A Simple Cascade NN Based Flux Estimator to Overcome Low Speed Problems in Sensor-Less Direct Vector Controlled IM Drives

A. Venkadesan, S. Himavathi and A. Muthuramalingam

Abstract The performance of sensor-less direct vector controlled IM drives to a large extent depends on the accuracy of field angle and resultant flux estimation. This in turn depends on the accuracy of estimated flux. Conventional voltage model used for flux estimation encounters major problems at low speeds/frequencies like integrator drift and stator resistance variation problems. These lead to significant error in the field angle and resultant flux estimation. To overcome these problems, a simple cascade Neural Network (NN) based flux estimator trained with input-output data including parameter variation is proposed in this paper. The suitability of the proposed flux estimator and its advantages over voltage model based flux estimator for field angle and resultant flux estimation is studied through extensive simulations and comprehensively presented.

Keywords Neural networks · Single neuron cascaded architecture · Flux estimator · Direct vector control · Sensor-less IM drives

A. Venkadesan (✉)
Department of Electrical and Electronics Engineering, Faculty of Engineering and Technology, SRM University, Kattankulathur, Kancheepuram 603 203, Tamil Nadu, India
e-mail: venkadesan.a@ktr.srmuniv.ac.in

S. Himavathi · A. Muthuramalingam
Department of Electrical and Electronics Engineering, Pondicherry Engineering College, Puducherry 605 014, India
e-mail: himavathi@pec.edu

A. Muthuramalingam
e-mail: armlingam@pec.edu

C. Kamalakannan et al. (eds.), *Power Electronics and Renewable Energy Systems*,
Lecture Notes in Electrical Engineering 326, DOI 10.1007/978-81-322-2119-7_156

156.1 Introduction

Advances in digital technology have made the vector control popular and realizable by industries. Depending on the method of measurement of field angle, the vector control can be divided into two sub categories: Direct Vector Control (DVC) and Indirect vector control. If the field angle is computed using the flux, it is termed as Direct Vector Control. In particular, sensor-less DVC is increasingly used in industries as it dispenses the use of a speed sensor which is bulky and requires maintenance. The performance of sensor-less DVC IM drives to a large extent depends on the accuracy of field angle and resultant flux estimation which in turn depends on the accurate knowledge of motor flux. Flux can be either measured or estimated. But measurement of flux using sensors is difficult and expensive. Hence flux is estimated from voltage model equations. The voltage model suffers from the problems of pure integrator and variation of stator resistance especially at low frequencies/speed [1–3]. Several techniques are proposed in the literature to overcome the problems of pure integrator [3]. To overcome the R_s variation problem methods for on-line R_s estimation are proposed in the literature [4, 5], but this in turn increases the complexity of the drive system. Neural Network (NN) based estimators provide an alternate solution for on-line flux estimation. It dispenses the direct use of complex mathematical model of the machine and hence overcomes the problems of integrator. They can be trained to be adaptive for parameter variations and hence dispenses the need for parameter estimation. Several Neural Network approaches are reported for online-flux estimation and it is currently under active area of research. A single layer feed-forward neural architecture is proposed for flux estimation [6]. A Heuristic Design methodology for Multilayer Feed-Forward NN architecture is proposed [7]. A compact NN model with desired accuracy assumes importance in real implementation of on-line flux estimator to ensure faster estimation for effective control. Single Neuron Cascaded (SNC) NN model is identified and shown to provide distinctly compact NN model for on-line flux estimation [8]. The application of single neuron cascaded neural architecture is explored for Model Reference Adaptive System based speed estimation scheme [9].

In this paper, a data based simple Cascade Neural Network is proposed for flux estimation to address the integrator drift and stator resistance variation problems in sensor-less direct vector controlled IM Drives. Using the data based NN flux estimator, field angle and resultant flux are computed. The suitability of the proposed NN based flux estimator and its advantages over voltage model based flux estimator for field angle and resultant flux estimation in sensor-less DVC IM drives is comprehensively presented through extensive simulations.

156.2 Sensor-Less Direct Vector Controlled IM Drives

The block diagram for the sensor-less DVC IM drive is shown in Fig. 156.1. Generally through a PI controller, the speed error signal is processed and the torque command is generated. It is combined with the flux command corresponding to the flux error to generate the common reference to control the motor current. The reference is used to produce the PWM pulses to trigger the voltage source inverter and control the current and frequency applied to the IM drive. The principal vector control parameters namely d-axis reference current (i^*_{ds}) and q-axis reference current (i^*_{qs}), which are dc values in synchronously rotating frame, are converted to stationary frame as phase current commands for the inverter with the help of a field angle (θ_e). The field angle and resultant flux can be computed using the d-axis rotor flux and q-axis rotor flux [2]. The equations are presented in (156.1)

$$\theta_{e,est} = \tan^{-1}\left(\frac{\psi^s_{qr}}{\psi^s_{dr}}\right); \quad \psi^s_{r,est} = \sqrt{\left(\psi^s_{dr}\right)^2 + \left(\psi^s_{qr}\right)^2} \tag{156.1}$$

The performance of sensor-less DVC IM drives to a large extent depends on the accuracy of field angle and resultant flux which is derived from the motor flux estimation. A Neural based flux estimator proposed in this paper is used to replace the voltage model based flux estimator.

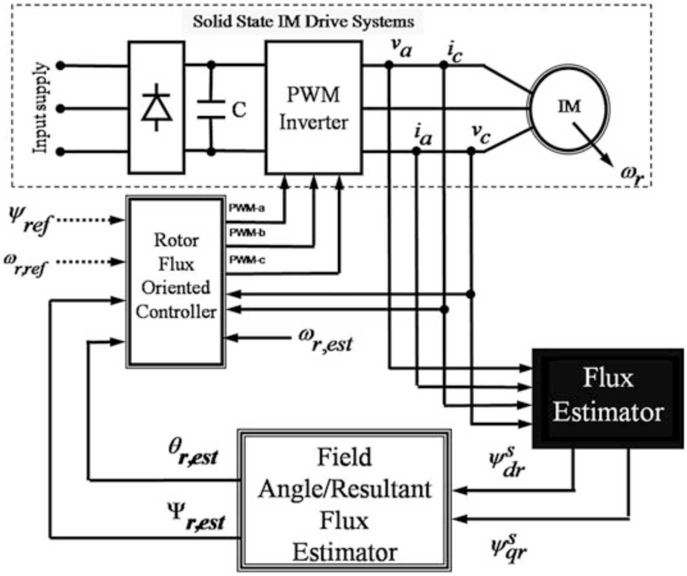

Fig. 156.1 Block diagram for sensor-less direct vector controlled IM drives

156.3 Voltage Model Based Flux Estimator and Its Limitations

The rotor fluxes can be computed using the voltage model equations [2] using the voltage and current signals. The voltage model equations are presented from (156.2) and (156.3).

$$\Psi_{ds}^{s} = \int (v_{ds}^{s} - R_s i_{ds}^{s})dt; \quad \Psi_{qs}^{s} = \int (v_{qs}^{s} - R_s i_{qs}^{s})dt \tag{156.2}$$

$$\Psi_{dr}^{s} = \frac{L_r}{L_m}(\Psi_{ds}^{s} - \sigma L_s\, i_{ds}^{s}); \quad \Psi_{qr}^{s} = \frac{L_r}{L_m}(\Psi_{qs}^{s} - \sigma L_s i_{qs}^{s}) \tag{156.3}$$

where,

$v_{ds}^{s}(v_{qs}^{s})$	Stator voltages d axis (q axis)
$i_{ds}^{s}(i_{qs}^{s})$	Stator currents d axis (q axis)
$\Psi_{ds}^{s}(\Psi_{qs}^{s})$	Stator flux d axis (q axis)
$\Psi_{dr}^{s}(\Psi_{qr}^{s})$	Rotor flux d axis (q axis)
$R_s(R_r)$	Stator resistance (rotor)
$L_s(L_r)$	Stator inductance (rotor)
L_m	Magnetization inductance
$\sigma = 1 - \frac{L_m^2}{L_r L_s}$	Leakage Co-Efficient

The voltage model equations encounter major drawbacks at low speeds/frequencies. They are integrator drift and parameter variation problems.

Integrator Drift Problem: The voltage model based flux estimation uses an integral function and hence suffers from the problems of pure integrator. A small dc bias in the measured signal for integration makes the estimated flux drift from the actual. This leads to large error in the field angle and resultant flux estimation which in turn deteriorates the performance of the IM drives.

Parameter Variation Problem: The voltage model equations are dependent on resistance R_s and inductances L_s, L_m, L_r. The variation of these parameters tends to reduce the accuracy of the flux estimation. Particularly, temperature variation of R_s becomes more dominant at low frequencies/speeds as small mismatch in R_s would cause the flux estimated to drift from the actual. This leads to large error in the field angle and resultant flux estimation and deteriorates the performance of the IM drives. Using a separate online Rs estimator would address the problem but this increases the complexity of the drive.

A cascade neural network can have any number of neuron in each layer and the number of layers and neurons/layer is heuristic. Hence a novel Single Neuron Cascaded Neural Network (SNC-NN), easy to design is proposed for flux estimation. Its performance is compared with conventional estimator.

156.4 SNC-NN Based Flux Estimator

To overcome the drawbacks of voltage model based flux estimator, a data based NN flux estimator is designed. The inputs to NN based flux estimator are direct and quadrature axis stator voltages $\left\{v_{ds}^{s}(k), v_{ds}^{s}(k-1), v_{qs}^{s}(k), v_{qs}^{s}(k-1)\right\}$ and stator currents $\left\{i_{ds}^{s}(k), i_{ds}^{s}(k-1), i_{qs}^{s}(k), i_{qs}^{s}(k-1)\right\}$ measured at kth and k − 1th sample. The outputs are the direct and quadrature axis rotor fluxes $\left\{\psi_{ds}^{s}(k),\ \psi_{qs}^{s}(k)\right\}$. Various Neural Network architectures and learning algorithms can be used to build the NN model. In this paper, a SNC neural architecture is used because it is simple and provides distinctly compact NN model [8–10] for on-line implementation with desired accuracy. The Single Neuron Cascaded architecture with multiple inputs/single output [8] is shown in Fig. 156.2. SNC-NN architecture consists of an input layer, hidden layers and an output layer. The first hidden layer receives only external signals as inputs. Other layers (M) receive external inputs and outputs from all previous (M − 1) layers. To create multilayer structure hidden layers are added one by one and the whole network trained repeatedly using the concept of moving weights so as to obtain compact network [8]. This process continues till the performance index is reached.

A three phase 1.1 kW, 4 poles, 415 V, 50 Hz induction motor is chosen for study. The motor parameters are as follows: R_s = 6.03 Ω, R_r = 6.085 Ω, $L_s = L_r$ = 0.5192 H, L_m = 0.4893 H, and J = 0.011787 kg m^2, B = 0.0027 kg m^2/s. The vector controlled drive is designed using Matlab and data has been obtained for

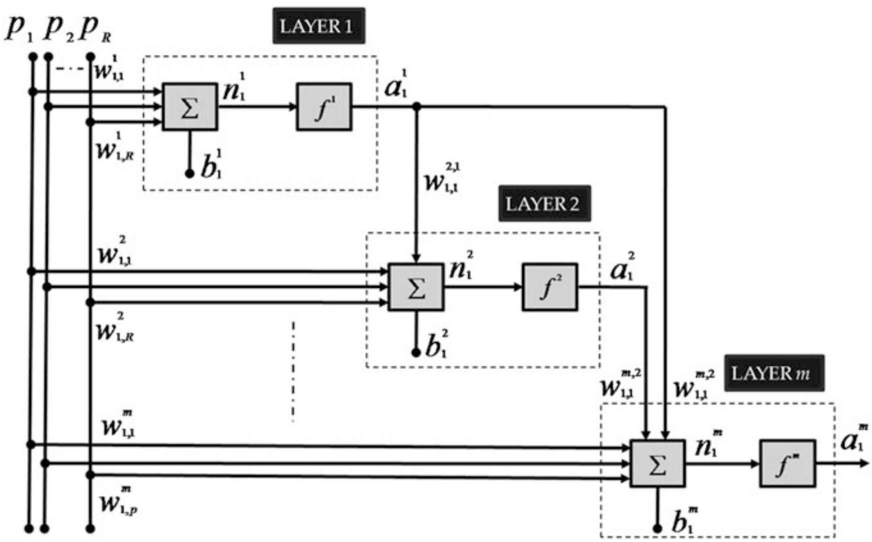

Fig. 156.2 SNC-NN with multiple inputs/single output

Table 156.1 Performance comparison of SNC-NN with SLFF-NN and MLFF-NN for on-line flux estimation

NN architecture	NN structure	Hidden neurons	Total parameters
SNC-NN	8-13(h*)-2	13	239
SLFF-NN	8-99-2	99	366
MLFF-NN	8-14-14-2	28	1,091

*h** hidden layer with single neuron

various operating conditions. Around 11, 244 data sets (input/output) are obtained through simulations for various operating conditions. In the literature, it is reported that the change in R_s may go up to 50 % [4]. Hence, to make SNC-NN robust to R_s variation, maximum of 50 % change in R_s variation is incorporated in the training data sets. The tan-sigmoid functions are chosen for hidden layers and pure-linear functions are chosen for output layer. The performance of SNC-NN architecture is compared with Single Layer Feed-Forward (SLFF) and Multilayer Feed-Forward (MLFF) architecture for on-line flux estimation. For performance comparison, all the three architectures are trained for the same accuracy with same input-output data, same Levenberg Marquardt learning algorithm. The performance of all the three architectures trained with same accuracy is compared in terms of hidden neurons and total parameters. The results obtained are presented in Table 156.1. The SNC-NN is shown to provide distinctly compact NN model for on-line flux estimation and hence found to be more suitable for on-line implementation of flux estimator. The obtained SNC-NN based flux estimator is used in the place of voltage model based flux estimator for field angle and resultant flux estimation.

156.5 Results and Discussions

The performance of NN based Flux Estimator and voltage model based flux estimator is compared for low speed/frequency problems namely integrator drift and R_s variation problem. All these problems are investigated for the drive operating at a very low speed of 1 rad/s under 50 % rated load.

156.5.1 Performance Comparison of Proposed Flux Estimator with Voltage Model Based Flux Estimator for Integrator Drift Problem

To investigate the dc drift problem, a dc bias of 5 % of the peak current is superimposed to the measured current. The performance of NN based flux estimator and voltage model based flux estimator is studied. The sample result for d-axis rotor

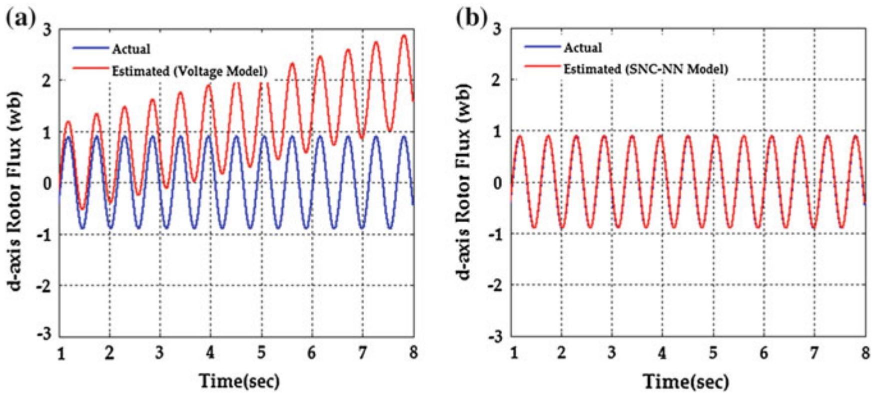

Fig. 156.3 d-axis rotor flux for integrator drift problem with 5 % dc bias **a** voltage model, **b** SNC-NN model

flux estimated from voltage model and NN based Flux Estimator is shown in Fig. 156.3a, b respectively. From the results obtained, it is clearly understood that d-axis rotor flux estimated from the NN based flux Estimator tracks the actual flux very well even in the presence of dc bias with the d-axis rotor flux MSE of 4.226×10^{-4}.

Thus NN based Flux Estimator based flux estimator is found to be less sensitive to dc bias problem. This is due to the inherent presence of saturating nonlinear activation function in the NN. Whereas, d-axis rotor fluxes estimated from the voltage model gets deviated from the actual and error in the d-axis rotor flux keeps on increasing with time. Thus it is understood that NN based Flux Estimator exhibits stable performance, where as voltage model shows unstable performance. The field angle estimated from the voltage model fails and gets deviated from the actual as presented in Fig. 156.4a. The field angle estimated from the NN based Flux Estimator tracks the actual closely with negligible error as shown in Fig. 156.4b.

156.5.2 Performance Comparison of Proposed Flux Estimator with Voltage Model Based Flux Estimator for Parameter Variation Problem

The performance of the NN based flux estimator and the voltage model based flux estimator is studied for field angle and resultant flux estimation for 50 % step variation in stator resistance. The resultant flux estimated from the voltage model oscillates around the actual as presented in Fig. 156.5a but the resultant flux from the NN based Flux Estimator tracks the actual closely with negligible error as shown in Fig. 156.5b. Thus the NN based estimator trained for parameter

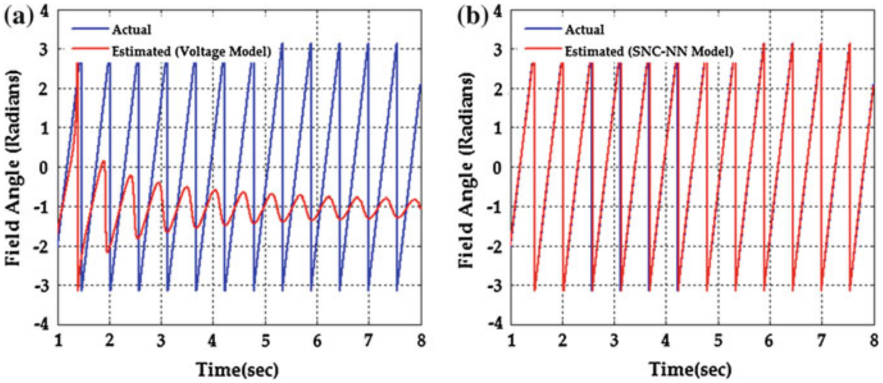

Fig. 156.4 Field angle for integrator drift problem with 5 % dc bias **a** voltage model, **b** SNC-NN model

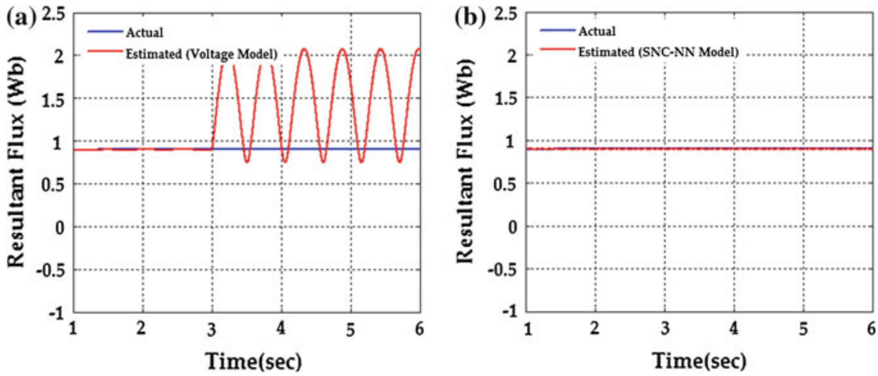

Fig. 156.5 Resultant flux for 50 % R_s variation **a** voltage model, **b** SNC-NN model

variations, exhibits robust flux estimation even in the presence of parameter variation. The voltage model can also be made robust to parameter variation with an additional on-line parameter estimator, which would increase the complexity of the drive system.

The Mean Square Error for the d-axis and q-axis rotor fluxes estimated from the proposed flux estimator and the voltage model based flux estimator for combinations of drift and parameter variation problems are consolidated and presented in Table 156.2. From Table 156.2, it is clearly observed that the SNC-NN model tracks the actual flux with good accuracy in the presence of drift and parameter variation.

Table 156.2 Performance comparison of the proposed flux estimator with the voltage model based flux estimator for drift and parameter variation problem

Change in R_s	dc bias superimposed to the signal	Proposed NN based flux estimator		Voltage model based flux estimator
		MSE for d-axis Flux	MSE for q-axis Flux	
50 %	5 % in voltage	2.769×10^{-4}	9.153×10^{-5}	MSE keeps increasing with time driving the system to instability
	5 % in current	7.138×10^{-4}	4.395×10^{-5}	
	5 % in voltage and current	1.100×10^{-3}	1.668×10^{-4}	

156.6 Conclusions

This paper presents a data based NN flux estimator to overcome the drawbacks of conventional voltage model based flux estimator at low speeds for field angle and resultant flux estimation in sensor-less DVC IM drives. A data based NN model is designed using SNC-NN architecture trained with data including parameter variation. The NN based Flux Estimator is shown to address the integrator drift and R_s variation problem at low speeds and found to outperform the voltage model based flux estimator. Hence it is concluded that a proposed data based NN flux estimator is accurate, simple, eliminates the separate need for parameter estimator and hence offers a promising alternative for field angle and resultant flux estimation in Sensor-less DVC IM drives.

References

1. Holtz J, Quan J (2003) Drift and parameter compensated flux estimator for persistent zero stator frequency operation of sensor-less controlled induction motors. IEEE Trans Ind Appl 39 (4):1052–1060
2. Bose BK (2005) Modern power electronics and AC drives. Prentice-Hall, India
3. Himavathi S, Venkadesan A (2011) Flux estimation methods for high performance induction motor drives—a survey. Electr India Mag 54(4):116–126
4. Karanayil B, Rahman MF, Grantham C (2007) Online stator and rotor resistance estimation scheme using artificial neural networks for vector controlled speed sensorless induction motor drive. IEEE Trans Ind Electron 54(1):167–176
5. Jaalam N, Haidar AMA, Ramli NL, Ismail NL, Sulaiman ASM (2011) A neuro-fuzzy approach for stator resistance estimation of induction motor. In: International conference on electrical, control and computer engineering, pp 394–398
6. Gadoue SM, Giaouris D, Finch JW (2009) Sensor-less control of induction motor drives at very low and zero speeds using neural network flux observer. IEEE Trans Ind Electron 56 (8):3029–3039
7. Venkadesan A, Himavathi S, Muthuramalingam A (2010) Design of feed-forward neural network based on-line flux estimator for sensor-less vector controlled induction motor drives. Int J Recent Trends Eng Technol 4(3):110–114

8. Venkadesan A, Himavathi S, Muthuramalingam A (2013) Performance comparison of neural architectures for on-line flux estimation in sensor-less vector controlled IM drives. J Neural Comput Appl 22(7–8):1735–1744
9. Venkadesan A, Himavathi S, Muthuramalingam A (2011) A novel SNC-NN-MRAS based speed estimator for sensorless vector controlled IM drives. Int J Electr Electron Eng 5 (2):73–78
10. Himavathi S, Muthuramalingam A, Venkadesan A, Sedhuraman K (2012) Nonlinear system modeling using single neuron cascaded neural network for real-time application. ICTACT J Soft Comput 2(3):309–318

Retraction Note to: An Independent Reconstruction Error Using Randomized Quantization

S. Arunadevi and S. Sathya

Erratum to:
Chapter 72 in: C. Kamalakannan et al. (eds.), *Power Electronics and Renewable Energy Systems*, DOI 10.1007/978-81-322-2119-7_72

The paper entitled "An Independent Reconstruction Error Using Randomized Quantization" by S. Arunadevi, S. Sathya, on pp. 743–751 of this volume, has been retracted due to a case of plagiarism.

The online version of the original chapter can be found at DOI 10.1007/978-81-322-2119-7_72

S. Arunadevi (✉) · S. Sathya
Department of Electronics and Communication Engineering, Dhanalakshmi Srinivasan Engineering College, Perambalur, Tamilnadu, India
e-mail: arunadevi.s90@gmail.com

C. Kamalakannan et al. (eds.), *Power Electronics and Renewable Energy Systems*,
Lecture Notes in Electrical Engineering 326, DOI 10.1007/978-81-322-2119-7_157

Author Index

A
Abdelaziz, Almoataz Y., 131, 553
Abhijeet, Redekar, 923
Akash Pattanaik, P., 245
AlbertSingh, N., 1585
Alex, Linss T., 953
Alexandar Beski, I., 873
Alexander, T. Jerry, 1537
Ali, Mohamed, 553
Alice Hepzibah, A., 973
Anand Kumar, K.S., 131, 553
Angel Viji, K.S., 1453
Anilkumar, G.V., 1273
Anitta, Pattu John Samuel, 829
Anjali, Dharme, 923
Anjappa, P., 563
Antony, Nidhin, 621
Anuraj, S., 1525
Aravind, C.V., 933
Arjun, P., 1183
Arul, R., 1407
Arun, 679
Arun Noyal Doss, M., 1
Arun, N., 373
Arunachalam, V., 341
Arunadevi, S., 743
Ashok Kumar, B., 183, 803
Atallah, Ahmed M., 553
Atul Kumar Mishra, D., 679
Augusteen, W.A., 1425
Auti, A.B., 275
Avirajamanjula, P., 811
Aysha, S., 643

B
Babu, Paduchuri Chandra, 453
Balamurugan, S., 91
Balasubramaniam, P.M., 1385
Banu, A. Shakila, 793
Barvin Banu, S., 1037
Begum, Subnum, 193
Bersis, C. Danya, 29
Bharani, R., 997
Bharathi Raja, G., 1183
Booma, Nagarajan, 237
Boopathi, C.S., 1273
Bosco, M. John, 1573
Bukya, Mohan, 591

C
Catherine, R.L. Helen, 19
Chairma Lakshmi, K.R., 545
Chanana, S., 853
Chandrashekar, A., 1173
Charles Raja, S., 1203
Chatterjee, Ananya, 193
Chauhan, Abhishek, 47, 321
Chellathurai, A. Samuel, 1109
Chitra, A., 1261
Chitra, R., 1377
Chouksey, Luckey, 245

D
Danya Bersis, C., 1445
Das, S.K., 485
Dash, S.S., 1, 29, 57, 351, 443, 453, 497, 653, 689, 709, 953, 1077, 1273, 1445
Deenadayalan, D., 873
Devaraj, D., 177
Devarajan, A.T., 1297
Devarajan, N., 1297
Devi Anusha, K., 425
Devi Maheswaran, V., 475
Devi, S., 941
Dhal, P.K., 665

C. Kamalakannan et al. (eds.), *Power Electronics and Renewable Energy Systems*,
Lecture Notes in Electrical Engineering 326, DOI 10.1007/978-81-322-2119-7

Dhayalini, K., 329
Dhivya, K., 313
DivyaNavamani, J., 67
Dubey, Hari Mohan, 573
Durairaj, S., 313, 373

E
Elavenil, P.E., 1007
Essaki Raj, R., 883
Ezhilarasan, G., 443, 653
Ezzat, M., 131

F
Francis, Tinu, 631

G
Gachhayat, Susanta Kumar, 953
Ganapathy, V., 1
Ganesan, P., 177
Ganeshprasad, G.G., 1149
Ganguly, Avik, 255
Gayathri Monicka, J., 285
Geethanjali, M., 941
Gokilapriya, D., 1037
Gokulakrishnan, P., 631
Gopikaramanan, R., 535
Gopinath, M., 985
Gorayan, R.S., 255
Govind, Greeshma, 611
Gowrinathan, M., 475
Gubbala, Srilakshmi, 145
Gunasundari, S., 1369

H
Helen Sulochana, C., 1117
Hemalatha, K., 285
Hemanth, S., 57
Himavathi, S., 1261, 1593

J
Jacob Raglend, I., 1127, 1309, 1545
Jaiganesh, R., 699
Jaikrishna, V., 953
Jamna, A., 361
Jamuna, V., 285, 361
Janakiraman, K., 1213
Janakiraman, S., 1369
Jayakumari, J., 1453
Jayasankar, K.C., 425, 997
Jebaseeli, E. Annie Elisabeth, 1017
Jegatheesan, R., 57
Jennela, Sravani, 225
Jeyakumar, M.K., 1099
Jobanarubi, Eswaramoorthi, 829
Jocobraglend, I., 1497
Joseph, Deepthi, 1467
Joseph, Lucina, 819
Joyal Isac, S., 1319
Joylin Rini, R., 973

K
Kalaiarasi, N, 1467
Kalaivani, R., 1007
Kalirasu, A., 497
Kamaraj, N., 183, 1349
Kannan, A., 1415
Kannan, G., 83, 305
Kannan, S., 9, 843, 1281, 1067
Kapil, P.N., 213
Karpagam, J., 383
Karthick, S.P., 19
Karthik, N., 1407
Karthikeyan, K., 621
Karthikeyan, S. Prabhakar, 1339, 1173
Karthikeyan, V.V., 1027
Karunanithi, K., 1067
Katta, Pradeep, 679
Kavitha, D., 465
Khan, K. Kareemulla, 591
Kumar Chinnaiyan, V., 91, 201, 265, 341, 383, 985
Kumar Sahoo, Sarat, 1309
Kumar, B. Ashok, 1349
Kumar, C., 535
Kumar, K. Chaitanya, 591
Kumar, R. Shiju, 1245
Kumar, R. Suresh, 611
Kumar, Sanjeev, 863

L
Lakshmanaprabu, S.K., 771
Lakshmi Ganesh, K., 295
Lakshmipathi, P., 563
Latha, S., 163, 407, 417
Lavanya, A., 67
Lavanya, Jay, 883
Lekshmi, Babu Saraswathi K., 1489
Lindsay, N. Mahiban, 1139

M
Mahalakshmi, M., 407
Mahesh, D., 1
Maheswaran, C.P., 1117
Maheswari, M., 611, 721
Mallick, Ranjan Kumar, 395
Manikandan, B.V., 1397
Manimegalai, D., 1289
Manimegalai, R., 819
Manivannan, D., 1213
Manju, A., 111
Manoharan, P.S., 39, 153
Margaret, Vijaya, 1149
Mary Anita, J., 1545
Mary, S. Anitha Janet, 1585
Mathew, Rini Valsa, 1585
Mayilvaganan, Arun Bhaskar, 689
Meena Alias Jeyanthi, K., 1497
Meenakumari, R., 829
Midhun, P.M., 601
Mini, M.V., 1517
Mirnalinee, T.T., 1183
Mithra, R., 121
Mohan Muralikrishna, G., 803
Mohanraj, K., 29, 1445
Mohanty, Mihir N., 395
Monasubramaniam, A., 111
Monica Subashini, M., 1127
MR, Rashmi, 1525
Murali, M.R.V., 417
Muthukumar, M.V., 497
Muthuramalingam, A., 1593
Muthuramalingam, M., 153
Muthuvel, K., 1537
Mynavathi, M., 91

N
Narasimha Rao, L.V., 893
Naresh, K., 563, 591, 893
Nargunam, A. Shajin, 1565
Nasir, Abdul Wahid, 731
Navauga, A., 67
Nayak, Pravati, 395
Nirmal Kumar, A., 383
Nithya Priya, R., 201
Nithya, R., 843

O
Orugu, Rangarao, 145

P
Padma Suresh, L., 1517
Padmini, S., 57
Palanivel, P., 811, 913
Pandit, Manjaree, 573
Pandiyarajan, A., 163
Pangavane, D.R., 275
Panigrahi, B.K., 573
Paramasivam, S., 1017, 1437
Parameswara Reddy, D., 509
Parvathy, A.K., 1139
Patel, Yashwant Singh, 193
Patnaik, Bibhudatta, 351
Pattnaik, Amruta, 395
Paul, G., 1509
Pillai, S.K., 1099
Prabha, S.U., 1385
Prabhakar Karthikeyan, S., 1127, 1309
Prakash, J., 1339
Prakash, T. Ruban Deva, 1245
Prasad, M.J. Hari, 1407
Prasad, R.S., 863
Preetha, M. Mary Synthuja Jain, 1573
Premaanand, N., 19
Premalatha, L., 1235
Premkumar, K., 1397
Priya Esther, B., 1309
Priya, G. Nalini, 1415
Priyadhershni, M., 265
Purushothaman, K.V., 1509
Puttalakshmi, G.R., 1437

R
Raghu, Winnie, 963
Raglend, Jacob I., 1173, 1339, 1489
Ragupathy, U.S., 121
Rahul, S., 903
Raj Kumar, V., 225
Raj, E. George Dharma Prakash, 1109
Raj, R. Sundar, 9
Raja, A. Sabari, 523
Raja, S. Charles, 1163
Rajagopal, S., 1077
Rajakarunakaran, S., 177
Rajan, C. Christober Asir, 665
Rajan, Christober Asir, 329
Rajan, K., 1467
Rajasekaran, D., 689
Rajeswari, V., 1557
Rama Reddy, S., 361

Ramesh Kumar, A., 1235
Ramesh, G.P., 933
Ramesh, V., 563, 591, 893
Ramkumar, A., 313, 373
Ramya, R., 783
Rao, K. Uma, 1149
Rathika, N., 903
Raveendhra, D., 47
Raveendhra, Dogga, 321
Ravikrishore, D., 893
Ravikumar, Premkumar, 829
Rayaguru, N.K., 653
Raymon, A., 1359
Razia Sultana, W., 1173
Reddy Swathi, K., 563
Rengaraj, R., 1425
Renuga, P., 465
Resmi, R., 1477

S
Sabarinath, P., 433
Sabura Banu, U., 731, 771
Sahoo, Sarat Kumar, 1127, 1173, 1339
Saikia, Arup Kumar, 213
Sakeenathul Kubra, K., 761
Saket, R.K., 131, 245, 553
Samanta, Chinmaya, 443, 653
Samantaray, Julie, 709
Sambath, S., 913
Sameh, W., 131
Santhiya, R., 201
Santhosh Rani, M., 709
Sapre, M., 275
Sarath, R., 1565
Saravanan, P., 1087
Saravanan, R., 433
Saravanan, S., 843, 1281
Saravanan, T.S., 963
Sasikala, R., 1027
Sathi, Rama Reddy, 237
Sathish Kumar, K., 1309
Sathishkumar, Shanmugam, 829
Sathiyamoorthy, S., 329
Sathya, S., 743
Sattianadan, D., 351
Satyanarayana, G., 295
Seenivasagam, L., 1359
Seenivasagam, V., 1377
Selvakumar, P., 643
Selvakumar, R.B., 1047
Selvan, N.B. Muthu, 1425
Selvi, K., 753, 761, 783
Semwal, S., 853, 863
Senthil Kumar, A., 903, 973, 1057
Senthilnathan, A., 201
Sharmila, S., 699
Sidthik, A. Sheik, 1359
Sindhuja, S., 1183
Singh, Albert, 1509
Singh, Munendra, 853, 863
Singh, Nitish Kumar, 193
Singh, Shailendra, 853
Singh, T.P., 275
Siva Ganesh, E., 1289
Siva Subramanian, S., 305
Sivaramakrishnan, N., 771
Sivasankar, G., 101, 1331
Somasekhar, K., 509
Sravan Kumar Reddy, Y., 453
Sreedendu, 1027
Sree Varshini, G.Y., 1163
Sreedevi, V.T., 475
Sridevi, R., 535
Sridhar, R., 1
Srikanth, K.S., 893
Srinivas, K., 145
Srinivasa Venkatesh, M., 803
Srinivasan, S., 523
Subashini, T.S., 1193, 1225
Subasri, C.K., 183, 1203, 1349
Subramani, C., 453, 689, 1273
Subramanian, Padma, 83, 305
Sudhakaran, M., 351
Suganthi, R., 985
Suganya, R., 1057
Sumithra, R.P., 1565
Sundarabalan, C.K., 753, 761
Surendran, Sumith, 1047
Suresh Kumar, K., 1319
Suresh Kumar, R., 721
Suresh Kumar, V., 1, 101, 1331
Suresh, Anjana, 1477, 1525
Suresh, L. Padma, 1537, 1557, 1573, 1585
Surya, M., 383
Suvitha, V., 509
Syam Pradeep, A, 1173
Syam, P., 485

T
Tejaswini, Navya, 453
Thakur, Padhmanabh, 47, 321
Thangaraj, C., 843, 1067, 1281
Thangavel, S., 721, 1027
Thansekhar, M.R., 433
Thirugnanasambandam, M., 177
Thyagarajan, K.K., 1087

U
Udaya Shankar, R.T., 83
Udhayashankar, C., 265
Uthirasamy, R., 121

V
Vaidehi, K., 1193
Vaishnavi, D., 1225
Valan Rajkumar, M., 39
Vanitha, V., 1477
Varghese, T., 1509
Vaz, P. Shirley, 753
Velayutham, R., 1289
Veni, S.H. Krishna, 1537
Venkadesan, A., 1273, 1593
Venkatesh, P., 91, 1163, 1203
Venkatesh, Yarralinganagari, 689
Vignesh, H., 679
Vijaya, S., 1057
Vijayakumar, K., 9, 67
Vijayakumari, A., 1297
Vinothkumar, N., 341
Visalakshi, S., 819
Vishnuram, Pradeep, 237
Vivekanandan, C., 721
Vrushali, Khatavkar, 923

W
Wahidabanu, R.S.D., 793
Warke, A.S., 275
Winnie Beulah, R., 1213

Y
Yasodha, T., 1497